These proceedings of the Ninth International Conference on Permafrost (NICOP) extend the documented legacy of permafrost related research begun in 1963 when the first International Conference was held in West Lafayette, Indiana, USA. NICOP also marks the 25th anniversary of the Fourth International Conference on Permafrost that was convened in Fairbanks in July 1983. It is imperative that we continue this international and long-ranging dialogue of cooperation on permafrost, particularly during a period of overall global warming. At no time in the past has our overall interest level in permafrost been greater. The number of papers published in these proceedings substantiates this interest. In addition to climate change, development in regions of permafrost is contributing additional stress to this thermally sensitive environment. This recent increased growth is often associated with resource development such as oil and gas, and various mineral resources.

The papers presented in these proceedings are diverse in both time and space; they cover results from field and laboratory studies, remote sensing, analyses and modeling – or some combination of these. Both scientific and engineering aspects of various permafrost issues are presented, and are often intertwined with each other. We hope these proceedings provide one more positive step in our understanding of the permafrost environment that intrigues us as scientists and engineers.

1

NICOP 2008

Ninth International Conference on Permafrost

Edited by
Douglas L. Kane
and
Kenneth M. Hinkel

NICOP 2008

Ninth International Conference on Permafrost

1

Edited by Douglas L. Kane and Kenneth M. Hinkel

Ninth International Conference on Permafrost

Proceedings of the Ninth International Conference on Permafrost
University of Alaska Fairbanks
June 29–July 3, 2008

Ninth International Conference on Permafrost

Edited by Douglas L. Kane and Kenneth M. Hinkel

Volume 1

Institute of Northern Engineering
University of Alaska Fairbanks
2008

Ninth International Conference on Permafrost
Edited by Douglas L. Kane and Kenneth M. Hinkel

Printed in the United States of America

Elmer E. Rasmuson Library Cataloging in Publication Data
International Conference on Permafrost (9th : 2008 : Fairbanks, Alaska)
Ninth International Conference on Permafrost /
edited by Douglas L. Kane and Kenneth M. Hinkel.
— Fairbanks, Alaska : Institute of Northern Engineering,
University of Alaska Fairbanks, 2008.
2 v., : ill., maps ; cm.
Includes bibliographical references and index.
June 29–July 3, 2008
1. Permafrost–Congresses. 2. Frozen ground–Congresses.
I. Title. II. Kane, Douglas L. II. Hinkel, Kenneth M.

GB641.I6 2008

ISBN 978-0-9800179-2-2 (v.1)
ISBN 978-0-9800179-3-9 (v.2)

Cover Photo: Low-Centered Polygons, North Slope, Alaska

Production Editors: Thomas Alton and Fran Pedersen

Kane, D.L. & Hinkel, K.M. (eds). 2008. *Ninth International Conference on Permafrost.* Institute of Northern Engineering, University of Alaska Fairbanks (2 Vols.), 2140 pp.

Contents

Volume 2

Preface

Since the first International Permafrost Conference convened in 1963, we have sustained an international scientific and engineering collaborative effort until we now are immersed in this, the Ninth International Conference on Permafrost (NICOP). Considerable change has occurred over the past 45 years, resulting in heightened interest in the permafrost environment and understanding of its many aspects. Participation by engineers and scientists in advancing our knowledge of permafrost as a thermally impacted medium has continued to grow in the wake of both resource development and climate change.

The University of Alaska Fairbanks (America's Arctic University) is an excellent choice for the location of this conference. Permafrost is ubiquitous in Interior Alaska, and it influences many aspects of our society. Our local field trips are arranged around some of the most interesting phenomena here in the zone of discontinuous permafrost, including the world famous Permafrost Tunnel, the Trans Alaska Oil Pipeline, evidence of anthropogenic impacts on permafrost, and thermokarsting of warm permafrost. Fairbanks is also a good starting point for trips to other parts of Alaska, including the North Slope, Seward Peninsula, Denali National Park (Mount McKinley), and many other adventures. We have also taken this opportunity to offer courses related to the permafrost environment for high school and elementary teachers, advanced graduate students, and working professionals.

The University of Alaska Fairbanks hosted the Fourth International Conference on Permafrost in 1983. It was at this meeting that the International Permafrost Association (IPA) was formally established. IPA members are truly pleased with the strong international flavor of this year's conference, with approximately 30 countries participating. IPA's uninterrupted activities over the past 25 years are partially responsible for this concerted effort to expand our understanding of the permafrost environment, both spatially and temporally. It is also, however, abundantly clear that much of our current interest in this environment is driven by climate change.

Currently, many aspects of permafrost research are receiving considerable attention. These include carbon release into the atmosphere, discharge from catchments dominated with permafrost, the role of gas hydrates in cold environments, degrading permafrost and thermokarsting, infrastructure design in a changing environment, and the overarching issue of climate change on this thermally sensitive environment. It is essential that our scientific and engineering communities help our societies adapt to living and working on warming permafrost. Permafrost degradation will affect all aspects of life in the high latitudes and high elevations. We must anticipate the changes in ecology, hydrology, and infrastructure construction that will accompany degradation of permafrost with a warming climate. That is the challenge facing permafrost scientists and engineers. It is our hope that by sharing our knowledge and understanding, we may better serve our nations and people.

Enjoy the conference. We hope you will go home with increased knowledge and an invigorated appetite for expanding our understanding of the environment we call "permafrost."

—Douglas L. Kane
Water and Environmental Research Center, Institute of Northern Engineering
—Larry D. Hinzman
International Arctic Research Center

Acknowledgments

We, the organizers of the Ninth International Conference on Permafrost (NICOP), cannot sufficiently express our gratitude to those who have made NICOP both possible and successful. There are those who contributed financially by keeping the cost of the registration low, supporting young investigators, helping defer the cost of the proceedings, and sustaining many other behind-the-scenes activities. There are those who served on the numerous committees associated with this conference at the local, national, and international levels; we hope they found this exercise to be professionally rewarding. Finally, there are those who served as associate editors and reviewers of the more than 400 papers submitted. This conference is advertised as an International Conference; to be truly successful, much work must be done to overcome language barriers. While not always finding success in bringing a paper to publication, the associate editors and reviewers performed in a very commendable manner. Thank you all for your help.

—Douglas Kane, Larry Hinzman, and the Local Organizing Committee

NICOP Organizing Team Members

General Chair	Douglas Kane
Co-Chair	Larry Hinzman
Publications	Douglas Kane, Kenneth Hinkel, Thomas Alton, Fran Pedersen
Conference Facilitator	Elizabeth Lilly
Technical Program	Larry Hinzman
Short Courses	Larry Hinzman, Michael Lilly, Yuri Shur
Exhibits - Trade Show	Michael Lilly
Public Affairs	Marmian Grimes, Jenn Wagaman, Cherie Solie
Fundraising	Dave Norton, Jerry Brown, Larry Hinzman, Michael Lilly, James Rooney, Douglas Kane
Finance	Michael Lilly
Website	Gary Whitton
Special Events/Social	Elizabeth Lilly, Deborah Bennett, Melanie Jackson, Chris Lace
Young Researchers	Guido Grosse, Katey Walter, Andrew Balsar, Oliver Frauenfeld
ICOP-IPA-IPY Celebration	Jerry Brown, Jess Walker, John Zarling
Field Trip Guides	Deanne Stevens

U.S. Permafrost Association Board of Directors

Kenneth Hinkel, President
Yuri Shur, President-Elect
Oliver Frauenfeld, Secretary
Michael Lilly, Treasurer
Anna Klene, Member
Jennifer Harden, Member
Larry Hinzman, IPA Representative
Jon Zufelt, Past President

NICOP Program Committee

Larry Hinzman, Chair
Jerry Brown
Doug Goering
Jennifer Harden
Kenneth Hinkel
Douglas Kane
Frederick Nelson
Vladimir Romanovsky
Katey Walter
Jon Zufelt

Local Field Trip Organizers

James Begét
Deb Bennett
Nancy Bigelow
Patty Burns
Ed Clarke
Billy Connor
Charles Collins
Tom Douglas
Doug Goering
Jack Hébert
Melanie Jackson
Elden Johnson
Torre Jorgenson
Elizabeth Lilly
Michael Lilly
O.D. Odsather
Vladimir Romanovsky
Yuri Shur
Diana Solie
Katey Walter
Kenji Yoshikawa

Extended Field Trip Organizers

Donald “Skip” Walker
Tom Hamilton
Bill Streever
Chien-Lu Ping
Robert Gieck
Gary Michaelson
Torre Jorgensen
Jesse Walker
Caryn Rae
Kenneth Hinkel
Jerry Brown
Deanne Stevens
Jim Beget
Chris Burn
Antoni Lewkowicz
Tom Krzewinski
Phil Brease
Nel Caine
Koren Nydick
Elden Johnson
John Zarling
Ed Clarke
O.D. Odsather
Lee Schoen

Additional people who have assisted in NICOP Organization

Danielle Jamieson
Dan White
Michelle Bartlett
Wendy Warnick
Helga Wilm

U.S. National Committee

Jerry Brown, Chair
Roger Barry
Julie Brigham-Grette
Jody Deming
Craig Dorman
Kenneth Hinkel
Larry Hinzman
Douglas Kane
Frederick Nelson
Vladimir Romanovsky
Bill Streever
Rupert "Bucky" Tart
Patrick Webber
Jon Zufelt

International Organizing Committee

Antoni Lewkowicz, Chair
David Gilichinsky
Huijun Jin
Truls Mølmann
Marcia Phillips

NICOP Sponsors

Universities
University of Alaska International Polar Year (Gold plus)
University of Alaska President's Fund (Gold)
Alaska University Transportation Center (Gold)
University of Alaska Fairbanks Institute of Northern Engineering (Silver)
University of Alaska Fairbanks International Arctic Research Center (Silver)
University of Alaska Fairbanks Experimental Program to Stimulate Competitive Research (EPSCoR) (Bronze)
University of Colorado-National Snow and Ice Data Center (Contributor)

Government Agencies
Alaska Division of Geological & Geophysical Surveys, Fairbanks (Gold)
U.S. National Science Foundation (Silver)
U.S. Geological Survey (Silver)
U.S. Army Cold Regions Research and Engineering Laboratory (Bronze)
U.S. Department of Energy (Bronze)
U.S. Arctic Research Commission (Brass)
U.S. Bureau of Land Management (Brass)
Denali Commission (Brass)
North Slope Science Initiative (Brass)
U.S. Minerals Management Service (Contributor plus)
U.S. Fish & Wildlife Service, Fairbanks Field Office (Brass)

Corporate and Non-Governmental Organizations
Arctic Foundations, Inc., Anchorage (Gold)
Alyeska Pipeline Company, Anchorage (Silver)
BP Foundation (Bronze)
International Permafrost Association (Bronze plus)
GW Scientific, Fairbanks (Bronze)
Duane Miller & Associates, Anchorage (Bronze)
CH2MHILL Energy & Power, Anchorage (Brass)
ConocoPhillips Alaska (Brass)
EBA Engineering Consultants Ltd., Canada (Brass)
Golder Associates, Anchorage (Brass)
Shannon & Wilson, Inc. Seattle (Brass)
BeadedStream, LLC, Anchorage (Contributor)
Hawk Consultants, LLC, Anchorage (Contributor)
Houston Advanced Research Center (HARC) (Contributor)
Northern Engineering & Scientific (Contributor)
Northern Geotechnical Engineering, Inc., Anchorage (Contributor)
R&M Consultants, Inc., Anchorage (Contributor)
Tryck Nyman Hayes, Inc., Anchorage (Contributor)
Resource Data, Inc., Anchorage (Sustaining)
URS Corporation, Anchorage (Sustaining)
Usibelli Foundation (Sustaining)
Harley H. Hightower, FAIA, Anchorage (Sustaining)

ICOP Donor Circle (Contributor)
Jerry and Celia Brown
Edwin Clarke
Hugh M. French
Don W. Hayley
C.W. "Bill" Lovell
J. Ross Mackay (Honorary Member)
Michael C. Metz
Frederick E. Nelson
Jim and Florence Rooney
Rupert "Bucky" Tart
Ted B. Trueblood
H. Jess Walker
John Zarling

Individuals
Joe Malen

In-Kind Sponsors
ABR, Inc., Environmental Research and Services
Mountain Studies Institute
Pogo Mine, Teck Cominco Limited
University of Alaska Toolik Field Station
University of Cincinnati
University of Colorado, Institute of Arctic and Alpine Research
U.S. Army CRREL Permafrost Tunnel
U.S. Geological Survey
U.S. National Park Service

Associate Editors

Lukas Arenson, BGC Engineering, Canada
James Bockheim, University of Wisconsin, US
Julie Brigham-Grette, University of Massachusetts, US
Sherry Cady, Portland State University, US
Billy Connor, University of Alaska Fairbanks, US
Scott Dallimore, Geological Survey of Canada, CA
Claude Duguay, University of Waterloo, CA
Oliver Frauenfeld, University of Colorado, US
Hugh French, University of Ottawa, CA
Guido Grosse, University of Alaska Fairbanks, US
Stephan Gruber, University of Zurich, CH
Jennifer Harden, U.S. Geological Survey, US
Charles Harris, Cardiff University, UK
Christian Hauck, University of Karlsruhe, DE
Don Hayley, EBA Engineering Consultants, Ltd., CA
David Hik, University of Alberta, CA
Kenneth Hinkel, University of Cincinnati, USA
Hans-Wolfgang Hubberten, Alfred Wegener Institute, DE
Ole Humlum, University of Oslo, NO
Elden Johnson, Alyeska Pipeline Service Company, US
Torre Jorgenson, ABR Inc., US
John Kimble, Consulting Soil Scientist, US
Peter Kuhry, Stockholm University, SE
Philip Marsh, Environment Canada, CA
Chris McKay, NASA, US
James McNamara, Boise State University, US
Julian Murton, University of Sussex, UK
Frederick Nelson, University of Delaware, US
Mark Parsons, University of Colorado, US
Marcia Phillips, Swiss Federal Institute for Snow and Avalanche, CH
Volker Rachold, International Arctic Science Committee, SE
Vladimir Romanovsky, University of Alaska Fairbanks, US
Sharon Smith, Geological Survey of Canada, CA
Steve Solomon, Geological Survey of Canada, CA
Ted Vinson, Oregon State University, US
Daniel Vonder Mühll, ETH Zurich, CH
Patrick Webber, Michigan State University, US
John Zarling, Zarling Aero and Engineering, US

Reviewers

Clint Adler, Alaska DOT&PF, US
Thomas A. Ager, US Geological Survey, US
H. Jonas Akerman, Lund University, SE
Michel Allard, Université Laval, CA
Dale T. Andersen, NASA Ames, US
Lesleigh Anderson, US Geological Survey, US
Pat Anderson, University of Washington, US
Oleg A. Anisimov, State Hydrological Institute, RU
Lukas U. Arenson, BGC Engineering, CA
Arnold Arnoldusson, Norwegian Inst. of Land Inventory, NO
Valery Astakhov, National Research Inst. of Remote Sensing, RU
Tezera F. Azmatch, University of Alberta, CA
Megan Balks, University of Waikato, NZ
Andrew W. Balser, University of Alaska Fairbanks, US
Rene Barendregt, University of Lethbridge, CA
Brian Barnes, University of Alaska Fairbanks, US
David L. Barnes, University of Alaska Fairbanks, US
William Barr, University of Calgary, CA
Roger G. Barry, National Snow and Ice Data Center, US
Doug Benn, University Centre in Svalbard, NO
Bruce Bennett, Yukon Department of Environment, CA
Ivar Berthling, Norwegian University of Sci.and Tech., NO
Peter Blanken, University of Colorado, US
James Bockheim, University of Wisconsin, US
Xavier Bodin, University Paris/Joseph Fourier University, FR
Jan Boelhouwers, Uppsala University Uppsala, SE
Julia Boike, Alfred Wegener Institute, DE
W. Robert Bolton, Alfred Wegener Institute, DE
Christian Bommer, Swiss Fed. Inst. for Snow …, CH
Philip Bonnaventure, University of Ottawa, CA
Matthew T. Bray, University of Alaska Fairbanks, US
Alexander Brenning, University of Waterloo, CA
Gabriele Broll, University of Vechta, DE
Troy Brosten, Boise State University, US
Jerry Brown, International Permafrost Association, US
Bruce Brunette, Alaska DOT&PF, US
Margo M. Burgess, Geological Survey of Canada, CA
Christopher R. Burn, Carleton University, CA
Fabrice Calmels, University of Alberta, CA
Philip Camill, Carlton College, US
Iain B. Campbell, Land & Soil Consultancy Services, NZ
Sean K. Carey, Carleton University, CA
James W. Cassie, BGC Engineering Inc., CA
Beata Casto, University of Buffalo, US
Jessica E. Cherry, University of Alaska Fairbanks, US
Jens H. Christensen, Danish Meteorological Institute, DK
Hanne H. Christiansen, University Centre in Svalbard, NO
Evgenii Chuvilin, Moscow State University, RU
Graeme G.C. Claridge, Land & Soil Consultancy Services, NZ
Edwin S. Clark, Soils Alaska, US
Ian D. Clark, University of Ottawa, CA
Mark Clark, Natural Resources Conservation Service, US
Peter Cleall, University of Cardiff, UK
Gary D. Clow, US Geological Survey, US
Michael Cole, ABR Inc., US
Charles Collins, US Army, ERDC/CRREL, US

Jean Côté, Université Laval Québec, CA
Michelle Côté, Geological Survey of Canada, CA
Nicole Couture, McGill University, CA
Patrick Crill, Stockholm University, SE
Ronald P. Daanen, University of Alaska Fairbanks, US
Scott Dallimore, Geological Survey of Canada, CA
Debendra K. Das, University of Alaska Fairbanks, US
Simon Davies, Colorado School of Mines, US
Gregory P. De Pascale, William Lettis & Assoc. Inc., US
Reynald Delaloye, University of Fribourg, CH
Philip Deline, Université de Savoie, FR
Jack Dennett, EBA Engineering Consultants Ltd., CA
Alexander Derevyagin, Moscow State University, RU
Bernhard Diekmann, Alfred Wegener Institute, DE
Wojciech Dobinski, University of Silesia, PL
Yongtao Dong, University of Alaska Fairbanks, US
Guy Dore, Universite Laval, CA
D.S. Drozdov, Earth Cryosphere Institute, RU
Caroline Duchesne, Geological Survey of Canada, CA
Alejandra Duk-Rodkin, Geological Survey of, CA
Larry Dyke, Geological Survey of Canada, CA
Mark Ednie, Geological Survey of Canada, CA
Markus Egli, University of Zurich, CH
Olaf Eisen, Alfred Wegener Institute, DE
Wendy Eisner, University of Cincinnati, US
David Esch, Alaska DOT&PF (retired), US
Bernd Etzelmüller, University of Oslo, NO
Eugenie Euskirchen, University of Alaska Fairbanks, US
Zhaosheng Fan, University of Colorado, US
Herman Farbrot, University of Oslo, NO
Alexander N. Fedorov, Melnikov Permafrost Institute, RU
Michael G. Ferrick, US Army, ERDC/CRREL, US
Javier Fochesatto, International Arctic Research Center, US
Steven L. Forman, University of Illinois-Chicago, US
Daniel Fortier, University of Alaska Fairbanks, US
Richard Fortier, Université Laval, CA
Walter J. Fourie, University of Alaska Fairbanks, US
Pierre Francus, Inst. National de la Recherche Scientifique, CA
Oliver W. Frauenfeld, University of Colorado, US
Regula Frauenfelder, University of Oslo, NO
Barry M. Freifeld, Lawrence Berkeley National Laboratory, US
Hugh M. French, University of Ottawa, CA
Duane Froese, University of Alberta, CA
Rina Garcia, Stockholm University, SE
Gunther Ghysels, Ghent University, BE
I. Gidley, University of Calgary, CA
Robert E. Gieck, University of Alaska Fairbanks, US
Ted Goebel, Texas A&M University, US
Douglas J. Goering, University of Alaska Fairbanks, US
Jules M. Goldspiel, Cornell University, US
Michael Gooseff, Pennsylvania State University, US
Jacob Gorelik, Earth Cryosphere Inst. SB RAS, RU
Sergey Goryachkin, Geography Institute, Moscow, RU
Raoul Granger, National Hydrology Research Centre, CA
Mikhail N. Grigoriev, Permafrost Institute Yakutsk, RU
Guido Grosse, University of Alaska Fairbanks, US
Ed Grozic, EBA Engineering Consultants Ltd., CA
Jocelyn Grozic, University of Calgary, CA
Hansueli Gubler, AlpuG Davos, CH
Mauro Guglielmin, Insubria University Varese, IT
Steve D. Gurney, University of Reading, UK
Örjan Gustafsson, Stockholm University, SE
Spencer Guthrie, Brigham Young University, US
Wilfried Haeberli, University of Zurich, CH
Birgit Hagedorn, University of Alaska Anchorage, US
Tristram C. Hales, Cardiff University, UK
Svein-Erik Hamran, University of Oslo, NO
Chris Hanks, Alexco Resource Corp., US
Jennifer Harden, US Geological Survey, US
Charles Harris, University of Cardiff, UK
Robert N. Harris, Oregon State University, US
Stuart A. Harris, Calgary Alberta, CA
Bent Hasholt, University of Copenhagen, DK
Andreas Hasler, University of Zurich, CH
Steven Hastings, San Diego State University, US
C. Haththatowa, University of Calgary, CA
Christian Hauck, Karlsruhe Institute of Technology, DE
Helmut Hausmann, Technical University of Vienna, AT
Jennifer Heldmann, NASA Ames, US
Karen S. Henry, ERDC/CRREL, US
Rita Hermanns, Friedlipartner AG, CH
Thomas Herz, University of Giessen, DE
Ulrike Herzschuh, Alfred Wegener Institute, DE
Gloria Hicks, National Snow and Ice Data Center, US
Christin Hilbich, Friedrich-Schiller-Universität Jena, DE
Kenneth M. Hinkel, University of Cincinnati, US
Larry Hinzman, University of Alaska Fairbanks, US
Richard Hodgkins, Loughborough University, UK
Martin Hoelzle, University of Zurich, CH
Ed T. Hoeve, EBA Engineering Consultants Ltd., CA
Igor Holubec, I. Holubec Consulting Inc., CA
Anne Hormes, University Centre in Svalbard, NO
William T. Horne, EBA Engineering Consultants Ltd., CA
Hans-Wolfgang Hubberten, Alfred Wegener Institute, DE
Leroy Hulsey, University of Alaska Fairbanks, US
Ole Humlun, University of Oslo, NO
James Hunter, Geological Survey of Canada, CA
Atsushi Ikeda, University of Tsukuba, JP
Thomas Ingeman-Nielsen, Tech. University of Denmark, DK
Arne Instanes, Opticonsult Bergen, NO
Kenneth C. Irving, University of Alaska Fairbanks, US
Ketil Isaksen, Norwegian Meteorological Institute, NO
Mamoru Ishikawa, Hokkaido University, JP
Michel Jaboyedoff, University of Lausnne, CH
Matthias Jakob, BGC Engineering, CA
Richard Janowicz, Yukon Dept. of Environment, CA
Alexander Jarosch, University of British Columbia, CA
A. Jayasinghe, University of Calgary, CA
Margareta Johansson, Lund University, SE
Elden R. Johnson, Alyeska Pipeline Service Co., US
Ken Johnston, Earth Tech, CA
H. Jonas Akerman, Lund University, SE
Ben Jones, US Geological Survey, US
Kevin W. Jones, EBA Engineering Consultants Ltd., CA
Torre Jorgenson, ABR Inc., US
Håvard Juliussen, University Centre in Svalbard, NO
Andreas Kääb, University of Oslo, NO
Mikhail Kanevskiy, University of Alaska Fairbanks, US
Julian Kanigan, Indian and Northern Affairs, CA
Kumari Karunaratne, Carleton University, CA
Andreas Kellerer-Pirklbauer, University of Graz, AT
Martina Kern-Luetschg, Cardiff University, UK
Maureen Ketzler, US Forest Service, US
Alexander Kholodov, University of Alaska Fairbanks, US
John Kimble, Consulting Soil Scientist, US
Lorenz King, University of Giessen, DE

Kurt Kjær, University of Iceland, IS
Anna E. Klene, University of Montana, US
Michael Knapp, Alaska DOT&PF, US
Christof Kneisel Universität Würzburg, DE
Steven V. Kokelj, Indian and Northern Affairs, CA
Else Kolstrup, University of Uppsala, SE
Vladimir S. Kolunin, Earth Cryosphere Institute, RU
P.Y. Konstantinov, Melnikov Permafrost Institute, RU
Demitri Konyushkev, Docuchaev Soils Institute, RU
Michael Krautblatter, University of Bonn, DE
Thomas Krzewinski, Golder & Associates, US
Bernd Kulessa, Swansea University, UK
Anna N. Kurchatova, Tyumen State Oil and Gas University, RU
Denis Lacelle, Canadian Space Agency, CA
Branko Ladanyi, Polytechnique Montréal, CA
Christophe Lambiel, University of Lausanne, CH
Hugues Lantuit, Alfred Wegener Institute Potsdam, DE
David M. Lawrence, NCAR, US
Daniel Lawson, US Army, ERDC/CRREL, US
Marc Lebeau, Université Laval Québec QC, CA
Anne-Marie LeBlanc, Université Laval, CA
Jonah Lee, University of Alaska Fairbanks, US
Marina Leibman, Earth Cryosphere Institute, RU
Mathias Leopold, University of Jena, DE
David W. Leverington, Texas Tech University, US
Antoni Lewkowicz, University of Ottawa, CA
Xin Li, World Data Center for Glaciology Lanzhou, CN
Jenny Liu, University of Alaska Fairbanks, US
Shuhuang Liu, US Geological Survey, US
Jerónimo López-Martínez, University of Madrid, ES
Lorene A. Lynn, University of Alaska Fairbanks, US
Jacek Majorowicz, Northern Geothermal Consultants, CA
Galina Malkova, Russian Academy of Sciences, RU
Michael Manga, University of California Berkeley, US
Jan Mangerud, University of Bergen, NO
William F. Manley, University of Colorado, US
Gavin K. Manson, Natural Resources, CA
Sergei Marchenko, University of Alaska Fairbanks, US
Laurent Marescot, ETH Zuerich, CH
Margarita Marinonva, California Inst. of Technology, US
Philip Marsh, Nat. Hydrology Res. Centre Environment, CA
Irene Marzloff, Johann Wolfgang Goethe Univ., DE
Norikazu Matsuoka, University of Tsukuba, JP
Hansruedi Maurer, ETH Zurich, CH
Galina G. Mazhitova, Komi Science Centre, RU
William D. McCoy, Univ. of Massachusetts, US
Les McFadden, University of New Mexico, US
A. David McGuire, University of Alaska Fairbanks, US
Robert McHattie, Alaska DOT&PF (retired), US
Christopher McKay, NASA Ames Research Center, US
Fiona McLaughlin, Dept. of Fisheries and Oceans, CA
Malcolm McLeod, Landcare Research Hamilton, NZ
Nicola McLoughlin, University of Bergen, NO
Michael C. Metz, M.C. Metz Associates, US
Franz Meyer, Alaska Satellite Facility Fairbanks, US
Hanno Meyer, Alfred Wegener Institute, DE
Keith Meyer, Michael Baker Jr. Corp., US
Gary J. Michaelson, University of Alaska Fairbanks, US
Fred A. Michel, Carlton University Ottawa, CA
Nicole Mölders, University of Alaska Fairbanks, US
Jack D. Mollard, J.D. Mollard and Associates, CA
Dan Moore, University of British Columbia, CA
George Moridis, Lawrence Berkeley Laboratories, US
Thomas Moses, Alaska DOT&PF (retired), US
Michael Mungoven, USDA-NRCS, US
Julian B. Murton, University of Sussex, UK
Mark Musial, Golder Associates, US
Philippe Nater, GeoNum GmbH, CH
Frederick E. Nelson, University of Delaware, US
William G. Nelson, University of Alaska Anchorage, US
Heng Joo Ng, Schlumberger, CA
Derick Nixon, Nixon Geotech Ltd., CA
F. Mark Nixon, Geological Survey of Canada, CA
Jeannette Noetzli, University of Zurich, CH
Rune S. Ødegård, University of Gjovik, NO
Jonathan O'Donnell, University of Alaska Fairbanks, US
Stanislav Ogorodov, Moscow State University, RU
C. Ordonez, University of Calgary, CA
Kirk Osadetz, Geological Survey of Canada, CA
Thomas Osterkamp, University of Alaska Fairbanks, US
Jim M. Oswell, Naviq Consulting Inc., CA
Sam Outcalt, University of Michigan (retired), US
P. Paul Overduin, Alfred Wegener Institute, DE
Ron Paetzold, Geo-Watersheds Scientific, US
Michael Palmer, Indian and Northern Affairs, CA
Charles Paull, Monterey Bay Aquarium Research Inst., US
David Payer, US Fish and Wildlife Service, US
Rorik Peterson, University of Alaska Fairbanks, US
Richard Petrone, Wilfred Laurier University, CA
Eva-Maria Pfeiffer, University of Hamburg, DE
Marcia Phillips, Swiss Fed. Inst. for Snow …, CH
Ryan D. Phillips, C-CORE St John's Newfoundland, CA
Chien-Lu Ping, University of Alaska Fairbanks, US
Albert Pissart, Université de Liege, BE
Vladimir V. Pitulko, Inst. for History of Mat. Culture, RU
Lawrence J. Plug, Dalhousie University, CA
Stefan Pohl, Nat. Hydrology Res. Centre Environment, CA
Wayne Pollard, McGill University, CA
Olga Ponomareva, Earth Cryosphere Institute, RU
Anupma Prakash, University of Alaska Fairbanks, US
Jon Price, University of Waterloo, CA
William Quinton, Wilfred Laurier University, CA
Charles Racine, US Army, ERDC/CRREL (retired), US
Miguel Ramos, University of Alcala, ES
Gareth Rees, Scott Polar Research Institute, UK
J. Repelewska-Pękala, University of Maria Curie, PL
Anette Rinke, Alfred Wegener Institute, DE
Dan Riseborough, Geological Survey of Canada, CA
Armin Rist, Swiss Fed. Inst. for Snow …, CH
Stephen D. Robinson, St. Lawrence University, US
Isabelle Roer, University of Zurich, CH
Vladimir Romanovsky, University of Alaska Fairbanks, US
Bård Romstad, University of Oslo, NO
Vladislav Roujanski, EBA Engineering Consultants Ltd., CA
Stephan Saboundjain, Alaska DOT&PF, US
Torsten Sachs, Alfred Wagener Institute, DE
Kazuyuki Saito, University of Alaska Fairbanks, US
Michael Schirmer, Swiss Fed. Inst. for Snow …, CH
Lutz Schirrmeister, Alfred Wegener Institute, DE
Michael Schlegel, GeoEngineers Inc., US
Martin Schnebelli, Swiss Fed. Inst. for Snow …, CH
Edward A.G. Schuur, University of Florida, US
Georg Schwamborn, Alfred Wegner Institute, DE
Charles A. Schweger, University of Alberta, CA
Dmitry Sergeev, Institute of Environmental Geoscience, RU
Enrique Serrano, University of Valladolid, ES

Jack Seto, BGC Engineering Inc., CA
Natsagdorj Sharkhuu, Mongolian Academy of Sciences, MN
Nicolai I. Shiklomanov, University of Delaware, US
Yuri Shur, University of Alaska Fairbanks, US
Andrew G. Slater, University of Colorado, US
Lee Slater, Rutgers University, US
Chuck Slaughter, University of Idaho, US
Bruce Smith, Worley Parsons, CA
Orson P. Smith, University of Alaska Anchorage, US
Scott Smith, Research Branch Agriculture and Agri-Food, CA
Sharon Smith, Geological Survey of Canada, CA
Chris Spence, National Hydrology Research Centre, CA
Sarah M. Springman, ETH Zurich, CH
Blaire Steven, University of Wyoming, US
Christopher W. Stevens, University of Calgary, CA
De Anne Stevens, Alaska Dept. of Natural Resources, US
Marc Stiglitz, Georgia Institute of Technology, US
Vladimir Stolbovoy, Joint Research Centre of European …, IT
Dmity Streletskiy, University of Delaware, US
Robert Striegle, US Geological Survey, US
Tetsuo Sueyoshi, Hokkaido University, JP
Brad Sutter, NASA Ames Research Center, US
John Inge Svendssen, University of Bergen, NO
David Swanson, US Forest Service, US
Eors Szathmary, Eötvös Loránd University , HU
Pavel A. Tarasov, Free University of Berlin, DE
Charles Tarnocai, Agriculture and Agri-Food, CA
Rupert G. Tart, Golder Associates Ltd., US
Alan E. Taylor, ASL Environmental Sciences Inc., CA
Robert O. Taylor, Natural Resources, CA
Randi Thompson, BGC Engineering Inc., CA
Gennady S. Tipenko, Russian Academy of Sciences, RU
Horacio Toniolo, University of Alaska Fairbanks, US
J. Kenneth Torrance, University of Carleton, CA
Thomas P. Trainor, Univeristy of Alaska Fairbanks, US
Richard Trimble, EBA Engineering Consultants Ltd., CA
Dario Trombotto, Ianigla-Cricyt-Conicet, AR
Merritt R. Turetsky, Michigan State University, US
Craig Tweedie, University of Texas El Paso, US
William Ussler, Monterey Bay Aquarium Res. Inst., US
Jef Vandenberghe, Vrije Universiteit, NL
B. Van Vliet-Lanoë, Univ. Sciences et Tech. de Lille, FR
Yurij K. Vasilchuk, Moscow State University, RU
Alexander Vasiliev, Earth Cryosphere Institute, RU
Gonçalo Vieira, University of Lisbon, PT
Ted Vinson, Oregon State University, US
Jason G. Vogel, University of Florida, US
Daniel Vonder Mühll, ETH Zurich, CH
William Waite, US Geological Survey, US
Mark Waldrop, US Geological Survey, US
Donald Walker, University of Alaska Fairbanks, US
Katey Walter, University of Alaska Fairbanks, US
James Walters, University of Northern Iowa, US
B. Wang, Geological Survey of Canada, CA
KaiCun Wang, University of Maryland, US
Jeff Warburton, University of Durham, UK
Patrick J. Webber, Michigan State University, US
Matthias Wegmann, Institute of Safety and Security, CH
Malte Westerhaus, University of Karlsruhe, DE
Kimberly Wickland, US Geological Survey, US
Jacek Wierzchos, University of Lleida, ES
Cort J. Willmott, University of Delaware, US
William Winters, US Geological Survey, US
Stephen A. Wolfe, Geological Survey of Canada, CA
Ute Wollschlaeger, University of Heidelberg, DE
Ming-ko Woo, McMaster University, CA
Fred Wright, Geological Survey of Canada, CA
Yladimir Yakushev, VNIIGAZ, RU
Daqing Yang, University of Alaska Fairbanks, US
Edward Yarmak, Arctic Foundations, Inc., US
Shiqiang Ye, BC Hydro, CA
Kenji Yoshikawa, University of Alaska Fairbanks, US
Kathy Young, York University, CA
Dmitry Zamolodchikov, Ctr. for Ecol. and Prod. of Forests, RU
John P. Zarling, Zarling Aero and Engineering, US
Jay Zarnetske, Oregon State University, US
Aining Zhang, Natural Resources, CA
Gordon Zhang, EBA Engineering Consultants Ltd., CA
Tingjun Zhang, University of Colorado Boulder, US
Xiong Zhang, University of Alaska Fairbanks, US
Yu Zhang, Natural Resources, CA
Shu-ping, Zhao, CAREERI CAS, CN
Sergei Zimov, Northeast Science Station, RU
Jon E. Zufelt, US Army ERDC/CRREL, US

Initial Disturbance and Recovery Measurements from Military Vehicle Traffic on Seasonal and Permafrost Terrain

Rosa T. Affleck
U.S. Army Engineer Research and Development Center, Cold Regions Research and Engineering Laboratory
Sally A. Shoop
U.S. Army Engineer Research and Development Center, Cold Regions Research and Engineering Laboratory
Charles M. Collins
U.S. Army Engineer Research and Development Center, Cold Regions Research and Engineering Laboratory
Ellen Clark
U.S. Army Garrison Alaska, Center for Environmental Management of Military Lands, Colorado State University

Abstract

Disturbance from off-road vehicle operations was measured to determine damage to the soil and the vegetation. A 20-ton Stryker vehicle was used for maneuver impact tests on various terrains at a training land in Alaska during winter and spring. The trafficking consisted of both single and multiple passes for straight and turning maneuvers. The wintertime maneuver test was conducted on frozen terrain with 10 cm of snow cover. The initial disturbance to the soil and vegetation was observed to be minimal during the winter maneuver test, which showed limited vegetative shearing or soil disturbance in the vehicle tracks. The initial disturbances during the spring maneuver tests were observed to be minimal on shallow thawed terrain and significant in some areas with deep thaw depth, high moisture content, and sparse vegetation cover. The locations where the initial survey points were taken were revisited during the growing season to measure the recovery. The recovery was measured almost every year for up to four years in some locations to examine and assess the rebounding of the vegetation and healing of the ruts. Soil erosion from flooding and soil slumping were observed on ruts or tracks during the first recovery visit. The results showed significant vegetation rebound after three years. Recovery rates varied significantly depending on the terrain, ground and soil conditions, and initial impact severity.

Keywords: permafrost; rutting; seasonal terrain; thawing condition; vegetation recovery; vehicle disturbance.

Introduction

A 20-ton Stryker was newly introduced to U.S. Army Alaska (USARAK) training lands to train and support the Stryker Brigade Combat Team (SBCT3) (Shoop et al. 2004). Vegetation recovery rates on non-seasonal terrain have been examined after being disturbed by military vehicles (Howard et al. 2007). However, disturbance information from this type of vehicle was limited and unknown on Alaska training lands, especially since USARAK used light vehicles prior to SBCT. The initial question was how much impact could be expected from the Stryker vehicle. Secondly, what are the expected recovery rates from various types of disturbance? These questions were important for the training land managers for planning, suitability, and rehabilitation management. Maneuver impact tests using a 20-ton Stryker vehicle were conducted in March and May of 2003. The tests were conducted at one location during winter with frozen ground and snow cover and at three locations during the spring breakup when soil strength was at its annual minimum immediately following the melting of seasonal frost. This study was an attempt to quantify the initial disturbance generated by 20-ton Stryker vehicle (Affleck et al. 2004, Affleck 2005). The test in March 2003 was conducted on a permafrost terrain, while the tests in May 2003 were conducted on a permafrost area and on two sites with seasonal frost.

Prior to this study, there had been few studies conducted on the long- and short-term effects of off-road vehicle traffic on arctic tundra and subarctic alpine tundra soils (Abele et al. 1984, Walker et al. 1977, 1987, Sparrow et al. 1978, Slaughter et al. 1990). These studies concluded that poorly drained soils underlain by permafrost are often most heavily damaged, and soil bulk densities were higher on traffic areas than on the undisturbed areas. In addition, their findings included that the disturbances were based on many factors, including vehicle type, acceleration, turning radius, speed, time of summer, number of passes, slope, and vegetation. However, these off-road vehicles are mainly used for recreational and transportation purposes in Alaska, are lighter in weight (less than 10,000 kg), and have lower contact pressures than the Stryker vehicle.

Approach

The maneuver impact tests were composed of spiral and multi-pass tests. For the spiral test, the vehicle performed turning maneuvers by traversing from a large radius to a small radius to examine the disturbance generated when the vehicle is turning. The multi-pass tests were composed of lanes with 1, 4, 8, and 13 passes. The maneuver impact tests were conducted at three locations in May 2003 during spring and in one location in March 2003 during winter.

Test Vehicle

The Stryker vehicle used during the test was an infantry carrier vehicle (ICV) with no additional armor; it weighed approximately 18,000 kg (40,000 lbs) when loaded. The vehicle configurations listed for the Stryker are based on one of its variants (Table 1). The eight-wheel-drive Stryker is a combat vehicle and consists of four axles with 44.3 cm (17.43 in.) of ground clearance (Fig. 1). Although the vehicle has the capacity to run under cross-country tire inflation, it was operated using on-road tire pressures of 550 kPa (80 psi) on all eight tires.

A Global Positioning System (GPS) unit was mounted on the Stryker vehicle to track its position. The GPS unit recorded the position data of the test at 1-s intervals. The GPS data were used to determine vehicle speed and turning radius.

The terrain disturbance measurement categories included an imprint, a scrape, or a combination of both, and a pile (Ayers et al. 2000, Haugen 2002, Haugen et al. 2002, Affleck 2005). An imprint is where soil and vegetation are compressed in the vehicle track. A scrape is where the soil and vegetation have been stripped away from the vehicle track. A pile disturbance is where soil and vegetation have been displaced from the vehicle track and piled on the side(s). The impact severity was characterized by the amount of vegetation disturbed and removed, and the amount of bare soil exposed along the track.

Test locations and conditions

The test sites are described in detail by Affleck (2005) and Affleck et al. (2004). The sites include Arkansas Range, Eddy Drop Zone, and Texas Range. The test conditions during the trafficking to quantify terrain disturbance are briefly described in Table 2. There was only one test site during winter season on limited snow cover.

Initial disturbance

The initial disturbance to soil and vegetation along the vehicle tracks in the maneuver test area was measured in August 2003. The guidelines were established using impact severity and its corresponding disturbed width using guidelines (Ayers et al. 2000, Haugen 2002, Haugen et al. 2002). Although the initial survey was conducted a few months after the maneuver tracking, changes in vegetation in terms of recovery were considered minimal or almost zero. The initial disturbances from the Stryker maneuver tests were thoroughly described by Affleck (2005) and Affleck et al. (2004).

Recovery measurements

Recovery surveys were conducted in May 2004, August 2006, and June 2007. Guidelines used to measure the recovery of the soil and vegetation were established using impact severity and its corresponding disturbed width, based on work by Ayers et al. (2000), Haugen (2002), and Haugen et al. (2002), and modified for seasonal and permafrost areas as listed in Table 3.

Percent recovery and recovery rate

An overall assessment is quantified based on percent recovery and recovery rate. Percent recovery is measured in terms of the soil and vegetation rebound for each monitoring

Table 1. Stryker vehicle mobility parameters.

Width, cm (in.)	265.4 (104.5)
Length, cm (in.)	693 (273)
Weight, kg (lb)	17,745 (39,120)
Contact pressure, kPa (psi)	193 (27.94)
Tractive force, asphalt, kN (lb)	125.8 (28,283)
Tractive force, ice, kN (lb)	17.4 (3,912)
Ground clearance, cm (in.)	44.3 (17.43)
% Slope performance: Frontal, side	60, 30
Cross-country tire pressure, kPa (psi)	275.8 (40)

Figure 1. Stryker disturbance test in March 2003 at the Texas Range site.

Table 2. Test site locations, terrain description, and conditions during tracking.

Test Sites		Arkansas Range (AR)		Eddy Drop Zone (EDZ)		Texas Range (TR)
Terrain description		Flat, seasonal		Flat, seasonal		Gently sloping permafrost
Vegetation		Grass and short bushes		Sphagnum moss, sedge, tall grass and thick bushes	Tall grass, bare ground	Sphagnum moss, sedge
Soil type		Silty sand (SM)		Silty sand (SM) with thick organic layer in dense vegetative areas		Peat, organics
Test section conditions		Wet	Dry	Dense vegetation	Sparse vegetation	Ice-rich, high water content
Spring thaw	Avg. water content (%)	49.3	33.9	94.5	36.2	315.7
	Avg. thaw depth (cm)	28.8	23.4	14.5	44.5	7.6
Winter	Snow depth (cm)	—	—	—	—	10.0

Table 3. Modified recovery impact severity guidelines for seasonal terrain.

Impact Severity (%)	*Guidelines*
0	No visible disturbance as compared to surrounding vegetation/area; **no depression of vehicle track or rutting**
100	Slight leaning of vegetation; vegetation may be leaning in the direction of the vehicle track instead of standing straight compared to surrounding vegetation; **minimal compression of vegetation and organic mat and depression of vehicle track or rutting still exist [≤ 7.6 cm (3 in.)] but vegetation cover** similar or same in size as surrounding vegetation; vehicle track only slightly visible
200	Leaning of vegetation, likely in the direction of vehicle tracking compared to surrounding vegetation; **depression of vehicle track or rutting still exists but vegetation cover** similar in size to surrounding vegetation; visibility of tracks; little to no disturbance of soil visible
40	Depression of vehicle track **narrowing and more shallow due to soil slumping, movement, or erosion**; bare soil visible; over one third of the vegetation not present compared to surrounding; vegetation growing in track not as fully grown or as large as surrounding vegetation **or other vegetation types growing along the tracks** (e.g., moss); if rocky soil, some rock visible in bare soil; **organic matter accumulating in tracks**
600	About one third of the area with growing vegetation; vegetation smaller than surrounding vegetation **or sign of other vegetation types growing along the tracks** (e.g., moss, dominant or invasive vegetation); significant amount of bare soil still exposed; if rocky soil, rocks visible on soil surface; depression of track visible; sign of **soil slumping, movement, or erosion in tracks**
800	Few vegetative species growing on vehicle path; vegetation present is much smaller and less developed than surrounding vegetation; depression of track visible; if in a rocky soil, increasing amount of rocks visible in track
100	Track is bare soil with no vegetation growing; depression of track visible; if in a rocky soil, rocks highly visible in track

time with respect to the initial disturbance at the same location. The equation used to calculate percent recovery for each monitoring time (or measurement date) is

$$\%\text{Recovery}_t = \left(\frac{IS_i - IS_t}{IS_i}\right)100 \qquad (1)$$

where IS_i is the impact severity during initial time and IS_t is the impact severity at the time of interest.

Recovery rate can be obtained by plotting the percent recovery with the time.

Results

Permafrost terrain

The disturbance from the Stryker vehicle during the winter test at Texas Range (TR) was generally in the imprint category in which the snow and vegetation were compressed by the tires, showing bare ground in some areas along the tracks (Fig. 2a). The initial impact severity values were mostly near 10%, with vegetation being flattened and with broken stems or branches as shown in Figure 2b. Because the ground was frozen during the test (and had sufficient bearing capacity), the ground showed no rutting or depression. Tracks were still visible after a year (Fig. 2c). However, it was fully recovered after 3.42 years, when tracks were very hard to find (Fig. 2d).

Because the thaw depth was minimal during the test, the initial impact severity during the spring test at Texas Range was mainly compression of the vegetation and organic layer down to the frozen layer, where some vegetation had been sheared off the track at a few locations due to the vehicle turning.

Seasonal terrain

The initial impact severity (IS_i) during the spring test at Arkansas Range and Eddy DZ varied tremendously depending on the soil condition and vegetation cover. In the wet section at Arkansas Range and the sparse vegetation areas at Eddy DZ, the IS_i was up to 100%, resulting in complete removal of the vegetation and displacement of soil with significant ruts along the tracks (Fig. 3a). Soil slumping occurred during the following spring thaw, and possibly soil settlement from water ponding in the area made the soil fill in the tracks as shown in Figure 3b. At Arkansas Range, soil slumping on the ruts' side walls occurred, possibly due to freezing and thawing effects. Both the soil erosion and slumping processes made the ruts more shallow and narrow over time. In addition, organics (dead leaves) accumulated on the tracks. Over time, other vegetation types were observed growing in the tracks (e.g., moss, dominant or invasive vegetation), as seen in Figure 3c, for example, and adjacent vegetation sprawled into the tracks. In dense vegetative areas and dry soil locations at both Arkansas Range and Eddy DZ, the initial disturbance ranged from minimal compression of vegetation and organic mat to slight vegetation removal, to deep ruts with some shearing of plant at roots and some bare soil exposed.

Recovery

The disturbances were grouped based on the initial impact severity. IS_i >50% was considered to be high initial impact, while IS_i <50% was defined as low initial impact. The percent recovery values were obtained using Equation 1, and then an average value was taken from both inner and outer tracks and for each measurement date.

The percent recovery varied significantly depending on the terrain, ground and soil conditions, and initial impact severity (Fig. 4).

(a) March 2003, initial disturbance.

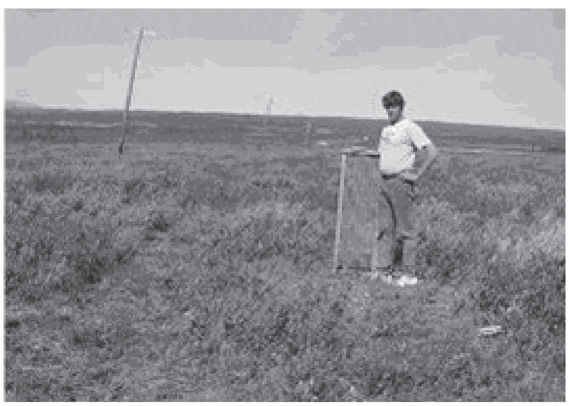

(b) Five months after trafficking.

(c) May 2004, one year and two months after trafficking. The area had just had a controlled burn.

Figure 2. Disturbance and recovery on tracks at Texas Range on permafrost.

(d) August 2006, 3.42 year after trafficking.

Figure 2. Continued.

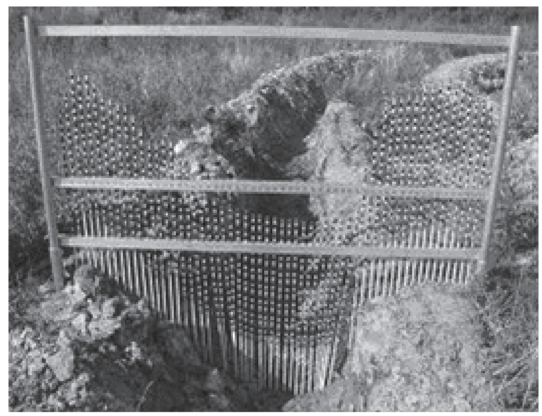

(a) August 2003, initial survey.

(b) May 2004, one year after.

(c) August 2006, 3.25 years after.

Figure 3. Left track disturbance and recovery on a track at Eddy DZ after 13 passes.

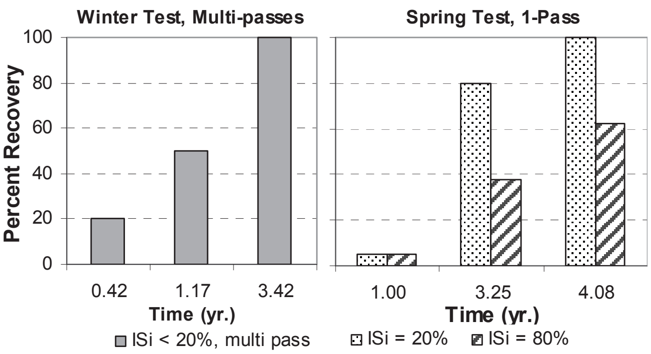

(a) Texas Range, permafrost terrain.

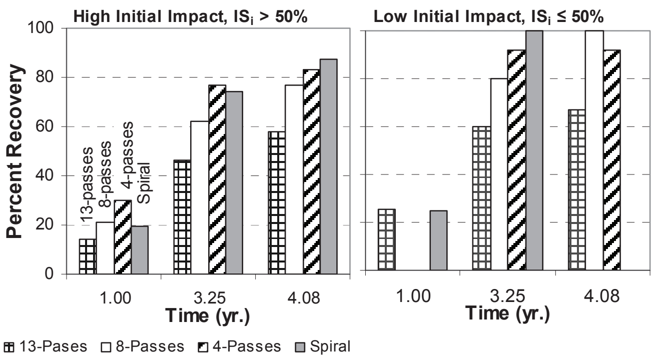

(b) Spring test disturbance at Arkansas Range.

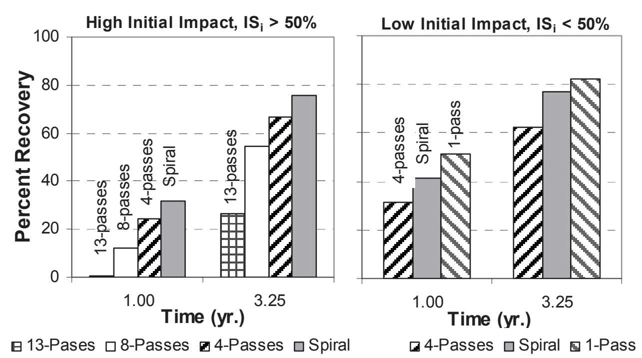

(c) Spring test disturbance at Eddy DZ, seasonal terrain.

Figure 4. Recovery rates at various locations from disturbance during winter and spring tests.

At the permafrost site (Texas Range), the recovery from the disturbance during the winter test produced a correlation with a rapid recovery of 100% after 3.42 year (Fig. 4a, left chart). On the other hand, the recovery for the spring test depended on the severity of the initial disturbance (Fig. 4a, right chart). 100% and 60% of recovery were found after 4 years for disturbances with initial impact severity of 20% and 80%, respectively.

Considerable differences in recovery rates were found at Arkansas Range and Eddy DZ from the disturbance generated by the Stryker vehicle during the spring tests (Figs. 4b & 4c). The percent recovery was higher and at a higher rate when the initial impact was less, but it also depended on the number of passes (Fig. 4b). For example, for initial high impact (severity of greater than 50%) after 4 years, approximately 58% and 87% recovery had occurred for the 13 passes and the spiral (single pass), respectively. However, with low initial impact (severity of less than 50%), the recovery rates were approximately 66% and 100% for the 13 passes after 4 years and for the spiral after 3.25 years, respectively.

Only up to 3.25 years of monitoring were conducted at Eddy DZ. The percent recovery was very limited for the 13-pass tracks, with zero recovery after the first year and only 26% after 3.25 years. During trafficking, the 13-pass tracks had less vegetation with bare ground compared to the rest of area at Eddy DZ. Overall, the recovery seemed to increase with a decreasing number of passes for initial impact severities greater than 50% (Fig. 4c, left chart). The recovery was a bit higher for low initial impact (severity less than 50%, Fig. 4c, right chart), and these tracks were in the dense vegetation area.

Summary and Conclusion

The initial disturbance from a Stryker vehicle at various sites and terrain conditions was assessed. Vegetation and surface recovery were monitored for up to 4 years in some sites. Percent recovery was quantified based on the impact severity for each measurement date with respect to the initial impact severity. Findings about the recovery can be summarized with the following:

1) The percent recovery and recovery rates varied significantly depending initial disturbance, which is a function of the terrain, ground and soil conditions and maneuver types (number of passes, tracks on turns and straight).

2) Recovery was rapid when the initial disturbance was low during winter with a snow cover on permafrost.

3) A higher rate of recovery was observed on areas with low initial disturbance of less that 50% impact severity.

4) There was very slow recovery after multi-pass trafficking and turns when the trafficking was on sparse vegetation, wet soils, and higher thaw depth areas.

5) The initial disturbance decreases and recovery rates increase with decreasing number of passes.

6) Overall the recovery from the vehicle impact of the Stryker vehicle is very promising as long as the tracks are allowed to heal over time.

Acknowledgments

Funding for the study was provided by the U.S. Army Garrison Alaska Directorate of Public Works and from AT42 High-Performance Ground Platform and Terrain Mechanics Modeling. The authors thank Jerry Reagan of the Cold Region Testing Center and his crew for conducting the Stryker maneuver tests at Donnelly Training Area. Technical support from U.S. Army Alaska staff, including Gary Larsen, Kevin Gardner, and Michael Davis; U.S. Army Alaska, Donnelly Training Area Range Control; and Sarah Brobst was greatly appreciated. We gratefully acknowledge Paul Ayers and Katie Simmons of the University of Tennessee for their technical support. The authors gratefully acknowledge the support provided by ERDC-CRREL staff, including Paul Richmond, Christopher Berini, Garrett Quillia, Maj. Douglas Anderson, the late Judy Strange, and Thomas Douglas.

References

Abele, G., Brown, J. & Brewer, M.C. 1984. Long-term effects of off-road vehicle traffic on tundra terrain. *Journal of Terramechanics* 21(3): 283–294.

Affleck, R.T. 2005. *Disturbance Measurements From Off-road Vehicles on Seasonal Terrain.* ERDC/CRREL Report TR-05-12. Hanover, NH: U.S. Army Engineer Research and Development Center, Cold Regions Research and Engineering Laboratory.

Affleck, R.T., Shoop, S., Simmons, K. & Ayers, P. 2004. Disturbance from off-road vehicle during spring thaw. *Proceedings, 12th American Society of Civil Engineers, International Winter Construction Symposium and Expo on Cold Regions Engineering, Alberta, Canada, 16–19 May 2004*.

Ayers, P., Vance, M., Haugen, L. & Anderson, A.B. 2000. *An Evaluation of DGPS-based Continuously Operating Vehicle Monitoring Systems to Determine Site-specific Event Severity Factors.* ERDC/CERL Technical Report TR-00-43. Champaign, IL: U.S. Army Engineer Research and Development Center, Construction Engineering Research Laboratory.

Haugen, L. 2002. *Design and Testing of a Vehicle Tracking System for Monitoring Environmental Impact at U.S. Army Training Installations.* M.S. Thesis. Fort Collins, CO: Colorado State University.

Haugen, L.B., Ayers, P.D., Anderson, A.B. & Nissen, P.E. 2002. Using GPS to evaluate movement patterns and impacts during training maneuvers. *Proceedings, 14th International Society for Terrain-Vehicle Systems (ISTVS), Vicksburg, Mississippi.*

Howard, H.R., Ayers, P.D. & Simmons, K.J. 2007. Vegetation rates after military training. *Proceedings, Joint North America, Asia-Pacific ISTVS Conference and Annual Meeting of Japanese Society for Terramechanics, Fairbanks, Alaska, June 23-26, 2007.*

Shoop, S., Affleck, R., Collins, C., Larsen, G. & Sullivan, P. 2004. Maneuver analysis methodology to assess vehicle impacts on training lands. *Journal of Terramechanics.*

Slaughter, C.W., Racine, C.H., Walker, D.A., Johnson, L.A. & Abele, G. 1990. Use of off-road vehicles and mitigation of effects of Alaska permafrost environments: a review. *Environmental Management* 14: 63–72.

Sparrow, S.D., Wooding, F.J. & Whiting, E.H. 1978. Effects of off-road vehicle traffic on soils and vegetation in the Denali Highway Region of Alaska. *Journal of Soil and Water Conservation* 33: 20–27.

Walker, D.A., Webber, P.J., Everett, K.R. & Brown, J. 1977. *The Effects of Low-pressure Wheeled Vehicles on Plant Communities and Soils at Prudhoe Bay, Alaska.* Special Report 77-17. Hanover, NH: U.S. Army Cold Regions Research and Engineering Laboratory.

Walker, D.A., Cate, D., Brown, J. & Racine, C. 1987. *Disturbance and Recovery of Arctic Alaskan Tundra Terrain: A Review of Recent Investigations.* CRREL Report 87-11. Hanover, NH: U.S. Army Cold Regions Research and Engineering Laboratory.

Erosion of the Barrow Environmental Observatory Coastline 2003–2007, Northern Alaska

A. Aguirre
The University of Texas at El Paso, El Paso, Texas, USA
C.E. Tweedie
The University of Texas at El Paso, El Paso, Texas, USA
J. Brown
International Permafrost Association, Woods Hole, MA, USA
A. Gaylord
Nuna Technologies, Homer, Alaska, USA

Abstract

The Barrow Environmental Observatory (BEO) is bounded to the east by the 10.7 km long Elson Lagoon shoreline of the Beaufort Sea. Rates of erosion along the 2 to 4 m high, ice and organic rich permafrost bluffs have been monitored annually at 14 transects since 2002 as part of the Arctic Coastal Dynamics (ACD) program. Continuous, ground-based Differential Global Positioning System (DPGS) surveys were conducted along the entire length of the BEO coastline in 2003, 2006, and 2007. The mean erosion rate during the four-year period was 2.3 m per year. A comparison of fall and summer erosion rates calculated from repeat DGPS surveys indicate similar amounts of erosion during fall 2006 (between August 2006 and June 2007, 8120 m^2) and summer 2007 (between June and August 2007, 7934 m^2). The total area lost to erosion during the four-year period was 9.8 hectares (average 2.5 ha/yr), which is almost twice the rate (1.3 ha/yr) calculated for the period 1979–2000 by previous studies

Keywords: ACD; bathymetry; coastal erosion; DGPS; ground ice; permafrost.

Introduction

Erosion of ice-rich, permafrost coastlines in the Arctic is limited to periods of ice-free seas. The duration and extent of seasonal ice-free seas in the Arctic is increasing (Serreze et al. 2007, Stroeve et al. 2007) and it is predicted that this in combination with increased storminess could increase rates of erosion experienced along arctic coastlines (Atkinson 2005). Increased rates of coastal erosion can impact communities, affect industry, and alter ecosystem structure and function in coastal terrestrial and marine ecosystems. Evidence supporting increased rates of erosion in the Arctic remain relatively scant and until recently the relationship between seasonal and interannual variations in erosion and storminess has been poorly studied. This study, linked to the Arctic Coastal Dynamics (ACD) program, documents the seasonal and interannual variations in coastal erosion along the Elson Lagoon coastline of the Barrow Environmental Observatory (BEO) situated on the Beaufort Sea coast of northern Alaska.

The Elson Lagoon shoreline is an ideal location to observe changing shoreline conditions. Coastal erosion research along this coastline dates back to 1948, is associated with the ACD program, and is situated on the BEO, a 7466 research preserve set aside by local land owners for research. Because of the availability of historical quantitative erosion data, there is potential in creating predictive models for shorelines with similar characteristics. Observing rapid change in high latitude shorelines creates urgency for these models to be developed. Until recently, observations have relied on measurements from sequential, high resolution imagery and repeat line-transect measurements made perpendicular to the coastline. Our additional results reported here are based on repeat, ground-based Differential Global Positioning System (DPGS) surveys that were conducted along the 10.7 kilometer length of the BEO coastline in August of 2003, 2006, and 2007. A similar survey was also conducted in June 2007 to begin to ascertain seasonal variations in the coastal erosion. This paper provides an update from on-going field studies, initial results presented at the eighth international permafrost conference in Zurich (Brown et al. 2003), and observations reported in the proceedings of the Arctic Coastal Dynamics workshops held in 2003 in St. Petersburg and in 2004 in Montreal (Serbin et al. 2004, Francis-Chythlook 2004, 2005, Francis-Chythlook & Brown 2005). Several papers report on regional erosion rates along the Chukchi Sea coast (Sturtevant et al 2005), the entire Beaufort Sea coast (Jorgenson & Brown 2005) and for a section of the Beaufort Sea coastline to the east that is directly exposed to the ocean (Mars & Houseknecht 2007).

The objectives of this continuing ACD project are to improve our understanding of rates and causes of coastal erosion and to assess their contributions to offshore sediment and carbon budgets and the impacts on living resources (Rachold 2004). Like many ACD-affiliated projects, this project also serves as a training ground for a new generation of young researchers and contributes to the International Polar Year and its legacy. Data from this project has been incorporated into the interactive and freely available Barrow Area Information Database-Internet Map Server (www.baidims.org) (Graves et al. 2004).

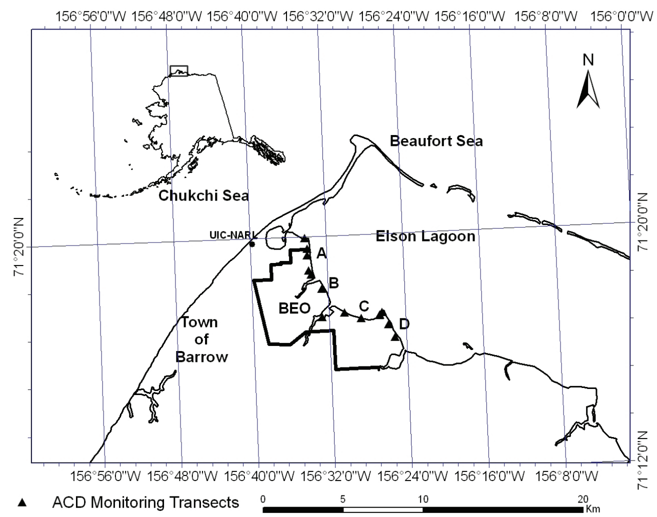

Figure 1. Location of the ACD observatory and key sites on the Elson Lagoon coastline of the BEO near Barrow, Alaska.

Study Area

The Barrow Environmental Observatory (BEO) is bounded on the east by the 10.7 kilometer-long Elson Lagoon shoreline (71°19'53", 156°34'4", Fig. 1). Elevations range from sea level to 4.4 m along this coastal stretch. Terrain is composed of ice wedge polygons, shallow elliptically shaped lakes, drained lake basins, and small ponds (Brown et. al 1980). The area is mainly composed of moist and wet tundra with acidic soils. The ACD observatory on the BEO coastline is divided into four segments with sections A, B, and D facing eastward and section C facing predominantly north. Water depth in Elson Lagoon ranges from 0.5 m to 3.5 m. The lagoon is bounded to the northeast by a series of low elevation barrier islands. Shallow but submerged bars lie at the mouth of most creeks draining from the BEO to Elson Lagoon and a submerged shoal extends northwest from Tekegakrok Point, which marks the junction between Sections C and D of the coastal observatory. Fourteen permanent ACD transect sites are oriented perpendicular to the coastline along the Elson Lagoon coast.

Methods

Field data collection utilized a Trimble NetRS GPS receiver with a Zephyr Geodetic antenna as a fixed Geodetic GPS base station located at the Barrow Arctic Science Consortium (BASC). This base station provides differential correction of data files at 1 second intervals as well as real time correction to field rover GPS units within approximately five kilometers and in line of sight of site of the Trimble HPB450 radio transmitter that is connected to the base station . The base station was upgraded in 2005 from a Trimble GPS 5800, which was used during the 2003 coastal survey described below. The rover system used for 2007 surveys included a Trimble R7 with internal radio that communicated with the base station radio transmitter for real time DGPS correction and a TSC2 survey controller that logged field data. Field surveys in 2003 and 2006 utilized a Trimble 5700 receiver, Zephyr antenna, and a Trimble TSC1 controller. All DGPS equipment was provided by UNAVCO (www.unavco.org) to the local science logistics provider (BASC).

Figure 2. Segment C facing east.

A total of four surveys of the 10.7 kilometer ACD BEO observatory were conducted. These included August 2003, 2006, and 2007 and June 2007. During each survey, field personnel walked along the top of the coastal bluff edge. The initial surveys for the 2003 season were conducted by Serbin et al (2003). In subsequent years surveys were conducted by the lead author of this paper following previously documented survey methodology documented in Serbin et al. (2003). For field surveys, the rover receiver was installed in a standard Trimble backpack configuration with the GPS antenna mounted on the bluff side of the backpack. After antenna height was corrected for the height of the field observer, this configuration allowed for the location of the horizontal and vertical position of the coastal bluff edge to be documented (Fig. 2).

Two survey methods were used. Real Time Kinematic (RTK) surveys were conducted whenever possible. This required a radio link to the base station. RTK surveys allow for instant DGPS processing and the acquisition of centimeter-accuracy horizontal and vertical location data. The second method utilized a Post-Processed Kinematic (PPK) survey style, which did not require a radio link, but instead relied on an unobstructed On-The-Fly (OTF) initialization period and post-survey differential correction with GPS data logged at the base station to provide field survey data with centimeter accuracy. For both survey types, the rover receiver was set to log data at a high resolution of one-second intervals to more accurately delineate the generally irregular coastal bluff edge. Repeat surveys using these vertically and horizontally centimeter-accurate field methods provide a means to accurately monitor the geospatial dynamics of the coastal bluff edge as it changes with coastal erosion.

DGPS survey data was downloaded from the controller and imported into Trimble Geomatic Office Software version 1.63 (TGO). Data was exported in text files suitable for ingestion by ESRI's ArcGIS (Workstation 9.2) Geographic Information System (GIS) software. Data from PPK surveys were processed by downloading base station files that were utilized for differentially correcting data collected by the

Table 1. Section length calculated for each DGPS survey.

Segment	Length (meters)			
	2003	**2006**	**Jun-07**	**Aug-07**
A	2923	2774	2683	2710
B	1666	1658	1568	1633
C	3449	3464	3377	3419
D	2643	2728	2651	2667
Total	**10681**	**10624**	**10279**	**10429**

Table 2. Total land area lost to erosion between sampling periods.

Segment	Erosion Area (m²)				
	Aug 03-Aug 07	Aug 03-Aug 06	Aug 06-Aug 07	Aug 06-June 07	June 07-Aug 07
A	16118	14143	1975	1375	600
B	9540	4584	4956	3156	1797
C	19237	16652	2584	666	1918
D	53130	46592	6539	2920	3619
Total	98025	81971	16055	8120	7934

Table 3. Total land area lost to erosion expressed as an annual rate.

Segment	Erosion Area (m² /year)		
	Aug 03–Aug 07	Aug 03–Aug -06	Aug 06–Aug 07
Years	4	3	1
A	4030	4714	1975
B	2385	1528	4956
C	4809	5551	2584
D	13282	15531	6539
Total	24506	27324	16055

Table 4. Total land area lost to erosion expressed as an annual rate per meter length of coastline.

Segment	Erosion Area (m² /year/segment length)		
	Aug 03–Aug 07	Aug 03–Aug -06	Aug 06–Aug 07
A	1.5	1.6	0.7
B	1.5	0.9	3.0
C	1.4	1.6	0.7
D	5.0	5.9	2.4
Mean	2.3	2.5	1.7

rover GPS unit using standard DGPS correction procedures. Processed data were exported as for that of the RTK surveys.

Processed DGPS survey data were imported to ArcGIS as X, Y point data and saved to a point shapefile. Erroneous points that resulted from poor GPS signal when field personnel traversed small coastal gullies were deleted. Using the polyline conversion tool in the ArcGIS extension AlaskaPak Version 2.0 for ArcGIS 9.2, point shapefiles were converted to polyline shapefiles. For each survey, the length of the coastline was computed for each of the four monitoring segments using the attribute data field calculator tool associated with the ArcGIS polyline tool (Table 1). Using the polyline shapefiles as a determinant location of the coastal bluff at each survey time, polygon shapefiles were created to establish the area of coastline lost to erosion for each monitoring segment for the following survey periods: August 2003 to August 2007, August 2003 to August 2006, August 2003 to June 2007, and June to August 2007. The area of each polygon shapefile was computed using the calculate area command from ArcGIS Toolbox. Rates of erosion were calculated for the following five periods by subtracting the total area of a preceding survey period from that of the most recent survey period: August 2003 to August 2007, August 2003 to August 2006, August 2006 to August 2007, August 2006 to June 2007, and June 2007 to August 2007. To enhance inter-comparison of erosion rates between segments of different lengths and different sampling periods, results were normalized by the length of the coastal segment at the earliest survey associated with a given survey period and reduced to a year-long time frame for survey periods spanning the 2003 to 2006 and 2007 periods (Table 4).

The establishment of the 14 coastal erosion monitoring transects (Fig. 1) oriented perpendicular to the coastline has been previously described by Brown et al. (2003). Since 2002, the distance from fixed markers along these linear transects to the coastal bluff and thaw depths have been measured. In 2003, 2006, and 2007, these measurements were made on the same day as the August DGPS surveys. While these survey methods do not permit the geospatial elucidation permissible from the repeat DGPS surveys, they are easy to perform, are part of the long-term ACD monitoring protocol, and are an excellent measurement to cross-check the accuracy of the DGPS surveys.

Results

Table 1 details the length of each coastal segment at each survey time. Section lengths were longest for Segments A and B in 2003 and Segments C and D in 2006. Lengths of the coastal bluff were shortest for Segments A, B, and C in June 2007 and for Segment D in 2003. Segment length is determined by the irregularity of the coastal bluff during each survey time period.

The calculated rates of total loss to erosion are given in Table 2. Overall, 9.8 hectares of tundra were lost to erosion between August 2003 and August 2007. Higher erosion rates were documented for Segments C and D in summer 2007 than in the Fall of 2006. Erosion loss was greatest in Segment D followed by Segments C, A, and B.

Mean annual erosion for all segments except Segment B was greater between 2003 to 2006 than between 2006 and August 2007 (Tables 3, 4). Erosion rates calculated for Segment B were greater between August 2006 and 2007 than during the period 2003 to 2006. Rates of erosion were greater in the Fall of 2006 for Segments A and B than in summer of 2007. As previously reported, Segment D had the highest rate of erosion when normalized by length of

Table 5. Distance between permanent markers and the coastal bluff edge since 2002 at ACD permanent line transects depicted in Figure 1.

Annual, total and average loss of coastline at permanent ACD line transects (m)								
Transect	2002	2003	2004	2005	2006	2007	total loss	m/yr
A1	92.2	89.2	88.1	86.2	76.0	75.0	17.2	2.9
A2	45.9	44.1	41.3	40.5	36.5	35.5	10.4	1.7
A3	110.4	109.1	-	107.3	105.0	103.9	6.5	1.1
A4	143.0	142.4	-	141.2	139.0	136.6	6.4	1.1
A5	56.0	55.0	-	53.6	53.2	50.8	5.2	0.9
B1	101.8	-	-	96.5	95.7	92.7	9.1	1.5
C1	-	72.4	70.9	-	68.8	68.2	4.2*	1.1
C2	-	37.7	-	-	29.3	28.6^	9.1*	2.3
C3	-	34.0	31.2	-	28.2	26.4^	7.6*	1.9
C4	-	97.3	95.6	91.9	88.0	80.8	16.5*	4.1
C5	38.0	37.0	34.6	34.8	-	34.3	3.7	0.6
D1	52.0	49.0	41.6	34.5	16.7	14.3	37.7	6.3
D2	54.9	53.2	51.5	44.7	38.7	35.6	19.3	3.2
D3	64.5	59.7	57.1	49.3	34.6	26.3	38.2	6.2

* Indicates total loss calculated between 2003 and 2007 instead of 2002 and 2007.
^ Indicates measurements made using the ArcGIS measuring tool due to erroneous field measurements.

coastline (Table 4). This rate is over three times the rate of loss recorded for the other segments during the period August 2003 and August 2007.

Annual rates of coastal retreat recorded using DGPS methods (Table 4) are similar to those measured using line-transect methods (Table 5).

Discussion

Similar to other studies focused on coastal erosion along Elson Lagoon (Brown et al. 2003, Serbin et al. 2004), this study documents substantial spatial and temporal variability in the rates of erosion. Within the 2003–2007 study period no segment monitored maintained a consistent temporal trend in the rate of erosion measured. Nonetheless, the DGPS study reported above has identified rates of erosion that are comparable to those that have used linear transect methods (Table 5) and GIS interpolation (Brown et al. 2003, Francis-Chythlook & Brown 2005, Serbin et al. 2004). Figure 3 illustrates a section of segment D on 2002 Quickbird panchromatic satellite image (Manley et al. 2005). The location of the coastline identified by DGPS surveys in 2003, 2006, and August 2007 are labeled. Relatively small scale sub decimeter-scale variability in the degree of coastal retreat between sampling periods can be observed. It appears that the variability in the rate of coastal erosion documented in this and other local studies is strongly related to this spatiotemporal heterogeneity.

Seasonally, erosion can begin as soon as the coastal bluffs thaw and Elson Lagoon becomes partially ice-free. This generally occurs around July 11th (Craig George unpublished data). Erosion ceases as bluffs freeze and the lagoon becomes ice covered, which has occurred around the 8th of October since 1988 (Craig George unpublished data). The process of shoreline retreat is enhanced by the undercutting of the coastal bluffs (thermo-erosion notches or niches) and removal by wave action of the slumped and thawed materials that can otherwise protect the coast from additional retreat (Walker 1991). Diurnal tidal movements are not considered to influence erosion in the Barrow area because they approximate only 0.3 m (Beal 1968, Mathews 1970). Brown et al. (2003) suggest the frequency, intensity, and duration of storms, and high water events affect seasonal to multi-decadal rates of retreat, whereas local spatial differences in erosion are generally attributed to the spatial variations in bluff elevation, ice and organic contents of exposed sediments, water depth, and wave fetch (Brown et al. 2003).

To better understand factors controlling the spatiotemporal variability in the patterns of coastal erosion along the Elson Lagoon coastline, a more thorough analysis of the interplay between the spatiotemporal dynamics of coastal erosion and other physical and climatic factors needs to be considered. These include the density of polygons and ice wedges, differences in land cover types, soil characteristics, and the elevation of the eroding coastline. The orientation of the coastline, offshore bathymetry, and the timing of freezing and thawing of the bluff, degree of storminess within a given sampling period are also important. These considerations fall beyond the scope of the current work, which is focused on updating the ACD time series for this section of coastline, but will be explored in a graduate thesis currently being developed by the lead author of this paper. Variations in seasonal soil thaw depths do not appear to play a role in erosion as regional thaw depths have been relatively consistent during the sample period (Nelson et al. 2008).

The DGPS survey method employed for this study demonstrates a potentially excellent method for further understanding how small-scale processes may control coastal erosion. Compared to line transect methods and GIS analysis, DGPS methods permit a greater consistency of measurement along the coast, provide better documentation of coastal shapes, provide more accurate and detailed products, and permit potentially more accurate volumetric calculations of erosion loss. DGPS surveys also appear to be more cost-effective than the acquisition and georectification of aerial or satellite imagery for the study area. The acquisition of imagery is costly and can be difficult to obtain due to the cloudy conditions that prevail during the arctic summer period. Nonetheless, DGPS surveys can be time consuming, require advanced training, and need to be performed at a relatively high frequency (at least twice in the summer, snow-free period) in order to best understand how climate and sea-state controls the seasonal and spatial dynamics of erosion. Products obtained from DGPS surveys are also particularly well suited to the development of process models that may help to predict future erosion patterns in the Barrow area and elsewhere along the arctic coastlines.

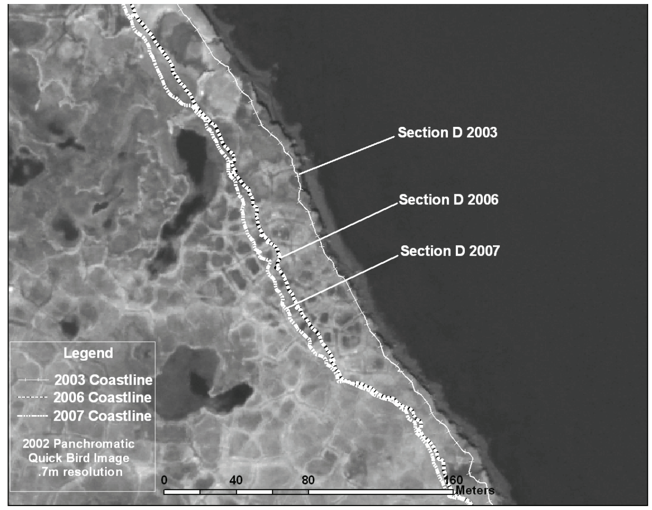

Figure 3. A section of segment D showing the location of the coastline in 2003, 2006, and August 2007 determined from DGPS surveys of the coastal bluff edge

Conclusion

Erosion rates along the Elson Lagoon coastline of the Barrow Environmental Observatory in northern Alaska, continue to be monitored as key contributions to the Arctic Coastal Dynamics Program, the International Polar Year, and a sustainable Arctic Observing Network. The Differential Global Positioning Systems approach employed provides a high-accuracy method to track coastline changes and to compute area and potentially volumetric losses due to erosion. The rates of coastal erosion documented in this study, like others in the Barrow area, confirm highly variable rates over time and space. Mean annual rates of erosion documented in this study are consistent with earlier reports, which further support the use of DGPS to monitor coastlines. Similar to Brown et al. 2003, who reported erosion rates between 1948–1949 and 1962–1964 we continue to document erosions rates for the Elson Lagoon between 1–3 m/yr. With the application of DGPS, however, we believe we can better determine where the higher erosion rates along this coastline are occurring and explore further questions such as why some areas are more vulnerable than others. We are currently evaluating the USGS Digital Shoreline Analysis System (DSAS) extension tool for ArcGIS to automate and standardize future analysis. Further research is needed to better affirm the primary controls of coastal erosion along this and similar sections of arctic coastline. This paper is a contribution to the International Polar Year (Project 90) by a member (lead author) of the Permafrost Young Researchers Network (PYRN).

Acknowledgments

The land occupied by the Barrow Environmental Observatory is owned by the Ukpeagvik Iñupiat Corporation (UIC) and has been designated for research and long-term observations. The Barrow Arctic Science Consortium (BASC), a non-profit organization dedicated to scientist/community collaboration, was designated by UIC to manage the BEO with support from the U.S. National Science Foundation (NSF). We are grateful to both UIC and BASC for the opportunity to establish and maintain our sites. NSF grants OPP9906692 and OPP0454996 (BAID) provided support. We also express appreciation to several undergraduate and graduate participants who assisted the authors in the field and with GIS support (Shawn Serbin, David Zaks, Eric Hammerbacher, Edith Jaurrieta Amorita Armendariz, Paulo Olivas, Ryan Cody, Rob Wielder, Sandra Villarreal, Santonu Goswami, and G. Walker Johnson). UNAVCO has generously provided DGPS support and training to field parties since 2002. Any opinions, findings, conclusion, or recommendations expressed in this paper are those of the authors and do not necessarily reflect the views of the National Science Foundation. Identification of specific products and manufacturers in the text does not imply endorsement by the National Science Foundation.

References

Atkinson, D.E. 2005. Observed storminess patterns and trends in the circum-Arctic coastal regime. *Geo-Marine Letters* 25: 98-109.

Beal, M.A. 1968. The seasonal variation in sea level at Barrow, Alaska. In: J.E. Sater (coord.), *Arctic Drifting Stations, 327-341.*

Brown J., Miller, P.C., Tieszen L. & Bunnell, F.L. 1980. *An Arctic Ecosystem: The Coastal Tundra at Barrow Alaska*. Stroudsburg, Pennsylvania: Dowden, Hutchinson and Ross, Inc., 571 pp.

Brown, J., Jorgenson, M.T., Smith, O.P. & Lee, W. 2003. Long-term rates of erosion and carbon input, Elson Lagoon, Barrow, Alaska. In: M. Phillips, S.M. Springman & L.U. Arenson, (eds.), *ICOP 2003 Permafrost: Proceedings of the 8th International Conference on Permafrost*. Netherlands: A.A. Balkema Publishers, 101-106.

Francis-Chythlook, O.P., 2004. *Coastal processes in Elson Lagoon, Barrow, Alaska*, M.S. Thesis. University of Alaska Anchorage, 130 pp.

Francis-Chythlook, O. 2005. Results of a wave climate study for Elson Lagoon, Barrow, Alaska. *ACD-Arctic Coastal Dynamics, 5th International Workshop, October 13-16, 2004, McGill University, Montreal, Canada. Reports on Polar and Marine Research* 506: 44-45.

Francis-Chythlook, O. & Brown, J. 2005. Additional erosion observations for the Elson Lagoon key site, Barrow, Alaska, *ACD-Arctic Coastal Dynamics, 5th International Workshop, October 13-16, 2004, McGill University, Montreal, Canada*, *Reports on Polar and Marine Research* 506: 38-41.

Graves, A., Tweedie, C.E., Zaks, D., Serbin, S., Manley, W., Brown, J. & Bulger, B. 2004. Spatial data infrastructure supports long term measurements to detect Arctic change. *Arctic Coastal Dynamics, Report of the 4rd International International Workshop. St. Petersburg, Russia, 10-13 November 2003.Reports on Polar and Marine Research.* 482: 29-30.

Jorgenson, M.T. & Brown, J. 2005. Classification of the Alaskan Beaufort Sea Coast and estimation of carbon and sediment inputs from coastal erosion. *Geo-Marine Letters* 25: 69-80.

Manley, W.F., Lestak, L.R., Tweedie, C.E. & Maslanik, J.A. 2005. *High-resolution Radar Imagery, Digital Elevation Models and Related GIS Layers for Barrow, Alaska.* Boulder, CO: National Snow and Ice Data Center. DVD.

Mars, J.C. & Houseknecht, D.W. 2007. Quantitative remote sensing study indicates doubling of coastal erosion rate in past 50 yr along a segment of the Arctic coast of Alaska. *Geology* 35: 583–586.

Matthews, J.B 1970. Tides at Point Barrow. *Northern Engineers* 2(2): 12-13.

Nelson, F.E., Shiklomanov, N.I., Streletskiy, D.A., Romanovsky, V.E., Yoshikawa,K., Hinkel, K.M. & Brown, J. 2008. A Permafrost Observatory at Barrow, Alaska: Long-term Observations of Active Layer Thicknesses and Permafrost Temperatures *Proceedings of the Ninth International Conference on Permafrost, Fairbanks, Alaska, June 29–July 3, 2008* (this proceedings).

Rachold V., Are, F.E., Atkinson, D.E., Cherkashov, G. & Solomon, S.M. 2004. Arctic Coastal Dynamics (ACD): an introduction. *Geo-Marine Letters* 25: 63-68.

Serbin, S., Graves, A., Zaks, A.D., Brown, J. & Tweedie, C.E. 2004. The utility of survey grade Differential Global Positioning Systems (DGPS) technology for monitoring coastal erosion. *Arctic Coastal Dynamics, Report of the 4rd International Workshop. St. Petersburg, Russia, 10-13 November 2003. Reports on Polar and Marine Research* 482: 52-56.

Serreze, M.C., Holland, M.M. & Stroeve, J. 2007. Perspectives on the Arctic's shrinking sea-ice cover. *Science* 31(5818): 1533-1536.

Stroeve, J., Holland, M.M., Mier, W., Scambos, T. & Serreze, M. 2007. Arctic sea ice decline: faster than forecast. *Geophysical Research Letters* 34(9): Art. No. L09501.

Sturtevant, P.M., Lestak, L.R., Manley, W.F. & Maslanik, J.A. 2005. Coastal erosion along the Chukchi coast due to an extreme storm event at Barrow, Alaska. *5th International Workshop, October 13-16, 2004, McGill University, Montreal, Canada. Reports on Polar and Marine Research.* 506:114-118.

Walker, H.J. 1991. Bluff erosion at Point Barrow and Wainwright, Arctic Alaska. *Z. Geomorh. N.F. Suppl.-Bd.* 81: 53-61.

Pore Water and Effective Pressure in the Frozen Fringe During Soil Freezing

Satoshi Akagawa
Hokkaido University, Sapporo, Japan

Syuhei Hiasa
West Nippon Expressway Co. Ltd., Osaka Japan

Syunji Kanie
Hokkaido University, Sapporo, Japan

Scott L. Huang
University of Alaska Fairbanks, Fairbanks, USA

Abstract

A model pipe (75 mm diameter, 29.5 mm length) is placed in NSF clay. Thin thermocouples attached to pressure gauges and markers monitor temperature. Five pressure gauges are placed along the pipe centerline and below the pipe: three in the vertical/radial direction, and two in the horizontal/hoop direction. As the frost bulb grows, the pipe moves up by 29 mm. Markers move away along the direction of heat flow during the early stage, but move upward with the model pipe once contained within the frost bulb. The pore-water pressure depresses in a temperature range corresponding to that of the frozen fringe. As the pore-water pressure depression reaches 35 kPa, the temperature is lowered by about 0.12°C. The effective pressure in the frozen fringe increases as temperature decreases, with the magnitude in the radial direction twice that in the hoop direction. The decrease of pore-water pressure is considered the driving force for ice lens formation, and the increase of effective pressure is the driving force for soil consolidation in the frozen fringe.

Keywords: effective pressure; frost heave mechanism; frozen fringe; unfrozen pore-water pressure.

Introduction

The subject of frost heave mechanism has been discussed and studied for a long time, yet it still attracts the attentions of scientists in the 21st century. Several models of the frost heave mechanism were proposed in the 1970s and 1980s (Miller 1978, Gilpin 1980, Takagi 1980), but they have not yet been verified empirically. The authors have attempted to verify those frost heave models empirically, and present results of the lab experiment in this paper.

Taber (1929) foresaw pore-water pressure depression in front of the segregating ice lens. Chamberlain and Gow (1978) speculated that the high consolidation of thawed sub-sea permafrost was due to the pore-water pressure depression as the ground became frozen. Gilpin (1980) and Miller (1978) proposed their frost heave models, and mentioned that the pore-water pressure depression in frozen fringe was the driving force sucking the water to the segregating ice lens. Akagawa (1988) observed consolidation in the frozen fringe during frost heaving with X-ray radiography technology and concluded that the consolidation was caused by pore-water pressure depression at the segregating ice lens.

Direct measurement of the pore-water pressure depression in the frozen fringe was first made by Radd and Oertle (1973) but was under closed system frost heave tests. Miyata and Akagawa (1998) tried to measure unfrozen pore-water pressure at the segregating ice lens in open system frost heave tests and concluded that the pore-water pressure depression was one-half of the value given by Generalized-Clausius-Clapeyron-Equation.

Despite intensive efforts taken to reveal the pore-water pressure depression at the segregating ice lens experimentally, none of them have received wide acceptance so far.

In this paper the total pressure and pore-water pressure in soil are presented. The pressure changes were monitored with frost heave tests in a 2D model. The relationship between the pressure measurements and the pressures depression in frozen fringe is discussed.

Experiment

Test apparatus and thermal condition

The experiment was conducted with an insulated soil box as shown in Figure 1 that was placed in a cold room in which temperature was maintained at 1.50 ± 0.5°C.

The box has inner dimensions of 500 mm in height, 500 mm in width, and 300 mm in depth. Two sides, the rear, and the bottom of the container were thermally insulated with Expanded Poly-Styrene. The front was covered with double Plexiglas to provide transparency and thermal insulation. The top side of the box was open to the air.

The experiment was initiated by circulating -10°C coolant as “thermal-shock,” and then the temperature was warmed to and kept at -4°C.

Monitored items and methods

During the experiment total pressure, pore-water pressure, soil deformation, and temperature of the model ground were monitored.

The total pressure gauge is 23 mm in diameter and 5 mm

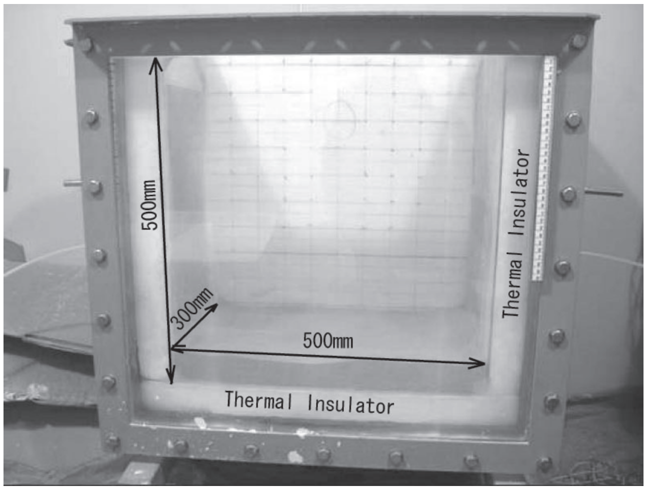

Figure 1. Insulated box used in axial-cylindrical frost heave test.

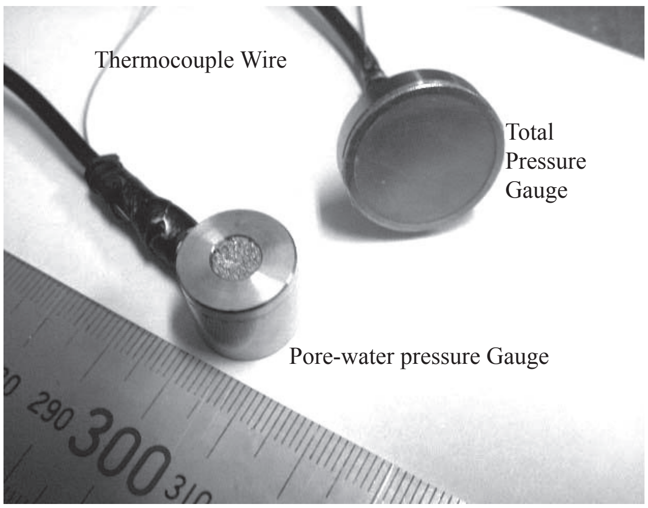

Figure 2. Total pressure and pore-water pressure gauges.

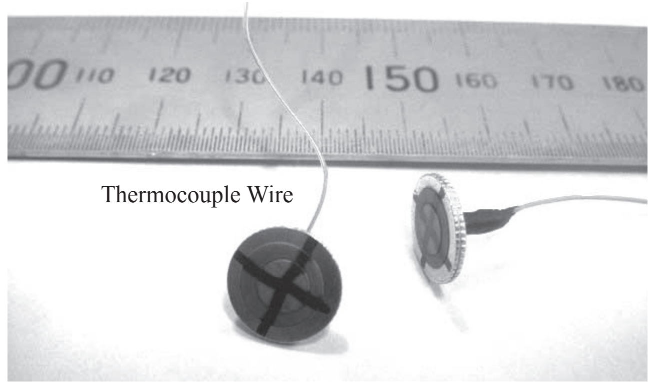

Figure 3. Marker with thin thermocouple.

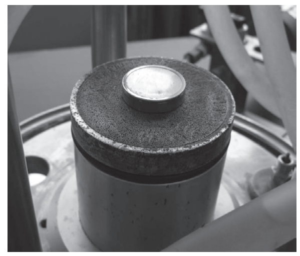

a) Total pressure gauge on the lower pedestal.

b) Cylindrical Plexiglas as soil container.

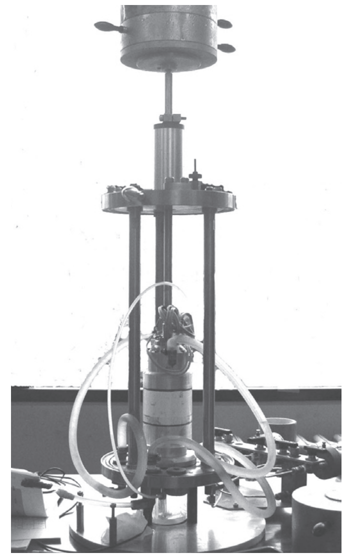

c) Pressure applied by dead weight through soil to total pressure gauge.

Figure 4. Total pressure gauge calibration.

in thickness, and the pore-water pressure gauge is 15 mm in diameter and 15 mm in thickness, as shown in Figure 2. The capacity of both types of transducers is 100 kPa.

Soil deformation was monitored with markers, which were placed between the front Plexiglas and test soil with a coating of grease to reduce the friction, as shown in Figure 3.

All the total pressure gauges were calibrated with the apparatus shown in Figure 4. One of the typical results obtained is shown in Figure 5. According to the calibration, the linearity of loading and unloading processes is considerably good, but it has hysteresis in loading and unloading.

Because the size of the experiment box was not large enough to utilize common thermocouples, the authors have used thin thermocouples, such as Omega TT-T-36, instead. Thin thermocouples, were attached to the pressure gauges and 20 of the markers as shown in Figures 2 and 3, in order to monitor the gauge and marker temperatures and to ensure the proper distance between the gauges and the cooling model pipe.

The temperature measurement method utilized in the experiment was traditional as shown in the Figure 6. However, the authors have confirmed the absolute accuracy of $\pm$ 0.02°C with this method by traceability.

The gauges and markers, with attached thermocouples, were placed in the model soil as shown in Figure 7.

In the vertical direction, five total pressure gauges were placed. Three of them were for vertical or radial total pressure, and the remaining two were for total pressure in horizontal or hoop direction. At about 12.5 mm below the model pipe, two total pressure gauges for radial and hoop direction and one pore-water pressure gauge were placed.

In the following sections, data obtained with these three groups of gauges are discussed.

Soil used and its preparation

Soil utilized in this experiment is commonly known as NSF clay with mineral composition of Pyrophyllite. This clay has relatively high frost heave susceptibility.

NSF clay powder was first mixed with distilled water with water content 1.5 times its liquid limit. It was then poured into the soil box in layers of 5 cm thick, and finally consolidated by dead weights with 10 kPa pressure. The front views of the

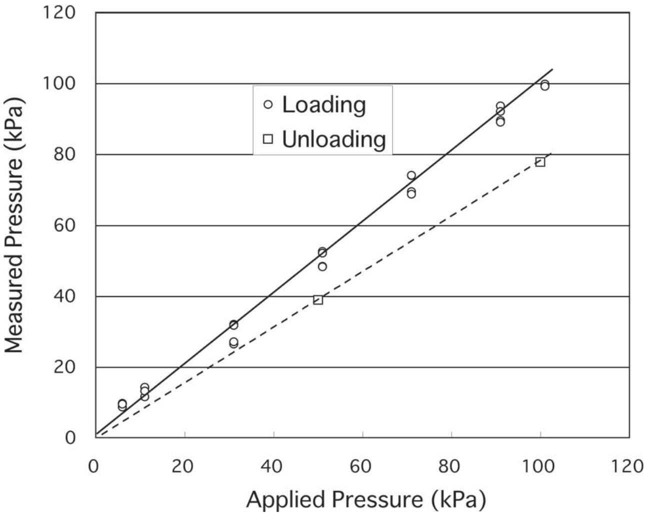

Figure 5. Typical calibration result of the total pressure gauge.

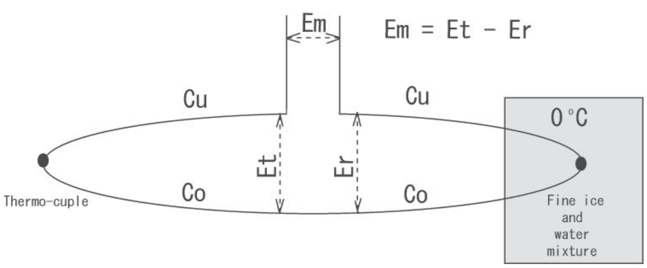

Figure 6. Thermocouple wiring.

soil box right after filling and at the end of consolidation are shown in Figure 8.

The consolidation behavior of NSF clay is shown in Figure 9. According to the e-log *P* relationship, the model soil made of NSF clay is normally consolidated and may cause a considerable amount of consolidation in frozen fringe when it freezes.

Thermal two-dimensionality

Prior to the main experiment the authors conducted a freezing test using agar instead of soil. Through this test we could verify the thermal dimensionality in 2D by checking the shape of the cylindrical frozen agar, which mimics growth of the "frost bulb" by a buried chilled gas pipeline in the arctic regions. As shown in Figure 10, the frost bulb is laterally symmetrical, and the lateral thermal two-dimensionality is presumed satisfied. In addition, the diameter of the frost bulb is almost the same in the middle and the rear end; the two-dimensionality in the pipe direction is considered satisfied for the rear half.

Test Results

Frost bulb growth

The frost bulb growth in elapsed time is shown in Figure 11. As time elapses, the diameter of the frost bulb is getting larger.

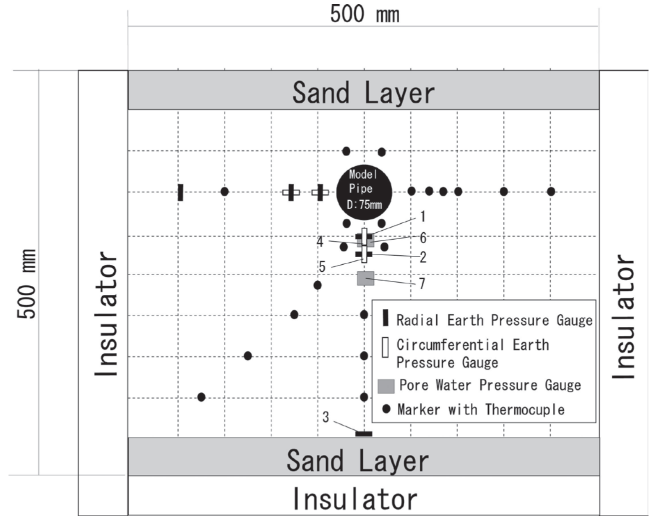

Figure 7. Locations of installed gauges and markers.

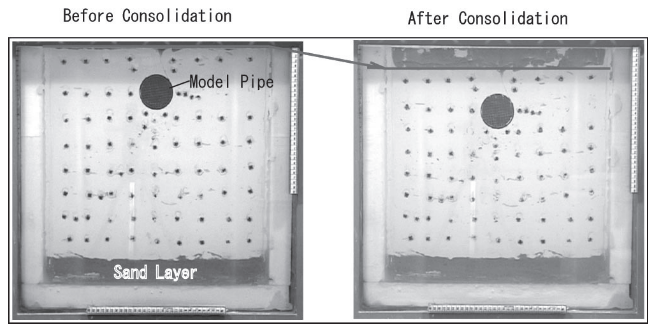

Figure 8. Initial and final condition of pre-consolidation at 10kPa pressure.

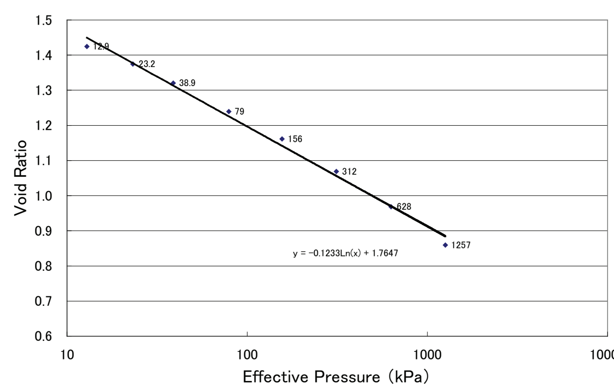

Figure 9. Consolidation behavior of saturated NSF model soil.

Upward movement of model pipe

Analyzing (x, y) coordinates of the markers, which were originally placed at the grid centers with 50 mm spacing on the front Plexiglas, 2D deformations of the model soil were recorded and are shown in Figure 12. As the frost bulb becomes larger, the model pipe is pushed up by 29 mm vertically, as shown in the figure. The movement of the markers during the experiment is also shown in the figure. Before the markers were enclosed by the growing frost bulb, they moved away along the direction of heat flow. However, as the markers were within the frost bulb, they moved upward with the model pipe.

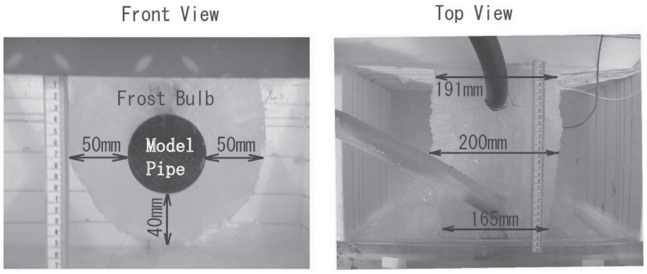

Figure 10. Frost bulb observed in preliminary experiment.

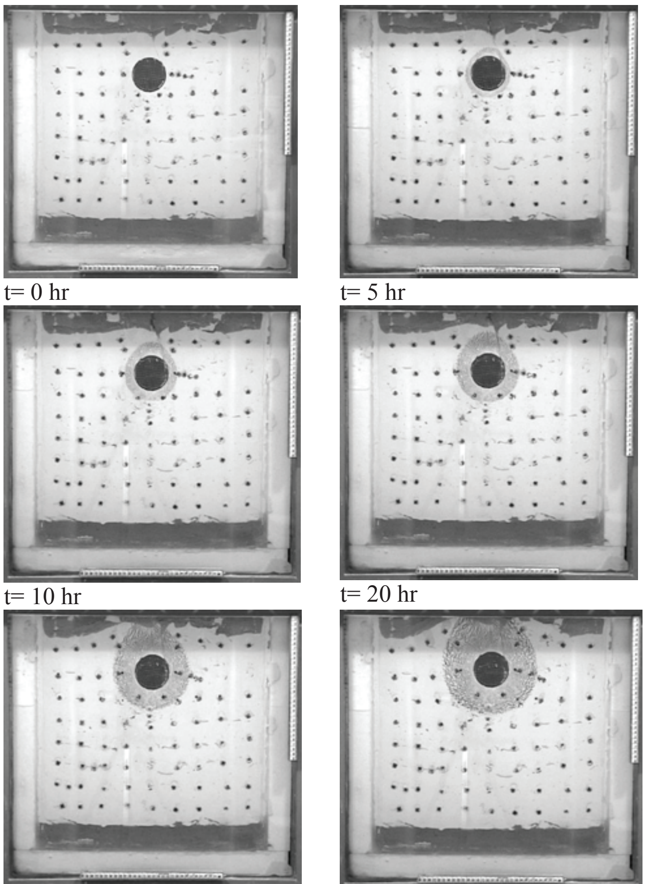

t= 0 hr
t= 5 hr
t= 10 hr
t= 20 hr
t= 40 hr
t= 80 hr

Figure 11. Frost bulb growth in elapsed time.

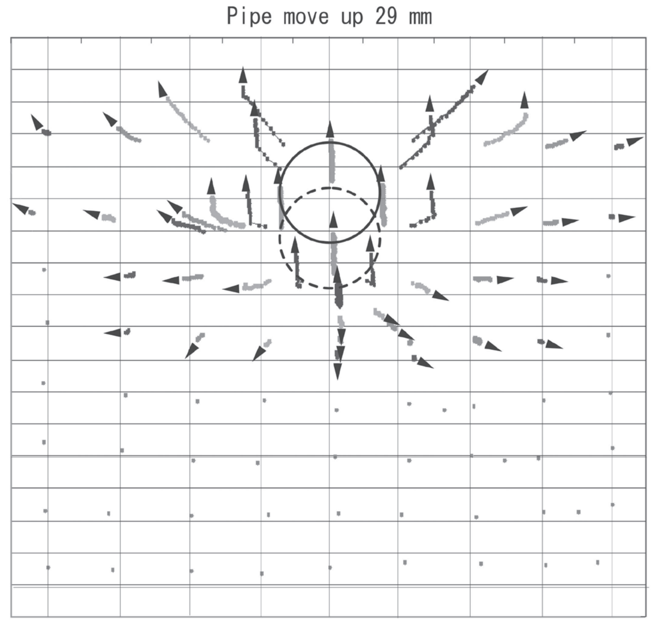

Figure 12. Model soil deformation with frost bulb growth.

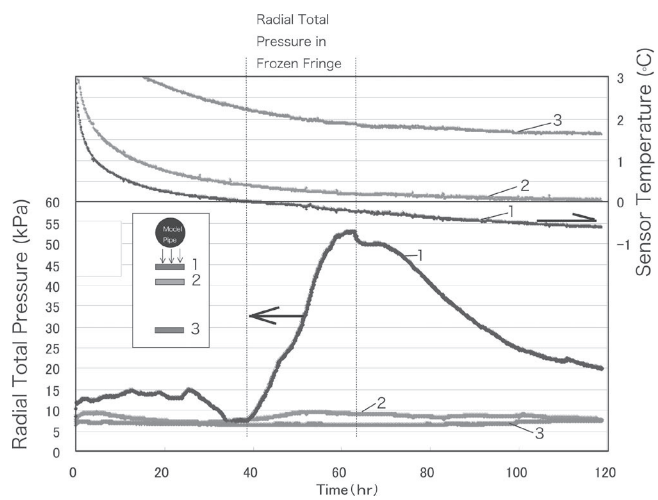

Figure 13. Radial total pressure below model pipe.

Monitored total and pore-water pressures

Three radial total pressures monitored with gauges Number 1–3, which were placed along the vertical pipe centerline are shown in Figure 13. The most adjacent gauge to the model pipe, Number 1, was captured by the frozen fringe at about 40 hours. This was recognized by its temperature shown in the figure. The frost bulb, however, did not enclose the other two gauges, Numbers 2 and 3, during the experiment. It is clearly shown in the figure that the radial total pressure rapidly increases when its temperature drops slightly below 0°C. It reaches a maximum pressure at about 60 hours, and then starts to decrease as the temperature approaches -0.2°C. Since this temperature range corresponds to that of a frozen fringe, the radial total pressure is presumed to have a sharp increase in frozen fringe and to decline in the much colder frozen portion in axial-symmetric freezing.

Two hoop total pressures, monitored with gauges Numbers 4 and 5, which were arrayed along the vertical pipe centerline, are shown in Figure 14. The frozen fringe captures the gauge next to the model pipe, Number 4, at about 40 hours. Similar to gauge Number 1, this is determined by its temperature at 0°C, as shown in the figure. Gauge Number 5 was not included in the frost bulb during the experiment.

A sharp increase of the hoop total pressure as its temperature dropped below 0°C was not seen in this case. However, a clear increase of the hoop total pressure was recorded after the gauge temperature fell below about -0.2°C, and it continued until the end of the experiment.

According to the data mentioned above, the hoop total pressure did not seem to change in the frozen fringe. Instead, it increased as the temperature dropped in the frozen soil.

Two pore-water pressures monitored with gauges Numbers 6 and 7, which also were placed along the vertical

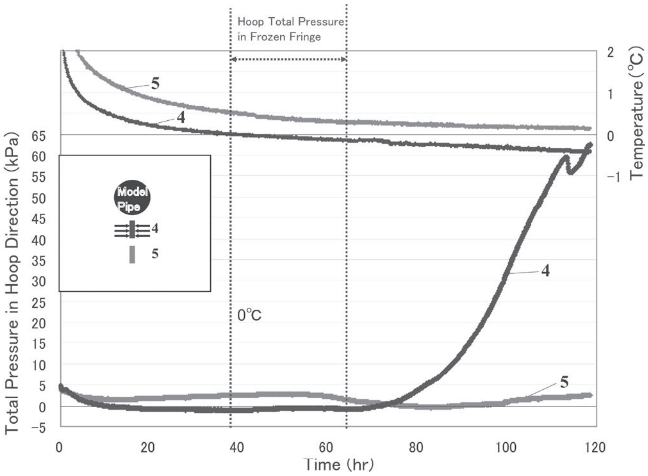

Figure 14. Hoop total pressure below model pipe.

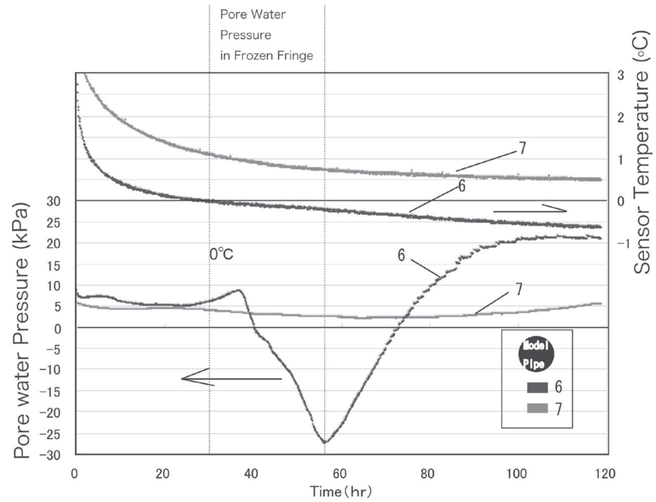

Figure 15. Pore-water pressure below model pipe.

pipe centerline, are shown in Figure 15. The most adjacent gauge to the model pipe, Number 6, was captured by the frozen fringe at about 40 hours. This is recognized by its temperature shown in the figure. Gauge Number 7 was not captured by the frost bulb during the experiment. It is clearly seen in the figure that the pore-water pressure, or unfrozen water pressure, in the frozen fringe sharply decreases when its temperature drops below 0°C and then starts to increase at about -0.2°C.

Discussion

Pore-water pressure in frozen fringe

As is clearly shown in Figure 15, the pore-water pressure depresses in a temperature range corresponding to that of the frozen fringe. Therefore, it infers that the unfrozen water pressure in the frozen fringe decreases as the local soil temperature becomes lower. During the period the unfrozen water pressure depression reached 35 kPa, temperature of the pressure gauge was lowered by about 0.12°C. This relationship between unfrozen water pressure and temperature seems not in good agreement with Generalized-Clausius-Clapeyron-Equation. However, if a certain amount of ice pressure is generated in the frozen fringe, it might likely agree with Generalized-Clausius-Clapeyron–Equation.

Effective pressure in the frozen fringe

The effective pressures in the radial and hoop directions calculated with the measured total soil and pore-water pressures are shown in Figure 16. As is clearly seen in the figure, the effective pressure in the frozen fringe increases as its temperature decreases. However, the magnitude of the effective pressure in the radial direction is about twice of that in the hoop direction.

Another noteworthy trend seen in the figure is that the effective pressure in the hoop direction after 90 hours, which corresponds to a well-frozen soil, continues to increase as time elapses and temperature becomes lower, whereas the effective pressure in the radial direction continues the decreasing trend.

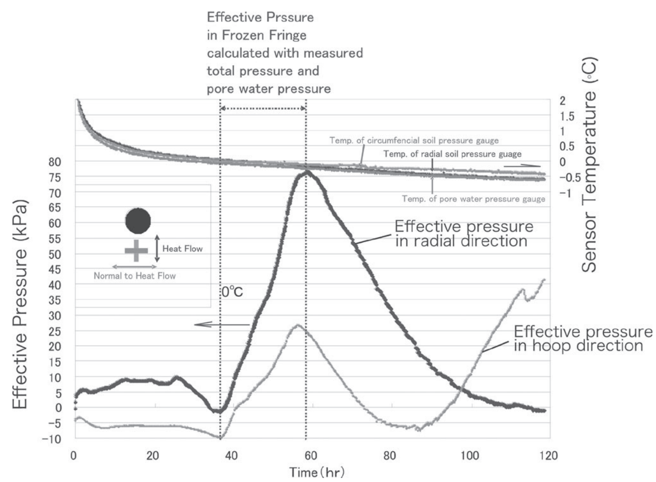

Figure 16. Effective pressures in radial and hoop directions in the frozen fringe.

Conclusions

Total pressure and pore-water pressure were directly measured in freezing soil during the 2D-model chilled gas pipeline experiments.

Because many features, such as frost bulb growth and upward movement of the model pipe, agreed well with the field experiment (Huang et al 2004), the observed pressures seem to be an indication of the real phenomena in freezing ground.

A significant finding from this experiment is that the pore-water pressure gauge has measured a clear pressure depression while it was in the frozen fringe. In addition, the effective pressures in the radial and hoop directions, which were calculated with the total pressure and pore-water pressure, showed steep increases in the frozen fringe.

The decrease of pore-water pressure was considered the driving force for ice lens formation, and the increase of the effective pressure was the driving force for consolidation in the frozen fringe.

References

Akagawa, S. 1988. Experimental study of frozen fringe characteristics. *Cold Regions Science and Technology* 15: 209-223.

Chamberlain, E.J. & Gow, A.J. 1978. Effect of freezing and thawing on the permeability and structure of soils. *Engineering Geology* 13: 73-92.

Gilpin, R.R. 1980. A model for the prediction of ice lensing and frost heave in soils. *Water Resources Research* 16(5): 918-930.

Huang S.L., Bray M.Y., Akagawa S. & Fukuda M. 2004. Field Investigation of Soil Heave by a Large Diameter Chilled Gas Pipeline Experiment, Fairbanks, Alaska. *J. Cold Regions Engineering* 18(1): 2-34.

Miller, R.D. 1978. Frost heaving in non-colloidal soils. *Proceedings of the Third International Conference on Permafrost, Edmonton*: 708-713.

Miyata Y. & Akagawa S. 1998. An experimental study of dynamic solid-liquid phase equilibrium in a porous medium. *JSME International Journal Series B* 41(3): 590-600.

Radd, F.J. & Oertle, D.H. 1973. Experimental pressure studies of frost heave mechanics and growth fusion behavior of ice. *Proceedings of the Second International Conference on Permafrost*: 377-384.

Taber, S. 1929. Frost heaving. *Journal of Geology* 37: 428-461.

Takagi, S. 1980. The adsorption force theory of frost heaving. *Cold Regions Science and Technology* 3: 57-81.

Coastal Processes and Their Influence Upon Discharge Characteristics of the Strokdammane Plain, West Spitsbergen, Svalbard

H. Jonas Akerman
Department of Physical Geography and Ecosystems Analysis, Lund University, Sweden

Abstract

Changes in Arctic sea ice conditions have affected conditions ashore along the west coast of Svalbard. Effects upon the discharge characteristics of a drainage basin close to the seashore are discussed. The area studied lies on the strandflat plain, south of Kapp Linné (78°04′N, 13°38′E). The anomalous discharge pattern of the Fyrsjöen Lake catchment area is described. Some years the outlet is blocked by ice-cemented storm ridges, delaying the spring peak flow several weeks and raising the lake level dramatically. Vast areas are flooded, affecting snowmelt, vegetation, and breeding birds of the area. The lake is then tapped during a few days with heavy flow, after which the discharge pattern returns to normal. This process is not unique, but rather common along the west coast of Spitsbergen. The special hydrographic and discharge conditions have an influence on the active layer, the permafrost, the vegetation, and the bird colonies of the area.

Keywords: arctic ecology; arctic sea ice; breeding birds; costal processes; polar hydrology; Svalbard.

Introduction

Sea ice is regarded as a key indicator and vital factor of climate change processes and has received much attention owing to the apparent reduction in coverage in the Arctic Sea (Parkinson et al. 1999, IPCC 2001, ACIA 2004). Since the potential impacts of these changes on climate, ecosystems, and lithosphere processes are great, sea ice is an important variable in any study of Arctic environmental change. The reduction in sea ice over the past several decades varies by region and season (Johannessen et al. 1995, 1999, Serreze et al. 2000, Serreze et al. 2003). The decrease in sea ice extent on the west coast of Svalbard is consistent with the general regional observations (Vinje 1976, 2001a, 2001b), and the periods with ice-free conditions have increased substantially. This has affected the hydrological and ecological environment of the Fyrsjöen catchment, which lies within an area where periglacial studies have been performed 1972–2004 (Åkerman 1980, 1992, 2005). Hydrological effects upon the active layer, river discharge, water balance, and the breeding birds also were monitored as a subproject.

A special focus has been directed toward changes in extreme runoff and floods that are likely to affect the depth of the active layer and the stability of the permafrost. This may lead to thermokarst processes and alter biological production and biodiversity within catchments near the coast. The status of ponds and wetlands, for which water levels are critical, determines whether these wetlands will become sources or sinks of CO_2 and CH_4.

Investigation Area

The investigation area is situated on the southern shore of the westernmost part of Isfjorden, central Spitsbergen (Fig. 1). The central west coast of Spitsbergen lies on the periphery of the extreme arctic zone. The moderating influence of the North Atlantic Ocean reduces temperature extremes and

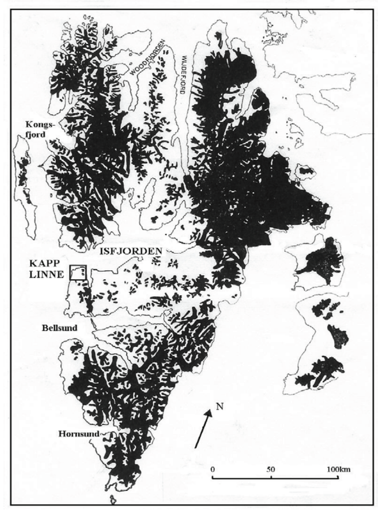

Figure 1. Svalbard and Spitsbergen with its glacial cover in black. The investigation area is indicated by a square

also brings more precipitation than is experienced at similar latitudes (Førland et al. 1997, Humlum 2002, Humlum et al. 2003).

The position on the border between maritime arctic and more continental arctic conditions explains the very great local climatic variations in Spitsbergen (Førland et al. 1997, Humlum et al. 2003). This is important for the interpretation of geomorphological and hydrological processes in an area with very few weather stations. The investigation area, however, offers the advantage of a permanent weather station situated not more than 6 km from the most distant monitoring site. The basic meteorological and climatological data have been obtained from this station.

The MAAT in the study area is -4.6°C, as measured at Isfjord Radio Station for the period 1935–1976 (Steffensen 1969, 1982, Førland et al. 1997 (Table 1). The estimated value for the normal period 1961–90 is -5.1°C (Førland et al 1997). The mean annual precipitation is 435 mm for the post-war period 1951–1975 (Steffensen 1982), and 443 mm during the full official record period (1935–1976), with a data gap during the war 1941–46. The estimated value for the normal period 1961–90 is 480 mm (Førland et al. 1997).

The official weather station was terminated in summer 1976, but an automatic station was established in 1996. After the termination of the official station in 1976, the author continued measurements of metrological and hydrological data within the study and catchment area. The records are covering the period up to 2003 with only minor gaps in the air temperature measurements. Unfortunately, there are long gaps in the measurements of precipitation. The annual course of air temperature and precipitation for Isfjord Radio are given as monthly means in Table 1 (c.f. also Akerman 1980, pp. 14-45, and Steffensen 1969, 1982, Førland et al 1997, Akerman 2005).

Objectives

The main objectives of this study are:

- To describe some of the hydrographical characteristics of the Fyrsjöen Lake catchment area.
- To give a simple description of the water balance of the catchment area.
- Describe how the blocking storm ridges are affecting the discharge pattern and the flooding of the catchment area.
- Illustrate how the flooding has affected the active layer in a small bog within the catchment.
- Investigate how the years of flooding have affected the breeding birds within the catchment.

Methods

Meteorological data have been obtained from the weather station at the nearby Kapp Linné station (Isfjord Radio). Additional precipitation data have been collected within the catchment during intensive study periods by the use of standard pluviometers and collectors. Winter precipitation and the effect of drifting snow (import to the catchment) have been studied through detailed snow surveys in late winters. The discharge in the outlet river needed different techniques during the violent peak flow and gentle normal flow. Water level has been measured with a fixed level gauge plus a recording level gauge put on the only rock outcrop along the short river. Propeller-type current meters applied in a simple traverse cableway have measured water speed during medium and peak flow. At lower flows, the water speed had to be measured with floats.

The highly variable cross-sectional area has been mapped every year or upon demand after "dam break flow" events (Pritchard & Hogg 2002). The dam break flow has here also been named "flush flow" in accordance with the terminology used for quick initial discharge in urban catchments. (Bertrand et al. 2002). Measurements started the first week of June and ended the first week of September. Hardly any flow was missed in May, but some years, flow in September has been missed.

Table 1. Official monthly and annual air temperature (°C) and precipitation (mm) (1935–1975) for Isfjord Radio. Data from Norsk Meteorlogisk Institutt, Oslo, Norway (Steffensen 1982).

Month	Temp °C	Precipitation (mm)
Jan	-10.7	37
Feb	-11.5	34
March	-12.2	34
April	-9.3	24
May	-3.3	25
June	+1.7	28
July	+4.7	38
August	+4.3	53
September	+1.1	47
October	-3.2	44
November	-6.8	40
December	-8.9	39
Annual	-4.6	443

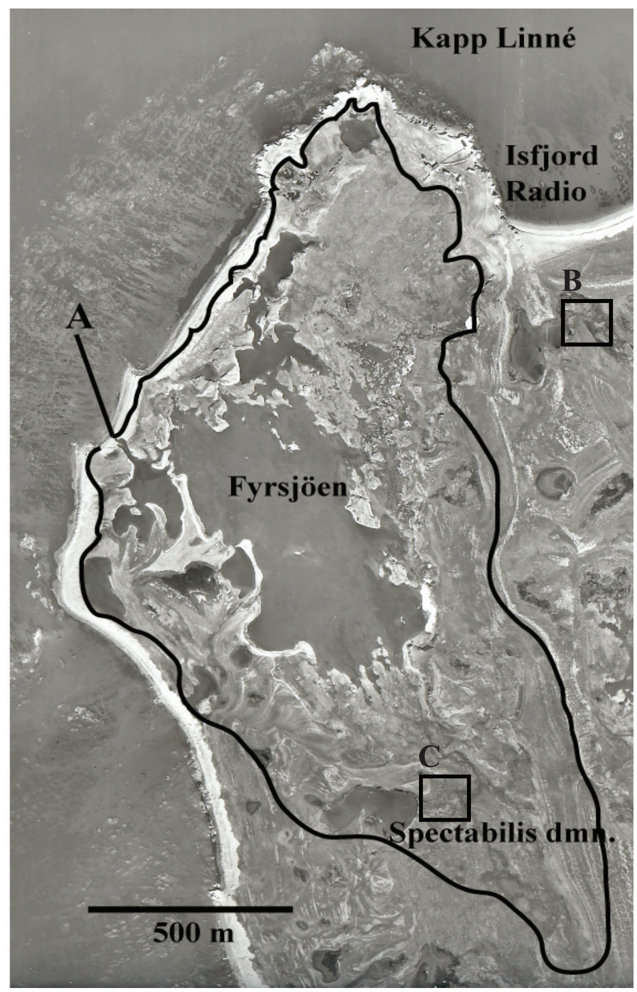

Figure 2. The Fyrsjöen catchment area. *A* indicates the short outlet river through the storm ridges; *B* shows the IPA active layer monitoring site AL3; and *C* is the active layer monitoring site next to the "Spectabilis" pond. (Aerial photograph; Norwegian Polar Institute, No. S69 2431, August 19, 1969.)

The active layer measurements followed the IPA methodology, but here only within a 20 x 40 m area (Brown et al. 2000). Readings were taken the last week of August. The nearest IPA standard site is 1.5 km away.

The breeding success and failure is based upon a nest inventory within the catchment prior to flooding events. This inventory has only been performed along the easily accessible bogs and shores and not upon the islands of the Fyrsjöen Lake. The post-flooding inventory was based upon the position of nests plotted on the 1:7000 topographical map in relation to the maximum water level (Akerman 1980). This makes the result of this part of the investigation relative only, but for the species studied it makes only a minor difference to the result.

Observations

Discharge and water balance

The annual course of flow in the catchment follows a characteristic pattern. In a normal year, the flow in June starts gradually along with the onset of the snowmelt. The catchment has no connection with higher levels (the water divide is 12–14 m. a. s. l.), nor has it connection with any glacier. The June part of the annual discharge is, as a mean, 16.1% (Figs. 3, 4), while July has 64.6%, August 19.2%, and September, only 0.01%. During flooding years, the dam breaks through, and flow normally does not start until July, giving July 77.7%, August 21.9%, and September 0.4% of the annual discharge. The low amounts in September are mainly explained by the fact that the catchment receives no contribution from meltwater from a glacier (cf. Killingtveit et al. 2003). The September precipitation and the active layer discharge flow are quantitatively of little importance. Typical daily discharge graphs are shown in Figure 5.

Despite some clear shortcomings in the measurements and gaps in the background meteorological data, an attempt to illustrate the water balance of the catchment has been performed. A common formula of the common water balance equation can be:

$$P - Q_{river} - Q_{ground} - ET \pm \Delta S = \epsilon \qquad (1)$$

where P is precipitation, Q_{river} is the river discharge, Q_{ground} is the groundwater discharge, ET is the evapotranspiration, ΔS is the storage changes, and ϵ is the error, all expressed in mm water. The error should end up close to 0 if all variables are measured correctly.

In this case the groundwater discharge can be ignored as we, as far as known, have permafrost in the entire catchment. There might be some uncertainties as we are close to the sea and the Lake itself might have some groundwater leakages. There is also a small karst sinkhole within the catchment, but this is, as far as can be judged, of minor quantitative importance.

Regarding evapotranspiration, the figure 80 mm/yr, used by Killingtveit et al. (2003), has been adopted. The storage component S is considered to be constant, as the water level in the lake at the end of the drainage season is down to a

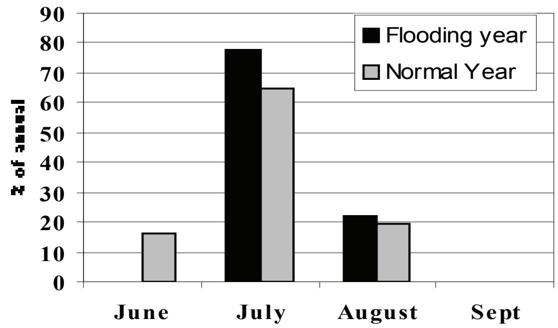

Figure 3. Runoff in the Fyrsjöen Lake catchment per month in % of the total 1974–2001. Note that September might be too low, as measurements some years could not be continued into this month.

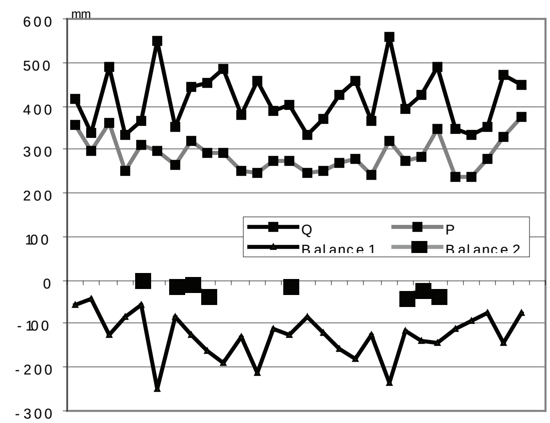

Figure 4. Runoff, precipitation, and hydrological balance for the Fyrsjöen Lake catchment area during the hydrological years (Sept–Aug) 1973/74 to 1999/2000. Q = discharge, P = precipitation-ET, water balance 1 = P–Q, and balance 2 = corrected water balance (considering the snow drift import) in mm during the hydrological years (Sept–Aug) 1974/75 to 1999/2000.

constant level with only marginal variations from year to year. Considering the annual budget, other storage components in this catchment are also of minor importance.

The discharge characteristic of the Fyrsjöen Lake catchment is shown in Figures 4 and 5 and Table 2, in which simple water balance figures are given also. The balance for each and every hydrological year is found negative—on an average -127 mm. The reasons for this lies partly in the precipitation or discharge figures, which may have some errors built in. But there is one factor not considered which became evident during the snow cover surveys within the catchment. Snow cover surveys have been performed in late winter during 8 different years.

The results are given in Figure 4 and Table 2. We find that the catchments contain on an average 100 mm more water equivalents than the winter precipitation measured indicates. The reason for this is the large amount of drifting snow that is accumulated in drifts mainly along the eastern "slopes" of the basin. The shallow basin gets a "precipitation import" through snowdrift mainly from the prevailing easterly winter winds.

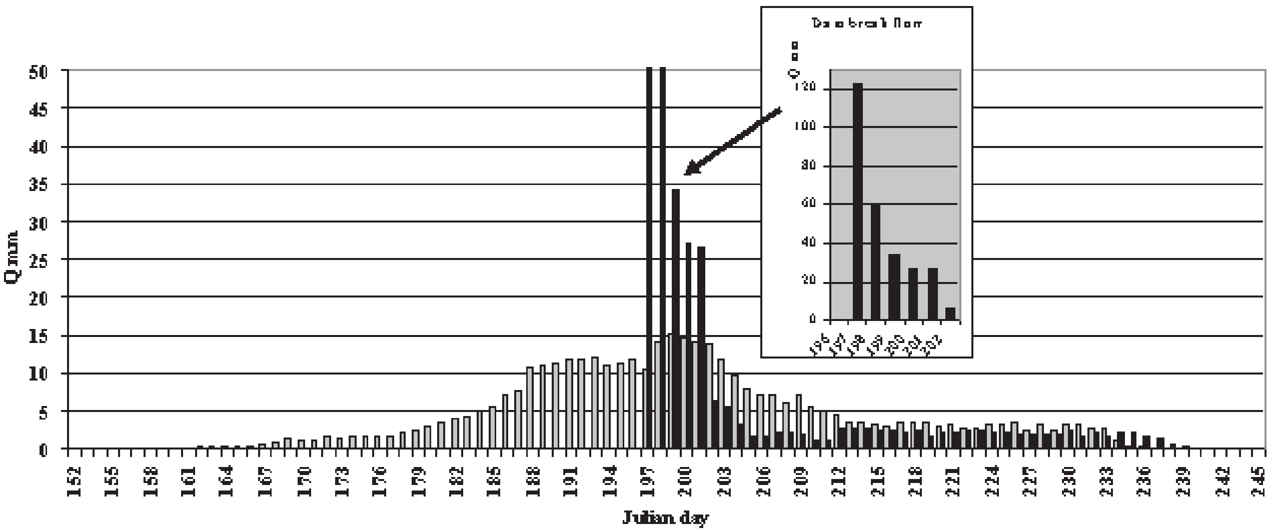

Figure 5. Daily discharge in the Fyrsjöen Lake outlet channel during a "normal" year—in this case 1995 (grey bars)—and a "flooding" year—in this case 1994 (black bars). A "flooding year "is a year with less sea ice and hence unprotected shores along which high blocking storm ridges are formed. Note that the discharge scale for the dam break flow days is different, with up to 120 mm the first day of the "flush."

Storm ridges

The storm ridges that are the cause of the blocked and delayed drainage of Fyrsjöen Lake are built up by the autumn and winter storms. These types of ridges have been observed in the mapping of the Svalbard coasts (Etzelmüller et al. 2003) and are by no means unique. In the coastal geomorphological mapping of Svalbard, they are classified as barriers (Ødegård et al. 1987, Høgvard & Sollid 1988). What is notable is that they now are formed almost every winter as a result of less sea ice along the coast (Fig. 6). Despite that this is indirect observation, they correspond well with the regional sea ice dynamics observed and monitored through RS (e.g., Vinje 1976, 2001, Shapiro et al. 2003).

The barriers vary in height according to the site, but in general they reach between 4 and 6 m above mean seawater level. They are built by coarse beach gravel, sand, and cobbles, typically with a large amount of seaweeds (kelp) mixed in and/or as a cover. In the frozen state, the ridges are like a concrete wall very resistant to melting. During melting, thermokarst features like collapsed thermokarst dolines appear in the surface, and some piping with a low amount of seepage may also occur. This seepage has not been measured, but is of minor importance.

Active layer

The active layer measured in the small bog next to the "Spectabilis dammen" pond follows the same general pattern as the active layer in the IPA bog site some 1.5 km to the north. The small "Spectabilis dammen" bog belongs to one of the bogs and other areas within the catchment that are flooded for years with a blocking storm ridge. The active layer during the investigation period is shown in Figure 7. The two bogs, which apart from size are as similar as can be, show the same general pattern regarding the active layer; that is, a gradual shallower active layer during the period 1972 to the mid-1980s, followed by an equally clear trend of increasing active layer depths. This pattern goes in perfect correspondence with the summer temperature DDT (degree days thaw) that is included in the figure.

However, if we separate the "normal years" and the "flooding years," we find that the "Spectabilis" bog has a deeper active layer (on an average 7 cm deeper) during a flooding year. This clearly indicates the importance of flooding also for the processes in the active layer and the top of the permafrost.

Table 2. Corrected hydrological balance for the Fyrsjöen Lake catchment area based upon snow surveys.

Hy.year	Vinter P mm	Balance mm	Snow in mm	Diff. mm	Corr. Balance
1977/78	267	-55	326	59	4
1979/80	292	-86	368	76	-10
1980/81	261	-123	378	117	-6
1981/82	304	-161	429	125	-36
1986/87	278	-125	391	113	-12
1993/94	298	-119	379	81	-38
1994/95	282	-141	402	120	-21
1995/96	287	-142	397	110	-32

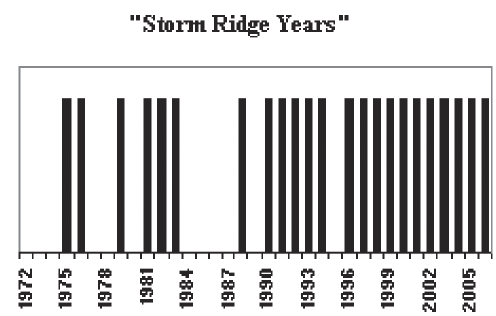

Figure 6. Years with and without larger storm ridges blocking the outlet river from the Fyrsjöen Lake catchment.

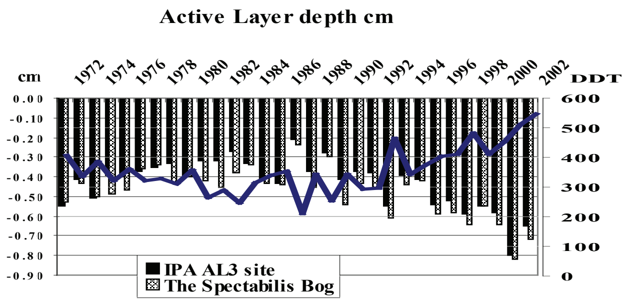

Figure 7. The active layer and the summer climate expressed in DDT (degree days thaw) 1972 to 2002 in the IPA monitoring site AL3 and in the "Spectabilis Bog."

Table 3. Breeding failure during a flooding year (1994) for seven regular breeding species within the Fyrsjöen catchment area.

Species	Nests/Failure	%
Stercorarius parasiticus	1/1	100
Sterna paradisea	26/5	21
Phalaropus fulicarius	6/3	50
Calidris maritima	3/2	66
Somateria molissima	26/5	21
Somateria spectabilis	10/4	40
Gavia stellata	2/2	100

Breeding birds

The breeding birds of the catchment area that have been monitored are shown in Table 3. We find that the Red-throated Diver (*G. stellata*) and the Arctic Skua (*S. parasiticus*) are the species strongest influenced in this case; but the Grey Phalarope (*P. fulicarius*), the less common King Eider (*S. spectabilis*), and the Purple Sandpiper (*C. maritima*) may also locally suffer a loss of 40 to 60% due to the flooding here.

This is, of course, only a very marginal loss considering the total population of these species along the coasts of Svalbard, but considering that this scenario is a trend that prevails, it might be of importance (Fig. 8).

Discussion

Changes in the duration of the open-water season will be critical to the future impacts of coastal and near-coastal processes and environments in the Arctic. An increasing storm frequency and sea level rise are the most well-known possible consequences of climate change, and the fate of sea ice may be equally or more important to natural and human coastal systems (Kerr 2002).

The stability of any coast is a function of the interaction between meteorological and oceanographic forces and the physical properties of coastal materials. The interaction between the atmosphere and the ocean that produces waves and storm surges is mediated by the presence and concentration of sea ice, while coastal materials are either strengthened or destabilized by the presence of permafrost, the abundance of ground ice, and associated temperature regimes (Are 1988; Kobayashi et al., 1999).

Coastal wetlands are likely to move farther inland, and

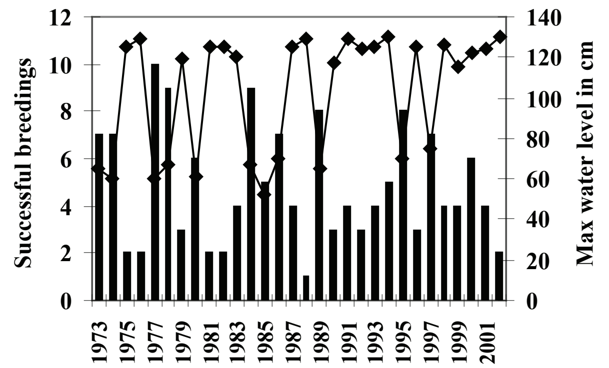

Figure 8. Successfully breeding pairs of King Eider in the Fyrsjöen catchment (bars) compared with the annual maximum water level above mean in cm.

Table 4. Line of observed related "events" from the global scale down to the species level.

A changing climate – a warmer Arctic
Less sea ice
Unprotected shores during winter storms
High ice-cemented storm ridges
Blocked river outlets
Blocked/delayed spring discharges
Anomalous drainage pattern
Flooding of floodplains, lakes, and bogs
Deepening of active layers
Changes in greenhouse gas exchanges
Disturbed plant communities
Breeding failures with birds

coastal flood events will increase. Salinity might increase in coastal marine ecosystems that are now freshened by terrestrial water discharge. If storm surges and coastal flood events increase in frequency and/or intensity, ecosystems in the affected areas are likely to be affected adversely.

This study, which may be summarized in Table 4, is an example of some of these problems.

Acknowledgments

Financial support was received from the Swedish Natural Sciences Research Council (NFR G.GU 3445 106-117), the Royal Physiographic Society in Lund and The Swedish Society for Anthropology and Geography.

References

ACIA. 2004. *Impacts of a Warming Arctic – Arctic Climate Impact Assessment*. Cambridge, UK: Cambridge University Press.

Akerman, H.J. 1980. *Studies on Periglacial Geomorphology in West Spitsbergen*. PhD thesis. Lunds Univ. Geografiska Inst. Ser. Avh. LXXXIX, 297 pp.

Akerman, H.J. 1992. Hydrographic characteristics of the Strokdammane Plain, West Spitsbergen, Svalbard. *Geografiska Annaler* (74A):2-3: 169-182.

Akerman, H.J. 2005. Slow slope processes and active layer 1972-2002, Kapp Linné, Svalbard. *Nor. Geogr. J.* 59: 116-128. Oslo. ISSN 0029-1951.

Are, F.A. 1988. Thermal abrasion of sea coasts (parts I & II) *Polar Geography and Geology* 12: 1-57.

Bertrand, J.L., Chebbo, G. & Saget, A. 1998. Distribution of pollutant mass vs volume in storm water discharge and the first flush. *Water Res.* 32: 2341-2356.

Brown, J., Hinkel, K.N. & Nelsson, P.E. 2000. The circumpolar active layer monitoring (CALM) programme: research design and initial results. *Polar Geography and Geology* 24: 165-258.

Etzelmüller, B., ØÅrd R.S. & Sollid, J.L. 2003. The spatial distribution of coast types on Svalbard. In: V. Rachold et al. (eds.), *Arctic Coastal Dynamics Report of the Third International Workshop, University of Oslo, Norway, 2–5 December 2002*. Bremerhaven: Alfred Wegener Institute for Polar and Marine Research.

Førland, E.J., Hanssen-Bauer, I. & Nordli, P.Ø. 1997. Climate statistics and long-term series of temperature and precipitation at Svalbard and Jan Mayen. *Klima* 21/97. Oslo: Norwegian Meteorological Institute.

IPCC. 2001. *Climate Change 2001: Synthesis Report. A Contribution of Working Groups I, II, and III to the Third Assessment Report of the IPCC.* Cambridge, UK, and New York, USA: Cambridge University Press, 398 pp.

Høgvard, K. & Sollid J.L. 1988. *Coastal map Svalbard B4 Bellsund,* 1:200,000. Department of Physical Geography, University of Oslo, Norway.

Humlum, O., Instanes, A. & Sollid, J.L. 2002. Modeling late 20th century precipitation in Nordenskiöld Land, Central Spitsbergen, Svalbard by geomorphological means. *Nor. Geogr. J.* 56: 96-103.

Humlum, O. et al. 2003. Permafrost in Svalbard: A review of research history, climatic background, and engineering challenges. *Polar Research* 22(2): 191-215.

Kerr, R. 2002. A warmer Arctic means change for all. *Science* 297: 1490-1492.

Kobayashi, N.J., Vidrine, C., Narin, R.B. & Solomon, S.M. 1999. Erosion of frozen cliffs due to storm surge on the Beaufort Sea Coast. *J. of Coastal Research* 15: 332-344.

Ødegard, R., Sollid, J.L. & Trollvik, J.A. 1987. *Coastal map Svalbard A3 Forlandssundet* 1:200,000. Department of Physical Geography, University of Oslo, Norway.

Parkinson, C.L., Cavalieri, D.J., Gloersen, P., Zwally, H.J. & Comiso, J.C. 1999: Arctic sea ice extents, areas, and trends, 1978-1996. *J. Geophys. Res*. 104: 20837-20856.

Johannessen, O.M., Miles, M. & Bj¢rgo, E. 1995. The Arctic's shrinking sea ice. *Nature* 376: 126-127.

Johannessen, O.M., Shalina, E. & Miles, M.W. 1999. Satellite evidence for an Arctic sea ice cover in transformation. *Science* 286: 1937-1939.

Killingtveit, Å., Pettersson, L.E. & Sand, K. 2003. Water balance investigations in Svalbard. *Polar Research* 22(2): 161-174.

Prichard, D. & Hogg, A.J. 2002. On sediment transport under dam-break flow. *J. Fluid Mech*. 4783: 265-274.

Serreze, M.C., Walsh, J.E., Chapin III, F.S., Osterkamp, T., Dyurgerov, M., Romanovsky, V., Oechel, W.C., Morison, J., Zbang, T. & Barry, R.G. 2000. Observational evidence of recent change in the northern high-latitude environment. *Climatic Change* 46(1-2): 159-207.

Serreze, M.C., Maslanik, J.A., Scambos, T.A., Fetterer, F., Stroeve, J., Knowles, K., Fowler, C., Drobot, S., Barry, R.G. & Haran, T.M. 2003. A record minimum arctic sea ice extent and area in 2002. *Geophysical Res. Letters* 30(3): 1110, doi:10.1029/2002GL016406, 2003.

Shapiro, I., Colony, R. & Vinje, T. 2003. April sea ice extent in the Barents Sea, 1850-2001. *Polar Research* 22(1): 5-10.

Steffensen, E. 1969. The climate and its recent variations at the Norwegian Arctic stations. *Metorol. Annaler* 5(8).

Steffensen, E. 1982. The climate at the Norwegian Arctic stations. *Klima* 5: 1-44.

Vinje, T. 1976: Sea ice conditions in the European sector of the marginal seas of the Arctic, 1966-1975. *Norsk Polarinst. Arbok* 1975, Norwegian Polar Institute: 163-174.

Vinje, T. 2001a Anomalies and trends of sea-ice extent and atmospheric circulation in the Nordic Seas during the period 1864-1998, *Journal of Climate* 14(3): 255-267.

Vinje, T. 2001b: Anomalies and trends of sea-ice extent and atmospheric circulation in the Nordic seas during the period 1864-1998. *Journal of Climate* 14: 255-266.

Forecasting Chemical Thawing of Frozen Soil as a Result of Interaction with Cryopegs

V.I. Aksenov
FSUE Fundamentproect, Moscow, Russia
N.G. Bubnov
Limited company Neivo, St.Peterburg, Russia
G.I. Klinova
FSUE Fundamentproect, Moscow, Russia
A.V. Iospa
FSUE Fundamentproect, Moscow, Russia
S.G. Gevorkyan
FSUE Fundamentproect, Moscow, Russia

Abstract

This paper suggests methods of forecasting chemical thawing of frozen soils interacting with cryopegs. We have performed experiments on chemical thawing of frozen soils at negative temperatures and have conducted theoretical research on the interaction between cryopegs and frozen soils. The results of our study are as follows: (1) Peculiarities of cryopeg occurrences across the Yamal Peninsula have been discovered; (2) Five types of cryopeg occurring throughout the Yamal Peninsula have been discovered, and cryopeg classification has been elaborated; (3) Basic patterns of chemical thawing of frozen soils have been identified; thus, experiments have shown the migration of unfrozen water and salt ions from the brine (mineralized water) to the frozen soil; (4) Three models of the most typical cryopeg occurrences across the Yamal Peninsula have been designed, and can be used for engineering purposes; and (5) New methods of forecasting the process of chemical thawing of frozen soils interacting with cryopegs have been suggested and are based on the empiric calculation formula (7) given in this paper.

Keywords: chemical thaw; cryopeg; frozen soil;, highly mineralized groundwater; pile; saline permafrost; saline soil; salt migration; thaw settlement.

Introduction

Yamal Peninsula (Western Siberia, Russia) (Fig.1) is one of the most promising Russian regions currently under intensive development. Primarily this involves exploration of a number of large oil and gas fields.

Modern marine and alluvial-marine deposits in the Pleistocene marine terraces and the deep Pre-Quaternary deposits scattered across Yamal Peninsula are rich in cryopegs.

Cryopegs are highly mineralized (saline) groundwater existing at temperatures below 0°C. Their temperature ranges from -12°C to almost 0°C. A change of temperature entails a change in the degree of cryopeg mineralization, which typically varies from 10 to 150 g/l (promille), but sometimes may be as high as 200 g/l.

Cryopegs pose a significant threat to pile foundations built in the permafrost region. Local thawing of soil adjacent to a brine lens may trigger further thawing of the soil along a pile trestle or a borehole. Such thawing is of chemical nature and occurs at temperatures below 0°C.

This paper deals with the interaction between natural brines (cryopegs) and frozen soil under continental conditions. These are characterized by lower temperatures compared to the subaqueous frost, as well as by certain peculiarities of the structure and composition of the rock mass. This difference can have a considerable effect on the interaction between the brines and the frost.

Cryopeg Distribution and Conditions for their Formation

In practice, civil engineers most commonly have to deal with "near-surface" cryopegs located at shallow depths. Such cryopegs are widely spread on laida (littoral marshy area flooded during the incoming tide and dry during tidal fall) and in the low reaches of rivers exposed to tide and surge, as well as at marine terraces formed by saline soils. However, they rarely occur at temperatures below -4ºC.

The laida and flood plain cryopegs were formed mainly as a result of decrease of temperature and freezing of enclosing deposits. They are located in areas adjacent to river flood plains, on sand spits, and in the rear part of flood plains. On laida the soil strata may be composed of just cooled soil containing cryopegs, of soil freezing only from the surface, or in form of soil frozen throughout the investigation depth interbedded by cooled soil lenses containing cryopegs.

The laida cryopegs feature the highest degree of salinity (up to 150 g/l) and, as a rule, low (up 10 m) water heads (Fig.1).

The flood plain cryopegs are characterized by a lower

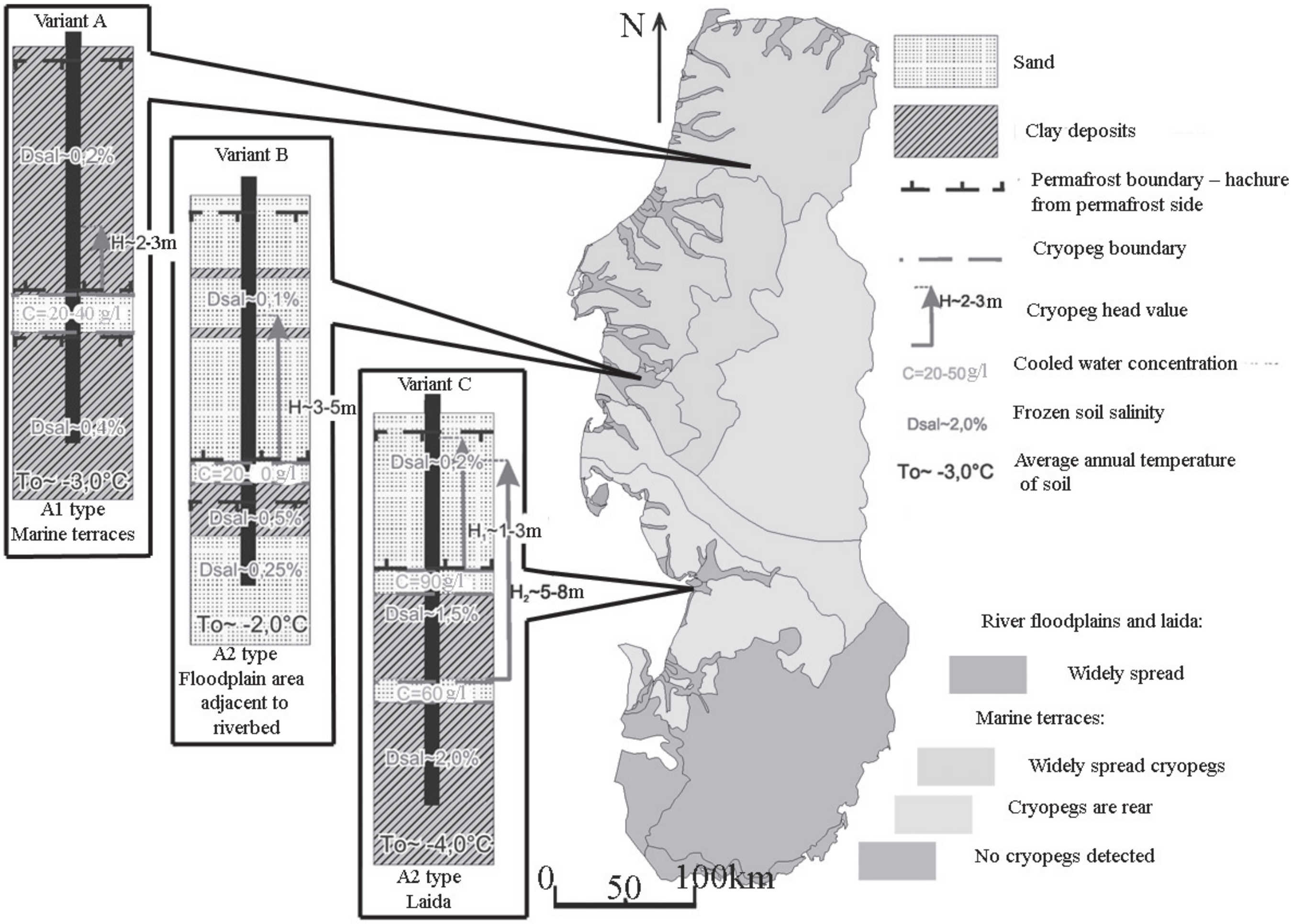

Figure 1. Distribution of cryopegs at Yamal Peninsula.

degree of mineralization (as a rule within 40–70 g/l), but slightly higher water heads. An upper layer of non-saline frozen soil 4–8 m thick is clearly distinguishable in the flood plain deposit profile. In laida this layer is of discontinuous nature and is thinner (2–6 m).

The marine terrace cryopegs occur in the form of relatively thin lenses at various depths and are confined to certain areas featured by enhanced salinity. Within these areas they are confined to local zones with temperatures higher than the background temperature. They are striped on the gently sloping hills, in depressions, on hasyrey (the bottoms of modern and ancient drained lakes), and in areas covered by shrub.

Over the last 40 years a number of researchers have studied cryopegs. As a result of their efforts several systems for classifying cryopegs according to their formation and distribution patterns were proposed and published. The most detailed classifications were proposed by N.V. Ivanova (Ivanova et al. 1992) and one suggested by I.D. Streletskaya (1991). In this paper we take the Streletskaya classification as the basis for our research, but we have modified it slightly to be consistent to the purposes of this study.

This classification is based on the conditions of cryopeg formation. All cryopegs are divided into groups, types, and sub-types (Table 1).

The groups are identified depending on cryopeg position in cryogenic strata (areas of active and passive cryodiagenesis). The cryopeg types are distinguished based on a set of genetic specificities, where the main attribute is the dynamic (period) of change of the cryogenic strata temperature. The sub-types are also identified based on the set of genetic specificities, but the main attribute is the trend (increase or decrease) of the cryogenic strata temperature.

The lenses are up to several meters thick and stretch for 100–300 m. They are featured by hydrostatic and cryogenic heads (10–36 m). The degree of cryopeg salinity is 5–35 g/l; water chemical composition is dominated by sodium chloride. The enclosing ground is represented by various types of sandy-clayey soils (D_{sal} = 0.1-1.0%). The salinity of cryopegs at all levels is 50–80 g/l, and their chemical composition is dominated by sodium chloride.

Cryopeg Impact on Ground Base

Cryopegs occur along the arctic sea coast at depths ranging from several meters to several hundred meters.

Two main factors are decisive in terms of modern distribution of frozen soils and cryopegs with marine-type salinity. The first factor involves sea water percolation through permafrost with the follow-on freezing. The second factor has to do with physical and chemical changes and desalination of the upper layer of permafrost during local warming. The frozen soil thawing and freezing processes are accompanied by salt differentiation between the liquid and solid phases as well as by change of the interstitial solution's concentration. As the interstitial water freezes, a small portion of salt dissolved in it is captured by ice crystals while another portion precipitates and the third portion is squeezed out into the underlying ground. All this enhances mineralization of the residual solution, which, in its turn, facilitates the formation of cryopegs.

In terms of chemical composition, the arctic coast cryopegs are similar to the sea water composition. They have marine-type salinity with the following ion concentration ratio:

$$Cl > SO_4 > HCO_3\ ;$$
$$Na > Mg > Ca.$$

The volume of cryopeg lenses in permafrost varies and depends on conditions under which such lenses are formed. Volume of the brine containing lenses formed in tectonic fractures may be large enough. Small lenses containing non-freezing brine solutions may be formed as a result of sea water percolation through the soft ground. The mechanism of their occurrence is as follows. When soil freezes due to the squeezing of salt out from the phase boundary, an area with low freezing temperature is formed near such a boundary. If the rate of salt diffusion is lower than that of freezing, the conditions favorable for normal crystallization occur below the enhanced salt concentration area. This triggers formation of a new ice sub-layer. Such overcooling of the brine solution caused by enhancement of salt concentration during soil freezing is one of the conditions for formation of a striped structure of frozen soil. In a situation where the brine solution remains unfrozen and the frozen soil enclosing a lens does not thaw, the cryopeg temperature should be the same as that of the enclosing frozen soil. But if the brine solution temperature differs from that of the frozen soil, their contact, depending on the external conditions, should result either in further overcooling of the brine solution with the follow-on freezing, or in thawing of the frozen soil (Gorelik & Kolunin 2002, Grigoryan et al. 1987).

Until now the processes of interaction between frozen soil and saline solutions were under researched. For a long time it was supposed that frozen soils were impenetrable to both water and brine solutions. But in recent years new information has been obtained on the development of the physical-chemical and the mass exchange processes occurring in frozen soils as a result of interaction with the saline solutions (Gorelik & Kolunin 2002, Grigoryan et al. 1987). Recently it was discovered that unfrozen moisture and salt ions migrate from a brine solution into a frozen soil. And here several mechanisms of ion migration are operating: diffusion, convection, and adsorption.

Depending on values and ratio of moisture potential gradient to that of ion concentration, moisture and salt migrate to and from the frozen soil. When brine solution concentration reaches the critical value, the dynamic equilibrium occurs, which leads to termination of the mass exchange process. These critical values of concentration depend on texture, mineral, and chemical composition of the frozen soils, as well as on their temperature. In case of sands interacting with the sodium chloride solution, such critical concentration is not less than 0.1 gram·mol per liter, and for clays it is equal to 5 gram·mol per liter.

The research results show that water and salt migration flows change with time. At the initial stage salt ions migrate and an insignificant amount of moisture is being transferred. Salt ions invading the frozen soil interact with soil mineral particles and with molecules of attached water and ice. Cations interact with the negatively charged surface of mineral particles, while anions interact with the positively charged surface of interstitial ice. In the beginning of the salt transfer process, intensity of anions migration in frozen soil is higher than that of cations. But later on, intensities of migration of anions and cations become almost the same.

Capacity of frozen soil to selectively transfer or hold certain types of ions plays an important role in the salt transport process. Such capacity of frozen soil depends on valence and mass of migrating ions, their hydratability, as well as on a structure of frozen soil pore space. And the structure of pore space of frozen soil, in its turn, depends on temperature and cryogenic morphology of frozen soil.

Mass transfer in frozen soils is possible only if there is a system of continuous water films oriented in the direction of the migration forces. Formation of segregated ice or ice-cement bands results in discontinuity of the active part of pore space participating in the mass transfer processes. This in its turn entails decrease of migration flow rate. This is why structure of pore space plays an important role in the migration processes.

If initial temperatures of soil and brine solution are the same, the phase changes associated with dissolution of interstitial ice contained in frozen soil occur at the interface of soil and brine solution. As a result the temperature of frozen soil will decrease.

In non-saline soils at temperatures below freezing point the relationship between unfrozen water W_w and temperature T is definitely described by the "unfrozen moisture curve." But in the case of saline soils the amount of unfrozen moisture (W_w) depends not just on temperature but also on concentration of interstitial solution. During the phase change process, concentration of interstitial solution changes according to the following formula:

$$C = \frac{C_O \cdot W}{W_w} \qquad (1)$$

where W – total humidity of frozen soil; W_w – content of frozen moisture in frozen soil; Co – initial concentration of interstitial solution. The W_w value can be easily determined from the formula proposed by Aksenov (1980):

$$W_w = 0{,}25 \cdot W_P + (W - 0{,}25 \cdot W_P) \cdot \frac{T_{bf}}{T} \qquad (2)$$

where W_p – humidity at plasticity limit; T_{bf} – temperature at which interstitial solution starts to freeze, determined from the formula:

Table 1. Classification of the North-Western Yamal Cryopegs (according to I.D. Streletskaya with partial modification).

Group	Type (Dynamics of cryogenic formation temperature)	Sub-type (Trend of cryogenic formation temperature)	Geomorphological level	Age and genesis of enclosing deposits	Composition of enclosing deposits and salinity of soils, D_{sal},%	Enclosing soil temperature, °C	Depth and absolute height, m	Head, m	Thickness lens,, m	Mineralization,, g/l
Active cryodiagenesis zone	A. Short term (average annual, 2 – 5 years, 11 years fluctuations of temperature)	A_1. Soil temperature rise	Marine terraces	m,pm I-II, sd II-IV	Sandy-loam and clayey Ds=0.2 - 0.8	-0.5÷-4	3 -12 0 ÷ +40	0.5-5.0	0,2-0,5	20-60
			Flood plain	am, lm IV	Sandy-loam and clayey Ds=0.05 - 0.5	-0.5÷-3	3 -10 0 ÷ +5	0.5-5.0	0,1-0,5	7-50
		A_2. Soil temperature drop	Flood plain (adjacent to river bed)	am IV	Sandy and sandy-loam Ds=0.05 - 0.7	-0.5÷-3	5-10 0 ÷ +5	2-6	0,1-0,5	7-50
			Flood plain (spit)	am IV	Sandy and clayey Ds=0.1 - 0.7	-3÷-5	6-10 0 ÷ +5	3-4	0,1-0,5	80-90
			Flood plain (hasyrey)	lmIV	Sandy-loam and clayey Ds=0.1 - 0.7	-3÷-5	2-10 0 ÷ -5	0.1-7	0,1-0,3	60-100
			Laida	mIV	Sandy and clayey Ds=0.5 - 3	-4÷-8	1-15 0 ÷ -10	0-10	0,1-0,5	70-150
Passive Cryodiagen. zone	B. Medium term (40-90 years fluctuations of temperature)	B_1-B_2. Soil temperature rise and drop	All levels	m,pm III	Sandy and sandy-loam Ds=0, 1-0,6	-3÷-5	15-40 -10÷ -40	10-35	0,3-12	50-80

$$T_{bf} = -1{,}83 \cdot \frac{C_O}{\mu} \qquad (3)$$

where μ – molecular mass of dissolved salt.

Patterns of Chemical Thawing of Frozen Soil as a Result of Interaction with Cryopegs

We conducted experimental research of a process of interaction between the NaCl solution and a frozen soil. Soil samples were placed into a 5 sm tall cylindrical container being 2 sm in diameter and were kept in a constant-temperature cabinet at a given temperature (below 0°C) during 2–3 days until soil phase changes were completed.

After that, a brine solution with the same temperature was poured on the upper surface of the sample. The soil container was sealed by a lid with a capillary. Soil thawing dynamics was assessed by rate of descent of the solution in the capillary. The side surface of the cylindrical container was covered by thermal insulating material, while the temperature at the container's upper and bottom surfaces was the same as the experiment temperature. By this we simulated one-dimensional interaction between the brine solution and the soil. Similar equipment and procedure of experiments were used by Gaidaenko (1990) and Ostroumov (1990).

Table 2. Constant factors of the formula (7).

	The opened system		The closed system	
	Case of sand	Heavy clay loam	Case of sand	Heavy clay loam
A_1	0,0752	- 0,3062	- 0,0692	– 0,0447
A_2	0,0588	- 1,0633	- 0,2205	0,0008
A_3	1,6036	0,7064	1,8014	1,7719
B_1	- 0,3029	1,9217	0,5746	0,3467
B_2	0,8455	8,0137	2,9339	1,0402
B_3	- 3,3278	2,0932	- 4,8438	- 6,6717

The results of our experiments are as follows. When temperature T = -1.8°C, a contact between frozen sand and brine solution (with concentration of 50 g/l) leads to a situation where chemical thawing of soil occurs during the first 20 hours. After that, interstitial moisture starts to refreeze. If solution concentration is 100 g/l, chemical thawing of soil proceeds continuously. In this case, when temperature T = -1.8°C, refreezing does not occur.

In the case of frozen clay, when temperature T = -1.8°C and brine solution concentration C = 100 g/l, the rate of chemical thawing is twice lower that for frozen sand, while refreezing starts in about 40 hours.

The rate of chemical thawing of frozen soils is influenced by a value of salt diffusion coefficient, which, in its turn, depends on many parameters. Primarily it depends on type of

Table 3. Rate and depth of chemical thawing of frozen soils as a result of interaction with cryopegs.

Cryopeg type and sub-type	Geomorphological level	Composition of enclosing deposits	Salinity, g/l	Enclosing soil temperature T, °C	Heat transfer system	Thawing rate V, sm/day	Thawing depth per 0.5 years h, m	Thawing depth per 1 year h, m
A_1	Marine terrace, flood plain	Clay loam	40	-1.5 < -2.0	Opened “	0.46 0	0.85 0	1,70 0
A_2	Floodplain (area adjacent to riverbed)	Sand	40	-1.5 -2.0 < -2.5	Opened “ “	0.94 0.36 0	1.71 0.66 0	3,42 1,32 0
A_2	Floodplain (hasyrey)	Clay loam	80	< -3.0	Closed	0	0	0
B	All levels	Sand	80	< -3.0	Closed	0	0	0

soil, thickness of water films in soil voids (pores), geometry and relative position of water films and ice crystals. For example, continuous ice beds prevent penetration of salt into soil. The coefficient of salt diffusion in frozen soil is calculated using the following formula:

$$D = W \cdot D_O \tag{4}$$

where D_O is the coefficient of salt diffusion in free water; in case of a NaCl, D_O is approximately 0.04–0.05 sm/h.

The rate of chemical thawing of frozen soil also depends on average density of brine solution-as brine solution density decreases, the duration of chemical thawing of soil increases.

We obtained a simple function that allows for calculating depth of chemical thawing of frozen soil exposed to saline solution:

$$h = h_1 \cdot \sqrt{t} \tag{5}$$

where h is the depth of soil layer thawed during an estimated time t; h_1 is the depth of soil layer thawed during the first day.

Our research demonstrates that when the temperature of brine solution is the same as temperature of frozen soil, the rate of chemical thawing of frozen soil depends on brine solution temperature and concentration in the following manner:

$$f(C,T) = (A_1 \cdot \ln C + B_1) \cdot T^2 + (A_2 \cdot \ln C + B_2) \cdot T + (A_3 \cdot \ln C + B_3) \tag{6}$$

where

$$V = \begin{cases} f(C,T) & at \quad f(C,T) \geq 0, \\ 0 & at \quad f(C,T) < 0; \end{cases} \tag{7}$$

where V is the soil thawing rate (sm/day); C is the brine solution concentration expressed in promille; T is the air temperature expressed in degrees Celsius. The factors A_i and B_i (i = 1, 2, 3) – constant values (experimentally obtained) (see Table 2).

The process of chemical thawing of soil described above will also occur under the foot of a pile driven into a borehole. When a borehole is being drilled, natural pressure of rock formation is released in the area where a pile is driven in.

Practical Examples

Physical and mechanical properties (strength and deformability) of marine deposits scattered along the Arctic coast depend on temperature, salinity, particle-size distribution, and humidity of marine sediments.

Depending on their deformability the Yamal Peninsula soils include hard frozen, plastic frozen, or cooled soils. Plasticity depends on soil type, temperature, and salinity that determine phase composition of interstitial solution and degree of soil cementation by interstitial ice. That is why it is expedient to link boundary of soil state change to phase composition of soil moisture.

Various states of frozen soils (hard frozen, plastic frozen, and cooled soil) also depend on interactions between the ground base and cryopegs. Chemical thawing of frozen soil is triggered by such interactions.

The comprehensive approach to studying distribution and classification of cryopegs, adopted by us, allowed for revealing patterns of cryopegs distribution within ground strata along the western coast of Yamal Peninsula. This makes it possible to assess soil variants as a base for pile foundations.

Let us consider these variants from the viewpoint of the possible load bearing capacity of piles.

Examples are based on typical soil conditions (in accordance with the survey of the Obskaya-Harasaway road (see Fig. 1).

Variant “a” (Fig. 1, variant A). A pile driven into frozen clay, saline soil taps low-pressurized low-mineralized cryopeg lens (C = 20–40 g/l) at a depth of H = 2–3 m. The temperature (T_o) of the saline clay soil of the marine terrace is minus 3°C. As a result, the pile surface is wetted with mineralized water (either fully or partially). Under such conditions the rate of chemical thawing of the soil amounts to zero (Table 3). However, given the above mineralization and temperature, there will be just a film of fresh ice forming in the pile contact area. In general, the bearing capacity of the pile will be largely unaffected. Tables containing construction standards can be used to calculate the bearing capacity.

Thus, if the temperature is minus 3°C and the salinity of clay soil is ~ 0.2%, shearing resistance of the soil adfreezing with the metal pile can be assumed equal to R_{af} = 150 kPa. If the temperature remains unchanged and the salinity amounts to 0.4%, design pressure under the pile butt-end can reach R = 550 kPa, which will ensure the bearing capacity of the pile.

Variant “b” (Fig. 1, variant B). A pile is driven into a frozen ground strata in the laida area adjacent to a riverbed. The upper part of the strata consists of slightly saline sands (D_{sal} = 0.1–0.15%). The bottom part is composed by clayey saline soils (D_{sal}=0.5%). A cryopeg lens penetrated by the pile is featured by high salinity (up to 70g/l). The pile driven into such a borehole is unlikely to have proper load bearing capacity since the rate of chemical thawing is high and equals to 0.36 sm/day (Table 3). Over half a year, chemical thawing along the level (r) can reach 0. 66 m (see Table 3). Bearing capacity of the pile in the lower part across the lateral adfreezing surface of saline (D_{sal} = 0.5%) clay soil is just as small. At a temperature of minus 2°C, R_{af} can amount to 30 kPa. In general, in the upper part of the pile, since soil is not frozen, sand will be thawed due to chemical thawing. In the bottom part of the pile there are plastic frozen soils with weak strength properties. Installation of a pile in such conditions is inexpedient and should be avoided. In such circumstances cooling systems may be used as a last resort.

Variant “c” (Fig. 1, variant C). A pile is driven into cooled soil in the bottom part of the section. The upper layer consisting of frozen sand may be 2–4 m thick. As a result of exposure to highly saline head water, chemical thawing of this layer may occur. The clayey saline soil strata (D_{sal} = 2.0%) may be interbedded by sand containing highly saline head cryopegs. In this situation a construction method based on preliminary thawing of ground strata should be used. The construction standards for thawed ground shall be used for determining strength properties.

Conclusion

Despite insufficient knowledge of the subject under investigation, limited experimental data, and challenges in meeting the set objectives, the research and studies performed by us allow for the first time to reveal basic patterns of change of physical and mechanical properties of frozen soil as a result of their interaction with cryopegs.

Our study comprised a number of experiments on chemical thawing of soils at a temperature ranging between -1.5°C and -6.0°C and with brine concentration ranging between 40 and 80 g/l. The analysis of the results yielded by our experiments enabled us to:

(1) discover basic interaction patterns between frozen soils and mineralized waters at below-zero temperatures;

(2) compile tables and devise formulas for calculating the rates of chemical thawing of frozen soils (see Formula (7), Table 4);

(3) suggest methods of assessing the bearing capacity of piles driven into the rock mass with cryopeg lenses. This allows us to determine whether it is possible to ensure the bearing capacity of pile bases (if there are any cryopegs present), or whether such a possibility is completely ruled out.

References

Aksenov, V.I. 1980. *Study on Mechanical Properties of Saline Soil as Building Bases.* Moscow: MISI, 24.

Gaidaenko, E.I. 1990. Effect of saline liquids on frozen soils and mortars. *Frozen Saline Soils as Foundations for Buildings*. Moscow: Nauka, 62-70.

Gorelik, Ya.B. & Kolunin, V.S. 2002. *Physics and Modeling of Cryogenic Processes in Crust.* Novosibirsk. Publishing House of Siberian Branch of Academy of Sciences, 317.

Grigoryan, S.S., Krass, M.S., Guseva, E.V. & Gevorkyan, S.G. 1987. *Quantitative Theory of Geocryological Forecast.* Moscow: Publishing House of Moscow University, 266.

Ivanova, N.V. et al. 1992. Patterns of cryopegs formation within Kara cryoartesian basin. *Formation of Cryolithozone Ground Water.* Yakutsk: Publishing House of Siberian Branch of Academy of Sciences, 18-34.

Ostroumov, V.E. 1990. Salt transfer in dispersed frozen soils under the influence of temperature gradient. *Frozen Saline Soils as Foundations for Buildings.* Moscow: Nauka, 45-55.

Streletskaya, I.D. 1991. *Patterns of distribution and Formation of Saline Frozen Soil and Cryopegs in North Western Yamal.* Moscow: Moscow State University, 21.

Permafrost and Cryopegs of the Anabar Shield

Sergey V. Alexeev
Institute of the Earth's Crust SB RAS, Irkutsk, Russia
Ludmila P. Alexeeva
Institute of the Earth's Crust SB RAS, Irkutsk, Russia
Alexander M. Kononov
Institute of the Earth's Crust SB RAS, Irkutsk, Russia

Abstract

The Anabar shield is characterized by continuous permafrost. The mean annual temperature of rocks reaches -15ºC, and the zero isotherm position is detected at depth 1000 m. According to the scheme of geocryological zonation, the ice-rich permafrost, underlain by dry permafrost, occurs down to a depth of 200 m; but the hydrogeological studies performed recently on the margins of the shield indicate possible availability of fresh groundwater within its field. Remarkably, this paper for the first time offers the theoretical model of cryopeg formation in crystalline rocks and a new type of permafrost structure. The study suggests that glaciation and marine transgressions have been identified as truly crucial events in the Pleistocene history of the shield. The glacial complexes experienced the processes of seawater-frozen rocks interaction, ground ice melting, and replacement of fresh groundwater with seawater. As a consequence, appropriate conditions were created for ice-rich permafrost and subpermafrost cryopegs to be derived in cryochrons.

Keywords: Anabar shield; brines; cryopegs; glaciation; permafrost; seawater.

Introduction

The Siberian platform is the most ancient and largest geological unit of Eurasia, in which a sustainable portion of rocks have been in a perennially frozen state since Early-Middle Pleistocene. Its northeastern part is occupied by the basement uplift that is the Anabar shield and is characterized by truly complicated natural and geocryological-hydrogeological conditions.

Lack of geocryological and hydrogeological information on the Anabar shield is primarily explained by its remoteness, as well as unavailability of data on deep drilling accomplished within the shield, and targeted survey. Therefore, identification of the main parameters of the Anabar shield permafrost and features of its evolution are key scientific goals. The profound knowledge to be gained will ensure understanding of the general pattern of the continental crust formation on Earth in the Late Cenozoic. The authors of this paper have compiled available data on geological features and the geocryological and hydrogeological settings of the Anabar shield. Paleogeocryological interpretation of these sources of information defined morphological and genetic specifics of the shield permafrost and the major phases of its evolution in the Late Cenozoic, as well as new types of the cryolithozone structure.

Presentation and Discussion of Results

Geology, geomorphology, and climate

The Anabar shield is composed of the Archean metamorphosed rocks of the granulite complex; for example, gneisses and crystalline schists (Fig. 1). They make up some

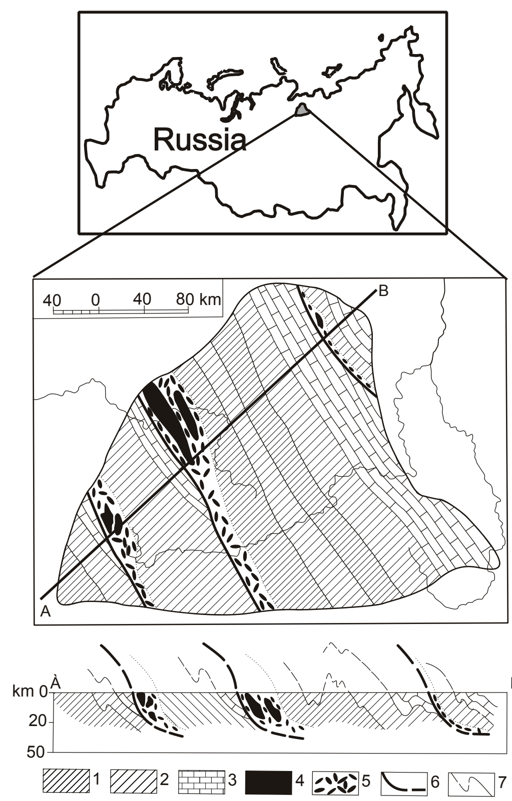

Figure 1. Geological structure of the Anabar shield (Rozen et al. 1986). 1 – Daldyn series, 2 – upper Anabar series, 3 – Khapchan series, 4 – cataclasite, phyllonite and diaphthorite of deep-seated shear zone and diaphthoresis, 5 – faults (mylonite and blastomylonite), 7 – folded structure (shown on section A–B).

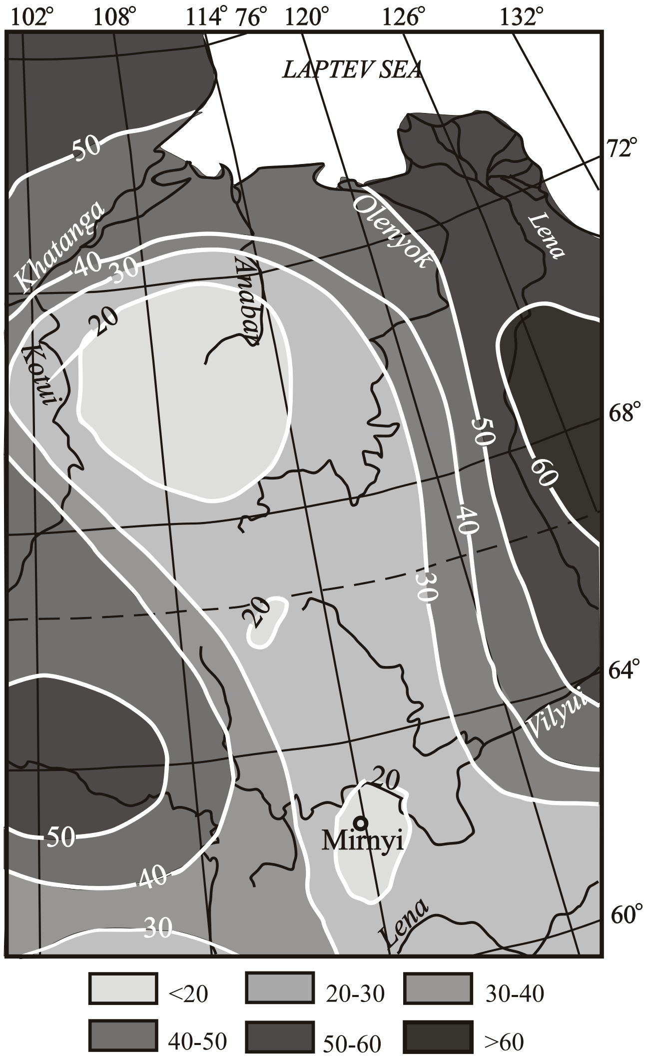

Figure 2. Heat flow values (mW/m^2) in the north of the Siberian platform (*Temperature, cryolithozone*… 1994)

rigid blocks, for instance, the Magan, Daldyn and Khapchan terrains, divided by thick zones of shearing and splitting striking towards the northwest (Rozen et al. 2002).

The Anabar shield is rimmed with a zone of flatly lying Proterozoic (peridotites, amphibolites, and pyroxenites) and Cambrian sedimentary rocks. Quaternary sediments are thin and are not widespread. The ancient magmatic rocks (granites and anorthosites) were formed in the Archean and Proterozoic cycles of volcanism, while young rocks represent Permian-Triassic "Siberian traps" making up thick covers, sills, and dykes. The common units of the Anabar shield structure are large fault dislocations.

The Anabar shield is one of the largest uplifts of the Mid-Siberian plateau. In relief the uplift looks like a deformed flat cupola with massive prominences separated by incised river valleys. A typical structural relief of the plateau was formed over the sedimentary rocks of monoclinal bedding composing the edges of the Anabar uplift. The maximum altitude of the plateau is 900 m in its central and southwestern parts. In the south and northeast, it reaches 600 m; in the southeast, it is 300–350 m; and near the eastern border, it is close to 200 m. The river valleys commonly occur in the zones of tectonic dislocations. They lack such forms of accumulation relief as the first floodplain terrace, river sand bars, spits, and flood lands.

The Anabar shield lies within the Siberian part of the sub-Arctic zone having a sharply continental climate. In the cold period, the climate is much affected by the Asian barometric maximum. The mean annual temperature of air varies from -13 to -15, while the mean minimum of air temperature ranges from -18 to -21°C (Gavrilova 1998). The amplitude of temperature variations reaches 56°C. In time of anticyclone, the air temperature inversion leads to a marked cooling of river valley bottoms. The annual amount of precipitation decreases south to north from 266 to 194 mm/yr. The steady snow cover is formed by early October, and it melts down in late May. On the wind-protected sites, the snow cover is commonly 66–73 cm deep, whereas in the open parts its depth decreases to 46–57 cm. The average value of snow density is 0.16–0.22 g/cm^3.

Geocryology and hydrogeology

The Anabar shield is located in the northern geocryological zone where permafrost is ubiquitous. Knowledge about the thermal status of frozen ground is insufficient and poor, because deep wells applicable for geothermal observations were not drilled. The highest mean annual temperature of rocks (-7…-9 °C) is typical for river valleys, gently sloping shores, and low interfluvial areas overlain with sandy and loam sandy fluvioglacial sediments. On the high, steep slopes and tops of the Anabar plateau, the mean annual temperature of rocks reaches -13…-15°C (Ershov 1989).

Considering geothermal parameters, the Anabar shield is regarded as the region with the coldest crust and the lowest heat flow (Balobaev et al. 1983). The temperature of rocks at depth 500 m amounts to -3…-5, and at depth 1000 m, it raises to -1…+1 °C. The heat flow values vary from 15 to 20 mWt/m^2 (Fig. 2).

It is currently believed that within the Anabar shield the cryolithozone has two layers. In the upper part of the shield and on its slopes, the thickness of permafrost reaches 150–200 m. It is underlain by dry rocks with negative temperature. Groundwater can occur only in the seasonally thawed layer and within closed taliks within river valleys. The total thickness of the cryolithozone is estimated to be over 1000 m (Fotiev 1978, Ershov 1989).

The authors of this paper propose that the sequence of perennially frozen rocks is composed of disconnected blocks and boulders bound by interstitial ice and dispersed material. The ice inclusions basically fill fractures of cleavage, chipping, as well as fractures of slip. The rocks of the Anabar shield inherit fractured and fracture-vein cryogenic structures producing shlierens, nests, and extensive veins. The pattern of fractures and ice-filled cracks essentially changes in massive rocks, and it is defined by the lithological, petrographic, and tectonic factors. In basalts, the net of cracks looks like columnar or pillar jointing (Fig. 3a). In granites and sandstones, the ice-containing cracks produce a system net (Fig. 3b), while in schists this is a wavy net (Fig.

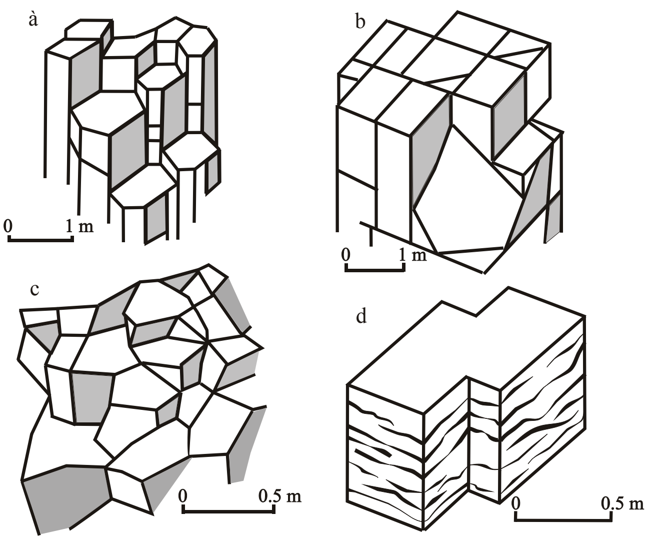

Figure 3. Structures of ice-filled fractures of the Anabar shield: a – polygonal (basalt), b – system (granite), c – chaotic (dolerite), d – wavy (schists).

3d), both occurring on the folds of longitudinal compression and near faults. In the fault zone, next to the ruptures and contact of intrusive rocks the dolerites display a chaotic net of cracks (Fig. 3c). The structure-forming ground ice has cement, infiltration, and sublimation genesis.

Hydrogeological studies performed recently on the margins of the Anabar shield indicate possible availability of fresh groundwater within its inner field (Solopanov & Tolstov 1996). This statement can be exemplified by the Tomtor pluton, hosting the unique deposit of rare-metal ores, located about 180 km east of the shield. The massif is composed of ultrabasic, alkaline, and carbonatite rocks. Geophysical surveys suggest that subpermafrost waters exist within the Anabar shield (Kalinin & Yakupov 1989).

At depths of 170–400 m, the wells penetrated artesian subpermarost waters of chloride-hydrocarbonate sodium composition with salinity of 225–770 mg/L. The head over the aquifer roof was 120–360 m. The well flow rate ranges from 2.4 to 7.0 m^3/day (Solopanov & Tolstov 1996). The geothermal observations in wells indicate that the temperature of rocks at the depth of zero ranges from -6.1 to -8.4°C, which corresponds to calculated estimates of mean annual temperature of rocks of the Anabar shield. The temperatures were measured at the Chair of Geocryology at Moscow State University.

Discussion

The interior of large massifs of crystalline rocks, for example, Baltic, Canadian, and Brazilian shields, contains chloride saline waters and brines of different salinity. Researchers have proposed alternative processes of evaporative concentration of seawaters and dissolution of halogene formations. In recent years, a number of published papers reported formation of chloride brines of the Baltic and Canadian shields due to cryogenic concentration of seawater (Herut et al. 1990, Szilder et al. 1995, Bottomley et al. 1999, Marion et al. 1999, Starinsky & Katz 2003).

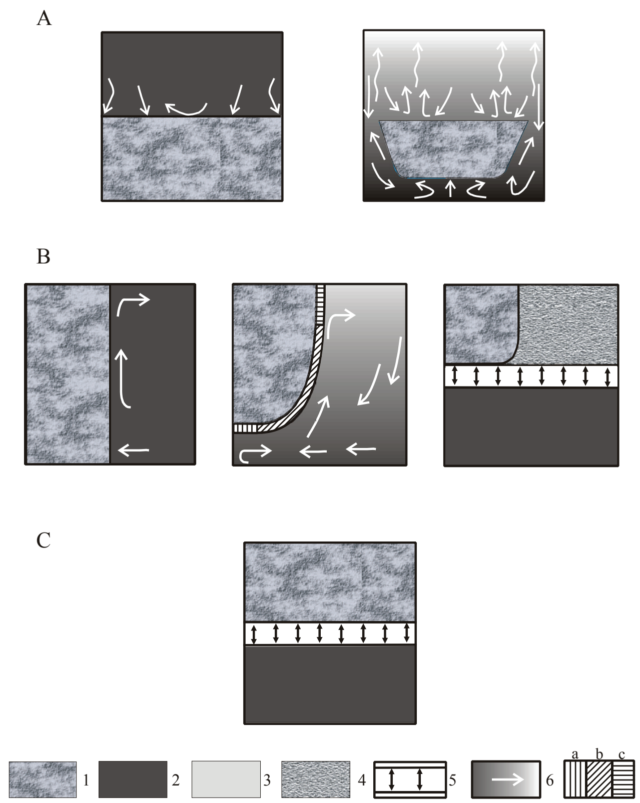

Figure 4. Phase interaction scheme in the brine-ice system (Alexeev 2000): 1 – initial ice, 2 – brine, 3 – diluted solution, 4 – secondary ice, layer of local equilibrium in the system and phase interaction at molecular diffusion, 6 – direction of density convection, 7 – hydrodynamic layer: a) zone of convection beginning and of the most active ice melting, b) zone of decreasing unequilibrium to ice, c) zone of neutral phase contact.

The principally new scenario is proposed as to how cryopegs could possibly be formed in the crystalline rocks of the Anabar shield. The theoretical background of the authors is based on some principal points.

1. Glaciation of the Anabar shield is an important factor of Pleistocene history. It resulted in formation of the thick glacial covers of the Antarctic type, or typical mountain-valley glaciers (Ershov 1990, 1998, Romanovsky 1993). Glaciation left a series of terminal moraines enclosed in each other. The glacier tongues also left moraines behind in the mountain valleys. The glaciers continuously covered the northern part of the Anabar plateau. Deglaciation caused formation of peculiar glacial complexes. They consist of the tongue basin or central depression.

2. The Pleistocene stage of the Anabar shield evolution is responsible for a significant number of marine transgressions, preconditioned by either active tectonic movements or glacial eustatic rises of the ocean level. The sea repeatedly reached the northern margin of the Anabar shield.

3. Marine transgressions proceeded with seawater of different salinity interacting with ice-rich frozen rocks. The phases interacted within the systems: "brine above ice" and "brine in the lateral contact with ice" (Alexeev 2000) (Fig. 4).

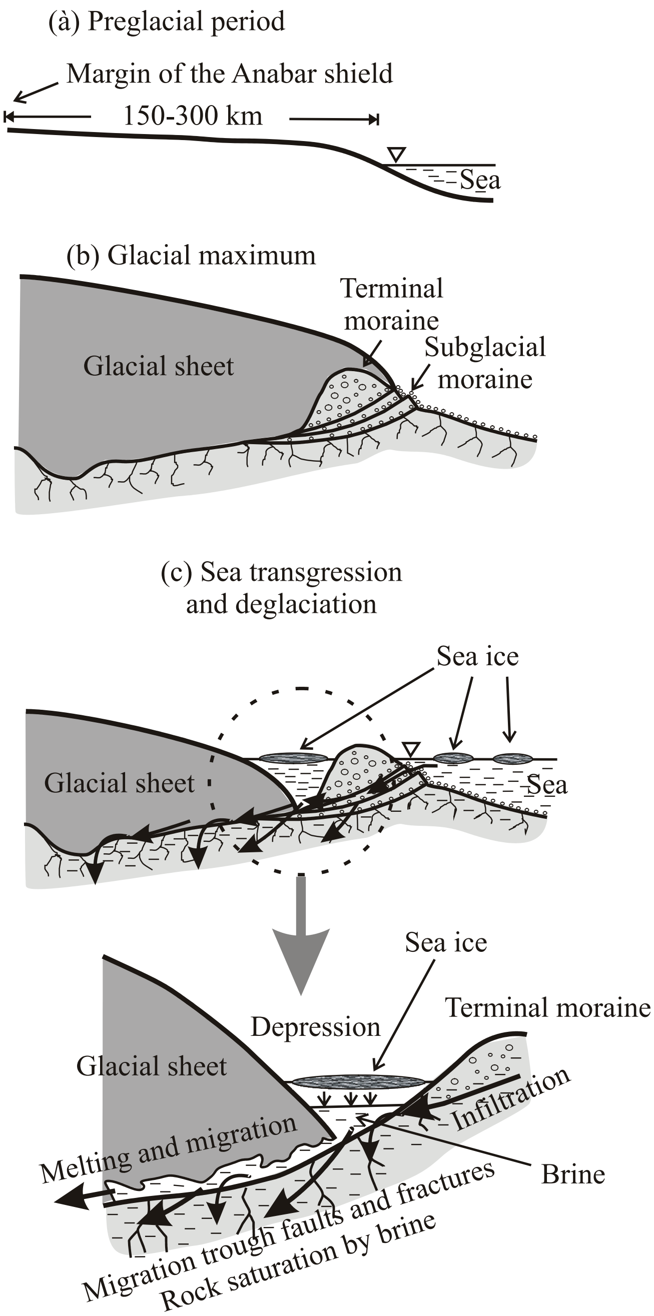

Figure 5. Cryopeg formation in crystalline rocks of the Anabar shield.

With sub-freezing air temperatures, the flooded part of the shelf turned into a peculiar cryogenic basin. Considering its functioning and final salinity, the cryogenic basin is similar to the classic sea evaporitic lagoon. However, the H_2O-solvent was removed due to the ice formation combined with sublimation, and it induced the change of the liquid phase volume and concentration of seawaters. Thus, in the time of glaciation and deglaciation it is suggested that the Anabar shield experienced the following events.

In the preglacial period, the Anabar shield and sea were separated by a narrow zone of intercalating continental and marine sediments extending for 150–300 km (Fig. 5). In time of glaciation, the entire marine material was dragged by a glacier to its termination. While advancing, it displaced a wide and massive terminal moraine forward. The bottom moraine formed in the base of a glacier. It consisted of weathering crust fragments and debris.

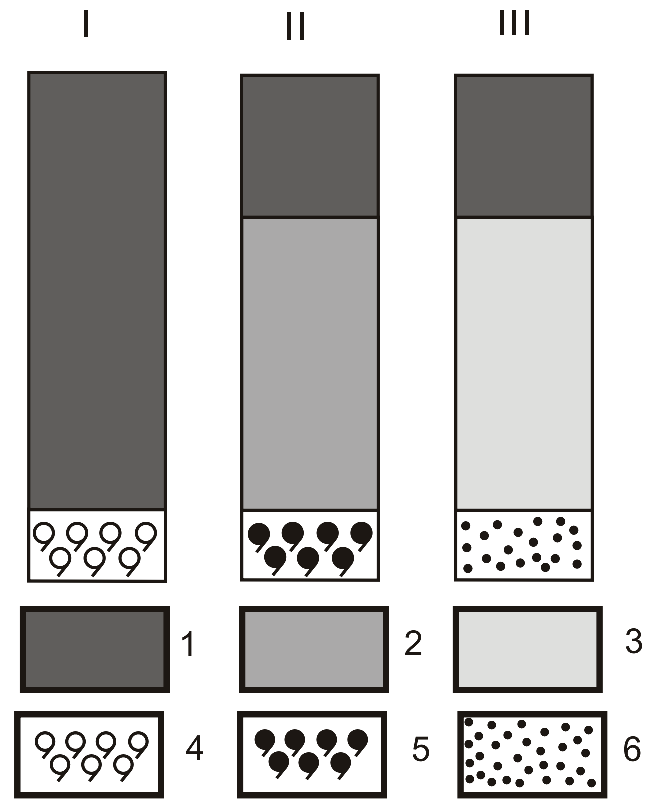

Figure 6. Permafrost structure of the Anabar shield (I and II are new types of permafrost structure, III – commonly accepted type).
1 – ice-rich frozen rocks, 2 – rocks filled by cryopegs, 3 – dry frozen rocks, 4 – rocks filled by subpermafrost fresh water, 5 – rocks filled by saline waters with positive temperature, 6 – dry rocks with positive temperature.

The glacier retreated when the climate turned warm, or if the amount of solid sediment diminished. Due to ice melting, the moraine material piled on the former glacier bed as a moraine line oriented across the valley.

The depression was formed between the glacier and deposited moraine. In the period of transgression, this depression was gradually filled with seawater infiltrating through a moraine either over the planes of scaly overthrusts or over the contact of rocks and lenses of dead ice. Their subsequent cooling was accompanied by ice formation in the near-surface space of depression, concentration, and subsidence of denser brine waters onto the water reservoir bottom. The stronger brines further migrated onto the dislocated bed of the ice shield through steeply dipping fractures of the tectonic zones and exogenous fracturing. If fissures in rocks were filled with ice, it actively melted, and a convective mass transfer took place. The brines also migrated towards the center of the depression along the thawed glacier base. The brines flew out of the depression, and the outflow was made up for new portions of seawater supplied from the moraine line.

During several tens of thousands of years of a transgressive regime, the crystalline rocks could have enclosed a considerable volume of brines. At the next stage of the Anabar shield evolution, the liquid phase in the crystalline rocks was stratified according to the density. This resulted in formation of a peculiar zonation marked by an increase of groundwater salinity at depth. Fresh and saline waters were frozen through, while the brines, when cooled, were transformed into cryopegs. We suggest that this scenario describes how conditions were created for formation of the cryolithozone, which consists of frozen and cryopeg-filled rocks.

Conclusions

Important conclusions have been derived due to the study performed:

1. The glaciation event was an important stage in the Late Cenozoic history of the Anabar shield development. The subsequently occurring deglaciation and transgression of the sea created conditions appropriate for formation in the crystalline rocks of the brines genetically related to seawater, which was infiltrated into crystalline rocks on the glacier/sea border.

2. In the Late Pleistocene cryochrons, the permafrost sequences were derived within the zone of exogenous fracturing. The profound cooling of crystalline rocks brought about cryogenic concentration of groundwater, increase in salinity, and formation of a thick zone of subpermafrost cryopegs.

Therefore, the formerly existing concept that groundwater is lacking within the shield is to be essentially reconsidered. Having considered available data, the proposal is to distinguish two alternatives types of cryolithozone structure with variable ratios of rocks having negative temperature (Fig. 6). The figure displays the relationships between different stages of cryogenic rocks.

When compiling a new map of geocryological conditions in East Siberia the newly recognized types (columns I and II) of cryolithozone, with possible presence of fresh groundwater and brines, should be included.

Acknowledgments

The authors express sincere gratitude to Tatiana Bounaeva for translation of the Russian text into English. The authors would like to thank the anonymous reviewers for the constructive comments and additional language improvement. This research has been carried out with the financial support of the Russian Fund for Basic Research (project 08-05-00086), Scientific School (9542.2006.5), and Polar Earth Science Program, Office of Polar Programs, National Science Foundation (ARC-0632400, ARC-0520578).

References

Alexeev, S.V. 2000. *The cryogenesis of groundwater and rocks as exemplified by the Daldyn-Alakit region of Western Yakutia.* Novosibirsk: Publ. SPC UIGGM SB RAS, 119 pp. (in Russian).

Balobaev, V.T., Pavlov, A.V., Perlshtein, G.Z. et al. 1983. *Thermal-physical researches of Siberian cryolithozone.* Novosibirsk: Nauka, 22-34 (in Russian).

Bottomley, D. J., Katz, A., Chan, L. H. et al. 1999. The origin and evolution of Canadian Shield brines: evaporation or freezing of seawater? New lithium isotope and geochemical evidence from the Slave Craton. *Chem. Geology* 155: 295-320.

Ershov, E.D. (ed.). 1989. *Geocryology of the USSR. Central Siberia.* Moscow: Nedra, 414 pp. (in Russian).

Ershov, E.D. 1990. *General Geocryology*. Moscow: Nedra, 559 pp. (in Russian).

Ershov, E.D. (ed.) 1998. *The Bases of Geocryology. Part 3. Regional and Historical Earth's Geocryology.* Moscow: Publ. of Moscow State University, 575 pp. (in Russian).

Fotiev, S.M. 1978. *Hydrogeothermal Peculiarities of the Permafrost of USSR.* Moscow: Nauka, 236 pp. (in Russian).

Gavrilova, M.K. 1998. *The Climates of the Earth Cold Regions.* Yakutsk: Publ. SB RAS, 206 pp. (in Russian).

Herut, B., Starinsky, A., Katz, A. et al. 1990. The role of seawater freezing in the formation of subsurface brines. *Geochim. Cosmochim. Acta* 54: 13-21.

Kalinin, V.M. & Yakupov, V.S. 1989. *Regional regularities of permafrost thickness behavior*. Yakutsk: Publ. SB RAS, 142 pp. (in Russian).

Marion, G.M., Farren, R.E. & Komrowski, A.J. 1999. Alternative pathways for seawater freezing. *Cold Regions Sci. Tech.* 29: 259-266.

Romanovsky, N.N. 1993. *The Bases of Lithosphere Cryogenesis.* Moscow: Publ. of Moscow State University, 335 pp. (in Russian).

Rozen, O.M., Vishnevsky, A.N., Glukhovsky, M.Z. et al. 1986. *Structure of the Anabar Shield Earth Crust.* Moscow: Nauka, 198 pp. (in Russian).

Rozen, O.M., Serenko, V.P., Spetsius, Z.V. et al. 2002. The Yakutian kimberlite province: disposition in the Siberian craton structure, composition peculiarities of the upper and lower crust. *Geology and Geophysics* 43(1): 3-26 (in Russian).

Solopanov, A.T. & Tolstov, A.V. 1996. Cryohydrogeological conditions of the Tomtor massif. Cryolithozone and groundwaters of Siberia. *Groundwaters and Icings*. Yakutsk: PI of SB RAS: 87-94 (in Russian).

Starinsky, A. & Katz, A. 2003. The formation of natural cryogenic brines. *Geochim. et Cosmochim. Acta* 67(54): 1475-1484.

Szilder, K., Lozowski, E.P. & Forest, T.W. 1995. One-dimensional freezing of seawater in constrained volume. *Can. Geotechn. Journal* 32, 1: 122-127.

Tectonics, geodynamics and metallogeny of the Sakha Republic (Yakutia) territory. 2001. Moscow: Nauka (Interperiodika), 571 pp. (in Russian).

Temperature, cryolithozone and radiogenic heat generation in the earth crust of the Northern Asia. Novosibirsk: Publ. SPC UIGGM SB RAS, 141 pp. (in Russian).

A First Estimate of Mountain Permafrost Distribution in the Mount Cook Region of New Zealand's Southern Alps

Simon Allen
Department of Geography, University of Canterbury, Christchurch, New Zealand
Ian Owens
Department of Geography, University of Canterbury, Christchurch, New Zealand
Christian Huggel
Glaciology, Geomorphodynamics & Geochronology, Department of Geography, University of Zurich, Zurich, Switzerland

Abstract

The heavily glaciated Mount Cook Region of New Zealand has experienced several recent large rock instabilities, but permafrost conditions related to these events remain unknown. This work presents the first systematic approach for investigating the distribution of mountain permafrost in New Zealand. At this level of the investigation, a first-order estimate is based upon the adaptation of established topo-climatic relationships from the European Alps. In the southeast of the study region, the permafrost estimate gives a reasonable correspondence with mapped rock glacier distribution but the maximum elevation of vegetation growth is situated 200 m beneath the lower limit of estimated permafrost. Extreme climate gradients exist and towards the humid northwest, where rock glaciers are absent and vegetation patterns give an unclear climate signal, large uncertainties remain. Data currently being recorded from a network of rock wall temperature measurements will help remove this uncertainty, and will allow distribution modeling that better accounts for the topographic complexities of this steep alpine region.

Keywords: permafrost distribution; rock instabilities; spatial modeling; Southern Alps; New Zealand.

Introduction

Internationally, mountain permafrost is a well recognized phenomenon in relatively low-angled debris-covered terrain where active rock glaciers produce distinctive landforms that indicate perennially frozen ground beneath. Previous research based upon the identification of active rock glaciers in the Southern Alps of New Zealand has suggested that permafrost probably occurs only sporadically within a very narrow altitudinal zone in the more arid areas of the Alps (Brazier et al. 1998). However, there has been no scientific consideration in New Zealand given to the likely wider distribution of permafrost within bedrock slopes, and in particular, on steep slopes which dominate at higher elevations throughout the Mount Cook Region (MCR). Recent large rock avalanches, including the spectacular summit failure of Mount Cook (McSaveney 2002) have awoken interest in the understanding of permafrost and slope stability interactions in the region. This paper aims to present the first results from permafrost distribution modeling for the MCR, based upon local application and calibration of topo-climatic relationships established in the European Alps. Initial validation of the estimated permafrost distribution is discussed on the basis of a rock glacier inventory and remote sensing-based vegetation mapping, and future research towards improved modeling in this region is introduced.

Background

Studies of permafrost processes in New Zealand are limited (Soons & Price 1990), with only a few detailed studies emerging from the identification and dating of rock glaciers within the Southern Alps. These studies have served to improve the chronology of Holocene glacial activity in the region (McGregor 1967, Birkeland 1982) and offer some insights regarding possible climate sensitivities of rock glaciers (Jeanneret 1975, Kirkbride & Brazier 1995). From the mapping and classification of periglacial landforms in the Ben Ohau Range, Brazier et al. (1998) suggested that permafrost distribution was more limited than would be expected based upon climatic boundaries identified in the European Alps (Haeberli 1985). In the driest, generally low-elevation mountains east of the Southern Alps, rock glaciers are absent and ice-free talus slopes dominate. In the more humid, maritime regions to the west where precipitation exceeds 10000 mm y^{-1}, glacier equilibrium line altitudes (ELAs) are low and temperate mountain glaciers dominate, with no active permafrost landforms evident (Augustinus 2002). Between these two extremes, within a narrow zone where precipitation does not exceed 1500 mm y^{-1} ELAs are higher, glacial ice is limited to debris-covered cirques, and more numerous permafrost landforms are found (Brazier et al. 1998).

Understanding permafrost distribution within complex steep mountain terrain is a relatively new field of scientific research largely stemming from European-based studies in relation to climate warming, permafrost degradation and related slope instability hazards (Gruber & Haeberli 2007). During the past 50 years, several large rock avalanche events have occurred within the MCR (McSaveney 2002), but in the complete absence of data regarding permafrost distribution in the steep terrain of the Southern Alps, the possible role of permafrost weakening within past or future detachment zones is uncertain.

In complex mountain terrain, variations in topography and related permafrost factors such as snow cover result in the necessary use of spatial modeling to achieve any realistic estimate of permafrost distribution (Etzelmüller et al. 2001). A hierarchy of modeling procedures has therefore been developed over recent years (Hoelzle et al. 2001). Readily applied empirical-statistical approaches relate documented permafrost occurrences to easily measured topo-climatic factors such as altitude, slope and aspect, air temperature, and solar radiation (e.g., Imhof 1996) and are particularly well suited for preliminary assessment and planning in relation to geotechnical hazards (Harris et al. 2001). A useful, and essential first step in these studies has been the adaptation of Haeberli's (1975) original topo-climatic key for predicting permafrost occurrence, which provides an immediate impression of likely permafrost distribution, and a basis from which local validation and more advanced modeling can proceed.

Study Region

The MCR is broadly defined here to encompass the 700 km^2 Aoraki Mount Cook National Park, extending west of the Main Divide into the Westland National Park and south to include the Ben Ohau Range (Fig. 1A). The region includes the highest mountains and the most heavily glacierised terrain of New Zealand's Southern Alps. Permanent snow covered peaks are found between 2500 and 3754 m a.s.l., with local relief in the order of 1000–2700 m. Moist westerly airflow perpendicular to the Main Divide, generates very high orographic rainfall amounts and creates an extreme precipitation gradient leeward of the Alps (Griffiths & McSaveney 1983). Glacial retreat since the Little Ice Age maximum has been most rapid during the mid 20th Century, leading to a 25% loss of total ice area in the Southern Alps during this past century, although some highly responsive glaciers have had notable periods of advancement over recent years (Chinn 1996).

Estimating Permafrost Distribution

Based on extensive geophysical and morphological investigations of rock glacier phenomena in the eastern Swiss Alps during the 1970s, Haeberli (1975) developed 'rules of thumb' for predicting permafrost occurrence. Stemming from these rules was the empirical topo-climatic key, incorporating the primary physical factors which influence permafrost distribution, determining both a zone of probable permafrost and the permafrost limit within a transitional zone termed "possible permafrost." These physical factors include significant aspect dependent radiation effects, altitudinal changes in air temperature, and topographically related snow cover variation (Etzelmüller et al. 2001). In relation to snow cover, gentle terrain situated at the foot of steeper slopes where long-lasting avalanche snow may accumulate can maintain cooler ground surface temperatures than steeper slopes of the same aspect. On flat terrain, the local permafrost distribution is determined more by air

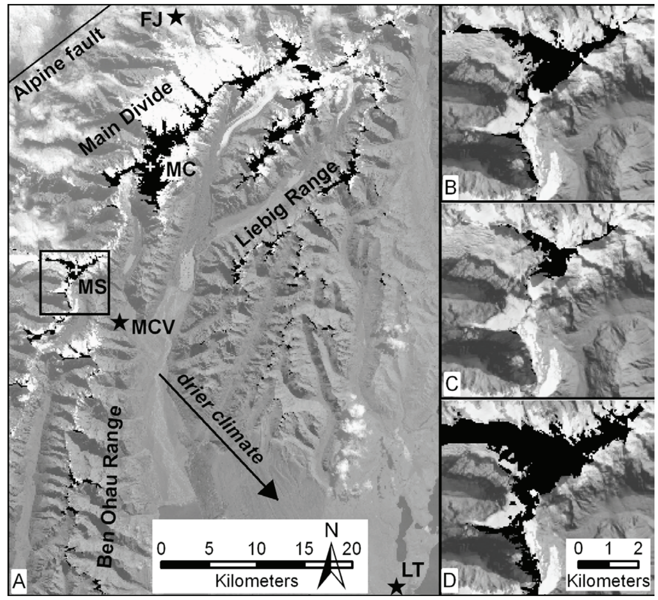

Figure 1. A) GIS-based modeling of possible steep permafrost distribution (black) in the MCR based upon adjustment of the original topo-climatic key (Haeberli 1975) using MAAT calculated from the Franz Josef (FJ), Mount Cook Village (MCV) and Lake Tekapo (LT) climate stations. Also shown are the locations of Mount Cook (MC, 3754 m) and Mount Sefton (MS, 3151 m), B) Closer view of the estimated permafrost terrain around the summit area of Mount Sefton, C) repeated for a 0°C isotherm rise of 200 m, and D) a 0°C isotherm lowering of 200 m. The base image used is an ASTER satellite mosaic from 2007.

temperature and snow cover than by radiation. Calibration of the key to local conditions in the MCR was based upon calculation of mean annual air temperature (MAAT) for the years 1982–2007 and the local 0°C isotherm elevation using daily temperature data from three climate stations located across the region (Fig 1A). For the eight primary slope aspects, the original elevation zones given in the topo-climatic key were either raised or lowered based upon the difference between the local elevation of the 0°C isotherm and the equivalent value from the Swiss Alps where the key was established. Topographic values for all analyses were extracted from the Landcare Research 25 m resolution South Island digital terrain model (DTM).

In an attempt to account for the significant climate gradients associated with the föhn effect which results from initially moist airflow across the Main Divide, the 0°C isotherm was calculated independently using MAAT measured at each of the three climate stations. Hydrological studies in the region have shown that rainfall gradients are approximately parallel to the Main Divide, with maximum rainfall measurements associated with the steepened terrain along the alpine fault (e.g., Griffiths & McSaveney 1983). Because of the effects of decreasing moisture towards the southeast on environmental lapse rates, the following values were used: Franz Josef, 0.005°C m^{-1} (Anderson 2003), Mount Cook Village, 0.0065°C m^{-1} , and Lake Tekapo, 0.0075°C m^{-1}. The latter two rates have not been directly measured, but were inferred from the nearest available

Table 1. Topo-climatic key for the estimation of permafrost distribution in the MCR adapted from Haeberli (1975).

Aspect	Permafrost possible		Permafrost probable	
	Steep slopes	Foot of slopes	Steep slopes	Foot of slopes
S	2280	1980	2480	2430
SE	2330	2180	2480	2580
E	2480	2280	2880	2580
NE	2730	2180	2880	2580
N	2880	2130	2880	2480
NW	2580	2030	2780	2430
W	2380	1980	2480	2330
SW	2230	1930	2280	2280
Flat Areas				
Wind-exposed		2480		2580
Wind-shielded		2530		2880
Variability				
Franz Josef (0.005 °C m^{-1})			270 m higher	
Lake Tekapo (0.0075 °C m^{-1})			190 m lower	

All elevations are given in metres above sea level (m). Values are based upon MAAT at Mount Cook Village (765 m) and an air temperature lapse rate of 0.0065°C m^{-1}. Variability is calculated using MAAT at Franz Josef (155 m) and Lake Tekapo climate stations (762 m) with given lapse rates.

measured locations where precipitation and humidity values are comparable (Brazier et al. 1998). Using a GIS procedure, the 0°C isotherm elevations were then interpolated between the three climate stations in a southeastern direction based upon distance from the alpine fault (Fig 1A). This modeling of 0°C isotherm elevations is a crude simplification, but for the purposes of an initial permafrost estimate, it is able to provide an approximation for the influence of moisture gradients prevailing across this region of the Alps.

Table 1 gives the adjusted permafrost elevation limits based upon the 0°C isotherm elevation of 2114 m calculated at the Mount Cook Village. This establishes a lower limit of permafrost in steep terrain (on slopes >20°) of 2880 m on sunny northern aspects, decreasing to 2230 m on shaded southern aspects. At Franz Josef, where a strong maritime climate prevails, the 0°C isotherm could be positioned up to 270 m higher, with a corresponding rise of the permafrost limits by the same amount, whereas these limits may be 190 m lower towards the drier climate at Lake Tekapo. At the foot of slopes (<20°), permafrost may be possible up to 750 m lower than on corresponding steeper slopes, but is probable at elevations only 400 m lower.

At elevations where possible steep permafrost is predicted along the Main Divide, glacial ice dominates much of the terrain with only limited exposed bedrock around ridge tops, on steep faces and rock outcrops (Fig 1A). In this region of the Alps, the average ELA is around 2000 m, well below the lower boundary of permafrost such that temperate glacial ice dominates, but areas of polythermal ice and associated permafrost interactions are likely within the higher elevation cliff and hanging glaciers (Etzelmüller & Hagen 2005). In the drier southeast, glacial growth is restricted with both talus and bedrock surfaces featuring prominently at elevations within the estimated permafrost terrain.

The accuracy of the selected lapse rates, MAAT, and resulting 0°C isotherm calculations will have a significant influence on the permafrost distribution estimate. This sensitivity is well illustrated for the area of the Main Divide around Mount Sefton (Figs. 1B-D). The current model estimates widespread permafrost surrounding the summit pyramid and along the ridges to the west and northeast. However, a 200 m lowering of the isotherm due to a colder MAAT or greater lapse rate selection would significantly increase the estimated possible permafrost distribution along all surrounding ridgelines and on all slope aspects. Under the scenario of a warmer MAAT or lower selected lapse rate resulting in a 200 m rise of the isotherm, the estimated permafrost terrain becomes mostly limited to the shaded aspects high on the summit area of Mount Sefton. While illustrating the sensitivity of the topo-climatic key to local calibration, this also gives some indication of the effect future climate warming could have on permafrost distribution in the region.

Local Validation Using Rock Glacier Inventory

Active and fossil periglacial landforms have been previously mapped in the Ben Ohau Range using a threefold classification of debris-covered glaciers, cirque-floor lobe forms, and talus rock glaciers (Brazier et al. 1998, Appendix 1). Although the Ben Ohau Range comprises only a small area of the much larger study region, it does contain the only known active permafrost forms in the region, and therefore is able to provide some initial local-scale validation of the permafrost distribution estimate. The original mapped landform data were transferred into a GIS inventory of active and fossil permafrost forms, with some positions and measurements reassessed using high resolution (0.61 m) QuickBird satellite imagery in combination with a DTM. A total of 70 permafrost forms were mapped according to their Rock Glacier Initiation Line Altitude (RGILA) position as measured from the foot of the talus. Active debris-covered glaciers are not necessarily indicative of permafrost conditions, but are included here to further illustrate the distinct landform zonation that occurs along this range (Brazier et al. 1998).

The active permafrost forms predominate on shaded aspects within a narrow 8.2 km north-south zone towards the centre of the Ben Ohau Range where the highest peaks are just above 2400 m (Fig. 2A). The RGILA of all active landforms would therefore be expected to lie mid-way between the permafrost limits estimated at the southern and northern ends of the range, but instead are positioned at altitudes 20 to 180 m lower (Fig. 2B). Permafrost originating at the foot of slopes might account for the preservation of some of these forms at lower elevations, but the possibility that the model estimate is too high within this area of the study region must also be considered. Although data are unavailable for northerly aspects, the aspect-related variability of the model from east through to west appears to match the distribution of active rock glaciers. No fossil permafrost forms are located within

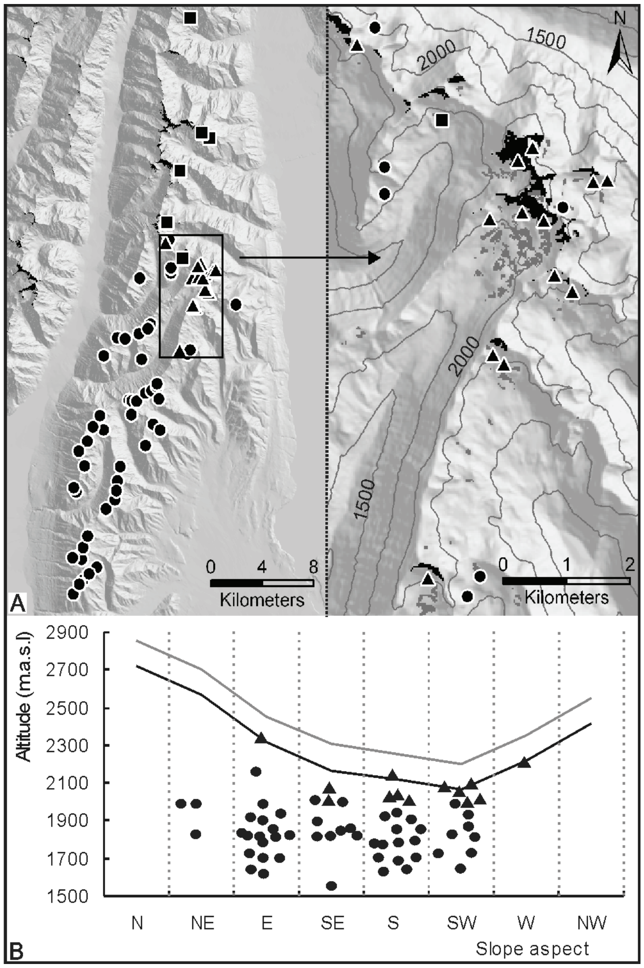

Figure 2. A) Modeled permafrost distribution on steep slopes (black) along the Ben Ohau Range compared with an inventory of active (triangle) and fossil (circle) rock glacier forms, and debris covered glaciers (square). Permafrost modeled at the foot of slopes is also shown (grey), based on slope curvature analyses. B) The spatial distribution of rock glacier forms is compared to steep permafrost lower elevation limits at the northern (grey) and southern (black) ends of the Ben Ohau Range.

the estimated permafrost terrain and most are positioned more than 200 m below the estimated boundary, which is greater than can be expected from 20th Century temperature warming in this region (Salinger 1979). The numerous fossil forms mapped at the southern end of the range are located at much lower altitudes, with surface dating suggesting that many of these forms are periglacial relics from the late Pleistocene (Birkeland 1982). Towards the northern end of the range, increased snowfall combined with topographic effects enables the growth of heavily debris covered cirque glaciers at higher elevations and neither active nor fossil permafrost forms are observed here.

Comparison with Vegetation Mapping

Modern remote sensing-based mapping techniques are able to provide a crude, indirect indication of likely permafrost distribution (Etzelmüller et al. 2001). The presence or absence of alpine vegetation is a particularly well known indicator of

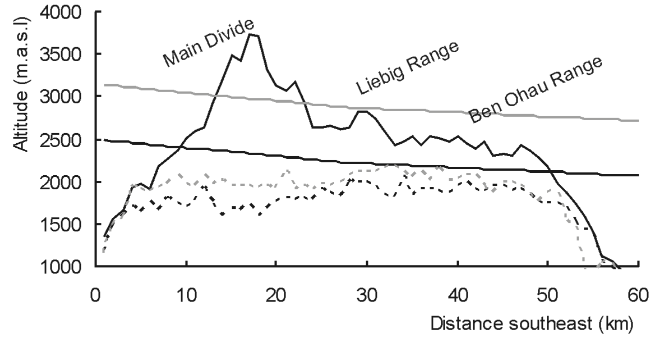

Figure 3. MAV (dashed) and corresponding minimum elevation of estimated permafrost distribution (solid lines) are plotted for steep northern (grey) and southwestern slopes (black) from northwest-southeast across the study region. The topographic profile with main mountain ranges labeled is also provided.

permafrost distribution in mid-latitude mountains (Haeberli 1975), and the inclusion of vegetation abundance mapping from satellite imagery has proven a useful parameter for improved distribution modeling (Gruber & Hoelzle 2001). In the current study, orthorectified 15 m resolution Advanced Spaceborne Thermal Emission and Reflection Radiometer (ASTER) imagery from 2007 was used to create a map of vegetation distribution for the entire study region. To achieve this, the Normalised Difference Vegetation Index (NDVI) was used, which is based upon the contrasting spectral response of healthy vegetation between the red and near infrared (NIR) wavelengths. Combined with a DTM, altitudinal patterns in vegetation distribution were analysed and compared with the estimated permafrost distribution. A comparison is made between the maximum altitude of alpine vegetation growth (MAV) and the estimated lower limit of steep permafrost distribution within every 1 km zone in a northwestern to southeastern direction across the Southern Alps, parallel to the climatic gradient (Fig. 3). To examine the influence of slope aspect on vegetation patterns and any relationship there might be to permafrost distribution patterns, analyses are included for both sunny northern aspects and shaded southwestern aspects. A slope curvature threshold was incorporated to ensure that only pixels with a small change in aspect were included, minimizing the risk of erroneous measurements around sharp terrain features.

In the drier mountains east of the Main Divide, such as the Liebig and Ben Ohau Ranges, the MAV on steep southwestern aspects is positioned at around 2000 m, and is consistently 200 m lower than the estimated lower boundary of possible permafrost for these slopes. Closer towards the Main Divide, this difference increases to over 400 m as the rise in permafrost limits is not matched by any rise in MAV. In fact, the fluctuating MAV decreases closer to the Main Divide possibly as a function of large maritime snowfalls combined with the effects of geomorphic and glacial disturbances. On northern slope aspects the MAV averages 150 m higher than on southwestern aspects, with some greater differences measured nearer to the Main Divide, but never coming close to reflecting the much greater differences that are expected between permafrost limits on these contrasting slope aspects. The lack of any strong MAV pattern across the study region suggests that the usefulness of vegetation as an indicator of likely permafrost distribution is very limited in the Southern Alps of New Zealand. While the presence of vegetation confirms the absence of permafrost, the absence of vegetation offers very little conclusive information as to the distribution of permafrost, particularly nearer towards the Main Divide.

Discussion

Application of topo-climatic relationships established within the Swiss Alps to a more maritime alpine region characterized by extreme climate gradients produces many challenges. MAAT and lapse-rate calibration parameters used here are based on low-elevation climate stations located some distance from the Main Divide, and with the absence of additional data, climate gradients across the highest terrain cannot be modeled with certainty. A current study is suggesting that maximum precipitation might exist very close to, and even leeward to the Main Divide (Kerr et al. 2007), which would likely raise the estimated permafrost limits near to this region. In addition to the effect that climate gradients will have on local MAAT, associated differences in factors such as cloudiness and precipitation will also influence the amount of variation within the topo-climatic key from northern to southern aspects. Heavy snowfall and maritime cloud cover near the Main Divide will influence solar radiation patterns at the ground surface, which largely determine the aspect variation within the key. Therefore, the assumption of uniform variation between slope aspects across the study region must be reconsidered in a more advanced approach to modeling permafrost distribution.

Comparison of modeled permafrost distribution with rock glacier inventories is a well-established approach (e.g., Imhof 1996), but was restricted in the current study by the limited spatial distribution of these landforms. Modern earth imagery such as QuickBird has significantly improved the ability to recognize and map permafrost features, but some subjectivity and potential for error remains in determining active from inactive landforms and defining parameters such as the RGILA. Vegetation patterns in relation to climate gradients and permafrost distribution were explored here on the fundamental basis of being absent or present, but given the ecological diversity that exists across the Southern Alps, more useful patterns might be observed within individual species or by using the NDVI to explore topographic patterns in plant biomass (Gruber & Hoelzle 2001).

Recent large rock failures in the European Alps have suggested that permafrost degradation is a serious concern in relation to climate warming and slope instability (Gruber et al. 2004). In the Southern Alps of New Zealand, the summit collapse of Mount Cook in 1991 detached from a maximum elevation of 3720 m on an eastern exposition (McSaveney 2002). This is well above the estimated lower boundaries of possible permafrost where 20th Century thawing may be expected. However, the large rock buttress involved in the failure extended down to a much lower elevation, and in complex, steep topography, the effects of three-dimensional thermal gradients must also be considered because of contrasting temperatures between colder and much warmer sunny slope expositions of the terrain (Noetzli et al. 2007). Furthermore, bedrock temperatures are complicated by the presence of steep ice bodies because heat exchanges associated with surface melting can induce significant thermal anomalies within the underlying bedrock (Huggel et al. 2008). Of the other large rock avalanche events occurring in the region over the past 50 years, three originated from within the estimated permafrost terrain, while another was initiated from an elevation approximately 140 m below the estimated lower permafrost boundary. In addition, two recent fatal rockfall events near the summits of Mount Cook and Mount Sealy further south, have also originated from within the estimated permafrost terrain.

On the basis of this initial estimate of permafrost distribution and the uncertainties it has raised, a field campaign was initiated during November 2007 measuring the spatial variation of rock surface temperatures on steep bedrock slopes over a 12-month period. Following the methodologies developed by Gruber et al. (2003), 15 miniature temperature data loggers were installed at elevations ranging from 2400 m to 3150 m on various slope aspects both immediately on the Main Divide and on the drier Liebig Range towards the southeast. In addition, a series of high elevation air temperature loggers have been installed across the region to better establish relationships with the low elevation, long term records from the Mount Cook Village climate station. Information regarding the spatial distribution of rock surface temperatures will be used to more accurately model and validate permafrost distribution across the region.

Conclusions

A first-order approach for permafrost distribution mapping in the Mount Cook Region of New Zealand's Southern Alps has been presented. Towards the southeast of the region a drier, more continental climate prevails, and the permafrost estimate gives reasonable correspondence with the limited distribution of active and fossil rock glaciers. Closer towards the Main Divide where conditions are more humid, the lower boundary of permafrost distribution is expected to be significantly higher, but rock glaciers are absent here preventing any potential for local validation. Similarly, modeled vegetation altitudinal limits across the region showed no relationship with the climatic gradients which are expected to influence permafrost distribution. Future modeling will incorporate rock wall temperature data to facilitate permafrost modeling which better accounts for the effects of solar radiation and topographic shading in this complex, steep mountain environment.

Acknowledgments

This paper has benefited significantly from support provided by the Glaciology, Geomorphodynamics & Geochronology Group, Department of Geography, University of Zurich. In particular, Stephan Gruber and Martin Hoelzle are thanked for their suggestions and advice. Fieldwork for this project is funded by the New Zealand Earthquake Commission. We thank Ray Bellringer of the Department of Conservation for his project support. Three anonymous reviewers provided thoughtful suggestions for an improved manuscript.

References

Anderson, B. 2003. *The response of Ka Roimata o Hine Hukatere Franz Josef Glacier to climate change.* Unpublished PhD Thesis, University of Canterbury.

Augustinus, P. 2002. Periglacial research in New Zealand: a review. *South African Journal of Science* 98: 64-70.

Birkeland, P.W. 1982. Subdivision of Holocene glacial deposits, Ben Ohau Range, New Zealand, using relative dating methods. *Geological Society of America Bulletin* 93: 433-449.

Brazier, V., Kirkbride, M.P. & Owens, I.F. 1998. The relationship between climate and rock glacier distribution in the Ben Ohau Range, New Zealand. *Geografiska Annaler* 80 A(3-4): 193-207.

Chinn, T.J.H. 1996. New Zealand glacier responses to climate change in the past century. *New Zealand Journal of Geology and Geophysics* 39: 415-428.

Etzelmüller, B. & Hagen, J.O. 2005. Glacier-permafrost interaction in arctic and alpine mountain environments with examples from southern Norway and Svalbard. In: C. Harris and J.B. Murton (eds.), *Crysopheric Systems: Glaciers and Permafrost. Geological Society Special Publication No. 242*, London.

Etzelmüller, B., Hoelzle, M., Heggem, E.S.F., Isaksen, K., Mittaz, C., Vonder Mühll, D., Odegard, R.S., Haeberli, W. & Sollid, J.L. 2001. Mapping and modeling the occurrence and distribution of mountain permafrost. *Norwegian Journal of Geography* 55: 186-194.

Griffiths, G.A. & McSaveney, M.J. 1983. Distribution of mean annual precipitation across some steepland regions of New Zealand. *New Zealand Journal of Science* 26: 197-209.

Gruber, S. & Haeberli, W. 2007. Permafrost in steep bedrock slopes and its temperature-related destabilization following climate change. *Journal of Geophysical Research* 112, doi:10.1029/2006 JF000547.

Gruber, S. & Hoelzle, M. 2001. Statistical modeling of mountain permafrost distribution: Local calibration and incorporation of remotely sensed data. *Permafrost and Periglacial Processes* 12: 69-77.

Gruber, S., Hoelzle, M. & Haeberli, W. 2004. Permafrost thaw and destabilization of Alpine rock walls in the hot summer of 2003. *Geophysical Research Letters* 31:L13504.

Gruber, S., Peter, M., Hoelzle, M., Woodhatch, I. & Haeberli, W. 2003. Surface temperatures in steep alpine rock faces-a strategy for regional-scale measurement and modeling. *PERMAFROST, Proceedings of the Eighth International Conference on Permafrost 2003*. Zurich: Swets & Zeitlinger, 325-330.

Haeberli, W. 1975. Untersuchungen zur Verbreitung von Permafrost zwischen Fluelapass und Piz Grialetsch (Graubunden). *Mitteilungen der Versuchsanstalt für Wasserbau, Hydrologie und Glaziologie der ETH Zurich* 17: 221.

Haeberli, W. 1985. Creep of mountain permafrost: internal structure and flow of alpine rock glaciers. *Mitteilungen der Versuchsanstalt für Wasserbau, Hydrologie und Glaziologie der ETH Zurich* 77: 142.

Harris, C., Davies, M.C.R. & Etzelmüller B., 2001. The assessment of potential geotechnical hazards associated with mountain permafrost in a warming global climate. *Permafrost and Periglacial Processes* 12: 145-156.

Hoelzle, M., Mittaz, C., Etzelmüller, B. & Haeberli, W. 2001. Surface energy fluxes and distribution models of permafrost in European mountain areas: an overview of current developments. *Permafrost and Periglacial Processes* 12: 53-68.

Huggel, C., Caplan-Auerbach, J., Gruber, S., Molnia, B. & Wessels, R. 2008. The 2005 Mt. Steller, Alaska, rock-ice avalanche: A large slope failure in cold permafrost. *Proceedings of the Ninth International Conference on Permafrost, June 28–July 3, 2008, Fairbanks, Alaska.*

Imhof, M. 1996. Modeling and verification of the permafrost distribution in the Bernese Alps, Western Switzerland. *Permafrost and Periglacial Processes* 7: 267-280.

Jeanneret, F. 1975. Blockgletcher in den Südalpen Neusee-lands. *Zeitschrift für Geomorphologie. NF* 19: 83-94.

Kerr, T., Owens, I. & Henderson, R. 2007. An extreme average annual precipitation gradient measured in a lee mountain catchment, South Island, New Zealand. *Geophysical Research Abstracts* 9(11607).

Kirkbride, M. & Brazier, V. 1995. On the sensitivity of Holocene talus-derived rock glaciers to climate change in the Ben Ohau Range, New Zealand. *Journal of Quarternary Science* 10: 353-365.

McGregor, V.R. 1967. Holocene moraines and rock glaciers in the central Ben Ohau Range, South Canterbury, New Zealand. *Journal of Glaciology* 6: 737-747.

McSaveney, M.J. 2002. Recent rockfalls and rock avalanches in Mount Cook National Park, New Zealand. *Geology Society of America, Reviews in Engineering Geology, XV*: 35-69.

Noetzli, J., Gruber, S., Kohl, T., Salzmann, N. & Haeberli, W. 2007. Three-dimensional distribution and evolution of permafrost temperatures in idealized high-mountain topography. *Journal of Geophysical Research* 112, doi:10.1029/2006JF000545.

Salinger, M.J. 1979. New Zealand climate: the temperature record, historical data and some agricultural implications. *Climate Change* 2: 109-126.

Soons, J.M. & Price, L.W. 1990. Periglacial phenomena in New Zealand. *Permafrost and Periglacial Processes* 1: 145-159.

The Perennial Springs of Axel Heiberg Island as an Analogue for Groundwater Discharge on Mars

Dale T. Andersen
Carl Sagan Center for the Study of Life in the Universe, SETI Institute, Mountain View, CA 94043, USA
Wayne H. Pollard
Department of Geography, McGill University, Montre´al, Que´bec, H3A 2K6, Canada
Christopher P. McKay
NASA Ames Research Center, Moffett Field, CA 94061, USA

Abstract

There are several regions on Earth where mean annual temperatures are well below freezing and yet liquid water persists. Such polar regions provide excellent analogues to study the hydrological cycle under conditions that have prevailed in the polar desert environment of Mars. In regions of continuous permafrost, fluxes of energy and water are strongly linked. However, most scientific studies of northern hydrology have been limited to surface process studies focusing on precipitation, snowmelt, evaporation, slope runoff, and stream flow. The springs located at Axel Heiberg Island provide insights into the limits of physical and biological processes associated with groundwater in cold polar deserts. These qualities make them valuable as analogues for groundwater activity on Mars. This paper summarizes the biophysical characteristics of several groups of perennial springs located in a range of settings on Axel Heiberg Island. Included are past and current hydrologic, microbiologic and geomorphic research and climate studies and their application as Mars analogues.

Keywords: astrobiology; groundwater; High Arctic; Mars; perennial springs; permafrost.

Introduction

Groundwater in regions of thick continuous permafrost

Several research groups have reported the occurrence of springs in the High Arctic. Spitsbergen, the largest island in the Svalbard archipelago, resides between 77° and 80°N where permafrost depths are estimated at 100–400 m. Roughly 60% of the island is covered in glaciers and a number of springs occur from Bockfjord in the northernmost part of the island to Sørkapp in the south (Banks et al. 1999, Lauritzen & Bottrell 1994). The Trollosen spring, a thermoglacial karst spring in South Spitsbergen, has a reported discharge rate of about 18 m^3/s of a turbid, 4°C water during the summer. Its flow is thought to originate from moulins on a glacier about 5 km distant. Nearby springs discharge water that is 12–15°C and seem to have a separate hydrothermal source with a subsurface temperature in the deep aquifer of at least 30°C (Lauritzen & Bottrell 1994). The thermal springs at Bockfjord are associated with local volcanic sources and geochemical evidence suggests that temperatures at depth reach between 130–180°C. They form travertine terraces with coatings of biofilms at the surface, and work is presently underway regarding the biological aspects of these springs primarily by the interdisciplinary, international Arctic Mars Analogue Svalbard Expedition (AMASE) team, which is creating a sampling and analysis strategy that could be used for future Mars research (Amundsen et al. 2004, Steele et al. 2004).

Grasby et al. (2003) have reported supraglacial sulfur springs located at 81°019′N, 81°359′W, in Borup Fiord Pass on northern Ellesmere Island in the Canadian high Arctic. Ten spring outlets were observed discharging from the surface of a 200 m thick glacier with active discharges estimated at 1 l/min at some locations and diffuse seeps elsewhere. The origins of the water were not reported, but a large ice-dammed lake located to the north of the spring sites may be a potential source along with basal melting of the glacier. To date, it is not clear if these springs are perennial or are seasonal. The spring outflows are located about 500 m from the terminus of the glacier depositing native sulfur, gypsum, and calcite onto precipitate mounds on top of the ice surface. Grasby et al. (2003) measured outflow temperatures of 1–2°C and reported smelling H_2S in and around the outlets. The water chemistry of the springs is different from local melt water with higher pH and conductivity values than local melt. Light and electron microscopy and culture-independent molecular methods provide evidence of a microbial community associated with the springs. The only other known perennial springs at these high latitudes are those located on Axel Heiberg Island in the Canadian high Arctic. We have identified several groups of perennial springs in a range of settings on Axel Heiberg Island located near the McGill Arctic Research Station (M.A.R.S.); the purpose of this paper is to describe these sites and review the research activities associated with them.

Study Site

Axel Heiberg Island

Axel Heiberg Island (Fig. 1) resides within the Sverdrup Basin, a pericratonic sedimentary trough encompassing roughly 313,000 km^2 and located within the Arctic Archipelago (Pollard et al. 1999). The axis of the basin strikes northeasterly from the Sabine Peninsula on Melville Island to the northwestern region of Ellesmere Island. Axel Heiberg is geologically complex, consisting of folded and faulted sedimentary rocks ranging

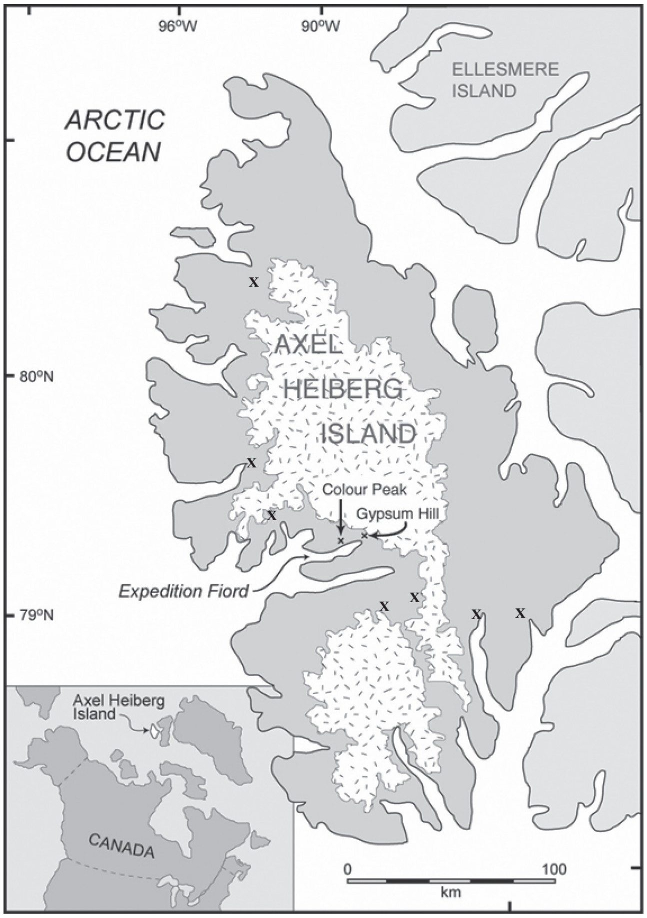

Figure 1. Map of Axel Heiberg Island. The x-marks show approximate locations of perennial springs.

from Triassic to Tertiary in age. Late Paleozoic evaporites locally intrude the overlying sedimentary/clastic rocks in a series of exposed piercement structures that occur mainly in line with the basin axis (Stephenson et al. 1992). The intrusions of the evaporites are typically associated with early Tertiary (Innuitian) orogenic activity and are mapped as Tertiary (Otto Fiord Formation) by Thornsteinsson (1971). However, the emplacement of the anhydrite structures at Expedition Fiord took place during an earlier tectonic phase prior to the mid Cretaceous (Embry & Osadetz 1988, Stephenson et al. 1992). Quaternary stream, deltaic, marine, and glacial sediments cover the valley floors and form raised shorelines.

There is considerable relief near the head of Expedition Fiord with peaks approximately 2000 m a.s.l. that decrease toward the fiord mouth. Breached anticlines produce asymmetrical ridges characterized by steep (70–80°) scarp faces and 25–35° dip slopes. In some locations, piercement structures create more regular and symmetrical hill and mountain features. Weathering of gypsum and anhydrite outcrops has given the diapirs very ragged, serrated profiles. Resistant volcanic sills and dikes have differentially eroded, leading to steep slopes mantled with coarse angular talus.

Glaciers currently cover 30–35% of Axel Heiberg Island, including the Stacie and Müller (McGill) Ice Caps and numerous outlet and valley glaciers. Small ice caps and isolated cirque and valley glaciers are widespread. At Expedition Fiord, the

	1998	1999	2000	2001	2002
January	-31.96	-32.6	-31.16	-32.42	-33.4
February	-34.38	-27.86	-23.83	-33.76	-35.24
March	-28.48	-17.89	-15.94	-30.02	-31.02
April	-16.65	-4.68	-4.88	-20.8	-25.07
May	-5.47	5.17	6.82	-10.13	-6.26
June	5.39	9.55	6.64	2.3	1.98
July	7.36	0.29	-2.64	5.23	4.42
August	2.86	-9.68	-13.88	3.34	4.08
September	0.1	-25.34	-23.89	-5.92	-2.61
October	-15.27	-31.69	-25.7	-20.3	-10.07
November	-23.55	-35.03	-24.48	-23.53	-26.93
December	-33.33	-35.58	-22.1	-26.28	-24.08
Mean	-14.45	-17.11	-14.59	-16.02	-15.35

Table 1a Mean Temp 1998-2002: -15.50 ¡C

	1998	1999	2000	2001	2002
January	0	0	0	0	0
February	0	0	0	0	0
March	0	0	0	0	0
April	1.07	10	17.65	0	0
May	7.79	160.68	211.4	2.7	4.65
June	162.13	286.55	207.19	92.62	83.51
July	228.66	57.35	20.62	163.09	135.61
August	91.36	0.29	0	114.09	128.17
September	36.51	0	0	7.89	13.34
October	0	0	0	0	8.96
November	0	0	0	0	0
December	0	0	0	0	0
Total	527.52	514.87	456.86	380.39	374.24

Table 1b Thawing index

	1998	1999	2000	2001	2002
January	-990.7	-1010.57	-965.81	-1004.93	-1035.31
February	-962.77	-780.15	-690.93	-945.34	-986.78
March	-882.79	-554.66	-494.18	-930.57	-961.77
April	-500.69	-150.44	-164.06	-624.09	-752.15
May	-176.43	-0.46	-0.07	-316.71	-198.68
June	-0.53	0	-8.12	-23.67	-25.12
July	-0.36	-48.27	-102.42	-1.03	-1.19
August	-2.8	-300.44	-430.37	-10.69	-1.72
September	-33.6	-760.32	-716.74	-185.55	-91.62
October	-473.34	-982.51	-796.72	-629.34	-321.25
November	-706.5	-1050.9	-734.33	-705.98	-807.98
December	-1033.3	-1102.8	-685.04	-814.7	-746.61
Total	-5763.8	-6741.6	-5788.8	-6192.6	-5930.2

Table 1c Freezing index

Figure 2. Gypsum Hill Springs, "Little Black Pond."

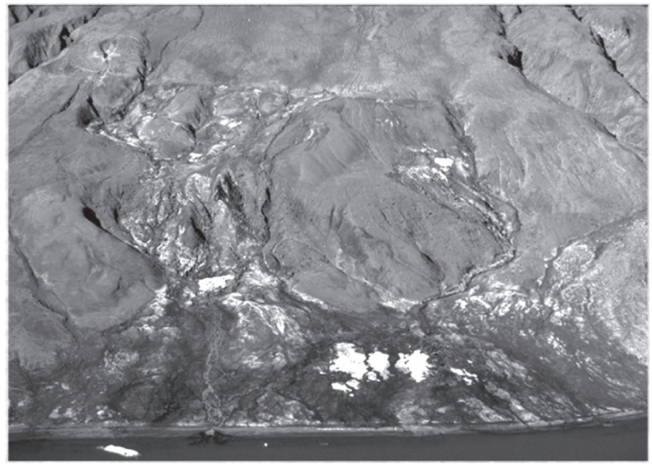

Figure 3. Colour Peak Springs.

White and Thompson glaciers converge roughly 10 km up valley from the head of the fiord, while the terminus of Crusoe glacier lies only a few kilometers west of the Expedition River Valley.

Climate/permafrost

The north and northwest Arctic Archipelago is characterized by polar desert conditions displaying very cold, dry winters and cool summers with maximum precipitation occurring in July. Intermittent climate records for the Expedition Fiord locale are available for the last 47 years, with a more complete record for the last 17 years.

Year-round data from an automatic weather station at Colour Lake (elevation 64 m a.s.l.) has been collected since 1992 indicates a mean annual temperature of -15.5°C with approximately 451 thawing degree-days and 6083 freezing degree-days during an average year (Andersen et al., this study). Tables 1a, 1b, and 1c list the mean average temperatures, thawing, and freezing index (degree-days below and above freezing) for each month during the years 1998–2002.

Permafrost depth has not been measured directly at Expedition Fiord; however, a permafrost thickness of > 400 m was documented in an exploration well at Mokka Fiord on the east side of Axel Heiberg Island, roughly 60 km from Expedition Fiord (Andersen 2004). Other exploration wells in the area reveal that permafrost is generally between 400–600 m thick. Permafrost features include extensive polygonal ice wedge development in unconsolidated fluvial and colluvial deposits at lower elevations.

McGill Arctic Research Station (M.A.R.S.)

The McGill Arctic Research Station is located 8 km inland at Expedition Fiord, Nunavut, on Central Axel Heiberg Island in the Canadian High Arctic (approximately 79º26′N, 90°46′W). Established in 1960 on the shores of Colour Lake, M.A.R.S. is one of the longest-operating seasonal field research facilities in the High Arctic, providing access to glacier, ice cap, and polar desert and tundra environments. Researchers utilizing M.A.R.S. have accumulated the longest continuous mass balance record for any High Arctic glacier (White Glacier). Past and current research conducted at the various springs has been carried out with support of this facility. The geomorphology, climate, chemistry and microbiology of the Gypsum Hill and Colour Peak Springs have been previously described by Pollard et al. (1999), Pollard (2005), Andersen et al. (2002), Heldmann et al. (2005a, b), Omelon et al. (2006) and Perreault et al. (2007), respectively.

Gypsum Hill springs: N79°24.247′, W090°43.968′

The Gypsum Hill spring site (Fig. 2) consists of approximately 40 springs and seeps on the northeast side of Expedition River, discharging along a band nearly 300 m long and 30 m wide between 10–20 m a.s.l. The springs are concentrated at the break in slope where bouldery colluvial materials overlap sandy outwash. The surface around the springs is littered by large boulders from both the till and exposed anhydrite. The area immediately surrounding the springs consists of small mounds separated by shallow gullies. There are outflows occurring in Expedition River; however, thick ice and snow in the winter and high stream flows during the summer have prevented determination of their exact locations. Pollard et al. (1999) estimated the total discharge of the Gypsum Hill Springs to be approximately 10–15 l/s. Spring outflow temperatures range from -0.5°C to 7°C. Major ion chemistry of the spring water is listed in Table 2. Analysis of the dissolved gases and bubbles in the spring water indicates that the source of the water is likely to be a combination of subglacial melt and lake water (Andersen 2004). Two nearby glacially-dammed alpine lakes, Phantom Lake and Astro Lake, provide large reservoirs of water and have basins residing upon gypsum-anhydrite piercement structures. Lake water is transported into the subsurface via permeable strata associated with the piercement structures. The water continues to flow along the subsurface salt strata to the spring sites, accumulating dissolved salts as it flows through this subsurface layer.

The composition of dissolved gases in the springs indicates that only 50% of the water comes from lake water and that the other 50% comes from glacial ice that has melted while isolated from the atmosphere. The dissolved gases in lake water reflect the equilibrium with the atmosphere based on the relative solubility of each gas. In contrast, air trapped in glacial

Table 2. Major ion chemistry of the spring water collected at Colour Peak, Gypsum Hill and Stolz Diapir outlets. *ORP values are reported as mV normalized to a hydrogen electrode (NHE).

	Colour Peak spring	Gypsum Hill spring	Stolz Diapir spring
Temperature (°C)	6.4	6.6	-1.05
pH	6.82	7.66	6.70
ORP (mV, NHE)*	-122.4	-97.1	--
Conductivity (mS/cm)	170	105	640
Density (g/cm^3)	1.114	1.056	--
Ca^{2+} (all in mol/kg)	0.0905	0.0574	0.032
Mg^{2+}	0.0130	0.0049	LDL
Na^+	2.30	1.5043	5.217
K^+	0.0048	0.0015	0.003
Cl^-	1.9324	1.0732	5.127
SO_4^{2-}	0.0240	0.0385	0.44
PO_4^{3-}	<0.5 mg/l	<0.5 mg/l	<0.5 mg/l
NO_3^-	0.001	LDL	LDL
DIC (mmol/l)	0.278	0.389	6.09
DOC (mg/l)	<0.2 mg/l	<0.2 mg/l	2.050
Alkalinity	0.0184	0.0155	--

ice has an atmospheric composition other than for Ne and He. These latter two gases are soluble in ice and would therefore be expected to diffuse through the ice. As an example, the ratio of N_2/Ar in lake water in equilibrium with the atmosphere is 37 while for air it is 84.

Colour Peak springs: N79°22.866', W091°16.270'

The Colour Peak Springs (Fig. 3) are located on the south-facing slope of Colour Peak at an approximate elevation of 100 m a.s.l., emerging from the top of the slope along a line nearly 400 m long. These springs are grouped into three distinct topographically controlled areas with 20 vents discharging directly into Expedition Fiord 300 m down slope. Major ion chemistry of the spring water is listed in Table 2. Interestingly, the springs on Axel Heiberg Island flow all year with little variation in their temperature and are not associated with volcanic activity.

Andersen et al. (2002) show that this can be explained by considering the flow through the subsurface salt layers. The flow enters the subsurface via the permeable strata associated with the salt diapirs that reside beneath the lakes, glaciers, and ice cap. At this depth the groundwater temperature is 0°C. The flow then proceeds below the surface to depths of at least 600 m and is warmed by the local geothermal gradient to temperatures up to 6°C. The flow rate to the surface is rapid enough that the temperature of the emerging groundwater does not change significantly from its initial value at depth.

Perreault et al. (2007) have speculated that sulfur-based metabolism may be the major source of biological energy production in these environments. Surveys of the microbial diversity in the sediments of these springs were conducted by analyzing denaturing gradient gel electrophoresis (DGGE) and clone libraries of 16S rRNA genes amplified with Bacteria and Archaea-specific primers. Dendrogram analysis of the DGGE banding patterns divided the springs into two clusters based on their geographic origin. Bacterial 16S rRNA clone sequences from the Gypsum Hill library (spring GH-4) classified into seven phyla (Actinobacteria, Bacteroidetes, Firmicutes, Gemmatimonadetes, Proteobacteria, Spirochaetes, Verrucomicrobia); δ- and γ-Proteobacteria sequences represented half of the clone library. Sequences related to Proteobacteria (82%), Firmicutes (9%), and Bacteroidetes (6%) constituted 97% of the bacterial clone library from Colour Peak (spring CP-1). Most GH-4 archaeal clone sequences (79%) were related to the Crenarchaeota while half of the CP-1 sequences were related to orders Halobacteriales and Methanosarcinales of the Euryarchaeota. Sequences related to the sulfur-oxidizing bacterium Thiomicrospira psychrophila dominated both GH-4 (19%) and CP-1 (45%) bacterial libraries and 56-76% of the bacterial sequences were from potential sulfur-metabolizing bacteria.

Figure 4. Wolf Diapir Springs.

Skaare Fiord Springs: N78°56.702', W088°17.666'

Sub-glacial discharge has been observed at an alpine glacier near the northeastern end of Skaare Fiord. The flow was discovered by Twin Otter pilots flying over the glacier during April 2002 when air temperatures were still well below freezing. Initial reconnaissance during the summer found an icing that was approximately 0.5km in diameter with red-tinted fine sediments covering the surface. The discharge was flowing from the central area of the icing at a rate of ~250 ml/sec, the water tasting strongly of iron, but not saline.

East Fiord springs: N79°30.109', W093°25.716'

In April 2007 during a wildlife survey, biologists from the Canadian Department of Environment reported to our research team a reddish staining on a glacier in the vicinity of East Fiord. Subsequent exploration of the area by helicopter located a large icing, stained with an iron-rich precipitate forming on and draping over the north edge of the unnamed glacier. Water was observed to be flowing from a series of outlets on top of the glacier about 20 m from the edge.

Figure 5. Stolz Diapir Spring

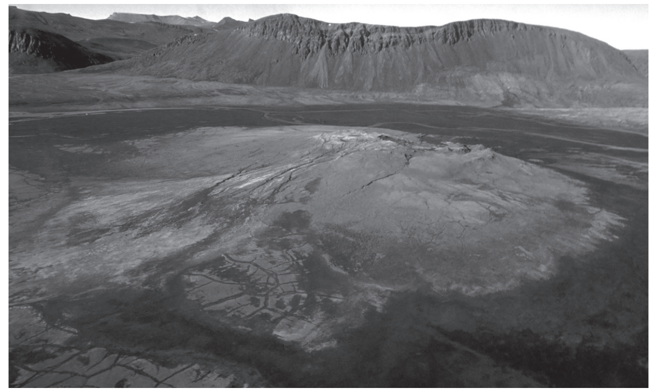

Figure 6. Middle Fiord Pingo with active outflow.

Wolf Diapir springs: N79°04.285', W090°12.755'

The Wolf Diapir site is characterized by a large mound of salt 3m in height and 3m in diameter that forms "fumarole-like" structure (Fig. 4). A saltpan extends about 0.5 km to the west. Water is present as a pool in the central portion of the structure, and during the winter months as temperatures decrease, the water level builds up and flows out and over the top producing a series of small terraces and rim pools on the NNE side of the structure. Increasing air temperatures in the summer allow for the dissolution of the salts (such as hydrohalite), and the spring water breaks through the sides and is released at the base lowering the water level. During July 2004, water flowing beneath and through the side of the structure was saline with a temperature of -3.5°C, pH of 6.4, and ORP of 60.0 (mV, NHE). Hydrogen sulfide was present in and around the discharge site.

Nine km SW of the Wolf Diapir Spring, a saline stream originating from beneath a landslide deposit with a flow rate of a flow of 10–12 L l/ss^{-1} occurs in the vicinity of Junction Diapir, originating on the south side of the dome and bounded by the Steacie Ice Cap. It has not been determined if this flow is perennial.

Stolz Diapir Springs: N79°05.343', W87°02.228'

At Whitsunday Bay a single spring discharges approximately 150 m up the south east side of Stolz Diapir and flows along a deep valley for 200m before it fans onto the Whitsunday River plain (Fig. 5). The position of the outflow moves up and down slope from year to year. Discharge is fairly constant at 40–50 l s^{-1} and the discharge temperature is constant at 1.2°C. Major ion chemistry of the spring water is listed in Table 2. In some years the outflow is marked by a single well-defined vent 40–50 cm in diameter while in others the outflow permeates through a layer of colluvial debris. This hypersaline spring produces a salt tufa deposit up to 5 m thick near the spring outlet and 1m thick near the valley mouth. In winter hydrohalite ($NaCl \cdot 2H_2O$) precipitates form a series of pool and barrage structures that staircase down the outflow channel. Several pools up to 10m wide and 3–5 m deep allow the water to cool in stages as it works its way down the valley with temperatures ranging from -10°C to -17°C in pools near the outlet to the eutectic point of the salts on the floodplain. The hydrohalite deposit merges with a fan-shaped icing that spreads on to the Whitsunday river flood plain. The source of recharge for the spring appears to be snowmelt that flows into and through the dome on the north west side of the diapir. The inflowing water is fresh, low conductivity (58.3 µS/cm) and near neutral pH (6.9). The inflowing water picks up the salts via dissolution of halite, which is present as large deposits at and near the surface of the diapir.

Bunde Fiord Ssprings: N80°22.749', W93°57.584'

Approximately 16 km SSW of Bunde Fiord, a large rectangular icing fills an east-west trending river channel where it dissects the northern edge of an anhydrite diapir abutting the far northwest end of the Mueller Ice Cap. The icing is roughly 200 m by 100 m, 2 m thick, and covered with a thick paste of precipitates and evaporates. The icing forms as a result of perennial flow from a series of small springs that exit the diapir 10–20 m above the base. The discharge is saline and flows into a small stream where it mixes with meltwater from local glacial sources. The stream contains numerous filamentous brown mats consisting of pennate diatoms.

Middle Fiord pingo: N79°43.653', W94°13.794'

At Middle Fiord a small spring flows from the side of a large pingo situated in the middle of a large floodplain 3 km downstream from Middle Fiord Glacier (Fig. 9). The pingo is 110 m in diameter and 20m high and is composed entirely of medium-grained sand and fine gravel. Water discharges at 0.5 to 1.2 l/s and at a temperature of 1.2°C from two or three closely-spaced outlets midway up the west side of the pingo.

Mars

Groundwater and the search for life on Mars

Despite the vast differences between the two planets today, Mars and Earth may have been much more similar early in their histories. If life developed on Mars as it did on early Earth, it may have faced an untimely extinction as the cryosphere of Mars enveloped the entire planet, its atmosphere thinned, and liquid water ceased to exist at the surface; or perhaps it has retreated to subsurface refugia. Nonetheless, even when Mars was wet it was probably cold. Thus the hydrological cycle in the coldest regions on Earth provides the best analog for a Martian hydrology. From studies of springs, rivers, and lakes in the polar regions, quantitative models have been developed that show how liquid water could have persisted on Mars even if mean annual temperatures were below freezing (Lee et al. 2001, Andersen et al. 2002, Heldmann et al. 2005a, b, McKay et al. 2004).

Springs, residual icings, pingos, and massive ground-ice deposits located in the Arctic (and Antarctic) provide opportunities to study microbial ecosystems in extreme polar environments. The ranges in temperature, pH, redox, nutrient availability, and the large seasonal variations in light have undoubtedly shaped the structure and function of the ecosystem as well as impacting the biological record left in the sediments. The planet Mars may have once hosted microbial ecosystems in a physical setting not too dissimilar to the Earth's polar regions. Determining the nature of the early Martian climate, the existence of subsurface water, or whether Mars ever gave rise to life will be aided by studies of terrestrial microbial ecosystems in regions of thick, continuous permafrost.

Acknowledgments

The authors acknowledge the support for fieldwork by the Canadian Polar Continental Shelf Project. The authors also wish to acknowledge support provided by NASA's Exobiology program, the Canadian Space Agency, the McGill University High Arctic Research Station, and the Natural Sciences and Engineering Research Council of Canada. Additional funding for student research was provided by the Department of Indian and Northern Affairs, Northern Scientific Training Program, and the McGill University Centre for Climate and Global Change Research.

References

Amundsen, H., Steele, A., Fogel, M., Mysen, B., Kiehle, J., Schweizer, M., Toporski, J. & Treiman, A. 2004. Life in a Mars analogue: Microbial activity associated with carbonate cemented lava breccia from NW Spitsbergen [Abstract]. *Fourteenth Annual V.M. Goldschmidt-Conference. Geochimica et Cosmochimica Acta 68 (11, Supplement 1):* A804.

Andersen, D. 2004. *Perennial springs in the Canadian High Arctic: Analogs of Martian hydrothermal systems*. Ph.D. Thesis. McGill University, Montreal.

Andersen D., Pollard W., McKay C., & Heldmann, J. 2002. Cold springs in permafrost on Earth and Mars. *J. Geophys. Res.* 10: 1029/2000JE001436.

Banks, D., Sletten, R.S., Haldorsen, S., Dale, B., Heim, M. & Swensen, B. 1998. The thermal springs of Bockfjord, Svalbard: occurrence and major ion hydrochemistry. *Geothermics* 27:445-467.

Embry, A.F. & Osadetz, K.G. 1988. Stratigraphy and tectonic significance of Cretaceous volcanism in the Queen Elizabeth Islands, Canadian Arctic Archipelago. *Can. J. Earth Sci.* 25: 1209-1219.

Gilichinsky, D., Rivkina, E., Bakermans, C., Shcherbakova, V., Petrovskaya, L., Ozerskaya, S., Ivanushkina, N., Kochkina, G., Laurinavichuis, K., Pecheritsina, S., Fattakhova, R. & Tiedje, J. 2005. *Biodiversity of cryopegs in permafrost. FEMS Microbiol. Ecol.* 53(1): 117-128.

Grasby, S.E., Allen, C.C., Longazo, T.G., Lisle, J.T., Griffin, D.W. & Beauchamp, B. 2003. Supraglacial sulfur springs and associated biological activity in the Canadian high arctic-signs of life beneath the ice. *Astrobiology* 3(3): 583-596.

Heldmann, J.L., Toon, O.B., Pollard, W.H., Mellon, M.T., Pitlick, J., McKay, C.P. & Andersen, D.T. 2005a. Formation of Martian gullies by the action of liquid water flowing under current Martian environmental conditions, *J. Geophys. Res.* 110: E05004, doi: 10.1029/2004JE002261.

Heldmann, J.L., Pollard, W.H., McKay, C.P., Andersen, D.T. & Toon, O.B. 2005b. Annual development cycle of an icing deposit and associated perennial spring activity on Axel Heiberg Island, Canadian High Arctic. *Arctic, Antarctic and Alpine Research* 37(1): 127-135.

Lauritzen, S.E. & Bottrell, S. 1994. Microbiological activity in thermoglacial karst springs, South Spitsbergen. *Geomicrobiology Journal* 12:161-173.

Lee, P., Cockell, C., Marinova, M., McKay, C. & Rice, J. 2001. Snow and ice melt flow features on Devon Island, Nunavut, Arctic Canada as possible analogs for recent slope flow features on Mars. Abstract #1809. *Lunar & Planetary Science Conference XXXII, March 2001*.

McKay, C., Andersen, D., Pollard, W.H., Heldmann, J., Doran, P., Fritsen, C. & Priscu, J. 2004. Polar Lakes, Streams, and Springs as Analogs for the Hydrological Cycle on Mars. In: T. Tokano (ed.), *Water on Mars and Life.* Berlin: Springer-Verlag, 219-233.

Omelon, C., Pollard, W. & Andersen, D. 2006. Geochemical evolution of perennial springs and the formation of travertines at Expedition Fiord Canadian High Arctic. *Applied Geochemistry* 21, 1-15.

Perreault, N., Andersen, D.T., Pollard, W.H., Greer, C.W. & Whyte, L.G. 2007. Culture independent analyses of microbial biodiversity in cold saline perrenial springs in the Canadian High Arctic. *Applied and Environmental Microbiology* 73(5): 1532-1543.

Pollard, W.H. 2005. Icing processes associated with high arctic perennial springs on Axel Heiberg Island. *Permafrost and Periglacial Processes* 16: 51-68.

Pollard W.H., Omelon, C., Andersen, D.T. & McKay, C.P. 1999. Perennial spring occurrence in the Expedition Fiord area of Western Axel Heiberg Island, Canadian High Arctic. *Canadian J. Earth Sci.* 36: 1-16.

Steele, A., Schweizer, M., Amundsen, H. & Wainwright, N. 2004. In-field testing of life detection instruments and protocols in a Mars analogue arctic environment [Abstract]. AbSciCon 2004, NASA Ames Research Center, Moffett Field, CA. *International Journal of Astrobiology*, *Supplement 1 (March)*: 24.

Stephenson, R., VanBerkel, J. & Cloethingh, S. 1992. Relation between salt diapirism and tectonic history of the Sverdrup Basin, Arctic Canada. *Canadian Journal of Earth Sciences* 29: 2640–2652.

Thorsteinsson, R. 1971. *Geology of Strand Fiord, District of Franklin.* 1:250,000. Map 1301A. Geological Survey of Canada. Map 1301A, scale 1: 250,000.

Geotechnical Considerations For Cut-Off Wall in Warm Permafrost

Steven L. Anderson, P.E.
Senior Geotechnical Engineer and Associate, Golder Associates Inc., Anchorage, AK
Thomas G. Krzewinski, P.E.
Senior Geotechnical Engineering Consultant and Principal, Golder Associates Inc., Anchorage, AK
Jim Swendseid, P.E.
Senior Mine Engineer, Teck Cominco Alaska Inc.

Abstract

A cut-off wall back dam has been designed for the existing tailings impoundment at the Red Dog Mine, Alaska. The planned cut-off wall, which is about 5,000 ft long and up to 170 ft deep, is located in an area of warm permafrost that consists of colluvium and alluvial materials overlying shale bedrock. The geotechnical program included a total of 41 boreholes on either side of the cut-off wall alignment. Geotechnical considerations included ice-rich and organic materials up to 19 ft thick and establishing design depths for the cut-off wall in frozen shale. These geotechnical issues have been addressed through a stable embankment design and deep excavation technology. Instrumentation and monitoring will be used to monitor the performance of the cut-off wall after construction is completed in the next two years.

Keywords: cut-off wall; dam design; geotechnical investigation; trench cutter.

Introduction

Teck Cominco Alaska Inc. (TCAK) commissioned Golder Associates (Golder) to design a Back Dam to minimize the potential for seepage at the southern end of the tailings impoundment at Red Dog Mine, Alaska. The Back Dam was designed for an elevation of 960 ft with a planned closure elevation of 986 ft.

The Red Dog Mine is located approximately 90 miles north of Kotzebue, Alaska at about 68 degrees latitude. The proposed Back Dam is located at the north end of the Overburden Stockpile, as shown in Figures 1 and 2.

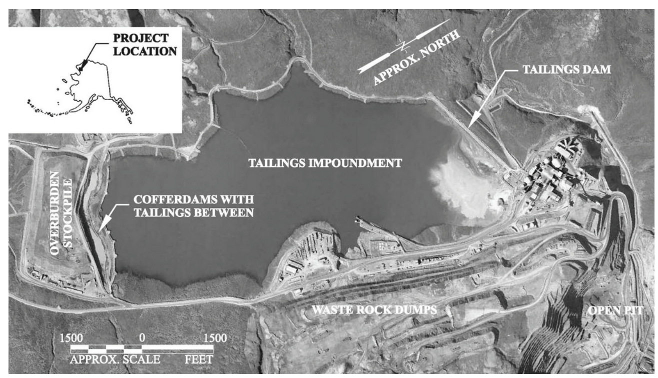

Figure 1: Back Dam location.

Background

Since 2002, the Back Dam design progressed through several stages and several options for reducing the seepage potential were reviewed. The initial design concept included construction of a cofferdam and installing a geomembrane liner on the upstream face of the Overburden Stockpile that would be keyed into silty native soil of relatively low permeability. Subsequently, TCAK constructed two waste rock cofferdams with a layer of geotextile and tailings placed between and a geotechnical investigation was performed by Golder in 2004 to verify the engineering parameters and assumptions used in the design. Based on the 2004 investigation results, ice-rich and organic materials were encountered below the proposed geomembrane liner and highly fractured bedrock was found near the liner key-in elevations.

During revision of the Back Dam design to account for the findings of the 2004 investigation, TCAK requested that the design should incorporate a cut-off to low permeability bedrock to reduce the risk of long-term seepage through the native materials and weathered bedrock. Several cut-off wall options were evaluated such as grouting, deep soil mixing, sheet piles, vibrated beam, a slurry trench, extending the geomembrane liner into a trench, and using a Bauer Cutter Soil Mixer (CSM). The option selected included constructing the cut-off wall with the Bauer CSM through an embankment between the Overburden Stockpile and the cofferdams.

In 2005 and 2006, Golder performed another geotechnical investigation along the southern cofferdam to determine the depth to low permeability bedrock. Ice-rich materials and organics were also encountered during this investigation and the low permeability bedrock was found to be up to about 170 ft below the proposed dam crest elevation of 960 ft.

Following the geotechnical investigation, the Bauer CSM was withdrawn as an option due to its very low production rates through rock and the amount of rock excavation expected. The Bauer CSM was replaced by a Bauer Trench Cutter.

Site Characteristics

Climate

The climate at the Red Dog Mine is characterized by long, cold winters and moderately warm, windy and somewhat rainy summers. The average annual temperature is 24°F (-4°C) with an air freezing index (AFI) of 4731°F-days and an air thawing index (ATI) of 1899°F-days. Total precipitation is generally between 10 to 13 inches per year and the average annual snowfall is 48 inches.

Thermal conditions

In the early 1980s the Red Dog Mine site was the subject of various feasibility and design studies. During this timeframe, approximately 50 thermistor strings were installed in geotechnical boreholes to provide information on the subsurface thermal regime of the area. These early readings are summarized in a monograph produced by the American Society of Civil Engineers (ASCE) (Hammer et al. 1985) that indicated relatively warm permafrost was present at the mine site and that surface water and shallow groundwater greatly influenced the thermal stability of the permafrost soils. Significant thaw bulbs were delineated surrounding streams in the area and the average temperature in a given area was significantly increased by poor drainage conditions and/or exposure to sunlight. In shaded areas with good drainage, temperatures averaged as low as 25°F (-3.9°C). In exposed areas with poor drainage, temperatures averaged as high as 31°F (-0.6°C) in frozen soils and some very poorly drained exposed areas found no permafrost present (to the depths explored).

Between 1995 and 1997, seven thermistor strings were installed within the Overburden Stockpile. Temperature readings from these thermistor strings indicate the permafrost has aggraded into portions of the stockpile and the depth to the top of permafrost varied between about 15 ft to 70 ft below the ground surface (Water Management Consultants 1999).

Thermistor readings were also taken during the 2005/2006 geotechnical investigation that indicated an average thaw depth of 18 ft below the native soil surface and average permafrost temperatures of about 31°F (-0.6°C). The deepest thaw depths were located near historic drainages.

Geology

The Overburden Stockpile site is reported to be generally underlain by a layer of unconsolidated, ice-rich, colluvial deposits, and interbedded Cretaceous age shale with inclusions of dark grey to brown sandstone.

Subsurface conditions

Subsurface conditions have been characterized near the proposed cut-off wall location from the geotechnical investigations performed in 2004 through 2006 that included 15 boreholes near the north face of the Overburden Stockpile and 26 boreholes along the southern cofferdam and near the abutments. The locations of these boreholes are shown in Figure 2 with subsurface profiles shown in Figures 3 and 4. These investigations also included test pits, thermistor string readings, packer tests, and laboratory testing.

- Fill materials were encountered on the haul roads, cofferdam, and Overburden Stockpile. The waste rock fill materials at the haul road and cofferdam generally had a composition of silty gravelly soil with occasional cobbles and boulders. Fill materials at the Overburden Stockpile mainly consist of Kivalina shale that had been stripped from the mining area.
- The native soils are colluvial and alluvial materials comprised of organic soil, ice and ice-rich soil, silty clayey soil and sandy gravelly soil.
    - Ice-rich and organic materials up to 14 ft and 19 ft thick were encountered near the cut-off wall alignment and below the Overburden Stockpile, respectively.
    - The silty clayey soil was loose to compact when thawed, averaged about 6 ft thick and generally thinned out toward the east.
    - The sandy and gravelly soil consists of silty sands to poorly graded sands and gravels that were typically compact to dense when thawed.
- The shale bedrock underlying the colluvial and alluvial materials was typically highly to completely weathered near the contact surface and became fresher with depth. The rock was generally fractured with a rock quality designation (RQD) of less than 20%. Rock strengths varied from weak (R2) to very strong (R5) with estimated uniaxial compressive strengths (UCS) up to 22,010 psi. The majority of bedrock encountered, about 75%, had a UCS less than 7,500 psi.

Design Considerations

Cut-off wall alignment

The cut-off wall alignment was selected to limit the amount of excavation into the Overburden Stockpile and minimize disturbance of the cofferdam. Using an excavation surface derived from the borehole and ground topography data, an alignment for the cut-off wall was developed based on the criteria that included:

- Maintaining the cut-off wall within the center of the constructed embankment to protect the cut-off wall from slope instability issues.
- Using 1H:2V (horizontal to vertical) slopes for the excavation prism starting a distance of 1.5 ft out from the alignment centerline at an elevation of 986 ft. The offset distance was based on a 3 ft cut-off wall width and the slope angle was based on the 2 to 1 stress distribution method, which is an empirical approach based on the assumption that the area over which the load acts increases in a systematic way with depth.

Cut slopes were developed based on natural slope angles with flatter cut slopes expected on the northern side of the alignment within the impoundment area. A limited amount of excavation into the cofferdam was considered tolerable depending on the seepage flows encountered after dewatering.

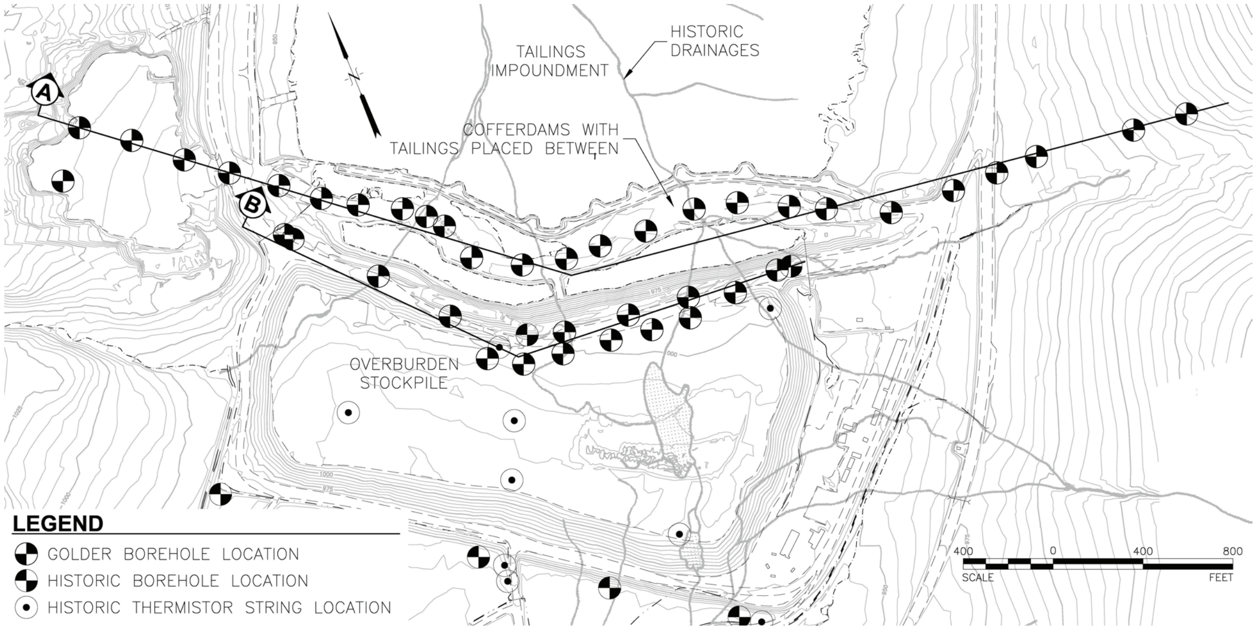

Figure 2. Borehole locations.

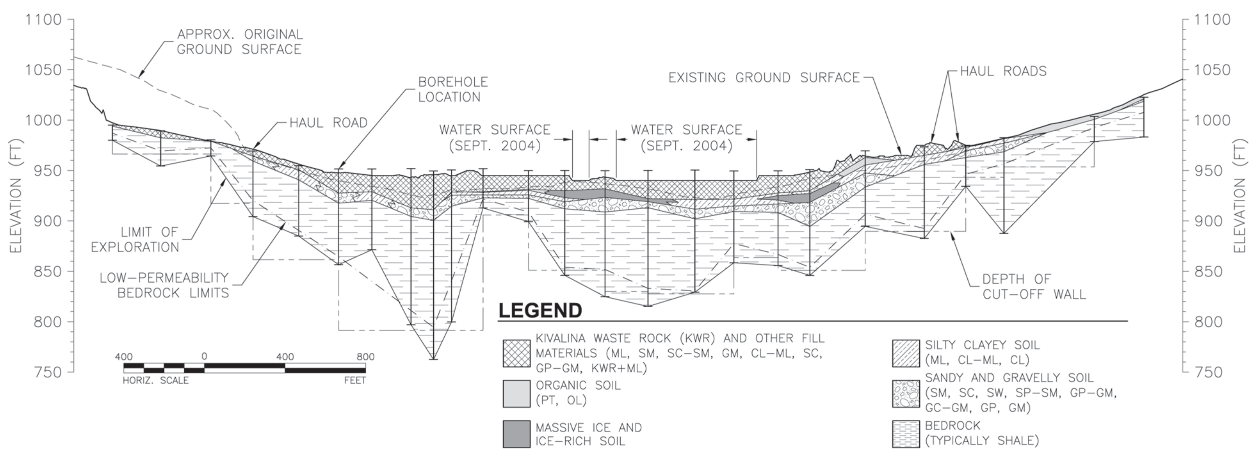

Figure 3. Section A through cofferdam.

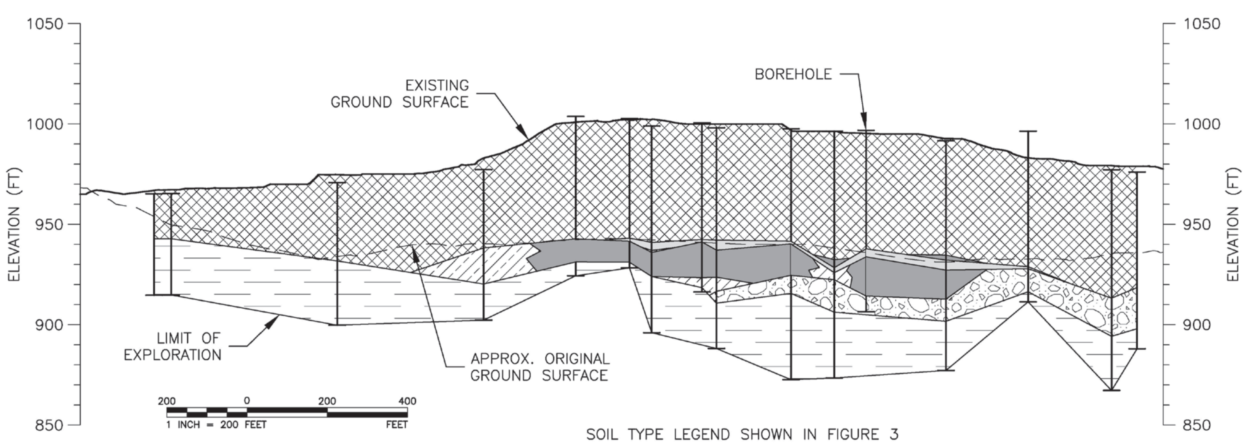

Figure 4. Section B through Overburden Stockpile.

Cut-off wall embankment section

The cut-off wall embankment will consist of a central section composed of select fill produced from screened crushed rock and compacted in controlled lifts to 95% maximum dry density (Modified proctor) to optimize strength and limit impacts from settlement. The select fill width was arbitrarily set at 20 ft for crest elevations of 986 ft and higher with 1H:3V side slopes. This provides a base width equivalent to the estimated deepest fill height (a criterion similar to what is used for impervious core dams) and keeps the select fill within the base excavation limits. The 20 ft width also allows for future raises, if required.

Rockfill, placed in controlled lifts and compacted with a minimum number of passes with a roller, will be used as fill outside of the select fill prism to provide additional stability with 3H:1V side slopes. The rockfill materials will be produced from waste rock from the mining operations or borrowed from other rock quarry areas. Acid producing rock will only be allowed on the upstream side of the cut-off wall. Some maintenance and additional fill placement is expected as the underlying ice-rich materials slowly thaw and consolidate, including some small slope failures and slumping due to as much as 9 ft of differential settlement, especially if the ice thaws quickly. The integrity of the cut-off wall, which is supported by the select fill section, will not be affected as these deformations will occur within the fill materials outside of the select fill section.

The proposed trench cutter and base carrier need a minimum work area of about 30 ft from the centerline of the cut-off wall alignment; therefore, the width of the embankment crest will be about 60 ft to keep the cut-off wall within the center of the embankment. As the cut-off wall construction needs a level work surface, stepped benches are required as the elevation increases at the abutments. In addition, a stepped bench is required at the deepest wall section due to the excavation limits of the proposed trench cutter. These benches were extended in stages to overlap gaps in the cut-off wall.

Cut-off wall panel target depths

The depth to low permeability bedrock, which was defined as having a permeability of 1 x 10^{-6} cm/sec or lower, was established during the 2005/06 geotechnical investigation. Permeability of the bedrock was typically determined using visual methods instead of the planned packer testing due to the frozen state of the rock. The visual criterion for apparent low permeability was one or less tight fractures per foot for a minimum length of three feet. Based on this criterion, the depth to apparent low permeability bedrock is shown in Figure 2. The cut-off wall panels will be keyed 3 ft into the apparent low permeability bedrock.

The deepest panel areas are located near historic drainages. These deeper zones of higher permeability bedrock are believed to be caused by freeze/thaw cycles and other weathering affects. The shallower panels are located outside of these historic drainages and in areas where the bedrock surface was encountered at a higher elevation. Therefore, these higher areas have not been exposed to the same degree of weathering and are less fractured at depth.

Thermal considerations

The cut-off wall is expected to be susceptible to degradation from freeze-thaw cycles; therefore, an insulated section will be installed to keep the frost penetration above the top of the cut-off wall. The insulation must also be wide enough to control frost penetration from the sides.

Due to the warm permafrost temperatures, which are near 31°F, the frozen conditions are not expected to affect the cut-off wall installation.

Instrumentation and monitoring

Instrumentation including thermistor strings, piezometers, and survey monuments will be important to monitor the performance of the seepage reduction structure. Thermistor strings will be installed to monitor degradation or aggradation of the permafrost. Standpipe piezometers will be installed to monitor water levels and seepage potential across the cut-off wall. Surficial survey monuments will be used to monitor settlement. Additional instruments installed within the cut-off wall itself, such as inclinometers and extensiometers to monitor vertical and horizontal movements, are important to monitor the performance of the cut-off wall.

Contingency options

In the event the cut-off wall does not perform as intended, as indicated by an increased head drop across the cut-off wall, some contingency options include jet grouting and permeation grouting. Jet grouting would likely be used for repairing higher than expected seepage in the fill and soils above the bedrock and possibly within the completely to highly weathered bedrock. Permeation grouting would be used to repair the bedrock. Water tests are typically performed prior to permeation grouting to evaluate the permeability of the rock and select the starting mix; therefore, this option would be the most successful under thawed conditions.

After the cut-off wall has been constructed, we expect the permafrost will aggrade into the fill embankment as it did into the Overburden Stockpile. Therefore, these contingency options will be considered following monitoring of the piezometers and thermistors strings.

Engineering Analyses

Engineering analyses performed for the design included seepage modeling, slope stability analyses (for the constructed embankment and cofferdam), hydrology and hydraulic analyses, thermal modeling, settlement, trench stability, and mix design of the cut-off wall materials. The following sections describe the results of the seepage analyses and mix design testing.

Seepage modeling

Potential seepage rates based on the cut-off wall design and future closure options were evaluated using the 2-D finite element program SEEP/W®. Analyses were carried out to evaluate seepage through the deepest section and the average section along the alignment. Some of the variables evaluated included:

- Changing the depth of the cut-off wall at the deepest section from 50 ft below the embankment to a 3 ft key into low permeability bedrock (10^{-6} cm/sec).
- Changing the hydraulic conductivity of the cut-off wall between 10^{-6} cm/sec and 5 x 10^{-7} cm/sec.
- Changing the hydraulic conductivity of the native soils and weathered/fractured bedrock, which were assumed to have the same permeability, between 10^{-3} cm/sec to 10^{-5} cm/sec (worst to best case).
- Changing the closure option from no tailings beach to a 900 ft tailings beach using 300 ft increments.

Results from the seepage modeling included the following:

- Keying the cut-off wall into low permeability bedrock decreased the flux values substantially assuming the worst-case (1 x 10^{-3} cm/sec) for the hydraulic conductivity of the native soils and weathered/fractured bedrock.
- For the best case native soils and weathered/fractured bedrock hydraulic conductivity, there was essentially no difference in flux values if the cut-off wall is installed at least 50 ft below the embankment fill whether it is keyed into the low permeability bedrock or not. Increasing the hydraulic conductivity of the native soils and weathered/fractured bedrock by an order of magnitude (average case of 1 x 10^{-4} cm/sec) about doubled the flux values.
- Assuming the native soils and weathered/fractured bedrock have at least a hydraulic conductivity of 1 x 10^{-4} cm/sec or less, seepage rates will still be relatively low if the cut-off wall terminates above the target depths.
- Adding a tailings beach may reduce the seepage flows up to 50%. A tailings beach that is 600 ft to 900 ft long will reduce seepage flows about 20% more than a tailings beach that is 300 ft long.
- The head drop across the wall could vary from 7 ft to 32 ft. The average head drop across the wall for all cases was 19 ft.
- Under completely thawed conditions, seepage flows should be expected to vary from about 30 gpm to 80 gpm for the entire cut-off wall alignment. Lower seepage values should be anticipated if:
  - The cut-off wall target depths can be achieved during construction;
  - The hydraulic conductivity of the cut-off wall or the low permeability bedrock is less than the design permeability of 1 x 10^{-6} cm/sec; and/or,
  - A tailings beach is constructed.

Mix design

The performance goals for the mix design were developed based on the engineering analyses described above. As settlements and stability are not expected to be a design concern, the minimum mix design compressive strength and deformity was determined qualitatively to be 100 psi and 5% strain, respectively, which should be greater than the surrounding soil. A minimum permeability of 1 x 10^{-6} cm/sec was selected based on the seepage analyses; however, a performance specification was provided based on a flux value of 0.007 gpm/ft width for a head loss of 23 ft and a minimum wall thickness of 2.6 ft to possibly reduce material quantities and save costs. This specification should provide a maximum flow rate of about 40 gpm across the entire cut-off wall.

Mix design testing was performed at Golder's laboratory in Burnaby, British Columbia, Canada using the following available materials:

- Potable water available at site (pH = 7)
- Type I cement meeting ASTM C150
- Bentonite meeting API 13A, Section 9
- ¾-inch minus crushed rock from site, which was passed through LA abrasion devise to simulate cuttings from the Trench Cutter

The mix design results are shown in Table 1. Based on the mix design testing results, Mix Design No. 4, which is 19% water, 10% cement, 3% bentonite, and 68% aggregate, met the performance criteria of 100 psi minimum compressive strength and a maximum permeability of 1 x 10^{-6} cm/sec at a strain of 5%. Additional testing will be performed by the contractor during construction to verify the field mixture continued to meet the performance specifications.

Current Construction Highlights

Excavation and embankment construction

Excavation and embankment construction is being performed by TCAK with construction quality control (CQC) provided by Golder. To date, the embankment has been constructed for about half the alignment and excavation depths have been similar to what was estimated from the design drawings. An example of some of the ice-rich materials encountered during the excavation is shown in Figure 5.

Slope stability was monitored on a daily basis during the embankment construction and slopes were flattened as necessary. Seepage flows through the cofferdam were generally low and easily controlled. However, seepage flows through the Overburden Stockpile were higher than expected and required construction of drainage trenches. A photograph of the constructed embankment is shown in Figure 6. Construction of the embankment is planned for next year with the majority of excavation occurring in the winter.

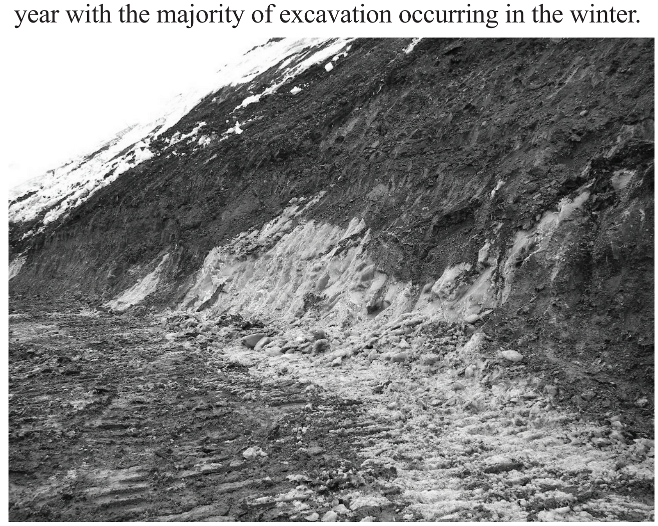

Figure 5. Massive ice encountered during excavation.

Table 1. Mix design results.

Mix Type	Sample Number	Age (days)	Wet Density (cm/sec)	Permeability Before Strain (cm/sec)	Maximum Deviator Stress (psi)	Tangent Modulus (tsf)	Maximum Strain (%)	Permeability After Strain (cm/sec)
Plastic Cement	1A	46	83	2.6E-07	231	2109	8.3	2.8E-7
	3A	19	78	6.3E-06	26	829	8.1	8.6E-6
Plastic Concrete	4B	42	129	6.8E-08	452	5127	7.7	8.4E-7
	4A	80	129	6.0E-08	514	3592	17.7	1.8E-6
	5A	19	131	3.5E-08	749	8135	1	6.9E-7

Strain of Sample 5A limited by capacity of load cell


Figure 6. Embankment with Bauer trench cutter.


Figure 7. Bauer cutter heads.

Cut-off wall construction

The cut-off wall is being constructed by Golder Associates Innovative Applications (GAIA), a wholly owned subsidiary of Golder's Canadian company providing specialized contracting services, with assistance from Bauer Maschinen. About 65 linear ft of cut-off wall has been constructed in 2007 to evaluate the performance of the cutter heads (Fig. 7), the slurry transport systems, and the mix design. Cut-off wall construction is scheduled to continue next year with two 12-hour shifts from May to October. The project is expected to be completed in 2009.

The cut-off wall is constructed by installing a series of primary and secondary panels. Construction begins by installing reinforced concrete guide walls to help support the near surface soils and provide alignment and continuity for the cut-off wall. Slurry is then introduced into the shallow trench between the guide walls and the panel is pre-excavated further to submerge the slurry pump on the trench cutter. Excavation continues with the trench cutter to the design depths. During this excavation, the slurry is recycled through a desander. The working slurry in the excavated column is then replaced with fresh slurry and the panel is completed by backfilling the column with tremied plastic concrete.

Conclusions

Based on the results of geotechnical investigations performed in warm permafrost for a cut-off wall in northwestern Alaska, ice-rich materials up to 19 ft thick were encountered in the overburden materials along the proposed alignment. In lieu of packer testing, which could not be performed in the frozen ground, a visual criterion was also developed to determine cut-off wall target depths in apparent low permeability bedrock. A cut-off wall up to 170 ft deep was required based on the borehole data.

To address the potential settlement issues from the melting ice-rich soils, a stable embankment design was developed that included excavating the ice-rich materials and constructing the central part of the embankment with select engineered fill. The cut-off wall will be constructed using a Bauer Trench Cutter that is capable of excavating into the bedrock to the design target depths. Plastic concrete slurry composed of aggregate, cement and bentonite will be used to backfill the excavation. Instrumentation and monitoring will be used to monitor the performance of the cut-off wall after construction is completed.

References

Hammer, T.A. et al. 1985. Ground temperature observations. *Thermal Design Considerations in Frozen Ground Engineering*: 8-52.

Water Management Consultants. 1999. The Phase II Hydrologic Characterization of the Tailings Impoundment. Report to Teck Cominco Alaska Inc.

Water Chemistry of Hydrogenous Taliks in the Middle Lena

N.P. Anisimova
Melnikov Permafrost Institute, SB RAS, Yakutsk, Russia
N.A. Pavlova
Melnikov Permafrost Institute, SB RAS, Yakutsk, Russia

Abstract

Based on the results of long-term investigation, this paper outlines the chemistry of groundwater of open and suprapermafrost taliks, occurring beneath the channel and arms, as well as in the low terraces of the Middle Lena River. This paper also illustrates the character of changes in the groundwater chemistry within the vertical profile and along the stretch of channel sediments forming an open talik under the Lena River; how these changes depend on surface water TDS fluctuations during the year-cycle; and specific features of mineral content of underlying bedrock. We have also regarded the impact of permafrost processes and human contamination in change of suprapermafrost talik groundwater chemistry.

Keywords: chemistry; hydrogenous taliks; open river talik; suprapermafrost talik.

Introduction

In Central Yakutia, with prevailing continuous permafrost, the groundwater in taliks is widely distributed under the Lena River channel, under lakes, cut-off meanders, and small rivers. Their chemistry is considerably affected by the geological and structural pattern of the territory, terrain type, geocryologic conditions, and the composition of recharge water.

There has been a thorough investigation of peculiarities of groundwater chemistry origins for taliks in the Middle Lena, where the river passes on from the Prilensky plateau region to the Central Yakutia lowland area. The valley's profile changes correspondingly from a narrow valley with steep rock sides to a vast terraced accumulative valley. The widest terraced part of the river valley situated on the western bank between the Tabaga and Kangalass bedrock fold is known as Tuymaada. It is 6–8 km wide. It includes two terraces and a flood plain which is separated from the main channel by numerous arms and islands. The width of the main channel of the Lena River at the town of Yakutsk is about 3 km. The Lena River flood plain is annually inundated by floodwater, its level above mean water reaching 8–10 m, according to long-term assessment. The flood plain topography is hilly, complicated by numerous narrow, semi-cut-off depressions and arcs. Arcs are made of fine and medium sand of channel facies, its surface covered by flood plain sabulous-loamy sediments 0.5–2.5 m thick. In the upper part of the cross section of semi-cut-off depressions and scourways we can identify a sabulous-loamy layer, up to 5 m thick. The combined thickness of the alluvial sediments, forming the flood plain, reaches 10–15 m.

Alluvial sediments in the Tuymaada region occur in Middle Jurassic rocks, upper layers of which are composed by clayey siltstone interbedded by fissured sandstones. Upstream the river, the thickness of Lower Jurassic terrigenous sediments is gradually diminishing; starting in the town of Pokrovsk the channel alluvium is underlain by carbonates.

The eastern low terraces are separated from the fourth one (Bestyakh) by a bench up to 20 m high. The depth of the river in the middle is 3–5 m, reaching 15–20 m along the fairway.

The spring flood of the river typically brings a rapid and high level rising. The main yield falls in the warm season. The winter period witnesses 9%–11% of the total yield. The river is completely frozen from the first half of November until the second half of May. It is mostly meltwater-recharged (50%), up to 35% rainfall-recharged, and about 15% of the recharge comes from ground water.

In the studied area permafrost covers all the territory, except for the Lena River channel and large lakes which are underlain by open taliks. The thickness of permafrost ranges from 20 to 450 m. The minimal thickness (20–50 m) is identified within low flood plain, under islands, and under some lake taliks. In the first and second fluvial terraces of the eastern bank (opposite Pokrovsk), separated from the channel by wide flood plain, the thickness of permafrost reaches 250–350 m; in the first fluvial terrace of the western bank (Yakutsk and suburbs) it makes 216–270 m, extending northwards up to 475 m (Khatyryk). Seasonal thawing depth depends on the general climate and a number of local factors: lithological composition of soils, their water-saturation, water permeability, shading effect, type of vegetation, the stage of the area in terrain, underlying bedrock temperature, etc. Depending on these factors the thickness of the seasonally thawing layer varies within quite a wide range (from 0.3 to 4.5 m).

The temperature of the permafrost within fluvial terraces is not uniform. The lowest temperatures (from -2.5°C to -4°C) occur in the ground that forms the flood plain, the surface of which is considerably swamped and peated. Within the first and second fluvial terraces the temperature is lower (from -0.9°C to -2.5°C), only in swamped and peated areas in the rear sides of the terraces the temperature falls to -3.6°C.

Research Methods

The existence of taliks in Lena River frozen ground is caused by the warming effect of river-, lake-, and suprapermafrost waters. According to the stage in the terrain, taliks are subdivided into river taliks, occurring in active channel sediments and bedrock immediately under the river, and terrace taliks, formed under flood plain and dead-channel lakes, or in depressions at the floors of arcs, ridges, and terrace slopes.

Initiated in the mid 1950s by the Permafrost Institute long-term investigations on water chemistry of hydrogenous taliks in the middle Lena valley have been continued. The investigations include drilling, water, and ground sampling for chemical analyses, temperature measurements in instrumented boreholes, as well as long-term observations of groundwater level and chemistry in taliks. Data obtained from long-term hydrogeochemical studies of open and suprapermafrost taliks occurring beneath the river channel and arms, as well as in the low and medium terraces in the Middle Lena valley were analyzed. This allowed us to determine variations in groundwater chemistry in relation to the dissolved solids concentration in source surface water in an annual cycle and to the composition of the underlying bedrock. An understanding was gained on the effects of cryogenic processes and anthropogenic contamination on talik water chemistry.

Results and Discussion

Open talik under the Lena River

The Lena River open talik was first tested in 1958 by a Gidroproekt Institute expedition in the Pokrovsk area. The 70–200 m deep drill holes completed on the islands and in the channel penetrated 27 m thick sandy-pebbled sediments and underlying fissured Cambrian limestone. During further investigation the groundwater of the Lena River talik was revealed in the Peschany island opposite Tabaga Point at the interval of 10.4–105.8 m, the water level settled at the depth of 4.37 m from earth surface. Among the water-bearing materials in Peschany island are anisometric quartzo-feldspathic sands, Quaternary gravels, and underlying fissured sands and Lower Jurassic siltstone. In channel sediments where there is no permafrost the water is non-artesian, and in the islands in conditions of active suprapermafrost forming, waters revealed in channel sediments have a slight pressure.

On the projection, the open talik zone contour repeats the contour of the channel zone. Its width ranges from 2.0 to 2.7 km.

Total dissolved solids (TDS) and chemistry of Lena River talik groundwater are not homogeneous judging by alluvial sediments cross section. In upper layers of channel sediments the chemistry of the water varies during the year according to the changes occurring in the composition of recharging surface water.

In winter water TDS reaches 500 mg/l with hydrocarbonate-chloride composition, and during the warm period it reduces down to 70–150 mg/l, when calcium and magnesium hydrocarbonates start prevailing.

In the bottom layers of the river talik alluvial zone the chemistry of water is affected by the mineralogical composition of the underlying bedrock. South from Pokrovsk, where channel sediments overlie Cambrian limestone, the chemistry of the bottom alluvial zone water is dominated by calcium and magnesium hydrocarbonates, and the TDS makes 330–570 mg/l (interval 33–70 m).

Downstream where Cambrian limestone dips below Jurassic sandstone in the basal levels of channel sediments, water, classified by the dominant dissolved ions, is mostly hydrocarbonate and natrium type with a TDS of 350–490 mg/l (Fig. 1).

The temperature in the Lena River channel ranges from 1°C to 4°C. On the old islands the soil is frozen down to 15-60 m deep. In the underlying talik, bedrock water is slightly over-mineralized. Thus, in fissured Cambrian limestone on the island opposing Pokrovsk, water TDS under the permafrost at a depth of 15 m made 500 mg/l, and its composition was hydrocarbonate magnesium-calcium; and on Ponomarev Island, opposing Yakutsk, under 25 m of permafrost, water revealed in Jurassic sandstone had a hydrocarbonate natrium composition, an increased content of chlorides, and TDS of about 1 g/l. Such composition occurs as a result of poor permeability under the permafrost.

The analysis of water chemistry in channel sediments of an open talik under the Middle Lena River (from Bulgunnyakhtakh to Namtsy) showed that there is no mineralized groundwater discharge into the channel from bedrock. The chemistry of the water revealed in the well under 173 m of permafrost in Jurassic sandstone in the western bank flood plain at Tabaga Point according is a bicarbonate-chloride sodium type (hereafter the water type name is given in increasing order of components), and TDS is 1.6 g/l.

Subpermafrost water of Middle Cambrian sediments, revealed in the well on the eastern bank of the Lena River (Krasny Ruchei, southern part of the studied territory) at a depth of 350 m is a bicarbonate-sulfate-chloride sodium type and TDS is 2 m/l.

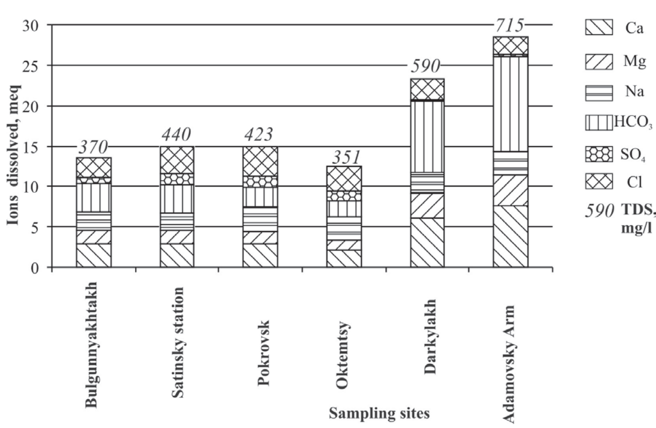

Figure 1. Changes in chemistry of groundwater under the Middle Lena.

Table 1. Water Chemistry of the Lena Riverside Arms in Tuymaada Valley (Makarov 1996).

Arm	pH	Minerals total, mg/l	Unit	Ca^{2+}	Mg^{2+}	$(Na+K)^{+}$	NH_4^{+}	HCO_3^{-}	SO_4^{2-}	Cl^{-}
Tabaga	7.5	178	mg/l	18	5.5	22	1.2	48	75	32
			meq%	39	20	41		24	48	28
Khatass	7.3	186	mg/l	30	8	27	1	82	36	43
			meq%	44	19	37		41	23	37
Khatass	5.9	163	mg/l	21	6	21.5	0.7	9	77	29
			meq%	42	20	38		6	62	32
Prigorodnaya	7.4	143	mg/l	24	6	21.5	1.2	55	41	25
			meq%	46	19	35		37	35	29
Zhatai	8.1	112	mg/l	17	6	17.5	0.7	54	21	24
			meq%	40	23	36		44	22	34
Tulagino	8.2	115	mg/l	21	7	13	0.4	78	17	18
			meq%	48	26	26		60	17	24

Although this water is high pressure artesian, its discharge to the surface is impeded by aquitard in the overlying zone (Beletsky & Kyrbasov 1972). The drilling of the aquitard consisting of marls interbedded with dolomites and limestone more than 100 m thick was completed starting from the depth of 50–75 m.

Suprapermafrost taliks

The suprapermafrost river talik under the arms of the Lena River was revealed during drilling by *Kommunvodstroi* Institution expeditions in 1932–1934. In 1960–1961 the Yakutsk Geological Board completed 15 drill holes with depths ranging from 12 to 76 m, aimed at estimating groundwater abundance under the Lena River channel near Yakutsk. The wide accumulative flood plain of the Lena River has numerous arms and lakes, flooded in spring. The taliks under them are closed. They are up to 40 m thick. The chemistry of talik water mostly depends on the surface water composition, but the discharges of surface- and suprapermafrost water from terraces also affects it.

Surface water TDS in the Tabaga, Khatass, Yakutsk, Zhatai, and Darkylakh arms situated on the western bank opposite Yakutsk, makes 50–60 mg/l in June, with an ionic composition dominated by calcium hydrocarbonates. At the end of summer it rises up to 170–180 mg/l, and natrium chlorides and sulphates prevail (Table 1). The highest values of water TDS in the river arms (up to 500 mg/l with dominating natrium chlorides) as well as in the main channel, are registered at the end of winter. In the river talik of the Adamovsky arm opposite Yakutsk the composition and mineralization of groundwater in winter (February) varies slightly along its profile; in the upper part (6–9 m deep) TDS makes about 620 mg/l with natrium and magnesium hydrocarbonates dominating, and in deeper layer (at interval of 12–15 m) it is slightly lower (470 mg/l) and has a natrium hydrocarbonate composition.

In the talik under the Darkylakh arm situated downstream, in the upper part of alluvial layer at a depth of 1–9 m, the TDS of the groundwater in April is about 500 mg/l; it has hydrocarbonate-chloride composition, not homogeneous by cations it contains.

The chemistry of water in suprapermafrost taliks under arms of the river which are close to Yakutsk is affected by contaminated suprapermafrost water runoff from urban areas to the alluvium. This is proven by an increased content of chlorine in the talik water and by its increased oxidability of 9.4 mg O_2/dm^3.

Increased accumulation of contaminants in alluvial sediments of river arms usually accompanies low permeability. Thus, for example, while constructing District 202 of Yakutsk, after an inwash of sand on the flood plain surface, TDS in channel sediments increased up to 1–2 g/l with a dominance of natrium chlorides and sulphates, which were being introduced with contaminated suprapermafrost water from the first fluvial terrace and were concentrating at permafrost table.

In the sediments making up the Lena River fluvial terrace suprapermafrost water-bearing taliks underlying minor arms and lakes are widely distributed. In the lower reaches of minor eastern-bank tributaries (Tamma, Lutenka, Menda, Suola) the thickness of river taliks in well-draining sandy-pebbled sediments makes 30–60 m and in some cases extends deeper into underlying bedrock. The maximal water-bearing capability of such arm taliks is indicated under minor arms within the Bestyakh terrace. Even though the channel is not wide (10–20 m) and surface flow is not permanent, here river taliks sustain during the winter as well, due to their increased water drainage and comparatively the high temperature of the permafrost. Thus, for example, water in a talik under the Tamma River dried channel in April (before flood) at a depth of 3–13 m has TDS of 200–300 mg/l. Its type is hydrocarbonate calcium-magnesium.

Increased thickness of river taliks under the Lena's eastern tributaries is indicated in the areas underlain by sandy-pebbled sediments covering fissured bedrock. Thus, in the lower reach of the Menda River the thickness of the aquifer talik reaches 60 m. At August testing the yield made 1.8 l/s, TDS – 200 mg/l, and the chemistry was dominated by calcium hydrocarbonates. The underflows beneath minor eastern tributaries discharge into the Lena River talik. In some cases, icing forms in areas near outlets of such rivers.

Minor western tributaries in Tuymaada Valley

(Shestakovka, Khatynnakh, Markhinka, and Zolotinka) do not have a year-round discharge, therefore during winter small river taliks sustain only in isolated, deep parts of the channels. In one of these river taliks in the lower reach of Markhinka at the end of winter (April) at a depth of 1.5 m, water had TDS of 238 mg/l, hydrocarbonate natrium-magnesium-calcium composition, and a high concentration of organic substances. Shestakovka River taliks occur under the lake-like widening of its channel in the lower reach. Here, TDS in water from the talik, revealed in sands in the interval of 1.0–4.5 m, varies during the year from 510 to 780 mg/l, while TDS in the river is considerably lower (50–95 mg/l). Talik water quality deterioration results from organic matter inflow from the seasonally freezing layer of the catchment area and from overlying stratum in the dried part of the channel.

Suprapermafrost aquifers in the first and second terraces of the Lena River also occur under lakes and cut-off meanders. The groundwater occurrence depth in lake taliks is subject to the depth of lake and in dried frozen parts of the basin corresponds to the thickness of newly formed permafrost. The thickness of taliks under small shallow lakes does not exceed 20 m and at a depth of 2–3 m and a width of 100–200 m it increases up to 30–40 m.

In taliks underlying continuously or periodically discharging lakes water TDS is not higher than 400–700 mg/l. The dissolved ionic type is hydrocarbonate, calcium, magnesium, and sporadically natrium. Under small static lakes no deeper than 1 m, taliks are thin (0.5–1.5 m). Their water TDS is often more than 1 g/l.

The majority of cut-off lakes in low terraces forming a beaded drainage become interconnected during high water. Nevertheless, the connection between their taliks is presently interrupted as a result of permafrost forming between the lakes in dry parts where there are roads.

In lower western terraces of the Lena River where saline lands are widely distributed under drying basins we can often indicate small freezing lake taliks with TDS of 2.5–4 g/l. In relict lake taliks under completely dried basins the TDS in some cases reaches up to 60 g/l, and the ionic composition is dominated by sulphates and chlorides, natrium and magnesium.

Increased salinity of the groundwater in lake taliks within the densely populated part of Tuymaada Valley is affected by human contamination of the territory (Anisimova et al. 2005).

The good quality of water in lakes and their taliks will retain only in case of them being non-stagnant and recharged by meltwater and slightly saline suprapermafrost water. On the western bank such lakes occur at the floor of the alluvial valley slope and on the eastern bank – at the floor of the fourth Bestyakh fluvial terrace. Such are, for instance, lakes to the south of Pavlovsk, where they are recharged not only by precipitation water, but also by intrapermafrost taliks occurring in the Bestyakh terrace. Said taliks discharge either in creek valleys, forming year-round flowing springs or forming submerged crop outs in some low-terrace lakes (Buluus, for instance). This thick intrapermafrost taliks' water is of low TDS and is hydrocarbonate magnesium-calcium and hydrocarbonate natrium type, but it cannot discharge into the Lena River talik due to the impedance of thick layers of low-terrace permafrost.

Conclusions

All stated above demonstrates that there are two crucial factors that affect the quality of water in open and suprapermafrost taliks: permeability rate determined by water circulation, and rechargeability with good quality water. Within the studied area the required properties are indicated only in one Lena River talik upstream from Pokrovsk where channel sediments are underlain by fissured limestone, and in the river taliks under right tributaries of Lena (Menda, Tamma, Lutenga).

In the Tuymaada Valley area, under the arms, yield horizon is confined only by the channel sediments zone. But in the vicinity of Yakutsk, the water chemistry of the river taliks deteriorates as a result of contaminated groundwater runoff of the active layer and suprapermafrost taliks from the urban area.

Acknowledgments

This study was supported by the RFBR grant 06-05-96087.

The authors are grateful to two anonymous reviewers for their helpful comments.

References

Anisimova, N.P., Pavlova, N.A. & Stambovskaya, Y.V. 2005. The influence of anthropogenic Contamination on groundwater chemistry in flood plain taliks and riverbed, Middle Lena River. Fundamental issues of water resources research and utilization. *Proceedings of a Scientific Conference, Irkutsk, Russia, September 20-24, 2005:* 339-340.

Beletsky, V.L. & Kyrbasov, P.V. 1972. *Saline Water in Middle Cambrian Sediments by the Lena River Streamside // Geocryological and Hydrogeological Research of Siberia.* Yakutsk: Yakutsk Book Publishing House, 164-167.

Makarov, V.N. 1996. *Environmental and Geochemical Profile of Tuymaada Valley //Environmental and Geochemical Issues in the Permafrost Region*. Yakutsk: SB RAS Institute of Permafrost Press, 3-34.

A New Hypothesis on Ice Lens Formation in Frost-Susceptible Soils

Lukas U. Arenson
BGC Engineering Inc., Vancouver, BC

Tezera Firew Azmatch
UofA Geotechnical Centre, Department of Civil and Environmental Engineering – University of Alberta,Edmonton, AB, Canada

David C. Sego
UofA Geotechnical Centre, Department of Civil and Environmental Engineering – University of Alberta,Edmonton, AB, Canada

Abstract

Generally it is accepted that frost heave is a one-dimensional process assuming that the ground conditions are homogeneous and the temperature gradient is one-dimensional. Unfrozen water is attracted to the base of the warmest ice lens for it to grow. Recent laboratory investigations suggest that the growth of ice lenses is more complex. Vertical ice veins form through the frozen fringe in a regular, hexagonal pattern reaching the freezing front. Based on these observations, a new hypothesis for ice lens formation is suggested. As suction builds within the frozen fringe, thin vertical cracks form that do not completely fill with ice, allowing a thin film of water to migrate from the unfrozen zone to the warmest ice lens. The existence of these vertical channels helps explain the measured ice lens growth considering the decreasing hydraulic conductivity in the frozen fringe as voids fill with ice. The tensile strength and the stress state of the soil that governs the crack pattern, therefore, control the ice lens growth and hence frost heave.

Keywords: frost heave; frost susceptibility; ice lens formation; hexagonal cracks.

Introduction

Saturated fine grained soils are known to form horizontal ice lenses when subjected to sub-zero temperatures. These ice lenses change the structure of the soil, generally associated with frost heaving. This change in structure as well as the expansion of these so-called frost-susceptible soils hasve to be taken into consideration when encountering such a soil as a construction or foundation material.

Phenomena associated with frost-susceptible soils have long been recognized by many researchers (e.g., Beskow 1935, Miller 1973, Penner 1959, Penner 1972, Taber 1929, Taber 1930). The basic mechanisms involved in frost heave were identified in the early days based on experimental evidences. Ice lenses form at a certain distance above the freezing front, and water from the unfrozen zone migrates towards the ice lens. Under thermal steady state the warmest ice lens continues to grow as long as water is available. Under transient conditions (penetrating frost front) the ice lens grows until, under some conditions still being debated, a new ice lens starts to form at a location below the initial one. By eliminating the water accessibility or reducing the hydraulic conductivity of the soil, frost heave is significantly reduced. In other words, the water migration towards the ice lens and its amount are the governing factors that contribute to ice lens development and frost heave under thermal steady state.

Based on experimental evidence this paper proposes a new hypothesis on ice lens growth, in particular on how water migrates towards the growing ice lens. The hypothesis assumes that the water migration from the unfrozen zone towards the ice lens is not a simple one-dimensional process. It is further thought that this new hypothesis may explain the phenomenon of frost heave better and may help in better quantifying the frost susceptibility and frost heave potential of freezing ground.

Ideas Behind Frost Heave Theories

Several theories and ideas have been proposed over the years that describe the thermodynamic processes involved in frost heave. Henry (2000) presents a thorough overview of available frost heave concepts. To date two main concepts are widely used to predict frost heave: (1) the segregation potential (SP) concept that was introduced by Konrad & Morgenstern (1980, 1982) and (2) the discrete ice lens theory proposed by Nixon (1991), which is an extension and modification of the rigid ice model by Gilpin (1980) and O'Neill & Miller (1985). Figure 1 shows the idealized frost heave concept generally used. Under a constant thermal gradient, the warm side of the ice lens at a certain time is at a temperature T_1 slightly colder than the temperature at the pore freezing front at the base of the frozen fringe, the partially frozen zone between the warmest ice lens and the freezing front. Water migrates through the unfrozen zone and the frozen fringe towards the warm side of the ice lens. Under saturated condition it can be assumed that the increase in pore water pressure in the unfrozen zone with depth is constant. At the interface between the ice lens and the water, the thermodynamic equilibrium requires that free energy of the ice equals that of the water. By using the Clapeyron equation, the suction at the interface between the ice and the water can be calculated. For example, if the temperature at the bottom of the ice lens is -0.1°C, the suction is -125 kPa

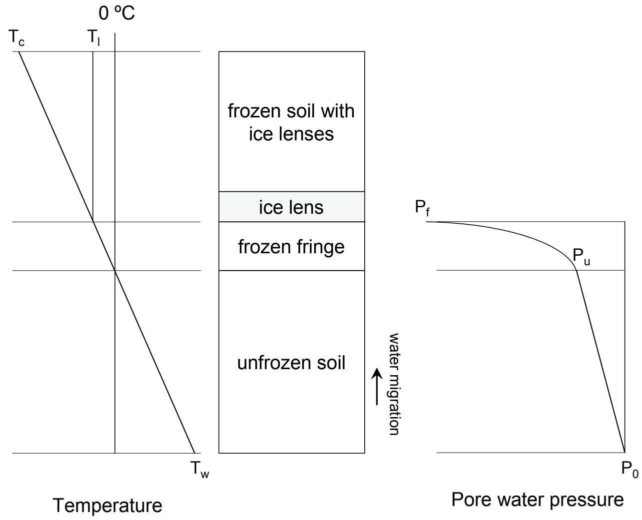

Figure 1. Temperature gradient and pore water pressure distribution und an idealized, one-dimensional ice lens growth scenario after Konrad (1989) and Nixon (1991). Significant suction is noted in the frozen fringe.

and for -0.2°C, the suction is -250 kPa. In order to satisfy the thermodynamic equilibrium, significant suction is required that rapidly decreases within the frozen fringe (Fig. 1).

Experimental Evidence

Recently a series of frost heave tests have beenwere carried out at the University of Alberta using novel visualization techniques. The one-dimensional freezing tests were performed on frost-susceptible Devon silt (Xia 2006). High resolution digital images were further utilized to measure ice lens growth with time under different temperature and stress conditions. Later, particle image velocimetry was applied to measure ice lens growth and soil consolidation during freezing on a microscopic scale (Arenson et al. 2007).

Ice lens structure and growth

The freezing tests clearly demonstrated that ice lens growth is not a simple one-dimensional process, but rather more complex. A snapshot from an early freezing stage (Fig. 2) shows that vertical ice veins precede the formation of the horizontal ice lens. The thin vertical ice vein nearly reaches down to the unfrozen zone through the frozen fringe. Even though the ice veins are not necessarily continuous, they grow more or less vertically on a continuous line. The thin nature of the ice veins makes them difficult to extract using digital image techniques (Fig. 3). However, it can be noted that the thickness of the ice veins does not change much with time in contrast to horizontal ice lenses.

The vertical ice lens structure was also observed when the sample was split at the end of the test (Fig. 4). The vertical ice veins of the frozen segment where well attached to the upper half, whereas a crack pattern was observed in the unfrozen half. The separation of the two halves occurred just below the final horizontal ice lens. In other words one sees on top of the frozen fringe when looking at the unfrozen section

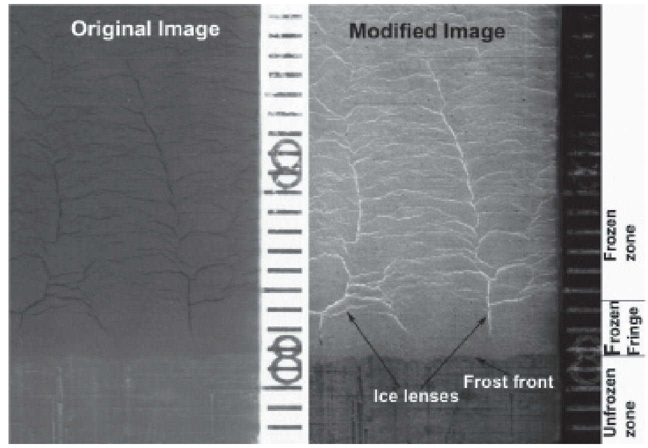

Figure 2. Original and modified image of ice lenses during one-dimensional freezing. The image was taken early during a freezing test at a high cooling rate. Scale in mm (after Xia, 2006).

(e.g., Fig. 4 right). The fact that the unfrozen part could be separated easily from the frozen part with the vertical ice veins attached to the frozen side indicates that there is only a weak bond between the unfrozen soil and the ice within the frozen fringe.

Analysis of the cross section confirms observations that were previously described during observations from the side as the sample froze. A regular pattern of vertical ice veins is formed along the height of the frozen section (Fig. 2). The existence of the vertical ice veins that precede horizontal ice lens formations is not a boundary effect occurring at the outer limit of the circular freezing test. On the contrary, a regular, hexagonal pattern forms throughout the whole cross section. Similar patterns were observed by Mackay (1974, McRoberts & Nixon 1975) for lake and marine clays, glacial tills, and mudflow deposits in permafrost areas of northern Canada. They also provide some theories of the reticulate ice lens growth mainly based on the idea of water being sucked from the clay resulting in suction cracks. Chamberlain and Gow (1979) also presented images of frozen silt that show the reticulate ice structure. They further suggest that there is a direct connection between the vertical ice veins and the vertical hydraulic conductivity of the freezing and frozen soil. However, no evidence or connection is shown between the vertical ice veins and the horizontal ice lenses.

The hexagonal pattern that was observed in the frozen fringe, i.e. the unfrozen side of the sample has a very strong resemblance to drying soils (Fig. 5). The size of the hexagonal elements in the freezing tests further depends on initial conditions, such as consolidation pressure or pore water salinity, and the boundary condition, such as temperature gradient or water availability. Figure 6 shows cross sections from three additional freezing tests. Test #1 (Fig. 4) was consolidated at a vertical pressure of 100 kPa, but frozen at 0 kPa pressure. Tests #4, #5, and #6 in Figure 6, on the other hand, were frozen under the consolidation pressures of 100 kPa, 200 kPa and 400 kPa, respectively. The horizontal ice lens and the frost heave rates decreased with increasing consolidation pressure as expected. In

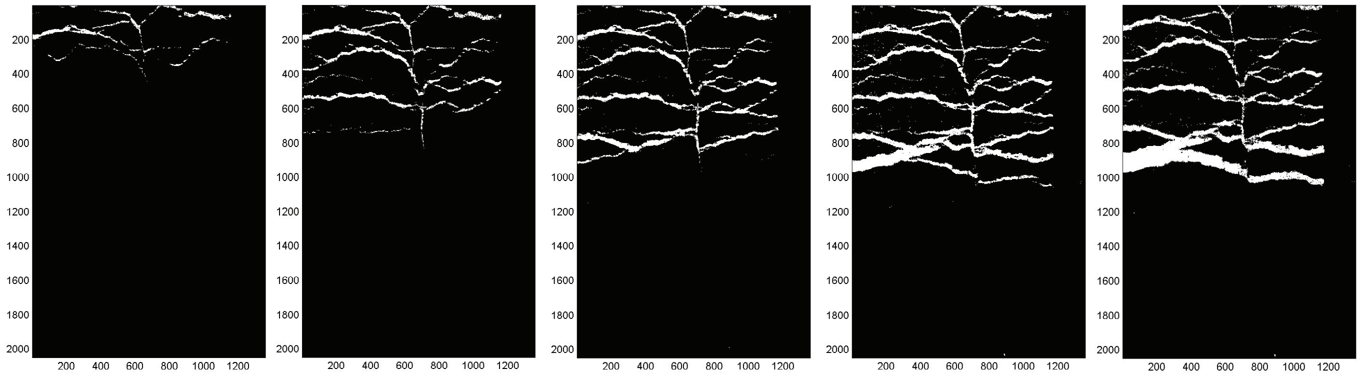

Figure 3. Digitally extracted ice lens structure with time for freezing test. The sequence shows the initiation of the final ice lens (Arenson et al. 2007).

addition, a change in the vertical ice structure can be noted. The size of the hexagonal elements increases with increasing pressure, i.e. the distance between the vertical ice veins increases. This was also visible in the pictures taken from the side of the freezing cell. The change in element size can be quantified by counting the number of full elements within a 50 mm x 50 mm square in the centre of the cross section. Even though the measure is quite rough it shows that with decreasing number of elements, i.e. increasing distance between the vertical ice veins, the final ice lens growth rate decreases. Test #1 and #4 showed similar heave rates of $2.64 \cdot 10^{-6}$ mm/s and Test #5 and #6 displayed values of 1.53 and $1.51 \cdot 10^{-6}$ mm/s, respectively (Xia 2006). The element count gives 18, 17, 11 and 10 hexagonal elements in the centre of the cross section. Even though only four tests are available the trend is convincing.

Hydraulic conductivity and water demand

The one-dimensional ice lens growth hypothesis assumes that all the water at the base of the growing ice lens migrates from the unfrozen soil through the partially frozen soil in the frozen fringe. Experiments on the hydraulic conductivity of partially frozen soils have shown that the permeability decreases rapidly as soon as pore ice forms (Aguirre-Puente and Gruson, 1983; Chamberlain and Gow, 1979; Konrad and Samson, 2000a; Konrad and Samson, 2000b; Williams and Burt, 1974). This reduction is caused by the decrease in void ratio as the pore water freezes and water migration to an ice lens is hindered. Williams and Burt (1974) present data for hydraulic conductivities *k* of silt as a function of temperature that show the rapid decrease in *k* from 10^{-6} m/s at -0.1°C to 10^{-11} m/s at -0.4°C, i.e. 5 orders of magnitude for 0.3°C temperature change. This decrease is not linear. A decrease of four orders of magnitude was actually recorded for the temperature drop from -0.1°C to -0.2°C. Similar trends were obtained by Horoguchi & Miller (1980). They further show a hysteresis effect that depends on whether the silt undergoes freezing or thawing. The hydraulic conductivities of the frozen silt (4-8μ) measured by Horoguchi & Miller (1980) ranged from $2 \cdot 10^{-8}$ m/s (0°C) to 10^{-12} m/s (-0.15°C). The rate of Williams & Burt (1974) are probably affected by the presence of lactose used in their experimental setup, indicating the challenges in measuring the hydraulic conductivity for partially frozen soils.

The authors are not aware of any experimental study that measures the hydraulic conductivity in the frozen fringe. A simple approach is therefore used to estimate the change in hydraulic conductivity *k* within the frozen fringe based on the soil-water characteristic curve (SWCC). Because the freezing process is somewhat similar to the drying process, the SWCC approach was judged to be suitable to estimate this change. The problem of using temperature dependent approximations, such as the temperature dependent permeability function suggested by Gilpin (1980), is that three-dimensional effects are excluded, and vertical flow of water from the unfrozen zone towards the growing ice lens is implied.

The Devon silt used for these investigations has an unfrozen, saturated hydraulic conductivity of $9.9 \cdot 10^{-10}$ m/s at an effective stress of 100 kPa. The moisture content at saturation was 26% with a porosity *n* of 40% (Xia, 2006). The volumetric water content changes in the frozen fringe when suction builds up (Fig. 1). Hence, the hydraulic conductivity changes. The hydraulic conductivity can, for example, be calculated after Fredlund and Xing (1994). The following parameters were utilized to calculate the hydraulic conductivity distribution (Fig. 7):

$a = 1.948$	parameter for Fredlund and Xing (1994)
$n = 2.708$	"
$m = 1.084$	"
$k_{sat} = 9.9 \times 10^{-10}$ m/s	saturated hydr. conductivity
$\theta = 15.6\%$	saturated vol. water content

The water requirement at the final ice lens can be calculated from the ice lens growth rate. For test #1 2.9×10^{-9} m³/s has to migrate from the unfrozen zone through the frozen fringe. Konrad (1994) showed that for temperatures close to 0°, theoretically the suction at an ice lens under atmospheric pressure increases linearly with decreasing temperature at a rate of 1250 kPa/°C. In test #1, a temperature gradient of 0.058°C/mm is applied at thermal steady state. With a frozen fringe thickness of 6 mm, the suction at the ice lens base is estimated to 438 kPa to satisfy the thermodynamic

Figure 4. Hexagonal structure of the vertical ice lenses. The frozen section is on the left, the unfrozen section on the right. The sample diameter is about 100 mm (Xia 2006).

Figure 5. Cracked earth inside the Ubehebe Crater, California (www.tawbaware.com).

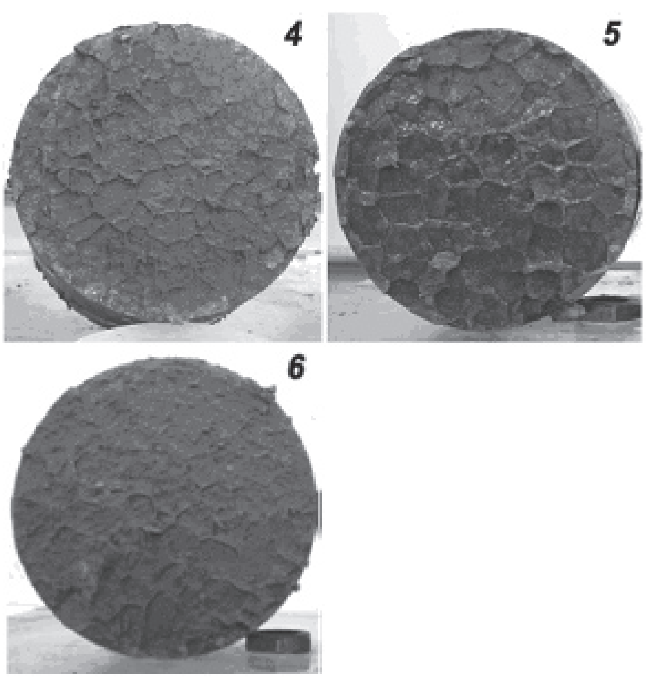

Figure 6. Cross sections after freezing for tests under different vertical pressure: #4: 100 kPa, #5: 200 kPa, #6: 400 kPa.

equilibrium. In an unfrozen state such suction would reduce the hydraulic conductivity in the Devon silt by more than 70%.

In order to estimate the amount of water flowing through the frozen fringe, an average value had to be determined. The average hydraulic conductivity k_{mv} can be calculated by assuming flow through a series of layers with changing hydraulic permeability and using Equation 1:

$$k_{mv} = \frac{\sum d_i}{\sum \frac{d_i}{k_i}} \tag{1}$$

Where d_i is the layer thickness and k_i the permeability. An exponential decrease in pore water pressure is further assumed in the frozen fringe towards the ice lens with no suction at the freezing front. This is a conservative approach since suction is most likely to penetrate into the unfrozen soil (Seto & Konrad 1994). Under these conditions, k_{mv} = 1.7 x 10^{-16} m/s, and a minimum of 8 x 10^{-18} m/s at the ice lens is determined for the frozen fringe in test #1 (Fig. 8). Utilizing Darcy's law a hydraulic gradient can be estimated. The average hydraulic gradient required in order to attract the necessary amount of water would be 17 x 10^6. This is significantly higher than the hydraulic gradient (~7000) that can be generated over the frozen fringe with a suction of 438 kPa.

Using the suction development at the ice lens and the SWCC may underestimate the hydraulic conductivity of the soil. However, even if the minimum hydraulic conductivity was capped at 1 x 10^{-14} m/s, the gradient would be in the order of 80,000. Such a cap would represent values measured for hydraulic permeability in frozen soils (Williams & Burt 1974).

Even though several assumptions had to be made that need further confirmation, and it may even be possible that the suction generated at the ice lens is capable of attracting enough water towards the ice lens, some concerns remain. If the suction reaches values of approximately 900 kPa it is possible that cavitation occurs under atmospheric conditions, i.e. as it reaches its vapor pressure, the pore fluid vaporizes and forms small bubbles of gas. According to the authors' knowledge no experimental evidence is available that shows the formation of gas bubbles at an ice lens.

New Ice Lens Growth Hypothesis

Based on recent laboratory investigations a new concept behind ice lens growth and frost heave is proposed. In 1979, Chamberlain & Gow (1979) presented similar ideas and experimental evidences. They showed that freezing and thawing caused a reduction in void ratio and an increase in vertical conductivity. The later was attributed to the formation of polygonal shrinkage cracks. However, no definite relationship could be established and the mechanisms observed have not been connected to ice lens formation and growth.

The new idea is based on water flow along vertical ice

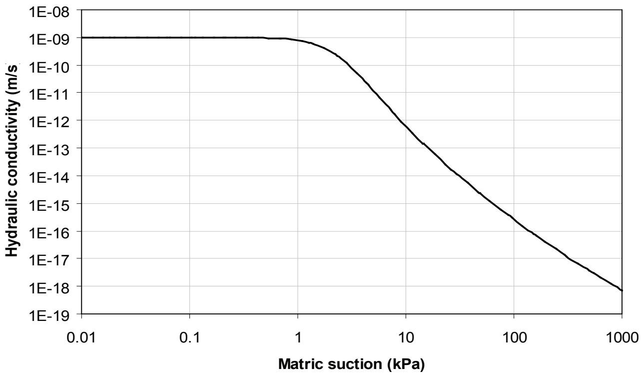

Figure 7. Hydraulic conductivity as a function of suction. Curve determined after Fredlund and Xing (1994).

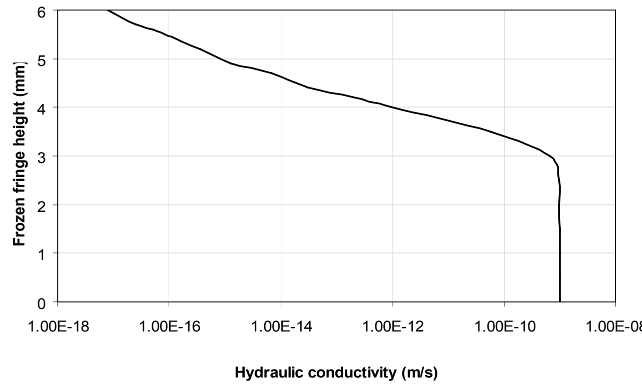

Figure 8. Hydraulic conductivity in the frozen fringe.

veins. As suction builds within the frozen fringe and the unfrozen soil below the freezing front, the soil reaching its tensile strength resulting in thin vertical cracks. These cracks are originally filled with water but will freeze rapidly as the freezing front penetrates. Between the vertical ice vein and the soil, a water film forms. This film is not the same as a water film that would form around a soil particle at thermal steady state, and may only be 60–100 nm thick at 0.1°C.

Instead of a one-dimensional water flow through the frozen fringe, that has a low hydraulic conductivity, water from the unfrozen zone migrates along the vertical ice veins towards the growing horizontal ice lens. By assuming laminar, incompressible, steady flow between two parallel plates (e.g., Streeter and Wylie 1985), a layer of 3 μm and a suction of 100 kPa would be enough to allow the necessary amount of water flow towards the ice lens in test #1. This simple calculation shows that significantly more water can migrate from the unfrozen soil to the growing ice lens along these ice veins at a much lower suction gradient than if it has to migrate through partially frozen pores of the frozen fringe. The thickness of the vertical ice lens did not change with time. It is assumed that no ice accumulation occurs because of the moving water film at the interface between the soil and the ice. Further, there is no major heat loss perpendicular to the ice vein that could lead to horizontal crystal growth. Figure 9 shows a schematic of the flow scheme based on this new concept.

Because water flow along vertical ice lenses controls the amount of water that migrates through the frozen fringe, it is basically the tensile strength of the soil at a certain stress state that governs ice lens growth. In order to attract sufficient water the suction may reach values that would cause tension cracking of the soil below the warmest ice lens. With a higher tensile strength, fewer vertical cracks can form, and therefore a lower number of preferential flow paths are available for water to migrate towards the ice lens. The application of a vertical stress, for example, changes the stress state of the Devon silt resulting in fewer cracks and therefore slower frost heave.

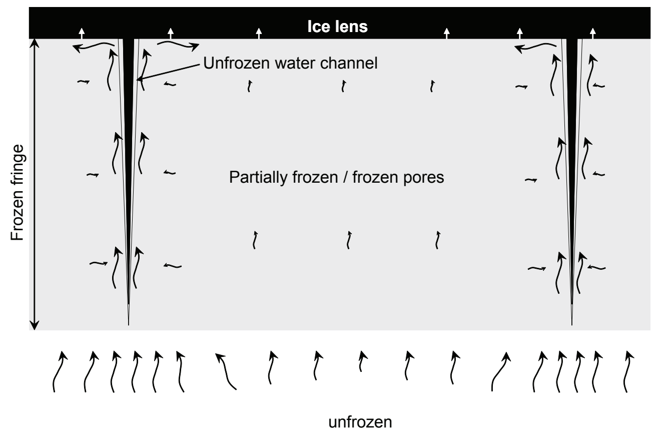

Figure 9. Water migration in freezing soils.

Conclusions

Based on experimental evidence a new hypothesis for a frost heave mechanism is proposed. The existence of vertical channels can explain the measured growth of the horizontal ice lenses considering the consolidation and the decreasing hydraulic conductivity in the frozen fringe. To date it is not clear how these vertical ice veins and water channels form. The tensile strength of the unfrozen soil may be reached as suction occurs. In addition, strain compatibility in the consolidation soil may also trigger the formation of vertical cracks.

However, the stress state and tensile strength of a soil basically govern ice lens growth because they controls the number of vertical cracks and vertical ice lenses that form in the frozen fringe.

A new series of one-dimensional freezing tests is currently being carried out at the University of Alberta Geotechnical Centre to improve our understanding of the hypothesis presented. The relationship between the hexagonal element sizes and frost heave rate will be studied in more detail using different soils as well as saline pore water. Saline pore water is known to change the size and shape of the ice lens pattern as well as the frost heave behavior (Arenson et al. 2006). The goal of this future research is to couple the tensile strength of a soil directly with frost heave potential.

Even though intense research has to be carried out in the future to support these ideas, the authors believe that it is time to move from a one-dimensional frost heave model towards a three-dimensional concept, even for one-dimensional freezing conditions.

Acknowledgments

The authors wish to acknowledge the valuable contributions obtained from three independent reviewers. They would further like to thank Andy Take from Queen's University for his support with the GeoPIV analysis. Tezera Firew Azmatch appreciated the financial support through the NSERC Discovery Grant held by Dr. Sego.

References

Aguirre-Puente, J. & Gruson, J. 1983. Measurement of permeabilities of frozen soils. In: T.L. Péwé and J. Brown (eds.), *4th International Conference on Permafrost, Fairbanks, AK, United States, July 17-22, 1983*: 5-9.

Arenson, L.U., Sego, D.C. & Take, W.A. 2007. Measurement of ice lens growth and soil consoliodation during frost penetration using particle image velocimetry (PIV), *60th Canadian Geotechnical Conference, Ottawa, ON*: 2046-2053.

Arenson, L.U., Xia, D., Sego, D.C. & Biggar, K.W. 2006. Change in ice lens formation for saline and non-saline Devon silt as a function of temperature and pressure. In: M. Davies & J.E. Zufelt (eds.), 1*3th International Conference on Cold Regions Engineering. American Society of Civil Engineers (ASCE), Orono, Maine, USA*: CD-Rom.

Beskow, G. 1935. Soil freezing and frost heaving with special applications to roads and railroads. *Swedish Geological Society, C, No. 375, Year Book No. 3*, Cold Region Research and Engineering Laboratory, Special Report 91-23: 41-157.

Chamberlain, E.J. & Gow, A.J. 1979. Effect of freezing and thawing on the permeability and structure of soils. *Engineering Geology* 13(1-4): 73-92.

Fredlund, D.G. & Xing, A.Q. 1994. Equations for the soil-water characteristic curve. *Canadian Geotechnical Journal* 31(4): 521-532.

Gilpin, R.R. 1980. A model for prediction of ice lensing and frost heave in soils. *Water Resources Research*, 16(5): 918-930.

Henry, K.S. 2000. *A Review of the Thermodynamics of Frost Heave.* CRREL Technical Report (TR 00-16): 25.

Horiguchi, K. & Miller, R.D., 1980. Experimental studies with frozen soil in an "ice sandwich" permeameter. *Cold Regions Science and Technology* 3(2-3): 177-183.

Konrad, J.M. 1989. Pore water-pressure at an ice lens: Its measurement and interpretation. *Cold Regions Science and Technology* 16(1): 63-74.

Konrad, J.M. 1994. 16th Canadian Geotechnical Colloquium - Frost Heave in Soils - Concepts and Engineering. *Canadian Geotechnical Journal* 31(2): 223-245.

Konrad, J.M. & Morgenstern, N.R. 1980. A mechanistic theory of ice lens formation in fine-grained soils. *Canadian Geotechnical Journal* 17(4): 473-486.

Konrad, J.M. & Morgenstern, N.R. 1982. Effects of applied pressure on freezing soils. *Canadian Geotechnical Journal* 19(4): 494-505.

Konrad, J.M. & Samson, M. 2000a. Hydraulic conductivity of kaolinite-silt mixtures subjected to closed-system freezing and thaw consolidation. *Canadian Geotechnical Journal* 37(4): 857-869.

Konrad, J.M. & Samson, M. 2000b. Influence of freezing temperature on hydraulic conductivity of silty clay. *Journal of Geotechnical and Geoenvironmental Engineering* 126(2): 180-187.

Mackay, J.R. 1974. Reticulate ice veins in permafrost, Northern Canada. *Canadian Geotechnical Journal* 11(2): 230-237.

McRoberts, E.C. & Nixon, J.F. 1975. Reticulate ice veins in permafrost, Northern Canada - Discussion. *Canadian Geotechnical Journal* 12(1): 159-162.

Miller, R.D. 1973. Soil freezing in relation to pore water pressure and temperature, *Second International Conference of Permafrost. Natl. Acad. Sci., Washington., Yakutsk, Siberia*: 344–352.

Nixon, J.F.D. 1991. Discrete ice lens theory for frost heave in soils. *Canadian Geotechnical Journal* 28(6): 843-859.

O'Neill, K. & Miller, R.D. 1985. Exploration of a rigid ice model of frozet heave. *Water Resources Research* 21(3): 281-296.

Penner, E. 1959. *The Mechanism of Frost Heaving in Soils.* Bulletin 225, U.S. Highway Research Board.

Penner, E. 1972. *Influence of Freezing Rate on Frost Heaving*. Highway Research Record 393, U.S. Highway Research Board.

Seto, J.T.C. & Konrad, J.M. 1994. Pore pressure measurements during freezing of an overconsolidated clayey silt. *Cold Regions Science and Technology* 22(4): 319-338.

Streeter, V.L. & Wylie, E.B. 1985. *Fluid Mechanics*. McGraw-Hill Book Company, 586 pp.

Taber, S. 1929. Frost heaving. *Journal of Geology* 37(5): 428-461.

Taber, S. 1930. The mechanics of frost heaving. *Journal of Geology* 38: 303-317.

Williams, P.J. & Burt, T.P. 1974. Measurement of hydraulic conductivity of frozen soils. *Canadian Geotechnical Journal* 11(4): 647-650.

Xia, D. 2006. *Frost Heave Studies Using Digital Photographic Technique.* M.S. Thesis. Edmonton, AB, Canada: University of Alberta, 165 pp.

Impact of the August 2000 Storm on the Soil Thermal Regime, Alaska North Slope

David E. Atkinson
International Arctic Research Center, University of Alaska Fairbanks, Fairbanks, Alaska 99775, USA
Larry Hinzman
International Arctic Research Center, University of Alaska Fairbanks, Fairbanks, Alaska 99775, USA

Abstract

The impact of a severe Alaska North Slope storm (August 2000) on the ground thermal regime along a north-south/coastal-inland transect was investigated. Using data gathered by the Water and Engineering Research Center at the University of Alaska Fairbanks, the storm was found to have a strong and widespread effect. Briefly, the storm initiated rapid cooling that was fairly uniformly expressed at all sites, despite their varying distances from the coast. At all of the sites 30 cm ground temperature dropped from 4°C to 1°C which, at the coastal sites, did not return to pre-storm summer levels before the initiation of winter despite two subsequent warm periods.

Keywords: Alaska; arctic storms; coastal; ground thermal regime.

Introduction

Storms in the arctic coastal zones have well-documented impacts on infrastructure and coastal morphometry via waves and storm surges (Rahold et al. 2005); however, the associated impacts on the ground thermal regime are not well documented. Gaining further insight into this issue is especially important in ice-rich regions where the seasonal freeze-thaw cycle is a critical underpinning to many derivative studies. A primary impact of storm passage is a rapid cooling of the entire active layer. This can act to prematurely shorten the thaw season by initiating early fall cooling. Focusing on a particularly severe storm (August 2000) and using a north-south/coastal-interior transect of meteorological and ground temperature data, this issue, one that has received virtually no specific treatment in the literature, is explored in detail.

The North Slope storm of August 10–12, 2000

In August of 2000, a strong storm moved from the north Chukotka coast, across the Chukchi Sea over to Alaska, and eastward along the North Slope coast. The storm strengthened to 996 millibars by August 11, when its center was positioned north of Prudhoe Bay (Fig. 1), and it developed a very strong pressure gradient to the west. The strong pressure gradient generated observed winds of 70 kts (36m/s), which caused the storm to develop heavy sea states that included a moderate surge and high waves. This event caused $7.7 million dollars in infrastructure damages along the North Slope, including the sinking of a barge (Koslow 2000). Unusual for Alaska, this event also caused substantial wind damage in the form of roof failure on many structures in Barrow.

The strength and orientation of the storm circulation (Fig. 2) allowed it to tap into a cold air mass situated over the mid/north Beaufort Sea (Fig. 3) and to draw it over and well south into the north Alaskan landmass. This rapid influx of cold air reduced air temperatures by up to 10°C in coastal areas (Fig. 4), from well above zero in the +6°C to +8°C range to below the freezing point, within a day.

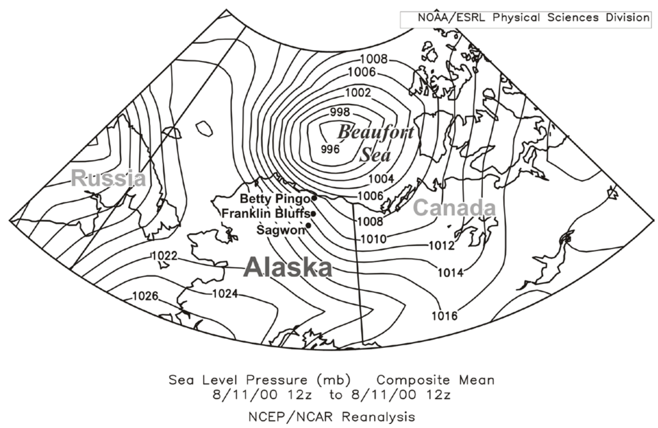

Figure 1. A plot of surface mean sea level pressure showing the August 2000 storm at peak intensity, 0300 AKT on August 11, 2000. The three ground temperature sites from which ground thermal and meteorological data were drawn are indicated. These locations are operated by the Water and Engineering Research Center at the University of Alaska Fairbanks as part of the "Kuparuk River Watershed Studies" project. Note closely-spaced pressure contours to the west of storm center. This flow pattern advected cold air over the North Slope region. (Pressure pattern data from the National Centers for Environmental Prediction/Department of Energy Reanalysis II, plotted at the National Oceanic and Atmospheric Administration's Earth Systems Research Laboratory [NOAA-ESRL]). AKT refers to Alaska Time.

Given its effect on air temperatures, the influx of cold air also likely had an impact on the ground thermal regime. It is the objective of this paper to examine the nature of this response at several locations in the North Slope of Alaska and to assess its possible impact at the seasonal time-frame.

Data and Methods

Meteorological and ground temperature data were obtained from monitoring sites operated as part of the Kuparuk River Watershed project by the Water and Engineering Research Center (WERC) at the University of Alaska Fairbanks (Kane & Hinzman 2000, Kane et al. 2000, Romanovsky

Table 1: The three main locations from which soil temperature profile data were drawn. The abbreviation for each station used in the text is given.

Site	*Sub-sites*	*Distance to coast (Prudhoe Bay)*
Betty Pingo	Upland (BPU)	12 km
	Wetland (BPW)	
Franklin Bluffs (FB)	--	70km
Sagwon (SW)	--	100km

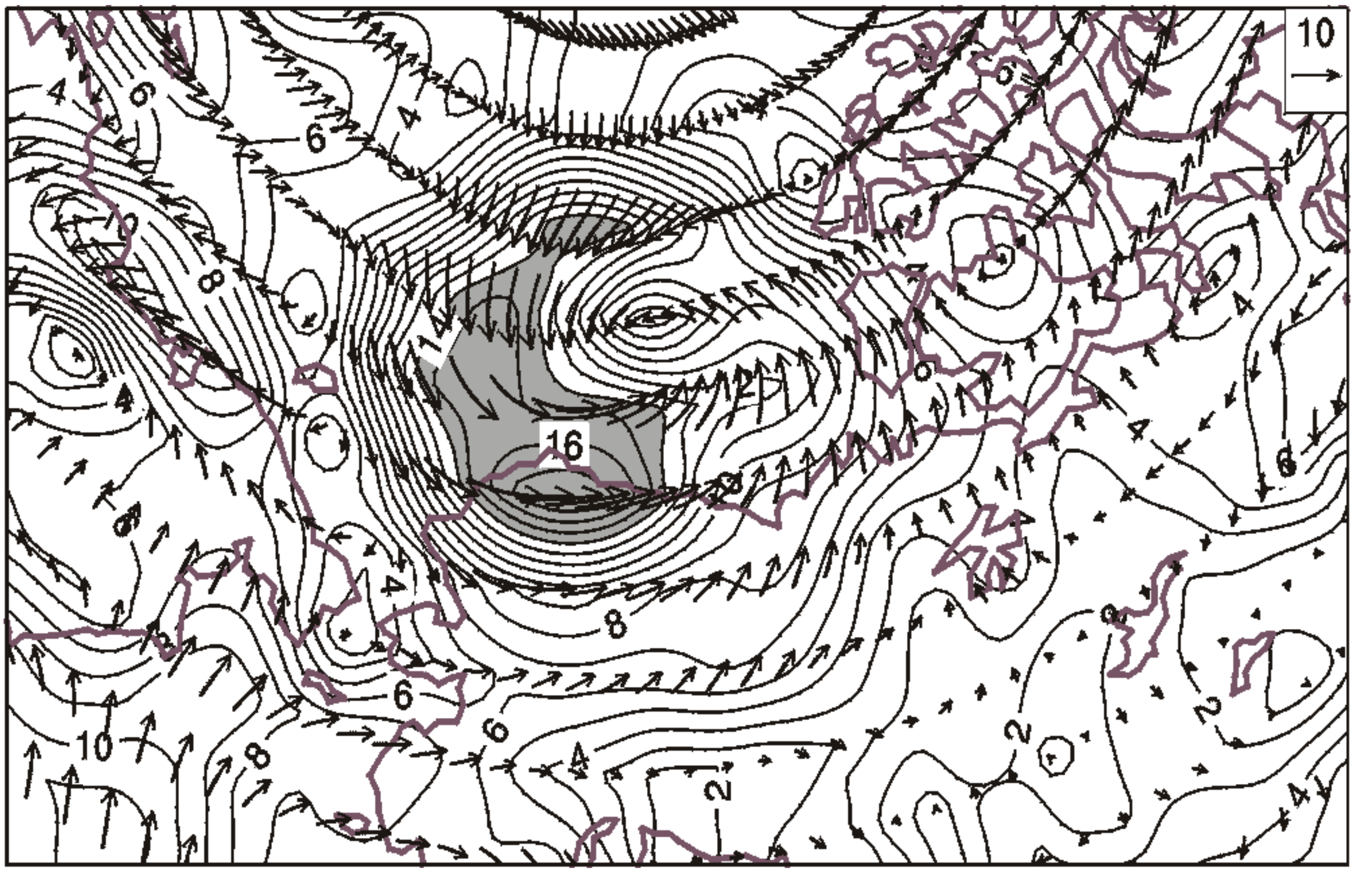

Figure 2. Wind speed isotachs (m/s) and direction vectors at the height of the storm (Aug. 10, 2100AKT). Shaded zone represents wind speeds exceeding 14 m/s.

& Osterkamp 2006). Four data sets were used from three separate locations (Table 1, Fig. 1).

This sampling methodology allowed a north-south transect to be examined with the three locations at successively greater distances from the coast. Storm winds and the strength of an advective temperature change can decrease with distance away from the coast due to a reduction of wind speed, brought about by increased surface roughness, and reduction of air/ground temperature gradient due to a longer exposure of the air mass to the modifying effects of the surface underneath (Wallace & Hobbs 2006, 404). In addition, the two locations at the Betty Pingo site allowed comparisons to be made between a saturated ("Wetland site") and non-saturated ("Upland site") ground. Data are available online at the WERC website (Kane & Hinzman 2000).

Analysis consisted of a direct examination of selected time series and a comparison between sites and between specific elements for the period of time surrounding the storm to determine timing and magnitude of temperature change at different levels. This was performed using a comprehensive plot on which time series from the four stations were laid out side-by-side (Fig. 5). Ground thermal data were recorded hourly at BPU and BPW and once daily at the FB and SW locations. At all locations, meteorological data were recorded once per hour; however, they were subset to once per day at FB and SW for comparison with the ground thermal data.

Results

The ground thermal regime at BPW and BPU responded rapidly to the initiation of cold air advection by the storm winds. The regular daytime cooling that was underway by mid-afternoon, August 10 (all time references are local time) was extended well below the daytime minimum (approximately 6–7°C) at the two sites compared to the preceding days. This coincided with the establishment of

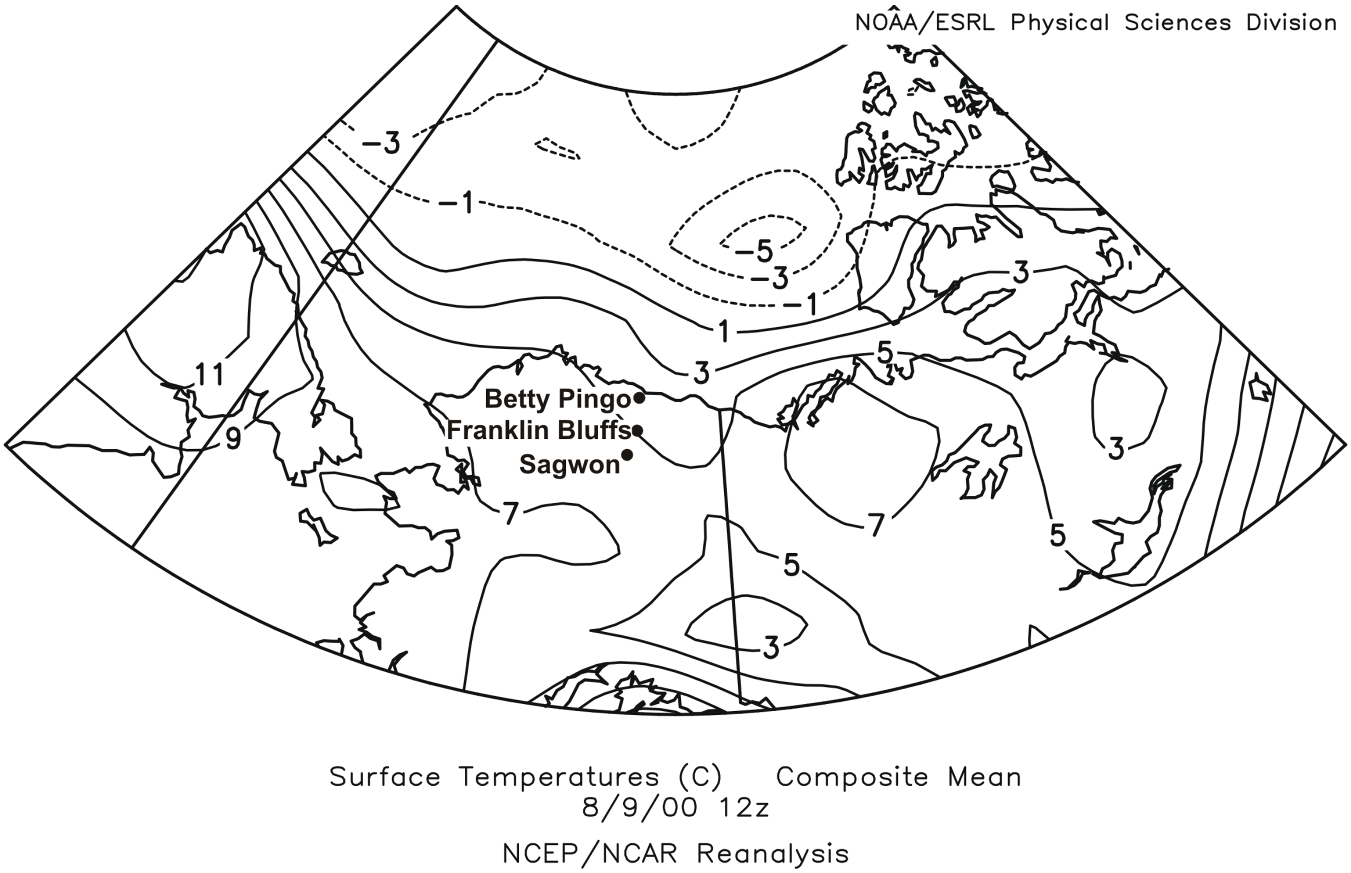

Figure 3: Surface air temperature distribution two days before the storm. Dashed isotherms indicate negative temperatures. Note the cold zone over the north/west Beaufort (circled). Rapid advection of this air mass along the trajectory indicated by the heavy arrow occurred as the storm moved along the north coast.

strong, persistent winds out of the west (Fig. 6 – BPU and BPW). At BPW air temperatures dropped 16°C, to -2°C, within one day and then dropped further the next day. The 5 cm soil depth temperature responded with a drop from ~7°C to 2°C in a 36-hour period. The 30 cm soil depth temperature dropped from 4°C to 2°C, and then further, down to 1°C, over the next few days. Similar patterns were observed at BPU, although at this location the air temperature drop was not as large, which meant the corresponding decrease in ground temperatures occurred slightly later. The main response difference observed between the BP wetland and upland sites was that soil temperatures at the wetland site exhibited a greater sensitivity to the air temperature forcing, especially 30 cm depth, from 5°C to 1°C at the upland site, whereas at the wetland site the 30 cm temperature change was from 4°C to 1.5°C. This is despite the fact that the upland site sensor is positioned slightly deeper, at 35 cm, and not 30cm. It was interesting to note, however, that the temperature drop at the 5 cm depth was greater at the wetland site, from 8°C to 2°C, whereas at the upland site, the 5 cm temperature change was from 7°C to 2°C.

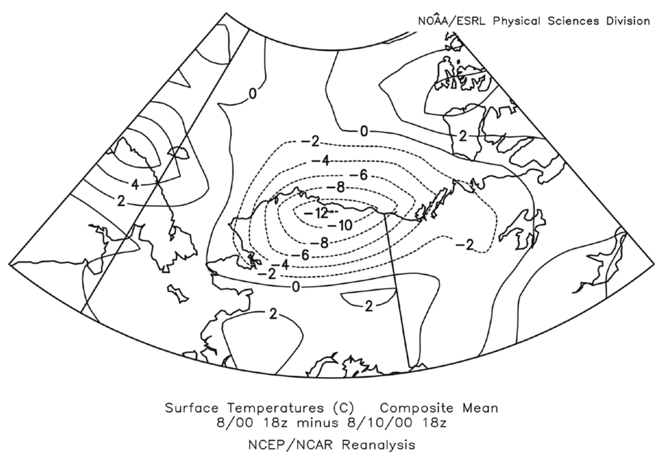

Figure 4. Surface air temperature difference plot, Aug. 11, 0900 AKT minus Aug. 10, 0900 AKT. This indicates the magnitude of temperature change in a 24-hour period over the north Alaska landmass. Dashed lines indicate negative temperature isotherms.

The data availably at FB and SW limited the detail of analysis but the major patterns were apparent. The same pattern of wind speed and direction observed at the BP sites prevailed at FB and SW—a strong peak in wind speeds developed out of the west. Although the two sites started with different air temperatures, at both locations air temperature had dropped to -2°C by the second day, representing decreases of 12°C (FB) and 10°C (SW). At both sites a drop in the 5 cm soil temperatures from 6°C to 2°C (FB) and from 9°C to ~1°C (SW) was observed, and in the 30 cm soil temperatures from 4°C to 1°C was observed.

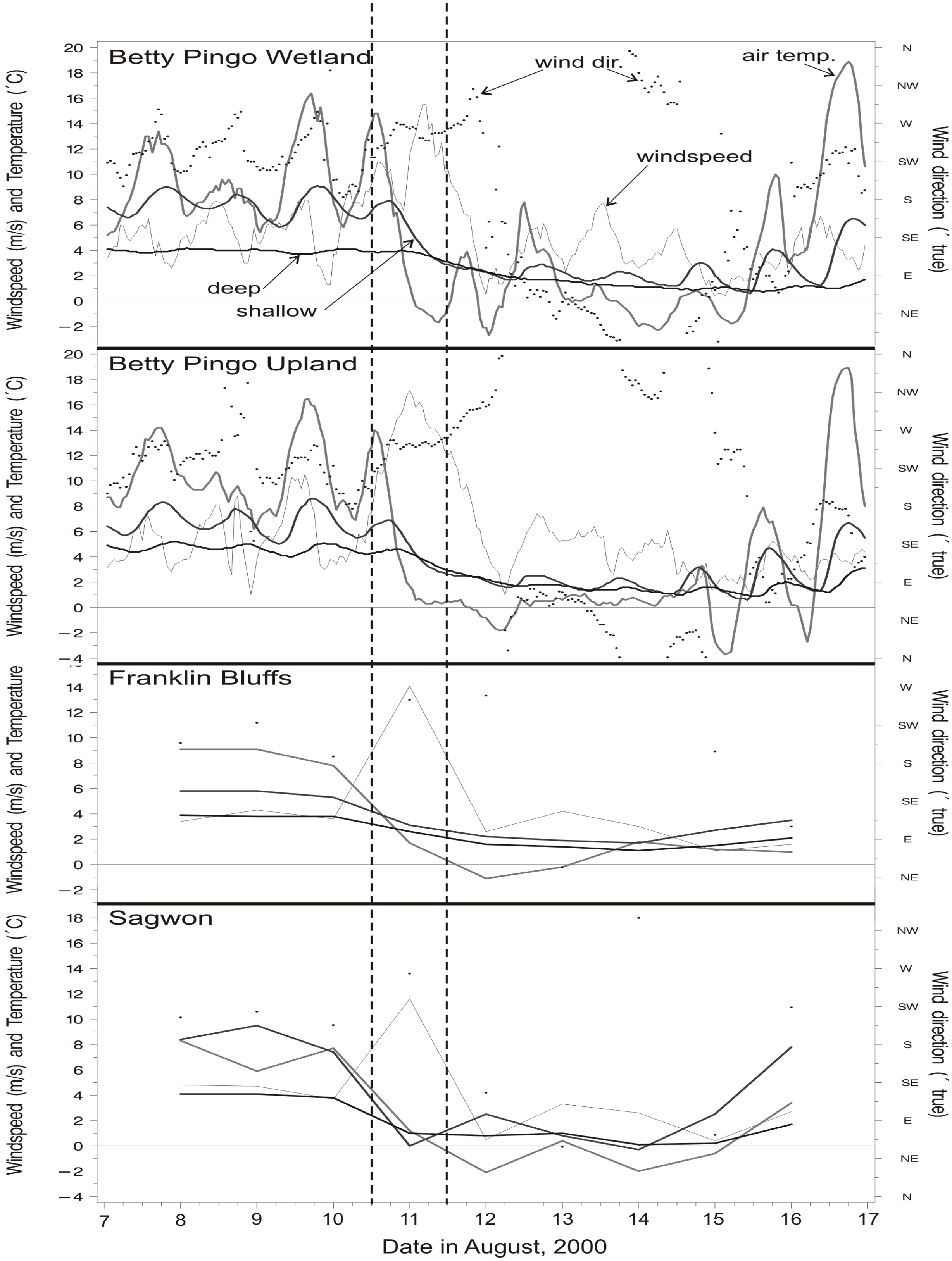

Figure 5. Winds, air temperature, and ground temperatures at the four sites. The following formatting scheme is applied to each plot: the dots represent wind direction observations in degrees true heading (vertical scale on the right), the thin black line represents wind speed (m/s), the thick light grey line represents air temperature (°C), the thick medium grey line represents a "shallow" ground temperature (°C), the thick black line represents a "deep" ground temperature (°C). The distinction "shallow" refers to the 5 cm soil depth at all sites and "deep" refers to 30 cm soil depth at all sites except Betty Upland, where it is 35 cm depth. The two vertical dashed lines represent the core of the storm from 1200 AKT, August 10 to 1200 AKT, August 11, 2007.

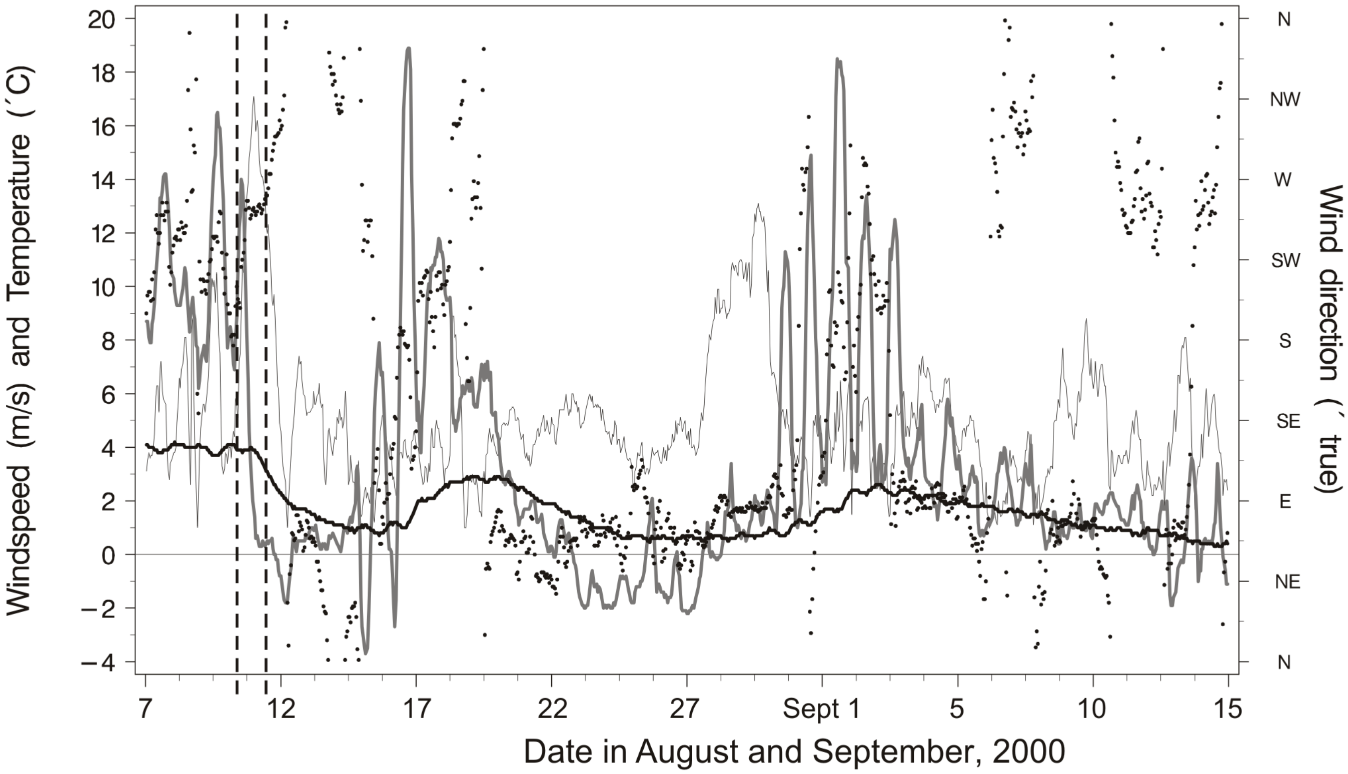

Figure 6. Wind speed and direction, air temperature, and 30 cm ground temperature at Betty Pingo Wetland. Storm time frame is indicated by the vertical dashed lines. Line schema is identical to that used in Figure 5.

Discussion and Conclusions

Examination of the longer-term implications of the storm-induced temperature drop at BPW site shows that, despite two very warm spells (air temperatures >15°C), the temperature at 30 cm does not again reach its summer levels (Fig. 7). This suggests that the influx of cold air from the storm was sufficient to set the stage for winter freeze-up; that is, it may be argued that without the contribution of this storm event, ground freeze-up would have occurred later in the fall. A more frequent occurrence of such storm events, which might accompany conditions of reduced sea-ice cover, could have the paradoxical effect of checking a summer ground thermal warming trend. Cooling did not seem to be quite as prominent at the inland sites (not shown): during the two warm episodes, 30 cm temperatures did warm to return almost to their pre-storm levels, although, as noted below, all sites cooled to a uniform extent.

Overall, the reach of the storm was considerable—marked effects on ground thermal regime were noted 100 km inland at Sagwon site, situated effectively at the foothills of the Brooks Range. Typically when an air mass is advected a long way over a surface, the lowest atmospheric layers begin to take on the temperature and moisture characteristics of the surface. In this case, that means the air mass should warm as it moves inland. However, the lowest air temperature reached during the event (start of August 12) at all four sites—that is, ~-2°C, was essentially the same. The ground thermal response was likewise uniform: at all sites the 30 cm soil temperature dropped to 1°C. This is indicative of the strength and persistence of the wind, that the air was moved so rapidly into the region that it underwent little modification in its lowest layers. Even though the peak wind speeds were progressively lower with increasing distance inland, they were still sufficient to move the advected air rapidly enough. Thus this one event affected soil temperatures to at least 30 cm depth over the bulk of the Alaska North Slope.

It is important to note that this particular event possessed unusual strength, which means it is unlikely that similar events observed on the north coast would be exert an influence as far inland as this event did. This is a question, however, that should be pursued in more detail to better understand the potential of increased summer storm activity on the ground thermal regime of the Alaska North Slope. It is clear that broader consideration of advected air masses and their relative frequency of occurrence over time could be a useful component of ground thermal regime to consider in more detail.

References

Kane, D.L., Hinzman, L.D., McNamara, J.P., Zhang, Z. & Benson, C.S. 2000. An Overview of a Nested Watershed Study in Arctic Alaska. *Nordic Hydrology* 31: 245-266.

Kane, D.L. & Hinzman, L.D. 2000. *Climate data from the North Slope Hydrology Research project*. University of Alaska Fairbanks, Water and Environmental Research Center. http://www.uaf.edu/water/projects/NorthSlope/ Fairbanks, Alaska, variously paged.

Koslow, M. 2000. *Climatology of Low Pressure Systems near Barrow, Alaska*. Unpublished monograph. University of Colorado, 18 pp.

Rahold, V., Are, F.E., Atkinson, D.E., Cherkashov, G. & Solomon, S.M. 2005. Arctic Coastal Dynamics: an introduction. *GeoMarine Letters* 25: 2-3.

Romanovsky, V. & Osterkamp, T. 2006. Interannual variations of the thermal regime of the active layer and near-surface permafrost in northern Alaska. *Permafrost and Periglacial Processes* 6: 316-335.

Wallace, J.M. & Hobbs, P.V. 2006. *Atmospheric Science: An Introductory Survey* (2nd ed.). New York: Academic Press, 483pp.

Global Simulation of Permafrost Distribution in the Past, Present, and Future Using the Frost Number Method

Tim Aus der Beek, Ellen Teichert
CESR, Center for Environmental Systems Research, University of Kassel, Germany

Abstract

Currently, about 39 mil km² of the world (including Antarctica) are covered by permafrost. One aim of this modeling experiment is to compare the current global permafrost distribution with its extent in the past and in future projections by integrating the well-known Frost Number method into the global hydrological and water-use model WaterGAP. The Frost Number is related to the zonal arrangement of permafrost and was slightly modified to test its receptivity of different snow parameter formulations. For past extents the Frost Number was averaged for 1901–1930 and set in contrast to present permafrost spreading (1971–2000). The future time slice was computed by averaging permafrost extent for 2071–2100, and was yet again compared with present and past permafrost extents. From the wide variety of climate scenarios, two contrasting IPCC-SRES scenarios, A1B and B1, were chosen. CO_2 and CH_4 feedback loops of melting permafrost were not considered in the model. To account for the specific variability of General Circulation Models (GCMs), two different GCMs were applied for both IPCC-SRES scenarios. Model results imply that the area of global permafrost occurrence decreased by 7% between past and present conditions, and future scenarios project that 30%–45% of the contemporary extent could be diminished by 2100. The application of different snow-parameter formulations yielded only minor changes in the quantification of the Frost Number.

Keywords: climate scenarios; Frost Number; global modeling; permafrost distribution; WaterGAP.

Introduction

The well-known Frost Number has proven its suitability for application to large geographical domains (Anisimov & Nelson 1997), but has never been operated on the global scale. The study presented hereby examines permafrost spreading on the global scale and, contrary to most other modeling efforts, considers three different time periods between 1901 and 2100. Future permafrost zonation is also used to roughly estimate the increase of atmospheric carbon content, released from formerly frozen grounds. The Frost Number method has been applied to several regions, such as the Northern Hemisphere (Anisimov & Nelson 1997), and has proven its suitability for the prediction of permafrost over large geographical domains by comparison with hard data (Anisimov & Nelson 1997). The Frost Number applied in this study relies on freezing and thawing indices based on air temperature (Frauenfeld et al. 2007) instead of modeled soil temperature, as in Stendel & Christensen (2002) or Lawrence & Slater (2005). Therefore, soil water processes and relic permafrost are not considered in the model.

Snow density, which is supposed to be crucial for the computation of snow cover and thus permafrost occurrence, was kept constant in earlier analyses (Anisimov & Nelson 1997). This model experiment also tests the variability of the Frost Number method by employing a snow-density routine. Furthermore, it introduces two different algorithms for the calculation of thermal conductivity of snow.

Methods

WaterGAP and data

To allow for a global application of the Frost Number method, it was incorporated into the hydrology and water-use model WaterGAP 2.1f (Water-Global Assessment and Prognosis), which computes daily water balances for a global 0.5°x0.5° grid with monthly hydrological outputs, such as river runoff and evapotranspiration (Döll et al. 2003). Due to its implemented soil routine, WaterGAP also offers good prerequisites for potential modeling of future active layer permafrost thawing. However, in this study the soil and runoff generation routine has not yet been linked to permafrost modeling.

The input data for past and current climate conditions used in this study consists of the CRU dataset (version TS 2.1, Mitchell & Jones. 2005), which has been compiled and regionalized by the Climate Research Unit (CRU) of the University of East Anglia, Norwich, UK. Air temperature and precipitation for both future scenarios were calculated by two different transient atmospheric General Circulation Models (GCMs) to account for the spatial variability of climate patterns in GCMs. The first GCM projection of air temperature and precipitation applied in WaterGAP is calculated by the Hadley Center Coupled Model (HadCM3), which has been developed at the Hadley Center for Climate Predictions and Observations in Exeter, UK (Gordon et al. 2000). ECHAM5, the second GCM, has been developed by the Max-Planck Institute for Meteorology (MPI) in Hamburg, Germany (Roeckner et al. 2006). Both GCMs have been scaled with the IPCC-SRES (Intergovernmental Panel on Climate Change – Special Report on Emission Scenarios) scenarios A1B and B1 (IPCC 2001). The A1B scenario is driven by very high economical outputs and energy demands, which nearly double today's CO_2 emissions and lead to an air temperature increase of 4.4°C (multi-model global mean) between 2000 and 2100. On the contrary, the B1 scenario projects CO_2 emissions slightly lower than today and an average air temperature increase of 3.1°C (multi-model global mean for 2100), which occurs in combination with a balanced economy and usage of alternative energy systems. CO_2 and CH_4 feedback loops of melting permafrost are not included in the data or model.

The Frost Number

The Frost Number method was developed by Nelson & Outcalt (1983, 1987) to predict and regionalize the presence and absence of permafrost on a large scale by calculation of degree-days of freezing (DDF) and thawing (DDT). The physical derivation and all computational details of the three different Frost Numbers (Air, Surface and Soil) are given in Nelson & Outcalt (1987).

The here-applied *Surface Frost Number* F_+ (equation 1) includes variables from the *Air Frost Number*, such as DDF and DDT, which are estimated from air temperature data for each grid cell. Furthermore, it also considers snow-cover properties at the earth surface, which can have large impacts on the process of soil freezing (Osokin et al. 2001). The *Surface Frost Number* has been applied in this study to analyze permafrost distribution for three different time periods: 1901–1930, 1971–2000, and 2071–2100. For all three time margins, F_+ has been averaged to a single value for each global grid cell to eliminate input inaccuracies caused by annual air temperature variations. The *Surface Frost Number* F_+ can be derived by

$$F_+ = \frac{DDF_+^{1/2}}{DDF_+^{1/2} + DDT^{1/2}} \tag{1}$$

where DDF_+ and DDT_+ are degree days of "surface" freezing and thawing (°C days). Due to this definition, F_+ ranges between 0 and 1, for which Nelson and Outcalt (1987) further derived threshold boundaries for different permafrost types, such as continuous ($F_+ \geq 0.67$), extensive discontinuous ($0.67 > F_+ \geq 0.6$), sporadic discontinuous ($0.6 > F_+ \geq 0.5$) and no permafrost ($F_+ < 0.5$).

We will only explain selected important formulations of the derivation of DDF_+ and DDT_+ to not repeat Nelson & Outcalt (1987). The main feature of F_+ is the integration of the snow cover, which is calculated by

$$\overline{Z}_s = \sin^2 \phi \{ \sum_{i=1}^{k} [(P_i / \rho_r)(k-(i-1))] / k \} \tag{2}$$

where $\overline{Z}_s$ is the average winter snow-cover depth, P_i is water-equivalent precipitation for months i (i = 1, 2, …, k), ρ_r is relative snow density of each cell, and Φ is the cell's latitude. The trigonometric function of equation (2) determines shorter and less pronounced thaws with increasing latitude, whereas the latter term weights snow falling early in the year at higher latitudes, simulating a more realistic snow-cover distribution. A description of the influence of intra-annual variability of snowfall on permafrost occurrence can be found in Zhang et al. (2001).

As snow density was kept constant in earlier applications of the Frost Number, this study explores the effects of applying two different formulations of snow density for the 1971–2000 period. First, snow density is set constant to 100 kg m^{-3} for all cells and F_+ is being calculated. For the second case, snow density ρ_s (in kg m^{-3}) for each cell is computed by

$$\rho_s = 545 * (5 - \overline{T})^{-1.15} + 50 \tag{3}$$

where $\overline{T}$ is the mean winter air temperature in °C. Equation (3) was defined by Meister (1986), who derived this air temperature–fresh snow density relationship by analyzing more than 850 snow-density measurements for three different climate regions. He also showed that, for stations below 1500 m.a.s.l., wind effects are negligible for the computation of snow density. In this study, snow density calculated by equation (3) has been limited to a maximum of 700 kg m^{-3}, which is concordant with the findings of Mellor & Mellor (1988). In general, equation (3) yields slightly higher snow-density values than in well-known functions described by Jordan (1991) and Hedstrom & Pomeroy (1998). Another modification from the original set of formulations provided by Nelson & Outcalt (1987) is the application of two regression functions of snow density and snow thermal conductivity (equations 4 and 5). Both methods have been applied for both versions of snow-density derivation for 1971–2000, resulting in a total of four different global computations of the Surface Frost Number for that period. Here and in previous studies on F_+, thermal conductivity of snow λ_s (in W m^{-1} K^{-1}) has been calculated with the formulation of Van Dusen (Paterson 1994: 205):

$$\lambda_s = 2.1 * 10^{-2} + 4.2 * 10^{-4} \rho_s + 2.2 * 10^{-9} \rho_s^{\ 3} \tag{4}$$

where snow density ρ_s is in kg m^{-3}. The second method of obtaining λ_s is given in Sturm et al. (1997) who found the following regression by the statistical evaluation of nearly 500 snow thermal conductivity measurements:

$$\lambda_s = 0.023 + 0.234 * \rho_s \quad \text{for } \rho_s \leq 0.156 \tag{5}$$

$$\lambda_s = 0.138 - 1.01 * \rho_s + 3.233 * \rho_s^{\ 2} \quad \text{for } \rho_s > 0.156$$

Equation (5) requires ρ_s in g cm^{-3} and yields λ_s in W m^{-1} K^{-1}. The computation of F_+ for all three time slices has been carried out with equations (3) and (5), whereas present conditions were additionally calculated by three combinations of constant ρ_s and equations (3) to (5).

So far, the Surface Frost Number has been applied to Canada (Nelson 1986), Russia, and the Northern Hemisphere (Anisimov & Nelson 1996, 1997). All modeling results were validated by comparison with measured permafrost extents and generally showed good agreements. A sensitivity analysis for the Surface Frost Number in combination with climate change scenarios has been conducted by Anisimov & Nelson (1996).

Results

The modeled global distribution of permafrost for all three time periods is shown in Figure 1. The zonal extent of all

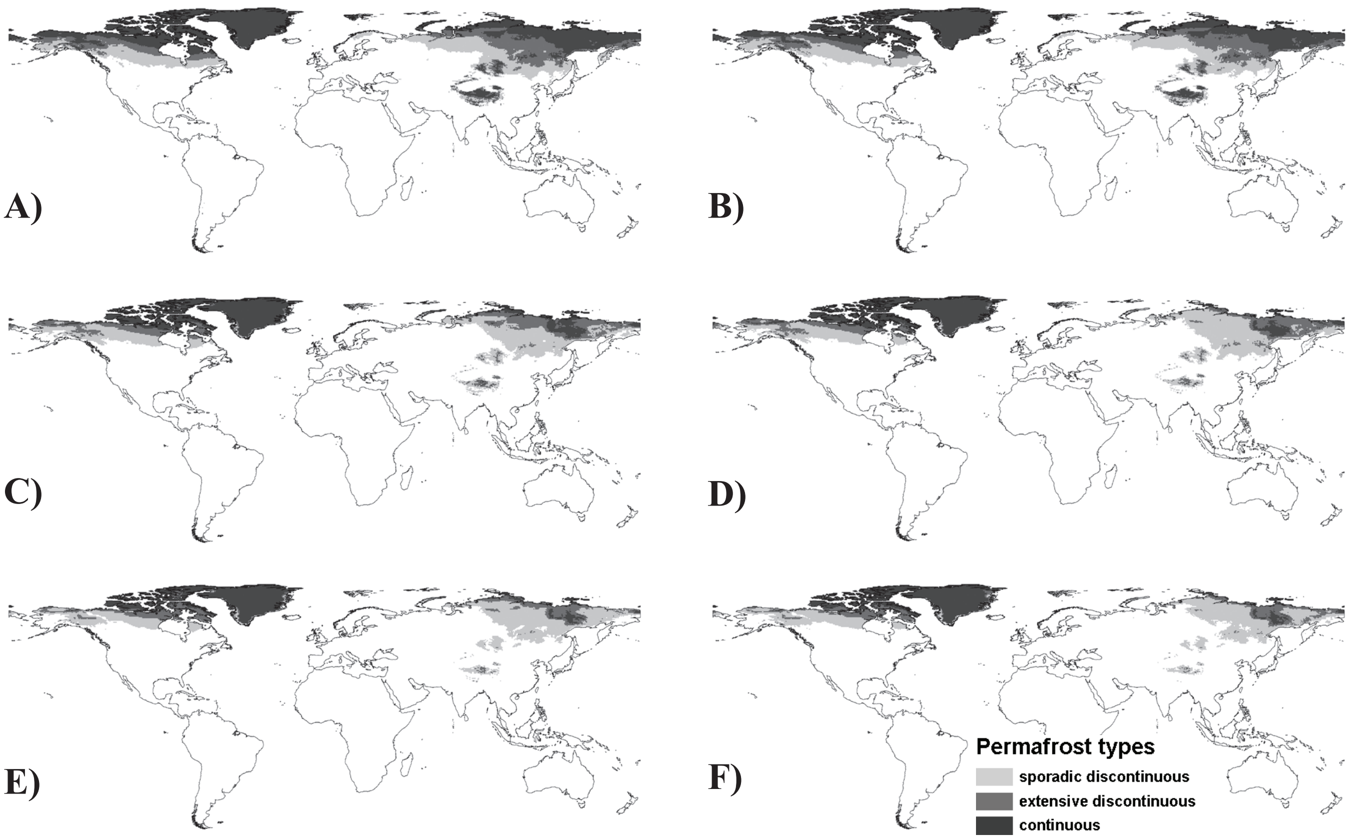

Figure 1. Global permafrost distribution modeling results (Surface Frost Number, using equations (3) and (5)). A): 1901-1930. B): 1971-2000. C): 2071-2100 (B1, HadCM3). D): 2071-2100 (B1, ECHAM5). E): 2071-2100 (A1B, HadCM3). F): 2071-2100 (A1B, ECHAM5).

permafrost calculations is given in Table 1. When comparing past and present conditions (Fig. 1A and 1B), it is noticeable that both, continuous and discontinuous permafrost boundaries, experience a moderate northeast shift. Due to the continental climate of the Eurasian permafrost regions, its degradation is more pronounced than for its North American counterpart. According to Table 1, the time period 1901–1930 featured 13% more continuous and 9% more discontinuous permafrost than today. An explanation for these findings can be derived by the analysis of air temperature data. Data analysis revealed that global average temperature in this modeling experiment increased by 0.5°C between both time periods, whereas the increase for permafrost regions averaged 0.7°C. Rising air temperature is strongly related to CO_2 emissions, which drastically increased since begin of industrialization.

Validation of present permafrost distribution

In order to assess the accuracy of the model results, we compared the Northern Hemisphere permafrost map of Brown et al. (1998) with the calculated present permafrost distribution. This was achieved by scaling the map to the 0.5° grid of WaterGAP. In general, total permafrost occurrence is underestimated by 7% (see Table 2), which could partially be explained by the model's inability to represent relic permafrost. The prediction of continuous and discontinuous permafrost cells is less accurate. However, this could be improved by adjusting the empirical threshold boundaries of the Frost Number. Additionally, we applied the map comparison algorithm *Kappa* (Pontius 2000) to contrast our results with the permafrost map. *Kappa* can vary between -1 and 1, where 1 describes a perfect fit and -1 is equivalent to a negative correlation of both maps. The global comparison yields a *Kappa* value of 0.67, whereas the comparison of the different permafrost zones yields a still acceptable value of 0.5.

A validation of simulated past permafrost distribution is not possible, as no permafrost map of this time period is available. However, as model results for past permafrost occurrence rely on the same climate data source as the validated present results, we can assume the results to be reasonable. In addition, Romanovsky (2005) found increasing permafrost temperatures for the last few decades at a multitude of boreholes. These outcomes support our model results of melting permafrost.

Future projections of permafrost distribution

The comparison of present and future permafrost occurrences (Fig. 1B versus 1C to 1F) can be discussed exemplarily for the HadCM3 climate forcing datasets. The pessimistic IPCC-SRES A1B scenario reveals significant zonal permafrost reductions of about 42% for the HadCM3 dataset (Fig. 1E). Once again, the impacts of climate change are more evident for the Eurasian continent, where continuous and extensive discontinuous permafrost is reduced to patches at the northeastern shoreline. Further, continuous permafrost with mid-continental exposition, such as in Mongolia and China, will be nonexistent. On the other side of the globe, modeled permafrost formations in Canada and Alaska undergo a northbound shift of 500 to 700 km. These findings can again be attributed to global warming. Thus, mean air temperature values of contemporary permafrost areas were compared to scenario temperatures for the same area. This revealed that the temperature increase was 15% (HadCM3) and 23% (ECHAM5) higher than the global average. Generally, the GCM ECHAM5 generates higher average air temperatures than HadCM3, and its combination with the IPCC-SRES A1B scenario yields with 11.6 million km² or -45% the strongest decrease of zonal permafrost arrangements of all four scenarios (see Table 1 and Fig. 1).

On the contrary, the optimistic IPCC-SRES B1 scenario indicates permafrost degradation of about 30% for both GCMs, whereas ECHAM5 again predicts higher losses than HadCM3. Since ECHAM5 triggers higher air temperature, much more continuous and extensive discontinuous permafrost is transformed to sporadic permafrost, which causes an increase of sporadic permafrost for this scenario. The spatial distribution of permafrost shows a less severe but yet significant shift of permafrost boundaries to the northeast. In contrast to the A1B scenario, northern Siberia still features a thick band of extensive discontinuous permafrost.

The conversion from continuous to discontinuous to no permafrost will have large impacts on society and climate. Nelson et al. (2002) describe how the permafrost-thawing processes already apparent cause soil instabilities; for example, by thermokarst, which render streets and buildings in Alaska and Canada useless. As permafrost regions are projected to be diminished by 7.7 to 11.6 million km² (see Table 1) during the next 100 years, the economical infrastructure expenses will rise dramatically for all circum-Arctic countries. In addition, large quantities of carbon are fixed in today's frozen ground which, if set free, can give impetus to feedback loops of an even more rapidly increasing climate. Zimov et al. (2006) state that the atmospheric global carbon budget rose by ~170 gigatons (GT) from preindustrial times to ~730 GT today. They further estimate that currently some 1980 GT are retained in glacier moraines, sediments beneath ice sheets, frozen Siberian loess, and steppe-tundra soils. If permafrost degradation follows the prediction of our analysis, about 600–900 GT of formerly frozen carbon will be released into the atmosphere and enhance already existent global warming until 2100.

The modeling results also suggest that the future rate of permafrost degradation will quadruple compared to today. During the last 70 years, annual global permafrost decline averaged ~23,000 km² per year, whereas the next 100 years will face an average loss of ~95,000 km² per year. In combination with the already described intensified global warming by carbon release from frozen ground, it is likely, that this average rate will rise even higher.

The Southern Hemisphere

Due to the fact that WaterGAP does not include Antarctica, Southern Hemisphere permafrost is very rare. The past time slice displays a total of four model grid cells containing discontinuous permafrost, which are reduced to three cells for contemporary conditions, and to none for all four future scenarios. The location of these cells in Argentina is concordant with the position of mountainous permafrost-

Table 1. Global area occupied by discontinuous and continuous permafrost in million km² (using equations 3 and 5). Values in parenthesis indicate percentage change to modeled 1971–2000 conditions.

	1901 – 1930	1971 - 2000	2071 – 2100 A1B, HadCM3	2071 – 2100 A1B, ECHAM5	2071 – 2100 B1, HadCM3	2071 – 2100 B1, ECHAM5
Sporadic discontinuous	9.5 (+ 2)	9.4 (0)	8.7 (-8)	8.2 (-13)	9.1 (-4)	9.5 (+1)
Extensive discontinuous	7.1 (+7)	6.7 (0)	2.9 (-56)	2.6 (-61)	4.3 (-35)	3.9 (-41)
Continuous	10.5 (+13)	9.4 (0)	3.1 (-67)	3.1 (-67)	4.4 (- 53)	4.1 (-56)
All permafrost regions	27.1 (+7)	25.5 (0)	14.7 (-42)	13.9 (-45)	17.8 (-30)	17.5 (-31)

Table 2. Global area occupied by discontinuous and continuous permafrost in million km² for 1971–2000 and comparison of different snow density ρ_s and thermal conductivity λ_s equations for the calculation of permafrost. Values in parenthesis indicate percentage change relative to permafrost map compiled by Brown et al. (1998). Anisimov & Nelson (1997) used different climate input and modeled Northern Hemisphere permafrost distribution (F_+) for 1961–1990 (using constant ρ_s (300 kg m^{-3}) and equation 4).

	ρ_s: equation (3) λ_s: equation (5)	ρ_s: constant λ_s: equation (5)	ρ_s: equation (3) λ_s: equation (4)	ρ_s: constant λ_s: equation (4)	Anisimov & Nelson (1997)	Permafrost map (Brown et al. 1998)
Sporadic discontinuous	9.4 (-17)	8.9 (-22)	9.7 (-15)	9.1 (-20)	8.1	11.4 (0)
Extensive discontinuous	6.7 (+24)	6.6 (+23)	6.8 (+26)	6.7 (+25)	5.6	5.4 (0)
Continuous	9.4 (-12)	9.7 (-9)	9.6 (-10)	9.9 (-7)	11.7	10.6 (0)
All permafrost regions	25.5 (-7)	25.2 (-8)	26.1 (-5)	25.7 (-6)	25.5	27.4 (0)

monitoring boreholes; for example, *Balcon I* at 32°57’43”S, 69°22’19”W (Trombotta et al. 1997), which are operated by the Global Terrestrial Network for Permafrost (GTNP).

Modification of the surface Frost Number

The aim of this model application was not only to predict global permafrost distribution, but also to test the framework of the Frost Number for the implementation of different formulations for snow density ρ_s and thermal conductivity λ_s. Table 2 compares the influence of these formulations on global permafrost distribution for contemporary conditions. The variation of total permafrost occurrence is rather small and lies within the range of one million km², whereas the combination of equations (3) (ρ_s calculated) and (4) (λ_s according to Van Dusen) yields the largest permafrost extent. Thus, as total permafrost occurrence is generally underestimated by the model, this combination of equations yields the smallest divergence (-5%) to the map of Brown et al. (1998). The lowest extent has been predicted by combining constant ρ_s and equation (5) (λ_s according to Sturm et al. 1997). The integration of equations (3) and (5) in the Frost Number calculations, which have also been used for the scenario estimates, generates mid-range permafrost spreading compared to other combinations. However, with 9.4 million km² of modeled continuous permafrost area, it also provides the smallest zonation of all four combinations.

Thermal conductivity of snow λ_s has been calculated using two different formulations, of which equation (5) generally yields lower values than equation (4) for ρ_s smaller than 345 kg m^{-3}, which holds true for most cells in this analysis. Table 2 shows that all permafrost calculations conducted with equation (5) feature smaller discontinuous and continuous permafrost extents than its counterpart equation (4). When snowfall occurs in the early stages of winter, low λ_s and thick snow layers can cause an insulation of the upper soil layer and thus prevent permafrost occurrence (Zhang et al. 2001). This effect is partially accounted for in equation (2), where snowfall early in the year is weighted higher than late snowfall.

There are two more options of snow-depth modeling, which could be applied for further studies on the Surface Frost Number. First, a physically detailed approach, which considers snow metamorphism and overburden (Jordan 1991). Secondly, if necessary input data are not available, a conceptual approach, as in Pomeroy et al. (1998), who suggest initializing annual snow density with 100 kg m^{-3} and add 25 kg m^{-3} for each month colder than 0°C.

In general, the comparison with results from a similar study conducted by Anisimov & Nelson (1997) shows good agreement for total permafrost extent. However, continuous permafrost is 25% lower, and discontinuous permafrost spreading is 15% higher in the current study. This could be explained by different climate data input, higher constant snow density, and an earlier and colder time period. Thus, in between the climate normal 1961–90 and 1971–2000, air temperature increase caused a transformation from continuous to discontinuous permafrost, which could explain some of the differences between both studies.

Conclusions

This model experiment projects that, due to climate change, increasing air temperatures do have a significant impact on global permafrost distribution and thawing. According to the model results, which esteem from two IPCC-SRES scenarios and two GCMs, future continuous permafrost will suffer the largest zonal reductions, which vary between -53% and -67% compared to today. Discontinuous permafrost faces two different pathways of decay, depending on its type. On the one hand, extensive discontinuous permafrost experiences losses between -35% and -61%. On the other hand, sporadic discontinuous permafrost faces moderate spatial changes between +1% and -13%, which is due to the conversion from continuous and extensive discontinuous to sporadic discontinuous permafrost. These thawing processes can have large impacts on urban infrastructure and can trigger feedback loops of enhanced global warming. The modeling results also show, that permafrost degradation in the next 100 years will progress much faster than during the last 70 years.

In this study, a validation of the Frost Number for present total permafrost occurrence has been carried out successfully. The general underestimation of modeled global permafrost extent can probably be addressed to the existence of relic permafrost which is not considered by the model.

The incorporation of additional snow parameter equations showed little sensitivity to the calculation of the Surface Frost Number.

Although the Surface Frost Number has proven its suitability to display contemporary permafrost distribution to some extent, the interpretation of all modeling results should be regarded with caution. Especially the interaction of transient GCMs, climate change scenarios, climate data-input uncertainties, and empirical model functions can lead to large inaccuracies in the prediction of permafrost occurrence. In this study, the main disadvantage of the Surface Frost Number can be seen in its dependence on climate input solely. Further, snow property calculations, such as modeled snow depth, should be subject to more physical approaches, which also consider snow typical processes, such as snow compaction (e.g., as in Jordan 1991). It is recommended further studies integrate soil properties, relic permafrost, and carbon and methane cycling in the assessment of climate change driven permafrost thawing. Potential candidates for the integration of soil features are formulations such as the Stefan Frost Number (Nelson & Outcalt 1987) or the more detailed Kudryavtsev solution, which is described in Anisimov et al. (2007).

Acknowledgments

We thank our colleagues, especially Florian Wimmer and Frank Voß, at the Center for Environmental Systems Research (CESR) for valuable discussions about the thermal properties of snow. We also gratefully acknowledge the helpful comments by two anonymous reviewers. This work was funded by the German Federal Ministry of Education and Research (FKZ:033762A).

References

Anisimov, O.A., Lobanov, V.A., Reneva, S.A., Shiklomanov, N.I., Zhang, T. & Nelson, F.E. 2007. Uncertainties in gridded air temperature fields and effects on predictive active layer modeling. *Journal of Geophysical Research* 112: F02S14.

Anisimov, O.A. & Nelson, F.E. 1997. Permafrost zonation and climate change in the northern hemisphere: results from transient general circulation models. *Climatic Change* 35: 241-258.

Anisimov, O.A. & Nelson, F.E. 1996. Permafrost distribution in the northern hemisphere under scenarios of climatic change. *Global and Planetary Change* 14(1-2): 59-72

Brown, J., Ferrians, O.J., Heginbottom, J.A. & Melnikov, E.S. 1998. *Digital Circum-Arctic Map of Permafrost and Ground-Ice Conditions*. Int. Permafrost Association Data and Information Working Group, Circumpolar Active-Layer Permafrost System, CD-ROM version 1.0. National Snow and Ice Data Center, U. of Colorado, Boulder, Colorado.

Döll, P., Kaspar, F. & Lehner, B. 2003. A global hydrological model for deriving water availability indicators: model tuning and validation. *Journal of Hydrology* 270: 105-134.

Frauenfeld, O.W., Zhang, T. & McCreight, J.L. 2007. Northern hemisphere freezing/thawing index variations over the twentieth century. *International Journal of Climatology* 27(1): 47-63.

Gordon, C.; Cooper, C., Senior, C.A., Banks, H., Gregory, J.M., Johns, T.C., Mitchell, J.F.B. & Wood, R.A. 2000. The simulation of SST, sea ice extents and ocean heat transports in a version of the Hadley Centre coupled model without flux adjustments. *Climate Dynamics* 16: 147-168.

Hedstrom, N.R. & Pomeroy, J.W. 1998. Measurements and modeling of snow interception in the boreal forest. *Hydrological Processes* 12: 1611-1625.

IPCC. 2001. *Special Report on Emissions Scenarios*. Cambridge: Cambridge University Press, 570pp.

Jordan, R. 1991. A one-dimensional temperature model for a snow cover. Technical documentation for SNTHERM.89. U.S. Army Corps of Engineers*, Cold Reg. Res. and Eng. Lab.*. Special Report 91-16.

Lawrence, D.M. & Slater, A.G. 2005. A projection of severe near-surface permafrost degradation during the 21st century. *Geoph. Res. Lett*. 32: L24401.

Mellor, M. & Mellor, A. 1988. Some characteristics of falling snow. *Cold Reg. Sc. and Tech.* 15: 201-206.

Meister, R. 1986. Density of new snow and its dependence on air temperature and wind. *Zürcher Geografische Schriften* 23: 73-79.

Mitchell, T.D. & Jones, P.D. 2005. An improved method of constructing a database of monthly climate observations and associated high resolution grids. *International Journal of Climatology* 25(6):693-712.

Nelson, F.E. 1986. Permafrost distribution in Central Canada: applications of a climate-based predictive model. *Annals of the Association of American Geographers* 76(4): 550-569.

Nelson, F.E., Anisimov, O.A. & Shiklomanov, N.I. 2002. Climate change and hazard zonation in the Circum-Arctic permafrost regions. *Nat. Hazards* 26:203-225.

Nelson, F.E. & Outcalt, S.I. 1987. A computational method for prediction and regionalization of permafrost. *Arctic and Alpine Research* 19(3): 279-288.

Nelson, F.E. & Outcalt, S.I. 1983. A frost index number for spatial prediction of ground-frost zones. *Permafrost: Fourth International Conference Proceedings*, I. Washington, DC: National Academy Press: 907-911.

Osokin, N.I., Samoylov, R.S., Sosnovskiy, A.V., Sokratov, S.A. & Zhidkov, V.A. 2000. Model of the influence of snow cover on soil freezing. *A. of Glaciology* 31: 417-421.

Paterson, W.S.B. 1994. *The physics of glaciers*. 3rd edition. Oxford: Pergamon Press, 481pp.

Pomeroy, J.W., Gray, D.M., Shook, K.R., Toth, P., Essery, R.L.H., Pietroniro, A. & Hedstrom, N. 1998. An evaluation of snow accumulation and ablation processes for land surface modelling. *Hydrological Processes* 12: 2339-2367.

Pontius, R.G. 2000. Quantification error versus location error in comparison of categorical maps. *Photogram. Engineering & Remote Sensing* 66(8): 1011-1016.

Roeckner, E., Brokopf, R., Esch, M., Giorgetta, M., Hagemann, S., Kornblueh, L., Manzini, E., Schlese, U. & Schulzweida, U. 2006. Sensitivity of simulated climate to horizontal and vertical resolution in the ECHAM5 atmosphere model. *J. of Climate* 19: 3771-3791.

Romanovsky, V.E. 2005. *How rapidly is permafrost changing and what are the impacts of these changes?* http://www.arctic.noaa.gov/essay_romanovsky.html.

Stendel, M. & Christensen, J.H. 2002. Impact of global warming on permafrost conditions in a coupled GCM. *Geophysical Research Letters* 29(13):1632.

Sturm, M. , Holmgren, J, Koenig, M. & Morris, K. 1997. The thermal conductivity of snow. *Journal of Glaciology* 43: 26-41.

Trombotto, D., Buk, E. & Hernandez, J. 1997. Monitoring of mountain permafrost in the Central Andes, Argentina. *Permafrost & Perigl. Proc* 8: 123-129.

Zhang, T., Barry, R.G. & Haeberli, W. 2001. Numerical simulations of the influence of the seasonal snow cover on the occurrence of permafrost at high latitudes. *Norsk geogr. Tidsskr*. 55: 261-266.

Zimov, S.A., Schuur, E.A.G. & Chapin III, F.S. 2006. Permafrost and the global carbon budget. *Science* 312(5780): 1612-1613.

Remote Sensing Data for Monitoring Periglacial Processes in Permafrost Areas: Terrestrial Laser Scanning at the Hinteres Langtalkar Rock Glacier, Austria

Michael Avian
Institute of Remote Sensing and Photogrammetry, Graz University of Technology, Austria
Andreas Kellerer-Pirklbauer
Institute of Geography and Regional Science, University of Graz, Austria
Arnold Bauer
Institute of Digital Image Processing, JOANNEUM RESEARCH, Graz, Austria

Abstract

This article discusses long-range terrestrial laser scanning (TLS) as a monitoring technique focusing on recent geomorphic changes at the near-terminus zone of the Hinteres Langtalkar rock glacier (46°59′N, 12°47′E). This rock glacier is characterised by extraordinarily high movement rates at its lower part since the mid-1990s. The surface of this collapsing part of the rock glacier is characterised by a very disturbed topography, which causes problems for terrestrial as well as remote sensing monitoring methods. The lack of textural information makes approaches such as optical flow detection in grey-scale images non-applicable at this study area. Long-range TLS is completing the dataset with distance measurements leading to 3D point clouds, which are afterwards converted into accurate 3D models. Analysis of surface kinematics derived from five digital elevation models (DEM) obtained during TLS campaigns between 2001–2006 shows promising results covering this lack of data in unfavourable terrain.

Keywords: Austrian Alps; high-resolution DEM; LIDAR; rock glacier kinematics; terrestrial laser scanning.

Introduction

Surface dynamics of rock glaciers are of increasing interest due to a high relationship to thermal conditions of permafrost areas. A few rock glaciers in the Alpine arc reacted to increasing air temperatures with extraordinarily high movement rates over several years (Roer et al. 2003). Most of them now show decreasing surface velocities (Delaloye et al. 2008). The Hinteres Langtalkar rock glacier changed its behavior most likely in 1994, moving over a prominent bedrock ridge into steeper terrain (Avian et al. 2005). Despite the remoteness of the location, a comprehensive monitoring network has been installed to get a better understanding of present processes, such as a geodetic survey (annually since 1998; Kienast & Kaufmann 2004), monitoring of the near-surface and surface thermal regime (since 2006 within the project ALPCHANGE), terrestrial laser scanning (2x2000, 2x2001, 2004, 2005, 2006, and 2007; cf. Bauer et al. 2003), and digital photogrammetry (1969, 1974, 1983, and 1997; cf. Kaufmann & Ladstädter 2004), providing data of different nature and in different resolutions in time and space. Long-range TLS ought to monitor the lowest part of the rock glacier to gather information about vertical surface changes and 3D movement rates.

Geographical Setting

The cirque-system Hinteres Langtalkar (46°59′N, 12°47′E) is situated in the Schober Mountains within the Hohe Tauern Range (Central Alps, Austria) (Fig. 1). The cirque-system is a hanging valley at the orographic right side of the Gössnitz Valley. The cirque covers an altitudinal range between

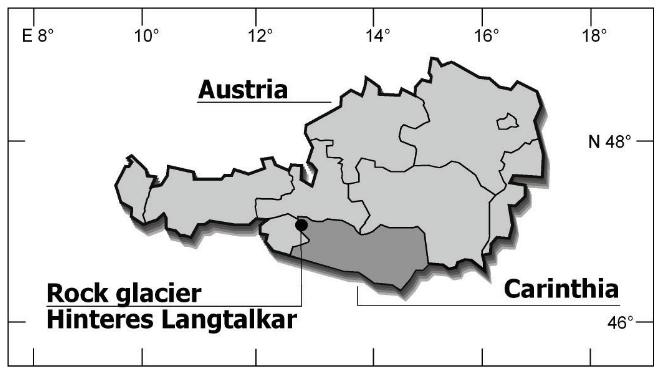

Figure 1. Location of Hinteres Langtalkar within Austria.

2300–3019 m a.s.l. The northwest facing tongue-shaped rock glacier itself covers the entire upper cirque floor with a lower margin at 2455 m a.s.l., root zones beginning in appr. 2700 m a.s.l, and a geometry of 600x300 m (Fig. 2). In general, rock glaciers are numerous in the Schober Mountains due to favorable geological conditions, leading to a total number of 77 intact rock glaciers (*cf.* Lieb 1998). Furthermore, the main range of the Central Alps (10 km to the N) causes pronounced continental climatic characteristics with a mean annual air temperature (MAAT) of 0°C at 2200 m a.s.l. and precipitation of ~1500 mm at 2000 m a.s.l. Glaciation in the Schober Mountains is developed only in some cirques and decreased rapidly during the last decades due to atmospheric warming (Kellerer-Pirklbauer & Kaufmann 2007). Auer et al. (2002) report a rising of the MAAT of 1.6°C since 1886 at the Hoher Sonnblick Meteorological Station (3106 m a.s.l., 15 km E of Hinteres Langtalkar) which is above the global average of 0.74°C (*cf.* IPCC 2007).

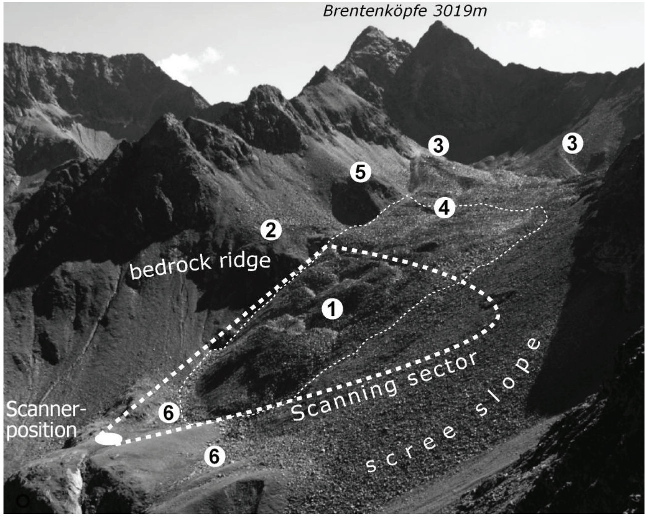

Figure 2. The cirque-system Hinteres Langtalkar including the monitoring configuration. Codes in photograph: (1) Area of intensive rock glacier movement and disintegration, (2) prominent bedrock ridge partly covered by periglacially weathered debris, (3) latero-terminal moraine ridges dating from the Little Ice Age (~1850 AD), (4) crevasses on rock glacier indicating high strain rates, (5) meteorological station and (6) fresh boulders spreading over alpine meadows adjacent to the rock glacier front. The thin dashed line comprises the recently fast-moving part of the rock glacier. Scanner position is in a distance of ~90 m to the rock glacier front (Photograph by Viktor Kaufmann 24.08.2003).

Methods

Laser scanning or LiDAR (Light detection and ranging) data have been used intensively for high mountain applications during the last decade. Examples are monitoring of glacier surface elevation changes by Airborne Laser Scanning/ALS (e.g., Baltsavias et al. 2001, Würländer et al. 2004) or TLS (e.g., Avian et al. 2007), monitoring of periglacial processes using TLS (e.g., Bodin et al. 2008), hazard monitoring by TLS (e.g., Conforti et al. 2005, Rabatel et al. 2007) or snow cover monitoring using TLS (Prokop 2007). Primary resulting digital elevation models (DEM) are used to consider surface elevation variations to quantify, for instance, glacier dynamics. Determination of horizontal flow fields with high-resolution DEMs was presented by e.g., Bucher et al. (2006) with the aid of the software IMCORR, using concepts from aerial image matching (cross correlation in grey-scale images).

The ability of TLS to acquire high-resolution 3D data of surface structures makes this technique an interesting instrument for measuring high mountain environments. The integrated measurement system is capable of describing 3D motion and deformation of rock glacier surface within a few hours measurement. It is a time-of-flight system that measures the elapsed time of the pulse emitted by a photo-diode until it returns to the receiver optics. Maximum range depends on the reflectivity of surface (which is favourable for snow and debris-covered terrain) and atmospheric visibility (best for clear visibility, bad for haze and fog). A measuring range of up to 2000 m allows hazardous sites to be easily measured from a safe distance. Since each single measurement consists of a multitude of laser-pulses, different measurement modes (“first pulse,” “last pulse,” “strongest pulse”) give proper results even during bad weather conditions and on poor surfaces like vegetated, moist, or roughly structured terrain that might otherwise lead to ambiguous measurements. Table 1 gives an overview of technical information concerning the long-range TLS Riegl LPM-2k.

Table 1. Scanner parameters and values of the used instrumentation Riegl LPM-2k Long-range Laser Scanner.

Scanner parameter	Value (range)
Measuring range for:	
- good diffusely reflective targets	up to 2500m
- bad diffusely reflective targets	>800m
Ranging accuracy	+50mm
Positing accuracy	+0.01gon
Measuring time / point	0.25s to 1s
Measuring beam divergence	1.2mrad
Laser wavelength	900nm
Scanning range	
- horizontal	400gon
- vertical	180gon
Laser safety class	3B, EN 60825-1
Power supply	11-18V DC, 10VA
Operation temperature range	-10 to +50°C

The measurement

Information at each individual measurement point includes the distance to the surface, the exact angular positions, the reflectance, and an estimated root mean square error (RMSE) of the distance measurement for reliability check. Measurements with an accuracy of distance better than 5 cm are automatically combined to a measurement grid. In general, several methodological, technical, and logistical problems are to be encountered when establishing an integrated monitoring system in this high alpine environment. These include among others the stability of device control software, the automatic sensor orientation, the high number of measurements, the compensation of weather influences, and the selection of reliable measurements. In addition, it is of particular importance to consider the highly heterogeneous surface in terms of material (rock, vegetation, and humidity in general) and structure. Many years of experience in the field of TLS (beginning in 2000) result in the development of a well-engineered, stable acquisition and analysis system, which in combination with expert field work, copes with all the conditions.

Data processing

The TLS dataset is converted to a DEM, which is a digital raster representation of surface topography. In general, a horizontal reference surface is used. However, topology is often highly varying in terms of inclination; for example, most of the potentially insecure surfaces are characterized by comparable steep fronts. In order to represent the surface data in best resolution, we generalize the DEM to an analytical reference model that best describes the global shape of the observed surface. To raster, a regularly spaced grid is defined on the reference model, and the "height" on every pixel is processed as normal distance to the reference surface. This data structure complies well with practical requirements such as difference measuring, volume change evaluation, and various visualization tasks. Neighbourhood relations of measured data points are directly described in the DEM structure; therefore, operating on DEMs allows quick access to the surface heights in a well-defined geometry. Direct mapping from the sensor spherical system to the DEM cartesian coordinate space would result in a sparse and non-uniform elevation map, especially at great distances. To avoid interpolation artefacts, the Laser Locus Method (Kweon et al. 1992) for DEM (Bauer et al. 1999) generation proves to be a robust tool for data acquisition from flat angles and supports error detection and utilization of additional confidence values provided by the range sensor. Since the DEMs of (temporally) different surface measurements are geo-referenced, simple differences between the DEMs reflect the changes in elevation. In consequence we can derive a full description of change in volume, spatial distribution of shape, or arbitrary profiles on the surface.

Single time-of-flight measurements are automatically combined to a measurement grid that enables the generation of a dense, enhanced DEM of the rock glacier surface. Repeatable sensor orientation is performed using reflective targets fixed on stable surfaces somewhere in the spherical field of view of the sensor. TLS measures the position of a theoretical, stable point on the surface within a given reference system.

Surface motion analysis

The DEM differences primarily only describe the vertical distance of the surface change. In order to understand the complex kinematics of rock glacier deformation – like the highly dynamic lowest part of the Hinteres Langtalkar rock glacier – further knowledge about the 3D surface motion patterns is required. Among others, Kääb et al. (2003) and Kaufmann & Ladstädter (2004) provide solutions to calculate the 3D motion by means of optical flow detection on the grey level images using correlation-based matching. This method is not applicable to the current laser scanning configuration, since similar reflectance conditions cannot be assured (basic requirement for robust matching). Tracking of objects on the surface can still be performed by the high-resolution surficial morphology provided by the DEM (despite the lack of textural information). Only on surfaces, where the structural surface changes are relatively small, state-of-art matching methods (cf. Paar & Almer 1993) obtain dense tracking vectors. In combination with the primarily obtained DEM differences mentioned above, this results in a three-dimensional vector field that describes the kinematic state of the rock glacier surface within the given periods.

Table 2: Periods of data acquisition and quality parameters. Data used for analysis discussed in this study are indicated in bold.

Period	total pts	used pts	PR (1)	OA (2)
07/2000	27048	26381	0.98	0.07
08/2000	**27048**	**26437**	**0.98**	**0.06**
07/2001	27048	26274	0.97	0.02
08/2001	**26910**	**26312**	**0.98**	**0.02**
08/2004	**20424**	**19818**	**0.97**	**0.02**
08/2005	**27048**	**17843**	**0.65**	**0.02**
09 2006	**7836**	**6048**	**0.77**	**0.02**
07/2007	6384	5739	0.90	0.02

(1) PR: point ratio = numbers of points used/total number of points measured. (2) OA: orientation accuracy [m].

Cross check with auxiliary data

To control the significance of the image matching data, cross checking with displacement rates from adjacent parts of the rock glacier were considered. Geodetic survey has been carried out in the middle part of the rock glacier (data kindly provided by V. Kaufmann) with its lower measurement boundary at the disintegrated lower part of the rock glacier. These campaigns provide verification data for the displacement vectors derived from image matching (Tab. 2). Some limitations in interpretation have to be considered due to distances of up to 60 m between scanning area and respective control points.

Results

Quality of data from image matching

To get more information about interpretability, a review of data quality is essential. In 2000–2005 the total number of acquired points is high with 20,000 to 30,000 per campaign. The surface topography of a rock glacier consists of boulders with sizes between a few decimeters up to some metres. This is of crucial importance in the face of a true reproduction of the real surface and subsequently in receiving reasonable results in terms of surface motion patterns. Due to problems with energy supply in 2006 and 2007, the scanning increment had to be reduced during these campaigns, leading to total point numbers below 10,000. This low number is unfavourable for interpolation and obtaining a DEM for an area-wide precise motion analysis. Orientation accuracy is satisfying for all periods with 0.02–0.07 m (Table 2).

Annual displacements from image matching

Results of the rock glacier motion analysis are given in mean annual horizontal displacement rates.

2000–2001: The stepped lowest part differentiates clearly in velocity patterns. The ridges show mean annual displacement rates of 0.78 ma^{-1} (max. 1.38 ma^{-1}) (Fig. 3A; zone 1), 0.95 ma^{-1} (max. 1.73 ma^{-1}) (Fig. 3A; zone 2), 1.38 ma^{-1} (max. 1.64 ma^{-1}) (Fig. 3A; zone 3), and 1.35 ma^{-1} (max. 1.75 ma^{-1}) (Fig. 3A; zone 4). The adjacent scree slope at the orographic left side of the rock glacier shows constant movement rates of 0.02–0.06 ma^{-1} over the entire scanning area.

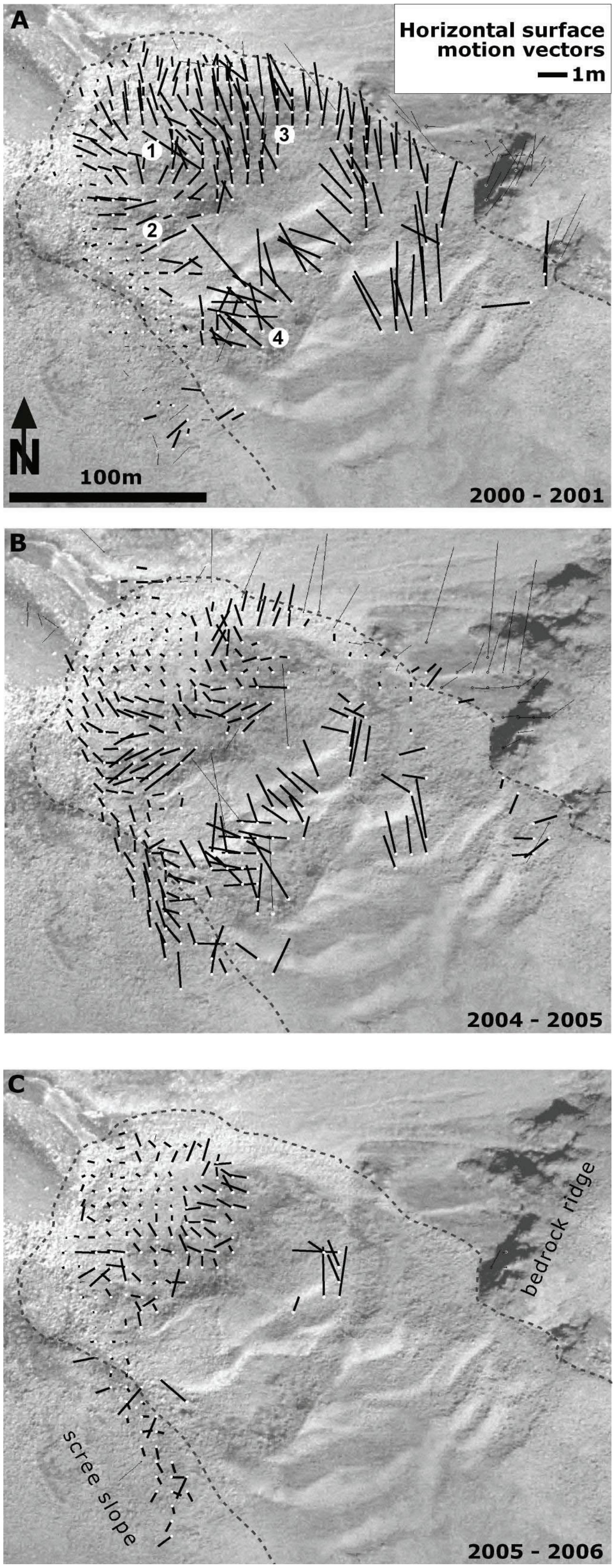

Figure 3. Horizontal displacement rates [ma^{-1}] for three annual periods: (A) 2000/01, (B) 2004/05 and (C) 2005/06. Motion vectors are obtained from DEM differences, DEMs were derived from TLS data. Numbers (1-4) indicate zones of different behaviour in terms of surface velocity; for details refer to text (Orthophotograph ©Nationalpark Hohe Tauern, 1998).

2004–2005: Quality of velocity data from this period tends to be unsatisfying in some areas. Distinct differentiation between obviously moving and akinetic areas at the margin of the rock glacier is not possible. Velocity patterns do not indicate a distinct border between the scree slope and the rock glacier body. Furthermore, displacement rates of 0.35–0.40 ma^{-1} seem to be unreasonable for this particular area. Surface topography on the rock glacier itself can be deduced from flow fields properly, as they show similar patterns as in the other periods.

2005–2006: Flow velocities and patterns are more difficult to interpret, although the ridges are detectable due to higher displacement rates (0.75 ma^{-1}). The main front shows rates around 0.15 ma^{-1}, the left margin is distinguishable towards the non-moving scree slope. Coarse point resolution leading to small spots of areal data does not allow reasonable interpretation of the upper part of the rock glacier tongue (cf. uppermost scanning area in Fig.2).

Direction of annual displacement vectors

Direction of movement at the terminus zone of the rock glacier shows outward movement of displacement vectors as expected. The ongoing development of the imbrication and the distinct shifting of detritus is visible in abrupt changes of the magnitude and direction of velocity vectors (Fig. 3, A-C, 1-4).

Cross checking with results from geodetic survey

Surface displacements derived from geodetic surveys in both periods at least coincide with displacement ranges obtained from TLS image matching (Tab. 3). However, substantial controlling is not possible due to poor data overlap. The main problems are hazardous working conditions for terrestrial monitoring, making geodetic or GPS surveys hardly feasible in the fast-moving sections of this rock glacier (up to 2.38 ma^{-1} in 2003–2004). The steep rock glacier's front surface changes rapidly in shape, texture, and object distribution. This results in unfavorable conditions for analysis of optical data; viewing angles nearly vertical or area-wide changes in surface cause problems in automatic detection).

High values at some areas of the right margin of the rock glacier, the bedrock, and vegetated areas are results due to unfavorable scanning geometry and therefore are not taken into account as the exact rock glacier extent is known from fieldwork.

Discussion and Conclusions

High-resolution DEMs derived from long-range terrestrial laser scanning are a good data basis for monitoring permafrost processes related to geo-hazards. Derivates like surface elevation changes and displacement vectors (in case of the availability of multi-temporal high-resolution DEMs) provide useful information about 3D surface dynamics. However, the quality of dataset s and concepts for calculating morphometric parameters have to be assessed critically. Point density is a crucial factor (cf. Bodin et al. 2008) as is the quality of the measurement itself (high point ratio and total point number). Remoteness (sufficient energy supply) and atmospheric conditions (e.g., air humidity) are crucial limiting factors. The exemplary study of the Hinteres Langtalkar rock glacier demonstrates the importance of independent control data for evaluation, and the problems in acquisition of the latter. High landscape dynamics – frequent shifting of material, block falls – inhibit terrestrial surveys. Methodological problems in automatic data interpretation (e.g., inadequate texture for photogrammetry) complicate remote sensing approaches. The current monitoring configuration lacks additional control targets in the vicinity of the upper rock glacier tongue on the bedrock. Large differences in velocity values of different periods do not allow the interpretation of recent processes precisely at present.

In terms of velocity patterns, topography, and surface modification, some considerations are appropriate. In the lowest section of the rock glacier front, the surface velocity is decreasing to the margin as expected. Flow patterns are detectable in step-like relief which geomorphodynamically results in a distinct surface topography (Figs. 2, 3). High velocities within ridges and sharp limits at the ridge fronts to slower areas support this assumption. The formation of the micro-relief within ridges is also visible in the displacement patterns. Surface velocity patterns also exhibit distinct differences between the main rock glacier body and adjacent permafrost areas at the orographically left side. At the beginning of the steeper part of the lower rock glacier tongue, varying directed vectors in both periods indicate non-laminar movement of that particular part and are therefore interpreted as intense modification and frequent shifting of the disturbed surface.

As this particular rock glacier shows extraordinary surface velocity rates (cf. Avian et al 2005, Roer et al. 2005), upcoming TLS campaigns on the middle and upper section of the rock glacier would enhance knowledge about methodological problems due to the availability of independent data derived from geodetic measurements.

Acknowledgments

These activities were carried out within the framework of the project ALPCHANGE (www.alpchange.at) funded by the Austrian Science Fund (FWF) through project no. FWF P18304-N10. We kindly acknowledge the help of Viktor Kaufmann (Institute of Remote Sensing and Photogrammetry, Graz University of Technology) for providing data from geodetic surveys. We also thank students of the Institute of Geography and Regional Science, University of Graz and the Institute of Remote Sensing, Graz University of Technology, Austria as well as several volunteers of the Nationalpark Hohe Tauern for their support during field campaigns.

Table 3. Annual horizontal displacement rates from geodetic measurements (based on unpublished data by V. Kaufmann) and image matching of adjacent areas.

Image matching	Geodetic survey	
displacement range [ma^{-1}]	Points	displacement [ma^{-1}]
2000/2001		
0.99 – 2.04	24	1.504
0.92 – 1.88	25	1.468
1.26 – 1.93	27	1.720
1.56 – 2.29	28	1.683
2004/2005		
1.05 - 1.98	24	2.017
0.97 – 1.89	25	1.734
no data	27	1.967
1.23 – 2.32	28	1.947

References

Auer, I., Böhm, R., Leymüller, M. & Schöner, W. 2002. Das Klima des Sonnblicks–Klimaatlas and Klimageographie der GAW-Station Sonnblick einschließlich der umgebenden Gebirgsregion. *Österreichische Beiträge zur Meteorologie und Geophysik* 28: 305 pp.

Avian, M., Kaufmann, V. & Lieb, G.K. 2005. Recent and Holocene dynamics of a rock glacier system–the example of Langtalkar (Central Alps, Austria). *Norsk Geografisk Tidsskrift* (Norwegian Journal of Geography) 59: 149-156.

Avian, M., Lieb, G.K., Kellerer-Pirklbauer, A. & Bauer, A. 2007. Variations of Pasterze Glacier (Austria) between 1994 and 2006 - Combination of Different Data Sets for Spatial Analysis. *Proceedings of the 9th International Symposium High Mountain Remote Sensing Cartography (HMRSC), Graz, Austria, September 14–22, 2006*: 79-88.

Baltsavias, E.P., Favey, E., Bauder, A., Boesch, H. & Pateraki, M. 2001. Digital surface modelling by airborne laser scannino and digital photogrammetry for glacier monitoring. *Photogrammetric Record* 17, 98: 243-273.

Bauer, A. & Paar, G. 1999. Elevation Modeling in Real Time Using Active 3D Sensors. *Proceedings of the 23rd Workshop of the Austrian Association for Pattern Recognition, AAPR, Robust Vision for Industrial Applications 1999. Steyr, Austria. May 27-28, 1999, Schriftenreihe der Österreichischen Computer Gesellschaft* 128: 89-98.

Bauer, A, Paar, G. & Kaufmann, V. 2003. Terrestrial laser scanning for rock glacier monitoring. *Proceedings of the Eighth International Conference on Permafrost, Zurich, Switzerland, 21-25 July 2003:* 55-60.

Bodin, X., Schoeneich, P. & Jaillet, S. 2008. High Resolution DEM Extraction from Terrestrial LIDAR Topometry and Surface Kinematics of the Creeping Alpine Permafrost: the Laurichard Rockglacier Case Study (French Southern Alps). *Proceedings of the Ninth International Conference on Permafrost, Fairbanks, Alaska, June 29–July 3, 2008* (this proceedings).

Bucher, K., Geist, Th. & Stötter, J. 2006. Ableitung der horizontalen Gletscherbewegung aus multitemporalen Laserscanning-Daten Fallbeispiel: Hintereisferner/Ötztaler Alpen. *Proceedings of Angewandte Geoinformatik 2006 – Beiträge zum AGIT-Symposium Salzburg, Salzburg, Austria, July 5-7, 2006*: 277-286.

Conforti, D., Deline, P., Mortasa, G. & Tamburini, A. 2005. Terrestrial scanning LiDAR technology applied to study the evolution of the ice contact Miage glacier (Mont Blanc, Italy). *Proceedings of the 9th Alpine Glaciological Meeting, Milano, Italy, February 24–25, 2005*: (digital media)

Delaloye, R., Perruchoud, E., Avian, M., Kaufmann, V., Bodin, X., Ikeda, A., Hausmann, H., Kääb, A., Kellerer-Pirklbauer, A., Krainer, K., Lambiel, C., Mihajlovic, D., Staub, B., Roer, I. & Thibert, E. 2008. Recent interannual variations of rock glaciers creep in the European Alps. *Proceedings of the Ninth International Conference on Permafrost, Fairbanks, Alaska, June 29–July 3, 2008* (this proceedings).

IPCC. 2007. *Climate Change 2007: The Physical Science Basis. Contribution of Working Group I to the Fourth Assessment Report of the Intergovernmental Panel on Climate Change.* S. Solomon, D. Qin, M. Manning, Z. Chen, M. Marquis, K.B. Averyt, M.Tignor and H.L. Miller (eds.). Cambridge, United Kingdom and New York, NY, USA: Cambridge University Press.

Kääb, A., Kaufmann, V., Ladstädter, R. & Eiken, T. 2003. Rock glacier dynamics: implications from high-resolution measurements of surface velocity fields. In: *Proceedings of the Eighth International Conference on Permafrost, 21-25 July 2003, Zurich, Switzerland* 1:501-506.

Kaufmann, V. & Ladstädter, R. 2004. Documentation of the movement of the Hinteres Langtalkar rock glacier. *Proceedings of the 20th Congress of the International Society for Photogrammetry and Remote Sensing, Istanbul, Turkey, July 12–23, 2004, IAPRS, 35, Part B7*: 893-898.

Kellerer-Pirklbauer, A. & Kaufmann, V. 2007. Paraglacial talus instability in recently deglaciated cirques: Schober group, Austria. *Proceedings of the 9th International Symposium High Mountain Remote Sensing Cartography (HMRSC), Graz, Austria, September 14–22, 2006:* 121-130.

Kienast, G. & Kaufmann, V. 2004. Geodetic measurements on glaciers and rock glaciers in the Hohe Tauern National park (Austria). *Proceedings of the 4th ICA Mountain Cartography Workshop*, *Vall de Núria, Catalonia, Spain, September 30–October 2, 2004*, Monografies tècniques 8, Institut Cartogràfic de Catalunya, Barcelona: 101–108.

Kweon, I.S. & Kanade, T. 1992. High-resolution terrain map from multiple sensor data. *IEEE Transactions on Pattern Analysis and Machine Intelligence* 14(2): 278-292.

Lieb, G.K. 1998. High mountain permafrost in the Austrian Alps. *Proceedings of the Seventh International Conference on Permafrost, Yellowknife, Canada, June 23–27, 1998*: 663-668.

Paar, G. & Almer, A. 1993. Fast hierarchical stereo reconstruction. In: *Proceedings of the Second Conference on Optical 3-D Measurement Techniques, Zurich, Switzerland*: 460-466,

Prokop, A. 2007. The application of terrestrial laser scanning for snow depth observation. *Geophysical Research Abstracts* 9: 07074.

Rabatel, A., Deline, P., Ravanel, L. & Jaillet, S. 2007. The use of laser scanning and terrestrial photogrammetry to quantify rock falls/avalanches in steep high-alpine rock walls. *Geophysical Research Abstracts* 9: 07170.

Roer, I., Avian, M., Delaloye, R., Lambiel, C., Dousse, J.-P., Bodin, X., Thibert, E., Kääb, A., Kaufmann, V., Damm, B. & Langer, M. 2005. Rock glacier "speed-up" throughout European Alps - a climatic signal? *Proceedings of the Second European Conference on Permafrost, Potsdam, Germany, June 12–16, 2005*: 101-102.

Würländer, R., Eder, K. & Geist, Th. 2004. High quality DEMs for glacier monitoring – image matching versus laser scanning. *International archives of Photogrammetry, Remote Sensing and spatial information science* XXXV (B7): 753-758.

Permafrost Temperatures and Erosion Protection at Shishmaref, Alaska

Mary T. Azelton
U.S Army Corps of Engineers, Alaska District, Anchorage, AK, USA
Jon E. Zufelt, PhD, PE
U.S Army Corps of Engineers, Engineer Research and Development Center Cold Regions Research and Engineering Laboratory, Ft. Richardson, AK, USA

Abstract

Shishmaref, Alaska, is located on Sarichef Island in the Chukchi Sea. Sarichef Island is composed of very fine-grained sand permafrost, most likely wind-blown deposits formed as dunes when global sea levels were much lower. With present-day sea levels and changing climatic conditions in the region, these permafrost soils are more susceptible to erosion from wind, wave, and ice forces. In recent years, erosion at Shishmaref has been more pronounced due to the changing climatic conditions in the region. To combat this erosion, several local protection projects have been constructed with varying degrees of success. In an effort to learn more about the thermal conditions of the permafrost at Shishmaref, ERDC-CRREL and the Alaska District installed a series of thermistor strings beneath these revetments. This data will allow us to gain an understanding of the temperature of the permafrost throughout the year and during periods of intense fall storm events.

Keywords: convective cooling; permafrost; Shishmaref.

Introduction

Shishmaref, Alaska is located on Sarichef Island, in the Chukchi Sea, just north of the Seward Peninsula. Shishmaref is 8.5 km from mainland Alaska, 210 km north of Nome, and 170 km southwest of Kotzebue. Shishmaref has a population of approximately 615, most of whom are Inupiat Eskimo. The people of Shishmaref live a traditional subsistence lifestyle.

Sarichef Island is a barrier island 4 km long by 0.7 km wide. The island is one of a string of barrier islands separating the Chukchi Sea from the Alaskan mainland. These islands are composed of very fine-grained sand-permafrost, most likely wind-blown deposits formed as dunes when global sea levels were much lower. With present-day sea levels and changing climatic conditions in the region, these permafrost soils are more susceptible to erosion from wind, wave, and ice forces.

Short period waves from locally generated storms appear to be the most problematic for the island. The shoreline is directly exposed to the southwesterly and northwesterly fetches across the Chukchi Sea and can experience moderately high waves under storm conditions. Such waves are generally in the 1.5 to 2.5 m high range with periods of 4 to 5 seconds based on observations at the bluff. Events with waves as high as 3 m have been estimated from observations during extreme storm conditions. These waves can cause severe erosion when coupled with high storm surge events. Fall storms can cause extreme erosion to the shoreline at Shishmaref. The wave action caused by these storms cuts into the banks and in the spring the banks that were undercut will thaw, drop, and wash away, thus exposing more frozen soils. Figures 1 and 2 illustrate how much damage can occur to the shoreline at Shishmaref due to one storm. Figure 3 illustrates the permafrost degradation seen at Shishmaref.

Figure 1. Shoreline fronting the Teacher's Quarters in July of 2004. Note steps to grass-covered bluff.

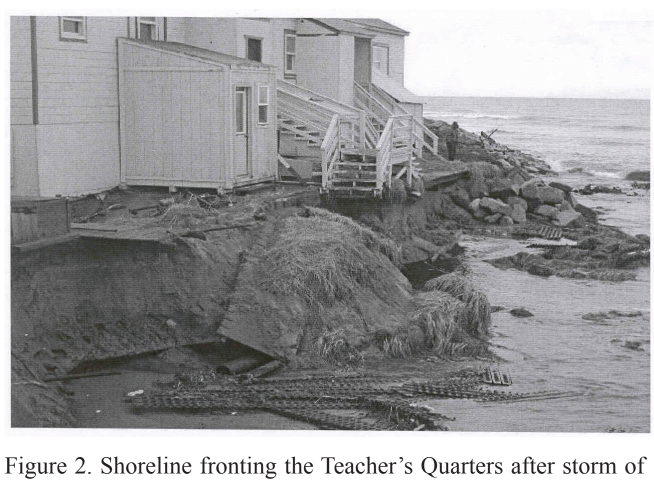

Figure 2. Shoreline fronting the Teacher's Quarters after storm of October of 2004.

Figure 3. Permafrost degradation at Shishmaref, Alaska showing exposed permafrost horizon.

Figure 4. USACE revetment fronting the Teacher's Quarters – summer 2005.

Figure 5. USACE revetment construction fall of 2007.

The frozen horizon can be clearly seen at the base of the bluff. Documented history of storm damage and coastal erosion problems at Shishmaref extends back more than 50 years and includes numerous reports by various consultants and State and Federal agencies, including the Alaska District, U.S. Army Corps of Engineers (USACE).

Erosion Protection

The community has tried many techniques throughout the years to arrest the erosion of their coastline including barrels, gabions, sandbags, and articulated concrete mat (AMC). All of these proved to be only temporary solutions as wave action and high water level events have all but destroyed these structures. Because the shoreline continues to recede, the community has moved houses and other structures back from the shoreline but they are quickly running out of room due to Shishmaref's limited size and soil conditions.

To combat the erosion several local erosion protection projects have been constructed with varying degrees of success. In 2004 the Bureau of Indian Affairs (BIA) constructed approximately 150 m of rock revetment. The Alaska District constructed approximately 70 m of rock revetment in the summer/fall of 2005, with the City of Shishmaref extending this effort by constructing an additional length of rock protection. In a continuing effort to protect the shoreline, the Alaska District will complete another 200 m of rock revetment in the fall of 2007 and summer of 2008. Figures 4 and 5 illustrate these construction efforts. Eventually the community would like to see their entire shoreline protected.

Permafrost Temperature Measurement

In an effort to learn more about the thermal properties of the permafrost at Shishmaref, the U.S. Army Corps of Engineers Engineer Research and Development Center-Cold Regions Research and Engineering Laboratory (ERDC-CRREL) and the Alaska District have installed a series of thermistor strings beneath several of the rock revetments placed at Shishmaref. This data will enhance existing knowledge of the temperature of the permafrost throughout the year at Shishmaref, as well as during intense fall storm events. With a better understanding of the permafrost conditions on Sarichef Island, USACE and other agencies will have more information with which to design stable erosion protection measures.

The Alaska District and CRREL installed the first thermistor string in the summer of 2005, coinciding with the construction of the USACE revetment fronting the school property. Figure 6 illustrates the placement of this thermistor string prior to covering with core rock. In addition, in the summer of 2006 a string of thermistors was placed beneath a gabion revetment built by the City of Shishmaref. Both of these strings were placed beneath the filter fabric prior to the placement of the core rock or the gabion baskets. The gabion revetment has subsequently been covered by the USACE rock revetment in the fall of 2007. In July of 2007 a vertical string, descending approximately 3.3 m was placed near Nayokpuk store and in August of 2007, a string was placed beneath the new USACE revetment along the shore fronting Nayokpuk store. This string was also placed between the filter fabric and the parent soil material.

All of the thermistor strings are connected to and read by Campbell Scientific CR10X data loggers and powered by three deep discharge gel-cell marine batteries. The thermistor strings are constructed from a multi-conductor cable with one of the conductors used as a common leg for the resistance measurement of each precision glass bead thermistor. Each thermistor location is isolated and waterproofed. The multi-conductor cable is protected by an outer conduit. The initial installation at the school property used a reinforced washing machine hose while later cables were protected with non-metallic liqui-tight conduit. Figure 7 shows the approximate location of each string on the island. Also included in this figure is the location of a proposed thermistor string in a relatively undisturbed portion of the shoreline. This string is intended to provide data on soil temperatures where convective cooling is not possible due to the native soil conditions and would be one of the last portions of the shoreline to be protected.

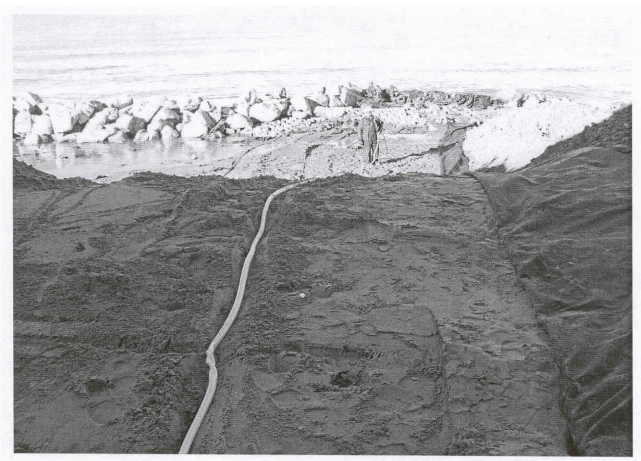

Figure 6. Thermistor string installation in the USACE revetment fronting the Teacher's Quarters.

Potential for convective cooling

There are several pieces of information that the Alaska District and CRREL hope to obtain from the data acquired from these thermistor strings. The first is a better understanding of the thermal interaction between the rock revetment and the natural soil materials at Shishmaref. The hope is to be able to establish where the active layer is generally located at the shoreline. The data will also be used to determine how the permafrost reacts to fall storm events. The data should show whether or not there are thermal fluxes in the soil temperatures during fall storms. Knowing whether or not the soil temperature fluctuates during these fall storms can enable a better understanding of when and what causes the shoreline permafrost to degrade and thus cause erosion.

Data provided by the thermistor strings may also provide knowledge of the link between the temperature of the permafrost and convective cooling. The fact that natural convection can have a large impact on heat transfer in a porous medium is well known (Goering 1995). In order to maintain stable permafrost, it is generally necessary to ensure that the mean annual surface temperature (MAST) is maintained below 0°C (Goering 1998). While the rock and gap sizes are greater than those recommended for efficient convective cooling, it is surmised that after a period of stabilization the revetment will help to maintain the MAST below 0°C, thus thermally stabilizing the permafrost.

Convective cooling is heat transfer by the natural upward flow of air from the relatively warmer object being cooled. Convective cooling techniques have been used with varying

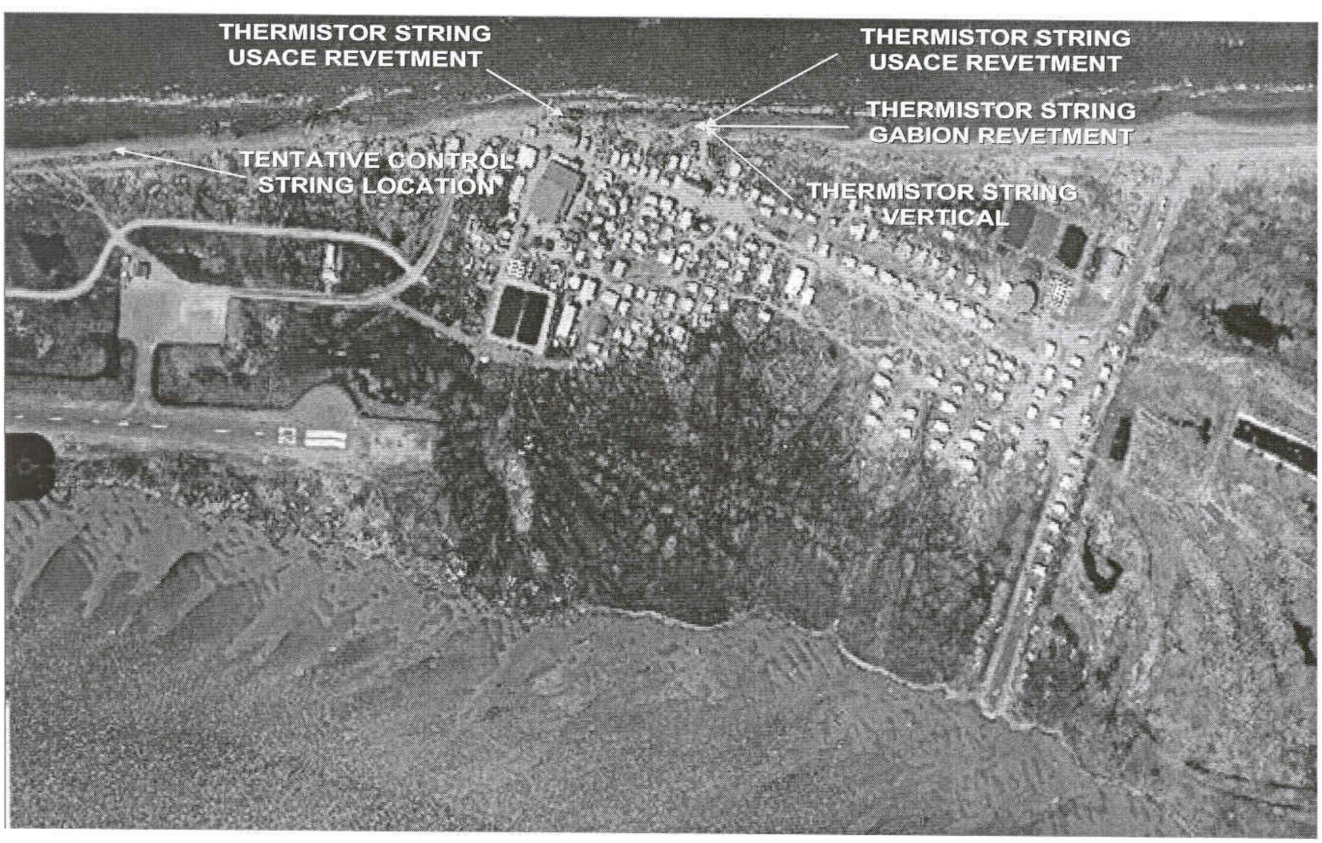

Figure 7. Thermistor string locations at Shishmaref.

degrees of success in road embankments in the Fairbanks, Alaska area. Several studies have previously been conducted on the use of Air Convection Embankments (ACE), which allow for natural convection of the pore air to occur within the embankment during the winter months (Goering 1998). Convection enhances the upward transport of heat out of the embankment during the winter months thus cooling the lower portions of the embankment and underlying foundation soil (Goering 1998). The cooling effect is achieved by maintaining a relatively small temperature difference during the winter compared with the summer. During the winter, colder pore air in the upper potion of the embankment will descend due to its greater density while warm pore air from the embankment base rises. This results in a pattern of convection cells within the embankment.

With the aid of convective cooling, the permafrost table should begin to rise. In order to achieve this cooling effect the embankment must be composed of a rock and gravel matrix, which is railroad ballast sized (0.05 to 0.075 m), poorly graded, and with a very low fines content (Goering 2003). Due to time, materials available, funding constraints, and coastal conditions the USACE revetments do not fully meet the criteria that best enhances convective cooling. It is still uncertain how much heat transfer will occur from the relative impermeable embankment base to the permeable revetment. The revetment that fronts the teacher's quarters at Shishmaref does not have a poorly graded rock/gravel matrix. The core layer in this revetment consists of dredge spoils with a high fines content. What may enhance convective cooling in this revetment is the armor rock layer. The armor layer in this revetment was constructed using selective placement. Selective placement is the careful selection and placement of individual armor stones to achieve a higher degree of interlocking. This 1 meter (approximate) thick layer of tightly knit rock may help to facilitate convection within the revetment. In the revetment fronting Nayokpuk store, once again the gradation of the gravel layer was not ideal to aid in convective cooling. Instead of a poorly graded material, the gravel in this revetment is closer to well-graded gravel. While not poorly graded gravel, the material used in the revetment should be clean enough (marginal amount of fines) to provide ample void space for convection to occur. It is hoped that the effects of convective cooling will be seen on the landward side of the revetment where a gravel layer has been placed to a thickness of 0.70 m. Water infiltration within the revetment during the spring and summer months may decrease the effects of convective cooling within the system. Presently there is not enough information to determine whether these revetments are helping combat permafrost degradation. Within 5 to 6 years enough data will have been collected so that the Alaska District and CRREL can do further analysis and then re-evaluate the effects of convective cooling.

Temperature data

The data gathered from the vertical thermistor string should allow us to confirm the general location of the active layer. It will also show the maximum and minimum annual permafrost temperatures. Preliminary data for the vertical string, and the string beneath the newest USACE revetment

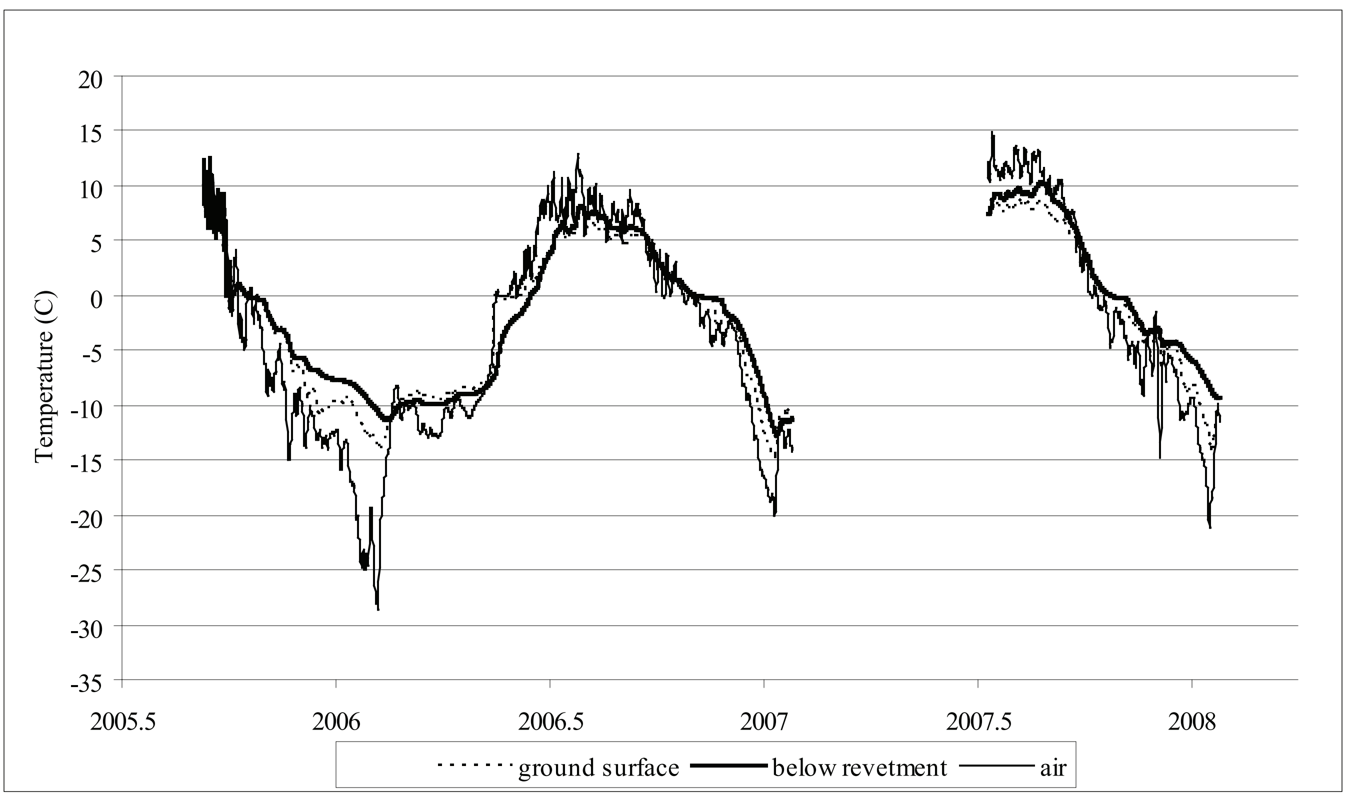

Figure 8. Graph of Temperature vs. Date for the thermistor string placed in the USACE revetment fronting the Teacher's Quarters.

should be available by the time of the presentation of this paper.

Figure 8 shows a graph of the data collected from the thermistor string beneath the USACE revetment fronting the Teacher's Quarters from September 2005 until January 2008. Gaps in data are due to power source difficulties. The data logger was originally placed on a trickle charger to keep the internal battery charged. Due to problems with power source reliability and the desire to keep the system maintenance-free, it was removed from line voltage and placed on the three deep discharge gel-cell marine batteries described above. From the data collected at this point it is apparent that the ground is staying relatively cool. The location of this thermistor string is beneath the filter cloth and just above the native soil. The core rock and armor stone of the shore protection are located vertically above the thermistors. Plotted on Figure 8 are the air temperature from a thermistor located approximately 3 m from the Teacher's Quarters, the ground temperature approximately 0.20 m below the surface, and the temperature beneath the core rock and armor stone. At the time of construction of this revetment, the native soil was contoured to match the final slope of the armor stone which resulted in the native soil, core rock, and armor stone attaining a temperature equivalent to the air temperature. Over the next month, all three temperatures on Figure 8 can be seen to follow the general decline of the air temperature. It can be seen from the period corresponding to the annual cycle of late 2005 to late 2006, the time that the soil temperatures were below 0^{o}C are longer than they were above 0^{o}C. This indicates that the mean annual soil temperature (both beneath the revetment and 0.2 m below the ground surface) is below 0^{o}C, one of the goals of convective cooling. There are some variations noted from year to year for the data presented. The maximum soil temperature beneath the revetment was approximately 8°C in the summer of 2006 and approximately 10°C in the summer of 2007. Similarly, the minimum soil temperature beneath the revetment was approximately -11°C in early 2006, -13°C in early 2007, and was still dropping at -9.6°C in mid-January 2008. This indicates that the base of the revetment is not below the permafrost table but within the active layer. Further data will allow the determination of whether the revetment is acting as an Air Convection Embankment

Summary

ERDC-CRREL and the Alaska District have installed several thermistor strings beneath shore protection projects at Shishmaref, Alaska on Sarichef Island. Data from the strings are beginning to show the variations in the temperature experienced over the annual cycle in the native soil beneath the revetment projects. It is hoped that the grading and selective placement of the armor stone of these revetments causes them to act as an Air Convection Embankment. An additional string placed vertically will supply information about the depth to the permafrost table and the thickness of the active layer.

In the future, along with continual data collection for the 4 strings currently in place a control string of thermistors will be placed at Shishmaref. Due to timing and funding constraints, the control string will be the final thermistor string placed on Sharichef Island. This string will be tentatively placed along the shoreline in the vicinity of the landing strip (as shown in Fig. 7). This area was chosen as a probable location because it will be one of the last areas impacted by revetment construction. Therefore, it should give us the longest period of record for temperatures on the unreveted shoreline. In April of 2008 a Ground Penetrating Radar (GPR) study will be will be conducted by the Alaska District and CRREL to aid in permafrost delineation, including depth to the permafrost table and the thickness of the permafrost layer. When this work is completed the Alaska District and ERDC-CRREL should have a through understanding of permafrost conditions in the vicinity of Shishmaref on Sarichef Island. Knowing the potential stability of the permafrost soils on Sharichef Island will enable the Alaska District and other Federal and State agencies make informed decisions regarding future shore protection and development opportunities.

References

Goering, D.J. 1998. Experimental Investigation of Air Convection Embankments for Permafrost-Resistant Roadway Design. *Proceeding of the 7th International Conference on Permafrost, Yellowknife, Canada, 1998*: 319-326.

Goering, D.J. 2003. Passively cooled railway Embankments for Use in Permafrost Areas. *Journal of Cold Regions Engineering* 17(3): 119-133.

Goering, D.J. & Kumar, P. 1995. Winter-time Convection in open-graded embankments. *Cold Regions Science and Technology* 24: 57-74.

Measuring Ice Lens Growth and Development of Soil Strains during Frost Penetration Using Particle Image Velocimetry (GeoPIV)

Tezera Firew Azmatch
UofA Geotechnical Centre, Department of Civil and Environmental Engineering, University of Alberta, Edmonton, AB, Canada
Lukas U. Arenson
BGC Engineering Inc., Vancouver, BC
David C. Sego
UofA Geotechnical Centre, Department of Civil and Environmental Engineering, University of Alberta, Edmonton, AB, Canada
Kevin W. Biggar
BGC Engineering Inc., Edmonton, AB

Abstract

The formation of ice lenses and the water migration during freezing of frost susceptible, fine-grained soils is a dynamic and complex process. Horizontal ice lenses and vertical ice veins form at different spacing, intervals, and growth rates as the pore freezing front penetrates into the ground forming a three dimensional ice lens pattern. One-dimensional step-freezing tests were carried out in a transparent freeze cell with frost susceptible Devon silt to study this effect in detail. Time-lapse photography and particle image velocimetry are used to identify the dynamics of the freezing processes. Three dimensional movements are used to measure the changes in ice lens growth and axial soil strain in-between ice lenses with time. The formation and growth rate of vertical ice veins are studied and local vertical strains are determined. Horizontal soil deformations are also investigated. The detailed strains and ice lens growth rates within freezing soils help in improving formulations for frost heave, strength, and deformation behavior of freezing and frozen soils.

Keywords: frost heave; frost susceptibility; ice lens formation.

Introduction

The formation of ice lenses and the water migration during freezing of frost susceptible, fine-grained soils is a dynamic and complex process. Horizontal ice lenses and vertical ice veins form at different spacing, intervals, and growth rates as the freezing front penetrates into the ground forming a three dimensional ice lens pattern. This pattern and the growth rates of the ice lenses strongly depend on the freezing boundary conditions, such as temperature gradient, cooling rate, or vertical pressures, and the characteristics of the soil, i.e. the grain size distribution, hydraulic conductivity, water availability, and pore water salinity (Konrad & Morgenstern 1982, Konrad 1994, Miller 1973, Penner 1972).

The formation of ice lenses is possible with the presence and migration of unfrozen water at temperatures below its freezing point (Konrad and Morgenstern 1980). It is believed that migration of the free water is induced by a temperature gradient within the soil that induces suction. The suction then drives the movement of free water to the growing ice lens. The flow of water towards the warmest ice lens is assisted by the formation of tension cracks, which increase the vertical hydraulic conductivity of the soil (Chamberlain & Gow 1979).

Freezing tests conducted at the University of Alberta (Xia 2006) have shown that ice lens growth is not a one-dimensional process. Horizontal ice lenses as well as vertical ice veins form as the soil freezes. The vertical ice veins develop a hexagonal crack pattern similar to that observed in drying soils (Arenson et al. in press).

The reticulate ice structure, also observed under natural freezing conditions (Mackay 1974), during freezing deforms the soil horizontally and vertically. When the final ice lens starts to form, part of the soil below the final ice lens consolidates, and part of the soil above the final ice lens heaves. Arenson et al. (2007) measured the vertical deformations in freezing soil and were able to explain the freezing process using these deformation results.

This work was continued, and this paper focuses on the formation of the vertical ice veins and the horizontal soil deformations. Results from the time-lapse photography presented by Xia et al. (2005) are re-analyzed using particle image velocimetery (PIV) to develop a better understanding of the formation and growth of ice structures.

Laboratory Tests

One-dimensional open system (access to water) step-freezing tests were carried out on Devon silt under different boundary conditions. The Devon silt has a liquid limit of 32%, plastic limit of 20%, and specific gravity of 2.65. The samples were frozen from the top downward. Two temperature baths control the temperature conditions at the top and the bottom of the sample to establish one dimensional

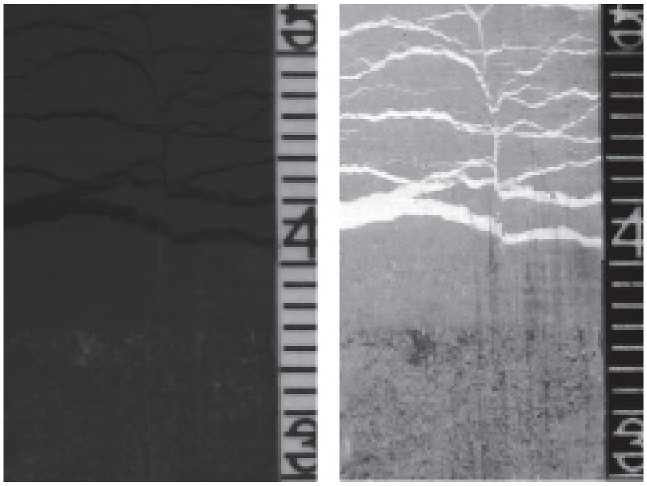

Figure 1. Original picture (left), and visible ice lens structure (right).

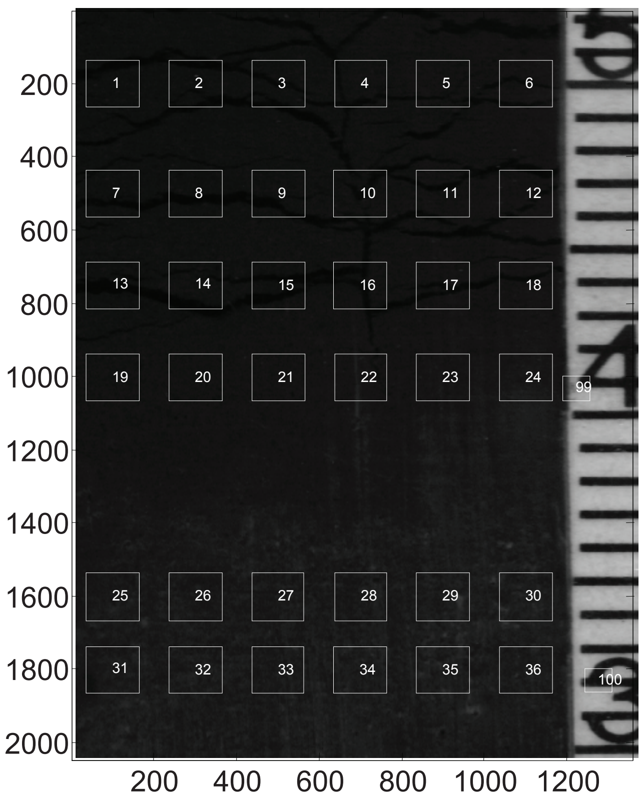

Figure 2. Initial patch locations; the scale is in pixels (1 pixel ~10 μm).

vertical freezing from the top downward.

A fluorescent tracer ($C_{20}H_{12}O_5$), which appears green in unfrozen water but colorless in ice under ultra violet light (Arenson & Sego 2006), was used to determine the frozen and unfrozen zone of the sample during freezing.

Time-lapse photography provided digital photo records to visually observe and document the freezing process. Details of the time-lapse photography technique and of the laboratory freezing tests used herein are presented in Xia et al. (2005) and Xia (2006).

Table 1. Test conditions.

Test #	T^1_{grad} (°C/m)	S^2 (g/L)	σ^3 (kPa)
1	58	0	0
4	58	0	100
8	58	10.2	0

[1] Temperature gradient at thermal steady state
[2] Salinity (NaCl)
[3] Vertical pressures during freezing

Image Analysis using GeoPIV

The digital images were analyzed using GeoPIV software, a MatLab module which implements particle image velocimetery (PIV) in a manner suited to geotechnical testing. This code has been programmed and successfully used for geotechnical laboratory testing to measure deformations in soils (White et al. 2003). It has also been used to determine the deformations in freezing soils (Arenson et al. 2007).

Figure 1 shows the original image and the corresponding ice lens structure for one of the images.

GeoPIV was used to measure the soil deformation. Geo PIV uses image texture to follow patches over a time series of pictures. A number of patches were defined on the sample and their movement was followed over time (Fig. 2).

Test Results and Image Analysis Results

Three tests from Xia et al. (2005) were analyzed in this paper. These tests were chosen because of their well defined vertical ice veins. The freezing test conditions are shown in Table 1. All the samples were initially consolidated at 100 kPa vertical pressure.

Ice Lens Growth and Deformation

The reticulate ice structures and cross sections of the frozen samples showing the hexagonal ice vein pattern are presented in Arenson et al. (in press). Figures 3 through 10 show various deformation results.

Vertical deformations

In the plots for vertical deformations (Figs. 3, 7) positive values indicate heave and negative values indicate consolidation.

It can be seen from Figure 3 (Test #1) that heaving starts at about 42 hours after the start of the test. By the time heaving has started the consolidation process is nearly complete. This means that heaving and consolidation are not occurring in parallel. Heaving starts almost after consolidation is complete. The heave rate and the consolidation rate are constant.

Figure 3 also indicates that P10 is undergoing heaving, and P22, P24, and P25 are consolidating. Hence, row 2 (containing patches P7–P12) is heaving, and row 4 (containing patches P19–P24) is consolidating. The final ice lens for this test is located between row 2 and row 4. This

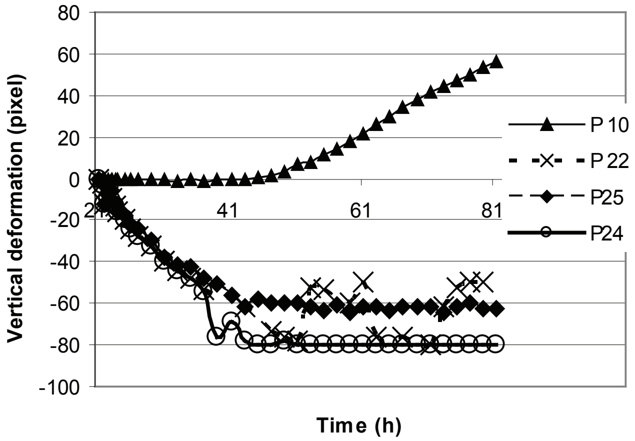

Figure 3. Vertical deformations for Test #1. P10 is located above the final ice lens. P22, P24 and P25 are located below the final ice lens.

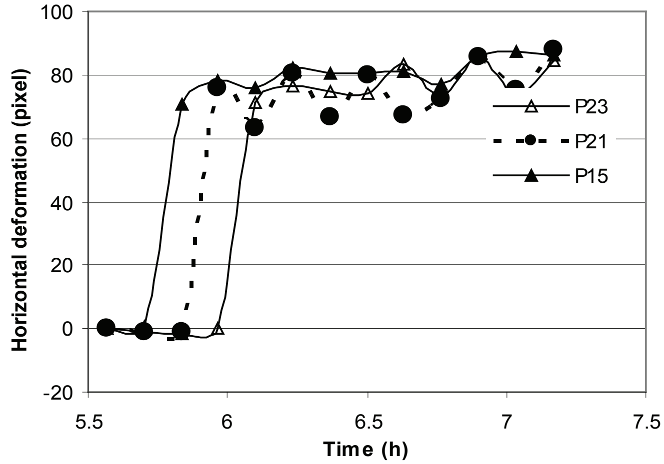

Figure 4. Horizontal deformations for Test #1.

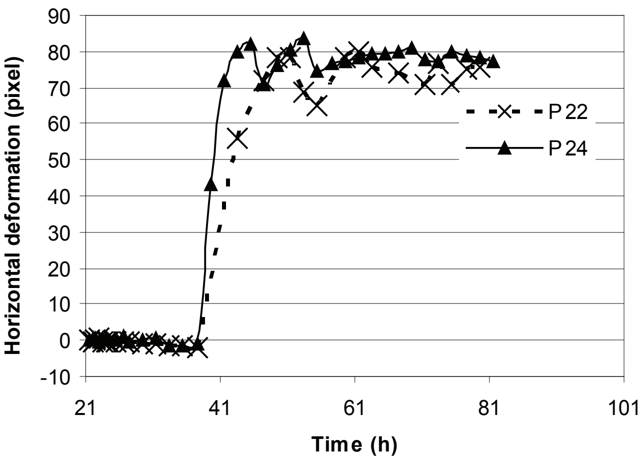

Figure 5. Horizontal deformations while a final vertical ice vein is being formed for Test #4.

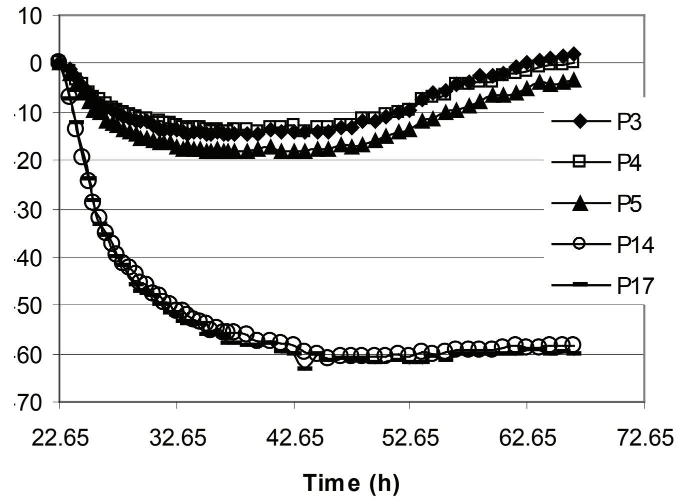

Figure 6. Horizontal deformations while an intermediate vertical ice vein is being formed for Test #4.

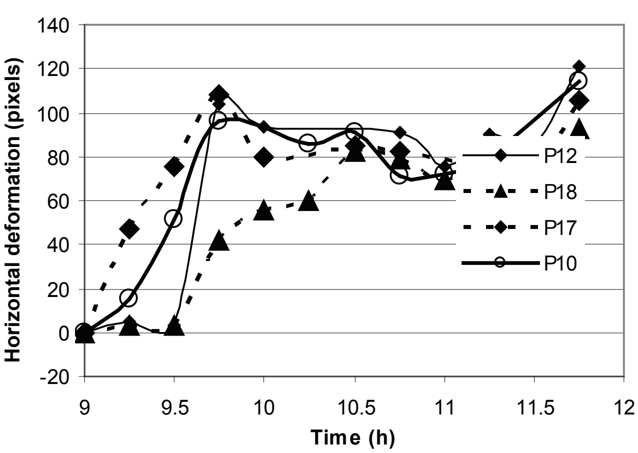

Figure 7. Vertical deformations while the final ice lenses are being formed for Test #8. P3, P4 and P5 are located above the final ice lens. P14 and P17 are located below the final ice lens.

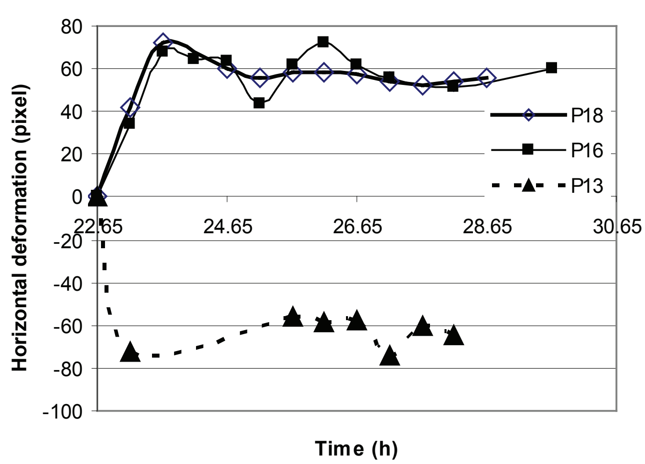

Figure 8. Horizontal deformations while a final vertical ice vein is being formed for Test #8. P13 is located to the left of the vertical ice vein. P16 and P18 are to the right of the vertical ice vein.

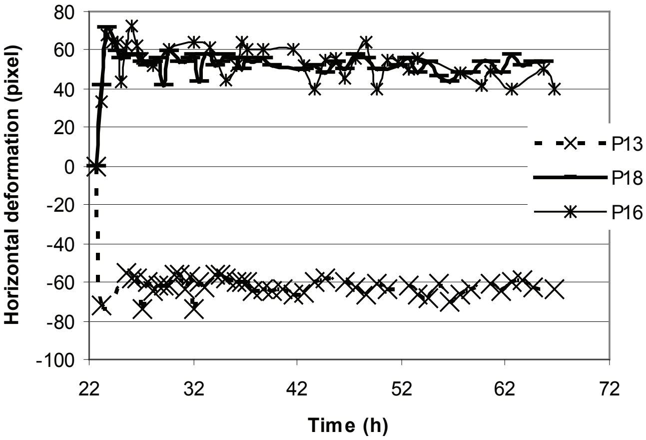

Figure 9. Horizontal deformations while a final horizontal ice lens is being formed for Test #8. P13 is located to the left of the vertical ice vein. P16 and P18 are to the right of the vertical ice vein.

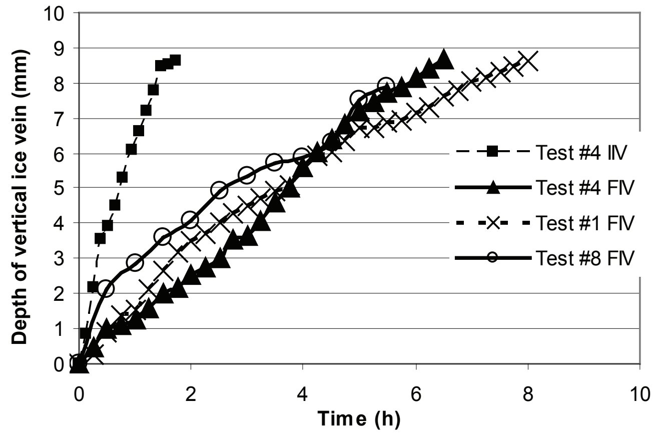

Figure 10. Rate of growth of the vertical ice veins (FIV=Final Ice Vein, IIV=Intermediate Ice Vein).

explains that water is being drawn from the region below the final ice lens. This water is then used to form the final ice lens. As the final ice lens forms, the regions above it start to heave, as observed by the movement of P10. Similar trends have also been observed by tracing other patches in the same test.

In Figure 7, all the patches are consolidating during the first 42 hours. After 42 hours, patches P3 and P4 start heaving, and patches P14 and P17 do not deform anymore. The final ice lens for this test started forming after about 42 hours. This indicates that the development of the final ice lens, hence frost heave, starts after the consolidation is complete. The final ice lens for this test is located between row 2 (containing patches P7–P12) and row 3 (containing patches P13–P18)

Figures 3 and 7 also indicate that the rate of heaving is smaller than the rate of consolidation. It can be concluded that the rate of ice formation is lower than the rate of water extraction from the soils.

Horizontal deformations

In Figure 3, it can be seen that heaving starts around 42 hours after the start of the test. This implies that the final horizontal ice lens starts to form after 42 hours. In Figure 4, it can be noted that the horizontal strains remain constant while the final ice lens is being formed. The same observation can be made in Figures 5, 6, and 8. This implies that the horizontal strains are due to the formation of the tension cracks and not due to the formation of the final horizontal ice lenses. The horizontal strains could therefore be assumed to originate from the formation of the vertical tension cracks, which are a result of the suction created by the temperature gradient. According to the authors, the mechanism of the formation of the vertical ice veins can be described as follows: First, suction is created in the frozen fringe, and tension cracks form; these tension cracks are then filled with water being removed from the soil, and finally, part of the water in the tension cracks freezes to form the vertical ice veins and part of it moves up to form the horizontal ice lenses behind the vertical ice veins. The formation of the tension cracks facilitates the flow of water by increasing the hydraulic conductivity of the soil. It is observed that tension cracks are formed prior to the formation of horizontal ice lenses (Arenson et al. in press).

While the soils are straining horizontally, water is being drawn to form the vertical ice veins and the horizontal ice lenses above their crack tip. Mackay (1974) states, “The vertical and horizontal ice veins are believed to have grown in shrinkage cracks with much of the water being derived from the adjoining clay.”

In most of the tests, the magnitude of the horizontal displacement is between 60 and 80 pixels (approximately 0.6–0.8 mmm). These could indicate that the thickness of the vertical tension cracks formed is almost constant. It can be observed from the digital images that the thickness of the vertical ice veins is the same for almost all the tests.

From Figures 8 and 9, it can be observed that the movements of P13 are in the opposite direction to that of P16 and P18. This is because the patches are located on different sides of the vertical ice vein. P13 is located to the left of the vertical ice vein, and P16 and P18 are located to the right of the vertical ice vein. Hence, their corresponding horizontal displacement is in a different direction but it displaces the same amount, indicating the opening of the vertical crack and the formation of the ice vein.

Rate of growth of vertical ice veins

Tension cracks always formed before the horizontal ice lenses. These tension cracks, which facilitate the flow of unfrozen water, are then filled partly by vertical ice veins.

Figure 10 shows the rate of growth of the vertical ice veins. The final ice veins (FIV) are defined as the vertical ice veins that form immediately before the start of the formation of the final horizontal ice lens. The intermediate ice veins are the vertical ice veins that form before the FIV. The rate of growth of the final vertical ice veins ranges from 1.22 mm/h to 1.57 mm/h. For Test #4, the rate of growth of the intermediate ice vein is 5.78 mm/h. Hence, the rate of growth

Table 2. Depth and growth rate of vertical ice veins.

Test #		Height of vertical ice vein (mm)	Growth rate (mm/h)
1	FIV	8.60	1.22
4	FIV	8.67	1.37
	IIV	8.60	5.78
8	FIV	7.91	1.57

of the IIV is higher than the rate of growth of the FIV.

The height of the vertical ice veins for the tests under consideration is about the same for all tests.

Conclusions

Particle image velocimetry (PIV) was used to measure soil deformations. Patches with a distinct characteristic were followed as the ice lenses formed and grew. The deformations measured were used to explain the freezing process and the resulting ice being formed.

The heaving process and the consolidation process were observed to take place at different times. Heaving followed immediately after consolidation was complete.

The horizontal strains were observed to be a result of the formation of the vertical tension cracks as the freezing front advanced.

The suction produced as a result of the temperature gradient caused tension cracks in the soil. The tension cracks, which increase the vertical permeability of the soil, were then filled with water. A channel formed where water can migrate from the unfrozen zone to the warmest ice lens. Part of the water moved up enhancing the development of a horizontal ice lens above the crack, and part of it froze inside the cracks, leading to the formation of the vertical ice veins.

The vertical tension cracks always formed before the horizontal ice lenses formed. Thus, the formation of the tension cracks, and hence the tensile strength of the soils, play a very important role in the freezing process.

Acknowledgments

The authors would like to thank Dr. Andy Take from Queens University for his support with the GeoPIV analysis. Tezera Firew Azmatch appreciated the funding through the NSERC Discovery Grant held by Dr. Sego.

References

Arenson, L.U., Firew Azmatch T. & Sego, D.C. 2008. A new hypothesis on ice lens formation in frost susceptible soils. *Proceedings of the Ninth International Conference on Permafrost, Fairbanks, Alaska, June 29–July 3, 2008* (this proceedings).

Arenson, L.U., Sego, D.C. & Take, W.A. 2007. Measurement of ice lens growth and soil consolidation during frost penetration using particle image velocimetry (PIV). *60th Canadian Geotechnical Conference, Ottawa, ON, October 21–24, 2007*: in press.

Arenson, L.U., Xia, D., Sego, D.C. & Biggar, K.W. 2006. Change in ice lens formation for saline and non-saline Devon silt as a function of temperature and pressure. *13th International Conference on Cold Regions Engineering. American Society of Civil Engineers (ASCE), Orono, Maine, USA*: CD-Rom.

Arenson, L.U. & Sego, D.C. 2006. The effect of salinity on freezing of coarse grained sands. *Canadian Geotechnical Journal* 43(3): 325-337.

Chamberlain, E.J. & Gow, A.J. 1979. Effect of freezing and thawing on the permeability and structure of soils. *Engineering Geology* 13(1-4): 73-92.

Konrad, J.M. 1989. Pore water-pressure at an ice lens: Its measurement and interpretation. *Cold Regions Science and Technology* 16(1): 63-74.

Konrad, J.M. 1994. 16th Canadian Geotechnical Colloquium - Frost Heave in Soils - Concepts and Engineering. *Canadian Geotechnical Journal* 31(2): 223-245.

Konrad, J.M. & Morgenstern, N.R. 1980. A mechanistic theory of ice lens formation in fine-grained soils. *Canadian Geotechnical Journal* 17(4): 473-486.

Konrad, J.M. & Morgenstern, N.R. 1982. Effects of applied pressure on freezing soils. *Canadian Geotechnical Journal* 19(4): 494-505.

Mackay, J.R. 1974. Reticulate ice veins in permafrost, Northern Canada. *Canadian Geotechnical Journal* 11(2): 230-237.

Miller, R.D. 1973. Soil freezing in relation to pore water pressure and temperature, *Second International Conference on Permafrost. National Academy of Sciences, Washington, Yakutsk, Siberia*: 344-352.

Nixon, J.F.D. 1991. Discrete ice lens theory for frost heave in soils. *Canadian Geotechnical Journal* 28(6): 843-859.

Penner, E. 1959. *The Mechanism of Frost Heaving in Soils.* Bulletin 225, U.S. Highway Research Board.

Penner, E. 1972. *Influence of Freezing Rate on Frost Heaving.* Highway Research Record 393, U.S. Highway Research Board.

Taber, S. 1930. The mechanics of frost heaving. *Journal of Geology* 38: 303-317.

White, D.J., Take, W.A. & Bolton, M.D. 2003. Soil deformation measurement using particle image velocimetry (PIV) and photogrammetry. *Geotechnique* 53(7): 619-631

Xia, D. 2006. *Frost Heave Studies Using Digital Photographic Technique.* M.S. Thesis. Edmonton, AB, Canada: University of Alberta, 165 pp.

Xia, D., Arenson, L.U., Biggar, K.W. & Sego, D.C. 2005. Freezing process in Devon silt – using time-lapse photography. *Proceedings, 58th Canadian Geotechnical Conference, Saskatoon, Saskatchewan. September 18–21.* CD-ROM

Evidence of Permafrost Formation Two Million Years Ago in Central Alaska

James E. Beget, Paul Layer, David Stone, Jeffrey Benowitz, Jason Addison
Department of Geology and Geophysics, University of Alaska Fairbanks, Fairbanks, AK, USA

Abstract

Ice wedge casts and thermokarst deposits near the base of loess cliffs at Gold Hill record a previously unrecognized cycle of transient climate cooling and permafrost formation followed by an interval of climate warming and permafrost degradation. The ice wedge casts and thermokarst features occur below the PA tephra (ca. 2.02 myr) and begin above loess recording the Reunion paleomagnetic excursion (ca. 2.14 myr). The dates indicate colder conditions and permafrost formation in central Alaska 2.14–2.02 million years ago and can be correlated with marine isotope stage 77, a time of significant global glaciation and cooling. Warmer conditions during marine isotope stage 76 thawed the permafrost and generated the ice wedge casts and thermokarst sediments preserved at Gold Hill today. Climate and permafrost in Alaska were responding rapidly to global climate forcing by two million years ago.

Keywords: Alaska; climate change; geochronology; loess, permafrost; Quaternary.

Introduction

Loess deposits are common across central Alaska, especially in low-lying areas near the Tanana and Yukon and other glacier-fed rivers. Large areas of ice-rich frozen ground in valley bottoms in central Alaska have formed in loess and reworked eolian silts. River erosion or human disturbance of loess at building, mining, and other construction sites sometimes reveal spectacular views of ice wedges, ice lenses, and other varieties of permafrost.

Pewe (1951) first recognized that the silts that blanket hillslopes and form thick deposits in valley bottoms near Fairbanks and other areas were eolian in origin, and suggested that the ice wedges and other periglacial features found in the loess were produced during the last ice age.

Large areas of valley-filling loess deposits were washed away and destroyed by hydraulic excavation and dredging during 20th century industrial scale gold mining operations near Fairbanks, Ester, Chicken, and other mining areas in central Alaska. When the mining operations stopped, cliffs of loess and other sediments 10–50 m thick were left in some areas. As a result of the gold mining, numerous bones and occasional frozen carcasses of bison, mammoths, and other extinct Pleistocene megafauna were collected from the loess and the alluvial gravels beneath the loess (Guthrie 1990).

The Troy L. Pewe Climatic Change Permafrost Reserve is located along the north side of the Parks Highway beginning about 3 km southwest of the University of Alaska Fairbanks campus. The site preserves the eastern part of an almost continuous vertical bluff of loess almost 5 km long produced by hydraulic mining in the Fairbanks area. The highest cliffs and the oldest deposits of loess occur at the eastern end of the Gold Hill exposure. The original surface of the loess sloped gently downwards to the south, and small "islands" of the original loess valley fill left by the mining operations are preserved on the south side of the Parks Highway.

Pewe (1975a, b) divided the loess at Gold Hill into four main stratigraphic units. A buried horizon containing logs and branches found near the middle of some loess sections was named the Eva Creek Forest Bed, while the upper loess

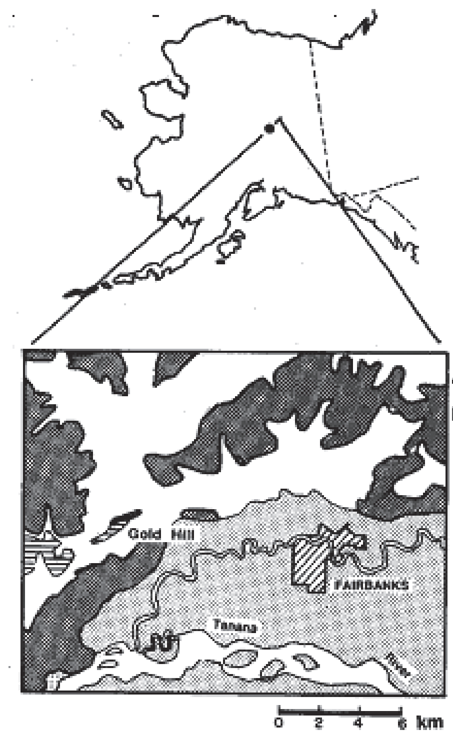

Figure 1. Location of the study site at Gold Hill and simplified Quaternary geology of the Fairbanks area. Light stiple = alluvium, dark stiple = pre-Quaternary bedrock, white = loess deposits, horizontally lined = gravel deposits exposed by mining. Figure modified from Westgate et al. (1990).

was assigned to the Goldstream Formation and the lower loess to the Gold Hill Formation. A basal forest bed occurred in a few sites and was named the Dawson Cut Forest Bed (Pewe 1975b). Pewe also recognized that numerous tephras are preserved in the loess. The base of the entire 30-m-thick loess section was originally estimated to be "Illinoian" in age, i.e., less than 200,000 years old (Pewe 1975a, Pewe & Reger 1989).

The first indication that Alaskan loess deposits might be much older came from the discovery that the loess

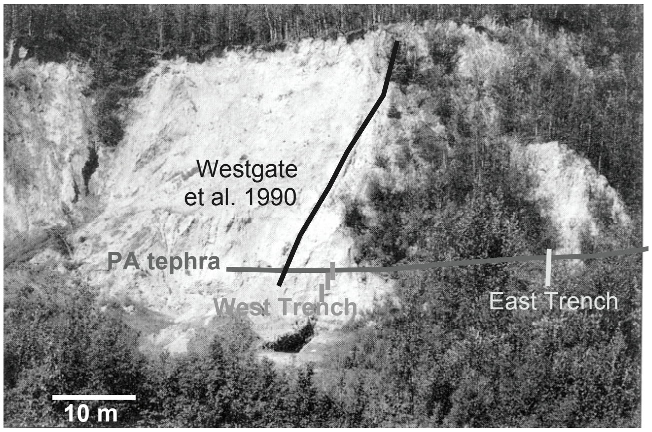

Figure 2. Location of the PA tephra and trenches excavated for stratigraphic and paleomagnetic studies at Gold Hill.

contained numerous paleosols, in addition to the Eva Creek and Bonanza Creek Forest Beds (Beget 1988, 1991). The sequences of multiple paleosols and interstratified loess deposits found at Gold Hill and other sites were interpreted as glacial-interglacial cycles, requiring an age for the loess significantly older than originally inferred by Pewe. These interpretations were supported by geophysical studies that demonstrated that loess deposited in glacial and interglacial periods had different magnetic properties, and that changes in environmental magnetic signals recorded in the loess could be used to produce proxy climate records through loess sections in Alaska that correlated with Milankovitch models of insolation changes and marine isotope records (Beget and Hawkins 1989, Beget et al. 1990, Beget 1996).

Westgate et al. (1990) used tephrochronology and paleomagnetic stratigraphy to determine that the PA tephra found at ca. 21 m depth at Gold Hill was deposited ca. 1.9 million years ago, and loess at the base of the Gold Hill section was as much as 3.1 million years old. Westgate and his co-workers took samples at 10 cm intervals, and found the upper loess was normally magnetized and correlative with the Brunhes paleomagnetic epoch. The lower part of the loess recorded mainly reversed magnetic fields, but in the overall reversely polarized section, there were magnetic reversals back to normal polarity at about 2.5 meters, 3.5 meters, 5.5 meters, and 8.2 meters below the PA tephra layer. The initial transition from normal to the reversely magnetized loess was correlated with the Brunhes-Matuyama boundary, and the two normal epochs below the PA tephra were assigned to the two Reunion subchrons (also known as the Huckleberry Ridge and Reunion events) in the Matuyama Paleomagnetic Chron. More recent work indicates the age of the PA tephra is 2.02 +/- 0.14 Ma (Westgate et al. 2003).

Here we report on the discovery of ice wedge casts, thermokarst features, and interstratified loess and paleosol sequences found below the PA tephra near the base of the Gold Hill section. We also present new paleomagnetic dates for the Gold Hill loess. Our data show that Alaskan loess deposits are surprisingly good recorders of short-lived geologic events, including transient shifts in climate and fluctuations in the earth's magnetic field. Paleoclimatic records from loess deposits are an important source of information about events in terrestrial areas of Alaska.

Field and Laboratory Methods

The PA tephra layer is located 11 m from the bottom of the loess section, and forms a distinctive marker bed that can be traced for more than 30 m across the lower part of the Gold Hill loess. The tephra bed is as much as 5 cm thick, although in most places it is broken into pods or two or more thinner layers. It was used as a datum from which local stratigraphic field measurements were taken at various points along the section.

Trenching and sampling were done to generate two new stratigraphic sequences: one about 5 m east of the long section studied by Westgate et al. (1990) and the second about 20 m to the east (Fig. 2). Both trenches were excavated to a depth of about 4 m and studied with the help of enthusiastic students (Naibert et al. 2005). The newly created loess exposures were then photographed and stratigraphically logged. At both sites, oriented samples were collected beginning at the PA tephra and continuing down to the bottom of the trenches. During sampling, a series of platforms were cut along the excavated exposure, and oriented plastic cube samples were taken at 5 cm intervals from undisturbed loess exposed in the face of the trenches for paleomagnetic analyses. Plastic vials of loose material were also collected every 2 cm for magnetic susceptibility measurements.

The oriented cubes were taken to the Paleomagnetic Laboratory at the University of Alaska Fairbanks, and successive alternating field demagnetization (11 steps) up to 100mT was applied to strip away the modern magnetic overprint and to determine the original polarity of the magnetic field at the time the loess was deposited. After some primary data analysis to locate points of interest in the section, the loess was sampled again with plastic cubes at 2 cm intervals from depths of 0.9 to 1.1 m, and from 2.9 to 3.1 m, for a more detailed examination of changes in magnetic inclination using alternating field demagnetization.

Stratigraphy and Structure

During the initial trenching and logging, it became apparent that loess just below the PA tephra had been locally involved in a series of post-depositional collapses. The PA tephra was deposited on the ground surface ca. 2 million years ago, and thus the topography and slumps that occurred near that time at Gold Hill can be reconstructed from the taphonomy of the PA tepha deposits. We note that a veneer of loose colluvium from 0.1–0.5 m thick is present on the surface at Gold Hill, but our excavations cut completely through the colluvium to expose the much more indurate early Quaternary loess. Our trenching sites were chosen specifically to determine the relationship between the deposits and stratigraphy in the trenches and the PA tephra.

Our excavations reveal the PA tephra was incorporated in local depressions and slumps in 4 distinct areas along the

30-m-long exposure. At the eastern pit, the tephra and the intercalated loess, which elsewhere are preserved in sub-horizontal beds, abruptly began to drop in elevation on each side of a 2-m-wide V-shaped depression, indicating the collapse had formed after the tephra was deposited, and that tephra and loess at the margin of the V-shaped depression was progressively slumping into the depression. Further excavations found pellets of the tephra and blocks of loess in a compact silt matrix within the depression. The V-shaped depression was excavated to a depth of 2 m where it became narrow and terminated. The morphology of the V-shaped depression, and the deformation of the sediment at the margins of the pit, are identical to modern ice wedge casts in the Fairbanks area, and the feature is interpreted as a 2 myr old ice-wedge cast.

At the western pit, a well-developed organic-rich paleosol occurs about 20–60 m thick above the PA tephra. This paleosol can be traced along much of the exposure above the PA tephra. The excavations in the western trench found bedded organic-rich sediment and loess and pods of PA tephra that had apparently collapsed into a broad depression. The organic material occurs in beds at angles up to 70°, together with loess and small pods of the PA tephra (Fig. 3). The depression is interpreted as having formed as part of a thermokarst zone.

At the far eastern of the PA exposure, a loess cliff exposed a 3-m-thick diamicton that could be traced 5 m across the section. The diamicton contained rounded to elongate silt and multi-colored paleosol clasts ranging from 0.5–10 cm in diameter disseminated in a dense, fine-grained matrix. The eastern margin of this deposit cuts across undisturbed loess below the PA tephra, and itself locally underlies the PA tephra and incorporates pods of the tephra. We interpret the diamicton as having formed by progressive collapse of wet, thawed pellets and blocks of sediment into a large thermokarst pit. Similar large pits are forming today at sites where frozen loess is thawing near Fairbanks (Shur et al. 2000). Bits of thawed ground can frequently be heard falling into thermokarst pits, and we suggest the abundant rounded clasts in this deposit accumulated in similar fashion in an ancient thermokarst collapse 2.0 million years ago.

The presence of ice wedge casts and thermokarst features below the PA tephra indicates climate in the Fairbanks cooled sufficiently prior to the deposition of the PA tephra to allow the formation of permafrost. The climate must have subsequently warmed and caused the permafrost to degrade and the thermokarst features to form. The warm period is tentatively correlated with the well-developed paleosol just above the PA tephra, as the presence of the strong paleosol records an interglacial period that occurred just after the PA tephra fall.

Paleomagnetic Record from the Trenches

New paleomagnetic data help to constrain the age of the periglacial features and the climate flucations recorded at the base of Gold Hill. The paleomagnetic data from our two new trenches predominantly display reversed magnetization, as expected in the Matuyama reversed polarity chron. Our data are generally consistent with the previously published age of the PA tephra and the paleomagnetic data from Westgate et al. (1990), and confirms that the loess below the PA tephra is indeed older than 2 million years. However, a comparison of the paleomagnetic data from our two new trenches and the trench of Westgate and his co-workers, reveals some differences. Our two new sections both contain a number of normally magnetized polarity samples that can be interpreted as recording a brief magnetic reversal within the upper part of the Matuyama chron that was not recognized in the trench studied by Westgate and his co-workers. This introduces the possibility that the creation and thawing of ice wedges and other kinds of permafrost may have disrupted the original loess deposits and affected the lateral continuity and preservation of the paleomagnetic record at Gold Hill.

Figure 3. Organic-rich silts and blocks of gleyed and unaltered loess filling a collapsed zone stratigraphically below the PA tephra in the western trench.

Our eastern trench contains a zone of magnetic polarity samples at 0.7 m below the PA tephra. The reversed signal occurs in five successive samples, leaving little doubt that it is a real reversal. Our western trench also produced evidence of this episode of normal magnetization, although it occurred in only one sample. Westgate et al. (1990) also found one point near this depth below the PA that appeared to record a transition to normal polarity, but they decided not to assign a reversal to this normal horizon. Based on the excellent signal in our eastern trench and the appearance of the same event in the two other trenches, we believe this is real polarity event. Because this is the first reversal below the PA tephra, we interpret this event as the Reunion event, dated to 2.14 million years ago.

The variability in the character of the magnetic signal between our two trenches and the Westgate trench is consistent with our recognition of ice wedge casts and thermokarst features in the loess at this depth in the loess. Since the loess below the PA tephra was locally disturbed by a cycle of formation and destruction of ground ice, the sedimentation rate and mode of deposition should vary from place to place across the exposure, just as we observe. Similarly, the low inclinations that both we and Westgate et al. (1990) observed in this area, likely reflect deformation of the sediment during the intrusion of ice wedges and slumping and relaxation of the sediment as the ground ice thawed. Indeed, when the sample locations of the paleomagnetic cubes are compared to the stratigraphic interpretations of the two trenches, it is clear the paleomagnetic samples from the eastern trench, where the Reunion event is best recorded, were taken from loess adjacent to an ice wedge cast, while paleomagnetic sampling in the western trench was inadvertently done partly excavated through a thermokarst deposit.

The short duration of the reversal ca. 0.7 m below the PA tephra in the Gold Hill loess is also consistent with our interpretation that this marks the Reunion event, as the Reunion event is consistently characterized as having been brief and transient where observed elsewhere on earth. The apparent brevity of the reversal and the lateral paleomagnetic inhomogeneity we find across the section is, therefore, supportive of our conclusion that permafrost, including ice wedges, formed and then thawed ca. 2.05 million years ago, shortly after the Reunion Chron.

Environmental Reconstruction

We collected samples for magnetic susceptibility measurements from both the eastern and western trenches. The susceptibility values averaged about 10 SI units, but systematic variations in magnetic susceptibility occurred through the sections, with massive unaltered loess having higher susceptibilities than loess from the paleosol zones. The pattern of environmental magnetism 2 million years ago closely resembles that from middle and late Quaternary loess sequences, suggesting that the susceptibility signal records both primary variations in wind strength and subsequent pedogenic alteration of the magnetic minerals in the loess (Beget 2001).

We used the ages of the PA tephra and the Reunion chron to control a linear interpolation model to estimate ages of sediments between these two well-dated points in our trenches at Gold Hill, and to evaluate the paleoclimatic inferences from the environmental magnetic record and the evidence of permafrost formation and disappearance.

The PA tephra occurs in a high susceptibility zone, and the age of the PA correlates well with a glacial interval recorded by marine isotope stage MIS 74 in global marine records (Shackelton et al. 1995). The paleosol just above the PA tephra has low susceptibility and is correlated with an interglacial episode recoded by MIS 73. The Reunion chron occurs during the MIS82-81 transition in the marine record, which is followed by a long and sustained global glacial event during MIS78 to MIS 76.

The top of the ice wedge casts and thermokarst features occurs between the PA tephra and the Reunion paleomagnetic chron, and the formation of ice wedges recorded at Gold Hill is therefore correlated with the unusually sustained glacial interval recorded by MIS 78–76. This glacial event produced a significant interval of cold climate 2.1 million years ago in central Alaska. The marine isotopic data suggests that

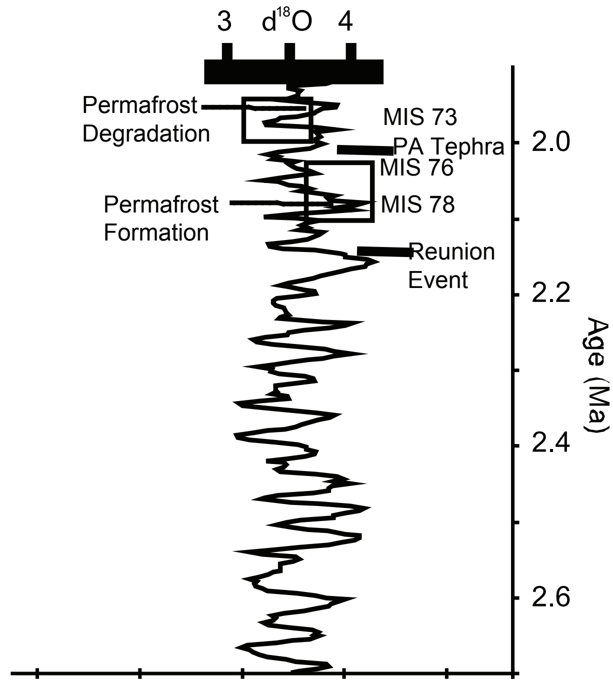

Figure 4. Standardized global marine isotopic record from Shakleton et al. (1995) covering the time period of the recorded by loess near the PA tephra at Gold Hill. Ground ice formed during a cold interval soon after the Reunion Chron (2.14 million years) and was destroyed during a subsequent interglacial interval. We correlate the cold interval with MIS 76–78 and the warm interval with MIS 73.

the MIS 78–76 glaciation was one of the longest and most intense until Middle Pleistocene time, resulting in as much as 70 m of sea level drop due to ice sheet growth on land (Pillans et al. 1998).

The fact that the PA tephra is locally incorporated in the ice wedge casts and thermokarst deposits, indicates warming and destruction of the ice wedges occurred after the PA tephra was deposited. We suggest this interval is correlative with MIS 73, a global warm interval recorded in marine records at about 1.9 million years ago. The correlations suggested by our discovery of ice wedge casts and thermokarst features, and our new age-dating model at Gold Hill, link evidence of rapid climate change in Alaska ca. 2 million years ago with the environmental magnetic proxy record of climate change from the loess, the paleosol evidence, the sedimentological record of permafrost formation and degradation, and the standard global climate record from isotopic studies of marine cores. We believe the excellent temporal correlations support the validity of our approach and the reliability of our conclusions.

Summary and Conclusions

We carried out stratigraphic, sedimentologic, and paleomagnetic studies of sediments in the lower part of the Gold Hill loess deposit, 3 km southwest of the University of Alaska Fairbanks. We report here on work done in two new trenches that were hand excavated by students participating in an NSF summer institute and by undergraduate and graduate students enrolled in the Geology and Geophysics program at the University of Alaska (Naibert et al. 2005).

The exposures in the two new trenches were photographed and stratigraphically logged. Oriented cubes and cylindrical cores were collected at regular intervals through the two new loess sections, starting from the prominent PA Tephra and extending down ca. 4 m.

The PA tephra, recently redated at 2.02 +/- 0.14 myr (Westgate et al. 2003), can be traced laterally across the exposure for 30 m, but the trenching revealed that the tephra layer was locally displaced by collapses, and was incorporated in deposits that had collected in small depressions stratigraphically below the level of the primary ash deposit. Excavation through the collapse deposits indicate that some of the collapse features are V-shaped and are interpreted as ice wedge casts, while others are broader, with irregular boundaries, and are interpreted as the products of thermokarst collapse pits.

The remnant magnetization recorded in the sets of oriented cubes and cylindrical cores taken from the two loess sections was measured at the University of Alaska-Fairbanks using a cryogenic magnetometer. Both alternating field and thermal demagnetization techniques were employed. Our data show that the section records predominantly reversed polarity, consistent with an age assignment within the Matuyama Reversed Chron. We identified a thin horizon of normal polarity at 0.7 m below the PA tephra. This event is well-preserved in our easternmost trench, but is recorded by only one point in our western trench. We correlate this event with the Reunion Chron dated to 2.14 million years ago. A transient normal polarity event at about the same stratigraphic position appears to be present in the paleomagnetic record of Westgate et al. (1990), although they did not assign it to any chron.

The variations between the paleomagnetic record of the Reunion event in these three trenches, excavated about 30 m apart, demonstrates that loess stratigraphy in this part of the Gold Hill section is complex and disturbed. This is consistent with the recognition of ice wedge casts and thermokarst features below the PA tephra. The strongest and thickest expression of the Reunion event occurs in samples taken down through undisturbed loess adjacent to an ice wedge cast in our eastern trench, while samples from our western trench intersect a thermokarst pit and show a weaker signal. More evidence of disturbance in this part of the loess section comes from low magnetic inclinations that characterize samples from this part of the section. The low inclinations are interpreted as a record of post-depositional deformation of the sediment associated with the growth of ice wedges and subsequent slumping and relaxation of the sediment as the ground ice thawed.

We also found systematic variations between magnetic susceptibility values from unaltered loess and those measured from loessic paleosols similar to those found in late Quaternary loess (Beget and Hawkins 1988; Beget 2001). The Reunion Chron and the PA tephra were used to develop a linear sedimentation rate model and to produce age estimates for the environmental magnetic record and unaltered loess interpreted as a glacial deposit and paleosols interpreted as interglacial deposits.

The stratigraphy and geochronology indicate ice wedges formed in central Alaska ca. 2.1 million years ago. The marine oxygen isotope record records a major, global glacial event at the same time, during MIS 78–76 (Shackleton et al. 1995, Pillans et al. 1998), suggesting the permafrost formed in response to global forcing. The permafrost degraded ca. 1.95 million years ago, at the same time as MIS 73, a global period of mild, interglacial temperatures.

Our study indicates that Alaskan permafrost was forming and degrading in response to changing global climate forcing by 2.14 million years ago. Some prior studies have suggested that the onset of glacial conditions in the Arctic was slow and gradual. In contrast, our work on permafrost history at Gold Hill indicates that Arctic climates have been fluctuating at the same rates and at the same times as global climate changes since earliest Pleistocene times.

Acknowledgments

Layer and Stone acknowledge funding from the National Science Foundation. Beget acknowledges funding from the U.S. Dept. of the Interior. Addison received funding from a University of Alaska Graduate Fellowship. Benowitz, also received funding from a University of Alaska Graduate Fellowship as well as additional funding from the Department of Geology and Geophysics of the University of Alaska Fairbanks.

References

Beget, J.E. 1988. Tephras and sedimentology of frozen loess: In: I.K Senneset (ed.), *Proceedings of the Fifth International Permafrost Conference, Trondheim, Norway, August 2-5, 1988*: 672-677.

Beget, J.E. 1991. Paleoclimatic significance of high latitude loess deposits. In: G. Weller (ed.), *Proceedings of the International Conference of the Role of the Polar Regions in Global Change, Fairbanks, Alaska, June 11–15, 1990*: 594-598.

Beget, J.E. 1996. Tephrochronology and paleoclimatology of the last interglacial-glacial cycle recorded in Alaskan loess deposits. *Quaternary International* 34–36: 121-126.

Beget, J.E., 2001. Continuous late Quaternary proxy climate records from loess in Beringia. *Quaternary Science Reviews* 20: 499-507.

Beget J.E. & Hawkins, D. 1989. Influence of orbital parameters on Pleistocene loess deposition in central Alaska. *Nature* 337: 151-153.

Beget, J.E., Stone, D.E. & Hawkins, D. 1990. Paleoclimatic forcing of magnetic susceptibility variations in Alaskan loess. *Geology* 18: 40-43.

Guthrie, D.R.. 1990. *Frozen Fauna of the Mammoth Steppe: The Story of Blue Babe*. Univ. Chicago Press, 338 pp.

Naibert, T.J., Domeier, M.M., Robertson, K.L., Fallon, J.F., Stone, D.B., Beget, J.E. & Layer, P.W. 2005. Re-evaluation of the magnetostratigraphy of the Gold Hill loess, Interior Alaska. American Geophysical Union. AGU Fall Meeting Abstracts, p. A96.

Pewe, T.L. 1951. An observation on wind-blown silt. *Journal of Geology* 59: 399-401.

Pewe, T.L. 1975a. Quaternary geology of Alaska. *U.S. Geological Survey Professional Paper 835*, 145 pp.

Pewe, T.L. 1975b. Quaternary stratigraphic nomenclature in central Alaska. *U.S. Geological Survey Professional Paper 862*, 32 pp.

Pewe, T.L., Berger, G.W., Westgate, J.A., Brown, P.M. & Leavitt, S. W. 1997. Eva interglaciation forest bed, unglaciated East-Central Alaska: global warming 125,000 years ago. *Geological Society of America Special Paper 319*, 54 pp.

Pewe, T.L.& Reger, D. 1989. Quaternary Geology and Permafrost along the Richardson and Glenn Highways between Fairbanks and Anchorage, Alaska. Fieldtrip Guidebook T102. *28th International Geological Congress*, Washington D.C., American Geophysical Union, 54 pp.

Pillans, B., Chappell, J., & Naish, T. R. 1998. A review of the Milankovitch climatic beat: template for Plio–Pleistocene sea-level changes and sequence stratigraphy. *Sedimentary Geology* 122: 5-21.

Shackleton, N.J, Crowhurst, S., Hagelberg, T., Pisias, N.G. & Schneider, D.A. 1995. A new Late Neogene time scale: application to leg 138 sites, *Proc. ODP Sci. Results* 138, 3-101.

Westgate, J.A., Stemper, B.A. & Péwé, T.L. 1990, A 3 m.y. record of Pliocene-Pleistocene loess in Interior Alaska: *Geology* 18: 858-861.

Westgate, J.A., Preece, S.J. & Pewe, T.L. 2003. The Dawson cut forest bed in the Fairbanks area, Alaska, is about 2 million years old. *Quaternary Research* 60(1): 2-8.

Recent Advances in Mapping Deep Permafrost and Gas Hydrate Occurrences Using Industry Seismic Data, Richards Island Area, Northwest Territories, Canada

Gilles Bellefleur
Geological Survey of Canada

Kumar Ramachandran
University of Tulsa

Michael Riedel
McGill University

Tom Brent
Geological Survey of Canada

Scott Dallimore
Geological Survey of Canada

Abstract

A 3D seismic reflection survey acquired by industry over the Mallik area in 2002 is used to map heterogeneities in permafrost and to determine the extent of gas hydrate occurrences beneath it. Seismic amplitude anomalies associated with lakes and drainage systems are observed in the 3D seismic data. Beneath lakes, the seismic data show weaker amplitudes, locally compromising images of the geology within and below the permafrost. On Richards Island, many of the lakes are deeper than the thickness of winter ice and have taliks that penetrate permafrost. Amplitude effects on the seismic data arise from velocity and attenuation variations associated with frozen and unfrozen parts of the permafrost. A 3D travel-time tomography algorithm was used to produce a map of the permafrost velocity structure. The 3D velocity map clearly reveals a heterogeneous velocity distribution, primarily related to thermal variations within the permafrost.

Keywords: gas hydrates; Mallik; Richards Island; seismic data; talik; tomography.

Introduction

The Mackenzie Delta area is characterized by a remarkable variability in permafrost conditions. In the central Mackenzie Delta, permafrost may be less than 80 m thick whereas in northern Richards Island it may be more than 700 m thick (Judge et al. 1987). This variability in part reflects a complex Quaternary history of surface temperatures and geologic processes (Taylor et al. 1996). As elaborated in more detail by Wright et al. (2008), lakes which cover between 20% and 50% of the landscape of the Mackenzie Delta area have played an important role in conditioning ground temperatures. Positive mean annual temperatures beneath the lakes (and indeed river channels or the ocean), if imposed for a significant amount of time, can thaw the permafrost, creating a thermal talik (above 0°C). More common perhaps, warmer permafrost beneath lakes affects the proportion of liquid water versus ice within the sediment matrix. Both conditions can modify the physical properties of sediments, affecting the propagation of seismic waves. Sediments with ice in the pore space are stiffer and characterized by higher seismic velocities whereas unfrozen sediments have lower velocities (Zimmermann & King 1986). Here, we show some effects of deep taliks on a 3D seismic reflection dataset acquired near the Mallik area on Richards Island (Fig. 1). Beneath lakes, the seismic data show weaker amplitudes, which locally compromise images of the geology within and below the permafrost. Direct seismic arrivals are used to produce a 3D velocity map of the permafrost. This map reveals a heterogeneous distribution of velocities, mostly related to variations in ice bonding within the permafrost. The 3D seismic data are also used to image and characterize gas hydrate accumulations beneath the permafrost.

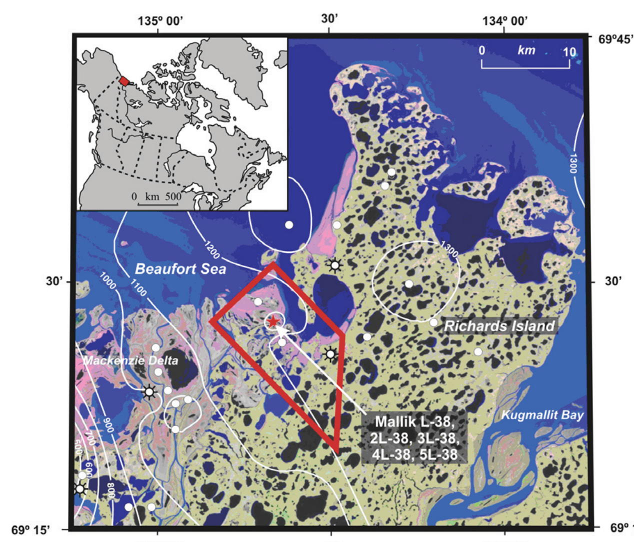

Figure 1. Location map showing the Mallik area in the Mackenzie Delta. The red polygon outlines the area covered by the 3D seismic survey used in this study. Small circles indicate well locations whereas larger circles with ticks show wells that intersected gas hydrate. Contours represent the base of the gas hydrate stability field.

Geological Setting

The 3D seismic survey used in this study is located in the western part of Richards Island in the Mackenzie River Delta on the coast of the Beaufort Sea (Fig. 1). The area straddles two physiographic regions identified by Rampton (1988), the Big Lake Delta Plain to the west which is influenced by active Mackenzie River deltaic deposition and older upland terrain referred to as the Tuktoyaktuk Coastlands. A shallow water embayment of the Beaufort Sea, referred to here as Mallik Bay, is also a dominant feature. Pleistocene sediments consisting mainly of glacial, marine, and fluvio-deltaic sediments are exposed at shallow depth beneath the Big Lake Delta plain and outcrop at the surface in the Tuktoyaktuk Coastlands. These deposits are underlain by older deformed deltaic Tertiary strata (Dixon 1995).

Interpretations of geophysical well logs from exploration wells in the area suggest that ice bonded permafrost beneath terrestrial areas is 600 to 650 m deep and that gas hydrates can occur to depths of 1150 m (Judge et al. 1987). Two major gas hydrate research well programs have been conducted at the Mallik site (Dallimore & Collett 2005) which is located at the apex of a regional anticline structure. Core studies and geophysical interpretations document that gas hydrate occurs in coarse-grained sandy sediments of the Mackenzie Bay and Kugmalit Tertiary sequences from 870 to 1100 m depth. The gas hydrate-bearing sediments are interbedded with silty sediments with little or no gas hydrate.

Approximately 50% of the surface area within the 3D seismic survey is affected by lakes, river channels, or the Mallik Bay. While no detailed bathymetric data are available, point soundings suggest water depths varying from less than 0.5 m to more than 6 m.

3D Seismic Data

The upper 2 s of a 3D seismic reflection dataset acquired during winter in 2002 has been made available to the Mallik 5L-38 science program through partnership with a joint venture of BP Canada Energy, Chevron Canada Resources, and Burlington Resources Canada. The 3D data were acquired with a combination of vibroseis and dynamite and covers approximately 130 km^2 that include four gas hydrate targeted wells and four industry wells drilled in the 1970s. The 3D acquisition geometry was designed to image conventional hydrocarbon accumulations located beneath permafrost and gas-hydrate zones (deeper than 1100 m). The initial data processing also focused on the imaging of the conventional gas-bearing structures, and the resulting 3D volume provides poor reflection images of the permafrost (above 600 m) and low fold in common-depth-point gathers in the gas-hydrate depth range (900–1100 m). For this study, we chose a dataset reprocessed to maintain the relative true-amplitude character of the data (Riedel et al. 2006).

Several areas of reduced seismic amplitude are observed in the true-amplitude 3D seismic dataset at depths exceeding 1 km (Fig. 2). Understanding these low-amplitude anomalies

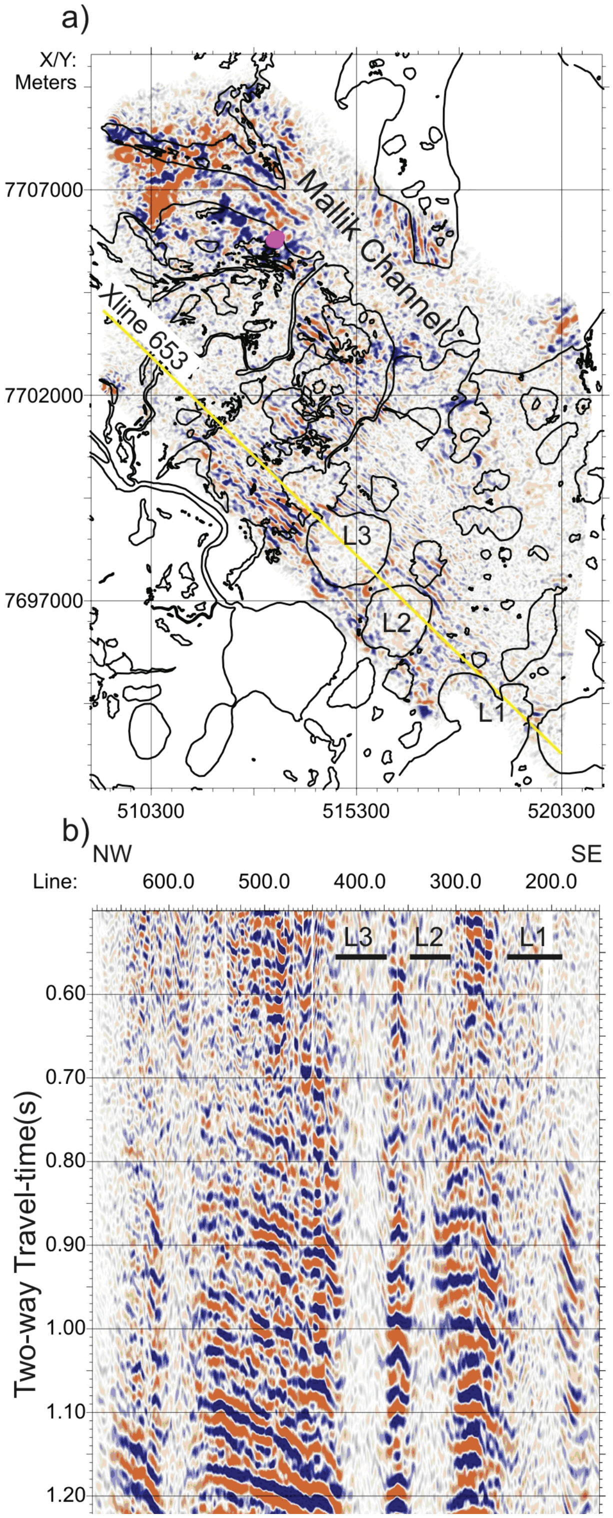

Figure 2. (a) Time slice from the true-amplitude 3D seismic data at 800 ms (approximately 1100 m). The purple dot shows the location of the Mallik wells. (b) Cross-line 653 showing reduction of amplitude beneath the lakes. The location of cross-line 653 is shown in (a) (yellow line). Colors represent seismic amplitudes (blue: negative amplitude; red: positive amplitude).

(also referred to as washout zones) is important for any gas-hydrate related interpretation. In the marine environment, wide-spread amplitude blanking has often been attributed to the presence of gas hydrate (Holbrook et al. 2001). At Mallik, the low seismic amplitude areas in the gas hydrate stability field (200 to 1100 m) may not indicate the presence of gas hydrates but instead likely result from variations of physical properties in permafrost, and more specifically to property changes associated with deep taliks.

A time slice from the 3D true-amplitude dataset, with an overlay of the hydrology, is shown in Figure 2. The time slice is located beneath the permafrost near the base of the gas hydrate stability field at 800 ms (approximately 1100 m depth). Areas of seismic blanking or reduced seismic amplitude are coincident with the location of large lakes. A seismic cross-section (Fig. 2b) shows that the reduced amplitudes beneath the lakes extend down to 1.3 seconds. Some reflections are also truncated underneath water bodies. This is particularly evident near the Mallik channel (Fig. 2a) and near lakes located in the southeast part of the time slice (L1, L2 and L3 on Figs. 2a, b). Some deeper water areas of Mallik Channel do show a response similar to that seen beneath the lakes (Fig. 2a). However, the river channels and many smaller lakes less than 300-400 m in diameter show no seismic amplitude reduction. Similar observations are made for shallow water areas located offshore.

The effect of ice bonding on seismic velocity is well documented. In water-saturated and unconsolidated sediments, velocity of P-waves varies significantly as a function of the fraction of pore water that is unfrozen (Zimmermann & King, 1986). Sediments with only ice in the pore space can have P-wave velocity as high as 4200 m/s whereas as sediments mostly filled with water have velocities near 1800 m/s. Other factors such as composition, density, porosity, and pressure also affect P-wave velocity of sediments. As reviewed by Wright et al. (2008) large lakes in the Richards Island area can have a significant talik beneath them. It is expected that sediments beneath those lakes will have a larger proportion of unfrozen water in the pore space and will be characterized by lower P-wave velocities. The unfrozen or partially unfrozen areas also attenuate seismic waves propagating through them more severely (the amplitude of waves in those areas is reduced more rapidly than within frozen permafrost) producing low amplitude areas in Figure 2.

Areas with lower velocity delay seismic waves propagating down to and up from deeper reflective geological structures. These delays, because they occur at shallow depths, must be taken into account during data processing to produce the most accurate images of deeper geological structures, and quantitative information about the velocity distribution of the permafrost is required to estimate proper static corrections. The velocity distribution can also provide information about the internal structure of the permafrost.

Velocity Structure of Permafrost

Direct P-wave travel-time tomography is used to produce a 3D velocity map of the permafrost. Tomographic inversion of first arrival travel-time data is a non-linear problem since both the velocity of the medium and the ray paths in the medium are unknown. The final solution is typically obtained by repeated applications of linearized inversion until model parameters (velocities) explain the observations (travel-times) within satisfactory criteria. More details about the tomography method can be found in Ramachandran et al. (2005).

The tomographic inversion of direct seismic arrivals resulted in a velocity model covering the area of the 3D survey and extending down to a depth of 500 m which is about 100 m above the base of permafrost. This model is divided into 50 m cubes. Approximately one million direct arrival travel-times were manually picked and used in the tomography. Figure 3 displays two depth slices from the reconstructed velocity model. The shallowest slice at 100 m shows a heterogeneous permafrost with P-wave velocities ranging from 1500 to 5000 m/s. As expected, lower velocities are found underneath lakes and drainage system and they likely correspond to areas of unfrozen permafrost. The deeper slice at 250 m is more homogeneous but still shows lower velocities beneath some lakes and the Mallik channel. At that depth, velocities beneath most lakes are slightly higher and may indicate the presence of a greater proportion of ice in the pore space of sediments, possibly related to a thermal gradient within some taliks. Some of the low-velocity areas beneath the lakes extend down to approximately 300 m (not shown) and have an inverted-cone shape (Fig. 4).

One way to assess the constraint on the velocity model is to count the number of rays passing through each cell. A large number of rays per cell is usually indicative of a well-constrained velocity. Figure 5 shows a depth slice at 100 m with the number of rays per cell. At this depth, all cells are cut by a large number of rays, except at the edge of the 3D velocity slice. At greater depths, the number of rays per cell is significantly lower. This is a result of the maximum source-receiver separation used during data acquisition. Larger source-receiver separations would be required to map velocity variations near the base of permafrost with travel-time tomography.

Gas Hydrates

Gas hydrate accumulations located onshore in Arctic permafrost regions are seen as a potential source of natural gas. Most known gas-hydrate occurrences in the Mackenzie Delta and Beaufort Sea areas were indirectly discovered or inferred from conventional hydrocarbon exploration programs. One of these occurrences, the Mallik gas hydrate field (Fig. 2), has received particular attention over the last 10 years. Two internationally-partnered research well programs have intersected three intervals of gas hydrates and have successfully extracted sub-permafrost core samples with significant amounts of gas hydrates (Dallimore & Collett

2005). The gas hydrate intervals are up to 40 m in thickness and have high gas hydrate saturation sometimes exceeding 80% of pore volume of unconsolidated sand with average porosities ranging from 25% to 40%. The gas hydrate intervals are located on the crest of the anticline between 900 m and 1100 m depths and do not exhibit large dips. Here, we refer to the three gas hydrate intervals as Zones A, B, and C (Dallimore & Collett 2005). Zone A is the shallowest gas hydrate interval whereas Zone C marks the base of the gas-hydrate occurrence at Mallik.

Sonic logging data acquired in two boreholes at Mallik show that P-wave velocity of sediments increases with concentration of gas hydrates (Guerin & Goldberg 2005).

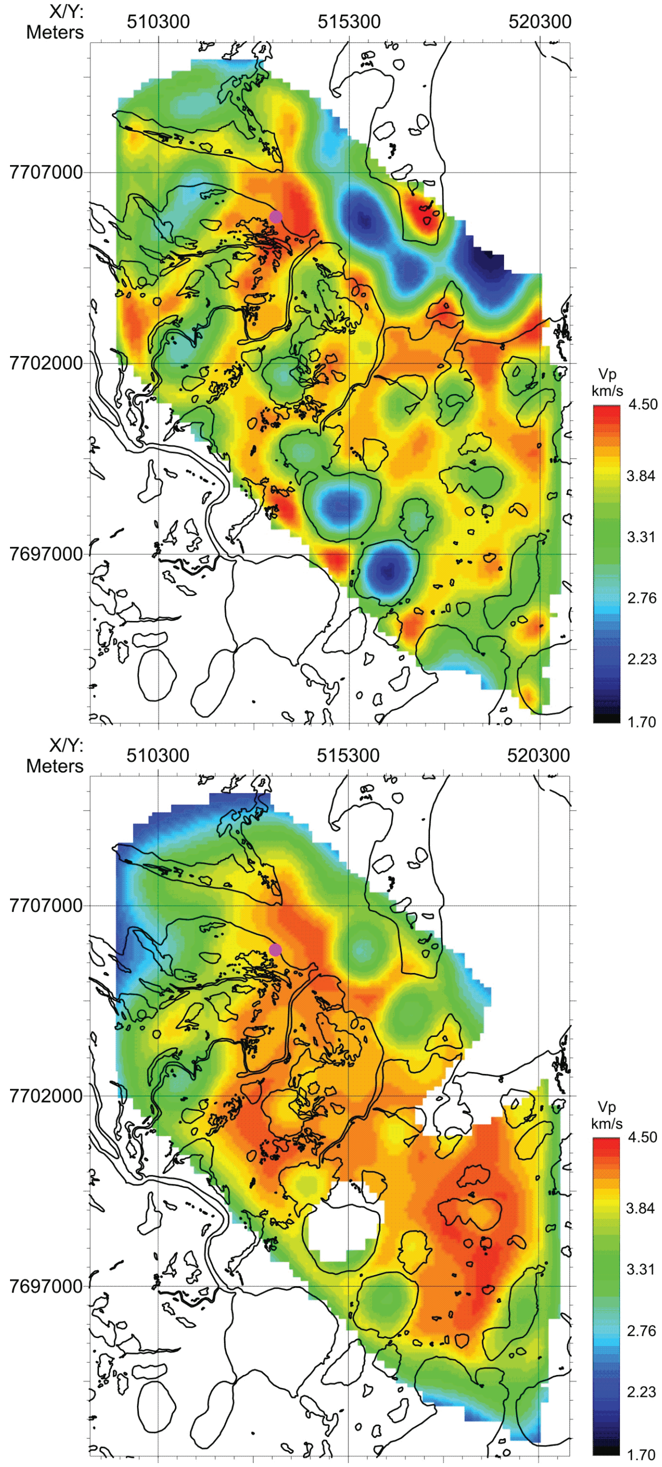

Figure 3. Depth slices through the 3D velocity model obtained from direct arrival travel-time tomography (top: depth slice at 100 m; bottom: depth slice at 200 m). Low-velocity areas are found beneath large lakes and deep water channels. The no-data areas on the deeper slice correspond to low-velocity zones not traversed by first-arrival rays which follow the fastest trajectory. Low-velocity zones will tend to be under-sampled as depth and source-receiver separation increase.

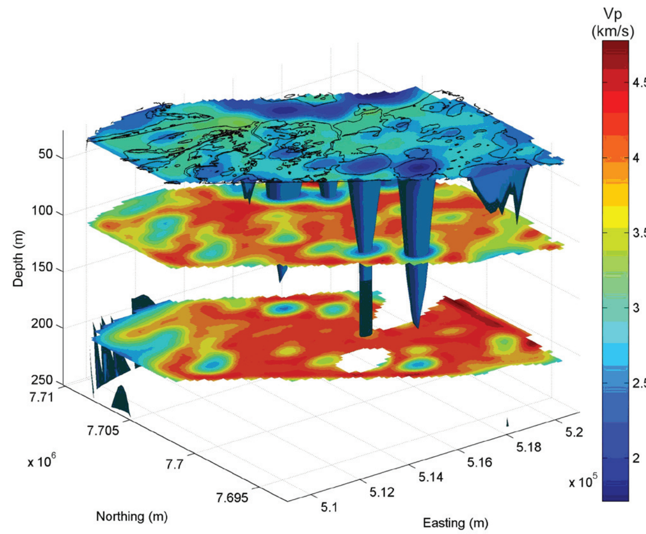

Figure 4. Plunge view to the NE showing three velocity slices (at 25 m, 100 m, and 200 m), natural drainage system and iso-surfaces set at 2.4 km/s. The iso-surfaces have an inverted-cone shape and are located beneath lakes and the Mallik water channel.

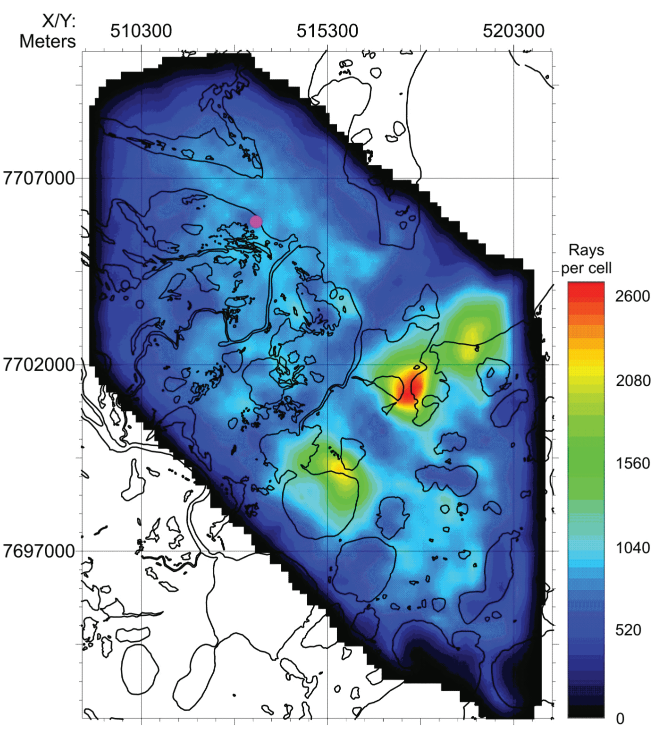

Figure 5. Depth slice at 100 m showing the number of rays per cell that constrained the velocity model shown in Figure 3. A large number of rays per cell is an indication of well-constrained velocity.

P-wave velocities range from 2400 m/s in sediments having no gas hydrates to 3200 m/s in strata with 80% pore occupancy by gas hydrate. This strong velocity contrast makes gas hydrates detectable with surface seismic reflection methods when they are found beneath the permafrost. They are difficult to detect when located within permafrost because of the limited or lack of velocity contrast with frozen sediments. On Mallik seismic records, the hydrate-bearing sediments are seen as bright reflections relative to a lower-amplitude surrounding background. Fortunately, there are no deep lakes close enough to the Mallik well site to distort seismic images.

While successfully used for determining in-situ properties of gas hydrates, boreholes alone cannot confirm lateral continuity of any of the three hydrate zones, which is required to provide reliable estimates of the resource in place. Here, we also used the 3D seismic data to assess the seismic characteristics of the zones to help define the lateral extent of the gas hydrates away from the wells. At the same time, we also wish to assess the influence of the local geology on the distribution of gas hydrates. Our seismic characterization approach relies strongly on well-log data in the gas hydrate intervals, seismic-to-well correlation, and acoustic impedance inversion. The seismic inversion generated an acoustic impedance (product of density and velocity) image of approximately 1.5 km^2 area around Mallik 5L-38 by matching a reflectivity model to the seismic data. We further extracted P-wave velocities from the impedances assuming no lateral variability in the density of the sediments. Overall the density is relatively constant throughout the entire gas hydrate interval and averages 2100 kg/m^3. We have attempted to convert P-wave velocity to gas hydrate concentration in pore-space by using the effective medium theory by Helgerud et al. (1999), in which gas hydrate supports the sediment matrix but does not cement sediment grains. In general, a very good correlation between the Mallik 5L-38 P-wave velocity logs and the inverted P-wave section is found for Zones B and C. Figure 6 shows maps of the inverted P-wave velocity for Zones B and C. Zone C reveals a complex pattern with large variation in P-wave velocity over distances less than a few hundred meters. This complex pattern could certainly be explained by lateral sediment heterogeneity and by spatial limitations of small-scale faults and other discontinuities. Zone C is more continuous and extends over a larger area than Zone B. P-wave velocities locally exceed 2900 m/s and correspond to sediments with high gas hydrate saturation (above 60%). These highly saturated sediments cover approximately 0.25 km^2. The area of highest gas hydrate concentrations for Zone B follows a N-S trend. Zone B is less continuous than Zone C and covers an area of approximately 0.1 km^2. The extent and geometry of Zones B and C defined from impedance inversion suggest that local geology plays a significant role in the distribution of gas hydrate at Mallik.

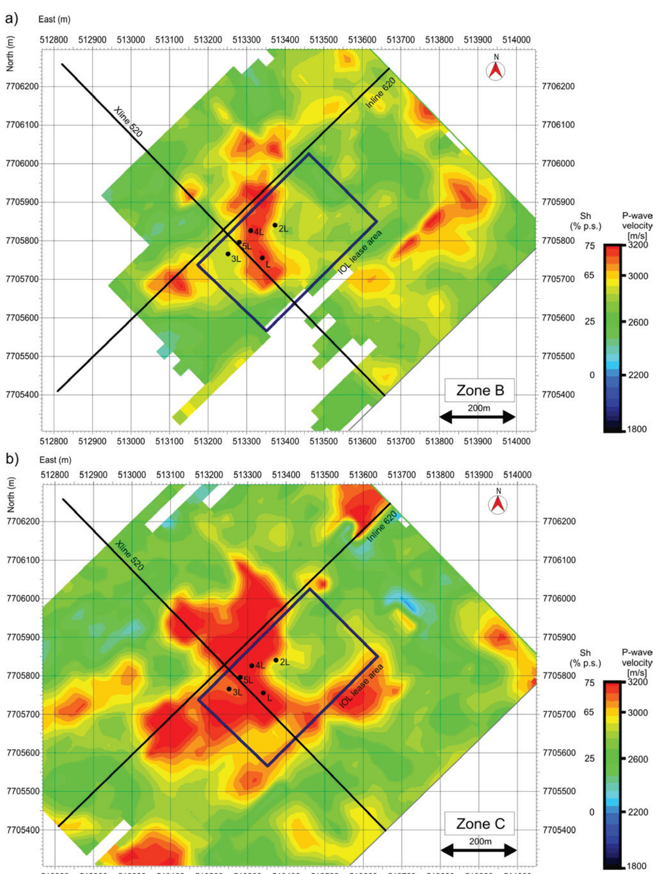

Figure 6. Velocity Map obtained from acoustic impedance inversion showing the extent of gas hydrate Zones B (top) and C (bottom). Color code shows P-wave velocity in m/s and gas hydrate concentration in percent of pore space (% p.s.). Gas hydrate Zone C is structurally complex with a center area of highest P-wave velocity and related gas hydrate concentration underneath the Mallik well sites. Zone B extends over a much smaller area than Zone C and is distributed along a N-S axis.

Conclusions

Lower seismic amplitudes are observed on the 3D Mallik data beneath some lakes and water channels. Amplitude effects on the seismic data arise from velocity and attenuation variations associated with frozen and unfrozen parts of the permafrost. A 3D velocity map of the permafrost obtained with direct arrival travel-time tomography indicates that some of the low-velocity areas beneath the lakes have an inverted-cone shape and extend down to approximately 300 m. Beneath the permafrost, results from acoustic impedance inversion indicate that sediments with high gas hydrate saturation near the Mallik well site extend over an area of 0.25 km^2 and suggest that lateral and depth-dependent geology variations play a significant role in the distribution of gas hydrates.

Acknowledgments

We acknowledge the international partnership that undertook the Mallik 2002 Gas Hydrate Production Research Well Program: the Geological Survey of Canada, Japan National Oil Corporation, GeoForschungsZentrum

Potsdam, U.S. Geological Survey, India Ministry of Petroleum and Natural Gas, BP/ChevronTexaco/Burlington joint venture parties, U.S. Department of Energy. The first 2 s of the Mallik 3D seismic data has been made available to the Mallik science program through partnership with the BP/ChevronTexaco/Burlington joint venture parties. Geological Survey of Canada contribution 20070388.

References

Dallimore, S.R. & Collett, T.S. 2005. Summary and implications of the Mallik 2002 gas hydrate production research well program. In: S.R. Dallimore & T.S. Collett (eds.), *Scientific Results from the Mallik 2002 Gas Hydrate Production Research Well Program, Mackenzie Delta, Northwest Territories, Canada.* Geological Survey of Canada. Bulletin 585: 36 pp.

Dixon, J. 19*95. Geological Atlas of the Beaufort-Mackenzie Area.* Geological Survey of Canada. Miscellaneous Report 59: 173 pp.

Guerin, G. & Goldberg, D. 2005. Modeling of acoustic wave dissipation in gas hydrate–bearing sediments, *Geochem. Geophys. Geosyst.* 6: Q07010, DOI: 10.1029/2005GC000918.

Helgerud, M., Dvorkin, J., Nur, A., Sakai, A. & Collett, T. 1999. Elastic-wave velocity in marine sediments with gas hydrates: Effective medium modeling. *Geophysical Research Letters* 26: 2021-2024.

Holbrook, W.S. 2001. Seismic studies of the Blake Ridge: Implications for hydrate distribution, methane expulsion, and free gas dynamics. In: C.K. Paull & W.P. Dillon (eds.), *Natural Gas Hydrates, Occurrence, Distribution and Detection.* AGU Geophysical Monograph Series 124: 235-256.

Judge, A.S., Pelletier, B.R. & Norquay, I. 1987. Permafrost base and distribution of gas hydrates. In: B.R. Pelletier (ed.), *Marine Sciences Atlas of the Beaufort Sea-Geology and Geophysics.* Geological Survey of Canada Miscellaneous Report 40: 39 pp.

Ramachandran K., Dosso, S.E., Spence, G.D., Hyndman, R.D. & Brocher, T.M. 2005. Forearc structure beneath southwestern British Columbia: A three-dimensional tomographic velocity model. *J. Geophys. Res.* 110: B02303, DOI: 10.1029/2004JB003258.

Rampton, V.N. 1988. *Quaternary Geology of the Tuktoyaktuk Coastlands, Northwest Territories.* Geological Survey of Canada, Memoir, 423 pp.

Riedel, M., Bellefleur, G., Brent, T., Dallimore, S.R. & Collett, T.S. 2006. Amplitude and frequency anomalies in 3D seismic data from the Mallik 5L-38 research site. *Geophysics*, 71: B183-B191, DOI: 10.1190/1.2338332.

Taylor, A.E., Dallimore, S.R. & Judge, A.S. 1996. Late Quaternary history of the Mackenzie-Beaufort region, Arctic Canada, from modelling of permafrost temperature, part 2--The Mackenzie Delta-Tuktoyaktuk coastlands. *Canadian Journal of Earth Science* 33: 62-71

Wright, J.F., Taylor, A.E. & Dallimore, S.R. 2008. Thermal impact of Holocene lakes on a permafrost landscape, Mackenzie Delta, Canada. *Proceedings of the Ninth International Conference on Permafrost, Fairbanks, Alaska, June 29-July 3, 2008* (this proceedings).

Zimmerman, R.W & King, M.S. 1986. The effect of the extent of freezing on seismic velocities in unconsolidated permafrost. *Geophysics* 51: 1285-1290.

Massive Ground Ice on the Ural Coast of Baydaratskaya Bay, Kara Sea, Russia

N.G. Belova, V.I. Solomatin, F.A. Romanenko
Lomonosov Moscow State University, Faculty of Geography, Moscow, Russia

Abstract

Massive ground ice on the coast of Baydaratskaya Bay (Kara Sea) is exposed on the western (Yugorski) side near the mouth of the Ngoyu-Yacha River. It reaches 7 m in thickness and lies in sandy stratum. The isotopic and chemical composition of the ice, complicated ice structure with several types of ice, ice deformations, and the lacustrine-alluvial origin of host sediments suggest a burial origin for the massive ice beds. Sands with massive ice are underlayed by clayey stratum which is related to the Kara diamicton stratigraphic unit. Massive ice beds are supposed to be the remains of outlet glaciers from Pai Khoi or Polar Ural, which were buried in lacustrine-alluvial (fluvioglacial) sediments in the Late Weichselian; this area wasn't covered by the Barents-Kara Ice Sheet at that time.

Keywords: Barents-Kara Ice Sheet; Late Weichselian glacial maximum; massive ground ice; paleogeography; Russian Arctic.

Introduction

It is now known that massive ground ice exposures on the coast of Baydaratskaya Bay (Kara Sea) are found in just one section – on Yugorski (western) side near the mouth of the Ngoyu-Yacha River (Fig. 1). The origin of these ice formations remains sharply controversial both locally and globally. There are two main points of view on massive ice origin: it could be buried glacial ice (in particular, basal ice of ice sheets) or intrasedimental ice, formed in pre-existing sediments. Any paleoreconstructions in this area would be imperfect without taking into account the origin of massive ice. For the purpose of making the question of massive ice origin clear at a local scale, an integrated study of thick (up to 7 m) massive ice beds was conducted 2005–2007 along the coastal bluffs of the area. The host strata and the relation to massive ice, ice structure, chemical composition of ice and host sediments, and isotopic composition of the ice have been studied to solve this problem.

Quaternary history of the study area

The Yugorski peninsula was supposed to be overridden by the Barents-Kara Ice Sheet no later than 90–80 ka BP, Marine Isotope Stage 5a–b (MIS 5a–b), i.e., at Early Weichselian. The Late Weichselian glacier limit didn't attain this area (see Fig. 1; based on Svendsen at al. 2004). During Holocene warming, this region was essentially reshaped by increased thermokarst activity (Romanenko et al. 2001).

Host Sediments: Stratigraphy and Relation with Massive Ground Ice

Composition and stratigraphy of host sediments

Near the mouth of the Ngoyu-Yacha River, the ridgy plain with an altitude of 27–35 m above sea level (a.s.l.) comes out to the Baydaratskaya Bay coast. In the coastal zone, this surface is strongly dissected by numerous thermokarst depressions known locally as "khasyreys" (The term is of Nenets origin (northwestern Siberia); an analogous term of Yakut origin is "alas"). The altitudes of many khasyreys are lower: up to 15–20 m. The elevated surfaces that have remained unaffected by thermokarst occupy a minor area compared to dissected ones.

The stratum of heavy consolidated fractured clays with scarce rounded boulders underlies many sections (Fig. 2), but on most of studied area it lies below sea level. In the upper part, clays are silty and contain occasional thin sand laminas (up to 0.5 cm thick) with fragments of shells.

Composite sandy stratum with clay bands, folds, lenses of well-rounded pebbles and gravel with fragments of sea shells overlap the clay unit at a stratigraphic disconformity (Fig. 2). The chemical composition of aqueous extract shows that this stratum is fresh (Fig. 6). The stratification features indicate the formation of these sediments by fluctuating stream activity. The alternating pebbly gravel layers with clayey layers, as well as the results of chemical analysis, indicates continental and coastal formational environments. Z.V. Aleshinskaya (pers. com.) came to the conclusion about the alluvial origin of the sandy stratum following analysis of diatom composition. On the pollen and spore diagram, the redeposited pollen of *Betula* sect*. Albae*, and *Pinus* is rather abundant, and there exists pollen of *Fagus* and *Juglans*. Spectra of a similar composition were detected in deposits of the Eemian-Early Weichselian (MIS 5d–e, c. 100–130 ka BP) of the Pai Khoi Ridge (Northern Ural); this may imply that a considerable part of spores and pollen was redeposited from older Pleistocene sediments (Andreev et al. 1998).

Gravel lenses and bands in the sandy stratum perhaps represent erosion activation phases on adjacent areas of the Polar Ural. Numerous facies boundaries in sandy-gravelly-pebbled stratum are possibly determined by alluvial redeposition on the lacustrine-alluvial plain. The ^{14}C dates from sandy sediments unaffected by thermokarst were 22 500±400 (detritus, GIN-13795) and 44 900±1100 (wood, GIN-13796) ^{14}C years BP. Peat lenses, which were formed during increased thermokarst activity at the surface of the sandy stratum, is characterized by a continuous

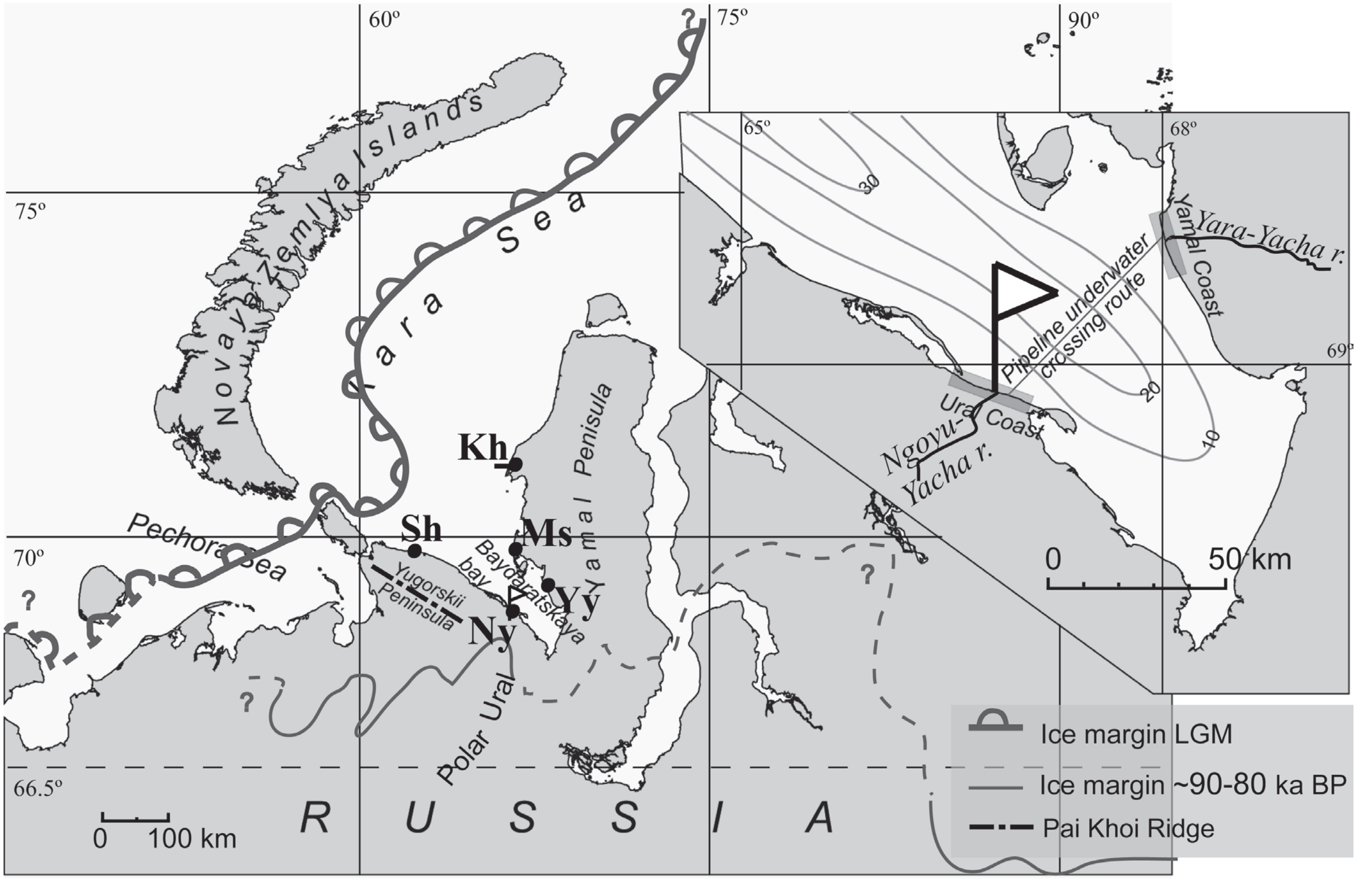

Figure 1. The area of investigations (marked by flag). Ice limits of the Late Weichselian glacial maximum (LGM) and Early Weichselian glacial maximum (90–80 ka BP) according to Svendsen et al. (2004). Ny – Ngoyu-Yacha River, Kh – Kharasavey River (northern Kara diamicton limit), Sh – Cape Shpindler, Ms – Marresale Station, Yy – Yara-Yacha River.

dated series (9 dates) from 10,900±120 (MSU-1362) and 8,210±110 (GIN-7862) to 4,140±70 (WAT-2895) ^{14}C years BP (Romanenko et al. 2001). It confines the period of sandy stratum formation at 11,000 yr BP.

On the opposite coast of Baydaratskaya Bay, near the mouth of the Yara-Yacha River, the same sandy stratum is exposed on coastal bluffs. Radiocarbon analysis using two *in situ* peat samples from lake sediments yielded an AMS radiocarbon age of 28 650±280 (AA-20 497) and 29 750±520 (AA-20 498) ^{14}C years BP (Gataullin & Forman 1997); and 19 560±330 ^{14}C years BP (GIN-8561) (Romanenko et al. 2001). It could be formed in the Middle-Late Weichselian (Romanenko et al. 2001). This confirms Middle-Late Weichselian age of sandy stratum on investigated area.

Relations between massive ground ice and host sediments

The principal singularity of the sandy stratum, which forms the surface with altitudes of 27–35 m a.s.l., is massive ground ice. Ice bodies are confined mainly to the highest parts of the unit that are least modified by thermokarst. They are recovered as close to the water edge, as near the highest altitudes of this surface – up to 15 m a.s.l.. Maximum dimensions of these massive ground ice bodies is up to 7 m thick (Fig. 3) and 150 m along the coastline.

Massive ground ice lies generally conformably with host strata. But fairly often the upper contact cuts the layers in the massive ice; in other words, this contact is erosional or it is a thaw unconformity. The erosional nature of the contact is obvious when massive ice is overlaid by several meters of sands with clear fluvial bedding (Fig. 4). Sometimes the upper contact is marked by c. 0.2 m of clay; thus it can be secondary.

At the lateral contact the ice bed is tapering out by ice layers, which are also conformable with host deposits (Fig. 2). Directly under the massive ground ice the deformed ice bands, dykes and elongated lenses are found with thicknesses up to 0.7 m; they disrupt the sand stratification or lie conformable with enclosing sediments. The ice of the bands and lenses is mostly transparent, often laminated owing to inclusions of host sediments, which lie in laminas parallel to ice bands. Tubular bubbles (c. 1 mm diameter and ≤2cm long) were often observed orthogonal to ice bands.

Cryostructures of Massive Ground Ice

Massive ice beds are composed of several types of ice. The majority of ice beds consists of laminated ice. This ice type is characterized by close alternation of layers (with 5–15 cm average thickness) of relatively transparent ice and muddy ice. The latter is due to suspended sand, clay

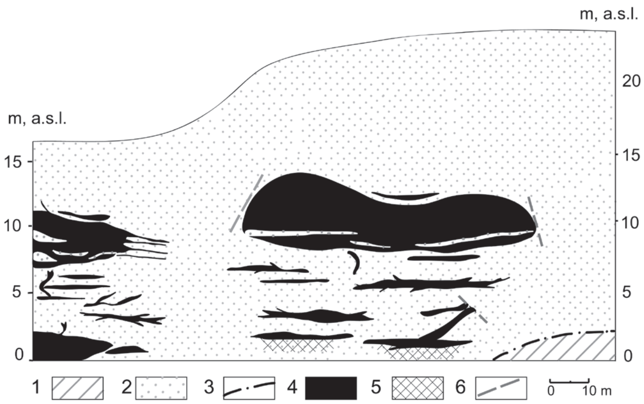

Figure 2. Stratigraphy of coastal bluffs (general scheme). 1- clays with boulders, 2 - sandy stratum, 3 – sediments strata's boundaries, 4 – ice, 5 – icy sediments, 6 - unclarified ice boundaries.

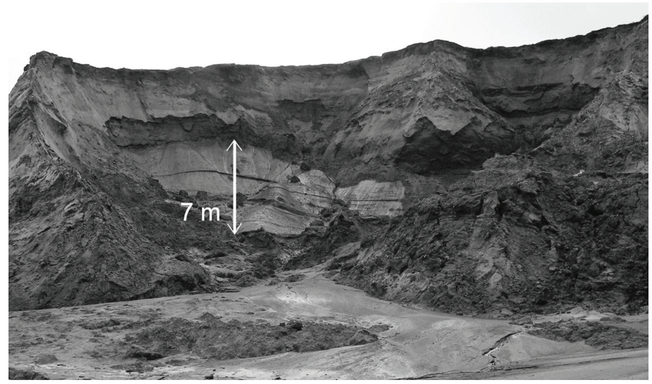

Figure 3. The thickest bed of massive ice (Photo by A.S. Iosimov).

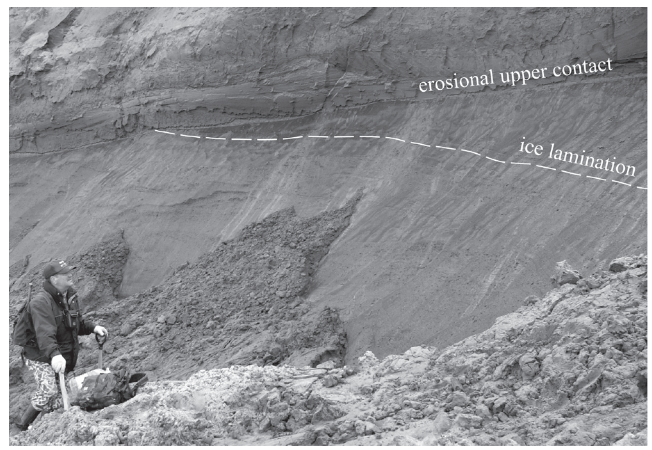

Figure 4. Erosional upper contact of massive ground ice (4 m thick). Ice bed is overlain by 8 m of sands.

and silt aggregates, several mm in diameter, and rounded or amorphous silty-clayey fragments up to several cm across (Fig. 5 a,b).

In the lower parts of the ice beds the mud content is usually higher than in the upper parts, and the laminations therefore become less distinct. Here it can be distinguished as the muddy ice subtype. Clay, silt and sand material in the ice beds corresponds to sands, silts and clays which enclose the massive ground ice. Generally, the layering of massive ground ice is subhorizontal, although it is more correct to note that it is subparallel to the upper ice bed boundary. Laminated ice has an average crystal diameter of 0.5–1.0 cm, and crystals are mostly isomorphic. In muddy ice layers with a great amount of sandy particles, the crystal size is much smaller. The laminated ice type becomes more complicated in places due to folds of different scales (Fig.5b), transparent ice inclusions, or sandy and clayey layers.

Thus, at the upper contact of the thickest massive ice bed, the upper 2 m of laminated ice are crumpled in recumbent folds above a subhorizontal shear plane. The limbs of the folds have amplitude of about 1 m.

Besides the laminated ice in the massive ice beds, there are also transparent and bubbly ice types (Fig. 5 c,d). Bubbly ice (bubbles are usually spherical, 0.5–3.0 mm diameter) is typical of the upper ice beds, and in the coastal section it gradually replaces laminated ice. By contrast, the transparent ice appears often to break through and sometimes draw apart the subhorizontal ice lamina. The thickness of such seams is up to 0.5 m; they often lie nearly vertically and sometimes bifurcate along several subparallel seams. In section they can have the form of a fold (Fig.6).

Transparent ice in its middle part often includes clay bands parallel to its boundaries (Fig. 5d, 6). The crystals of transparent ice can be 25 cm across.

For massive ground ice, independent of the ice type, clayey and sandy layers of different thickness (from several cm up to 0.5 m, usually about 10–20 cm) are typical. Thick ground layers are more frequent in the lower reaches of the ice beds; these layers can lie parallel to each other, form lenticular structures, and sometimes cut the subhorizontal ice layers.

Chemical and Isotopic Composition

Chemical analysis

In 2005–2007, the massive ice beds, ice bands and lenses in the underlying sediments (melt ice) and host sediments (from sediments aqueous extract) were sampled for chemical analysis. All the samples turned out to be fresh water– the mineralization of all of them is less than 200 mg/l. But composition and the ratio between different chemical ions varies substantially (Fig. 7). In massive ground ice, Ca^{2+} and Na^{+} cations and HCO_3^- (rarely SO_4^{2-}) are predominant. But in ice bands and lenses from below the massive ice beds HCO_3^- is completely absent. Aqueous extract from sediments shows that here chemical composition is somewhat different – Ca^{2+}, K^+, Na^+ and SO_4^{2-} predominate.

Isotopic analysis

The first results of stable isotope measurements in massive ice beds near the mouth of the Ngoyu-Yacha River were obtained concurrent with discover in 1990 (Konyakhin et al. 1991). Based on this data, the ^{18}O isotope values vary from -17.5 to -25.5‰ (relative to SMOW standard) in transparent ice and from -18.4 to -22.4‰ in bubbled ice. The analytical results of samples from 2006 confirmed the significant spread

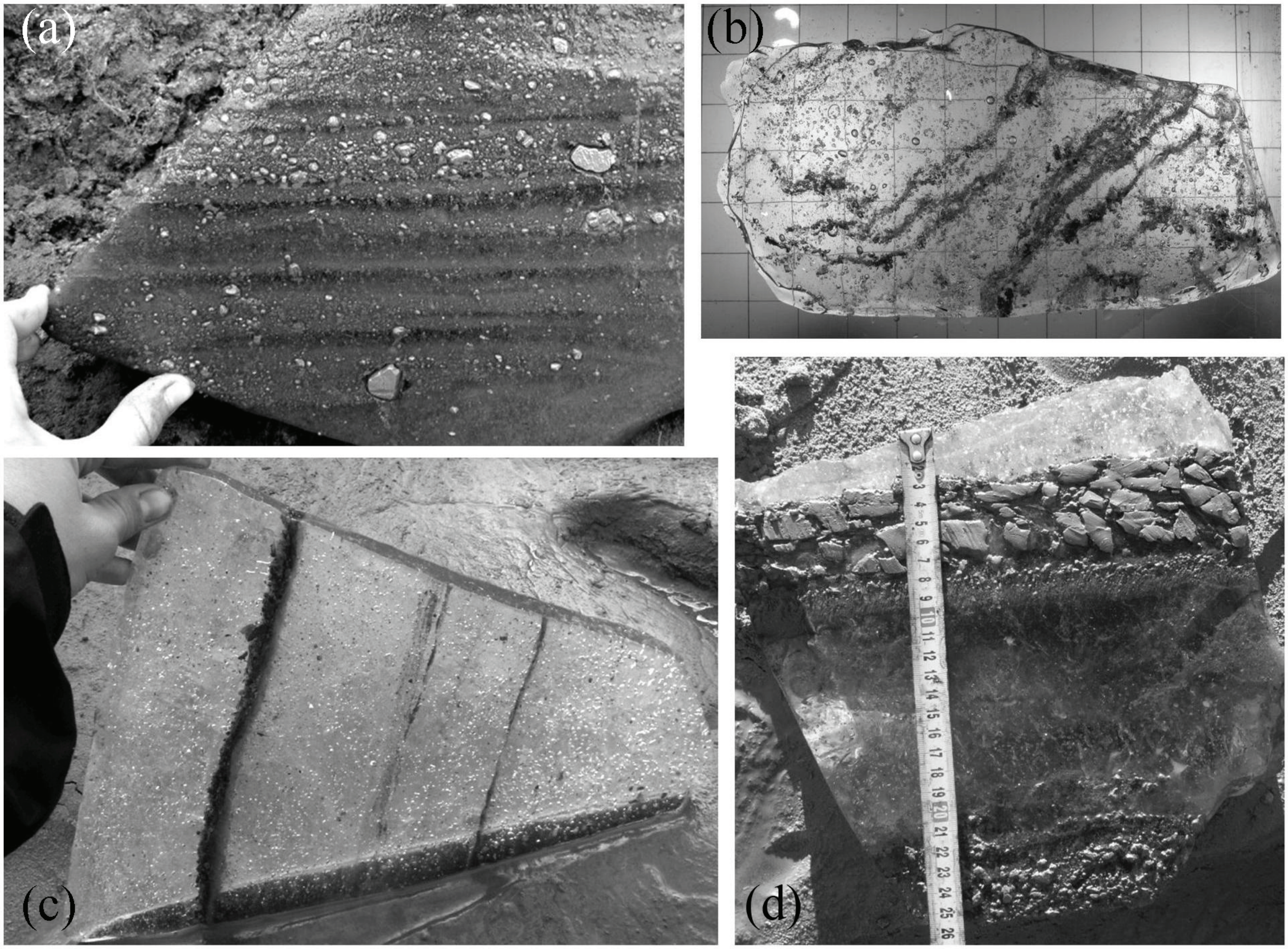

Figure 5. Types of massive ice: (a) laminated ice; (b) laminated deformed ice (1 cm mesh); (c) bubbly ice; (d) transparent ice with clayey band.

of values established earlier. A massive ice bed, 3.5 m in thickness, has been sampled in one vertical section at every 30–40 cm (Belova et al. 2007). Sampled ice is homogeneous; it is presented by laminated type except for the upper 30 cm where it slips into laminated, but clearer, bubbly ice. Here the dispersion turned out to be significant—at about 7‰ for $\delta^{18}O$ and about 45‰ for δD (Fig. 8).

Interpretation and Discussion

Composition and stratigraphy of host sediments

The lowest stratigraphic unit in the sections studied is represented by clays with boulders, and this unit can be related to the Kara diamicton. It is an informal stratigraphic unit first defined near Marresale station by V.N. Gataullin (Gataullin 1988; see Fig. 1). Kara diamicton is widespread on the western Yamal Peninsula, but has yet to be identified north of 70º50′N (Kharasavey River mouth; Forman et al. 2002). Near the Marresale station its uppermost facies is represented by massive to crudely stratified clayey silty diamicton without any glaciotectonic structures and with random pebbles and occasional sand horizons <1 cm thick. This description is almost identical to that for one of the clay units near the mouth of the Ngoyu-Yacha River. At Marresale station, the upper facies of the diamicton is interpreted by investigators as a supraglacial meltout till formed by the release of glacial debris from stagnant glacier ice. Based on finite radiocarbon and luminescence ages of ca. 35,000 to 45,000 yr obtained from the immediately overlying Kara diamicton Varjakha peat and silt (informal unit), the last glaciation was >40,000 yr ago (Forman et al. 2002). Thus, at the study area, the last large-scale glaciation was presumably also earlier than Middle Weichselian.

In such a case, massive ice beds in a sandy unit overlying what is probably Kara diamicton couldn't be the remains of a large ice sheet. Furthermore, they lie in lacustrine-alluvial sediments, so the lack of typical moraine deposits can be explained by their origin as remains of local glaciers (probably outlet glaciers of local Ural glaciation). This fact is confirmed by implication of spore-pollen spectra data, which is similar to Eemian-Early Weichselian one in Pai Khoi Ridge deposits (central part of Yugorski peninsula, northern part of Ural). Based on dates of the enclosing sediments, this glaciation could have occurred in Late Weichselian (MIS 2).

In the northern part of the Yugirski peninsula at Cape

Figure 6. Fold formed by transparent ice in laminated ice with subhorizontal bedding.

Shpindler (Fig. 1), a somewhat similar assumption was made. Possibly glacier ice was flowing northward from the hills in the Pai-Hoi uplands on the Yugorski Peninsula, 468m a.s.l., which may have acted as an ice sheet nucleation area during the Early Weichselian glaciation (Svendsen et al. 2004). However, at the study area it is difficult to assume the same scenario because typical moraine sediments are absent.

The unconformable upper contact of the massive ice unit in some places can be the result of thaw layer deepening or increased thermokarst activity during Holocene warming. But in many sections where the surface is unaffected by thermokarst and massive ice is overlaid by more than 8 m of sediments, this unconformity was evidently formed at the same time as the massive ground ice. This fact contradicts the intrasedimental hypothesis of massive ice formation but can be explained within the framework of a burial origin.

The ice bands and lenses and dykes in the host sediments most likely were formed by segregation and injection processes during permafrost aggradation following the burial of portions of the outlet glaciers.

Ice structure

The ice types described here can be observed in the case of buried glacier or under intrasedimental ice origin. Similar ice types were described in other massive ice exposures; for example, in massive ice at Tuktoyaktuk Coastlands in western Arctic Canada, which is supposed to be buried basal ice of the Laurentide Ice Sheet (Murton et al. 2005). There the laminated type of ice from this study can be related to aggregate-poor ice facies altering with pure ice facies.

Ice deformations, which are poorly explained by the intrasedimental hypothesis of massive ice origin, provide much stronger evidence of massive ice burial. For example, the observed folded transparent band could be formed as a result of ice removal in horizontal flatness, which deformed a previously intact band (such transparent bands form in bodies of contemporary glaciers).

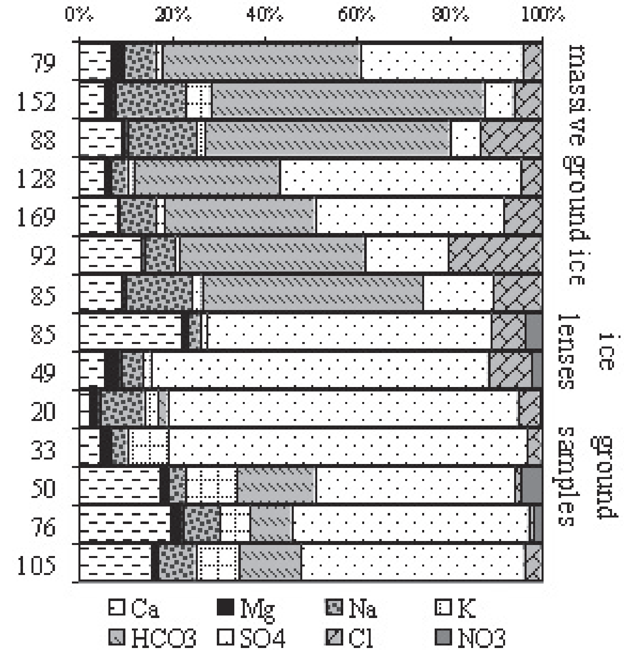

Figure 7. Mineralization (Y-axis, mg/l) and percentage of chemical components in massive ice, host sediments and ice bands and lenses in host sediments.

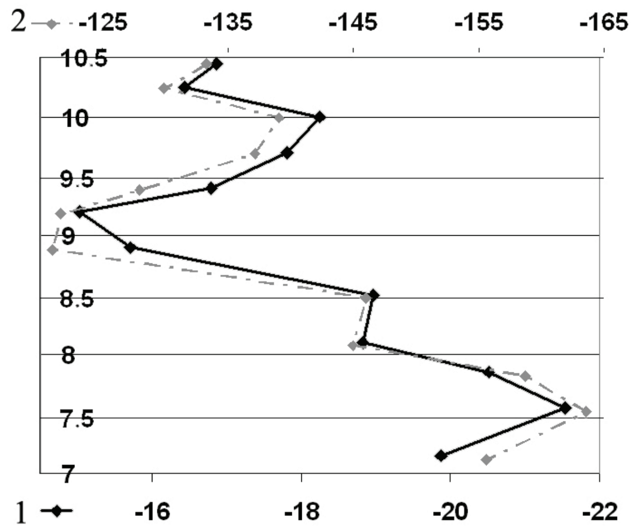

Figure 8. Vertical profiles of the ^{18}O (1) and D (2) isotope values in the massive ground ice body 3.5 m thick. Y-axis shows altitudes, a.s.l.

Chemical and isotopic composition

The chemical composition of massive ice and host sediments is slightly different, which testifies against the hypotheses of underground origin of massive ground ice.

Ice bands and lenses are similar to sandy strata by the ratio of chemical components' content, which confirms their intrasedimental origin. The absence of HCO_3^- in these ice formations is typical for stagnant water (Alekin 1970). It supports the formation of these lenses in a closed system during freezing and consolidation of enclosing lacustrine-alluvial sediments.

The rather large amplitude of oscillation of the ^{18}O and D isotope values tells about the impossibility of this massive intrasedimental ice bed forming only by the segregation process. On the contrary, this data doesn't contradict the possibility of basal glacial ice burial.

Conclusions

Based on these data, we can suppose that the complicated sandy-pebble stratum, which encloses massive ground ice, was formed in conditions of periglacial lacustrine-alluvial flat with the demolition of the material from adjacent parts of the Polar Ural. During Middle-Late Weichselian, as the result of intensive entry of alluvial-proluvial or fluvioglacial sediments and reformation of river channels ice bodies, apparently remnants of Ural's outlet glaciers could be buried. Later on they were periodically destroyed by thermokarst and buried again, which caused complicated construction of ice beds. The last regional glaciation occurred earlier in this area, probably during Early Weichselian.

Acknowledgments

We are grateful to S.A. Ogorodov for logistical support of fieldwork, and to the Russian Foundation of Basic Research, projects 05-05-64883 and 05-05-64872, for financial support.

References

Alekin, O.A. 1970. The foundations of hydrochemistry. Leningrad: Hydrometeorology Publishing, 442 pp. (in Russian).

Andreev, A.A., Tarasov, P.E., Romanenko, F.A., Sulerzhitskii, L.D. & Terekhov, K.I. 1998. Vegetation of the western coast of Baydaratskaya Bay at the end of the Late Pleistocene. *Stratigraphy and Geological Correlation* 6(5): 520-525.

Belova, N.G., Solomatin, V.I., Romanenko, F.A., Olyunina, O.S. & Ogorodov, S.A. 2007. New materials on massive ground ice at the eastern coast of Yugorski peninsula. *Proceedings of the international conference "Cryogenic resources of polar regions"*. Salekhard: Vol.1: 198-200 (in Russian).

Forman, S.L., Ingólfsson, Ó., Gataullin, V., Manley, W.F. & Lokrantz, H. 2002. Late Quaternary stratigraphy, glacial limits, and paleoenvironments of the Marresale area, western Yamal Peninsula, Russia. *Quaternary Research* 57: 355–370.

Gataullin, V.N. 1988. Upper Quaternary Deposits of the Western Coast of the Yamal Peninsula, Russia.// Ph.D. thesis abstract, Federal Geological Institute, 26 pp. (in Russian).

Gataullin, V.N. & Forman, S.L. 1997. Stratigraphy of upper Quaternary sediments in Western Yamal as a key for last glacial paleogeography reconstructions. // Problems of the cryolithology of Earth. International conference proceedings. Pushchino, 1997: 246-249.

Konyakhin, M.A., Ampleeva, T.V. & Nikolaev, V.I. 1991. An occurrence of massive ground ice in Upper Pleistocene deposits, the Uralian Coast of the Baydaratskaya Bay. *Materials of Glaciological Researches* 72: 227-228 (in Russian).

Murton, J.B., Whiteman, C.A., Waller, R.I., Pollard, W.H., Clark, I.D. & Dallimore, S.R. 2005. Basal ice facies and supraglacial melt-out till of the Laurentide Ice Sheet, Tuktoyaktuk Coastlands, western Arctic Canada. *Quaternary Science Reviews* 24: 681-708.

Svendsen, J.I., Alexanderson, H., Astakhov, V.I., Demidov, I., Dowdeswell, J.A., Funder, S., Gataullin, V., Henriksen, M., Hjort, C., Houmark-Nielsen, M., Hubberten, H.W., Ingólfsson, Ó., Jakobsson, M., Kjær, K.H., Larsen, E., Lokrantz, H., Lunka, J.P., Lysa, A., Mangerud, J., Matiouchkov, A., Murray, A., Möller, P., Niessen, F., Nikolskaya, O., Polyak, L., Saarnisto, M., Siegert, C., Siegert, M.J., Spielhagen, R.F. & Stein, R. 2004. Late quaternary ice sheet history of northern Eurasia. *Quaternary Science Reviews* 23: 1229-1271.

Romanenko, F.A., Voskresenskiy, K.S., Tarasov, P.E., Andreev, A.A., Nikolaev, V.I. & Sulerzhitskiy, L.D. 2001. The relief and loose sediments forming features on the Western Yamal and Baydaratskaya Bay coast (Kara Sea). *Problems of general and applied geoecology of the North.* Moscow: MSU Publishing, 41-68 (in Russian).

A Direct Method for Obtaining Thermal Conductivity of Gravel Using TP02 Probes

Hui Bing
State Key Laboratory of Frozen Soil Engineering, Cold and Arid Regions Environmental and Engineering Research Institute, CAS, Lanzhou, China

Ping He
Tunnel and Underground Engineering Research Center, Ministry of Education, Beijing Jiaotong University, Beijin, China

Norbert I. Koemle
Space Research Institute, Austrian Academy of Science, Graz, Austria

Wenjie Feng
State Key Laboratory of Frozen Soil Engineering, Cold and Arid Regions Environmental and Engineering Research Institute, CAS, Lanzhou, China

Abstract

Gravel was used as one of the effective measures to decrease the temperature of embankment during construction of the Qinghai-Tibet Railway. Thermal conductivity is one of the most relevant material parameters needed for the design and construction of roads and railways, especially in permafrost regions. We report on the measurement of the thermal conductivity of gravel (with grain size between 5 cm and 8 cm, which was widely adopted during construction of the Qinghai-Tibet Railway) using Thermal Properties sensors (TP02) made in Netherlands, which allowed a direct measurement of local thermal conductivity. Two conditions of the gravel are preformed: (1) natural convection exists in the gravel, and (2) there is only heat conductivity in the gravel by setting the boundary temperature and constrained convection using agar gel embedded in the gravel. We describe the data evaluation and present the results of the experiments.

Keywords: agar gel; gravel; natural convection; permafrost regions; Qinghai-Tibet Railway; thermal conductivity.

Introduction

In many physical and engineering problems thermal conductivity of the materials used is one of the key parameters that, to a high extent, control the thermo-physical behavior of the system. For example, during construction, the distribution of artificial or naturally generated underground heat determines the stability of the roadbed and thus the safety of the pathways. This is especially important in permafrost regions, like the areas transected by the Qinghai-Tibet Railway. The permafrost layer of the road contains high ice content, making it susceptible to consolidation if thawing occurs. If thawing consolidation takes place beneath engineering structures such as roadway embankments and buildings, the consolidation of the foundation soils typically results in instability and failure of the structures.

Thawing-unstable permafrost provides a very significant challenge to engineers working on the Qinghai-Tibet Railway. Over the years, techniques for avoiding damage to engineering structures because of thaw settlement have remained high on the research agenda for the Chinese government and scientific researchers, although the railway was test run on July 1, 2006. Roadbed embankments typically have a large influence on the thermal regime of the ground when they are constructed in permafrost regions. In order to maintain the stability of the embankments, gravel embankments and slopes are used to avoid thawing-settlement in permafrost regions. But there is some dispute over temperature decreasing degree of various conditions for the complicity of the thermal conductivity determination.

Goering (1996, 2000) studied temperature decreasing of gravel embankments in winter using the dynamic of porous medium. Temperature reductions will reduce or eliminate the tendency for the subsurface permafrost to thaw, thereby protecting the embankment structure from damage due to thaw-settlement. Due to the macropore characteristic of the gravel, cool and warm air in winter and summer can change reciprocally, shielding heat (Sun & Ma 2003). Under the condition of temperature fluctuation and knowing the heat diffusion coefficient of the gravel, thermal conductivity can be obtained by calculating the equivalent heat capacity (Sun et al. 2002, 2005). Therefore, thermal conductivity is a key heat parameter in indicating the heat condition for designing the gravel embankments and slopes. Thermal conductivity of the various materials can be obtained by experiment, but it is difficult to gain the conductivity for gravel of large grain size. However, Thermal Properties sensors (TP02) supplied by IWF and produced by the Hukseflux company allow direct measurement of local thermal conductivity. This research has resulted in a number of indoor experimental studies which can be utilized in field research and numerical modeling of the convection embankments for protecting a wide variety of structures from thawing-settlement damage. Nevertheless, many unsolved problems still remain.

Experimental Apparatus and Materials

Experimental apparatus

The goal of our experiments was to measure the thermal conductivity of gravel used in roadbed engineering. The tests were performed in a thermally controlled environment, namely a climate chamber (Fig. 1). The chamber allowed establishment of a homogeneous temperature environment in the range of -40°C to +70°C. The inner size of the chamber is approximately 100 cm × 100 cm × 100 cm. Two big fans on the inside back of the chamber are used to control the temperature of the chamber to a prescribed value. Also, the air humidity inside the chamber can be controlled externally and set to a given temperature. During operation the power device of the chamber must be cooled by a cold water circuit.

The second major device used in the experiments was the sample container (Fig. 2). It is of rectangular shape (70 cm × 70 cm × 35 cm) and its sides are thermally insulated. The bottom of the container is connected to a circuit which connects to a cooling machine working with alcohol as the cooling agent. The bottom temperature of the container can be set to a certain value, so the upper and bottom temperature of the sample in the container can be controlled by setting the temperature on the chamber and the cooling machine to whatever temperature gradient wanted for the experiments.

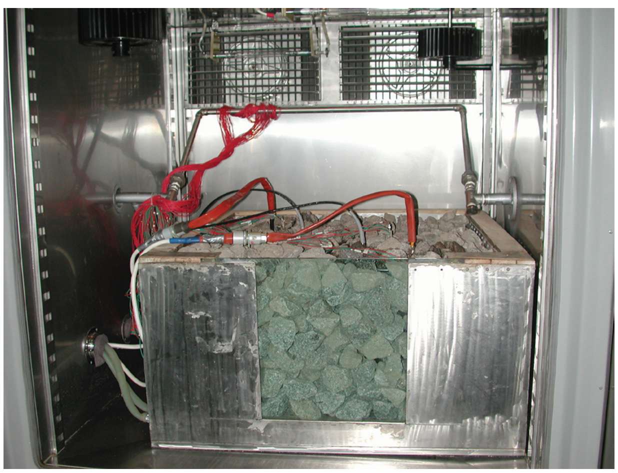

Figure 1. Climate chamber and container used in the experiments.

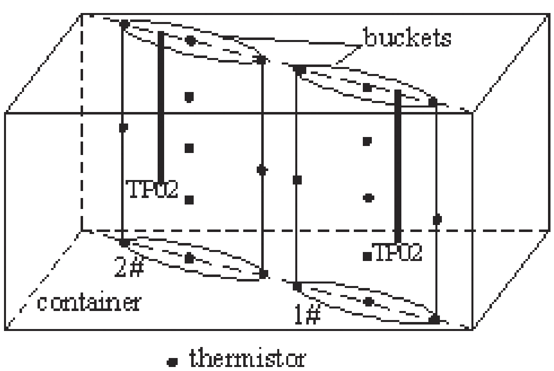

Figure 2. Schematic charts of the experimental apparatus.

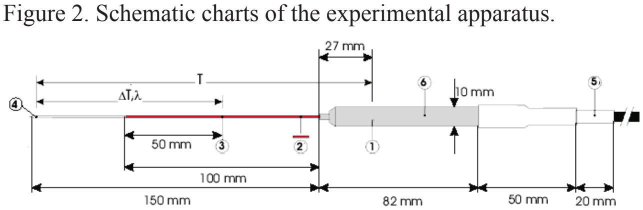

Figure 3. Dimension and buildup of Hukseflux TP02 thermal conductivity probes, which were used to obtain the thermal conductivity data presented in this paper. The sensors including the needle are hermetically sealed in a stainless steel casing, which makes them suitable also for vacuum application.

The third device used was two big stainless steel buckets 32 cm in inner diameter and 30 cm in height. The buckets were filled with gravel and put in the diagonal place of the container; the container was filled with gravel, too.

Measurement sensors

Two types of sensors inserted in the gravel were used in our experiments for measuring the thermal conductivity λ. Thermistors were distributed among the gravel uniformly, which can be seen in Figure 2, to monitor the temperature variations of the gravel during the periods of cooling and heating. The other sensors are two TP02 probes (Fig. 3), which were put in the two buckets. It allows a classical method of getting the thermal conductivity value. The sensor needle of the Hukseflux TP02 probe consists of a needle with two thermocouple junctions (one of which acts as a reference) and a heating wire. It is inserted into the medium that is investigated. In the base, a temperature sensor is mounted. The probe has a heater resistance per meter of 75.52 Ω, a length of 150 mm, and a diameter of 1.5 mm. Its maximum operating temperature is T_{max} = 135°C. To get reasonable results of thermal conductivity, the sensor has to be inserted into the sample at least to the upper end of the thin needle, better up to the base. The principle relies on the unique property of a line source: after a short transient period the temperature rise, ΔT, only depends on heater power, Q, and medium thermal conductivity, λ:

$$\Delta T = (Q/4\pi\lambda)(\ln t + B) \tag{1}$$

with ΔT in K, Q in W/m, λ in W/mK, t the time in *s* and B a constant.

The thermal conductivity can be calculated from two measurements at t_1 and t_2 (Seiferlin et al. 1996). For TP02, both t_1 and t_2 are higher than 60s, and typically 100s apart. Now ΔT the temperature difference between t_1 and t_2

$$\lambda = (Q/4\pi\Delta T)\ln(t_2/t_1) \tag{2}$$

The signal of TP02 is the function of the natural logarithm of time. The different steps of signal analysis for evaluating the thermal conductivity from the measured temperature signal of a heated thin-wire sensor can be seen in Figure 4. In every individual measurement, the graph in the logarithmic time scale should also be visually inspected to see where the linear part heat can be used for the evaluation of λ.

To estimate the length of the transient part of the signal, one can use the following formula (Hukseflux TP02 manual):

$$t_{transient} = \frac{10D^2}{a} \tag{3}$$

Hereby, the transient time is proportional to the medium thermal diffusivity a, and the probe cross section (D is the diameter).

Experimental procedure

The gravel we used in our experiment is widely adopted in the convection roadbed along Qinghai-Tibet Railway. The porosity of the gravel with grain size of 5 cm–8 cm has been experimentally determined as n = 0.48. Figure 2 also shows the schematic charts of the experimental apparatus used in our experiment. We filled the two buckets (#1 and #2) and the container with gravel at random. It was possible to make a large number of measurements over a number of days under this condition, when the cooling fans of the chamber were switched off temporarily and thus no forced air convection took place in the chamber.

In order to investigate the thermal conductivity of gravel without convection, we used agar gel, filling the pores of gravel. It was also used for calibration in the experiments. This is a water gel, of which the ingredients can be bought in every pharmacy. The agar itself does not significantly influence the thermal, but eliminates the effects of convection. At 20°C and 0°C, its thermal conductivity is 0.60 W/mK and 0.57 W/mK, respectively. The temperature dependence of the thermal conductivity is 0.0015 W/mK/°C.

Two different grain size gravel measurements were done at room temperature. After the investigation, the calibration of the probes was performed.

Data Evaluation

The criterion for natural convection

The Rayleigh number is a key similarity parameter investigating the natural convection in the porous medium (Sun et al. 2004). Whether natural convection will take place depends on the shape and the boundary of the porous medium. Based on the research on the convection of gravel, the Rayleigh number is defined as

$$R_a = \frac{\rho_0 g \beta K H \Delta\theta}{\mu \alpha_t} \tag{4}$$

It is the product of Darcy number $D_a = K/H^2$ and the Rayleigh number of pure fluid $Ra' = \beta g\ H^3\Delta\theta/\mu a_t$, where ρ_0 is the density of the pore air (kg·m^{-3}), g is gravity acceleration (m·s^{-2}), β is the coefficient of thermal expansion (K^{-1}), and K is the permeability of the gravel (m^2), which is difficult to obtain, and generally it is estimated by the semi-rational formula as follows (Goering, 1998):

$$K = \frac{1}{5}\left[\frac{(1-n)^2}{n^3}\left(\frac{f_0}{100}\sum \frac{p_m}{d_m}\right)^2\right]^{-1} \tag{5}$$

where f_0 is the shape factor of gravel ranging from 6.0 of sphere to 7.7 of corner edge shape, and p_m is the percent of average grain size, d_m, in gravel. In the experiments, the permeability of the gravel is 4.83 × 10^{-6}m^2 determined experimentally. H is the height of the gravel (m), and $\Delta\theta$ is the temperature difference between the lower and upper boundary in the experiment (K); μ is dynamic viscosity of the pore air (N·s·m^{-2}) influenced by temperature, and it is of 1.158 × 10^{-5} N·s·m^{-2}～1.700 × 10^{-5} N·s·m^{-2} under the temperature of between -20° to 40°, and a_t is the volumetric heat capacity of the pore air (m^2·s^{-1}).

There is a critical Rayleigh number, Ra_c, depending on the shape and boundary conditions of the porous medium (Bear 1972). When Ra is less than Ra_c, the component of air among gravel is zero, so there is only pure heat conductivity; however, natural convection is taking place when Ra is greater than or equal to Ra_c. The critical Rayleigh number Ra_c can be calculated under different boundary conditions (Kong et al. 1996). In the experiments, it is a two-dimensional square region, all-around waterproof, and boundary temperatures are stable with side insulation, so $Ra_c = 4\pi^2 = 39.47$. The Rayleigh number, Ra, is 67.83 in the minimum temperature difference between the lower and upper boundary, greater than the critical Rayleigh number, Ra, 39.47; so before filled with agar gel during the experiment, heat conductivity exists in the gravel, but natural convection as well.

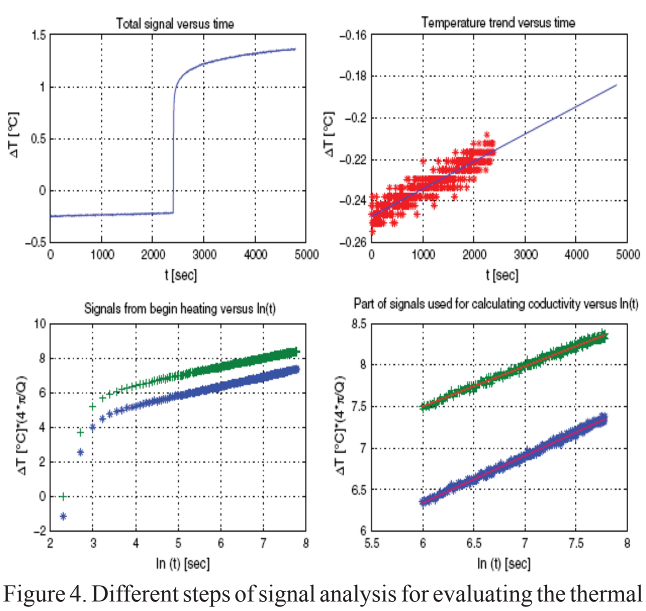

Figure 4. Different steps of signal analysis for evaluating the thermal conductivity from the measured temperature signal of a needle probe. Upper left: measured temperature increase in response to sensor heating. Upper right: evaluation of the general temperature trend in the sample before heating. Lower left: corrected (green) and uncorrected (blue) temperature increase in response to sensor heating over a logarithmic time coordinate; only the heated part of the signal is plotted here. Lower right: part of the signal used for the evaluation of the thermal conductivity.

Thermal conductivity of gravel with convection

Figure 5 shows the variation of thermal conductivity of existing natural convection in gravel. It can be seen that the thermal conductivity increases in positive temperature and decreases in negative temperature, so it is good for heat exchange in summertime for road stability in permafrost regions. There is the same trend in the temperature gradient (Fig. 6). It means that there exists natural convection to a negative temperature gradient (bottom temperature is grater than the upper temperature), and there is only heat conductivity to a positive temperature gradient (bottom temperature is lower than the upper temperature). Under this condition, the bottom temperature is higher than the upper boundary temperature. Due to the existence of natural convection, the heat transferred from the lower to upper is greater than the conditions where there is only heat conductivity. With the increasing of the temperature gradient, the effect is more obvious. The advantage of gravel roadbeds and slopes is active protection of the permafrost, especially in summertime with high temperatures. The results can be used in numerical modeling of the variation of temperature field of the roadbed.

From the experiment graph of the thermal conductivity of gravel with convection, we know the thermal conductivity with convection, but in our experiment using TP02 probes, we do not know how much the convection affects the thermal conductivity, namely temperature.

Thermal conductivity of gravel filled with agar

Our experiments with gravel, agar gel, and the composite sample (gravel with air, and gravel with agar gel filled) offer the possibility to test some simple formulas predicting the conductivity of two component samples practically, since we have both conductivity measurements of the single components and measurements of the sample containing both components in a known volume ratio.

In order to eliminate the effects of convection, the thermal conductivity measurements were done by filling the gravel with agar gel. The thermal conductivity of the composite sample is 1.6 W/mK in positive temperature, and 3.0 W/mK when freezing. Then the simplest way to predict the effective conductivity of the composite sample would be

$$\lambda = n\lambda_a + (1-n)\lambda_s \tag{6}$$

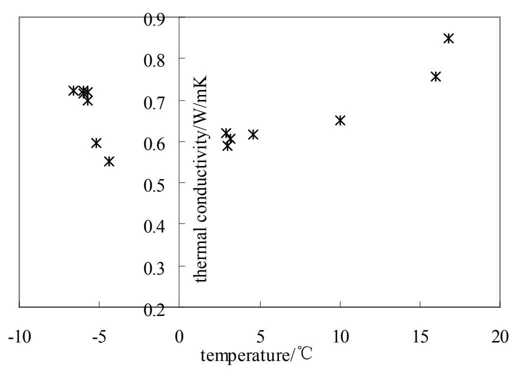

Figure 5. The variation of thermal conductivity with temperature when there is existing natural convection.

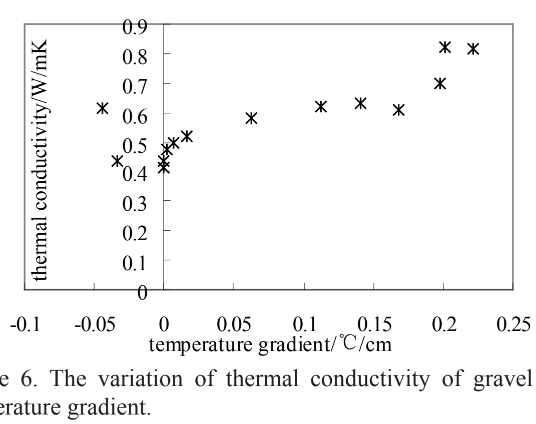

Figure 6. The variation of thermal conductivity of gravel with temperature gradient.

where n is the porosity of the gravel (equivalently n is the volume ratio filled with the agar gel); λ_a is the thermal conductivity of agar gel, and the change is very little with temperature; and λ_s is the conductivity of granite stones.

The porosity n of the composite sample (respectively the fraction filled by the agar gel) has been experimentally determined as $n = 0.48$. The calculation value of the thermal conductivity of gravel filled with agar gel is 1.692 W/mK in positive temperature, and 2.964 W/mK when freezing.

Different grain-size thermal conductivity measurement at room temperature

At room temperature, different grain size gravel measurements were done. One is of grain size between 1 cm and 2 cm, and the porosity of it is 37.9%; the other is of grain size between 2 cm and 4 cm, and the porosity is 40%. It can be seen from Figure 7 that the bigger the grain size or porosity, the greater is the thermal conductivity.

Conclusions

1. The thermal conductivity measurements of gravel using TP02 probes give a simple and direct way to obtain results. To the temperature and the temperature gradient with air convection, the thermal conductivity increases in positive, and decreases in negative.
2. With the agar gel filled and using one simple formula, the calculation value of the thermal conductivity of gravel is 1.692 W/mK in positive temperature, and 2.964 W/mK when freezing.
3. The bigger the grain size or porosity, the greater is the thermal conductivity.
4. We studied the thermal conductivity of gravel with air convection, but it is still a question as to how much the convection affects the thermal conductivity and the temperature in the roadbed. A solution to this is expected in our future work.

Acknowledgments

Funding for this work was provided by the National Key Basic Research and Development Foundation of the Ministry of Sciences and Technology of China (Grant No. 2002CB412704), National Natural Science Foundation of

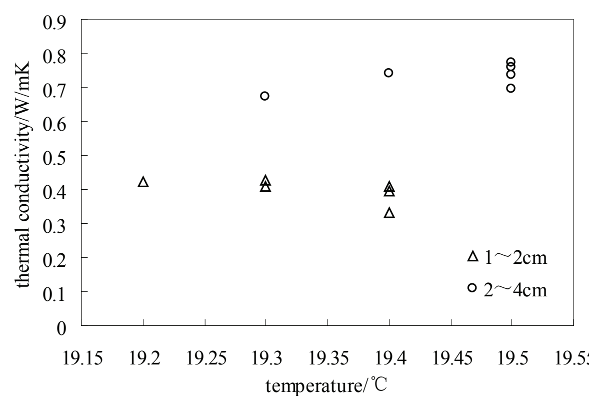

Figure 7. Thermal conductivity of different grain sizes.

China (No. 50778012, No. 40501016), the National Natural Science Foundation for Basic Talents Training in Special Subject of Glaciology and Cryopedology (No. J0630966).

References

Bear, J. 1972. *Dynamics of Fluids in Porous Medium*. New York: Elsevier.

Goering, D.J. 1998. Experimental investigation of air convection embankment for permafrost-resistant roadway design. *Proceeding of the Seventh International Conference on Permafrost. Yellowknife, NWT, Canada*.

Goering, D.J. & Kumar, P. 1996. Winter-time convection in open-graded embankments. *Cold Regions Science and Technology* 24: 57-74.

Goering, D.J., Instanes, A. & Knudsen, S. 2000. Convective heat transfer in railway embankment ballast, *Proceedings of the International Symposium on Ground Freezing and Frost Action Soils, Louvain-la-Neuve, Belgium. A.A. Balkema, Rotterdam*, 31-36.

Hukseflux Thermal Sensors: TP02 probe for thermal conductivity measurement, 2003. User manual, 26 pp.

Kong, X.Y., Lu, D.T., Xu, X.Z. & Wang X.D. 1996. Study on convection in porous medium. *Advances in Mechanics* 26: 510-520.

Seiferlin, K., Koemle, N.I., Kargl, G. & Spohn, T. 1996. Tine heat source measurements of the thermal conductivity of porous HO ice, CO ice and mineral powders under space conditions. *Planet Space Science* 44: 691-704.

Sun, X.B., Xu, X.Z., Lai, Y.M. & Li, D.Q. 2002. Determination of thermal diffusivity and conductivity on ballast. *Journal of Glaciology and Geocryology* 24: 790-795.

Sun, Z.Z. & Ma, W. 2003. Effects of ballasts on temperature of embankment in permafrost region. *Journal of Railway Engineering Society* 4: 59-61.

Sun, X.B., Xu, X.Z., Lai, Y.M., Li, D.Q., Wang, S.J. & Zhang, J.Z. 2004. Experimental research of thermal diffusivity and conductivity in embankment ballast under periodically fluctuating temperature, *Cold Regions Science and Technology* 38: 219-227.

Sun, X.B., Xu, X.Z., Lai, Y.M. & Fang, M.X. 2005. Evaluation of fractured rock layer heights in ballast railway embankment based on cooling effect of natural convection in cold regions. *Cold Regions Science and Technology* 42: 120-144.

The Effect of Near-Freezing Temperatures on the Stability of an Underground Excavation in Permafrost

Kevin L. Bjella , P.E.
Cold Regions Research and Engineering Laboratory, Fairbanks, AK, USA

Abstract

Changes in tunnel geometry have occurred to the Cold Regions Research and Engineering Laboratory (CRREL) Permafrost Tunnel in Fox, Alaska, since excavation in the mid-1960s. Frozen silt deformation has occurred in the rear of the horizontal adit, and a portion of the gravel roof in the lower winze chamber has detached from the silt strata above. Both of these deformations are attributable to thermal changes in the facility that have raised the overall temperature to near-freezing. Temporary modifications to the air-chilling system have decreased the temperature to an average of -7.0°C for the winter months and -3.5°C for the summer months, and early data from a monitoring program indicate the creep rate has slowed significantly.

Keywords: creep; frozen gravel; frozen loess; ice wedges; massive ice; permafrost tunnel.

Introduction

The CRREL Permafrost tunnel is located 16 km north of Fairbanks in Fox, Alaska (Fig. 1).The facility consists of a 110 m long horizontal adit excavated in frozen loess and a 45 m long winze that extends obliquely down to the underlying frozen gravels. Changes have occurred to the geometry of the tunnel since the excavation was conducted in the mid to late 1960s. Specifically deformation of the frozen silt has occurred in the rear of the adit, and a rooffall of the gravel layer has occurred in the room at the bottom of the winze. Investigation of the deformation was conducted in May of 2006 to ascertain what measures could be taken to prevent further deformation (Bjella et al., in press).

Background

This tunnel is composed of two portions: the adit (a nearly horizontal passage from the surface into a mine), which was driven by the U.S. Army Corps of Engineers using continuous mining methods in the winters of 1963–64, 1964–65, and 1965–66 (Sellman 1967), and the winze (an inclined adit), which was driven by the U.S. Bureau of Mines from 1968 to 1969 using drill and blast, thermal relaxation, and hydraulic relaxation methods (Chester & Frank 1969).

The adit was driven into a nearly vertical silt escarpment at the margin of Goldstream Creek Valley. This valley was historically mined for placer gold, and the escarpment was created by this activity. The geology consists of silt deposits that are Wisconsin to recent in age and eolian in nature derived from the Alaska Range. The silts overlie gravels of Nebraskan age derived from the surrounding hills of the Yukon–Tanana Upland terrain, and they in turn overlie Pre-Cambrian Birch Creek schist bedrock (Sellman 1967). The natural surface over the axis of the tunnel rises gently from the top of the 10 m escarpment and preferentially drains towards Goldstream Creek to the west and Glenn Creek to the north. The overburden is approximately 8 m deep at the rib-sets near the portal, 12 m deep at the rear of the adit, and approximately 17 m deep over the gravel room.

The tunnel contains many periglacial features found in fine-grained permafrost, such as thick segregated ice, massive ice (ice wedges and thaw ponds), and erosional and climate change boundaries marking depositional events, all of which are readily seen in the walls and roof of the adit and winze. The mode of permafrost formation was generally syngenetic, and the ice wedges are probably segments of larger ice wedge polygon complexes. Sellman (1967) suggested that two major silt units with separate ice wedge development exist in the adit. Moisture contents for the silt range from 39% to 120% with an average of 77% (Sellman 1967). The lower winze gravels have an average moisture content of 13.5% (Law 1987).

When the tunnel was constructed, it was realized that warm summer temperatures would adversely affect the stability of the facility, and therefore a mechanical air-chilling unit was installed. This unit, which is housed outdoors,

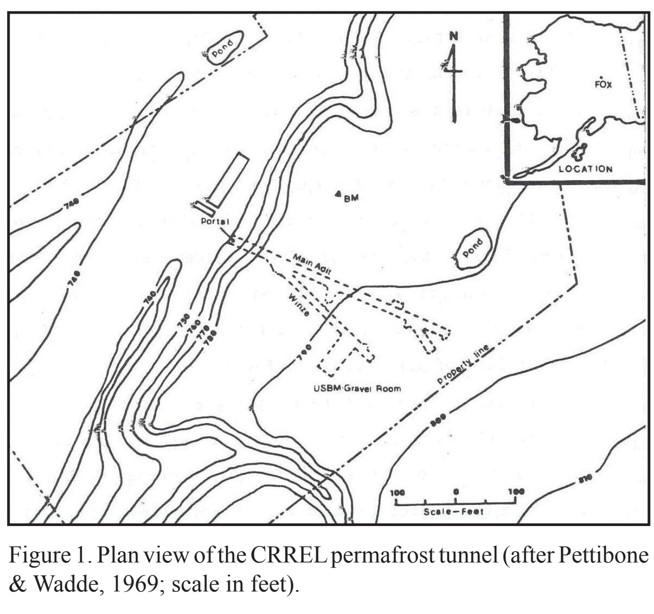

Figure 1. Plan view of the CRREL permafrost tunnel (after Pettibone & Wadde, 1969; scale in feet).

circulates liquid refrigerant through a series of loops that are embedded in the active layer over the portal bulkhead. One of these loops is circulated through a blower unit that hangs inside the tunnel between the bulkhead and the rib-sets and this serves to cool the interior air. This mechanical system was designed to run only during the months when outdoor ambient temperatures are above freezing.

Now inaccessible at the end of the adit are three approximately 1 m diameter ventilation shafts that were augured down from the surface to the tunnel. These were designed to aid in natural convection cooling in the winter while the portal doors were opened. These were problematic to maintain, as surface water would migrate along the shaft, thaw the permafrost, and form a conduit for surface water to travel to the tunnel, eventually occluding the vent. Each subsequent vent was installed after the failure of the previous. Sometime after 1993, the last of the three vents froze shut and has not been operable since. To aid in cooling the rear of the adit since that time, fans have been used to circulate the winter air after opening the portal doors.

The continuous mining method utilizing the Alkirk Miner simultaneously cut two 2 m circular arcs, side by side. After this pass was complete to the end of the adit at 110+00 (110 m, where 0+00 is the inside wooden bulkhead), a portion of the floor was lowered using a Joy 10 RU coal cutter, which resembled a large, multi-angle chainsaw. This started near the bulkhead and continued to approximately midway at 50+00, where the floor begins to incline noticeably to meet the elevation of the Alkirk pass at 62+0.5. The winze begins at 30+00 and drops obliquely at an incline of 14% for 45 m, passing into the gravel unit and ultimately into the weathered bedrock, where the Gravel Room was excavated (Pettibone 1973). At the time of excavation, portions of the Gravel Room roof consisted of a gravel layer up to 2 m thick below the overlying silt unit (Garbeil 1983).

Silt deformation

Beginning at the portal and moving towards the face (rear), the adit retains the original excavated geometry. An examination of the area near the portal reveals that this location has not experienced any appreciable deformation, probably because of the proximity to the portal doors during winter cooling and the proximity to the mechanical chilling unit during summer cooling. At 50+00, the "switch room," measuring 6×6 m, was excavated on the south side of the adit, and it appears that the roof in this area may have dropped some amount corresponding to the 12 m roof span. A transverse-oriented crack, about 4 cm wide, crosses the roof in this area. It is ice-filled, which suggests a cyrostructural origin and not a tension crack from deformation. Otherwise, from the portal to approximately 75+00, there is no perceptible deformation to suggest structural instability. In fact, for most of this portion of the adit, the Alkirk Miner profile is still visible in the roof, suggesting that the material is relatively stable and has not moved or deformed since the time of excavation.

At approximately 75+00 the roof begins to perceptibly sag and at 80+00 fallen slabs of silt up to 0.25 m in thickness are lying on the floor; the adit is then completely blocked by low-hanging and fallen soil layers at 90+00 (Fig. 2). The overhead layers of soil delaminate from the bedded soil above and creep down towards the floor hanging from the wall/roof intersection. This portion of the adit has evidence of paleo-alluvial deposition and erosion (Sellman 1967) where the poorly-graded silt contains interbedded layers of gravelly sandy silt, millimeters to centimeters in thickness. These layers are the preferential locations of the overhead detachment yielding the laminated structure (Bjella et al., in press). The slow deformation towards the floor can then give way to an abrupt release of portions up to 4 m^2 when the tensile strength of the soil is exceeded on either end of the catenary. Except near the portal, approaching the face, and in close proximity to cryological ice features, the silt in the adit and upper 30 m of the winze appears to have undergone little deformation since emplacement and retains a massive cryological structure appearance. No subsidence is noticed at the surface directly above this deformation.

The winze was excavated using drill and blast methods starting at a low hanging ledge at 30+00. This ledge was the pullout location for the shuttle car used to move waste material out of the adit from the Alkirk machine. Because of the excavation method, the winze retains a much rougher appearance than the adit and is shallower in geometry. There is no evidence through the entire length that this ramp has undergone deformation to any significant degree.

Gravel deformation

The Gravel Room, which is located at the foot of the winze and extends to the southwest, was the focus of subsurface mining studies in the late 1960s. The room is 9×21 m and was excavated in the gravel and bedrock below the overlying silt unit. This silt/gravel boundary at the time of excavation was approximately 2 m above the level of the roof of the Gravel Room. It was recognized that this gravel material, with its much higher unit weight than the silt unit to which it is bonded (2080 kg/m^3 for the gravel vs. 1600 kg/m^3 for the silt), could separate and fall in rooms of large roof span.

Investigators have repeatedly studied this parting potential through the years, with two investigations utilizing a warming study to understand the temperature dependence on creep and separation of the two soil units (Pettibone 1973, Garbeil 1983, Huang 1985, 1986). Two multiple-position borehole extensometers were installed during the 1983 study, with one end anchored in the silt unit and the other anchored in the gravel roof. Specific parting of 0.0084 mm/d was noted between the silt and gravel units when temperatures achieved their highest readings of -1.9°C during the study. Overall vertical closure rates for the room during April 1983 were 0.010 mm/day at -3.7°C, and in July 1983 the closure accelerated to 0.053 mm/d at -1.9°C.

The Gravel Room roof fell to the floor, approximately 25 m^3, after a 6.2 Richter magnitude earthquake struck the Fairbanks region in October 1995. The boundary of the dropped material is coincident with the wall that was installed to facilitate warming of the roof in 1983 and is shown in Figure 2. No subsidence is noticed at the surface due to this roof fall.

Additional observations

On the north side of the adit at 80+00 is a 5×5 m side area referred to as Sayles's Room (also called the Crystal Room). It is divided from the adit by a lumber frame and a heavy tarpaulin, and inspection revealed a large ice wedge on the western wall that widens where it meets the roof and then spreads out to almost room-width across the roof towards the adit. The adit at this stationing is overlain by massive ice, but to what degree is uncertain. The roof in Sayles's Room is supported by a 3 m long steel beam resting on 15×15 cm timbers, which are the remnants of previous creep testing.

Opposite Sayles's Room on the southeast end of the adit, at approximately 95+00, a 16×6 m crosscut exists that departs at a 36° angle. This room is now inaccessible because of the deformation in the adit, and anecdotal information implies that an ice wedge feature is exposed in the southwest wall of this room adjacent to the adit. Also, in the north wall of the adit at 75+00, there is a complex configuration of massive ice consisting of ice wedges, pond ice, and 5 to 15 cm -thick ice lenses. Because of the close proximity of the adit deformation, the Sayles's Room ice wedge, the cross-cut ice wedge, and the massive ice complex at 75+00; and based on the polygonal nature of ice wedge complexes (Williams & Smith 1989, Murton & French 1994), this intersection may be coincident with the near-center of an ice wedge polygon complex (Bjella et al., in press).

Analysis

Creep reference locations

Creep reference locations were installed in May of 2006 to specifically measure the change in dimension of selected areas of the facility. Seven were established in the adit and two in the winze and were designed to be measured with a metal tape extensometer which measures the relative distance to the nearest 0.01 mm. Each location consists of four attachment points of 0.95 cm diameter × 20 cm long lag eye-bolts screwed into the soil. Two of the points are located at mid-height of opposing walls, approximately perpendicular to the axis of the tunnel. The other two are located in the roof and floor in the same plane as the wall points, and are approximately mid-distance between the walls. The locations are prefixed with *A* for adit or *W* for winze and numbered starting with "1" continuing toward the face. Location A3 consists of only floor and roof points.

The creep stations are shown in Figure 2 and listed in Table 1 with distances from the bulkhead. The stations in the winze are measured from adit location A1. There have been three measurements conducted at all locations starting in May of 2006, with the most recent in July of 2007. The results of the measurements are listed in Table 1. On either side wall near

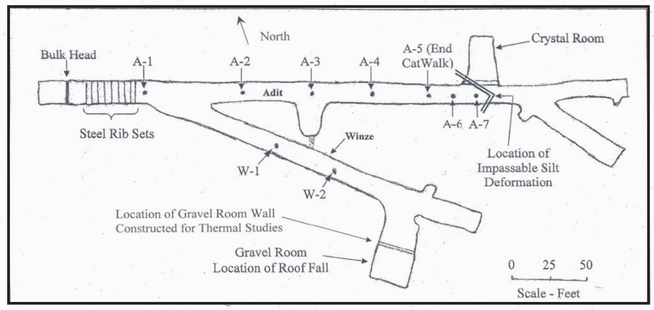

Figure 2. Detailed tunnel plan showing locations of deformation and creep monitoring locations (scale in feet).

the bulkhead are 0.95 cm lag bolts located in vertical 10×10 cm timber posts and these serve as a permanent extensometer reference location to verify continued accuracy of the tape extensometer measurements.

Wu (1985) measured nineteen vertical and nine horizontal convergence stations in both the adit and winze over a 287-day period. Four vertical and two horizontal points appear to have been within approximately 3 m of the newly established creep reference locations in the adit. Two vertical and two horizontal points appear to have been within these same limits of the newly created creep reference locations in the winze. Wu's locations, total convergence, and rate are listed in Table 1.

Temperatures

In May of 2006, temperature measurements were taken utilizing thermistors located approximately every 3.0 m horizontally and at 1.0 m vertically from the floor, both in the air and at soil depths of 0.15 m, 0.40 m, and 0.60 m. The tunnel air near the portal was approximately -3.0°C, and the rear adit air was approximately -1.7°C. The temperature gradient near the portal was 5.6°C/m with depth into the wall, with the ambient air colder than the wall. The gradient at 83+00 was 0.42°C/m, with the ambient air warmer than the wall. The crossover (0°C/m) where the temperature of the ambient air is the same as the wall temperature takes place at approximately 75+00, where the silt deformation begins. The temperature at the top of the winze was -3.0°C, the bottom of winze -2.7°C, and the Gravel Room measured -2.2°C. The mechanical cooling unit was delivering approximately -5.0°C air, and it is unknown at what depth into the wall the soil temperature reaches equilibrium with the local permafrost.

Pettibone (1973) reported that in February of 1969 the gravel room was approximately -8.3°C, and in March it was -6.7°C. During the period mid-April to mid-June 1969 the temperature was -3.9°C. Linnell & Lobacz (1978) reportthat immediately after tunnel excavation the face experienced temperatures down to -9.0°C in the winter months when natural convection was being utilized through the vent system.

Temperatures measured by Wu from October 4, 1983, to February 28, 1984, show that the adit roof in the area corresponding to A4 to A7 ranged from -3.8 to -2.5°C with

Table 1. Creep measurements.

Location	Stationing (m)	*Creep (mm)	*Rate (mm/day)	†Creep (mm)	†Rate (mm/day)	‡Wu ID	‡Creep (mm)	‡Rate (mm/day)
A1 Vertical	16+50	-1.35	0.004	-0.07	0.006			
A1 Horizontal		-0.05	0.000	-0.65	0.005			
A2 Vertical	40+00	-5.35	0.017	-0.30	0.003			
A2 Horizontal		-4.95	0.016	-0.05	0.000			
A3 Vertical	54+00	-9.75	0.031	-0.85	0.007			
A4 Vertical	63+00	-9.80	0.031	-0.20	0.002	VA8	-3.96	0.014
A4 Horizontal		-5.70	0.018	-1.25	0.010			
A5 Vertical	75+00	-14.4	0.045	-.850	0.007	VA5	-5.16	0.018
A5 Horizontal		-14.3	0.045	-2.60	0.022	HA3	-3.53	0.012
A6 Vertical	80+00	-25.9	0.082	-2.80	0.023	VA4	-7.29	0.025
A6 Horizontal		-21.9	0.069	-2.30	0.019	HA2	-6.65	0.023
A7 Vertical	85+00	-51.2	0.161	-7.55	0.063	VA3	-14.2	0.050
A7 Horizontal		-31.5	0.099	-4.50	0.038			
W1 Vertical	30+00	-10.9	0.034	-2.70	0.023	VB3	-4.72	0.017
W1 Horizontal		-22.7	0.071	-4.05	0.034	HB2	-5.72	0.020
W2 Vertical	42+00	-15.9	0.050	-2.25	0.019	VB6	-5.41	0.019
W2 Horizontal		-17.5	0.055	-3.25	0.027	HB3	-5.38	0.019
Reference	0+00	-1.70	0.005	-1.00	-0.008			

* 5/17/2006 to 3/31/2007 (318 days)
† 3/31/2007 to 7/29/2007 (120 days)
‡ 5/17/1983 to 2/28/1984 (287 days)

the warmest temperatures at the end of the measurement period. The winze roof temperatures in the area of W1 to W2 for the same period ranged from -5.2 to -3.1°C, again with the warmest temperatures at the end of the period. Johanssen (1993) details the beginning of silt deformation that has altered the wooden frame for the door leading into Sayles room, and he reports the rear of the adit is approaching 0.0°C. At that time the vent system was operable; therefore, this system must have become unusable after that date. It is unknown if the mechanical system has degraded over the years, but it could be assumed that the system has only decreased in efficiency.

The temperature distribution measured in May of 2006 (-3.0°C at the portal, -1.7°C rear of adit) demonstrated that the air delivered in the summer from the chilling unit and the winter ambient air from the open portal doors was not being circulated to the rear of the adit or bottom of the winze in an effective manner. Because of this, starting on July 17, 2006, air temperatures at the front of the adit near A1, back of the adit near A6, and bottom of the winze near W2 have been recorded daily. The wall soil temperature near A4 at a wall depth of 0.15 m and 1.5 m above the floor has also been measured since that time. A plot of this data from Jan. 1, 2007 to March 19, 2007 is shown in Figure 3. Previous studies (Wu 1985, Law 1987) have shown considerable seasonal temperature variations of approximately 4°C, and daily variations of up to 1.0°C, and this was confirmed by our measurements.

Discussion

The larger scale deformation that has been occurring in the CRREL Tunnel for the last two decades appears to be attributable to the gradual increase in tunnel temperatures due to air-handling issues. No measurements or comparisons have been made to determine if a correlation exists with recent climate change. In an effort to slow deformation, a portable blower unit with 45 cm -diameter flexible ducting delivering approximately 0.55 m^3/sec was placed outdoors of the portal and routed approximately 60 m down the adit in February of 2007. The blower unit was moved inside the tunnel under the chilling unit when the chilling unit was turned on for the summer season. The point in time when the blower was first added is shown in Figure 3, and the temperatures decreased substantially to -7.5°C at the back of the adit by March 19, 2007, twelve days prior to the second creep reference location measurements. The temperatures during the third creep reference location measurements on July 29, 2007, averaged -3.5°C for the air near station A6. The creep rate at the rear of the tunnel has slowed by a factor of approximately 3 from the second measurement to the third, and the rate for the winze locations during the same period has slowed by approximately a factor of 2. This creep rate reduction corresponds with the modifications to the cooling system.

To illustrate temperature sensitivity in the near freezing range from -2.0° to -1.0°C for ice-rich fine-grained soil, we compare three uniaxial constant-stress tests (creep) conducted by the author on intact CRREL Tunnel cores

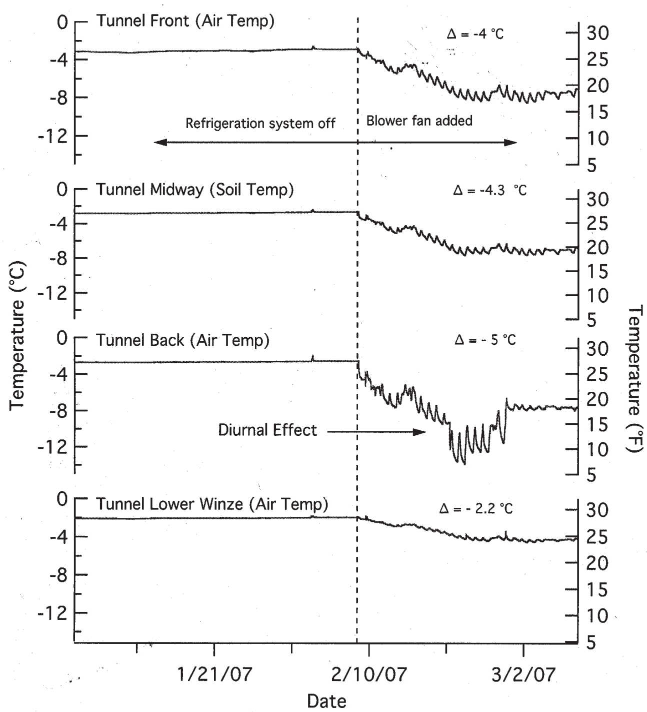

Figure 3. Tunnel facility temperatures.

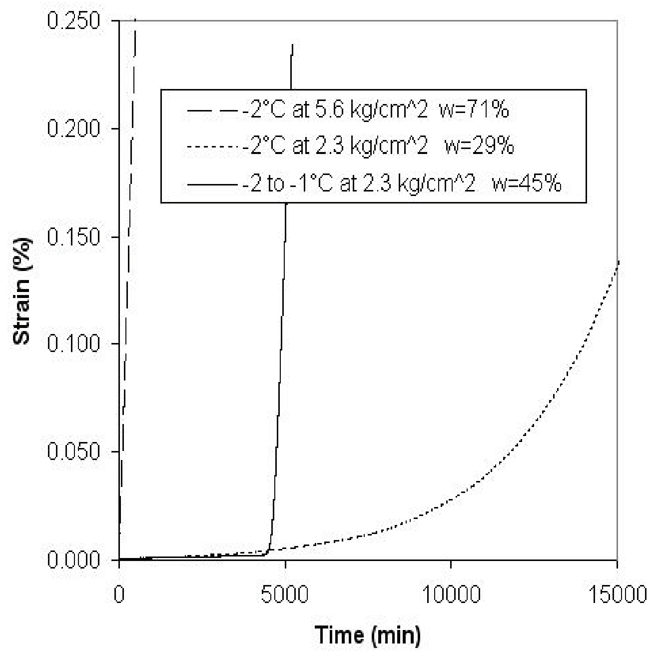

Figure 4. Temperature dependence of tunnel silt.

measuring 100.0 mm in length and 55.0 mm in diameter. These cores were taken from the left wall at approximately 74+00 and 0.3 m above the floor. One test was conducted at an axial stress of 5.6 kg/cm^2, and the second at 2.3 kg/cm^2 (approx. stress due to overburden), both at a constant -2.0°C. The third test was conducted at 2.3 kg/cm^2 with a temperature step from -2.0 to -1.0°C at 4500 min. For the third test the strain rate accelerates from 4.0 x 10^{-9} (s^{-1}) to 3.0 x 10^{-6} (s^{-1}) in 18 hr (Fig. 4).

In another example of temperature sensitivity, Zhu & Carbee (1987) conducted uniaxial constant-stress tests with remolded CRREL Tunnel silt. For medium density samples of approximately 1.2 g/cm^2 and moisture contents of 43%, it was found that for an applied stress of approximately 7.0 kg/cm^2, the time to failure dropped from 29,000 min at -2.0°C, to 70 min at a temperature of -1.0°C.

Conclusions

The adit deformation coincides with the reduction of facility cooling via natural convection and forced mechanical chilling, which has raised the rear adit air temperature to near freezing. This is in comparison to temperatures measured after excavation in the late 1960s. In addition it appears the rear of the adit is composed of a higher density of cryological structures than is evident in the rest of the facility. Exactly how the structural integrity of the frozen silt with emplaced massive ice bodies is affected by warmer temperatures is at best very complex. However, it can be assumed that across the soil mass as a whole, the non-homogenous thermal conductivity and strength properties due to these ice bodies, and the silt deformation caused by the emplacement, only serves to weaken the total soil mass, especially at the soil/ice margins.

This higher density of massive ice features is coincident with a change in soil gradation towards the rear of the adit, from poorly-graded silt, to poorly-graded silt with interbedded layers of larger grain size, resulting in preferentially weaker -bonded frozen soil. These weaker bonds and massive ice/soil margins are the location for detachment when the temperature is raised to near zero.

The winze and Gravel Room experience warmer temperatures than historical for the same reasons as the adit. These warmer temperatures have weakened the bond between the frozen gravel comprising the roof and the silt unit above, causing detachment during a past dynamic event. These warmer temperatures, large roof span, and historical parting studies have contributed to this parting.

Due to the addition of the blower and ductwork, there has been a reduction in rear adit temperature to an average -7.0°C for the winter months, and -3.5°C for the summer months, which has reduced the creep movement by a factor of 3. The temperature reduction in the winze has reduced the creep by a factor of 2. Continued reduction of the temperature to a maximum of -5.0°C for all portions of the facility during all seasons would be expected to reduce the deformation to the slower rates experienced prior to the extreme deformation of the rear of the adit.

Acknowledgments

Stephanie Saari and Art Gelvin of CRREL contributed greatly to the information provided in this report. The tunnel upgrades and ongoing data collection would not have been as successful and efficient without their specific and dedicated technical expertise.

Also, we wish to thank Dr. Gang Chen of the University of Alaska Fairbanks, Department of Mining Engineering, and Dr. Scott Huang of the University of Alaska Fairbanks, Department of Geological Engineering, for the use of the tape extensometer and general comments.

References

Bjella, K.L., Tantillo, T.J, Weale, J.C. & Lever, J.H. 2006. *The CRREL Permafrost Tunnel.* Technical Report (in press). Hanover, NH: Cold Regions Research and Engineering Laboratory, 69 pp.

Chester, J.W. & Frank, J.N. 1969. *Fairbanks placers fragmentation research final report*. Minneapolis: Twin Cities Mining Research Center, U.S. Bureau of Mines, Heavy Metals Program, 52 pp.

Garbeil, H.M. 1983. *Temperature effects upon the closure of a gravel room in permafrost.* M.S. Thesis. University of Alaska Fairbanks, 134 pp.

Huang, S.L. 1985. Temperature and time effects on the closure of a gravel room in permafrost. *Bulletin of Association of Engineering Geologists* 22(2): 53-65.

Huang, S.L. & Aughenbaugh, N.B. 1986. Stability study of CRREL Permafrost Tunnel. *ASCE Journal of Geotechnical Engineering* 112(8): 777-790.

Johansen, N.I. (1993.) *CRREL Permafrost tunnel after event*. Video.

Johansen, N.I. & Ryer, J.W. 1982. Permafrost creep measurements in the CRREL tunnel. *Proceedings of the Third International Symposium on Ground Freezing, Hanover, New Hampshire.* Hanover, New Hampshire: U.S. Army CRREL, 61-63.

Law, K.H. 1987. *Time-dependent bearing capacity of frozen ground*. M.S. Thesis. University of Alaska Fairbanks, 129 pp.

Linell, K.A. & Lobacz, E.F. 1978. Some experiences with tunnel entrances in permafrost. *Proceedings of the Third International Conference on Permafrost, 1978, Edmonton, Alberta:* 814-819.

Murton, J. B. & French, H.M. 1994. Cryostructures in permafrost, Tuktoyaktuk coastlands, western arctic Canada. *Canadian Journal of Earth Sciences* 31: 737-747.

Pettibone, H.C. 1973. Stability of an underground room in frozen gravel. In *Permafrost: North American contribution to the Second International Conference*, Washington: National Academy of Sciences, 699-706.

Pettibone, H.C. & Waddell, G.G. 1969. Stability of an underground room in frozen, gold-bearing strata, Fairbanks, Alaska. *Seventh Annual Northwest Mining Association Convention, Spokane, Washington*. U.S. Bureau of Mines Heavy Metals Program, 14 pp.

Sellmann, P.V. 1967. *Geology of the USA CRREL Permafrost Tunnel in Fairbanks, Alaska*. Technical Report 199. Hanover, NH: Cold Regions Research and Engineering Laboratory, 22 pp.

Williams, P.J. & Smith, M.W. 1989. *The frozen earth: Fundamentals in geocryology*. Cambridge, U.K.: Cambridge University Press.

Wu, M.C. 1985. *The temperature and geometry influences on an underground opening in the frozen ground*. M.S. Thesis. University of Alaska Fairbanks, 186 pp.

Zhu, Y. & Carbee, D.L. 1987. *Creep and Strength Behavior of Frozen Silt in Uniaxial Compression.* CRREL Report 87-10. Hanover, NH: Cold Regions Research and Engineering Laboratory, 67 pp.

Distribution of Permafrost Types and Buried Ice in Ice-Free Areas of Antarctica

J.G. Bockheim
University of Wisconsin, Madison, WI, USA

I.B. Campbell
Land & Soil Consultancy Services, Nelson, New Zealand

M. Guglielmin
Insubria University, Varese, Italy

J. López-Martínez
University of Madrid, Madrid, Spain

Abstract

Only 0.35% (49,800 km²) of Antarctica is ice-free. We have divided the continent into nine major ice-free regions and estimated the distribution of permafrost by form: (i) buried ice within the upper 100 cm; (ii) ice-cemented permafrost with the surface within the upper 70 cm; (iii) ice-cemented permafrost with the surface below 70 cm; and (iv) dry-frozen permafrost with the surface below 70 cm. For each of these categories, permafrost distribution was divided into continuous, discontinuous, and sporadic or no permafrost. Based on preliminary analysis, 43% of the ice-free areas contain ice-cemented permafrost in the upper 70 cm, followed by dry-frozen permafrost (41%), and buried ice (13%). Permafrost is continuous throughout East Antarctica and along the Antarctic Peninsula and the surrounding islands at elevations generally above 40 m a.sl. Along the Antarctic Peninsula, discontinuous permafrost exists at elevations between 40 and 20 m a.s.l, and permafrost is either sporadic or lacking below 20 m a.s.l.

Keywords: ANTPAS; Antarctica; dry-frozen permafrost; ice-cemented permafrost; permafrost mapping.

Introduction

Only 0.35% or 49,800 km² of the Antarctic region (≥60ºS) is ice-free (Fig. 1). At 24,200 km² the Transantarctic Mountains (TAM), which extend 2,600 km from North Victoria Land (69ºS) to the Roberts Massif in the upper Scott Glacier region (86º30′S), are the largest ice-free area (Table 1).

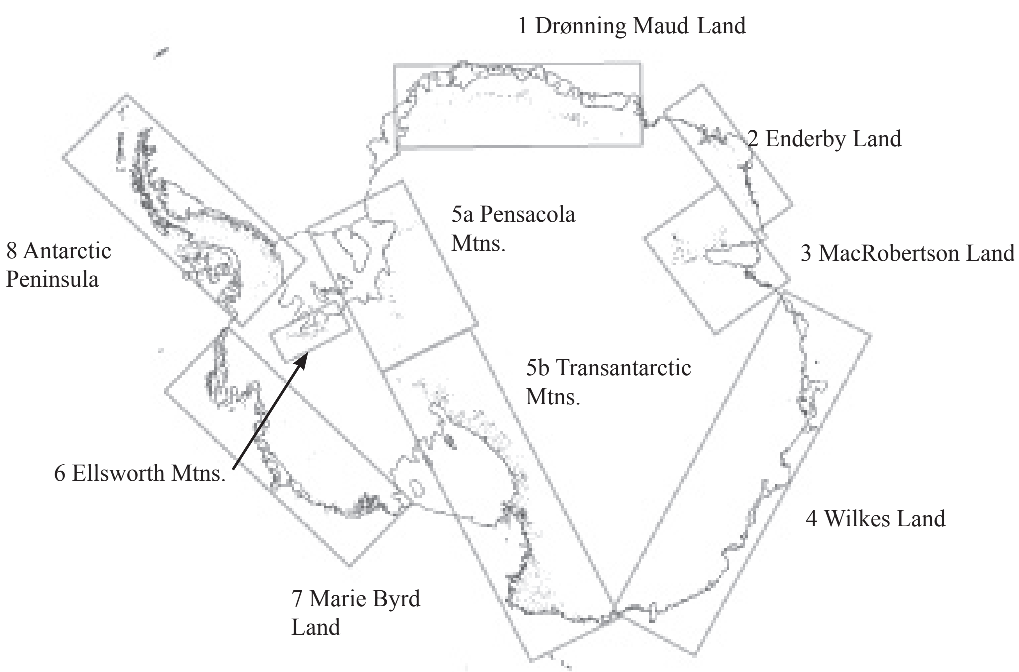

Figure 1. Major ice-free regions of Antarctica (after Greene et al. 1967). Ice-free areas are shown with dots, with each dot accounting for 15 km². Areas delineated using the Antarctic Digital Database V. 4.0 and ArcGIS V. 9.1 by D. Smith of the Australian Antarctic Division.

The Antarctic Peninsula and its offshore islands constitute the next largest ice-free region at 10,000 km2 (Table 1), followed by MacRobertson Land, Drønning Maud Land, and the Ellsworth Mountains. The Pensacola Mountains, Enderby Land, Marie Byrd Land, and Wilkes Land each contain 1500 km2 of ice-free area, or less.

Bockheim (1995) prepared the first permafrost map of ice-free areas in Antarctica. He showed that permafrost was limited to ice-free areas and that all of East Antarctica and most of West Antarctica contain continuous permafrost. Discontinuous permafrost was present from 66ºS to 63ºS along the Antarctic Peninsula and its offshore islands. Sporadic permafrost was limited to the South Orkney Islands. Zotikov (1963) showed the distribution of subglacial permafrost in Antarctica.

The following is a review of permafrost conditions in Antarctica by region. In the Sør Rondane Mountains of Drønning Maud Land (region 1), ice-cemented permafrost occurs at depths ranging from 7 to 80 cm, and dry permafrost is common (Sekyra 1969, Vtyurin 1986, Matsuoka et al. 2006). McNamara (1969) reported the top of ice-cemented permafrost at 75 cm in Enderby Land (region 2) and a limited amount of dry-frozen permafrost. Since the climate in MacRobertson Land (region 3) is comparable to that of Enderby Land, we suggest that the permafrost conditions are likewise comparable. It is likely that dry-frozen permafrost exists in the southern Prince Charles Mountains. Wilkes Land (region 4) contains two major ice-free areas, the Bunger Hills and the Windmill Islands. According to Blume & others (2002), the top of ice-cemented permafrost occurs at 30 to 80 cm throughout the Windmill Islands.

Observations from the Pensacola Mountains (region 5a) (Parker et al. 1982) imply that the ice-cemented permafrost surface occurs at 20 to 45 cm. In that dry-frozen permafrost exists in the Ellsworth Mountains, which occur at a similar latitude and proximity to the Ronne Ice Shelf, it is likely that dry-frozen permafrost exists in portions of region 5a.

For convenience we subdivided the Transantarctic Mountains (TAM; region 5b) into three subregions based on latitude: North Victoria Land (69º30′–75ºS), the central TAM (75º–80º30′S), and the southern TAM (80º30′–86º30′S). Campbell & Claridge (2006) reviewed permafrost properties throughout the TAM, noting that the active layer ranges from <5 cm in inland and upland regions to 80 cm in coastal areas. The moisture content of ice-cemented permafrost is greatest in coastal areas, where snowfall and regelation are common, and lowest in inland areas, where the moisture content may be <1%. In North Victoria Land (NVL), the active layer ranges from 10 to 30 cm in thickness (Guglielmin 2006). Whereas ice-cemented permafrost and buried ice are common, dry-frozen permafrost was not observed in NVL (Guglielmin & French 2004). However, in the Rennick Glacier-Talos Dome areas of interior NVL, ice-cored moraines are common beside blue-ice glacier margins (Denton et al. 1986). Elsewhere the surface of ice-cemented permafrost occurs at 8 to 70 cm; dry-frozen permafrost exists in the Morozumi Range.

Early permafrost studies in the central TAM largely were limited to observations and measurements of the growth of patterned ground (Berg & Black 1966, Black 1973), and core logs collected in 1970–1975 during the Dry Valley Drilling Project (DVDP) (McGinnis 1981). Using a combined dataset that included nearly 1000 shallow (<1.5 m) excavations, Bockheim & others (2007) provided a map at a scale of 1:2 million showing the distribution of permafrost in the MDVs. Their data suggested that about 55% of the permafrost was ice-cemented, 43% was dry-frozen, and buried ice comprised at least 2% of the ice-free area. Permafrost form was related to climatic zone, age of sediments, and local site factors.

The Ellsworth Mountains (region 6) can be divided into the Heritage Range, which contains localized areas of glacial drift, and the Sentinel Range, which contains primarily arétes and nunataks (Denton et al. 1992). We were unable to find information about permafrost conditions in Marie Byrd Land (region 7).

The Antarctic Peninsula (region 8) can be divided into five latitudinal subregions: (1) Palmer Land and Alexander Island (68–76ºS), (2) Graham Land and the Palmer Archipelago (63–68ºS), (3) the James Ross Archipelago (65º30–67ºS), (4) the South Shetland Islands (61–63ºS), and (5) the South Orkney Islands (60–61ºS). Permafrost depths bear a strong relation to latitude along the Antarctic Peninsula. Along the Trinity Peninsula and offshore islands, the surface of ice-cemented permafrost occurs at 25 cm (Everett 1976). In the South Shetland Islands, the top of ice-cemented permafrost exists at 25 cm to more than 100 cm, with about 50% of sites examined having permafrost in the upper 70 cm (López-Martínez et al. 1996, Serrano et al. 1996, Bölter et al. 1997, Blume et al. 2002, López-Martínez & Serrano 2002, Vieira et al. 2007). The surface of ice-cemented permafrost occurs at 40 to 200 cm in the South Orkney Islands (Holdgate et al. 1967, O'Brien et al. 1979).

To address the need for a permafrost map for Antarctica, a joint committee was appointed at the Seventh International Conference on Permafrost in Zurich by the International Permafrost Association (IPA) and the Scientific Committee on Antarctic Research (SCAR). In November 2004 the International Workshop on Antarctic Permafrost and Soils, sponsored by the U.S. National Science Foundation, was held in Madison, Wisconsin. A task force under the auspices of ANTPAS, the Antarctic Permafrost and Soils group (http://erth.waikato.ac.nz/antpas/) was established to begin preparing a permafrost and ground-ice map of Antarctica, with subgroups responsible for key ice-free areas. This manuscript is in response to this mandate and is intended to accompany these maps.

Methods

Ice-free areas in Antarctica, defined here according to the Antarctic Treaty (http://www.scar.org/treaty) as all lands >60ºS, were delineated using the Antarctic Digital Database version 4.0 (http://www.add.scar.org/) and ArcGIS 9.1 by D. Smith of the Australian Antarctic Division. Ice-free areas were divided into nine regions using the subdivisions of

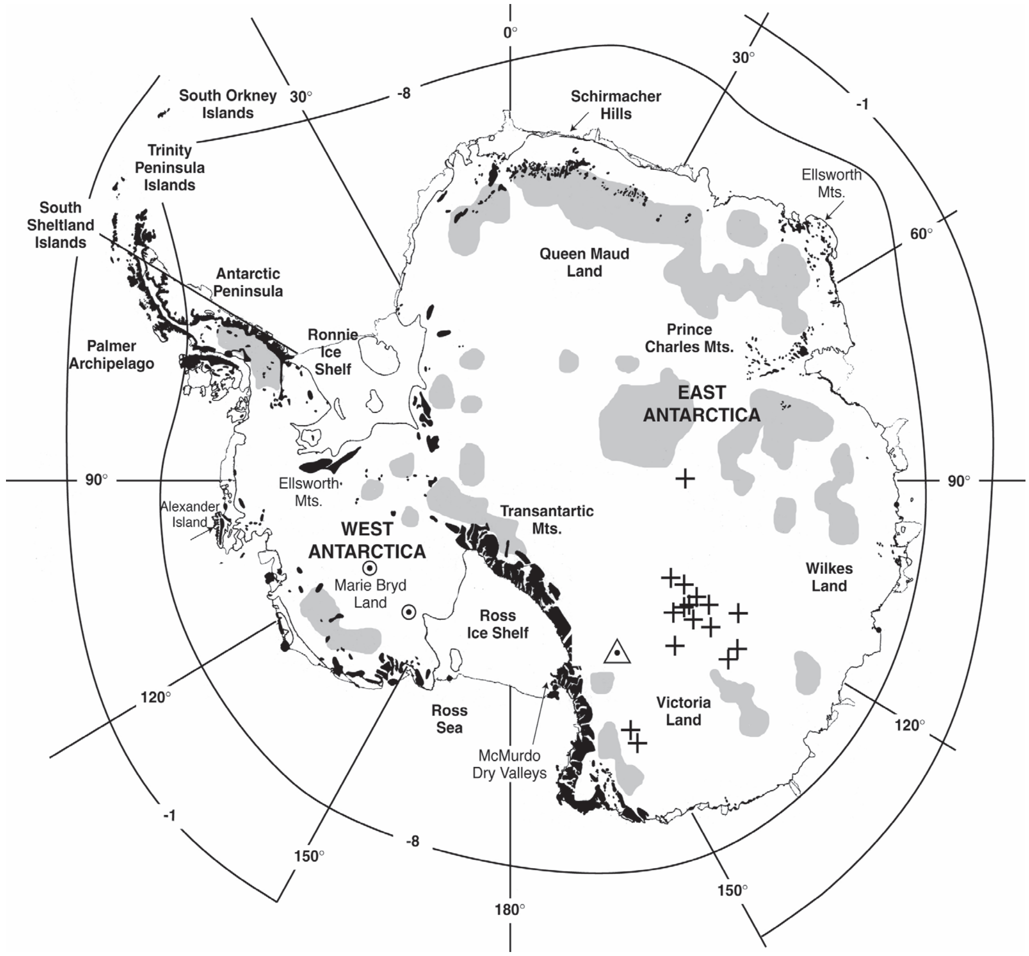

Figure 2. Provisional distribution of permafrost in Antarctica. Ice-free areas are shown in black; grey areas represent the likely location of subglacial permafrost; and crosses indicate the existence of subglacial lakes. The -1°C and -8°C isotherms represent the likely distribution of discontinuous and continuous permafrost, respectively, based on correlations from the Northern Hemisphere (Bockheim 1995).

Greene & others (1967) (Fig. 2). Expert permafrost scientists working in Antarctica were contacted and asked to assist in preparing the following legend: (i) buried ice within the upper 100 cm; (ii) ice-cemented permafrost with the surface within the upper 70 cm; (iii) ice-cemented permafrost with the surface greater than 70 cm; and (iv) dry-frozen permafrost with the surface below 70 cm. For each of these categories, permafrost distribution was divided into

(i) continuous, (ii) discontinuous, and (iii) sporadic or no permafrost. The legend included a color scheme for permafrost maps. In Antarctica, the active layer either grades into ice-cemented permafrost or, in dry areas, into dry-frozen permafrost. In the latter case, the active layer can only be differentiated from dry-frozen permafrost from temperature monitoring.

The distribution of permafrost form by region was determined from the ANTPAS database for regions 4, 5b, 6, and 8 (Table 1). To determine permafrost distribution for the remaining regions, we utilized published data from regions 1, 2, 3, and 7 and inferences from diagnostic ground criteria for regions 5b and 7. These criteria included a stippled pattern and medial moraines on 1:250,000 topographic maps for ice-cored drift and strongly developed patterned ground on high-resolution land satellite images and proximity to stream, lakes, and ponds for ice-cemented permafrost. The remaining areas, particularly in interior mountains and broad central valleys, were assigned to dry-frozen permafrost. The 20 m contour was used to delineate areas where the top of ice-cemented permafrost occurred below 70 cm along the Antarctic Peninsula and its offshore islands.

We were unable to locate sufficient permafrost information for mapping regions 2 (Enderby Land), 3 (MacRobertson Land), 5a (Pensacola Mountains), and 7 (Marie Byrd Land); however, we provide brief summaries of information existing for these areas. Maps (not included in this brief report) were developed for the more-studied regions 1, 4, 5b, 6, and 8, which account for about 38,000 km2 or 85% of the ice-free areas in Antarctica. Because of insufficient data, we were unable to show permafrost thickness and temperatures on the maps.

Table 1. Database and proposed map scales for permafrost mapping in Antarctica.[1]

No.	Region	Subregion	Proposed Map scale	Data available Soils	Data available Permafrost	Electronic data archive	GIS
1	Queen Maude Land	Fimbulheimen	1:1000K	?	?	?	?
		Sør Rondane Mtns.	1:500K	Y	Y	?	?
2	Enderby Land	Scott Mtns.-Amundsen Bay	1:500K	?	?	?	?
3	MacRobertson Land	Mawson Escarpment	1:250K	?	?	?	?
		Prince Charles Mtns.	1:500K	?	?	?	?
		Grove Mtns.	1:250K	Y	Y	?	?
4	Wilkes Land	Windmill Islands	1:50K	Y	Y	?	?
5a	Pensacola Mtns.	Shackleton Range	1:500K	N	N	N	N
		Paxutent Range	1:500K	N	N	N	N
		Thiel Mtns.	1:250K	N	N	N	N
5b	Transantarctic Mtns.	North Victoria Land (69–75ºS)	1:1000K	Y	Y	Y	Y
		Central Victoria Land (75–80º30'S)	1:1000K	Y	Y	Y	Y
		S. Victoria Land (80º30'–86º30'S)	1:1000K	Y	Y	Y	Y
6	Ellsworth Mtns.	Heritage Range	1:500K	Y	Y	Y	N
		Sentinel Range	1:500K	Y	Y	Y	N
7	Marie Byrd Land	Ford Ranges	1:250K	?	?	?	?
8	Antarctic Peninsula	Palmer Land & Alexander Island	1:1000K	?	?	?	?
		Graham Land & Palmer Archipelago	1:1000K	?	?	?	?
		James Ross Archipelago	1:200K	Y	Y	Y	Y
		South Shetland Islands	1:200K	Y	Y	Y	Y
		South Orkney Islands	1:200K	Y	Y	Y	Y

[1] ? = availability of data uncertain; Y = data available; N = data not available; electronic data archive = data available in spreadsheets; GIS = Geographic Information System.

Results

More than 80% of the ice-free area of Antarctica contains continuous permafrost (Table 2). Discontinuous and sporadic permafrost occurs only along the tip of the Antarctic Peninsula and its offshore islands.

The dominant permafrost form is ice-cemented permafrost within 70 cm of the surface, accounting for 43% of the ice-free area in Antarctica. Ice-cemented permafrost is prevalent in coastal areas, including Wilkes Land, Enderby Land, and the Antarctic Peninsula and its offshore islands, and accounts for 60%–93% of the area (Table 2). In terms of total area, ice-cemented permafrost within 70 cm of the surface is most abundant in the Transantarctic Mountains (8000 km^2) and the Antarctic Peninsula (6000 km^2).

Dry-frozen permafrost accounts for 41% of the total ice-free area (Table 3) and is most abundant in Queen Maud Land, the Pensacola Mountains, and the Ellsworth Mountains, accounting for 59%–65% of the area (Table 1). The Transantarctic Mountains contain 11,600 km^2 of dry-frozen permafrost, 57% of the total area.

The total area of buried ice is not completely known. We suggest that this form of permafrost comprises 13% of the total ice-free area (Table 2). Buried ice is most abundant in the Transantarctic Mountains and along the Antarctic Peninsula. Deep (>70 cm) ice-cemented permafrost primarily occurs in coastal areas of East Antarctica and along the Antarctic Peninsula

Table 2. Preliminary estimation of permafrost distribution in Antarctica by region (bold face = estimates).

Region	Area (km^2)	% Ground ice	% Ice-cemented <70 cm	% Ice-cemented >70 cm	% Dry frozen
1	3400	2	58	4	36
2	1500	2	60	30	8
3	5400	6	44	2	48
4	700	2	93	5	0
5a	1500	6	32	0	60
5b	24200	18	33	1	48
6	2100	6	35	1	59
7	1000	2	33	0	65
8	10000	15	60	5	20
Total	49800				

Discussion

Permafrost is dominant in ice-free areas of Antarctica, which contain till-covered and bedrock surfaces occupying 49,800 km^2 of the entire continent. The distribution of permafrost in continental Antarctica is continuous except along the outer Antarctic Peninsula (ca. ≤63ºS) with the

Table 3. Estimated permafrost areas in Antarctica by subregion.

	km^2			
Region	Ground ice	Ice-cemented <70 cm	Ice-cemented >70 cm	Dry frozen
1	68	1972	136	1224
2	30	900	450	120
3	324	2376	108	2592
4	14	651	35	0
5a	90	480	30	900
5b	4356	7986	242	11616
6	126	735	0	1239
7	20	330	0	650
8	1500	6000	500	2000
Total	6828	21430	1501	20341
	13.1	*43.0*	*3.0*	*40.8*

northern boundary roughly following the -8ºC isotherm for mean annual air temperature. Recent findings (Serrano & López-Martinez 2000, Vieira et al. 2006) have validated Bockheim's (1995) proposal that the southern limit is defined by the -1ºC isotherm for mean annual air temperature. In the South Shetland Islands discontinuous permafrost exists at elevations between 40 and 20 m a.s.l, and permafrost is either sporadic or lacking below 20 m. In this area, altitude, topography, soil characteristics, and slope orientation affect permafrost occurrence and distribution.

In the South Shetland and South Orkney Islands, the active layer thickness appears to be strictly related to surface characteristics such as snow distribution and vegetation type and coverage (Cannone et al. 2006).

Ice-cemented permafrost within the upper 70 cm is the dominant form in Antarctica, accounting for 43% of the ice-free area. This type of permafrost occurs in coastal areas and adjacent to water bodies and on predominantly younger land surfaces throughout the continent. Dry-frozen permafrost is unique to Antarctica and occurs on predominantly older land surfaces especially in broad valleys in the McMurdo Sound area and inland mountains throughout the continent. It accounts for 41% of the ice-free area. Buried ice is ubiquitous in Antarctica in ice-cored moraines of Holocene age along major outlet glaciers and the coast. Ice buried by drift occurs along the Polar Plateau. Buried ice overlain by ablation till occurs sporadically and in places in thought to be of Miocene age (Sugden et al. 1999).

Conclusions

This text is intended to accompany maps at different scales depicting permafrost and buried ice of the Antarctic region (≥60ºS). Based on our analysis, 43% of the ice-free areas contain ice-cemented permafrost in the upper 70 cm, followed by dry-frozen permafrost (41%), and buried ice (13%). Permafrost is continuous throughout East Antarctica and along the Antarctic Peninsula and the surrounding islands at elevations above 40 m. Discontinuous permafrost exists at elevations between 40 and 20 m, and permafrost is either sporadic or lacking in coastal areas below 20 m.

Acknowledgments

This report is the collective effort of the IPA working group on Antarctic Permafrost and Periglacial Environments. The authors gratefully acknowledge the contributions of ANPAS members, including M. Balks, G.G.C. Claridge, N. Matsuoka, M. McLeod, M. Ramos, E. Serrano, D. Smith, G. Vieira, and others.

References

Berg, T.E. & Black, R.F. 1966. Preliminary measurements of growth of nonsorted polygons, Victoria Land, Antarctica. American Geophysical Union, *Antarctic Research Series* 8: 61-108.

Black, R.F. 1973. Growth of patterned ground in Victoria Land, Antarctica. In: *Permafrost: North American Contribution, Second International Conference; Genesis, Composition, and Structure of Frozen Ground and Ground Ice, National Academy of Sciences, Washington, DC*, 193-203.

Blume, H.-P., Kuhn, D. & Bölter, M. 2002. Soils and landscapes. In: L. Beyer & M. Bölter (eds.), *Geoecology of Antarctic Ice-Free Coastal Landscapes*. Berlin: Springer-Verlag.

Bockheim, J.G. 1995. Permafrost distribution in the Southern Circumpolar Region and its relation to the environment: a review and recommendations for further research. *Permafrost & Periglacial Processes* 6: 27-45.

Bockheim, J.G., Campbell, I.B. & McLeod, M. 2007. Permafrost distribution and active layer depths in the McMurdo Dry Valleys, Antarctica. *Permafrost & Periglacial Processes* 18: 217-227.

Bölter, M., Blume, H.-P., Schneider, D. & Beyer, L. 1997. Soil properties and distributions of invertebrates and bacteria from King George island (Arctowski Station), maritime Antarctic. *Polar Biology* 18: 295-304.

Campbell, I.B. & Claridge, G.G.C. 2006. Permafrost properties, patterns and processes in the Transantarctic Mountains region of Antarctica. *Permafrost & Periglacial Processes* 17: 215-232.

Cannone, N., Ellis Evans, J.C., Strachan, R. & Guglielmin, M. 2006. Interactions between climate, vegetation and active layer in Maritime Antarctica. *Antarctic Science* 18(3): 323-333.

Chambers, M.J.G. 1966b. Investigations on patterned ground at Signy Island, South Orkney Islands: II. Temperature regimes in the active layer. *British Antarctic Survey Bulletin* 10: 71-83.

Denton, G.H., Bockheim, J.G., Rutford, R.H. & Andersen, B.G. 1992. Glacial history of the Ellsworth Mountains, West Antarctica, pp. 403-432. *In* Webers, G.F., Craddock, C. & Splettstoesser, J.F. (eds.) *Geology and paleontology of the Ellsworth Mountains, West Antarctica*. Geol. Soc. Am. Memoir 170.

Denton, G.H., Bockheim, J.G., Wilson, S.C. & Schlüchter, C. 1986. Late Cenozoic history of Rennick Glacier and Talos Dome, northern Victoria Land, Antarctica. In: Stump, E. (ed.) *Geological Investigations of Northern Victoria Land*. American Geophysical Union, Antarctic Res. Ser. 46:339-375.

Everett, K.R. 1976. *A survey of the soils in the region of the South Shetland Islands and adjacent parts of the Antarctic Peninsula*. Institute of Polar Studies, Report No. 58, Ohio State University, Columbus, OH, 44

Estimation of Ice Wedge Volume in the Big Lake Area, Mackenzie Delta, NWT, Canada

Jenifer A. Bode
Department of Geography, University of Calgary, Calgary, Canada
Brian J. Moorman
Department of Geography, University of Calgary, Calgary, Canada
Christopher W. Stevens
Department of Geoscience, University of Calgary, Calgary, Canada
Steve M. Solomon
Natural Resources Canada, Halifax, Nova Scotia, Canada

Abstract

With potential development of the Mackenzie Gas Pipeline in northern Canada, it becomes increasingly necessary to understand all aspects of the permafrost environment affected by this project. A major concern with development is terrain disturbance within the Kendall Island Bird Sanctuary, resulting in an alteration of the subsurface thermal regime. Warming of the subsurface could lead to the melting of excess ground ice causing further subsidence. A combination of Ground Penetrating Radar (GPR) and remote sensing data were used to map the distribution of excess ground ice. The volume of wedge ice was calculated and then combined with a high-resolution digital elevation model to determine the location and amount of potential subsidence that could be induced by melting of subsurface excess ground ice. Although the distribution of excess ice in the Big Lake area is not uniform, its presence is substantial enough that melting may result in significant terrain alteration.

Keywords: Big Lake; digital elevation model; ground penetrating radar; ground subsidence; ice wedges; Mackenzie Delta.

Introduction

Several large hydrocarbon fields have been discovered in the Mackenzie Delta area, NWT, Canada (Fig. 1). One of these is the Taglu gas field which is estimated to contain 2.8 trillion cubic feet of natural gas and natural gas liquids (Imperial Oil Resources Limited 2004). The Taglu field is located within the Kendall Island Bird Sanctuary. Alteration of the landscape in this area could alter sensitive bird habitat.

There is concern that with alteration of the landscape there will be a disturbance of the subsurface thermal regime which could lead to the melting of ground ice. The objective of this research is to estimate the volume of ice contained within ice wedges in order to calculate the potential subsidence and terrain disturbance that could result from the warming of the subsurface. This study focuses solely on ice wedges as they contribute to significant volumes of excess ice in the study area.

Ice wedge formation has been widely studied (Mackay 1974, Murton & French 1993, Murton 2001). However, estimating ice wedge volume has remained difficult as measuring the depth and shape in the subsurface is usually limited to coring. Obtaining core data is expensive and logistically very difficult at Big Lake, so alternative methods were used in an attempt to quantify ice wedge volume. Their linear dimensions and width are in some cases relatively easy to measure photogrammetrically, but their depth is difficult to measure by drilling due to the narrow shape of the wedge.

Previous studies (Arcone et al. 1982, Kasper 1996, Hinkel et al. 2001, Fortier & Allard 2004, Munroe et al. 2007) have shown that it is possible to identify the location of ice wedges using Ground Penetrating Radar (GPR). However, estimates of ice wedge volume have not been determined using GPR. For this project we use GPR and a geographic information system to measure the length, width, and depth of the ice wedges and estimate the total volume of ice and maximum potential subsidence.

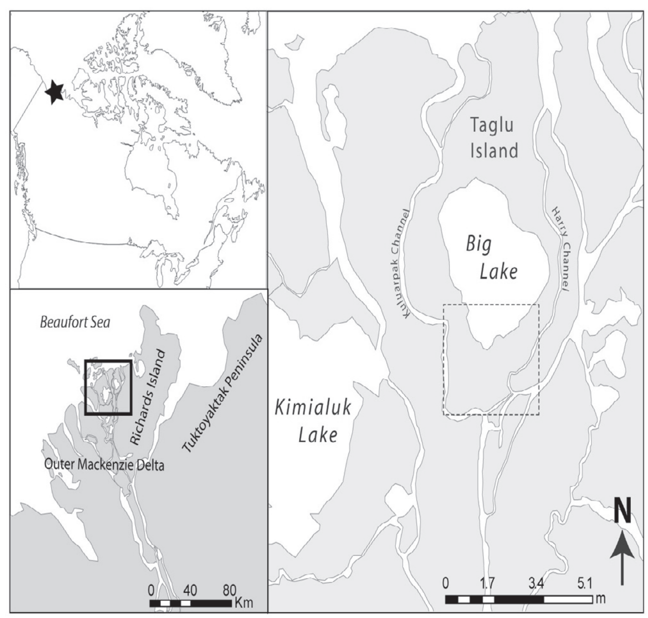

Figure 1. Location of the study area in the outer Mackenzie Delta, NWT, Canada. The study site, located south of Big Lake, is outlined with a dashed line.

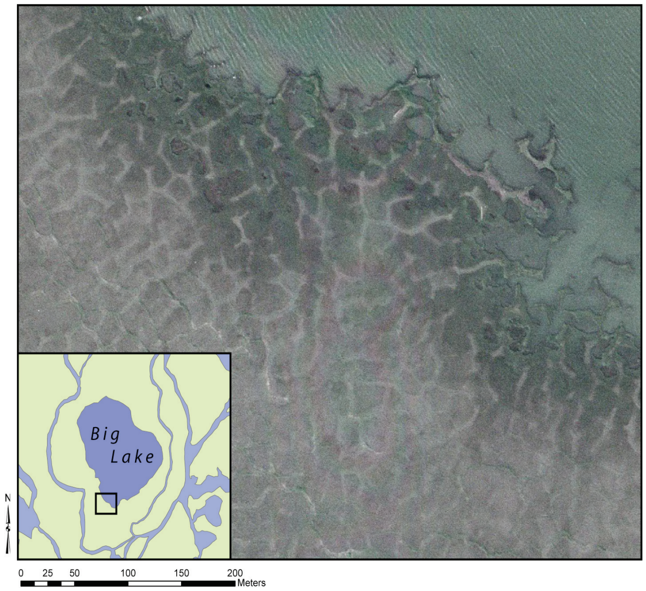

Figure 2. A portion of the aerial photo that shows the surficial expression of ice wedges in the southern portion of Big Lake.

Excess Ground Ice and Land Subsidence

Extraction of natural gas, and subsequent reduction of reservoir pressure, has previously been shown to cause subsidence of the overlying sediment (Geertsma 1973, Doornhof 1992, Teatini et al. 2005). At the Taglu site subsidence from gas extraction is estimated to be a maximum of 0.38 m in the center of the subsidence bowl (Haeberle et al. 2004). However, these estimates do not account for the thawing of permafrost and melting of excess ground ice (Haeberle et al. 2004, Haeberle et al. 2005). The center of the subsidence bowl is located just south of the southern shore of Big Lake; therefore it is likely that subsidence will lead to inundation of the surrounding terrain and expansion of the lake. With inundation, the water will act as a heat source and warm the subsurface (Williams & Smith 1989). If excess ground ice is present, a warming of the subsurface could result in a positive feedback mechanism of excess ice melt causing further subsidence.

Study Area

The Mackenzie Delta is the second largest arctic delta in the world and is a product of the largest river in Canada, the Mackenzie River. The delta is composed of many islands one of which is Taglu Island (Fig. 1). This region of the delta was likely ice free around 12.5 ka BP (Duk-Rodkin & Lemmen 2000). Permafrost beneath the Island extends 500–620 m (Taylor et al. 2000). On the southern tip of Taglu Island a Circumpolar Active Layer Monitoring (CALM) grid indicates an average active layer depth of 95 cm (average from 1998–2002)(Brown et al. 2003). Shallow drilling data indicated fine-grained sand overlain by silt and a thin layer of organic peat. Excess ground ice in the form of ice lenses ranges from 20–50% by volume in the upper 6 m (Traynor & Dallimore 1992).

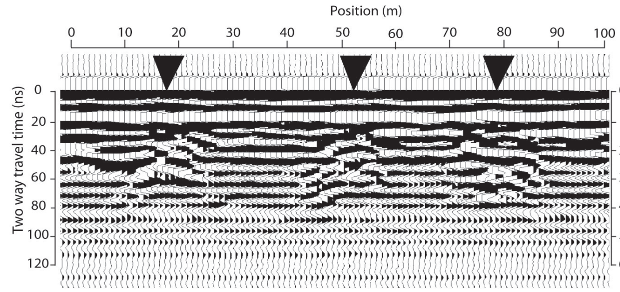

Figure 3. A 100 MHz GPR profile that shows the location of ice wedges. The ice wedges are indicated by the triangles above the profile.

The most prominent feature of Taglu Island is Big Lake which occupies 25% of the island (Fig. 1). Big Lake lies between two levees created by Kulurpak channel to the west and Harry channel to the east. The low lying land surrounding the lake is periodically flooded in the spring when the river overtops the levees. Flooding also occurs in the fall due to flooding from infrequent storm surges. However, Big Lake is cut off from the main channel for most of the year making it a low closure lake (Mackay 1963). The lake is surrounded by low centered, (Traynor & Dallimore 1992) non-oriented ice wedge polygons with an average diameter of approximately 20 m.

This study focuses on the southwestern shore of Big Lake where the estimated subsidence bowl is centered and the largest amount of data is available. The borders of the study area were determined by the availability of elevation data and the extent of the modeled subsidence bowl.

Methods

Volumetric estimates of ice wedges have previously been determined using aerial photos (Pollard & French 1980). However we use a combination of remote sensing and geophysical data to estimate the volume of ground ice. Aerial photography was used to determine the length and width of the ice wedges (Fig. 2) and GPR data were used to determine ice wedge depth. From these three variables, the volume of ice can be estimated using:

$$V = ½ * L * W * (D-D_{AL}) \qquad (1)$$

where L is the total length of ice wedges visible on the aerial photographs, W is the average width of the ice wedges, D is the average depth of the ice wedges, and D_{AL} is the average active layer depth. This is assuming a triangular cross-section of the ice wedges. Field observations from the study area suggest that a triangular cross-section is a reasonable assumption (Mackay 1963).

The GPR response to ice wedges is based on the dielectric contrast between frozen sediment and ice. Radar patterns produced by ice wedges include secondary reflections from the reverberation of energy within the ice and hyperbolic reflections from the wedge acting as a point source (Arcone et al. 1982). Hyperbolas are frequently centered at the top

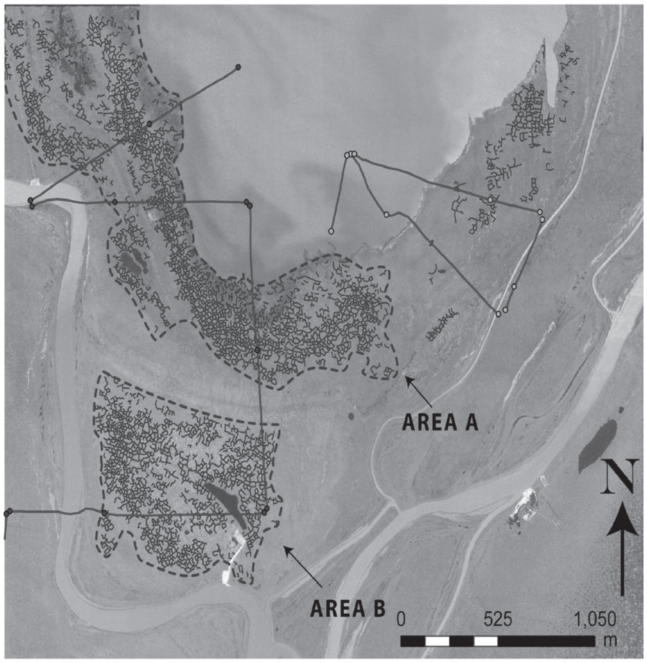

Figure 4. All the ice wedges digitized in the study area. The two areas where ice wedges are concentrated are outlined with the dashed line. Area A is the focus of this paper. The GPR transects surveyed in this study are indicated by the solid black lines.

(Fig. 3) and at the base of the ice wedge (Fortier & Allard 2004).

In March of 2007, GPR data was collected at the Taglu site using a PulseEKKO 100 with 100 MHz antennas and a 400 V transmitter. The GPR antennas were pulled behind a Tucker Sno-Cat® traveling at a constant speed of 5 km/hr. The vehicle was able to keep a steady speed higher than the resolution of the GPS. Data were collected in continuous mode and the average step size was 0.9 m. A total of 22 GPR transects were collected around the southern half of Big Lake (Fig. 4). The location of the GPR transects was determined with a GPS receiver that automatically tagged every trace with its position and elevation as it was collected. An average velocity for frozen sediment (0.1 m/ns) was used to convert travel time measurements to calculated radar depth.

Aerial photographs (Indian and Northern Affairs Canada 2004) of the southern portion of Taglu Island were used to identify the spatial extent of ice wedges (Fig. 4). The photographs were taken in August 2004 and have a resolution of 1.25 m. Every ice wedge was digitized to measure the length, which was used to calculate the total length of all visible ice wedges within the study area. To determine the average width, the trough of the ice wedge was measured from aerial photos. The trough width is not always equal to the actual ice wedge width however they are often comparable as shown in the data of Kokelj et al. (2007). Measurements were made at the mid-point between the junctions of the ice wedge using the measure tool in ArcGIS.

Ice wedge depths were calculated from the hyperbolic reflections caused by the base of the wedge. The depth to the bottom of the ice wedges was more difficult to determine since it was not always possible to interpret the basal reflections of the wedges from the GPR profile.

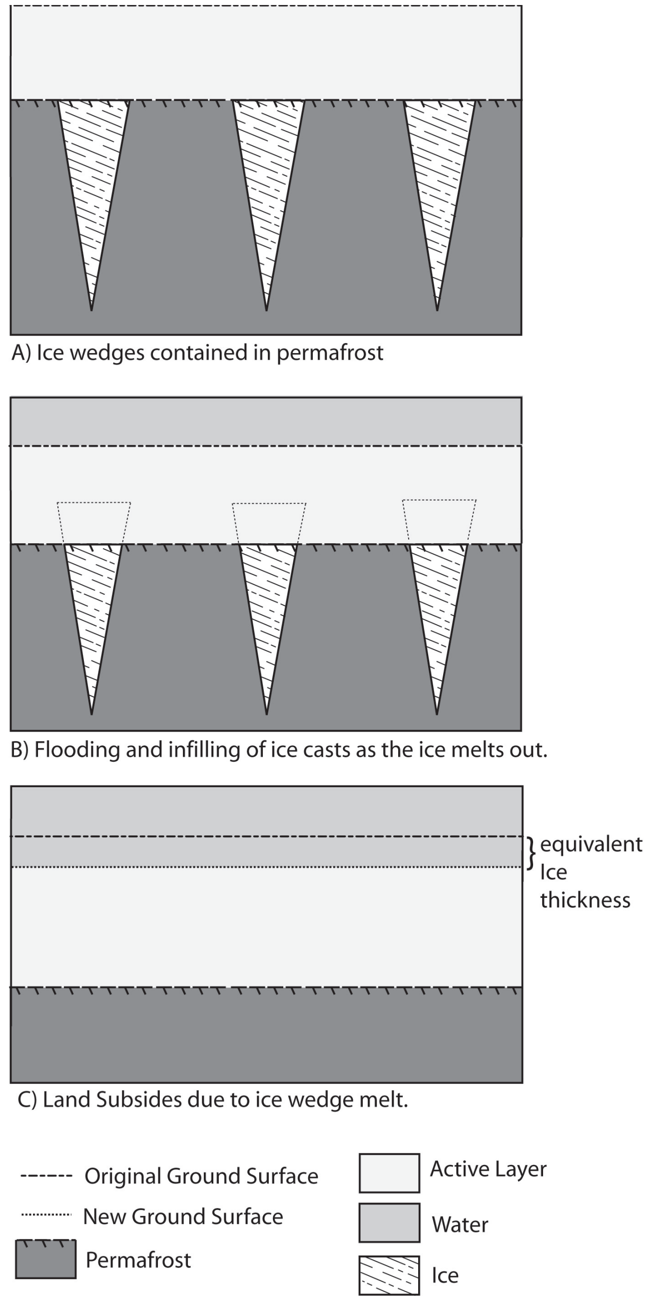

Figure 5: Schematic illustration of ground subsidence caused by flooding of the landscape (A), deepening of the active layer (B), and melt of the equivalent ice thickness (C).

Here we consider the worst-case scenario where all of the volume of ice melts. Little research has been conducted to address the nature of ground subsidence caused by ice wedge degradation. Therefore, a uniform approach to ground subsidence was adopted. The term *equivalent ice thickness* was used to represent the estimated volume of ice wedge ice uniformly distributed over the study area (Fig. 5). The ice wedge volume was divided by the total area underlain by ice wedges in Area A to determine the equivalent ice thickness. The equivalent ice thickness was then applied uniformly over Area A and subtracted from a digital elevation model

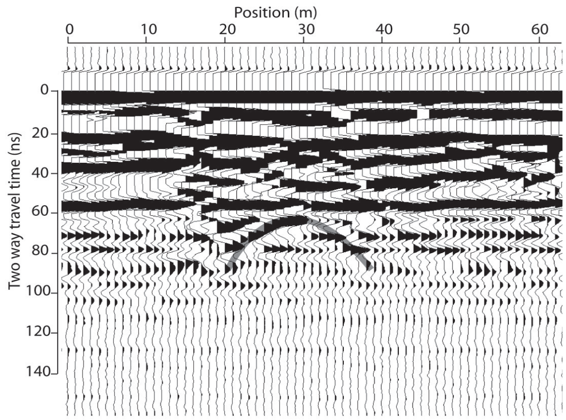

Figure 6. A portion of a GPR transect that shows the bottom of an ice wedge (highlighted). The bottom of the ice wedge is at the top of the hyperbola.

(DEM). The draft version of a DEM created from 1:30,000 air photos was obtained from the Northwest Territories Centre for Geomatics. The vertical accuracy of the DEM is ±1.5 m and is therefore not sufficient to obtain accurate results of subsidence due to ice wedge melting. However, we use it here for illustrative purposes since it is the best available dataset. DEMs developed from LiDAR are more appropriate for these types of analyses, but there are no publicly available data for this location.

Results

The ice wedges in the study area were primarily concentrated in two locations; the southwestern edge of Big Lake (Area A) and the southern portion of Taglu Island (Area B) (Fig. 4). Since the area of ice wedges closest to Big Lake would be most affected by lake expansion, Area A was the focus of this investigation. The total area of Area A is 2,940,040 m^2. The total length of ice wedges in this area was 95,525 m. The average width of the ice wedges was 3.9 m ±0.5 m (n = 225, max. = 5.8 m, min. = 1 m). The ice wedges ranged from 3.5 to 4 m in depth (n = 12) (Fig. 6). Minimum and maximum subsidence scenarios were both calculated as the number of ice wedge depth measurements was limited.

Using Equation 1 the volume of ice in Area A was calculated to be 471,655 m^3 using the minimum depth estimate and 754,650 m^3 using the maximum depth estimate. These volumes were then divided by the total area of Area A to calculate equivalent ice thicknesses of 0.17 m and 0.27 m for the minimum and maximum scenarios.

Figure 7 illustrates the effect of surface subsidence from the melt out of ice wedges on surface topography and shore location.

Discussion

The potential resultant area flooded by the melt out of ice wedges is likely to be irregular in character; however, with a uniform subsidence using the previously discussed equivalent ice thicknesses, a minimum of 274,790 m^2 of land would be flooded by ice melt alone (Fig. 7). With the

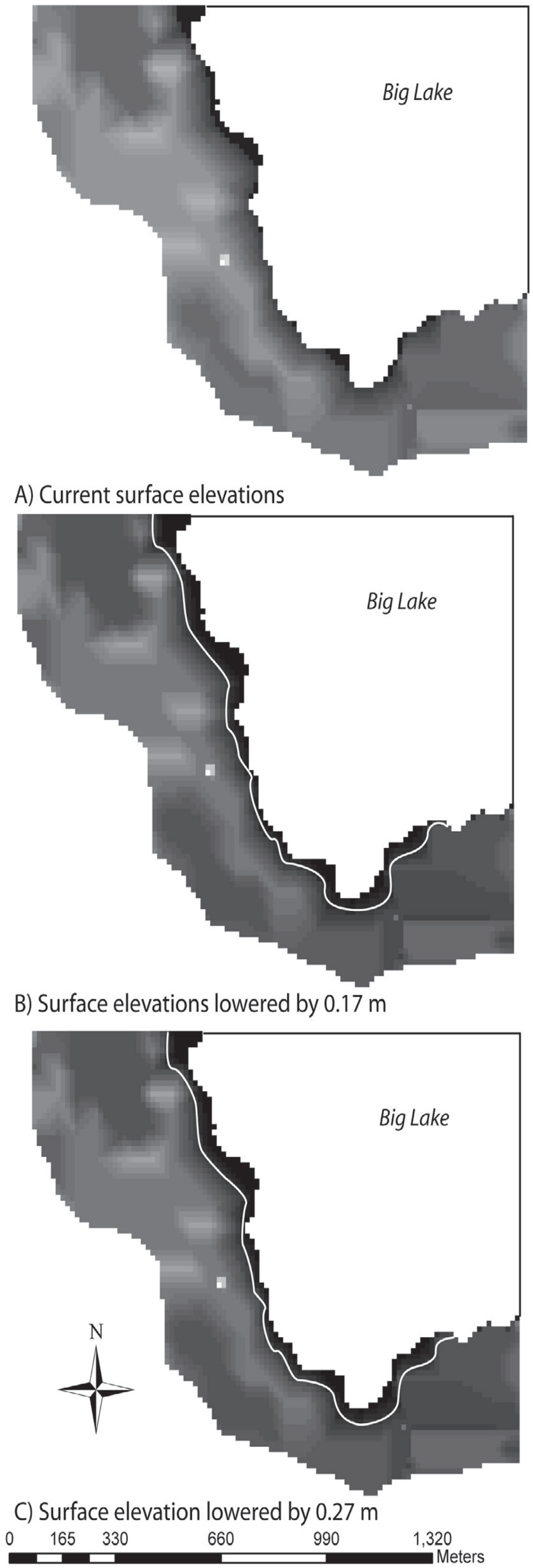

Figure 7. Topography of Area A to the southwestern edge of Big Lake. A) Displays the current terrain elevations (Northwest Territories Centre for Geomatics 2004), B) surface elevations minus 0.17 m and C) surface elevations minus 0.27 m. The 0.9 m white line in B and C indicates the extent of lake expansion. The water level at Big Lake, according to the dataset is 0.9 meters above sea level (m a.s.l.) therefore anything below 0.9 m a.s.l. will become flooded.

Figure 8. Flooded ice wedge polygons in the Mackenzie Delta. Subsidence appears to be spatially variable.

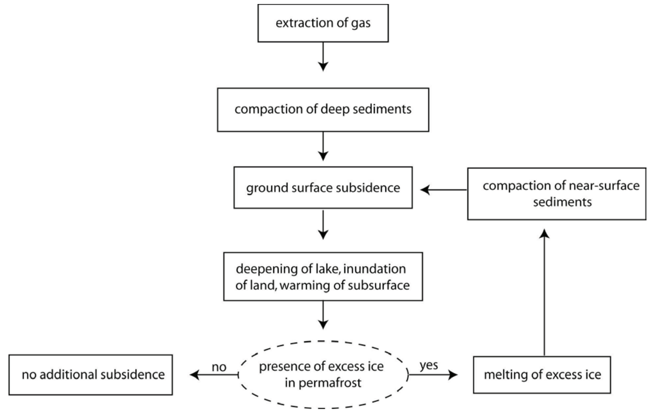

Figure 9. Flow chart illustrating the positive feedback that could be initiated by ground subsidence induced by natural gas extraction.

maximum depth scenario 343,715 m^2 would be flooded. The shoreline would move inland by over 75 m in some locations. These estimates are based on land below 0.9 m a.s.l. becoming flooded as that is the lake level from the DEM. Under a scenario of irregular subsidence concentrated at the zones immediately surrounding the central axes of the wedges, much greater flooding would occur reaching completely across Area A. Figure 8 illustrates another area in the Mackenzie Delta where irregular flooding of ice wedge polygons has occurred.

This study focused only on a small area on the southern part of Taglu Island due to the availability of elevation data and imagery. Ice wedges can also be seen on the northern portion of Taglu Island, therefore there is potential for ice wedge melt and flooding over a greater area surround the lake. Additionally, smaller bodies of ice, such as ice lenses, were resolved from GPR profiles. These ice lenses, if melted, would also cause ground subsidence.

For this initial estimate, subsidence was calculated using the equivalent ice thickness, therefore, the spatial variability in ice content is not taken into account. The actual character of subsidence may play a significant role in determining the resultant topography and the extent of flooding. Additionally, it is possible that the ice at depth could be maintained even with a deepening of the active layer. Consequently, we have calculated the worst case scenario where ice wedges completely melt. It should also be noted that these maps do not take into account the modeled subsidence bowl caused by natural gas extraction, as discussed earlier.

If considering the compounded effects of ground subsidence caused by both ice wedge melt and natural gas extraction over half of the study area would be flooded. Subsidence caused by gas extraction is estimated to be up to 0.38 m (Haeberle et al. 2004). If this subsidence were to occur a positive feedback loop could be initiated (Fig. 9). With initial subsidence, flooding could occur causing melt of excess ground ice leading to further subsidence and flooding. However, it must be acknowledged that there is also the potential that permafrost and ice wedges could remain stable and potentially even cool if flooding remains shallow.

Although the objectives of this research focused on assessing subsidence due to ice wedge melt, there are other potential causes of terrain disturbances. For example, climate warming could cause a deepening of the active layer and the melting of ground ice. Eustatic sea level rise and changes in the magnitude of seasonal flooding could also lead to excess ice melt. There are other processes that could result in changes of surface elevation such as isostatic rebound, sediment compaction, and frost heave.

This work builds on the study of Pollard and French (1980) which only used aerial photos and estimations of ice wedge depth. The result of this current research provides an initial attempt to estimate ice wedge volume using a combination of aerial photos and GPR data. Further verification of ice cross-sectional area, geometry near the junction of ice wedges, the character of ice wedge degradation due to flooding, and excess ice in other forms is required to further refine the quantification of excess ice and impact of subsidence and flooding.

Conclusions

Estimation of excess ice content from drilling is time consuming, difficult, expensive, and only provides point source data. Using GPR and aerial photographs, an estimation of ice wedge ice volume can be made over a large area in a relatively short time. The surficial expression of ice wedges at this location made it possible to measure their total length and width from aerial photographs. GPR was used successfully to identify the base of the ice wedges and determine ice wedge depth. By combining this data, the total volume of excess ice contributed by ice wedges was estimated. Applying these estimates to a DEM allowed for predictions to be made of the role of ice wedges may have on terrain subsidence and subsequent flooding. At the Taglu site the estimated ice volume is significant enough that if the subsurface warms and melts excess ice, subsidence leading to extensive flooding of land could occur.

Acknowledgments

Financial support for the research was provided by NSERC. The authors thank Chevron and the crew at Camp Farewell for accommodations and hospitality. The authors would also like to thank Steve Kokelj for providing insight and information.

References

Arcone, S.A., Sellmann, P.V. & Delaney, A.J. 1982. *Radar Detection of Ice Wedges in Alaska.* U.S. Army Cold Regions Research and Engineering Laboratory: CRREL Report 82-43, 15 pp.

Brown, J., Hinkel, K. & Nelson, F. (comp.). 2003. Circumpolar Active Layer Monitoring (CALM) program network: description and data. In: M. Parsons & T. Zhang (eds.), International Permafrost Association Standing Committee on Data Information and Communication (comp.). 2003. *Circumpolar Active-Layer Permafrost System, Version 2.0.* Boulder, CO: National Snow and Ice Data Center/World Data Center for Glaciology. CD-ROM.

Doornhof, D. 1992. Surface subsidence in The Netherlands: the Groningen gas field. *Geologie en Mijnbouw* 71: 119-130.

Duk-Rodkin, A. & Lemmen, D.S. 2000. Glacial history of the Mackenzie Region. In: L.D. Dyke & G.R. Brooks (eds.), *The Physical Environment of the Mackenzie Valley, Northwest Territories: A Base Line for the Assessment of Environmental Change.* Geological Survey of Canada Bulletin 547: 11-20.

Fortier, D. & Allard, M. 2004. Late Holocene syngenetic ice wedge polygons development, Bylot Island, Canadian Arctic Archipelago. *Canadian Journal of Earth Sciences* 41: 997-1012.

Geertsma, J. 1973. Land subsidence above compacting oil and gas reservoirs. *Journal of Petroleum Technology* 25: 734-744.

Haeberle, D.C., Pakal, R., Asmann, M. & Duffy, B.W. 2004. Taglu surface subsidence study. *Northern Gas Project Joint Review Panel.* http://www.ngps.nt.ca/ Upload/Proponent/Imperial %20Oil%20Resources%20 Ventures%20Limited/IORVL_R2_NRCAN_004%20 Attach_2.04-1_Taglu_Surface%20_Subsidence_ Study_Report. pdf. Retrieved February 25, 2007.

Haeberle, D.C., Hsu, S. & Asmann, M. 2005. Taglu surface subsidence study - addendum. *Northern Gas Project Joint Review Panel.* http://www.ngps.nt.ca/ Upload/ Proponent/Imperial %20Oil%20Resources%20Ventures%20Limited/IORVL_R2_NRCAN_004%20Attach_2.04-1_Taglu _Surface%20_Subsidence_Study_ Report_ Addendum.pdf. Retrieved February 25, 2007.

Hinkel, K.M., Doolittle, J.A., Bockheim, J.G., Nelson, F.E., Paetzold R., Kimble, J.M. & Travis R. 2001. Detection of subsurface permafrost features with ground penetrating radar, Barrow, Alaska. *Permafrost and Periglacial Processes* 12: 179-190.

Imperial Oil Resources Limited. 2004. *Application for the Approval of the Development Plan for Taglu Field: Project Description.* Calgary: Submitted to National Energy Board.

Indian and Northern Affairs Canada. 2004. *Mackenzie Valley Airphoto Project.* 2004, Airphoto 1:30,000 [Photo No. 500769]. Yellowknife, NWT.

Kasper, J. 1996. *Geomorphic, Geophysical and Quaternary Studies of Ice and Soil Wedge Features in the Foucault River valley, Northern Quebec.* Ph.D. Thesis. Université Laval, 277 pp.

Kokelj, S.V., Pisaric, M.F.J. & Burn, C.R. 2007. Cessation of ice-wedge development during the 20th century in spruce forests of eastern Mackenzie Delta, Northwest Territories, Canada. *Canadian Journal of Earth Sciences* 44: 1503-1515.

Mackay, J.R. 1963. *The Mackenzie Delta area, N.W.T.* Canadian Department of Mines and Technology Geographical Branch Memoir 8, 202 pp.

Mackay, J.R. 1974. *The Rapidity of Tundra Polygon Growth and Destruction, Tuktoyaktuk Peninsula-Richards Island Area, N.W.T.* Current research Part A Geological Survey of Canada paper 74-1A: 391-392.

Munroe J.S., Doolittle, J.A., Kanevskiy, M.Z., Hinkel, K.M., Federick, E.N., Jones, B.M., Shur, Y. & Kimble, J.M. 2007. Application of ground penetrating radar imagery for three-dimensional visualization of near-surface structures in ice-rich permafrost, Barrow, Alaska. *Permafrost and Periglacial Processes* 18: 309-321.

Murton, J.B. & French, H.M. 1993. Thaw modification of frost fissure wedges, Richards Island, Pleistocene Mackenzie Delta, western Arctic Canada. *Journal of Quaternary Science* 3: 185-196.

Murton, J.B. 2001. Thermokarst sediments and sedimentary structures, Tuktoyaktuk Coastlands, western arctic Canada. *Global and Planetary Change* 28: 175-192.

Northwest Territories Centre for Geomatics, 2004. *Mackenzie Valley Gas Project files, D5 Contours and DEMS.* Indian and Northern Affairs Canada.

Pollard, W.H. & French, H.M. 1980. A first approximation of the volume of ground ice, Richards Island, Pleistocene Mackenzie Delta, Northwest Territories, Canada. *Canadian Geotechnical Journal* 17: 509-516.

Taylor, A., Burgess, M.M., Judge, A.S. & Allen, V.S. 2000. Deep Ground Temperatures. In: L.D. Dyke & G.R. Brooks (eds.), *The Physical Environment of the Mackenzie Valley, Northwest Territories: A Base Line for the Assessment of Environmental Change.* Geological Survey of Canada Bulletin 547**,** 153-158.

Teatini, P., Ferronato, M., Gambolati, G., Bertoni, W. & Gonella, M. 2005. A century of land subsidence on Ravenna, Italy. *Environmental Geology* 47: 831-846.

Traynor, S. & Dallimore, S.R. 1992. *Geological Investigations of Proposed Pipeline Crossings in the Vicinity of Taglu and Niglintak Islands, Mackenzie Delta, NWT*. Geological Survey of Canada, Open File Report 2552, 109 pp.

Williams, P.J. & Smith, M.W. 1989. *The Frozen Earth: Fundamentals of Geocryology.* Cambridge: Cambridge University Press, 360 pp.

High-Resolution DEM Extraction from Terrestrial LIDAR Topometry and Surface Kinematics of the Creeping Alpine Permafrost: The Laurichard Rock Glacier Case Study (Southern French Alps)

Xavier Bodin, Philippe Schoeneich
University Paris Diderot (Paris 7)/Institute of Alpine Geography, Joseph Fourier University, Grenoble, France
Stéphane Jaillet
EDYTEM laboratory, University of Savoie, Le Bourget-du-Lac, France

Abstract

The most common landforms associated with the creep of Alpine permafrost are the rock glaciers, the morphology of which reflects the complex processes of the internal deformation of the ice and debris mixture. In the present study, a terrestrial LIDAR device was employed to scan, at a sub-decimeter resolution, the surface of the Laurichard active rock glacier (Southern French Alps). Two points-clouds were generated at one-year interval (Sept. 2005 and Sept. 2006) and processed in order to produce two high-resolution digital elevation models (DEMs) and to compare them. Different methods were used in order to extract small-scale topography, quantify interannual surface changes, and determine the kinematic behavior of the creeping mass. For a better understanding of rock glacier dynamics, the results have also been compared to the geodetic measurements annually over a 20-year period, and to the geophysical evidences of rock glacier internal structure.

Keywords: alpine permafrost; French Alps; high-resolution DEM; LIDAR; rock glacier morphology; surface kinematics.

Introduction

The long term, steady-state and slow deformation of ice-supersaturated sediments, which generates specific landforms called rock glaciers, is dependent on various parameters such as the ice/debris mixture thickness, the local slope angle, the ice and water content, or the depth of the basal shear zone (Haeberli 1985, Barsch 1992, Arenson et al. 2002, Haeberli et al. 2006). Recent investigations have also suggested that, at an interannual scale, the main controlling factor of rock glacier deformation rate may be the thermal state of the permafrost body (Ikeda 2004, Roer et al. 2005, Kääb et al. 2006).

Previous studies on rock glacier surface kinematics have classically used remote-sensing techniques (Kääb et al. 1998, Kaufmann et al. 2005), which provide a good spatial resolution but only on mid- to long-term trends of the creeping activity, or geodetic surveys (Delaloye 2004, Lambiel & Delaloye 2004, Kaufmann et al. 2006), which are often carried out at an annual time-scale but with a limited spatial resolution.

Recent development of the LIDAR (Light Detection And Ranging) technique allows fast and accurate acquisition of the topography with very high resolutions. Using terrestrial devices, several millions of points may be acquired in one day, and entire slopes (≈10^4 m^2) and landforms may be scanned. Therefore, it appears a promising tool to produce high-resolution digital elevation models (HR-DEMs) that have, until now, rarely been used to study surface changes and related processes in the glacial (Bauer et al. 2003, Avian & Bauer 2006) or periglacial geomorphology.

In this study, a medium-range terrestrial LIDAR was employed during two successive years to scan the surface of a rock glacier.

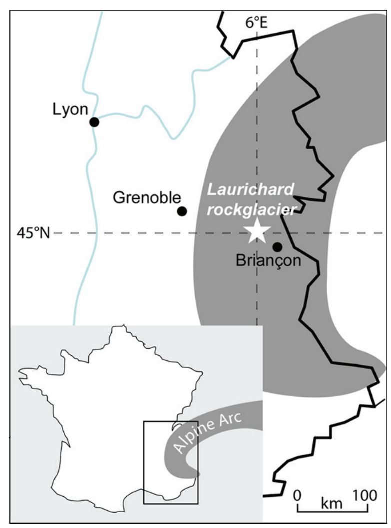

Figure 1. Location of the Laurichard rock glacier, in the Southern French Alps.

The investigated landform is the Laurichard rock glacier in the Southern French Alps (Fig. 1), which is a 500 m long, tongue-shaped, active rock glacier. As it is surveyed since 1979 with annual geodetic measurements of 28 marked blocks (Francou & Reynaud 1992), its mean surface velocities are known to range from 0.2 m/yr at the root and at the front to 1.2 m/yr in its steepest central part.

Beyond the necessity to test the applicability of the terrestrial LIDAR on a very rough and complex terrain, the main goals of this study were to perform multi-scale morphometric measurements, to quantify the interannual surface changes, and to determine the kinematic behavior of the creeping mass.

Acquiring High-Resolution DEM in an Alpine Environment

Data acquisition

The device (Ilris-3D, Optech; wavelength: 1500 nm) used in the present study is able to acquire 2500 points per second, with a centimetre accuracy (8 mm at 100 m) and at a maximal range of about 1000m. The limiting factors that can reduce the LIDAR measurements quality are the presence of non-reflective surfaces, such as snow, and the occurrence of very humid or foggy atmospheric conditions.

The small-scale morphology of the rock glacier, composed of extensive (longitudinal ridges) or compressive (transversal convex ridges and furrows) flow structures, has made it imperative to multiply the angles of view. Hence, during the two field campaigns (September 2005 and September 2006) four stations and 14 to 17 scenes (between 1 and 4 per station) were necessary each time to scan the whole surface of the rock glacier and to minimise shadowed areas (Fig. 2). In addition, five fixed points, outside the rock glacier, were measured with DGPS (Differential GPS), enabling a centimeter precision for the georeferencing of each DEM.

With a mean resolution of 7 cm (it varies according to the distance between the LIDAR and the target) two clouds of 10–15 millions points were generated.

Data processing

The raw datasets, that consist in x, y, and z coordinates (reflectance and colorimetric information have not been used), have to undergo several processing steps before being usable for further treatments. The PolyWorks (© InnovMetrics 2005) software, dedicated to the processing of 3D point clouds, was hence used to:

1. align and adjust the scenes together, thanks to common overlapping areas,
2. reduce the redundancy where a high density is not necessary,
3. grid the data to obtain either a polygonal model or a regularly spaced model,
4. georeference one polygonal model, thanks to using the DGPS points by the manual recognition of the blocks, and
5. align the two polygonal models on their common stable parts.

Finally, three types of processed data are available for further analysis: initial point clouds (17 in 2005, 14 in 2006, plus the 2 final aligned ones); two polygonal models (one per year); and two regularly-spaced models (one per year, at resolution of 0.5 and 1 m).

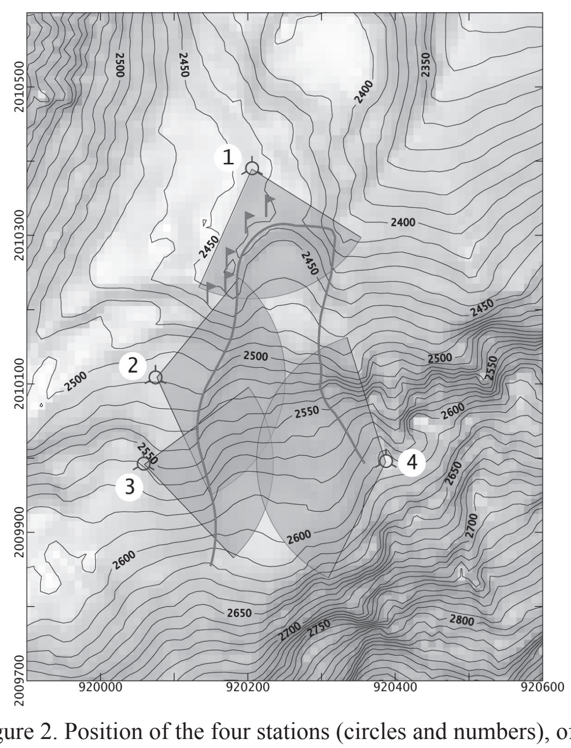

Figure 2. Position of the four stations (circles and numbers), of the corresponding scanning windows (circle portions) and of the fives fixed points (flag) used to scan the surface of the rock glacier (bold line). Geographic coordinates and elevations are in meters.

The Use of High-Resolution DEM to Quantify Rock Glacier Morphology and Surface Kinematics

Morphometric analysis of the rock glacier

Because of the presence of snow on the upper part of the rock glacier during the 2006 campaign, only the 2005 data were used.

First, a detailed map of the main morphological features has been established and verified in the field (Fig. 3). Interesting elements, such as the limits of the different flowing units or the variable roughness of the surface, can be extracted.

Second, the use of morphometric parameters has allowed a fine quantitative description of the rock glacier topography. Slope, microtopography (μz) after Kääb (2005), and roughness (ρz) index were computed along the main flow line by the following formulas:

$$\mu z_n = \frac{\sum_{n+2}^{n-2} z_n}{5} - \frac{\sum_{n+25}^{n-25} z_n}{51} \tag{1}$$

$$\rho z_n = z_n - \frac{\sum_{n+10}^{n-10} z_n}{21} \tag{2}$$

This allows several parts with homogeneous morphometric characteristics to be distinguished (Fig. 4):

a) the scree slope at the contact between the rock wall (slope >37°) is marked on its upper part by a deep concavity, which actually corresponds with the "randkluft" of the rock glacier (massive ice is commonly observed);
b) the upper convex part of the central slope where transversal microtopography is almost absent due to high, extensive flow;

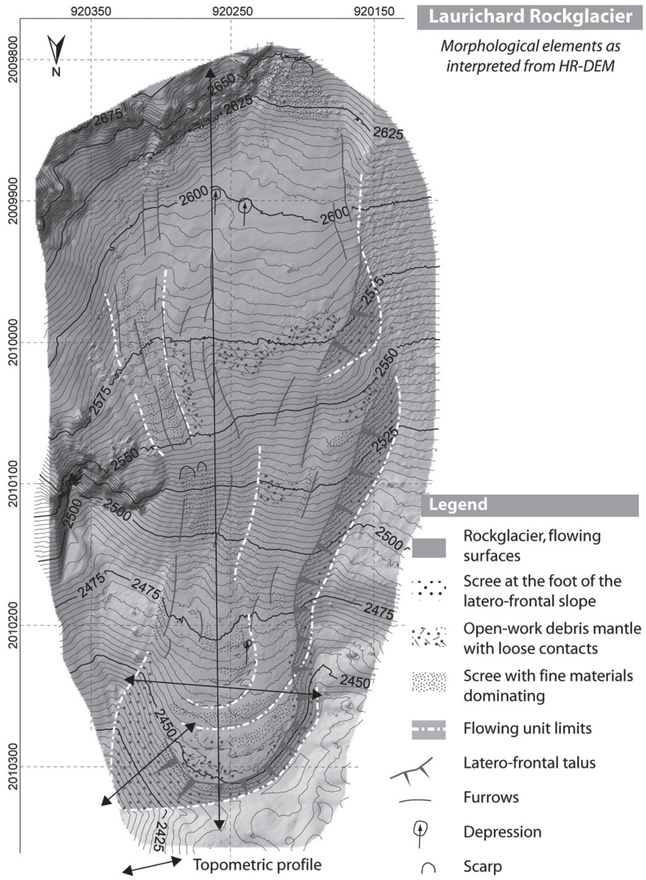

Figure 3. Morphological map of the rock glacier from the 2005 HR-DEM. Coordinates are in meters and equidistance of the contour lines is 2.5 m. Please note that, for aesthetic reasons, north as been placed at the bottom.

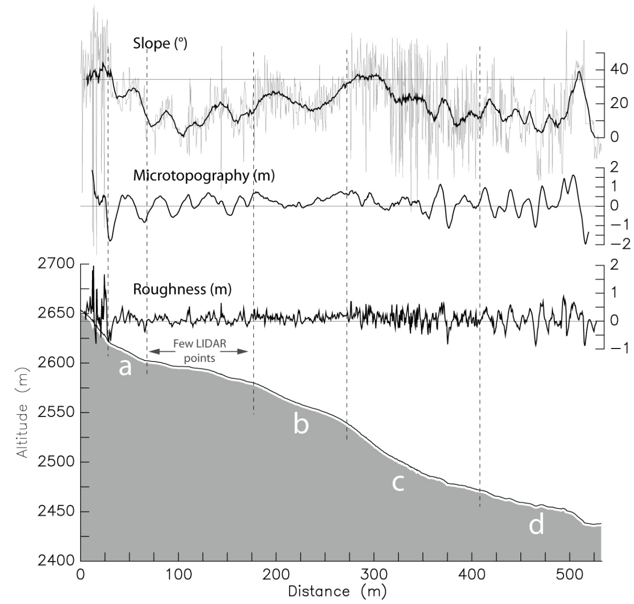

Figure 4. Longitudinal profile of the rock glacier with computed values of slope, microtopography, and roughness.

c) the lower concave part of the central slope, which is characterized by a high roughness, related to the presence of numerous large boulders and, at the bottom, by transverse ridges and furrows;

d) the gently sloping tongue of the rock glacier shows several ridges, and the roughness index suggests smaller boulders.

As a rock glacier is commonly interpreted as a creeping mixture of debris and ice (Haeberli 1985, Barsch 1992), it may be assumed that those morphometric measurements partly reflect the dynamics of the landforms.

Long-term deformation of the rock glacier

The digitizing of contour lines obtained through photogrammetric restitution of 1975 aerial photos (topographic map IGN 3436ET, 1:25000) has provided a DEM (at a grid resolution of 10 m) of the rock glacier region. The comparison between this 10 m DEM (which displays quite poor accuracy of +/-5m) and the 2005 HR-DEM allows us to roughly estimate the characteristics of the Laurichard rock glacier flow (Fig. 5). It appears that the frontal zone has advanced by about 11 m, displacing a volume of rock and ice of approximately 50,000 m^3 in 30 years. An interesting feature is the clear inflexion of the flow towards its right, in a local valley axis.

Interannual comparison of HR-DEM

Due to the coarse detritic cover of the rock glacier, made up of decimeter to meter-sized boulders without fine material, the surface roughness appears to be greater than the spatial resolution of the HR-DEM. Furthermore, the variability of the point density, from place to place and from one HR-DEM to the other, may lead to an heterogeneous quality of the reproduction of the surface by the models. Thus, as a smoothing of the "noisy" blocky surfaces would have induced an additional inaccuracy and would have limited the detection of infra-meter surface movements, direct comparisons were performed by two different means.

With the first method, the PolyWorks software computes the distance between each cell of the 2005 polygonal model and the closest cell of the 2006 polygonal models. A directional constraint is set by a 3D vector which specifies in which direction the comparisons have to be performed. Thus, maps of "directional differences" can be computed for various 3D vectors.

This method shows some of the main components of the surface movement, such as the downstream progression of the ridge that appears to be larger in the main flow axis of the landform (Fig. 8). The larger movement on the right side of the rock glacier seems also to be confirmed, and the fall of blocks from the top of the front or the individual movements of big boulders can be easily detected.

The second method consists in the use of topographic profiles along which 2005 and 2006 surfaces are compared. Vertical changes as well as horizontal differences can then be computed.

Specific patterns of rock glacier movement can therefore be visualized. The frontal advance is detected by the uprising of the surface, which decreases toward the foot of the talus (Fig. 6 A). Erosion by the fall of blocks from the upper part of the front is also perceptible at some places by a lowering

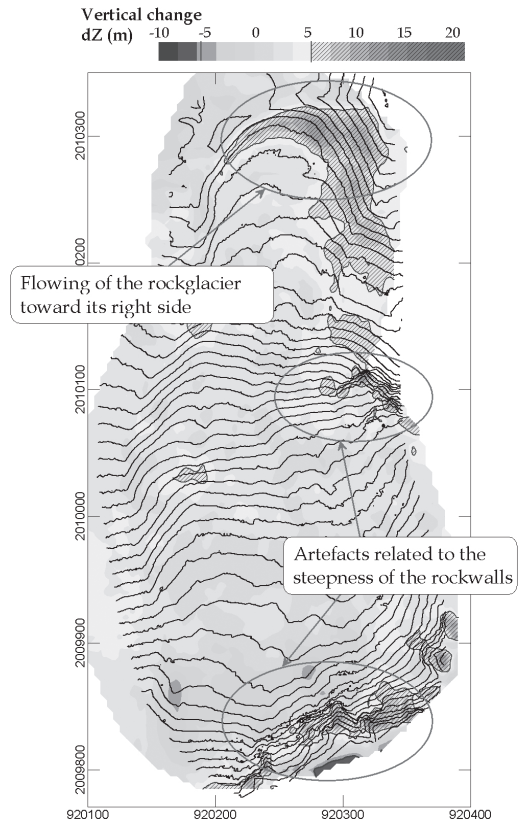

Figure 5. Vertical changes (in meters) between 2005 HR-DEM and 1975 DEM.

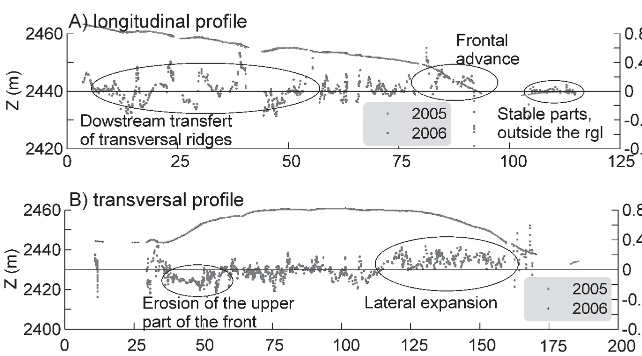

Figure 6. Vertical changes between 2005 and 2006 on a longitudinal and a transversal profile.

of the surface at the top and a subsequent rising at the foot, which corresponds to the deposit.

This method also permits to quantification of the downstream progression of the ridges (from 0.2–0.6 m/yr on the tongue) and the advance of the latero-frontal talus that appears to range from 0–0.6 m/yr (Fig. 7).

Discussion on the Rock Glacier Dynamics and Discussion

The rock glacier advance

The latero-frontal edges of the rock glacier were frequently perpendicular to the line-of-sight of the LIDAR, and this has locally improved the quality of the HR-DEM and facilitated surface changes quantification on those specific sectors.

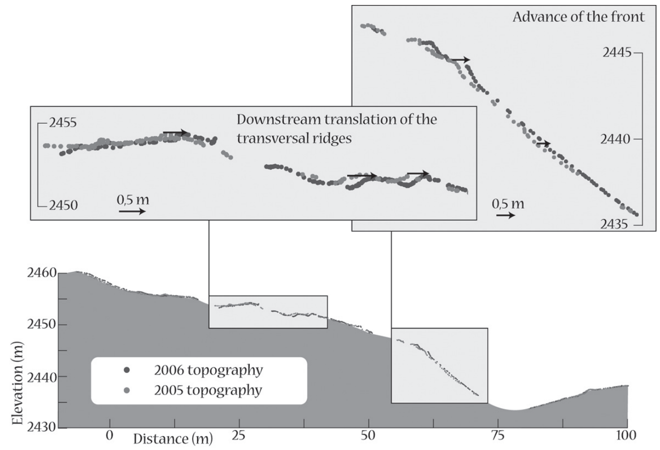

Figure 7. Surface changes between 2005 and 2006 on a longitudinal profile showing the tongue of the rock glacier.

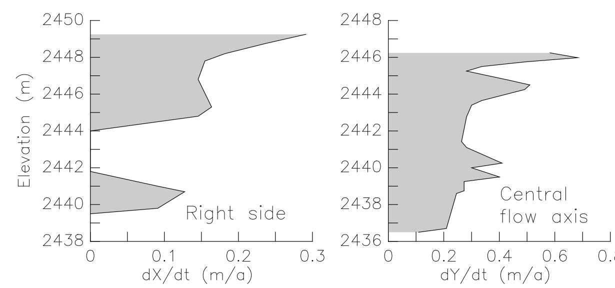

Figure 8. Vertical profiles showing the horizontal advance rate of the latero-frontal edges of the rock glacier (see Fig. 3 for location).

Hence, measure of the horizontal movement of visible boulders allows the drawing up ofvertical profiles of the advance of the rock glacier edges (Fig. 8). Those show an increase of the advance rate toward the top of the front, as well as marked ruptures that are visible at different levels in the profiles.

Although this kind of measurement has to be carefully interpreted due to the roughness of the surface and to individual boulder movements that may introduce noise in the values, several remarks can be made concerning the advance of the rock glacier.

First, the linear to parabolic shape of the vertical profiles is similar to those observed by Kääb & Reichmuth (2005) on the front of two rock glaciers. For the Murtèl case, they found that its frontal part is affected by a downslope creep of a surface layer (which acts as a "conveyor belt") and a thaw settlement that reveal an excess ice content of about 60%–70%.

Second, the presence of a non-moving layer is observed within the vertical profiles of the right side of the Laurichard rock glacier. This may approximately correspond to the level of the bedrock (as suggested by surrounding evidence) and may be interpreted as evidence of the presence, immediately above, of a shear zone (Arenson 2002) where a large part of the total deformation occurs.

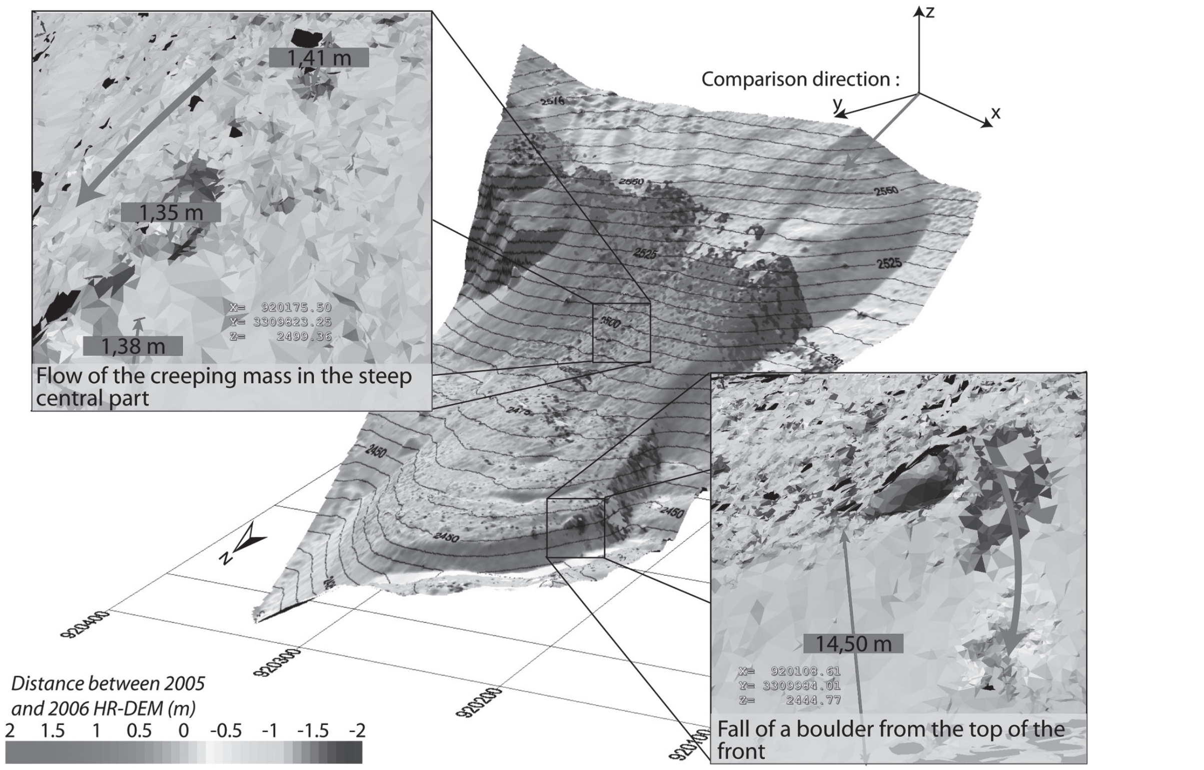

Figure 9. Map of the "directional difference" (direction of comparison shown in the upper right corner) between 2005 and 2006 HR-DEM. The inserts present some details of typical surface changes, such as the individual movements of boulders in the steep central part or the fall of a block from the front. The downstream progression of the ridge is also clearly visible.

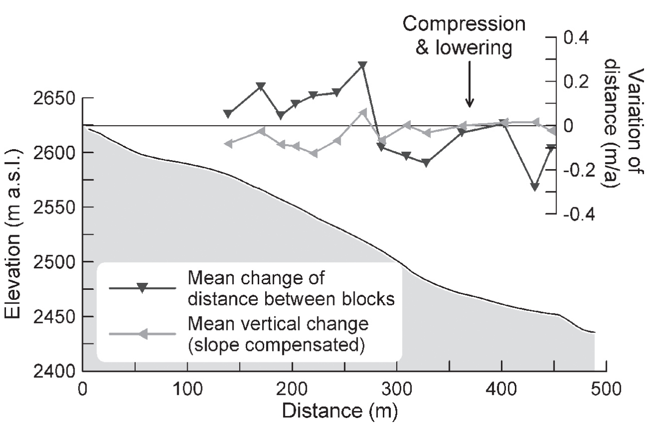

Figure 10. Surface variations of the Laurichard rock glacier after the long-term geodetic survey (mean 1986–2006 values).

Implications for the long-term geodetic survey

The annual measurements with the LIDAR device have suggested that the flow of the rock glacier may partly turn to its right, following a local valley axis. Between 1975 and 2005, the right side of the rock glacier advanced by about 14 m (+/-5 m) in that direction, and the corresponding 2005–2006 advance was around 0.3 m on the top of the latero-frontal talus.

Therefore it can be assumed that the surface changes observed with the long-term geodetic survey along the main axis of the rock glacier (Fig. 10) will reflect this specific behavior.

As a consequence, the small mean lowering of the surface (indicated by the calculated slope compensated variation of surface, data from 1986 to 2006) which accompanies the local compression of the tongue has to be interpreted in different ways. It may be a consequence of the global dynamics of the rock glacier, as well as an impact of the thaw settlement that would be associated to the global warming of the last two decades.

Conclusion

The terrestrial LIDAR technique has been employed to produce two high-resolution DEMs of the Laurichard rock glacier in two successive years. The morphology of the landform has been analyzed, thanks to mapping and to morphometric parameters. The depicted flowing structures clearly reveal the creep of the ice and debris mixture. This has also been studied through interannual comparisons of the HR-DEM, which allows general or detailed quantification of the surface kinematics of the rock glacier. By comparing with the results of a long-term geodetic survey, it appears that more detailed studies, for example with a regular (every 5 years) survey of the rock glacier, are necessary to develop models of the rock glacier dynamics.

Acknowledgments

This work has been possible thanks to collaboration between the Institute of Alpine Geography (Grenoble, France) and EDYTEM laboratory (Le-Bourget-du-Lac, France). The authors are indebted to R. Delunel, J. M. Krysiecki, and

A. Rabatel, as well as to the "Chalet-Laboratoire" of the Lautaret Pass (S. Aubert, P. Choler) for their help during the field campaigns. The unpublished data of the geodetic survey of Laurichard have been made available by the courtesy of L. Reynaud and E. Thibert.

References

Arenson, L., Hoelzle, M. & Springman S. 2002. Borehole deformation measurements and internal structure of some rock glaciers in Switzerland. *Permafrost and Periglacial Processes* 13: 117-135.

Avian, M. & Bauer, A. 2006. First results on monitoring glacier dynamics with the aid of terrestrial Laser Scanning on Pasterze Glacier (Hohe Tauern, Austria). *Grazer Schriften der Geographie und Raumforschung* 41: 27-36.

Barsch, D. (1992). Permafrost Creep and Rockglaciers. Permafrost and Periglacial Processes 3: 175-188.

Bauer, A., Paar, G. & Kaufmann, V. 2003. Terrestrial laser scanning for rock glacier monitoring. *8th International Conference on Permafrost, Zürich, Balkema:* 55-60.

Delaloye, R. 2004. *Contribution à l'étude du pergélisol de montagne en zone marginale*. PhD. Thesis. Université de Fribourg: 260 pp.

Francou, B. & Reynaud L.. 1992. 10 years of surficial velocities on a Rock glacier (Laurichard, French Alps). *Permafrost and Periglacial Processes* 3: 209-213.

Haeberli, W. 1985. *Creep of Mountain Permafrost: Internal Structure and Flow of Alpine Rock Glaciers*. Zürich, ETH. 142 pp.

Haeberli, W., Hallet, B., Arenson, L., Elconin, R., Humlum, O., Kaab, A., et al. 2006. Permafrost creep and rock glacier dynamics. *Permafrost and Periglacial Processes* 17(3): 189-214.

Ikeda, A. 2004. *Rock Glacier Dynamics near the Lower Limit of Mountain Permafrost in the Swiss Alps.* PhD. Thesis. University of Tsukuba: 107 pp.

Kääb, A. 2005. *Remote Sensing of Mountain Glaciers and Permafrost Creep.* University of Zürich: 266 pp.

Kääb, A., Frauenfelder, R. & Roer, I. 2006. On the response of rockglacier creep to surface temperature increase. *Global and Planetary Change* 56(1-2): 172-187.

Kääb, A., Gudmundsson, G.H. & Hoelzle, M. 1998. Surface deformation of creeping mountain permafrost. Photogrammetric investigations on Murtel rock glacier, Swiss Alps. *Proceedings of the Seventh International Conference on Permafrost, Yellowknife, Canada, Université de Laval*: 531-537.

Kääb, A. & Reichmuth, T. 2005. Advance mechanisms of rock glaciers. *Permafrost and Periglacial Processes* 16: 187-193.

Kaufmann, V., Ladstädter, R. & Kienast, G. 2007. 10 years of monitoring of the Doesen rock glacier (Ankogel group, Austria) - A review of the research activities for the time period 1995–2005. *5th ICA Mountain Cartography Workshop, Bohinj, Slovenia*: 128-144.

Kaufmann, V., Ladstädter, R. & Lieb, G.K. 2006. Quantitative assessment of the creep process of Weissenkar rock glacier (Central Alps, Austria). 8th International Symposium on High Mountain Remote Sensing Cartography, *Grazer Schriften der Geographie und Raumforschung, Band* 37, 77-86.

Lambiel, C. & Delaloye, R.. 2004. Contribution of RTK GPS in the study of creeping mountain permafrost. Examples from the Western Swiss Alps. *Permafrost and Periglacial Processes* 15: 229-241.

Roer, I., Avian, M., Delaloye, R., Lambiel, C., Dousse, J.-P., Bodin, X., et al. 2005. Rockglacier "speed-up" throughout European Alps - a climatic signal? *2nd European Conference on Permafrost, Potsdam, Alfred-Wegener-Stiftung:* 99-100.

Comparison of Exposure Ages and Spectral Properties of Rock Surfaces in Steep, High Alpine Rock Walls of Aiguille du Midi, France

Ralph Böhlert, Stephan Gruber, Markus Egli, Max Maisch, Dagmar Brandová & Wilfried Haeberli
Department of Geography, University of Zurich, Zurich, Switzerland

Susan Ivy-Ochs, Markus Christl
Institute of Particle Physics, ETH Zurich, Zurich, Switzerland

Peter W. Kubik
Paul Scherrer Institut, c/o Institute of Particle Physics, ETH Zurich, Zurich, Switzerland

Philip Deline
Laboratoire EDYTEM, Université de Savoie, Le Bourget-du-Lac, France

Abstract

Among various factors, permafrost and frost-thaw cycles play an important role for the stability of steep rock slopes in high alpine regions. Climate change in general and local temperature and precipitation trends in particular are likely to influence permafrost and, consequently, also the stability of rock walls. As stress relief following deglaciation can be excluded at Aguille du Midi (France), rockfall activity is mainly related to changes in permafrost and frost-thaw cycles. To put modern observations of possible climate-induced rockfalls into perspective, information on past rockfall activity is required. In this study, we investigated a combination of surface exposure dating and spectrometry to derive a correlation between rock surface ages and their spectral properties in homogenous lithology. The surface ages found varied from less than 2,000 years to around 40,000 years, and showed a clear correlation with reflectance behavior in the range 380–580 nm. These results may be a first step towards the possible generation of spatial data fields of age distribution in steep rock walls. This may provide deeper insights into spatial and temporal rock-wall development of permafrost in high alpine permafrost environments.

Keywords: cosmogenic nuclide dating; permafrost; reflectance spectroscopy; steep rock slope stability; surface exposure dating.

Introduction

Permafrost thaw is an important process which affects the stability of steep bedrock slopes in many alpine areas (cf. Haeberli et al. 1997, Gruber & Haeberli 2007). Slope failures, like rockfalls, landslides and debris flows, that are assumed to be triggered by changes in the permafrost conditions are known from numerous locations in high mountains and especially in the Alps (e.g., Haeberli 1992, Deline 2001, Noetzli et al. 2003, Schiermeier 2003, Gruber et al. 2004a). These processes cover magnitudes from small rockfalls to huge rockslides (Bergsturz). In comparison with debris-covered slopes, rock faces react quickly to climate change. This is due to the absence of a block layer (Mittaz et al. 2000, Hoelzle et al. 2001) and corresponding direct coupling of surface and subsurface conditions, combined with low water content and small transfer of latent heat during melt. This rapid reaction, together with the effect of destabilization, makes rockfalls due to permafrost degradation a likely and perceivable impact of climate change in the near future (Gruber et al. 2004a).

While recent advances in permafrost modeling have enabled the derivation of permafrost maps for steep bedrock (Gruber et al. 2004b), information about long-term rockfall activity is required to put recent observations and changes in temperature into a long-term perspective.

Besides radiocarbon dating and luminescence methods, the usage of cosmogenic nuclides has become a central technique to gain information about landform ages and landform-modification processes such as rockfalls. An overview of the spectrum of dated landforms and commonly used nuclides is given, for instance, in Gosse & Phillips (2001) and in Ivy-Ochs & Kober (2006). In relation to glacio-geomorphological questions, the determination of ^{10}Be- and ^{26}Al-concentrations in the surface of moraine boulders and polished bedrock is of great interest. Ivy-Ochs et al. (2006) summarized results from the European Alps. Whereas, numerous ages from late glacial moraines are available, data from polished bedrock (indicating deglaciation at higher altitudes) or from areas that were not glaciated during the Last Glacial Maximum (LGM) are sparse. Except for investigations in the Grimsel Pass region in central Switzerland (Ivy-Ochs 1996, Kelly et al. 2006), so far no dating has been carried out at higher-elevation sites.

Remote sensing techniques with multispectral and hyperspectral sensors are widely used to investigate different aspects of mountain areas. Kääb et al. (2005) provide an overview of air- and spaceborn remote sensing methods that are applicable for glacier and permafrost hazard assessment and disaster management. Other approaches discuss methodologies for mapping glacio-geological features such as trim lines or terminal moraines in order to reconstruct glacier changes and related past climate (e.g., Huh et al. 2006). Spectral field measurements and airborn hyperspectral data have enabled an approach to date and map other geomorphic features such as arid and semi-arid alluvial fans (Crouvi et al. 2006). The development of a rock coating significantly influences the overall reflectance of the surface. The redness of rock material or soil is directly related to the age. In oxidizing environments and increasing weathering time, color hues become redder and chromas become brighter (rubification). This fact is, among others, used in the calculation of the profile development index which gives a direct indication of soil age (e.g., Harden, 1982, Goodman et al., 2001).

In this paper, we present a pilot study to investigate the potential of combined imaging spectrometry and exposure dating to derive approximate surface ages in steep bedrock walls of homogeneous lithology. The geometric and radiometric correction of hyperspectral imagery over steep terrain is challenging but generally possible (cf. Gruber et al. 2003). The spatial data fields of estimated age resulting from this method would allow deriving the area and relative frequency of surfaces that belong to a certain age class and that are uninterrupted by older surfaces over a certain distance. This information is related to the frequency of rockfall events during a certain period and is a useful long-term background for assessing whether presently observable, large rockfall shows an unusual abundance as suggested by the relevance of permafrost for slope stability.

Our hypothesis is that the surface ages in this high alpine region can be directly related to the redness of the rocks. The redder a rock surface is, the higher the age that should be measured.

Geological and Physical Setting

Aiguille du Midi (3842 m a.s.l.) is situated some four kilometres south of Chamonix in the Western Alps in France. Whereas most of the peaks surrounding Chamonix are only reachable by making trips of several days with high alpine equipment, Aiguille du Midi is easily accessible by cable car and therefore an ideal study site.

Geologically, this area is part of the Mont-Blanc massif (Spicher 1980) and is made up of the so-called Mont-Blanc Granite with an age of roughly 300 Ma (von Raumer & Bussy 2004, Bussy et al. 2000). This granite type is of a very quartz-rich quality and thus suitable for surface exposure dating with ^{10}Be.

During LGM, the uppermost part of the Aiguille du Midi SSE-face, where the samples were taken, was most probably not glaciated. Paleogeographical reconstructions based on trimline mapping by Coutterand & Buoncristiani (2006) and Kelly et al. (2004) showed that Aiguille du Midi was, during this time, a Nunatak bounded in the east by the Mer de Glace, in the north by the Glacier de l'Arve, and in the west by the Glacier des Bossons. Apart from local glaciations in the less steep parts of the wall, the influence of glacial ice masses on exposure ages can be excluded.

We chose our sampling sites based on visually identifiable differences in color on photographs taken from a helicopter.

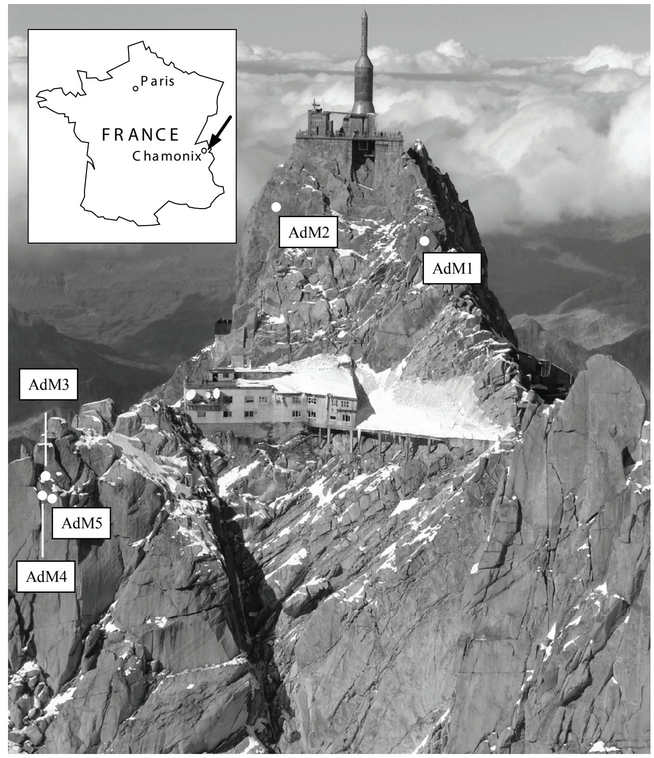

Figure 1. Overview of the sampling locations at Aiguille du Midi.

The hypothesis was that intensively red-colored parts in the rock wall were exposed to weathering over a longer time period than fresh gray ones, and consequently should have a higher age. This assumption is based on field observations at the adjacent Drus, where, besides several smaller events, a huge rockfall occurred in 2005 (Ravanel 2006). The gray-colored area that came to light clearly contrasts to the surrounding, more or less reddish, and obviously older parts of the wall.

Sample AdM1 was taken at a conspicuously red spot, whereas AdM2 was gathered from a gray part of the wall, where no red coloring was seen. AdM4 and AdM5 can be placed somewhere in between with respect to color. Thereby, sample AdM5 presented a more intensive coloration than AdM4. All these sampling places had a slope ≥ 79°. The slope at AdM3 was, however, only 49°. This sample was the only one that was partly covered by lichen, probably due to an increased water availability resulting from melting snow. For this reason spectral analysis was not applicable, and AdM3 was not taken into account for further interpretation. We concluded that the rock surfaces should have the following order of age: AdM1 > AdM5 >AdM4 > AdM2.

Rock samples were taken with hammer, chisel, and a drilling machine. After Masarik & Wieler (2003), marginal sampling places were excluded in order to avoid edge effects. To calculate the influence of shielding caused by the surrounding topography, azimuth-dependent angles were extracted from the map.

Methodology

Surface exposure dating

Approximately 500–1000 g of each rock sample were crushed and sieved. A grain-size fraction of 0.5 to 1 mm was used. Pure quartz was separated by selective chemical dissolution (Kohl & Nishiizumi 1992, Ivy-Ochs 1996). This method is based on the fact that feldspars and micas dissolve in 4% HF more quickly than quartz does. At least six HF steps were used to obtain very pure quartz as reflected by the low Al concentration (less than 100 ppm). ^{9}Be carrier was added to the dried quartz, which was then completely dissolved with concentrated HF in a microwave. Be and Al were separated using a cation exchange column. The Be hydroxides were precipitated, dried, and calcined at 850°C to BeO.

The $^{10}Be/^{9}Be$ ratios were measured at the ETH/PSI Zürich Tandem Accelerator Mass Spectrometry (AMS) Facility (Synal et al. 1997).

In order to calculate ^{10}Be ages, a simple exposure history was assumed, specifically that all ^{10}Be measured was produced in the rock surface during the latest period of exposure and that the rock surface did not suffer significant erosion. Any earlier exposure, even at greater depth below the original surface, will make the "measured" age an upper limit for the true exposure age of the sample's surface.

Ages were calculated using the ^{10}Be production rate of 5.1 ± 0.3 atoms gram-1 year-1 at sea level and high latitude (Stone 2000). Production rates were scaled to the specific sample locations according to Stone (2000) and corrected for sample thickness (assuming an exponential depth profile) and topographical (skyline) shielding (Dunne et al. 1999) (Table 2).

Laboratory reflectance spectroscopy

Rock surface spectra were measured in the laboratory using an ASD FieldSpec Pro Fr spectro-radiometer, a Spectralon reference panel, and a Thermo Oriel irradiance source. The hematite spectrum was taken from the Jet Propulsion Laboratory (JPL) Spectral Library (HEMATITE 0-1A). In order to identify absorption features for measurement, continuum removal was applied to the data. This is a means of normalizing reflectance spectra to allow comparison of individual features from a common baseline. Continuum removal (Clark & Roush 1984, Kruse et al. 1985, Green & Craig 1985) was performed in ENVI 4.1 to facilitate the comparison of individual absorption features between different objects. In this method, a convex hull (the continuum) of a reflectance spectrum is divided by the spectrum itself and thus results in values ranging from 0-1. The convex hull is built utilizing straight line segments that connect local reflectance maxima.

Elemental composition by X-ray fluorescence measurements

The elemental composition of the rock samples was analyzed by X-ray fluorescence (XRF) spectrometry. After crushing the rock samples to a size of <1mm, around 10 g of rock material were milled to <50 µm in a tungsten carbide disc swing mill (Retsch® RS1, Germany). 4 g of rock powder was mixed with 0.9 g of Licowax® C Micro-Powder PM (Clariant, Switzerland), pressed into a 32 mm pellet, and analyzed using an energy dispersive XRF spectrometer (SPECTRO X-LAB 2000, SPECTRO Analytical Instruments, Germany).

Table 1. Elemental composition of the samples.

	Samples Aiguille du Midi 1-5					Statistics	
Element [%]	AdM1	AdM2	AdM3	AdM4	AdM5	Mean	SD
CaO	0.87	0.87	1.44	1.17	1.31	1.13	0.26
MgO	0.62	0.60	0.37	0.39	0.56	0.51	0.12
K_2O	5.09	5.22	4.91	5.28	5.37	5.17	0.18
Na_2O	3.12	2.84	2.74	2.80	2.78	2.86	0.15
Al_2O_3	13.62	13.58	13.67	13.82	12.89	13.52	0.36
Fe_2O_3	1.43	1.64	1.85	1.70	2.23	1.77	0.30
SiO_2	70.32	68.73	67.27	70.09	66.56	68.60	1.67
MnO	0.02	0.03	0.033	0.04	0.049	0.04	0.01
P_2O_5	0.06	0.07	0.072	0.07	0.091	0.07	0.01
TiO_2	0.26	0.30	0.310	0.31	0.334	0.30	0.03
ZrO_2	0.02	0.02	0.022	0.02	0.022	0.02	0.00
BaO	0.07	0.08	0.098	0.08	0.080	0.08	0.01
Rb_2O	0.03	0.03	0.031	0.03	0.034	0.03	0.00
WO_3	0.05	0.05	0.045	0.06	0.036	0.05	0.01
LOI	3.43	0.55	0.63	3.57	0.53	1.74	1.61
Total	99.02	94.61	93.49	99.43	92.89		

Elemental composition of the samples based on XRF measurements. Values are converted into oxide contents. LOI = Loss on ignition. The low standard deviation (SD) values indicate a comparable composition and demonstrate the homogeneity of the lithology.

Table 2. List of samples and calculated surface exposure ages.

	Samples Aiguille du Midi 1-5				
	AdM1	AdM2	AdM3	AdM4	AdM5
Elevation (m a.s.l)	3800	3810	3750	3740	3740
Sample thickness (cm)	2.5	3.5	5.5	2.5	4.0
Surface dip (°)	85	85	49	79	79
Quartz (g)	58.13	57.03	58.26	56.77	56.68
^{10}Be (10^4 atoms g^{-1})	157.63	6.03	24.28	24.84	28.28
Measurement error (%)	3	9.2	5	4.6	5.2
Production rate not corrected (atoms g^{-1} yr^{-1})	75.59	76.00	73.57	73.17	73.17
Shielding factor	0.559	0.559	0.898	0.627	0.627
Production rate corrected for shielding, sample thickness and surface dip (atoms g^{-1} yr^{-1})	41.24	41.11	62.85	44.77	44.34
^{10}Be date (yr)	**38,600±1200**	**1,470±140**	**3,870±200**	**5,560±260**	**6,390±330**

Samples organized by sample name. The reference production rate is scaled for sample altitude and latitude after Stone (2000) and corrected for sample thickness (assuming exponential attenuation of cosmic rays at depth and an attenuation length of 150 g cm-2) and skyline shielding (Dunne et al. 1999).

Results

Elemental composition

Results from XRF measurements show after conversion into oxide contents a very similar composition (Table 1.). The high quartz content of the Mont-Blanc granite is represented by high amounts of SiO_2. Other important constituents of the rock samples are Al_2O_3 and potassium oxide. The total values of over 90% mean that almost all possible compounds were measured.

The comparable composition of the samples is an important indication that observed differences in color are not due to inhomogeneities in lithology.

Surface exposure ages and comparison with measured spectra

The intensively red colored sample AdM1 shows the highest age, followed by AdM5, AdM4, and AdM2, where no coloring occurred. This is in agreement with the above-stated hypothesis and the sample description (Table 2).

Generally, the ^{10}Be ages, especially AdM1, are remarkably old, and the differences in age are very big. But these ages have to be interpreted as maximum exposure ages of the rock surface, as long as erosional processes can be excluded.

Looking at the measured spectra (Fig. 2), a well-pronounced correlation between surface exposure ages and the corresponding spectral signature in the range of approximately 380–580 nm is identifiable after continuum removal. As a reference, a piece of unweathered fresh rock was also analyzed (AdMf).

According to the visual impression, the curve progression of AdM2 is shaped very similarly to the one of the unweathered sample. With increasing surface exposure ages and thus more pronounced weathering, a decrease in feature depth is ascertainable. A comparison with the continuum-removed spectrum of hematite permits the conclusion that the spectra evolution with increasing age is influenced, at least partly, by hematite formation (Fig. 2). Thus, hematite content and its effects on rock surface color can be interpreted as the main feature required in regard to the generation of spatial data fields of age distribution in rock walls.

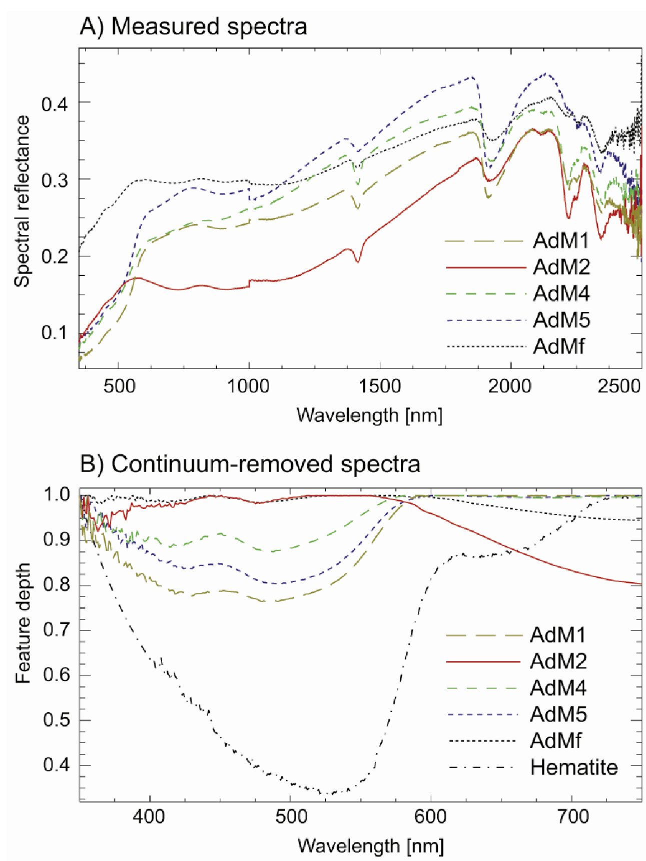

Figure 2. Measured and continuum-removed spectra. The arrow indicates the influence of the Fe-Oxide content with age.

Discussion and Conclusions

We showed that analyzing spectral properties of rock surfaces in steep walls with homogeneous lithology may be a tool to estimate the age distribution and related past rockfall activity in high alpine environments. The redder a rock surface, the longer this rock was exposed to weathering. In numerous cases, the correlation of rockfall initiation to changes in the permafrost conditions is rather weak, and related forecast and mitigation possibilities are limited (Gude & Barsch 2005). Not only permafrost thawing but also other processes like general frost-thaw activities (physical weathering), seismic (neotectonic) activity, or stress relief following deglaciation could induce rockfalls. Furthermore, non-erosive cold-based glacier ice can complicate the erosion history of rock surfaces (Briner et al. 2006). Due to the topographic situation of the investigated sites, however, at least one process affecting the stability of rock walls can be excluded. A stress-relief following deglaciation of (cold-based) glacier ice did not occur because no glaciers covered the rock walls during (and after) the LGM. Rockfall is predominantly due to permafrost changes and frost-thaw activities. Although neotectonic activities have been rather low, their influence on rockfalls cannot be fully excluded. The used approach, therefore, will not allow direct reconstruction of past permafrost conditions. However, it can give indications about past and present-day rockfall activities. From this, the influence of permafrost on rock wall stability can be deduced at least partially. Inasmuch as global warming in general and local temperature and precipitation trends in particular are likely to influence the permafrost significantly, the stability of rock walls will also be affected.

The relationships found look promising; however, they certainly represent only a first impression and further investigations in this field will be necessary to establish this approach as a commonly usable application. Doubtless, of great importance is the enlargement of the survey sample size in order to be able to generate statistical correlations between surface exposure ages and spectral properties. Therefore, the latter have to be translated into quantifiable values.

In the present study, we tried to keep as many factors constant as possible. Potential follow-up studies will have to deal with the influence of variable slope aspect and altitudes and different lithologies. Steep places at high elevations should be preferred. Sampling locations that are situated too low are not suitable due to lichen growth disturbing the spectral signal. The same is true for flat spots where snow cover can develop more easily and remain for a longer time. A fundamental problem will be the difficulty in accessing appropriate sites. There is, however, great potential for further efforts.

Acknowledgments

This research is supported by the Swiss National Science Foundation grant number 20-109565/1. We would like to thank Jürg Schopfer for providing support in the spectro lab. Easy access to Aiguille du Midi was possible thanks to the generous help of the Compagnie du Mont Blanc (Chamonix) and particularly of Emerick Desvaux. We are, furthermore, indebted to Anne Hormes and to an unknown reviewer for their helpful comments on an earlier version of the manuscript.

References

Briner, J.P., Miller, G.H., Davis, P.T. & Finkel, R.C. 2006. Cosmogenic radionuclides from fiord landscapes support differential erosion by overriding ice sheets. *GSA Bulletin* 118: 406-420.

Bussy, F., Hernandez, J. & von Raumer, J. 2000. Bimodal magmatism as a consequence of the post-collisional readjustment of the thickened variscan continental lithosphere (Aiguilles Rouges/Mont-Blanc massifs, western Alps). *Transactions of the Royal Society of Edinburgh: Earth Sciences* 91, 1-2: 221-223.

Clark, R.N., & Roush, T. L. 1984. Reflectance spectroscopy: Quantitative analysis techniques for remote sensing applications. *Journal of Geophysical Research* 89(B7): 6329-6340.

Couterrand, S. & Buoncristiani, J.-F. 2006. Paléogeographie du dernier macimum glaciere du Pleistocène de la Region du Mont Blanc, France. *Quartenaire* 17(1): 35-43.

Crouvi, O., Ben-Dor, E., Beyth, M., Avigad, D. & Amit, R. 2006. Quantitative mapping of arid alluvial fan surfaces using field spectrometer and hyperspectral remote sensing. *Remote Sensing of Environment*, 104: 103-117.

Deline, P. 2001. Recent Brenva rock avalanches (Valley of Aosta): New chapter in an old story? *Suppl. Geogr. Fis. Dinam. Quat*.: 55-63.

Dunne, J., Elmore, D. & Muzikar, P. 1999. Scaling factors for the rates of production of cosmogenic nuclides for geometric shielding and attenuation at depth on sloped surfaces. *Geomorphology* 27: 3-11.

Goodman, A.Y., Rodbell, D.T., Seltzer, G.O. & Mark, B.G. 2001. Subdivision of glacial deposits in southeaster Peru based on pedogenetic development and radiometric ages. *Quaternary Research* 56: 31-50.

Gosse, J.C. & Phillips, F.M. 2001. Terrestrial in situ cosmogenic nuclides: theory and application. *Quaternary Science Reviews* 20: 1475-1560.

Green, A.A., & Craig, M.D. 1985. Analysis of aircraft spectrometer data with logarithmic residuals. *Proceedings, AIS workshop, 8-10 April, 1985.* JPL Publication 85-41, Jet Propulsion Laboratory, Pasadena, California: 111-119.

Gruber, S. & Haeberli, W. 2007. Permafrost in steep bedrock slopes and its temperature-related destabilization following climate change. *Journal of Geophysical Research* 112, F02S18, doi:10.1029/2006JF000547.

Gruber, S., Hoelzle, M. & Haeberli, W. 2004a. Rock wall temperatures in the Alps: Modelling their topographic distribution and regional differences. *Permafrost Periglacial Processes* 15(3): 299-307.

Gruber, S., Hoelzle, M. & Haeberli, W. 2004b. Permafrost thaw and destabilization of Alpine rock walls in the hot summer of 2003, *Geophysical Research Letters* 31, L13504, doi:10.1029/2004GL020051.

Gruber, S., Schläpfer, D. & Hoelzle, M. 2003. Imaging spectrometry in high-alpine topography: The derivation of accurate broadband albedo. *Proceedings of the the 3rd EARSeL Workshop on Imaging Spectroscopy, Oberpfaffenhofen, Germany, 13–16 May 2003*: 10 pp.

Gude, M. & Barsch, D. 2005. Assessment of geomorphic hazards in connection with permafrost occurrence in the Zugspitze area (Bavarian Alps, Germany). *Geomorphology* 66: 85-93.

Haeberli, W., Wegmann, M. & Vonder Mühll, D. 1997. Slope stability problems related to glacier shrinkage and permafrost degradation in the Alps. *Eclogae Geologicae Helveticae* 90: 407- 414.

Haeberli, W., 1992. Construction, environmental problems and natural hazards in periglacial mountain belts. *Permafrost and Periglacial Processes* 3: 111-124.

Harden, J.W. 1982. A quantitative index of soil development from field descriptions: examples from a chronosequence in central California. *Geoderma* 28: 1-28.

Hoelzle, M., Mittaz, C., Etzelmüller, B. & Haeberli, W. 2001. Surface energy fluxes and distribution models of permafrost in high mountain areas: An overview of current developments. *Permafrost and Periglacial Processes* 12: 53-68.

Huh, K.I., Csatho, B., van der Veen, C.J. & Ahn, Y. 2006. Reconstructing Holocene glacier changes in west Greenland from Multispectral ASTER imagery. *EOS* 87, Fall Meeting Supplement, Abstract C11A-1134.

Ivy-Ochs, S. 1996: *The dating of rock surfaces using in situ produced 10Be, 26Al and 36Cl, with examples from Antarctica and the Swiss Alps*. Ph.D. thesis, ETH Zürich, No. 11763, 196 pp.

Ivy-Ochs, S., Kerschner, H., Reuther, A., Maisch, M., Sailer, R., Schaefer, J., Kubik, P.W., Synal, H.-A. & Schlüchter, C. 2006. The timing of glacier advances in the northern European Alps based on surface exposure dating with cosmogenic ^{10}Be, ^{26}Al, ^{36}Cl, and ^{21}Ne. In: L.L. Siame, D.L. Bourlès & E.T. Brown (Eds.), *In Situ-Produced Cosmogenic Nuclides and Quantification of Geological Processes: Geological Society of America Special Paper 415*: 43-60.

Ivy-Ochs, S. & Kober, F. 2006. Exposure geochronology. In: S.A. Elias (Ed.), *Encyclopedia of Quaternary Sciences:* 435-445.

Kääb, A., Huggel, C., Fischer, L., Guex, S., Paul, F., Roer, I., Salzmann, N., Schlaefli, S., Schmutz, K., Schneider, D., Strozzi, T. & Weidmann, Y. 2005. Remote sensing of glacier- and permafrost-related hazards in high mountain: an overview. *Natural Hazards and Earth System Sciences* 23: 1-28.

Kelly, M.A., Ivy-Ochs, S., Kubik, P.W., von Blanckenburg, F. & Schlüchter, C. 2006. Chronology of deglaciation based on 10Be dates of glacial erosional features in the Grimsel Pass region. Central Swiss Alps. *Boreas* 35: 634-643.

Kelly, M.A., Buoncristiani, J.-F. & Schlüchter, Ch. 2004. A reconstruction of the last glacial maximum (LGM) ice-surface geometry in the western Swiss Alps and contiguous Alpine regions in Italy and France. *Eclogae Geologicae Helveticae* 97: 57-75.

Kohl, C.P. & Nishiizumi, K. 1992. Chemical isolation of quartz for measurement of in-situ produced cosmogenic nuclides. *Geochemica et Cosmochimica Acta* 56: 3583-3587.

Kruse, F. A., Raines, G. L. & Watson, K. 1985. Analytical techniques for extracting geologic information from multichannel airborne spectroradiometer and airborne imaging spectrometer data. *Proceedings, International Symposium on Remote Sensing of Environment, Thematic Conference on Remote Sensing for Exploration Geology, 4th, Environmental Research Institute of Michigan, Ann Arbor:* 309-324.

Masarik, L. & Wieler, R. 2003. Production rates of cosmogenic nuclides in boulders. *Earth and Planetary Science Letters* 216: 201-208.

Mittaz, C, Hoelzle, M. & Haeberli, W. 2000. First results and interpretation of energy-flux measurements over Alpine permafrost. *Annals of Glaciology* 31: 275-280.

Noetzli, J., Hoelzle, M. & Haeberli, W. 2003. Mountain permafrost and recent Alpine rock-fall events: A GIS-based approach to determine critical factors. *8th International Conference on Permafrost, Int. Permafrost Assoc., Zurich, Switzerland*.

Ravanel, L. 2006. *Contribution à l'étude des écroulements dans les parois à permafrost de la haute montagne alpine. L'éxemple du Petit Dru (massif du Mont-Blanc) depuis la fin du Petit Age Glaciere*. Master's thesis, Université de Savoie, 116 pp.

Schiermeier, Q. 2003. Alpine thaw breaks ice over permafrost's role. *Nature* 424: 712.

Spicher, A. 1980. *Tektonische Karte der Schweiz*. Schweizerische Geologische Kommission (Hrsg.).

Stone, J.O. 2000. Air pressure and cosmogenic isotope production. *Journal of Geophysical Research* 105 (B10), 23: 753-759.

Synal, H. A., Bonani, G., Döbeli, M., Ender, R.M., Gartenmann, P., Kubik, P.W., Schnabel, Ch. & Suter, M. 1997: Status report of the PSI/ETH AMS facility. *Nuclear Instruments in Physics Research* B (123): 62-68.

von Raumer, J.F. & Bussy, F. 2004. Mont Blanc and Aiguille Rouges – Geology of their polymetamorphic basement (external massifs, France-Switzerland). *Mémoires de géologie (Lausanne)* 42, 203 pp.

—*Plenary Paper*—

Heat and Water Transfer Processes in Permafrost-Affected Soils: A Review of Field- and Modeling-Based Studies for the Arctic and Antarctic

Julia Boike
Alfred Wegener Institute for Polar and Marine Research, Telegrafenberg A43, 14473 Potsdam, Germany
Birgit Hagedorn
Environment and Natural Resources Institute, University of Alaska, Anchorage, Anchorage, 99501, USA
Kurt Roth
Institute of Environmental Physics, University of Heidelberg, 69120 Heidelberg, Germany.

Abstract

The main field experiments and modeling results of heat and moisture transfer processes of the Arctic and Antarctic are reviewed, following the historical development. Agreement exists that heat is mainly transferred via conduction in Arctic and Antarctic soils, but that latent heat and vapor migration are important factors for the thermal dynamic. Factors determining amount and type of heat transfer are soil water content and temperature gradient between atmosphere and soil.

Keywords: Antarctic; Arctic; heat transfer; permafrost; thermal processes; water transfer.

Introduction

An apparent discrepancy exists between numerical modeling results and field observations indicating water and vapor transfer in frozen soils. The latter includes depth hoar formation under snow, direct measurements of vapor flux out of the ground (e.g., Santeford 1978, Woo 1982), desiccation of upper soil layers (Hinzman et al. 1991) and ice growth from field and lab experiments (Parmuzina 1978, Chen & Chamberlain 1988) and accumulation of ice at the base of the active layer/top of permafrost (Yershov 1998, Solomatin & Xu 1994).

Due to page limits, we review available literature on heat and water transfer processes in Arctic and Antarctic soils only; thus results from alpine, high elevation and temperate regions are excluded from this paper. Furthermore, we limited the review of heat and water transfer modeling to studies for which field data are available.

The very different climate conditions in the Arctic and Antarctic are reflected in the soil systems. While Arctic soils generally have free liquid water in active layer during summer, Antarctic soils are hyperarid in the dry valleys around the Ross Sea but gradually approach wetter conditions towards the east and Antarctic Peninsula (Beyer et al. 1999 and references within). These differences are reflected in motivation and approaches to model water and heat transport processes thus both regions are described separately. A quantitative understanding of the processes underlying the thermal and hydraulic dynamics of permafrost soils is paramount to anticipate consequences of a changing atmospheric forcing as well as to improve the parameterization of the soil-atmosphere interaction in climate models.

Thermal dynamics of permafrost-affected soils

The major stages for the seasonal thermal dynamics of the active layer at a permafrost site consists of four different characteristic periods: (i) cold period, (ii) warming period, (iii) thawed period, (ix) isothermal plateau. During the *cold period*, temperatures are well below 0°C. Most of the soil water is frozen and the entire ground may be considered as a solid medium. With the sun rising in late spring and the onset of snow melt, ground temperatures rise quickly, soil water content changes following the soil freezing characteristic curve. This *warming period* is terminated by the thawing front, a macroscopic phase boundary that separates partially frozen ground from the completely unfrozen soil during the *thawed period.* The propagation of the thawing front consumes a large proportion of the energy input from the positive net radiation. As the energy balance becomes negative in fall, the soil cools down to 0ºC starting to freeze from the surface. Upon further cooling the reverse phase transition sets in, from liquid to solid. It releases large quantities of latent heat and thereby opposes the cooling. This leads to a rapid equilibration of the temperature at 0 ºC in the entire thawed zone, indicated by the practically vertical isotherms. This is often referred to as the closing of the zero-curtain (Outcalt et al. 1996, Outcalt et al. 1990). As the active layer turns isothermal, large quantities of latent heat need to be removed to allow further cooling. This leads to the *isothermal plateau* where soil temperatures stay near 0 ºC for an extended time. It is eroded from above and from below, where temperatures in the air and in the underlying perennial ice are well below the freezing point. Eventually, the isothermal plateau disappears, giving way to the *cooling period* where regular conduction removes the remaining surplus heat from the active layer. It is transferred through the snow layer, which is a major modulating factor, to the atmosphere.

While thermal processes may be the same in wet soils of east Antarctica and Antarctic Peninsula, in the hyperarid soils of dry valleys the isothermal plateau due to release of latent heat does not exist. However, based on changes in air temperature and lack of incoming radiation, temperature gradient in soils reverses in October, which causes a quasi-isothermal soil during a short period of time (Hagedorn et al. 2007, Pringle et al. 2003) but this isothermal temperature is well below 0ºC.

Heat and water transfer processes

Permafrost-affected soil can potentially have five components (soil matrix, ice, water vapour, water, air). Conduction, heat transfer through gradients, is widely accepted to be the dominant mechanism of heat transfer in soils. Other nonconductive heat transfer mechanisms associated with the convection of water, either in the liquid or in the vapor phase, are possible with appropriate gradients (pressure, gravitational, density, vapor pressure, and chemical). A good summary of potential heat transfer processes in permafrost affected soils is provided by Kane et al. (2001). They summarized the importance of non conductive heat transport based on data sets from Alaska as the following: (i) infiltration and refreezing of water in frozen soil accelerates warming of soil; (ii) free convection of fluids is not an important heat transfer process; (iii) migration of water and vapour could be important but has not been quantified yet. The large value of the enthalpy of evaporation, which exceeds that of melting by a factor of 7.4, makes vapor an efficient means for the transport of thermal energy.

Heat and Water Transfer Processes in Permafrost-Affected Soils: Arctic

Most of the available English-language literature up to the end of 1990s is reported from Alaskan sites and is based on temperature and electric potential measurements and one dimensional thermal diffusion modeling. When the snow cover becomes isothermal and snow melt starts during the warming period, the soil rapidly warms at all depths, presumably because of the infiltration and refreezing of snow melt water and of migrating vapor into the frozen soil. Most studies agree that nonconductive heat transfer processes must be responsible for the rapid warming of the soil (Putkonen 1998, Hinkel & Outcalt 1994).

Conversion of latent heat is thought to be most important during the summer when moisture evaporates from the surface and the active layer thaws. Evaporation consumes 25–50% of the total incoming energy at a Siberian study site on Northern Taymyr peninsula (Boike et al. 1998) and 30–65% in northern Alaska (Kane et al. 1990). According to Outcalt et al. (1998), evaporative cooling at the surface of the active layer was responsible for the deviation between observed and modeled soil temperatures of the active layer and upper permafrost. Thawing of the active layer is another important sink for thermal energy. It consumes up to 40% of the total net radiation at the Siberian site (Boike et al. 1998). Generally, a high percentage of the total heat flux into the ground (between 70 and 100% is converted into latent heat (Rouse 1984, Boike et al. 1998). Conduction of heat, transport of thermal energy by convection of water, either in the liquid or vapor phase, has been discussed. Hinkel et al. (1993) identified infiltration of summer precipitation as an effective method to transfer heat to the base of the active layer, especially in drained, organic soils. Pore water convection during the summer thaw period, driven by the density inversion of water, has been proposed as the initiator for the formation of sorted circles (Krantz 1990, Ray et al. 1983), but Hallet (1990) argued that this process is unlikely and that it has not been observed in finer-grained sediments typically found in patterned ground. Putkonen (1998) calculated a Peclet number much smaller than 1 for this site and concluded that advection of heat due to water motion is negligible.

When net radiation decreases during the fall, the soil is cooled to a practically isothermal condition, the so-called zero curtain at 0°C. The large amount of latent heat which must be removed from the profile through an almost isothermal soil stabilizes soil temperatures at 0° for a prolonged time. Hinkel & Outcalt (1993, 1994) suggested that internal distillation driven by osmotic gradients transfer heat across this isothermal zone. In contrast, Romanovsky & Osterkamp (2000) accurately predicted soil temperatures for sites in Central and North Alaska during the freeze back using a conductive heat exchange model by including effects of unfrozen water and therefore excluding moisture migrating as a transport mechanism. Snow melt infiltration was the only non conductive heat transfer responsible for soil warming.

Putkonen (1998) estimated that the maximal possible vapor and latent heat flux under given soil thermal properties was two orders of magnitude smaller than conductive heat transport, hence being insignificant for western Spitsbergen. Through the application of electronic instrumentation measurement techniques, such as Time Domain Reflectometry for determination of soil moisture in frozen soils, highly precise and frequent temperature and moisture data have been obtained from various field sites. Roth & Boike (2001) found an excellent agreement between projected and measured temperatures for the cold period which demonstrates that during this time, heat transport on Spitsbergen (Bayelva site) can be described by effective conduction. Furthermore, they found that the production of latent heat and the associated migration of water vapor is an important agent in the thermal dynamics at this site for all four periods and that it is the dominating process in the isothermal plateau since heat conduction is practically negligible there. Unimpeded vapor migration is possible down to some 0.9 m, restricted by a massive ice rich layer. This contrasts findings of sites for which it was stipulated that upon closing of the zero curtain, internal distillation and water advection cease for the rest of the winter (Hinkel & Outcalt 1994, Romanovsky & Osterkamp 2000).

Differences in latent heat production using the model by Roth & Boike (2001) were presented by Overduin & Kane (2006). Their patterned ground site, covered by mud boils, is located in Northern Alaska (Galbraith Lake). One of the contrasting differences in winter heat transfer processes was the continuous latent heat production after freeze back until spring in the middle part of the profile It is hypothesized that water advection in the frozen soils was possible through the unfrozen water film attached to the soil particles. Subsequent freezing of water was the source of the latent heat production, resulting in ice formation and large heave rates in the center of the mudboil. While these two Arctic sites are very similar in terms of soil parent material, surface cover and topography, the soil water/ice content and climate conditions vary. Firstly, the site at Galbraith lake is water saturated, thus the pore spaces are filled with ice during winter. The soil at the Bayelva site is water saturated only in the lower part of the profile below about 0.7 m depth. Secondly, Galbraith, located in the Arctic climate is much colder (average January air temp. ~ -24°C) compared to the warmer, maritime influenced Svalbard climate (average January air temp. ~ -13°C). In addition, Galbraith has no or little snow cover, whereas the Bayelva site experiences a snow depth up to about 1 to 1.5 m, modulating the ground thermal regime and thus reducing the thermal gradient between air and soil temperature. It is postulated that the large temperature gradient at Galbraith Lake was also responsible for the large heave (up to 12 cm) which is about an order of magnitude higher compared to the Bayelva site (about 2 cm).

Heat and Water Transfer Processes in Permafrost-Affected Soils: Antarctic

Due to the very dry climate in dry valley soils of Antarctica, the majority of water is present as ice which occurs 0.1 to 0.5 m below surface in approximately 36% of soils in Antarctica (Bockheim 2002). Liquid water is limited to scarce infiltration after snow events (Friedman 1978, Gooseff et al. 2003), water films adsorbed to grain boundaries (Anderson & Morgenstern 1973), and to brines in ice cement (Dickinson & Rosen 2003). Only a small fraction of water is present as water vapor, which is the phase that is transported between atmosphere, soil pore space and ice. The main motivation to study vapor transport and thermal regime in Antarctic soils of Dry Valleys is to estimate the stability of subsurface ice in Antarctic soils, since this ice is important for geomorphologic development of patterned ground formation, e.g. contraction cracks (Sletten et al. 2003) and since Antarctic soils are the best terrestrial analogue to Martian soils (Schorghofer 2005).

Sugden et al., (1995) and van der Wateren & Hindmarsh (1995) did the first back on the envelope calculation of vapor transport to evaluate the stability of ground ice using steady state vapor diffusion modeling. Both yielded very different results; Sudgen et al. (1995) used geothermal gradients to determine soil and ice temperature and assumed vapor saturated atmosphere. He estimated sublimation rates of 10^{-4}mm a^{-1}; van der Wateren & Hindmarsh (1995) used meteorological data and assumed vapor unsaturated atmosphere and estimated a rate of 1 mm a^{-1}. This fast sublimation rate could be confirmed in a more detailed modeling approach by Hindmarsh et al. (1998).

McKay et al. (1998) calculated vapor transport using soil temperature, air temperature and relative humidity records collected at Linnaeus Terrace (1550 to 1700 m elevation). Parameters like tortuosity and porosity were determined on investigated soil material. Thermal conductivity was modeled from temperature profiles and yielded 0.6±0.1 $Wm^{-1}K^{-1}$ for dry soil and 2.5±0.5 $Wm^{-1}K^{-1}$ for ice cement which are close to values determined by Putkonen et al. (2003). Based on Fick's diffusion they found that ice is lost at rates at ~0.2 mm a^{-1}, highlighting the very dry atmospheric conditions in the dry valleys. Based on a comparison between frost point of atmosphere and ice cemented soil they suggest that increase of 40% moisture to all humidity values could stabilize ground ice.

Schorghofer (2005) modeled ice sublimation in Beacon Valley (~1500 m asl.) constrained by climate and soil temperature data and found rates comparable to those of McKay et al. (1998). He found that advection caused by changes in surface pressure has negligible effect on sublimation. By exploring possible scenarios to stabilize subsurface ice, he suggests a decrease in annual air temperature by 5°C or increase in relative humidity of 50%, a rather unrealistic value.

Hagedorn et al. (2007) modeled vapor transport based on multi-year climate and soil temperature record in Victoria Valley which is about 400 m asl. and where ice occurs 0.2 to 0.4 m below surface. Vapor transport is calculated using Fick's diffusion incorporating a reaction term for ice precipitation and allowing vapor diffusion into the ice cement. Initially a linear vapor density gradient between ice cement and atmosphere was assumed. Using this approach they yielded sublimation rates close to those observed by McKay et al (1998). However, part of the vapor is transported from ice surface into the ice cement and most of it precipitates in upper ice cement slowly closing the pore space. Transient ice will form in dry soil during winter but completely disappears during beginning of summer. Snow cover will reduce vapor loss to atmosphere but to completely offset sublimation rates it would need to remain for several months. As suggested by McKay et al. (1998) and Schorghofer (2005) they also found that decreasing air temperature or increasing moisture will reduce sublimation but those scenarios do not seem to be very realistic under current climatic conditions. The most likely process which stabilizes ground ice in Antarctica seems to be occasional recharge by snow melt water.

Studies modeling thermal conductivity and heat fluxes based on field measurements are rare in Antarctic soils of the Dry Valleys. Putkonen et al. (2003) measured the sensible heat flux based on the difference between measured net radiation and ground heat flux in Beacon Valley using in situ measurements of soil thermal properties and 1-dimensional thermal conductivity model (Putkonen 1998). At this site, soils consist of ~20 cm dry sublimation till underline by massive ice. They found that mean annual ground heat flux is close to zero indicating long term thermal equilibrium. The annual mean net radiation is positive (24 Wm^{-2}) suggesting a net advection of sensible heat into atmosphere from this area. Measured values for thermal conductivity in dry debris are ~2 times smaller (0.2 $Wm^{-1}K^{-1}$) as values found from modeling (see above 0.4 $Wm^{-1}K^{-1}$). The difference between modeled and measured values may well be in the range of the instrument uncertainty.

Pringle et al. (2003) used temperature data collected on three sites from Table Mountain with different lithology and ice contents to calculate apparent thermal diffusivity (ADT). They found strong dependence of ADT with abundance of ice and determined an ice-fraction dependency of heat capacity of 1.7 to 1.8 $MJm^{-3}\,°C^{-1}$ causing a range of conductivity of ice rich soils between 2.5 to 4.1 $Wm^{-1}\,°C^{-1}$. Pringle et al. (2003) treated the heat transfer as purely conductive due to the very dry conditions and absence of liquid water. The lower value of heat conductivity is in good agreement with values from Putkonen et al. (2003) found for the massive ice. The generally low thermal conductivity found in Antarctic soils is an order of magnitude lower as in Arctic soils (6-26 times lower) reflecting the very dry conditions.

Summary and Future Potentials

Arctic versus Antarctic heat and water transfer processes

Other than during freeze back and snow melt infiltration, heat is largely transferred through conduction in soils at both regions. In non saturated Arctic soil, vapor migration occurs during all thermal periods while water advection occurs in frozen saturated soils. In dry Antarctic soils, vapor diffusion is a main process of water transport. The total amounts of water transferred are generally rather small; however, over longer terms could be significant, for example for the formation of patterned ground features (for example circles, ice wedges).

Snow melt is an important event for recharge of ground ice in Antarctica and a significant latent heat input for Arctic soils.

Factors affecting the heat transfer processes

The main factors determining the heat transfer are (i) phase composition of soil (specifically available pore space) which enables vapor diffusion and/or water advection (ii) the temperature gradient between atmosphere and soil which is largely affected by the snow cover.

What should happen next?

We need further detailed case studies (experimental and modeling) to face the challenge of highly nonlinear and strongly coupled processes which lead to a complex phenomenology. We still lack accurate methods for measuring relevant state variables of the system, for example the phase density of ice or water vapor, and even more so by the lack of sufficiently accurate instruments for measuring fluxes of thermal energy and of water. The processes of water and heat dynamics in permafrost soils, i.e. their potential relative weight should be assed quantitatively which is a topic of a future publication

Acknowledgments

We would like to thank Pier Paul Overduin for discussion about this topic.

References

In the following, references are organized geographically (Arctic versus Antarctic). Not all literature from Alaska is cited in the text since many references are repetitive.

Arctic

Boike, J., Roth, K. & Overduin, P.P. 1998. Thermal and hydrologic dynamics of the active layer at a continuous permafrost site (Taymyr Peninsula, Siberia). *Water Resources Research* 34(3): 355-363.

Chen, G. & Chamberlain, E.J. 1988. Observations of moisture migration in frozen soils during thawing. *Proceedings of the Fifth International Conference on Permafrost, V. 1, Trondheim, Norway, 2–5 August 1988:* 308-312.

Hallet, B. 1990. Self-organization in freezing soils: From microscopic ice lenses to patterned ground, *Can. J. Phys*. 68: 842-852.

Hinkel, K.M., Outcalt, S.I. & Nelson, F.E. 1990. Temperature variation and apparent diffusivity in the refreezing active layer, Toolik Lake, Alaska. *Permafrost and Periglacial Processes* 1: 265-274.

Hinkel, K.M. & Outcalt, S.I. 1993. Detection of nonconductive heat transport in soils using spectral analysis. *Water Resour. Res*. 29: 1017-1023.

Hinkel, K.M., Outcalt, S.I. & Nelson, F.E. 1993. Near-surface summer heat-transfer regimes at adjacent permafrost and non-permafrost sites in Central Alaska. *Proceedings of the Sixth International Conference on Permafrost, Beijing, China, 5–9 July 1993:* 261-266.

Hinkel, K.M. & Outcalt, S.I. 1994. Identification of heat transfer processes during soil cooling, freezing, and thawing in Central Alaska. *Permafrost and Periglacial Processes* 5: 217-235.

Hinkel, K.M. & Outcalt, S.I. 1995. Detection of heat-mass transfer regime transitions in the active layer using fractal geometric parameters. *Cold Regions Science Technology* 23: 293-304.

Hinkel, K.M. 1997. Estimating seasonal values of thermal diffusivity in thawed and frozen soils using temperature time series. *Cold Regions Science Technology* 26: 1-15.

Hinzman, L.D., Kane, D.L., Benson, C.S. & Everett, K.R. 1991. Hydrologic and thermal properties of the active layer in the Alaskan Arctic. *Cold Regions Science and Technology* 19: 95-110.

Kane, D.L., Gieck, R.E. & Hinzman, L.D. 1990. Evapotranspiration from a small Alaskan arctic watershed. *Nordic Hydrol*. 21: 253-272.

Kane, D.L., Hinzman, L.D. & Zarling, J.P. 1991. Thermal response of the active layer to climatic warming in a permafrost environment. *Cold Regions Science and Technology* 19: 111-122.

Kane, D.L., Hinkel, K.M., Goering, D. J., Hinzman, L.D. & Outcalt, S.I. 2001. Non-conductive heat transfer associated with frozen soils. *Global and Planetary Change* 29: 275-292.

Krantz, W.B. 1990. Self-organization manifest as patterned ground in recurrently frozen soils. *Earth Sci. Rev*. 29: 117-130.

Nelson, F.E., Outcalt, S.I., Goodwin, C.W. & Hinkel, K.M. 1985. Diurnal thermal regime in a peat-covered palsa, Toolik Lake, Alaska: *Arctic* 38(4).

Osterkamp, T.E. & Romanovsky, V.E. 1999. Evidence for warming and thawing of discontinuous permafrost in Alaska. *Permafrost Periglacial Processes* 10: 17-37.

Outcalt, S.I. & Hinkel, K.M. 1989. Night-frost modulation of near-surface soil-water ion concentration and thermal fields. *Physical Geography* 10: 336-348.

Outcalt, S.I., Nelson, F.E. & Hinkel, K.M. 1990. The zero-curtain effect: Heat and mass transfer across an isothermal region in freezing soil. *Water Resources Research* 26(7): 1509-1516.

Outcalt, S.I. & Hinkel, K.M. 1996. Thermally driven sorption, desorption, and moisture migration in the active layer in Central Alaska. *Physical Geography* 17: 77-90.

Outcalt, S.I., Hinkel, K.M., Nelson, F.E. & Miller, L.L. 1998. Estimating the magnitude of coupled-flow effects in the active layer and upper permafrost, Barrow, Alaska U.S.A. *Proceedings of the Seventh International Conference on Permafrost*: 869-873.

Overduin, P.P. & Kane, D.L. 2006. Frost boils and soil ice content: Field observations. *Permafrost and Periglacial Processes* 17: 291-307.

Parmuzina, O.Y. 1980. Cryogenic texture and some characteristics of ice formation in the active layer (in Russian). In: A.I. Popov (ed.), *Problems of Cryolithology*, V. 7. Moscow: Moscow Univ. Press, 1978, 131-152 (English translation *Polar Geogr. Geol*.: 131-152).

Putkonen, J. 1998. Soil thermal properties and heat transfer processes near Ny-Alesund, Northwest Spitsbergen, Svalbard. *Polar Research* 17(2): 165-179.

Ray, R.J., Krantz, W.B., Caine, T.N. & Gunn, R.D. 1983. A model for sorted patterned-ground regularity. *J. Glaciol*. 29: 317-337.

Romanovsky, V.E. & Osterkamp, T.E. 1995. Interannual variations of the thermal regime of the active layer and near-surface permafrost in northern Alaska. *Permafrost and Periglacial Processes* 6: 313-335.

Romanovsky, V.E. & Osterkamp, T.E. 2000. Effects of unfrozen water on heat and mass transport processes in the active layer and permafrost. *Permafrost and Periglacial Processes* 11: 219-239.

Roth, K. & Boike, J. 2001. Quantifying the thermal dynamics of a permafrost site near Ny-Ålesund, Svalbard. *Water Resources Research* 37(12): 2901-2914.

Rouse, W.R. 1984. Microclimate of arctic tree line 2. Soil microclimate of tundra and forest. *Water Resour. Res*. 20: 67-73.

Santeford, H.S. 1978. Snow soil interaction in interior Alaska. In: S.C. Colbeck & M. Ray (eds.), *Modeling of Snow Cover Runoff.* Cold Reg. Res. and Eng. Lab., Hanover, New Hampshire, 311-318.

Solomatin, V.I. & Xu, X. 1994. Water migration and ice segregation in the transition zone between thawed and frozen soil, *Permafrost Periglacial Processes* 5: 185-190.

Woo, M.K. 1982. Upward flux of vapor from frozen materials in the High Arctic. *Cold Regions Science Technology* 5: 269-274.

Yershov, E.D. 1998. *General Geocryology.* New York, NY: Cambridge Univ. Press.

Antarctic

Anderson, D.W. & Morgenstern, N.R. 1973. Physics, chemistry, and mechanics of frozen ground: A review. *Proceedings of the Second International Conference on Permafrost, Yakutsk, USSR*. Washington, DC: National Academy of Sciences Press.

Beyer, L., Bockheim, J.G., Campbell, I.B. & Claridge, G.G.C. 1999. Review: Genesis, properties and sensitivity of Antarctic Gelisols. *Antarctic Science* 11(4): 387-398.

Bockheim, J.G. 2002. Landform and soil development in the McMurdo Dry Valleys, Antarctica: A regional synthesis. *Arctic Antarctic and Alpine Research* 34: 308-317.

Dickinson, W.W. & Rosen, M.R. 2003. Antarctic permafrost: An analogue for water and diagenetic minerals on Mars. *Geology* 31: 199-202.

Friedman, E.I. 1978. Melting snow in the dry valleys is a source of water for endolithic microorganisms. *Antarctic Journal of the United States* 13: 162-163.

Gooseff, M.N., Barrett, J.E., Doran, P.T., Fountain, A.G., Lyons, W.B., Parsons, A.N., Porazinska, D.L., Virginia, R.A. & Wall, D.H. 2003. Snow-patch influence on soil biogeochemical processes and invertebrate distribution in the McMurdo Dry Valleys, Antarctica. *Arct. Antarct. Alp. Res*. 35: 91- 99.

Hagedorn, B., Sletten, R.S. & Hallet, B. 2007. Sublimation and ice condensation in hyperarid soils: Modeling results using field data from Victoria Valley, Antarctica. *Journal of Geophysical Research* 112.

McKay, C.P., Mellon, M.T. & Friedman, E.I. 1998. Soil temperature and stability of ice-cemented ground in McMurdo Dry Valleys, Antarctica. *Antarctic Sciences* 10: 31-38.

Pringle, D.J., Dickinson, W.W., Trodahl, H.J. & Pyne, A.R. 2003. Depth and seasonal variations in the thermal properties of Antarctic Dry Valley permafrost from temperature time series analysis. *J. Geophys. Res*. 108(B10): doi:10.1029/2002JB002364.

Putkonen, J.K., Sletten, R.S. & Hallet, B. 2003. Atmosphere/ice energy exchange through thin debris cover in Beacon Valley, Antarctica. *Proceedings of the Eighth International Conference on Permafrost, Zürich, Switzerland.*

Schorghofer, N. 2005. A physical mechanism for long-term survival of ground ice in Beacon Valley, Antarctica. *Geophys. Res. Letters* 32: L19503, doi:10.1029/2005GL023881.

Sletten, S.R., Hallet, B. & Fletcher, R.C. 2003. Resurfacing time of terrestrial surfaces by the formation and maturation of polygonal patterned ground. *Geophys. Res*. 108(E4), 8044: doi:0.1029/2002JE001914.

Sugden, D.E., Marchant, D.R., Potter, N., Souchez, R.A., Denton, G.H., Swisher, C.C. III. & Tison, J.-L. 1995. Preservation of Miocene glacier ice in East Antarctica. *Nature* 376: 412-414.

van der Wateren, D. & Hindmarsh, R. 1995. Stabilists strike again. *Nature* 376: 389-391.

Estimation of Hydraulic Properties in Permafrost-Affected Soils Using a Two-Directional Freeze-Thaw Algorithm

W. Robert Bolton
Alfred Wegener Institute for Polar and Marine Research
Julia Boike
Alfred Wegener Institute for Polar and Marine Research
Pier Paul Overduin
Alfred Wegener Institute for Polar and Marine Research

Abstract

In this study, a two-directional freeze-thaw (TDFT) algorithm is used to estimate the hydraulic conductivity and storage capacity of permafrost-affected soils. The physically based TDFT algorithm is based upon the Stefan equation. The algorithm is driven by both the surface temperature and temperature at a specified depth and uses physical properties of the soil (bulk density, porosity, soil moisture, organic and mineral fraction, and freezing temperature of water) as input variables. The TDFT is tested in a wet valley bottom and along a relatively dry hill slope in the Imnavait Creek Watershed, Alaska. Results indicate that the timing of thaw/freezeback periods, the maximum thaw depth, and latent heat effects are accurately simulated. Using the TDFT algorithm to derive hydraulic variables is an improvement from the previous methods used to represent the active layer in hydrological modeling studies.

Keywords: active layer; hydraulic conductivity; hydrologic modeling; permafrost; porosity.

Introduction

In (sub-) arctic environments, most biologic, geomorphic, hydrologic, and ecologic processes take place within the active layer —the thin soil layer above the permafrost that seasonally freezes and thaws (Kane et al. 1991, Hinzman et al. 1998, Woo 2000). The depth of the active layer, as well as the rate of seasonal freezing and thawing, is dependent upon a number of factors including soil properties (thermal conductivity, bulk density, moisture content, vegetation type/thickness), meteorologic conditions (air and surface temperature, presence of snow cover), and disturbance (either anthropogenic or natural disturbance such as wildfire) (Woo 1986). As each of these factors are spatially and temporally variable, the position of the freeze-thaw interface is also spatially and temporally variable (Woo & Steer 1983).

Hydrologically speaking, the (sub-) arctic environment is unique in that the thermal and hydrologic regimes of the soil (permafrost versus non-permafrost) can vary greatly over short horizontal spatial scales, with depth, and over time. It is well documented that the hydraulic conductivity of ice-rich permafrost soils can be several orders of magnitude lower than their unfrozen counterparts (e.g., Burt & Williams 1976, Kane & Stein 1983). Furthermore, ice-rich conditions at the freeze-thaw interface significantly reduce the permeability of the soil, effectively limiting the soil water capacity of the soil (Dingman 1975, Woo 1990).

However, the point and hill slope scale understanding of permafrost soils, specifically the effect of the freezing and thawing of the active layer on hydrologic proceses, have not been adequately or systematically incorporated into meso-scale hydrologic models (Vörösmarty et al. 1993). Representation of the active layer in previous modeling studies includes switching soil properties for the winter and summer periods (Sand & Kane 1986) and use of a simple square root of time function to estimate the active layer depth (Zhang et al. 1998, Schramm et al. 2007). Thermal models are absent in most hydrologic models because of computational time requirements and complexities in model coupling.

Fox (1992) introduced a physically-based one-directional freeze-thaw (ODFT) algorithm for estimating the position of the freeze-thaw interface. The ODFT is driven by surface temperature. Woo et al. (2004) modified the ODFT by inverting the equations and driving the algorithm in two-directions by using temperatures at the surface and at a specified depth in the soil column. This two-directional freeze-thaw (TDFT) algorithm improves the representation of the freeze-thaw interface during the freezeback period.

The objective of this paper is to present a method for estimating hydraulic conductivity and effective porosity (proxy for soil storage capacity) using the TDFT algorithm.

Methods

Overview of the TDFT algorithm

The main difference between frozen and thawed soils is the difference in hydraulic conductivity and storage capacity, both a function of amount of pore ice in the soils (Woo 1986). In our conceptualization of the arctic hydrologic regime, frozen soils are represented with a very low hydraulic conductivity, while thawed soils within the active layer are represented with a larger hydraulic conductivity. Effective porosity (P_{eff}) is used as a proxy for storage capacity. In frozen soils, the presence of pore ice reduces the effective porosity of the soil.

The freeze-thaw interface in the active layer is determined using the TDFT algorithm. The physically-based TDFT algorithm is based upon the Stefan's equation of heat conduction (Jumikis 1977). One of the assumptions of the Stefan equation is that sensible heat effects are negligible. This assumption typically holds in soils with high moisture contents (Lunardini 1981). The algorithm requires inputs for each soil layer: specified depth, bulk density, porosity, fraction of organic and mineral soils, soil moisture content, the threshold for freezing the soil moisture, and minimum unfrozen water content in frozen soils. For each soil layer, the thermal conductivity and the energy required to freeze or thaw that soil layer is calculated. The algorithm is driven by the surface temperature and temperature at the bottom of the soil column. At each time step, the energy available to freeze/thaw the soil is determined using a simple 'degree-day' formulation. The amount of energy available is compared to the amount of energy required to freeze/thaw a soil layer. The total amount of freezing or thawing of the soil layers is determined by the total amount of energy available from the surface and at the bottom of the soil column. The procedures for determining the thermal conductivity, the energy available for freezing/thawing the soils, and determination of the total freezing and thawing of the soil layers are described in detail in Woo et al. (2004). In our formulation, the TDFT is slightly modified such that soil thawing from the bottom of the soil column is not allowed.

Estimation of hydraulic properties

The next steps are to estimate the freeze-thaw interface, the hydraulic conductivity, and the effective porosity. After each time step, the total thawed thickness and frozen thickness (D_t and D_f, respectively) of each soil layer are determined. The position of the freeze-thaw interface is estimated for each soil layer, from the surface downward, by evaluating the thermal condition of the neighboring soil layers. For example, if soil layer X_{+1} is completely frozen ($D_t = 0.0$), while soil layer X_{-1} is completely thawed (D_t = soil layer thickness), then we assume that the active layer is developing and the position of the freeze-thaw boundary is located at D_t depth from the top of the soil layer, X. By evaluating each soil layer after each time step, multiple freeze-thaw interfaces within the soil column are possible.

Once the D_t and D_f are determined for each soil layer, the hydraulic conductivity for each soil layer is estimated using a simple weighting function. For each soil layer, the frozen and thawed hydraulic conductivity are specified. If the entire soil layer is either frozen or thawed, the appropriate hydraulic conductivity is assigned to that soil layer. If the freeze-thaw interface is located within a soil layer, the horizontal (K_H) and vertical hydraulic (K_V) conductivities are determined using simple weighting functions:

$$K_H = \frac{K_f D_f + K_t D_t}{D} \tag{1}$$

$$K_V = \frac{D}{\left[\dfrac{D_f}{K_f} + \dfrac{D_t}{K_t}\right]} \tag{2}$$

where $K_{f,d}$ are the frozen and thawed hydraulic conductivities, and D is the total thickness of the soil layer.

The effective porosity for each soil layer is simply estimated from the fractional components of the soil layer:

$$P_{eff} = 1.0 - F_m - F_o - F_{ice} \tag{3}$$

where $F_{m,o,ice}$ are the fractional components of mineral, organic, and ice.

Results

Evaluation of the TDFT

The TDFT algorithm is tested in the Imnavait Creek Watershed, Alaska (68°30′N, 149°15′W). Two sites, one in a valley bottom and one along a hill slope, are selected for testing. Compared with the hill slope site, the valley bottom site has a thick surface organic layer (0.3 m versus 0.2 m) and has a high soil moisture content. Table 1 shows the soil properties used to test the TDFT. The soil moisture content of each soil layer is the linear interpolation of field measurements to the center of each soil layer.

The surface temperature sensors used in the valley and hill slope sites are located at 2 and 7 cm below the land surface, respectively. Ground temperature measurements, located at 98 and 69 cm below the ground surface, were used for valley bottom and hill slope sites. In our simulations, the ground temperature can only be used in the soil freezing process (soils are not allowed to thaw from depth).

Initial simulations resulted in an underestimation of the maximum thaw depths at each site, probably as a result of underestimation of the amplitude of fluctuation of the ground surface temperature. The timing of the beginning of thaw/freezeback process was also slightly offset from measured field data. To better estimate ground surface temperatures, the near-surface soil temperatures were estimated via extrapolation of amplitude to the surface (Fig. 1). This resulted in an amplification of annual surface temperature fluctuation by 5% at the valley bottom and by 38/27% for temperatures above/below 0°C at the hill slope site. We explain the difference in amplitude by differences in near-surface moisture availability. Compared to the dry hill slope site, the wet valley bottom site has a high thermal diffusivity in the near surface soils. The combination of the high thermal diffusivity as well as the near proximity to the ground surface result in a much smaller surface temperature adjustment at the valley bottom site. Figure 2 displays the simulated freeze-thaw interface compared with measured soil temperatures and soil moisture content at each site.

Table 1: Soil properties of the valley bottom and hill slope sites.

Layer	Soil Depth (cm)	Valley Bottom Site				Hill Slope Site			
		Bulk Density (kg/m^3)	Porosity (%)	Organic / Mineral Fractions	SMC / SMC min	Bulk Density (kg/m^3)	Porosity (%)	Organic / Mineral Fractions	SMC / SMC min
1	10	150	80	0.20 / 0.0	0.45 / 0.05	150	80	0.20 / 0.0	0.40 / 0.06
2	10	260	63	0.37 / 0.0	0.60 / 0.15	560	63	0.37 / 0.0	0.40/ 0.04
3	10	855	55	0.25 / 0.2	0.55 / 0.14	1530	40	0.0 / 0.6	0.38 / 0.10
4	10	1530	48	0.0 / 0.48	0.48 / 0.14	1530	40	0.0 / 0.6	0.40 / 0.12
5	10	1530	40	0.0 / 0.6	0.40 / 0.06	1530	40	0.0 / 0.6	0.40 / 0.12
6	10	1530	40	0.0 / 0.6	0.40 / 0.06	1530	40	0.0 / 0.6	0.40 / 0.12
7	10	1530	40	0.0 / 0.6	0.40 / 0.05	1530	40	0.0 / 0.6	0.40 / 0.12
8	15	1530	40	0.0 / 0.6	0.40 / 0.05	1530	40	0.0 / 0.6	0.40 / 0.12

SMC / SMC min: Volumetric soil moisture content / Volumetric unfrozen water content of frozen soil.

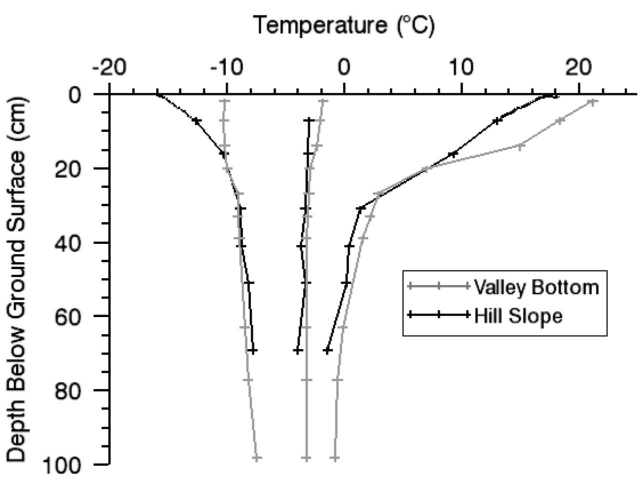

Figure 1. Trumpet curves showing the minimum, maximum, and average temperatures at the valley bottom site (light line) and hill slope site (dark line) for 2003. The "+" indicates location of measurements.

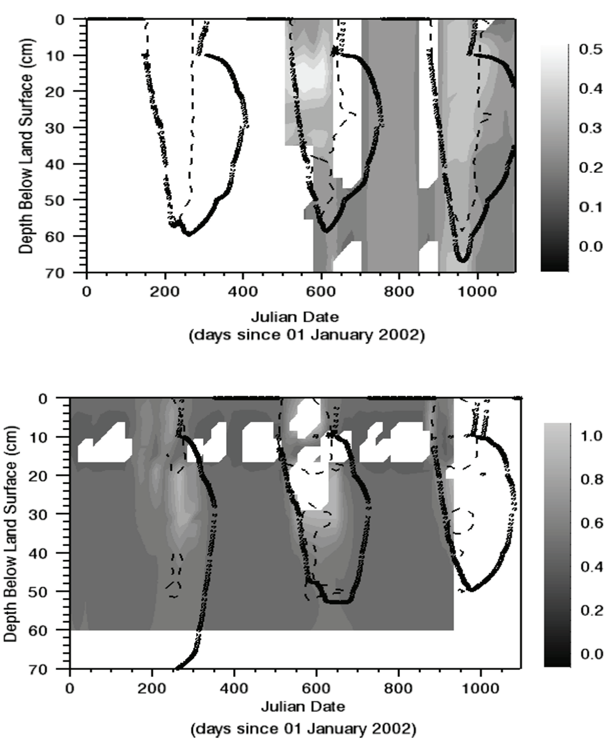

Figure 2. Comparison of the simulated freeze-thaw interface (dark dots) in the valley bottom (top panel) and hill slope (bottom panel) sites with the -0.1°C isotherm (dark dashes) and unfrozen soil moisture content (background). Color bar indicates volumetric soil moisture content. Solid white regions indicate missing data.

For these simulations and comparisons, daily temperature and soil moisture data measured at 12:00 are used. Results indicate that for most years, the TDFT algorithm is able to simulate the beginning of thaw, the maximum thaw depth, and freezeback period. The latent heat effect during the freezeback period is also represented. Estimated porosities derived from these simulations are shown in Figure 3.

Discussion and Conclusions

The seasonal freezing and thawing of the active layer and the associated changes in hydraulic properties are defining features of arctic hydrologic systems. Despite the known importance of the active layer in hydrologic systems, it has been poorly represented in meso-scale hydrologic models. The TDFT algorithm provides a foundation for estimating the freezing and thawing of the soils, hydraulic conductivity, and storage capacity of the soils.

The TDFT, based upon the Stefan equation, assumes that sensible heat effects are negligible. Care must be taken when applying the TDFT in drier areas, where sensible heat fluxes may be an important component of the energy balance. A basic understanding of the physical system being modeled is critical before applying the TDFT.

Using the TDFT to estimate hydraulic properties is an improvement over previously used methods in that 1) changes in the thermal and hydrologic regimes are continuously and adequately captured over time; 2) the ability to simulate the freezeback period allows for longer (year-to-year) simulations, whereas the other methods such as using the

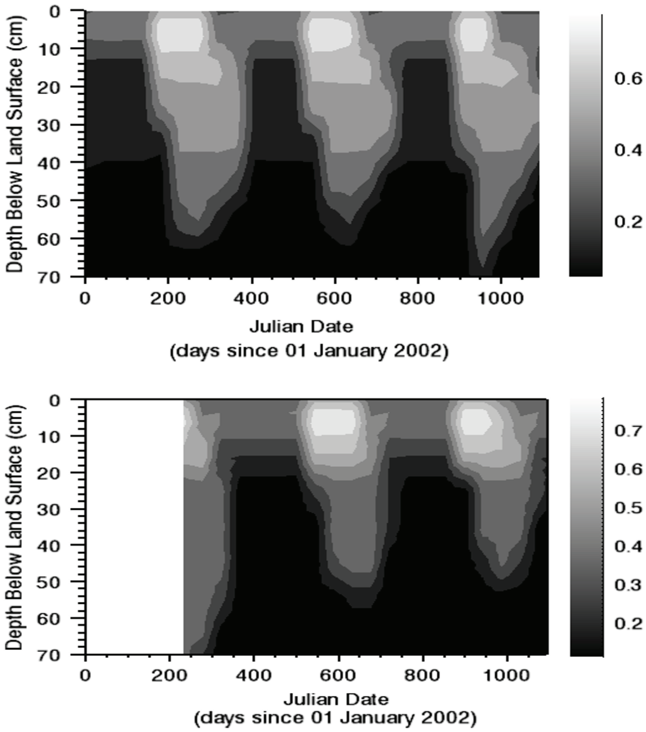

Figure 3. Simulated soil porosity at the valley site (top panel) and hill slope (bottom panel). Solid white regions indicate missing data.

square root of time function is only able to simulate the thawing process; 3) the TDFT is physically based, requiring no prior calibration; and 4) the TDFT is computationally cheap.

The depth and rate of thawing/freezing of the active layer are both spatially and temporally variable. As a result the hydraulic properties of the soils are spatially (x-, y-, and z-directions) and temporally (both short and long term) variable. Accurate freeze-thaw boundary simulations using the TDFT algorithm are highly dependent upon accurate surface temperature data. In order to take full advantage of the TDFT derived variables in (spatially-distributed) meso-scale models, a method needs to be developed to obtain accurate spatial and temporal surface temperatures from within the modeling area.

Acknowledgments

We gratefully acknowledge financial support by a Heimholtz Young Investigator Grant (VH-NG 203) awarded to Julia Boike. We also appreciate the helpful suggestions of the reviewers.

References

Burt, T. & Williams, P. 1976. Hydraulic conductivity in frozen soils. *Earth Surficial Processes* 1(4): 349-360.

Dingman, S.L. 1975. *Hydrologic effects of frozen ground.* Special Report 218. U.S. Army Cold Regions Research and Engineering Laboratory.

Fox, J.D. 1992. Incorporating freeze-thaw calculations into a water balance model. *Water Resources Research* 28: 2229-2244.

Hinzman, L., Goering, D. & Kane, D. 1998. A distributed thermal model for calculating soil temperature profiles and depth of thaw in permafrost regions. *Journal of Geophysical Research* 103(D22): 28,975-28,991.

Jumikus, A.R. 1977. *Thermal Geotechnics*. Rutgers University Press, 375 pp.

Lunardini, V. 1981. *Heat transfer in cold climates.* New York: Van Nostrand Reinhold, 731 pp.

Kane, D., Hinzman, L. & Zarling, J. 1991. Thermal response of the active layer to climatic warming in a permafrost environment. *Cold Regions Science and Technology* 19(2): 111-122.

Kane, D.L. & Stein, J. 1983. Water movement into seasonally frozen soils. *Water Resources Research* 19(6): 1547-1557.

Sand, K. & Kane, D.L. 1986. Effects of seasonally frozen ground in snowmelt modeling. In: D.L. Kane (ed.), *Proceedings of the Cold Regions Hydrology Symposium.* American Water Resources Association, 321-327.

Schramm, I., Boike, J., Bolton, W.R. & Hinzman, L. 2007. Application of TopoFlow, a spatially distributed hydrologic model to the Imnavait Creek Watershed, Alaska. *Journal of Geophysical Research* 112:G04S46, doi:10.1029/2006JG000326.

Vörösmarty, C., Gutowski, W., Person, M., Chen, T.-C. & Case, D. 1993. Linked atmosphere-hydrology models at the macroscale. In: W. Wilkinson (ed.), *Macroscale Modeling of the Hydrosphere.* No. 214 in International Association of Hydrological Sciences, 3-27.

Woo, M.-K. 1986. Permafrost hydrology in North America. *Atmosphere-Ocean* 24(3): 201-234.

Woo, M.-K. 1990. Permafrost hydrology. In: T. Prowse, C. Ommanney, & M.-K. Woo (eds.), *Northern Hydrology, Canadian Perspectives, Proceedings of the Northern Hydrology Symposium.* Canadian National Hydrology Research Institute Science Report 1: 63-76.

Woo, M.-K. 2000. Permafrost and Hydrology. In: N. Nuttal & T.V. Callaghan (eds.),, *The Arctic: Environment, People, Policy.* Harwood Academic Publications, 57-96.

Woo, M.-K., Arain, M.A., Mollinga, M. & Yi, S. 2004. A two-directional freeze and thaw algorithm for hydrologic and land surface modeling. *Geophysical Research Letters*: L12501, doi:10.1029/ 2004GL019475.

Woo, M.-K. & Steer, P. 1983. Slope hydrology as influenced by thawing of the active layer. *Canadian Journal of Earth Science* 20: 978-986.

Zhang, Z., Kane, D. & Hinzman, L. 2000. Development and application of a spatially-distributed Arctic hydrological and thermal process model (ARHYTHM), *Hydrological Processes* 14: 1017-1044.

Engineering Solutions for Foundations and Anchors in Mountain Permafrost

Ch. Bommer
WSL, Swiss Federal Institute for Snow and Avalanche Research SLF, 7260 Davos Dorf, Switzerland
H.R. Keusen
Geotest AG, 3052 Zollikofen, Switzerland
M. Phillips
WSL, Swiss Federal Institute for Snow and Avalanche Research SLF, 7260 Davos Dorf, Switzerland

Abstract

Various technical solutions for foundations and anchors of infrastructures in permanently frozen ground are examined. Focus is placed on different categories of infrastructures and their sensitivity to changing subsurface conditions, primarily caused by modifications in the ice and water contents of the permafrost. The requirements for infrastructures with high safety standards such as cableway stations and pylons are determined by factors including the mass of the building, its serviceability, dynamic forces engendered by the cable mechanism, and the bearing capacity of the ground. In contrast, the conditions for a structure such as an alpine hut are mainly given by the relatively low mass of the building, snow loads, wind effects, and the bearing capacity of the ground. It is crucial that design considerations involve an integral approach and take into account the influences of global warming and the more intensive time and cost factors required to complete a project.

Keywords: anchor; bearing capacity; foundation; mountain permafrost; serviceability.

Introduction

Changing subsurface conditions represent the main problem for infrastructures in mountain permafrost. The reasons for changing subsurface conditions can be global warming, construction work, an existing infrastructure, or a combination of these, and can lead to permafrost ice warming, melting, and finally to complete degradation. After the soil and rock characteristics, ice content and temperature strongly affect the subsurface conditions and play a vital role in controlling the deformation behaviour and the bearing capacity of infrastructures.

On the other hand, the serviceability determines the maximal allowable vertical and horizontal displacements of an infrastructure. The serviceability requirements depend on building categories (Table 1). Cableway stations and pylons or pipelines are highly sensitive to differential displacements, resulting in a higher urgency for repairs after displacements, whereas communication structures (e.g., telecommunication antennae) or alpine huts and mountain restaurants react less delicately. Therefore, the building category controls the differential deformation sensitivity or the serviceability respectively.

Combining the controlling subsurface conditions with the serviceability of an infrastructure is an essential step in the development of an adequate foundation concept. In addition, the mass of the building, snow loads, dynamic loads and the influences of present and future global warming must be considered. Depending on the subsurface and load conditions, anchor reinforcements for the foundation may be necessary. In this paper, we examine engineering solutions for foundations and anchors for various building categories in mountain permafrost.

Design Considerations

Time and cost intensity

The time and cost intensity required for the construction of infrastructure in mountain permafrost is higher in comparison with infrastructure located in permafrost-free terrain. The site investigation in particular requires a longer period of time. If the first site study indicates a possible permafrost occurrence, the preliminary study should take in account further *in situ* investigations to determine the characteristic geotechnical parameters. In addition to the typical examinations regarding the foundations, measurements of temperature and deformation should be carried out for at least one year prior to construction. With the resulting data, a first evaluation of the ice content, ground temperature, active layer thickness and deformation rate can be carried out. Sustainable design considerations can only be ensured with this crucial information.

The following additional factors can also have a time and cost-increasing effect: the obtention of approval to build outside an official construction zone; the environmental impact assessment of the projected structure; climatic conditions such as snow, air temperature or altitude; the logistics like accessibility and transportation; and the short time frame available for construction at high altitudes. All these factors account for a significantly higher time and cost intensity for infrastructures in mountain permafrost.

Effects on the ground and structure

For the design of infrastructure in mountain permafrost it is important to consider the effects on the ground. The main effects are due to the dead and live loads induced by an infrastructure. Other effects include heat input/thermal disturbance from building activity or the long-term thermal and mechanical influences of the infrastructure itself and those caused by global warming. Excavation activities also affect the ground. A warming of the excavated slope can cause instabilities and rockfall. In summary, there are mechanical influences (load), which change the stress condition, and there are thermal influences (heat exchange), which can change the geotechnical parameters of the ground. An appropriate design must take into account the geotechnical and thermal effects with respect to the bearing capacity, sliding and toppling (ultimate limit state [ULS]). The definition of ULS is satisfied if all design loads are below the ground resistance calculated for the section under consideration (Swisscode SN 505267).

The effects of modifications on the structure itself are as important as the effects on the ground. The allowable effects with respect to the deformation and creep rates are dependent on the serviceability of the infrastructure, which is usually defined in the service criteria agreements (Swisscode SN 505267) as an allowed inclination angle of a structure due to differential settlements. This inclination angle consists of a ratio of the differential settlement to the size (length) of the structure. In Table 1 the sensitivity limits for serviceability are given for different building categories. Not incorporated in Table 1 is the time factor, such as how fast a displacement takes place. Other effects on the structure, such as natural hazards in the vicinity or geotechnical and technical difficulties, are determined by the risk analysis. The aim of the latter is to identify all kinds of risks that could influence both the construction and use of an infrastructure. A consideration of all these effects on the structure is necessary for the design with respect to the serviceability (serviceability limit state [SLS]).

The ultimate and serviceability limit states result in two allowable values for the foundation pressure or anchor tension. Depending on the smaller value, the size and shape of a foundation or the type and length of an anchor are determined. Hence, only an integral design consideration, which includes all the above-described factors, ensures the sustainability of an infrastructure.

Table 1. Assessment of different building categories with the sensitivity limit for serviceability and the need for repairs.

Building categories	Sensitivity limit for serviceability: Uniform displacement	Sensitivity limit for serviceability: Differential displacement[1]	Urgency for repairs after displacement
Cableway station	moderate	high	high
Cableway pylon	moderate	high	high
Communication structure	low	high	moderate
Mountain hut	low	moderate	low
Mountain restaurant	low	moderate	moderate
Pipeline	high	high	high
Snow supporting structure	low	moderate	moderate

[1] e.g., leading to tilting and cracking of the structure.

Impact of global warming

Global warming shows an elevation dependency, whereby the warming at high elevation sites in the Alps may be more pronounced than at low elevations (Beniston & Rebetez 1996). The exact consequences are difficult to define, but the general warming tendency will lead to long-term degradation of mountain permafrost and a deepening of the active layer. Warming permafrost ice increases the creep ratio and decreases shear strength, which can lead to more pronounced mass movements. Melting of the permafrost ice induces horizontal (creep) and vertical displacements (settlement) and elevated pore water pressures (Andersland & Ladanyi 2004, Esch 2004). Ice segregation can cause uplift of infrastructures and terrain and lead to rock instabilities. These various impacts of global warming on an infrastructure in mountain permafrost must be considered during the design process with respect to the total service life of a building.

Technical Solutions

Shallow foundations

Foundation systems depend on load and subsurface conditions as described above. A shallow foundation transfers building loads to the ground very near the surface. Shallow foundations include, for example, single foundations, strip foundations, and slab-on-grade foundations. Therefore, if the subsurface consists of stable rock or the design loads are rather small, a shallow foundation type is suitable. In mountain permafrost, shallow foundations are common, because the subsurface conditions often consist of stable rock with high strength. On this account, cableway stations and pylons, mountain restaurants, and huts are often built with a shallow type of foundation such as single, strip or slab-on-grade foundations. Figure 1 shows the strip foundation of the

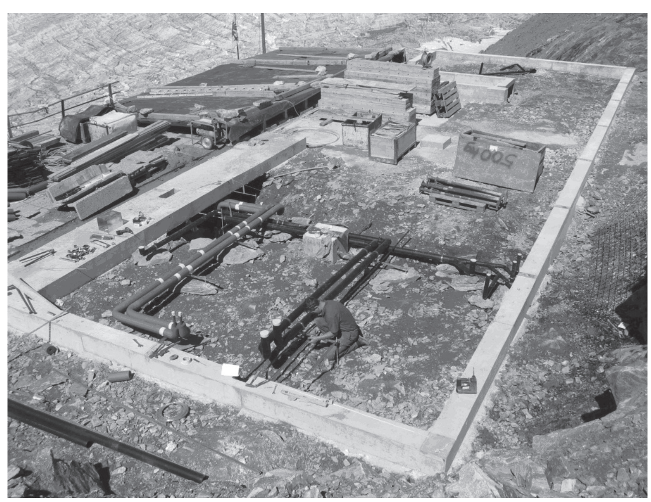

Figure 1. Strip foundation of new Finsteraarhorn mountain hut, Swiss Alps (Photograph: Ruch Architects, Meiringen 2003).

new Finsteraarhorn SAC (Swiss Alpine Club) mountain hut in the Swiss Alps.

Other reasons to choose a shallow foundation wherever possible are the complicated accessibility and transportation of heavy equipment for the excavation and material to the construction site. Shallow foundations are less complicated to implement than deep ones and therefore cheaper compared to all other types of foundations.

Deep foundations

As their name suggests, deep foundations are distinguished from shallow foundations by the depth to which they are embedded into the ground. The main reasons a geotechnical engineer would recommend a deep foundation over a shallow one are large design loads, high ice contents, warm permafrost at shallow depth or other site constraints such as unstable and complex geology. Deep foundations in mountain permafrost include drilled piles, shafts and piers. Drilled micropiles are often used for the construction or restoration of cableway stations and pylons. Permafrost degradation and active layer deepening can lead to a decrease in the bearing capacity of the ground, requiring additional anchors for the stabilisation of an existing structure – depending on the building category and its sensitivity limit for serviceability. In mountain permafrost the most practicable way to carry out this type of stabilisation is to drill a hole, place a threaded bar (micropile) and inject grout under high pressure into the surrounding clefts and fissures to increase the stability and bearing capacity. This is not a sustainable solution but it helps to allow continuation of the operation of an infrastructure without altering its location. For cableway stations and pylons in particular, this approach represents a cost-efficient and thus attractive way of restructuring.

Flexible structures

The latest technical experiences indicate that for locations with ice-rich permafrost, flexible systems are best adapted to meet the serviceability requirements. Laterally adjustable cableway pylons or three-point bearings for structures such as cableway stations (Phillips et al. 2007, Walser, pers. com.) and mountain restaurants are examples of these. Differential settlements within a three-point bearing do not generate internal constraints; this type of system can therefore extend the service life of a structure. Figure 2a shows one of the three-point bearings of a mountain restaurant in Ischgl, Austria. If settlement occurs, the steel construction can be uplifted hydraulically and steel plates can be inserted between the concrete support and the steel structure (Fig. 2b). The repositioning in this particular case takes place once a year and can be carried out in a few hours.

Snow nets (snow supporting structures) represent another flexible solution that is ideal for mountain permafrost. The hinged supports are mounted on ball joints, which allow them to swivel in a certain range. This behavior is particularly useful in creeping permafrost terrain and raises the service life of this type of avalanche defense structure (Phillips 2000). Experience in the Swiss Alps over the last decade shows that it is not sustainable to construct snow nets if the creep rates exceed 5 cm/year (Margreth 2007) and that floating foundations (steel bed plates) should be used in strongly creeping permafrost (Phillips & Margreth 2008, this proceedings).

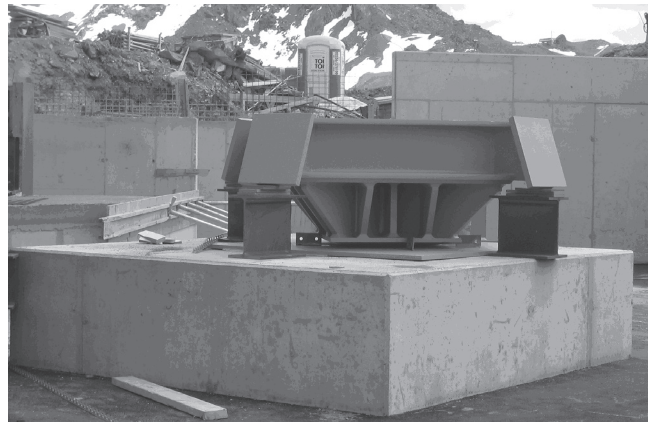

Figure 2a. Point bearing of a steel structure on a single concrete foundation, Ischgl, Austria (Photograph: M. Walser, Ischgl 2004).

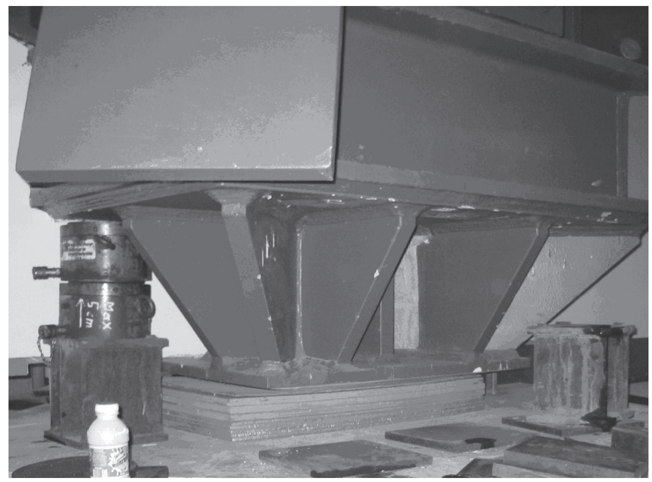

Figure 2b. Repositioning point bearing with hydraulic press, inserted steel plates, Ischgl, Austria (Photograph: M. Walser, Ischgl 2005).

Substrate structure

It is common practice to modify the substrate structure if necessary by replacing poorly graded material or broken rock with a well-graded gravely material. The modified substructure helps to uniformly distribute the load over an inhomogeneous surface. Compaction should take place in layers with a water content of the material close to the w_{opt} (Phillips et al. 2007). This facilitates the compaction work and increases the compactness of the packing (Soil Compaction Test, ASTM D698, Proctor 1933). A reinforcement consisting of steel nets or geotextile is possible. The reinforcement increases the bearing capacity, resulting in a higher design load and an even load distribution.

Insulation and cooling systems

To prevent heat transfer into the permafrost body (e.g.,

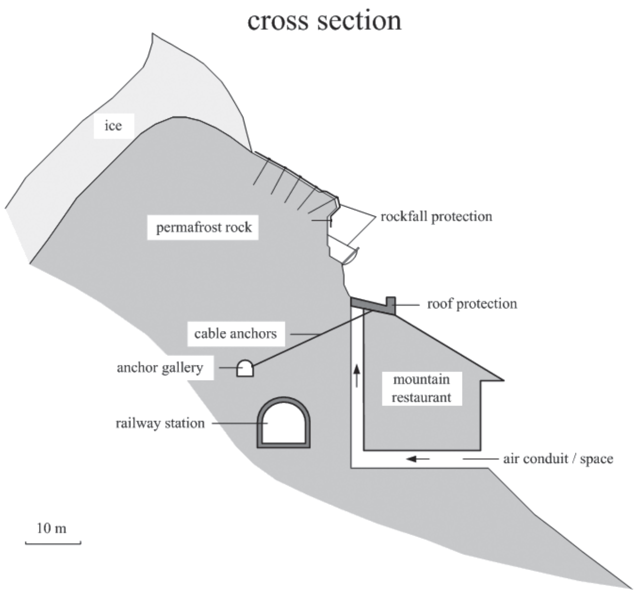

Figure 3. Scheme of air conduits, anchorage and anchor gallery, Jungfraujoch, Switzerland (after Keusen & Amiguet 1987).

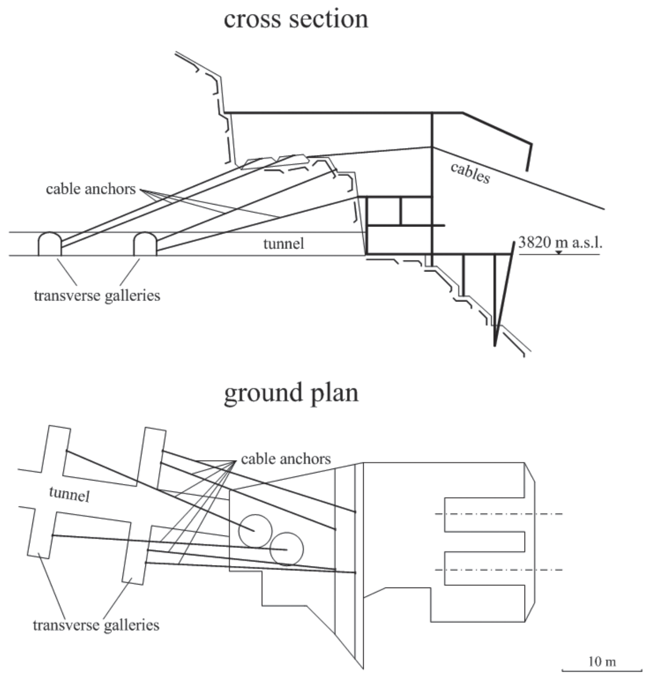

Figure 4. Scheme of anchorage including the transverse galleries, Klein Matterhorn, Switzerland (after Keusen & Haeberli 1983).

hydration heat emanating from curing concrete or conductive heat transfer from a heated structure above), a layer of insulation with high compressive strength (e.g., extruded polystyrene) should be placed between the foundation and the ground. Air conduits/spaces beneath a foundation and external wall represent another solution to protect the underlying permafrost (Fig. 3). These passive cooling systems are common, whereas experience with more sophisticated passive cooling systems (e.g., thermosyphons) is practically non-existent in the Alps. Active cooling systems (e.g., powered ventilation system) are used in individual cases but are not widespread in mountain permafrost infrastructures.

Anchors

Ground anchors normally consist of steel reinforcing bars or cables with a grout coating or a grout anchorage body (tieback). Rock or soil anchors can be installed prestressed or non-prestressed, respectively—prestressed is common practice. The non-prestressed are soil or rock nails and usually fully grouted. The force transmission of an anchor is based on a frictional bond between the grout and the surrounding ground. Anchors therefore react in a sensitive manner to changing subsurface conditions such as permafrost warming accompanied by loss of ice. The main implication of warming is reduced shear strength of anchors that can lead to a decreasing external bearing capacity and consequently, to accelerated deformation or failure of the supported structure.

The subsurface conditions, the size of the induced force and the risk potential of a failing structure determine the anchoring concept. In mountain permafrost most of the designed anchors are tied in bedrock. High stress and strain anchors with a large risk potential, such as those used for cableway stations and other exposed infrastructures, should be installed within an anchor gallery to avoid problems associated with injection anchors (e.g., freezing of grout, changing subsurface conditions) and to allow anchor replacements. Where possible, monitored anchors and load cells should be used. Figures 3 and 4 show two possible solutions for anchor galleries. In Figure 3, the rockfall and snow load roof protections of the mountain restaurant, Jungfraujoch, Switzerland, anchored with several high stressed cable anchors are illustrated (Keusen & Amiguet 1987). Figure 4 shows the traverse galleries from the access tunnel, used for anchorage of the cables and steel construction of the cableway station, Klein Matterhorn, Switzerland (Rieder et al. 1980, Keusen & Haeberli 1983). Drilling and prestressing of the anchors as well as the continued observation of the anchors occurs from the anchor gallery. This design approach ensures reliable monitoring, resulting in a higher factor of safety. Small stress and strain anchors such as those used for mountain huts, defence and communications structures, with a smaller risk potential, can be carried out with standard anchors without an anchor gallery. Margreth (2007) describes the important criteria and implications to install an anchor in mountain permafrost such as e.g., warming of the mixing water to a certain temperature to allow the curing of the injected grout in the anchor hole before freezing takes place.

In either case a monitoring and maintenance concept is highly recommended. It is compulsory for all prestressed permanent anchors to have accessible anchor heads over their service life. For high stress and strain anchors a permanent monitoring with load cells is a desirable objective. Likewise, there should be an anchor system redundancy, in order to allow maintenance work without safety reduction or interruption of operation.

Conclusions

The design consideration has to incorporate that the time and cost factors are higher for construction of an infrastructure in mountain permafrost in comparison with an infrastructure located in permafrost-free terrain. In particular the logistics such as the accessibility and transportation contribute to increasing time and cost for infrastructures in mountain permafrost. The necessity of undertaking extensive geotechnical investigations at least one year in advance of the start of construction also significantly extends the design and construction phase. The influences of present and future global warming, including the natural hazards involved, must be considered in the design of mountain infrastructure as well.

Various engineering solutions in mountain permafrost are affected by global warming and have been modified or restructured. Flexible technical solutions are well adapted to permafrost undergoing modification. In some cases, inappropriate technical solutions have been used and various mistakes have been made. Hence, development of guidelines for infrastructures in mountain permafrost is necessary to limit both cost and risk factors. The Swiss Federal Institute for Snow and Avalanche Research SLF is currently developing recommendations for infrastructures in alpine permafrost which should be published in 2009.

Acknowledgments

This research is supported by the Swiss Federal Office of Transportation FOT, armasuisse Real Estate and the Canton Valais. It is carried out in collaboration with the Swiss Alpine Club. The authors are thankful to W.J. Ammann and other anonymous reviewers of this paper for their helpful comments and suggestions.

References

Andersland, O.B. & Ladanyi, B. 2004. *An Introduction to Frozen Ground Engineering, XII*. Hoboken, New Jersey: John Wiley & Sons, Inc., 363 pp.

Beniston, M. & Rebetez, M. 1996. Regional behavior of minimum temperatures in Switzerland for the period 1979–1993. *Theoretical and Applied Climatology* 53(4): 231-243.

Esch, D.C. (ed.). 2004. *Thermal analysis, construction, and monitoring methods for frozen ground.* Technical Council on Cold Regions Engineering monograph. Reston, VA: American Society of Civil Engineers, 492 pp.

Keusen, H.R. & Amiguet, J.-L. 1987. Geologie, Felseigenschaften, Permafrost. *Schweizer Ingenieur und Architekt* (30-31): 905-906.

Keusen, H.R. & Haeberli, W. 1983. Site investigation and foundation design aspects of cable car construction in alpine permafrost at the „Chli Matterhorn," Wallis, Swiss Alps. *Permafrost Fourth International Conference*: 601-604.

Margreth, S. 2007. Defense structures in avalanche starting zones. *Technical Guideline as an aid to enforcement*. Bern and Davos: FOEN, SLF, 101 pp.

Phillips, M. 2000. *Influences of snow supporting structures on the thermal regime of the ground in alpine permafrost terrain.* Davos: Swiss Federal Institute for Snow and Avalanche Research SLF, 146 pp.

Phillips, M., Ladner, F., Müller, M., Sambeth, U., Sorg, J. & Teysseire, P. 2007. Monitoring and reconstruction of a chairlift midway station in creeping permafrost terrain, Grächen, Swiss Alps. *Cold Regions Science and Technology* 47(1-2): 32-42.

Phillips, M. & Margreth S. 2008. Effects of ground temperature and slope deformation on the service life of snow-supporting structures in mountain permafrost: Wisse Schijen, Randa, Swiss Alps. *Proceedings of the Ninth International Conference on Permafrost, Fairbanks, Alaska, June 29–July 3, 2008* (this proceedings)

Proctor, R.R. 1933. Fundamental principles of soil compaction. *Engineering News-Record* (9-13).

Rieder, U., Keusen, H.R. & Amiguet, J.-L. 1980. Geotechnische Probleme beim Bau der Luftseilbahn Trockener Steg-Klein Matterhorn. *Schweizer Ingenieur und Architekt* (18): 428-431.

Swisscode, SN 505267, 2003. *Geotechnical Design SIA 267.* Zurich: Swiss Society of Engineers and Architects, 104 pp.

Carbon, Nitrogen, and Phosphorus Interactions in the Hyporheic Zones of Arctic Streams that Drain Areas of Continuous Permafrost

William B. Bowden, Morgan J. Greenwald
Rubenstein School of Environment & Natural Resources, University of Vermont, Burlington, VT, USA
Michael N. Gooseff
Department of Civil & Environmental Engineering, Pennsylvania State University, University Park, PA, USA
Jay P. Zarnetske
Department of Geosciences, Oregon State University, Corvallis, OR, USA
James P. McNamara, John Bradford, Troy Brosten
Department of Geosciences, Boise State University, Boise, ID, USA

Abstract

In arctic streams, permafrost may influence hydrological and biogeochemical processes that control carbon and nutrient dynamics. We examined interactions among these processes in a fast-flowing, cobble-bottom stream and a slow-flowing, peat-bottom stream near Toolik Lake, within the foothills region of the Brooks Range, Alaska. Using a combination of ground penetrating radar, physical probing, and conservative solute injection experiments, we found that the thaw depths within the cobble-bottom stream were considerably deeper than in the peat-bottom stream. The maximum extent of hyporheic penetration followed a similar trend, but in both streams the hyporheic depth was less than the maximum extent of thaw. Hyporheic regeneration of N and P (estimated as mass fluxes) were in reasonable stoichiometric agreement. However, regeneration of C (estimated by whole-stream metabolism) was much greater than regeneration of either N or P, indicating considerable internal recycling of these essential elements.

Keywords: biogeochemistry; hyporheic zones; nutrients; thaw bulbs; tundra streams..

Prior to our current research, virtually nothing was known about hyporheic dynamics in Arctic streams draining areas with continuous permafrost. Substantial evidence from temperate streams suggests that the hyporheic zone can be an important site of organic matter turnover and a source of regenerated nutrients. However, permafrost exerts strong influences on surface processes that we initially thought might alter the structure and function of the hyporheic zone in Arctic streams. However, initial results reported by Edwardson (1997) and Edwardson et al. (2003) showed that hyporheic dynamics in the Kuparuk River, on the eastern North Slope of Alaska, were similar to those observed in temperate streams. In particular, we found that geomorphic profiles of stream channels (longitudinal more so than lateral) provide the necessary hydraulic gradients to drive hyporheic exchange through the streambed, as shown by Harvey and Bencala (1993) and Kasahara and Wondzell (2003). We also showed that biogeochemical processing in the hyporheic zone was important, potentially supplying from 14 to 162% of the benthic N uptake requirements in the Kuparuk River.

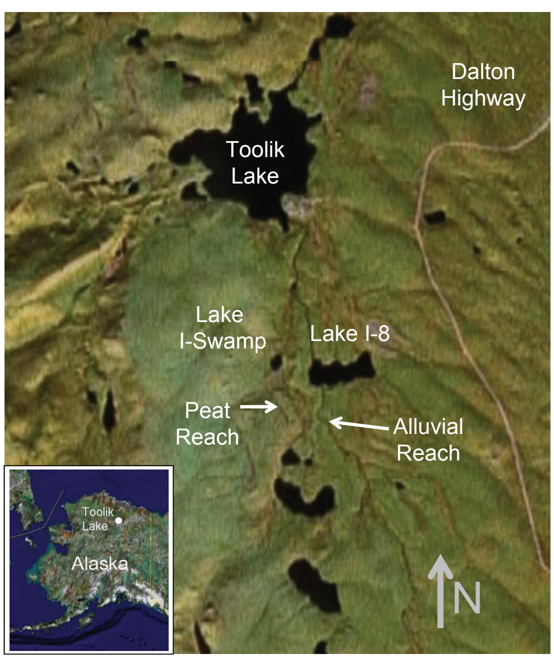

Figure 1. Location of the study streams. (Colored illustration available on CD-Rom.)

The purpose of this paper is to integrate the results of our work on hyporheic dynamics in tundra streams with results from a separate study of whole-stream metabolism in similar streams. These two studies provide insight into interactions among carbon, nitrogen, and phosphorus dynamics in the hyporheic zones of arctic tundra streams that overlie continuous permafrost.

Site Description and Methods

Study sites

The study area (Fig. 1) was located on the North Slope of the Brooks Range in Alaska, near the Toolik Field Station (68°38′N, 149°36′W), about 180 km south of the Arctic Ocean. Two common stream geomorphologic types occur on the tundra landscapes in this area: (a) high-gradient, alluvial streams with alternating riffle-pool sequences and (b) low-gradient, peat-bottom streams with a "beaded" morphology in which large, deep pools are connected by narrow, deep runs. We located two streams that represent these contrasting tundra stream types and that lie parallel to each other within a series of lakes and connecting streams that flow north into Toolik Lake. Kling et al. (2000) referred to these two stream reaches as the inlets to Lakes I-8 and I-Swamp in the I-Series. These two streams are of the same order, have the same aspect, and drain similar landscapes. They differ in that the alluvial reach has a higher gradient and drains an area that has no lakes, while the peat stream has a lower gradient and drains an area with several lakes.

Ground penetrating radar

We used ground penetrating radar (GPR) to establish the boundary between the thawed sediments in the active layer under the stream (the thaw bulb) and permafrost (Bradford et al. 2005, Brosten et al. 2006). We used a commercial pulsed radar system with 200 MHz antennas and high-powered transmitter (1000V) to maximize penetration beneath the streambed. The antennas and GPR control equipment were placed in the bottom of a small rubber boat, and pulled steadily across the stream and banks on either side while triggering the radar at a constant rate. While acquiring data, we were careful to maintain a steady pull rate while minimizing downstream drift. Additional details of GPR data acquisition are provided by Bradford et al. (2004). In addition to acquiring the radar profiles, we measured depth to permafrost on the stream banks and shallow (<0.5 m) margins of the streams by pressing a metal probe through the active layer to the point of refusal.

Solute injection experiments

We performed solute injection experiments (SIEs) using Rhodamine WT (RWT) in June and August 2005 in each stream to determine the extent of hyporheic exchange within the thaw bulb. A metering pump dripped RWT into the stream at a constant rate at the top of the reach until the surface water RWT concentration reached a plateau in the fully mixed zone of the streams (20–50 downstream from the injection point). During each SIE, and for a period following the tracer injection, surface and subsurface water were sampled at regular intervals. Subsurface samples were obtained via a set of nested mini-piezometers that spanned the depth of the thawed zone in each stream (3 depths in the alluvial stream and 2 depths in the peat stream). For the alluvial SIE, samples were taken every 20 min for the first hour, and every 30 min hourly thereafter, until the end of the experiment (~2.5 h). The peat SIE was longer, and so the later samples were taken approximately every two hours to the end of the experiment (6 and 9.7 h in two experiments). Samples were returned immediately to the laboratory for analysis of RWT concentration using a Turner Designs 10-AU fluorometer. For each mini-piezometer location, a tracer breakthrough curve (RWT concentration vs. time) was obtained for the surface water and each subsurface location sampled for each SIE. We used these data to establish the depth and timing of surface water penetration into the hyporheic zone of the two stream reaches. Details for these approaches are provided in Zarnetske (2006), Zarnetske et al. (2007), and Greenwald (2007).

Water chemistry

Four times during the summer of 2005 (Alluvial: 29 June, 4 July, 1 August, 15 August; Peat: 27 June, 1 July, 29 July, 10 August), surface and subsurface water from 9 sub-sites within both streams were sampled and analyzed for concentrations of nitrate (NO_3), ammonium (NH_4), soluble reactive phosphorus (SRP), dissolved oxygen (DO) and dissolved organic carbon (DOC). For each stream, the results from the first two sampling dates were averaged and reported as June data, and the results from the last two sampling dates were averaged and reported as August data. Early summer chemistry data were paired with the June SIE data, and late summer chemistry data were paired with the August SIE data.

Concentrations of DO in surface and subsurface water samples were measured in the field with a WTW Oxi 340i handheld dissolved oxygen meter. The reported accuracy for this dissolved oxygen meter is +0.01 mg/L (WTW, Weilheim, Germany). However, under the conditions in which we used this equipment, we assumed a more conservative estimate of accuracy of +0.1 mg/L. All other water samples were filtered through 0.45 μm, 25 mm diameter, cellulose acetate syringe filters and kept on ice for transport to the laboratory.

Ammonium and SRP analyses were done within 48 hours at the Toolik Field Station. Ammonium analyses were performed using the orthophthaldialdehyde (OPA) method (Holmes et al. 1999). SRP analysis was performed using the colorimetric molybdate blue method (Murphy and Riley 1962). Nitrate samples were immediately frozen at the field station, then transported to the University of Vermont's Rubenstein Ecosystem Science Laboratory in Burlington, Vermont, USA, where they were analyzed within 6 months by the cadmium reduction technique (Askew & Smith 2005, p. 123). DOC samples were preserved with 6N hydrochloric acid to a pH of 2, transported to the Ecosystems Center in Woods Hole, Massachusetts, USA, and analyzed by the persulfate-ultraviolet method within 6 months (Baird 2005, p. 23). We combined the RWT tracer and water chemistry data to estimate net nutrient regeneration rates using methods described by Greenwald (2007).

Whole-stream metabolism

We calculated net ecosystem metabolism (NEM) with the whole-stream, open-system, single station approach described by Marzolf et al. (1994) as refined by Young and Huryn (1998). We measured reaeration using the sound pressure method developed for these streams by Morse et al. (2007). Estimates of ecosystem respiration (ER) were corrected for the presence of low light levels at solar midnight, as described by Cappelletti (2006). Gross primary production is the difference between NEM and ER (where ER <0; i.e., a consumption of DO).

Results and Discussion

Stream characteristics

Despite their close proximity (less than 1 km), the two study streams were geomorphically distinct. Both streams are underlain by permafrost. However, the gradient of the alluvial stream was 0.7%, and the substrate was a mix of cobble and boulders, while the gradient of the peat stream was 0.03%, and the substrate was a mix of peat and silt (Fig. 2).

We used ground penetrating radar (GPR) to image the progression of thaw depth from May–September 2004 in the thawed zone under the alluvial and peat streams (Brosten et al. 2007). Permafrost depths interpreted from GPR data were constrained by both recorded subsurface temperature profiles and by pressing a metal probe through the active layer to the point of refusal. We found that the thaw bulb developed differently within the two stream environments. Thaw depths within the alluvial stream increased in thickness up to 2.5 m by the end of the summer (Fig. 3) but to a maximum of only 1.5 m (and generally <1 m) in the peat-bottom stream (Fig. 4). By late August and early September, the alluvial site began to refreeze. while the peat-bottom site continued to thaw; thaw depths had not receded at the peat-bottom sites by our last site visit in September. These results indicate distinctly different responses to the seasonal thermal input. Rapid heat absorption and loss occurs in the cobble-bottom alluvial stream while peat insulates the permafrost and introduces a lag in the seasonal thermal profile.

Using conservative tracer additions, we found that transient storage indicators such as mean storage residence time, storage zone area, hydraulic retention, and storage exchange rates were sensitive to discharge and strongly correlated with total stream power (Zarnetske et al. 2007). However, the relationship between transient storage and extent of thaw was less clear. Transient storage indicators increased with increasing thaw depths under base- and low-flow conditions, but these relationships diminished at high flow. We found good correlations between the Darcy-Weisbach friction factor of these channels and several metrics of transient storage, in agreement with previous studies (e.g., Bencala & Walters 1983, Harvey & Wagner, 2000). We found that stream power was a good predictor of transient storage characteristics because it normalizes simple characteristics of hydraulics and morphology, thereby allowing better comparisons across streams that differ widely in these characteristics (Fig. 2). Our results in arctic streams are comparable to those in temperate streams (Legrand-Marcq & Laudelout 1985, D'Angelo et al. 1993, Harvey et al. 2003) indicating that our findings are likely transferable to non-

A

B

Figure 2. Overview of the alluvial (A) and peat (B) stream reaches. (Colored illustration available on CD-ROM.)

A B

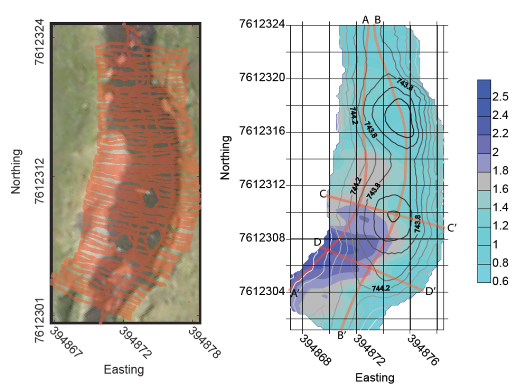

Figure 3. Thaw depth thickness in the alluvial reach. The left panel (A) shows an areal view of the reach with the GPR tracks (light grey) overlain. The right panel (B) shows an interpretation of the maximum thaw depth thickness in August 2005. (Colored illustration available on CD-Rom.)

A B

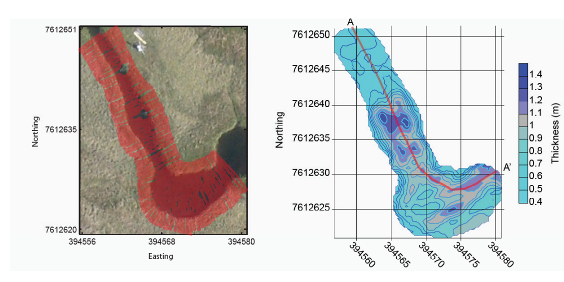

Figure 4. Thaw depth thickness for a portion of the peat reach. The left panel (A) shows an areal view of the reach with the GPR tracks overlain. The right panel (B) shows an interpretation of the maximum thaw depth thickness in August 2005. (Colored illustration available on CD-ROM.)

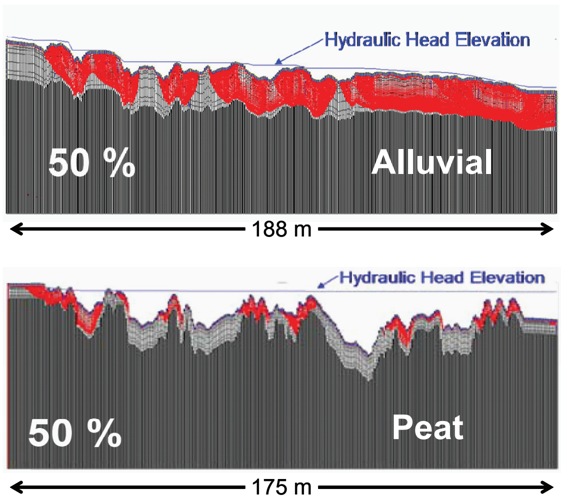

Figure 5. Zones of hyporheic exchange (black flow lines) in the alluvial (upper panel) and peat (lower panel) reaches for combined MODFLOW and MODPATH simulations in which the active layer (grey areas) was 50% of the observed maximum in each reach. See Zarnetske (2006) for details. (Colored illustration available on CD-ROM.)

arctic streams.

Hyporheic exchange depths in the cobble-bottom and peat-bottom streams (Fig. 5) were constrained in part by depths of thaw beneath these two streams and in part by the texture of the substrate, both of which are controlled by stream gradient. In the cobble-bottom stream–which had a greater depth of thaw–stream water penetrated the hyporheic zone to a depth of up to 54 cm. In the peat-bottom stream, which had a much shallower depth of thaw, the actively functioning hyporheic zone was limited to a depth of 10 cm or less. In both streams, we found that the maximum extent of hyporheic penetration was much less than the maximum extent of thaw.

Combining our estimates of hydraulic exchange between the open channel and the hyporheic zone with analyses of hyporheic nutrient concentrations in these reaches (Table 1) provided an estimate of hyporheic regeneration. Total N regeneration in the alluvial reach was about 9.3 µmoles m^{-2} h^{-1}, primarily as nitrate (7.9 µmoles m^{-2} h^{-1}). The P regeneration rate was 0.54 µmoles m^{-2} h^{-1} for N:P regeneration molar ratio of 17:1. Total N regeneration in the peat stream was 5.3 µmoles m^{-2} h^{-1} based on a release of ammonium (6.8 µmoles m^{-2} h^{-1}) and an uptake of nitrate (-1.5 µmoles m^{-2} h^{-1}). The P regeneration rate was very low, at 0.05 µmoles m^{-2} h^{-1} for an N:P regeneration molar ratio of 105:1. Thus, hyporheic regeneration in the alluvial reach was in approximate stoichiometric balance (16:1), while regeneration of P in the peat stream was considerably less than expected.

The ratios of N and P regeneration can also be compared to estimates of hyporheic C processing based on whole-stream estimates of ecosystem respiration measured in these stream reaches in a previous year (W.B. Bowden, unpublished data, 2001). Cappelletti (2006) observed that even in a modestly productive river (the Kuparuk River), the vast majority of total ecosystem respiration could be attributed to hyporheic respiration. Ecosystem respiration in both stream reaches was similar at ~30 mmoles m^{-2} h^{-1}. Thus, the observed C regeneration ratios relative to N and P were roughly 3 orders of magnitude greater than the expected C:N (~7:1) and C:P (~106:1) ratios. This suggests that a considerable quantity of N and P liberated in the course of decomposition in the hyporheic zones of these streams is reutilized before it leaves the hyporheic system.

Table 1. Connectedness-weighted, season-averaged concentrations of nutrients in the hyporheic zones of the alluvial and peat stream reaches. See Greenwald (2007) and Greenwald et al. (in press) for details about seasonal nutrient concentrations.

Nutrient	Stream type: Alluvial	Stream type: Peat
Nitrate (µM)	5.75	7.49
Ammonium (µM)	0.20	0.52
Phosphate (SRP) (µM)	0.02	0.03

These results show that gradient strongly influences the spatial and temporal extent of thawed sediments in streams that drain permafrost-dominated landscapes. Gradient controls substrate particle sizes, which in turn controls the hydraulic and—peat is deposited—the thermal conductivities of stream substrates. Thus, steeper streams have coarser substrates and conduct heat energy and water more effectively to depth than is the case in less-steep streams that accumulate fine organic sediments. The result is that the thaw bulb (active layer) below alluvial streams is deeper than it is beneath peat streams. For similar reasons, the zone of active hyporheic exchange is thicker in alluvial streams than it is in peat streams. However, we found that the thaw depth was thicker than the zone of active hyporheic exchange in both stream types.

The hyporheic zones in these streams were biogeochemically active. In the alluvial reach, the hyporheic zone was a source of NH_4, NO_3, and PO_4 and a sink for DO. In the peat stream, the hyporheic zone was a strong source of NH_4, a weak source of PO_4, and sink for NO_3 and DO. The total regeneration of N and P was in reasonable stoichiometric balance in the alluvial reach, while in the alluvial reach less P was regenerated than expected based on the N regeneration. However, based on C regeneration (respiration), far less N and P were regenerated from the hyporheic zones of either stream than expected. This suggests the potential for substantial re-immobilization of N and P mineralized from organic matter decomposition in the hyporheic zones of these streams. The relative importance of net nutrient regeneration from the hyporheic zones of these streams versus internal recycling of nutrients within these hyporheic zones is still poorly known. In addition, it is not clear how factors such as geomorphic form, stream network characteristics (e.g., stream order), or landscape characteristics (e.g., young versus old glacial ages) influences this balance.

Acknowledgments

We thank Julia Larouche, Kenneth Turner, Joel Homan, Tom Crumrine, and Adrian Green for field and laboratory assistance and Alan Howard for statistical advice. Kenneth Edwardson contributed valuable information and insight to our comparisons of net nutrient regeneration rates in North Slope streams. We also thank the staff of the Toolik Field Station and VECO Polar Resources for logistical support. The material presented in this paper is based upon work supported by the National Science Foundation under Grant No. OPP-0327440.

References

Askew, E.F. & Smith, R. 2005. Inorganic nonmetallic constituents. In: A.D. Eaton, L.S. Clesceri, E.W. Rice & A.E. Greenberg (eds.), *Standard Methods for the Examination of Water and Wastewater*. Baltimore, MD: Port City Press, 123.

Baird, R.B. 2005. Aggregate organic constituents. In: A.D. Eaton, L.S. Clesceri, E.W. Rice & A.E. Greenberg (eds.), *Standard Methods for the Examination of Water and Wastewater.* Baltimore, MD: Port City Press, 23.

Bencala, K.E. & Walters, R.A. 1983. Simulation of solute transport in a mountain pool-and-riffle stream: a transient storage model. *Water Resources Research* 19: 718-724.

Bradford, J.H., McNamara, J.P., Bowden, W.B. & Gooseff, M.N. 2005. Imaging depth-of-thaw beneath arctic streams using ground-penetrating radar. *Hydrological Processes* 19(14): 2689-2699.

Brosten, T.R., Bradford, J.H., McNamara, J.P., Zarnetske, J.P., Gooseff, M.N. & Bowden, W.B. 2006. Profiles of temporal thaw depths beneath two arctic stream types using ground-penetrating radar. *Permafrost and Periglacial Processes* 17: 341-355.

Cappelletti, C. 2006. *Photosynthesis and respiration in an arctic tundra river: modification and application of the whole-stream metabolism method and the influence of physical, biological, and chemical variables*. M.Sc. Thesis. Burlington, VT: University of Vermont.

D'Angelo, D.J., Webster, J.R., Gregory, S.V. & Meyer, J.L. 1993. Transient storage in Appalachian and Cascade mountain streams as related to hydraulic characteristics. *Journal of the North American Benthological Society* 12: 223-235.

Edwardson, K.J. 1997. *Characterizations of hyporheic influences on the hydrology and biogeochemistry of arctic tundra streams.* M.Sc. Thesis. Durham, NH: University of New Hampshire.

Edwardson, K.J., Bowden, W.B., Dahm, C. & Morrice, J. 2003. The hydraulic characteristics and geochemistry of hyporheic and parafluvial zones in arctic tundra streams, North Slope, Alaska. *Advances in Water Resources* 26: 907-923.

Harvey, J.W. & Bencala, K.E. 1993. The effect of streambed topography on surface-subsurface water exchange in mountain catchments. *Water Resources Research* 29: 89-98.

Harvey, J.W., Conklin, M.H. & Koelsch, R.S. 2003. Predicting changes in hydrologic retention in an evolving semi-arid alluvial stream. *Advances in Water Resources* 26: 939-950.

Harvey, J.W. & Wagner, B.J. 2000. Quantifying hydrologic interactions between streams and their subsurface hyporheic zones. In: J.B. Jones & P.J. Mulholland (eds.), *Streams and Ground Waters*. San Diego, CA: Academic Press, 3-44.

Holmes, M., Aminot, A., Kerouel, R. Hooker, B.A. & Peterson. B.J. 1999. A simple and precise method for measuring ammonium in marine and freshwater ecosystems. *Canadian Journal of Fisheries and Aquatic Science* 56(10): 1801-1808.

Greenwald, M.J. 2007. *Hyporheic exchange and biogeochemical processing in arctic tundra streams.* MSc. Thesis. Burlington, VT: University of Vermont.

Greenwald, M.J., Bowden, W.B., Gooseff, M.N , Zarnetske, J.P., McNamara, J.P., Bradford, J.H. &. Brosten, T.R. In press. Hyporheic exchange and water chemistry of two arctic tundra streams of contrasting geomorphology. *Journal of Geophysical Research – Biogeosciences*.

Kasahara, T. & Wondzell, S.M. 2003. Geomorphic controls on hyporheic exchange flow in mountain streams. *Water Resources Research* 39: 1005, doi:1010.1029/2002wr001386.

Kling, G.W., Kipphut, G.W., Miller, M.C. & O'Brien, W.J. 2000. Integration of lakes and streams in a landscape perspective: the importance of material processing on spatial patterns and temporal coherence. *Freshwater Biology* 43: 477-497.

Legrand-Marcq, C. & Laudelout, H. 1985. Longitudinal dispersion in a forest stream. *Journal of Hydrology* 78: 317-324.

Marzolf, E.R., Mulholland, P.J. & Steinman, A.D. 1994. Improvements to the diurnal upstream-downstream dissolved oxygen change technique for determining whole-stream metabolism in small streams. *Canadian Journal of Fisheries and Aquatic Sciences* 51: 1591-1599.

Morse, N., Bowden, W.B., Hackman, A., Pruden, C., Steiner, E. & Berger, E. 2007. Using sound pressure to estimate reaeration in streams. *Journal of the North American Benthological Society* 26(1): 28-37.

Murphy, J. & Riley, J.P. 1962. A modified single solution method for the determination of phosphate in natural waters. *Anayitica Chimica Acta* 27: 31-36.

Young, R.G. & Huryn, A.D. 1999. Effects of land use on stream metabolism and organic matter turnover. *Ecological Applications* 9: 1359-1376.

Zarnetske, J.P., Gooseff, M.N., Brosten, T.R., Bradford, J.H., McNamara, J.P. & Bowden, W.B. 2007. Transient storage as a function of geomorphology, discharge, and permafrost active layer conditions in Arctic tundra streams. *Water Resources Research* 43: W07410, doi:10.1029/2005WR004816.

Zarnetske, J.P., Gooseff, M.N., Bowden, W.B., Greenwald, M.J., Brosten, T.R., Bradford, J.H. & McNamara, J.P. Influence of morphology and permafrost dynamics on hyporheic exchange in arctic headwater streams under warming climate conditions. *Geophysical Research Letters* (in review).

Zarnetske, J.P. 2006. *Headwater hyporheic zones in a warming arctic climate: an assessment of hyporheic dynamics across distinct geomorphic and permafrost conditions.* M.Sc. Thesis. Logan, UT: Utah State University.

Geomorphology and Gas Release from Pockmark Features in the Mackenzie Delta, Northwest Territories, Canada

R.G. Bowen
Diversified Scientific Solutions, 3439 Fulton Road, Victoria, B.C., V9C 3N2
S.R. Dallimore, M.M. Côté, and J.F. Wright
Geological Survey of Canada- Pacific, P.O. Box 6000, Sidney, B.C., V8L 4B2
T.D. Lorenson
United States Geological Survey, 345 Middlefield Road, M.S. 999, Menlo Park, CA 94025

Abstract

Field investigations were undertaken to study the geomorphology and permafrost conditions of more than 20 methane-venting pockmark features in a pond west of Middle Channel, Mackenzie Delta. The flux of methane to the atmosphere from these pockmarks is estimated to be 5.07 x 10^5 m^3 yr^{-1}. Terrestrial permafrost around the pond is ~60 m thick and likely formed within Holocene deltaic sediments. However, the site is located only 2 km from a major permafrost boundary where permafrost thickens over a short distance to more than 400 m. Mean annual pond-bottom temperature is above 0°C, creating the potential for talik formation, and hence gas migration pathways, beneath the pond. Isotopic analysis indicates that the methane is of thermogenic origin, and is similar in composition to the gas of the nearby Niglintgak gas field.

Keywords: climate change; gas hydrates; Mackenzie Delta; methane seeps; pockmarks.

Introduction

Interest in the occurrence of greenhouse gases within permafrost, particularly methane, has grown in recent years with the consideration of the effects of climate warming and the continued expansion of engineering activity in the Arctic. The potential release of methane as free gas fluxing from arctic lakes is recognized as a possible positive climate change feedback mechanism (Walter et al. 2006), as is gas release from dissociating gas hydrates beneath transgressed areas of the Arctic Shelf (Taylor et al. 2002, Paull et al. 2007). Gas leakage from deeper hydrocarbon occurrences are also of interest in areas underlain by large sedimentary basins. Finally, shallow occurrences of free gas have been recognized as a potential geohazard to hydrocarbon exploration and development (Collett & Dallimore 2002).

This paper describes a number of small gas seeps and one prolific seep which occur in a pond in the outer Mackenzie Delta, NWT, Canada (Fig. 1A). The site is of historical interest, as natural gas was first observed discharging from the pond in 1963 by Dr. Ross Mackay (pers. com. 1991). During the course of three field seasons approximately twenty small gas seeps and one large seep have been investigated. The large seep has a conical bed form depression similar to pockmark features described offshore (Hovland & Judd 1988). This paper describes permafrost conditions, geomorphology and geotechnical properties of the site, and quantifies the geochemistry and gas flux from the large seep.

Permafrost and Physiographic Setting

The depth of ice-bonded permafrost in the outer Mackenzie Delta has been estimated from geophysical well logs, hydrocarbon exploration wells (Smith & Judge 1993), and deep sounding electromagnetic transects (Todd & Dallimore 1998). Ground temperature data are also available from instrumented wells (Taylor et al. 1998). Using these data, the base of ice-bonded permafrost and intervals where stable methane hydrate can occur was modeled with physiographic boundary constraints.

Permafrost distribution beneath terrestrial areas is variable (Fig. 1A), reflecting a complex Quaternary paleoclimate and depositional history (Taylor et al. 1996). To the east of Middle Channel, older pre-Holocene sediments outcrop or occur at shallow depths beneath a thin veneer of Holocene deltaic sediments. Permafrost beneath land areas is 250 to 600 m thick. To the west of Middle Channel, Holocene deltaic sediments dominate the near-surface geology, and permafrost thins over a few kilometers to approximately 60 m (Fig. 1B). Reflecting this spatial change in ground temperatures, methane hydrate is not stable to the west of Middle Channel, whereas to the east, the base of the methane hydrate phase boundary may be 400 to 700 m deep (Fig. 1C).

The pond containing the pockmarks is 3 km from the Beaufort Sea and is connected to Middle Channel to the east via a small side channel and to the Beaufort Sea via a meandering channel to the west. The pond is tidally influenced and is highly turbid in summer due to the inflow of silt-laden Mackenzie River waters. The terrain in the vicinity of the pond is <2 m above sea level, and thus the site is susceptible to flooding during river breakup and Beaufort Sea storm surges. Pond sediments consist of uniform, dark brown mud with occasional organic inclusions including twigs and rootlets.

Estimates of the shallow terrestrial ground temperature regime are available from a temperature cable ~5 km south

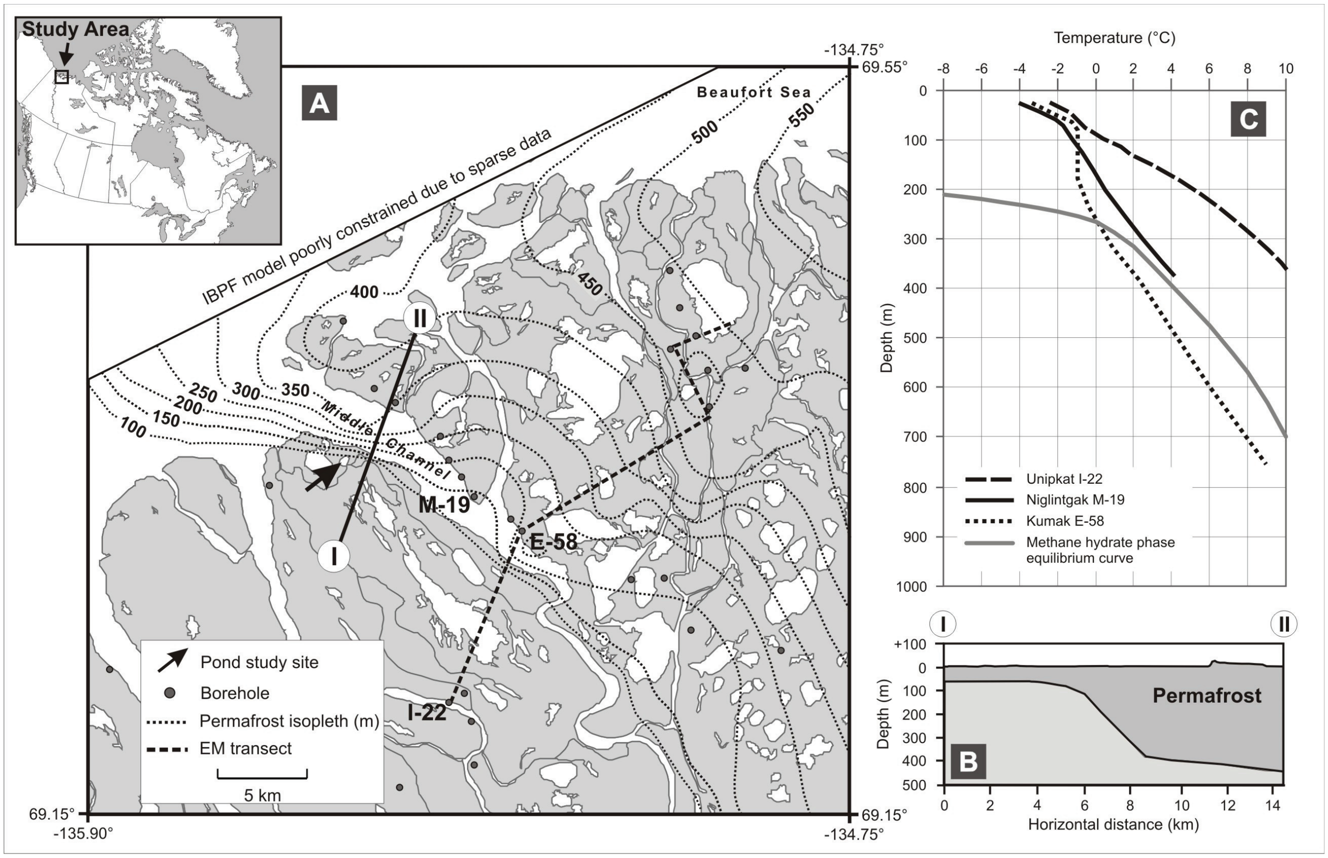

Figure 1. (A) Outer Mackenzie Delta near Middle Channel showing pockmark research site. Contours are of the base of ice-bonded permafrost, modeled using interpretations from geophysical well logs (Smith & Judge 1993), a deep sounding electromagnetic transect (Todd & Dallimore 1998), and boundary constraints established from the surficial geology. (B) The depiction of the base of permafrost from point I to II has been derived from the modeled data. (C) Ground temperatures from three instrumented wells (Taylor et al. 1998), methane hydrate phase equilibrium curve is from Sloan (1998).

of the pond site (Dyke, pers. com.) and a deeper installation 12 km south of the site (Dallimore & Matthews 1997). These studies reveal mean annual ground temperatures of this portion of the outer Mackenzie Delta are -4 to -6°C. Mean annual air temperatures measured at a site 20 km to the east are approximately -11°C (National Snow and Ice Data Centre 2007).

Vemco Minilog-T temperature loggers (temperature range -4 to +20°C, resolution 0.1°C) were deployed at the bed of the large pockmark site to record daily bottom water temperatures. The annual mean bottom temperature from August 10, 2006, to August 10, 2007, at ~9 m depth was 4.1 ± 0.1°C. Water depths of the main pond are generally <1.5m, and as a result, late winter ice typically contacts the bed in these areas lowering the annual mean temperatures to 2 to 3°C.

Bathymetry and Pockmark Morphology

The pond investigated in this study is heart-shaped and 25 hectares in surface area. Water depths vary from 1–2 m with the exception of the large seep/pockmark feature which is ~10 m deep. During the summers of 2006 and 2007, ~20 small but continuously active seeps were observed within the pond. Typically these seeps had surface bubble plumes which were 0.5 to 1.5 m in diameter. Physical inspection of six of these seeps revealed that sediment strength in the vicinity of the seeps was very weak, with 0.3 to 1.0 m deep conical depressions in the pond bed. Many seeps were discharging gas through orifices that were approximately 5 cm in diameter. In addition to the continuous seeps, small episodic gas discharges were observed throughout the pond, and occasionally on land, suggesting that gas is venting to the surface over a large area.

A boat equipped with a LCX-19C sonar and Global Positioning System (GPS) system was used to collect a series of survey transects over the large seep and the surrounding area. The bubble plume area at the surface of this seep varied from 2 to 5 m in diameter. The plume within the water column was visible from the sonar acoustic data as an area of intense acoustical backscatter due to the sonic reflection of the bubbles. Examination of the sonar data adjacent to the plume as well as several data points that penetrated the plume enabled the construction of depth interpolations, where the sonar data were giving false bottom data due to the strong reflection of bubbles from the plume. A digital terrain model was generated from the corrected sonar data (Fig. 2). The pockmark feature was ~10 m deep and conical in shape with a diameter of about 24 m at 3.5 m depth tapering to a flatter base of ~5 m diameter. The slopes were relatively steep with average dips of 20 to 25° (mean 22.4 ± 0.7°). The volume below a depth of 3.5 m was approximately 5400 m³.

Bearing Strength of Pockmark Sediments

A Seabed Terminal Impact Newton Gradiometer (STING) was used to estimate the dynamic bearing strength of the lake bed sediments across the main pockmark feature. This device measures the kinematic dynamics of the probe during the deceleration as it penetrates bottom sediments (Mulhearn 2002). The STING was configured with a 1 m shaft and a 35 mm foot. A boat survey transect was established using a taught surface line. The instrument was allowed to free-fall from the water surface at 1–3 m intervals along the transect line. Each point on the transect consisted of four discrete drops that were averaged to yield a mean. The instrument sampled every 0.0005 seconds allowing construction of a bearing strength vs. depth profile.

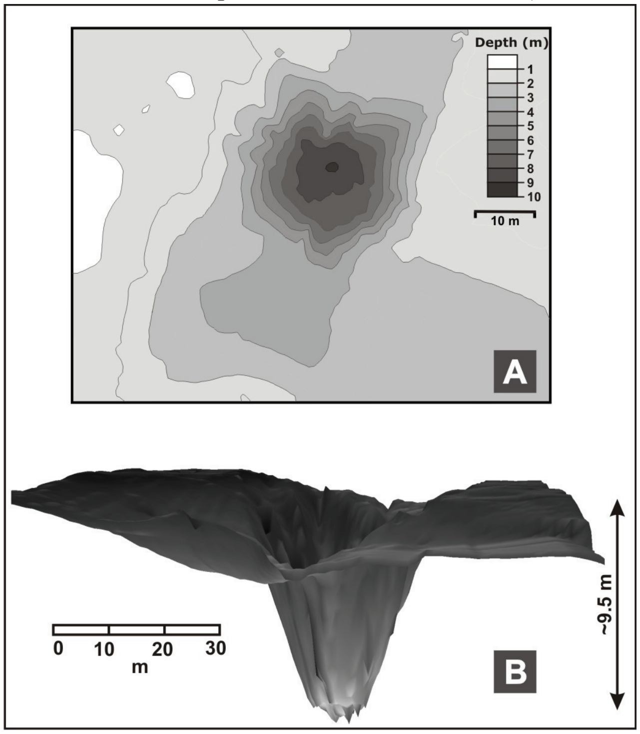

Figure 2. (A) Plan view and (B) sun-shaded perspective view of seep digital elevation model generated from sonar transects.

Figure 3 shows an east–west transect of 12 STING deployments across the pockmark feature. With the exception of deployments 11 and 12, the sediments from 0–25 cm depth are very weak, with bearing strengths below 20 kPa. At many sites (i.e., deployment 5, 6, 7, and 9, 10) the water sediment interface is barely discernible, and the bearing strength vs. depth shows only a small increase to maximum depth of penetration (limited by frictional effects). Several deployments do show some change in bearing strength vs. depth which are interpreted to be harder sediment layers. No STING measurements were obtained outside of the pockmark. However, estimates of the surface bearing strength in the shallow areas of the pond were made by several walking/wading transects. For the most part, the sediment interface could bear a person's weight, suggesting that near-surface bearing strengths likely exceed 200 kPa. STING data from the channel to the south of the pond showed near-surface bearing strengths as high as 400 kPa.

Gas Flux Measurements

Summer

An instrument was developed to measure gas flux from the large seep site (Fig. 4). The flux instrument, which was modified over several field seasons, consisted of a gas collection funnel and a chimney assembly.

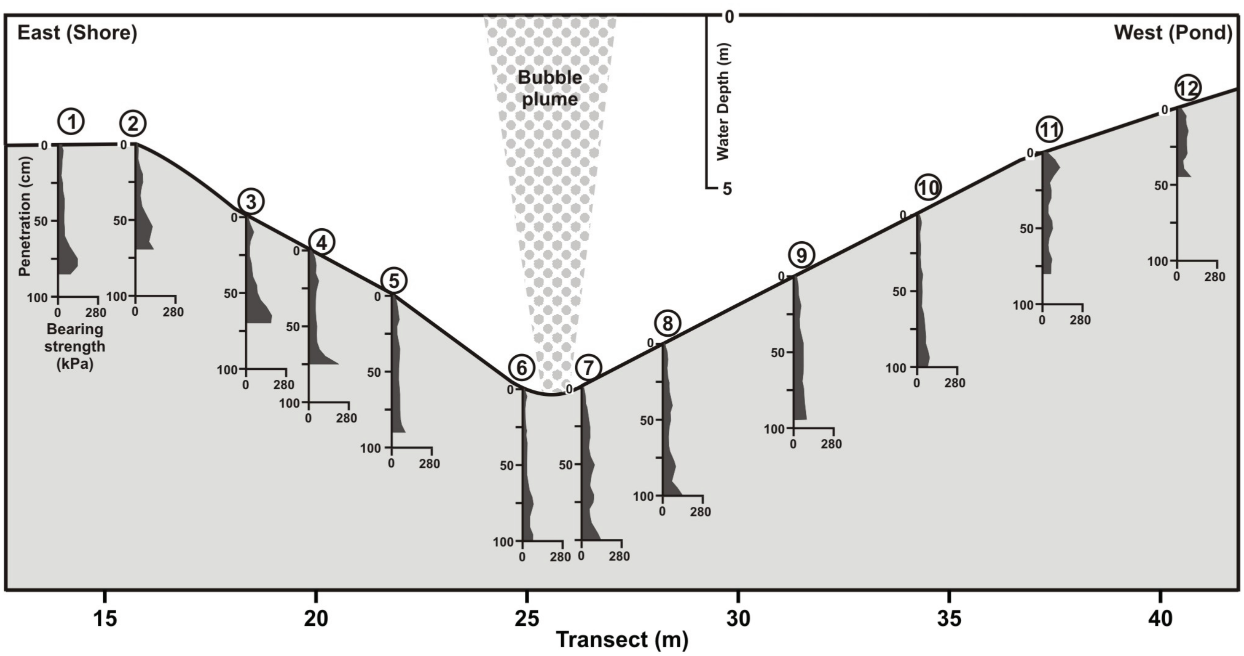

Figure 3. Seabed Terminal Impact Newton Gradiometer (STING) transect of seep. Profiles are averaged from four individual penetrations at each site.

Gas flow was measured with an airflow anemometer which was installed in the centre of the 10 cm chimney assembly. Anemometers are routinely used by industry for measuring flow through ducts. The anemometer internally logged data at 1-second intervals. To verify this measuring technique, the anemometer was calibrated at the Alaron Instruments wind tunnel calibration facility with an estimated instrument accuracy of ±3%. Calibration coefficients were applied to the raw data to produce corrected data. Further bench testing of the chimney assembly was undertaken by utilizing a 10 cm tube outfitted with a calibrated ultrasonic time of flight system. Airflow was measured by both the anemometer and the ultrasonic system with flux results yielding equal values at steady state flow.

The gas plume consisted of an upwelling convection current of gas bubbles and entrained water. The plume diameter and intensity at the surface varied constantly, shifting its position as much as 2 m over intervals of minutes. For this reason the collection funnel deployed in 2007 had a 9 m cross-sectional dimension with much of the funnel submerged to reduce wind and wave loading.

Figure 4. Seep collection flux meter used in 2007. Instrument consists of a 9 m collection funnel, most of which is submerged to reduce wind and wave loading, and a 10 cm chimney assembly in which the airflow anemometer was housed.

Figure 5 presents data from a 40 min deployment in August 2007. The data show 1-minute averaged flux rates between 0.36 and 0.86 m^3min^{-1}, with mean of 0.59 m^3min^{-1} and a standard deviation of 0.09. Marked increases and decreases in flux over a period of minutes are consistent with visual observations at the surface and measurements with a smaller collection funnel carried out in 2006.

Fall/winter

Field visits to the pond seep site were carried out in the fall and late winter. In late October, approximately 10 cm of ice had formed over the main pond, covering all but the main pockmark area where turbulence had resulted in a 19 m diameter ice-free area as measured by a laser range finder. While in some other locations in the outer Mackenzie Delta, holes in the ice persist through the winter, by March the only evidence of the large seep was a slight doming of the ice surface and the conspicuous occurrence of tension cracks radiating out from the dome. Drilling through the ice near the centre of the seep revealed ice thickness of less than 50 cm; in contrast, typical pond ice thicknesses were 1.2–1.8 m. While preparing for a through-ice ROV deployment in March 2007, a pressurized pocket of gas was penetrated at the ice-water interface which discharged a column of gasified water ~10 m high for about 1 minute.

Attempts to measure winter flux were undertaken by placing the chimney assembly directly over a 25 cm auger hole through the ice. The flow rates varied significantly as gas accumulated under the ice plate before venting in strong bursts. These bursts were short-lived lasting about 1 second followed by short periods with low flow, or even back flow, as water drained back into the auger hole. Burst intervals were

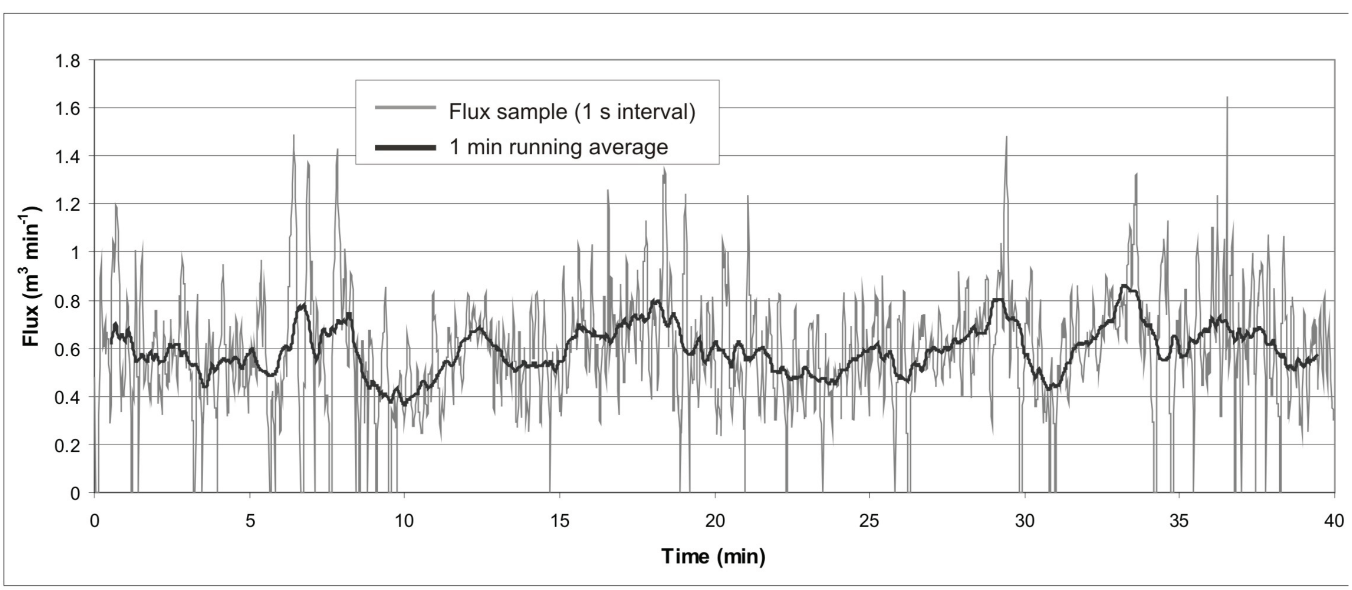

Figure 5. Flux data collected in August 2007. Grey line depicts flux data sampled at 1 s sampling interval. Black line shows the 1 min running average flux.

Table 1. Seep gas analysis from large pond seep.

Sample	CO_2 (ppm)	CO_2 *13C (ppt)	CH_4 (ppm)	CH_4 *13C (ppt)	C_2H_6 (ppm)	C_2H_6 *13C (ppt)
[1]SS-1	1030	-36.2	884400	-43.6	63	N/D
SS-2	1940	-48.8	849100	-43.2	230	-27.8
SS-3	1960	-24.5	976800	-43.0	140	N/D
[2]Nig field	9000	N/D	981900	N/D	6900	N/D

[1] SS = Gas samples collected from large seep; [2] Nig = Niglintgak gas field sample (Shell Canada Ltd. 2004a); N/D = no data

every 2–5 seconds as observed from recorded video. The measured gas flux values were influenced by the constrains of the ice plate, the possible release of gas through the radial ice cracks and the small diameter of the auger hole and were therefore too complex to resolve credible flux rates.

Geochemistry

The * [18]O and *D composition of mixed waters collected over the seeps were found to be identical to local surface water elsewhere in the pond and channels. This suggests that there are no large discharges of deeper connate waters associated with the seeps. The hydrocarbon gases from the pond seep are mainly methane with minor higher hydrocarbon homologues (Table 1). The carbon isotopic content of the methane suggests that it is of thermogenic origin. The carbon dioxide isotopic composition, however, is very light. Under some circumstances, if methane oxidation is a dominant process, then methane of microbial genesis may be mistaken for thermogenic methane. While the carbon dioxide isotope values are unusual, further evaluation of the data shows that the volume of methane is quite large relative to carbon dioxide, which is the opposite of what would be expected from the process of methane oxidation. In addition, the ethane carbon isotopic composition is of thermogenic origin. Thus the balance of data suggests the hydrocarbon gases have a thermogenic origin. The Niglintgak gas field produces a similar dry gas and may be the ultimate seep gas source.

Discussion

Formation of pockmark features

The presence of free gas in unconsolidated sediments can reduce the effective stress regime and, in turn, the sediment-bearing capacity. Identification of small orifices with almost no sediment strength, and the weak bearing strengths recorded by the STING survey over the large seeps suggest this possibility. Video from a winter ROV survey showed light sediment and fine organic material being liberated from the sediment interface into the water column by gas discharge. In some cases, gas discharge was associated with exposed root mats and organic debris which were free of sediment. The weakening of the strength of the sediments and the force of gas bubbles at the sediment interface provide a mechanism for the mobilization and exhumation of the bottom sediments and seems a possible factor in the formation of the pockmark features described.

A simple three-dimensional model can be constructed assuming 60 m of ice-bonded terrestrial permafrost with mean annual temperatures of -4°C, a basal temperature regime of 1°C for the 600 m diameter pond and 4°C for the 30 m diameter main pockmark. Applying a similar modeling methodology to that described by Taylor et al. (this volume) a through-going talik is created through the terrestrial permafrost if the pond existed on the landscape for 1000 years. The gas migrations appear to be associated with networks of root mats and organic debris. These networks may create vertical gas migration pathways, which may be a factor affecting the location of the seep/pockmarks within the larger pond.

Source of gas feeding the seeps

The seeps described in this paper are quite remarkable in both the volume of gas released and their apparent longevity. Based on an average flux rate of 0.59 $m^3 min^{-1}$, the large seep is releasing 3.10 x 10^5 m^3 of methane (2.99 x 10^5 m^3 at 0°C, 1 bar) on an annual basis. Short-term flux measurements carried out on several of the small seeps suggest rates for some of these are as high as 0.13 $m^3 min^{-1}$. In total, for the entire pond area (1 large seep, 20 small seeps), we estimate at least 5.07 x 10^5 m^3 (at STP) of gas is released annually. As the large seep feature has a similar appearance, and is virtually in the identical location to that observed by Dr. Mackay in 1963, it is not unreasonable to assume that during the past 44 years 2.23x10^7 m^3 (at STP) or almost 0.8 billion ft^3 of gas has been released from the 21 seeps. Clearly a significant source of gas accumulation is feeding these seeps continuously.

The closest known conventional gas field is the Niglintgak field located approximately 5 km to the east. This field, which contains approximately 2.8 x 10^{10} m^3 (~1 TCF) of recoverable gas, forms one of three anchor fields for the proposed Mackenzie Valley Gas pipeline project. The gas-bearing horizons occur at 760 m depth (Shell Canada Ltd. 2004b), with a similar dry gas chemistry to the pond seep samples (Table 1). Smith and Judge (1993) have identified gas hydrates in several Niglintgak wells at depths as shallow as 660 m. Assuming vertical gas migration is most likely where permafrost is absent and gas hydrate is not stable, the abrupt transition to the west of Middle Channel (Fig. 1) is an obvious potential lateral migration path to the near surface. However, further investigation is required to confirm this.

Conclusions

The following conclusions can be drawn from this study:

1) Approximately 20 small and 1 very large gas seeps have been characterized at a small terrestrial pond in the outer Mackenzie Delta;
2) The hydrocarbon gases being released are predominantly methane with minor higher hydrocarbon homologues (Table 1). The carbon isotopic content of methane and ethane indicates that the gas is of thermogenic origin;

3) Pockmark features are formed in the pond bed by vertical gas migration, causing sediment weakening and exhumation. The small seeps typically have small 0.5–1.0 m deep pockmarks, while the large seep has a 10 m deep pockmark;
4) Flux of methane to the atmosphere from these seeps is estimated to be 5.07 x 10^5 m^3 annually which, when considered over 44 years of activity, suggests a large supply of gas at depth;
5) The permafrost setting of the pond likely exerts control over the migration of gas to the surface with the site occurring at a major permafrost/gas hydrate boundary. The proximity of a large gas field down-dip and the similarity of gas geochemistry suggests a candidate for the source of the gas is the Niglintgak gas field.

Acknowledgments

The fieldwork is supported by the Polar Continental Shelf Project and the Aurora Research Institute. Financial support has been provided by the Panel for Energy Research and Development and the Geological Survey of Canada. Larry Greenland and William Hurst are thanked for their excellent field assistance. Mark Nixon's knowledge and field experience were very much appreciated. Dr Ross Mackay is gratefully acknowledged for his suggestion to embark on the study.

References

Collett T.S. & Dallimore, S.R. 2002. Detailed analysis of gas hydrate induced drilling and production hazards. *Proceedings of the Fourth International Conference on Gas Hydrates, Yokohama, Japan, May 19-23, 2002*: 1:47-52.

Dallimore, S.R. & Matthews, J.V., Jr. 1997. The Mackenzie Delta borehole project. Environmental Studies Research Funds Report No. 135, National Energy Board, Calgary, CD-ROM.

Hovland, M. & Judd, A.G. 1988. *Seabed Pockmarks and Seepages. Impact on Geology, Biology and the Marine Environment*. London: Graham & Trotman Ltd., 293 pp.

Mulhearn, P.J. 2002. *Influences of penetrometer probe tip geometry on the bearing strength estimates for mine burial prediction*. Australia: DSTO Aeronautical and Maritime Research Laboratory, 20 pp.

National Snow and Ice Data Centre. 2007. Geological Survey of Canada active-layer monitoring system documentation for Global Geocryological Database. http://nsidc.org/forms/ggd353_or.html

Paull, C.K., Ussler, W., Dallimore, S.R., Blasco, S.M., Lorenson, T.D., Melling, H., Medioli, B.E., Nixon, F.M., & McLaughlin, F.A. 2007. Origin of pingo-like features on the Beaufort Sea shelf and their possible relationship to decomposing methane gas hydrates. *Geophysical Research Letters* 34: (January 5, 2007) DOI 10.1029/2006GL027977.

Shell Canada Ltd. 2004a. Application for approval of the development plan for the Niglintgak field, Project Description, section 5.4 Functional Criteria. www.ngps.nt.ca/applicationsubmission/nig.html

Shell Canada Ltd. 2004b. Application for approval of the development plan for the Niglintgak field, Project Description, section 2.3 Petrophysics. www.ngps.nt.ca/applicationsubmission/nig.html

Sloan, E.D., Jr. 1998. *Clathrate Hydrates of Natural Gas*. New York: Marcel Dekker Inc., 705 pp.

Smith, S.L. & Judge, A.S. 1993. Gas hydrate database for Canadian Arctic and selected east coast wells. Geological Survey of Canada, Open File 2746, 54 pp.

Taylor, A.E., Dallimore, S.R., & Judge, A.S. 1996. Late Quaternary history of the Mackenzie-Beaufort region, Arctic Canada, from modelling of permafrost temperature. 2. The Mackenzie Delta-Tuktoyaktuk coastlands. *Canadian Journal of Earth Science* 33: 62-71

Taylor, A.E., Burgess, M.M., Judge, A.S., Allen, V. & Wilkinson, A. 1998. *Canadian Geothermal Data Collection - Deep permafrost temperatures and thickness of permafrost; Global Geocryological Database, CAPS version 1*. Colorado: International Permafrost Association and the National Snow and Ice Data Centre, CD-ROM.

Taylor A.E., Dallimore, S.R., Hyndman, R.D. & Wright, J.F. 2002. Comparing the sensitivity of terrestrial and marine gas hydrates to climate warming at the end of the last ice age. *Proceedings of the Fourth International Conference on Gas Hydrates, Yokohama, Japan, May 19-23, 2002*: 1:63-70.

Taylor, A.E., Dallimore, S.R. & Wright, J.F. This volume. Thermal impact of Holocene lakes on a permafrost landscape, Mackenzie Delta, Canada.

Todd, B.J. & Dallimore, S.R. 1998. Electromagnetic and geological transect across permafrost terrain, Mackenzie River Delta, Canada. *Geophysics* 63: 1914-1924.

Walter, K.M, Zimov, S.A., Chanton, J.P., Verbyla, D., & Chapin F.S., III. 2006. Methane bubbling from Siberian thaw lakes as a positive feedback to climate warming. *Nature* 443: 7 Sept 2006.

Current Capabilities in Soil Thermal Representations Within a Large-Scale Hydrology Model for Regions of Continuous Permafrost

Laura C. Bowling
Purdue University, West Lafayette, IN, USA
Keith A. Cherkauer
Purdue University, West Lafayette, IN, USA
Jennifer C. Adam
Washington State University, Pullman, WA, USA

Abstract

Despite the fact that warming in the Arctic has been greater than the global average and hydrological changes may provide important feedback responses to global climate, until fairly recently many global climate models that used to generate future climate projections have neglected the influence of permafrost on water and energy exchange in high latitude regions. At the scale of such models, the complexities of representing water and thermal exchange in permafrost systems are further compounded by the necessity for computational efficiency, coarse spatial resolution and the inability to fully describe the current state of the system. In this presentation, we explore successes and on-going challenges in simulating seasonal and decadal permafrost dynamics for the arctic region, with specific examples based on simulations using the Variable Infiltration Capacity (VIC) model, a macroscale land surface scheme. Considerable challenges still exist in appropriate definition of boundary conditions and with respect to near-surface runoff generation.

Keywords: Arctic; ground ice; hydrology; modeling; permafrost; wetlands.

Introduction

Observations of dramatic hydrologic change in permafrost environments in recent years have led to increased interest in the large-scale interactions of permafrost with surface water hydrology under a changing climate. Opposing changes in Siberian lake extent have been observed, which can be attributed to differences in discontinuous versus continuous permafrost by allowing or preventing drainage (Smith et al. 2005, Grippa et al. 2007). Observed trends in streamflow in some north-flowing arctic rivers, particularly in the winter season, may also be associated with increasing seasonal thaw and the melt of excess ground ice (Adam & Lettenmaier 2008, Cherry et al. 2006). In addition, there is continued evidence that the treatment of permafrost in the land surface schemes of global climate models can yield large sensitivities in remote teleconnections for future climate scenarios (Saha et al. 2006, Gagnon & Gough 2005). Although mathematical models of permafrost have existed for quite some time, many of these modeling efforts are poorly suited for investigating the complex interactions of the active layer hydro-thermal regime and water and energy interactions governing hydrologic response across the circumpolar arctic (Ishikawa & Saito 2006).

Representation of the spatial distribution of permafrost, particularly in alpine areas, has often relied on GIS-based empirical/statistical relationships to estimate the probability of permafrost presence at gridded locations based on proxy variables, such as snow basal temperatures (Julian & Chueca 2007), air temperature (Juliussen & Humlum 2007) and terrain parameters and land cover (Etzelmueller et al. 2007). These techniques have recently also been extended to non-alpine domains (Anisimov et al. 2002).

The state of the art in permafrost temperature modeling is typically associated with the detailed multi-dimensional modeling performed in the design of cold regions engineered structures (Zhang et al. 2006) or the evaluation of complex physical structures (Noetzli et al. 2007, Ling & Zhang 2004). Such models are often not capable of hydrologic analysis so physically detailed. Spatially distributed watershed models suitable for permafrost domains have also been developed (Zhang et al. 2000, Kuchment et al. 2000). These can be extremely useful for investigation of hydrothermal interactions at the scale of small watersheds, but more regional application is limited due to the required computational times.

Presently, the representation of permafrost within global climate models primarily includes a finite difference or finite element solution of the heat diffusion equation. The PILPS 2(e) land surface model intercomparison experiment compared simulated output from 23 land surface schemes applied to the Torne-Kalix River basin in Northern Sweden, an area of seasonally frozen ground. At the time of that experiment (2002), 16 of the 21 participating models represented soil freezing through some implementation of the heat diffusion equation (Bowling et al. 2003). The remaining models either did not include soil freezing or used a temperature index to restrict soil water movement. Due in large part to computational considerations, however, these early attempts at including physically-based permafrost algorithms within GCMs required simplifications regarding boundary and initial conditions, the energy effects of phase change and the number of solution elements.

The objective of this paper is to document the current representation of permafrost within the Variable Infiltration Capacity (VIC) model (version 4.1.0 r5), macroscale hydrology model/land surface scheme that has been adapted for applicability in arctic domains, and to explore the sensitivities and limitations of the current approach.

The Variable Infiltration Capacity Model

The variable infiltration capacity model

The Variable Infiltration Capacity (VIC) model is a water and energy balance hydrologic model suitable to application at large scales, typically applied at grid scales ranging from 0.125–2.0 degrees latitude by longitude (Nijssen et al. 2001, Su et al. 2005). It is similar to land surface parameterization schemes used in regional and global climate models, however, the VIC model is typically applied in an off-line mode, using historic meteorological observations or downscaled and bias-corrected climate model output, then calibrated and evaluated with respect to observed surface hydrology. General model structure is documented in Liang et al. (1994, 1996), Cherkauer and Lettenmaier (1999), and Cherkauer et al. (2003). In this section we wish to document the model structure as it pertains to simulation of surface water hydrology in permafrost domains.

Soil thermal solution

The core of the soil thermal solution is a finite-difference solution of the heat diffusion equation (Cherkauer & Lettenmaier 1999). The thermal solution takes into account the energy associated with phase change and freezing point depression by the soil matrix. Infiltration, percolation and baseflow are calculated based on the total and unfrozen soil moisture contents. The finite difference solution includes specification of thermal nodes that are independent of the model soil moisture layers, allowing for flexibility in the specified depth to the bottom boundary and number of solution nodes.

In addition, the bottom boundary condition can be specified as either a constant temperature or zero flux boundary. Typically, a constant temperature boundary condition is invoked by fixing the mean temperature of the annual thermal damping depth (approximately 3–4 m depth). A zero flux boundary condition is applied at a solution damping depth at least three times deeper than the thermal damping depth.

Figure 1 illustrates the influence of the bottom boundary condition on the equilibrium temperature profile. For the base simulation (gray, solid line) the model was run with a no flux boundary condition at a depth of 25 m, and spun-up for 100 years of constant 1998 weather conditions. Observed meteorology, soil temperature and soil conditions from the Betty Pingo research site, near Prudhoe Bay, Alaska, collected by the Water and Energy Research Center (WERC) at the University of Alaska Fairbanks (UAF) were used. The black line represents a similar simulation, using a 4 m damping depth, with the bottom temperature set equal to the final 4 m temperature derived from the no flux solution. The dashed lines represent repeated 100 year simulations, with an imposed air temperature gradient of 0.094°C/decade, chosen to represent the recent observed rate of change in the Arctic (Polyakov et al. 2003). It was anticipated that this example would illustrate that under the imposed temperature trend, the no flux boundary condition would allow the profile temperatures to migrate away from the equilibrium solution, while the constant temperature boundary would not. What is perhaps more striking is that in both cases, the constant temperature solution diverges substantially from the no flux equilibrium profile, resulting in colder (and more reasonable) near-surface temperatures. The zero flux boundary condition appears to be allowing the accumulation of excess heat in the bottom of the soil column, leading to excessive warming in long-term simulations. This could illustrate that a constant flux boundary, that would pass this excess heat to the deeper soil layer would be more appropriate (Zhang et al. 2003). Or it may be due to solution error associated with the choice of damping depth such as that documented by Alexeev et al. (2007). Both of these will be explored in the future.

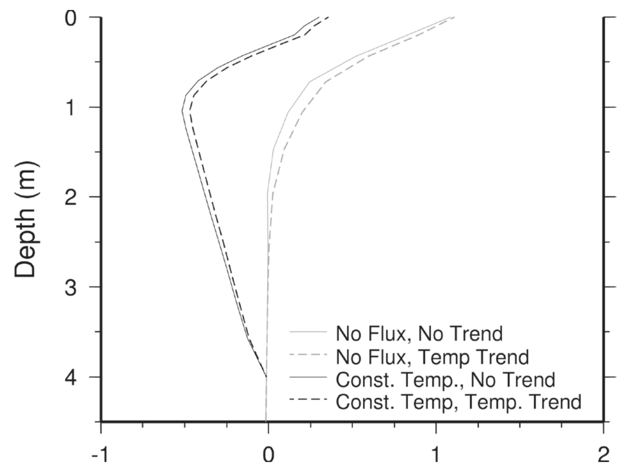

Figure 1. Illustration of the choice of boundary condition (no flux or constant temperature) on the soil temperature profile at equilibrium. Simulations were run for 100 years under constant 1998 conditions (solid lines). Simulations were then repeated (dashed) with an imposed air temperature trend of 0.094°C/decade.

Solution dynamics and node distribution

The original VIC thermal solution used an explicit solution technique with iteration at the top boundary to close the surface energy balance. The imposed node distribution allowed for three fixed nodes in the top 20 cm of soil, with nodes linearly distributed between 20 cm and the specified damping depth. Both of these simplifying assumptions contributed to model instability, particularly in the presence of dry soils or extreme temperatures. Rather than solve the heat equation explicitly for each node, an implicit Newton-Raphson method has been implemented to solve soil temperatures and ice contents simultaneously. In the rare event of non-convergence, the method defaults to the explicit solution. Because the greatest variability in temperature occurs at the near surface thermal nodes, the nodes are distributed exponentially with depth.

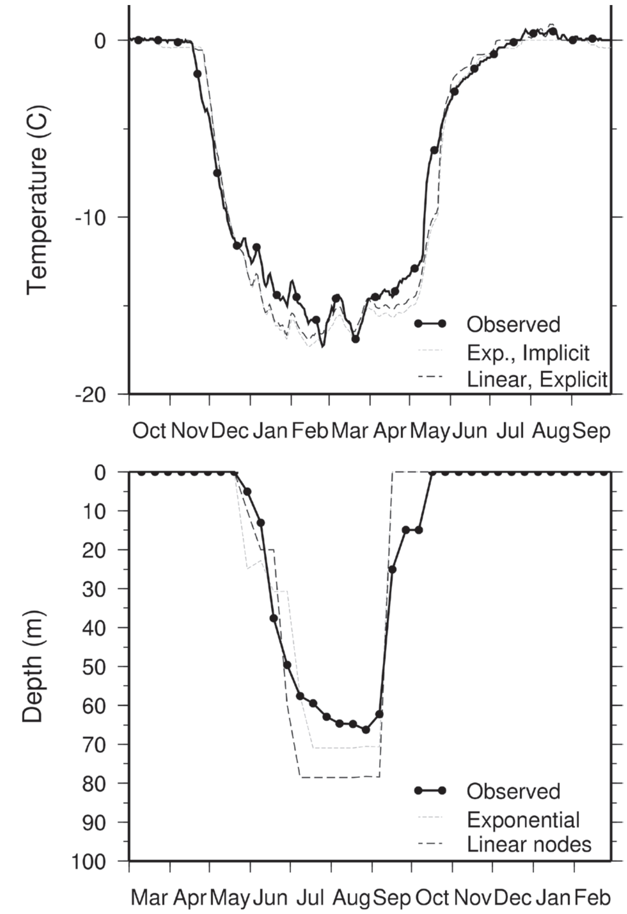

Figure 2. Example application of the VIC model to a point centered on the WERC Betty Pingo research site near Prudhoe Bay Alaska. (top) Simulated and observed 60 cm soil temperatures and (bottom) The location of the simulated and observed 0°C isotherm.

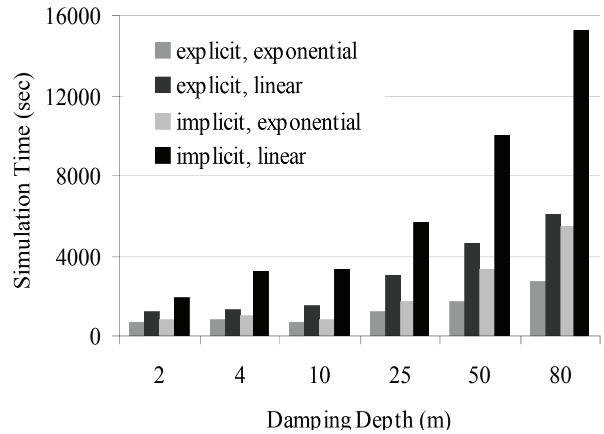

Figure 3. Comparison of system CPU times for a 100 year simulation with different damping depths using the explicit and implicit solutions and exponential and linear node distributions.

A grid transformation is performed in which the physical system exists in exponential space, while the heat equations are solved in linear space.

As shown in Figure 2 (top), when sufficient solution nodes are specified, there is negligible difference between the temperature solutions obtained from either the exponential or linear node distribution. This example utilized a constant temperature boundary at 4 m, with 20 solution nodes. Observed temperatures are taken from the WERC Betty Pingo site. The implicit or explicit solution also does not influence the predicted temperature. The benefit of the exponential node distribution is realized in more typical simulations, utilizing fewer nodes (Fig. 2). In this case, only 7 solution nodes were used, and it can be seen that by concentrating more nodes in the area of maximum change, the exponential node distribution is better able to capture the depth of the observed 0^oC isotherm.

Fewer solution nodes are advantageous with respect to total simulation time, as illustrated in Figure 3. In this case the model was run for several damping depths, with the number of solution nodes adjusted for each depth. With a linear distribution, the number of nodes was set equal to the damping depth plus 8, while only 1/3 as many nodes were used for the exponential distribution (with a minimum of 6 nodes). Overall the implicit solution is more time consuming than the explicit solution, in part because the implicit solution currently updates temperature dependent variables with each iteration, while the explicit scheme does not. By reducing the total number of solution nodes, however, the exponential distribution reduces the overall simulate time so that the implicit, exponential solution is faster than the explicit, linear solution.

Excess ground ice and ground subsidence

Excess ground ice, defined as an ice concentration above what could be held as liquid water in the soil column where the ground completely thawed, exists in various parts of the Arctic. As excess ice melts in response to climatic warming, the ground collapses and the excess meltwater is expelled to the surface. Because of ground subsidence, the water-holding capacity of the soil column is diminished. An excess ground ice and ground subsidence algorithm has been introduced to the VIC model. Each layer of the soil column is initialized with an ice fraction, which may exceed the soil porosity. Figure 4 illustrates how the expanded column depth is calculated based on the input soil column depth and ice fractions.

The expanded column depth does not change until the ice fraction to porosity ratio falls below a pre-specified ratio, f_{ice}. Even at very low temperatures, there can be a small amount of liquid water in the soil column due to freezing point depression (cf. Eq. 14 of Cherkauer & Lettenmaier 1999), therefore f_{ice} should be set to a value somewhere between 0.5 and just below 1.0, with a lower value causing subsidence to occur at warmer temperatures. After subsidence, all parameters dependant on the soil layers are updated.

Surface water interactions

As shown by Ling & Zhang (2003), shallow arctic thaw lakes can be significant sources of heat to sub-lake taliks and the surrounding permafrost. Surface water storage in small (sub-grid) lakes and wetlands is represented in the VIC model utilizing an input depth-storage relationship to determine

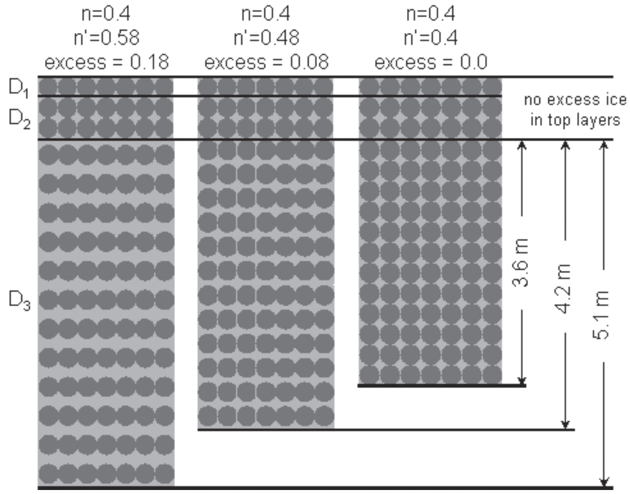

Figure 4. Example of an application of the VIC excess ice and subsidence algorithm in which the excess ice fraction in the third soil layer is initialized to 0.18 (left column). As the excess ice melts, the depth of the third soil layer decreases, and the effective porosity (*n'*) also decreases. Once effective porosity reaches soil porosity (*n*), the soil no longer subsides (right column).

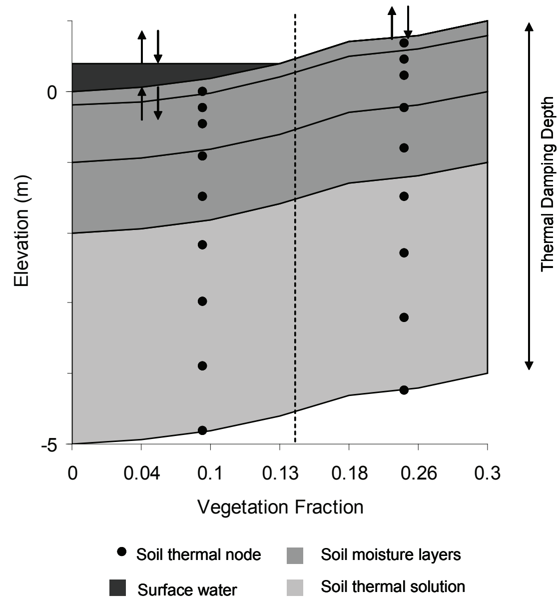

Figure 5. Illustration of the soil thermal solution for the wetland fraction of a VIC grid cell. The flooded fraction is determined using the land surface profile input as a depth-area curve. Soil temperatures are resolved independently for the flooded and upland fractions and then averaged.

spatial variability in surface water extent based on the stored volume (Cherkauer et al. 2003). The temperature profile and evaporation from stored water is resolved using an implicit one dimensional thermal model, based on Hostetler & Bartlein (1990). The original model assumed a no flux boundary condition at the lake bottom and did not resolve sub-lake soil temperatures. As illustrated in Figure 5, recent enhancements to the lake algorithm extend the thermal solution into the soil column, with a bottom boundary condition determined by the soil thermal model. Solar radiation through shallow water and conductive heat transfer from the water to the soil are balanced by the ground heat flux at the soil/water interface. The number of thermal solution nodes in the surface water is variable depending on water depth. To resolve energy instabilities in very thin water layers, the lake algorithm collapses to solve together with the surface soil layer, similar to the solution for thin snowpacks described by Cherkauer et al. (2003). This enhancement allows for exploration of the interaction of surface water storage and the soil thermal regime within the macroscale model. These interactions are further explored in Chiu et al. (these proceedings).

Discussion

Long-term simulation of the soil temperature profile requires a computational damping depth that greatly exceeds the thermal damping depth. The use of exponentially-distributed thermal nodes that are separated from the soil moisture layers results in reduced computation time, while the application of an implicit solver for the sub-surface heat equation results in greater numerical stability. There are still many issues to explore regarding the selection of appropriate damping depths and the start-up time required to

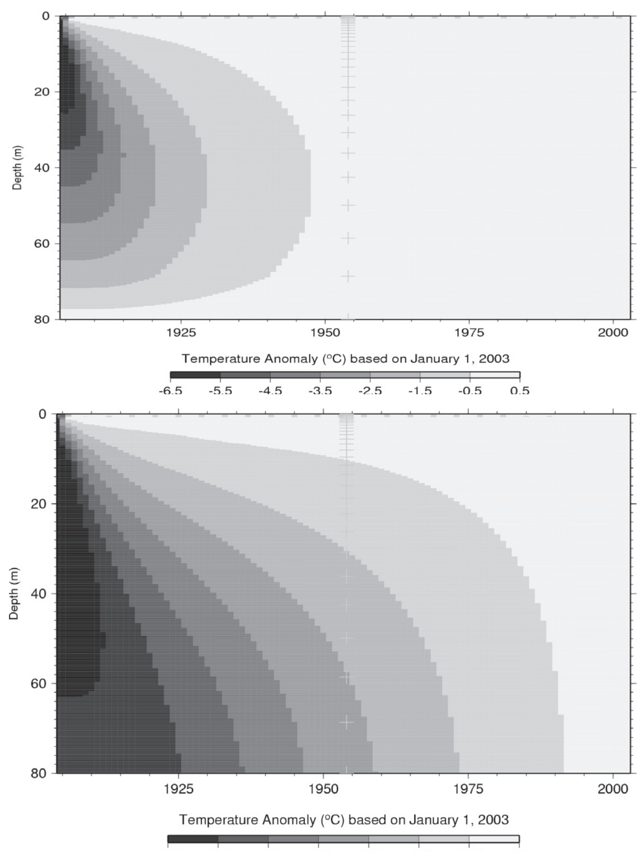

Figure 6. Assessment of the simulation time required to remove start-up anomalies with an implicit solution using exponentially-distributed nodes (shown by cross-hatches): constant temperature boundary condition (top), zero flux boundary condition (bottom).

reach stability. Figure 6 shows the temperature anomaly over time at each solution node for both the constant temperature and zero flux boundary conditions. The implicit solution and exponential node distribution were used in both cases. Temperature anomalies were calculated as the difference between the temperature on January 1 of each year, and the temperature on January 1 of the last year of simulation, so that small anomalies imply a temperature equilibrium has been reached. For the constant temperature scenario, equilibrium is reached after about 45–50 years of simulation. With the zero flux solution, it is not clear that equilibrium is reached after 100 years of simulation.

Summary

Recent studies have explored issues of computational stability, the role of excess ground ice, and permafrost/wetland interactions within the VIC land surface model. Representation of excess ground ice which exceeds the porosity of the undisturbed soil is essential for duplicating the water balance in some watersheds, especially those experiencing significant permafrost change. In other regions, the interaction between permafrost and surface water storage can be explored by resolving soil thermal fluxes under surface lakes and wetlands. These computational advances allow initial exploration of the role of large-scale permafrost-hydrology interactions on the dynamics of surface water and ground ice storage. Considerable challenges still exist in identifying the role of scale in permafrost representation, and with respect to near-surface runoff generation and the interactions between permafrost change and wetland extent.

Future work will proceed in several areas, including:

- Understanding of the problem of excessive warming in the no-flux boundary solution.
- Improved representation of runoff dynamics in permafrost areas, including the representation of subsurface water movement as a perched layer on top of the frozen transitional zone.
- Interaction between the ground subsidence algorithm and the wetland surface elevation profile, allowing dynamic increases in wetland extent associated with permafrost melt.

Acknowledgments

Funding for this research has been provided by NASA through the Northern Eurasia Earth Science Partnership Initiative (NEESPI). We acknowledge the efforts of M. Pan for implementation of the implicit solution method in the VIC model.

References

Adam, J.C. & Lettenmaier, D.P. 2008. Application of new precipitation and reconstructed streamflow products to streamflow trend attribution in Northern Eurasia. *Journal of Climate,* accepted.

Alexeev, V.A., Nicolsky, D.J., Romanovsky, V.E. & Lawrence, D.M. 2007. An evaluation of deep soil configurations in the CLM3 for improved representation of permafrost. *Geophysical Research Letters* 34(9): 9502.

Anisimov, O.A., Shiklomanov, N.I. & Nelson, F.E. 2002. Variability of seasonal thaw depth in permafrost regions: A stochastic modeling approach. *Ecological Modelling* 153(3): 217-227.

Bowling, L.C., Lettenmaier, D.P., Nijssen, B., Graham, L.P. et al. 2003. Simulation of high latitude hydrological processes in the Torne-Kalix basin: PILPS Phase 2(e) 1: Experiment description and summary intercomparisons. *Global and Planetary Change* 38(1–2): 1-30.

Cherkauer, K.A. & Lettenmaier, D.P. 1999. Hydrologic effects of frozen soils in the upper Mississippi River basin. *Journal of Geophysical Research 104*(D16): 19599-19610.

Cherkauer, K.A., Bowling, L.C. & Lettenmaier, D.P. 2003. Variable Infiltration Capacity cold land process model updates. *Global and Planetary Change* 38: 151-159.

Cherry, J.E., Alexeev, V., Liepert, B., Groisman, P. & Romanovsky, V. 2006. Acceleration of the arctic water cycle: Evidence from the Lena basin, Siberia. *EOS Transactions, American Geophysical Union* 87(52; Suppl.), Suppl. 26 Dec.

Etzelmueller, B., Farbrot, H., Gudmundsson, A., Humlum, O., Tveito, O.E. & Bjornsson, H. 2007. The regional distribution of mountain permafrost in Iceland. *Permafrost and Periglacial Processes* 18(2): 185-199.

Gagnon, A.S. & Gough, W.A. 2005. Climate change scenarios for the Hudson Bay region: An intermodel comparison. *Climatic Change* 69(2-3): 269-297.

Grippa, M., Mognard, N.M., LeToan, T. & Biancamaria, S. 2007. Observations of changes in surface water over the western Siberia Lowland. *Geophysical Research Letters* 34: L15403, doi:10.1029/2007GL030165.

Hostetler, S.W. & Bartlein, P.J. 1990. Simulation of lake evaporation with application to modeling lake level variations of Harney-Malheur Lake, Oregon, *Water Resources Research* 26 (10): 2603-2612.

Ishikawa, M., & Saito, K. 2006. Frozen ground sciences influencing climate and water cycle; reviews and perspectives. *Seppyo (Journal of the Japanese Society of Snow and Ice)* 68(6): 639-656.

Julian, A. & Chueca, J. 2007. Permafrost distribution from BTS measurements (Sierra de Telera, central Pyrenees, Spain); assessing the importance of solar radiation in a mid-elevation shaded mountainous area. *Permafrost and Periglacial Processes* 18(2): 137-149.

Juliussen, H. & Humlum, O. 2007. Towards a TTOP ground temperature model for mountainous terrain in central-eastern Norway. *Permafrost and Periglacial Processes* 18(2): 161-184.

Kuchment, L.S., Gelfan, A.N. & Demidov, V.N. 2000. A distributed model of runoff generation in the permafrost regions. *Journal of Hydrology* 240(1-2): 1-22.

Liang, X., Lettenmaier, D.P., Wood, E.F. & Burges, S.J. 1994. A simple hydrologically based model of land surface water and energy fluxes for GSMs. *Journal of Geophysical Research* 99(D7): 14,415-14,428.

Liang, X., Wood, E.F. & Lettenmaier, D.P. 1996. The soil moisture parameterization of the VIC-2L model: evaluation and modifications. *Global and Planetary Change* 13: 195-206.

Ling, F. & Zhang, T. 2003. Numerical simulation of permafrost thermal regime and talik development under shallow thaw lakes on the Alaskan Arctic coastal plain. *Journal of Geophysical Research* 108(D16): doi:10.1029/2002JD003014.

Ling, F. & Zhang, T. 2004. A numerical model for surface energy balance and thermal regime of the active layer and permafrost containing unfrozen water. *Cold Regions Science and Technology* 38(1): 1-15.

Nijssen, B., Schnur, R. & Lettenmaier, D.P. 2001. Global retrospective estimation of soil moisture using the Variable Infiltration Capacity land surface model, 1980-1993. *Journal of Climate* 14: 1790-1808.

Noetzli, J., Gruber, S., Kohl, T., Salzmann, N. & Haeberli, W. 2007. Three-dimensional distribution and evolution of permafrost temperatures in idealized high-mountain topography. *Journal of Geophysical Research* 112(F2): doi:10.1029/2006JF000545.

Polyakov, I., Bekryaev, R.V., Alekseev, G.V., Bhatt, U.S., Colony, R.L., Johnson, M.A., Makshtas, A.P. & Walsh, D. 2003. Variability and trends of air temperature and pressure in the maritime Arctic, 1875-2000. *Journal of Climate* 16 (12): 2067-2077.

Saha, S.K., Rinke, A., Dethloff, K. & Kuhry, P. 2006. Influence of a complex land surface scheme on arctic climate simulations. *Journal of Geophysical Research* 111(D22): doi:10.1029/2006JD007188.

Smith, L.C., Sheng, Y., MacDonald, G.M. & Hinzman, L.D. 2005. Disappearing Arctic Lakes, *Science* 308, 3 June: 1429.

Su, F., Adam, J.C., Bowling, L.C. & Lettenmaier, D.P. 2005. Streamflow Simulations of the Terrestrial Arctic Domain*, Journal of Geophysical Research* 110: D08112, doi:10.1029/2004JD005518.

Zhang, M., Yuanming, L., Fujun, N. & Shusheng, H. 2006. A numerical model of the coupled heat transfer for duct-ventilated embankment under wind action in cold regions and its application. *Cold Regions Science and Technology* 45(2): 103-113.

Zhang, Y., Chen, W. & Cihlar, J. 2003. A process-based model for quantifying the impact of climate change on permafrost thermal regimes. *Journal of Geophysical Research* 108(D22): doi:10.1029/2002JD003354.

Zhang, Z., Kane, D.L. & Hinzman, L.D. 2000. Development and application of a spatially-distributed arctic hydrological and thermal process model (ARHYTHM). *Hydrological Processes* 14(6): 1017-1044.

Effects of Soil Cryostructure on the Long-Term Strength of Ice-Rich Permafrost Near Melting Temperatures

M.T. Bray

University of Alaska Fairbanks, Departments of Civil and Environmental Engineering, Fairbanks, Alaska, USA

Abstract

Stress relaxation tests were performed to look at the effect of cryostructure on the long-term strength of ice-rich permafrost. Cryostructures of tested soils include micro-lenticular, remolded-massive, reticulate-chaotic, and wedge ice. Soils with remolded-massive structure shows long-term strengths three to four times greater than undisturbed soils, suggesting that data extrapolation from remolded soils to undisturbed soils can be non-conservative. Samples with reticulate-chaotic structure showed higher long-term strength in the tested temperature range than samples with micro-lenticular structure and wedge ice structure. Long-term strength relationships with temperature are presented.

Keywords: long-term cryogenic structure; cryostructure; ice-rich; long-term strength; permafrost; stress relaxation.

Introduction

Only a few published studies include information on the long-term strength behavior of ice-rich permafrost. In most cases, remolded samples are used for a variety of reasons. Remolded samples usually contain a *massive* cryostructure unless special efforts are made to create a different cryostructure. The cryostructure is the pattern of ice inclusion found in a frozen soil. Soils with *massive* structure may, but in many instances for ice-rich permafrost, do not represent the actual permafrost soil that is present. It has been recognized that the texture has an influence on the resulting strength and creep behavior (e.g., Sayles & Carbee 1981). A few studies have investigated the creep behavior of ice-rich permafrost samples (undisturbed cores) (Arenson & Springman 2005, McRoberts et al. 1978, McRoberts 1988, Savigny & Morgenstern 1986). Savigny & Morgenstern (1986) briefly explored the effects of cryostructure on the behavior of clay permafrost and found that the prominent ice veins or lenses had a large impact on the resulting creep behavior. Research in Russia showed that the orientation of segregated ice in frozen soil also had an impact on the shear strength (e.g., Pekarskaya 1965, Vialov et al. 1965). Shear strength in the direction of ice lenses was lower than the shear strength perpendicular to ice lenses.

The primary purpose of this program is to examine the impact of cryostructure on the long-term strength of ice-rich permafrost.

Materials and Methods

Soils and cryostructure

The soils used in this testing program are taken from the CRREL permafrost tunnel at Fox, Alaska. A detailed discussion of the permafrost geology and cryostructures is presented by Bray et al. (2006).

Permafrost in the CRREL permafrost tunnel is ice-rich, syngenetic permafrost deposit of Pleistocene age and is commonly referred to as the "Ice Complex" or "Yedoma" (Shur et al. 2004). This syngenetic permafrost deposit is characterized by sediments that typically contain 40–60% segregated ice by volume and large, 2–5 m wide, dark colored ice wedges. The syngenetic permafrost is representative of the original permafrost formed during deposition and sedimentation. The other defining feature of the tunnel is that extensive secondary modification occurred due to thermal-fluvial erosion that operated preferentially along the ice wedges. The resulting deposits are characterized by epigenetic permafrost with cryostructures that are different from the original syngenetic permafrost.

Cryostructures within the tunnel deposits are strong indicators of the original syngenetic and secondary refrozen deposits. *Micro-lenticular* cryostructure is the primary diagnostic cryostructure of the original permafrost. *Layered* and *lenticular-layered* cryostructures are also characteristic of the original permafrost. The modified permafrost deposits either contain *massive* or *reticulate-chaotic* cryostructures. In this study, soils with *micro-lenticular*, *massive* (i.e., *remolded-massive)*, and *reticulate-chaotic* cryostructures were used (Fig. 1). Also included is massive *wedge ice.*

Micro-lenticular cryostructure consists of thin, straight to wavy lenticular shaped ice lenses that essentially saturate the soil. Lenses are less than 0.5 mm in thickness and usually less than 4–10 mm long. Microscopic analysis shows that the soil particles are essentially suspended in an ice matrix. Typical water contents by weight are 90–130%. Frozen bulk densities range from 1.26 to 1.34 g/cm^3. *Horizontal micro-lenticular* and *vertical micro-lenticular* cryostructure is referred to below. Horizontal indicates ice lenses are perpendicular to applied principal stress. Vertical indicates ice lenses are parallel with applied stress.

Massive cryostructure consists of silt cemented together without visible segregated ice. Microscopic analysis from *massive* structures in the tunnel silts show that ice in excess of pores does exist, indicating that the soil was in a supersaturated condition when refrozen. This was confirmed by gravimetric water contents between 50–70%. Saturation for these soils is normally 30–40%.

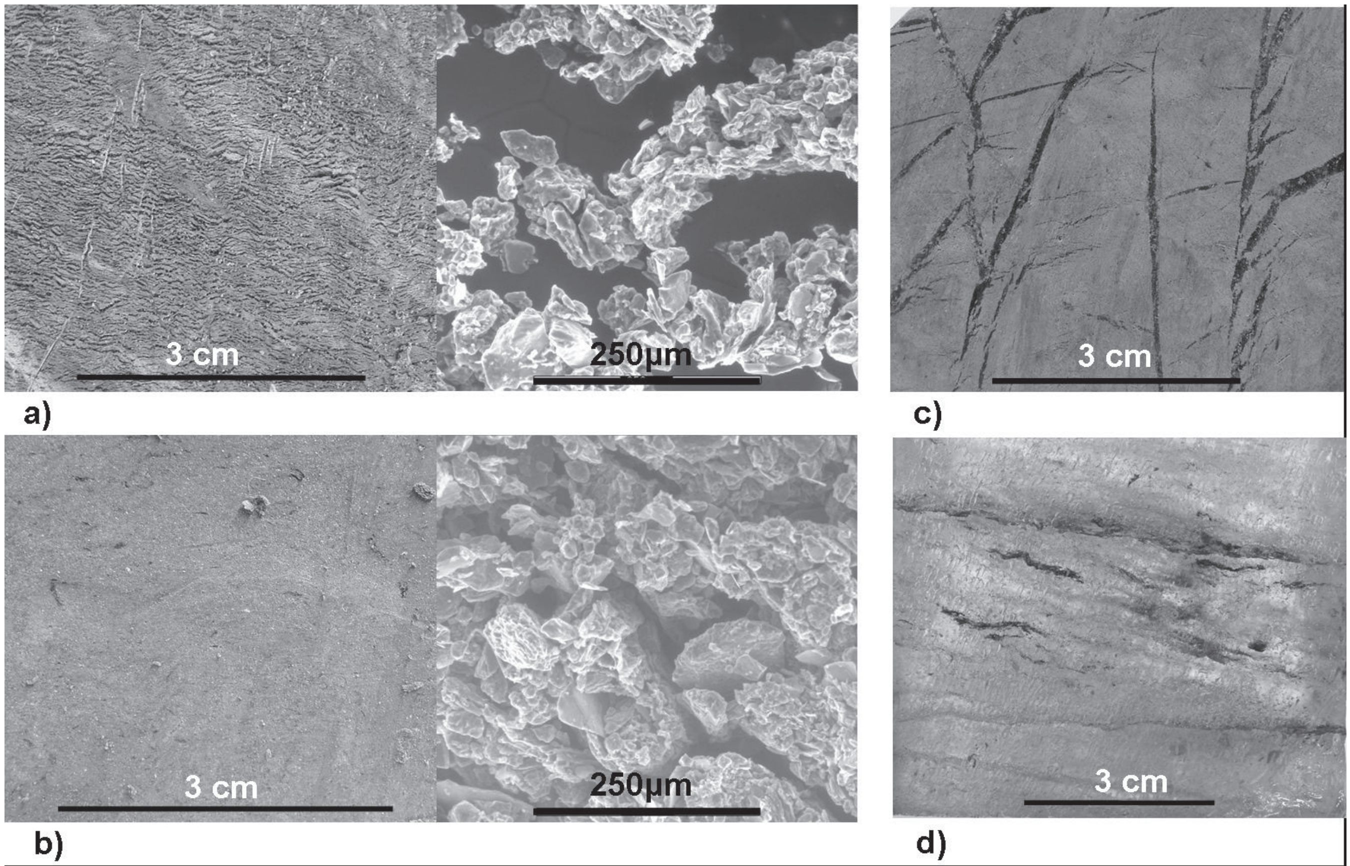

Figure 1. Images of cryostructures: a) *Micro-lenticular* cryostructure. To the right is a micro-scale image taken with an ESEM, b) *Massive* cryostructure. To the right is micro-scale image taken with an ESEM. c) *Reticulate-chaotic* cryostructure consists of larger ice lenses with massive soils between them, d) *Wedge ice*. Dark inclusions are foliation planes and sedimentation zones. Typically they run from 0° to 15°. Scales are indicated.

Remolded-massive structure represents a soil that has been reconstituted and then frozen quickly to produce *massive* cryostructure. A slurry was prepared and placed in a plastic cylinder. The sample was then vibrated to increase settlement. The sample was allowed to drain 24 hours under gravitation and then was frozen at -45ºC. The result was very little ice segregation and uniform *massive* silt. Frozen bulk densities range from 1.52 to 1.58 g/cm^3. Remolded samples were prepared from a slurry made of material from the CRREL tunnel, which had water contents ranging from 60–65%. Final drained water contents ranged from 48–52% by weight. This represents the lower range of water contents as seen from silts with *massive* structure found in the permafrost tunnel.

Reticulate-chaotic structure is characterized by randomly oriented ice lenses, 1–5 mm in thickness, and 1–5 cm in length. The silt between segregated ice lenses is *massive.* Frozen bulk density ranges from 1.33 to 1.51 g/cm^3. This structure most commonly occurs with clear ice deposits (non-foliated ice, thus not wedge ice) that we classify as thermokarst cave ice; another term used in the North American literature is *pool ice* (Mackay 1988 p. 87, 1997 p. 20). It occurs in the saturated sediments along the erosional-depositional surface. *Reticulate-chaotic* structure can be found in some silt deposits along the erosional surface without thermokarst cave ice, but it will always be found with thermokarst cave ice deposits in the tunnel. When found in association with thermokarst cave ice, the lenses are largest near the clear ice deposits.

Wedge ice was taken from large syngenetic ice wedges. They are brown to gray in color due to soil particles along foliations and organic staining. The wedges are generally 2–5 m in width with the bottom portions observed.

Testing

Undisturbed samples of syngenetic and epigenetic permafrost, along with samples remolded from the same silt, were tested. Relaxation tests were the main testing method and were performed on two electro-mechanical screw driven load frames.

All tests were conducted within a temperature range from -0.3°C to -3.1°C. Temperature stability was generally better than +/- 0.10°C for the duration of the tests. The two electro-mechanical screw driven frames were placed within a cold room that was maintained at -5°C. Insulated chambers were then placed around the sample. Temperature of the sample area was maintained using 20 liter recirculating water baths with temperature stability of +/- 0.10°C, by running the fluid through a convection driven heat exchanger located in the insulated chambers. These convection driven temperature controlled environments tended to promote substantial sublimation problems. In order to prevent sublimation of soil samples, latex membranes were placed around the sample with good results.

Relaxation tests

One of the primary focuses of the testing program was the utilization and application of relaxation tests. Relaxation tests allow for the testing of one sample as compared to a set of identical samples. The inherent variability of undisturbed soils made the use of relaxation tests an attractive alternative.

The relaxation tests were conducted by quickly loading (10–20 mm/min) the sample with a high capacity spring (approx. 71 kN/cm) placed in series with the sample to a prescribed stress level. The stress level was at least 50% of the instantaneous strength. The lower load applying platen was then fixed (stationary). As the elastic strain in the spring is released, the soil undergoes creep deformation and stress relaxation. Movement of the lower platen was monitored with an LVDT (i.e., machine relaxation) and two LVDT's were used to monitor the creep deformation occurring within the sample. The load was monitored with an electronic load cell. Temperatures were monitored by two thermistors at the sample surface. All data was automatically collected at 5 sec to 30 min intervals. Tests were typically run for 300 to 1000 hours. The longest test ran for about 2000 hours.

Long-Term Strength

The long-term strength can be defined as the stress above which deformations no longer attenuates (Tsytovich 1975, Vyalov 1980). Alternatively creep strengths are commonly predicted by recording the time to failure for a given stress. Failure is adopted as the transition from secondary to tertiary creep or a strain of 20% (Andersland & Ladanyi 1994). Strength versus time is plotted to represent ultimate creep strength. A direct experimental approach to determining the long-term strength is outlined by Tsytovich (1975) and Vyalov et al. (1966). The two approaches outlined are the ball plunger and the dynamometer, from which the long-term strength is defined as the stress at which deformation ceases (or a prescribed conditional stability is met). Thus, these approaches give directly the value of long-term strength.

The test procedures used in this work are similar to the dynamometer techniques. In many instances complete stabilization was difficult to reach, therefore two strain rates of 2.083 x 10^{-6} hr^{-1} and 2.083 x 10^{-7} hr^{-1} were considered as conditional stability states, as was done by Vyalov et al. (1966). The first strain rate condition will henceforth be referred to as "*stability condition 1*" and the second as "*stability condition 2*." Consequently, the definition of long-term strength in this work is the stress at which the conditional stability criterion is met.

Results and Discussion

Table 1, Figure 2, and Figure 3, show the long-term strengths as determined directly from relaxation tests based on the conditional stability criteria. Table 2 shows long-term

Table 1. Summary of long-term strengths for stability conditions 1 and 2.

vertical micro-lenticular (VML)		
Long-term strength (kPa) Stability Condition 1	Long-term strength (kPa) Stability Condition 2	Temperature (°C)
69.2	39.9	-0.77
46.0	23.0	-0.86
217.4	153.0	-2.78
horizontal micro-lenticular (HML)		
Long-term strength (kPa) Stability Condition 1	Long-term strength (kPa) Stability Condition 2	Temperature (°C)
56.4	33.9	-.077
48.5	27.2	-0.82
162.3	113.1	-1.81
115.7	74.8	-1.86
127.2	84.7	-1.82
209.5	161.2	-2.81
remolded-massive (RM)		
Long-term strength (kPa) Stability Condition 1	Long-term strength (kPa) Stability Condition 2	Temperature (°C)
72.5	60.7	-0.3
146.2	142.0	-0.5
136.0	130.2	-0.5
270.9	256.7	-1.0
259.0	236.6	-1.0
286.9	278.8	-1.0
532.8	506.2	-2.0
509.9	484.2	-2.0
695.4	654.6	-3.0
715.2	676.8	-3.0
reticulate-chaotic (RC)		
Long-term strength (kPa) Stability Condition 1	Long-term strength (kPa) Stability Condition 2	Temperature (°C)
86.9	63.6	-0.88
154.7	118.0	-1.85
140.0	110.0	-1.85
183.3	138.2	-2.08
213.0	151.1	-2.79
wedge ice (IW)		
Long-term strength (kPa) Stability Condition 1	Long-term strength (kPa) Stability Condition 2	Temperature (°C)
95.8	39.3	-0.44
131.0	63.0	-0.96
123.2	60.1	-0.95
101.3	42.5	-1.86
113.6	53.4	-1.86
117.7	58.6	-3.10
113.4	59.0	-3.10

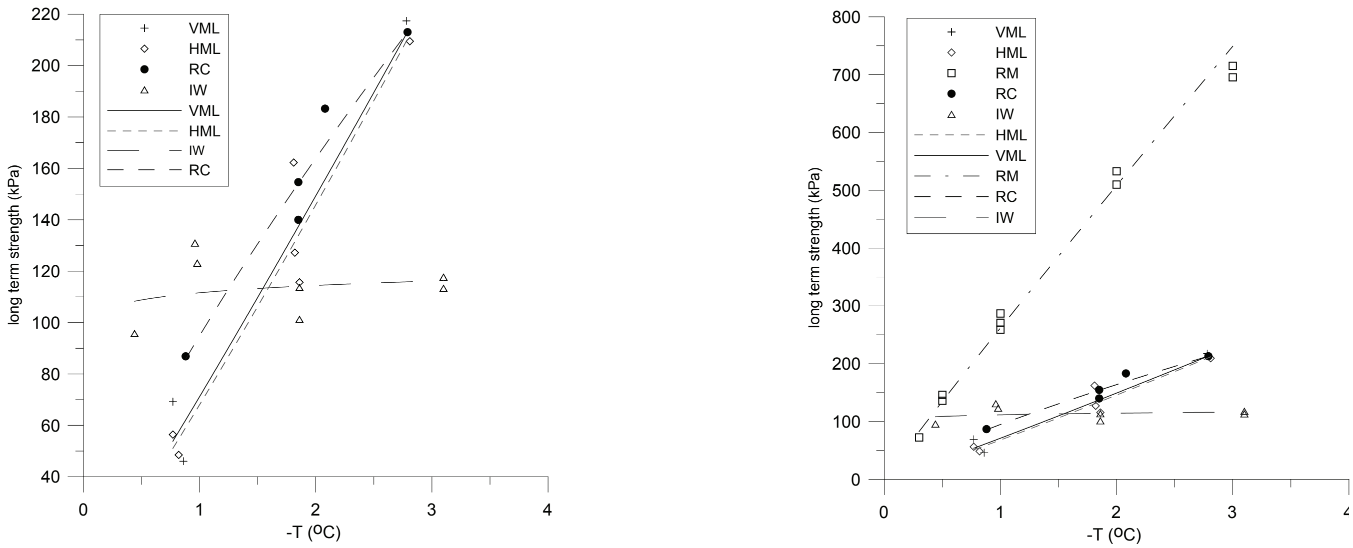

Figure 2. Long-term strength for stability condition 1.

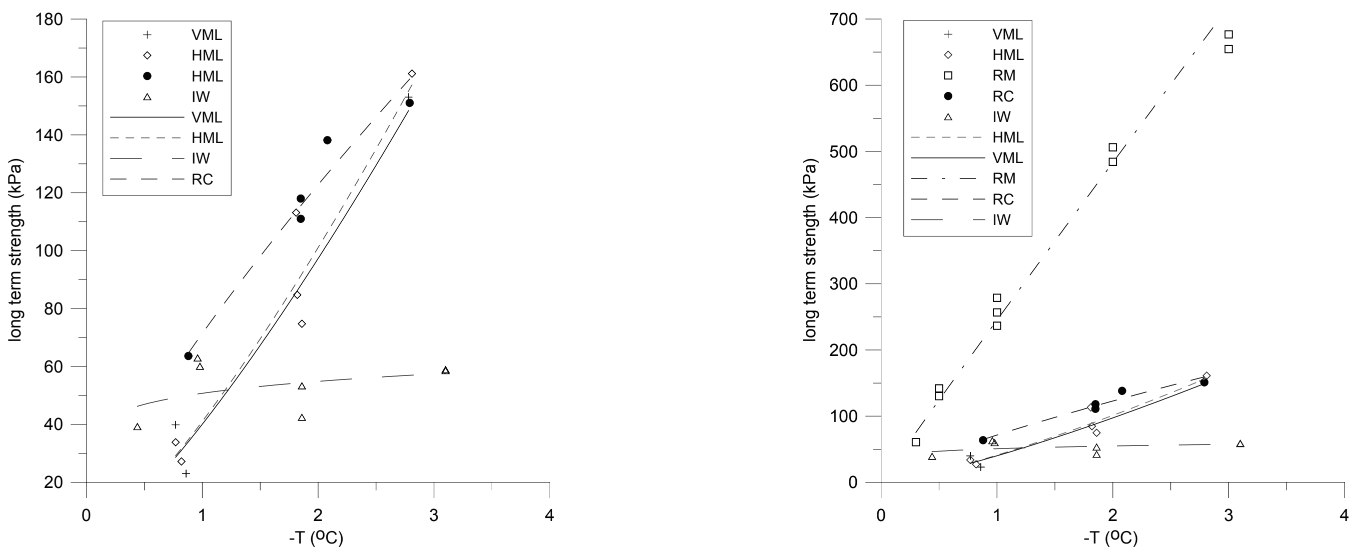

Figure 3. Long-term strength for stability condition 2.

strengths for Fairbanks silt from outside sources. Long-term strength as a function of temperature can be modeled by equation 1.

$$\sigma_{lt} = A\left|\theta\right|^{b} \tag{1}$$

where A and b are experimentally determined parameters. Values for A and b as a function of cryostructure are shown in Table 3 and 4. The value of σ_{lt} has units of kPa. A has units of kPa°C^{-b}. Temperature, θ, is the temperature in degrees Celsius below 0°C.

For soils with *micro-lenticular* structure, the value of b>1 results in concave upwards inflection of any extrapolation of the curve. The temperature range represented by this data is the zone of the most intense change in unfrozen water content. As the temperature decreases, the long-term strength generally increases at a slower rate. Therefore, extrapolation of the given equation to lower temperatures should give larger values of long-term strength than would be expected.

The long-term strength of soils with *vertical micro-lenticula*r (VML) and *horizontal micro-lenticular* (HML) structure are similar as seen from the parameters A and b as well as Figure 2 and Figure 3. Soil with *remolded-massive* (RM) cryostructure shows higher long-term strength as compared to natural soils; the strength is 3 to 4 times larger for RM soils than undisturbed soils. This is significant in that extrapolation of results from remolded soils to undisturbed soils is not conservative, based on our data.

In situ massive silts from the permafrost tunnel were not tested directly using the relaxation method. A small number of massive silt specimens were tested under uniaxial constant stress conditions. Results suggest that the in situ massive silts show higher deformation for a given stress than soils with micro-lenticular structure. Results from soils with *remolded-massive* structure should not be extrapolated to the in situ massive silts.

Table 2. Long-term strength data summary for Fairbanks silt and other ice-rich silt.

long-term strength (kPa) stability condition 1	long-term strength (kPa) stability condition 1	Temperature (ºC)	soil	source	comments
319.7	228.5	-2.0	Fairbanks silt	Yuanlin & Carbee 1987	low density, remolded
62.9	35.4	-1.7	Fairbanks silt	Thompson & Sayles 1972	Lab test on undisturbed cores
46.8	26.3	-1.7	Fairbanks silt	Thompson & Sayles 1972	Permafrost tunnel closure rates
*note: above values are based on steady state power law creep relationships					
100 Year Strength Approximations					
$\sigma_{100\ yrs}$	Temperature (ºC)	soil	source	comments	
191.2	-0.5	Fairbanks silt	Yuanlin & Carbee 1987	med. density, remolded	
343.2	-1.0	Fairbanks silt	Yuanlin & Carbee 1987	med. density, remolded	
608.0	-2.0	Fairbanks silt	Yuanlin & Carbee 1987	med. density, remolded	
864.0	-3.0	Fairbanks silt	Yuanlin & Carbee 1987	med. density, remolded	
29.3	-1.7	Fairbanks silt	Ladanyi et al. 1991	pressuremeter relaxation, field, med. strains	
133.8	-1.7	Fairbanks silt	Ladanyi et al. 1991	pressuremeter relaxation, field, low strains	
171.0	-1.0	Norman Wells silt	McRoberts et al. 1978	lab tests, undisturbed cores, ice-rich	
220.0	-3.0	Norman Wells silt	McRoberts et al. 1978	lab tests, undisturbed cores, ice-rich	

Soils with *reticulate-chaotic* (RC) structure show a slight increase in long-term strength over soils with *micro-lenticular l*structure under the temperature range tested. Extrapolation of the RC curve to colder temperatures would suggest lower long-term strengths.

The *wedge ice* (IW) shows small increase of long-term strength with temperature. Significant scatter of experimental data exists. Only at -0.44ºC is a drop in strength observed. Under the temperature range observed, the long-term strength can be considered constant. At a temperature of approximately -1.5ºC, the long-term strength of *wedge ice* falls below that of the ice-rich soils. The largest drop in long-term strength for the stability condition 2 is for *wedge ice.*

Comparison with previous works

Table 2 shows strength data for Fairbanks silt (Ladanyi et al. 1991, Thompson & Sayles 1972, Yuanlin & Carbee 1987) along with data for ice-rich silts (McRoberts et al. 1978). Data is reduced from steady state creep rates and primary creep equations. Yuanlin & Carbee (1987) worked with remolded Fairbanks silt from the permafrost tunnel. For low density (1.07–1.10 g/cm^3), the strength corresponding to stability conditions 1 and 2 were 319.7 kPa and 228.5 kPa at -2°C. Values were obtained from tests with strains rates greater than 2.88 x 10^{-4} hr^{-1}. Hundred year long-term strength (data extrapolated to 100 years) for medium density silt (1.18–1.23 g/cm^3) yielded strengths of 191.2 kPa, 343.2 kPa, 608.0 kPa, and 864 kPa at temperatures of -0.5°C, -1°C, -2°C, and -3°C, respectively. The strength data for soils with *remolded massive* structure falls between the low and medium density silts. The dry densities for soil with *remolded-massive* structure are close to the low density silts.

Ladanyi et al (1991), performed in situ pressuremeter relaxation tests in the permafrost tunnel. For medium strains, 100 year strength is equal to 29.3 kPa. For low strains, the 100 year strength is equal to 133.8 kPa. Test temperatures varied from -1.7°C to -2°C. Thompson & Sayles (1972) measured closure rates of the permafrost tunnel and performed laboratory creep tests of undisturbed soil cores. Based on steady state creep rates for laboratory tests, the strengths are 62.9 kPa and 35.5 kPa (for strain rate of 2.083x10^{-6} hr^{-1} and 2.083x10^{-7} hr^{-1}, respectively) at -1.67°C. Test strain rates were greater than 0.0018 hr^{-1}. Steady state creep conditions for the tunnel closure data yielded strength values of 46.8 kPa and 26.3 kPa. McRoberts et al (1978) reported 100 year strengths for ice-rich Norman Wells silt with strength value of 171 kPa and 220 kPa at temperatures of -1°C and -3°C, respectively. Based on water contents listed in the field study reports from the permafrost tunnel, the soil tested was most likely *micro-lenticular*. Detailed permafrost descriptions were not available. Generally, the field tests yielded lower strengths as compared to the relaxation tests in this study. It is important to note that results of the laboratory tests on undisturbed soils are extrapolations from higher strain rates under which the tests were conducted to lower strain rates. Experience indicates that extrapolation to lower strain rates generally will yield lower strengths. The low strain conditions (Ladanyi et al. 1991) are in the same range as soils with *micro-lenticular* structure. The -1°C strengths are generally higher for ice-rich Norman Wells silt as compared to soils with *micro-lenticular* and *reticulate-chaotic* structure. The -3°C long-term strengths are comparable.

Conclusions

The aim of this study was to explore the effects of the cryostructure on the long-term strength of ice-rich permafrost soils. Long-term strength data directly from relaxation tests yield comparable results to other testing methods. Soils with *remolded-massive* structure had long-term strengths 3 to 4 times greater than the undisturbed soils. In the temperature

Table 3. Experimental parameters A and b for Eq. 1 for stability condition 1.

Cryostructure	Temp range (°C)	A ($kPa^{\circ}C^{-b}$)	b (dimensionless)
VML	-0.77 to -2.78	40.057	1.2806
HML	-0.77 to -2.81	41.043	1.3004
RM	-0.3 to -3.0	244.980	0.9798
RC	-0.88 to -2.79	0.1128	0.7817
IW	-0.44 to -3.10	50.747	0.0365

Table 4. Experimental parameters A and b for Eq. 1 for stability condition 2.

Cryostructure	Temp range (°C)	A ($kPa^{\circ}C^{-b}$)	b (dimensionless)
VML	-0.77 to -2.78	40.057	1.2806
HML	-0.77 to -2.81	41.043	1.3004
RM	-0.3 to -3.0	244.980	0.9798
RC	-0.88 to -2.79	0.1128	0.7817
IW	-0.44 to -3.10	50.747	0.0365

range tested, soils with *reticulate-chaotic* structure have greater long-term strength than soils with *micro-lenticular* structure or *wedge ice.* The long-term strength for *wedge ice* had little temperature influence in studied range. Soils with *horizontal* and *vertical micro-lenticular* structure had similar long-term strength patterns.

Acknowledgments

This research was funded by NSF Alaska EPSCOR grant 0701898. Dr. Yuri Shur's advice and feedback are appreciated.

References

Andersland, O.B. & Ladanyi, B.L. 1994. *An Introduction to Frozen Ground Engineering.* New York: Chapman & Hall, 352 pp.

Arenson, L.U. & Springman, S.M. 2005. Triaxial constant stress and constanst strain rate test on ice-rich permafrost samples. *Canadian Geotechnical Journal* 42: 412-430.

Bray, M.T., French, H.M. & Shur, Y. 2006. Further Cryostratigraphic Observations in the CRREL Permafrost Tunnel, Fox, Alaska. *Permafrost and Periglacial Processes*, 17: 233-243.

Ladanyi, B., Touileb, B. & Huneault, P. 1991. Pressuremeter stress relaxation testing in a permafrost tunnel. *Proceedings of the Geotechnical Engineering Congress, Boulder, CO, 1991,* 1-11.

Mackay, J.R. 1988. Catastrophic lake drainage, Tuktoyaktuk Peninsula area, District of Mackenzie. *Current Reasearch, Part D, Geological Survey of Canada, Paper* 88-1D: 83-90.

Mackay, J.R. 1997. A full-scale experiment (1978-1995) on the growth of permafrost by means of lake drainage, western Arctic coast: a discussion of the method and some results. *Canadian Journal of Earth Sciences,* 34: 17-34.

McRoberts, E.C. 1988. Secondary creep interpretation of ice-rich permafrost. *Proceedings of the Fifth International Conference on Permafrost, Trondheim, Norway, August 2-5, 1988*: 1137-1142.

McRoberts, E.C., Law, T.C. & Murray, T.K. 1978. Creep tests on undisturbed ice-rich silt. *Third international permafrost conference* 1: 539-545.

Pekarskaya, N.K. 1965. *Shear strength of frozen ground and its dependence on texture*. CRREL, Technical translation AD 715 091. Hanover, NH: 97 pp.

Savigny, K.W. & Morgenstern, N.R. 1986. Creep behaviour of undisturbed clay permafrost. *Canadian Geotechnical Journal* 23(4): 515-526

Sayles, F.H. & Carbee, D.L. 1981. Strength of frozen silt as a function of ice content and dry unit weight. *Engineering Geology* 18: 55-65.

Shur, Y., French, H.M, Bray, M.T. & Anderson, D.A. 2004. Syngenetic permafrost growth: cryostratigraphic observation from the CRREL tunnel near Fairbanks, Alaska. *Permafrost and Periglacial Processes* 15(4): 339-347.

Thompson, E.G. & Sayles, F.H. 1972. In situ creep analysis of room in frozen soil. *Journal of the Soil Mechanics and Foundation Division* 98: 899-915.

Tsytovich, N.A. 1975. *The Mechanics of Frozen Ground.* Washington, DC: Scripta Bood Compnay, 426 pp.

Vialov, S.S., Gmoshinskii, V.G., Gorodetskii, S.E., Grigorieva, V.G., Zaretskii, Iu.K., Perkarskaya, N.K. & Shusherina, E.P. 1965. The strength and creep of frozen soils and calculations for ice-retaining structures. *Izd Akademii Nauk SSR Moscow (1962), CRREL Translation 76,* Hanover, NH: 301 pp.

Vyalov, S.S., Gorodetskii, S.E., Ermakov, V.F., Zatsarnaya, A.G. & Pekarskaya, N.K. 1966. *Methods of Determining Creep, Long-Term Strength, and Compressibility Characteristics of Frozen Soils.* Moscow: Nauka, 109pp. NRC technical translation 1364.

Vyalov, S.S., Dokuckayev, V.V. & Sheynkman, D.R. 1980. Ground-ice and ice-rich ground as structure foundations. *CRREL Translation 737*. Hanover, NH: 159 pp.

Yuanlin, Z. & Carbee, D.L. 1987. *Creep and Strength behavior of frozen silt in uniaxial compression: CRREL Report 87-10.* Hanover, CRREL, 67 pp.

Warming of Cold Permafrost in Northern Alaska During the Last Half-Century

Max C. Brewer
U. S. Geological Survey, 4200 University Drive, Anchorage, Alaska 99508-5021, USA
Huijun Jin
State Key Laboratory of Frozen Soils Engineering, 326 W. Donggang Rd., Lanzhou 730000 China

Abstract

Climatic warming has not resulted in measurable thawing of the cold (-5 to -10°C) permafrost in northern Alaska during the last one-half century. The maximum depths of summer thaw at five locations near Barrow, Alaska, in 2005 were within the ranges of the depths obtained at those exact same locations during the early 1950s. However, there has been a net warming of about 2°C at the upper depths of the permafrost column at two of the locations. Thawing of permafrost from above (increase in active layer thickness) is determined by the summer thawing index for the specific year, while any warming or cooling of the upper permafrost column results from the cumulative effect of changes in the average annual air temperatures over a period of years, assuming no change in surface conditions. Theoretically, thawing from the base of permafrost should be negligible even in areas of thin (about 100-200 m) permafrost in northern Alaska.

Key words: cold permafrost; climatic warming; northern Alaska; thawing.

Introduction

The U.S. Geological Survey (USGS) initiated a program for studying permafrost temperatures, based at Barrow, in northern Alaska beginning in 1949. The objective was to assist the U.S. Navy in solving some of the engineering problems being encountered in their oil and gas exploration of Naval Petroleum Reserve No. 4 (NPR-4). It rapidly became apparent that several areas of science and engineering would be involved in the solution of the problems. The Navy's problems included drilling bits frozen into wellbores, well-casing collapse, saline waters encountered in seismic shot holes in supposedly deep permafrost areas, obtaining year-around water supplies, obtaining electrical grounds for communications, overland transportation, and differential settlements and frost heaves in airstrips and in building foundations and floors.

Barrow is on the coast at the northernmost point (71°20′N) of land in Alaska (Fig. 1). It has an arctic marine climate with short, cool (maximum temperature +24°C, average about 4°C) summers and long, cold (minimum temperature -49°C) winters. The average annual air temperature was -12.2°C during the period from 1922 to 2004. The sun sets for the year on November 19 and does not show above the horizon again until January 24; it rises on May 10 and does not set again until August 2. Precipitation is light, about 53 mm of "drizzle-type" rain in summer, and 244 mm in the form of hard-packed snow, density about 0.4 g cm^{-2}, in winter (Black 1954), but the evaporation rate is low. Light winds are almost constant, fall storms are common, and blizzards occur frequently during the winter. The ocean is frozen over for 8 to 10 months of the year. The inland coastal plain is a flat-lying, treeless, roadless, tundra-covered area with a vast multitude of shallow lakes and ponds. For biologically oriented scientists, it is a priceless wetland; for engineers, it is a mosquito-infested swamp land in summer

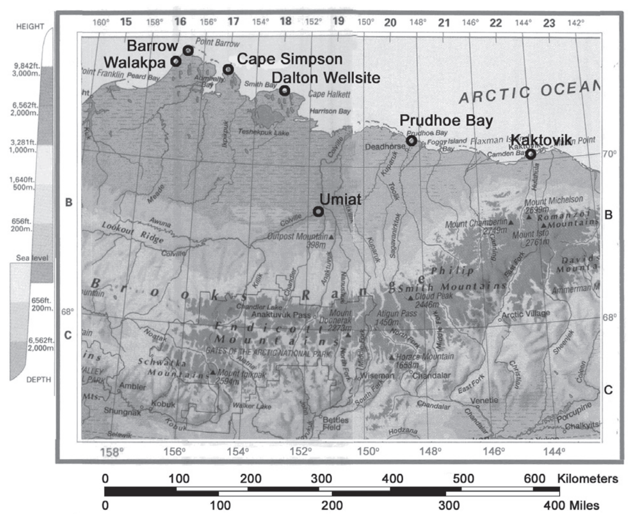

Figure 1. Permafrost study areas.

and a desolate wasteland in winter, although that is the best season for trafficability. For the Eskimo people it is, and has been for more than 6,000 years, home. The permafrost table is at depths ranging from 0.3 to about 1.0 m.

The permafrost temperatures were obtained using thermistor cables permanently frozen into the boreholes with readings obtained weekly in the shallow (0.3 to 40 m) holes, less frequently in the deeper (200 to 2000 m) oil wells abandoned during the late 1940s and the 1950s. The deeper measurements were concentrated on the solution of the problem of well-casing collapse. One very important scientific finding from those studies was that when the geothermal gradients from depth were projected upwards in some of the wells, they suggested a warming of 2 to 4°C in the upper approximately 100 m of the permafrost column (Brewer 1958a, Lachenbruch & Brewer 1959, Lachenbruch et al. 1962, Lachenbruch and Marshall, 1986, Lachenbruch et al. 1987). Lachenbruch (pers. com.) calculated that, for the warming from surface effects to have reached depths on the order of 100 m, the warming would need to have commenced about the year 1860, the estimated end of the Little Ice Age.

During the next century, an even greater change in climate in Alaska has been projected by some researchers, often using 1980 (at Barrow, the end of a mini-cooling period (Fig. 2)) as a temperature reference base. By 2100, the IPCC and HadCM2 modeling have projected a warming of 2.8°C (in the range of 1.1 to 5.0°C) in spring, summer, and fall, and 5.6°C (with a range of 2.2 to 8.9°C) in winter. Earlier measurements in more than 100 boreholes with depths ranging from 0.3 to 30 m, to more than 100 m, and on some occasions up to 650 m, on the North Slope in the 1950s and early 1960s were obtained by scientists from the USGS (Brewer 1958a, b, Lachenbruch & Brewer 1959, Lachenbruch et al. 1962, Lachenbruch and Marshal 1986, Lachenbruch et al. 1982, 1988). In addition, yearly permafrost temperature measurements were obtained along the Trans-Alaska Pipeline and at other locations in Alaska in the late 1970s (Osterkamp et al. 1994, Osterkamp & Romanovsky 1999) by a research team led by Jerry Brown, which re-occupied some of the earlier Barrow boreholes (Jin & Brewer 2002, Jin et al. 2002, Romanovsky et al. 2002), by Clow, who took over the Lachenbruch and Brewer ONPRA permafrost temperature measurement program on the Arctic Coastal Plain and Foothills (Clow & Urban 2002), and by other individuals. However, the IPCC appears to have ignored the fact that Alaska is a big area (1.5 million km^2), is surrounded on three sides by oceans/seas, that the state essentially has five climate zones, and that a cooler summer, when thawing occurs, and a warmer winter can produce a positive average annual air temperature (AAAT). Some of the reports contain a paucity of information regarding surface conditions in the areas where the temperatures were measured; the difference in snow conditions, especially the densities, preferring to use the term "temperature offset" to encompass the unknowns; vegetative covers; active layer conditions; or differences in elevations.

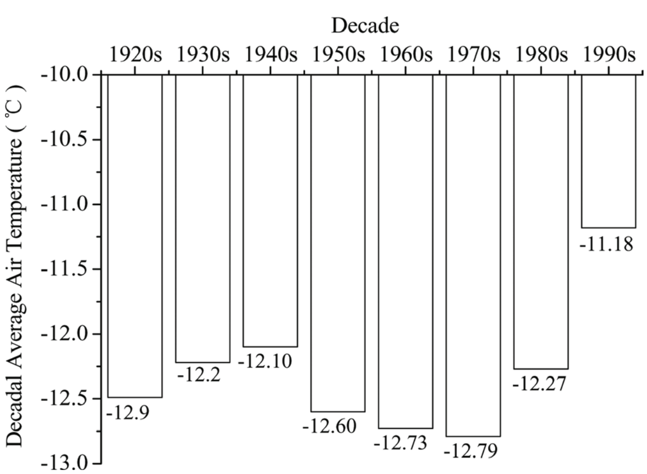

Figure 2. Decadal variations in average annual air temperatures at Barrow, Alaska, during the 20th Century.

Weather Bureau records (Fig. 2) for Barrow, Alaska, from 1922 to date indicate a decadal warming trend from the 1930s through the 1940s, a cooling from about 1950 through about 1975, the year that a major portion of the construction equipment and materials could not reach Prudhoe Bay because of the Arctic Ocean pack ice, followed by a warming trend that accelerated in the 1990s. Romanovsky provided the authors with a copy of the AAATs for Barrow from 1922 to 2004 that indicated no overall average change in the AAATs during that period.

Many modelers on climatic-warming-related degradation of permafrost have predicted significant and rapid losses of permafrost, both in thickness and areal extent in Alaska and in other regions. In so doing, the modelers have had to make many assumptions, including that the changes in air temperatures and the changes in depths to the permafrost table move in lock-step. However, the rate of dispersing the heat received downward in the permafrost profiles and the thicknesses of those profiles to absorb the heat are important factors. Of even greater importance are the complicated interactions between the atmosphere and the permafrost table, particularly those impacts involved because of the intervening poorly understood and little-studied active layer.

Study Regions

The wide, flat-lying, tundra-covered coastal plain of northern Alaska is characterized by "cold (-5 to -10°C) permafrost"; a multitude of 1- to 3-m-deep lakes; grasslands interspersed with areas of low-center ice-wedge polygons; high-center polygons adjacent to small breaks in topography, often associated with lake basins or minor drainage patterns; and meandering streams. The vegetation overlying the dominant silts and fine sands is thin (5 to 10 cm), as are the peats which are often confined to the low-center polygonal areas. MacCarthy (1952) reported an average of approximately 1 m per year of coastal erosion between Barrow and Kaktovik, approximately 560 km to the east. However, the averaging obscures the fact that the natural erosion geographically has been very uneven during the 20th century. Reportedly, the erosion has been as much as 800 m in the area of Cape Halkett (200 km east) since 1913 and a recorded 400 m at the Dalton Wellsite (Fig. 1) since 1980. The Native coastal settlements of Birnik, dating back 800 to 1000 years, and at Walakpa with an age of approximately 6,000 years still remain. The bluff at Walakapa, 17 km southwest of Barrow, retreated a measured 10.2 m between 1951 and 1997.

Umiat (69°22′N, 152°08′W, 81 m in elevation) is located in the Colville River Valley, which traverses the rolling hill country on the northern front of the Brooks Range. The vegetation tends to be tall grasses and low shrubs with birch near the river.

While the Alaskan arctic and subarctic meteorological data are sparse geographically and of limited history, the Weather Bureau's reported average annual air temperatures (AAATs) through 1954 for Barrow (-12.2°C), Kaktovik (-12.0°C), and Umiat (-12.1°C) 120 km inland were very similar, even though the first two have arctic marine environments and the latter the greater extremes of an arctic continental climate. The similar AAATs obscure the fact that the cumulative centigrade degree days of thawing for Barrow averaged 268, and for Umiat 916 during the 1950s.

Because the wind blows almost continually at Barrow, Umiat, and Kaktovak, the snow crystals are broken up and packed much like fine sand, and the snow pack develops a density of about 0.4 g cm^{-3}. The majority of the snowfall arrives during three periods: early fall before the air temperatures drop much below -20°C, during the annual early January warming period of two to three weeks, and in the late spring (April and May). Thus, its cumulative effect as a ground insulator is highly variable. Another imponderable cumulative effect is the amount of evaporative cooling of the ground resulting from the frequency, sometimes almost daily, of the July, August, and occasionally early September "drizzle-type" precipitation with the ever-present windy conditions.

Methodology

The shallow temperature cables, permanently installed, were used to investigate temperatures beneath various natural surface environments (dry grasslands, wet meadows, low- and high-center polygons, old poorly vegetated beach ridges, an active beach, shallow and moderate-to-deep lakes and lagoons, lake and ocean ice, and the near-shore Arctic Ocean) and beneath engineering structures (various types and sizes of buildings, airstrips, roads, various thicknesses of gravel fill, and beneath a recently artificially drained shallow (0.5 m) lake). Most of these study sites were located within about 8km of the Barrow Weather Station (71°18′N, 156°47′W) and thus were assumed to be impacted by relatively similar air temperatures, precipitation, and winds. The accuracy of the thermistors was 0.02°C, their sensitivity was 0.006°C. Similar shallow temperature study programs, on much reduced scales, were initiated near Umiat in 1951. The depths of thaw measurements data presented are from some of those studies, plus updates from 2001 and 2005 in northern Alaska.

Results and Discussions

Permafrost

"Cold (-10 to -5°C) permafrost," ice-wedge polygons, and wetlands are prominent characteristics of the Alaskan Arctic. The measured thicknesses of permafrost vary greatly at the same latitude, from less than 200m to an unusual thickness of 685m in the Prudhoe oilfield. Lachenbruch et al. (1987) believe that thickness resulted from anomalous thermal conductivity because of the unusual thickness of gravel swept down from the Brooks Range by the Sagavanirktok River. At Umiat, the thickness of permafrost ranges from 213 to 322m within a horizontal distance of 2.4km. That rapid change in the thickness may have resulted from changes in the course of the Colville River. Brewer (1958a) also found

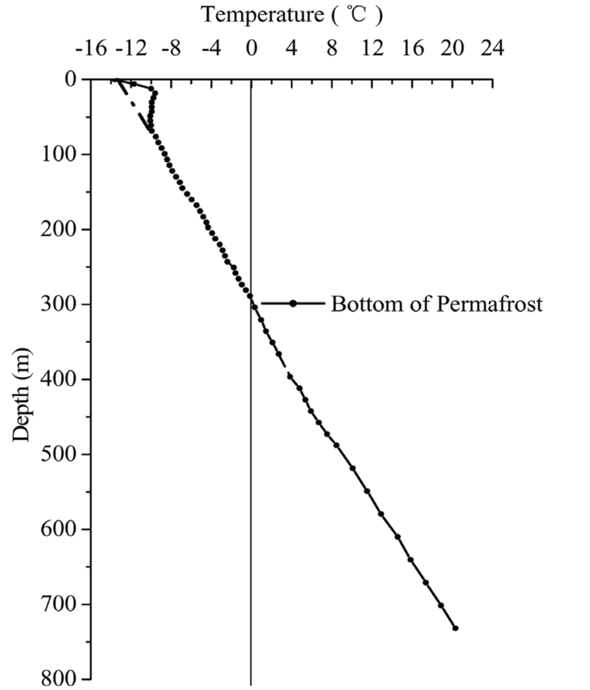

Figure 3. Thermal profile for Simpson 28 Well 112 km southeast of Barrow, Alaska. The broken line at depths of 0-80 m is the linear projection based on the thermal gradient from below.

that the temperatures at depths of 20 m (depth of significant annual change of 0.01 to 0.03°C) within a radius of 8 km from the Weather Bureau Station at Barrow varied from -7.3 to -10.7°C, to +1.0°C beneath a freshwater lake 2.8 m in depth.

The geothermal profile for Simpson Well 28 (Fig. 3) obtained two years after installation of the cables in the wellbore and, projected upwards, is one of those used by Brewer (1958b), Lachenbruch & Brewer (1959), and Lachenbruch et al. (1962) to suggest a warming of the upper part of the permafrost by 2 to 4°C during the previous century. The consistent slope of the profile below 70m suggests a remarkably steady surface environment (air temperature, precipitation, and vegetative cover) for the previous several centuries.

The geothermal profiles in Figure 4 were obtained at the end of the unusually warm 1954 summer, from within a horizontal radius of approximately 5 km near Barrow. The figure is intended to illustrate the relative impacts of various natural surface covers on the near-surface temperatures. The temperatures at 2 m are at the maximum for the year although, because of the phase lag, those below that depth will continue to rise for several weeks or months thereafter.

The permafrost temperatures at a red grass low-center polygonal area in 1954, and from a replacement cable installed in the same spot by Kenji Yoshikawa in 2001, are shown in Figure 5 (Romanovsky et al. 2002). The cumulative maximum warming indicated was 1.69°C at about the 11 m depth. The vegetative cover in Figure 5, except for the wetness (a bit drier), the area was little changed after 47 years. However, the data in Table 1 indicate a minor greater measured maximum depth of thaw (thickness of the active layer) in 1954.

The 1950s cooling (0.80°C at a depth of 4.7 m) beneath the adjacent, unusually wide polygonal trough, about 10 m distant, was much greater than at the same depth beneath the polygon. This was in spite of the fact that the trough quickly accumulated a thickness of about 1.0 m of drifted, hard-packed snow (insulating effect is over compensated by the additional time required for melting (Drew et al. 1958)), whereas the top of the polygon rarely had more than 4 to 10 cm of snow cover in winter due to the ever-prevailing winds. Permafrost temperatures at depths of 30 m at other Barrow installations indicate a cooling of 0.23 to 0.30°C during the period 1953-1960.

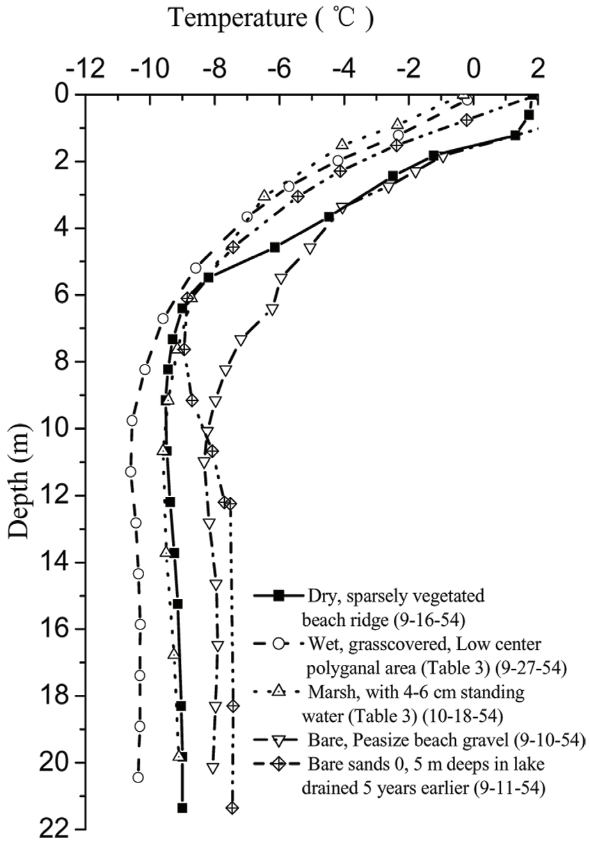

Figure 4. Geothermal profiles beneath different surface covers within a radius of 5 km, Barrow, Alaska.

The temperature profiles (Fig. 6), obtained weekly from a frozen-in cable beneath a high-center polygon, indicate a cooling of the permafrost of about 0.37°C, at 4.7m, between the years 1953 and 1960. A repeat of the measurements in 2001 indicates a cumulative warming of the permafrost at that depth of 1.66°C during the intervening 41 years.

Table 1. Maximum depths (cm) of thaw, Barrow, Alaska.

Date	Dry, high-center polygon with good drainage	Date	*Low-center polygonal area with 4-10 cm standing water	Date	Marsh with 4-6 cm standing water and moss/grass
9-08-52	48.3	9-01-52	25.4	9-07-53	26.7
9-07-53	55.9	9-07-53	27.3	7-27-54	26.7
9-14-54	63.5	8-23-54	30.5	9-15-56	26.7
8-25-56	41.3	8-25-56	25.4	8-05-57	28.6
		9-07-57	33.0	8-18-58	31.8
				9-15-59	29.2
Averages	52.3		28.3		28.3
9-08-05	47.2		34.0		19.1**

* No visible change in surface cover during 1951-2005. This site is shown in Figure 5 and 6.

** Area had more and taller grasses in 2005.

The year 1953 had a very cool summer, and 1954 and 1957 had unusually warm summers.

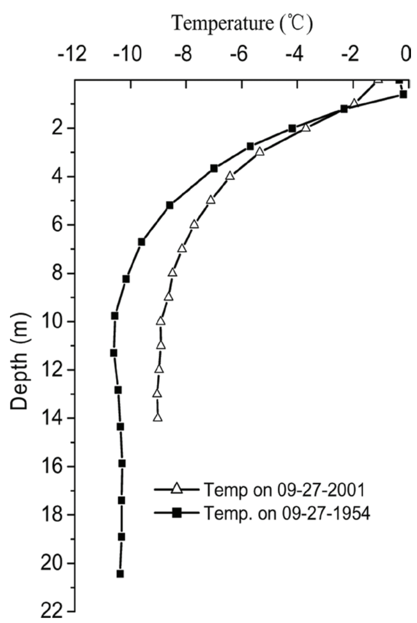

Figure 5. Geothermal profile beneath low-center polygon area with 4-10 cm standing water at Barrow, Alaska. This site had the coldest temperature measured at 20 m in Northern Alaska.

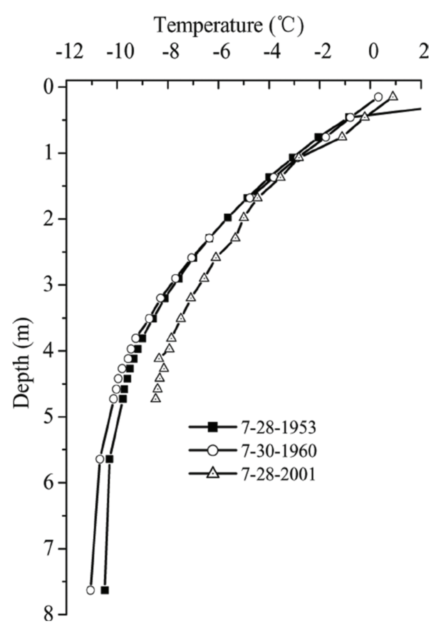

Figure 6. Geothermal profiles for a high-center polygon, Barrow, Alaska.

An illustration of the impact on permafrost temperatures resulting from modifying the surface is shown in Figure 7. Tracked personnel vehicles, traversing a moderate slope at Umiat during a spring/summer, caused the tundra in the trail to become badly damaged. The thermistor cables installed beneath the bare trail and in an adjacent undamaged area two years later indicated that the active layer beneath the trail had deepened from about 0.6m to about 1.5m, but that the annual permafrost temperatures had decreased by about 1.3°C at 6.1m. In other words, the active layer was increasing in thickness at the expense of thawing a bit of the upper permafrost, while at the same time the annual average temperatures of the underlying permafrost were decreasing. The same phenomena occur in gravel fills at Barrow, and it was the basic tenant behind the construction, in 1955, of the permanent roads and airstrips for the radar stations along the Alaskan Arctic coast and for the permanent drilling pads and other facilities constructed in the Prudhoe Bay oilfields. The 1.5m of fill cools and brings the top of the permafrost into the base of the fill in cold permafrost areas, thus providing a solid foundation.

Depths of thaw

Since deepening of the active layer and/or permafrost thaws only when the temperatures are above freezing for an extended period of time, the annual change in the thawing index tends to provide far greater insights regarding the near-surface permafrost than do the changes in the annual average air temperatures.

The cumulative °C-days of thaw at Barrow in 1950 and 1952 (Table 2) were about the same, approximating the decadal average, but the average annual air temperature in 1952 was 2°C colder than in 1950, indicating colder winter air temperatures, which have nothing to do with the thawing of permafrost or the active layer.

The maximum depths of summer thaw were obtained using a pointed steel rod, 0.64 cm in diameter, pushed to refusal (sounded like hitting concrete) at an average of 4 points at about 1 m distance surrounding the thermistor cables (Tables 1 and 3). The measurements generally were made in early September, as there usually is little thaw of permafrost, or warming of lake (Brewer 1958b, Drew et al. 1958), after the first week in August in northern Alaska.

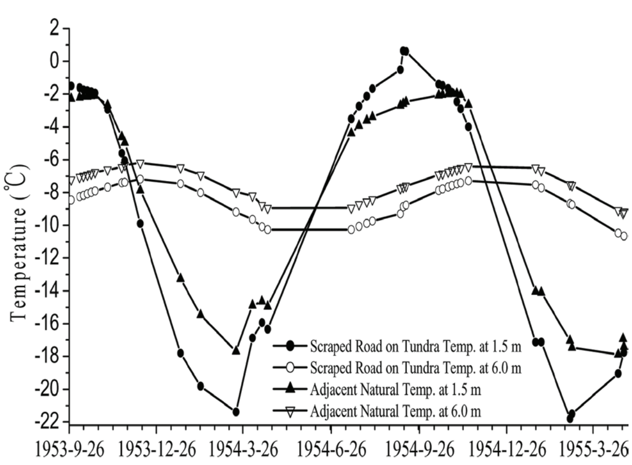

Figure 7. Time-temperature series beneath damaged and adjacent undamaged tundra, 1953-1955, Umiat, Alaska.

Summary and Conclusions

Observation over the last 50 years indicates that in Arctic Alaska there definitely has been a warming of the upper layer of permafrost, and just as definitely there has been no thawing of the permafrost during the same 50 years because the depths of thaw have remained unchanged.

Projecting temperatures upwards in permafrost is a relatively easy and scientifically repeatable way to study climate change because the equilibrium geothermal profile has long been established, the impacts of the active layer are avoided, and only heat conduction is involved. This was the approach used by Brewer and Lachenbruch in 1958, 1959, and 1962 when they noted an apparent warming of 2-4°C in the upper permafrost. The big problem is bridging the complicated active layer, which is subject to short-term cyclical changes and numerous unknown factors, to connect with the atmosphere where most climatic measurements are being obtained.

Table 2. Average annual air temperature (AAAT) and thawing index (TI) at Barrow, Alaska during 1950-1960.

Year	AAATs (°C)	TI (°C·d)
1950	-10.6	284
1951	-11.4	448
1952	-12.8	264
1953	-13.3	186
1954	-11.8	472
1955	-14.8	116
1956	-13.9	121
1957	-12.3	324
1958	-11.5	384
1959	-13.6	198
1960	-13.3	154
1950-1960 Average	-12.7	268
2000	-11.8	304
2001	-11.9	220

Table 3. Maximum depths (cm) of thaw in adjacent dry and wet areas (Figure 7 and text), Barrow, Alaska.

Date	Grass-covered, high-center Polygon	Adjacent 1- m deep wet polygonal trough
09-05-53	29.2	33.0
09-04-54	36.8	
08-22-55	28.6	
09-14-56	31.8	
09-09-57	41.7	
09-10-58	33.0	35.6
09-11-59	25.4	26.7
09-10-60	27.9	27.9
1953-1960 average	31.8	30.8
9-08-05	28.2	36.1

Brewer (1958b), Lachenbruch & Brewer (1959), and Lachenbruch et al. (1962) discussed an apparent warming of permafrost in Arctic Alaska beginning about 1860, the estimated end of the Little Ice Age, without making any predictions regarding the future. But many recent publications have discussed air temperature warming in Arctic Alaska beginning about 1980, the end of a mini-cooling period at Barrow (Fig. 2), projecting temperatures forward and suggesting worldwide implications. Projecting forward from an extreme point in a cycle would appear to be of questionable scientific validity.

Chronicling climatic change is a long-term multi-faceted endeavor that necessitates the observation of numerous potentially impinging aspects of nature, not just changes in temperature. Obtaining those needed observations sometimes is hampered by the fact that advancements in the technologies in instrumentation, communications, and transportation have outstripped the willingness and ability of researchers to obtain field observations, i.e., one can rapidly acquire data without the needed field environmental information concerning how the data may have been or are being compromised by extraneous factors.

The many mixed views on the changes in permafrost and its distribution under a changing climate have highlighted the paucity of integrated scientific knowledge and information, due to a lack of long-term observations, as recorded by Hinzman et al. (2005).

A determination of the actual effects of the active layer, which lies between the permafrost and the atmosphere and hence the correlations between the permafrost and climatic change, is the biggest problem. At least a proximate solution, which cannot be derived by imagery or modeling, is critical.

References

Black, R.F. 1954. Permafrost: a review. *Bulletin of the Geological Society of America* 65: 839-856.

Brewer, M.C. 1958a. The thermal regime of an arctic lake. *American Geophysical Union, Transactions* 39: 278-294.

Brewer, M.C. 1958b. Some results of geothermal investigations of permafrost in northern Alaska. *American Geophysical Union, Transactions* 39: 19-26.

Clow, G.D. & Urban F.E. 2002. Large permafrost warming in Northern Alaska during the 1990s determined from GTN-P borehole temperature measurements. *American Geophysical Union, Fall Meeting 2002, Abstract* #B11E-04.

Drew, J.V., Tedrow, J.C.F., Shanks, R.E. & Koranda, J.J. 1958. Rate and depth of thaw in Arctic soils. *American Geophysical Union, Transactions* 39: 697-701.

Hinzman, L.D., Bettez, N.D., Bolton, W.R. & Chapin, F.S. 2005. Evidence and implications of recent climatic change in Northern Alaska and other Arctic regions. *Climatic Change* 72: 251-298.

Jin, H.J. & Brewer, M.C. 2002. Correlating changing annual air and permafrost temperatures in northern Alaska. *Abstracts: AGU Fall Meeting*, San Francisco, CA, 6-10 December 2002.

Jin, H.J., Brewer, M.C. & Perkins, R.A. 2002. Ground Temperatures across the Old and New Roads at Mile 130, Richardson Highway during 1954-1962. *Cold Regions Engineering: Cold Regions Impacts on Transportation and Infrastructure*: *Proceedings of the 11th International Conference*, May 20–22, 2002, Anchorage, Alaska. K.S. Merrill (ed.). ASCE, Washington D.C., 724-735.

Lachenbruch, A.H. & Brewer, M.C. 1959. Dissipation of the temperature effect of drilling a well in Arctic Alaska. Washington D.C.: *U. S. Geological Survey Bulletin*, 1083-C, USGPO, 73-109.

Lachenbruch, A.H., Brewer, M.C., Greene, G.W. & Marshall, B.V. 1962. Temperatures in permafrost. *Temperature: Its Measurement and Control in Science and Industry*, Vol. 3. New York: Reinhold Publishing Co., 791-803.

Lachenbruch, A.H., Sass, J.H., Marshall, B.V. & Moses, T.H. Jr. 1982. Permafrost, heat flow, and the geothermal regime at Prudhoe Bay, Alaska. *Journal of Geophysical Research* 87(B11): 9301-9316.

Lachenbruch, A.H. & Marshall, B.V. 1986. Changing climate geothermal evidence from permafrost in the Alaskan Arctic. *Science* 234: 689-696.

Lachenbruch, A.H., Sass, J.H., Lawver, L.A. & Brewer, M.C. 1987. Temperature and depth of permafrost on the Alaskan arctic slope. In: Tailleur I. and Weimer P. (eds.), *Alaskan North Slope Geology*, Vol. 2. Society of Economic Paleontologists and Mineralogists, Pacific Section: Bakersfield, CA, USA, 545-558.

Lachenbruch, A.H., Cladouhos, T.T. & Saltus, R.W. 1988. Permafrost Temperature and the Changing Climate. In: *Permafrost, 5th International Conference on Permafrost*, Vol. 3. S. Kaare (ed.). Trondheim, Norway: Tapir Publishers, 9-17.

MacCarthy, G.R. 1952. Geothermal investigations on the Arctic slope of Alaska. *American Geophysics Union Transaction* 33: 589-593.

Osterkamp, T.E., Zhang, T. & Romanovsky, V.E. 1994. Evidence for a cyclic variation of permafrost temperatures in Northern Alaska. *Permafrost and Periglacial Processes* 5: 137-144.

Osterkamp, T.E. & Romanovsky, V.E., 1999. Evidence of warming and thawing permafrost in Alaska. *Permafrost and Periglacial Processes* 10(1): 17-37.

Romanovsky, V.E., Yoshikawa, K., Brewer, M.C., Jin, H.J. & Brown, J. 2002. A permafrost observatory at Barrow, Alaska. In: *Proceedings of the Arctic System Science Program All-Hands Workshop*, February 20-23, 2002. J. Overpeck (ed.). Fairbanks, AK: Arctic Research Consortium of the United States, 196.

Characterization and Classification of Topsoils as a Tool to Monitor Carbon Pools in Frost-Affected Soils

Gabriele Broll
University of Vechta, Vechta, Germany
Charles Tarnocai
Research Branch, Agriculture and Agri-Food Canada, Ottawa, Canada

Abstract

Many frost-affected soils contain large pools of carbon that are very sensitive to climate change. Detailed mapping of topsoils and their spatial variability could help to improve the reliability of soil carbon data. The topsoil, which acts as the interface between vegetation and subsoil, is an indicator of ecosystem change. The objective of this paper is to give an overview of developments in topsoil/humus form characterization and classification. This information can be used to show the spatial variability of topsoils and, thus, carbon pools, as well as the biological activity in the Arctic. Identification, sampling, and analysis of representative pedons for the soil and humus forms will improve the quality of the data required for upscaling and, additionally, will provide information on the soil biocoenoses, all interacting organisms living in soil. Special requirements for frost-affected sites should be considered when topsoils are mapped.

Keywords: carbon stocks; permafrost-affected soils; seasonally frozen soils; soil biocoenoses; topsoil.

Introduction

Many frost-affected areas (perennially or seasonally frozen) with large carbon stocks are very sensitive to climate change. Topsoils or humus forms are the interface between vegetation and subsoil (Fig. 1). They can act as indicators for changes of ecosystems driven by climate change or land-use change. Up to now new approaches of international working groups to characterize and to classify topsoils and/or humus forms are ignoring frost-affected sites. On the other hand, topsoils of subarctic and arctic sites will probably change quickly due to climate warming, wild fires, and flooding.

Objectives of this paper are:

- To present developments in characterization and classification of topsoils and humus forms, which could be used in the Arctic and Subarctic;
- To show examples for spatial variability of topsoils and thus carbon pools as well as biological activity in the Arctic and Subarctic;
- To present ideas how knowledge about topsoils can help to improve the interpretation of carbon data, which is of special interest for the northern environment containing large carbon pools.

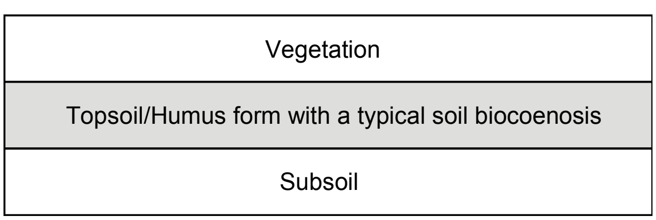

Figure 1. Topsoil as interface between vegetation and subsoil, acting as habitat for a typical soil biocoenosis and being a product of the soil organisms based on litter input and mineral components.

Characterization, Classification, and Indicator Function

Topsoils and humus forms include litter (L), in many cases organic horizons (OF/F, OH/H), and the A horizon. In agricultural areas, the A horizon is in almost all cases the only part of the topsoil. Thus, soil structure and the quality of the soil organic matter as results of the soil biological activity can be used for characterizing the topsoils. In forests usually different organic layers indicate different decomposition rates. Modeling approaches focusing on organic layers help to improve predictions for changes of carbon pools in the environment (e.g., Akselsson et al. 2005). In the Subarctic and Arctic there are different types of topsoils, from the more or less pure geological substrate to thick organic layers.

The topsoil acts as habitat for the soil organisms, and at the same time it is a product of the soil organisms. The humus form is the mirror of the soil biocoenosis, their composition, and their activity result in different decomposition rates. So why not look for the soil organisms and their activity directly? It is time-consuming as well as costly and requires specialists. This should be done for representative monitoring sites which could then serve as reference sites. Humus forms can be used as indicators for environmental change instead of the soil organisms themselves. Humus form data could be made available for large areas within a relatively short time. Their description is quite easy to learn and probably new remote sensing methods will be available in the future, but first, worldwide accepted guidelines for characterizing and classifying topsoils have to be developed.

A first step in this direction was made in cooperation with the FAO that has a draft for characterizing topsoils. One outcome of a FAO project was that in principle, a great coincidence between characterizations of humus types and

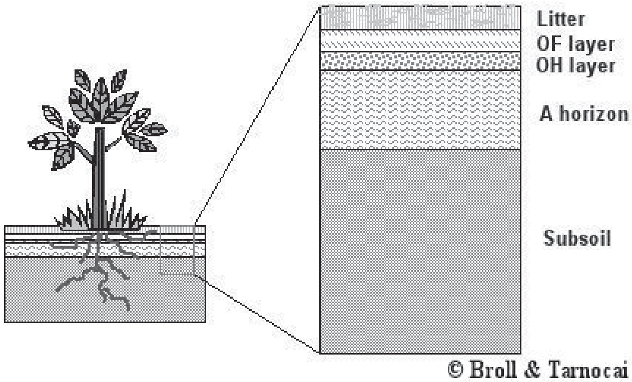

Figure 2. Appearance of carbon in the vegetation and in different soil horizons; example for non-frost-affected soils.

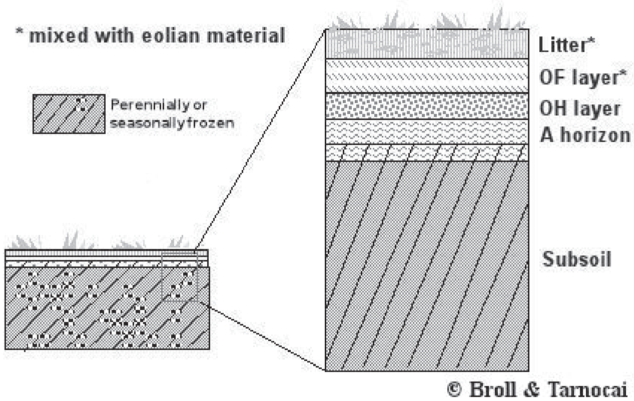

Figure 3. Appearance of carbon in the vegetation and in different soil horizons; example for static frost-affected soils.

topsoils exists which appears to be an appropriate basis for further correlation, and, finally, incorporation in the World Reference Base for Soil Resources. This could promote worldwide use of this system. In case of forest sites, the topsoil characterization can be improved by incorporation of humus typology using qualifiers for the organic layers. In case of grassland or arable land usually lacking organic layers, topsoil characterization can be improved by using qualifiers for soil biological activity in the A horizon. The biological qualifiers provide a good basis for soil quality assessment besides chemical and physical qualifiers (Broll et al. 2006).

Looking at the carbon pools specifically in non-frost-affected soils, carbon is stored in the vegetation, in the organic layers, in the A horizon, and in the subsoil, where generally only small amounts of carbon are found (Fig. 2). The carbon stocks in the topsoil depend on site conditions such as moisture.

Looking at frost-affected soils of the Arctic, especially those perennially frozen, only little amounts of carbon are stored in the actual vegetation but large amounts can be stored in the soil, both in the topsoil and in the subsoil (Figs. 3, 4).

The topsoil can have, for example, a thick moss layer on wet sites. In the boreal region, about one-third of the carbon

Figure 4. Turbic cryosols and static cryosols at Pangnirtung Pass on Baffin Island, Canadian Arctic.

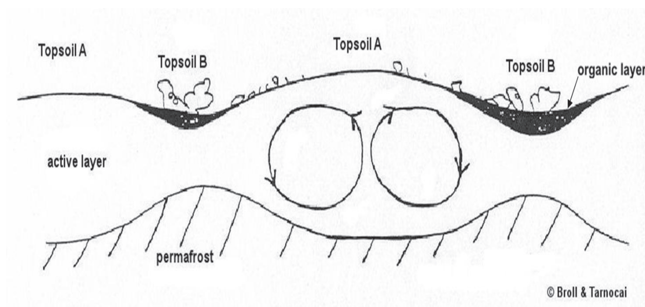

Figure 5. Turbic cryosol with two different topsoils occurring regularly in the landscape (modified after: Heal et al. 1998).

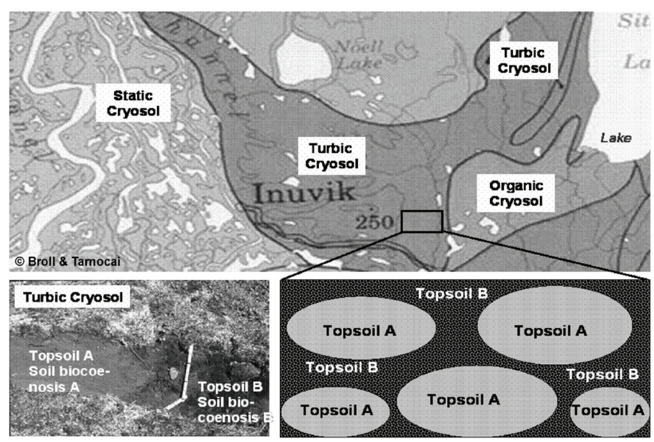

Figure 6. Distribution of Cryosols, topsoils, and soil biocoenoses in the Canadian Arctic (Mackenzie River delta area).

is in the vegetation and two-thirds in the soil. Very often the topsoil in the Arctic is enriched with eolian material. Due to formerly warmer climate along with high production of biomass, large amounts of carbon can be found also in the subsoil, where the carbon is stored in the permafrost.

Turbic Cryosols (cryoturbated, permafrost-affected soils) (Fig. 4) contain larger amounts of carbon than Static Cryosols (non-cryoturbated, permafrost-affected soils) (Tarnocai et al. 2003, Tarnocai & Broll 2008) and show even more specific

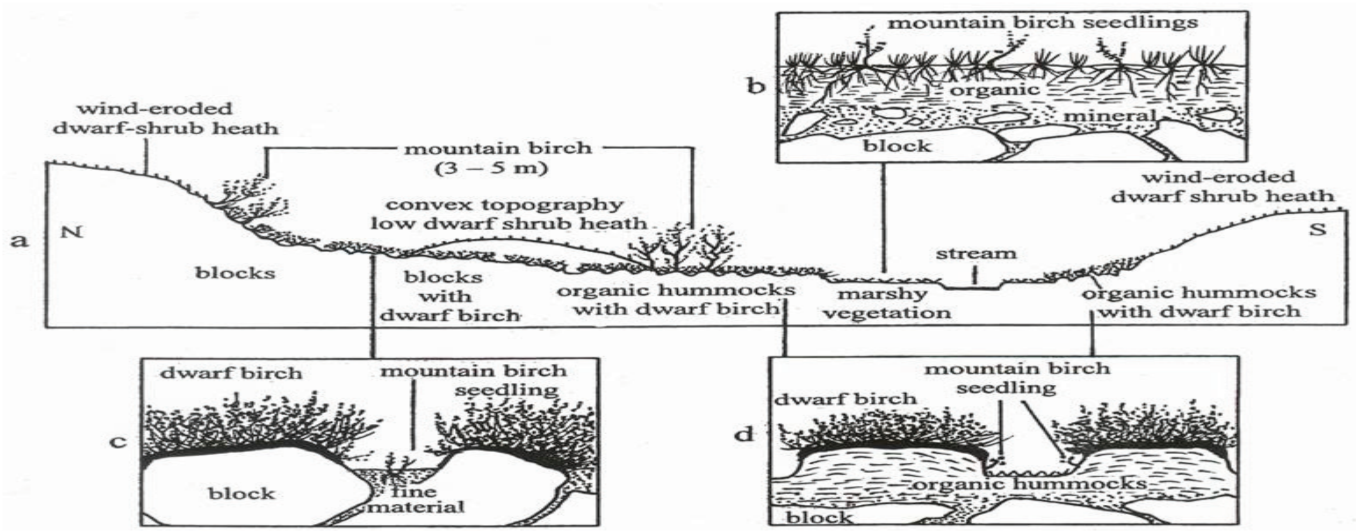

Figure 7. Spatial variability: Topsoils and carbon sequestration depending on microtopography in the Finnish Subarctic (Holtmeier et al. 2003).

Figure 8. Landscape mosaic in the treeline ecotone on Mt. Rodjanoaivi, subarctic Finland.

properties concerning carbon pools. Organic layers are drawn into the subsoil due to cryoturbation and, on the other hand, geological substrate-like till can be brought to the surface producing topsoil with very low amounts of carbon. Moreover, carbon can be enriched above the permafrost table.

In case of Static Cryosols, topsoils are relatively homogenous. In case of Turbic Cryosols two different topsoils occur (Figs. 4, 5). These topsoils are not unique for certain areas like Pangnirtung Pass on Baffin Island (Fig. 4); they are widespread in the Arctic. These frequently appearing features can be mapped in the field as well as by remote sensing and thus used for modeling and upscaling.

Spatial Variability and Upscaling

Turbic Cryosols show a regular pattern of topsoils due to cryoturbation (Figs. 5, 6). Because of insulation effects of the organic layer, the active layer under topsoil B is shallower than that under topsoil A. In general, topsoil A has low amounts of carbon whereas topsoil B contains high amounts of carbon (Broll et al. 1999). In case of climate warming, cryoturbation will stop and vegetation succession will start from topsoil B to topsoil A. At the optimum stage the plant cover will be continuous, and it will be very difficult to tell the differences between the two topsoils at the surface. On the other hand, this can be very helpful for a quick monitoring of environmental change in the Arctic.

Detailed investigations of topsoils including soil organisms (species, activity) on representative sites would enable making predictions for soil biocoenosis, decomposition, etc. for large areas. This could be interesting, especially in those areas where detailed soil mapping is already available like in the Mackenzie River delta area (Fig. 6). Similar approaches are tested in temperate regions already (Beylich et al. 2006).

This approach of upscaling soil ecological properties via topsoil mapping is relatively easy on flat areas. In mountainous areas the relief plays an important role for the distribution of soils especially because of creating different drainage and thus soil moisture conditions. This affects the topsoils and the related carbon stocks (Figs. 6, 7).

Although those sites like in the Finnish Subarctic looks quite heterogenous; a regular pattern can be identified which occurs all over in the Subarctic: dry wind-exposed heath, boulders with fine material in between, small organic hummocks etc. (Figs. 6, 7) (Broll et al. 2007).

Because topsoils are habitats for characteristic soil biocoenoses, soil ecological processes like decomposition are correlated with the topsoil type (Nadelhoffer et al. 1992, Broll 1994, Müller et al. 1999) Since the topsoil pattern shows a certain regularity, geostatistical methods could be applied to get from the plot scale to the landscape scale (Joschko et al. 2007).

Conclusions

- Topsoils are good indicators for ecosystem changes in the Arctic and Subarctic.
- Detailed information on topsoils in soil mapping protocols can improve the data quality for upscaling of carbon data, can help modeling soil ecological processes and provide information on the soil biocoenoses.
- Combination of spatial soil data with spatial humus form data and vegetation data could help to reduce the number of carbon analysis or help to extrapolating existing data.
- Identification and characterization of topsoils should be included in the Minimum Soil Dataset for Cryosols to provide first information on the biological activity of the site.
- Some existing long-term monitoring sites already include the characterization of topsoils. This knowledge can also be applied to the Arctic.

References

Akselsson, C., Berg, B., Meentemeyer, V. & Westling, O. 2005. Carbon sequestration rates in organic layers of boreal and temperate forest soils – Sweden as a case study, *Global Ecology and Biogeography* 14: 77–84.

Beylich, A., Broll, G., Höper, H., Römbke, J., Ruf, A., & Wilke, B.-M. 2006. Boden als Lebensraum für Bodenorganismen: Bewertung im Rahmen von Planungsprozessen. *Bodenschutz* 2: 49-53.

Broll, G. 1994. Influence of the Soil Mosaic on Biodiversity at Heath Sites in the European Subarctic. *Transactions 15th World Congress of Soil Science (Mexico)*, Vol. 4a, 220-231.

Broll, G., Brauckmann, H.-J., Overesch, M., Junge, B., Erber, C., Milbert, G., Baize, D. & Nachtergaele F. 2006. Topsoil characterization – recommendations for revision and expansion of the FAO-Draft (1998) with emphasis on humus forms and biological features. *Journal of Plant Nutrition and Soil Science* 169(3): 453-461.

Broll, G., Holtmeier F.-K., Anschlag, K., Brauckmann, H.-J., Wald, S. & Drees B. 2007: Landscape mosaic in the treeline ecotone on Mt Rodjanoaivi, Subarctic Finland. *Fennia* 178(2) (in press).

Broll, G., Tarnocai, C. & Müller, G. 1999. Interactions between vegetation, nutrients and moisture in soils in the Pangnirtung Pass area, Baffin Island, Canada. *Permafrost and Periglacial Processes* 10: 265-277.

Heal, O.W., Broll, G., Hooper, D.U., McConnell, J., Webb, N.R. & Wookey, P.A. 1998. Impacts on global change on tundra soil biology. In: O.W. Heal, T.V. Callaghan, J.H.C. Cornelissen, C. Körner, & S.E. Lee (eds.), *Global change in Europe´s cold regions.* Ecosystems Research Report No. 27, Brussels, 65-134.

Holtmeier, F.-K., Broll, G., Müterthies, A. & Anschlag, K. 2003. Regeneration of trees in the treeline ecotone: northern Finnish Lapland. *Fennia* 181: 103-128.

Joschko, M., Oehley, J., Gebbers, R., Wiemer, M., Timmer, J. & Fox, C. 2008. A spatial approach to soil ecological experimentation at landscape scale. *Journal of Plant Nutrition and Soil Science* (in press).

Müller, G., Broll, G. & Tarnocai, C. 1999. Biological activity as influenced by microtopography in a Cryosolic soil, Baffin Island, Canada. *Permafrost and Periglacial Processes* 10: 279-288.

Nadelhoffer, K.J., Giblin, G.R., Shaver, G.R. & Linkins, A.E. 1992. Microbial processes and plant nutrient availability in arctic soils. In: F.S. Chapin (ed.), *Arctic ecosystems in a changing climate. An ecophysiological perspective.* San Diego, California: Academic.

Tarnocai, C. & Broll, G. 2008. Soil Organic Carbon Stocks in the Northern Permafrost Region and Their Role in Climate Change. *Proceedings of the Ninth International Conference on Permafrost*, *Fairbanks, Alaska, June 29–July 3, 2008* (this proceedings).

Tarnocai, C., Kimble, J. & Broll, G. 2003. Determining carbon in Cryosols using the Northern and Mid Latitudes Soil Database. In: M. Phillips, S. Springman, & L.U. Arenson (eds.), *Proceedings of the Eighth International Conference on Permafrost*, *Zurich, Switzerland, 21–25 July 2003.* Lisse: Balkema Publishers, 1129-1134.

The International Permafrost Association: 1983–2008

Jerry Brown, President IPA
International Permafrost Association, Woods Hole, MA, USA
Hugh French, Professor Emeritus, Past President IPA
Departments of Geography and Earth Sciences, University of Ottawa, Ottawa, Canada
Cheng Guodong, Academician, Past President IPA
CAREERI, Chinese Academy of Sciences, Lanzhou, China

Abstract

The International Permafrost Association (IPA) was founded in July 1983, at Fairbanks, Alaska, during the Fourth International Conference on Permafrost. The four founding members were Canada, China, the USSR, and the United States. The IPA presently has 26 members. The primary purposes of the IPA are to convene international conferences to facilitate communication and to develop and exchange information related to permafrost research and engineering. Beginning in 1963, international permafrost conferences have been held in Canada, China, Norway, USSR (Russia), Switzerland, and the United States. Working groups, task forces, and committees undertake specific projects and collaborate with other international organizations. Accomplishments include establishment of the Global Geocryological Data (GGD) system, an international permafrost glossary, a permafrost map of the Northern Hemisphere, an inventory of carbon content of northern soils, bibliographies, and publication of *Frozen Ground*. Several major international programs and long-term observing networks initiated by the IPA contribute to the 2007–2008 International Polar Year (IPY).

Keywords: frozen ground; history; IPA; IPY; permafrost; periglacial.

Background

The geopolitical situation that evolved after the Second World War focused attention upon the high northern latitudes. Russian experience of permafrost conditions was more extensive, more advanced, and better documented than in North America (e.g., see Shiklomanov 2005). For example, the Permafrost Institute, a branch of the USSR Academy of Sciences, Moscow, had been established in Yakutsk, Siberia, in 1939, and Russian language permafrost texts had been published from the 1930s onwards (e.g., see Sumgin 1927/37, Shvetsov 1956). By the late 1940s and early 1950s, the importance of the Russian permafrost literature was beginning to be appreciated in North America (Muller 1943, see French & Nelson 2008). As a consequence, the USA and Canadian governments established research agencies and organizations to promote scientific understanding of these regions.

In the USA, the Snow, Ice and Permafrost Research Establishment (SIPRE) and the Arctic Construction Frost Effects Laboratory, later to become the Cold Regions Research and Engineering Laboratory (CRREL), in Hanover, New Hampshire, and the Arctic Research Laboratory (ARL) in Alaska, were established, and the U.S. Geological Survey began extensive field investigations. In Canada, the Division of Building Research (DBR), National Research Council of Canada (NRCC), the Polar Continental Shelf Project (PCSP) and the Geological Survey of Canada (GSC) started to support permafrost-related investigations in the north. The Arctic Institute of North America (AINA) was set up as a bi-national organization with headquarters in Montreal and Washington. Several monographs and publications document some of these early North American undertakings (see French & Nelson 2008).

The First International Conference on Permafrost (ICOP), held at Purdue University, Indiana, in 1963, was an initiative to promote communication and understanding between Soviet and North American permafrost scientists and engineers. This was the first major contact between Russian and western scientists (Brown & Walker 2007). The Second ICOP was held in Yakutsk, Siberia, in 1973, where it was mutually agreed that further conferences would be advantageous to all concerned. At the Third ICOP in Edmonton, Canada, in 1978, the desirability of establishing an organizational structure that would ensure the continuation of these conferences was discussed. Accordingly, the NRCC, through its Bureau of International Relations and the DBR, established a task force in 1981 to draft a set of organizational rules. This was chaired by Lorne Gold, Head of the DBR, NRCC, and the members were Fred Roots, Science Advisor, Environment Canada, John Fyles, Head of the Division of Terrain Sciences, Geological Survey of Canada, and Hugh French, Chairman, Permafrost Sub-committee, ACGR, NRCC. Representatives of the Bureau of International Relations, NRCC, provided advice at meetings of the group.

Formation of the IPA

At the Fourth ICOP in 1983, held at the University of Alaska-Fairbanks, Alaska, Hugh French, leader of the Canadian delegation, convened a special meeting of the leaders of the official delegations from the USA, USSR, and China. Professor T.L. Péwé (USA), Academician P.I. Mel'nikov

(USSR), and Professor Shi Yafeng (China) attended this meeting together with advisors (Fig. 1). Unofficially, these four countries subsequently became known as the "Big Four." It was agreed to form an international association.

The primary mandate of the newly formed association was to organize and promote international conferences on permafrost at regular five-year intervals. A secondary role was to encourage and facilitate the international exchange of scientific information among permafrost scientists and engineers. The agreement to form the association was announced at the closing ceremony; the Executive Committee consisted of Academician Mel'nikov, President, Professor Péwé, Vice-President, and Professor J. Ross Mackay, Secretary-General. The terms of office were for five years. The NRCC, through its Bureau of International Relations, agreed to provide funding to support the activities of the Secretary-General. The creation of the IPA Council was announced, and countries wishing to join the Association were asked to name an organization or representative. The Council was to

Figure 1. Participants in the founding meeting of the IPA, held at Fairbanks, Alaska, in 1983. Front row: Louis DeGoes, Li Yusheng, Shi Yafeng, J. Ross Mackay, P.I. Mel'nikov, T.L. Péwé, G.H. Johnston, N.A. Grave. Back row: Zhao Yuehai, Cheng Guodong, H.M. French, Jerry Brown. Photograph taken by J.A. Heginbottom.

meet at regular intervals, minimally at the beginning and end of each international conference on permafrost. At the closing ceremony it was immediately clear that, in addition to USA, Canada, China, and the USSR, a number of other countries were interested in becoming members of the IPA.

Three of the first acts of the Association in Fairbanks were to: (1) modify the constitution to allow for a Second Vice-President, (2) appoint a Nominations Committee in order to allow a new Executive to be elected at the 1988 Conference, and (3) plan to seek affiliation with other international scientific bodies. Dr. Kaare Flaate (Norway) was elected to the Executive Committee as a second Vice-President, and Norway agreed to host the Fifth ICOP in Trondheim in 1988.

The detailed history of the IPA is chronicled in its News Bulletin *Frozen Ground,* which started as informal notes by the Secretary General in 1986, and became a formal publication starting in 1989. All issues are found on the IPA website. The following sections report on the development and accomplishments of the Association. Hereafter, specific issues of *Frozen Ground* are cross-referenced, for example, as (FG 30). The following presents both administrative details and some of the major accomplishments of the IPA since 1983.

Administrative Activities

Council, Executive Committee, and Secretariat

Membership on the Council is through adhering national or multinational organizations as full voting members or as non-voting associates or individuals in countries where no Adhering Body exists. The IPA is governed by its Council and elected Executive Committee officers. Members of the Executive Committee are listed in Table 1. The Council currently consists of representatives from 24 Adhering Bodies and two Associate members having an interest in any aspect of theoretical, basic, and applied frozen ground research, including permafrost, seasonal frost, artificial freezing, and periglacial phenomena.

Attendance at the first council meeting on August 5, 1987, in Ottawa, Canada, included 15 Adhering Bodies together

Table 1. Executive Committees of the International Permafrost Association 1983–2008

	1983–1988	1988–1993	1993–1998	1998–2003	2003–2008
President	P.I. Mel'nikov U.S.S.R.	T.L. Péwé USA	Cheng Guodong China	H.M.French Canada	J. Brown USA
Vice President	T.L. Péwé USA	Cheng Guodong China	N.N. Romanovskii Russia	F.E. Are Russia	C. Harris U.K.
Vice President	K. Flaate Norway	V.P. Mel'nikov U.S.S.R	H.M. French Canada	W. Haeberli Switzerland	G. Perlshtein Russia
Secretary General	J. Ross Mackay Canada	J. Ross Mackay Canada	J. Brown USA	Replaced by Secretariat	Replaced by Secretariat
Members				J. Brown, USA T. Mølmann, Norway Zhu Yuanlin, China	H.-W. Hubberten Germany D.W. Hayley Canada Zhu Yuanlin Ma Wei, China

with representatives from France (joined 1988) and Sweden (joined 1990) as observers. Other members soon followed: Denmark (1989), Spain and Southern Africa (1993), Mongolia and Kazakhstan (1995), Austria (1998), Iceland (2003), and New Zealand (2005). Portugal and South Africa were approved as Associate members in 2005. Each member pays an annual membership fee established by the Council.

The Constitution and Bylaws were adopted at the first council meeting. Since then, five modifications have been approved (December 1992, June 1998, March 2003, June 2005, Potsdam; and May 2006). These largely involved membership and working party activities.

The Council elects the Executive Committee and approves the formation and review activities of Committees, Working Groups, and Task Forces. It also approves the venue for each ICOP. The Council met in ten locations:

Ottawa, Canada (1987, FG 2).
Trondheim, Norway (1988, FG 4).
Quebec City, Canada (1990; FG 7).
Beijing, China (1991 during INQUA, FG 10).
Washington, DC (1992 during INQUA, FG 12).
Beijing, China (1993, FG 14).
Berlin, Germany (1995 during INQUA, FG 18).
Yellowknife, Canada (1998, FG 22).
Zurich, Switzerland (July 2003, FG 27).
Potsdam, Germany (June 2005, FG 29).

Starting in 1990, the Council issued a series of recommendations that include specific activities and topics of international scope (see summaries of Council meetings in *Frozen Ground*). These include statements on mapping, long-term monitoring, modeling, climate change, data acquisition and archiving, terminology, coordination with other international organizations and programs including both the Northern and Southern Hemisphere, and mid- and low-latitude mountains and plateau regions.

The Executive Committee is elected by Council every five years. Although members do not represent their own country, the four countries with significant areas of permafrost have always been represented on the Committee. A representative from the forthcoming international conference is also a member. A geographic and disciplinary balance of membership is also maintained. The first formal meeting of the Executive Committee took place in Oslo in September 1985. The Council has met formally 27 times.

The Secretary General first resided at the University of British Columbia, Canada (J. Ross Mackay, 1983–1993) and then in Washington DC, USA (Jerry Brown, 1993–1999). In 1998 the position of Secretary General was replaced by a Secretariat. This was initially located at the Institute of Geography, University of Copenhagen, Denmark (1999–2001) and is now at the University Centre on Svalbard (UNIS), Norway (2001–2009). Hanne H. Christiansen has been responsible for the Secretariat since 1999. In both locations, national research agencies and institutions have provided financial support. Major responsibilities include preparation and distribution of *Frozen Ground*, maintenance of the IPA webpage, coordination of administrative, Executive Committee and Council affairs, and international representation. The IPA web is currently hosted by the Department of Geosciences, University of Oslo.

International affiliations

The IPA became an Affiliated Organization of the International Union of Geological Sciences (IUGS) in July 1989. In 1996 the IPA and the International Geographical Union (IGU) signed an agreement that formalized a joint Periglacial Commission. This agreement recognized the longtime relationships between periglacial and permafrost researchers, the foundations of which are recorded in the pages of the Polish journal *Builetyn Peryglacjalny*. The IGU-IPA agreement was modified in 2004 with the formation of the new Commission on Cold Regions Environments.

Agreements also exist to share joint working groups, committees, or projects with the International Union of Soil Science (IUSS), the Scientific Committee for Antarctic Research (SCAR), and the International Arctic Science Committee (IASC). A Memorandum of Understanding was signed in 2004 between IPA and the World Climate Research Programme project "Climate and Cryosphere" (CliC). Although no formal agreement exists with the International Union of Quaternary Research (INQUA), close working relations are maintained with the Quaternary communities. Similarly, ties are maintained with the International Society for Soil Mechanics and Geotechnical Engineering (ISSMGE) and the newly formed International Association of Cryospheric Sciences.

Technical Activities

Conferences and workshops

Starting in 1983, the International Permafrost Association assumed responsibility for scheduling the ICOP meetings at five-year intervals. A written invitation for the proposed conference is required for IPA Council approval. The President of the IPA formally convenes the opening and closing sessions of each conference. In 1998 an International Advisory Committee for ICOP was formed to facilitate continuity in the planning of conferences. The host country is responsible for the financial support, technical organization, and publications. Field trips in or to permafrost areas are required as part of the program. The host country is responsible for the organization and financing of the conferences. The eight international conferences to date are:

First: 11–15 November, 1963, Purdue, Indiana, USA.
Second: 12–20 July, 1973, Yakutsk, Siberia, USSR.
Third: 10–13 July, 1978, Edmonton, Alberta, Canada.
Fourth: 17–22 July, 1983, Fairbanks, Alaska, USA.
Fifth: 2–5 August, 1988, Trondheim, Norway.
Sixth: 5–9 July, 1993, Beijing, China.
Seventh: 23–27 June, 1998, Yellowknife, Canada.
Eighth: 20–25 July, 2003, Zurich, Switzerland.

Over the span of these forty years, approximately 2500 individuals from 36 countries have participated in the eight conferences. Short reports on each conference, including numbers of attendees, papers in proceedings, field trips, and related publications for all eight conferences are reported elsewhere (Brown & Walker 2007). From 2008 onwards, conferences will take place on a four-year cycle with an official intervening regional conference. During the Eighth ICOP, the Troy L. Péwé Award was established to recognize the best presentation by a young researcher.

The IPA has also sponsored a number of regional permafrost conferences. These include the Fourth Canadian permafrost Conference (Québec, 1990), two European permafrost conferences (Rome, 2001: Potsdam, 2005), and the First Asian Conference on Permafrost (Lanzhou, 2006). In addition, the annual Russian geocryology conferences (e.g., Pushchino; Salekhard), and several cryopedology and soils meetings (e.g., Copenhagen, Syktyvkar, Madison, Arkhangelsk) have been sponsored by the IPA.

Workshops also play an important role in implementing IPA-related projects. The following are the major such meetings; results are reported in *Frozen Ground*:

Global Geocryological Data workshop (1994).

International workshop on processes and ability to detect change (1995).

Mountain permafrost and monitoring (1997).

International workshop on permafrost monitoring and databases (2000).

International symposium on mountain and arid land permafrost (2001).

Circumpolar Active Layer Monitoring (CALM) workshop (2002).

Arctic Coastal Dynamics workshops (annual 1999-2006).

Permafrost and Climate in the 21st Century (PACE21) workshop (2004).

Antarctic workshops (2004, 2007).

Asian permafrost mapping workshop (2006).

Working parties

Since 1998 many of the IPA activities between conferences have been undertaken by committees, working groups, and task forces (collectively referred to as *working parties*). Annual reports of working parties are published in *Frozen Ground* and archived on the IPA website. At the 1988 Council meeting in Trondheim, three standing committees and six working groups were established. New working groups were added and some goals modified prior to, or at, the 1993 Council. During the intervening years and at the 1998 Yellowknife Council meetings, major revisions were made to the organization of working parties. New guidelines were developed and included the formation of Task Forces (see FG 22). During the 2003 Council meeting, several Task Forces became working groups, and existing working groups were redefined. A total of ten working groups, several with subgroups, are presently active and are joint with other international organizations:

Standing Committees:

Data, Information and Communication

International Advisory Committee for International Permafrost Conferences

Working Groups:

Antarctic Permafrost and Periglacial Environments (SCAR)

Coastal and Offshore Permafrost (IASC and LOICZ)

Cryosols (IUSS)

Glaciers and Permafrost Hazards in High Mountains (IACS)

Isotopes and Geochemistry of Permafrost

Mapping and Modeling of Mountain Permafrost

Periglacial Landforms, Processes and Climate (IGU)

Permafrost and Climate (IGU)

Permafrost Astrobiology

Permafrost Engineering (ISSMFE)

Since 1998, working party reports covering the previous five years have been published as part of the program for the international conferences on permafrost. In 2007 a review was undertaken by an ad hoc committee on working parties to provide recommendations on the present activities and future directions. These will be discussed at the 2008 Council meetings. Future activities will be approved between then and the next regional and international conferences in 2010 and 2012, respectively.

Major Accomplishments

By 1988 the IPA was serving as a catalyst and organizer of several major international activities.

Database

A common challenge facing many field-oriented disciplines is access to international data sets and the subsequent preservation or archiving of these data. The lack of readily available, international permafrost-related data sets was recognized by the IPA prior to, and during, the 1988 Trondheim conference. A Working Group on Permafrost Data was formed and an international data workshop was subsequently convened in 1994 in Olso. The result was development of the Global Geocryological Database (GGD), the basis of which is identification and description of data sets beginning in a metadata format. The National Snow and Ice Data Center took the lead in populating the GGD with both metadata and data. For the 1998 and 2003 conferences, the compilations of the GGD were provided on CD-ROM, entitled Circumpolar Active-Layer Permafrost System (CAPS) (Barry et al. 1995, NSIDC 1998, IPA SCDIC 2003, Parsons et al. 2008). The CAPS/GGD products are available on line at the NSIDC Frozen Ground Data Center.

Terminology

By the time the IPA was established, it was clear that the major terminological problem associated with permafrost, as defined in North America, Russia, and China, arose from the fact that ground at or below 0°C may, or may not, be frozen. Put simply, permafrost is not necessarily frozen because soil and rock, for a variety of reasons (salts, pressure, etc.), may exist in an unfrozen state at temperatures below 0°C. This prompted the Permafrost Subcommittee of the Associate Committee on Geotechnical Research, NRCC, to establish a terminology working group in 1985. In its report (ACGR 1988), "cryotic" terminology was re-introduced in an attempt to accommodate the unfrozen nature of certain permafrost situations. The IPA Council approved a Working Group on Permafrost Terminology in 1988 and encouraged production of a multi-language glossary of permafrost and related ground ice terms (van Everdingen 1998). Although this glossary did not resolve the problem, the permafrost community has, for the first time in its history, a working document that describes permafrost terminology in twelve languages. This represents a major achievement.

International permafrost map

Prior to 1983, the mapping of permafrost had been undertaken using different classifications by different national organizations. The need existed for a circum-arctic map based on a common classification. An informal group representing members of the United States Geological Survey (USGS), the Geological Survey of Canada, and the Institute for Hydrogeology and Engineering Geology (VSEGINGEO), Russia, was spearheaded by the IPA Secretary General (J. Brown) and started work in the early 1990s. A generalized legend based on permafrost continuity, ground ice content, and physiography was applied to existing permafrost maps and, after several meetings and numerous editorial discussions by the authors and the USGS cartographers, a map at 1:10,000,000 was finalized and published (Brown et al. 1997). It was subsequently digitized and made available in ArcInfo. The digitized product has been used extensively by the modeling communities and others involved in climate research. Building on this existing map, a new international map based on spatial and temperature variations of permafrost terrain is a logical next step.

Observational networks

The IPA has taken the leadership in initiating and coordinating several international, long-term monitoring networks and related data acquisition programs. The IPA entered into a cooperative partnership with the World Meteorological Organizations (WMO) and the Food and Agriculture Organization (FAO) of the United Nations to facilitate development and coordination of the Global Terrestrial Network for Permafrost (GTN-P) (Burgess et al. 2000). The GTN-P consists of two components: the borehole measurements or Thermal State of Permafrost (TSP) and the Circumpolar Active Layer Monitoring (CALM) network. Both TSP and CALM are included in the IPA-coordinated International Polar Year (IPY) Project 50 "Permafrost Observatory Project: A Contribution to the Thermal State of Permafrost." This currently consists of 150 CALM sites (Nelson et al. 2004, Shiklomanov et al. 2008) and approximately 500 borehole temperature sites in both hemispheres. Also included are the boreholes developed under the PACE program (Harris 2008) and the Norwegian TSP boreholes. At least 15 countries are participating in GTN-P, primarily with national funding.

A second major network exists in the Arctic Coastal Dynamics (ACD) program. Following a 1999 workshop, a science plan under the Working Group on Coastal and Offshore Permafrost was developed and project status was approved by the International Arctic Science Committee. There are approximately 30 key coastal sites located around the Arctic Ocean. ACD developed a database of several thousand coastal segments.

Publications

In addition to those previously mentioned, numerous publications have arisen from IPA working parties, projects, and related activities. Some of these include:

Bibliographies of published literature (e.g. Brennan 1983, 1988, 1993, Mullins 2003).

An annotated bibliography on climate change (Koster et al. 1994).

Soil carbon map (Tarnocai et al. 2003).

Periglacial manual (IPA web accessible).

In addition, the Wiley journal *Permafrost and Periglacial Processes (PPP)* has published a number of special issues on mountain permafrost (PPP3), climate change (PPP4), grèzes litées (PPP6), frozen ground (PPP7), cryostratigraphy (PPP9), cryosols (PPP10), PACE (PPP12), hydrology, climate and ecosystems (PPP14); periglacial processes and instrumentation (PPP14), CALM (PPP15), PACE21: mountain permafrost (PPP15), and a special issue in honor of J. Ross Mackay at the time of his 90th birthday (PPP18).

Several other journals serve the international geocryology communities. For example, since 2002, the *Reports on Polar Research* of the Alfred Wegener Institute for Polar and Marine Research (Bremerhaven, Germany) have contained an annual issue devoted to the results of the ACD workshops. Other journals have also devoted special issues to IPA-sponsored activities: these include the *Norwegian Journal of Geography, Polar Geography and Geology, Southern African Journal of Science, Global and Planetary Change, Cold Regions Science and Technology,* and *Journal of Geophysical Research.*

Conclusions

The International Permafrost Association has established itself as a productive international organization.

Geocryology is now recognized as a cold-climate discipline that integrates permafrost science and permafrost engineering. Permafrost is recognized as an important component of the cryosphere.

Specific achievements under the IPA include the production of a multi-language glossary, publication of a digitized, circum-arctic map of permafrost and related ground ice conditions, and the establishment of the global geocryological database system and several monitoring networks.

The IPA legacy that is resulting from both the IPY and existing activities includes: (i) establishment of networks of active layer and permafrost temperature observatories, (ii) development of a sustainable geocryological database, and (iii) fostering a new generation of geocryologists through the activities of the Permafrost Young Researchers Network.

These collective activities will further develop and sustain international activities, particularly those related to the state and fate of permafrost in relation to a changing climate.

Acknowledgments

The IPA and this report contribute to the activities of the International Polar Year. Numerous individuals and organizations have contributed to the success of the IPA. Special thanks must go to the Bureau of International Relations, National Research Council of Canada, for the initial funding of the activities of the IPA Secretary General, Professor J. Ross Mackay, between 1983 and 1993, and to the U.S. National Science Foundation, USA, for funding the activities of the IPA Secretary General, Jerry Brown. Since 1998, Hanne H. Christiansen has been responsible for the successful operation of the IPA Secretariat, assisted by Angélique Prick (2005–2007), and most recently by Herman Farbrot. Funding of this Secretariat has been provided by the Danish Polar Centre, Barlindhaug, and the Research Council of Norway. Ole Humlum (University of Oslo) has provided valuable assistance and support for the IPA webpage.

References

Associate Committee on Geotechnical Research 1988. *Glossary of permafrost and related ground-ice terms*. National Research Council of Canada. Ottawa, Technical Memorandum No. 1242, 156 pp.

Barry, R.G., Heginbottom, J.A. & Brown, J. 1995. Workshop on Permafrost Data Rescue and Access. 3-5 November 1994, Oslo, Norway. *Glaciological Data Report GD-28.* World Data Center for Glaciology (Snow and Ice), Boulder, CO, 134 pp.

Brennan, A.M. 1983. Permafrost bibliography update, 1978-1982. *Glaciological Data Report GD-14*. World Data Center for Glaciology (Snow and Ice), Boulder, CO, 336 pp.

Brennan, A.M. 1988. Permafrost bibliography update, 1983-1987. *Glaciological Data Report GD-21*. World Data Center for Glaciology (Snow and Ice), Boulder, CO, 225 pp.

Brennan, A.M. 1993. Permafrost bibliography update, 1988-1992. *Glaciological Data Report GD-26.* World Data Center for Glaciology (Snow and Ice), Boulder, CO, 401 pp.

Brown, J., Ferrians, O.J., Jr., Heginbottom, J.A. & Melnikov, E.S. 1997. Circum-Arctic map of permafrost and ground-ice conditions. *U.S. Geological Survey Circum-Pacific Map CP-45*, 1:10,000,000, Reston, Virginia.

Brown, J. & Walker, H.J. 2007. Report from the International Permafrost Association: A brief history of the International Permafrost Conferences (1963-2003). *Permafrost and Periglacial Processes* 18: 385-392.

Burgess, M. Smith, S.L., Brown, J., Romanovsky, V., & Hinkel, K. 2000. Global Terrestrial Network for Permafrost (GTNet-P): Permafrost monitoring contributing to global climate observations. *Geological Survey of Canada, Current Research 2000-E14*, 8 pp.

French, H.M., & Nelson, F.E. 2008. The permafrost legacy of Siemon Muller (*this proceedings*).

Harris, C. 2008. Recent warming of European Permafrost: evidence from PACE boreholes and other monitoring networks (*this proceedings*).

IPA Standing Committee on Data Information and Communication, comp. 2003. *CAPS: Circumpolar Active-Layer Permafrost System, Version 2.0*, M. Parsons & T. Zhang (Eds.), National Snow and Ice Data Center, Boulder, CO, CD-ROM.

Koster, E.A., Nieuwenhuijzen, M.E. & Judge, A.S. 1994. Permafrost and Climatic Change: An Annotated Bibliography. *Glaciological Data Report GD-27*. World Data Center for Glaciology (Snow and Ice), Boulder, CO, 94 pp.

Mullins, T. 2003, Permafrost and Frozen Ground Bibliography, 1978-2003. *Glaciological Data Report GD-31*. World Data Center for Glaciology (Snow and Ice), Boulder, CO, 1128 pp.

National Snow and Ice Data Center 1998. *CAPS: Circumpolar Active-Layer Permafrost System, Version 1.0.* National Snow and Ice Data Center, Boulder, CO, CD-ROM.

Nelson, F.E. (Ed.) 2004. Special Issue: Circumpolar Active Layer Monitoring (CALM) Workshop. *Permafrost and Periglacial Processes* 15(2): 99-188.

Parsons, M.A. et al. 2008. Managing Permafrost Data: Past Approaches and Future Directions (*this proceedings*).

Shvetsov, P.F. 1956. *Basic concepts and terms in geocryology.* Inst. Merzlotovedeniya, Akad. Nauk SSSR, 16 pp. (in Russian).

Shiklomanov, N.I. 2005. From exploration to systematic investigation: Development of geocryology in 19th- and early-20th century Russia. *Physical Geography* 26: 249-263.

Shiklomanov, N., Nelson, F.E., Streletskyi, D.A., Hinkel, K.M. & Brown, J. 2008. The Circumpolar Active Layer Monitoring (CALM) Program: Data Collection, Management, and Dissemination Strategies (*this proceedings*).

Sumgin, M.I. 1927, 1937. Soil Permafrost within the USSR. *Vladivostok: 1st edition; Moscow-Leningrad: 2nd edition, Acad. Nauk SSSR*, 372 pp. (in Russian).

Tarnocai, C., Kimble, J. & Broll G. 2003. Determining carbon stocks in Cryosols using the northern and mid Latitudes soil database. *Proceedings of the Eighth International Conference on Permafrost, Zurich, Switzerland, July 21-25, 2003:* 1129-1134.

van Everdingen. R.O. 1998. *IPA Multi-Language Glossary of Permafrost and Related Ground-Ice Terms in Chinese, English, French, German, Icelandic, Italian, Norwegian, Polish, Romanian, Russian, Spanish and Swedish.* Arctic Institute of North America, Calgary, Canada.

Experimental Study of the Thermal Conductivity of Frozen Sediments Containing Gas Hydrates

B.A. Buhanov
Department of Geocryology, Geological Faculty, Moscow State University, Russia
E.M. Chuvilin
Department of Geocryology, Geological Faculty, Moscow State University, Russia
O.M. Guryeva
Department of Geocryology, Geological Faculty, Moscow State University, Russia
P.I. Kotov
Department of Geocryology, Geological Faculty, Moscow State University, Russia

Abstract

In this paper, the authors present the results of laboratory measurements of the thermal conductivity of artificial hydrate-bearing sediments under frozen conditions and atmospheric pressure. Frozen hydrate-saturated samples were maintained in a quasi-stable condition due to the so-called "self-preservation" effect of gas hydrates at negative temperatures. We determined the structure and thermal and physical properties of gas hydrate-bearing sediments, including the thermal conductivity. The results were then compared to properties of similar frozen sediments containing no methane hydrate. Experimental data showed that the thermal conductivity is very different for hydrate-bearing sediments in the self-preserved state than for similar ice-bearing sediment samples. This difference depends on the type of sediments and on structure-textural transformations which occur in the porous medium during self-preservation of hydrate-bearing samples. This difference increases with increasing hydrate saturation and volumetric hydrate content and with the decrease of dry density.

Keywords: frozen sediment; gas hydrate; hydrate-bearing sediments; self-preservation; thermal conductivity.

Introduction

Gas hydrates are ice-like crystalline substances that form from water and gas (of comparatively low molecular weight) under certain thermobaric conditions. Gas hydrates are a highly concentrated source of natural gas (mainly methane), and are considered to represent a promising new energy resource due to their extensive geographic occurrence. It is known that gas hydrates can exist naturally at both positive and negative temperature. According to drilling data and other indirect indicators, gas hydrates occur in permafrost environments in several regions of North Siberia and in on-shore/off-shore regions of the Canadian Arctic (Judge et al. 1994; Judge & Majorowicz 1992, Yakushev & Chuvilin 2000). Most known concentrations of permafrost gas hydrate occur below the permafrost table (e.g., Mallik), at temperatures well above 0°C (Henninges et al. 2005) However, several occurrences of intrapermafrost gas hydrates have been documented (Dallimore & Collett 1995, Dallimore et al. 1996, Ershov et al. 1991). It is difficult to identify and quantify gas hydrates occurring within frozen sediments using traditional geophysical techniques (mainly seismic) because of the similar geophysical response of gas hydrates and pore ice in frozen sediments. This is assumed to be due to the similarity between many of the physical properties of ice and gas hydrates (Table 1). However, the authors note that the thermal conductivity of ice and gas hydrate differ significantly, raising the possibility of employing thermal conductivity measurements to identify gas hydrates occurring within permafrost.

The anomalously low thermal conductivity of gas hydrates was discovered by Stoll & Bryan (1979), and was later confirmed by many other studies (Sloan 1998). Experimental data indicate that the thermal conductivity of gas hydrate (~0.5 $Wm^{-1}C^{-1}$) is similar to that of water (~0.6 $Wm^{-1}C^{-1}$), and is approximately 5 times lower than the thermal conductivity of ice (~2.2 $Wm^{-1}C^{-1}$).

The first technical study of the thermal properties of gas hydrate-bearing sediments was conducted by Groysman (1985), in which he compared the thermal properties of gas hydrate-bearing sandstone in the frozen and unfrozen states. These experiments indicate that the heat capacity per unit mass of frozen and gas hydrate-bearing sandstone differed little from each other, but the thermal conductivity of a gas hydrate-saturated sandstone was 70% lower than that of the frozen (ice-bearing) sample (Groysman 1985). Asher (1987) experimentally showed that the thermal conductivity of frozen sand is 80% higher then that of hydrate-saturated sand, but did not present any quantitative data about the degree of hydrate saturation of the investigated sediments. Wright et al. (2005) employed a needle probe to measure the thermal conductivities of laboratory specimens and recovered core from the gas hydrate-bearing reservoir at the Mallik gas hydrate production research site in Canada's Mackenzie Delta. Their measurements were obtained within a temperature-controlled pressurized test chamber designed to maintain thermodynamically stable gas hydrate.

Table 1. Comparison of physical properties of ice, SI and SII hydrate (Sloan 1998).

PROPERTY	ICE	STRUCTURE I	STRUCTURE II
Number of H_2O molecules	4	46	136
H_2O diffusion jump time (μsec)	21	>200	>200
Dielectric constant at 273 K	94	~58	~58
Isothermal Young's Modulus at 268 K (10^9 Pa)	9.5	8.4 (est)	8.2 (est)
Poisson's ratio	0.33	~0.33	~0.33
Bulk modulus at 272 K (GPa)	8.8	5.6	N/A
Shear modulus at 272 K (GPa)	3.9	2.4	N/A
Velocity ratio (comp./shear) at 272 K	1.88	1.95	N/A
Linear thermal expansion at 200 K (K^{-1})	56 x 10^{-6}	77 x 10^{-6}	52 x 10^{-6}
Adiabatic bulk compression at 273 K (GPa)	12	14 (est)	14 (est)
Speed Long Sound at 273 K (km/sec)	3.8	3.3	3.6
Density (g/cc)	0.917	0.91 (at 273 K)	0.94 (at 273 K)
Thermal conductivity at 263 K ($Wm^{-1}C^{-1}$)	2.23	0.49±0.02	0.51±0.02

Their data also indicated that the thermal conductivity of frozen (ice-bearing) samples is considerably higher than that of the same samples containing gas hydrate at temperatures above 0°C. They presented data on the thermal conductivity of frozen hydrate-bearing sediments with values 20–25% higher than the thermal conductivity of the unfrozen hydrate-bearing samples. Their results suggest that the thermal conductivity of gas hydrate-bearing sediments in the frozen/unfrozen state is dependent on the relative proportions of gas hydrate/ice and gas hydrate/water, respectively.

Waite et al. (2007) also used the needle probe technique to study the thermal conductivity of gas hydrate, and demonstrated weak temperature and pressure dependencies for thermal conductivity of gas hydrate. On the basis of the experimental data and analysis of published works they concluded that the thermal conductivity of hydrate-containing sediments at positive temperatures does not depend on the ratio of hydrate and water in the porous media.

Gas hydrates in frozen sediments can exist in a "relict" state for long periods of time due to the self-preservation effect (Ershov et al. 1991, Dallimore et al. 1996). The determination of in situ thermal conductivity anomalies may represent a potential exploration tool for gas hydrate identification and quantification within the upper horizons of permafrost. This notion forms the motivational basis for undertaking the experimental study of the thermal conductivity of frozen, hydrate-containing sediments under the non-equilibrium conditions ($p<p_{eq}$), as presented in this paper.

Methods

To facilitate the study of thermal conductivity of frozen hydrate-bearing sediments at negative temperature, we prepared artificial hydrate-saturated samples of sand, silty sand, and sandy loam, including samples collected from permafrost regions. A summary of sample characteristics is presented in Table 2.

For each individual laboratory test, a sample holder containing a test specimen was loaded into a high-pressure cell designed for the formation of gas hydrate within artificial or natural porous media, under controlled pressure and temperature conditions (Chuvilin & Kozlova 2005). After hermetically sealing the test cell, the cell was purged of air and charged with methane gas by slowly increasing cell pressure to about 8–10 MPa. The cell was maintained at room temperature while temperature and pressure conditions were stabilized, after which the cell was cooled to about 1–2°C. Under these conditions the process of gas hydrate formation was spontaneously initiated, as indicated by a sharp pressure drop within the cell. After the termination of hydrate accumulation within the sediment, the test cell was cooled to about -7 to -8°C, freezing any residual pore water which had not transformed to gas hydrate. The test cell was then transferred to a cold room maintained at a temperature of about -8°C. The cell was subsequently depressurized to 1 atmosphere, after which the test cell was opened and the sample removed.

The self-preservation effect of gas hydrates at negative temperatures facilitates the maintenance of the frozen hydrate-bearing samples in a quasi-stable state (at atmospheric pressure) during subsequent measurements of thermal conductivity. This also facilitates determination of the composition, structure and selected properties of gas hydrate-bearing samples, including the thermal-conductivity (λ), gravimetric water content (W_g), density and gas content. Definition of the sample's gas content was carried out by means of measurement of gas released in the course of defrosting of the sample placed in saturated NaCl solution. Then we calculated dry density (ρ), porosity (φ), volumetric hydrate content H_v (H_v=V_H·100% /$V_{sam,}$ where V_H is volume of hydrate, V_{samp} is volume of the sample), hydrate saturation S_h (S_h = H_v /φ ,%); ice saturation S_i (S_i = I_v /φ ,% where I_v is volumetric ice content). The results were then compared to measurements of the properties in samples without methane hydrates.

Thermal conductivity measurements were obtained using the thermal properties analyzer KD2, which is a registered trademark of Decagon Devices, Inc. The pocket-sized KD2 uses a single sensor (needle probe) to measure thermal conductivity and thermal resistivity of the test sample.

Table 2. Characteristics of soils.

Type of sediment	*Particle size distribution, %*			*Particle density, ρ_s, g/cm³*	*Plastic limit, W_p, %*	*Liquid limit, W_L %*	*Salinity, %*
	1–0.05 mm	0.05–0.001mm	<0.001 mm				
Silty sand	84	14	2	2.65	-	-	0.089
Sand	94.8	3.1	2.1	2.65	-	-	0.012
Sandy loam	41.8	53.7	4.5	2.7	20	33	0.693

The unit employs the transient line heat source method to calculate and display the thermal conductivity within 90-seconds. A detailed description of the transient line heat source method is presented by Bristow et al. 1994.

The small-diameter needle probe (1.2 mm diameter by 65 mm long) results in very little compaction during installation and allows for a short heating time, thereby minimizing any thermally-induced disturbance to gas hydrate or ice in the vicinity of the probe. The KD2 needle probe contains both a heating element and a thermistor. The controller module contains a battery and a 16-bit microcontroller, which automatically calculates the thermal-conductivity from temperature-time data.

The KD2 is rated for operation across a temperature range from -20 to +40°C, and measures thermal conductivity in the range from 0.01 to 2.0 $Wm^{-1}C^{-1}$ with a rated accuracy of ±5% to about 2.0 $Wm^{-1}C^{-1}$ with an accuracy ± 10%.

During the measurement, temperature increases by about 0.5°C. Since the sample temperature during measurement is in the range of -7 to -8°C, we assume that this small temperature increase does not significantly influence the phase composition of water either through ice melting or hydrate decomposition. Since the measurement is obtained at atmospheric pressure (i.e., outside of the gas hydrate pressure-temperature stability field), some portion of the hydrate in sediment pores dissociates progressively with time. However, the rate of dissociation is assumed to be very slow due to the self-preservation effect and according to our estimation does not influence the thermal field of the sample during the 90 second period of measurement.

To facilitate insertion of the needle probe, a small hole was drilled into the frozen test sample, the diameter of which corresponded to the diameter of the probe. The chilled needle probe was inserted full-length into the hole, such that a tight fit was obtained. Thermal contact between the probe and the sediment was maximized by use of a thermal paste with a thermal conductivity of 1.0 $Wm^{-1}C^{-1}$. For each sample, multiple measurements of thermal conductivity were obtained over a reasonable time period that allowed any thermal disturbances within the test sample to dissipate between measurements. With constant negative ambient temperatures being maintained, subsequent consecutive measurements were made at longer time intervals to document the change in thermal conductivity with time (assuming slow but progressive gas hydrate dissociation under the "self-preserved" condition). At the same time the gas content was determined with accuracy of 2–3%.

The KD2 thermal analyzer was also employed to measure the thermal conductivity of frozen control sediments having similar physical properties but without hydrate.

Results of Experimental Research

Frozen hydrate-containing samples of sand, silty sand, and sandy loam were prepared for thermal conductivity measurement. For each sample tested, we determined water content, dry density, porosity, gas hydrate saturation, and ice saturation. Thermal conductivity measurements (Table 3) were obtained using a needle probe and KD2 thermal analyzer.

Data from experiments indicate that the thermal conductivities of hydrate-bearing sediments were considerably lower than those obtained for similar ice-bearing sediments. The maximum difference (by more than a factor of 5) was observed for silty sand with an initial water content of 21%, and a high pore hydrate-saturation. We speculate that this large difference in measured thermal conductivities may be a reflection of the comparatively low thermal conductivity of methane hydrate forming on the surfaces bridging individual sediment particles within the bulk sediment. In the experiments conducted by Wright et al. (2005) the difference in the thermal conductivities of hydrate-saturated sand vs. frozen sand containing no hydrate is noticeably smaller, not exceeding 70%. However their data were obtained for thermodynamically stable gas hydrate under controlled temperatures and elevated pressures (in the order 5–8 MPa). In our case, thermal conductivity measurements were obtained at atmospheric pressure and freezing temperatures favourable for the self-preservation of pore-space gas hydrate. It is possible that the structural characteristics of sediments containing self-preserved gas hydrate are significantly different than the structural characteristics of sediment containing thermodynamically stable gas hydrate. One plausible explanation may be the formation of numerous microcracks and pinholes within the gas hydrate crystal matrix during partial dissociation of hydrate in the self-preserved condition. The formation of such microcracks in hydrates following depressurization to one atmosphere has been described previously by Ershov et al. (1990). The presence of microcracks in pore-space gas hydrate may result in a substantial reduction of the thermal conductivity of hydrate-bearing sediments, in comparison to frozen samples containing no gas hydrate.

The smallest differences between the thermal conductivity

Table 3. Thermal conductivity for frozen hydrate-saturated sediment samples (*t* = -7 to -8°C).

Type of sediment	Wg, %	Dry density, ρ_s, u.f.	Porosity, ϕ, u.f.	Hv,%	Sh, %.	Si, %	λ_{hyd}, $Wm^{-1}C^{-1}$	λ_{fr} $Wm^{-1}C^{-1}$
Sand	10	1.23	0.55	12	23	6	0.76	1.30
Silty sand	10	1.52	0.42	8	20	23	1.07	1.74
	15	1.51	0.43	13	32	32	0.5	1.9
	17	1.53	0.42	14	40	34	0.46	2.14
	21	1.37	0.48	25	52	18	0.44	2.32
Sandy loam	17	1.55	0.42	22	59	16	1.24	1.93
	17	1.55	0.42	15	34	35	1.59	1.93

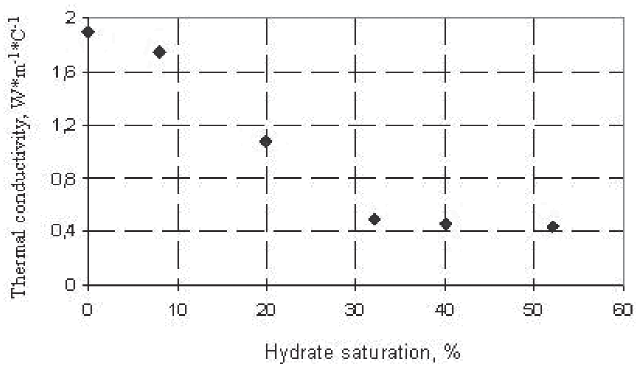

Figure 1. Influence of hydrate saturation on thermal conductivity in frozen silty sand sample (*t* = -7 to -8°C).

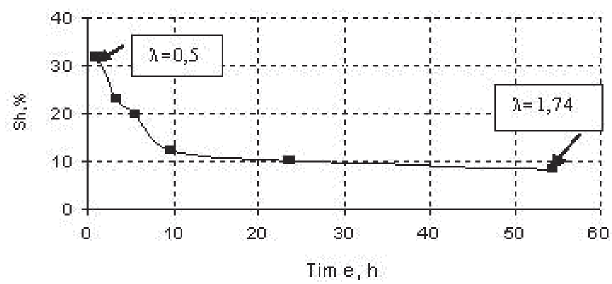

Figure 2. Methane hydrate dissociation kinetic in frozen silty sand sample and thermal conductivity (*t* = -7 to -8°C).

of frozen hydrate-bearing vs. ice-bearing samples (30–50%) were observed in samples of sandy loam (Table 3), characterized by comparatively high dry density (1.55 g/cm^3) and low porosity (~0.42). This result may be explained by the absence of hydrates at contacts between sediment particles, despite the relatively high hydrate content. Comparatively little difference in the thermal conductivity of frozen hydrate-bearing vs. ice-bearing samples was observed for sand having an initial water content of 10%. Note that hydrate saturation of this sample was 2.5 times lower than that of the silty sand having an initial water content of 21%. The large difference between the thermal conductivity of frozen hydrate-bearing and ice-bearing samples representing more dispersed sediments may be associated with structure-textural peculiarities in sediments containing self-preserved pore-space gas hydrate. However, this question requires additional investigation.

Thus, our data indicate that for self-preserved gas hydrate at atmospheric pressure, higher hydrate-saturation is associated with decreased thermal conductivity (Fig. 1).

Additional experiments to measure thermal conductivity during dissociation of pore-space hydrate in silty sand (W_{in}=15%) were conducted at negative temperatures (Fig. 2). Note that the degree of pore saturation with hydrate decreases over time as a result of the slow dissociation of pore hydrate in the self-preserved state, accompanied by an apparent increase in thermal conductivity from 0.5 $Wm^{-1}C^{-1}$ at the beginning of the experiment, to 1.74 $Wm^{-1}C^{-1}$ at the end of the testing period

The observed increase in thermal conductivity at the end of the experiment can be explained by a progressive decrease in the amount of pore-space hydrate and a corresponding increase in the amount of pore ice as dissociation progresses at temperatures below 0°C. Ice is exposed to processes of metamorphism which causes decrease of its porosity. Given that the process of hydrate dissociation in porous media at atmospheric pressure is poorly understood, it is desirable to undertake special micro-morphological studies designed to clarify the specifics of thermal conductivity in frozen hydrate-bearing sediments under non-steady state conditions.

Conclusion

A technique for obtaining rapid measurements of the thermal conductivity of self-preserved hydrate-bearing sediments at atmospheric pressure were was established.
Experimental data confirm that the thermal conductivity of self-preserved hydrate-bearing sediments is considerably lower than that of similar ice-bearing sediments, and that this discrepancy increases with increasing of hydrate saturation and volumetric hydrate content, and with decreasing dry density. This difference is also more apparent in uniform sands than in more dispersed sediments such as sandy loam.

Experimental results show that the thermal conductivity of frozen hydrate-containing soils increases with time because of the pore gas hydrate dissociation at non-equilibrium conditions.

Our results show the possibility of using thermal conductivity to single out frozen hydrate containing layers both in stable and metastable states.

Acknowledgments

This research was funded by the program Russian Foundation Basic Research No. 05-05-39019 and No. 06-05-91573. We thank the anonymous referees for various suggestions to improve the manuscript. Special thanks to J.F. Wright for his valuable advice and help to correct the English.

References

Asher, G.B. 1987. *Development of a computerized thermal conductivity measurement system utilizing the transient needle probe technique: an application to hydrates in porous media*. Dissertation T-3335, Colorado School of Mines, Golden, Colorado.

Bristow, K.L., White, R.D. & Kluitenberg, GJ. 1994. Comparison of single and dual probes for measuring soil thermal properties with transient heating. *Australian Journal of Soil Research* 32: 447-464.

Chuvilin, E.M. & Kozlova, E.V. 2005. Experimental estimation of hydrate-containing sediments stability. *Proceedings of the Fifth International Conference on Gas Hydrates. Thermodynamic Aspects. V.5. Trondheim, Norway:* 1562-1567.

Dallimore, S.R. & Collett, T.S. 1995. Intrapermafrost gas hydrates from a deep core hole in the Mackenzie Delta, Northwest Territories, Canada. *Geology* 23: 527-530.

Dallimore, S.R., Chuvilin, E.M., Yakushev, V.S. Grechischev, S.E., Ponomarev, V. & Pavlov A. 1996. Mackenzie Delta, N.W.T., Canada. *Proceedings of the 2nd International Conference on Natural Gas Hydrates, France, Toulouse*: 525-531.

Ershov, E.D., Lebedenko, Yu.P, Chuvilin, E.M. & Yakushev, V.S. 1990. Experimental investigations of microstructure of ice–methane hydrate agglomerate. *Engineering Geology* 3: 38-44 (in Russian).

Ershov, E. D., Lebedenko, Yu.P., Chuvilin, E.M., Istomin, V.A. & Yakushev V.A. 1991. Peculiarity of gas hydrates existence in the permafrost. *Reports of Academy of Sciences USSR* 321: 788-791 (in Russian).

Groysman, A.G. 1985. *Thermophysical properties of gas hydrates*. Novosibirsk, 94 pp.

Henninges, J., Schrötter, J., Erbas, K. & Huenges, E. 2005. Temperature field of the Mallik gas hydrate occurrence – implications on phase changes and thermal properties. In: S.R. Dallimore and T.S. Collett (eds), *Scientific Results from the Mallik 2002 Gas Hydrate Production Research Well Program, Mackenzie Delta, Northwest Territories, Canada*. Geological Survey of Canada, Bulletin 585.

Judge, A.S., Smith, S.L. & Majorowicz, J.A. 1994. The current distribution and thermal stability of gas hydrates in the Canadian Polar Regions. *Proceedings of the Fourth International Offshore and Polar Engineering Conference, Osaka, Japan, The International Society of Offshore and Polar Engineers:* 307-313.

Judge, A.S. & Majorowicz, J.A. 1992. Geothermal conditions for gas hydrate stability in the Beaufort-Mackenzie area: the global change aspect. *Global and Planetary Change* 98: 251-263.

Sloan, E.D. 1998. Physical/chemical properties of gas hydrates and application to world margin stability and climatic change. In: J.-P. Henriet & J. Mienert (eds.), *Gas Hydrates: Relevance to world margin stability and climate change.* Geological Society, London, Special Publication 137: 31-50.

Stoll, R.D. & Bryan, G.M. 1979. Physical properties of sediments containing gas hydrates. *Journal of Geophysical Research* 84: 1629-1634.

Waite, W.F., Stern, L.A., Kirby, S.H., Winters, W.J. & Mason, D.H. 2007. Simultaneous determination of thermal conductivity, thermal diffusivity and specific heat in sI methane hydrate. *Geophysical Journal International* 169: 767-774.

Wright, J.F., Nixon, F.M., Dallimore, S.R., Henninges, J. & Côté, M.M. 2005. Thermal conductivity of sediments within the gas-hydrate-bearing interval at the JAPEX/JNOC/GSC et al. Mallik 5L-38 gas hydrate production research well. In: S.R. Dallimore & T.S. Collett (eds), *Scientific Results from the Mallik 2002 Gas Hydrate Production Research Well Program, Mackenzie Delta, Northwest Territories, Canada*. Geological Survey of Canada, Bulletin 585.

Yakushev, V.S. & Chuvilin, E.M. 2000. Natural gas and hydrate accumulation within permafrost in Russia. *Cold Regions Science and Technology* 31: 189-197.

Permafrost Dynamics Within an Upper Lena River Tributary: Modeled Impact of Infiltration on the Temperature Field Under a Plateau

Sergey Buldovich
Moscow State University, Geological Faculty, Moscow, Russia
Nikolai Romanovskiy
Moscow State University, Geological Faculty, Moscow, Russia
Gennadiy Tipenko
Institute of Environmental Geoscience, Russian Academy of Sciences, Moscow, Russia
Dmitry Sergeev
Institute of Environmental Geoscience, Russian Academy of Sciences, Moscow, Russia
Vladimir Romanovsky
Geophysical Institute, University of Alaska Fairbanks, USA

Abstract

In southern Yakutia where permafrost is discontinuous, the numerous taliks on the watershed divide surface provide ideal conditions for groundwater feeding. This groundwater discharges locally in the bottom of valleys. Climate change produces differences in permafrost configuration (geometry). It affects the interaction between underground and fluvial waters through changes in the volume of talik reservoirs. This interaction leads to changes in river discharge, especially in the winter. To describe this interaction, the authors developed an efficient numerical method for solving coupled groundwater flow and phase-change heat transfer problems in porous media. The first results of modeling showed that the watershed divides without permafrost became colder because the descending cold infiltration water is directed toward the ascending heat flow. The developed approach seems to be instrumental in analyzing the peculiarities of discharge dynamics of the Lena River tributaries.

Keywords: climate change; discontinuous permafrost; groundwater flow; numerical modeling; water infiltration.

Introduction

Introduction

The problem of discharge dynamics of the great Siberian rivers and the affect on permafrost conditions is the topic of this paper.

The site of our investigation is located on a plateau with monoclinal bedding of Mesozoic rock in the upper part of the Lena basin. The study area is situated in uplands and mountain foothills where permafrost is the warmest in the region (it is still widespread but discontinuous). This region is between the Aldan and Timpton Rivers (centered at 57°N and 125°E), and, more specifically, within the basin of the Chulman River, right tributary of the Aldan River which is a right tributary of the Lena River. Geologically, this region is located in the central part of the Mesozoic Chulman Depression. This territory is well-studied in geocryological and hydrogeological aspects and is representative in Southern Yakutia as the region with discontinuous permafrost (Chizhov et al. 1975). The water catchment areas are situated predominantly at 850–950 m a.s.l.. The typical depth of valleys is 150–200 m. Locally, the valley depth increases up to 950 m. The density of the river network is very high. The water-collecting areas are flat and have the width of 2–3 km. The steepness of slopes is 10–20º. Permafrost distribution is closely related with different elements of the relief. It exists under slopes and in the valley bottoms. The permafrost thickness varies from ten m to 100–150 m and more. The mean annual permafrost temperatures (MAPT) vary from -0.5 to -2.0ºC rarely to -5.0ºC. The permafrost-free flat surfaces of hilltops are the areas where snowmelt and rain waters percolate into the deeper rock horizons. In these areas the active layer in well-drained coarse sediments, and weathered bedrock is very deep (down to 5 m).

The long-term dynamics of precipitation regime and river discharge demonstrate a tight correlation during most of the year. However, they have opposite tendencies in June and September–October. This fact shows the complexity of water balance within the Southern Yakutia watersheds. Here the groundwater (interpermafrost and subpermafrost) storage and icings are important components of the regional discharge. Recently observed total increase in the annual amount of precipitation goes together with a relatively stable dynamics of evapotranspiration (Berezovskaya et al. 2005).

We suppose the principal factor of river discharge tendencies is an interaction between variable permafrost massifs and underground water-flow intensity. Such assertion has no evident analogs in recent investigation results and requires combined theoretical and field studies.

In this paper, we present some preliminary results of permafrost-hydrosphere interaction modeling.

Methods

Problem definition

We developed a schematization of permafrost-hydrogeological and meteorological conditions and governing pro-

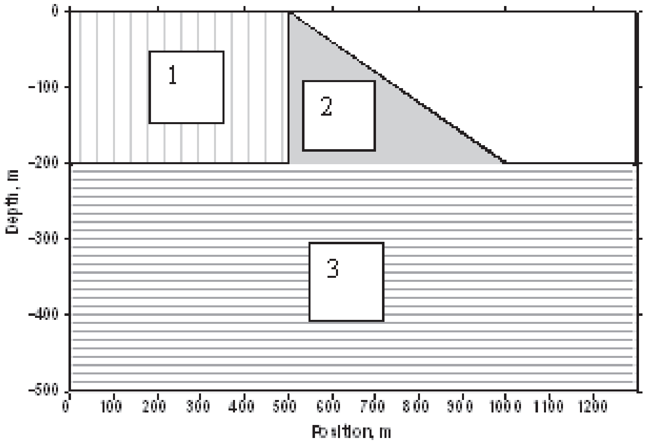

Figure 1. The geometry of the computational domain.

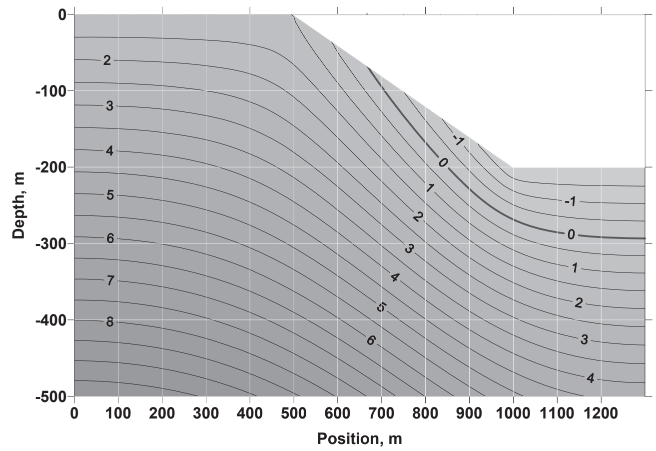

Figure 2. Temperature field without water-flow.

cesses that were used for the formulation of a mathematical model. This model allows the assessment of river discharge dynamics under the influence of permafrost and climate change in the upper part of the Lena River basin.

The hydrogeological setting depends on permafrost conditions. In spring and summer, the feeding of the groundwater takes place due to vapor condensation and percolation of snowmelt and rain waters through the vast watershed taliks situated on the flat hilltops. The vertical zones of air-dry fractured bedrock, periodical saturation, and constant saturation are located within unfrozen massifs of intensively fractured and weathered bedrock. The area and volume of the above-mentioned zones constantly change during the year. In spring, the snowmelt water and atmospheric precipitation start to infiltrate into and through a thick zone of airing (50–150 m and more) and increase the volume of saturation by the groundwater zone. The water movement is very fast and is accompanied by increasing water level in the massif of bedrock and by forming so-called infiltration knolls (reaching up to tens of meters in thickness). Groundwater feeding by atmospheric precipitation stops when the air temperature drops below 0°C in early winter and the active layer freezing starts. Starting from this moment, the gradual decrease of infiltration knolls begins. It is linked with groundwater discharge through open river taliks on the valley bottoms and icing forming. The groundwater transit pass way under the slopes is situated below the bottom of ice-bonded permafrost. This intensive flow of subpermafrost groundwater eventually forms a layer with high water permeability. However, in the lower parts of the slopes, the subpermafrost water head has a level up to 10 m above the permafrost table.

The analysis of available data shows that climate change can affect the groundwater recharge, out-flow, and discharge by the following factors or processes: (1) the expansion or contraction of the area of watershed open taliks; (2) a shift in the duration and timing of seasonal freezing and thawing that controls the time of infiltration and feeding of the groundwater reservoirs; and (3) changes in the amount of atmospheric precipitation.

In an epoch of climate warming and increased precipitation, we should expect the increase in the groundwater discharge in the valleys. There is a very important problem about the time lag of the pressure water waves. They form during the summer under the watershed divides and move toward the valley bottoms during the autumn and early part of the winter.

Research Strategy

The goal of the research presented here is to evaluate the impact of climate and permafrost changes on hydrological dynamics. To achieve this goal, we developed an efficient numerical method for solving coupled fluid flow and the phase-change heat transfer problem in porous media.

Because of the baffling complexity of the problem, the calculations were organized in three stages. *Foremost, we solved the two-dimensional heat transfer problem while taking into account the permanent continuous annual infiltration*. The goal of this stage was the retrieval of equilibrium spatial configuration of permafrost massif under condition of water flow in zones of suspended water and water saturation. In considered conditions, the influence of convective heat transfer on the permafrost develops not only because of the convective transport of the heat, but also because of the redistribution of the direction and intensity of the geothermal heat flow. As a result of this stage, the calculated configuration (geometry) of the permafrost massif in the computational domain was used as the base for the *second stage of modeling, when we are solving the phreatic flow problem with variable infiltration feeding*. In this case, the shape of the ice-bonded permafrost massif was assumed stable because the typical time of its change is much larger than the time scale of changes in the groundwater flow field. The model will allow understanding of the groundwater head level regime within the watershed divide taliks, the transfer of the head wave along the way of water flow under the permafrost, and water discharge dynamics in the valley during the year. Lastly, at *the third stage of modelin,g we plan to investigate the seasonal freezing as well as the full dynamics of the permafrost and taliks-configuration*

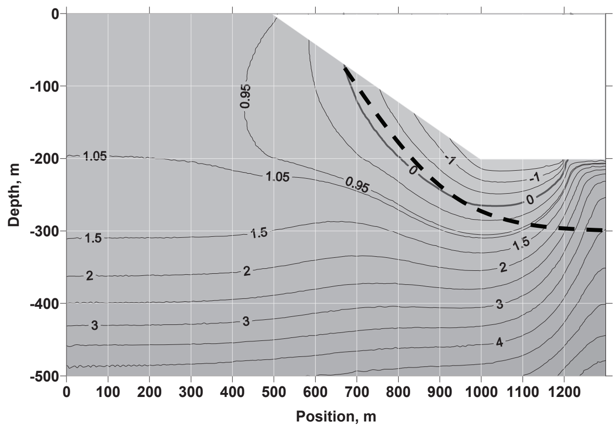

Figure 3.The temperature field in the run with a water-flow. The dashed line shows the zero-temperature isotherm for the run where the convection was not taken into account.

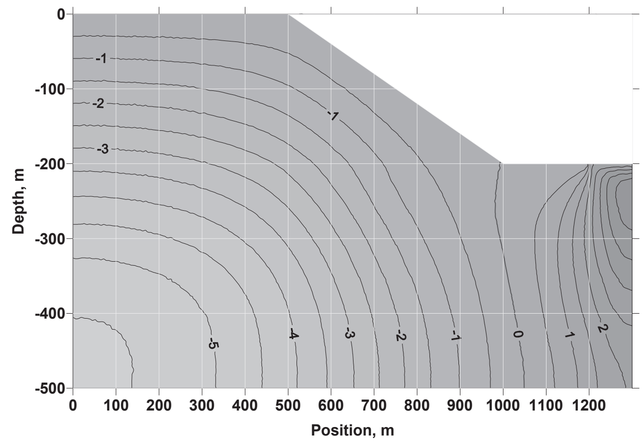

Figure 4. The difference in the temperature between "convective" and "conductive" runs.

development by taking into account the variability of climate and convective heat transfer in the bedrock. The seasonal freezing affects the period, the area, and the patterns of groundwater infiltration. The area of taliks within the watershed divide, and the amount of precipitation controls the volume of groundwater reservoir (storage).

Thus, these three stages of modeling will allow the obtaining of quantitative characteristics of the link between climate change and the hydrological dynamics within a typical site in the southern part of the Lena River basin.

Methods of Modeling and Assumptions

We performed the first stage of the modeling with the following principal simplification to describe the natural conditions. The original numerical model was prepared by G.Tipenko (Sergueev et al. 2003). We assumed that the temperature and water-flow fields can be represented by the two-dimensional vertical section across a river valley because of the elongated shape of the watershed divides. The hydrological and thermal physical properties of sediments and bedrock are sectionally continuous and isotropic.

Because the divide valley is symmetrical, we modeled a fragment between the vertical axis of the watershed divide and the center of an adjacent valley (Fig. 1). The geometry of this area corresponds to a real relief fragment near the town of Chulman in southern Yakutia. The calculation domain contains three blocks (Fig. 1). The width of the flat divide surface is 1000 m (block #1), the horizontal lengths of the slope is 500 m, and the valley depth is 200 m (block #2). The width of the valley's bottom is 600 m. The bottom of the computation area is at 300 m below the bottom of the valley and at 500 m below the top of the divide surface (block #3).

The position of low limit of permeability corresponds to the real data about zone of active water exchange in this region (about 200–300 m).

At the first stage of modeling we use some simplifications of real rules of the water migration. The zone of suspended water is replaced by the zone of full saturation (block #1). Within this zone an effective permeability of rocks was selected to ensure the correspondence to unit value of head gradient as in condition of descending water flow. Thus in condition of flow norm as W_{in} m/year the hydraulic conductivity in the zone of suspended water should be $k_f = W_{in}/365$ m/day (W_{in} is the rate of the infiltration).

The block #2 is water-impermeable because it represents permafrost; therefore there is not any infiltration in the upper part of the valley slope. This assumption explains the absence of the horizontal spread of water from the block #1.

The hydraulic conductivity of the seepage is determined by the reverse calculation from the shape of seepage level surface under the watershed divide under condition of infiltration. We use the value of transmissivity T = 45 m^2/day. This value corresponds to the hydraulic conductivity k_f = 0.15 m/day in condition of seepage thickness at 300 m. It corresponds very well with real mean conductivity of terrigenous rocks in southern Yakutia.

The left- and right-side borders of the computational area are "heat-proof" (zero value of heat flux in the "Second Type" boundary conditions). At the bottom of the computational domain, we set the heat flux q_{dp} = 0.043 W/m^2. At the upper boundary, we prescribed the "First Type" boundary condition as the temperature +1ºC at the hilltop divide surface and some rule of variability of temperature in the valley system. Within the entire bottom of the valley, the surface temperature was set at -2ºC. On the slopes, the temperature has a linear spatial trend from +1ºC on the limit of the hilltop divide surface to -2ºC at the foot of the slope. The chosen initial ground conditions values are theoretically typical for the area (Chizhov et al. 1975).

The surface of the slope and the lower and side limits of the computational domain are hydraulically impermeable. On the top of the divide and at the bottom of the valley we use the "First Type" hydraulic boundary conditions as head values that correspond to the altitude of the relief surface. The permafrost is also impermeable to water-flow in our model.

Results

To describe the influence of infiltration and convective heat transfer on the temperature field dynamics in the thawed zone, we implemented the plain conductive heat transfer computation as the first step of modeling. Here we did not have a riverbed talik in the valley. In this case, we obtained the maximal thickness of the permafrost at 93 m (Fig. 2).

At the second step of modeling, we increased the surface temperature in the 100-m band from the middle part of the river main channel in the valley up to +2ºC. This increase was held for a sufficient time for the occurrence of the riverbed talik as the zone of subpermafrost water discharge and icing formation that exists in reality.

At the third step of modeling, we resolved a coupled groundwater flow and phase-change heat transfer problem in porous media. The surface temperature in the middle part of the valley was +0ºC. The calculation was performed for the 10,000 yr time period to reach the new equilibrium for the temperature field (Fig. 3) and obtain the field of the water head that corresponds to the new geometry of the permafrost massif.

The numerical modeling resulted in following qualitative and quantitative conclusions. Because the descending cold infiltration water is directed toward the ascending heat flow, the watershed divides without permafrost became colder. This cooled area exists not only in the zone of suspended water, but also in water-saturated rock massif up to 200 m below the surface of saturation. This effect is a result of high importance of the vertical component of the water flow in the area between model blocks 1 and 3 where the groundwater flow changes its direction. As a result, a non-gradient temperature field was formed in the zone of suspended water.

The migration of groundwater from cooled divide massif to the valley was accompanied by temperature decrease under the slope and increase in permafrost thickness there. In the valley the convective open talik became stable, and temperature around it increased in comparison with the case without convective heat transfer. This change was not only a consequence of the convective heat flux, but also a result of decrease in the geothermal heat flux from the lower part of the calculation domain because it was shifted from the watershed to the valley.

The influence of the water-flow on the temperature field was illustrated by calculation of the difference between "convective" and "conductive" runs (Fig. 4). The considerable decrease in the temperature in the zone of descending groundwater flow and vertical heat flux from the bottom was obviously noticeable (left part of the figure). On the contrary, in the zone of water discharge into the riverbed talik, the temperature increased (right part of the figure). The separation zone, where the influence of the water-flow on the temperature is insignificant, was located under the lower part of the slope.

Conclusion

The basic conclusion from our numerical modeling is that *even at large depth the temperature distribution and the permafrost configuration (geometry) are sensitive to the percolation of surface water from snowmelt and from liquid precipitation and to amount and pass ways of groundwater infiltration within the thawed zones in sediments and fractured bedrock*. As a result of permafrost degradation related to climate warming, the areas of groundwater feeding and the reservoir capacity of fissured/fractured bedrock increase in size and the river discharge changes.

Considered mechanisms of interaction between permafrost and underground discharge have a regional importance.

We are planning to study these effects during the next stage of modeling. The model must be calibrated using real hydrological and hydrogeological data. A proposed approach could be used to explain the complicated picture of real tendencies in relationships between changes in atmospheric precipitation and river discharge.

Acknowledgments

This work is supported by grants from NASA THP Discovery Investigation "Current climate changes over Eastern Siberia and their impact on permafrost landscapes, ecosystem dynamics, and hydrological regime" and "Permafrost Dynamics within the Northern Eurasia Region and Related Impacts on Surface and Sub-Surface Hydrology" and by research grants from the Russian Fund of Basic Research (#06-05-64959a and 05-05-64390a).

References

Berezovskaya, S., Yang, D. & Hinzman, L. 2005. Long-term annual water balance analysis of the Lena River. *Global and Planetary Change* 48: 84-95.

Chizhov, A.B., Buldovich, S.N. & Chizhova, N.I. 1975. Hydrogeological condition of Chulman Depression. In: *Southern Yakutia*. MGU Publ: 291-311 (in Russian).

Sergueev, D., Tipenko, G., Romanovsky, V. & Romanovskii, N. 2003. Mountain permafrost thickness evolution under influence of long-term climate fluctuations (results of numerical simulation). *Proceedings of the Eighth International Conference on Permafrost, Switzerland, July 2003*, 2: 1017-1021.

Permafrost Distributions on the Seward Peninsula: Past, Present, and Future

Robert C. Busey
International Arctic Research Center, University of Alaska Fairbanks, USA
Larry D. Hinzman
International Arctic Research Center, University of Alaska Fairbanks, USA
John J. Cassano
UC Boulder, Colorado, USA
Elizabeth Cassano
UC Boulder, Colorado, USA

Abstract

Current observations show the Seward Peninsula sits on the margin of the continuous/discontinuous permafrost transition in western Alaska, U.S.A. This region of subarctic Alaska could be viewed as a proxy for a warmer Arctic, due to the broad expanses of tussock tundra, invading shrubs, and fragile permafrost. With average annual air temperatures just below freezing and very warm permafrost, the area is susceptible to dramatic change in response to a warming climate. Ground temperatures were estimated using observed meteorological and GCM-simulated forcing of the TTOP soil temperature model, making it possible to investigate the potential rate and mechanisms of change in frozen ground distribution past, present, and future.

Keywords: climate change; IPCC projections; numerical soil temperature model; permafrost; TTOP.

Introduction

The Seward Peninsula of Alaska, USA is located in the western part of the state (Figure 1). As estimated by the International Permafrost Association (2003), the northern part of the peninsula is underlain by continuous permafrost while the southern part, with its higher mean annual air temperatures and a maritime coast, is underlain by discontinuous permafrost.

Villages on the peninsula are located primarily near the coast, but many subsistence activities take place in the interior. Active local economic development includes placer and hard rock gold mining, as well as reindeer herding. Future mining will create a need for a denser road network. With ground underlain by warm permafrost, the economic cost of maintaining current and establishing new infrastructure is expected to rise in a warmer climate due to thawing of permafrost. The economic future of the peninsula is dependent on an accurate projection of permafrost distribution and state.

Permafrost sensitivity is affected by changes in a transitional climate and will shape the economic future on the peninsula. In this paper, permafrost extent is estimated for three periods: the early 20th century, the early 21st century, and the late 21st century using the TTOP numerical model.

Methods

Detailed knowledge about permafrost is difficult to ascertain without extensive research. To develop a better understanding of permafrost distribution on the larger scale we often use models. A model is a way of simplifying the complex natural environment into something more manageable.

In this study, permafrost thermal composition on the Peninsula is estimated using the TTOP numerical model with a spatial resolution of 100 m. The TTOP model is one way of determining the thermal offset between the ground surface and the top of the permafrost table (Smith & Riseborough 1996). TTOP was originally developed by Smith & Riseborough (1996) and is an equilibrium numerical model, which assumes quasi-steady state conditions for each year (Riseborough 2007). The TTOP model was selected because it is numerically efficient so performing calculations over a large domain such as the Seward Peninsula at a relatively high horizontal resolution is not an obstacle. In this study, to reduce the impact of interannual climate variation, several years are averaged together. The three time periods modeled in this study show thermal change over centennial scales. The components of the thermal offset calculation are outlined in Equation 1 below.

$$
\begin{aligned}
T_T &= \frac{n_T k_T I_{AT} - n_F k_F I_{AF}}{k_F P}, T_T < 0 \\
T_T &= \frac{n_T k_T I_{AT} - n_F k_F I_{AF}}{k_T P}, T_T > 0
\end{aligned}
\tag{1}
$$

In Equation 1, T_T is the temperature at the top of the perennially frozen or unfrozen ground (°C). Each variable on the right-hand side of Equation 1 is a function of spatial position except the annual cycle (365 days), P. I_{AT} and I_{AF} are the annual air temperature thawing and freezing indices (°C-days), which are calculated for each time period using another model, MicroMet—a quasi-physically-based program that uses climate forcing to distribute meteorological parameters across a physical domain and will be described in more detail below (Liston & Elder 2006). The annual freezing index is the summation of mean daily air

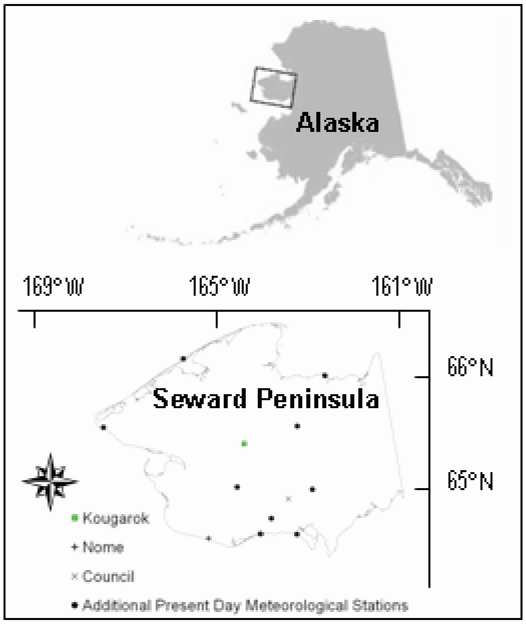

Figure 1 The study area, Seward Peninsula in Western Alaska, USA. Model comparison data are from Kougarok, the square in the interior of the Peninsula. Verification data comes from Kougarok and Council, the *x* symbol in the interior of the peninsula. Nome, the largest community on the peninsula, is the + symbol along the southern coast of the peninsula.

temperatures below freezing at a single point for a one-year period. The annual thawing index is the sum of average daily air temperatures above freezing over the year. N-factors are a way of relating air temperature to soil surface temperature, simplifying the heat transfer relationship between air and the soil surface (Lunardini 1978). N-factors parameterize effects such as radiative heating, evaporative cooling in summer, or snow insulation in winter. For the above freezing and below freezing air-soil surface interface relationship, n-factors are represented as n_T and n_F, respectively (Lunardini 1978). In this study, these two components vary as a function of the primary vegetation group in each cell. In the TTOP equation, thawed and frozen bulk thermal conductivities of the soil in the active layer are represented by k_T and k_F. These two thermal conductivity parameters vary spatially across the peninsula and are based on values from a soil classification map created by the Natural Resources Conservation Service (Van Patten 1990). The next several sections will discuss these components in more detail.

To calculate the annual freezing and thawing air temperature indices across the peninsula (I_{AT} and I_{AF} from Equation 1), the program MicroMet was used. MicroMet is a quasi-physically-based meteorological forcing model (Liston & Elder 2006). MicroMet distributes common meteorological variables, like air temperature, relative humidity, precipitation (solid and liquid), wind speed, and wind direction, across a physical domain. Originally developed for a domain on the North Slope of Alaska, it has been used successfully in other Arctic areas and locations around the world (Liston & Elder 2006). Quasi-physically-based means the point data (e.g., from a meteorological station) are adjusted through physical parameterizations to a common elevation of sea level when appropriate, such as with air temperature. Next, these point data are gridded horizontally across the domain using the Barnes objective distribution scheme (Barnes 1973, Koch et al. 1983). Finally, the interpolated data are adjusted vertically back to a realistic topographic distribution using the model and elevation data from the digital elevation. In this study, MicroMet distributes the meteorological data daily in one-year intervals. At the end of each one-year period the annual freezing and thawing air temperature indices (I_{AF} and I_{AT}) are calculated for each point in the Seward Peninsula domain.

GIS components

When applying the TTOP equations across the Seward Peninsula domain several variables vary spatially. Both MicroMet and TTOP use a Digital Elevation Model (DEM) with the same 100 m horizontal resolution. In addition, a vegetation map is used both by MicroMet (for solid precipitation distribution) and TTOP (the n-factor values are a function of vegetation type). The plant types in this digital map include three types of tundra in varying degrees of wetness, forest, shrub land, water bodies, and barren lands (Thayer-Snyder 2005). The vegetation type in each pixel controls the n-factors (n_t and n_f in Equation 1). Surface n-factor relationships in each vegetation class are primarily calculated using several years of data collected by our established long-term meteorological stations (http://www.uaf.edu/water/projects/atlas/atlas.html) on the peninsula and are supplemented with n-factor values compiled by Lunardini (1978).

The U.S. Natural Resources Conservation Service (NRCS) completed an extensive soil examination covering the Seward Peninsula area (Van Patten 1990). This digital map of peninsula soils serves as the basis for estimating subsurface thermal properties (k_t and k_f in Equation 1). These data are generally qualitative and are divided into 24 landscape groups. In the report, each landscape group has at least one subsurface soil profile typical to that class. To make this map useful in the permafrost extent modeling, quantitative data collected by Ping et al. (2005) was used to estimate thermal conductivity of the mineral soils identified by Van Patten (1990). Using the mineral content of the soil from Ping et al (2005), bulk thermal conductivity over the active layer was estimated using Johansen's method outlined in Farouki (1981). In addition, surface vegetation and subsurface organic layer thermal conductivity were measured by our group during the 2007 field season on the northern part of the peninsula. These values were used for all organic soils mentioned in the typical soil profiles of Van Patten (1990). Frozen organic thermal conductivity is estimated using prior work by Hinzman et al. (1991).

Early 20th century permafrost extent

For the early 20th century permafrost distribution, a single meteorological record from the peninsula (Nome) is available from the National Climate Data Center. Using

MicroMet, annual freezing and thawing air indices for the hydrologic years 1908 to 1918 are calculated. The mean annual air temperature over this period for the Kougarok site is -2.9°C. Since there is just a single point in the domain, MicroMet performs only a vertical temperature adjustment (using the adiabatic lapse rate) across the peninsula. The period 1908 to 1918 was chosen as the earliest continuous segment in the Nome period of record. In summer when sea ice is absent, Nome has a maritime climate rather than the continental climate that is typical of the interior of the peninsula. Temperatures in Nome are also warmer compared to the northern coast of the peninsula. Using only one station observation therefore leaves considerable uncertainties, but it is the only record available for this era.

Present-day permafrost extent

Present-day permafrost extent is estimated using data from significantly more meteorological stations in the region. Data sources include the Natural Resources Conservation Service (NRCS) Snow Telemetry (SNOTEL) sites, Bureau of Land Management (BLM) Remote Automated Weather Stations (RAWS), National Weather Service (NWS) sites, and University of Alaska Fairbanks Water and Environmental Research Center (WERC) sites.

All of these sites record hourly air temperature, relative humidity, wind speed, and wind direction. Additionally, many, but not all, log precipitation. The period of interest is an average of the hydrologic years 2001 to 2004 with the mean annual air temperatures over this period -3.2ºC (Table 2). The recent period was selected because a number of new meteorological stations came online during this time compared to the previous decade.

Late 21st century permafrost extent

Permafrost temperatures at the end of the 21st century are estimated using output from the 13 Intergovernmental Panel on Climate Change (IPCC) fourth assessment report (AR4) General Circulation Models (GCMs) (2007). See Table 1 for a list of the GCMs. These models show considerable variability in their climate projections. For example, at the Kougarok K2 station grid point, the intermodel variation in mean air temperature ranged from -8.7°C (FGOALS 1.0g) to 4.6°C (IPSL CM4). The climate forcing for the GCM output is based on the SRES A1B scenario and encompasses the interval 2092 to 2100 with the exception of the NCAR model, which has an interval of 2092 to 2099. The A1B scenario is driven by technological and economic advancement across the globe with a balanced increase in energy use. Grid points from the GCM output located over the Seward Peninsula are used by MicroMet to downscale meteorological parameters on the peninsula.

For the future distribution experiments, MicroMet is run with data from each GCM individually. An average temperature at the top of the permafrost for each GCM is computed and then averaged over the decade to smooth interannual variability. Finally, a multi-model mean of these late 21st century runs is computed for brevity.

Table 1. IPCC AR4 Models used for late 21st century extent and mean air temperature over the period 2092 to 2100 at Kougarok site K2.

IPCC SRES A1B GCMs	Mean Air Temperature, Degrees Celsius
Canadian Centre for Climate Modelling and Analysis (Canada) CGCM 3.1	2.7
Centre National de Recherches Météorologiques (France) CNRM CM3	-3.2
Commonwealth Scientific & Industrial Research Organization (Australia) Mk 3.0	0.6
Geophysical Fluid Dynamics Laboratory (USA) CM 2.0	-1.7
Geophysical Fluid Dynamics Laboratory (USA) CM2.1	-0.3
Goddard Institute for Space Studies (USA) AOM	-0.4
Goddard Institute for Space Studies (USA) Model E R	-4.7
Institute of Atmospheric Physics (China) FGOALS 1.0g	-8.7
Institut Pierre Simon Laplace (France) IPSL CM4	4.6
Center for Climate System Research (Japan) 3.2 medres	0.3
The Max Planck Institute for Meteorology (Germany) Echam 5	-1.3
Meteorological Research Institute (Japan) MRI CGCM2.3.2a	-4.9
National Center for Atmospheric Research (USA) NCAR CCSM3.0 (2092–2099 mean)	-0.7

Results

Permafrost temperatures for the early 21st century (2001–2004) are shown in Figure 2. For verification, observed temperature data from two pairs of meteorological stations operated by WERC in Kougarok and Council were compared to the calculated TTOP model results for the present TTOP model output. Kougarok and Council are located in the interior of the peninsula as seen in Figure 1. These four sites are located in three different vegetation types as well as three separate soil classes. A Mann-Whitney *U* test, similar to Student's *t* test but more appropriate for these data, is true at the 0.1 significance level, suggesting good agreement between the calculated TTOP temperature and the observed top of permafrost temperature. With regard to the precision of the modeling results, the mean absolute error is 1.8°C. Site-specific information is shown in Table 2, which is an overview of the climate and permafrost temperatures at one of the Kougarok sites.

In Figure 2, areas with above-freezing TTOP temperatures, which could indicate a talik below the active layer and thawing permafrost or a permafrost-free area, are generally limited to mountains and related features. However, in the south, some areas with a thicker organic base are also estimated to be experiencing thaw.

Table 2. Climate statistics at Kougarok site K2.

K2 Site	Mean Annual Air Temperature	Observed TTOP	Calculated TTOP	Difference (Observed – Calculated)
		Degrees Celsius		
2001	-2.5	-3.7	-3.0	-0.7
2002	-4.4	-2.7	-4.6	1.9
2003	-2.1	-2.5	-3.0	0.4
2004	-3.7	--	-4.6	--

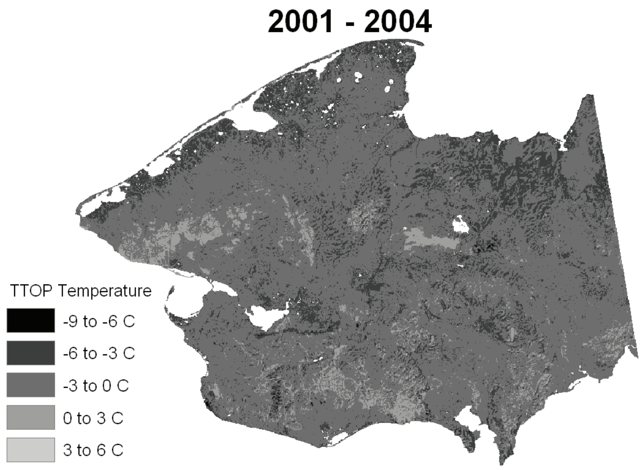

Figure 2. Present-day estimated permafrost temperatures.

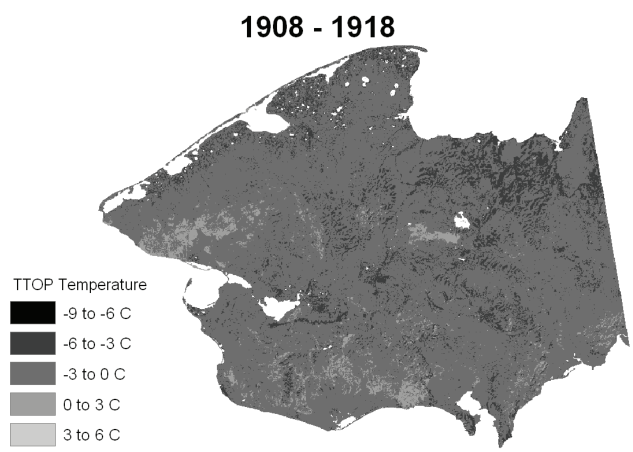

Figure 3. Early twentieth century estimated permafrost temperatures.

One current MicroMet limitation is the lack of an algorithm for calculating wintertime temperature inversions. If included, there would potentially be more land surface estimated as underlain by continuous permafrost in the interior. Winter temperature inversions occur when air temperatures are well below freezing and there has been no wind, which allows air temperatures to stratify vertically with the coldest temperatures at the lowest elevations. Steep thermal gradients develop until the wind mixes the air column again. This is not expected to be a major limitation, as the Seward Peninsula seldom experiences calm winds for extended periods. It is possible that for estimating present

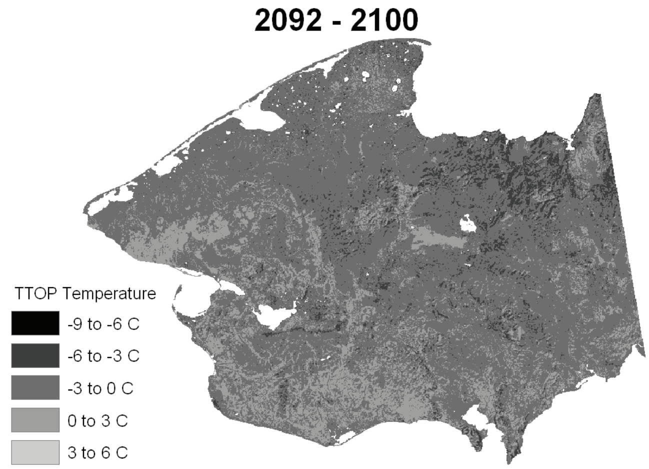

Figure 4. Late 21st century estimated permafrost temperatures.

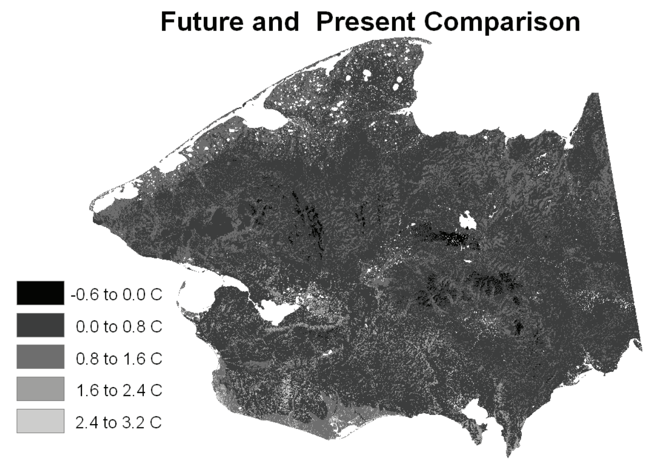

Figure 5. Temperature difference between the future distribution and the present distribution. Higher temperatures represent warmer future conditions.

extent satellite measured ground surface temperatures could allow consideration of winter inversions in future research.

Modeled permafrost temperatures for the early 20th century (1908–1918) displayed in Figure 3 are similar to the present day TTOP results (Fig. 2). In reality the TTOP temperatures for this earlier time should be a bit lower due to using a single weather station in Nome as the only climate forcing point in the domain used by MicroMet. Points further north in the interior would better capture the continental climate for the landscape away from the ocean. Additional experiments are planned to test this hypothesis. Another similarity to the present is that only the mountainous areas, which are dominated by coarse mineral soil, are thawed or thawing. This is probably related to the reduced water content in these coarse soils and the corresponding higher thermal conductivity compared to the valley bottoms, where there is a thick layer of organic mat above the fine-grained mineral soil. About 8% of the area has TTOP temperatures above freezing.

In contrast, permafrost extent for the end of this century (2092–2100) shown in Figure 4 based on the IPCC SRES A1B scenario shows much warmer temperatures across the peninsula. Much of the near-surface landscape in the south and low-lying areas will likely have temperatures at the base of the active layer rise above freezing.

A summary figure comparing the difference between the late 21st century results of the IPCC SRES A1B scenario to the present estimated TTOP temperatures is shown in Figure 5. A plot comparing the early 20th century permafrost temperatures to the present is not shown because the temperatures were similar. In Figure 5, the greatest difference in temperature is concentrated along the coasts. Several small areas in Figure 5 show colder temperatures between the future and the present. These are high in the mountains and are probably skewed by the IAP FGOALS 1.0 g GCM, which predicts future air temperatures 5° colder than the present. Additionally, the increase of thawing landscape between now and the future begins to encompass more of the lower, flatter terrain that is also ice-rich. Charon (1995) estimated permafrost thickness on Cape Espenberg, the northernmost part of the peninsula, to be 158 m. Thus, permafrost is unlikely to thaw completely, but the surface conditions, where there is the highest diversity of plants and organisms, will change.

Conclusion

Permafrost temperatures over the Seward Peninsula of Alaska were modeled over 3 time intervals approximately 80 years apart. Early 20th century simulated permafrost conditions are similar to current estimated permafrost temperatures. When conducting numerical modeling, it is important to start with a simulation that estimates the present conditions well. Comparison of permafrost temperatures modeled with TTOP to observations from four UAF WERC climate stations on the peninsula shows they are statistically similar. In the future, permafrost degradation is likely to accelerate (Fig. 5). This will probably result in additional thermokarst development, because much of the areas predicted to warm are ice-rich valley bottoms. Higher permafrost temperatures and unfrozen talik formation will likely have a mixed effect on local industry, such as mining and reindeer herding, on the peninsula. The logistics of getting to these locations will increase in difficulty, since road maintenance costs are likely to be higher.

Acknowledgments

Support for this research was provided by the U.S. National Science Foundation under the Arctic System Science Programs (Grant Number OPP-0328686 and OPP-0229649). We would like to thank the people of the Seward Peninsula for assisting us in conducting this research. We also acknowledge international modeling groups for providing their data for analysis and the Program for Climate Model Diagnosis and Intercomparison for collecting and archiving the model data.

References

Barnes, S.L. 1973. *Mesoscale Objective Analysis Using Weighted Time-series Observations*. NOAA Tech. Memo. ERL NSSL-62, National Severe Storms Laboratory, Norman, OK 73069, 60 pp. [NTIS COM-73-10781].

Charon, S.D. 1995. *Changes in late Pleistocene and Holocene sedimentation, North Killeak Lake, Bering Land Bridge, National Preserve, Western Alaska.* M.S. Thesis, University of Massachusetts Amherst.

Farouki, O. 1981. *Thermal Properties of Soils.* U. S. Army Cold Regions Research and Engineering Laboratories, Hanover, NH. CRREL Monograph 81-1.

Hinzman, L.D., Kane, D.L., Gieck, R.E. & Everett, K.R. 1991. Hydrologic and thermal properties of the active layer in the Alaskan Arctic. *Cold Regions Science and Technology* 19: 95-110.

International Permafrost Association Standing Committee on Data Information and Communication (comp.). 2003. *Circumpolar Active-layer Permafrost System, Version 2.0.* M. Parsons & T. Zhang (eds.). Boulder, CO: National Snow and Ice Data Center/World Data Center for Glaciology. CD-ROM.

IPCC. 2007. *Climate Change 2007: The Physical Science Basis. Contribution of Working Group I to the Fourth Assessment Report of the Intergovernmental Panel on Climate Change.* S. Solomon, D. Qin, M. Manning, Z. Chen, M. Marquis, K.B. Averyt, M. Tignor & H.L. Miller (eds.). Cambridge, United Kingdom and New York, NY, USA: Cambridge University Press, 996 pp.

Koch, S.E., DesJardins, M. & Kocin, P.J. 1983. An interactive Barnes objective map analysis scheme for use with satellite and conventional data. *J. Clim. and Appl. Meteorol*. 22: 1487-1503.

Liston, G.E. & Elder, K. 2006. A meteorological distribution system for high-resolution terrestrial modeling (MicroMet). *Journal of Hydrometeorology* 7: 217-234.

Lunardini, V.J. 1978. Theory of n-factors and correlation of data. *Proceedings of the Third International Conference on Permafrost, Edmonton, Alberta, July 10–13, 1978:* 41-46.

Ping, C., Michaelson, G.J. & Dai, X.Y. 2005. *NSF-ATLAS Winter C-flux Project.* URL: http://www.joss.ucar.edu/atlas/seward_cd/tables/group_ps.htm. Boulder, CO, variously paged. November 2

Riseborough, D.W. 2007. The effect of transient conditions on an equilibrium permafrost-climate model. *Permafrost and Periglacial Processes* 18: 21-32.

Smith, M.W. & Riseborough, D.W. 1996. Permafrost monitoring and detection of climate change. *Permafrost and Periglacial Processes* 7: 301-310.

Thayer-Snyder, C.R., Maier, H.A & Walker, D.A. 2005. *A Preliminary Landsat MSS-Derived Land-Cover Map of the Seward Peninsula, Alaska.* http://www.geobotany.uaf.edu/. Fairbanks, AK, variously paged. November 2

Van Patten, D. 1990. *Soil investigation of Seward Peninsula area, Alaska*. USDA-NRCS (SCS). U.S. Gov. Print. Office, Washington, DC.

Soil and Permafrost Properties in the Vicinity of Scott Base, Antarctica

I.B. Campbell
Land & Soil Consultancy Services, Nelson, New Zealand
G.G.G.Claridge
Land & Soil Consultancy Services, Nelson, New Zealand

Abstract

The southern tip of Ross Island is the location of two bases: Scott Base and McMurdo Station. The soils in this area are formed from thin volcanic drift over volcanic bedrock materials, and the active layer averages around 30 cm thick. The permafrost is predominantly ground ice, but ice wedges are present and extend into the volcanic bedrock. Extensive ground surface modifications have resulted in loss of permafrost ice, the formation of hummocky and patterned ground, and extensive surface soluble salt precipitation. Low albedo contributes to soil warming and moisture evaporation. Chemically, the soils are influenced by their proximity to the sea. They contain small amounts of soluble salts and are strongly alkaline. They are very little weathered and most of the clay fraction is derived from mechanical rock breakdown. Significant contaminations with heavy metals, wood, metal and fabric materials, and hydrocarbons have resulted from human occupation.

Keywords: Antarctic permafrost; Antarctic soils; human disturbance; Ross Island; Scott Base.

Introduction

Ross Island is a large volcanic island (area approximately 1350 km^2) situated at the southern margin of the Ross Sea and at the edge of the Ross Ice Shelf (Fig. 1). It comprises several extinct volcanoes and the active Mt. Erebus, 3740 m in elevation. Small ice-free areas occur in eastern and northwestern coastal areas (the location of several penguin rookeries), around the central summit crater, and at the southern tip of the island at the end of the narrow Hut Point Peninsula. Permanent research station occupation was established on the southeastern end of Hut Point Peninsula at Scott Base and at McMurdo Station on the southwestern end (some 4 km apart) in 1956/57 but at that time, little consideration was given to the nature of the soils, the permafrost or other environmental issues that are at the forefront today.

Since establishment of these bases, considerable land surface changes have occurred through construction of roads and pipelines, ground surface leveling for building sites and storage of materials, installation of communications, and extensive ground scraping for aggregate requirements, coupled with retreat of snow and ice cover. These have dramatically altered the original permafrost conditions in the modified areas.

The advent of the Antarctic Treaty (1959) and the Protocol on Environmental Protection to the Antarctic Treaty System (1991) have now provided a framework within which environmental management is expected to occur. This report gives an outline of the soil and permafrost conditions observed in the southern Ross Island area to provide a basis for future management considerations. Information and data have been obtained from general observations since the 1970s as well as from experimental, soil sampling, and monitoring activities through the 1990s.

Environmental Background

Ross Island is part of the McMurdo Volcanics Group, the rocks at Hut Point Peninsula being primarily scoriaceous flows and tuffs around 1.5 my old (Kyle 1981). The present hilly topography has been little modified by glacial erosion and is largely inherited from the previous volcanic activity with cones and craters forming distinctive local features. The soil forming material is a patchy thin cover of till, dominated by fragmental volcanic rock with a stony sandy gravel texture that becomes coarser with increasing depth (Table 1). Small partly rounded basaltic clasts are sometimes present, and also some granite and sandstone in the upper horizons. The latter rock materials are believed to be derived from the mainland, some 70 km to the west during the last glacial period (Ross Glaciation, Denton et al. 1971) when ice filled McMurdo Sound and covered Hut Point Peninsula.

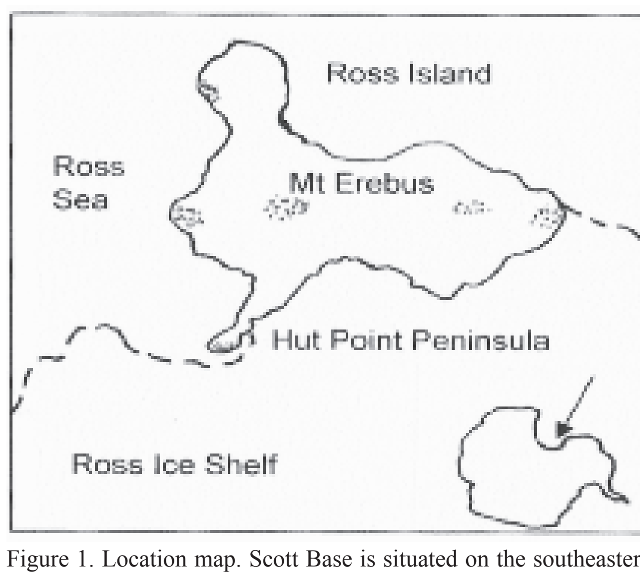

Figure 1. Location map. Scott Base is situated on the southeastern end of Hut Point Peninsula. Dotted areas are bare ground locations.

Table 1. Particle size fractions for a typical soil from volcanic materials near Scott Base.

	Weight fractions % of whole soil				
Depth cm	75 -2mm	75 -20mm	20 -5mm	5 -2mm	<2mm
0-0	42	4	18	20	58
0-7.5	56	37	19	--	44
7.5-15	65	36	10	19	35
15-30	74	46	12	16	26
30-45	61	34	13	14	39

Figure 2. Average active layer thickness and active layer and permafrost H_2O% (gravimetric) for 21 dry sites (left) and 21 wet sites (right).

The major features of the climate of the Hut Point Peninsula area are a mean annual temperature of -20°C at Scott Base (-18°C at McMurdo) and precipitation equivalent of about 200 mm. Temperatures average from around -30°C in winter months to -4°C in December and January but with occasional days in which summer temperatures may reach +6°C. Precipitation is difficult to assess accurately as much snow accumulates as drift from surrounding sea ice. Periodic summer snowfalls occur, however. Much of the landscape is snow covered in early December with maximum thaw taking place by late December to early January. The December/January thaw period is usually accompanied by small water flows from thawing snow banks, etc., but most of the snow is lost by ablation with only occasional surface soil moistening. Vegetation is restricted to sparse moss and lichen patches.

Soils

The soils of the Hut Point Peninsular area are unweathered and belong to weathering stage I which includes soils less than 50,000 years old (Campbell & Claridge 1975, 1987). They typically have a boulder or pebble pavement of angular scoriaceous basalt which is unweathered apart from a patina or thin varnish that gives upper black coloured clast surfaces a distinct luster. Ventiforms are absent although some clast abrasion is occasionally seen. The undersides of surface clasts commonly have a thin grayish brown calcareous coating and occasionally a thin precipitate of soluble salts. The carbonate was thought to have been derived from wind-deposited dusts originating from the mainland (Blakemore & Swindale 1958) but given the granite erratics that are present and the known fluctuations of the Ross Ice Shelf, the carbonate may have originated from the till materials. Below the stony surface pavement, the soil is grayish brown (10YR 5/2-2.5Y5/2) loose sandy stony gravel with the coarse fraction increasing with depth (Table 1).

Figure 3. Ice wedge formed in tuffaceous volcanic bedrock in a cut section for pipeline construction, near Scott Base.

A weakly-developed vesicular structure, formed as a result of freezing when the soil is moist, may be present in the top few centimeters. The soil passes abruptly into hard ice-cemented and unweathered permafrost. The active layer thickness ranges from near ground surface alongside permanent snow patches to around 60 cm on well-drained windy surfaces that have little snow accumulation. In well-drained sites, the soils have a low moisture content (gravimetric), averaging around 0.5% in the surface horizon and increasing with depth to around 8% above the permafrost.

Permafrost Properties

Physical characteristics

The permafrost in the Hut Point Peninsula region has been observed in the course of a number of investigations including general soils investigation, leaching and contamination studies (Claridge et al. 1999, Sheppard et al. 2000), from experimental disturbance of permafrost (Balks et al. 1995), as part of long-term monitoring studies (Paetzold et al. 2000), and from casual observations during domestic activities.

Examinations from shallow drilling (approximately 1.5 m deep) showed that the average depth of the permafrost table was approximately 30 cm at well-drained sites such as ridge surfaces (Fig. 2). In gullies or nivation cirques where water flows are occasionally present, the active layer thickness averaged 18 cm. At the edge of a permanent snow pack, the permafrost table was at the ground surface but increased to 20 cm some 20 m from the snow pack. The frozen water content (gravimetric) of the permafrost increases from around 10% near the permafrost table to 140% at greater depths with ice layering commonly occurring as ground ice. Our shallow drilling revealed that ground ice was present in the volcanic rock below the cover materials, with ice wedges and sand wedges being observed in the volcanic bedrocks in excavated

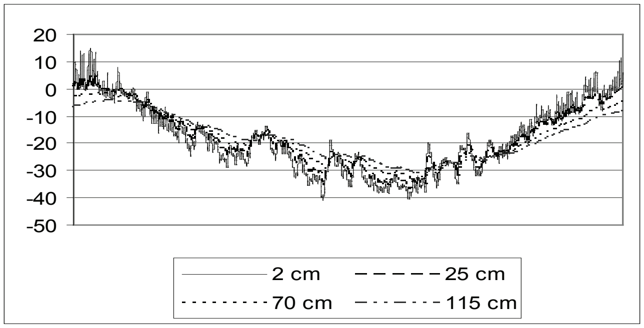

Figure 4. Hourly plots of temperatures (°C) at four depths in 2002 from the CALM site near Scott Base.

roadway sections (Fig. 3). In some places, massive stagnant ice was observed in exposures where regolith removal had given rise to accelerated thaw and ground slumping.

Thermal characteristics

Soil temperature plots from hourly measurements in 2002 at a CALM recording site near Scott Base (Paetzold et al. 2000) are shown in Figure 4. Mean annual soil and permafrost temperatures at four of the depths (2, 25, 70, and 115 cm) from which temperatures were recorded are all similar (approximately -18°C) and are close to the mean annual 1992 air temperature recorded at the site (-19.3°C). The 2 cm depth temperatures range from 14.2°C (January 11) to -40.7°C in mid June. At 115 cm, (approximately 85 cm below the permafrost table, the annual temperature ranged from -4°C to -19°C. At the 2 cm depth, there were 45 freeze/thaw cycles through the period from December 2 to January 31 with soil temperatures remaining above 0°C periodically for 15 days. As soil warming commences after the winter minimum temperatures, the temperature at all depths is briefly isothermal (-23°C) around late August and again in late February when the temperature was -6°C (Fig. 4). In summer months, diurnal temperature changes may reach 16°C while in winter months temperature changes in excess of 20°C occur over short periods due to weather events.

Experimental soil and permafrost disturbance

The moisture content, evaporation rate and soil radiation balance were investigated at an experimental site near Scott Base in January, 1994 (Balks et al. 1995, Campbell et al. 1997). The active layer (approximately 30 cm) was removed from 300 m^2 of eastward-facing, gently-sloping ground and observations were made and compared with those from an undisturbed immediately adjacent similar-sized area.

Observations from neutron probe access tubes to 1.2 m depths in the undisturbed sites showed low moisture contents in the active layer, very high ice contents in the upper part of the permafrost, and decreasing amounts with increasing depth. At the disturbed site, thawing of the permafrost began immediately with some of the thaw water apparently accumulating in the upper permafrost zone, judged by the neutron probe measurements which showed considerably higher moisture/ice contents compared with the undisturbed

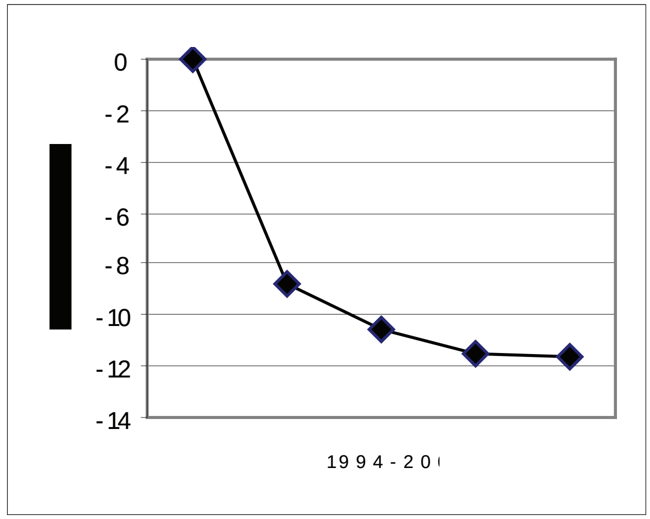

Figure 5. Average ground shrinkage values for 7 tube sites over 6 years at an experimental site near Scott Base.

site. Over the following six years, ice was lost from the disturbed site at a diminishing rate as measured by the amount of ground shrinkage against the access tubes (Fig. 5).

Evaporation rates were measured on undisturbed and the disturbed soil using small lysimeters over six days (Balks et al 1995). For the undisturbed dry soil, the evaporation loss was less than 0.1 mm/day and 1.1 mm/day at a site that was wetted from an adjacent snow melt. For the disturbed soils, initial evaporation rates of 1.5 mm/day and 3 mm/day were measured, but these rates declined as the soil surface became lighter-coloured on drying. These rates are similar to those observed in moist soils in the Dry Valley region (Campbell 2003).

The soil radiation balance was also measured at the disturbed and undisturbed sites (Balks et al. 1995, Campbell et al. 1997) over four days, and albedo measured during the 3-hour period of highest solar angle averaged 0.048 on the undisturbed surface with a similar value on the moist disturbed surface. On the dried disturbed surface, the values averaged 0.112 with more solar radiation being reflected from the disturbed dry surface than the undisturbed and the disturbed moist surface.

Disturbances caused by logistical activities

Soil and permafrost disturbance from logistical activities are widespread in the southern Hut Point Peninsula area and have primarily been caused by ground scraping to provide fill material for construction sites. In some places, only shallow scraping occurred with the active layer being removed but at other sites, repeated ground scraping into the scoria bedrock has removed meters of material. The shallow scraping was observed to result in rapid permafrost thaw with ground shrinkage causing patterned ground to form within three years, due to melting of ice wedges. It was noted that, in places, the ground surface was partly covered with large rock slabs indicating that the ice wedges and ground ice were largely within the volcanic bedrock. A reticular

Table 2. Components of the <2 µm fraction. Mc mica, Vt vermiculite, Chl chlorite, FeC iron-rich chlorite, Sm smectite, Qtz quartz, Fel feldspar, Hb hornblend, SRO short-range order material.

Depth	Mc	Vt	Chl	FeC	Sm	Qtz	Fel	Hb	SRO
cm				% of <2 mm fraction					
0-4	30		10	25	5	15	15		
4-30	30	5	5	20	7	15	15	5	
30-90	10	5		5	5	5	15		55
>100	10	3	2	5	5	5	15		55

Table 3. Composition of water extracts of soil, ms conductivity of 1:5 soil water extract $mScm^{-1}$.

Depth	pH	EC	Na	Ca	Mg	K	Cl	SO_4	CO_3
cm		mS	Millimoles charge/100g (me%)						
0-5	9.1	186	185	8.3	7.8	1.6	120	1.0	81.7
5-30	9.1	4.2	59	4.3	0.9	0.3	17	0.1	47.4
30-90	9.2	3.5	16	1.3	0.4	0.2	9.9	0.15	8.4
>100	9.4	3.2	16	1.2	0.4	0.7	10.8	0.1	7.7

patterned ground network was present in a few places on the deeply cut surfaces near McMurdo Station suggesting that ice wedges may at times penetrate some depth into the bedrock. At one locality on a ridge that had been scraped, grey quartzofeldspathic sand was noted in a crack that was presumed to be the remains of a sand wedge. Scraping on sloping ground that was underlain by stagnant ice resulted in extensive instability in the early 1980s, with repeated ground slumping and formation of thermokarst terrain (Campbell & Claridge 2003). In most places, ground disturbance is followed by the precipitation of a surface cover of soluble salts.

Examinations of areas in which fill materials have been deposited have not revealed any indications of recent ice accumulation consistent with the reformation of icy permafrost. The gravimetric moisture content was found to vary with depth and probably reflects the moisture content of the materials when deposited.

Soil Chemical Properties

Soil chemistry and mineralogy

The soils at southern Ross Island are very little weathered and contain only small amounts of the fine-earth fraction. Extractable Fe_2O_3, the usual measure of mineral breakdown, and release of iron is also very low, about 0.3% of the fine earth fraction, while clay contents (<2 µm) are around 6%, relatively high for Antarctic soil indicating mechanical breakdown of rock particles, largely the glassy component of the basaltic scoria parent material. The clay fraction of the surface material (Table 2) (0–30 cm) contains mica (illite?), chlorites, and some smectite, as well as clay-size quartz and feldspar, all consistent with much of the clay fraction, apart from the smectite, being derived from materials transported from the mainland, rather than from breakdown of the basaltic rocks. The smectite could have been derived from weathering of the glassy material in the basalt but this has not been investigated.

Within the ice-cemented permafrost, which was accessed by drilling, the clay fraction is dominated (50%) by palagonitic material showing only short-range order and may have been derived from breakdown of glassy material within the basalt.

The soils of the southern Ross Island area are heavily influenced by their proximity to the ocean, in contrast to most of the soils from the Transantarctic Mountains (Campbell & Claridge 1987). They are strongly alkaline, with pH values above 9. They contain moderate amounts of water-soluble salts (Table 3), in contrast to some of the older soils of the Transantarctic Mountains, and the salts are dominantly chlorides of sodium with lesser amounts of calcium and magnesium. The proportion of sulphate ion is very low while nitrate is below the limit of detection.

There is very little difference in the composition of the salts in the active layer of the soil and the salts in the underlying permafrost which was sampled to 1.5 m. At a site where the active layer had been removed and the underlying permafrost had thawed and a new active layer formed, the salts contained within the thawed permafrost had migrated to the surface giving an extensive surface efflorescence of halite. At sites that had not been scraped, only very small efflorescence’s were visible. The ions within the surface efflorescence’s are in the same proportion as those within the soil indicating no differences in mobility of the ions over the distances involved.

It is not clear whether the salts within the permafrost are residual and relate to previous glacial conditions or whether the salts may migrate into the permafrost under current conditions as thin films of concentrated solutions with low melting points as described by Ugolini & Anderson (1973).

Lithium chloride-leaching experiments

In order to assess the potential for salts or contaminants to move within the soils at southern Ross Island, the mobility of lithium chloride, which was added to the soil surface, was studied (Claridge et al. 1999). In this experiment, lithium chloride solution was applied to the soil surface at two sites, one a dry ridge and the other a moist depression, then sampled over several years at and downslope from the application sites, then analysed for lithium.

The results of this experiment showed that at the dry sites, substances added to the soil surface, such as airborne salts or spilt contaminants, will mainly penetrate only a small distance into the soil, related to the particle size and permeability of the soil. A small proportion may penetrate further down by capillary action until the soil temperature reaches freezing point at the permafrost table. Solutions concentrated by freezing and evaporation may also enter the permafrost through cracks and pores as indicated by detectable lithium within the permafrost. At the moist site, lithium was detected several meters downslope after three years indicating that downslope movement of contaminants can occur given sufficient moisture.

Table 4. A 0-2 cm, B 2-10 cm, C 10-20 cm, D 20-30 cm. Con – control site; Sp – contaminated site; THP – total petroleum hydrocarbons (mg/kg);, hyd – hydrocarbon degraders (no./g).

	pH		Org C		THP		Hyd	
	Con	Sp	Con	Sp	Con	Sp	Con	Sp
			%			$X10^4$		$X10^4$
A	8.4	7.8	0.1	5.1	<20	3.3	3.3	1.3
B	9.1	8.8	0.1	3.4	<20	2.5	230	1.4
C	8.9	9.8	0.09	1.6	<20	0.1	13	8.3
D	9.3	9.8	0.06	0.08	<20	0.1	13	3.5

Contaminations of soils around Scott Base

Detailed studies of the contamination of soils around Scott Base were made by Sheppard et al. (2000). Day-to-day activities can result in many kinds of contaminants being added to the soil surface, more especially in the past when management procedures were less concerned with environmental protection. A range of macro-contaminants such as wood, plastic, fibre, metals, etc. as well as odours from fuel spills were detected. The organic carbon content in the soils adjacent to the base was generally higher than at undisturbed sites, indicating the presence of intrusive organic material, which may have ranged from wood fragments to exhaust materials.

Acid extracts of the soils, designed to estimate heavy metal contamination, showed that the soils adjacent to the base were measurably contaminated with Ag, As, Cd, Cu, Pb and Zn, with the highest amounts in sites where materials had been dumped or stored.

The saline, oxidizing, and alkaline environment of the soils and the variations of these conditions within the soil profiles were considered to cause the episodic mobilization and retention of heavy metals in response to freeze-thaw cycles and the movement of water through the soils. Heavy metals can be bound to the surface of the clay particles within the soil, such as the smectites or the short-range order of palagonitic clays, and this may prevent their removal, while the more soluble constituents may be leached out.

Effect of fuel oil spills

Accidental fuel spills can arise from a variety of causes and several spill sites have been noted around Scott Base (Aislabie et al. 2004). The most obvious affect on soil properties is that the soil becomes darker and absorbs more heat, so that soil temperatures may rise by as much as 10°C, possibly causing some thawing of the underlying permafrost. Fuel-affected soils are sometimes weakly hydrophobic with the potential to alter the soil moisture regime and change other soil properties, some of which are shown in Table 4. Hydrocarbon-contaminated sites have slightly lower pH values, especially in the surface layer, increased organic carbon contents, much higher total petroleum hydrocarbons (TPH), and very much larger contents, by five orders of magnitude, of hydrocarbon-degrading bacteria, although total bacterial counts are more or less the same.

If left undisturbed, fuel-contaminated sites have the potential to self-remediate, as the hydrocarbons are used as an energy source by some organisms, as discussed by Aislabie et al. (2004).

Hydrocarbon spills that are sufficiently large may wet the active layer and pond on the ice-cemented permafrost and spread over a much larger area than the surface spill. Liquid hydrocarbons may also penetrate into the permafrost along cracks and fissures filled with unfrozen saline solutions. While no major spills of this sort are known around Scott Base, they have been observed elsewhere in the McMurdo Sound region.

Conclusions

Properties of the soils at southern Ross Island reflect their youthfulness, being exposed to weathering since the retreat of Ross I ice in the late Last Glaciation. The permafrost table is present at a relatively shallow depth compared with that is soils of other coastal locations in the McMurdo Sound region because the combination of low albedo and high moisture availability results in more energy being expended in moisture phase change rather than in soil heating to greater a depth. Variations in depth to the permafrost table are due to differing site moisture availability. Soil disturbance and removal of the active layer soon results in permafrost thawing and ground instability with patterned ground forming where ice wedges have melted and ground slumping where massive stagnant ice is present. Ground ice and ice wedges are common in the volcanic bedrock.

The soils are strongly alkaline because of the marine influence, and salts have penetrated far into the underlying permafrost and are rapidly precipitated at the ground surface after the removal of metres of bedrock permafrost.

As well as the physical and chemical changes resulting from disturbance to the active layer and the permafrost, soils in the region are contaminated from a wide variety of macro-substances, and also by a range of heavy metals and hydrocarbons. Experiments have shown that the movement of contaminants through the soil is small in dry sites but greater in moist sites. The levels of hydrocarbons in the soils can be reduced by biodegrading bacteria.

Acknowledgments

The support provided by the New Zealand Antarctic Programme over a number of years and the contributions from various colleagues is gratefully acknowledged.

References

Aislabie, J.M., Balks, M.R., Foght, J.M. & Waterhouse, E.J. 2004. Hydrocarbon spills on Antarctic Soils: Effects on management. *Environmental Science and Technology* 38: 126.

Balks, M.R., Campbell, D.I., Campbell, I.B. & Claridge, G.G.C. 1995. *Interim results of 1993/94 soil climate, active layer and permafrost investigations at Scott Base, Vanda*

Station, and Beacon Heights, Antarctica. University of Waikato Antarctic Research Unit Special Report No. 1, 1-64.

Blakemore, L.C. & Swindale, L.D. 1958. Chemistry and clay mineralogy of a soil from Antarctica. *Nature* 182: 47-48.

Campbell, D.I., MacCulloch, R.J.L & Campbell, I.B. 1997. Thermal regimes of some soils in the McMurdo Sound region, Antarctica. In: W.B. Lyons & C Howard-Williams (eds.), *Ecosystem Processes in Antarctic Ice-free Landscapes.* Rotterdam: Balkema, 45-55.

Campbell, I.B. 2003. Soil characteristics at a long-term ecological research site in Taylor Valley, Antarctica. *Australian Journal of Soil Research* 41: 351-364.

Campbell, I.B. & Claridge, G.G.C. 1975. Morphology and age relationships in Antarctic soils. In: R.P. Suggate & M.M. Cresswell (eds.), *Quaternary Studies.* Royal Society of New Zealand Bull. 13, 83-88.

Campbell, I.B. & Claridge, G.G.C. 1987. *Antarctica: Soils, Weathering Processes and Environment*. Amsterdam: Elsevier, 368 pp.

Campbell, I.B. & Claridge, G.G.C. 2003. Thermokarst landforms in the Transantarctic Mountains region of Antarctica. *Proceedings of the Eighth International Conference on Permafrost, Zurich, Switzerland, July 21-25, 2003:* 119-124.

Claridge, G.G.C., Campbell, I.B. & Balks, M.R. 1999. Movement of salts in Antarctic soils: Experiments using chloride. *Permafrost and Periglacial Processes* 10: 223-233.

Denton, G.H., Armstrong, R.I. & Stuvier, M. 1971. The late Cenozoic glacial history of Antarctica. In K.K. Turekian (ed.), *The Late Cenozoic Glacial Ages.* Yale University Press, 267-306.

Kyle, P.R. 1981. Glacial history of the McMurdo Sound region as indicated by the distribution and nature of McMurdo Volcanic Group rocks. In: L.D. McGinnis (ed.), *Dry Valley Drilling Project.* Am. Geophys Union Antarct. Resc. Ser. 33, 403-412.

Paetzold, R.F., Balks, M.R., Aislabie, J., Kimble, J.M. & Campbell, I.B. 2000. In: J.A. Adams & A.K. Metherall (eds.), *Soil 2000: New Horizons for a new century. Australia and New Zealand Second Joint Soils Conference.* Christchurch: NZ Society of Soil Science , 167.

Sheppard, D.S., Claridge, G.G.C. & Campbell, I.B. 2000. Metal contamination of soils at Scott Base, Antarctica. *Applied Geochemistr.* 15: 513-530.

Ugolini, F.C. & Anderson, D.M. 1973. Ionic migration and weathering in frozen Antarctic soils. *Soil Science* 115: 461-470.

Patterned Ground Features and Vegetation: Examples from Continental and Maritime Antarctica

N. Cannone

Dept. Biology and Evolution, Ferrara University, Corso Ercole I d'Este, 32, 44100 - Ferrara, Italy

M. Guglielmin

DBSF, Insubria University, Via J.H. Dunant, 3, 21100 - Varese, Italy

Abstract

The relationships between vegetation patterns and periglacial features and their underlying ecology are still poorly understood and lack specific investigations in Antarctica. Here we present the preliminary results on vegetation colonization of different types of sorted patterned ground and gelifluction features (stone-banked lobes and terracettes) in two sites at James Ross Island and four sites in Northern Victoria Land. The paper aims to a) understand the relationships between the patterns of vegetation colonization and the investigated periglacial features; b) compare the characteristics of vegetation patterns in similar periglacial features in two geographically remote sites of Maritime and Continental Antarctica; and c) compare the observed patterns of vegetation with those described by literature for the High Arctic. Vegetation relations with the periglacial features show some common patterns between Maritime and Continental Antarctica. Frost creep/gelifluction processes and frost heave are much more effective than grain size as limiting factors for vegetation development.

Keywords: gelifluction features; Continental Antarctica; Maritime Antarctica; patterned ground; vegetation.

Introduction

Periglacial landforms are widespread in the polar regions of both hemispheres (French 2007). While several authors have focused on the relationships between vegetation colonization and the periglacial landforms in the Arctic (i.e., Britton 1957, Billings & Mooney 1959, Jonasson & Sköld 1983, Anderson & Bliss 1998, Matthews et al. 1998, Cannone et al. 2004, Walker et al. 2004), this topic has been poorly addressed in Antarctica (i.e., Heilbronn & Walton 1984). Moreover, to our knowledge, until now there are not specific investigations providing the comparison of the vegetation patterns in relation to periglacial landforms in Maritime and Continental Antarctica.

The aims of this paper are:

1) to understand the relationships between the patterns of vegetation colonization and the type and characteristics of the most widespread periglacial features;

2) to compare the characteristics of the periglacial features and of their related vegetation patterns in geographically remote sites of Maritime and Continental Antarctica: and

3) to compare the patterns observed in Antarctica with those described by literature for the High Arctic.

Study Areas

Two geographically remote areas of Antarctica were selected for this investigation (Fig. 1): James Ross Island, located on the eastern side of the Antarctic Peninsula and used as a template of Maritime Antarctica, and Northern Victoria Land, located at East Antarctica and used as a template of the conditions of Continental Antarctica.

Maritime Antarctica

At James Ross Island, two different sites (about 20 km from each other) were investigated: the Rink Plateau (named Rink in this paper) (63°55′S, 58°10′W) and Lachman Crags (named Lachman in this paper) (63°54′S, 57°35′W).

At James Ross the climate is a cold, dry maritime climate, with a mean annual air temperature of -6.7°C (referred to the period 1996–2004) (Mori et al. 2007) and mean annual precipitation of about 200 mm/yr water equivalent (Strelin & Sone 1998).

Rink site is a relatively high elevation plateau (400 m a.s.l.) delimited by a sharp and almost vertical scarp. This site is characterized by the occurrence of several periglacial features and a small ice cap located in the upper part of the plateau. The outcropping bedrock is composed of Cenozoic lavas and pyroclastites underlain by Cretaceous sedimentary rocks (Strelin & Malagnino 1992, Carrizo et al. 1998).

Lachman site includes different types of environments (i.e., valley bottoms, raised beaches, slopes) at elevations ranging between 0 and 200 m a.s.l. and characterized by a high frequency of periglacial features. The outcropping bedrock is volcanic with the occurrence of different types of deposits ranging from morainic and slope deposits, to raised beaches.

Northern Victoria Land

The climate of Northern Victoria Land is frigid Antarctic, with a mean annual air temperature of -18°C and precipitation, always in the form of snow, between 100 and 200 mm (Grigioni et al. 1992).

Four different sites were selected: Tarn Flat (74°59′S, 162°37′E), Boulderclay (74°44′S, 164°05′E), Gondwana (74°36′S, 164°12′E), and Apostrophe Island (73°30′S, 167°50′E).

All these sites are located along the coast, with the exception of Tarn Flat, at elevations ranging from 20 to 150 m a.s.l. These sites are characterized by the occurrence of different types of periglacial features occurring on different outcropping rock and deposits ranging from gabbro and metamorphic rocks (Apostrophe Island and Gondwana) to granites and morainic deposits (Tarn Flat and Boulderclay).

The vegetation both at James Ross and at Victoria Land is a cryptogamic nonvascular tundra, including different moss- and lichen-dominated associations (Longton 1979). Descriptions of the moss and lichen flora and of the main vegetation communities of Victoria Land have been provided by several authors (Kappen 1985, Castello & Nimis 1995, Seppelt et al. 1995, 1996, Seppelt & Green 1998, Smith 1999, Cannone 2005, 2006).

Methods

Geomorphology

The geomorphological study was performed by field surveys. All the periglacial landforms occurring in each selected study site were recorded and classified. Only in some representative cases, the groups of landforms selected for the vegetation survey were also morphometrically characterized through profiles and visual descriptions. In addition, the thickness of the active layer was measured by frost probing and, where logistical conditions allowed enough time, also by measuring the ground temperature at different depths following the method proposed by Guglielmin (2006).

Trenches were dug into the ground to investigate the internal structure of the features and for sampling.

Vegetation survey

The vegetation was sampled in 50 × 50-cm plots. Two (occasionally three) plots were set up at each of the selected landforms. All of the plots were located in morphologically homogeneous microhabitats within the landforms. All of the moss and lichen species occurring in the plot were recorded and their percentage cover estimated visually. Microtopography and surface-soil texture were assessed visually in each plot. Species nomenclature follows Castello & Nimis (2000), Øvstedal & Smith (2001) and Castello (2003) for lichens, and Ochyra (1998) and Seppelt & Green (1998) for bryophytes.

Results

Maritime Antarctica

At James Ross Island several types of periglacial features were analyzed, including sorted, patterned ground (debris island; sorted polygon; sorted stripes), terracettes, and stone-banked lobes (Rink & Lachman). The geomorphological survey pointed out that, within each site, the high- and low-centered patterned ground shows similar size (Table 1), which is about twofold larger at Lachman than at Rink. The measured frost table depth ranged from 40 cm at Rink and 80 cm at Lachman. In many cases, groundwater flow filled the trenches. The height of the investigated terracettes and of the stone-banked lobes ranges between a few decimeters up to 1.6 m. At Lachman, vegetation colonization shows clear patterns. The average total vegetation coverage is highest on the sorted stripes, decreases to the terracettes, and is lowest on the stone-banked lobes. High-centered and low-centered patterned ground show opposite colonization patterns, with the highest coverage on the border of the low-centered and on the center of the high-centered patterned ground (Table 1). The total vegetation coverage shows differences considering separately the different parts of the landforms (i.e., border and center of sorted patterned ground, tread and riser of both terracettes and stone-banked lobes, fine- and coarse-grained parts of the sorted stripes). As could be expected, the higher values of coverage characterize the elements with finer texture, ranging from the fine part of the sorted stripes (with the highest average coverage recorded >80%), to the treads of the terracettes and the center of sorted high-centered patterned ground (with similar values ranging around 35%), to the treads of stone-banked lobes (c. 25%). In the coarser sediments, vegetation coverage is relatively high on the border of sorted patterned ground (ranging from 14% on high-centered to 48% on low-centered). On the other hand, coverage decreases sharply when considering the coarse part of the sorted stripes and the treads of terracettes, while the riser of stone-banked lobes is devoid of vegetation. In the sorted stripes the vegetation (occurring only on the fine-grained part) is dominated by crustose microlichens with scattered mosses. Similar floristic composition and dominance (crustose microlichens such as *Psoroma*, foliose lichens as *Leptogium* and scattered mosses) characterize the flat part of the terracettes, the center of sorted patterned ground and the flat of stone-banked lobes. The border of sorted patterned ground is mainly colonized by different species of mosses and macrolichens (*Usnea* and *Stereocaulon*).

The high-centered patterned ground shows opposite vegetation colonization patterns between Lachman and Rink, where the stony border shows higher vegetation coverage (60%) than the finer center (1%). At Rink the low-centered patterned ground shows similar patterns to those of Lachman, although with lower vegetation coverage, with higher coverage on the border (21%) than the center (8%). However, the patterns of floristic composition are similar indicating similar environmental and ecological gradients but different intensity of ground disturbance. On the other hand, at Rink the center of all the patterned ground is mainly colonized by crustose microlichens (i.e., *Psoroma*) and mosses, and the vegetation of the borders is composed of mosses (more than 15%) and, only as subdominants, by macrolichens (*Usnea* and *Leptogium*). At Lachman the depressed fine center of the low-centered patterned ground is homogeneously colonized (average coverage 11%) by crustose microlichens (*Psoroma*, *Ochrolechia*) and mosses (*Andreaea*, *Polytrichum*) and by a black crust of *Nostoc*. The border of the low-centered patterned ground shows lower average vegetation coverage (48%) with the prevalence of mosses (*Bryum*, *Andreaea*) and of epilithic foliose and fruticose lichens (*Leptogium*, *Usnea*). Among the rarest periglacial features at Lachman, there are

Table 1. Average total vegetation coverage and floristic composition of the different elements of the investigated features at two sites (Rink and Lachman) of James Ross Island (Maritime Antarctica). The features are listed in order of decreasing total vegetation coverage (+ = less than 1%). Legend: A = Lachman; B = Rink; 1 = fine grained sorted stripes; 2 = tread terracettes; 3 = center of sorted patterned ground; 4 = tread stone-banked lobes; 5 = border of sorted patterned ground; 6 = coarse grained sorted stripes; 7 = riser terracettes; 8 = riser stone-banked, *low-centered patterned ground, ° high-centered patterned ground, ND not determinable.

Site	A	A	A	A	B	A	A	B	A	A
Feature Characteristics	1	2	3	4	5	5	6	3	7	8
% Total Vegetation Coverage	85	45	35° 11*	30	60° 21*	14° 48*	5	1° 8*	1	0
Mosses	10	5	10	5	15	15	5	5		
Fruticose lichens			1	+	5				+	5
Foliose lichens	+	5	1	5	5	5		+	+	
Crustose lichens	75	35	20	20	1	1	1	5	+	
Algae and Cyanobacteria			5		1	1	+	+		
% Blocks	10	10	10	15	75	45	65	15	75	70
Width (cm)	125	158	116°128*	78	52° 49*	116°128*	90	52° 49*	ND	ND
Length (cm)		125	163° 165*	284	75° 76*	163° 165*		75° 76*	ND	ND
% Pebbles	10	20	20	15	25	40	30	15	20	30
% Gravel	20	20	30	25	0	<5	<5	30	<5	0
% Sand and finer material	60	50	40	45	0	10	<5	40	<5	0

Table 2. Average total vegetation coverage and floristic composition of the different elements of the investigated features at four sites (Tarn Flat, Boulderclay, Gondwana, Apostrophe Island) of Victoria Land (Continental Antarctica). The features are listed in order of decreasing total vegetation coverage (+ = less than 1%). Legend: A = Tarn Flat; B = Boulderclay; C = Gondwana; D = Apostrophe Island; 1 = riser terracettes; 2 = tread stone-banked lobes; 3 = tread terracettes; 4 = border of sorted patterned ground; 5 = center of sorted patterned ground; 6 = tread stone-banked lobes; 7 = riser stone-banked lobes; ° high-centered patterned ground, ^ debris island, ND not determinable.

Site	D	D	D	C	B	A	A	C	C	C	A	A	C	C
Feature Characteristics	1	2	3	4	5	4	3	2	7	5	1	5	3	1
% Total Vegetation Coverage	45	45	35	30	25	20	15	15	10	5	1	1	1	1
Mosses	5	5	15	1	20			+	1	+				
Fruticose lichens	10	10		1										
Foliose lichens	10	20	1	5		5	5							
Crustose lichens	30	15	30	25	5	15	15	15	10	5	1	1	1	5
Algae and Cyanobacteria								+		+				
Width (cm)	4.5	1.2	4.5	148°	75^	80	80	265	ND	148°	80	80	127	ND
Length (cm)	2.7	4.3	2.7	183°	85^	40	40	295	ND	183°	40	40	92	ND
Height (cm)	29	n.d	n.d.	25°	n.d.	n.d.	n.d.	n.d.	28	25°	10	n.d-	n.d.	14
Slope (°)	27	5	2	1	0	1	5	24	42	2	40	1	6	44
% Blocks	65	45	20	85	5	95	35	30	65	10	70	5	40	65
% Pebbles	<5	10	15	5	15	<5	45	30	15	35	10	5	20	20
% Gravel	15	10	15	5	45	<5	5	30	10	30	10	10	20	10
% Sand and finer material	15	35	50	5	35	0	15	10	5	25	10	80	20	5

frost boils, developing on sandy ground close to the raised beach and showing occasionally salt efflorescence. These features are extensively colonized by mosses (*Polytrichum* spp. and *Dicranum* spp.) located on the raised centers.

Continental Antarctica

In Northern Victoria Land in order to achieve a comparable data set, we only considered the same types of periglacial features investigated in Maritime Antarctica. The features that were analyzed were sorted patterned ground (debris island at Boulderclay, high-centered patterned ground at Tarn Flat, Gondwana, Apostrophe Island), terracettes (Tarn Flat, Gondwana, Apostrophe Island), and stone-banked lobes (Gondwana, Apostrophe Island).

From the geomorphological point of view, the absence of low-centered patterned ground and the thinner frost table (from 15 to 50 cm of depth) is remarkable with respect to the values recorded in Maritime Antarctica. No groundwater flow was found in any of the trenches. The height of the investigated terracettes and of the stone-banked lobes is surely much smaller than in Maritime Antarctica, ranging between 10 cm up to 35–40 cm.

In Northern Victoria Land vegetation shows different colonization patterns with higher total vegetation coverage on the tread of terracettes, tread of the stone-banked lobes, and coarse border of high-centered patterned ground and debris island, whereas the riser of stone-banked lobes and terracettes are characterized by a very low total coverage.

Tarn Flat and Gondwana show similar patterns of vegetation colonization both for terracettes and high-centered patterned ground concerning the total coverage and the floristic composition. The tread of terracettes and the center of high-centered patterned ground in these sites are colonized by microcrustose lichens (*Lecidella siplei*), and the slope of terracettes and coarse border of patterned ground are characterized by epilithic foliose lichens (i.e., *Umbilicaria*) and crustose placodioid lichens (i.e., *Buellia frigida* and *Rhizocarpon* spp.). At Apostrophe Island the high-centered patterned ground shows vegetation patterns similar to those observed both at Tarn Flat and Gondwana.

On the contrary, at Apostrophe Island vegetation composition of the gelifluction features is different with the strong ingression of foliose (*Umbilicaria*) and fruticose (*Usnea*) lichens accompanied by crustose lichens (*Buellia frigida*) mainly on the risers of terracettes and on the treads of stone-banked lobes.

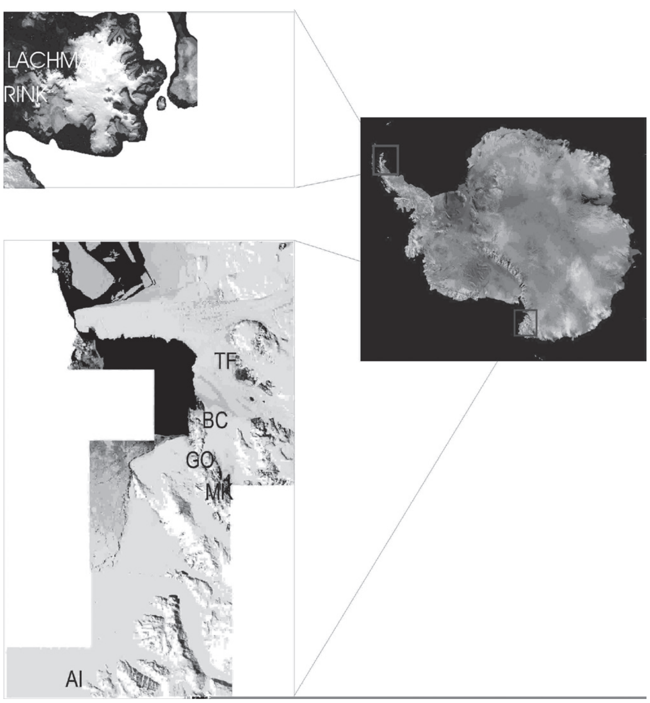

Figure 1. Location of the study sites at James Ross Island (Maritime Antarctica) and Victoria Land (Continental Antarctica). Legend: AI Apostrophe Island, BC Boulderclay, GO Gondwana, TF Tarn Flat. (Images from Landsat Image Mosaic of Antarctica, LIMA, International Polar Year 2007–2008 Project by BAS, USGS, NSF).

Discussion and Conclusions

The results obtained in all the investigated sites underline that grain size is not an effective factor in shaping the vegetation distribution patterns in the analyzed features.

The progressive decreasing sequence of vegetation coverage found through the periglacial landforms at Lachman suggest an important role of the frost creep/gelifluction processes as limiting factors for vegetation development. The estimated higher water content within the active layer and the higher height of the frost creep/gelifluction features in Maritime Antarctica than in Victoria Land can suggest that these processes are more intense in the former than in the latter areas. On the other hand, from the fabric of the pebbles in the trenches, the layer involved in the sorting or in the preferential orientation is much thinner (data not shown) than the recorded frost table depth. This pattern is opposite to what was already stressed by Cannone et al. (2004) for the High Arctic, where the substrate disturbance associated with gelifluction landforms does not affect the integrity of the upper soil layer.

Moreover, Northern Victoria Land (Gondwana and Tarn Flat) show similar conditions to what was found at Lachman. The higher vegetation cover of the gelifluction landforms at Apostrophe Island could be related more to the edaphic conditions of the site (high level of nutrients; higher water availability; see Cannone et al., in press) than to the active-layer thickness or to the depth of gelifluction processes.

The similar vegetation patterns at Rink (maritime Antarctica) and in all the selected sites at Northern Victoria Land are contrasting with those of Lachman.

At this site, the frost heave may be weaker than in the other sites not only due to milder conditions, but also due to the high salt content of the ground.

The analyses carried out at Victoria Land (as a template of Continental Antarctica) and at James Ross Island (as a template of Maritime Antarctica) indicate that there are some common patterns between these two geographically remote regions of Antarctica. In particular, the patterns of vegetation distribution (in terms of vegetation coverage, but not for the floristic composition) of the sorted patterned ground of Rink (James Ross Island) are more similar to those of all the investigated locations of Victoria Land than to the other site at James Ross Island (Lachman).

Similar evidences concern the colonization patterns of terracettes, with the patterns observed at Rink being more similar to those of Victoria Land than of Lachman.

On the other hand, the stone-banked lobes show similar trends in all the investigated sites, although at James Ross Island the differences between tread and riser are much more evident than at Northern Victoria Land.

Acknowledgments

Thanks to PNRA for the logistical support in Victoria Land. Thanks to DNA, PNRA and IAA for their logistical support and cooperation in Maritime Antarctica, with special reference to Dr. Jorge Strelin, Dr. Toni Curtosi, and Dr. Rodolfo del Valle. We want to thank also Enrique Serrano and an anonymous reviewer for their precious suggestions and comments.

References

Anderson, DG. & Bliss, LC. 1998 Association of plant distribution patterns and microenvironments on patterned ground in a polar desert, Devon Island, N.W.T., Canada. *Arct. Alp. Res.* 30: 97-107

Billings, W.D. & Mooney, H.A. 1959. An apparent frost-hummock sorted polygon cycle in the alpine tundra of Wyoming. *Ecology* 40: 16-20.

Cannone, N. 2005. Moss and lichen flora of Victoria Land Continental Antarctica along a latitudinal transect. *Terra. Antarctica Reports*, 11, 1-9.

Cannone, N. 2006. A network for monitoring terrestrial ecosystems along a latitudinal gradient in Continental Antarctica. *Antarctic Science*, 18(4): 549-560.

Cannone, N., Guglielmin, M. & Gerdol, R. 2004. Relationships between vegetation patterns and periglacial landforms in northwestern Svalbard. *Polar Biology* 27: 562-571.

Cannone, N., Wagner, D., Hubberten, H.W., & Guglielmin, M. 2007. Biotic and abiotic factors influencing soil properties across a latitudinal gradient in Victoria Land, Antarctica. *Geoderma*, in press.

Carrizo, H.G., Torielli, C.A., Strelin, J.A. & Muñoz, C.E.J. 1998. Ambiente eruptivo del grupo volcanico Isla James Ross en Riscos Rink, Isla James Ross, Antartida. *Revista de la Associación Geológica Argentina* 53: 469-479.

Castello, M. & Nimis, P.L. 1995. The lichen vegetation of Terra Nova Bay Victoria Land, Continental Antarctica. *Bibliotheca Lichenologica* 58: 43-55.

Castello, M. & Nimis, P.L. 2000. A key to the lichens of Terra Nova Bay Victoria Land, Continental Antarctica. *Italian Journal of Zoology*, Supplement, 1: 175-184.

French, H. 2007. *The Periglacial Environment* (3rd Ed.). London: John Wiley and Sons, 478 pp.

Grigioni, P., De Silvestri, L., Pellegrini, A. & Sarao, L. 1992. Some climatological aspects in the Terra Nova Bay area, Antarctica. In: M. Colacino, G. Giovanelli & L. Stefanutti (eds.), *Italian Research on Antarctic Atmosphere*. Bologna: SIF: 97-121.

Guglielmin, M. 2006. Ground surface temperature (GST), active layer, and permafrost monitoring in continental Antarctica. *Permafrost and Periglacial Processes* 17(2): 133-143.

Heilbronn, T.D. & Walton, D.W.H. 1984a. Plant colonization of actively sorted stone stripes in the Subantarctic. *Arct. Alp. Res.* 16: 161-172.

Jonasson, S. & Sköld, S.E. 1983. Influences of frost-heaving on vegetation and nutrient regime of polygon-patterned ground. *Vegetatio* 53: 97-112.

Kappen, L. 1985. Vegetation and ecology of ice-free areas of northern Victoria Land, Antarctica: 1. The lichen vegetation of Birthday Ridge and an inland mountain. *Polar Biology* 4: 213-225.

Matthews, J.A., Shakesby, R.A., Berrisford, M.S. & McEwen L.J. 1998 Periglacial patterned ground on the Styggedalsbreen Glacier foreland, Jotunheimen, Southern Norway: Micro-topographic, paraglacial and geoecological controls. *Permafrost Periglac.* 9: 147-166.

Mori, J., Fukui, K., Sone, T., Strelin, J., & Torielli, C. 2007. Internal structure of stone-banked lobes and terraces on Rink Plateau, James Ross Island, Antarctic Peninsula region. *Polish Polar Research* 281: 23-30.

Ochyra, R. 1998. *The Moss Flora of King George Island, Antarctica*. Cracow: Polish Academy of Sciences, W. Szafer Institute of Botany, 279 pp.

Øvstedal, D.O. & Smith, R.I.L. 2001. Lichens of Antarctica and South Georgia. Cambridge: Cambridge University Press, 405 pp.

Seppelt, R.D., Green, T.G.A. & Schroeter, B. 1995. Lichens and mosses from the Kar Plateau, Southern Victoria Land, Antarctica. New Zealand *Journal of Botany* 33: 203–220.

Seppelt, R.D., Green, T.G.A. & Schroeter, B. 1996. Additions and corrections to the lichen flora of the Kar Plateau, Southern Victoria Land, Antarctica. *New Zealand Journal of Botany* 34: 329-331.

Seppelt, R.D. & Green, T.G.A. 1998. A bryophyte flora for Southern Victoria Land, Antarctica. *New Zealand Journal of Botany* 36: 617-635.

Strelin J.A. & Malagnino, E.C. 1992. Geomorfologia de la Isla James Ross. In: C.A. Rinaldi (Ed.), *Geología de la Isla James Ross, Antártida*. Instituto Antártico Argentino, Buenos Aires: 7-36.

Strelin, J.A. & Sone, T. 1998. Rock glaciers on James Ross Island, Antarctica. In: A.G. Lewkowicz & M. Allard (Eds.), *Permafrost – Proceedings of the 7th International Permafrost Conference, Yellowknife, Canada. Collection Nordicana, Université Laval 57*: 1027-1032.

Walker, D.A., Epstein, H.E., Gould, W.A. et al. 2004. Frost boil ecosystems: Complex interactions between landforms, soils, vegetation and climate.

Rainfall-Runoff Hydrograph Characteristics in a Discontinuous Permafrost Watershed and Their Relation to Ground Thaw

Sean K. Carey
Department of Geography and Environmental Studies, Carleton University, Ottawa, Ontario, Canada K1S 5B6

Chris M. DeBeer
Centre for Hydrology, University of Saskatchewan, Saskatoon, Saskatchewan, Canada S7N 5C8

Abstract

Rainfall-runoff hydrographs were analyzed for 49 rainstorms over 5 years in a 7.6 km^2 alpine discontinuous permafrost watershed to assess the effect of seasonal thawing on hydrograph parameters. Hydrographs were analyzed for 11 common characteristics including runoff ratio, initial abstraction, recession coefficient, and several parameters related to shape of the hydrograph. Runoff ratios varied between 0 and 0.33 (average 0.09) and declined throughout the summer, reflecting increased active layer storage. Hydrograph recessions were steeper immediately post-freshet and flattened as the summer progressed, as flow pathways descended into soils with lower transmissivities. There was no relation between antecedent wetness and timing response, indicating that saturated areas of the catchment exist near the stream throughout the season, facilitating rapid runoff. Results indicate that at this scale, permafrost and active layer depth exert a strong influence on the stormflow hydrograph.

Keywords: discontinuous permafrost; hydrograph analysis; hydrology; recession; runoff.

Introduction

Watersheds underlain with discontinuous permafrost show a high degree of spatial variability in the timing and magnitude of hydrological processes (Carey & Woo 2001a, Spence & Woo 2003). Due to the relatively impermeable nature of permafrost, percolation is restricted and the soil storage capacity reduced, resulting in greater volumes of event water (both meltwater and rain) being conveyed to the stream from perched unconfined aquifers (Quinton & Marsh 1998, Carey & Woo 2001b). Following snowmelt, thaw of seasonally frozen ground increases the thickness of the active layer, enhancing basin storage and altering flow pathways (Bowling et al. 2003, Carey & Quinton 2004). As the ground thaws, the water table descends into deeper soil layers with reduced saturated hydraulic conductivity, stormflow response is dampened. In contrast, catchment areas without permafrost infiltrate and percolate meltwater and rainwater to the deeper regional groundwater table without generating significant lateral flow.

Rainfall-runoff events in permafrost basins are flashy, with accentuated peaks, extended recessions, and low baseflow contributions (Dingman 1973, McNamara et al. 1998). The mechanisms of runoff production in permafrost catchments has emphasized rapid surface and near-surface flow in porous organic soils that are ubiquitous surface cover, preferential flow pathways through interconnected surface depressions, soil conduits, and rills, particularly during the snowmelt period (Hinzman et al. 1993, McNamara et al. 1998, Quinton & Marsh 1999, Carey & Woo 2001a). As the active layer thaws and the saturated layer descends, rapid runoff declines and these runoff pathways become less effective in conveying water to the drainage network. In addition to changes in vertical soil hydraulic properties, the areal extent of runoff generation declines following snowmelt. When the saturated layer resides within near-surface organic soils, water from slopes and upland areas can be conveyed rapidly to the stream and the source area for runoff generation is relatively large and the basin is highly connected. However, as the water table drops into the mineral substrate, hill slopes and areas away from the stream become disconnected, reducing the contributing source area (Carey & Woo 2001b). The total percentage of the basin underlain by permafrost is important as seasonally frozen soils have predominantly vertical water flux throughout the year, and basin comparison studies in zones of discontinuous permafrost reveal significant differences in streamflow properties and hydrochemistry based upon permafrost disposition (McLean et al. 1999, Petrone et al. 2007).

A significant amount of research in discontinuous permafrost environments has investigated runoff mechanisms at the hillslope or plot scale (Carey & Woo 2001b, Spence & Woo 2003). This process information has not been linked to larger scale basin flow attributes. For example, in a continuous permafrost environment, McNamara et al. (1998) studied temporal variations in runoff properties over a cascading range of watershed scales and related hydrograph characteristics to the influence of permafrost. A similar exercise in discontinuous permafrost environments would provide validation that processes operating at small scales are manifested in the streamflow hydrology at the basin scale.

Hydrograph analysis continues to be a widely utilized and practical assessment tool of basin storages and in the calibration of many hydrological models (i.e. Tallaksen 1995, Szilagyi & Parlange 1998). Response times, runoff ratios and recession parameters provide first-order information as to catchment functioning. In this regard, hydrograph analysis remains a useful tool to evaluate whether conceptual and numerical models of runoff generation derived from plot and slope studies are applicable to the entire catchment, which integrates areas of seasonal and permafrost soils. It is the objective of this paper to evaluate five years of summer stormflow data to improve understanding of how heterogeneous discontinuous permafrost basins deliver water to the stream. Hydrograph parameters will be compared with precipitation characteristics and antecedent conditions such as flow and time of year (as a surrogate for ground thaw). The influence of increased basin storage on rainfall-runoff relations will be determined and results compared with knowledge of processes at smaller scales. The snowmelt period will not be considered.

Study Area

The study was conducted within Granger Basin (60º32′N, 135º18′W), a small headwater catchment of the Wolf Creek Research Basin, located approximately 15 km south of Whitehorse, Yukon (Fig. 1). The climate is subarctic continental, which is characterized by a large temperature range, low relative humidity, and low precipitation. Mean annual (1971–2000) temperature at the Whitehorse airport (706 m above sea level) is -0.7ºC, with mean January and July temperatures of -17.7ºC and +14.1ºC, respectively, although winter and summer extremes of -40ºC and 25ºC are not uncommon. Mean annual precipitation is 267.4 mm, of which 145 mm falls as rain.

The drainage area of Granger Basin is approximately 7.6 km^2, and the elevation ranges from 1310 to 2250 m a.s.l. The lower half of the basin and most of the stream channel has a fairly gentle slope (~4°), however the upper portion of the basin is considerably steeper (~15-25°). Throughout the basin there are several small (~0.01 km^2) ponds, and a permanent snowpack near the summit of Mount Granger.

Granger Basin lies within alpine and shrub-tundra ecological zones, with vegetation consisting predominantly of various willow (*Salix spp.*) and birch (*Betula spp.*) shrubs. A significant portion of the upper basin on the slopes of

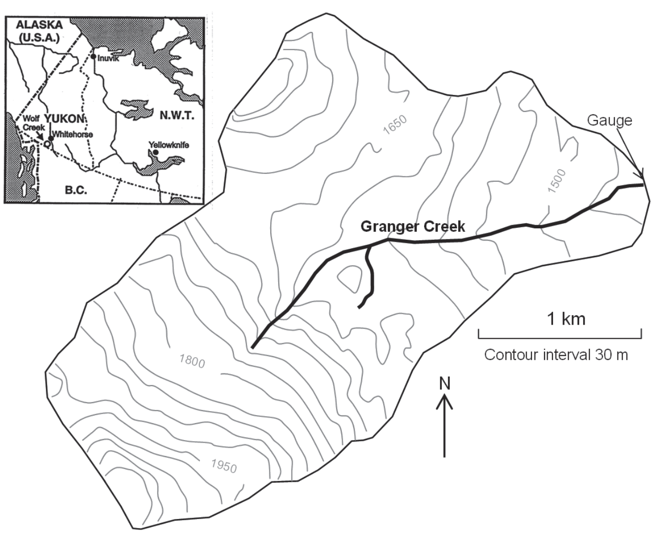

Figure 1. Map of Granger Basin. Inset is location within northwestern North America.

Mount Granger is covered with talus and bedrock outcrops. The lithology of the basin is predominantly sedimentary, comprising limestone, sandstone, shale, and conglomerate. A mantle of glacial till overlies most of the bedrock, ranging up to several meters in thickness. Fine-textured alluvium is found along much of the valley floor where the main channel resides, while colluvial deposits are more common along upper slopes away from the main valley. Soils are primarily orthic eutric brunisols with textures ranging from sandy loam to gravelly sandy loam. These are fairly well-drained soils with coarse parent materials. Surface organic soils range from 0.1 to 0.4 m in thickness, and are deepest in riparian areas and north-facing slopes throughout the basin, becoming thinner and more scattered in higher elevation and south-facing areas. Using the BTS method, it is estimated that approximately 70% of the basin is underlain with permafrost (Lewkowicz & Ednie 2004).

Methodology

Field data

Spring and summer discharge data were collected for Granger Creek over five years from 1999 to 2003 using an electronic stage recorder (Ott) placed inside a stilling well at the basin outlet. Measurements of stage were recorded at 15-minute intervals. A stage-discharge rating curve was developed by manual gauging of the stream at least 10 times per year. Rainfall data were collected using a Texas Instruments tipping bucket rain gauge, part of a nearby meteorology station (Fig. 1), measured rainfall depths in 0.1 mm increments and summed to the total number of these increments of each 30-minute period.

Hydrograph analysis

Hydrographs selected for analysis were taken after the snowmelt period (15 June) to eliminate diurnal fluctuations and mixed runoff signals. Visual inspection of the hydrographs was used to determine which events were suitable for analysis, and the selection criteria was based on distinct and isolated response events. In most cases, only storms >4 mm with one continuous or near continuous (<1 hour of no precipitation) event were chosen. In certain instances, additional precipitation following the peak in discharge prevented the determination of certain response factors. In these cases, the multiple input and flow peaks were treated as a single event to calculate runoff ratios and recession trends. Selected hydrographs were then isolated and analyzed separately.

The separation of stormflow runoff, *R*, and baseflow components was carried out using a straight line drawn from the initial rise in flow to the point of greatest curvature on the recession limb (Fig. 2). The rational for this procedure was that previous research in permafrost environments had justified this method based upon the properties of permafrost soils (McNamara et al. 1998, Carey & Woo 2001b).

Hydrograph parameters were determined as shown in Figure 2. Input starts at time t_{w0} and ends at time t_{we}, and total storm duration, T_w is given by, $T_w = t_{we} - t_{w0}$. Total precipitation

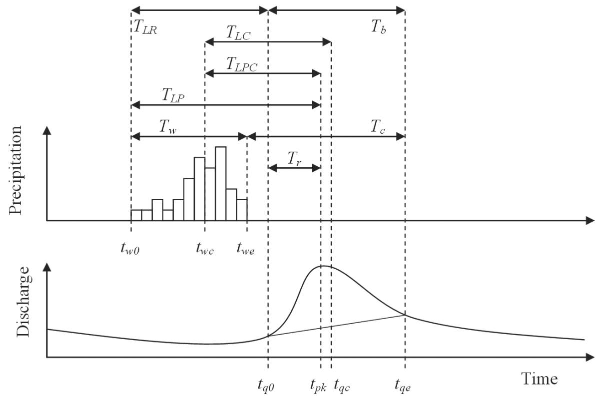

Figure 2. Hydrograph and precipitation parameters measured for analysis. Terms are provided in the text below.

is P_t. Stream response begins at time t_{q0} and ends at time t_{qe}, peaking at time t_{pk}. The time duration of the storm hydrograph is $T_b = t_{qe} - t_{q0}$. The time of rise specifies the period of increasing discharge, or rising limb, and is determined as: $T_r = t_{pk} - t_{q0}$. Time of concentration, T_c, defined as the time required for the water to travel from the most hydraulically distant part of the contributing area to the basin outlet is: $T_c = t_{qe} - t_{we}$. The time between the beginning of input and the initial hydrograph response, known as the response lag is: $T_{LR} = t_{q0} - t_{w0}$. Initial abstraction, P_{abst}, is as precipitation that falls prior to the initial rise in the storm hydrograph. The lag to peak discharge, T_{LP}, measures the time between the beginning of input and the hydrograph peak: $T_{LP} = t_{pk} - t_{w0}$. The center of mass, or centroid, of both input and runoff is useful in characterizing time lags. In determining the centre of mass, or centroid, for the input hyetograph, t_{wc}, the input values, W_i, measured for i = 1, 2, n time periods of equal length as:

$$t_{wc} = \sum_{i=1}^{n} W_i t_i \Big/ \sum_{i=1}^{n} W_i \tag{1}$$

The centroid of the response hydrograph, t_{qc}, is determined in the same fashion, summing the event-discharge-weighted time values for equal length periods, and dividing by the sum of the event discharge values for each period:

$$t_{qc} = \sum_{i=1}^{n} Q_i t_i \Big/ \sum_{i=1}^{n} Q_i \tag{2}$$

The centroid lag is defined as the period of time between the respective center of mass of the input and runoff events: $T_{LC} = t_{qc} - t_{wc}$. The centroid lag to peak is the interval from the input center of mass to the peak discharge: $T_{LPC} = t_{pk} - t_{wc}$.

Hydrograph recessions were analyzed for all of the selected stormflow events. The recession curve conveys information about watershed characteristics and storage properties, as it represents the natural storage that feeds the stream after the input has ceased. Numerous studies have focused attention on this part of the hydrograph, and many models have been develop to describe the decline in streamflow because of the importance in certain areas of hydrological application, including forecasting and water resource planning (see Tallaksen 1995 for review). Additionally, recession analysis has been used widely in permafrost environments (Dingman 1973, McNamara et al. 1998, Carey & Woo 2001b).

The most basic model for describing the recession is the linear-reservoir model of response, where water storage recharge and evaporation are neglected, given as:

$$q = q_0 e^{(-t/t^*)} \tag{3}$$

where q is discharge, q_0 is the discharge at $t = 0$ (the beginning of the recession), t is time, and t^* is the recession parameter, also known as the turnover time, that describes the decay for the draining aquifer. The linear-reservoir model of watershed response has the advantage that it is simple and that t^* is a widely used parameter for inferring watershed characteristics. However, this model is recognized as being valid over a limited range of the recession period (Tallaksen 1995).

Results

Post-freshet hydrographs (15 July to 15 September) are shown above in Figure 3. The interruption in the hydrographs in August 2003 was due to mechanical failure of the logger. Maximum annual flows occurred during snowmelt freshet (not shown) in May and early July when 30 to 50% of the annual precipitation was released over a several-week period. Following freshet, streamflow gradually declined throughout the summer and fall, with rainfall-runoff stormflow events superimposed on the seasonal recession. Discharge rates were typically below 0.4 m^3s^{-1} following snowmelt, and gradually declined to ~0.05 m^3s^{-1} before stream gauging ceased prior to freezing. The 2000 hydrograph shows greater flows than other years, with baseflow rates of ~0.25 m^3s^{-1} in early summer, which later rose to 0.3 m^3s^{-1} triggered by a series of storms in late August. By late September 2000, the flow rate had fallen to ~0.2 m^3s^{-1}.

Rainfall from 15 June to 15 September over the five years was 141, 234, 141, 130, and 129 mm for 1999 to 2003, respectively. In 1999, 2001, and 2002, ~8 rainfall events following the snowmelt period were >4 mm in magnitude, whereas 2000 and 2003 were wetter with 15 and 13 events >4 mm, respectively. The average rainfall for all storms (including those not analyzed) over all years was 8.1 mm with a maximum of 31.8 mm. Rainfall intensities varied from 0.2–2.6 mm hr^{-1}, averaging 0.8 mm hr^{-1}. Storms selected for analysis ranged between 2 and 48 hours with an average of 6 hours.

Hydrograph timing response

During the 5-year study period, 49 rainfall-runoff stormflow events passed the selection criteria and were analyzed for response lags and time durations. A summary of the hydrograph parameters is presented in Table 1. A Spearman rank (Sr) correlation coefficient matrix ($p < 0.05$) of all measured variables was performed to explore relations among hydrograph parameters, rainfall and date (Table 2). Response lags (T_{LR}) ranged between 0 and 11.2 hours, with an average time of 2.4 hours. McNamara et al. (1998) reported a mean response time of 2.15 hours (range 0–6

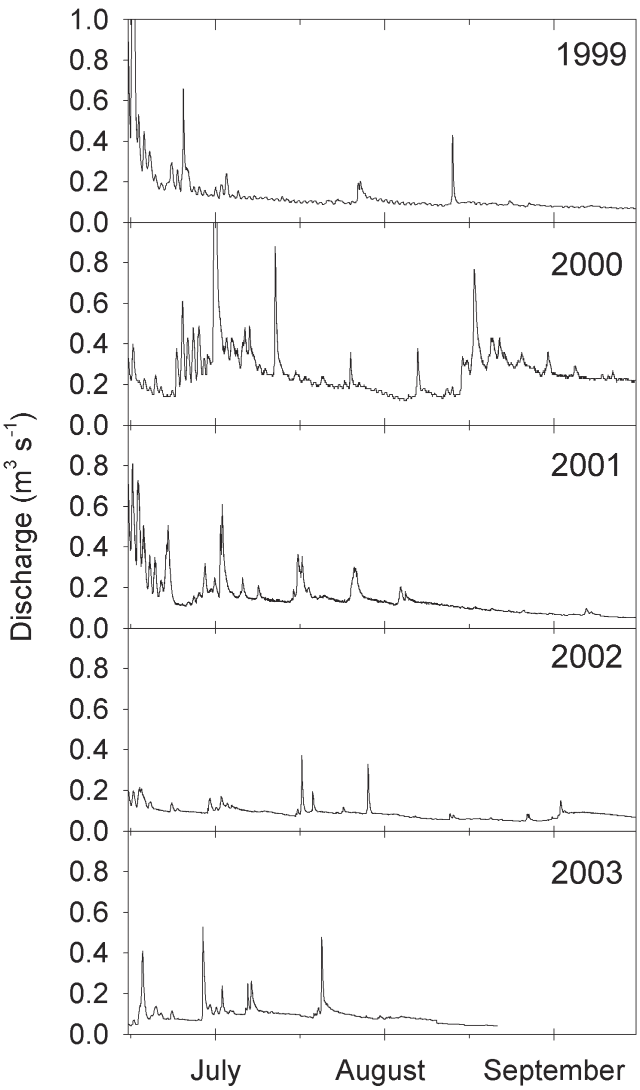

Figure 3. Post-freshet hydrographs (15 June–15 September) for Granger Basin, 1999–2003.

hours) for Imnavait Creek, a continuous permafrost basin (2.2 km²) in northern Alaska. Compared with temperate basins, the average response time was rapid, and the results are consistent with Church (1974) who also reported that rapid response times are a characteristic of northern rivers.

Initial abstractions (P_{abst}) were low, ranging from 0 to 4.1 mm with an average of 1.1 mm. An unexpected significant positive relation existed between P_{abst} and antecedent discharge, (Q_{ant}) (Sr = 0.32), indicating that more water was abstracted when the catchment was wettest. On the other hand, watershed wetness as represented 5-day antecedent rainfall (P_{5day}) showed no relation with P_{abst}. A lack of correlation between P_{abst} and wetness indices has been reported previously for subarctic and arctic watersheds (Dingman 1973, McNamara et al. 1998, Carey & Woo 2001b), and is typically attributed to limited subsurface storage capacity due to the presence of permafrost.

The time of rise (T_R) for most hydrographs was similar to the duration of precipitation (T_W). The lag to peak (T_{LP}), centroid lag to peak (T_{LPC}), and centroid lag (T_{LC}) were short,

Table 1. Summary of hydrograph parameters for 49 storms. Terms are defined in text.

Hydrograph Parameter	Mean	Standard Deviation	Maximum	Minimum
R/P_t	0.09	0.09	0.33	0.00
t^* (h)	41.70	32.20	163.10	7.70
P_{int} (mm)	0.79	0.84	5.20	0.18
P_{abst} (mm)	1.05	0.96	4.10	0.00
P_{5d} (mm)	7.72	6.81	29.30	0.00
T_w (h)	12.19	8.70	46.00	0.50
T_{LR} (h)	2.44	2.72	11.25	0.00
T_r (h)	9.56	6.52	33.50	2.00
T_{LP} (h)	11.83	6.47	34.75	3.50
T_{LPC} (h)	5.80	3.38	18.75	0.36
T_{LC} (h)	8.07	3.15	16.10	1.37
T_b (h)	25.21	13.81	72.50	6.50
T_c (h)	15.29	7.97	45.50	4.00

with averages of 11.8, 5.8, and 8.1 hr, respectively. This is in contrast to values of T_{LP} and T_{LC} of 17.8 and 34.8 hr for Imnavait Creek reported by McNamara et al. (1998). The centroid lag for Granger Basin was closer to the average of 19.5 hr reported by Holtan & Overton (1953) in a study of 40 streams in the conterminous United States, ranging from 76 km² to 3200 km² in basins that are much larger than the study catchment. Both T_{LP} and T_{LC} were positively correlated (Sr = 0.31 and 0.29, respectively) with Q_{ant}.

Runoff ratios (R/P_t) were highly variable, ranging between 0 and 0.33, with an average of 0.1. These values were low when compared with studies from other permafrost basins and hill slopes (Dingman 1971, Slaughter et al. 1983, Woo 1983, McNamara et al. 1998, Carey & Woo 2001b). Seasonally, higher runoff ratios were associated with early periods following melt when the frost and water table was near the surface, and ratios progressively diminished as summer progressed and the active layer thickened (Fig. 4a). A strong negative relationship existed between runoff ratio and Julian Day (Sr = -0.74). Runoff ratio increased with Q_{ant} (Sr = 0.55), yet there was no significant relation between runoff ratio and P_{5day}. Additionally, there was no relation between runoff ratio and total rainfall and rainfall intensity.

Streamflow recessions

Hydrograph recessions were observed to be temporally variable, with steeper recession limbs characteristic of earlier season discharge events that flattened out as summer progressed (Fig. 4b). Values of the t^* parameter ranged between 7.7 and 163.1 hr with an average of 41.7 hr, which compared well with other permafrost and organic-covered permafrost basins of similar area. For example, Dingman (1971) reported an average t^* of 39 hours for Glenn Creek, Alaska, while McNamara et al. (1998) found this value to be 30.2 hours for Imnavait Creek. There was a strong positive relationship between t^* and Julian Day (Sr = 0.69) indicating that as the season progresses and soils thaw, runoff reached the stream through deeper, less conductive soils. As would be expected, t^* increased with decreasing runoff ratio (Sr =

Table 2. Spearman rank correlation matrix. Values in bold are significant at the 95% confidence level. Terms defined in text.

	Julian Day	P_t	Q_{ant}	R/P_t	$t*$	P_{int}	P_{abst}	P_{5d}	T_w	T_{LR}	T_r	T_{LP}	T_{LPC}	T_{LC}	T_b	T_c
Julian Day	**1.00**	**-0.35**	**0.69**	**-0.74**	0.23	0.03	0.23	0.05	0.24	0.23	-0.12	-0.12	-0.25	-0.04	-0.01	-0.24
P_t		**1.00**	-0.10	**0.55**	0.11	0.13	**0.32**	**0.45**	0.19	0.24	0.17	**0.31**	0.23	**0.29**	0.20	0.17
Q_{ant}			**1.00**	**-0.66**	-0.07	-0.25	0.07	0.10	0.26	0.15	0.04	0.08	-0.11	0.12	0.06	-0.17
R/P_t				**1.00**	0.04	-0.02	-0.04	0.19	0.01	-0.13	0.26	0.20	0.25	0.24	**0.31**	**0.47**
$t*$					**1.00**	0.29	**0.30**	0.02	**0.61**	0.24	**0.46**	**0.44**	0.04	0.24	**0.53**	0.23
P_{int}						**1.00**	-0.21	0.12	**-0.44**	-0.26	-0.23	**-0.46**	**-0.43**	**-0.50**	**-0.29**	-0.14
P_{abst}							**1.00**	0.10	**0.50**	**0.68**	-0.11	0.21	0.02	0.27	0.08	0.07
P_{5d}								**1.00**	-0.04	0.17	-0.08	-0.03	0.08	0.08	-0.03	-0.06
T_w									**1.00**	**0.43**	**0.59**	**0.78**	**0.35**	**0.57**	**0.66**	0.23
T_{LR}										**1.00**	-0.18	**0.34**	0.04	0.14	-0.09	-0.12
T_r											**1.00**	**0.78**	**0.64**	**0.63**	**0.88**	**0.53**
T_{LP}												**1.00**	**0.69**	**0.68**	**0.67**	**0.41**
T_{LPC}													**1.00**	**0.60**	**0.41**	**0.33**
T_{LC}														**1.00**	**0.80**	**0.74**
T_b															**1.00**	**0.76**
T_c																**1.00**

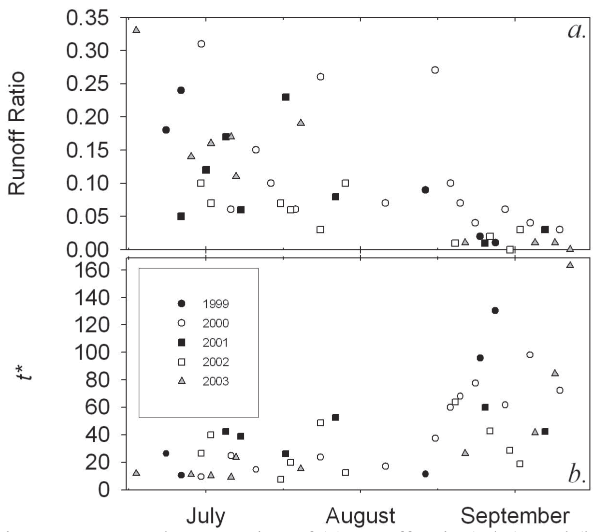

Figure 4. Seasonal progression of (a) runoff ratio (R/P_t), and (b) recession parameter, $t*$, for 49 stormflow events between 1999 and 2003.

-0.66). Recession constants were compared with total rainfall (P_t), antecedent wetness indices (Q_{ant}, P_{5day}), and other storm characteristics to assess for any influence of input volume, intensity, or watershed wetness, yet these relations were poorly defined and not statistically significant at the 95% confidence level.

Discussion and Conclusion

Simple analysis of stormflow hydrographs provide useful insight into the dynamics of runoff generation as permafrost-underlain catchments, unlike more temperate catchments, undergo significant physical changes throughout the summer due to ground thaw. For example, the decline in runoff ratio implies a widespread increase in soil storage capacity as the active layer becomes thicker and soils dry. Large rainfall events late in the summer must overcome significant storage deficits to generate even small volumes of runoff. Increasing $t*$ indicates water inputs take progressively longer to reach the stream due the gradual deepening of the flow pathways into less transmissive soil layers. Results from Granger Basin compare well with others reported in permafrost regions (Dingman 1973, Slaughter et al. 1983, McNamara et al. 1998) and support conceptual models of runoff generation being controlled by the relation between frost and water table positions for this environment (Carey & Woo 2001b).

Hydrograph lag-time indices had little correspondence with time of year or wetness, implying at the basin scale, these variables were not controlled explicitly by permafrost-related processes, but rather to other catchment characteristics (which may be affected by the presence of permafrost). The lack of correlation between response lags (T_{LR}), initial abstractions (P_{abst}), and measures of basin wetness such as antecedent discharge (Q_{ant}) and 5-day rainfall (P_{5day}) indicate that certain areas of the basin (footslopes of permafrost-underlain slopes and riparian areas) remain wet, contributing water rapidly to the stream after rainfall begins. The spatial extent of these wet areas expands and contracts away from the stream based on time of year and basin wetness, which is reflected by the declining trend in runoff ratios (R/P_t) throughout the summer. This process is similar to that reported by Quinton & Marsh (1998) and Carey & Woo (2001b), whereby hill slopes become effectively disconnected from the stream as the season progresses.

The recession coefficient, $t*$, was strongly related to time of year and runoff ratio, yet had no relationship with precipitation characteristics. Shallow thaw depths in the early summer lead to rapid drainage of the slopes through near-surface organic soils and preferential pathways that are well-linked. As the active layer deepens, the water table descends atop the frost table, and rainfall is able to percolate into deeper, less permeable, mineral soils. The hydraulic conductivity of mineral soils is typically orders of magnitude less than organic soils (Carey & Woo 2001b), resulting in increased transmission times to the stream and larger $t*$.

Hydrograph parameters investigated in Granger Basin, a discontinuous permafrost alpine basin, indicate that at the headwater scale, streamflow response reflects the influence of permafrost throughout the post-freshet season. Hydrological models that use these parameters in calibration must consider their temporal dependent nature.

Acknowledgments

This work is funded by research grants from the Natural Sciences and Engineering Research Council of Canada, the Canadian Foundation for Climate and Atmospheric Sciences, and the Northern Scientific Training Program. The support of Glenn Ford and Ric Janowicz of the Water Resource Branch, Yukon Environment, and John Pomeroy, University of Saskatchewan is gratefully acknowledged.

References

Bowling, L.C., Kane, D.L., Gieck, R.E., Hinzman, L.D. & Lettenmaier, D.P. 2003. The role of surface storage in a low-gradient Arctic watershed. *Water Resources Research* DOI: 10.1029/2002WR0014466.

Carey, S.K. & Quinton, W.L. 2004. Evaluating snowmelt runoff generation in a discontinuous permafrost catchment using stable isotope, hydrochemical and hydrometric data. *Nordic Hydrology* 35: 309-324.

Carey, S.K. & Woo, M-K. 2001*a*. Slope runoff processes and flow generation in a subarctic, subalpine environment. *Journal of Hydrology* 253: 110-129.

Carey, S.K. & Woo, M-K. 2001*b*. Spatial variability of hillslope water balance, Wolf Creek basin, subarctic Yukon. *Hydrological Processes* 15: 3113-3132.

Chacho Jr., E.F. & Bredthauer, S. 1983. Runoff from a small subarctic watershed, Alaska. *Proceedings, Fourth International Conference on Permafrost, National Academy Press, Washington, D.C.*, 115-120.

Church, M. 1974. Hydrology and permafrost with reference to northern North America, In: *Proc. Workshop Seminar on Permafrost Hydrology, Canadian National Committee*. Ottawa: IHD, 7-20.

Dingman, S.L. 1966. Characteristics of summer runoff from a small watershed in central Alaska. *Water Resources Research* 2: 751-754.

Dingman, S.L. 1973. Effects of permafrost on stream flow characteristics in the discontinuous permafrost zone of central Alaska. *North American Contribution to Second International Conference of Permafrost, National Academy of Sciences, Washington, D.C.,* 447- 453.

Hewlett, J.D. & Hibbert, H. 1967. Factors affecting the response of small watersheds to precipitation in humid regions. In: Sopper, W.E. & Lull, H.W. (eds.), *Forest Hydrology*. Oxford: Permagon Press, 275-290.

Hinzman, L.D., Kane, D.L. & Everett, K.R. 1993. Hillslope hydrology in an Arctic setting, *Proceedings, Sixth International Conference on Permafrost, South China Press, Beijing,* 257-271.

Kane, D.L. Bredthauer, S.R. & Stein, J. 1981. Subarctic snowmelt runoff generation. In: Vinson, T.S. (ed.), *Proceedings of the Specialty Conference on The Northern Community, ASCE, Seattle, Washington,* 591-601.

Kane, D.L., Hinzman, L.D., Everett, K.R. & Benson, C.S. 1989. Hydrology of Imnavait Creek, and arctic watershed. *Holarctic Ecology* 12: 262-269.

Lewkowicz, A.G. & Ednie, M. 2004. Probability mapping of mountain permafrost using the BTS method, Wolf Creek, Yukon Territory, Canada. *Permafrost and Periglacial Processses* 15: 67-80.

MacLean, R., Oswood, M.W., Irons III, J.G. & McDowell, W.H. 1999. The effect of permafrost on stream biogeochemistry: a case study of two streams in the Alaskan (U.S.A.) taiga. *Biogeochemistry* 47: 239-267.

McNamara, J.P., Kane, D.L., & Hinzman, L.D. 1998. An analysis of streamflow hydrology in the Kuparuk River Basin, Arctic Alaska: a nested watershed approach. *J. of Hydrol.* 206: 39-57.

Petrone, K.C., Jones, J.B., Hinzman, L.D. & Boone, R.D. 2006. Seasonal export of carbon, nitrogen, and major solutes form Alaskan catchments with discontinuous permafrost. *Journal of Geophysical Research* 111: DOI: 10.1029/2005JG000055.

Pomeroy, J.W. & Granger, R.J. (eds.) 1999. *Wolf Creek Research Basin: Hydrology, Ecology, Environment.* Saskatoon: Environment Canada, 160 pp.

Quinton, W.L. & Marsh, P. 1998. The influence of mineral earth hummocks on subsurface drainage in the continuous permafrost zone. *Permafrost and Periglacial Processes* 9: 213-228.

Quinton, W.L. & Marsh, P. 1999. A conceptual framework for runoff generation in a permafrost environment. *Hydrological Processes* 13: 2563-2581.

Slaughter, C.W. & Kane, D.L. 1979. Hydrologic role of shallow organic soils in cold climates. *Proceedings, Canadian Hydrology Symposium 79: Cold Climate Hydrology, National Research Council of Canada, Ottawa,* 380-389.

Slaughter, C.W., Hilgert, J.W. & Culp, E.H. 1983. Summer streamflow and sediment yield from discontinuous-permafrost headwater catchments. *Proceedings, Fourth International Conference on Permafrost, National Academy Press, Washington, D.C.,* 1172-1177.

Spence, C. & Woo, M-K. 2003. Hydrology of subarctic Canadian Shield: soil-filled valleys. *Journal of Hydrology* 279: 151-166.

Szilagyi, J. & Parlange, M.B. 1998. Baseflow separation based on analytical solutions of the Boussinesq equation. *Journal of Hydrology* 204: 251-260.

Tallaksen, L.M. 1995. A review of baseflow recession analysis. *Journal of Hydrology* 165: 349-370.

Woo, M.K. & Steer, P. 1982. Occurrence of surface flow on arctic slopes, southwestern Cornwallis Island. *Canadian Journal of Earth Sciences* 19: 2368-2377.

—Plenary Paper—

Innovative Designs of the Permafrost Roadbed for the Qinghai-Tibet Railway

Guodong Cheng
State Key Laboratory of Frozen Soil Engineering, Cold and Arid Regions Environmental and Engineering Research Institute, Chinese Academy of Sciences, Lanzhou, 730000, China

Qingbai Wu
State Key Laboratory of Frozen Soil Engineering, Cold and Arid Regions Environmental and Engineering Research Institute, Chinese Academy of Sciences, Lanzhou, 730000, China

Wei Ma
State Key Laboratory of Frozen Soil Engineering, Cold and Arid Regions Environmental and Engineering Research Institute, Chinese Academy of Sciences, Lanzhou, 730000, China

Abstract

Under global warming scenarios, the traditional method of simply increasing the thermal resistance by raising the embankment height and using insulating materials has been proven ineffective in warm and ice-rich permafrost areas and, therefore, could not be used in the Qinghai-Tibet Railway engineering. Instead, an alternative "cooled-roadbed" approach was developed and used to lower the ground temperature in order to maintain a perennially frozen subgrade. The concept that local and site-specific factors play an important role in the occurrence and disappearance of permafrost has helped us to devise a number of measures to cool down the roadbed. For example, we can adjust and control heat transfer by using different embankment configurations and fill materials. The Qinghai-Tibet Railway project demonstrates that a series of alternative roadbed-cooling methods can be used to lower the temperature of permafrost beneath the embankment and to stabilize the roadbed. These methods include solar radiation control using shading boards, heat convection control using ventilation ducts, thermosyphons, air-cooled embankments, and heat conduction control using "thermal semi-conductor" materials, as well as combinations of the above-mentioned three control measures. This roadbed-cooling approach provides not only a solution for engineering construction in sensitive permafrost areas, but also a countermeasure against possible global warming.

Keywords: cooled roadbed; global warming; Qinghai-Tibet Railway; warm permafrost.

Introduction

The Qinghai-Tibet Railway, 1142 km from Golmud to Lhasa, crosses 632 km of permafrost terrain of which 275 km is warm permafrost (mean annual ground temperature between 0 and -1°C) and 221 km is ice-rich permafrost (ice content >20% by volume). The section that is underlain by both warm and ice-rich permafrost is 134 km in distance (Wu et al. 2002). At the beginning of the Qinghai-Tibet Railway project, Chinese scientists and engineers were confronted with two unfavorable factors: the "warm" nature of the plateau permafrost and scenarios of global warming. Finding a solution for building the railway and keeping it operational and stable under such conditions became one of the greatest challenges (Cheng & Wu 2007). Observations along the Qinghai-Tibet Highway indicate that, after the road surface was paved with asphalt, talik pockets developed in 60% of the paved sections due to increased thawing. All that happened in warm permafrost areas. Approximately 85% of the damage to highway embankments is caused by thaw settlement of ice-rich permafrost (Wu et al. 2002). The performance of the Qinghai-Tibet Highway and other engineering structures in permafrost areas indicates that the traditional design method of simply increasing the thermal resistance by raising the embankment height and using insulating materials can no longer meet operational and safety needs. An alternative "cooled-roadbed" approach was developed and used to lower the underlying ground temperature, especially in areas of warm and ice-rich permafrost. Otherwise, it is difficult to maintain a stable roadbed (Cheng 2004a, 2005a). It has long been known that local and site-specific factors (e.g., slope aspect, soil type, etc.) have a significant impact on the occurrence and disappearance of permafrost. With the same concept, we devised and used a number of measures to cool down the roadbed for the Qinghai-Tibet Railway. These methods include adjusting and controlling the amount of solar radiation, heat convection, and heat conduction, as well as combinations of the above-mentioned measurements, by using different embankment configurations and fill materials (Cheng 2004b, 2005b).

Controlling Solar Radiation

The combination of low latitude and high altitude makes solar radiation on the Qinghai-Tibet Plateau one of the strongest in the world. Shading the surface from solar radiation can effectively lower the ground temperature (Kondratyev 1996). Feng et al. (2006) investigated the effect of awnings and measured the ground surface temperature at 14:00 over the course of a one-year period at the Fenghuoshan area. The surface temperature was 8–15°C lower inside the awnings than outside, and the maximum temperature difference can reach 24°C. But awnings are not suited on the plateau due to the strong wind. Consequently, shading boards were

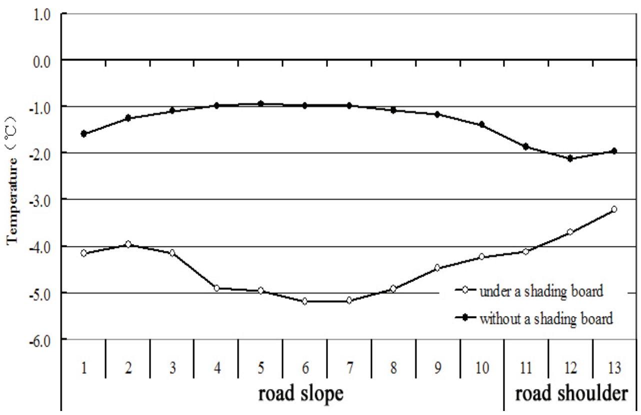

Figure 1. The variation of soil temperature under a shading board.

installed on embankment side slopes at Beiluhe to study the cooling effect. Observations show that the mean annual slope-surface temperature under the board was 3.2°C lower than that outside the board (Fig. 1) and 1.5°C lower than that of the natural ground surface (Yu et al. 2007a).

The original embankment fill may become loose and weak after undergoing repeated freeze–thaw cycles. Shading boards can reduce the number of these cycles and can also protect the embankment from the impact of wind action and erosion caused by the rain.

Altering Convection Patterns

Crushed rocks, ventilation ducts, and thermosyphons (or thermal tubes) were used in the Qinghai-Tibet Railway engineering to adjust and control convection patterns within embankments (Fig. 2).

Crushed rocks

On the Qinghai-Tibet Plateau, crushed rocks over permafrost act as "thermal semi-conductor" materials. In winter, the air is colder than permafrost; this induces R-B convection within the crushed rocks. As a result, permafrost releases heat into the air. In summer, the air is warmer than permafrost. Since the cold air is heavier and sinks to the bottom, no convective heat transfer takes place, and heat exchange is mainly in the form of conduction. Because of the small contact areas between the crushed rock and the low thermal conductivity of the air, the crushed rocks act as thermal insulators and reduce the amount of heat gained by the underlying permafrost from the air. The imbalance of increased heat releases in winter and reduced heat gains in summer produces a net heat release over the course of one year and thus lowers the underlying ground temperature (Cheng & Tong 1978, Goering & Kumar 1996, Goering 2003, Cheng et al. 2007a). When crushed rocks are placed on sloping surfaces, the chimney effect develops if the slope angle is sufficiently big. This chimney effect also lowers the underlying ground temperature (Cheng et al. 2007a).

On the Qinghai-Tibet Plateau, wind speeds are stronger in winter than in summer; 75% of the strong winds occur in winter. Therefore, wind-forced convection in crushed rocks

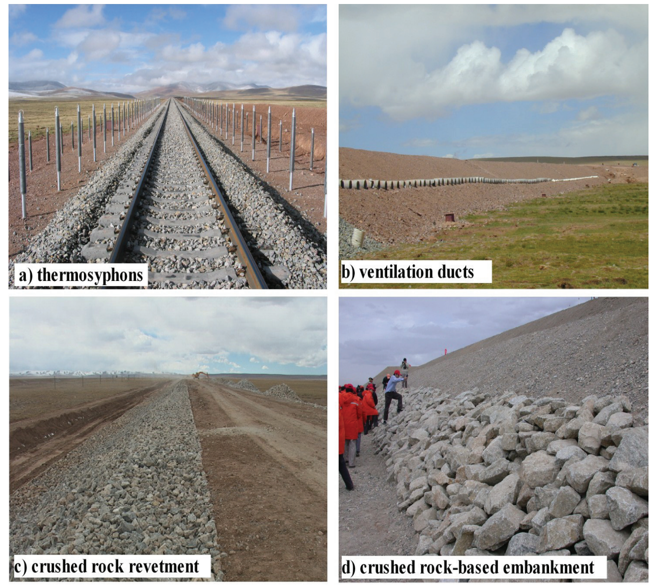

Figure 2. Measures adjusting and controlling convection.

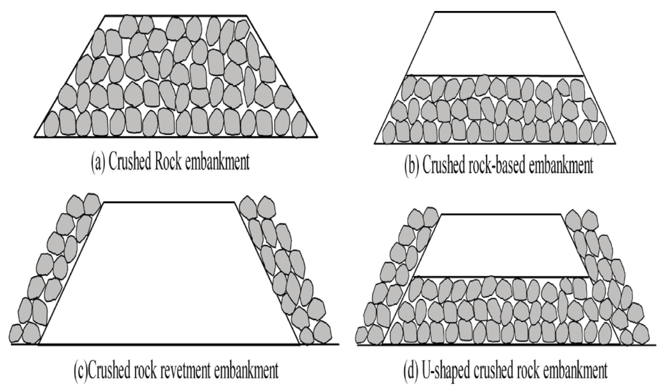

Figure 3. Different types of crushed-rock embankment.

is greater in winter than in summer, causing a cooling effect in the underlying ground (Cheng et al. 2007b).

The use of crushed rocks in embankments during the Qinghai-Tibet Railway construction took several different forms and configurations: crushed-rock embankment, crushed rock-based embankments, crushed-rock revetments embankments, and U-shaped crushed-rock embankments (Fig. 3).

Crushed rock-based embankments

The railway design standard in China requires that the soil layer beneath the railroad tracks be at least 2.5 m thick. A rock layer is often placed at the base of the embankment, so a crushed-rock embankment (Fig. 3a) is changed into a crushed rock-based embankment (Fig. 3b). This type of embankment covers 130 km of the Qinghai-Tibet Railway. The base of the embankment is usually between 1.0 and 1.2 m thick and consists of crushed rocks of 20–30 cm in diameter. The overlying soil layer ranges in thickness from 2.5 to 10 m.

Ground temperature monitoring was carried out on rock-based embankments at seven sites. Monitoring data

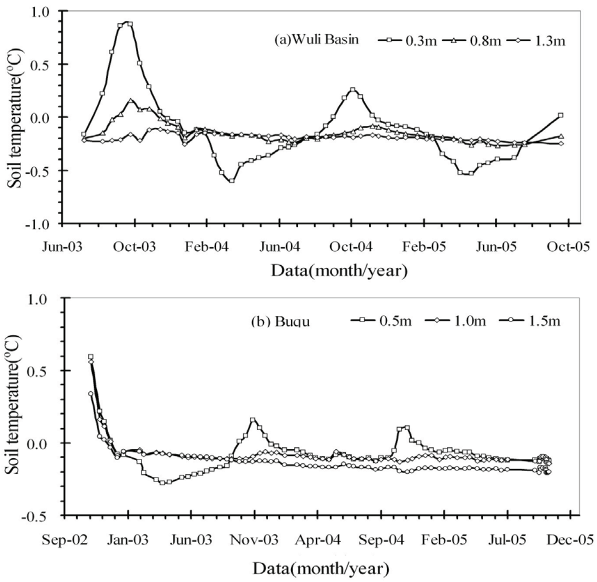

Figure 4. The variation of soil temperature under crushed rock-based embankment in warm permafrost areas.

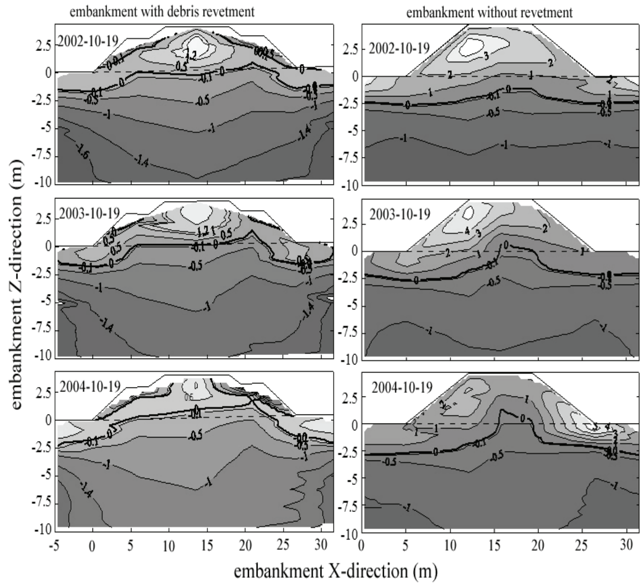

Figure 5. Comparison of soil temperatures under embankment with and without crushed-rock revetment.

indicates that the permafrost table beneath the embankment had raised at most sites by as much as between 1.8 and 2.6 m. Ground temperature near the permafrost table showed a cooling trend. However, at Wuli Basin and the Buqu River, where the mean annual ground temperature is warmer than -0.5°C, the ground temperature near the permafrost table did not show a clear cooling trend (Wu et al. 2006a) (Fig. 4), indicating that the cooling effect of crushed rocks is greatly reduced due to the overlying soil layer. Therefore, we cannot rely on the rock-based embankment alone to ensure a stable roadbed; additional cooling techniques are required.

A comparison study was made on the cooling effect of open and closed crushed rock-based embankment at Beiluhe. *Closed* means that the crushed rocks on the embankment side slopes are covered with a soil layer of 20 cm thick. *Open* means that the crushed rocks are not covered by a soil layer and are exposed to the air on either side of the embankment. At Beiluhe, the crushed-rock layer at the base is 1.2 m thick, consists of crushed rocks of 20–30 cm in diameter, and is overlain by a 2.5 m thick soil layer. At this site, wind speeds are also much higher in winter than in summer. For example, the average wind speed in winter is 5–8 m/s and is mainly from the east-northeast, roughly perpendicular to the embankment. The average wind speed in summer is 2–3 m/s and is mainly from the north-northwest. Observations indicate that, due to the overlying soil layer, natural convection in the closed rock layer is weak. On the other hand, the wind-forced convection dominates and is strong in the open crushed-rock layer. In the open crushed-rock layer, natural convection takes place in winter only when the wind speeds are low. Wu et al. (2006b, 2007) conclude that open crushed-rock layers at the base of the embankment have a greater cooling effect than its closed counterparts, because the ground temperature beneath open rock layers is 2–4°C lower than that beneath closed rock layers.

Crushed-rock revetments embankment

Crushed rocks are placed on embankment side slopes to cool down the roadbed (Fig. 3c). Approximately 37 km of the embankment along the Qinghai-Tibet Railway is covered with crushed-rock revetments. The revetment is 80–100 cm thick and is made up of crushed rocks of two different sizes: 8–10 cm and 20–30 cm in diameter.

A comparison is made between embankments with and without crushed-rock revetments at Beiluhe on the Tibet Plateau. At this site, the mean annual air temperature is -3.8°C, and the mean annual ground temperature is between -1.4 and -1.6°C. Two different rock sizes are used in the revetment. The side slopes of one section of the embankment are covered with rocks 5–8 cm in diameter. The revetment is 80 cm in thickness and is 4.1 m in height. A neighboring section is covered with rocks of 40–50 cm in diameter. The revetment is also 80 cm in thickness and is 4.8 m in height. The height of the traditional embankment (without a crushed-rock revetment) is 4.5 m. Temperature readings were taken from the 10 cm depth below the crushed-rock surface. The results show that summer temperature in the crushed-rock (5–8 cm in size) revetments, regardless of their aspect, is lower than that of the unrevetted counterparts, due to the insulating action of crushed rocks. In winter, the opposite is true, indicating the development of air convection in rock revetments (Saboundjian & Goering 2003). Temperature measurements from boreholes drilled at the center of the general and crushed-rock (5–8 cm in size) revetment embankments indicate that the magnitude of temperature decrease in the revetment embankment is greater than that in the general embankment. The temperature within 2 m of the surface is still decreasing under the revetment embankment, displaying a greater cooling effect (Fig. 5). Three years after completion of the above embankments, the permafrost table had risen slightly into the unrevetted embankment.

In contrast, the permafrost table had moved well into the embankment fill for most of the embankments with crushed-rock (40–50 cm in size) revetments. The overall temperature in the crushed-rock revetment embankment is lower than that in the general embankment. This demonstrates the cooling effect of crushed-rock (40–50 cm in diameter) revetments (Sun 2006).

Laboratory models and field data indicate that placing rock revetments of different thicknesses on embankment side slopes can reduce the differential thaw depth. This may help prevent differential thaw settlement and longitudinal cracking in the embankment (Yu 2006).

U-shaped crushed-rock embankments

As the cooling effect of crushed rocks is reduced due to the overlying soil layer, crushed rocks are placed on side slopes of rock-based embankments to form U-shaped crushed-rock embankments (Fig. 3d) in order to strengthen the thermal stability. Although it is too early to draw any conclusions, preliminary results show that it has an even greater cooling effect than both the rock-based and rock-revetted embankments (Ma et al. 2007).

Zhang et al. (2005, Niu et al 2006) completed a numerical simulation on three different embankments: the traditional embankment with ballasts, the rock-based embankment, and the U-shaped crushed-rock embankment. The objective was to evaluate the impact of future climatic warming on the embankment thermal regime. The model assumes an increase of 2.6°C in mean annual air temperature over the next 50 years. The initial mean annual air temperature used in the model is -4.0°C. The embankment height is 5.0 m; crushed rocks are 10 cm in size; the crushed-rock layer at the base is 1.5 m thick; the overlying soil layer is 3.5 m thick; the rock revetment is 1.6 m thick. The model shows that in 50 years, the permafrost table under the traditional embankment will be lowered to a depth of 7.4 m, and this will reduce the stability of the embankment due to the thaw settlement and subsidence. The permafrost table under the rock-based embankment will be very close to the natural ground surface, but its overall temperature will be warm and close to 0°C. For the U-shaped rock embankment, the permafrost table will be above the natural ground surface and in the base layers of crushed rocks. The overall temperature will be 0.25–0.3°C lower than the rock-based embankment, improving the thermal stability.

The crushed rocks layer used in the Qinghai-Tibet Railway engineering have a cooling impact on the underlying ground, but they are not as effective as theoretically predicted. This may have been caused by fine soil grains within the crushed rocks layer. These soil grains reduce the porosity of the rock layer and thus decrease the cooling effect. Fine-grained soils can find their way into the crushed-rock openings during the construction; wind can also blow them into the openings. Necessary measures should be taken in the future to prevent this from happening.

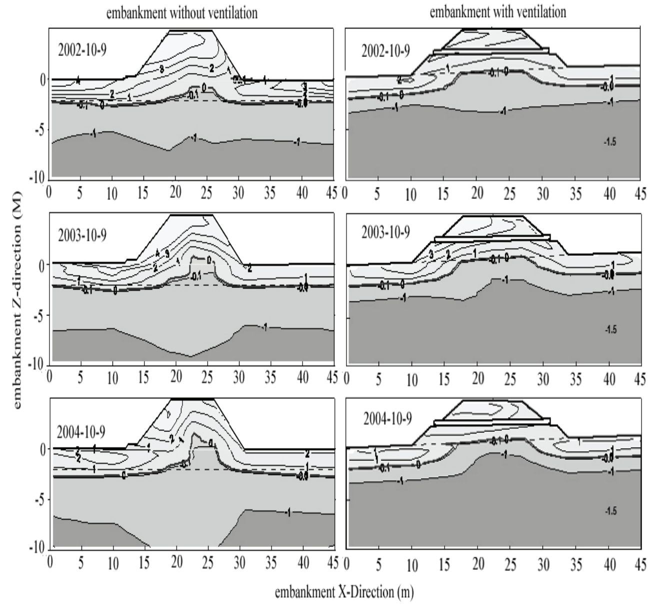

Figure 6. Comparison of soil temperature under embankment with and without ventilation ducts.

Ventilation ducts

Field experiments on ventilation ducts were carried out using PVC and concrete ducts at Beiluhe (Fig. 2b). These ducts are either 30 cm or 40 cm in diameter; the distance between two neighboring ducts is 2 times the duct diameter. They are buried into the embankment 0.5–0.7 m from the original ground surface.

The mean annual air temperature on the Tibet Plateau is, on average, about 3°C colder than the mean annual ground surface temperature. Consequently, embedding air ducts in embankments can effectively lower the underlying ground temperature. Field observations show that air ducts do lower ground temperatures. Ventilation ducts buried below and near the original ground surface have a greater cooling impact than those buried in higher positions (Niu et al. 2006). For embankments with ducts buried below and close to the original ground surface, the permafrost table moved up to the same level as the original ground surface three years after embankment construction (Fig. 6). The -1°C isotherm continued to rise, showing a clear cooling trend (Fig. 5). Temperature data indicate that the air temperature within the ventilation ducts is just 1.6–1.8°C higher than the air temperature, while the embankment surface temperature is 45°C higher, and the natural ground surface temperature is 2.5°C higher than the air temperature (Niu et al. 2007).

Air ducts increase the heat loss of the underlying soil during winter; they also increase the heat absorbed by the underlying soil in summer. To enhance the cooling effect of air ducts, an experiment was conducted to investigate the impact of a temperature-controlled ventilation system where one or both ends of the air ducts are installed with shutters that open and close automatically with changes in air temperature. The shutter has a temperature sensor and a control unit. It closes when the ambient air temperature is higher than a pre-set value. The temperature data measured from the inner walls of the ventilation ducts indicate that ducts with shutters are 1°C colder than those without. The mean annual ground temperature measured at a depth of 3.5 m beneath the embankment with shuttered air ducts is 0.45°C lower than that beneath the embankment installed with normal air ducts (Yu et al. 2007b).

To further improve the cooling effect, an experiment was carried out on an embankment ventilated by perforated air ducts at Beiluhe. Because of the holes in the duct wall, the heat exchange between the air inside the duct and surrounding soils is greatly increased, and the cooling effect is improved (Hu et al. 2004).

Thermosyphons

Thermosyphons were installed in over 34 km of the Qinghai-Tibet Railway embankment (Fig. 2a). Based upon the embankment height, thermosyphons of different length (7 m, 9 m, and 12 m) were inserted either vertically or at an angle into the shoulder or the foot of side slopes. The lower end is usually 2–3 m below the permafrost table.

Experiments on actual embankments at Qingshuihe show that thermosyphons do lower the ground temperature and make the permafrost table move upwards. As the "radius of influence" of a thermosyphon is about 1.8 m, the suggested distance between the thermosyphons is 3 m (Pan et al. 2003). Numerical modeling suggests that the cooling effect both in the embankment and at the foot of side slopes is greatest when the incline angle of the thermosyphons (installed at the foot of side slopes) is 25–30° (Yang et al. 2006).

Altering Heat Conduction

When water is frozen, its thermal conductivity increases by 4 times, from 0.45 to 2.2 W/m·K. This characteristic of water can be used to manufacture a material with a much greater thermal conductivity in the frozen state than in the thawed state. The material, similar to a "thermal semi-conductor" will lower the ground temperature by increasing heat loss in winter and decreasing heat gain in summer. Yu (2006) completed a laboratory experiment by placing layers of a water-absorbing material, separated by layers of air, in a sealed container. Water was added to the container. The result indicates that, when the material froze, its thermal conductivity changed from 0.11 W/m·K to 1.2 W/m·K, an increase of about 10 times. So far, this study has not been applied to cold regions engineering.

Combined Control Measures

The three different measures (e.g., adjusting radiation, adjusting convection, and adjusting conduction) can be combined in engineering practices to improve the cooling effect.

Dry bridges

Dry bridges totaling 125 km in length were built in ice-rich and extremely unstable permafrost sections along the Qinghai-Tibet Railway. Piles 1.2 m in diameter were buried 25–30 m into the ground to form a solid foundation. Since the dry bridges became operational, the deformation has been less than 2 mm on average, with a maximum of 5 mm.

Dry bridges can lower the ground temperature, as they can shade the ground from the sun; the air can freely flow through it. They possess good mechanical stability and can support heavy loads. They are effective means of ensuring the stability of roadbeds in ice-rich and sensitive permafrost. Dry bridges can also provide a migration route across the railroad for wild animals on the plateau. A numerical simulation on the dry bridge at Qingshuihe shows that the bridge has a cooling effect because the mean annual permafrost temperature under the bridge is lower than that without the bridge (Xiao et al. 2004).

Combining shading boards and crushed-rock revetments

Li et al. (2007) studied a different embankment configuration by combining shading boards with crushed-rock revetments. This configuration not only can shade the embankment from the sun but also can make good use of natural convection in crushed rocks to lower the ground temperature. The shading boards can also reduce the amount of fine-grained soil getting into the openings of crushed rocks. A numerical model was developed for this combined configuration to calculate the optimum values for the shading board height, for the thickness of rock revetments, for the embankment height, and for the size of crushed rocks. Li et al. (2007) proposed an optimum design for this type of embankment configuration.

Combining thermosyphons and insulating board

Wen et al. (2005) numerically simulated another embankment configuration that combines insulating board with thermosyphons. The board is embedded near the base of the embankment (0.5 m above the original ground surface). The model indicates that, assuming a mean annual air temperature of -3.5°C and a 2°C increase in air temperature on the plateau over the next 50 years, the stability of all three types of embankments (e.g., normal embankments, embankments installed with thermosyphons, and embankments with insulating boards) will without exception be compromised. However, if thermosyphons are combined with insulating board, the embankments will have a greater resistance to global warming and will remain stable.

Combining crushed-rock revetments and insulating board

Zhang et al. (2005) studied the effect when insulating board is embedded at a 0.8 m depth beneath the surface of rock-reveted embankments. The numerical model indicates that the temperature measured from the middle portions of the embankment is lower when insulating boards are used.

Conclusions

Under the global warming scenario, the "cooled roadbed" approach must be used for road design and construction in "warm" and ice-rich permafrost. This approach changes the design philosophy from traditional insulation to alternative cooling to better deal with possible global warming.

Combining solar radiation control, heat convection control, and heat conduction control can achieve a better cooling effect on the roadbed. Shading boards, crushed rocks, ventilation ducts, thermosyphons, and dry bridges were all used in the Qinghai-Tibet Railway engineering and have proven successful in lowering the ground temperature and in ensuring the roadbed stability.

Further studies are necessary to quantify and to optimize various measures employed in the Qinghai-Tibet Railway project.

Acknowledgments

The authors sincerely thank Dr. Baolai Wang for editing the English version of the article. This work was supported by a grant of the Knowledge Innovation Program of the Chinese Academy of Sciences (Grant no. KZCX1-SW-04) and the Outstanding Youth Foundation Project, the National Natural Science Foundation of China (Grant No. 40625004).

References

Cheng, G.D. & Tong, B.L. 1978. Experimental research on an embankment in an area with massive ground ice at the lower limit of alpine permafrost. *Proceedings of the Third International Conference on Permafrost, Ottawa.* National Research Council of Canada 2: 199-222.

Cheng, G.D. 2004a. Principle of thermal insulation for permafrost protection. *Cold Regions Science and Technology* 40: 71-79.

Cheng, G.D. 2004b. Influences of local factors on permafrost occurrence and their implications for Qinghai-Tibet Railway design. Science in China, Series D: *Earth Sciences* 47(8): 704-709.

Cheng, G.D. 2005a. Permafrost studies in the Qinghai-Tibet Plateau for road construction. *Journal of Cold Regions Engineering* 19(1): 19-29.

Cheng, G.D. 2005b. A roadbed cooling approach for the construction of Qinghai-Tibet Railway. *Cold Regions Science and Technology* 42: 169-176.

Cheng, G.D. & Wu, T.H. 2007. Responses of permafrost to climate change and their environmental significance, Qinghai-Tibet Plateau. *Journal of Geophysical Research* 112: F02S03, doi:10.1029/2006JF000631.

Cheng, G.D., Lai, Y.M., Sun, Z.Z. & Jiang, F. 2007a. The "thermal semi-conductor" effect of crushed rocks. *Permafrost and Periglacial Processes* 18: 151-160, doi:10.1002/ppp.575.

Cheng, G.D., Sun, Z.Z. & Niu, F.J. 2007b. Application of the roadbed cooling approach in Qinghai-Tibet railway engineering. *Cold Regions Science and Technology:* doi:10.1016/j.coldregions.2007.02.006 (in press).

Feng, W.J., Ma, W., Li, D.Q. & Zhang, L.X. 2006. Application investigation of awning to roadway engineering on the Qinghai-Tibet Plateau. *Cold Regions Science and Technology* 45: 51-58.

Goering, D.J. & Kumar, P. 1996. Winter-time convection in open graded embankments. *Cold Regions Science and Technology* 24(1): 57-74.

Goering, D.J. 2003. Passively cooled railway embankments for use in permafrost areas. *Journal of Cold Regions Engineering* 17(3): 119-133.

Hu, M.J., Wang, R., Ge, X.R., Shi, X.F. & Huang, M.K. 2004. An experimental study on the cooling effect of perforated ventilation pipes embedded in the Qinghai-Tibet Railway roadbed. *Chinese Journal of Rock Mechanics and Engineering* 23(24): 4195-4199 (in Chinese with English abstract).

Kondratyev, V.G. 1996. Strengthening railroad base constructed on icy permafrost soil. *Proceedings of the Eighth International Conference on Cold Regions Engineering, Fairbanks:* 688-699.

Li, N., Kang, J.M. & Quan, X.J. 2007. Study on cooling mechanism of a new type ripped-stone embankment in high temperature area. *Chinese Journal of Geotechnical Engineering* 29(3): 425-429 (in Chinese with English abstract).

Ma, W., Feng, G.L., Wu, Q.B. & Wu, J.J. 2007. Analyses of temperature fields under the embankment with crushed-rock structures along the Qinghai-Tibet Railway. *Cold Regions Science and Technology:* doi:10.1016/j.coldregions.2007.08.001 (in press).

Niu, F.J., Cheng, G.D., Xia, H.M. & Ma, L.F. 2006. Field experiment study on effects of duct-ventilated railway embankment on protecting the underlying permafrost. *Cold Regions Science and Technology* 45(3): 178-192.

Niu, F.J., Liu, X.F., Ma, W., Wu, Q.B. & Xu, J. 2007. Monitoring study on the boundary thermal conditions of duct-ventilated embankment in permafrost regions. *Cold Regions Science and Technology:* doi:10.1016/j.coldregions.2007.07.004 (in press).

Pan, W.D., Zhao, S.C., Xu, W.Z., Yu, S.S. & Ma, W.D. 2003. Application of thermal probe to enhance thermal stability of roadbeds in plateau permafrost areas. *Journal of Glaciology and Geocryology* 25(4): 433-438 (in Chinese with English abstract).

Saboundjian, S. & Goering, D.J. 2003. Air convection embankment for Roadway: A field experimental study in Alaska. *Publication at the 82nd Annual Meeting of the Trasportation Research Board, Washington, DC.*

Sun, Z.Z. 2006. *Study on the crushed rock revetment embankment in permafrost regions of Qinghai-Tibet Railway.* Ph.D. Thesis, Cold and Arid Regions Environmental and Engineering Research Institute, Chinese Academy of Sciences (in Chinese with English abstract).

Wen, Z., Sheng, Y., Ma, W., Qi, J.L. & Wu, J.C. 2005. Analysis on effect of permafrost protection by two-phase closed thermosyphon and insulation jointly in permafrost regions. *Cold Regions Science and Technology* 43: 150-163.

Wu, Q.B., Liu, Y.Z. & Zhang, J.M. 2002. A review of recent frozen soil engineering in permafrost regions along Qinghai-Tibet Highway, China. *Permafrost and Periglacial Processes* 13(3): 199-205.

Wu, Q.B., Cheng, G.D., Ma, W., Niu, F.J. & Sun, Z.Z. 2006a. Technical approaches on permafrost thermal stability for Qinghai-Tibet Railway. *Geomechanics and Geoengineering: An International Journal* 1(2): 119-127.

Wu, Q.B., Dong, X.F. & Jiang, G.L. 2006b. Cooling effect differences of soil beneath open and closed block-stone embankments. *Chinese Journal of Rock Mechanics and Engineering* 25(12): 2565-2571 (in Chinese with English abstract).

Wu Q.B., Cheng H.B., Jiang G.L., Ma W. & Liu Y. Z. 2007. Cooling mechanism of embankment with block stone interlayer in Qinghai-Tibet railway. *Science in China, Series E* 50(3): 319-328.

Xiao, J.Z., Lai, Y.M., Zhang, X.F., Yu, W.B. & Zhang, S.J. 2004. Three dimensional temperature character analysis of a dry bridge on the Qinghai-Tibet Railway. *Journal of Glaciology and Geocryology* 26(4): 426-434 (in Chinese with English abstract).

Yang, Y.P., Zhou, S.H. & Wei, Q.C. 2006. Effect simulation of different incline angles of thermosyphons used in Qinghai-Tibet railway permafrost embankment. *China Civil Engineering Journal* 39(3): 108-113 (in Chinese with English abstract).

Yu, Q.H. 2006. *Study on the heat conduction process of roadbeds in permafrost region and new control methods.* Ph.D. Thesis, Cold and Arid Regions Environmental and Engineering Research Institute, Chinese Academy of Sciences (in Chinese with English abstract).

Yu, Q.H., Niu, F.J., Pan, X.C., Bai, Y. & Zhang, M.Y. 2007a. Investigation of embankment with temperature-controlled ventilation along the Qinghai-Tibet Railway. *Cold Regions Science and Technology:* doi:10.1016/j.coldregions.2007.07.002 (in press).

Yu, Q.H., Pan, X.C., Cheng, G.D. & He, N.W. 2007b. An experimental study on the cooling mechanism of a shading board in permafrost engineering. *Cold Regions Science and Technology:* doi:10.1016/j.coldregions.2007.07.003 (in press).

Zhang, M.Y., Lai, Y.M., Liu, Z.Q. & Gao, Z.H. 2005. Nonlinear analysis for the cooling effect of Qinghai-Tibet Railway embankments with different structures in permafrost regions. *Cold Regions Science and Technology* 42: 237-249.

Does Permafrost Deserve Attention in Comprehensive Climate Models?

Jens Hesselbjerg Christensen and Martin Stendel
Danish Meteorological Institute, Copenhagen, Denmark

Peter Kuhry
Stockholm University, Sweden

Vladimir Romanovsky and John Walsh
University of Alaska Fairbanks, USA

Abstract

Traditionally, from a climate modeling perspective, permafrost is looked upon as a phenomenon impacted by climate change. However, it is well recognized that thawing permafrost may create climate feedback loops via changes in greenhouse gas emissions and surface hydrology. Only recently, these effects are being introduced in comprehensive climate models. The thermal properties of permanently frozen regions on the other hand have not been much explored in this context, mainly because models rarely resolve soil layers deeper than a few meters. One reason comes from the still rather poor ability of climate models to simulate realistic snowpack behavior, which is vital to allowing for a realistic depiction of below-surface properties. Here, we stress the sensitivities of near-surface atmospheric temperatures to inadequacies in the description of soil processes including retreat of permafrost to deeper layers under warming conditions.

Keywords: global climate; permafrost modeling; regional climate change; systematic errors.

Introduction

A major effort in the development of comprehensive climate models is devoted towards a reduction in systematic errors. In general, the better a model can reproduce in a satisfactory manner observed climate statistics, the higher its credibility in simulating climate change. But the demand for accurate representation of climate variables is changing steadily as the application of models for climate change research and demand for realistic climate projections increase. Efforts in the 1990s were concentrated on getting a realistic energy balance at the top of the atmosphere energy balance, along with a realistic annual cycle in mean climate variables such as mean sea level pressure, temperature, and precipitation. The field has moved forward, and focus is now set on other aspects of the climate system, including the ocean, sea ice, and land-surface processes. Furthermore, higher moments of climate variables are being assessed. This includes, for example, the ability to reproduce observed trends or the entire spectrum of daily precipitation intensities and temperature variables. The understanding of models' ability to reproduce these features has become the cornerstone in identifying model shortcomings and gives a clear hint to the modeler on where to improve model descriptions (e.g., IPCC 2007).

Despite the ongoing improvement of models and the associated enhanced credibility in climate change projections, the deficiencies in the models are still limiting their ability to provide detailed regional projections where systematic errors are indisputable. Examples are errors in the ability to capture the overall distribution of sea ice, the seasonality of snow cover, and more complex inefficiencies due to erroneous atmospheric or oceanic circulation. In applying such models to investigate the influence of anthropogenic climate changes, it becomes vital to keep in mind these model deficiencies as they may leave an imprint on the resulting climate projections. Here we discuss the complexity of such errors and how they may be interpreted. We focus on the role of permafrost as a key to improvement of model behavior in the Arctic and, hence, add to an improved understanding of the future behavior of permafrost in a warming world.

Understanding Modeled Climate Change

Global climate change in the Arctic

The ability to simulate present-day climate conditions by a climate model is well depicted by characteristics of the dynamics of the atmosphere. Hence, if the position of the storm tracks is erroneous, the details of the simulated climate cannot be accurate and must be erroneous even if the model validates well with statistical properties of temperature and precipitation, for example. To a certain extent, it simply must be an artifact of the way the model is constructed and less due to a correct depiction of the physical processes. Thus the ability to simulate aspects of the North Atlantic Oscillation (NAO) and atmospheric blocking events becomes of particular relevance for the Arctic. According to the recent Intergovernmental Panel on Climate Change (IPCC 2007), models have continued to improve in their ability to represent some of the main observed NAO-related characteristics. However, there are still major discrepancies in their ability to represent blocking frequency. The implications of this will tend to manifest themselves in inadequate depictions of precipitation and temperature patterns, but these may be obscured by the presence of other systematic errors, resulting in error cancellations, that may not easily be depicted from model validation analyses.

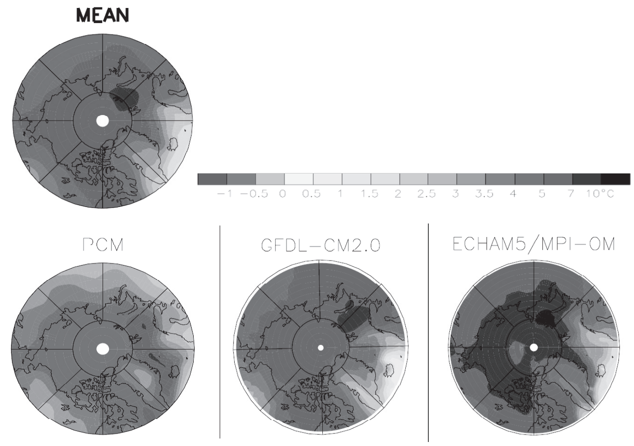

Figure 1. Maps of composite (based on 21 models) and 3 individual model simulated annual mean temperature change (2080–2099 vs. 1980–1999) for the IPCC A1B SRES scenario. From IPCC (2007).

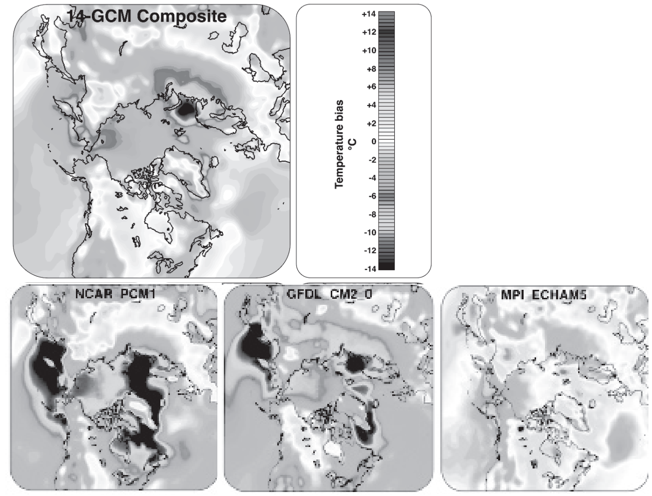

Figure 2. Maps of composite (based on 14 models) and 3 individual model temperature biases for winter (1958–2000). From Walsh et al. (2007).

Changes in temperature and sea ice

In IPCC (2007), the temperature within the Arctic is assessed to increase at a higher rate than globally, confirming results from previous IPCC reports and ACIA (2005). For the IPCC SRES A1B scenario, the annual mean Arctic temperature increase by the end of the 21st century is projected to be about twice that of the global mean (5°C–7°C vs. 2.5°C–3.5°C) (IPCC 2007, Christensen et al. 2007). Figure 1 shows an extract of an evaluation of 21 model simulations of global change under the A1B scenario (from Christensen et al. 2007), highlighting 3 models—the NCAR PCM, GFDL CM2.0, and MPI ECHAM5—as well as the 21-model mean. It is evident that these 3 individual models qualitatively show the same climate change response, but the magnitude of the change differs by several °C, with the PCM model exhibiting the lowest degree of warming, and the ECHAM5, the highest degree of warming, while the GFDL CM2.0 model is close to the ensemble mean.

It is interesting to note, however, that the projected climate signals to some degree are caused by quite different mechanisms. Figure 2 shows an extract of an analysis of the performance of 14 model simulations for the period 1958–2000 from Walsh et al. (2007). Again the ensemble mean behavior is shown along with the same 3 individual models. A common feature for most of the models, reflected by the ensemble mean, is a clear cold bias in the Barents Sea due to a tendency to simulate too much sea ice, with the MPI model being a clear exception. At the same time, the greatest warming by the end of the century is simulated exactly over this region in the ensemble mean as well as by the individual models. In the NCAR and GFDL models, this is partly reflecting the bias in present-day sea ice conditions, while in the MPI model this apparently cannot be the case. Note also that, in general, the largest warming occurs in the area with too much ice (strong cold bias) under present-day conditions, and in the NCAR model in particular, even though we here compare winter with annual mean. Thus, to some extent, the results are at the regional scale clearly subject to the systematic errors in the present-day simulations. Using an ensemble of models masks this deficiency.

Therefore, maps of warming must be carefully analyzed, and data cannot be used in a region with nonlinear feed backs such as the presence and absence of sea ice without further analysis.

Changes in snow conditions

Snow cover presents a challenge to models, and the issue is further complicated by a rather incomplete verification database. Apart from very few sites, the information available is only snow cover extent. While this is a similar challenge as for sea ice, there is much less constraint on the temperature below the snow seal. In the ocean, temperatures are well approximated by -1.7°C under sea ice, while soil temperatures can go well below -10°C in some places. Therefore, the ability to simulate snow cover realistically is essential.

According to the IPCC (2007), models are now more consistent in their simulation of snow cover than previously. Problems remain, however, and Roesch (2006) showed that the recent models predict excessive snow water equivalent in spring, likely because of excessive winter precipitation. The magnitude of these model errors is large enough to affect continental water balances. Snow cover area is well captured by the recent models, but interannual variability is too low during melt. Moreover, many models are able to reproduce the observed decline in annual snow cover area for the period 1979 to 1995, and most models capture the observed decadal-scale variability over the 20th century. Despite this, some of the models still exaggerate snow covered areas in spring and summer. This has obvious consequences for any analysis on permafrost-related properties using such models.

Implications for changes in permafrost

Re-inspection of Figure 1 reveals that the largest warming, apart from that occurring over the Arctic Ocean, is seen

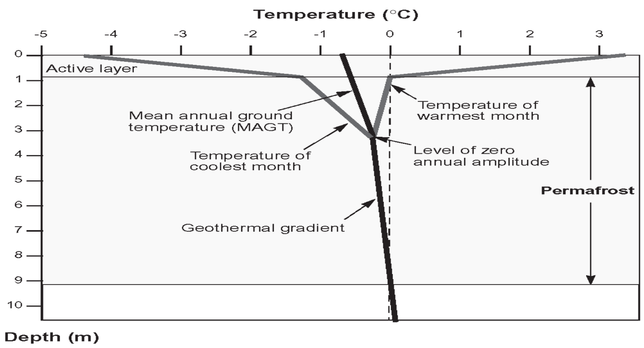

Figure 3. Schematics of temperature profiles at a permafrost site. Fat horizontal stippled line indicates an arbitrarily chosen lowest soil model level as typically represented in a climate model.

over the northern-most part of the continents, for several reasons. Firstly, the warming associated with the reduced sea ice cover simulated by all models has an impact mainly in spring and autumn. During these periods, relatively warm and moist air is more likely to influence these regions due to the lack of sea ice cover in a longer period, while in summer and winter the atmospheric conditions in this aspect will be more like present day. Thus the largest signal in the warming comes from the change in the seasonality of the sea ice. This in turn has implications for the poleward advection of heat in the shoulder seasons as well, leading to enhanced warming. But the albedo feedback from reduced snow cover from the return of sun light in spring to late autumn is also likely to contribute to the enhanced warming. Any bias in the seasonality of sea ice or snow cover will strongly impact this warming signal. This immediately implies that simulated permafrost properties are impacted by a model's ability to capture the present-day conditions as well as respond to increased greenhouse forcing in an adequate way.

Figure 3 illustrates the classical depiction of temperature profiles at a site underlain by permafrost. This schematic picture also shows how the typical representation of the soils in a GCM is handled. The lowest layer in the soil is located somewhere above the level with zero annual amplitude. Typically, GCMs adopt a zero heat flux adjustment at the lowest level in order to avoid an artificial energy source or sink. This implies that instead of allowing for heat penetration into the deeper soils, heat accumulates near the lowest level if the general model behavior reflects a warming, as indeed is the case unanimously in the Arctic under global warming. Therefore, in the model, once the possible nonlinear jump due to changes in snow cover conditions (earlier melt and later reoccurrence) has expressed itself at a grid point underlain by permafrost, heat can start to accumulate in the shallow soils, starting from below. This in turn will show up as a faster warm-up and, subsequently, thaw of the permafrost conditions than should be expected if the excess heat were allowed to propagate into greater depth. Recently, it has been demonstrated that indeed such behavior is found using the CLM land surface scheme (Alexeev et al. 2007, Nicolsky et al. 2007). Therefore, these authors proposed a procedure to parameterize the existence of deeper soil layers. In their idealized case study, the CLM was driven off-line with observations from one winter season, and the authors were able to show how heat was effectively transported to further depth, avoiding a pile-up of excess heat near the deepest model levels. The implications are important not only for the depiction of soil temperature behavior. Once a region experiences strong warming due to modified snow-cover insulation conditions, permafrost erroneously warms up too fast below the active layer, implying excess heat capacity during the cold season which in turn may lead to too-warm conditions close to the surface as well. Thus a feedback mechanism is initiated that may induce further warming, which at least partly is induced by the imperfect lower-boundary condition. The implications for the interpretation of direct GCM model-based soil temperatures are therefore severe; the induced warming and subsequent thawing of permafrost will take place too quickly. Moreover, when more advanced permafrost models are used to provide detailed information about changes in permafrost conditions, the simulated permafrost properties will be impacted by the biased precipitation, snow, and near-surface temperature provided to it by the GCM.

Conclusion

Here we have highlighted some of the well-known deficiencies of most state-of-the-art climate models. It is also clear, however, that some models appear to be less prone to some of the errors we have discussed here. In particular, a few of today's models are capable of reproducing crucial aspects of the climate system in the Arctic. In order to provide reliable climate change scenarios in areas underlain by permafrost, we have illustrated the need to single out some of today's GCMs that are representing with reasonable accuracy the atmospheric circulation, sea ice distribution, and general aspects of snow cover for the present climate Furthermore, we have demonstrated that there is a need to introduce a more sophisticated treatment of soil processes which includes information about soil thermal development even at considerable depth, as this has the potential to further improve the ability of climate models to simulate arctic climate, hence increasing credibility of arctic climate change projections.

Finally, the importance of permafrost in high-latitude climate change implies a need for accurate representations of the soil vertical profiles of conductivity, porosity, and other parameters affecting soil temperature and moisture content.

Acknowledgments

This research was partly funded by the Polar Earth Science Program, Office of Polar Programs, National Science Foundation (ARC-0612533), and by the EU Sixth Framework Programme, Global Change and Ecosystems sub-programme, CARBO-North Project (contract number 036993).

References

ACIA. 2005. *Arctic Climate Impact Assessment*. NY: Cambridge University Press, 1042 pp.

Alexeev, V.A., Nicolsky, D.J., Romanovsky, V.E. & Lawrence, D.M. 2007. An evaluation of deep soil configurations in the CLM3 for improved representation of permafrost. *Geophys. Res. Lett.* 34: L09502, doi:10.1029/2007GL029536.

Christensen, J.H., Hewitson, B., Busuioc, A., Chen, A., Gao, X., Held, I., Jones, R., Kolli, R.K., Kwon, W.-T., Laprise, R., Magaña Rueda, V., Mearns, L., Menéndez, C.G., Räisänen, J., Rinke, A., Sarr, A. & Whetton, P. 2007. Regional Climate Projections. In: S. Solomon, D. Qin, M. Manning, Z. Chen, M. Marquis, K.B. Averyt, M. Tignor, & H.L. Miller (eds.), *Climate Change 2007: The Physical Science Basis. Contribution of Working Group I to the Fourth Assessment Report of the Intergovernmental Panel on Climate Change.* Cambridge, UK, and New York, NY: Cambridge University Press.

IPCC. 2007. *Climate Change 2007: The Physical Science Basis. Contribution of Working Group I to the Fourth Assessment Report of the Intergovernmental Panel on Climate Change.* S. Solomon, D. Qin, M. Manning, Z. Chen, M. Marquis, K.B. Averyt, M. Tignor, & H.L. Miller (eds Cambridge, UK, and New York, NY: Cambridge University Press.

Nicolsky, D.J., Romanovsky, V.E., Alexeev, V.A. & Lawrence, D.M. 2007. Improved modeling of permafrost dynamics in a GCM land-surface scheme. *Geophys. Res. Lett.* 34:L08501, doi:10.1029/2007GL029525.

Roesch, A. 2006. Evaluation of surface albedo and snow cover in AR4 coupled climate models. *J. Geophys. Res.* 111:D15111, doi:10.1029/2005JD006473.

Walsh, J.E., Chapman, W.L., Romanovsky, V., Christensen, J.H. & Stendel, M. 2007. Global climate model performance over Alaska and Greenland. *J. Clim.* (in revision),

—*Plenary Paper*—

Trace Gas Budgets of High Arctic Permafrost Regions

Torben R. Christensen
Dept. of Physical Geography and Ecosystem Analyses, Lund, Sweden, and Abisko Scientific Research Station, Abisko, Sweden
Thomas Friborg
Institute of Geography, Copenhagen University, Øster Voldgade 10, DK-1350 Copenhagen K, Denmark
Margareta Johansson
Dept. of Physical Geography and Ecosystem Analyses, Lund, Sweden, and Abisko Scientific Research Station, Abisko, Sweden

Abstract

Trace gas fluxes in tundra regions have attracted substantial attention in recent years because of the large quantity of carbon stored in tundra soils and the associated feedbacks to climate change. Major international assessments (e.g., ACIA, IPCC) have not been able to come up with a conclusive answer as to trace gas budgets of the Arctic. Here we find that the Circumpolar North is roughly in balance with respect to carbon dioxide exchanges, with some regions showing signs of current losses and others showing sings of current carbon sinks. Taking into account methane emissions over a decadal timescale, however, the Circumpolar North is considered a current source of radiative forcing. Whether this source functioning will continue or increase into the future is uncertain and depends on the fate of permafrost, soil moisture, and surface hydrology.

Keywords: Arctic tundra; carbon dioxide (CO_2); methane (CH_4); permafrost regions; trace gas flux.

Introduction

Arctic terrestrial ecosystems have attracted major attention in the context of global carbon cycling in recent years (ACIA 2005, Millenium Ecosystem Assessment 2005, McGuire et al. 2007). A reason for this is that Arctic terrestrial ecosystems store a significant proportion of the global stock of soil organic carbon (C). In the arctic tundra proper, some 121-191 Gt of C are stored, or approximately 12-16% of the estimated world total (McKane et al. 1997, Tarnocai et al. 2003). Arctic permafrost regions are predicted to undergo significant changes due to anthropogenic climate impacts (Kittel et al. 2000, IPCC 2001, Wookey 2002, ACIA 2005, Lawrence and Slater 2005). These changes and the feedbacks they engender could change the climatic conditions that have allowed the development of such large soil C stocks in the Arctic (Gorham 1991, Shaver et al. 1992, McKane et al. 1997, Hobbie et al. 2000). Extensive regions of the High Arctic that lack substantial C stocks and currently have very limited rates of atmospheric exchange could develop dynamic C cycles. Climate driven changes in plant community structure, specifically shifts from herbaceous and cryptogamous dominance to systems dominated by ericaceous and woody species, are also likely to change ecosystem C dynamics and balance.

Arctic soils are often wet and, when waterlogged, become anoxic. Anoxic soils often accumulate C in the form of peat (Gorham 1991, Clymo et al. 1998) and release methane (CH_4), a radiatively important trace gas (Matthews and Fung 1987, Joabsson and Christensen 2001, Öquist and Svensson 2002). Methane flux is rarely a quantitatively important component in the ecosystem C balance but it can play a disproportionately important role in terms of greenhouse gas forcing (gram for gram methane in the atmosphere has 23 times the radiative forcing potential of CO_2).

Permafrost environments are very dynamic with respect to trace gas exchanges and there are important interactions between permafrost dynamics and, in particular methane emissions both in terrestrial (Christensen et al. 2004) and thaw lake ecosystems (Walter et al. 2006). Here we briefly review the current state of budgets for the northern permafrost regions with respect to observational data on seasonal and annual CO_2 and CH_4 fluxes.

Mechanisms

Processes controlling trace gas budgets in arctic ecosystems vary across a continuum of space (plot to region) and time (minutes to decades), and varying classes of biological complexity (e.g. from individual species, through trophic interactions, to whole ecosystems). Thus, determining an accurate C budget for the Arctic requires an extensive and sustained observational capacity, which incorporates measurements and instrumentation that are sensitive to processes influencing C uptake, storage and loss. The latter is arguably the greatest source of current scientific uncertainty due to significant uncertainties remaining in the mechanistic understanding of processes controlling C losses, whereas accurate scaling across space and time is perhaps more constrained by logistical and funding limitations. Here, we discuss the importance of several crucial processes controlling C uptake, loss and storage in arctic tundra. Factors that are important for scaling process studies across space and time are considered below.

There are a finite number of basic processes involved in controlling CO_2 exchange. Net ecosystem production (NEP) of organic carbon is the net product of two independent processes that drive the uptake and release of C; gross primary production (GPP) and respiration (both autotrophic and heterotrophic, CO_2 as well as CH_4; Fig. 1). The net

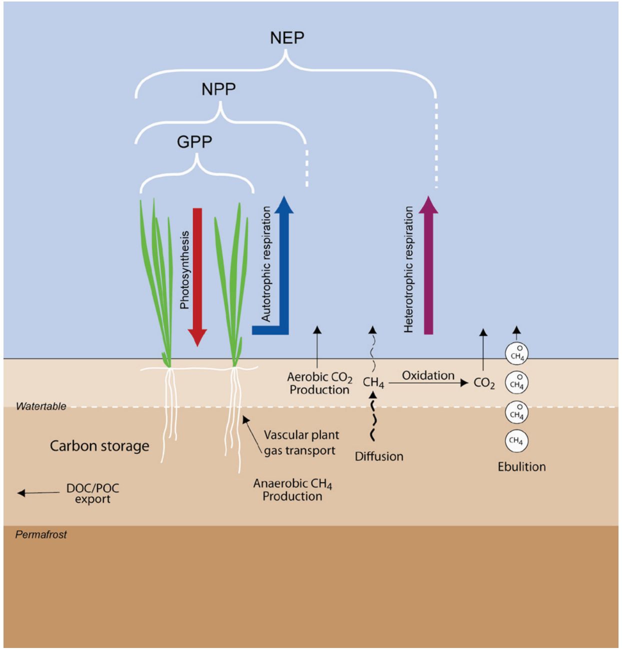

Figure 1. Schematic diagram of the processes governing the net balance of CO_2 and CH_4 fluxes in typical permafrost regions.

annual C budget of a given ecosystem is also affected by export of dissolved and particulate organic C in ground and streamwater flows (Michaelson et al. 1998, Tipping et al. 1999, Cole et al. 2002, Judd and Kling 2002), which are relatively unknown for the Arctic. In addition to the capacity for C transport in Arctic soils and streams (Kling et al. 1991, Judd and Kling 2002) there are minor releases of volatile organic compounds (Kesselmaier et al. 2002) contributing to a full C budget. The net annual C balance or budget is, hence, the result of both independent and coupled (e.g., Boone et al. 1998, Högberg et al. 2001) processes that often respond differentially to the same abiotic forcing factors which makes interpretation and prediction of their quantitative impact a major challenge.

The net emission of CH_4 from a given ecosystem is also the result of a complex set of independent processes that regulate production, oxidation and transport (Fig. 1). Controls on these processes include soil temperature, plant species composition (and functional type), and factors that influence the redox potential (Eh) of the soil environment (e.g. the position of the water table) (Moore and Knowles 1989, Christensen 1993, Funk et al. 1994, Yavitt et al. 1997, Bellisario et al. 1999, Christensen et al. 1999, 2000, Joabsson and Christensen 2001, Öquist and Svensson 2002, Sjögersten and Wookey 2002, Blodau and Moore 2003, Ström et al. 2005). Also, as is the case for CO_2 exchange, the temporal dynamics of net CH_4 fluxes between a given landscape and the atmosphere can be highly variable due to contrasting processes controlling exchange at different times of the year. Permafrost dynamics impact all these factors (Fig. 1) in arctic, subarctic and some boreal ecosystems. Thus, changes in the permafrost regime (Christensen et al. 2004, Lawrence and Slater 2005, Walter et al. 2006) will have fundamental consequences for CO_2 and CH_4 fluxes in the Arctic.

Seasonal Flux Dynamics

Figure 2 illustrates critical components controlling the seasonal dynamics of C exchange in a simplified arctic tundra ecosystem. Within the four seasons (I-IV in Figure 2) there are important, and at times very different, processes acting which are resulting in the net effect of the individual seasons on the annual budget. Critical facets of early-season conditions - such as a substantial C loss during spring melt and early summer due to release of trapped CO_2, and possibly a hindered onset of photosynthesis due to dry early summer conditions - can seriously affect the annual budget.

In midsummer again water deficit can be important as a limiting factor for photosynthesis, while a very warm summer has the potential to stimulate respiration (including root respiration) more than photosynthesis (in particular in dry years) so these effects together can be very important for the annual budget (Crawford et al. 1993, Marchand et al. 2005, Kwon et al. 2006). In the third season, a mild autumn followed by the delayed appearance of a consistent snowcover could be critical for processes involved in C fluxes. Usually photosynthesis will decline regardless of warm "Indian" summer conditions that will stimulate respiration for as long as the soils remain unfrozen (or contain free water). So a mild autumn may also be a very important triggering factor for C losses on an annual basis (Jackovitz-Korchinsky et al. in prep.). The critical factors for determining the annual carbon budget of a simplified arctic tundra are summarized in Table 1, which includes examples of factors that can affect seasonal processes (δa, δb, δc, δd) occurring in season I (spring), II (summer), III (autumn) and IV (winter) and, therefore estimation of annual budgets. The annual budget can then be summarised as Equation 1 (below) where k is a site specific productivity factor and δ represents seasonal factors that indicate the positive or negative effects that each season is having on the net annual balance.

$$C_{annual} = k * (\delta a + \delta b + \delta c + \delta d) \quad (1)$$

Importantly, there may be several complications associated with this very simplified model. For example, an early freeze-up in season III, which would tend to increase net C uptake in a given year through preventing respiratory C losses in a lengthy autumn, may act very differently during the subsequent year depending upon whether or not the soil is underlain by permafrost. In a permafrost free setting, where there are still unfrozen conditions and substantial microbial activity beneath the freezing front, there is the chance for a substantial winter-time build-up of CO_2 below the frozen ice and soil layer, which in turn may affect the δa in the subsequent year through a substantial and potentially pulsed release of trapped CO_2. In continuous permafrost this hand-over effect from one year to the next may be less apparent.

Nonetheless, Equation 1 may be useful for comparing annual budgets between ecosystems, studies and sites to determine factors controlling not only intra-site inter-annual variability but also for comparing why different sites appear with different annual budgets. The discussion on estimates of annual fluxes below rationalizes why such differences in annual budgets can be found both within and between sites.

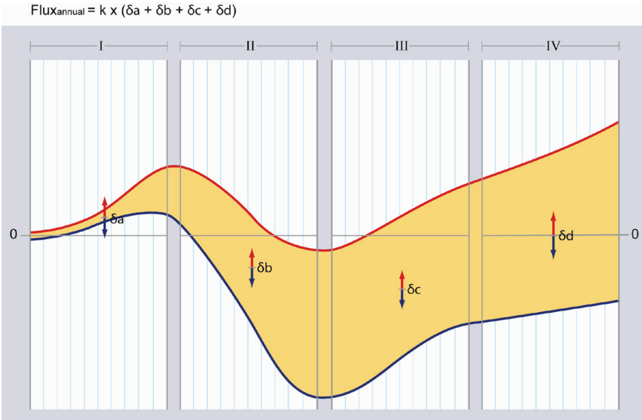

Figure 2. Conceptual model for the seasonal dynamics of accumulated carbon exchange with the atmosphere in a tundra ecosystem. The four different seasons determining the annual balance are indicated starting with the Spring (I) defined as the time from snowmelt until the carbon balance turns negative. The reverse point defines the end of the following period defined as Summer (II). Autumn is from the turning point of the carbon balance to the onset of permanent snowcover (III) and winter is the permanent snow covered period (IV). Examples of critical parameters for the annual total budget outcome in these individual parts of the season are shown in table inserted below.

Table 1. Examples of requirements for δx (Fig. 2) to be:

	Positive	Negative
δa	Short (little snow);	Long and cold;
	Soil moisture limitation;	Little trapped CO_2
	Lots of trapped CO_2	
δb	Short and warm.	Long and cold.
	Moisture limitations on	No moisture deficit for GPP
	GPP; Insect outbreaks	
δc	Long and dry	Short; Early freeze-up
δd	(snowcover) long	(snowcover) short

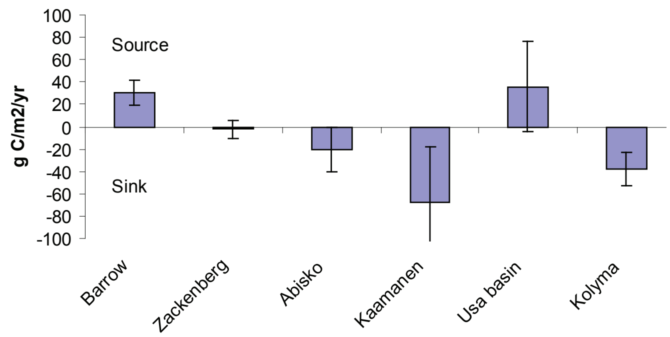

Figure 3. A compilation of annual C budgets based on measurements at sites ranging from Alaska over Greenland, northern Scandinavia and north-eastern European Russia to NE Siberia. (Data from Oechel et al. 2000, Nordstroem et al. 2001, Soegaard et al. 2000, Christensen et al. 2000, Aurila et al. 2004, Jackovitz-Korchinsky et al. in prep, Heikkinen et al. 2003 and Corradi et al. 2005.)

Trace Gas Budgets

Annual estimates

Due to the natural interannual variability determined by the factors discussed above it is extremely difficult to ascertain the C budget status of any tundra ecosystem from single year or even 2-3 year studies. The degree of variability between years is generally quite high. The longest series of annual C balance estimates for tundra ecosystems is from N Alaska, where chamber flux measurements in the 1970's and 1980's, and eddy correlation measurements in more recent years, have indicated a shift from sink to source by the early 1990's, after which there was a tendency for the system to tend towards sink status despite remaining a net source (Oechel et al. 2001). Regardless of these rather dramatic fluctuations in annual budgets over decadal time scales, tundra sites in northern Alaska have also shown relatively stable summertime uptake rates of 40 to 70 g C m^{-2} $season^{-1}$ (Spring to Fall) in recent years (Kwon et al. 2006), emphasising the importance of the shoulder season for determining the variability between years.

Other sites where full annual budgets have been monitored include Stordalen in northern Sweden (Jackovitz-Korchinsky et al. in prep.) and Kaamanen in northern Finland (Aurela et al. 2002, 2004). From NE Greenland there are several years of full seasonal flux observations available both from wet tundra fen and dry heath sites and annual budgets have been estimated at an overall balance close to zero (Soegaard et al. 2000, Nordstroem et al. 2001, Groendahl et al. 2006). In Siberia an annual sink estimate of 38 g C m^{-2} $year^{-1}$ was measured in tussock tundra in NE Siberia (Corradi et al. 2005).

The status of C exchange in the Circumpolar North based on the few actually observed annual C budgets indicate that Arctic terrestrial ecosystems are functioning with significant spatial and temporal heterogeneity with some regions being sources of carbon to the atmosphere (mostly dry and mesic ecosystems) and some regions sinks (mostly wet tundra) (Fig. 3).

From the available circumpolar data it is very difficult to provide a straight answer to the question of whether the Arctic tundra is a source or a sink of atmospheric carbon. There was a time in the 1990s where there was a tendency for the studies and sites that represented the larger areas of tundra to show source activity (northern Alaska and European Russia, Figure 3) but this pattern has changed since the vast NE Siberian tundra became represented by Corradi et al.'s (2005) study (Fig. 3). Taking into account the error bars also shown in Figure 3 it is impossible, given the currently available measured annual carbon budgets, to say for certain that the overall carbon balance of the Circumpolar North should be different from equilibrium.

Greenhouse gas budgeting

Few of the annual budgets referred to above include observations of CH_4 emissions. Where such combined measurements are available on an annual basis, i.e. at Stordalen (Sweden), Kaamanen (Finland) and Kolyma (NE Siberia), the contribution of CH_4 to the actual net annual carbon exchanges (NEP, Figure 2) amounts to 10-25% of the heterotrophic respiration (Jackovitz-Korchinsky et al. in prep, Corradi et al. 2005).

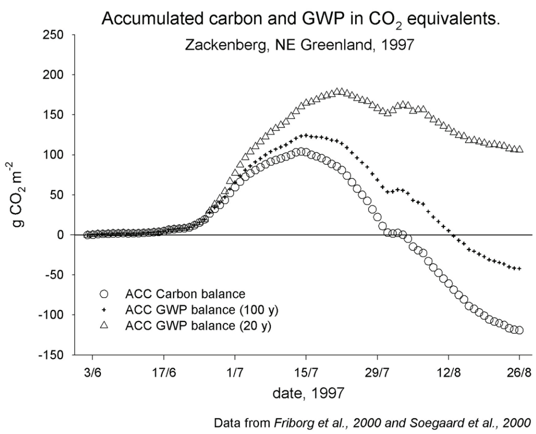

Figure 4. An accumulated greenhouse gas budget (CO_2 and CH_4 as CO_2 equivalents) for a northern wet tundra site versus one of CO_2 only (from ACIA, 2005 based on data in Soegaard et al. 2000 and Friborg et al. 2000).

Since CH_4 is a greenhouse gas with a radiative forcing potential 23 times greater (expressed as gram per gram) than that of CO_2 (in a 100 yr time perspective), the emissions of methane from wet tundra ecosystems, in particular, must be taken into account in any attempt to document the radiative forcing capacity of arctic landscapes (Johansson et al. 2006). For tundra ecosystems where a third commonly studied greenhouse gas, nitrous oxide (N_2O), is assumed to be rarely exchanged with the atmosphere due to nutrient limitations, estimates of total greenhouse gas fluxes are usually confined to the combined effects of CO_2 and CH_4 exchange. Here a complicating factor is time. Most tundra ecosystems have accumulated carbon over many thousands of years. Over such a period the accumulated and reduced radiative forcing potential of CO_2 uptake is a stronger factor than that of accumulated CH_4 emissions (Frolking et al. 2006). However, in most greenhouse gas budgets, focus is generally directed to the immediate emissions and possible changes that may occur and what impact these will have on climate as this responds to change over the coming decades. Over decadal time scales, most wet tundra CH_4 emissions will be a stronger greenhouse forcing factor acting on climate than the CO_2 uptake. Typical calculations of such a total GHG budget may look like that illustrated in Figure 4, which has been derived for the Zackenberg eddy tower site in NE Greenland by applying two typical CH_4 greenhouse warming potentials of 63 for a 20 yr time perspective and 23 for a 100 yr time perspective respectively (Friborg et al. 2004, ACIA 2005).

Many dry/mesic tundra ecosystems have minimal CH_4 emissions, if any, and CO_2 budgets are balanced around zero or are actual sources of C to the atmosphere, However, we conclude that arctic tundra regions should currently be considered a net contributor to greenhouse warming because wet tundra ecosystems are likely to be sources of climate warming over the next few decades due to strong CH_4 emissions. Whether this source functioning will continue into the future without acclimation is uncertain. In all likelihood, this may depend on the response of permafrost that appears to be warming, soil moisture status that appears to be variable with moisture levels increasing in some regions and drying in other regions. A further factor is the future state and carbon fixing potential of the High Arctic.

Current research infrastructure, monitoring and international and scientific coordination will not be sufficient to answer such questions. To further understand the significance of arctic environmental change for global greenhouse warming potential, new and concerted efforts need to be sustained to investigate further and adequately measure processes modulating C flux in arctic tundra and how C fluxes in arctic landscapes vary across multiple scales of space and time.

Conclusions

Throughout the Holocene, most tundra in the Arctic has been a net sink for carbon due to low rates of decomposition and loss relative to rates of uptake. Based on the few observed annual carbon budgets in the Circumpolar North, the current status of carbon exchanges indicates that Arctic terrestrial ecosystems are dynamic and heterogeneous, with some regions being sources of carbon to the atmosphere (mostly dry and mesic ecosystems) and some regions being sinks (mostly wet tundra). If the measurements from sites in N America and North Eurasia are assumed representative for these vast regions, then source and sink areas are roughly balanced.

Current global and regional climate modeling of predicted future states of arctic precipitation dynamics and hydrological balance are highly uncertain (ACIA, 2005). The models must be better parameterized and validated in order to constrain predictions of future soil hydrological states that will determine the magnitude and of C efflux from arctic tundra and the dynamics and the composition (CO_2, CH_4, VOCs etc.) of that exchange (Sitch et al. 2007).

Many dry/mesic tundra ecosystems have minor CH_4 emissions if any, and CO_2 budgets are balanced around zero or are actual sources. However, wet tundra ecosystems are likely to enhance radiative forcing over decadal time scales through the emission of CH_4. As such, arctic tundra and small lake regions should be concluded to currently be acting as a source of greenhouse warming. Whether this source functioning will continue or increase into the future is uncertain and will depend on the fate of permafrost, soil moisture and surface hydrology and the future state of ecosystem structure and function in the high arctic. To decrease uncertainty and improve our fundamental understanding of carbon balance at high northern latitudes new novel and concerted research and monitoring efforts need to focus over decadal time scales.

Acknowledgments

This paper forms the foundation for an updated presentation at NICOP 2008 representing an extract from a larger review under preparation in an IASC supported process (the FATE group and a continued follow-up from a 2003 workshop at Skogar, Iceland) that has involved contributions from a range of people in addition to the current authors including: C. E. Tweedie, P. M. Crill, J. A. Gamon, L. Groendahl, J. Gudmundsson, Y. Harazono, F. Huemmrich, C. Lloyd, P. J. Martikainen, W.C. Oechel, H. Oskarsson, N. Panikov and P.A. Wookey.

References

ACIA, 2005. *Arctic Climate Impact Assessment.* Cambridge University Press. 1042 pp.

Aurela, M., Laurila, T. & Tuovinen, J.P. 2002. Annual CO2 balance of a subarctic fen in northern Europe: Importance of the wintertime efflux. *Journal of Geophysical Research-Atmospheres* 107: art-4607.

Aurela M, Laurila T. & Tuovinen, J.P. 2004. The timing of snow melt controls the annual CO2 balance in a subarctic fen. *Geophysical Research Letters* 31.

Bellisario L.M., Bubier J.L., Moore, T.R. & Chanton, J.P. 1999. Controls on CH4 emissions from a northern peatland. *Global Biogeochemical Cycles* 13: 81-91.

Blodau, C. & Moore, T.R. 2003. Experimental response of peatland carbon dynamics to water table fluctuation. Aquatic Sciences 65: 47-62.

Boone, R.D., Nadelhoffer, K.J., Canary, J.D. & Kaye, J.P. 1998. Roots exert a strong influence on the temperature sensitivity of soil respiration. *Nature* 396: 570-572.

Christensen, T.R. 1993. Methane emission from Arctic tundra. *Biogeochemistry* 21:117-139.

Christensen, T.R., Jonasson, S., Callaghan, T.V., Havström, M. & Livens, F.R. 1999. Carbon Cycling and Methane Exchange in Eurasian Tundra Ecosystems. *Ambio* 28: 239-244.

Christensen, T.R., Friborg, T., Sommerkorn,M., Kaplan, J., Illeris, L., Soegaard, H., Nordstroem, C. & Jonasson, S. 2000. Trace gas exchange in a high-arctic valley 1. Variations in CO2 and CH4 flux between tundra vegetation types. *Global Biogeochemical Cycles* 14, 701-713.

Christensen, T.R., Johansson, T., Malmer, N., Åkerman, J., Friborg, T., Crill, P., Mastepanov, M. & Svensson, B. 2004. Thawing sub-arctic permafrost: Effects on vegetation and methane emissions, *Geophysical Research Letters* 31: L04501, doi:10.1029/2003GL018680.

Clymo, R..S., Turunen, J. & Tolonen, K. 1998. Carbon accumulation in peatlands. *Oikos* 81: 368-388.

Cole L., Bardgett, R.D., Ineson, P. & Adamson J.K. 2002. Relationships between echytraeid worms (Oligochaeta), climate change, and the release of dissolved organic carbon from blanket peat in northern England. *Soil Biology and Biochemistry* 34: 599-607.

Corradi, C., Kolle, O., Walter, K., Zimov, S.A. & Schulze, E.D. 2005. Carbon dioxide and methane exchange of a north-east Siberian tussock tundra. *Global Change Biology* 11: 1910-1925.

Crawford, R.M.M., Chapman, H.M., Abbott, R.J. & Balfour, J. 1993. Potential impact of climatic warming on arctic vegetation. *Flora* 188 (4): 367-381.

Friborg, T., Christensen, T.R., Hansen, B.U., Nordstroem, C. & Soegaard, H. 2000. Trace gas exchange in a high-arctic valley 2. Landscape CH4 fluxes measured and modeled using eddy correlation data. *Global Biogeochemical Cycles* 14: 715-723.

Friborg, T., Soegaard, H., Christensen, T.R., Lloyd, C.R. & Panikov, N.S. 2003. Siberian Wetlands: Where a sink is a source. *Geophysical Research Letters* 30: 2129.

Frolking, S., Roulet, N. & Fuglestvedt, J. 2006. The impact of a northern peatland on the earth's radiative budget: sustained methane emission versus sustained carbon sequestration. *Journal of Geophysical Research-Biogeochemistry* 111: G01008, doi:10.1029/2005JG000091.

Funk, D.W., Pullman, E.R., Peterson, K.M., Crill, P.M. & Billings WD. 1994. Influence of water-table on carbon dioxide, carbon monoxide, and methane fluxes from taiga bog microcosms. *Global Biogeochemical Cycles* 8: 271-278.

Gorham, E. 1991. Northern peatlands: role in the carbon cycle and probable responses to climatic warming. *Ecological Applications* 1: 182-195.

Groendahl, L., Friborg, T. & Soegaard, H. 2006. Temperature and snow-melt controls on interannual variability in carbon exchange in high Arctic. Theoretical and Applied Climatology, doi: 10.1007/s00704-005-0228-y.

Heikkinen, J. E. P., Virtanen, P. T, Huttunen, J. T., Elsakov, V. & Martikainen, P. J. 2004. Carbon balance in East European tundra. *Global Biogeochemical Cycles* 18: 10.1029/2003GB002054.

Hobbie, S.E., Schimel, J.P., Trumbore, S.E. & Randerson, J.P. 2000. Control over carbon storage and turnover in high-latitude soils. *Global Change Biology* 6 (Suppl. 1): 196-210.

Högberg, P., Nordgren, A., Buchmann, N., Taylor, A.F.S, Ekblad, A., Högberg, M.N., Nyberg, G., Ottosson-Lofvenius, M. & Read, D.J. 2001. Large-scale forest girdling shows that current photosynthesis drives soil respiration. *Nature* 411: 789-792.

IPCC 2001. *Climate Change 2001: Synthesis Report.* A Contribution of Working Groups I, II and III to the Third Assessment Report of the Intergovernmental Panel on Climate Change. Watson, R.T. and the Core Writing Team (eds.). Cambridge, U.K., and New York: Cambridge University Press, 398 pp.

Joabsson, A. & Christensen, T.R. 2001. Methane emissions from wetlands and their relationship with vascular plants: an Arctic example. *Global Change Biology* 7 (8): 919-932.

Johansson, T., Malmer, N., Crill, P.M., Mastepanov, M. & Christensen, T.R. 2006. Decadal vegetation changes in a northern peatland, greenhouse gas fluxes and net radiative forcing. *Global Change Biology* 12: 2352–2369.

Judd, K.E. & Kling, G.W. 2002. Production and export of dissolved C in arctic tundra mesocosms: the roles of vegetation and water flow. *Biogeochemistry* 60(3): 213-234.

Kesselmeier, J. et al. 2002. Volatile organic compound emissions in relation to plant carbon fixation and the terrestrial carbon budget. *Global Biogeochemical Cycles* 16: 1–9.

Kittel, T.G.F., Steffen, W.L. & Chapin, F.S. III. 2000. Global and regional modelling of Arctic boreal vegetation distribution and its sensitivity to altered forcing. *Global Change Biology* 6: 1-18.

Kling, G.W., Kipphut, G.W. & Miller, M.C. 1991. Arctic Lakes and streams as gas conduits to the atmosphere: implications for tundra carbon budgets. *Science* 251(4991): 298-301.

Kwon, H.-J., Oechel, W. C., Zulueta, R. C. & Hastings, S.J. 2006. Effects of climate variability on carbon sequestration among adjacent wet sedge tundra and moist tussock tundra ecosystems. *Journal of Geophysical Research* 111, G03014, doi:10.1029/2005JG000036.

Lawrence, D.M. & Slater, A.G. 2005. A projection of severe near-surface permafrost degradation during the 21st century. *Geophysical Research Letters* 32 (24): Art. No. L24401.

Marchand, F.L., Mertens, S., Kockelbergh, F., Beyens, L. & Nijs, I. 2005. Performance of High Arctic tundra plants improved during but deteriorated after exposure to a simulated extreme temperature event. *Global Change Biology* 11 (12): 2078-2089.

Matthews, E. & Fung, I. 1987. Methane emission from natural wetlands: Global distribution, area, and environmental characteristics of sources. *Global Biogeochemical Cycles* 1: 61-86.

McGuire, A.D., Chapin, F.S. III, Wirth, C., Apps, M., Bhatti, J., Callaghan, Y., Christensen, T.R., Clein, J.S., Fukuda, M., Maximov, T., Onuchin, A., Shvidenko, A. & Vaganov, E. 2007. Responses of high latitude ecosystems to global change: Potential consequences for the climate system. In: *Terrestrial Ecosystems in a Changing World.* Edited by Canadell, J.G., Pataki, D.E. & Pitelka, L.F.), pp. 297-310. The IGBP Series, Springer-Verlag, Berlin Heidelberg.

McKane, R.B., Rastetter, E.B., Shaver, G.R., Nadelhoffer, K.J., Giblin, A.E., Laundre, J.A. & Chapin, F.S. III. 1997. Reconstruction and analysis of historical changes in carbon storage in arctic tundra. *Ecology* 78: 1188-1198.

Michaelson, G.J., Ping, C.L., Kling, G.W, & Hobbie, J.E. 1998. The character and bioactivity of dissolved organic matter at thaw and in the spring runoff waters of the arctic tundra north slope, Alaska. *Journal of Geophysical Research* – Atmospheres 103 (D22): 28939-28946.

Millenium Ecosystem Assessment. 2005. *Ecosystems and human well-being: Current state and trends.* Findings of the Condition and Trends Working Group. Millennium Ecosystem Assessment Series. Island Press, Washington.

Moore, T.R. & Knowles, R. 1989. The influence of water-table levels on methane and carbon dioxide emissions from peatland soils. *Canadian Journal of Soil Science* 69: 33-38.

Nordstroem, C., Soegaard, H., Christensen, T.R., Friborg, T. & Hansen, B.U. 2001. Seasonal carbon dioxide balance and respiration of a high- arctic fen ecosystem in NE-Greenland. *Theoretical and Applied Climatology* 70: 149-166.

Oechel, W.C., Vourlitis, G.L., Hastings, S.J., Zulueta, R.C., Hinzman, L. & Kane, D. 2000. Acclimation of ecosystem CO2 exchange in the Alaskan Arctic in response to decadal climate warming. *Nature* 406: 978-981.

Öquist, M.G. & Svensson, B.H. 2002. Vascular plants as regulators of methane emissions from a subarctic mire ecosystem. *Journal of Geophysical Research* 107: (D21). 4580, doi:10.1029/2001JD001030.

Shaver, G.R., Billings, W.D., Chapin, F.S., Giblin, A.E., Nadelhoffer, K.J., Oechel, W.C. & Rastetter, E.B. 1992. Global change and the carbon balance of arctic ecosystems. *BioScience* 42: 433-441.

Sitch, S, McGuire, A.D., Kimball, J., Gedney, N., Gamon, J., Emgstrom, R, Wolf, A., Zhuang, Q. & Clein, J. 2007. Assessing the circumpolar carbon balance of arctic tundra with remote sensing and process-based modeling approaches. *Ecological Applications* 17: 213–234.

Sjögersten, S. & Wookey, P.A. 2002. Spatio-temporal variability and environmental controls of methane fluxes at the forest-tundra ecotone in the Fennoscandian mountains. *Global Change Biology* 8: 885-894.

Soegaard, H., Nordstroem, C., Friborg, T., Hansen, B.U., Christensen, T.R. & Bay, C. 2000. Trace gas exchange in a high-arctic valley 3. Integrating and scaling CO2 fluxes from canopy to landscape using flux data, footprint modeling, and remote sensing. *Global Biogeochemical Cycles* 14: 725-744.

Ström, L., Mastepanov, M. & Christensen, T.R. 2005. Species-specific effects of vascular plants on carbon turnover and methane emissions from wetlands. *Biogeochemistry* 75: 65-82.

Tarnocai, C., Kimble, J. & Broll, G. 2003. Determing carbon stocks in Cryosols using the Northern and Mid Latitudes Soil Database. In: *Permafrost.* Edited by Phillips, M., Springman, S.M. & Arenson, L.U. Proceedings of the Eighth International Conference on Permafrost, 21-25, Zurich Switzerland. (Vol. 2, p. 1129-1134). Lisse, The Netherlands: Sets & Zeitlinger B.V.

Tipping, E., Woof, C., Rigg, E, Harrison, A.F., Ineson, P., Taylor, K., Benham, D., Poskitt, J., Rowland, A.P., Bol, R. & Harkness, D.D. 1999. Climatic influences on the leaching of dissolved organic matter from upland UK moorland soils, investigated by a field manipulation experiment. *Environment International* 25: 83-95.

Walter, K.M., Zimov, S.A, Chanton, J.P., Verbyla, D. & Chapin, F.S. 2006. Methane bubbling from Siberian thaw lakes as a positive feedback to climate warming. *Nature* 443, 71–75.

Wookey, P.A. 2002. Tundra. *Encyclopedia of Global Environmental Change*. Vol. 2: *The Earth system – biological and ecological dimensions of global environmental change,* edited by H.A. Mooney and J. Canadell. London: Wiley, pp. 593-602.

Yavitt, J.B., Williams, C.J. & Wieder, R.K. 1997. Production of methane and carbon dioxide in peatland ecosystems across north America: Effects of temperature, aeration, and organic chemistry of peat. *Journal of Geomicrobiology* 14: 299-316.

Interannual Variations in Active Layer Thickness in Svalbard

Hanne H. Christiansen
The University Centre in Svalbard, UNIS, P.O. Box 156, 9171 Longyearbyen, Norway,
Ole Humlum
Institute of Geoscience, University of Oslo, P.O. Box 1041 Blindern, 0316 Oslo, Norway
The University Centre in Svalbard, UNIS, P.O. Box 156, 9171 Longyearbyen, Norway

Abstract

Long-term monitoring of active layer thickness and top permafrost thermal state has been ongoing since the year 2000 in the UNISCALM site on a loess-covered terrace in Adventdalen, central Svalbard. The site has proved to be excellent for studying the effects of meteorological variables such as air temperature and cloud cover on active layer thickness. The active layer thickness varied from 74 to 105 cm in the UNISCALM site since 2000. This fairly-large interannual active layer thickness variation reflects extremely shallow thaw in 2005. The top permafrost is warm, and no two-sided freezing occurs. This makes the site susceptible to the meteorological variations with MAAT variations, with MAAT variations between -1.7ºC and -6.1ºC recorded over the 2000 to 2007 monitoring period.

Keywords: active layer; CALM; interannual variations; monitoring, permafrost temperature; Svalbard.

Introduction

Svalbard is located in a high arctic maritime setting, exposed to significant interannual meteorological variations similar in magnitude to modeled climatic changes during the 21st century. Permafrost is classified as continuous (Humlum et al. 2003), and several characteristic periglacial landforms, such as rock glaciers, ice-wedges, and pingos, all show widespread permafrost existence. The mean annual air temperature (MAAT) at sea level has varied, however, between -1.7ºC and -6.1ºC in the period 2000–2006, measured at the official meteorological station at Longyearbyen airport (www.met.no).

MAAT for the year 2006 was 4.4ºC above the average for the entire period of meteorological measurements in Svalbard, but the warming mainly occurred in winter, with the summer average temperature 6.3ºC (June, July, and August) closer to the average of 4.4ºC (1912–2007 summers), but still warmer than ever recorded before. The 2007 summer temperature was higher still, at 6.4ºC. As ground thaw progression measurements exist since 2000, we can study how much and how quickly the active layer responded to the recent warm years.

Circumpolar Active Layer Monitoring (CALM) network sites exist in Svalbard, mainly along the west coast (Brown et al. 2000). The UNISCALM site, located in the most continental central part of Svalbard, is probed regularly during the thawing season from May to September to follow the thaw progression. Inside the UNISCALM site, active layer and top permafrost temperatures are measured directly in the sediment. This combination of measurements enables a good understanding of how the active layer has responded to recent meteorological variations.

The UNISCALM site

Adventdalen is one of several large valleys that dissect the mountainous landscape in central Svalbard. The UNISCALM site is located at 10 m a.s.l. in the central lower part of Adventdalen at 78º12′N, 15º45′, on a Late Holocene loess-covered terrace. The upper 1.3 m of sediment consists of horizontally layered silt-dominated sediments (Christiansen et al. in prep).

UNISCALM extends over a 100 x 100 m grid, with 10 m grid size spacing. It was established in mid-summer of 2000. It is being measured by physical probing of all 121 grid points from 8 to 15 times during the thawing season from May–September each year to follow the seasonal thaw progression and record the active layer thickness (ALT). As the grid was established in July 2000, only four measurements were carried out that year. The location of the grid is marked by small wooden pegs extending 5 cm above ground. The repetitive seasonal measurements are taking place in the same hole each summer to follow thaw progression in each grid point. Each year the location of the probe hole is moved slightly from the year before, to avoid measuring into earlier years' sites. Three persons have done the measurements in the eight-year period, usually by only one person during each season.

To investigate spatial variability within the UNISCALM site over the eight-year period, a normalized variability index (Iv) was calculated for each grid node (Hinkel & Nelson 2003) for the ALT measurements in late summer. If Iv varies only slightly between years, the interannual node variability (INV) is small (Hinkel & Nelsen 2003), indicating a high degree of consistency in thaw depths over the eight-year period. If Iv varies much between years, local factors may have a large influence on ALT.

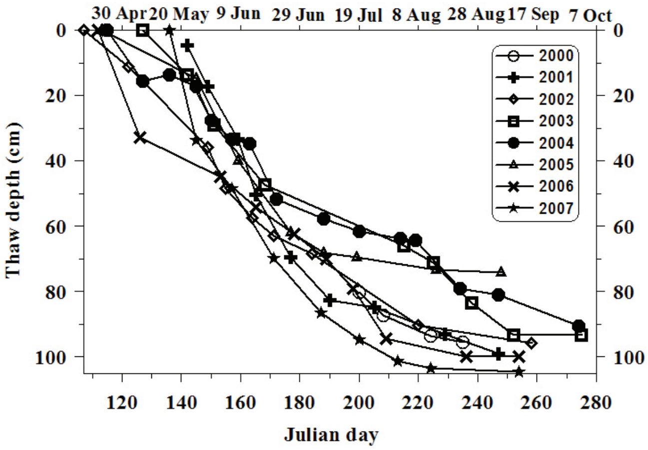

Figure 1. Thaw progression in the UNISCALM site calculated as the average from all 121 grid points at each date.

Active layer temperatures have been measured at the centre on the UNISCALM grid since it was established in summer 2000. Data are obtained by miniature dataloggers of the Tinytag type, with external sensors inserted horizontally directly into the ground at 0, 10, 20, 50, and 110 cm depths in the active layer and one was placed vertically into the top permafrost by drilling. Air temperature at 20 cm above ground is also measured by a Tinytag datalogger with an external sensor, also located at the site of the ground thermal profile, but built into a well-ventilated cairn of rocks. The resolution of the Tinytags is ±0.1ºC and the recording interval is one hour. Snow depths are measured manually on a regular basis during winters at the site of the active layer ground temperature profile.

Meteorology

The nearest official meteorological station to the UNISCALM site is the Longyearbyen airport, 9 km to the west, at the mouth of Adventdalen. It is situated at 28 m a.s.l. but closer to the sea than UNISCALM. This station has operated since 1975, but older data exist from nearby stations, and a homogenized data series exists for the entire period since the first meteorological records in 1912 (Førland et al. 1997).

Mean annual air temperatures (MAAT) has varied from -12ºC to -1.7ºC in the 1912–2006 recording period (www.met.no), partly because of warming since the Little Ice Age, but also because of large interannual temperature variations, which are natural in the maritime setting of Svalbard. The average MAAT for the entire period of measurements is -6.1ºC (www.met.no). The interannual variations are largest during winter, while summer temperatures vary significantly less. This causes a somewhat reduced meteorological influence on ALT, as summer temperatures typically exert large meteorological control.

The annual precipitation varies from 100–200 mm (www.met.no). It is evenly distributed throughout the year, but shows large interannual variation. During the winter, most precipitation falls as snow. Wind activity causes exposed areas at the UNISCALM site in the flat valley bottom to have only a shallow snow cover. This allows good energy exchange between atmosphere and ground.

Table 1. UNISCALM data and statistics based on data from the Longyearbyen airport meteorological station.

	2000	2001	2002	2003	2004	2005	2006	2007
Active layer (cm)	95	99.	96	93	91	74	100	105
Max (cm)	110	119	108	108	107	92	116	121
Min (cm)	81	83	83	70	70	51	85	90
TDD thaw start	12 Jun	8 June	25 May	1 June	21 May	28 May	8 April	9 May
TDD thaw end	22 Aug	4 Sep	15 Sep	9 Sep	30 Sep	5 Sep	11 Sep	11 Sep
TDD at thaw end	391	544	609	546	567	600	708	620
TDD total	560	643	680	576	581	637	749	687
TDD % at thaw end	70 %	85 %	90 %	95 %	98 %	94 %	95 %	90 %
Rain (mm)	43.5	40.6	40.6	26.4	69.9	40.4	63.1	31.2
Cloud cover (%)	68.4	73.6	75.4	77.2	76.0	77.9	74.3	70.1
Wind speed (m/s)	4.1	4.3	3.9	3.7	4.1	4.8	4.5	4.3

Results

Thaw progression

Thawing degree-days (TDD) start when continuous positive air temperatures start in the spring. TDD thaw end is the date of the UNISCALM active layer measurement. TDD to thaw end is the amount of TDD during the recorded active layer thawing period, calculated from average daily temperature values. TDD total is for the entire year from the beginning of continuous daily positive air temperatures to the last day of the year. TDD at thaw end is the % TDD recorded at the time when the active layer measurement was done. Rain is the amount of precipitation falling during the month of June, July and August. Cloud cover (% of the sky with cloud cover) and wind speed are the means for the TDD thawing period. In 2007 TDD total and TDD at thaw end could not be calculated as the year was not over at the time of paper submission.

The average ALT recorded in the UNISCALM site was 94 cm for the 2000–2007 period with large interannual variations; the minimum was 74 cm in 2005, while 105 cm was the maximum in 2007. Thawing started as early as the end of April (2002 and 2006), and as late as end of May 2001 and 2007 (Fig. 1 and Table 1). The largest interannual variation in thaw progression occurred in the uppermost 40 cm (Fig. 1). These large differences are mainly controlled by the timing of snowmelt. No thawing is recorded until the surface is snow-free. In a year with very early thaw, such as in 2006 when continuous positive air temperatures were recorded from April 8 with a few subsequent short cold periods, thawing was very early. In contrast, in 2005 thawing was very slow for the first month because of a more protracted snowmelt period. The 50 cm thaw depth was reached in the same period June 4–19 in all years. Below this depth, some interannual variation exists, but with maximum thaw depths reaching 90–100 cm in most years. In 2005 the active layer, however, only reached down to 74 cm as late as September 5. In 2000, the active layer was already 95 cm by August 22. There is generally a correlation between the ALT and the TDD at the time of the active layer recording, but 2005 was clearly anomalous (Fig. 2).

Summer air temperatures (June, July, and August) exhibited less variability than other months, in the entire study period. The coldest summer was 2000, and the warmest summer was 2007. The active layer was 4.7 cm thicker in 2007 than in 2006, although the summer air temperature was only 0.1ºC higher in 2007, and TDD at the end of thaw (Table 1) was higher in 2006 than in 2007, because thawing had already started by April of 2006. The low correlation between ALT and summer air temperature (Fig. 2) largely reflects the influence of the anomalous years in 2000 and 2005. This means that something other than air temperature can have significant influence on ALT in some years. The difference cannot be explained by bad timing of the active layer measurements, as 94% of the annual TTD (Table 1) had occurred at the time of active layer recording in 2005. Only 70% of the annual TDD had occurred in 2000 at the time of active layer recording, so most likely the active layer was somewhat deeper this year, which most likely would locate it closer to most of the other years. In all other years, the ALT was recorded when around 85–98% of the TDD had occurred, indicating that normally the active layer develops in early to mid September.

Precipitation in the form of rain could affect ground thawing. Although there is rather large interannual variation in the amount of summer rain in the study period (Table 1), there is no correlation between the amounts of summer rain and the active layer depths (Fig. 2). Actually, the 2007 summer with only 31.3 mm rain had the deepest thaw of 104.6 cm.

The mean cloud cover in the entire thaw season varied on average from 68–78% and had the best correlation with ALT. ALT decreased when the cloud cover increased (Fig. 2). This indicates that increasing amounts of direct radiation increase thawing in this valley-bottom site. Increasing mean wind speeds over the summer generally increase the ALT, but again this correlation becomes low when including the year 2005.

Spatial variation

The UNISCALM site has a characteristic spatial thaw pattern (Fig. 3) with the deepest active layer in the southern

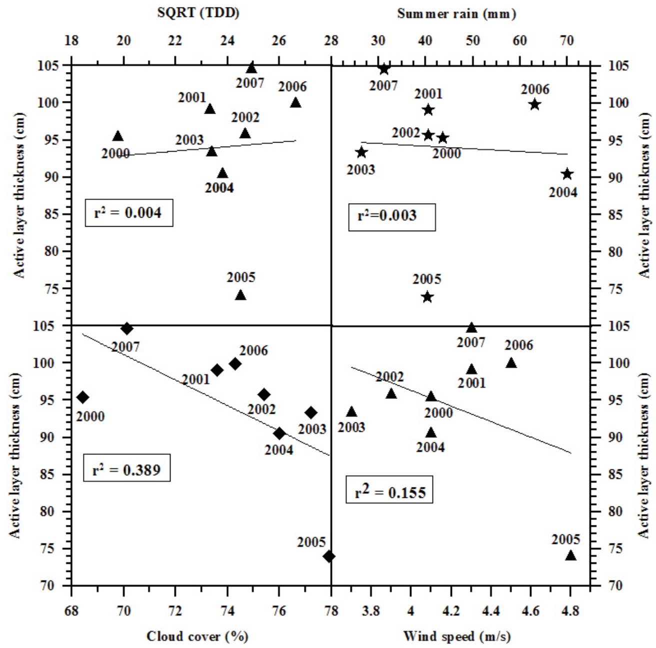

Figure 2. UNISCALM active layer thickness correlated to meteorological parameters in the 2000–2007 period. Correlations include data from all years 2000–2007.

and northeastern part, while the northwestern corner consistently had the thinnest active layer. The maximum grid node point ALT was as deep as 92–121 cm (Table 1)—all in the southern part of the grid during the 2000–2007 period (Fig. 3). The spatial thaw pattern is reproduced in all years except in 2005, where thawing in the southern part was particularly shallow: only 60–70 cm in several areas consisting of more points. The entire southern part of the grid had shallower thaw in 2005 than in all other years. This year, thawing was thinnest in the southern part of the grid, while it was deeper and not far from the depths recorded in the other years in the northern part of the grid.

The average interannual grid node variability (INV) is 18.5% for the entire site, with a maximum of 46% and a minimum of 3.3% for the individual grid nodes. The areas with high INV (Fig. 4) are exactly the areas with relatively shallow thaw in summer 2005. Otherwise, the INV values are fairly low, showing little interannual thaw variability and a generally consistent thaw pattern.

Temperature in the active layer

Active layer and top permafrost thermal monitoring was continuous, except for two summer breaks in the ground surface temperature in the summers of 2001 and 2004. Data from a borehole 100 m away, also on the loess-covered terrace, were used to substitute the missing values in 2004, while data from another flat ground surface site 2.5 km further up the Adventdalen were used in the 2001 period. The air temperature recording was first established in October 2000, so data from the Adventdalen site was also used in the first months.

The annual ground temperature distribution is presented from September 1–August 31 in the following year for all

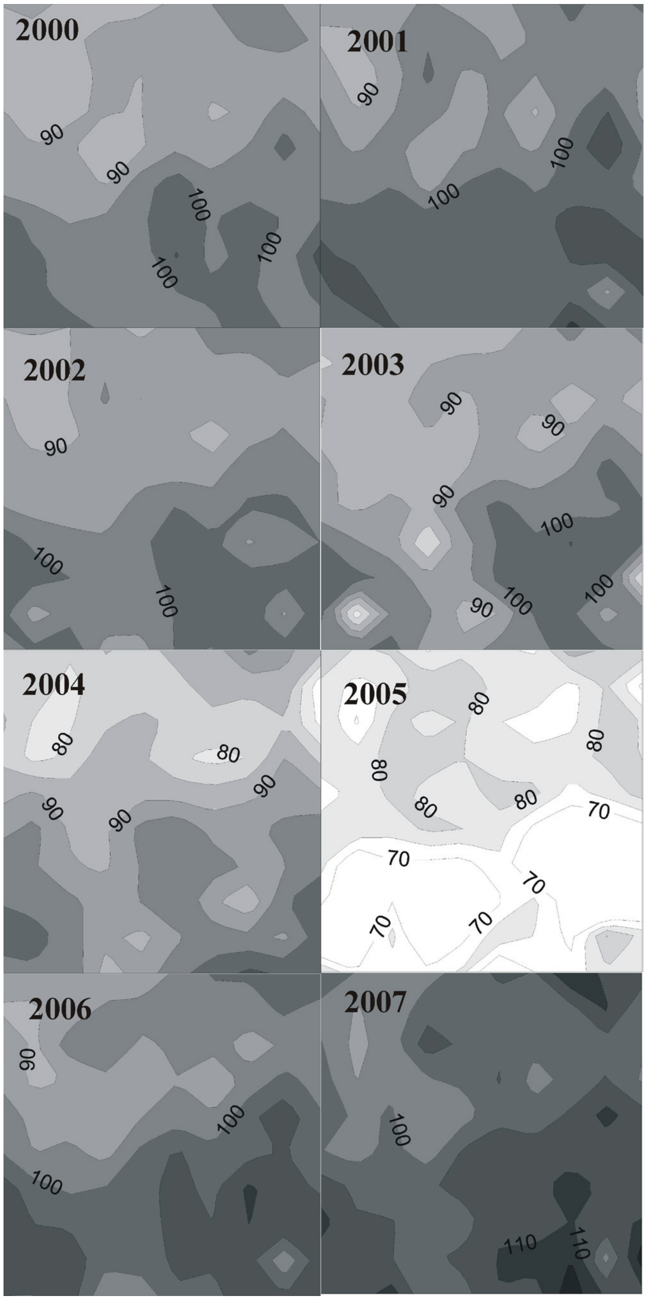

Figure 3. Spatial distribution of the active layer thickness in the UNISCALM site, mapped using the kriging interpolation method (Golden Software, 2002), and a grid spacing of 11 m, based on the 10 m grid node measurements. N is towards the top.

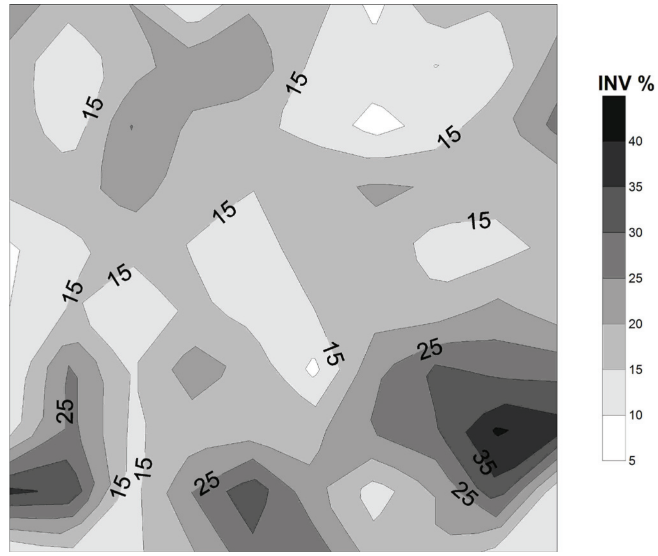

Figure 4. Interannual grid node variability (INV) for the period from 2000–2007. The mean for the entire grid is 18.5%. Based on the kriging interpolation method (Golden Software, 2002), with a grid spacing of 11 m of the 10 m grid node measurements.

years (Fig. 5). There is large interannual variation especially in the winter ground temperatures, while the summer temperatures have much less variation between the years, as for the air temperature conditions. The thermal conditions in the summer of 2005 are not significantly different from the other summers (Fig. 4). The phase change during freezing in autumn occurs mainly from the top down, so that the zero curtain is much shorter in the top than at the bottom of the active layer. The difference is up to 2 months before the bottom of the active layer is completely frozen and further cooling can occur. It is mainly the top 70–50 cm of the active layer that experiences significant cooling with temperatures below -10ºC, whereas the lower part of the active layer and top permafrost, especially in the last two years, have not reached temperatures below -10ºC. Also, in the last 3 winters, relatively longer periods of warming of the ground have occurred with ground temperatures as high as -4ºC in almost the entire active layer (Fig. 5).

Figure 3. Spatial distribution of the active layer thickness in the UNISCALM site, mapped using the kriging interpolation method (Golden Software, 2002), and a grid spacing of 11 m, based on the 10 m grid node measurements. N is towards the top.

MAAT varied from -6.2°C to -3.2°C in the study period, while MAGST varied from -5.7°C to -2.2°C and MAGT at 110 cm, in the top permafrost, varied from -5.8°C to -3.6°C (Fig. 6).

Thus, the largest annual variation was at the ground surface, and it occurred in just three consecutive years. The highest mean annual ground temperature was found at 10 cm depth in three of the seven years; thus the theoretical ground temperature profile (Smith & Riseborough 2002) did not occur in all years. There is very large interannual variation in the mean annual ground temperature conditions.

The almost vegetation-free UNISCALM site at the exposed valley-bottom terrace has a generally thin snow cover from late September or October to April or May, with a maximum of 20–30 cm snow depth. Despite the shallow snow, annual surface offsets (Smith & Riseborough 2002) from 2.0–0.4ºC occurred. The n-factor (Carlson 1952) varied from 0.57–0.93 despite the shallow snow cover. The annual thermal offsets (Smith & Riseborough 2002) varied from 2.0–0.1 ºC.

Annual ALT was calculated from the interpolated ground thermal data by locating the lowest position of the 0ºC isotherm in Figure 5. This shows active layer values from 98–105 cm, which is comparable to the UNISCALM-

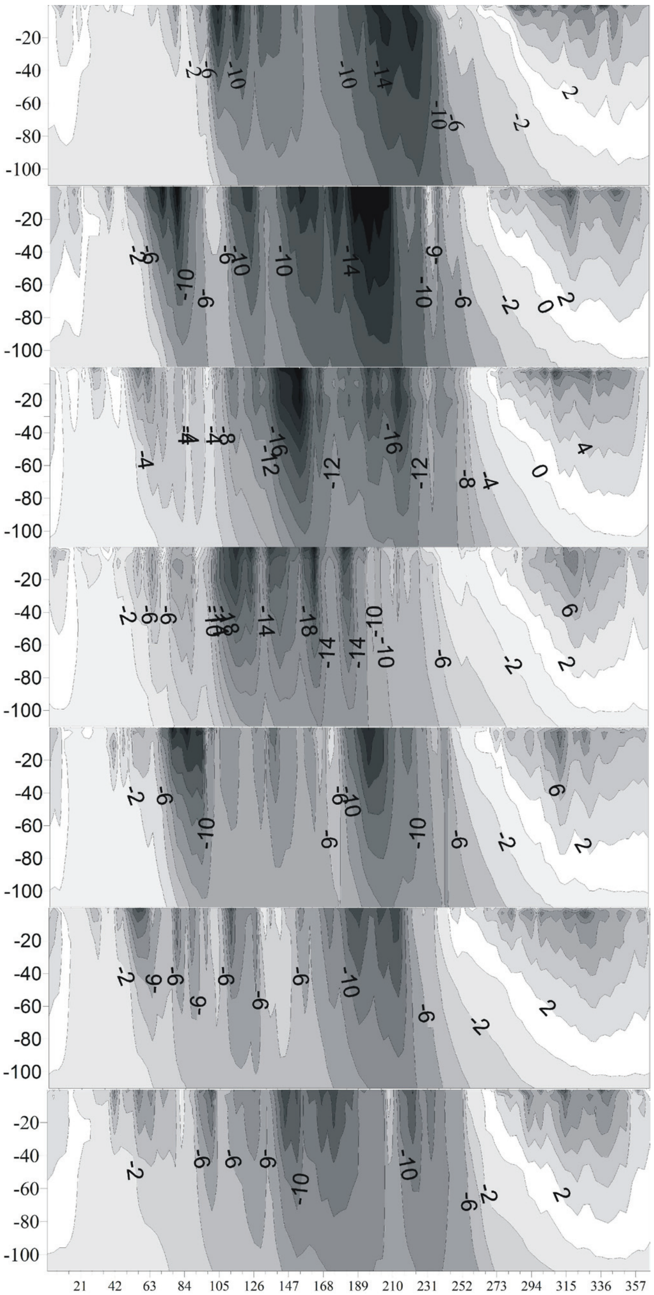

Figure 5. Active layer and top permafrost temperatures in the UNISCALM site measured by miniature loggers with temperature sensors at 0, 10, 20, 50, and 110 cm depths. The annual ground temperature distribution is presented from September 1–August 31 in the following year, and the units on the x-axis are therefore days after September 1. The upper plot is 2000–2001, while the lowermost is 2006–2007.

measured average values, but with less interannual variation. This is especially true in 2005 when the calculated active layer was 102 cm, and thus not as shallow as the clear minimum in the UNISCALM data. The timing of the calculated active layer is much earlier than the measured values in UNISCALM—up to 2 months, but typically one to four weeks.

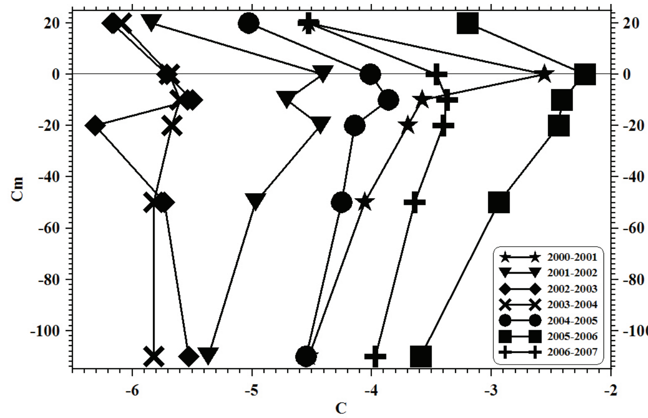

Figure 6. Annual mean temperature distribution from 20 cm above ground down through the active layer and into the top permafrost in the UNISCALM site. Data is from Tinytag miniature dataloggers.

Discussion and Conclusions

In the fine-grained UNISCALM loess site in the Adventdalen valley bottom setting, the active layer varied from 0.74–1.04 m in the 2000–2007 period. Fourteen km further into Adventdalen on the exposed Janssonhaugen sandstone bedrock hill, the active layer varied from 1.5–1.8 m in the 2000–2006 period (Harris et al. submitted).

Sediments are often assumed to experience less interannual active layer variation due to the effect of ice-rich conditions in the transient layer between the active layer and permafrost top (Shur et al. 2005). The active layer monitoring data from bedrock and sediment in Adventdalen, however, show variation of the same size. Therefore the transient layer is presumably not ice-rich in the UNISCALM site, enabling large interannual fluctuations in ALT.

The recorded 30 cm interannual ALT variation in the UNISCALM seems to be mainly controlled by meteorological conditions. However, there is not only a simple correlation between TDD and ALT, but most likely also the cloud cover influences ALT, as this parameter has the highest correlation with ALT for the entire 2000–2007 study period (Fig 3). Thus direct solar radiation seems to affect ALT at this site. This seems most likely due to the relatively low water vapor and dust content in the High Arctic atmosphere in combination with a dark-colored sediment surface with very little vegetation, which will have a low albedo. This combination promotes ground heating during direct radiation in summer. Also the water content in the site is fairly low during most of the summer, as only a little summer rain falls, as stressed by the missing correlation between summer rain and ALT. Finally the UNISCALM site is dry due to the local topography, without drainage from surrounding areas, which further supports it being most likely relatively ice-poor in the top permafrost. Water contents of only 10–18% of the dry soil weights were measured in summer 200 0, with the largest values down through the active layer (Oht 2002).

It is mainly the relatively shallow thaw depths from the end of the 2005 summer that cause large INV in the southern end of the UNISCALM site. We do not think that these values represent bad probing, as the thaw progression curve is consistent through the summer with no significant jumps. Comparing the calculated active layer depth of 102 cm from the temperature profile in the middle of the UNISCALM site to the entire UNISCALM average ALT of 74 cm, and studying the typical annual distribution of ALT in the entire UNISCALM site in 2005, show that the southern part experienced significantly reduced thawing this summer.

In the UNISCALM site, the ALT is largely controlled by the air temperature and radiation, with the warmest conditions occurring in the last two warm years. ALT increased 21 cm from 2005–2007 according to the average UNISCALM data (Fig. 4), but only 3 cm according to the ground thermal data (Fig. 5). This large difference between the two methods must lead to precautions when interpreting the direct effect of climatic variations on the ALT.

The significant surface offsets existing every year of the study period show that the winter influence of even a shallow snow cover of 20–30 cm significantly reduces the ground cooling. Also, there is a clear thermal offset causing the top permafrost in the UNISCALM site to be a relatively warm, 0 to -2ºC, during summer with no significant two-sided freezing in autumn. These conditions and the generally low assumed ice content in the top permafrost make the UNISCALM site very susceptible to meteorological variations, as it has experienced in the last 8-year period. This first overall data analysis from the UNISCALM site shows that this site is a good monitoring site for recording the response of climatic variations to the state of the top permafrost and active layer, but also that several factors affect the atmosphere and ground interaction in the maritime Svalbard setting, such as the Adventdalen site.

The UNISCALM site experienced much larger interannual variations than what is recorded in another flat High Arctic sediment CALM site, the ZEROCALM-1 site in northeast Greenland (Christiansen 2004). This is most likely due to the much-more maritime setting of Svalbard compared to the Zackenberg area in northeast Greenland.

Acknowledgments

Several persons have been our field assistants during the UNISCALM measurements. We extend our thanks to all of them for patiently writing down numbers. A special thanks to Sigurd D. Nerhus, who conducted the UNISCALM measurements in 2006 and 2007. The University Centre in Svalbard, UNIS, is thanked for providing funding for the equipment used to operate the UNISCALM site. The measurements from 2007 are part of the International Polar Year project "Permafrost Observatory Project: A Contribution to the Thermal State of Permafrost in Norway and Svalbard," supported by the Research Council of Norway, grant no. 176033/S30. Thanks to the two anonymous reviewers and the review editor for constructive comments. Thanks to our colleague Doug Benn for improving the English of the paper.

References

Brown, J. Hinkel, K.M. & Nelson, F.E. 2000. The Circumpolar Active Layer Monitoring (CALM) Program: Research Designs and Initial Results. *Polar Geography* 24: 165-258.

Carlson, H. 1952. *Calculation of Depth of Thaw in Frozen Ground.* Frost Actions in Soils: A Symposium. Washington DC: Highway Research Board Special Report 2, National Research Council, 192-223.

Christiansen, H.H. 2004. Meteorological Control on Interannual Spatial and Temporal Variations in Snow Cover and Ground Thawing in Two Northeast Greenlandic Circumpolar-Active-Layer-Monitoring (CALM) Sites. *Permafrost and Periglacial Processes* 15: 155-169.

Christiansen, H.H., Hormes, A. & Snowball. I. (in prep.) High resolution Late Holocene loess record with syngenetic ice-wedges in Adventdalen, Svalbard. *The Holocene.*

Førland, E.J., Hanssen-Bauer, I. & Nordli, P.Ø. 1997. *Climate statistics and long-term series of temperature and precipitation at Svalbard and Jan Mayen.* DNMI Klima rapport 21/97, 72 pp.

Harris, C., Arenson, L.U. Christiansen, H.H., Etzelmüller, B., Frauenfelder, R., Gruber, S., Haeberli, W., Hauck, C., Hölzle, M., Humlum, O., Isaksen, K., Kääb A., Lehning, M. Lütschg, M.A., Matsuoka, N., Murton, J., Nötzli, J., Phillips, M., Ross, N., Seppälä, M., Springman, S. & Vonder Mühll, D (submitted). Permafrost and climate in Europe: Geomorphological impacts, hazard assessment and geotechnical response. *Earth Science Reviews*.

Hinkel, K.M. & Nelson, F.E. 2003. Spatial and temporal patterns of active layer thickness at Circumpolar Active Layer Monitoring (CALM) sites in northern Alaska, 1995–2000. *Journal of Geophysical Research* 108: D2:ALT 9: 1-13.

Humlum, O., Instanes, A. & Sollid, J.L. 2003. Permafrost in Svalbard: A review of research history, climatic background and engineering challenges. *Polar Research* 22: 191-215.

Oht, M. 2002. *Impact of meteorological factors and local conditions on active layer depth and temperature, Adventdalen Area in central Spitsbergen, Svalbard.* Unpublished M.Sc. thesis, 77 pp.

Shur, Y., Hinkel, K.M. & Nelson, F.E. 2005. The transient layer: Implications for geocryology and climate-change science. *Permafrost and Periglacial Processes* 16: 5-17.

Smith M.W. & Riseborough, D.W. 2002. Climate and the limits of permafrost: a zonal analysis. *Permafrost and Periglacial Processes* 13: 1-15.

Experimental Study of the Self-Preservation Effect of Gas Hydrates in Frozen Sediments

E.M. Chuvilin
Department of Geocryology, Geological Faculty, Moscow State University, Russia
O.M. Guryeva
Department of Geocryology, Geological Faculty, Moscow State University, Russia

Abstract

Gases released from shallow frozen sediments may include methane from the dissociation of relict gas hydrate maintained by self-preservation. A series of experiments to substantiate this possibility were conducted. This research involved artificial formation of methane hydrate in frozen sediments, including samples recovered from gas shows in permafrost horizons, and studying the effect of self-preservation of gas hydrates in frozen soil samples at decreased pressure. The experiments show that self-preservation of gas hydrates in frozen sediments is enhanced by low formation temperatures, high ice content, and low sediment gas permeability.

Keywords: dissociation; gas hydrate; self-preservation.

Introduction

The presence of gas hydrate in permafrost has been confirmed by hydrate found in core samples and by indirect evidence in various regions of the world (e.g., Canadian Arctic, Alaska, and northern Siberia). Hydrate-containing samples have been recovered from permafrost and subpermafrost layers in the Mackenzie Delta (Dallimore & Collett 1995, Dallimore et al. 1999). In addition, there is evidence that self-preservation of relict methane hydrate, made possible by the continual frozen nature of the sediment, occurred in the upper permafrost layers (Dallimore et al. 1996).

Numerous hydrate shows were also indirectly found in Russia above a depth of 200 m in northwest Siberia and other regions containing permafrost (Are 1998, Chuvilin et al. 1998, Skorobogatov et al. 1998, Yakushev & Chuvilin 2000). These "relict" gas hydrates may have formed during glacial periods. Subsequently, glacial retreat induced metastable preservation of the hydrate by self-preservation (Ershov et al. 1991, Stern et al. 2001, Istomin et al. 2006).

Gas hydrate self-preservation phenomenon can be defined as a very slow decomposition of gas hydrates when the external pressure drops below a three-phase equilibrium pressure of the gas-ice-hydrate system at sub-zero (below -3 to -2°C) temperature as a result of thin ice film emergence on the gas hydrate surface (Istomin et al. 2006).

This effect was initially discovered and described in detail between 1986 and 1992, by researches from Canada (Ottawa National R&D Center) and Russia (VNIIGAZ and Moscow State University) (Davidson et al. 1986, Handa 1988, Ershov et al. 1989, 1991). The term "gas hydrate self-preservation" was introduced by Russian researches after several laboratory experiments revealed that gas hydrate decomposition came to a virtual halt when hydrate particles became covered by a thin ice shell at the initial decomposition stage.

Japanese scientists from Hokkaido Institute (HNIRI) studied methane hydrate decomposition kinetics and the self-preservation effect using X-ray diffraction. They showed that at temperatures above -84°C there are two stages in methane hydrate dissociation. Initially, hydrate dissociates rapidly (during first 10 minutes) then the rate of hydrate decomposition abruptly decreases due to the formation of an ice film on the surface of hydrate. The slow rate of decomposition is controlled by the conditions of methane diffusion through the pores or boundary of ice crystals (Takeya et al. 2002).

Research on the kinetics of gas hydrate decomposition at temperatures below 0°C revealed irregularly low rates of methane hydrate dissociation at temperatures between -31°C and -2°C, which was termed "anomalous preservation" of gas hydrates (Stern et al. 2001).

German scientists studied anomalous preservation of CH_4 and CO_2 hydrates and structural transformation of ice at low temperatures using neutronography and scanning electron microscopy (Kuhs et al. 2004). They determined that the lower temperature boundary of methane hydrate self-preservation occurs at -33°C; at temperatures below this threshold the ice structure does not inhibit gas diffusion, while gas diffusion becomes hindered as the ice structure changes at -33°C.

Using field data from gas shows in shallow permafrost and laboratory research of gas hydrate behavior at negative temperatures, we can identify the so-called metastable zone of gas hydrates. This zone is located above the stability zone of gas hydrates where the temperature conditions are favorable for the self-preservation effect (Fig. 1).

These self-preserved shallow-depth gas hydrates are presently under non-equilibrium conditions and pose a serious geological hazard to drilling exploration in these regions. The dissociation of shallow metastable methane hydrate may also contribute to global warming by adding significant amounts of methane, a greenhouse gas, to the atmosphere.

Since relict gas hydrates are poorly understood, experimental research on the self-preservation effect of gas hydrates in frozen sediments under non-equilibrium conditions is of significant importance.

Methods

Experiments on the self-preservation of gas hydrate in frozen sediments under non-equilibrium conditions were conducted on natural samples from Vorkuta, Russia, located 160 km beyond the Arctic Circle. Cores were collected from permafrost horizons exhibiting gas release at the Yamburg gas field (dust sand, depth: 63 m) and the Bovanenkovo gas field (light loam, depth: 65 m) (Table 1). The initial sediment water contents ranged from 10 to 20%.

The experimental technique is based on physical modeling of water phase transitions and frozen methane hydrate-saturated samples in pressure chambers (Chuvilin & Kozlova 2005a). Methane (99.98% pure) was used to form hydrate at temperatures between ~0.5 and 2.0°C in two partially water saturated 9-cm long sediment samples with 4.6 cm and 6.8 cm diameters. The pressure chambers were filled to 6-7 MPa. After hydrate formation stopped, the pressure chamber containing the test sample was cooled to -8°C freezing any remaining free water and pushing the hydrate deeper into

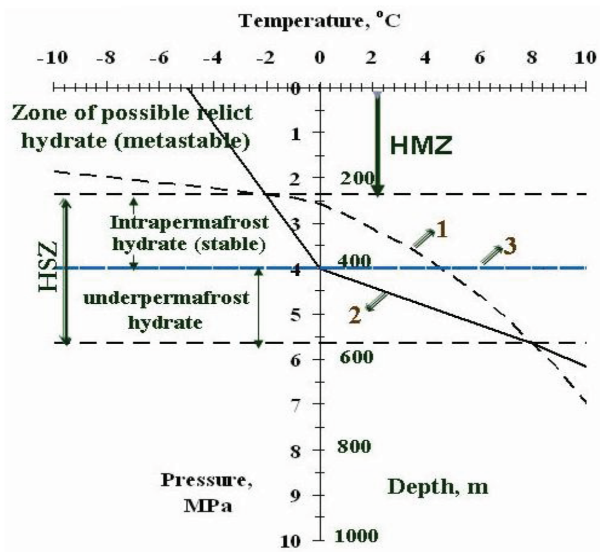

Figure 1. Conditions of gas hydrate occurrence in permafrost environments. **1** - Equilibrium curve of methane-hydrate stability in water-gas medium; **2** – Ground temperature profile; **3** - Permafrost boundary; **HSZ** - Hydrate stability zone; **HMZ** – Hydrate metastability zone.

the stability field. The experimental technique is described in detail in Chuvilin et al. (2003).

The hydrate content and hydrate coefficient (share of water which has transformed in hydrate) were determined from changes in thermobaric conditions incorporating compressibility according to Mendeleyev-Clapeyron equation:

$$m_G = \frac{P_i \cdot V \cdot M}{R \cdot T_i \cdot z},$$

where P_i is pressure at a point in time i (MPa); V is free volume of the pressure chamber (cm^3); M is molar mass of gas (g/mol); R is absolute gas constant (N·m/K ·mol); T_i is temperature at a point in time i (K); z is gas compressibility.

After chamber pressure was vented to atmosphere, the chamber was opened in a cold room at -8°C. Detailed petrophysical analyses were performed on the frozen hydrate within 30 minutes of it being taken out of the chamber. Petrophysical analyses included macro- and micromorphological observations, calculation of water content, density, gas and hydrate content, porosity, hydrate coefficient, degrees of hydrate, and ice pore saturation. Gas content was measured by thawing in a solution of NaCl. Quantification of methane hydrate dissociation assumed a hydrate number of 5.9.

Remaining frozen hydrate-bearing sediment samples were stored on weighing devices for extended periods of time at freezing temperatures. Sublimation of the ice was reduced by a thin ice coating on the samples. Samples were monitored for over a month, during which time volumetric hydrate content Hv (Hv =VH·100% /Vsamp where VH is volume of hydrate, Vsamp is volume of the sample), hydrate saturation Sh (Sh = Hv /ϕ, % where Hv is volumetric hydrate content, and ϕ is sample porosity); ice saturation Si (Si = Iv /ϕ, % where Iv is volumetric ice content) and hydrate coefficient K_h (share of pore water which has transformed in hydrate) were calculated.

Experimental Results

In general, the test samples were characterized by homogeneous sediment structure and uniform distribution of hydrate and ice in the pore space resulting from an initial uniform water distribution (Chuvilin & Kozlova 2005b). The samples were also characterized by massive cryohydrates.

Table 1. Characteristics of soils.

Type of sediment	Particle size distribution, %			Particle density, ρ_s, g/cm^3	Plastic limit, W_p, %	Liquid limit, W_l, %	Salinity, %
	1-0.05 mm	0.05-0.001mm	<0.001 mm				
Silty sand	84	14	2	2.65	-	-	0.089
Sandy loam	41.8	53.7	4.5	2.68	11	15	0.075
Light loam	63.5	25.5	11.0	2.7	20	33	0.693

Table 2. Properties of frozen hydrate-saturated sediment samples.

Parameters	Silty sand		Silty sand		Sandy loam		Light loam	
	$p>p_{eq}$	$p<p_{eq}$	$p>p_{eq}$	$p<p_{eq}$	$p>p_{eq}$	$p<p_{eq}$	$p>p_{eq}$	$p<p_{eq}$
Gravimetric water content (W_g, %)	14		18		18		20	
density (ρ, g/cm³)	1.76		1.63		1.68		1.82	
Porosity (ϕ)	0.41		0.44		0.47		0.43	
Hydrate coefficient (K_h)	-	0.68	0.74	0.66	0.30	0.23	0.12	0.11
Hydrate pore saturation (S_h, %)	-	45	50	42	23	15	11	10
Ice pore saturation (S_i, %)	-	15	8	15	20	28	67	68
Volumetric hydrate-content (H_v, %)	-	18	22	20	11	7	5	4

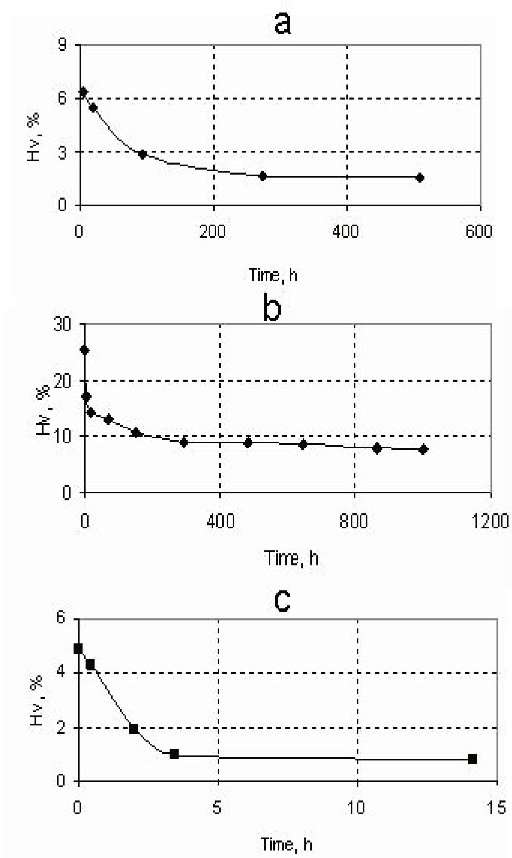

Figure 2. Methane hydrate dissociation kinetics in hydrate saturated frozen sediment after release of pressure to 0.1 MPa (atmospheric pressure).
a - sandy loam (W_g= 18%, t = -7.0°C);
b - silty sand (W_g= 18%, t = -6.5°C);
c - light loam (W_g= 20%,t = -5.0°C).

The sample properties are presented in Table 2. The porosity of the artificially hydrate-saturated sediment samples ranged from 0.41 to 0.47. The proportion of water incorporated into hydrate (K_h) in the silty sand sample (W_g=18%) (under equilibrium condition prior to pressure release) was 0.74, with a hydrate pore saturation (S_h) of 50%. 30-minutes after pressure release K_h and S_h decreased to 0.66 and 42% respectively. The light loam sample (W_g = 20%) had a K_h of 0.12 and S_h of 11% under equilibrium conditions. These values decreased to 0.11 and 10% respectively after pressure release. Thus, hydrate distribution in the finer-grained sediments was more dispersed and the pore saturation was lower. After pressure release, there is an intense decomposition of pore-space hydrate, followed by a more gradual decomposition (Fig. 2).

Our experimental data show that self-preservation reduces decomposition of pore-space hydrate in all samples. The self-preservation effect forms a thin ice film around particles of dissociating gas hydrate at temperatures below 0°C. As a result of this effect, hydrate can remain in a metastable condition for a long time.

As hydrate saturation decreases, ice content (S_i) increases (Fig. 3). At the beginning of the experiment (before gas release) hydrate saturation was 50%, and ice saturation was 8% in the silty sand sample. After 845 hours, gas hydrate saturation decreased to 13%, and ice saturation increased to 43%.

Self-preservation of gas hydrate in frozen sediment depends on many factors such as thermobaric conditions, hydrate and ice saturation, gas permeability, structure of organic-mineral skeleton of sediment, pore water salinity, and structure of hydrate, including micromorphology.

Ice formed during freezing of residual pore water which has not transformed into hydrate plays a special role in the self-preservation of gas hydrates. Occurrence of this ice promotes gas hydrate stability in a porous medium. As a rule, samples of frozen hydrate with greater ice content after pressure release are more prone to self-preservation. The presence of clay particles increases gas hydrate dispersion and reduces, but does not eliminate, the self-preservation

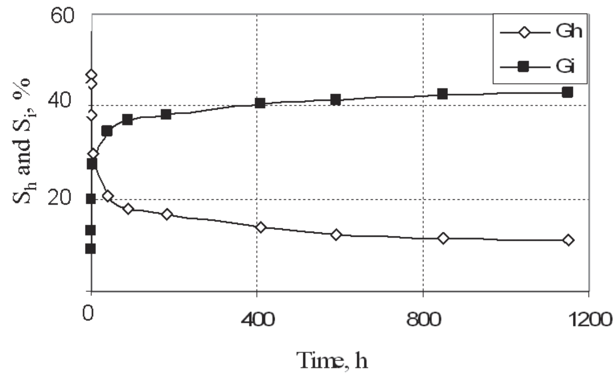

Figure 3. Change in methane hydrate saturation (S_h) and ice saturation (S_i) in hydrate-saturated silty sand (W_g=18%, t = -6.5 °C) after pressure release to 0.1 MPa.

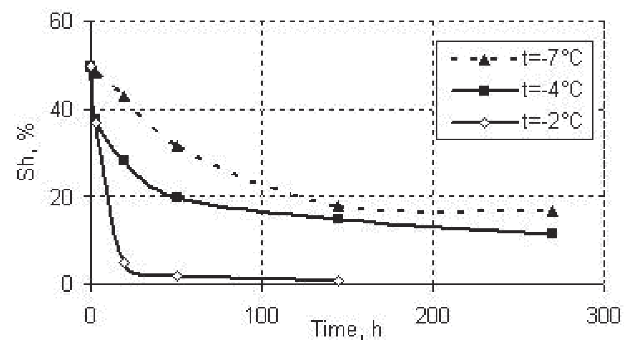

Figure 4. Methane hydrate dissociation kinetics in artificially hydrate-saturated frozen silty sand (W_g=14%) after pressure release to 0.1 MPa.

effect even in loamy deposits. Presence of salt in hydrate containing sediments also reduces the self-preservation effect. Thus, in light loam the intensive reduction of hydrate content after pressure release can be connected with the higher salinity (to compare to other samples) (Table 1, Fig. 2).

Results of experiments on sand and loam samples show that the intensity of pore gas hydrate dissociation sharply decreases with lower temperatures. In the silty sand sample (W_g=14%, initially about 45% hydrate saturation at all temperatures) hydrate saturation after pressure release decreased to 5% at -2°C in 20 hours, 28% at -4°C, and 43% at -7°C (Fig. 4). After 150 hours at -2°C, little hydrate remained, however, at -4°C and -7°C decomposition was sharply decreased.

Pore-hydrate dissociation practically ceases at lower temperatures. Because experimental temperatures compare favorably to natural temperatures (-5°C to -7°C) for permafrost sediments at the Yamburg and Bovanenkovo gas fields, it is possible for *in situ* gas hydrate to remain in a metastable condition for long periods of time.

In addition, the weight of overburden and high ice content of sediments provide additional stability to the metastable hydrate.

Conclusions

Experiments were conducted on kinetics of gas hydrate dissociation. Our experiments conducted on core samples confirm the self-preservation of natural pore-space gas hydrates. The conditions promoting self-preservation of natural gas hydrates are: low temperature, high ice content, low gas permeability, and overburden pressure. However, increased sediment temperature and pore water salinity, and gas hydrate dispersion in fine-grained sediment reduce the self-preservation effect.

Acknowledgments

This research was funded by the Russian Foundation Basic Research Program No 05-05-39019 and 06-05-91573. We thank the anonymous referees for various suggestions to improve the manuscript.

References

Are, F.E. 1998. Problem of deep-earth gases emission to the atmosphere. *Cryosphere of the Earth* II:42-50 (in Russian).

Chuvilin, E.M., Yakushev, V.S. & Perlova, E.V. 1998. Gas and gas hydrates in the permafrost of Bovanenkovo gas field, Yamal Peninsula, West Siberia. *Polarforschung 68* (erschienen 2000): 215-219.

Chuvilin, E.M., Kozlova, E.V., Makhonina, N.A. & Yakushev V.S. 2003. Experimental investigation of gas hydrate and ice formation in methane-saturated sediments. *Proceedings of the 8th International Conference on Permafrost, Zurich, Switzerland:* 145-150.

Chuvilin, E.M. & Kozlova, E.V. 2005a. Research of formation of frozen gas hydrate-saturated sediment. *Earth Cryosphere Journal*, 9:73-80 (in Russian).

Chuvilin, E.M. & Kozlova E.V. 2005b. Experimental estimation of hydrate-containing sediments stability. *Proceedings of the 5th International Conference on Gas Hydrates. Thermodynamic Aspects, v.5, Trondheim, Norway*: 1562-1567.

Dallimore, S.R. & Collett, T.S. 1995. Intrapermafrost gas hydrates from a deep core hole in the Mackenzie Delta, Northwest Territories, Canada. *Geology* 23: 527-530.

Dallimore, S.R., Chuvilin, E.M., Yakushev, V.S. Grechischev, S.E., Ponomarev, V. & Pavlov A. 1996. Field and laboratory characterization of intrapermafrost gas hydrates, Mackenzie Delta, N.W.T., Canada. *Proceedings of the 2nd International Conference on Natural Gas Hydrates, Toulouse, France*: 525-531.

Dallimore, S.R., Uchida, T. & Collett T.S. 1999. Summary. In: S.R. Dallimore, T.Uchida, T.S. Collett (eds), *Scientific results from JAPEX/JNOC/GSC Mallik 2L-38 Gas Hydrate Research Well, Mackenzie Delta, Nothwest Territories, Canada*. Geological Survey of Canada, Bulletin 544:1-17.

Davidson, D.W., Garg, S.K., Gough, S.R., Handa, Y.P., Ratcliffe, C.I., Ripmeester, J.A., Tse, J.S. & Lawson W.F. 1986. Laboratory analysis of a naturally occurring gas hydrate from sediment of the Gulf of Mexico. *Geochimica et Cosmochimica Acta* 50: 619-623.

Ershov, E.D., Lebedenko, Yu.P., Chuvilin, E.M., Istomin, V.A. & Yakushev, V.A. 1989. Problems of hydrate formation in the permafrost. *Permafrost exploring, MSU*: 50-63 (in Russian).

Ershov, E.D., Lebedenko, Yu.P., Chuvilin, E.M., Istomin, V.A. & Yakushev V.A. 1991. Peculiarity of gas hydrates existence in the permafrost. *Reports of Academy of Sciences USSR* 321: 788-791 (in Russian).

Istomin, V.A., Yakushev, V.S. Mokhonina, N.A., Kwon, V.G. & Chuvilin, E.M. 2006. Self-preservation phenomenon of gas hydrate. *Gas industry of Russia* Digest 4: 16-27.

Kuhs, W.S., Genov, G., Staykova, D.K. & Hansen, T. 2004. Ice perfection and onset of anomalous preservation of gas hydrates. *Physical Chemistry and Chemical Physics* 6: 1-6.

Skorobogatov, V.A., Yakushev, V.S. & Chuvilin, E.M. 1998. Sources of natural gas within permafrost North-West Siberia. *Proceedings of the 7th International Permafrost Conference, Yellowknife, Canada*: 1001-1007.

Stern, L.A, Circone, S., Kirby, S.H. & Durham, W.B. 2001. Anomalous Preservation of Pure Methane hydrate at 1 atm. *Journal of Physical Chemistry* 105: 1756-1762.

Takeya, S., Ebinuma, T., Uchida, T., Nagao, J. & Narita, H. 2002. Self-preservation effect and dissociation rates of CH_4 hydrate. *Journal of Crystal Growth:* 237-239, Part 1: 379-382.

Yakushev, V.S. & Chuvilin, E.M. 2000. Natural gas and hydrate accumulation within permafrost in Russia. *Cold Regions Science and Technology* 31:189-197.

Effects of Recent Climate Change on High Mountains of Western North America

John J. Clague
Simon Fraser University

Abstract

Pronounced step-wise atmospheric warming during the 20th century reduced ice cover in mountains by 25–50 percent. Net changes in average annual and mean summer temperatures responsible for this remarkable deglacierization are less than 2°C, a small fraction of the warming that occurred at the end of the Pleistocene. Yet the effects of these changes on mountain landscapes have been profound. Alpine permafrost, which expanded during the Little Ice Age, now appears to be thinning and disappearing in many areas. Loss of alpine permafrost and glacier downwasting appear to be partly responsible for accelerated mass wasting and catastrophic rock-slope failures in high mountains. New lakes appeared during the Little Ice Age when glaciers advanced across streams and rivers and blocked drainage. Most of these lakes drained one or more times during the 20th century, producing catastrophic floods orders of magnitude larger than normal nival or rainfall floods. In some instances, lakes have appeared upvalley of former, drained ones as glaciers have continued to retreat under a warming climate. Lakes also formed behind Little Ice Age end moraines when glaciers retreated in the early 20th century. Moraine dams are vulnerable to failure because they are steep-sided and consist of loose sediment. Outburst floods from lakes dammed by glaciers and moraines erode, transport, and deposit huge amounts of sediment over distances tens of kilometers. They broaden flood plains, destroy pre-flood channels, and create a new braided planform. The changes can persist for decades after the flood.

Keywords: climate change; deglacierization; jökulhlaup; landslides; Little Ice Age; permafrost thaw.

Introduction

Alpine glaciers in the Northern Hemisphere achieved their greatest extent of the Holocene during the "Little Ice Age" (AD 1200–1900; Holzhauser 1985, Grove 1988, Wiles et al. 1999, Luckman 2000, Luckman & Villalba 2001). Although Earth's climate was highly variable during this period, alpine glaciers grew episodically but progressively larger, culminating with the maximum advances of the Little Ice Age in the late 17th to mid 19th centuries.

Climate variability during the Little Ice Age (Moberg et al. 2005) probably was caused by a combination of forcing mechanisms (Mann et al. 1998). Explosive volcanism has contributed to Northern Hemisphere temperature changes during the past 600 years (Bradley & Jones 1993, Briffa et al. 1998), and some glacier advances coincided with intervals of elevated volcanic aerosols in the atmosphere (Porter 1986). Some researchers have argued that solar activity influenced the climate of the past millennium (Lean et al. 1995, Crowley & Kim 1996, Crowley 2000); indeed, periods of late-Little Ice Age moraine formation generally coincide with solar minima (Lawrence 1950, Wiles et al. 2004, Luckman & Wilson 2005). In addition, ocean-atmosphere interactions influenced atmospheric circulation and thus glacier behavior during the past millennium (Hendy et al. 2002, Nesje & Dahl 2003, Lewis & Smith 2004*,* Mann et al. 2005). Ruddiman (2003) suggested that widespread farm abandonment during the Black Death plagues and attendant reforestation may explain the cool phases of the Little Ice Age by changing concentrations of atmospheric carbon dioxide and methane.

The Little Ice Age ended about 100 years ago when climate around the world began to warm. Glaciers in most mountain ranges in the Northern Hemisphere, including those in western North America, receded during the first two decades of the 20th century. Some glaciers advanced in the 1920s but underwent rapid and extensive recession over the next three decades. Most glaciers advanced small distances between the 1950s and early 1980s but since then have retreated. Today most glaciers are 25% to 50% smaller than at the end of the Little Ice Age.

Net changes in average annual and mean summer temperatures responsible for glacier and climate change during and following the Little Ice Age are less than 2°C (Mann et al. 1998). This amount is a small fraction of the total warming that occurred during the demise of Northern Hemisphere ice sheets at the end of the Pleistocene. Corresponding changes in mean and seasonal precipitation in most areas also are relatively small. Yet these changes have had significant effects on high mountain environments and on rivers flowing from these mountains. This paper summarizes and discusses these effects.

Permafrost Thaw and Deglacierization

An increase in large landslides in northern British Columbia during the 20th century (Geertsema et al. 2006) may be related to warming or thaw of alpine permafrost and deglacierization. Permafrost expanded in high mountains during the Little Ice Age but now appears to be thinning and disappearing there (Zhang et al. 2006). Alpine permafrost has a complex and patchy distribution that is controlled mainly by altitude, material properties, snow cover, and topography. A rough estimate can be made of changes in the extent of permafrost in high mountains of North America using independently determined temperature changes, bearing in mind that permafrost distribution is affected by more than

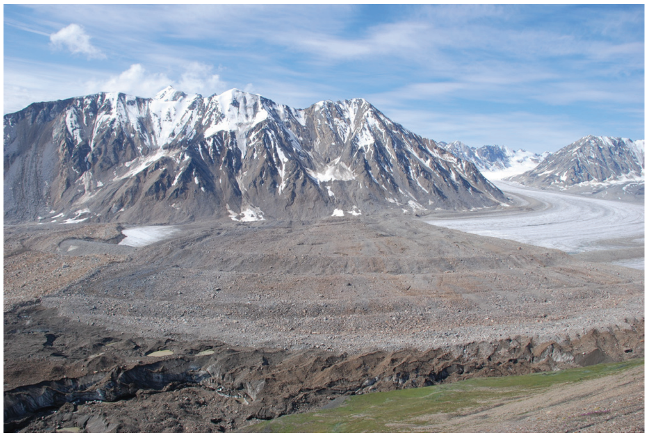

Figure 1. Landslide deposit on Black Rapids Glacier, Alaska. The rock avalanche was triggered by a large earthquake in November 2002, but loss of glacier ice on the source slope may have contributed to the failure. The landslide scarp is indicated by an arrow.

just temperature. Using a range of mean annual temperature of 2°C on timescales of decades and an adiabatic lapse rate of 4°C/km–6°C/km, the limit of permafrost shifted vertically 300–500 m during the Little Ice Age. The average rise in the limit of alpine permafrost in the 20th century, during which climate warmed 0.6°C–0.8°C, may have been 100–200 m. These values may not seem significant, but even greater reductions in permafrost can be expected through the remainder of this century. Even 20th century warming and loss of permafrost have been implicated by recent instability of slopes in some mountain ranges (Watanabe et al. 2000, Gruber et al. 2004). Further, permafrost warming alone, without thaw, may increase the likelihood that rock slopes will fail (Davies et al. 2001, Harris et al. 2001). Sediments may mobilize as debris flows when their interstitial ice thaws (e.g., Bovis & Jakob 2000), and masses of rock may fail, generating rockslides and rock avalanches when ice within the fractures undergoes repeated thawing and freezing.

Another consequence of increased thaw of permafrost in high mountains is that many active rock glaciers will cease moving. Evidence has been reported that formerly active rock glaciers became less active or even fossil landforms in the 20th century (McCarroll et al. 2001, Baroni et al. 2004).

Glacier downwasting and retreat appear to be partly responsible for some catastrophic rock-slope failures in high mountains (Evans & Clague 1994, Evans & Clague 1999, Holm et al. 2004). Many marginally stable slopes that were buttressed by glacier ice during the Little Ice Age failed after they became deglaciated in the 20th century (Fig. 1). A factor that possibly has contributed to such failures is steepening of rock slopes by cirque and valley glaciers during the Little Ice Age.

These effects are most pronounced in mountain ranges with the largest ice cover, because it is there that ice losses in the 20th century have been greatest. An extreme example is Glacier Bay, which until the end of the 18th century was covered by glacier ice. Since then, Glacier Bay has become deglaciated with the loss of over 1000 km^2 of ice in 200 years. This amount of ice lost is so great that the land is rising due to isostatic rebound (Larson et al. 2005).

Figure 2. Summit Lake, located in the northern Coast Mountains of British Columbia. The lake is impounded by Salmon Glacier (background) and has drained and refilled more than 40 times over the past 47 years.

Outburst Floods

New lakes appeared in the mountains of western North America when glaciers advanced across streams and blocked drainage during the Little Ice Age (Fig. 2). The histories of these lakes are poorly known except in the 20th century when most of them drained one or more times, producing catastrophic floods (jökulhlaups) orders of magnitude larger than normal nival or rainfall floods (Fig. 3, Costa & Schuster 1988, Clague & Evans 1994, and references therein). These floods have occurred during a period of warming climate due to progressive wastage of the glacier dam and the formation of subglacial, supraglacial, or ice-marginal channels. Lakes may also form during rapid glacier advances ("surges").

New lakes also formed behind Little Ice Age end moraines as glaciers retreated in the late 19th and early 20th century (Fig. 4; Costa & Schuster 1988, O'Connor & Costa 1993, Clague & Evans 1994, Clague & Evans 2000). Moraine dams are vulnerable to failure because they are steep-sided and consist of loose sediment. Irreversible rapid incision of the dam may be caused by a large overflow triggered by an ice avalanche or rockfall. Other failure mechanisms include earthquakes, slow thaw of ice within the moraine, and removal ("piping") of fine sediment from the moraine. "Outburst floods" from lakes dammed by glaciers and moraines erode, transport, and deposit huge amounts of sediment over distances tens of kilometers (Fig. 5).

Outburst floods from glacier- and moraine-dammed lakes display an exponential increase in discharge, followed by a gradual or abrupt decrease to background levels as the water supply is exhausted. Peak discharges are controlled by lake volume, dam height and width, the material properties of the

Figure 3. Jökulhlaup caused by the sudden drainage of Summit Lake, north of Hyder, Alaska.

dam, failure mechanism, and downstream topography and sediment availability. Floods from glacier-dammed lakes tend to have lower peak discharges than those from moraine-dammed lakes of similar size. This is because enlargement of tunnels within ice is a slower process than overtopping and incision of sediment dams.

Floods resulting from failures of glacier and moraine dams may transform into debris flows as they travel down steep valleys. Such flows can only form and be sustained on slopes greater than 10°–15°, and only where there is an abundant supply of sediment in the valley below the dam. Entrainment of sediment and woody plant debris by floodwaters may cause peak discharge to increase down valley, which has important implications for hazard appraisal.

Outburst floods from lakes dammed by moraines and glaciers commonly alter river flood plains tens of kilometers from the flood source (Fig. 5). The floodwaters erode, transport, and deposit huge amounts of sediment. They commonly broaden flood plains, destroy pre-flood channels, and create a new multi-channel, braided planform. The changes can persist for decades after the flood, although rivers quickly reestablish their pre-flood grades by incising the flood deposits.

Climate is an important determinant of the stability of moraine and glacier dams. Most moraine-dammed lakes formed in the last century as glaciers retreated from bulky end moraines constructed during the Little Ice Age. The lakes soon began to fail as climate warmed. With continued warming and glacier retreat, the supply of moraine-dammed lakes susceptible to failure will be exhausted, and the threat they pose will diminish (Clague & Evans 2000). Glacier-dammed lakes typically have gone through a period of cyclic or sporadic outburst activity, lasting up to several decades, since climate began to warm in the late nineteenth century. The cycle of outburst of floods from any one lake ended when the glacier dam weakened to the point that it could no longer trap water behind it. However, with continued glacier retreat, the locus of outburst activity may, in some cases, shift up-glacier to sites where new lakes develop in areas that are becoming deglaciated (Geertsema & Clague 2005).

Figure 4. Moraine-dammed lake in the Bishop River watershed, southern Coast Mountains, British Columbia.

Figure 5. Flood-devastated west fork of Nostetuko River valley, British Columbia. The photograph was taken in 1998, one year after an outburst flood from moraine-dammed Queen Bess Lake.

Changes to Streams

Fluctuations of glacier margins on timescales of decades and centuries can mobilize sequestered glaciogenic sediment. During glacier advance, initial incision due to increased competence of meltwater streams is quickly followed by aggradation as sediment supply increases (Maizels 1979). Sediment stored within and beneath glaciers is delivered at an increasing rate to fluvial systems as glaciers advance (Karlén 1976, Maizels 1979, Leonard 1986, Leonard 1997, Karlén & Matthews 1992, Lamoureux 2000). Similarly, subglacial erosion increases during glacier advance, and meltwater may carry more sediment into river valleys than at times when glaciers are more restricted. Paraglacial sediment pulses may propagate rapidly downstream in narrow mountain valleys when glaciers advance to maximum positions and, subsequently, as they begin to retreat. Glacier retreat typically exposes large areas of unstable, poorly vegetated sediment that is easily transferred to the fluvial system, causing valley-wide aggradation and complex changes in channel planform (Church 1983, Desloges & Church 1987, Gottesfeld & Johnson-Gottesfeld 1990, Brooks 1994, Ashmore & Church 2001, Clague et al. 2003, Wilkie 2006).

Increased glacial erosion and sediment production during glacier advance, coupled with climatically induced changes in discharge and sediment yield, can cause rivers to aggrade their beds. Sediment delivery to streams in the Coast Mountains of British Columbia, for example, increased during the Little Ice Age, and the streams responded by aggrading their channels and braiding over distances up to tens of kilometers down valley from glaciers (Church 1983, Gottesfeld & Johnson-Gottesfeld 1990, Wilkie 2006). Subsequently, during the 20th century, the streams incised their Little Ice Age deposits and reestablished single-thread channels characteristic of periods of lower sediment flux.

Conclusion

Climate warming during the 20th century and the first decade of the present century has caused changes in the pace of geomorphic processes in mountains in western North America and elsewhere. Rapid, large-scale deglacierization and thaw of alpine permafrost have increased the incidence of landslides and debris flows in mountains. Lakes that formed against retreating glaciers and end moraines have drained suddenly, catastrophically altering valley bottoms far downstream. Changes in sediment delivery to streams have altered local base level and channel planform in mountain valleys. If the forecasts of climate modelers are correct, loss of glacier ice and alpine permafrost will continue and perhaps accelerate through the remainder of this century.

References

Ashmore, P. & Church, M. 2001. *The Impact of Climate Change on Rivers and River Processes in Canada*. Geological Survey of Canada Bulletin 555, 58 pp.

Baroni, C., Carton, A. & Seppi, R. 2004. Distribution of behaviour of rock glaciers in the Adamello-Presanella Massif (Italian Alps). *Permafrost and Periglacial Processes* 15: 243-259.

Bovis, M.J. & Jakob, M. 2000. The July 29, 1998, debris flow and landslide dam at Capricorn Creek, Mount Meager volcanic complex, southern Coast Mountains, British Columbia. *Canadian Journal of Earth Sciences* 37: 1321-1334.

Bradley, R.S. & Jones, P.D. 1993. 'Little Ice Age' summer temperature variations: their nature and relevance to recent global warming trends. *The Holocene* 3: 367-376.

Briffa, K.R., Jones, P.D., Schweingruber, F.H. & Osborn, T.J. 1998. Influence of volcanic eruptions on Northern Hemisphere summer temperature over the last 600 years. *Nature* 393: 450-455.

Brooks, G.R. 1994. The fluvial reworking of late Pleistocene drift, Squamish River drainage basin, southwest British Columbia. *Géographie physique et Quaternaire* 48: 51-68.

Church, M. 1983. Pattern of instability in a wandering gravel bed channel. In: J.D. Collinson & J. Lewin (eds.), *Modern and Ancient Fluvial Systems*. International Association of Sedimentologists Special Publication 6: 169-180.

Clague, J.J. & Evans, S.G. 1994. *Formation and Failure of Natural Dams in the Canadian Cordillera*. Geological Survey of Canada Bulletin 464, 35 pp.

Clague, J.J. & Evans, S.G. 2000. A review of catastrophic drainage of moraine-dammed lakes in British Columbia. *Quaternary Science Reviews* 19: 1763-1783.

Clague, J.J., Turner, R.J.W. & Reyes, A. 2003. Record of recent river channel instability, Cheakamus Valley, British Columbia. *Geomorphology* 53: 317-332.

Costa, J.E. & Schuster, R.L. 1988. The formation and failure of natural dams. *Geological Society of America Bulletin* 100: 1054-1068.

Crowley, T.J. 2000. Causes of climate change over the past 1000 years. *Science* 289: 270-277.

Crowley, T.J. & Kim, K.-Y. 1996. Comparison of proxy records of climate change and solar forcing. *Geophysical Research Letters* 23: 359-362.

Davies, M.C.R., Hamza, O. & Harris, C. 2001. The effect of rise in mean annual temperature on the stability of rock slopes containing ice-filled discontinuities. *Permafrost and Periglacial Processes* 12: 137-144.

Desloges, J.R. & Church, M. 1987. Channel and floodplain facies in a wandering gravel-bed river. In: F.G. Ethridge & R.M. Flores (eds.), *Recent Developments in Fluvial Sedimentology*. Society of Economic Paleontologists and Mineralogists, Special Publication 39: 99-109.

Evans, S.G. & Clague, J.J. 1994. Recent climatic change and catastrophic geomorphic processes in mountain environments. *Geomorphology* 10: 107-128.

Evans, S.G. & Clague, J.J. 1999. Rock avalanches on glaciers in the Coast and St. Elias Mountains, British Columbia. *Proceedings of the 13th Annual Vancouver Geotechnical Conference, Vancouver, BC*. Richmond, BC: BiTech Publishers, 115-123.

Geertsema, M. & Clague, J.J. 2005. Jökulhlaups at Tulsequah Glacier, northwestern British Columbia, Canada. *The Holocene* 15: 310-316.

Geertsema, M., Clague, J.J., Schwab, J.W. & Evans, S.G. 2006. An overview of recent large catastrophic landslides in northern British Columbia. *Engineering Geology* 83: 120-143.

Gottesfeld, A.S. & Johnson-Gottesfeld, L.M. 1990. Floodplain dynamics of a wandering river, dendrochronology of the Morice River, British Columbia, Canada. *Geomorphology* 3: 159-179.

Grove, J.M. 1988. *The Little Ice Age*. London: Methuen Press, 498 pp.

Gruber, S., Hoelzle, M. & Haeberli, W. 2004. Permafrost thaw and destabilization of alpine rock walls in the hot summer of 2003. *Geophysical Research Letters* 31(13): 4 pp.

Harris, C., Davies, M.C.R. & Etzelmuller, B. 2001. The assessment of potential geotechnical hazards associated with mountain permafrost in a warming global climate. *Permafrost and Periglacial Processes* 12: 145-156.

Hendy, E.J., Gagan, M.K., Alibert, C.A., McCulloch, M.T., Lough, J.M. & Isdale, P.J. 2002. Abrupt decrease in tropical Pacific sea surface salinity at the end of Little Ice Age. *Science* 295: 1511-1514.

Holm, K., Bovis, M. & Jakob, M. 2004. The landslide response of alpine basins to post-Little Ice Age glacial thinning and retreat in southwestern British Columbia. *Geomorphology* 57: 201-216.

Holzhauser, H. 1985. Neue Ergebnisse zur Gletscher- und Klimageschichte des Spätmittelalters und der Neuzeit. *Geographica Helvetica* 40: 168-185.

Karlén, W. 1976. Lacustrine sediments and tree limit variations as evidence of Holocene climatic variations in Lappland, northern Sweden. *Geografiska Annaler* 58: 1-34.

Karlén, W. & Matthews, J.A. 1992. Reconstructing Holocene glacier variations from glacial lake sediments: Studies from Nordvestlandet and Jostedalsbreen-Jotunheimen, southern Norway. *Geografiska Annaler* 74: 327-348.

Lamoureux, S. 2000. Five centuries of interannual sediment yield and rainfall-induced erosion in the Canadian High Arctic recorded in lacustrine varves. *Water Resources Research* 36: 309-318.

Larson, C.F., Motyka, R.J., Freymueller, J.T., Echelmeyer, K.A. & Ivins, E.R. 2005. Rapid viscoelastic uplift in Southeast Alaska caused by post-Little Ice Age glacial retreat. *Earth and Planetary Science Newletters* 237: 548-560.

Lawrence, D.B. 1950. Glacier fluctuations for six centuries in southeastern Alaska and its relation to solar activity. *Geographical Review* 40: 191-222.

Lean, J., Beer, J. & Bradley, R. 1995. Reconstruction of solar irradiance since 1610: implications for climate change. *Geophysical Research Letters* 22: 3195-3198.

Leonard, E.M. 1986. Varve studies at Hector Lake, Alberta, Canada, and the relationship between glacial activity and sedimentation. *Quaternary Research* 25: 199-214.

Leonard, E.M. 1997. The relationship between glacial activity and sediment production: evidence from a 4450-year varve record of neoglacial sedimentation in Hector Lake, Alberta, Canada. *Journal of Palaeolimnology* 17: 319-330.

Lewis, D. & Smith, D. 2004. Dendrochronological mass balance reconstruction, Strathcona Provincial Park, Vancouver Island, British Columbia, Canada. *Arctic, Antarctic, and Alpine Research* 36: 598-606.

Luckman, B.H. 2000. Little Ice Age in the Canadian Rockies. *Geomorphology* 32: 357-384.

Luckman, B.H. & Villalba, R. 2001. Assessing the synchroneity of glacier fluctuations in the western Cordillera of the Americas during the last millennium. In: V. Markgraf (ed.), *Interhemispheric Climate Linkages*. New York: Academic Press, 119-140.

Luckman, B.H. & Wilson, R.J.S. 2005. Summer temperatures in the Canadian Rockies during the last millennium; a revised record. *Climate Dynamics* 24: 131-144.

Maizels, J.K. 1979. Proglacial aggradation and changes in braided channel patterns during a period of glacier advance: an Alpine example. *Geografiska Annaler* 61: 87-101.

Mann, M.E., Bradley, R.S. & Hughes, M.K. 1998. Global-scale temperature patterns and climate forcing over the past six centuries. *Nature* 392: 779-787.

Mann, M.E., Cane, M.A., Zebiak, S.E. & Clement, A. 2005. Volcanic and solar forcing of the tropical Pacific over the past 1000 years. *Journal of Climate* 18: 447-456.

McCarroll, D., Shakesby, R.A. & Matthews, J.A. 2001. Enhanced rockfall activity during the Little Ice Age; further lichenometric evidence from a Norwegian talus. *Permafrost and Periglacial Processes* 12: 157-164.

Moberg, A., Sonechkin, D.M., Holmgren, K., Datsenko, N.M. & Karlén, W. 2005. Highly variable northern hemisphere temperatures reconstructed from low- and high-resolution proxy data. *Nature* 433: 613-617.

Nesje, A. & Dahl, S.O. 2003. The 'Little Ice Age' – only temperature? *The Holocene* 13: 139-145.

O'Connor, J.E. & Costa, J.E. 1993. Geologic and hydrologic hazards in glacierized basins in North America resulting from 19th and 20th century global warming. *Natural Hazards* 8: 121-140.

Porter, S.C. 1986. Pattern and forcing of Northern Hemisphere glacier variations during the last millennium. *Quaternary Research* 26: 27-48.

Ruddiman, W.F. 2003. The anthropogenic greenhouse era began thousands of years ago. *Climatic Change* 61: 261-293.

Watanabe, T., Nakamura, N. & Khanal, N.R. 2000. Mountain hazards in the Kanchanjunga area, eastern Nepal; landslides developed on lateral moraines. *Jounal of Nepal Geological Society* 22: 525-532.

Wiles, G.C., Barclay, D.J. & Calkin, P.E. 1999. Tree-ring dated 'Little Ice Age' histories of maritime glaciers from western Prince William Sound, Alaska. *The Holocene* 9: 163-173.

Wiles, G.C., D'Arrigo, R.D., Villalba, R., Calkin, P.E. & Barclay, D.J. 2004. Century-scale solar variability and Alaskan temperature change over the past millennium. *Geophysical Research Letters* 31: L15203.

Wilkie, K.M.K. 2006. *Fluvial Response to Late Holocene Glacier Fluctuations in the Nostetuko River Valley, Southern Coast Mountains, British Columbia*. M.Sc. Thesis, Simon Fraser University, Burnaby, BC, 84 pp.

Zhang, Y., Chen, W. & Riseborough, D.W. 2006. Temporal and spatial changes of permafrost in Canada since the end of the Little Ice Age. *Journal of Geophysical Research* 111, D22: 14 pp.

A Model of Permafrost Distribution and Disturbance Sensitivity for Denali National Park, Using Soil-Ecological Site Inventory Information

Mark H. Clark
USDA-Natural Resources Conservation Service, Palmer, Alaska, USA

Abstract

A soil-ecological site survey of Denali National Park and Preserve (Denali) completed in 2004 by the Natural Resources Conservation Service is used to provide a map of Gelisols, soils with permafrost within 2 m of the surface, and their sensitivity to disturbance. Three sensitivity classes are assigned, based on similarities in the degree and rapidity of change to soil properties and plant communities following disturbance, as well as return interval to the pre-disturbance condition. The model aggregates ecological sites into groups with similar plant community structure and species richness, two elements useful in evaluating wildlife habitat. Dynamic soil properties, such as thickness of organic mat, depth to water table, and permafrost, may also be estimated for the various ecological states identified for each sensitivity class. This information is useful for estimating transient carbon budgets in soils and hydrologic functions, as well as indicating soils that are likely to be impacted by climate change. Gelisols considered highly sensitive to disturbance comprise 118,185 ha, or about 4% of Denali. Moderately sensitive Gelisols comprise 445,192 ha, or 18% of Denali. Gelisols considered low in sensitivity include 391,760 ha, or about 16% of Denali.

Keywords: ecological site inventory; Gelisols; permafrost; soil survey.

Introduction

The northern region of Denali includes areas lying north of the Alaska Range summit. This represents a subset of the Polar Domain described by Bailey (1994) and lies within the zone of discontinuous permafrost (Péwé 1975). The "Interior" climate of the northern part of Denali is continental, with long cold winters and short warm summers, relatively low precipitation, with a significant moisture deficit during the growing season (Patric & Black 1965).

Gelisols, soils with permafrost within 2 m of the surface (Soil Survey Staff 2006), are widely distributed within the northern part of Denali and generally absent in the remainder of the Denali south of the Alaska Range summit (Fig. 1). Gelisols are common to gently sloping, infrequently flooded surfaces throughout the boreal forest biome and lower elevations of the alpine life zone (Fig. 1) Gelisols are defined as having permafrost. However, extensive areas alternate between a poorly-drained, ice-rich condition, and a well-drained, permafrost-free state due to disturbance such as fire and post-disturbance plant succession. In this application, the definition of Gelisols includes those soils that have permafrost within 2 m of the soil surface under potential natural vegetation. Soils that are permafrost-free, with early to mid-succession communities and soil morphological properties that suggest that permafrost is present under potential native vegetation, are also considered Gelisols.

Variable rates of thaw, recession of water tables, and return intervals to the pre-burn condition are common to Gelisols following disturbance (Dyrness 1982). These differences are documented in the Ecological Site or Landtype (Bailey 1994) descriptions for each Gelisol soil component provided in the soil-ecological site survey of Denali National Park and Preserve (Denali) (Clark & Duffy 2004). The purpose of this poster is to provide a distribution map of Gelisols in Denali and present a model of sensitivity of Gelisols to disturbance based on ecological Landtypes.

Methods

The sensitivity of Gelisols to disturbance and lowering or loss of permafrost is modeled using a two-step process. The first step includes deriving a map of the distribution of Gelisols in Denali. This is accomplished using the soil-ecological survey database (Clark & Duffy 2004) to develop criteria and the spatial data to illustrate the map and provide associated statistics. Map units consisting of at least 15% Gelisols are aggregated into a map for consideration in the development of the disturbances sensitivity model (Fig. 1). The second step includes assigning map units into three sensitivity classes based on similar response to disturbance as defined in the ecological landtype descriptions. Significant soil properties associated with each disturbance class are then derived from the ecological landtype database.

Both static and dynamic site and soil properties are determined as useful to the model. Soil texture and overall thickness of the surface mineral layer are important static soil properties useful in determining sensitivity. A soil's ability to conduct heat increases as particle sizes increase (Jury et al. 1991). Soils with a low sand and rock fragment content conduct heat less effectively than soils with high sand or rock fragment content. Soils with high silt content have lower thermal conductivity and are most likely to experience a slower rate of permafrost recession and more rapid return to pre-burn condition than coarse textured soils. Soils with high sand and rock fragment content are less likely to have the potential for permafrost, because the high thermal conductivity promotes summer warming and prevents frost from persisting through the summer months. Dynamic soil and site properties for each ecological landtype are useful to document transitional states between the non-permafrost and permafrost condition and provide a time-line for change between each pathway element. Dynamic soil properties important to the model include organic mat thickness, depth to permafrost, and depth to water table perched above the permafrost.

Fire is the only major disturbance factor available for use in the criteria. Anthropogenic disturbance in Denali is minimal, and flooding and landslide activity is primarily limited to soils other than Gelisols. The criteria assumes that a level of fire intensity common to the boreal biome and alpine life zone has occurred, including a mosaic pattern of scorched and unburned ground, and only partial incineration of the surface organic mat where burned. Fire disturbance is infrequent on soils with permafrost within the alpine life zone. The assignment of sensitivity classes to Gelisols within the alpine life zone are based on similar soils from within the boreal biome. Criteria used to assign three categories of sensitivity are outlined below.

Gelisols that are highly sensitive to disturbance, are rarely or non-flooded, and have a surface mineral soil layer consisting of 50 to 100 cm of silt loam, or stratified fine sand and silt with few rock fragments over sandy and gravelly alluvium with variable rock fragment content. Soil properties and plant communities associated with this sensitivity class are represented by ecological landtype Loamy Frozen Terraces-131B_104 (Clark & Duffy 2004). Thermal conductivity properties of the silt or stratified surface mineral soil layer are relatively low ranging, from about 0.25 to 1.4 cal $cm^{-1}s^{-1}$ $^{o}C^{-1}$ (Jury 1991). However, the thin nature of the surface mantle does not significantly retard surface warming following disturbance, and subsequent recession of permafrost is relatively fast. The high thermal conductivity of the underlying sand and gravel is estimated at 4.5 cal $cm^{-1}s^{-1}$ $^{o}C^{-1}$ (Jury 1991), and the porous nature of these coarse texture materials likely contributes to rapid warming and recession of permafrost in these soils. Landforms associated with the highly sensitive class include stream terraces, alluvial fans, and high positions on flood plains (Fig. 2). Climax plant communities from this class include shrub birch (*Betula glandulosa*)-bog blueberry (*Vaccinium uliginosum*)/moss scrub within the alpine life zone; and black spruce (*Picea mariana*)-tamarack (*Larix laricina*)/Labrador tea (*Ledum groenlandicum*) woodland within the boreal biome. Soils included in this class include Typic Historthels, Ruptic-Histic Aquiturbels, Fluvaquentic Historthels, and Typic Aquiturbels subgroups of US Soil Taxonomy (Soil Survey Staff 2004).

Gelisols that are moderately sensitive to disturbance are loamy throughout the soil profile, with 15 to 40% rock fragments in the upper 100 cm of soil. Soil properties and plant communities associated with this sensitivity class are represented by ecological landtype Gravelly Frozen Slopes, M135A_180 (Clark & Duffy 2004). These soils have intermediate levels of thermal conductivity related to the moderate level of rock fragments and loamy soil matrix, which overall exchange heat at a slower rate than soils of the first class. Landforms associated with this sensitivity class include till plains, all positions on glaciated low mountains, and on lower mountain slopes of non-glaciated mountains (Fig. 3). This class mostly consists of gelisols within the alpine life zone, commonly with a climax plant community of shrub birch-mixed ericaceous shrub/sedge (*Carex spp*.) scrub. Soils in this sensitivity class include Typic Historthels and Glacic Folistels subgroups of US Soil Taxonomy (Soil Survey Staff 2004).

Soils with permafrost that are considered to have a low sensitivity to disturbance (Fig. 4) are rock-free with silt or stratified fine sand and silt textures over 100 cm thick and have soils with near-surface water tables associated with cottongrass (*Eriophorum spp.*) tussock late succession communities. Soil properties and plant communities associated with this sensitivity class are represented by ecological landtype: Loamy Frozen Slopes, Wet-131B_402 (Clark & Duffy 2004). This group has soil texture of silt loam, loam, or stratified loamy surface layers with relatively low thermal conductivity properties ranging from 0.25 to 1.4 cal $cm^{-1}s^{-1}$ $^{o}C^{-1}$ (Jury 1991). Landforms associated with the low sensitivity class include loess covered plains, hills, and stream terraces (Fig. 4). Climax plant communities include black spruce-tamarack/tussock cottongrass woodland within the boreal biome and tussock cottongrass/mixed ericaceous shrub meadow in the alpine life zone. Soils in this sensitivity class include Typic Histoturbels, Typic Historthels, and Typic Umbrothels subgroups of US Soil Taxonomy (Soil Survey Staff 2004).

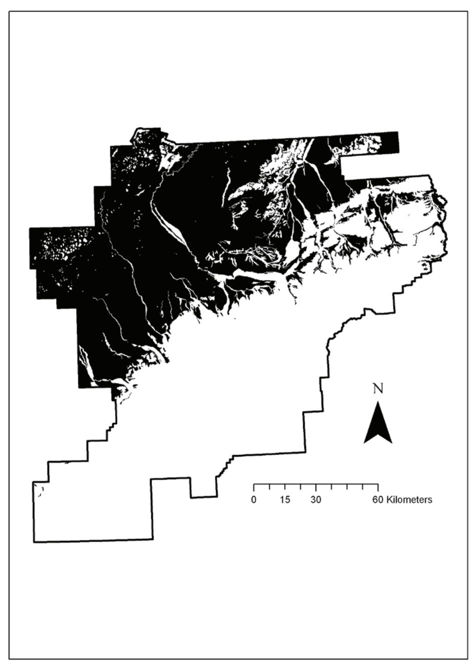

Figure 1. Distribution of soil map units consisting of at least 15% Gelisols in Denali.

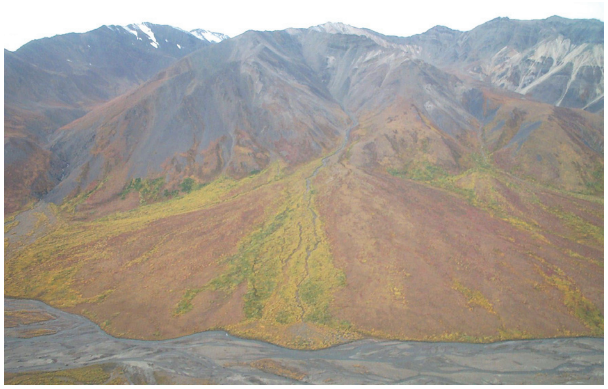

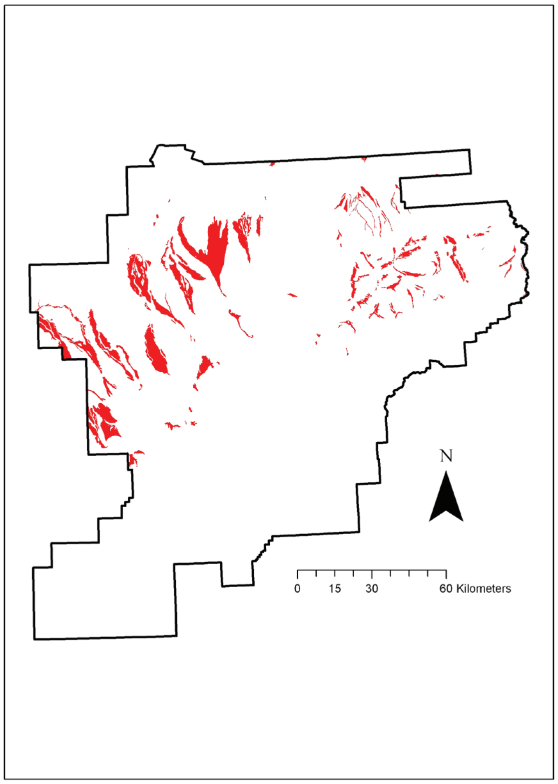

Figure 2. Upper: Alluvial fan with Gelisols illustrated in the foreground with shrub birch-bog blueberry/moss scrub typical of a Gelisol sensitive to disturbance. Lower: Gelisols highly sensitive to disturbance or temperature change are represented in black and total 118,185 ha, or about 4% of Denali.

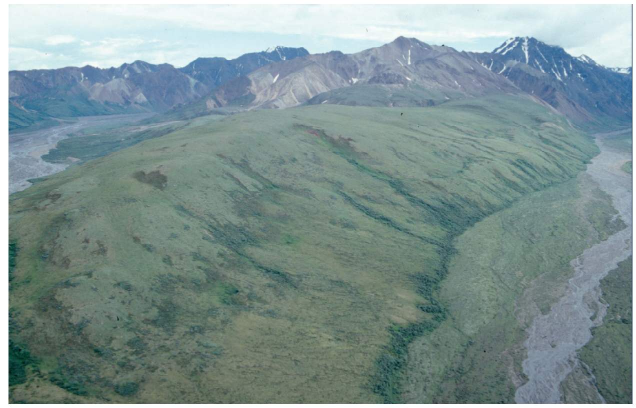

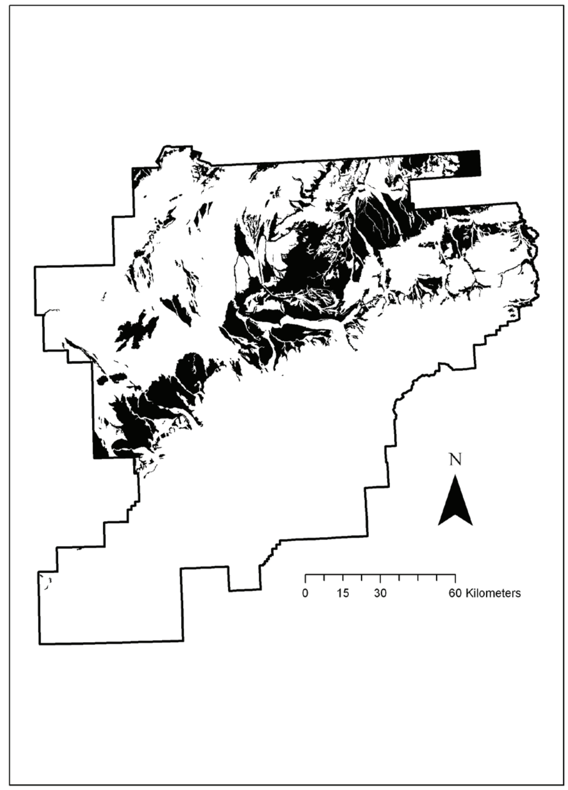

Figure 3. Upper: Glaciated mountains with shrub birch-mixed ericaceous shrub/sedge scrub illustrated in the light tonal areas of the foreground. Soils are primarily Gelisols that are moderately sensitive to disturbance. Lower: Gelisols moderately sensitive to disturbance are represented in black and total 445,192 ha, or 18% of Denali.

Results

Distribution of soil map units with Gelisols in Denali is provided in Figure 1. This illustrates map units containing soil components with permafrost that comprise 15% or more of the map unit. The total distribution of map units that meet these criteria encompasses 931,000 ha, or about 38% of the park. Soil map units with Gelisols highly sensitive to disturbance or temperature change are represented in black, and total 118,185 ha, or about 4%, of Denali (Fig. 2). The high thermal conductivity property of soils is considered an important factor in the high sensitivity of these soils to change following disturbance Permafrost is observed to drop rapidly to below 200 cm of the ground surface within one to three years following fire in this class. Return to the pre-burn condition in the black spruce type in Interior Alaska is suggested as 50 to 70 years Foote (1976) and Viereck (1973). However, based on tree core observations in Denali, a return interval of 100 to 150 years is estimated for this sensitivity category. Gelisols within the boreal biome that are included within this class have a single climax and two distinctive transitional plant communities, suggesting that significant changes in dynamic soil properties following disturbance are associated with a diverse array of wildlife habitat types, especially within the boreal biome.

Soil map units with Gelisols moderately sensitive to

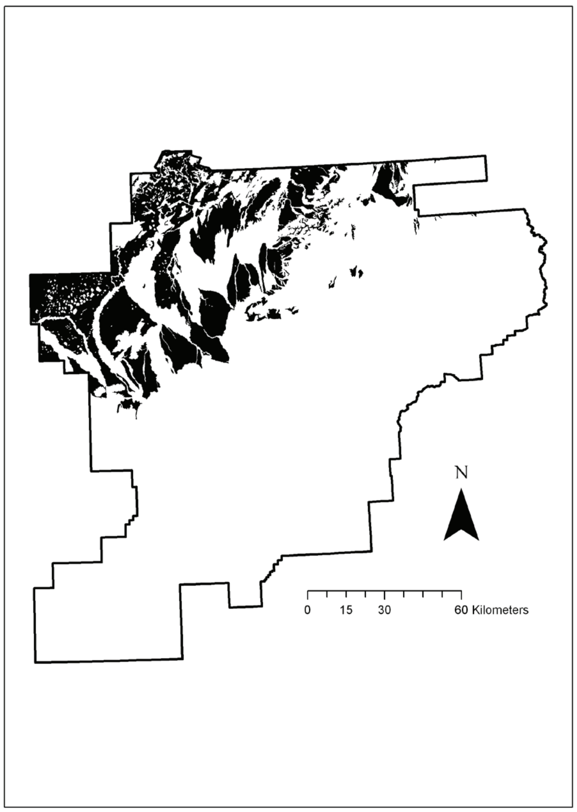

Figure 4. Upper: An extensive loess plain with black spruce/ericaceous shrub woodland and Gelisols with low sensitivity to disturbance. Lower: Gelisols with low sensitivity to disturbance are represented in black and total 391,760 ha or about 16% of Denali.

disturbance or temperature change are represented in black in Figure 5 and total 445,192 ha, or 18% of Denali. The moderate thermal conductivity property of soils is considered an important factor of change in this class. Loss of permafrost to depths below 200 cm is observed at three to five years following fire, and is significantly longer than that observed for the previous class. However, the return to the pre-burn condition is similar to that of the highly sensitive soils: about 130 years. A single climax plant community consisting of shrub birch-mixed ericaceous shrub/sedge scrub has been identified, suggesting a moderately low level of diversity in terms of habitat types.

Soil map units with Gelisols that have low sensitivity to disturbance are represented in black in Figure 7 and total 391,760 ha, or about 16% of Denali. The relatively low thermal conductivity property of soils is attributed to the minimal change on these soils following disturbance. Gelisols within this sensitivity class are observed to experience only slight lowering in depth to permafrost, rarely exceeding 200 cm depth unless associated with localized massive ice degradation. Site and soil characteristics typically return to the pre-burned condition within 25 years, based on tree core observations. Several ecological landtypes are included in this sensitivity class, each with unique climax vegetation and seral communities. Black spruce woodlands with various understory including ericaceous shrub, cottongrass tussock are common late succession communities within the boreal biome and tussock cottongrass/mixed ericaceous shrub meadow in the alpine life zone. Several community types are identified for this sensitivity class. However, most types are similar in terms of species composition, with only subtle differences apparent between succession states.

References

Bailey, R.G., P.E. Avers, T. King & W.H. McNab (eds.), 1994. *Ecoregions and Subregions of the United States* (map). 1:7,500,000. USDA Forest Service. Washington, DC. With supplementary table of map unit descriptions, compiled and edited by W.H. McNab and R.G. Bailey.

Clark, M.H. & Duffy, M. 2004. *Soil Survey of Denali National Park and Preserve Area, Alaska.* Available on Web Soil Survey. http://websoilsurvey.nrcs.usda.gov/app/WebSoilSurvey.aspx.

Dyrness, C.T. 1982. *Control of depth to permafrost and soil temperature by the forest floor in black spruce/feathermoss communities.* U.S. Department of Agriculture, Forest Service. Research Note PNW-396.

Foote, M.J. 1976. *Classification, description, and dynamics of plant communities following fire in the taiga of Interior Alaska.* Fire effects study. U. S. Department of Agriculture, Forest Service, Institute of Northern Forestry. Final report. BLM contract No. 53500-ct2-224.

Viereck, L.A. 1973. Wildfire in the taiga of Alaska. *Quaternary Research* 3(3): 465-495.

Jury, W.A.;. Gardner, W.R & Gardner, W.H. 1991. *Soil Physics*. New York, NY: John Wiley and Sons, Inc.

Patric & Black. 1965.

Péwé, T.L. 1975. *Quaternary geology of Alaska.* Geologic Survey Professional Paper 835. Washington, DC: U.S. Govt. Printing Office.

Soil Survey Staff. 2004. *Keys to Soil Taxonomy*. 10th ed. U.S. Department of Agriculture, Natural Resources Conservation Service.

A Multi-Disciplinary Approach to Assess the Impact of Global Climate Change on Infrastructure in Cold Regions

Jim Clarke
BP Exploration, Sunbury, UK

Clark Fenton
Imperial College, London, UK

Antonio Gens
Universitat Politècnica de Catalunya, Barcelona, Spain

Richard Jardine, Chris Martin, David Nethercot
Imperial College, London, UK

Satoshi Nishimura
Port and Airport Research Institute, Yokosuka, Japan, formerly Imperial College, London, UK

Sebastia Olivella
Universitat Politècnica de Catalunya, Barcelona, Spain

Catherine Reifen, Paul Rutter, Fleur Strasser, Ralf Toumi
Imperial College, London, UK

Abstract

Imperial College London is researching with BP some potential impacts of future climate change. BP has a significant number of facilities in cold high-latitude regions, where global climate models predict significant rises in air and ground surface temperature. This could impact on the state and extent of permafrost, potentially posing risks to facilities, infrastructure, and operations (ACIA 2005). The paper reviews the research, focusing on an exemplar study region in eastern Siberia. The key elements included: (1) Developing an approach to provide a best estimate of future climate change. (2) An engineering geological appraisal of the ground conditions in the study region. (3) Performing a parametric study of geothermal conditions in the study region using finite element thermal analyses. (4) Developing a Thermal-Hydraulic-Mechanical modeling approach for assessment of climate change impact on specific engineering facilities. (5) Developing a methodology for incorporating potential climate change considerations into engineering decision-making and design.

Keywords: climate change; engineering adaptation; engineering geology; GCM modeling; Siberia; thermal modeling.

Introduction

This paper describes research by Imperial College London commissioned by BP Research. The objective was to provide BP with a process for assessing the likely effects of climate change on the integrity of its engineered facilities. The original brief was to:

- Describe the potential impact of changes in local climatic conditions on BP's current operations between now and the 2050s.
- Determine the potential vulnerability of new projects should existing design parameters remain unchanged.
- Provide a process to evaluate BP's exposure to damaging or beneficial effects of climate variability.
- Provide guidelines for the design of structures and infrastructure that anticipate potential future climactic changes in the region of interest.

A generic process has been developed to assess the potential exposure of future projects to climate change, but it became clear during the early parts of study that the outputs of General Circulation Models (GCM) used to predict climate change are not easily converted into data that can be used for engineering design. It was therefore decided to focus particular attention on the possible engineering consequences of air warming on the temperature profiles of frozen ground, the potential effects of permafrost thawing, and the difficulties of operating facilities in permafrost areas. This required the development of new modeling techniques for the assessment of climate change-induced effects on pipelines, foundations, and slopes in regions of existing permafrost.

An area of eastern Siberia was chosen as a relevant example, in order to validate the process,and to demonstrate the potential importance of climate change to BP operations.

Climate Modeling as a Geotechnical Input

The climate data used in this study is based on the predictions of seventeen coupled Atmosphere Ocean General Circulation Models (AOGCM) included in the IPCC Fourth Assessment Report (IPCC 2007), whose data is available from the Coupled Model Intercomparison Project (see URL: https://esg.llnl.gov:8443). These models were chosen because they have provided climate predictions under the conditions of the SRES A2 emissions scenario (Nakicenovic et al. 2000) adopted in this study, which is a standard pessimistic projection of greenhouse gas emission.

Coupled AOGCMs are the most sophisticated tools available for modeling current and future climate. All models used in this study have produced simulations of 20th Century climate that have been validated against appropriate contemporary observations. Climate models perform better at large spatial scales (such as global mean predictions), than at regional or local level, but there is nevertheless reasonably good agreement between modeled and observed temperature trends in Siberia and other cold regions. Careful statistical assessments indicate that the most reliable predictions are made by averaging the results of all available models to form a multi-model ensemble mean.

The multi-model ensemble mean air temperature (defined as the temperature at 2 m above the ground surface) was compared with the corresponding European Centre for Medium-Range Weather Forecasts 40 Year Re-analysis (ERA-40) observational dataset (Simmons & Gibson 2000) for each study area over the 1958–1998 period. Corrections were applied to the entire 1940–2059 time-series based on the difference between modeled and observed 40–year monthly mean temperature from 1958–1998, in an attempt to eliminate model bias as far as possible. The same process was applied to the corresponding multi-model mean time-series for snow depth. Each model time-series was then considered to correspond to the relevant 2.5° x 2.5° ERA-40 grid cell, which is equivalent to an area of approximately 150 km (east-west) by 280 km (north-south) in the study region. In all cases, the processed time-series represents a significantly larger area than would ideally be required for the thermal ground modeling, but further improvements in resolution would require better coverage of local station data than is currently available. An example of the model output is included in Figure 4, along with the predictions for changes in the ground thermal regime discussed below.

Height corrections were applied to produce both air temperature and snow depth time-series for different elevations. Temperature was adjusted based on mean monthly lapse rates derived from linear regression of the corresponding ERA-40 temperature, available for six elevations between 0 and 3000 m above sea level (m a.s.l.). Snow depth was adjusted in the accumulation phase based on a simple model describing orographic enhancement of precipitation (Roe et al. 2002), for which mean slope and wind speed data were taken from ERA-40. In the melting phase, snow depth was adjusted based on a combination of air temperature and solar radiation (Cazorzi & Fontana 1996), the former being dependent on the height correction applied to the temperature time-series. The final predicted mean monthly time-series were validated against local data and appear to be consistent with conditions in the study areas.

Project Geotechnical Strategy

The strategy developed for assessing the impact of climate change in cold regions has involved geotechnical research and development in four main areas:

1. Assessing the regional engineering geology and geomorphology of the study region, including identification of potential geohazards.
2. Reviews of present conventional frozen ground engineering practice.
3. Developing rigorous geothermal analytical tools and applying these on a regional basis.
4. Exploring and developing the potential of THM modeling in cold region engineering applications.

This work has led to a practical process for assessing geotechnical impact of climate change in cold regions that involves a hierarchy of risk assessment activities. The level of sophistication adopted for the risk assessment reflects the severity of potential adverse effects to BP's infrastructure and operations. The consequence assessment is carried out at a regional scale and incorporates consideration of the local ground conditions (identification of geohazards), the climate modeling outputs (sensitivity of hazard to climate change) and the inventory of BP's infrastructure (exposure and vulnerability).

The following three-level approach is recommended:

- Low-consequence hazards addressed through check-lists combined with simple accepted empirical methods.
- Intermediate-level cases to be tackled through regional (or site-specific) uncoupled geothermal modeling predictions combined with well-established conventional geocryological engineering approaches.
- Potentially high-consequence hazards to be addressed by advanced site-specific THM modeling.

The results obtained from any one of these approaches should confirm or challenge the initial assessment and could lead to a higher level of investigation.

Engineering Geology and Geomorphology

A region of eastern Siberia around Lake Baikal (Fig. 1) was chosen as the main focus for investigating the geotechnical impacts of climate change in an area of variable permafrost. The local geological, geographical, and climatic setting was assessed through an extensive review of published data, including geological and geocryological maps, consulting reports as well as interviews with local and international specialists. A brief reconnaissance field trip was also undertaken. The work was limited by the remote, undeveloped nature of the region. The data availability to western parties was also limited by a combination of material sensitivity, geographic location of resources, and translation requirements. A good data set is crucial to the recommended process and, to progress this study, the current assessment was augmented by reference to data from analogous geological and geocryological settings around the world.

Data requirements

The inputs needed to assess the geotechnical impact of climate change on permafrost are driven by the requirements of the geothermal modeling analyses discussed below. The key data requirements are:

- Comprehensive local climate records.
- Geographical and geomorphological information.

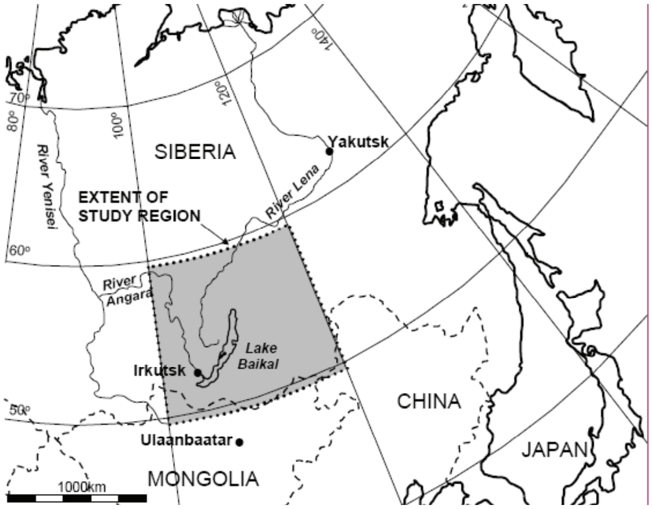

Figure 1. Study region and vicinity map.

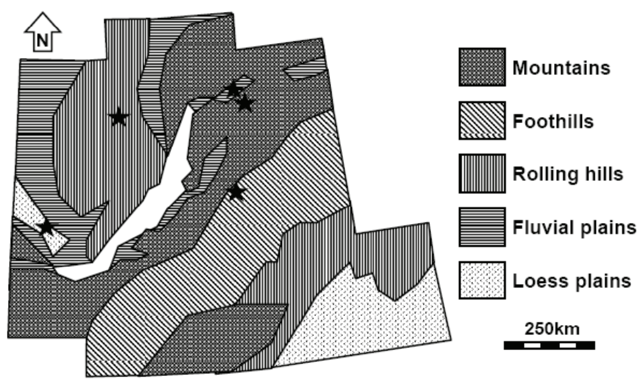

Figure 2. Classification into five geomorphological units. Black stars show location of "exemplar" study areas.

- Surface and deeper geology.
- Geocryology, including ground thermal regime and geothermal material properties.
- Land use and forest fire records.
- Inventory of relevant infrastructure.

Regional setting of study area

Ground conditions vary considerably over the area selected for detailed study, which is outlined in Figure 1 and measures approximately 1300 km east-west and 1100 km north-south. The topography ranges from high-relief mountains (Baikal, Patoma, and Khamar Daban ranges) to low-lying fluvial plains towards Mongolia and along the Angara River valley. The geology varies from relatively flat-lying undisturbed sedimentary rocks of the Siberian platform, to much older highly deformed and metamorphosed rocks along the active Baikal rift zone. The significant variation in relief has a profound effect on the observed climatic conditions, the vegetation, drainage characteristics, and hence the permafrost distribution within the region, which varies from being absent to continuous.

Geomorphological units and expected ground conditions

In order to assess the ground conditions across the study region, five geomorphological units were defined, which encompass broadly similar physical characteristics, as shown in Figure 2.

Once these geomorphological units were defined, five "exemplar" study areas were selected (Fig. 2), which provided representative settings for the associated climate modeling, geothermal ground modeling and engineering geological terrain analysis.

Remote sensing data (Shuttle Radar Topography Mission [SRTM] topographic survey data) was used to produce a Digital Elevation Model (DEM), allowing detailed assessment of elevation, slope angle, slope aspect, and drainage characteristics within each study area. This terrain analysis could be further enhanced in future applications by incorporating higher resolution datasets.

Geological, geocryological, and geotechnical characteristics were interpreted for each study area, based on literature review and field reconnaissance, assigning data where necessary from other global analogues. The latter included representative vegetation and ground void ratio profiles for each study area, which provided best-estimate, lower-bound, and upper-bound parameters for geothermal numerical modeling in each setting.

Although this investigation has included a thorough review of all of the readily available data, there is significant uncertainty associated with the age, provenance, and hence accuracy of some of the available information. The current review is considered adequate for a preliminary research study, which could be compared with the feasibility or possibly appraisal stage of a large civil engineering project. However, detailed site-specific information and further analysis would be essential before progressing to any preliminary design stage.

Geocryological Engineering

Civil engineering activity in the North American cold regions prompted rapid development from the 1960s of specialist geotechnical tools, analyses and practices, as detailed in Andersland & Ladyanyi (2004), for example. Similar work was undertaken from an earlier date in the Former Soviet Union, although much of the output was published in Russian and is less well known in the West. The paradigms, practices, and design codes applied in North America and the Former Soviet Union are substantially different.

Some of the practical geocryological engineering topics that are important to the proposed risk assessment and design processes are highlighted below.

Geocryological analysis: elements, options, and strategy

Geocryological engineering analysis involves many elements; the relative significance of which depends on the nature of the engineering problem of interest. For example, thermal (T), hydraulic (H), and potentially chemical (C) elements are more important than the mechanical (M) element in water discharge or contaminant transport problems. However, it is essential to address the mechanical element when assessing the viability, stability, and serviceability of facilities, pipelines and slopes.

Checklists, definitions, and indices

The essential precursor for all rational geocryological analyses is the information gathering and data access. Geothermal modeling is only possible when adequate climate, geology, and ground temperature data exist, including the local air-to-ground temperature conversion factors, which are influenced by local vegetation, soil types, topography, and weather patterns.

Ground behaviour associated with thermal regime changes

Engineering activities and climate change trends are both likely to modify the ground's thermal regime. Significant deterioration of the engineering properties of frozen soil is expected as temperatures increase, potentially leading to difficulties with embedded structural elements such as foundations and pipelines. Potentially severe phenomena may be encountered in soils or rocks that become unstable as they thaw. It is also well known that frozen soils show very strongly time-dependent behaviour: creep movements can be large in the field and field strengths may be far lower than are seen in laboratory loading tests.

Furthermore, the thawing of frozen open ground can lead to substantial settlements and large transient pore-water pressures. In cold regions, slope stability is dominated by thermal effects. Slopes sited in permafrost areas experience annual cycles of thawing and freezing in their active layers, experiencing seasonal downslope creep. Large-scale instabilities can also occur as a result of changes in ground surface conditions or sub-surface hydrology.

Construction itself may generate more significant thermal changes in foundation soils and rocks than those expected from climate change alone. Insulation elements, air ducts, or active cooling systems are often designed and installed to improve foundation behaviour, and these could be required more extensively to cope with climate change.

A key issue in pipeline engineering is the effect on the ground thermal regime of heat flow to or from the pipeline and its products. Thawing induced by running warm oil in pipelines buried in frozen ground can induce melting, settlement, strength loss, and even floatation. Elevated sections may be utilised, but these require piled foundations that can cope with the possible geotechnical consequences of climate change. On the other hand, ice migration and growth caused by running chilled gas in buried unfrozen ground can cause serious differential heave in pipelines installed in discontinuous permafrost regions. It is therefore vital to consider all potential damage processes within the risk assessment process.

Thermal Modeling and Permafrost Mapping

In order to make reasonable assessments of how slopes, foundations and pipelines may respond to climate change, it is necessary to be able to reliably predict how ground temperatures and properties will react over tens of metres of depth. GCM models incorporate sophisticated formulations that address temperature variations within the atmosphere and oceans, and offer projections as to how the climate may change in the future. However, the near-surface temperature of the ground is usually considered in a simplistic manner, for example, by assuming a constant ratio between air and ground temperature changes, and little attention is given to what may happen at greater depths. The GCMs therefore fail to predict the considerable time lag between climate change and ground response, potentially resulting in gross overestimates of the depth of permafrost melting expected by any given date, the degree of ground warming, and, therefore, of permafrost degradation and infrastructure distress.

Simple models have been proposed to relate air and ground temperatures; however, the Authors' work has shown that the thermal conductivity is complex and nonlinear in permafrost, and a fundamental analytical treatment is necessary to predict the variations with time of the thermal regime, extending tens of metres beneath the ground surface. A fundamentally formulated regional approach has been developed for the present study. A new Finite Element Code (FEM FATALE, Nishimura 2007a) was written to perform rigorous thermal analyses efficiently for multiple vertical profiles. The code can also be applied to any other specific site, for which detailed information is available.

The model is based on non-linear heat conduction theory, with material properties that effectively vary with unfrozen water content and hence temperature. The thermal properties of water, ice, and the soil minerals are fixed, and the global properties at any point in the ground profile depend on the ground's porosity profile (which is input on the basis of the engineering geology assessment described above) and a specific function that relates the degree of ice saturation to temperature. The code also incorporates latent heat effects. The effects of the seasonally-variable snowcover are modeled explicitly. The surface energy transfer is modeled using the n-factor approach (Lunardini 1978), making careful distinctions between summer values and times when the ground is snow-covered, when n is taken as unity. These purely thermal regional analyses do not consider pore fluid migration or ground deformations; these features are covered by the more sophisticated, fully-coupled THM approach reported later.

The purely thermal approach has been applied on a regional basis by considering multiple analyses of the development of permafrost in the circum-Baikal region, covering the period 1940 to 2059. Climate predictions have been applied to stereotypical ground profiles that were selected to encompass the range of geological/geotechnical conditions that might reasonably be expected within the five geomorphological units in the study region. An extensive parametric study has been performed with FEM FATALE to produce time-series predictions for ground temperature and ice content profiles from ground level to 100 m depth, considering the effects of different surface elevations, porosity profiles, snow cover, and natural geothermal gradients; the output data providing the basis of a large-scale risk assessment process for climate change-induced hazards. Examples of some predictions are shown in Figures 3 and 4; substantial warming and thawing is indicated over the next 50 years within

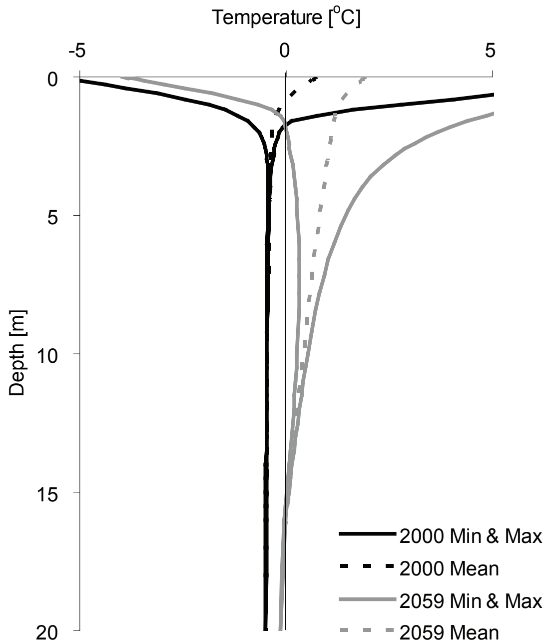

Figure 3. Example of simulated geothermal curves: case of stratigraphy with 1 m colluvial soil (assumed porosity, ∅ = 0.4) and 9 m weathered rock (∅ reducing from 0.4 to 0.04 with depth) overlying base rock (∅ = 0.04) in the rolling hills study area, 643 m a.s.l. (assuming air-surface thawing index, n_t = 0.6).

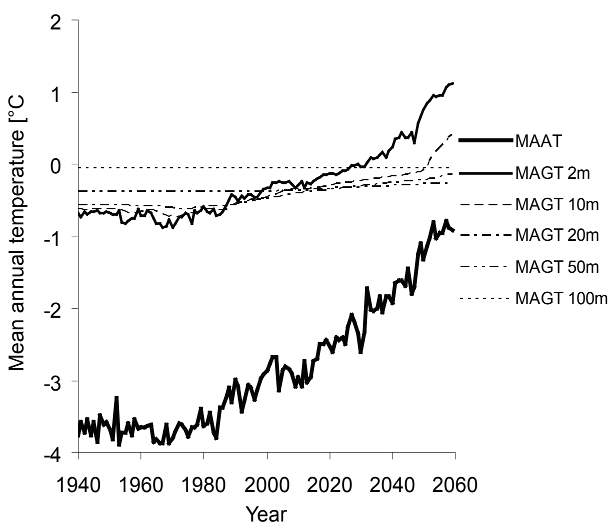

Figure 4. Predicted time-series of temperature at different depths, for example shown in Figure 3.

the top 20 m that would have a considerable negative impact on foundations, pipelines, and slopes.

In addition, a new method has been developed for correlating, synthesising, and presenting the time-dependent evolution of geocryological conditions in a series of layered maps. The approach interfaces data from DEM and GCM sources with the FEM FATALE thermal analyses. The approach has been used to successfully predict, from first principles (i.e., “Type A” prediction, Lambe 1973), the current and historical extent of permafrost in each geological study area, and can be used to produce maps of future distribution of permafrost and its thermal characteristics. Engineering geocryological analyses may be performed based on these data to predict the geotechnical impact for a particular facility or area.

Fully-Coupled Finite Element Analysis

In cases where the consequences of the expected ground temperature changes are sufficiently significant, more rigorous THM analyses of the interconnected thermal (T), hydraulic (H) and mechanical (M) processes may be deemed necessary. THM analyses incorporate predictions for ground movements, soil stresses, and changes in state, along with possible ground failure and soil-structure interaction. While THM models offer potentially powerful tools for assessing climate change impact, they are rarely conducted in practice: their complexity, incompletely developed formulation, and long computational run times limit their current appeal. Assessing, developing, and demonstrating THM applications in cold region geotechnical engineering was an important aspect of the present study, even though THM analyses are likely to be reserved for high-consequence cases.

THM-analysis has been developed intensively for high-temperature problems, particularly related to nuclear waste disposal. However, its application to frozen soils has concentrated on frost heave, and its potential use in permafrost problems has only been noted recently. The group collaborated with colleagues at UPC Barcelona for this purpose, running and developing with them their sophisticated THM programme CODE-BRIGHT (Olivella et al. 1996, Gens 2008). The main aims of the THM component of the study, and the achievements made, were:

- An assessment of the difficulties in applying THM-analysis to permafrost problems. Potential problems have been identified and solutions found that will enable a wider range of applications.
- Developing a robust overall THM modeling framework capable of embracing future sub-model developments. The formulation requires additional features that are important in ice-rich permafrost, including the development of large creep strains under load and the potential for extreme pore pressure generation during thawing.
- A new framework of describing stresses in frozen soils. This development has opened a way for recently developed soil model elaborations to be directly applied in frozen ground modeling.
- Successful back analyses of practical pipeline frost heave problems, which demonstrate the potential for THM analysis in cold region engineering applications.

Freezing ground water migration problems such as frost heaving around chilled pipelines can be simulated with reasonable accuracy by the CODE-BRIGHT model in its current state; the case study outlined below is provided as an illustration. THM analyses undertaken with the code for this project provide good predictions of the frost heave measured in a carefully controlled, long-term field test involving chilled gas running in a frost susceptible unfrozen silty soil (Slusarchuk et al. 1978). Figure

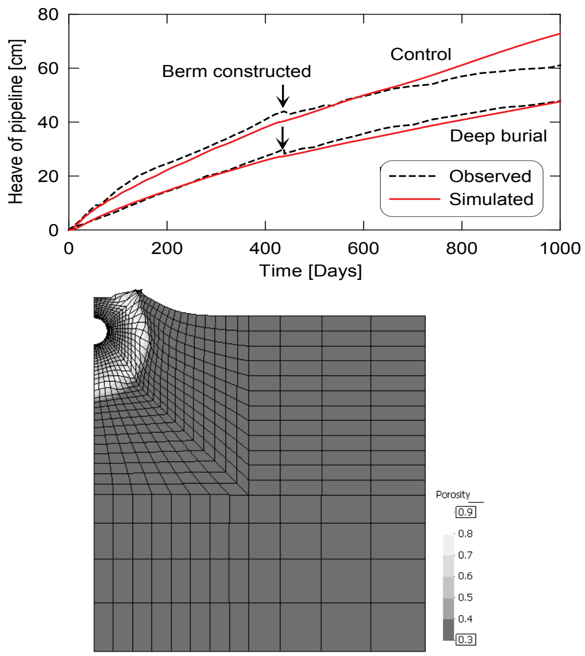

Figure 5. Top: Comparison between observed and measured heave of pipeline buried at two different depths. Bottom: Deformed mesh showing simulated pipeline heave and porosity contours in "Control" case at day 1000.

5 shows the generally good agreement between the observed and simulated heave of pipelines buried at two different depths; 'Control' and 'Deep burial' (Nishimura 2007b).

The THM model's fully-coupled treatment allows far more generalised situations to be considered than conventional engineering geocryological methods. Three-dimensional soil-structure interaction in discontinuous permafrost can be considered, in principle, without many additional modifications.

Conclusions

- A multi-disciplinary approach has been developed to assess the impact of climate change on infrastructure; this has been applied in an exemplar cold region of eastern Siberia.
- The effect of air temperature change on ground temperature profiles has been identified as being of critical significance to facilities and ground conditions in areas of variable or discontinuous permafrost.
- An integrated regional assessment approach has been developed that combines climate modeling data, engineering geology assessments, remote sensing data, and geocryological engineering methodologies to produce regional ground condition predictions.
- More advanced fully-coupled THM approaches have also been explored for site-specific application in critical cases. Key development targets have been identified for future THM modeling research.
- The research predicts that climate change will have a considerable impact on ground conditions in the study region over the next 50 years. However, the effects will be less severe than might be anticipated from studies that do not model the ground response with the same level of sophistication.

Acknowledgments

The Authors thank BP for their permission to publish and acknowledge the modeling groups for providing their data for analysis, PCMDI for collecting and archiving model output, and the JSC/CLIVAR Working Group on Coupled Modeling for organizing model data analysis activity. The multi-model data archive is supported by the Office of Science, U.S. Department of Energy. ERA-40 data have been obtained from the ECMWF data server. We would also like to acknowledge assistance from Arup Geotechnics London with the SRTM processing and terrain analysis.

References

ACIA. 2005. *Arctic Climate Impact Assessment*. Cambridge University Press, 1042 pp.

Andersland, O.B. & Ladanyi, B. 2004. *Frozen Ground Engineering*, John Wiley & Sons, 384 pp.

Cazorzi, F. & Fontana, G.D. 1996. Snowmelt modeling by combining air temperature and a distributed radiation index, *Journal of Hydrology* 181: 169-187.

Intergovernmental Panel on Climate Change. 2007. *Climate Change 2007: The Scientific Basis.* Contribution of Working Group I to the Fourth Assessment Report of the Intergovernmental Panel on Climate Change. Cambridge, UK: Cambridge University Press,

Gens, A. 2008. *Soil-environment interactions in geotechnical engineering*. Rankine Lecture. Presented 21 March 2007. *Geotechnique* (in press).

Lambe, T.W. 1973. Predictions in soil engineering. *Geotechnique* (23)2: 149-202.

Lunardini, V.J. 1978. Theory of n-factors and correlation of data. *Proceedings of the Third International Conference on Permafrost, Edmonton, Alberta*: 41-46.

Nakicenovic, N. et al. 2000. *Special Report on Emissions Scenarios: A Special Report of Working Group III of the Intergovernmental Panel on Climate Change.* Cambridge, UK: Cambridge University Press.

Nishimura, S. 2007a. *Assessment and prediction of circum-Baikal permafrost development over period 1940-2059.* Imperial College Internal Report.

Nishimura, S. 2007b. *THM-Coupled Finite Element Analysis of Soil Freezing: Formulation and Application.* Imperial College Internal Report.

Olivella, S., Gens, A., Carrera, J. & Alonso, E.E. 1996. Numerical formulation for a simulator (CODE_BRIGHT) for the coupled analysis of saline media. *Engineering Computations* 13(7): 87-112.

Roe, G.H. et al. 2002. Effects of orographic precipitation variations on the concavity of steady-state river profiles. *Geology* 30(2): 143-146.

Simmons, A.J. & Gibson, J.K. 2000. *The ERA-40 Project Plan.* ERA-40 Project Report Series No. 1. Reading, UK: ECMWF, Shinfield Park, 63 pp.

Slusarchuk, W.A., Clark, J.I., Nixon, J.F., Morgenstern, N.R. & Gaskin, P.N. 1978. Field test results of a chilled pipeline buried in unfrozen ground. *Proceedings of the Third Intl. Conf. on Permafrost, Edmonton, Alberta*: 878-883.

Freezeback of an Anthropogenic Talik Within Tailings at Nanisivik Mine, Canada

Geoff Claypool, P.Eng.
BGC Engineering Inc.

James W. Cassie, P.Eng.
BGC Engineering Inc.

Robert Carreau
Breakwater Resources Ltd.

Abstract

Following 26 years of successful mining, the tailings facility at the Nanisivik Mine site was reclaimed between 2004 and 2005. The objective of the reclamation plan for the tailings facility was to use the cold environmental conditions to encapsulate the tailings in permafrost, thereby limiting the potential for negative environmental impacts over the long term. During reclamation planning, a talik was identified within the tailings deposit. The talik was studied in detail due to its unknown effect on the stability of the adjacent tailings retention dike and the effect of freezeback on surface water quality, and to assess the time required for freezeback to occur. This paper summarizes the studies undertaken to characterize the talik and assess freezeback, ,and includes performance monitoring undertaken to date.

Keywords: cryoconcentration; freezeback; Nanisivik; pingo; tailings; talik.

Introduction

Nanisivik Mine is located at the northern end of Baffin Island in the Territory of Nunavut in the Canadian Arctic. The mine operated from 1976 to 2002, during which time sulphide ore was mined to produce lead and zinc concentrates. The tailings generated during the mining process were initially deposited directly into West Twin Lake (WTL). However, as additional mining reserves were identified, the West Twin Lake reached its storage capacity, and it became necessary to identify further storage options to keep the mine in production. Construction of a frozen tailings retention dike permitted the continued use of the West Twin Lake area until closure of the mine in 2002. During tailings deposition in the West Twin Disposal Area (WTDA), a partial water cover was maintained over most of the tailings. In areas where the tailings were aerially exposed, or where only a thin water cover was maintained, permafrost aggraded into the tailings. In areas where a deeper water cover was maintained, the tailings remained in a thawed state. As such, a talik, a zone of thawed materials surrounded by permafrost, formed within the tailings deposit.

Between 2002 and 2004, development of the Final Closure and Reclamation Plan (FCRP) for the West Twin Disposal Area was undertaken. This included characterization and delineation of the talik and an assessment of the potential effects of freezeback of the talik anticipated during closure. The talik delineation and characterization program was undertaken by conducting a detailed geotechnical drilling investigation which included installation of several types of monitoring instrumentation. Freezeback assessment of the talik included geothermal modeling to predict the rate of talik freezeback and assessing the potential for pingo growth, frost-heave and generation of high pore pressures within the center of the talik and its effect on the stability of the adjacent dike.

Figure 1. Regional location map – Nanisivik Mine.

Between 2004 and 2005, the reclamation plan for the West Twin Disposal Area was implemented. The partial water cover was removed from the tailings pond and a permafrost aggradation cover was constructed over the tailings to promote the freezeback of the talik. Additional instrumentation was installed after construction of the cover to monitor ground temperatures, pore pressures, and water quality in the talik during freezeback. This paper provides a summary of the talik characterization and assessment work that was completed and a summary of the monitoring data collected during the initial years of talik freezeback.

Background

Location and climate

The Nanisivik Mine Site is located on the northern end of Baffin Island in the Canadian Arctic, as shown on Figure 1.

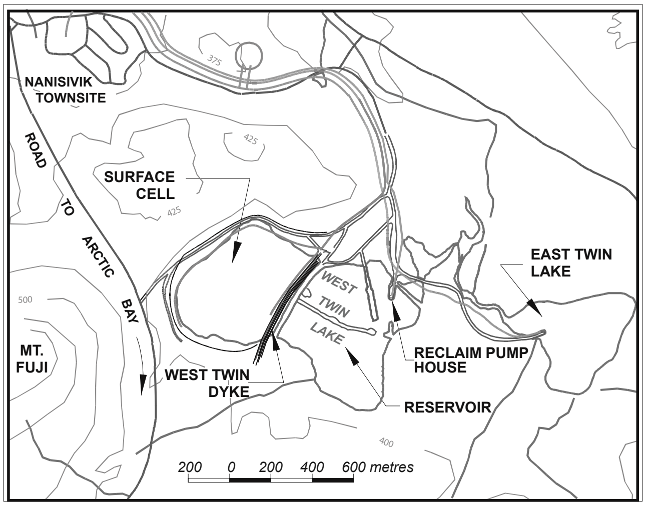

Figure 2. West Twin Disposal Area.

Based on the available climate record from the Nanisivik airport (1971–2006) the mean annual air temperature (MAAT) is approximately -14.8°C and the mean annual precipitation is 282 mm/yr.

Permafrost

Nanisivik is located in the region of continuous permafrost. Permafrost has been observed to extend to a depth of at least 430 m, as observed in a borehole drilled from the underground workings. Ground conditions in the area have been characterized by NRC (1995) as having the potential for medium amounts of ground ice (as high as 20%) and mean annual ground temperatures colder than -10°C. This has been verified by ground temperature measurements at various locations around the mine site as cold as -13°C at depth. The depth of the active layer in natural ground has been observed to average between 1 m to 2 m below ground surface.

Tailings deposition practices

Tailings were initially deposited sub-aqueously into WTL beginning in 1977. Based on the known mine reserves at the time, WTL had sufficient tailings storage capacity for the life of the mine. Mine reserves, however, continued to expand each year and by the mid 1980s, it was apparent that continued production would exceed the storage capacity of WTL. In 1988, an approval was received from the Northwest Territories Water Board to begin surface deposition of tailings at Nanisivik. To accommodate this, WTL was divided into two sections using an earthen dike, as shown on Figure 2. The dike was constructed using a north/south trending causeway that was developed by beaching of tailings in the lake as a foundation. The eastern portion of the lake, the Reservoir, retained its original lake level and was used as a stand-by when surface disposal was not practical (i.e. during annual dike construction periods). The western part of the lake, the Surface Cell, became the main deposition area for the tailings and accommodated sub-aerial tailings.

On-land deposition of tailings in the Surface Cell commenced on August 27, 1990. Tailings discharge in the Surface Cell continued throughout the 1990s, permitted by annual raises of the West Twin Dike in 2 m increments. Tailings continued to be discharged mainly from the northwest corner of the Surface Cell with a deeper section of the pond in the southeast corner for water reclamation and mineral processing purposes. In total, it is estimated that 6.5 million m^3 of tailings were deposited into the Surface Cell between 1978 and 2002.

It should be noted that tailings were deposited subaqueously into the area later known as the Reservoir between 1976 and 1990. The discharge of tailings generally took place near the current location of the West Twin Dike resulting in the aggradation of the tailings deposit in a southeasterly direction into the Reservoir. Tailings deposition along an east-west trending line from the centrer of the West Twin Dike resulted in exposure of a tailings causeway in the Reservoir by 1988. This causeway eventually became the foundation for the east/west arm of the Test Cell Dike. Tailings deposition along a northwest-southeast trending line resulted in a second tailings causeway near the reclaim water pumphouse, which was exposed by 1992. This causeway eventually became the foundation for the north/south arm of the Test Cell Dike. The Test Cell Dike was constructed in 2000 and 2001, increasing the storage capacity of the Test Cell thereby allowing for the additional placement of tailings into the Test Cell. Deposition of tailings at the base of the West Twin Dike in 2000 resulted in aerial exposure of tailings in the Reservoir and Test Cell. In total, it is estimated that 3.5 million m^3 of tailings have been deposited into the Reservoir and Test Cell since 1978.

Talik Characterization and Delineation

Geotechnical drilling investigation

In 2002 and 2003, a total of 44 boreholes were drilled in the Surface Cell, Test Cell Dike, and at the base of the West Twin Dike. The drilling was completed using a diamond drill coring rig and chilled brine was used as a drilling fluid to enable core recovery of frozen tailings. The following points summarize the significant observations recorded during the geotechnical drilling investigation:

- The maximum thickness of tailings contained within the Surface Cell was approximately 34 m.
- The maximum thickness of tailings contained within the Test Cell was 20 m.
- During the drilling investigation, thawed tailings were encountered in both the Surface Cell and Test Cell.
- Artesian pore pressures were encountered in the Surface Cell talik.
- The frozen tailings were generally observed to be ice-poor. However, some ice lenses were observed in the frozen tailings. It was unclear if the ice formed in-situ or was encapsulated during deposition.

Select samples collected during the drilling process were forwarded for geotechnical testing. The following points summarize the geotechnical characteristics of the tailings:

- The grain size distribution was variable ranging from 95% sand-sized particles to 95% silt-sized particles.
- Specific gravity ranged from 3.9 to 4.5.
- The tailings generally had a saturation value of greater than 90%.
- The frozen bulk density of the tailings ranged from 2100 to 3500 kg/m^3, with the lowest values associated with samples containing visible ground ice.
- The thermal conductivity of the tailings was measured to be approximately 1.9 W/(m·°C) at room temperature and 3.2 W/(m °C) at -15°C.

A number of monitoring instruments were installed during the geotechnical investigation to further characterize the subsurface conditions. Thermistors and thermocouples were installed to assess geothermal conditions and vibrating wire piezometers were installed to monitor pore pressures within the thawed tailings. Monitoring wells were also installed to assess the pore water quality in the taliks.

Geothermal monitoring data indicated near 0°C temperatures within the talik. Ground temperatures within the thawed zones were observed to be as cool as -0.2°C, indicating freezing point depression. Piezometers installed in the Surface Cell talik indicated artesian pore pressures 3 m to 4 m above ground surface.

The results of the geotechnical investigation and the available historical information on tailings deposition was used to estimate the size of the Surface Cell and Test Cell taliks. Based on the analysis, it was estimated that the Surface Cell and Test Cell taliks contained approximately 2,000,000 m^3 and 1,000,000 m^3 of thawed tailings, respectively, which was approximately 30% of the tailings contained within the facility.

Technical Analyses

Due to the unknown effect of the freezeback of the taliks on the stability of the West Twin Dike, the surface of the reclamation covers or the water quality of the entire system, a number of technical analyses were undertaken. The following sections summarize the objectives and results of each analysis.

Geothermal modeling

Geothermal modeling of the Surface Cell talik was completed to predict the rate of permafrost aggradation into the talik. The results of the modeling were to be used to direct future monitoring efforts and to estimate the time required to achieve various benchmarks during closure.

The geothermal modeling was completed using the commercially available software Temp/W produced by GeoSlope International. The model was calibrated using the geothermal data collected in an area of recently deposited tailings, and by comparing the predicted freezeback thermal regime to the observed freezeback thermal regime over a one year period.

Once the model was calibrated, several analyses were conducted to assess the variability and sensitivity of the results to initial thermal conditions, global warming, snow cover, and the placement of the shale as a cover material. Additionally, an envelope of freezeback times was developed, based on the results of the parametric analyses.

The following is a list of the principal conclusions derived from the geothermal analysis of the Surface Cell talik:

1. There is minimal sensitivity in the predicted depth of permafrost aggradation of the various parameters in the initial 5 years.
2. Permafrost aggradation reaches a depth of 17 m (the base of the West Twin dike) between 7 and 8 years after the initial winter following completion of reclamation activities.
3. Permafrost aggradation reaches an elevation of 365 m, a depth of approximately 23 m, between 13 and 15 years after the initial winter.
4. Depending on the modeled scenario, permafrost aggradation reaches an elevation of 353 m, a depth of approximately 35 m, between 27 and 32 years after the initial winter.
5. The results were not sensitive to assumed global warming values.

Effect of high pore pressures on dike stability

The effect of high pore pressures in the Surface Cell talik on the stability of the West Twin dike were assessed due to the artesian piezometric conditions encountered during the geotechnical investigation.

The artesian pore pressures are thought to be attributed to the process of pore water expulsion that occurs during freezing of saturated soils. McRoberts and Morgenstern (1975) attributes the pore water expulsion process to the fact that when the ice-water interface progresses through a freezing saturated soil, water may be expelled from the ice interface, depending upon soil type and stress level. If no drainage of the excess pore pressures is permitted, then the system is considered closed. If drainage is allowed, the system is considered open.

Useful information can be found on the topic of pore pressures generated by pore water expulsion through the study of pingos. Pingos are intrapermafrost ice-cored hills, typically conical in shape, that grow and persist only in a permafrost environment (Mackay 1998). Many pingos form in the bottoms of old lakes that drained rapidly. They form in response to the development of excessive pore water pressures and differential permafrost thickness. Mackay et al. (1972) suggests that pore pressures generated by pore water expulsion in growing pingos can exceed 80% of the total overburden pressure, even beneath permafrost 40 m thick. Additionally, Mackay (1978) notes that pressure transducers installed in one sub-pingo water lens measured a hydrostatic head of 22 m above lake bottom.

Due to the fact that no evidence of hydraulic connectivity between the Surface Cell talik and the Reservoir was defined during the geotechnical investigation, the Surface Cell talik is considered to be a closed system. As such, the pore pressures within the Surface Cell talik are expected to continue to rise

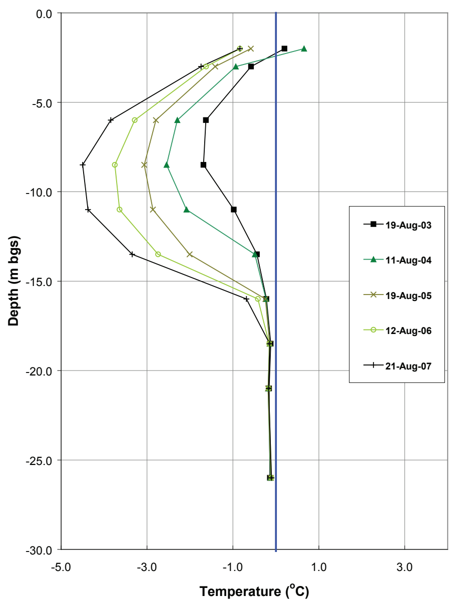

Figure 3. Geothermal monitoring data from edge of Surface Cell talik (BGC03-09).

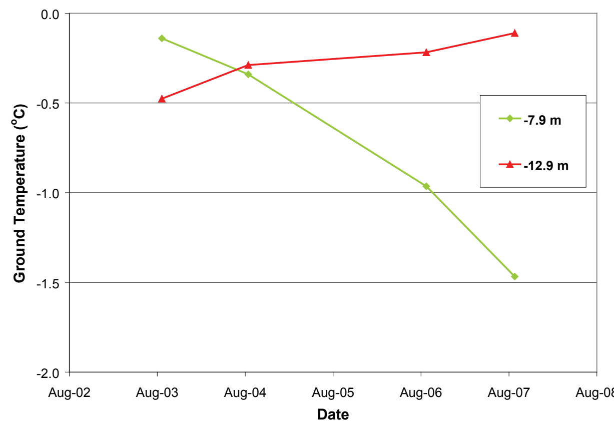

Figure 4. Geothermal data from center of Surface Cell talik (BGC03-10).

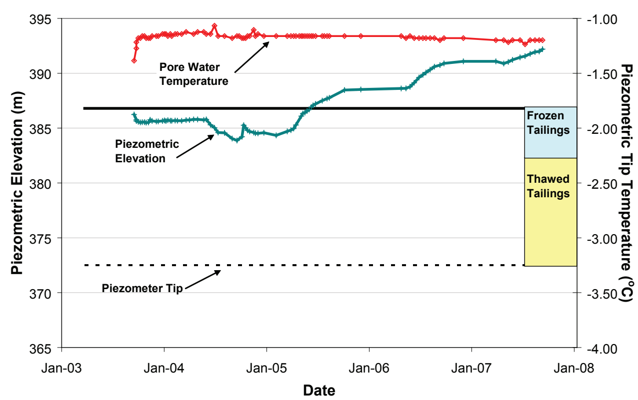

Figure 5. Piezometric monitoring data from Surface Cell (BGC03-35).

as freezeback of the talik progresses. Conversely, due to the presence of a hydraulic connection between the Test Cell alik and the Reservoir, the Test Cell talik is considered an open system. However, the flow path is lengthened by the permafrost aggradation which has occurred beneath the Test Cell Dike. As such, the pore pressures within the Test Cell talik may continue to rise as freezeback progresses, however at a much slower rate than they are anticipated to increase in the Surface Cell talik.

Since the West Twin Dike would remain in place during closure, it was important to determine the effect of the high pore pressures on the long term stability of the dike. As such, a stability analysis was completed assuming a portion of the talik extended beneath the base of the dike, which was considered a conservative assumption. A variety of pore pressure conditions were applied to the thawed zone and the effect of these pore pressures on the stability of the dike were noted. The analysis suggested that pore pressures corresponding to 12 m of artesian head would be required to reduce the Factor of Safety against sliding to 1.0. However it should be noted that the results were sensitive to the configuration of the talik. For example, if the pore pressures were confined deeper beneath the base of the dike, it was found that higher pore pressures could be experienced without affecting the stability of the dike.

Pingo growth potential

The potential for pingo growth was assessed due to the potential deformation it could cause to the physical integrity, and the overall effectiveness, of the surface reclamation cover.

Based on the extensive research by Mackay and others, there are several occurrences required to initiate the growth of a pingo, as summarized below from Mackay (1998):

1. A lake, sufficiently deep to form an underlying talik, must drain, allowing permafrost to aggrade into the underlying talik.

2. If there is at least one large and relatively deep residual pond without any permafrost directly beneath it, then expelled pore water can discharge into the unfrozen basin that underlies the residual pond and a pingo is unlikely to grow.

3. If at least one residual pond of sufficient size and critical depth exists so that the bottom sediments gradually freeze downward, the pressure exerted by the groundwater flow from the large lake bottom area of aggrading permafrost acts like an hydraulic jack (Gasanov 1978) on the much smaller area of the frozen bottom of the residual pond to dome it up and so to initiate pingo growth.

As can be inferred from the research, pingo formation results from a very delicate balance of gradual permafrost aggradation, pore water expulsion, and resultant overburden heaving, in combination with the differential in-situ conditions from the residual pond area to the perimeter lake bottom area. For the case of drained lakes that do not lead to the formation of a pingo, the expelled pore water must either report to the surficial pond (through some vertically oriented talik) or a cryopeg must form at depth below the frozen lake bottom.

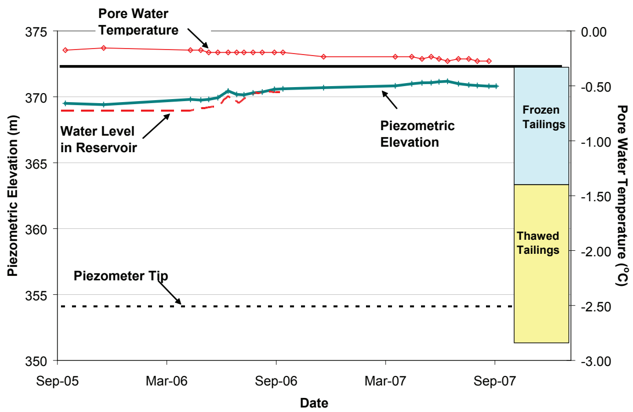

Figure 6. Piezometric monitoring data from Test Cell talik.

In comparison to the pingos formed in the Mackenzie Delta area, the following differences are suggested with respect to the Surface Cell and Test Cell taliks:

1. The remnant pond on the surface of the tailings has been completely removed and the cover has been sufficiently graded such that no residual pond can be formed.
2. Since the pond was completely removed, permafrost aggradation has been quite rapid, as inferred from the geothermal monitoring data collected to date. Due to the rapid aggradation of permafrost, and the high specific gravity of the tailings, the overburden pressure acting on top of the talik was expected to increase soon after completion of the cover.
3. Since there is no remnant pond, there is limited differential in the permafrost aggradation conditions from the previously existing pond area to the surrounding tailings surface.

As a result, instead of a pingo forming, it was considered more likely that a cryopeg would form at depth in the Surface Cell. Based on the monitoring data collected to date, this appears to be the case as no surficial indications of pingo growth have been observed while the pore pressures within the talik continue to increase.

Hydraulic fracturing

Hydraulic fractures occur in frozen ground whenever the fluid pressure exceeds the tensile strength of the enclosing frozen material plus the least compressive principal total stress (Mackay 1998). Hydraulic fractures are of significance significant with respect to reclamation of the WTDA because they could result in the release of pore water from the taliks at surface.

Hydraulic fracturing was thought to be possible in two scenarios during freezeback of the taliks. One area is a hydraulic fracture propagating vertically from the talik to the surface of the Surface Cell. The second is at the base of the West Twin Dike where the fracture could propagate upwards from the talik near the foundation of the dike to surface. Since the freezeback of the top 4 to 5 m of tailings was expected to occur rapidly during the first winter, the water pressure would have to exceed 110 kPa to 135 kPa (the approximate overburden pressure) plus the tensile strength of the frozen tailings for the first scenario to occur. Additionally, the overburden pressure in the area of the talik that underlies the dike is estimated to be approximately 400 kPa. For hydraulic fracture propagation to be initiated, this overburden pressure plus the tensile strength of the frozen tailings must be exceeded.

Table 1. Water quality testing Surface Cell talik.

Instrument	Year	pH	*Total Zinc Concentration*
BGC05-11	2005	10.9	*0.01*
	2006	11.3	*0.08*
	2007	10.5	*0.09*
BGC05-12	2005	10.3	*0.54*
	2006	10.3	*0.29*
	2007	*9.7*	*0.17*

Considering the rapid permafrost aggradation rate into the talik, it was considered unlikely that extremely high pore pressures would develop during the initial freezing period. By the time the pore pressures increased to the values required for fracturing, a frozen layer of sufficient thickness, and of significant frozen density, would likely be in place. Therefore, it was considered unlikely that hydraulic fracturing would occur.

To date, no observations of hydraulic fracturing have been noted. Although, the pore pressures have been observed to be somewhat cyclical potentially indicating that the pore pressures are relieved by some means, at certain times of the year.

Talik Freezeback Monitoring

Instrumentation and monitoring program

After completion of the reclamation covers, an additional twenty instruments were installed to monitor the freezeback of the talik. Thermistors were installed to monitor ground temperatures, vibrating wire piezometers were installed to monitor pore pressures within the talik, and monitoring wells were installed to monitor changes in pore water quality within the talik.

The instrumentation has been monitored regularly since installation. Monitoring is undertaken by site staff on a bi-weekly basis from May through October, and two to three additional times throughout the winter months.

Geothermal monitoring

The thermistors in the Surface Cell monitored since 2003 provide an excellent record of freezeback of the talik. The data from one instrument, BGC03-09, is provided in Figure 3.

Only the data from mid-August of each year is illustrated to provide a clear indication of progression of the freezing front into the talik. As can be seen, the -1°C isotherm has progressed from approximately 11 m below ground surface (bgs) in 2003 to approximately 16 m bgs in 2007. This compares favorably with the predictions made during the geothermal modeling analysis which was predicted for this location. Additional geothermal monitoring data is presented in Figure 4.

The data on Figure 4 is derived from thermistor BGC03-10 which was installed near the center of the talik. As can be seen, nodes within 10 m of the surface are cooling with time, as expected. However, nodes below 10 m have experienced a small degree of warming over the monitoring period. This suggests that heat flow from the surrounding tailings, which are actively freezing, is towards the centrecenter of the talik.

Piezometric monitoring

The piezometers in the Surface Cell monitored since 2003 provide an excellent record of pore pressure in response to freezeback of the talik. The data from one instrument, BGC03-35, is provided in Figure 5.

As can be seen, the pore pressures were not artesian when monitoring began in 2003. This was due to the proximity of the instrument to the former location of the retained pond that used to be contained in the Surface Cell. As the water was removed form the Surface Cell during reclamation activities, the pore pressures in this part of the talik initially reduced. During the first winter after the pond was removed, the pore pressures began to rise in response to freezeback of the talik. This rise in pore pressures suggests that that the system is closed and that pore pressures are not being relieved. Additionally, the vibrating wire piezometers are equipped with a thermistor node at the tip of the instrument. The data collected from this thermistor node suggests the pore water temperature is approximately -1.2°C, indicating a freezing point depression of at least this amount in the centrer of the talik. In contrast, piezometric monitoring data from the Test Cell talik is provided on Figure 6.

As can be seen, the pore pressures in the Test Cell talik are not artesian and tend to mirror the water level in the nearby Reservoir. This suggests hydraulic connectivity between the Test Cell talik and the Reservoir, as was anticipated. Also of note, the pore water temperature measured in the Test Cell talik was approximately -0.2°C, indicating only a slight amount of freezing point depression.

Pore-water quality monitoring

Water samples have been collected from the Surface Cell and Test Cell taliks once a year since completion of the surface reclamation covers in 2005. The data is summarized in Table 1.

The main conclusion drawn from the data is that metals concentrations are highest in the centrer of the talik (BGC05-12) compared to the edge of the talik (BGC05-11). Since the degree of freezing point depression is related to solute concentration, the data suggests that a higher degree of freezing point depression can be expected in the centrer of the talik. This is verified by the monitoring data reviewed earlier which suggested a freezing point depression of at least -1.5°C near the centrer of the talik, compared to -0.2°C along the edge of the talik.

Summary

The freezeback of the tailings at the Nanisivik Mine is a unique process which required detailed study, assessment, and ongoing monitoring to understand the significance with respect to reclamation and long term environmental impacts. Monitoring undertaken to date has supported the conclusions of many of the technical studies undertaken during the development of the reclamation plan.

Acknowledgments

The authors would like to acknowledge Breakwater Resources Ltd. for their permission to publish this paper. We would also like to acknowledge site staff for their meticulous efforts in collecting the monitoring data under challenging conditions.

References

Gasanov, S. 1978. Cyrolithogenesis as an independent hydrothermal type of sedimentary process. *Proceedings 3rd International Conference on Permafrost, Part 1: English translations of twenty-six of the Soviet papers*. National Research Council of Canada, Ottawa, Ontario, NRCC 18119: 225-244.

Mackay, J.R., Rampton, V.N. & Fyles, J.G. 1972. Relic Pleistocene permafrost, western Arctic, Canada. *Science* 176: 1321-1323.

Mackay, J.R. 1978. Sub-Pingo Water Lenses, Tuktoyaktuk Peninsula, Northwest Territories. *Canadian Journal of Earth Sciences* 15: 1219-1227.

Mackay, J.R. 1998. Pingo Growth and Collapse, Tuktoyaktuk Peninsula Area, Western Arctic Coast, Canada: A Long Term Field Study. *Geographie Physique et Quaternaire* 52: 271-323.

McRoberts, E.C. & Morgenstern, N.R. 1975. Pore Water Expulsion during Freezing. *Canadian Geotechnical Journal* 12: 130 - 139.

Natural Resources Canada (NRC) 1995. Canada – Permafrost 1995. *The National Atlas of Canada, 5th Edition.* Published by the National Atlas Information Service, Canada Centre for Mapping, Geomatics Canada and the Terrain Sciences Division, Geological Survey of Canada, Natural Resources Canada 1995.

Geologic Controls on the Occurrence of Permafrost-Associated Natural Gas Hydrates

Timothy S. Collett
U.S. Geological Survey, Denver, Colorado, USA

Abstract

With an increasing number of highly successful gas hydrate field studies, significant progress has been made in addressing some of the key issues on the formation, occurrence, and stability of gas hydrates in nature. The concept of a gas hydrate geologic system as a subcomponent of a conventional oil and gas petroleum system is gaining acceptance. The primary goal of this report is to compare and contrast several permafrost-related gas hydrate systems in order to better understand the geologic controls on the formation and occurrence of gas hydrates. This report focuses on the results of the recently completed BP Exploration Mount Elbert project, which successfully cored, logged, and tested a gas hydrate accumulation on the North Slope of Alaska in the spring of 2007. The Mount Elbert Test, along with the Canadian Mallik 2002 project, have for the first time allowed the rational assessment of the physical response of permafrost-associated gas hydrate occurrences to production.

Keywords: Alaska; Arctic; Canada; gas hydrate; resources.

Introduction

Gas hydrates are naturally occurring 'ice-like' combinations of natural gas and water that have the potential to provide an immense resource of natural gas from the world's oceans and polar regions. Gas hydrates are known to be widespread in permafrost regions and beneath the sea in sediments of outer continental margins. The amount of natural gas contained in the world's gas hydrate accumulations is enormous, but these estimates are speculative and range over three orders-of-magnitude, from about 2,800 to 8,000,000 trillion cubic meters of gas. Milkov et al. (2003) recently reported that the volume of gas trapped in global gas hydrate accumulations was actually in the range of 3,000 to 5,000 trillion cubic meters, which is 1/7 to 1/4 of some of the more widely cited estimates. By comparison, conventional natural gas accumulations (reserves and technically recoverable undiscovered resources) for the world are estimated at approximately 440 trillion cubic meters as reported by Ahlbrandt (2002). Despite the enormous range in reported gas hydrate volumetric estimates, even the lowest reported estimates seem to indicate that gas hydrates are a much greater resource of natural gas than conventional accumulations. However, it is important to note that none of these assessments has predicted how much gas could actually be produced from the world's gas hydrate accumulations.

Arctic Gas Hydrate Accumulations

Gas hydrate in onshore arctic environments is typically closely associated with permafrost. It is generally believed that thermal conditions conducive to the formation of permafrost and gas hydrate have persisted in the Arctic since the end of the Pliocene (about 1.88 Ma). Maps of present day permafrost reveal that about 20 percent of the land area of the northern hemisphere is underlain by permafrost (Fig. 1). Geologic studies (Molochushkin 1978) and thermal modeling of subsea conditions (Osterkamp & Fei 1993) also indicate that permafrost and gas hydrate may exist within the continental shelf of the Arctic Ocean. Subaerial emergence of portions of the Arctic continental shelf to current water depths of 120 m (Bard & Fairbanks 1990), during repeated Pleistocene glaciations, subjected the exposed shelf to temperature conditions favorable to the formation of permafrost and gas hydrate. Thus, it is speculated that 'relic' permafrost and gas hydrate may exist on the continental shelf of the Arctic Ocean to present water depths of 120 m. In practical terms, onshore and nearshore gas hydrate can only exist in close association with permafrost, therefore, the map in Figure 1 that depicts the distribution of onshore continuous permafrost and the potential extent of "relic" sub-sea permafrost also depicts the potential limit of onshore and nearshore gas hydrate.

This paper deals with the assessment of the geologic factors that control the occurrence of gas hydrates. This assessment will be conducted mainly though the examination of several relatively well-characterized gas hydrate accumulations in northern Canada and the United States.

Mackenzie Delta, Canada – Mallik gas hydrate accumulation

Assessment of gas hydrate occurrences in the Mackenzie Delta-Beaufort Sea area have been made mainly on the basis of data obtained during the course of hydrocarbon exploration conducted over the past three decades (Dallimore et al. 1999). Prior to the more recently completed Mallik gas hydrate research drilling programs (Dallimore & Collett 1995, 2005, Dallimore et al. 1999), the most extensively studied gas hydrate occurrences in the Mackenzie Delta-Beaufort Sea region were those drilled in the onshore Mallik L-38 and Ivik J-26 wells (Bily & Dick 1974) and those in the offshore Nerlerk M-98, Koakoak O-22, Ukalerk C-50, and Kopanoar M-13 wells (Weaver & Stewart 1982). On

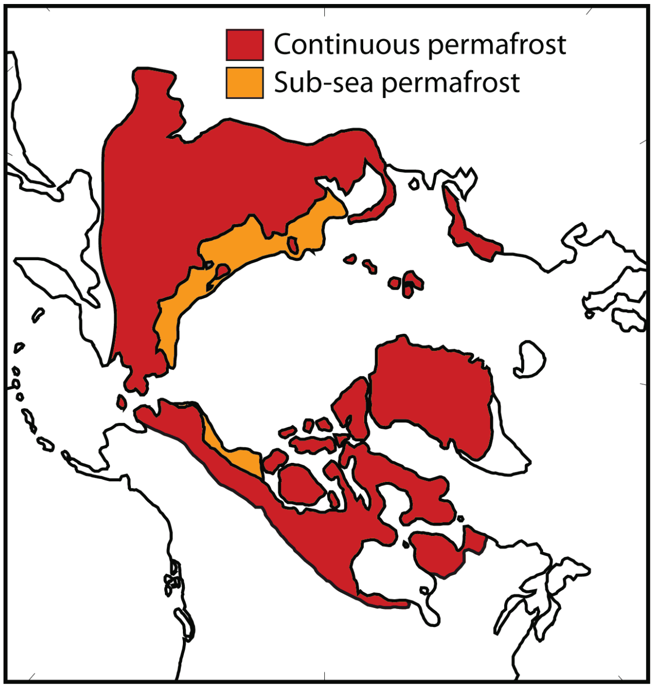

Figure 1. Distribution of permafrost in the Northern Hemisphere.

the basis of open-hole well log evaluation, it is estimated that Mallik L-38 encountered about 100 m of gas-hydrate-bearing sandstone, and Ivik J-26 penetrated about 25 m of gas hydrate. Analyses of open-hole well logs and mud-gas logs indicate that the offshore Nerlerk M-98 well penetrated about 170 m of gas-hydrate-bearing sediments, while the Koakoak O-22, Ukalerk C-50, and Kopanoar M-13 wells drilled approximately 40 m, 100 m, and 250 m of gas hydrate respectively. In all four cases, the well-log inferred gas hydrate occurs in fine-grained sandstone rock units.

During a permafrost-coring program in the Taglu area on Richards Island in the outer Mackenzie Delta, ice-bearing cores containing visible gas hydrate and possible pore-space gas hydrate were recovered (Dallimore & Collett 1995). The visible gas hydrate occurred at a depth of about 330 to 335 m and appeared as thin ice-like layers that released methane upon recovery.

Estimates of the amount of gas in the gas hydrate accumulations of the Mackenzie Delta-Beaufort Sea region vary from 9.3 to 27 trillion cubic meters (Smith & Judge 1995, Majorowicz & Osadetz 1999, 2001); however, these estimates are generally poorly constrained. A more detailed study by Osadetz and Chen (2005) resulted in an estimate that is within the same bounds given by Majorowicz and Osadetz (2001) and range between 1.0 to 10 trillion cubic meters of gas within the permafrost associated gas hydrate accumulations of the Beaufort Sea-Mackenzie Delta region.

The JAPEX/JNOC/GSC Mallik 2L-38 gas hydrate research well, drilled in 1998 near the site of the Mallik L-38 well (Fig. 2), included extensive scientific studies designed to investigate the occurrence of in situ natural gas hydrate in the Mallik field area (Dallimore et al. 1999). Approximately 37 m of core were recovered from the gas hydrate interval

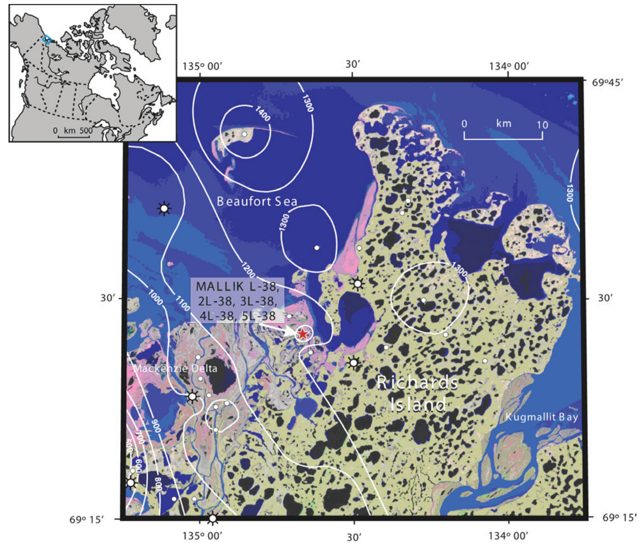

Figure 2. Location of the JAPEX/JNOC/GSC et al. Mallik 3L-38, 4L-38, and 5L-38 gas hydrate production research wells, Mackenzie Delta, Northwest Territories. Base map is a false-color mosaic constructed from a Landsat V image taken July 8, 2002. Contours indicate depth to the base of the gas hydrate stability zone in meters. Symbols include small circles as well locations, larger circles with ticks are wells containing gas hydrate (Dallimore & Collett 2005)

(878–944 m) in the Mallik 2L-38 well. Pore-space gas hydrate and several forms of visible gas hydrate were observed in a variety of unconsolidated sands and gravels interbedded with non-hydrate bearing silts. The cored and downhole logged gas hydrate occurrences in the Mallik 2L-38 well exhibit both high electrical resistivities and rapid acoustic velocities. In total, the gas hydrate-bearing strata was approximately 150 m thick within the depth interval from 889 to 1101 m.

Because of the success of the 1998 Mallik 2L-38 gas hydrate research well program, the Mallik site has been elevated as an important gas hydrate production test site with the execution of two additional gas hydrate production research programs: (1) The Mallik 2002 Gas Hydrate Production Research Well Program, and (2) 2006–2008 JOGMEC/NRCan Mallik Gas Hydrate Production Research Program.

In June of 2005, the partners in the Mallik 2002 Gas Hydrate Production Research Well Program publicly released the results of the first modern, fully integrated field study and production test of a natural gas hydrate accumulation (Dallimore & Collett 2005). From December 25, 2001 through March 15, 2002 the Mallik 2002 Gas Hydrate Production Research Well Program drilled three wells (the JAPEX/JNOC/GSC et al. Mallik 3L-38 and 4L-38 observation wells and Mallik 5L-38 gas hydrate production test well) in the Mallik Gas Hydrate Field on Richard's Island in the Mackenzie Delta, Northwest Territories, Canada.

The Mallik 5L-38 well cored and recovered gas hydrates and associated sediments from an interval between 880-1150 m depth (Fig. 3). These cores were the subject of intensive examination by members of the Mallik research team. Detailed information on the geology, geochemistry, geotechnical, and microbiological properties of gas hydrate bearing sediments was complemented by an extensive research geophysics program, which included both surface seismic surveys and downhole logging studies. Downhole measurements allowed for direct estimates of in situ permeability, gas hydrate content, and investigations of the occurrence of natural fractures.

Rather than carry out long term production testing during the Mallik 2002 effort, a decision was made to conduct carefully controlled production experiments. The response of gas hydrates to heating and depressurization was evaluated with careful attention to accurately measure both input conditions and reservoir responses. The overall goal was to combine the science and production program to allow for calibration and refinement of reservoir simulation models capable of predicting long-term reservoir response. Pressure draw down experiments were designed to study the response of gas hydrate to a reduction in formation pressure conditions. The results of three short duration gas hydrate tests demonstrate that gas can be produced from gas hydrates with different concentrations and characteristics, exclusively through pressure stimulation. The data supports the interpretation that the gas hydrates are much more permeable and conducive to flow from pressure stimulation than previously thought. Thermal stimulation experiments were designed to destabilize gas hydrates by using circulated hot water to increase the in situ temperature. A five-day experiment was undertaken within a 17-m-thick section of highly concentrated gas-hydrate-bearing strata. Gas was continuously produced throughout the test at varying rates with maximum flow rate reaching 1500 cubic meters per day. The total volume of gas produced was small, reflecting that the test was a controlled production experiment rather than a long duration well test.

The Mallik 2002 production research well program proved for the first time that gas production from gas hydrates is technically feasible. The Mallik 2002 thermal and depressurization production data have allowed the calibration of several reservoir models used to simulate the thermal and depressurization tests. Part of the calibration process has been the recognition that gas hydrate deposits are much more permeable than previously thought. The Mallik data allowed for the rational assessment of the production response of a gas hydrate accumulation if the various tests were extended far into the future. These studies show that among the possible techniques for production of natural gas from in situ gas hydrates, depressurization will produce more gas than just heating the formation. However, the combination of heating and depressurizing the gas hydrate at the same time will produce the greatest amount of gas. Project-supported gas hydrate computer production simulations, including those performed by Lawrence Berkeley National Laboratory, have shown that under certain geologic conditions gas can be produced from gas hydrates at very high rates, exceeding several million cubic feet of gas per day.

The following discussion dealing with the 2006–2008 JOGMEC/NRCan Mallik Gas Hydrate Production Research Program has been taken almost entirely from a news article appearing in the Spring/Summer 2007, U.S. Department of Energy, Office of Fossil Energy, National Energy Technology Laboratory, Fire in the Ice, Methane hydrate newsletter (available at http://www.netl.doe.gov/tech nologies/oilgas/publications/Hydrates/Newsletter/HMNewsSpringSummer07optmiized.pdf; viewed August 16, 2007). The 2006–2008 JOGMEC/NRCan Mallik Gas Hydrate Production Research Program is being conducted to mainly monitor long term production behavior of gas hydrates. The Japan Oil, Gas, and Metals National Corporation (JOGMEC) and NRCan are leading this research program. Aurora College/Aurora Research Institute is acting as the operator for the field program. The primary objective of the winter 2007 field activities was to install equipment and instruments to allow for long term production testing of several gas hydrate intervals during the winter of 2007–2008. Drilling rigs were used to re-enter and deepen the Mallik 2L-38 and Mallik 3L-38 wells (Fig. 3). Each well was also logged with various tools to establish formation properties prior to testing. After completing operations in the Mallik 2L-38 and 3L-38 wells, a short pressure draw down production test was conducted to evaluate equipment

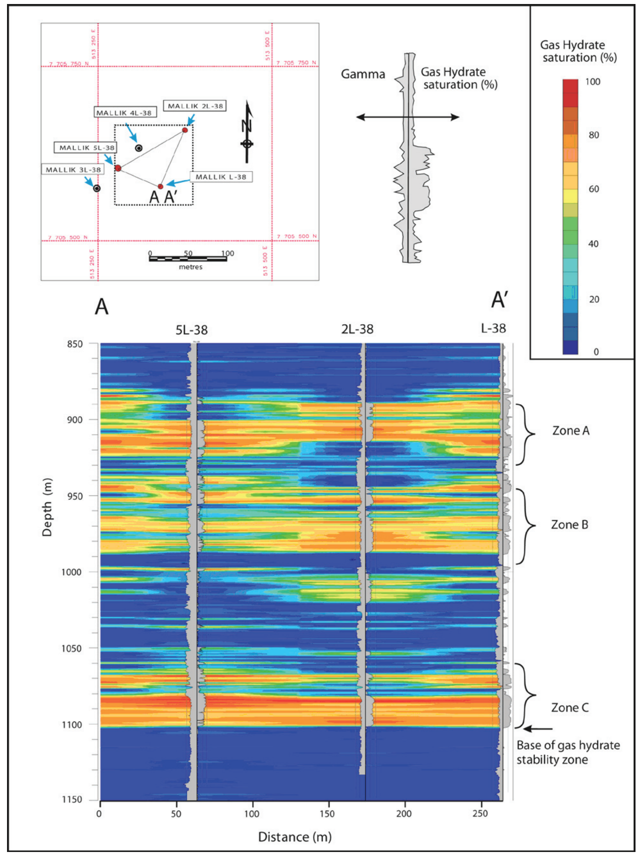

Figure 3. Fence diagram showing well-log-derived gas hydrate concentrations and natural gamma-ray logs for Imperial Oil Ltd. Mallik L-38, JAPEX/JNOC/GSC Mallik 2L-38, and JAPEX/JNOC/GSC et al. Mallik 5L-38 wells. The well locations are shown on the location map (Dallimore & Collett 2005).

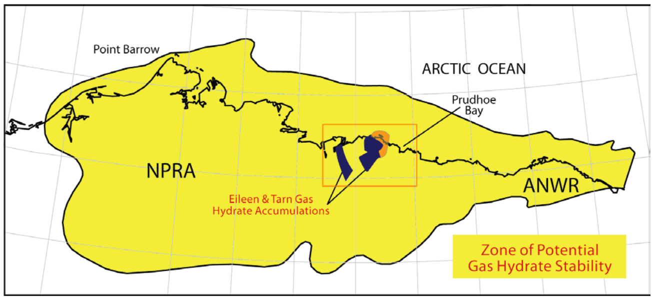

Figure 4. Map of the Alaska North Slope gas hydrate stability zone. Also shown is the location of the Eileen and Tarn gas hydrate accumulations (Collett 1993).

performance and short term producibility of the gas-hydrate-bearing section. A 12-m-thick gas hydrate interval near the base of the gas hydrate stability zone was tested for 60 hours. The test results were described as 'encouraging', documenting "robust" gas flow rates. Important observations were also made in terms of produced water and the sediment response to production. The JOGMEC/NRCan Mallik gas hydrate production research program is currently planning operations for the 2007–2008 winter program.

North Slope, Alaska, USA – Eileen gas hydrate accumulation

On the North Slope, the subsurface temperature data, needed to assess the distribution of the gas hydrate stability zone, comes from high-resolution, equilibrated well-bore surveys in 46 wells and from well log estimates of the base of ice-bearing permafrost in 102 other wells (Collett 1993). The methane-hydrate stability zone in northern Alaska, as mapped in Figure 4, covers most of the North Slope. The offshore extent of the gas-hydrate stability zone is not well established; however, 'relic' permafrost is known to exist on the Beaufort Sea continental shelf to a present water depth of 90 m (Osterkamp & Fei 1993).

Before the recently completed coring and downhole logging operations in the BP Exploration (Alaska) Mount Elbert well in Milne Point, the only direct confirmation of gas hydrate on the North Slope was obtained in 1972 with data from the Northwest Eileen State-2 well located in the northwest part of the Prudhoe Bay Field. Studies of pressurized core samples, downhole logs, and the results of formation production testing have confirmed the occurrence of three gas-hydrate-bearing stratigraphic units in the Northwest Eileen State-2 well (Collett 1993). Gas hydrates are also inferred to occur in an additional 50 exploratory and production wells in northern Alaska based on downhole log responses calibrated to the known gas hydrate occurrences in the Northwest Eileen State-2 well. Many of these wells have multiple gas-hydrate-bearing units, with individual occurrences ranging from 3- to 30-m-thick. Most of the well-log inferred gas hydrates occur in six laterally continuous sandstone and conglomerate units; all are geographically restricted to the area overlying the eastern part of the Kuparuk River Field and the western part of the Prudhoe Bay Field

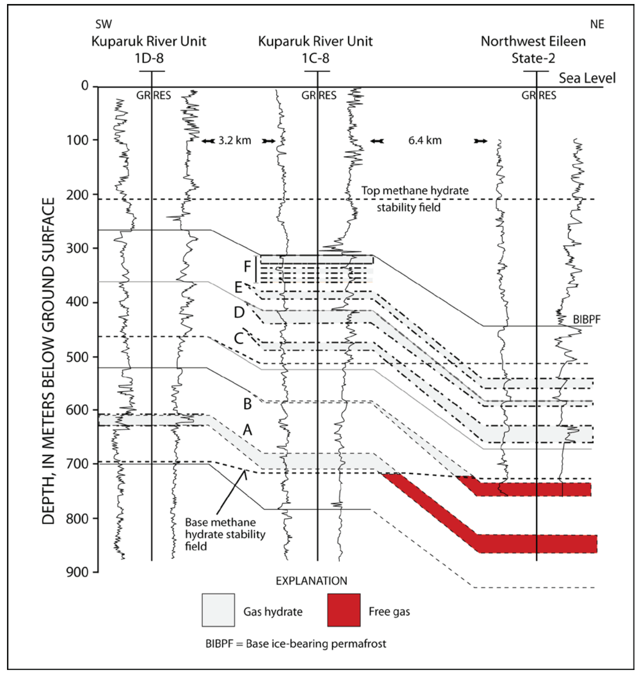

Figure 5. Cross section showing the lateral and vertical extent of gas hydrates and underlying free-gas occurrences in the Prudhoe Bay-Kuparuk River area in northern Alaska. See Figure 6 for location of cross section. The gas-hydrate-bearing units are identified with the reference letters A through F (Collett 1993).

(Figs. 5, 6). The six gas-hydrate-bearing sedimentary units have each been assigned a reference letter, Units A through F, with Unit A being the stratigraphically deepest (Fig. 5). Three-dimensional seismic surveys and downhole logs from wells in the western part of the Prudhoe Bay Field indicate the presence of several large free-gas accumulations trapped stratigraphically down-dip below four of the log-inferred gas hydrate units (Figs. 5, 6 Units A through D). The total mapped area of all six gas hydrate occurrences is about 1643 km^2; the areal extent of the individual units ranges from 3 to 404 km^2. The volume of gas within the gas hydrates of the Prudhoe Bay-Kuparuk River area, which has come to be known as the Eileen Gas Hydrate Accumulation, is estimated to be about 1.0 to 1.2 trillion cubic meters, or about twice the volume of known conventional gas in the Prudhoe Bay Field (Collett 1993).

The 1995 National Oil and Gas Resource Assessment, conducted by the U.S. Geological Survey, focused on assessing the undiscovered conventional and unconventional resources of crude oil and natural gas in the United States. This assessment included for the first time a systematic resource appraisal of the *in-place* natural gas hydrate resources of the United States onshore and offshore regions (Collett 1995). The onshore portion of the assessment dealt with most of northern Alaska, in which it was estimated that there may be as much as 590 trillion cubic feet of in-place gas trapped in gas hydrates.

Under the Methane Hydrate Research and Development Act of 2000 (renewed in 2005), the U.S. Department of Energy (DOE) funds laboratory and field research on both

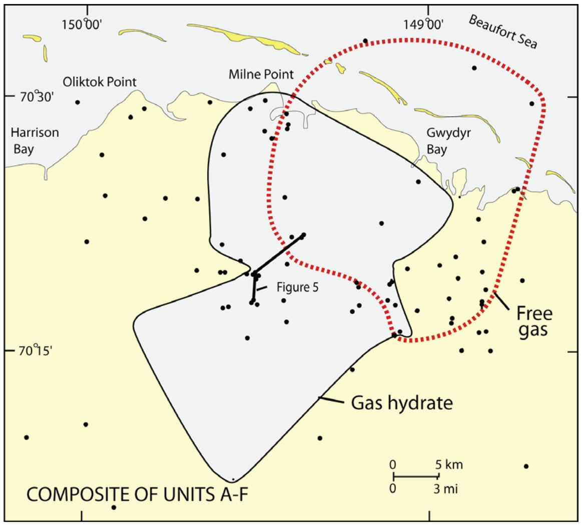

Figure 6. Composite map of all six gas-hydrate/free-gas units (Units A-F) from the Prudhoe Bay-Kuparuk River area in northern Alaska. Also shown is the location of the cross section in Figure 5 (Collett 1993).

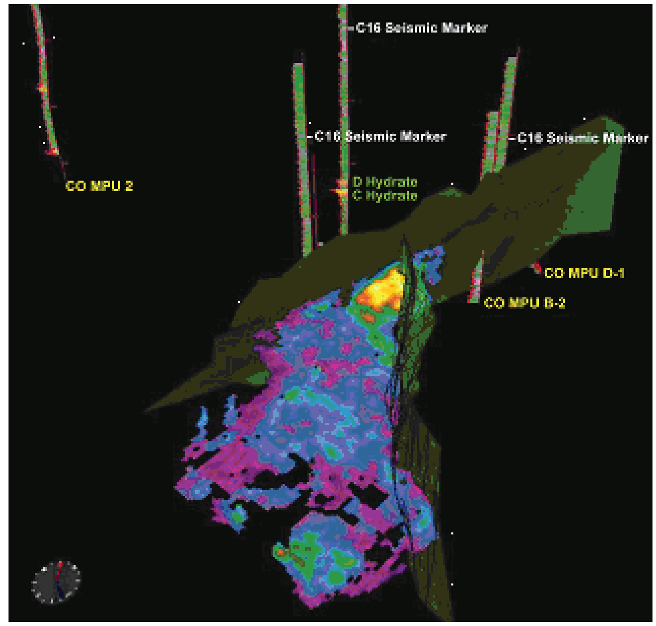

Figure 7. Three-dimensional seismic amplitude map of the Mount Elbert gas hydrate prospect within a three-way fault-bounded closure. Also shown is the location of nearby well locations.

Arctic and marine gas hydrates. Among the current Arctic studies, BP Exploration (Alaska), Inc. and the DOE have undertaken a project to characterize, quantify, and determine the commercial viability of gas hydrates and associated free gas resources in the Prudhoe Bay, Kuparuk River, and Milne Point field areas on the Alaska North Slope. Ultimately, this project could determine if gas hydrates can become a part of the Alaska North Slope gas-resource portfolio.

The following discussion dealing with the BP Exploration (Alaska) Inc. (BPXA) Mount Elbert Gas Hydrate Stratigraphic Test Well has been taken almost entirely from a news article appearing in the Winter 2007, U.S. Department of Energy, Office of Fossil Energy, National Energy Technology Laboratory, Fire in the Ice, Methane hydrate newsletter (available at http://www.netl.doe.gov /technologies/oilgas/publications/Hydrates/Newsletter/HMNewsWinter07.pdf; viewed August 16, 2007). On February 18, 2007, a team of scientists concluded an extensive data collection program in the Mount Elbert Gas Hydrate Stratigraphic Test Well drilled in the Milne Point area on the Alaska North Slope; it yielded one of the most comprehensive datasets yet compiled on naturally-occurring gas hydrates. This project began in earnest in 2002, following BPXA's response to a DOE request for proposals to evaluate the gas hydrate resources on the North Slope. Over the following three years, the project team conducted regional geological, engineering, and production modeling studies through collaborations with the University of Alaska (Fairbanks), the University of Arizona, and Ryder-Scott Company. In 2005, extensive analysis of BPXA's proprietary 3-D seismic data and integration of that data with existing well log data (enabled by collaborations with the U.S. Geological Survey, the Bureau of Land Management, and Interpretation Services, Inc.), resulted in the identification of more than a dozen discrete and mapable gas hydrate accumulations within the Milne Point area. Because the most favorable of those targets was a previously undrilled, fault-bounded accumulation (Fig. 7), BPXA and the DOE decided to drill a vertical stratigraphic test well at that location (named the 'Mount Elbert' prospect) to acquire critical reservoir data needed to develop a longer-term production testing program.

The Mount Elbert gas hydrate stratigraphic test well was designed as a 22-day program with the planned acquisition of cores, well-logs, and downhole production test data. A surface hole was first drilled and cased to a depth of 595 m. The well was then continuously cored to a depth of 760 m with chilled oil-based drilling fluid using the wireline-retrievable coring system. This core system delivered 85% recovery through 154 m of gas hydrate and water-bearing sandstone and shale. The coring team processed these cores on site and collected subsamples for analyses of pore water geochemistry, microbiology, gas chemistry, petrophysical properties, and thermal and physical properties. Core samples were also stored in liquid nitrogen or transferred to pressure vessels for future study of the preserved gas hydrates. After coring, the well was reamed and deepened to a depth of 915 m, and the well was surveyed with a research-level wireline logging program including magnetic resonance and dipole acoustic logging, resistivity scanning, borehole electrical imaging, and advanced geochemistry logging. Following logging, Schlumberger Modular Dynamic Testing (MDT) was conducted at four open-hole stations in two sandstone reservoirs. Each test consisted of flow and shut-in periods of varying lengths, with one lasting for more than 13 hours. Gas was produced from the gas hydrates in each of the tests.

Gas hydrates were expected and found in two stratigraphic sections. An upper zone, (Unit D) contained ~14 m of gas hydrate-bearing reservoir-quality sandstone. A lower zone, (Unit C), contained ~16 m of gas hydrate-bearing reservoir. Both zones displayed gas hydrate saturations that varied with reservoir quality as expected, with typical values between 60% and 75%. Presently, the project research partners are in the process of fully analyzing and integrating all the data collected from the Mount Elbert test well, including re-calibration of the initial geological and seismic models for the site.

Conclusion

Despite the apparent obstacles to the development of gas hydrate resources, it is important to remember that extraordinary technological developments in the petroleum industry—three-dimensional seismic techniques, secondary recovery methods, and horizontal drilling, for example—have allowed the extraction of resources once thought to be unavailable. Natural gas hydrates may also become economically extractable. On-shore Canada and Alaska are proven exploration targets for gas hydrates. The first commercial production of gas hydrates is likely to occur in either northern Alaska or Canada, where gas from gas hydrates will either support local oil and gas field operations or be available for commercial sale, if and when suitable gas pipelines are constructed. It is important to highlight that on the North Slope of Alaska, critical drilling and transportation infrastructure exists, which will allow gas hydrate prospects to be drilled and produced from existing installations.

Acknowledgments

This contribution was partially funded by both the U.S. Department of Energy (under the Interagency Agreement No. DE-AI21-92MC29214) and the U.S. Bureau of Land Management (under the Interagency Agreement No. LAI -02-0015).

References

Ahlbrandt, T.S. 2002. Future petroleum energy resources of the world. *International Geology Review* 44(12): 1092-1104.

Bard, H.B. & Fairbanks, R.G. 1990. U-Th ages obtained by mass spectrometry in corals from Barbados, sea level during the past 130,000 years. *Nature* 346: 456-458.

Bily, C. & Dick, J.W.L. 1974. Natural occurring gas hydrates in the Mackenzie Delta, Northwest Territories. *Bulletin of Canadian Petroleum Geology* 22/3: 340-352.

Collett, T.S. 1993. Natural gas hydrates of the Prudhoe Bay and Kuparuk River area, North Slope, Alaska. *American Association of Petroleum Geologists Bulletin* 77/5: 793-812.

Collett, T.S. 1995. Gas hydrate resources of the United States. In: D.L. Gautier, G.L. Dolton, K.I. Takahashi & K.L. Varnes (eds.), *1995 National Assessment of United States Oil and Gas Resources* on CD-ROM: U.S. Geological Survey Digital Data Series 30, CD-ROM.

Dallimore, S.R. & Collett, T.S. 1995. Intrapermafrost gas hydrates from a deep core hole in the Mackenzie Delta, Northwest Territories, Canada. *Geology* 23: 527-530.

Dallimore, S.R. & Collett, T.S. (eds.) 2005. *Scientific Results from the Mallik 2002 Gas Hydrate Production Research Well Program, Mackenzie Delta, Northwest Territories, Canada.* Geological Survey of Canada Bulletin 585, two CD-Rom set.

Dallimore, S.R., Uchida, T. & Collett, T.S. 1999. Scientific *Results from JAPEX/JNOC/GSC Mallik 2L-38 Gas Hydrate Research Well, Mackenzie Delta, Northwest Territories, Canada.* Geological Survey of Canada Bulletin 544, 403 pp.

Majorowicz, J.A. & Osadetz, K.G. 1999. *Basic Geological and Geophysical Controls Bearing on Gas Hydrate Distribution and Volumes in Canada.* Geological Survey of Canada Open-File Report, 35 pp.

Majorowicz, J.A. & Osadetz, K.G. 2001. Gas hydrate distribution and volume in Canada. *American Association of Petroleum Geologists Bulletin* 85/7: 1211-1230.

Milkov, A.V., Claypool, G.E., Lee, Y-J., Xu, W., Dickens, G.R., Borowski, W.S. & the Ocean Drilling Program Leg 204 Scientific Party. 2003. In situ methane concentrations at Hydrate Ridge, offshore Oregon: New constraints on the global gas hydrate inventory from active margins. *Geology* 31(10): 833-836.

Molochushkin, E.N. 1978. The effect of thermal abrasion on the temperature of the permafrost in the coastal zone of the Laptev Sea. *Proceedings of the Second International Conference on Permafrost, Takutsk, USSR, July 13-28, 1973.* Washington D.C.: National Academy of Sciences, 90-93.

Osadetz, K.G. & Chen, Z. 2005. A re-examination of Beaufort Sea – Mackenzie Delta Basin gas hydrate resource potential using a petroleum system approach. *Proceedings of the Fifth International Conference on Gas Hydrates, Trondheim, Norway, June 13-16, 2005*, 11 pp.

Osterkamp, T.E. & Fei, T. 1993. Potential occurrence of permafrost and gas hydrates in the continental shelf near Lonely, Alaska. *Proceedings of the Sixth International Conference on Permafrost, Beijing, China, July 5-9, 1993* Washington, D.C.: National Academy of Sciences, 500-505.

Smith, S.L. & Judge, A.S. 1995. Estimates of methane hydrate volumes in the Beaufort-Mackenzie region, Northwest Territories: Geological Survey of Canada, *Current Research 1995-B*: 81-88.

Weaver, J.S. & Stewart, J.M. 1982. In situ hydrates under the Beaufort shelf. In: M.H. French,. (ed.), *Proceedings of the Fourth Canadian Permafrost Conference, 1981*. National Research Council of Canada, The Roger J.E. Brown Memorial Volume: 312-319.

Laboratory Simulations of Martian Debris Flows

François Costard
UMR 8148 IDES Interactions et Dynamique des Environnements de Surface, Université Paris-Sud 11, 91405 Orsay France
Emeric Védie, Marianne Font, Jean-Louis Lagarde
UMR CNRS 6143 «M2C» Université de Caen, 2-4, rue des Tilleuls, 14 032 CAEN Cedex, France

Abstract

Small gullies observed on Mars could be formed by groundwater seepage from underground aquifers or may result from the melting of near-surface ground ice at high obliquity. To test these different hypotheses, a laboratory simulation has been performed. An experimental slope was designed to simulate debris flows over sand dunes with various slope angles, different granulometry, and permafrost characteristics. Preliminary results suggest that the typical morphology of gullies observed on Mars can be best explained by the formation of linear debris flows related to the melting of near-surface ground ice with silty materials. This physical modeling highlights the role of the active layer during debris flow formation.

Keywords: debris flows; gullies; Mars; physical modeling.

Introduction

The recent discovery of groundwater seepage and surface runoff on Mars suggests the local occurrence of subsurface liquid water at mid and high latitudes during recent periods. They have been proposed to result from subsurface seepage of water (Malin & Edgett 2000), brines (Andersen et al. 2002), near-surface ice melting at recent periods of high obliquity (Costard et al. 2002), snowmelt in more recent periods (Christensen 2003), geothermal heating (Mellon & Phillips 2001), or liquid CO_2 breakout (Musselwhite et al. 2001). Among this large variety of surface runoff features, an unusual example of debris flows over sand dunes retains our attention. These debris flows are characterized by (1) their localisation over sand dunes, (2) a typical morphology with long and narrow channels, and (3) the development of networks made of long, parallel down-dip flows (Fig. 1). The exact process of their formation still remains speculative. This study focuses on the formation of that typical morphology by means of various laboratory simulations within a cold room. According to these experiments, we discuss the possibility of explaining these gullies over sand dunes as a consequence of surface and near-surface melt of volatile-rich material. In this study, we describe how the depth of the active layer helps us to understand better the formation of Martian linear gullies observed in the Russell Crater. Such interpretation has important consequences in terms of recent climate change on Mars. We show that the characteristics of these typical linear Martian gullies are consistent with some external processes triggered by seasonal melting at high obliquity.

Gullies on Mars

Morphological characteristics

The observation of small gullies on Mars was one of the more unexpected discoveries of the Mars Observer Camera (MOC) aboard the Mars Global Surveyor spacecraft (Malin & Edgett 2000). *Debris flow* is the term used by Malin and Edgett (2000) to describe a downslope flow of debris mixed with a significant amount of water within the walls of impact craters. They mostly occur in a latitudinal band higher than 30°, with preferential pole-facing gullies in the southern mid-latitudes (Balme et al. 2006). A large majority are sited on the inner walls of impact craters and are occasionally found on central peaks of impact craters (Balme et al. 2006). They often become narrower and shallower downslope, are often slightly sinuous, and sometimes display complex morphologies such as levees, tributaries and streamlining around obstacles.

The upper part of most debris flows has a steeper slope that is dissected by channels, often sinuous, whereas thick accumulations of debris cover the bases of escarpments. The upper part of the slopes (mostly south-facing slopes in the Southern Hemisphere) exhibits alcoves. They are also characterized by their distinct V-shaped channels with well-defined levees. Individual channels exhibit low sinuosity and deep erosion down to the fans that bury the lower parts of the crater walls.

Most of the gullies observed on Mars are preferentially located at latitude higher than 30°. Therefore, they are located in regions where the Martian permafrost is supposed to contain ground ice in the near subsurface (Mellon & Phillips 2001).

Perched aquifer

Various mechanisms have been proposed for the formation of gullies by water. According to Malin and Edgett (2000), debris flows would result from springs fed by shallow aquifers. Water usually emerges from the lower part of the slope producing springs. According to that hypothesis, however, under hydrostatic pressure, springs may occur in the upper part of hills or slopes. The sources of this water can freeze on the surface. When the hydrostatic pressure oversteps the lithostatic pressure, the discharge can occur. The main problem is the difficulty for a shallow aquifer

Figure 1. Linear gullies over sand dune in the inner part of the Russell Crater on Mars. One can note the presence of sinuosity near the crest rim. HIRISE image PSP_002904_1255 (25 cm/pixel). Width of the image: 5 km. Light from the left. Credit: NASA/JPL/University of Arizona.

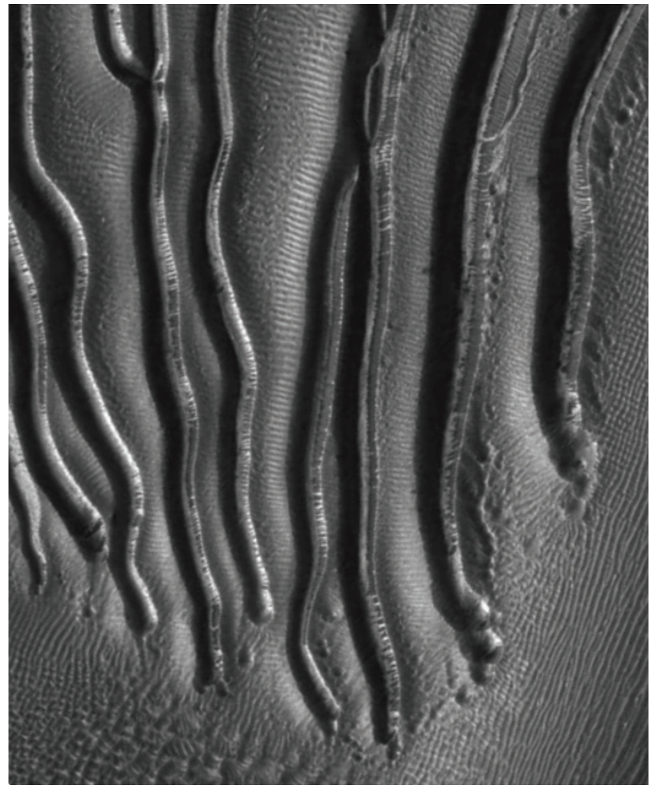

Figure 2. Close-up over the terminal part of gullies on the megadune. HIRISE image PSP_002904_1255 (25 cm/pixel). Width of the image: 1 km. Light from the left. Credit: NASA/JPL/University of Arizona.

to survive in equilibrium at such shallow depths under the cold ambient conditions. One possibility is to suppose a concentration of brines within the aquifer (Mellon et al. 2001).

CO_2 frost cover

Current seasonal defrosting has been proposed to explain gullies on hill slopes (Bridges et al. 2001) or over dunes (Reiss & Jaumann 2002). Recent HIRISE images clearly show a blanketing of CO_2 frost covering the south flank of dunes. Dark spots observed on the top of the dunes are attributed to the sublimation of CO_2 (Mangold et al. 2003). The possibility of snowmelt is not excluded (Lee et al. 2001; Christensen 2003).

Ice-rich deposit and obliquity scenario

This ground ice may represent one source of liquid water for the debris flows. However, this conclusion is contradictory with the usual consideration that liquid water cannot exist at the surface because of the low pressure and temperatures. This implies either that the ice-water is not pure or that climatic conditions were warmer in the recent past.

Ice-water doped with salts or CO_2 clathrates has been reported in different ways (Hoffman 2000, Ishii & Sasaki 2004). At least, it could explain gullies of the south polar regions, at 70°S, where temperatures are very cold; that is, 190 K of mean annual temperatures. According to terrestrial analogs in periglacial regions, Costard et al. (2002) have discussed the possibility of explaining some of these landforms by debris flows only due to surface and near-surface (<10 m) melt of volatile-rich material at high obliquities. Recent climatic changes may be possible considering the large pseudo-cyclic variations of the obliquity of the planet (Laskar et al. 2004). Variations of the orbital parameters are probably required to generate a subsurface melting of the supposed ice-rich permafrost or seasonal frost in these regions, thus allowing other processes to occur such as transient melting of ice-water (Costard et al. 2002).

Terrestrial analogs

On Earth, debris flows occur in periglacial environments when soils begin to be heavily saturated with water after the melting of the snow cover and/or the ground ice (Coussot et al. 1998). The initiation process of flow is still not fully understood. This initiation can be either due to water saturation by a peak intensity of rainfall events or to a rapid snowmelt (or melting of ground ice) with subsequent saturation or to a seismic event. Field observations indicate that snow cover plays an important role in the dynamic of debris flows. The duration of these debris flows is extremely variable and may occur as single or multiple waves. The deposition occurs along the narrow channel in levees of very coarse materials with boulders.

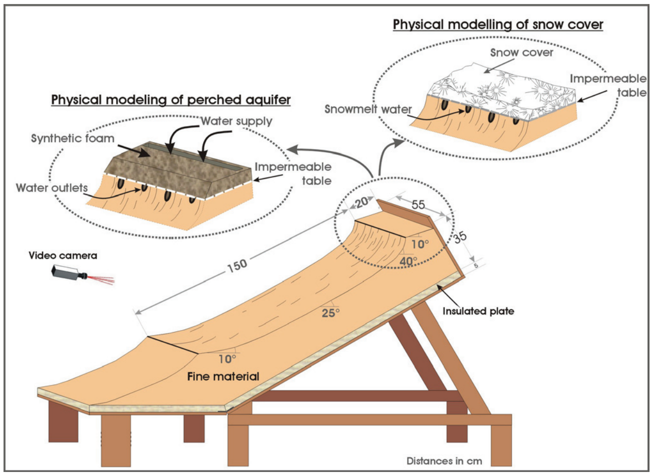

Figure 3. Global overview of the experimental setup and experimental configurations for two types of water supply (perched aquifer and snow cover).

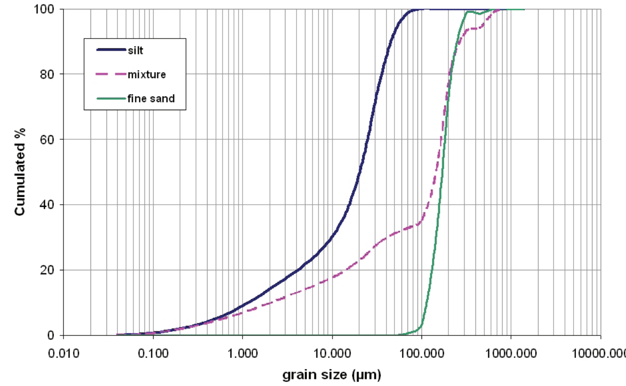

Figure 4. Grain size distribution of materials used for the experiment.

Gullies Over Sand Dunes

Russell Crater, a 200 km large crater located at 55°S and 347°W, exhibits various dune fields. One of them is relatively high (500 m) and covered by relatively low albedo volcanic sands. The SW flank of the megadune exhibits a few hundred long and narrow linear gullies, first discovered by Mangold et al. (2003). Gullies are about 2.5 km in length, and their mean slope is 10°. They start from regularly spaced small alcoves just under the crest of the dune, which is the steepest part of the dune (Fig. 1). Individual gullies exhibit linear and narrow channels with a loose pattern of connections.

Levees are observed on both sides of these channels as continuous and narrow ridges. These levees characterize a flow with a yield strength (Coussot et al. 1998) that corresponds to the minimal shear strength before flow. They are typically associated with flows containing 50% to 90% solid particles (silt to pebble size).

Relatively small distal-lobes are found lower down at the end of the channels at the foot of hill slopes. But gullies without terminal deposits are especially visible on the flank of dunes in the Russell Crater (Fig. 2). From a high-resolution HIRISE image (Fig. 2), most of the terminal deposits do not exhibit terminal lobes, but rather a concentration of small pits of unknown origin (thermokarst process ?).

These dune gullies present sinuosity and connections with a geometry that allows the calculation of flow properties, like the velocity and the viscosity (Mangold et al. 2003). The exact process of their formation over sand dunes, however, still remains speculative.

Terrestrial analogs for these typical linear gullies are unknown, justifying the use of laboratory experiments to try to understand the processes and conditions of the formation of these gullies.

Laboratory Simulations

Many factors work simultaneously in the triggering of debris flow, and their interdependence makes their analysis very difficult. High-resolution images are not completely appropriate in assessing the main parameters affecting the dynamic of debris flow. Laboratory simulation studies provide an opportunity for more detailed monitoring than can be done from imagery. The purpose of the study is to test qualitatively the influence of different parameters on the formation of linear gullies.

Methodology

Physical modeling has been developed in order to simulate the development of some typical gullies observed over Martian sand dunes in the Russell Crater. The major purpose of the experiment was to examine the respective effects of slope angle, material, and permafrost. To simulate a periglacial environment, these experiments require a cold room wide enough to receive an experimental slope (Fig. 3). We used the facility at the University of Caen/CNRS, France in a laboratory dedicated to physical modeling in geomorphology (Font et al. 2006).

Experimental setup

Our small-scale experiment was composed of a rectangular box of 2.5 m by 0.55 m wide and 0.50 m depth in which reconstituted debris from fine sand or silt materials was saturated with water (Figs. 3, 5). Morphologies are tested, with a median slope gradient of 15°, whereas the top and bottom slope gradients are constant (8° and 50° respectively). In order to simulate the periglacial environment, the slope was frozen from the surface, and permafrost was created at depth (0.50 m) with a temperature of -10°C.

The experiment procedure allowed the simulation of natural water supply for the debris flow formation. Two types of water supply were tested (Fig. 3):

1. To simulate perched aquifer, solid and porous synthetic foam was placed on the top of the rim crest. Then during thawing, a controlled water supply was injected into the foam.

2. Inflowing snowmelt water during thawing was simulated using fine particles of ice (<1 mm) covering all of the upper part of the slope.

Figure 5. Close-up of the apparatus used in the physical modeling of debris flows.

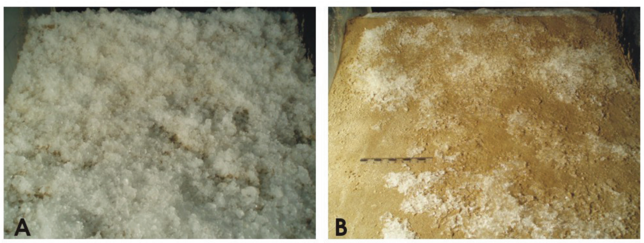

Figure 6. Experimental slope before (A) and after (B) snowmelt. In the laboratory simulation, the snow blanket is covering all of the slope. In that typical situation, no debris flows are observed probably because the snow blanket has a too wide-spread effect during the melting.

Ice-rich permafrost and control of the active layer

For each experiment, the material was initially saturated just before freezing. The thermal stability of the experiment was controlled by using 10 thermocouples at various depths. After freezing, the surface of the frozen soil is then progressively (and naturally) warmed to induce a controlled active layer formation. Thawing of the upper few mm of permafrost was done with an average air temperature of 18°C, giving rise to an active layer of 1 mm to 1 cm thick. Figures 3 and 5 outline the experiment.

Here, we assumed that liquid water was stable on the surface of Mars. The Martian gravity was not taken into account, and we assumed that the scale effect was not a limited factor. Our cold room is not a climatic chamber, so we do not control the atmospheric pressure and the thermodynamic aspect of the debris flow process. Here, the objective was mainly to simulate linear gullies as those observed on Mars in order to evaluate the respective influence of different parameters in terms of the efficiency of different parameters on the formation of these typical linear gullies.

Results

We carried out 42 experiments over two years. Data from a few tens of experimental gullies formation are presented here. They attest to the efficiency of periglacial processes

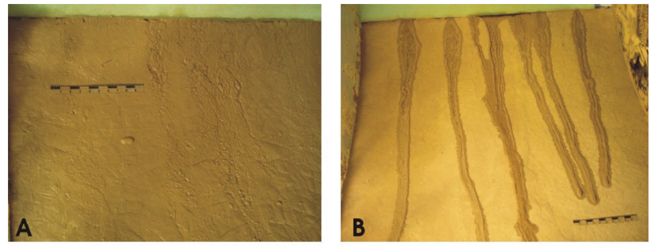

Figure 7. Effect of active layer thickness in a permafrost environment. A: diffused flow on surface with an active layer up to 10 mm. B: localized debris flows with an active layer of 1 mm thick. A relatively thin active layer strongly favors the formation of long and narrow linear gullies like those observed on Mars. Here, narrow gullies are preferentially formed by the water supply in the debris from the progressive thawing of the ice-rich permafrost, which occurs along a significant length of the flow.

that control both erosion and changes in gully morphology: (1) near-surface permafrost leads to a rather low sinuosity of the channel; (2) effects of silty material lead to increase the length/width ratio of the channel.

Blanket of snow or effect of the active layer?

From the experiment, the melting of the snow and the interstitial ice leads to the saturation level being reached within the layer of weathered debris. The decrease of the shear strength of the debris by water saturation is probably responsible for repeated debris flow episodes. According to the Christensen hypothesis (2003), gullies were created by trickling water from melting snowpacks, not by underground springs or pressurized flows. We did several simulations with a blanket of snow on the slope. The subsequent melting of snow deposits all over the slope has no effect on gully formation (Fig. 6B). However, underground springs or pressurized flows (either by a simulated perched aquifer or by inflowing snowmelt water from the rim crest, Fig. 3), both induced the melting of near-surface permafrost and the subsequent formation of linear gullies (Fig. 7B). To obtain such linear gullies, we need a clean pulse of water; the melting of the blanket of snow has a too wide-spread effect to trigger this kind of pulse.

Longitudinal variation and width/length ratio of gullies

According to Johnson (1970), debris flow deposits exhibit a variation of their morphologies in agreement with successive waves of debris. A plan view of the experiment (Fig. 8) shows the supposed waves and deposits formed by successive waves of debris. Figure 9 shows a comparative study between a terminal lobe from our laboratory simulation and a high-resolution image of the terminal lobe of two gullies on the megadune.

From various experiments with both silt and fine sand frozen material, carried out with the same volume of water supply and similar active layer thickness, it appears that silt material strongly favours the total length of debris flows (Table 1). The implication for Mars is to suppose that Martian dunes in the Russell Crater are made of silty materials. This interpretation is in agreement with the low

Figure 8. Narrow gullies with lateral levees and relatively small terminal lobes. The morphological characteristics of these gullies on sand are similar to those found on Mars in the Russell Crater. On the top: sinuous channels on the rim crest (like those observed on Mars). In the middle: connections between gullies and variation of their growth by successive wave of debris due to several pulses of water from the rim crest. The analogy with Figures 1 and 2 is striking.

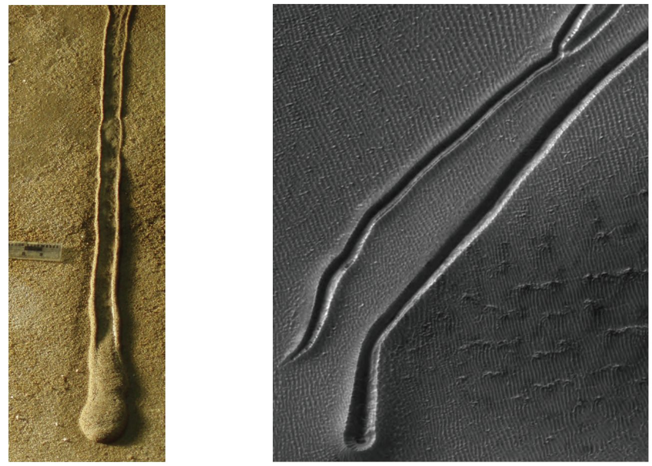

Figure 9. Comparative study of the development of lateral levees and terminal lobe between our experiment (left) and on Mars (right: HIRISE image PSP_002904_1255 (25 cm/pixel). Width of the image: 500 m. Light from the left. Credit: NASA/JPL/University of Arizona.

Table 1. Morphological properties of experimental debris flows obtained by the thaw of the ice-rich permafrost (protocol using synthetic foam).

Material	Lenght/width	% of length incised	% of levees
Sand	23	34	26
Sand/silt mixture	41	34	48
Silt	86	32	66

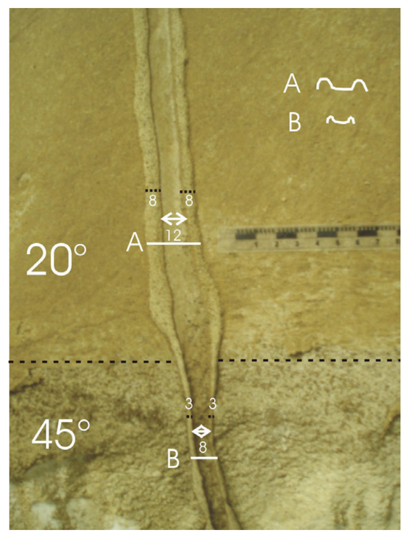

Figure 10. Variations of levees width in relation to slope angle. As on Martian gullies, levees are larger on the lowest slope. Laboratory simulation with fine sand.

albedo, which should be volcanic sands. The composition of these debris flows over sand dunes supposes finer particles than usual terrestrial debris flows (Mangold et al. 2003). In our experiment, the existence of linear gullies implies the incorporation of meltwater in the debris. This is only possible if thawing of the ground occurs along a significant length of the flow.

Levees and channel connections

Figure 9 shows a comparative study between a terminal lobe from our laboratory simulation and a high-resolution image of the terminal lobe of two gullies on the megadune.

The morphological change of the levees (Fig. 10) is related to the variation of velocities which results from the small change in slope gradient. This observation is in agreement both with characteristics of Martian gullies (Mangold et al. 2003) and rheological properties of terrestrial debris flows (Johnson & Rodine 1984).

Conclusion

Laboratory experiments have been undertaken to explore processes involved in gully formation over a sand dune in the Russell Crater. Debris flows over dunes involve either water formation from external processes (Mangold et al. 2003) or subsurface aquifers. The comparison between Martian and laboratory simulations leads to the conclusion that a periglacial environment could explain many of the described features in the Russell Crater. More than 40 laboratory simulations have been proposed in order to understand the formation of gullies over sand dunes on Mars. We used various materials (sand, silt), different slope angles, and different depths of active layers.

Our experiments suggest that the morphology of gullies found on Mars implies the presence of ice-rich permafrost with a relatively thin active layer. In any case (whatever the origin of the water—melting of snow, perched aquifer, or melting of permafrost), the active layer, together with the permafrost, controls the typical morphology of these linear gullies

The best analogy was observed with experimental permafrost made of silty materials with a very thin active layer (higher length/width ratio and percent of total length limited by levees: Table 1).

This preliminary work shows that a periglacial environment and the presence of near-surface permafrost could explain the formation of the Martian gullies. This hypothesis is consistent with some external process triggered by seasonal melting at high obliquity.

In the near future, we plan to test other debris flow formations with lower slope angle in agreement with both slopes from Russell Crater and Martian gravity.

Acknowledgments

This program is supported by "Programme Reliefs de la Terre" INSU, CNRS, France, and GDR mutations polaires: société et environnement.

References

Balme, M, Mangold, N., Baratoux, D., Costard, F., Gosselin, M., Masson, Ph., Pinet, P. & Neukum, V. 2006. Orientation and distribution of recent gullies in the southern hemisphere of Mars: Observations from HRSC/MEx and MOC/MGS data, 111, E05001.

Christensen, P.R. 2003. Formation of recent Martian gullies through melting of extensive snow deposits. *Nature* 163(8), Feb. 22: 116.

Costard, F., Forget, F., Mangold, N. & Peulvast, J.-P. 2002. Formation of recent Martian debris flows by melting of near-surface ground ice at high obliquity. *Science* 295: 110-113.

Coussot, P., Laigle, D., Arattano, M., Deganutti, A. & Marchi, L. 1998. Direct determination of rheological characteristics of debris flow. *J. Hydraul. Eng.* 124: 865-868.

Font, M., Lagarde, J.-L., Amorese, D., Coutard, J.-P., Dubois, A., Guillemet, G., Ozouf, J.-C. & Védie, E. 2006. Physical modelling of fault scarp degradation under freeze/thaw cycles. *Earth Surf. Process. Landforms* 31(14): 1731-1745. doi:10.1002/esp.1371.

Johnson, A.M. 1970. *Physical Processes in Geology*. New York: W.H. Freeman, 576 pp.

Johnson, A.M. & Rodine, J.R. 1984. *Debris flow.* In: D. Brundsen & D.B. Prior (eds.), *Slope Instability*. New York: John Wiley, 257-361.

Hoffman, N. 2000. White Mars: A new model for Mars' surface and atmosphere based on CO_2. *Icarus* 146: 326342.

Laskar, J., Correia, A., Gastineau, M., Joutel, F., Levrard, B. & Robutel, P. 2004. Long term evolution and chaotic diffusion of the insolation quantities of Mars. *Icarus* 170: 343-364.

Lee, P., Cokell, C.S., Marinova, M., McKay, C.P. & Rice, J.W. Jr. 2001. Snow and ice melt flow features on Devon Island, Nunavut, Arctic Canada as possible analogs for recent flow features on Mars (abstract 1809). *Lunar. Planet. Sci. Conf. 32th.*

Ishii, T. & Sasaki, S. 2004. Formation of recent Martian gullies by avalanches of CO_2 frost. *Lunar Planet. Sci. Conf., 35th*, #1556.

Malin, M.C. & Edgett, K.S. 2000. Evidence for recent groundwater seepage and surface runoff on Mars, *Science* 288: 2330-2335.

Mangold, N., Costard, F. & Forget, F. 2003. Debris flows over sand dunes on Mars: Evidence for liquid water, *J. Geophys. Res*. 108.

Mellon, M.T. & Jakosky, B.M. 1993. Geographic variations in the thermal and diffusive stability of ground ice on Mars. *J. Geophys. Res.* 98: 3345-3364.

Mellon, M.T. & Phillips, R.J. 2001. Recent gullies on Mars and the source of liquid water. *J. Geophys. Res.* 106: 23165-23180.

Musselwhite, D.S., Swindle, T.D. & Lunine, J.I. 2001. Liquid CO_2 breakout and the formation of recent small gullies on Mars. *Geophysical Research Letters* 28(7): 1283-1286.

Piqueux, S., Byrne, S. & Richardson, M.I. 2003. Sublimation of Mars' southern seasonal CO_2 ice cap and the formation of spiders, *Journal of Geophysical Research* 108(3).

Reiss, D. & Jaumann R. 2002. Spring defrosting in the Russell Crater dune field—Recent surface runoff within the last Martian year. (abstract 2013). *Lunar Planet. Sci. Conf. 33th.*

Schorghofer, N. & Edgett, K.S. 2006. Seasonal surface frost at low latitudes on Mars. 11 *Icarus* 180: 321-334.

Stewart, S.T. & Nimmo, F. 2002. Surface runoff features on Mars: Testing the carbon 14 dioxide formation hypothesis. *J. Geophys. Res.* 107(E9): 5069.

Treiman, A.H. 2003. Geologic settings of Martian gullies: Implications for their origin. *J. Geophys. Res.* 108(E4): 8031.

Modeling the Erosion of Ice-Rich Deposits Along the Yukon Coastal Plain

Nicole J. Couture
Geography Department, McGill University, Montreal, Canada
Md. Azharul Hoque
Geography Department, McGill University, Montreal, Canada
Wayne H. Pollard
Geography Department, McGill University, Montreal, Canada

Abstract

The Yukon Coastal Plain is an area of ice-rich deposits along the Canadian Beaufort Sea and has been identified as highly vulnerable to the effects of sea-level rise and climate warming. Erosion is a function of the composition and morphology of coastal features, as well as wave energy. This paper outlines a simple model that considers these factors. Variations in ground ice contents and onshore and nearshore morphology are examined, as is their effect on the coastal dynamics of the region. Ice volumes are variable, ranging 52% to 84% by volume. A wave climate for the region is hindcast from historical climate records with offshore significant wave heights averaging between 0.32 and 0.45 m. Modeled wave energy shows that cross-shore energy is up to four times greater than longshore. Net longshore sediment transport is westward at all sites although the magnitude varies. Potential erosion is appraised.

Keywords: Beaufort Sea; coastal erosion; erosion model; ground ice; wave climate; Yukon Coastal Plain.

Introduction

Climate changes in the Arctic will have profound impacts on the permafrost coastline of Canada's Beaufort Sea. In addition to warmer air and sea temperatures, changes are expected in several other primary environmental forcings on permafrost coastal systems such as relative sea level (RSL), storminess, and the duration and extent of the open water season. The Yukon Coastal Plain is considered to be in a submergent area (Forbes 1980), with current rates of RSL rise estimated to be approximately 3.5mm/a (Manson et al. 2002). These increases in sea level will be magnified by oceanic thermal expansion which will contribute to the region's sensitivity to erosion (Shaw et al. 1998). Lambert (1995) suggested an increase in the frequency of storms under a warming climate and Solomon et al. (1994) have shown that there is a strong correlation between storm intensity and coastal erosion along the Beaufort Sea. The coast of the Beaufort Sea is micro-tidal with astronomical tide heights less than 0.5 m, so waves play a strong role in coastal change. This is particularly true during the open water season, when sea ice does not dampen wave development. Impacts of climate change along the Yukon Coastal Plain go beyond a physical response. The oil and gas industry are concerned about the effect of shoreline changes on infrastructure and exploration activities. Erosion and changes in the nearshore ecology also have the potential to directly affect local communities since hunting, fishing, and trapping are economic and cultural mainstays for many aboriginal communities along the coast. Numerous historical and archeological sites in the region have already been destroyed by erosion and a number of others are threatened.

The goal of this paper is to outline a simple erosion model to predict how ice-rich coastlines along the Beaufort Sea will respond to changes in climate. A wave climate is hindcast-based on historical climate data and is then used to calculate the potential wave energy available for erosion and sediment transport. The properties of the coastal bluffs are considered in determining spatial variability in erosion potential. The future susceptibility of the different coastline types is considered, based on predicted changes in environmental forcings for the region.

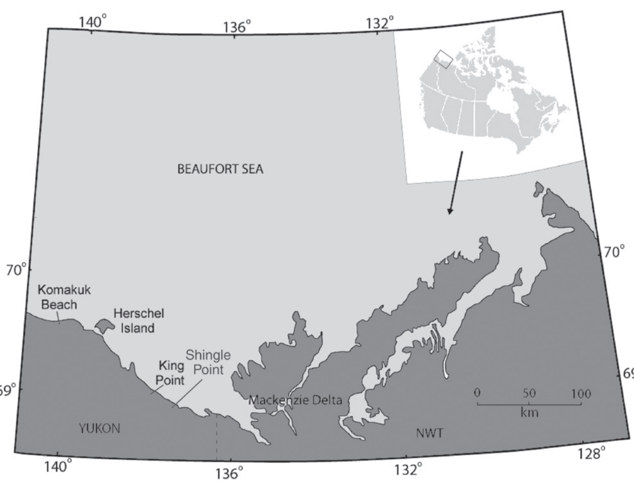

Figure 1. Location map showing the study region and sites along Canada's Yukon Coastal Plain.

Study Area

Canada's Yukon Coastal Plain, located along the Beaufort Sea west of the Mackenzie Delta (Fig. 1), is a lowland of dissected and hilly tundra about 250 km long and 10–30 km wide. Offshore, the continental shelf slopes gently to the shelf break located at about 80 m water depth (Hill et al. 1991). The shelf is relatively narrow, ranging from 40 km wide and sites in the western area to over 150 km wide at the Mackenzie

Delta. This region is classified as having a low arctic climate, with a mean annual temperature of -11°C and mean annual precipitation between 200 and 300 mm. The coastal plain is largely an erosion surface cut into Tertiary sandstone and shale. Most of it was covered by a lobe of the Laurentide ice sheet known as the Buckland Glaciation in the early Wisconsin, as well as by a later stillstand or re-advance known as the Sabine Phase. Surficial deposits reflect this history, with the coast east of Herschel Island being covered by glacial outwash plains and fans, moraines, and fine-grained lacustrine sediment. Moraines make up ice-pushed ridges or else blanket rolling to hummocky topography likely resulting from thermokarst activity (Rampton 1982). West of Herschel Island, the plain was unaffected by the Buckland Glaciation and is made up of coastal lagoons, coalesced deltas, and alluvial fans (Rampton 1982). Most of the flat or gently sloping landscape is covered by organic deposits and peat beds are common, particularly in lacustrine basins (Rampton 1982). Beaches along the coast are generally narrow and are backed by coastal bluffs that can be up to 90 m high. Permafrost along the Yukon coast is continuous and reaches depths of approximately 300 m (Smith & Burgess 2000). The ice content of these soils is high due to the presence of pore ice and thin ice lenses, abundant ice wedges, and beds of massive ice. Subsea ice-bonded permafrost is present below the Beaufort Sea in water depths up to 100 m (Mackay 1972, Dallimore et al. 1988, Dyke 1991). Three sites along the coastal plain were selected for study: Komakuk Beach, King Point, and Shingle Point.

Methods

Coastal composition and morphology

The presence of ground ice in coastal soils constrains the sediment content and influences the coast's susceptibility to erosion. To assess ice content along the Yukon Coastal Plain, a morphological model was developed based on a method first presented by Pollard & Couture (1999). The model calculates the total volume of ground ice for different terrain units along the coast by determining how much of each different type of ground ice is contained within that segment. Three types of ground ice are considered in the calculations: 1) pore ice and thin lenses of segregated ice, 2) wedge ice, and 3) beds of massive ice. As part of the Arctic Coastal Dynamics (ACD) project, a detailed segmentation of the Canadian Beaufort Sea coastline was conducted based on predominant landforms, surficial materials, permafrost conditions, and coastal processes. This initial segmentation was then refined using direct field observations, as well as data from Rampton (1982), Wolfe et al. (2001), and Harper et al. (1985). The percentage of ice content for each type of ground ice was first established, then the volume of each ice type in a terrain unit is determined. Finally, the percentages of total ice content by volume for each terrain unit are calculated.

Wave hindcasting

Meteorological data was obtained from Environment Canada weather observing stations at Komakuk Beach and Shingle Point and from a Campbell Scientific automatic weather station set up at King Point in 2004. Average hourly wind speed and direction were considered for the open water period for the years 2004–2006. The open water period is based on normals of median sea-ice concentration data from the Canadian Ice Service for the period 1971–2000. For the Yukon coast, ice concentrations fall below 5/10 during the last week of June, and open water lasts until the first week of October. Data from the King Point observing station was first adjusted to the 10 m level. Wind speed measurements from the three overland stations were then converted to overwater values to account for differences in roughness between the two surfaces, using commonly used empirical coefficients (Resio & Vincent 1977, cited in Kamphuis). The wind data were then used to model deepwater waves, following the JONSWAP method:

$$H_s = \frac{\lambda u^2}{g} \qquad (1)$$

where H_s = significant wave height for a fully developed sea (m), λ = dimensionless coefficient (approximately equal to 0.243), u = wind speed (m/s), and g = gravitational acceleration (9.8 m/s^2).

In the above calculations, shoreline orientation at each site was accounted for, and only offshore winds were considered to be capable of wave generation; winds blowing from a landward direction were set to 0. The waves are not considered to be fetch-limited, so the values are for a fully developed sea. Although only local winds are used to derive the offshore wave climates characteristics, the JONSWAP method considers the entire wave spectrum, so low frequency swell waves, which may be generated a great distance from the area of interest, are included in the calculated outputs. Nevertheless, swell waves are rare in the study region and are low when they are seen (Forbes 1997).

Wave energy and material transport

As waves approach shore, the bottom of the wave begins to interact with the seabed and shoaling begins. The wave is slowed, the wavelength becomes shorter, successive waves begin to pile up, and the heights of the waves increase until they steepen to the point that they break on the shore. The energy they contain is thereby liberated to effect sediment transport and erosion. If a wave approaches the shore at an angle, the portion of the wave closer to shore will slow first, while the deeper portion remains unaffected. As a result, the wave is refracted, or bent, so that the wave crest more closely parallels the shore. Standard equations based on linear wave theory were used to convert the deepwater waves to nearshore ones and determine the height of the breaking wave. Wave energy was then calculated based on the following equation:

$$E = \frac{\rho g H_b^2}{8} \quad (2)$$

where E = energy per area (N/m^2), ρ = density of seawater (1025 kg/m^3), g is as noted above, and H_b = breaking wave height.

The energy term was separated into its component vectors to give longshore and cross-shore values. Sediment transport in the longshore direction is given by the CERC expression (Kamphuis 2000):

$$Q = 330 H_b^{5/2} \sin 2\alpha_b \quad (3)$$

where Q = volume of transported material (m^3/h) and α_b = the incident angle of breaking wave.

Results

Wind data for the three-year period under consideration are shown in Figure 2. The importance of using site- specific wind data has been noted by earlier studies (Pinchin &and Nairn 1987), and is highlighted here by the differences between the stations examined. The coastal plain is narrowest in the west, and at Komakuk Beach, the close proximity of the British Mountains contribute to channeling the winds in an east-west direction. Offshore waves were hindcast from these winds producing average significant wave heights ranging up to approximately 0.5 m. Details of the significant wave heights for the three sites are given in Table 1.

The breaking wave heights are used to generate wave energy for each modeled wave, which is then broken down into a crossshore component (X) and a longshore one (Y) (Table 2). The proportion of energy going into each component is dependent on the incident angle of the nearshore wave which is, in turn, a factor of the original wind direction and the degree of wave refraction that occurs. This angle also governs which direction the longshore current will take (overall east or west, in the cases examined here). Net annual longshore energy is obtained by subtracting the total longshore in one direction from the total in the opposite direction. Using Equation 3, the potential net volume of sediment transported by the longshore wave energy can be calculated for the three-year period examined (Table 3). Although these calculations indicate potential transport of several thousands of cubic metres of sediment, the amount transported at Shingle Point is nevertheless not considered to be significant, if one considers that the uncertainty of the method is on the order of 10–-20%.

In order to assess how this potential sediment transport might affect coastal retreat at the study sites, the actual volume of material in the bluff needs to be considered. At Komakuk Beach, coastal bluffs are approximately 3 m high and consist of fine-grained lacustrine material. Ground ice comprises 61% by volume of the coastline. At King Point, cliffs up to 30 m high are made up of morainic material. The presence of beds of massive ice contributes to a very high ice content of 84%. At Shingle Point, the 10 m high bluffs are also morainic in origin, but their ice content is only 52%.

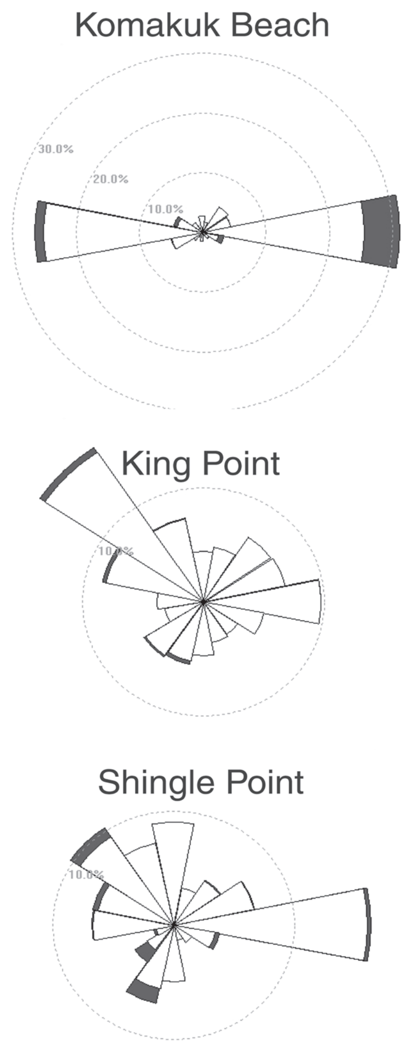

Figure 2. Wind roses showing frequency and magnitude of winds. Shaded areas indicate winds in excess of 37 km/hr, a common criteria for storm winds.

Figure 3 provides an indication of how these values compare to other sites along the Yukon coast.

Based on cliff heights and the percentage of ice they contain, the volume of sediment for a section of the coast extending 1 m inland can be calculated for each segment of coastline under study:

$$V = lh(1 - PIV) \quad (4)$$

where V = volume of sediment in a homogeneous coastline segment based on ACD project criteria (m^3),
l = length of the coastline segment (m),
h = height of the coastal bluff, and
PIV = percentage of ice from all sources of ground ice.

Entire segments of coastline are used to account for the fact that not all sediment being transported alongshore at any one point is necessarily sediment eroded from the coastline at that particular point. Rather, some of it has been supplied from further up the coast and is simply in transit. It

Table 2. Cross shore (X) and longshore (Y) components of modeled wave energy.

Site	Total X (N/m^2)	Total Y (N/m^2)	Eastward Y* (N/m^2)	Westward Y* (N/m^2)	Ratio X/Y
Komakuk	15.7 X 10^5	5.2 X 10^5	0.7 X 10^5	4.6 X 10^5	3.0
King Pt.	13.4	3.4 X 10^5	1.3 X 10^5	2.1 X 10^5	4.0
Shingle Pt.	16.0	4.5 X 10^5	2.2 X 10^5	2.2 X 10^5	3.6

* These represent only general direction of Y component. Actual movement of material is parallel to the shore at each site.

Table 3. Modeled longshore sediment transport for 2004–06.

Site	Q (m^3)
Komakuk	3.2 X 10^5 towards the west
King Pt.	0.5 X 10^5 towards the west
Shingle Pt.	0.1 X 10^5 towards the west (not significant)

Table 4. Volume of sediments and erosion rates for the different coastline segments in this study.

Site	Segment length (m)	Volume of sediments (m^3)	Annual sediment transport (m^3)	Potential retreat (m/yr)
Komakuk	6020	0.70 X 10^4	10.6 X 10^4	15.1
King Pt.	2990	1.43 X 10^4	1.8 X 10^4	1.3
Shingle Pt	8850	4.23 X 10^4	0.3 X 10^4	0

is therefore more realistic to integrate erosion over a longer length of homogeneous coastline. Total sediment transport for the 3-year period of study was averaged to arrive at a potential annual rate of transport. Assuming that this volume of sediment is being removed from the segment of coastline under consideration, then based on the volume of the sediments in the segment, a potential rate of annual coastline retreat is calculated (Table 4).

Discussion and Conclusions

This study examines nearshore wave energy generated through hindcasting. Previous studies have modeled potential erosion through wave climate analysis (Solomon et al. 1994, Hequette & Barnes 1990), but used offshore waves only so the results cannot be directly compared. Different techniques for nearshore wave transformation produce varying results (Pinchin & Nairn 1987) and the results of this study will need to be validated using measured nearshore waves. Previous work usually considers only storm winds and waves in their evaluation of erosion. We chose to examine all waves because several processes unique to arctic coasts can provide material for erosion between storms. Figure 4 shows two types of failures along coastal bluffs—retrogressive thaw slumps and block failures—that are common in ice-rich environments such as the Yukon Coastal Plain. In both cases, material is available close to the waterline and so is potentially subject to erosion by even moderate wave action. The erosion of the sediment from such failures may not result in any immediate retreat in the shoreline position, but once that material is removed, the toe of the bluff is not longer protected from direct wave action and subsequent shoreline retreat can proceed more rapidly. This study only examines three years of data and so does not necessarily reflect the

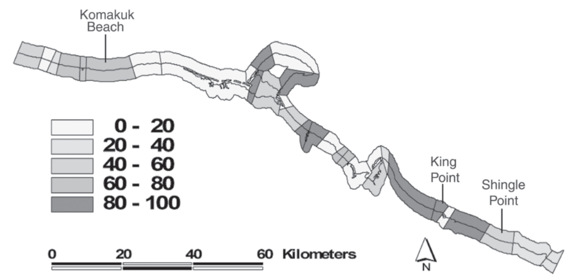

Figure 3. Ground ice volumes (by percentage) for different terrain units along the Yukon Coastal Plain.

longer term retreat rates resulting from these types of slopes failures

The modeled results can be considered acceptable given that the annual erosion rates are of the same order of magnitude as measured rates for the region (e.g., Harper 1990, Solomon 2005). Although the rate for Komakuk Beach shown here is higher than ones reported in earlier studies (0.76 m/a in Forbes 1997), this may be due to the fact that, rather than contributing to active erosion, the majority of the wave energy is devoted to transporting the high sediment loads being input from two rivers to the east of the site..

The simple erosion model in this study provides a first approximation of the influence of wave energy on coastal retreat rates. However, this model can only hope to explain some of the lower- level coastal landscape features. Coastal dynamics are extremely complex and are also influenced by currents, wave refraction around major features such as Herschel Island, river inputs of sediment, shoreface profiles, and ice-push events. The larger landscape structures like spits and barrier islands are likely controlled by major storm events. This is underscored by the fact that even though sediment transport at Shingle Point is shown to be not significant, a major spit does exist at this site. Improvements to the model presented here can be made by extending the length of the data set (preferably to at least 15 years), by validating the hindcast wave climate, and by incorporating grain size into the sediment transport equation since the one used for this study assumes that all transported material is sand. Fetch length was considered to be unlimited as soon as ice concentrations fell below 5/10, but its variability with time and direction should be part of future work. An examination of crossshore sediment transport is also planned. 4a) Ab) Episodic events such as these deliver sediments to the beach that can be subsequently removed by even moderate wave activity. The model could be used to examine future erosion rates, but several factors would need to be considered including changes to sea ice extent.

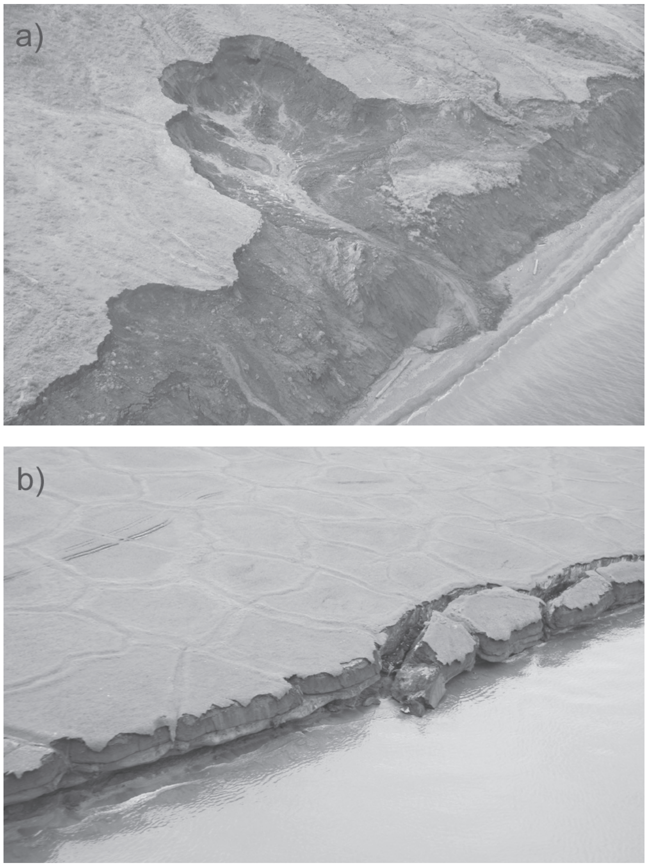

Figure 4. a) A retrogressive thaw slump near King Point and b) a block failure near Komakuk Beach. . Episodic events such as these deliver sediments to the beach that can be subsequently removed by even moderate wave activity.

Acknowledgments

Financial assistance was provided by ArcticNet NCE (1.2, 1.2 and 2.4), the Natural Science and Engineering Research Council of Canada, and Fond québécois de la recherche sur la nature et les technologies. Fieldwork was made possible by the Polar Continental Shelf Project and the Northern Scientific Training Program. We would also like to thank the Alfred Wegener Institute for Polar and Marine Science (Potsdam), Herschel Island Territorial Park, Ivvavik National Park, the Aurora Research Institute, S. Solomon, H. Lantuit, G. DePascale, T. Haltigin, and D. Leitch. Comments by S. Ogorodov and an anonymous reviewer are very much appreciated.

References

Dallimore, S.R., Kurfurst, J.J. & Hunter, J.A.M. 1988. Geotechnical and geothermal conditions of near-shore sediments, southern Beaufort Sea, Northwest Territories, Canada. *Proceedings of Fifth International Permafrost Conference*, *Trondheim, Norway*: 127-131.

Dyke, L.D. 1991. Temperature changes and thaw of permafrost adjacent to Richards Island, Mackenzie Delta, N.W.T. *Canadian Journal of Earth Sciences* 28: 1834-1842.

Forbes, D.L. 1980. *Late Quaternary sea level in the Beaufort Sea.* GSC Paper 80 (1B), 75-87.

Forbes, D.L. 1997. *Coastal erosion and nearshore profile variability in the southern Beaufort Sea, Ivvavik National Park, Yukon Territory.* Geological Survey of Canada, Open File 3531, 28 pp.

Harper, J.R., Reimer, P.D., & Collins, A.D. 1985. *Canadian Beaufort Sea physical shore zone analysis*. Geological Survey of Canada, Open File Report 1689, 105 pp.

Héquette, A. & Barnes, P.W. 1990. Coastal retreat and shoreface profile variations in the Canadian Beaufort Sea. *Marine Geology* 91: 113-132.

Hill, P.R., Blasco, S.M., Harper, J.R. & Fissel, D.B. 1991. Sedimentation on the Canadian Beaufort Shelf. *Continental Shelf Research* 11: 821-842.

Kamphuis, J.W. 2000. *Introduction to Coastal Engineering and Management*. Singpore: World Scientific Publishing, 437 pp.

Lambert, S.J. 1995. The effect of enhanced greenhouse warming on winter cyclone frequencies and strengths. *Journal of Climate* 8: 1447-1452.

Mackay, J.R., 1972. The world of underground ice. *Annals of the American Association of Geographers* 62: 1-22.

Manson, G.K., Solomon, S.M. & MacDonald, A. 2002. Describing Beaufort Sea coastal climate variability. *Reports on Polar and Marine Research* 413: 31-33.

Pinchin, B.M. & Nairn, R.B. 1987. *Beaufort Sea coastal sediment study: evaluation of inshore wave climate and coastal sediment transport techniques at King Point, Yukon*. Toronto, Ontario: Keith Philpott Consulting Limited.

Pollard, W.H. & Couture, N.J. 1999. *The use of morphological methods to estimate ground ice volumes along the Canadian Beaufort Sea coast.* Report for the Geological Survey of Canada (Atlantic), 30 pp.

Rampton, V.N. 1982. *Quaternary Geology of the Yukon Coastal Plain*. Geological Survey of Canada Bulletin 317, 49 pp.

Shaw, J., Taylor, R.B., Forbes, D.L., Ruz, M.-H. & Solomon, S. 1998. *Sensitivity of the coasts of Canada to sea-level rise.* Geological Survey of Canada Bulletin 505, 79 pp.

Smith, S., & Burgess, M. 2000. *Ground temperature database for northern Canada*. Geological Survey of Canada, Open File 3954, 28 pp.

Solomon, S.M., Forbes, D.L. & Keirstead, B. 1994. *Coastal impacts of climate change: Beaufort Sea erosion study*. Geological Survey of Canada, Open-File 2890.

Solomon, S.M. 2005. Spatial and temporal variability of shoreline change in the Beaufort-Mackenzie region, Northwest Territories, Canada. *Geo-Marine Letters* 25: 127-137.

Wolfe, S. A., Kotler, E. & Dallimore, S. R. 2001. *Surficial characteristics and the distribution of thaw landforms (1970–1999), Shingle Point to Kay Point, Yukon Territory*. Geological Survey of Canada, Open File 4115, 18 pp.

Dynamics of Patterned Ground Evolution

James G.A. Croll
University College London, London, England WC1 E 6BT

Abstract

New dynamic mechanisms for the formation of a number of different forms of patterned ground are postulated to result from alternations of solar energy reaching the ground surface. Extensions of the thermo-mechanical processes widely believed to power the growth of ice wedge polygons are suggested to contribute to the dynamic evolution of many patterned ground features, such as sorted and unsorted stone circles, polygons, nets, stripes and steps. hummocks, frost mounds, palsas, and pingos. For each, fluctuations in solar energy at various temporal scales are argued to provide at least part of the dynamic driving force in what might be referred to as thermo-mechanical ratchet processes. While these ratchet models appear to be supported by past field observation, new field data are clearly needed if they are to be adequately assessed as to whether they might better explain the formation of many forms of patterned ground.

Keywords: contraction; cracking; expansion; patterned ground; periglacial morphologies; ratchet; thermal loading.

Introduction

Many forms of patterned ground within periglacial environments have been the subject of long-standing fascination. From the formation of geometrically patterned ground, to the sometimes distinctive mounds developing out of otherwise flat areas of permafrost, to the hummocks and other regular geometric patterns observed over ground subject to seasonal freeze-thaw cycles, much has been written as to their possible causes. Understanding of the processes responsible for their initiation and growth is of significance in relation to the interpretation of past climatic conditions through the observation of the relic geomorphic features remaining long after previous permafrost has receded. It is therefore not surprising that the processes which might have been responsible for the growth of these various forms of patterned ground have occupied considerable research attention. In many cases there is widespread agreement on the processes involved in these formations while in others there remains considerable uncertainty.

This paper approaches the subject of the mechanical causes of these various features from a somewhat different perspective. It postulates dynamic mechanisms that are in some form the result of alternations of solar energy reaching the ground surface. It suggests that these alternations of solar energy produce warming periods when the frost layer, or permafrost where it is present, is subject to horizontal compressive forces arising from the restrained, lateral, thermal expansion. During subsequent cooling, tension forces will accompany the restrained thermal contraction. Because of differential mechanical properties exhibited by ice and ice-rich ground at high and low temperatures, or under compression and tension, certain forms of deformation will accumulate to form morphological features through processes that might be generically referred to as thermal ratchets. Of particular interest here is how these processes might be at work in the development of patterned ground and as such is intended to complement earlier work dealing with the development of various forms of surface mound (Croll 2004, 2007b).

Ice wedges and ice wedge polygons are widely accepted to be the result of a form of this thermo-mechanical ratchet process. This was recognised by Lachenbruch (1964) and further elaborated from the field observations of Mackay (1974, 2000) and Mackay & Burn (2002). In this model of the formation of ice wedges and ice wedge polygons, the thermal ratchet process relies upon the cyclic compressive and tensile energies being dissipated through two very different processes. During seasonal warming, the compression phase, the release of stored energy is through an outward shoving of ground material, particularly within the active layer, giving rise to upward shearing and folding into the typical forms of rampart either side of the ice wedge. During seasonal cooling, the tensile phase, the dissipation of energy is the result of brittle tensile fracture, preferentially accumulating in the growing ice wedge. Over many such cycles the outward and upward movement of permafrost and active layer material compensates the growth in volume of the peripheral ice wedges. Yet surprisingly, the elegant logic of this seasonally driven thermal ratchet model process has not been transferred into efforts to better understand other periglacial phenomena occurring at possibly different spatial and temporal scales. As the following suggests, a related from of thermal ratchet model may also be responsible for the development of some of the many patterned ground features so eloquently described by Washburn (1979).

Stone Circles and Polygons

While reasons have in the past been proposed for the horizontal movements needed to form such curious features as the sorted stone circles of Figure 1(a), or polygons of Figure 1(b), etc, none of them appear to be entirely convincing or able to account for all such features. Encouraged by field measurements showing clear patterns of outward radial movements of the surface materials, from the centres of well formed stone circles (see e.g., Hallet et al. 1986), there have been many attempts to explain the formation of stone circles in terms of the development of convection motions within the active layer. Indeed, during the 1980s the convective cell model seems to have become the dominant explanation for the growth of stone circles (Gleason et al. 1986, Ray et al. 1983).

There are, however, fundamental problems with these models based as they are upon density differences largely resulting from variations in moisture content of the soil. First, the forces required to not just power the outward radial surface motion of the fines, but also shift the considerable weight of the border stones to allow the surface layers to be subducted beneath, would seem to be very much higher than any generated by the relatively small changes in soil density,and this does not even include the very considerable forces needed to visco-plastically distort the soil layers. Just as the density differences due to thermal gradients were held to be insufficient to drive a convection cell at the scale required for stone circles (Morgenstern 1932), it would appear that the forces due to density differences are also inadequate. Even the measurements of outward deformations of the soil surface do not appear to support the hypothesis of buoyancy driven convection. Accurate readings taken in western Spitzbergen clearly show radial deformation rates increasing away from the centre of the monitored stone circles (see Fig. 5, Hallet et al. 1986). Were the driving mechanism to be convection, very simple considerations of mass conservation would predict that the outward deformation rates would decrease with radial distance form the centres.

There appear to be similar problems with some of the more recent hypotheses for the development of stone circles and ice wedge polygons, even though results from computer generated models appear to support them (Kessler et al. 2003, Plug et al. 2002). Space does not allow fuller discussion. While it is likely that no single explanation will be able to account for all motions involved in the formation of periglacial morphologies, the following would appear a feasible explanation for at least some of the features outlined in classic texts such as Washburn (1979) and French (1996).

Role of thermal ratchetting

To illustrate how thermal-mechanical ratchet processes could be at work in the horizontal motions of both top soil and stones, consider a typical stone lying at surface level a distance h from the centre of a stone circle having radius r that is in the process of forming, as depicted in Figure 2. Here “circle” will be assumed to cover the case where the circular diameters are such that they would overlap were it not for the development of interacting polygons, nets, etc. Putting aside for the moment the question of what governs the characteristic dimensions of the stone circles, of current concern is the process that continues to drive the outward movement of the stones and surface material once the basic geometric patterns have been defined. In early autumn the seasonally unfrozen ground will start to refreeze. Initially this surface freezing and thawing would be governed by

Figure 1 (a). Examples of sorted stone circles.

Figure 1 (b). Examples of stone polygons.

circadian periodicities, for which the temperatures would follow a pattern similar to that shown in Figure 2(a). Each night the typical stone will be locked into the downwardly propagating freezing layer as suggested at time (1) in Figure 2(b). With the frozen layer being grounded within the stone boundary rampart, a drop in surface temperatures will develop tensile stresses in the frozen surface layer, as a result of the constrained contraction – time (2). Desiccation and even discrete cracks, associated with the development of the tensile stress, will attract moisture that at the low temperatures will turn to ice – time (3) in a similar way to ice wedge polygons. When temperatures begin to increase towards morning, the frozen ground will start to develop compressive stress as a consequence of the restraint to the expansion that would otherwise occur. Because the frozen layer of soil is likely to have fairly high compressive strength the overall radial forces being developed will be in certain ground conditions sufficiently high to dislodge the stone and cause it to move outward – time (4). At least in early autumn and spring the nocturnal frozen layer will completely thaw during the high diurnal warmth, leaving the stone and adjacent soil permanently moved out a small distance, δu, as shown at time (5). And so the process will continue with the radial distances moved increasing as the circadian fluctuations in temperature are increased.

To provide an indication of the levels of radial deformation and force developed during a typical circadian period, consider a nocturnally frozen layer of thickness 10 mm, having a coefficient of linear thermal expansion α = 50x10^{-6}/°C, subject to an increase in temperature ΔT = 10°C during

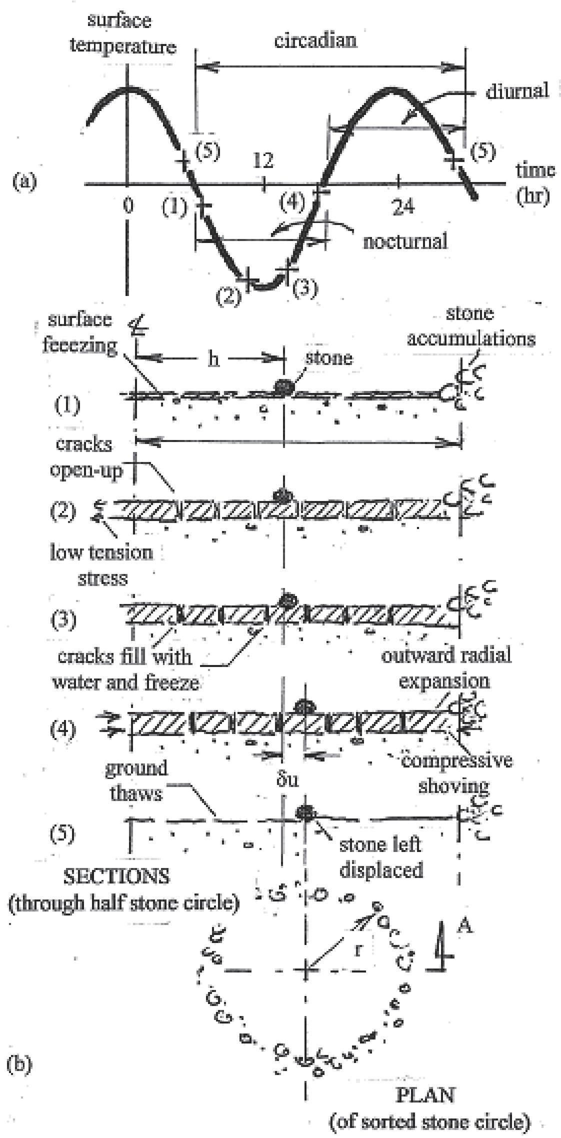

Figure 2. Schematic representation of (a) typical autumnal circadian thermal cycle acting on a stone circle, showing (b) typical half cross sections taken at times indicated.

the diurnal warming and prior to any melting. If there were no radial restraint, the outward radial deformation of a stone at a distance of, say, h = 1500 mm from the circle centre, would be $\delta u = \alpha \, \Delta T \, h$ = 1.3 mm/d. These rates of outward deformation are consistent with those recorded by Hallet et al. (1986). In that they are predicted to increase linearly with the distance from the centre of the stone circle, the deformation profiles are, in contrast with those predicted from the convection cell model, also in accord with those recorded by Hallet et al. (1986). If the outward radial deformation was to be fully restrained by the stone boundary, the radial stress σ_r developed in the frozen soil, assumed to have a modulus of elasticity E = 1 GPa, would be $\sigma_r = \alpha \, \Delta T \, E$ = 0.5 MPa. With the frozen layer of thickness 10 mm, a single stone of diameter 50 mm would attract a radial force of 250 N, or nearly 60 lbf, enough to dislodge even the most recalcitrant of stones. While it is difficult to conceive of soil convection developing force levels of this magnitude, the above scoping calculations suggest that a combination of thermal expansion and contraction is well capable of providing the driving force for the development of stone circles.

Even when the frozen layer ceases to completely thaw and starts to propagate downward, there may be short, daily or possibly longer, timescales over which a surface melt allows the stone to be ratcheted out a little further in much the same way as that described above. Under these circumstances the mechanism discussed in Figure 2 would operate in the diurnally thawed layer above the seasonal, downwardly-propagating frozen layer. Longer period thermal cycles could also be operating in the seasonally frozen ground in much the same way as they do in the growth of ice wedge polygons. As discussed below, these longer-term thermal cycles could play an important part in the determination of the characteristic dimensions of the rock or stone circles.

Controls of characteristic dimensions

While the above appears to provide a very plausible mechanism for driving the development of stone circles, it does not directly explain the mechanics whereby the stone circles are formed in the first instance and what it is that determines for a particular set of circumstances the characteristic radii for the rock circles, polygons, etc. In a given location and within a particular set of thermal climatic conditions, the characteristic dimensions of any stone circles appear to be fairly robust. If the forcing mechanism derives from a ratchet process driven by fluctuations in thermal loading, like that described above, then the nature of the mechanics involved but at longer timescales could also determine the characteristic dimensions that can be achieved. There are a number of mechanical processes that could be controlling these characteristic dimensions.

At annual timescales the depth of the thermal wave would determine not just the thickness of the frozen ground but also the depth and the spacing of any cracks connecting up to form crack-wedge polygons. This form of tensile energy relief could influence the typical dimensions of the eventual stone polygons, in much the same way as they control the characteristic dimensions of the ice wedge polygons within the deeper permafrost.

Another potentially controlling factor could be the shear capacity between the frozen layer and the underlying unfrozen ground. For a given set of ground conditions, the total shear capacity resisting an outward radial expansion would increase linearly with increasing radius of the stone circle. For a given range of thermal loading, which for a fully restrained expansion would control the maximum compressive force developed, the radius of accumulating stones would be increased until such time as the thermally dependent compressive force just equilibrates the shear resistance inhibiting radial movement. The most extreme thermal loading could be controlled by relatively short term thermal cycles, with moderately large temperature fluctuations but for which the frozen ground might be expected to retain high stiffness, or it could be the longer-term, annual seasonal, thermal cycles involving much larger average temperature fluctuations but for which the visco-plastic response would imply that the frozen ground has a lower effective stiffness to thermal straining. Whichever exerts the most extreme compressive loading will control, for a given set of prevailing underlying shear strength properties, the maximum or characteristic radius of the stone circle – or polygon where these start to overlap. The stone ramparts could be caused by shoving actions similar to the processes responsible for the formation of ramparts at the edges of expanding lake ice (Gilbert 1890, Hobbs 1911, Scott 1927).

Another possible mechanical condition that could control the characteristic radii would be the development of a form of upheaval buckling of the frozen layer, similar to the process recently described for the possible formation of pingos (Croll 2004, 2007a,b). Depending upon the thickness of the frozen layer and the thermal compression developed when during the spring its average temperature is increased, it is possible that the characteristic radius could be controlled by thermal uplift buckling. While such an upward doming would likely be recovered when the frozen ground thaws, the sloping sides and the surface melt in spring prior to this recovery might also contribute to the outward movement of any surface material to the lower edges of the buckled dome.

Development of differential frost heave

Once sorting of the type described above has taken place, there will be spatial inhomogeneity in the thermal conductivity of the surface layers. Peripheral stone or rock mounds with air voids will be likely to have a lower than average thermal conductivity with the result that downward growth of the circadian, seasonal or other periodicity growth of the frozen layer will be retarded around the periphery. The more rapid downward propagation over the central regions would induce greater rates of frost heave in these areas. If sufficiently large, this form of differential frost heave could elevate the central regions sufficiently that gravity might also lead to larger stones and rocks being moved towards the outer periphery. Even if the slopes are not sufficient to induce purely gravity-related sliding of the larger particles, a form of Moseley-Davidson thermal ratchet, similar to that described by Croll (2006) and believed to be the cause of insolation creep (Moseley 1855, Davison 1888), could be operating. However, on this basis the differential frost heave would be the result of the sorting not its cause.

Sorting through erosion

The thermal ratchet model described above would also account for the finer soil particles also being gradually shoved out to form peripheral edge ramparts, like those shown in Figure 1. Why these fines do not remain could be accounted for by subsequent differential surface erosion. Surface runoff from the elevated edge ramparts and selective erosion of the fines within these peripheral accumulations would wash back into the lower central regions of the circle/polygon. In certain circumstances it is likely that summer surface water or wind action could see the accumulated finer soil at the outer edges being eroded back to fill the fissures and pores left by the melting of ice from the previous winter's cracking action. This additional form of mass movement would accentuate the process of soil sorting whereby the centres of the circle are gradually colonised by finer particles and the outer edges by those of larger dimension.

High-centred stone circles

It is interesting to speculate as to why in seemingly more restrictive circumstances the larger stones accumulate not at the outer boundaries but at the centres of the graded stone circles, polygons, etc. It seems plausible, as suggested by Washburn (1979), that these stone accumulations may be an advanced form of the stone polygon. The corner nodes of the polygonal array may eventually attract, through a process similar to that described above, the accumulations previously occurring at the edges of the polygon. These nodes would then become the centres of arrays of essentially high-centred triangles, the triangular array representing the congugate of the original polygonal array. High-centred, sorted, or unsorted circles may either be the result of collapse of the underlying ice wedges at the boundaries, or in active permafrost be the result of a compression failure at the centre of the circle. Such failures might involve a process of upheaval buckling similar to that described recently in relation to the development of hummocks, frost mounds, palsas, and pingos (Croll 2007a,b).

Other Permafrost Features

Descriptions of many periglacial geomorphic features are consistent with the role of thermal ratchet processes like those described above being ubiquitous. Stone nets, stripes, and steps appear to be driven by mechanisms similar to those described above, but with the intervention of gravity the geometric patterns become orientationally distorted. Stone pavements and string bogs appear to have many features in common with the process described above for the formation ice wedge polygons. High-centred polygons seem to share a close resemblance to and possible similarity in origin to the pingo. As observed by Washburn (1979, p. 135) "some ice-wedge polygons enclose small pingo-like ice cored mounds."

Mention should also be made of frost-creep in the context of ratchetting processes. In this case the ratchet mechanism within currently accepted models is somewhat different, and thought to involve a combination of frost-heave occurring normal to the slope, followed by a thaw that results in a stone or other object settling vertically under the action of gravity. The result is a gradual downward motion accompanying each freeze-thaw cycle. Space does not permit consideration of the extent to which those phenomena, explained in terms of solifluction and gelifluction, might also have contributions from the thermo-mechanical ratchet processes outlined above.

In all of these surface motions, it is possible to construct models that could be complementing the processes currently considered to provide the driving force.

Some Closing Remarks

One of the purposes of this paper has been to suggest a form of dynamic mechanisms that may be contributing to the initiation and development of various forms of patterned ground. Thermo-mechanical ratchet processes, derived from fluctuations in the levels of solar radiation reaching the earth's surface, are suggested to contribute to the formation of rather more periglacial processes than currently accepted. The dynamic mechanism for the formation of various forms of patterned ground is postulated to result from alternations of solar energy reaching the ground surface. Extensions of the thermo-mechanical processes widely believed to power the growth of ice wedge polygons have been postulated to contribute to the dynamic evolution of many patterned ground features, such as sorted and unsorted stone circles, polygons, nets, stripes, and steps. Simple calculations have demonstrated that outward radial displacements of the frozen surface soil are consistent with previous field measurements. They also show that the levels of force generated when the expansions are restrained are large enough to account for the outward shoving of the stone ramparts.

Similar processes have recently been discussed (Croll 2007a,b) for the development of hummocks, frost mounds, palsas, and pingos. For each, fluctuations in solar energy at various temporal scales are argued to provide at least part of the dynamic driving forces in what might be referred to as thermo-mechanical ratchet processes.

While these ratchet models appear to be supported by past field observation, new field data are clearly needed if they are to be adequately assessed as to whether they might better explain the formation of many forms of patterned ground. Field tests would need to be devised that would allow, for example, the radial displacement rates to be correlated with the thermal conditions and especially temperature alternations. To be adequate, these measure-ments would need to be recorded continuously over full circadian cycles at the times of the year when motions are at their greatest. They would need to monitor variations in both the thickness and temperature gradients through the thickness of the frozen layer at circadian and other periodicities. If such data are to be adequately interpreted, it will be important to measure the site-specific coefficient of thermal expansion, modulus of elasticity, and other thermo-mechanical properties of the frozen soil.

As is becoming clear in evidence from recent planetary probes, many of the surface features being observed on the other planets and their satellites (see e.g., Kuzmin 2002, Yoshikawa 2002) would appear to have close relationships with similar features on Earth. Improved understanding of the mechanics responsible for developing these features will be essential if these observations are to allow better understanding the origins of the solar system, including a more complete appreciation of the nature and influences of present and past climatic conditions.

It is also becoming clear that closely related morphological features exist at very small scale in the behaviour of asphalt (Croll 2005a, 2006, 2007c). In these analogous cases similar forms of thermo-mechanical ratchet processes would appear to be responsible. Again, better understanding of the mechanics will be essential if future design and maintenance strategies can be expected to reduce the currently high maintenance costs for asphalt pavements. To capture all these phenomena, account must be taken of the relationships linking the thermal periodicities and the spatial scales.

Fluctuations in levels of solar energy and the operation of various forms of thermo-mechanical ratchet process seem to be rather more common in the shaping of environments, including periglacial environments, than is currently recognised. This paper represents a small start towards suggesting for patterned ground a new classification based upon the form of the thermo-mechanical ratchet processes that might be at work in their formation.

Acknowledgments

Financial support to cover attendance at the 2008 NIPC has been provided by a fellowship from the Leverhulme Foundation, whose support is gratefully acknowledged. Being relatively new to this fascinating field, I have relied heavily upon the excellent descriptions in books by French (1996) and Washburn (1979) and the impressive series of papers by Mackay. I have also benefited from private correspondence with Professors Mackay and Burn, whose efforts to correct many misunderstandings and provide references that might put me on a more correct path are gratefully acknowledged. In preparing this revised version of the original paper, I have also benefited from the comments of two anonymous referees, whose perceptive and helpful comments I hope to have at least partially addressed.

References

Croll, J.G.A. 2004. An Alternative Model for "Pingo" Formation in Permafrost Regions. *Proceedings of 21st International Congress of Theoretical and Applied Mechanics*, *August, 2004*, *ICTAM-04, Warsaw*:15-21.

Croll, J.G.A. 2005a. Thermal buckling of pavement slabs. *Proceedings of the Institution of Civil Engineers 2005, Transportation Vol. 158 (May)*: 115-126.

Croll, J.G.A. 2005b. *Pulsatile motion of solids.* Internal report. University College London.

Croll, J.G.A. 2006. From asphalt to the arctic: new insights into thermo-mechanical ratchetting processes. Presented at *Third International Conference on Computational Mechanics*, *Lisbon, Portugal, 5–8 June, 2006*.

Croll, J.G.A. 2007a. Thermal ratchet uplift buckling and periglacial morphologies. Presented at *International Conference Cryogenic Resources of Polar Regions*, *Salekhard City, Russia, 17–22 June, 2007.*

Croll, J.G.A. 2007b. Mechanics of thermal ratchet uplift buckling in periglacial morphologies, *Proceedings of the SEMC Conference*, *Cape Town, South Africa, September, 2007.*

Croll, J.G.A. 2007c. Thermal ratchetting in the blister buckling of asphalt pavements. *International Journal of Pavement Engineering* (in press).

Davison, C. 1888. Note on the movement of scree material. *Quarterly Journal of the Geol Soc*. (4): 232-238.

French, H.M. 1996. *The Periglacial Environment*, second edition. Addison Wesley Longman Ltd

Gilbert, G.K. 1890. *Lake Bonneville.* U.S. Geological Survey Monograph 1, 1890, 438pp.

Gleason, K.J., Krantz, W.B., Caine, N., George, J.H. & Gunn, R.D. 1986. Geometric aspects of sorted patterned ground in recurrently frozen soil. *Science* 232: 216-220.

Hallet, B. & Prestrud, S. 1986. Dynamics of periglacial stone circles in western Spitsbergen. *Quarternary Research* 26: 81-99.

Hobbs, W.H. 1911. Requisite conditions for the formation of ice ramparts. *Journal of Geology* 19: 157-160.

Kessler, M.A. & Werner, B.T. 2003. Self-organisation of sorted patterned ground. Science 299: 380-383.

Kuzmin, R.O., Ershow, E.D., Komarow, I.A., Kozlov, A.H. & Isaev, V.S. 2000. The comparative morphometric analysis of polygonal terrain on Mars and the Earth high latitude areas, *Lunar and Planetary Science* 33: 2000.

Lachenbruch, A.H. 1962. Mechanics of thermal contraction cracks and ice-wedge polygons in permafrost. *Geological Society of America*, Special paper 70, 69 pp.

Mackay, J.R. 1974. Ice-wedge cracks, Garry Island, NWT. *Journal of Earth Science* 11: 1366-1383.

Mackay, J.R. 2000. Thermally induced movements in ice-wedge polygons, Western Arctic coast: A long term study. *Geographie physique et Quarternaire* 54: 41-68.

Mackay, J.R. & Burn, C.R. 2002. The first 20 years (1978-79 to 1998-99) of ice-wedge growth at the Illisarvik experimental drained lake site, western Arctic coast, Canada. *Canadian Journal of Earth Sciences* 39(1): 95-111 and (39)11: 1657-1674.

Moseley, H. 1855. Descent of a solid body on an inclined plane when subject to alternations in temperature, *Proceedings of the Royal Society VII*, *April, 1855*: 341.

Plug, L.J. & Werner, B.T. 2002. Non-linear dynamics of ice-wedge networks. *Nature* 417: 929-933.

Scott, I.D. 1927. Ice-push on lake shores*, Michigan Academy of Science, Arts, and Letters* 7: 107-123.

Strathan, I. 1977. *Earth Surface Sediment Transport*. Clarendon Press.

Washburn, A.L. 1979. *Geocryology: A Survey of Periglacial Processes and Environments*, Second edition. London, England: Edward Arnold Ltd.

Yoshikawa, K. 2000. Contraction cracking and ice-wedge polygons in Mars. *Second International Conference on Mars Polar Science and Exploration*, *August, 2000*: 186-187.

Legacy and Accomplishments of Frozen Ground Engineering Studies in Alaska 60 Years Ago

Margaret Cysewski
University of Alaska Fairbanks, Department of Civil and Environmental Engineering, Fairbanks, Alaska, USA
Yuri Shur
University of Alaska Fairbanks, Department of Civil and Environmental Engineering, Fairbanks, Alaska, USA

Abstract

One of the most extensive frozen ground engineering studies in the world was started in Alaska in 1945. It was led by the U.S. Army Corps of Engineers and has remained the most ambitious project in frozen ground engineering research. The name of the project was "Investigation of airfield construction in arctic and subarctic regions." This paper presents a review of some parts of this project, which paved the way for numerous further studies.

Keywords: aerial photographs interpretation; foundations design and construction; n-factor; permafrost; thermal conductivity.

Introduction

One of the most extensive frozen ground engineering research programs was conducted 60 years ago in Alaska. It was led by the St. Paul District of the U.S. Army Corps of Engineers and was a most ambitious project in frozen ground engineering research. The purpose of the program was "to determine design methods and procedures to be used in military construction in arctic and subarctic regions" (U.S. Army 1950). This goal was achieved, and results of the studies were widely used in military manuals for arctic and subarctic construction. The results have also contributed to contemporary knowledge on permafrost, and some of these became a starting point for numerous later studies.

The program integrated direct frozen ground engineering with supplementary studies. The direct frozen ground engineering studies consisted of the construction of sections of runways, with different types of embankments, insulation, and surfaces, and buildings with different types of foundations. These construction sections were conducted at Fairbanks Research Area with "the purpose of providing an opportunity to observe various types of structures erected on permafrost under conditions that would be known and recorded from the beginning to the conclusions of operations" (U.S. Army 1950). The study also included the monitoring of existing runways and buildings, and their impact on permafrost. These existing facilities were at the Northway Airfield, Eielson Air Force Base (near Fairbanks), and Ladd Air Force Base (Fort Wainwright).

The supplementary studies included development of methods for aerial photographic reconnaissance in permafrost regions, applicability of geophysical methods to permafrost investigations, thermal properties of frozen and unfrozen soils, and literature research.

In this paper, we describe the most notable studies and their results, which were presented in 1950 within the comprehensive report (U.S. Army 1950) by the Corps of Engineers and in several reports on the supplementary studies.

Design and Construction Studies at Fairbanks Research Area

Numerous experiments were conducted at the Fairbanks Research Area. They included the evaluation of terrain modifications (Area No. 1), different types of runways (Area No. 2), and different building foundations (Area No. 3) in the permafrost region.

Area No. 1 included three 61 m by 61 m sections of different surface conditions. Section A was an undisturbed area with natural vegetation. In Section B, trees and bushes were removed, but the surface vegetation cover was left. In Section C, all vegetation was removed with the top 40 cm of soil. Then another 10 m by 30 m section, Section D, had all the vegetation removed with the top 30 cm of soil. This section was then backfilled with sand to the original ground line and paved with 15 cm of concrete. Then the section was divided in three equal sections where two were colored white and black, and the third was left its natural gray color.

Monitoring of permafrost conditions in Area No. 1 included observations of the ground temperature to a depth of 10 m, the supra-permafrost ground water level, the vertical movement of the soil surface, probing to the permafrost table, and testing of the soil moisture content and density.

The report presents mean monthly soil temperature data for Sections A, B, and C from July 1946 to November 1948, and the positions of the permafrost table in 1947 and 1948. The studies in Area No. 1 are well-known from Linell (1973), who presented 17 years of observations of the positions of the permafrost table in Sections A, B, and C. Recent positions of the permafrost table are evaluated by Douglas et al. (in these proceedings).

The soil temperature data for Section D covered only one year of observations. At the end of summer 1948, the depth to the permafrost table under each part of Section D was about 2.5 m. The authors of the report concluded that "concrete surface color whether black, gray or white under the test conditions has no appreciable effect on depth of thaw" (U.S. Army 1950). It seems to us that the period of observation was too short for such conclusion.

Area No. 2 included 26 runway test sections of approximately 250 m by 60 m each. The natural vegetation was removed from the site, and the upper soil was stripped to various depths from 0.3 m to 1.2 m. The thicknesses of embankment of test sections varied from 0.6 m to 3.6 m, with 1.2 m thickness for most sections. Two sections had gravel surfaces, while the others had asphalt or concrete surfaces. Some sections were insulated with 7.5 cm and 15 cm thick foamglas, 15 cm and 30 cm thick cell concrete, and 15 cm thick compacted moss. Fifteen sections were not insulated.

The data presented in the report on ground temperatures and soil freezing and thawing in the runway test sections cover only one year of monitoring and are of very limited value. However, one conclusion is worth mentioning: it was found that "the ground temperature below the insulation is cooler in summer and warmer in winter than if the insulation were not present. The net effect is that the mean annual ground temperature is about the same, whether or not insulation is used" (U.S. Army 1950). This conclusion has not appealed to many arctic engineers, and thermal insulation is still often considered as a trusted measure of permafrost protection under roads and airfields in any permafrost area. Nidowicz and Shur (1998) analyzed data presented in several works from Alaska, Canada, and Russia which also show that thermal insulation has either no effect or increases the mean annual soil temperature. Thermal insulation is effective in areas of cold permafrost because it decreases the depth of seasonal thawing and protects upper ice-rich permafrost, while at the same time, the increase in permafrost temperature does not impact the integrity of structures in these areas. In the discontinuous permafrost zone, thermal insulation does not protect permafrost from degradation. The permafrost protective effect of thermal insulation in any permafrost area is greatly increased with the addition of a soil cooling system, such as heat pipes or ventilated ducts. These cooling systems make the soil colder under thermal insulation in the winter, and thermal insulation decreases heat flow into the soil in the summer.

Eleven buildings were built in 1946–1947 in Area No. 3 to study the stability of different types of foundations. Five of them were built on gravel pads where the thickness ranged from 0.6 m to 1.8 m, with concrete or insulated wood floors placed on the ground. Two buildings had 60 cm high crawl spaces, where one of them had wood skirting. One building had an open crawl space that was 1.2 m high.

Building No. 11 was constructed on a gravel pad of 1.5 m thickness. It was based on a 48 cm thick concrete slab containing a layer of continuous hollow tile that was open to air on both sides. Ventilation of the foundation was not sufficient, and the permafrost thawed to a depth of 3.2 m under the center of the building in 1948. The monitoring data of the settlement of building corners in 1948 to 1964 were presented by Linell and Lobacz (1980). The maximum thaw settlement from 1948 to 1964 reached 75 cm. The buildings, also, were left unheated from 1957 to 1964 which did not stop the thaw settlement during this period.

Building No. 10 was built on piles with an open crawl space of 1.2 m. One pile at the southwest corner did not refreeze and frost jacked 18 cm during 1947–1957. Posts supporting two porches were installed in the active layer and frost jacked 40 cm in the same period (Linell & Lobacz 1980).

During initial observations covered by the report, it was found that seasonal vertical movement depends on the thickness of the gravel pads for buildings with floors placed on the ground. Movement was less than 2 cm for Building No. 4 constructed on a 1.8 m thick pad and more than 12 cm movement for Building No. 8 which was constructed on the natural surface. Data show this dependence greatly decreases when the thickness of the pad reaches 1.2 m.

Lobacz and Quinn (1966) analyzed the performance of buildings from their construction in 1946 until 1954, and found that the gravel pads did not protect the buildings from permafrost degradation and had "appreciable amounts of vertical settlement" (Lobacz & Quinn 1966). The thermal insulation of the floors slightly improved the foundations' integrity. They also found that buildings on piles with open crawl spaces performed well when "piles are firmly bonded in permafrost" (Lobacz & Quinn 1966).

The special project on the Navy monotube test piling was not successful. A steel pile of 18 m length and another steel pile of 12 m length were installed by steam thawing of the permafrost during November 13–20, 1947. The loading was concluded on December 12, 1947. It is possible that the method of pile installation was chosen because of the contemporary belief that "Piles cannot be driven into permafrost by the usual methods. It is therefore necessary to resort to a preliminary thawing of the ground by steam points" (Muller 1947). But the same source warned that "at a depth of 5 or 6 meters below the permafrost table the freezing of a pile to permafrost takes about a month and a half to 2 months. Only after that time can the pile be loaded with the calculated weight of the projected structure" (Muller 1947). Both statements do not specify the permafrost conditions for which they are applicable. At the test site, freezeback did not occur, and the piles experienced rapidly accelerating settlement, even after a part of the load was taken away.

The permafrost temperature at the site was close to 0°C, and only lack of experience can explain the chosen method of pile installation in warm permafrost and the pile loading shortly after the pile's installation. Even six months later, in June 1948, soil temperature was above 0°C throughout the length of both piles (U.S. Army 1950). The experiment did produce one interesting result, where thermistors were installed in the pipes attached to the piles showed an increase in soil temperature during the settlement of the piles.

The full history of the Fairbanks Research Area was recently briefly described by Henry and Bjella (2006).

N-Factor

One of the long-lasting results of the studies at the Fairbanks Research Area is the way of correlating air and surface temperatures. "Since air temperatures are generally available and surface temperatures are not, a study has been made of data from Fairbanks, Alaska to determine the relation between a thawing or freezing index calculated from air temperature and indexes calculated from the temperatures of different types of surfaces with the thermocouples so installed that they were partially embedded in the surfaces" (U.S. Army 1950, Carlson 1952). As a result of the Corps of Engineers studies, the correlation factor, which is now known as the n-factor, was proposed to evaluate a surface thawing or freezing index from the known air thawing of freezing index. With time, the n-factor approach became a very powerful tool in arctic engineering and permafrost studies.

The set of data for the correlation factors (n-factors) for different types of surfaces was developed on the basis of surface temperature measurements at the Fairbanks Research Area and air temperature measurements at the Weeks Airfield in 1947 and 1948. The correlation factors founded in the study were later included in countless works. We highly value this part of the study, as well, because it had a great impact on the development of engineering methods of the evaluation of soil freezing and thawing and permafrost methodology. We should observe that the air and surface temperature measurements were taken at two separate sites, which could have compromised the data, especially for winter conditions. The Fairbanks Research Area is on a gentle south-facing slope, and the Weeks Airfield was located on the flat surface of a low terrace of the Chena River. The distance between sites was 5 km, and the difference in elevation was about 10 m. This elevation difference in Fairbanks, which is famous for winter inversions, can partly explain why the winter n-factors for concrete and asphalt surfaces without snow were as low as 0.7. We also suspect that the snow was not completely plowed from the thermistor locations to protect them from damage.

Permafrost Existence and Thermal Offset

In the Russian book, *General Permafrost Studies,* by Sumgin et al (1940), the authors of the report identified the following equation as "a definite contribution" which describes "the conditions necessary for the existence of permafrost" (Main Report 1950):

$$k_f T_f \tau_f > k_u T_u \tau_u, \tag{1}$$

f = factors in the equation during freezing
u = factors during thawing
k = coefficient of thermal conductivity
T = average temperature of the ground at depth h
τ = time during freezing or thawing.

The equation (1) was found by Krylov (1934) from the Stephan equation for soil freezing and thawing, with an assumption that permafrost exists if freezing is greater than thawing.

$$\sqrt{\frac{2k_f(T-T_f)\tau_f}{L}} > \sqrt{\frac{2k_u(T-T_f)\tau_u}{L}} \tag{2}$$

At sites where the bottom of the active layer merges with the permafrost table, the depth of the seasonal freezing is equal to the depth of the active layer defined by seasonal thawing. Kudriavtsev (1954) named the freezing associated with the left part of the equation (1) as the potential freezing. The authors of the comprehensive report finally presented the equation (3) in the following form (U.S. Army 1950, Carlson 1952):

$$\frac{k_f}{k_u} > \frac{I}{F} \tag{3}$$

I = thawing index at the soil surface,
F = freezing index at the soil surface.

The authors of the report noticed that the ratio in the left part of equation (3) is greater than one, if the thermal conductivity of soil in the frozen state is greater than its thermal conductivity in the unfrozen state. They concluded that "permafrost can exist even though the thawing index is greater than the freezing index" (U.S. Army 1950).

The greater the thermal conductivity of the frozen soil than the unfrozen soil also leads to the decrease of the soil mean temperature at the bottom of the active layer in comparison with the temperature at the soil surface. Kudriavtsev (1954) used the Russian term *temperaturnaya sdvizhka* to describe this effect. Burn (1988) and, Romanovskiy & Osterkamp (1995) use the term *thermal offset*, and Shur & Jorgenson (2007) literally translated the Russian term as *the thermal shift*. Kersten (see below) showed that the thermal conductivity of coarse well-drained soils in the frozen state can be smaller than their thermal conductivity in the thawed state. In this case, the disparity (3) should be rewritten as

$$\frac{k_f}{k_u} < \frac{I}{F} \tag{4}$$

From (4) we can conclude that permafrost can be absent even though the freezing index of the soil surface is greater than the thawing index. In this case, the thermal offset (thermal shift) has the opposite sign. To be consistent, we should consider the negative thermal offset (which is usually referred to as the thermal offset) and the positive thermal offset.

Thermal Properties of Frozen and Unfrozen Soils

The Corps of Engineers contracted the research of the thermal properties of soil, with objectives "to determine under varying conditions of temperature, moisture, bulk density, and composition the thermal properties of representative soils and organic material from Alaska" (Kersten 1949). The study was conducted at the Oak Street Laboratories of the Engineering Experimental Station of the University of Minnesota. Miles S. Kersten, Associate Professor of Civil Engineering, was in immediate charge of the investigation. Procedures and results were presented in a report (Kersten 1949) and numerous publications since then.

Soils from Alaska included Chena River gravel, sand, silty clay loam, silt loam, and peat from Fairbanks; sand and silt loam from Northway; and clay from Healy. To cover a wider range of soil properties, some soils from other regions were also studied.

Soil was placed in a hollow cylinder for thermal conductivity tests. Boundary conditions at the inside face of a hollow soil cylinder were kept at a constant heat flow. Constant temperature was the boundary condition on the outside face. Temperature was measured at two points in the inside face and two points at the outside face. To evaluate the coefficient of thermal conductivity the following equation was used:

$$q = \frac{\dfrac{k(A_2 - A_1)}{\ln(A_2 / A_1)}(T_1 - T_2)}{r_2 - r_1} \quad (5)$$

where:
q = measured rate of heat flow,
k = coefficient of thermal conductivity,
A_2 = area of outside face of soil cylinder,
A_1 = area of inside face of soil cylinder,
T_1 = temperature at inside face,
T_2 = temperature at outside face,
r_2 = outside radius,
r_1 = inside radius.

This equation can be transformed into the commonly used equation, written for one unit of length:

$$q = \frac{2\pi k(T_1 - T_2)}{\ln(r_2 / r_1)} \quad (6)$$

The equations define steady-state heat flow between two cylindrical surfaces having constant temperatures consequently T_1 and T_2. This is not the case for the test conditions dealing with a composed hollow cylinder with prescribed heat flux at one surface and prescribed temperature at the other. To satisfy the boundary conditions expected in equations (5) and (6), the heat flow (voltage and amperage of the heater) at the inner face was manually adjusted to reach the desired temperature at this face of the hollow cylinder filled with soil. Measurements were taken when temperature variations were less than 1% during a five-hour period.

The thermal conductivity of soils was studied using a wide range of soil densities and water contents at average temperatures of 70, 40, 25, and 20°F. The temperature difference between sides of the soil cylinder was 10°F. This means that for the average temperature of 25°F, it was 30°F on the hot face of the soil cylinder and 20°F on the cold face.

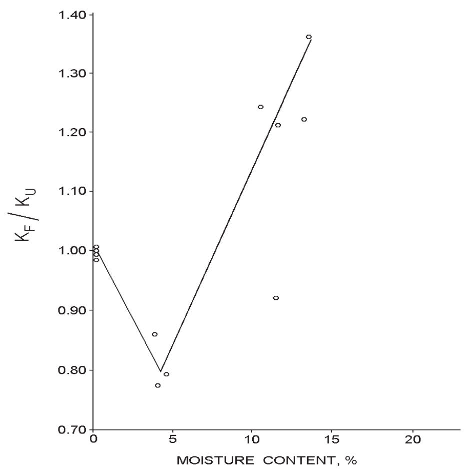

Figure 1. Ratio of soil thermal conductivity in frozen state to thermal conductivity in unfrozen state (from Kersten 1949).

After the tests, the moisture content of sandy soils at the cold side of the specimens was greater by a few percentages than on the warm side, and some mass transfer occurred during the tests. This could be driven by extremely high temperature gradients which were about 6°C over 5 cm.

Experimental data show that over a wide range of soil moisture content, the ratio of soil thermal conductivity in a frozen state is greater than the thermal conductivity of the same soil in an unfrozen state. This is because the thermal conductivity of ice is four times greater than the thermal conductivity of water. This rule is practically always applicable to fine soils. Kersten also found that, at low water content, the thermal conductivity of unfrozen soil is greater than the thermal conductivity of frozen soil, and the ratio k_f/k_{un} is less than one (Fig. 1). This was because of the separation of soil particles and the disturbance of thermal contacts between particles by ice during freezing, and an increase in soil porosity (Gavriliev 2004). It is a very rare situation for fine soils, but it is a common one for well-drained coarse soils.

Thermal conductivity of a few soils were compared (Kersten 1949) with limited data obtained by the Corps of Engineers New England Division, Boston, by a different method on the same soils. Values found by the University of Minnesota are less than those of the Boston study, but the difference does not exceed 10%.

Kersten did not test the frozen soils in their natural state. Soils from Alaska were remolded, and different water contents were assigned that were limited by saturation. In natural conditions, permafrost soils often have water content sufficiently greater than soils studied by Kersten. This limitation was later overcome by Slusarchuk and Watson (1975). Extensive research of thermal conductivity of surface covers was done by Gavriliev (2004).

Aerial Photo Interpretation for Permafrost Identification

As a part of the research, the U.S. Army Corps of Engineers funded and provided field support of the studies

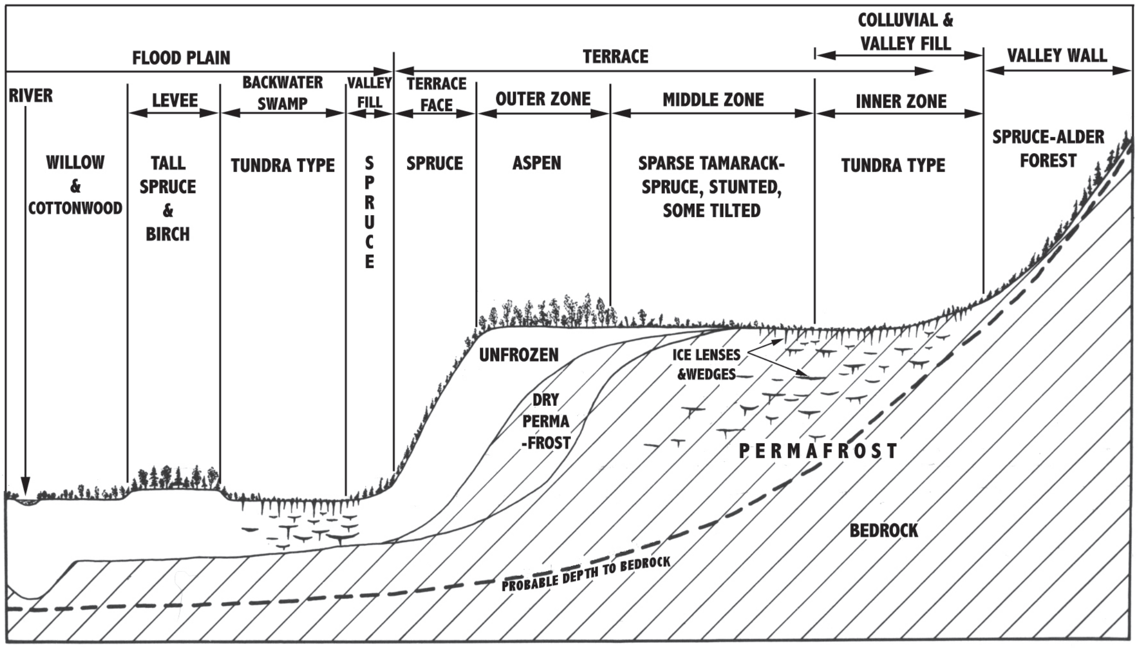

Figure 2. Possibly the first permafrost-relief-vegetation sequence (from Frost 1950).

by Purdue University. The purpose was to evaluate soils and permafrost conditions in Alaska by means of aerial photographs. Colonel Yoder, one of the leaders of the project, described expectations in the following words: “In relatively undeveloped regions, such as in the Territory of Alaska, aerial photographs can be used to great advantage in locating airports, highways, railroads, bases, etc. In a few hours’ time, a general engineering soil map can be produced which will show the good, poor, and intermediate soil areas evaluated on the basis of anticipated performance of engineering structure. Thus, the poor soil areas can be eliminated almost entirely by study of the aerial photographs, and the field investigation can be concentrated on those areas best suited to construction” (Frost 1950).

Scientists from Purdue University spent five summers in Alaska, gathering information which helped to develop techniques of aerial photograph interpretation. Field work was conducted in Interior Alaska, Seward Peninsula, Yukon-Kuskokwim Delta, Arctic Slope, and Arctic Coastal Plain. “When possible, such studies were made by ‘on the spot’ sampling with the aerial photographs in hand” (Frost 1950). As a result of the field studies and analysis of the field data, aerial photo patterns related to permafrost conditions were developed. They include vegetation, topography, drainage, erosion, and some direct indicators of permafrost conditions. With the information from the aerial photographs and ground reconnaissance, engineering soils maps can be made for finding suitable construction sites. These maps can shorten the preliminary investigation and eliminate the need for costly, extensive preliminary drilling (Frost 1950). This work became widely known from the extensive paper presented by R.E. Frost in a symposium, *Frost Action in Soils,* and published in the proceedings of this symposium (Frost 1952).

The report compiled by Frost (1950) for the Corps of Engineers consists of several examples of aerial photographs and descriptions of land forms and vegetation in relation to permafrost in Alaska. Figure 2, from the report, presents the typical profile through a river valley in the discontinuous permafrost zone showing patterns of permafrost existence and absence in relation to relief and vegetation. It is possible that this figure is the first permafrost profile of such kind in permafrost literature.

Frost’s report outlines a comprehensive approach to applications of aerial photography to permafrost studies. It stimulated similar studies in Russia (Protas’eva 1967) and Canada (Brown 1964, 1966). It was also the first step in the series of studies which led to the effective application of terrain unit analysis to permafrost investigations for the Trans-Alaska Pipeline. Kreig and Rigert (1982) improved and effectively applied aerial photo interpretation and application of the terrain analysis to geotechnical investigations for the pipeline, with the acknowledgement Frost’s report. Roger Brown (1970) in his book, *Permafrost in Canada*, also acknowledged the pioneering studies by Purdue University in Alaska and later in Canada, which “justified the belief in the applicability of airphoto interpretation methods for preliminary site surveys in permafrost areas” (Brown 1970). The method, which was initially solicited for engineering investigations for airfields in the Arctic, finally became an interdisciplinary tool of arctic and subarctic scientific studies and applied investigations of different scales and for multiple purposes.

Stoeckeler, who worked with the Purdue University team, studied a relationship between permafrost and vegetation. He found that vegetation is not a good indicator of permafrost presence in areas where the permafrost table is lower. “The presence of the permafrost table at a depth of 6 feet or more from the ground surface has little or no deleterious effect on tree growth, with the possible exception to deep rooted trees like balsam poplar, cottonwood, and jack pine. Therefore, vegetation alone can be employed only as an indicator of soil conditions to a relatively shallow depth" (Stoeckeler 1949). This message, from 1949, still remains relevant to permafrost and many other studies in the discontinuous permafrost zone.

Conclusions

In the 1940s, the St. Paul District of the U.S. Army Corps of Engineers carried out pioneering research. This paved the way for future intensive research of frozen ground engineering in Alaska, as well as around the world.

Investigations by the Minnesota and Purdue Universities were funded by the Corps of Engineers for specific engineering tasks, as parts of the project. Their immense impact on permafrost studies over the last 60 years proved that there is nothing more valuable than good science.

Acknowledgments

We wish to thank Jerry Brown, Hugh French, and Mikhail Kanevskiy for helpful discussions and advice.

This work was supported by the Alaska EPSCoR, (NSF award 0701898 and NSF grant ARC 0454939). Any opinions and findings expressed in this material are those of the authors and do necessarily effect the views of the NSF.

References

Brown, R.J.E. 1964. *Permafrost Investigations on the Mackenzie Highway in Alberta and Mackenzie District*. Ottawa: National Research Council of Canada, Division of Building Research, 36 pp.

Brown, R.J.E. 1966. Influence of vegetation on permafrost. *Proceedings of the Permafrost International Conference, Lafayette, Indiana, November 11–15, 1963:* 20-25.

Brown, R.J.E. 1970. *Permafrost in Canada.* Toronto: University of Toronto Press, 234 pp.

Burn, C.R. & Smith, C.A.S. 1988. Observations of the thermal offset at several sites near Mayo, Yukon Territory, Canada. *Arctic* 41(2): 99-104.

Frost, R.E. 1950. *Evaluation of soils and permafrost conditions in the Territory of Alaska by means of aerial photographs.* USA: U.S. Army: 110 pp.

Frost, R.E. 1952. Interpretation of permafrost features from airphotos. *Frost Action in Soils: A Symposium, Highway Research Board Special Report No. 2*. Washington, DC: National Research Council, 223-246.

Gavriliev, R.I. 2004. Thermal properties of soils and surface covers. In: D.C. Esch (ed.), *Thermal Analysis, Construction, and Monitoring Methods for Frozen Ground.* Reston: American Society of Civil Engineers, 277-294.

Henry, K.S & Bjella, K. 2006. History of the Fairbanks permafrost experiment station, Alaska. *Proceedings of the 13th International Symposium on Cold Regions Engineering 2006: Current Practices in Cold Regions Engineering, Orono, Maine, July 23–26, 2006:* 11 pp.

Kersten, M.S. 1949. *Final report laboratory research for determination of the thermal properties of soils.* St Paul, MN: University of Minnesota, 227 pp.

Kreig, R.A. & Reger, R.D. 1982. *Air-photo analysis and summary of landform soil properties along the route of the Trans-Alaska Pipeline System*. Fairbanks: Alaska Division of Geological & Geophysical Surveys, 149 pp.

Krylov, M.M. 1934. The thermal analysis of soil freezing. *Engineering bulletin* 10: 53-59 (in Russian).

Linell, K.A. 1973. Long-term effects of vegetation cover on permafrost stability in an area of discontinuous permafrost. *Proceeding of the Second International Conference on Permafrost, Yakutsk, U.S.S.R., July, 13–28, 1973*: 688-693.

Linell, K.A. & Lobacz, E.F. (eds.). 1980. *Design and construction of foundations in areas of deep seasonal frost and permafrost*, *CRREL Special Report 80-34.* Hanover: U.S. Army Cold Regions Research and Engineering Laboratory, 310 pp.

Lobacz, E.F. & Quinn, W.F. 1966. Thermal regime beneath buildings constructed on permafrost. *Proceedings of the Permafrost International Conference, Lafayette, Indiana, November 11–15, 1963:* 247-252.

Muller, S.W. 1947. *Permafrost or Permanently Frozen Ground and Related Engineering Problems.* Ann Arbor: J.W. Edwards, 230pp.

Nidowicz, B. & Shur, Y. 1998. Pavement thermal impact on discontinuous permafrost. *Proceedings of 9th International Conference on Cold Regions Engineering: Cold Regions Impact on Civil Works, Duluth, Minnesota*, *September 27–30, 1998*: 34-45.

Protas'yeva, I.V. 1967. *Aeromethods in Geocryology*. Moscow:,Nauka, 196 pp (in Russian).

Romanovsky, V.E. & Osterkamp, T.E. 1995. Interannual variations of the thermal regime of the active layer and near-surface permafrost in Northern Alaska. *Permafrost and Periglacial Processes* 6(4): 313-335.

Shur, Y.L. & Jorgenson M.T. 2007. Patterns of permafrost formation and degradation in relation to climate and ecosystems. *Permafrost and Periglacial Processes* 11(1): 7-19.

Slusarchuk, W.A. & Watson, G.H. 1975. Thermal conductivity of some ice-rich permafrost soils. *Canadian Geotechnical Journal* 12: 413-424.

Stoeckeler, E.G. 1948. *Identification and evaluation of Alaskan vegetation from airphotos with reference to soil, moisture and permafrost conditions: A preliminary paper*. St. Paul: U.S. Army, 103 pp.

Sumgin, M.I., Kachurin, S.P., Tolstikhin, N.I. & Tumel', V.F. 1940. *General permafrost science*. Moscow: U.S.S.R. Academy of Sciences, Moscow-Leningrad, 340 pp.

United States Army, Corps of Engineers, St. Paul District 1950. Main Report and Appendix III, *Comprehensive report, investigation of military construction in arctic and subarctic region: 1945–1948*. USA: U.S. Army, 68 pp. & 22 pp.

High-Resolution Surface and Subsurface Survey of a Non-Sorted Circle System

Ronald Daanen
Geophysical Institute, University of Alaska Fairbanks, Fairbanks, Alaska
Vladimir Romanovsky
Geophysical Institute, University of Alaska Fairbanks, Fairbanks, Alaska
Donald (Skip) Walker
Department of Biology and Wildlife, University of Alaska Fairbanks, Fairbanks, Alaska
Mike LaDouceur
Geophysical Institute, University of Alaska Fairbanks, Fairbanks, Alaska

Abstract

Non-sorted circle patterned ground features are abundant in the Arctic tundra. These features show large variability in active layer depth in summer and heave in winter. There is a lot of research devoted to measuring active layer depth, yet little is known about small-scale variability of the active layer in patterned ground systems. The active layer is sometimes used as an indicator of a warming climate which is not always correct. The active layer depth varies from year to year as it freezes and thaws. It also expands and shrinks as it accumulates ice and loses ice. We have conducted two surveys, one in the spring of 2007 and one in the summer of 2007. The surveys were taken from the Biocomplexity research site near Franklin Bluffs, North Slope Alaska. We were able to reference the surveys points to a deep well located near the site that is used for deep-permafrost temperature sampling. The well is 60 m deep and, therefore, permanently anchored in the permafrost. The surface elevation is recorded in a 25 cm dense grid over an area of 10 by 10 m. The plot contains approximately 20 non-sorted circles. The average surface elevation in winter was 85 cm below the reference point, and in the summer it was 97 cm below the reference point. This means that there was a 12 cm surface elevation difference. We suggest multiple mechanisms that could explain this amount of heave. Current active layer development shows a decreasing trend (smaller active layers over time) with long-term observations near our site, in contrast to the annual average soil temperatures that are increasing. Reasons for a decreasing trend may include a lack of a warming trend in summer, changes in thermal conditions, and greening of the Arctic, which may lead to increased transpiration rates and absorption of incoming shortwave radiation. Long-term observation of surface movement in this grid will reveal more detailed information on the behavior of ice accumulation in the active layer.

Keywords: active layer; non-sorted circles; permafrost; snow; soil; survey.

Introduction

During the annual cycle, arctic soils form an active layer in the summer that refreezes during the fall and winter. In this paper, we present a high-resolution elevation dataset of a non-sorted circle system on continuous permafrost near Franklin Bluffs, Alaska. Non-sorted circles are defined as "semi barren areas in the tundra that lack a border of stones" (Washburn 1956). The non-sorted circle system is defined here as interacting areas of vegetated and semi-barren surfaces. The system can be as small as a single non-sorted circle with its surrounding vegetation. This vegetation zone can be anywhere from 10 cm to 10 m. The vegetated surface is generally underlain by a well-developed, organic layer several centimeters thick.

Besides these data we also provided information on the soil climate (soil temperature and moisture content) at the time the survey was done, as well as historical climate variation from the area, to put the elevation data from the survey in perspective.

The survey helped our understanding of the processes of frost heave and thaw settlement. Frost heave and thaw settlement (consolidation) is scale dependent and can be viewed as one-dimensional on a landscape scale (Brown et al. 2000, Hinkel & Nelson 2003). The Circumpolar Active Layer Monitoring (CALM) sites are treated as a landscape scale measurement, where it takes many measurements to determine the average active layer depth for a region, to eliminate any local heterogeneity. On a smaller scale, however, it is a three-dimensional process. Small heterogeneities in topography, vegetation, and organic layer thickness, are observed at a typical plot scale of a 100 m^2. Micro climate at the soil surface generated by vegetation and micro relief has a strong effect on the soil surface energy balance. Soil climate, driving freezing and thawing processes, depends on: the micro climate above the soil, soil properties, wetness, and permafrost conditions below the active layer. Frost heave, driving freezing and thawing processes, causes the soil surface to move up and down within the season and between annual cycles. This aspect of movement of the soil surface is also called ice segregation and thaw settlement. These two processes are not monitored in the CALM sites and it is therefore not possible to monitor the loss and gain of ground ice within and between the annual cycles. This loss or gain of ground ice has only a limited effect on the active layer depth, due

Figure 1. Ice lens formation in silty clay loam.

to the limited amount of soil present in the ice rich transient layer (Pullman et al. 2007, Shur & Jorgenson 2007).

The annual soil surface movement is driven by frost heave or frost action, where the strongest movement is expected in frost susceptible soils. During freezing these soils accumulate ice in the form of lenses that form perpendicular to the temperature gradient (Cheng 1983, Kokelj & Burn 2005, Kokelj et al. 2007, Mackay 1983). This is also called secondary frost heave (Miller 1980). This process drives an expansion of the soil which exceeds the difference in density between water and ice. For secondary frost heave to take place water needs to flow to the freezing front, driven by cryostatic suction, to make this expansion possible (Daanen et al. 2007). The source of this water is still not resolved in the literature. Many models require an unlimited water supply to be able to generate the amount of frost heave observed. In a laboratory setup it was found that even without adding water to a frost susceptible soil during one dimensional freezing it was possible to generate heave beyond the expansion of water alone (Daanen unpublished data). This process can be explained as drying of the soil between the ice lenses (Daanen et al. 2007). The dry soil occupies a volume and in addition the ice occupies a volume.

The interannual soil movement is caused by segregated ice at the bottom of the active layer, which can cause thaw settlement (Pullman et al. 2007). Slow refreezing at the bottom of the active layer in the fall generally causes larger ice lenses compared to the upper active layer, where freezing is faster. Formation and loss of this ice depends on many of the same energy balance processes as mentioned above but in addition, it depends on variations in hydrological conditions between years (Kokelj & Burn 2005).

Soil surface movement is generally hard to detect due to a lack of a proper reference point in the tundra. Romanovsky (Walker et al. 2004) and Washburn (Washburn 1997) have used permafrost anchors as a reference point to measure the difference between frost heave in non-sorted circles and vegetated tundra. This method is good when the anchors are deep enough to prevent them from heaving out of the ground on a longer time span. Satellite observations through interferometry would be an option when data is available during a small window in the fall before freezing and spring if the signal is not distorted by the snowpack. Differences between seasons may be too small to detect. Global Positioning System (GPS) equipment could be used to identify the movement of the soil surface; however accuracy of the equipment in elevation differences is a concern (Berthling et al. 2003).

Methods

For this study we used a deep borehole casing as a reference point to survey our site with a total station, at a resolution of 25 cm. The borehole is 60 m deep (with at least 59 m anchored in permafrost) located near Franklin Bluffs along the Dalton Highway, Alaska. The site was part of a biocomplexity study "Biocomplexity associated with biogeochemical cycles in arctic frost-boil ecosystems," which ended in 2006 (Walker et al. 2004). The site can be described as "mesic" or "zonal" and therefore a good representation of the regions in terms of vegetation and soil climate conditions (Walker et al. 2004). The annual average air temperature in the region is -11.3°C. The silty clay loam soils at the site are frost susceptible and generate a lot of segregated ice lenses during freezing (Fig. 1).

These soils are capable of forming and sustaining non-sorted circles, for a more detailed description of the internal workings of these system we refer to Daanen et al. (2007). These non-sorted circles provide a heterogeneous soil and soil surface that causes a large spatial variability in the active layer depth and frost heave level (Kade et al. 2006, Walker et al. 2004). Due to the scale of the non-sorted circles we chose to survey our plot with a resolution of 25 cm to capture the smaller nuances of relief between the non-sorted circles and the surrounding tundra.

We surveyed the site with a Leica TPS400 series total station using the deep permafrost borehole as a reference point (±0.03 m). The first survey was done in the April of 2007 well before the onset of snowmelt. The second survey was done in August of 2007 near the point of maximum thaw depth. In addition to the soil surface survey we also measured the snow depth in winter and the thaw depth in the summer. Measurements of the air temperature, soil temperature, and soil moisture are collected at the site using a datalogger and presented later in the results section.

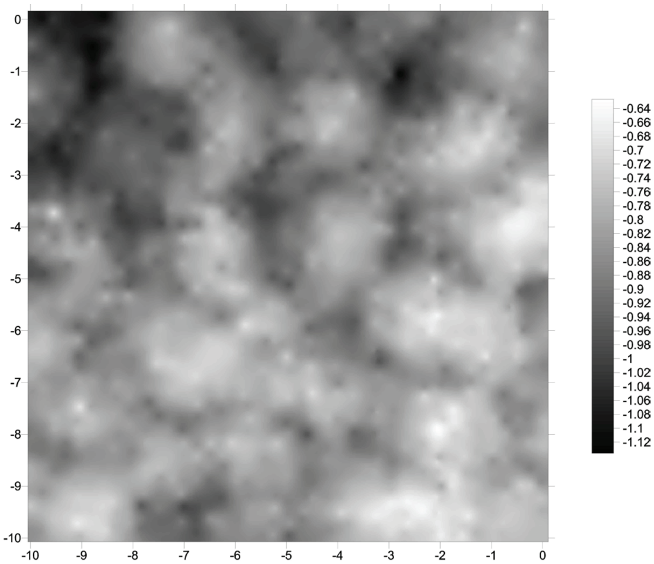

Figure 2. Elevation of the grid in winter relative to the fixed well casing (units are meters), April 26, 2007.

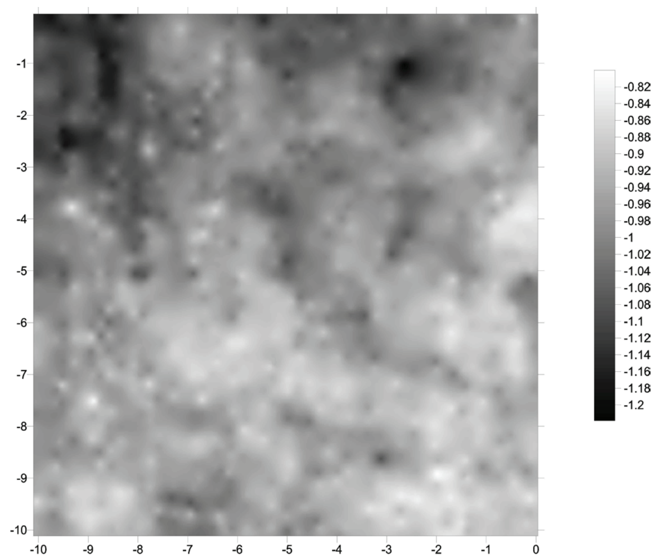

Figure 3. Elevation of the grid in summer August 27, 2007, relative to the fixed well casing (units are meters).

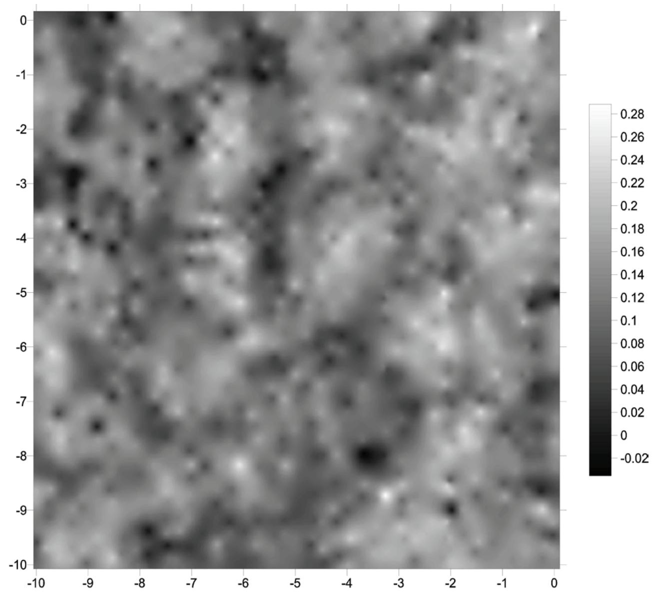

Figure 4. Elevation differences between summer and winter for the Franklin Bluffs site (units are meters). This plot represents frost heave.

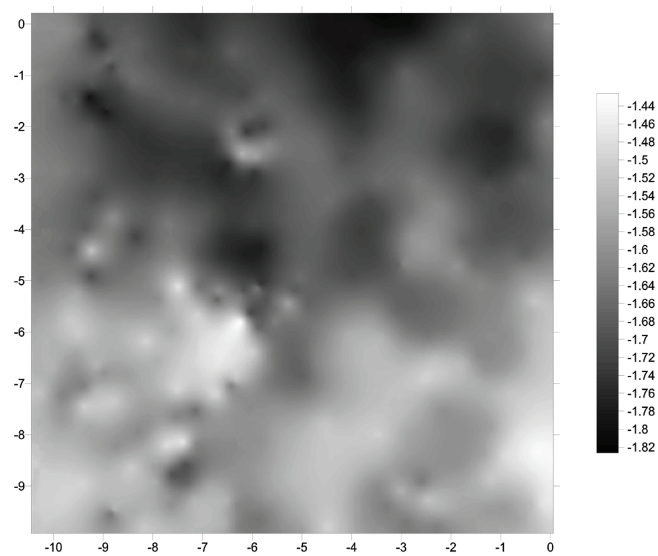

Figure 5. Permafrost table elevation for the site relative to the well casing on August 28, 2007 (units are meters)

Results

The spatial distribution of surface elevation in winter and summer is shown in Figure 2 and 3, respectively.

The winter results show a clear distribution of non-sorted circles in the lighter areas where the surface is raised above the inter circle areas (approximately 25 non-sorted circles within the domain of 10 x 10 m). Compared with Figure 3 the non-sorted circles are more visible due to increased frost heave in the circles. From Figure 3 the elevations still show the non-sorted circles, which implies that the elevation gain during freezing is not all lost during the summer thaw. Also visible from both illustrations is the gentle slope from upper left to lower right or from northwest to southeast.

We found that there was on average a 12 cm elevation difference between the summer and winter conditions. The scales on Figures 2 and 3 have an offset; for the lowest point 8 cm and the highest point 18 cm relative to the well casing.

The elevation difference for each observation point between the two data sets is given in Figure 4. Areas with the greatest difference are shown in the lighter shades. The non-sorted circles are also distinctly visible as areas with the greatest amount of annual frost heave.

The permafrost table elevation map is given in Figure 5.

The active layer depth is the difference between the surface elevation in summer and the permafrost table. A map of this depth is given in Figure 6. The average depth measured in the grid was 65.9 cm with a standard deviation of 7.8 cm. This depth is on track with active layer depths measured

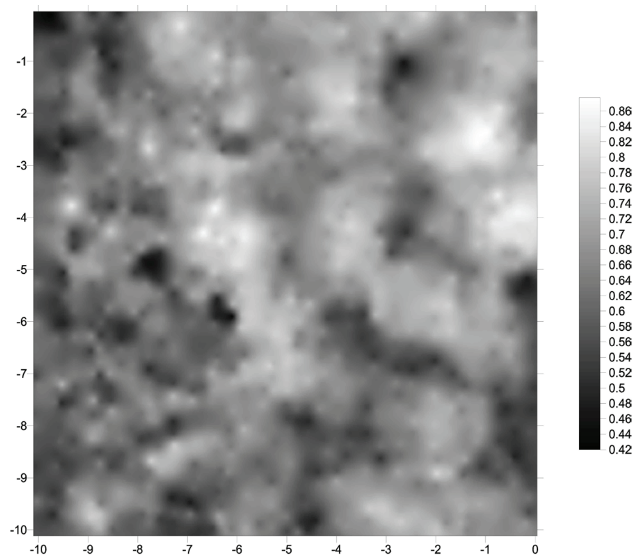

Figure 6. Active layer depth generated from the difference between the surface elevation and the permafrost table elevation (units are meters).

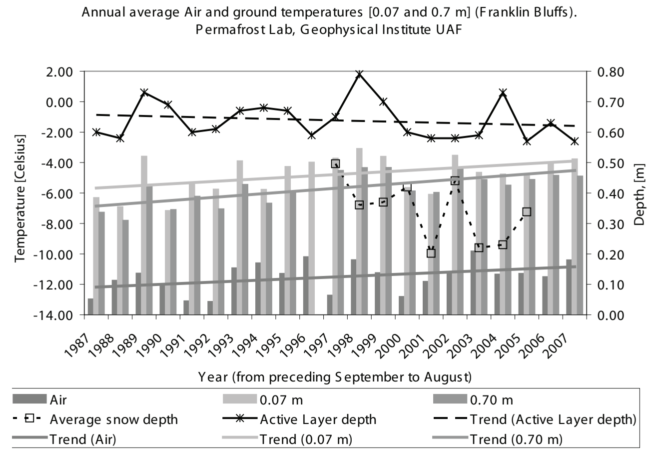

Figure 7. Long-term trends in active layer depth, air temperature, soil temperature (0.0 and 0.7 m), and snow depth near Franklin Bluffs, Alaska, from 1987–2007.

over a long period for the area as part of the long-term permafrost observation network (Fig. 7). Figure 7 also shows the trends in air and soil temperature over the past 20 years near Franklin Bluffs, Alaska. Over that period following the trend lines the annual average air temperature increased by 1.334°C, the soil at 0.07 m increased by 1.774°C, the soil at 0.7 m increased 2.34°C and the active layer depth decreased 0.036 m. Observed surface and permafrost temperatures north of our field site shows an even stronger warming trend then shown here (Romanovsky et al. 2008).

The active layer depth at the Franklin Bluffs site is measured by the permafrost laboratory at the Geophysical Institute as part of the long-term permafrost observation network. These measurements are taken in a larger 100 by 100 m grid surrounding the deep permafrost temperature well. The average thaw depth measured for long-term observations for Franklin Bluffs was 57.1 cm for August 28, 2007. The standard deviation for the larger grid was 10.4 cm.

To compare current soil conditions to recent years, we present daily air and soil temperature data in Figure 8. These data show that the winter was cooler then previous winters, and the summer was warmer than previous summers. Soil moisture data from the same period is given in Figure 9.

These soil moisture data suggest that the active layer was drying over the period presented here. This may lead to decreased frost heave during next season.

Discussion

The observed movement of the soil surface resulted in an average 12 cm of annual heave. These 12 cm cannot be explained by expansion due to phase change alone, because there is a limited amount of water in the active layer. The mineral soils have approximately 40% moisture by volume that would only result in 3 cm of heave during refreezing of the active layer. In non-frost-susceptible soils a similar amount of heave was observed in Canada (Mackay & Burn 2002). In our site, the soils are frost susceptible and water can move during freezing. However there are no obvious other large water reservoirs in the area that are close enough to make a difference to the amount of heave. The small slope to the site would drain the water just as fast as it would add water to the site. Our hypothesis is that there is additional water contained inside the soil profile, like water stored in small surface depressions and thick organic layers (inter circle area). It was observed during our spring measurements that there was no ice in the depressions where there is normally water in summer. Part of this water could have been absorbed by the freezing mineral soil, which is cooling more rapidly than the organic soils in between the non-sorted circles (Daanen et al. 2007). Additional heave can be attributed to drying of the soil as it freezes water from the soil segregates and forms ice lenses while the soil dries out. Air would replace water in the pore spaces and increase the volume of the soil column and the soil skeleton supports the overburden. Evidence was found that larger cracks within the active layer are ice free (Romanovsky pers. com.). A last reason for the low elevation of the soil surface could be attributed to the dry soil conditions during the summer survey see Figure 9. There are clay minerals in the soil profile that may have the potential to shrink as the soil dries. It has to be noted that the inter circle areas did not shrink significantly (Fig. 3).

The average active layer depths within the surveyed grid are 65.9 cm and the average active layer depth in the larger long-term grid is 57.1 cm. The difference can be explained by a difference in drainage, the surveyed grid is better drained due to small relief compared to the larger grid sampled. The draining of water would result in less ice buildup in the active layer and therefore less energy required for thawing the profile. Improved drainage also affects the vegetation at the site, which tends to have less moss than the wet vegetation plot down slope of the surveyed grid.

The active layer depth compared with other sites along

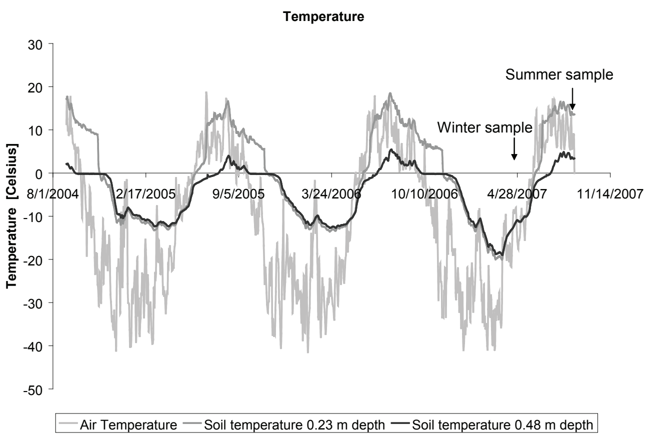

Figure 8. Air and soil temperature near the surveyed grid.

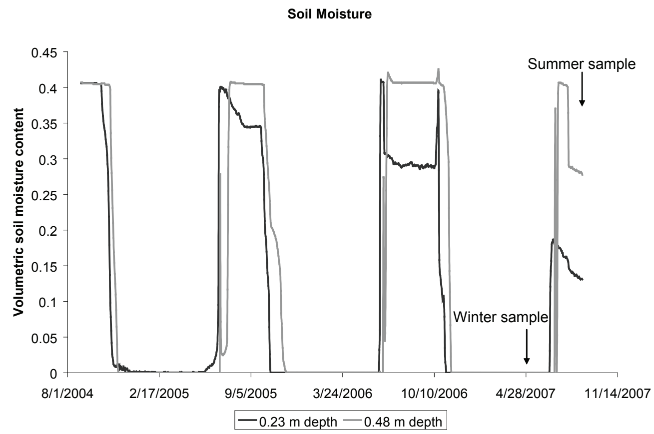

Figure 9. Soil moisture near the surveyed grid.

the Dalton Highway shows no trend that can be related to soil climate (Romanovsky et al. 2008). This is caused by differences in vegetation, with a much more developed vegetated/organic mat in the south compared to the vegetated/organic mat in the north.

The active layer depth over time shows a slight decreasing trend even though the soil temperature shows a trend toward warmer conditions (Fig. 7). There are many reasons to explain the trend. The summer air temperature did not increase. Average annual temperatures from the more recent period do not show a major trend toward warming conditions. The winter of 2006/2007 was colder (Fig. 8) than normal due to less snow compared with normal conditions, the snow data are not in the graph due to malfunction of the probe. The colder soils take longer to warm up and thaw. The dry conditions over the summer months had a reducing effect on the thermal conductivity of the organic layer. Another reason for a limited active layer depth could be loss of segregated ice near the bottom of the active layer. The potential loss of segregated ground ice is what we will measure during future surveys when we compare different years. The last reason is related to long-term observations of "greening" in the Arctic (Jia et al. 2003). Increased vegetation or Leaf Area Index (LAI) may be responsible for increased insulation (boundary layer), shading or transpiration at the site during the summer which leads to shallower thaw depths, even though the average annual temperatures have increased. Cooler conditions due to increased evapotranspiration have been observed on Banks Island where a constant wind made soils of southwest facing slopes cooler in summer (French 2007). In our situation an increase in LAI leads to increased radiation adsorption which causes increased transpiration rates. The spatial distribution of the vegetation in the non-sorted circle system shows that vegetated surfaces have shallower thaw depth.

Results from the survey also show the large variability in heave and thaw in a relatively small area of 10 x 10 m. Driven by increased insulation of the vegetation and underlying organic mat the energy flux through the surface is greatly reduced (Daanen et al. 2007). The heterogeneity on the soil surface causes temperature differences in the soil during freezing. This leads to cryostatic suction toward cooler areas where ice accumulates as the water freezes. Cryoturbation in the non-sorted circles reduces vegetation succession which keeps the non-sorted circles semi-barren and poorly insulated.

Conclusions

A high-resolution elevation survey of a non-sorted circle ecosystem near Franklin Bluffs, Alaska, shows substantial soil surface movement. The average elevation difference between summer and winter sampling is 12 cm. This heave cannot be explained with expansion of water due to phase change. Other explanations for the large difference are additional water from organic material froze as ice lenses in the mineral soil, ice lens formation in conjunction with soil freeze drying, and soil shrinkage due to dry conditions in summer.

The long-term active layer observations do not show a clear trend with average air and soil temperatures in our records. Some reasons suggested here are that the summer is not warming enough to affect the active layer, and the increased greening of the Arctic may lead to increased transpiration by the vegetation. More data is needed to identify a set of reasons that can fully explain the variability and behavior of the active layer system.

Heterogeneity of the soil surface vegetation causes heterogeneity in soil surface movement (frost heave) due to preferential ice accumulation in the semi-barren areas called non-sorted circles. The same vegetation pattern also causes preferential active layer development and thaw settlement.

Acknowledgments

This research was funded by the Polar Earth Science Program, Office of Polar Programs, National Science Foundation Grant No. ARC-0612533, OPP-0120736 ARC-0632400, and ARC-0520578.

References

Berthling, I., Etzelmuller, B., Eiken, T. & Sollid, J.L. 2003. The rock glaciers on Prins Karls Forland: corrections of surface displacement rates. *Permafrost and Periglacial Processes* 14: 291-293.

Brown, J., Nelson, F.E. & Hinkel, K.M. 2000. The circumpolar active layer monitoring (CALM) program research designs and initial results. *Polar Geography* 3: 165-258.

Cheng, G. 1983. The mechanism of repeated-segregation for the formation of thick layered ground ice. *Cold Regions Science and Technology* 8: 57-66.

Daanen, R.P., Misra, D. & Epstein, H.E. 2007. Active-layer hydrology in non-sorted circle ecosystems of the arctic tundra. *Vadose Zone Journal (accepted)*.

French, H.M. 2007. *The Periglacial Environment*. West Sussex, Chichester: Wiley.

Hinkel, K.M. & Nelson F.E. 2003. Spatial and temporal patterns of active layer thickness at Circumpolar Active Layer Monitoring (CALM) sites in northern Alaska, 1995-2000. *Journal of Geophysical Research-Atmospheres* 108 (D2).

Jia, G.S.J., Epstein, H.E. & Walker, D.A. 2003. Greening of arctic Alaska, 1981-2001. *Geophysical Research Letters* 30(20).

Kade, A., Romanovsky, V.E. & Walker, D.A. 2006. The n-factor of nonsorted circles along a climate gradient in Arctic Alaska. *Permafrost and Periglacial Processes* 17(4): 279-289.

Kokelj, S.V. & Burn, C.R. 2005. Near-surface ground ice in sediments of the Mackenzie Delta, Northwest Territories, Canada. *Permafrost and Periglacial Processes* 16(3): 291-303.

Kokelj, S.V., Burn, C.R. & Tarnocai, C. The structure and dynamics of earth hummocks in the subarctic forest near Inuvik, Northwest Territories, Canada. *Arctic Antarctic and Alpine Research* 39(1): 99-109.

Mackay, J.R. 1983. Downward water movement into frozen ground, western arctic coast, Canada. *Canadian Journal of Earth Sciences* 20: 120-134.

Mackay, J.R. & Burn, C.R. 2002. The first 20 years (1978-1979 to 1998-1999) of active-layer development, Illisarvik experimental drained lake site, western Arctic coast, Canada. *Canadian Journal of Earth Sciences* 39(11): 1657-1674.

Miller, R.D. 1980. *Freezing phenomena in Soil. Applications of Soil Physics.* New York: Academic Press, 254-299.

Pullman, E.R., Jorgenson, J.C. & Shur, Y. 2007 Thaw Settlement in Soils of the Arctic Coastal Plain, Alaska, *Arctic, Antarctic, and Alpine Research* 39(3): 468-476.

Romanovsky, V.E., Marchenko, S., Daanen, R.P., Sergeev, D.O. & Walker, D.A. 2008. Soil climate and frost heave along the Permafrost/Ecological North American Arctic Transect. *Proceedings of the Ninth International Conference on Permafrost*, *Fairbanks, Alaska, June 29–July 3, 2008* (this proceedings).

Shur, Y.L. & Jorgenson, M.T. 2007. Patterns of permafrost formation and degradation in relation to climate and ecosystems, *Permafrost and Periglacial Processes* 18(1): 7-19.

Walker, D.A., Epstein, H.E., Gould, W.A., Kelley, A.M., Kade, A.N., Knudson, J.A., Krantz, W.B. Michaleson, G., Peterson, R.A., Ping, C.L., Raynolds, M.A., Romanovsky, V.E. & Shur, Y. 2004. Frost-boil ecosystems: complex interactions between landforms, soils, vegetation, and climate. *Permafrost and Periglacial Processes* 15: 171-188.

Washburn, A.L. 1956. Classification of patterned ground and review of suggested origins. *Geological Society of America Bulletin* 67: 823-866.

Washburn, A.L. 1997. *Plugs and Plug Circles; a Basic Form of Patterned Ground, Cornwallis Island, Arctic Canada; Origin and Implications*. Seattle, WA, United States (USA): University of Washington, Quaternary Research Center.

Effect of Adsorbed Cations on Unfrozen Water in Silty Soil as Determined Using the NMR Method

Margaret M. Darrow
University of Alaska Fairbanks

Scott L. Huang
University of Alaska Fairbanks

Satoshi Akagawa
Hokkaido University

Go Iwahana
Hokkaido University

Abstract

To investigate adsorbed cations effects on the unfrozen water in frozen soil, laboratory experiments were conducted on Hanover silt. Monovalent and divalent cation treatments were prepared by exchanging the soil's adsorbed cations in saturated salt solutions. Laboratory experiments included measuring unfrozen water content with pulse NMR, T2 relaxation time, ζ-potential, and specific surface area. T2 relaxation time provides insight into unfrozen water changes during freezing. As the soil temperature decreases from -0.2°C to -2°C, the T2 net magnetization signal strength decreases rapidly, and subsequently levels off for temperatures colder than -2°C. This may indicate a reduction in the mobility of unfrozen water, as it is restricted under the influence of surface potential. Monovalent cation-treated samples have shorter T2 relaxation times than divalent cation-treated samples, suggesting less mobility of unfrozen water in monovalent-saturated soil. The monovalent cation-treated samples also demonstrated greater ζ-potentials, resulting in thicker unfrozen water films.

Keywords: cation; frozen soil; mobility; NMR; T2; unfrozen water; ζ-potential.

Introduction

The presence of unfrozen water in frozen soil is an integral part of frost heave theory, permafrost studies, and frozen ground engineering. Since unfrozen water was first identified by Bouyoucos (1917, 1920), numerous different methods have been used to measure it. Tice et al. (1978, 1982) presented the nuclear magnetic resonance (NMR) method as a viable technique to measure the unfrozen water content. While the NMR method has been used by these and other researchers to quantify unfrozen water, no reference has been made to spin-spin relaxation measurements (T2) or their meaning as related to the behavior of unfrozen water in frozen soil.

As part of a larger research project, we investigated the unfrozen water content using the NMR method, ζ-potential, and other chemical and mineralogical properties of natural soil and its associated cation-treated samples. In this paper, we present NMR free-induction decay (FID) data and spin-spin relaxation (T2) data for a silty soil, and investigate the effects of cation treatments upon T2 relaxation time and ζ-potential.

Methods

Soil preparation

Hanover silt loam (HS) was sieved following the procedure implemented by Rieke et al. (1983), and all organic matter was removed from the original soil sample. This sieved soil is referred to as the "Baseline" (BSLN) sample. The results of a semi-quantitative x-ray diffraction (XRD) analysis indicated that the HS BSLN sample contained illite/mica, kaolinite, chlorite, and interlayered smectite, as well as other non-clay mineral species. The total percentage of phyllosilicates in the HS BSLN sample was 20.8%. In order to investigate the effects of surface chemistry on the unfrozen water content, cation treatments were applied to the BSLN soil. Four different salts, magnesium chloride ($MgCl_2$), calcium chloride ($CaCl_2$), sodium chloride (NaCl), and potassium chloride (KCl), were used for the various treatments. For a complete description of the cation treatment preparations, see Darrow (2007).

ζ-potential measurements

In certain clay minerals, the negative potential at the Stern layer is manifested as the ζ-potential, which can be quantified by placing a dilute soil suspension into an electric field. The negatively-charged soil particles will migrate toward the positive pole, while the remaining cation swarm in the fluid will migrate toward the negative pole. The ζ-potential is the negative potential formed at the shearing surface of the soil particle (Greenland & Hayes 1978). The ζ-potential depends on the type of cations adsorbed within the Stern layer. Thus, changing the adsorbed cations on the mineral surface affects the measured ζ-potential and the overall double layer thickness.

The ζ-potential of the HS BSLN and cation treatments was determined using a Zeta-Meter. To begin the sample preparation, 0.5 g of each sample was placed into a scintillation vial, to which distilled, deionized water was added. After the soil was completely saturated, the vial was shaken vigorously in order to suspend most of the soil particles. A small portion of the suspension was taken from the vial and mixed with additional distilled, deionized water to create a dilute suspension for ζ-potential measurements. The amount of suspension removed and diluted was not exact; instead, these samples were prepared "by eye," having the concentration necessary to provide adequate particle tracking under the Zeta-Meter microscope (Zeta-Meter Inc. 1975). The dilute suspension was poured into the Zeta-Meter's electrophoresis cell, and the time necessary for each of 50 soil particles to travel 120 μm at room temperature was recorded. The dilute suspension was replaced after 15 to 25 particles were tracked. This ensured that the heat added by the Zeta-Meter components had a minimal effect on the ζ-potential measurements. Once all 50 particles were tracked, the time measurements and charts available in the Zeta-Meter manual (1975) were used to calculate the ζ-potential of the soil particles.

As a fine-grained soil may contain several different types of clay minerals, its measured ζ-potential will form a wide particle-charge distribution curve, demonstrating the range of the ζ-potential for all clay minerals present (Riddick 1968). The median ζ-potential value for each bulk soil sample was calculated from the particle-charge distribution curve, using a procedure outlined by Riddick (1968).

Unfrozen water measurements using NMR

FID and T2 measurements were made using a pulse NMR. NMR measurements were made at the following temperatures: -0.2°C, -0.5°C, -1°C, -2°C, -3°C, -4°C, -5°C, -7.5°C, -10°C, -15°C, and -20°C. After these measurements were completed, the sample was warmed to above freezing, and FID and T2 measurements were made at 10°C. The moisture content of the soil was determined at the above-freezing temperature, and the unfrozen water content, w_U, at each sub-freezing temperature was calculated by:

$$w_U = \frac{w_{10^o C} \cdot x_T}{x_{10^o C}} \qquad (1)$$

where $w_{10^o C}$ is the measured gravimetric water content at 10°C, $x_{10^o C}$ is the NMR signal amplitude at 10°C, and x_T is the NMR signal amplitude at the corresponding sub-freezing temperature. All w_U values presented here are gravimetric water contents, and NMR signals used in these calculations represent FID peak times. Likewise, T2 net magnetization signal strength amplitudes presented are the peak values measured for each temperature.

Results

ζ-potential measurements

Figure 1 contains the ζ-potential particle-charge distribution curves for the HS BSLN sample and corresponding cation treatments, and the median ζ-potential values for the five HS samples are summarized in Table 1. The range for the Na^+ sample is larger than the other samples, resulting in a wider curve. The median ζ-potential values for the monovalent cation-treated samples are greater (i.e., more negative) than the divalent cation-treated and BSLN samples.

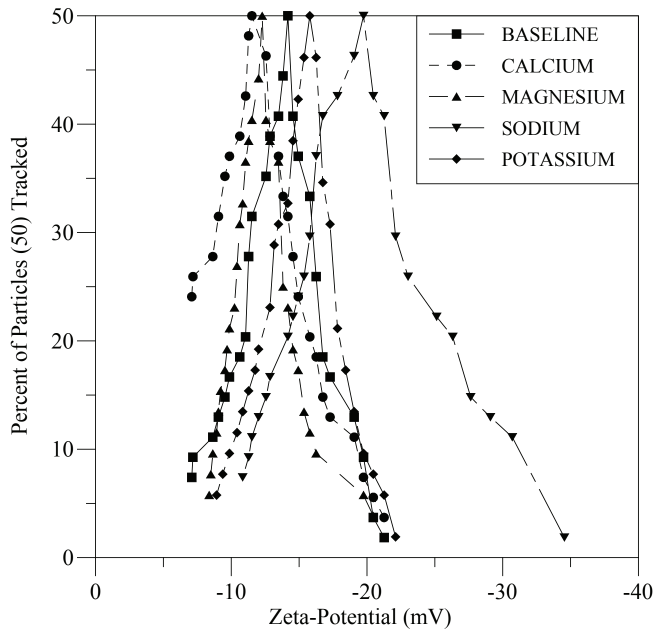

Figure 1. ζ-potential particle-charge distribution curves for the HS BSLN sample and corresponding cation treatments.

Table 1. Summary of ζ-potential median values for HS BSLN and corresponding cation treatments.

Sample	ζ-potential median values (mV)
BSLN	-14.17
Ca^{2+}	-11.76
Mg^{2+}	-12.28
Na^+	-19.74
K^+	-15.79

Unfrozen water measurements

The w_U data for HS BSLN sample and corresponding cation treatments calculated using the FID peak times are presented in Figure 2. The K^+-treated sample has the highest w_U at a given temperature, followed by the Na^+-treated sample. The w_U of the three remaining samples are very close to one another over the range of temperatures measured. The overall trend is similar for each sample, with the w_U steadily decreasing in an exponential fashion with decreasing temperature.

A plot of T2 net magnetization signal strength versus temperature for the HS samples is shown in Figure 3. The trends in these data are noticeably different from those in Figure 2. For each sample, the T2 signal strength decreases rapidly from -0.2°C to -2°C. There is little change in the T2 signal strength at temperatures colder than -2°C until -20°C, at which point the T2 signal strength drops close to 0 for all samples. This noticeable break at -2°C suggests a difference in the behavior of the unfrozen water at this temperature.

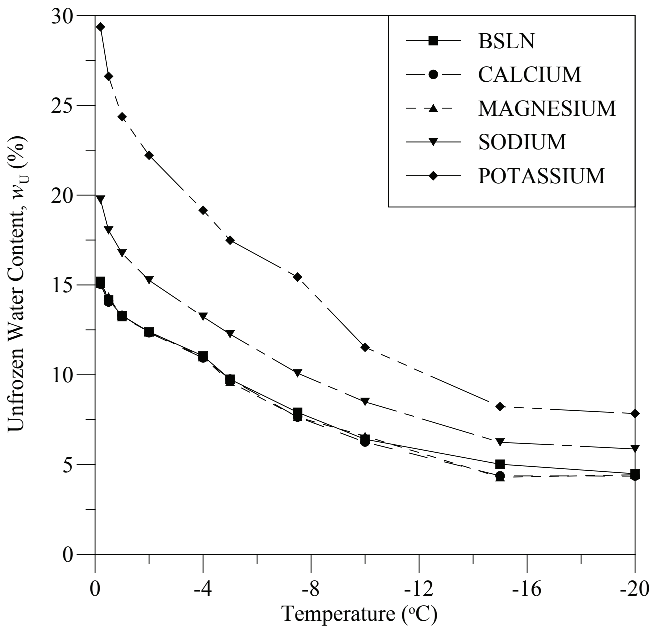

Figure 2. Unfrozen water content, w_U, versus temperature for HS BSLN and corresponding cation treatments.

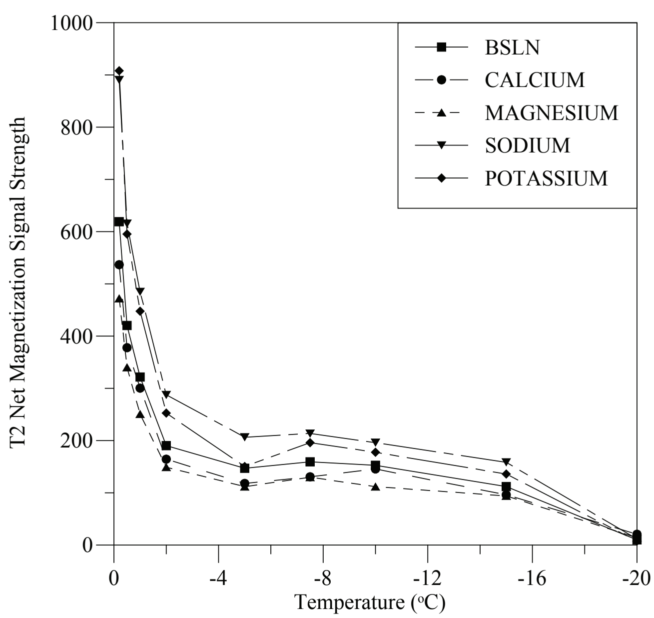

Figure 3. T2 net magnetization signal strength versus temperature for HS BSLN and corresponding cation treatments.

The raw T2 signal data was processed to yield T2 relaxation times, which are presented in Figure 4. While these data demonstrate more scatter than those in the previous figures, T2 relaxation time also decreases in an exponential fashion with decreasing temperature. Although not shown in Figure 4, T2 relaxation times were also calculated for each sample at 10°C. These times ranged from 1.69 ms to 2.59 ms, with the monovalent cation-treated samples demonstrating the shorter times.

The thickness of the unfrozen water film in each sample was calculated at each temperature using the w_U data presented in Figure 2, the measured HS specific surface area of 9.25

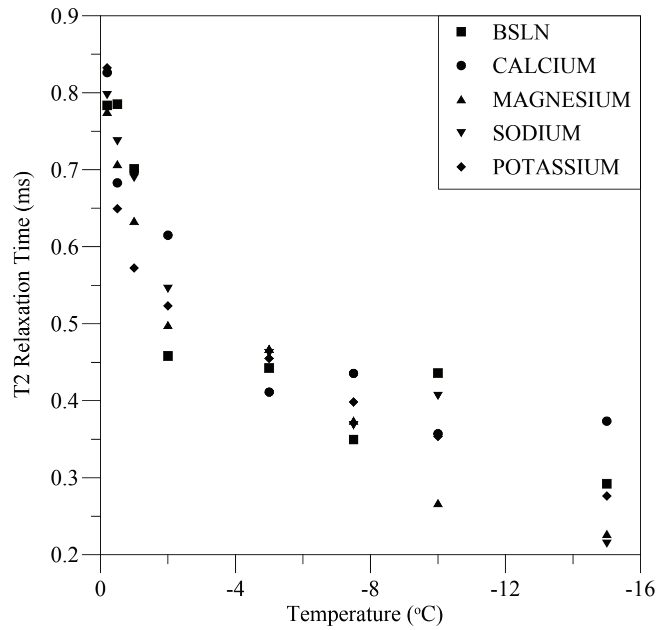

Figure 4. T2 relaxation time versus temperature for HS BSLN and corresponding cation treatments.

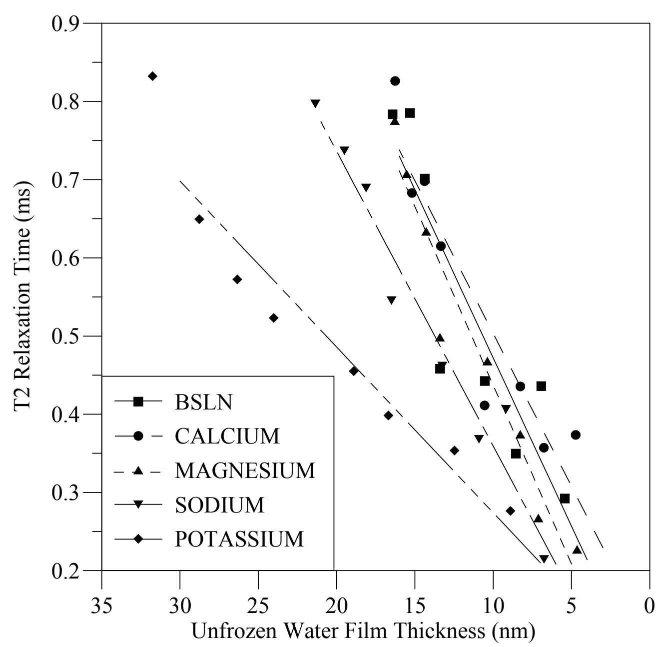

Figure 5. T2 relaxation time versus calculated unfrozen water film thickness for HS BSLN and corresponding cation treatments. Linear trend lines are shown for each data set.

m^2/g, and water densities for each sub-freezing temperature interpolated from published data (Hodgman 1956). The calculated thicknesses are plotted against T2 relaxation times for each corresponding temperature, as shown in Figure 5. For all samples, T2 relaxation time decreases with decreasing unfrozen water thickness in a linear fashion. This is indicated by the best-fit linear trend lines, with coefficients of determination (r^2) ranging from 0.81 to 0.96.

Discussion

While NMR FID signal strength data is a useful means of quantifying the unfrozen water content in a frozen soil, T2 data may yield important information about unfrozen water mobility.

Kojima and Nakagami (2002) used the magnetic resonance imaging (MRI) technique to investigate water mobility in the gel-layer of a drug. They found that the T2 relaxation time of the outer portion of the gel-layer was close to that of free water. However, in the inner portion of the gel-layer, the T2 relaxation time progressively decreased, suggesting that the water mobility around the core interface became highly restricted.

Similar interpretations can be made from the data presented here. In Figure 3, the rapid decrease in T2 net magnetization signal strength from -0.2°C to -2°C may indicate the freezing of water within the soil pores and capillaries, and some reduction in the thickness of the unfrozen water layers around individual soil particles. In Figure 5, for any given unfrozen water thickness, the monovalent cation-treated samples have shorter T2 relaxation times than the divalent cation-treated and BSLN samples. This suggests less mobility of unfrozen water in the monovalent cation-treated samples than in the divalent cation-treated samples. The monovalent cation-treated samples also demonstrated the greatest ζ-potentials of the sample group, resulting in their thicker unfrozen water films.

T2 relaxation times within water "layers" around the soil particles were calculated by taking the difference of the T2 signal strength at two sequential temperature readings. Unfrozen water "layers" with smaller numeric values are closer to the soil particle surface. These results, presented in Figure 6, demonstrate scatter because of the calculation method and variations within the data; however, generally T2 relaxation time decreases exponentially with decreasing distance to the soil particle surface.

Conclusions

The NMR method is a useful means for quantifying the unfrozen water content of a frozen soil through FID signal strength data. The results presented here indicate that T2 net magnetization signal strength and resulting T2 relaxation time provide insight into the mobility of unfrozen water. The rapid decrease in the T2 signal strength from -0.2°C to -2°C and the subsequent leveling off of the signal for temperatures colder than -2°C indicate a reduction in the mobility of the unfrozen water, as the unfrozen water becomes more restricted by the proximity of the soil particles' surfaces.

T2 relaxation time decreases linearly with the decreasing thickness of unfrozen water films. Soil saturated with monovalent cations demonstrates shorter T2 relaxation times than that saturated with divalent cations. The monovalent cation-treated soil also demonstrates greater ζ-potential, resulting in thicker unfrozen water films. Thus, the predominantly adsorbed soil cations strongly affect T2 relaxation time and the mobility of unfrozen water. T2 relaxation time decreases exponentially with decreasing unfrozen water "layers"; however, the effect of cation treatments on the water "layers" is not well-defined for this soil.

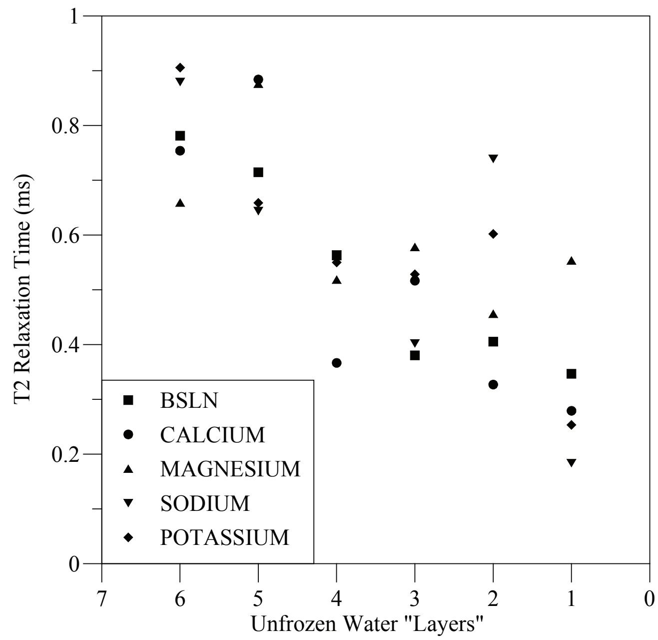

Figure 6. T2 relaxation time versus unfrozen water "layers." Each "layer" represents the difference in T2 signal strength at two sequential temperature readings. Unfrozen water "layers" with smaller numeric values are closer to the soil particle surface.

Acknowledgments

The authors would like to thank the National Science Foundation for providing financial support to the first author for her doctoral studies.

References

Bouyoucos, G. 1917. *Classification and Measurement of the Different Forms of Water in the Soil by Means of the Dilatometer Method*, Technical Bulletin 36, Michigan: Michigan Agricultural College Experiment Station.

Bouyoucos, G. 1920. A new classification of the soil moisture. *Soil Science* 11 (1): 33-47.

Darrow, M.M. 2007. *Experimental Study of Adsorbed Cation Effects on the Frost Susceptibility of Natural Soils*. Ph.D. thesis. Fairbanks: University of Alaska Fairbanks, 257 pp.

Greenland, D.J. & Hayes, M.H.B. (eds.) 1978. *The Chemistry of Soil Constituents*. New York: John Wiley & Sons.

Hodgman, C.D. (ed.) 1956. *Handbook of Chemistry and Physics*. Cleveland: Chemical Rubber Publishing, Co.

Kojima, M. & Nakagami, H. 2002. Investigation of water mobility and diffusivity in hydrating micronized low-substituted hydroxypropyl cellulose, hydroxypropylmethyl cellulose, and hydroxypropyl cellulose matrix tablets by magnetic resonance imaging (MRI). *Chem. Pharm. Bull.* 50(12): 1621-1624.

Riddick, T.M. 1968. *Control of Colloid Stability through Zeta Potentia*. New York: Zeta-Meter, Inc.

Rieke, R.D., Vinson, T.S. & Mageau, D.W. 1983. The role of specific surface area and related index properties in the frost heave susceptibility of soils. *Proceedings, Permafrost: Fourth International Conference, Fairbanks, Alaska, July 17-22, 1983*: 1066-1071.

Tice, A.R., Burrous, C.M. & Anderson, D.M. 1978. Determination of unfrozen water in frozen soil by pulsed nuclear magnetic resonance. *Proceedings, Third International Conference on Permafrost, Edmonton, Alberta, July 10-13, 1978*: 149-155.

Tice, A.R., Oliphant, J.L., Nakano, Y. & Jenkins, T.F. 1982. *Relationship between the Ice and Unfrozen Water Phases in Frozen Soil as Determined by Pulsed Nuclear Magnetic Resonance and Physical Desorption Data*, Hanover: CRREL Report 82-15.

Zeta-Meter, Inc. 1975. *Zeta-Meter Manual*. New York: Zeta-Meter, Inc.

Changes in Active Layer Thickness and Seasonal Fluxes of Dissolved Organic Carbon as a Possible Baseline for Permafrost Monitoring

S.P. Davydov

Northeast Science Station Pacific Institute of Geography, Far-Eastern Branch of Russian Academy of Sciences, Cherskii, Republic Sakha (Yakutia), Russia

D.G. Fyodorov-Davydov

Institute of Physicochemical and Biological Problems in Soil Science of RAS, Pushchino, Moscow Region, Russia

J.C Neff

Geological Sciences and Environmental Studies, University of Colorado at Boulder, Boulder, CO 80309, USA

N.I. Shiklomanov

Department of Geography, University of Delaware, Newark, DE 19716, USA

A.I Davydova

E-mail: sdavydov@cher.sakha.ru

Abstract

This study investigates the relationship between changes in active layer thickness (ALT) above permafrost and the discharge of dissolved organic carbon (DOC) in streams of the Kolyma Lowland, northeastern Siberia. The results of observations indicate that the increase in ALT began in northern taiga landscapes in 2001–2005 and 2007. The contribution of melted ice from the thawed permafrost layer to the regional runoff is estimated to be 5–10% of the annual precipitation. The Kolyma Lowland is underlain by ice- and organic-rich Pleistocene deposits (Yedoma or Ice Complex). The observed increase in ALT results in involvement of ancient DOC in a contemporary biochemical cycle. This phenomenon is reflected by the structure and age of the DOC in streams in the fall. The observed effect of the increase in ALT on DOC potentially allows the use of radiocarbon dating for the integrative assessment of permafrost conditions over large territory.

Keywords: ALT monitoring; DOC; transitional layer; Yedoma.

Introduction

During the last decade, a great amount of research has underlined an increase of Siberian river discharge into the Arctic Ocean (Peterson et al. 2002, McCleland et al. 2004). This process has many sources, and permafrost thawing is among them. This study investigates the proposal to examine dissolved organic carbon (DOC) in seasonal streams for permafrost monitoring of the Arctic ecosystem.

The Kolyma Lowland occupies the northeast of the vast Siberian Coastal Plains. The region is characterized predominantly by continental climate (Table 1). The greatest positive changes of the study area occurred during recent years.

The lowland is wholly underlain by continuous permafrost that is the most ancient underground ice formation of Eurasia since the Pliocene Age. The total thickness of frozen sediments is 500–650 m with a mean temperature of permafrost from -3° to -11°C (Fyodorov-Davydov & Davydov 2006). Northern ecosystems of the Kolyma Lowland are underlain by ice-rich loess sediments with high organic content are called the Yedoma Suite or Ice Complex in Russia. Yedoma deposits are mid to Late Pleistocene continental loamy sediment with ice wedges. The total ice content in yedoma (sedimentary soil and ice wedges combined) is on average 75% (Gasanov 1971, Kholodov et al. 2003). The mean organic content in these sediments is

Table 1 Meteorological characteristic* of the study area.

	Period	aver	max	min
Mean Annual temperature, ^{o}C	1980 –2007	-10.8	-7.6 (2007)	-13.2
Mean summer temperature, ^{o}C	1980 –2007	10.7	14.9 (2007)	8.3
Mean sum positive summer temperature, ^{o}C	1980 –2007	993.6	1371.3 (2007)	670.7
Mean Annual precipitation, mm	1980 –2007	224.0	322.1 (2006)	146.1

*data of meteorological station “Cherskii.”

estimated to be from 5–12 kg/m3 (Kholodov et al. 2003) to 21 kg/m3 (Zimov et al. 2006, Zimov et al. 2006a).

The upper layer (0.1–2.0 m) of yedoma was thawed during the climatic optimum of the Holocene (6.3–9.6 thousand years ago for northeast Siberia). The consequent refreezing resulted in formation of a secondary frozen layer, called the transitional Layer (TL) (Shur 1988). This layer forms a boundary between the active and older permafrost layers of a yedoma.

Methods

Monitoring of changes in active layer thickness

The North-East Science Station (NESS) has carried out

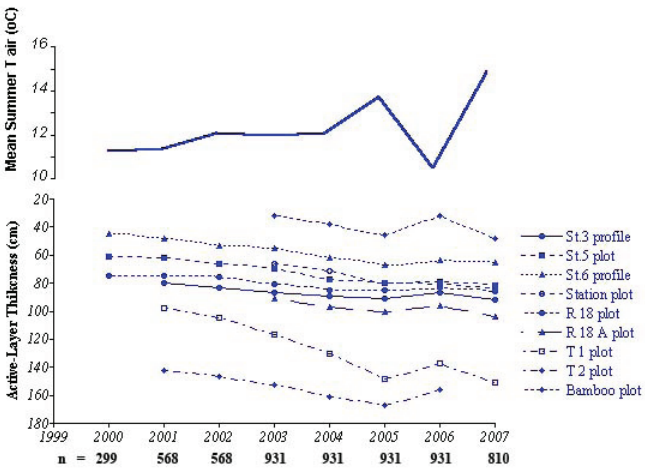

Figure 1. Annual dynamics of active layer thickness in different sites of the upland landscape of the Kolyma lowland; *n* – numbers of observation points on each year.

research of seasonal changes in ALT for more than 20 years. Since 1996, this study has been extended by participation in the network of the Circumpolar Active Layer Monitoring (CALM) Project. Sediments of the upper part of the permafrost and soils of the watershed area, both upland and lowland streams, have loamy and loamy sandy grading of soils. Therefore, measurements of seasonal changes in ALT were made by steel probes with length more than the maximum depth of the active layer. This method has an accuracy of 1–2 cm. We also used thermologgers, which were installed in thermometric boreholes.

Long-term observations for seasonal changes of ALT were made on 9 sites (Fig. 1). Each of 7 plots has 121 data points and different grids for measurements: one plot, 10 x 10 m; five plots, 1 x 1 m; and one plot, 0.5 x 0.5 m. Two profiles have 64 data points.

ALT monitoring started in all sites after the melting of snow cover. Observations were made once in 2 weeks (for profiles) or once in the beginning of every month (for plots) during the warm season. Every year the maximum of ALT was determined in the beginning of soil freezing in all points for each site.

Determination of volumetric soil moisture content

We used two methods for determination of volumetric soil moisture content in transitional horizon soils and permafrost of watersheds: (1) direct measurement of volumetric soil moisture content of undisturbed drilling soil sample; and (2) calculating the method by the N.A. Tsytovich equation (Gasanov 1971).

$$V_i = \frac{\gamma}{\Delta_i} * \frac{W_s - W_{ms}}{1 + W_s} \tag{1}$$

where

V_i = volumetric soil moisture content, %;

W_s = the gravimetric water content of frozen soil in % of soil dry weight,

W_{ms} = quantity of unfrozen water in % soil dry weight; mean content for sediments of the transitional horizon and yedoma is 2% unfrozen water for study area.

γ = density of the frozen soil of undisturbed structure, g/cm^3; mean density for sediments of the transitional horizon and yedoma 1.8 g/cm^3 for study area.

Δ_I = ice density, g/cm^3

Figure 2. Some types of cryogenetic textures of transitional layer.

Calculation of contribution of the release water partitioning by percentage of summer precipitation

For calculations of percentage of the release water partitioning of total summer precipitation we used the equation

$$P_{ALT}(\%) = \frac{\Delta_{ALT} * 0.3}{S_{\Sigma}} * 100\% \tag{2}$$

where

P_{ALT} = percentage of the release water partitioning of total summer precipitation, %;

Δ_{ALT} = annual gradient of thawing ALT, mm;

0.3 = mean part of the volumetric soil moisture content for transitional horizon of study area;

S_{Σ} = total summer precipitation, mm.

Results and Discussion

Changes in active layer thickness and hydrologic regime

Observational studies of active layer monitoring sites are characterized by different variants of the larch taiga landscapes and dispose at some watersheds of upland streams. Their active layer is characterized mainly by the soil cover of loamy cryohydromorphic soils (Cryozems and Gleyzems). Cryozems occupy more than 80% of soils (Fyodorov-Davydov & Davydov 2006). We used various methods of observation for ALT (profiles and plots) at Circumpolar Active Layer Monitoring (CALM) and North-East Science Station (NESS) sites from upland landscapes.

The observed increase in ALT is characteristic for all sites in 2001–2005. The correlation between ALT and mean summer temperatures reaches 0.96, and the maximal observed increase in ALT reaches 40% from long-term mean on some sites, which suggests that the increase in annual thawing has resulted from the abnormally high summer temperatures (Fig. 1).

The TL is characterized by very ice-rich cryogenetic textures that presented a predominance of lens-wicker, ataxitic, and lens-layered cryotextures (Fig. 2). Measurements

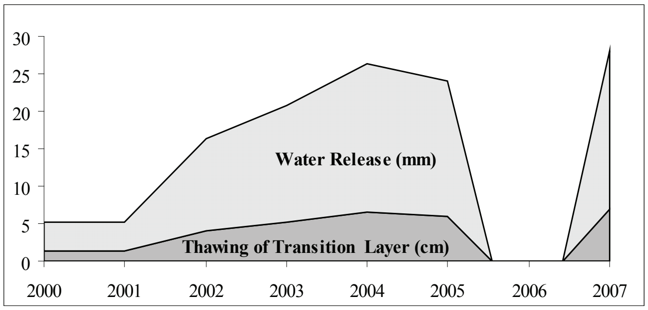

Figure 3. The relationship between thawing of the transitional layer and water release from melting permafrost.

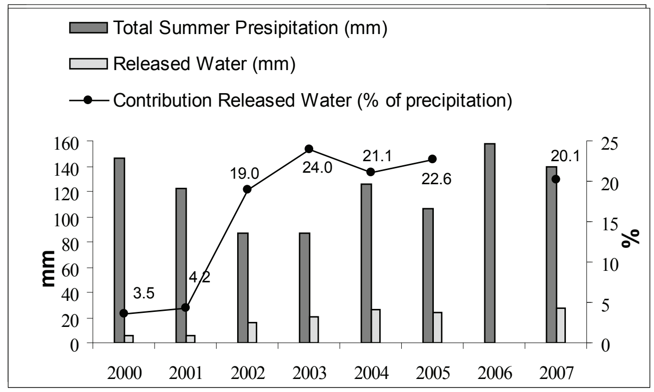

Figure 4. The contribution of the total annual water flux from the degrading transitional layer, estimated by percentage of summer precipitation.

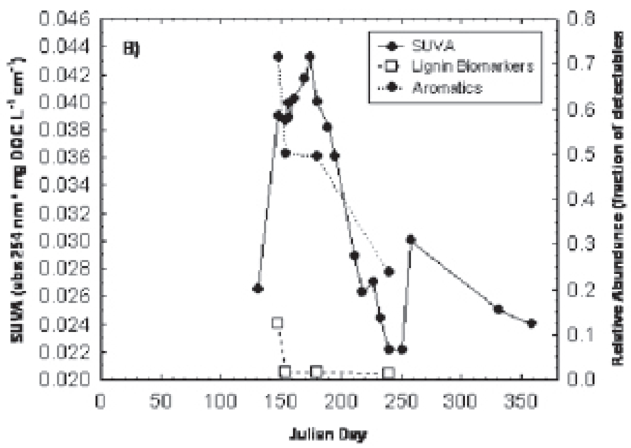

Figure 5a. Seasonal changes for lignin biomarkers, aromatics, and SUVA values (specific ultraviolet absorbance at 254 nm) for DOC (Neff et al. 2006).

of volumetric soil moisture content (10 cm above frozen horizon) indicate that the mean moisture content is 25% for the AL (n=128) and 55% for the TL and upper permafrost horizons (n=104) in a 10 cm layer lower depth of seasonal melting. Observations of soil moisture content were conducted at the end of the thawing season or at the beginning of winter for landscapes of watershed. We used direct or calculation methods for estimation of volumetric soil moisture. To preliminarily evaluate the release of water from the thawing of the upper permafrost, we considered the difference in volumetric water content between active and underlying transitional layers. The 30% difference translates to a 3 mm thick layer of water for each cm of thawed soil (Fig. 3). Due to moisture saturation characteristic of low-lying surfaces, wetlands were not considered for analysis.

The observed increase in ALT results in degradation of the TL. In 2003–2005 and 2007 at several sites, the transient horizon has degraded completely, causing thawing of deeper, perennially frozen layers. In 2006 the mean temperature decreased, and the summer precipitation abnormally increased, perhaps stimulated by the ice cover reduction at the East-Siberian Sea in last years. In this season the ALT decreased and there was a pause in the annual degradation of the TL. The release water and DOC fluxes stopped from the older permafrost layer. In 2007 the mean summer temperature vastly increased. That initiated thawing of the horizon, which was frozen in the previous season, and re-thawing of the TL with the formation of a new portion of release water (Fig. 3).

When the upper horizon of permafrost is thawing, a saturated layer is formed, and its water takes part in the seasonal hydrological cycle. Processes of transpiration have little influence on the release water fluxes from the permafrost, since plants vegetation of watershed landscapes in the middle of August–beginning of September basically has finished. In the same period, water migration in the upper soil horizon does not occur for the absence of soil freezing.

The contribution of the released water to the regional water runoff is estimated as 5–10% of the 280 mm of mean annual precipitation and reaches 20% of mean summer precipitation (Fig. 4).

Age and structure of dissolved organic carbon

A relatively thin layer of earth materials between the ground surface and the top of the permafrost undergoes an annual cycle of freezing and thawing (active layer) and is an important component of the Arctic ecosystem. A systematic and widespread increase in the thickness of the active layer could lead to changes in the biochemical cycle of high latitudes. Moreover, the TL and the yedoma contain a high level of dissolved organic carbon (DOC) held by frozen sediments and ice wedges. The significant increase of thawing leads to the involvement of buried, dissolved organic matter in the contemporary carbon biogeochemical cycle.

Strong seasonal trends in carbon age and chemical composition of DOC during the seasonal thawing were shown by Neff et al. (2006). Concentrations of lignin and aromatics of DOC in runoff of upland streams are decreasing from spring to fall (Fig. 5a), while relative DOC age is increasing (Fig. 5b). However, such trends are not evident in lowland streams located in the Kolyma flood plain, underlain by relatively young Holocene permafrost (Fig. 5b). The seasonal increase of DOC radiocarbon age can indicate the involvement of ancient carbon in contemporary hydrobiochemical cycles. A high water flux from the thawed horizon provides an effective vehicle for DOC to reach

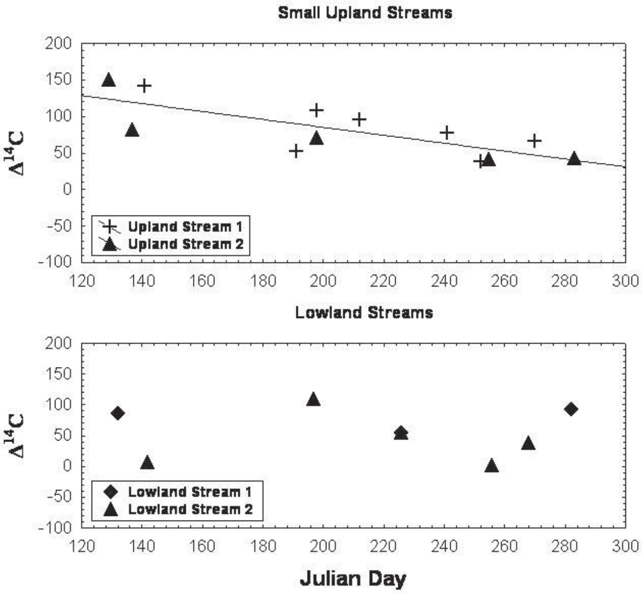

Figure 5b. Small upland streams – seasonal changes in the Δ14C content and the Δ14C of DOC. Lowland streams that drain seasonally flooded, modern permafrost – seasonal distribution of the Δ14C of DOC (Neff et al. 2006)

streams. However, the limited biochemical data (one, 2003 year) does not allow us to reach a definite conclusion about carbon release and migration due to an increase in annual thaw propagation. It is probable that the part of seasonally-released DOC, which remains in soil, migrates upward through the soil profile due to freezing and influences the age and structure of the DOC during consecutive thawing seasons.

Chemical composition and age of DOC can be measured in autumn, at the end of thawing season, when the ALT is maximal.

Conclusions

The results of observations suggest a progressive increase in active layer thickness in the Kolyma Lowland.

The observed changes in active layer thickness result in metachronous degradation of the ice- and organic-rich transitional layer.

The total annual water flux from the degrading transient layer can reach 20% of the total summer precipitation during dry and warm thawing seasons.

The seasonal dynamic of DOC composition and age suggests the involvement of ancient carbon previously stored in the upland (yedoma) sediments in contemporary hydrobiochemical cycles.

The relationship between degradation of the transient layer and DOC age and chemical composition can potentially allow the use of these characteristics for the integrative assessment of permafrost condition over a large territory at the end of the warm season.

Acknowledgments

Support was provided by CALM II project (NSF OPP 0352958), NSF RAISE projects, and the Russian Academy of Science.

References

Fyodorov-Davydov, D.G. & Davydov S.P. 2006 Seasonal thawing of soils on the north of the Kolyma Lowland. *Soil Processes and Spatio-Temporal Organization of Soils*. Moscow: Nauka, 455-471 (in Russian).

Gasanov, S.S. 1971. Volume ice content of frozen sediments. *Periglacial processes* 38: 167-180 (in Russian).

Kholodov, A.L., Rivkina, E.M., Gilichinsky, D.A. Fyodorov-Davydov, D.G., Gubin, S.V., Sorokovikov, V.A., Ostroumov, V.E. & Maksimovich, S.V. 2003. Estimation of the organic carbon input into Arctic Ocean due to erosion of the East-Siberian seashore. *Kriosphera Zemli* 7(3): 3-12 (in Russian).

McClelland, J.W., Holmes, R.M., & Peterson, B.J. 2004. Increasing river discharge in the Eurasian Arctic: Consideration of dams, permafrost thaw, and fire as potential agents of change. *J. Geophysical Research-Atmospheres* 109.

Neff, J.C., Finlay, J.C., Zimov, S.A., Davydov, S.P., Carrasco, J.J., Schuur, E.A.G. & Davydova A.I. 2006. Seasonal changes in the age and structure of dissolved organic carbon in Siberian Rivers and streams. *Geophysical Research Letters* 33(23).

Peterson, B.J., Holmes, R.M., McClelland, J.W., Vorosmarty, C.J., Lammers, R.B., Shiklomanov, A.I., Shiklomanov, I.A. & Rahmstorf, S. 2002. Increasing river discharge to the Arctic Ocean. *Science* 298(5601): 2171-2173.

Shur, Y.L. 1988 The upper horizon of permafrost soil. *Proceedings of the Fifth International Conference on Permafrost, Norway*: 867–871.

Zimov, S.A., Schuur, E.A.G. & Chapin, F.S. 2006. Permafrost and the global carbon budget. *Science* 312: 1612-1613.

Zimov, S.A., Davydov, S.P., Zimova, G.M., Davydova, A.I., Schuur, E.A.G., Dutta, K. & Chapin, F.S. 2006a. Permafrost carbon: Stock and decomposability of a globally significant carbon pool. *Geophysical Research Letters* 33.

Geophysical Mapping of Ground Ice in the Western Canadian Arctic

Gregory P. De Pascale
William Lettis & Associates, Inc., Walnut Creek, California, USA
Wayne H. Pollard
McGill University, Montreal, Quebec, Canada

Abstract

Warming in the Arctic is occurring sooner and more rapidly than was initially expected and is predicted to increase with time. The nature and distribution of ground ice is one of the most unpredictable geological variables in near-surface materials characterized by continuous permafrost. It is also the main reason permafrost is considered vulnerable to climate warming. In this study, coordinated measurements by two complementary geophysical tools—capacitive-coupled resistivity (CCR) and ground penetrating radar (GPR)—were used to map ground ice and cryostratigraphy at King Point and Richards Island in the western Canadian Arctic. Validation of geophysical interpretations was accomplished using adjacent natural exposures. The synergenistic benefits of using these two geophysical tools permitted accurate mapping of various types of ground ice including massive ice, and wedge ice, and detection of the top of the massive ice bodies.

Keywords: climate change; ground ice; ground penetrating radar; massive ice; resistivity.

Introduction and Significance of Ground Ice

The primary goals of this paper are (1) to characterize ground ice conditions at two ice-rich sites in the Western Canadian Arctic, and (2) to demonstrate the complementary nature of GPR and CCR data in the analysis of ground ice in continuous permafrost. The nature and distribution of ground ice is one of the most unpredictable geological variables in surficial sedimentary deposits characterized by continuous permafrost (Pollard & French 1980). Volumetric ground ice contents can range from <10% in relatively dry permafrost to >90% in ice-rich permafrost containing massive ice (Mackay & Dallimore 1992). Massive ground ice is defined as ice greater than 1 m thick with a gravimetric water content exceeding 250% on a dry weight basis (Permafrost Subcommittee 1988). Ice content patterns are often related to soil texture and depositional and freezing histories. In this classification, ground ice occurrence ranges from disseminated ice crystals in a soil matrix (pore ice) to discrete V-shaped linear networks of vertically foliated ice (wedge ice) to thick (10–20 m), horizontally continuous layered bodies of nearly pure segregated ice that often extends for several km^2. The significance of ground ice pertains to its geomorphic and geologic role in landscape development and geotechnical characteristics. The former includes various processes and landforms associated with either ground ice aggradation, like frost heave or the formation of ice-cored landforms, or with ground ice degradation, particularly thermokarst and associated ground ice subsidence. Ultimately, ground ice is a hazard for northern development, and disturbance of sites with ground ice present can cause thermokarst and disturbance of wildlife habitat, and create concerns with traditional land uses.

For this study, we selected two sites in the Western Canadian Arctic: King Point on the Yukon coast and a site on Northern Richards Island in the Mackenzie Delta Region of the Northwest Territories (Fig. 1).

The King Point site was selected because ground ice conditions have been well documented (Pollard & Dallimore 1988) and is known for having different types of ground ice present and visible in a large retrogressive thaw slump. Previous ground ice research in this area involves a series of cryostratigraphic studies based on detailed examination of ground ice exposures along the Yukon coast (Harry et al. 1988, Pollard & Dallimore 1988). In each case, massive ice interpreted as intra-sedimental ice was documented between 3–5 m below the surface. This research also describes a widespread thaw unconformity, which in some cases truncates massive ice (Harry et al. 1988) and the burial and preservation of surface snow patches (Pollard & Dallimore 1988). In each case, these studies provide compelling evidence of extensive massive ice and a previous deep thaw event that lead to truncation of Pleistocene ice wedges. The retrogressive thaw slump at King Point permitted direct validation of geophysical data (Fig. 2).

The Richards Island site was selected because of the presence of a large retrogressive thaw slump that is approximately 250 m long and 5 to 10 m high (Fig. 3).

This slump is unreported in the literature and appears to have formed sometime between 2005 and 2006. Again, the access to this site permitted direct comparison of the geophysical data with the stratigraphy in the natural exposure.

Methods and Data Acquisition

In this study, two geophysical tools, capacitive-coupled resistivity (CCR) and ground penetrating radar (GPR), were used to map ground ice occurrence at two sites that have not previously been investigated. Fieldwork was conducted in March 2005 and March 2006 using geophysical techniques. Winter fieldwork permitted smooth survey lines due to snow cover and noise-free datasets because during winter the active

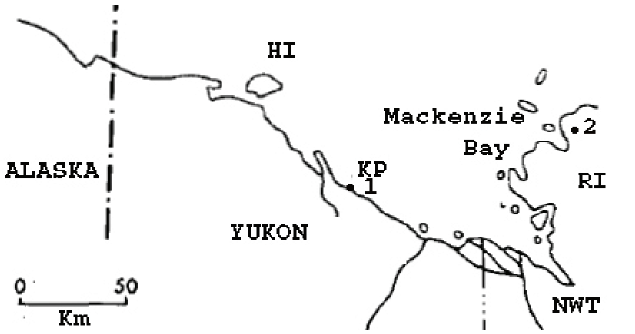

Figure 1. Map of two study sites with 1) King Point and 2) Ground Ice slump on Richards Island. HI is Hershel Island, RI is Richards Island.

Figure 2. Oblique air photo showing the King Point site. Note the coalescing coastal landslides and the small ice wedge melt ponds and polygonal ground in the foreground.

layer is frozen. Ground resistivity and radar techniques give valuable information about subsurface conditions based on different electromagnetic properties of sediments. Electrical resistivity determines the subsurface resistivity distribution from induced current measurements made at the ground surface. From these measurements, the specific resistivity of subsurface materials can be determined. The resistivity of a material can be calculated using Ohm's law: R = V/I (resistance = voltage/current).

For geoelectrical measurements of ground resistivity, Ohm's Law is used in its differential vector form: $\rho = E/J$, where ρ is resistivity, E is electric field, and J is current density. By measuring an electric field at a known current, it is possible to calculate the resistance of the total volume of material between the transmitter and receiver to the depth of detection limit of the transmitter signal (Loke & Barker 1996). Resistivity techniques work well in regions of permafrost because there is a marked increase in electrical resistivity of water that occurs at the phase change from liquid to solid water (Hoekstra et al. 1975, Wolfe et al. 1996, Calvert et al. 2001, Calvert 2002, Hauck 2002, Hauck et al. 2003 De Pascale et al., in press). In permafrost regions resistivity will vary directly as a function of the ice content and type; for example, sediments with low ice contents are generally conductive and typically have low resistivity values. Massive ice will generally have higher resistivity values than pore ice. Sediments with high ice content will generally have resistivities higher than sediments without ground ice present, but lower resistivities than sediments containing massive ice.

Capacitive-coupled resistivity (CCR) surveys are a recent advancement in electrical resistivity mapping. Other workers have used Direct Current (DC) resistivity with success for mapping permafrost and ground ice (Kneisel et al. 2000, Hauck & Kneisel 2006), although this techniques is not as effective in cold continuous permafrost. For a detailed review of the theory behind capacitive-coupled resistivity, see Timofeev et al. (1994). As with DC resistivity, CCR uses two dipoles. In principal, current is applied to the ground by a transmitter via capacitive-coupling and the resulting potential is measured at the receiver dipole. Two previous studies using CCR techniques in permafrost were not able to distinguish between massive ice and glaciofluvial sediment with ice contents >30% (Wolfe et al. 1996), but Calvert (2002) noted that two-dimensional resistivity measurements were acquired relatively quickly in areas of ground ice. In another recent study, different resistivity techniques are compared in an area of mountain permafrost in the Swiss Alps (Hauck & Kneisel 2006). In that environment, permafrost conditions are very different from the Mackenzie Delta region; for example, mid-latitude alpine permafrost is much warmer and wetter (higher liquid water content), and contains little ground ice (extensive massive ice is largely absent), and bedrock plays an important control on landscape development. These differences limit the applicability of comparing the geophysical results between these two permafrost regions. The only study to combine CCR and GPR data in continuous permafrost regions (De Pascale et al., in press), was also the first occasion where methodology for CCR data acquisition was discussed.

Ground penetrating radar (GPR) is another geophysical tool that has been used increasingly over the last 30 years for a wide range of subsurface mapping applications. By transmitting an electromagnetic pulse into the ground and recording the travel time of reflections caused by contrasts in dielectric properties, GPR measurements are used to characterize the structure and stratigraphy of near-surface geology. Previous studies have used GPR to study permafrost (Doolittle et al. 1990, Hinkelet et al. 2001, Moorman 1994, 1995, Arcone et al. 1998, Moorman et al. 2003) and massive ground ice (Dallimore & Davis 1987, Dallimore et al. 1992, Robinson 1994). These studies have shown that GPR data reliably indicate contacts between ice and frozen sediments, ice and solid rock, and frozen and thawed regions. The only study to-date that has integrated GPR and CCR techniques to map massive ice in permafrost was De Pascale et al., in press.

In this study, geophysical surveys were conducted in March 2005 and March 2006 with air temperatures between -15ºC and -40ºC, and the ground surface was covered by wind-crusted snow. Ground resistivity was measured using a Geometrics OhmMapper TR1 system, with operating frequencies in the range of 8 to 32 kHz using a dipole-dipole transmitter and receiver. Current is run along the transmitter's

Figure 3. Photo showing the retrogressive thaw slump on Richards Island. Note person for scale and exposed white ice wedges.

dipole cables with the dipoles acting as one plate of a capacitor and the ground as the other. The resulting voltage, measured at the receiver dipole, is proportional to the ground resistivity between the two dipoles and the initial current emitted from the transmitter. The apparent resistivities are calculated from the measured resistances using the geometric factor, which corresponds to the distance between the transmitter and receiver. Multiple passes are made along each survey line to gather data over a range of n-spacings, which is the ratio of the distance between the transmitter and receiver and the dipole spacing, permitting resistivity measurements of the materials at several depths. By increasing the distance between the transmitter and receiver, a larger survey line is created, giving a greater depth of investigation. In this study, the initial n-spacing was used for two passes at each site in order to ensure data reliability and measurement consistency. The GPR system used was a MALA controller with RTA antennas operating at 50 MHz and 250 MHz. The controller triggers pulses of energy that are transmitted into the surface by the antenna which acts as a band-pass filter, emitting sine waves with the center frequency determined by the antenna. Since penetration depth of a GPR signal depends on the antenna frequency and the electromagnetic properties of the subsurface materials, the frozen ice-rich nature of our sites was favorable for penetration depths on the order of ~15 m at the frequencies used. Due to the lack of topography at the sites, static corrections were unnecessary. Sediment and ice were sampled from Richards Island for petrographic and geochemical analysis, and the results from these data are forthcoming.

Data processing

The CCR data were reduced using the DataMap 2000 software (Geometrics 2001), while inversions were completed using the two-dimensional inversion software RES2DINV (Loke & Barke 1996). These CCR data were transferred to RES2DINV, where filtering techniques such as despiking were employed to remove outliers and smooth the datasets with a 3-point running average. Data were plotted in a pseudo-section, where the depth scale is calculated as a function of the separation between the dipoles. A pseudo-section is a geometrical view of the measured apparent resistivity dataset, whereas the inversion model shows the true resistivity for each model block, which is calculated independent of the resistivities of the surrounding model blocks. Interpretations of the CCR models were constrained by other subsurface information available at each of the sites, including the natural exposures in the retrogressive thaw slumps and ice wedge troughs. GPR data were processed using the ReflexW software package. Processing involves time-zero surface correction and horizontal filtering of the direct coupling wave. This processing is standard for GPR data and removes system noise that could mask real data. Because of the frozen nature of the field sites, penetration depth estimates assumed a dielectric constant of 6 ($v = 0.12$ m/ns) for frozen sediments and a dielectric constant of 3 ($v = 0.16$ m/ns) of ground ice. Generally we used an average of $v = 0.14$ m/ns due to the varied nature of these sites.

Results

At King Point we conducted a 225 m 2-D transect parallel and approximately 5–10 m from the Yukon coast. This survey intersected several ice wedge troughs that were visible on the surface. The setting varied from ice wedge terrain, as detected by low-center polygons on the surface, to terrain with massive ice exposed in a large retrogressive thaw slump (Fig. 4).

On Richards Island we surveyed a 250 m long 2-D transect parallel and above a retrogressive thaw slump. In the exposure, ice wedges, massive ice, and stratigraphic relationships were logged using digital cameras to map site conditions during the survey for geophysical validation (Fig. 5).

King Point results

Based on our surveys we were able to map out ground ice distribution at the site. The CCR data detected wedge ice (2500 to 500 Ohm.m), massive ice (5000–10000 Ohm.m) and variations in the depth to top of massive ice. The depth of the top of massive ice is extremely variable, which is expressed as a wavy, however continuous surface and varies between 3.5 to 7 m below ground surface. The RMS value for this site was 17.4%, which is a suitable error considering the variance in resistivities of these materials. With the GPR data, we were able to show strong reflectors at two levels, with the upper reflections being mainly horizontal to wavy and extending to a depth of ~50 ns, and the lower interface appearing at ~100 ns and exhibiting more variations in topography.

Stratigraphic information from adjacent coastal exposures and retrogressive slump were used to help guide the interpretation. The region between the two areas of high reflections contains semi-horizontal structures. These areas correspond to regions of massive ice occurrence. Estimated depths were calculated using a velocity of 0.14 m/ns assuming a combination of frozen sediments and areas of massive ice. Using these depths, the upper reflections extend to ~3.5 m, and the tops of the lower reflections are at ~7 m. The semi-

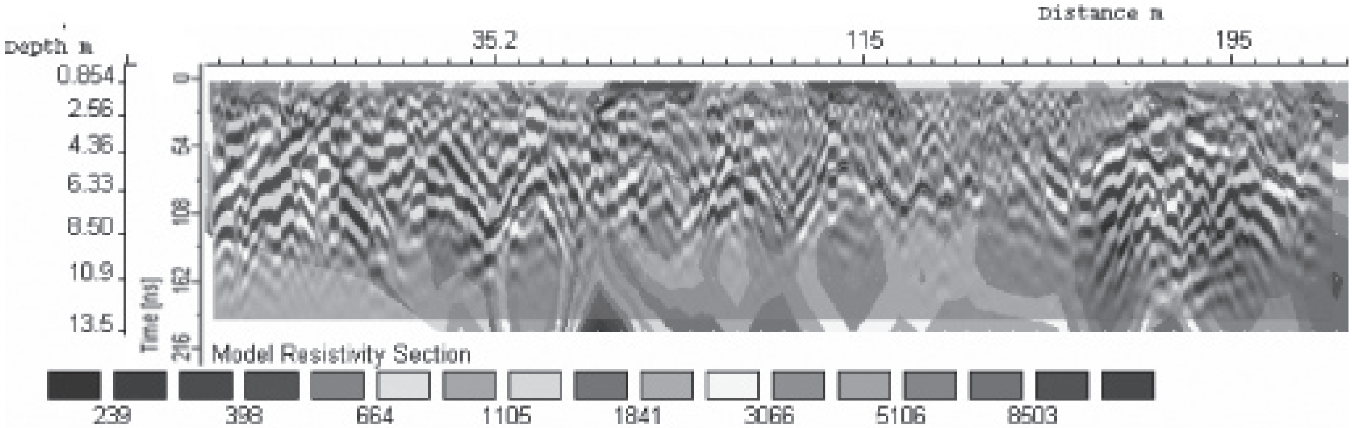

Figure 4. Combined CCR and GPR (50 MHz) data for the King's Point study site. A west-to-east transect with higher zones of resistivities (shown in red) corresponding with massive ground ice distribution and the dark brown which corresponds with wedge ice. Note the prominent reflector in pink that corresponds with the yellow increase in resistivity values and ground ice content (found between 3 and 6 m below ground surface). The increase in resistivity values east of station 160 corresponds with the transition between polygonal ground (wedge ice) and massive ice with no surface expression.

horizontal structures at approximately 3.5 m corresponds to the depth in the CCR data where resistivity levels become much larger below 3.5 m; this is the contact between frozen sediments to ice-rich frozen sediments. This could possibly be the maximum depth of the frozen Hypsithermal active layer, as noted in other sites in the Western Arctic (De Pascale et al., in press). Data with both systems were difficult to resolve below 13 m at this site. Wedge ice was detected between stations 35 and 150, and expressed as oval-shaped zones of higher resistivities with zones of lower resistivities between these zones of wedge ice. East of station 160, there is a transition from an area with ice wedges to massive ice, and there is a marked increase in resistivity values at this contact. The GPR data shows a decrease in signal attenuation east of station 160, which is consistent with massive ground ice occurrence due to a decrease in electrical conductivity.

Richards Island results

As with the King Point surveys, we were able to map the ground ice distribution at this site. The CCR data detected wedge ice (2,600 to 5,000 Ohm.m), massive ice (10,000 to 60,000 Ohm.m), and depth to the top of the massive ice. The RMS value for this site is 16.1%. The depth to the top of the massive ice varies from 7 to 8 m below ground surface. With the GPR data, we were able to detect strong reflectors at two levels, with the upper reflectors being subhorizontal to wavy and continuous for up to 60 m over a ~200 m section of the transect. The upper interface was ~100 ns and the lower interface appearing at ~225 ns. The upper interface corresponds with the top of the massive ice, while the lower interface is beyond the depth of the exposure. This reflector could be the base of the massive ice. Using these depths, the upper reflections extend from 6 to 8 m below the ground surface, while the lower reflector was at ~16 m. There was good agreement between the geophysical data and exposure adjacent to the transect, which permitted direct validation to the geophysical results. From the geophysical data, the contrast between pore-ice- rich sediments and the underlying massive ice was easily obtained. The lithologies of the materials under the major GPR reflector would be difficult to interpret without the CCR data, which demonstrated large variations in resistivity. However, this dielectric contrast between the massive ice and overlying sediments caused a strong reflector to be present in the GPR data. This contact was detected with both systems and showed 2 to 3 m of hummocky subsurface topography. The location of the ice wedges was easily detected due to geometry and increase in resistivity values, and from ice wedge troughs on the surface. Overall, the amount of massive ice found at this site permitted deeper investigations than at the Kings Point site.

Conclusions

Massive ground ice, wedge ice, ice-rich sediments, the active layer, a thaw unconformity corresponding to the hypsithermal paleo-active layer, as well as basic stratigraphic relationships found in the surrounding sediments were mapped. The two-dimensional geometry of ice bodies was obtained using these two geophysical techniques. Massive ice was consistently found at depths greater than 4 m, a depth corresponding with the Hypsithermal thaw unconformity, although modern wedge ice is often encountered at depths less than 2 m. It was found that that the hummocky surface of the massive ice body and the top of ice wedges were variable at both locations. This was possibly due to differential melting during the hypsithermal, prior to re-aggredation of permafrost within this section. A number of authors (e.g., Burn 1997, French 1998) describe the hypsithermal as a well-developed, shallow thaw unconformity in permafrost exposures in numerous locations throughout the western Canadian Arctic that appears between 2–3 m below the ground surface as an abrupt change in ice content, ice chemistry, soil colour,

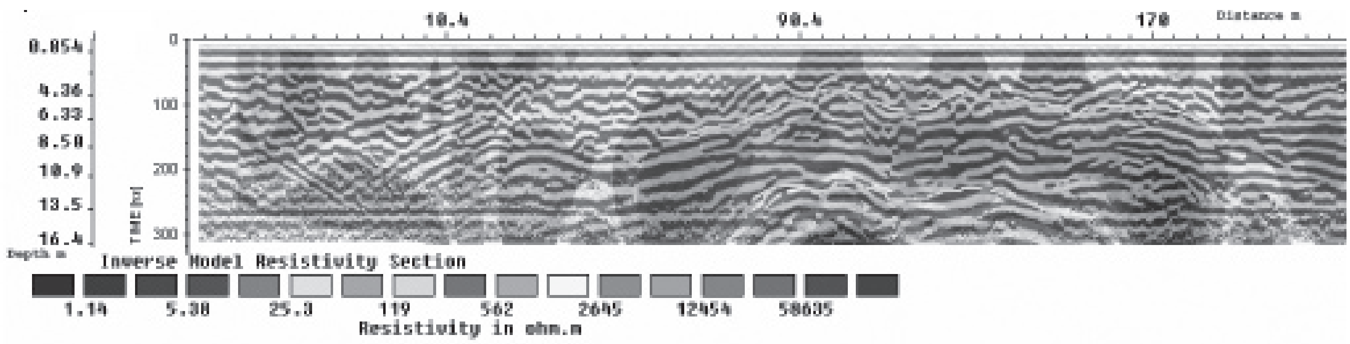

Figure 5. Combined CCR and GPR (50 MHz) data for the Richards Island site in a west-to-east transect. Higher zones of resistivities (shown in red) correspond with massive ground ice distribution. Note the anticline at station 90 m at a depth of approximately 14, and how there is a reduction in resistivities that corresponds with anticline structures found at depth. Green picks outline top and base of massive ice body. Note the wedge ice at stations 10 and 20 at depths near the surface and below 6 m.

organic content, and cryostructure. Examination of the King Point exposure revealed a number of these features, as well as several truncated ice-wedge tops (Harry et al. 1985) at a depth of ~2.5–3.0 m. The strong reflector at between 3 to 5 m depths seen in both the GPR and CCR data is interpreted as this transition. Dating of organic material (French 1998) from the overlying thawed zone from other sites confirms that this unconformity is related to an early Holocene warm interval referred to as the Hypsithermal (8.0–9.0 ka BP), when active layers were 2–2.5 times deeper than present. Another important finding is the large variation in resistivity values, almost a magnitude in the case of this study, for similar types of ground ice found in different settings. Coastal ground ice exposures have lower resistivity values than those found inland, and this is most likely due to the higher levels of cations present in the system from proximity to saline coastal conditions. The overall reduction in depth of investigation between our coastal site (King Point) and our inland site (Richards Island), suggests that the influence of coastal cations reduces the electrical resistivity values for all materials at a site. Because of this, more work needs to be undertaken to better understand the resistivity "signatures" of continuous permafrost.

Fieldwork on ground ice characterization at Richards Island in the Mackenzie Delta and King Point on the Yukon Coast, utilizing non-invasive geophysical methods like CCR and GPR, provided an opportunity to assess the synergistic benefits of using two complementary geophysical systems. Our results support previous research showing that, individually, CCR and GPR are useful tools for obtaining general subsurface information in permafrost (e.g., Calvert 2002, Dallimore & Davis 1987, Arcone et al. 1998, Moorman et al. 2003, De Pascale et al., in press), and clearly show the added value that results by combining their outputs. This study, based on the examination of sites at King Point and Richards Island, together with De Pascale et al. (in press), which focuses on massive ice in coarse-grained sediments, illustrates the enhanced benefit of integrating two complimentary geophysical techniques. These techniques detect and map the distribution of permafrost materials and structures containing ground ice, and if GPR is properly constrained using CCR data, a more accurate estimate of depth is possible. There was excellent agreement between these two systems that permit accurate mapping of ground ice locations. To our knowledge this is the first report of the young retrogressive thaw slump on Richards Island. Future work with these techniques can help us to better understand complex ground ice settings where various different ground ice are present, without damaging the natural environment using these non-destructive methods. To date our research has used observed cryostratigraphic relationships (nature sections or boreholes) and surface geomorphic expression (ice wedges polygons) to constrain our interpretation of subsurface permafrost conditions. Like any form of remote sensing, confidence levels increase when ground truthing confirms interpretations based on proxy data. For example, given the range of resistive values we have observed for massive ice, we are reasonably confident that in areas of deep continuous permafrost, where surface geomorphology does not indicate any unusual hydrologic phenomenon (e.g., saline ground water), we can detect the location, extent, and thickness of a massive ice unit. We are also confident that the distinct pattern of reflection together with resistivity can detect ice wedges, even relict ice wedges beneath a thaw unconformity. Ultimately, with the appropriate configuration (antenna frequency, spacing, …) of equipment, the combination of GPR and CCR is an effective and non-invasive technique to detect and map ground ice.

Acknowledgments

Funding for this research was provided by a NSERC Discovery Grant, ArcticNet, the Canadian Space Agency, and a PERD/DIAND financial agreement managed by R. Gowan with McGill University (W. Pollard). Field support for this research was provided by the Aurora Research Institute (ARI) in Inuvik and was conducted under NWT research License numbers 13560 and 13753 and Inuvialuit Land Administration (ILA) License number 03TIN055. The authors would like to thank an anonymous reviewer for the very helpful comments and suggestions. G.P.D would like to thank the professional development program William Lettis & Associates for supporting this work.

References

Arcone, S.A., Lawson, D.E., Delaney, A.J., Strasser, J.C. & Strasser, J.D. 1998. Ground penetrating radar reflection profiling of groundwater and bedrock in an area of discontinuous permafrost. *Geophysics 63*: 1573-1584.

Burn, C. 1997. Cryostratigraphy, paleogreography and climate change during the early Holocene warm interval, western Arctic coast. *Canadian Journal of Earth Sciences* 34, 912-925.

Calvert, H.T. 2002. Capactive-coupled resistivity survey of ice-bearing sediments, Mackenzie Delta, Canada. *Society of Exploration Geophysicists, 72nd annual meeting, Salt Lake City, UT, Oct. 2002*. Society of Exploration Geophysicists, Tulsa, OK, USA.

Calvert, H.T., Dallimore, S.R. & Hunter, J.A. 2001. Application of Geophysical Techniques For Mapping of Ice-Bearing Sediments, Mackenzie Delta, Western Arctic, Canada. *Conference on the Geophysical Detection of Subsurface Water on Mars,* 674 pp.

De Pascale, G.P., Williams, K.W., Pollard, W.H. In Press. Geophysical mapping of ground ice using a combination of capacitive coupled resistivity and ground penetrating radar, NWT, Canada. *Journal of Geophysical Research – Earth Surface.*

Doolittle, J.A., Hardisky, M.A. & Gross, M.F. 1990. A ground penetrating radar study of active layer thicknesses in areas of moist sedge and wet sedge tundra near Bethel, Alaska, USA. *Arctic and Alpine Research 22:* 175-182.

French, H.M. 1998. An appraisal of cryostratigraphy in North-West Arctic Canada. *Permafrost and Periglacial Processes* 9: 297-312.

Harry, D.G., French, H.M. & Pollard, W.H. 1985. Ice wedges and permafrost conditions near King Point, Beaufort Sea Coast. *Current Research, Part E, Geological Survey of Canada, Paper 85-1A,* 111-116.

Harry, D.G., French, H.M. & Pollard, W.H. 1988. Massive ground ice and ice-cored terrain near Sabine Point, Yukon Coastal Plain. *Canadian Journal of Earth Sciences* 25: 1846-1856.

Hauck, C. 2002. Frozen ground monitoring using DC resistivity tomography. *Geophysical Research Letters 29(*21): 2016.

Hauck, C. & Kneisel, C. 2003. Application of a capacitively coupled resistivity system for mountain permafrost studies and implications for the interpretation of resistivity values. *Proceedings of the Eighth International Conference on Permafrost, Zurich 2003*: 55-56.

Hauck, C. & Kneisel, C. 2006. Application of capacitively-coupled and DC electrical resistivity imaging for mountain permafrost studies. *Permafrost and Periglacial Processes* 17: 169-177.

Hauck, C., Muhll, D.V. & Maurer, H. 2003. Using DC resistivity tomography to detect and characterize mountain permafrost. *Geophysical Prospecting 51*: 273-284.

Hoekstra, P., Sellmann, P.V. & Delaney, A. 1975. Ground and airborne resistivity surveys of permafrost near Fairbanks, Alaska. *Geophysics* 40: 641-656.

Kneisel, C., Hauck, C. & Vonder Mühll, D. 2000. Permafrost below the timberline confirmed and characterized by geoelectrical resistivity measurements, Bever Valley, Eastern Swiss Alps. *Permafrost and Periglacial Processes* 11: 295-304.

Loke, M.H. & Barker, R. 1996. Rapid least-squares inversion of apparent resistivity pseudo-sections using a quasi-Newton method. *Geophysical Prospecting* 44: 131-152.

Mackay, J.R. 1972. The world of underground ice. *Annals of the Association of American Geographers* 62: 1-22.

Mackay, J.R. & Dallimore, S.R. 1992. Massive ice of the Tuktoyaktuk area, western Arctic coast, Canada. *Canadian Journal of Earth Sciences* 29: 1235-1249.

Moorman, B.J., Robinson, S.D. & Burgess, M.M. 2003. Imaging periglacial conditions with ground-penetrating radar. *Permafrost and Periglacial Processes 14:* 319-329.

Permafrost Subcommittee, Associate Committee on Geotechnical Research. 1988. *Glossary of Permafrost and Related Ground-Ice Terms*. National Research Council of Canada. Technical Mem. No. 142, 156 pp.

Pollard, W.H. & Dallimore, S.R. 1988. Petrographic characteristics of massive ground ice, Yukon Coastal Plain, Canada. *Proceedings of the Fifth International Conference on Permafrost, VI, Trondheim, Norway, Tapir Publishers,* 224-229.

Pollard, W.H. & French, H.M. 1980. A first approximation of the volume of ground ice, Richard Island, Pleistocene Mackenzie delta, NWT. *Canadian Geotechnical Journal* 17: 509-516.

Robinson, S.D. 1994. Geophysical studies of massive ground ice, Fosheim Peninsula, Ellesmere Island, Northwest Territories. *Current Research 1994-B, Geol. Surv. Can.*, Ottawa, Ont.: *11-18.*

Timofeev, V.M., Rodozinski, A.W., Hunter, J.A. & Douma, M. 1994. A new ground resistivity method for engineering and environmental geophysics, *Proceedings of the Symposium on the Application of Geophysics to Engineering and Environmental Problems, EEGS*: 701-715.

Wolfe, S.A., Burgess, M.M., Douma, M., Hyde, C. & Robinson, S.D. 1996. Geological and Geophysical Investigations of the Canamera Carat Lake Esker- Delta Complex, Slave Geological Province, NWT. *Geol. Surv. Can.,* Ottawa, Ont., 38 pp.

Recent Interannual Variations of Rock Glacier Creep in the European Alps

Reynald Delaloye, Eric Perruchoud
Department of Geosciences, Geography, University of Fribourg, Switzerland
Michael Avian, Viktor Kaufmann
Institute of Remote Sensing and Photogrammetry, Graz University of Technology, Austria
Xavier Bodin
Institute of Alpine Geography, Joseph Fourier University, Grenoble, France
Helmut Hausmann
Institute of Geodesy and Geophysics, Vienna University of Technology, Austria
Atsushi Ikeda
Graduate School of Life and Environmental Sciences, University of Tsukuba, Japan
Andreas Kääb
Department of Geosciences, University of Oslo, Norway
Andreas Kellerer-Pirklbauer
Institute of Geography and Regional Science, University of Graz, Austria
Karl Krainer
Institute of Geology and Paleontology, University of Innsbruck, Austria
Christophe Lambiel
Institute of Geography, University of Lausanne, Switzerland
Dragan Mihajlovic, Benno Staub
Institute of Geography, University of Bern, Switzerland
Isabelle Roer
Department of Geography, University of Zurich, Switzerland
Emmanuel Thibert
Cemagref, Grenoble, France

Abstract

Recent interannual variations of rock glacier surface motion are compared for 16 landforms monitored for a few years in various parts of the European Alps. Large fluctuations have been observed particularly since 2002. Most investigated rock glaciers have shown a similar behavior whatever their location in the Alpine arc, their size, or their velocity. The observed interannual variations appear to be primarily related to external climatic factors rather than to internal characteristics. They are mostly well correlated with mean annual ground surface temperature shifts with a delay of a few months, reflecting the thermal wave propagation deeper into permafrost. Seasonal factors may also play a significant role: a lower intensity of winter ground freezing and/or a larger winter snow accumulation appear to facilitate a higher rate of rock glacier surface motion.

Keywords: creep; European Alps; interannual variations, rock glaciers; surface motion.

Introduction

Rock glaciers act as sediment conveyors in cold periglacial mountain environments. Where a rock glacier is perched on a steep valley side, it may be the source of slope instability processes (mainly rock falls and debris flows). Any change in the rate of permafrost creep may modify the delivery of loose materials at the rock glacier snout and affect the frequency, the magnitude, and even the type of related slope instabilities (e.g., Roer et al. 2008). In this context, and paying regard to the ongoing climate warming trend, there is an increasing request in the densely inhabited European Alps for precise and up-to-date data documenting the evolution of the high-altitude permafrost environment. In addition to the assessment of longer term (decadal to pluri-decadal) changes affecting rock glacier dynamics, which can be precisely determined by airborne photogrammetric analysis (Kääb et al. 2003), documentation of the short-term (interannual and even seasonal) variations is needed. Two decades after the pioneer work on the Gruben rock glacier (Haeberli 1985), the systematic survey of annual velocities was reinitiated a few years ago by several research teams by means of terrestrial measurements. This paper provides a first comparison of time series that have been measured since 1999/2000 or later on a sample of 16 rock glaciers located in six regions of the Alpine arc.

Background

Mostly located in the lower half of the mountain discontinuous permafrost belt, Alpine rock glaciers are rather warm. They may move relatively fast and are highly sensitive to small temperature changes (Kääb et al. 2007).

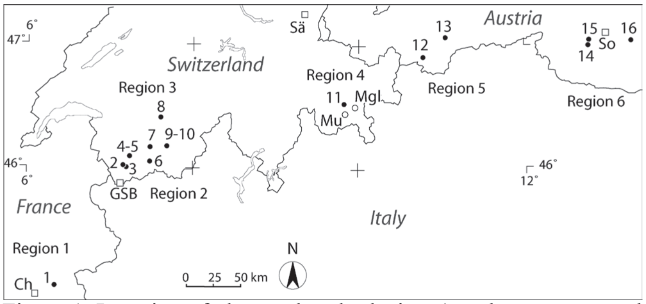

Figure 1. Location of observed rock glaciers (numbers correspond to Table 1). Other cited rock glaciers : Mu: Murtèl; Mgl : Muragl. Regions: 1. southwestern Alps (France), 2. western Swiss Alps (Valais), 3. northwestern Swiss Alps (Bernese Alps), 4. eastern Swiss Alps (Upper Engadine), 5. western Austrian Alps, 6. central Austrian Alps. Weather stations : Ch: St.-Christophe-en-Oisans; GSB : Grand-St-Bernard; Sä : Säntis; So : Sonnblick.

Three types of temporal variability in surface motion are superimposed on a secular time scale in response to ground surface temperature variations (e.g., Kääb et al. 2007, Perruchoud & Delaloye 2007): a decadal to pluri-decadal trend, interannual variations, and a seasonal rhythm. Non-thermally induced changes in rock glacier dynamics (e.g., topography effect) may also influence the creep rate particularly at longer time scales, whereas the infiltration of snowmelt water (Ikeda et al. 2008) and the influence of subpermafrost groundwater (Haeberli 1985, Krainer & Mostler 2006) are also advanced as controlling factors at shorter time intervals. The early measurements on the Gruben rock glacier already indicated that strong short-term velocity variations occur where the permafrost base is above bedrock, and that these variations can be different in lower and upper rock glacier parts (Haeberli 1985).

Studies carried out in various parts of the Alps (e.g., Roer et al. 2005, Kääb et al. 2007, Kaufmann et al. 2007) have shown that the motion of alpine rock glaciers has drastically accelerated since the 1980s, probably in response to an increase in permafrost temperature consecutive to warmer air temperatures. For the past 15 years or so, however, no clear further warming trend has been visible in the borehole temperatures time series on the Murtèl rock glacier in the eastern Swiss Alps (Vonder Mühll et al. 2007).

Seasonal variations have been reported for several rock glaciers (Haeberli 1985, Kääb et al. 2003, Hausmann et al. 2007a, Perruchoud & Delaloye 2007), whereas almost constant annual velocities have also been observed (Krainer & Mostler 2006), particularly where permafrost is reaching into bedrock as on the Murtèl rock glacier (Haeberli et al. 1998). Where existing, seasonal fluctuations can be large, reaching up to 50 % from the annual mean. They occur every year more or less at the same time but are not fully synchronous for all rock glaciers. Highest velocities are reached in most cases between summer and early winter, whereas the lowest values are usually observed in spring or early summer. The seasonal increase in velocity can be rapid and connected to the snowmelt process (Perruchoud & Delaloye 2007) or slower and delayed (Kääb et al. 2007). On the Muragl rock glacier (eastern Swiss Alps), the annual amplitude of the seasonal rhythm varies significantly, the winter/spring decrease being reduced by warmer winter ground surface temperature (Kääb et al. 2007).

Interannual Velocity Survey and Dataset

Interannual velocities are surveyed by terrestrial measurements (geodetics or real-time kinematic GPS) with accuracy in the mm to cm range. The annual campaign at each rock glacier is carried out as closely as possible on the same date - ideally by late summer - in order to avoid an effect of potentially strong seasonal variations on the reliability of the data. Ten to more than 100 marked points, covering part or the whole of the rock glacier or disposed along longitudinal and/or transversal profiles, are surveyed. The compared value is then the mean horizontal velocity for all moving points with uninterrupted series. This value is considered to be a proxy for the activity of a whole rock glacier, keeping in mind that local differences in flow rates and amplitudes of annual changes are probable.

The 16 observed rock glaciers (Fig. 1) are located in six distinct regions and are briefly described hereafter and in Table 1. There is a distance of 600 km between Laurichard (southwest) and Dösen (east) rock glaciers.

Region 1: Southwestern Alps (France)

Laurichard is a tongue-shaped rock glacier which displays longitudinal furrows in its steepest part and transversal ridges near the edge. Surface velocities have been measured since 1983 (Francou & Reynaud 1992) along a 420 m long longitudinal profile of 17 painted blocks. Mean horizontal velocity over the 1983–2007 period is 0.75 ma^{-1}.

Region 2: Western Swiss Alps (Valais)

Mille is a rock glacier looking inactive on morphological criteria (Delaloye 2004), however moving slowly in its steeper lower half (0.02 to 0.05 ma^{-1}).

Aget-Rogneux is a low active back creeping push-moraine located in the Little Ice Age forefield of a small vanished glacier (Lambiel & Delaloye 2004).

Mont-Gelé B and C are two coalescent small rock glaciers. Whereas Mont-Gelé B is moving faster, the deformation of Mont-Gelé C is much reduced despite an apparently higher ice content (Lambiel & Delaloye 2004).

Tsarmine is a tongue-shaped, currently very active rock glacier ending at the top of a steep gully and providing large amounts of loose materials. Local disturbances of the block surface point to a recent drastic acceleration of the rock glacier movement (Lambiel et al. 2008).

The Becs-de-Bosson rock glacier is an active feature consisting of two adjacent lobes. There is no permafrost—and no creep—in the rooting zone of the rock glacier due to the former development of a local glacier during the Little Ice Age. Significant seasonal variations are observed on the whole rock glacier (Perruchoud & Delaloye 2007).

HuHH1 and HuHH3 are two adjacent multilobate rock glaciers situated below cirques. Both landforms are of similar size and showed maximum horizontal velocities up to 4 ma^{-1} in 2003/04 (Roer 2007).

Region 3: Northwestern Swiss Alps (Bernese Alps)

Furggentälti is a small, tongue-shaped rock glacier with annual surface displacement currently 5 to 10 times larger than during the period 1960–1974 (Mihajlovic et al. 2008). Seasonal fluctuations were observed in 1998/99.

Table 1. Alpine rock glaciers with annual surface velocity survey.

N°	Name	Coordinates	Elevation m a.s.l.	Area km^2	Aspect	Available data	Mean horizontal velocity (2003/04) ma^{-1}	Relative drop (2004-2006) %
1	Laurichard	45°01'N, 06°24'E	2424-2644	0.08	N	1999-...	1.03	-40
2	Mille	46°01'N, 07°12'E	2340-2430	0.02	NE	2003-...	0.05	-61
3	Aget-Rogneux	46°01'N, 07°14'E	2810-2890	0.03	SE	2001-...	0.20	-50
4	Mont-Gelé B	46°06'N, 07°17'E	2600-2740	0.02	NE	2000-...	1.20	-81
5	Mont-Gelé C	46°06'N, 07°17'E	2620-2820	0.05	N	2000-...	0.22	-42
6	Tsarmine	46°03'N, 07°30'E	2480-2650	0.04	W	2004-...	-	-
7	Becs-de-Bosson/Réchy	46°10'N, 07°31'E	2610-2850	0.10	NW	2001-…	0.97	-36
8	Furggentälti/Gemmi	46°24'N, 07°38'E	2450-2650	0.03	N	1994-...	3.08	-52
9	HuHH1	46°11'N, 07°43'E	2630-2780	0.04	NNW	2001-2005	1.26	-
10	HuHH3	46°11'N, 07°43'E	2515-2650	0.05	NW	2002-...	1.78	-52
11	Büz North (Trais Fluors)	46°32'N, 09°49'E	2775-2840	0.02	NE	1998-2005	0.74	-
12	Ölgrube	46°54'N, 10°45'E	2380-2810	0.21	W	2000-2005	1.50	-
13	Reichenkar	47°03'N, 11°02'E	2310-2750	0.27	NE	1998-2006	3.15	-9
14	Weissenkar	46°57'N, 12°45'E	2610-2720	0.15	W	1999-...	0.08	-41
15	Hinteres Langtalkar	46°59'N, 12°46'E	2455-2700	0.15	NW	1999-...		
	(upper part)		>2655	0.06			0.18	-28
	(lower part)		<2655	0.09			2.22	-21
16	Dösen	46°59'N, 13°17'E	2340-2650	0.19	W	1995-...	0.26	-19

Region 4: Eastern Swiss Alps (Upper Engadine)

The Büz North (Trais Fluors) pebbly rock glacier comprises two superimposed lobes, 70 and 90 m long. At the beginning of the survey in 1998, no pronounced morphological expression of flow was noticed. However, the movement turned out to be in the order of 1 ma^{-1} and more (Ikeda et al. 2008, Kääb et al. 2007).

Region 5: Western Austrian Alps

Ölgrube rock glacier consists of two lobes of varying activity. Maximum annual velocities (1.5 ma^{-1}) occur in the central lower part. Seasonal variations were observed with a velocity decrease of about 50% during winter 2003 (Krainer & Mostler 2006, Hausmann et al. 2007a).

Reichenkar is a 1400 m long, very active tongue-shaped rock glacier. Highest velocity (up to 3 ma^{-1}) occurred in 2003/04. No seasonal variation was noticed in 2002 and 2003 (Krainer & Mostler 2006, Hausmann et al. 2007a, b).

Region 6: Central Austrian Alps

Weissenkar is a slowly moving, tongue-shaped rock glacier consisting of an upper lobe overriding a lower one, and characterized by well developed furrows and ridges at the entire lower half. Weissenkar rock glacier moves on average 0.02 to 0.11 ma^{-1} (Kaufmann et al. 2006).

Hinteres Langtalkar houses a highly active, tongue-shaped rock glacier advanced over a prominent terrain ridge into steeper terrain most likely in 1994 (Avian et al. 2005). Several transverse crevasses have developed since (e.g., Roer et al. 2008). The current movement pattern differentiates a faster lower part and a substantially slower upper part.

Dösen is a tongue-shaped rock glacier. Displacement measurements started in 1995—including photogrammetric work of the preceding period until 1954—revealing mean velocity rates of 0.13–0.37 ma^{-1} (Kaufmann et al. 2007).

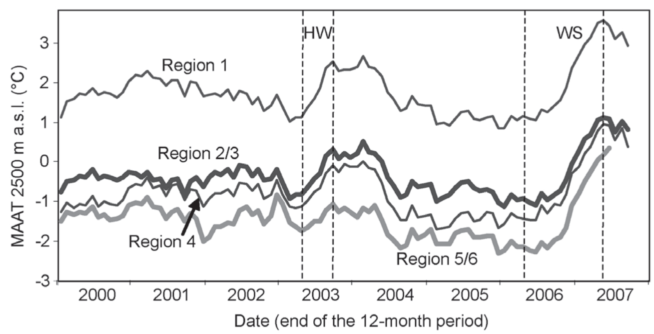

Figure 2. Mean annual air temperature (12-month running mean) standardized at 2500 m a.s.l. (gradient: -0.56°C/100 m). HW: heat wave 2003; WS: warm swell 2006/07. Region 1: St. Christophe, 1570 m a.s.l. (Météo-France). Region 2/3: Grand-St-Bernard, 2472 m a.s.l. (MeteoSwiss). Region 4: Säntis, 2490 m a.s.l. (MeteoSwiss). Region 5/6: Sonnblick, 3105 m a.s.l. (ZAMG –Central Institute for Meteorology and Geodynamics).

MAAT and MAGST in 2000–2007

Air temperature

The 1987–2007 mean annual air temperature (MAAT) in the Alps was on average 1°C to 2°C warmer than during the preceding decades. Since 2000, two extreme, warm climatic events affected the Alpine region: the heat wave of summer 2003 and the 2006/07 warm swell, namely 15 months of quasi continuous, large, positive temperature anomaly between April 2006 and June 2007 (except August 2006). The 2003 heat wave induced a rapid warming of MAAT towards values exceeding those of earlier and later years (except in the Austrian Alps), and the 2006/07 event resulted in an exceptionally high MAAT, which exceeded everywhere the 2003 value by 0.5°C to 1.5°C (Fig. 2).

Ground surface temperature

There are no boreholes on the 16 observed rock glaciers, except a shallow one (6 m) at Trais Fluors. Ground surface temperature is nevertheless monitored on several of them. Variations of the mean annual ground surface temperature (MAGST)

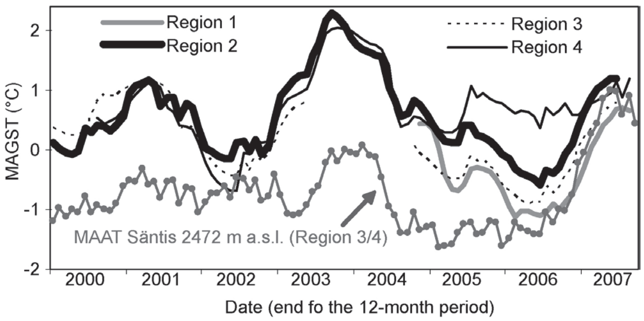

Figure 3. Interregional comparison of MAGST behavior in the western and central Alps (12-month running mean). Region 1: Laurichard rock glacier (average of 2 sites of measurement). Region 2: Becs-de-Bosson/ Réchy (2). Region 3: Furggentälti/ Gemmi (1). Region 4: Trais Fluors (1).

are used as a proxy for the permafrost thermal regime at shallow depth, even if the intensity of the winter cooling and summer warming (freezing and thawing index) should not be neglected. The snow cover buffers the ground-atmosphere heat exchanges for a long part of year, varying annual snow cover conditions alter the behavior of MAGST in comparison with MAAT: both are not evolving in a parallel way (Fig. 3). Despite the effect of snow, a homogeneous MAGST behavior is observed at the regional scale (e.g., Delaloye & Monbaron 2003). The larger variations of MAGST are also similar at the interregional scale in the Alps with, however, some differences in 2005–2006—colder values in the western regions 1–3 (Fig. 3). Three periods of warmer MAGST occurred in 2001, 2003/04 and 2007, with the 2003/04 event as the warmest.

Both 2003 and 2006/07 warm climatic events did not affect MAGST in the same way. In 2003 a strong MAGST increase already had occurred during the winter due to earlier snow insulation (e.g., Vonder Mühll et al. 2007); a second phase of warming succeeded in summer and was caused by the heat wave. An extremely high MAGST value was reached by the end of 2003. In 2006/07, the situation was the reverse. Later and lesser snowfalls in early winter favoured the cooling of the ground surface in spite of the persistence of mild air temperature. The extremely high MAAT was strongly attenuated in MAGST.

Results

Despite variable size, morphology, complexity of flow field, mean annual velocity, seasonal rhythm, etc., the compared rock glaciers have shown a rather homogeneous and synchronous behavior (Fig. 4). Three phases of higher creep rate can be quoted in 2000/01, 2003/04, and 2006/07. They all followed immediately a period of warmer MAGST.

Every rock glacier reached an absolute or relative maximal creep rate in 2003/04 before a drastic drop occurred for most of them between 2004 and 2006 (up to -81%, Table. 1). The drop was generally stronger to the west (Regions 1–3) than to the east (Regions 5–6). Stationary or slightly increased velocities were observed everywhere in 2006/07.

The situation in 2000/01 was more contrasted. A peak rate of deformation occurred in Region 4 and was also almost reached in Region 1. Relative maxima are reported from Regions 3 and 6 (no data in Region 2) whereas no maximum is documented in Region 5. Neighboring regions did not display similar behavior in rock glacier movement.

Discussion

Neglecting small differences in interannual variations that may be due to either internal and topographical characteristics of the rock glaciers or to the variability of the seasonal rhythm or to a shift in the measurement date, the rather homogeneous behavior of Alpine rock glaciers allows us to state that: (1) the driving processes are likely to be the same for all observed rock glaciers; (2) there should be a common climatic control of the permafrost creep rate; (3) a dominant effect of active layer solifluction or surface boulder creep can be excluded, as corroborated, for instance, by borehole deformation measurements on the Trais Fluors rock glacier (Ikeda et al. 2008).

As the interannual changes of surface motion appear to be mostly correlated to the evolution of the MAGST with a delay of a few months (Fig. 4) - the warmer the MAGST, the larger the velocity, - one can infer that they should be caused by a thermally induced process. The delay being not long enough for the surface thermal signal to penetrate deeply into permafrost, interannual changes would thus be primarily caused by shifts in the deformation rate of shallow permafrost layers mostly located—if existing—above the shear horizon.

Higher creep rates should also be caused by the development of a thick winter snow cover, which during early summer provides more meltwater to penetrate into a warm rock glacier system. This process is evoked by Ikeda et al. (2008) to explain the high activity of the Trais Fluors rock glacier in 2001. In that region, the snow cover in winter 2000/01 was much deeper than for both the previous and the following winters. The unusually high amount of meltwater in early summer 2001 is advanced as a factor which facilitated permafrost creep. A similar situation occurred in the Laurichard area in the French Alps. The snow accumulation (2.42 m we) recorded that winter on the Sarennes glacier at a distance of 24 km was 0.65 m we above the 1984–2007 mean and the only value exceeding 2 m we since 1995 (Fig. 5). Among the six regions defined in this study, both Laurichard and Trais Fluors regions are the most exposed to southerly precipitations, a situation which prevailed in winter 2000/01.

Changing interannual creep rates may finally be related to the intensity of winter ground freezing. Where data is available, the maximal activity of rock glaciers appears to be linked to lower freezing index values. In the western and eastern Swiss Alps, the highest annual velocities occurred after the warmest winters on the ground surface, in 2001 and 2003 (Fig. 6). On the Muragl rock glacier, close to Trais Fluors, seasonal velocity surveys carried out between 1998 and 2003 (Kääb et al. 2007) showed that, contrary to other winters, the velocity of the rock glacier did not decrease during winter 2000/01. The higher annual velocity was caused by the absence of a winter deceleration.

Conclusions and Perspectives

Rapid and slow rock glaciers have shown mostly a similar kind of annual velocity variations in the whole arc of the

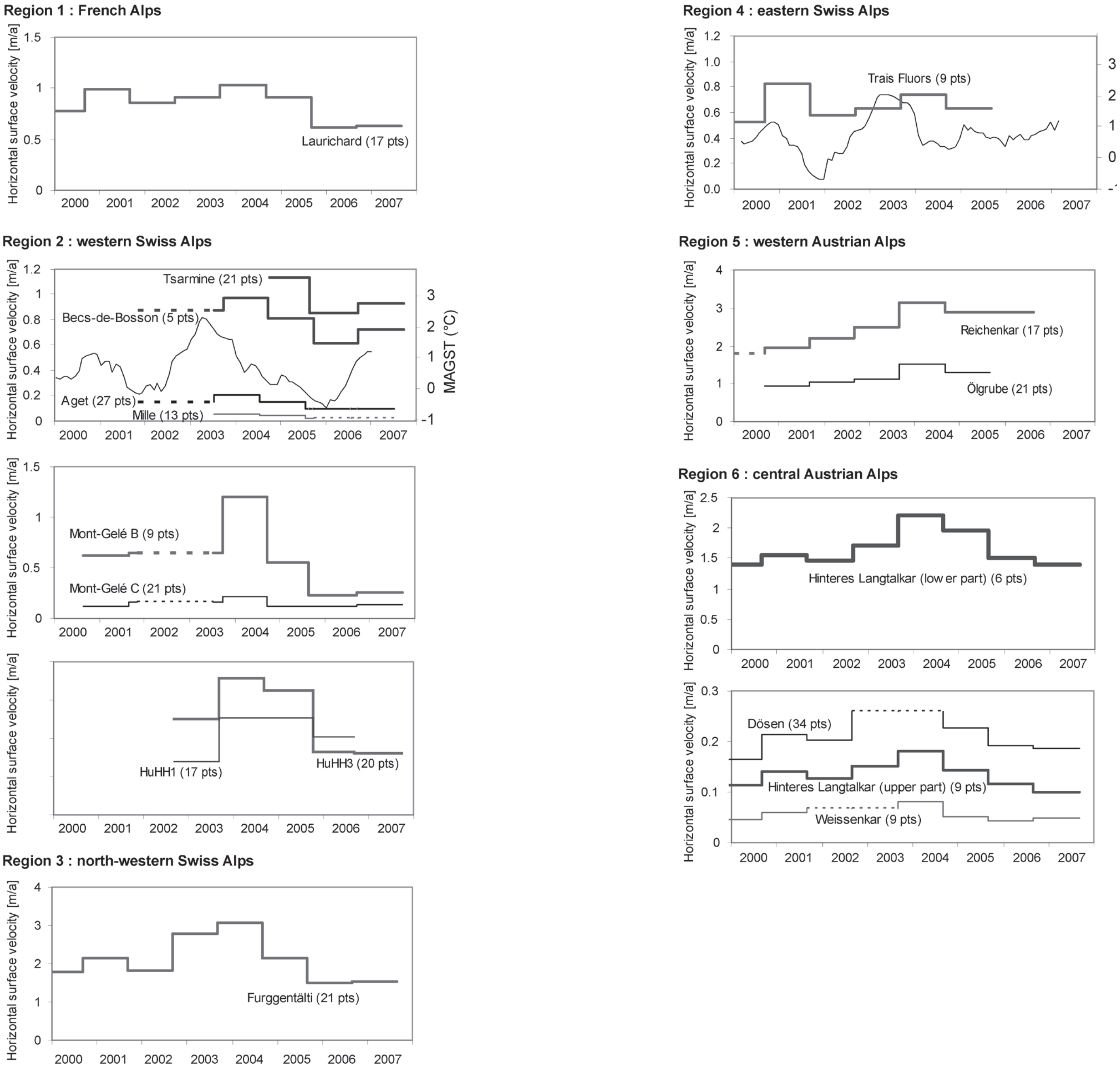

Figure 4. Annual horizontal velocities of alpine rock glaciers. The velocity scale is not identical on every graph. Dotted lines indicate a 2-year interval of measurement. Mean annual ground surface temperature (MAGST) at Becs-de-Bosson and Trais Fluors rock glaciers are inserted in the respective chart with date corresponding to the median of the 12-month period.

European Alps since 2000. Interannual variations of rock glacier dynamics appear so far—with probably a few exceptions—to be primarily related to external climatic factors rather than to the internal characteristics of the rock glaciers. They are mostly well related to shifts in mean annual ground surface temperature with a few months of time lag reflecting the delay in propagation of corresponding anomalies deeper into permafrost. Seasonal factors may also play an important role. A lower intensity of winter ground freezing and/or a larger amount of winter (October–May) snowfall facilitate a higher rate of annual rock glaciers surface motion.

The set of 16 rock glaciers is representative of six alpine regions. It establishes a pioneer network for the observation of short-term variations of rock glacier activity. The first synthetic results strongly encourage the continuation of the monitoring effort and the extension of the network to further regions, particularly in the southern Alps for which such data is still mostly lacking. The availability of uninterrupted series, complemented by ground surface temperature and snow data acquired on the rock glaciers or in their close vicinity, will serve a more precise identification and quantification of the factors driving the short-term behavior of permafrost creep rate in temperate mountain areas.

Acknowledgments

Special thanks are due to both reviewers and to the reviewer editor for their comments, and to all involved in the field survey campaigns for their inestimable contribution.

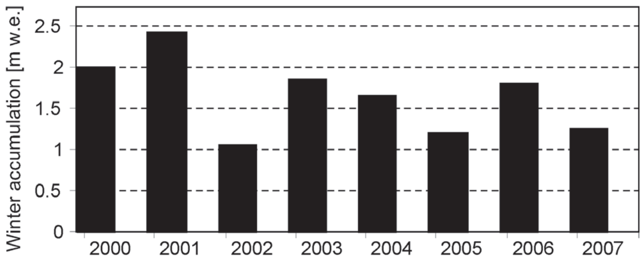

Figure 5. Winter snow precipitations (cumulative amount from October to April in meters of water equivalent, m we) recorded at Sarennes Glacier (French Alps).

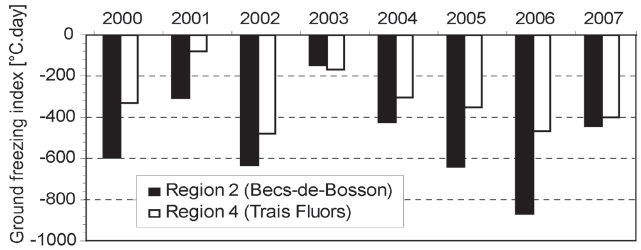

Figure 6. Interregional comparison of ground freezing index in the Swiss Alps.

References

Avian, M., Kaufmann, V. & Lieb, G.K. 2005. Recent and Holocene dynamics of a rock glacier system – the example of Langtalkar (Central Alps, Austria). *Norwegian Journal of Geography* 5: 149-156.

Delaloye, R. & Monbaron, M. 2003. Snow effects on recent shifts (1998-2002) in mean annual ground surface temperature at alpine permafrost sites in the western Swiss Alps. *Eighth Conference on Permafrost, Zurich 2003, Extended Abstracts*: 23-24.

Delaloye, R. 2004. *Contribution à l'étude du pergélisol de montagne en zone marginale*. Ph.D. Thesis, University of Fribourg, Switzerland, *GeoFocus* 10.

Francou, B. & Reynaud, L. 1992. 10 years of surficial velocities on a rock glacier (Laurichard, French Alps). *Permafrost and Periglacial Processes* 3: 209-213.

Haeberli, W. 1985. Creep of mountain permafrost: internal structure and flow of Alpine rock glaciers. *Mitteilung VAW/ETH Zurich* 74.

Haeberli, W., Hoelzle, M., Kääb, A., Keller, F., Vonder Mühll, D. & Wagner, S. 1998. Ten years after drilling through the permafrost of the active rock glacier Murtèl, eastern Swiss Alps: answered questions and new perspectives. *Proceedings of the Seventh International Conference on Permafrost, Yellowknife,* Nordicana 57: 403-410.

Hausmann, H., Krainer, K., Brückl, E. & Mostler, W. 2007a. Creep of Two Alpine Rock Glaciers – Observation and Modelling (Ötztal- and Stubai Alps, Austria). *Grazer Schriften der Geographie und Raumforschung* 43: 145-150.

Hausmann, H., Krainer, K., Brückl, E. & Mostler, W. 2007b. Internal Structure and Ice Content of Reichenkar Rock Glacier (Stubai Alps, Austria) Assessed by Geophysical Investigations. *Permafrost and Periglacial Processes* 18: 351-367.

Ikeda, A., Matsuoka, N. & Kääb, A. 2008. Fast deformation of perennially frozen debris in a warm rock-glacier in the Swiss Alps: an effect of liquid water. *Journal of Geophysical Research* (in press).

Kääb, A., Kaufmann, V., Ladstädter, R. & Eiken, T. 2003. Rock glacier dynamics: implications from high-resolution measurements of surface velocity fields. *Proceedings of the Eighth International Conference on Permafrost, Zurich,* Balkema : 501-506.

Kääb, A., Frauenfelder, R. & Roer, I. 2007. On the response of rockglacier creep to surface temperature increases. *Global and Planetary Change* 56(1-2): 172-187.

Kaufmann, V., Ladstädter, R. & Lieb, G.K. 2006. Quantitative assessment of the creep process of Weissenkar rock glacier (Central Alps, Austria). *Proceedings of the Eighth High Mountain Remote Sensing and Cartography Symposium, La Paz, Bolivia, March 20-27, 2004*: 77-86.

Kaufmann, V., Ladstädter, R. & Kienast, G. 2007. 10 years of monitoring of the Doesen rock glacier (Ankogel group, Austria) - A review of the research activities for the time period 1995-2005. *Proceedings of the Fifth Mountain Cartography Workshop, Bohinj, Slovenia, March 29–April 1, 2006*: 129–144.

Krainer, K. & Mostler, W. 2006. Flow velocities of active rock glaciers in the Austrian Alps. *Geografiska Annaler, Series A: Physical Geography* 88(4): 267–280.

Lambiel C. & Delaloye R. 2004. Contribution of real-time kinematic GPS in the study of creeping mountain permafrost: examples from the Western Swiss Alps. *Permafrost and Periglacial Processes* 15: 229-241.

Lambiel, C., Delaloye, R., Strozzi, T., Lugon, R. & Raetzo, H. 2008. ERS InSAR for detecting the rock glacier activity. *Proceedings of the Ninth International Conference on Permafrost, Fairbanks, Alaska, June 29–July 3, 2008* (this proceedings).

Mihajlovic, D., Staub, B., Nussbaum, A., Krummenacher, B. & Kienholz, H. 2008. Twenty years of permafrost research on the Furggentälti rock glacier, Western Alps, Switzerland. *Proceedings of the Ninth International Conference on Permafrost, Fairbanks, Alaska, June 29–July 3, 2008* (this proceedings).

Roer, I. 2007. Rockglacier kinematics in a high mountain geosystem. *Bonner Geographische Abhandlungen* 117.

Roer, I., Kääb, A. & Dikau, R. 2005. Rockglacier acceleration in the Turtmann valley (Swiss Alps) - probable controls. *Norwegian Journal of Geography* 59(2): 157–163.

Roer, I., Haeberli, W., Avian, M., Kaufmann, V., Delaloye, R., Lambiel, C. & Kääb, A. 2008. Observations and considerations on collapsing active rockglaciers in the Alps. *Proceedings of the Ninth International Conference on Permafrost, Fairbanks, June 29–July 3, 2008* (this proceedings).

Perruchoud, E. & Delaloye, R. 2007. Short-term changes in surface velocities on the Becs-de-Bosson rock glacier (western Swiss Alps). *Grazer Schriften der Geographie und Raumforschung* 43: 131-136.

Vonder Muehll, D., Noeztli, J., Roer, I., Makowski, K. & Delaloye, R. (eds). 2007. *Permafrost in Switzerland.* PERMOS Reports 4 & 5 (2002/03 & 2003/04). Swiss Acad. of Sciences.

Ground-Based LIDAR Data on Permafrost-Related Rockfall Activity in the Mont Blanc Massif

Philip Deline, Stéphane Jaillet, Antoine Rabatel, Ludovic Ravanel
EDYTEM Lab, Université de Savoie, CNRS, Le Bourget-du-Lac, France

Abstract

It is hypothesized that climatic warming since 1980 increases rock wall instability in high mountains due to permafrost degradation. This is supported by the observation of ice in several rockfall scars. Due to a lack of systematic observations, magnitude and frequency of high mountain rock failures remain poorly known. As part of the French-Italian *PERMAdataROC* project, we apply ground-based LIDAR to monitor instability on representative permafrost-affected rock walls (3000 to 4650 m a.s.l.) in the Mont Blanc massif. Initial results indicate that rockfall activity probably relates to different conditions at the 3 reported sites. The Piliers de Frêney and Grand Pilier d'Angle, both above 4000 m, are virtually stable (0 m^3 of rockfalls) and indicate conservation of permafrost at high altitudes even on south-facing rock walls. With a probably critical state of permafrost, Tour Ronde E-Face and Arête Freshfield NE-Face (3460–3792 m) released ca. 1000 m^3 of rockfall from 2005–2007. On Les Drus (2700–3700 m a.s.l.), 560 m^3 of rockfalls were observed; we argue that these occur due to slope readjustment to the 2005 rock avalanche and are not directly linked to permafrost degradation.

Keywords: LIDAR; Mont Blanc massif; *PERMAdataROC* project; permafrost; rockfall; terrestrial laser scanning.

Introduction

Recently, large rock and rock/ice avalanches have occurred in high mountain areas worldwide (*e.g.,* Kolka-Karmadon, Caucasus 2002, Huggel et al. 2005). In the Alps, Brenva Glacier (1997), Punta Thurwieser (2004), the west face of Les Drus (2005), and the east face of Monte Rosa (2006, 2007) are the most recent examples (Deline 2001, Noetzli et al. 2003, Fischer et al. 2006, Ravanel 2006). In addition, innumerable smaller rockfalls detached from steep rock walls during the hot summer of 2003 (Gruber et al. 2004). The hypothesis that the increase of high mountain rock wall instability relates to permafrost changes gains force (Haeberli et al. 1997, Gruber & Haeberli 2007) from the fact that (1) ice was observed in many starting zones; (2) the mean annual air temperature in the Alps has increased more than 1°C during the 20^{th} Century; and (3) the warming trend has accelerated since 1980.

However, frequency and volume of instability events in high mountains are still poorly known because of the lack of systematic observations, and ongoing permafrost changes in rock walls remain poorly understood due to the difficulties in carrying on in situ measurements. So far, permafrost studies are mainly based on modeling, with a few existing instrumented sites.

The PERMAdataROC project

The *PERMAdataROC* project aims at studying the relation between permafrost degradation and high mountain rock wall instability in two west Alpine areas, the Mont Blanc massif and the Matterhorn, based on the interface of three research assignments (Ravanel & Deline 2006).

The first assignment deals with the collection, maintenance and analysis of recent rockfall/rock avalanches in the Mont Blanc massif in a data base, based on (1) systematic survey of slope instability events (localisation, exposition, time, meteorological conditions, snow conditions, estimated volume, path) carried out by local, trained people (mountain guides, rescue people, hut keepers) in collaboration with the researchers; (2) digitalisation of the events in a GIS; and (3) analysis of the topographical, geological and climatic parameters of the affected rock walls. This data base is complemented by past events that are documented by newspapers, hut, and guide books, as well as previous studies and guide interviews.

The second research assignment deals with measuring and the thermal regime in rock walls. The instrumentation (thermistors at 5, 10, 30, and 55 cm depth) and measurement of relevant properties (albedo, irradiation, thermical conductivity) of rock wall superficial layer and surface at the selected study sites, combined with high altitude climatic data recorded by a movable automatic weather station, will contribute to validate the models of temperature distribution and variations.

The third research assignment is provided by the monitoring of the instability of representative rock walls, by (1) frequently repeated surveys with long-range ground-based LIDAR (LIght Detection And Ranging) and terrestrial photogrammetry, and (2) the installation of a geophone network in one of the study sites to determine the frequency and volume of rockfalls, considering variable parameters (altitude, aspect, slope angle, lithology, fracturing, shadow effect, height drop).

Italian (CNR-IRPI Torino, ARPA Valle d'Aosta and FMS Courmayeur) and French (EDYTEM Lab) partners are involved in the *PERMAdataROC* project, with collaboration with the GGG of University of Zürich.

Here we present initial results of the monitoring of the

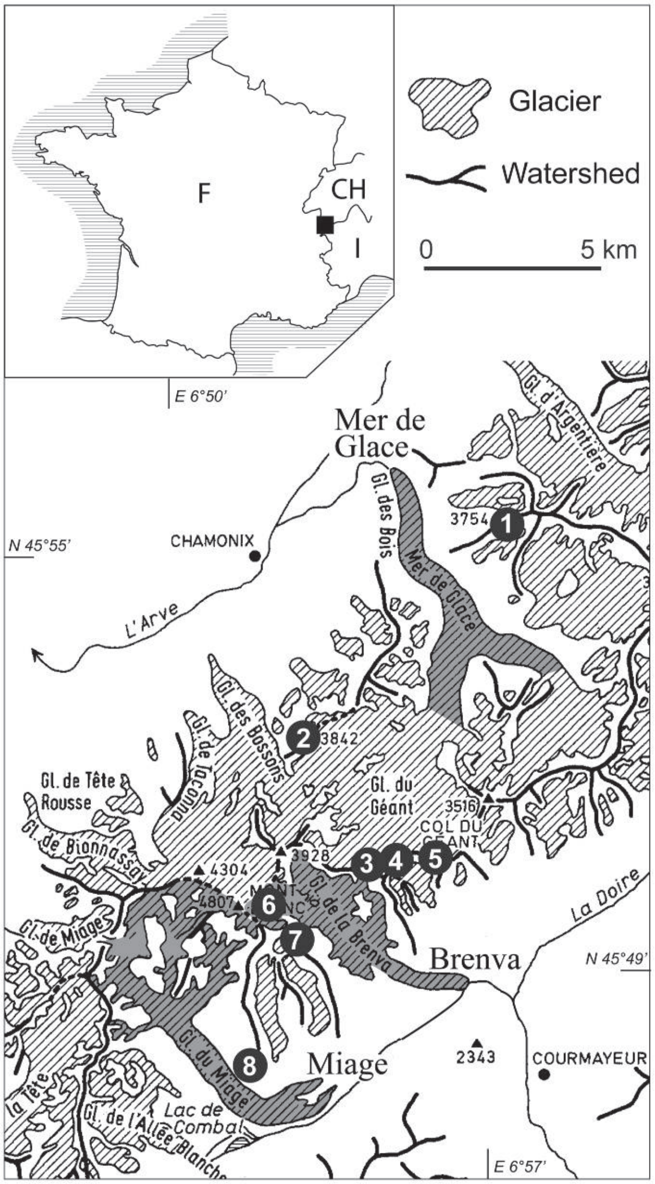

Figure 1. Location map of GB-LIDAR surveyed sites in the Mont Blanc massif within the framework of the *PERMAdataROC* project. 1: Drus; 2: Aiguille du Midi; 3: Tour Ronde-Arête Freshfield; 4: Aiguilles d'Entrèves; 5: Grand Flambeau; 6: Piliers du Frêney-Grand Pilier d'Angle; 7: Aiguilles Blanches de Peuterey; 8: Vallon du Miage. Largest glaciers are highlighted. This paper presents initial results from sites 1, 3, and 6.

instability of rock walls at three sites in the Mont Blanc massif since 2005.

Study Area

The Mont Blanc massif covers an area of approximately 350 km², 40% of which is glacierized. It reaches its highest point at 4808 m a.s.l., but many of its granitic, fractured faces, peaks, and aiguilles stand well above 3000 m. The water divide between Rhône and Pô basins is a 35 km long crest line which always exceeds 3300 m and is often higher than 4000 m. Being one of the most active uplift spots in the Alps (>1.5 mm.an^{-1}), the massif is not only characterized by very high, but also steep faces and rock walls.

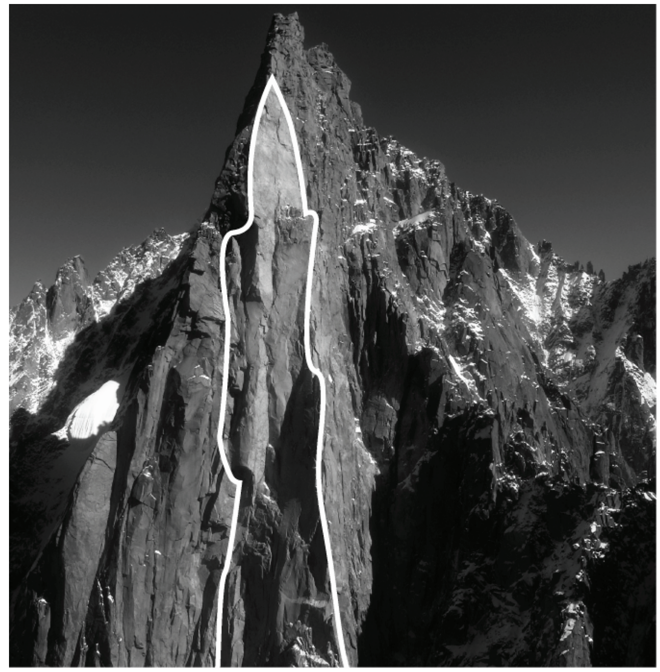

Figure 2. Upper part of the west face of Les Drus. The upper part of the 2005 rock avalanche scar is delimited by the white line. To survey the face, the ground-based LIDAR is set up on Les Flammes de Pierre (crest on bottom right).

Seven study sites from 3000 to 4650 m with different aspects were selected in the Mont Blanc massif within the *PERMAdataROC* project (Fig. 1): the west face of Les Drus, a >70° rock wall between 2700 and 3700 m affected by a series of rockfalls since 1950 with increasing magnitude until June 2005, when collapse of the Pilier Bonatti generated a rock avalanche of >250,000 m^3 (Fig. 2) (Ravanel 2006); the surveyed area at Les Drus is between 3000 and 3700 m; the Piton Central of the Aiguille du Midi (3770–3842 m) which towers above the cable car station, with all aspects; the east face of the Tour Ronde, and the NE-facing Arête Freshfield which develops at the south (3460–3792 m), where rockfalls have been active for several years; the west face of the Aiguilles d'Entrèves (3490–3591 m); the Grand Flambeau (3410–3561 m), close to the Helbronner cable car station, with all aspects; the east-facing Piliers de Frêney (4000–4650 m) and the south face of the Grand Pilier d'Angle (4050–4308 m), on the south side of Mont Blanc summit, and the NW face of the Aiguille Blanche Nord de Peuterey (4000–4103 m). These high elevation sites are complemented by a low-elevation control site (2200–2700 m) without permafrost, on the SW-facing side of the Vallon du Miage.

Methods

Since June 2005, ground-based LIDAR measurements are realised seasonally (summer/autumn) or annually at the eight sites in the Mont Blanc massif, using helicopter or cable cars for access. Data are processed for calculating high-resolution (centimeter-scale) triangulated irregular networks (TIN). Volumetric changes, extracted on the rock faces by comparing the successive TINs, represent the fallen rocks between the measurement periods (Ravanel & Deline 2006).

LIDAR survey

LIDAR measurements are performed using an Optech® ILRIS 3D ground-based LIDAR. This laserscanner works at distances of up to 800 m if surface reflectivity and visibility are good. The angle of view is 40°×40°, and the sampling rate reaches a maximum frequency of 2000 points per second. At a distance of 100 m, the laser beam diameter is about 30 mm (perpendicular shot), and the accuracy on a flat surface is about 3–5 mm. The LIDAR point to point distances on the rock walls we are surveying range between 61 mm and 246 mm (in 2006 and 2007), on the closest and farthest areas, respectively.

Data processing

Data processing (Rabatel et al., submitted) is realised using InnovMetric PolyWorks® software, with (1) alignment of individual point clouds using the IMAlign module: they are merged with a rototranslation matrix into a unique local reference system, after cleaning individual scans from outliers (Fig.3); and (2) creation of the TIN using the IMMerge module.

The computation of the fallen rock volume in a rock wall between two successive field work campaigns is achieved with the PolyWorks® IMInspect module, which compares two point clouds and quantifies the thickness changes. A reference plan is built, and the volume between the surface topography and this plan is computed for each date.

Error estimation

The total uncertainty can be estimated by the quadratic sum of the different independent errors in the processing. (1) LIDAR error is 3–5 mm at 100 m (manufacturer data). (2) TIN is interpolated from existing points of the global point cloud (set of 3D images). To merge it into a unified polygonal mesh, most parameter values are calculated using input point cloud values. Due to the average mesh used, the TIN construction error is ca. 7 cm. (3) To be compared, diachronous TINs have to be very overlapped. But because of very large TINs, there is a TIN overlapping error, which is 5 cm as measured by Polyworks. This yields an overall uncertainty of 9 cm, which is reduced by directly comparing the point clouds.

Mask effect

Masks result from (1) the topography of the rock wall (roofs, ledges, corners, spurs); (2) the common scarcity of sites to set up the LIDAR (e.g., for the west face of Les Drus, there is only one possible on Les Flammes de Pierre: Fig. 2); and (3) the snow cover, whose extension differs each year. Masks could represent an important part of the surface surveyed, and appear as holes in the TINs. This is particularly

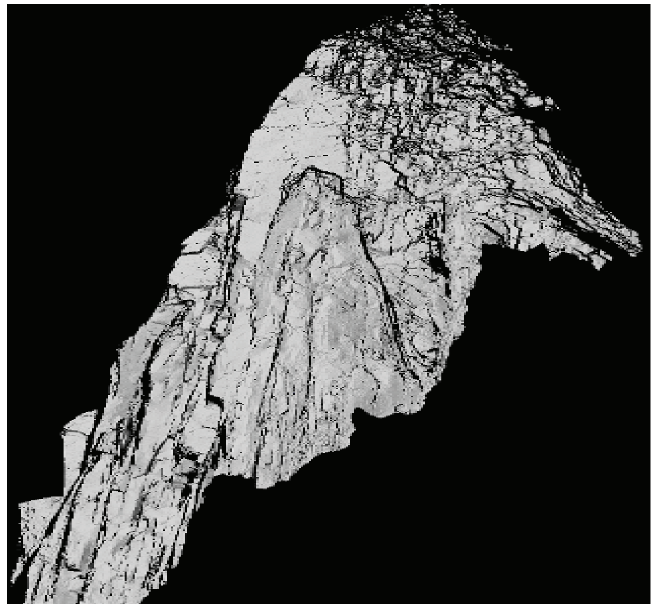

Figure 3. Point clouds of the west face of Les Drus derived from LIDAR surveys (left: October 2005; right: October 2006). The height of the 2005 rock avalanche scar here represented is 500 m.

the case if there are no multiple viewing angles (Les Drus), or if the snow-ice cover is important (Peuterey).

The Polyworks® IMEdit module allows to reduce their extension. The hole area is first selected. A tool allows the holes to fill automatically using irregular triangles. Only the maximum distance between the vertices of a triangle has to be specified. The longer this distance, the greater resulting size of the plugged hole.

Results

We present initial results from three of the seven high-elevation selected sites in the Mont Blanc massif: (1) the west face of Les Drus; (2) the east face of the Tour Ronde and the NW side of the Arête Freshfield; and (3) the Piliers de Frêney and the south face of the Grand Pilier d'Angle (Table 1).

West face of Les Drus

Comparison of October 2005 and October 2006 TINs reveals a detachment from the 2005 rock avalanche scar of height rock elements of a volume ≥1 m³: five boulders are ≤6 m³, and three are larger. At about 3600 m a.s.l., a notch of 29×10×1.8 m (426 m³) is present on the 2006 TIN; the rocks reached the small debris-covered glacier of Les Drus, at the foot of the west face. Lower on the rock wall, two elements of 19 and 84 m³ also collapsed in this one-year period. In total, 546 m³ of rock were released in the surveyed area between October 2005 and October 2006.

The third survey, carried out at the end of September 2007, shows reduced rockfall activity over the period extending from October 2006 to September 2007: only one small rockfall occurred (22 m³), out of the 2005 scar.

Table 1. Rockfall data from LIDAR surveys (2005–2007).

Site	Period of measurement (d/m/y)	Surface of surveyed area by LIDAR (m²)	Volume of rockfalls (m^3) Total	Volume of rockfalls (m^3) 2 main	Mean rock wall retreat rate in surveyed area ($mm\ a^{-1}$)	Extreme distance of point to point on rock wall (mm)
Drus (W face)	11/10/2005–11/10/2006	70,500	546	426 + 84	7.7	Not calculated
	12/10/2006–24/09/2007		22	-	0.3	71–208
Piliers de Frêney - Grand Pilier d'Angle (S face)	14/07/2005–10/10/2005	115,600	0	0	0.0	Not calculated
	11/10/2005–30/06/2006		0	0	0.0	Not calculated
	01/07/2006–13/10/2006		0	0	0.0	61–246
	14/10/2006–12/10/2007		0	0	0.0	61–246
Tour Ronde (E face) – Arête Freshfield (NE face)	13/07/2005–18/07/2006	67,400	536	382 + 154	8.4	Not calculated
	19/07/2006–12/10/2006		0	0	0.0	75–207
	13/10/2006–12/10/2007		448	448	6.6	75–207

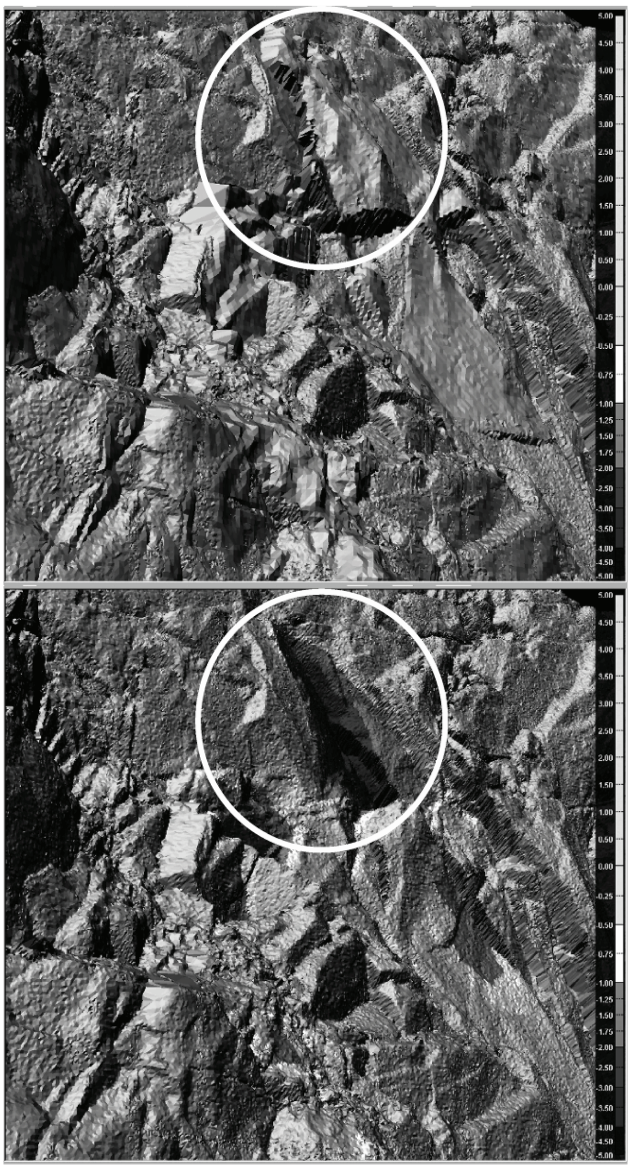

Figure 4. East face of the Tour Ronde TIN (detail). The view focuses on the area affected by the main rockfall between July 2005 (top box) and July 2006 (bottom box). Dimensions of the main scar (visible in bottom box circle) are 17.5×7.8×4.3 m, with a volume of 382 m^3 (image size: ca. 45 m × 45 m).

East face of La Tour Ronde-NE face of Arête Freshfield

At the Tour Ronde, the evolution of the surface topography of the east face between July 2005 and July 2006 shows two main rockfall events, with a volume of 382 m^3 (Fig. 4) and 154 m^3 (main scar sizes are 17.5×7.8×4.3 m and 15.1×9.3×1.4 m, respectively). The total volume of these two rockfall reaches 536 m^3.

The comparison of LIDAR measurements for the second period, between July 2006 and October 2006, shows no significant change during the 2006 summer.

During the third, and last, period of survey, no change was observed on the east face of Tour Ronde. On the other hand, at least two rockfalls occurred on the NE side of the Arête Freshfield, involving a set of large boulders (total volume: 448 m^3) which detached from a small area where bedrock is highly dislocated.

Piliers de Frêney-south face of Grand Pilier d'Angle

Five successive LIDAR surveys performed since July 2005 display no change on the rock walls during a period of 27 months, including 3 summers. Mask effects are important, due to the rough topography of the area (large pillars separated by deep couloirs) and the unique site available to set up the ground-based LIDAR. Thus, only a part of this area is surveyed, but no significant rockfall was observed over the 115,000 m^2 it represents.

Discussion and Conclusions

Results indicate that rockfall activity probably relates to different conditions at the three sites.

On the west face of Les Drus, the rockfalls which occurred probably represent slope readjustment after the large rock avalanche of 2005 and are not directly related to permafrost degradation. For example, the detachment of 84 m^3 between October 2005 and October 2006 is due to the fall of an individualized, hanging, and poorly-rooted slice. Moreover, the small pieces of rock (<1 m^3) identified between 2005 and 2006 were probably destabilized during the fall of the largest element (426 m^3). Lastly, no rockfall occurred into the 2005 scar between 2006 and 2007: this suggests that the mesoscale slope readjustment in the scar is now achieved.

But it is noteable that a new permafrost active layer forms in the 2005 rock avalanche scar.

On the other hand, on the east face of La Tour Ronde and on the NE side of the Arête Freshfield, the rockfalls (2005–2006: 536 m^3; 2006–2007: 448 m^3) probably result from permafrost degradation. This is suggested both by (1) the high rock fall activity during recent years: the normal route to the summit of Tour Ronde is not used when snow cover has melted; and (2) the modeling of the surface temperature of rock walls in alpine areas with similar weather conditions. For instance, mean annual surface temperatures range between -2°C and -4°C at Junfraujoch at 3500–3750 m a.s.l. for E/NE aspect (Gruber et al. 2004: Fig. 2), without taking into account the local topography of the rock faces.

Contrary to the two others sites, the area of the Piliers de Frêney and the south face of the Grand Pilier d'Angle show stable conditions. The results suggest that no or very occasional degradation of the permafrost occurs at very high altitude (>4000 m), including south-facing rock walls like the Grand Pilier d'Angle. Several large grey scars at the foot of the Piliers de Frêney and the nearby Piliers du Brouillard and Mont Maudit, which clearly contrast to the reddish surrounding granite, indicate that rockfalls and rock avalanches have occurred at elevations greater than 4000 m; but preliminary studies (Böhlert et al. 2008) suggest that these grey scars could have formed before 1,500 yr BP, during previous Holocene cold periods.

Given that high-alpine rock walls are a poorly known system, the introduced methodology shows a great potential to reveal quantitative data on geomorphological processes in permafrost-affected rock walls

Acknowledgments

The paper benefited from critical comments by the two anonymous referees, one of them also improving the English. Thanks to all partners of the *PERMAdataROC* project. The European Union (FEDER), the Town Council of Chamonix, and the Conseil Général de la Haute-Savoie are acknowledged for funding. This paper is part of the Interreg IIIA France-Italy # 196 *PERMAdataROC* project.

References

Deline, P. 2001. Recent Brenva rock avalanches (Valley of Aosta): new chapter in an old story? *Supplemento Geografia Fisica e Dinamica Quaternaria* 5: 55-63.

Böhlert, R., Gruber, S., Egli, M., Maisch, M., Brandová, D., Haeberli, W., Ivy-Ochs, S., Kubik, P.W. & Deline, P. 2008. Comparison of exposures ages and spectral properties of rock surfaces in steep, high Alpine rock walls—a field study at Aiguille du Midi, France. *Proceedings of the Ninth International Conference on Permafrost, Fairbanks, Alaska, June 29–July3, 2008* (this proceedings).

Fischer, L., Kääb, A., Huggel, C. & Noetzli, J. 2006. Geology, glacier retreat and permafrost degradation as controlling factor of slope instabilities in a high-mountain rock wall: the Monte Rosa east face. *Natural Hazards and Earth System Sciences* 6: 761-772.

Gruber, S. & Haeberli, W. 2007. Permafrost in steep bedrock slopes and its temperature-related destabilization following climate change. *Journal of Geophysical Research* 112:F02S18, doi: 10.1029/2006JF000547.

Gruber, S., Hoelzle, M. & Haeberli, W. 2004. Permafrost thaw and destabilization of Alpine rock walls in the hot summer of 2003. *Geophysical Research Letters* 31, L13504, doi: 10.1029/2004GL020051.

Haeberli, W., Wegmann, M. & Vonder Mühll, D. 1997. Slope stability problems related to glacier shrinkage and permafrost degradation in the Alps. *Eclogae Geologicae Helvetiae* 90: 407-414.

Huggel, C. Zgraggen-Oswald, S., Haeberli, W., Kääb, A., Polkvoj, A., Galushkin, I. & Evans, S.G. 2006. The 2002 rock/ice avalanche at Kolka/Karmadon, Russian Caucasus: assessment of extraordinary avalanche formation and mobility, and application of QuickBird satellite imagery. *Natural Hazards and Earth System Sciences* 5: 173-187.

Noetzli, J., Hoelzle, M. & Haeberli, W. 2003. Mountain permafrost and recent Alpine rock fall events: a GIS-based approach to determine critical factors. *Proceedings of the 8th International Conference on Permafrost, Zürich, Switzerland, August, 2003*: 827-832.

Rabatel, A., Deline, P., Jaillet, S. & Ravanel, L., submitted. Rock falls in high-alpine rockwalls quantified by terrestrial LIDAR measurements. A case study in the Mont Blanc area. *Geophysical Research Letters*.

Ravanel, L. 2006. *Contribution à l'étude des écroulements dans les parois à permafrost de la haute montagne alpine. L'exemple du Petit Dru (massif du Mont Blanc) depuis la fin du Petit Age Glaciaire)*. MSc thesis, Université de Savoie, 116 pp.

Ravanel, L. & Deline, P. 2006. Nouvelles méthodes d'étude de l'évolution des parois rocheuses de haute montagne: application au cas des Drus. *Actes du Colloque Géologie et risques naturels: la gestion des risques au Pays du Mont-Blanc, Sallanches, France, November 18, 2006*: 48-53.

Use of Ground-Penetrating Radar to Characterize Cryogenic Macrostructures in Southern New Jersey, USA

Mark Demitroff
Department of Geography, University of Delaware, Newark, DE USA
James A. Doolittle
National Soil Survey Center, USDA-NRCS, Newtown Square, PA, USA
Frederick E. Nelson
Department of Geography, University of Delaware, Newark, DE, USA

Abstract

The Pine Barrens of southern New Jersey has a well-documented periglacial legacy, evidenced by traces of relict frost fissures and related deformational structures. This study measures the potential of three-dimensional ground-penetrating radar (3D GPR) techniques to detect and identify subsurface cryogenic macrostructures investigated previously in the region, including deformed wedges, sediment-filled pots, and frost-fissure casts. Radar images are especially useful where infill is sandy, and the host sediments are indurated. Although geometric relations between cryostructures are more subtle than in the few contemporary permafrost environments where 3D GPR has been employed and interpretation is more difficult, the ability of 3D GPR to detect networks of fossil features warrants further investigation. The methodology complements traditional field observation and appears to have considerable potential as a tool for detecting and analyzing networks of relict subsurface permafrost features.

Keywords: cryostructures; ground-penetrating radar; New Jersey Pine Barrens; permafrost; remote sensing; thermokarst.

Introduction

The Pine Barrens of southern New Jersey is a highly weathered landscape lying 50 to 150 km beyond the maximum extent of late Pleistocene ice sheets. Its regolith repeatedly experienced cold, dry, and windy conditions during the late Pleistocene, leaving behind a long-debated fossil signature of climate change (Wolfe 1953, Newell & Wyckoff 1992, Demitroff 2007). Permafrost was present in at least three intervals during the last 200,000 years (French et al. 2007). Various periglacial geomorphic processes operated intermittently in the region, including thermal-contraction cracking, desiccation, and thermokarst displacement.

Alternating cold and warmer intervals created a complex suite of distinctive soil phenomena in southern New Jersey (French & Demitroff 2003, French et al. 2003, 2005), including sand-wedge casts, "soil wedges," and thermokarst features. We refer to these features collectively as cryogenic macrostructures (Huijzer 1993). Recent investigations (French & Demitroff 2001, French et al. 2003, 2005) indicate that the coarse-textured soils, sparse vegetation, and thin snow cover of the region during cold intervals favored deep frost penetration. Gravel-rich hilltops and proximal slopes composed of near-surface gravelly colluvium are the best locations to observe macrostructures, because the features are best preserved in such topographic situations. This study evaluates the ability of ground-penetrating radar (GPR) to image cryogenic macrostructures on both two-dimensional (2D) radar records and three-dimensional (3D) pseudo-images.

Frost-Fissure Casts

Sand-wedge casts

Ice wedges are commonplace in contemporary Arctic landscapes. This was not the case in Pleistocene New Jersey. Moisture was minimal when thermal-contraction cracking occurred in the Pine Barrens, so open fissures were mostly filled with wind-blown sands instead of ice. Primary mineral-filled frost cracks are called *sand wedges* (Murton et al. 2000). Pine Barrens sand wedges were epigenetic. They are found just below the uppermost 0.5 to 1.0 m of the soil surface, range in depth from 1.5 to 3.0 m, and average from 20 to 40 cm in width. Two distinct types of sand-wedge-cast forms are recognized in southern New Jersey, "older" (Fig. 1A) and "younger" (Fig. 1B), based on luminescence ages (French et al. 2003). Both exhibit variable spacing (10 to 40 m apart), although smaller sand-wedge casts can grade toward closer spacing.

Older sand-wedge casts typically extend 2–3 m below the surface and are found in higher landscape positions. They contain slightly indurated, fine loess-like to medium sand laminae that stand in sharp contrast to the indurated enclosing matrix, which is interpreted as a fragipan. Small amounts of near-vertically oriented gravels are present towards wedge tops. Luminescence dates indicate that these structures are Early Wisconsinan (Oxygen Isotope Stage 4 [OIS-4]), Illinoisan (OIS-6), or even older structures. Younger sand wedges are 1 to 2 m in depth and can be located across various landscape elevations. They are filled with coarse, loosely packed sand grains that that have been less abraded by wind than those found in older macrostructures. Infill is massive, and lacks the vertical foliation common to older

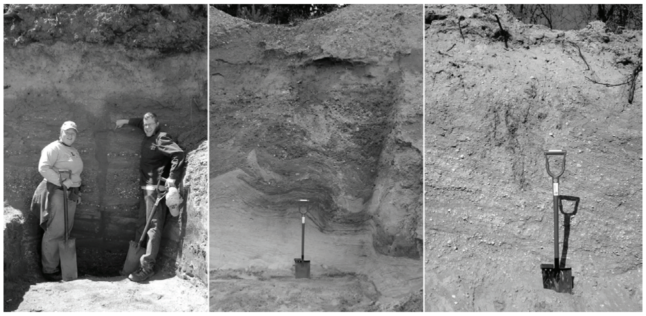

Figure 1. Examples of frost-fissure cast forms at study sites. (A) Older sand-wedge cast, Dorchester. (B) Younger sand-wedge cast, Unexpected 1. (C) "Soil wedge," Unexpected 1.

sand-wedge casts. Luminescence dating indicates that they formed during the Late Wisconsinan (OIS-2).

Soil wedges

In addition to sand-wedge casts, smaller, more closely spaced (2 to 6 m) wedge casts (Fig. 1C) have been described in the Pine Barrens (French et al. 2003). These structures are shallower in depth (<1.5 m) and often narrower in width than sand wedges. Due to their superposition on older features, these structures may be of similar age or possibly younger than the late Wisconsinan sand-wedge casts (OIS-2). Little is known of the dynamics of these features, which have been termed *soil wedges* by Romanovskij (1985). They appear to be artifacts of a dry, cold period at the end of the late Wisconsinan. Active soil wedges have been described from Siberia, but are uncommon under current climatic conditions. Their origin is attributed to cryodesiccation in a seasonally frozen soil layer. Permafrost need not be present for such wedges to form (Jahn 1975, French & Demitroff 2001).

Thermokarst-Modified Wedges

Deformed wedges

Downslope from salients and relict plateaus, the fragipan, which preserves the wedge features, dissipates and the moisture gradient increases. Accompanying this change is modification of upland sand wedges into deformed, furrow-like structures (Fig. 2A) up to 3 m by 3 m. These features are created through deformation of the original macrostructures by thaw erosion, gullying, cryoturbation, and slumping (French et al. 2005). The modifications occurred during periods of climatic amelioration and permafrost degradation, approximately 30 ka (French et al. 2007).

Sediment-filled pots

Associated features known as sediment-filled pots (Fig. 2B) occur at the intersection of deformed wedges. These kettle-like features appear as large elongated to bulbous shaped structures up to 3 to 5 m wide, extend 3 to 4 m below the surface, and extend horizontally up to a few meters in distance. Sediment-filled pots are complex vessels of sands, and silty-to-clayey-to-gravelly diamict.

Figure 2. Examples of thermokarst-modified wedges at study sites. (A) Modified sand wedge, Unexpected 2 (B) sediment-filled pot, Unexpected 2.

Locations and Methods

Study sites

Sites investigated in this study are located in two commercial sand and gravel operations in southern New Jersey where various cryogenic macrostructures have been identified. The sites are referred to as the Dorchester (39.29013˚N, 74.95023˚W) and the Unexpected (originally named Brimfield Crossing) (39.56707˚N, 74.91448˚W) sites. The Dorchester site is in an area of Aura sandy loam, with 0 to 2 percent slopes. The Unexpected site is located in an area of Downer loamy sand, with 0 to 5 percent slopes. The very deep, well-drained Aura and Downer soils were formed in unconsolidated alluvial sediments on the Outer Coastal Plain's Bridgeton Formation. Aura soils are moderately deep (50 to 100 cm) to fragipan. Aura is a member of the coarse-loamy, siliceous, semiactive, mesic Typic Fragiudults family. Downer is a member of the coarse-loamy, siliceous, semiactive, mesic Typic Hapludults family. At the Unexpected site, the upper 25 to 50 cm surface materials had been removed in preparation for mining. A very dense and compact B horizon is also present at the latter site.

Field methods

Survey grids were established at each site. At the Dorchester site, a 2.5 × 2.5 m grid was established immediately behind an excavation wall that contained an older sand-wedge cast. Traverse-line spacing was 25 cm. Two grids were established at the Unexpected site. A 20 × 15 m grid was established near an excavation wall containing deformed wedges, soil wedges, and sediment-filled pots. A 20 × 13 m grid was established near an excavation wall that contained younger sand-wedge casts and soil wedges. For each of these grids, the traverse line spacing was 50 cm.

All grids were established across recently cleared, accessible, and level areas adjacent to excavation walls. For each grid, two parallel axis lines were laid out and spaced either 2.5 m (Dorchester) or 20 m (Unexpected) apart. Along these two parallel axes, survey flags were inserted into the ground at a spacing of 25 cm (Dorchester) or 50 cm (Unexpected), and a reference line was extended between matching survey flags on opposing sides of the grid using a graduated rope. GPR traverses were conducted along this reference line (the X-axis). A 400 MHz antenna was pulled along the graduated rope, which was stretched across the soil surface, and, as it passed each 50 cm (Dorchester) or 100 cm (Unexpected) graduation, a mark was impressed on the radar record. Following completion of a transect, the reference line was moved to the next pair of survey flags to repeat the process.

The radar unit is the TerraSIRch Subsurface Interface Radar (SIR) System-3000, manufactured by Geophysical Survey Systems, Inc. (GSSI; Salem, New Hampshire, USA). The system consists of a digital control unit (DC-3000) with keypad, SVGA video screen, and connector panel, weighs about 4.1 kg (9 lbs), and is backpack portable. The system requires two people to operate.

The *RADAN for Windows* (version 5.0) software program developed by GSSI was used to process the radar records. Processing included: setting the initial pulse to time zero, color table and transformation selection, marker editing, distance normalization, range gain adjustments, high-pass filtering, and migration. The Super 3D QuickDraw program developed by GSSI was used to construct 3D pseudo-image of the radar records.

Calibration

Ground-penetrating radar is a time-scaled system measuring the time required for electromagnetic energy to travel from the antenna to an interface (e.g., soil horizon, stratigraphic layer) and back. To convert the travel time into a depth scale, either the velocity of pulse propagation or the depth to a reflector must be known. The relationships among depth (D), two-way pulse travel time (T), and velocity of propagation (v) are described in the following equation (Daniels 2004):

$$v = 2D/T \tag{1}$$

The velocity of propagation is principally affected by the relative dielectric permittivity (ε_r) of the profiled material (s) according to the equation (Daniels 2004):

$$\varepsilon_r = (C/ v)^2 \tag{2}$$

where C is the velocity of propagation in a vacuum (0.298 m ns^{-1}). Velocity is expressed in meters per nanosecond (m ns^{-1}). In soils, the amount and physical state (temperature dependence) of water have the greatest effect on ε_r and v. The velocity of propagation through the upper part of the soil profile at each grid site was based on the measured depth and the two-way pulse travel time to a known buried reflector, and using equation (1). At the Unexpected Site, the estimated velocity of propagation was 0.119 m ns$^{-1,}$ and the relative dielectric permittivity was 6.3 m ns^{-1}. At the Dorchester Site, the estimated velocity of propagation was 0.136 m ns$^{-1,}$ and the relative dielectric permittivity was 4.8. Daniels (2004) has detailed GPR processing techniques for those who wish to go beyond the scope of this paper.

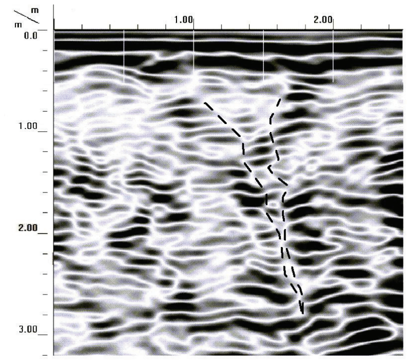

Figure 3. An older sand-wedge cast is faintly expressed in this radar record from the Dorchester site.

Results

Dorchester site

The radar record in Figure 3 was obtained immediately behind an excavation wall in which a well-documented sand-wedge cast (French & Demitroff 2001, French et al. 2003) was exposed. The depth and distance scales are expressed in meters, with depth based on an estimated velocity of propagation of 0.136 m ns^{-1}. A majority of the radar reflections are of moderate to high signal amplitude (darker images) and appear nearly level to slightly inclined. These characteristics are considered typical of fluvial to marine-marginal Coastal Plain sediments. However, these reflectors are not laterally continuous, but appear segmented, with noticeable breaks appearing on the radar record. On radar records, segmentation can be caused by truncation of layers, lateral gradation in the degree of contrast between reflectors, and/or superposition and cancellation of reflected signals.

A sand-wedge cast can be identified on this radar record between the 1.0 and 1.6 m marks at the surface (Fig. 3). Segmented lines highlight the inferred boundary of this sand wedge. The fissure is most clearly expressed in the upper meter of the radar record, where the loosely cemented, smaller grain-sized infill contrasts with the encircling very hard, indurated, and coarser sandy-gravelly matrix. Sand wedges display a wide variety of geometric forms and structures. They may consist of massive or highly stratified materials, have sharp and planar to diffuse and irregular boundaries, and can be wedge-shaped and tapered to irregular, or bulbous (Murton et al. 2000). The morphological characteristics of older sand-wedge casts, in particular, do not favor radar interpretations, owing to their, narrow width and indurated infill. Below depths of about 1 meter, the thin width, tortuous vertical descent, and variable physical properties of the wedge casts contribute to poor, ambiguous boundary expression with the host materials.

In Figure 4 an exposed sand-wedge cast is located on the wall of the excavated pit. All radar traverses were conducted parallel to the X-axis (right foreground). Radar traces were sampled more continuously along this axis, and reflectors are more strongly represented, with little distortion, along it. Along the Y-axis, however, data were not recorded continuously but were instead interpolated over a 25 cm

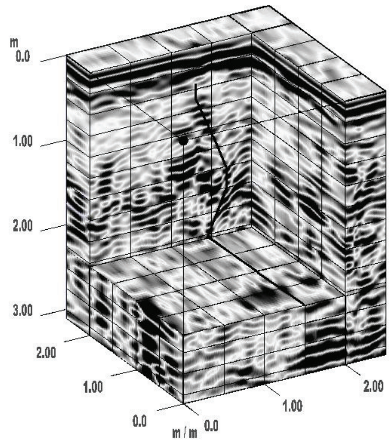

Figure 4. A 3D pseudo-image cube of the Dorchester grid area, with a 2.0 by 2.0 by 2.3 m inset removed.

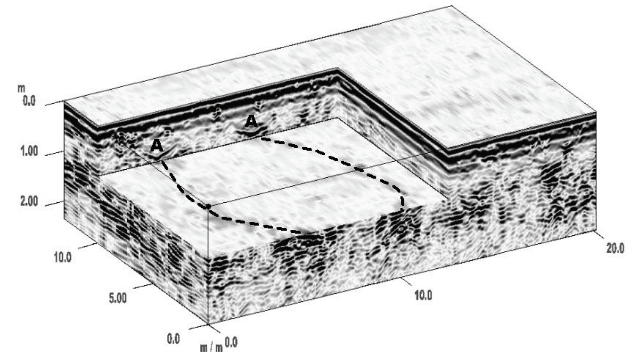

Figure 5. A 3D pseudo-image cube of the Unexpected grid area has subsurface furrows. In this image, a 12.0 m× 10.0 m× 1.0 m inset has been removed.

interval (the distance between radar traverses). As a result, some subsurface information was lost during interpolation, and features appear smudged, less resolved, and more generalized along the Y-axis.

In Figure 4, a bold dashed line emphasizes the inferred centerline of the ancient sand-wedge cast on the back wall and base of the cutout section. The wedge is more evident on the back wall of the cutout. Along its base, only a very weakly expressed and ambiguous trace of very low signal amplitudes (white color) marks the inferred location of the wedge. This frost crack, while evident, was not clearly expressed on either the 2D radar records or the 3D pseudo images prepared from data collected with the 400 MHz antenna. Interpretations are ambiguous and, without knowledge of its location, the fissure may have been missed using GPR. Older sand-wedge casts often defy visual detection as well, requiring careful site preparation and prior familiarity with feature identification. Wedge borders are often faint, with little contrast between infill and enclosing sediments. Wedge outlines may not be fully apparent until hours after excavation. Upon exposure to air, the loose sandy infill dries more rapidly than denser enclosing sediments, creating visible differences in tonal contrast.

Unexpected site

At the Unexpected site, two small grids were established near areas of known cryogenic macrostructures. One grid was established near an area underlain by younger sand-wedge casts and soil wedges that were traced backward and downslope along an excavation wall. Figure 5 is a 3D pseudo-image of the 20 m × 13 m grid area. In this image, the excavation wall parallels the X-axis (right foreground). A 12.0 m × 10.0 m × 1.0 m inset has been removed. All radar traverses were conducted parallel to the X-axis.

The grid was established across an area recently cleared of forest vegetation. In Figure 5, the occasional, high-amplitude, hyperbolic reflections apparent in the upper 70 cm of the image may represent larger tree roots. In general, subsurface reflectors apparent in this pseudo-image suggest the dominance of linear, level to slightly inclined interfaces. These reflectors are presumed to represent the boundaries of contrasting stratigraphic layers within the fluvial sediments.

Along the back wall of the cutout, two perceptible, high-amplitude concavities with downturned reflection patterns are apparent at depths ranging from 70 to 100 cm (“A” in Fig. 5). These features probably represent a continuation of the younger sand-wedge casts clearly visible in the front-wall exposure. Though discontinuous, faint, and somewhat ambiguous, these structures appear to form lineations that extend across the base of the cutout. These lines appear to represent the traces of wedges running parallel to the slope. Beneath the traces are areas with more complex reflector patterns on the front wall of the diagram (right foreground). This plot represents a front-to-back view of a transitional zone, in which sediments that formerly contained little ice (foreground) grade into those that were once ice-rich (30 m beyond the study plot)(Demitroff 2007).

Thermokarst involutions observed by French & Demitroff (2001) and French et al. (2005) were just 30 m downslope from the back of this study plot. Fissures, marked in bold dashed lines on Figure 5, are oriented directly toward these deformed sediments. Recent excavations in this vicinity revealed a younger sand-wedge cast (Fig. 1B) superimposed upon a load-deformed portion of an involution (Demitroff 2007). The underlying thermokarst-affected layer appears to have been deformed by thawing of an ice-rich wedge aligned with the slope-oriented fissures demarcated on the radar image. Older frost cracks appear to have been modified along a moisture gradient. Forms are modified gradually along such gradients, from sand wedges to deformed wedges to thermokarst involutions. Younger sand-wedge casts and soil wedges are little deformed, because thermokarst appears not to have developed during late Wisconsinan (OIS-2) warming (French et al. 2007). Although linkages may be extrapolated from the radar image, their true relationships will soon be revealed as the intervening 30 m of forest is removed and quarrying continues. In the Pine Barrens, younger wedge structures commonly form within earlier cryogenic macrostructures, as these are the most likely locations for

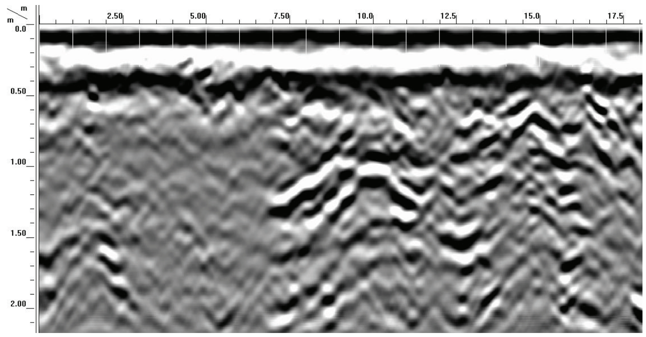

Figure 6. The radar record from the Line Y =10 m at the second Unexpected site.

stress to be relieved during episodes of cracking.

At the Unexpected site, a second grid was established near an exposure containing soil wedges, modified sand wedges, and sediment-filled pots. An 18 m section of a radar record from this site is shown in Figure 6. The number, intensity, and geometry of subsurface reflectors vary across this radar record. The left part of this diagram is comparatively devoid of high-amplitude reflectors, and may be underlain by more homogenous and less anisotropic materials. The right part of this diagram contains multiple, irregularly shaped and sized reflectors, which form a distinct zone about 10 m wide. However, most individual reflectors within this zone are less than 2 to 3 m wide.

The number and complexity of reflectors confound individual interpretations. It is assumed that this portion of the radar record consists of multiple strongly deformed layers and inclusions of soil materials that vary in grain-size distribution, moisture content, and/or density. This portion of the radar record is believed to represent a complex of cryogenic macrostructures. The difficulty in using a planar view is the diverse orientations of many wedge-like features. If viewed from an oblique angle, the radar image may be difficult to interpret. In some cases, the upper portion of a wedge may be perpendicular to the ground, and the lower portion sharply angled.

Figure 7 is a 3D pseudo image of a 20 m × 15 m survey area at Unexpected. In Figure 7, all radar traverses were conducted parallel to the X-axis (right foreground). The base of the cutout contains a diversity of both linear and curved features that vary in width and are not evenly distributed beneath the grid area. Linear features were interpreted as representing deformed wedge furrows (Fig. 2A). Large circular-to-elongate patterns evident on the base of the cutout are interpreted as sediment-filled pots (Fig. 2B).

Figure 8 documents the excavation wall when it had progressed midway across the former GPR grid site. Several well-defined deformed wedges (1st, 2nd and 5th arrows, left to right) and sediment-filled pots (3rd and 4th arrows) are exposed in the pit wall (Fig. 8). Dark patches mark their presence along the diagonal line. The fifth feature is just outside the study bounds. These features support earlier GPR interpretations. The loose, light-colored, aeolian structure-fill markedly contrasts with the indurated, orange/

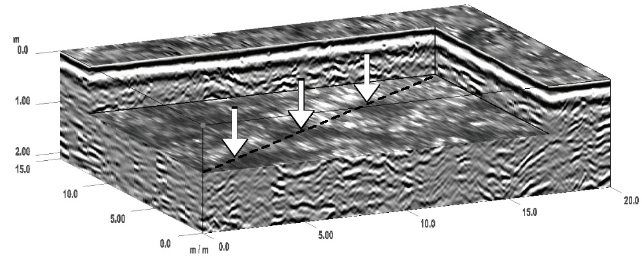

Figure 7. A 3D GPR pseudo-image from the grid site. In this image of the 20 m x 15 m survey area, a 17 m x 12 m x 0.95 m volume has been removed. The dashed diagonal line indicates the location of the wall section of Figure 8 when the photo was taken. Three white arrows mark the location of sand-filled cryogenic macrostructures marked by the inner arrows on Figure 8.

Figure 8. The second Unexpected site with half the soil diagonally removed by excavation. Arrows indicate the locations of larger (eolian) sand-filled cryogenic macrostructures. Smaller periglacial structures occupy the intervening space.

red-colored host materials. Here, the macrostructures are infilled with fine to medium sand with some sandy gravel diamict. Their loosely packed materials contrast with the indurated enclosing matrix of sands and gravel (French et al. 2003). The indurated layers helped to preserve these features as permafrost thawed (French et al. 2005).

Conclusions

GPR has been used extensively in glacial and periglacial environments (Munroe et al. 2007, Woodward & Burke 2007), where ground ice provides sharp radar reflection contrast with other frozen sediments. Near Barrow, polygonal ice -wedge networks provided impressive geometric patterns in 3D radar images (Munroe et al. 2007). This study indicates that not all paleoperiglacial landscapes are so amenable to ground-penetrating radar application. Relict macrostructures are problematic: (1) primary and secondary fill often provides little contrast with host sediments; (2) subsequent, often polycyclic, modification creates complex, indistinct boundaries; (3) many relict structures are smaller than their Arctic counterparts; and, at least in the Pine Barrens, (4) complete geometric expression of frost-crack polygons is absent. Although rarely observed in plain view, deformed wedge/furrows may form incomplete polygons or lineations parallel to the slope gradient. The absence of well-defined polygons in the uplands indicates that conditions were marginal for their development (French et al. 2003).

Ground-penetrating radar can be used to help locate and characterize various buried cryogenic macrostructures. Uplands of the Pine Barrens are a protean landscape, an epigenetic tableau that was repeatedly subjected to the waxing and waning of ice-marginal periglacial conditions. The broad suite of composite cold-climate structures present can be baffling, even with careful field scrutiny by experts. In the absence of heavy excavation equipment, the well-developed dense fragipan of the Pine Barrens drastically limits a three-dimensional perspective of cryogenic macrostructures. In lieu of arduous quarrying, radar records are a useful tool for use in identifying the presence, size, and directional trend of generic structures. However, only careful excavation can reveal a structure's origins with certainty.

The study areas have favorable soil properties (i.e., low in clay, soluble salt, and moisture content) for the use of GPR. The features under investigation often lack sufficient contrast and/or have geometrical forms that limit the amount of energy that is reflected back to the radar antenna. Owing to the limited size and complexity of many cryogenic macrostructures in southern New Jersey, some of these features are more difficult to recognize than in other regions such as in Wisconsin (Doolittle, unpubl.).

In southern New Jersey, older sand-wedge casts are narrow and indurated, making detection by GPR alone difficult. Delineation is often problematic even under visual scrutiny in pit sections. The steep inclination and tortuous nature of the wedges produces weak, nearly indistinguishable reflections that are difficult to trace laterally in plan view and preclude recognition of the full extent of their traces. Narrow wedges can be indistinguishable on radar records. Wider deformed sand wedges and related thermokarst features are much more amenable to interpretation. These structures are more nearly linear and are often slope-aligned, producing recognizable GPR images. Boundaries between cryogenic macrostructures and host sediments can be complicated where sloughing of sediments and reworking from the sides has occurred through thaw erosion, gullying, and slumping, especially with deformed wedges and sediment-filled pots. Intricate arrangements of segmented, inclined, or contorted subsurface reflectors, separated by abrupt vertical fissures, may serve to identify these features on radar records.

Acknowledgments

Students from the University of Delaware Geography and Geology Field Geomorphology course in Spring 2006 provided field assistance. Aggregate extraction operations access was kindly provided through Dave Hergert (Mays Landing Sand and Gravel) and another operator who wishes to remain unacknowledged. MD thanks both for long-term support of his field investigations. Manufacturers' names are provided for specific information, and use does not constitute endorsement.

References

Daniels, D.J. 2004. *Ground Penetrating Radar*, 2nd Edition. London, UK: The Institute of Electrical Engineers, 726 pp.

Demitroff, M.N. 2007. *Pine Barrens Wetlands: Geographical Reflections of South Jersey's Periglacial Legacy.* Masters Thesis. University of Delaware, Newark, DE, 224 pp.

French, H.M. & Demitroff, M. 2001. Cold-climate origin of the enclosed depressions and wetlands ('spungs') of the Pine Barrens, southern New Jersey, USA. *Permafrost and Periglacial Processes* 12: 337-350.

French, H.M. & Demitroff, M. 2003. Late-Pleistocene periglacial phenomena in the Pine Barrens of southern New Jersey: GANJ Field Excursion Guide, October 11, 2003. In: M.J. Hozik & M.J. Mihalasky (eds.), *Field Guide and Proceedings, 20th Annual Meeting of the Geological Association of New Jersey, October 10-11, 2003*: 117-142.

French, H.M., Demitroff, M. & Forman, S.L. 2003. Evidence for Late-Pleistocene permafrost in the New Jersey Pine Barrens (Latitude 39°N) Eastern USA. *Permafrost and Periglacial Processes* 14: 259-274.

French, H.M., Demitroff M. & Forman, S.L. 2005. Evidence for Late-Pleistocene thermokarst in the New Jersey Pine Barrens (Latitude 39°N) Eastern USA. *Permafrost and Periglacial Processes.* 16: 173-186.

French, H.M., Demitroff M., Forman, S.L. & Newell, W.L. 2007. A chronology of Late Pleistocene permafrost events in southern New Jersey, Eastern USA. *Permafrost and Periglacial Processes* 18: 49-59.

Huijzer, A.S. 1993. *Cryogenic Microfabrics and Macrostructures: Interrelations, Processes, and Paleoenvironmental Significance.* Ph.D. dissertation, Vrije Universiteit, Amsterdam, 245 pp.

Jahn, A. 1975. *Problems of the Periglacial Zone* (*Zagadnienia strefy peryglacjalnej*). Translated from Polish. Warszawa, POL: Polish Scientific Publishers, 223 pp.

Munroe, J.S., Doolittle, J.A., Kanevskiy, M.Z., Hinkel, K.M., Nelson, F.E., Jones, B.M., Shur, Y. & Kimble, J.M. 2007. Application of ground-penetrating radar imagery for three-dimensional visualization of near-surface structures in ice-rich permafrost, Barrow, Alaska. *Permafrost and Periglacial Processes* 18: 309-321.

Murton, J. B., Worsley, P. & Gozdzik, J. 2000. Sand veins and wedges in cold aeolian environments. *Quaternary Science Reviews* 19: 899-922.

Newell, W.L. & Wyckoff, J.S. 1992. Paleohydrology of four watersheds in the New Jersey Coastal Plain. In: G.S. Gohn (ed.), *Proceedings of the 1988 U.S. Geological Survey Workshop on the Geology and Geohydrology of the Atlantic Coastal Plain*. United States Geological Survey, Circular 1059, 23-28.

Romanovskij, N.N. 1985. Distribution of recently active ice and soil wedges in the USSR. In: M Church & O. Slaymaker (eds.). *Field and Theory: Lectures in Geocryology.* Vancouver, BC: University of British Columbia Press, 154-165.

Wolfe, P.E. 1953. Periglacial frost-thaw basins in New Jersey. *Journal of Geology* 61: 133-141.

Woodward, J. & Burke, M.J. 2007. Applications of ground-penetrating radar to glacial and frozen materials. *Journal of Environmental and Engineering Geophysics* 12(1): 69-86.

Tomodensitometric Analysis of Basal Ice

Matthew Dillon, Daniel Fortier, Mikhail Kanevskiy, Yuri Shur
University of Alaska Fairbanks, Institute of Northern Engineering, Fairbanks, Alaska, U.S.A.

Abstract

Basal ice of contemporary glaciers was studied in an attempt to find convincing evidence of a genesis of buried glacial ice in permafrost. As a part of this study, tomodensitometric scans of basal ice from the Matanuska Glacier in Alaska were made using a micro-computed tomographic scanner. Scans are an excellent complement to field studies of cryostructures because of the level of detail obtained regarding the ice distribution. Two- and three-dimensional models were generated from the scans and were used to study patterns of ice distribution, the volume of ice, sediment, and gas inclusions.

Keywords: basal ice; buried glacial ice; computed tomography; cryostructure; Matanuska Glacier; x-ray.

Introduction

X-ray computed tomography, also known as tomodensitometry, has been widely used in two- and three-dimensional (3-D) visualization of the internal structures of various materials since its inception (Ambrose & Hounsfield 1973). Tomodensitometry is a computer-controlled x-ray photography procedure. By taking a single x-ray photo from multiple angles, a 3-D interpolation of the interior of the sample can be revealed. Tomodensitometry usage is expected to undergo sustained growth due to the relatively low cost of scanner apparatus, the non-destructive aspect of its application, the clear penetration of x-rays into samples, and the high resolution imaging potential related to advances in computing power. One of the immediately recognizable benefits of tomodensitometry is that it is a non-destructive technique. Non-biological objects, such as soils, remain structurally unaffected by x-ray radiation.

In soil sciences, tomodensitometry has been used in multiple ways. Porosity has been calculated by separating phase components post-scanning by Alshibli et al. (2006) and Rachman et al. (2005). By various methods, many typical soil index properties have been determined, such as bulk density distribution, water content distribution, and mineral type distribution (Phogat et al. 1991, Macedo et al. 1998, Rogasik et al. 1999, Pralle et al. 2001, Pedrotti et al. 2004). Computer simulations using real-world geometries of soils for determination of hydraulic conductivity have been performed by Fourie et al. (2007) and Bastardie et al. (2003).

In fresh-water ice studies, tomodensitometry has been used to characterize air inclusions in river ice to aid in synthetic aperture radar interpretation of river ice (Gherboudj et al. 2007).

In permafrost studies, Torrance et al. (in press) used tomodensitometry to study the pattern of ice lenses in soil. Calmels et al. (2004, 2008) used tomodensitometry to image faulted ice and sediment layers in palsas, to infer direction of soil freezing and to provide volumetric content of ice, gas, and sediment components. The thresholding technique used to determine the volumetric contents and the error associated with it has not, however, been specified.

This paper presents some results of tomodensitometric studies of basal ice of glaciers. To the best of our knowledge, this is the first time that this technique has been used to study the structure of basal ice of glaciers. Basal glacier ice is formed at the bed of glaciers due to several processes, such as entrainment and incorporation of sediments by overriding ice, regelation, glacio-hydrologic supercooling, glaciotectonics, basal freeze-on, ice segregation, and downward propagation of cold temperatures in the sediment at the glacier bed (Sharp et al. 1994, Knight 1998, Lawson et al. 1998). We want to develop a classification of basal ice cryostructures for permafrost studies to identify and to distinguish basal glacier ice buried in the permafrost from other types of massive ice (e.g., massive segregated ice and injection ice); however, this paper only addresses the application of tomodensitometry to basal ice analysis. It is focused mainly on the technical aspects of 2-D and 3-D imaging of the samples in order to extract key parameters such as basal ice structure and the volumetric contents of its phase components.

Methods

Sampling

Field work was conducted at the Matanuska Glacier, Alaska (61°46′11″N, 147°44′3″W). We logged, sketched, and photographed the cryofacies and cryostuctures of several basal ice exposures. The description of the basal ice cryostratigraphy is beyond the scope of this paper, and those results will be presented elsewhere. Cores were retrieved from the exposures using a CRREL-SIPRE corer barrel. The cores were covered in plastic wrap and aluminum foil and brought back frozen to the laboratory.

In the lab, cores approximately 50 mm in diameter and 50 mm tall were extracted from the large-barrel cores to accommodate the maximum sample size that the scanning equipment can accept. These smaller cores were wrapped in plastic wrap to prevent sublimation, as well as in cellulose insulation, encased in a hollow plastic container, and kept in a freezer at -10°C

Tomodensitometry

The scans were acquired with a Skyscan 1172™ scanner, equipped with a rotating scan platform, a stationary camera, and an x-ray source. The scans were commenced in a cold room environment at -6°C. In order to ensure adequate "penetration" of the x-rays through dense materials, the scans were performed at 80 kV and 100 µA, the highest voltage and current permitted by the system. An exposure time of 1264 ms, a rotation step of 0.3°, and a scanning domain of 360° were experimentally determined to maximize scan quality. The camera's pixel size was 34.46 µm.

Image processing methods

The scanner results are a "stack" of grayscale images that represent the total volume for the sample. Reference volumes 27.57 mm high by 27.57 mm wide by 13.71 mm deep were selected from each scanned core for streamlined analysis. The resized samples had a pixel size of 68.93 µm. Each image is 400 pixels by 400 pixels and 1 pixel thick. One unit pixel in the image is also called a voxel for 3-dimensional image data. Each voxel is assigned a grayscale value based on its density relative to that of gas—low density values are black pixels with a grayscale value of 0; high density values are white pixels with a grayscale value of 255. All the shades of gray vary linearly between grayscale values of 0 and 255. The Mathworks MATLAB R2007a™ Image Processing Toolbox software was used to process the volume's grayscale values that are obtained from the scanner.

The samples contain three components: gas, ice, and sediment. These components were separated in the scans using a thresholding technique which reassigns a range of

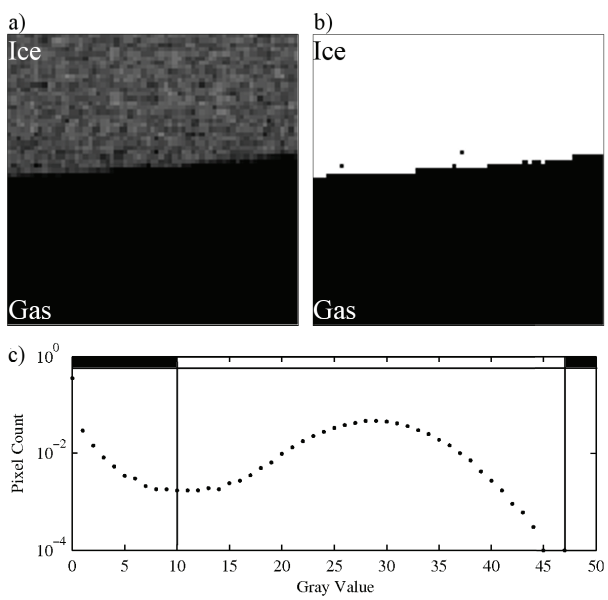

Figure 1. Scan images of an ice cube edge made of de-aired and de-ionized water. a) Cross sectional scan image of ice and gas before thresholding (varying gray values represents ice, black is gas). b) Cross sectional scan image of ice and gas after applying threshold limits at 10 and 48. c) Histogram of grayscale values for the cross section, threshold limits of 10 and 48 define grayscale values for ice.

grayscale values to white, while everything outside of this range is black. Threshold values were determined from the grayscale histogram on scans of ice made of de-aired and de-ionized water (Fig. 1a). By determining the minima of the gray values on the histogram (Fig. 1c), the limits of thresholding can be applied at these points for a binary image (Fig. 1b). For this study, ice was found to generally range between 10 and 48 in grayscale values, based on several scans of pure ice. Therefore gas was defined as 0–9, ice as 10–48, and sediment as 49–255 grayscale values. The threshold values were applied to the raw scan images (Fig. 2a) to create component reduced images (Fig. 2b).

Volumetric content profiles of gas, ice, and sediment were generated in an iterative process by thresholding each individual slice. Microvariations with height were derived by obtaining a content profile for a cryostructure. The volumetric contents for each component were then calculated using

$$\%Volume_{component} = \frac{\Sigma Voxels_{x-y}}{\Sigma Voxels_{0-255}} \qquad (1)$$

where x and y are the range of grayscale values for the component (0–9 for gas, 10–48 for ice, 49–255 for sediment).

We created 3-dimensional models in MATLAB from the 2-dimensional cross section images (Fig. 3). To smooth the data for enhanced processing, and to attempt to account for the partial volume effect (the probability that more than one phase can exist in a single voxel), cross sectional images were eroded and dilated with a kernel of 1 pixel in 2-D (Fourie 2007). The models were created using the "isosurface" function, which creates a three-dimensional contour line representing an area of constant density.

Volumetric component content profiles for two samples are presented in Figure 4. A set of profiles for each component was generated for each sample by determining the percent area occupied by each component in each cross sectional image. By calculating the average for each component profile in each sample, an approximation of the sample's typical component contents was determined. The standard error, σ_{mean}, was calculated by using the standard error of the mean method

$$\sigma_{mean} = \frac{\sigma}{\sqrt{n}} \qquad (2)$$

where σ is the standard deviation of the profile, and n is the number slices in the profile.

Results

Many samples with different cryostructures were sampled and scanned, but for the sake of illustration, only one cryostructure will be presented. This type of cryostructure is called *suspended-intergranular* (Fortier et al., in submission) which defines a cryostructure with the sediments located between ice crystals. Two samples (I and II) of this basal

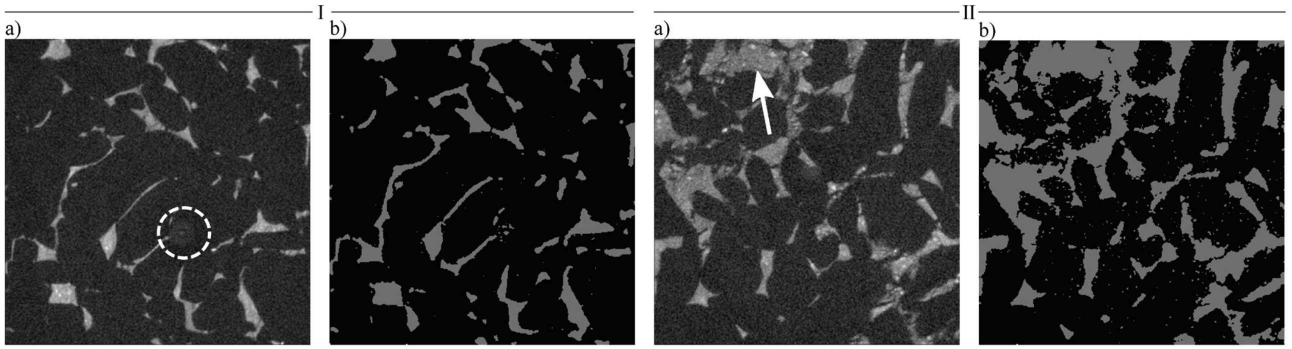

Figure 2. Cross sections from 2 scans of basal glacier ice. a) Raw scans of suspended-interganular cryostructure. Coarser and denser mineral grains are observable (arrow). A ring artifact (circle) is observable on both scans; b) processed images after thresholding showing the three phase components (air is not visible in images at this scale).

ice are presented in Figure 2. Both samples are very ice-rich with volumetric amount of ice 86% for sample I and 66% for sample II.

Figure 2a for both samples shows a raw scan image of the suspended-intergranular cryostructure. In the upper left corner of Figure 2a for sample II, the various mineral grains (see arrow) in the sediment may be observed due to the varying densities as reflected in the grayscale. A ring artifact (circle) is observable on the raw scans, as well (Fig. 2a, sample I).

After applying the threshold values, the complexity of the scan image may be decreased by reducing it into its 3 phases for structural analysis. Figure 2b for both samples shows the results of thresholding. The grey, black, and white represent the sediment, ice, and gas, respectively. Gas bubbles (white) are hardly visible due to their small size and low concentration. The ring artifact has been suppressed by the thresholding technique in Figure 2b.

Figure 3 is a series of 3-D models of the samples with the suspended intergranular cryostructure presented in Figure 2. Figure 3a models the ice, sediment, and gas components together. Figure 3b models the ice component only and shows the ice-rich nature of the samples. Figure 3c models the sediment component only and shows that the sediments are located in between the sub-rounded grains of ice (or ice crystal aggregates).

By applying Equation (1) to each cross section, volumetric profiles for the samples were produced (Fig. 4). The total volume of each phase is given for each cross section (because each cross section has a thickness of 1 voxel) taken along the x-y plane and plotted against the vertical location. The profile for the ice (Fig. 4a) shows a 10% decrease and a 20% increase in ice content from the bottom to the top of samples I and II, respectively, while the sediment (Fig. 4b) shows a 10% increase and a decrease of 20% in samples I and II, respectively. The gas (Fig 4c) remains close to constant (0.10–0.20% and 0.25–0.55%, I and II, respectively) in content which indicates a fairly uniform distribution in the samples. By applying Equation 1 to the entire reference volume, the total volumetric content for each phase was determined (Table 1).

Table 1. Average volume per component and associated error.

	Component Volume (%)		
	Ice	Gas	Sediment
Suspended Intergranular I	85.50±0.16	0.16±0.01	14.34±0.16
Suspended Intergranular II	66.05±0.38	0.38±0.01	33.58±0.39

Discussion

Settings should be consistent, because scan results are highly dependent on the scanner settings. Appropriate settings for voltage, current, pixel size, and exposure time must be determined via calibration with a known substance, such as pure ice.

Ice scans, however, require a sub-freezing temperature-controlled environment to avoid thawing of the sample during testing. Under these conditions, detailed testing and evaluation of an individual sample can be repeated. This is a challenging operation because temperatures colder than -6°C often resulted in mechanical problems in the scanner apparatus, such as the sample stage freezing in place instead of rotating, and the sample door freezing open.

By using a computational software package, such as MATLAB™, quantification of the phase components is a powerful alternative to traditional destructive lab techniques, such as oven drying of samples.

Thresholding effects

Determination of appropriate levels for thresholding is the most critical aspect to this study, as well as the most difficult. Under- and over-estimation of a component can occur if the selected threshold range is too small. While calibration with ice serves as a good reference point, it is not perfect. Scan output data is based on the attenuation of x-rays through a sample; however, the attenuation is not only dependent on the material it is passing through, but on the surrounding materials at any given point, as well. The results of overestimating the selection are exemplified by the slight difference in the boundaries between the ice and sediments in Figure 2b.

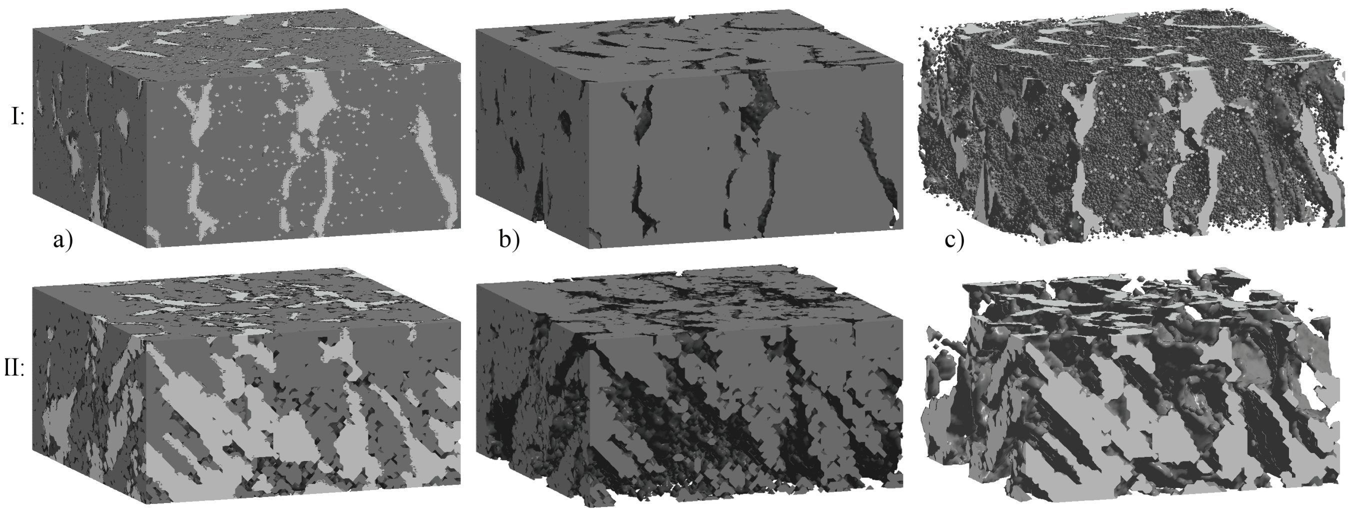

Figure 3. Three-dimensional images created for samples I and II. a) Combined ice and sediment, b) ice component, c) sediment component. Volume dimensions: 25.57 mm by 27.57 mm by 13.71 mm. It is important to note that the 3-D renderings have lighting effects on them. This creates the shading observable on the models which make it possible to distinguish depth in the image.

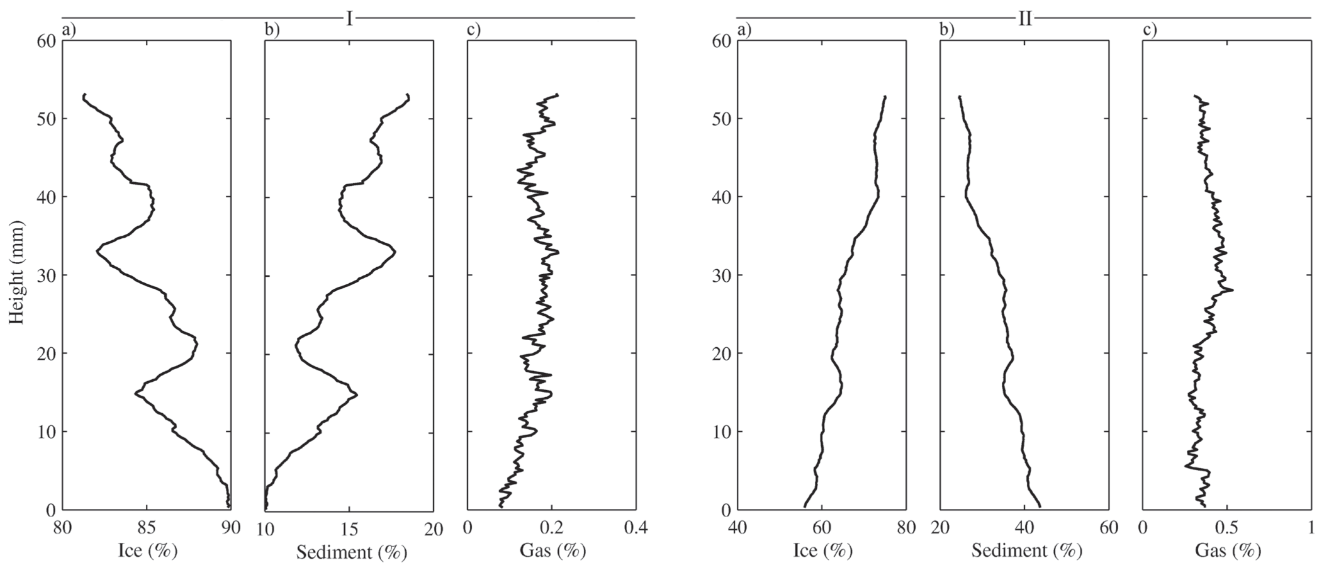

Figure 4. Volumetric content of ice, soil, and gas phases in samples I and II with suspended-intergranular cryostructure.

Cryostructure visualization and phase component quantification

Traditionally, cryostructures are evaluated and classified via visual inspection, typically from cores of frozen soil. When viewing an exposure, the investigator is usually limited to a 2-D view of the cryostructure. The scanner results can be viewed in 2-D "slices," which allow for an in-depth comparison with detailed exposure descriptions from the field.

After applying the limits of thresholding to the cross sections, it became easier to focus on the general structures and patterns in each sample. However, identification of mineral grains is not possible anymore because the thresholding lumps the full range of mineral densities together. A solution to this would be to apply more threshold limits in a series of steps, to show varying degrees of mineral density, however, this study focused on the cryostructure of the sample, so this was not performed. Thus, a side-by-side analysis of the raw scans images and the images with thresholding in 2-D is very beneficial. For instance, Figure 5 shows well the presence of sand grains in the sediments which can not be observed on a processed image. On the other hand, visualization of gas bubble distribution in a section is better realized with a processed scan signal.

Visualization of cryostructures was greatly aided by utilizing both cross sectional images, and 3-dimensional isosurfaces. Three-dimensional spatial relationship between the phase components is a great advantage of tomodensitometry, because of the ease of generating 3-dimensional models. Gas bubble distribution in ice has traditionally been a very difficult subject to study, because of the inherent problems and time requirements related to generating thin sections

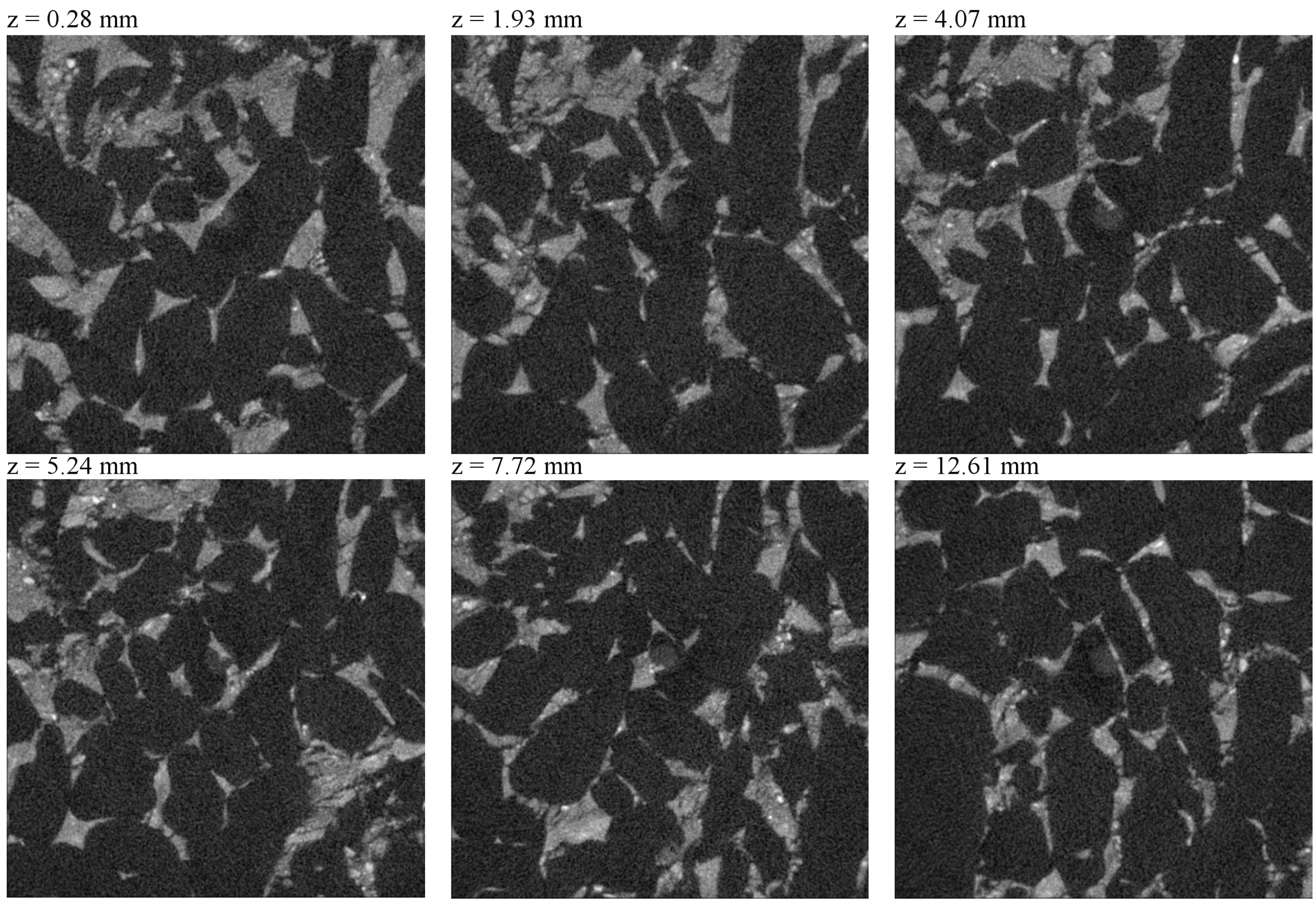

Figure 5. Sequence of cross sectional height for sample II with suspended-intergranular cryostructure. Dark areas are less dense materials such as gas and ice, while light areas are denser, such as different minerals in the sediments. All image dimensions are 27.57 mm by 27.57 mm. The position of a cross section in the sample is denoted by the "z" measured from the bottom of the sample.

(Gherboudj et al. 2007). The cross sectional images show the spatial distribution of components against each other. By comparing cross sections throughout an entire sample (Fig. 5), evaluation of structure and phase component variation along the sample's height is possible.

Understanding how components relate and are distributed in a volume is easily aided by the isosurfaces. These are models of the boundary between one component, and the rest of the sample. These models can "strip away" all of the other components in a sample, and isolate one to have a better representation of its 3-D structure. In Figure 3b, for instance, it can be observed that the samples are mainly composed of ice, which is typical of a suspended cryostructure. The ice content and its geometry typically vary between two samples. In Figure 3c, it can be observed that the sediment particles are located at the junction and in-between the ice grains. This is easier to see than in the 2-D scans. By analyzing a large number of samples, statistics can be derived to obtain a range of values for a given cryostructure type.

The determination of the individual components relies on the output from the thresholding of the original scan data. Once the components have been divided, the calculation of their volumetric content are found using Equation 1.

Traditionally, in the lab, methods for the calculation of volumetric ice content for frozen soil cores requires measurements of the bulk volume of a core, then oven drying the sample, determining the gravimetric water content, and determining, finally, the volumetric ice content. By utilizing the methods presented, all of the intermediate steps may be bypassed, and, the original specimen is completely preserved.

Conclusions

X-ray computed tomography can become a powerful complementary method to traditional field observations and laboratory work. Cross sectional images generated from scans may be viewed as raw images and as images with thresholding. Raw cross sections have the advantage of showing a complete picture of any plane in the sample. Cross sections that have thresholding allow for more direct interpretation of structure in the sample, which aids in cryostructure classification. Three-dimensional models reveal variations of cryostructures in three-dimensions, a key element for generating a new classification. In terms of cryostructure classification, this would be one more method in the field of cryostratigraphy.

Tomodensitometry has applications in many other cold region studies, such as evaluation of cryostructures in permafrost, and evaluation of river ice, icings, glaciers, and sea ice. Besides being an important tool for research, the practical applications for determining component contents is important in many frozen ground engineering design considerations.

Acknowledgments

We would like to thank the UAF Research Center's Undergraduate Research Symposium and Flint Hills Resources for providing funds to M.D. for this study and Alaska EPSCoR for providing support for technical training. The authors are appreciative of the support received by Skyscan, Inc. This work was supported by the USA National Science Foundation by grants EPS-0346770 to D.F. and M.K., and ARC-0454939 to M.D. and Y.S. Any opinions and findings expressed in this material are those of the authors and do not necessarily reflect the views of the funding agencies. The authors are especially thankful for the constructive comments and advice offered by the reviewer.

References

Alshibli, K.A., Alramahi, B.A. & Attia, A.M. 2006. Assesment of spatial distribution of porosity in synthetic quartz cores using microfocus computed tomography. *Particulate Science and Technology* 24: 369-380.

Ambrose, J. & Hounsfield, G. 1973. Computerized transverse axial tomography. *British Institute of Radiology* 46: 148-149.

Bastardie, F., Capowiez, Y., de Dreuzy, J.R. & Cluzeau, D. 2003. X-ray tomographic and hydraulic characterization of burrowing by three earthworm species in repacked soil cores. *Applied Soil Ecology* 24: 3-16.

Calmels, F. & Allard, M. 2004. Ice segregation and gas distribution in permafrost using tomodensitometric analysis. *Permafrost and Periglacial Processes* 15: 367-378.

Calmels, F. & Allard, M. 2008. Segregated ice structures in various heaved permafrost landforms through CT scan. *Earth Surface Processes and Landforms* 33: 209-225.

Fourie, W., Said, R., Young, P. & Barnes, D.L. 2007. The simulation of pore scale fluid flow with real world geometries obtained from x-ray computed tomography. *Proceedings of the COMSOL Conference, October 4–6, 2007.*

Gherboudj, I., Bernier, M., Hicks, F. & Leconte, R. 2007. Physical characterization of air inclusions in river ice. *Cold Regions Science and Technology* 49: 179-194.

Knight, P.G. 1998. The basal ice layers of glaciers and ice sheets. *Quaternary Science Reviews* 16: 975-993.

Lawson, D.E., Strasser, J.C., Evenson, E.B., Alley, R.B., Larson, G.J. & Arcone, S.A. 1998. Glaciohydraulic supercooling: a freeze-on mechanism to create stratified, debris-rich basal ice: I. Field evidence. *Journal of Glaciology* 44: 547-567.

Macedo, A., Crestana, S. & Vaz, C.M.P. 1998. X-ray microtomography to investigate thin layers of soil clod. *Soil & Tillage Research* 49: 249-253.

Pedrotti, A., Pauletto, E.A., Crestna, S., Holanda, F.S.R., Cruvinel, P.E. & Vaz, C.M.P. 2005. *Soil & Tillage Research* 80: 115-123.

Phogat, V.K., Aylmore, L.A.G. & Schuller, R.D. 1991. Simultaneous measurement of the spatial distribution of soil water content and bulk density. *Soil Science Society of America Journal* 55: 908-915.

Pralle, N., Bahner, M.L. & Benkler, J. 2001. Computer tomographic analysis of undisturbed samples of loose sands. *Canadian Geotechnical Journal* 38: 770-781.

Rachmanm, A., Anderson, S.H. & Gantzer, C.J. 2005. Computed-tomographic measurement of soil macroporosity parameters as affected by stiff-stemmed grass hedges. *Soil Science Society of America Journal* 69: 1609-1616.

Rogasik, H., Crawford, J.W., Wendroth, O., Young, I.M., Joschko, M. & Ritz, K. 1999. Discrimination of soil phases by dual energy x-ray tomography. *Soil Science Society of America Journal* 63: 741-751.

Sharp, M., Jouzel, J., Hubbard, B. & Lawson, W. 1994. The character, structure and origin of the basal ice layer of a surge-type glacier. *Journal of Glaciology* 40: 327-340.

Torrance, J.K., Elliot, T., Martin, R. & Heck, R.J. In Press. X-ray computed tomography of frozen soil. *Cold Regions Science and Technology*.

New Patterns of Permafrost Occurrence in a Mountain Environment, Based on an Example from the Tatra Mountains, Poland, and Abisko Area, Sweden

Wojciech Dobinski

University of Silesia, Faculty of Earth Sciences, Department of Geomorphology, ul. Będzińska 60, 41-200 Sosnowiec, Poland

Abstract

At present, research into the occurrence of mountain permafrost concentrates on its relationship to the currently changing climate. Modern research shows that in northern Scandinavia the permafrost extent is much wider than it has been believed so far. Comparative studies on the occurrence of permafrost in the Tatra Mountains and in the Abisko area concern both active and fossil permafrost. A set of geophysical research into permafrost of the Tatra Mountains and the Abisko area conducted in similar geological and climatic conditions reveals that two similar high-resistivity anomalies can be distinguished in both places. Shallower anomalies were interpreted as permafrost which is connected with current climate (contemporary permafrost). Deeper ones were interpreted in two ways: in the Tatra Mountains, as a layer of dry, much older, probably fossil permafrost, whereas in the Abisko area, as thermal differentiation within the permafrost layer occurring there, which probably indicates climate variability in the Holocene.

Keywords: Abisko; electroresistivity; fossil permafrost; geophysics; permafrost occurrence; tomography; Tatra Mountains.

Introduction

Recent decades show an increased interest in issues related to permafrost occurrence in mountain environment (Harris 2001, Gorbunov 2003, Haeberli 2003). The main research concentrates on the most current problem in earth sciences, which is climate warming and its impact on the components of earth surface. The frozen lithosphere (cryolithosphere), including seasonal snow cover, permafrost, glaciers and continental glaciers, as well as floating ice (Dobinski 2006), is the most sensitive to climate change. The predicted consequences of climate warming and their social aspect result in research being predominantly focused on the active layer and subsurface layer of permafrost.

Research into mountain permafrost in the Tatras and in Abisko is conducted in areas where permafrost occurrence is relatively poorly recognized (Svensson 1986). As a result, the main aim of this project is to determine permafrost extent and its forms of occurrence, its geophysical properties, probable origin and evolution and its relationships to the warming climate.

The first results of the research conducted in the Abisko area were presented last year (Dobinski 2007). Here a new hypothesis of permafrost occurrence in mountainous areas will be presented, based on geophysical data collected by the author and published last year.

Location

The survey areas—the Abisko Mountains (A) and the Tatra Mountains (B)—are located far away from each other, at a distance of 2100 km (Fig.1). Despite a relatively big latitude gradient, both areas of detailed surveys have properties that suggest the necessity of comparing one to the other. Two meteorological stations operating in the Tatras indicate a mean annual air temperature (MAAT) similar to the one in the survey area. The MAAT of Kasprowy Wierch stands at -0.8°C at the altitude of 1986 m a.s.l. and of Łomnicki Szczyt at -3.8°C at the altitude of 2632 m a.s.l. (Dobinski 1997, Niedzwiedz 1992) In the Abisko area, close to the research station ANS at the altitude of 388 m a.s.l., MAAT stands at -0.8°C and in the mountainous areas nearby, it drops to -4.0°C (Ridefelt & Boelhouwers 2006, Jonasson 1991). Nearby Tarfala Research Station (1151 m a.s.l.) has MAAT of -3.9°C, which is similar to the one measured on Łomnicki Szczyt.

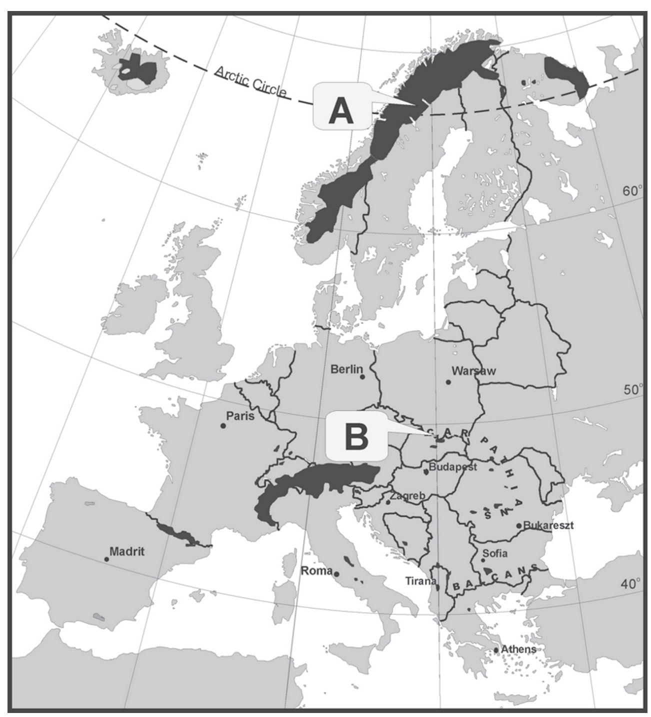

Figure 1. Location of the research areas within the map of mountain permafrost in Europe (modified from Dobinski 2005).

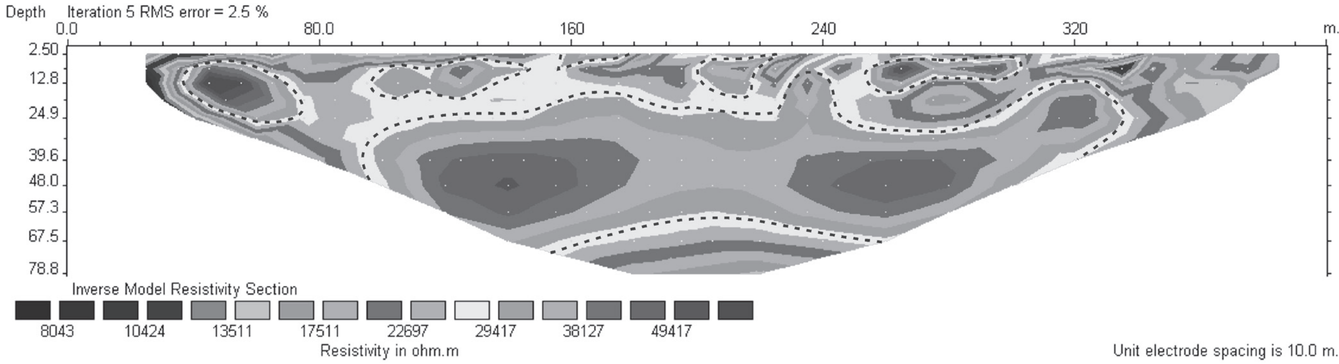

Figure 2. ERT profile performed on the mouton in the Abisko area. High-resistivity anomalies surrounded by the dashed line. Note high-resistive area at a depth of 25–65 m.

Nearby Tarfala Research Station (1151 m a.s.l.) has a MAAT of -3.9°C, which is similar to the one measured on Łomnicki Szczyt.

Both of these mountain regions underwent glaciation several times in the Pleistocene. It finished about 10,000 years BP in the Tatra Mountains (Baumgart-Kotarba & Kotarba 1995) and about 9,000 years BP in the Abisko area (Karlen 1979). Glaciation significantly altered the relief of the areas; in the final stage of evolution they were affected by periglacial processes, which ultimately shaped their relief. A considerable difference between the two areas observed in their topography lies mainly in the difference in relative altitude. In the Tatras, relative altitudes are much higher and due to this fact the mountains are steeper than the ones in the Abisko area. Such a topography results in lower dynamics, compared to the Tatras, of geomorphological processes occurring in the Abisko Mountains at present. Steep slopes in the Tatra Mountains, dominating above the permanent snow line, prevent formation of glaciers.

Geophysical surveys in northern Sweden were conducted on a granite mouton—a tor-like bare rock polished by the glacier—(ca. 450 m a.s.l.) located about 20 km west of Abisko, ca. 200 m north of the Kiruna–Narvik Road, near the Bjorkstugans station, beyond the exact mountain area. This mouton, not very high and with a bit fractured surface, was chosen as a particularly suitable area to be compared with the granite dome of Kasprowy Wierch, the Tatras, Poland, where electroresistivity and electromagnetic profiling was also performed. The mouton is slightly covered with glacial blocky deposits which accompany a slightly weathered *in situ* granite. It is partly overgrown with moss and grass, and wherever there are more deposits, a process of frost sorting can be observed. In Poland, the surveys were carried out on the dome summit of Kasprowy Wierch, which is also built of granite and has a 4 m thick cover weathered *in situ* in periglacial conditions and which is mostly overgrown with grass.

Methods

The following geophysical methods were applied in the surveys on the occurrence of mountain permafrost in the Abisko area and the Tatras: one-dimensional (1D) DC resistivity soundings (e.g., Vonder Mühll 1993), two-dimensional (2D) resistivity tomography (e.g., Kneisel 2006), shallow and deep electromagnetic soundings (EM) (Hauck et al. 2001), and measurement of bottom temperature of the winter snow cover (BTS) (Haeberli 1973). Such methods are quite commonly used in geophysical surveys on detection and mapping of permafrost in a mountain environment and can be said to be standard at present (Vonder Mühll et al. 2001, Hauck 2001).

Abisko area, Sweden

Two intersecting electrical resistivity profiles were carried out in the NS and WE directions. The WE profile was 200 m in length and had electrodes spaced at 2.5 m intervals. Suitable terrain conditions and the assumptions underlying the survey, which aimed at detection of permafrost at a considerable depth, resulted in the second profile being carried on the distance of 400 m, with electrode spacing of 10 m (Fig. 2). The electromagnetic method was chosen under similar assumptions. In the surveys, a EM-34 conductivity meter with a variable transmitter-receiver spacing was used, which allowed reaching the depth of about 80 m below the ground surface.

Kasprowy Wierch, Tatra Mountains, Poland

On Kasprowy Wierch, two 200 m 2D electroresistivity tomography with electrodes spaced at 2.5 m intervals and shallow electromagnetic sounding surveys were carried out. One of the ERT profiles was located above the tourist path and ran along it, while the other descended from the summit. Additionally, BTS temperature measurements were made on the summit dome and in the surrounding area.

Results

Mouton in the Biorkstugans area, Abisko.

The interpretation of the second profile, running N-S, reaches the depth of almost 80 m, and it presents a significant variation in resistivity values, but they all occur in a high value range. Note that the interpretation of the research in the second ERT profile probably did not include the active layer, the thickness of which in such an environment varies

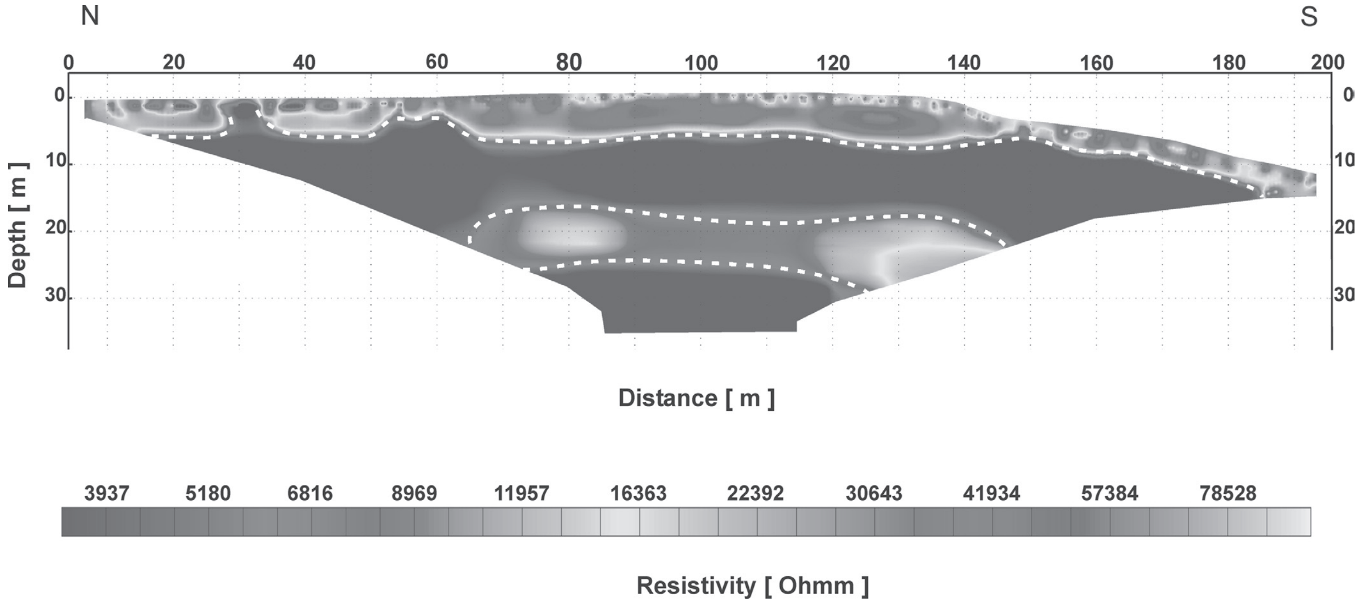

Figure 3. ERT profile performed on Kasprowy Wierch. High-resistivity anomalies surrounded by the dashed line. Note high-resistive area at the depth 15–25 m, and different vertical scale. (Due to appear in Hauck, C. & Kneisel, C. (in press), *Applied Geophysics in Periglacial Environments*. Cambridge University Press, reproduced with permission.)

between 1.5–2.5 m (Knutsson 1980) or more. At a depth of 3–15 m, a series of high-resistivity anomalies can be observed; their resistivity values range between 30 and 50 kOhmm, and they form an unclear layer. Below the depth of 25 m resistivity drops to around 20–30 kOhmm and it increases again to 30–50 kOhmm at the depth between 30 m and 60 m. In deeper places, resistivity falls again to stand at about 17 kOhmm or more. Lower resistivity values, below 10–13 kOhmm, are registered exclusively on the edges of the survey site; that is, in the places where the area could have been locally watered, as there is a river flowing nearby and the terrain there is wet. The profile does not show any anomalies characteristic of deep fractures. The image of the two high-resistivity anomalies, especially the deeper one, has a characteristic, more or less horizontal course.

The results are supported by deep electromagnetic soundings made by means of EM-34 conductivity meter. The findings of these surveys reveal variation in electromagnetic conductivity in various depths. The map of electromagnetic conductivity created for the depth of 15 m shows very little variation in values within the 3.2–4.0 mSm range. At the depth of 30 m, conductivity falls to 1.7–2.1 to rise again to 8.4–11.0 mSm at the depth of 60 m.

Kasprowy Wierch, Tatra Mountains, Poland

In the 2D resistivity tomography (Fig. 3) made on Kasprowy Wierch, two distinct high-resistivity anomalies can be distinguished. The first one, of a horizontal course, is discontinuous, and its fragments come over the surface. Electrical resistivity interpreted in it indicates the values from 30–90 kΩm. Such high electrical resistivity is characteristic of both: coarse blocky cover with numerous air voids and of places of permafrost occurrence (Dobinski et al. 2006, Vonder Mühll 2001).The layer is 3–4 m thick and its upper end is at a depth of 1–2 m. The horizontal arrangement of anomalies can be regarded as permafrost, whereas single, small, high-resistivity anomalies which come over the surface are probably air voids in blocky-cover. The layers below the delineated limit can be treated as a homogenous granodiorite massif with characteristic resistivity of approximately 4 kΩm. In its upper sections there can be fractures. In the massif, at the depth of 15–25 m, another high-resistivity anomaly, of 15–60 kΩm resistivity can be identified.

BTS temperatures measured on the summit dome of Kasprowy Wierch range from -2.7°C in the place of southern exposure, to -3°C on the summit, to -3.2°C in the place of slight northwest aspect (Dobiński 2004). In both places**,** high-resistivity anomalies running near the surface and much more deeply are observed. The shallow ones can be interpreted as active permafrost**;** the one connected with contemporary climate, where ice may occur. If we accept a highly probable assumption that geological structure in the survey sites, which are built of granite, is uniform, the change in resistivity and electromagnetic conductivity values should be mainly attributed to physical factors other than petrographic variety of rocks. A deep fracture would be accompanied by the infiltration of water of meteoric origin (Kasprowy Wierch) and of water coming from the stream and small water reservoirs near the mouton (Abisko). Such a change would rather lead to a decrease in resistivity values due to permafrost degradation and higher conductivity of water.

Discussion

Resistivity values and those of electromagnetic conductivity which occur on the mouton in the Abisko area, as well as resistivity values and BTS temperatures in the

Tatra Mountains, indicate that in both places high-resistivity anomalies should most likely be interpreted as permafrost occurrence, which would comply with the recent findings on permafrost occurrence in the Abisko area (Johansson et al. 2006) and in the Tatras (Dobinski et al. 2006). The results of surveys conducted both on Kasprowy Wierch and on the mouton in the Björkstugans area reveal that permafrost occurrence in both areas is probably not always accompanied by the occurrence of ground ice. Thus, the most likely interpretation of the obtained results is that these deep high-resistivity anomalies should also be regarded as occurrence of dry permafrost, older than permafrost present above it, which has relic character. This is the most probable hypothesis as it is commonly known that permafrost occurrence in the world is mostly the effect of Pleistocene cooling and such is its age (French 1996).

The thesis is supported in publications of other authors who have conducted surveys in this area. Ekman (1957) confirms the presence of at least 70 m thick permafrost near the Låkktajåkka tourist station at the altitude of 1220 m a.s.l.; that is a few kilometers away from the survey site. A borehole directly documenting this fact was drilled there in 1941. Another place where 20 m thick permafrost occurs is the Moskogaisa mine near Lyngen in Norway, at the altitude of 750 m a.s.l. (Ekman 1957). Relic and active permafrost is also distinguished in Scandinavian mountains by King (1984, Table 6, p. 36), who states that an active layer of relic permafrost is 4 m deep. He estimates the thickness of relic permafrost at 50–100 m and of active one at 40–140 m. A similar regularity is also registered in the Tatras (Dobinski et al. 2006), where under a layer of active permafrost there is probably fossil permafrost at the depth of about 15–25 m.

Fossil permafrost presence is documented in other places as well. The 100 m deep borehole drilled in March 2000 near the Tarfala Research Station (MAAT between -6 and -7°C) showed a temperature of -2.8°C in 100 m depth. Linear extrapolation of the borehole temperatures suggests permafrost thickness of 350 m (Isaksen et al. 2001). It is not possible for permafrost of such thickness to be solely an effect of contemporary climate influence (Lunardini 1995).

In the Alps (Zermatt) and in southern Scandinavia (Jotunheimen), a regularity similar to the one occurring in the Tatras (Kasprowy Wierch) and in the Abisko area can be observed. In 2D resistivity tomography performed near Stockhorn, one can distinguish two distinct high-resistivity anomalies, the first one in the 1–7 m depth and the second at the depth of about 20 m and more (Hauck 2001). Permafrost thickness in this place is estimated at about 160 m (King 2001), so both anomalies that occur there probably indicate its presence. A similar situation is on Jotunheimen (Fig. 6a) (Hauck et al. 2004), where a high-resistivity anomaly is visible in the lower part of the profile. Permafrost thickness for the borehole drilled in this area is estimated to be 380 m (Isaksen et al. 2001), which indicates that this high-resistivity anomaly might be interpreted as probable fossil permafrost. The possibility of its presence in this area is acknowledged by other researchers as well. (Ødegård et al. 1996). Nevertheless, as the resolution of the 2D resistivity tomography model decreases near the model boundary, the possibility of an inversion artifact must also be taken into account in the deeper part of both sections

The above assumptions are supported by an analysis of climate evolution in northern Scandinavia after glaciation. Long-term climatic history, deglaciation, and tree limit changes in the Holocene have been described mainly by Karlén (1976, 1979). The deglaciation of the Tornetrsk area took place around 9000^{14}C years BP (Karlen 1979). This information leads to the conclusion that in the mountain region of Abisko, in the entire Holocene period, temperature did not rise enough to reach MAAT >0°C, whereas in lower places the warming period was too short. During the Holocene there was not a period of time long enough to allow for a complete degradation of permafrost in the survey area. Rough estimates show that such an evolution took place in the Tatras too (Dobinski 2004).

Conclusions

Geophysical surveys carried out in the Abisko area indicate that active permafrost occurrence in this region is not solely limited to mountain and hill areas above 800 m a.s.l. (Jeckel 1988), and to muirs and palsa, but is also possible in other, lower places which are not covered with vegetation but constitute exposed convex forms (moutons) (Johansson et al. 2006). Thus, the occurrence of altitudinal and latitudinal permafrost probably overlaps.

Surveys on permafrost in Scandinavia and published results show that mountain permafrost, just like permafrost in western Siberia, reflects climatic fluctuations dating from at least postglacial period and that it occurs in both active and fossil forms. This allows for a more synthetic view on permafrost occurrence in the world. The published data indicate that such a hypothesis could also be applied in other mountain areas. Although it can be put forward at the present stage of research, it requires verification. It is impossible to prove the existence of permafrost by using the geophysical methods alone.

Acknowledgments

Geophysicists K. Wzietek and B. Zogala supported the field measurement and its interpretation. The constructive and helpful comments of two anonymous referees are gratefully acknowledged. Sincere acknowledgments go to Mira Jach for her work in translating the text into English. The work was financed from the funds of the University of Silesia, Research Project MNiSW: N306 052 32/3405 and EU ATANS Grant (Fp6 506004).

References

Baumgart-Kotarba, M. & Kotarba, A. 1995. High-mountain environment of the Tatras in the period of Pleistocene and Holocene transition. *Biuletyn Peryglacjalny* 34: 37-51.

Dobinski, W. 2007. First results of the geophysical research of the lower border of permafrost occurrence in the Abisko area, Lappland, Sweden. *Geophysical Research Abstracts* 9, 03075, 2007 SRef-ID:1607-7962/gra/EGU2007-A-03075.

Dobinski, W. 2006. Ice and environment: A terminological discussion. *Earth-Science Reviews* 79(3-4): 229-240.

Dobinski, W. 2005. Permafrost of the Carpathian and Balcan Mountains, Eastern and Southeastern Europe. *Permafrost and Periglacial Processes* 16(4): 395-398.

Dobinski, W. 2004. Wieloletnia zmarzlina w Tatrach: geneza, cechy, ewolucja. *Przegląd Geograficzny* 76(3): 327-343.

Dobiński, W. 1997. Distribution of mountain permafrost in the High Tatras based on Freezing and thawing indices. *Biuletyn Peryglacjalny* 36: 29-37.

Dobinski, W., Żogała, B. & Wziętek, K. 2006. Geophysical investigation of the contemporary and Pleistocene permafrost in the Kasprowy Wierch, Tatra Mountains, Poland. *Przegląd Geofizyczny* 51(1): 71-82.

Ekman, S. 1957. Die Gewasser des Abisko–Gebietes und ihre Bedinungen. *Kungl. Svenska Vetenskapsakademiens Handlingar* 6 (6): 172 pp.

French, H.M. 1996. *The Periglacial Environment*. Longman, 341 pp.

Gorbunov, A.P. 2003. *Vietchnaya merzlota gor ot ekvatora do poljarhyh shirot* (Permafrost of the mountains from equator up to polar latitudes), Almaty, 124 pp. (in Russian).

Haeberli, W. 1973. Die Basis-Temperatur der winterlichen Schneedecke als moglicher indikator für die Verbreitung von permafrost in den Alpen. *Zeitschrift für Gletscherkunde und Glazialgeologie* 9(1–2): 221-227.

Haeberli, W. 2003. Report of the Eight International Conference on Permafrost. *Frozen Ground* 27: 3-5.

Hauck, C. 2001. *Geophysical methods for detecting permafrost in high mountains.* PhD thesis, Laboratory for Hydraulics, Hydrology and Glaciology (VAW), ETH Zurich, Switzerland. *VAW-Mitteilung* 171: 215 pp.

Hauck, C., Gugielmin, M., Isaksen, K. & Vonder Mühll, D. 2001. Applicability of frequency-domain and time-domain electromagnetic methods for mountain permafrost studies. *Permafrost and Periglacial Processes* 12: 39-52.

Hauck, C., Isaksen, K., Vonder Mühll, D. & Sollid, J.L. 2004. Geophysical surveys designed to delineate the altitudinal limit of mountain permafrost: An example from Jotunheimen, Norway. *Permafrost and Periglacial Processes* 15: 191-205.

Harris, C. 2001. Editorial. *Permafrost and Periglacial Processes* 12: 1.

Isaksen, K., Holmlund, P. & Sollid, J.L., 2001. Three deep alpine permafrost boreholes in Svalbard and Scandinavia. *Permafrost and Periglacial Processes* 12: 13-25.

Jeckel, P., P. 1988. Permafrost and its Altitudinal zonation in northern Lappland. *Proceedings of the Fifth International Conference on Permafrost, Trondheim, Norway, 2–5 August 1988*: 170-175.

Johansson, M., Christensen, T.R., Akerman, H.J. & Callaghan, T.V. 2006. What determines the current presence or absence of permafrost in the Torneträsk Region, a sub-arctic landscape in northern Sweden? *Ambio* 35(4): 190-197.

Jonasson, C. 1991. Holocene Slope Processes of Periglacial Mountain Areas in Scandinavia and Poland. *UNGI Rapport 79*. Uppsala University, Department of Physical Geography.

Karlén, W. 1976. Lacustrine sediments and tree-limit variations as indicators of Holocene climatic fluctuations in Lappland, northern Sweden. *Geografiska Annaler* 58A(1–2): 1-33.

Karlén, W. 1979. Deglaciation dates from northern Swedish Lappland. *Geografiska Annaler* 61A(3–4): 203-210.

King, L. 1984. Permafrost in Skandinavien–Untersuchungsergebnisse aus Lappland, Jotunheimen und Dovre/Rondane. *Heidelberger Geographische Arbeiten* 76: 125 pp.

King L. 2001. News from members, Germany. *Frozen ground* 25: 25-26.

Kneisel, C. 2006. Assessment of subsurface lithology in mountain environments using 2D resistivity imaging. *Geomorphology* 80: 32-44.

Knutsson, S. 1980. Permafrost i Norgevägen. *Byggmästaren* 10: 8-11.

Lunardini V.J. 1995. Permafrost formation time. *CRREL Report 95-8*: 44 pp.

Niedźwiedź T. 1992. Climate of the Tatra Mountains. *Mountain Research and Development*, 12(2): 131-146.

Ødegård, R.S., Hoelzle, M., Johansen, K.V. & Sollid, J.L. 1996. Permafrost Mapping and Prospecting in Southern Norway. *Norsk Geografisk Tidsskrift* 50: 41-54.

Ridefelt, H. & Boelhouwers, J. 2006. Observations on regional variation in solifluction landform morphology and environment in the Abisko region, northern Sweden. *Permafrost and Periglacial Processes* 17: 253-266.

Svensson, H. 1986. Permafrost. Some morphoclimatic aspects of periglacial features of Northern Scandinavia. *Geografiska Annaler* 68A(3): 123-130.

Vonder Mühll, D. 1993. Geophysikalische Untersuchen im Permafrost des Oberengadins. *Mitteilungen der Versuchsanstalt für Wasserbau, Hydrologie und Glaziologie* 122: 222 pp.

Vonder Mühll, D., Hauck C., Gubler H., McDonald R. & Russill, N. 2001. New geophysical methods of investigating the nature and distribution of mountain permafrost with special reference to radiometry techniques. *Permafrost and Periglacial Processes* 12: 27-38.

Permafrost Dynamics at the Fairbanks Permafrost Experimental Station Near Fairbanks, Alaska

T.A. Douglas
Cold Regions Research and Engineering Laboratory Fairbanks, AK

M. Torre Jorgenson
Alaska Biological Resources, Fairbanks, AK

M.Z. Kanevskiy, V.E. Romanovsky, Y. Shur, K. Yoshikawa
University of Alaska Fairbanks, Fairbanks, AK

Abstract

The Fairbanks Permafrost Experimental Station was established in 1945 near Fairbanks, Alaska. In 1946 vegetation was removed from two plots (the Linell plots) to investigate the impacts of vegetation disturbance on permafrost degradation. We revisited the sites in 2007 to evaluate the permafrost table using probes and direct current electrical resistivity. The permafrost table has expanded downward to 9.8 m at a site where all surface vegetation and organic material was removed. The permafrost surface has remained at 4.7 m depth since 1972 at a second site where vegetation was removed but organic material was left intact. In 2005 a Circumpolar Active Layer Monitoring Network (CALM) site was established at an undisturbed plot nearby to provide a baseline assessment of the permafrost. The response of permafrost at the site to the hypothesized future climatic warming of the Alaskan Interior can be assessed, once a long-term record is available.

Keywords: boreal forest; electrical resistivity; monitoring; permafrost degradation; vegetation disturbance.

Introduction

Permafrost in thermal equilibrium can be drastically affected by disturbances such as clearing vegetation (Linell 1973, Nicholas & Hinkel 1996), forest fires (Viereck 1982, Burn 1998, Hinzman et al. 2003), or climatic change (Shur & Jorgenson 2007). The Fairbanks Permafrost Experiment Station near Fairbanks, Alaska (64.877°N, 147.670°W) was established by the U.S. Army in 1945 as a location where geotechnical, geophysical, and engineering studies could be performed on permafrost. The site has a rich history and was designated as a National Geotechnical Experimentation Site in 2003. In 1946 vegetation was removed from two plots at the site (the Linell plots) to investigate the impacts of vegetation disturbance on permafrost degradation. This paper summarizes the results of recent investigations focused on measuring the current state of permafrost at the site. Our results provide information on permafrost degradation where vegetation disturbance has lead to a change in the thermal regime either through engineering activities, fire, or climatic change. Permafrost at the study site is considered "warm" (the mean annual air temperature is -3.3°C) and mean annual temperatures in the area are increasing. As a consequence, future degradation of permafrost during climate warming can be assessed once a long-term record is available from the site.

Results

Linell plots and Circumpolar Active Layer Monitoring site

In 1946 three square plots 61 m on a side (3721 m^2) were identified at the Fairbanks Permafrost Experiment Station to investigate the influence of vegetation removal on permafrost (Linell 1973). Herein these plots are referred to as the *Linell plots*. One of the Linell plots was left undisturbed to preserve the subarctic taiga forest with dense white and black spruce. Vegetation was removed from the other two plots. One plot was stripped of trees by hand but the roots and organic mat were left intact (Fig. 1) while at the other plot all of the vegetation and surface organic material were removed (Fig. 2). Linell (1973) described permafrost degradation at the two disturbed sites 26 years later. In the completely disturbed site the thaw depth reached 6.7 m after 26 years while at the partially disturbed site the melting expanded to a depth of

Figure 1. The Linell plot where trees and shrubs were removed, but the organic mat and roots were left intact. From the U.S. Army Corps of Engineers, Permafrost Division, 1950.

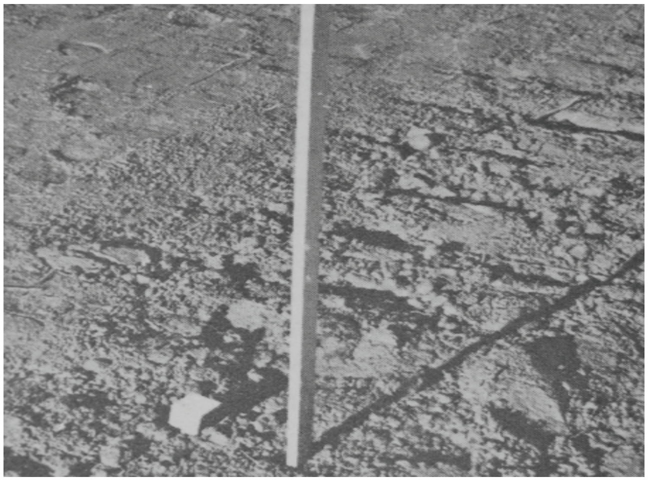

Figure 2. The completely disturbed Linell plot where trees, shrubs, the organic mat and roots were removed. From the U.S. Army Corps of Engineers, Permafrost Division, 1950.

Figure 3. The CALM site at the undisturbed plot in August 2006.

4.7 m. The results showed that permafrost degradation is linked to surface vegetation disturbance and that in warm permafrost random, mixed, low vegetation will not provide a stable thermal regime for permafrost.

In 2005 a Circumpolar Active Layer Monitoring Network (CALM) site was established in the undisturbed Linell plot. Thaw depths have been measured yearly in early October at 121 locations on an 11 by 11 cell grid with 3 m spacing. This provides thaw depth measurements over a 33 by 33 m (1089 m^2 area). Moss thickness and total thaw depth were measured and recorded at each probe location. In the fall of 2007 direct current electrical resistivity measurements were made along an 85 m long line at both of the disturbed Linell plots to quantify the state of permafrost 61 years after modification. A borehole was installed at the completely disturbed plot in 2007 to measure the current thaw depth and to ground truth the geophysical measurements.

Climate, soils, vegetation and permafrost in Interior Alaska

Fairbanks, located in Interior Alaska, has a continental climate with a mean annual temperature of -3.3°C and

Figure 4. A photograph in August 2007 of the Linell plot where in 1946 the surface vegetation was removed but the organic material was left intact.

typical monthly average temperatures of 20.2°C in the summer (July) and -31.7°C in the winter (January). Absolute extremes range from -51°C to 38°C (Jorgenson et al. 2001). The average annual wet precipitation is 407 mm and the typical average annual snowfall is 1.7 m. The Fairbanks Permafrost Experimental Station site sits on a gently sloping southward facing hill 6 km north of Fairbanks, Alaska.

Soils in the study area consist of tan silt and wind blown loess near the surface and grey silt at depths below 1.4 m. Permafrost gravimetric percent moisture contents range from 26% to 41% for the frozen silts which makes this relatively low moisture content permafrost (Linell 1973). The thin (2 to 32 cm thick) surface peaty organic mat has a gravimetric moisture content as high as 258% (Linell 1973). Organic rich silt and peat layers are common as are layers and inclusions of charcoal.

Vegetation at the Fairbanks Permafrost Experimental Station (Fig. 3) is typical of the Alaskan Interior- subarctic taiga forest with white and black spruce towering above a thick moss layer interspersed with low-bush cranberry and Labrador tea. Feather and sphagnum moss and woody debris cover the terrain surface (Hamilton et al. 1983).

Forest succession following disturbance is evident at both Linell plots. At the two disturbed plots dead or dying shrubs covered in moss are being replaced by white and black spruce and birch trees. The trees are taller at the less disturbed site where the surface vegetation was removed but the organic material was left intact (Fig. 4).

Permafrost in Interior Alaska is discontinuous, generally underlying north facing slopes and valley bottoms (Jorgenson et al. 2001). A detailed description of the types of permafrost in the Alaskan Interior is provided in Osterkamp et al. 2000). The thickest permafrost at the Fairbanks Permafrost Experimental Station, 60 m, is near Farmers Loop Road and the thickness decreases with increasing elevation. The mean annual temperature at 10 m depth from 1946 to 1972 was -0.5°C (Linell 1983).

Circumpolar Active Layer Monitoring site measurements

Thaw depths at the CALM site from 2005 to 2007 are generally between 20 and 80 cm (excluding moss) in early October (Table 1). Moss thickness ranges from 0 to 32 cm (Fig. 5). Linell (1973) presents consistent thaw depth readings of ~85 cm at the undisturbed plot from 1946 to 1972. This suggests recent climatic warming in the Alaskan Interior (1.5°C warmer at Fairbanks from the 1960s to the 1990s (Osterkamp & Romanovsky 1999)) may not be greatly affecting thaw depths at the Fairbanks Permafrost Experiment Station. In all three years of measurements the shallower moss cover is associated with deeper thaw depths.

Geophysical measurements at the Linell plots

Direct current (DC) electrical resistivity measurements have been used to quantify the presence of permafrost at many locations worldwide (e.g., Gilmore & Clayton 1995, Hauck et al. 2003, Hauck & Kneisel 2006). The electrical resistivity of a soil is controlled by its mineralogy, porosity, moisture content, cation/anion concentration of moisture, temperature, and whether the pore water is frozen or thawed. The resistivity (ρ) values of frozen soil are generally 10- to 1000 times greater than those of unfrozen or brine-rich soils (Harada & Yoshikawa 1996).

Direct current electrical resistivity measurements were run across the two disturbed Linell plots in September 2007 to quantify current thaw depths. We used two-dimensional resistivity profiling (IRIS instruments; Syscal pro R1 48-72 channel) for this investigation using a Wenner electrode configuration. The DC resistivity sounding employed four electrodes for measurement whereby a current (I) was delivered and received between the outer two electrodes and the resulting potential difference (V) was measured between the inner two electrodes. For this array on the ground surface, an apparent resistivity (ρ_a) between electrodes separated by distance (a) is:

$$\rho_a = 2\pi a(V/I) \tag{1}$$

The inversion analysis was performed with changing values of resistivity and layer thickness by using the linear filter method for a one-dimensional investigation (Das & Verma 1980). We do not have measurements of pore water salinity or moisture content across the resistivity lines and this limits the confidence of our interpretation of the resistivity measurements. However, based on the data presented in Linell (1973), the soil moisture contents, the soil temperature, and our probing and borehole measurements we are confident the resistivity markers we interpret as the upper boundary of the permafrost table are accurate.

For the acquisition of the two-dimensional apparent resistivity data we used multi-channel, equally spaced electrodes at 1.5 m for the minimally disturbed Linell plot and 2 m for the completely disturbed Linell plot. Each measurement was repeated up to 16 times, depending on the variance of the results. Two-dimensional model interpretation was performed using RES2DINV (Geotomo software) which performs smoothing and constrained inversion using finite difference forward modeling and quasi-Newton techniques (Loke & Barker 1996).

Resistivity profiles across the disturbed Linell plots show that in one case the permafrost continues to degrade while in another a small zone of potentially refrozen material has been recreated since 1973 (Linell 1973). Figure 6 includes a DC resistivity cross section of the plot where surface vegetation was cleared by hand but the surface organic material was left intact. Undisturbed permafrost is present at 0 m on the line (x-axis). The dark mass to the right center of the plot corresponds with a low lying grassy area along the DC resistivity line with standing water and minimal shrubs or trees. This wet soil affects DC resistivity measurements and yields an apparent highly resistive mass at a depth of 3 m that is not present based on frost probing. This is signified by the bulbous mass with resistivities >200 Ω-m from 34 to 47 m along the section. To the left (east) the resistivities that are >200 Ω-m likely signify permafrost at 9 m depth. This depth to permafrost was confirmed at two locations with an expandable frost probe. Figure 7 includes a DC resistivity cross section of the plot where surface vegetation and organic material were removed in 1946. Undisturbed permafrost is present from 0 to 25 m on the line (x-axis). A borehole encountered permafrost at 9.8 m (Fig. 8) which corresponds with the tabular region (black) consistently yielding a resistivity of >450 Ω-m.

Table 1. A summary of the summer average temperatures, active layer depth, and moss thickness from 121 points at the undisturbed Linell plot (CALM site) for 2005–2007.

Year	May-October mean air temperature (˚C)[1]	Mean thaw depth without moss (cm)	Mean moss thickness (cm)
2005	13.7	44.5	13.0
2006	12.6	40.1	13.5
2007	12.9	43.7	13.6

[1]Alaska Climate Research Center.

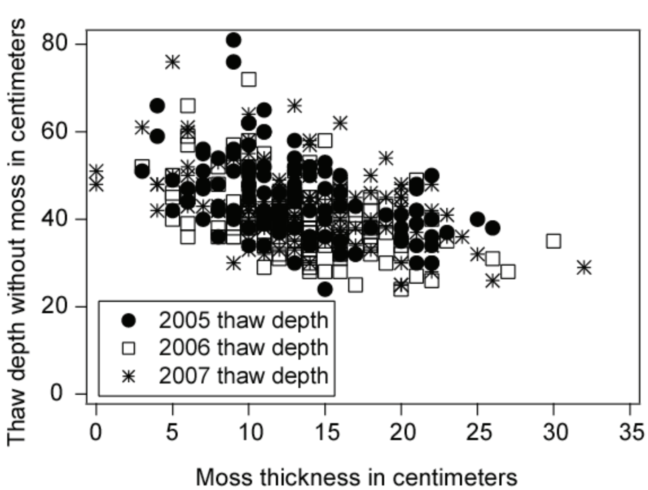

Figure 5. The relationship between moss thickness and thaw depth at the pristine Linell plot (CALM site) for 2005 to 2007.

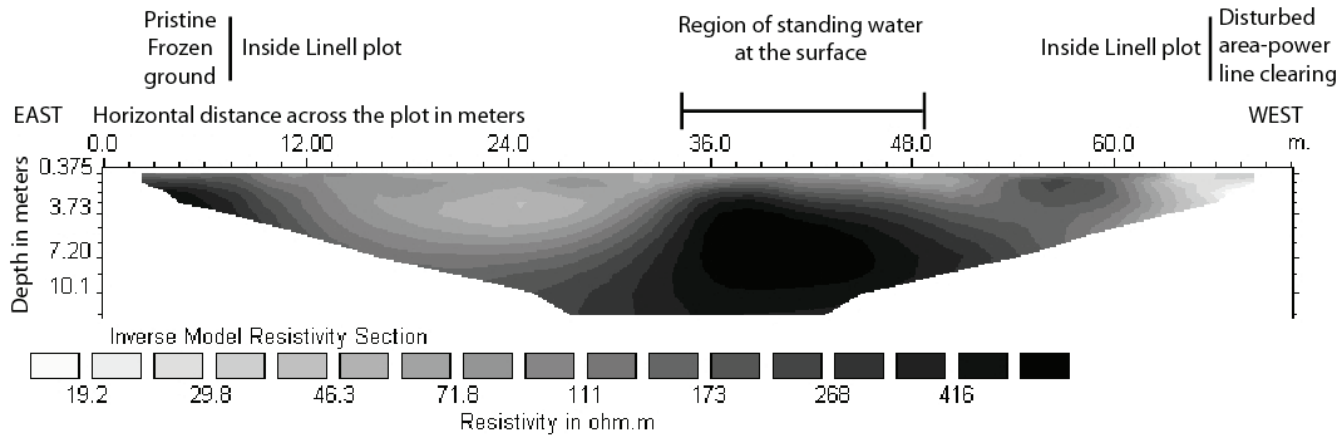

Figure 6. A direct current resistivity profile across the Linell plot where, in 1946, the surface vegetation was removed but roots and organic material were left intact. The unit electrode spacing is 1.5 m.

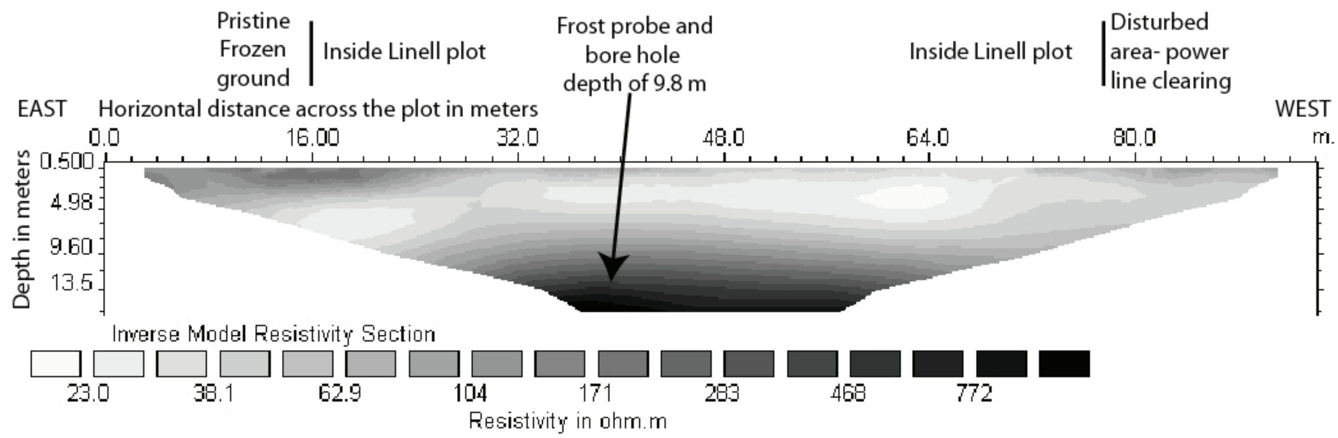

Figure 7. A direct current resistivity profile across the Linell plot where, in 1946, the surface vegetation, roots, and organic material were removed. The unit electrode spacing is 2 m. The arrow denotes where a borehole encounters permafrost at 9.8 m depth (Fig. 8).

The DC resistivity values here are ~450 to 800 Ω-m when permafrost is encountered. This is on the low end for studies reporting resistivity values for permafrost. Hoekstra and McNeill (1973) report values of 300 to 7000 Ω-m for "Fairbanks silt" with the values approaching 800 Ω-m for "Fairbanks silt" at -5°C. This is within the range of values we measured for soils that are similar to Fairbanks silt. Harada et al (2000) report values of 2100 and 12,000 Ω-m for permafrost at the Caribou-Poker Creek Research Watershed (CPCRW) located 20 km north of our study site. Yoshikawa et al. (2006) report values of 1000 to 14,000 Ω-m for permafrost at the top of a pingo at the CPCRW and 600 to 10,000 Ω-m for frozen ground at a pingo located 4 km west of the Fairbanks Permafrost Experimental Station. Permafrost in northern Quebec (Seguin and Frydecki 1994) yields values between 1000 and 5000 Ω-m. DC resistivity values are strongly controlled by the moisture content and the salinity (or conductivity) of the permafrost. In the Fairbanks area the mean annual temperature is -3.3°C. The permafrost is roughly 0.5°C to 1°C (Fig. 8) which is considered warm for permafrost. As a consequence, there is likely unfrozen water in the pore spaces of silt rich sediment at the top of the permafrost table. This could result in lower resistivity values than are measured at locations where colder temperatures and less unfrozen water are present.

A summary of our measurements combined with the data reported by Linell (1973) is provided as Figure 9. Permafrost destruction at the site where surface vegetation was removed but organic material was left intact appears to have ceased since 1973. While probing along the DC resistivity line at the site we identified a thin (50 cm) frozen layer between 1 and 1.5 m depth. This likely signifies a zone of aggrading permafrost. At the site where all vegetation and surface organic material were removed the depth to permafrost has increased to 9.8 m depth (based on frost probing and a bore hole installed at this location in the fall of 2007 that yielded temperatures below freezing at 9.8 m depth in October 2007 and January 2008 (Fig. 8).

If one assumes a maximum volumetric ice content of ~30%, the loss of 9.8 m of ice at the disturbed site and 4.7 m of ice at the partially disturbed site would lead to subsidence of ~2.9 m and ~1.4 m, respectively. This assumes all the ice was lost (as melt water) through evapotranspiration or subsurface flow which is not likely. The ground surface appears visibly

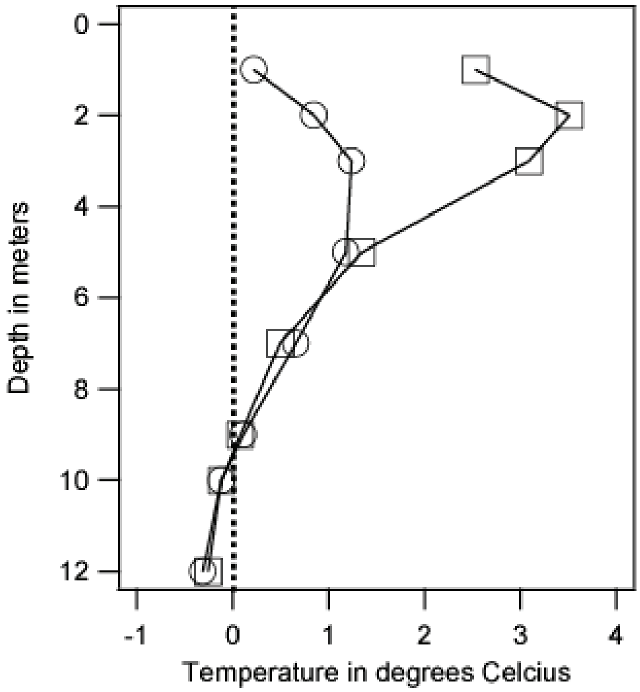

Figure 8. Borehole temperatures on October 19, 2007 (open boxes) and January 20, 2008 (open circles) at the Linell plot where surface vegetation, roots, and organic material were removed.

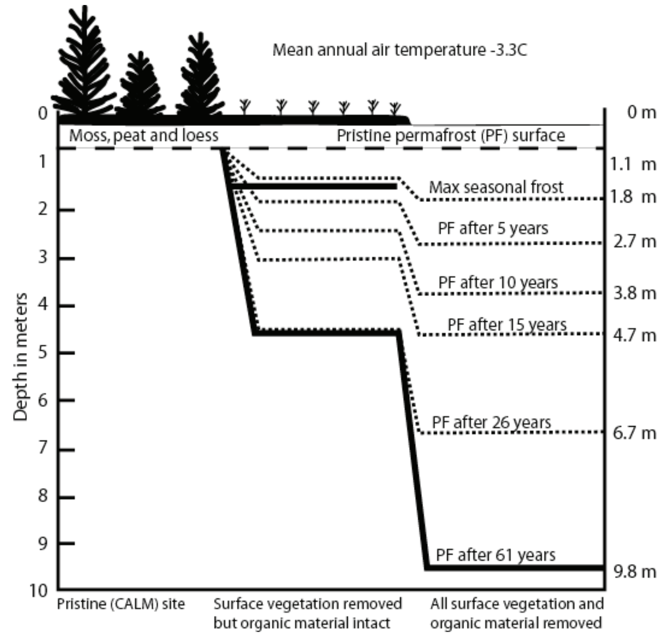

Figure 9. A cross section based on Linell, 1973. Vegetation removal from the two disturbed sites occurred in 1946. The bold line denotes the measurements collected in the fall of 2007, representing 61 years since disturbance.

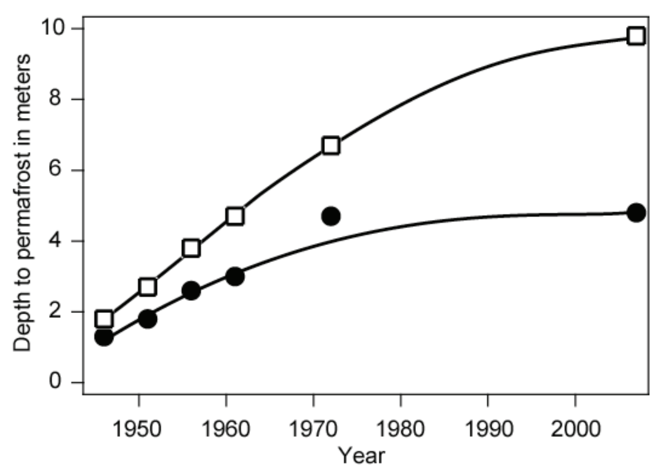

Figure 10. Permafrost degradation at the disturbed Linell plots. Boxes denote the site where surface vegetation and organic material were removed, and circles denote the site where surface vegetation was removed but organic material was left intact.

depressed at the two disturbed Linell plots compared to the edges of the plots and to the control plot. However, the degree of subsidence cannot be ascertained beyond a visual estimation due to a lack of high resolution elevation measurements at the site prior to disturbance in 1946.

Discussion

Comparing the results from this investigation with that of Linell (1973) it is apparent that at both of the plots where vegetation was removed the permafrost expanded downward for the first 26 years while the permafrost table eventually stabilized at the partially disturbed site. This is likely due to the reestablishment of a boreal forest at the site within 25 years. This forest succession did not lead to the upward migration of the permafrost table, most likely due to the fact that ambient temperatures in the area are relatively warm. However, the small frozen layer at roughly 1.5 m depth at this site may signify that an epigenetic (downward freezing) regime is currently in place.

At the site where all the surface vegetation and organic material were removed the permafrost surface has migrated downward for the past 35 years. Vegetation is continuing to evolve and is currently transitioning from a shrub, birch, and willow forest to one with a higher density of spruce trees and moss. The downward migration of the permafrost surface has not been linear in nature (Fig. 10). In fact, the rate of permafrost degradation at both of the disturbed sites is best represented by a second order polynomial.

Since the climate of Interior Alaska has warmed slightly over the past three decades it is possible some of the permafrost degradation at the Linell plots is attributable to climatic change. The downward migration of the permafrost surface may be augmented by warming temperatures in addition to the changing thermal regime caused by vegetation disturbance. Thaw depths at the pristine Linell plot (the CALM site) are ~80 cm and are within the range of values presented by Linell (1973) for the period from 1946 to 1972. The recent establishment of a Circumpolar Active Layer Monitoring Network (CALM) site at the undisturbed Linell plot will provide a baseline of the current and future state of permafrost which can be assessed once a long-term record (>10 years) has been measured.

Conclusions

Based on the results from this and previous studies, it is evident that the downward degradation of permafrost is highly dependent on the type of surface degradation and time. This has ramifications for forest succession following fire or human-caused disturbances to vegetation in permafrost terrains.

This study supports previous work showing that vegetation disturbance greatly affects permafrost stability. The regrowth of boreal forest vegetation at the partially disturbed Linell plot has lead to the cessation of permafrost degradation. In fact, a thin layer of frozen ground slightly below the typical thaw depth may be evidence of the reestablishment of permafrost. The site with greater vegetation disturbance has exhibited permafrost degradation since 1946, but the rate of degradation is not linear and is decreasing as the re-establishment of boreal forest continues. Resistivity values we measured for permafrost (~450 to 800 Ω-m) are relatively low compared to measurements in ice-rich permafrost. However, our site is characterized by low-moisture-content silts. Further studies of the thermal state and moisture content of the frozen silt at the site are warranted. Finally, ambient air temperatures have increased over the past few decades in the study area, and they are expected to continue to increase in the future. Though thaw depths in the permafrost at the CALM site appear to be somewhat stable since 1946, we will only be able to determine how future warming will continue to affect permafrost at the site with continued monitoring.

Acknowledgments

Many people donated time, equipment, and information to support this collaborative study. Site history was provided from Charles Collins and Karen Henry of CRREL. Field assistance from Stephanie Saari, Art Gelvin, Allan Delaney, Charles Collins, and Tohru Saito has been invaluable. Beth Astley shared her geophysical information for Birch Hill and Farmers Loop. Comments from two anonymous reviewers and Editor D. Kane strengthened the manuscript.

References

Burn, C.R. 1998. The response (1958–1997) of permafrost and near-surface ground temperatures to forest fire, Takhini River valley, southern Yukon Territory. *Canadian Journal of Earth Science* 35: 184-199.

Das, U.C. & Verma, S.K. 1980. Digital linear filter for computing type curves for the two-electrode system of resistivity sounding. *Geophysical Prospecting* 28: 610-619.

Gilmore, T.J. & Clayton, E.A. 1995. Mapping the top of the permafrost using surface direct current resistivity survey. *Environmental Geology* 30(1/2): 29-33.

Hamilton, T.D., Ager, T.A. & Robinson, S.W. 1983. Late Holocene ice wedges near Fairbanks, Alaska, U.S.A.: Environmental setting and history of growth. *Arctic and Alpine Research* 15(2): 157-168.

Harada, K. & Yoshikawa, K. 1996. Permafrost age and thickness near Adventfjorden, Spitsbergen. *Polar Geography* 20: 4, 267-281.

Harada, K., Wada, K. & Fukuda, M. 2000. Permafrost mapping by transient electromagnetic method. *Permafrost and Periglacial Processes* 11: 71-84.

Hauck, C., Mühll, D.V. & Maurer, H. 2003. Using DC resistivity tomography to detect and characterize mountain permafrost. *Geophysical Prospecting* 51(4): 273-284.

Hauck, C. & Kneisel, C. 2006. Application of capacitively-coupled and DC electrical resistivity for mountain permafrost studies. *Permafrost and Periglacial Processes* 17: 169-177.

Hinzman, L.D., Fukuda, M., Sandberg, D.V., Chapin III, F.S. & Dash, D. 2003. FROSTFIRE: An experimental approach to predicting the climate feedbacks from the changing boreal fire regime. *Journal of Geophysical Research* 108(D1): 8153.

Hoekstra, P. & McNeill, D. 1973. Electromagnetic probing of permafrost. National Academy of Sciences, National Research Council. *Proceedings of Permafrost: North American contribution to the Second International Conference:* 517-526.

Jorgenson, M.T., Racine, C.H., Walters, J.C. & Osterkamp, T.E. 2001. Permafrost degradation and ecological changes associated with a warming climate in central Alaska. *Climatic Change* 48: 551-579.

Linell, K.A. 1973. Long-term effects of vegetative cover on permafrost stability in an area of discontinuous permafrost. National Academy of Sciences, National Research Council. *Proceedings of Permafrost: North American contribution to the Second International Conference:* 688-693.

Loke, M.H. & Barker, R. D. 1996. Rapid least-squares inversion of apparent resistivity pseudosections by a quasi-Newton method. *Geophysical Prospecting* 44(1): 131-152.

Nicholas, J.R.J. & Hinkel, K.M. 1996. Concurrent permafrost aggradation and degradation induced by forest clearing, central Alaska, U.S.A. *Arctic and Alpine Research* 28(3): 294-299.

Osterkamp, T.E. & Romanovsky, V.E. 1999. Evidence for warming and thawing of discontinuous permafrost in Alaska. *Permafrost and Periglacial Processes* 10: 17-37.

Osterkamp, T.E., Vierick, L., Shur, Y., Jorgenson, M.T., Racine, C., Doyle, A. & Boone, R.D. 2000. Observations of thermokarst and its impact on boreal forests in Alaska, U.S.A. *Arctic, Antarctic and Alpine Research* 32(3): 303-315.

Seguin, M.-K. & Frydecki, J. 1994. Semi-quantitative geophysical investigations of permafrost in northern Quebec. *Journal of Applied Geophysics* 32: 73-84.

Shur, Y.L. & Jorgenson, M.T. 2007. Patterns of permafrost formation and degradation in relation to climate and ecosystems. *Permafrost and Periglacial Processes* 18: 7-19.

U.S. Army Corps of Engineers, Permafrost Division. 1950. *Investigation of Military Construction in Arctic and Subarctic Regions, Comprehensive Report 1945-48; Main Report and Appendix III - Design and Construction Studies at Fairbanks Research Area.* ACFEL Technical Report 28.

Viereck, L.A. 1982. Effects of fire and firelines on active layer thickness and soil temperatures in interior Alaska. *Proceedings of the Fourth Canadian Permafrost Conference. National Research Council of Canada Calgary: Ottawa, Ontario:* 123-135.

Yoshikawa, K. & eight others. 2006. Comparison of geophysical investigations for detection of massive ground ice (pingo ice). *Journal of Geophysical Research* 111(E06S19): 10 pp.

Recent Advances in Russian Geocryological Research: A Contribution to the International Polar Year

D.S. Drozdov, G.V. Malkova, V.P. Melnikov
Earth Cryosphere Institute, Russian Academy of Sciences, Siberian Branch, Tyumen, Russia

Abstract

Fifty years have passed since the previous Polar Year (1957–1959). After the relatively cold climatic period of 1950–1960, the abrupt warming of air and ground temperatures was evident for the north of Russia. The geocryological observations suggest that the rise in ground temperature slowed down in the early 1990s; the recent trend of changes in geocryological conditions is uncertain. Ongoing and future permafrost research and modeling of permafrost evolution under the impact of climate change and man-induced development should be based on wide-ranging scenarios. Generally, the permafrost and climatic trends show that there will be no significant changes in geocryological conditions in the upcoming 20 to 25 years. The decreasing continentality of the climate can increase the extent of destructive cryogenic processes on the continent and in the coastal zone, especially in the case of significant impact caused by development. Cryogenic structure of permafrost will control significantly the activity of external processes.

Keywords: air and ground temperatures; cryogenic processes; GIS; geocryological monitoring; geosystem; permafrost change.

Introduction

The International Polar Year (IPY) provides one of the most significant events for geocryologists. Fifty years have passed since the previous Polar Year (also International Geophysical Year, 1957–1959). Some of its participating Russian geocryologists are still active (G.F. Gravis, A.V. Pavlov, M.M. Koreisha, and others). The end of the 1950's was a time of rather cold climate and the main investigations in the permafrost zone concerned cryogenic structure of the upper permafrost layers. At present, due to the concerns for global warming, the main attention is focused on the problem of permafrost degradation and destructive external processes, especially in case of man-made impacts. The basic problem is the study of seasonal and annual changes in climate and permafrost conditions and their interaction. Our contemporary investigations are coordinated with numerous international IPY programs: Arctic Circumpolar Coastal Observatory Network (ACCO-Net) and our Coastal Cryolithozone of the Russian Arctic (COCRA); Thermal State of Permafrost and our International Network of Permafrost Observatories (INPO); Greening of the Arctic: Circumpolar Biomass (GOA) and, also, various Russian Integrative and Regional Programs to assess permafrost changes. Collecting and processing of climatic and geocryological data are performed using GIS-techniques applied to models at global, regional, and localscales.

The IPY research in the Eurasian polar region concerns the following general items (Melnikov et al. 2007):

- Contemporary changes in climate and sea hydrodynamics in Arctic regions;
- Geocryological structure and cryogenic features;
- Continental and subsea permafrost formation and evolution;
- Natural and man-made cryogenic physical and geological processes;
- Permafrost monitoring (including coastal permafrost);
- Development of GIS databases and maps as conceptual and graphical models;
- Development of the new techniques for permafrost research.

This report highlights some of the recent results from these investigations with a focus on Western Siberia.

Geosystem Approach and Processing of Geocryological Data

Geocryological studies, mapping, and monitoring of the northern territories affected by climate change and intensive development are aided by global, regional, and local GIS applications. Digital maps of onshore and offshore areas with attribute databases of geomorphology, landscapes, lithology, soil properties, geocryological conditions, bathymetry, etc. are efficient tools for the analysis of available data and for assessing the environment (Melnikov & Minkin, 1998). A wide-ranging generalization of information from databases, and the compilation and redrafting of thematic digital maps, makes it possible to reflect the present-day state, trends and dynamics of coastal processes (Drozdov et al. 2005).

The landscape (geosystem) approach is used to pass from the low hierarchical level to the higher level (and vice versa) while processing the data. This is necessary for the collection and generalization of primary data with the development of general small-scale maps, on the one hand, and for displaying general regional regularities on the large-scale maps, on the other hand. The landscape maps display geomorphology, lithology, geocryology, vegetation and their longitudinal and altitudinal zonality. Thus, it reflects the main features and properties of the modern environment. The overlay of the landscape and climatic maps allows one to generate spatial geocryological forecast as an element of general environmental forecast.

Climate-Permafrost Relationships: General Regularities

Global and regional modes are used to predict the evolution of permafrost as related to the climatic and economic conditions. Extrapolation of contemporary permafrost and climate trends indicates that there will be no significant changes in geocryological conditions in the upcoming 20 to 25 years. But the decreasing climatic continentality (Fig. 1) can accelerate the development of the destructive cryogenic processes, causing permafrost degradation. In the areas with significant summer warming (e.g., in Western Siberia), the active layer thickness should increase, and thermokarst, thermal erosion, and cryogenic landslides should be more intense. In the areas with prevailing winter warming, intensification of frost heave, cryogenic cracking, and ground-ice formation are predicted. Global and regional GIS and databases are used to reveal and describe these phenomena.

The most negative tendency for the permafrost stability is expected for the regions where climate warming is accompanied by continued economic development. The potential decrease in the permafrost stability in this case is not related to climatic feedback effects caused by development, as there are no direct evidences for this process (Pavlov & Malkova 2005).

The long-term prognosis (20 to 50 years) is developed from the assessment of Russian permafrost sensitivity to the short-term climatic change (one year). This assessment is based on temperature and precipitation calculations. The basic argument for the short-term prognosis is the changing of the active layer thickness and moisture. Thus, according to a short-term prognosis of the geocryological processes, no catastrophic events were expected in 2006 and this forecast proved to be correct (Gravis & Konchenko 2007). In 2007, cryogenic processes were expected to be more active in the eastern regions of Russia, and to result in disturbance of the natural landscapes. This forecast is yet to be verified.

It is established for the offshore Arctic areas that changes of coastal destruction are rhythmical and have no meaningful trend. All temporal anomalies in the coastal destruction rate are synchronous with the climatic fluctuations, including characteristics of sea hydrodynamics and the state of ice in the Arctic seas. The smoothed hydrodynamic forecast makes it possible to assume a subsequent stable rate of coastal destruction that would not exceed contemporary rates by more than 10%–20%. If all other conditions are equal, the dominant role in coastal processes is related to the spatial

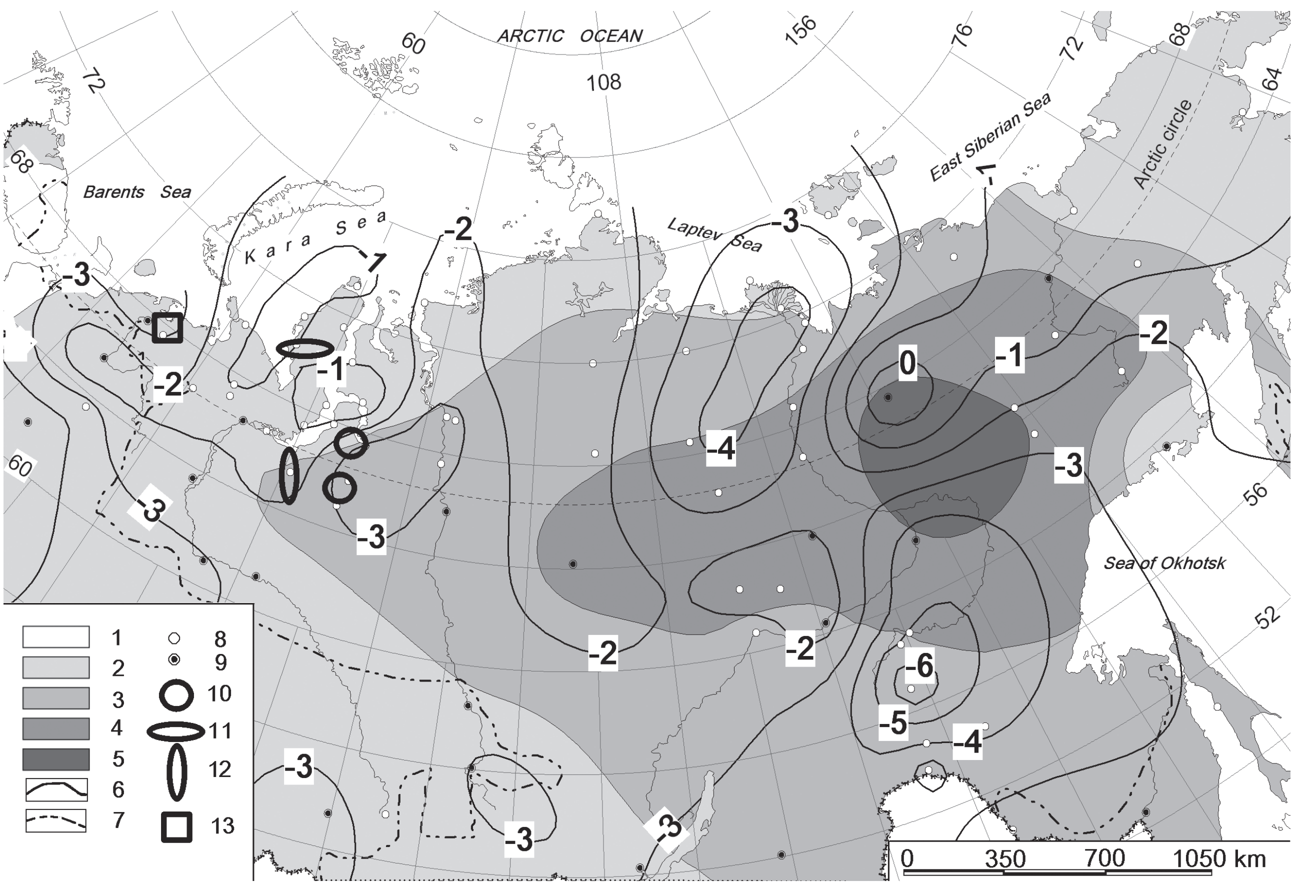

Figure 1. Map of climate continentality change owing to climate warming (amplitude contraction map). *1 – 5 – Annual amplitude of air temperature, °C: 1 – 20-30; 2 – 30-40; 3– 40-50; 4 –50-60; 5 – 60-70. 6 – change of annual amplitude since 1970, °C; 7 – southern limits of cryolithozone; 7 – 8 – weather stations with weather record: 7 – less then 100 years, 8 – more then 100 years; 10 – 13 – ECI SB RAS geocryological key-sites at: 10 – Urengoy gas-field, 11 – Yamal (Marre-Sale), 12 – Nadym, 13 – Pechora River mouth (cape Bolvanskii).*

variability of the cryogenic structure of permafrost (Vasiliev et al. 2005). The thermal erosion of the seacoast is considered to be the most destructive process, particularly in the case of ice-rich permafrost. Some anomalies are evident during the last decade, such as the correlation with fluctuations in the coverage of sea ice.

Monitoring of Unique Regions and Territories

Mapping and monitoring of unique territories are based on the regional and local landscape maps as the graphical tools. GIS techniques are used for the multivariate generalization of the experimental field data and for developing maps of the different conditions. Repeated geocryological surveys (for example, for the territory of Urengoy gas field, Western Siberia) show there have been no statistically significant changes in the permafrost temperature during the last several years. Compilation of these repeated maps is based on the reprocessing of existing data and on geocryological parameters aided by the new annual observations. Unfortunately, these regime data do not characterize all types of the geosystems. This limits the comprehensiveness of the repeated mapping.

Our experience in using insufficient data sets for compiling prognostic geocryological and environmental maps in the regions of new economic development is of particular interest. These maps are extremely important for feasibility studies and for the potential environmental impact assessment.

The medium-scale maps (1:100,000 to 1:200,000) of the natural and disturbed ecosystems, engineering-geocryological conditions, external geological processes, and permafrost stability were developed using GIS modeling (Drozdov et al. 2007). Expected gas and oil pipeline corridors cover about 3000 km^2. These are wide swaths of land ranging from 20 to 70 km as in: a) the Vankor oilfield to the north and to the south in Western Siberia; b) the Bovanenkovo deposit to the south in Western Siberia; and c) the northern branch of VSTO pipeline in East Siberia to the Pacific Ocean (Ust-Kut–Lensk–Aldan–Tynda). New geocryological information of limited extent made it possible to display up-to-date ground temperature and cryogenic processes in these regions.

Geo-Indicators of Cryogenic Processes

New data necessary for the reconstruction of Pleistocene-Holocene evolution and assessment of cryogenic stability of Russian Arctic are developed from offshore, on-shore and coastal expeditions. Geocryological structure, geocryological conditions, ice-content, ice-complex distribution, and external processes were examined in the European and Siberian North and in the coastal zone of Barents, Kara and Laptev seas. Some new conclusions can be made.

The investigations in Yenisey Bay (Kara Sea coastal zone) showed that polygenetic Pleistocene plains have very different geological and cryological characteristics. The sites with displaced sandy and loamy sediments and low ice content can be found in close proximity to the territories with horizontal sediment bedding and the presence of the ice complex. Sometimes, the ice-complexes occur in several layers. The alternation of ice-rich and ice-poor sites is observed along the coast; they are characterized by different rates of thermal abrasion and thermal erosion. Numerous slopes subjected to strong thermal erosion is indicative of the presence of ice-complexes even in the case when the latter cannot be diagnosed by either standard landscape surveys and remote sensing in this northernmost region of the Yenisey River (Streletskaya et al. 2007).

The traditional on-shore and coastal regime investigations that have been carried over a long time at the Bolvanskii key-site in the mouth of Pechora River (Barents Sea) were accompanied by seismic surveys. Geophysical seismic research and monitoring were conducted to analyze slope stability. This special seismic technique is based on theoretical relationships and experimental correlation between seismic characteristics of the soil and stress-strain condition of the soil massif. A very important feature of this technique is the opportunity to monitor and predict initial changes of the slope stability before significant change occurs. The length of forecasts range from months to several years. The error in expected spatial discontinuity does not exceed several meters (Skvortsov & Drozdov 2003). Repeated investigations during 2002–2006 showed that the relaxation of the stress-strain conditions took place, and slope stability increased. This micro-landscape mapping indicated that an existing crack on the surface, indicative of a weakened zone, became less noticeable from year to year. The seismic research, extended to the offshore zone, showed that the permafrost table is found at a depth of 8 m under the beach and descends to about 20 m at a distance of 200 m offshore (Skvortsov et al. 2007).

The theory of "landslide plains" explains how the changing of soil-biota conditions causes the new cryogenic landslides and how the new brine laden horizons are entrained into the active layer within the period of about 300 years (Leibman & Kizyakov 2007).

Frost heave and permafrost degradation are the main cryogenic processes in central part of Western Siberia. Complex monitoring near the town of Nadym revealed natural and anthropomorphic changes of landscape. The old peat mounds resulting from heaving are growing and new mounds continue to appear. The growth of the peat mounds is most active in the coldest winters; in milder winters, it is less intense. In contrast there are other processes like the increase in the active layer thickness and the rise of ground temperature. Temperature rise was very pronounced at the end of the 20th century. Locally it caused significant degradation of the permafrost. This tendency is moderated now, and geocryological conditions have become more stable. Man-made development increase permafrost degradation (Moskalenko & Ponomapeva 2006).

The micromorphological indicators of cryogenic conditions and processes during the early Cenozoic have been studied. The so-called cryogenic type of microstructure of sub-aerial sediments has been described. It is widespread and very stable. It can be traced in polygenetic syn-cryogenic and epicryogenic soils presently frozen or thawed. The established differences in the microstructure of Quaternary and Late-Cenozoic sediments make it possible to reconstruct features of paleo-cryogenic origin and the sequence of permafrost aggradation and degradation cycles for the past 3,000,000 years (Slagoda 2003).

Geocryological Monitoring in the Important Economic Regions

The important economic regions in the permafrost zone are influenced by substantial development that, together with the natural climate fluctuations, change landscapes and geocryological conditions. The studies of ecological and geocryological regimes concern both spatial and temporal description and forecast changes to the properties of the geological environments. Several key sites are located in Western Siberia and the European North in different natural settings and under different cryological conditions: for example, at Urengoy gas field, near the town of Nadym, on the Yamal peninsula, and on the mouth of Pechora River (Fig. 1). The landscapes, external processes, cryolithology, active layer, and ground temperature are studied there. These studies are important both for the ecological and geological estimation of current state of the territories and for detection of general regularities governing the observed changes.

Changes of average annual ground temperature are smoothed in comparison to external changes (e.g., in air temperature). They make it possible to observe general cryological trends not hidden by the highly variable fluctuations and extremes. At Urengoy gas field, the ground temperature measurements were made in 1974, 1975, 1977, 1978, 1992, 1993, 1994, 1997, 1999, 2005, 2006, and 2007.. According to these data, the temperature of the permafrost increased approximately 1°C during the period 1975–1993 owing to the natural climatic warming. Land use changes added an extra 1°C to 2.5°C, but this ground temperature rise is located close to human constructions. Changes in the ground temperature are not identical at the different landscapes (geosystem rank). They vary over wide limits. In the southern forest-tundra the ground temperature increase ranges from 0.6°C to 2.1°C. In northern forest-tundra and southern tundra, its increase is somewhat lower (0.1°C to 1.6°C, Drozdov 2002). The continuous temperature observations of 1994–1999 testify to the retardation in the increase of the frozen ground temperature. In the next five years, a decrease in ground temperature was registered at some sites. The pattern of ground temperature change in the southern forest-tundra landscape zone is shown in Figure 2.

For areas with high shrubs, where much snow is accumulated during winter and where the frozen ground temperature at the beginning of the warming cycle was close to 0°C, the degradation of permafrost was observed. The top of the degrading permafrost can be found at a depth of approximately 10 m. Analogous processes occur at the forested sites. The thawing of ground has not ceased. At some tundra and boggy sites, the warming of permafrost was followed by significant

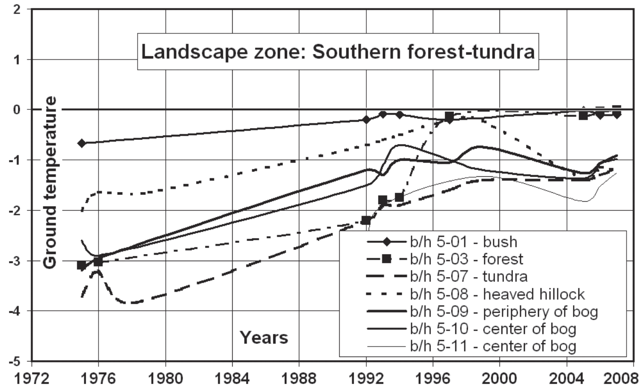

Figure 2. Ground temperature changes in southern forest-tundra at ~10 m depth (Urengoy gas field, Western Siberia) *b/h – borehole number and type of landscape site.*

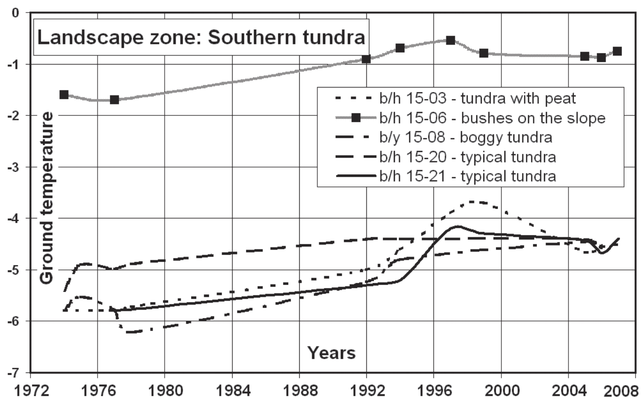

Figure 3. Ground temperature changes in southern tundra at ~10 m depth (Urengoy gas field, Western Siberia); *b/h – borehole number and type of landscape site.*

cooling in the mid 1990's. The more significant freezing can be found on hillocks. It is interesting that the temperature conditions in different geosystems become closer to one another under the impact of recent temperature changes; in the areas with degrading permafrost, the ground temperature is close to 0°C; in the areas with stable permafrost, it varies from -1°C to -1.4°C.

The same processes can be observed in the southern tundra landscape zone, but they occur generally under conditions of lower mean temperatures (Fig. 3).

All the geosystems are characterized by some temperature maximum in the mid-1990s. In most of the boreholes, temperatures at the depth of 10 m were very similar and rather cold: from -4°C to -5°C for the typical conditions.

A common feature for the northern part of Western Siberia is the rise in the ground temperature in the last three years (2005–2007). In the previous years, a decrease in the ground temperature took place. Thus, it is difficult to judge the real temperature trend in this region

The spatial and temporal distribution of permafrost temperatures are displayed on a series of temperature maps of Urengoy gasfield area, Western Siberia (Fig. 4). The first temperature map (B) is compiled on the basis of the results of the geocryological surveys in the period 1972 to 1977;

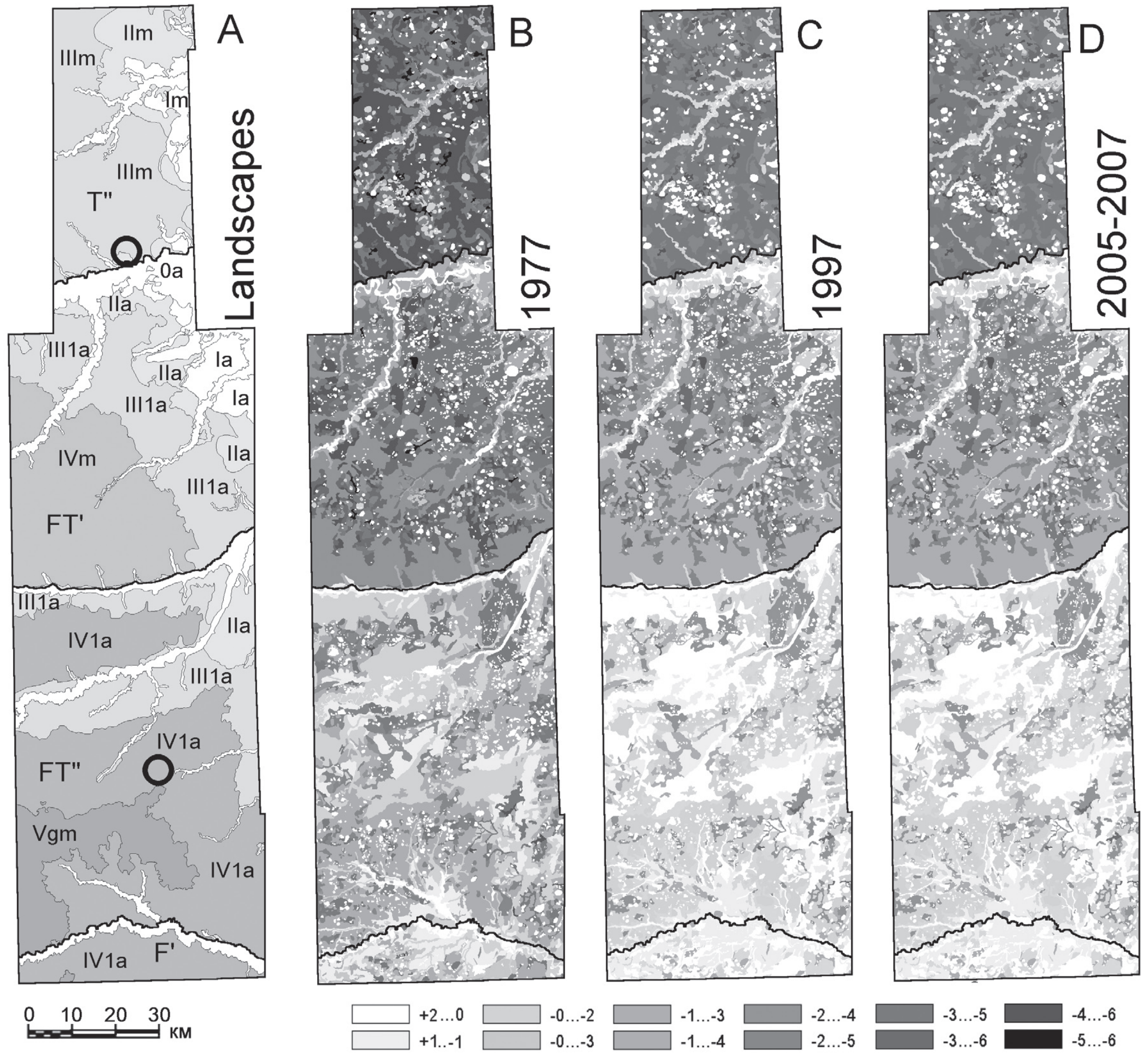

Figure 4. Natural dynamics of permafrost temperatures at the territory of Urengoy gas field (Western Siberia). *A – geosystem types (the larger letters – indexes of landscape zones; the smaller letters – landscape type index – number of geomorphologic level and genesis; black circle – geocryological regime key-site); B, C, D – ground temperature at 1977 (B), at 1997 (C) and at 2005-2007 (D).*

the second map (C) is drawn according to the data of the repeated simplified survey and thermal observations (1992 to 1997); the third map (D) is created on the basis of new thermal observations (1999, 2005 to 2007). Examining the gray-scale saturation of these maps, one can see that maps B and C reflect an average increase in the ground temperature of approximately ~1°C over a span of 20 years. Maps C and D indicate the absence of considerable temperature change during the last decade.

Conclusions

After the relatively cold period of the late 1950s, the decades of the 1970s and 1980s were characterized by the sharp warming of air and ground in the north of Russia. According to geocryological observations, the rise in ground temperatures slowed down and practically stopped since the middle 1990s. This invites us to assume that the warming tendency can be replaced by a cooling tendency. However, the recent short period of 2005–2007 showed an increase in ground temperatures. Thus, the real trend of modern geocryological condition is not factually clear. The modeling of permafrost evolution concerning the climatic and industrial influences should be performed for an ensemble of the scenarios. Extrapolation of contemporary permafrost climatic trends shows that there will be no significant changing of geocryological conditions in the coming 20 to 25 years, but the reduction of climatic continentality can increase the development of the negative cryogenic processes related to the increase in the active layer thickness, permafrost degradation, thermokarst, thermal erosion, and landslide activation in regions of summer warming. The most hazardous changes are expected in the regions, where climatic warming is accompanied by active land use change caused by development. The long-term prognosis (20 to 50 years) can provide an assessment of permafrost sensitivity to the short-term climatic changes that differ from year to year in the Russian North.

The seacoast thermal erosion is considered to be stable and rhythmic and shows no significant trend. Some anomalies are observed during the last decade and are associated with fluctuations in sea ice coverage. The activity of coastal processes relies on the spatial variability of the coastal cryogenic structure. The theory of "landslide plains" explains how the changing soil-biota conditions cause the new cryogenic landslides and the inclusion of new brine laden horizons into the active layer.

The knowledge of recent geocryological regularities allows the development of the medium-scale map-models of natural and man-influencedt geosystems, engineering-geocryological conditions, geo-environmental situation and permafrost stability, even in case of insufficient data.

GIS-techniques, geosystem methods, new meteorological and geocryological data, different landscape-geocryological field experiments, geophysics, and lab analyses allow us to extend our knowledge about permafrost and its interactions with other environments within programs of IPY.

Acknowledgments

We express our deep gratitude for scientific and financial support to the Russian Foundation of Basic Research, the Russian Academy of Sciences (grant 05-05-64215), the Tyumen Governor, the U.S. National Science Foundation (ARC-0632400, ARC-0520578), the "Okeangeologiya" Scientific Research Institute, "Urengoygazprom" Company, and Yenisey Shipping.

References

Drozdov D.S., Korostelev Yu.V., Malkova G.V., Melnikov E.S., Soromotin A.V., Ukraintseva E.A. & Chekrygina S.N. 2007. Preliminary geocryological and environmental mapping of the areas of perspective economic activity. *Cryogenic resources of polar regions: Int. conf., Vol. II. Salekhard, June 2007*: 264-266.

Drozdov D.S. 2002. GIS investigations at geocryological monitoring of Urengoy oil-gas field (the northern part of Western Siberia). *Ecology of northern territories of Russia: Conf., Vol. 1, Archangelsk, June, 2002*, 89-94 (in Russian).

Drozdov D.S., Rivkin F.M., Rachold V., Ananjeva-Malkova G.V., Ivanova N.V., Chehina I.V., Koreisha M.M., Korostelev Yu.V. & Melnikov E.S. 2005. Electronic Atlas of the Russian Arctic Coastal Zone. *Geo-Marine Letters* 25(2-3): 81-88.

Gravis G.F. & Konchenko L.A. 2007. Cryogenic geological processes: problems of the short-term forecast. *Cryogenic resources of polar regions: Int. Conf., Vol. I. Salekhard, June 2007:* 131-133.

Leibman M.O. & Kizyakov A.I. 2007. Cryogenic landslides of the Yamal and Yugorsky peninsular. *Moscow: Earth Cryosphere Institute SB RAS,* 206 pp.

Melnikov E.S. & Minkin M.A. 1998. About strategy of development of electronic geoinformation systems (GIS) and databases in geocryology. *Earth Cryosphere* II(3): 70-76 (in Russian).

Melnikov V.P., Vasilyev A.A., Gravis G.F., Drozdov D.S., Leibman M.O., Malkova G.V., Melnikov E.S., Moskalenko N.G., Pavlov A.V., Ponomareva O.E., Skvortsov A.G., Slagoda E.A. & Smetanin N.N. 2007. Contemporary state, stability and dynamics of permafrost zone: international polar year, first decisions. *Cryogenic resources of polar regions: Int. Conf., Vol. I. Salekhard, June 2007*: 21-25.

Moskalenko N.G. & Ponomareva O.E. The temperature of the permafrost at largely hilly peat bogs in the northern taiga of Western Siberia and the forecast of its change. *Earth Cryosphere Assessment: Theory, Applications and Prognosis of Alterations.: Proceedings of the International Conference. Tyumen, 2006, Vol. 1*: 90-93.

Pavlov A.V. & Malkova G.V. 2005. Contemporary climate changes in the northern Russia: Album of general maps. *Novosibirsk, Academic publishing house "Geo",* 54 pp. (in Russian).

Pavlov A.V., Malkova G.V. & Skachkov Yu.B. 2007. Model Tendencies in the Evolution of Thermal state of cryolithozone under the climate changes. *Cryogenic resources of polar regions: Int. Conf., Vol. I. Salekhard, June 2007*: 34-38.

Skachkov Yu.B., Skryabin P.N. & Varlamov S.P. 25 years long monitoring of cryolithozone at Chabyda Station in Central Yukutia. *Cryogenic resources of polar regions: Int. Conf., Vol. I. Salekhard, June 2007*: 167-170.

Skvortsov A.G. & Drozdov D.S. 2003. Stress-strain conditions and stability of the Arctic coastal slopes: assessment using seismic surveys. *Permafrost: 8th International conference on permafrost: Extended abstracts. Zurich, ICOP, 2003*: 149-150.

Skvortsov A.G., Malkova G.V., Sadurtdinov. M.R. & Tsarev A.M. 2007. Geocryological conditions of the coastal part of the Pechora bay shelf in the region of Bolvansky-permanent-state-station according to the prospecting seismology data. *Cryogenic resources of polar regions: Int. conf., Vol. I. Salekhard, June 2007*: 170-173.

Slagoda E.A. Cryogenic deformations of the Cenozoic sediments at Baikal flexure. 2003. *Reports to the Academy of Sciences,* Vol. 393, No 8, part 1: 1105-1109 (in Russian).

Streletskaya I.D., Vasiliev A.A., Drozdov D.S. & Kanevskiy M.Z. 2007. Ice complex of Western Taymyr *Cryogenic resources of polar regions: Int. Conf., Vol. I. Salekhard, June 2007*: 99-102.

Vasiliev A.A., Ostroumov V., Rachold V. & Sorokovikov V.A. 2005. An Application of a Markov-chain model of shore erosion for describing the dynamics of sediment flux. *Geo-Marine Letters* 25(2-3): 196-203.

High-Resolution Numerical Modeling of Climate Change Impacts to Permafrost in the Vicinities of Inuvik, Norman Wells, and Fort Simpson, NT, Canada

C. Duchesne
Geological Survey of Canada, Ottawa, Ontario, Canada
J.F. Wright
Geological Survey of Canada, Sidney, British Columbia, Canada
M. Ednie
Geological Survey of Canada, Ottawa, Ontario, Canada

Abstract

Transient numerical ground temperature modeling conducted within an ARC-GIS-resident spatial analysis system was employed to predict the current and future distribution and character of permafrost in three study areas of the Mackenzie River Valley. Future impacts of progressive climate warming to 2055 were also predicted. Modeling results illustrate the variability in the evolution of permafrost characteristics, such as active layer and talik development, for representative terrain types. A clear north-to-south trend towards higher ground temperature was confirmed, paralleled by a north-to-south decrease in the areal extent and thickness of permafrost. Predicted ground thermal conditions for 2055 show minor changes at the base of permafrost, with the most substantive permafrost degradation being realized through the deepening of the active layer and the development of taliks in the top few to several meters below the ground surface.

Keywords: active layer; climate warming; Mackenzie River; numerical model; talik.

Introduction

The Mackenzie River Valley is characterized by widespread permafrost terrain of thickness ranging from more than 600 m in areas of the Mackenzie and Beaufort coastal plain, to only a few tens of metres or less in the southern extent of the valley (Judge 1973, Taylor et al. 1998). Heginbottom et al. (1995) mapped the continuous, discontinuous, and sporadic zones of permafrost in Canada, but at finer scales the distribution and character of permafrost are not well known. Numerical ground temperature models integrated within a geographic information system (GIS) provide a means for estimating the current distribution and character of permafrost across extensive geographic regions, and for generating time-series predictions of future impacts to permafrost under a progressively warming climate. This paper presents modeling results for three study areas in the Mackenzie River Valley (Fig. 1): Fort Simpson located in the discontinuous zone (15,405 km^2), Norman Wells overlapping the discontinuous and continuous zone (12,117 km^2) and Inuvik in the continuous zone (9089 km^2).

Numerical Models

Smith and Riseborough (1996) have proposed a simple analytical relation (TTOP) demonstrating direct linkages between key climate and terrain factors influencing ground temperatures. Under assumed thermal equilibrium, the model estimates the mean annual temperature at the top of permafrost (TTOP) or, when permafrost is not present, the mean annual temperature at the base of the annual freeze-thaw layer (TBAL). The model was applied to regional mapping of permafrost distribution in Norway's mountainous regions (Juliussen & Humlum 2007), and in the Mackenzie River Valley (Wright et al. 2003). For investigations of the transient impacts of climate change, the T-ONE one-dimensional, finite-element, heat conduction model provides reliable solutions to ground thermal problems in both natural and engineered environments (Goodrich 1982).

Both the TTOP and T-ONE models utilize similar model parameters representing the dominant climate and terrain factors

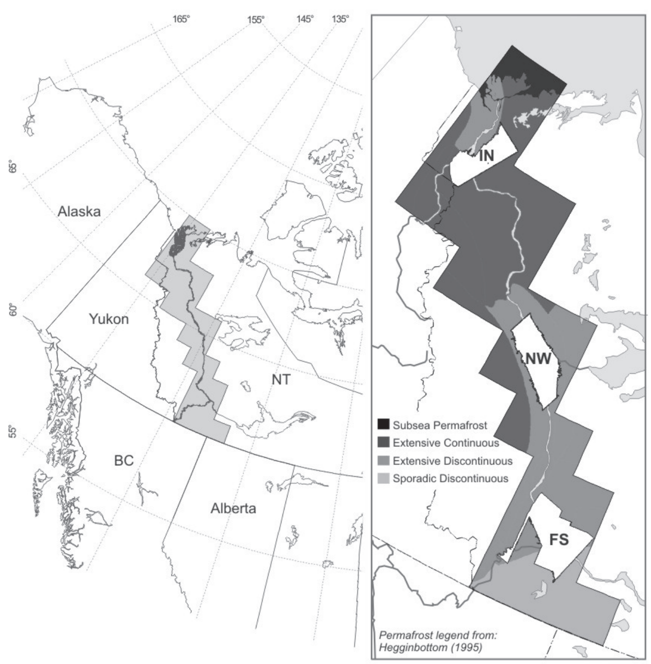

Figure 1. General and detailed location of the study areas modeled, northwestern Canada. IN: Inuvik, NW: Norman Wells, FS: Fort Simpson.

influencing the ground thermal state. The two models have been integrated within an ARC-GIS platform, enabling a quasi 3-dimensional grid space for generating predictions of permafrost occurrence, distribution, and temperature at local and regional scales, over selected time frames of interest.

Methods

Modeling parameters

To successfully apply the models to regional-scale mapping of permafrost, it is necessary to specify model parameter values which adequately reflect prevailing terrain and climate conditions within the study regions. The influence of atmospheric climate on the ground thermal regime is assumed to be primarily a function of air temperature as represented by thawing and freezing degree-day indices, and assumes that heat transfer in permafrost terrain is dominated by conductive processes (Outcalt et al. 1990). Thus, heat transfer through convective transport of water vapour and air within soil pore spaces, and the transient influences of rainfall infiltration and surface runoff (mass fluxes) are not considered. The use of seasonal n-factors links atmospheric temperatures to the ground thermal regime (Lunardini 1981) and provides a simplified representation of the influence of the buffer layer in modulating heat flow between the atmosphere and the ground surface. The summer vegetation cover is represented as a thawing n-factor, while the influence of snow cover is assumed to be implicit in the freezing n-factor (Wright et al. 2003, Jorgensen & Kreig 1988). Local topographic influences (as represented by a potential insolation index Ip), were not considered in this work in order to limit the number of unique terrain conditions modeled.

The general distribution of earth materials was obtained from available regional surficial geology maps (Hughes et al. 1972, Hanley et al. 1973, Rutter et al. 1980) supporting the assignment of model parameter values representing soil bulk density, soil mineralogy, and soil texture (Wright et al. 2003). These values are subsequently used for estimating the frozen/ unfrozen thermal conductivity (Johansen 1975) and specific heat capacity of surficial materials.

Information about the nature and extent of surface vegetation cover was obtained from conventional polygon maps based on regional surveys, and from multi-spectral classifications of Landsat TM satellite imagery at 30 m spatial resolution (GNWT Forest Management Division 2002). Integration of these data sources provided a basis for the assignment of seasonal n-factor values and soil moisture levels (Wright et al. 2003).

Calibration and validation

The GIS coupled T-ONE model was initially calibrated and validated using the TTOP analytical solution (Wright et al. 2003; Wright et al. 2001, unpubl.). Under conditions of thermal equilibrium, TTOP and T-ONE predictions of the temperature at the top of permafrost are virtually identical, meaning that although the model calibration was conducted using the computationally simple TTOP model, identical results regarding the presence/ absence of permafrost within the borehole dataset would have been obtained using the computationally more complex T-ONE finite element model. The model is capable of adequately reproducing observed trends in the regional distribution of permafrost occurrence and thickness within these regions, as documented in records from 154 geotechnical boreholes located in undisturbed, natural terrain (IPL 1982). Overall, the calibrated model correctly predicted the presence/ absence of permafrost in 134 of 154 cases (87%), and reasonably predicts the thickness of permafrost as compared to regional observations and limited borehole data (Wright et al. 2003). Also, the north-south distribution of ground temperatures data as estimated by TTOP agrees favourably with limited ground temperature data for the Mackenzie Valley presented by Judge (1973).

Climate and model equilibrium

The TTOP equilibrium ground temperature model was used to conduct an initial assessment of the likely range of ground temperatures expected within the individual study areas and supported the specification of initial equilibrium ground temperature profiles. Although true thermal equilibrium is never achieved between atmospheric climate and the ground thermal regime, initial conditions for forward modeling (including assumed equilibrium ground temperature profiles) were established circa 1730 AD (Ednie et al. 2008). This provided a basis for estimating current (year 2000) ground temperature profiles in support of transient ground thermal modeling through to 2025 and 2055, (although, due to space constraints, only results for 2000 and 2055 are presented in this paper). This approach was motivated by the observation that ground temperatures at numerous sites within the more southerly extents of permafrost terrain in the Mackenzie Valley appear to be near-isothermal close to 0°C (Smith et al. 2005), which we interpret as an indication that ground temperatures have been warming for an extended period of time. Measured and proxy records also suggest that there has been no extended period of stable climate in the northern hemisphere during the past few hundred years (Ednie et al. 2008). Figure 2 illustrates the initial equilibrium temperature and reconstructed paleo-climate trends used by the forward model to generate estimates of the current (year 2000) ground thermal state.

Burn et al. (2004) ranked scenarios from seven Global Climate Models (GCMs) and presents a series of plausible projections of climate warming in the Mackenzie Valley over the next 55 years. The median warming scenario with a temperature increase (over 1961–90 normals) of 1.3°C and 2.9°C for 2025 and 2055, respectively, was used to specify rates of regional climate warming in the Fort Simpson and Norman Wells study area. Since 1980, the recorded data for the Inuvik area indicate a steady increase in mean annual air temperature (Environment Canada 2002). Imposing a best-fit line through the data record suggests an increase in MAATs by 2000 which is well beyond the median warming scenario presented by Burn et al. (2004). Hence, for the Inuvik study area only, we have opted to extend the trend in recorded MAAT though to 2055, as this describes a more realistic scenario of future climate warming for this area (Fig. 3). With this trend, the MAAT for 2055 falls just below the projection for maximum warming as proposed by Burn (2004). For comparison purposes, modeling was also

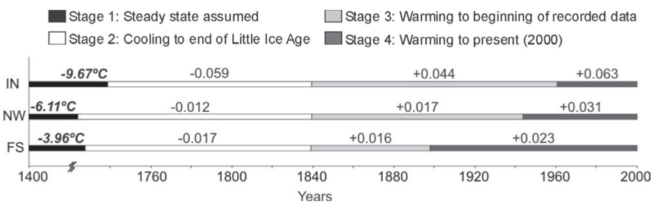

Figure 2. Paleo-climate trend used in the modeling. Stage 1: equilibrium temperature; Stage 2 to 4: subsequent ramps applied in °C/year.

conducted following an extension of the trend in recorded MAATs through to 2025, followed by a slight warming to 2055 based on the median warming ramp of +0.006ºC per year as specified by Burn et al (2004).

Configuration of the problem space

The T-ONE model was initiated using a single-layer geological substrate for all terrain types except in organic terrain, for which a two-layer substrate was modeled. In both cases, simulations were run at 6 hour time steps with grid spacing of 0.01 m at the ground surface exponentially increasing to a maximum of 8 m at greater depths. The depth of the grid was optimize according to TTOP estimation of the base of permafrost and was set at a minimum of 45 m in the Fort Simpson study area to 167 m in the Fort Good Hope region. A lower boundary heat flux of -40 mWm^{-2} was assumed. Within each 30 m grid element, ground temperatures were calculated at the specified depths below ground surface and iterated at successive time steps extending over the specified time intervals of interest (2000, 2025, and 2055). Model outputs are provided as a mean annual ground temperature.

T-ONE Modeling Results

Transient ground temperature modeling enables prediction of the incremental impacts to permafrost in response to a changing climate, and provides estimates of the timing of those changes. Typical model outputs include mean annual ground temperature profiles, permafrost distribution and thickness, active layer development and talik formation. A talik in this context is defined as the thawed layer between the seasonal active layer and the top of permafrost.

Inuvik

In general, moraine deposits cover ~45% of the Inuvik study area, with glaciofluvial/alluvial deposits occupying ~33%. Vegetation is dominated by shrubs (31%) followed by open black spruce (24%) and mixed forest (14%). Modeling using the extended trend in recoded MAATs predicts that 100% of the Inuvik area is underlain by permafrost at both 2000 and 2055. Mean ground temperatures at year 2000 range between -1.7°C in barren lichen cover underlain by glaciofluvial/alluvial deposits to -0.08°C in deciduous forest underlain by moraine deposits, increasing to -0.38°C and -0.01°C, respectively, by 2055 (Table 1).

Overall permafrost thickness ranges from ~40 m to over 150 m for white spruce on coarse-grained sediments. Modeling of

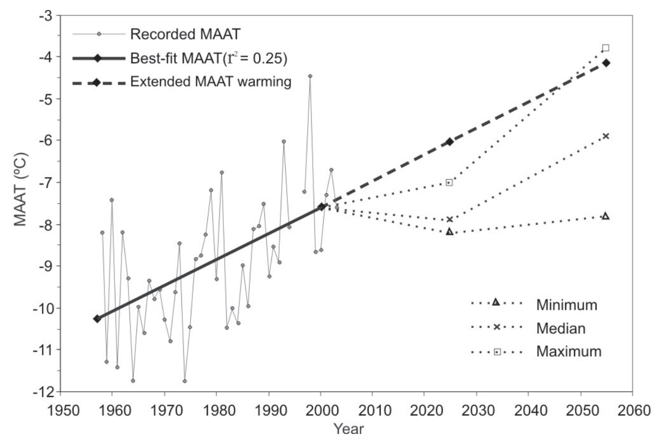

Figure 3. Minimum, mean, and maximum climate scenarios (Burn 2004) and extended trend of the 1970–2000 MAAT data for Inuvik.

Table 1. Predicted areal extent of permafrost and range of mean annual ground temperature (TTOP) in terrain modeled (excluding water bodies and bedrock) for each study area.

		Current conditions (2000)			Warming to 2055		
	% of study area modeled	% Frozen	Ground Temp. Min. (ºC)	Ground Temp. Max. (ºC)	% Frozen	Ground Temp. Min. (ºC)	Ground Temp. Max. (ºC)
IN	85.5	100	-1.65	-0.08	100	-0.38	-0.01
NW	79.6	96.0	-0.60	+2.13	85.9	-0.25	+2.90
FS	94.9	22.3	-0.24	+2.93	17.2	-0.02	+3.72

present-day (2000) conditions predicts the absence of taliks overlying permafrost in the Inuvik area. Representative cases in Table 2 highlight the presence of thick permafrost in open and closed black spruce forests through to 2055 with increases in thaw depth of less than 1 m. Permafrost in shrub- and deciduous-dominated terrain is marginally thinner, with thaw depths of between 0.5 m and 3 m in 2000, with the development by 2055 of substantial taliks of up to 4.5 m for shrubs and 9 m for deciduous forest. Figure 4 shows the changes in permafrost thickness, thaw depth, and talik development for representative terrain units. The results for the median warming scenario presented by Burn et al. (2004) predicts slightly thinner seasonal active layers and more subdued talik development.

Norman Wells

About 50% of the Norman Wells study area is underlain by moraine deposits, followed by eolian/lacustrine deposits (18%) and glaciofluvial/alluvial deposits (12%). The dominant vegetation class is open black spruce forest (37%), followed by open white spruce (10%) and mixed forest (10%). The model predicts permafrost underlying 96% and 86% of the Norman Wells study area in 2000 and 2055, respectively (Table 1). Present-day (2000) ground temperatures range from -0.6°C to 2.1°C, with taliks over permafrost present in 13% of the study area). Continuous permafrost underlies

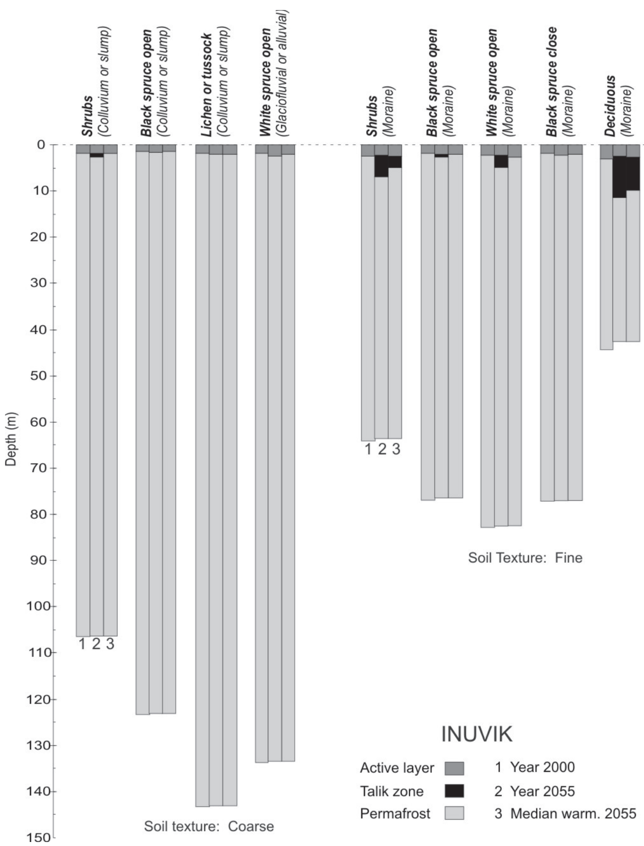

Figure 3. Summary of predicted active layer, talik and permafrost for representative terrain units in the Inuvik study area, 2000 and 2055; and 2055 median warming model of Burn (2004).

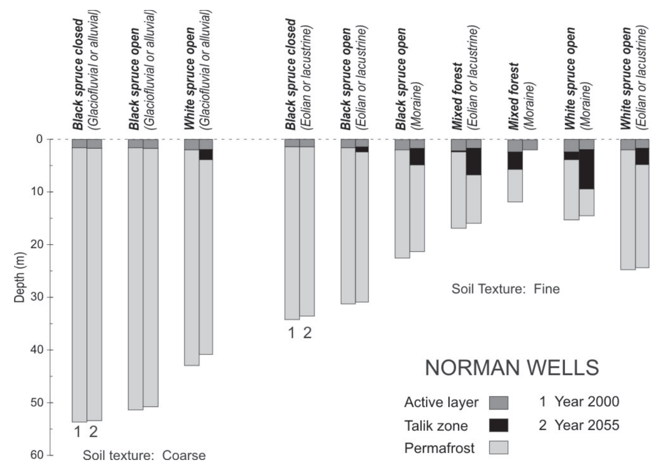

Figure 4. Summary of modeling results for representative terrain units in the Norman Wells study area.

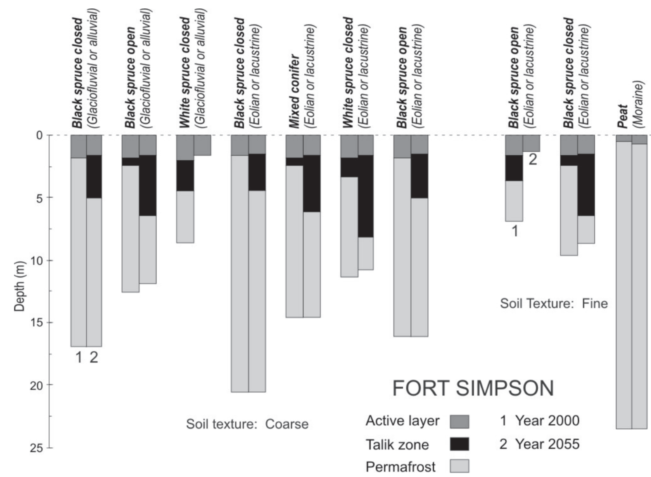

Figure 5. Summary of modeling results for representative terrain units in the Fort Simpson study area.

the majority of vegetation classes with the exception of deciduous forest (90% unfrozen), and fens and graminoids (100% unfrozen). Permafrost thickness ranges from 2.4 m under some deciduous forests to greater than 60 m beneath undifferentiated spruce, with a predicted thaw depth range from 0.6 m to 6.3 m. By 2055, relatively thin permafrost underlying deciduous forests, shrubs, and mixed forest is predicted to thaw completely, and for most representative terrain units, substantial taliks up to 8 m in thickness are predicted to develop under open white spruce on moraine. Table 2 and Figure 5 indicate changes in thaw depth ranging from a few centimetres to several meters, with complete permafrost thaw in the case of shrubs on moraine deposits. Only minimal permafrost thaw is predicted for open black spruce forest underlain by coarse-grained glaciofluvial/alluvial deposits.

Fort Simpson

Moraine deposits underlie ~65% of the Fort Simpson area, followed by eolian/lacustrine and glaciofluvial/alluvial deposits, which underly about 24% and 8% of terrain, respectively. Closed black spruce and open black spruce forests each cover ~24% of the study area, with closed white spruce occupying ~12%. Modeling predicts that approximately 22% of the Fort Simpson study area is underlain by permafrost, decreasing to about 17% by 2055 (Table 1). Estimated current (2000) ground temperatures range from about -0.24°C in peat bogs to almost 3°C in graminoids underlain by till. In 2000, taliks are predicted to overlie 54% of permafrost (11% of the study area). Overall, permafrost thickness ranges from just a few meters to 20 m or more in peat bogs. Relatively thick permafrost will persist in peat bogs and closed black spruce forests through 2055 (Table 2). Permafrost thaw during this period varies significantly between vegetation classes, ranging from less than 1 m in peat plateaus to 5–6 m beneath white spruce forests. Under current conditions, the model estimates that permafrost temperatures in the Fort Simpson region are only slightly below freezing, and that most permafrost-bearing terrain will remain marginally frozen (near-isothermal close to 0°C) through to 2055. However, permafrost beneath some black and white spruce forests is predicted to disappear by 2055. The thickness of the thaw layer above permafrost is predicted to increase by 3–5 m by 2055, with the exception of peat bogs that will see only small changes in thaw depth and permafrost thickness (Fig. 5).

Table 2. Modeling results of representative terrain types.

Study area	Vegetation cover	Surficial geology	% area cover	Ground[1] Temperature (°C)		Active[2] layer depth (m)		Thaw depth[3] (m)			Permafrost thickness (m)		
				2000	2055	2000	2055	2000	2055	Chg	2000	2055	Chg
IN	Open B.Sp.	Moraine *(fine)*	22.6	-0.84	-0.01	1.80	2.00	1.80	2.74	**0.94**	75.08	73.78	**-1.3**
Modeled area: 9089 km^2	Shrubland	Moraine *(fine)*	27.6	-0.50	-0.01	2.42	2.20	2.42	6.98	**4.56**	61.76	56.53	**-5.23**
	Closed B.Sp.	Moraine *(fine)*	0.83	-0.95	-0.02	1.79	2.29	1.79	2.29	**0.5**	75.42	74.71	**-0.71**
	Closed	Moraine *(fine)*	0.67	-0.08	-0.01	3.05	2.41	3.05	11.41	**8.36**	41.23	31.25	**-9.98**
	Open W.Sp.	Glacioflu. or allu. *(coarse)*	0.09	-1.19	-0.01	1.87	2.43	1.87	2.43	**0.56**	131.9	131.5	**-0.4**
NW	Open B.Sp.	Moraine *(fine)*	23.5	-0.05	-0.01	2.16	1.81	2.16	5.37	**3.21**	20.5	16.69	**-3.81**
Modeled area: 12117 km^2	Open B.Sp.	Lacustrine or eoli. *(fine)*	6.7	-0.26	-0.01	1.67	1.62	1.67	2.71	**1.04**	30.54	29.29	**-1.25**
	Open B.Sp.	Glacioflu. or allu. *(coarse)*	3.3	-0.38	-0.01	1.75	2.22	1.75	2.22	**0.47**	50.30	49.74	**-0.56**
	Closed B.Sp.	Moraine *(fine)*	3.2	-0.14	-0.01	2.12	2.00	2.12	2.22	**0.10**	24.64	21.83	**-2.81**
	Shrubland	Moraine *(fine)*	2.4	-0.01	1.89	2.41	2.00	7.13	np[6]	**-**	3.08	0.00	**-3.08**
FS	Closed B.Sp.	Lacustrine or eoli. *(fine)*	3.6	-0.01	-0.01	1.62	1.44	2.55	6.82	**4.27**	7.19	2.09	**-5.10**
Modeled area: 15405 km^2	Shrubland	Moraine *(fine)*	4.5	1.89	3.03	2.00	1.62	np	np	**-**	np	np	**-**
	Closed B.Sp.	Lacustrine or eoli. *(coarse)*	2.8	-0.05	-0.01	1.76	1.44	1.76	4.48	**2.72**	19.30	16.34	**-2.96**
	Bog	Moraine *(fine)*	2.9	-0.24	-0.02	0.65	0.76	0.65	0.76	**0.11**	23.94	23.57	**-0.37**
	Closed B.Sp.	Glacioflu. or allu. *(coarse)*	1.4	-0.01	1.75	2.00	1.62	4.68	np	**-**	4.38	0.00	**np**

1 TTOP if permafrost is present, otherwise temperature at base of seasonal freeze/thaw layer.

2 Thickness of ground surface layer that thaws and refreezes seasonally.

3 Cumulative depth of thaw over permafrost including the active layer and underlying talik where present.

np – no permafrost; chg. – change; B.Sp. – *Picea mariana*; W.Sp. – *Picea glauca*; Glacioflu. – glaciofluvial; allu. – alluvial; eoli. – eolian

Discussion

Our modeling results illustrate the variability in permafrost evolution for different terrain conditions (i.e., combinations of surficial materials and vegetation cover), under a continued climate warming. Where not already the case circa year 2000, ground temperatures are predicted to progressively warm towards isothermal, followed by the development and deepening of talik zones above permafrost. The formation of taliks has also been predicted by Kane et al. (1991). At the same time, the base of permafrost will slowly degrade upward towards the deepening talik zone. Latent heat effects are implied by the general increase in warming rates once ground temperatures increase above 0°C. For peat bogs characterized by relatively high heat capacities, active layer thickening and permafrost degradation is minimal within the time frames modeled. The model suggests that for much of Norman Wells and Inuvik terrain, only modest changes in permafrost thickness will be realized during this period, although increases in thaw penetration will be substantial for certain terrain types. The results may be summarized using the permafrost classification system of Shur & Jorgenson (2007). MAAT in the Inuvik area ('"climate driven,"' even with a warming trend) would still be cold enough to sustain permafrost. In contrast, in the Fort Simpson area much of the terrain would be underlain by '"climate-driven, ecosystem-protected"' permafrost where disturbance (e.g., change in the insulation layer) can cause the complete degradation of the permafrost with no re-establishment of initial permafrost conditions.

Numerical modeling affords a systematic and rigorous means for assessing ground thermal characteristics across extensive geographic areas. In the case of the TTOP and T-ONE models employed in this study, limited ground truthing and statistical validation of modeling outputs have established a reasonable level of confidence in model performance within the broader

Mackenzie Valley. While the T-ONE model generates apparently precise predictions (to multiple decimal points) of permafrost attributes such as temperature and thickness, it would be prudent to apply appropriate caution when evaluating model predictions, given that a -0.1°C change in ground temperature is equivalent to ~5 m of permafrost in typical surficial sediments. Also, we have noted that in the Inuvik area particularly, the model appears to overestimate active layer thickness and therefore possibly future rates of thaw penetration (Nixon, pers. com.). This may be related to our use of a one-layer system in which latent effects of excess ice and/or organic veneer are not adequately simulated.

Conclusion

Modeling of present-day (2000) ground thermal conditions confirms a clear north-to-south trend towards warmer ground temperatures, paralleled by a north-south decrease in areal extent and thickness of permafrost. The results also illustrate a north-to-south increase in thaw depth and development of taliks above the permafrost table. Predicted ground thermal conditions for 2055 (with a warming climate) confirms minor degradation at the base of permafrost with the greatest permafrost degradation occurring in the top few to several meters below the ground surface.

References

Burn, C.R., Barrow, E. & Bonsal, B. 2004. Climate change scenarios for Mackenzie River valley. *57th Canadian Geotechnical Conference, Québec,* 7A, Vol. 2: 2-8.

Ednie, M., Wright, J.F. & Duchesne, C. 2008. A Paleo-climatic reconstruction for transient ground thermal modeling in the Mackenzie River valley. *Proceedings of the Ninth International Permafrost Conference, Fairbanks, Alaska, June 28–July 3, 2008* (this proceedings).

Environment Canada. 2002. *Canadian Climate Normals: Canadian Monthly Climate Data and 1943–2000 Normals*. Environment Canada: Ottawa, CD-ROM.

GNWT Forest Management Division. 2002. *Northwest Territories Land Cover Classification.* Raster digital data, unpublished.

Goodrich, L.E. (1982). *An introductory review of numerical methods for ground thermal regime calculations*. National Research Council of Canada, DBR Paper 106, 133 pp.

Hanley, P.T., Hodgson, D.A., Hughes, O.L., Kurfurst, P.K., Lawrence, D.E., Zoltai, S.C., Pettapiece, W.W. & Pilon, J. 1973. *Surficial Geology and Geomorphology Maps of Fort Norman, Carcajou Canyon, Norman Wells and Sans Sault Rapids Map Areas, Mackenzie Valley.* Geological Survey of Canada, Open File 155.

Hegginbottom, J.A., Dubreuil, M.A. & Harker, P.T. 1995. Canada, Permafrost. In: *National Atlas of Canada. 5th ed*., Natural Resources Canada, MCR 4177.

Hughes, O.L., Hodgson, D.A. & Pilon, J. 1972. *Surficial Geology, Fort Good Hope, Arctic Red River, Fort McPherson, District of Mackenzie, Maps and Legend.* Geological Survey of Canada, Open File 97.

Interprovincial Pipe Lines (NW) Ltd. 1982. *Norman Wells Pipeline Project - Delineation of Permafrost Distribution by Geophysical Survey.* Summary Report KMP 0 to 868.3 to the National Energy Board, December 1982.

Johansen, O. 1975. *Thermal Conductivity of Soils*. Ph.D. Thesis. Trondheim, Norway. (CRREL Draft Translation 637, 1977, Ad 044002).

Jorgenson, M.T. & Kreig, R.A. 1988. A model for mapping permafrost distribution based on landscape component maps and climatic variables. *Proceedings of the Fifth International Conference on Permafrost, Trondheim, Norway,* 1*:* 176-82.

Judge, A.S. 1973. *Thermal Regime of the Mackenzie Valley: Observations of the Natural State.* Report 37-38, Environmental Social Committee, Northern Pipelines, Task Force on Northern Oil Development, Government of Canada, 177 pp.

Juliussen, H. & Humlum, O. 2007. Towards a TTOP ground temperature model for mountainous terrain in central-eastern Norway. *Permafrost and Periglacial Processes* 18: 161-184.

Kane, D.L., Hinzman, L.D. & Zarling, J.P. 1991. Thermal response of the active layer to climatic warming in a permafrost environment. *Cold Regions Science and Technology* 19:111-122.

Lunardini, V.J. 1981. *Heat Transfer in Cold Climates*. Toronto: Van Nostrand Reinhold Company, 731 pp.

Outcalt, S.I., Nelson, F.E. & Hinkle, K.E. 1990. The zero curtain effect: heat and mass transfer across an isothermal region in freezing soil. *Water Resources Research* 26: 1509-1516.

Rutter, N.W., Minning, G.V. & Netterville, J.A. 1980. Surficial Geology and Geomorphology, Fort Simpson, District of Mackenzie. *Geological Survey of Canada, Preliminary Map 3-1978*.

Shur Y.L. & Jorgenson, M.T. 2007. Patterns of permafrost formation and degradation in relation to climate and ecosystems. *Permafrost and Periglacial Processes* 18: 7-19.

Smith, S.L., Burgess, M.M., Chartrand, J. & Lawrence, D.E. 2005. *Digital Borehole Geothechnical Database for the Mackenzie Valley/Delta Region.* Geological Survey of Canada, Open File 4924, 30 pp.

Smith, M.W. & Riseborough, D.W. 1996. Permafrost Monitoring and Detection of Climate Change. *Permafrost and Periglacial Processes* 7: 301-309.

Taylor, A., Burgess, M., Judge, A., Allen, V. & Wilkinson, A. 1998. Canadian Geothermal Data Collection - Deep permafrost temperatures and thickness of permafrost. In: *International Permafrost Association, Data and Information Working Group, comp. Circumpolar Active-Layer Permafrost System (CAPS).* Boulder, Colorado: NSIDC.

Wright, J.F., Duchesne, C., Nixon, F.M. & Côté, M.M. 2001. *Ground Thermal Modeling in Support of Terrain Evaluation and Route Selection in the Mackenzie River Valley.* Summary Report, CCAF Project A073, Natural Resources Canada, 53 pp.

Wright, J.F., Duchesne, C. & Côté, M.M. 2003. Regional-scale permafrost mapping using the TTOP ground temperature model. *Proceedings of the Eighth International Conference on Permafrost, Zurich, Switzerland, 2003*: 1241-1246.

Variable Rate Modeling of Fluvial Thermal Erosion

L. Dupeyrat
UMR8148-IDES, CNRS-UPS, bât 509, Université Paris-Sud-11, 91405 Orsay, France
R. Randriamazaoro
Labo.P.M.T.M. Bat : L2, Institut Galilée Université Paris 13, Av. J. B. Clément 93430 Villetaneuse, France
F. Costard
UMR8148-IDES, CNRS-UPS, bât 509, Université Paris-Sud-11, 91405 Orsay, France
E. Carey Gailhardis
UMR8148-IDES, CNRS-UPS, bât 509, Université Paris-Sud-11, 91405 Orsay, France

Abstract

In periglacial regions, frozen river banks are affected by thermal and mechanical erosion. In Siberia, bank retreat of up to 40 m per year is observed. This thermal erosion occurs during a few weeks, at springtime, with high enough water temperatures and river discharges. Until now, models of thermal erosion have been based on the assumption of a constant melting rate. We have developed a more general model at variable rate, whose solution is calculated with the integral method. Results of this model are compared with experiments, carried out in a cold room. The model has contributed to better understanding of the roles of each parameter during the thermal erosion process. The duration of such an acceleration phase is systematically studied.

Keywords: ablation; heat balance integral method; periglacial river; permafrost; phase change; thermal erosion.

Introduction

Most periglacial rivers exhibit a breakup period and a flood season associated with high discharge rates and high water temperatures. The Lena River in Siberia and its tributaries can be divided into two classes (1) the Lena basin outlet and (2) the southern sub-basins (Aldan, upper Lena, Vilui valley). A relatively low stream temperature variation and a high discharge variation characterize the Lena basin outlet. The stream temperature varies from 0°C to 14°C, and the discharges can reach 100,000 m^3/s in early June (Gautier et al. 2003, Liu et al. 2005, Yang et al. 2002). In the second case, the southern sub-basins are characterized by relatively high stream temperature and low discharge. For these rivers, stream temperatures are up to 4°C higher than those of the Lena outlet (Liu et al. 2005) and can reach 18°C; the discharges are about ten times smaller than those in the Lena basin outlet (Liu et al. 2005, Yang et al. 2002). During the break-up and flood seasons the water flow in permanent contact with frozen river banks induces both a fluvial thermal and mechanical erosion. This problem is non-linear because it involves a moving boundary (an interface between solid and liquid) whose location is unknown. Until now, models of thermal erosion based on the assumption of a constant melting rate for a constant convective flux at the interface have been used to study thermal erosion of ice and permafrost (Costard et al. 1999). The objective of this study is to propose a model of thermal erosion of permafrost without the simplified assumption of a constant melt rate. Once validated by the comparison with laboratory experiments, the model will be applied to the Siberian rivers case.

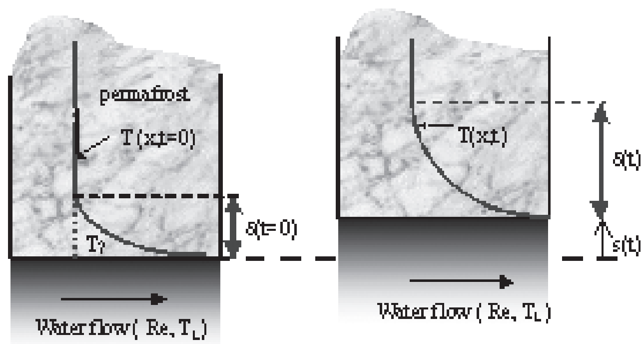

Figure 1. (a) The initially isothermal permafrost (T_∞) is suddenly heated by a permanent water flow (Re, T_L). After a rapid transient phase, the interface reaches the melting temperature (T_m=0°C). Then the thermal erosion initiates, and the interface starts to move. (b) The interface progressively moves. Its instantaneous position and erosion rate are given by s(t) and ds/dt. The instantaneous thickness of the thermal boundary layer is δ(t).

The Ablation Model at Variable Rate

Mathematical model

A semi-infinite permafrost sample initially at a uniform negative temperature (T_∞) is suddenly heated by a turbulent water flow of permanent temperature (T_L) and discharge (Q_L) (Fig. 1).

We suppose that all the sediment is immediately swept away by mechanical action of the water flow. The heat transfer occurs by conduction inside the permafrost (Eq. 1). At the permafrost-water interface, the convective heat flux from the water flow must balance the latent heat absorbed by melting, added to the conductive heat flux in the solid (Eq. 2).

$$\frac{\partial T}{\partial t} = \left(\frac{k}{\rho.c_p}\right)\frac{\partial}{\partial x}\left(\frac{\partial T}{\partial x}\right) \qquad x \geq s(t) \tag{1}$$

$$h(T_L - T_m) = \rho L \frac{\partial s}{\partial t} - k\left(\frac{\partial T}{\partial x}\right)_{x=s} \quad x = s(t) \tag{2}$$

where k [W m^{-1} K^{-1}], ρ [kg m^{-3}], cp [J kg^{-1} K^{-1}] and L [J/kg] are the thermal conductivity, the density, the specific heat, and the latent heat of melting of the permafrost, and h [W m^{-2} s^{-1}] is the heat transfer coefficient between turbulent water and permafrost.

Resolution by the heat balance integral method

The heat-balance integral method consists of integrating the heat conduction equation (Eq. 3) over the thermal layer $\delta(t)$. It is based on the assumption of a quadratic boundary layer temperature (Eq. 4).

$$\frac{\partial}{\partial t}\int_s^{\delta} T dx = \left(\frac{k}{\rho.c_p}\right)\left[\left.\frac{\partial T(x,t)}{\partial x}\right|_{x=\delta} - \left.\frac{\partial T(x,t)}{\partial x}\right|_{x=s}\right] \tag{3}$$

$$T(x,t) = T_\infty\left[-2\left(\frac{x-s}{\delta-s}\right) + \left(\frac{x-s}{\delta-s}\right)^2\right] \quad s(t) < x < \delta(t), \tag{4}$$

The temperature distribution (Eq. 4) is substituted in Equation 1 and the heat equation is integrated (Eq. 3), applying boundary and initial conditions. Then, solutions in a-dimensional form are obtained (Goodman 1958). The system of Goodman (1958) is solved for every time t during the thermal erosion process in order to get the instantaneous thermal boundary layer $\delta(t)$ and eroded thickness $s(t)$ (Randriamazaoro et al. 2007).

Results

Both the thermal boundary layer and the ablation rate increase (acceleration phase) and stabilize (stationary phase) towards asymptotic values (Eqs. 5, 6), which correspond to the solutions of the constant rate-melting model (Aguirre et al. 1994, Costard et al. 2003).

$$\delta_{lim} = \frac{2.k.L}{c_{p.}.q_{conv}} \tag{5}$$

$$\left(\frac{ds(t)}{dt}\right)_{lim} = \frac{q_{conv}}{\rho L + \rho.c_{p.}(T_\infty - T_m)} \tag{6}$$

where q_{conv} is the heat flux exchanged by convection at the interface between the water flow and the permafrost and includes both the effects of water temperature and discharge (Eq. 7).

$$q_{conv} = h.(T_L - T_f) \tag{7}$$

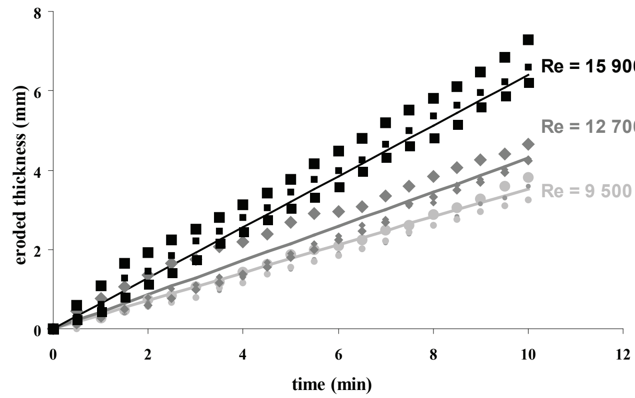

Figure 2. Measurements of eroded thickness of pure ice initially at –7.5°C, heated by a turbulent water flow at 5.5°C. In 10 minutes, the measured eroded thickness of the ice sample is 3.5 mm, 4.5 mm, 6.5 mm for Re=9500, 12,700, and 15,900 respectively.

Our model is validated by measurements of instantaneous eroded thickness of ice and permafrost samples in contact with a turbulent water flow in a cold room (Costard et al. 2003). One set of experiments is done on ice samples at an initial temperature equal to -7.5°C and the water temperature remains at 5.5°C during the experiments. Different Reynolds numbers are investigated. The ablation rate increases with the Reynolds number (Fig. 2).

Experiments suggest that the eroded thickness increases linearly with time (Fig. 2). Considering a stationary erosion rate, the measured erosion rate of ice is equal to 0.35 mm/min, 0.45 mm/min, and 0.65 mm/min for Re = 9500, 12,700, and 15,900 respectively. We tested our model to these particular experimental conditions (Fig. 3). The model predicts a first phase of acceleration during which both the thermal boundary layer and the erosion rate increase (Fig. 3). This first phase lasts a few minutes. The asymptotic values of the calculated ablation rate (Fig. 3) are consistent with the measured values (Fig. 2).

Other experiments are done on frozen ice sand samples (initially at –7.5°C) with different massic ice contents (ω=20%, 80%) and are compared with pure ice (Fig. 4). The turbulent water flow remains at 5.5°C and the Reynolds number is equal to 15,900.

The model is applied to these particular conditions, and again the experiments and the model are consistent (Figs. 4, 5).

The effects of the water temperature and the ice temperature are also investigated. The effects of the water temperature are predominant, whereas the effects of the ice temperature are very weak. The erosion rate increases with water temperature, ice temperature, and Reynolds number and decreases with the ice content. The model at variable rate predicts a first acceleration phase whose duration is typically greater for smaller erosion rates.

Then the model is applied to the Lena River. The convective heat flux is calculated (Eq. 7) for water temperature between 0°C and 20°C and for water discharges between 0 m^3/s and 120,000 m^3/s. The heat transfer coefficient h is estimated,

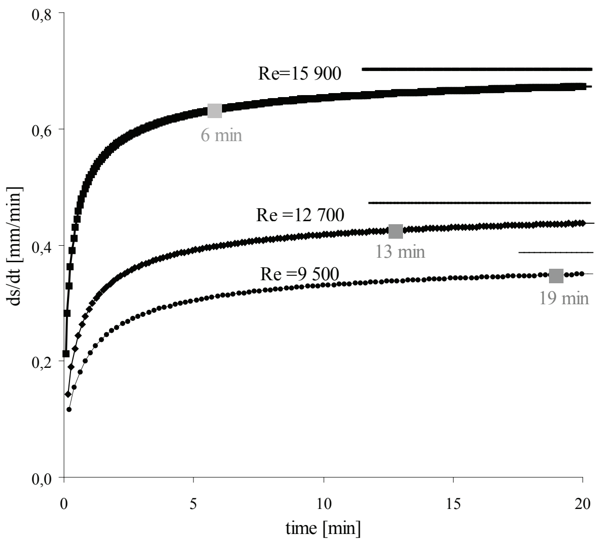

Figure 3. Theoretical erosion rate as a function of time for a water temperature equal to 5.5°C, an ice temperature equal to 7.5°C and different Reynolds numbers (Re=9500, 12,700, and 15,900) applied to the geometry of our hydraulic channel. The erosion rate increases rapidly (acceleration phase) and stabilises (stationary phase). The duration of the acceleration phase is calculated from the time necessary to reach 90% of the asymptotic value. The greater the Reynolds number, the greater the erosion rate and the smaller the duration of the acceleration phase. Measured values (Fig. 2) are consistent with the asymptotic calculated values.

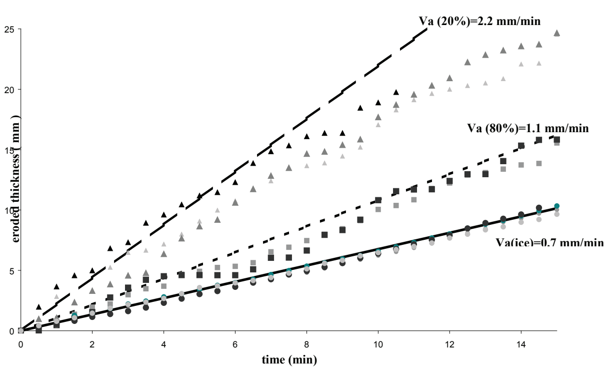

Figure 4. Measurements of eroded thickness of pure ice and sandy permafrost with different ice contents, initially at −7.5°C, heated by a turbulent water flow (5.5°C and Re=15,900). In 10 minutes, the measured eroded thickness is about 6 mm, 11 mm, 18 mm for pure ice, permafrost with ω=80%, and ω=20% respectively. Linear fit gives measured erosion rates equal to 0.7 mm/min, 1.1 mm/min and 2.2 mm/min for pure ice, permafrost with ω=80% and ω=20% respectively.

using the empirical law of Lunardini (1986) (A=0.0078, α=0.3333, β=0.9270) and the Manning equation applied to the geometry of the channel (Eqn. 8) (Costard et al. 2003).

$$h = A\left[\left(\frac{\sqrt{s}}{n}\right)^{3/5} l^{\,3/5-\beta}\right]\left[\mathrm{Pr}^{\,\alpha}\,\frac{k_w}{\upsilon_w{}^{\beta}}\right]Q^{\,\beta-3/5} \tag{8}$$

where S = 0.0001 m/m, n = 0.1, l = 10 km, k_w, v_w, Pr are the

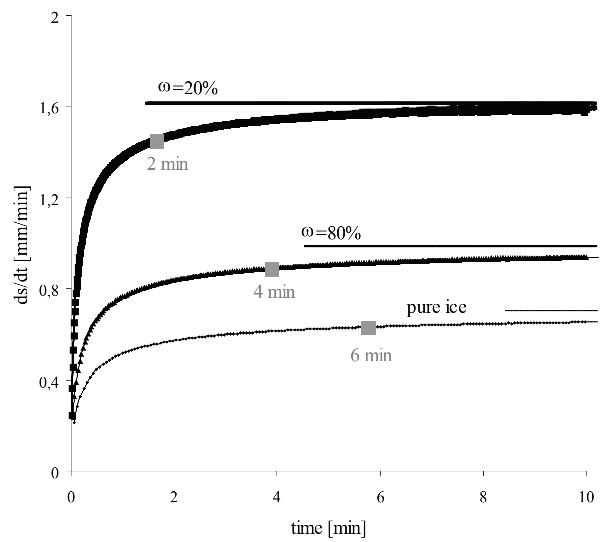

Figure 5. Theoretical erosion rate as a function of time for a water temperature equal to 5.5°C, an ice temperature equal to 7.5°C a Reynolds number equal to 15,900, applied to the geometry of our hydraulic channel. The erosion rate increases rapidly (acceleration phase) and stabilizes (stationary phase). The smaller the ice content, the greater the erosion rate and the smaller the duration of the acceleration phase. Measured values are consistent with the asymptotic values.

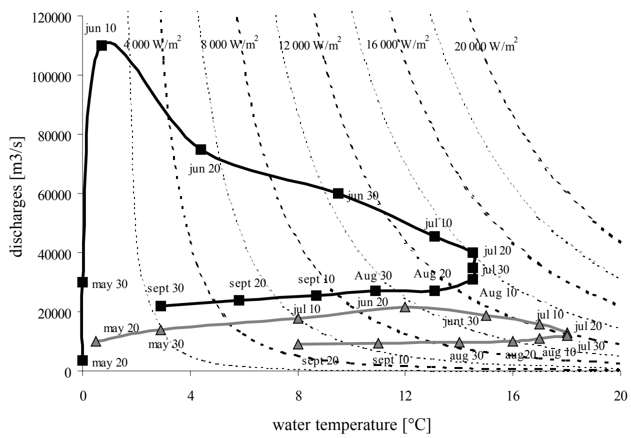

Figure 6. Diagram of heat flux versus discharge and water temperature.
---------- Isoflux lines (2 000 – 20 000 W/m²)
■ Water mean temperatures and discharges in the Lena basin outlet (Yang et al. 2002, Liu et al. 2005)
Δ Water mean temperatures and discharges in the Lena sub-basins (Aldan, Upper Lena, Vilui basin (Liu et al. 2005)).

longitudinal slope, the Manning roughness coefficient, the width of the river, the thermal conductivity of water [W m^{-1} K^{-1}], the cinematic viscosity of water [m^2 s^{-1}], and the Prandtl number, respectively.

Isoflux lines are plotted from the calculated values of the convective heat flux (Fig. 6). On this diagram, simultaneous measurements of water temperatures and discharges in the Lena basin outlet and the southern Lena sub-basins (Yang et al. 2002, Liu et al. 2005) every 10 days during the flood season are reported.

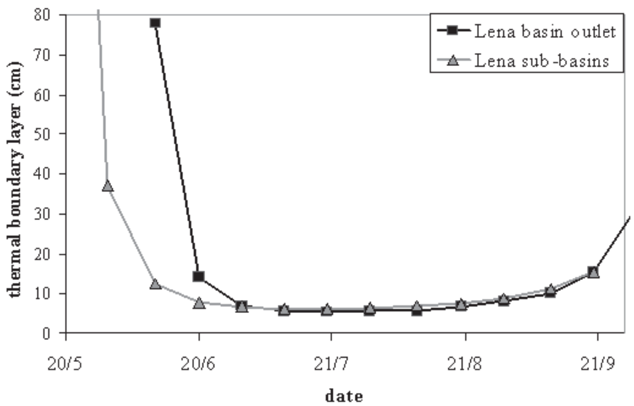

Figure 7. Evolution of the calculated thermal boundary layer thickness for the Lena basin outlet and the Lena sub-basins.

As expected, the heat flux increases when the water temperature and the discharge increase simultaneously from May to mid-June. By contrast, from June to July the water temperature is still increasing, while the discharge decreases by about 50%, and a positive trend of the heat flux is still observed. The maximum (12,000 W/m² and 14,000 W/m² for the southern Lena sub basin and for the Lena basin outlet, respectively) of the heat flux occurs during July when water reaches its maximum temperature. It appears that the convective heat flux evolution mainly depends on the water temperature evolution for Siberian rivers during the flood season. The heat flux variation for the Aldan, Upper Lena, and Vilui Rivers is similar to the one of the Lena basin outlet. The relative higher values of water temperatures for the southern Lena sub-basin are compensated by the relative higher values of the discharges for the Lena basin outlet.

With regards to specific heat flow, the application of the model of variable rate on pure ice or permafrost should allow determination of the thermal boundary layer thickness (Fig. 7), the ablation rate, and the duration of the acceleration phase (Fig. 8).

The greater the convective heat flux, the greater the erosion rate and the smaller the duration of the acceleration phase. The most favorable conditions to get the longer acceleration phase are obtained for the smaller values of the erosion rate at the beginning (early May) or at the end (October) of the flood season. For example, considering a small thermal erosion rate 0.06 mm/min (early May), the acceleration phase should last about 14 days.

Conclusions

A model of the fluvial thermal erosion has been formulated at variable rate. This mathematical model has been applied to a typical frozen river bank in permanent contact with a turbulent water flow. The expressions of the instantaneous melting thickness, ablation rate, and thermal boundary layer have been obtained by integral method and validated by experiments on ice samples. An acceleration phase occurs at the beginning of the process. The duration of this acceleration phase is quantified. Typically, the acceleration phase lasts longer for a low ablation rate. The ablation rate increases with water temperature and discharge and decreases with ice content. The effects of stream temperature and discharge can be represented by the convective heat flux. The heat flux along the river banks are identical for the Lena basin outlet and for the southern Lena basin because relative higher values of stream temperatures for the southern Lena sub-basin are compensated by the relative higher values of the discharges for the Lena basin outlet. From our studies, the stream temperature is an important parameter which controls the evolution of the erosion rate during the flood season. Further studies will take into account the possible effect of global warming on the thermal erosion rate.

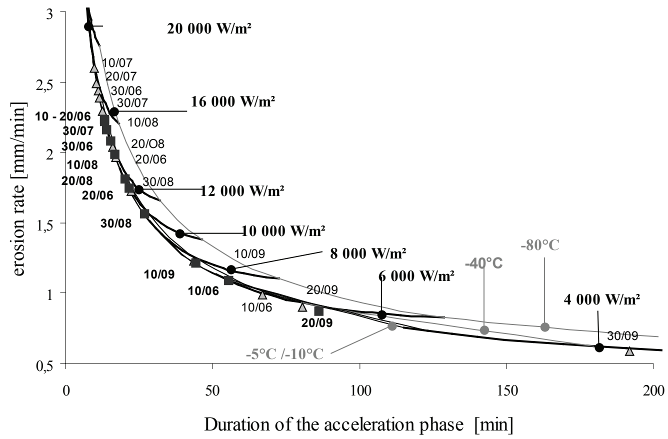

Figure 8. Diagram of ablation rate and duration of acceleration phase for various convective heat flux and ice temperature) –
━━ Isoflux lines (4000–20,000 W/m^2)
—— Isothermal lines (-10°C to -80°C)
□ Ablation rate and duration of the acceleration phase in the Lena basin outlet
Δ Ablation rate and duration of the acceleration phase in the Lena tributaries (Aldan, Upper Lena, Vilui basin).

Acknowledgments

Hydrological data were obtained from the Hydro-Meteorological Center under the auspices of the Permafrost Institute at Yakutsk. This program is supported by "Programme Reliefs de la Terre" INSU, CNRS, France, and GDR «mutations polaires: société et environnement».

References

Aguirre-Puente, J., Costard, F. & Posado-Cano, R. 1994. Contribution to the study of thermal erosion on mars. *Journal of Geophysical Research* 99: 5657-5667.

Costard, F. & Aguirre-Puente, J. 1999. Martian fluvial-thermal erosion: laboratory simulation. *Journal of Geophysical Research* 104: 14.091-14.098.

Costard, F., Dupeyrat, L., Gautier, E. & Carry-Gailhardis, E. 2003. Fluvial thermal erosion investigation along a rapid eroding river bank: application to the Lena river (central Siberia). *Earth Surface Processes and Landforms* 29: 1349-1359.

Gautier, E., Brunstein, D., Costard, F. & Lodina, R. 2003. Fluvial dynamics in a deep permafrost zone: the case of the middle Lena river (Central Yakutia). *Proceedings of the eighth International Permafrost Conference, Switzerland, Zurich, July 21-25, 2003:* 271-275.

Goodman, T.R. 1958. The heat-balance integral and its applications to problems involving a change phase. *Transaction ASME* 80: 335-342.

Liu, B., Yang, B. Ye & Berezovskaya, S. 2005. Long-term open-water season stream temperature variations and changes over Lena River Basin in Siberia. *Global and Planetary Change* 48: 96-111.

Lunardini, V.L., Zisson, J.R. & Yen, Y.C. 1986. *Experimental Determination of Heat Transfer Coefficients in Water Flowing Over Horizontal Ice Sheet.* CREEL Report 86-3. US Army Cold Regions Research and Engineering Laboratory.

Randriamazaoro, R., Dupeyrat, L., Costard, L. & Carey-Gailhardis, E. 2007. Fluvial thermal erosion: heat balance integral method. *Earth Surface Processes and Landforms* 32: 1828-1840.

Yang, D., Douglas, L.K., Hinzman, L., Zhang, T. & Ye, H. 2002. Siberian Lena River hydrologic regime and recent change. *Journal of Geophysical Research* 107: 4694. DOI : 10.1029/2002JD002542.

Modeling Mountain Permafrost Distribution: A New Permafrost Map of Austria

Barbara Ebohon
Department of Geography and Geology, University of Salzburg, Austria
Lothar Schrott
Department of Geography and Geology, University of Salzburg, Austria

Abstract

Alpine permafrost response is very sensitive to climate change. Thus, it is of great interest to estimate and assess permafrost distribution in high mountain areas. In this study, the permafrost distribution of the Austrian Alps was modeled by using commands of the programs PERMAKART (for steep slopes) and PERM (for footslope-positions) which were applied in a DTM with a resolution of 50 m. Possible and probable permafrost areas of the Austrian Alps comprise approximately 1600 km². The potential permafrost area has been compared with BTS, spring temperature measurements, alpine meadows, and isotherms of the MAAT (mean annual air temperature). The results of the validation show that the map still needs some improvement on a local scale, but simulates the possible and probable permafrost distribution of the Austrian Alps as a good general overview.

Keywords: alpine permafrost; Austrian Alps; simulation; validation.

Introduction

Several studies carried out in the Austrian Alps have shown permafrost distribution above approximately 2500 m a.s.l. (Lieb 1998). Current global warming already causes a degradation of permafrost in some mountain regions.

Of particular interest are areas with discontinuous permafrost on steep talus slopes and rock walls. Due to the absence of a blocky layer, rock faces react quickly to climate change compared with debris-covered slopes (Gruber et al. 2004, Mittaz et al. 2000). In densely populated and developed mountain areas (e.g., ski resorts, etc.), where a degradation of permafrost, in particular at its lower limit could cause enhanced debris flow and rockfall activity, mapping and modeling of permafrost distribution is an important prerequisite to prevent natural hazards and risks.

In Switzerland, Haeberli has already started to publish profound knowledge about permafrost distribution in the year 1975. Afterwards a lot of empirical models were developed (e.g., PERMAKART: Keller 1992, PERMAMAP: Hoelzle 1994, PERM: Imhof 1996, PERMAMOD: Frauenfelder 1998). Now, also complex process-oriented models (e.g., PERMEBAL: Stocker-Mittaz et al. 2002), which are based on the particular understanding of the energy fluxes between permafrost and the atmosphere (Hoelzle et al. 2001, Etzelmueller et al. 2001), are already available. However, until recently, the possible and probable permafrost distribution in Austria has been mapped and modeled for only a few local regions (e.g., parts of the High and Low Tauern range) (Lieb 1996, Lieb 1998, Kellerer-Pirklbauer 2005).

Compared to Switzerland, Austria has much less direct (e.g., BTS, geophysics) and indirect data of permafrost occurrence; therefore, modeling of permafrost distribution is just slightly developing.

The aim of this study is to model the permafrost distribution for the entire Austrian Alps by adjusted lower limits for possible and probable permafrost with a simple model considering the relation between slope, altitude, aspect, and permafrost occurrence. In this approach, the often-used trisection of sporadic (<30%), discontinuous (30–80%) and continuous (>80%) permafrost (Nyenhuis 2006) is applied, where sporadic equals possible and discontinuous equals probable permafrost.

Table 1. Values used for the simulation.

	Permafrost possible (sporadic)		Permafrost probable (discontinuous)	
	Steep Slopes	Foot-slope positions	Steep Slopes	Foot-slope positions
N	2300 m a.s.l.	1690 m a.s.l.	2500 m a.s.l.	2410m a.s.l.
NE	2450 m a.s.l.	2100 m a.s.l.	2600 m a.s.l.	2500m a.s.l.
E	2575 m a.s.l.	2220 m a.s.l.	2720 m a.s.l.	2520m a.s.l.
SE	2700 m a.s.l.	2230 m a.s.l.	2850 m a.s.l.	2630m a.s.l.
S	2900 m a.s.l.	2340 m a.s.l.	2900 m a.s.l.	2690m a.s.l.
SW	2650 m a.s.l.	2230 m a.s.l.	2850 m a.s.l.	2630m a.s.l.
W	2600 m a.s.l.	2160 m a.s.l.	2700 m a.s.l.	2510m a.s.l.
NW	2530 m a.s.l.	2120 m a.s.l.	2580 m a.s.l.	2470m a.s.l.
Flat areas	Permafrost possible (sporadic)		Permafrost probable (discontinuous)	
Wind-exposed	2590m a.s.l.		2710m a.s.l.	
Sheltered from wind	2640m a.s.l.		2900m a.s.l.	

Although such a map has, inherently, a limited accuracy, it allows approximations of the permafrost distribution on a national scale and enables comparisons with other Alpine provinces and countries (Frauenfelder et al. 1998).

Austria is positioned at the edge of the eastern margin of the Alps. The absolute heights of mountain ranges decline from west to east in Austria, so that the permafrost areas have their maximum extension in the western federal states.

Methods

The first well-known permafrost model in Central Europe, known as PERMAKART, has been introduced by Keller (1992). PERMAKART is implemented into the GIS-software ARC INFO. On the basis of the topo-climatic key from Heaberli (1975), which analyses the relation between slope, altitude, aspect, and permafrost occurrence, the model is able to distinguish between probable, possible, and no permafrost.

The model PERM (Imhof 1996) is also mostly based on the topo-climatic key from Heaberli (1975), but has been implemented into the raster-GIS-system IDRISI. For the calculation of the foot-slope positions, the differentiating GIS-System didn't offer the same possibilities as ARC VIEW. Therefore, foot-slope positions are generated manually through a smoothing of the DTM.

To work in detectible paces, every step was reproduced in ArcGIS9. Since the empirical values for the simulation (limits of possible and probable permafrost distribution related to altitude, aspect, slope- and footslope-positions) were originally deduced and calibrated for the Upper Engadine in the eastern Swiss Alps (Haeberli 1975), it was necessary to adjust them to the eastern Alps. Values of the lower limits of discontinuous permafrost in the central Alps of Austria were used after Lieb (1998) to model the probable permafrost distribution. Since values for the lower limit of possible permafrost were not available, they have been deduced from the relation between lower limits of possible to probable permafrost in Switzerland.

For the calculation of the lower limit of permafrost for wind-exposed areas, mean elevation values of steep slopes are generated for probable and possible permafrost. Concerning regions of possible permafrost, the lower limit for wind-sheltered areas lays 50 m above the one for wind exposed regions. For wind-sheltered areas, the highest value (2900 m a.s.l.) is used to determine the lower boundary of probable permafrost.

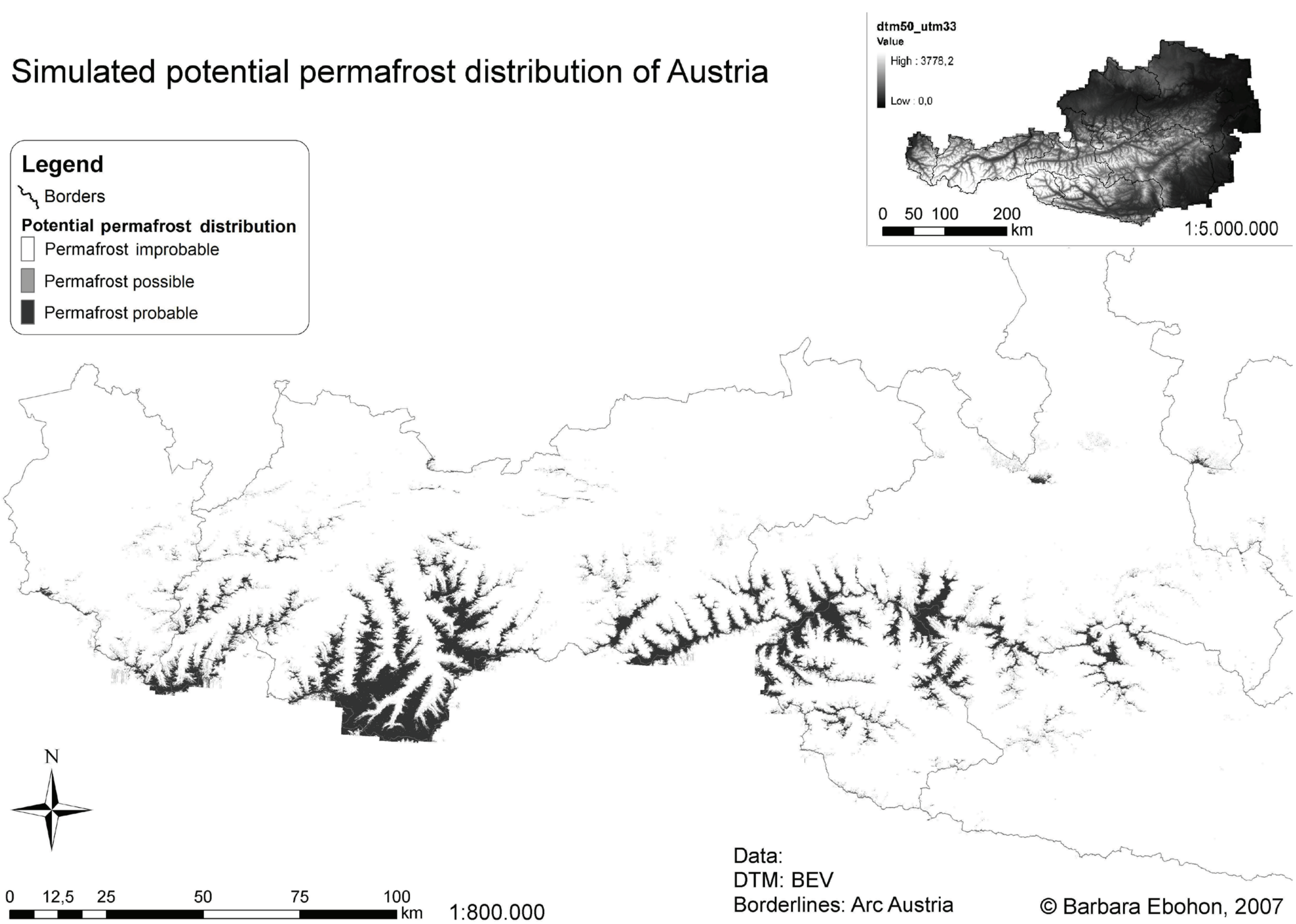

Figure 1. Map of the permafrost distribution of Austria showing the total permafrost territory of about 1600 km² (The difference between possible and probable permafrost can not be seen in this resolution: for higher resolution please see Figs. 5 and 6.).

Previous studies using PERMAKART and PERM show that this application of permafrost modeling, utilized on a nationwide scale, allows good approximations of permafrost distribution.

In a first approach, queries similar to the model PERMAKART (Keller 1994) were used to simulate permafrost of steep slopes. A map of inclination was produced and utilized to highlight all areas above the limits of possible and probable permafrost steeper than 10°, subdivided into different aspects.

The footslope-positions were worked out through a calculation of the curvature similar to the model PERM (Imhof 1992): First the DTM was smoothed, and then the original DTM was subtracted from the smoothed DTM. Areas which show values above zero are supposed to be convex regions, while all values below zero show concavities. In a next step, a map which pointed out all regions flatter than 10° was produced. This step allowed determining all flat and concave areas.

Afterwards all areas steeper than 10° were extracted and hemmed with a 150 m buffer. Following those queries, areas could be extracted which are concave, flat, and not more than 150 m away from steep slopes. On these footslope-positions the values for possible and probable permafrost were applied.

In this context, Haeberli (1975) and Etzelmueller (2001) stated that, in flat areas, the influence of air temperature is much more important than differences in radiation. Following that, flat, concave (troughs), and convex (domes) areas with less than 10° inclination above the lower limit of possible and probable permafrost were pictured.

All queries were summed and applied on a DTM with a resolution of 50 m using the UTM-coordinate system.

Table 2. Comparison of the results from the model starting to calculate steep slopes at 5° and at 10° inclination.

	5°model	10° model
Permafrost possible	711 km²	721 km²
Permafrost probable	899 km²	873 km²
Permafrost distribution (total)	1610 km²	1594 km²

Table 3: Relative permafrost areas of Austria (%) by federal states.

	Permafrost total	Permafrost possible	Permafrost probable
Burgenland	0.00	0.00	0.00
Carinthia	1.65	0.87	0.78
Lower Austria	0.00	0.00	0.00
Upper Austria	0.04	0.03	0.01
Salzburg	2.76	1.48	1.28
Styria	0.05	0.05	0.00
Tirol	9.28	3.84	5.44
Vorarlberg	1.90	1.28	0.61
Vienna	0.00	0.00	0.00
Austria	1.90	0.86	1.04

Results and Validation

Results

The permafrost map displays areas with improbable (equals no permafrost), possible, and probable permafrost and gives an overview of regional differences. At first sight, there is a strong dominance of permafrost occurrence in the western higher part of Austria, whereas the eastern part shows a somewhat patchy distribution.

To pay attention to different inclination thresholds discussed in the literature (5°/10°), two models with different conditions were applied. It is surprising that there are hardly differences in the calculated permafrost areas between the model which started calculating steep slopes at 5° inclination and the second one taking 10° into consideration. In the calculations that follow, the results of the 10° model were used.

Modeling results show that 1.9% of the territory of Austria can be assigned to mountain permafrost. This corresponds to an area of approximately 1600 km².

In Tyrol, 9.3% of the area is underlain by permafrost. This is a significant proportion compared to values for Switzerland (between 4 and 6%). Estimates for Salzburg, Vorarlberg, and Carinthia vary between 2 and 3%.

Validation

Validation was primarily a comparing of the modeling results with data from basal snow temperature measurements (BTS) and spring water temperatures.

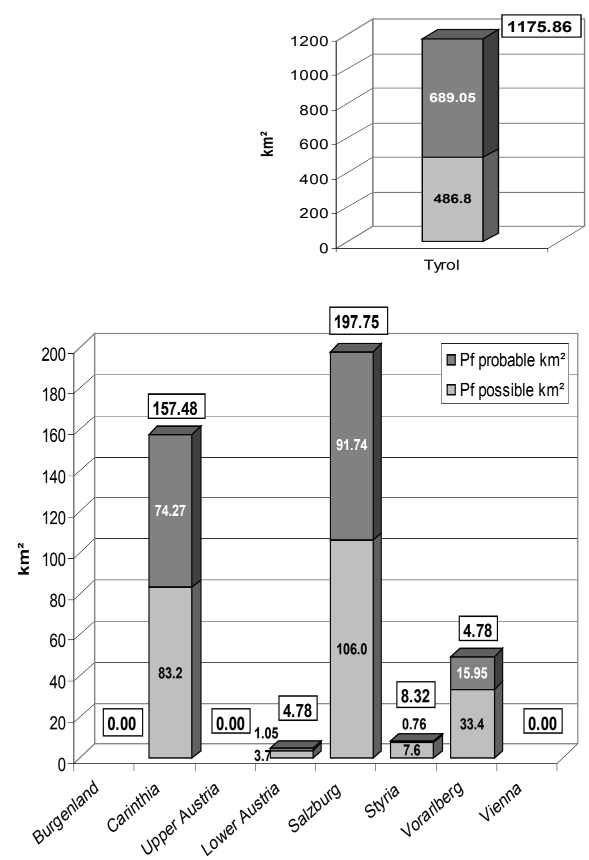

Figure 2a, 2b. Potential permafrost distribution of Austria in km².

Summarizing all measurements from local study sites such as Kaisergratspitz, Oelgrube, Sulzkar, Goessnitzvalley/ Langvalley, Hoher Sonnblick, Doesener Valley, Reisseck, and Hafergruppe, data from 300 point measurements allow a quick and reasonably good approximation of regional permafrost distribution.

Following the comparison between the simulated area with the measuring points, 48.7% of the measurements (BTS, spring water temperatures) match the three simulated categories (no PF, possible PF, probable PF). However, it should be noted that many points are just slightly outside the simulated permafrost area and probably a problem of DTM resolution or imprecise information of the point measurements which were mostly analogue and subsequently digitized for the validation. Combining the two categories, "PF possible" and "PF probable," into one entire zone, already 71.1% of the point measurements (BTS and spring water temperature data) used for validation accord with this calculation. Zoning the area of simulated permafrost after different exposures, it should be stated that N, NE, and SE are mapped well, and E, S, and SW are relatively well-presented. W and NW need further investigation on a local scale.

It can also be mentioned, that areas of rockslopes without vegetation, extracted from CORINE-Data 2000 (Aubrecht 1998), often match the modeled areas of permafrost.

Comparing the simulated permafrost area with the distribution of alpine meadows (CORINE 2000), only about 3% (44.5 km²) of simulated potential permafrost distribution intersects with them (Fig. 5). It has to be considered that permafrost and vegetation exclude each other often, but not always. It is notable that most intersections are northerly exposures. Therefore, northern aspects should be investigated more precisely on a local scale (e.g., grain size analyses, lithology, etc.).

It is well known that permafrost probably exists above certain threshold values concerning the MAAT (mean annual air temperature). Following this approach, another adjustment is made through the comparison of simulated permafrost areas with calculated isotherms based on MAAT from 1961–1990 and a total of 117 measurement stations and contour lines. The calculated isotherms mostly lay some few meters above the contour lines applied by Lieb (1996), who used the threshold of 2250 m a.s.l. for discontinuous permafrost

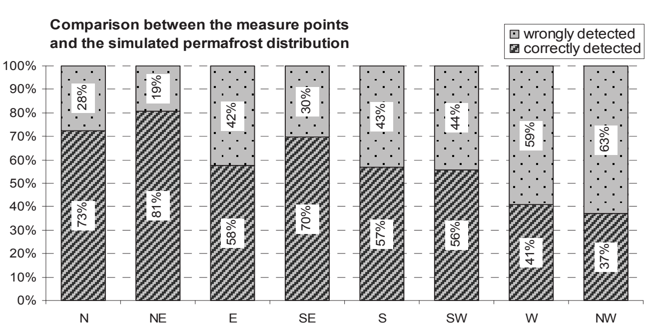

Figure 3. Comparison between measurement points (BTS, spring water temperatures) and permafrost occurrence (simulated permafrost distribution), differentiated in aspects.

and 3250 m a.s.l. for continuous permafrost. Comparatively, areas above the -2°C isotherm refer to discontinuous permafrost, while areas above the -6°C isotherm point to continuous permafrost. It must be stated, that only a small zone of continuous permafrost can be expected in Austria because most of the areas above -6°C MAAT are occupied by glaciers. In the N, NW, and NE aspects, the borderlines of discontinuous permafrost match the modeled area quite well, while in the SW, S, and SE aspects, borderlines are much lower than the limit of simulated permafrost.

Discussion

In summary, the simulation gives a useful overview of possible and probable permafrost distribution in the Austrian Alps. There are, however, still some unsolved problems and inaccuracies. As Keller & Hoelzle (1996) stated, one big issue is the appointment of the critical inclination, which differentiates between steep and moderate slopes. The approach presented has shown that there are minor differences between the permafrost areas calculated with the two models (5 and 10° inclination), but it remains unclear whether a threshold above 10° would show better results.

Also, the distinction between western and eastern Austria should be analyzed in more detail according to well-known temperature differences.

Improvements to this study would also be achieved by including more data on rock glaciers and higher resolution DTM data to better represent the strongly differentiated relief of the Austrian Alps.

Moreover, the distinction between the two categories—"permafrost possible" and "permafrost probable"—is still problematic because the data used on existing permafrost occurrences are based on point measurements (BTS and spring temperatures) only. The interpolation of these data produces simulated lower boundaries of permafrost distribution with limited accuracy. A further problem is related to the semantic differentiation of possible and probable permafrost, and to the unknown quantitative proportion of permafrost in these categories (Heginbottom 2002).

There are also problems with the values used themselves: they represent only mean values derived from one region in the Upper Tauern. Because of a lack of values for other areas, they were used to model the permafrost distribution for the entire area of Austria.

To improve the accuracy of the regional permafrost distribution map, more validation data from BTS measurements and field geophysics are needed. Furthermore, data should be more uniformly distributed over the Austrian territory.

It would then be possible to rework the empirical approach and to derive values for permafrost distribution. The more empirical data available, the better the adjustment to regional and local conditions would be.

Lieb (1996) stated that the difference between N and S orientation concerning intact rock glaciers is about 273 m (mean value for entire Austria). Whether the accuracy can be raised by adjusting the permafrost boundaries to this value is still an open question.

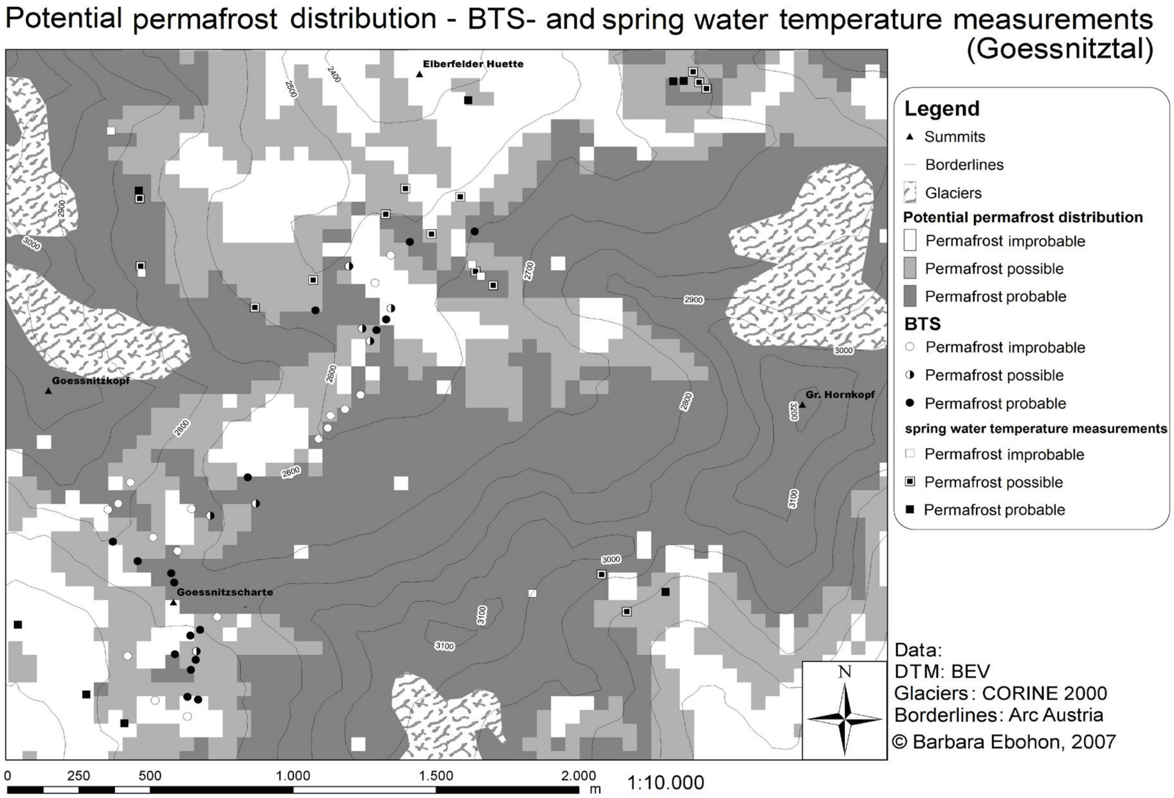

Figure 4. Permafrost distribution compared with BTS data and spring temperature measurements (data: G.K. Lieb, pers.com.).

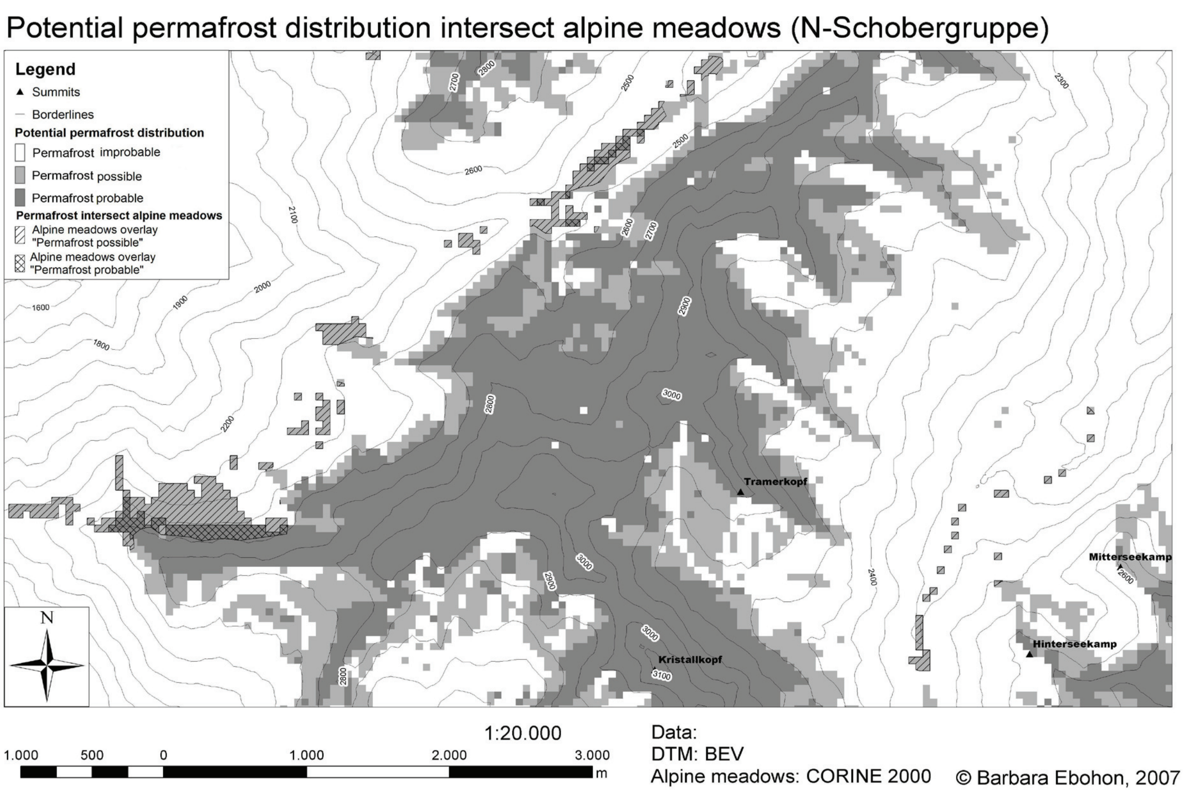

Figure 5. Comparison of simulated permafrost distribution with vegetation (alpine meadows).

Another important issue is the indication of permafrost areas at lower altitudes than expected, which is probably only possible to be pictured through a physically based model. This kind of model is able to reproduce the energy balance, and therefore, can record those areas and should be further developed in future.

Acknowledgments

We gratefully acknowledge the valuable comments by two anonymous reviewers.

Data were kindly provided by:

- Karl Krainer (University of Innsbruck): data from basal snow temperature measurements (BTS).
- Gerhard Karl Lieb (University of Graz): data from basal snow temperature measurements (BTS) and spring water temperature measurements.
- Wolfgang Schöner (ZAMG): Project PERSON (Permafrost-monitoring Sonnblick) GZ BMLFUW-UW.1.3.2/0528-V/5/2005 by order of Lebensministerium.
- Herbert Formayer (University of Natural resources and Applied Life Sciences, Vienna, Austria): Calculated Isotherms.
- Michael Avian (Graz, University of Technology).
- BEV: DTM.

References

Aubrecht, P. 1998. *CORINE Landcover Österreich. Vom Sattelitenbild zum digitalen Bodenbedeckungssatz*. Wien: Umweltbundesamt Monographien, 93: 59 pp.

Etzelmueller, B., Hoelzle, M., Heggem, E.S.F., Isaksen, K., Mittaz, C., Vonder Muehll, D., Ødegård, R.S., Haeberli, W. & Sollid, J.L. 2001. Mapping and modelling the occurrence and distribution of mountain permafrost. *Norwegian Journal of Geography* 55(4): 186-194.

Frauenfelder, R., Allgöwer, B., Haeberli, W. & Hoelzle, M. 1998. Permafrost investigations with GIS – a case study in the Fletschhorn area, Wallis, Swiss Alps. *Proceedings of the 7th International Conference on Permafrost, Yellowknife, Canada, June 23–27, 1998*: 291-295.

Gruber, S., Hoelzle, M. & Haeberli, W. 2004. Rock wall temperatures in the Alps: Modelling their topographic distribution and regional differences. *Permafrost and Periglacial Processes* 15(3): 299-307.

Haeberli, W. 1975. *Untersuchungen zur Verbreitung von Permafrost zwischen Flüelapass und Piz Grialetsch (Graubünden)*. Zürich: Mitteilung der Versuchsanstalt für Wasserbau, Hydrologie und Glaziologie der ETH Zürich, 17: 182 pp.

Heginbottom, J.A. 2002. Permafrost mapping: a review. *Progress in Physical Geography* 26(4): 623-642.

Hoelzle, M. 1994. *Permafrost und Gletscher im Oberengadin—Grundlagen und Anwendungsbeispiele für automatisierte Schätzverfahren*, Zürich: VAW Mitteilung der Versuchsanstalt für Wasserbau, Hydrologie und Glaziologie der ETH Zürich, 132: 121 pp.

Hoelzle, M., Mittaz, C., Etzelmller, B. & Haeberli, W. 2001. Surface energy fluxes and distribution models of permafrost in European mountain areas: an overview of current developments. *Permafrost and Periglacial Processes* 12(1): 53-68.

Imhof, M. 1996. PERM – ein Programm für die automatische Kartierung von Permafrost in den Schweizer Alpen. In: W. Haeberli, M. Hölzle, J.P. Dousse, J.M. Gardaz, M. Imhof, F. Keller, P. Kunz, R. Lugon & E. Reynard, *Simulation der Permafrostverbreitung in den Alpen mit geographischen Informationssystemen. Arbeitsbericht NFP 31*. Zürich: vdf Hochschulverlag, 15-34.

Keller, F. 1992. Automated mapping of mountain permafrost using the program PERMAKART within the geographical information system ARC/INFO. *Permafrost and Periglacial Processes* 3(2): 133-138.

Keller, F. 1994. *Interaktionen zwischen Schnee und Permafrost. Eine Grundlagenstudie im Oberengadin*. Zürich: Mitteilungen der Versuchsanstalt für Wasserbau, Hydrologie und Glaziologie der ETH Zürich, 127: 145 pp.

Keller, F & Hölzle, M. 1996. PERMAKART und PERMAMAP. In: W. Haeberli, M. Hölzle, J.P. Dousse, J.M. Gardaz, M. Imhof, F. Keller, P. Kunz R. Lugon, & E. Reynard, *Simulation der Permafrostverbreitung in den Alpen mit geographischen Informationssystemen, Arbeitsbericht NFP 31*. Zürich: vdf Hochschulverlag, 35-46.

Kellerer-Pirklbauer, A. 2005. Alpine permafrost occurrence at its spatial limits: First results from the eastern margin of the European Alps. *Norwegian Journal of Geography* 59: 184-193.

Lieb, G.K. 2007. personal comment (29.1.2007).

Lieb, G.K. 1996. *Beiträge zur Permafrostforschung in Österreich*. Arbeiten aus dem Institut für Geographie der Karl-Franzens-Universität Graz, 33: 223 pp.

Lieb, G.K. 1998. High-Mountain permafrost in the Austrian Alps (Europe). *Proceedings of the 7th International Conference on Permafrost, Yellowknife, Canada, June 23–27, 1998*: 663-668.

Mittaz, C., Hoelzle, M. & Haeberli, W. 2000. First results and interpretation of energy flux measurements over alpine permafrost. *Annals of Glaciology* 31: 275-280.

Nyenhuis, M. 2006. *Permafrost und Sedimenthaushalt in einem alpinen Geosystem.* Bonn: Bonner Geographische Abhandlungen 116: 142 pp.

Stocker-Mittaz, C., Hoelze, M. & Haeberli, W. 2002. Modelling alpine permafrost distribution based on energy-balance data: a first step. *Permafrost and Periglacial Processes* 13(4): 271-282.

Establishing Initial Conditions for Transient Ground Thermal Modeling in the Mackenzie Valley: A Paleo-Climatic Reconstruction Approach

M. Ednie
Geological Survey of Canada, Ottawa, Ontario, Canada
J.F. Wright
Geological Survey of Canada, Sidney, British Columbia, Canada
C. Duchesne
Geological Survey of Canada, Ottawa, Ontario, Canada

Abstract

The Geological Survey of Canada has implemented a GIS-coupled, finite-element ground thermal model for simulating the response of permafrost in the Mackenzie Valley to progressive climate change. Near-isothermal ground temperature profiles observed in southern portions of the Valley indicate that ground temperatures are presently in disequilibrium with the current climate, and have likely been warming for many decades or centuries. Finite-element methods require specification of initial conditions from which forward modeling can proceed. However, due to the lack of detailed information about current ground temperatures in the region, initial ground temperature profiles for forward modeling must be estimated based on available proxy data. In this work, climate trends observed in the paleo-climatic record are used to reconstruct regional air temperature trends over the past several hundred years. Numerical simulations using this paleo-climate reconstruction successfully reproduce the essential characteristics of the ground temperature regime as observed in borehole records.

Keywords: climate change; numerical model; permafrost; Mackenzie Valley.

Introduction

The Geological Survey of Canada has implemented the T-ONE one-dimensional finite-element ground thermal model (Goodrich 1982) into an ArcGIS platform to simulate the response of permafrost in the Mackenzie valley to progressive climate change. The purpose of the model is to facilitate rigorous and systematic study of the climate-driven evolution of regional ground temperatures as expressed in the present and future distribution and thickness of permafrost (Duchesne et al. 2008). Finite-element models require specification of initial conditions from which forward modeling can proceed, including an initial ground temperature profile for each geographic grid location modeled. Given the limited availability of actual data from instrumented boreholes, present-day ground temperature profiles can be estimated based on transient modeling from an assumed earlier period of quasi-equilibrium to the present. Apart from an initial ground temperature profile, our configuration of the T-ONE model requires specification of rates of change in atmospheric temperature (upper boundary condition) to drive the model according to past and/or future scenarios of climate change, and specification of the regional geothermal heat flux (lower boundary condition). For modeling near-surface ground temperatures, initial profiles can be equilibrated to the atmosphere and ramped using short meteorological data sets (Möldes & Romanovski 2006). However, the deeper ground thermal regime will continue to reflect aspects of the initial climate (such as the presence of deep permafrost) during the equilibrium period even when the ground surface is exposed to sustained atmospheric warming. The specification of initial ground temperature profiles and the time frame selected for modeling from past to present can potentially exert a strong influence on model predictions of the current ground thermal state. Available borehole observations in the discontinuous permafrost zone of the Mackenzie Valley frequently identify near-isothermal conditions close to 0ºC, implying that present day permafrost is in disequilibrium with the current atmospheric temperature regime. This notion is consistent with the observed progressive increase in mean annual air temperatures throughout the Mackenzie Valley during the past century. Taking into account this historic warming trend, we are unlikely to establish a reasonable representation of current ground thermal conditions by employing present-day, or even 20th century climate conditions as a starting point for forward modeling.

This paper describes the reconstruction of mean annual air temperature (MAAT) trends for the Fort Simpson region, NWT, using available climate records and proxy reconstructions of paleo-climatic data to (1) identify a suitable period of quasi-stable regional climate for estimating initial equilibrium ground temperature profiles, and (2) establish an appropriate scenario of climate change from past to present to facilitate prediction of present and future permafrost conditions. We have also compared the results of both equilibrium modeling (driven by contemporary climate data) and transient modeling (from past to present) to ground temperature profiles from selected boreholes in the Mackenzie Valley to illustrate the importance of initial conditions and specification of an appropriate start date for forward modeling.

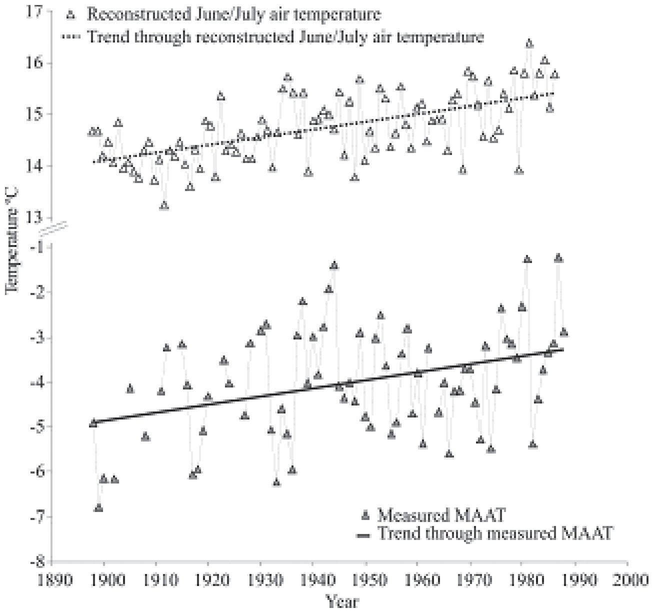

Figure 1. Best-fit lines through MAAT of measured June/July for Fort Simpson and of summer temperature reconstructions (Szeicz & MacDonald 1995) for the period 1898–1988.

Climate Data

Mean annual air temperatures from climate records

We have consolidated available climate data for the study area, consisting of two daily mean air temperature series. (Environment Canada 2002). The most recent data (for the period 1963–2002) were combined with older data (1898–1963) to produce a single continuous temperature series of daily averages. MAAT was calculated from the daily mean values from January 1 through December 31.

Proxy data for reconstructing paleo-climatic trends

A variety of different proxy records can be used to reconstruct past climatic conditions (Gajewski & Atkinson 2003), such as tree rings, lake sediments, ice cores, etc. Proxy data requirements for this study include: acceptable temporal resolution, ready availability, and suitable spatial extent of the reconstruction (site specific, regional, hemispherical, or global). Of these proxy types, tree rings satisfy the majority of the requirements. A limitation of the temperature reconstructions from tree rings is that they are specific to summer temperatures only and lack the contribution of winter months on the MAAT (Jones et al. 2003). A summer air temperature (June/July) reconstruction by Szeicz and MacDonald (1995) was selected out of a group of available data sets. The authors used age-dependent tree ring modeling to derive estimates of average summer air temperatures from AD 1638–1988. Their study provides important information on climate change trends over a relatively long time period for a region that is geographically consistent with the Fort Simpson study area. The data used for the climate reconstruction are available from the NOAA paleoclimatology web site (http://www.nc dc.noaa.gov/paleo/recons.html.)

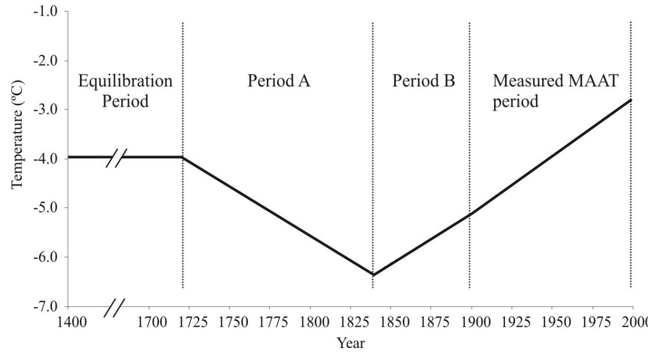

Figure 2. Reconstructed MAATs from 1720–1897 following trends in Group A and Group B, and measured MAAT from 1898–2000 with best fit line for Fort Simpson.

Mann et al. (1999) documented mean annual air temperature anomalies specific to the northern hemisphere for the period 1000–1998, based on tree ring and ice-core data. The reconstructed climate data are presented as MAAT anomalies relative to the 1961–1990 northern hemispherical mean. We used data for the period 1400–1746 to estimate a long-term MAAT representative of an extended period of quasi-stable climate assumed to exist prior to 1750. In this work, the hemispheric temperature anomalies provided by Mann et al. (1999) were examined for general climate trends in order to establish a long term deviation from the 1961–1990 air temperature normal (-3.72ºC) for Fort Simpson. Although not ideal for our purposes, the lack of available data alternatives has dictated that we rely on hemispheric rather than regional proxies to establish regional paleo-climatic trends prior to 1900.

Methods

Available temperature records and proxy climate data (Begin et al. 2000) indicate that Canada's western Arctic has experienced significant variations in mean annual air temperature over the past 250 years, with a modest cooling during the Little Ice Age followed by a progressive warming of climate from the early 1800s to present. As such it would be inappropriate to attempt to reproduce current permafrost conditions in the Mackenzie Valley by relying only on an equilibrium model of the ground thermal state. Neither would it be appropriate to initiate transient numeric modeling at any time during the past century or so without having initial ground temperature profiles specific to the time of initiation of the transient model.

Model initialization at quasi-equilibrium

In order to implement the transient numeric model, we specify a time at which a state of quasi-equilibrium was assumed to exist between atmospheric temperatures and the ground thermal state, from which forward modeling is initiated. For modeling purposes we assume the existence of an extended period of quasi-equilibrium prior to about 1750 AD, characterized by a long-term mean annual air temperature for Fort Simpson of about -4°C, based on the work of Mann et al. (1999). These equilibrium ground temperature profiles serve as the starting point for forward modeling from past to present (i.e. AD 2000), through incorporation of the paleo-climatic trends described below.

Identification of paleo-climatic trends

We examined the relations between measured and reconstructed summer air temperatures and measured MAAT using simple linear regression. A low correlation (R2 = 0.14) for measured summer temperature regressed against measured MAAT indicates that summer temperatures are ideal predictors of MAAT for the Fort Simpson study area, although other studies have used summer temperatures in such a context (Juliussen & Humlum 2007).

A higher R2 value was obtained for winter air temperatures (December/January/February) regressed against measured MAAT. However, given the lack of reliable proxy data representative of regional winter temperatures, summer temperature reconstructions from tree-ring data were employed in this work. Linear regression of available data described trends in measured MAAT for Fort Simpson and the reconstructed June/July tree-ring temperatures for the period 1898–1988 (Fig. 1).

As mentioned above, the weak correlation between measured June/July air temperature and MAATs from climate records inhibits the direct use of predictive models for estimating past MAATs from proxy indicators of mean summer temperature. Alternatively, the slopes of the best fit lines through recorded MAATs and reconstructed June/July temperatures are very similar, being 0.018ºC/year and 0.015ºC/year, respectively. According to the general trends, MAAT has increased by about 1.8ºC over the past 100 years, and reconstructed June/July temperatures have increased by a similar amount (1.5ºC). Based on this similarity, it is feasible to use the reconstructed summer temperature trends as an indicator of general trends in regional MAAT. Therefore, the recorded MAAT for the year 1898 for Fort Simpson is used as an anchor point from which to transform the temperature trends observed within the summer proxy data to estimate MAAT for the entire proxy period. This transformation must be used with caution as previous studies, together with the relation mentioned above, suggest that summer temperatures explain less yearly variance than winter temperatures and can lead to potentially flawed indications of past climate if summer values alone are used to reconstruct yearly temperatures (Jones et al. 2003). Linear regression was also used to characterize the general trends in summer temperature data for discrete time intervals prior to 1898 (i.e. the beginning of recorded temperature data).

A three-year running average was applied to the tree-ring temperature reconstruction of Szeicz and MacDonald (1995) to clarify general trends in the data (Fig. 2). According to the smoothed data, a general cooling trend from quasi-equilibrium at 1746 reached a minimum temperature around 1838. This cooling period was followed by a general warming trend through to the present.

Based on the general trends observed, the reconstructed summer temperature data were partitioned at AD 1838, corresponding to the apparent minimum temperature of the contemporary Little Ice Age. The paleo-climate record was separated into two periods: period A from 1746–1838 and period B from 1839–1897 (Fig. 2). Period A is characterized by a pronounced cooling trend. A best fit line through the data (r^2 = 0.41) indicates a cooling rate of 0.0171ºC/year over 92 years with a total change in temperature of 1.57Cº. Period B is characterized by a warming trend from 1838 to the start of the modern temperature record in 1898. Based on a best-fit line through the data, mean annual air temperatures warmed by 0.98Cº during this 58 year period at a rate of 0.0169ºC/year.

A best-fit line through the modern MAAT record for Fort Simpson (r^2 = 0.27) was used to specify an anchor point from which the trends identified in Figure 1 were used to estimate MAAT previous to the modern record. At the beginning of period A, the observed trend was forced backward by 25 years to 1721, intersecting with the assumed long-term equilibrium MAAT of -3.96ºC. This allowed for a smooth transition from the assumed long-term MAAT to the cooling trend characteristic of period A. Figure 3 shows the equilibration period using an average value from 1400–1720, reconstructed MAATs between 1721 and 1898 and the MAAT trend at Fort Simpson determined from the modern temperature record, which together comprise the paleo-climate scenario employed in transient ground thermal modeling from 1721 to present.

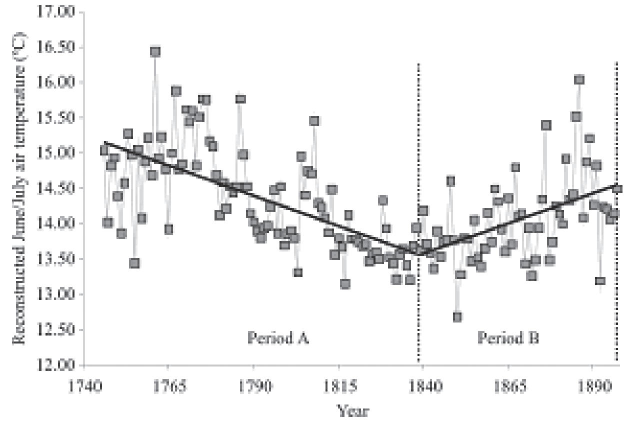

Figure 3. Reconstructed summer air temperatures from Szeicz & MacDonald (1995) smoothed wit h a 3-year running mean.

Comparison of modeled vs. recorded ground temperature

To facilitate evaluation of the influence of initial conditions and start date on model predictions, six measured ground temperature profiles from the Fort Simpson area are compared to results of transient numerical modeling, using the temperature reconstruction and an equilibrium solution based on the 1971–2000 normal. The boreholes are a part of a Geological Survey of Canada network for observing permafrost conditions throughout the Mackenzie Valley. The physical parameters assumed for each borehole site and corresponding modeling run are presented in Table 1. At this point it would prove useful to give a simple description

Table 1. Parameters recorded at each borehole and associated modeling properties.

Borehole properties				Modeled properties				
Borehole	Vegetation	Surficial geology	Material	Saturation (Sr)	NT	NF	Bulk density (Kg/m^3)	Texture
94TC1	Closed bs.	Glacio-lacustrine	Sand	0.80	0.55	0.24	1500	Coarse
97TC1	Aspen	Glacio-lacustrine	Silt	0.55	0.30	0.90	1500	Fine
97TC2	Closed bs.	Glacio-lacustrine	Sand	0.80	0.24	0.55	1500	Coarse
97TC4	Open bs.	Glacio-lacustrine	Fine sand	0.85	0.24	0.60	1500	Fine
99TC1	Open bs	Glacio-lacustrine	1.5 of organic over silt	1.0	0.14	0.50	300/ 1500	1.5 organic over fine
99TC2	Fen	Glacio-lacustrine	7 m organic over clay	1.0	0.12	0.70	300/ 1500	7 m Organics over fine

Note: Sr refers to soil water content in terms of the degree of pore saturation; bs. refers to Black spruce (*Picea mariana*).

of the mechanics of the T-ONE model. A more complete description of model parameters can be found in Duchesne et al. (2008) and Wright et al. (2003, 2001). Annual air temperature trends are incorporated in the model through seasonal thawing and freezing degree days. N-factors reflect the thermal off-set between ground surface and atmospheric temperatures. The thawing (summer) n-factor incorporates effects of vegetation on the ground thermal regime, while the effect of winter snow pack is assumed to be implicit in the freezing (winter) n-factor.

Moisture content is described in terms of the degree of pore saturation, based on porosity values derived from specifications of dry bulk density of earth materials. The model assumes a purely conductive heat flow, following the assumption that conduction is the dominant heat transfer process in permafrost landscapes (Hinkle & Outcalt 1994, Outcalt et al. 1990). The effect of latent heat due to the freezing of water or the thawing of ice is incorporated in the model. In the cases present in this paper, the one-dimensional modeling space was set at depth of 45 m with grid spacing ranging from 0.01 m at the surface to 2.0 m at depth. The lower boundary condition is defined in terms of geothermal heat flow, set at a regional value of -0.40 Wm^{-2} (Judge 1975).

The transient model was equilibrated using a -3.96ºC MAAT, with forward modeling initiated at 1721, following the generalized climate change scenario described in Figure 3 to the year 2000. For comparison purposes, a separate equilibrium solution was obtained for each borehole case using a MAAT of -3.01ºC, which is representative of the 1971–2000 climate normal at Fort Simpson.

Results and Discussion

The results of two modeling solutions (transient and equilibrium) were compared with measured ground temperature profiles from six boreholes located in the vicinity of Fort Simpson, NWT (Fig. 4). The largest discrepancy between modeled and measured ground temperatures occurs at borehole 97TC1, a deciduous forest site on glacio-lacustrine silt. Both transient and equilibrium modeling confirm the absence of permafrost at this site, but modeled ground temperatures are about 1ºC warmer than recorded values. This result may indicate an error in the specification of n-factor values for this vegetation category, as comparatively few deciduous cases were included in the initial parameter calibration process (Wright et al. 2003). For cases where borehole data show the presence of permafrost, both transient and equilibrium modeling predict ground temperatures slightly warmer than those observed in the borehole record. In general, the transient model captures the near-isothermal character of ground temperatures in boreholes 94TC1, 97TC2, 97TC4, and 99TC2, although transient model predictions for the latter are somewhat warmer than measured values, and equilibrium predictions even more so. In all cases except 99TC1 equilibrium modeling predicts ground temperatures at depth that are significantly warmer than those indicated by borehole data.

A close agreement of ground temperatures between measured values and those predicted by T-One transient modeling is observed at borehole 97TC4, with the prediction of 8 m of permafrost being close to that indicated in the borehole (~9 m), although a somewhat deeper thaw zone is indicated by the transient model in the upper few metres of the profile. In contrast, equilibrium modeling predicts substantively warmer ground temperatures with unfrozen conditions throughout the profile.

At borehole 97TC2, measured permafrost temperatures tend towards colder values at depths below about 5 m. This again confirms the notion that permafrost is progressively warming from the surface downward in response to climate warming during the past century or so. Transient modeling predicts the isothermal tendencies apparent in this borehole data, but predicts significantly warmer ground temperatures at depth. Actual permafrost thickness at this site is not known, but based on the temperature at the bottom of the profile, the transient model prediction of 22 m of permafrost is likely a reasonable estimate. In contrast, the equilibrium modeling based on the 1971–2000 normal significantly over-predicts ground temperatures at depth and grossly under-predicts permafrost thickness at this site.

Boreholes 99TC1 and 99TC2 are located in strikingly different settings, although they are separated by a distance of only about 10 m. Site 99TC1 is located on a raised peat plateau, while 99TC2 is situated in a wet collapse feature

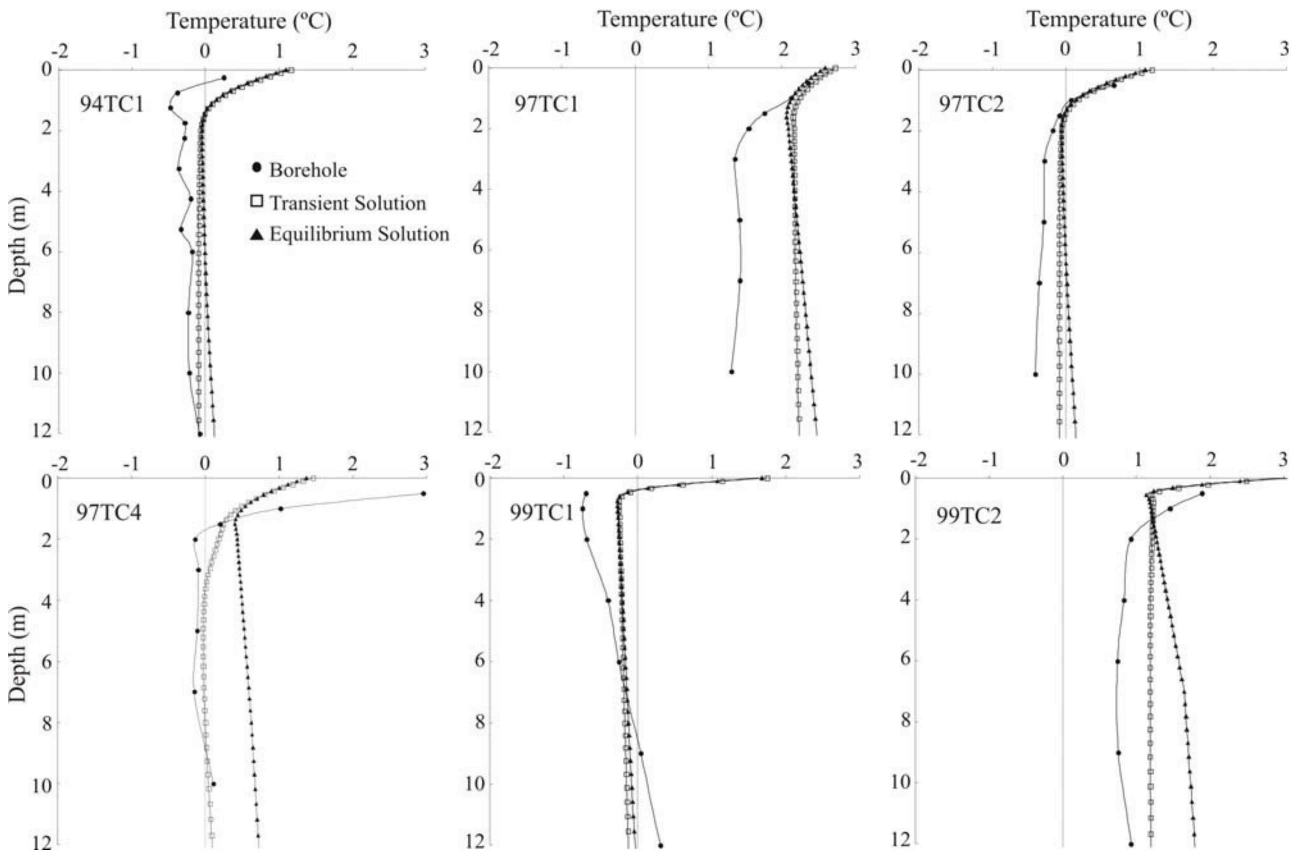

Figure 4. Measured ground thermal profiles from boreholes and results from a transient model using the climate reconstruction and an equilibrium solution based on 1971–2000 climate normal for the Fort Simpson area.

immediately adjacent to the peat plateau. Both sites are separated from an extensive fenland by a low ridge only a few metres wide. Recorded temperatures indicate that 99TC2 is unfrozen as correctly predicted by both transient and equilibrium modeling. The transient solution over-predicts ground temperatures at depth by about 0.5°C, while the equilibrium model over-predicts by about twice that amount. Borehole 99TC1 is characterized by a steep temperature gradient with uncharacteristically cold temperatures (~-0.8°C) at the near-surface, with unfrozen conditions below about 9 m depth. When examining this profile it is useful to consider that the raised peat plateau is about 2 m higher than the surrounding terrain. It is potentially exposed on its western face to winds from an extensive fen immediately adjacent to the site. Consequently, this site may experience reduced snow accumulation and therefore more direct exposure to cold winter temperatures at the ground surface. The presence of a 1.5 m layer of peat also insulates the ground during the summer months, promoting potentially colder near-surface ground temperatures. On the other hand, given the perhaps anomalously cold permafrost temperatures at 99TC1, the relatively shallow depth of permafrost at this site may reflect the influence of the adjacent fenland and/or its close proximity to the collapsed bog feature. Indeed, neither model adequately reproduces the ground thermal characteristics at this site, possibly due to the role of non-conductive and/or significant lateral heat fluxes in this environment.

In general, both the transient and equilibrium models tend to over-predict ground temperatures to some degree, relative to the borehole measurements. While near-surface ground temperature predictions are similar, the equilibrium model tends towards warmer temperatures at the base of the profiles. This difference can be explained by two factors: (1) the transient model was equilibrated at a slightly colder MAAT leading to a greater initial depth of permafrost circa 1721, and (2) transient modeling simulated approximately 100 years of cooling through to the end of the Little Ice Age (circa 1840) before warming to present-day conditions. It is also possible that the assumed thermal equilibrium between the atmosphere and ground circa 1700 is invalid, with either colder temperatures prevailing at that time or during some period earlier in the proxy record.

The differences between recorded borehole temperatures and the predictions of equilibrium modeling (as shown in Figure 4) illustrate that current ground temperature profiles are not in equilibrium with the modern climate regime, and that current ground temperatures at depth are colder than would be expected based on late 20th century climate. Furthermore, the near-isothermal character of ground temperatures observed in the majority of boreholes is not reflected in the equilibrium modeling, but is characteristic of the transient modeling from circa 1721, in spite of the 100 years or more of cooling prior to 1840. The results of equilibrium modeling based on a late 20th century climate are likely to underestimate permafrost occurrence and thickness and to overestimate ground temperatures at depth. Although the transient modeling predicts somewhat warmer ground temperatures in comparison to available measured ground temperature profiles, the general characteristics of the ground thermal regime in permafrost environments are reasonably well replicated.

Conclusion

Using available proxy records to identify general trends in the paleo-climatic record, a reasonable estimation of regional trends in MAAT was reconstructed from an assumed quasi-stable climate prior to the mid-1700s through to present day. Trends in summer air temperature deviation determined from proxy data (1740–1890) were transformed into estimates of annual temperature trends in MAAT for the Fort Simpson region and intersected with the centurial trend identified in the modern temperature record (1900–2000). Transient numeric ground thermal modeling driven by this reconstructed climate scenario captures the general characteristics of the current ground thermal regime in the southern extent of permafrost terrain, as indicated by the congruency between model predictions and borehole measurements. Differences between recorded borehole temperatures and the results of equilibrium modeling (based on the 1971–2000 climate normal) indicate that ground temperatures in the Fort Simpson region are not in thermal equilibrium with the current climatic regime. Our results suggest that permafrost models incorporating present day or even 20th century climate will not adequately reproduce the essential characteristics of the current permafrost regime, and so are unlikely to produce reliable predictions of the future evolution of permafrost when standard scenarios of climate warming are applied. The results also indicate that there is considerable opportunity for improvement of our transient ground thermal modeling capability, including refinement of the paleo-climate trends established for forward modeling from past to present. A detailed analysis of modeling outputs from this work, together with additional comparisons of modeling results with more widely distributed borehole temperature records, will support refinement of model parameter assignments and increase confidence in model performance for regional and local-scale applications.

References

Begin, C., Michaud, Y. & Archambault, S. 2000. Tree-ring evidence of recent climate changes in the Mackenzie Basin, Northwest Territories. In: L.D. Dyke and G.R. Brooks (eds), *The Physical Environment of the Mackenzie Valley, Northwest Territories: a base line for the Assessment of Environmental Change*. Ottawa: Geological Survey of Canada, Bulletin 547: 65-77.

Duchesne, C., Wright, J.F. & Ednie, M. 2008. High resolution numerical modeling of climate change impacts to permafrost in the vicinities of Inuvik, Norman Wells, and Fort Simpson, NWT, Canada *Proceedings of the Ninth International Permafrost Conference, Fairbanks, Alaska, June 29–July 2, 2008* (this proceeding).

Environment Canada. 2002. Canadian Climate Normal: Canadian Monthly Climate Data and 1943–2000 Normal. Environment Canada: Ottawa. CD-ROM.

Gajewski, K. & Atkinson, D.A. 2003. Climatic change in northern Canada. *Environmental Reviews* 11(2): 69-102.

Goodrich, L.E. 1982. An introductory review of numerical methods for ground thermal regime calculations. Division of Building Research, National Research Council of Canada. *DBR Paper* No. 106, 133 pp.

Hinkle, K.E. & Outcalt, S.I. 1994. Identification of heat transfer processes during soil cooling, freezing, and thawing in Central Alaska. *Permafrost and Periglacial Processes* 5: 217-235.

Jones, P.D., Briffa, K.R. & Osborn, T.J. 2003. Changes in the Northern Hemisphere annual cycle: Implications for paleoclimatology. *Journal of Geophysical Research* 108(D18): 13-1-13-7.

Judge, A.S. 1975. Geothermal studies in the Mackenzie Valley by the Earth Physics Branch. In: Geothermal Service of Canada, *Geothermal Series No.2*. Ottawa: Energy Mines and Resources Canada, 12pp.

Juliussen, H. & Humlum, O. 2007. Towards a TTOP ground temperature model for mountainous terrain in Central-Eastern Norway. *Permafrost and Periglacial Processes* 18: 161-184.

Mann, M.E., Bradley, R.S. & Hughes, M.K. 1999. Northern hemisphere temperatures during the past millennium: Inferences, uncertainties, and limitations. *Geophysical Research Letters* 26(6): 759-762.

Möldes, N. & Romanovski, V.E. 2006. Long-term evaluation of the hydro-thermodynamics soil-vegetation scheme's frozen ground/permafrost component using observations at Barrow, Alaska. *Journal of Geophysical Research* 111: D04105.

Outcalt, S.I., Nelson, F.E. & Hinklel, K.E.. 1990. The zero curtain effect: heat and mass transfer across an isothermal region in freezing soil. *Water Resources Research* 26: 1509-1516.

Szeicz, J.M. & MacDonald, G.M. 1995: Dendroclimatic reconstruction of summer temperatures in Northwestern Canada since A.D. 1638 based on age-dependent modeling. *Quaternary Research* 44: 257-266.

Wright, J.F., Duchesne, C. & Côté, M.M. 2003. Regional-scale permafrost mapping using TTOP ground temperatures model. *Proceedings of the Eight International Permafrost Conference, Zurich, Switzerland, July 21-25, 2003*: 1241-1246.

Wright, J.F., Duchesne, C., Nixon, F.M. & Côté, M.M. 2001. Ground thermal modeling in support of terrain evaluation and route selection in the Mackenzie River valley, *CCAF Project A073*. *Summary Report*. Ottawa: Natural Resources Canada, 53 pp.

Seasonal Variations of Surface Radiowave Impedance of Frozen Ground

V.N. Efremov
Melnikov Permafrost Institute, SB RAS, Yakutsk, Russia

Abstract

The depth of superficial seasonal thawing observed in permafrost bodies with a thickness of hundreds of meters results in substantial seasonal variations in radiowave impedance for radio frequencies. This report outlines the results of an investigation of seasonal variations of radiowave impedance in Central Yakutia at a frequency range of 10–1000 kHz. The peculiarities of seasonal variations in the region include a significant influence of thawed layer conductivity on wave impedance magnitude and phase angle at the freezing of the seasonally thawed layer. This report reveals and analyzes the diverse nature and degree of seasonal variations of wave impedance magnitude, phase angle, and apparent resistivity in different frequencies during seasonal ground freezing and thawing at two sites of differing landscape but identical geological structure. Subsurface conductivity structure models were suggested, reflecting results of radiowave impedance sounding on the sites. Stabilization of apparent resistivity level change was registered in the period from August to October.

Keywords: frozen ground; seasonal variations; seasonally thawed layer; surface radiowave impedance.

Introduction

Our work during past years (Efremov 2007) was aimed at assessing physical properties of frozen ground, based on surface wave impedance (Wait 1962) or input impedance (Berdichevsky 1966) measurements.

$$Z = \frac{E_x}{H_y} = |Z| e^{-i\varphi} \tag{1}$$

The results of mathematical simulation demonstrated that radiowave sounding, used to study the structure and properties of permafrost, must involve measurement of surface wave impedance at a frequency range of 10–1000 kHz (Efremov 1995). The range of frequencies includes very-low-frequency (VLF from 10 kHz to 30 kHz), low-frequency (LF from 30 kHz to 300 kHz), and, partially, medium-frequency (MF from 300 kHz to 1000 kHz) belonging to the radio-frequency spectrum, propagating above the ground surface. For frozen ground, VLF sounding conduction currents prevail, which make it possible to assess frozen rocks resisitivity. At frequencies of 30–1000 kHz (LF-MF) the influence of displacement currents increases, but does not dominate. At these frequencies, there is a possibility of assessing resistivity and other physical properties of frozen ground, as a result of processing and interpretation of surface wave impedance measurement data.

To interpret the measured data, we use two components of wave impedance: |Z| magnitude and φ phase angle, as well as apparent resistivity that is determined using these components, taking into account the displacement currents (Veshev, Egorov 1966).

$$\rho = \frac{|Z|^2}{2\pi f \mu \cdot \sin 2\varphi} \tag{2}$$

Nevertheless, measurements of surface wave impedance within LF and MF bands, could be considerably affected by the conductive layer, formed in an active layer on the frozen ground surface as a result of seasonal thawing. The freeze-thaw cycle of the seasonally thawed layer is the reason for seasonal variations in components of surface radiowave impedance.

Results and Discussion

Some regional results

The results of surface radiowave impedance measurements in Central Yakutia and in numerical simulations demonstrate that the seasonal variations are significant and have some regional peculiarities. The region is characterized by a relatively deep seasonal thawing of permafrost, making 1.5–2 m, while its thickness is 300–400 m. With freezing of the seasonally thawed layer, its resistivity increases, and the phase angle grows at all frequencies. At frequencies of f >300 kHz at freezing we observe a significant increase of phase angle, and wave impedance magnitude grows, due to upper layer longitudinal conductivity reduction. At frequencies of f <300 kHz the wave impedance magnitude increase is less significant due to the effect of the formation of a cumulative non-conductive layer of frozen unconsolidated deposit above a more conductive layer composed of frozen rocks, in accordance with a two-layer model. At thawing of the seasonally-thawed layer, phase angle decreases as well as the wave impedance magnitude, which is more significant at f >300 kHz. The phase angle reduction, since some size of magnitude of longitudinal conductivity, is dependent on resistance permafrost (for example 0.05 $\Omega^{-1}\cdot$m for ρ=1000 Ω·m), accepts an asymptotic value. The decrease of wave impedance magnitude is proportional to the increase of longitudinal conductivity of such layers. We observed a sufficient convergence of apparent resistivities within MF range and seasonally thawed layer resistivity at

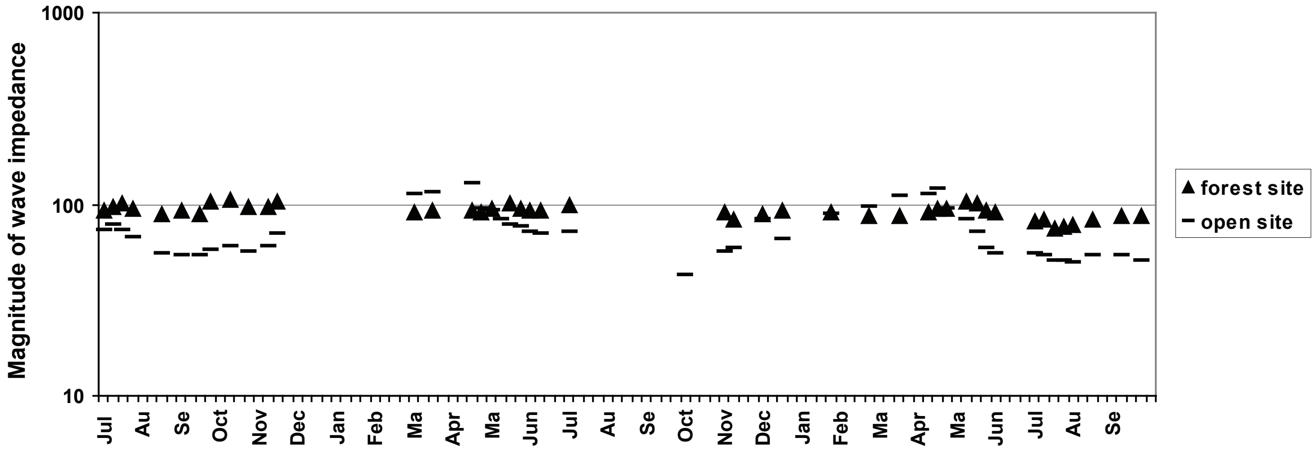

Figure 1. Seasonal variations of magnitude of wave impedance in MF (549 kHz) in test sites from July 2005 to September 2007.

constant current, which speaks to a significant influence of the seasonally thawed layer on wave impedance magnitude within the given range, as shown in the following.

According to experimental data obtained along the 200 km-long highway at the same sites (first in August, then in April of the following year), the fluctuation at LF, caused by the seasonally thawed layer (STL) freezing, gave on average: for wave impedance +18%, for phase angle +19°. At higher frequencies, in MF range, the fluctuation of wave impedance reached +40%, and phase angle fluctuation made +16° on average.

The increase of wave impedance magnitude at STL freezing, as well as the increase of this fluctuation at higher frequencies of the field were expected and totally fit into the results of numerical simulation (Efremov 1995). The increase of phase angle with freezing of the seasonally-thawing layer indicates that there is a thin conductive layer within the permafrost, and that the effect produced by this layer during the warm period is partially mitigated by the presence of a conductive seasonally thawed layer. This suggestion is proven by the results of numerical simulation for the frequency dependence of surface wave impedance for permafrost including a thin conductive layer.

Other factors than thawing, resulting in seasonal variations of surface impedance, may be abundant rainfall, or long absence of precipitation. In the first case, resistivity decreases and permittivity of the seasonally thawed layer increases as a result of the moistening; in the second case we see an inverse effect as a result of dehydration of the upper layer, evaporation, and gravitational moisture transfer to the bottom of the permafrost.

Results in test sites

Over the last years, observations of surface impedance seasonal variation were carried out in Central Yakutia at two test sites located 200 m away from each other in the same geological conditions, but in different landscapes – in forest with thawing of the ground down to 1.3 m, and in open space with thawing down to a depth of 1.9 m. The area where the sites are located is composed of sandy-loamy deposits with a total thickness of 30 m, overlying frozen rocks up to 300 m deep. Geological and geocryological profiles of both sites are typical for Central Yakutia.

The surface impedance measurements were carried out using reception of horizontal electric-field component E_x on a symmetric ungrounded receiver circuit, and of horizontal magnetic component of the field H_y - on a frame magnetic antenna. The measurements were carried out at the same sites with periodicity of 1–2 weeks during the warm period and on occasional days of thaw during winter. A surface impedance indicator IPI-1000 (Parfentyev & Pertel 1991) was used as a measuring instrument. The instrument represents a selective microvoltmeter, phase-angle meter, operating within a frequency range of 10–1000 kHz and measuring the magnitude of wave impedance accurate within 5%, and a phase angle inaccuracy rate of 1°.

The results of observations showed that the profiles of seasonal variations of complex wave impedance components for forest- and open sites do not have distinctions of kind (Figs. 1, 2).

At the forest site, the variations of surface radiowave impedance magnitude were not as significant, as variations of phase angle, with a range of deviation reaching 35°. At the open site, on the contrary, there was not as substantial a variation in phase angle as there was in surface radiowave impedance magnitude, reaching 58%. This difference can be explained by the presence of a thin conductive layer at different depths and by distinctions in cryogenic structure of the ground at the sites, resulting in different subsurface conductivity structures. According to the sounding data interpretation, at the forest site a conductive layer is indicated at the bottom of unconsolidated deposits, and in the open site at the bottom of a seasonally thawed layer. This presumes different subsurface conductivity structures, different depth of sounding on the sites, and consequently a different level of influence of conductive layers constituting the ground. The range of seasonal variations of apparent resistivity is wider at the open site than at the forest one. This can be explained by higher ice content in the ground and a thicker seasonally thawed layer at the open site.

At each of the sites, the components of wave impedance and the apparent resistivity seasonal variations profiles

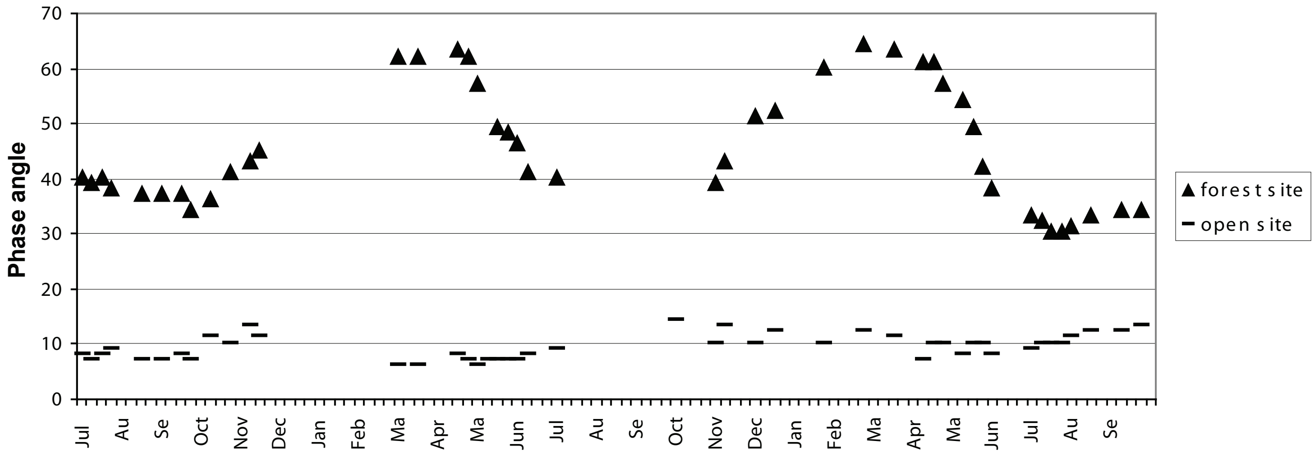

Figure 2. Seasonal variations of phase angle in MF (549 kHz) in test sites at period from July 2005 to September 2007.

substantially differ for different frequencies (Figs. 3, 4).

At the forest site, a sudden increase of phase angle within LF and MF (VLF remaining almost unchanged) was observed since the freezing of the seasonally thawed layer started in October and finished in April of the next year (Fig. 2). Here, the wave impedance magnitude decreased to VLF by the end of April and did not significantly change in higher frequencies (below than 800 kHz). Decrease of wave impedance magnitude reaching 56% occurs here in higher frequencies (higher then 800 kHz) during the period of intensive STL thawing from April until July. During the same period, at the forest site, we observed a rapid decrease of phase angle in LF-MF range, reaching 34°, apparent resistivity increasing within VLF and decreasing within MF (Fig. 4).

At the open site, the growth of wave impedance magnitude and of apparent resistivity occurs in LF-MF range, at freezing of the STL during the period from November until April of the following year and is accompanied by a slight decrease of impedance magnitude in VLF. At STL thawing during the period from April until June, wave impedance magnitude and apparent resistivity decrease within LF-MF and increase within VLF (Fig. 3). During the same period, the phase angle decreases within the range of frequencies lower than 400 kHz. During the period from May until July, the phase angle increases at high frequencies (higher than 800 kHz). It is essential to note that in 2007, STL thawing led to a more abrupt decrease of wave impedance magnitude within LF-MF than in the previous years.

Based on the analyses of our experimental data, we suggest four-layer and five-layer models of subsurface conductivity structure of the sites for warm and cold periods of the year, shown in Tables 1 and 2.

Besides STL freezing and thawing, seasonal variations of the surface radiowave impedance in Central Yakutia, a region of high temperature permafrost, are substantially influenced by temperature variations in the layer of annual temperature fluctuations (to a depth of 3 m). These temperature variations can result in changes of the resistivity. This part of the ground is freezing, and consequently, resistivity increases during the period from November until April. From May until July, while ground temperature rises, a decrease of resistivity is recorded in this part of the ground; and from August until October the resistivity change stabilizes. In the open site, the stabilization of wave impedance magnitude changes, phase angle, and correspondingly of apparent resistivity is indicated within the LF-MF band during the period from June until September. This is the result of compensation of the effect of a non-conductive layer made of frozen unconsolidated deposits, by the effect of the conductive STL (Fig. 4). Based on the results of numerical simulation, full compensation can be achieved under the condition given by (Efremov 1995):

$$\frac{h_1}{\rho_1} = \frac{h_2}{\rho_3} \tag{3}$$

where h_1/ρ_1 is the longitudinal conductivity of seasonally thawed layer; h_2 is the thickness of frozen unconsolidated deposits; ρ_3 is the resistivity of frozen rocks. It is significant to note that the levels of stabilization of wave impedance magnitude changes and apparent resistivity are lower in 2007 than in 2005 and 2006.

Over the last years, both open and forest sites have depicted a trend towards decrease of ground resistivity variations amplitude, correlated with decrease of freezing degree and increase of thawing degree (Fig. 4). These changes can be explained by increased snow cover thickness and warming of the climate. The increase of thawing depth is evidenced by measurements of thawing at sites with the help of a test prod. All this indicates a connection between seasonal variations of surface radiowave impedance and climatic changes.

Conclusions

Regional peculiarities of surface radiowave impedance seasonal variations for frequencies ranging between 10 – 1000 kHz have a significant influence on the thawed layer conductivity magnitude and the increase of phase angle at

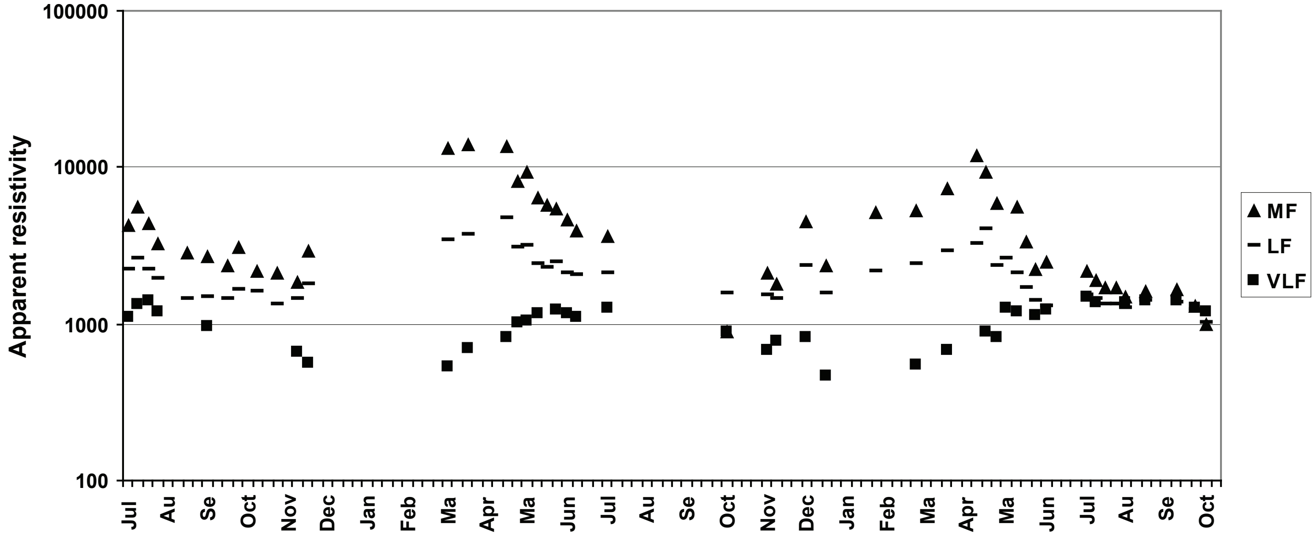

Figure 3. Seasonal variations of apparent resistivity (Ω·m) in MF-LF-VLF in the open site from July 2005 to October 2007.

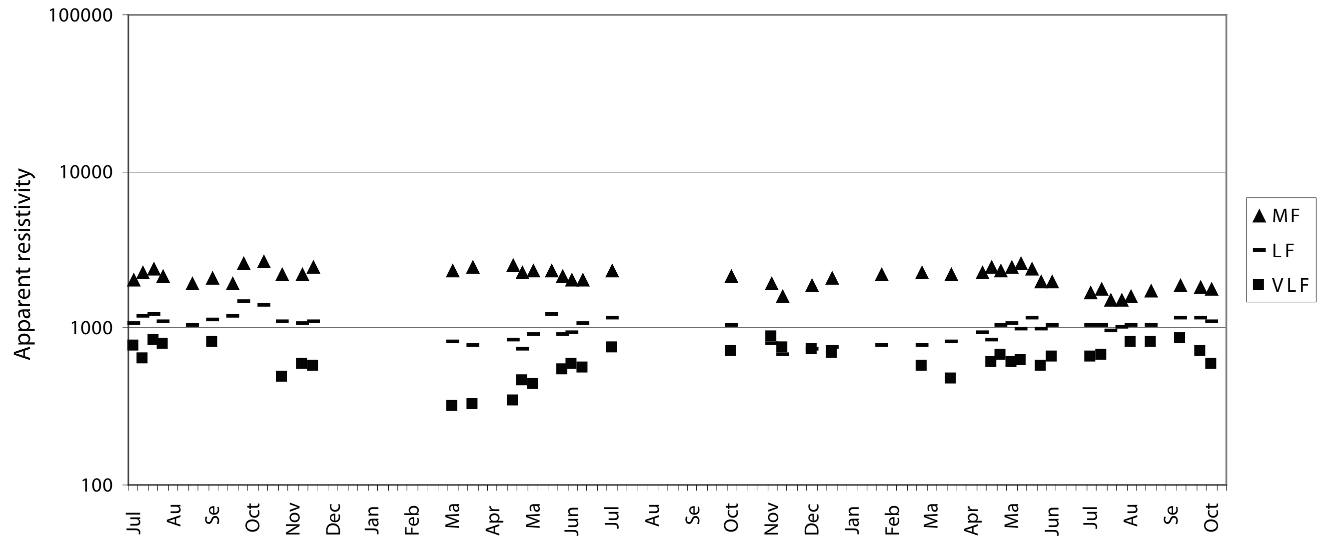

Figure 4. Seasonal variations of apparent resistivity (Ω·m) in MF-LF-VLF in the forest site from July 2005 to October 2007.

freezing of the seasonally thawed layer. This fact proves that within permafrost there is a thin conductive layer of cryolithological nature.

Seasonal variations in surface radiowave impedance components differ dramatically by character and degree of change in sites with differing landscapes, resulting from different geocryologic profiles. Besides, there is a difference in character and degree of change for different frequencies of 10–1000 kHz range at one and the same site. It results in the necessity to consider seasonal changes in frozen ground research by radiowave methods. On the other hand, the analysis given about seasonal variations of the surface radiowave impedance at various frequencies will allow gaining more specific information on the geocryological structure of the ground and the dynamics of seasonal changes occurring in it.

Freezing and thawing of the upper layer, to a considerable extent, change the subsurface conductivity structure of permafrost and the ratio of conductive and non-conductive layers within it. This consequently changes the ratio of conduction and displacement currents for the given frequency, which in its turn determines the phase angle. Therefore seasonal changes in the upper layer at thawing can hide (and at freezing intensify) the anomalies caused by conductive bodies within permafrost.

Stabilization of components of wave impedance and apparent resistivity during the period from August until October, caused by the compensation of influence from frozen unconsolidated deposits by conductivity of the seasonally thawed layer, gives us a chance to assess the resistivity of frozen rocks according to measured apparent resistivity. The period from August until October is the

Table 1. Models of the subsurface conductivity structure of the frozen ground in the forest site.

	April-November	December-March
1	Conductive layer	Medium resistivity layer
2	Variable high-resistivity layer	Variable high-resistivity layer
3	Very-high-resistivity layer	Very-high-resistivity layer
4	High-resistivity layer	High-resistivity layer

Table 2. Models of the subsurface conductivity structure of the frozen ground in the open site.

	April-November	December-March
1	Conductive layer	Medium-resistivity layer
2	Thin conductive layer	Variable high-resistivity layer
3	Variable high-resistivity layer	Very-high-resistivity layer
4	Very-high-resistivity layer	High-resistivity layer
5	High-resistivity layer	

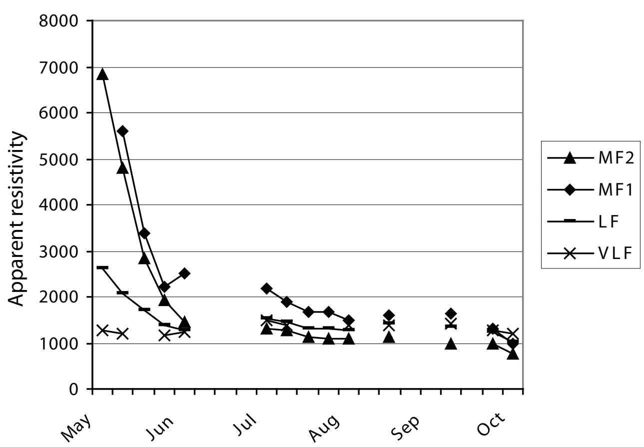

Figure 5. Seasonal variations of apparent resistivity (Ω·m) in MF-LF-VLF in open site at period from May 2007 to October 2007.

most practical for research of frozen rocks using radiowave methods in Central Yakutia and other regions, similar by climatic and geocryologic profiles.

Correlation of the seasonal variations of the surface radiowave impedance magnitude and phase angle with the degree of ground freezing and depth of thawing, allows us to assume the possibility of monitoring of changes in frozen ground caused by climatic changes.

References

Berdichevsky, M.N. 1968. *Electrical Exploration by Magnetotelluric Sounding Method (Elektricheskaya razvedka metodom magnitotelluricheskogo profilirovania).* Moscow: Nedra, 255 pp (in Russian).

Efremov, V.N. 1995. Surface impedance in permafrost at radio frequencies. In: *Geophysical Investigations in Yakutia (Geofizicheskie issledovania v Yakutii)*. Yakutsk: Izd-vo Yakutskogo Universiteta, 70-80 (in Russian).

Efremov, V.N. 2007. On the real time tentative estimation of physical properties of frozen soils during radio impedance express-sounding. In: *Cryogenic Resources of Polar Regions. Proceedings of the International Conference in Salekhard City, West Siberia, June, 2007*. Pushchino 2: 311-313 (in Russian).

Parfentiev, P.A. & Pertel', M.I. 1991. A device for measuring VLF and LF surface impedance. In: *The Earth-Ionosphere Low-Frequency Waveguide (Nizkochastotnyi volnovod Zemlya-ionosfera)*. Alma-Ata: Golym, 133-135 (in Russian).

Veshev, A.V. & Egorov, V.A. 1966. *On Methodology for Observing and Interpreting the Results of Studies on the Fields of Radio Broadcast Stations*. Voprosy Geofiziki: Uchenye zapiski LGU, 329(16): 172-189 (in Russian).

Wait, J.R. 1962. *Electromagnetic Waves in Stratified Media. International Series of Monografs in Electromagnetics Waves.* Pergamon, Toronto, 3: 372 pp.

Using Indigenous Knowledge to Assess Environmental Impacts of Overland Travel Routes, Arctic Coastal Plain of Alaska

Wendy R. Eisner
Department of Geography and Environmental Studies Program, University of Cincinnati, Cincinnati, OH 45221-0131 USA
Kenneth M. Hinkel
Department of Geography, University of Cincinnati, Cincinnati, OH 45221-0131 USA
Benjamin M. Jones
Alaska Science Center, U.S. Geological Survey, Anchorage, AK 99508-4664 USA
Christine J. Cuomo
Institute for Women's Studies and Dept. of Philosophy, University of Georgia, Athens, GA 30602-2305 USA

Abstract

The overland travel routes from Barrow, Alaska, to inland regions are assessed using indigenous knowledge of Iñupiaq elders and hunters, as well as historic documents, aerial photos, and satellite imagery. Route information is superimposed on a satellite image within a geographic information system to identify areas of observed impact. The overall pattern for summer travel routes has not changed significantly over the past 50 years, despite the change from travel by foot and river boats to motorized vehicles, predominantly all-terrain vehicles. Route elements have altered, however: whereas traditional routes depended on conveyance by boat and included waterways, modern traffic detours around lakes and streams, are increasing the impact on tundra vegetation, soil, and permafrost.

Keywords: Alaska; GIS; indigenous knowledge; off-road vehicles; permafrost; thermokarst; trails.

Introduction

The traditional travel routes of the Iñupiaq people are an important and useful area of study for cultural geographers and anthropologists. Ethnographic studies have recognized so-called traveling landscapes as a rich repository of information about hunting and fishing resources, trading relations and kinship ties, and survival mechanisms. Our current research in northern Alaska utilizes indigenous knowledge (IK) of elders and hunters, who have primary and secondary information on natural and anthropogenic landscape changes. During the course of interviews with Iñupiaq elders from Barrow, Atqasuk, and Wainwright, informants repeatedly called attention to their present and past travel routes for both summer and winter travel. We consequently began to examine this information to determine how and why inland travel routes have changed, and to assess the impact of routes on the landscape.

We have collected and georeferenced relevant Iñupiaq summer inland travel information in a Geographic Information System (GIS) database. This includes overland trails on the tundra and river routes that utilize watercraft. Our informants have indicated on maps and satellite images the routes currently in use, as well as traditional routes that have been abandoned due to changes in ground-cover, hydrology, transportation technology, and viability (that is, the route no longer leads to useful sites). We are able to compare modern routes to those of the traditional Iñupiaq route system that existed in the 1950s (Spencer 1959), or before the proliferation of affordable snowmachines and All-Terrain Vehicles (ATVs). We also utilized some inland travel route information from the 1970s (Tremont 1987) and, more recently, trails that are visible on 1:50,000 color infrared (CIR) photography captured for the Barrow Peninsula in 2005.

The objective of this report is to identify the changes in travel routes on the Barrow Peninsula over the past half-century, assess the cause for route changes, and identify visible effects on the landscape. We will focus only on terrestrial travel in the summer period, when the potential for damage to the tundra is maximal. The use of snowmachines has, until recently, been restricted to winter and will not be considered here.

Background

The pre-motorized Iñupiat had a variety of reasons for traveling long distances inland, and food acquisition was just one of these. Spencer (1959) writes that the main interaction between the *nuunamiut* (inland Iñupiat) and the *tareumiut* (coastal Iñupiat) was based on organized trade. Trade was important for commodity exchange, but also vital for maintaining social ties and enabling groups to achieve economic stability. Trading generally commenced at specific times of the year, and often centered around traditional trading sites or areas. Other reasons to travel include accessing seasonal hunting and fishing areas, attendance at festivals, and travel to engage in warfare (Burch 2005).

The mode of transportation depended on the season of travel and the terrain along the specific route. The method of conveyance depended to a large degree on the season. Some portion of summer and early fall travel was simply done on foot. The traveling *umiaq*, a skin boat which is a smaller version of the whaling *umiaq*, was used to travel the rivers and lakes between May and October. The loaded *umiaq* was difficult if not impossible to navigate in head- or cross-winds, and was often towed from the banks by dogs and family members (Spencer 1959, Burch 2005, Flossie Itta in Atqasuk August 2003 interview, Roy Nageak Sr. of Barrow in August 2006 interview). Rivers and streams were usually only deep enough for continuous travel in the spring; by summer gravel bars and boulders posed considerable obstacles. A sledge was often part of the boatload, and could be used when ice was encountered. In areas where the waterways were blocked or not connected, the travelers would portage. Overland travel was most intense during the summer and covered the maximum territory because people were accessing distant trading centers.

Several of our informants spoke of traditional travel by boat along inland waterways, and informants still use larger, motorized boats along the sea coast and bays. When feasible, they will enter larger, deeper rivers to navigate to their summer camps. Thus, boats still provide a viable alternative for moving large amounts of supplies to inland sites. The *umiaq* is no longer used for inland travel, having been effectively replaced by ATVs in the snow-free period. Similarly, snowmachines have entirely replaced dog teams for spring and winter travel. However, whereas a snowmachine can pull a large sledge with supplies, the ATV remains largely a single-person transport unit. One strategy is for inhabitants to haul their goods to summer camps while the snow cover is still in place. More recently, we have noticed a disturbing trend of snowmachine use on the tundra after snowmelt.

Dramatic change to summer tundra travel was triggered by the introduction of motorized vehicles for personal use. Commercially-manufactured, one-passenger ATVs for personal use became common in northern Alaska during the 1960s. Before that time, overland vehicles such as Caterpillar tractors were used exclusively by industry and government due to the excessive cost.

The introduction of the ATV has caused long-term effects not only on the environment, but on the traditional culture of the North Slope communities as well. Hunters are now able to make longer journeys inland after game. These are not expeditions, but short-term hunting forays based on expediency or opportunity, and can be made by an individual traveling with light gear. The Iñupiaq people are no longer dependent on waterways, but instead have to navigate along high, dry ground and are forced to avoid the wettest, marshiest areas. Streams, the former transportation arteries of inland travel routes, are now obstacles.

Study Area and Methodology

The Arctic Coastal Plain of northern Alaska is a flat, low-lying region of tundra vegetation with numerous thaw lakes developed in ice-rich permafrost**.** Approximately 22% of the land area on the Barrow Peninsula north of ~71° latitude (which constitutes the area of study for this article) is covered with thaw lakes, and at least 50% is scarred by basins formerly occupied by lakes (Hinkel et al. 2003). In this cold maritime climate, the seasonal thaw zone (active layer) is typically less than 50 cm deep.

Over the past four years, our team has conducted extensive interviews with over 40 Iñupiaq elders and hunters from Barrow, Atqasuk, and Wainwright. These interviews have focused primarily, but not exclusively, on thaw-lake dynamics. We integrated interview methods to include unstructured talks (Bernard 2002) as well as semi-directive interviews (Huntington 2000, Fox 2002), a format which encourages informants to speak freely about their observations and knowledge of environmental changes. During videotaped interviews, informants located sites on detailed 2002 Landsat 7+ satellite images and USGS topographic maps. Afterwards, the interviews were logged and all sites located on maps were geocoded and entered into an ArcGIS database.

We also utilized 1:63,360 and 1:50,000 scale CIR aerial photography captured for the Barrow Peninsula in 1979 and 2005, respectively.

Analysis

Comparison of modern and traditional summer routes

The modern summer travel routes on the Barrow Peninsula identified by the majority of IK holders are shown in Figure 1. These closely coincide with the traditional trade routes mapped by Spencer (1959), shown in Figure 2. Both show two main trails extending southward from the traditional village of Barrow, and generally heading toward the Inaru River and Admiralty Bay. However, there are substantial changes that occurred over the half-century period.

The first modern summer travel route (Fig. 1: Route A) begins at Isatquaq Lagoon near the eastern end of the Wiley-Post Airport runway. It runs in a southerly direction along the banks of an existent lake (Iksrugagvik: I; Note that all letters and numbers within parentheses refer to figure labels). The trail, which mainly follows the course of the Avak River, crosses Iksrugagvik Creek beyond the lake at Maloney Bridge (M) which was constructed by Roy Nageak Sr. about ten years ago to enable ATVs to cross. The route continues eastward along the Avak River, going past several recently drained lake basins (Sikiluk—K—is one named) and then toward Iko Bay and associated inlets.

The second modern summer travel route (Fig. 1: Route B) is an important link between Barrow and inland settlements. It originates near Imaiqsaun Lake (also called Fresh Water Lake) slightly south of Barrow, and runs along the margin of Pinguatchaiq Lake (P) towards the Sungugruak Lake (S) complex. It passes to the east of the now drained Ikkalgugruaq Lake (G) and then splits toward either eastward to Iviksuq (V) or continuing north toward Puluyaaq (U), both important historic settlements. This demarcates the limit of the routes as specified by our informants, although some indicated that the eventual goal was access to Admiralty Bay.

Both traditional routes (Fig. 2; digitized from Spencer's 1959 map) joined a larger network of trade routes across

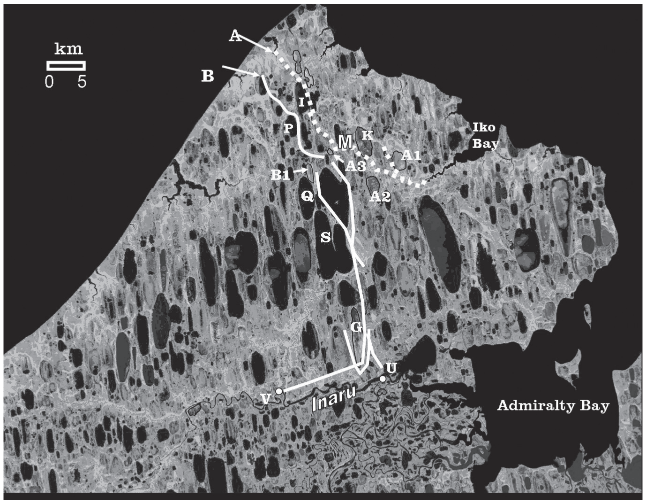

Figure 1. Modern summer travel routes A (dotted line) and B (solid line). Route information is superimposed on a 2002 Landsat 7+ satellite image within a GIS. Labels refer to place names and sites discussed in text.

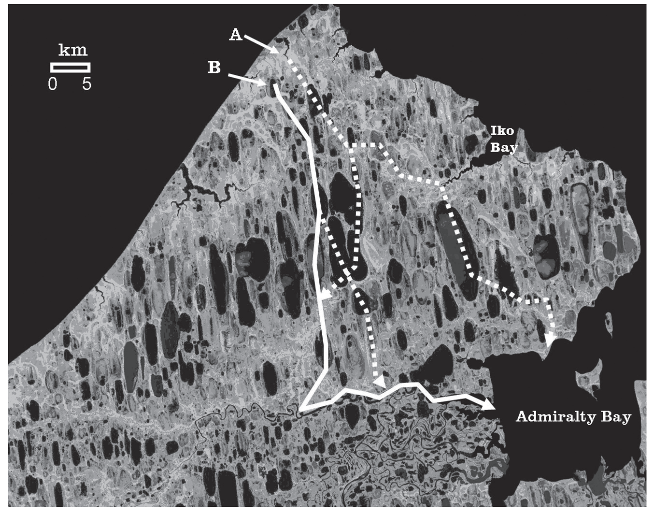

Figure 2. Traditional summer travel routes digitized from Spencer (1959).

northern Alaska and northwestern Canada. Beginning near Barrow, they utilize different streams and water bodies to eventually reach Admiralty Bay. From there, they traveled eastward to Lake Teshekpuk, and finally to the mouth of the Colville River, where there was an important trading center. Spencer (1959) noted that the people from Barrow took the inland fresh-water routes because often during the trading periods—early spring or fall—the sea ice posed too great an obstacle for safe travel along the coast of the Beaufort Sea. By contrast, the inland route through the rivers and lakes eventually arrived at Admiralty Bay, which was usually relatively ice-free at these times.

It is striking that the traditional route and the modern route are so similar, given the drastically different methods of conveyance. Modern routes are mainly used by hunters on ATVs and skirt around the lakes, often following raised shorelines. By contrast, the map by Spencer (1959) demonstrates traditional routes A and B taking full advantage of the lakes and streams for water passage. Several of our informants indicated that, in some places near Barrow, streams were artificially extended across shallow drainage divides to connect with nearby streams and thus reduce the number of portages.

We also compared these routes to those identified in a Minerals Management Service (MMS) survey report from 1987 (Tremont 1987). On the Barrow Peninsula, these routes coincide neither with our map nor with Spencer's traditional trading routes. The MMS map appears to follow waterways, but there is no indication as to whether these are river routes for boat traffic, ATVs trails, or even snowmachine trails.

Both the traditional and modern Route A (Figs. 1, 2) pass along the shores of three drained lake basins (Sikiluk (K), A1 and A2) that are shown as extant lakes prior to 1955. Interviewed Iñupiat noted that these lakes drained recently, although they were unable to specify the timing of these events. Another small basin (A3) was identified from satellite imagery as having drained between 1955 and 2002 (Hinkel et al. 2007). Route B passes along the margin of another drained lake basin (B1), identified by our informants on satellite imagery as having drained in the past 50 years. The southerly basin was formerly Ikkalgugruaq Lake (G) which drained in 1985 based on IK and satellite imagery. Lake drainage or changes in lake level would almost certainly necessitate changes in the route. One of the most experienced modern hunters in the Barrow area, Roy Nageak Sr. explained that he often chose the dry, flat shore on one side of the lakes as optimal for ATV travel.

Satellite imagery and aerial photography

The extent of permanent damage to the tundra from vehicular traffic is evident from the scars caused by vegetation disruption that are visible in aerial photography and high-resolution satellite imagery. We have examined the impacts on the area around Imaiqsaun Lake by using aerial photographs from 1979 and 2005 (Fig. 3). Because this lake was for many years an important source of fresh water for the Barrow community, there is a gravel road approaching it from the north that is visible on both photos. A seismic trail, dating to earlier times, can be seen to the far east in both photos. However, a very distinct ATV trail is apparent in the 2005 image. It departs from the gravel road going southeast, traveling along the dryer and elevated shoreline of an old drained lake basin. Eventually it converges with the traditional route as it follows the modern route B. We can detect the seismic trails in both the 1979 and 2005 photos, indicating visible damage persisting over 25 years. The impact of ATV use in the 2005 photo suggests recent and ongoing damage.

Modern routes are not absolutely fixed in space, and even traditional routes show deviations. This is especially true in the vicinity of Sungugruak Lake (S), where the narrow land bridge between Sungugruak and Qimuksiq Lake (Q) was breached around 1992. This narrow stretch of land was traditionally used as a corridor to access the hunting

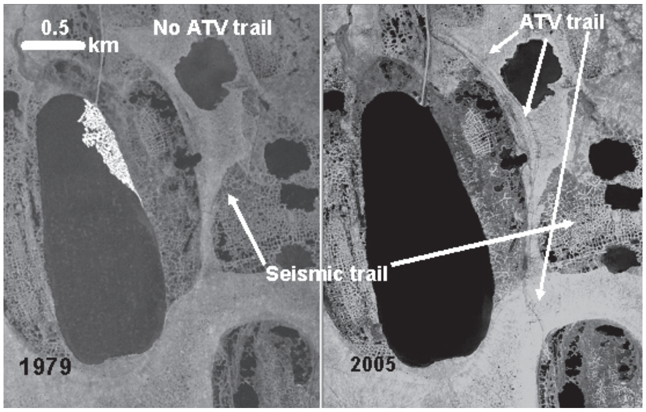

Figure 3. CIR aerial photography captured for the Barrow Peninsula showing ATV and seismic trails in 1979 (1:63,360) and 2005 (1:50,000).

and fishing cabins on the south side Sungugruak Lake. The Miller family of Barrow has a cabin on the south side of Lake Sungugruak; since the neck was breached in 1992, the family must travel a greater distance to reach their cabin (Donna Miller of Barrow in August, 2004 pers. comm.). The modern trails also diverge and converge as they approach cabins and popular hunting and fishing areas.

Discussion

The consequences of ATV usage on the culture and landscape of the Arctic Coastal Plain is profound. The inland regions have become increasingly accessible, but as more people travel the routes, they are subject to heavy vehicular traffic. This damages the vegetation, disrupts the protective organic mat, and destabilizes the underlying permafrost. Past researchers recognized and monitored the deleterious effects of motorized vehicles of all sorts on permafrost landscapes (Brown 1997, Lawson 1986, Nelson et al. 2003, Slaughter et al. 1990). They found that the long-term impacts depended to a large extent on the specific environmental setting: vegetation type and density, ice-content of permafrost, and soil type. The severity of impact also depended on the intensity of human use such as traffic frequency, vehicle weight and width, and even vehicle operation (Slaughter et al. 1990). A comprehensive study by Lawson (1986) emphasized that the ice content of the sediments, coupled with elevation and slope, were the most important factors in determining impact severity. Lawson (1986) also differentiated between the relative impacts of types of activities and their subsequent level of disturbance. Footpaths, even when they get heavy use, do not have the equivalent impact as off-road vehicles. Vehicle weight and the tearing effect of spinning, rough-studded tires are critical factors.

Repeated use by ATVs will eventually disrupt the surface vegetation to the extent that thermokarsting can occur. Depending on the topography of the landscape and the ice-content of the sediments, subsidence, melting wedge ice, slope instability, and lake drainage are a few of the possible outcomes.

Hunters that travel modern routes are cognizant of the environmental effects of ATVs and modern hunting practices, but feel they are caught in a double bind. In a recent interview, Roy Nageak Sr. (Barrow, August 2006 interview) said that the area around Maloney Bridge (Fig. 1, M) is getting swampier due to heavy traffic, and that he would soon be forced to move the bridge. Another hunter, Evelyn Donovan (Barrow, April 2006 interview) reported that the stream near the bridge is getting deeper, and expressed concern about the impact of increased traffic on the tundra. Roy explained that he sometimes “kicked himself” for building the bridge, since it facilitates ease of travel and focuses traffic along the route near the bridge, thus exacerbating damage to the tundra. He explained that the increased use was justified because of the rising cost of purchased food, giving the people of Barrow little choice but to depend to a greater extent on subsistence hunting. At the same time, the increase in gasoline prices has put pressure on hunters to economize by taking shorter routes. Whereas it used to take Roy more than half a day to get to the caribou hunting grounds on his ATV, by taking the bridge shortcut, he can reduce his travel time to an hour.

A recent study (Sonnenfeld 2002) showed an increase in disorientation and loss of geographic knowledge among the Iñupiat who travel on the North Slope. Although the study did not differentiate between summer and winter travel, nor did the author discuss the recent changes in transport mode as a factor in this disorientation, he did note how the loss of traditional knowledge has diluted the wayfinding ability of Iñupiat. During our own interviews, some informants were very outspoken in their concern that younger members of the community did not have the necessary skills to safely navigate in the tundra environment, especially in winter when the surface appears uniform (Thomas Itta Sr. Atqasuk, August 2004 interview). Further afield, Yup’ik Elders have voiced serious concerns about the inexperience of young people when it coincides with their increased travel through the tundra on ATVs and snowmachines (Bradley 2002). Again, during interviews in which we specifically asked about changes to the tundra, some informants expressed frustration at what they perceived as their own reduced knowledge of the landscape. They noted that, either they only went inland during the winter when the tundra was snow-covered and hence observed no changes, or else that they traveled through the landscape on their ATVs too quickly to notice any significant changes.

Concluding Remarks

There are a number of preventative and mitigation measures that have been recommended for addressing tundra disturbance due to ATV traffic. Residents and especially experienced hunters recognize that some terrain types are more resistant to disturbance, and therefore they may be interested in working with scientists to select routes which avoid sensitive areas (Slaughter et al. 1990). Regulation of ATV use may not be a realistic alternative, but the use of synthetic surface protection materials has been successful in some areas. In a 2006 interview, Roy Nageak Sr. said that he recommended to the North Slope Borough that small portions of Route A be covered with a high-strength polymer ground stabilizing mesh. Use of this protective cover would have the dual advantage of directing traffic to a specific track, thus spatially restricting the damage, and stabilizing the vegetation and soil beneath the mesh. Ground stabilizing mesh is already being used in high-traffic areas within Barrow city limits, but is quite expensive.

The IK GIS enables us to compare earlier movements of peoples with current tundra usage and in assessing natural versus anthropogenic landscape change. By combining IK, information gathered from historic reports, and modern aerial photography, we are able to hypothesize causes for route modification or disappearance, and add a new perspective as to how human activities translate to the local landscape.

We can also observe how indigenous communities are adjusting to the impacts of landscape change and how they may be initiating or enhancing some of these changes themselves. Recently, we have noticed a somewhat alarming trend. Visible from the air are heavily traveled tracks across the tundra which extend from Barrow southward to near the Inaru River. The tracks are wide because the damage to the tundra causes local ponding, requiring users to shift to one side or the other. Further, conversations with local residents indicate that it is no longer uncommon for people to use snowmachines on the bare tundra in summer, especially in spring when heavy loads of goods are hauled to inland sites on attached sledges. The snowmachine track and sledge runners tear up the vegetation mat, and the large number of travelers exacerbates the damage. Concerned individuals have installed protective synthetic mats near traffic funneling points such as bridges, but this is a local and temporary solution. It is our hope that the information collected on routes and trail damage will enable community leaders to forecast how the landscape, travel routes, and access to resources will evolve in the future.

Acknowledgments

This work was supported by the National Science Foundation (NSF) under grants BCS-0548846, ARC-0539167, and OPP-0240174 to WRE. Any opinions, findings, conclusions, or recommendations expressed in this material are those of the authors and do not necessarily reflect the views of the NSF. Use of trade, product, or firm names is for descriptive purposes only and does not imply endorsement by the U.S. Government. We are grateful for logistical support from the Barrow Arctic Science Consortium and the Ukpeagvik Iñupiaq Corporation. We thank our Iñupiaq collaborators, especially Mr. Thomas Itta Sr. (deceased), Mrs. Flossie Itta, Mr. Roy Nageak Sr., Mr. Ron Brower Sr., and our translator and community liaison, Mrs. Lollie Hopson. The authors would like to thank Drs. Guido Grosse and William Manley for their very helpful reviews.

References

Bernard, H.R. 2002. *Research Methods in Anthropology*, 3rd Ed. Walnut Creek: Altimira Press.

Bradley, C. 2002. Traveling with Fred George: The Changing Ways of Yup'ik Star Navigation in Akiachak, Western Alaska. In: I. Krupnik & D. Jolly (Eds.), *The Earth is Faster Now: Indigenous Observations of Arctic Environmental Change*, Fairbanks, AK: Arctic Research Consortium of the United States, 241-264.

Brown, J. 1997. Disturbance and recovery of permafrost terrain. In: R.M. Crawford (Ed.), *Disturbance and Recovery in Arctic Lands: An Ecological Perspective*. Dordrecht: Kluwer Academic, 167-178.

Burch, E.S. Jr. 2005. Alliance and Conflict: The World System of the Iñupiaq Eskimos. Lincoln: University of Nebraska Press.

Fox, S. 2002. These things are really happening: Inuit perspectives on the evidence of climate change in Nunavut. In: I. Krupnik & D. Jolly (Eds.), *The Earth is Faster Now: Indigenous Observations of Arctic Environmental Change*, Fairbanks, AK: Arctic Research Consortium of the United States, 13-53.

Hinkel, K.M., Eisner, W.R., Bockheim, J.G., Nelson, F.E., Peterson, K.M. & Dia, X.Y. 2003. Spatial extent, age and carbon stocks of drained thaw lake basins on the Barrow Peninsula, Alaska*. Arctic, Antarctic, and Alpine Research* 35(3): 291-300.

Hinkel, K.M., Jones, B.M., Eisner, W.R , Cuomo, C.C, Beck, R.A. & Frohn, R. 2007. Methods to assess natural and anthropogenic thaw lake drainage on the western Arctic Coastal Plain of Northern Alaska. *Journal of Geophysical Research* 112: F02S16, doi:10.1029/2006JF000584.

Huntington, H.P. 2000. Using traditional ecological knowledge in science: Methods and applications. *Ecological Applications* 10: 1270-1274.

Lawson, D.E. 1986**.** Response of permafrost terrain to disturbance: A synthesis of observations from northern Alaska, USA**.** *Arctic and Alpine Research* 18: 1-17.

Nelson, F.E., Brigham, L., Hinkel, K.M., Parker, W., Romanovsky, V.E., Smith, O., Tucker, W. & Vinson, T. 2003. *Climate Change, Permafrost, and Impacts on Civil Infrastructure*. Special Report 01-03, Permafrost Task Force, U.S. Arctic Research Commission, Arlington, VA, 72 pp.

Slaughter, C.W., Racine, C.H., Walker, D.A., Johnson, L.A. & Abele, G. 1990. Use of off-road vehicles and mitigation of effects in Alaska permafrost environments: A review. *Environmental Management* 14(1): 63-72.

Sonnenfeld, J. 2002. Social dimensions of geographic disorientation in Arctic Alaska. *Etudes Inuit Studies* 26(2): 157-173

Spencer, R.F. 1959. *The North Alaskan Eskimo: A Study in Ecology and Society***.** Government Printing

Office, Smithsonian Institution, Bureau of American Ethnology, Bull. No. 171, 490 pp.

Tremont, J.D. 1987. *Surface Transportation Networks of the Alaskan North Slope*. OCS Report MMS 87-0010, Anchorage, Alaska: Minerals Management Service, 96 pp.

Permafrost in Iceland: Thermal State and Climate Change Impact

Bernd Etzelmüller
Department of Geosciences, University of Oslo

Thomas V. Schuler
Department of Geosciences, University of Oslo

Herman Farbrot
Department of Geosciences, University of Oslo

Águst Guðmundsson
Jardfrædistofan Geological Services, Reykjavik, Iceland

Abstract

This paper provides an overview of distribution and thermal characteristics of mountain permafrost in Iceland. Borehole temperature monitoring since summer 2004 and simple distribution modeling suggest widespread mountain permafrost in Iceland above 800 to 900 m a.s.l. The permafrost temperatures are close to 0ºC and some tens of meters thick in the elevation range of 800 to 1000 m a.s.l. At that elevation, the permafrost distribution is mainly governed by the distribution of snow, while above 1200 m a.s.l. smaller areas of continuous permafrost do exist. This presentation presents new borehole temperature data that have been collected until the summer 2007 and associated numerical modeling of snow influence on ground temperatures.

Keywords: ground temperatures; Iceland; modeling; permafrost.

Introduction

Within the context of climate-permafrost relationships in the North Atlantic region, Iceland represents a link between Scandinavia and Greenland. The regional distribution of permafrost in Iceland has been addressed by means of gridded mean annual air temperatures (MAAT) for the 1961–1990 period interpolated from point meteorological data (Etzelmüller et al. 2007) (Fig. 1). Etzelmüller et al. (2007) showed that MAAT~-3ºC gives an indication of the lower limit of widespread permafrost in Iceland, not regarding snow conditions or topographic aspect variability. Figure 1 suggests the presence of widespread mountain permafrost outside the already known sporadic permafrost zone in central Iceland. The lower limit increases in elevation towards the southeast, with elevations between 800 m a.s.l. in the north and more than 1000 a.s.l. in the southern part of Iceland. Permafrost is also predicted on the highest mountain peak areas along the southeastern coast above c. 900 m a.s.l. This paper presents new data series and modeling exercises to elaborate the influence of surface temperature and snow variation on permafrost temperatures in Iceland.

Setting

Iceland is located where the asthenospheric flow under the Mid-Atlantic Ridge interacts and mixes with a deep-seated mantle plume (Shen et al. 1998, Wolfe et al. 1997). This implies generally high geothermal heat fluxes due to heat conduction from the partly molten layer at approximately 10°-km depth (Flóvenz & Sæmundsson 1993). Iceland is characterized by maritime conditions with cool summers and mild winters. In the lowland areas, the MAAT for the 1961–1990 period was 4°–5°C in southern parts, 3°–4°C in the eastern and western parts, and 2°–3°C in northern, coastal parts of the country (Tveito et al. 2000). A large part of the precipitation falls with winds prevailing from eastern and southern directions (Einarsson 1984). Thus, mean annual precipitation increases from above 500 mm in the central and northern parts of the country to more than 3000 mm in the southeast.

In four boreholes, ground temperatures were monitored since 2004 (Farbrot et al. 2007) (Fig. 1). They are located in central and northeastern Iceland at ~890–930 m a.s.l. All boreholes are relatively shallow (12–22 m deep), penetrating through a shallow sediment cover into basaltic bedrock. All sites are on elevated plateaus, and significant slopes are more than 100 m away from the boreholes. The sites are not vegetated and are exposed to wind drift of snow.

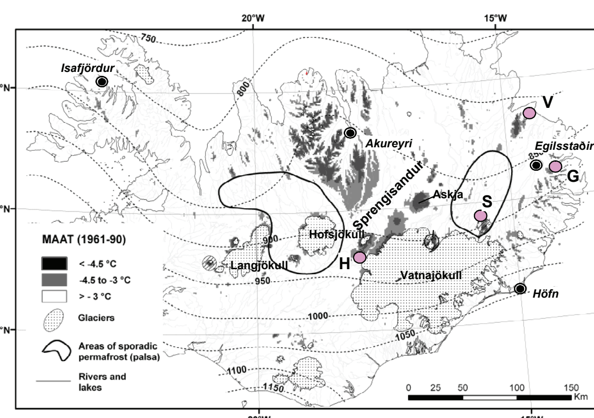

Figure 1: Key map and permafrost map of Iceland (based on Etzelmüller et al. 2007). G=Gagnheiði; S=Snæfell; V=Vopnafjörður; H=Hágöngur. The dotted contour lines indicate the lower limit of permafrost based on the distribution of MAAT~-3ºC.

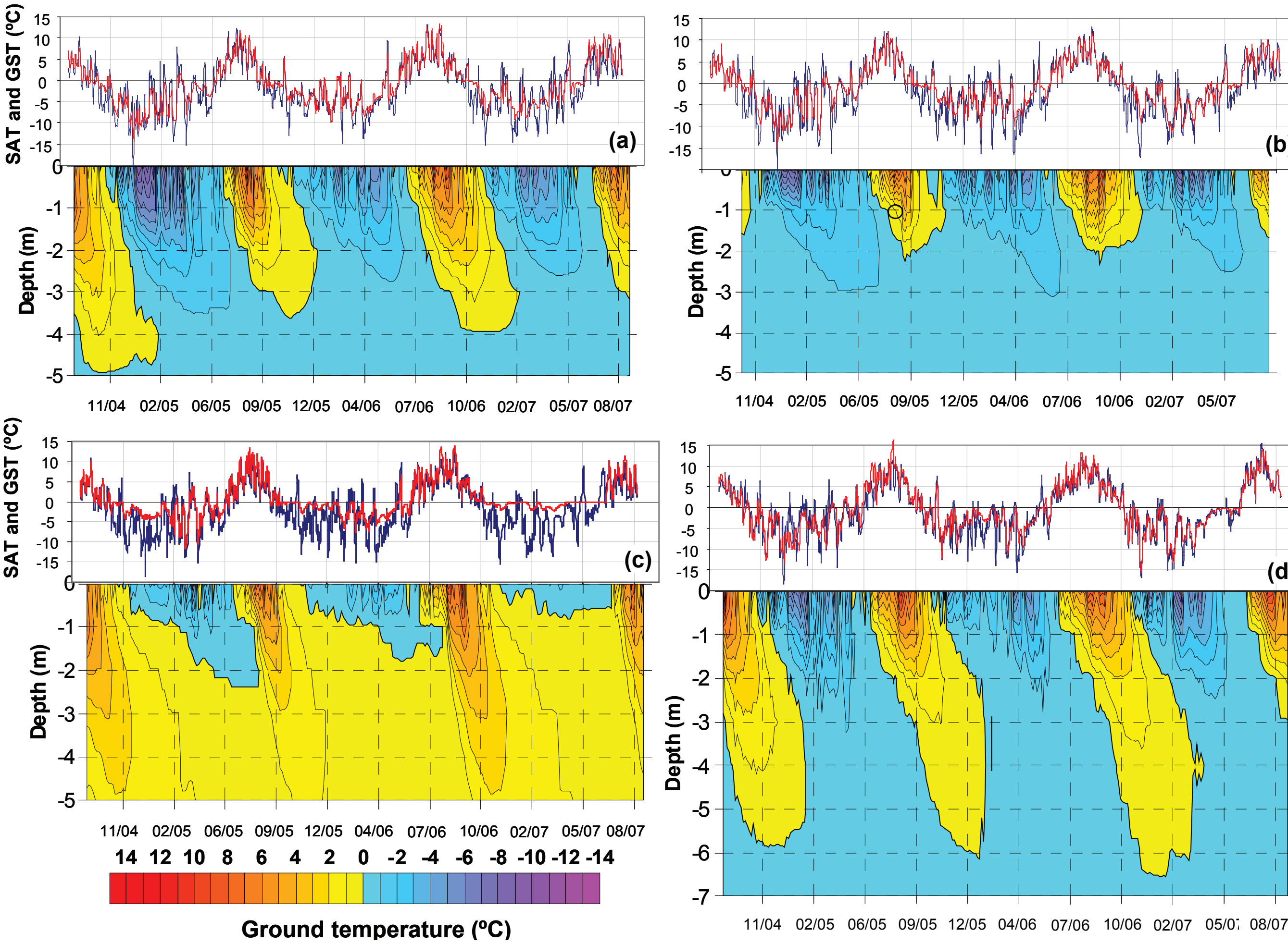

Figure 2: Depth-time series for air, surface, and ground temperatures at the four monitoring stations. The upper graph show SAT (surface air temperature) (blue) and GST (ground surface temperature) (Red) during the measurement period (August 2004 to August 2007). The lower diagram shows an interpolated depth-time series of ground temperatures. The contour interval is 1ºC, (**a**) Gagnheiði, (**b**) Snæfell, (**c**) Vopnafjörður, and (**d**) Hágöngur.

Methods and Results

Temperature monitoring and analysis

Instrumentation: All boreholes were initially equipped with UTL-1 miniature temperature dataloggers (MTDs) having an accuracy of ±0.27°C or better (cf., Hoelzle et al. 1999). In August 2005, the boreholes at Snæfell and Gagnheiði were equipped with thermistor chains consisting of 26 and 15 YSI S40006 thermistors, respectively. These thermistors have an absolute accuracy of ±0.05°C (Vonder Mühll 1992). Close to each borehole, single MTDs, measuring at intervals of 2 hours, were installed near the ground surface (i.e., at 1–5-cm depth) to record ground surface temperature (GST) and in radiation shields 1.5 m above ground to measure surface air temperatures (SAT). At Gagnheiði, the SAT from the meteorological station was used. Minor data gaps existed for air temperature measurements, which were filled in using linear regression to one of the other stations, usually with a $R^2>0.95$. More details of borehole location and characteristics are given in Farbrot et al. (2007).

Calculations: A set of parameters is calculated, representing an average over the three seasons reaching from September 1 to August 31 (Table 1). The frost number for air (F) and ground surface ($F+$) are calculated following Nelson and Outcalt (1987):

$$F = \sqrt{DDF_a} / \left(\sqrt{DDF_a} + \sqrt{DDT_a} \right) \quad (1)$$

and

$$F_+ = \sqrt{DDF_s} / \left(\sqrt{DDF_s} + \sqrt{DDT_s} \right) \quad (2)$$

where DDF are freezing degree days, DDT are thawing degree days and the indexes a and s refer to air and surface, respectively. The n-factors simply follow the equation

$$n_T = DDT_s / DDT_a \text{ and } n_F = DDF_s / DDF_a$$

for the freezing factor n_F and the thawing factor n_T, respectively, $TTOP$ (top of permafrost) temperatures are estimated following, for example, Smith & Riseborough (2002):

$$TTOP = (r_K * n_T * DDT_a - n_F * DDF_a) / P \qquad (3)$$

where P is the period (365 days) and r_K is the quotient between thermal conductivity of soil in thawed and frozen state, respectively. Values of thermal conductivity are taken from literature, with values varying between 1.7 and 1.9 $Wm^{-2}K^{-1}$ (Flóvenz & Sæmundsson 1993).

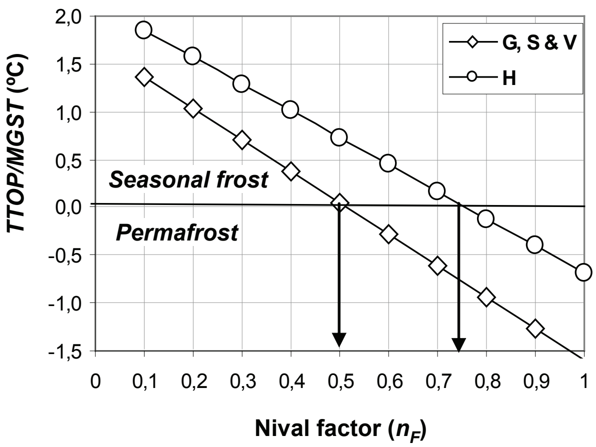

Figure 3: Modeled *TTOP* as a function of n_F, *G, S,* and *V* stands for Gagnheiði, Snæfell, and Vopnafjörður, respectively. For the three stations, it is assumed *DDF=1200* and *DDT=620* according to the last three seasons average (*MAT=-1.6ºC*), *H* stands for Hágöngur, assuming *DDF=1030* and *DD=780* (*MAT=-0.7ºC*), $r_K=1$ and $n_T=1$, as calculated from temperature measurements at the permafrost stations.

Results: The three records from Gagnheiði, Snæfell, and Vopnafjörður are highly correlated with respect to air temperatures with similar annual pattern, and have corresponding DDF_a and DDT_a values. Snæfell is slightly warmer than the two other stations (Table 1). However, ground temperatures are dissimilar (Fig. 2). The Vopnafjörður borehole has no permafrost and only shallow seasonal frost. The two others have permafrost, with *TTOP* temperatures above -0.5ºC. The active layer thickness was higher at Gagnheiði (3.5–4.5 m) than on Snæfell (~2 m), despite higher GST and SAT at the Snæfell station. This is due to higher water content at Snæfell, as discussed in Farbrot et al. (2007). The SAT at the Hágöngur station was slightly higher than the three others (0.7° to 0.8ºC); however, marginal permafrost is present, with an active layer thickness of ~5 m.

It is obvious that permafrost existence and temperatures are highly related to the snow cover at the stations. At the Vopnafjörður station the n_F-factor was at 0.5 or below, while all other stations showed n_F-values *>0.7*, up to *>0.9* (Hágöngur station). We have no recordings of snow cover thickness. All sites are wind-exposed, and thick snow accumulations are unlikely. According to Smith & Riseborough (2002) the obtained nival factors correspond to average snow depths of below 0.2 m, which is in accordance to winter observations at the field stations. No stations show persistent <0ºC winter temperatures, but numerous events of melting episodes throughout the season (Fig. 2). This has two effects: First, snow cover becomes isothermal even with low thicknesses because of latent heat release during refreezing, leading to lower n_F-factors. Second, snow cover decreases and occasionally disappears during these episodes, allowing

Table 1: Summary of temperature recordings at the four measurement stations calculated over three seasons. *SAT*= Mean surface air temperature. *GST* = mean ground surface temperature. *DDF* = freezing degree days. *DDT* = thawing degree days for air and surface (index *a* and *s*). n_T = thawing n-factor. n_F = freezing (nival) n-factor. *F* and *F+* are the frost number for air and surface. respectively. *TTOP* is *measured* mean temperature at the top of permafrost or the bottom of seasonal freezing.

Location	Period	SAT	GST	DDF_a	DDT_a	DDF_s	DDT_s	n_T	n_F	F	F+	TTOP
Vopna	2004/05	-1.7	0.1	1261.2	627.7	629.7	663.2	1.06	0.50	0.59	0.50	1.0
Vopna	2005/06	-1.6	0.4	1225.9	638.6	500.2	648.1	1.01	0.41	0.58	0.47	0.8
Vopna	2006/07	-1.4	1.1	1099.6	601.4	153.7	545.0	0.91	0.14	0.57	0.34	1.1
3-years average		***-1.6***	***0.5***	***1195.6***	***622.6***	***427.9***	***618.8***	***0.99***	***0.35***	***0.58***	***0.44***	***1.0***
Hágöng	2004/05	-0.6	-0.3	941.0	727.4	927.0	834.0	1.15	0.99	0.53	0.53	-0.2
Hágöng	2005/06	-1.1	-0.1	1109.5	706.4	784.0	751.9	1.06	0.71	0.56	0.51	-0.2
Hágöng	2006/07	-0.3	-0.1	1018.7	894.2	890.6	841.4	0.94	0.87	0.52	0.50	-0.1
3-years average		***-0.7***	***-0.2***	***1023.0***	***776.0***	***867.2***	***809.1***	***1.05***	***0.86***	***0.53***	***0.51***	***-0.2***
Gagn	2004/05	-1.6	-1.4	1164.9	601.8	1060.2	549.3	0.91	0.91	0.58	0.57	-0.15
Gagn	2005/06	-1.9	-0.9	1238.9	620.0	933.0	593.1	0.96	0.75	0.59	0.55	-0.15
Gagn	2006/07	-1.5	-0.5	1135.4	599.3	829.9	659.0	1.10	0.73	0.58	0.54	-0.1
3-years average		***-1.6***	***-0.9***	***1179.7***	***607.0***	***941.0***	***600.5***	***0.99***	***0.80***	***0.58***	***0.55***	***-0.1***
Snæfell	2004/05	-1.5	-0.9	1232.1	690.9	952.1	622.3	0.90	0.77	0.57	0.54	
Snæfell	2005/06	-1.6	-0.8	1252.9	655.9	870.7	570.5	0.87	0.69	0.58	0.54	-0.55
Snæfell	2006/07	-1.4	-0.5	1112.9	591.8	826.9	628.1	1.06	0.74	0.58	0.54	-0.55
3-years average		***-1.5***	***-0.8***	***1199.3***	***646.2***	***883.2***	***607.0***	***0.94***	***0.74***	***0.58***	***0.54***	***-0.55***

subsequent cold penetration, resulting in higher n_F-factors. This is especially obvious at the Vopnafjörður station, where deep seasonal frost could develop late in the 2004/05 season after a strong melting episode. The Hágöngur station showed less strong melting episodes. At the Vopnafjörður station, temperature decreases with depth with values <0.4ºC at -20 m. This indicates possibly relic permafrost below 25 m or so (cf. Etzelmüller et al. 2007, Farbrot et al. 2007).

Simple TTOP modeling following Equations (1) and (2) indicate that at the three stations of Vopnafjörður, Gagnheiði, and Snæfell, permafrost persists above a nival factor of n_F >0.5, while the Hágöngur station would produce positive "TTOP" with n_F-factors <0.75 (Fig. 3), showing virtually no snow during the winter season. Etzelmüller et al. (2007) proposed a limit of *MAAT=-3ºC* (normal period 1961–1990) for the lower limit of widespread permafrost in Iceland and Scandinavia. Theoretical considerations based on the TTOP model indicate a minimum n_F-factor of ~0.3 for TTOP <0 and MAAT=-3ºC. Since temperatures during the normal period 1961–1990 were about 1º to 2ºC lower than during our study (Farbrot et al. 2007), the Vopnafjörður station possibly had permafrost during at least the major part of the last century. Measured TTOP temperatures were lowest on Snæfell, which seems to have the most stable permafrost (Table 1). The two other permafrost stations show TTOP-temperatures very close to 0ºC, and seem to be in a stage of degrading. When modeling TTOP temperatures according to Equation (3), the r_K values are close to unity, indicating mostly similar TTOP than GST. This is possibly because of water advection and the influence of unfrozen water content close to 0ºC.

Modeling of ground temperatures

To investigate the sensitivity of ground temperatures to changes in snow coverage, we employ a numerical 1-D heat conduction model. We use an n-factor approach to derive GST from SAT and change the values of n to represent situations of different snow coverage. Based on the results, we discuss possible changes that may have led to the recent deterioration of permafrost at Vopnafjörður

Heat-conduction modeling principles: A numerical 1-D model of heat conduction is used, which accounts for latent heat and is forced by annual, monthly or daily GST input values (cf. Farbrot et al. 2007). The model solves the heat conduction equations following:

$$\rho\, c\frac{\partial T}{\partial t} = -k\frac{\partial^2 T}{\partial z^2} \tag{4}$$

(e.g., Williams & Smith 1989). As boundary conditions, we prescribe time series of GST and the geothermal heat flux

$$Q_{geo} = -k \cdot \partial T / \partial z \tag{5}$$

at depth, Q_{geo} was sat to 0 for shallow modeling domains below 30 m. Values for Q_{geo} were obtained from Flóvenz & Sæmundsson (1993), and must be regarded as regionally applicable values rather than local estimates. The thermal properties of the ground are described in terms of density ρ, thermal conductivity *k* and heat capacity *c*. Typical values for Icelandic basalt were derived from the literature (Flóvenz & Sæmundsson, 1993). In our model, we consider the change of latent heat *L* due to phase changes of the pore water by describing a temperature-dependent heat capacity $c_{(T)}$. In a small temperature interval between T_1 (-0.1ºC) and T_2 (0ºC) around the freezing temperature, we add the effect of latent heat release to the heat capacity of the substrate c_0 (e.g., Wegmann et al. 1998).

$$c_{(T)} = c_0 + \frac{L}{(T_2 - T_1)} \tag{6}$$

Any effects of heat advection related to groundwater flow are neglected in this study. The heat conduction equation (Equation [4]) was discretized along the borehole depth using finite differences, and subsequently solved by applying the method of lines (Schiesser 1991).

Calibration run: For this study, the study sites of Vopnafjörður (no permfrost) and Gagnheiði (warm and shallow permafrost) were selected. The model was calibrated using measured ground temperatures, and the values of *w* (volumetric water content) and *k* were adjusted to match modeled and measured temperature distributions, annual amplitudes at a given depth, and modeled and measured thicknesses of the active layer (Fig. 4). Generally, the fit revealed R^2-values of *>0.9*. The model performance was lower during spring and fall, most probably due to advective processes which are not accounted for, or deficits of the modeling approach because of lacking prescription of important processes. Values for material properties are taken from literature. The calibration indicates relatively dry

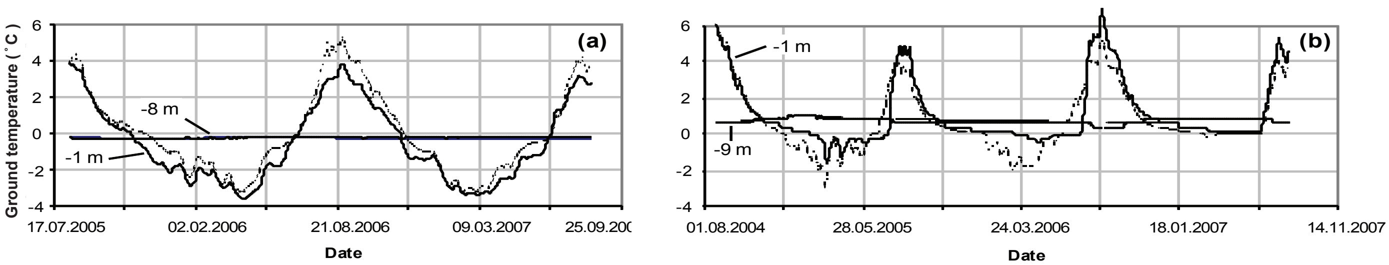

Figure 4: Examples of fit for modeled and measured ground temperatures in depth (8 and 9 m) and close to the surface (1 m). (a) Gagnheiði, (b) Vopnafjörður. Solid line is "modeled"; dashed line is "measured."

conditions at both sites, with volumetric water contents of below 5% (Farbrot et al. 2007).

Simulation run: To investigate the sensitivity of ground temperatures to changes in snow coverage, we use an n-factor linking GST to SAT and change the values of n_F to represent different situations. We prescribe SAT as a sinusoidal variation of specified amplitude around a specified annual mean temperature. Winter temperatures (defined as <0ºC) were damped using the n_F-factor.

Snow cover effect was simulated by changing n_F-factors, and SAT varies around a mean of *-1.6ºC* with amplitude of *9ºC* (Table 2). The n_F-factor was kept constant throughout the winter. For the Gagnheiði station, stable snow cover corresponding to n_F-factors <0.5 will lead to an almost instantaneous development of taliks. A smaller influence of snow coverage ($n_F>0.5$) is conserving the permafrost situation at Gagnheiði. This corresponds well with the TTOP analysis described previously, even if the TTOP approach produces errors especially close to 0ºC (Riseborough 2007). The same is valid for the Vopnafjörður station. Here, further warming of the ground is continued with $n_F<0.3$, while $n_F=0.4$ *to 0.6* results in a situation with no or very limited ground temperature trends, even after *40 years* of model run. This indicates that the measured n_F-factor (0.14) for the 2006/07 season at Vopnafjörður (Table 1) was exceptionally low. With $n_F=0.7$ permafrost aggregates after 7 years of model run. This is also in rough correspondence to Figure 3

In a second simulation, we evaluated the impact of changing SAT on ground temperatures, assuming a constant snow cover like that observed during the three years of recent monitoring. We introduced a step change of ~1ºC warming for Gagnheiði ($n_F=0.7$, *MAT=-0.6ºC)* and cooling for Vopnafjörður station ($n_F=0.45$, *-2.8ºC)*. For the Gagnheiði station, a talik appears after c. 8 years, and permafrost is degraded within 50 years. This is roughly in accordance to the analysis shown in Farbrot et al. (2007). For the Vopnafjörður station the model produces permafrost after c. *15 a* with instant cooling to *-2.8 ºC* and a $n_F=0.45$. The air temperature value corresponds roughly to MAAT during the last normal period 1961–1990 in eastern Iceland close to 900 m a.s.l. After 50 years, permafrost is modeled to be approximately 10 m thick. This clearly demonstrates that permafrost at Vopnafjörður most probably has been degrading during the last decades, and that there might still be relic permafrost. It seems certain that the site had permafrost conditions during the Little Ice Age, since there is plenty of geomorphological evidence, such as rock-glaciers and well-developed patterned ground features.

Table 2: Simulation for varying snow conditions. The model was forced with a sinusoidal curve, with MAT of -1.6ºC and air temperature amplitude of 9ºC. AL=active layer depth; SF=seasonal frost depth after 20 years; GT=ground temperature; T=Tallilk, PF=permafrost. The initial ground temperatures were sat to the measured temperatures from 1.6.2007.

	Gagnheiði		**Vopnafjörður**			
n_F	G T response	AL (m)	G T response	SF (m)	A L (m)	PF thick after 20 a
0.1	T > 1 a		Warming	< 1.5		
0.2	T > 1 a		Warming	< 2		
0.3	T > 2 a		Warming	< 2.5		
0.4	T > 3 a		Stable (no PF)	< 3		
0.5	T > 12 a		Stable (no PF)	< 3.5		
0.6	Stable	> 5	Stable (no PF after 40 a)	< 4		
0.7	Stable	> 3.8	PF > 7 a		4.5	7 m
0.8	Stable	> 3.6	PF > 4 a		4	8 m
0.9	Stable	> 3.4	PF > 3 a		3.5	10 m

Summary and Conclusions

A three-year monitoring series of air and ground temperatures is presented for four permafrost stations in Iceland. Permafrost is warm, and in a degrading stage at two stations. At one, permafrost is absent, and this study indicates that permafrost may have existed at this station during some part of the last century. Snow is the decisive factor for permafrost distribution in elevation ranges between 800 m and 1000 m a.s.l. in Iceland, which corresponds to MAAT during the last normal (1961–1990) period of around -3*ºC*. A $n_F>0.6$ seems necessary to keep permafrost stable in the elevation ranges below 1000 m a.s.l. in Iceland. The study demonstrates the sensitivity of ground temperatures to small changes in air temperatures and snow cover in the maritime mountains of Iceland. As ground temperatures are major decisive factors for understanding a suite of geomorphological processes, the understanding of the impact of expected climate warming on this environment is crucial.

Acknowledgments

This study was financed by the Norwegian Research Council (project 157837/V30). Jardfrædistofan Geological Services, Reykjavik, Iceland, and the Department of Geosciences, University of Oslo, Norway. The paper was certainly improved by the helpful comments by two anonymous reviewers. We want to thank all mentioned persons and institutions.

References

Einarsson, M.Á. 1984. Climate of Iceland. In: H. Van Loon (Editor), Climate of the oceans: World survey of climatology. Elsevier Science Publishers, pp. 673-698.

Etzelmüller, B. et al. 2007. The regional distribution of mountain permafrost in Iceland. *Permafrost and Periglacial Processes* 18(2): 185-199.

Farbrot, H. et al. 2007. Thermal characteristics and impact of climate change on mountain permafrost in Iceland. *Journal of Geophysical Research* 112: F03S90, doi:10.1029/2006JF000541.

Flóvenz, O.G. & Sæmundsson, K. 1993. Heat flow and geothermal processes in Iceland. *Tectonophysics* 225: 123-138.

Hoelzle, M., Wegmann, M. & Krummenacher, B. 1999. Miniature temperature dataloggers for mapping and monitoring of permafrost in high mountain areas: First experience from the Swiss Alps. *Permafrost and Periglacial Processes* 10(2): 113-124.

Nelson, F.E. & Outcalt, S.I. 1987. A Computational method for prediction and regionalization of permafrost. *Arctic and Alpine Research* 19(3): 279-288.

Riseborough, D. 2007. The effect of transient conditions on an equilibrium permafrost-climate model. *Permafrost and Periglacial Processes* 18(1): 21-32.

Schiesser, W.E. 1991. The numerical method of lines: integration of partial differential equations. Academic Press, San Diego, CA, USA, 326 pp.

Shen, Y., Solomon, S.C., Bjarnason, I.T. & Wolfe, C.J. 1998. Seismic evidence for a lower-mantle origin of the Iceland plume. *Nature* 395(6697): 62-65.

Smith, M.W. & Riseborough, D.W. 2002. Climate and the limits of permafrost: A zonal analysis. *Permafrost and Periglacial Processes* 13(1): 1-15.

Tveito, O.E. et al. 2000. Nordic temperature maps. Report No. 09/00, DNMI, Oslo.

Vonder Mühll, D. 1992. Evidence of intrapermafrost groundwater flow beneath an active rock glacier in the Swiss Alps. *Permafrost and Periglacial Processes* 3(2): 169-173.

Wegmann, M., Gudmundsson, G.H. & Haeberli, W. 1998. Permafrost changes in rock walls and the retreat of alpine glaciers: A thermal modelling approach. *Permafrost and Periglacial Processes* 9: 23-33.

Williams, P.J. & Smith, M.W. 1989. The frozen Earth: Fundamentals of geocryology. Cambridge University press, Cambridge, 300 pp.

Wolfe, C.J., Bjarnason, I.T., VanDecar, J.C. & Solomon, S.C. 1997. Seismic structure of the Iceland mantle plume. *Nature* 385(6613): 245-247.

Present and Past Distribution of Mountain Permafrost in the Gaissane Mountains, Northern Norway

Herman Farbrot
Department of Geosciences, University of Oslo and Norwegian Meteorological Institute, Norway
Ketil Isaksen
Norwegian Meteorological Institute, Norway
Bernd Etzelmüller
Department of Geosciences, University of Oslo, Norway

Abstract

The Gaissane Mountains, situated in northern Norway, reach elevations above 1000 m a.s.l. Our study area contains a range of active and relict periglacial features as well as numerous landforms related to the Pleistocene ice sheet. The distribution of permafrost in the mountains has been investigated through basal temperature of snow (BTS) measurements, continuous ground surface temperature (GST) measurements, and electrical resistivity tomography. Solar radiation and the presence or absence of coarse blocks are the two main factors controlling the thermal regime of regularly snow-covered ground. At fairly snow-free sites, the investigations indicate that mountain permafrost is common in the area above 350–450 m a.s.l. On the summits, about 1000 m a.s.l., geomorphic evidence combined with GST measurements suggest that the permafrost probably shows great antiquity, possibly prevailing since the last interglaciation.

Keywords: Gaissane Mountains; palaeopermafrost; permafrost mapping.

Introduction

In southern Norway, the lower regional altitudinal limit of mountain permafrost decreases eastwards with increasing continentality. The investigated sites in southern Norway have in common that the BTS variance to a great extent is explained by elevation, whereas the effect of solar radiation is secondary (Etzelmüller et al. 2003). Although Reusch (1901) a century ago recognized permafrost as a common phenomenon at high altitudes in northern Norway, few quantitative studies on mountain permafrost have been conducted in this area. Rather most investigations have focused on periglacial geomorphology and in particular palsas (Isaksen et al. 2008 and references therein). Gridded mean annual air temperature (MAAT) maps, however, indicate a similar altitudinal gradient for discontinuous permafrost limits also in northern Norway, decreasing from over 1000 m a.s.l. in coastal sites down to below 400 m a.s.l. in interior, more continental areas (Etzelmüller et al. 2008, Isaksen et al. 2008).

The aim of this study is to investigate occurrences of mountain permafrost in the Gaissane Mountains, northern Norway, by using measurements of ground surface temperature (BTS and Miniature Temperature Dataloggers [MTDs]) and electrical resistivity tomography (ERT). The factors controlling the distribution of permafrost are discussed. In addition, the distribution of paleopermafrost is briefly discussed based on geomorphic mapping.

Setting

The Gaissane Mountains are situated southwest of the Varanger Peninsula (70°N, 25°E) in the county of Finnmark, northern Norway (Fig. 1). The mountains reach elevations above 1000 m a.s.l. Western and southwestern parts of Norway are mostly influenced by western, Atlantic air flows bringing unstable weather patterns with high winter temperatures and moist air, whereas eastern parts of northern Norway are frequently dominated by Eurasian high-pressure systems involving stable air with high summer temperatures and low winter temperatures for long periods of time (Johannessen 1970). The official weather station closest to the field area is Banak (5 m a.s.l.), 20 km to the north. There, MAAT

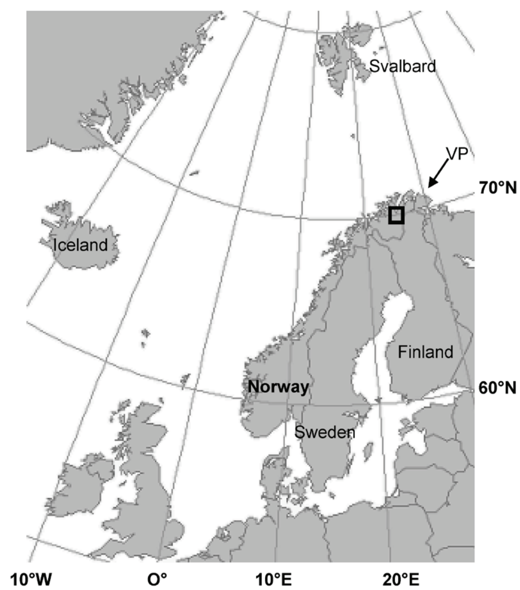

Figure 1. The Gaissane Mountains are situated in northern Norway, southwest of the Varanger Peninsula (VP).

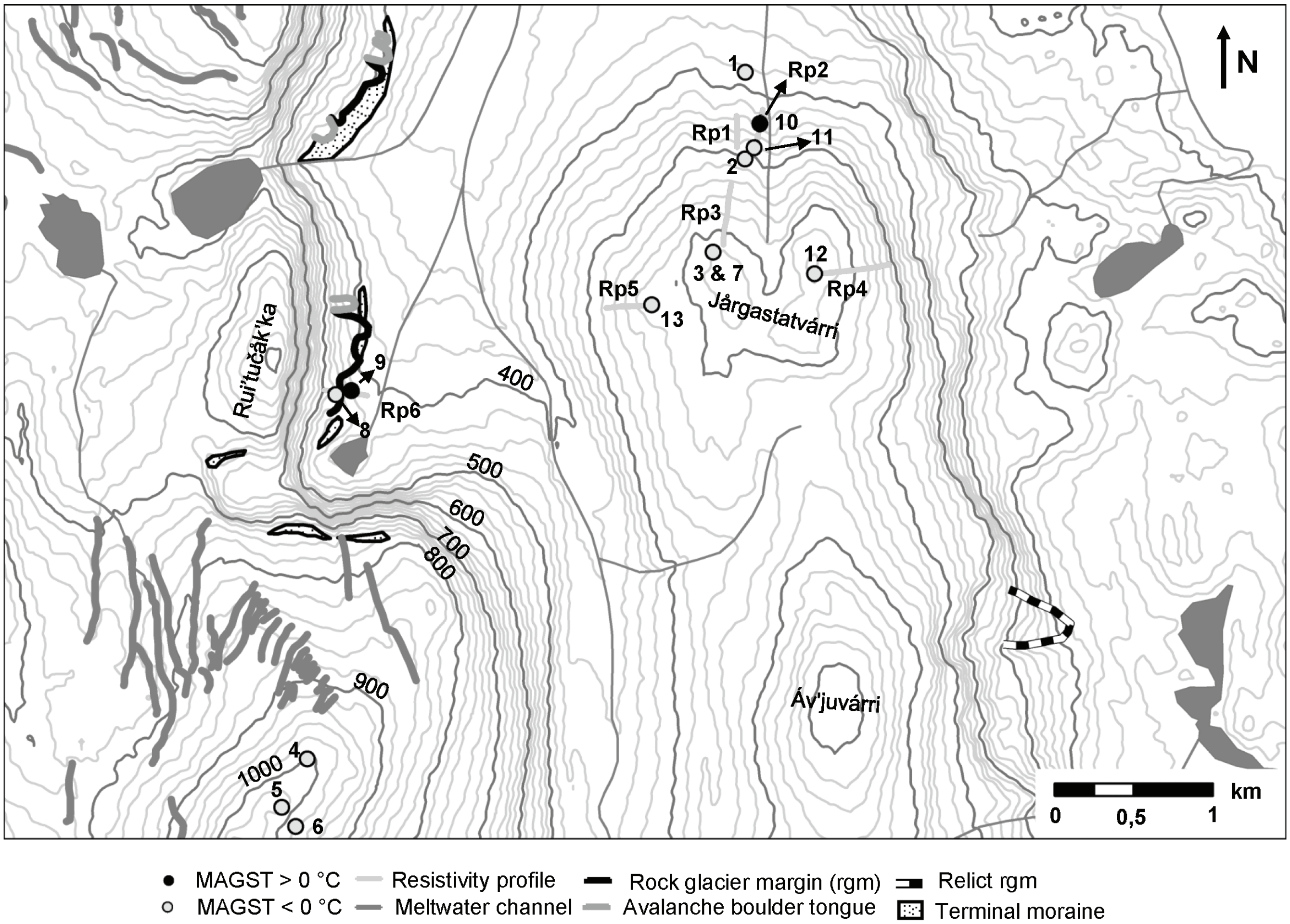

Figure 2. Map of the field area in Gaissane Mountains containing the positions of the ERT profiles (Rp1-6), MTDs and some geomorphic features. Letters refer to the MTDs in Table 1. The westernmost rock glaciers partly cover morainic ridges of presumable Preboreal age (Kellerer-Pirklbauer 2008).

(1961–1990) is 0.6°C and mean annual precipitation 345 mm. The winds are strong during winter, and above the forest line (250–300 m a.s.l.) extensive snow cover is commonly restricted to depressions.

The field area contains a range of active and relict periglacial features including rock glaciers, solifluction lobes, ploughing boulders, and patterned ground, as well as numerous landforms related to the Scandinavian ice sheet. The field area is situated well inside the glacial limit of the Younger Dryas ice; however, the summits were nunataks at that time (Marthinussen 1960).

Methods and Results

MTDs

13 UTL-1 MTDs were used during the period 2003–2006, 12 measuring ground surface temperatures and one measuring air temperature (Fig. 2, Table 1). The thermistors have a temperature range of −29° to +39°C, and the accuracy of the sensors are ±0.27°C (Hoelzle et al. 1999). The MTD data is probably not representative for long-term ground surface temperature conditions, since the observational period was characterized by considerably higher air temperatures than normal (1961–1990). By correlating the daily ground surface means with daily air temperature means from the weather station at Banak, a simple linear regression model was established. Using MAAT from Banak as independent variable, mean annual ground surface temperatures (MAGSTs) for the normal period 1961–1990 were estimated for the MTD sites. For these estimates to be reliable, we only used data from more or less snow-free sites, as indicated by the existence of high-frequency temperature fluctuations during winter (MTDs 1, 3-5, 8-13). The assumption is, thus, that these areas also remained snow free during the normal period 1961–1990 (cf., Farbrot et al. 2007). In general, a R^2 of > 0.70 (for all records: $p << 0.001$) was achieved in these analyses. Fitting a linear trend line through the estimated MAGST from the MTD sites indicate that the MAGST 0°C-isotherm of fairly snow-free sites is found at ~350 m a.s.l.

One year of air temperature measurements at an elevation of 614 m a.s.l. (MTD 7) combined with corresponding measurements from Banak weather station (5 m a.s.l.) reveal a mean altitudinal lapse rate of ~ -0.005°C m^{-1}. This fits well with investigations by Laaksonen (1976) indicating a similar mean vertical temperature gradient for Fennoscandia and in particular other investigations from northern Norway indicating comparable lapse rates (Isaksen et al., in prep.).

Table 1. Measured and estimated ground surface and air temperatures at the MTD sites in the Gaissane Mountains. MTD 10–13 were operating less than a year, but have been used for estimation of MAGST. MGST = Mean ground surface temperature, FDD = freezing degree days, TDD = Thawing degree days, MAAT = Mean annual air temperature, MAGST = Mean annual ground surface temperature, N = number of values in the statistical analyses, R^2 = Goodness-of-fit of a straight line fitted by least squares to the points.

	1	2	3	4	5	6	7 (Air)	8	9	10	11	12	13
Elevation (m a.s.l.)	389	508	614	1002	1034	982	614	471	428	433	487	643	593
MGST 03-04 (°C)	-	0.5	-1.1	-2.7	-2.8	-0.5	-	-	-	-	-	-	-
FDD 03-04	-	748	1379	1620	1692	783	-	-	-	-	-	-	-
TDD 03-04	-	942	977	634	683	597	-	-	-	-	-	-	-
MGST 04-05 (°C)	-	0.8	-0.9	-2.2	-2.4	-2.1	-0.9 (air)	0.3	1.3	-	-	-	-
FDD 04-05	-	679	1327	1501	1600	1211	1381	917	830	-	-	-	-
TDD 04-05	-	957	988	705	729	429	1048	1010	1291	-	-	-	-
MGST 05-06 (°C)	-	0.5	-0.8	-2.4	-2.4	-1.4	-	0.1	1.4	-	-	-	-
FDD 05-06	-	789	1254	1456	1439	1075	-	998	841	-	-	-	-
TDD 05-06	-	965	976	594	549	577	-	1051	1334	-	-	-	-
Est. MAGST (°C)	-0.4	-	-2.2	-3.5	-3.6	-	-	-0.8	0.2	0.4	-1.1	-1.6	-1.7
N	313	1039	1039	1039	1039	1039	398	725	725	336	336	333	335
R^2	0.853	-	0.887	0.812	0.788	-	0.895	0.804	0.884	0.705	0.887	0.913	0.892
Est. MAAT (°C)	-1.3	-1.9	-2.5	-4.1	-4.5	-4.3	-2.5	-1.8	-1.7	-1.5	-1.7	-2.6	-2.3
Est. surface offset (°C)	0.9	-	0.3	0.6	1.0	-	-	0.9	1.9	1.9	0.5	1.0	0.6

Hence, the measured mean lapse rate is assumed fairly representative for the 1961–1990 period, and, thus, MAATs for this period can be estimated for the MTD sites (Table 1), thereby enabling estimates of the surface offset (i.e., MAGST–MAAT). Surface offsets are mainly less than 1°C at dry sites without pronounced snow cover (Table 1). This fits with investigations from southern and northern Norway (Isaksen et al. 2007, 2008) and Iceland (Farbrot et al. 2007). From this approach, permafrost should be common at locations with thin or no snow cover above the elevation of the –1°C-isotherm. Using the assumed mean altitudinal lapse rate of –0.005°C m^{-1}, the –1°C-isotherm is found at ~330 m a.s.l. in the field area.

BTS

Basal temperature of snow (BTS) measurements involve measuring temperatures at the bottom of the snow cover when the temperatures have stabilized before onset of melting. Under a thick, dry snow cover (>0.8–1.0 m) the ground surface temperature is mainly controlled by heat conduction from the subsurface, thereby reflecting the thermal regime of the ground. Permafrost is considered probable if BTS values <–3°C, possible if values are between –2° and –3 °C and improbable if values > –2°C (Haeberli 1973).

Table 2. Parametric (Pearsons r) correlation matrix for BTS as dependent variable and selected topographic attributes and presence and absence of coarse blocks at the ground surface expressed as a dummy variable. PR = Potential radiation, N = 163.

	Elevation	PR	Coarse blocks	Snow depth	Wetness index
BTS	-0.065	0.445*	-0.604*	0.289*	0.092

* Correlation is significant at the 0.01 level (2-tailed)

In March 2004, February 2005, and February 2006, a total of 334 BTS measurements were obtained. The measuring points' topographical characteristics such as elevation, slope, and aspect were estimated from a DEM with 25 m grid spacing (© Statens Kartverk). Further, the annual potential solar radiation (PR) was estimated based on the SRAD topographic model (Wilson & Gallant 2000). A potential topographic wetness index—defined as the quotient of the specific upstream area and the surface slope—was estimated based on Beven & Kirkby (1979). In addition, the surficial material type (presence or absence of coarse blocks) was recorded at each measuring

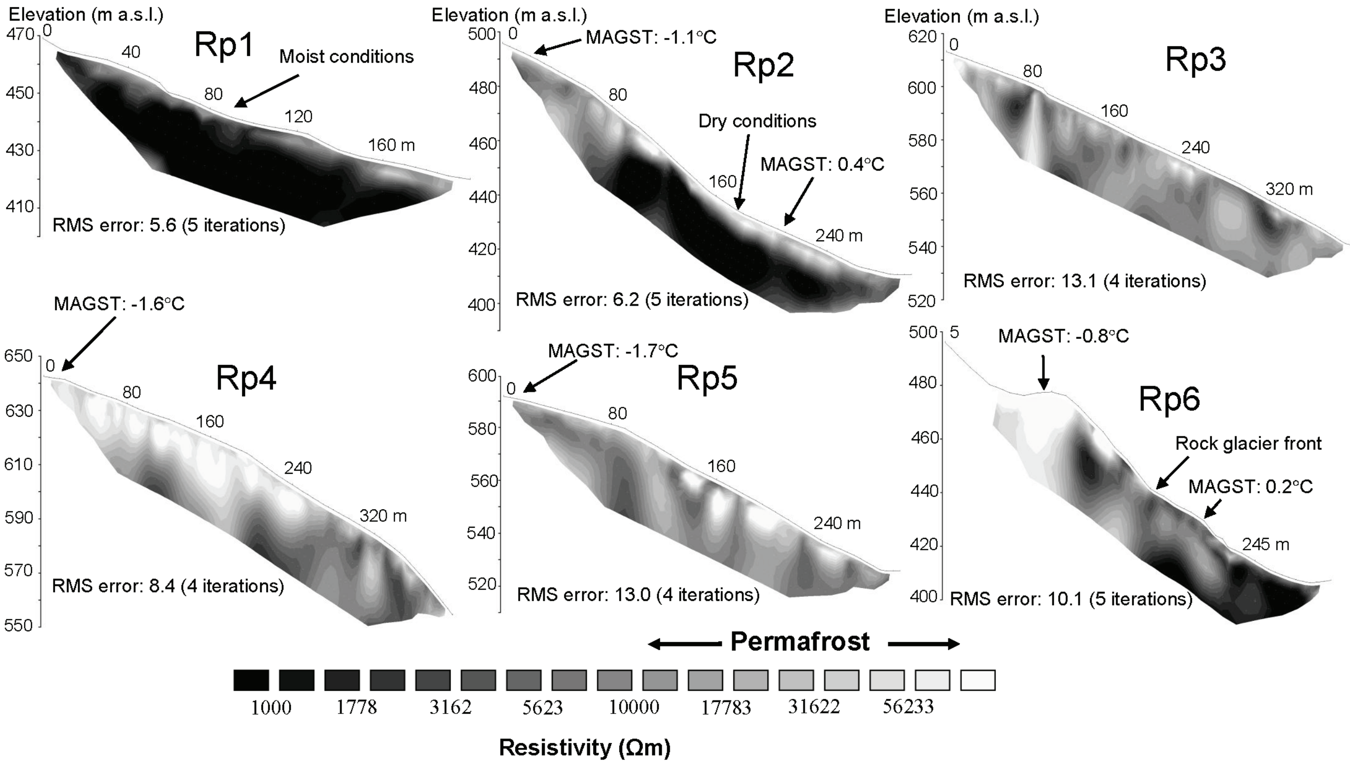

Figure 3. ERT profiles obtained in the Gaissane Mountains (for location, see Fig. 2). There is an overall increase in resistivity with elevation. The profiles indicate permafrost at elevations >450 m a.s.l., which corresponds well with estimated MAGSTs along the profiles.

site. Mean values were computed within diameters ≤10 m with consistent topographical and ground surface characteristics to try to overcome the problem of micro-scale variability and spatially clustered data (cf., Brenning et al. 2005), and these means (N=163) were used in the further analyses. From the correlation analysis, it is evident that PR and the presence or absence of coarse blocks, expressed as a dummy variable (1 means coarse material is present; 0 means coarse material is absent), are the major factors controlling BTS (Table 2). Mean BTS value for sites with coarse blocks is ~2.2°C lower than for sites without. However, the coarse-grained sites reveal less PR than the fine-grained sites. This effect is excluded by subtracting the assumed effect of lower PR on BTS values from the linear regression, thereby indicating that the effect of coarse blocks lowers the mean BTS value with 1.6°C. A linear regression model with the presence or absence of coarse blocks and PR as independent variables, explains 65% of the BTS variability. No significant correlation was found between BTS and elevation (at the 0.01 level [2-tailed]). Correlation between BTS and snow depth is significant but weak.

Electrical resistivity tomography

Electrical resistivity tomography (ERT) measurements are conducted by inserting an electrical current into the ground via two current electrodes. The resulting electrical potential between two other electrodes is measured, and from these measurements the true resistivity of the ground can be estimated. The existence of ice in the ground increases the resistivity markedly since the resistivity of ice is several orders of magnitude higher than water. Thus, resistivity measurements are highly valuable for detecting and characterizing ice-bearing permafrost (e.g,. Hauck & Vonder Mühll 2003). Six two-dimensional ERT profiles have been obtained in the field area (Fig. 3). Resistivity profile 1 (Rp1) is the lowermost profile (~400 m a.s.l.) across presumably permafrost free ground as indicated by BTS measurements. Hence, this profile presumably represents bedrock resistivities, thereby indicating that resistivity values >10 000 Ωm can serve as a conservative estimate for permafrost. This assumption corresponds well with the MTD measurements (Fig. 3). Generally, there is an overall increase in resistivity with elevation, and the profiles indicate permafrost above ~450 m a.s.l. Furthermore, Rp 6, a longitudinal profile along a rock glacier, indicates ice rich subsurface conditions within the rock glacier, although the possibility of air-filled cavities causing the high-resistive zone can not be excluded from the ERT measurements solely (cf., Hauck et al. 2004).

Discussion

BTS variability

The BTS measurements indicate that solar radiation and the presence or absence of coarse blocks are the two main factors controlling the thermal regime at snow covered sites (Table 2). The influence of PR is greater than what is found in southern Norway where ground thermal regime is highly correlated with elevation and to a lesser extent PR (Isaksen et al. 2002, Heggem et al. 2005). This difference seems plausible as the solar height is lower in northern Norway.

The occurrence of openwork blocky debris in the field area is clearly a cooling factor for ground surface temperatures. Similar results have been found in a range of studies (e.g., Harris & Pedersen 1998), and recently in southeastern Norway (Juliussen & Humlum 2007). This is presumably due to air circulation within the voids, which was indicated by several observations of air ventilation funnels through the snow cover in wintertime.

The lack of significant correlation between BTS and elevation probably reflects that the BTS points are mainly scattered between 300 and 600 m a.s.l., and a greater elevation span would have increased the correlation (cf., Brenning et al. 2005), as obtained for the MTDs. The mentioned elevation range obviously shows large snow cover, soil moisture and vegetation cover variations, covering the elevation signal in the statistical analysis (cf., Isaksen et al. 2002).

Present permafrost distribution

No borehole temperature measurements are available within the field area, so identification of mountain permafrost relies on indirect methods. Below the forest line of about 250–300 m a.s.l., winter snow cover is fairly extensively developed, so permafrost is presumably absent there due to the insulating effect of snow (cf., Johansson et al. 2006). The lowermost presumably active rock glaciers in the area have their margins at ~430 m a.s.l., and both BTS and ERT measurements indicate that these features contain permafrost at present.

The consistency of the independent indirect methods (Table 3) leads to the conclusion that mountain permafrost is common above 350–450 m a.s.l. As all BTS measurements rely on point measurements with a stable snow cover of a least 80 cm, this should imply that these points represent warmer ground conditions compared to areas with limited snow cover, due to the isolating effect of snow (cf., Jeckel 1988). Developed snow covers are limited in the field area due to low precipitation and strong winds. Thus, the aerial extent of permafrost is presumably greater than indicated by BTS measurements (cf., Sollid et al. 2003). The permafrost distribution pattern indicated fits generally well with Johansson et al. (2006), stating that permafrost is common in the tundra zone above the forest line in the Torneträsk region, northern Sweden. The pattern also agrees with investigations by King & Seppälä (1987) in north-western Finland which indicate a lower limit of discontinuous permafrost of 300–500 m a.s.l. based on geoelectrical soundings.

Past permafrost conditions

Several relict periglacial landforms in the field area point to a cooler environment in the past than at present. Such landforms include a rock glacier, terminating in the birch forest, with its fronts at 180 m a.s.l., presumably relict tundra polygons, ploughing boulders found in the birch forest, and extensive areas of vegetated patterned ground. The low-elevation rock glacier witnesses a past lower limit of permafrost at least 200 m below the present.

The past lower limit of mountain permafrost in the field area were obviously variable during the Holocene climate fluctuations

Table 3. Elevation of different environmental parameters and permafrost limits indicated by different indirect approaches. See text for details.

Environmental parameter/ permafrost limit	Elevation (m a.s.l.)
Tree line	250-300
Blockfield limit	~800
BTS	?
Estimated MAGST	350
ERT measurements	~450
-1°C isotherm	330
Active rock glacier	430

(cf., Kukkonen & Šafanda 2001). However, on the summits of about 1000 m a.s.l., a different picture emerges. The blockfields of the summit areas show no signs of Holocene modification. The lateral meltwater channels eroded into the blockfields together with the terminal moraines found on top (cf., Marthinussen 1960) indicate a pre-Late Glacial Maximum age of the blockfield and subsequent survival underneath cold-based, non-erosive ice. This interpretation is supported by investigations of blockfields on the Varanger Peninsula (Fjellanger et al. 2006). According to Heikkilä & Seppä (2003) maximum annual air temperatures in Fennoscandia were approximately 1.5–2.0°C higher during the mid-Holocene thermal optimum (HTO) than the reconstructed mean temperature of the last 200 years. Assuming a roughly equal coupling between air and ground surface temperatures, sub-zero MAGST probably still occurred in the summit areas of about 1000 m a.s.l. during HTO. This is based on the assumption that the summits have prevailed bare-blown, with limited influence of changes in the Holocene wind and precipitation patterns. Thus, although warm periods have occurred during the Holocene, affecting thermal regime and the permafrost thickness, permafrost conditions have presumably prevailed in the summit areas. This is supported by numerical modelling of permafrost in bedrock in northern Fennoscandia during the Holocene by Kukkonen & Šafanda (2001). Hence, assuming cold-based ice in the summit areas at least during the last glaciation, permafrost at these elevations probably is of considerable age, potentially spanning the Weichselian.

Conclusions

Based on these investigations the following conclusions concerning mountain permafrost in the Gaissane Mountains seem supported:

- At present permafrost is common above 350–450 m a.s.l.
- Coarse, openwork blocks tend to reduce ground surface temperatures significantly.
- The permafrost in the summit areas at about 1000 m a.s.l. is of considerable age, possibly prevailing since the last interglaciation.

Acknowledgments

This study was financed by the Norwegian Research Council (project no. 157837/V30) and the Department of

Geosciences, University of Oslo. We also want to thank M. Avian, M.K. Bagge-Lund, J. Fjellanger, R. Frauenfelder, H. Juliussen, A. Kellerer-Pirklbauer, B. Larsen, and L. Sørbel who participated in the field work. Andreas Kellerer-Pirklbauer and Rune S. Ødegård reviewed an earlier version of the manuscript. We thank all individuals and institutions for their contributions.

References

Beven, K.J. & Kirkby, M.J. 1979. A physically-based, variable contributing area model of basin hydrology. *Hydrological Sciences Bulletin* 24: 43-69.

Brenning, A., Gruber, S. & Hoelzle, M. 2005. Sampling and statistical analyses of BTS measurements. *Permafrost and Periglacial Processes* 16: 383-393.

Etzelmüller, B., Berthling, I. & Sollid, J.L. 2003. Aspects and concepts on the geomorphological significance of Holocene permafrost in Southern Norway. *Geomorphology* 52: 87-104.

Etzelmüller, B. et al. 2008. Mapping and modelling the distribution of permafrost in the Nordic countries. *Proceedings of the Ninth International Conference on Permafrost, Fairbanks, Alaska, June 29–July 3, 2008* (this proceedings).

Farbrot, H. et al. 2007. Thermal characteristics and climate change impact of mountain permafrost in Iceland. *Journal of Geophysical Research* 112, doi:10.1029/2006JF000541.

Fjellanger, J., Sørbel, L., Linge, H., Brook, E.J., Raisbeck, G.M. & Yiou, F. 2006. Glacial survival of blockfields on the Varanger peninsula, northern Norway. *Geomorphology* 82: 255-272.

Haeberli, W. 1973. Die Basis Temperatur der winterlichen Schneedecke als möglicher Indikator für die Verbreitung von Permafrost. *Zeitschrift für Gletscherkunde und Glazialgeologie* 9: 221-227.

Harris, S.A. & Pedersen, D.E. 1998. Thermal regimes beneath coarse blocky material. *Permafrost and Periglacial Processes* 9: 107-120.

Hauck, C., Isaksen, K., Vonder Mühll, D. & Sollid, J.L. 2004. Geophysical surveys designed to delineate the altitudinal limit of mountain permafrost; an example from Jotunheimen, Norway. *Permafrost and Periglacial Processes* 15: 191-205.

Hauck, C. & Vonder Mühll, D. 2003. Inversion and interpretation of two-dimensional geoelectrical measurements for detecting permafrost in mountainous regions. *Permafrost and Periglacial Processes* 14: 305-318.

Heggem, E.S.F., Juliussen, H. & Etzelmüller, B. 2005. Mountain permafrost in Central-Eastern Norway. *Norsk Geografisk Tidskrift-Norwegian Journal of Geography* 59: 94-108.

Heikkilä, M. & Seppä, H. 2003. A 11,000 yr palaeotemperature reconstruction from the southern boreal zone in Finland. *Quarternary science reviews* 22: 541-554.

Hoelzle, M., Wegmann, M. & Krummenacher, B. 1999. Miniature temperature dataloggers for mapping and monitoring of permafrost in high mountain areas: First experience from the Swiss Alps. *Permafrost and Periglacial Processes* 10: 113-124.

Isaksen, K., Farbrot, H., Blikra, L.H., Johansen, B. Sollid, J.L. & Eiken, T. 2008. Five year ground surface temperature measurements in Finnmark, Northern Norway. *Proceedings of the Ninth International Conference on Permafrost, Fairbanks, Alaska, June 29–July 3, 2008* (this proceeedings).

Isaksen, K., Hauck, C., Gudevang, E., Ødegård, R.S. & Sollid, J.L. 2002. Mountain permafrost distribution on Dovrefjell and Jotunheimen, southern Norway, based on BTS and DC resistivity tomography data. *Norsk Gografisk Tidsskrift-Norwegian Journal of Geography* 56: 122-136.

Isaksen, K., Sollid, J.L., Holmlund, P. & Harris, C. 2007. Recent warming of mountain permafrost in Svalbard and Scandinavia. *Journal of Geophysical Research* 112, doi:10.1029/2006JF000522.

Jeckel, P.P. 1988. Permafrost and its altitudinal zonation in N. Lapland. In: K. Senneset (ed.), *Proceedings of the Fifth International Conference on Permafrost, 1988*: 170-175.

Johannessen, T.W. 1970. The climate of Scandinavia. In: C. C. Wallén (ed.), *Climates of Northern and Western Europe.* Amsterdam: Elsevier Publishing company, 23-80.

Johansson, M., Christensen, T.R., Åkerman, J.H. & Callaghan, T.V. 2006. What determines the current presence or absence of permafrost in the Torneträsk region, a sub-arctic landscape in northern Sweden? *Ambio* 35: 190-197.

Juliussen, H. & Humlum, O. 2007. Towards a TTOP ground temperature model for mountainous terrain in central-eastern Norway. *Permafrost and Periglacial Processes* 18: 161-184.

Kellerer-Pirklbauer, A. 2008. The Schmidt-hammer as a Relative Age Dating Method for Rock glacier Surfaces: Examples from Northern and Central Europe. *Proceedings of the Ninth International Conference on Permafrost, Fairbanks, Alaska, June 29–July 3, 2008* (this proceedings).

King, L. & Seppälä, M. 1987. Permafrost thickness and distribution in Finnish Lapland; results of geoelectric soundings. *Polarforschung* 57: 127-147.

Kukkonen, I.T. & Šafanda, J. 2001. Numerical modelling of permafrost in bedrock in northern Fennoscandia during the Holocene. *Global and Planetary Change* 29: 259-273.

Laaksonen, K. 1976. The dependence of mean air temperatures upon latitude and altitude in Fennoscandia (1921–50). *Ann. Academ. Scient. Fennicae A III* 119, 19 pp.

Marthinussen, M. 1960. Marginal substages and drainage during deglaciation in the Repparfjord-Stabbursdal area, western Finnmark (in Norwegian). *Norges Geologiske Undersøkelse* 213: 118-169.

Reusch, H. 1901. Some contributions towards an understanding of the manner in which the valleys and mountains of Norway were formed (in Norwegian). In: *NGU Yearbook 1900*. Kristiania: Norwegian Geological Survey, 124-263.

Sollid, J.L., Isaksen, K., Eiken, T. & Ødegård, R.S. 2003. The transition zone of mountain permafrost on Dovrefjell, southern Norway. *Proceedings of the Eighth International Conference on Permafrost, Zurich, Switzerland*: 1085-1089.

Wilson, J.P. & Gallant, J.C. (eds). 2000. *Terrain analysis: Principles and applications*. New York: John Wiley & Sons, 512 pp.

Recent Changes in Ground Temperature and the Effect on Permafrost Landscapes in Central Yakutia

A.N. Fedorov
Melnikov Permafrost Institute SB RAS, Yakutsk, Russia

P.Y. Konstantinov
Melnikov Permafrost Institute SB RAS, Yakutsk, Russia

Abstract

The main objective of this paper is to determine the state of permafrost landscapes in Central Yakutia under recent climate change. Air and ground temperature data from monitoring sites of the Melnikov Permafrost Institute and records from weather stations at Yakutsk, Churapcha, and Pokrovsk are used. Analysis of the data indicates that the Pokrovsk records are most suitable for evaluating long-term ground temperature variations in Central Yakutia. A good correlation has been found between the data from monitoring sites and the Pokrovsk weather station. During the last several decades, major increases in ground temperature occurred in the early to mid 1980s and the early 1990s. At present, some cooling of ground temperature is observed, although air temperature shows an increasing trend. However, there is a high risk for active development of cryogenic processes in forest-free areas that can cause permafrost degradation and terrain disturbance. Thermokarst is actively developing in some areas of Central Yakutia. Disturbed landscapes, primarily the deforested anthropogenic complexes affected by agriculture, tree removal, or burning, are most sensitive under the current climate change.

Keywords: climate change; cryogenic process; ground temperature; permafrost landscape; thermokarst.

Introduction

Ground temperature is an important cryoecological characteristic of permafrost-affected landscapes. Its influence on the state and dynamics of permafrost landscape is difficult to overestimate. Analyses of the recent data from thermal monitoring sites in Central Yakutia are presented in the Russian permafrost literature (Skryabin et al. 1998, Varlamov et al. 2002, Pavlov 2003, Konstantinov et al. 2006, Pavlov & Malkova 2005, and others). These studies document ground temperature and thaw depth variability and indicate that ground temperatures show both an increasing and decreasing trend in the region where air temperatures are increasing. However, observations at monitoring sites are too short and do not provide sufficient information to evaluate long-term trends in natural processes. Direct field observations of the ground temperature regime in Central Yakutia are available only for the period since 1980.

Weather station records have to be used, therefore, in order to understand the long-term dynamics of ground temperatures. Vasiliev & Torgovkin (1996), Gilichinsky et al. (2000), and Romanovsky et al. (2007) analyzed ground temperature records from Yakutian weather stations for various depths and various periods and determined trends. Most weather stations in Central Yakutia demonstrate a strong increasing trend in ground temperature. Vasiliev & Torgovkin (1996) examined the period 1967-1992 when the largest increase in air temperature was observed in Central Yakutia. The period 1951-1996 was analyzed in Gilichinsky et al. (2000) and the value of this work is in comparing temperature trends in different regions of the Russian permafrost zone. Romanovsky et al. (2007) calculated trends in ground temperature at 1.6 m depth along the Tiksi-Yakutsk-Nagorny transect in Yakutia. The authors analyzed the spatial variability of ground temperatures and found that temperatures were increasing at some sites and decreasing at others during the period from 1956 to 1990.

The paper discusses the results of long-term observations on permafrost terrain dynamics at the Yukechi, Neleger, Spasskaya Pad, and Umaibyt sites near Yakutsk, and the variations in meteorological elements based on Yakutsk and Pokrovsk weather station records (Fig. 1).

The main objective of this paper is to determine the state of permafrost landscapes in Central Yakutia under recent climate change. Retrospective analysis of ground temperatures provides a basis for assessing changes in the thermal state of cryogenic landscapes. However many factors make such assessment difficult, such as the differences in soil conditions between weather stations, the inhomogeneities in data records due to relocation, and the indirect effects of anthropogenic disturbance of surrounding

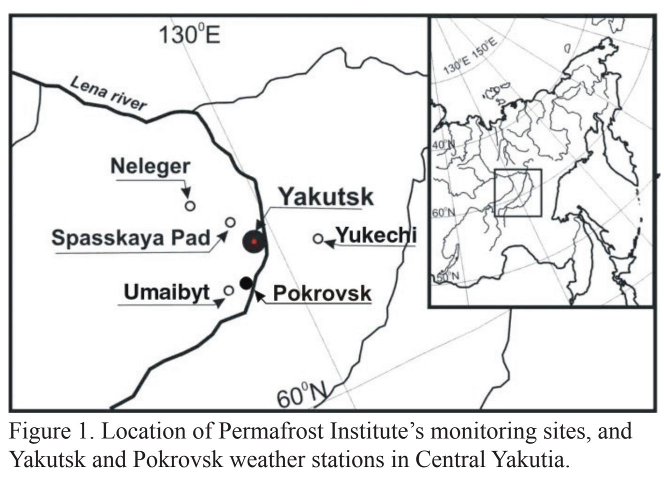

Figure 1. Location of Permafrost Institute's monitoring sites, and Yakutsk and Pokrovsk weather stations in Central Yakutia.

areas. Analysis of long-term ground temperature variations at weather stations during the entire period of instrumental observations will enable us to determine the development of cryoecological stresses in Central Yakutia, which is important for understanding the dynamics of cryogenic landscapes and for environmental protection planning.

Data Sources and Research Methods

Continuous ground temperature measurements in Central Yakutia have been made since 1931 (weather stations at Yakutsk and Pokrovsk). To determine representativeness of ground temperature records, data for depths of 1.6 and 3.2 m from the Yakutsk and Pokrovsk weather stations over the period 1931-2006 have been examined. The weather station data allow an assessment of both mean monthly and interannual variations in ground temperature. Based on the data analysis, Pokrovsk has been chosen as the most representative station for Central Yakutia. A measurement site at Pokrovsk was relocated in 1941. This move had little effect on the ground temperature record, because the new site was very similar to the older one in landscape and soil conditions. A site of the Yakutsk weather station was moved in 1964. The new and old sites differed greatly in landscape conditions, resulting in significant differences between the temperature series. Moreover, the Yakutsk data show virtually no variation after 1989 because of the change in the suprapermafrost water regime. This was a major reason for choosing the Pokrovsk records. Correlation coefficients between the mean annual ground temperatures at 1.6 and 3.2 m in Pokrovsk and Yakutsk are 0.85 and 0.88, respectively, at p=0.05 (during the period from 1965 to 1988 when the uniformity of measurement conditions was not disturbed by relocations or man-induced change in suprapermafrost water level).

Data obtained from the Yukechi, Umaibyt, Dyrgabai, and Tabaga monitoring sites, as well as the Neleger and Spasskaya Pad intensive observation sites, have been used to examine the effects of climate change on permafrost landscapes. These sites include measurements of ground temperature, thaw depth and active-layer moisture content, as well as observations of changes in microrelief and landscape at the facies level (Fedorov 1996, Fedorov et al. 1998, Konstantinov et al. 2001, Fedorov & Konstantinov 2003, Fedorov et al. 2003, Konstantinov et al. 2006). Ground temperatures at Spasskaya Pad and Neleger correlate well with the Pokrovsk weather station data. For example, the correlation coefficient of mean monthly temperatures at 3.2 m between Pokrovsk and the monitoring sites from October 2000 to September 2005 is 0.89 for Spasskaya Pad and 0.92 for Neleger. Such close relationship allows us to rely on the Pokrovsk records to analyze the long-term dynamics of ground temperatures and permafrost landscapes. We must also note that air temperature variations are relatively uniform across Central Yakutia. Correlation coefficients between locations are 0.89-0.98 (Skachkov 2001). In view of different record lengths and relocations of other weather stations, this fact allows us to use the Pokrovsk record as a basis for documenting long-term ground temperature variations (since 1931) in Central Yakutia.

Results

Interannual variations of ground temperature

A depth of 3.2 m was selected to analyze the long-term ground temperature variability, because materials at this level are perennially frozen. Temperature variations in the upper permafrost have a strong impact on the landscape and control degradation or recovery of the environmental conditions. An increase in temperature triggers cryogenic processes, while a decrease improves the stability of the upper permafrost.

The mean annual ground temperature at Pokrovsk for the period examined is -2.4°C and the standard deviation of the series is 0.44. The amplitude of annual means is 1.8°C, with a minimum of -3.3°C and a maximum of -1.5°C. The mean annual ground temperature has increased by 0.7°C over the period, with a trend of 0.1°C/decade (Fig. 2).

The time series of mean annual ground temperature shows a cyclic and progressive variation with an average period of 9.6 years. The maximum period is 12 years and the minimum is 8 years. Relatively high temperatures (the positive phase of the cycle) are observed in the mid 1930s, early 1940s, late 1940s-early 1950s, late 1950s-early 1960s, late 1960s-early 1970s, early 1980s-middle 1980s, early 1990s, and late 1990s-early 2000s. Two positive phases that occurred in the early 1940s and the late 1950s-early 1960s are less pronounced than the others. The temperatures series shows increasing values both for the positive and negative phases.

The most significant increases in ground temperature occurred in the early to mid 1980s and in the early 1990s, when the periods with maximum temperatures were longest and the periods with minimum temperatures were short. The temperature series before the 1980s can be characterized as stable, with alternating positive and negative phases.

Analysis of mean annual air temperature variations indicates that significant warming began in the late 1980s. Since then, the temperature series has changed from its normal pattern (Fig. 3). The mean annual air temperature at

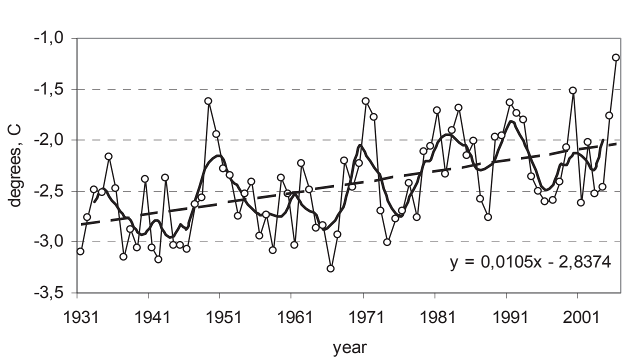

Figure 2. Interannual ground temperature variation at 3.2 m depth for the Pokrovsk weather station.

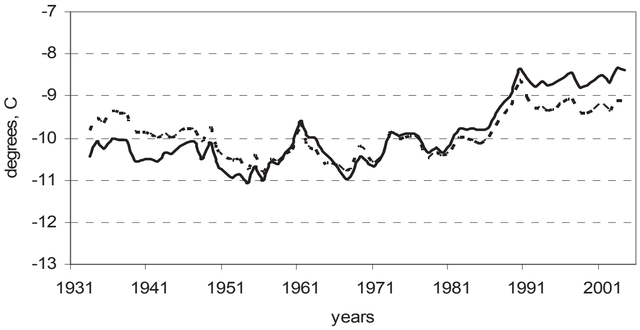

Figure 3. Variations in mean annual air temperature for Yakutsk (solid line) and Pokrovsk (dash line).

Yakutsk for the period from 1988–2005 was -8.5°C, while the long-term average had been -10.2°C (Handbook on the USSR Climate 1989). It is evident that the increase in ground temperatures from the early to mid 1980s was not due to a rise in air temperature. Being an integrating environmental parameter, ground temperature is not always consistent with variations of individual elements, such as mean annual air temperature or precipitation. We also note that air temperatures were higher at Pokrovsk than at Yakutsk until the mid 1950s, nearly identical between the mid 1950s and the mid 1970s, and colder since the mid 1970s to the present. This variation is likely due to circulation processes, since an anthropogenic factor has been ruled out by researchers (Skachkov 2001). However the increasing amplitudes of mean annual air temperature since the 1990s require a detailed analysis to determine the cause.

Of special interest is the change in ground temperature since 1980, with distinct cooling continuing to the present (Fig. 4a). Varlamov et al. (2002) attributed this cooling to the effect of snow cover. However the magnitude of the cooling is not so significant relative the entire series as to ameliorate the cryoecological stress (Fig. 2). There has been a steady increase in air temperature during this period in Central Yakutia (Fig. 4c), suggesting that Varlamov et al. are correct in relating the ground cooling to changes in snow cover. The variations in early winter (October, November and December) precipitation, which has an important effect on the permafrost temperature regime, provide some support to this view (Fig. 4b).

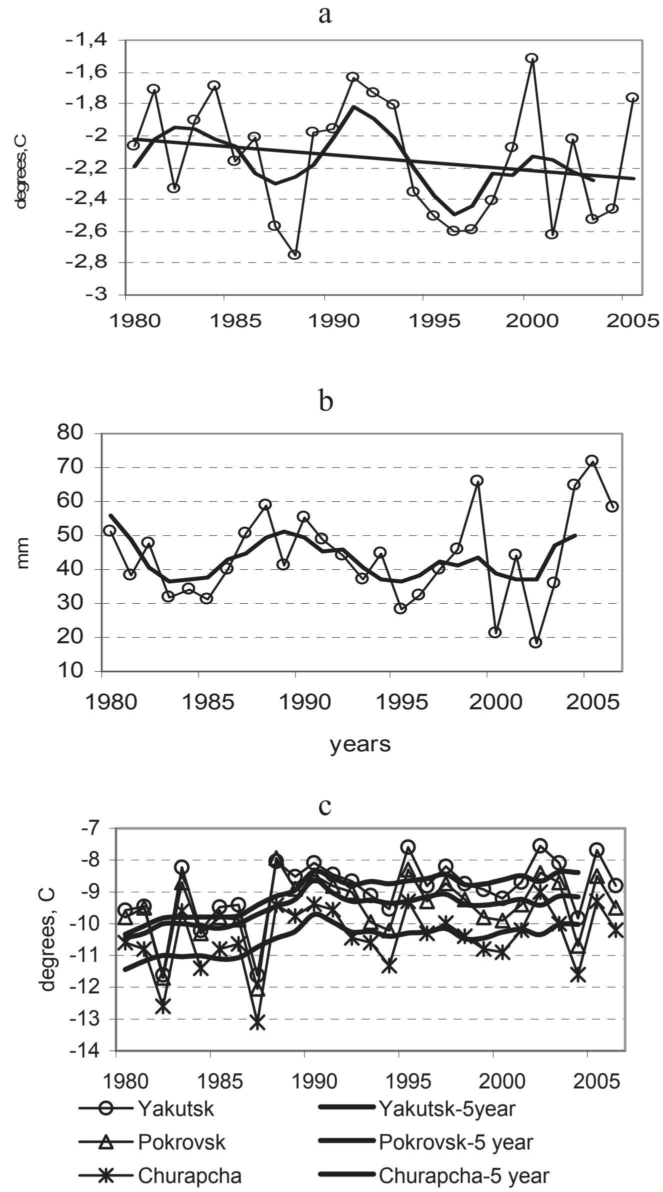

Figure 4. Ground temperature at 3.2 m for Pokrovsk (a) early winter precipitation for Yakutsk (b) and mean annual air temperature for Yakutsk, Pokrovsk and Churapcha (c) between 1980 and 2005. Thin lines – annual means, thick lines – 5-year running means.

Response of permafrost landscapes to impacts under present climatic conditions

Post-disturbance changes in permafrost and cryogenic landscapes have been studied during recent years as part of the Permafrost Institute's projects (Bosikov 1998, 2004, Fedorov et al. 1998, 2003, Gavriliev et al. 1999, 2005, Fedorov 2006). Thermokarst research is a major component in these investigations. Thermokarst studies are carried out at the Yukechi, Neleger, Spasskaya Pad and Umaibyt sites near Yakutsk.

The sites are heavily underlain by ground ice and contain numerous alases. Excess ice in permafrost is the main cause for thermokarst development. Central Yakutia, primarily between the Lena and Amga rivers, is dominated by ice-rich permafrost landscapes. The presence of wedge ice is readily identified by cemetery mounds on alas slopes and thaw depressions on the disturbed surfaces.

Generally, in Yakutia ice-rich permafrost landscapes are of limited distribution and occupy only near 10% of the region (Bosikov 1978), mainly within the densely populated areas such as the Lena-Amga watershed and the Viluy and Kolyma basins. However, thermokarst is not always active in ice-rich terrain. There are strong self-preservation forces in the landscapes that enable them to adjust and resist climate warming.

Climate plays a special role in thermokarst development. In Central Yakutia, thermokarst is actively developing in the previously disturbed areas since the 1990s when air temperatures began increasing throughout the region. The landscapes disturbed by fire, forest harvesting and land clearing for agriculture have become an indicator of the impact of recent climate change on permafrost. Ground ice at these sites occurs at shallow depths, on average within 2 to 2.2 m of the surface. The long existence of the landscapes in an artificial state cannot but leave a trace. The active layer becomes heavily desiccated, requiring more heat for thawing compared to wet soils in forest. As a result, seasonal thaw reaches the tops of ice wedges in critical years, causing ice melting and ground subsidence.

Gavriliev et al. (2001) obtained original data on thermokarst activity at the Kerdyugen site located near the village of Tabaga in the vicinity of Yakutsk. They observed rapid development of initial thermokarst forms in an abandoned farm field. In the field, which was little affected by thermokarst in 1987, shallow thaw pits covered about half of the field surface by 1993; currently the entire 100 ha field is disturbed by thermokarst. Recent monitoring studies have shown that, during the periods of notable climatic stresses, the ecological state of anthropogenic landscapes significantly degrades. This causes abandonment of agricultural lands.

We conducted detailed thermokarst investigations at the Yukechi site which is situated on the right bank of the Lena River 50 km east of Yakutsk. The area is characterized by extensive development of thermokarst landforms. Recent climate warming has intensified thermokarst activity in the existing thaw depressions and accelerated the rates of ground subsidence (Fig. 5). In central portions of young water-filled thermokarst depressions 2 to 2.5 m in depth, an average rate of surface subsidence is 5–10 cm/yr.

Interesting data were obtained from the areas that had not been affected by cryogenic processes previously. These are flat treeless interalas areas with no visible indications of thermokarst such as thaw troughs over ice wedges. Such sites are experiencing subsidence in response to climatic stress.

Our investigations since 1992 show that this process has a distinctive trend. At many observation points, the ground surface has subsided 20–30 cm between 1992 and 2006 (Fig. 6). This subsidence can be attributed primarily to climate warming. The treeless landscapes with the desiccated active layer are most sensitive to climatic warming and most threatened by further disturbances.

Analysis of the obtained data indicates that subsidence at these sites develops impulsively, showing some rhythm. For example, significant subsidence occurred in 1995–1996, 2000–2001 and then in 2004 and 2006. These settlements are more directly related to variations in precipitation rather than to changes in ground or air temperatures. The years when settlement was initiated (1995, 2000 and 2004) were characterized by lower precipitation following the previous rainy season, while subsidence in 2006 was related to anomalously high rainfall. Initiation of deep subsidence is also related to moisture content of the active layer, starting in the seasons with high soil moisture contents (1995, 2000 and 2006).

Thus, the last two decades with maximum increases in air

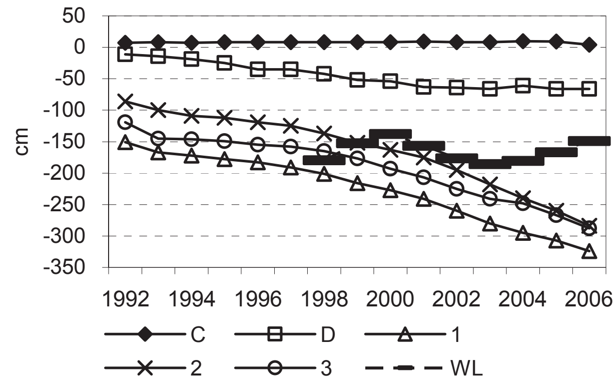

Figure 5. Surface subsidence at plot 2, Yukechi (well-drained inter-alas area). C – reference point, undisturbed inter-alas area, D – initial thaw depression, 1-3 – polygon centres within large thaw depressions, WL – water level.

and ground temperatures are very sensitive to changes in meteorological conditions. Thawing of the top of ice wedges and subsidence of the ground surface occur in 2–3 year intervals. This is apparently related to the general increase in annual air temperature from the average by up to +1.4°C and annual ground temperature from the average by up to +0.6°C which creates instability in the state of permafrost. The activation of subsidence on existing thermokarst depressions and directed subsidence of well-drained, flat interalas meadows are a dramatic indicator of current climatic changes in Central Yakutia.

The present response of disturbed areas underlain by ice-rich permafrost was investigated at the Neleger site in the vicinity of Yakutsk (Fig. 1).

It was found that cryogenic processes are most active during the first 5–6 years after disturbance, after which the processes stabilize and conditions develop for the recovery of permafrost terrain. If the forest cover is re-established over this period, the disturbed area is no longer the locus of ecological risk. At Kys-Alas (the Neleger site), which is underlain by ice-rich sediments, intensive thermokarst development with surface subsidence up to 10–15 cm began after the area was clear cut of trees in 1996. Subsidence continued to 2001, and then, between 2001 and 2004, the surface heaved due to refreezing of the thawed layer and exceeded the initial level. In 2004–2006, relative stability was observed (Fig. 7). The oversaturation of the active layer in the first few years after tree removal, as well as periodic strong cooling of the ground in early winter due to low snowfall in the winters of 2001/2002, 2002/2003 and 2003/2004, caused ground thawing to cease. An ice-rich layer formed at a depth of 110–180 cm which now acts as a protective layer.

The depth of thaw at this site has not exceeded 110 cm in recent years. Freezing of the oversaturated soils caused heaving and the relative surface levels have risen, on average, by 10–15 cm (Fig. 7). This mechanism of permafrost stabilization appears to be the main condition for recovery and optimization of the permafrost landscapes which are in a critical state.

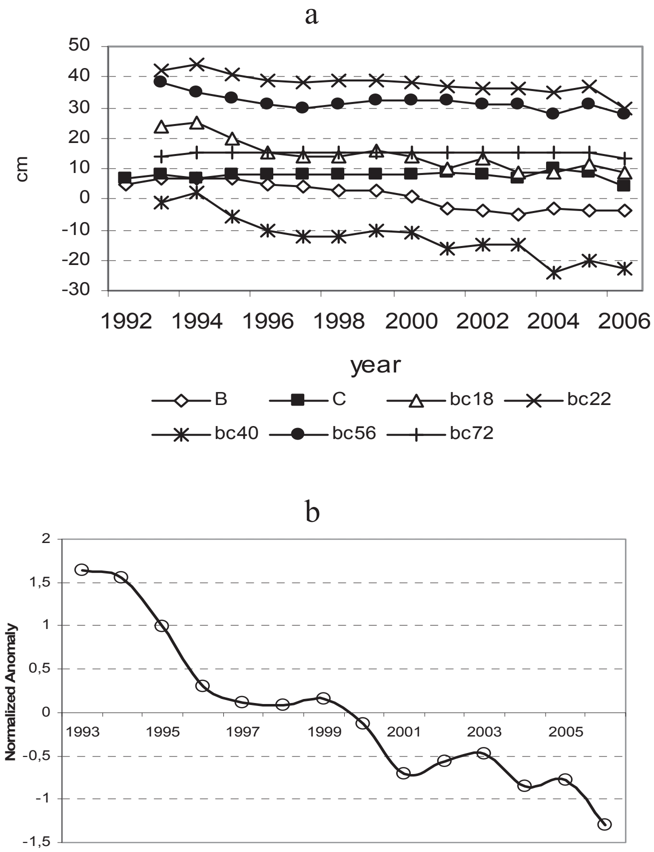

Figure 6. Surface subsidence in a well-drained inter-alas area, plot 2, Yukechi (a – observed values, b – averaged normalized anomalies) B and C – markers on stable flat surfaces; bc18, bc22, bc40, bc56 and bc72 – markers on relatively stable, flat surfaces near the slope of small thaw depressions. Normalized anomalies were calculated for each year as follows: $A = (i-i_{av})/\delta$ where i is the value for a given year; i_{av} is the long-term mean of a continuous series; δ is the root-mean-square deviation of a series.

Conclusion

In conclusion, recent variations in air and ground temperatures are reflected in the change of permafrost landscapes in Central Yakutia. A good correlation between the mean monthly ground temperatures at Spasskaya Pad and Neleger and the Pokrovsk records has allowed construction of a reliable retrospective scheme for ground temperature variations in Central Yakutia. It should be noted that ground temperature data from most other stations are inhomogeneous due to instrument relocations and human impacts. The ground temperature diagram shows that relatively high temperatures from the 1980s to present have been stressful for permafrost landscapes, resulting in fairly active development of cryogenic processes. Disturbed areas are most sensitive, particularly where trees have been removed for land use (croplands and cuts). Such permafrost landscapes are more vulnerable and sensitive to meteorological variations under the current climate warming. On the other hand, our results also indicate that permafrost landscapes are capable of self-stabilization. This mechanism is relatively strong, so thermokarst development is as yet limited.

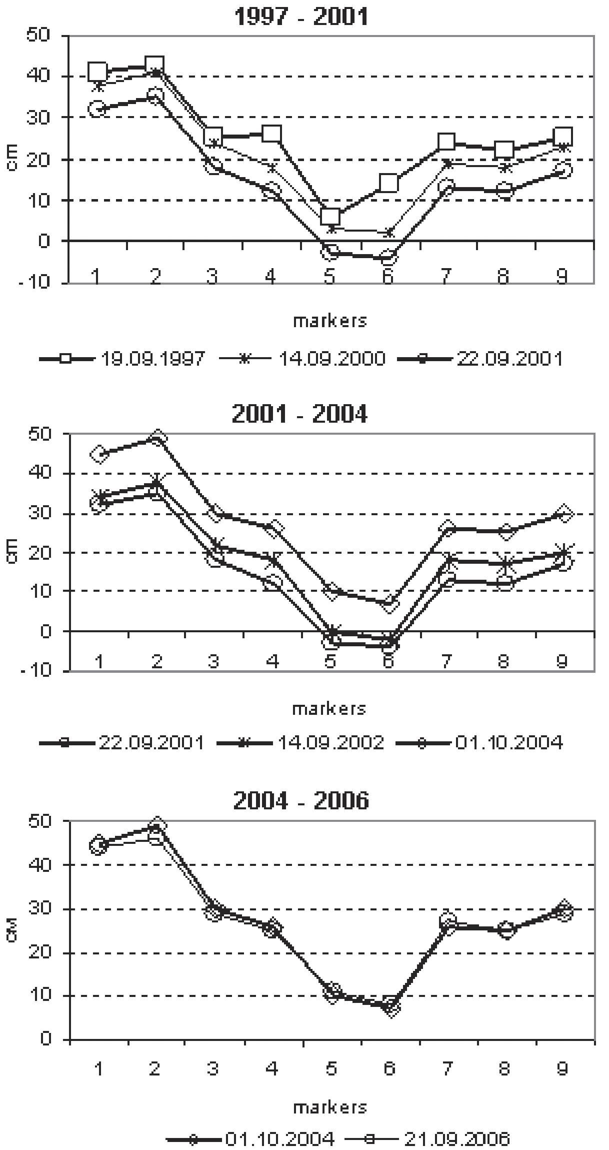

Figure 7. Changes in relative surface elevation at Kys-Alas, the Neleger site.

References

Bosikov, N.P. 1978. Alas coverage in Central Yakutia. In: *Geocryological Conditions in Mountains and Plains of Asia (Geokriologicheskie uslovia v gorakh I na ravninakh Asii)* (in Russian). Yakutsk: IMZ SO AN SSSR, 113-118.

Bosikov, N.P. 1998. Wetness variability and thermokarst dynamics in Central Yakutia. In: *Geocryological Problems (Problemy geokriologii)* (in Russian). Yakutsk: Izd-vo SO RAN, 123-127.

Bosikov, N.P. 2004. Man-caused thermokarst destruction of inter-alas landscapes in the Lena-Amga watershed (in Russian). *Kriosfera Zemli* VIII(4): 12-14.

Fedorov, A.N. 1996. Effects of recent climate change on permafrost landscapes in Central Sakha. *Polar Geography* 20(2): 99-108.

Fedorov, A. 2006. Present post-disturbance dynamics of permafrost in Central Yakutia. *Symptom of Environmental Change in Siberian Permafrost Region*. Sapporo: Hokkaido University Press, 225-231.

Fedorov, A.N., Gavriliev, P.P. & Konstantinov, P.Y. 2003. Study of the permafrost dynamics at Spasskaya Pad (in Russian). *Nauka i Obrazovanie* 3: 62-65.

Fedorov, A.N. & Konstantinov, P.Y. 2003. Observations of surface dynamics with thermokarst initiation, Yukechi site, Central Yakutia. *Proceedings of the 8th International Conference on Permafrost, Zurich, Switzerland, July 21-25, 2003*. Vol. 1: 239-243.

Fedorov, A.N., Konstantinov, P.Y., Vassiliev, I.S., Bosikov, N.P. Torgovkin, Y.I. & Samsonova, V.V. 1998. Observations of permafrost-landscape dynamics related to anthropogenic disturbances, Yukechi study site, Central Yakutia. *Proceedings of the Seventh International Conference on Permafrost, Yellowknife, Canada, June 23--27, 1998*: 259-263.

Gavriliev, P.P., Ugarov, I.S. & Efremov, P.V. 1999. The Permafrost-ecological monitoring of the agricultural lands in Central Yakutia (in Russian). *Kriosfera Zemli* 3: 92-99.

Gavriliev, P.P., Ugarov, I.S. & Efremov, P.V. 2001. *Permafrost and Ecology of Agricultural Landscapes in Taiga Areas, Central Yakutia (Merzlotno-ekologicheskie osobennosti taezhnykh agrolandshaftov Centralnoi Yakutii)* (in Russian). Yakutsk: Permafrost Institute Press, 195 pp.

Gavriliev, P.P., Ugarov, I.S. & Efremov, P.V. 2005. Cryogenic processes and ice-rich permafrost sensitivity to climate change and surface disturbance, Central Yakutia (in Russian). *Nauka i Obrazovanie* 4 (40): 84-87.

Gilichinsky, D.A., Bykhovets, S.S., Sorokovikov, V.A. et al. 2000. Use of the data of hydrometeorological survey for century history of soil temperature trends in the seasonally frozen and permafrost areas of Russia (in Russian). *Kriosfera Zemli* IV(3): 59-66.

Handbook on the USSR Climate, Vol. 24. Yakut ASSR 1989. (*Nauchno-prikladnoi spravochnik po klimatu SSSR. Vyp. 24. Yakutskaya ASSR)* (in Russian). Leningrad: Gidrometeoizdat, 608 pp.

Konstantinov, P.Y., Argunov, R.N., Gerasimov, E.Y. & Ugarov, I.S. 2006. On the relationship between seasonal thaw depth and interannual variation of mean annual ground temperature (in Russian). *Kriosfera Zemli* X(3): 15-22.

Konstantinov, P.Y., Rusakov, V.G. & Fukuda, M. 2001. Thermal regime of the upper permafrost layers in taiga landscapes, Yakutsk Area, 1996-2000. *Proceedings of the Ninth Symposium on the Joint Siberian Permafrost Studies between Japan and Russia in 2000, Sapporo, Japan, January 23-24, 2001*: 204-209.

Pavlov, A.V. & Malkova, G.V. 2005. *Recent Climatic Changes in Northern Russia (Sovremennye izmenenia klimata na severe Rossii)* (in Russian). Novosibirsk: Geo Publ., 54 pp.

Pavlov, A.V. 2003. Permafrost and climate changes in northern Russia: observations and forecasts (in Russian). Izvestia RAN. *Seria Geograficheskaya* 6: 39-50.

Romanovsky, V.E., Sazonova, T.S., Balobaev, V.T., Shender, N.I. & Sergueev, D.O. 2007. Past and recent changes in air and permafrost temperatures in eastern Siberia. *Global and Planetary Change* 56(3-4): 399-413.

Skachkov, Y.B. 2001. *Recent Climate Warming and Thermal Stability of Upper Permafrost in Central Yakutia.* Ph.D. Thesis Abstract (Termicheskaya ustoichivost' verkhnikh gorizontov kriolitozony Centralnoi Yakutii pri sovremennom potemplenii klimata. Avtoref. dis. kand. geogr. nauk) (in Russian). Yakutsk, 25 pp.

Skryabin, P.N., Varlamov, S.P. & Skachkov, Y.B. 1998. I*nterannual Variability of Ground Temperatures in the Yakutsk Area (Mezhgodovaya izmenchivost teplovogo rezhima gruntov rajona Yakutska)* (in Russian). Novosibirsk: SB RAS Press, 144 pp.

Varlamov, S.P., Skachkov, Y.B. & Skryabin, P.N. 2002. *Thermal Regime of Permafrost Landscapes in Central Yakutia (Temperaturnyi rezhim merzlotnykh landshaftov Centralnoi Yakutii)* (in Russian). Yakutsk: Permafrost Institute Press, 218 pp.

Vasiliev, I.S. & Torgovkin, Y.I. 1996. The influence of climate on temperature and thickness of the active layer. In: T*he Influence of Climate on Permafrost Landscapes in Central Yakutia (Vlianie klimata na merzlotnye landshafty Centralnoi Yakutii)* (in Russian). Yakutsk: Permafrost Institute Press, 37-45.

Methodical Design for Stability Assessments of Permafrost-Affected High-Mountain Rock Walls

Luzia Fischer
Glaciology, Geomorphodynamics & Geochronology, Department of Geography, University of Zurich
Christian Huggel
Glaciology, Geomorphodynamics & Geochronology, Department of Geography, University of Zurich

Abstract

Slope stability of steep rock walls in glacierised and permafrost-affected high-mountain regions is influenced by a number of different factors and processes. For an integral assessment of slope stability, a better understanding of the predisposing factors is particularly important, especially in view of rapid climate-related changes. This study introduces a methodical design that includes suitable methods and techniques for investigations of different predisposing factors in high-mountain rock walls. Current state-of-the-art techniques are reviewed, and their potential application for in situ and remote studies is assessed. A comprehensive array of analyses and modeling tools is presented, including data-acquisition methods and subsequent stability analyses. Based on two case studies of recent slope instabilities in the European Alps, the effective application and coupling of measurements, analyses, and modeling methods are shown.

Keywords: climatic change; high-mountain rock walls; investigation techniques; predisposing factors; slope stability.

Introduction

Hazards related to rockfall, rock avalanches and combined rock/ice avalanches from steep glacierised and permafrost-affected rock walls pose a significant threat to people and infrastructure in high mountain regions. Due to ongoing climatic change, a widespread reduction in stability of formerly glacierised and perennially frozen slopes might occur and result in a shift of hazard zones (Haeberli et al. 1997, Harris et al. 2001, Fischer et al. 2006). A major problem is the possible increase in magnitude and frequency of slope failures.

Slope stability of steep rock walls in glacierised and permafrost-affected high-mountain regions is influenced by a number of different factors such as topography, geological and geomechanical characteristics, hydrology as well as glaciation, permafrost distribution, and thermal condition. Gradual or abrupt changes in one or more of these factors may reduce the slope stability and eventually lead to a rockfall event. Among these factors, permafrost and glaciers are particularly prone to rapid changes in relation to ongoing climate change. Although these two factors are, together with the hydrological regime, assigned a likely important role in current and future slope destabilization, the effects are not clearly understood. A better understanding of the factors and mechanisms determining the slope stability of steep rock walls is thus a key factor and needs basic research.

The complexity of slope stability problems requires a number of different investigation and modeling techniques to consider the relevant physical processes and factors. However, high-mountain rock walls are an extremely challenging environment for currently existing technology and related investigations for a number of reasons. Often, the hazard source areas are situated in remote high-mountain regions and the on-site access to steep rock walls is mostly very difficult or prohibitively dangerous due to existing slope instabilities. Furthermore, the steepness complicates applications of airborne investigation techniques.

This article provides a review of current local-scale investigation techniques and introduces a multidisciplinary methodical design for comprehensive, stability-directed investigations of predisposing factors in steep, high-mountain rock walls which adequately considers the particular difficulties of steep and partly inaccessible ground conditions, based on a combination of on-site and remote methods. The design presented here does not claim to provide a complete approach; rather it bases itself on investigation techniques and analyses that were applied and tested within past and ongoing projects. Also, the rapidly advancing technology may require extension and adaptation of the design in the future.

Factors Influencing Slope Stability

Predisposing and triggering factors can be distinguished with respect to slope stability of rock walls. In the following, a short definition of the two different types of factors is given. Proposed methodical design for slope stability assessment is mainly focused on the investigation of predisposing factors; analyses of triggering factors usually require permanent monitoring methods.

Predisposing factors are physically measurable processes and parameters that permanently affect stress and strain fields in a flank, also in the stable state. They can be broadly categorized in topographical, geomorphological, geological, hydrological, and several other physically-based factors. In high-mountain areas, permafrost and glaciers are two additional important factors (Fig. 1).

Triggering factors can vary in time, space, and magnitude and eventually provoke slope failure. They include, for example, earthquakes, rainfall and snowmelt events that can result in increased water pressure, and rather seldom in high-mountain areas, human interactions.

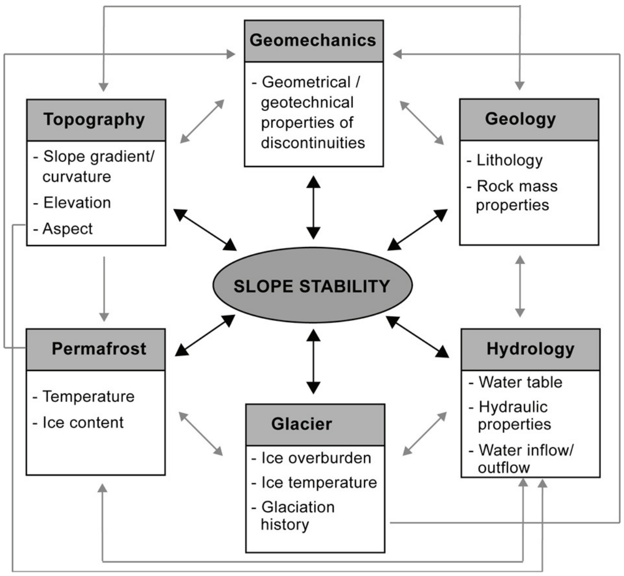

Figure 1. Predisposing factors influence the slope stability and have complex interactions among themselves which are represented by arrows.

Predisposing factors have complex interactions among themselves that influence slope stability (Fig. 1). Topography is a fundamental parameter for slope stability. Slope angle and morphology are important factors for the occurrence and spatial distribution of slope instabilities due to their strong influence on stress and strain fields within a flank. Topography is closely connected to the geological setting and the geomorphological history of a rock wall (erosion, glacial overburden), which, in turn, also effectively influence the geomechanical setting.

The geological setting is determined by the lithology and the geotechnical properties of the rock mass. The geological structures, i.e. discontinuities such as joints, bedding planes, schistosity, and fault zones are fundamental for slope stability, especially their geometrical and geotechnical characteristics. The shear strength as a major parameter for stability is directly related to the geotechnical properties such as cohesion, friction angle, aperture, infilling, and weathering.

Permafrost occurrence in a rock wall can strongly influence the geotechnical parameters of discontinuities, depending on ice content and temperature. The shear strength of ice-bonded discontinuities is strongly affected by the thermal regime in the sub-surface and may be reduced by a rise in temperature or finally the melting of ice-filled rock joints (Davies et al. 2001, Gruber & Haeberli 2007, Harris et al. 2001). This, in turn, also influences the hydrological regime, and may, for instance, result in an increase of the water pressure. The hydraulic setting in a steep rock wall is closely connected to the topography, geological setting, geomechanical characteristics, glaciation, and permafrost occurrence. Changes in water table and water pressure may significantly change the shear strength of the rock mass and therefore exert a strong influence on the slope stability.

Glacier ice may influence slopes differently. Hanging glaciers may have an impact on the thermal, hydraulic, and hydrologic regime in adjacent areas (Haeberli et al. 1997). The erosion by and retreat and down-waste of valley glaciers, in turn, may induce long-term change in the stress field inside the rock wall (Wegmann et al. 1998, Eberhardt et al. 2004).

Among the factors outlined in Figure 1, glaciation and permafrost are presently those subject to the most direct and rapid changes due to climatic change. Changes in these parameters can significantly influence other factors such as hydrology, geomechanical and geotechnical properties in particular. The response of steep high-mountain rock walls to changes in these predisposing factors is, at the same time, strongly conditioned by the topography and the geological setting, in particular by the geometrical and geotechnical characteristics of discontinuities (Ballantyne 2002).

Investigation Techniques and Methodology

Data acquisition

In this section, current state-of-the-art techniques for the investigation of the predisposing factors are illustrated, while in the following section subsequent analyses and processing methods are described (Fig. 2).

In situ field investigations are useful to obtain detailed data. Traditional geological in situ field studies are necessary to achieve data on geological and geomechanical characteristics of the rock mass. The lithological and geomorphological setting as well as geological structures can be mapped, and a preliminary assessment of the intact rock mass properties can be achieved, for example, using the Schmidt hammer method (Aydin & Basu 2005). The geomechanical and geotechnical properties of discontinuities can be assessed by measuring parameters such as orientation, frequency, spacing, aperture, and surface characteristics based on the application of rock mass classification systems (Hack 2002, Hoek & Brown 1997, Wyllie & Mah 2004). In case of inaccessible ground conditions, these types of investigations can also be conducted in the surrounding area with similar lithological and geomechanical settings. Limited observations of the hydrological regime can also be done in situ and from photographs; for instance, observations of water inflow or outflow in a mountain flank.

Point measurements of near-surface rock temperatures using temperature loggers installed a few cm to dm below the surface can constrain permafrost distribution and the prevailing thermal regime (Gruber et al. 2003). Nearby boreholes equipped with temperature loggers give an indication of temperature distribution at depth.

Geophysical techniques are powerful methods for the investigation of subsurface characteristics, but in steep rock walls difficult and complex in their application and therefore rarely exploited until now. Georadar, electrical resistivity tomography, and refraction seismic can be applied for the determination of subsurface structures and the distinction between frozen and thawing rock sections (Hauck et al. 2004, Heincke 2005, Krautblatter & Hauck 2007).

Remote sensing-based techniques are crucial due to the inaccessibility of wide areas of high-mountain walls.

Terrestrial and aerial imagery can be used for identifying

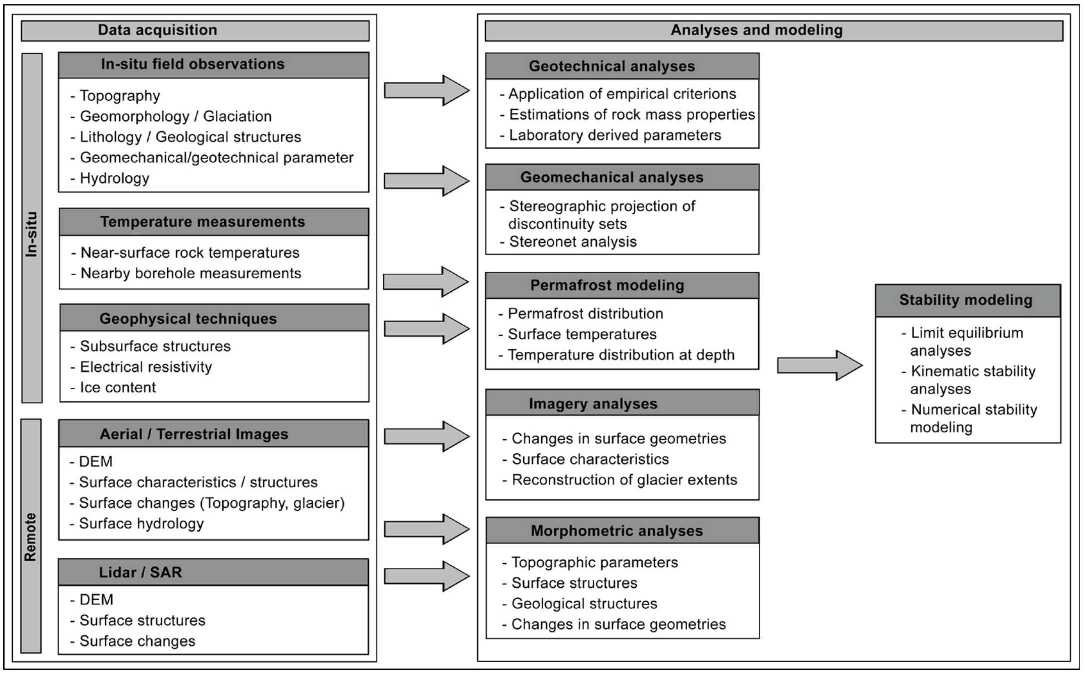

Figure 2. Methodical design for the assessment of slope stability in high-mountain areas containing different insitu and remote sensing-based methods. The upper part shows techniques for the data collection, the lower part processing and analyses of acquired data.

geological structures and surface changes with respect to ice cover and topography. Aerial photography can also be used for the generation of digital elevation models (DEMs), the measurement of terrain displacements and for detailed interpretations (Baltsavias et al. 2001). In some specific studies, terrestrial photography was used for identifying changes with respect to ice cover and slope instabilities on steep ice faces (Fischer et al. 2006, Kääb et al. 2005). These studies have shown the considerable potential of such image analyses which should be further exploited. Automatic cameras are a commonly applied tool for monitoring acute slope instabilities.

Airborne and terrestrial laser scanning (LiDAR) is a rapidly emerging and highly promising tool for acquiring very high-resolution DEMs for high-mountain areas, and thus for detecting small-scale topographic structures (Baltsavias et al. 2001, Janeras et al. 2004). Laser scanning applications from helicopter allow perpendicular recording of LiDAR data and simultaneous acquisition of digital photographs with little geometric distortion (Skaloud et al. 2005). Repeated measurements are the basis for deriving topographic changes. Ground-based synthetic aperture radar (SAR) technology is a capable tool for slope deformation studies (Atzeni et al. 2001, Singhroy & Molch 2004).

Analyses and modeling

Lithological and geomorphological data can be displayed on a map in a GIS for further applications or comparison with other parameters. The geomechanical and geotechnical data measured during fieldwork typically have to be processed to get required parameters for stability modeling by using empirical criteria and rock mass classification systems (Hack 2002, Hoek & Brown 1997) or with adequate laboratory tests. Geomechanical data such as the orientation of discontinuities can be displayed in stereographic projections and may be applied subsequently for kinematic analyses, limit equilibrium analyses, and numerical modeling (Stead et al. 2006).

For the modeling of permafrost distribution a number of models with varying levels of sophistication and at different spatio-temporal scales have been developed (Hoelzle et al. 2001, Gruber et al. 2003). The three-dimensional temperature distribution and its evolution with climatic change is an important component for rock slope stability considerations and has been assessed using numerical modeling by coupling a surface energy balance model with a subsurface heat conduction scheme (Noetzli et al. 2007). A modeling scheme that would directly include modeled permafrost distribution within slope stability models has yet to be developed, but it can be considered for the model assumptions.

Geophysical investigations can mainly be used as boundary conditions and reference values either for permafrost modeling or for analyses of the subsurface structures.

The most common application of remotely sensed image data consists of the interpretation and classification of the image content. Terrestrial and aerial imagery can be used for the identification and mapping of different surface features in steep rock walls and also their temporal changes. Digital aerial as well as terrestrial photos have considerable potential for quantitative analyses of geomorphic structures and changes in a rock wall by georeferencing or matching images based on a high-resolution DEM or photogrammetric techniques (Roncella et al. 2005).

DEMs represent the core of any morphometric investigation of predisposing factors. They can be obtained from stereo aerial and high-resolution terrestrial photos but also from LiDAR data (Kääb et al. 2005). From these DEMs, topographic parameters, large-scale morphotectonic features,

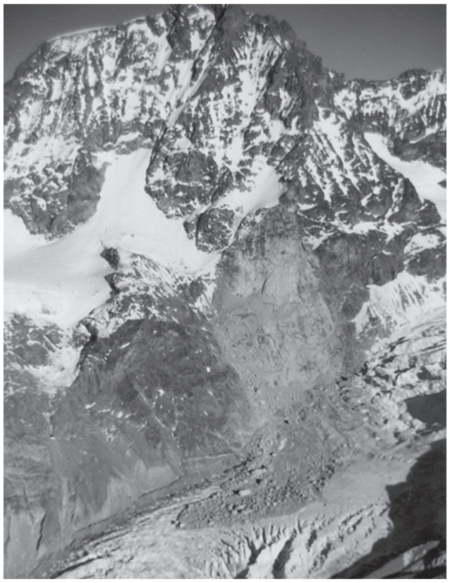

Figure 3. The western flank of the Piz Morteratsch with the Tschierva glacier in the foreground. Visible in the middle of the photo is the detachment zone of the 1988 rockfall and the deposits on the glacier (photo by A. Amstutz, 1988).

and geological structures can be extracted. A promising, yet not fully exploited method is the coupling of laser scanning data with photogrammetric analyses and terrestrial imagery analyses to extract important topographic and structural-geological parameters from DEMs. Main discontinuity sets can be distinguished and their geometrical pattern determined. Therefore, a preliminary assessment of potentially unstable areas may be performed based on geomechanical parameters with limit equilibrium and kinematic analyses using the data from in situ measurements or even only based on DEM analyses (Derron et al. 2005, Stead et al. 2001). Further structural and stability analysis with a DEM is made possible by the recent development of geologically oriented GIS tools (Günther 2003, Jaboyedoff et al. 2004).

For more complex slope stability assessments numerical methods are required. Numerical techniques used for rock slope analyses are generally divided into continuum and discontinuum approaches, or when combined, hybrid approaches (Barla & Barla 2001, Eberhardt et al. 2004, Stead et al. 2001, Stead et al. 2006). Numerical modeling is in fact a powerful tool for the assessment of failure mechanisms, but the level of topographic and geotechnical detail needed can limit the application.

Case Studies

Tschierva rock avalanche event

The Tschierva rock avalanche occurred on October 19, 1988, from the western flank of Piz Morteratsch (3751 m a.s.l., in the Engadin, Switzerland) on Tschierva glacier with an estimated volume of approximately $0.3x10^6$ m^3 (Fig. 3).

For the re-analyses of the Tschierva rock avalanche, detailed numerical slope stability modeling was proposed. Therefore, in situ fieldwork and subsequent geotechnical and morphometric analyses have been done to obtain required

Figure 4. The Monte Rosa east face with the Belvedere glacier in the foreground (photo by L. Fischer, 2004). The detachment zone of the ice avalanche (2005) is marked with a black circle, the one of the rock avalanche (2007) in white.

accurate data (Fischer et al. 2007). The steps described here generally follow the scheme from Figure 2.

The in situ field observations included:

- Preliminary analyses of rock mass properties (lithology, discontinuities, fault zones, water occurrence).
- Characterization of discontinuities (discontinuity sets, orientation, density, condition, aperture, filling).
- Surveying of detachment zone and adjacent area with manual rangefinder.

Subsequent complementary analyses included:

- Geotechnical and geomechanical analyses by using field data, stereographic plots, and empirical criterions.
- Photogrammetric analyses of aerial images for the evaluation of topographic changes.
- Analyses of aerial and terrestrial photos for detecting geological structures and water occurrence.
- Modeling of permafrost distribution.
- Reconstruction of glacier extents based on satellite images and historical topographic maps.

Numerical slope stability modeling was then performed with the 2-D distinct-element method model UDEC (by Itasca) to examine the possible failure mechanisms. Modeling of the unloading of the Pleistocene glacial overburden showed that subsequent redistribution of stress and strain fields in the flank had a strongly controlling influence on the geometry of the detachment zone. A sensitivity analysis of geotechnical parameters showed that the cohesion of the discontinuities was a fundamental parameter. The stability modeling for dry conditions also revealed that the failure mechanism was a combination of shear failure along preexisting discontinuities and development of brittle fractures propagation through the intact rock mass.

Coupled hydro-mechanical modeling demonstrated that slope stability was very sensitive to changes in water pressure. The existing fault zone crossing the rock slope induced an elevated water inflow due to the higher permeability and might therefore be, together with the long-lasting effects of ice unloading, a main factor for the slope instability.

Instabilities in the Monte Rosa east face

The Monte Rosa east face, Italian Alps, is one of the highest flanks in the Alps (2200–4600 m a.s.l.). Steep hanging glaciers and permafrost cover large parts of the wall (Fig. 4). Since the end of the Little Ice Age (~1850), hanging glaciers and firn fields have retreated continuously. During recent decades, the glaciers of the Monte Rosa east face experienced an accelerated and drastic loss. Some glaciers have completely disappeared. New slope instabilities and detachment zones developed and resulted in enhanced rockfall and debris flow activity (Kääb et al. 2004, Fischer et al. 2006). In August 2005, an ice avalanche with a volume of more than $1x10^6$ m^3 occurred, and in April 2007, a rock avalanche of about $0.3x10^6$ m^3 detached from the upper part of the flank.

The main focus of the investigations of the Monte Rosa east face was the assessment of the influence of glacier retreat and permafrost degradation on the current and possible future rockfall and ice avalanche activity (Fischer et al. 2006).

During field studies, the following data were compiled:

- Detailed geological and geomorphological mapping.
- Current glacier extents.
- Detailed map of the current detachment zones of mass movement activities.

Due to difficult and dangerous in situ access, this information was collected from distant ground-based and air-borne observations.

Further analyses included:

- Modeling of the permafrost distribution.
- Reconstruction of glacier extents since the early 20th century based on orthophotos and terrestrial photos.

The results were compiled in a GIS, and the overlay of each investigated factor revealed spatial as well as temporal linkages between investigated processes and their influence on the formation of new detachment zones.

The most important findings were that most detachment zones in the Monte Rosa east face are located in areas where surface ice has recently disappeared. In addition, many detachment zones are located at the altitude of the lower boundary of the estimated permafrost distribution, where presumably warm and degrading permafrost exists. A striking result is also that many detachment zones are situated in transition zones between orthogneiss and paragneiss. These findings demonstrate that the formation of detachment zones mostly seems to be caused by a combination of different factors.

Conclusion and Perspectives

The investigation of slope stability in steep, high-alpine rock walls is a major challenge, chiefly due to the difficulties in data acquisition and the complexity of the factors and processes influencing slope stability. In each case, the proceeding has to be adapted, and different methodologies have to be applied concerning the possibilities of data acquisition and the required stability modeling method.

The case study of the Tschierva rockfall shows that the appropriate method combination, including classic geological field investigation techniques, terrestrial and aerial image analyses, and permafrost modeling, allows the performance of detailed numerical slope stability modeling and the evaluation of possible failure mechanisms.

The much larger Monte Rosa east face, with surface and subsurface ice subject to extremely fast changes, represents the most challenging high-mountain conditions and required a more remote-based approach. However, local field surveys could be integrated for a comprehensive spatial and temporal analysis of predisposing factors and their interaction.

In the future, measurement, analytical, and modeling tools will be further advanced. For instance, ground-based SAR and helicopter-based LiDAR have only very recently been applied on large high-mountain walls and should be further developed. Advances are also expected with regard to a more comprehensive integration of high-technology data into slope stability assessment methods.

Acknowledgments

This project is funded by the Swiss National Science Foundation (project no. 200021-111967). We acknowledge constructive comments made by two reviewers and editors.

References

Aydin, A. & Basu, A. 2005. The Schmidt hammer in rock material characterization. *Engineering Geology* 81: 1-14.

Atzeni, C., Basso, M., Canuti, P., Casagli, N., Leva, D., Luzi, G., Moretti, S., PieraccinI, M., Sieber, A.J. & Tarchi, D. 2001. Ground-based radar interferometry for landslide monitoring and control. *Proceedings of the ISSMGE Field Workshop on Landslides and Natural/ Cultural Heritage Trabzon (Turkey), August 23–24, 2001*: 195-209.

Ballantyne, C.K. 2002. Paraglacial Geomorphology. *Quarternary Science Reviews* 21: 1935-2017.

Baltsavias, E.P., Favey, E., Bauder, A., Boesch, H. & Pateraki, M. 2001. Digital surface modelling by airborne laser scanning and digital photogrammetry for glacier monitoring. *Photogrammetric Record* 17(98): 243-273.

Barla, G. & Barla, M. 2001. Investigation and modelling of the Brenva Glacier rock avalanche on the Mount Blanc Range. *Proceedings of the ISRM Regional Symposium Eurock 2001, Espoo, Finlandia, 3-7 giugno, 2001*: 35-40.

Davies, M.C.R., Hamza, O. & Harris, C. 2001. The effect of rise in mean annual temperature on the stability of rock slopes containing ice-filled discontinuities. *Permafrost and Periglacial Processes* 12 (1): 137-144.

Derron, M.-H., Jaboyedoff, M. & Blikra, L. H. 2005. Preliminary assessment of rockslide and rockfall hazards using a DEM (Oppstadhornet, Norway). *Natural Hazards and Earth System Sciences* 5: 285-292.

Eberhardt, E., Stead, D. & Coggan, J.S. 2004. Numerical analysis of initiation and progressive failure in natural rock slopes - the 1991 Randa rockslide. *Int. J. Rock Mech. Min. Sci.* 41: 69-87.

Fischer, L., Kääb, A., Huggel, C. & Noetzli, J. 2006. Geology, glacier retreat and permafrost degradation as controlling factors of slope instabilities in a high-mountain rock wall: the Monte Rosa east face. *Natural Hazards and Earth System Sciences* 6: 761-772.

Fischer, L., Huggel, C. & Lemy, F. 2007. Investigation and modelling of periglacial rockfall events in the European Alps. *EGU - Geophysical research abstracts*.

Gruber, S. & Haeberli, W. 2007. Permafrost in steep bedrock and its temperature-related destabilization following climate change. *Journal of Geophysical Research* 112: F02S18.

Gruber, S., Peter, M., Hoelzle, M., Woodhatch, I. & Haeberli, W. 2003. Surface temperatures in steep alpine rock faces – A strategy for regional-scale measurement and modeling. *Proceedings of the 8th International Confernce on Permafrost 2003, Zurich, Switzerland*: 325-330.

Günther, A. 2003. SLOPEMAP: programs for automated mapping of geometrical and kinematical properties of hard rock hill slopes. *Computer and Geosciences* 29: 865-875.

Hack, R. 2002. An evaluation of slope stability classification. *Proceedings of ISRM EUROCK 2002, Portugal, Madeira, Funchal, Nov. 25-28, 2002*: 3-32.

Haeberli, W., Wegmann, M. & Vonder Mühll, D. 1997. Slope stability problems related to glacier shrinkage and permafrost degradation in the Alps. *Eclogae geologicae Helvetiae* 90, 407-414.

Harris, C., Davies, M.C.R. & Etzelmüller, B. 2001. The assessment of potential geotechnical hazards associated with mountain permafrost in a warming global climate. *Permafrost and Periglacial Processes* 12 (1): 145-156.

Hauck, C., Isaksen K., Vonder Mühll, D. & Sollid, J.L. 2004. Geophysical surveys designed to delineate the altitudinal limit of mountain permafrost: an example from Jotunheimen, Norway. *Permafrost and Periglacial Processes* 15: 191-205.

Heincke, B. 2005. Determination of 3-D fracture distribution on an unstable mountain slope using georadar and tomographic seismic refraction techniques. *Doctoral thesis*, ETH Zurich.

Hoek, E. & Brown, E. 1997. Practical estimates of rock mass strength. *Int. J. Rock. Mech. Min. Sci. Abstr*. 27 (3): 1165-1186.

Hoelzle, M., Mittaz, C., Etzelmüller, B. & Haeberli, W. 2001. Surface energy fluxes and distribution models relating to permafrost in European mountain permafrost areas. *Permafrost and Periglacial Processes* 12: 53-68.

Jaboyedoff, M., Baillifard, F., Philippossian, F. & Rouiller, J.-D. 2004. Assessing fracture occurrence using "weighted fracturing densit": a step towards estimating rock instability hazard. *Natural Hazards and Earth System Science* 4: 83-93.

Janeras, M., Navarro, M., Arnó, G., Ruiz, A., Kornus,W., Talaya, J., Barberá, M. & López, F. 2004. LIDAR applications to rock fall hazard assessment in Vall de N´uria. *Proceedings of the 4th ICA Mountain Cartography Workshop, Vall de Núria, Catalonia, Spain*.

Kääb, A., Huggel, C., Barbero, S., Chiarle, M., Cordola, M., Epinfani, F., Haeberli, W., Mortara, G., Semino, P. Tamburini, A. & Viazzo, G. 2004. Glacier hazards at Belvedere glacier and the Monte Rosa east face, Italian Alps: Processes and mitigation. *Proceedings of the Interpraevent 2004 – Riva/Trient*.

Kääb, A., Huggel, C., Fischer, L., Guex, S., Paul, F., Roer, I., Salzmann, N., Schlaefli, S., Schmutz, K., Schneider, D., Strozzi, T. & Weidmann, I. 2005. Remote sensing of glacier- and permafrost-related hazards in high mountains: an overview. *Natural Hazards and Earth System Sciences* 5: 527-554.

Krautblatter, M. & Hauck, C. 2007. Electrical resistivity tomography monitoring of permafrost in solid rock walls. *Journal of Geophysical Research* 112: F02S20.

Noetzli, J., Gruber, S., Kohl, T., Salzmann, N. & Haeberli, W. 2007. Three-dimensional distribution and evolution of permafrost temperatures in idealizes high-mountain topography. *Journal of Geophysical Research* 112: F02S13.

Roncella, R. Forlani, G. & Remondino, F. 2005. Photogrammetry for geological applications: automatic retrieval of discontinuity in rock slopes. *Proceedings of SPIE-IS&T Electronc Imaging, SPIE* 5665: 17-27.

Skaloud, J., Vallet, J., Keller, K., Veyssiere, G. & Kölbl, O. 2005. HELIMAP: Rapid large scale mapping using handheld LiDAR/CCD/GPS/INS sensors on helicopters. *Proceedings of ION GNSS 2005 Congress, Long Beach, California*.

Singhroy, V. & Molch, K. 2004. Characterizing and monitoring rockslides from SAR techniques. *Advances in Space Research* 33: 290-295.

Stead, D., Eberhardt, E., Coggan, J. & Benko, B. 2001. Advanced numerical techniques in rock slope stability analyses-applications and limitations. *Proceedings of the International Conference on Landslides-Causes, Impacts and Countermeasures, Davos 2001*: 615-624.

Stead, D., Eberhardt, T. & Coggan, J.S. 2006. Developments in the characterization of complex rock slope deformations and failure using numerical modeling techniques. *Engineering Geology* 83: 217-235.

Wegmann, M., Gudmundsson, G.H. & Haeberli, W. 1998. Permafrost changes in rock walls and the retreat of Alpine glaciers: a thermal modelling approach. *Permafrost and Periglacial Processes* 9: 23-33.

Wyllie, D.C. & Mah, C.W. 2004. *Rock Slope Engineering,* 4th ed. New York: Spon Press, 431 pp.

Permafrost in Marine Deposits at Ilulissat Airport in Greenland, Revisited

Niels Foged
Arctic Technology Centre, Department of Civil Engineering, Technical University of Denmark, DK-2800 Kgs. Lyngby, Denmark

Thomas Ingeman-Nielsen
Arctic Technology Centre, Department of Civil Engineering, Technical University of Denmark, DK-2800 Kgs. Lyngby, Denmark

Abstract

Ilulissat Airport was constructed in 1982 to 1984 after detailed geotechnical investigations as the construction site included up to 12 m thick basins of marine clay deposits. Despite soil temperatures of approximately -3°C the soil appeared unfrozen from 4 m to 5 m below ground surface due to a high residual salt content in the porewater. However, in the less saline top zone massive ice layers were found constituting up to 30% by volume. These formations, representing a typical example of saline permafrost, caused the planned position of the runway to be shifted towards the northwest and the layers to be removed and replaced with compacted blasted rock fill. However, a test fill of 2.5 m of rock fill and coarse gravel was constructed in the abandoned area in order to establish experiences for future constructions. Background, previous findings, and present activities are also topics in an accompanying paper, Ingeman-Nielsen et al. (2007).

Keywords: airport; construction; embankment; freezing point depression; saline permafrost; test fill.

Introduction

In Greenland it has been very difficult and costly to establish the traffic infrastructures necessary for the development of a modern society under the present physiographic and climatic conditions. The establishment of the airport in Ilulissat (Jakobshavn) was a milestone in a traffic project based on the aircraft type DASH-7, which could land on a short 700 m "Short Take Off and Landing" – STOL runway with an in-flight angle of 7.5° instead of the normal 3°. At present 7 airports of this type are operational and more will be established. Ilulissat Airport was the first to be constructed using rock fill on rock outcrops and marine clay under permafrost. Consequently, the geotechnical investigations started in 1978 were very detailed and led to new findings on saline clay permafrost published by Foged and Bæk-Madsen (1980).

Investigations in 1978–1982

Ilulissat Airport was constructed in 1980–1984 two km north of the town on a plain area with shallow rock outcrops surrounded by marine clay deposits. It is situated in discontinuous permafrost and project investigations from 1978 to 1985 focussed on the thermal state of these deposits and the geotechnical properties of frozen and unfrozen clay being the possible foundation for the runway embankment, taxiway, and terminal area. The soil investigations were carried out for Asiaq–Greenland Survey (Previously Grønlands Tekniske Organisation) by the Danish Geotechnical Institute with the senior author being responsible for special field and laboratory work.

Engineering geology

Ilulissat is located in the central bay of West Greenland, which was glaciated repeatedly during Quaternary but most soil formations relate to the last Weichselian-glaciation (Wisconsin) and to the late-glacial and Holocene deglaciation. Onshore, the most important deposits are local side moraines and glaciomarine clay and silt sediments overlain by Holocene solifluction deposits and topsoil in the form of only slightly decomposed peat. According to Bennike and Björck (2002) the innermost part of the bay near to Jakobshavn was not deglaciated before earliest 9600 years before present (BP). The glaciomarine sediments were deposited at a relative high sea level of >50 m above present. The saline pore water is maintained to a high degree as desalination due to freshwater percolation was not effective during the Holocene climatic optimum between 8000 and 5000 years BP (Weidick 1968, Foged 1979, and Foged & Bæk-Madsen 1980). After 5000 years BP it is assumed that the climate caused permafrost to develop as seen today.

Geotechnical investigations

The distribution of sediments, permafrost, and bedrock of gneiss was delineated using engineering geological field survey and aerial photos, Figure 1. This work was supplemented with geophysical investigation by means geoelectrical measurements using Wenner configurations for subsurface mapping of the marine clay basins and Schlumberger electrical soundings to delineate geological and permafrost boundaries. In connection with this more than 70 boreholes were carried out using a self-transportable rotary core drilling rig, indispensable in the very wet muskeg peat and solifluction soil top-layer. A number of boreholes were equipped with soil temperature PT-100 sensors sat down in PEL-tubes with an antifreeze liquid. The sensors were generally measured manually during the investigation and construction periods.

Figure 1. Orthophoto of the Ilulissat Airport. The test fill and the present research area is located at the southeastern corner on the solifluction slope. Equidistance is 2 m. ©Asiaq 2000.

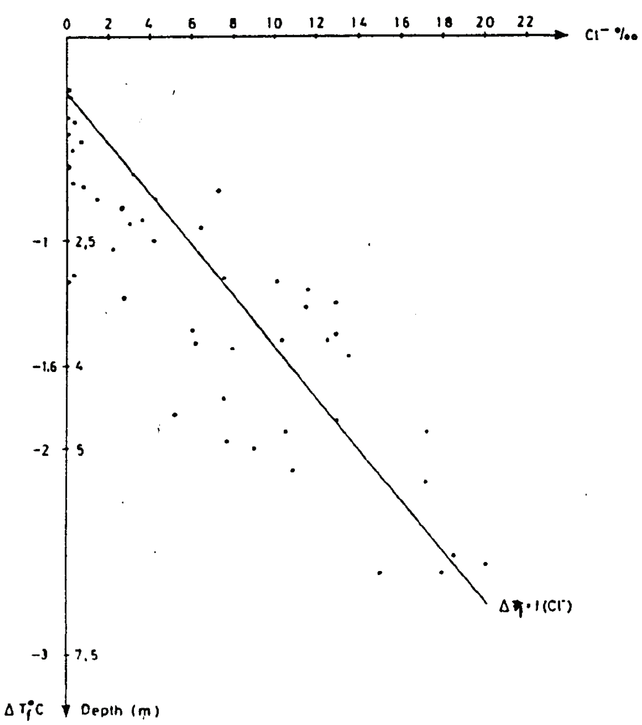

Figure 2. Salinity as function of depth in boreholes and the estimated minimum freezing point depression.

Table 1. Chemical composition of pore water (g/l).

Borehole No.	Depth (m)	w (%)	Ca^{+} (g/l)	Mg^{++} (g/l)	K^{+} (g/l)	Na^{+} (g/l)	Cl^{-} (g/l)
79005	3.1	30.3	0.66	0.44	0.22	5.45	11.72
79011	5.0	34.1	0.65	0.36	0.30	4.84	10.26
79012	3.6	46.4	0.35	0.18	0.23	2.59	6.03
79012	8.0	63.4	0.35	0.25	0.24	3.94	8.52
Seawater			0.40	1.35	0.38	10.50	19.00

Collected soil specimens were stored in their frozen state and transported to the laboratories in Denmark for geotechnical classification properties as water content w (%), bulk density ρ_b (g/cm^3) using the Archimedes principle of volume determination with buoyancy in chilled trichlorethene, void ratio and saturation degrees of water and ice, S_r and $S_{r,ice}$ (%), using the specific soil particles density of ρ_s = 2.75 g/cm^3 and ρ_{ice} = 0.917 g/cm^3. The salinity variations in the pore water were established as the chloride content Cl^- (grams per liter = g/l or ‰) using $AgNO_3$–titration on diluted samples. Some additional tests on the cation-distribution by means of specific electrodes are shown in Table 1. Consequently, it was considered that Cl^- might be a useful indicator of the total ion content in the pore water as also shown by Foged (1979).

On intact core samples from the borings the freezing point depression ΔT_f was found by means of controlled, very slow thawing from the storage temperature. The results are shown together with the measured chloride content and the estimated minimum freezing-point depression as function of Cl^- in Figure 2.

Generally, the thawing showed a general transition over a wide temperature range, which also was seen in a series of consolidation tests carried out with well-controlled temperature steps of 1°C from -9°C to 0°C and continuous deformation registrations and further ordinary loadings shown in Figure 3. The example relates to borehole 78020 Lab.No. 156 from the depth of 3.2 m on frozen clay with a water content of 31.5% and Cl^-=13.0 g/l. From a geotechnical viewpoint it was very interesting that the test specimen after the controlled drained thawing, which caused 7.8% of deformation, showed an apparent preconsolidation of 210 kPa much higher than the in situ stress level of σ_o<55 kPa, due to desiccation of the clay structure by ice lenses. The sample appeared in thawed condition as a fissured silty clay. Another finding was that the drainage process takes place under partially frozen conditions, as seen from the step function of deformation in Figure 3.

Permafrost

The investigations showed the presence of saline marine clays in most depressions in bedrock, with sediment thicknesses up to 12 m. From a theoretical viewpoint this is a permafrost formation as temperatures below a thin active layer (0.2 m to 0.8 m at the time of drilling) were between

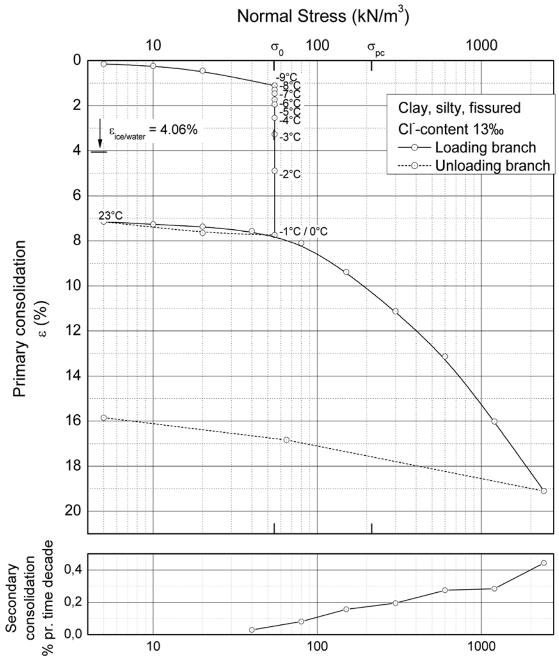

Figure 3. Sample deformation under controlled thawing followed by ordinary consolidation in a number of loading steps.

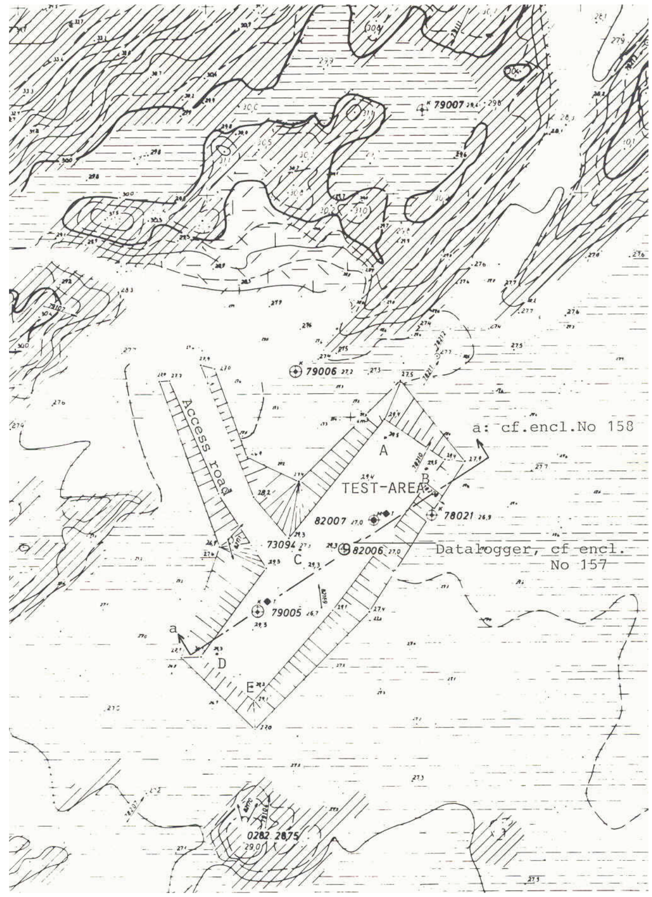

Figure 4. Test site at the south eastern corner of the present runway.

-1°C and -3.5°C. Technically however, it was obvious that the clay material was only partially frozen and often unfrozen below a depth of 4 m to 5 m b.g.s. The cause was also found by geoelectrical measurements showing extreme low electrical resistivity (<4 ohmm) and as previously shown by chemical analyses, which showed that the pore water changed gradually with depth from fresh water at the surface towards seawater at depths >5 m. The varying concentrations of pore water salinity give rise to various freezing-point depressions down through the deposits. Consequently, the thermal stability is very vulnerable to changes in the heat flux as the latent heat of soil layers may be limited. The clay formations showed variable freezing point depressions from -1°C to -3.5°C. Generally we found under 0.5 m active layer a 2 m to 4 m thick layer of frozen ice-rich clay was found underlain by unfrozen clay at soil temperatures of -3°C down to bedrock.

Furthermore, the geotechnical strength and deformation properties in such deposits must also vary with the thermal state from frozen deposits to unfrozen soil resulting in low shear and deformation properties. This would be of critical importance, when a runway is to be constructed on an embankment of up to 5 m of rock fill on top of such deposits.

Evaluations done related to the construction

Fine-grained deposits will always cause freezing point depression because of capillary tension in the pores, (Williams 1967, Pusch 1979, Tsytovich 1975) and parts of the water may remain unfrozen down to a temperature of -10°C. However, the combination with varying salinity in the pore water we found in literature only some results with the same tendency described by Young et al. (1979). It was characteristic for the area and other locations in Ilulissat (Olesen 2003), that a considerable part of the pore water is frozen at a depth of 4 m to 5 m below ground surface. The soil exhibits properties of unfrozen material in spite of temperatures of -2°C to -4°C. Consequently, only a limited heat capacity is available when temperature conditions change in the area due to constructions (and as seen today climatic changes). At that time we could not find practical experiences from the Arctic that could be directly applied.

The initial program showed major problems with two basins situated in the southeastern part of the area. The partly frozen and unfrozen sediments up to 12 m in thickness gave rise to latent risk of settlements caused by thawing and ordinary consolidation due to applied load from the construction. These conditions motivated the final choice of location for the runway as shown on Figure 1. Even with this choice, critical soil conditions were met to a minor extent along the runway and it was decided to excavate these small basins and to substitute the clay with compacted rock fill.

Test fill

With a view to future road construction, terminal area, and extensions of the runway, investigations were initiated in a test fill being placed in the critical area in combination with continuous recording of temperature in representative borings under and outside the test fill. The results have been

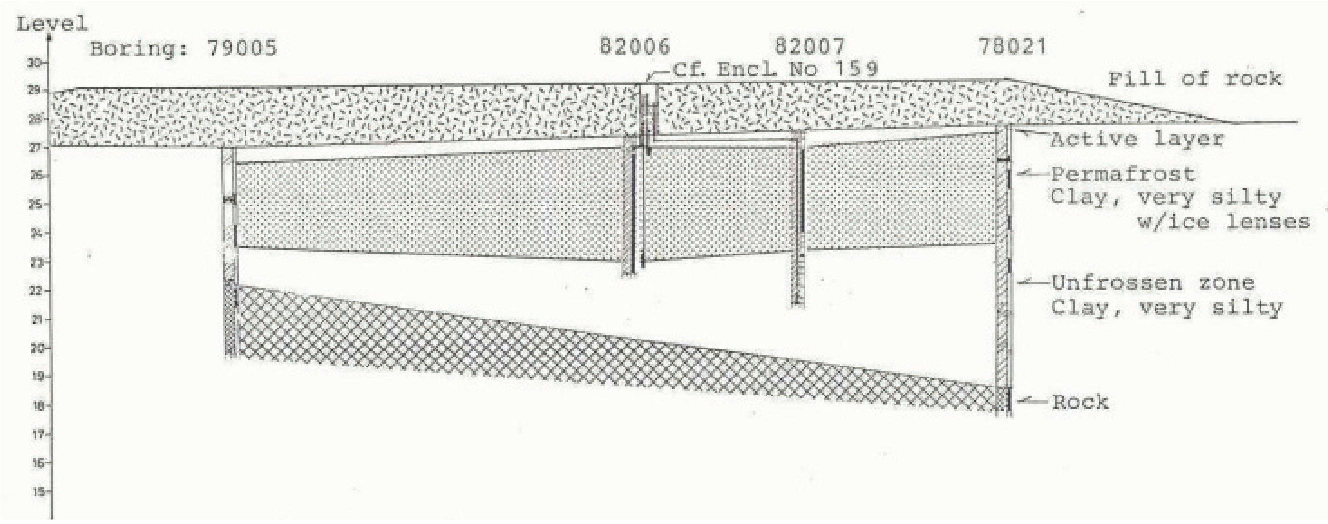

Figure 5. Cross section in the test fill along A-B.

the background for a M.S. project at the DTU Institute for Geology and Geotechnical Engineering in cooperation with the Danish Geotechnical Institute with the senior author as supervisor. The topic for the master thesis by Civil Engineer M.S. Søren Frederiksen (1993) was: "Foundation in Permafrozen Areas" reflecting construction methods of a fill area of compacted blasted rock fill. The technical details and the results through the initial observational period (approximately 5 years) and later on have never been published.

Ilulissat Airport and Test Fill

The test site was placed before construction of the runway as shown on Figure 4 and with a cross section as shown in Figure 5 in a typical basin of marine clay in the southeastern part of the airport area. The test fill was constructed along with some instrumented boreholes with deformation gauges and temperature sensors. The test fill was observed for 5 years during and after construction of the airport and in 2007 found intact and partly operational. The original technical findings are reported by the Danish Geotechnical Institute Geotechnical report No. 9 Jakobshavn Ilulissat. Temperaturmålinger. Prøvefelt. dated 1985-04-23 to Grønlands Tekniske Organisation (Asiaq-Greenland Survey).

The soil and permafrost conditions relate to boreholes 78021, 79005, 82006, and 82007 of which 78021 was selected for presentation in Figure 6. The soil formations consist of marine clay and silt deposits, being part of the marine Quaternary clay formation found up to approximately 50 m a.s.l. in Ilulissat. The profile shows diluted seawater content in the top zone and occurs presently partly permafrozen and unfrozen as previously discussed. The test site was established close to the present safety zone with a typical ca. 2.5 m thick layer of blasted rock fill overlain by some graded coarse gravel similar to the safety zone. For control of the changes in temperature in the test fill and the underlying marine clay a series of continuous temperature measurements were carried out in the boreholes 79005, 82006, and 82007. The deformation gauges were placed at the bottom and top of the real permafrost layer and at the original terrain surface under the test fill. Secured by a measuring well as seen in the cross section the settlement gauges were placed inside a lubricated tube to secure free motion. Furthermore 5 fixed measuring points were established on the top of the test fill in the graded gravel.

The boreholes outside the construction area show a slight tendency of temperature rise (1°C to 2°C) during the period until 1984. Below the test fill a yearly mean temperature of -4°C was found in 2 m depth rising to -3°C at 4 and 5.5 m of depth before filling up (1980 to 1982). After construction (1982 to 1984) values of -5.5°C to -3.5°C were found. The technical conclusion was that the 2.5 m rock fill and graded coarse gravel isolate against conductive heat during summer and allows enhanced convective heat transfer during winter resulting in approximately 1°C to 1.5°C lower yearly mean temperature. The settlement measurements show at all gauges and defined points less than 1 mm to 3 mm mainly reversible deformation, which are at the limit of the measuring resolution. Consequently, it must be stated that during the short control period the effect of filling up with 2.5 m of very coarse grained fill of blasted rock with a top layer of graded gravel must be considered positive.

In 1993 Søren Frederiksen visited the Ilulissat Airport area and downloaded from the data logger a full set of data from 1984 to 1987. He also collected a new series of measurements.

Below the test fill the original surface showed total settlements of 3 cm and the boundaries to top and bottom of originally permafrozen clay were unchanged. However, the top of the test fill showed continued settlements of up to 7 cm over the total period. The time series of the temperature sensors in boreholes B82006 and B82007 show that the upper limit of permafrost rises and a larger part of the original soil maintains permafrozen as expected.

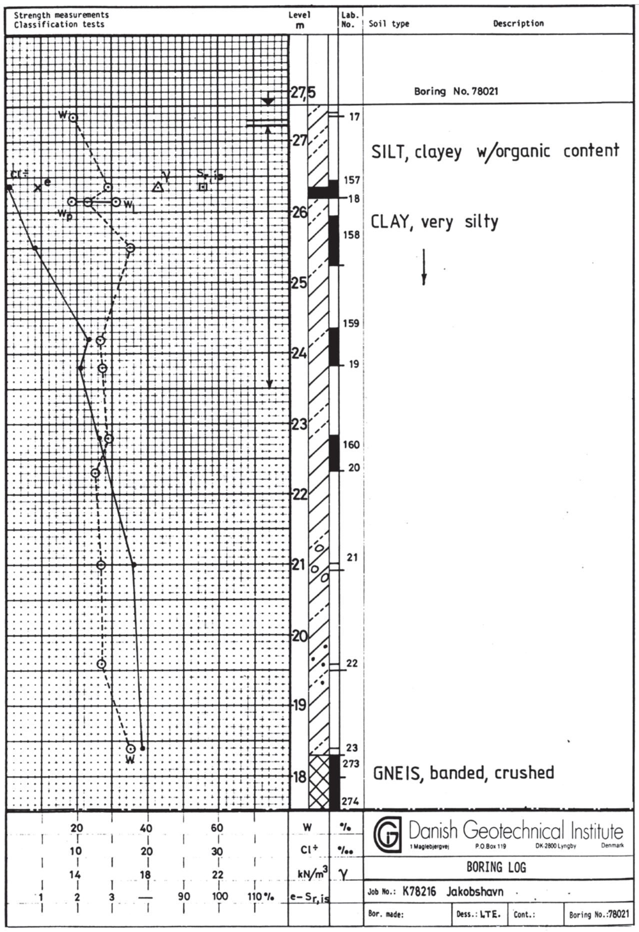

Figure 6. Typical original borehole diagram for borehole 78021 from the test fill showing the discussed soil classification parameters.

Figure 7. Photo of the tilt and heave of the fence pile due to a horizontal slide of the rock fill slope guided by deformation in the active layer.

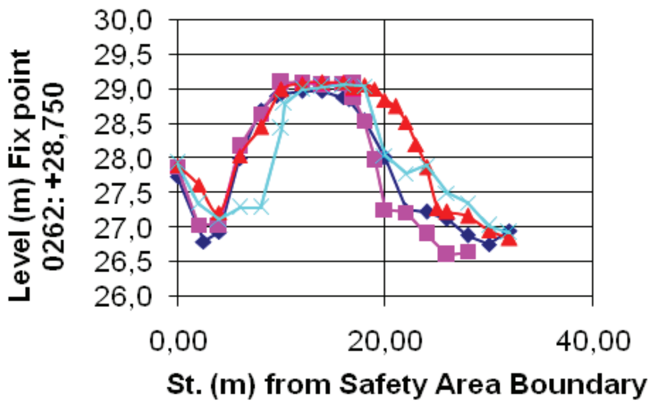

Figure 8. Results of a leveling of the test fill carried out in June 2007.

Ilulissat Airport and test fill, revisited in 2007

In the NSF ARC-0612533 project "Recent and future permafrost variability, retreat and degradation in Greenland and Alaska: An integrated approach" this area was chosen as a type locality for permafrost studies in saline clay related to infrastructures. In June and August 2007 we revisited the area after 25 years of operation and found the constructions in very fine condition with only minor failures and deformations at the boundary of the test fill as seen on Figure 7. The slope of the test fill has moved horizontally due to a failure in the active layer which also turns the airport fence approximately 30°C. Søren Frederiksen showed some vertical deformation due to frost heaving of the pile.

In 1993 Søren Frederiksen observed somewhat less heave of the fence piles, however he did not observe any sliding. Consequently, it must be concluded that the present climate since 1993, which had the lowest registered temperatures since the construction of the airport, might have caused changes in the shear strength or changed the thickness of the active layer allowing for a failure to take place. We performed a levelling of the test fill surface in June 2007. The results for 4 sections A-D with a distance of 10 m perpendicular to the fence with station 0 at the safety zone boundary are shown in Figure 8. The failure zone in the test fill is found between St. 17 and 19 and in front of the test fill the sloping side and the soil layers in front of it show obvious horizontal displacement approximately 0.5 m away from the constructed test fill boundary. The fence is deformed similarly. In comparison to the levelling performed in the period of 1982 to 1987 and in 1993 the central part of the test fill shows only very little deformation as the level is found to a value of approximately +29 comparable to the earlier levelling results of +29.15 to +29.30 in July 1993.

Conclusions

The present contribution and an accompanying contribution, Ingeman-Nielsen et al. (2007), to NICOP 2008 present the new findings together with an overview of the project investigations done during the period of 1978 to 1984.

The geotechnical deformation and strength properties were studied in detail and influenced the final design and construction very distinctly. It was decided to keep the runway away from the deep basins of marine clay for stability and settlements reasons. Under the runway and taxiway and in the terminal area frost susceptible soils were substituted by rock fill.

These decisions led to a generally very stable runway, taxiway, and terminal area. According to interviews with the technical personnel at the airport only one repair has been performed of the asphalt concrete layer in an area where settlements occurred due to some natural silt and clay being left under the bearing layer during construction of compacted rock fill and coarse gravel fill.

The behavior of the test fill slope shows the present climatic change might explain a boundary failure and horizontal deformation in front of the test fill causing the Airport fence to tilt and heave.

Consequently, the detailed studies carried out in 1978 to 1985 have led to safe construction with very little need for repair and maintenance. We will continue the permafrost studies in the coming period as part of the present NSF ARC-0612533 project "Recent and future permafrost variability, retreat and degradation in Greenland and Alaska: An integrated approach." The locality is a well documented example on saline permafrost under discontinuous permafrost condition.

Acknowledgments

The original investigations were performed by the Danish Geotechnical Institute for Grønland Tekniske Organisation (now ASIAQ) on behalf of Grønlands Luftshavns Væsen GLV (now Mittarfeqarfiit). During design and construction of Jakobshavn Airport the senior author had a very close cooperation with Civil Engineer Poul Væver-Petersen from the Danish/Greenlandish consultant Nielsen & Rauschen-berger (now NIRAS). Permission to publish and valuable discussions with lead members and employers of the mentioned institutions are gratefully acknowledged. Furthermore, the work done in the M.S. Thesis by Civil Engineer Søren Frederiksen, INUPLAN, Nuuk, Greenland has been of great value.

The later part of this research was funded by the Polar Earth Science Program, Office of Polar Programs, National Science Foundation (ARC-0612533).

References

Bennike, O. & Björck, S. 2002. Chronology of the last recessionof the Greenland Ice Sheet. *Journal of Quaternary Science* 17 (3): 211-219.

Christiansen H.H. & Humlum, O. 2000. Permafrost. In: B.H. Jakobsen, J. Böcher, N. Nielsen, R. Guttesen, O. Humlum & E. Jensen (eds.), *Topografisk Atlas Grønland*. Copenhagen: C.A. Reitzets Forlag, 32-35.

Danish Geotechnical Institute. *Geotechnical Reports related to K78216 Jacobshavn*. (Restricted, internal, unpublished).

Foged, N. 1979. *Engineering Geological Investigations of Quaternary Marine Clay Deposits on West Greenland*. Ph.D .Thesis. The Institute for Applied Geology. Technical University of Denmark,. (In Danish with English Overview).

Foged, N. & Bæk-Madsen, C. 1980. Jakobshavn Airport. thermal stability in marine deposits. *Proceedings of 2nd International Symposium on Ground freezing, Trondheim, Norway.* Reprint 1-10.

Frederiksen, S. 1993. *Foundation in Permafrozen Areas. A Blasted Rock Test Fill Influence on the Thermal Conditions.* M.S. Thesis. Institute for Geology and Geotechnical Eng.

Olesen, O.B. 2003. *Shallow Borehole Temperatures, Ilulissat, Greenland.* Greenlandic Geological Survey (GEUS). Distributed by National Snow and Ice Data Center/ World Data Center for Glaciology.Digital Media.

Pusch, R. 1979. Unfrozen water as a function of clay microstructure. *Engineering Geology* 13: 157-162.

Tsytovich, N.A. 1975. *The Mechanics of Frozen Ground.* New York: McGraw-Hill Book Company.

Weidick, A. 1968. *Observations on Some Holocene Glacier Fluctuations in West Greenland.* Meddelelser om Grønland, Bd. 165, Nr. 6, København.

Williams, P.J. 1967. *Properties and Behavior of Freezing Soils,* Norwegian Geotechnical Institute, Publ. No. 72, Oslo, Norway.

Young, R.N., Cheung, C.H. & Sheeran, D.E. 1979. Prediction of salt influence on unfrozen water content in frozen soils. *Engineering Geology* 13: 137-155.

Genesis of Reticulate-Chaotic Cryostructure in Permafrost

Daniel Fortier
University of Alaska Fairbanks, Institute of Northern Engineering, Fairbanks, U.S.A.
Mikhail Kanevskiy
University of Alaska Fairbanks, Institute of Northern Engineering, Fairbanks, U.S.A.
Yuri Shur
University of Alaska Fairbanks, Department of Civil and Environmental Engineering, Fairbanks, U.S.A.

Abstract

Cryostratigraphic studies in the CRREL permafrost tunnel in Alaska revealed the presence of multi-directional ice veins in the permafrost which was described as reticulate-chaotic cryostructure. Our hypothesis relates the formation of this cryostructure to inward freezing of saturated sediments trapped in underground channels cut in the permafrost by thermo-erosion. The multi-directional reticulate ice veins were formed in the sediments deposited in the underground channels after the cessation of the underground water flow. This hypothesis was confirmed by laboratory experiments which reproduced reticulate-chaotic cryostructures and thaw unconformities in the sediments similar to those observed in the CRREL permafrost tunnel.

Keywords: CRREL tunnel; freezing cell; ground ice; ice segregation; reticulate cryostructure; underground thermo-erosion.

Introduction

The CRREL permafrost tunnel (≈ 64°57′N, 147°37′W) is located near Fairbanks, Alaska. In the 1960s, a 110-m long tunnel and an inclined winze were excavated in the ice-rich silt and the underlying fluvial gravel that locally form the permafrost. The geology, the cryostratigraphy, the chronology of the tunnel, and the properties of the permafrost were described in many publications (Sellmann 1967, 1972, Pettibone & Waddell 1973, Huang et al. 1986, Hamilton et al. 1988, Long and Pewe 1996, Shur et al. 2004, Bray et al. 2006). The stratigraphy of the permafrost exposed in the tunnel and in the winze consists of an ice-saturated gravel deposit unconformably covering weathered schist bedrock. Fluvial sandy silts overlay the gravelly unit and are covered by partially reworked eolian silts. The latter are syngenetic in nature, ice-rich, and characterized by a micro-lenticular cryostructure and, to a lesser extent, by layered and lenticular-layered cryostructures (Shur et al. 2004; Bray et al. 2006, Kanevskiy et al. 2008).

This paper focuses on the genesis of reticulate-chaotic cryostructures firstly described in the CRREL permafrost tunnel by Shur et al. (2004). The reticulate-chaotic cryostructures are associated with stratified sediments or massive ice bodies enclosed in the frozen ground or cross-cutting ice wedges. A reticulate cryostructure develops when ice crystals oriented in the direction of freezing and growing into the still unfrozen sediments are intersected by crystals of other orientation (Shumskii 1964a). Mackay (1974) proposed that the preferred growth of reticulate ice veins was linked to the restriction of an upward flow of water which prevented the maintenance of a stationary freezing plane and the growth of horizontal ice lenses. Murton and French (1994) mentioned that it is unclear why some reticulate cryostructures are regular and others are irregular. Our hypothesis is that reticulate-chaotic cryostructures observed in the CRREL permafrost tunnel were formed in a closed-system by inward freezing of saturated sediments deposited in underground thermo-erosion channels or gullies. The objective of this study was to reproduce in the laboratory inward freezing of saturated sediments in underground channels analogs in order to support our interpretations of reticulate-chaotic cryostructures genesis.

Methods

Field methods

Cryostratigraphic studies, performed in the CRREL permafrost tunnel in 2004–2006 (Shur et al. 2004, Bray et al. 2006), revealed the occurrence of a cryostructure named reticulate-chaotic. We logged and sketched the permafrost stratigraphy of exposures with reticulate-chaotic cryostructures enclosed in syngenetic permafrost. Samples were retrieved, described, and analyzed for their ice content. The grain size distribution of the sediments was obtained using sieves and an hydrometer (ASTM D422 2008). We studied the morphology and the density of reticulate ice veins and ice lenses within the sediments. Special attention was paid to the contact between the sediments with reticulate-chaotic cryostructure and the enclosing original syngenetic permafrost.

Laboratory methods

To reproduce reticulate-chaotic cryostructures, we conducted 20 laboratory experiments. We used a temperature-controlled environmental chamber to freeze sediments in PVC cells at temperature between -20°C and -25°C for at least six hours. Saturated sand or silt at room temperature were poured

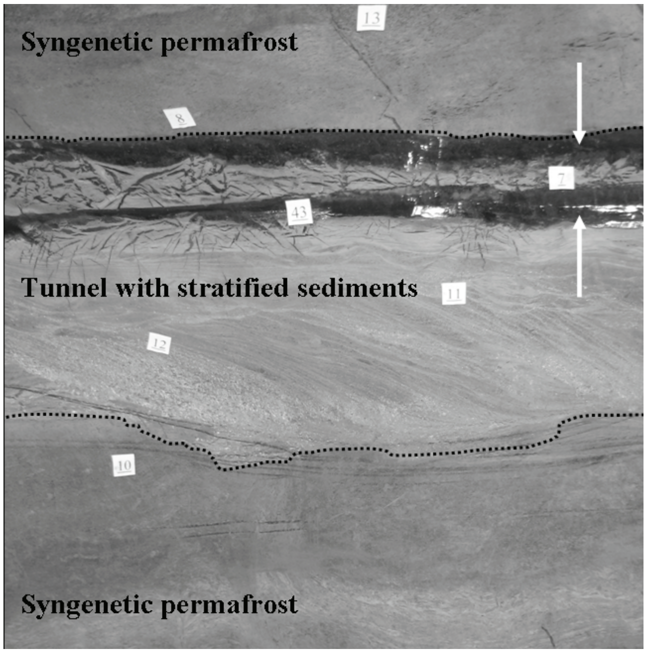

Figure 1. Underground channel filled with stratified sediments enclosed in syngenetic eolian silt. The erosion unconformities are outlined by dotted lines. The upper part of the underground channel contains layers of clear ice (arrows) underlain by stratified sediments dissected by reticulate-chaotic ice veins. The white paper scales are 2.5 x 2.5 cm.

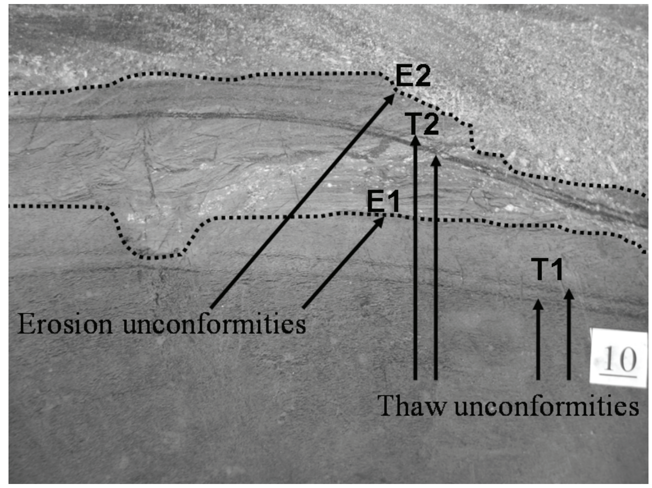

Figure 2. Close-up of erosion and thaw unconformities shown in Figure 1. The lowermost erosion unconformity (E1) is older and located at the bottom of the ice-poor stratified silts. Ice lenses located at the boundary with the underlying ice-rich syngenetic eolian silts mark the location of the thaw unconformity (T1) associated with E1. The uppermost erosion unconformity (E2) is younger and located at the bottom of the ice-poor stratified sand and gravel. The younger thaw unconformity T2 associated with this erosion boundary is marked by ice lenses located in the previously deposited sediments. The paper scale is 2.5 x 2.5 cm.

in the cells and allowed to freeze. After two days, a core was extracted from the central part of the frozen sediments to produce a cavity. A portable carbide and diamond crown drill was used for this procedure. The coring stopped at 5 cm to 10 cm above the bottom of the cells. The environmental chamber was then set to -5°C and kept at this temperature for one day to allow frozen soils to warm-up to this temperature. The cavity was used as an analog for underground thermo-erosion channels enclosed in permafrost. Cavities were filled with well-mixed supersaturated sediments previously kept at temperature between 1°C to 4°C. We used clay, silt, and sand sediments to test the effect of soil texture on the configuration of the cryostructures. We used soils with 80% and 150% gravimetric water content to test the effect of water content on the density of reticulate ice veins. Slices of frozen soil approximately 5 cm thick cut from the extracted cores and conditioned to -5°C were used as lids to close the underground channel analogs. The samples were allowed to freeze back in situ at a temperature of -5°C for 7 days to 14 days depending on the size of the freezing cells.

We used three different sizes of circular freezing cells to test the effect of underground channel size on the development of ground ice cryostructures. The first type of cell was 30 cm in diameter, 37 cm tall and covered by a 10 cm thick layer of mineral wool. The bottom and the top of the cell were covered by a 5 cm thick extruded polystyrene layer. The second type of cell was 17 cm in diameter, 75 cm tall and insulated by 5 cm thick extruded polystyrene rings. The third type of cell was 10 cm in diameter, 30 cm tall and covered by a 3 cm thick insulation layer. This cell was equipped with a consolidation device and cooled by thermal baths from the top and the bottom of the cell.

After the experiment, the frozen samples were extracted from the cells and cut into slices about 5 cm thick. The cryostructures were described. We analyzed the ice content of cores 2.5 cm in diameter extracted from the center and the side of the underground channel analogs slices. The geometric configuration of the ground ice formed and the contact with the enclosing sediments were described and compared to field observations in the CRREL permafrost tunnel.

Results

Field observations

Twenty ice wedge exposures can be observed in the adit of the CRREL permafrost tunnel. With the exception of one, all the observed ice wedges are showing signs of thermo-erosion. Remains of ice wedge with shapes atypical of syngenetic ice-wedge growth were observed at the erosion boundaries. Some ice wedges were cut by underground channels and gullies filled with sediments cutting across or enclosed in ice wedges. These underground channels are also enclosed in the syngenetic eolian silt surrounding the ice wedges (Fig. 1).

The syngenetic undisturbed permafrost comprises organic-rich fine eolian silts with abundant rootlets, oxydo-reduction stains, and millimeter-to-centimeter thick peat layers (Fig. 1). The permafrost is characterized by an ice-rich micro-lenticular cryostructure with gravimetric water contents usually above 100%.

Figure 3. Typical reticulate-chaotic cryostructure with multi-directional interconnected ice veins and ice lenses. The handle of the knife is about 6 cm long.

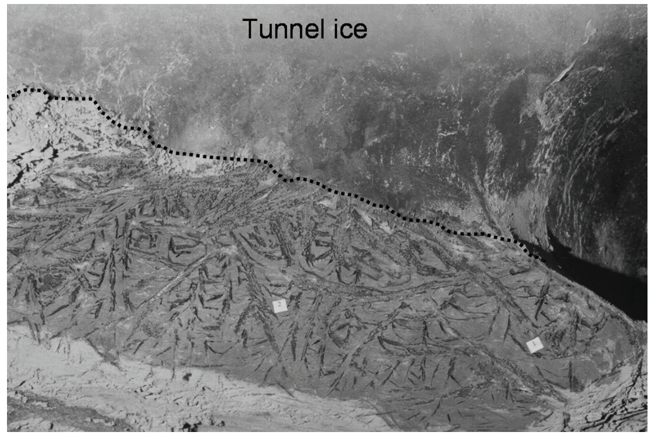

Figure 4. "Tunnel ice" underlain by sediments with high-density reticulate-chaotic cryostructure. The white paper scales are 2.5 x 2.5 cm.

The underground channels could often be traced over several meters. They had a slight inclination and flat to bowl-shape channel bottom. The channels were outlined by erosion unconformities at their contact with the syngenetic undisturbed permafrost (Fig. 2). In the underground channels, the sediments were mostly stratified and clearly different than the surrounding syngenetic eolian silt (Figs. 1, 2). For instance, in Figure 1, the underground channel is filled with ice and silty sands and gravels having oblique, cross, wavy, and horizontal stratifications (see also Fig. 2). The average gravimetric ice content of the cross-stratified sands in the underground channel is 44.6% (n = 8), whereas it is 107.7% (n =17) in the surrounding syngenetic permafrost.

In some cases the underground channels were only partially incised in the wedges and extended in the adjacent underground channels previously cut in the syngenetic permafrost. Among the observed channels, the grain-size fraction and the stratification patterns varied which suggests the occurrence of different sources of sediments and depositional modes, probably related to distinct thermo-erosion events along similar flow paths.

Along the boundaries of the underground channels, thaw unconformities were observed (Fig. 2). They were marked by a continuous ice lens a few millimeter-thick sub-parallel to the channel boundaries. The thaw unconformities were usually located a few millimeters to a few centimeters in the syngenetic permafrost surrounding the underground channels. The permafrost between the erosion boundary and the thaw unconformity did not have a micro-lenticular cryostructure. This indicates that after deposition of the saturated sediments, the release of heat from the water trapped in the underground channels melted the ground ice of the adjacent syngenetic permafrost. Freezeback of the thawed sediment created an ice lens marking the thaw unconformity. When underground channels were observed to cut through prior channels the thaw unconformities were located in the sediment of the eroded channels (Fig. 2). Thaw unconformities were also observed in the ice wedges cut by channels. Millimeter-thick ice lenses, often with elongated air bubbles aligned perpendicular to the thaw unconformity, were intercalated between the ice wedge and the sediments of the underground channels.

Usually, the sediments deposited in the underground channels were characterized by a reticulate-chaotic cryostructure made of multi-directional interconnected ice veins and ice lenses (Fig. 3).

Close to the underground channel boundaries, the ice veins were aligned perpendicular and the ice lenses parallel to the erosion unconformities. The concentration of ice veins and ice lenses were higher close to the channel boundaries, especially but non-exclusively at the bottom of the channels and decreased toward the center of the channel (Fig. 4). In the underground channels, the layers of sediments with reticulate-chaotic cryostructure were sometimes intercalated with centimeter-thick layers of clear ice with mineral or organic inclusions (Fig. 1).

About 60% of the underground channels cutting through the ice wedges and the enclosing syngenetic permafrost were partially or entirely filled by sub-horizontal non-foliated ice bodies (Fig. 4). The ice was clear to whitish, sometimes with orange to dark-brown bands in the central part and contained embedded organic matter. The ice had a columnar crystalline structure and bubble trains that suggested inward freezing. In the literature, this type of ice was previously called "thermokarst-cave ice" (Shumskii 1964b, Bray et al. 2006) or "pool ice" (Mackay 1988, 1997). We propose the term *tunnel ice* to describe massive ice bodies formed by inward refreezing of water trapped in underground thermo-erosion pipes, channels, and tunnels (Fortier et al. 2007). Usually at the bottom of these *tunnel ice* bodies we observed a sub-horizontal layer of sediment with a reticulate-chaotic cryostructure (Fig. 4).

Laboratory observations

The experiments in the laboratory reproduced reticulate-chaotic cryostructures similar to those observed in the field (Fig. 5). They were formed in the underground channel analogs during freezeback of the sediments.

The density of ice veins and ice lenses was always greater along the walls of the channel analogs than in the central part,

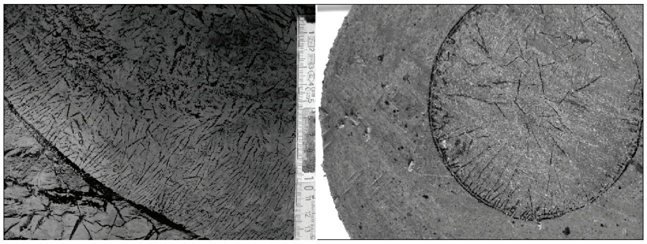

Figure 5. Comparison of field (A) and laboratory (B) observations. (A) Portion of an underground channel. The boundary (lower left corner) of the channel is outlined by a mm-thick ice lens. The sediments in the channel (right corner) are characterized by a reticulate-chaotic cryostructure (B) Channel analog 8 cm in diameter showing an ice lens at the channel boundary and reticulate-chaotic cryostructure similar to what was observed in the field (A).

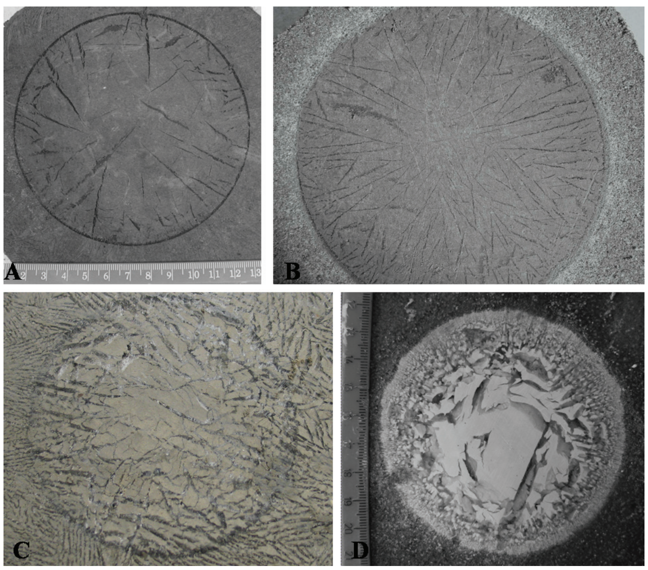

Figure 6. Cross-sections of channel analogs 8 cm in diameter with reticulate-chaotic cryostructures. (A) syngenetic eolian silt from the CRREL permafrost tunnel, 80% water content slurry; (B) fine silt <75µm, 80% water content, slurry; (C) fine silt <75µm and clay, 150% water content slurry; (D) clay, 150% water content slurry.

independent of grain-size and water content of the sediments (Fig. 6). Figures 6 and 7 show that the ice veins and ice lenses are often interconnected close to the boundary of the channel analog. In cross section, the ice veins were mostly aligned normal to the boundary. They extended toward the center with many ice lenses connected sub-perpendicular to them. The pattern of ice veins was more chaotic in the center of the channel analogs (Fig. 7). Consolidated sediments produced thin ice veins.

We observed thaw unconformities at the boundary of some underground channel analogs. On Figure 8, the ground ice in the frozen sediment enclosing the channel analog melted and secondary ice lenses were formed after freezeback.

Larger and thicker ice veins and ice lenses were formed in larger freezing cells. We used silt with a grain size fraction <75 µm and a water content of 150% for the slurry. Figure 9 shows that a thick ice lens was formed at the channel analog boundary. Large multi-directional ice veins were formed in the center of the channel analog.

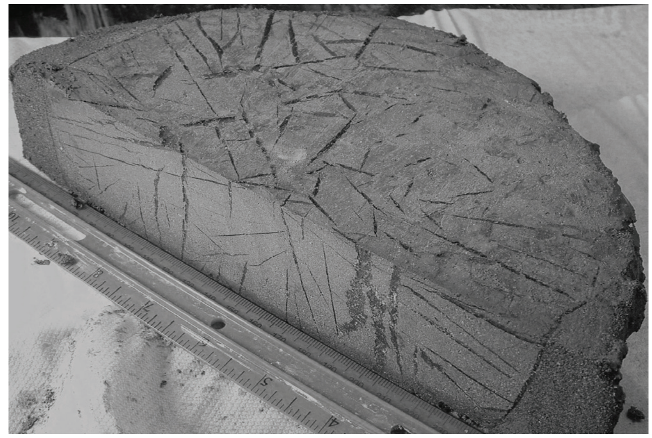

Figure 7. Cross-sections of a channel analog 25 cm in diameter (silt <75 µm, 150% water content slurry) with interconnected multi-directional ice veins and ice lenses. Note the similarity with reticulate ice veins of Figures 3 and 4.

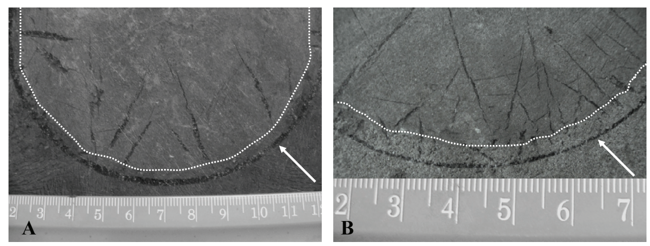

Figure 8. Cross-sections of channel analogs 8 cm in diameter showing thaw unconformities (arrows) located in the enclosing frozen ground. The dotted lines indicate the channel analog boundaries. (A) fine eolian silt from the CRREL permafrost tunnel with 80% water content. (B) coarse eolian silt from the CRREL permafrost tunnel with 80% water content.

We observed that fine-grained sediments produced more and larger ice veins and ice lenses than coarse-grained sediments. In Figures 6A and 6B, eolian silt from the CRREL tunnel was used for the experiment. In the experiment of Figure 6C, we used a mix of silt with a grain size fraction <75 µm and kaolinite clay. Experiments with clay soils are presented in Figures 6D and 10. The fine sediments produce a well-developed reticulate-chaotic cryostructure with a high density of ice veins and ice lenses. Figure 10 shows that the chaotic nature of the cryostructure and the formation of a thick ice lens at the channel analog boundary were better expressed in clay sediments.

In Figure 8A the gravimetric ice content of the sample after freezing was 122% at the channel boundary and 51% in the center whereas it was 58% at the channel boundary and 53% in the center in Figure 8B.

Discussion

Mechanism of reticulate-chaotic cryostructure formation

We observed in our experiments that saturated and super-saturated sediments trapped in frozen cavities (underground channel analogs) and submitted to slow inward freezing develop a reticulate-chaotic cryostructure. After deposition of the sediment, release of heat from water trapped in the

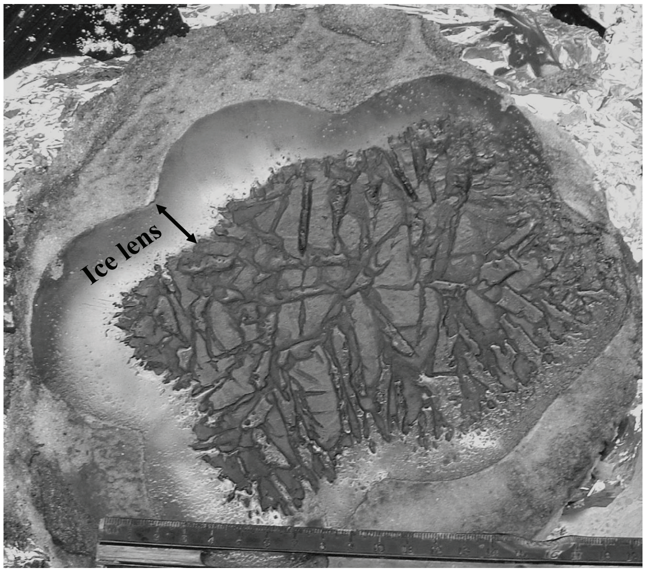

Figure 9. Cross section of a large channel analog formed in a large freezing-cell. A thick lens of pure ice was formed along the channel boundary between the coarse frozen sand and the fine silt (dark colored) in which large interconnected multidirectional reticulate ice veins were formed. The gravimetric ice content of the silt is 287%.

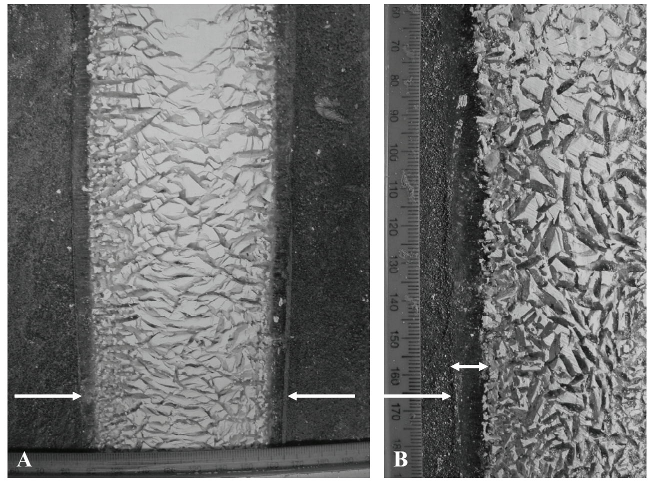

Figure 10. (A) longitudinal cross-section of a channel analog 8 cm in diameter. (B) Close-up of (A) showing a well-developed ice-rich reticulate-chaotic cryostructure in clay (150% water content slurry) with a thick ice lens (arrows) at the channel boundary.

sediment can melt the ground ice in the adjacent frozen sediments (Fig. 7). Inward freezing of the sediment creates one or more ice lenses at or close to the channel boundary (Figs. 6, 7, 8, 9, 10). Thicker ice lenses and larger reticulate ice veins were developed in: (1) slow freezeback scenarios (large freezing cells), (2) sediments with high water content, and (3) fine-grained sediments (fine silt and clay) (Figs. 6C, 6D, 9, 10). Due to redistribution of water in a closed system, the periphery of the underground channels analogs contained more ground ice than the center. At the beginning of freezing the uniform propagation of the freezing front inward created similarly aligned reticulate ice vein along the channel boundary. The chaotic nature of the reticulate ice veins is better expressed towards the center of the channels due to the slowing down and uneven inward propagation of the freezing front in sediments with lower water contents.

Formation of reticulate-chaotic cryostructures in the CRREL permafrost tunnel

Our experiments support the idea that reticulate-chaotic cryostructures were formed in relation to thermo-erosional events in the CRREL permafrost tunnel. A widespread network of underground channels was developed and buried during the syngenetic aggradation of the permafrost. The channels enclosed in the syngenetic eolian silt and cutting through the ice wedges were formed by underground thermo-erosion (Péwé 1982, Fortier et al. 2007). The stratified sediments in the tunnel were deposited by water flowing into the underground channels and after the cessation of the underground flow, either due to blockage or after the surface run-off period. The multi-directional ice veins observed in the sediments filling up the channels and at the base of the non-foliated *tunnel ice* bodies were formed after inward freezing of the sediments. Slow freezeback of supersaturated fine-grained silt developed dense reticulate-chaotic cryostructure patterns with thick ice veins.

Conclusion

Freezing of sediments trapped in underground channels cut by thermo-erosion in the permafrost that are submitted to inward freezing develops a reticulate-chaotic cryostructure. Availability of water, its ability to move through the sediments, and the rate of freezing can create thick ice lenses at the channel boundary and large multi-directional reticulate ice veins in the sediments. The irregular nature of the reticulate-chaotic cryostructure is linked to the uneven propagation of the freezing front in a closed-system with limited water supply. The reticulate-chaotic cryostructure is often observed close to or in contact with *tunnel ice* bodies. This type of ice is formed by inward freezing of water trapped in the underground channels. Our results help to identify ground ice associated with the process of underground thermo-erosion in permafrost exposures.

Acknowledgments

Special thanks are owed to the Fairbanks Office of the Cold Regions Research and Engineering Laboratory for access to the CRREL permafrost tunnel. Margaret Cysewski, Matthew Dillon, and Eva Stephani provided great assistance in field and in the laboratory. The reviewers and the associate editor are gratefully acknowledged for their suggestions to improve the manuscript. This work was supported by the National Science Foundation by grants (EPS-0346770) to Daniel Fortier and Mikhail Kanevskiy and (ARC–0454939) to Yuri Shur. Any opinions and findings expressed in this material are those of the authors and do not necessarily reflect the views of the funding agencies.

References

American Society of Testing and Materials. 2008. ASTM D 422 (Reapproved 1998): Standard test method for particle-size analysis of soils. A*nnual Book of ASTM Standards.* West Conshohocken, Pennsylvania: ASTM, (accessed online).

Bray, M.T., French, H.M. & Shur, Y. 2006. Further cryostratigraphic observations in the CRREL permafrost tunnel, Fox, Alaska. *Permafrost and Periglacial Processes* 17: 233-243.

Fortier, D., Allard, M. & Shur, Y. 2007. Observation of rapid drainage system development by thermal erosion of ice wedges on Bylot Island, Canadian Arctic Archipelago. *Permafrost and Periglacial Processes* 18: 229-243.

Gell, W.A. 1978. Ice-wedge ice, MacKenzie Delta – Tuktoyaktuk peninsula area, N.W.T., Canada. *Journal of Glaciology* 20: 555-562.

Hamilton, T.D., Craig, J.L. & Sellmann, P.V. 1988. The Fox permafrost tunnel: a late Quateranry record in central Alaska. *Geological Society of America Bulletin* 100: 948-969.

Huang, S.L., Aughenbaugh, N.B. & Wu, M.-C. 1986. Stability study of CRREL permafrost tunnel. *Journal of Geotechnical Engineering* 112: 777-790.

Kanevskiy, M., Fortier, D., Shur, Y., Bray, M. & Jorgenson, T. 2008. Pleistocene syngenetic permafrost in the CRREL permafrost tunnel at Fox, Alaska. *Proceedings of the Ninth International Conference on Permafrost, Fairbanks, Alaska, June 29–July 3, 2008* (this proceedings).

Long, A. & Pewe, T.L. 1996. Radiocarbon dating by high-sensitivity liquid scintillation counting of wood from the Fox permafrost tunnel near Fairbanks, Alaska. *Permafrost and Periglacial Processes* 7: 281-285.

Mackay, J.R. 1988. Catastrophic lake drainage, Tuktoyaktuk Peninsula area, District of Mackenzie. In: *Current Research*, *Part D*. Geological Survey of Canada, Ottawa, Ontario, Paper 88-1D: 83-90.

Mackay, J.R. 1997. A full-scale field experiment (1978–1995) on the growth of permafrost by means of lake drainage, Western Arctic Coast: a discussion of the method and some results. *Canadian Journal of Earth Sciences* 34: 17-33.

Murton, J.B. & French, H.M. 1994. Cryostructures in permafrost, Tuktoyaktuk coastlands, western arctic Canada. *Canadian Journal of Earth Sciences* 31: 737-747.

Pettibone, H.C. & Waddell, G.G. 1973. Stability of an underground room in frozen gravel. *Proceedings, American Contribution, Second International Conference on Permafrost, Yakutsk, U.S.S.R., July 13-28, 1973.* Publication 2115. Washington, D.C.: National Academy of Sciences: 699-706.

Péwé, T.L. 1982. *Geologic Hazards of the Fairbanks Area, Alaska*. College, Alaska, Division of Geological and Geophysical Surveys. Special Report 15, 109 pp.

Sellmann, P.V. 1967. *Geology of the USA CRREL Permafrost Tunnel Fairbanks, Alaska*. Hanover, New Hampshire, Cold Regions Research and Engineering Laboratory. Technical Report 199, 22 pp.

Sellmann, P.V. 1972. *Geology and Properties of Materials Exposed in the USA CRREL Permafrost Tunnel.* Hanover, New Hampshire, Cold Regions Research and Engineering Laboratory. Report 177, 16 pp.

Shumskii, P.A. 1964a. Principal of Structural Glaciology. New York: Dover Publications, 497 pp.

Shumskii, P.A. 1964b. Chapter IX. Ground (subsurface) ice. In: P.F. Shvetsov, B.N. Dostovalov (eds.), *Principles of Geocryology (Permafrost Studies*). Academy of Sciences of the USSR, 1959. V.A. Obruchev Institute of Permafrost Studies: Moscow: 247-327 (in Russian). National Research Council of Canada, Ottawa, Technical Translation 1130, 118.

Shur, Y., French, H.M., Bray, M.T. & Anderson, D.A. 2004. Syngenetic permafrost growth: cryostratigraphic observations from the CRREL tunnel near Fairbanks, Alaska. *Permafrost and Periglacial Processes* 15: 339-347.

Fast Permafrost Degradation Near Umiujaq in Nunavik (Canada) Since 1957 Assessed from Time-Lapse Aerial and Satellite Photographs

Richard Fortier, Ph.D.
Centre d'études nordiques, Université Laval, Québec (QC), Canada G1V 0A6
Bernard Aubé-Maurice, M.Sc.
Département de géologie et de génie géologique, Université Laval, Québec (QC), Canada G1V 0A6

Abstract

The spatio-temporal evolution of lithalsas and thermokarst ponds near Umiujaq in Nunavik (Canada) was studied using time-lapse aerial photographs collected in 1957, 1983, and 2003, and IKONOS satellite images taken in 2005 to assess the permafrost degradation. Nine typical sectors located in valleys totalizing a survey area of 2.245 km^2 were selected. The areas occupied by the lithalsas and thermokarst ponds were respectively 0.421 and 0.024 km^2 in 1957 (18.8 and 1.1% of the survey area) and 0.251 and 0.066 km^2 in 2005 (11.2 and 3.0%). The permafrost extent decreased 40%, while the thermokarst one increased 175% in 48 years. According to the climate data from Environment Canada, the mean annual air temperature was quite variable over the study period but increased 3°C during the last 15 years. Climate warming is therefore the main driver of permafrost degradation, but other concurrent mechanisms affecting the thermal balance of permafrost exacerbate the observed degradation.

Keywords: climate warming; lithalsas; mapping; permafrost degradation; thermokarst ponds; time-lapse aerial photographs.

Introduction

Both palsas and lithalsas are cryogenic mounds formed in frost-susceptible marine sediments under a cold climate (Pissart 2002). They are important components of the periglacial landscape in the discontinuous permafrost zone in Nunavik (Canada). The tops of these periglacial features stand a few meters above the surrounding ground due to the accumulation of segregation ice; their mineral cores are ice-rich and they have a diameter of a few tens of meters making them easily recognizable on aerial photographs even at a scale as large as 1:40,000. They are an excellent indicator of the presence of ice-rich permafrost. While the palsas are covered by peat, the lithalsas are free of peat cover (Pissart 2002) and their surfaces are dotted with frost boils. Permafrost degradation due to climate warming and eventually the thawing of lithalsas leave ramparted thermokarst ponds (Luoto & Seppälä 2003, Pissart 2002).

Based on paleoecological studies of permafrost peatlands (Allard & Seguin 1987b), the inception of palsas occurred during cold periods of the Holocene with a maximum extent during the Little Ice Age (LIA), but they are now decaying in response to climate warming. The thawing of palsas and lithalsas located in the discontinuous permafrost zone along the east coast of Hudson Bay, Nunavik (Canada), was studied respectively by Payette et al. (2004) and Vallée & Payette (2007). Their results show continuous permafrost degradation during the 20th century. Between 1957 and the beginning of the 21st century the area occupied by ice-rich permafrost decreased by 84% and 23% respectively at the southern and northern limits of the discontinuous permafrost zone. Permafrost loss was compensated by a concurrent gain in thermokarst ponds. The subsidence of palsas surfaces due to the ground ice melting was of the order of 1 to 1.5 m from 1993 to 2003 (Payette et al. 2004). According to Payette et al. (2004), the main climatic driver for accelerated permafrost thawing was snow precipitation. The hydric conditions affect also the dynamics of lithalsas and control in part their decay (Vallée & Payette 2007).

The purpose of the present study is to map the spatial distribution of lithalsas and thermokarst ponds near Umiujaq in Nunavik (Canada) using time-lapse aerial photographs and satellite images to assess the permafrost degradation since 1957. The comparison of these photographs will allow the evaluation of the decrease of ice-rich permafrost extent. Since the thermal regime of the lithalsas is closely related to climate changes, the assumption of permafrost degradation due to climate warming recently observed in Nunavik (Chouinard et al. 2007) will be thus verified.

Study Area

The study area is located in the discontinuous permafrost zone close to the Inuit community of Umiujaq on the east coast of Hudson Bay, Nunavik, Canada (Figs. 1, 2). The deglaciation of the area took place 7600–7300 years ago. Marine sediments were then deposited in deep valleys. After emergence, the deposits were eroded and colonized by vegetation, and ice-rich permafrost aggraded. Large fields of lithalsas are found in the valleys.

Lithalsas and Thermokarst Ponds

An example of a recent collapse of a lithalsa due to climate warming and an expansion of a thermokarst pond to the detriment of the lithalsa is shown in Figure 3. According to field observations including deep temperature profiles

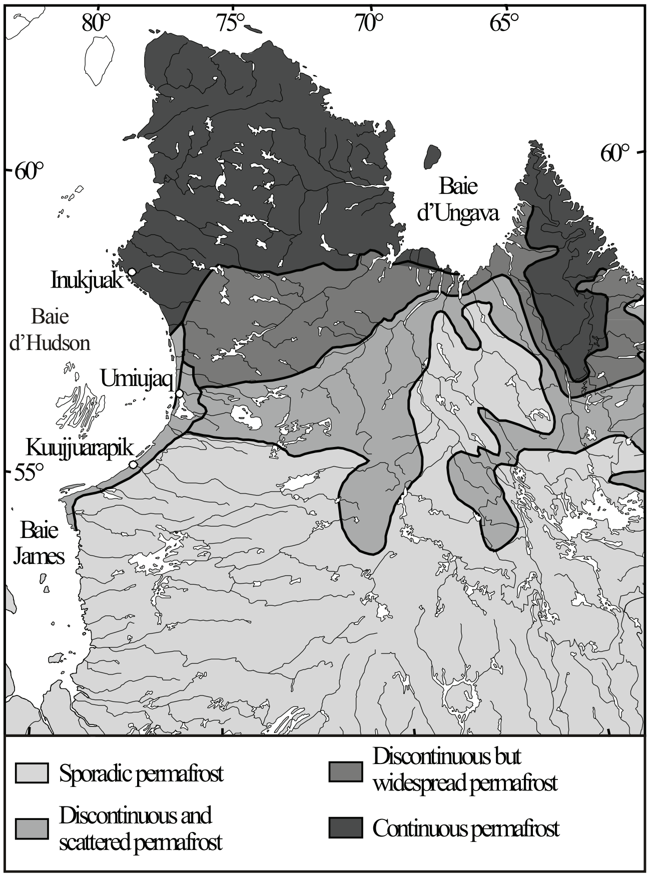

Figure 1. Map of permafrost distribution in Nunavik, Canada (modified from Allard & Seguin 1987a). Location of the Inuit communities of Kuujjuarapik, Umiujaq and Inukjuak along the east coast of Baie d'Hudson.

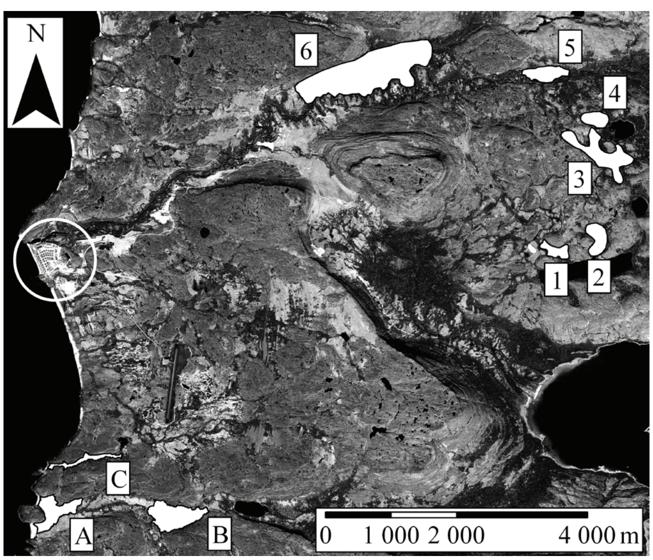

Figure 2. IKONOS satellite image of Umiujaq taken on July 26th 2005. Location of the Inuit community of Umiujaq (white circle) and the nine sectors (white areas identified with a number or a letter) mapped in the present study.

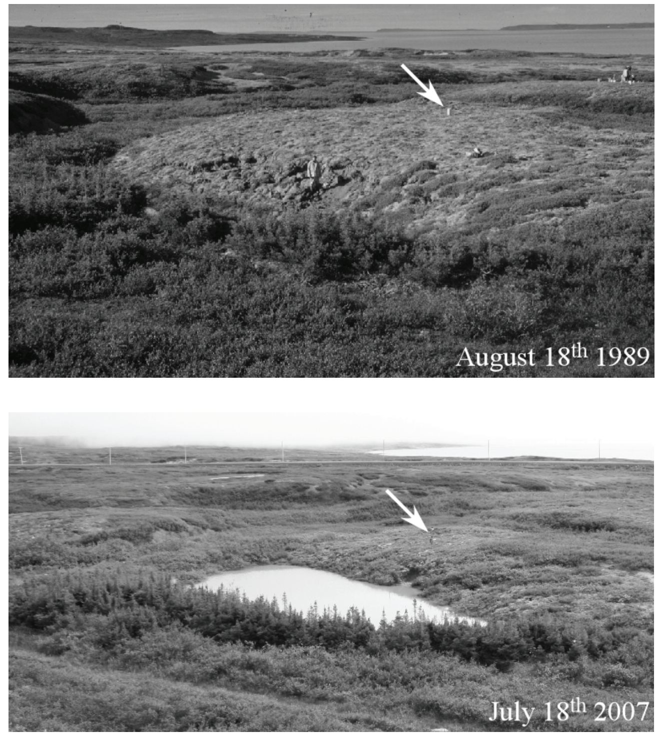

Figure 3. Example of permafrost degradation in 18 years from August 1989 to July 2007. The thermokarst pond on the left overruns progressively to the right the lithalsa. The arrow indicates the location of a thermistor cable. Note the man in the forefront near the small active layer detachment failure on August 18th 1989 for the scale. The road leading to the airport of Umiujaq in the background in 2007 was not yet built in 1989.

near Umiujaq, a typical lithalsa has a diameter of 40 m and a height of 2.5 m above the surrounding ground; the active layer is 1.5 m thick and the permafrost base is 12.5 m deep. The average volumetric ice content of the ice-rich core is 50%. For a permafrost thickness of 11 m, the total thickness of segregated ice lenses is then 5.5 m. The difference of 3 m between the frost heaving of the lithalsa surface and the ice accumulation is due to the irreversible over-consolidation of marine sediments occurring during freezing. These sediments were first deposited in a normally consolidated state before freezing. The formation of segregation ice fed by cryosuction can induce a decrease in void ratio as high as 30% of the saturated sediments in the freezing fringe (Konrad & Seto 1994). Therefore, after the permafrost thaws, a depression filled with water as deep as 3 m is left (2.5–5.5 m or 30% decrease in void ratio of a 10 m thick sediment layer). Due to solifluction on the lithalsa slopes there is an accumulation of materials on its sides explaining the remnant ring-shaped rampart left around the thermokarst pond (Fig. 3). Typically, a rampart is 3 m wide and 1 m high above the surrounding ground for an approximate volume of 350 m^3. This volume accounts for about 0.30 m (350 m^3 over a surface area of 1250 m^2) of the depression left. Following the water budget, drainage system and sediments permeability, the thermokarst pond can be more or less filled with water (Yoshikawa & Hinzman 2003).

Methods

Three series of aerial photographs collected in 1957 (series A-15618, Natural Resources Canada), 1983 (series Q83857 and Q83858, Ministère des Ressources naturelles et de la Faune, Québec) and 2003 (series Q03201, Ministère des Ressources naturelles et de la Faune, Québec), and one IKONOS satellite image taken in 2005 (Fig. 2) were used to map the spatio-temporal evolution of the lithalsas and thermokarst ponds. The snow cover was not totally melted in the series of aerial photographs taken on June 18, 1957 (Fig. 4A) making difficult the delineation of the thermokarst ponds. The aerial photographs in 1983 and 2003 cover only the west part of the satellite image including the village and airport infrastructures (Fig. 2). The satellite image was provided in a digital format, already orthorectified according to a digital elevation model of the world, and georeferenced.

Nine sectors typical of the lithalsas fields found in the study area and totaling a survey area of 2.245 km^2 were selected (Fig. 2). The mapping of permafrost degradation was carried out using ArcMap from ESRI. The satellite image allowed not only the delineation of the limits of lithalsas and thermokarst ponds in 2005 but also the georeferencing and rectification of the aerial photographs before mapping these periglacial features in 1957 and 1983. Based on numerous tie points selected and identified on both satellite image and aerial photographs, the georeferencing and rectification of the digitized aerial photographs were performed for each sector. The stereoscopic view of the aerial photographs in 1957, 1983, and 2003 allowed the delineation of the limits of lithalsas and thermokarst ponds. The lithalsas and thermokarst ponds look like heaved forms and ramparted depressions filled with water respectively and can be easily identified and mapped on the aerial photographs. However, only the water surface was mapped. These limits were then reported on different layers in ArcMap. Because the aerial photographs in 2003 and the satellite image in 2005 were so close in time, there was no real change in permafrost extent. However, the stereoscopic view of the photographs in 2003 was quite useful for delineating the lithalsas and thermokarst ponds on the satellite image in ArcMap.

Results

Spatial distribution of lithalsas and thermokarst ponds

An example of permafrost degradation mapping between 1957 and 2005 for Sector 1 (Fig. 2) is given in Figure 4. Permafrost degradation was already occurring in 1957 under the form of small thermokarst ponds mainly located along the northern valley wall and east of Sector 1 (Fig. 4E). The decrease in permafrost extent is major in the 48 years from 1957 to 2005. Most of the permafrost degradation visible in 2005 has taken place principally along the northern valley wall where the thermokarst ponds have replaced the lithalsas (Figs. 4G, 4H, 5).

The statistics on the areas occupied by the lithalsas and thermokarst ponds in 1957 and 2005, and the difference in areas between 1957 and 2005 appear in Table 1 not only for Sector 1 but also for the other sectors. The numbers of lithalsas or thermokarst ponds mapped in each sector and the numbers of vanished lithalsas or appeared thermokarst ponds between 1957 and 2005 are also given in Table 1.

The permafrost and thermokarst extents were also mapped on the aerial photographs taken in 1983 only for Sectors A, B, and C covered by this series of aerial photographs (Table 1). The rate of permafrost degradation increased in recent years from an annual loss rate of 380 m^2 or 0.8% between 1957 and 1983, to 640 m^2 or 1.6% between 1983 and 2005.

Spatial accuracy of the mapped areas

The spatial accuracy of the areas occupied by the lithalsas and thermokarst ponds is evaluated to 20% and 60% respectively. It depends on the spatial resolution of the aerial photographs and satellite image and the capability of the cartographer to delineate accurately the limits of the lithalsas and ponds. According to statistics drawn from the mapping, the average areas occupied by a lithalsa and a pond are 1200 m^2 and 130 m^2 respectively. If these areas are assumed to be perfect circles, the average radius is 20 m for a lithalsa and 6 m for a pond. The pixel side of the aerial photographs and satellite image is about 0.8 m. If an accuracy of ±2 m for the radius is supposed to take into account the spatial resolution and the error on the limit delineation, respective accuracies of ±250 and ±80 m^2 are found for the areas occupied by a lithalsa and a pond. For the photographs taken in 1957, the spatial accuracy of the areas occupied by the ponds is likely higher than 60% due to the snow cover still present at that time in the depressions between the lithalsas hiding the ponds (Fig. 4A).

Discussion

Climate variability

According to Chouinard et al. (2007), the surface temperature at the end of the LIA in Nunavik was colder of 1°C in comparison to the reference period 1961–1990.

Climatic data are available for the Inuit communities of Kuujjuarapik and Inukjuak respectively 160 km south and 250 km north of Umiujaq (Figs. 1, 6). No trend in snowfall is obvious over the record period (Fig. 6A). However, a marked trend to climate warming of at least 3°C is observed since 1992 (Figs. 6B, 6C). The mean annual air temperature is well above the average air temperature found for the reference period 1961–1990 plus one standard deviation since 1998 except for 2004.

Permafrost degradation

The thermal regime of permafrost is closely related to climate changes, and the main mechanism of permafrost decay is climate warming. Permafrost thawing is a long-term process due to the latent heat of fusion of ice delaying the impacts of climate warming on permafrost. The permafrost degradation already observed in 1957 (Figs. 4A and 4E) was therefore inherited from climate warming of 1°C since the LIA (Chouinard et al. 2007). In 1957 the lithalsas were probably not yet in equilibrium with the climate and permafrost degradation was still in progress.

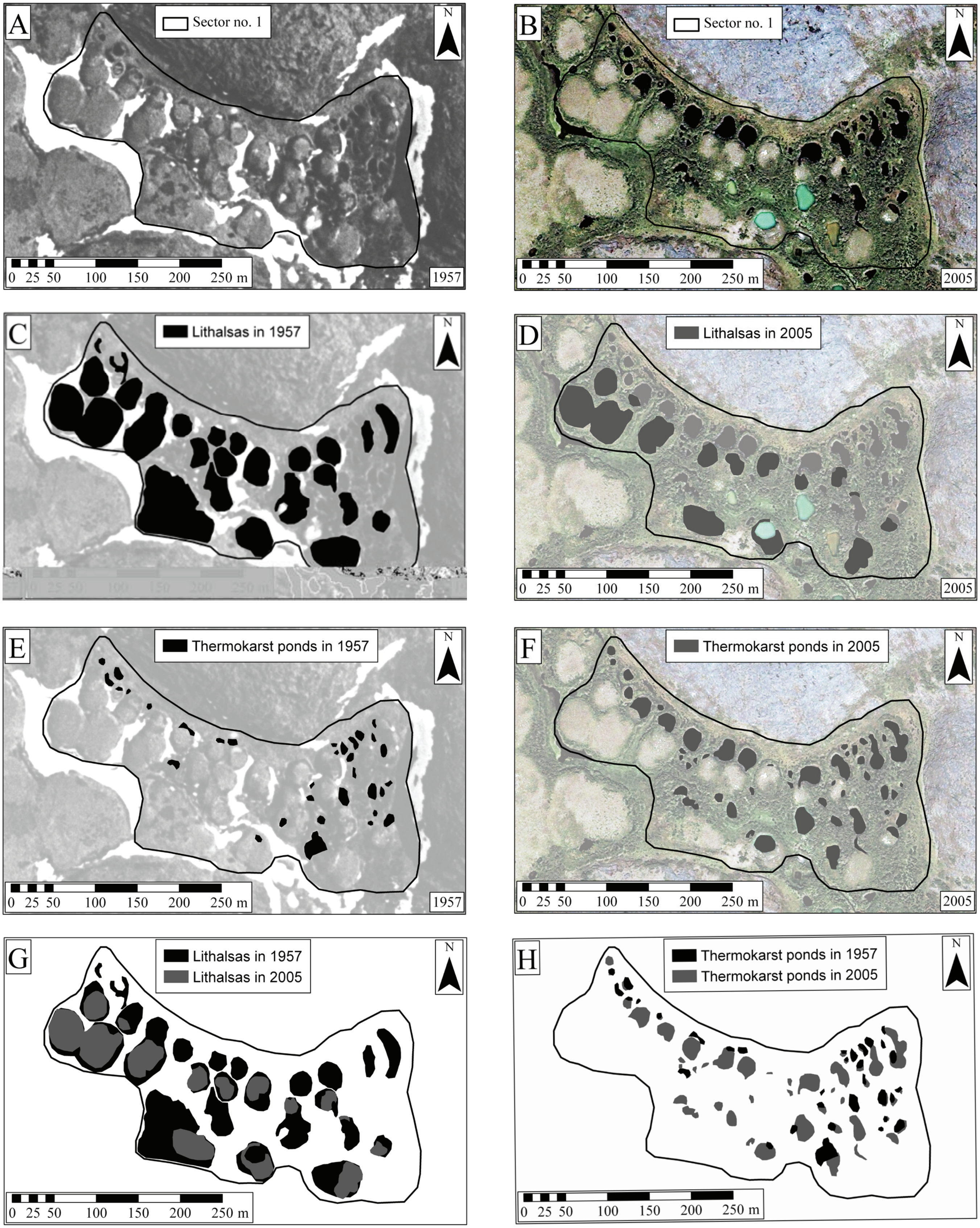

Figure 4. A) Study area no. 1 in 1957 (aerial photograph no. 39, series A-15618, reproduction authorized by the Minister of Public Works and Government Services of Canada 2007, courtesy of the National Air Photo Library, Mapping Services Branch, Natural Resources Canada). B) Study area no. 1 in 2005 (IKONOS satellite photograph). Spatial distributions of lithalsas in 1957 (C) and 2005 (D), and thermokarst ponds in 1957 (E) and 2005 (F). Superposition of spatial distributions of lithalsas (G) and thermokarst ponds (H) in 1957 and 2005.

Table 1. Areas occupied by lithalsas and thermokarst ponds in 1957, 1983 (sectors A, B, C) and 2005.

Lithalsas										
Sectors		Land occupation in 1957		Land occupation in 1983[5]		Land occupation in 2005		Difference in area between 1957 and 2005		
no.	(x 10^3 m^2)	(x 10^3 m^2)[1]	(%)	(x 10^3 m^2)[1]	(%)	(x 10^3 m^2)[1]	(%)	(x 10^3 m^2)[2]	(%)[3]	(%)[4]
1	71	29 (24)	40.8			11 (14)	15.5	-18 (-10)	-25	-62
2	118	11 (22)	9.3			4 (13)	3.4	-7 (-9)	-5.9	-64
3	297	61 (52)	20.5			35 (46)	11.8	-26 (-6)	-8.8	-43
4	83	18 (23)	21.7			7 (16)	8.4	-11 (-7)	-13.3	-61
5	129	21 (28)	16.3			6 (15)	4.7	-15 (-13)	-11.6	-71
6	1014	230 (103)	22.7			161 (97)	15.9	-69 (-6)	-6.8	-30
A	190	23 (16)	12.1	21 (14)	11.1	15 (13)	7.9	-8 (-3)	-4.2	-35
B	268	19 (21)	7.1	14 (16)	5.2	9 (11)	3.4	-10 (-10)	-3.7	-53
C	75	9 (10)	12.0	6 (6)	8.0	3 (3)	4.0	-6 (-7)	-8.0	-67
Subtotal (A+B+C)	533	51 (47)	9.6	41 (36)	7.7	27 (27)	5.1	-24 (-20)	-4.5	-47
Total	**2245**	**421 (299)**	**18.8**			**251 (228)**	**11.2**	**-170 (-71)**	**-7.6**	**-40**

Thermokarst ponds										
Sectors		Land occupation in 1957		Land occupation in 1983[5]		Land occupation in 2005		Difference in area between 1957 and 2005		
no.	(x 10^3 m^2)	(x 10^3 m^2)[1]	(%)	(x 10^3 m^2)[1]	(%)	(x 10^3 m^2)[1]	(%)	(x 10^3 m^2)[2]	(%)[3]	(%)[4]
1	71	3 (33)	4.2			8 (51)	11.3	5 (18)	7.0	167
2	118	1 (17)	1.7			5 (21)	4.2	4 (4)	2.5	150
3	297	1 (10)	0.3			9 (50)	3.0	8 (40)	2.7	800
4	83	1 (14)	1.2			7 (27)	8.4	6 (13)	7.2	600
5	129	1 (19)	0.8			8 (32)	6.2	7 (13)	5.4	700
6	1014	2 (12)	0.2			8 (46)	0.8	6 (34)	0.6	300
A	190	3 (22)	1.6	4 (18)	2.1	4 (19)	2.1	1 (-3)	0.5	33
B	268	7 (70)	2.6	9 (86)	3.4	11 (95)	4.1	4 (25)	1.5	57
C	75	4 (37)	5.3	6 (41)	8.0	6 (50)	8.0	2 (13)	2.7	50
Subtotal (A+B+C)	533	14 (129)	2.6	19 (145)	3.6	21 (164)	4.0	7 (35)	1.3	50
Total	**2245**	**24 (234)**	**1.1**			**66 (391)**	**3.0**	**42 (157)**	**1.9**	**175**

The data in parentheses are the numbers of lithalsas or thermokarst ponds mapped in each sector.
The data in parentheses are the numbers of vanished lithalsas or appeared thermokarst ponds between 1957 and 2005 in each sector.
Difference relative to the area of each sector.
Difference relative to the area occupied by the lithalsas or thermokarst ponds in each sector in 1957.
Only Sectors A, B and C are covered by the aerial photographs taken in 1983.

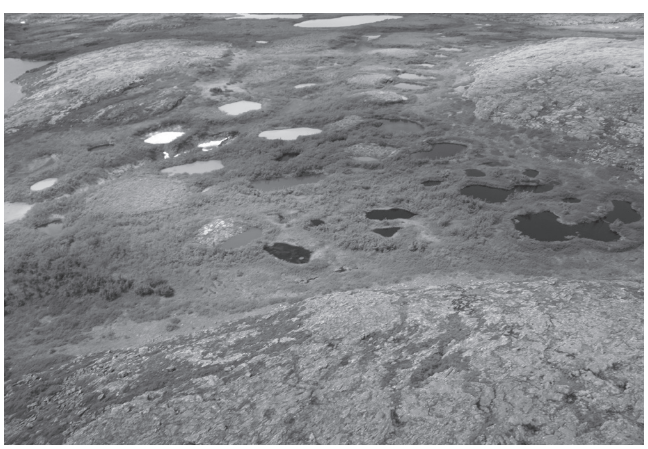

Figure 5. Aerial view of the sector no. 1 looking to the west taken on July 14, 2007. The presence of thermokarst ponds is more important close to the northern valley wall than in the middle of the sector.

From 1957 to 1983, the climate was more or less stable (Fig. 6), but the permafrost was still decaying at a loss rate of 0.8%/year for Sectors A, B, and C (Table 1). However, due to the trend of climate warming of 3°C over the last 15 years (Fig. 6), the rate of permafrost decay increased to a value of 1.6%/year between 1983 and 2005. The variability of annual snowfall without any trend (Fig. 6A) can be ruled out as a potential explanation of permafrost decay. Even if the actual climate stabilizes, permafrost decay will continue until a new thermal equilibrium is reached.

In addition to climate warming, other concurrent mechanisms affect the thermal balance of permafrost and exacerbate its degradation. The melting of ground ice in excess induces a differential thaw subsidence more important on the warmer sides of a lithalsa than its top. The subsidence is progressing from the sides to the top of the lithalsa (Fig. 3). Thaw subsidence allows the formation of a small thermokarst pond and the

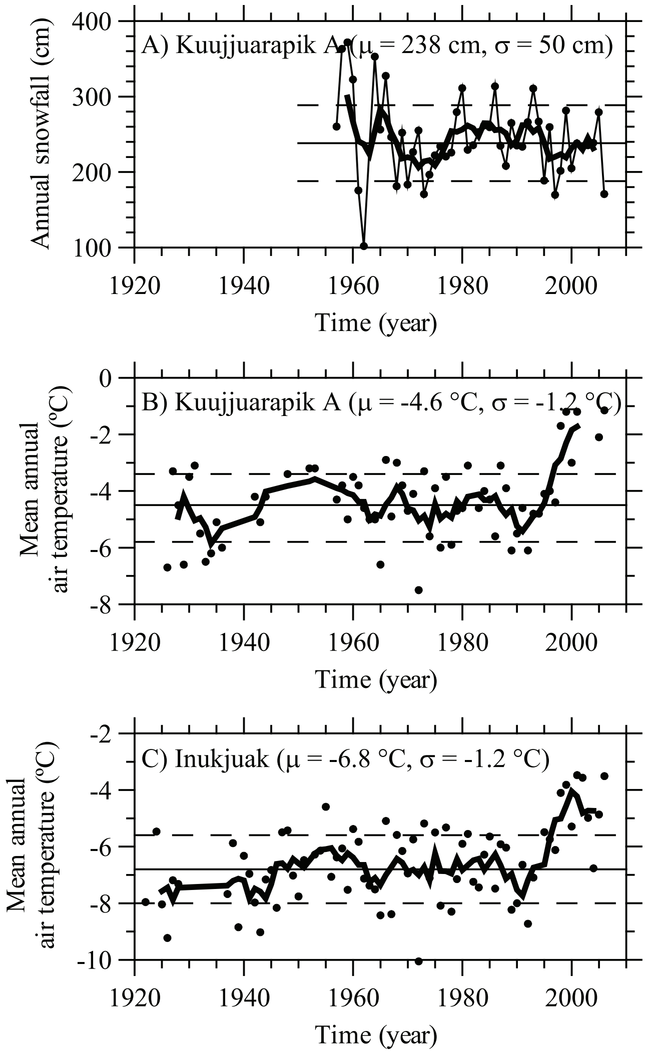

Figure 6. A) Annual snowfall at Kuujjuarapik A. Mean annual air temperature at Kuujjuarapik A (B) and Inukjuak (C). Climate data from Environment Canada. Thick lines correspond to a 5-year running average through mean annual snowfall or air temperature. Full and dotted horizontal lines are respectively the average and ±standard deviation (values in parentheses) of snowfall or air temperature over the reference period 1961-1990.

accumulation of snow. Freezing of the active layer underneath the thermokarst

pond is delayed the next winter due to the latent heat of freezing of water while the thermal insulation of thick snow cover also prevents further ground freezing. In addition, the vegetation growth under less severe climatic conditions favors the accumulation of snow in winter. These multiple degradation mechanisms have a snow ball effect. As soon as permafrost warming begins, these mechanisms operate and eventually can cause the lithalsa disappearance even if the climate is stabilized at some point. The warmest lithalsas, such as the ones close to the valley walls where the marine deposits are thinner and the heat flow is higher due to the high thermal conductivity of rock close to the surface are more susceptible to disappear first (Figs. 4A, 4B, and 5). The heat coming from running water on the valley walls can also contribute to permafrost warming.

Conclusions

Widespread and fast permafrost degradation is currently occurring at Umiujaq, Nunavik (Canada). These changes in the periglacial landscape were documented using time-lapse aerial photographs collected in 1957, 1983, and 2003, and satellite images taken in 2005. The rate of permafrost degradation increased over the last two decades due to a trend to climate warming of 3°C observed in Nunavik since 1992. At the annual loss rate of 1.6% found between 1983 and 2005, the disappearance of ice-rich permafrost will occur in this region through the next five to ten decades.

Acknowledgments

We would like to express our sincere gratitude to the Inuit community of Umiujaq for their hospitality and friendly support. The research presented herein was supported by the NSERC. Thanks are addressed to Nicolas Bélanger for his help in the mapping. The manuscript was substantially improved following the constructive comments from anonymous reviewers.

References

Allard, M. & Seguin, M.K. 1987a. Le pergélisol au Québec nordique: bilan et perspective. *Géographie physique et Quaternaire* 41: 141-152.

Allard, M. & Seguin, M.K. 1987b. The Holocene evolution of permafrost near the tree line, on the eastern coast of Hudson Bay (northern Quebec). *Canadian Journal of Earth Sciences* 24: 2206-2222.

Chouinard, C., Fortier, R. & Mareschal, J.-C. 2007. Recent climate variations in the subarctic inferred from three borehole temperature profiles in Northern Quebec, Canada. *Earth and Planetary Science Letters*, doi: 10.1016/j.epsl.2007.09.017.

Konrad, J.-M. & Seto, J.T.C. 1994. Frost heave characteristics of undisturbed sensitive Champlain Sea clay. *Canadian Geotechnical Journal* 31(2): 285-298.

Luoto, M. & Seppälä, M. 2003. Thermokarst ponds as indicators of the former distribution of palsas in Finish Lapland. *Permafrost and Periglacial Processes* 14: 19-27.

Payette, S., Delwaide, A., Caccianiga, M. & Beauchemin, M. 2004. Accelerated thawing of subarctic peatland permafrost over the last 50 years. *Geophysical Research Letters* 31(18): 1-4.

Pissart, A. 2002. Palsas, lithalsas and remnants of these periglacial mounds. A progress report. *Progress in Physical Geography*, 26(4): 605-621.

Vallée, S. & Payette, S. 2007. Collapse of permafrost mounds along a subarctic river over the last 100 years (northern Québec). *Geomorphology* 90(1-2): 162-170.

Yoshikawa, K. & Hinzman, L.D. 2003. Shrinking thermokarst ponds and groundwater dynamics in discontinuous permafrost near Council, Alaska. *Permafrost and Periglacial Processes* 14: 151-160.

An Integrative Observation of Kinematics and Geophysical Parameters of Gianda Grischa Rock Glacier, Upper Engadine, Swiss Alps

Regula Frauenfelder
Department of Geosciences, University of Oslo, Norway
now at Norwegian Geotechnical Institute, Oslo, Norway

Christian Hauck
Institute for Meteorology and Climate Research, Forschungszentrum Karlsruhe, University of Karlsruhe, Germany

Christin Hilbich
Department of Geography, University of Jena, Germany

Christof Kneisel
Department of Physical Geography, University of Würzburg, Germany

Martin Hoelzle
Department of Geography, University of Zurich, Switzerland

Abstract

An integrative analysis of rock glacier kinematics and ice content is presented using photogrammetric analyses and different geophysical techniques. The studied rock glacier system is situated in the eastern Swiss Alps, and comprises forms of different activity. Geophysical surveys (electrical resistivity measurements, refraction seismics) have been performed on one active rock glacier, an inactive one, as well as on a relict part underlying the active rock glacier. The highest resistivity values representing ice rich permafrost were obtained on the active rock glacier. The inactive and relict parts showed lower resistivity values. The results of the Electrical Resistivity Tomography (ERT) correspond well with the results of the seismic survey. Based on streamline interpolations, the active rock glacier is estimated to be min. 4 to 5 ka old, assuming a constant creep rate. Ground surface temperatures on this rock glacier vary strongly between years, mainly in response to the prevalent atmospheric conditions (air temperature, snow cover); this is also reflected in the year-to-year fluctuations of active layer thickness visible in the geophysical soundings.

Keywords: geophysics; ground surface temperatures; kinematics; photogrammetry; rock glaciers; Swiss Alps.

Introduction

Rock glaciers are complex morphological structures and can exhibit a large variability concerning kinematics, subsurface properties like ice content and porosity, and genesis. They are usually divided into three classes concerning their ice content and kinematics: (1) active (supersaturated with ice and creeping), (2) inactive (degrading ice and/or almost no creeping) and (3) relict (free of ice, no creeping).

In this contribution an integrative analysis of rock glacier kinematics and geophysical surveying is presented using photogrammetric analyses and different geophysical techniques. The study site is a complex, multi-unit rock glacier system in the eastern Swiss Alps. The objective of the study is (a) to link the kinematic behaviour to the subsurface properties and their temporal evolution, and (b) to get insights into the reaction of such a multi-unit rock glacier system to climate forcing. For this purpose, geophysical monitoring profiles have been installed for periodic measurements of electrical resistivity and seismic P-wave velocity in addition to ground surface temperature monitoring and kinematic velocity measurements. The presented rock glacier system is composed of active, inactive, and relict rock glacier bodies of similar nature and settings (e.g., headwall geology, cleavage, weathering conditions, slope angle, regional climate), thus enabling the simultaneous investigation of different forms that differ, most probably, mostly in their temporal history.

Geographic Setting

The Gianda Grischa rock glacier system is situated on the western slopes of Piz Julier (3384 m a.s.l.) in a side valley of Julier Pass, eastern Swiss Alps. The rock glacier system consists of three individual landforms (Fig. 1): (A) a W-exposed active rock glacier, overlaying (B) an older, possibly relict part, and (C) a W- to SW-oriented inactive rock glacier.

The active rock glacier (A) is c. 1000 m long and between 170 and 390 m wide and is situated between 2540 and 2800 m a.s.l. This rock glacier exhibits a flat root zone separated from its moderately inclined tongue by a steep slope. While the flatter areas show some ridges and furrows, such structures are absent in the steep slope. Of the possibly relict part (B), underlying the active rock glacier, only the tongue is visible, which is c. 100 m long and 100 m wide. The surface of this part is composed of small rocks and pebbles overgrown by vegetation (alpine grasses, dwarf willows, etc.). The inactive rock glacier (C) is 780 m long and 300 m wide; its surface consists of a very coarse top layer and shows a conspicuous ridge-and-furrow topography.

The area was covered by a small mountain glacier during the Egesen stage of the Younger Dryas cold phase. In the subsequent warming periods, this glacier decayed. During the Little Ice Age the catchment area of the currently active rock glacier (A) was already free of surface ice, while the

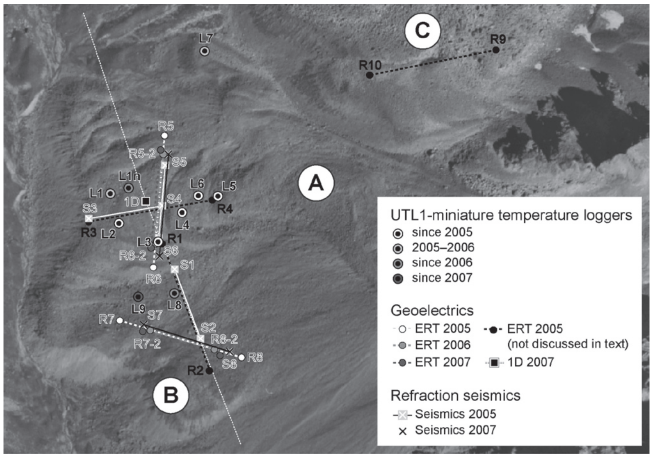

Figure 1. Aerial photograph of the Gianda Grischa rock glacier system with measurement locations: UTL1-miniature temperature loggers (dotted circles), electrical resistivity tomography (ERT) profiles (R1–R10, circles), one-dimensional sounding (rectangle), refraction seismics profiles (S1–S8, crosses). (A) active rock glacier, overlaying (B), an older, possibly relict part, (C) inactive rock glacier. Black-and-white aerial photograph from swisstopo, 11. 8. 1998, Flight-line 152, Image-No. 4647.

root zone of the presently inactive rock glacier (C) was still covered by a small cirque glacier. Today, both cirques are free of surface ice except for some small pluriannual ice patches.

Methods

Velocity measurements and streamline calculations

Using photogrammetrically derived digital elevation models and scanned aerial photography, ortho-images with 0.2 m resolution were computed digitally. From these digital ortho-images, horizontal surface displacements were derived using an image correlation technique described in detail in Kääb & Vollmer (2000). The age structure of the rock glacier surface was assessed from streamlines interpolated from the obtained surface velocity field. Assuming steady-state conditions, these streamlines represent the trajectories of specific particles on the surface and can thus be used to obtain rock glacier age estimates (for more details, cf. Kääb et al. 1998). The actual advance rate can be considerably smaller than the surface velocity, and therefore, surface ages obtained on the base of surface velocity streamline interpolations constitute a minimum age. Kääb (2005) derived empirical values of rock glacier advance rates and found that the total age of the considered rock glaciers is 2–5 times higher than the minimum age obtained for the surface.

Ground surface temperature measurements

Miniature temperature datalogger devices have been installed at six locations on rock glaciers (A) and (B) in summer 2005. One of these loggers had to be moved to a new location in 2006, and two additional loggers were installed in 2006 and 2007, respectively. Six of the loggers record the ground surface temperature (GST) at shallow depths, two loggers measure GST in air voids of the coarse blocky layer; all loggers measure in a 2h-interval. The thermistor used is a TMC-1T with a temperature range of -29°C to +39°C, with an accuracy given by the manufacturer of better than 0.25°C (cf. Hoelzle et al. 1999 for an in-depth discussion of the applied devices).

Geoelectrical techniques

Geoelectrical sounding techniques are based on the electrical resistivity differences between different subsurface materials. For a given frequency, resistivity depends mainly on the material type and the unfrozen water content of the sample (Hoekstra & McNeill 1973). Resistivity values for mountain permafrost targets can be very high and can vary over a wide range from 1–10 kOhm.m to a few MOhm.m (e.g., Haeberli & Vonder Mühll 1996). The method has been successfully applied to detect and characterize different permafrost structures in mountain terrain in various studies (e.g., Ishikawa et al. 2001, Isaksen et al. 2002, Hauck & Vonder Mühll 2003, Marescot et al. 2003).

Depending on the lateral heterogeneity and the target depth, one-dimensional (1D) vertical electrical soundings (VES) or two-dimensional (2D) electrical resistivity tomography (ERT) surveys can be conducted. For monitoring purposes, ERT measurements are repeated at certain time intervals using a permanently installed electrode array. This fixed-electrode array effectively filters resistivity variations due to variable electrode contacts or geological background variations, as mainly temporal resistivity changes are determined.

In our study, we used an "OYO McOhm" instrument for VES and a "SYSCAL Junior Switch system (IRIS)" as well as a "Geotom (Geolog)" instrument for ERT measurements. Electrode spacing of the initial surveys was 5 m, for the monitoring surveys 2 m spacing was employed in order to achieve a better resolution within the active layer. ERT data sets were inverted using the software package RES2DINV (Loke & Barker 1995). Further details on particularities of geoelectric applications in mountain permafrost are, for example, given in Kneisel & Hauck (2008).

Refraction seismics

Seismic investigations are based on different velocities of acoustic waves in subsurface materials. Energy from the seismic source is transported in waves and both reflected and refracted at interfaces. Refraction seismics concentrates on the first arrivals of the signal. The method is well suited to determine the presence or absence of ice, particularly in loose sediments. Differences in seismic velocities occur between frozen and non-frozen areas: permafrost is usually indicated by higher values, due to interstitial ice. Typical seismic velocity values for unfrozen loose sediments are lower than 1500 m s^{-1}, but can reach up to almost 4000 m s^{-1}, when icebound (Maurer & Hauck 2007).

In this study, a 12-channel "Geometrics Seismograph" equipment with a sledge-hammer as source was applied. Geophone spacing was 10 m, with six shot points.

Results and Discussion

Kinematics and age estimates

Horizontal average annual surface velocities were determined photogrammetrically between 1971 and 1998 (Fig. 2a). During the 27 years under observation, the active rock glacier crept downslope with an average velocity of approximately 0.4 to 0.5 ma^{-1}, reaching maximum velocities of up to 1 ma^{-1}. Compared to other rock glaciers in the region, Gianda Grischa is deforming at a considerable rate (e.g., Murtèl rock glacier: v_{max} = 0.2 ma^{-1}, Muragl rock glacier: v_{max} = 0.5 ma^{-1}, cf. Kääb 2005). Both the inactive rock glacier and the possibly relict part showed no statistically significant movement in the period 1971–1998.

More recent velocity measurements are not available yet, but are envisaged in the near future, in order to relate the kinematics to the results of the ongoing measurements of thermal and geophysical properties.

Rock glaciers are formed by the continuous deformation of ice-rich debris material, with the result that the age of the surface becomes greater along the flowlines from their root zone to their front. Minimum surface age estimates obtained from photogrammetric streamline interpolations are in the order of 4 to 5 ka (Fig. 2b). Both frontal lobes of the spatulate tongue seem to be of comparable age and lie on the overridden, older tongue which shows no movement.

Considering that such surface ages constitute a minimum age and that the total age of the rock glacier can be up to 2–5 times higher than the minimum age obtained for its surface (see above, section 'Methods') implies that this rock glacier presumably began to evolve during the early Holocene (for a more detailed discussion cf. Frauenfelder et al. 2005).

Ground surface temperature

Mean annual air temperature (MAAT) at the front of the rock glacier, at an altitude of 2540 m a.s.l., is approximately -1.1°C, as derived by Hoelzle & Gruber (2008). Ground surface temperature (GST) measurements are ongoing since autumn 2005 at different sites at altitudes between 2586 and 2640 m a.s.l. Mean annual GST on the active rock glacier was between -1.0 and -2.1°C at five out of seven sites during 2005–2006. During 2006–2007 MAGST was negative at one out of six sites (Table 1).

These year-to-year fluctuations are in good agreement with the prevalent atmospheric conditions (air temperature, snow cover) in the area. The MAAT measured at the nearby Murtèl-Corvatsch station showed a very cold winter 2005/2006, contrasted by a very warm winter 2006/2007 (Fig. 3).

Snow cover conditions (thickness and duration), both influencing the ground thermal regime, were normal during winter 2005/2006 as compared to the existing measurements since 1972. In contrast to this, snow cover thickness during winter 2006/2007 was the thinnest ever recorded in the last 35 years. Under normal conditions, winter 2006/2007 would have been one of the coldest recorded, due to the lacking isolation of the snow cover. However, winter 2006/2007 was characterized by a record warm period, lasting from September 2006 until May 2007. This fact is well represented

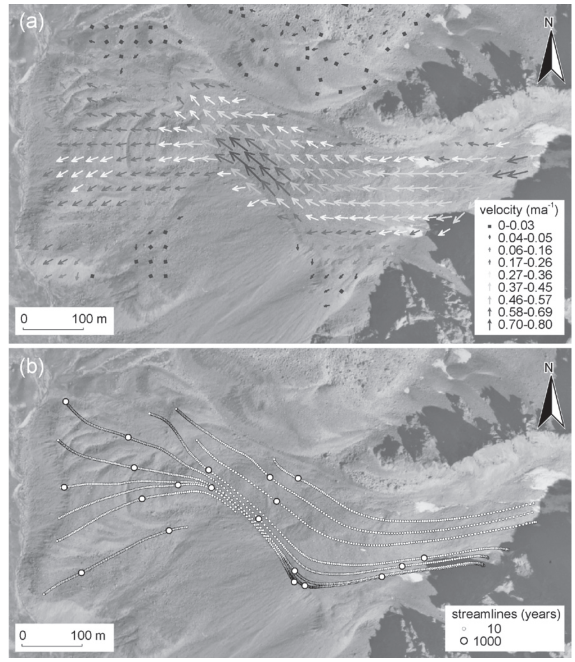

Figure 2. Photogrammetrical measurements on the Gianda Grischa rock glacier system: (a) Horizontal average annual surface velocities between 1971 and 1998; (b) Streamline calculations. Black-and-white aerial photograph from swisstopo, 11. 8. 1998, Flight-line 152, Image-No. 4647.

Table 1. Mean annual ground surface temperatures (MAGST), as measured at different sites on the active and the relict rock glacier from 2005 (resp. 2006) until 2007 (resp. 2006). Abbreviations: Instal. = Date of installation; De-instal. = Date of de-installation.

ID	Instal.	De-instal.	Altitude [m a.s.l.]	MAGST 05/06 [°C]	MAGST 06/07 [°C]
L1	31.8.2005	18.9.2006	2604	-2.102	--
L1n	18.9.2006	ongoing	2615	--	+2.028
L2	31.8.2005	ongoing	2608	+0.215	damaged
L3	31.8.2005	ongoing	2616	+0.508	+2.045
L4	31.8.2005	ongoing	2623	-2.029	-0.150
L5	31.8.2005	ongoing	2640	-1.936	+0.157
L6	31.8.2005	ongoing	2628	-0.970	+1.276
L7	31.8.2005	18.9.2006	2622	-1.507	--
L8	18.9.2006	ongoing	2603	--	+2.348

in the MAGST measured on the rock glacier (Fig. 3).

As the measurements show, winter 2006–2007 was characterised by warm air temperatures, combined with thin snow cover. Although the thin snow cover allowed a certain amount of ground cooling and thereby partly outbalanced the influence of the warm air temperatures, the overall result of these atmospheric conditions was considerably "warm" GSTs on the rock glacier.

Geophysical subsurface characterisation

ERT surveys have been performed on both the active (A) and the inactive (C) rock glacier, as well as on the possibly relict part (B) underlying the active rock glacier. As a complementary method, seismic surveys have been

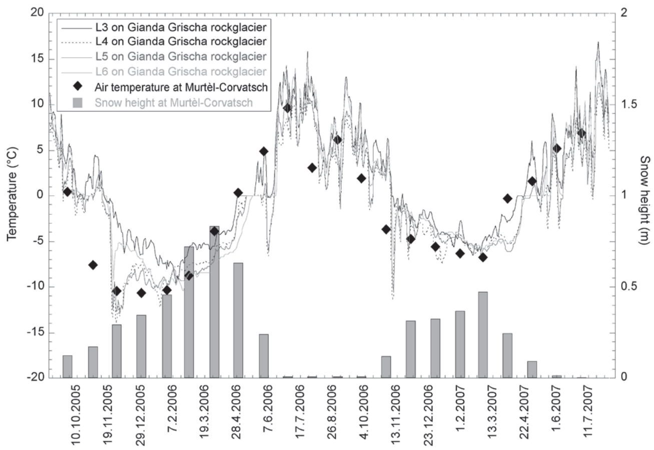

Figure 3. Ground surface temperatures (GSTs) in the period 2005–2007 as measured continuously at four locations on the active rock glacier, and air temperature and snow depth measurements from the nearby Murtèl-Corvatsch weather station.

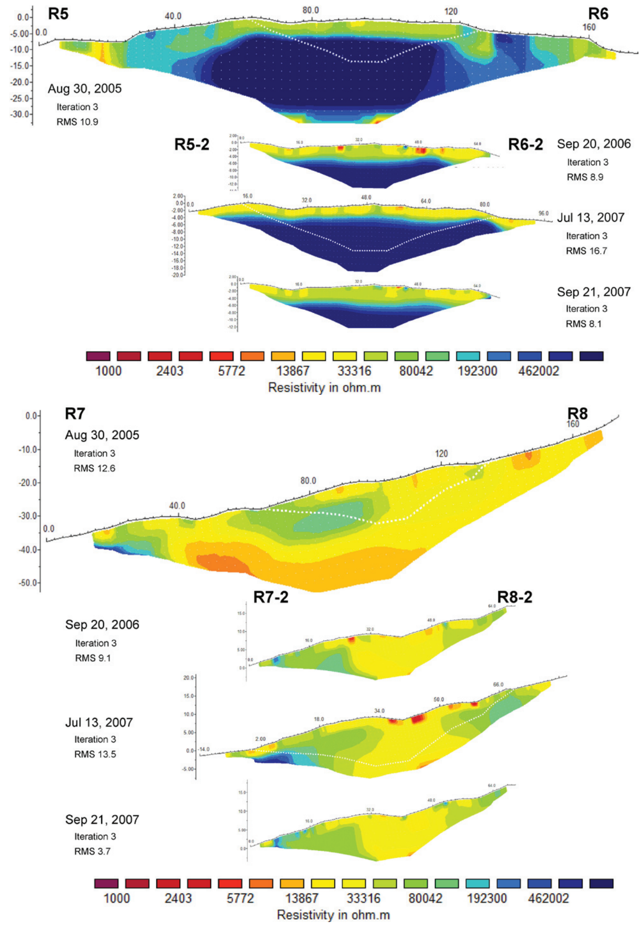

Figure 4. Results of the Electrical resistivity tomography (ERT) measurements: (top) Transversal profile on the active rock glacier (profile line R5–R6); (bottom) longitudinal profile over the edge of the active rock glacier onto the underlying, older (possibly relict) part (profile line R7–R8). R#-numbers refer to the measurements in 2005 (5 m spacing), R#-2-numbers refer to the monitoring profiles from 2006 and 2007 (2 m spacing).

conducted on the active and relict part. The aim was to confirm or contradict the geomorphological and kinematic evidence and to roughly estimate the ice content in the different rock glaciers.

On the active rock glacier (A) the active layer is comparably thick with about 4–5 m (in September, Fig. 4, top) and resistivity values between 30 and 50 kOhm.m. The maximum investigation depth is c. 30 m (obtained with a 5 m spacing profile in August 2005). From this profile a lense-shaped structure is visible with maximum values between c. 200 and >500 kOhm.m. The lateral extent of this high resistive anomaly coincides with the morphological and kinematic evidence for recent high activity. Beneath the maximum, resistivities decrease again indicating a decreasing ice content below 20–25 m depth. Even though this latter interpretation is supported by an additional ERT profile along the rock glaciers flowline (not shown here) and by the VES results (Fig. 5, Table 2), this result remains uncertain, as the reliability of the ERT profiles decreases with depth due to the high resistivity and the limited penetration depth (cf. Hauck & Vonder Mühll 2003, Marescot et al. 2003).

The corresponding seismic results show a similar active layer depth (August measurement) and a high velocity layer below the active layer, with maximum velocities between 2500–4000 ms^{-1} (Fig. 6), indicating the possibility of a significant ice layer, the velocity of ice being 3500 ms^{-1}. Both measurements are in good accordance with evidence from comparable blocky rock glaciers (e.g., rock glacier Murtèl, Maurer & Hauck 2007) and strongly suggest the presence of ice-rich permafrost or even massive ice cores. The depth of the bedrock could not be estimated conclusively.

Measurements on the inactive rock glacier (C, not shown here) and on the possibly relict part (B, Fig. 4, bottom) show significantly lower, but still comparably high resistivity values around c. 50 kOhm.m.

Although the inactive rock glacier showed no statistically significant movement in the period 1971–1998, the results of the ERT survey may indicate the presence of strongly degraded subsurface ice with higher amounts of unfrozen water which no longer has the appearance of one massive and supersaturated ice core. The resistivity values of this inactive rock glacier correspond well with the ERT results from other permafrost landforms with less (but still significant) ice content (cf. Hilbich et al. 2008b). The same is true for the older part, underlying the active rock glacier, which was mapped as relict due to its geomorphological habitus (lateral and frontal sides with low slope angles, collapsed inner structure, considerably dense vegetation cover) and the absence of measurable movement.

On the other hand, the lack of seasonal changes in most parts of the profile may indicate an absence of significant ground ice, as this would lead to, for example, a significant deepening of the surficial unfrozen layer between July and September.

Similarly, the observed seismic velocities are lower than in the active rock glacier, but still high enough to indicate possible ice occurrences. The depth of the relict part of the rock glacier is estimated around 25 m. At shallower depths, the comparatively small P-wave velocities suggest air-filled

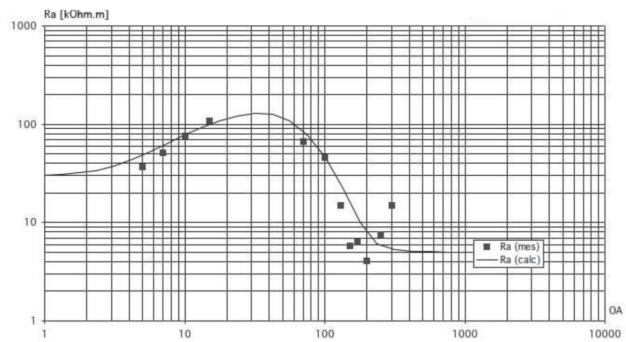

Figure 5. Sounding curve of the one-dimensional sounding (1D) on the active rock glacier (A in Fig. 1).

voids or cavities not only on the inactive and relict rock glacier, but also on the margins of the active one (Fig. 6). As these voids can cause equally high resistivities as massive ground ice, some heterogeneity concerning the ice content on the active rock glacier can, therefore, not be excluded.

The VES results confirm the general findings from the active rock glacier with a 4 m thick active layer (30–65 kOhm.m) and an approximately 20 m thick permafrost layer below (> 250 kOhm.m). Below this layer, the presence of two increasingly apparent resistivity measurements may indicate the bedrock layer or a possible further relict permafrost occurrence some 50–60 m below the surface, which was shielded from atmospheric conditions by the overlying, presently active rock glacier. Even though geomorphic evidence of a relict rock glacier below at least parts of the active rock glacier (cf. above) may argue for the latter, the geophysical evidence is too scarce to allow a reliable interpretation.

Geophysical monitoring

Two profiles were chosen as future monitoring profiles: R/S5–6 on the active rock glacier and R/S7–8 on the possibly relict part (cf. Fig. 1). To better resolve the active layer and the upper part of the permafrost, where seasonal and long-term changes will be largest, a reduced electrode spacing of 2 m was chosen. Up to now, measurements were conducted on September 20, 2006, July 13, 2007, and September 21, 2007. Due to the use of a different ERT instrument in July 2007, these measurements have slightly larger penetration depths.

For the active rock glacier profile the ERT monitoring results show a significant increase in the thickness of the unfrozen layer (low resistivity values) from July to September 2007. A similar thickening, but much smaller, can be seen from September 2006 to September 2007, indicating warmer subsurface conditions in 2007 than in 2006, which is also confirmed by the MAGST measurements (see above). In contrast to this, no such effects can be found on the possibly relict part. Differences can be seen in the lower part of the slope, where the profile nears the active rock glacier, but a clear seasonal increase of the unfrozen layer thickness as well as an interannual signal are missing. From this finding may be deduced that the ice content is low or absent in most of profile R7–8, as a significant ice content would lead to seasonal resistivity contrasts near the interface between

Table 2. Apparent resistivities and thickness of the layers in the 1D model, as shown in Figure 5.

Layer	Resistivity [kOhm.m]	Thickness [m]
1	30–65	3–5
2	>250	20 (–40)
3	5–10	∞

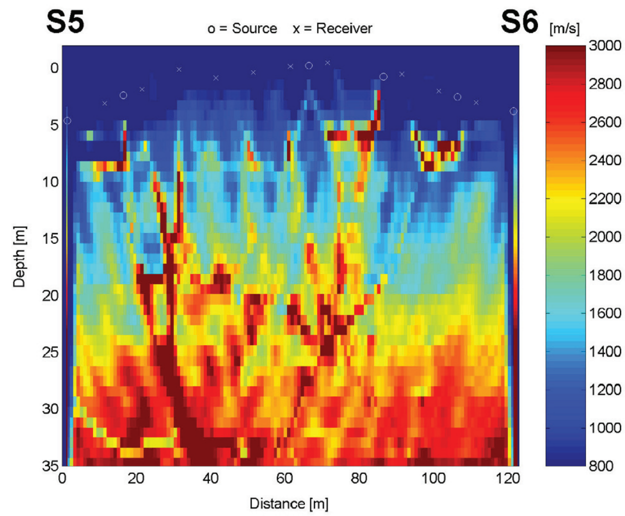

Figure 6. Results of the refraction seismics measurements on the active rock glacier (profile line S5–S6).

the active layer and the permafrost body (cf. Hauck 2002, Kneisel 2006, Hilbich et al. 2008a). This is further supported by the very small vertical resistivity gradient throughout most parts of the profile. An exception may be the lowest part of the profile, where the resistivity increases strongly with depth.

Conclusions and Perspectives

The present study shows that a sound combination of different photogrammetrical, geophysical, and meteorological methods can reveal new insights about individual rock glaciers or even complex rock glacier systems. Photo-grammetrical measurements (velocity, streamlines) help to identify moving and non-moving parts and allow age constraints to be derived. Geophysical surveys give insights into the composition and about the ice content of the studied features. Ground surface temperature measurements and additional meteorological data (such as air temperature, snow cover thickness and duration from nearby meteorological stations) give further information that helps to better understand observed kinematic behaviour, such as, short-term velocity changes as recently reported from many Alpine rock glaciers (e.g., Ikeda et al. 2003, Lambiel & Delaloye 2004, Roer et al. 2005).

In summary, our data show a connection between lower resistivities, larger unfrozen water content, and higher MAGST, with higher creep velocity and vice-versa. More extensive and repeated monitoring is necessary, however, to reliably link the kinematic behaviour to the thermal and subsurface properties.

Once longer time-series of such combined measurements are available, this data will help to explain climate forcing impacts on mountain permafrost, such as the above mentioned observed recent increase in rock glacier velocity. The presented monitoring approach will then enable the assessment of future changes of rock glacier dynamics and their causes in the atmosphere and the subsurface. These data can be used as much needed input and forcing variables in permafrost evolution models.

Acknowledgments

This study has been financially supported by the Swiss Academy of Sciences ("Reisestipendien in Botanik, Zoologie und Erdwissenschaften") and the Department of Geosciences, University of Oslo. We would also like to thank an anonymous reviewer for his constructive comments, which greatly helped to improve the manuscript.

References

Frauenfelder, R., Laustela, M. & Kääb, A. 2005. Relative age dating of Alpine rock glacier surfaces. *Zeitschrift für Geomorphologie N.F.* 49(2): 145-166.

Haeberli, W. & Vonder Mühll, D. 1996. On the characteristics and possible origins of ice in rock glacier permafrost. *Zeitschrift für Geomorphologie* 104: 43-57.

Hauck, C. 2002. Frozen ground monitoring using DC resistivity tomography. *Geophysical Research Letters* 29 (21): 2016, doi: 10.1029/2002GL014995.

Hauck, C. & Vonder Mühll, D. 2003. Inversion and interpretation of 2-dimensional geoelectrical measurements for detecting permafrost in mountainous regions. *Permafrost and Periglacial Processes* 14(4): 305-318.

Hilbich, C., Hauck, C., Hoelzle, M., Scherler, M., Schudel, L., Voelksch, I., Vonder Mühll, D. & Mäusbacher, R. 2008a. Monitoring mountain permafrost evolution using electrical resistivity tomography: A 7-year study of seasonal, annual, and long-term variations at Schilthorn, Swiss Alps. *Journal of Geophysical Research* 113: F01S90.

Hilbich, C., Hauck, C., Delaloye, R. & Hoelzle, M. 2008b. A geoelectric monitoring network and resistivity-temperature relationships of different mountain permafrost sites in the Swiss Alps. *Proceedings of the Ninth International Conference on Permafrost, Fairbanks, Alaska* (this proceedings).

Hoekstra, P. & Mc Neill, D. 1973. Electromagnetic probing of permafrost. In: F.J. Sanger & P.J. Hyde (eds.), *Proceedings of the Second International Conference on Permafrost*. National Academy of Sciences, Washington DC: 517-526.

Hoelzle, M., Wegmann, M. & Krummenacher, B. 1999. Miniature temperature dataloggers for mapping and monitoring of permafrost in high mountain areas: First experience from the Swiss Alps. *Permafrost and Periglacial Processes* 10(2): 113-124.

Hoelzle, M. & Gruber, S. 2008: Borehole and ground surface temperatures and their relation to meteorological conditions in the Swiss Alps. *Proceedings of the Ninth International Conference on Permafrost, Fairbanks, Alaska* (this proceedings).

Ikeda, A., Matsuoka, N. & Kääb, A. 2003. A rapidly moving small rock glacier at the lower limit of the mountain permafrost belt in the Swiss Alps. *Proceedings of the Eighth International Conference of Permafrost*, Zurich, Switzerland, Swets & Zeitlinger, Lisse: 455-460.

Isaksen, K., Hauck, C., Gudevang, E., Ødegård, R.S. & Sollid, J.L. 2002. Mountain permafrost distribution in Dovrefjell and Jotunheimen, southern Norway, based on BTS and DC resistivity tomography data, Norwegian Journal of Geography 56: 122–136.

Ishikawa, M, Watanabe, T. & Nakamura, N. 2001. Genetic difference of rock glaciers and the discontinuous mountain permafrost zone in Kanchanjunga Himal, Eastern Nepal. *Permafrost and Periglacial Processes* 12(3): 243-253.

Kääb, A. 2005. *Remote sensing of mountain glaciers and permafrost creep*. Zurich: University of Zurich, Switzerland, Physische Geographie 48, 264 pp. (ISBN 3 85543 244 9)

Kääb, A., Gudmundsson, G.H. & Hoelzle, M. 1998. Surface deformation of creeping mountain permafrost. Photogrammetric investigations on Murtèl rock glacier, Swiss Alps. *Proceedings of the Seventh International Permafrost Conference, Yellowknife, Collection Nordicana* 57, Centre d'Etudes Nordiques, Université Laval, Canada: 531-537.

Kääb, A. & Vollmer, M. 2000. Surface geometry, thickness changes and flow fields on creeping mountain permafrost: automatic extraction by digital image analysis. *Permafrost and Periglacial Processes* 11: 315-326.

Kneisel, C. & Hauck, C. 2008. Electric methods. In: Hauck, C. & Kneisel, C. (eds.), *Applied Geophysics in Periglacial Environments*. Cambridge: Cambridge University Press, in press.

Kneisel, C. 2006. Assessment of subsurface lithology in mountain environments using 2D resistivity imaging. *Geomorphology* 80: 32-44.

Lambiel, C. & Delaloye, R. 2004. Contribution of real-time kinematic GPS in the study of creeping mountain permafrost: examples from the Western Swiss Alps. *Permafrost and Periglacial Processes* 15: 229-241.

Loke, M.H. & Barker, R.D. 1995. Least-squares deconvolution of apparent resistivity. *Geophysics* 60: 1682-1690.

Marescot, L., Loke, M.H., Chapellier, D., Delaloye, R., Lambiel, C. & Reynard, E. 2003. Assessing reliability of 2D resistivity imaging in permafrost and rock glacier studies using the depth of investigation index method. *Near Surface Geophysics* 1(2): 57-67.

Maurer, H. & Hauck, C. 2007. Geophysical imaging of alpine rock glaciers. *Journal of Glaciology* 53(180): 110-120.

Roer, I., Kääb, A. & Dikau, R. 2005. Rock glacier acceleration in the Turtmann valley (Swiss Alps). *Norwegian Journal of Geography* 59(2): 157-163.

Deployment of a Deep Borehole Observatory at the High Lake Project Site, Nunavut, Canada

Barry M. Freifeld
Lawrence Berkeley National Laboratory, Berkeley, CA, USA

Eric Chan and Tullis C. Onstott
Princeton University, Princeton, NJ, USA

Lisa M. Pratt and Adam Johnson
Indiana University, Bloomington, IA, USA

Randy Stotler, Brian Holden and Shaun Frape
University of Waterloo, Waterloo, Ontario, Canada

Susan M. Pfiffner and Sarah DiFurio
University of Tennessee, Knoxville, TN, USA

Timo Ruskeeniemi
Geological Survey of Finland, Espoo, Finland

Ian Neill
Zinifex Canada Inc., Ontario, Canada

Abstract

We deployed a deep permafrost observatory in a borehole at the High Lake Project Site (67°22′N, 110°50′W), Nunavut, Canada with the aims of (1) investigating the physical and chemical limitations on microbial life within such environments, (2) developing life-detecting technologies for the exploration of life on Mars, and (3) constraining the hydrological and thermal parameters relevant to the evolution of permafrost and groundwater flow in these environments. The High Lake Project Site is located in an Archean mafic volcanic belt, with permafrost extending down to 458±5 m depth. The borehole, drilled to a total depth of 480 m, provides multifunctional monitoring capability: subpermafrost geochemical sampling, thermal profile, and estimation of hydraulic and thermal formation properties. The primary sampling objectives are delineating salinity gradients, gas concentration, pH, pe, microbial abundance, community structure, and activity, as well as isolating pristine subpermafrost brine for future studies. A multimode fiber-optic cable, along with a heat-trace cable, was installed to perform distributed temperature-perturbation sensor (DTPS) measurements along the entire length of the borehole. Following successful installation of the borehole observatory, we acquired a thermal perturbation dataset and obtained estimates for formation thermal conductivity and heat flux.

Keywords: borehole observatory; climate change; geothermal profile; microbial sampling; permafrost instrumentation; permafrost thickness.

Introduction

Given that global climate models predict the greatest increases in temperature at arctic latitudes, permafrost is increasingly looked upon as a harbinger of climate change (Anisimov et al. 2007). Borehole thermal profiles provide information on past ground-surface temperature histories (GSTH) not available from atmospheric temperature records collected prior to the twentieth century (Lachenbruch & Marshall 1986, Harris & Chapman 1997). To invert thermal profile data for estimating GSTH, thermal properties need to be constrained. Prior studies have either used laboratory measurements performed on drill cores or cutting fragments, or have used estimates based on lithologic descriptions (Taylor et al. 2006, Majorowicz & Safanda 2001).

Understanding a permafrost site's hydrogeological and thermal conditions is important for predicting the destabilization of permafrost by construction activities, assessing mine inflows, contaminant transport risks, and for the design of tailing and waste rock impoundments (Harris 1986). Given that the economic activities in arctic Canada are predominantly (diamond and metal) mining, as well as oil and gas exploration and production, engineering the necessary infrastructure and assessing the impact that infrastructure has on the natural environment requires understanding both present site conditions and evolving climatic conditions.

In the summer of 2007 we installed a multifunctional borehole observatory at the High Lake Project Site (67°22′N, 110°50′W), in Nunavut Territories, Canada, with the aim of acquiring a broad spectrum of environmental data. Within the permafrost, a distributed thermal perturbation sensor (DTPS) was used to measure the thermal profile; based on these temperature data, we can estimate formation thermal conductivity. Beneath a pneumatic packer located above the base of the permafrost, a U-tube geochemical sampling system acquired fluid samples for delineating gas concentration, pH, pe, microbial abundance, and community structure and

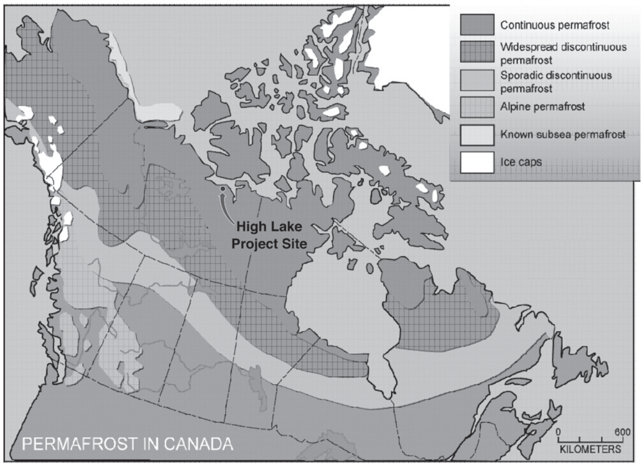

Figure 1. High Lake Project Site Location in Nunavut Territories, Canada. Permafrost base map from NRC Atlas Website, http://atlas.nrcan.gc.ca/.

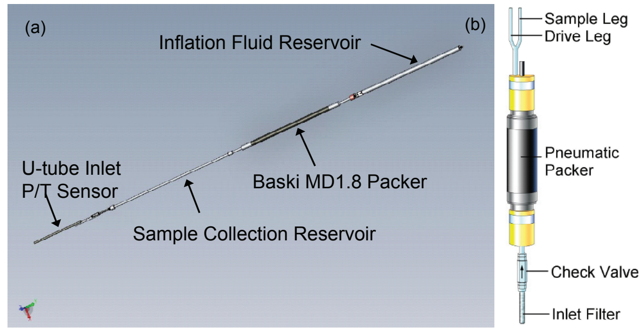

Figure 2. (a) High Lake bottom hole assembly showing the sequence of components from bottom to top (left to right on the schematic). (b) Conceptual layout of a U-tube sampler. The Sample Collection Reservoir formed the "U" portion of the U-tube at High Lake.

activity, as well as isolating pristine subpermafrost brine for future studies (Freifeld et al. 2005). A pressure-temperature sensor collocated with the U-tube sampling inlet facilitated estimation of hydraulic conductivity.

This paper presents the thermal and hydrologic data collected following installation of the U-tube and DTPS and contains a preliminary interpretation of these data. One of the unique results of our field program was our method of using *in situ* data to estimate formation thermal conductivity with high spatial resolution. This approach—resulting in better estimates of formation thermal conductivity, as contrasted to using laboratory derived values—can reduce uncertainty in prediction of GSTH when inverting borehole temperature measurements.

High Lake Site and Observatory Description

Site description

The High Lake Project Site, shown in Figure 1, is located in an Archaen Mafic volcanic belt, with permafrost extending down to 460 m on a mining exploratory lease originally purchased by Wolden Resources and currently operated by Zinifex Canada Inc. All of the work was conducted within a 75 mm diameter borehole, designated HL03-28. HL03-28 was initially drilled in 2003 to a length of 335 m (depth 304 m) as part of Wolfden Resource's characterization of base metals for potential economic extraction from the High Lake volcanogenic massive sulfide deposit. In July 2006, our project team cored continuously to lengthen HL03-28 to 535 m. After removing an ice blockage that formed in the borehole during the previous season, we installed a permanent borehole observatory.

Borehole observatory

The High Lake borehole observatory targeted both the permafrost region for geothermal investigation and the subpermafrost formation for estimation of hydrologic properties and collection of fluid samples. The instrumentation at the bottom of the borehole, consisting of a pneumatic packer, a U-tube sampling system with a sample fluid reservoir, and a pressure-temperature sensor, are collectively referred to as the bottom hole assembly (BHA). The fluid, electrical, and fiber-optic lines running between the BHA and the surface are referred to as the deployment string.

Figure 2(a) shows a schematic of the High Lake BHA. With an overall length of 14.9 m, the BHA is composed of (from top to bottom) a fluid reservoir for packer inflation, a pneumatic packer (Baski Model MD18, Denver, CO, USA), a sample fluid collection reservoir, a pressure-temperature sensor (In-situ Level Troll 500, Fort Collins, CO, USA) and a U-tube inlet composed of a 40 μm sintered stainless steel filter and a check valve.

Prior to deployment of the BHA, the fluid reservoir was filled with 3 lL of propylene glycol. Propylene glycol was chosen because of its low freezing point and its inability to permeate through the rubber packer gland. To inflate the packer, we applied a N_2 head to the reservoir (using a 6.4 mm stainless steel tube), forcing the fluid into the packer and inflating the packer gland. The central mandrel of the packer served as a conduit for transport of sampled fluid and electrical signals between the surface and the BHA.

A traditional U-tube sampler, as shown in Figure 2(b), is composed of a looped tube, forming a "U" that is open to the formation via a check valve. To recover a sample, compressed N_2 gas, applied to the drive leg, forces the check valve to close, and fluid is transported up the sample leg to the surface. At High Lake, the inlet filter and check valve were both located beneath a 7 lL sample collection reservoir. Using a small, 6.4 mm-diameter inner tube terminating 10 cm from the bottom of the sample collection reservoir (to form a sample leg), the outer large diameter cylinder served the function of the traditional U-tube drive
independent sample lines that ran up to the surface.

The DTPS deployed at High Lake consisted of an HDPE jacketed multimode fiber-optic cable that runs from the top of the packer fluid reservoir up to a Distributed Temperature Sensor (DTS; Agilent Technologies Manufacturing GmbH & Co. KG, Model N4385A, Böblingen, Germany) located at

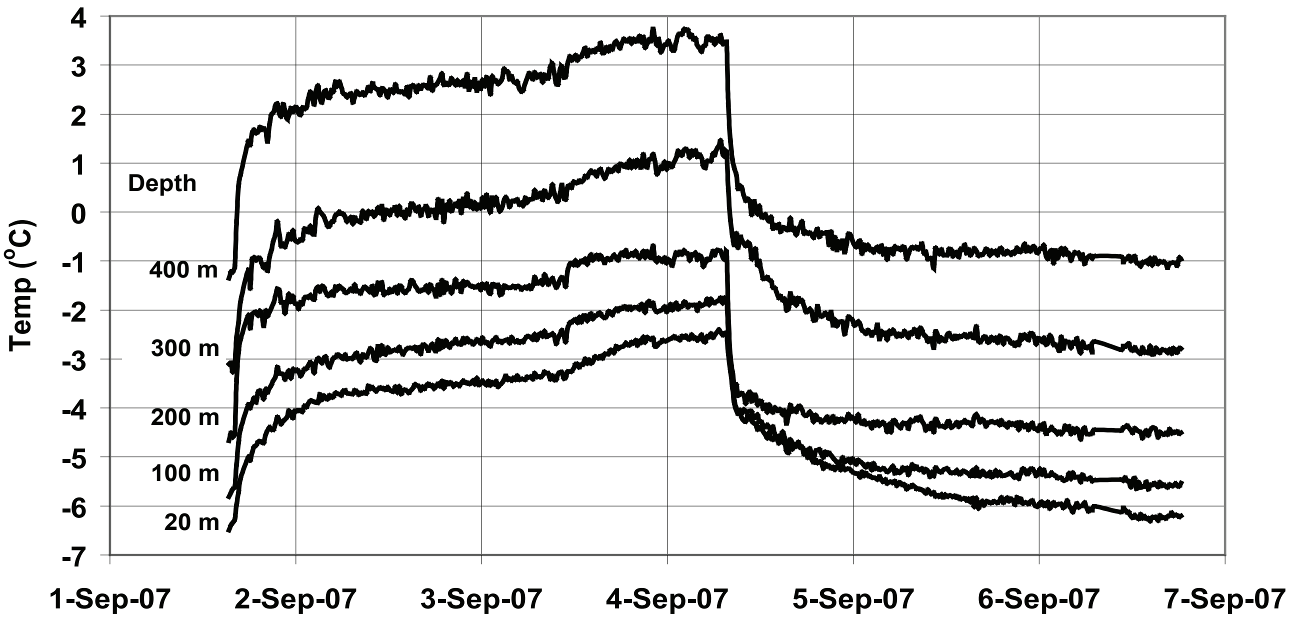

Figure 3. High Lake thermal profiles acquired using a distributed temperature sensor. Heating was initially conducted at a rate of 16.8 W/m for 43 hours, followed by heating at 20.5 W/m for 21 hours. Following the geothermal gradient, the thermal profiles go from coolest (shallowest) to warmest (deepest).

the surface. The DTS uses a laser backscattering technique to measure temperature with a 1 m spatial resolution along the length of the fiber. An overview of the DTS technology as applied to environmental monitoring can be found in Selker et al. (2006). Parallel to the fiber-optic cable is a two-conductor 14 AWG direct burial (outdoor) cable shorted at the bottom, which provides uniform heating along the length of the well when current is applied.

Following the wellbore completion process, the temperature was allowed to equilibrate for 1 month before thermal data were collected. To conduct the DTPS measurement, we first acquired a baseline thermal profile. While energizing the heater cable, additional thermal profiles were obtained at 15-minute intervals to record the thermal transient during heating. After 64 hours of monitoring the heating, the generator was turned off, and cooling was monitored for an additional 58 hours. Figure 3 shows a limited subset of the hundreds of thermal transients recorded.

Results

Fluid sampling

Immediately after deployment of the borehole observatory, the U-tube was operated five times over a span of three days, recovering a total of approximately 60 lL. Although samples were still contaminated with $CaCl_2$ saturated drilling fluids used during the removal of the ice plug a few days earlier, the salinity declined five-fold with the purging of wellbore fluids. The sampling lines eventually froze, despite the fact that heat was being applied at a rate of 20 W/m in an attempt to keep the sample lines flowing. The thermal data (discussed later in detail) show borehole temperatures approaching –7°C and moderate to high formation thermal conductivity, indicating the potential for rapid heat loss of the sampling system. In retrospect, an insulated hose encompassing both the sampling lines and the heat-trace cable would have ensured the continued operation of the sampling system.

Hydraulic conductivity

During operation of the U-tube sampling system, the bottomhole pressure was continuously recorded using a pressure/temperature sensor located near the inlet of the U-tube sampling system (Fig. 4). The U-tube sampling event corresponds to a sharp increase in pressure (over several minutes) immediately followed by a rapid decrease in pressure, as the compressed gas is vented from the sampling tubing. As fluid reenters the borehole, the downhole pressure rebounds. As shown in Figure 4(b), the increase in pressure occurs in two distinct phases: (1) a slow pressure increase immediately after sampling and venting of the sample lines, which corresponds to filling of the downhole sample reservoir, and (2) a quicker increase, which corresponds to filling of the small-diameter sampling lines that run up to the surface.

To estimate the hydraulic conductivity of the formation beneath the packer, we apply Thiem's Equation. Assuming a homogeneous confined radial aquifer, the hydraulic conductivity is:

$$K = \frac{Q}{2\pi\left(h(r) - H\right)L} \ln \frac{r}{R} \tag{1}$$

where Q is the volumetric flux into the borehole, L the length of the packed-off interval, r the radius of the well, R the radius to a fictitious constant head boundary (assumed to be 2 m), and $h(r)$ (determined in the next section to be 349 m H_2O) and H are the heads at these two locations.

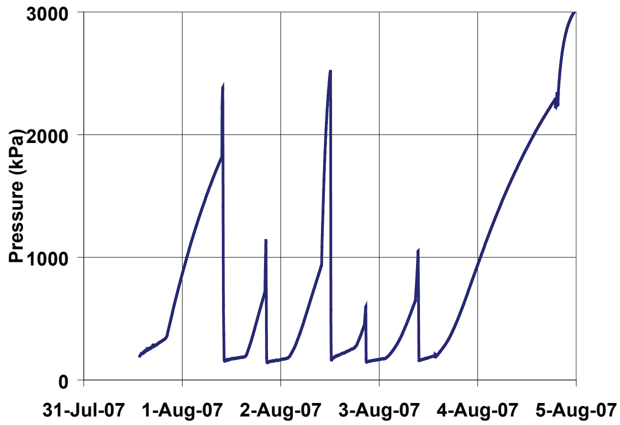

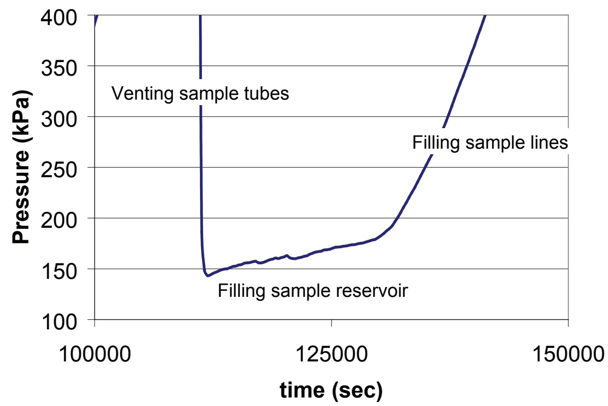

Figure 4. (a) Pressure response during U-tube sampling events as measured near the U-tube inlet. (b) Following acquisition of a U-tube sample and sample line N_2 gas venting, the pressure rebounds slowly as the sample reservoir fills, followed by a quicker rebound during filling of the small diameter sample lines.

To apply Thiem's equation, which requires steady-state conditions, we assume that the head H within the sample reservoir represents a pseudo-steady head of 18 m (Figure 4b)—justified because the change in head (3 m over several hours) is small compared to $h(r)–H$. Q, is assumed equal to the flux into the sample reservoir, determined as the product of the change in the fluid height within the sample reservoir (per unit time) and the reservoir's cross-sectional area.

Given the geometry of the High Lake borehole, the hydraulic conductivity K is estimated to be 2.3×10^{-11} m/s. This exceptionally small conductivity is typical of unfractured igneous rocks.

Permafrost thickness and hydrostatic head

Our results provide the best measured thickness of permafrost in this region, as other nearby estimates by the Geological Survey of Canada are from much shallower boreholes (e.g., Taylor et al. 1998). A linear extrapolation through the lower 120 m of fiber-optic temperature sensor data, with the addition of the discrete data point measured by the Level Troll pressure-temperature sensor (Figure 5), indicates that the base of the permafrost is at 458±5 m, where the depth uncertainty is based upon propagating a temperature error of ±0.1°C into the depth estimate. A small correction (+0.025°C) has been applied to account for the thermal perturbation created near the base of the well during the wellbore completion process, following the method suggested by Lachenbruch & Brewer (1958). By plotting the temperatures measured after wellbore completion as a function of $Log_e(t/(t\text{-}s))$, where t is the time elapsed since wellbore completion and s is the duration of the thermal perturbation (assumed to be 1.25 days), we correct for the effect of cooler water being introduced deeper in the borehole during the completion process (Figure 6).

The steady-state subpermafrost hydrostatic pressure can also be estimated by plotting pressure as a function of $Log_e(t/(t\text{-}s))$—referred to as a Horner Plot in well test literature. Using the pressure data from the Level Troll pressure-temperature sensor, we determined the hydrostatic pressure at a depth of 430 mbgs to be 3420 kPa. This is equivalent to a freshwater head of 349 m or a water table at 81 mbgs.

Thermal perturbation measurements

The DTPS experiment was conducted over a span of five days, with 63 hours of heating and 58 hours of cooling (Figs. 3, 5). To interpret the acquired thermal transients, we used a one-dimensional radial model explicitly incorporating the fluid-filled borehole and steel casing, surrounded by rock with homogeneous thermal properties, to invert cooling data. The formation of ice, which was observed to occur at depths shallower than 30 mbgs during cooling (as indicated by the thermal transients remaining stable near the freezing point of the borehole fluid [–4.5°C] for several hours), was not explicitly incorporated, but will be in future analyses. Heating data are not used, because small variations in spatial distance between the fiber-optic cable and the heating cable create large differences in temperatures. During cooling, however, conduction of heat tends to homogenize temperatures near the wellbore, making the simulations insensitive to the exact separation between the heating cable and monitoring fiber.

Figure 7 shows modeled cooling transients as a function of rock thermal conductivity, with data shown for selected depths. The model data are shown as lines and the measurements are shown as points. Using the one-dimensional radial model to invert the DTPS data, thermal conductivity is estimated along the wellbore with a spatial resolution equivalent to the 1 m resolution of the DTS (Fig. 8). The results shown in Figure 8 are consistent with the borehole lithology and literature values (Clauser & Huenges 1995), in which lower thermal conductivity felsic metavolcanic strata overly mafic metavolcanic strata. The exceedingly high thermal conductivities are attributed to zones in which the core was observed to consist of at least 50% pyrite.

Heat flux

Using the baseline temperature profile (Fig. 5) and the thermal conductivity profile (Fig. 8), the vertical heat flux

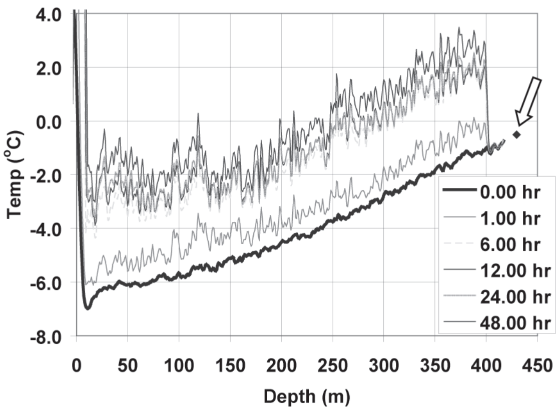

Figure 5. Thermal profiles acquired using a DTS. The lowest profile is the baseline prior to heating and cooling. The arrow points to a temperature measurement provided by the downhole Level Troll pressure-temperature sensor.

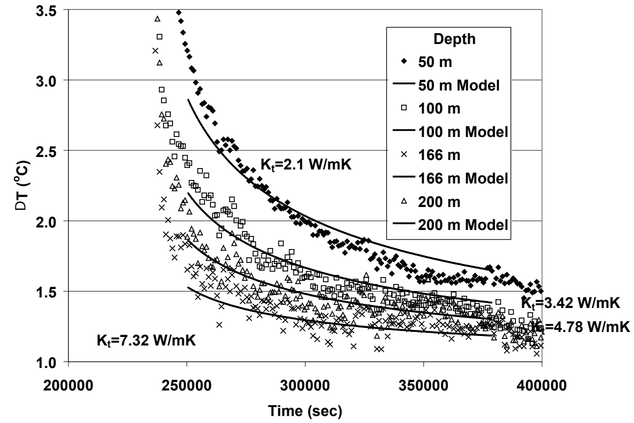

Figure 7. One-dimensional thermal simulations of DTPS testing showing modeled cooling transients along with select measurements. Time is measured from start of heating.

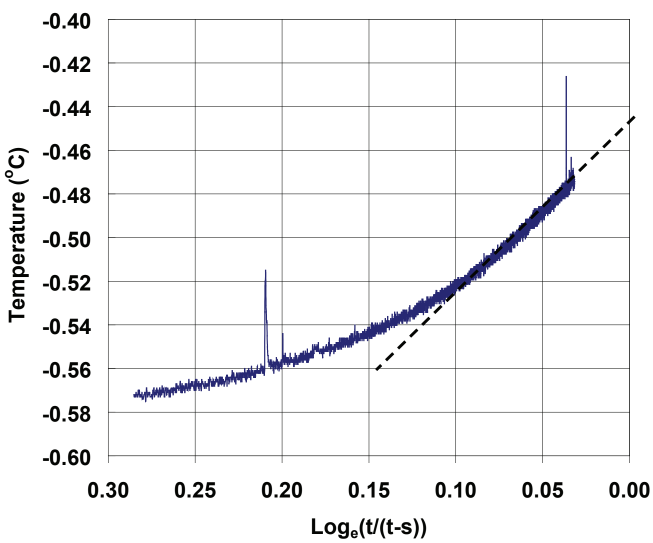

Figure 6. Temperatures measured in HL03-28 at a depth of 430 m following the wellbore completion process, as suggested by Lachenbruch & Brewer (1959) to determine undisturbed conditions. The temperatures extrapolated along the dotted line indicate the well is still 0.025°C cooler than at equilibrium.

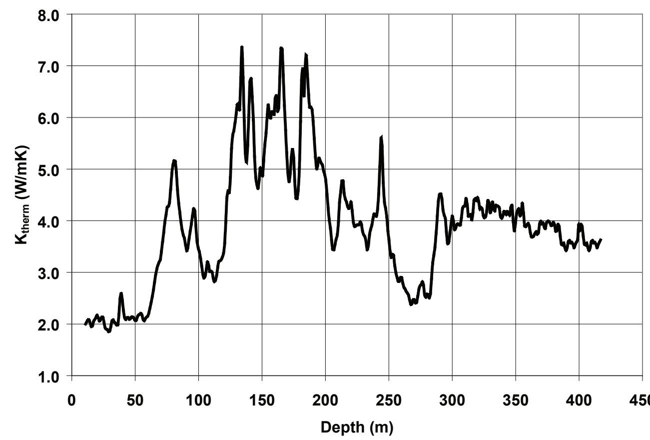

Figure 8. Thermal conductivity as a function of depth using a 1-D model to invert DTPS data. The results are consistent with lithology, in which shallow tuffs are underlain by ore-bearing mafic intrusives.

can be estimated in the vicinity of the wellbore. Using averaged values for thermal conductivity within the felsic metavolcanic units at a depth of 50 to 100 m, we estimate a heat flux of 30 mW/m^2, whereas at a depth between 300 and 400 m, the heat flux is much greater, 70 mW/m^2. The value of 70 mW/m^2 is considerably greater than the average value of 46±6 mW/m^2 reported for two wells 320 km south of High Lake by Mareschal et al. (2004) at Lac du Gras, Nunuvut, Canada. It is also greater than the value of 54.1 mW/m^2 estimated by inversion of thermobarometric data by Russell & Kopylova (1999) at the Jericho Kimberlite Pipes located 230 km southwest of High Lake. The much higher heat flow at High Lake can probably be attributed to the effect of the massive volcaniclastic sulphide deposit that can act as a conduit for conduction of heat to the surface.

The reduction in the estimated heat flux observed at the shallower depths (50 m to 100 m) at HL03-28 is consistent with other studies investigating GSTH. This change in heat flux is apparent in Superior Province temperature logs (Shen & Beck 1992), temperature logs from three borehole in northern Québec (Chouinard et al. 2007), and also in temperature profiles reported in the Canadian Arctic Archipelago (Taylor et al. 2006). However, without more detailed information on the three-dimensional shape of the High Lake ore body, which could influence lateral heat flux, and/or the regional history of snow cover, which would impact vertical heat flux (Stieglitz et al. 2003), it is impossible to know how much of the observed warming can be attributed solely to changes in GSTH.

Conclusions

We have deployed a multifunctional borehole observatory at the High Lake Project Site, which includes a bottomhole assembly for subpermafrost geochemical sampling using a

U-tube sampler located beneath a packer, and a pressure/temperature sensor for monitoring hydrologic conditions. The deployment lines contained a distributed thermal perturbation measurement system, consisting of a fiber-optic cable for distributed temperature measurements, and a heat trace cable to uniformly heat the wellbore.

Given the interest in using borehole temperature profiles as an indicator of paleoclimate, we have demonstrated a methodology for using the DTPS data for estimating formation thermal conductivity as a function of depth with meter-scale resolution. Having *in situ* estimates for thermal properties can reduce uncertainty in inverting borehole temperature profiles, leading to more accurate delineations of ground surface temperature history (GSTH). Future work using the High Lake data set will estimate the GSTH using the detailed thermal conductivity profile and the measured baseline temperature profile.

Acknowledgments

This work was supported by a grant from the NASA Astrobiology Institute (NASA NNA04CC03A). Additional support was provided through the Geological Survey of Finland, Espoo, Finland, POSIVA Oy, Finland, SKB, Sweden, and the Nuclear Waste Management Organization, Ontario, Canada. The authors wish to recognize the invaluable assistance and logistic support provided by Zinifex Canada Inc. in giving access to the High Lake Project Site. We thank Stefan Finsterle, Jacek A. Majorowicz and Alan E. Taylor, who provided numerous constructive comments on this manuscript. We also wish to acknowledge the generous loan of the Agilent DTS by Agilent Technologies.

References

Anisimov, O.A., Vaughan, D.G., Callaghan, T.V., Furgal, C., Marchant, H., Prowse, T.D., Vilhjálmsson, H. & Walsh, J.E. 2007. Polar regions (Arctic and Antarctic). In: M.L. Parry, O.F. Canziani, J.P. Palutikof, P.J. van der Linden & C.E. Hanson (eds.), *Climate Change 2007: Impacts, Adaptation and Vulnerability. Contribution of Working Group II to the Fourth Assessment Report of the Intergovernmental Panel on Climate Change*, Cambridge: Cambridge University Press, 653–685.

Clauser, C. & Huenges, E. 1995. Thermal conductivity of rocks and minerals. In: T.J. Ahrens (ed.), *Rock Physics and Phase Relations: A Handbook of Physical Constants*. American Geophysical Union.

Freifeld, B.M., Trautz, R.C., Yousif K.K., Phelps, T.J., Myer, L.R., Hovorka, S.D. & Collins, D. 2005. The U-Tube: A novel system for acquiring borehole fluid samples from a deep geologic CO_2 sequestration experiment. *J. Geophys. Res.* 110: B10203, doi:10.1029/2005JB003735.

Harris, R.N. & Chapman, D.S. 1997. Borehole temperatures and a baseline for 20th-Century global warming estimates. *Science* 275: 1618–1621.

Harris, S.A. 1986. *The Permafrost Environment.* London, England: Biddles Ltd., Guildford and King's Lynn. 276 pp.

Lachenbruch, A.H. & Brewer, M. 1959. Dissipation of the temperature effect in drilling a well in arctic Alaska, United States Geological Survey Bulletin 1083-C, 73–109.

Lachenbruch, A.H. & Marshall, B.V. 1986. Changing climate: geothermal evidence from permafrost in the Alaskan Arctic. *Science* 234: 689–696.

Mareschal, J.C., Nyblade, A., Perry, H.K.C., Jaupart, C. & Bienfait, G. 2004. Heat flow and deep lithospheric thermal structure at Lac de Gras, Slave Province, Canada. *Geophys. Res. Lett*. 31: L12611, doi:10.1029/2004GL020133.

Majorowicz, J.A. & Safanda, J. 2001, Composite surface temperature history from simultaneous inversion of borehole temperatures in western Canadian plains. *Global and Planetary Change* 29: 231–239.

Russell, J.K. & Kopylova, M.G. 1999. A steady state conductive geotherm for the north central Slave, Canada: Inversion of petrological data from the Jericho Kimberlite pipe. *J. Geophys. Res.* 104: 7089–7101.

Selker, J.S., Thévenaz, L., Huwald, H., Mallet, A., Luxemburg, W. van de Giesen, N., Stejskal, M., Zeman, J., Westhoff, M. & Parlange M.B. 2006. Distributed fiber-optic temperature sensing for hydrologic systems. *Water Resour. Res.* 42: W12202, doi:10.1029/2006WR005326.

Shen, P.Y. & Beck, A.E. 1992. Paleoclimate change and heat flow density inferred from temperature data in the Superior Province of the Canadian Shield. *Palaeogeogr., Palaeoclimatol., Palaeoecol. (Global Planet. Change Sect.)* 98: 143–165.

Stieglitz, M., Déry, S.J., Romanovsky, V.E. & Osterkamp, T.E. 2003. The role of snow cover in the warming of arctic permafrost. *Geophys. Res. Lett.* 30(13): 1721, doi:10.1029/2003GL017337.

Taylor, A.E., Burgess, M.M., Judge, A.S., Allen, V.S. & Wilkinson, A. 1998. Canadian Geothermal Data Collection—Deep permafrost temperatures and thickness of permafrost. In:*Circumpolar Active Layer Permafrost System (CAPS), Version 1.0*. Compiled by International Permafrost Association, Data and Information Working Group, National Snow and Ice Data Center, University of Colorado, Boulder, CO. CD-ROM.

Taylor, A.E., Wang, K., Smith, S.L., Burgess, M.M. & Judge, A.S. 2006. Canadian Arctic permafrost observatories: detecting contemporary climate change through inversion of subsurface temperature time series. *J. Geophys. Res.* 111: B02411, doi:10.1029/2004JB003208.

The Permafrost Legacy of Siemon W. Muller

Hugh M French
10945 Marti Lane, North Saanich, British Columbia, Canada
Frederick E. Nelson
Department of Geography, University of Delaware, USA

Abstract

Siemon W. Muller's contribution to permafrost engineering in North America is widely recognized. His status in this field derives from a 1943 US Army engineering manual, compiled from translated Soviet literature and prepared to alleviate problems experienced during construction of the Alcan (Alaska) Highway. Muller's status in permafrost science is derived from the same source, but in this context his contribution is less well defined. A previously unpublished manuscript by Muller, drafted prior to 1963, could have made a contribution to permafrost *science* as significant as his earlier effort was to permafrost *engineering*. It would also have encouraged development of a holistic approach to geocryology in North America, similar to that developed in Russia and China, as opposed to the dualism that evolved between permafrost science and permafrost engineering in the mid-century North American literature.

Keywords: geocryology; history of science; North America; permafrost engineering; permafrost science.

Introduction

Siemon W. Muller is generally regarded as the "father" of permafrost studies in North America. Muller used the term *permafrost*, which he apparently calqued from Russian (Kabakchi & Butters 1989, French & Nelson 2008), to describe the perennially frozen and often ice-rich terrain encountered during construction of the Alcan (Alaska) Highway in 1942–43. He documented the engineering problems associated with construction in ice-rich permafrost terrain in a US Army handbook, first printed in 1943 and subsequently declassified and printed in book form in 1947 (Muller 1943, 1947). This book formed the framework for North American permafrost engineering over the next two decades.

Less clear is Muller's legacy as regards permafrost science in North America. A monograph by Stephen Taber (1943), published virtually simultaneously, provided a more thorough discussion of the genesis and evolution of perennially frozen ground in Alaska. The present paper draws upon a previously unpublished manuscript completed by 1963 (French & Nelson 2008) and speculates about how Muller's contribution to permafrost science might have been enhanced if this manuscript had been published at that time. The near-complete manuscript was found in 1996 in his files.

The Man

Of critical significance to Muller's permafrost legacy was his Russian heritage. He was born in Blagoveshchensk, eastern Russia, near the border of Manchuria. He left Russia shortly after the Russian revolution and moved to the US in 1921. His fluency in Russian allowed him to introduce Russian permafrost knowledge into North America at a time when few North American scientists were fluent in Russian and there were few contacts between Soviet and North American scientists.

Contrary to what one might expect, permafrost was a distinctly subsidiary interest for Muller, and he never contributed to its primary literature. The central focus of his research was the Triassic paleontology and stratigraphy of western Nevada. His teaching responsibilities at Stanford University, where he studied and worked for more than 40 years, included courses in historical geology, paleontology, stratigraphy, and the geology of California.

During the 1930s, Muller developed a close collaboration with the USGS geologist Henry Ferguson. They worked together on the geology of western Nevada, and Muller assumed a part-time affiliation with the USGS. Muller's knowledge of stratigraphy, structural geology, and field methods, combined with his knowledge of Russian, explains why he was approached by the US Army in 1942 to give geological advice during construction of the Alcan Highway. The outstanding merit of the 1943 US Army handbook was its accurate, well-organized summary of early Russian permafrost literature. This allowed others to solve the many permafrost engineering problems encountered in wartime projects in Alaska and northern Canada.

Upon his return to academia in 1945, Muller resumed his teaching responsibilities and collaborative research with Henry Ferguson. He also began teaching a course on permafrost. His only graduate student to concentrate on permafrost was Troy Péwé (PhD Stanford, 1953) but others, such as Lou deGoes and some USGS staff at Menlo Park, probably attended his classes. Muller published virtually nothing on permafrost during the remainder of his career. The unpublished book manuscript referred to above appears to have been his only attempt to add to the permafrost literature. We can only speculate about the reasons why he did not bring the book to publication (see French & Nelson 2008).

The Growth of Geocryology in the USSR

The occurrence of perennially frozen ground in northern North America had been known in general terms for more than a century by the time of Muller's 1943 report (e.g., Leffingwell 1919; see French 2003, 29–34). By the early 1930s the extent of frozen ground in both Alaska and northern Canada was reasonably well known. However, a detailed understanding of the permafrost terrain of central Alaska was still lacking.

By contrast, the Russian experience with frozen ground was far more extensive (see Shiklomanov 2005). This was because an Institute of Permafrost had been established in Yakutsk by the USSR Academy of Sciences in 1939. Also, the movement of population, often penal in nature, to the more remote parts of Siberia had begun. The boreal forest was being removed and agriculture started. Russian-language texts soon summarized extensive knowledge about permafrost (e.g., Sumgin 1927, 1937), and the first edition of what was to become the standard Russian text on permafrost for the next 25 years, *Obshcheye Merzlotovedeniya (General Permafrostology*), was published in 1940 (Sumgin et. al. 1940). By the late 1950s, a major publication by the V.A. Obruchev Institute of Permafrost Studies, Moscow, entitled *Osnovy geokriologii (merzlotevedeniya) (Principles of Geocryology*) (Shvetsov & Dostovalov 1959) had appeared. This text was divided into two volumes: Part I – General Geocryology and Part II – Engineering Geocryology. The science and engineering aspects of permafrost were explicitly linked in one discipline: geocryology. A similar approach to geocryology developed later in China (Academia Sinica 1975, Zhou et al. 2000).

The Emergence of Permafrost Science and Permafrost Engineering in North America

In North America, the most significant early advances in understanding permafrost phenomena were made in a series of laboratory experiments by Stephen Taber, an American engineer. In a number of papers published between 1916 and 1930, he examined the mechanics of frost action and the process by which ice segregates in freezing soil (Taber 1929, 1930). These were seminal contributions, soon followed by Swedish studies of frost heaving, especially as they applied to roads and buildings, and then by Japanese military engineers in Manchuria during the Second World War (see Sugaya 1956). It was in a similar context that Muller became involved, in 1942–43, in construction of the Alcan Highway (Fig. 1).

In the same year that Muller's US Army handbook appeared, Stephen Taber published a monograph-length paper summarizing available knowledge on perennially frozen ground in Alaska (Taber 1943). This paper describes the climatic and vegetation conditions associated with perennially frozen ground and related geomorphological processes, including freezing and thawing, frost heaving, and mass wasting. It also discusses the Quaternary-age gravels and silts that overlie bedrock in Alaska, their frozen nature, and the occurrence of ground ice, both in bedrock and surficial sediments. Finally, a sequence of Pleistocene events is set out, involving successive periods of sediment deposition, deep freezing, deep thawing and erosion, and refreezing.

Taber's 1943 monograph, rather than Muller's, might more properly be regarded as the beginning of modern permafrost science in North America. Not only does it discuss the conditions associated with permafrost occurrence (as does Muller's), but also it considers the Pleistocene history and origin of permafrost and ground ice as mentioned above. These became central themes in permafrost science in North America in the second half of the 20th century. Examples are T.L. Péwé's Pleistocene and Quaternary geology work in Alaska, J.R. Mackay's permafrost and ground-ice-related studies in the western Canadian Arctic, and A.L. Washburn's concern for solifluction and mass-wasting processes. It is significant that Taber used the term "perennially frozen ground" and made no mention of either "permanently frozen ground" or "permafrost." The latter were the two terms used by Muller in his 1943 manual. Permafrost is now, of course, generally referred to as being "perennially" rather than "permanently" frozen ground.

Muller's primary concerns in his 1943 manual were the geotechnical and engineering problems associated with ice-rich permafrost terrain. His admirably explicit treatment

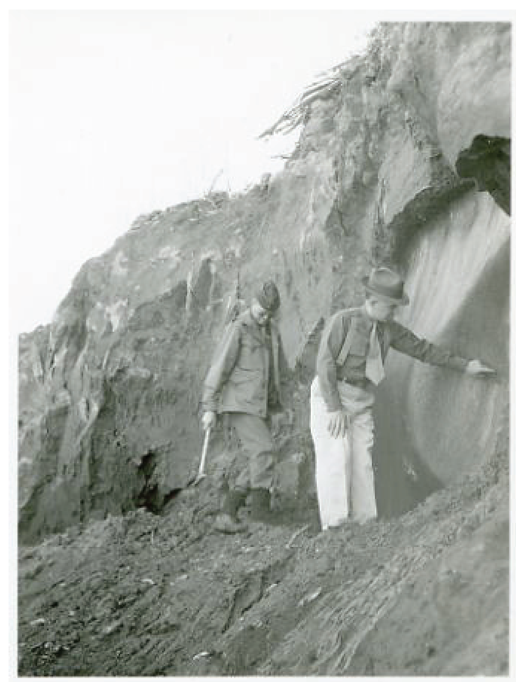

Figure 1. Photo of Siemon Muller in 1944, near Fairbanks, Alaska, with Roy Earling, President of the U.S. Smelting, Refining, and Mining Company, and Fairbanks Exploration Company. Muller is wearing the clothes of a US Army officer, but with no insignia or rank; he was a civilian. The sediments that enclose the ice wedges are part of the Goldstream Formation of Wisconsinan age (~120,000 to 10,000 years ago). The upper 1.5 m (above the ice wedges) is Holocene-age sediment (Ready Bullion Formation). Caption details supplied by T.L. Péwé, December 1996. Source of photo: unknown.

of these issues promoted the formation of governmental research agencies involved with cold regions geotechnical engineering in both the US and Canada (e.g., the Snow, Ice and Permafrost Research Establishment [SIPRE], later to become the Cold Regions Research and Engineering Laboratory [CRREL], in Hanover, New Hampshire, and the Division of Building Research [DBR], National Research Council of Canada [NRCC], in Ottawa, Ontario); and the emergence of professional groups such as the Technical Committee on Cold Regions Engineering (TCCRE) of the American Society of Civil Engineers (ASCE), the Cold Regions Engineering Division of the Canadian Society of Civil Engineering (CSCE), and the Cold Regions Geotechnology Division of the Canadian Geotechnical Society (CGS).

The Muller and Taber publications of 1943 are complementary. Symbolically, they mark the beginning of a dualism that continues in North America between the literature of permafrost science and permafrost engineering. Attempts were initially made to bridge the divide, as personified by the close collaboration between Roger Brown and Hank Johnston at the NRCC (e.g., Brown & Johnston 1964, Johnston et al. 1963), and various USGS reports on permafrost terrain problems in Alaska (e.g., Hopkins et al. 1955, Lachenbruch 1962, Ferrians et al. 1969). However, it is fair to conclude that cold regions engineering soon developed as a separate discipline, only to be reunited with permafrost science every five or ten years at the international permafrost conferences.

"Frozen in Time" – The 1963 Manuscript

Muller's previously unpublished manuscript (French & Nelson 2008) indicates that he was acutely aware of the imbalance between permafrost science and permafrost engineering in his 1943 monograph. It is clear that in the 15 years following his return to academia in 1945, he closely followed the permafrost literature in both North America and the USSR. Not only did he attempt to update the North American engineering practices described in his 1943 manual, but also he attempted to incorporate Russian understanding of permafrost science. Several examples can be offered.

First, Muller was aware of the importance of the unusual permafrost conditions that characterize the base of the active layer and the top of permafrost. This is why he used the term *active zone* rather than the more conventional term *active layer* that dominated the North American literature. The evolution of his ideas concerning near-surface permafrost terrain is illustrated in Figures 2 and 3, where Muller's 1943 diagram is compared with a reworked version in the later manuscript. In Figure 3b Muller indicates that the active zone is composed of two layers: a near-surface layer that freezes and thaws annually and a lower layer ("pereletok") that might remain frozen in certain years of cooler summers and thawed in others of warmer summers. This reflected the Russian permafrost literature. Nearly 30 years were to pass

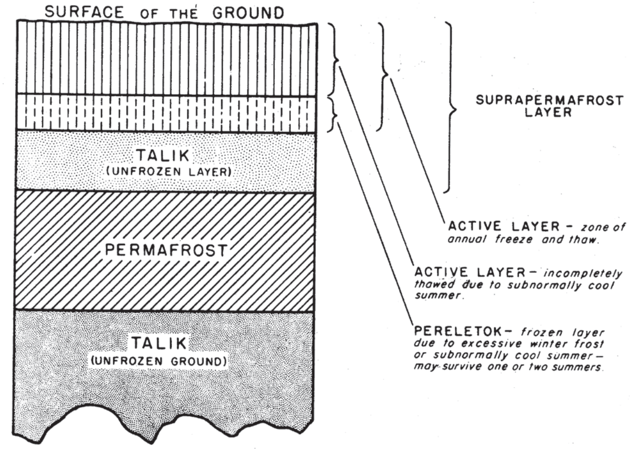

Figure 2. Muller's 1943 Figure 5, entitled "Diagram showing the different layers in the permafrost area."

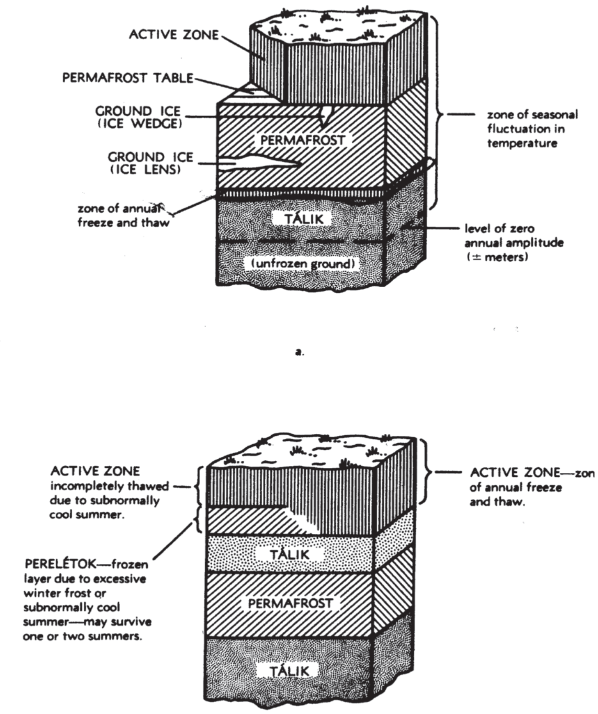

Figure 3. The 1963 manuscript's Figure 1, entitled "Diagrams of profiles with permafrost."

before a three-layer concept of the active layer-permafrost interface was formally introduced into the North American literature (Shur 1988, Shur et al. 2005). This ice-rich zone has been termed the *transient layer*.

It is now clear that the depth of the active layer fluctuates on both yearly and decadal time scales. It promotes an ice-rich layer (or "zone") at the active layer-permafrost interface. Current global warming concerns also focus attention upon this ice-rich layer; for example, it is central to the second phase of the Circumpolar Active Layer Monitoring (CALM II) program (Nelson et al. 2004).

Second, Muller understood the complex role played by vegetation over permafrost distribution and nature. Even before 1943, there was a large Russian literature available on

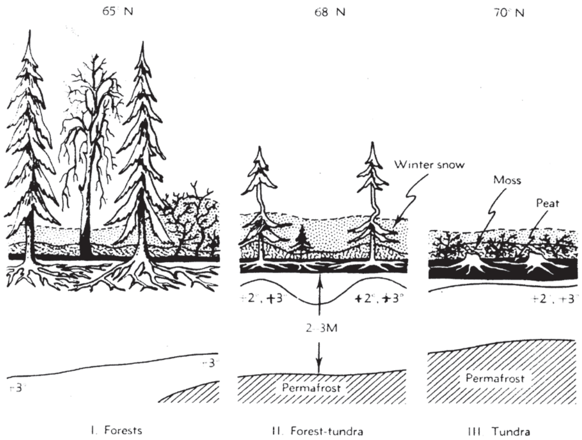

Figure 4. The 1963 manuscript's Figure 47, entitled "The combined effect of moss, peat, and snow on the distribution of roots and on the summer ground temperatures in forests, forest-tundra, and tundra, at latitudes of 65ºN, 68ºN and 70ºN."

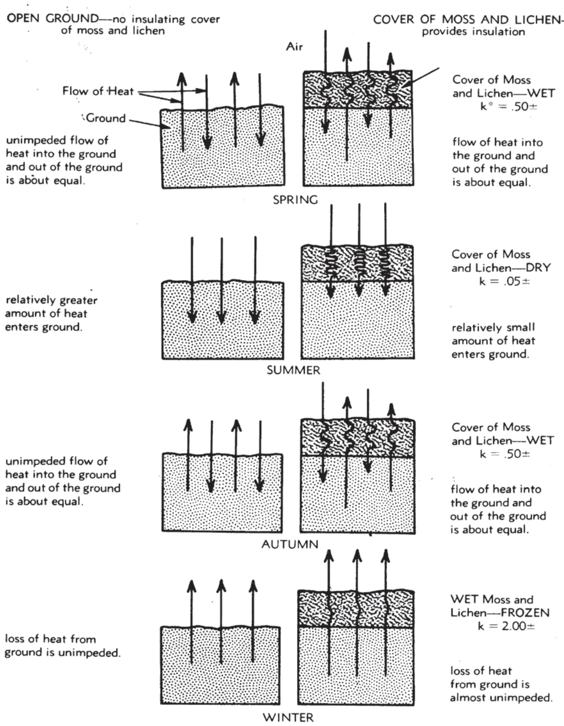

Figure 5. The 1963 manuscript's Figure 4, entitled "Flow of heat between air and ground in tundra country."

this topic (e.g., Sumgin et al. 1940, Tyrtikov 1956). Muller relied heavily on a text by A.A. Grigor'yev (1956) describing the vegetation of the Russian subarctic and tundra. For example, an elegant figure summarizes the effects of moss, peat, and snow on vegetation in the forest, forest-tundra, and tundra at latitudes of 65°, 68°, and 70°N (Fig. 4). It was not until after Muller had drafted his manuscript, and translations of the 1959 *Principles of Geocryology* had appeared, that North American permafrost scientists began to appreciate the importance of vegetation (e.g., Brown 1966, 1970).

The importance ascribed by Muller to the influence of vegetation was also a precursor to modern studies of permafrost, ground climate, and the "n-factor" (e.g., Lunardini 1978, Klene et al. 2001). For example, Figure 5 summarizes his discussion of the effects of soil thermal conductivity (k) upon heat flow in "open ground" (i.e., tundra with no insulating cover of moss and lichen) and in terrain where a cover of moss and lichen provides insulation.

Third, Muller expanded the treatment of ground ice in his 1943 manual by discussing ground ice in the context of cryostructures and cryotextures. This Russian approach (Vtyurin 1965) was far more advanced than the descriptive classification used in North America at the time (e.g., Pihlainen & Johnston 1963), since it inferred genesis and implied permafrost history. The cryostratigraphic approach to permafrost history only developed in North America three decades later (e.g., Mackay 1974, Burn et al. 1986, Murton & French 1993).

In other ways, too, Muller was ahead of his time. For example, he used some of the "cryo" terminology of K. Bryan (1946). At the time, this was largely rejected by the academic community. He thereby avoided the semantic pitfalls associated with the terms *frozen* and *unfrozen*, an ambiguity that continued into the 1990s (Burn 1998). Also, in his discussion of "cryogenic" weathering, he relied on Soviet literature that preceded later research, demonstrating the existence of microbiological processes at sub-zero temperatures (e.g., Gilichinsky et al. 1995).

Finally, many engineering concepts in the earlier text were upgraded to incorporate advances in the 1950s. For example, the manuscript reveals that Muller clearly understood the significance of moisture migration in freezing soils and its relevance to frost heave and ice segregation. Following recent Soviet work (Bozhenova 1957), Muller illustrated how moisture migrates in freezing soils (Fig. 6). Although this was confirmed by the subsequent work of E. Penner (1959), it was not until 20 years later that its geomorphological significance was recognized (e.g., Cheng 1983, Mackay 1983).

One of the last meetings Muller attended before his death in 1970 was a USGS seminar dealing with the Alaska North Slope. When Muller raised a concern about the engineering planning of the proposed pipeline, the USGS scientist A.H. Lachenbruch (1970, J5) responded that "substantial unsolved problems have received remarkably little attention." One is tempted to speculate about the impact Muller's then-unpublished text might have had on the subsequent construction of the TAPS Pipeline later in that decade.

Conclusions

Muller's pioneering status in North American permafrost engineering is well deserved. Viewed from the privileged position of hindsight, however, one can argue that his 1943 monograph neglected permafrost science. Undoubtedly, the realities of wartime explain this.

Muller's "lost" manuscript was an attempt to rectify this deficiency, but unfortunately and for unknown reasons, he abandoned his nearly completed project, never to return to it.

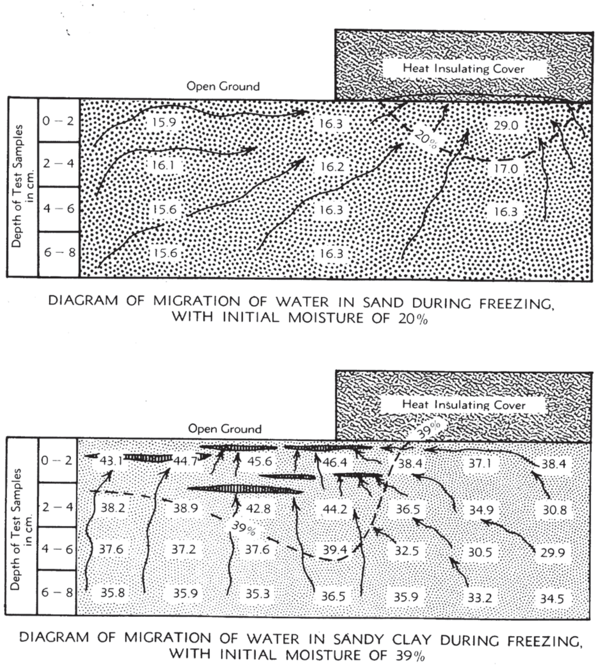

Figure 6. The lower two diagrams of the 1963 manuscript's Figure 13, entitled "Diagrams of migration of water in sand (sandy clay) during freezing with initial moisture contents of 13%, 20%, and 39%."

Muller's manuscript, if published in 1963 at the time of the First International Conference on Permafrost, would have advanced permafrost science in North America in the same way that his 1943 US Army handbook became a benchmark for permafrost engineering in North America. It contained concepts and information that would have advanced permafrost science in North America by at least two decades. But even more important, by integrating permafrost science with permafrost engineering, Muller would have promoted a holistic approach to geocryology in North America. This would have made the study of permafrost in North American more similar to the discipline of geocryology that developed in both Russia and China.

Acknowledgments

HMF acknowledges the late Troy L. Péwé, who instilled in him an appreciation of the legacy of Siemon Muller and who passed to him, in 1995, many of Muller's books, papers and photographs. Jerry Brown and an anonymous reviewer provided helpful comments on the manuscript

References

Academia Sinica. 1975. *Permafrost*. Lanzhou: Research Institute of Glaciology, Cryopedology and Desert Research, China, 124 pp. (in Chinese). (National Research Council of Canada, Ottawa, Technical Translation, 2006 (1981), 224 pp.).

Bozhenova, A.P. 1957. Physical phenomena and processes in freezing and frozen grounds. *Merzylykh Gruntov, Institut Merzlotevedeniya*, Akad. Nauk SSSR, 3: 23-27 (in Russian).

Brown, R.J.E. 1966. Influence of vegetation upon permafrost. In: *Proceedings, Permafrost International Conference, Washington, D.C.*, National Academy of Science – National Research Council, Publication 1287, 20-25.

Brown, R.J.E. & Johnston, G.H. 1964. Permafrost and related engineering problems. *Endeavour* XXIII(89): 66-72.

Bryan, K. 1946. Cryopedology – the study of frozen ground and intensive frost action with suggestions on nomenclature. *American Journal of Science* 244: 622-42.

Burn, C.R. 1998. The active layer: two contrasting definitions. *Permafrost and Periglacial Processes* 9: 411-416.

Burn, C.R., Michel, F.A. & Smith, M.W. 1986. Stratigraphic, isotopic and mineralogical evidence for an early Holocene thaw unconformity at Mayo, Yukon Territory. *Canadian Journal of Earth Sciences* 23: 794-803.

Cheng, G. 1983. The mechanism of repeated-segregation for the formation of thick layered ground ice. *Cold Regions Science and Technology* 8: 57-66.

Ferrians, O.J., Jr., Kachadoorian, R. & Greene, G.W. 1969. Permafrost and related engineering problems in Alaska. *United States Geological Survey Professional Paper* 678, 37 pp.

French, H.M. 2003. The development of periglacial geomorphology: 1-up to 1965. *Permafrost and Periglacial Processes* 14: 29-60.

French, H.M. & Nelson, F.E. (eds.) 2008. *Frozen in Time: a Manual on "Permafrost and Engineering Problems" by S. W. Muller.* New York: American Society of Civil Engineers, Technical Committee on Cold Regions Engineering, in press.

Gilichinsky, D., Wagener, S. & Vishnevetskaya, T.A. 1995. Permafrost microbiology. *Permafrost and Periglacial Processes* 6: 281-291.

Grigor'yev, A.A. 1956. *The Subarctic*. Moscow: Institute of Geography, USSR Academy of Sciences, 223 pp. (in Russian).

Hopkins, D.M., Karlstom, T.D. & others. 1955. Permafrost and groundwater in Alaska. *United States Geological Survey Professional Paper* 264-F, 113-146.

Johnston, G.H., Brown, R.J.E. & Pickersgill, D.N. 1963. *Permafrost Investigations at Thompson, Manitoba: Terrain studies*. Ottawa: Division of Building Research, National Research Council, Technical Paper 158, 51 pp.

Klene, A.E., Nelson, F.E., Shiklomanov, N.I. & Hinkel, K.M. 2001. The N-Factor in natural landscapes; variability of air and soil-surface temperatures, Kuparuk River Basin, Alaska, USA. *Arctic, Antarctic and Alpine Research* 33: 140-148.

Lachenbruch, A.H. 1962. Mechanics of thermal-contraction cracks and ice-wedge polygons in permafrost. *Geological Society of America, Special Paper* 70, 69 pp.

Lachenbruch, A.H. 1970. Themal considerations in permafrost. In: W.L. Adkison & M.M. Brosgé (eds.), *Proceedings of the Geological Seminar on the North Slope of Alaska*. Pacific Section, American Association of Petroleum Geologists, Los Angeles, J1-J5.

Leffingwell, E. de K. 1919. The Canning River region, northern Alaska. *United States Geological Survey Professional Paper* 109, 251 pp.

Lunardini, V. 1978. Theory of n-factors and correlation of data. *Proceedings of the Third International Conference on Permafrost, Edmonton, Alberta, Canada 10–13 July 1978:* 40-46.

Mackay, J.R. 1974. Reticulate ice veins in permafrost, Northern Canada. *Canadian Geotechnical Journal* 11: 230-237.

Mackay, J.R. 1983. Downward water movement into frozen ground, western arctic coast. *Canadian Journal of Earth Sciences* 20: 120-134.

Muller, S.W. 1943. *Permafrost or Permanently Frozen Ground and Related Engineering Problems*. United States Geological Survey, Strategic Engineering Study, Special Report No 62, Intelligence Branch Office, Chief of Engineers, U.S. Army, 136 pp.

Muller, S.W. 1947. *Permafrost or Permanently Frozen Ground and Related Engineering Problems.* Ann Arbor, MI: J. W. Edwards, 231 pp.

Murton, J.B. & French, H.M. 1994. Cryostructures in permafrost, Tuktoyaktuk coastlands, western Arctic, Canada. *Canadian Journal of Earth Sciences* 31: 737-747.

Nelson, F.E., Shiklomanov, N.I., Hinkel, K.M. & Christiansen, H.H. 2004. Introduction: the Circumpolar Active Layer Monitoring (CALM) Workshop and the CALM II Program. *Polar Geography* 28: 253-266.

Penner, E. 1959. The mechanism of frost heaving in soils. *Highway Research Board, Bulletin* 225: 1-13.

Péwé, T.L., 1953. *Geomorphology of the Fairbanks Area, Alaska*. Ph.D. Dissertation, Stanford University, 308 pp.

Pihlainen, J.A. & Johnston, G.H. 1963. *Guide to a Field Description of Permafrost*. Ottawa: National Research Council, Associate Committee on Soil and Snow Mechanics, Technical Memorandum 79, 23 pp.

Shiklomanov, N.I., 2005. From exploration to systematic investigation: development of geocryology in 19th- and early-20th-Century Russia. *Physical Geography* 26: 249-263.

Shur, Y. 1988. The upper horizon of permafrost soils. *Proceedings of the Fifth International Conference on Permafrost, Trondheim, Norway, 2–5 August, 1988:* 867-871.

Shur, Y., Hinkel, K.M. & Nelson, F.E. 2000. The transient layer: implications for geocryology and climate-change science. *Permafrost and Periglacial Processes* 16: 5-18.

Shvetsov, P.F. & Dostovalov, B.N. (eds.) 1959. *Osnovy geokriologii (merzlotovedeniya) (Fundamentals of geocryology)*. Moscow: Collected publications by staff members of the USSR Academy of Sciences, Institute of Permafrost, Parts I and II, USSR Academy of Sciences Press (in Russian).

Sugaya, J. 1956. *Congelation-structure and frost-heaving ratio at Assan, Manchuria*. Ottawa: Canada Defence Research Board, Translation T 54 J (from unpublished manuscript) by E. R. Hope, 18 pp.

Sumgin, M.I. 1927, 1937. *Soil Permafrost within the USSR.* Vladivostok: 1st edition; Moscow – Leningrad: 2nd edition, Academii Nauk USSR, 372 pp. (in Russian).

Sumgin, M.I., Kachurin, S.P., Tolstikhin, N.I. & Tumel, V.F. 1940. *Obshche merzlotovedeniya (General Permafrostology).* Moscow – Leningrad: USSR Academy of Sciences, 340 pp. (in Russian).

Taber, S. 1929. Frost heaving. *Journal of Geology* 37: 428-461.

Taber, S. 1930. The mechanics of frost heaving. *Journal of Geology* 38: 303-317.

Taber, S. 1943. Perennially frozen ground in Alaska; its origin and history. *Geological Society of America Bulletin* 54: 1433-1548.

Tyrtikov, A.P. 1956. The effect of vegetation on perennially frozen soil. In: *Data on the principles of the study of frozen zones in the earth's crust*, Issue III, Institute of Permafrost Studies, USSR Academy of Sciences, Moscow. (in Russian). (National Research Council of Canada, Ottawa, Technical Translation 1088 (1964), 69-90).

Vtyurin, B.I. 1965. *Cryogenic Structure of Quaternary sediments*. Moscow: Nauka, Academy of Sciences USSR, 151 pp. (in Russian).

Zhou, Y., Gou, D., Cheng, G. & Li, S. 2000. *Geocryology in China*. Lanzhou: Cold and Arid Regions Environmental and Engineering Research Institute (CAREERI), Chinese Academy of Sciences, 450 pp. (in Chinese).

Seasonal Thaw of Soils in the North Yakutian Ecosystems

D.G. Fyodorov-Davydov, A.L. Kholodov,V.E. Ostroumov, G.N. Kraev, & V.A. Sorokovikov
Institute of Physicochemical and Biological Problems in Soil Science, Russian Academy of Sciences, Pushchino, Moscow

S.P. Davydov
Northeast Science Station, Pacific Institute of Geography, Far East Branch, RAS, Chersky, Sakha (Yakutia) Republic, Russia

A.A. Merekalova
Geographical Faculty, Lomonosov State University, Moscow, Russia

Abstract

The active layer thickness (ALT) in tundra ecosystems of North Yakutia is controlled by soil texture. Normal thaw depth in zonal soils of sandy tundra are about 50–105 cm, while in soils of loamy tundra it is 35–70 cm. In the intrazonal ecosystems, the seasonal thaw depth is smaller than in complementary zonal ecosystems. Studies in the Kolyma Lowland show that the ALT pattern is subject to climatic zonality. ALT reaches 27–37 cm in the Arctic tundra subzone; in the Typical tundra it is 41–42 cm, and 43–49 cm in the Southern tundra. In the Northern taiga, the thaw depth under positive microrelief elements varies between 43 and 90 cm in loamy soils and between 65 and 120 cm in sandy soils. According to our data, the active layer in Yana-Indigirka and Kolyma Lowlands experienced a progressive thickening over the 2000–2006 period.

Keywords: active layer; climate; permafrost; Russia; soils.

Introduction

The monitoring of the active layer thickness (ALT) plays an important role in global permafrost observation efforts. During the 1996–2006 period, extensive active-layer field observations were conducted in North Yakutia under the auspices of the international Circumpolar Active Layer Monitoring (CALM) program (Brown et al. 2000). An analysis of empirical data and previously published information (e.g., Karavaeva 1969, Garagulya et al. 1970, Savvinov 1976, Soloviev 1978, Elovskaya et al. 1979, Perfilieva et al. 1991) have revealed spatial and temporal patterns of seasonal thaw for one of the least investigated regions. Special emphasis was placed on analysis of the active layer response to changing air temperature attributable to climate variability and change.

Analysis, conducted in permafrost regions of West Siberia, indicates pronounced deepening of seasonal thaw over the decades (Moskalenko 2001, Melnikov et al. 2004, Pavlov et al. 2004). No long-term measurements of the active layer depth are known from North Yakutia. In this paper we investigate the spatial and temporal ALT trends for North Yakutia and its relation to landscape and climatic variables. Due to the lack of adequate long-term empirical information, this study is focused primarily on recent changes in the active-layer thickness.

Study Area

The study was conducted primarily in the tundra zone of North Yakutia and Northern taiga subzone of the Lowlands (Fig. 1). The observational sites were selected to represent characteristic landscapes of both bioclimatic zones.

The tundra zone of Yakutia occupies the coast and islands of East-Siberian and Laptev seas and extends to 250–300 km inland. Based on climatological and geobotanical criterion, it is subdivided into Arctic, Typical, and Southern tundra subzones. The territory is largely underlain by ice-rich loamy sediments of the Late Pleistocene yedoma formation, which was subject to extensive thermokarst and thermoerosion processes since the Holocene optimum. The topography is represented by alternating yedoma uplands and thermokarst depressions (alases). Upland surfaces are covered by low shrub/sedge/green moss, sedge/green moss/dryas, or green moss/osier associations, and characterized by zonal Cryozem or Gleyzem (*Glacic Haploturbels, Typic Haploturbels,* and *Typic Umbriturbels*) soils. The microrelief is represented by frost mounds. Alases are predominantly occupied by polygonized bogs. A few areas in the tundra zone are underlain by well-drained sand deposits covered by low shrub/lichen and green moss/low shrub/lichen associations with Podbur (*Spodic Psammoturbels*) soil representing a zonal soil type. The microrelief is characterized by frost mounds and hummocks.

The sites representative of the Northern taiga are underlain by loam and sands. Vegetation is characterized by larch forest with the low shrub/lichen, lichen/green moss, and low shrub/green moss/lichen associations often growing under shrub storey. Cryogenic microrelief is less expressed in Northern taiga than in tundra. Flood-plain landscapes are spotty and include drained river banks and different types of bogs. Sedge/green moss/willow and *calamagrostis* associations are found near the river channels. Frost mounds are abundant and pronounced, and they are associated with the Alluvial soddy gleyic (*Typic Umbriturbels*) soils. There is a huge variety of flood-plain bogs.

The climate of Yakutia's tundra zone is severe and strongly continental. The mean annual air temperature in tundra zone varies between -11.5°C and -15.0°C. The mean

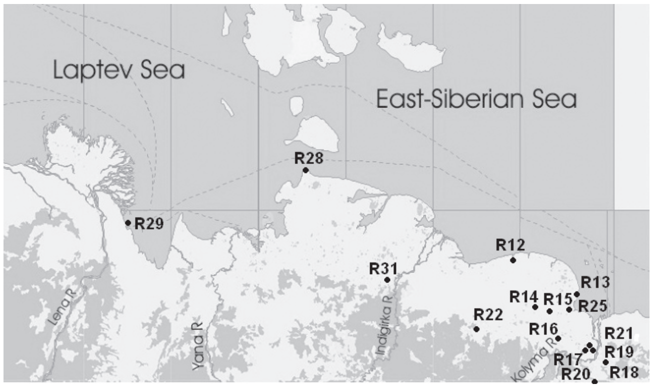

Figure 1. Map of the North Yakutia lowland with the CALM-site locations: R12 - Bolshaya Kuropatochya River (plakor and slope); R13 - Malyi Chukochiy Cape (plakor and alas); R14 - Bolshaya Chukochya River; R15 - Malaya Konkovaya River (plakor and alas); R16 - Segodnya Pingo; R17 - Akhmelo Channel; R18 - Mountain Rodinka; R19 - Glukhoe Lake; R20 - Malchikovskaya Channel; R21 - Akhmelo Lake; R22 - Alazeya River; R25 - Yakutskoe Lake; R28 - Svyatoy Nos Cape; R29 - Bykovsky Cape (plakor and alas); R31 - Allaiha River.

air temperature in January is -29.0°C to -37.5°C. The mean July air temperature varies between 2.5°C and 5.0°C in Arctic tundra and between 6.5°C and 11.5°C in Typical and Southern tundra.

The area is underlain by continuous low-temperature permafrost that is 500–650 m thick. The coldest permafrost (-10°C to -12°C) is found in the yedoma uplands of the tundra zone. Alases and areas underlain by sand are characterized by higher permafrost temperatures (-8°C to -10°C). The permafrost temperature of the Northern taiga varies within a -5°C to -8°C range and can be warmer near large streams.

Observational Program

An array of 19 active layer monitoring sites was established following standardized CALM procedure (Brown et al. 2000) in the following North Yakutian subregions: Bykovskii Peninsula, Yana-Indigirka Lowland, and Kolyma Lowland (Fig. 1). Sixteen sites are located in tundra, while the remaining three sites are situated in the Northern taiga zone. Each site consists of a regular 1 ha grid. ALT observations are carried out by graduated metal rode at 10 m interval, yielding 121 point measurements per each site. The points were arrayed with 10 m spacing in aligned rows. A set of supplementary sites of variable sizes was established in landscapes under-represented by the primary CALM sites. A detailed description of sites and observation methodology is provided in Fyodorov-Davydov et al. (2004).

Spatial Controls of Active Layer Thickness at Different Scales

The thickest active-layer of 110–125 cm was found in sandy dunes, while minimum ALT (15–30 cm) was observed at sphagnum- and/or grass/green moss-covered polygonized bogs and palsas, underlain by peat soils.

In zonal tundra, ALT usually corresponds well to soil texture. Mean multi-year ALT values for sandy Podbur soils are about 50–105 cm, with maximum recorded thaw depth reaching 120–150 cm. Loamy Cryozem and Gleyzem soils are characterized by 35–70 cm ALT with the maximum reaching 75–80 cm (Table 1).

Observations in the Kolyma Lowland, the region with the highest number of sites, showed that ALT generally corresponds to climatic zonality. For similar yedoma watersheds with zonal tundra vegetation, frost mound microrelief, and Cryozem soils, the mean multi-year ALT values increase from north to the south (Table 2). The typical ALT value for northern-most Arctic tundra is about 27–37 cm, followed by 41–42 cm in Typical tundra and 43–49 cm in southern most Southern tundra. Microtopographically, the zonal ALT pattern is better expressed for frost mounds than intermound depressions. The overall ALT difference between Northern and Southern tundra locations is about 12–22 cm. ALT difference within frost mounds increases to 30 cm, and decreases to 10–13 cm for intermound depressions (Table 3).

Sandy tundra soils are located predominantly in the northeast of the Kolyma Lowland (so called Khallerchinskaya tundra) and distributed in a narrow latitude belt within the Southern tundra subzone. Due to meridian distribution of the sandy soil, the ALT there differs more than in loamy soils characteristic of yedoma landscapes (Table 4). For instance, on the sandy sites with zonal vegetation, the ALT within the mounds increased to 35–53 cm from north to the south (1.7–2.0 times), and to 18–41 cm (1.4–1.8 times) for intermound depressions. ALT in polygonal crack areas does not express any latitudinal zonality.

The mean ALT generally increases along the tundra-taiga direction (Table 2). However, the spatial heterogeneity of landscapes also increases from north to south as the timber stand, soil and vegetation types, slope angles, and exposure play a more pronounced role. Within the Northern taiga subzone, the ALT for loamy soils ranges between 43 and 91 cm (Table 3) and between 65 and 119 cm for sandy soils (Table 4). At the same time, at the zonal boundary, the ALT in the forests is thinner than in tundra. Trees (larch) decrease the soil temperature by (a) shading ground surface; (b) creating a shielding effect through their horizontal root systems; (c) creating an additional organic soil horizon (forest litter); (d) promoting the wide occurrence of mosses; and (e) significantly delaying snow melt. As a result, in the northeast of Kolyma Lowland, the mean ALT in sandy soils of Northern taiga (R19) was up to 5–15 cm less than in its tundra analogue (R21).

The differences of seasonal thaw depth between intrazonal landscapes are determined by soil moisture and the presence and thickness of peat horizons in the soil profile. Along streams, alluvial soddy gleyic soils of riverbanks thaw to 35–90 cm, alluvial peat-gley soils of the central part of the floodplain active layer extend to 20–50 cm. In thermokarst depressions (alases), Gleyzem soils of well drained sites thaw to 25–55 cm, and the ALT at polygonized bogs with Peat-Gleyzem soils is 10–35 cm. Since the bogs are more

Table 1. The active layer thickness in different sites of observation.

Region	Subzone	Site number	Site name	Lat.	Long.	Landscape	Texture of soils parent material	Observation years	Active layer thickness, cm		
									mean values (different years)	min values (different years)	max values (different years)
Yana-Indigirka Lowland	Arctic tundra	R28	Svjatoy Nos cape	72°52′	141°01′	zonal site, plakor	loam	2001	38	16	60
	Typical tundra	R31	Allaiha River	70°33′	147°26′	zonal site, plakor	loam	2004-2006	41.5	2-28	64-65
Bykovskiy Peninsula	Arctic tundra	R29	Bykovskiy Cape	71°47′	129°25′	zonal site, plakor	loam	2003-2006	32	6-22	45-50
						alas	loam	2004-2006	30	13-20	44-53
Kolyma Lowland	Arctic tundra	R12	B.Kuropatochya River	70°55′	156°38′	zonal site, plakor	loam	1996	37	18	58
						zonal site, slope	loam	1996	27	8	48
	Typical tundra	R13	Cape M.Chukochiy	70°05′	159°55′	zonal site, slope	loam	1999-2006	42	14-37	43-64
						alas	loam	2000-2006	39	8-24	46-80
		R25	Yakutskoe Lake	69°51′	159°30′	zonal site, slope	loam	1999-2006	41	0-29	40-73
	Southern tundra	R14	B.Chukochya River	69°29′	156°59′	zonal site, slope	loam	1996-2006	42.5	3-20	54-66
		R15	M.Konkovaya River	69°23′	158°28′	zonal site, plakor	loam	1999-2006	39	14-18	50-65
						alas	loam	1996-2006	32	3-11	45-65
		R22	Alazeya River	69°19′	154°59′	zonal site, plakor	loam	1998-2005	49	1-31	70-80
		R16	Segodnya Pingo	69°05′	158°54′	polygonized bog	sand	1996-2006	41	10-25	58-100
		R21	Akhmelo Lake	68°50′	161°02′	zonal site	sand	1996-2006	92	7-56	107-145
		R17	Akhmelo Channel	68°49′	161°26′	flood-plain	loam	1996-2006	49	13-33	67-97
	Northern taiga	R19	Glukhoe Lake	68°48′	160°58′	zonal site, plakor	sand	1996-2006	81	5-51	107-148
		R18	Mountain Rodinka	68°45′	161°30′	zonal site, slope	loam	1998-2006	78.5	25-31	107-135
		R20	Malchikovskaya Channel	68°31′	161°26′	flood-plain	loam	1996-2006	52	2-32	77-108

Table 2. The active-layer thickness for zonal series of loamy soils.

Subzone	Latitude	Site number	Site name	Active layer thickness in different year (cm)										Mean multiyear values
				1996	1998	1999	2000	2001	2002	2003	2004	2005	2006	
Arctic tundra	70°55′	R12	B.Kuropatochya River	27-37	-	-	-	-	-	-	-	-	-	-
Typical tundra	70°05′	R13	Cape M.Chukochiy	-	-	37	33	38	44	49	-	50	43	42
	69°51′	R25	Yakutskoe Lake	-	-	23	37	38	47	-	-	55	45	41
Southern tundra	69°29′	R14	B.Chukochya River	43	41	38	41	-	-	-	-	48	44	42.5
	69°19′	R22	Alazeya River	-	46	46	-	-	50	-	51	53	-	49
Northern taiga	68°45′	R18	Mountain Rodinka	-	72	74	75	75	76	81.5	85	85	83	78.5

frequent and extensive in flood plains and alases than in well-drained areas, the mean ALT values are significantly lower compared to adjacent zonal ecosystems. In the sandy Khallerchinskaya tundra, the ALT depends on the thickness and composition of soil organic horizons. In polygonized bogs this corresponds to different stages of bog formation. For younger bogs, ALT varies from 47–55 cm, 18–27 cm in later stages of bog development and peat formation, and 33–60 cm in bogs characterized by the peat degradation stage. Mean ALT at the standard 100x100 m R16 site, covering the different stages of polygonized bogs, was about 1.5 times less than in the microplakor with zonal sandy soil, and about 2.2 times less than at the analogous R21 site characterized by a zonal landscape of sandy tundra.

Table 3. The mean values of active-layer thickness for zonal series of loamy soils under different microrelief elements.

Subzone	Latitude	Site name	ALT under different microrelief elements (cm)	
			mounds	depressions
Arctic tundra	70°55′	B.Kuropatochya River	38	26
Typical tundra	70°05′	Cape M.Chukochiy	46	31
	70°02′	B.Chukochya River (lower stream)	45	23
Southern tundra	69°33′	B.Chukochya River (middle stream)	56.5	28
	69°19′	Alazeya Rive	68	36
Northern taiga	68°51′	Arbyn Lake	43-44	32
	68°44′	Mountain Rodinka	60-90	45-60
	68°44′	Komarok Brook	54-91	39
	68°33′	Duvany Yar	57-60	44.5
	68°30′	Malchikovskaya Channel	64-70	-

Temporal Active Layer Dynamics

Annual ALT observations indicate a pronounced thickening of the active layer over 2000-2005 for both zonal and intrazonal soils of the Kolyma Lowland. This period was characterized by high summer temperatures. Based on observations at the Chersky Meteorological Station, the mean summer air temperatures over the 2000–2005 period were 11.3°C-13.7°C, a significant increase compared to the 1998–1999 minimum of 8.3°C-9.8°C. Due to warming, 10 of 12 sites demonstrated an ALT increase (r=0.67-0.96, n=10). In 2003, the thickening of the active layer became evident at all tundra (R13, R14, R21, R22, and R25) and Northern taiga (R18 and R19) zonal ecosystems, as well as at the majority of intrazonal landscapes including flood plains (R17), alases (R13A), and polygonized bogs (R16).

The maximum increase in ALT was observed in sandy Podbur soils and varies from 32 cm (40% from the multi-year mean) in taiga (R19, Fig. 2A), up to 40 cm (44%) in tundra (R21, Fig. 2B). An extremely high increase of 26 cm (65%) was found in the polygonized bogs of the Khallerchinskaya tundra (R16, Fig. 2C), where the relative increase of ALT was higher than at the zonal sites. The greatest ALT sensitivity to the increase of summer temperatures was realized at sites characterized by more advanced stages of bog development and covered by green moss and green moss/lichen/sedges. For these sites, a comparison with ALT data from the mid-1990s indicates an ALT increase of 11–18 cm, or 27%–51%, from the multi-year mean. By contrast, at the younger bogs covered with sedge/sphagnum, the ALT increase did not exceed 3%.

For loamy cryosol soils within the tundra zone, the relative ALT increase is reduced from north (Typical tundra) to south (Southern tundra).

At the upland site of the East Siberian Sea coast (R13), the ALT has increased by 13 cm (33%) (Fig. 2D), in the mid-stream of Bolshaya Chukochya River (R14) by 10 cm (24%) (Fig. 2E), and in the similar landscape at the tundra/taiga boundary (R22) by only 7 cm (14%) (Fig. 2F). In the

Table 4. The values of active layer thickness for zonal series of sandy soils on different nanorelief elements.

Subzone	Latitude	Site name	Active layer thickness in different nanorelief elements (ñm)			
			hummocks of mounds	mounds	depressions	polygonal cracks
Southern tundra	69°35'	Stanovaya	-	51	-	-
	69°23'	Laiydoskoe Lake	-	59	50	-
	69°23'	B.Konkovaya River	78	71	62,5	-
	69°10'	B.Pokhodskoe Lake	-	65	52	46
	69°08'	Golyavino Lake	-	50	-	-
	69°05'	Segodnya Pingo	71	63	61	51
	68°54'	Vankhotveem River	93	89	82	66.5
	68°51'	Arbyn Lake	77-88	70-83	63-75	56
	68°50'	Akhmelo Lake	102-105	98-104	89-91	-
	68°48'	Stadukhinskaya Channel	-	86	68	36
Northern taiga	69°12'	Kray Lesa	-	70	-	-
	68°48'	Glukhoe Lake	-	65-119	-	-

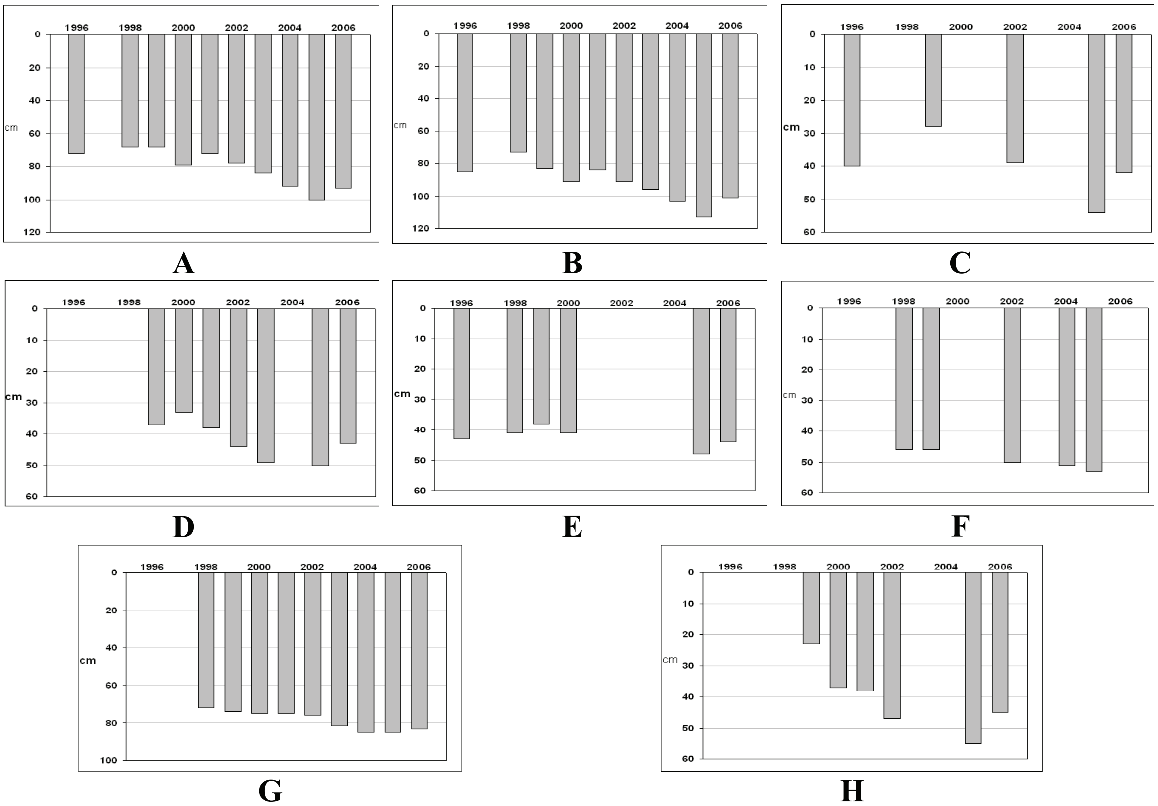

Figure 2. The annual dynamics of active layer thickness in different sites of the Kolyma lowland: A - Glukhoe Lake, R19; B - Akhmelo Lake, R21; C - Segodnya Pingo, R16; D - Malyi Chukochii Cape, R13; E - Bolshaya Chukochya River, R14; F - Alazeya River, R22; G - Mountain Rodinka, R18; H - Yakutskoe Lake, R25.

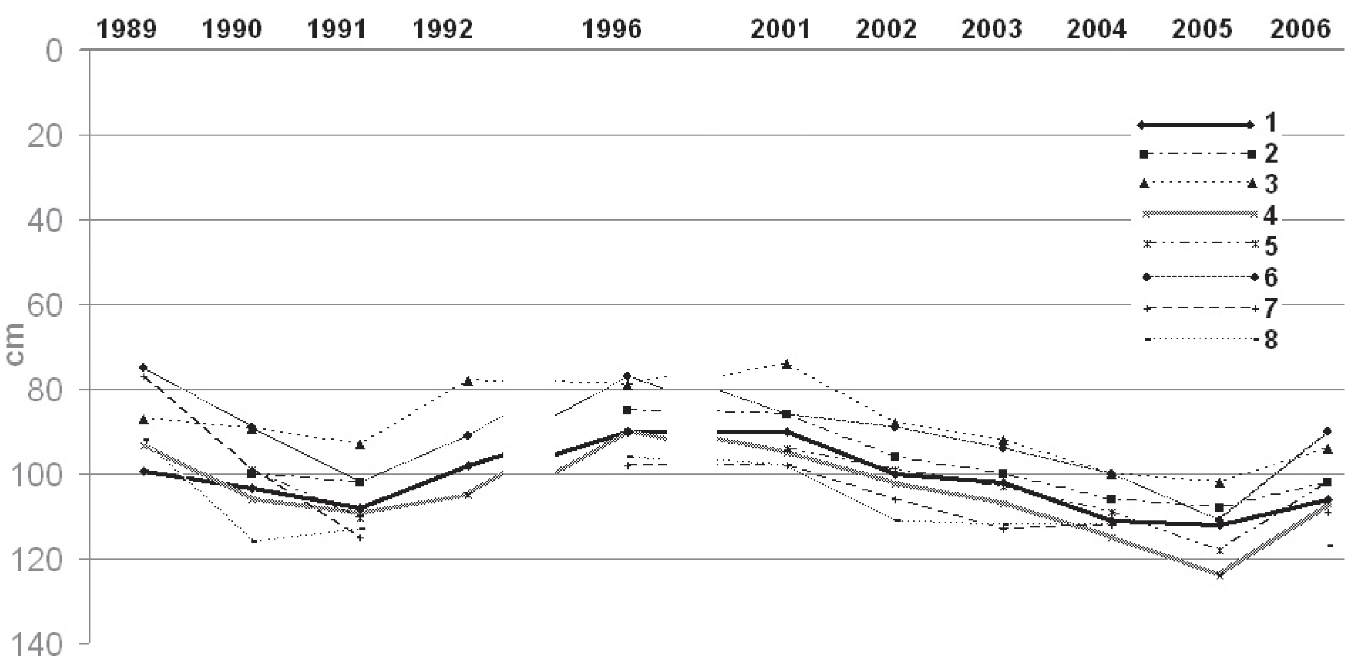

Figure 3. Annual dynamics of active-layer thickness under different micro- and microrelief elements at a tundra site near Akhmelo Lake. Legend: 1 - top of a hillock (microplakor), hummocks on the surface of mounds; 2 - top of a hillock, between hummocks in the limits of mounds; 3 - top of a hillock, between mounds; 4 - slope of a hillock (microslope), hummocks on the surface of mounds; 5 - slope of a hillock, between hummocks in the limits of mounds; 6 - slope of a hillock, between mounds; 7 - microdepression, bare spot medallions; 8 - microdepression, ridges surrounding spot medallions.

Northern taiga subzone (R18), ALT increased by 13 cm (17%) (Fig. 2G).

An even greater thaw increase of 32 cm (80%) (Fig. 2H) was observed at the other northern site (R25), located on a steep (20°–25°) southeast slope, where the ice-rich layer common to yedoma is absent.

Low summer temperatures in 2006 (10.5°C) led to a relative decrease in ALT (3%–36%) from the multi-year mean. However, ALT has never reached the level of cold of the 1998–1999 years (Fig. 2).

An increase of ALT during the investigation period was also observed at the nearby Yana-Indigirka Lowland. In 2004–2006, the mean ALT increased from 38 to 44 cm at the upland site of Typical tundra subzone (R31). On the Bykovskiy Peninsula site (R29), no significant ALT changes were obtained in either upland yedoma or alas landscapes.

The longest ALT record is available for a site established near Akhmelo Lake. Figure 3 shows temporal ALT variability at the Akhmelo site for different landscape elements over the 1989–2006 period. In 1991, the ALT reached 93–115 cm under different landscape elements in response to a high mean summer air temperature of 14.9°C.

In the mid-1990s, the active layer thinned to 74–98 cm, and beginning in 2002, ALT began to increase. In 2004–2005, the majority of the landscape elements exceeded the 1991 ALT level by 4 to 14 cm. Based on the long-term record presented in Figure 3, we can assume that the progressive increase in ALT observed over the Kolyma and Yana-Indigirka Lowlands is not attributable to irreversible global change processes, but rather show a thermal maximum of a century-scale cycle of unknown period.

Conclusions

1. The ALT in the tundra zone of North Yakutia varies significantly depending on soil texture. The mean multi-year ALT values within the positive microrelief elements are 50–105 cm for sandy Podbur soils and 35–70 cm for loamy Cryozem and Gleyzem soils.

2. The distribution of ALT in yedoma uplands and slopes is strongly influenced by climatic zonality (subzonality), which is more pronounced within positive microrelief elements than within depressions.

3. In general, the soils of flood plains, thermokarst depressions (alases), and polygonized bogs have thinner ALT than soils of corresponding zonal ecosystems. The difference in ALT between intrazonal landscapes is determined by soil moisture and thickness of peat horizons in the soil profiles.

4. The majority of soils at Northeast of Yakutia (Kolyma and Yana-Indigirka Lowlands) experienced a pronounced (14%–80%) increase in ALT over the 2000–2006 period.

Acknowledgments

This research in supported by the U.S National Science Foundation (grant OPP-9732051). We are also grateful to the Civil Research and Development Fund (GAP project RUS2-1468) in assisting us in logistical organization of the field campaign.

References

Brown, J., Hinkel, K.M. & Nelson, F.E. 2000. The circumpolar active layer monitoring (CALM) program: research designs and initial results. *Polar Geography* 24(3): 165-258.

Elovskaya, L.G., Petrova, E.I. & Teterina, L.V. 1979. *Soils of North Yakutia.* Novosibirsk: Nauka, 303 pp (in Russian).

Fyodorov-Davydov, D.G., Sorokovikov, V.A., Ostroumov, V.E., Kholodov, A.L., Mitroshin, I.A., Mergelov, N.S., Davydov, S.P., Zimov, S.A. & Davydova, A.I. 2004. Spatial and temporal observations of seasonal thaw in the Northern Kolyma Lowland. *Polar Geography* 28(4): 308-325.

Garagulya, L.S., Kudryavtsev, V.A., Kondratieva, K.A. & Maksimova, L.N. 1970. Influence of geological-geographical factors on the temperature regime of active layer grounds in the north part of Yana-Indigirka basin. *Permafrost Researchings X*, Moscow: Moscow University Publishing, 59-79 (in Russian).

Karavaeva, N.A. 1969. *Tundra Soils of North Yakutia*. Moscow: Nauka, 205 pp (in Russian).

Melnikov, E.S., Leibman, M.O., Moskalenko, N.G. & Vasiliev, A.A. 2004. Active-layer monitoring in the cryolithozone of West Siberia. *Polar Geography V* 28(4): 267-285.

Moskalenko, N.G. 2001. The seasonal soil thawing in natural and disturbed ecosystems of West Siberian northern taiga. *Abs. of the Third International Conference on Cryopedology: Dynamics and Challenges of Cryosols, Copenhagen, August 20-24, 2001*.

Pavlov, A.V., Skachkov, Yu.B. & Kakunov, N.B. 2004. An interaction between the active layer depth changing and meteorological factors. *Earth Cryosphere* VIII (4): 3-11 (in Russian).

Perfilieva, V.I., Teterina, L.V. & Karpov, N.S. 1991. *Vegetation Cover of Yakutia Tundra Zone*. Yakutsk, 192 pp (in Russian).

Savvinov, D.D. 1976. *Hydrothermic Regime of Soils within the Permafrost Zone*. Novosibirsk: Nauka, 254 pp.(in Russian).

Soloviev, P.A. 1978. Thickness of surface seasonally frozen ground on the territory of Yakutia. *Geocryological and Hydrogeological Researching in Yakutia*. Yakutsk: 3-12 (in Russian).

Emplacement of Lobate Rock-Glacier Landforms and Landscape Modification, Mareotis Fossae, Mars

S. van Gasselt
Freie Universitaet Berlin, Planetary Sciences and Remote Sensing, Malteserstr. 74-100, D-12249 Berlin, Germany
E. Hauber
German Aerospace Center (DLR), Institute of Planetary Research, D-12489 Berlin, Germany
A.P. Rossi
RSSD of ESA. ESTEC, NL 2200 AG, Noordwijk, The Netherlands
G. Neukum
Freie Universitaet Berlin, Planetary Sciences and Remote Sensing, Malteserstr. 74-100, D-12249 Berlin, Germany

Abstract

The so-called fretted terrain at the Martian dichotomy boundary exhibits a variety of creep-related morphologies generally known as lobate debris aprons and lineated valley fills. These features usually occur along troughs and circumferentially to remnant massifs. We here report on investigations of debris aprons and adjacent terrain in the Tempe Terra/Mareotis Fossae region and provide observational evidence for several phases and mechanisms of debris supply at remnant massifs comprising rock fall and large-scale landsliding and terminating with deposition and disintegration of a widespread surficial mantling deposit. The mantling deposit disintegrates by processes similar to thermokarstic degradation as indicated by heavily dissected areas and characteristic shallow and aligned circular depressions. Comparisons of theoretically derived cross-section profiles to topographic measurements along and across lineated-valley fill units, as well as lobate debris aprons, provide additional clues that such creep-related landforms are currently degrading,. It is also shown that a considerable volume of debris/ice is transported along the intra-highland valleys. Such processes might even be active today, as geomorphologic features appear pristine, and crater-size frequency measurements yield ages in the range of 50–100 Ma only. Such observations confirm modeling results of the stability of ground ice on Mars. Various phases of emplacement and degradation confirm theories about cyclic re-deposition of volatiles caused by the changes of the configuration of orbital parameters of Mars.

Keywords: climate; Mars; periglacial; planetary permafrost; rock glaciers.

Introduction

A variety of landforms indicates the possible existence of past or present ice in the near subsurface of Mars (Sharp 1973, Carr 1977 Rossbacher & Judson 1981, Lucchitta 1981). Among the most prominent ice-related features are lobate debris aprons. They have been interpreted to be a mixture of rock particles and ice (Squyres 1978, 1979) analogous to terrestrial rock glaciers, i.e., debris transport systems comprising a mixture of rock fragments and segregational and/or interstitial ice (Barsch 1996). The analogy between terrestrial rock glaciers and Martian lobate debris aprons is mainly based on (a) their lobate shape, (b) the cross-sectional convex-upward profile, (c) characteristic sets of ridges and furrows, and (d) their relationship to adjacent regions indicative of permafrost-related morphologies. Lobate debris aprons have been observed primarily along steep escarpments near the dichotomy boundary (Squyres 1978, 1979, Mangold 2001) and the large impact basin of Hellas Planitia (Squyres 1979, Crown et al. 2002). Rock glaciers are sensitive indicators for the climatic environment during their formation and are thought to be possible large and accessible water reservoirs (Whalley & Azizi 2003). Morphologies of lobate debris aprons in Tempe Terra are similar to terrestrial talus rock glaciers (Whalley 1992, Barsch 1996) which are usually derived from footslope debris situated underneath steep wall-rock of mountainous permafrost environments.

Settings and Observations

The Tempe Terra/Mareotis Fossae region (Fig. 1) is located between 270°E–294°E and 46°N–54°N and is characterized by the steep dichotomy escarpment and the so-called fretted terrain (Sharp 1973) which separates the study area into the southern highland assemblages and a region known as the northern lowland plains. Young surficial deposits interpreted as features related to creep of ice and debris (Squyres 1978, 1979) and mapped as Amazonian surficial units by Scott & Tanaka (1986) fill broad fretted channels of the heavily deformed Noachian highlands, extend from the dichotomy escarpment in northern direction, and are located circumferentially to knobs and remnants of the Noachian basement. The north-south extent of the fretted terrain in our study area varies between 60 km to 170 km. The undissected upland has an elevation of -2700 m at 294°E and about 0 m at 280°E. The lowland has its highest elevations also in the western part of the study area and slopes gently (~0.1°) towards NE, reaching minimum elevations of -4500 m at the eastern border of the study area. Elevation difference between uplands and lowlands decreases from 3000 m to 1500 m.

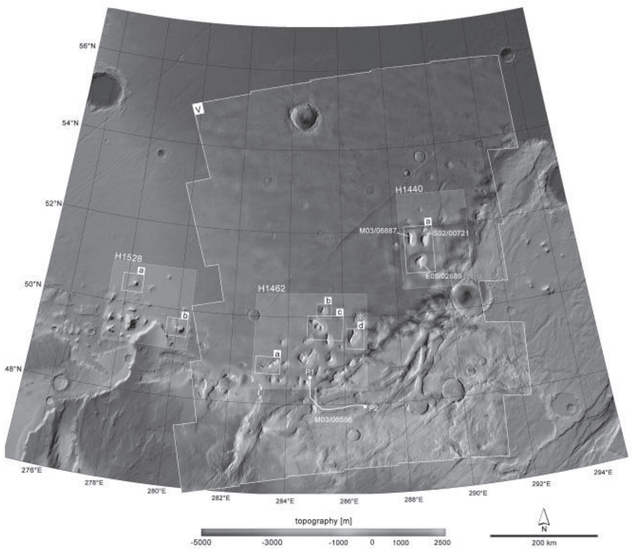

Figure 1. Study area in the Tempe Terra/Mareotis Fossae region as represented by the Viking global image mosaic (MDIM-2.1) superimposed on MOLA (MEGDR) topographic data and location of image scenes discussed in the text; [V] manually processed medium-resolution Viking image mosaic; H1528, H1462, H1440 refer to HRSC image numbers discussed in the text; lettered boxes and white outlines refer to sub-scenes depicted from HRSC image data; individual MOC scenes used in this study are labeled accordingly; P1-P2: topographic profile discussed in the text.

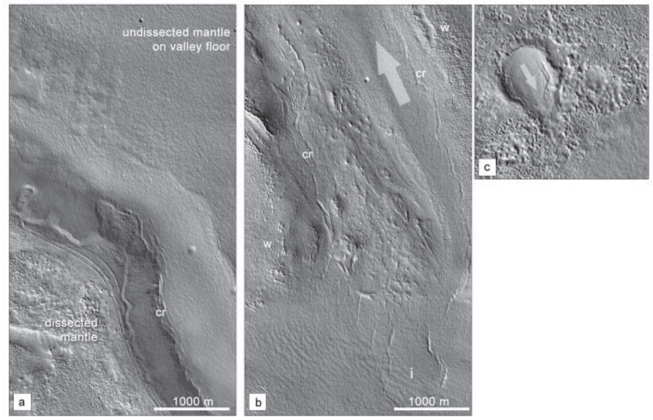

Figure 2. MOC sample scenes of the dichotomy boundary. (a) fretted channel floor (right) and wall (lower left). A mantling deposit is intact on the valley floor, but heavily degraded on the uplands. Crevasses [cr] on the floor of the fretted channels are characteristic of creep and flow of ice and debris. Parallel thin ridges 15–20 m wide run at constant elevations along the upper channel wall. (b) Floor of a fretted channel is covered by a mantling deposit. Crevasses [cr] are situated near the channel walls [w]. They also outline an impact crater completely buried by the mantle [i]. (c) Impact crater filled by mantling deposit. The mantle seems to have flowed out of the crater, scale is 1000 m across.

This difference is slightly less than that reported from the dichotomy boundary on the eastern hemisphere of Mars, i.e., Deuteronilus, Protonilus and Nilosyrtis Mensae, with 2-6 km. Highlands have a generally flat surface, sloping at an angle of less than 0.1° when measured perpendicular to the dichotomy boundary. The surfaces of very large upland segments bounded by fretted channel have larger slopes toward the lowlands (1–2°) and might be tilted as blocks. Such fretted channels have steep walls and flat floors (Squyres 1978), the latter of which are often characterized by so-called “lineated valley fill” (Squyres 1978, 1979}, which is interpreted as material comparable to that of lobate debris aprons but confined to the valley extent. In the study area, fretted valleys have uniform widths of 5–10 km and constant depths of a few hundred meters. The morphologic boundary between highland and lowland areas is characterized by two and sometimes three distinct components: (a) a steep upper slope, i.e., the wall-rock, (b) an intermediate shallow-sloped unit with downslope facing striae, and (c) the highly textured apron (Carr 2001). An intermediate unit is only rarely observed at isolated remnants. At a few sample locations we measured the angles of intermediate units (6°–8°) and angles of debris aprons (2°–4°).

Mantling deposit

A mantling deposit can be observed at scarps and channels near the dichotomy boundary (Fig. 2) as well as around isolated remnant massifs and aprons (Fig. 3) that are located in the lowlands. The deposit does not show any preference to geographical or topographic location, thus, covering all parts of the study area. This observation is based on high-resolution image data (1.5–12 m/pixel) taken with the Mars Orbiter Camera (MOC) that clearly show surfaces at the dichotomy boundary that are covered by that deposit. The mantling deposit is often degraded by erosion, resulting in surfaces whose texture are highly variable, ranging from smooth over stippled, pitted, or knobby to heavily etched. In some places the mantling is completely removed. The disintegration process seems to be controlled by slope aspect, the southern (sun-lit) slopes being more affected than northern slopes.

On the floors of some fretted channels we identify crevasse-like features (Fig. 2). Their specific geometry resembles that of terrestrial chevron crevasses in glaciers, (e.g., Benn & Evans 2003, Menzies 2002). Lineations correspond to longitudinal or transversal lineations and are frequently observed at terrestrial features indicative of creep of ice and debris. Such lineations can be observed at small scales as illustrated in Figure 2. Other lineations are formed by ridges that are thin (15–20 m wide) and extend at approximate constant elevations along upper channel walls; they seem to be genetically connected to the mantling deposit (Fig. 2a). A thick mantling is also observed in a number of image scenes covering the remnant massifs of the Tempe Terra lowland: as seen in Figure 3a, the surface of three debris aprons (A-C) appears relatively smooth although different sets of transversal ridges on the apron can still be observed. The crest of remnant A is characterized by a scalloped and fretted depression (d) and sets of elliptical and aligned shallow depressions on the eastern slope which have a dimension of few tens of meters. Both the crest depression as well as the slope depressions are located in a mantling deposit and

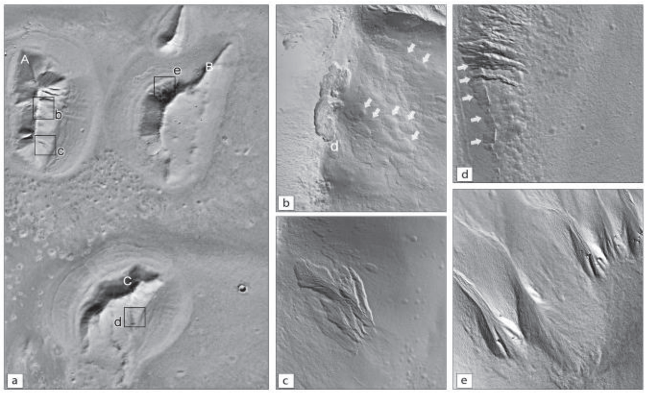

Figure 3. Sample scenes of HRSC in orbit 1440 covering the easternmost study area. Labeled black boxes in (a) refer to MOC sample scenes (b-e). All scenes show indications for the disintegration of a thick mantling deposit. (b) Unusual scalloped depression at remnant crest and elliptical depressions at eastern wall (arrows). (c) Overlapping gullied slide flows. (d) Small slide flows incised into the footslope talus of remnant C. All incision start at the boundary (arrows) between talus and debris apron and are located in a mantling deposit. (e) Slide flows incised into surficial mantling deposit of remnant B.

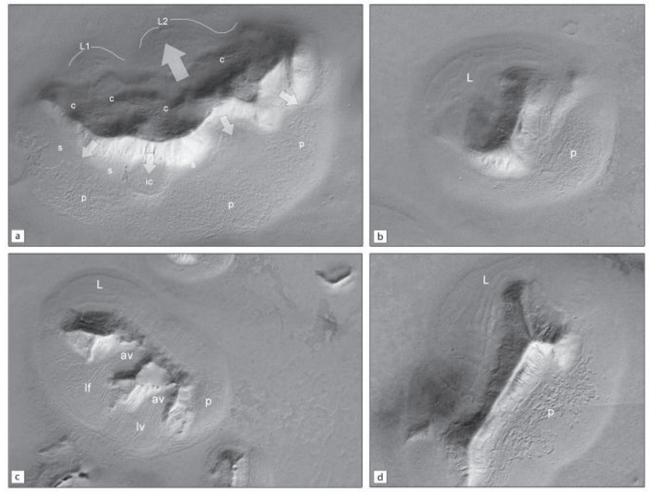

Figure 4. Sample scenes of HRSC in orbit 1462 covering the central lowlands of Tempe Terra. (a) Arcuate remnant massif characterized by an inclined surface tilting towards northern direction; two main directions of transport are observed: large lobes form in northern direction [L1-L2], large coherent debris masses with a pitted surface [p] advance in southern direction. An impact crater [ic] has been completely filled by erosional debris. The talus shows a generally smooth surface texture [s]. Arcuate and sub-parallel furrows on remnant indicate extensional flow [c]. (b) Small isolated remnant knob located northeast of remnant shown in (c); northern apron texture is characterized by ridges and furrows [L], southern apron has a pitted appearance [p]. (c) Alcoves [ac] are incised into remnant massif forming Accumulation zones of debris that is subsequently transported downslope as seen in longitudinal surface lineations. (d) Elongated remnant massif with well-defined crest exhibits transversal ridges and furrows [L] on northern apron and a pitted surface [p] on southern apron. Note also, all aprons are comparable in size when related to the remnant massif.

are indicative of material removal. Mantling-related mass-wasting features are shown in 3c–e where gullied slide flows initiate instantaneously somewhere at the mid-slope, overlap partly and produce faint terminal depositional fans (Fig. 3c, d) that are indicative of dry mass-wasting processes.

As seen in Figure 3d, gullied slide flows can be related to a boundary where the remnant talus abuts the mantling deposit. While the northern sets of slide flows are deeply incised and well expressed, the southern are shallower (Fig 3e).

Disintegration texture

Many debris aprons in Tempe Terra are characterized by surface textures indicative of disintegration of either the surficial mantling deposit or the main debris/ice body. As shown in Figure 4, a slightly northwards inclined and elongated remnant shows a well-pronounced debris apron emerging near the foot of a remnant. While the northern debris apron is characterized by at least two large lobes with transversal ridges (L1–L2), the southern apron is more homogeneously developed with a highly pitted surface texture (p). Below the southern scarp, talus forms as expressed by a relatively smooth texture (s). Eroded remnant material has filled an old impact crater (ic). The southern scarp of the remnant is relatively steep when compared to the northern remnant slope. Flow ridges (c) indicate that material is eroded as coherent sheet and thus contributes to the development of the northern apron. Arrangements of transversal ridges and furrows located on a northern apron and a pitted surface texture located on the southern apron is observed in the scenes depicted in Figures 4b, d. In Figure 4b, the shapes of the remnant massif and debris apron are more circular and the remnant slope angles are approximately comparable in the north and south. However, the northern remnant slopes is composed of a single large bowl-shaped depression in which material is collected from the wall-rock and subsequently transported downslope towards the plains. In Figure 4d, the pitted surface in the south has not reached the terminal area of the apron but is restricted to the remnant footslope. Figure 4c shows well-expressed alcoves (av) at the southwestern remnant slopes and longitudinal sets of furrows and ridges (lf, lv) in the direction of maximum slope gradient. The pitted surface texture seen in Figures 4a, b and d is here restricted to a small area of the southeastern debris apron (p) while lobes (L) are again restricted to the northern apron. In the westernmost region of the Tempe Terra study area, remnants and aprons are developed slightly differently when compared to those in the central and easternmost areas. Northern apron slopes show a ridge-and-furrow texture but it extends asymmetrically farther away from its source. Contrasting to this, the remnant in Figures 5b–b′ is heavily dissected by alcoves and cirque-like features. Towards the north, longitudinal and transversal ridges and furrows prevail while towards the south aprons merge with the apron of the dichotomy escarpment and show sets of depressions at various sizes. For few aprons crater-size measurements could be obtained to derive ages (Fig. 6). Elliptical depressions indicate deformation of impact craters after apron emplacement. In order to obtain the last

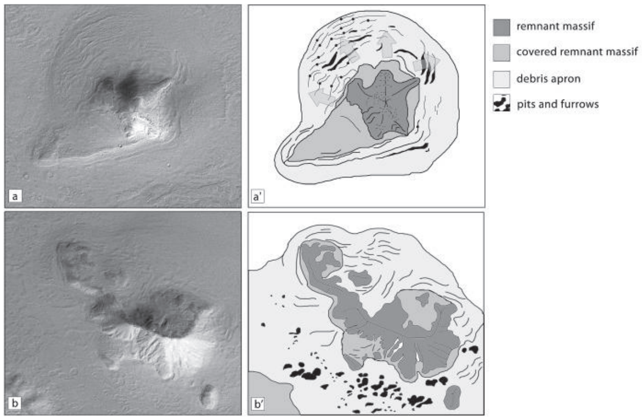

Figure 5. Sample scenes of HRSC in orbit 1528 and schematic maps covering lobate debris aprons of the westernmost study area. Labeled boxes refer to labels in Figure 1; [a–a′] isolated small remnant massif with circumferential lobate debris apron, northern apron shows pattern of ridges and valleys characteristic of compressional flow (ridges) and extensional flow (furrows); [b–b′] flow lineations at debris apron are in longitudinal configuration below alcove depression facing northeast and in transversal configuration under remnant scarp. Southern apron is characterized by pitted texture indicative of degradation.

resurfacing period only fresh-appearing craters have been mapped. Measurements provided ages in the range of 0.01 to 0.05 Ga which is consistent with data obtained from other debris apron (Squyres 1978, Mangold 2003, Berman et al. 2003, Head 2005, Li 2005, van Gasselt 2007).

Geomorphometry

Lobate debris aprons were digitized using a common GIS environment (Fig. 7). We derived geographic coordinates, topographic elevations, lengths, areas and volumes and made simplifications with respect to the (a) base of the debris apron, which was assumed to be horizontal and flat (Barsch 1996), and (b) to the volume of that part of the remnant massif located below its visible extent, i.e., covered by apron debris. In plan view, the remnants north of the dichotomy boundary in Tempe Terra have a more or less irregular polygonal shape and a rugged top, in contrast to the more flat-topped mesas of the type locations in Elysium or Arabia Terra (Mangold & Allemand 2001). The cross-sectional shapes of the aprons are convex upward and steepening towards the terminus of the apron (Fig. 8). The length of debris aprons varies between 1.4 km to 6.3 km averaging at ~4.0 km in northern direction and ~3.5 km in southern direction. The average lengths of aprons are significantly less than values provided by Mangold (2001) with 10.8 to 33 km, and also less than those given by Carr (2001) and Colaprete & Jakosky (1998) with 15 km. Thicknesses of (upper) remnant massifs in Tempe Terra range from ~20 m to ~1100 m. The thickness of aprons varies between ~70 m and ~600 m under the assumption of a flat base. Minimum thickness values are lower than those given by Mangold (2001) (276 m) for the Deuteronilus area, maximum values are about the same. Volumes of debris aprons at Tempe Terra range from <10 km³ to ~300 km³ with a mean surface

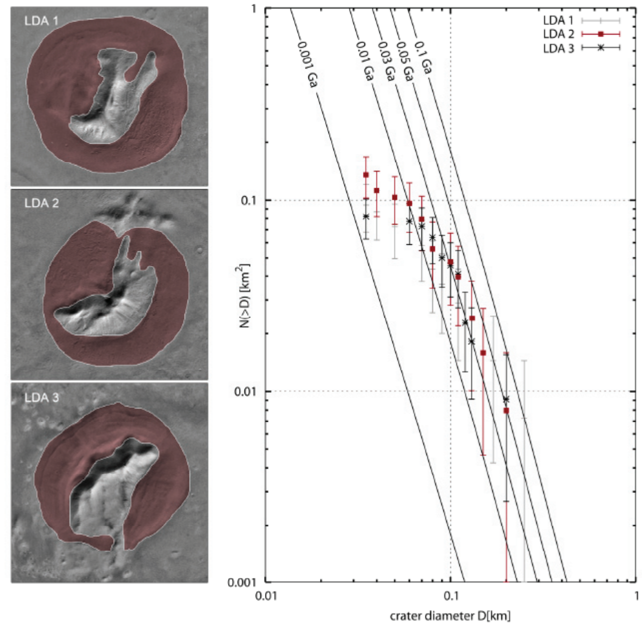

Figure 6. Ages derived for debris-apron surfaces of the central and eastern part of the study area. Stair-stepped distribution indicates multiple episodes of erosional activity, derivation of isochrones (in Ga) are based on Hartmann and Neukum (2001) with the polynomial production function coefficients by Ivanov (2001); for a discussion on errors, see Neukum et al. (2004).

area of ~282 km² (Fig. 7). The remnants have a mean size of ~115 km² (15 to >1000 km²) and a mean volume of ~21 km³ (<5 to 200 km³). As Barsch (1996) summarizes, there might be a close relationship between the source area of debris production and the surface area of a (terrestrial) rock glacier at the footslope with values between 1:1.36 to 1:4.4 (Wahrhaftig & Cox 1959, Barsch 1977, Gorbunov 1983). From 27 observations at Tempe Terra we obtain a factor of 2 for the remnant size when compared to the area occupied by the debris apron. Mangold (2001) calculated the basal shear stress and obtained values in the range of σ = 34–108 kPa for the Deuteronilus/Protonilus Mensae areas. These values are lower than photoclinometrically derived values by Squyres (1978). For the Tempe Terra region we obtain values between 6.7–82.4 kPa for average apron lengths, with an average of ~38 kPa. The calculated values are not consistent with basal shear stresses given for terrestrial rock glaciers by Whalley (1992) with 100–300 kPa. This may indicate an ice content which is higher (Hauber et al. 2007) than typically considered for rock glaciers or very low strain rates due to a low shear stress. Inactive rock glaciers tend to have generally lower slopes as either debris material was eroded or volatiles were removed, subsequently causing thermokarstic degradation of the rock-glacier surface (Barsch 1996, Ikeda & Matsuoka 2002, Berthling et al. 1998).

Discussion and Conclusions

Image data provide observational evidence for the existence of a widespread mantling deposit in the Tempe Terra/Mareotis Fossae region which covers not only debris

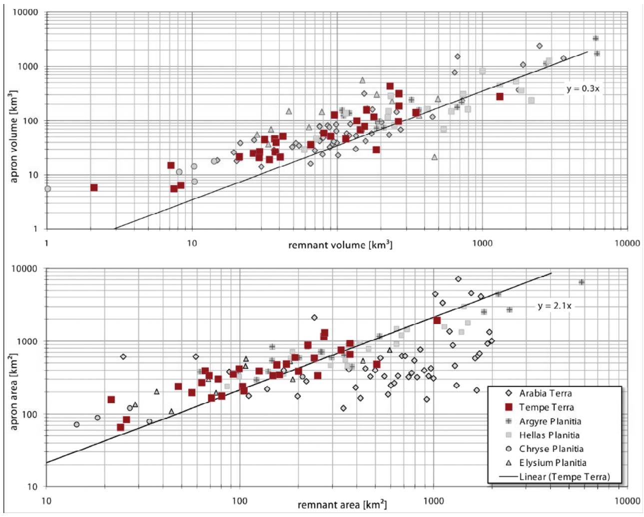

Figure 7. Plot of derived ratios between volumes (a) and areas (b) of remnant massifs and debris aprons as indicator for the degradational state. Values of Tempe Terra massifs and debris aprons (dark squares) are approximated by linear fit.

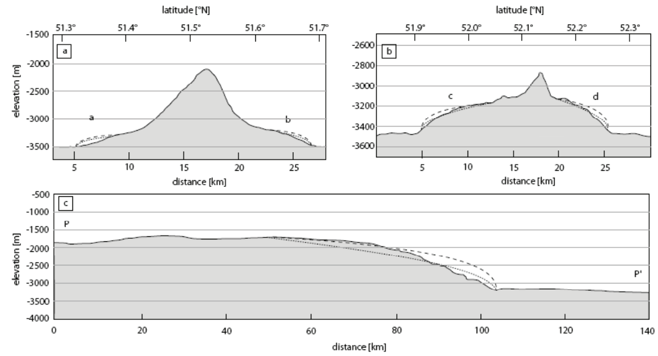

Figure 8. MOLA-based topographic profiles across debris aprons (a, b) and along fretted channel (c) and theoretic profiles of debris aprons obtained from equation derived by Paterson (2001).

aprons of the lowlands but also the escarpment of the Martian dichotomy boundary. At the dichotomy escarpment this mantling deposit shows several characteristics of creep and deformation as well as for processes of disintegration similar to thermokarstic degradation of ice-rich surface materials. Indicators for the mobility of that mantling deposit are found at various locations.

We confirm the presence of a mantle at latitudes higher than ~30–50° as inferred from global-scale roughness maps (Kreslavsky 2000) and directly observed in MOC images (Carr 2001, Malin 2001). Flow lineations on debris aprons resemble closely features known from terrestrial rock glaciers comprising various sets of transversal and longitudinal ridges and furrows indicative of differential movements controlled by subsurface topography. At several locations in Tempe Terra, southward-facing debris aprons show a pitted surface texture that is interpreted as indicators for thermokarstic degeneration and loss of volatiles subsequently leading to collapse and formation of shallow depressions or pits. Their restricted extent suggests control by sun-irradiation (Rossi et al. 2008). Shallow depressions form primarily in mantling material covering remnant massifs whereas pits and furrows are more often observed on the debris-apron surface. Degradation of surfaces is also confirmed by observations of theoretically derived cross-profiles of debris aprons and lineated valley fill units. Both creep-related landforms show an unsatisfactory fit to the model curve. The convex-upward shape of lineated valley fill at the entrance of fretted channels shows not only debris transport perpendicular to valleys walls but also in parallel direction. This furthermore indicates that flow lineations seen in lineated valley fill deposits are not only caused by compression but also by the downslope movement along the valley. It is suggested that the main processes of landsliding and rockfall had come to an end and that subsequent deposition of a mantling deposit caused smoothing of the underlying topography and allowed formation of such slides and gullied flows. Resurfacing ages of 0.01 to 0.05 Ga are consistent with ages obtained from other debris apron locations on Mars. Geomorphometrically derived area ratios of the depositional zone and source area show values that are comparable to estimates given in Barsch (1996) for terrestrial rock glaciers, indicating that the genetic configuration is comparable. Geologically recent degradational and thermokarstic processes are in good agreement with modeling work of obliquity variations of the planet's rotational axis and variations of the planet's eccentricity and precession (Murray et al. 1973, Pollack 1979, Toon et al. 1980, Jakosky et al. 1995). It was shown that prolonged periods of higher obliquity lead to mobilization of volatiles at the poles and to precipitation at lower latitudes (Levrard et al. 2004). This process (a) might have lead to saturation of remnant-related talus deposits with ice causing subsequently creep of debris, and (b) also contributed to a mid-latitudinal mantling deposit (Rossi et al. 2008).

References

Barsch, D. 1977. Eine Abschätzung von Schuttproduktion und Schutttransport im Bereich aktiver Blockgletscher der Schweizer Alpen, Z. *Geomorph. Supp.* 28: 148-–160.

Barsch, D. 1996. *Rockglaciers: indicators for the present and former geoecology on high mountain environments.* Berlin, Germany: Springer, 331 pp.

Benn, D.I. & Evans, D.J.A. 2003. *Glaciers and glaciation*. London, England: Arnold, x+734 pp.

Berman, D.C., Hartmann, W.K. & Crown, D.A. 2003. Debris aprons, channels, and volcanoes in the Reull Vallis region of Mars. In: *Lun. Planet. Sci. Conf. Abs., XXXIV, #1879, 12-17 March.* CD-ROM. League City, Tex., USA: Lun. Planet. Inst.

Berthling, I., Etzelmüller, B., Eiken, T. & Sollid, J.L. 1998. Rock glaciers on Prins Karls Forland, Svalbard. I: internal structure, flow velocity and morphology. *Permafrost Perigl. Proc.* 9(2): 135-145.

Carr, M.H. & Schaber, G.G. 1977. Martian permafrost features. *J. Geophys. Res.* 82(11): 4039-4054.

Colaprete, A. & Jakosky, B.M. 1998. Ice flow and rock glaciers on Mars. *J. Geophys. Res.* 103(E3): 5897-5909.

Crown, D.A., Pierce, T.L., McElfresh, S.B.Z. & Mest, S.C. 2002. Debris aprons in the eastern hellas region of mars: Implications for styles and rates of highland degradation. In: *Lun. Planet. Sci. Conf. Abs., XXXIII, #1642*. CD-ROM. League City, Tex, USA.

Gasselt, van S., Hauber, E. & Neukum, G. 2007. Cold-climate modification of Martian landscapes: A case study of a spatulate debris landform in the Hellas Montes region, Mars. *J. Geophys. Res.* 112 (E09006).

Gorbunov, A. 1983. Rock glaciers of the mountains of middle Asia. *Proceedings of the Fourth International Conference on Permafrost, Fairbanks, Alaska*: 359-362.

Hartmann, W.K. & Neukum, G. 2001. Cratering chronology and the evolution of Mars. *Space Sci. Rev.* 96(1-4): 165-194(30).

Hauber, E., van Gasselt, S., Chapman, M.G. & Neukum, G. 2007. Geomorphic evidence for former lobate debris aprons at low latitudes on Mars: indicators of the Martian paleoclimate. *J. Geophys. Res.* 112: E09006, doi:10.1029/2006JE002842.

Head, J.W., Neukum, G., Jaumann, R. et al. 2005. Tropical to mid-latitude snow and ice accumulation, flow and glaciation on Mars. *Nature* 434: 346-351.

Ikeda, A. & Matsuoka, N. 2002. Degradation of talus-derived rock glaciers in the Upper Engadin, Swiss Alps. *Permafrost Perigl. Proc.*13(2): 145-161.

Ivanov, B.A. 2001. Mars/Moon cratering rate ratio estimates. *Space Sci. Rev.* 96(1-4): 87-104(18).

Jakosky, B.M., Henderson, B.G. & Mellon, M.T. 1995. Chaotic obliquity and the nature of the Martian climate. *J. Geophys. Res.* 100(E1): 1579-1584.

Kreslavsky, M. & Head, J.W. 2000. Kilometer-scale roughness of Mars: results from MOLA data analysis. *J. Geophys. Res.* 105: 26,695-26,712.

Laskar, J., Correia, A.C.M., Gastineau, M., Joutel, F., Levrard, B. & Robutel, P. 2004. Long term evolution and chaotic diffusion of the insolation quantities of Mars. *Icarus* 170(2): 343-364.

Levrard, B., Forget, F., Montmessin, F. & Laskar, J. 2004. Recent ice-rich deposits formed at high latitudes on Mars by sublimation of unstable equatorial ice during low obliquity. *Nature* 431: 1072-1075.

Li, H., Robinson, M.S., & Jurdy, D.M. 2005. Origin of Martian northern hemisphere mid-latitude lobate debris aprons. *Icarus* 176(2): 382-394.

Lucchitta, B.K. 1981. Mars and Earth–comparison of cold-climate features. *Icarus* 45(2): 264-303.

Lucchitta, B.K. 1984. Ice and debris in the fretted terrain, Mars. *J. Geophys. Res.,* Supp. 89(B1): B409-B419.

Mangold, N. 2001. Lobate debris aprons as potential targets for ground ice detection analogs to terrestrial rock glaciers. In: *Conf. Geophys. Detect. Subsurf. Water Mars, #7009.* Houston, Tex., USA: Lun. Planet. Inst.

Mangold, N. & Allemand, P. 2001. Topographic analysis of features related to ice on Mars. *Geophys. Res. Lett.* 28(3): 407-410.

Mangold, N. 2003. Geomorphic analysis of lobate debris aprons on Mars at Mars Orbiter Camera scale: evidence for ice sublimation initiated by fractures. *J. Geophys. Res.* 108(E4): 8021.

Menzies, J. (ed.) 2002. *Modern and Past Glacial Environments.* Oxford, England: Butterworth-Heinemann, xxii+5543 pp.

Milliken, R.E., Mustard, J.F. & Goldsby, D.L. 2003. Viscous flow features on the surface of Mars: observations from high-resolution Mars Orbiter Camera (MOC) images. *J. Geophys. Res.* 108(E6): 5057.

Murray, B.C., Ward, W.R. & Yeung, S.C. 1973. Periodic insolation variations on Mars. *Science* 180(4086): 638-640.

Mustard, J.F., Cooper, C.D. & Rifkin, M.K. 2001. Evidence for recent climate change on Mars from the identification of youthful near-surface ground ice. *Nature* 412: 411–414.

Neukum, G., Jaumann, R., Hoffmann, H. et al. 2004. Recent and episodic volcanic and glacial activity on Mars revealed by the High Resolution Stereo Camera. *Nature*. 432: 971-979.

Paterson, W.B. 2001. *The Physics of Glaciers*, 3rd ed. London, England: Butterworth-Heinemann, ix+496 pp.

Pollack, J.B. 1979. Climatic change on the terrestrial planets Icarus 37(3): 479-553.

Rossbacher, L.A., & Judson, S. 1981. Ground ice on Mars—inventory, distribution, and resulting landforms. *Icarus* 45(1): 39-59.

Rossi, A.P., van Gasselt, S., Pondrelli, M., Zegers, T., Hauber, E. & Neukum, G. 2008. Periglacial landscape evolution at Lower Mid-Latitudes on Mars: The Thaumasia Highlands, *Proceedings of the Ninth International Conference on Permafrost, Fairbanks, Alaska, June 29–July 3, 2008* (this proceedings).

Scott, D.H. & Tanaka, K.L. 1986. *Geologic map of the western equatorial region of Mars*. 1:15,000,000. Map I-1802-A. U.S. Geol. Surv. Misc. Inv. Ser.

Squyres, S.W. 1978. Martian fretted terrain: flow of erosional debris. *Icarus* 34(3). 600-613.

Squyres, S.W. 1979. The distribution of lobate debris aprons and similar flows on Mars. *J. Geophys. Res.* 84(B14): 8087-8096.

Sharp, R.P. 1973. Mars: fretted and chaotic terrains. *J. Geophys. Res.* 78: 4073-4083.

Toon, O.B., Pollack, J.B., Ward, W., Burns, J.A. & Bilski, K. 1980. The astronomical theory of climatic change on Mars. *Icarus* 44(3): 552-607.

Wahrhaftig, A.L. & Cox, A. 1959. Rock glaciers in the Alaska Range. *Bull. Geol. Soc. Am.* 70: 383-436.

Whalley, W. 1992. A rock glacier in South Ellendalen, Lyngen Alps. *Norsk Geografisk Tidsskrift* 46: 29-31.

Whalley, W.B. & Azizi, F. 2003. Rock glaciers and protalus landforms: analogous forms and ice sources on Earth and Mars. *J. Geophys. Res.* 108(E4): 8032.

Climatic Change and Fluvial Dynamics of the Lena River (Siberia)

Emmanuèle Gautier
University Paris 8, CNRS UMR 8591 Laboratory of Physical Geography, F-92195 Meudon Cedex, France

François Costard
CNRS UMR 8148 IDES Interactions et Dynamique des Environnements de Surface, Université Paris 11, F-91405 ORSAY Cedex, France

Daniel Brunstein
CNRS UMR 8591 Laboratory of Physical Geography, F-92195 Meudon, France

Julien Hammadi
University Paris 8, Dep. Geography, F-93526 Saint-Denis Cedex, France

Alexander Fedorov
Melnikov Permafrost Institut, Siberian Branch Russian Academy of Science, Yakutsk, Republic of Sakha, 677010, Russia

Daqing Yang
Water and Environmental Research Center, University of Alaska Fairbanks, AK 99775, USA

Abstract

It has been recently reported that climatic change greatly influences Arctic rivers. The Yakutia region is a particularly interesting area for its spectacular floods, for its lowest temperature records, as well as for its maximum thickness of permafrost. The hydrology of the Lena and its tributaries is characterized by an extremely episodic flow regime. In spring during the break up period, the joined increase of the water discharge and stream temperature contributes to an active thermal erosion along the frozen river banks. Here we report recent climatic change in Central Siberia, and its impact on the thermal erosion. We first point out three major evolutions since the 1990s: a reduction of the river ice thickness in winter, a pronounced increase of the stream temperature in the spring, and a slight increase of the discharge during the break up period (May–June). A GIS analysis based on aerial pictures and satellite images highlights the impact of the water-warming on the frozen banks. The vegetated islands appear to be very sensitive to the water temperature increase, showing an acceleration of head retreat (+21%–29 %).

Keywords: climatic change; fluvial dynamics; fluvial islands; GIS analysis; Lena River; thermal erosion.

Introduction

The Lena River is one of the largest Arctic rivers located in a permafrost environment. With its huge basin (2.49 million km²) and its south-north orientation (exceeding 4000 km) the Lena crosses several latitudinal belts (Fig. 1). Central Siberia is one of the coldest and driest zones (with mean temperature of 9°C and mean precipitation of 190 mm yr^{-1}) and has very thick and continuous permafrost (1500 m). For these reasons, the hydrology of the Lena and its tributaries is characterized by an excessive fluvial regime and exhibits a spectacular flood mostly controlled by periglacial dynamics. This study examines current climatic change and its impacts on the middle Lena River dynamics, from the Tabaga gauging site (located upstream of Yakutsk) to the junction of the Aldan River (Fig. 1). From the beginning of November to May, a continuous ice cover can be observed as thick as 2 m in Central Siberia; the discharge of the Lena River is low, 900–1500 $m^3.s^{-1}$ (Tabaga gauging site). The break up starts around May 15 for the Lena, corresponding to an increase of the stream temperature up to 18°C from May to July and to a rise of the water level up to 8–10 m, which inundates flood plain and islands. Highest floods occur generally in June and can be 50,000 $m^3.s^{-1}$ at Tabaga. Then, in July, the discharge rapidly decreases. The fluvial landforms consist of a large number of shallow, wide channels that are between several hundred meters and three kilometers wide. These multiple channels are separated by sandy bars and large forested islands. Downstream of Yakutsk, the flood plain width can be up to 25 km and exhibits various thermokarstic landforms due to the local melting of the continuous permafrost.

During the annual fluvial outburst (May–June), the joined increase of river water temperature and discharge induces the propagation of a thawing line within the frozen riverbank. The interaction between thermal erosion and fluvial erosion during the flood creates specific forms on the banks (‘thermo erosive niches’) and locally causes important bank retreat (Are 1983, Jahn 1975, Walker & Hudson 2003). Our previous studies highlighted the spatial and temporal variability of the thermal and mechanical erosion on banks of the middle Lena River. We showed that the island heads are particularly subjected to this erosion process, with mean values of 15 m year and maximal values of 20 m, and an exceptional rate up to 40 m was measured locally (Gautier et al. 2003, Costard & Gautier 2007).

Arctic regions respond disproportionately to global warming. In Yakutia, a mean air temperature increase of 1.2°C was registered since the end of the 1980s; this impacts directly the permafrost temperature (Fedorov & Konstantinov 2003,

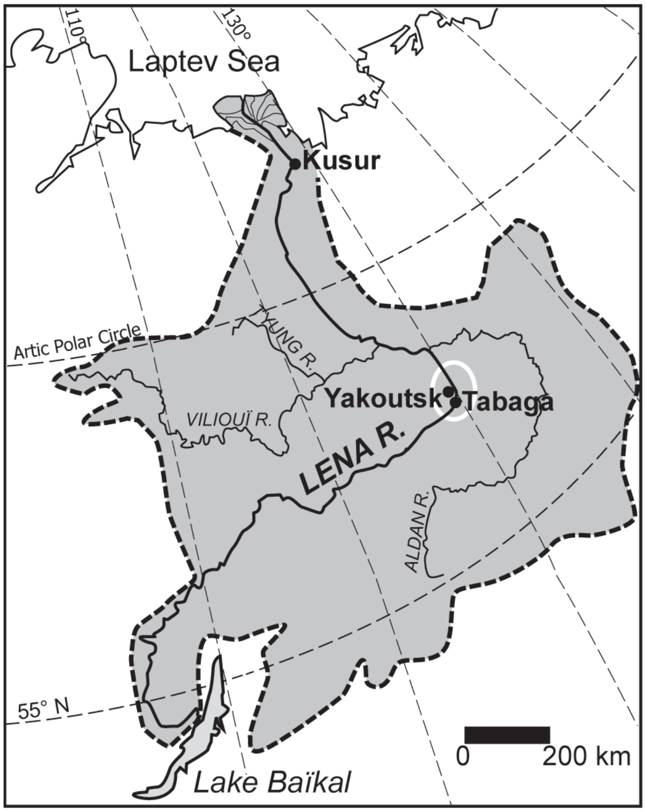

Figure 1. The Lena Basin and the study zone.

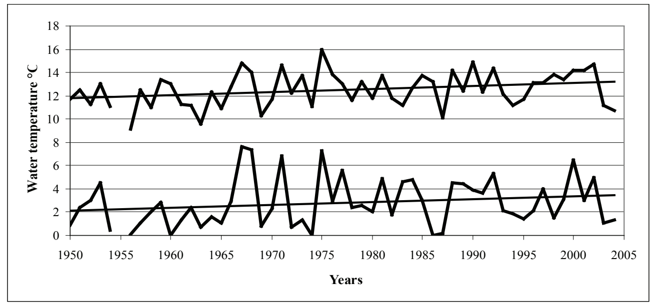

Figure 2. Water temperature of the Lena River since 1950 (May: below and June: above).

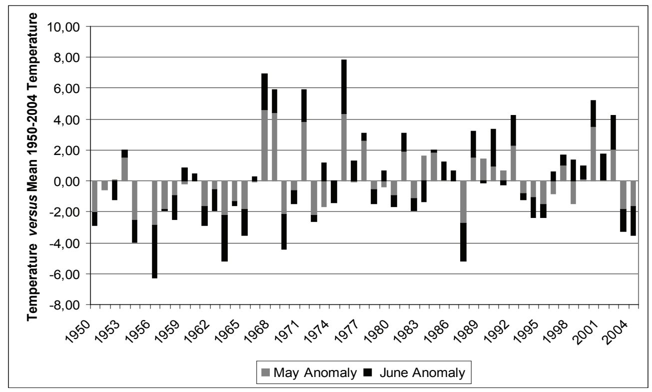

Figure 3. Anomaly of stream temperature in May and June (1950–2004, in °C).

Pavlov 1994). The thickening of the active layer reinforced by the increasing precipitation related to cyclone activity in the North Atlantic provokes a marked rise of the Arctic rivers discharge (Peterson et al. 2002, Serreze et al. 2000, Yang et al. 2002). Therefore, the objective of the present study is (1) to characterize precisely the hydro-climatic change in Central Siberia (water, air, permafrost temperatures, and river discharge) and (2) to quantify the impact of the change on erosion and sedimentation processes on the Lena River near Yakutsk.

Data and Methods

Firstly, the study is based on different sources of environmental data such as climatic data (air, permafrost, and river water temperatures) since the 1950s. We especially examined the water temperature because of its impact on thermal erosion (Costard et al. 2003). Parameters concerning the river were also detailed: discharge, water level, thickness of river ice during the winter, and date of the beginning of the outburst since 1936 at the Tabaga gauging site.

Secondly, we conducted a 35 years diachronic GIS analysis (1967–2002) of 300 km of the fluvial landforms on the Lena River upstream and downstream of Yakutsk in order to evaluate the effects of recent global warming on the mobility of the fluvial units. On aerial pictures (Corona declassified pictures, 1967 and 1980) and satellite images (Landsat 4–7: 1992, 1999, and 2002), landforms were precisely analyzed. The delineation (1) of the channel banks and (2) of the vegetated island banks allows us to quantify their erosion rates since 1967. The position of the islands in the channel, their area, and their form were also determined. Finally, we examined the correlation between the erosion rate variations and the various hydrometeorological variables (discharge, stream temperature, river ice thickness).

Hydro-Climatic Change and Morphodynamics Disruption

Influence of current climatic change on hydrology

All studies concerning Siberia clearly identify the signs of climatic change in the 1980s or at the beginning of the 1990s. On the right bank of the Lena River, 50 km southeast of Yakutsk, A. Fedorov & P. Konstantinov (2003) clearly underline a strong air temperature change, the mean temperature since 1992 being 1.2°C higher than for the whole period (1931–2002). Furthermore, the period 1992–2002 was marked by a pronounced raise of the summer temperature. Correlatively, since the beginning of the 1980s, the soil temperature at 3.2 m depth is also characterized by positive anomalies (Fedorov & Konstantinov 2003). This observation agrees with D. Yang et al. (2002), who show a strong warming in winter and spring over the Lena basin.

On the middle Lena River, the stream temperature has undergone an important change since 1950, that is characterized by positive trends during the flood season (May and June) up to 2°C (Fig. 2). More precisely, the river temperature increase has been particularly pronounced since

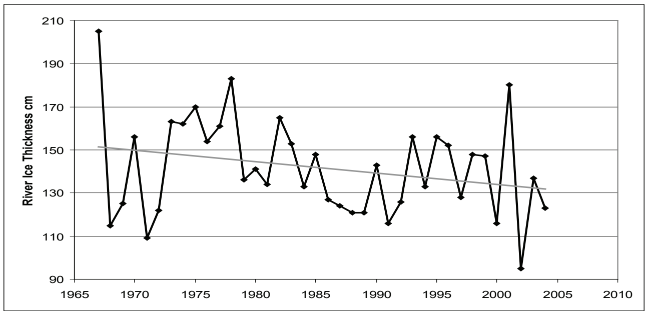

Figure 4. River ice thickness of the Lena River at the Tabaga gauging station since 1967.

1990: +0.73°C (May) and +0.97°C (June) (Costard et al. 2007).

On Figure 3 two periods can be seen: the first 25 years are characterized by an important variability, whereas water temperature since 1975 is more regular and generally marked by positive anomalies. The frequency of temperature anomaly is particularly significant; between 1950 and 1975, positive anomalies of water temperature occurred every 4 years in May and every 2.66 years in June; during the period 1976–2004, they were registered every 1.87 year in May and 1.71 in June (Fig. 3).

The ice cover of the river is the third factor showing a marked evolution. From the beginning of November, a continuous ice cover can be observed as thick as 2 m. Even if the ice cover varies greatly each winter, Figure 4 clearly shows its thinning since 1967. Before 1987, the river ice thickness was 1.48 m on average during winter and exceeded 1.5 m every two years. From 1987 to 2004, the mean thickness was 1.34 m and exceeded 1.5 m every 4.25 years.

The water discharge of the Lena River shows a strong interannual irregularity. Because of this irregularity, it is difficult to detect easily a possible hydrologic change. However, two signs seem to reveal a recent evolution. First, a very moderate increase of 3% of the discharge can be noticed at Tabaga since the 1980s. The winter undergoes greater water discharge since the 1980s, particularly at the end of the cold season (March–April: +22%-23%, Fig. 5). The break up period (May–June) is characterized by a slight but progressive increase: +4% for 1980–1992 and +7% since 1992.

Second, the frequency of abundant discharge has clearly increased during the last 25 years. In April, the frequency of the highest discharge doubled: discharge exceeding 1000 $m^3.s^{-1}$ (the mean discharge) was registered nine times between 1936 and 1980 (i.e. every 4.88 years), and it has occurred ten times since 1980 (every 2.4 years). In May, the frequency of discharge higher than 15,000 $m^3.s^{-1}$ also doubled (frequency of 7.33 years before 1980, frequency of 3.42 after). Furthermore, the evolution of the discharge in May is particularly marked for the period 1996–2004, that underwent repeated high water discharge exceeding by 22%–57% the mean value. The evolution is less clear for June and July. June discharge is characterized by the strongest interannual variability; the highest water levels were registered between 1956 and 1963,

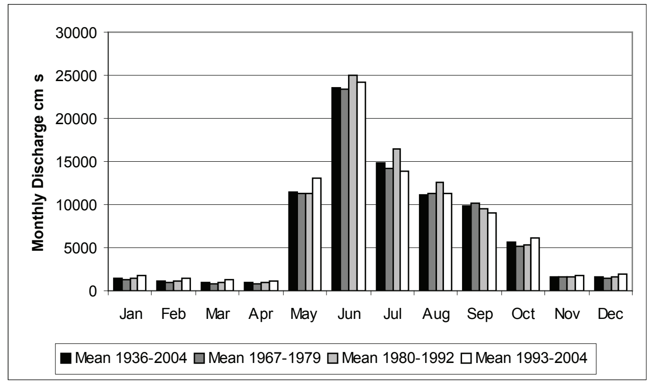

Figure 5. Evolution of water discharge of the Lena River since 1936 (Tabaga gauging station).

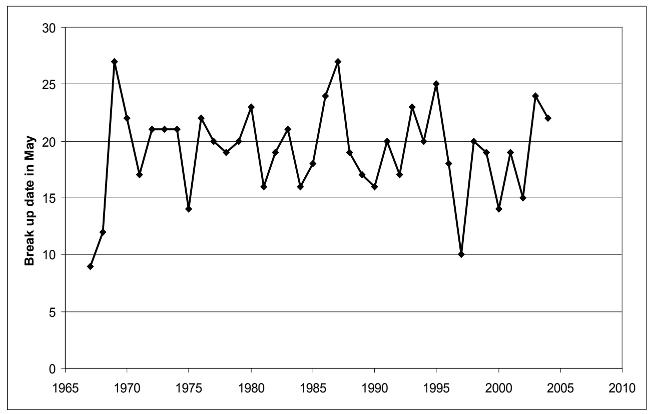

Figure 6. Break up date in May on the Lena River at Tabaga since 1967.

corresponding to a period of low water temperature (Fig. 2). However, an increase of high discharge was also observed since 1980; discharge exceeding 30,000 $m^3.s^{-1}$ was registered six times between 1936 and 1980 (i.e. frequency of 7.33 years), and this value was reached five times for the period 1981–2004 (every 4.8 years). May and June discharges are inversely correlated; it must be remembered that the local inundation is controlled by the flood wave coming from the south and the water provided by the thawing active layer and by the snowmelt. No important rainfall or groundwater supply sustains the river discharge in Central Siberia during summer.

Therefore, the relative abundance of water discharge in May and June must be examined with regards to the break up date. The date of the beginning of the break up is highly variable in May; at Tabaga, it occurs generally around May 15–20, rarely before May 10 or after May 25 (Fig. 6). No important change can be seen nowadays concerning the date of break up. An early break up generally induces an important discharge in May; on the contrary a late break up favors a higher discharge in June.

Impact of hydro-climatic change on fluvial landforms

The middle Lena River develops a multiple-channel pattern. Two types of channels can be distinguished: (1) wide active channels (some of them are dewatered at the end

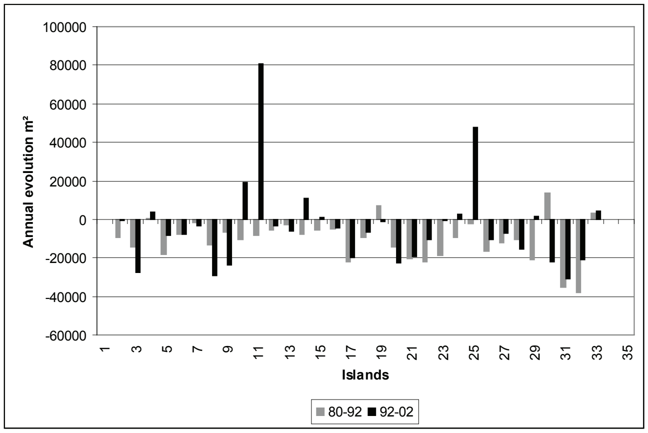

Figure 7. Area evolution of 35 islands since 1980.

of summer and during winter); (2) small sinuous and narrow branches crossing islands and flood plain (these channels are inundated only during the flood peak). A previous study based on satellite image analysis documented the erosion rates on main channels banks (Costard et al. 2007, Costard & Gautier 2007). Actually, for the 1967–2002 period, the mean retreat of the channel banks was low or moderate, with an average value of 2 m per year; maximal values of 14–18 m per year were registered locally. These values must be considered with regard to the active channel width; the bank retreat represents only 0.05%–0.1% of the main channel width. For this reason, active channels remained relatively stable during the study period; no migration or avulsion was observed on the middle Lena River.

The large, forested islands represent important mesoforms of the hydrosystem. Just upstream of Yakutsk, because of the widening of the flood plain, the Lena River forms huge islands. Several km long, these islands are densely vegetated. We could classify these islands in three types: (1) T1: islands located in the central part of the channel; (2) T2: islands located near the river bank and (3) T3: islands located downstream of an unvegetated bar (Costard et al. 2007). We noticed that island heads undergo a stronger erosion than channel banks, with mean value of 15 m per year. The erosion is located on the head of the island; therefore, the island migrates progressively downstream, keeping its general shape. Most interesting is the variability of the island head retreat depending on its type. T1 and T2 islands are subjected to a higher erosion rate, with mean bank retreat of 20 m per year and maximal retreats exceeding 40 m. Because of the position of these islands, the river water is in permanent contact with the frozen banks during the flood, and the thawed sediments are swept away by the current; thus thermal and mechanical erosion are jointly at work, explaining the rapid migration of the form. For the third type, the upstream bar protects the island head from rapid erosion (7 m per year).

The diachronic study of the fluvial landforms since 1967 (date of the first picture) reveals a disruption of the river morphodynamics, that is expressed by the island mobility. For the three types of islands, a marked acceleration of erosion was measured since 1992. Actually, the mean erosion rate of T1 islands increased by 29% (reaching 23 m per year) and by 22% for T2 islands (21 m per year). T3 Islands also undergo a rapider migration (+21%).

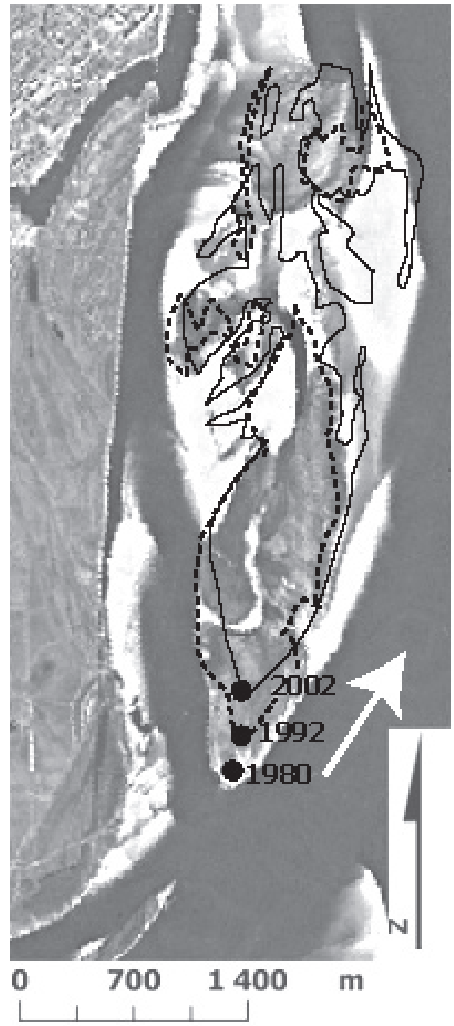

Figure 8. Evolution of an island located upstream of Yakutsk (1980–2002). Lines: limit of the perennial vegetation; points: island head; background image: Corona 1980 (adapted from Hammadi 2007).

The erosion of the island heads could have just implied a progressive reduction of the island areas. In fact, the evolution of islands is relatively complex.

The comparison of the total area of 35 islands located just upstream of Yakutsk between 1967 and 2002 reveals two main models of evolution (Fig. 7). The first model is a progressive decrease of the island area; this evolution is noticeable especially for small islands that are disappearing. On the contrary, eight islands undergo a greater sedimentation on their downstream part, that compensates for the head retreat. An important aggradation on bars located downstream of these islands is observed (Fig. 8). This evolution model is generally observed on very large islands. This accelerated deposition is accompanied by vegetation colonization on the middle part and tail of the island.

Discussion

The hydro-climatic change on the middle Lena River is complex. The discharge increase (+3%) at Tabaga is less pronounced than on the low Lena River at Kusur. B.J. Peterson et al. (2002) calculated for six large Eurasian Arctic rivers (including the low Lena River at Kusur) a mean annual rate of discharge increase of 7%. At Kusur, the spring discharge increases strongly (Yang et al. 2002). But, the dam regulation on the Viliou river (an important tributary of the Lena River, Fig. 1) has a strong influence on the water temperature and discharge on the low Lena River (Liu et al. 2005, Ye et al. 2003). On the contrary, we can consider that the hydrological change of the middle Lena River mainly depends on climatic change, because of the lack of large dams in the upper Lena basin. In this part of the valley, the most significant sign of a possible hydrologic change is the increasing frequency of high discharge, especially in May.

The accelerated erosion on island heads induces an increase of sediment supply in the channel. But, the progressive growth of several islands lets us suppose that the greatest part of the sediment load (mainly sand) provided by the thermal and mechanical erosion process does not migrate over long distances downstream and accumulates on wide bars and long islands. One of our projects is to evaluate precisely in the field this erosion and sedimentation rhythm.

Two hypotheses can be proposed to explain the accelerated erosion of island heads. The first is the increase of the discharge during May and June. The increasing frequency of high discharge in May and June is certainly an important factor of fluvial bed erosion. It has been demonstrated that the duration of efficient discharge determines the bank retreat. But the observed hydrological change alone seems too weak to explain such an aggravation of erosion rates. The second hypothesis is the impact of the water temperature during the flood season by up to 2°C. Actually, the ablation model developed by F. Costard et al. (2003) and R. Randriamazaoro et al. (2007) helped to determine the role of different factors (mainly discharge, permafrost, air and water temperatures, and Reynolds Number) on thermal erosion. Relative effects of water temperature and discharge have been studied separately. The model demonstrates that water temperature is four times more important than Reynolds Number. The measured increase up to 2°C of the stream temperature alone could increase the erosion rate respectively by 26% and 16% in May and June. The laboratory simulation experiment and the physical approach (Costard et al. 2003) demonstrated that exceptional erosion rates can be best explained together with a high water temperature, and mechanical erosion in association with some particular geometry of the channel. In the near future, a more precise numerical modeling will take into account the impact of global warming on the erosion rate for fluvial systems in a periglacial environment.

A last but very important factor must also be taken into account: the vegetation. The islands are densely vegetated with pioneer bushes on freshly dewatered areas and mature forests on stable and higher zones. This vegetation cover seems not to protect efficiently the island heads against the erosion: the thermal process during the flood destabilizes the thawed and non-cohesive deposits. But, the progressive colonization by pioneer sequences (mainly composed by *Salix*) on the middle and downstream section of the island exerts a great control on the sedimentation. The sediment trapping effect of the vegetation is well known (Gautier & Grivel 2006, Hickin 1984, Steiger & Gurnell 2003). For this reason, one of our future objectives is to examine precisely interactions between river and vegetation dynamics.

Conclusion

In the case of the Lena River, fluvial islands are indicative of ongoing dynamic change; the islands express the readjustment of the fluvial system to physical factors (increasing water temperature and secondly, increasing discharge). This study clearly highlights the first sign of destabilization of the fluvial bed directly related to global warming and it appears that climatic change has a strong impact on fluvial forms of this Arctic river. The increasing water temperature directly impacts the erosion rate of the islands, and a greater instability of these fluvial forms is clearly observed. Furthermore, we previously demonstrated that the middle Lena River is a low-energy fluvial system in spite of its great floods, because of its very gentle slope and the brevity of the morphogenic discharge (Gautier & Costard 2000). Thus, the rapidity of the fluvial form readjustment is indicative of the very deep impact created by the present climatic change. It can be supposed that continuation of the recent global warming will induce an increasing destabilization of the river banks and amplify the sediment supply in the riverbed. For society, the increasing mobility of the fluvial bed and the increasing flooding represent very important risks: the great majority of towns and industrial infrastructures are installed on the river banks. The Lena River represents also a major transportation axis in winter and summer. The precise quantification and location of erosion will participate to the prevention of the risk.

Acknowledgments

Hydrological data were provided by the Hydrometeorological Center of Yakutia, under the auspices of the Permafrost Institute at Yakutsk. This program is supported by “Programme Reliefs de la Terre” INSU, CNRS, France, and GDR «Mutations Polaires: Société et Environnement».

References

Are, F.E. 1983. Thermal abrasion on coasts, *Proceedings, Fourth International Conference on Permafrost, Fairbanks, Alaska*. Washington DC: National Academy Press, 24-28.

Costard, F., Dupeyrat, L. Gautier, E. & Carey-Gailhardis, E. 2003. Fluvial thermal erosion investigations along a rapidly eroding river bank: application to the Lena River (central Yakutia). *Earth Surface Processes and Landforms* 28: 1349-1359.

Costard, F. Gautier, E., Brunstein, D. Hammadi, J. Fedorov, A. Yang, D. & Dupeyrat, L. 2007. Impact of the global warming on the fluvial thermal erosion over the Lena River in Central Siberia. *Geophys. Res. Lett*. 34(14): Art. No. L14501 JUL 18 2007.

Costard, F. & Gautier, E. 2007. The Lena River: main hydromorphodynamic features in a deep permafrost zone. In: A. Gupta (ed.), *Large Rivers: Geomorphology and Management*. John Wiley, 225-232.

Fedorov, A. & Konstantinov, P. 2003. Observations of surface dynamics with thermokarst initiation, Yukechi site, Central Yakutia. In: M. Philips, S. Springman & L.U. Arenson (eds.), *Proceedings of International Permafrost Conference, Zurich*: 239-243.

Gautier, E. & Costard, F. 2000. Les systèmes fluviaux à chenaux anastomosés en milieu périglaciaire: la Léna et ses principaux affluents en Sibérie Centrale. *Géographie Physique et Quaternaire* 54(3): 327-342.

Gautier, E. Brunstein, D. Costard, F. & Lodina, R. 2003. Fluvial dynamics in a deep permafrost zone: the case of the middle Lena River (Central Yakutia). In: M. Philips, S. Springman & L.U. Arenson (eds.), *Proceedings of International Permafrost Conference, Zurich*: 271-275.

Gautier, E. & Grivel, S. 2006. Multi-scale analysis of island formation and development in the Middle Loire River, France. In: J.S. Rowan, R.W. Duck & A. Werrity (eds.), *Sediment Dynamics and the Hydromorphology of Fluvial Systems*. IAHS Pub. 306: 179-187.

Hammadi, J. 2007. *Impact du Changement Climatique sur l'érosion Thermo-Dynamique des Berges de la Léna (Sibérie Centrale)*. Geography Master Research, Univ. Paris 8, 150 pp.

Hickin, E. 1984. Vegetation and river channel dynamics. *Canadian Geographer* 28: 111-126.

Jahn, A. 1975. *Problems of the Periglacial Zone*, Washington DC: Warzawa, 223 pp.

Liu, B. Yang, D. Ye, B. & Berezovskaya, S. 2005. Long-term open-water season stream temperature variations and changes over Lena River Basin in Siberia. *Global and Planetary Change* 48(1-3): 96-111.

Pavlov, A.V. 1994. Current change of climate and permafrost in the Arctic and Subarctic of Russia, *Permafrost Periglacial Processes* 5: 101-110.

Peterson, B.J., Holmes, R.M,. McClelland, J.W., Vörösmarty, C.J., Lammers, R.B., Shiklomanov, A.I., Shiklomanov, I.A. & Rahmstorf, S. 2002. Increasing river discharge to the Arctic Ocean. *Nature* 298: 2171-2173.

Randriamazaoro, R. Dupeyrat, L. Costard, F. & Carey-Gailhardis, E. in press. Fluvial thermal erosion: heat balance integral method. *Earth Surface Processes and Landforms*.

Steiger, J. & Gurnell, A.M. 2003. Spatial hydrogeomorphological influences on sediment and nutriment deposition in riparian zones: observations from the Garonne River, France. *Geomorphology* 49: 1-23.

Walker, H.J. & Hudson, P.F. 2003. Hydrologic and Geomorphic Processes in the Colville Delta, Alaska. *Geomorphology*, 56: 291-304.

Yang, D., Kane, D., Hinzman, L., Zhang, X,. Zhang, T. & Ye, H. 2002. Siberian Lena River hydrologic regime and recent change. *J. of Geophys. Res.* 107(D23): 4694-4703.

Ye, B., Yang, D. & Kane, D. 2003. Changes in Lena River streamflow hydrology: human impacts vs. natural variations, *Water Resources Research*, 39(8): 1200, doi: 10.1029/2003WR001991.

Inter-Alas Agricultural Landscapes and Active Layer Trends and Dynamics in Response to a Warming Climate in Central Yakutia

P.P. Gavriliev
Melnikov Permafrost Institute, SB RAS, Yakutsk, Russia

Abstract

This report presents the new long-term (1989–2006) data on monitoring of diverse reaction of active layer, permafrost table, and agricultural landscapes to the climate warming. We have investigated the genuine patterns in the dynamics of progressive development of anomalous cryogenic processes and phenomena, such as intensive degradation of the ice complex up 0.5–0.9 m during sporadic anomalously warm summer-autumn seasons, rich in precipitation; 2.9 times increase in the depth to the permafrost table; sudden activation of different stages of thermokarst, from barely visible *bylar* to young lake thermokarst within 15–18 years, in conditions of rapid climate warming (about 0.09°C/year) and diverse agricultural land use.

Keywords: agricultural landscape; climate warming; ice complex; permafrost process; thermokarst.

Introduction

The peculiarities of formation, stages, and activations of cryogenic processes and phenomena, which cause fundamental changes in thermal condition of permafrost, active layer, and cryogenic relief of geosystems, are permanently in the focus of interest of renowned scientific centres, and their significance needs to be periodically defined more precisely because new data permanently occur. Since the 1950s a great number of works exploring these issues was published and much progress achieved in understanding anthropogenic and natural cryogenic processes and phenomena in northern regions and countries of the world (Russia, Yakutia, western Siberia, Alaska, northern Canada, etc.) (Soloviev 1959, Kachurin 1961, Grechishchev et al.1980, Feldman 1984, Shur 1988, Pewe 1954, Washburn 1988, Osterkamp & Romanovsky 1998, Osterkamp et al. 2000, Gilichinsky & Kimble 1997, Racine et al. 1998, Gavriliev 2001).

Many works, summarizing the available data, state that in context of global climate changes and intensive natural resource development, different regions differ in pace and scale of changes in geocryologic conditions and development of cryogenic processes.

Huge agricultural land resources of Yakutia occupy 67,435.6 thousand ha or 22.2% of its total area. From 20 to 60% of large masses of taiga, valley, and shallow valley soils are underlain by shallow (1–2.5 m) permafrost with wedge ice (ice complex). Considerable areas of territory of the north and the subarctic are characterized by low resistivity to anthropogenic impact (Grechishchev et al. 1980, Gavriliev 2001). Melioration and agricultural development of the permafrost-covered area result in both, advantages, and, in some cases, irreversible negative cryogenic processes and their consequences for the northern nature and ecosystems (Gavriliev 2001). In permafrost area and, especially, in the areas of ice complex distribution, cryogenic (cryogeological) processes activation and the way they influence stability and transformation processes of agricultural and natural permafrost landscapes is very specific and still needs to be thoroughly investigated, taking into account the rapid climate warming (about 0.09°C/y) and existence of a variety of ways of agricultural land use.

This work aims at revealing patterns of permafrost processes dynamics, specifically patterns of activation of initial stages of thermokarst in agriculture-affected lands with ice complex sediments at present day.

This study is a continuation of our earlier work (Gavriliev & Efremov 2003).

Research Methods

In 1989–2006 Melnikov Permafrost Institute, SB RAS, carried out monitoring of active layer, frost phenomena, and permafrost and wedge ice tables (up to 10–15 m deep) in taiga, alas, and valley landscapes, both natural and agricultural, in different physical-geographical regions of Yakutia (Fig. 1). This monitoring network, being multipurpose, includes 6 test sites and 36 experimental plots.

In 1989–2006 we have implemented monitoring observations of dynamics of seasonal thawing-freezing depth, water-saturation and temperature of soil; identified their hydrophysical properties and plasticity; studied the peculiarities of grain-size classification and cryogenic structure of close-to-surface tables of permafrost and ice wedge (ice complex sediments), development of cryogenic and post-cryogenic processes and phenomena, as well as parameters of soil cover (snow, moss layer, forest floor, etc.). In investigating the regularities of permafrost processes and phenomena dynamics, we used detailed permafrost and landscape methods and topographic shoots(at scale range 1:100–1:5,000), and photointerpretation, used in geocryology. The methods for cryogenic processes investigation are specified in works (Grechishchev et al. 1979, 1980, Shur 1988, Pavlov 1997, Gavriliev & Efremov 2003).

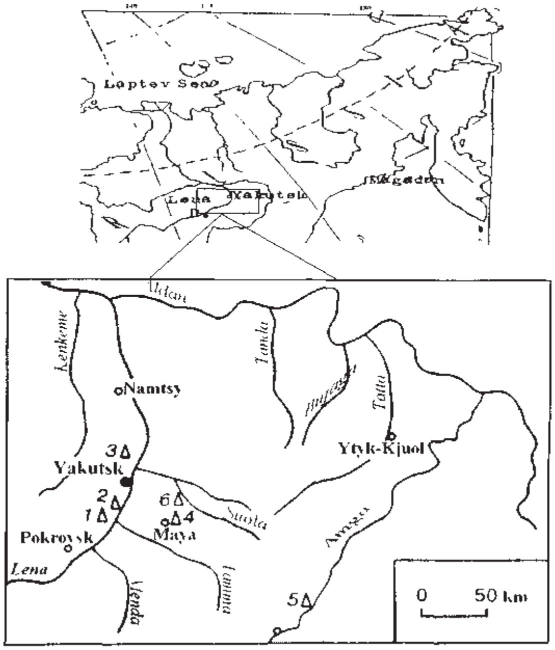

Figure 1. Location of monitoring sites. Sites indicated by triangles: 1–Kerdyugen, 2–Khatassy, 3–Spasskaya Pad', 4–Maia (Dyrgebai), 5–Amga, 6–Khorobut.

Results and Discussion

Diverse reaction of ice complex soils, active layer, and agricultural landscapes to the climate warming and agricultural development

Central Yakutia is among the regions in the north of Russia with maximal effect of global climate warming, reaching 2–2.5°C (Pavlov 2000). According to the data from weather stations of the region, dramatic changes of climate elements were registered during the past 25 years, including: 14 warm winters and 6 anomalously warm winters with air temperatures exceeding the normal by 3–4°C, and during some months by 5–8°C. There was not one cold winter (Skachkov 2000 et al.).

The amount of precipitation ranged during warm period ±1.5–3 times of the regular one, this included anomalously warm and dry summer of 1998 and mean annual air temperature higher than the normal by 4.5°C, as well as increase of snow cover height in some years by 1.5–3 times of the background value, and in subsidence by 1.4–3 times higher than background standard, according to the data of snow survey.

It was determined that during past 15–20 years in central Yakutia at high rate of climate warming and ice complex landscape surface disturbance, a trend towards permafrost degradation is indicated. Thus, in inter-alas areas, depending on landscape-anthropogenic conditions, at forest stubbing, and agricultural development, mean annual temperatures of perennially frozen ground rose to 1.5–2.5°C.

At sporadic inter-alas areas of agricultural landscapes of sixth-seventh terraces of the River Lena, an unprecedented high thawing rate of ice-rich permafrost was indicated, reaching 0.5–0.9 m during some excessively rainy, relatively warm summer-autumn seasons (1994, 1997, 2004–2006), preceded by anomalously warm winters. In 1989–2006 the trend of ice complex soils thawing in inter-alas areas of agricultural landscapes averaged from 0.03 to 0.27 m/y, and in the natural (undisturbed) landscapes, it is considerably lower: from 0.007 to 0.01 m/y (Figs. 2, 3).

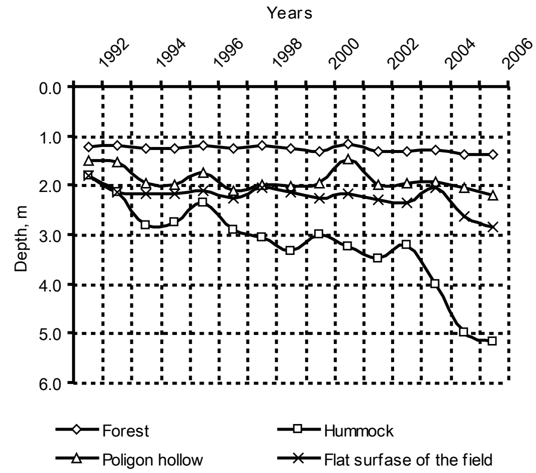

Figure 2. Dynamics of thaw depth at Dyrgebai site on the right bank of the River Lena, 1992–2006.

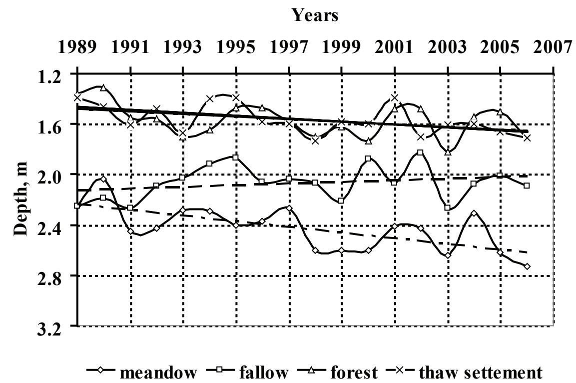

Figure 3. Dynamics of seasonal thaw depth at Kerdyugen site on the left bank of the Lena River, 1989–2006.

During the period of 1993 to 2006 anomalously intensive increase of perennially frozen ground occurrence depth was registered, making 2.9 times, at permafrost and wedge ice thawing starting from 1.8 to 5.17 m. At the same time the thickness of thawed zone in the upper layer of the ice complex ground (Δh_i) in Dyrgebai site at Abalakh (sixth) terrace of the Lena River made, correspondingly, from 0.3–0.5 m to 1.5–3.7 m, which resulted in intensive development of thermokarst subsidence, deformation, and surface degradation in various types of cryogenic relief: from hardly-visible thermal subsidence (undeveloped *bylar*) to undeveloped lake thermokarst (see further).

According to the degree of dangerousness and non-dangerousness of the results of reaction–development of undesirable geocryologic and soil processes caused by surface disturbance, different types of agricultural landscapes form the following consequences (in descending order): inter-alas fallows, used as pastures, in case of wedge ice immediately beneath the seasonally thawed layer (STL); inter-alas irrigated farming areas (fallows, sowed grasslands) at presence of wedge ice in the zone of potential seasonal thawing; inter-alas fallows where wedge ice occurs out of STL; irrigated valley lands; irrigated alas lands; shallow valley haylands; and natural alas lands (alas landscapes).

Along with an overall positive trend of permafrost degradation (thawing), we can note some short-term fluctuations (rhythms, reflecting cycles ranging between 3–4 and 9–11 years), activations and fadings of negative and positive nature (i.e., permafrost table descending and ascending). These fluctuations of seasonal thawing depth reduce, to considerable extent, the danger of fundamental disturbance of frozen-complex ground stability eventually resulting in occurrence of low-grade anthropogenic landscapes and lake thermokarst, but not inevitably.

Activation of natural-anthropogenic cryogenic processes and phenomena in inter-alas agricultural landscapes

New spatial-temporal patterns were revealed in cryogenic processes and phenomena dynamics in inter-alas lands of permafrost agricultural landscape complexes in nowadays conditions.

The analysis of results of long-term research work (1989–2006) on agricultural landscapes condition in Central Yakutia revealed, within the mentioned above landscapes, the activation of destructive cryogenic processes, related with the general 1.5–2.5°C increase of mean annual air temperature in the region and increasing anthropogenic stress.

Yu.L. Shur, a well-known permafrost scientist, has noticed: "There are few thermokarst observations and they refer to initial stages of the process. Such observations applied to areas with ice complex sediments include two or at the most three stages of thermokarst relief development: undeveloped bylar, mature bylar, iyo" (1988, 106).

Our field observations conducted in 1989–2006 in the agricultural areas, which are situated on the V–VII medium-height terraces of the middle Lena River on its left (Kerdyugen site) and right (Maia site) banks and are underlain by ice-rich permafrost, identified and assessed 8 and 12 manifestations of anomalous natural-anthropogenic cryogenic processes and phenomena, respectively. These include:

1) inter-alas surfaces unaffected by cryogenic processes (thaw subsidence, thermal erosion, frost fracture, etc.);
2) polygonally fractured areas;
3) undeveloped bylar, i.e., flat area, affected by separate micro-subsidential crater 0.3 m depth above ice wedges;
4) destabilized (weakened) areas in active layer and disruption of sensitivity of ice complex grounds with subsurface voids, loose sediments, i.e., with drastic changes in permafrost soil composition, construction and in all properties;
5) anomalously rapid surface deformations and active layer destruction by thermokarst subsidences of various forms and sizes (up to 1.8 m and more);
6) bylar, i.e,. deformated area with subsidences and polygonal shallow gullies network above ice wedges (at 0.3–0.5 m depth);
7) iyo, i.e., feeble shallow gully with water within bylar limits;
8) thermokarst mound, i.e., deformated area with bumpy-hollow microrelief;
9) hollow-like subsidence (subsidence hollow gullies, extended in one direction (e.g., in direction of dyodya);
10) subsidence thermoerosion formations (focuses of thermoerosion draft);
11) initial thermokarst depression (or primary areal thermokarst) without lake, but still watering in some particular rainy periods (2005–2007). These thermokarst phenomena often cause permafrost bogging.
12) undeveloped (young) thermokarst lake (dyodya).

These results improve and significantly enlarge already-known patterns of thermokarst formation development stages (Soloviev 1959, Shur 1988, Gavriliev & Efremov 2003, and others). Besides, they evidence an anomalously rapid progressive development of thermokarst stages, not sufficiently studied before.

Activation of primal thermokarst (or primal areal thermokarst)

Five thermokarst stages are observed *in situ* at Dyrgebai test site. For rather short period (1991–2006) clearly-defined primal thermokarst depression with polygonal bumpy-hollow microrelief without lake, but watering in particularly rainy periods (2005 and 2006) formed in one of the key areas of Dyrgebai. For the last 15 years, the longitudinal profile of the primal thermokarst depression (or primal areal thermokarst) increased from 6.2 m in 1994 up to 101.3 m in 2006 (or by 16.3 times), its width—from 40–50 m (by 12.5 times), and its depth increased from 0.35–2.1 m (by 6 times).

The most rapid surface subsidences (14–24 cm/y) above the thawing ice wedge occurred in central watered areas of developing thermokarst depression (primal areal thermokarst). Thus interpolygonal surface hollow gully deformation is 2.02 m, and in polygonal block, which replaces ice wedge, deformation is 0.95 m (*vide* Figs. 2, 3). No significant surface level depression of permafrost agricultural landscapes was noticed in the droughty basin-like subsidences in inter-alas arable lands, grassland, and long-fallow soils.

Other test sites Dyrgebai and Kerdyugen saw correspondingly 11 and 6 similar primal thermokarst depressions develop with the same polygonal microrelief. Three of them in inter-alas agricultural landscape Dyrgebai revealed a tendency of passing onto undeveloped thermokarst lake stage.

Activation of undeveloped thermokarst lake

Here and there in the agricultural lands, small thermokarst lakes form (dyodya, tympy) in taiga inter-alas areas at upper relatively flat and concave meso-relief areas of fifth-seventh terraces in the middle Lena river. For development of these natural-anthropogenic lakes at least 10 factors and criteria are needed:

1) ice complex within the potential (maximum) depth of the seasonal thawing;

2) climatic conditions: humid and warm years;

3) permafrost-hydrological conditions and criteria for thermokarst lake development, including:

- assemblage of effect of several water delivery sources (types): atmospheric (P_{os} = precipitation), hillside (deluvial) ($S_n > S_{om}$ = the recharge from surface-water exceeds their discharge), permafrost (W_m and $W_{лв}$ = water amount from structure-formative permafrost ices thawing and from ice wedge thawing to depths h_m accordingly), suprapermafrost water input ($S_{мв}$) of active layer to subsidence (or basin) from outer spillway, and water does not drain from closed subsidence and thermokarst basins $W_{лв}$ and $S_{ом}$;
- drastic increase of permafrost water source fraction $W_{лв}$, $W_{тв}$ and $S_{мв}$ during the undeveloped or young lake formation as a result of intensive permafrost and wedge ice thawing;

4) geological and geomorphological conditions: undrained area with slopes of less than 0.5°;

5) positive subsidence water balance formation;

6) ice content of ice complex grounds of more than 50-60% of their volume;

7) water cover appearing in subsidence or thermokarst depression having width exceeding the critical value: from 0.7–1.0 up to 1.5–1.8 m (Feldman 1984);

8) area of thermokarst depression should be rather large for spontaneous thermokarst;

9) activation of mechanisms of self-enhancement of permafrost processes and phenomena;

10) irrational land use.

Undeveloped (young) thermokarst lakes are developed and evolve mostly at fallows and along the arable lands edges, sometimes at very various territories. For example, four lakes formed at test site Dyrgebai, two lakes at Kerdyugen site, and at other inter-alas masses such as Khaya-Yurdya, Urasalakh, etc. All dyodyas have rounded shape, with the diameter from 25–80 m, basin depth from 1.5–6 m, and sides are abrupt. These dyodya formed about 35–60 or more years ago as a result of forest clearance, soil cover removal and thawing of large ice aggregation etc. Thermokarst lake (dyodya) #4 at Dyrgebai test site is the youngest one; it formed only 20 years ago after agricultural development of the area.

Conclusions

1. Rather realistic reaction (weak, moderate, strong) of the soils active layer, permafrost processes and ice complex table of inter-alas agricultural landscapes up to 10 m deep to discontinuous climate warming and various ways of agricultural land use.

2. Results and data obtained during 18 years of integrated monitoring observations (1989–2006) helped to reveal spatial-temporal patterns in progressive development of anomalous natural-anthropogenic permafrost processes and phenomena, which were not sufficiently studied before. That includes the research of 6 thermokarst stages from bylar to young lake thermokarst at rapid climate warming (about 0.09° C/y) and various ways of land use.

3. Rhythmical and trend patterns of dynamics of seasonal thawing depth, permafrost processes and table fluctuation of ice complex grounds of inter-alas agricultural areas, which were not sufficiently studied before are nowadays revealed.

4. If the present tendency of climatic warming in central Yakutia with air temperature trend around 0.09°C/y and agricultural land use ratio increase keep on, the possibility of activation (manifestation) of permafrost processes and especially that of thermokarst remains very high.

References

Feldman, G.M. 1984. *Thermokarst and permafrost (Termokarst i vechnaia merzlota)* (in Russian). Novosibirsk:Nauka, 260 pp.

Gavriliev, P.P. 2001. Dangerous natural and anthropogenic processes and difficult ecological situations (geographical, geocryological and soil aspects). In: *Permafrost and ecological peculiarities of taiga landscapes in Central Yakutia (Merzlotno-ecologicheskieosobennostitaezhnykhagrolandshaftov Tsentralnoi Yakutii)* (in Russian). Yakutsk: Izd-vo Instituta Merzlotovedenia SO RAN, 113-148.

Gavriliev, P.P. & Efremov, P.V. 2003. Effects of cryogenic processes on Yakutian landscapes under climate warming. *Proceedings of the Eighth International Conference on Permafrost, Zurich, Switzerland, July 21–25, 2003*: 277-282.

Gilichinsky, D. & Kimble, J. (eds.) 1997. *Cryosols in classification hierarchy. Advances on fundamental research of the Earth cryosphere in Arctic and Subarctic; Proc. intern, conf., Pushchino, 22–26 April, 1996 (Special issue)*. Novosibirsk: Nauka, 3-6.

Grechishchev, S.E., Chistotinov, L.V. & Shur, Yu.L. 1980. *Cryogenic physical and geological processes and their prediction (Kriogennye fiziko-geologicheskie protsessy i ikh prognoz)* (in Russian). Moscow: Hedra, 380 pp.

Kachurin, S.P. 1961. *Thermokarst in the USSR area (Termokarst na territorii SSSR)* (in Russian). Moscow: Izd-vo AN USSR, 291 pp.

Osterkamp, T.E. & Romanovsky, V.E. 1998. Recent changes in permafrost and active layer conditions in Alaska. *Proceedings of 49th Arctic Science Conference/lARC Inauguration American Association, 25–28 October, 1998,* Fairbanks: University of Alaska, 61-62.

Osterkamp, T.E., Viereck, L., Shur, Y. et al. 2000. Observations of thermokarst and its impact on boreal forests in Alaska, U.S.A. *Arctic, Antarctic, and Alpine Research,* 32(3): 303-315.

Pavlov, A.V. 1997. Permafrost-climatic monitoring of Russia: methods, observation results, prediction (in Russian, abstract in English). In: *Earth Cryosphere (Kriosfera Zemli)* 1(1): 47-58.

Pavlov, A.V. 2000. Results of the International Conference "Monitoring of cryosphere", Pushchino, 1999 (in Russian, abstract in English). In: *Earth Cryosphere (Kriosfera Zemli)* 4(1): 44-51.

Pewe, T.L. 1954. *Effect of permafrost on cultivated fields, Fairbanks Area Alaska*. Geol. Surv. Bull. 989-F. Washington,164-186.

Racine, C.H., Jorgenson, T.M. & Walters J.C. 1998. Widespread and rapid permafrost degradation on the Tanana Flats in Central Alaska. *Proceedings of 49th Arctic Science Conference/lARC Inauguration American Association, 25-28 October, 1998.* Fairbanks: University of Alaska, 186-187.

Shur, Yu.L. 1988. *Upper layer of permafrost and thermokarst (Verkhniy gorizont tolschi merzlykh porod itermokarst)* (in Russian). Novosibirsk: Nauka, 213 pp.

Skachkov Yu.B. 2000. Present-day climate changes in Central Yakutia. In: *Climate and Permafrost:complex research in Yakutia (Klimat i merzlota: kompleksnye issledovanie v Yakutii)* (in Russian). Yakutsk: Izd-vo Instituta Merzlotovedenia SO RAN, 113-148.

Soloviev, P. A. 1959. *Cryolithozone of the northern part of the interfluve Lena and Amga interfluve (Kriolitozona severnoi chasti Leno-Amginskogo mezhdurechia)* (in Russian). Moscow: Izd-vo AN USSR, 144 pp.

Washburrn, A.L. 1988. *The world of cold. Geocryological research (Mir kholoda. Geokriologicheskie issledovania)*(in Russian). Moscow: Progress, 384 pp.

A Model for Calculating the Effective Diffusion Coefficient of Water Vapour in Snow

Rev Gavriliev
Melnikov Permafrost Institute SB RAS, Yakutsk, Russia

Abstract

A model is proposed for calculating the effective diffusion coefficient of water vapour for snow to account for its particulate structure. This is an improvement of the model presented in Gavriliev (2004), based on more adequate treatment of heat and mass transfer in snow. The model considers a cubic cell containing a spherical particle with point contacts on the apexes. The vapour concentration distribution on the particle surface is controlled by its temperature field. The temperature field is calculated based on generalized conduction theory for composite bodies, represented in the model by ice and vapour-air mixture. A quantitative relation between the diffusion coefficient of water vapour in snow and the snow density is established which provides a good explanation for the large scatter of experimental data. Because of the particulate structure of snow, the diffusion coefficient of vapour in snow is several times greater than the molecular diffusion coefficient of vapour in air (six times for compact snow).

Keywords: air; diffusion coefficient; snow; vapour flux.

Introduction

Experimental values for the vapour diffusion coefficient in snow, D_s, reported in the literature (Yosida 1950, Pavlov 1962, Kuvaeva 1966, Morozov 1967, Saveliev et al. 1967, Kolomyts 1971, Sommerfeld et al. 1986, Fedoseeva & Fedoseev 1988, Nikolenko 1988, Voitkovskii et al. 1988) scatter widely. There is also no agreement among authors whether this parameter depends on snow temperature, density or structure. The average D_s values measured in experiments vary from 0.17 to 1.20 cm²/s, although the authors used the same standard methods, a crystallizer pan or cans. Some writers (Woodside 1958, Dyunin 1961) adopted the air diffusion coefficient of 0.20 cm²/s at 0°C in their theoretical analyses of the heat and mass transfer in snow, assuming that the coefficients for vapour and air are approximately equal. The experimental results indicate, however, that the measured coefficients of diffusion of water vapour in snow are much larger than the molecular diffusion coefficient in air (4 to 6 times in Yosida [1950] and Pavlov [1962]). Yosida and Pavlov attribute this to the fact that in snow the water vapour is transferred not only by microscopic diffusion across the pores (free diffusion in air), but also by the passage through snow flakes, in which vapour is condensed on one side and evaporates from the other (macroscopic or hand-to-hand diffusion). In both cases, however, the mechanism of vapour transfer through the pore space is the same, namely, the molecular (free) diffusion of vapour-air mixture. Vapour is transferred in the pore space of snow due to the temperature gradient which establishes a vapour pressure gradient. The present author is of the opinion that the large differences in the diffusion coefficients of vapour in snow and in air are due to the particulate structure of snow, because actually vapour evaporates from the entire particle surface. Previous investigators estimated the vapour flux caused by the temperature gradient based on the plane area of a particle (the crystallizer model), which is evidently less than the area of its evaporating surface, i.e., as if the vapour flux is artificially increased. It should be borne in mind that instrumental measurements give the effective values of vapour diffusion coefficient in a unit area.

In order to prove this idea, a model for calculating the vapour diffusion coefficient was proposed by the author (Gavriliev 2004) which took into account the particulate structure of snow. The first attempt of model representation of snow structure to study vapour diffusion in snow was undertaken by Auracher (1978). Auracher's model consisted of plates of ice oriented either perpendicular or parallel to the flow, and the results were very dependent on the assumptions made. More recently, Colbeck (1993) proposed a particle-to-particle model. He considered a cubic packing of non-contacting, equally spaced spheres of ice in the air space. The vapour flux between particles was estimated using the electrostatic analogy. Colbeck found that the effective coefficient of vapour diffusion in snow D_s is related to the porosity of snow m according to

$$D_s = D_m \left[m^n + 10.0\,(1-m)^{0.51} \right] \tag{1}$$

where D_m is the coefficient of vapour diffusion in air and n is the exponent (n = 0, 1, 2, …). The D_s expression is highly insensitive to the exponent n and for practical purposes it can be taken equal to zero.

There are, however, several objections to the particle-to-particle model of Colbeck. First, the model virtually neglects the effect of vapour bypass around the particles through the free pore space, because by analogy with the electric force lines, the vapour flow lines close on the particles. So, Colbeck had to introduce the first term in Eq. (1) in order to obtain the coefficient of vapour diffusion in air D_m, when the particles disappear, i.e., at m = 1. Second, Colbeck's model assumes that the particles are isothermal, resulting in increased temperature gradients across the pores. The vapour flux is thus overestimated.

The model proposed in Gavriliev (2004) develops a very different approach to accounting for the vapour flow and temperature distribution, although it is outwardly similar to Colbeck's model in that it considers a cubic packing of spherical particles, but the particles have point contacts. Based on this model, a linear relation was found between the vapour diffusion coefficient in snow and snow porosity. Clearly some simplifying assumptions have to be made, as in any model investigation. The purpose of this paper is to improve my earlier model by treating heat transfer in snow in a more adequate way.

A Revised Model of Vapour Diffusion Flux in Snow

An outline of the proposed model is as follows. Since snow is cooled from above, the vapour concentration increases downwards. The vapour and heat flows move in the same direction, from the soil to the snow surface (upward). Snow has a complex multi-branch openwork structure with numerous contacts between particles. Modeling of this structure is a difficult task. However, some important advances have recently been made in three-dimensional modeling of snow structure, based on X-ray microtomopgraphic images of snow samples. Two lines of modeling research can be identified. The first one involves the development of simple physical models, based on Kelvin and Langmuir-Knudsen equations, to describe the isothermal and temperature gradient metamorphism of snow (Flin et al. 2003, 2005). Another approach is discrete element modeling (DEM) (Kaempfer et al. 2005, 2007). This snow model has an explicit geometric structure composed of large aggregate of discrete, individual snow grains with axisymmetric particle shapes, including spheres, tapered cylinders, and elongated or oblate spheroids and ellipsoids. The model was used by Kaempfer et al. to reproduce experimentally the radiative and heat transfer in snow. The above models provide realistic representation of the snow structure. However their application to the analysis of heat and mass transfer involves some difficulties. Usually in such a case, the model schemes are simplified; for example, the random structure is replaced by an ordered structure. The simplest models of mixture structure are based on the following rule (from chaos to order) (Dulnev & Zarichnyak 1974): the effective generalized conduction coefficients are equal for the ordered and chaotic systems, if their structures are similar and the properties and volumetric concentrations of the components are the same. This is the case for the model with changing particle shapes developed by the present author to calculate the thermal conductivity of snow (Gavriliev 1996, 1998). The model consists of three intersecting ellipsoids of revolution in a cubic cell and adequately reflects the main features of metamorphic changes in snow structure through the whole cycle from deposition to the glacial state. Depending on snow porosity, particles attain a large variety of shapes, such as stellar, needle, irregular, rounded, faceted and rounded cubical. It is a three-dimensional, ordered and rigid model with coordinate number 6. Contact spots exist where the model figure contacts with the planes of the cubic cell. The size of contact spots and the model porosity are determined by the semi-axes ratio of the ellipsoids of revolution. The model porosity ranges from 0 to 1. The model is purely geometrical and the system's porosity is changed by assigning ellipsoid parameters with no consideration of snow metamorphism.

For the vapour diffusion study, we have restricted ourselves to the special case of the model where the particles have a spherical shape (Gavriliev 2004), and are arranged cubically. In snow, the vapour evaporates from the upper surface of a lower-lying particle and, due to the temperature gradient, moves upward to the lower surface of a higher particle where it condenses in nearly the same amount according to the thermodynamic equilibrium condition. Therefore it is sufficient to consider one of the two processes, evaporation or condensation (the hemisphere scheme in the model). Evaporation has been chosen for the present research. The temperature field in the snow cover gives rise to concentration gradients, thus controlling the rate of vapour diffusion. There is no reverse transport of vapour in snow.

The earlier work (Gavriliev 2004) considered the scheme shown in Figure 1 for a hemisphere in a semicubical cell. At the tops, the particle has a plane of contact with other particles. The bottom $(y = 0)$ and the top $(y = R)$ of the sphere are maintained at constant temperatures t_1 and t_2 $(t_1 > t_2)$, which cause constant vapour concentrations c_1 and c_2 $(c_1 > c_2)$. Since vapour evaporation is a surface phenomenon, along the heat flow axis oy the vapour concentration distribution on the sphere's surface $c(y)$ or $c(x)$ is given over a range from c_1 to c_2.

Snow sublimation is a diffusive process and can be described by Fick's Law. According to the principles of Maxwell's diffusional theory of evaporation (Dyunin 1961), the general equation for the rate of evaporation of a body of arbitrary shape is

$$\frac{dM}{dt} = -\int_S D_o \, grad \, c \, \overline{dS} \tag{2}$$

where dM/dt is the diffusive flux of vapour from the surface; D_o is the general coefficient of diffusion of vapour which depends on molecular diffusion and the character of medium movement relative the body; S is the surface area; $\overline{dS}$ is the vector element of surface area; and c is the weight concentration of vapour in air.

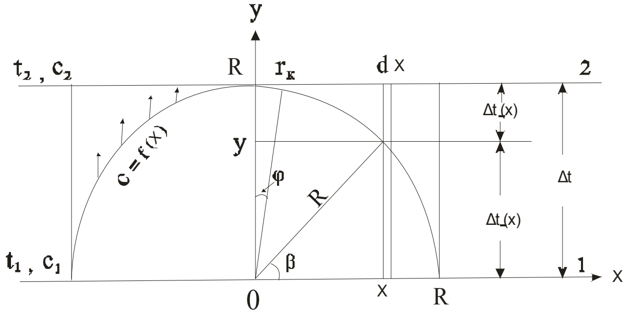

Figure 1. Schematic model of evaporation, vapour diffusion and snow temperature (Gavriliev 2004).

Since the exact theory of evaporation of solids is extremely complex, it is common to consider only the case of steady-state evaporation: $i = dM/dt$ = const. From Eq. (2) it follows that the amount of vapour in the space above the hemisphere depends on the surface area of evaporation and the vapour concentration gradient. The larger is the specific surface area, the more vapour is formed. The particulate structure of a body facilitates water evaporation. This can explain the great difference between the vapour diffusion coefficient in snow and that in air.

For the scheme shown in Figure 1, the concentration gradient in Eq. (2) is taken to be that outside the sphere, i.e., in the region R-y, and considered are the external surface of the sphere S and its differential dS. In the previous work (Gavriliev 2004), an error was made in selecting these parameters when y was taken instead of R-y and the differential dS was calculated from the bottom area of the sphere, i.e., the vapour flux within the sphere was computed.

The differential of the external surface of the sphere is $dS = 2\pi x dl$ (here $dl = (dy^2 + dx^2)^{1/2}$ is the arc length of the sphere's external surface intercepted by an inclined ring with radii x and $x+dx$). Taking into account that $y = (R^2 - x^2)^{1/2}$, we obtain

$$dS = \frac{2\pi R\, x\, dx}{\sqrt{R^2 - x^2}} \quad .$$

Considering the above remarks, the vapour flux i through the cylindrical region of the model is written:

$$i = -D_m \int_{S_c}^{S} \frac{c(y) - c_2}{R - y}\, dS =$$

$$= 2\pi R\, D_m \int_{r_c}^{R} \frac{[c(x) - c_2]\, x\, dx}{\left(R - \sqrt{R^2 - x^2}\right)\sqrt{R^2 - x^2}} \tag{3}$$

where r_c and S_c are the radius and the area of the contact spot at the top of the sphere. In this equation, the concentration gradient is reckoned from c_2.

The distribution of vapour concentration on the particle surface, *c(x),* is controlled by temperature. For an approximate estimate of this parameter, Kaganer's (1966) solution for the sphere with two contact areas was used in Gavriliev (2004) (see Fig. 1). The problem assumes that heat is transferred only through the contact surfaces of the particles, i.e., there is no heat transport across the pore space. This assumption is not entirely correct for snow and is only valid for very low temperatures (about -20°C or lower) when the diffusive transport of vapour is comparatively small and heat is predominantly transferred by conduction.

In the general case, calculation of the temperature distribution on the surface of a snow grain should account the additional heat convection by vapour diffusion due to a temperature gradient. This can be done by using the effective thermal conductivity of air λ_{ae}, which incorporates the thermal effect of vapour transfer in snow by thermal diffusion (Gavriliev 1998).

$$\lambda_{ae} = \lambda_{\mathrm{a}} + \frac{L\, D_{\mathrm{s}}\, e_o}{R_{\mathrm{v}}\, T^2}\left(\frac{L}{\mathrm{R_v}\, E} - 1\right)\exp\left[\frac{L\,(T - T_o)}{R_{\mathrm{v}}\, T_o\, T}\right] \tag{4}$$

where λ_a is the thermal conductivity of calm air; $e_o = 6.1 \cdot 10^2$ Pa is the saturation vapour pressure at 0°C (T_o = 273 K); $R_v = 4.6 \cdot 10^2$ J/(kg·K) is the gas constant of water vapour; T is the absolute temperature; L is the latent heat of ice sublimation; and D_s is the diffusion coefficient of water vapour in snow.

For calculating λ_{ae} within the model space, however, the molecular diffusion coefficient of vapour, D_m, should be used in Eq. (4). The equation for the temperature dependence of D_m at atmospheric pressure (1 atm) given by Kikoin (1976) is

$$D_m = D_0 \left(\frac{T}{273}\right)^{1.5} \tag{5}$$

where D_0 is the diffusion coefficient for vapour at 0°C (T_0 = 273 K).

The D_0 values for water vapour in air reported in the literature (see references in Gavriliev 2004) vary from 0.205 to 0.277 cm²/s, the more frequent values being within the range of 0.230 to 0.277 cm²/s. Jumikis (1962) gives D_0 = 0.426 cm²/s, the value which was obtained in a test with similar conditions to the crystallizer experiments but stands out of the common range. In this study, the value chosen for D_0 is 0.25 cm²/s.

The thermal conductivity of air in relation to temperature may be calculated by an equation given by Vargaftik (1963)

$$\lambda_{\mathrm{a}} = \lambda_0 \left(\frac{T}{273}\right)^{0.82} \tag{6}$$

where $\lambda_0 = 0.0244$ W/(m·K) is the thermal conductivity of air at 0°C (T_0 = 273 K).

The temperature dependence of the effective thermal conductivity of air, based on Eqs. (5) and (6), is shown in Figure 2.

An approximate estimation for the temperature distribution on the surface of a snow particle can be obtained based on the theory of generalized conductivity of composite bodies. The distortion of flow lines in the system components is usually neglected, which introduces some errors into the calculations. However, these errors are largely removed by fragmenting the elementary cell by adiabatic and isothermal planes and by using the arithmetic means of thermal conductivity (Dulnev & Zarichnyak 1974).

Let us consider the scheme in Figure 1, assuming that only point contacts exist between the spherical particles. Select a circular ring with width dx and inner radius x. The heat flux Q is the same across the particle (1) and the medium (2):

$$dQ = -\lambda_1 \frac{\Delta t_R}{y}\, dS = -\lambda_2 \frac{\Delta t_2}{R - y}\, dS \tag{7}$$

where λ_1 and $\lambda_2 = \lambda_{ae}$ are the thermal conductivities of the ice particle and the air with water vapour, respectively (the effective coefficient); dS is the cross-section area of the ring; $\Delta t_R(x) = t_R(x) - t_1$ and $\Delta t_2(x) = t_2 - t_R(x)$ are the temperature

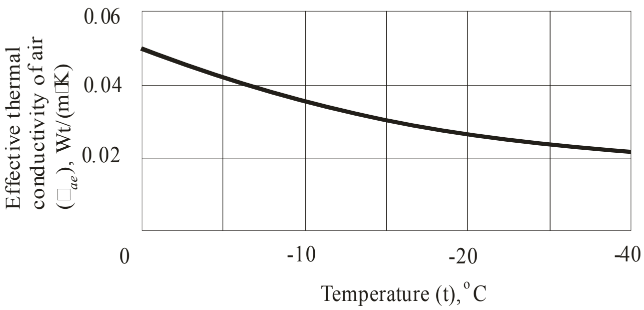

Figure 2. The effective thermal conductivity of air in snow versus temperature.

differences on the particle surface and in the air space of the circular ring, respectively; $\Delta t_R(x)$ is the temperature of the sphere's surface at points (x and y) of intersection with the cylindrical ring. Eq. (7) is valid for any radius x.

Considering expressions $y = (R^2 - x^2)^{1/2}$ and $\Delta t_R(x) + \Delta t_2(x) = \Delta t$ (the total temperature difference in the cell $t_2 - t_1$), the equation

$$\frac{\Delta t_R(x)}{\Delta t} = \frac{1}{1 + \dfrac{\lambda_1}{\lambda_2}\left(\dfrac{1}{\sqrt{1 - x^2/R^2}} - 1\right)} \qquad (8)$$

is obtained from Eq. (7) for the relative temperature difference over the particle surface.

Hence it follows that the temperature distribution on the particle surface depends on the ratio between the thermal conductivities of the particle and the pore medium (Fig. 3). Taking into account the effective thermal conductivity of air, curves 6–8 fit for snow over a temperature range 0 to -10°C.

Because the vapour in snow is saturated, its concentration is determined using the well-known equation

$$c = \frac{c_0\, T_0}{T} \exp\left(\frac{22.46\, t}{T}\right) \qquad (9)$$

where $c_0 = e_0 \mu_l / R_v T_0$ is the vapour concentration at T_0; μ_l is the molecular weight of the vapour.

When the temperature distribution at the particle surface is given by curves 6-8 (Fig. 3) (within the temperature range of 0 to -10°C), the calculations of vapour concentration with Eq. (9) result in a single curve (with few departures) relating the relative difference in vapour concentration over the sphere, $\Delta C_R(x)/\Delta C$, and the dimensionless coordinate x/R (Fig. 4). For convenience of integration in Eq. (3), this curve is expressed by the equation

$$\frac{\Delta C_R(x)}{\Delta C} = 2.4\frac{x}{R} - 1.4\frac{x^2}{R^2} \qquad (10)$$

where $\Delta C = C_1 - C_2$ is the maximum difference in vapour concentration between the equatorial and vertex planes of the spherical particle; $\Delta C_R(x) = C_R(x) - C_2$ is the vapour concentration difference over the particle surface relative the vertex plane.

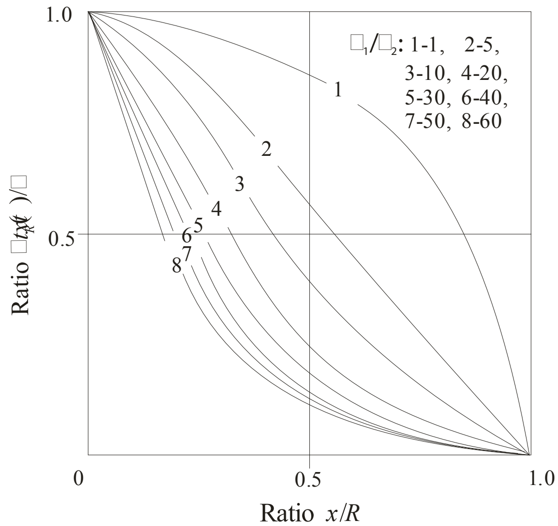

Figure 3. The distribution of the relative temperature difference over a spherical particle at various ratios between thermal conductivities of ice (1) and pore space (2).

Since the particles have only point contacts ($r_c = 0$), Eq. (43) is integrated over dx from 0 to R. Then the vapour flux in the cylindrical region of the model will be calculated using the equation:

$$i = -2\pi R\, D_m (C_1 - C_2) \int_0^R \frac{\left(2.4\dfrac{x}{R} - 1.4\dfrac{x^2}{R^2}\right) x\, dx}{\sqrt{R^2 - x^2}\left(R - \sqrt{R^2 - x^2}\right)} =$$

$$= -2\pi R\, D_m (C_1 - C_2)(1.2\pi + 0.3). \qquad (11)$$

Effective Diffusion Coefficient of Vapour in Snow

The effect of the particulate structure of snow on the vapour diffusion coefficient is estimated as above by comparing the vapour flux calculated by Eq. (11) and the flux through the bottom of the cylindrical region $i_{fl} = -\pi R D_s'(c_1 - c_2)$ where D_s' is the effective diffusion coefficient for vapour in the cylindrical region of the snow model. Then we obtain, as above, the equation

$$D_s' = K\, D_m \qquad (12)$$

where $K = 2(1.2\pi + 0.3)$ is a parameter for the particulate structure of snow which shows how many times the vapour diffusion coefficient in snow is greater than that in air due to the increased evaporation area of snow particles.

For the considered case of the vapour concentration distribution near the surface of the spherical snow particle, we have a different value of K which is equal to 8.2.

When the contribution of a through space to vapour diffusion is taken into account, the total diffusion coefficient is calculated by the equation in Gavriliev (2004)

$$D_s = D_m\, \left[1 + 1.5(K - 1)(1 - m)\right] \qquad (13)$$

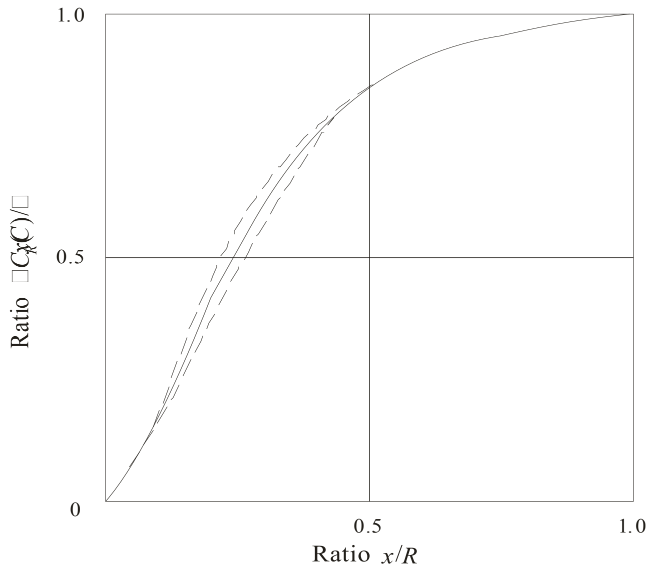

Figure 4. The distribution of the relative vapour concentration difference on the surface of a spherical snow particle.

where $0.33 \le m \le 1$. At $m = 1$, we have $D_s = D_m$, and at $m = 0.33$, $- D_m = K D_m$.

Thus the diffusion coefficient of water vapour in snow depends on porosity (density).

Discussion of Results

Computations have been made for snow densities varying from 0.1 to 0.4 g/cm^3 ($m = 0.56 \div 0.89$). The obtained values of the diffusion coefficient for snow, D_m (cm^2/s), range from 0.55 to 1.45 and are compatible with the experimental results of most workers. It is interesting to compare the relative effective coefficients of vapour diffusion in snow (D_s/D_m) calculated by Eq. (1) (Colbeck 1993) and Eq. (13) (Gavriliev 2004). Figure 5 shows that the D_s/D_m ratio values from Colbeck's equation are invariably higher than those obtained by Eq. (13). The possible explanation is that calculations with the particle-to-particle model use the overestimated vapour flux due to the increased temperature gradient across the pores and the adding of the first term in Eq. (1) which leads to the results higher by unity. Curve 2′ for the results obtained without adding the first term in Eq. (1) agree better with our results (curve 1). It should be noted that actual computations with the particle-to-particle model led Colbeck to Eq. (1) that did not include the first term which was added later so that the logical reasoning would be complied for $m = 1$. Colbeck (1993) admitted that, because of the above reasons, the D_s/D_m values obtained by Eq. (1) were higher (4 to 7) than the D_s/D_m range (3.5 to 5) found by Yosida (1950).

Figure 5 also shows the experimental results of the authors mentioned in this paper. It is evident that there is no clear relationship between D_s/D_m and snow density and that the data scatter from 0.6 to 5.1. This is probably due to the effect of snow temperature on the measured coefficient of vapour diffusion in snow observed in the experimental data of Morozov (1967), Kolomyts (1971) and Nikolenko (1988). Most of the experimental data are lower than the theoretical results. Further investigations will be made to find an explanation.

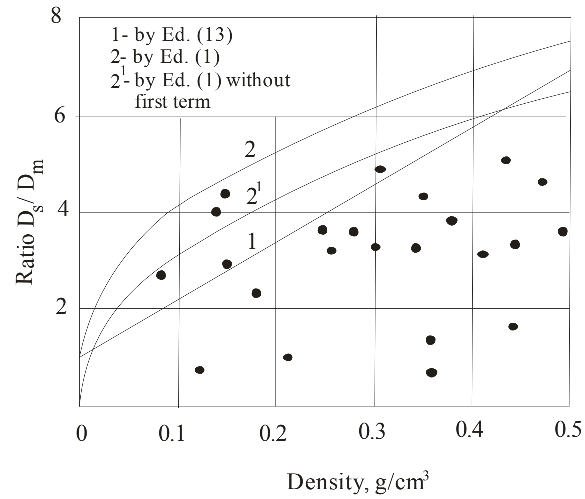

Figure 5. D_s/D_m ratio vs. snow density.

It is interesting to note that, according to the proposed model, the diffusion coefficient of vapour in snow can reach a maximum of 2.06 cm^2/s at a porosity of 0.33, or a porosity of about 0.62 g/cm^3. This can be considered to be a purely theoretical value for dry snow which is hardly possible in real situations.

Conclusions

A model was developed to describe the process of water vapour diffusion in snow which takes into account the particulate structure of snow. Based on this model, a linear relation was found between the vapour diffusion coefficient and snow density. It has been theoretically established that because of the particulate structure of snow, the effective diffusion coefficient of vapour in snow is many times that of water vapour in air (up to six times for compacted snow).

Acknowledgments

The author is grateful to the Associate Editor of the Conference Proceedings and two anonymous reviewers for their valuable comments. The work described here was supported by the Russian Foundation for Basic Research (Grant 06-05-96126).

References

Auracher, H. 1978. Heat transfer in frost and snow. *International Heat Transfer Conference*. Washington, D.C.: Hemisphere, 25-30.

Colbeck, S.C. 1993. The vapor diffusion coefficient for snow. *Water Resources Research* 29(1): 109-115.

Dulnev, G.N. & Zarichnyak, Y.P. 1974. *Thermal Conductivity of Mixtures and Composite Materials (Teploprovodnost smesei I kompozitsionnykh materialov)* (in Russian). Leningrad: Energia, 263 pp.

Dyunin, A.K. 1961. *Snow Evaporation (Isparenie snega)* (in Russian). Novosibirsk: Izd-vo SO AN SSSR, 119 pp.

Fedoseeva, V.I. & Fedoseev, N.F. 1988. Estimation of the diffusion coefficient of water vapour in snow (in Russian). *Meteorologia i Gidrogeologia* 2: 132-136.

Flin, F., Brzoska, J.-B., Lesaffre, B., Coleou, C. & Pieritz, R.A. 2003. Full three-dimensional modeling of curvature-dependent snow metamorphism: first results and comparison with experimental tomographic data. *Journal of Physics D: Applied Physics* XXXVI(10): 49-54.

Flin, F., Brzoska, J.-B., Pieritz, R.A., Lesaffre, B., Coleou, C. & Furukawa, Y. 2006. A tentative model for the temperature gradient snow metamorphism and its first validations on X-ray microtomographic data. *Proceedings of the 8th International Conference on X-Ray Microscopy, Institute of Pure and Applied Physics Conference Series 7*: 306-308.

Gavriliev, R.I. 1996. A mathematical model for calculating thermal conductivity of snow subject to metamorphism. *Proceedings of the Fifth International Symposium on Thermal Engineering and Science for Cold Regions, Ottawa, Canada, May 19-22, 1996*: 516-521.

Gavriliev, R.I. 1998. *Thermal Properties of Soils and Ground Covers in Permafrost Areas (Teplofizicheskie svoistva gornykh porod I napochvennykh pokrovov)* (in Russian). Novosibirsk: Izd-vo SO RAN, 280 pp.

Gavriliev, R.I. 2004. On the diffusion coefficient of water vapour in snow cover (in Russian). *Kriosfera Zemli* VIII(2): 74-81.

Jumikis, A. 1962. Vapor diffusion in freezing soil systems of very large porosities. *Highway Research Board Bulletin* 331: 28-45.

Kaempfer, T.U., Hopkins, M.A. & Perovich, D.K. 2007. A three-dimensional microstructure-based photon-tracking model of radiative transfer in snow. *Journal of Geophysical Research* 112, D24113, doi: 10.1029/2006JD008239.

Kaempfer, T.U., Schneebeli, M. & Sokratov, S.A. 2005. A microstructural approach to model heat transfer in snow. *Geophysical Research Letters* 32, L21503, doi: 1029/2005GL023873.

Kaganer, M.G. 1966. Contact heat transfer in granular material under vacuum (in Russian). *Inzhenerno-Fizicheskiy Zhurnal* II(1): 30-37.

Kikoin, I.K. (ed.). 1976. *Handbook of Physical Quantities (Tablitsy fizichekikh velichin)* (in Russian). Moscow: Atomizdat, 1008 pp.

Kolomyts, E.G. 1971. *The Snow Structure and Regime in West-Siberian Taiga (Struktura I rezhim snezhnoi tolshi Zapadno-Sibirskoi taigi)* (in Russian). Leningrad: Nauka, 174 pp.

Kuvaeva, G.M. 1966. Determination of the coefficient of water vapour diffusion in snow. *Proceedings of the Third Trans-Caucasian Conference on Snow Cover, Avalanches and Glaciers in the Caucasian Mountains (in Russian)*: 75-79.

Morozov, G.A. 1967. Calculation of snow density changes due to water vapour diffusion, convection and sublimation (in Russian). *Meteorologia i Gidrologia* 6: 98-104.

Nikolenko, A.V. 1988. Laboratory-determined characteristics of water vapour diffusion in snow cover (in Russian). *Materialy Gliatsiologicheskikh Issledovanij* 62: 90-96.

Pavlov, A.V. 1962. Thermophysical properties and thermal balance of snow cover in the Moscow area. In: *Materials for the Study of Frozen Zones in the Earth Crust (Materialy k ucheniu o merzlykh zonakh zemnoi kory)* (in Russian). Moscow: Izd-vo AN SSSR, 3-35.

Saveliev, B.A., Laptev, M.P. & Lapteva, N.I. 1967. The structure, composition and physical-mechanical properties of snow in the Khibin mountains and their changes during metamorphism. In: *Snow and Avalanches in the Khibin (Sneg i laviny Khibin)* (in Russian). Moscow: Izd-vo MGU, 201-239.

Sommerfeld, R.A., Friedman, I. & Nilles, M. 1986. The fractionation of natural isotopes during temperature gradient metamorphism of snow. In: H.G. Jones & W.J. Orville-Thomas (eds.), *Seasonal Snowcovers: Physics, Chemistry, Hydrology*. Dordrecht: D. Reidel Publishing Company, 95-106.

Vargaftik, N.B. 1963. *Reference Book on Thermophysical Properties of Gases and Fluids Spravochnik po teplofizicheskim svoistvam gazov I zhidkostei)* (in Russian). Moscow: Fizmatgiz, 708 pp.

Voitkovskii, K.F., Golubev, V.N., Sazonov, A.V. & Sokratov, S.A. 1988. New data on the water vapour diffusion coefficient in snow (in Russian). *Materialy Gliatsiologicheskikh Issledovanij* 63: 76-81.

Woodside, W. 1958. Calculation of the thermal conductivity of porous media. *Canadian Journal of Physics* 37(7): 112-118.

Yosida, Z. 1950. Heat transfer by water vapour in snow cover. *Teion Kagaki* 5: 93-100.

Recent and Projected River Runoff Changes in Permafrost Regions of Eastern Siberia (Lena River Basin)

A.G. Georgiadi
Institute of Geography RAS, Moscow, Russia
I.P. Milyukova
Institute of Geography RAS, Moscow, Russia
E.A. Kashutina
Institute of Geography RAS, Moscow, Russia

Abstract

During the last decades the permafrost regions in the Lena River basin, Eastern Siberia, have experienced substantial climate warming. The analysis of long climatic and hydrological series revealed an inhomogeneous distribution of climate warming over the territory. Climate warming is shown to be accompanied by pronounced runoff changes, particularly in the cold season, that also exhibit significant space-time inhomogeneity. According to the hydrological modeling results, the expected anthropogenic climate warming in the 21st century can cause more perceptible runoff changes in the Lena River basin, as compared with the recent climate change. The hydrology-related consequences of climate warming are evaluated from a macro-scale monthly water-balance model (Georgiadi & Milyukova 2002, 2006).

Keywords: eastern Siberia; monthly water-balance model; permafrost; river runoff changes; scenarios of global climate warming.

Introduction

The river flow forming in the cryolithic zone of Eurasia, especially within the largest river basins (Lena, Enisey, Ob'), has a strong effect on the regional climate and the surrounding seas, affecting the chemical composition of water, the sea ice formation, and the circulation in the Arctic Ocean and the North Atlantic. Changes of the river runoff can have a pronounced effect on the processes involved.

During the recent decades significant global climate warming has been observed. Climate warming has been the largest in Northern Eurasia, particularly in the permafrost regions of Eastern Siberia (IPCC 2001). These changes include the winter air temperature and overall soil temperature rise (Varlamov et al. 2002). Regional climate changes are accompanied by river runoff changes in Eastern Siberia (Georgievsky et al. 1999, Savelieva, et al. 2000, Yang et al. 2002, Simonov & Khristoforov 2005, Berezovskaya et al. 2005, Georgiadi et al. 2006).

According to model forecasts of the climate change caused by the increased atmospheric greenhouse gases, the most perceptible changes take place in the permafrost regions of Eastern Siberia (IPCC 2001). Regional climate warming will cause a considerable increase in soil temperature and consequent permafrost thawing (Anisimov et al. 1997, Demchenko et al. 2002, Malevsky-Malevich et al. 2000). Such changes can alter the river runoff, particularly its intra-annual distribution (Georgiadi & Milyukova 2006). Possible changes of freshwater and heat flows going into the Arctic Ocean have potentially important implications for the ocean circulation and climate outside the region.

Until now, the processes regulating the river runoff in the large basins of the cryolitho zone have not been well studied, particularly the geographical (spatial and temporal) structure of their response to recent and projected global climate warming.

The Lena River basin in Eastern Siberia was selected as the main subject of investigation. It is one of the world's largest basins and occupies the area of 2,488,000 km^2 and extends as far as 4400 km. The basin is almost completely covered with deep permafrost ground whose upper active layer thaws out during the short summer season. In addition, the Lena basin is characterized by a small anthropogenic influence owing to a low population density. Analysis of the Lena basin is also facilitated by large intensive research programs carried out by Russian, bilateral, and international teams in the last 15 years.

The main objectives of this investigation is to analyze spatial and temporal heterogeneities of the recent river runoff changes over the Lena River basin, as well as to compute river runoff changes caused by the projected global climate warming.

Recent River Runoff Changes

The investigation of a spatial-temporal structure of the long-term runoff changes in the Lena River basin is based on the analysis of long-term series of hydrometric observations which are conducted on the national network of gage stations. Long-term series of annual, seasonal, and monthly runoff values for large, medium, and small representative river basins and annual and monthly series of air temperatures and precipitation are analyzed for characteristic zonal-landscape conditions. At the initial stage, the following methods were used:

1) Method to compare the characteristics of mean annual, seasonal, and monthly values of hydrological and climatic changes for the two periods: from the start of records to 1980 and from 1981 to the end of the 1990s and the beginning of the 2000s. It is the latter period alone, when the regional climate warming is most intensive.

2) Method of cumulative sum of normalized values which was traditionally used in the USSR and Russia to study the cycles of long-term changes in hydrological and climatic elements.

$$C_{si} = \sum (K_i - 1) / C_v \, , \; K_i = E_i / E_m \, , \qquad (1)$$

where C_v is the coefficient of variation, E_i is the value of the element for the i-year, E_m is the mean value of the element, K_i is the modulus coefficient of the element, C_{si} is the cumulative sum of the normalized values of the hydrological and climatic element.

Climatic changes

It follows from the calculations performed that in the period of the intensive regional climate warming, the annual air temperature rises considerably, with the temperature rise being distributed inhomogeneously over the territory of the Lena River basin. The maximal rise is registered in the central, eastern, and southern parts of the basin.

The character of the basin-averaged air temperature changes (provided that we do not consider the features of their spatial distribution) agrees with the classical idea, i.e. the most noticeable changes occur in the cold season of the year and insignificant warming and even temperatures fall in the summer-autumn period are observed. At the same time considerable spatial variation of changes throughout the year is typical for the basin.

Considerable spatial variation is also characteristic of the changes in average monthly precipitation values, especially in the summer.

The analysis of the cumulative sum curves of annual air temperatures indicates that beginning in the 1980s, the climate warming, which was synchronous enough in different parts of the Lena River basin, was recorded. The change of precipitation in this period is less homogeneous over the basin's territory.

River runoff changes

According to the analysis of the cumulative sum curves of the annual river runoff in different parts of the Lena River basin, the phase of the increase in the annual river runoff is observed in most of the basin during the last 15-25 years.

Only in some of the rivers, in the southern left-bank basin and in the upper course of the Lena, is the trend for the runoff decrease revealed.

The comparison of cumulative sum curves of annual and winter (November-April) river runoffs for the long period of observations (1935-2005) yields three types of their combinations (the list and the position of gage stations are shown in Figure 1):

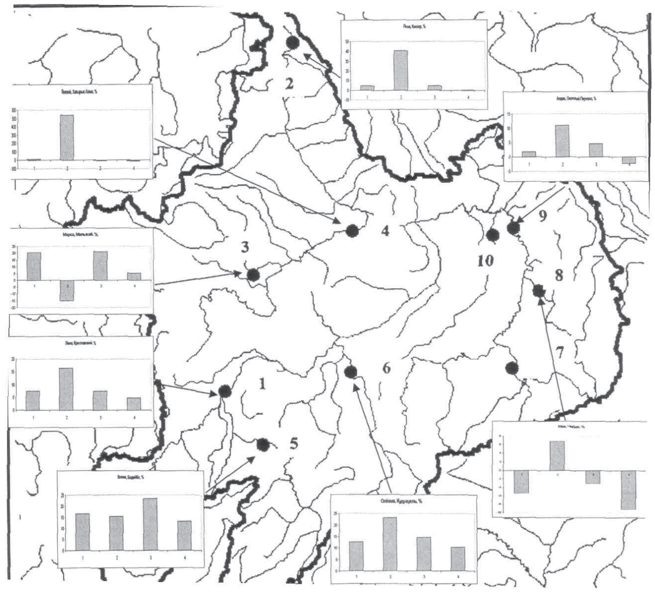

Figure 1. Deviations of mean annual and seasonal runoff for the period 1981-2005 and the period from the start of records to 1980 (in percent). Designations of diagram columns: 1 is the annual runoff; 2 is the winter (November-December) runoff; 3 is the flood (May-June); 4 is the low water (July-October). 1) Lena, Krestovsky; 2) Lena, Kyusyur; 3) Markha, Malyukai; 4) Vilyui, Khatyryk-Khomo; 5) Vitim, Bodaibo; 6) Olekma, Kudu Kuel; 7) Uchur, Chyul'byu; 9) Aldan, Okhotsky Perevoz; 10) Amga, Buyaga.

1) Phases of the annual and winter river runoff increase and decrease are almost synchronous, but for the winter runoff, these are usually better defined (Lena, Krestovsky; Vitim, Bodaibo; Olekma, Kudu Kuel; Aldan, Okhotsky Perevoz; Uchur, Chyul'byu; etc.).

2) Phases of the annual and winter runoff increase and decrease during the long period of observations can coincide or be asynchronous (Markha, Malyukai).

3) Relatively short and less intensive phases of the annual runoff increase and decrease are observed against the background of the long phases of increasing and decreasing winter runoffs (Lena, Kyusyur; Amga, Buyaga).

The comparison of intra-annual runoff changes in the Lena River basin for the periods considered shows the following (Fig. 1):

1) In the downstream of the Lena River, the most noticeable runoff increase occurs in the cold season of the year, while in the southern and southwestern mountain parts of the basin (with discontinuous and sporadic permafrost and more pronounced underground flow), the changes in runoff intra-annual distribution are more homogeneous and normally more intensive in all seasons of the year, as compared with the other parts of the basin.

2) The most noticeable increase in the Lena River runoff in the cold season is observed in the downstream of the Aldan and Vilyui rivers confluence.

3) The increase in the river runoff during the cold season in the downstream of the Aldan River can be related to the change of climatic conditions in its basin.

4) The considerable runoff increase in the lower portion of the Vilyui River in many respects can be connected with its artificial regulation as a result of the dam construction. This factor plays the main role in the winter runoff increase in the downstream of the Lena River.

Projected River Runoff Changes

Monthly water-balance model (MWBM)

The monthly water-balance model (MWBM), developed by the Institute of Geography of RAS to calculate hydrological consequences of the expected global climatic changes, was used to evaluate the large-scale hydrological changes (Georgiadi & Milyukova 2002, 2006). It can be referred to the category of macro-scale hydrological models with monthly resolution which are actively developed in the recent years (Willmott et al. 1985, Yates & Strzepek K. 1994, etc).

The model describes the main processes of the land hydrological cycle: infiltration and accumulation of water in the active layer; evaporation (based on the modified Tornthwite method (Willmott et al. 1985)); freezing and thawing of ground by using the Pavlov (1979) and the Belchikov & V.I.Koren methods (1979) which have been established as a simplified solution of the classical Stefan problem as applied to permafrost grounds; snow accumulation and snowmelt based on the Komarov method (Manual… 1989); formation of the surface flow and runoff from the active layer; and formation of the ground flow and river runoff.

The model allows for macro-scale inhomogeneity of hydrometeorological fields and other characteristics of the territory (permafrost, soil, hydrogeology). Such an approach provides the required accuracy in modeling climate changes that is achieved in the experiments with general atmosphere and ocean circulation models. The model calculations are performed in the regular grid cells. The existing version of the model employs a uniform spatial grid whose change makes it possible to take into account the main macro-scale inhomogeneity of the relief, the features of permafrost grounds including their active layer and hydrometeorological characteristics. The model is elaborated to estimate the changes of multi-year average characteristics of the water balance.

The principal approach to the account of inhomogeneity of the hydrogeological structure is to divide the underground zone into layers and calculate the runoff from each of them using our scheme of income and discharge of water for these layers.

The results of numerical experiments with ECHAM4/OPYC3 (Max Plank Meteorological Institute, Germany) and GFDL-R30 (Geophysical Laboratory of Hydrodynamics of the Princeton University, USA) were used based on the A2 family scenarios of global socio-economic changes in the 21st century from the last SRES scenario series accepted in the IPCC program. Calculations were made for the averaged conditions of the two periods (2010-2039, 2040-2069).

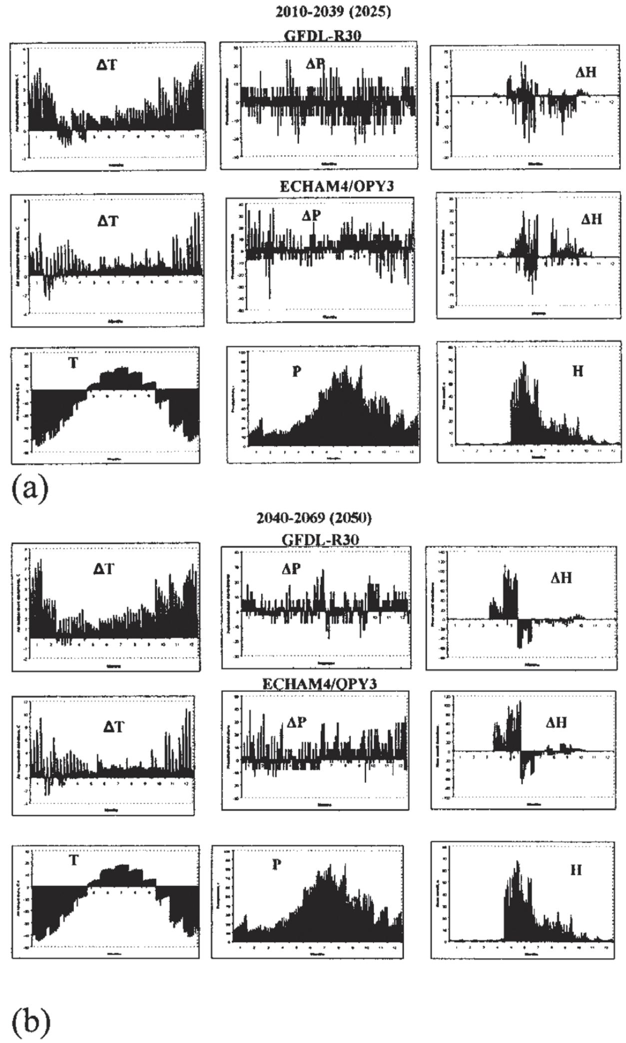

Figure 2. Deviations of mean monthly air temperatures (ΔT, °C), atmospheric precipitation (ΔP, mm) and river runoff (ΔH, mm) from their modern values generalized in the regular grid cells covering the plain part of the Lena basin, with regard for climate warming in 2010-2039 (a) and in 2040-2069 (b) by using scenarios of the Geophysical Laboratory of Hydrodynamics of the Princeton University (USA) and the Max Plank Meteorological Institute (Germany). The last line of figures shows mean monthly air temperatures (T, °C), atmospheric precipitation (P, mm), and stream flow (H, mm) under the modern climate conditions.

Discussion of modeling results for the plain part of the Lena River basin

Climatic conditions are shown in Figure 2. According to the considered scenarios for a plain in the central part of the Lena River basin, the climate is expected to warm essentially and more intensive in the middle of the 21st century.

Thus according to the scenario of the Max Plank Meteorological Institute, the climate warming can be more perceptible. Both scenarios predict a better pronounced air temperature increase in the cold period of the year, which is likely to lead to its duration reduction. The character of changes in atmospheric precipitation is more complicated. According to the both scenarios, the tendency towards the precipitation increase is to be evident as late as the mid-21st century.

It should be noted that the character of annual distribution of scenario changes of monthly average air temperatures and precipitation is very similar to the appropriate changes observed in this region during the last decades of the modern climate warming, though it differs from the current changes in scale.

Hydrological conditions are also shown in Figure 2. According to the climatic scenarios developed by the Geophysical Laboratory of Hydrodynamics, Princeton University and the Max Plank Meteorological Institute for the plain part of the Lena River basin, during the first thirty years of the current century it is not likely to expect any noticeable increase in both annual river runoff and river runoff for the spring-summer flood period (three months with the greatest monthly flow). For the two scenarios realized, a significant increase in annual and spring flood runoffs is expected to occur by the middle of the 21st century.

It should be noted that the distribution of the possible changes in the river runoff over this part of the basin is characterized by essential spatial inhomogeneity which is to be reduced appreciably by the middle of the century.

Both scenarios suggest significant changes in the intra-annual stream-flow distribution. Thus in the first third of the century, both scenarios give similar changes in the wave of the spring-summer flood, whereas the river runoff changes following the main wave of high water may be of absolutely opposite character. By the middle of the century, both scenarios give, in essence, the same pattern of changes in the intra-annual stream-flow distribution: the wave of spring-summer high water is to be shifted (with the form and volume of water nearly unchanged) one month backward, as compared with the current situation. By the way, the character of changes in the intra-annual stream-flow distribution in the Lena River basin is identical to the similar changes in the Volga River basin with the probable global climate warming in the current century.

The following conclusions can be made as to the probable impacts of the predicted climate warming in the central plain part of the Lena River basin.

1. According to the considered scenarios, the essential climate warming is likely to be expected, and in the middle of the 21st century this is to be even more intensive.

2. The character of the intra-annual distribution of the scenario changes in monthly mean air temperatures and precipitation is rather similar to the appropriate alterations observed in this region during the last decades of the modern climate warming, but differs from the recent climate warming in scale.

3. According to the climatic scenarios, a significant increase, both in annual runoff and in spring-summer flood runoff, is likely to be expected by the middle of the current century.

4. Quite a significant change in the character of the annual stream-flow distribution may take place. By the middle of the century, the both scenarios give, in essence, the same pattern of changes in the intra-annual stream-flow distribution: the wave of spring-summer high water is to be shifted one month backward, as compared with the current situation.

This study was supported by NASA grant NNG06GH41G and the Russian Fund on Basic Research grant 07-05-12085-ofi.

Acknowledgments

The authors are grateful to Dr. R. Leemans, who contributed global a database on the modern climate, prepared in the International Institute of Applied System Analysis, Laxenburg, Austria.

References

Anisimov, O.A., Shiklomanov, N.I. & Nelson, F.E. 1997. Effects of global warming on permafrost and active-layer thickness: results from transient general circulation models. *Global and Planetary Change* 15(2): 61-77.

Belchikov, V.A. & Koren, V.I. 1979. Model of snow melting and rain runoff forming for forest watersheds. *Proc. of Hydrometeocenter of the USSR* issue 218: 3-21. (in Russian)

Berezovskaya, S., Yang D. & Hinzman, L. 2005. Long-term annual water balance analysis of the Lena River. *Global and Planetary Change* 48: 84-95

Demchenko, P.F., Velichko, A.A., Eliseev, A.V. Mokhov, I.I. & Nechaev, V.P. 2002. Dependence of permafrost conditions on global warming: comparison of models, scenarios, and paleoclimatic reconstructions. *Izvestiya, Atmospheric and Oceanic Physics* 38(2): 143-151. Translated from Izvestiya AN. Fizika Atmosfery i Okeana, Vol. 38, No. 2, 2002, 165–174. English Translation Copyright © 2002 by AIK

Georgiadi, A.G. & Milyukova, I.P. 2002. Possible scales of hydrological changes in the Volga river basin during anthropogenic climate warming. *Meteorology and Hydrology* No. 2: 72-79. (in Russian)

Georgiadi, A.G. & Milyukova, I.P. 2006. Possible river runoff changes in the largest river basins of the Russian Plain in the 21st century. *Water management complex of Russia* No. 1: 62-77. (in Russian)

Georgievsky, V.Yu., Ezhov, A.V., Shalygin, A.L., Shiklomanov, I.A. & Shiklomanov, A.I. 1999. Evaluation of possible climate change impact on hydrological regime and water resources of the former USSR rivers. *Meteorology and Hydrology* No. 11: 89-99. (in Russian).

IPCC 2001. *Climate Change 2001: The Scientific Basis. Contribution of Working Group I to the Third Assessment Report of the Intergovernmental Panel on Climate Change* (J.T. Houghton, Y. Ding, D.J. Griggs, M. Noguer, P.J. van der Linden, X. Dai, K. Maskell & C.A. Johnson [eds.]). Cambridge, UK, and New York, NY: Cambridge University Press, 881 pp.

Malevsky-Malevich, S.P., Molkentin, E.K, Nadyozhina, E.D. & Shklyarevich, O.B. 2001. Numerical simulation of permafrost parameters distribution in Russia. *Cold Regions Science and Technology* 32: 1-11.

*Manual on hydrological forecasts. Issue 1: Long-term forecasts of water regime of rivers, lakes and water reserve*s. 1989. Leningrad: Gidrometeoizdat, 358 pp. (in Russian).

Pavlov, A.V. 1979. *Thermophysics of Landscapes*. Novosibirsk: Nauka, 285 pp. (in Russian).

Savelieva, N.I., Semiletov, I.P., Vasilevskaya, L.N. & Pugach, S.P. 2000. A climate shift in seasonal values of meteorological and hydrological parameters for Northeastern Asia. *Progress in Oceanography* 47(2-4): 279-297.

Simonov, Yu.A. & Khristoforov, A.V. 2005. Analysis of long-term stream-flow variability in the Arctic Ocean basin rivers. *Water Resources* 32(6): 645-652. (in Russian).

Varlamov, S.P., Skachkov, Yu.B. & Skryabin, P.N. 2002. *Ground Temperature Regime of Central Yakutia Permafrost Landscapes*. Yakutsk: SB RAS, 218 pp. (in Russian).

Willmott, C.J., Rowe, C.M. & Mintz, Y. 1985. Climatology of the terrestrial seasonal water cycle. *Journal of Climatology* 5: 589-606.

Yang, D., Kane, D.L., Hinzman, L.D., Zhang, X., Zhang, T. & Ye, H. 2002. Siberian Lena River hydrologic regime and recent change. *Journal of Geophysical Research* 107(d 23, 4694): 14-4 – 14-10.

Yates, D. & Strzepek, K. 1994. *Comparison of Models for Climate Change Assessment of River Basin Runoff*. WP-94-45, IIASA, Laxenburg, Austria. 48 pp.

Permafrost Analogues of Martian Habitats

David A. Gilichinsky
Soil Cryology Laboratory, Institute of Physicochemical and Biological Problems in Soil Sciences, Russian Academy of Sciences, Pushchino, Russia

Abstract

Terrestrial permafrost, inhabited by viable microorganisms, represents a range of possible extraterrestrial cryogenic ecosystems on Earth-like planets without obvious surface ice, such as Mars. In a balanced permafrost environment, cells survive significantly longer than in other habitats. If life existed during the early stages of Martian development, then remnants of primitive forms may be found within frozen material that protects them against unfavorable conditions. This paper considers (a) the suggested age of Antarctic permafrost as an analogue somewhat closer to that of Mars than Arctic permafrost, (b) that free water can only exist on Mars in the form of cryopegs, as formed when Mars became dry and cold, (c) volcano-ice interactions in permafrost areas as one way to have liquid water on Mars, and (d) soil cover as a distant model of the Martian active layer.

Keywords: astrobiology; cryopegs; Mars; microorganisms; permafrost; volcanoes.

Introduction

Temperature is the fundamental aspect of the environment, where it acts as a regulator of physicochemical reactions and forms the basis of biological processes. Hard data indicate that biota survive over geological periods at temperatures <0°C within permafrost (for a recent overview, see Steven et al. 2006) down to -27°C (Gilichinsky et al. 2007a), and in ice sheets in Greenland (Miteva et al. 2004), the Tibetan Plateau (Christner et al. 2003), and in Antarctica down to -50°C (Abyzov 1993). In such environments, the dehydration leads to a considerable decrease of biochemical activities. This allows the survival of an ancient microbial lineage that can physiologically and biochemically adapt much longer than it would in any other known habitat.

The ability of microorganisms to survive on a geological scale forces us to redefine the spatiotemporal limits of the terrestrial and extraterrestrial biospheres and suggests that mechanisms of such adaptation might operate for millions of years. The long-term subzero temperature regime of the cryosphere is not limiting but rather a stabilizing factor. Organisms adapted to such balanced conditions represent a significant part of the biosphere—the cryobiosphere.

The cells, their metabolic by-products and bio-signatures (bio-minerals, bio-molecules, bio-gases), found in the Earth's cryosphere provide a range of analogues that could be used in the search for possible ecosystems and potential inhabitants on extraterrestrial cryogenic bodies. If life ever existed on other planets during the early stages of development, then its traces may consist of primitive cell forms. Similar to the Earth, they might have been preserved and could be found at depths within the ice or permafrost.

Microorganisms isolated from the ice cores of both hemispheres have been interpreted to be Earth's most representative analogues of icy inhabitants on Jupiter's ice-covered moon Europa, icy moon in Saturn's system Enceladus, and ice caps on Martian poles. Because ice thaws under geostatic pressure even at subzero temperatures, the existence of very old microorganisms is unlikely on the mentioned moons and caps.

The most inhabited and ancient part of the cryobiosphere's permafrost, being up to several hundred meters deep, harbors significant numbers of viable microorganisms, adhered on soil particles, and represents a wide range of possible cryogenic ecosystems for planets without obvious surface ice. Most intriguing are the traces of past or existing life on Mars, of interest due to upcoming missions. Because of unfavorable factors, life is unlikely to exist on the surface, and no terrestrial habitats duplicate Martian conditions. Anderson et al. (1972) and Cameron & Morelli (1974) first advanced the idea of using the terrestrial permafrost analogues, and the present paper considers these analogues as a bridge to Martian habitat and possible life forms. "Mars-Odyssey" observations of neutron fluxes that found water in the subsurface layer (Boyton et al. 2002) indicated Mars as a "water-rich planet." Hence, the requisite conditions for life have a place that makes the analogous models more or less realistic.

Soil Cover

Water ice within the top meters of the high-latitude regolith, as well as visual similarities on the Earth's and Martian surface—polygons formed by frost cracking—leads to consideration of the frost affected, seasonally thawed soil cover with mean annual temperature below 0°C underlain by permafrost as an extraterrestrial model. The leading factor in differentiation of these soils, named Cryosol, is temperature crossing through 0°C, resulting in freezing-thawing processes and ice-water phase exchange. The temperature oscillations crossing through the freezing point are also observed on the Martian surface. With respect to Mars, it is important to note that cryosol microbial communities, formed under the impact of multi-time freezing-thawing stress, did not change under such stress. Their maximal number and biodiversity correlate with the horizon A, decrease with

depth to the surface beneath the seasonal thaw layer, and have the accumulative sharp peak on the permafrost table. In spite of the tundra, the day surface is under the influence of solar radiation; the snow and vegetation covers decrease and minimize this impact, as well as temperature oscillations. Thus, Arctic cryosol has
distant similarities with the Martian surface.

The surface conditions in the Antarctic desert (the intensive level of solar radiation, the absence of snow and vegetation covers, and on account of the ultra-low subzero temperatures which can be as low as -60°C) and on Mars are closer. At elevations above 1500 m, there are no summer air temperatures above freezing. However, the surface temperatures of soil or rock can be 15°C warmer than the air due to solar heating; they may exceed 0°C for several hours (McKay et al. 1998), and for short periods even reach 10°C (Campbell & Claridge 1987). In addition to sharp temperature oscillations and high insolation, the main similarity between the Antarctic Dry Valleys and Mars is the vertical structure of their "active layers." In the Dry Valleys the upper 10–25-cm-thick sandy layer does not form a stable soil cover on the ice-cemented permafrost table. It is dry (W~2%) and lacks ice-cement due to sublimation. This dry-frozen permafrost—frosty, in the present author's terms—throughout the upper 100 cm (including the active layer) covers ~60% of the Dry Valleys area (Bockheim et al. 2007). The overcooled ground, with no water and thus no ice, is often mobilized by storm winds similar to the instability of Martian dunes. Such layering structure and distribution of water ice within the first surface meter on Mars is proposed according to HEND/Odyssey and MOLA/MGS data (Mitrofanov et al. 2007).

The upper ~2 cm layer of the Dry Valley surface often contains a low number of viable cells in comparison with the underlying horizons (Horowitz et al. 1972). In some cases, these microorganisms cannot be isolated on agar plates, correlating with a poor diversity of bacterial phylotypes, a low number of mycelia fungi strains, and a minimum of chlorophyll content. The occurrence and biodiversity of microorganisms is higher at depth than in the top of the active layer, and suggests that a search for life on Mars should not sample the surface but the bottom of the "active layer." In particular, because the upper horizons contain low cell counts, Antarctic frosty soils are useful for testing equipment for searching for life on Mars.

Cryolithosphere

It has been established that numerous (up to a dozen millions cells/g) and various ecological and morphological viable microbial groups have survived under permafrost conditions since the time the permafrost formed. They are the only known living organisms preserved over a geologically significant time. This approach is relevant to questions concerning the protective properties of permafrost, especially for astrobiology, because the Odyssey's discovery of water ice within the top meters of the high-latitude regolith points to the existence of near-surface permafrost on Mars. It also raises the question of liquid water presence as a necessary condition for life forms. Unfrozen water films play the leading role in the preservation of microorganisms. These films coat the soil particles and protect the viable cells adhered onto their surface from mechanical destruction by growing crystals of intrusive ice, and make possible the mass transfer of microbial metabolic by-products in permafrost, thus preventing the cells biochemical death (Gilichinsky et al. 1993). Therefore, the unfrozen water might be considered as a main ecological niche where the microorganisms might survive. In fine dispersed Arctic permanently frozen sediments at temperatures -3 to -12°C, the amount of unfrozen water can be estimated as 3–8% by weight. Because of temperatures below -20°C in the coarse Antarctic Valley's sands, the unfrozen water values are so small that the instrumental methods fail to record them. The unfrozen water must, therefore, only be firmly bound "liquid" water with binding molecules, and indicates a "biologically dry" environment. Based on experiments, Jakosky et al. (2003) calculate that liquid water can exist at ice grain-dust grain and ice grain-ice grain contacts above about -20°C. Below this temperature, water would not be present in soils in sufficient thickness and amount to physically allow the presence of microorganisms; i.e., this temperature is the lowest at which life can function. Both conclusions are not fully clear at this moment and not quite correct: First, R. Sletten has determined that, for Victoria Valley, the unfrozen water is ~2% at -20°C and ~1.5% at -30°C due to the salt content. The same amount of unfrozen water is expected in Beacon Valley, where the soil has a higher salt content (Gilichinsky et al. 2007). Second, considerable research has shown that microorganisms metabolize at extremely low temperatures in ice and permafrost—between -10 and -20°C (Rivkina et al. 2000, 2004; Carpenter et al. 2000; Bakermans et al. 2003; Junge et al. 2004), and down to -28 and -35°C (Gilichinsky et al. 2007a; Panikov & Sizova 2007). Mars polar and high-latitude temperatures rise above this level (up to 0°C for hours), and similar to cryptoendolithic microbial communities within Antarctic sandstone (Friedmann 1982) make the near-surface past and present permafrost layers potentially favorable sites to search for evidence of life. Probably, in such ecological niches, thin brine films might be formed within Martian permafrost as proposed by Dickinson & Rosen (2003) through their studies of minerals and accumulation of ground ice on Table Mountain, Sirius Group sediments.

From the astrobiological point, it is important that the permafrost, where 92–98% of water is in solid state, and subzero temperatures slack off the cumulative effects of background terrestrial gamma radiation on cells for thousands and millions of years. The lower the water content and the rate of metabolic processes, the less is the radio lesions of biological objects. This is why the irradiation sensitivity of soil microorganisms at temperatures above 0°C, differs from the sensitivity of microorganisms preserved in permafrost. Responses of the permafrost microbial complex to irradiation in nonfrozen and frozen states is different. At the irradiation

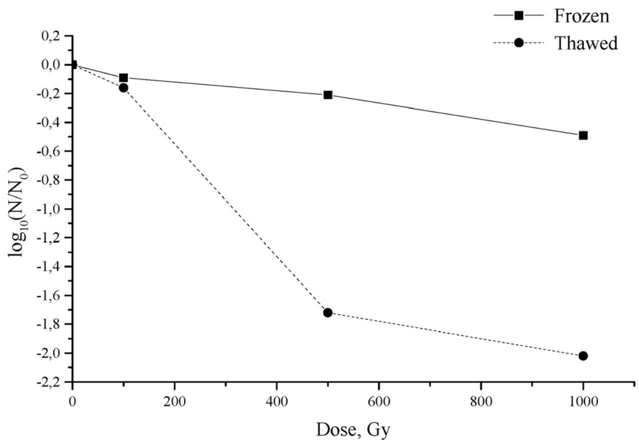

Figure 1. Differences in microbial complex survival rates after γ-irradiation in frozen or thawed state.

dose of 1 kGy, there is one magnitude difference in the number of viable cells between the nonfrozen and frozen samples (Gilichinsky et al. 2007b), and the cell survival rate was estimated to be, respectively, 1% and 10% from the initial number (Fig. 1). In the model γ-irradiation, the dose of 5 kGy was lethal for microorganisms in the nonfrozen samples.

The *in situ* measurements in the boreholes on the Eurasian northeast showed that the dose received by the immured bacteria in frozen sands and loams is about 2 mGy per year. Taking into account the oldest, ~3 Myr, late Pliocene age of permafrost and bacteria, the total dose received by cells would be 5–6 kGy. Under these conditions, most of the cells survived. This fact shows that freezing increased the cells' resistance to radiation and uniqueness of permafrost as an environment, where microorganisms display a high resistance to radiation. From these data the doze from radionuclides diffused through the permafrost is not fatal, but should be large enough to destroy the DNA of ancient viable cells. Their viability and growth implies the capacity for DNA repair, probably in the frozen environment; i.e., at the stable rate of damage accumulation, a comparable rate of repair also exists (Gilichinsky 2002). This is why the "biologically dry" (at temperatures deep below -20°C) Antarctic permafrost, with extremely low and inaccessible organic matter, is nevertheless inhabited by up to 10^4–10^5 viable cells/g, providing an analogue for the Martian ecosystem.

Antarctic Permafrost

Antarctic desert deposits beneath the frosty active layer are unexpectedly icy (Table 1); that is, of the same order as the more humid Arctic. This means that ground ice instability due to the processes of sublimation at ultra low humidity and air temperature is in a very thin surface layer only, and revises the earlier thesis of dry Antarctic permafrost. This is why we can also expect the existence of high icy subsurface layers on Mars.

Permafrost on Earth and Mars vary in age, from a few million years found on the Earth to a few billion years on Mars (Carr 2000, Baker 2004, Tokano 2005). Such a difference in time scale would have a significant impact on the possibility of preserving life on Mars because the number and biodiversity of microorganisms decrease with increasing permafrost age. This is why the longevity of life forms preserved within the Arctic permafrost can only work as an approximate analogue for Mars. The suggested age of Antarctic permafrost (~30 Myr) is somewhat closer to that of Mars. A number of studies indicates that the Antarctic cryosphere began to develop soon after the final breakup of Gondwana and the isolation of the Antarctic continent. It is believed to have been started on the Eocene-Oligocene boundary (Barrett 1996, Wilson et al. 1996, DeConto & Pollard 2003). The discussion of Neogene stability has focused mainly on the state of the ice sheet, which is the most variable part of the cryosphere. Permafrost is the more stable end-member of the cryosphere, and the conditions needed for ice degradation, even if they existed in the climatic optimum, are not enough to thaw the permafrost. Permafrost degradation is only possible when mean annual ground temperatures, -28°C now, rise above freezing; i.e., a significant warming, 25°C or more, is required to degrade the permafrost once formed. There is no evidence to date of such significant temperature variation, which indicates that the Antarctic climatic and geological history was favorable for the formation and persistence of pre-Pliocene permafrost. Antarctic permafrost may, therefore, be more than 30 Myr old (Gilichinsky et al. 2007a) and date from Antarctic ice sheets predicted in early Oligocene times (Zachos et al. 2001).

Table 1. Ice content (I, %) in Taylor Valley permafrost sands.

depth, m	1	3	6	8.8	10	12	15	18
I, %	50	30	26	30	27	30	34	52

Viable microorganisms were isolated from the cores taken in Beacon Valley from beneath an 8.1 Myr volcanic ash layer that has been interpreted as a direct air-fall deposit (Sudgen et al. 1995), and this age is supported by several studies (Schäfer et al. 2000). The age of isolated communities remains controversial because the recent investigation has questioned this age relation, and the calculations indicate that sublimation rates would be too high for the ice to persist for 8.1 Myr (Ng et al. 2005). However, the last paper of Bidle et al. (2007) isolated microorganisms from the ice beneath this ash; these authors again affirm the 8.1 Myr age. From an age perspective, the Glacigene Sirius Group sediments on Mount Feather may be even older. They were estimated to be at least 2 Myr in age (Webb & Harwood 1991) and possibly as old as 15 Myr (Marchant et al. 1996). The ages for the superficial deposits, where bacteria were sampled in the permafrost, are 5 Myr (Wilson et al. 2002). If this age is correct, these are, to date, the oldest confirmed viable microorganisms discovered in permafrost and the oldest viable communities reported on the Earth (Gilichinsky et al. 2007a).

Permafrost distribution in Antarctica is well described by Bockheim (1995). It would be advantageous to locate relics of the oldest Antarctic permafrost. These are possibly to be found at the high hypsometric levels of ice-free areas such as the Dry Valleys, along the Polar Plato and Trans-Antarctic mountains, on Northern Victoria Land. It is desirable to date the layers within them and test for the presence of viable cells. The limiting age, if one exists, within the most ancient Antarctic permafrost cores, where the viable organisms were no longer present, could be established as the age limit for life preservation within permafrost at subzero temperatures. Any positive results obtained from the Antarctic microbial data will extend the geological scale and increase the known temporal limits of Cryobiosphere; i.e., duration of life preservation. The author proposes this activity in accordance with the resolution of the International Workshop on Antarctic Permafrost and Soils (Madison 2004) and in the frame of the IPY ANTPAGE project, which has the following objectives:

- To integrate existing geological records and produce a thematic map of areas where climate and geological history of the last dozens of millions years were favorable for formation and persistence of early Oligocene permafrost and identify the most suitable drilling sites.
- To develop the hand-carried equipment for sterile drilling and sampling, and use these boreholes and cores for ground radiation and temperature measurements, cosmogony dating, ice and organic content, textural and chemical composition, microbial, pollen, diatom, and microfauna analysis.
- To develop the methods of direct dating of permafrost using the cosmogony radionuclides in ice-cement and segregated ice as a natural chronometer and biological clock, based on the racemization rates and differences of microbial communities immured in permafrost.
- To provide arguments that the Antarctic permafrost may have existed earlier than the Arctic permafrost by a factor of ten, and present the Earth's model with only one cold pole in the Southern Hemisphere during this period.
- To define the limit of dormancy of frozen life on Earth and in ancient permafrost on other planets and, potentially, provide a model for Martian ecosystems.

Volcanoes

Despite active volcanism, permafrost often exists on slopes of high-elevation or high-latitude volcanoes in places such as Hawaii, Iceland, Mexico, Peru, North America, and Antarctica. One way to have liquid water on Mars at shallow depths would be through subglacial volcanism. Such volcano-ice interactions could be going on beneath the polar caps of Mars today, or even within the adjacent permafrost around the margins of the ice caps. Basalt lava fields are common on Martian surfaces and some cinder cones have been found near the polar caps. The rover traces on the terrestrial ash fields and Martian surface, as well as the chemical composition of basalts on Earth and Mars, are similar (Squyres et al. 2006). This is why permafrost research on terrestrial volcanoes is expected to be a valuable step in understanding extraterrestrial volcanoes as one of the Earth's analogue. The main question is whether such ecological niches as volcanoes and associated environments contain microbial communities. The task is to find thermophylic microorganisms associated with volcanoes that have been deposited with products of eruption, and that have then survived in permafrost after the freezing of scoria and ash. Our study was carried out on the Kluchevskaya Volcano Group (Kamchatka Peninsula) which was formed starting from the late Pleistocene (Braitseva et al. 1995). The mean annual ground temperature decreases from -1°C on the lower boundary of permafrost (~900 m) to -7°C at 2500 m (Abramov et al. 2007). During the volcano eruptions in the last 2000–3000 yr, the thick (12–16 m) layers of volcanic ash, sand, and scoria accumulated on the elevations occupied by permafrost and at that time became frozen. The last eruption was in 1975–76, and ~500 km^2 were covered by scoria and ash (Fedotov & Markhinim 1983). The cores extracted from the borehole crossing these young volcano deposits contained biogenic CH_4 (up to 1900 μl/kg) and viable bacteria, including thermophilic anaerobes (10^3 cells/g), and among them, methanogens growing on CO_2+H_2. Because thermophiles have not previously been found before in permafrost, the only way for these bacteria to appear within frozen volcanic horizons is through the eruption of a volcano or its surrounding associated strata. The important conclusion is that thermophiles might survive in permafrost and even produce the biogenic gases. For future space missions, the permafrost volcano areas are promising test sites and provide opportunities to study analogues of possible Martian ecosystems. Their original microbial communities represent an analogue for Martian communities. The methanogenic bacteria found at such sites can likely adapt to temperatures <0°C as compared to other studied groups of anaerobes.

Cryopegs

Microorganisms have survived in natural conditions at subzero temperatures in ice and permafrost, but also have been reported to survive at above zero temperatures for dozens to hundreds of millions of years in amber (Cano & Borucki 1995) and saliniferous sediments (Vreeland et al. 2000), respectively. All these very different environments have common features: complete isolation, stability, aridity, and waterproof-ness, and represent the niches where microorganisms retain viability in the absence of free water. Based on the present study, it is possible that microorganisms might also survive in closed ancient aquatic ecosystems. Such habitats have overcooled water lenses formed during the Quaternary when the dynamics (transgression and regressions) of the Polar Ocean of the High Arctic favored the formation of overcooled brines (cryopegs) against a cold climatic background. Freezing in cryopegs is prevented by freezing-point depression due to the dissolved-solids content of the pore water. The cryopegs are embedded in permanently frozen coastal Pleistocene/Holocene marine strata. They are the only hydrological systems on the Earth with permanent subzero temperatures, high salinity, and isolation from external factors throughout their geologic history.

Cryopegs were exposed by boreholes along the Polar Ocean coastal zone with mean annual ground temperatures varying between -2 and -12°C on Cape Barrow (Alaska), the Barents Sea coast, the Yamal Peninsula (surrounded by the Kara Sea), and the Kolyma lowland (East Siberian Sea). At the last site the cryopegs are confined to a 20-m-thick marine horizon, sandwiched between non-saline terrigenous layers at depths of 40–50 m below the tundra surface (the mean annual ground temperature varying -9 to -11°C). Finely dispersed sand and sandy loams were deposited in shallow lagoons at temperatures slightly above 0°C. After regression of the Polar Ocean, the water-bottom sediments were exposed sub-aerially and froze. Because of the pressure caused by freezing, water was released as the freezing front penetrated downward. This was accompanied by a freezing out of salts in the water to form lenses of overcooled sodium chloride brines with salinities of 170–300 g/L. Later, the marine horizon was buried by a 15–20–m-thick unit of lacustrine-alluvial late Pleistocene icy complex that was built up under harsh climate conditions, was syngenetically frozen and has never thawed. Within the marine horizon, the lenses occur at different depths, their thickness varying 0.5–1.5 m and their width 3–5 m. Some of them represent non-artesian water, and some exist under low pressure with a hydrostatic head. Different salinities of the brines confirm their lenticular nature and isolated bedding.

Bacteria isolated from cryopegs not only were adapted to subzero temperatures, but also were tolerant to the high salt concentrations. What is more, detected microorganisms are both halophilic and psychrophilic organisms, and have never been isolated from natural habitats. In the cold saline conditions of cryopegs, special communities were formed. Active adaptation to low temperatures of already-studied bacteria gives hope that fully active and reproducing bacteria can be discovered in saline habitats at subzero temperature. Biotic survival in the aquatic environment on a geological time scale indicates unknown bacterial adaptations. The microbial activity detected in cryopegs at temperatures as low as -15°C documents the fact that subzero temperatures themselves do not exclude biochemical reactions and provides reason to conclude that in overcooled water the metabolic strategy of microbial survival operates, and that this strategy does not accept that cells can multiply *in situ* (Gilichinsky et al. 2005).

The salt tolerance may be associated with cold tolerance. Experimental data showed that in the presence of 25% NaCl halophiles survive better than non-halophiles under low (-20 to -80°C) temperatures (Mancinelli et al. 2002). Mars is a cryogenic planet where free water only has the opportunity to exist in the presence of high solute content, probably as brine lenses within permafrost. These brines, like their terrestrial analogues, may contain microorganisms adapted to low temperature and high salinity. This is why unique halo/psychrophilic communities preserved hundreds of thousands of years in mineral-enriched Arctic cryopegs provide the plausible prototype for Martian microbial life (Gilichinsky et al. 2003), either as an "oasis" for an extant, or the last refuge of an extinct biota (Mancinelli et al. 2002).

Conclusion

The future mission priorities for the search for life on Mars must be based on studies of the most probable environments in which the life might be found, and the maximum period of time over which such life could be preserved. This is why terrestrial subsurface frozen layers represent the analogues of extraterrestrial cryobiosphere, where the probability of finding life is the highest. Hemolithotrophic psychrotolerant anaerobes with their unique mechanisms to assimilate CO_2 are more like life- forms on Mars, which has no free oxygen; as well, cryopeg halo/psychrophilic communities provide the other prototype for Martian microbial life.

Acknowledgments

This research was supported by the Russian Fund for Basic Research (grant: 07-05-00953) and NASA Astrobiology Institute. Special thanks to Dr. Sandra Ponder (Australian Antarctic Center) for editing the manuscript.

References

Abramov, A., Gruber, S. & Gilichinsky, D. 2008. Mountain permafrost on active volcanoes: Field data and statistical mapping, Kluchevskaya Volcano group (Kamchatka). *Permafrost and Periglacial Processes* (in press).

Abyzov, S. 1993. Microorganisms in the Antarctic ice. In: E.I. Friedmann (ed.), *Antarctic Microbiology*. New York: Wiley-Liss, Inc., 265-296.

Anderson, D., Gatto, L. & Ugolini, F. 1972. An Antarctic analog of Martian permafrost terrain. *Antarctic J. USA* 7: 114-116.

Baker, V. 2004. A brief geological history of water on Mars. In: *Origin, Genesis, Evolution and Diversity of Life*. Dordrecht, The Netherlands: Kluwer Publishers, 619-631.

Bakermans, C. et al. 2003. Reproduction and metabolism at -10°C of bacteria isolated from Siberian permafrost. *Environmental Microbiology* 5(4): 321-326.

Barrett, P. 1996. Antarctic paleoenvironment through Cenozoic times: A review. *Terra Antarctica* 3: 103-119.

Bidle, K., Lee, S., Marchant, D. & Falkowski, P. 2007. Fossil genes and microbes in the oldest ice on Earth. / *PNAS* 104 (33), 13455-13460.

Bockheim, J.G. 1995. Permafrost distribution in the southern circumpolar region and its relation to the environment: A review and recommendations for further research. *Permafrost Periglacial Processes* 6: 27-45.

Bockheim, J., Campbell, I. & McLeod, M. 2007. Permafrost distribution and active-layer depths in the McMurdo Dry Valleys, Antarctica. *Permafrost and Periglacial Processes* 18: 217-227.

Braitseva, O. et al. 1995. Ages of calderas, large explosives craters and active volcanoes in the Kuril-Kamchatka region, Russia. *Bulletin Volcanology* 57: 383-402.

Cameron, R. & Morelli, F. 1974. Viable microorganisms from ancient Ross Island and Taylor Valley drill core. *Antarctic J. USA* 9: 113-116.

Campbell, I. & Claridge, G. 1987. *Antarctica: Soils, Weathering Processes and Environment.* Amsterdam: Elsevier Science Publishers, 368 pp.

Cano, R. & Borucki, M. 1995. Revival and identification of bacterial spores in 25 to 40 million year old Dominican amber. *Science* 268(5213): 1060-1064.

Carpenter, E., Lin, S. & Capone, D. 2000. Bacterial activity in South Pole snow. *Applied Environmental Microbiology* 66(10): 4514-4517.

Carr, M. 2000. Martian oceans, valleys and climate. *Astron. Geophys.* 41(3):20-26.

Christner, B. et al. (2003). Bacterial recovery from ancient glacial ice. *Environmental Microbiology* 5: 433-436.

DeConto, R. & Pollard, D. 2003. Rapid Cenozoic glaciation of Antarctica induced by declining atmospheric CO_2. *Nature* 421(6920): 245-249.

Dickinson, W. & Rosen, M. 2003. Antarctic permafrost: An analogue for water and diagenetic minerals on Mars. *Geology* 31(3): 199-202.

Fedotov, S. & Markhinim, Y. 1983. *The Great Tolbachik Fissure Eruption:Geological and Geophysical Data 1975-1976.* England: Cambridge University Press.

Friedmann, E.I. 1982. Endolithic microorganisms in the Antarctic cold desert. *Science* 215: 1045-1053.

Gilichinsky, D., Soina, V. & Petrova, M. 1993. Cryoprotective properties of water in the Earth cryolithosphere and its role in exobiology. *Origin of Life & Evol. Biosph*. 23(1): 65-75.

Gilichinsky, D. et al. 2003. Supercooled water brines within permafrost–an unknown ecological niche for microorganisms: A model for astrobiology. *Astrobiology* 3(2): 331–341.

Gilichinsky, D. et al. 2005. Biodiversity of cryopegs in permafrost. *FEMS Microbioogy Ecology* 53(1): 117-128

Gilichinsky, D.G. et al. 2007a. Microbial populations in Antarctic permafrost: Biodiversity, state, age, and implication for astrobiology. *Astrobiology* 7(2): 275-311.

Gilichinsky, D. et al. 2007b. Bacteria in permafrost. In: R. Margesin, F. Schinner, J-C. Marx, & C. Gerday (eds.) *Psychrophiles: From Biodiversity to Biotechnology,* Chapter 6. Springer Verlag, 83-102.

Horowitz, N., Hubbard, J., & Cameron, R. 1972. Microbiology of Dry Valleys of Antarctica. *Science* 176: 242-245.

Jakosky, B. et al. (2003). Subfreezing activity of microorganisms and the potential habitability of Mars polar regions. *Astrobiology* 3(2): 343-350.

Junge, K., Eicken, H. & Deming, J. 2004. Bacterial activity at -20°C in Arctic wintertime sea ice. *Applied Environmental Microbiology* 70: 550-557.

Kapitsa, A. et al. 1996. A large deep freshwater lake beneath the ice of central East Antarctica. *Nature* 381: 684–686.

Mancinelli, R. et al. 2004. Brines and evaporates: Analogs for Martian life. *Advances Space Research* 33(8): 1244-1246.

Marchant, D. et al. 1996. Late Cenozoic Antarctic paleoclimate reconstructed from volcanic ashes in the Dry Valleys region of southern Victoria Land. *GSA Bulletin* 108: 181-194.

McKay, C. et al. 1998. Soil temperatures and stability of ice-cemented ground in the McMurdo Dry Valleys. *Antarctic Science* 10(1): 31-38.

Miteva, V. et al. 2004. Phylogenetic and physiological diversity of microorganisms isolated from a deep Greenland glacier ice core. Applied Environmental Microbiology 70(1): 202-213.

Mitrofanov, I. et al. 2007. Water ice permafrost on Mars: The layering structure and surface distribution according to HEND/Odyssey & MOLA/MGS data. *Geophysical Research Letters* 34, L18102.

Ng, F. et al. 2005. Fast growing till over ancient ice in Beacon Valley, Antarctica. *Geology* 33: 121-124.

Priscu, J. et al. 2000. Perennial Antarctic lake ice: An oasis for life in a polar desert. *Science* 280: 2095-2098.

Rivkina, E. et al. 2000. Metabolic activity of permafrost bacteria below the freezing point. *Applied Environmental Microbiology* 66(8): 3230-3233.

Rivkina, E. et al. 2004. Microbial life in permafrost. Advances Space Research 33(8): 1215-1221.

Schaefer, J. et al. 2000. The oldest ice on Earth in Beacon Valley, Antarctica: New evidence from surface exposure dating. *Earth Planetary Science Letters* 179: 91-99.

Squyres, S. et al. 2006. The Opportunity Rover's Athena science investigation at Meridian Planum, Mars. *Science* 306: 1698-1703.

Steven, B. et al. 2006. Microbial ecology and biodiversity in permafrost. *Extremophiles* 10: 259-267.

Sugden, D. et al. 1995. Preservation of Miocene glacier ice in East Antarctica. *Nature* 376: 412-414.

Tokano, T. (ed.) 2005. *Water on Mars and Life.* Springer.

Vreeland, R., Rosenzweig, W. & Powers, D. 2000. Isolation of a 250 million-year-old halotolerant bacterium from a primary salt crystal. *Nature* 407(6806): 897-900.

Webb, P-N. & Harwood, D 1991. Late Cenozoic glacial history of the Ross Embayment, Antarctica. *Quaternary Science Review* 10: 215-223.

Wilson, G. et al. 1996. Coring for microbial records of Antarctic climate. *Antarctic J. USA* 31: 83-86.

Wilson, G. et al. 2002. The Mount Feather diamicton of the Sirius Group: An accumulation of indicators of Neogene Antarctic glacial and climatic history. *PALEO* 182: 117-131.

Zachos, J. et al. 2001. Trends, rhythms, and aberrations in global climate 65 Myr to present. *Science* 292(5517): 686-693.

Microbial Diversity in a Permafrost Environment of a Volcanic-Sedimentary Mars Analog: Imuruk Lake, Alaska

Felipe Gómez, Olga Prieto-Ballesteros, David Fernández-Remolar, José Antonio Rodríguez-Manfredi,
Maite Fernández-Sampedro, Marina Postigo Cacho, Josefina Torres Redondo, Javier Gómez-Elvira
Centro de Astrobiologia (CAB) INTA-CSIC. Carretera de Ajalvir Km 4 Torrejón de Ardoz Madrid 28850, Spain

Ricardo Amils
Centro de Astrobiologia (CAB) INTA-CSIC. Carretera de Ajalvir Km 4 Torrejón de Ardoz Madrid 28850, Spain and Centro de *Biología Molecular (UAM-CSIC), Universidad Autónoma de Madrid, Cantoblanco, Madrid 28049, Spain*

Abstract

Permafrost has attracted considerable interest from an astrobiological point of view (Wynn-Williams & Edwards 2000), due to the recently reported results from the Mars Exploration Rovers. The possible existence of past or present water in the subsurface of the red planet increases the probabilities of life existence on Mars. Considerable studies have been developed on extreme ecosystems and permafrost, in particular, to evaluate the possibility of life on Mars. The biodiversity of permafrost located on the Bering Bridge National Preserve has been studied. Different conventional (enrichment, isolation) and molecular ecology techniques (cloning, fluorescence in situ probe hybridization-FISH) have been used for isolation and bacterial identification.

Keywords: Alaska; astrobiology; biodiversity; Imuruk Lake; permafrost.

Introduction

Due to reported Mars surface environmental conditions (Klein 1978) (oxidative stress, high UV radiation levels, etc.) the possibility for life development in the surface of the red planet is very small. The identification of water-ice on the subsurface on Mars by the Thermal Emission Spectrometer onboard the Mars Odyssey (Kieffer & Titus 2001) and from the High Energy Neutron Detector (Litvak et al. 2006) has important astrobiological connotations, because in addition to being a potential source for water, these locations are shielding habitats against the harsh conditions existing on the planet, like UV radiation (Gomez, et al. 2004, Gomez et al. 2007).

Several authors have discussed similarities between Earth and Martian permafrost (Frolov 2003) and the structures that could play a protective role for subsurface ecosystems (Gilichinsky et al. 2007).

Chemolithotrophic microorganisms have the ability to use inorganic compounds, like reduced minerals, as energy sources for metabolism in isolated environments of the subsurface. Better understanding of permafrost ecosystems on Earth is needed to evaluate the possibilities that life could have developed in these types of structures on Mars. Permafrost on Earth is located at circumpolar latitudes. Of special interest is the permafrost on volcanic areas due to their similarities with Mars geology (Dyar & Schaefer 2004).

Future space missions will be focused on searching for life on the subsurface of Mars. New techniques and methodologies for studying these putative habitats need to be developed (Frolov 2003).

Material and Methods

Imuruk Lake campaign

We identified an interesting volcanic area associated with permafrost in the region of Imuruk Lake (Alaska). An exploration campaign was developed during July 2005 to study the geology and microbiology of the area. Imuruk Lake is located at 65.6ºN, 163ºW. This region is a volcanic area in the Bering Land Bridge National Preserve (Fig. 1).

The 2005 campaign was developed in the eastern part of the lake, near Nimrod Hill. Previous geologic studies (Hopkins 1963) of the area have been reported. The area is characterized by volcanic formations with basaltic composition. Some basalt lava flows are present. Over the lava structures there are two covers with different composition: the first is a wind blown silt layer, and the second is a peat cover at the top. Some intermediate terraces can be found around the hill with sedimentary material.

With the idea of future development of instrumentation for automated remote life detection systems on permafrost, three main objectives were considered during the expedition: (1) permafrost localization by geophysical techniques and drilling; (2) microbial diversity analysis, with special interest on deeper parts of the column, the oldest part of the permafrost (pattern preservation of biosignatures in cold environment is of extraordinary astrobiological interest); and (3) understanding cold ecosystems to facilitate permafrost niche detection and mapping.

An Arctic area has been selected for permafrost characterization. Field camping was developed on the Bering Land Bridge National Preserve (Fig. 1). Permafrost was localized using geophysical sounding techniques over several traverse lines on the Imuruk Lake area. A particular place for sampling was chosen, and a borehole 4 m deep

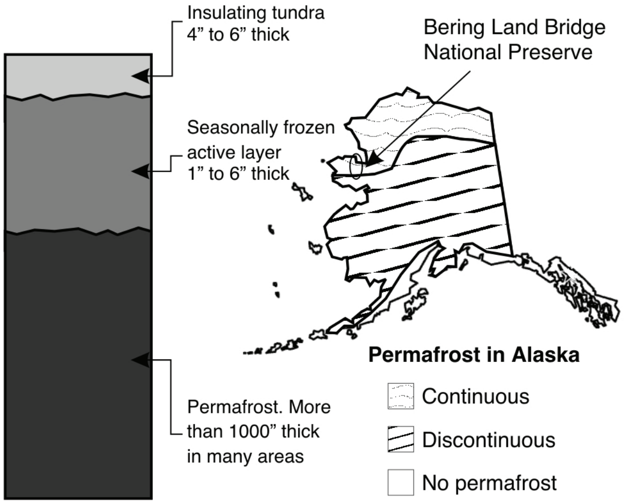

Figure 1. Bering Land Bridge National Preserve situation. Imuruk Lake is located on a volcanic area.

was drilled for sampling along the soil column. The active layer at the surface and subsequent permafrost were sampled at several depths. Samples were used for biodiversity determination using complementary techniques.

Geophysical studies

Permafrost depth was identified by geophysical techniques (electric tomography sounding, ERT). *Syscal KID Swich-24* equipment was used. Thirteen parallel lines were deployed from the lake to the top of the hill (see Prieto et al. in this issue for details). Each tomographic line was 48 mm long, separation between electrodes was 2 m, and the space between lines was 15 m.

Temperature recording during core sampling indicated a permafrost depth of around 30 cm, but tomographic data indicated that permafrost began at a mean depth of 0.50 m from the surface. After tomographic data interpretation a place for drilling was chosen.

Stratigraphic column

A portable drilling system was used for stratigraphic sampling at different depths. A Cardi E-400 fuel-powered system was adapted for core retrieval. The dimension of the pits was 0.5 long and 50 mm diameter. Pits could joint each other to obtain a maximum depth core of 4 m. Microbiological studies were performed over tomographic Line 11 core. Maximum depth on this drill was 3.6 m.

Microbial diversity studies

From ERT studies, a particular place was chosen for drilling and sampling at several depths. Proximity of permafrost to the surface was the criterion chosen for drilling. Several core depths were chosen for microbiological analysis (Table 1). Some ice pockets were detected in Line 11 (Fig. 2). From every core depth selected for sampling, two aliquots were used: the first for direct media inoculation, and the second for hybridization analysis. In the second case, the first step was to fix the sample with formaldehyde as soon as possible

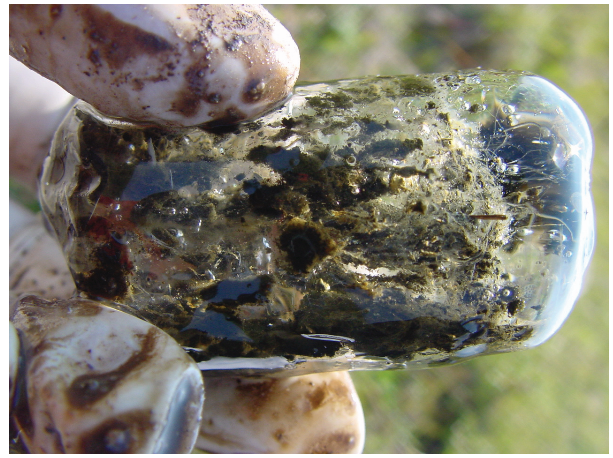

Figure 2. An 0.8 m deep sample from tomographic Line 11.

in order to maintain the structure of the microbial population without any alteration. These fixed samples were transported to the laboratory for further processing and hybridization with DNA probes of different specificity (species, genus, and phylum).

Two different methodologies for microbial population analysis were used:

(1) media inoculation for microbial enrichment: Three different media were chosen for microbial growth: chemolithotrophic media enriched with ferrous iron, heterotrophic organic media and several anaerobic specific media enriched with different energy sources (methanol, formate, proteolytic and volatile fatty acid). Growth was followed by optical density at 580 nm in a WPA Lightwave spectrophotometer. Qualitative values for growth were assigned depending on the slope of the growth curve. After growth, microbial populations were identified by 16S rRNA amplification of DNA, cloning, and sequencing.

(2) Fluorescence in situ hybridization techniques (FISH) with specific DNA probes, used for microorganism identification: The DNA probes used on this study were specific for *Bacteria* and *Archaea* domains, Alfa-, Beta-, and Gamma-proteobacteria subclasses, a CF (Cytophaga-Flavobacterium cluster) and a HGC (High G+C content bacterial cluster) specific group probes. Samples were directly fixed on the field with formaldehyde (4% v/v) and incubated at 4°C for 2 h. After incubation, samples were washed twice with PBS and filtered. Filters were stored under frozen conditions in PBS-ethanol (1:1). Samples from several depths were chosen for further analysis with different DNA-specific probes. Cell density was determined by cell counting with a microscope. Filters were dried and maintained at low temperature until further processing in the lab.

Results and Discussion

Thirteen transects along Nimrod Hill were chosen for electrical resistivity tomography studies, and thirteen tomography lines were obtained. The existence of different resistivity values along the lines at different depth determined the presence of several units. Typical resistivity values of pits and sedimentary units were recorded. The tomography diagrams obtained from the 13 lines were used for permafrost localization (Fig. 3) to determine the drilling points (vertical arrow in Fig. 3) and the sampling depths for microbiology analysis. Samples were taken at 30 cm, 1 m, 1.5 m, 2.1 m, 3.1 m, and 3.6 m. From every sample, two aliquots were taken.

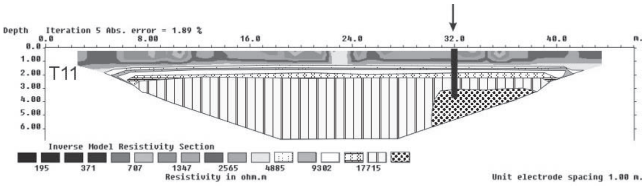

Figure 3. Electrical Resistivity Tomography for Line 11. This section was chosen for drilling a 4 m deep borehole for microbial sampling.

Microbial growth was observed in most of the media. Table 1 shows the results obtained on the inoculated media after 72 h of incubation at 12°C: - is no growth; +/- is less growth to +++, much growth; *Gas* indicates gas production during growth); Fe^{2+} indicates basal media enriched with ferrous iron on aerobic conditions; *Het.* indicates enriched media for heterotrophic bacteria cultures under aerobic conditions; *P* indicates media enriched with peptone and yeast extract for proteolytic bacteria and cultured under anaerobic conditions; *M* indicates methanol-enriched media under anaerobic conditions; *F* indicates formaldehyde-enriched media under anaerobic conditions; and *VFA* indicates volatile fatty acid (C2 plus C4) enriched media under anaerobic conditions.

The most efficient growth (Table 1) was obtained using

Table 1. Growth obtained on different inoculated media after 72 h of incubation at 12°C.

	Fe^{2+}	**Het.**	**P**	**M**	**F**	**VFA**
T11-1 (30 cm)	-	+++	+++ Gas	+++	++	++ Gas
T11-2 (1 m)	+/-	Gas	Gas	++	+	+
T11-3 (1.5 m)	+/-	++	+	++	++	++
T11-4 (2.1 m)	+/-	+++	++	+	+	+
T11-5 (3.1 m)	+/-	++	++	+	+	+
T11-6 (3.6 m)	+	+++	+++	++	++	++

Table 2. Biodiversity from sample point T11-1 after microbial enrichment in several media and cloning and sequencing the 16S rDNA from total extracted DNA. T11-1 is the 30 cm. deep sample from transect T11. Media: VFA Minimal media enriched with Volatile Fatty Acids. F: minimal media enriched with Formaldehyde. P: minimal media enriched with Peptone and Yeast Extract, M: minimal media enriched with Methanol, LB: Organic media for heterotrophic aerobic bacteria. Fe^{2+}: minimal media enriched with ferrous iron. N.D.: no data.

Culture	Blast result (NCBI database)	Gene Bank ID number	Query coverage	Max. Ident
T11-1 VFA	Unc. Proteobacterium	EF699933.1	100%	99%
	*Shigella flexneri*FBD002	EU009187.1	100%	99%
	Unc. Archaeon SPS46	AJ606292.1	10%	100%
	Unc. Propionibacterium 402C1	AM420143.1	100%	100%
T11-1 F	*Psychrobacter sp*. 9B	AY689064.1	100%	98%
	Antarctic sea water bac. BSW10170	DQ064630.1	100%	98%
T11-1 P	Unc. Archaeon SPS33	AJ606279.1	19%	100%
T11-1 M	*Citrobacter koseri* CP000822.1	CP000822.1	100%	92%
T11-1 LB	*Psychrobacter sp*. 9B	AY689064.1	100%	98%
	Antarctic sea water bac. BSW10170	DQ064630.1	100%	98%
T11-1 Fe^{2+}	N.D.			

heterotrophic media under aerobic and anaerobic conditions inoculated with samples from all along the column. There was no obvious relationship between depth and bacterial growth, indicating that viable bacteria are present along the column at all depths. Chemolithotrophic media produced less efficient growth, indicating that chemolithotrophs were not present in high numbers on these ecosystems. The opposite was observed for heterotrophic microorganisms, which have both aerobic and anaerobic representatives. Different microorganisms are present in the Imuruk Lake permafrost, since different media gave positive growth. In the case of sample T11-1, growth was observed in heterotrophic media under aerobic conditions and in the basal media under anaerobic conditions enriched with peptone plus yeast extract, methanol, formaldehyde, and volatile fatty acids. There was also gas production in the media enriched with peptone and yeast extract and VFA. These cultures inoculated with sample T11-1 were used for total DNA extraction, amplification, cloning and sequencing of the 16S rRNA gene (Table 2). Gas production could be congruent with the presence of methanogenic bacteria (Kotsyurbenko 2005). Amplification, cloning, and sequencing of the 16S rRNA confirmed this observation.

The 16S rDNA amplification from DNA extracted from cultures allowed identification of the presence of members of the *Psychrobacter* genus (Table 2). Also, the presence of some members of *Propionibacterium* genus, characterized by anaerobic growth using fatty acids for energy uptakes with production of propionic acid, was confirmed. Some uncultured Antarctic sea water representatives were also identified by 16S rRNA sequencing.

Soil samples from several depths were hybridized with specie- or genera-specific DNA probes and compared with universal staining (DAPI) for cell counting and evaluation of cell density along the column. Figure 4 shows a universal stained microbial preparation of a sample from tomographic Line 11 obtained at a depth of 2 m. Bacterial counting by light microscopy was used for cell density quantification. Figure 4 shows the population gradient (cells/gr of soil) with depth.

The presence of active bacteria on frost soil was determined by FISH techniques (Fig. 5). Hybridization of the RNA probe is done over the 16S rRNA, thus only active bacteria, which are sometimes uncultivable, can be detected. This technique requires the sample to be fixed at the moment of sampling to ensure the viability of the 16S rRNA molecule population.

Population gradient along the core (Fig. 5) was determined by direct counting of stained samples from 30 cm, 1 m, 1.5 m, 2.1 m, 3.1 m, and 3.6 m depth. Hybridized samples with genera- and group-specific DNA probes were counted to evaluate the correspondent percentage of the cell population (Fig. 5).

Bacterial density decreased with depth (Fig. 5), which is congruent with a permafrost model. An active layer develops during the summer on the first 50 cm cross section of the crust, and soil became completely frost down to this depth all through the year. This active layer develops a dense active bacterial population that is reduced during winter due

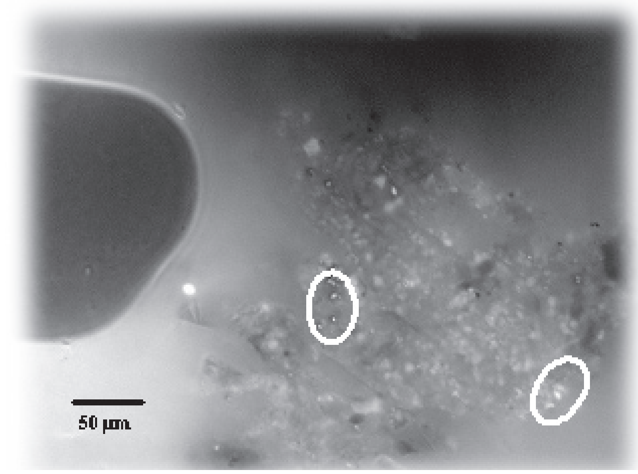

Figure 4. Soil sample from tomographic Line T11 stained with DAPI and used for cell quantification. Bacteria are the white spots inside the circle.

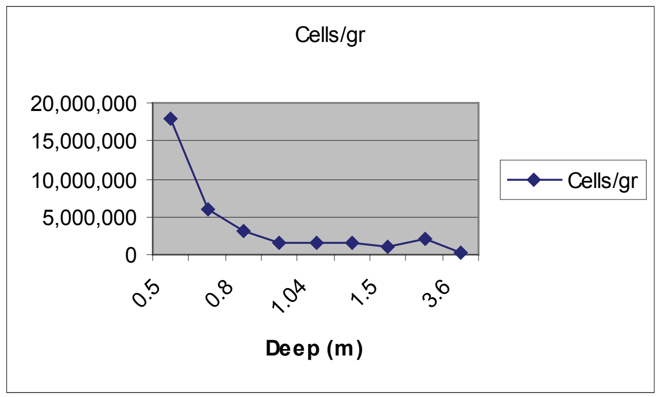

Figure 5. Population density (cells per gram of soil) gradient along the borehole from tomographic Line 11.

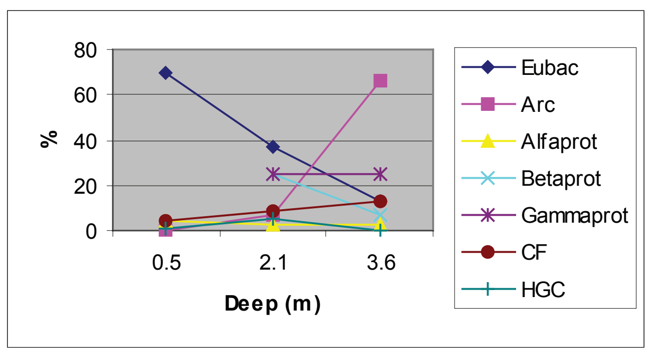

Figure 6. Percentage of different group pf microorganisms along the T11-1. Column identified by FISH techniques.

to lower temperatures. The permafrost model is congruent with lower bacterial density on soil frosted year-round. An interesting result was the location of active bacteria under 50 cm depth. 16S rRNA sequencing results confirmed the presence *Psychrobacter* gen. representatives, corroborating the results obtained in culture experiments and underlying the identification of active microorganisms on the frosted layer of the soil.

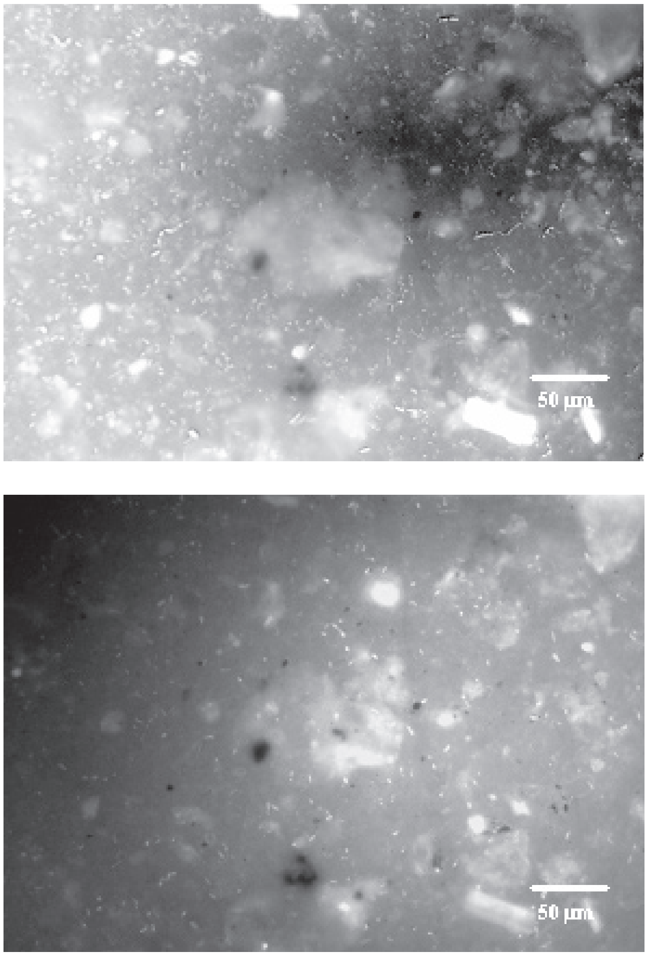

Figure 7. Universal staining DAPI preparation of a sample from the culture T-11-6 soil in heterotrophic media (top). Same culture preparation hybridized with *Alfaproteobacteria*-specific DNA probe labeled with CY3 fluorophore. Bacteria are small white spots.

The cell density decreased with depth; the lower the depth, the lower the bacterial population—a consequence of the harsh conditions of permafrost environments. Not only is reduction of the bacterial number the interesting data reported by these experiments, but also the fact that several microorganism groups were detected all along the column (Fig. 6). The percentage of every group varied with depth. On the first 50 cm of the soil column the main microbial population was composed by *Bacteria*. The presence of this type of microorganisms is constantly reduced with depth. While members of the domain *Archaea* have a low representation in the upper part of the column, its population increased with depth.

The Archaea identified on the grown media T11-1 P and T11-1 VFA (Table 2) are closely related to acetoclastic and hydrogenotrophic methanogens (Kotsyurbenko 2003).

The viability of microorganisms on the permafrost was tested by sample inoculation on growth media and following the growth of the cultures. Figure 7 shows bacteria preparation from the aerobic heterotrophic media inoculated with a 3.6 m deep sample from T11 borehole. The quantification of every metabolic group of bacteria was done by comparison of the total bacteria stained with the universal stain DAPI (Fig. 7, top) and the positive hybridization signals with group specific DNA probes (Fig. 7, bottom).

Conclusions

Abundant cells per mg of sample were detected in the first 60–70 cm of the column (the permafrost active layer). Accordingly to in situ hybridization and metabolic analysis, an active microbial layer was detected on the first 60–70 cm. Hybridization with specific 16S rRNA probes reported the presence of a high number of microorganisms from the *Bacteria* domain in the upper part of the column, which is congruent with the higher temperature reached at this depth during the summer. In contrast, deeper samples gave decreasing numbers for members of the bacterial domain, while the cell density for *Archaea* started to grow. From 2.1 m depth to the 3.6 m, the *Archaea* are the most abundant, and it correlates with the fact that, at this depth, the soil is permanently frozen. The production of gas and the identification of archaeal-related sequences on the T11-1 enrichment cultures are congruent with the presence of methanogenic *Archaea* and with the permafrost model.

These results are congruent with a putative ecosystem completely isolated from the surface and protected against possible harsh atmospheric conditions with the production of methane. The detection of this type of ecosystem in permafrost increases the possibility of existence of life in other planetary bodies like planet Mars, especially after the detection of methane in the Mars atmosphere by the Mars Express Planetary Fourier Spectrometer (Formisano et al. 2004).

Acknowledgments

The 2005 expedition to Imuruk Lake was supported by Centro de Astrobiologia-INTA (Spain). The laboratory experimental procedures were supported by Grant ESP 2006-06640 "Desarrollo de Tecnología para la identificación de vida de forma automática" from the Spanish Government. We thank the Bering Land Preserve staff (U.S. National Parks) for their help, especially Dr. Chris Young and INTA and Dr. Juan Pérez-Mercader for helping us during the campaign and later experimental work development.

References

Dyar, M.D. & Schaefer, M.W. 2004 Moessbauer spectroscopy on the surface of Mars: Constraints and expectations. *Earth and Planetary Science Letters* 218: 243-259.

Formisano, V., Atreya, S., Encrenaz, T., Ignatiev, N. & Giuranna, M. 2004 Detection of methane in the atmosphere of Mars. *Science 306*: 1758-1761.

Frolov, A. 2003 A review of the nature and geophysical studies of the thick permafrost in Siberia: Relevance to exploration on Mars. *J. Geoph. Res.* 108(E4): 8039-8046. doi:10.1029/2002je001881.

Gilichinsky, D.A., Wilson, G.S., Friedmann, E.I., McKay, C.P., Sletten, R.S., Rivkina, R.M., Vishnivetskaya, T.A., Erokhina, L.G., Ivanushkina, N.E., Kochkina, G.A., Shcherbakova, V.A., Soina, V.S., Spirina, E.V., Vorobyova, E.A., Fyodorov-davydov, D.G., Hallet, B., Ozerskaya, S.M., Sorokovikov, V.A., Laurinavichyus, K.S., Shatilovich, A.Y., Chanton, J.P., Ostroumov, V.E. & Tiedje, J.M. 2007. Microbial populations in Antarctic permafrost: Biodiversity, state, age, and implication for astrobiology. *Astrobiolog* 7(2): 275-311.

Gomez, F., Grau-Carles, A., Vázquez, L. & Amils, R. 2004 UV radiation effects over microorganisms and study of protective agents. *ESA SP-545*: 21-25.

Gómez, F., Aguilera, A. & Amils, R. 2007. Soluble ferric iron as an effective protective agent against UV radiation: Implications for early life. *Icarus.* doi:10.1016/j.icarus.2007.04.008

Hopkins, D.M. 1963 Geology of the Imuruk Lake area, Seward Peninsula, Alaska. *U.S. Geological Survey Bulletin* 1141-C: C1-C101.

Kieffer, H.H. & Titus, T.N. 2001 TES mapping of Mars' north seasonal cap. *Icarus* 154: 162-180.

Klein, H.P. 1978. The Viking biological experiments on Mars. *Icarus* 34: 666-674.

Kotsyurbenko, O.R. 2005. Trophic interactions in the methanogenic microbial community of low-temperature terrestrial ecosystems. *FEMS Microbial. Ecol.* 53: 3-13.

Kotsyurbenko, O.R., Chin, K.J., Glagolev, M.V., Stubner, S., Simankova, M.V., Nozhevnikova, A.N. & Conrad, R. 2003. Acetoclastic and hydrogenotrophic methane production and methanogenic populations in an acidic West-Siberian peat bog. *GenBank ID number: AJ606292 (s*ubmitted 08-Nov-2003). Unpublished.

Litvak, M.L., Mitrofanov, I.G., Kozyrev, A.S., Sanin, A.B., Tretyakov, V.I., Boynton, W.V., Kelly, N.J., Hamara, D., Shinohara, C. & Saunders, R.S. 2006. Comparison between polar regions of Mars from HEND/Odyssey data. *Icarus* 180(1): 23-37.

Prieto-Ballesteros, O., Fernández-Remolar, D.C., Gómez, F., Torres Redondo, J., Fernández-Sampedro, M., Martín Redondo, M.P., Rodriguez-Manfredi, J.A., Gómez-Elvira, J. & Gómez-Ortíz, D. 2008. Astrobiological applications of the studies on the permafrost of the Imuruk Lake basaltic field area (Alaska). *Proceedings of the Ninth International Conference on Permafrost, Fairbanks, Alaska, June 29–July 3, 2008* (this proceedings).

Wynn-Williams, D.D. & Edwards, H.G.M. 2000. Antarctic ecosystems as models for extraterrestrial surface habitats. *Planetary and Space Science* 48: 1065-1075.

Thermal Dynamics of the Active Layer Along a Hydrologic Gradient Bordering Lakes in the McMurdo Dry Valleys, Antarctica

Michael N. Gooseff
Department of Civil & Environmental Engineering, Pennsylvania State University, University Park, PA 16802
J. E. Barrett
Department of Biological Sciences, Virginia Polytechnic Institute, Blacksburg, VA 24061
Scott Ikard
Geology & Geological Engineering Department, Colorado School of Mines, Golden, CO 80401
Melissa Northcott
Geology & Geological Engineering Department, Colorado School of Mines, Golden, CO 80401
Cristina Vesbach
Department of Biology, University of New Mexico, Albuquerque, NM 87108
Lydia Zeglin
Department of Biology, University of New Mexico, Albuquerque, NM 87108

Abstract

With little precipitation (<10 cm water equivalent annually as snow), soils of the McMurdo Dry Valleys (MDV) have limited water available to support hydrological or biogeochemical processes. Active layer depths across most of this landscape are <1 m. Saturated sediments are obvious in wetted margins on the shorelines of lakes, extending for up to ~10 m into a zone where typically arid MDV soils prevail. We propose that wetted margins of MDV lakes will differ from arid soils across the rest of the landscape in their active layer depth and temperature regimes because of the consistent presence of water within these wetted margins. We have monitored temperatures along a wetted margin of Lakes Fryxell, Bonney, and Joyce. During the austral summer, we found that drier soils promoted shallower thaw depths and that, at the same depths, wet soils generally had lower temperatures and smaller diurnal fluctuations than dry soils.

Keywords: active layer; Antarctica; McMurdo Dry Valleys; temperature time series.

Introduction

Soil temperature dictates physiological constraints on biological activity (Kirshbaum 1994) and is especially important in the McMurdo Dry Valleys (MDV) of Antarctica (Fig. 1) where temperature is a primary control over biogeochemical cycling and biotic communities (Doran et al. 2002b, Parsons et al. 2004, Aislabie et al. 2006). Similarly, soil moisture is a limiting factor in Antarctic soil ecosystems where low temperatures severely limit the availability of liquid water (Kennedy 1993). Most soil studies in the MDV have emphasized the top 10 cm of the soil profile, within the active layer that is generally 60 cm thick (Campbell et al. 1998).

There has been extensive research on active layer thermal dynamics in the Arctic, with emphasis on numerical modeling of these dynamics (Hinkel 1997), and their response to changing climate (Hinkel et al. 2001). Arctic active layer soils exhibit seasonal changes in surface energy balances comparable to those in the MDV, though the magnitudes and types of energy exchange differ greatly due to the presence of extensive vegetation in the Arctic, as well as substantial spring snowmelt infiltration and rain infiltration during the summer. There have been several studies of permafrost and active layer processes in the Victoria Land (Bockheim et al. 2007, Guglielmin 2006), but little attention has been paid to active layer thermal dynamics on floors of the MDV, particularly with respect to dependence upon soil moisture. Bockheim and Tarnocai (1998) note that most of the surficial permafrost in the MDV is dry permafrost, which has very low water content (<5%), and Pringle et al. (2003) have documented thermal properties of MDV permafrost and active layer from two fairly high elevation sites in the region.

The shores of MDV water bodies are continually proximal to liquid water during the austral summer, and wick water from the lake and stream edges to the dry mineral soil. These wetted margins are visually apparent, and represent a hydrologic gradient in soil moisture from saturated at the water body to dry conditions at distal locations. Around lakes, Gooseff et al. (2007) found that the dimensions of these wetted margins vary as a function of both shore slope and depth of the active layer. We propose that, because these wetted margins represent an obvious gradient of soil moisture, the active layer thermal dynamics across these wetted margins should vary, with general soil moisture condition, due to the differences in thermal conductivity and heat capacity of the soil matrix with changes in soil moisture status.

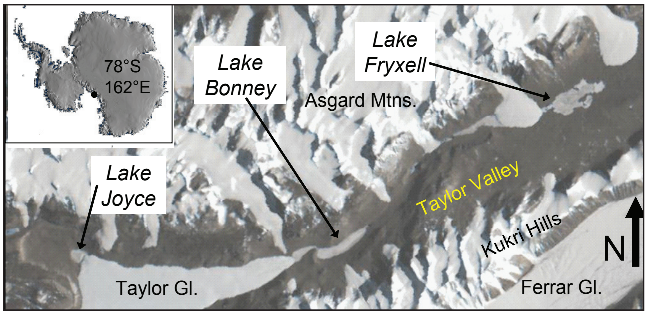

Figure 1. Map of Taylor Valley, Antarctica and Lakes Joyce, Bonney and Fryxell.

Table 1. Distances to thermocouple strings from the edge of the lake, in meters (XX), and depth of deepest thermocouple, in meters (YY), in the format XX,YY. All thermocouples are spaced by 10 cm vertically on a string. The number of thermocouples at a location is determined by the depth of penetration possible when deployed, with a maximum of 0.5 m depth.

	Study Plot		
String	*Lk. Fryxell*	*Lk. Bonney*	*Lk. Joyce*
I	0.0, 0.50	0.0, 0.35	0.0, 0.35
II	0.2, 0.50	0.20, 0.32	0.2, 0.30
III	5.1, 0.45	1.89, 0.50	1.75, 0.40
IV	10.3, 0.45	3.64, 0.50	3.20, 0.33
V	11.3, 0.33	5.42, 0.50	3.80, 0.17

Site Description and Methods

Site description

The MDV are located on the western edge of the Ross Sea, at approximately 78°S 162°E. The climate is cold, with annual mean temperatures of -20°C, and dry, with <10 cm precipitation (all as snow) annually (Doran et al. 2002a). The water balance of closed-basin lakes on the valley floors are maintained by incoming glacial meltwater stream flow and losses due to annual ablation of perennial ice covers, and evaporation of open water "moats" that form along the lake shores during the austral summer. Thus, lake shore soils and sediments are immediately adjacent to liquid water for approximately 2.5 months annually. Due to the dry nature of the MDV and the presence of continuous permafrost, these shoreline sediments wick lake water several meters inland from the shoreline.

Methods

In January 2005, we deployed thermocouple strings with 10 cm vertical spacing along transects across wetted margins of the north shore of Lake Joyce, the south shore of the east lobe of Lake Bonney, and the north shore of Lake Fryxell (Fig. 1). Five thermocouple strings were deployed at each lake-side location (Fig. 2A): String I at the water edge, String II 20 cm from the shoreline, String III at a point bisecting the wetted margin, String IV just before the outside edge of the wetted margin, and String V outside of the wetted margin (Fig. 2B, Table 1). Thus we collected active layer temperature data across three hydrologic gradients, from saturated conditions at String I to dry conditions at

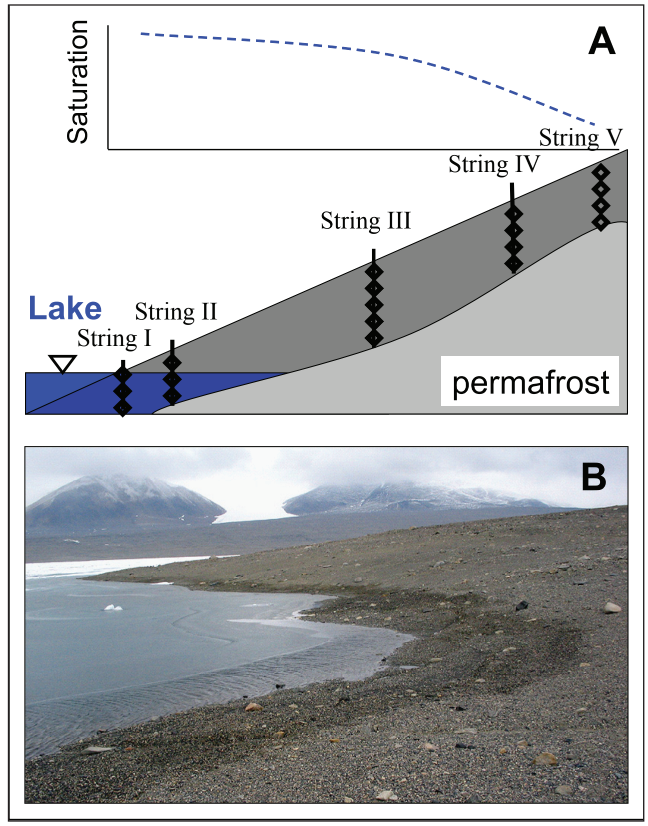

Figure 2. (A) General layout of thermocouples along transects, across wetted margins, (B) wetted margin around Lake Fryxell, extending ~10 m from shoreline.

String V. Thermocouple strings were built in a lab prior to deployment and then inserted into the ground using a thin steel rod attached to the end of the thermocouple string. The rod was subsequently removed after being inserted to the point of refusal.

At each transect, thermocouple data was collected by a Campbell Scientific CR-10XT datalogger via an AM-25T multiplexer. In addition, a thermistor was also deployed which collected air temperature data near the soil surface, in a shaded location. During the 2004-05 and 2005-06 field seasons, we were able to visit the dataloggers intermittently. Records are not continuous for the entire time of deployment due to datalogger failures. At Lake Joyce, data was collected on a 4 h interval from 18–22 Jan. 2005, from 12 Jul. to 15 Dec. 2005, and on a 15 min interval from 27 Dec. 2005 to 04 Jan. 2006. At Lake Fryxell, data was collected on a 15 min interval from 18–25 Jan. 2005, on a 4 h from 02 Jul. to 05 Dec. 2005, on a 1 h interval from 07 Jan. to 01 Feb. 2006, and on a 4 h interval from 01 Feb. to 30 Jan. 2007. At Lake Bonney, data was collected on a 15 min interval from 15–22 Jan. 2005, and on a 4 h interval from 03–30 Jan. 2006, and from 14 Dec. 2006 to 02 Feb. 2007.

We analyzed the collected subsurface temperature data by calculating 1) total degree-days of thaw (DDT) for each thermocouple record and 2) the daily amplitudes of temperature at every site, for days on which complete data collection was available (539 d at Lake Fryxell, 81 d at

Lake Bonney, and 166 d at Lake Joyce). We then computed frequency-duration curves (FDCs) using these data to illustrate comparisons among the thermocouple strings at each site, along the hydrologic gradients. Temperature FDCs that plot to the right on such graphs indicate a greater proportion of large diurnal cycles compared to those that plot toward the left. Our expectation is that thermocouple records in the drier shore sediments (i.e., Strings IV and V) will have greater diurnal variation than strings in more saturated conditions (Strings I-III). Because each thermocouple string is not deployed to a common depth, we cannot compare all FDCs on the same plot. Thus, for a more fair comparison, we have only plotted FDCs for thermocouple strings that have common or very similar depths (within 3 cm of each other). From Lakes Fryxell and Bonney, we plot only Strings III, IV and V. From Lake Joyce, we plot only Strings II, III, and IV.

Results and Discussion

Temperatures in the subsurface vary throughout the year from -50°C to just above 10°C. At Lake Fryxell, the time series data indicate a tight coupling of the temperature records near the shore (Strings I and II) and increasing vertical temperature gradients at more distal locations (Strings III, IV, and V) (Fig. 3). Similar patterns are evident from data collected at Lake Bonney (Fig. 4) and Lake Joyce (Fig. 5). It is worth noting that none of these locations appear to go through an extensive periods of zero-curtain condition during thawing (Figs. 3–5), as has been observed in arctic active layers (Hinkel et al. 2001). The only freeze-up data available is from Lake Fryxell, which does indicate a few days of zero-curtain condition close to the shorelines (Strings I and II) at Lake Fryxell (Fig. 3).

The vertical temperature gradients (Figs. 3–5) are not perfectly comparable as the thermocouples are deployed at different absolute depths along each thermocouple string. Despite these differences, these gradients are approximately comparable for Strings I-IV at Lake Fryxell, as the penetration depths are 50 cm, 50 cm, 45 cm, and 45 cm, respectively. At Lake Bonney, Strings III, IV, and V are all deployed to the same depths, and it is evident that String IV appears to have the greatest diurnal fluctuation in temperature, at the 10 cm depth (Fig. 4). At Lake Joyce, String IV is offset by 3 cm from Strings II and III (Fig. 5).

To compare integrated heating among locations along the soil moisture gradients, the DDT values are presented in Table 2. As expected, there is a pattern of diminishing degree-days above freezing with increasing depth. Similar to the analyses of temperature time series, these data are not ideally comparable among thermocouple strings within a site because of different absolute depths. The vertical pattern exceptions are String II and String V at Lake Fryxell, and String I at Lake Bonney. These unexpected results are likely due to one of three explanations: (1) surface evaporation which may drive cooling in the upper layers of the soil, (2) longitudinal movement of cool water from

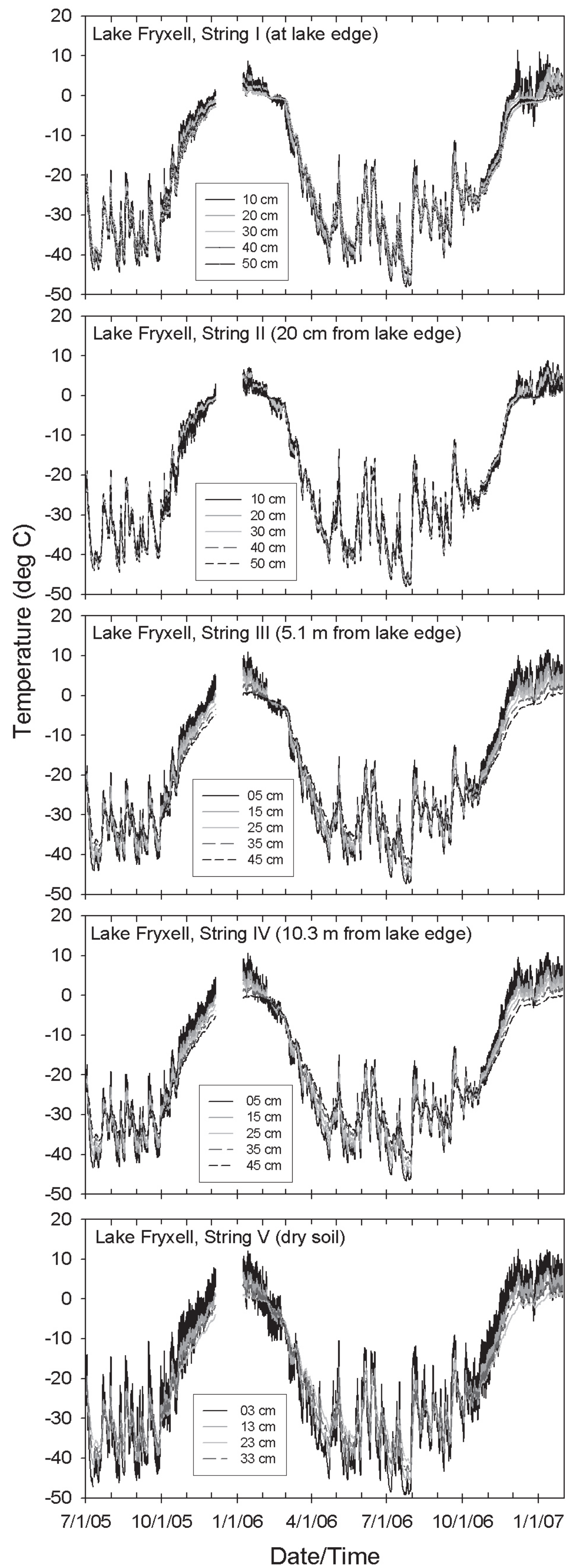

Figure 3. Lake shore soil temperatures from thermocouple strings I through V at Lake Fryxell.

Table 2. Degree-days of thaw (DDT, °C·d) for entire temperature records of thermocouples and thermistors. The table is organized by thermocouple string and position along the string with 1 = shallowest and 5 = deepest.

	Thermocouple String				
TC#	I	II	III	IV	V
			Lake Fryxell		
Air			274.8		
1	264.7	230.0	427.5	384.2	543.0
2	173.2	178.8	292.5	245.5	300.9
3	140.4	162.7	173.1	126.4	39.2
4	83.3	99.0	92.7	53.7	140.8
5	41.0	114.9	16.9	0.00	-
			Lake Bonney		
Air			234.4		
1	40.0	100.8	348.0	425.3	447.7
2	60.5	110.9	240.2	327.4	312.8
3	67.7	78.0	146.4	203.1	190.8
4	64.9	78.1	74.0	118.4	107.5
5	-	-	16.8	60.0	39.0
			Lake Joyce		
Air			53.5		
1	97.4	86.0	134.3	160.3	157.5
2	83.5	81.0	84.3	81.8	104.1
3	35.4	49.1	47.1	36.5	-
4	10.0	15.2	20.7	13.3	-
5	-	-	3.6	-	-

the shoreline outward toward the dry soils, or (3) change in surface conditions. String I at Lake Bonney was found to be inundated at the surface in Jan. 2006, due to rising lake levels. Thus the temperature signal at this location becomes more representative of benthic interaction with a water column than a soil exposed to atmosphere. The longitudinal movement of water is a possibility at String II at Lake Fryxell, given that the water at the lake shore (String I) is generally cooler within the same ~depths (positions 4 and 5).

The comparisons of temperature dynamics are also informed by the frequency analysis of diurnal temperature amplitudes (Fig. 6). At the Lake Fryxell transect, the diurnal amplitudes of temperatures increase for near-surface thermocouples from String III to IV to V, with similarities between III and IV, and much more variable overall at V (red curves, Fig. 6A). The same pattern exists at the thermocouples in the 2nd position (green curves, Fig. 6A), but changes at the 3rd thermocouple position, with Strings III and V similar in their FDC curves, and that of IV being generally less variable (blue curves, Fig. 6A). This is unexpected, and may be due to (1) the fact that these mid-transect locations are buffered at depth because of greater soil moisture or (2) lateral movement of water (i.e., along a direction that is parallel to the shoreline), which was not investigated here. At Lake Bonney, String IV is more variable at thermocouple positions 1 and 2, than Strings III and V (red and green curves, Fig. 6B). Similar to the patterns observed at Lake Fryxell, this sequence changes at position 3, and String IV becomes generally less variable than Strings III and V (blue curves, Fig. 6B). This

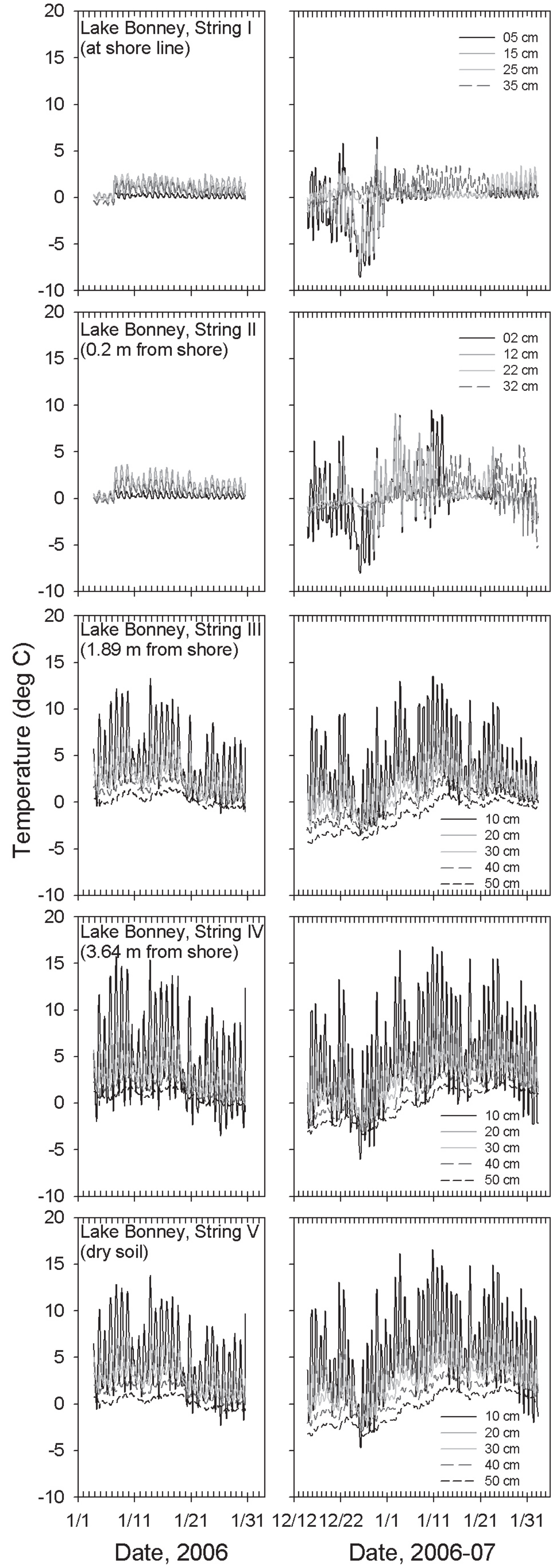

Figure 4. Lake shore soil temperatures from thermocouple strings I through V at Lake Bonney.

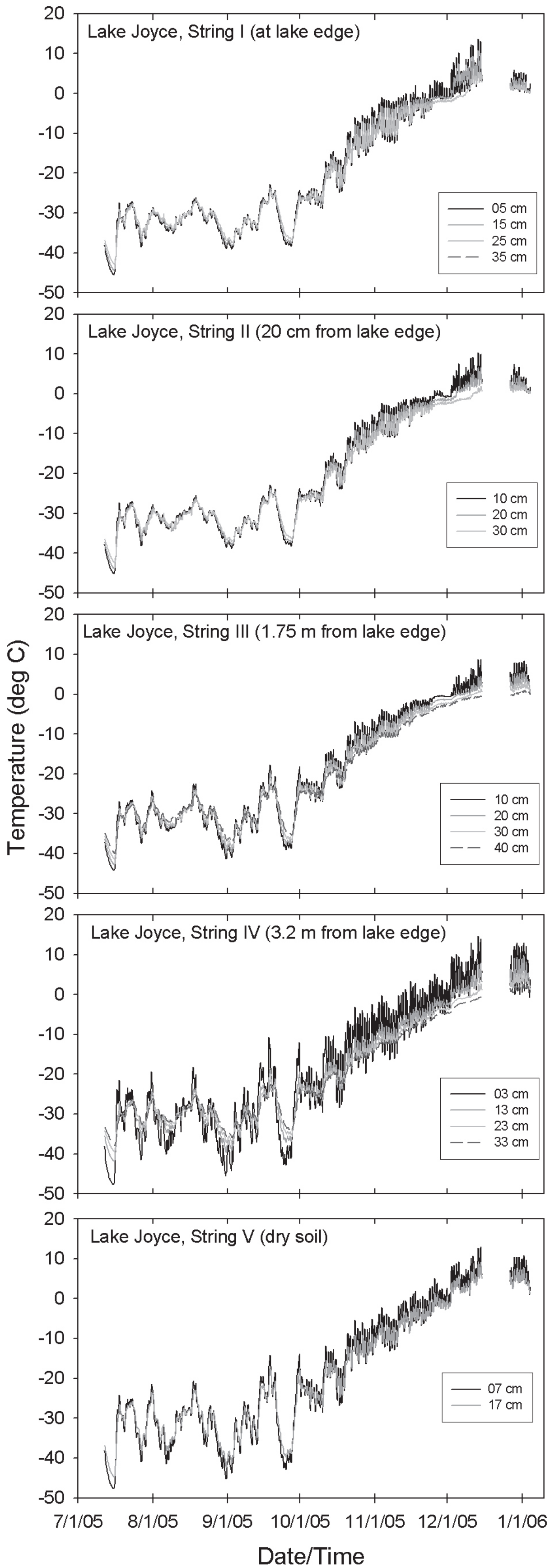

Figure 5. Lake shore subsurface temperatures from thermocouple strings I through V at Lake Joyce.

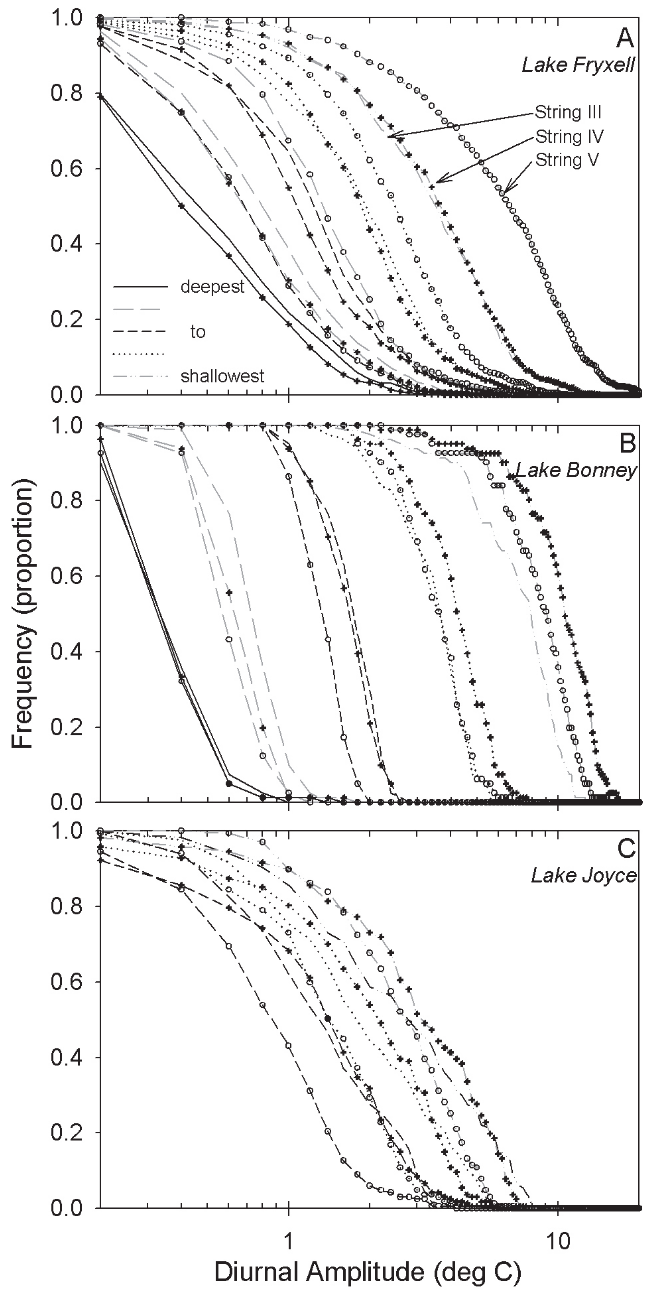

Figure 6. Frequency-duration curves (FDCs) for daily amplitudes in soil temperatures at A) Lake Fryxell, B) Lake Bonney, and C) Lake Joyce. Each curve represents the entire record for a single thermocouple. Strings with comparable depths of thermocouple deployments are presented for comparison. Strings are distinguished by symbols on the curves: nearest the lake has no symbol, the next one out has a cross symbol, and the furthest an open circle. Similar depths are indicated by pattern.

may indicate here too that String III is well buffered because of (1) enhanced soil moisture at depth at this position, (2) this mid-transect location is a transition point between the influence of convected heat from either longitudinal (i.e., away from the shoreline) flowing water from the shore to the dry soils, or (3) the influence of lateral flow of water not investigated here. At Lake Joyce, there is a consistent pattern of String IV having greater diurnal variability, in general, than String V at thermocouple positions 1, 2, and 3 (red, green, and blue lines, respectively, Fig. 6C). At the 4th thermocouple position (next to deepest), String V is much more variable in daily temperature fluctuation than String III at Lake Fryxell (black curves, Fig. 6A), and very similar for Strings III-V at Lake Bonney (gray curves, Fig. 6B). At the deepest thermocouple location (positions 5) temperature amplitudes are similarly buffered at Strings III and IV at both Lake Fryxell (Fig. 6A) and Lake Bonney (Fig. 6B).

These three sets of results generally support our expectation, that drier soils would be warmer and more variable than wetter soils. In particular, this notion is supported by the evident temperature time series magnitudes, which are greater at the distal thermocouple strings than at the near-shore strings, as well as by the general patterns of increased DDF at the distal locations compared to the nearshore locations. Finally, for the most part, locations that have less soil moisture are more variable in daily temperature amplitude than more saturated soils.

Conclusions

We found that, in general, soils with little soil moisture were warmer and more variable in temperature than wetter soils. This investigation focused on locations of soil moisture gradients near three lakes in the MDV, which may host variable microbial communities due to potential dependence upon habitat conditions, namely soil temperature and water content. These factors also influence biogeochemical processes across these hydrologic gradients.

Acknowledgments

The authors gratefully acknowledge Raytheon Polar Services Corp., Petroleum Helicopters, Inc., and UNAVCO for logistical and field support, and the McMurdo Long Term Ecological Research project. This research was funded by the National Science Foundation under collaborative research grants OPP 03-38267, 03-36970, and 03-38174. Any opinions, findings, and conclusions or recommendations expressed in this material are those of the author(s) and do not necessarily reflect the views of the National Science Foundation.

References

Aislabie, J.M., Chhour, K.L., Saul, D.J., Miyauchi, S., Ayton, J., Paetzold, R.F. & Balks, M.R. 2006. Dominant bacteria in soils of Marble Point and Wright Valley, Victoria Land, Antarctica. *Soil Biology & Biochemistry* 38: 3041-3056.

Bockheim, J.G. & Tarnocai, C. 1998. Nature, occurrence and origin of dry permafrost. *Proceedings of the Seventh International Permafrost Conference*, 57-63.

Bockheim, J.G., Campbell, I.B. & McLeod, M. 2007. Permafrost distribution and active-layer depths in the McMurdo dry valleys, Antarctica. *Permafrost and Periglacial Processes* 18(3): 217-227.

Campbell, I.B., Claridge, G.G.C., Campbell, D.I. & Balks, M.R. 1998. Permafrost properties in the McMurdo Sound-Dry Valley region of Antarctica. *Proceedings of the Seventh International Permafrost Conference*, 121-126.

Doran, P.T., McKay, C.P., Clow, G.D., Dana, G.L., Fountain, A.G., Nylen, T. & Lyons, W.B. 2002a. Valley floor climate observations from the McMurdo dry valleys, Antarctica, 1986–2000. *Journal of Geophysical Research* 107(D24): 4772, doi:10.1029/2001JD002045.

Doran, P.T., Priscu, J.C., Lyons, W.B., Walsh, J.E., Fountain, A.G., McKnight, D.M., Moorhead, D.L., Virginia, R.A., Wall, D.H., Clow, G.D., Fritsen, C.H., McKay, C.P. & Parsons, A.N. 2002b. Antarctic climate cooling and terrestrial ecosystem response. *Nature* 415: 517-520.

Gooseff, M.N., Barrett, J.E., Northcott, M.L., Bate, D.B., Hill, K., Zeglin, L., Bobb, M. & Takacs-Vesbach, C. 2007. Controls on soil water dynamics in near-shore lake environments in an Antarctic polar desert. *Vadose Zone Journal* 6: 841-848.

Guglielmin, M. 2006. Ground surface temperature (GST), active layer and permafrost monitoring in continental Antarctica. *Permafrost and Periglacial Processes* 17(2): 133-143.

Hinkel, K.M. 1997. Estimating seasonal values of thermal diffusivity in thawed and frozen soils using temperature time series. *Cold Regions Science and Technology* 26(1): 1-15.

Hinkel, K.M., Paetzold, F., Nelson, F.E. & Bockheim, J.G. 2001. Patterns of soil temperature and moisture in the active layer and upper permafrost at Barrow, Alaska: 1993–1999. *Global and Planetary Change* 29(3–4): 293-309.

Kennedy, A.D. 1993. Water as a limiting factor in the Antarctic terrestrial environment: A biogeographical synthesis. *Arctic and Alpine Research* 25(4): 308-315.

Kirschbaum, M.U.F. 1995. The temperature-dependence of soil organic-matter decomposition, and the effect of global warming on soil organic-C storage. *Soil Biology & Biochemistry* 27: 753-760.

Parsons, A.N., Barrett, J.E., Wall, D.H., & Virginia, R.A. 2004. Soil carbon dioxide flux from Antarctic Dry Valley soils. *Ecosystems* 7(3): 286-295.

Pringle, D.J., Dickinson, W.W., Trodahl, H.J. & Pyne A.R. 2003. Depth and seasonal variations in the thermal properties of Antarctic Dry Valley permafrost from temperature time series analysis. *Journal of Geophysical Research* 108(B10): 2474, doe:10.1029/2002JB002364.

The Mechanism of Ice Formation in Connection with Deformation of the Freezing Layer

J.B. Gorelik
Earth Cryosphere Institute SB RAS, Tyumen, Russia

Abstract

The freezing of a closed volume of water-saturated sands is considered in this report. The separate clay body may be situated inside sand. Only the freezing layer may be deformed under action of cryogenic pressure. It is shown that a layer of ice may be formed in the volume. For its formation, it is necessary that the effective radius of the water-supplying area be more than some critical value. In this condition, the frozen layer is similar to the frozen part of a pingo with a water lens in its base. In the opposite case, only the frozen soil with different ice content may be formed. If the vertical length of the clay body is less than some limit, it will be pulled out from its sandy environment or it will be broken along some of its horizontal cross section.

Keywords: cryogenic pressure; deformations; frozen layer; ice content.

Introduction

Thick ice bodies are spectacular features of the permafrost environment. The mechanisms of formation of some of them are still debatable and there are ten hypotheses concerning their formation. They are subdivided into two groups: a) ice body formed inside the ground; b) ice body formed on the surface of the ground and then buried by alluvium. Different viewpoints on this problem are reflected in several books and in numerous articles. Recently some articles were published where mechanisms from both of these groups are discussed and differences in ideas are not resolved.

The idea of ice body formation as a result of segregation or injection is mostly found among hypotheses of the first group. The burial of glacial ice is the most recognized hypothesis of the second group. Existing approaches cannot completely explain ice body formation under certain conditions, as well as structure ice and structure of the enclosing sediments.

The mechanism of ice body formation is proposed in this paper. It attempts to explain a number of important characteristics of the structure of ice body deposits.

Deformations of Freezing Layer

Let us consider the freezing of a closed volume of water-saturated soil which includes clay and sand. The bottom and sides of this volume are formed by dense clay with sand inside it. It is assumed that a separate clay body may be situated inside the sand (Fig. 1). Additional assumptions are: 1) the freezing layer is connected rigidly with clay sides of the volume and 2) the additional water supply of the considered volume may be realized from the sands which are outside of the clay sides. Thus, only the freezing layer may be deformed in such a system. These deformations are caused by cryogenic pressure which arises in a closed system, with increase in the volume of freezing water due to a difference in the density of water and ice.

During freezing of a closed volume, the cryogenic pressure increases, causing the plate of freezing ground to curve upwards. The upward-directed force acts on the central clay body while it is freezing; simultaneously the opposite direction force acts on the freezing layer and holds it back from deformations. The force causes tension stresses in the horizontal direction at the unfrozen part of the clay body. These stresses have a maximum at the contact of frozen and unfrozen parts, and they increase in time. When the cohesion value of the unfrozen material is reached, then the clay body is broken along this frozen/unfrozen contact. The crack between broken parts is filled with water which freezes, resulting in ice body formation. For analysis of the transformations in the system, it is necessary to consider the deformation process of the freezing layer first.

For general consideration, let us introduce the "closing" depth of the volume h_0. It determines the freezing depth at which surface water is not connected with freezing soil. The source of surface water in Figure 1 is nonessential anymore. It is assumed that the deformations of the freezing layer at all clay bodies and at the peripheral water-supplying zone are negligible. We use R_w and R_f for the effective radii of the water-supplying zone and of the rigid connection contour accordingly. The inequality takes place in general: $R_w \geq R_f$ (Fig. 1). Assuming that the thickness of the frozen layer, h, is much less than the value of R_f, its mechanical behavior may be described as deformations of the thin plate. Real configuration of all the elements of the considered system is very complicated. Theoretical analysis may be realized for the system with any symmetry. Later on, we shall use the mechanical analog of the Figure 1 scheme,where all vertical walls are cylindrical. This analog has the axis symmetry. In this analog, the vertical deformation of freezing layer ζ_r is the function of the radial coordinate r and time t.

It is considered that the deformations of the freezing layer are started after freezing of the surface sources of water. These deformations are limited if the acting stresses are smaller than the long-term strength of frozen sands, and they are increased with no limit in the opposite case. The attenuated deformations are described by the equation of

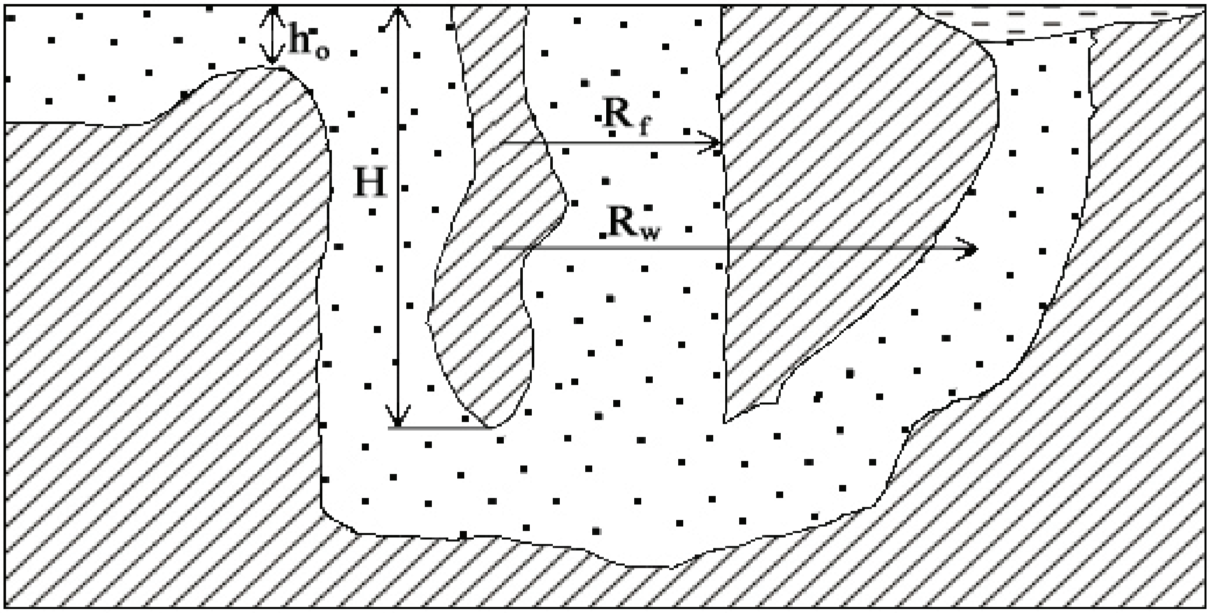

Figure 1. The scheme of closed volume before freezing. - clay, - sands, - surface basin. The notation of the values is in the text.

hereditary creep theory (the instantaneous deformations are negligible):

$$\varsigma_r(t) = t_r^{-1}\int_0^t \varsigma_r^u(\tau)\cdot \exp\left[-(t-\tau)/t_r\right]d\tau \quad (1)$$

where E, v, η are elastic modulus, the Poisson ratio and viscosity coefficient of frozen sand; $t_r = 2(1+v)\eta/E$ is relaxation time; $\zeta_r^u(t)$ is elastic solution of the task (its change in the time is due to the slow change of cryogenic pressure and of the thickness of the freezing layer at the same time). The characteristics of frozen soils should be defined from the tests with attenuated deformations. Methods and results of the frozen soils tests, both for the attenuated and for no-limited deformations are fully presented by Grechishev (1963). The constant E should be defined at the stabilized state in the tests of frozen sample and constant η should be defined by measuring the deformations rate through the same tests in the beginning of the test. Then equation (1) describes satisfactorily these experimental data of frozen sand attenuated deformations in time. For frozen sands, the relaxation time is not more than 15 days as a rule. For a closed system, the elastic bend, ζ_r^u, is defined by equation:

$$D\cdot\Delta^2\varsigma_r^u = -\rho_s gh + P_c - \rho_w g\varsigma_r^u \quad (2)$$

where P_c is the value of cryogenic pressure; ρ_s, ρ_w are the densities of frozen soil and of pore water; $D=Eh^3/12(1-v^2)$ – plate rigidity; Δ is the Laplasian operator; g is acceleration of gravity. The term $\rho_s gh$ is the pressure associated with weight of the freezing layer and the term $\rho_w g\zeta_r^u$ is pressure due to Archimedean force. The last arises owing to deformations inequality of the plate as it takes place for floating plates (Timoshenko 1967). It is important that the elastic reaction from the sandy bed to the freezing plate is absent because the effective stresses are equal to zero in a closed system (Gorelik 2007b). The last statement is true for the uniform loadings acting on the plate, considered here. The value $P=P_c -\rho_s gh$ defines the prevalence of cryogenic pressure over pressure of the freezing layer weight. It is always positive in a closed system, and it is upward-directed.

We shall consider the non-limit deformations only at the stage of stationary creep. These deformations may be described by the viscous-plastic soil flow model. The scheme of this flow is analogous to the flow of the viscous-plastic liquid in the cylindrical tube. At the stage of stationary creep, the freezing layer is shifted continuously relative to the clay walls of the volume. The elastic deformations are negligible, and the kern of the flow may be considered as rigid. Near the walls, there is a thin layer which is deformed as viscous uncompressible liquid. The beginning of the creep stage occurs when the intensity of the stress at the attenuated deformations stage reaches the value of long-term strength of frozen sands on the contour of the rigid connection. The definite values of abundance P_s and of freezing depth h_s correspond to execution of this criterion. The rigid kern velocity of the flow v_s for $h\geq h_s$, $P\geq P_s$ is defined by expression:

$$v_s = -\frac{\tau_s}{\eta}(R_f - r_s) + \frac{P}{4\eta h}(R_f^2 - r_s^2) \quad (3)$$

where r_s is rigid kern radius. For running values of h and P it is defined by $r_s=2\tau_s h/P$; τ_s is long-term strength of frozen sands defined under shear-tests of the samples. The viscosity coefficient, η, in equation (3) is different than its value in equation (1) in general, and it must be defined under the same shear-tests during stationary creep stage. The shear-test may be realized by the rotation of a frozen soil tube with acting axial force as presented by Grechishev (1963).

Both cryogenic pressure P_c in equation (2) and the abundance P in equation (3) are not determined up to now. For its determination it is necessary to use the equation of water mass conservation in a closed system:

$$\frac{1}{\pi R_f^2}\int_0^{R_f} \varsigma_r 2\pi r dr = \qquad (4)$$

$$= \left(\frac{\rho_w n_u - \rho_i n_f}{\rho_w \sqrt{n_u n_f}} + \frac{\Delta\rho_{wi}}{\rho_w}(\alpha^2 - 1)\right)(h - h_0)$$

Here: ρ_i is the density of ice; $\Delta\rho_{wi}=\rho_w-\rho_i$; n_u, n_f are the soil porosities at the unfrozen and frozen states (they are constants here); $\alpha=R_w/R_i\geq 1$; $h\geq h_0$. For the determination the value of P in equation (3) it is necessary to derive the relation (4) over t taking into account $v_s=\partial\zeta_r/\partial t$ for the creep stage. In the equation (4) the average deformation of freezing layer (left part) is proportional to its thickness after closing the system. It occurs because of change it porosity migration of water from peripheral parts of the system (right part). These deformations are purely connected with nonzero densities difference $\Delta\rho_{wi}$. It may be shown that $\zeta_r=0$ for all r if we shall take on formally $\Delta\rho_{wi}=0$ in equation (4). Later on, we take the simple form of the relation between frozen depth and time: $h=(\beta t)^{0.5}$, where β is a constant proportional annual mean surface temperature and to the value of n_f^{-1}.

The written equations and the formulated additional conditions are sufficient to determine cryogenic pressure and deformations of the freezing layer in time. The behavior of the value P as a function of the freezing depth is shown on Figure 2a at the following initial data: $E=10^8$ Pa, $\eta=10^{13}$ $Pa{\cdot}sec$, $\tau_s=1.8{\cdot}10^5$ Pa, $R_f=300$ m, $h_0=0$ m, $n_u=0.3$, $n_f=1.5n_u$, $\beta=1.3{\cdot}10^{-7}$ m^2/sec, $\alpha^2=7$. It can be seen that the value of P has a bend at the deformations transition to the stationary creep stage.

The criterion of breaking of the central clay body may be written as: $P=cR_c/R_f$. Here c is the cohesion of the unfrozen clay and R_c is the radius of the central clay body. The clay bodies may be broken at any deforming stage (if, of course, the freezing depth will reach the needed value). For example, the dotted line on Figure 2a demonstrates the breaking stress with the parameters: $c=0.5{\cdot}10^5$ Pa, $R_f=300$ m, $R_c=50$ m. Figure 2b shows the correlation between bend lines of the freezing layer before and after breaking of the central clay body. At the breaking at the attenuated deformations stage, the bend line from double convex is transforming to the convex one. The experimental modeling of this process shows that this transformation is accompanied by increasing of the temperature and abrupt falling of the cryogenic pressure. Electromagnetic emission and crack formation in the freezing layer were observed during the process. But the frozen layer was unbroken as whole (Gorelik 2007a).

The further fluent lifting of the broken (upper) clay body part is possible, together with the frozen layer itself, for breaking at the stationary creep stage.

The breaking criterion does not take into account the vertical length of the clay body, H. But such interval of values H exists ($0\leq H\leq H^*$) that for every H from this interval the clay body will be pulled out from its sandy couch before it will be broken. The limiting value H^* is defined by two conditions: 1) the vertical stress at the contact of frozen and unfrozen parts reaches the value of c and 2) the upward-directed force is equal to the sum of the unfrozen part weight and the friction force at its lateral contact with sands. The expression for H^* is:

$$H^* = h^* + \frac{cR_c}{\Delta\rho_{sw} g R_c + 2\tau_t}; \qquad (5)$$

where τ_t is the lateral stress of the friction; h^* is the freezing depth at which the unlimited in vertical direction clay body is broken. Similar conditions can be used to develop the equation for the freezing depth h^{**} at which the pulling out takes place at any H from the interval.

The ice body must be formed directly under the base of the clay body on its pulling out. The main tendencies in the deformation of the freezing layer under this process will be the same as at its breaking.

Water Flows and Ice Accumulation

All deformations of the freezing layer in a water-saturated closed system are connected with water inside this system. So, the deformations are negligible near the points of the rigid connection contour, and water is driven away from the freezing front here. The water flows to the freezing front in this area. It means that the porosity, n_f, is a function of radial coordinate r in general and it cannot take arbitrary values (as it is considered above approximately). The function $n_f(r)$ characterizes the local ice accumulation along the freezing layer by coordinate r. As it was noticed above, the constant β is proportional to n_f^{-1}; then the freezing layer thickness h_r at any radial point is connected with it at the points of the rigid connection contour h by dependence: $h_r=h(n_u/n_f(r))^{0.5}$. To find the function $n_f(r)$ it is necessary to use an additional correlation as the local equation of the skeleton's mass conservation (Gorelik 2007b):

$$(n_f - n_u)\partial z_f / \partial t = -(1 - n_f)v_f \qquad (6)$$

where $\partial z_f/\partial t$, v_f are the rates of the freezing front movement and lifting of the upper surface of freezing layer relatively to the unfrozen part of the volume ($v_f=\partial\zeta_r/\partial t$ at the attenuated deformations stage and $v_f=v_s$ at the stationary creep stage). Between values of $\partial z_f/\partial t$, v_f and $\partial h_r/\partial t$ the connection exists: v_f-$\partial z_f/\partial t=\partial h_r/\partial t$ (Fig, 2c).

The rate v_s does not depend on r at the stationary creep stage and the values of n_f, v_s and $\partial z_f/\partial t$ may be calculated as functions of parameter α (Fig. 2d). Such critical value α^* exists that for $\alpha<\alpha^*$ $n_f<1$ and $n_f=1$ in the opposite case (for $n_u\approx 0.25$ we have $\alpha^*\approx 4.5$). With the increasing of α from one to α^* the value of n_f increases to one monotonously. The rate $\partial z_f/\partial t$ is less than zero always in this case. For $\alpha\to\alpha^*$ we have $n_f\to 1$ and very icy soil is formed. For $\alpha\geq\alpha^*$ only

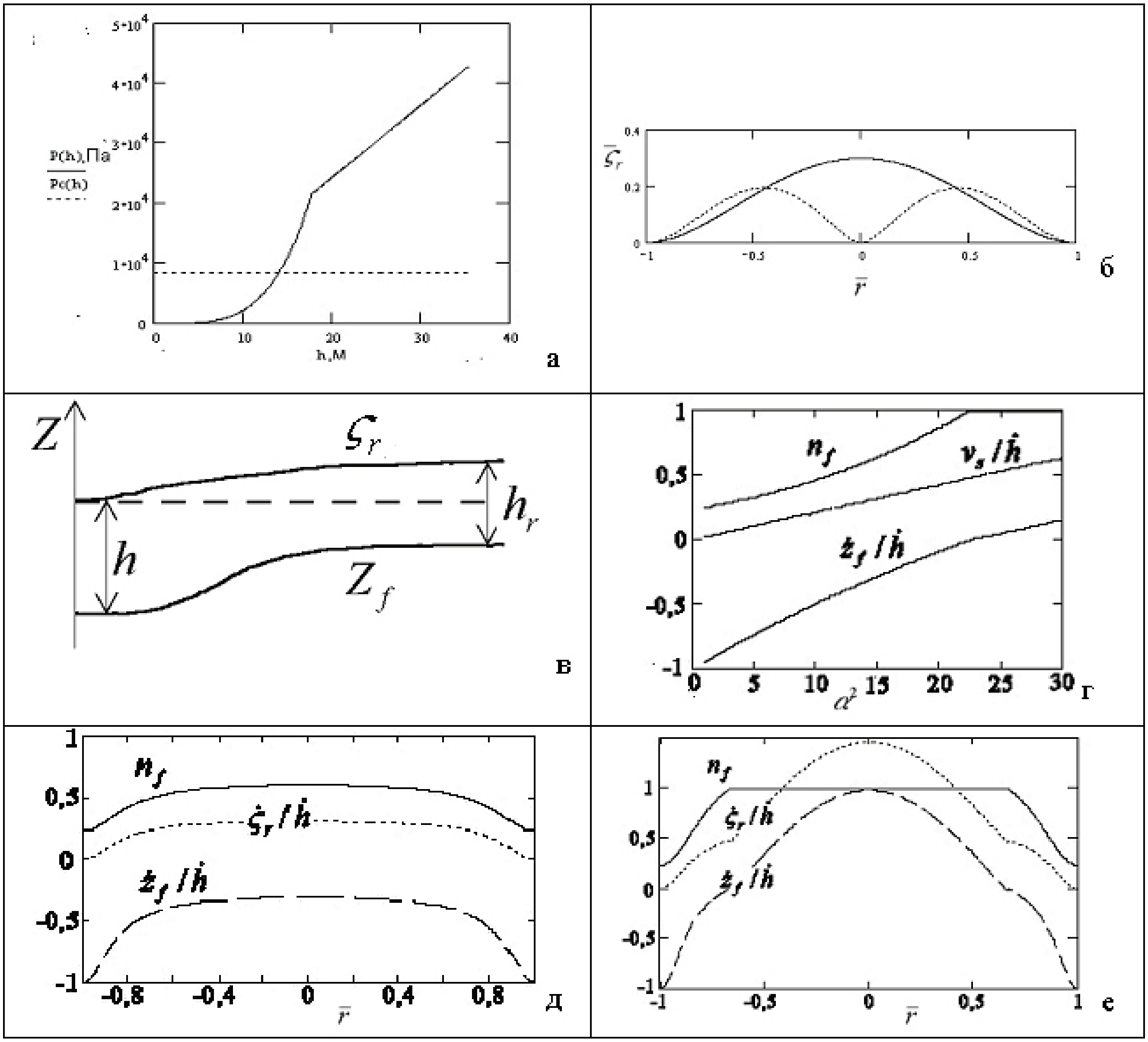

Figure 2. The characteristics of cryogenic pressure, deformations and ice accumulation at the freezing of closed volume: a) the dependence of cryogenic pressure abundance on freezing depth (continuous line), dotted line is the breaking stress in the central clay body; b) the bend lines before (dotted line) and after (continuous line) the break of the central clay body (in non-dimensional coordinates); c) the scheme of frozen layer near the points of rigid connection; dotted line is the initial position of the ground surface; d) the dependences of frozen soil porosity, relative velocities of deformations and of freezing on value of α at the stationary creep stage; e) the dependences of frozen soil porosity, relative velocities of deformations and of freezing on non-dimensional coordinate r at attenuated deformations stage (α=3.5<α^*); f) the dependences of frozen soil porosity, relative velocities of deformations and of freezing on non-dimensional coordinate r at attenuated deformations stage (α=4.8>α^*).

clear ice is formed and rate $\partial z_f/\partial t$ is more than zero. The last means that the freezing front is retired from the unfrozen soil, and a clear water lens is formed under the ice body. The vertical thickness of the lens should increase with time. All these transformations may be interpreted as changes in the character of ice accumulation at the variation of the radius R_w and at fixed radius R_f.

At the attenuated deformations stage, the value of n_f is a function of r. In this case the critical value α^* exists also: if $\alpha<\alpha^*$, we always have $n_f<1$ for all values of r from the deformations zone, and if $\alpha>\alpha^*$, the area with radius R_α exists inside the deformations zone ($R_\alpha<R_f$) where n_f=1 for all the values of r from this area (for $n_u\approx0.25$ we have $\alpha^*\approx4.2$). For $\alpha=\alpha^*$, we have R_α=0 and the value of R_α is increased with increasing of α.

The dependence of the functions n_f, v_s and $\partial z_f/\partial t$ on r for $\alpha<\alpha^*$ is shown on Figure 2e. In this case we have $n_f<1$, $\partial z_f/\partial t<0$ for all $r\leq R_f$. For $\alpha>\alpha^*$ the limited area with n_f=1 and $\partial z_f/\partial t>0$ is present inside the deformations zone (Fig. 2f). It means that the kern of the clear ice is formed in the freezing layer. This kern is surrounded by very icy soil, and the water lens underlies the kern. This structure of the frozen layer is

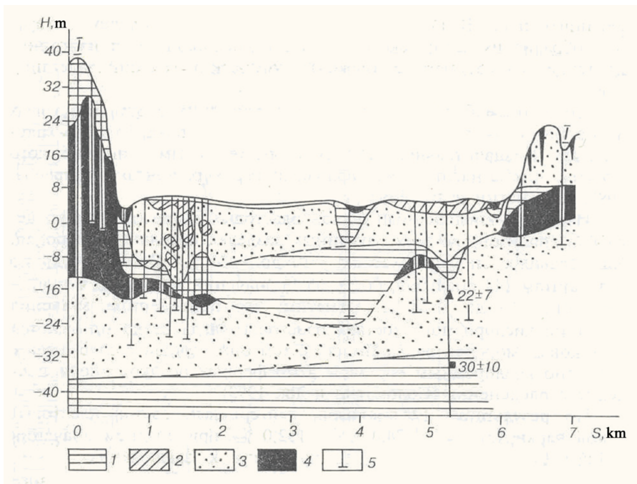

A

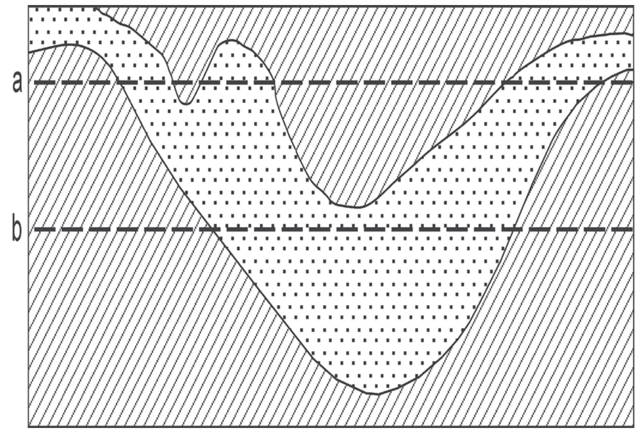

B

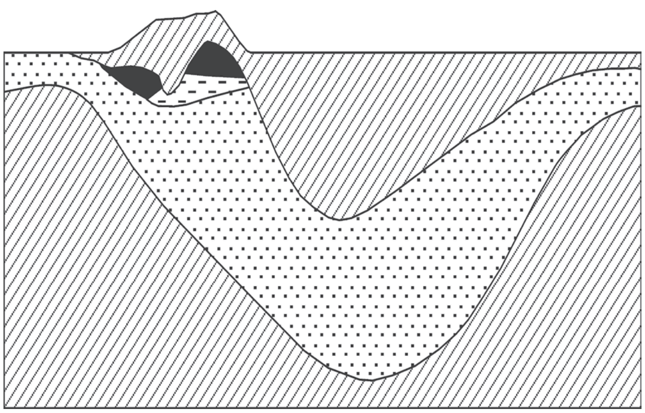

B-a

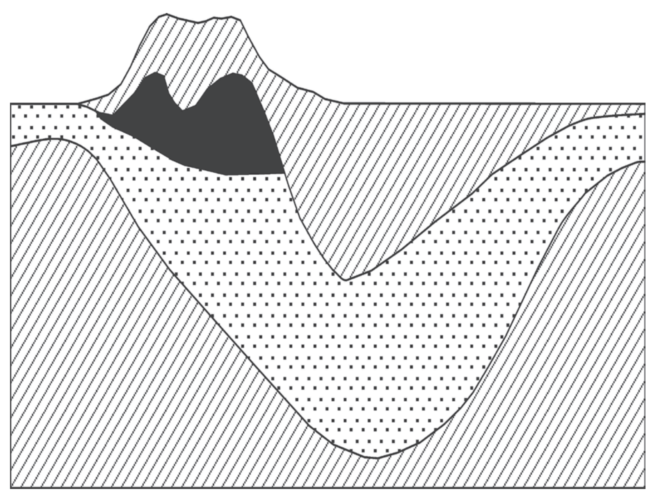

B-b

Figure 3. The sections of ice body deposits: A) the cross section of the Se-Yaha river valley, 1-clay, 2-clay loam, 3-sand, 4-ice, 5-borehalls (Solomatin & Konyahin 1997); B), B-a), B-b) the hypothetic section for different stages of the freezing, -ice, - -water lens. The other notations and clarifications are on the Figure 1 and in the text.

analogous to the structure of a pingo, which is presented by Mackay (1978). The likeness of the structures of some ice body deposits and a pingo is noted by Fotiev (2003).

Geological Aspects of the Considered Problem

The soil section in Figure 1 has a specific structure characterized by the certain combination of sand and clay. The important role in a ice body formation belongs to the lower clay layer which forms bottom and walls of the volume. Continuous bodies of massive ice widely occur on the Yamal Peninsula. It is interesting to compare their occurrence and relationship with the surrounding soil with a soil section in Figure 1? Although field descriptions and photographs of the sections with ice bodies are presented in many publications, information about soil beneath ice bodies is limited. However, the clay layer is found under sands, which underlain ice (Velikotsky 1987, Baulin et al. 1996, Solomatin & Konyahin 1997, Dubikov 2002, Streletskaya & Leibman 2002, Fotiev 2003, Shpolanskaya et al. 2006). The role of the lower clay layer in an ice body formation has not been previously discussed. All the sections described in these papers have had a three-layer structure before ice formation: clays, sand, and clay. It created the conditions for freezing of the sands in a closed system. For example, Figure 3A shows such a section presented by Solomatin and Konyahin (1997). It shows that the ice bodies are covered by clay, and they have sand in its bedding everywhere, but under these sands, the clay layer is present. Without ice (before freezing), the section has a three-layer structure. It is of interest to deduce the role of each of the layers in the ice body formation. Let us consider the question for the hypothetic section presented in Figures 3B, 3B-a, and 3B-b for different stages of freezing (the small and big tongues in upper clay layer are analogs of small and big clay bodies in the sands of Figure 1). Figure 3B shows this section before freezing. The dotted lines a-a and b-b are the positions of the freezing front at intermediate and final stages of freezing (in assumption that mass transfer processes are absent in the system). Figure 3B-a shows separate fragments of the ice body, water lens, and deformations of the separate layer boundaries and the surface of the massif at the intermediate stage. Figure 3B-b shows the final form of the ice body and final deformations of the layers and boundaries.

In this process, the lower clay layer is a confining layer at the bottom and walls of the closed volume. There is a solid connection between the freezing layer and these walls. Without this connection, the cryogenic pressure that occurs will not be enough to deform the upper layers. The lower clay layer is not deformed at ice body formation process as a rule.

The sandy layer is the main water-containing and water-conductive layer. The ice accumulation and deformations of the upper layer and the structure and composition of the ice body are essentially connected with an extension of this layer in horizontal and vertical directions. At the deforming of the upper layer, the fractures and cavities are formed between the upper and sandy layers. As far as cohesion of sand is equal to zero and under an impact of the water flow, sand partially fills these defects. Hence, the upper boundary of the sands has to take on a subhorizontal position under the water lens and ice bodies (Figs. 3A, 3B-a, 3B-b).

The upper clay layer is the main layer which is subjected to transformations during ice body formation. Configuration of the ice body depends on size and configuration of this clay layer. The only clay composition of this layer is not obligated, but if clay is present here, the freezing layer moves its unfrozen parts upwards. Deformations arise and expand at mostly weak parts of the layer (Figs. 3B, 3B-a). Its more solid parts (as the big tongue on Fig. 3B-a) hold the freezing layer from deformations. (On the real section of Fig. 3A it is the central clay body. It is possible that the upper left part of the clay layer on this section is broken during ice body formation.) At the final stage, the solid parts of the layer may be deformed, too. For example, the big tongue of Figure 3B-b has some rotation to the right. It may be cracks formation in the tongue's body at this rotation. The upper boundary of the ice takes over the configuration of the lower boundary of the upper clay layer (Fig. 3B-b).

Acknowledgments

The author is indebted to Professor S.E. Grechishchev and to Professor S.M. Fotiev for discussing the problem and for their useful criticisms.

References

Baulin, V.V., Aksenov, V.I. & Dubikov, G.I. 1996. Permafrost conditions of development of Bovanenkovo gas-field. In: V. Tsibulsky (ed.), *Geotechnical Monitoring of Yamal Oil- and Gas-Fields*. Tyumen: Institute of Northern Development SB RAS, 3-238.

Dubikov, G.I. 2002. *Composition and Cryogenic Structure of Permafrost in West Siberia*. Moscow: GEOS Publishing House, 248 pp.

Fotiev, S.M. 2003. Ice bed genesis in the Yamal marine deposits. *Earth's Cryosphere* 1, VII: 63-75.

Gorelik, J.B. 2007a. Shift in ice cover deformations under freezing in a closed system. *Proceedings of the International Conference "Cryogenic Resources of Polar Regions," Salechard, Russia, June 17–21, 2007*: 125-128.

Gorelik, J.B. 2007b. On regimes of ice formation during freezing of the ground. *Earth's Cryosphere* 4(XI): 42-49.

Grechishchev, S.E. 1963. Creep of the frozen soils under complex stressed state. In: K. Voytkovsky (ed.), *Strength and Creep of Frozen Soils.* Moscow: USSR Academy of Sciences

Mackay, J.R. 1978. Sub-pingo water lenses, Tuktoyaktuk Peninsula . *Canadian Journal of Earth Sciences* 8(15): 1219-1297.

Shpolanskaya, N.A., Streletskaya, I.D. & Surkov, A.V. 2006. Cryolithogenesis in Arctic shelf (recent and relict). *Earth's Cryosphere* 3(X): 49-60.

Solomatin, V.I. & Konyahin, M.A. 1997. Cryolithogenesis and stratigraphy of the Central Yamal frozen soils formation. In: E. Melnikov (ed.), *Results of the Earth's Cryosphere Fundamental Researches in Arctic and Sub-Arctic*. Novosibirsk: Nauka, 173-182.

Streletskaya, I.D. & Leibman, M.O. 2002. Cryogeochemical interrelation of massif ground ice, cryopegs, and enclosing deposits of Central Yamal. *Earth's Cryosphere* 3(VI): 15-24.

Timoshenko, S.P. 1967. *Plates and Shells*. Moscow: Nauka, 626 pp.

Velikotsky, M.A. 1987. Dislocations and ice bodies in quaternary sediments of the Yamal Peninsula. In: A. Popov (ed.), *Cryogenic Processes*. Moscow: Moscow State University, 48-59.

Technocryogenesis Controls on the Permafrost Environment and Geotechnical Factors in Towns of the Permafrost Zone

V.I. Grebenets
Geographical Faculty, Lomonosov State University, Moscow, Russia

Abstract

Currently, due to the significant landscape modification that alters the thermal and mass exchange between permafrost and the atmosphere, special geocryological conditions are formed in urbanized areas of the permafrost zone. It is suggested that the specificity of changes in geocryological, landscape, geoecological and geotechnical environments should be delineated with the technocryogenesis concept, which has four basic features. Technocryogenesis is the specific exogenous process taking place in urbanized areas of the cryolithozone (1); it occurs at the contact of technogenic loads and the permafrost environment (2); it has an irreversible character (3); and appears as specific natural geocryological complexes (4). Regional studies of technocryogenesis revealed its varied influence on permafrost and ecological environments and geotechnical condition.

Keywords: cryogenic processes; deformation; permafrost degradation; technocryogenesis; temperature regime.

Introduction

Currently, due to significant landscape modifications that have altered the thermal and mass balance between the permafrost and the atmosphere, special geocryological conditions are developed in urbanized areas of permafrost. In addition, engineering and mechanical loads force permafrost soils to change physical, thermal, and mechanical properties. Consequently, the soil temperature beneath the affected surface rises and dangerous cryogenic processes are activated. This results in the overall reduction of geotechnically stable areas.

Methods

To study the relation between the permafrost conditions and geotechnical environments, we measured the temperature of permafrost in boreholes. This was done in built-up areas, and the results were compared to the thermal field that existed before construction. Geodetic survey data of the surface prior to embankment construction was also analyzed to determine the trends and rates of cryogenic processes taking place at the study sites. Visual and instrumental observations of the state of buildings and constructions were collected.

Results

There are several types of forces acting on permafrost soils in urban basements, as described below:

Mechanical disturbance

Exploitation of soils for basement construction, borrowing and excavation, and mining and tunneling, alter the strength capacity and continuity of the permafrost. Dirt piles, montons, and embankments favor either formation of permafrost bodies or permafrost degradation.

Technogenic inundation and salinization

The release of unrefined effluents on the daylight surface, accidental release from sewerage, and penetration of contaminants into the active layer notably alter the geochemistry of soils. This has been observed in Yakutsk, Vorkuta, Igarka, and many others towns in the permafrost zone. For instance, soil water of the active layer in Norilsk (where there exist the largest nonferrous-metal industries in the world) is rich in sulfates and chlorides, making the environment aggressive to the foundation concrete. The maximal salinity is found in areas being built up at the outset of the Northern exploration– up to 21 mg/l is the concentration of salts in sands under the Nickel Plant built in 1940 (Grebenets 1988). Chemical contamination of soils lowers the freezing temperature, increases active layer thickness, and favors thawing of ice-rich sediments with consequent thermokarst.

Alteration of surface thermal conditions

The vast majority of both domestic and rural areas of northern towns are free of vegetation and covered with asphalt. Asphalt allows soil heat flow to increase due to summer heating and winter cooling from snow clearing. Observations showed that the snow collecting areas have warmer (by 2–3°C) permafrost than that under the snow cleared roads. Ventilating cellars lower the soil temperature due to shading in summer and protection from snow accumulation in winter. Correct operation of a ventilating cellar could lower the permafrost temperature by 2–4°C. However, multiple failures in service were found and include the following: missing the solid waterproof cover and catch-water drains; malfunctioning of the sanitation system; insufficient number of weep holes in ventilating cellars or weep holes covered with snow; and low altitude of ventilating cellars turning them into encatchments. Serious service failures were found in 85% of the buildings in Dudinka. Failures favored degradation of permafrost, resulting in local taliks or warmer soil body formation as well as formation of non-anchored permafrost bodies. Bedding courses without lateral watertight faces have a generally negative influence on permafrost (Grebenets 2003). The bedding courses consist of roughly sorted coarse grained wastes including crushed rock, pebble, and sand that could be easily supplemented with construction debris or snow. Moss and vegetation is covered, consequently increasing heat flux into the soils. Moreover, due to high filtration coefficient of 10 to 50 m/day, the bedding course material is permeable for surface waters. For example, residential 9-storey buildings on Laureatov st., Norilsk were constructed in 1975–1980 having 2–3 m to 8–10 m of the bedding course in the basement damaged several years after due to a reduction in the soil bearing capacity. The soil temperature under the bedding courses changes in range from -2.5°C to +2°C (Grebenets 2001).

Thermal forcing

Enhanced flow of heat into the soil from industries, residential buildings and communications, water released in rural areas or accidentally, lack of storm canalization, will all lead to permafrost degradation. Large heat-emitting utility collectors contribute most to permafrost warming. The collectors in Talnakh, Vorkuta, Dudinka, and other populated towns represent a distributed net of technogenic systems dug 4 to 6 m into the soil. We recorded above zero temperatures in the annual thermal regime of the collectors, which is the reason the thaw bulb is expanding. There were icings found in winter, while snow melt water and effluents flow in summer. The thermal forcing could be prevented if the collectors were laid on the ground like those in the Yamburg and Novozapolyarnyi settlements.

We suggest that technogenic impacts are the reason for the change in the soil temperature profile. Measurements in a deep borehole in downtown Norilsk evidence the temperature increase at a depth of 20–60 m by 0.5°C to 1°C during the period 1955–1985. Geothermal studies in a 135 m borehole in the suburbs of Norilsk revealed a increase of temperature over the last 50 years from -3.5 or -4°C to -1.5 or -2°C at a depth of 20 to 90 m. It is thought that temperature changes below the 15–20 m layer is not controlled by seasonal changes in climate parameters, and thus are associated with continuous technogenic pressure. It is confirmed by air temperature data recorded at meteorological stations in Norilsk during the period 1933–2005 and at Dikson (1917–2003); the data do not evidence any regional air temperature warming. However, the permafrost temperature before the construction in the 1940s varied from -0.1 or -0.5°C to -6 or -7°C, and the soil temperature in domestic areas was -3°C (Sheveleva & Khomichevskaya 1967). By the year 2005, it had risen up to -2.5°C. Consequently, great warmed areas appeared and hugh technogenic taliks formed over about 30% of the territory. Thermokarst is indicated as the asphalt breaks up, and due to the increase in the active layer depth, the frost heaving of soils and foundations is widespread in built-up areas.

The temperature regime changes, with subsequent lowering of the bearing capacity of the soils and activation of dangerous cryogenic processes. This has led to a growing number of deformed buildings and constructions. More than 75% of buildings in the permafrost zone of Russia are built on frozen basements, with permafrost supporting the basement. Under the tendency for permafrost degradation in the largest towns of the permafrost zone (Grebenets & Sadovsky 1993, Grebenets 2003), the increase of the soil temperature, often supplemented by ground thaw, consequently lowers the bearing capacity of the frozen foundation. The deepening of seasonal thaw expands the zone of cryogenic weathering of concrete. Acting together, these processes lead to mass destruction of buildings and constructions. Currently, 60% of buildings are deformed in Igarka, Dikson, and Vilyuysk; literally 100% in tribal settlements of Taymyr Autonomous District; and around 40% in Vorkuta. The number of deformed constructions in Norilsk Region of northern Siberia during the last 10 years has markedly exceeded that of the last 50 years. Currently, there are nearly 300 large buildings in towns of the Norilsk Industrial Region that are significantly deformed due to unfavorable permafrost, and geological consequences arose. More than 100 objects were in the state of failure, with 50 of the 9-storey and 5-storey buildings constructed during 1960–1980 recently being deconstructed.

A growing number of building breakdown, constructions, water lines, oil lines, and industries causes increased technogenic pressures on permafrost in urbanized areas, leading to new changes in the permafrost and forming a new geocryological environmental reality. Due to the factors of physical and economical geography, industrial exploration of permafrost is spotty. Permafrost in urbanized areas can be characterized by the altered intensity of cryogenic processes that have taken place in the region, or even a new set of processes. Occurrence, activity, intensity, reversibility, the formation of a paragenic series of geocryological phenomena, together with other characteristics of the cryogenic processes on urbanized areas, significantly differ from that of natural areas or those having no analogues in the natural environment.

Specific naturally-technogenic geocryological complexes form in urbanized areas. Each identity has various permafrost dynamics that differ from that under natural conditions. There were thirteen (13) basic identities marked in the territory of Norilsk Industrial Region (Grebenets 2001), ranging from technogenic badlands (tailing dams, waste and ash disposal areas) where permafrost is disturbed and the natural landscape destroyed, to relatively weakly modified sites in tundra and forest tundra where the active layer deepens due to an increase in thermal conductivity of soils impacted by acid rains and technogenic salinization. Listed below are the natural-technogenic geocryological identities allocated for Yamburg gas-condensate field:

1) sites currently occupied with gas-preparation facilities; having water drains; systems for basement soil cooling; with the geotechnical state and engineering geocryological conditions being stable;

2) urban areas having water drains in operation; regular snow removal; on-ground utilities; maintained with ventilating cellars; with a tendency for aggradation of permafrost and controlled damping of cryogenic processes;

and lacking deformation of buildings or constructions;

3) sites with residential and service buildings built during the 1980–1990s, among which are many that are heat emitting; these are areas with degrading permafrost and multiple deformation of buildings and constructions;

4) sites of the infrastructural objects including rural areas where the objects are being used on disturbed permafrost; having extensive warming and thawing areas; intensive thermokarst and frost heaving; with a number of objects being destroyed or even being in the breakdown state;

5) areas occupied with coarse wastes and where rubbish accumulation takes place; where permafrost warming occurs due to chemical reactions;

6) linear zones along multiple pipelines where the conditions of heat exchange on the surface are significantly modified; with active frost heaving of pipeline supports; thermokarst and thermoerosion development;

7) relatively stable tundra areas of thermokarst, thermoerosion, and gully expansion along heavy vehicle pathways.

Nonstandard permafrost-ecological problems arise under housing compaction or reconstruction of objects in areas of continuous (years to decades) technogenic loading on permafrost basements. For example, in Talnakh in northern Siberia, to provide stable building constructions on the spot where old buildings were located for 25–30 years and then demolished, the pile footing depth needed to be increased by 50 to 75%. Rebuilding the areas of recently deconstructed buildings in Yakuts and Norilsk resulted in tackled the serious problem connected with anthropogenic cryopegs. The aggressive medium actively corroded ferroconcrete piles of the new buildings.

Conclusions

Permafrost dynamics in towns, involving the state, temperature, bearing capacity, seasonal thaw depth, and activity of cryogenic processes is controlled by the following factors: 1) geocryological (features and properties of permafrost before construction); 2) geotechnical (town-planning parameters, technogenic impact type, intensity and effective area); and 3) temporal (duration of influence and climate changes). Factors could often act multi-directionally, at various scales, and asynchronously; this results in spotty pattern of permafrost change in the urbanized areas.

It is suggested that the specificity of changes in geocryological, landscape, geoecological and geotechnical environments should be delineated with the technocryogenesis concept having four basic features. Technocryogenesis is the specific exogenous process taking place in urbanized areas of the cryolithozone (1); occurring at the contact of technogenic loads and the permafrost environment (2); having irreversible character (3); and appearing as specific natural geocryological complexes (4). Regional studies of technocryogenesis revealed its varied influence on permafrost and ecological environments and geotechnical condition.

The study of technocryogenesis accounting for the size of the town system, number of elements involved and duration of interaction with nature, and permafrost stability is thought to present interest. The important issue is to assess technocryogenesis interaction with climate change trends at the regional scale for permafrost areas.

Acknowledgments

This work was funded by the Russian Programme of Scientific Schools Support, grant 4861.2006.5.

References

Grebenets, V.I. 2003. Geocryological-geoecological problems occurring in urbanised territories in Northern Russia and methods for improvement of foundations. *Proceedings of the Eighth International Conference on Permafrost, Zurich, Switzerland, July 21–25, 2003* 1: 303-307.

Grebenets, V.I. & Sadovskii, A.V. 1993. Climate warming vs thermal regime of the northern city basements. *Osnovaniya, fundamenty i mekhanika gruntov* (*Basements, Foundations, and Soil Mechanics)* 5: 27-30.

Grebenets, V.I. 2001. Specific technogenic ecosystems formation in Norilsk Industrial Region. *Proceedings of the Second Russian Conference on Geocryology, Moscow, June 1—3, 2005* 4. Engineering Geocryology: 59—65.

Grebenets, V.I. 1998. Study of technogenic inundation and salinization in Norilsk Industrial Region. *Kriosfera Zemli* (*Earth Cryosphere)* 2 (1): 44-48.

Sheveleva, N.S. & Khomichevskaya, L.S. 1967. *Geocryology of Northern Yenisei Region*. Moscow: Nauka, pp.

A Study of High Arctic Retrogressive Thaw Slump Dynamics, Eureka Sound Lowlands, Ellesmere Island

J.D. Grom
McGill University, Montreal, Canada
W. H. Pollard
McGill University, Montreal, Canada

Abstract

To better understand retrogressive thaw slump dynamics and their potential response to a warming climate, this study investigates the form and process of a thaw slump located in the Eureka area of Ellesmere Island in the Canadian High Arctic and attempts to identify microclimatic variation induced by its morphology. Preliminary analysis indicates that microclimates develop at the ablating ice face and within the mudflow that potentially create a feedback process for headwall retreat. Furthermore, trends in development indicate spatial variation in energy input and morphological influence on the landform.

Keywords: massive ground ice; retrogressive thaw slump; thermokarst.

Introduction

Polar regions are expected to exhibit a strong response to projected warming trends, and a significant concern is the expansion of thermokarst—land surface affected by permafrost degradation—and the resulting terrain instability throughout the Arctic. Retrogressive thaw slumps, a type of erosional backwasting resulting from the exposure of ice-rich permafrost, are a prominent thermokarst feature in arctic landscapes and have a profound potential for landscape alteration (Fig. 1). They consist of three main structural components: 1) a nearly vertical "headwall" made up of permafrost soil; 2) a steeply inclined (20°–80°) "headscarp" of ice-rich sediment acting as a thermal erosion belt; and 3) the slump floor, consisting of a low-angle (1°–10°) mud pool expanding to form a lobate pattern at the base of the slump (Burn & Lewkowicz 1990, de Krom 1990, Lantuit & Pollard 2005). The headwall and headscarp are the most dynamic components of the thaw slump and contribute the thaw material, flow deposits, and water accumulation of the mud pool. The landform often has a characteristic "horse-shoe" or linear shape and typically ranges from tens to hundreds of meters in length and width (Barry 1992, Lantuit & Pollard 2005). Retrogressive thaw slumps are initiated by various activities and are sensitive to climate and morphology, providing for periods of activity and stabilization (Burn & Lewkowicz 1990).

Rates of retreat for active retrogressive thaw slumps are variable and dependent upon climate and morphology, including slope, rate and patterns of erosion, and ground ice distribution and quantity (McRoberts & Morgenstern 1974). Radiation and sensible heat transfer have been identified as the principal energy sources for ice face ablation (Burn & Lewkowicz 1990, Lewkowicz 1986a, b, Robinson 2000); therefore, warm and clear days are the most conducive to retrogressive thaw slump activity and headwall retreat.

In an attempt to further define controlling parameters on retrogressive thaw slump development, this study investigates the potential formation of a microclimate existent within the retrogressive thaw slump as compared to the surrounding area, with increased temperatures developing at the ice face during periods of high incoming shortwave radiation (↓K), creating a positive feedback for melt of the ice face and headwall retreat. This paper also describes the methodology used to quantitatively define associated process and morphology. Field activities, including the collection of microclimate and morphologic data, were performed at a retrogressive thaw slump near Eureka, Ellesmere Island, Nunavut, Canada, over a 17-day period. Data were then analyzed to describe retrogressive thaw slump activity and characterize the development of a microclimate unique to the landform.

Study Area

Field observations were conducted from July 3–22, 2007, in the Eureka Sound Lowlands, located at the Fosheim Peninsula of Ellesmere Island, in the Nunavut Territory of Northern Canada (Fig. 2). Specific data collection focused

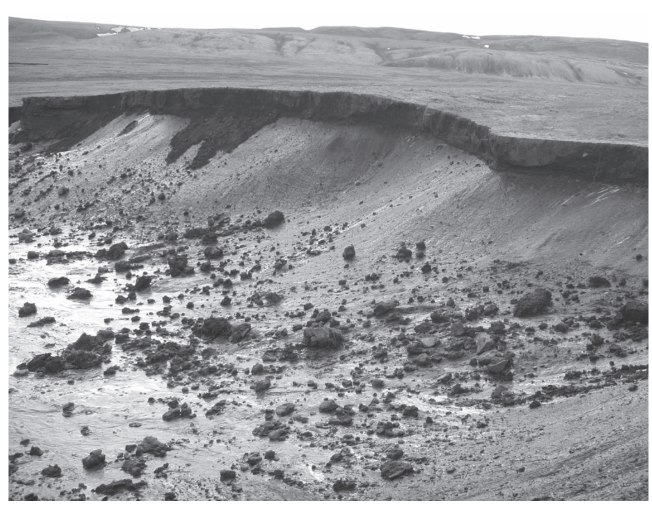

Figure 1. Photograph of retrogressive thaw slump, July 4, 2007.

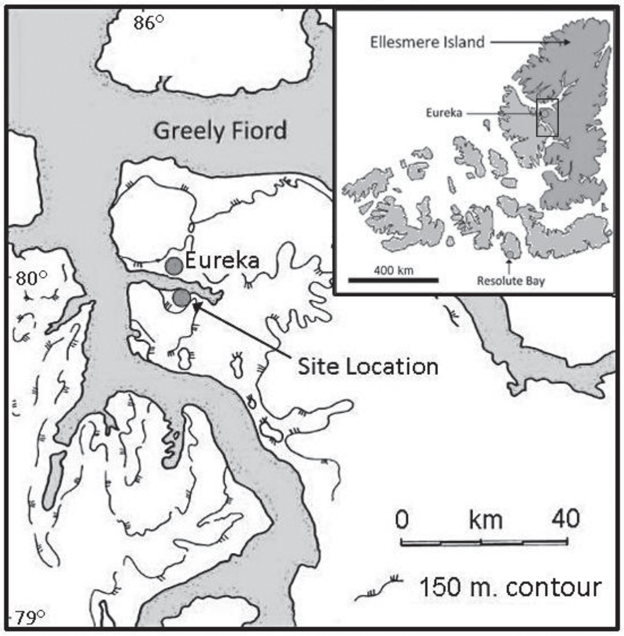

Figure 2. Map of site location and Canadian Archipelago. (150 m contour obtained from Pollard & Bell 1998).

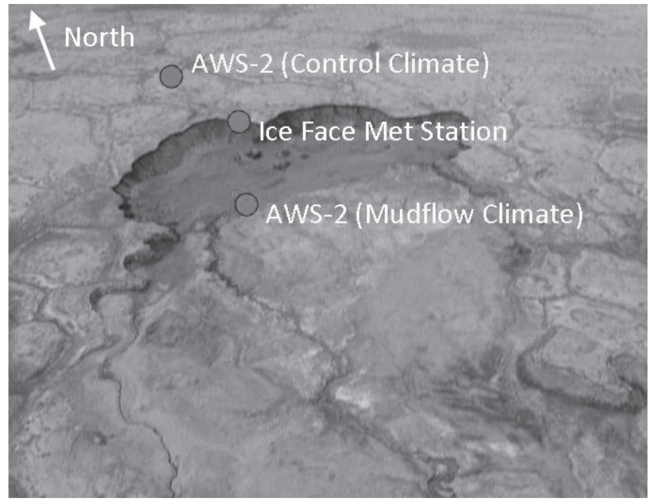

Figure 3. Oblique overhead photograph of retrogressive thaw slump investigated in study, including headwall, mudflow, micrometeorological equipment.

on a southerly-oriented, active, retrogressive thaw slump located at 79°53.782′N, 85°59.357′W, approximately 10 km southeast of Eureka. This region is a polar desert, experiencing an average mean annual air temperature (MAAT) of -19.7°C and an average of 64 mm of precipitation per year, 60% of which is snow (Pollard & Bell 1998, Pollard 2000). Permafrost thickness can exceed depths of 500 m, with active layer depths ranging from 0.15–0.9 m and an extrapolated mean ground surface temperature of -20.8°C (Robinson 1993, Robinson 2000). Regional topography consists of broad, undulating lowlands.

Massive ground ice up to 17 m thick is present throughout the Eureka Sound Lowlands, and as such, substantial thermokarst activity is found along slopes experiencing active erosion and/or former thermokarst events (Robinson 2000). Ice exposures, the majority of which are overlain by marine sediments of varying thickness, are often up to 8 m thick and result in retrogressive thaw slump activity and development. Field studies performed in 1991/1992 at the nearby Hot Weather Creek revealed at least 20 active thaw slumps within an 80 km^2 area (Robinson 2000). Average rates of retreat for the duration of the study ranged from 8–14 m/year for high-angle slumps and 5–9 m/year for low-angle slumps, indicating the importance of morphology in ablation of the ice face. Additionally, several active and inactive retrogressive thaw slumps were observed in the vicinity of the studied thaw slump during the recent site reconnaissance.

Field Methods

Morphology

The outline of the headwall was identified on July 12, 2007, using differential global positioning satellite (DGPS), and aerial photographs were obtained for the site. Headwall retreat was obtained manually by installing a series of 10 coupled stakes along the headwall and measuring the change in distance between the stakes and headwall using a 50-m tape measure. Measurements were recorded to the nearest millimeter; however, accuracy was possible to the nearest centimeter.

Additionally, headwall retreat was obtained for the portion of the headwall situated directly above the ice face meteorological station in order to integrate morphologic and climatic data impacting the landform. The headwall was measured 4 times over the 17-day period, including July 5, July 6, July 12, and July 22. Surface angles were obtained at the beginning of the site investigation using a handheld abney level for the inactive portion of the slump mudflow and the surrounding terrain in addition to 10 points along the ice face corresponding to the aforementioned locations of headwall retreat measurement.

A profile of the ice face was obtained in the vicinity of the ice face meteorological station in order to characterize ground ice and stratigraphy. Additional samples were obtained from the ice face for the laboratory determination of gravimetric moisture-content in order to determine the volumetric latent heat of the ice to be applied in future analysis in conjunction with the ice face meteorological weather station data to gain insight to the energy balance at the ablating ice face.

Microclimate

In order to investigate the potential formation of a microclimate induced by retrogressive thaw slump morphology, two automatic weather stations were strategically placed at the site; one weather station was placed within the slump mudflow (AWS-1), approximately 78 m from the ice face and headwall, and the second was placed atop the slump (AWS-2), approximately 67 m upslope of the headwall, in order to represent the control climate (Fig. 3). It should be noted that AWS-1 could not be placed closer to the headwall as originally intended due to the viscous nature of the mudflow, making it inaccessible to installation and repeated access. The placement of these stations was

Figure 4. Ice face meteorological station.

intended to capture the microclimates within the thaw slump in comparison to the surrounding area, or the control climate, using the data collected from AWS-1 and AWS-2, respectively. Both of the stations were equipped with an SP-LITE silicon pyranometer (measuring ↓K), an HMP45C shielded thermistor and relative humidity probe (measuring ambient temperature and atmospheric relative humidity), an RM Young wind monitor (measuring wind speed and direction), and a barometric pressure sensor. AWS-2 was also equipped with a temperature sensor, measuring subsurface temperatures at depths of 50 and 70 cm below surface grade. It should be noted that the temperature sensors and SP-LITE, which provide the basis of data for this analysis, are considered accurate within ±0.35°C and approximately ±2 W/m^2, respectively. Climate data were scanned at 60-second intervals and compiled to produce 1-hour averages. Data output was stored on automated data loggers (AWS-1 and -2: Campbell Scientific CR10X; ice face station: Campbell Scientific CR10).

Additional instrumentation was suspended approximately 0.5 to 1 m above the ice face in order to provide additional quantification to retrogressive thaw slump microclimate development, in addition to defining the microclimate and energy activity at the ablating ice face (Fig. 4). This station was equipped with an NR–LITE (measuring net radiation), an HMP45C shielded thermistor and relative humidity probe, and a model 014A wind speed sensor.

Results and Discussion

Morphology

The observed retrogressive thaw slump consisted of 2 well-developed units, consisting of a layer of massive ice with an average surface exposure of approximately 4 m, overlain by massive sandy/clayey silt with a depth of 0.8–1.0 m; refer to Figure 1. The massive ice unit consisted of an intersedimental ice unit with exposed ice wedges embedded throughout.

The headwall of the retrogressive thaw slump was horseshoe-shaped and approximately 240 m along its perimeter. Retreat was variable among the points of measurement along the headwall - spaced at 24-m intervals along the perimeter, ranging from 1.5–5.6 m over the 17-day period (Fig. 5). Greater retreat was observed along the central portion of the headwall as opposed to the sidewalls, further contributing to its horseshoe-shaped morphology. This trend reflects the characteristic pinching of the sidewall attributed to lower ice angles, as identified in previous investigations (Barry 1992). However, it should be noted that no significant trend was observed between ice angle and cumulative headwall retreat in this study. Therefore, the spatial variation in headwall potentially reflects differences in ablation of the underlying massive ice in response to differences in energy distribution and morphology, including both depths of the overburden and ice and terrain angles.

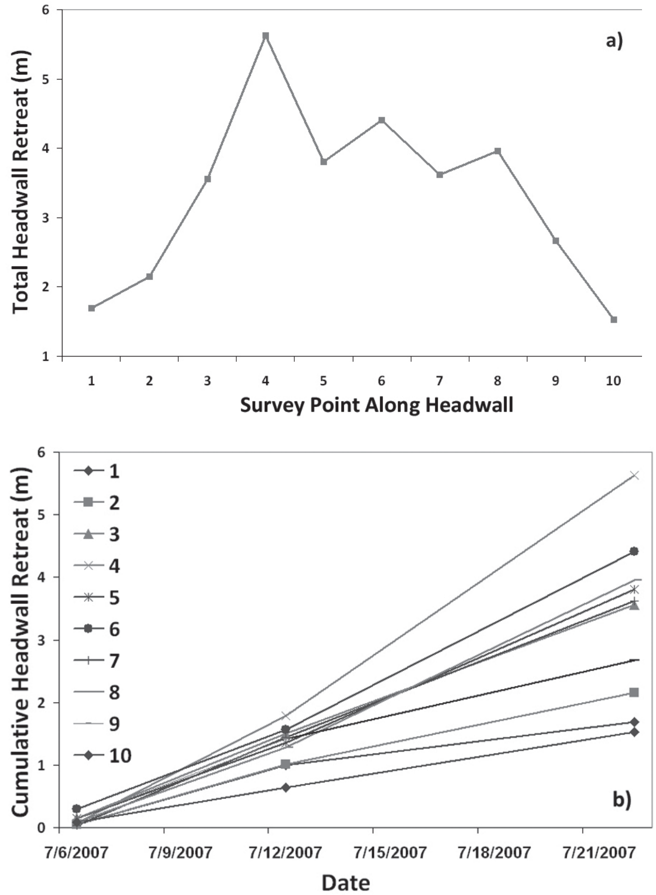

Figure 5. a) Total headwall retreat observed at studied retrogressive thaw slump, with each number representing a survey point spaced in 24-m intervals, moving west to east along the headwall. b) Retreat at all 10 survey points along the headwall over time.

Microclimate

Previous studies have identified solar radiation as providing a primary energy contribution to ablation, and therefore headwall retreat, of retrogressive thaw slumps (Lewkowicz 1985, Pufahl & Morgenstern 1980). It has been noted that net radiation alone can accurately capture approximately 60% of the variation in energy available for ablation (Lewkowicz 1986b) and that ice face orientation, which impacts periods of direct ↓K exposure, influences ablation rates (Lewkowicz

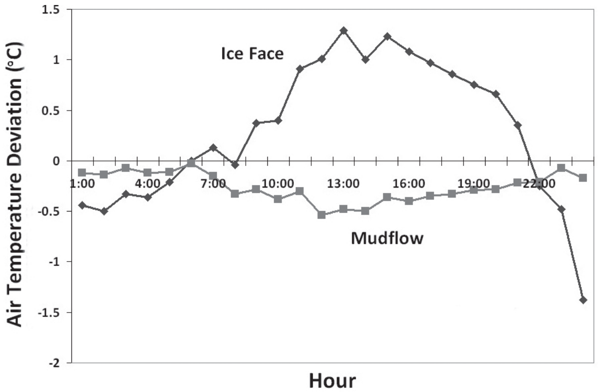

Figure 6. Air temperature deviation from control climate at ice face and within mudflow on a sunny day.

1988). An additional study also observed relatively high near-surface temperatures within the active portion of a retrogressive thaw slump (Mackay 1978). Data provided by the current study indicate that the influence of ↓K, which is inherently related to net radiation, is potentially further exaggerated by a feedback process that induces increased temperatures within the thaw slump, specifically at the ice face, during periods of high ↓K.

Initial analysis suggests the potential creation of unique microclimates existing near the ice face and in the mudflow in comparison with the surrounding climate. Temperatures appear to be heightened at the ice face in response to increased amounts of ↓K, whereas the temperatures are simultaneously slightly dampened at the automatic weather station located within the mudflow, potentially due to increased evaporation. In 119 of the hourly cases in which the ice face air temperature was greater than the control temperature by at least 0.35°C, 117 (98%) were under conditions of ↓K exceeding 250 W/m^2. In addition, of the 28 hourly cases in which mudflow air temperature was at least 0.35°C less than the control temperature, 27 (96%) were accompanied by a ↓K greater than 250 W/m^2.

Figure 6 displays a characteristic response of these spatial temperature differences on July 19, 2007, a relatively sunny day, characterized as having an average daily ↓K exceeding 250 W/m^2. As displayed, temperatures are increased up to 1.3°C at the ice face as compared to the control temperature and are decreased by 0.5°C within the mudflow, with an average increase of 0.29°C at the ice face and an average decrease of 0.26°C within the mudflow for the day. ↓K on July 19, 2007, averaged 315.6 W/m^2 (min 141.2 W/m^2, max 500.6 W/m^2), and the studied portion of the ice face received direct solar radiation from approximately 10:00–20:00, which strongly correlates to the period of observed increase in ice face air temperature. Winds were northerly/northeasterly with an average speed of 3.4 m/s, and air temperatures averaged 12.5°C ± 6.4°C (Fig. 7).

In contrast, the above air temperature deviations are not displayed during periods of low ↓K. Under these conditions, temperature deviations at the ice face and within the mudflow are minor, supporting the hypothesis that ↓K is a controlling factor in microclimate development. These

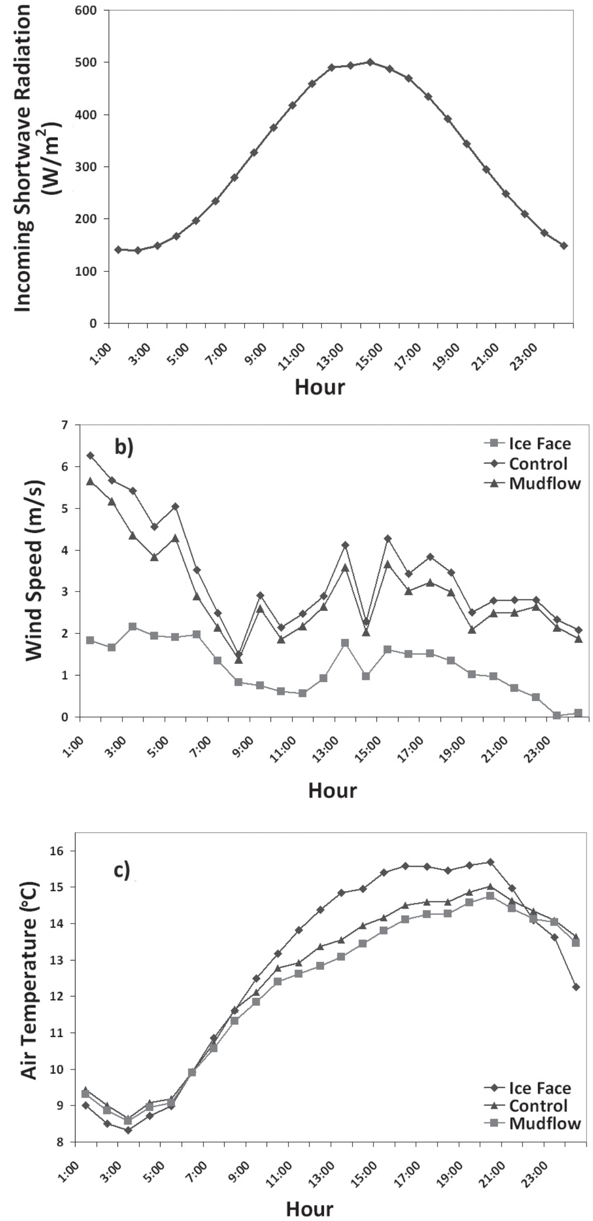

Figure 7. a) ↓K (measured at AWS-2), b) wind speed, and c) air temperature trends for July 19, 2007.

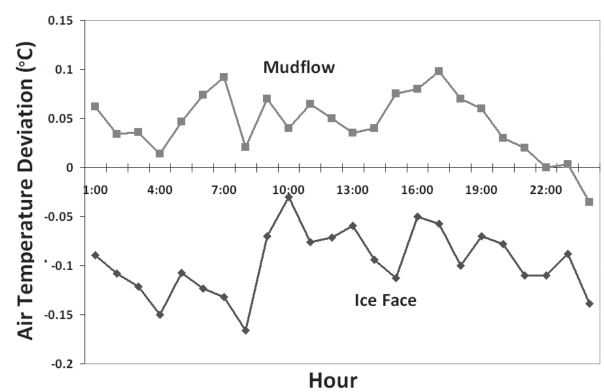

Figure 8. Air temperature deviation from control climate at ice face and within mudflow on a cloudy day.

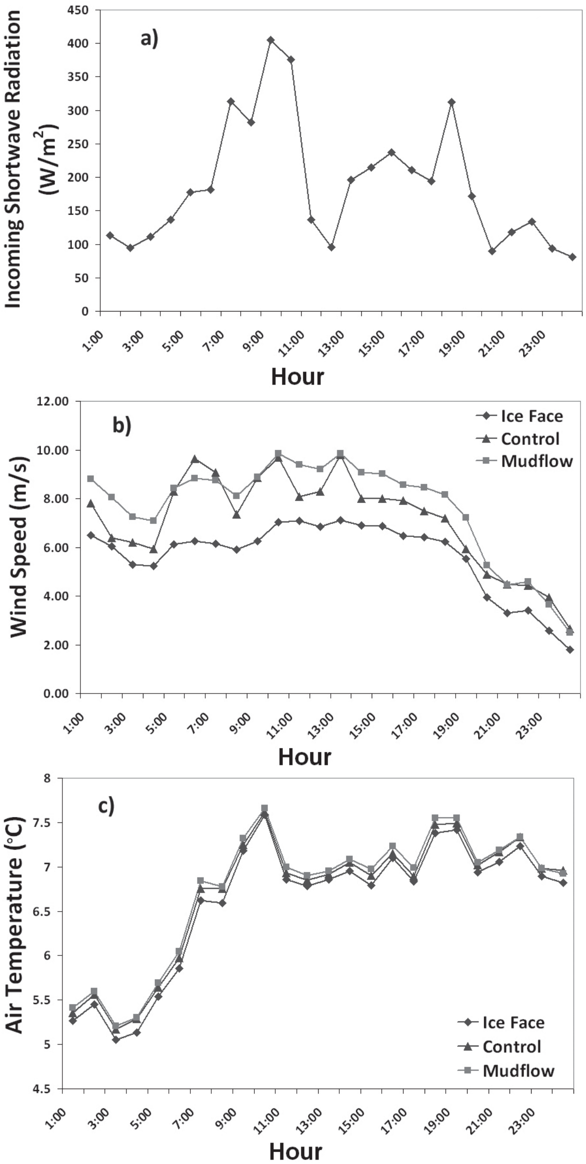

Figure 9. a) ↓K (measured at AWS-2), b) wind speed, and c) air temperature trends for July 7, 2007.

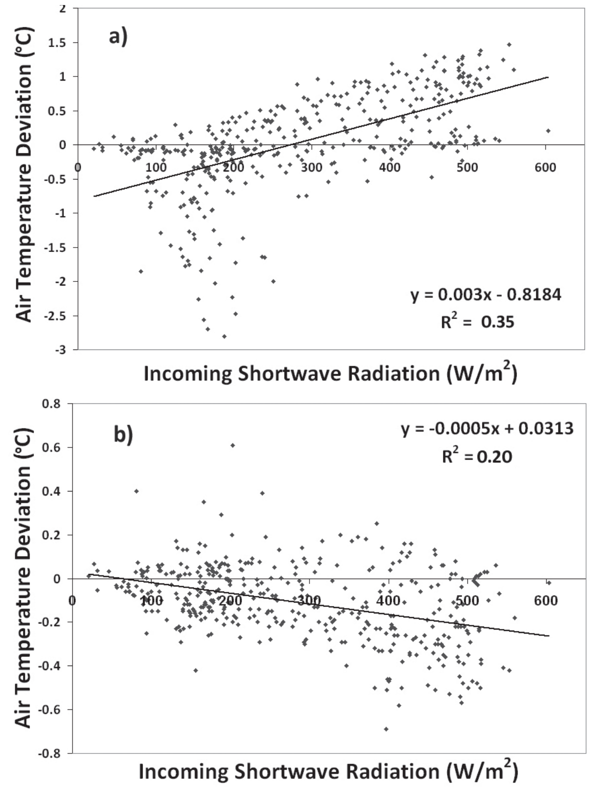

Figure 10. a) Ice face air temperature deviation versus ↓K, and b) mudflow air temperature versus ↓K; July 6–22, 2007.

trends are displayed in Figure 8, which displays temperature deviation trends on July 7, 2007, a relatively cloudy day, characterized by an average ↓K of 186.6 W/m^2. Additionally, southerly winds with an average speed of 7.1 m/s and an average daily air temperature of 6.7°C were observed on this day (Fig. 9). Under these circumstances, average daily air temperature deviations are -0.1°C and 0.0°C for the ice face and mudflow, respectively. It should be noted that trends within this range are considered relatively insignificant due to the aforementioned accuracy of the temperature sensor.

In order to further support the formation of spatial microclimates within the retrogressive thaw slump, a regression analysis was performed on the full dataset of temperature deviations and ↓K (Fig. 10). This analysis reveals significant trends between air temperature deviations from the control temperature under increasing ↓K conditions, identifying an overall positive trend in air temperature difference at the ice face ($p < 0.001$) and a significant but slight decrease in mudflow air temperature ($p < 0.001$). It should be noted that the r^2 values are relatively low for the ice face air temperature ($r^2 = 0.35$) and mudflow ($r^2 = 0.20$); however, this indicates the influence of additional factors in the formation of the observed microclimates and supports the need for additional investigation.

It is suspected that these deviations are the result of retrogressive thaw slump morphology (i.e., ice angle, sediment content, slump shape) and the associated differences in parameters such as albedo and wind speed. This could also be related to spatial differences in ablation rate previously identified, in which microvariations in energy input were identified as the most likely factor contributing to these conditions (Lewkowicz 1985). Additional investigation of available microclimate data is required in order to further define the conditions observed in field data.

It should be noted that climate data were also obtained from the nearby Eureka Weather Station and compared to the data obtained at the site. Previous studies have displayed that temperatures are typically significantly warmer in the Fosheim Peninsula as compared to the nearby Eureka Weather Station (Atkinson 2000). The site control station recorded temperatures in average exceedance of 4°C as compared to measurements reported from Eureka, and measured and reported temperatures rarely coincided with one another (Fig. 11). These differences, in addition to the microscale variations measured at the site, display the need for location-specific on-site weather measurements when investigating process-based dynamics of a landform.

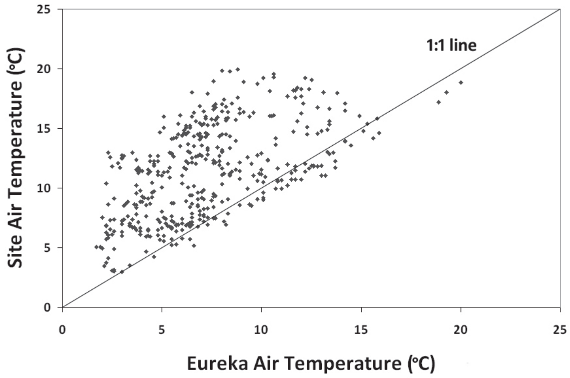

Figure 11. Recorded site air temperature vs. air temperature recorded at the Eureka Weather Station, July 4–22, 2007.

Summary and Conclusions

This study describes the methodology developed to capture and explore the dynamic interaction of climate and morphology in retrogressive thaw slump activity. The 17-day study period represents the most annually active period of ablation and headwall retreat, which was variable along various points of the headwall. These variations have previously been linked to changes in angle of the underlying ice face. However, this study does not support the sole influence of ice angle and indicates that additional investigation addressing the interplay of morphology and surficial energy activity is required.

Additionally, significant temperature variations in microclimates were identified at the site, specifically in the vicinity of the ice face. Preliminary analysis indicates that ↓K influences these conditions and further supports the importance of solar radiation on ablation and retrogressive thaw slump activity, as identified in previous studies. Further definition of these temperature variations is required to understand their formation and impact on retrogressive thaw slump morphology.

Microclimate data derived at the ablating ice face during this study are also being analyzed to further quantify the energy balance. These investigations will provide important information into retrogressive thaw slump process and provide the foundation for understanding the potential responses under altering climate conditions.

Acknowledgments

This research was supported by the Natural Science and Engineering Research Council of Canada (W. Pollard) and ArcticNet (W. Pollard). Exceptional logistic support was provided by Polar Continental Shelf Project (PCSP). J.D. Grom is supported by the Natural Science and Engineering Research Council of Canada (W. Pollard), ArcticNet (W. Pollard), and McGill University. Aerial photographs and DGPS data were generously performed by T. Haltigin, and excellent and much appreciated field assistance was provided by P. Budkewitsch, M. Ecclestone, and T. Haltigin. Dr. I. Strachan also contributed to helpful discussions in developing research methods. This manuscript has been enhanced by the insightful recommendations of three anonymous reviewers.

References

Atkinson, D.E. 2000. Modelling July mean temperatures on Fosheim Peninsula, Ellesmere Island, Nunavut. *Geological Survey of Canada* 529: 99-111.

Barry, P. 1992. *Ground Ice Characteristics in Permafrost on the Fosheim Peninsula, Ellesmere Island, N.W.T.: A Study Utilizing Ground-Probing Radar and Geomorphological Techniques*. M.Sc. thesis, Montreal, Quebec: McGill University, 135 pp.

Burn, C.R. & Lewkowicz, A.G. 1990. Retrogressive thaw slumps. *The Canadian Geographer* 34: 273-276.

de Krom, V. 1990. *A Geomorphic Investigation of Retrogressive Thaw Slumps and Active Layer Slides on Herschel Island, Yukon Territory.* M.Sc. thesis, Montreal, Quebec: McGill University, 157 pp.

Lantuit, H. & Pollard, W.H. 2005. Temporal stereophotogrammetric analysis of retrogressive thaw slumps on Herschel Island, Yukon Territory. *Natural Hazards and Earth System Sciences* 5: 413-423.

Lewkowicz, A.G. 1985. Use of an ablatometer to measure short-term ablation of exposed ground ice. *Canadian Journal of Earth Sciences* 22: 1767-1763.

Lewkowicz, A.G. 1986a. Headwall retreat of ground-ice slumps, Banks Island, Northwest Territories. *Canadian Journal of Earth Sciences* 24: 1077-1085.

Lewkowicz, A.G. 1986b. Rate of short-term ablation of exposed ground ice, Banks Island, Northwest Territories, Canada. *J. of Glaciology* 32: 511-519.

Lewkowicz, A.G. 1988. Ablation of massive ground ice, Mackenzie Delta. *Proceedings of the Fifth International Conference on Permafrost, Trondheim, Norway. August 1988*: 605-610.

Mackay, R.J. 1978. The surface temperature of an ice-rich melting permafrost exposure, Garry Island, Northwest Territories. *Geological Survey of Canada*. 78-1A: 521-522.

McRoberts, E.C. & Morgenstern, N.R. 1974. The stability of thawing slopes. *Canadian Geotechnical J.* 11: 447-269.

Pollard, W.H. 2000. Ground ice aggradation on Fosheim Peninsula, Ellesmere Island, Nunavut. *Geological Survey of Canada* 529: 325-333.

Pollard, W.H. & Bell, T. 1998. Massive ice formation in the Eureka Sound Lowlands: a landscape model. *Proceedings of the Seventh Canadian Permafrost Conference, Yellowknife, NWT, June 1998*: 903-908.

Pufahl, D.E. & Morgenstern, N.R. 1980. The energetics of an ablating headscarp in permafrost. *Canadian Geotechnical Journal* 17: 487-497.

Robinson, S.D. 1993. *Geophysical and Geomorphological Investigations of Massive Ground Ice, Fosheim Peninsula, Ellesmere Island, Northwest Territories.* M.Sc. thesis, Kingston, Ontario: Queen's University, 171 pp.

Robinson, S.D. 2000. Thaw-slump-derived thermokarst near Hot Weather Creek, Ellesmere Island, Nunavut. *Geological Survey of Canada* 529: 335-345.

Distribution of Thermokarst Lakes and Ponds at Three Yedoma Sites in Siberia

Guido Grosse
Geophysical Institute, University of Alaska Fairbanks, USA
Vladimir Romanovsky
Geophysical Institute, University of Alaska Fairbanks, USA
Katey Walter
Institute of Northern Engineering / International Arctic Research Center, University of Alaska Fairbanks, USA
Anne Morgenstern
Alfred Wegener Institute for Polar and Marine Research, Potsdam, Germany
Hugues Lantuit
Alfred Wegener Institute for Polar and Marine Research, Potsdam, Germany
Sergei Zimov
Northeast Science Station, Cherskii, Russia

Abstract

Thermokarst lake formation in ice-rich yedoma deposits in north Siberia has a major impact on regional landscape morphology, hydrology, and biogeochemistry. Detailed assessment of lake distribution characteristics is critical for understanding spatial and temporal lake dynamics and quantifying their impacts. The distribution of thermokarst ponds and lakes at three different sites with ice-rich permafrost (Bykovsky Peninsula, SW Lena Delta, and Cherskii) in northeast Siberia was analysed using high-resolution remote sensing and geographical information system (GIS) tools. Despite similarities in geocryological characteristics, the distribution of thermokarst lakes differs strongly among the study regions and is heavily influenced by the overall hydrological and geomorphologic situation as a result of past lake-landscape dynamics. By comparing our high-resolution water body dataset with existing lake inventories, we find major discrepancies in lake distribution and total coverage. The use of low-resolution lake inventories for upscaling of thermokarst lake-related environmental processes like methane emissions would result in a strong underestimation of the environmental impacts of thermokarst lakes and ponds in Arctic lowlands.

Keywords: lake distribution; remote sensing; Siberia; thermokarst lakes; yedoma.

Introduction

Global lake inventories currently used in Earth system modeling contain only lakes larger than 10 ha (Lehner & Döll 2004, Downing et al. 2006). Most of these lakes are found in the Northern Hemisphere; that is, in permafrost-influenced or formerly glaciated regions. In permafrost regions with unconsolidated sediments most of the lakes are thermokarst lakes or ponds which formed due to the melting of massive or segregated ground ice and subsequent surface settlement. Thermokarst lakes are a major component of vast arctic and subarctic landscapes in Siberia, Alaska, and Canada. Thermokarst lakes and ponds can laterally expand by thermo-erosion and thaw slumping along shores. Usually a positive relation is established between thaw subsidence, horizontal basin extension, and water body growth, resulting in continued thawing of underlying permafrost and thermo-erosion on its margins. This runaway effect is mostly dependent on ground ice content in the underlying permafrost, and it continues going until thawed-out sediments form an insulating layer preventing further thawing and subsidence. Consequently, ice-rich unconsolidated permafrost deposits like those of the widespread Late Pleistocene Yedoma Suite in northeast Siberia (Schirrmeister et al. 2008) are especially vulnerable to thermokarst development initiated by natural or anthropogenic environmental change.

Regional medium-resolution studies aimed at the classification and spatial analysis of thermokarst lakes in Arctic regions were mostly based on Landsat satellite imagery, which has proven valuable for water body detection (e.g., Frazier & Page 2000). Such studies were conducted for the North Alaska Coastal Plain (Sellmann et al. 1975, Frohn et al. 2005, Hinkel et al. 2005), the Siberian Lena Delta (Morgenstern et al. 2008), the Lena-Anabar Lowland (Grosse et al. 2006), and the Tuktoyaktuk Peninsula (Côté & Burn 2002). These and other works reveal a very large number of lakes and ponds between 1–10 ha for most permafrost lowland areas. Based on field experience and spatially limited aerial surveys, it is known that there is very likely an even larger number of thermokarst ponds smaller than 1 ha.

The lacking representation of small lakes and thus bias towards large lakes in existing global lake inventories might result in a strong underestimation of the environmental impact of thermokarst lakes, which would seriously hamper the understanding of their role in the Arctic hydrological cycle and global biogeochemical cycles. First qualitative and quantitative studies on the environmental impact of thermokarst lakes over both geological and historical time frames suggest a potentially large role of such lakes in the

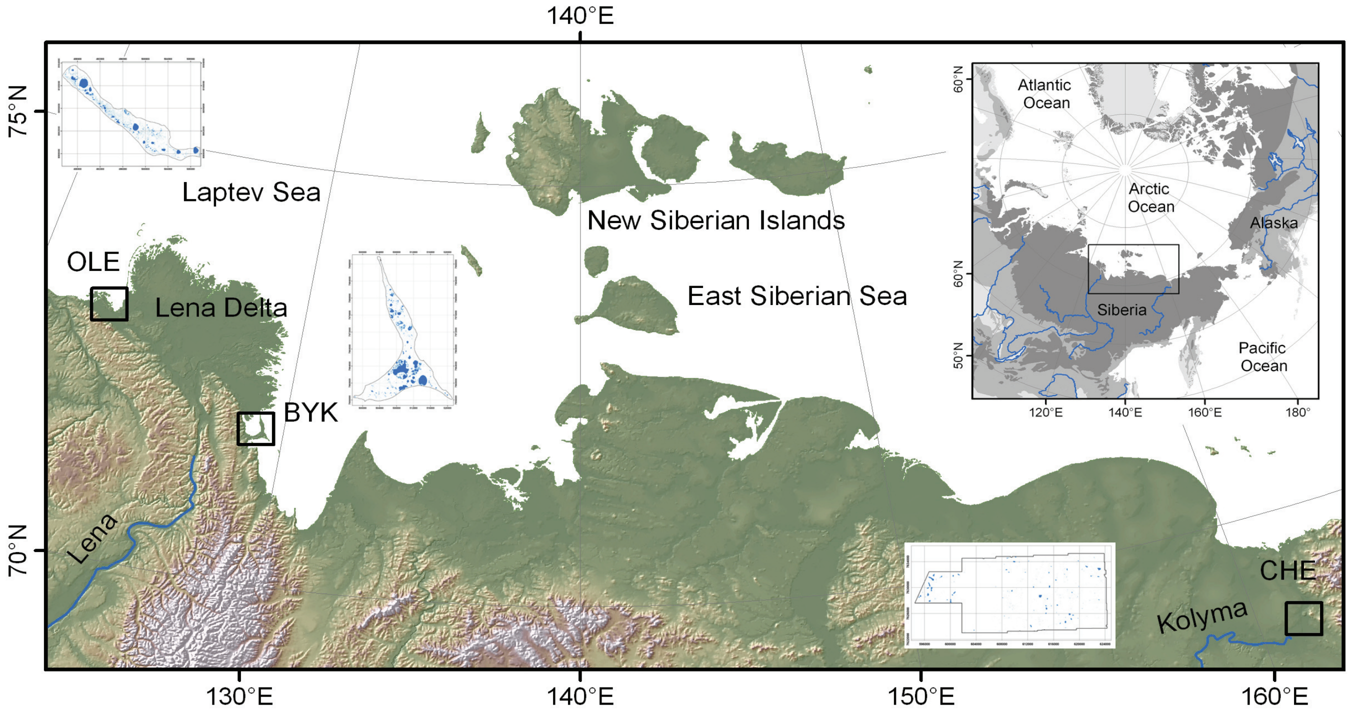

Figure 1. Relief map showing the location of the three study sites: Olenek Channel (OLE), Bykovsky Peninsula (BYK), and Cherskii (CHE) in NE Siberia including maps showing the lake distribution. Small inset in upper right indicates the location of the large map (black rectangle) in Siberia and the distribution of continuous (dark grey) and discontinuous permafrost (medium grey) after Brown et al. (1998).

arctic carbon cycle by unlocking vast amounts of permafrost-stored organic carbon and thus also for global climate dynamics (Zimov et al. 1997, Walter et al. 2006, Walter et al. 2007). Other studies indicate e.g., the impact of arctic wetland and lake distribution on atmospheric circulation patterns (Gutowski et al. 2007). Many studies also show that small water bodies in permafrost lowlands, e.g., polygonal ponds, are an important component for methane emissions from tundra wetlands (e.g., Wagner et al. 2003, Schneider et al. in review). To quantify the environmental impact of such arctic lakes and ponds it is necessary to have detailed information on their distribution and extent.

Several studies suggest a direct connection between thermokarst lake distribution and underlying permafrost characteristics, as well as between lake dynamics and permafrost dynamics. Widespread lake drainage in the discontinuous permafrost zone is related to a beginning disappearance of permafrost due to current climate warming (Yoshikawa & Hinzman 2003, Smith et al. 2005, Riordan et al. 2006). On the contrary, in the continuous permafrost zone an increase in lake area was observed in Western (Smith et al. 2005) and Eastern Siberia (Walter et al. 2006), but not on the Alaskan North Slope (Riordan et al. 2006, Hinkel et al. 2007). Most of these studies are based on the medium-resolution (30–80 m) Landsat satellite data record spanning about 35 years and some additionally involve historical aerial photography. However, although Landsat data may be sufficient to detect complete drainage and drying of some large lakes or the formation of new large lakes, it has serious limitations in detecting changes in lake extent due to thaw slumping and thermo-erosion. A high-resolution dataset of recent lake and pond distribution in combination with historical imagery would form an excellent base for studying change in lake extent and link these changes to permafrost or climate dynamics.

In this study a dataset of recent thermokarst lake and pond distribution on ice-rich yedoma deposits is developed based on high-resolution (1–2.5 m) satellite remote sensing data for three sites in Northeast Siberia and then compared with data from the Global Lake and Wetland Database (GLWD: Lehner & Döll 2004).

Study Region

All three study sites are situated in the continuous permafrost region of northeast Siberia (Fig. 1). The size of the study areas, a set of basic environmental characteristics, and information about the geocryology are provided in Table 1. The Bykovsky Peninsula (BYK) is situated southeast of the Lena River Delta. The peninsula is surrounded on three sides by large bays and the Laptev Sea. It is an erosional remnant of a Late Pleistocene accumulation plain consisting predominantly of silty to sandy ice-rich permafrost deposits of the yedoma (Grosse et al. 2007). Lakes, predominantly of early Holocene thermokarstic origin, are abundant at BYK (Grosse et al. 2005). They are located either on the yedoma uplands or as lake remnants and polygonal ponds in drained lake basins. These basins were formed by large thermokarst lakes during the early Holocene climate warming. They subsequently shrunk or drained after the middle Holocene due to climate deterioration and coastal erosion, leaving behind lake remnants and drained lake basins, which upon freezing

Table 1. General environmental characteristics of the study areas.

Parameter	OLE	BYK	CHE
Location	72.94°N 122.90°E	71.80°N 129.30°E	68.75°N 161.33°E
Study area (ha)	7982	17 009	28 897
Permafrost depth (m)	200–600	500–600	400–500
Active layer depth (m)	0.3–0.6	0.3–0.6	0.3–1.5
Annual ground temperature (20 m depth) (°C)	-9– -11	-9 – -11	-3 – -11
Climate data for closest weather station (Rivas-Martínez 2008):			
Station name	Tiumyati	Bukhta Tiksi	Nizhniye Kresty
Measurement period	1948–60	1984–94	1984–94
Annual air temperature (°C)	-14.5	-13.2	-11.6
Annual precipitation (mm)	206	427	294
Vegetation zone	Tundra	Tundra	Taiga / Tundra
Yedoma thickness (m)	~ 8[d]	< 50[b]	< 40
Gravimetric ice content (%)	88[c]	116[c]	< 80[a]
Ice wedge width / length (m)	3-5 / 9	6 / 40	3 / 40
Organic carbon content (%)	3.0[c]	4.7[c]	~2[a]

[a] Zimov et al. 1997
[b] Grosse et al. 2007
[c] Schirrmeister et al. 2003
[d] Schirrmeister et al. 2008

could support formation of polygonal ponds (Grosse et al. 2007). The land surface at BYK ranges from 0–45 m a.s.l. The study area around Cherskii (CHE) is part of the Kolyma fluvial lowland and located in the surroundings of the Rodinka hill (351 m a.s.l.). The wide, undulating slopes of this hill are mantled by ice-rich deposits of the yedoma stretching down to the banks and flood plain of the Kolyma River.

The study area in the southwest Lena River Delta along the Olenek channel (OLE) is part of an erosional remnant of Late Pleistocene sediments incorporated into the Holocene river delta architecture. It has the form of a peninsula and is bordered by the Laptev Sea and the wide channels of the delta. The permafrost deposits consist of ice-poor fluvial sands (ca. 0–17 m a.s.l.) overlain by yedoma (Schirrmeister et al. 2003) (Table 1). The topography is dominated by a flat plain with some thermo-erosional valleys and thermokarst basins. Water bodies are abundant in sizes ranging from polygonal ponds to large thermokarst lakes.

Remote Sensing Data

Spatially high-resolution recent satellite imagery was acquired from all three study sites to study thermokarst lake distribution and extent (Table 2). All images are from the snow-free early summer period.

For the BYK and the OLE sites two Spot-5 images were georeferenced to topographic maps of scale 1:100,000, for CHE several Ikonos-2 images were ortho-rectified (Table 2). All imagery used in this study is panchromatic and showed excellent contrasts for land-water separation.

Table 2. Satellite imagery used for mapping lake distribution.

Site	Platform	Date	Ground Resolution
BYK	Spot-5	2006-07-09	2.5m
OLE	Spot-5	2006-07-08	2.5m
CHE	Ikonos-2	2002-07-09	1.0m

Table 3. Main parameters of lakes and ponds in the study areas.

Parameter	OLE	BYK	CHE
Number of water bodies N	15,012	13,001	1348
Total water body area A (ha)	1059.6	2622.1	242.3
Limnicity (%)	13.3	15.4	0.8
Largest lake size (ha)	196.19	605.00	16.71
Mean water body size (ha)	0.0706	0.2017	0.1797
Median water body size (ha)	0.0088	0.0075	0.0115
Normalized per 10 000 ha:			
Number of water bodies N	18,808	7644	466
Total water body area A (ha)	1327.6	1541.6	83.8

Methods

A simple density slice classification was applied to the most recent images at each site to distinguish water and land in the panchromatic imagery. A threshold that best separated image pixel values (Digital Numbers, DN) of water from land was chosen. Usually, there is a strong difference in reflectance between water bodies (dark or black, low DN) and bare or vegetated land surfaces (bright, high DN). A visual comparison was conducted to verify the classification. The DN of some lakes was found to be influenced by either very shallow water levels (probably less than 1 m), resulting in higher DN due to reflectance of the lake bottom, or turbid water with high sediment suspension, resulting in higher DN from the sediment load. On some lakes remaining lake ice (highly reflective, very high DN) resulted in misclassification. Additional misclassifications occurred for pixels associated with deep thermo-erosional valleys and steep north-facing cliffs or slopes. In both cases shadows were misclassified as water. These misclassifications were corrected by applying manually generated masks in ArcGIS™ to either exclude pixel (shadows, stream water bodies, man made structures) or to include pixel (lake ice, turbid and shallow water) from the lake dataset. Based on our visual examination and manual correction the resulting datasets can be considered a conservative minimum of standing water bodies in the study areas.

Based on the ground resolution of the available imagery, a minimum of 5 pixels was considered acceptable for successful water body detection. For better comparison between all study areas we therefore only included and analyzed standing water bodies larger than 0.003 ha. Since our classification approach was conservative and aiming at open water surfaces, we assume to have missed especially small ponds overgrown by vegetation in our inventory. At BYK, three thermokarst lagoons were included in the dataset, since they morphologically belong to the peninsula. Eventually, ArcGIS™ was used to analyze the spatial distribution of water bodies in the resulting datasets. The resulting dataset was then compared with the GLWD dataset (Lehner & Doell 2004) for all study areas.

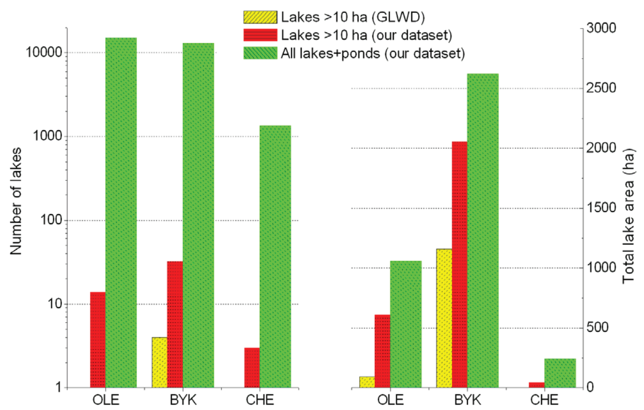

Figure 2. Comparison between GLWD (Lehner & Döll 2004) and high-resolution lake inventory for all study sites.

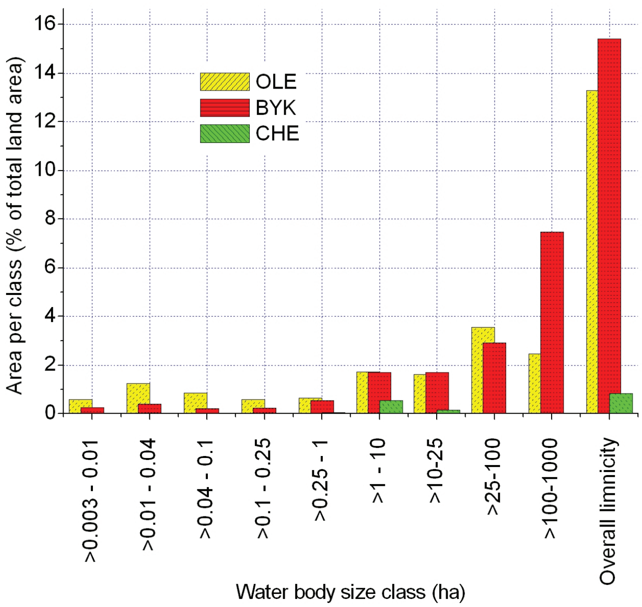

Figure 3. Histogram of total water body surface area for various sizes classes. Last bar shows the overall limnicity in the study areas.

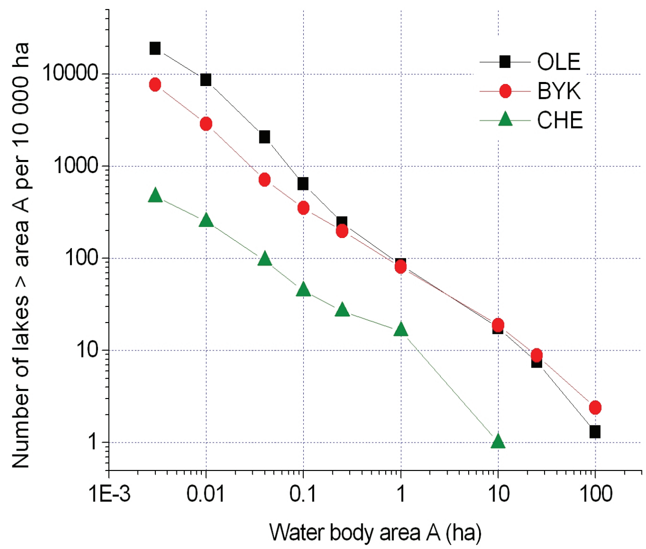

Figure 4. Area-normalized distribution of water bodies per 10,000 ha in the study areas as total number N of water bodies > area A.

Results

Despite similar basic geocryological conditions at all three sites (ice-rich yedoma deposits), the distribution of thermokarst lakes strongly differs among them. A total number of 29,361 lakes >0.003 ha were classified in the study areas (Table 3). The highest lake cover by land area (limnicity) was found at BYK (15.4%), closely followed by OLE (13.3%). Though CHE is the largest study area, its lake portion is lower than at both other sites by more than one order of magnitude (0.8 %).

Of the lakes >10 ha (49 lakes), 14 belong to OLE (609 ha), 32 to BYK (2053 ha), and 3 to CHE (44 ha) (Fig. 2). When comparing the water body distribution in various size classes, strong differences between the three study sites become even more obvious (Fig. 3). The OLE region has more than double the number of small ponds (0.003–0.01 ha) when compared to the BYK region, and almost 50-fold that of the CHE region. This disparity is also expressed in the low mean lake size for OLE. The dominance of lake numbers in the OLE area is true for all size classes except the three largest (>5 ha), where BYK dominates.

Comparing the area-normalized (per 10,000 ha) number N of water bodies larger than area A versus the area A in a logarithmic scaled diagram reveals an almost linear trend for the lake size distribution in all three study sites (Fig. 2). The possibility of describing a lake distribution with such a power law function of type $y=ax^b$ is well known from investigations of other large lake inventories (Lehner & Döll 2004, Downing et al. 2006). It seems to be also applicable to the NE Siberian dataset of comparably small-sized thermokarst lakes investigated in this study. However, obviously for the CHE water bodies the trendline is situated about one order of magnitude below BYK and OLE.

Comparison of lake density between the sites shows a generally highly dense water body population at OLE due to a large amount of small ponds, the clustering of water bodies and thus lake density at BYK, and the overall sparse lake cover at CHE. At CHE, the presence of Rodinka hill in the study area and the lack of lakes on the bedrock hill itself creates an additional cause for the scarcity of lakes. However, it appears not to be the main reason, since flat areas with unconsolidated yedoma farther away from the hill also have much lower lake densities then OLE or BYK. Image analysis and ground truthing reveal that the large lakes in the BYK area usually occur in deep thermokarst basins (subsided up to 40 m below surrounding surface) and often are only the lake remnants of previously partially drained lakes. Many polygonal ponds are situated in these drained basins. Small ponds and medium lakes are found on the yedoma uplands with poor drainage. Yedoma uplands with many thermo-erosional valleys do not contain many lakes. At OLE, most of the numerous, small ponds are found on the yedoma upland. There are only a few large, drained thermokarst basins. Remarkably, the OLE area is relatively homogeneously covered with numerous small ponds, while these small water bodies occur in irregular patterns at BYK and CHE. There are comparably few small thermokarst lakes at CHE. Many of

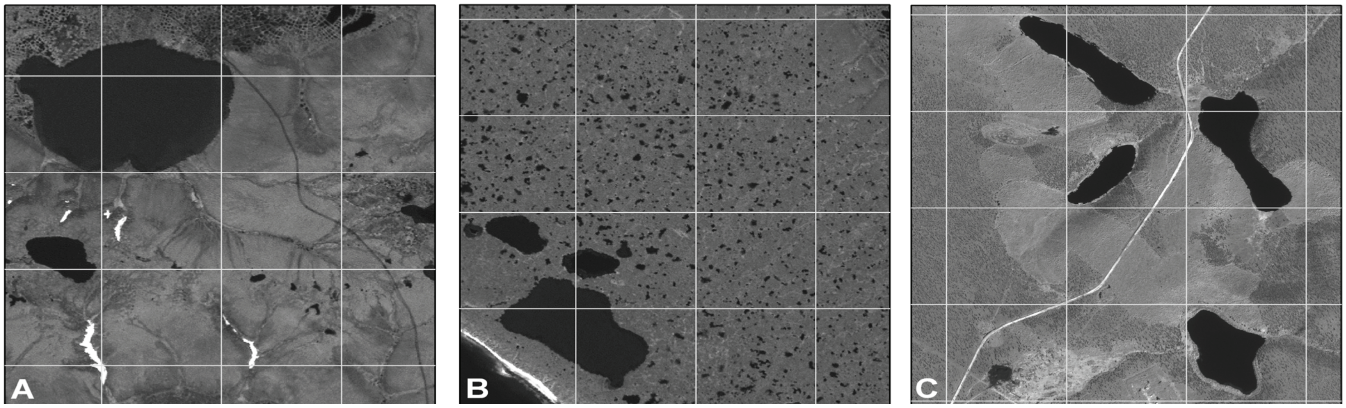

Figure 5. Subsets of study areas displaying characteristic landscape and lake patterns for all three sites. A – BYK; B – OLE; C – CHE. Image grid spacing is 600 m.

these were formed due to human activity in the area around the settlement of Cherskii, adding an artificial component to the natural lake distribution. Similar, at BYK human impact resulted in the drainage of several small lakes along vehicle tracks in the tundra. In contrary to CHE, the overall lake population is very high at BYK and therefore the human influence on the lake distribution characteristics is probably negligible here.

A comparison of our detailed water body dataset with the lakes in the GLWD (Lehner & Döll 2004) reveals large discrepancies in number and area of thermokarst lakes larger than 10 ha (minimum size GLWD) (Fig. 2). As a result, GLWD limnicity at OLE (1.1%), BYK (6.8%), and CHE (0.0%) is significantly lower than in our dataset for the same lake size category (7.6%, 12.1%, and 0.2% respectively). A large percentage of the total water body area (<10 ha) that is important for hydrological and biogeochemical cycles is currently not inventoried and used in environmental modeling (not inventoried water body area per 10 000 ha land area at OLE: 42.7%, BYK: 21.6%, and CHE: 82.2%).

Discussion

Thermokarst lake distribution in our study areas seems to be strongly connected to hydrological and geomorpho-logical factors rather than to geocryology alone. At BYK, a strong thermokarst relief developed during the Late Pleistocene-Holocene transition and many first-generation thermokarst basins and thermo-erosional valleys were formed (Fig. 5A). A large number of second-generation lakes appeared during the Holocene in drained basins. OLE is dominated by a flat yedoma surface with only some thermokarst basins and valleys. Also, yedoma thickness is considerably less than at both other sites with possibly impacts on lake expansion dynamics. The poorly drained upland plain is densely and relatively homogeneously packed with a large number of first generation lakes (Fig. 5B). At CHE (Fig. 5C) the yedoma is mantling the rolling slopes around Rodinka Hill. Comparably few small water bodies occur, but proportionally many medium-sized first-generation lakes. Compared to both other study sites, lakes are less abundant, most likely due to better overall drainage. However, there are plain regions east of Rodinka Hill with the same deposits but still very low lake density.

Vegetation either growing or floating in the lake can pose a challenge for any water-land classification method, be it manual or fully automated. Careful image interpretation, field experience, and in some cases ground truthing are required. We estimate the effect of unclassified water due to vegetation on the order of <2% of the overall water body area for some lakes. Seasonal hydroclimatology can also have an effect on lake surface area especially for lakes with shallow basin topography. While many of the ponds certainly fall into this category, many of the typical thermokarst lakes in ice-rich permafrost do not. These usually have steep banks and a more pronounced basin morphology resulting predominantly in vertical lake level changes rather than lateral lake area changes during seasonal water level variations. Many of the larger lake basins have subsided tens of meters below the surrounding land surface and are surrounded by steep banks. Lake extent changes for such thermokarst lakes are more related to thermoerosion, thaw slumping, or drainage than just seasonal water level changes.

A lake change study for the study areas is still in progress. The time series of lake extent for the BYK site will range for the period from 1951–2008, providing an observational high-resolution dataset for 57 years. For OLE and CHE the time series span a period of 42 and 37 years, respectively.

Conclusions

High-resolution satellite imagery provides the opportunity to characterize the distribution of thermokarst lakes on yedoma deposits in high detail. Spatial analysis of thermokarst features plays an important role in understanding thermokarst dynamics in northern regions and impacts on the global hydrological and biogeochemical cycles. It was shown that thermokarst lake distributions at three yedoma sites differ greatly. Lake distribution is distinguishable for areas with first and second generation lakes. Our comparison with the GLWD lake dataset demonstrates the necessity to quantify northern lakes; that is, thermokarst lakes, in a much higher detail than currently available. Any quantification and upscaling of thermokarst lake-related parameters like methane emission might be biased due to the exclusion of a large number of small lakes and ponds not represented in current global databases. This highlights the need for more intense research on thermokarst distribution and lake dynamics.

Acknowledgments

Grosse and Walter were partially funded by University of Alaska IPY fellowships. Spot imagery for OLE and BYK was provided through the OASIS program. Ikonos imagery for CHE was provided through the NSF AON project.

References

Brown, J., Ferrians, O.J., Jr., Heginbottom, J.A. & Melnikov, E. 1998. Circum-Arctic Map of Permafrost and Ground-Ice Conditions. In: M. Parsons & T. Zhang (eds.), International Permafrost Association Standing Committee on Data Information and Communication (comp.). 2003. *Circumpolar Active-Layer Permafrost System, Version 2.0.* Boulder, CO: National Snow and Ice Data Center/World Data Center for Glaciology. CD-ROM.

Côté, M.M. & Burn, C.R. 2002. The oriented lakes of Tuktoyaktuk Peninsula, Western Arctic Coast, Canada: A GIS-based analysis. *Permafrost and Periglacial Processes* 13: 61–70.

Downing, J.A., Prairie, Y.T, Cole, J.J., Duarte, C.M., Tranvik, L.J., Striegl, R.G., McDowell, W.H., Kortelainen, P., Caraco, N.F., Melack, J.M. & Middelburg, J.J. 2006. The global abundance and size distribution of lakes, ponds, and impoundments. *Limnology and Oceanography* 51(5): 2388–2397.

Frazier, P.S. & Page, K.J. 2000. Water Body Detection and Delineation with Landsat TM Data. *Photogrammetric Engineering & Remote Sensing* 66(12): 1461-1467.

Frohn, R.C., Hinkel, K.M. & Eisner, W.R. 2005. Satellite remote sensing classification of thaw lakes and drained thaw lake basins on the North Slope of Alaska. *Remote Sensing of Environment* 97: 116-126.

Grosse, G., Schirrmeister, L., Kunitsky, V.V. & Hubberten, H.-W. 2005. The use of CORONA images in Remote Sensing of periglacial geomorphology: An illustration from the NE Siberian coast. *Permafrost & Periglacial Processes* 16: 163-172.

Grosse, G., Schirrmeister, L., Malthus, T.J. 2006a. Application of Landsat-7 satellite data and a DEM for the quantification of thermokarst-affected terrain types in the periglacial Lena-Anabar coastal lowland, *Polar Research* 25(1): 51-67.

Grosse, G., Schirrmeister, L., Siegert, Ch., Kunitsky, V.V., Slagoda, E.A., Andreev, A.A. & Dereviagyn, A.Y. 2007. Geological and geomorphological evolution of a sedimentary periglacial landscape in Northeast Siberia during the Late Quaternary, *Geomorphology* 86(1-2): 25-51.

Gutowski, W.J., Wei, H., Vörösmarty, C.J. & Fekete, B.M. 2007. Influence of Arctic Wetlands on Arctic Atmospheric Circulation. *Journal of Climate* 20: 4243–4254.

Hinkel, K.M., Frohn, R.C., Nelson, F.E., Eisner, W.R. & Beck, R.A. 2005. Morphometric and Spatial analysis of thaw lakes and drained thaw lake basins in the western arctic coastal plain, Alaska. *Permafrost & Periglacial Processes* 16: 327-41.

Hinkel, K.M., Jones, B.M., Eisner, W.R., Cuomo, C.J., Beck, R.A. & Frohn, R. 2007. Methods to assess natural and anthropogenic thaw lake drainage on the western arctic coastal plain of northern Alaska. *Journal of Geophysical Research* 112: F02S16.

Lehner, B. & Döll, P. 2004. Development and validation of a global database of lakes, reservoirs and wetlands. *Journal of Hydrology* 296: 1–22.

Morgenstern, A., Grosse, G. & Schirrmeister, L. 2008. Genetical, Morphological, and Statistical Classification of Lakes in the Permafrost-dominated Lena Delta. *Proceedings of the Ninth International Conference on Permafrost, Fairbanks, Alaska, June 29–July 3, 2008* (this proceedings).

Riordan, B., Verbyla, D. & McGuire, A.D. 2006. Shrinking ponds in subarctic Alaska based on 1950–2002 remotely sensed images. *Journal of Geophysical Research* 111: G04002.

Rivas-Martínez, S. 2008. Worldwide Bioclimatic Classification System. Phytosociological Research Center, Spain. Online database, http://www.globalbioclimatics.org

Schirrmeister, L., Kunitsky, V.V., Grosse, G., Kuznetsova, T., Meyer, H., Derevyagin, A., Wetterich, S. & Siegert, Ch. 2008. The Yedoma Suite of the northeastern Siberian shelf region – characteristics and concept of formation. *Proceedings of the Ninth International Conference on Permafrost, Fairbanks, Alaska, June 29–July 3, 2008* (this proceedings).

Schirrmeister, L., Kunitsky, V.V., Grosse, G., Schwamborn, G., Andreev, A.A., Meyer, H., Kuznetsova, T., Bobrov, A. & Oezen, D. 2003. Late Quaternary history of the accumulation plain north of the Chekanovsky Ridge (Lena Delta, Russia) - a multidisciplinary approach. *Polar Geography* 27: 277-319.

Schneider, J., Grosse, G. & Wagner, D. (in review). Land cover classification of tundra environments in the arctic Lena Delta based on Landsat 7 ETM+ data and its application for upscaling of methane emissions. *Remote Sensing of Environment.*

Sellmann, P.V., Brown, J., Lewellen, R.I., McKim, H. & Merry, C. 1975. *The Classification and Geomorphic Implications of Thaw Lakes on the Arctic Coastal Plain, Alaska.* United States Army, CRREL Research Report 344, 21 pp.

Smith, L.C., Sheng, Y., MacDonald, G.M. & Hinzman, L. D. 2005. Disappearing Arctic Lakes. *Science* 308: 1429.

Wagner, D., Kobabe, S., Pfeiffer, E.-M. & Hubberten, H.-W. 2003. Microbial controls on methane fluxes from a polygonal tundra of the Lena Delta, Siberia. *Permafrost and Periglacial Processes* 14: 173-185.

Walter, K.M., Edwards, M.E., Grosse, G., Zimov, S.A. & Chapin, F.S., III. 2007. Thermokarst lakes as a source of atmospheric CH4 during the last deglaciation. *Science* 318: 633-636.

Walter, K.M., Zimov, S.A., Chanton, J.P., Verbyla, D. & Chapin, F.S., III. 2006. Methane bubbling from Siberian thaw lakes as a positive feedback to climate warming. *Nature* 443: 71-75.

Yoshikawa, K. & Hinzman, L.D. 2003. Shrinking thermokarst ponds and groundwater dynamics in discontinuous permafrost near Council, Alaska. *Permafrost & Periglacial Processes* 14: 151-160.

Zimov, S.A., Voropaev, Y.V., Semiletov, I.P., Davidov, S.P., Prosiannikov, S.F., Chapin, F.S., III, Chapin, M.C., Trumbore, S. & Tyler, S. 1997. North Siberian lakes: a methane source fueled by Pleistocene carbon. *Science* 277: 800-802.

The Cooling Effect of Coarse Blocks Revisited: A Modeling Study of a Purely Conductive Mechanism

Stephan Gruber, Martin Hoelzle

Glaciology, Geomorphodynamics and Geochronology, Geography Department, University of Zurich, Switzerland

Abstract

Coarse blocks are a widespread ground cover in cold mountain areas. They have been recognized to exert a cooling influence on subsurface temperatures in comparison with other types of surface material and are employed in man-made structures for ground cooling and permafrost protection. The contrast in heat transfer between the atmosphere and the ground caused by thermally driven convection in winter and stable stratification of interstitial air during summer is usually invoked to explain this "thermal diode" effect. Based on measurements and model calculations, we propose an additional cooling mechanism, which is independent of convection, and solely functions based on the interplay of a winter snow cover and a layer of coarse blocks with low thermal conductivity. The thermal conductivity of a block layer with a porosity of 0.4 is reduced by about an order of magnitude compared to solid rock. We use a simple and purely conductive model experiment to demonstrate that low-conductivity layers reduce the temperature below the winter snow cover as well as mean annual ground temperatures by comparison with other ground materials. Coarse block layers reduce the warming effect of the snow cover and can result in cooling of blocky surfaces in comparison with surrounding areas in the order of one or several degrees. The characteristics of this mechanism correspond to existing measurements.

Keywords: coarse blocks; heat transfer; mountain permafrost; rock glacier; snow cover; thermal offset.

Introduction

Coarse blocks are a common surface cover in many cold and temperate mountain ranges. They have a cooling influence on ground temperatures compared with fine-grained soil or bedrock in otherwise similar settings (cf. Haeberli 1973, Harris 1996, Gorbunov et al. 2004, Juliussen & Humlum 2008). This cooling effect makes blocky substrates interesting for construction in cold regions (e.g., Goering & Kumar 1996, Guodong et al. 2007) and it is a significant factor influencing the distribution and characteristics of permafrost (Haeberli 1975). Therefore, the understanding and quantification of this cooling effect is important for spatial modeling of permafrost, estimation of its characteristics, and assessment of its temporal evolution.

Measurements in coarse blocky substrate as well as their interpretation are faced with a number of difficulties. To begin with, it is difficult to define the surface of a blocky substrate. Point measurements are bound to either the interstitial air or large clasts and integral macroscopic properties of the blocky material, such as temperature or albedo, are difficult to determine. Similarly, on a macroscopic scale, snow is partly deposited in a volume rather than on a discrete surface because the geometric surface roughness and the depth of voids can have the same order of magnitude as snow thickness itself. Despite these difficulties, a number of processes that may be responsible for the cooling effect of coarse blocks have been proposed and analyzed (e.g., Hanson & Hoelzle 2004, Juliussen & Humlum 2008, see Herz 2006 for a comprehensive review).

These processes are: (a) free convection; (b) forced convection; (c) chimney effect; (d) evaporation/sublimation/ice melt; (e) snow deposition deep into the active layer; and (f) protruding blocks reducing the insulating effect of the snow cover. While all of these processes are plausible, little is known about their relative importance and about the dependence of this importance on environmental conditions. However, understanding the importance of each process is vital to further progress.

One way to achieve this is the joint analysis of model results and measured data. The deviation between model and measurements is bound to contain (among other errors) the error produced by not including an important process in the model. Using such experiments, we were surprised to find that the thermal conductivity of the near-surface material decisively controls ground temperatures below the snow cover. For example, the depression of winter temperatures measured on coarse block fields (cf. BTS on coarse blocks, Haeberli 1973, 1975) in the Murtèl/Corvatsch area (Fig. 1) could be reproduced with two models (TEBAL, Gruber 2005; SNOWPACK, Bartelt & Lehning 2002) that do not include the process of air movement in blocks (cf. Frey 2007). This suggests that at this site, either convection is of secondary importance after an effect related to thermal conductivity, or, that errors in both models resulted in temperature depressions similar to those measured.

In this paper we explore and describe this combined effect of near-surface thermal conductivity and snow pack using a simplified model. While subject to strong generalization with respect to the measured situation, the simple model used here allows to isolate and properly demonstrate the relevant process in a framework that is easily traceable. The cooling mechanism, which we propose, does not contradict existing and well-established research on convective heat transport in coarse blocks (e.g., Goering & Kumar 1996, Guodong et al. 2007). Instead, it offers an explanation of measured cooling where snow cover is thick and signs of significant convection are absent.

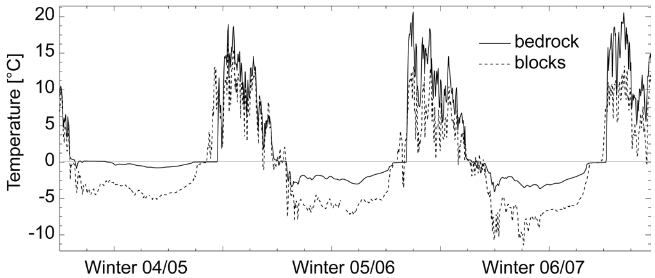

Figure 1. Near-surface temperatures at the rock glacier Murtèl. The solid line shows average daily temperatures 10 cm deep in bedrock adjacent to the rock glacier front. The dashed line shows daily temperature measurements about 50 cm deep within the blocky surface of the rock glacier. These measurements were taken around midnight and therefore have a cold bias during the snow-free time when significant diurnal amplitudes exist.

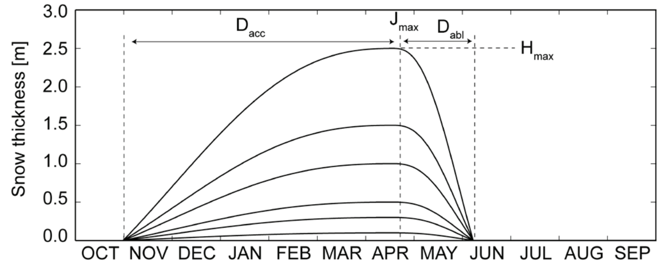

Figure 2. Synthetic snow cover evolution using H_{max} of 2.5, 1.5, 1.0, 0.5, 0.3, and 0.1 m.

Model Experiment with Synthetic Data

Based on a model experiment, we intend to illustrate that a lower thermal conductivity of near-surface material causes lower temperatures below the winter snow cover and that this also affects mean temperatures at greater depth. The model is reduced to only conductive components and effects of, e.g., water percolation or phase change are neglected. That way, this mechanism can be studied in isolation from other effects.

Model description

The model contains a finite-difference Crank-Nicolson solution of the heat conduction equation with no treatment of phase change or advective heat transport. The snow pack and the uppermost 5 m of the ground are discretized with a spacing of 0.1 m. Below, the interval gradually increases down to 15 m. The snow cover is added and depleted in steps of 0.1 m. Available model parameters are: maximum snow cover thickness (H_{max}), duration of the accumulation (D_{acc}) and ablation (D_{abl}) periods, date of maximum snow cover thickness (J_{max}), phase lag of temperature cycle (L), mean surface temperature (M), surface temperature amplitude (A), and the thickness of the block layer (B).

Equation (1) describes the temporal evolution of the snow cover thickness H (Fig. 2). The parameter Δt ranges from 0 to 1 and describes the relative distance to J_{max}, where $\Delta t=0$ at the date of J_{max} and $\Delta t=1$ at the dates of D_{acc}.and D_{abl}.

$$H = H_{\max} \cdot \left(1 - \left(\frac{e^{-\Delta t^{2.5}} - 1}{e - 1}\right)\right) \quad (1)$$

The influence of the snow cover on ground temperatures in nature has three main causes: (a) thermal insulation; (b) reduction in albedo; and (c) advection of latent heat because melt energy is required to remove the snow. In this model, only (a) is considered because the effect of thermal insulation is of interest here.

Ground properties

The snow cover has a uniform density of 280 kg m^{-3}, a thermal conductivity of $k_S = 0.13$ W m^{-1} K^{-1}, and a volumetric heat capacity of $c_S = 5.4\times10^5$. The thermal conductivity of the ground is $k_G = 2.5$ W m^{-1} K^{-1} and the volumetric heat capacities of the ground and block layers are $c_G = 1.6\times10^6$ J m^{-3} K^{-1} and $c_B = 0.8\times10^6$ J m^{-3} K^{-1}. This is based on typical rock thermo-physical properties (Cermák & Rybach 1982) and a porosity of the block layer, which is assumed to be 0.4–0.5. For the block layer, different thermal conductivities k_B are considered between that of pure rock (2.5 W m^{-1} K^{-1}) and a rather low estimate (0.2 W m^{-1} K^{-1}). The low values of thermal conductivity for the block layer are in accordance with values in the range of 0.3 W m^{-1} K^{-1} published for dry sand and for theoretical values when calculating a mixture of rock and air using the geometric mean that usually approximates random aggregates rather well.

Boundary conditions

A harmonic temperature boundary condition (Dirichlet) representing seasonal variation drives the heat conduction scheme at its upper boundary for the duration of several hundred years. This condition ($T_{surface}$) is prescibed at the snow surface during winter and at the ground surface during summer. It is described by Equation (2), where φ is the duration of one seasonal cycle (one year). Similar to conditions at Murtèl/Corvatsch, we assume M = -2.5°C, A = 10°C, L = 45, J_{max} = 105, D_{abl} = 50, D_{acc} = 170, where $D_{abl/acc}$, J and L are given in days and days of the year, respectively.

$$T_{surface} = \sin\left(-(t+L)\frac{2\pi}{\varphi}\right) \cdot A \cdot M \quad (2)$$

Results

The insulating influence of the winter snow cover increases with thicker snow cover (Fig. 3). The temperature T_0 refers to the temperature at the ground surface. Changing the thermal conductivity of the block layer modifies the warming influence of the snow cover (Fig. 4A) and, in accordance with observations (Fig. 1), lower temperatures are modeled under the snow when using lower thermal conductivities of the near-surface, which are characteristic of the block layer. During winter, the heat conduction through the snow pack is very small and, as a consequence, the heat conduction from deeper ground layers

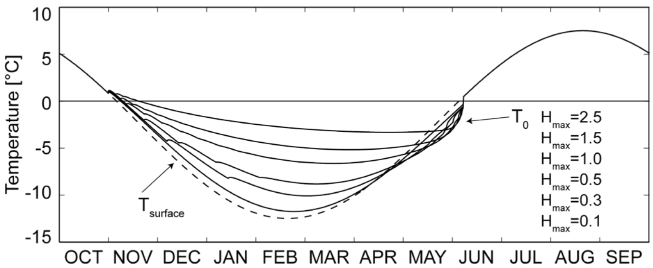

Figure 3. Temperature evolution at the ground surface during one year and for diverse snow cover conditions defined by H_{max}. All cases have a thickness of the block layer B = 3 m and a thermal conductivity of the block layer k_B = 0.2 W m^{-1} K^{-1}. The dashed line represents the prescribed surface temperature $T_{surface}$. In the cooling phase, slight kinks are visible in the temperature curve. These are unimportant artifacts from the simple modeling scheme in which discrete elements of 0.1 m are added or removed as the snow pack evolves.

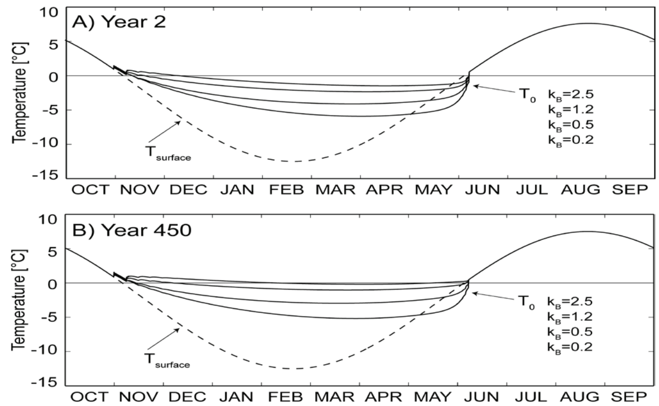

Figure 4. Temperature evolution at the ground surface during two different model years for a maximum snow thickness H_{max} = 1.5 m and a thickness of the blocky layer of B = 3 m. Different curves refer to different thermal conductivities of the block layer k_B.

dominates the temperatures at the snow/ground interface. The BTS method (Haeberli 1973) exploits this effect. If the thermal conductivity of the near-surface ground layer is significantly lower, then the relative importance of heat transfer through the snow increases and temperature at the snow/ground interface will respond more to atmospheric forcing. This is also visible in Fig. 1, where both time series contain similar temperature fluctuations in winter and where these fluctuations are more pronounced in the blocks.

It is now important to know whether this effect only results in lower temperatures under the snow cover, or, whether it also influences mean ground temperatures. In Fig. 4B we can see that over the course of about 450 modeled years, all temperatures have warmed with respect to Figure 4A, indicating exactly this effect over the longer term. This is also visible in the transient response of temperatures at 10 m depth (Fig. 5). After initialization with a temperature of M = −2.5°C and constant boundary conditions having the same mean, temperatures equilibrate at much higher levels due to the insulating effect of the winter snow. This insulating effect is modulated by the thermal conductivity of the blocky layer. These results can be explained as follows: The mean annual ground temperature (at some shallow depth) in first approximation contains a weighted average of surface temperatures. The weight and relative importance of winter temperatures in this average is reduced by the insulating effect of the snow cover (cf. Zhang et al. 2001) that impedes the heat transfer between the (snow) surface and the ground. Where the thermal conductivity of the near surface is low, the heat transfer in snow-free conditions is already slow. As a consequence, the contrast between summer and winter conditions is smaller than for situations with high thermal conductivity of the subsurface. The relative cooling effect of blocky material (compared to many other surfaces) is essentially an effect of reduced warming. This effect is a thermal filter with an effectiveness that is dependent on the thermal contrast between summer and winter conditions. A block layer reduces the overall thermal conductivity of the ground-atmosphere interface and thus reduces the contrast between summer and winter.

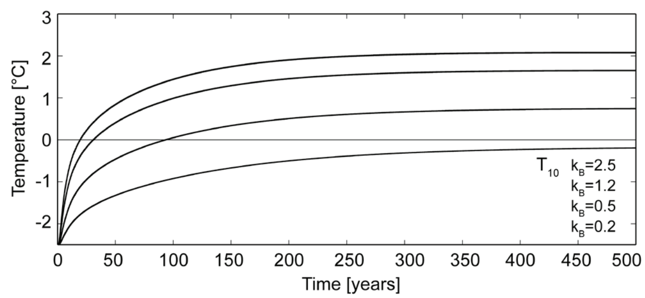

Figure 5. Temperature evolution at a depth of 10 m below the ground surface (T_{10}) during 500 model years for a maximum snow thickness H_{max} = 1.5 m and a thickness of the blocky layer of B = 3 m. Different curves refer to different thermal conductivities of the block layer k_B.

Discussion

This experiment illustrates that the temperature below the winter snow cover as well as mean annual ground temperatures at greater depth can be significantly reduced solely based on the low thermal conductivity of blocky material. The use of a one-dimensional scheme together with macroscopic properties of block layers is a challenging concept because the size of individual clasts can exceed the vertical discretization interval by far. Nevertheless, as long as the majority of clasts do not exceed the thickness of the block layer, this approximation should produce acceptable results, because the overall conductive heat transfer is impeded by the small surface of the contacts between individual pieces of rock. The comparison of modeling results with measurements, however, has to employ either spatial averaging or deeper measurements in order to average lateral variability (cf. Frey 2007, Hoelzle & Gruber 2008). Using the geometric average as an approximate mixing model (Clauser & Huenges 1995), the thermal conductivities of coarse blocks (cf. Binxiang et al. 2004) and sand should be the same because both materials have similar constituents and a similar porosity. This is only true for completely dry material because sand or other soil material usually holds significant amounts of water due to capillary forces in the more abundant small pores. This likely

Table 1. Example of the net effect of diverse near-surface layers.

Block layer thermal conductivity	Heat flux at lower boundary condition 0.0 W m^{-2}	0.06 W m^{-2}
k_B=2.5 W m^{-1} K^{-1}	4.6 °C	4.7 °C
k_B=1.2 W m^{-1} K^{-1}	4.1 (0.5) °C	4.3 (0.4) °C
k_B=0.5 W m^{-1} K^{-1}	3.2 (1.4) °C	3.5 (1.2) °C
k_B=0.2 W m^{-1} K^{-1}	2.3 (2.3) °C	3.2 (1.5) °C

Subsurface warming for a 3 m thick near-surface layer with diverse thermal conductivities and two different lower boundary conditions. The second column (zero heat flux) represents the conditions shown in Fig. 5. Warming values refer to final subsurface warming at a depth of 3 m with respect to the mean (prescribed) surface temperature (M). Numbers in brackets express this warming as relative cooling with respect to pure rock (2.5 W m^{-1} K^{-1}).

results in a distinctively higher overall thermal conductivity in fine-grained soil than in coarse material.

In many publications, the effect of ground cooling in block slopes is referred to as thermal offset, in analogy to common terminology in the Arctic. The thermal offset described in the Arctic is caused by seasonal differences in the properties of the active layer, which are due to the contrast in thermal conductivity between water and ice. This usually results in a curved temperature profile and a marked temperature difference between the top and bottom of the active layer. Convection of air would be similar to a temporary increase in the thermal conductivity and resembles this pattern. The mechanism we propose here, produces no temperature difference between the top and bottom of the active layer, and this behavior corresponds with several existing measurements (Juliussen & Humlum 2008, Hoelzle & Gruber 2008).

A block layer of very low thermal conductivity results in a strong thermal gradient with depth in the presence of a geothermal heat flux. This effect can reduce the relative ground cooling (Table 1) and varies with the thickness of the block layer and with the heat flux across it. In mountain areas, the deeper heat flux is usually reduced (Kohl 1999) and spatially highly variable (Gruber at al. 2004). Additionally, the advection of subsurface ice (moving rock glacier) and transient effects can reduce or even invert the heat flux in the uppermost tens of meters.

The effect of reduced warming by the snow cover as proposed here does not preclude the presence of additional processes that lead to relative ground cooling. Depending on environmental conditions, other processes may even be more important. The most prominent other process that is described in the literature is the circulation of air caused by temperature-driven free convection. This effect and the effect proposed in this paper are complementary in some way: conditions of little snow cover favor the effect of advection and reduce the purely conductive mechanism described here, whereas a thick snow cover inhibits convection and gives rise to the full effect of low thermal conductivity. Conditions may vary on a continental scale (low/high precipitation areas), locally (wind-swept ridge or snow-filled depression) or with time (dry winter, climate change). Because the proposed effect is "relative cooling by reduced warming," it cannot result in ground temperatures significantly below the MAAT as has been observed for block surfaces with strong air movement (e.g., Gorbunov et al. 2004, Delaloye et al. 2003).

Conclusion and Outlook

We have presented a simple and purely conductive mechanism that can cause lower temperatures at the snow/ground interface as well as lower mean ground temperatures in coarse blocky surfaces as compared to bedrock or fine-grained material. This mechanism is not an alternative but rather an extension of existing theory, and it can at least partly clarify previously unexplained measurement results.

The quantitative understanding of the influence of each proposed mechanism and its sensitivity to material properties and environmental conditions is an important topic for future research. This will determine, for instance, which processes have to be included in a specific model and which are of secondary importance, only. The creative combination of both modeling and measurements is expected to be a viable means to achieve this. Additionally, methods for the delineation of block fields (cf. Heiner et al. 2003, Gruber & Hoelzle 2001) are important because this can strongly improve the quality of simulations, even with simple methods.

Acknowledgments

We are grateful to S. Bircher and E. Frey who contributed to the ideas presented here with their MSc theses as well as many discussions and experiments. Three anonymous reviewers have provided valuable feedback—the question of the lower boundary condition being our favorite by far.

References

Bartelt, P. & Lehning M. 2002. A physical SNOWPACK model for the Swiss avalanche warning. Part I: numerical model. *Cold Regions Science and Technology* 35: 123-145.

Binxiang, S., Xuezu, X., Yuanming, L,, Dongqing, L., Shuangjie, W. & Zhang, J. 2004. Experimental researches of thermal diffusivity and conductivity in embankment ballast under periodically fluctuating temperature. *Cold Regions Science and Technology* 38: 219-227.

Cermák, V. & Rybach, L. 1982. Thermal conductivity and specific heat of minerals and rocks. In: G. Angeneister (ed.), *Landolt-Börnstein Zahlenwerte und Funktionen aus Naturwissenschaften und Technik, Physikalische Eigenschaften der Gesteine (V/1a)*, Berlin: Springer, 305-343.

Clauser, C. & Huenges, E. 1995. Thermal conductivity of rocks and minerals. In: T.J. Ahrens (ed.), *Rock Physics and Phase Relationsóa Handbook of Physical Constants*, *AGU Reference Shelf,* 3: 105-126.

Delaloye, R., Reynard, E., Lambiel, C., Marescot, L. & Monnet, R. 2003. Thermal anomaly in a cold scree slope, Creux du Van, Switzerland. *Proceedings of the 8th International Conference on Permafrost, Zurich, 2003*, Vol. 1: 175-180.

Frey, E.A. 2007. *Messung und Modelllierung der Basistemperatur der alpinen Schneedecke*. Unpublished MSc thesis, Department of Geography, University of Zürich, Switzerland, 95 pp.

Goering, D.J. & Kumar, P. 1996. Winter-time convection in open-graded embankments. *Cold Regions Science and Technology* 24: 57-74.

Gorbunov, A.P., Marchenko, S.S. & Seversky, E.V. 2004. The thermal environment of blocky materials in the mountains of Central Asia. *Permafrost and Periglacial Processes* 15: 95-98.

Gruber, S. 2005. *Mountain permafrost: transient spatial modeling, model verification and the use of remote sensing*. PhD thesis, Department of Geography, University of Zurich, Switzerland, 123 pp.

Gruber, S. & Hoelzle, M. 2001. Statistical modelling of mountain permafrost distribution – local calibration and incorporation of remotely sensed data. *Permafrost and Periglacial Processes* 12: 69-77.

Gruber, S., King, L., Kohl, T., Herz, T., Haeberli, W. & Hoelzle, M. 2004. Interpretation of geothermal profiles perturbed by topography: The Alpine permafrost boreholes at Stockhorn Plateau, Switzerland. *Permafrost and Periglacial Processes* 15: 349-357.

Guodong, C., Yuanming, L., Zhizhong, S. & Fan, J. 2007. The "thermal semi-conductor" effect of crushed rock. *Permafrost and Periglacial Processes* 18: 151-160.

Haeberli, W. 1973. Die Basis-Temperatur der winterlichen Schneedecke als möglicher Indikator für die Verbreitung von Permafrost in den Alpen. *Zeitschrift für Gletscherkunde und Glazialgeologie* 9: 221-227.

Haeberli, W. 1975. Untersuchungen zur Verbreitung von Permafrost zwischen Flüelapass und Piz Grialetsch (Graubünden). Zürich, *Mitteilungen der Versuchsanstalt für Wasserbau, Hydrologie und Glaziologie* 17: 221pp.

Hanson, S. & Hoelzle, M. 2004. The thermal regime of the active layer at the Murtèl rock glacier based on data from 2002. *Permafrost and Periglacial Processes* 15: 273-282.

Harris, S.A. 1996. Lower mean annual ground temperature beneath a block stream in the Kunlun Pass, Qinghai Province, China. *Proceedings of the 5th Chinese Permafrost Conference, Lanzhou, 1996*: 227-237.

Heiner, S., Gruber, S. & Meier, E. 2003. The spatial extend and characteristics of block fields in alpine areas: evaluation of aerial photography, LIDAR and SAR as data sources. *Extended abstract volume of the 8th International Conference on Permafrost, Zurich, 2003*: 59-60.

Herz, T. 2006. *Das Mikroklima grobblockiger Schutthalden der alpinen Periglazialstufe und seine Auswirkungen auf Energieaustauschprozesse zwischen Atmosphäre und Lithosphäre*. PhD thesis, Department of Geography, University of Giessen, Germany, 207 pp.

Hoelzle, M. & Gruber, S. 2008. Borehole and ground surface temperatures and their relationship to meteorological conditions in the Swiss Alps. *Proceedings of the 9th International Conference on Permafrost 2008*, Fairbanks, Alaska, USA.

Juliussen, H. & Humlum, O. 2008. Thermal regime of openwork block fields on the mountains Elgåhogna and Sølen, central-eastern Norway. *Permafrost and Periglacial Processes* 19: 1-18.

Kohl, T. 1999. Transient thermal effects at complex topographies, *Tectonophysics* 306: 311-324.

Zhang, T., Barry, R.G. & Haeberli, W. 2001. Numerical simulations of the influence of the seasonal snow cover on the occurrence of permafrost at high latitudes. *Norwegian Journal of Geography* 55: 261-266.

Interrelation of Cryogenic and Hydrologic Processes on Small Streams and Catchments of Central Yamal

A.A. Gubarkov
Tyumen Oil and Gas University, Tyumen, Russia
M.O. Leibman
Earth Cryosphere Institute SB RAS, Tyumen, Russia

Abstract

Small streams of the Yamal Peninsula provide the best opportunity to study the interrelation of cryogenic and hydrologic processes. A case study on the test river Panzananayakha was undertaken to assess catchment morphogenesis, water flow, and sediment transport in relation to cryogenic processes. Which dominating cryogenic processes most affect the river channel depends on channel morphology. In V-shaped valleys the low valley slopes end directly in the channel, and the influence of cryogenic landsliding on hydrologic processes dominates. Ice wedges close to the surface produce bead-shaped channels that slow the stream velocity. Cryogenic processes directly affect sediment transport as well. The complex cryogenic and hydrologic processes which are characteristic for upper, middle, and lower stream courses in the small catchments are specified. Channel processes include bottom and lateral thermoerosion. Trans-catchment processes include transitional landslides, earth flows, and ravine thermoerosion.

Keywords: bead-shaped channel; cryogenic processes; hydrologic processes; landslides; thermoerosion.

Introduction

More than 90% of the rivers in tundra regions can be considered as small rivers less than 10 km in length. These small rivers comprise more than 80% of the total length of all rivers. Small rivers in the cryolithozone are characterized by the interaction and interrelation of cryogenic and hydrologic processes. These processes result in specific valley slopes and bottom shape, stream mode and transport of sediments. The same scale of cryogenic and hydrologic processes in these small catchments is the main reason for such a relation. On middle-length and long rivers, the impact of cryogenic processes on a channel is not observed as the mass waste processes are not capable of changing the stream direction, or creating a full or even partial damming of the water flow.

The main cryogenic process affecting water and sediment runoff of these small rivers is thermoerosion, cryogenic landslides (active-layer detachments and earth flows), and thermokarst.

Thermoerosion studies have been carried out since the middle of 19th century. The Yamal Peninsula is discussed in numerous publications including: Kosov & Konstantinova (1973), Malinovskiy (1980), Dan'ko (1982), Sidorchuk (1999), Voskresensky (2001). Typically thermoerosion occurs only at the end of summer or in the fall when the active layer reaches its maximum depth. Dan'ko (1982) suggests that thermoerosion is possible during different periods of warm time of the year. Malinovskiy (1980) measured the ability of water flow to carry sediment load and bottom sediments under thermoerosion and found typical values of 700 g/l.

Sidorchuk (1999) conducted observations on the Bovanenkovo gas field at Central Yamal in 1987–1995 and found the hydrologic and morphometry factors of ravine erosion and thermoerosion in both natural and anthropogenic environments. Voskresenskiy (2001) emphasized the need to consider the complex interactions between thermoerosion and thermokarst. These studies showed an obvious relationship between the density of ravines and thermokarst distribution on the Yamal Peninsula.

The interrelation of thermoerosion and thermokarst is also discussed by Romanovsky (1961) who concluded that lake thermokarst and thermoerosion in alases result in a united system of erosion-thermokarst depressions, through which runoff of water and sediment takes place. Romanenko (1997) studied tundra lakes in the Siberian Arctic. He has showed that the proportion of erosion-thermokarst lakes at the Bovanenkovo gas field is maximal in all of northern Siberia and accounts for 15% of the total lake distribution of this region.

Study of the cryogenic landsliding (Leibman & Kizyakov 2007) shows that the greatest influence on water and sediment runoff, and the evolution of channels and valleys of small rivers is induced by landslides (both active-layer detachments and earth flows). Important features of landslides are the speed of descent, volume of the landslide body, and position on the valley slope. This last feature determines whether the landslide body has the potential to block the valley and small stream channel, and therefore, creates a temporary lake in the stream channel or valley. The duration of cryogenic landslides varies from several hours to minutes, while the lifetime of a resulting dammed lake depends on the time needed for the stream to cut through the dam formed by the landslide body. One directly observed dammed lake drained 11 years after a landslide event.

The level of activity of the erosion, transport and accumulation during the warm period in relation to a complex of natural factors can vary considerably from year to year. As determined from theoretical assumptions, laboratory tests and field observations, thermoerosion is most active in the

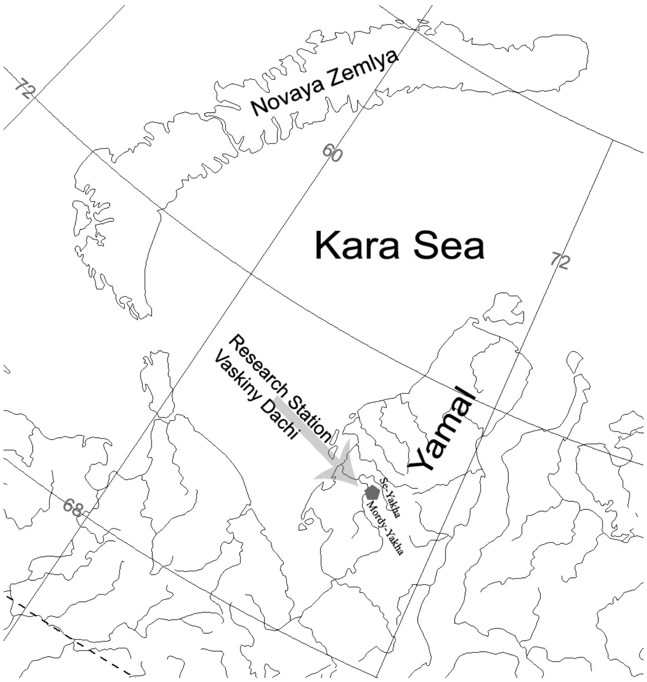

Figure 1. The study area on Central Yamal in the vicinity of Research station Vaskiny Dachi.

summer-fall, when air temperature and , water temperature are the highest. The heat energy of the flow is enough to melt permafrost under such conditions. This is especially true in cases where there is sufficient energy of flow to erode the thawed active layer soils first. However on Central Yamal in summer-fall, the slopes are protected by vegetative cover and thus are hard to erode. The active layer deposits consolidate and aggregate with time while the thaw depth increases, reducing the ability of the erosion of the active layer as well as underlying permafrost. Erosion of sands is easier compared to clayey and organic soils but the active-layer depth in sands is much higher. Consequently to promote thermoerosion in permafrost, intensive rains are required to provide the power of flow sufficient to erode the active-layer deposits. According to Russian Hydrometeorological Service records very intense rainstorms in these tundra regions occur once in 30 years, and intense showers occur only once in 10-20 years. More typical are drizzling rain, which do not increase streamflow sufficiently to allow intensive thermoerosion. Thermoerosion in summer-fall period most likely occurs in interrelation with cryogenic landslides and thermal denudation or other slope displacements forming cracks or bare surface.

Methods and Study Area

Both remote-sensing and land-based data were used to obtain information on cryogenic and hydrologic features in the study area. Both 1:25000 topographic maps and 1:10000 aerial photos were digitized and interpreted. Interpretation included counting and measuring both hydrological and cryogenic features. These features were then evaluated by field measurements.

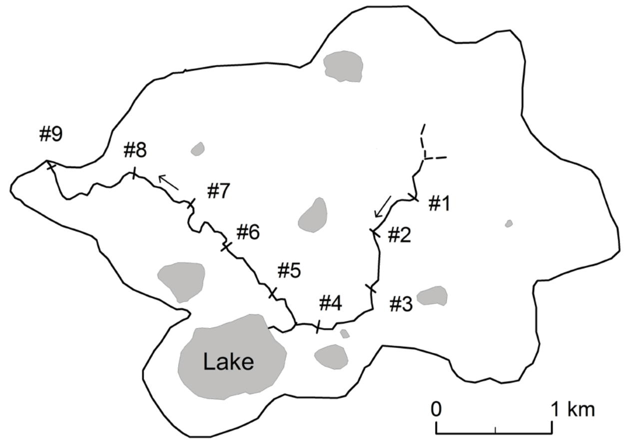

Figure 2. Panzananayakha river catchment. Numbers refer to section lines where water discharge was measured.

The test river Panzananayakha, which is 7 km in length and has a catchment area of 8 km^2, is representative of small rivers of the Central Yamal as shown from analysis of maps of various scale and field studies in the basin of Se-Yakha and Mordy-Yakha rivers and their tributaries. Average river length in this region is 5.99 km.

Land-based studies were used to determine features of beam-shaped river-channel forms, including width, length and depth, as well as stream velocity. Turbidity was measured in both middle and small sized rivers. This was done by water sampling, filtering, drying, and weighing the dried solids.

Field studies at the research station “Vaskiny Dachi” (Fig. 1) were undertaken in 2005–2007, considered the regime and morphology of temporary non-channel and channel streams, small rivers with catchment area under 10 km^2, and a middle-length river (catchment area about 3000 km^2).

The temporary non-channel and channel streams were located on 25 shear surfaces of landslides, in 3 thermocirques, and 3 ravines. Channel features, as well as water and sediment runoff were observed in 4 small and 1 middle-length rivers. On the Panzananayakha test river, all morphometry features of its channel, including landslides, thermokarst forms, erosion, and hydrology were measured (Fig. 2). In addition, alternation of erosive and accumulation zones, and channel shape along the crosscuts were studied in the test river valley.

Results and Discussion

In some years, the slope erosion in the spring may account for up to 75% of annual erosion (Dan’ko 1982). This suggests that most of the erosion is confined to frozen deposits (thermoerosion), including both active-layer deposits and permafrost that are in a frozen state. In the late summer–fall period, as mentioned above, thermoerosion and erosion are limited by active-layer properties and vegetative cover. However, according to our observations, the processes of cryogenic landsliding promoting thermoerosion and erosion events are most active during this period.

Table 1. Depth of shear surface against surrounding slope, and depth of thermoerosion landforms against the landslide shear surface at the upper, middle and lower portions of the landslide slope.

Landslide #	Depth of shear surface, m			Depth of thermoerosion landforms, m		
	upper	middle	lower	upper	middle	lower
1	-3.3	-3.8	-9.5	-1.2	-1.2	-0.2
2	-0.5	-3.1	2.5	-0.5	-2.1	-0.4
3	-3.5	-2.5	-0.5	-1	-1.1	-0.8
4	-4.2	-3.4	-2.2	-1.2	-1.2	-0.3
5	-5.7	-5.7		-0.2	-1.5	
6	-2.1	-1.8		0	-0.2	
7	-1.7	-2.3		-0.2	-1.7	
8	-3.7	-5.8		-1.2	-0.1	
9	-5.3	-6.2		-0.1	-1	
10	-3.7			-1		
11	-5.3			-0.9		
Average	-3.5	-3.8	-3.9	-0.7	-1.1	-0.4

After landslide shear surfaces are exposed, they are susceptible to heavy erosion and thermoerosion, and as a result a significant quantity of sediments are often delivered into the stream network (Leibman & Streletskaya 1997). Under the influence of temporary stream erosion/thermoerosion, troughs develop in a specific sequence. We subdivide these into three zones of down slope thermoerosion: sediment mobilization (upper), sediment transition (middle), and sediment accumulation (lower). All three zones are developed only when the landslide body entirely moves away from the shear surface.

Cross-sections were set and slope morphology measured in the upper, middle, and lower portions of slope. Results are presented in Table 1.

Analysis of Table 1 shows that there is a relation between the depth of thermoerosion against the landslide shear surface and the depth of shear surface against the surrounding slope or hilltop edges. This relation is directly proportional in the sediment mobilization zone, and inversely proportional in the accumulation zone as shown on cross-sections of the landslide shear surfaces and erosion troughs (Fig. 3). In the upper portion of the landslide shear surface, the increase of the erosion trough depth is observed when landslide shear surface is deeper than the slope surface. This is due to the higher relief potential energy when the shear surface is deeper. At the same time, runoff from the catchment does not contain a high sediment load due to the vegetation coverage. That is why the erosional ability of the water flow in the sediment mobilization zone of a landslide shear surface is the highest.

In the lower portions of the landslide slope, the depth of the erosion troughs is less when the shear surface is deeper. This is a result of increased input of sediment from the higher shear surface rim. For this reason, maximum runoff observed in the lower portion of the shear surface performs minimal erosion because the sediment load

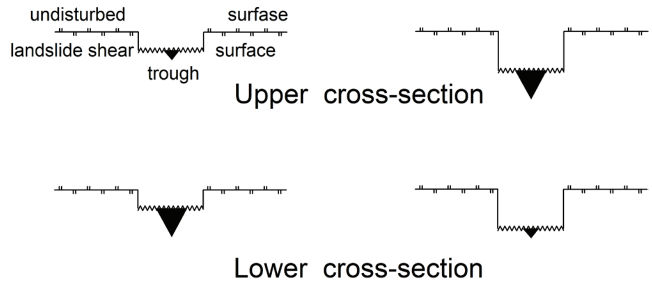

Figure 3. Erosion/thermoerosion trough in relation to the depth of cryogenic landslide shear surface cut into a slope surface in the zones of sediment mobilization (upper cross-section) and sediment accumulation (lower cross-section).

exceeds the potential eroding ability of the water flow.

In the middle portion of the slope, the depth of the shear surface cutting does not affect the erosion trough depths because up slope and down slope patterns compensate for each other.

Water runoff is higher here than at the upper cross section but erosion potential is used to transport larger sediment load (Fig. 3).

The most pronounced combined effect of cryogenic and hydrologic processes is the formation of thermoerosion pits and "tunnel thermoerosion" (term introduced by Poznanin 1995) in headwater gullies. Our observations are generalized in Figure 4. At the initial stage of snowmelt at the gully headwater, water flow and thermoerosion occur (Fig. 4, I). During melt, a thermal pit forms at the uppermost point of the headwater. These pits gradually increase in depth. Our measurements show that the depth of thermal pits changes from 2 to 6 m. Since the active-layer at the gully slopes is typically oversaturated with meltwater, they often start to creep, resulting in the formation of an earthflow. The snow surface may be dammed by the landslide mass, and thermoerosion may continue beneath the snowpatch undersurface as tunnel erosion (Fig. 4, II). It often takes 5–10 days for the landslide mass to cover the snow patch surface, and therefore exclude surface runoff. Finally the water-cut pit may be filled by collapsed pit walls and landslide masses so that runoff is forced back to the surface (Fig. 4, III). The entire cycle of thermal pit-tunnel thermoerosion process starting with spring snowmelt takes approximately one month.

In the upper cross-section (Fig. 4, I–III-A) both the depth and width of the gully can change from stage I through to stage III. However, in the lower cross-section (Fig. 4, I–III-B) only the width of the gully increases with time and the proportion of snow and silt deposits on top the snow change, with the ratio of snow decreasing.

River sediment transport is affected by processes in the inflowing ravines. In the ravine networks, the influence of erosion and thermoerosion on the river sediment transport is determined by the river length. The shorter the river, the greater the impact. Turbidity of the river may change twice depending on the remoteness of the inflowing ravine. This effect is much less significant in the middle-length rivers. For instance, our measurements in Se-Yakha river, a middle-

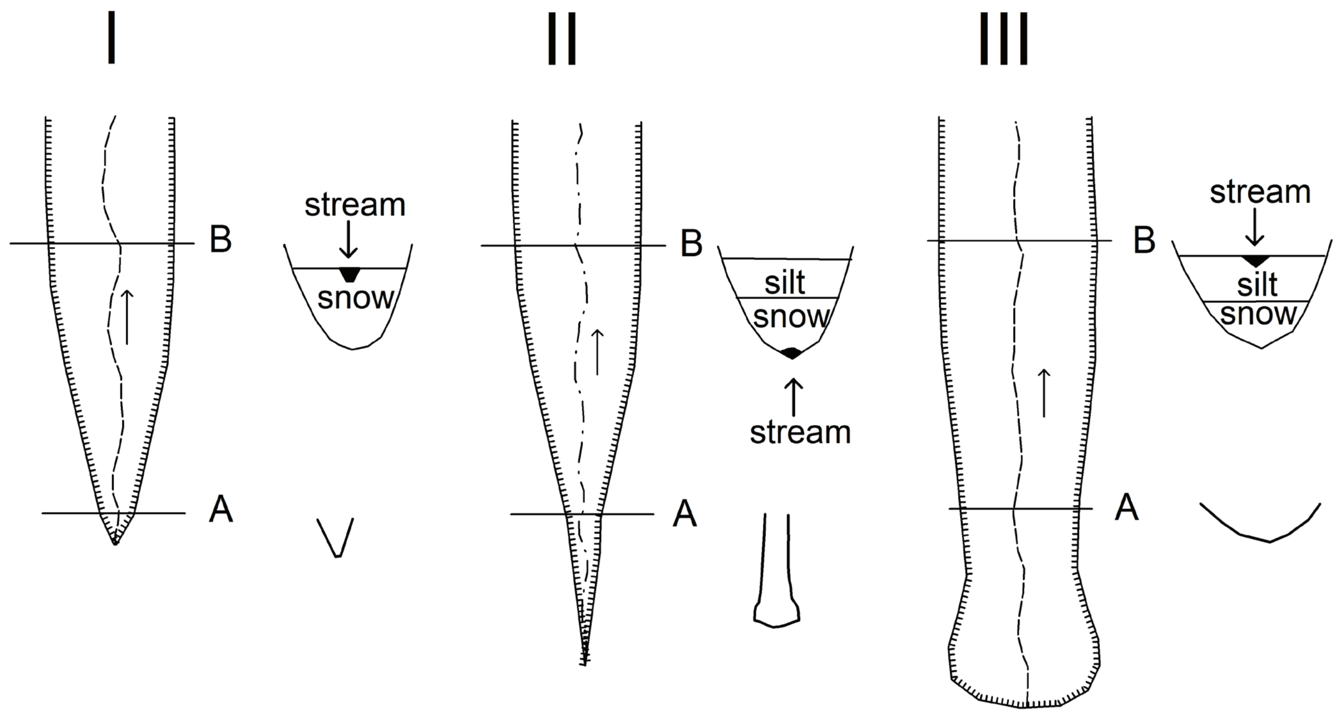

Figure 4. Stages of gully development and formation of thermoerosion water-cut pit: I, initial period of snowmelt on top of the surface of snow patch in the gully; II, the period thermoerosion water-cut pit formation and of meltwater flow below the snow patch; III, collapse of thermoerosion water-cut pit walls; A, plan (left) and cross-section (right) in the upper course of the gully; B, the same in the lower course.

length river in Central Yamal, showed that at the end of August 2007 turbidity was as high as 90 g/m^3, which is several orders of value higher than sediment runoff measured at the same time in the majority of small rivers-tributaries of Se-Yakha.

The cryogenic factors not only increase the sediment runoff, but also reduce it. Reduction of the sediment runoff in small rivers occurs when bead-shaped and dammed river channel features are formed. These can result first from polygonal structures and second from landsliding. In the upper stream of Panzananayakha river in August 2007, sediment runoff was as high as 5120 g/m^3 resulting from activation of erosion and thermoerosion. But in the middle course, sediment runoff reduced to 3 g/m^3 because of precipitation of sediments in the bead-shaped features. Analysis of aerial photography allows us to conclude that for the majority of small rivers with active cryogenic processes at the river banks sediment fans are formed at the ravine mouths, and landslide bodies often descend to the valley bottom and into the channel. Erosion and thermoerosion fans are comparable in size with the width of the valley bottom and river channel, and the lifetime of these fans is longer when compared to dammed lakes resulting from landslide activity.

Dams formed out of landslide bodies loaded in the valley bottom and small river channel may be 2–3 m high. They prevent any sediment transport downriver. After the dams' breakout on former flooded valley bottom, sheet runoff prevails over linear runoff that does not promote erosion, and also slows the sediment transport. The upper course of the test river Panzananayakha and river Halmeryakha at the study area show such features.

Mouth areas of small rivers inflowing into bigger rivers are separated from the river channel of a higher grade by the flood plain with numerous lakes. So, on the way to this channel small river sediment load precipitates within the flood plain lakes.

In small river catchments interrelation of channel and cryogenic processes is common. Depending on slope gradient, lengths and shape, as well as cryogenic features, different cryogenic slope and thermokarst processes are controlling the river runoff.

Small rivers with intensive linear and side erosion trigger landsliding to produce dammed lakes. The lifetime of these lakes is several years, thus prolonging the water cycle time by two to four orders of magnitude (Tab. 1). Thus on small streams even a single landslide event may affect river runoff for several years.

Polygonal ice-wedge features occurring close to the surface and subject to thermokarst, produce bead-shaped channels which last much longer compared to the dammed lakes. Being larger in volume, these channel features have a major impact on the water cycle. They reduce water runoff in the channel by three to four orders of magnitude as follows from measurements presented in Table 2.

Cryogenic processes determine the particularities of the sediment transport through the channel depending on their location at the upper, middle or lower course. Cryogenic landsliding at the upper course expose surface deposits which are eroded into the channel. Prior to the removal of dammed lakes, as mentioned above, the sediment load settles in these lakes, but after the dammed

Table 2. Cryogenic and hydrometric features measured in the upper, middle and lower course of Panzananayakha River.

Distance of the section line from the river head, km	River course	Water discharge, m^3/s	Volume of bead-shaped forms, m^3	Volume of dammed lakes, m^3	Time of water cycle, hour	Cryogenic/ hydrological features observed upstream from the section line
1.5	Upper	0.005	0	0	3	None
1.5	Upper	0.005	205	0	11	Ice wedges/Bead-shaped forms
1.5	Upper	0.005	0	50	3	Landslides/Dammed lakes
1.5	Upper	0.005	0	1700	94	Landslides/Dammed lakes
3	Middle	0.0075	2800	0	104	Ice wedges/Bead-shaped forms
5	Lower	0.015	1185	0	22	Ice wedges/Bead-shaped forms
	Total		4190	1700	220	

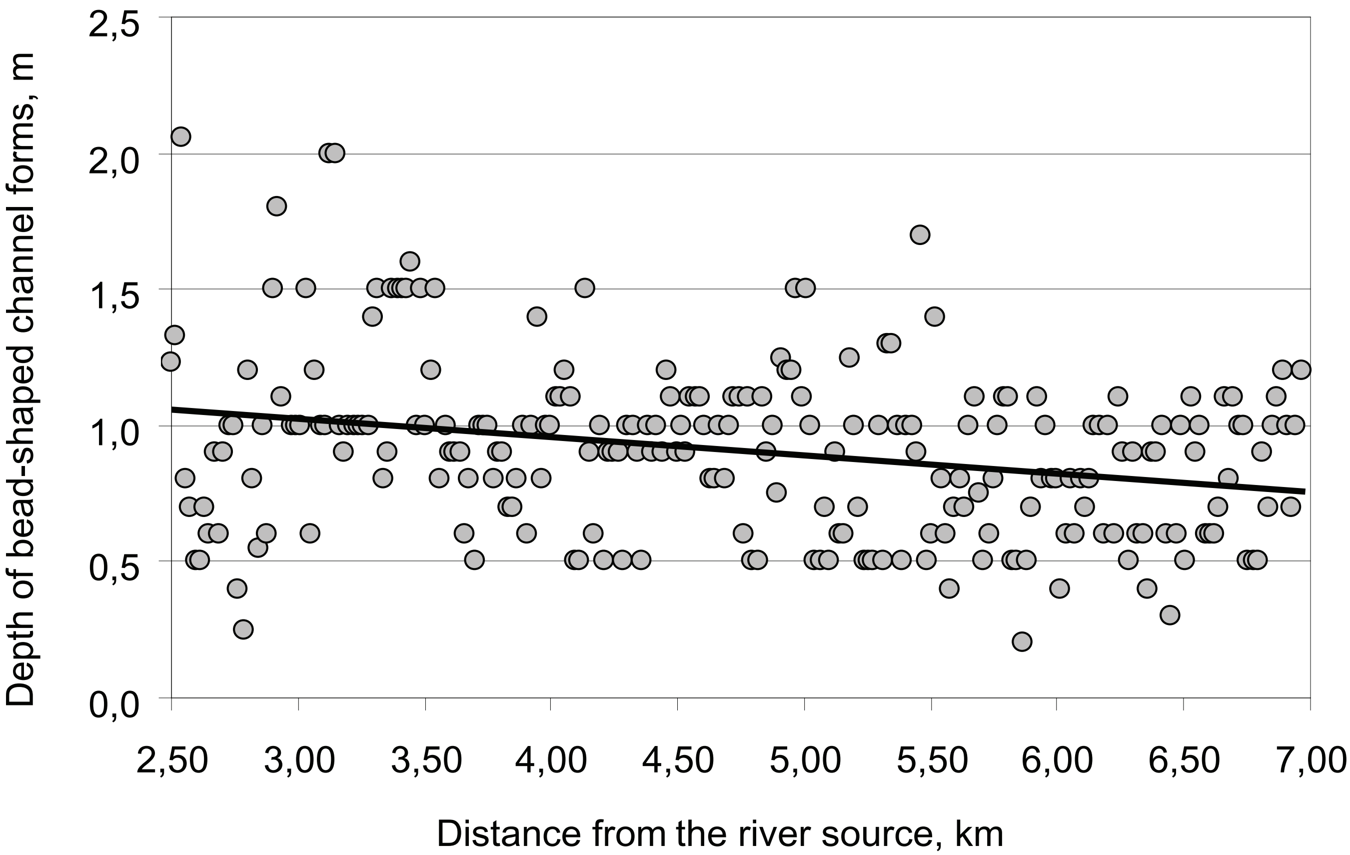

Figure 5. Depth of bead-shaped channel forms in the middle and lower courses of Panzananayakha River in relation to the distance from the river source.

lakes drain the sediment is transported downstream to fill in the bead-shaped forms of the middle course. In the lower course though there are no bare surfaces produced by landsliding, the water discharge is much higher than in the upper course, sediment load is reduced by middle-course bead shaped forms, so that the water flow can produce both thermokarst and erosive work in the lower course. Bead-shaped forms appear due to heat transfer, and sediment runoff increases due to erosive work in the sides and bottom of the valley. As a result, bead-shaped forms are filled in with the sediment and their depth reduces downstream as measured in the lower course of the test river (Fig. 5).

Conclusions

Interrelation of hydrologic and cryogenic processes in the small river catchments differs spatially. Valley slopes can be subdivided by temporary streams and small river banks and channels in the upper, middle and lower portions of the river valley. Activity of the erosion and thermoerosion in temporary stream network on slopes of the river valleys is determined by domination of landslide processes. Concave bare or sparsely vegetated landslide shear surfaces concentrate water runoff into temporary channels that are easier to erode. Hydrological processes depend on the position against the landslide headwall and on the depth of shear surface cutting into the surrounding slopes. Temporary streams on landslide affected slopes are important sources of sediment runoff in the small rivers.

In a small river catchment, interrelation of the hydrologic and cryogenic processes occurs in many locations. Depending on the catchment morphometry, the dominating cryogenic process affecting the river channel differs. In the V-shaped valley slopes, the influence of cryogenic landsliding on hydrologic processes dominates: dammed lakes are formed, which may exist from many years and increase the storage time of the water cycle.

In the U-shaped valleys, ice wedges are found close to the surface, and bead-shaped channels are formed. These bead-shaped channels may slow down the water cycle in the streams, exceeding the effect of dammed lakes as bead-shaped channels occur more regularly. All together they store a greater volume of water, and may exist much longer.

Cryogenic landsliding results in the active sediment washout from the exposed landslide shear surfaces into a channel, and the "bead" forms, occurring on adjacent portions of the channel are filled with these sediments. However when landslide bodies still dam the channels, they interfere with sediment transport and thus promote longer existence of bead-shaped channels downstream.

The complexes of cryogenic and hydrologic processes, characteristic for upper, middle and lower stream courses in the small catchments are: (1) a landslide complex in the upper course with subsidiary bottom thermoerosion and the prevalence of accumulation instead of sediment erosion; (2) thermokarst complex of the middle course with an equilibrium of accumulation and sediment erosion; and (3) thermoerosion complex of the lower course with subsidiary thermokarst, and a prevalence of sediment erosion over sediment accumulation.

Cryogenic and hydrologic processes are important drivers in the formation of the Arctic landscapes. Therefore, understanding the interrelation of these processes is a prerequisite for successful maintenance of infrastructure in the Arctic.

References

Dan'ko, V.K. 1982. *The regularities of the thermoerosion process development in the north of West Siberia.* Candidate dissertation. Moscow: PNIIIS Publisher, 20 pp. (in Russian)

Kosov, B.F.& Konstantinova, G.S. 1973. Ravine density in the north of West Siberia. In: *Natural conditions of the West Siberia*. Moscow: Moscow University Press, 104-115 (in Russian).

Leibman, M.O. & Kizyakov, A.I. 2007. *Cryogenic landslides of the Yamal and Yugorsky peninsular*. Moscow-Tyumen: IKZ SO RAN, 206 pp. (In Russian).

Leibman, M.O. & Streletskaya, I.D. 1997. Land-slide induced changes in the chemical composition of active layer soils and surface-water run-off, Yamal Peninsula, Russia. *Proceedings of the International Symposium on Physics, Chemistry, and Ecology of Seasonally Frozen Soils, Fairbanks, Alaska, 1997:* 120-126.

Malinovskiy, D.V. 1981. The particularities of the thermoerosion development on western Yamal peninsula. In: *Natural conditions of the West Siberia*. Moscow: Moscow University Press, 130-137 (in Russian).

Poznanin, V.L. 1995. *Nature of ravine thermoerosion.* Doctor of science dissertation. Moscow: Moscow University Press, 33 pp. (in Russian).

Romanenko, F.A. 1997. *Formation of the lake basins on Siberian Arctic plains*. Candidate dissertation. Moscow: Moscow University Press, 25 pp. (in Russian).

Romanovskiy N.N. 1961. Erosion-thermokarst depressions in the North of Maritime lowlands of Yakutiya and Novosibirsk islands. In: *Permafrost Studies (Merzlotnye Issledovaniya)* 1. Moscow: Moscow University Press, 124-144 (in Russian).

Sidorchuk, A.Yu. 1999. The sediment balance on ravine catchments. In: A.Yu. Sidorchuk & A.V. Ram (eds.), *Erosion Processes at Central Yamal.* Saint-Petersburg: 242-252 (in Russian).

Voskresenskiy, K.S. 2001. *The Modern Relief-Forming Processes on Plains of the Northern Russia*. Moscow: Moscow University Press: 264 pp. (in Russian).

Periglacial and Permafrost Map of Signy Island, South Orkney Islands, Maritime Antarctica

M. Guglielmin
Insubria University, Via Dunant, 3, 21100 Varese, Italy
D. Boschi
Insubria University, Via Dunant, 3, Varese, Italy
Carlo D'Agata
Milano University, Earth Sc. Dep., Via Mangiagalli 34, Milano, Italy
C. Ellis-Evans and M.R. Worland
British Antarctic Survey, Natural Environment Research Council, Madingley Road, Cambridge CB3 0ET, United Kingdom

Abstract

Signy Island was one of the first Antarctic locations to be the subject of a detailed periglacial landform study which was completed in the 1960s. Several periglacial features such as patterned ground, block stripes, and gelifluction lobes have been analysed and monitored. More recently, the relationships between different vegetation coverage, soil type, and the underlying permafrost have also been studied. In this paper we present a geomorphological map of Signy Island that has been mapped with particular reference to the occurrence of periglacial landforms. Geomorphological features were mapped at 1:10,000 scale during the austral summer of 2004/05. A highly simplified permafrost model (PERMDEM) based on the digital elevation model and the air lapse temperature have been here presented and tested by comparing the distribution of some periglacial features together with thermal profiles and trenches excavated in the main geomorphological areas of interest.

Keywords: gelifluction; Maritime Antarctica; modeling; patterned ground; periglacial features; permafrost.

Introduction

Studies of permafrost distribution in Antarctica have recently been developed through the IPY–ANTPAS initiative and other linked research programs (Bockheim et al. 2008). Nevertheless in the South Orkneys, as in other parts of the maritime Antarctic, permafrost is still poorly understood. As far as we are aware, no permafrost maps of Maritime Antarctica have been produced, although some papers have presented information related to permafrost distribution such as; models of net radiation balance (Vieira & Ramos 2003), permafrost thermal profiles (e.g., Chen 1993), and active layer thermal regimes (Ramos & Vieira 2003, Cannone et al. 2006, Guglielmin et al. in press). Periglacial landforms have received more attention resulting in the production of maps for the South Shetlands (e.g., Serrano & Lopez Martinez 2000, Serrano et al. 1996, Zhu et al. 1996) and other islands (i.e., Mori et al. 2007, Strelin & Sone 1998). Investigations by Chambers (1966a, b, 1967, 1970) into periglacial processes such as frost heave, frost creep, and solifluction would have benefited from both permafrost and periglacial geomorphology maps. Signy Island, South Orkney Islands, provides a unique opportunity in Antarctica to compare new data on the active layer thermal regime with previous Signy Island data collected in 1963 by Chambers (1966b).

The main aims of this paper are to provide a preliminary permafrost and periglacial map of Signy Island and to analyze possible relationships between the mapped periglacial features, permafrost distribution, and some climatic factors such as air temperature, global radiation, and snow cover.

Study Area

Climatic and geological constraints

Signy Island (60°43′S, 45°38′W) in the South Orkney Islands is located in the maritime Antarctic and is characterized by a cold oceanic climate with a mean annual air temperature of around -3.5°C; mean monthly air temperature above 0°C for at least one, but up to three months each summer; and annual precipitation of around 400 mm, primarily in the form of summer rain and cloud cover of 6–7 okta year-round. The climatic records indicate a progressive warming of air temperatures of 2°C ± 1 over the past 50 years (Turner et al. 2005).

The substrate is mainly quartz-mica-schist, although in some parts of the island there are small marble outcrops (Matthews & Maling 1967). Half of the island is covered by an ice cap that is currently rapidly shrinking.

Glacial evolution

According to Sudgen & Clapperton (1977), during the Last Glacial Maximum (17,000–18,000 years BP) Signy Island was completely covered by the South Orkneys ice cap with the former coastline extended to the actual 130-150 contour b.s.l. The reduction of the ice cap has not been investigated in detail although some authors indicate a major period of shrinkage between 9000 and 6000 years BP (e.g., Nakada & Lambeck 1988), while others suggest that the disappearance of the ice cap occurred some time before 7000 yr BP (Herron and Anderson 1990).

Deglaciation has been confirmed by lake formation dated

Figure 1. Location of the study area. The black dot indicates the CALM grid. The black thick line indicates the extent of the glacier in 2004.

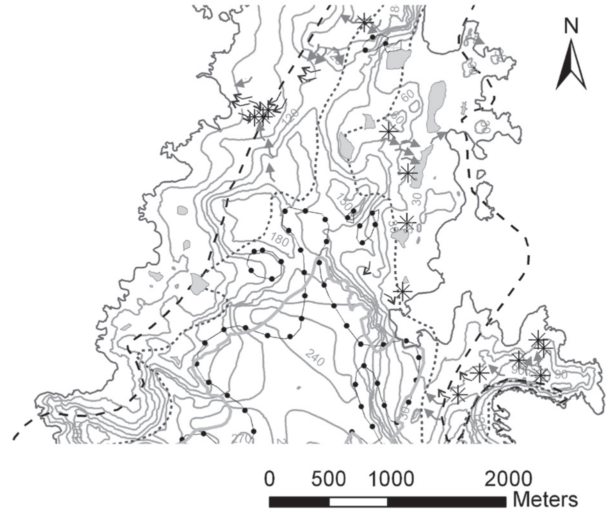

Figure 2. Geomorphological sketch of the center part of the Signy Island. Legend: 1) rock glacier; 2) gelifluction lobes; 3) soil stripes; 4) patterned ground; 5) glacier boundary 5000–3000 BC; 6) glacier boundary 400–600; 850–1000; 1150–1300 AD; 7) glacier boundary 600–850; 1000–1150; 1300–1450 AD; 8) extent of the glacier in 2004. The glacier limits at point 5–7 are suggested by Smith (1990).

between 5890 ± 60 14C yr BP at Heywood Lake and c. 5700 yr BP at Sombre Lake (Jones et al. 2000) and later by the oldest moss banks developed at c. 5500 yr BP (Smith 1990). During the middle and upper Holocene, different phases of cooling and warming occurred as established by proxy data. Radiocarbon data from the moss banks indicate several glacial advances between 1250 and 1600 AD and two advances between 1700 and 1850 AD (Smith 1990). Paleolimnological studies carried out particularly on Sombre and Heywood lakes suggest a different Holocene evolution characterized by cool conditions and slow sedimentation and colonization rates between c. 5900-3800 yr BP, followed by evidence for a late "Holocene climate optimum" (c. 3300–1200 yr BP) and finally a cooling period (Jones et al. 2000). More recently there is evidence of a strong reduction in size of the glaciers with an increase in new deglaciated areas of 35% between 1949 and 1989, (Jones et al. 2000) and an even faster shrinkage in the last 20 years.

Permafrost distribution and periglacial landforms

Permafrost on Signy Island was considered discontinuous by Chambers (1966b) with variable active layer thicknesses ranging from 40 cm in moss sites to more than 2 m in well-drained coarse deposits.

Most of the island is covered by cryptogamic vegetation which has a distinct influence on the ground surface temperature (GST) and also in some cases on the active layer thickness (Cannone et al. 2006, Guglielmin et al. in press).

During the austral summer of 2004/2005 a permanent CALM grid (40 x 50 m with the nodes every 10 m) was installed under the auspices of the framework of the project "Permafrost and Global Change in Antarctica II (PGCAII)" established by the Insubria University and the British Antarctic Survey (BAS) with logistical support by PNRA and BAS. An automatic station monitored the temperature of the active layer at 4 different points within a CALM grid located on a flat summit behind the Signy research station (Fig. 1). The system also recorded the main climatic elements at the site.

Despite the clear and innovative studies on the periglacial processes involved in the production of sorted and unsorted circles, sorted stripes and "stone streams" carried out here in the 1960s by Chambers (Chambers 1966a, b, 1967, 1970) few geomorphological studies have been conducted since. However there have been a few studies investigating weathering processes (e.g., Hall 1986, 1987, 1988, 1990).

Chambers emphasized in his works that only the upper part of the active layer (40-60 cm) was involved in sorting, gelifluction, and ice segregation.

Methods

During the austral summer of 2004/2005, two of the authors made a geomorphological survey of the island at the scale of 1:10,000 with particular attention to the periglacial and permafrost features. Transversal trenches were dug at the site of some selected periglacial features to explore their internal structure and to sample soils and underlying deposits.

Additionally, some trenches and pits were excavated to measure the active thermal profile and describe the main soil characteristics in different geomorphological areas and in different quaternary deposits.

Each trench and pit was included in a GIS system with the geomorphological map. Boreholes were drilled down to 2.5

m at Spin Drift Col and on the upper part of the Backslope close to the Signy research station (Fig. 1) to sample frozen ground. The digital elevation model (DEM) developed by BAS has a pixel of 7.5 m.

The permafrost model (PERMDEM) has been developed to obtain a mean annual GST (MAGST) using the available DEM of the island as an input to produce a map of the mean annual air temperature (MAAT) and a map of the global annual radiation (direct plus diffuse short wave).

The first map was achieved by applying the adiabatic lapse rate calculated between the only two available automatic weather stations (AWS) (Fig. 1). The lapse rate for 2006 was 0.011°C/m.

The solar radiation analysis tools calculate insolation across a landscape or for specific locations, based on methods from the hemispherical viewshed algorithm (Rich 1990), as further developed by Fu & Rich (2002). The total amount of radiation calculated for a particular location or area is given as global radiation.

Considering that snow/ice-free ground surfaces suffer GST almost always warmer than the air temperature we used the annual global radiation map (calculated for 2006) to compute a correction factor *Ir* to add to the obtained MAAT value according to the equation:

$$MAGST = MAAT + Ir \qquad (1)$$

where *Ir* is calculated as the regression between the difference ΔT (MAGST-MAAT) of two monitored points of the CALM grid (bare grounds) and the global annual radiation compiled in the same points.

Finally, the permafrost map was tested comparing the obtained modeled results with the temperatures measured in the excavated trenches and in the monitored boreholes.

Results

Geomorphological mapping

An example of a very simplified geomorphological map is shown in Figure 2. The symbols that represent periglacial features (patterned ground; soil stripes; gelifluction lobes) indicate the areas in which more than 10 single features occur. Neither patterned ground nor soil stripes are differentiated between sorted and unsorted in this simplified sketch. In the field, low-centered sorted circles, sorted stripes and stone-banked lobes are the most widespread. Low-centered sorted circles are the most widespread form of patterned ground and show a high level of size variability with diameter ranging between 2 and 5 m.

Low-centered sorted circles occur preferentially in flat and depressed areas at altitudes lower than 80 m. High-centered sorted circles are less frequent than smaller ones (ranging between 10 and 150 cm) and generally occur on flat summits at higher altitudes. Unsorted circles occur quite often and generally have a size similar to the high-centered sorted circles, but do not show a clear distribution pattern. In some depressed and peaty areas, frost boils also occur with a diameter of between 0.2 and 0.7 m. No ice wedge

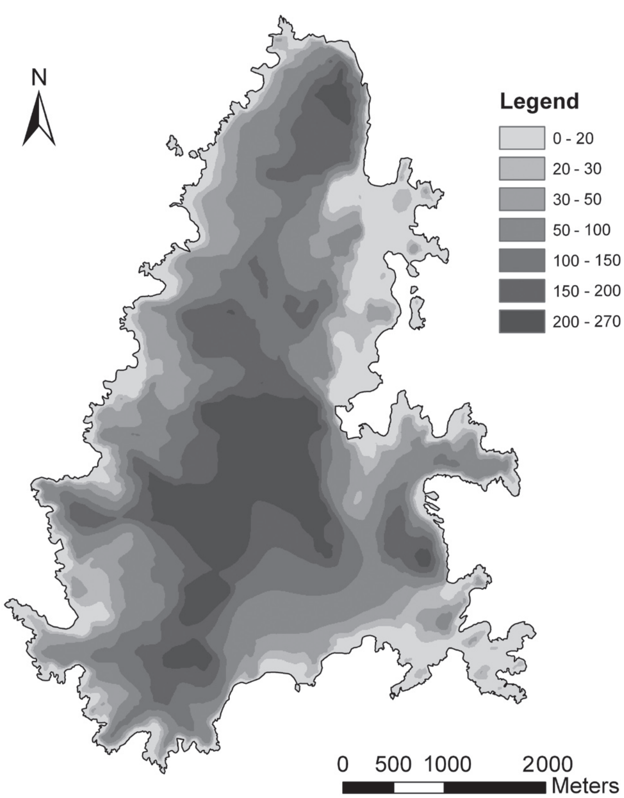

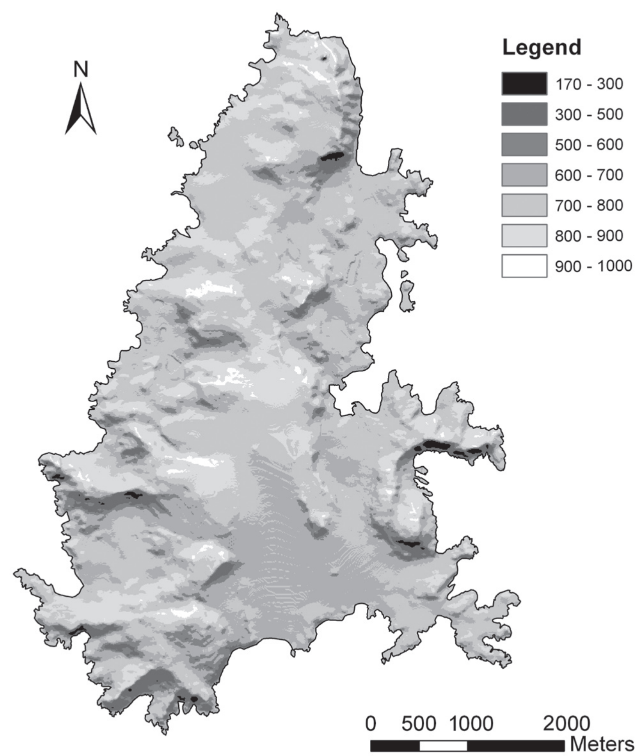

Figure 3. a) DEM classified according the elevation (m a.s.l.); b) global radiation (W/m^2) for the austral summer 2005/2006 (December 2005–February 2006).

polygons or sand wedge polygons were found. Only some poorly defined frost fissure polygons occur on the flat and highest ice-free areas of the island. Soil stripes are mainly sorted with a width ranging from 10 to 210 cm at the same site. Soil stripes are developed on glacial till and on colluvial deposits with slopes greater than 4°-6°. Transitional features from low-centered circles to sorted stripes are also present. Usually the coarse bands are raised with respect to the fine ones although sometimes can occur the opposite as unsorted stripes can occur very close to the sorted ones. Also soil stripes frequently end with low lobes (less than 1 m).

Gelifluction lobes are the most common periglacial feature which often occur on the same slope with a high variability of shape and dimension from stone-banked terracettes to lobes and stone streams (in Chambers *sensu*) and sometimes combine to form sheets. The gelifluction features are almost all stone-banked and develop on a wide range of slopes, but always greater than 4°-5° and show frontal ramps between 0.5 to 3 m in height. On the western side of the island moss-banked lobes which can be over 3 m high at the frontal ramp are quite widespread.

Only one active rock glacier has been detected on the island just northward of Sombre Lake. The rock glacier shows a convex profile along the flow direction and a very steep frontal scarp indicating the presence ice within it.

Permafrost distribution and modeling

PERMDEM is a very simplified model (derived by PERMACLIM, Guglielmin et al. 2003) which uses available climatic data (air temperature) and data automatically

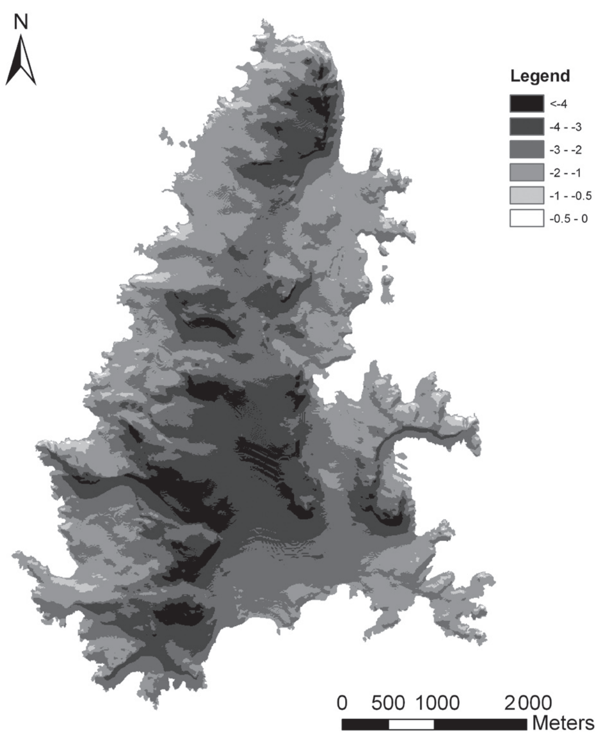

Figure 4. PERMDEM map of the Signy Island. The results MAGST are always negative, and only in less than 0.2% of the total area MAGST is between 0 and -0.%°C.

achievable by DEM that can influence the GST and consequently the permafrost distribution.

Figure 3 shows the DEM (classified according to the altitude 3a) and an example of the global radiation for the austral summer of 2005/2006 (3b).

From these layers and applying equation (1), a MAGST map has been obtained (Fig. 4). This model shows that permafrost conditions in 2006 (MAGST < 0°C) occur over the entire island from the sea shoreline upward. The model also shows that aspect and slope are important factors when considering global radiation and therefore the radiative balance and the energy balance of the surface. The major part of the ice-free areas of the island have a MAGST between -1°C and -2°C (41%) and between -2° and -3°C (34%), while only 4% have a temperature greater than -1°C.

The known effects of vegetation cover (Cannone et al. 2006, Guglielmin et al. in press) are not considered here, but the extensive cover of some mosses like *Sanionia* can significantly cool the surfaces. In contrast, the widespread black lichens (*Usnea*) and the patchy grasses can warm the surfaces compared to levels predicted by the model. Moreover, due to a lack of data on snow cover, thickness, and permanence on the island, its effect is also disregarded. The estimation of the snow cover from the preliminary observations of the available aerial and satellite images is difficult due to the high degree of cloud cover present for the majority of the time. From historical records and field data the depressions on the west side and on the south side of the island have the maximum snow accumulation and are more protected from the catabatic winds coming from Coronation Island. In 2006 the CALM grid remained completely snow free for all of the year suggesting that, at least for the year under study, the surface energy balance was not influenced on the exposed summit of the island and reasonably on the northward slopes.

The trenches carried out between December 2004 and the beginning of January 2005 had a target depth of 1 m. In several cases it was not possible to achieve this depth because (a) the water flow above the frost table filled the trench or (b) the presence of large boulders which prevented the holes from being dug. In the case of (a) above and where trenches could be dug to 1m depth, the frost table was found to be between 20 and 60 cm in depth. In all other cases, the 0° isotherm depth was estimated from the thermal profile according to Guglielmin (2006) and was estimated to range between 50 and 250 cm. Where the trenches were deeper than frost table, ice-cemented permafrost and subordinately ground ice (segregated ice) was found.

Discussion and Conclusions

The field excavations and the permafrost model indicate that permafrost does occur everywhere, although the periglacial features occurring on Signy Island do not provide conclusive evidence of permafrost because there is a lack of permafrost indicators such as ice wedge or sand wedge polygons and frost mounds. The gelifluction features do

Table 1. Distribution of the investigated periglacial features respect the MAGST classes calculated by PERMDEM for 2006. Legend: 1) -1<MAGST<1.5; 2) -1.5<MAGST<-2; 3) -2<MAGST<-2.5; 4) -2.5<MAGST<-3; 5) -3<MAGST<-3.5; 6) -3.5<MAGST<-4.

	N	1	2	3	4	5	6
Patterned Ground	14	28.5	43	28.5	0	0	0
Un/sorted Stripes	11	0	36	46	18	0	0
Gelifluction Lobes	23	30.5	30.5	17	4	9	9

not show any clear pattern with aspect and seem to prefer the areas where MAGST is higher (Table 1) confirming the conclusion of Vieira and Ramos (2003) for Livingston Island. The distribution of the different types of patterned ground seems to reflect their different genetic processes.

PERMDEM appears to be appropriate for use in Maritime Antarctica to model permafrost distribution because it requires only a minimum of air temperature data and a reasonably good DEM. The results obtained could certainly be improved by the inclusion of the effects of vegetation and snow cover. On the other hand PERMDEM indicates clearly that permafrost conditions are actually present everywhere on the Island even in the beach deposits.

The major limit of the model is that the *Ir* factor is actually calculated using only two points (the only two points located on bare ground and monitored all year round). It may be that the quite strong difference between the measured MAGST for the two areas of bare ground studied are related not only to the incoming radiation but also to difference of latent heat. The two sites were located less than 60 m apart and at the same altitude, but one had a southwestern aspect and the other a northeastern aspect.

The success of the model (more than 90% of accuracy) for the particular year studied may partly be due to the low snow cover for that year. As there was actually little snow cover, the lack of data on snow conditions had little effect on the predictions of the model.

It seems reasonable to conclude that, in any case, there are no altitudinal boundaries for permafrost occurrence at Signy Island as suggested by Serrano & Lopez Martinez (2000) for the South Shetlands and that permafrost is continuous and not discontinuous as suggested by Chambers (1966a). Further developments are required to improve the model and its calibration, especially to model active layer and permafrost thickness. Also more detailed geomorphological analyses of the periglacial features occurring on this unique island are required in order to understand their genesis and evolution in this period of climatic change.

Acknowledgments

We thank BAS and PNRA for their logistic and financial support of this research in the frame of the joint project “Permafrost and Global Change in Antarctica II (PGCAII).” We thank also BAS for permission to use and elaborate on the DEM data of Signy Island. Special thanks to James Bockheim, whose comments and suggestions allowed us to improve this paper significantly.

References

Bockheim, J.G., Campbell, I.B., Guglielmin, M. & López-Martínez J. 2008. Distribution of permafrost and ground ice in the Antarctic region. *Proceedings of the Ninth International Conference on Permafrost, Fairbanks, Alaska, June 29-July 3, 2008* (this proceedings).

Cannone, N., Ellis Evans, J.C., Strachan, R. & Guglielmin, M. 2006. Interactions between climate, vegetation and active layer in Maritime Antarctica. *Antarctic Science*,18(3): 323-333.

Chambers, M.J.G. 1966a. Investigations of patterned ground at Signy Island, South Orkney Islands: I. Interpretation and mechanical analyses. *Brit. Antarct. Surv. Bull.* 9: 21-40.

Chambers, M.J.G. 1966b. Investigations of patterned ground at Signy Island, South Orkney Islands: II. Temperature regimes in the active layer. *Brit. Antarct. Surv. Bull.* 10: 71-83.

Chambers, M.J.G. 1967. Investigations of patterned ground at Signy Island, South Orkney Islands: III. Miniature patterns, frost heaving and general conclusions. *Brit. Antarct. Surv. Bull.* 12: 1-22.

Chambers, M.J.G. 1970. Investigations of patterned ground at Signy Island, South Orkney Islands: IV. Long-term experiments. *Brit. Antarct. Surv. Bull.* 23: 93-100.

Chen, X. 1993. Permafrost around CGWS, Antarctica. *Proceedings of the Sixth International Conference on Permafrost, Beijing, China. July 5-9, 1993:* 84-88.

Fu, P. & Rich, P.M. 2002. A geometric solar radiation model with applications in agriculture and forestry. *Computers and Electronics in Agriculture* 37: 25-35.

Guglielmin, M. 2006. Ground surface temperature (GST), active layer, and permafrost monitoring in continental Antarctica. *Permafrost and Periglacial Processes* 17(2): 133-143.

Guglielmin, M., Aldighieri, B. & Testa, B. 2003. PERMACLIM: a model for the distribution of mountain permafrost, based on climatic observations. *Geomorphology* 51: 245-257.

Guglielmin, M., Ellis Evans, C.J. & Cannone, N. in press. Active layer thermal regime under different vegetation conditions in permafrost areas. A case study at Signy Island (Maritime Antarctica). *Geoderma*.

Hall, K. 1986. Rock moisture content in the field and the laboratory and its relationship to mechanical weathering studies. *Earth Surf. Proc. Landf.* 11: 131-142.

Hall, K. 1987. The physical properties of quartz-micaschist and their relationship to mechanical weathering studies. *Earth Surf. Proc. Landf.* 12: 137-149.

Hall, K. 1988. A laboratory simulation of rock breakdown due to freeze–thaw in a maritime Antarctic environment. *Earth Surf. Proc. Landf.* 13: 369-382.

Hall, K. 1990. Mechanical weathering rates on Signy Island, maritime Antarctic. *Perm. Perigl. Proc.* 1: 61- 67.

Herron, M.J. & Anderson, J.B. 1990. Late Quaternary glacial history of the South Orkney Plateau, Antarctica. *Quaternary Research* 33: 265-275.

Jones, V.J., Hodgson, D.A. & Chepstow-Lusty, A. 2000. Palaeolimnological evidence for marked Holocene environmental changes on Signy Island, Antarctica, *The Holocene* 10(1): 43-60.

Matthews, D.H. & Maling, D.H. 1967. The geology of the South Orkney Islands: I Signy Island. *Falkland Islands Dependencies Survey Scientific Reports* 25: 32 pp.

Mori, J., Fukui, K., Sone, T., Strelin, J. & Torielli, C. 2007. Internal structure of stone–banked lobes and terraces on rink plateau, James Ross Island, Antarctic peninsula region. *Polish Polar Research* 28(1): 23-30.

Nakada, M. & Lambeck, K. 1988. The melting history of the late Pleistocene Antarctic ice sheet. *Nature* 333 (6168): 36-40.

Ramos, M. & Vieira, G. 2003. Active layer and permafrost monitoring in Livingston Island, Antarctic. First results from 2000 to 2001. In: M. Phillips, S.M. Springman, L. Arenson (eds.), *Proceedings of the 8th International Conference on Permafrost, Zurich, Switzerland.* Lisse: Balkema Publishers, 929-933.

Rich, P.M. 1990. Characterizing plant canopies with hemispherical photography. In: N.S. Goel & J.M. Norman (eds.), Instrumentation for studying vegetation canopies for remote sensing in optical and thermal infrared regions. *Remote Sensing Reviews* 5: 13-29.

Serrano, E. & Lopez-Martinez, J. 2000. Rock glaciers in the South Shetland Islands, Western Antarctica. *Geomorphology* 35: 145-162.

Serrano, E., Martınez de Pison, E. & Lopez-Martınez, J., 1996. Periglacial and nival landforms and deposits. In: J. Lopez-Martınez, M.R.A. Thomson & J. Thomson (eds.), *Geomorphological Map of Byers Peninsula, Livingston Island, BAS Geomap Series, 5A.* Cambridge: British Antarctic Survey, 28–34.

Strelin, J.A. & Sone, T. 1998. Rock glaciers on James Ross Island, Antarctica. *Proceedings of the Seventh International Conference on Permafrost*, *Yellowknife, Canada, 23–27June, 1998:* 1027-1032.

Sugden, D.E. & Clapperton, C.M. 1977. The maximum ice extent on island groups in the Scotia Sea, Antarctica. *Quaternary Research* 7: 268-282.

Smith, R.I.L. 1990. Signy Island as a paradigm of biological and environmental change in Antarctic terrestrial ecosystems. In K.R. Kerry & G. Hempel (eds.), *Antarctic ecosystems. Ecological change and conservation*. Berlin: Springer-Verlag, 32-50.

Turner, J., Colwell, S.R., Marshall, G.J., Lachlan-Cope, T.A., Carleton, A.M., Jones, P.D., Lagun, V., Reid, P.A. & Iagovkina, S. 2005. Antarctic climate change during the last 50 years. *International Journal Climatology*, 25: 279-294.

Vieira, G. & Ramos, M. 2003 Geographic factors and geocryological activity in Livingston Island, Antarctica. Preliminary Results. *Proceedings of the Eighth International Conference on Permafrost, Zurich, Switzerland, 21–25 July 2003:* 1183-1188.

Development and Initial Evaluation of a Daily DEM-Based Active Layer Heave and Subsidence Model

Davor Gugolj
Terrapoint Canada Inc., Calgary, AB, Canada

Brian J. Moorman
Department of Geography, University of Calgary, Calgary, AB, Canada

Matthew P. Tait
Department of Geomatics Engineering, University of Calgary, Calgary, AB, Canada

Abstract

Daily permafrost active layer heave and subsidence was simulated for a 1 km^2 study area in the Mackenzie Delta, NWT for a period of one year. This study involved the development and application of a simplified methodology for assessing the dynamic nature of the active layer. It is based on the adaptation and integration of previously developed empirical and theoretical relationships related to the formation of segregated ice within frozen soil. The model requires a limited dataset including: general soil characteristics, a representation of the terrain in form of a digital elevation model, and regional weather records. The model was able to simulate the active layer thermal regime, yielding thaw depth values well within the range of measured observations. Likewise, daily changes in ground surface elevation across the study area due to formation or melt of segregated ice lenses agreed with direct measurements.

Keywords: heave; permafrost; segregation ice; subsidence; thermal modeling.

Introduction

Freezing and thawing of the active layer and the resultant heaving and subsidence of the ground surface are of particular significance in the Arctic regions, as the vertical movement of the ground surface throughout the year presents a hazard for the infrastructure. With an expected increase in the production of oil and natural gas in the Canadian Arctic, and associated infrastructure development, frost heaving may become a significant engineering issue, as well as a safety hazard (Bergquist et al. 2003, Palmer & Williams 2003). Various efforts have been made to predict and prevent active layer heave and subsidence from an engineering point of view, especially for prevention of gas pipeline buckling and road pavement heave (Konrad 1994, Palmer & Williams 2003). The dynamic nature of the active layer also presents challenges in assessing the subsidence caused by the oil and natural gas extraction in the permafrost-rich Arctic regions. Precise monitoring of terrain deformation through methods such as differential interferometric synthetic aperture radar (DInSAR) requires an accurate assessment of the state of the active layer at the date of acquisition. To address this issue, an active layer heave and subsidence model was developed that provides daily estimates of the thermal state of active layer, cumulative active layer heave or subsidence and the resulting ground surface elevation change.

To enable easy application of the model in a variety of permafrost terrain, the model complexity is reduced to require minimal input parameters. These parameters include a single sampling of terrain (elevation) and soils data, as well as regional weather data or that from nearby weather stations. All other required parameters are derived from such inputs based on empirical and theoretical relationships.

Study area

The model was tested at a site approximately two kilometers upland from Reindeer Station, NWT on the East Channel of the Mackenzie River (68.68°N, 134.06°W), and forty kilometers north of Inuvik, NWT, as shown in Figure 1. The site is one square kilometer of rolling tundra in the Caribou Hills, with a local relief of 20 meters, on an elevated bench overlooking the Mackenzie Delta. This hummocky upland terrain features a variety of soil types, ranging from peat to clayey silt colluvium derived from carbonate tills. The vegetation in the area is typified by dwarf shrubs, sedges, and herbs characteristic of a tundra environment, with willow and ground birch occupying the transitional zone between the tree-line and the tundra. The climate of the area can be characterized as very cold and dry, with a mean yearly temperature of -8.8°C and mean annual precipitation of 248.4 mm at Inuvik, for the years 1971-2000. Snowfall can occur in any month of the year, contributing an average of 167.9 mm SWE annually, and remaining on the ground for up to 8 months of the year (Environment Canada 2005).

Data

Minimizing the amount of input data required to simulate the active layer heave and subsidence is pertinent to providing a very simple, yet accurate model that can be applied in a variety of scales and environments. Weather data can be obtained from a climatological record at a nearby station, or from an in-situ weather station set up in the study area. For this study, climatological records for Environment Canada station *Inuvik A*, at Inuvik, NWT were used. Daily air temperature, precipitation, wind, and snow records for the years 1995 to 2006 were used (Environment Canada 2005). Terrain is represented in form of a digital

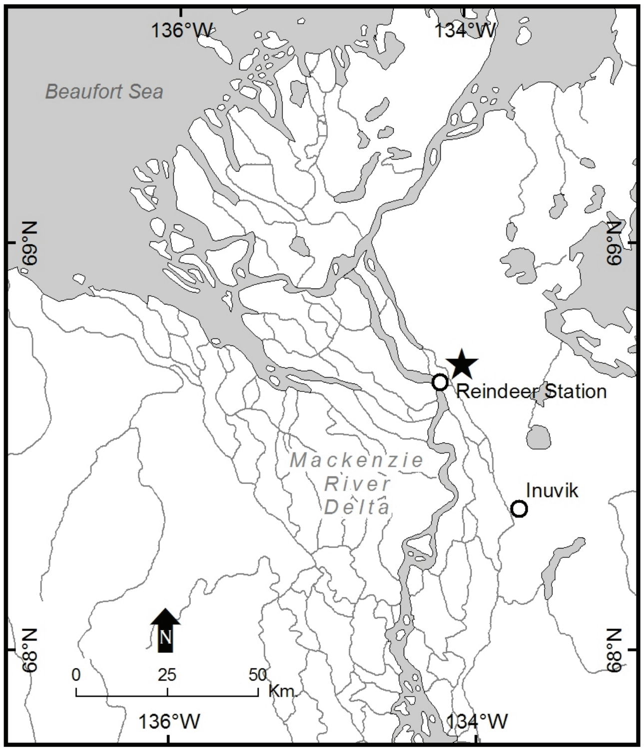

Figure 1. The star indicates the location of the study site in the Mackenzie Delta.

elevation model (DEM), which was created from a leveling survey conducted in the summer of 2004. A DEM with a 50-m resolution was generated from a dataset of 3962 points uniformly distributed across the study area. In addition, soil properties, water content, the presence and depth of the organics/peat layer, and active layer depth were obtained from a dataset of 36 sampling points also collected in the summer of 2004. Particle size analysis and moisture measurements were performed on the soil data, to obtain the necessary input parameters for the model. A 30-sample set of snow depth measurements was obtained at the study site in March of 2006, to be used to verify the predictions of the snow model.

Methodology

The simulation of the motion of the active layer was comprised of three sub-models. A snow distribution model was developed to predict the snow depth at the study site, in order to estimate the upper boundary (surface) thermal condition to be used in the thermal regime model, a thermal regime model estimated the temperature of the soil at different depths and so provided the location and character of the frost and thaw fronts, and an active layer heave/subsidence model calculated the amount of segregation ice formed or melted, and therefore the daily change in surface elevation

Snow distribution model

Spatial distribution of snow is fundamental for predicting the extent of permafrost in Arctic environments. Since snow acts as an insulator to the ground below, areas with long periods of thick snow cover usually remain permafrost free, while lack of snow cover promotes cooling of the soil and thus the growth of permafrost. Historically, the modeling of snow movement has been done through a variety of approaches, including empirical relationships between snow and wind, wind-tunnel testing, as well as one-dimensional and two-dimensional numerical models that predict the patterns of snow erosion and accumulation in a specified area (Liston & Sturm 1998, Pomeroy et al. 1993, 1997, Pomeroy & Li 2000).

Using a DEM of the study area in a geographic information system (GIS) environment, as well as the daily snowfall records and prevailing wind direction data from the weather station, the accumulation and redistribution of snow on the site was calculated. Implementation into a raster-based GIS environment was done through an iterative process using a 3 x 3 cell kernel which calculated the erosion or accumulation of snow in a given raster cell based on the above empirical relationships, as well as terrain characteristics. The results of this snow distribution model were then input into the thermal regime model.

Thermal regime model

Numerical models are generally the most popular approach to simulating and forecasting the thermal regime of active layer and permafrost (Miller 1979, Kane et al. 1991, Pustovoit 2000, Woo et al. 2004).

Determination of the thermal regime in this model was done using a simplified finite difference function (Rankinen et al. 2004) for calculating the ground temperature at a given depth. This calculation is based on a minimal set of environmental parameters, which include air temperature, snow depth, deep layer soil temperature at a known depth, and soil characteristics from field measurements. The thermal regime at each sampling point was calculated daily for each sample point for a period from July 1, 2002 to December 31, 2005. Allowing the model to stabilize for approximately 550 days before the needed values (years 2004-2005), the initial conditions were set sufficiently.

In order to provide an accurate estimate of the position of the freezing front within the soil, soil temperature was calculated at 1.0 cm increments to a maximum depth of 1.0 meter. Assuming a continuous flux between the soil surface and the air, through the snowpack and peat layers, surface temperature for every point was determined on a daily basis. Thermal properties of snow and peat were assumed to be constant over the study period.

Although snow becomes denser after snowfall, there was no practical solution to account for this change in density and thermal properties. However, on the tundra where considerable wind speeds are found at the ground surface, fresh snow quickly becomes reworked and reaches a steady state dense snow pack. Snow density value of 250 kg m^{-3} was used to represent tundra snowpack that was a few days to a week old. The thermal properties of snow used in this study reflect this density value (Williams & Smith 1989).

The model assumes that the soil properties below the surface (or peat layer where present) are homogeneous and do not vary with depth. This simplification of natural processes is necessary as the thermal properties of soil data at varying depths were not available for this study. Future versions of the model could include such variability.

The presence of water and ice close to the freezing temperature has significant effect on the thermal properties of frozen soils (Williams & Smith 1989). Therefore, thermal properties of soils must be modified accordingly for the proper interpretation and analysis of thermal conditions in the ground and for carrying out thermal calculations. Since the thermal conductivity and heat capacity of the soil were not measured for the soil samples, representative value for silty clay was obtained from Williams & Smith (1989) and used for all sampling locations. Silty clay, as defined in Williams & Smith (1989), was chosen as it was fairly representative of the soil samples obtained in the study area. The model accounts for the variability in thermal conductivity of soil with change in temperature, as well as adjusting for the variability of heat capacity due to influences from the ratio of unfrozen water and ice content in the soil, as well as those from the soil temperature.

It is argued that the water in soils freezes over a range of temperatures, depending on the chemical and geological properties of the host soil (Williams & Smith 1989). The frost front, defined as the location within the soil where the segregation ice will begin to form, often occurs close to the 0ºC isotherm, and the exact temperature varies with the aforementioned soil properties. Konrad & Morgenstern (1981) argue that the frost front for fine sands or coarse silts occurs very close to the 0°C isotherm. The present study therefore assumes that the frost front coincides with the 0°C isotherm based on the amount of fines present in the soil samples.

To identify the location of the frost front within the calculated thermal regime, the model identifies the location of the 0°C isotherm within the soil for each day, and returns the depth at which the frost front resides. The algorithm automatically recognizes the upper and lower temperatures on either side of the freezing front, and calculates the temperature gradient at the location. Since the thickness of the frozen fringe is fairly small (1.0 cm) it is assumed that the temperature gradient is linear. The model is robust enough to account for dual frost fronts that may occur as the freezing descends from the surface, and ascends from the underlying permafrost. In such situations, both depths and associated temperature gradients are used for the calculation of heave. The same function is used to identify the depth of thaw, as the soil is thawing during the warmer months. The location of the thaw front is identified, as well as the temperature gradient across it, and is used for subsidence calculations.

Heave and subsidence model

In its simplest form, the theory of frost heave is based on the freezing of water that is arriving at the freezing front in a saturated soil, as well as freezing of in-situ pore water. Formation of segregated ice lenses in the soil due to these

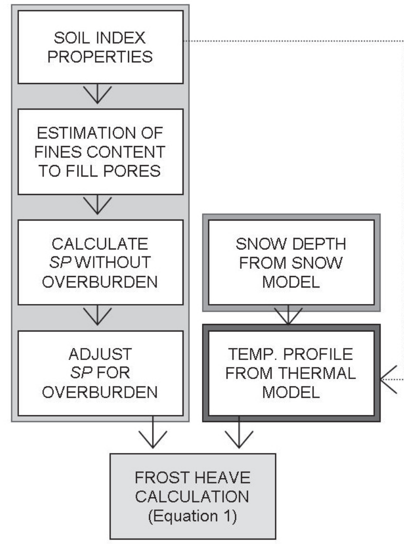

Figure 2. Model flowchart for calculating frost heave.

two phenomena cause significant structural disturbances in the soil. Segregated ice occurs as pure ice layers or lenses, millimeters to meters thick, within the soil. When ice lenses form, the overlying soil is pushed up (heaved) to accommodate for the volume of the ice itself, thus causing heaving at the ground surface. During the melt season, the disappearance of the ice lenses through melting causes weakening of the soil structure, which is often followed by collapsing of the ground surface (Konrad 1999).

The segregation potential model developed by Konrad & Morgenstern (1980) offers a very simple, but highly sensitive approach to simulating frost heave using a minimal set of input variables and is based on the concept of a segregation potential parameter (*SP*). Konrad (1999) defined a relationship between the *SP* parameter and four key soil properties (fines content, clay mineralogy, soil fabric, overburden pressure) and created a simple, soil index-based derivation of the *SP* parameter and the resulting frost heave. The amount of frost heave Δh (mm) that occurs during a given time interval Δt (s), is therefore defined as:

$$\frac{\Delta h}{\Delta t} = 1.09(SPgradT) \tag{1}$$

where *SP* is the calculated segregation potential value, and *gradT* defines the temperature gradient across the frozen fringe, as derived in the thermal regime model. Figure 2 summarizes this approach.

Required soil index properties were calculated for each sampling point from the samples obtained at the study site. Daily segregated ice content was calculated for each of 110 points across the study site and the depth at which it formed was identified. In situations where dual frost fronts occurred, both depths were identified and the amount of segregated ice was summed for a daily total. The calculations were performed for all days where freezing occurred, until the two freezing fronts converged and the soil was completely frozen.

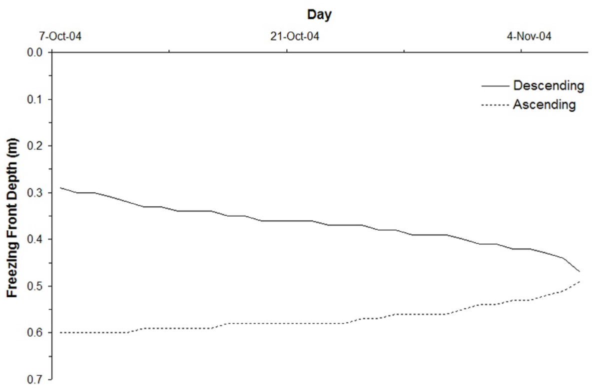

Figure 3. The progression of freezing front with time, for the end of the freeze-up period in year 2004.

During the thaw season, the amount of subsidence was calculated as the thaw front descended through the segregated ice formed during the previous year's freezing period. If the thaw depth coincided with the location of an ice lens, it was assumed that the entire ice lens that formed at that given depth will be melted and the ground surface will subside by the thickness of the lens. Changes in thermal properties of the soil due to presence of ice lenses were not accounted for. Elevation of each sampling point was modified daily, based on the amount of heave or subsidence that occurred. Heave and subsidence amounts were output into a database to be used in further spatial analyses.

Results and Discussion

Snow distribution model

The simplified approach to snow modeling provided a sufficient snow surface to be used in this model. Statistical comparison of the predicted snow surface and the set of 30 observed snow points show that the minimum and maximum snow depths are within one centimeter of each other, and the model overestimates the mean by 0.11 cm. The standard deviations of the two datasets are within 0.69 cm, indicating a similar variance of snow depths throughout the study area. The estimated snow distribution displayed the expected pattern, with thicker snow found in sheltered areas and thin snowpack on exposed slopes.

While having a more complex snow model (e.g., Liston & Sturm 1998, Pomeroy et al. 1993) would possibly be beneficial to accurately assess the daily snow cover over the study area, the method presented here is suitable for predicting the snow cover based on a minimal number of input parameters.

Thermal regime model

The thermal regime for all 110 locations was calculated for the test period (January 1, 2002, to December 31, 2005). In order to assess the change in elevation at each point due to heave and subsidence, the test period was considered to be from the first day of freeze-up in 2004 to the last day of thaw in 2005, thereby providing one full cycle of heave and thaw. Through the thermal model, these days were found to be October 7, 2004, and September 24, 2005, respectively.

As expected, the temperatures at depth respond well to the oscillations in air temperature, but with diminishing amplitude and an increasing phase lag with increasing depth. Figure 3 illustrates the depth of the frost fronts predicted for a selected station over time. The model successfully simulates the convergence of the descending and ascending freeze fronts in the soil, to completely freeze up the active layer.

Averaged across all locations, the depth of thaw for 2004 was found to be 56 cm. This is within the range of values measured in the Mackenzie Delta area. Kokelj & Burn (2005) estimate the thaw depth on the uplands near Inuvik to be between 30 and 100 cm. The thaw results also were validated by frost probing conducted through the summer.

To achieve a complete freeze-up the soil took an average of 40 days, starting on October 7, 2004. The soil was found to remain completely frozen for most locations until between May 15, 2005, and June 5, 2005. The average depth of thaw in 2005 was found to be 52 cm, with most locations achieving their maximum thaw depth by mid-September, approximately a week prior to the first day of freeze-up.

Heave and subsidence model

The amount of segregated ice, and therefore the amount of surface upheaval, was found to be an average of 10.33 cm per station during the freeze-up period in 2004. Approximately 78% of segregation ice formed at the descending frost front, at depths less than 30 cm below ground. This facilitated a fairly fast melt of the bulk of the segregated ice, as on average, the thaw front achieved a depth of 30 cm in approximately 35 to 40 days. Ignoring possible resultant alterations to the soil fabric and any factors that may inhibit the soil from returning to its original state, the subsidence due to melt of segregated ice has been modeled to be an average 9.10 cm. This therefore suggests that the soil does not return to its baseline elevation, and that an average of 1.24 cm of segregated ice remains into the next freeze-up season. This is a function of colder temperatures experienced in the second model year.

Figure 4a depicts the predicted progression of segregated ice formation through time at one sampling point. As the ground begins to freeze, the steep thermal gradient across the freezing front initially causes a significant amount of segregated ice to form. With a decrease in the gradient, less ice is formed, reaching a minimum at zero as either all water in the soil is frozen, or the two freezing fronts converge. Due to the lag time in the response to surface temperature changes at depth, the thermal gradient across the descending freezing front is always much steeper than that moving upwards from the permafrost below. Thus, the amount of segregated ice formed at the descending freezing front contributes much more to the total ice content, while leaving the majority of ice lenses within the first few tens of centimeters below the surface. This is also supported by the results presented in Figure 4b, showing the progression of the thaw front though the soil, as well as the associated subsidence due to melt of

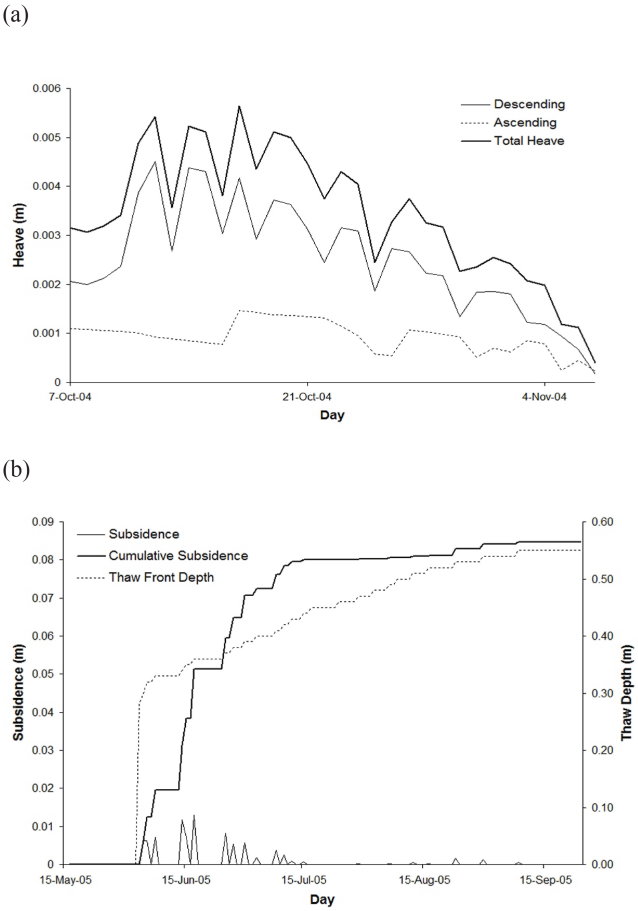

Figure 4. (a) Generation of segregated ice lenses (and therefore heave) at the descending and ascending freezing fronts at point #54, during the freeze-up season in 2004 (b) Progression of the thaw front during the melt season in 2005 and the consequent subsidence due to melt of ice lenses, for point #54.

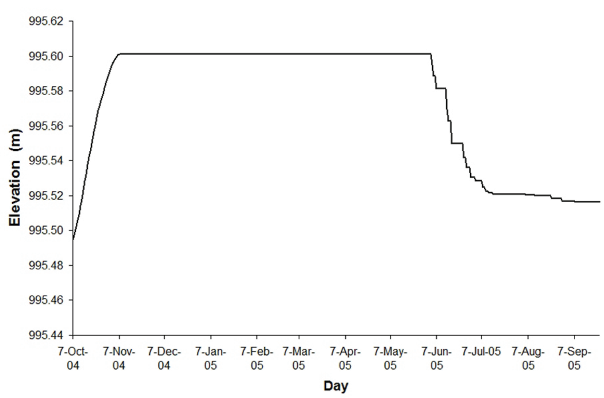

Figure 5. Predicted elevation changes during the study period (2004-2005) due to formation and melting of segregated ice at point #54.

ice lenses. Figure 5 illustrates the annual cycle of ground surface heave and subsidence due to formation and melt of segregated ice for a single sampling point, during the testing period. The overall change in elevation at the end of the melt period in 2005 is shown in Figure 6. As the thaw depths in 2005 did not reach all of the segregated ice that was formed in 2004, a lift in the ground surface is observed across the whole study area. Biggest elevation changes are seen in the northeastern quadrant of the study area, where the ground has been raised by up to 2.4 cm.

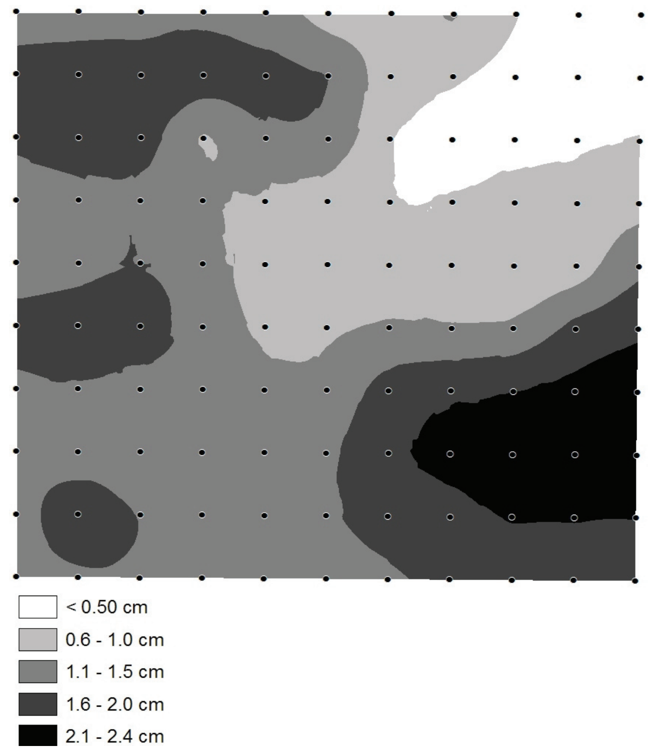

Figure 6. Total predicted change in elevation for the study area, after the melt season of 2005.

Conclusions

This work provides a simplified methodology for predicting active layer heave and subsidence on a daily basis based on a limited number of parameters. The approach integrated and modified a number of previously developed methodologies for snow distribution modeling, calculation of freezing soil thermal regimes and the formation of segregated ice within frozen soil.

The snow distribution and thermal models produced estimates that closely matched measured values at the test site. Based on the predicted frost and thaw front depths, the heave/subsidence model was able to simulate the daily changes in the surface elevation due to formation and melt of segregated ice lenses, also yielding values within the expected ranges for the area.

The model is also able to take into account inter-annual weather variability and the resultant changes in the depth of thaw and longer term surface elevation change resulting from changes to the active layer.

Future refinements of the active layer motion model presented in this study will focus on capturing the characteristics of layered soils. As well, implementation of lateral exchanges of heat and water would allow for full three-dimensional predictions of the thermal regime and have characteristics, thereby accounting for natural variations in microclimatic and terrain conditions that may play a role in the formation of segregated ice.

Acknowledgments

The authors would like to express gratitude to Jeff Williams for field data collection and analyses, as well as to Imperial Oil Limited and NSERC for financial assistance and Steve Solomon and the Geological Survey of Canada for logistical assistance.

References

Bergquist, C.L., Graham, P.P., Johnston, D.H. & Rawlinson, K.R. 2003. Canada's Mackenzie Delta: fresh look at an emerging basin. *Oil and Gas Journal* 101: 42-46.

Environment Canada. 2005. National Climate Data and Information Archives. *Online.* <http://www.climate.weatheroffice.ec.gc.ca/climateData/canada_e.html> Accessed December 15, 2005.

Kane, D.L., Hinzman, L.D. & Zarling, J.P. 1991. Thermal response of the active layer to climate warming in permafrost environment. *Cold Regions Science and Technology* 19: 111-122.

Kokelj, S.V. & Burn, C.R. 2005. Geochemistry of the active layer and near-surface permafrost, Mackenzie delta region, Northwest Territories, Canada. *Canadian Journal of Earth Sciences* 42: 37-48.

Konrad, J.M. 1994. Sixteenth Canadian Geotechnical Colloquium: Frost heave in soils: concepts and engineering. *Canadian Geotechnical Journal* 31: 223-245.

Konrad, J.M. 1999. Frost susceptibility related to soil index properties. *Canadian Geotechnical Journal* 36: 403-417.

Konrad, J.M. & Morgenstern, N.R. 1980. A mechanistic theory of ice lens formation in fine grained soils. *Canadian Geotechnical Journal* 17: 473-486.

Konrad, J.M. & Morgenstern, N.R. 1981. The segregation potential of a freezing soil. *Canadian Geotechnical Journal* 18: 482-491.

Liston, G.E. & Sturm, M. 1998. A snow-transport model for complex terrain. *Journal of Glaciology* 44: 498-516.

Miller, T.W. 1979. The surface heat balance in simulations of permafrost behaviour. *Journal of Energy Resources Technology* 101: 240-250.

Palmer, A.C. & Williams, P.J. 2003. Frost heave and pipeline upheaval buckling. *Canadian Geotechnical Journal* 40: 1033-1038.

Pomeroy, J.W., Gray, D.M. & Landine, P.G. 1993. The prairie blowing snow model: characteristics, validation, operation. *Journal of Hydrology* 144: 165 - 192.

Pomeroy, J.W. & Li, L. 2000. Prairie and Arctic aerial snow cover mass balance using a blowing snow model. *Journal of Geophysical Research* 105: 26619-26634.

Pomeroy, J.W., Marsh, P. & Gray, D.M. 1997. Application of a distributed blowing snow model to the Arctic. *Hydrological Processes* 11: 1451-1464.

Pustovoit, G.P. 2000. Calculation of permafrost temperature. *Soil Mechanics and Foundation Engineering* 37: 27-31.

Rankinen, K., Karvonen, T. & Butterfield, D. 2004. A simple model for predicting soil temperature in snow-covered and seasonally frozen soil: Model description and testing. *Hydrology and Earth System Sciences* 8(4): 706-716.

Williams, P.J. & Smith, M.W. 1989. *The Frozen Earth: Fundamentals of Geocryology*. Cambridge: Cambridge University Press, 306 pp.

Woo, M.K., Arain, M.A., Mollinga, M. & Yi, S. 2004. A two-directional freeze and thaw algorithm for hydrologic and land surface modeling. *Geophysical Research Letters* 31: L12501.

Shear Strength of Ice-Filled Rock Joints

Friederike K Günzel
University of Brighton, Brighton, UK

Abstract

Ice-filled rock joints are a common feature of high mountain permafrost areas. Warming of these joints in rock can lead to instabilities and rockfall events. In the following study, a series of direct shear tests was performed with artificial samples simulating ice-filled rock joints. The direct shear tests were carried out in two testing modes: constant strain and constant stress. In constant stress tests, the ice-filled joints show a parabolic relationship between normal stress and shear stress unlike the linear relationship usually found in mineral filled rock joints (Barton 1974). Constant stress tests were also conducted in which the samples were allowed to warm up until failure occurred while a constant normal stress and a constant shear stress were applied. Different failure modes could be identified, either driven by breaking the connection of ice and concrete or ductile deformation of the ice or a combination of both.

Keywords: direct shear; ice strength; rock joints; rock slopes; shear strength.

Introduction

In recent years, increased numbers of landslide and rockfall events have been reported in high mountain areas (Gruber et al. 2004). A connection between the landslide events and the warming of permafrost due to increasing mean annual air temperatures was observed in landslide events, such as the Val Pola Landslide in 1987 (Dramis et al. 1995).

Earlier laboratory experiments, carried out on a geotechnical centrifuge (Davies et al. 2003 and Günzel & Davies 2006) showed that ice-filled joints in rock are stable as long as the temperature of the ice is low (below about 2°C); however, both the strength and stiffness of ice in the joint reduce if the temperature rises closer to melting point. This leads to a reduction in strength of the rock joint which, if it is critical to maintaining slope stability, can result in slope failure or rockfall. However, the stability increases again when the ice from the joint melts and the rock surfaces come into contact with each other. That means that slope failure can occur at a joint during warming of the permafrost ice, even if a slope is stable both when the rock joints contain "cold" ice and when no ice is present. Slope failure might be avoided if these critical joints can be identified and stabilised temporarily during the period when the ice is warming and when the shear capacity of the joint is below that required for stability.

The current study systematically uses direct shear testing to investigate the shear strength of an ice-filled rock joint during warming of permafrost.

Laboratory Methods

Preparation of samples

In the study, artificial samples made of high-strength concrete (Densit Ducorit D4) were used. To simulate the roughness of the rock joint surfaces, a regular saw-tooth surface was used with the dimensions as shown in Figure 1. Regular, saw-toothed surfaces are a commonly used idealisation of rough rock surfaces in the literature (de Toledo & de Freitas 1993). The dimensions of the samples were 59mm x 59mm to fit inside a 60mm square shear box.

A thermocouple was cast into the concrete samples with the sensitive tip in a small cavity at the centre of the sample surface (Fig. 2). This allowed the temperature of the ice to be measured during the shear tests.

Initial tests were carried out without ice to establish the friction of the concrete surface. Then two different types of ice-filled samples were prepared: concrete-ice samples (Fig. 3) and sandwich samples (Fig. 4).

The concrete-ice samples consist of a concrete block with saw-toothed surface overlaid by an equally thick ice block (Fig. 3). This sample type simulates an ice-filled joint, with

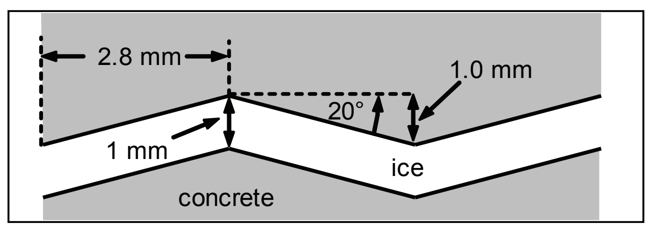

Figure 1. Dimensions of the saw-tooth surface.

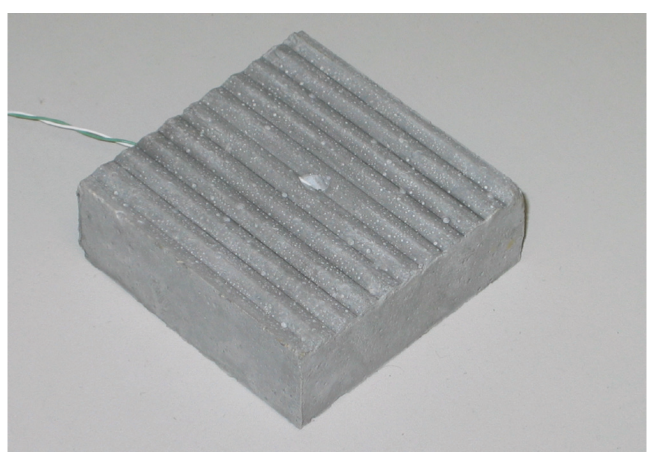

Figure 2. Concrete block with cast saw-tooth surface; the small cavity in the center holds the tip of the thermocouple.

Figure 3. Concrete-ice sample after a constant strain test with normal stress = 207 kPa.

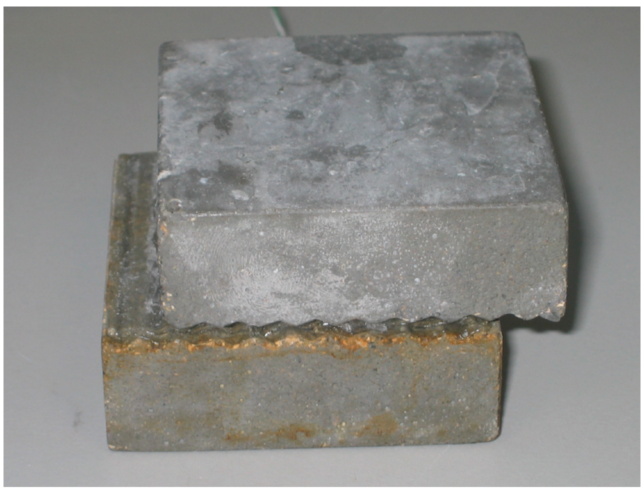

Figure 4. Sandwich sample after a constant stress test with normal stress = 207 kPa.

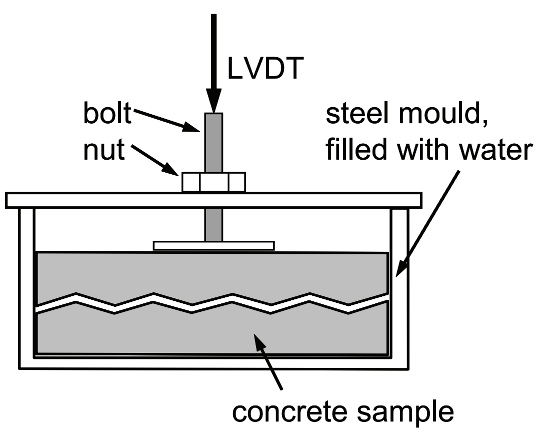

Figure 5. Preparation of sandwich sample.

the ice thickness being much larger than the amplitude of the surface roughness. The concrete-ice samples are prepared by placing concrete blocks into moulds filled with water and allowing them to freeze.

The sandwich samples consist of two saw-toothed concrete blocks with a 1mm thick layer of ice in-between (Fig. 4). This sample type simulates an ice thickness equal to the amplitude of the surface roughness. These samples are prepared as illustrated in Figure 5. The two concrete blocks are immersed in water in a mould. A bolt is glued to the top block. The top block is then lifted by turning the nut against the lid of the mould while the movement is measured with an LVDT (Linear Variable Displacement Transducer). After that, the surplus water on top of the sample is drained, and the sample is frozen.

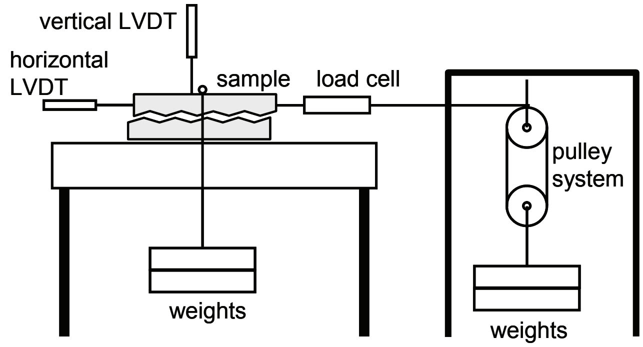

Figure 6. Schematic overview over experimental set-up of the constant strain test.

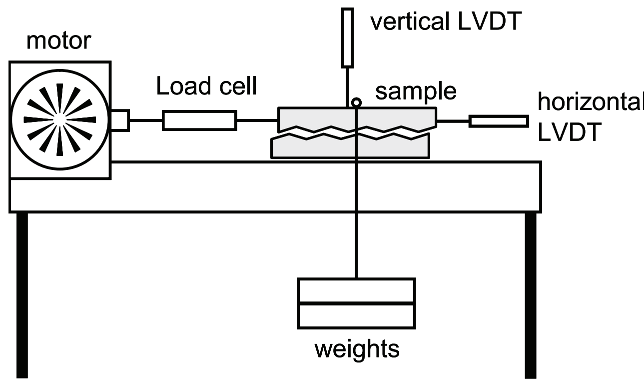

Figure 7. Schematic overview over experimental set-up of the constant stress tests.

Direct shear tests

Two different modes of direct shear tests were carried out in this study: constant strain tests and constant stress tests. Schematic overviews of both testing modes are shown in Figures 6 and 7. Normal stress is provided by hanging weights. Horizontal and vertical displacements are measured with LVDTs.

In the constant strain tests, shear stress is applied by an electric motor pushing the upper part of the sample while the lower part remains stationary. The shear stress is measured with a load cell. These tests were carried out at -2°C and -4°C, with normal stresses ranging between 135 kPa and 620 kPa. This is equivalent to a depth of 5–25 m below ground. This depth is above the range of the annual freeze-thaw depth of 5±2 m in the Alpine periglacial belt reported by Matsuoka et al. (1998). However, with increasing air temperatures, the freeze-thaw depth can be

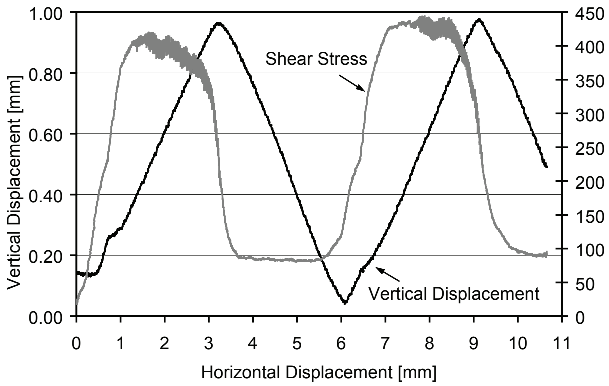

Figure 8. Vertical displacement and shear stress vs. horizontal displacement of a shear experiment without ice (normal stress = 207 kPa).

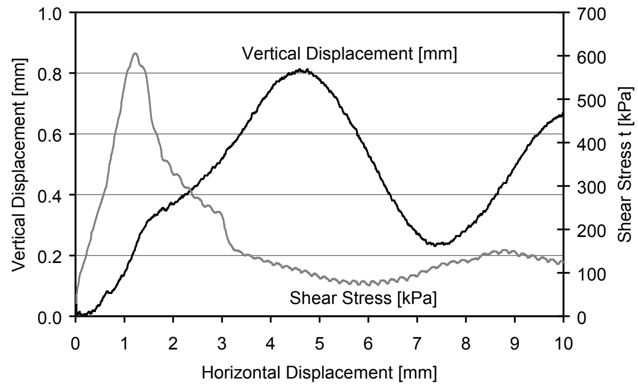

Figure 10. Results of a constant strain shear experiment with a concrete-ice sample at -2°C (normal stress = 207 kPa).

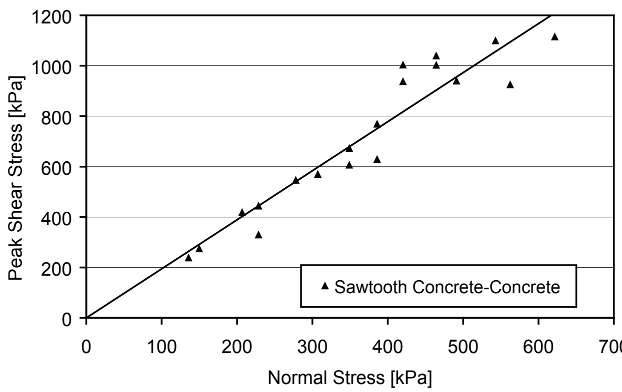

Figure 9. Overview of peak shear test results of concrete samples.

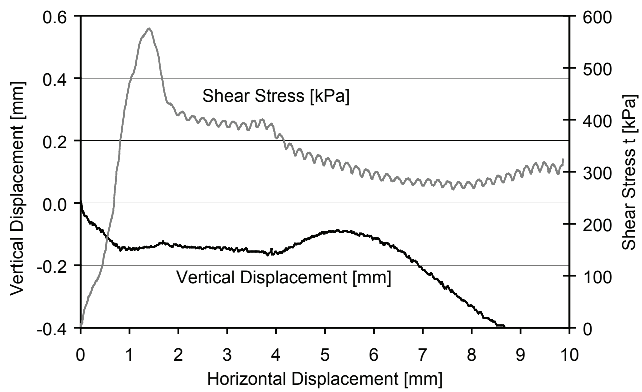

Figure 11. Results of a shear experiment at constant strain with a concrete-ice sample. Temperature = -4°C, normal stress = 562 kPa.

expected to increase.

A constant horizontal displacement rate of 0.47 mm/hour was used for all tests. However, earlier studies (Barnes et al. 1971) found that not only the temperature, but also the strain rate, has a significant effect on the shear strength of an ice-granite interface. Also, failure of a rock slope is not controlled by constant strain, but rather by constant stress.

Therefore the shear box was modified to be able to apply a constant shear stress rather than a constant strain onto the concrete ice samples and the sandwich samples. Here, the motor was replaced by a pulley system and weights to apply a constant shear stress to the samples. The sample temperature was then increased slowly until the sample failed.

Cold room

The experiments were carried out in a cold room. To ensure a constant temperature of the sample during the defrosting cycles of the cooling element, the shear box was encased inside a Styrofoam box with 100 mm wall thickness. However, the electric motor of the shear box apparatus caused the temperature inside the Styrofoam box to increase during the constant strain tests. Therefore it was very difficult to control the temperature of the sample and subsequently the temperatures at failure varied by about 0.5 C.

Experimental Results

Samples without ice

To establish the frictional resistance of the concrete samples without ice, direct shear tests were carried out with normal stresses between 135 kPa and 620 kPa. The typical response of a sample is shown in Figure 8. Here the shape of the saw tooth surface is clearly visible from the vertical displacement. The development of the shear stress follows the same pattern with the maximum shear stress during the uplift of the top sample.

Figure 9 shows the maximum measured shear stresses of all concrete samples plotted against the normal stress applied to the sample. As expected, there is a clear linear relationship between the normal stress and the shear stress. The scatter of data above a normal stress of 400 kPa is due to abrasion of the concrete samples during the test.

Constant strain tests with concrete-ice samples

A total number of 26 constant strain tests were carried out at two different temperatures: -2°C and -4°C. Depending on the normal stress, the vertical displacement during the test showed different behaviour (Figs 10,11): at low normal stresses, the vertical displacement clearly reproduces the shape of the saw-toothed surface, albeit with a slightly reduced amplitude (Fig. 10). This behaviour can be

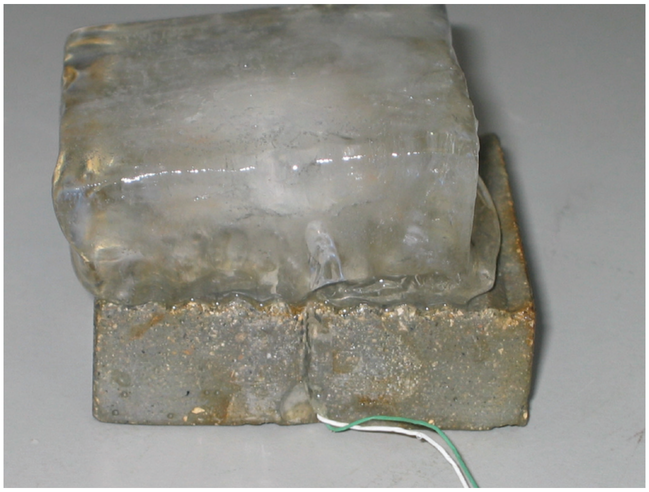

Figure 12. Shear deformation of a concrete-ice sample after a constant strain test with normal stress = 490 kPa.

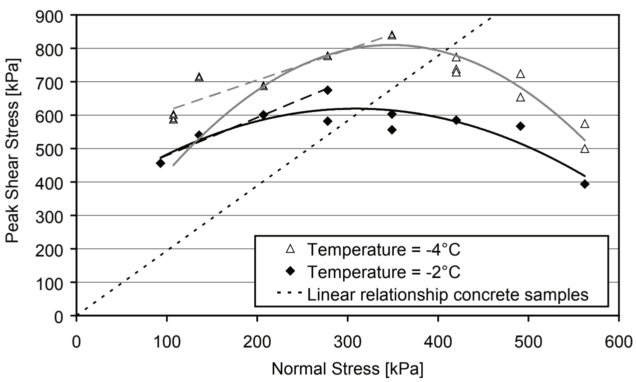

Figure 13. Peak shear test results from concrete-ice samples in constant strain tests.

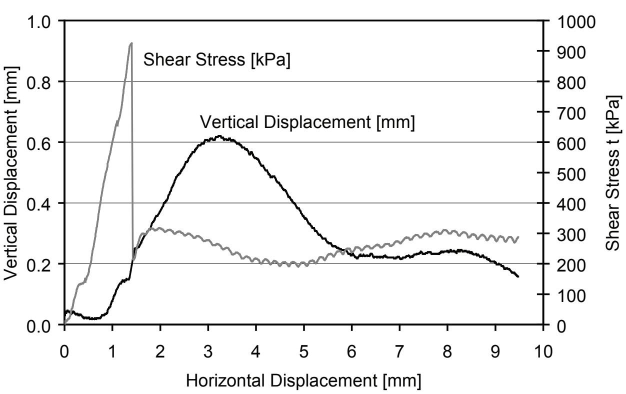

Figure 14. Results of a constant strain shear experiment with a sandwich sample at -5°C (normal stress = 490 kPa).

interpreted as the ice becoming detached from the concrete surface, and the behaviour of the sample is mainly defined by the friction between surfaces of the ice and the concrete (Fig. 3). However, at high normal stresses, no dilation of the sample was observed (Fig. 11). Here the deformation of the sample is mostly due to a shear deformation of the ice itself rather than the sliding of ice over concrete. At the end of these tests, the ice was still firmly attached to the concrete surface (Fig. 12). No granularisation of the ice comparable

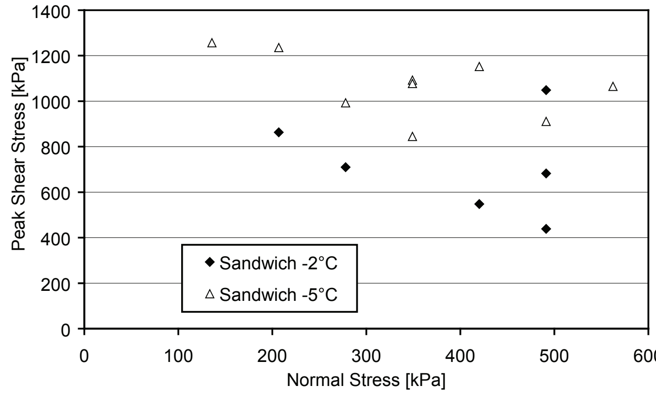

Figure 15. Overview of peak shear test results of sandwich samples in constant strain tests.

to the "rubblisation" reported by Yasufuku et al. (2003) was observed. It should be noted, that the initial stiffness of the samples is approximately the same, irrespective of the type of deformation.

The two different mechanisms of deformation also become apparent in the relationship of maximum shear stresses and normal stresses at failure (Fig. 13): at low normal stresses, the relationship between maximum shear stress and maximum normal stress appears to be linear (dashed lines in Fig. 13), which is in agreement with the behaviour of mineral-filled rock joints (Barton 1974). However, at normal stresses, above 220 kPa and 300 kPa for -2°C and -4°C, respectively, this relationship becomes parabolic. This result agrees with the parabolic strength envelopes of ice found by Fish & Zaretsky (1997).

Constant strain tests with sandwich samples

The constant strain tests with sandwich samples were carried out at -2°C and -5°C. Unlike the concrete-ice samples, the sandwich samples dilated even at high normal stresses (Fig. 14). It is also noticeable that the shear stress maximum forms a very sharp peak with a sudden drop when the ice becomes detached from the concrete surface. Again, the initial stiffness of the sample is very similar to the stiffness of the concrete-ice samples. Due to the sharp peak, a considerable scatter of the maximum strength at failure is to be expected (Fig. 15). It is unlikely that the scatter is enhanced to a large extent by the sampling rate: the shear stress increased with a rate of approximately 10 kPa per minute, so that with a one-minute sampling rate, the error would be not more than 10 kPa. Despite the large scatter, a decrease of the maximum shear stress with increasing normal stress can be observed.

Constant stress test

The tests were started at an ice temperature of approximately -5°C, and then the temperature was increased at a rate of about 0.3°C per hour until failure occurred. These shear tests were carried out at normal stresses between 136 kPa and 630 kPa. The typical result of a constant stress shear test with a concrete-ice sample is shown in Figure

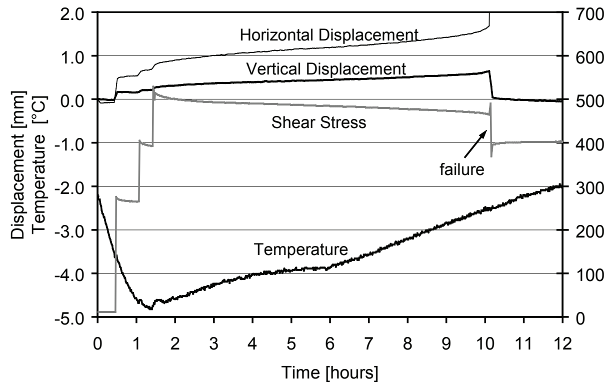

Figure 16. Results of a constant stress experiment (concrete-ice sample, normal stress = 207 kPa) plotted against time.

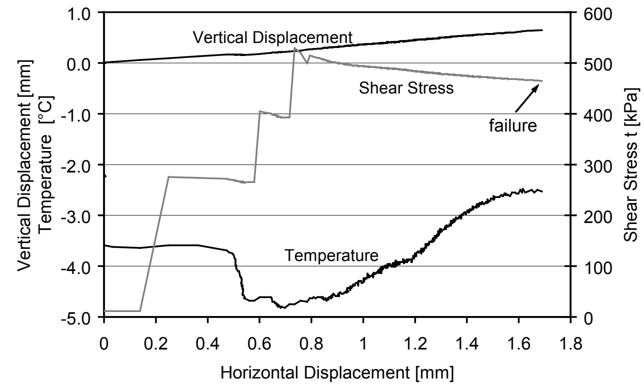

Figure 17. Results of a constant stress experiment (concrete-ice sample, normal stress = 207 kPa) plotted against horizontal displacement.

16 (plotted against time) and Figure 17 (plotted against horizontal displacement). The results for concrete-ice samples and sandwich samples are very similar. The steps of the shear stress at the beginning of the test correspond to adding weights to the pulley system. The decrease of stress during the test is due to friction in the pulley system: the tension in the nylon rope connecting the sample with the weight slackens slightly as the sample deforms, due to creep in the ice prior to failure. The apparent change of the rate of temperature increase is due to the increasing rate of horizontal deformation immediately before failure of the sample.

The horizontal displacement during the constant stress tests was considerably slower than during the constant strain tests; it varied between 0.002 mm/hour and 0.06 mm/hour. The deformation rate increased with increasing shear stress, but no significant change could be observed for increasing normal stress or temperature. The horizontal displacement at failure was between 1.5 mm and 2.5 mm, similar to the displacement at failure of the constant strain tests. The vertical displacement decreased with increasing normal stress.

Figure 18 shows the variation of failure temperature depending on normal stress and shear stress for concrete-ice samples and sandwich samples. The data points represent the shear stress at failure versus the normal stress acting on the sample. The temperature distribution for both sample types is very similar, with the only difference being that the failure temperatures of the sandwich samples were about 0.5°C lower than the concrete-ice samples. The data show decreasing failure temperatures with increasing shear stresses. However, the failure temperatures increase with increasing normal stresses throughout the test series up to normal stresses of 630 kPa. This behaviour differs from the constant strain experiment where, at normal stresses above 300 kPa, a decrease of failing temperature with increasing normal stress was observed (Fig. 13).

Figure 18 also shows the failure envelope of the concrete samples. It can be seen that, at low temperatures and low normal stresses, the ice-filled joints have a higher shear strength than joints without ice-filling.

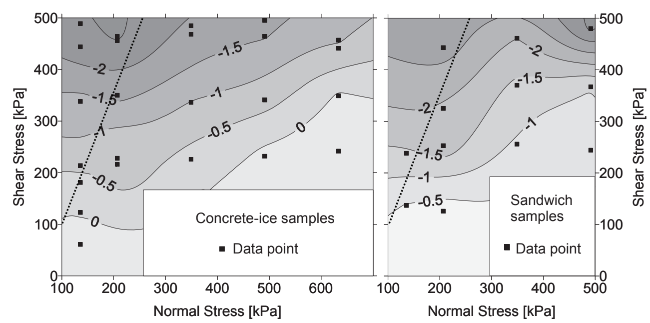

Figure 18. Temperatures at failure (measured by the sensor in the middle of the sample) during constant stress tests with concrete-ice samples (left) and sandwich samples (right). The dotted lines represent the linear relationship between shear stress and normal stress obtained for the concrete samples.

Discussion

Depending on sample type (concrete-ice or sandwich) and test type (constant stress or constant strain), three different types of deformation could be identified:

1. Deformation driven by breaking of the connection between the ice and the concrete surface;
2. Deformation driven by shear deformation of the ice itself; and
3. Combination of the deformation types 1 and 2.

In the constant strain tests with concrete-ice samples at low normal stresses, the first type of deformation is predominant. Indicators for this type of failure are the extent of the dilation of the samples during the test (Fig.10) and the visual examination of the sample after the test (Fig. 3) that clearly shows the ice being detached from the concrete surface. However, the same sample type shows ductile deformation of the ice at high normal stresses. Here the samples show no net dilation during the test (Fig. 11); any local dilation that may be present in the sample is counteracted by the ductile deformation of the ice, which is clearly visible in the sample after the test (Fig. 12).

In the constant-strain tests of the sandwich samples, a combination of the first two failure modes is observed. Visual examination of the samples showed the ice detached from one of the concrete surfaces. However, these samples show a reduced dilation of 0.4mm–0.6mm (Fig. 14) indicating that sliding of the ice over the concrete surface is not the only type of deformation in these samples. The other type of deformation may be shear deformation of the ice itself. The maximum shear strength reduces with increasing normal stress (Fig. 15), again indicating shear deformation of the ice.

Constant-stress experiments with both sample types show that here the predominant type of deformation is breaking the connection between the ice and the concrete. This observation is consistent with the data shown in Figure 18, where the shear stress at failure increases rather than decreases with normal stress for a constant temperature.

Conclusions and Outlook

In this study, three different failure modes of ice-filled joints could be distinguished. This adds to the understanding of the failure mechanisms of rock slopes in warming permafrost conditions.

Several issues that have not been considered to date will be addressed in the near future:

- The strength of ice depends on the strain rate; constant strain tests need to be carried out with the same strain rate as observed in the constant stress tests.
- Creep measurements of ice at constant temperatures, rather than increasing temperatures, need to be conducted.
- The strain rate measured in the laboratory needs to be compared with strain rates measured in full scale rock slopes rather than small-scale centrifuge model tests.

Acknowledgments

All experiments were carried out at the geotechnical laboratories of the University of Dundee, UK.

References

Barnes, P., Tabor, D. & Walker, J.C.F. 1971: The friction and creep of polycrystalline ice. *Proceedings of the Royal Society, London (Series A)* 324: 127-155.

Davies, M.C.R., Hamza, O. & Harris, C. 2003: Physical modelling of permafrost warming in rock slopes. *Proceedings of the Eighth International Conference on Permafrost, Zürich, Switzerland, July 21-25, 2003:* 169-174.

de Toledo, P.E.C. & de Freitas, M.H. 1993: Laboratory testing and parameters controlling the shear strength of filled rock joints. *Géotechnique* 42(1): 1-19.

Dramis, F., Govi, M., Guglielmin, M. & Mortara, G. 1995: Mountain permafrost and slope instability in the Italian Alps: the Val Pola Landslide. *Permafrost and Periglacial Processes* 6: 73-82.

Fish, A.M. & Zaretsky, Y.K. 1997: Ice strength as a function of hydrostatic pressure and temperature. *CRREL Report 97-6.*

Gruber, S., Hoelzle, M. & Haeberli, W. 2004: Permafrost thaw and destabilization of Alpine rock walls in the hot summer of 2003. *Geophysical Research Letters* 31:L13504.

Günzel, F.K. & Davies, M.C.R. 2006: Influence of Warming Permafrost on the Stability of Ice Filled Rock Joints. *Proceedings of the Sixth International Conference on Physical Modelling in Geotechnics, Hong Kong, August 4-6, 2006:* 343-348.

Matsuoka, N., Hirakawa, K., Watanabe, T., Haeberli, W. & Keller, F. 1998: The role of diurnal, annual and millennial freeze-thaw cycles in controlling Alpine slope instability. *Proceedings of the Seventh International Conference on Permafrost, Yellowknife, Canada, June 20-24, 1998:* 711-717.

Yasufuku, N., Springman, S.M., Arenson, L.U. & Ramholt, T. 2003: Stress-dilatancy behaviour of frozen sand in direct shear. *Proceedings of the Eighth International Conference on Permafrost, Zürich, Switzerland, July 21-25, 2003:* 1253-1258.

An Analysis of Land Suitability for Urban Construction in Permafrost Regions

Igor E.Guryanov
Melnikov Permafrost Institute, SB RAS, Yakutsk, 677010, Russia

Abstract

Natural conditions of sites varying in favorability for urban construction are discussed, based on the example of Yakutsk, northeastern Russia. Their role in overall land suitability is shown. Relationships between the initial land suitability level and the resulting ecological situation at the townsite are analyzed, with particular reference to the permafrost region.

Keywords: conditions; ecological situation; factors; land suitability; permafrost; urban construction.

Problem Statement

The common feature of community infrastructures in permafrost regions is the lower structural and maintenance safety of buildings and facilities compared to more temperate regions, and the frequent performance problems resulting from permafrost thawing due to anthropogenic changes. It is, therefore, important to determine to what extent these deficiencies are related to the design and construction solutions, the choice of which is dictated indispensably by considerations of economics.

Construction Area Quality Factors

Depending on the favorability of environmental conditions, areas vary in suitability for urban development. Development of the areas of limited suitability results in an additional burden on the urban environment. Development of unsuitable areas aggravates the situation, producing complex engineering and ecological problems.

The suitability of any area for urban land use is predetermined by five basic factors characterizing the general conditions for construction:

1) The geology of the area and the geological processes and features anticipated to occur beneath buildings and structures.

2) The topography of the area which affects the convenience of service lines.

3) The hydrogeology and the surface and subsurface drainage conditions.

4) The hydrology of rivers and lakes.

5) The thermal regime and the air and water quality.

These factors are analyzed during the planning process in order to create the most favorable conditions and control the quality of construction sites. Inadequate consideration or neglect of any of these environmental factors reduces the overall suitability of the construction area. Since the factor combinations are always specific, suitability evaluations are only made for specific areas.

Factor Assessment Criteria

First factor (geological conditions)

- Favorable conditions: Homogenous soils or rocks that are good foundation material for conventional foundation types; the stability and adequate performance of engineering structures are guaranteed;
- Provisionally favorable conditions: Ground properties that call for some restrictions of the effects from buildings and other structures to ensure their stability and good performance; special foundation types, soil improvement, and other measures can be applied;
- Unfavorable conditions: Weak soils that require special foundation designs, soil improvement, structural measures. and stringent controls on construction and maintenance.

Second factor (topography)

- Favorable conditions: Lowlands with slopes of 0.5 to 10%, local relief of up to 10 m, and low horizontal dissection (erosional incisions spaced at least 2 to 5 km apart).
- Provisionally favorable conditions: Slopes less than 0.5% and 10 to 20% in the lowlands and up to 30% in the mountains; 10 to 25 m local relief; moderate horizontal dissection with incisions spaced at 0.5 to 2 km.
- Unfavorable conditions: Slopes greater than 20% in the lowlands and greater than 30% in the mountains; local relief greater than 25 m; and high horizontal dissection with less than 0.5 km spacing between incisions (Solodukhin 1985).

Third factor (hydrogeology and drainage)

- Favorable conditions: Groundwater occurs lower than the foundation bottom; no protective measures against the influence of groundwater are required.
- Provisionally favorable conditions: Special precautions are required to ensure adequate construction and maintenance of buildings and structures (water proofing, drawdowning, drainage, corrosion control, etc.).
- Unfavorable conditions: A complex system of special measures must be taken to prevent the adverse effect of groundwater on the construction and maintenance of engineering structures and their performance.

Fourth factor (flooding hazard):

- Favorable conditions: Areas unflooded by 1% probability flood events (one in one hundred years).
- Provisionally favorable conditions: Areas that are not

flooded in a 4% probability flood event (one in 25 years).

- Unfavorable conditions: Areas liable to flooding during >4% probability flood events (more than one in 25 years) (Lomtadze 1978).

Fifth factor (temperatures and water and air quality)

Only two categories—favorable conditions and unfavorable conditions—are identified, based on the atmospheric circulation patterns and the environmental quality standards.

In accordance with favorability, provisional favorability, and unfavorability of each factor, study areas are categorized as suitable, limited suitable, and unsuitable.

Analysis of Land Suitability for Construction

The actual approaches to urban development in permafrost regions will be illustrated below, using the example of Yakutsk which faces the typical problems.

Considering the first factor of land suitability for urban construction which characterizes the geological structure and related geological processes, it should be noted that the special design and construction methods for engineering work in permafrost areas have less than one century of history (USSR Building Code 2.02.04-88, 1990). Based on technical experience, special-purpose permafrost zonation of Russia has been made, and special requirements for design and construction of foundations and buildings have been elaborated. However, the need for special foundation types and structural improvements, as well as the special considerations for construction and operation stages, imply the overall unfavorability of engineering-geological conditions. It means that any permafrost area is essentially unsuited for urban construction, and strict solutions to the problems posed by the first factor require that in each specific case, proper weight should be given to the other factors in order to prevent them from adding to adverse effects on the engineering geological conditions.

By the second factor (topography), the townsite of Yakutsk located on the first and second terraces of the Lena River has a general slope of much less than 0.5% per 10 km or more, and the distance between frequent oxbow depressions is about 1 km. These conditions are provisionally favorable, making the townsite limited suitable by the second factor which affects the quality of utility lines and roads.

Moreover, because of the flatness of the townsite, surface and subsurface (active layer) drainage is in fact lacking. In other words, the area is unsuited for urban development in terms of the third factor, since the problems of inundation and salinization remain unsolved due to the technical complexity. The 370 years of continuous anthropogenic saturation and salinization of the soils, as well as leaking service pipes, have resulted in cryopegs in the low-lying areas with salinities of up to 10 g/l. These cryopegs contain Na and Mg chlorides aggressive to foundation concrete.

Within the city limits, the first river terrace is from 93–95 m to 97 m in elevation. Surface runoff and drainage occur very slowly, from Lermontov Street to Khabarov and Chernyshevsky Streets. The lack of drainage results in frost jacking of the structures and frost cracking beneath the buildings. With the construction of a new residential district, Mirkorayon 202, on the Lena floodplain filled to a 97-m elevation, the first-terrace area between Lermontov and Khabarov Streets has become a depression, and drainage in the active layer has been disrupted.

The fourth factor (hydrological conditions) is of prime importance for Yakutsk, as it lies in the Lena Valley. Floods to levels between 1% and 4% probability make the area that of limited suitability for urban development, while the zones with levels of less than 4% probability are classified as unsuited. Flood levels of the Lena River in the Yakutsk area are 96.36 for 1% probability events and 95.46 for 4% floods. Since the level at Khabarov Street near the town dam is 95.5 m, the first terrace is entirely an area of limited suitability for construction.

Filling of the floodplain area for new construction is estimated by the project designer, Giprokomminstroy, to add 40 cm to flood levels, and a 4% probability flood thus would reach 95.86 m. As a result, the first terrace has become a flood-risk area, making the developed parts of the city unsuited in terms of the building standard. This change in the situation has already resulted, in that every spring flood-control action has to be taken along the first-terrace slope.

By the fifth factor, atmospheric quality, the urban land-use suitability is not evaluated. However, its ecological implications should be given consideration, because, being located in the river valley, Yakutsk is influenced by temperature inversion during the winter. The inversion is several hundreds of meters in vertical extent and up to 10º in temperature difference; the number of days with fog is up to 56 during the winter months. Weak air movement results in heavy air pollution with the maximum permissible concentrations exceeded by 10 to 20 times. The average maximum exceeding of the standards is 3–8 for SO_2, 9 for CO, 5 for NO_2, and 10–17 for H_2S. These levels are above high and harmful air pollution thresholds (Central Research and Design Institute on Urban Development 1986). The development of the floodplain has increased trapping of pollution emissions within the city area.

According to the recommended environmental criteria for urban areas (Central Research and Design Institute on Urban Development 1986), Yakutsk is now an extremely unfavorable (critical) zone in terms of air and water quality, as well as soil and vegetation conditions.

Osipov (2004), in his analysis of environmental problems in Russia, presents environmental degradation zonation of the country. The map shows that in the permafrost zone, local areas of degradation are those affected by mining activities. No degradation is indicated for the Yakutsk area. However, the above discussion makes us conclude that Yakutsk appears to be the only community in the permafrost zone where the arduous situation has resulted solely from the absence of an orderly pattern of development. The oldest city erected on permafrost has been an experimental plot with both building successes and failures.

Construction and Maintenance Problems at Yakutsk

The critical engineering and ecological situation has resulted in significant negative consequences, which are listed below in a decreasing order of the number of affected buildings and structures.

1. Anthropogenic salinization of the foundation materials and related reduction in the frozen soil strength and bearing capacity.

2. Warming and thawing of the underlying frozen ground due to insufficient heights of air space between the buildings and the ground surface, primarily due to overall saturation of the townsite soils resulting from the lack of surface runoff and hydraulic discharge of the active layer.

3. Repeated or contingent leaks from the internal, external, district and main water and heat lines into the ground near or below the buildings. Leakage results in large thaw bulbs, foundation settlement, and structural damage.

4. Concrete deterioration in the foundation sections within the layer of seasonal thaw due to frost and chemical action. Capillary suction of groundwater from the active layer to the masonry walls of the mid-20th century or older buildings (a demolished building on Ordzhonikidze Square, a number of buildings on Lenin, Khabarov, and Bestuzhev-Marlinsky Streets) and gradual damage to the bearing walls leading to complete failure.

5. Frost cracking in the foundation soil during the winter months resulting in damage to the basement walls.

Of about 500 residential and public buildings examined at Yakutsk, 182 buildings, or 36.4% of major infrastructure, show various levels of deformation. It is not surprising, since Yakutsk, which initially had no sanitary or storm sewer systems, is the oldest community on permafrost.

The current situation on the Yakutsk townsite calls for the following immediate measures:

1. Prohibit new construction in the floodplain areas. Develop measures aimed at minimizing the adverse effects of the built-up floodplain sections on the remainder of the townsite.

2. Establish, by the city of Yakutsk Department of Housing and Municipal Services, a special supervisory service for performance control, repair, and reconstruction of the district utility systems and the sewage main.

3. Prepare alternative reconstruction plans for the areas of sporadic construction, providing for green recreational zones to reduce the total burden on the city.

4. Enforce the re-opening of the Yakutsk permafrost station which would, at the initial stage, be subordinate to the Federal Emergency Management Department's Monitoring and Prediction Centre. Based on the existing experience (USSR Committee for Construction's Institute of Foundations and Underground Structures 1982), this station should be charged with developing a single network of thermal and level monitoring network of the city area and building sites. In the first years, the station should prepare regular reports on the permafrost conditions at the city and the performance of the existing infrastructure.

The recommended measures are certainly of regulative character and cannot be expected to solve the general problem. Land quality remediation is a task for many decades to come. City expansion should be diverted away from the inversion-affected valley (an ecological objective) and the low terraces of the Lena River (a planning objective). It is evidently the only way to improve the urban land use quality.

General Evaluation of Permafrost-Affected Infrastructure

Despite the diversity of construction conditions in northern communities, it is of interest to compare the infrastructure conditions survey data, since these figures provide some indication of the general situation. At Norilsk, for example, about 300 of the 1000 buildings examined required foundation stabilization; about 40 buildings are reconstructed and repaired annually by a specialized engineering company. At Chita, 132 of 526 buildings investigated (25.1%) are damaged or distressed. In the communities located on the Arctic coasts, 30% of the buildings show signs of deformation. Mosgiptotrans, the railroad design company of Moscow, reports that 27.4% of the northern railroad embankments show deformation. With Yakutsk, these findings indicate that, on average, 30% of the infrastructure in the permafrost areas is in distress, irrespective of its type.

An analysis of the survey results for 114 damaged buildings in Magadan Province showed that 25% of the cases were due to improper site investigation and design, 17% due to inadequate site preparation and poor foundation construction, and 58% due to maintenance deficiencies. It follows that at least 83% of the problems are caused by errors in evaluation of construction conditions, and this corresponds to the lower level of the probable number of problem buildings. Thus, neglect of the urban construction quality of an area as a whole and individual construction sites produces a practically exact range: 25–30% damaged buildings. This range means that the precision of achieving a design purpose, expressed as the confidence probability of a target result, corresponds to the square root of variance. Hence urban development can be viewed as a stochastic process characterized by a normal distribution; i.e., the system control of the urban design and construction process is entirely absent. This is the reality of the urban development process in the permafrost regions.

Conclusions

The neglect of technical requirements in the construction practice in the North has no objective reasons. The northern communities that came into existence in recent decades are characterized by the same failure rate as Yakutsk with its 375-year history. The only way to solve the problem is enact into law and enforce the current urban construction regulations for permafrost areas discussed above.

References

Central Research and Design Institute on Urban Development. 1986. *Recommendations on Environmental Protection in Regional Planning*. Moscow: Stroyizdat, 160 pp.

Lomtadze, V.D. 1978. *Engineering Geology. Special Engineering Geology*. Leningrad: Nedra Publ., 496 pp.

Osipov, V.I. 2004. Ecological problems in Russia. *J. Geoecology. Engineering Geology, Hydrogeology and Geocryology* 1: 5-12.

Solodukhin, M.A. 1985. *Engineering-Geological Investigations for Industrial and Civil Construction.* Moscow: Nedra Publ., 225 pp.

USSR Building Code 2.02.04-88. Foundations in Permafrost. 1990. Moscow: USSR Committee for Construction Press, 56 pp.

USSR Committee for Construction's Institute of Foundations and Underground Structures. 1982. Recommendations on Monitoring of Foundations in Permafrost. Moscow: Stroyizdat, 33 pp.

A New Permafrost Map of Quebec-Labrador Derived from Near-Surface Temperature Data of the Moderate Resolution Imaging Spectroradiometer (MODIS)

Sonia Hachem
Centre d'Études Nordiques, Département de Géographie, Université Laval, Quebec, Quebec, Canada
Michel Allard
Centre d'Études Nordiques, Département de Géographie, Université Laval, Quebec, Quebec, Canada
Claude Duguay
Department of Geography, Faculty of Environmental Studies, University of Waterloo, Waterloo, Ontario, Canada

Abstract

Data obtained from spaceborne platforms offer a significant advantage for studies conducted in arctic and subarctic areas where measurement stations are geographically scattered. The Land Surface (skin) Temperature (LST) products of the Moderate Resolution Imaging Spectroradiometer (MODIS), aboard NASA's Terra and Aqua satellite platforms, were retrieved over continuous and discontinuous permafrost zones. A temporal interpolating model was applied to fill gaps due to extensive periods of cloudiness (more than 50% of cloudy days per year were observed from 2000 to 2005). Mean annual and monthly near-surface temperatures, as well as freezing (Fi) and thawing indices (Ti) and the ratio (Ti/Fi), were calculated pixel by pixel over the six complete annual temperature cycles for large geographical areas. This approach provides a new and original view of surface temperature patterns over Quebec-Labrador. It is suggested that conditions favourable for permafrost have recently moved northward.

Keywords: freezing index; land surface temperature; MODIS; permafrost boundaries; thawing index.

Introduction

Many authors have mapped the spatial distribution of permafrost in the past using various climatological and terrain parameters. For this purpose, different methods for interpolating climate data between dispersed stations were used. The first maps used mean annual air temperature isotherms (Brown 1960, 1970, Heginbottom 1984, Johnston 1981), some added mean July air temperatures (Allard & Séguin 1987), and included typical permafrost landform reconnaissance (Allard & Séguin 1987, Brown 1979, Harris 1982, Jorgenson & Kreig 1988, Rochefort & Payette 2001). Others have used thawing and freezing indices to delineate permafrost zones (Hinkel et al. 2001, Nelson 1986, Nelson & Outcalt 1987, Riseborough & Smith 1998). Recently, active layer thaw depth has also been mapped from these indices (Hinkel & Nicholas 1995, Riseborough 2003, Shiklomanov & Nelson 1999, 2002), and improved by n-factors (Klene et al. 2001, Riseborough 2004, Shur & Slavin-Borovskiy 1993).

The arctic and the subarctic regions are remote areas where to install and maintain measurement stations is technically difficult and excessively expensive. Even so, it remains necessary to assess surface temperatures over the landscape to monitor the climate. The large swath scanned by satellite sensors allows for broad-scale mapping in a single satellite overpass. As satellite sensors measure radiative temperatures at the atmosphere/surface boundary. The satellite temperatures are called "skin" surface temperatures or near-surface temperatures. Mapping at a regional scale a subsurface phenomenon such as permafrost using satellites is hence a challenge. But since permafrost owes its existence basically to the surface temperature regime, mapping this controlling variable seems to be the most logical approach. Hence, this type of measurement is physically different from those collected with temperature sensors (thermistors) either in the air or in the ground, usually at depths of 2 to 10 cm.

The MODIS sensor aboard the Terra and Aqua satellites was chosen for three main reasons. First, the Land Surface Temperature (LST) product is distributed online where it is easily and rapidly accessible. Second, this product is retrieved by two satellites that overpass the same region twice daily: in the morning and in the evening. Third, the spatial resolution chosen (pixel size of 1 km²), on one hand, is coarse enough to compute and store regional mapping, and on the other hand, is small enough to keep an acceptable accuracy for delimiting boundaries over vast landscapes. The LSTs are tile-shape distributed. Each tile is a piece about 1113 km by 1113 km in 1200 rows by 1200 columns, in a sinusoidal map projection. Three tiles (h14v02, h14v03 and h13v03) are needed to cover the entire Quebec-Labrador area. The LSTs used herein start on February 24, 2000, for Terra, and from July 4, 2002, for Aqua, and end on May 31, 2005, for both satellites.

Skin temperature validations were made previously for different landscapes, Lake Titicaca (Wan et al. 2002), rice fields (Coll et al. 2005) and homogeneous landscapes on the Tibetan Plateau (Wang et al. 2007), using field radiance measurements. Stations used for each of these studies were comprised within 1 km². The amount of radiation reaching the satellite radiometer is modified by both atmospheric water vapour effects and surface emissivity effects (spectral

Table 1. Comparison between TM, Ti and Fi from Reference calculation with the ones calculated from the fitted sinusoidal equations Tair_sin et LST_sin.

	Mean annual TM		Degree-days of thawing (Ti)		Degree-days of freezing (Fi)	
	REF/ Tair_sin	REF/ LST_sin	REF/ Tair_sin	REF/ LST_sin	REF/ Tair_sin	REF/ LST_sin
R^2	0.90447021	0.4955715	0.47103442	0.20069824	0.85643988	0.83075603
rmse	0.656	1.6044	189.6851	370.4642	232.7709	251.3852
P-value	0.0001	0.0001	0.0001	0.0101	0.0001	0.0001

and angular) over the land. The very complex (e.g.,, heterogeneity of mixed land covers) effect produced suggest that for them accuracy can only be done in a few special cases, when surface and atmospheric properties are very well known (Prata 2000). For the present study, instead of radiance measurements, the available stations, which were far apart from each other, collected ground temperatures and meteorological data. As these stations represent several tundra landscapes (low and sparse vegetation), comparisons between LST pixel values and ground station temperatures cannot be used to validate LST for a particular square kilometer. Nevertheless, the evaluation of the level of agreement between MODIS LST (LST data) and near-surface air temperature measurements (Tair data) at 2–3 m above ground, at ground-based stations located in the continuous permafrost zones of northern Quebec and Alaska, yielded a very good correlation ($R^2 > 0.81$; $4.41 < RMSE < 6.89$; $-3.58 <$ mean bias < 5.92). From this first assessment, it was deemed feasible to try to use MODIS LST products to map the surface temperatures dictating the presence of permafrost and its thermal regime (Hachem 2007).

Temporal Interpolation

The Arctic is known for its high cloudiness weather regime. This persistent cloudiness is evident through the analysis of measurements from 15 stations in Alaska and northern Quebec. The year had been divided in two parts to simplify calculations. As summer begins on June 1 and ends on September 30, it is composed of the four warmest months of the year. The additional months are defined as winter, i.e., from October 1 to May 31. All stations taken together showed a number of cloudless days of 23 (19%) during summer and of 88 (36%) during winter, summing to slightly more than a hundred days per year. As LSTs are measured at cloud-sensitive Earth-emitted thermal infrared wavelengths, for each cloudy day, LSTs are missing. Over a year, there are many weeks during which the presence of a cloud cover prohibited the determination of surface temperatures by space-based thermal infrared sensors. This setback was partly overcome through developing a statistical model of the temporal LSTs distribution.

Mathematically, the annual distribution of temperatures can be expressed by the following sinusoidal function:

$$T_t = T_m - A_0 . \cos\left(\frac{2\pi t}{P} - \phi\right) \qquad (1)$$

where T_t is the measured temperature at time t, T_m is the mean annual temperature, A_0 is the amplitude, P is the period (a constant equal to 365 days), and ϕ is the phase (Williams & Smith 1989).

From this equation mean annual temperature (T_m) is directly given, freezing (F_i) and thawing indices (T_i) are obtained by calculating the integrals under the sinusoidal curve, corresponding to the sum of negative temperatures (freezing degree-days) and positive temperatures (thawing degree-days), respectively (i.e., consecutive winter and summer). The sinusoidal curve was calculated to fit to LSTs and Tair data. Results from this calculus were named LST_sin, and Tair_sin, the sin abbreviation refer to the fitted sinusoidal equation.

As Tair were measured at field stations, we also calculated the Tm, Fi, and Ti as it is usually done, and named the results from these calculations REF.

We compared Tm, Fi, and Ti calculated with the year-by-year fitted equations from LSTs (LST_sin) and Tair (Tair_sin) data with Tm, Fi, and Ti calculated the usual way from Tair (REF). The LSTs used for comparison were taken from pixels which coordinates include a meteorological station in the field.

Table 1 shows statistical analyses of the different calculated Tm, Ti, and Fi. There are very good correlations between Tm and Fi, calculated from the LST dataset and recorded air temperatures, and a good correlation between the two sets for Ti (Hachem 2008). The statistical model gives excellent results for the two Tair datasets (REF and Tair_sin), which validates the use of this model. It still provides good results when REF is compared with LST_sin. Nevertheless, Ti correlations are very low (Table1). This is not necessarily related to the model used or to the absence of cloudy day values. Actually, Ti is known to be a highly variable parameter, as well as between two consecutive years than between stations only a few meters apart (Klene 2000).

The statistical algorithm was devised to derive the equation of the sinusoidal curve that best fits MODIS LST for each year of data and for each image pixel. Through applying that relationship to LST data over the pixels, Fi and Ti maps were drawn.

A New View of Quebec-Labrador Permafrost Distribution

Tm, Fi, and Ti maps description

The Tm, Fi, and Ti maps (not presented here) are an average over six years, from 2000 to 2005, and correspond to

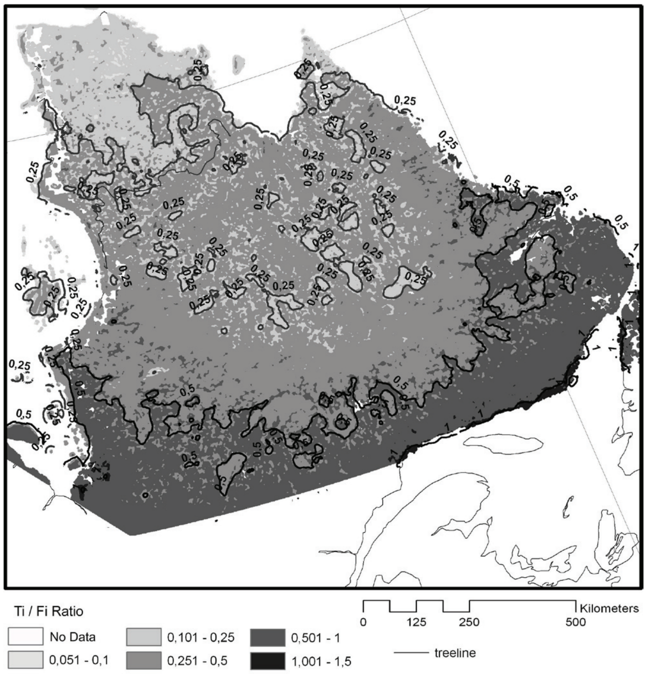

Figure 1. Ti/Fi ratio map.

Figure 2. After Payette & Rochefort (2001). A: continuous permafrost zone. B: discontinuous permafrost zone; B¹: more than 50% of permafrost; B²: less than 50% of permafrost; B³: maximal concentration of cryogene hillock and plateaus formed in Tyrrell Sea loamy silt. C: sporadic permafrost (less than 2%). D: annual frozen soils. Otish (1) mounts and Groulx mounts (2) are two high summit permafrost enclaves in sporadic permafrost zone. Chic-Choc mounts (3) and Lac des Cygnes mount (4) are high summit permafrost enclaves in annual frozen soil zone. (R. is used to indicate "reservoir," i.e., La Grande Reservoir.)

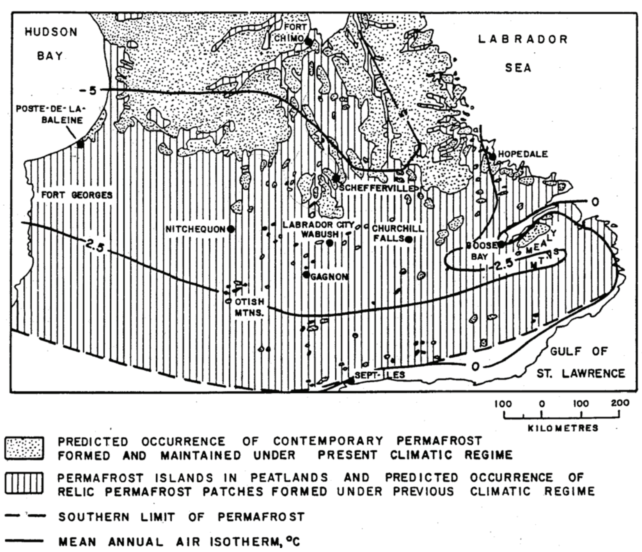

Figure 3. Discontinuous permafrost (Brown 1979).

a mixture of temperatures from different cover types included within a single pixel (1 km²). They all show a similar climate pattern (latitudinal, altitudinal, continental distribution, and large lakes). Colder areas are northernmost. The central section of northern Quebec is colder than coastal areas–a poorly documented observation until now as no stations are located on the high central plateaus of the peninsula. Also, due to Hudson Bay influence and barrier effects by the Torngat Mountains, the east coast of the Quebec-Labrador peninsula is colder than the west coast. Moreover, the maps show that large water bodies produce colder microclimates that influence the surrounding land areas (within 2 pixels of water bodies). However, in the continuous permafrost zone, large river basins show warmer temperatures than the surrounding plateaus (Hachem 2008). The high elevated topography is easily identifiable because of the cold tops which are colder than the plains.

The Ti/Fi ratio map

Anisimov & Nelson (1997) used Fi and Ti ratios to estimate the presence or absence of permafrost. If F_i is greater than T_i, it means that the mean annual temperature is below 0°C, suggesting that permafrost is likely to be present. Whereas if F_i is less than T_i, then the heat gain in summer is large enough to counterbalance the heat loss in winter, hindering permafrost to form, or in areas where it is present, leading to its disappearance over time. In addition, if T_i increases over time and remains greater than F_i, it can be deduced that the active layer is thickening, leading to the progressive disappearance of permafrost from the top downward. Here, we used the T_i/F_i ratio (Fig. 1) to provide a first estimate of the presence or absence of permafrost.

However, this estimate could be improved either by calculating the frost number (Nelson & Outcalt 1987) or by including the "buffer" information (Riseborough 2004). The frost number is defined by Nelson & Outcalt (1987) as a dimensionless ratio using freezing and thawing degree-day sums and gives a device for portraying the distribution of contemporary permafrost at continental scales. The "buffer layer" effect, often integrated in the n-factor, corresponds to the impact of factors affecting heat exchanges between the atmosphere and the ground surface (i.e., vegetation, organic layer, snow cover).

The Ti/Fi ratio map (Fig. 1) is divided into three main parts, by two isolines. The 0.25 isoline (i.e., when Fi is four times as large as Ti) corresponds and follows nearly the southern limit of the continuous permafrost drawn by Payette & Rochefort (2001), based on general knowledge of landforms and vegetation zones (Fig. 2), which corresponds also to the +10°C isotherm of the mean air temperature of the warmest month of the year (Allard & Séguin 1987). Herein, July was used as the warmest.

The 0.5 isoline (i.e., when F_i is twice as large as T_i)

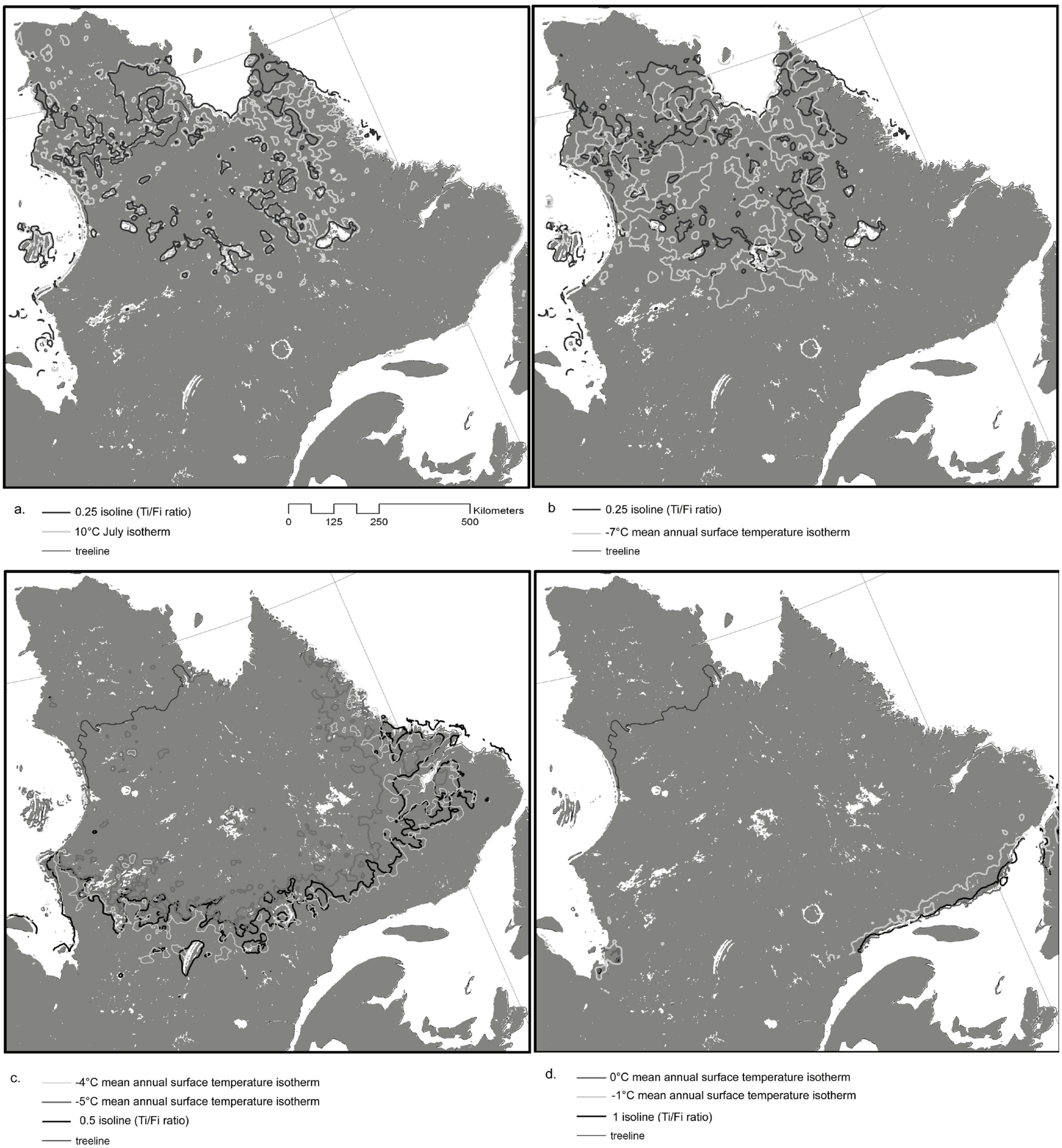

Figure 4. Comparisons of different potential limits of permafrost.

corresponds rather well to the known southern limit of the Brown's (1979) sporadic permafrost zone drawn by Figure 3.

Therefore, this first map is a promising starting point to pursue the next mapping steps.

Northern Quebec-Labrador permafrost limits

A consensus exists in the literature that permafrost extent can be mapped in three categories: continuous, discontinuous, and sporadic or isolated patches. The categories are not perfectly established and depend on what characteristics are mapped (e.g., percentage of frozen soil actually related to ground ice conditions, or air isotherms) and on mapping scale (Heginbottom 2002). While mapping the northern Quebec-Labrador peninsula one limiting criteria chosen by Allard & Séguin (1987) was the +10°C isotherm for the warmest month of the year (corresponding to the tree line) as the boundary between discontinuous and continuous permafrost. The limit between discontinuous and sporadic permafrost was roughly the -−1°C isotherm of mean annual air temperature. Inclusion of other information such as topography, physiography, surface geology, soil moisture, content vegetation, and snow cover would help to better define boundaries and map distribution of permafrost patches in greater detail.

A relatively good correspondence appears between key Ti/Fi ratio contour lines and key isotherms that are generally used for interpreting the boundaries of permafrost zones. For instance, Figure 4a shows the excellent correspondence between the 0.25 Ti/Fi ratio contour line and the +10°C July isotherm, both measured with the MODIS sensor, therefore supporting the idea that this contour fits roughly with the boundary between continuous and discontinuous permafrost. It is to be noted, however, that this line was further north than the tree line during the period 2000–2005, which agrees with observed recent climate warming. This suggests that climate conditions propitious for continuous permafrost are currently moving northward. The -7°C mean annual surface temperature (MAAT) isotherm derived by MODIS on Figure 4b is likely a better approximation of the diffuse boundary between widespread (>50%) and scattered discontinuous permafrost (<50%) than what was previously estimated. The overlapping 0.5 Ti/Fi ratio contour line and -5°C MAAT isotherm in Figure 4c can be associated with the southern limit of discontinuous permafrost. Finally, sporadic occurrences of permafrost can occur as far south as the 0°C MAAT isotherm, in good correspondence with Brown's permafrost map (Fig. 4d).

Conclusion

We developed a statistical model that uses MODIS LST to map mean monthly and annual surface temperatures as well as freezing and thawing indices, as an alternative to conventional ground-based measurements which are spatially limited. Thermal permafrost limits were added through the calculation and mapping of the Ti/Fi ratio contour lines. These maps compare rather well with maps drawn by previous authors based on ground-collected data. They can be used only as a first approximation since other (local) factors such as snow cover, vegetation, and organic layers—variable with moisture content—create a "buffer" effect between the atmosphere and the surface which is not included in the Ti/Fi ratio.

These maps bring in new knowledge regarding the spatial distribution of temperatures across northern Quebec-Labrador. In an upcoming study, maps similar to the ones presented in this paper will be produced to encompass the entire pan-arcticArctic domain. They could be improved if n-factors are available. Also it would be possible to input the Ti in different models calculating active layer thickness (TTOP [Riseborough 2003], the frost number [Nelson & Outcalt 1987], or the GIPL model [Sazonova & Romanovsky 2003]). This approach with MODIS data is also a new tool available for monitoring surface temperature changes at a high spatial resolution.

References

Allard, M. & Séguin M.K. 1987. Le pergélisol au Québec nordique: bilan et perspectives. *Géographie physique et quaternaire* 41(1): 141-152.

Anisimov, O.A. & Reneva, S. 2006. Permafrost and Changing Climate: The Russian Perspective. *Ambio* 35(4): 7 pp.

Brown, R.J.E. 1960. The distribution of permafrost and its relation to air temperature in Canada and the USSR. *Arctic* 13(3): 163-177.

Brown, R.J.E. 1970. *Permafrost in Canada, Its Influence on Northern Development.* Toronto: University of Toronto Press.

Brown, R.J.E. 1979. Permafrost distribution in the southern part of the discontinuous zone in Québec and Labrador. *Géographie physique et quaternaire* 33(3-4): 279-289.

Coll, C., Caselles, V., Galve, J.M., Valor, E., Niclos, R., Sanchez, J.M. & Rivas, R. 2005. Ground measurements for the validation of land surface temperatures derived from AATSR and MODIS data. *Remote Sensing of Environment* 97: 288-300.

Hachem S. 2008. *Cartographie des températures de surface, des indices de gel et de dégel de la répartition spatiale du pergélisol, à l'aide du Moderate Resolution imaging Spectroradiometer (MODIS)*. Thèse de Doctorat. Département de Géographie, Université Laval, 144 pp.

Hachem, S., Duguay, C.R. & Allard, M. 2007. Comparison of MODIS-derived Land Surface Temperatures with Near-Surface Soil and Air Temperature Measurements in Continuous Permafrost Terrain. (submitted)

Harris, S.A. 1982. Identification of permafrost zones using selected permafrost landforms. *Proceedings of the Fourth Canadian Permafrost Conference, Calgary, Alberta, March 2–6, 1981*: 49–57.

Heginbottom, J.A. 1984. The Mapping of Permafrost. *Canadian Geographer* 28(1): 78-82.

Heginbottom, J.A. 2002. Permafrost mapping: a review. *Progress in Physical Geography* 26(4): 623-642.

Hinkel, K.M. &Nicholas, J.R. 1995. Active layer thaw rate at a boreal forest site in Central Alaska, USA. *Arctic and Alpine Research* 27(1): 72-80.

Hinkel, K.M., F. Paetzold, F.E. Nelson &Bockheim, J.G. 2001. Patterns of soil temperature and moisture in the active layer and upper permafrost at Barrow, Alaska 1993-1999. *Global and Planetary Change* 29(3-4): 293-309(17).

Johnston, G.H. 1981. *Permafrost, Engineering Design and Construction.* Toronto:Wiley, 540 pp.

Jorgenson, M.T. & Kreig, R.A. 1988. A model of mapping permafrost distribution based on landscape component maps and climatic variables. *Fifth International Conference on Permafrost, August 2–5, 1988, Trondheim, Norway.* Tapir.

Klene, A.E. 2000. *The N-Factor in Natural Landscapes: Relations between Air and Soil-Surface Temperatures in the Kuparuk River Basin, Northern Alaska.* Publications in Climatology 53. Newark: University of Delaware, Center for Climatic Research, 85 pp.

Klene, A.E., Nelson, F.E. & Shiklomanov, N.I. 2001. The n-factor as a tool in geocryological mapping: seasonal thaw in Kuparuk River basin, Alaska. *Physical Geography* 22(6): 449-466.

Nelson, F.E. 1986. Permafrost distribution in central Canada: applications of a climate-based predictive model. *Annals of the Association of American Geographers* 76: 550-569.

Nelson, F.E. & Outcalt, S.I. 1987. A computational method for prediction and regionalization of premafrost. *Arctic and Alpine Research* 19(3): 279-288.

Payette, S. & Rochefort, L. 2001. *Ecologie des tourbières du Québec-Labrador.* Québec: Presse de l'Université Laval.

Prata, A.J. 2000. The proposed global land surface temperature product for ENVISAT's AATSR: Scientific basis, algorithm description and validation protocol. *ERS-ENVISAT Symposium, 16-20 October, 2000, Gothenburg, Sweden.*

Riseborough, D.W. 2003. Thawing and freezing indices in the active layer. *8th International Conference on Permafrost, 22-25 July, 2003, Zurich, Switzerland.* Lisse: Swets and Zeitlinger.

Riseborough, D.W. 2004. *Exploring the Pparameters of a Simple Model of the Ppermafrost Relationship. Geography and Environmental Studies.* Ottawa: Carleton, 310 pp.

Riseborough, D.W. & Smith, M.W. 1998. Exploring the limits of permafrost. *Seventh International Conference on Permafrost, Yellowknife, Canada.* Québec, Québec, Canada: Université Laval, Centre d'Etudes Nordiques.

Sazonova, T.S. & Romanovsky, V.E. 2003. A model for regional estimation of temporal and spatial variability of active layer thickness and mean annual ground temperatures. *Permafrost and Periglacial Processes* 14: 125-139.

Shiklomanov, N.I. & Nelson, F.E. 1999. Analytic representation of the active layer thickness field, Kuparuk River Basin, Alaska. *Ecological Modelling* 123: 105-125.

Shiklomanov, N.I. & Nelson, F.E. 2002. Active layer mapping at regional scales: a 13 year spatial time series for Kuparuk Region, North Central Alaska. *Permafrost and Periglacial Processes* 13: 219-230.

Shur, Y.L. & Slavin-Borovskiy, V.B. 1993. N-factor maps of Russian permafrost region. *Sixth International Conference on Permafrost, July, 1993, Wushan Guangzhou, China.* Beijing: South China University of Technology Press.

Wan, Z., Zhang, Y.-L., Zhang, Q.-C. & Li, Z.-L. 2002, Validation of the land surface temperature products retrieved from terra moderate resolution imaging spectroradiometer data. *Remote Sensing of Environment* 83(1-2): 163-180.

Wang, K., Wan, Z., Wang, P., Liu, J. & Sparrow, M. 2007. Evaluation and improvement of the MODIS land surface temperature/emissivity products using ground-based measurements at a semi-desert site on the western Tibetan Plateau. *International Journal of Remote Sensing* 28: 2549-2565.

Williams, P.J. & Smith, M.W. 1989. *The Frozen Earth: Fundamentals of Geocryology.* Cambridge: Cambridge University Press, 306 pp.

—*Plenary Paper*—

Research Challenges for Permafrost in Steep and Cold Terrain: An Alpine Perspective

Wilfried Haeberli
Glaciology, Geomorphodynamics & Geochronology, Geography Department, University of Zurich, Switzerland
Stephan Gruber
Glaciology, Geomorphodynamics & Geochronology, Geography Department, University of Zurich, Switzerland

Abstract

The past few decades have seen a rapid development and progress in research on permafrost in mountain areas with complex and rugged topography such as the European Alps. At the same time, it becomes increasingly clear that climate change impacts have the potential to severely affect future living conditions in areas with steep and cold terrain by influencing the chain of surface processes that link debris production via rock fall to talus/moraine formation, creep deformation of frozen deposits, and material evacuation by debris flows and fluvial transport. Key scientific challenges relate to special aspects induced by complex topography. Corresponding aspects are briefly outlined concerning the relation between the atmosphere and the permafrost in areas with highly variable snow cover and potentially strong lateral energy fluxes, permafrost thermal conditions in mountains with pronounced microclimatic asymmetries, the destabilization of steep to near-vertical rock walls and degrading permafrost, the flow and stability of ice-rich frozen debris with increasing subsurface temperature and melt water availability, interactions between glaciers and permafrost under conditions of rapid if not accelerating change, 4D-evolution of permafrost in rugged mountain topography, and hazards from permafrost slopes in densely populated high-mountain chains.

Keywords: climate change; cold regions; mountains; natural hazards; permafrost; slope stability.

Introduction

The first contributions in the Proceedings of the International Permafrost Conferences about permafrost in mid-latitude, high-altitude mountain regions started to appear in the late 1970s (e.g., Barsch 1978, Fuji & Higuchi 1978, Gorbunov 1978, Haeberli 1978, Harris & Brown 1978). This indicates the essential beginning of systematic research on permafrost in high-mountain areas and led to a first visibility peak at the International Workshop on Mountain Permafrost in Interlaken 1991 with a first set of overview papers (cf. situation reports by Barsch 1992, Guodong & Dramis 1992, Haeberli 1992, Harris & Corte 1992, King et al. 1992, Lautridou et al. 1992). During its rather young history, research on permafrost in steep and cold terrain developed and expanded rapidly. Perhaps the most important impulse was the EU-funded PACE project (Permafrost and Climate in Europe, Harris et al. 2001). The subsequent progress and increase in visibility is impressing: high-mountain permafrost is now described for many regions (for instance, Isaksen et al. 2007, Jin et al. 2000, Marchenko 2007, Trombotto 2000) and is regularly included in international assessments on cryospheric conditions, especially as related to climate change (IPCC 2007, UNEP 2007, cf. also Harris 2008).

Climate change indeed constitutes a major challenge for the science of mountain permafrost as it concerns a phenomenon that depends on atmospheric conditions in a complex way, is not directly accessible through visual observation, often involves logistic problems with difficult access and strikingly lacks observational series over extended time periods. As a consequence, even key questions are still open for detailed investigations. The present contribution focuses on special aspects related to rugged topography and steep terrain. It is primarily built on experience from the European Alps as summarized in recent reviews (Harris et al. 2008, Gruber & Haeberli 2008, Haeberli & Gruber 2008) and briefly outlines a set of high-priority research topics covering process understanding, numerical modeling and the anticipation/assessment of potential climate change impacts. The basic structure of the considered geo-system (Fig. 1) as is characteristic for mountain ranges with transitional to continental climate—where glacier equilibrium lines are far above the 0°C-annual isotherm—is the process chain leading from debris production via rock fall to debris cone or moraine formation, creep deformation of frozen deposits and sediment evacuation to larger valleys by fluvial transportation and debris flows.

In the following discussion, the most important conclusions based on existing knowledge are briefly outlined and major challenges concerning research on mountain permafrost are discussed. We thereby distinguish seven major topics: (1) atmosphere-permafrost coupling in complex topography; (2) permafrost thermal conditions inside mountains; (3) destabilization of permafrost rock walls; (4) flow and stability of ice-rich frozen debris; (5) glacier/permafrost interactions; (6) 4D-evolution of permafrost in mountain topography; and (7) hazards related to rock falls and debris flows from permafrost slopes.

Topics (1) to (5) are related to necessary improvements of our process understanding. The spatio-temporal consideration, on the other hand, is more and more urgently needed for realistically assessing consequences and impacts from continued atmospheric warming. The discussion

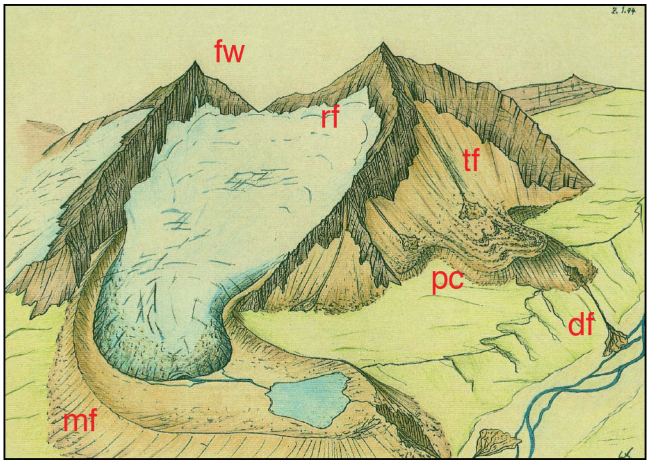

Figure 1. Scheme of the characteristic process chain in cold mountain areas: frost weathering (fw) and debris production, rock fall (rf), talus (tf) or moraine formation (mf), permafrost creep (pc), evacuation by fluvial transport and debris flows (df). Adapted from Haeberli (1996).

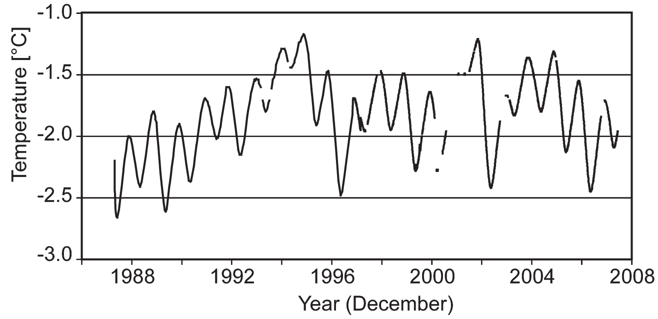

Figure 2. Borehole temperatures in the active Murtèl rock glacier. The winters of 1996, 2002 and 2006 had thin snow cover causing strong ground cooling despite relatively warm air temperatures.

therefore also includes two central aspects—topics (6) and (7)—related to the assessment of local, regional and global impacts of climate change and the anticipation of corresponding hazard potentials.

Atmosphere-Permafrost Coupling in Complex Topography

The now 20 years old series of borehole temperatures in the Murtèl rock glacier (Fig. 2) clearly shows the important influence of the winter snow cover on near-surface ground temperatures. This effect of snow on relations between the atmosphere and the permafrost has been investigated using measurements (Keller & Gubler 1993) and snow/permafrost models (e.g., Lütschg et al. 2003). A number of studies also address the cooling influence that coarse blocks exert on ground temperatures when compared with lower porosity or finer-grained surface materials (Hanson & Hoelzle 2004, Hoelzle & Gruber 2008).

The effect of topography on temperatures in steep rock has been investigated with measurements (Gruber et al. 2003) and model experiments (Gruber et al, 2004 a, b, Noetzli et al. 2007, Salzmann et al. 2007). Despite significant progress in understanding these processes of atmosphere-permafrost coupling, the high spatial variability of surface micro-climatology and subsurface properties in mountain terrain makes the generalization of findings to larger areas difficult. One example is the thermal effect of thin and intermittent snow cover in rock faces that has not been quantified to date.

The role of heat advection by moving water or air in sediments or in cleft systems is a further set of processes that is little understood but that bears high relevance for the anticipation of climate change impacts (fast thaw along frozen joint systems and corresponding rock fall) and for the understanding of permafrost dynamics (Gruber & Haeberli 2007). Especially lateral transfer of sensible as well as latent heat through ventilation effects in steep, coarse-grained debris or by melt water in heavily fissured, near-vertical rock walls appear to be essential.

Permafrost Thermal Conditions Inside Steep Mountains

Measured borehole temperatures (Harris et al. 2003, Gruber et al. 2004c, Isaksen et al. 2007) and combined time-dependent energy balance and heat diffusion modeling for complex topography (Noetzli et al. 2007) now document the main thermal characteristics of cold mountains. Summits can be frozen to depths of nearly 1000 m, and often have strongly asymmetrical thermal fields with steeply inclined isotherm configurations and predominant lateral heat flow from warmer to colder outer rock walls. The uppermost parts of such ridges and summits are essentially decoupled from geothermal heat and, due to their geometry, enable thermal disturbances to penetrate from two or more sides. Atmospheric warming during the 20th century has caused pronounced thermal anomalies to depths of about 50–70 m below surface. In perennially frozen debris (talus, moraines, rock glaciers) with high ice contents near the lower boundary of local permafrost occurrence, temperatures below the depth of zero annual amplitude have, in places, reached phase equilibrium condition (pressure melting) throughout (zero or near-zero heat flow).

The formation and existence of unfrozen zones within permafrost (taliks) as documented, for instance, in the borehole through Murtèl rock glacier in the Swiss Alps (Vonder Mühll et al. 2003), constitutes a disturbance and heterogeneity for subsurface heat and energy flow. Positive feedback between energy input and hydraulic permeability most likely causes such effects to be widespread in warm permafrost, to increase in importance with continued warming and often to dominate over heat conduction through extended subsurface layers.

The occurrence and intensity of corresponding processes, however, are hardly known and most difficult to predict. Individual observations at high-mountain railway and cable car stations (Fig. 3) point to the importance of the

Figure 3. A roof protects tourists from melt water that only recently began to percolate through the rock mass above the tunnel inside the Jungfraujoch rock crest, 3500 m asl, Swiss Alps.

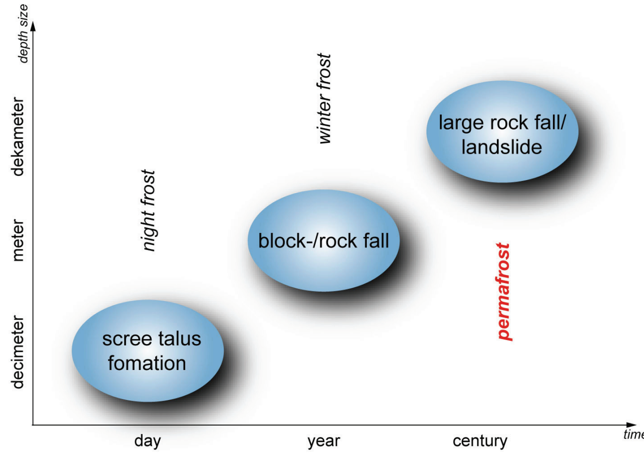

Figure 4. Scales of frost weathering and gravity driven mass wasting in rock walls.

phenomenon (Gruber & Haeberli 2007) and approaches to scientifically investigate these phenomena are now being developed (Hasler et al. 2008). Geophysical tomography (seismic refraction, electrical resistivity, Hauck & Vonder Mühll 2003, Krautblatter et al. 2007, Sass 2003), drilling/borehole temperature monitoring in fissured rock with warm permafrost (cf. Vonder Mühll et al. 2008) and the combination of heat diffusion modeling with other sources of information (Noetzli et al. 2008) for defining the conductive part of changes in the subsurface thermal field appear to be the most viable research avenue.

Destabilization of Permafrost Rock Walls

It is now quite well understood that frost-induced processes of rock destruction act on scales of time and depth that are often—but not always—connected via heat diffusion (Fig. 4). Seasonal to perennial frost, strong spatial temperature gradients in ridges and the availability of snowmelt water in active layers are likely to promote ice segregation involving depth scales of decimeters to tens of meters. Laboratory investigations (Davies et al. 2001) indicate that critical temperatures for the destabilization of frozen rocks with ice-filled cracks on steep slopes can also be reached at temperatures of -1 or -2°C. With continued warming, permafrost in cold mountains reaches such critical temperatures over more and more extended areas and over increasing depths. As a consequence, the probability of large rock falls from warming permafrost in steep to near-vertical rock walls is increasing. The process of rock destabilization by permafrost thaw is supported by observational evidence and theoretical consideration (Gruber & Haeberli 2007). However, we know little about the dominant processes responsible. Frequent rock fall during the extremely hot and dry summer 2003 in the Alps occurred in July, long before the active layer reached its maximum depth and long before it exceeded maximum thaw depths of previous years based on pure heat conduction modeling (Gruber et al. 2004c). Failure is therefore likely to have taken place under the influence of factors other than pure thaw to excessive depths. This finding points to the role of fast linear thaw along joint systems by heat advection during water transport. The influence of melt water penetrating into partially frozen rock may also be a reason for the strikingly high proportion of detachment zones from partially or at last strongly asymmetrically frozen summits and crests with marginal or even absent permafrost on the warm side. Reanalysis of recent rock falls (cf. Fischer et al. 2006, Noetzli et al. 2003) using energy balance modeling for defining pre-failure thermal conditions in the detachment zones is presently being undertaken in the Swiss Alps. International collaboration and exchange of information is important in order to expand the sample size and to enable reliable statistical analysis.

Flow and Stability of Ice-Rich Frozen Debris

The number of observations concerning flow phenomena in mountain permafrost using high-precision photogrammetry, geodesy and borehole measurements as combined with relative and absolute age dating and numerical modeling is rapidly increasing. The corresponding evidence now provides a quite coherent image of the processes, which govern cumulative long-term deformation of perennially frozen debris (talus, moraines etc.) containing ice in excess of the pore volume available between the rock particles under unfrozen conditions (Haeberli et al. 2006). Corresponding steady-state creep of ice-supersaturated debris over millennia—most probably since the end of the last Ice Age—led to the formation of the widespread and spectacular landforms called (active) rock glaciers. A major part of the straining obviously takes part within discrete shear horizons. The deforming fine-grained material from the upper part of talus cones thereby carries large blocks at its surface, which were deposited at the foot of the same talus cones, ride along the flow trajectory with maximum (surface) speed and, therefore, fall over the rock glacier front (where the creeping fine-grained material is exposed again), are overridden and

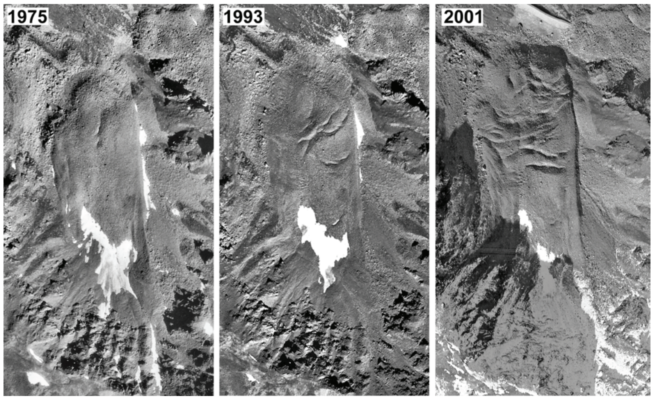

Figure 5. Grueo 1 rock glacier in the Turtmann Valley (Swiss Alps) showing signs of accelerating flow and intense crevasse formation (from Roer 2007).

form a saturated "structured" permafrost layer at depth with damped creep behavior. Seasonal and inter-annual variations of surface velocity can be observed where the permafrost base is not in bedrock but in non-frozen sediments.

The most surprising recent observation concerns the spectacular inter-annual variations of flow velocity as documented over wide areas in the European Alps in connection with the extremely hot/dry summer of 2003 (Delaloye et al. 2008, Kääb et al. 2006). Many rock glaciers with fronts near the local boundary of permafrost occurrence accelerated their flow speed almost simultaneously in the same year 2003 by a factor of two to five or even more and then more steadily decelerated to average long-term flow rates over the following about three years with less extreme conditions. The processes explaining this striking regional-scale phenomenon still remain to be explained (Roer et al. 2008). Rheological softening of ice/rock-mixtures by permafrost warming at temperatures close to phase equilibrium and at depths close to the expected shear horizons may have been part of the answer (Kääb et al. 2007). Increased melt water infiltration into already "temperate" or at least very warm permafrost may have been another contribution (Ikeda et al. 2007). Higher water pressure causing softening of subpermafrost sediments may also have come into play and enhanced mobility within the shear horizon itself cannot be excluded either. Continued high-resolution flow observations will help clearing the difficult question about corresponding interactions between the processes mentioned. Already now, however, the stability problem connected with warm permafrost in rock glaciers on steep mountain slopes received a new dimension. With the formation of striking crevasse patterns as a result of accelerated flow (Fig. 5, Roer et al. 2005), strong heterogeneities with respect to cohesion, hydraulic permeability and stress distribution developed within the creeping permafrost: possibilities for the triggering of debris flows and even landslides in such cases is no more restricted to the over-steepened frontal parts of rock glaciers alone (cf. Arenson et al. 2002).

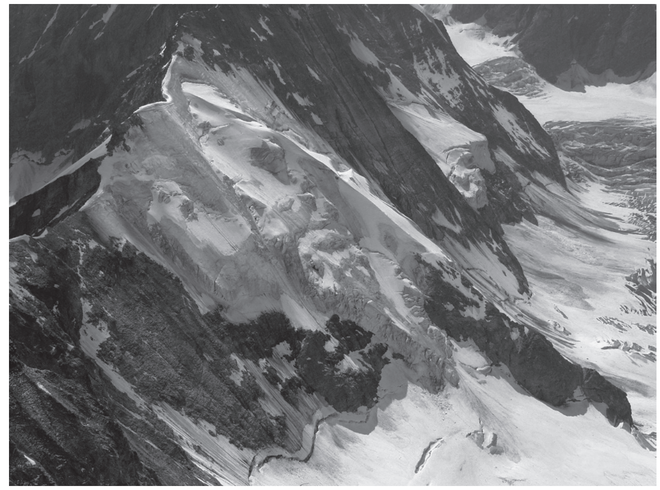

Figure 6. Hanging glaciers and ice faces on the northern side of the ridge extending between the Matterhorn and the Dent d'Herens along the border between Switzerland and Italy. Interactions between polythermal surface ice and subsurface permafrost are complex, especially with conditions of rapid atmospheric warming. Photo by S. Gruber.

Glacier-Permafrost Interactions

Interactions between glaciers and permafrost are widespread in regions with moderately to strongly continental climate, because the equilibrium line on glaciers is situated inside zones and altitudinal belts with discontinuous and continuous permafrost occurrence. Information concerning this important aspect is sparse at present (Haeberli 2005), especially because the scientific communities involved in permafrost and glacier research still communicate far too little. Results from geophysical soundings, miniature temperature data-logging, shallow borehole observations and photogrammetric movement determinations show that subsurface ice in glacier forefields successively exposed since the end of the Little Ice Age is often polygenetic (Kneisel 2003). It is most likely derived from recent ground freezing in cold microclimates of formerly temperate bed parts after glacier retreat, preservation of former subglacial permafrost underneath cold marginal parts of polythermal glaciers, burial of "dead ice" from the glacier itself or a combination of these processes. Ice-containing parts of morainic deposits commonly show signs of lateral flow and vertical displacements (heave, subsidence, cf. Kääb & Kneisel 2006).

Most important questions concern the evolution of permafrost in recently deglaciated moraines under the influence of changing surface conditions and continued atmospheric warming at lower altitudes and the thermal structure and stability of high-altitude hanging glaciers in steep, perennially frozen rock walls at higher elevations (cf. Gruber & Haeberli 2007). The stability of often polythermal hanging glaciers with temperate and permeable firn behind and above cold and rather impermeable cliffs (Fig. 6) and their thermal and hydraulic interaction with the permafrost inside the underlying rock walls (Lüthi & Funk 1997) may indeed constitute a key factor concerning large ice/rock avalanches with extremely far runout (Haeberli et al. 2004, Huggel et al. 2005). At a different level of process understanding, another common phenomenon deserves much more attention: basal regelation layers of glaciers are nothing else than epigenetic permafrost in fine grained sediments—often with large amounts of excess ice and ice lenses—attached to the base and deforming under peak stresses and at maximum strain rates of the corresponding glaciers. Improved knowledge about the rheology of the involved creep phenomena would provide essential insights with respect to non-isotropic flow characteristics of ice sheets, glaciers and rock glaciers.

Spatial Patterns and 4D-Evolution of Permafrost in Mountain Topography

Spatial distribution patterns of permafrost in complex high-mountain topography can be estimated by distributed modeling of the surface energy balance and sub-surface heat transfer. However, this implies knowledge of surface and sub-surface characteristics, proper initialization techniques, as well as methods for snow redistribution by wind and avalanches (Gruber 2007). Full energy balance models (e.g., Lehning et al. 2002) can make use of high (hourly or more frequent) time resolution, and thus resolve effects like the diurnal variability of convective cloud formation that often can have an essential influence on spatial ground temperature distribution.

A variety of models from empirical-statistical to more process-oriented approaches have so far been used with considerable success (Etzelmüller et al. 2001, Gruber & Hoelzle 2001). The Swiss Federal authorities have now produced a 1:50,000 map of permafrost distribution for the entire Swiss Alps. The model used for producing this map is more empirical-statistical but includes a discrimination between steep rock faces with little snow and less inclined slopes with thick winter snow (Gruber et al. 2006). First experiments with coupling regional climate models and GIS-based impact models indicate that warming trends are stronger in north-facing (shadow) than on sunny south-exposed slopes, because the relative influence of sensible heat effects in comparison to solar radiation is stronger (Salzmann et al. 2007). First successful attempts have also been made to couple surface energy balance with heat diffusion at depth for high mountains (Noetzli et al. 2007).

The main steps to follow this successful development consist in expanding such spatial modeling to all cold mountains on earth based, for instance, on SRTM or ASTER digital elevation and global climate data or model scenarios. Another important progress would be to further improve and validate modeling also on less inclined slopes covered by thicker and more irregular snow cover including cases with high ice contents using transient modeling. A possible result could be the coupling of thermal and geomorphic spatial models such as the modeling of creep phenomena as demonstrated in first encouraging attempts by Frauenfelder (2005). There is, undoubtedly, a long way to go for even

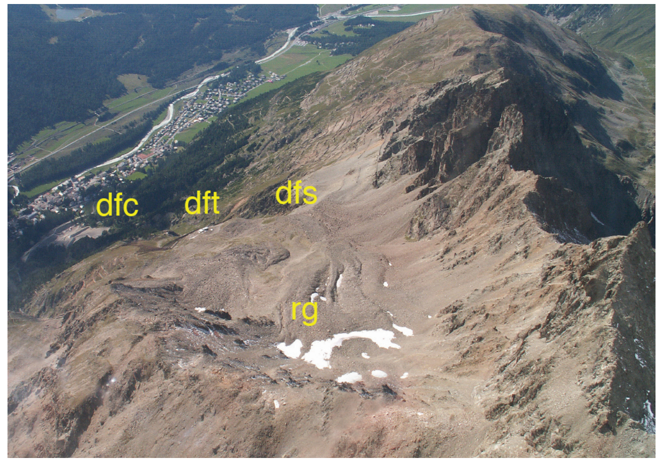

Figure 7. Creeping permafrost (rock glaciers rg) and debris flow starting zone (dfs), trajectory (dft) and cone (dfc) above Potresina (Swiss Alps). Note recently constructed avalanche and debris flow retention dam on cone. Photo by C. Rothenbühler.

partially reaching such research goals. However, already relatively rough approaches and early accomplishments could help with making it clear to scientists as well as policymakers and the public that permafrost belongs to the primary characteristics of cold mountain areas, that it relates to many other phenomena like snow, glaciers, erosion or slope stability, and that atmospheric warming causes growing disequilibria already now but even much more so in the foreseeable future.

Hazards Related to Rock Falls and Debris Flows from Permafrost Slopes

Debris flows from rock glaciers and moraines in permafrost areas (Fig. 7) can be among the largest debris flow events in mountain areas and cause devastating damage to settlements and infrastructure in valley bottoms.

Large-scale rock falls from steep to near-vertical rock faces seem to take place at increasing frequency and can propagate to areas far below timberline. They can dangerously erode or mobilize thick snow packs, glaciers, or water bodies, thereby undergo process changes, transform into high-speed flows or trigger flood waves which can reach extremely far runout distances and cause severe damage to human lives and economy. In the Swiss Alps, for instance, the 500,000 m^3 debris flow at Guttannen in 2005—probably the largest during decades back in time—started from a large moraine accumulation where (rather marginal) permafrost may have helped to transfer the water runoff from extreme precipitation to cross the flat cirque floor and to reach the steep outer moraine slopes. In the valley bottom, the large deposited debris volume dammed the Aare river which itself had peak flood discharge and soon started to overflow the debris dam and to cut a new bed on the other side of the principal road. As a logical consequence, the large river reached and damaged the village before heavy machines could cut an opening through the road and force the river back into its abandoned bed.

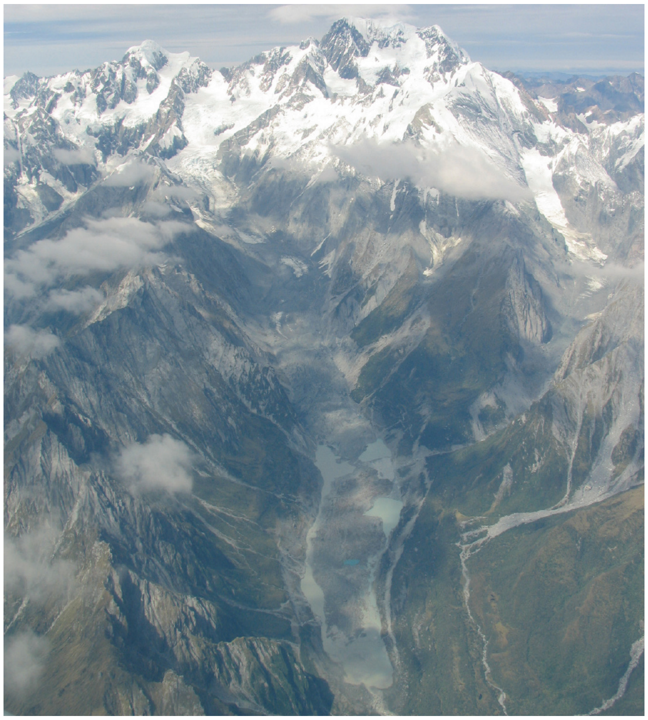

Figure 8. Disintegrating glacier tongue and formation of a large lake in the New Zealand Alps. Such lakes constitute an increasing hazard potential with respect to flood-waves triggered by rock falls from deglaciated slopes and/or slopes with warming and degrading permafrost. Photo by M. Hoelzle.

In the Caucasus, a combined ice/rock avalanche from the perennially frozen north wall of Dzimarai Khkok near Kazbek volcano eroded a medium size debris-covered glacier almost entirely. The mobilized mass squeezed out large amounts of probably subglacial water, turned into a high-speed two-phase mass flow and traveled over a runout distance of about 33 kilometers. Rivers from tributary valleys were dammed by the deposits to form lakes drowning parts of a local village and constituting a flood wave threat to people even in settlements situated far downstream (Haeberli et al. 2004, Huggel et al. 2005). Despite large uncertainties involved with the present understanding about the exact triggering and flow mechanisms of such events, hazard potentials from similar future phenomena must be anticipated and assessed at the best possible level of experience and knowledge.

GIS-based models to estimate flow paths and runout distances of ice/rock avalanches and debris flows in rugged high-mountain topography exist and can be applied already now (Huggel et al. 2003, Noetzli et al. 2006). Perhaps the most urgent need concerns the possibility of large ice/rock falls into existing lakes or lakes that newly form as a consequence of glacier retreat and downwasting (Haeberli & Hohmann 2008, Fig. 8). Debuttressing of formerly glacierized valley walls in combination with permafrost warming could thereby be an especially critical condition. In fact, primary factors influencing the stability of steep permafrost slopes are:

- slope inclination and topographically unsupported parts;
- geological structure (layer dipping, crack density and orientation);
- permafrost conditions (temperature, ice content, hydraulic permeability); and
- topographic evolution (erosion, glacier vanishing, earlier events).

Among these factors, permafrost and glacier conditions are changing most rapidly. Together with slope inclination, they can be spatially modeled in order to find most critical factor combinations. In a second step, possible flow trajectories of avalanches from such sites and their potential interactions and process chains involving snow, glaciers and/or water bodies could be modeled in order to detect places of highest risk. Such preliminary analyses over large areas would help to direct more detailed geological investigations and to establish focused monitoring or adequate protection measures. Integrative hazard assessment is far more than an academic idea: the potential for very large catastrophes is neither negligible nor undetectable. It rises at an accelerating rate with continued deep warming of high mountain permafrost, rapid glacier vanishing and drastic changing of alpine landscapes and habitats.

Further Issues and Perspectives

Besides the concrete challenges mentioned with respect to the described specific topics, three important challenges can be envisaged for future research on mountain permafrost: (a) holistic understanding; (b) increasingly quantitative methods; and (c) applied research. Holistic understanding is the broad understanding of all permafrost and its role in mountain landscapes. Our understanding at present is largely focused on special cases such as rock glaciers or steep bedrock but in fact, most permafrost has characteristics that lie in between these two cases and that are poorly constrained. Also, the transient interaction between permafrost and glaciers or the long-term influence of permafrost on the evolution of mountain topography remains largely unknown. Quantitative methods are necessary in order to understand and disentangle processes of increasing complexity. This requires not only infrastructure (such as data and models), but also novel concepts for the validation of models and for the analysis of uncertainty and scale issues that are among the most prominent characteristics of quantitative research in mountain areas. Applied research, for example in collaboration with public authorities or operators of high-elevation infrastructure, helps to transfer knowledge and evidence between researchers and people who work in permafrost environments on a daily basis, and, it is important in order to remain focused on research areas of direct importance to society.

Acknowledgments

Our special thanks go to all friends and colleagues who share with us the fascination and learning process related to mountain permafrost research. Their scientific progress, open discussions and feedbacks formed the basis of this review. An anonymous reviewer provided constructive comments.

References

Arenson L.U. 2002. Unstable Alpine permafrost: a potentially important natural hazard: Variations of geotechnical behaviour with time and temperature. Ph.D. Thesis No 14801, Inst. for Geotechnical Engineering, ETH, Zurich, 271.

Barsch, D. 1978. Active rock glaciers as indicators for discontinuous alpine permafrost – an example from the Swiss Alps. *Proceedings of the Third International Conference on Permafrost*, NRC Ottawa, 1, 349-3353.

Barsch, D. 1992. Permafrost creep and rock glaciers. *Permafrost and Periglacial Processes* 3/3: 175-188.

Davies, M., Hamza, O. & Harris, C. 2001. The effect of rise in mean annual temperature on the stability of rock slopes containing ice-filled discontinuities, *Permafrost Periglacial Processes* 12(1): 137-144.

Delaloye, R., Perruchoud, E., Avian, M., Kaufmann, V., Bodin, X., Hausmann, H., Ikeda, A., Kääb, A., Kellerer-Pirklbauer, A., Krainer, K., Lambiel, C., Mihajlovic, D., Staub, B., Roer, I. & Thibert. E. 2008. Recent interannual variations of rock glaciers creep in the European Alps. Proceedings of the 9th International Conference on Permafrost 2008, Fairbanks, Alaska, USA. This volume.

Etzelmüller, B., Hoelzle, M., Soldjørg, Flo, Heggem, E., Isaksen, K., Mittaz, C., Vonder Mühll, D., Ødegard, R.S., Haeberli, W. & Sollid, J.L. 2001. Mapping and modelling the occurrence and distribution of mountain permafrost. *Norsk Geografisk Tidsskrift* 55: 186-194.

Fischer, L., Kääb, A., Huggel, C. & Noetzli, J. 2006. Geology, glacier changes, permafrost and related slope instabilities in a high-mountain rock wall: Monte Rosa east face, Italian Alps. *Natural Hazards and Earth System Science* 6: 761-772.

Frauenfelder, R. 2005. Regional-scale modeling of the occurrence and dynamics of rockglaciers and the distribution of paleopermafrrost. Schriftenreihe Physische Geographie: Glaziologie und Geomorphodynamik 45, University of Zurich, 202 pp.

Fujii, Y. & Higuchi, K. 1978. Distribution of alpine permafrost in the northern hemisphere and its relation to air temperature. *Proceedings of the Third International Conference on Permafrost*, NRC Ottawa, 1, 367-371.

Gorbunov, A.P. 1978. Permafrost in the mountains of central Asia. *Proceedings of the Third International Conference on Permafrost*, NRC Ottawa, 1, 372-377 (in Russian).

Gruber, S. 2007. MTD: a mass-conserving algorithm to parameterize gravitational transport and deposition processes using digital elevation models. *Water Resources Research* 43, W06412, doi:10.1029/2006WR004868.

Gruber, S. & Haeberli, W. 2007. Permafrost in steep bedrock slopes and its temperature-related destabilization following climate change. *Journal of Geophysical Research* 112: F02S18, doi:10.1029/2006JF000547.

Gruber, S. & Haeberli, W. 2008. (in press) Mountain permafrost. Mountain Permafrost. In: *Permafrost Soils,* edited by: Margesin, R., Biology Series, Springer.

Gruber, S. & Hoelzle, M. 2001. Statistical modelling of mountain permafrost distribution – local calibration and incorporation of remotely sensed data. *Permafrost and Periglacial Processes* 12(1): 69-77, doi: 10.1002/ppp.374.

Gruber, S., Haeberli, W., Krummenacher, B., Keller, F., Mani, P., Hunziker, G., Hölzle, M., Vonder Mühll, D., Zimmermann, M., Keusen, H.-R., Götz, A. & Rätzo, H. 2006. Erläuterungen zur Hinweiskarte der potentiellen Permafrostverbreitung in der Schweiz 1:50'000. Bundesamt für Umwelt (BAFU) / Swiss Federal Office for the Environment.

Gruber, S., Hoelzle, M. & Haeberli, W. 2004a. Permafrost thaw and destabilization of Alpine rock walls in the hot summer of 2003. *Geophysical Research Letters* 31: L13504, 4pp, doi:10.1029/2006JF000547.

Gruber, S., Hoelzle, M. & Haeberli, W. 2004b. Rock wall temperatures in the Alps – modelling their topographic distribution and regional differences. *Permafrost and Periglacial Processes* 15(3): 299-307, doi: 10.1002/ppp.501.

Gruber, S., King, L., Kohl, T., Herz, T., Haeberli, W. & Hoelzle, M. 2004c. Interpretation of geothermal profiles perturbed by topography: the Alpine permafrost boreholes at Stockhorn Plateau, Switzerland. *Permafrost and Periglacial Processes* 15(4): 349-357, doi:10.1002/ppp.503.

Gruber, S., Peter, M., Hoelzle, M., Woodhatch, I. & Haeberli, W. 2003. Surface temperatures in steep Alpine rock faces: a strategy for regional-scale measurement and modelling. *Proceedings of the 8th International Conference on Permafrost 2003*, Zurich, Switzerland: 325-330.

Guodong, Ch. & Dramis, F. 1992. Distribution of mountain permafrost and climate. *Permafrost and Periglacial Processes* 3/2: 83-91.

Haeberli, W. 1978. Special aspects of high mountain permafrost methodology and zonation in the Alps. *Proceedings of the Third International Conference on Permafrost*, NRC Ottawa, 1: 379-384.

Haeberli, W. 1992. Construction, environmental problems and natural hazards in periglacial mountain belts. *Permafrost and Periglacial Processes* 3/2: 111-124.

Haeberli, W. 1996. On the morphodynamics of ice/debris-transport systems in cold mountain areas. *Norsk Geografisk Tidsskrift* 50: 3-9.

Haeberli, W. 2005. Investigating glacier-permafrost relationships in high-mountain areas: historical background, selected examples and research needs. In: Harris, C. & Murton, J. B. (eds): Cryospheric Systems: Glaciers and Permafrost, The Geological Society of London, Special Publication 242, 29-37.

Haeberli, W. & Gruber, S. 2008. (in press) Global warming and mountain permafrost. In: *Permafrost Soils,* edited by: Margesin, R., Biology Series, Springer.

Haeberli, W. & Hohmann, R. 2008. Climate, glaciers and permafrost in the Swiss Alps 2050: scenarios, consequences and recommendations. Proceedings of the 9th International Conference on Permafrost 2008, Fairbanks, Alaska, USA. This volume.

Haeberli, W., Hallet, B., Arenson, L., Elconin, R., Humlum, O., Kääb, A., Kaufmann, V., Ladanyi, B., Matsuoka, N., Springman, S. & Vonder Mühll, D. 2006. Permafrost creep and rock glacier dynamics. *Permafrost and Periglacial Processes* 17/3: 189-214. (doi: 10.1002/ppp).

Haeberli, W., Huggel, C., Kääb, A., Zgraggen-Oswald, S., Polkvoj, A., Galushkin, I., Zotikov, I. & Osokin, N. 2004. The Kolka-Karmadon rock/ice slide of 20 September 2002: an extraordinary event of historical dimensions in North Ossetia, Russian Caucasus, *Journal of Glaciology* 50/171: 533-546.

Hanson, S. & Hoelzle, M. 2004. The thermal regime of the active layer at the Murtèl rock glacier based on data from 2002. *Permafrost Periglacial Processes* 15(3): 273-282.

Harris, C. 2008. (Plenary presentation), Proceedings of the 9th International Conference on Permafrost 2008, Fairbanks, Alaska, USA. This volume.

Harris, C., Haeberli, W., Vonder Muehll, D. & King, L. 2001. Permafrost monitoring in the high mountains of Europe: the PACE Project in its global context. *Permafrost and Periglacial Processes* 12(1): 3-11

Harris, C., Arenson, L.U., Christiansen, H.H., Etzelmüller, B., Frauenfelder, R., Gruber, S., Haeberli, W., Hauck, C., Hölzle, M., Humlum, O., Isaksen, K., Kääb, A., Lehning, M., Lütschg, M.A., Matsuoka, N., Murton, J.B., Nötzli, J., Phillips, M., Ross, N., Seppälä, M., Springman, S.M. & Vonder Mühll, D. 2007. (In review.) Permafrost and climate in Europe: geomorphological impacts, hazard assessment and geotechnical response. *Earth Science Reviews.*

Harris, C., Vonder Mühll, D., Isaksen, K., Haeberli, W., Sollid, J., King, L., Holmlund, P., Dramis, F., Guglielmin, M. & Palacios, D. 2003. Warming permafrost in European mountains. *Global and Planetary Change* 39: 215–225.

Harris, S. & Brown, R.J.E. 1978. Plateau Mountain: a case study of alpine permafrost in the Canadian Rocky Mountains. *Proceedings of the Third International Conference on Permafrost*, NRC Ottawa, 1, 386-391.

Harris, S. & Corte, A. 1992. Interactions and relations between mountain permafrost, glaciers, snow and water. *Permafrost and Periglacial Processes* 3/2: 103-110.

Hasler, A., Talzi, I., Beutel, J., Tschudin, C. & Gruber, S. 2008. Wireless sensor networks in permafrost research – concept, requirements, implementation and challenges, Proceedings of the 9th International Conference on Permafrost 2008, Fairbanks, Alaska, USA. This volume.

Hauck, C., & Vonder Mühll, D. 2003. Inversion and interpretation of two-dimensional geoelectrical measurements for detecting permafrost in mountainous regions. *Permafrost Periglacial Processes* 14: 305-318.

Hoelzle, M. & Gruber, S. 2008. Borehole and ground surface temperatures and their relationship to meteorological conditions in the Swiss Alps, Proceedings of the 9th International Conference on Permafrost 2008, Fairbanks, Alaska, USA. This volume.

Huggel, C., Kääb, A., Haeberli, W. & Krummenacher, B. 2003. Regional-scale GIS-models for assessment of hazards from glacier lake outbursts: evaluation and application in the Swiss Alps. *Natural Hazards and Earth System Sciences* 3 (6): 647-662.

Huggel, C., Zgraggen-Oswald, S., Haeberli, W., Kääb, A., Polkvoj, A., Galushkin, I. & Evans, S.G. 2005. The 2002 rock/ice avalanche at Kolka/Karmadon, Russian Caucasus: assessment of extraordinary avalanche formation and mobility, and application of QuickBird satellite imagery. *Natural Hazards and Earth System Sciences* 5: 173-187.

Ikeda, A., Matsuoka, N. & Kääb, A. 2008 (in press). The role of liquid water in the fast deformation of perennially frozen ground. A case study on a rock glacier in the Swiss Alps. *Journal of Geophysical Research.*

IPCC 2007. Climate Change 2007. Intergovernmental Panel on Climate Change, Cambridge and New York. Various reports.

Isaksen, K., Sollid, J., Holmlund, P. & Harris, C. 2007. Recent warming of mountain permafrost in Svalbard and Scandinavia*. Journal of Geophysical Research* 112: F02S04, doi:10.1029/2006/F000522.

Jin, H., Li, S., Cheng, G., Wang, S. & Li, X. 2000. Permafrost and climate change in China. *Global and Planetary Change*. 26 (4), 387-404.

Kääb, A., Frauenfelder, R. & Roer, I. 2006. On the response of rockglacier creep to surface temperature increases. *Global and Planetary Change* 56(1-2): 172-187.

Kääb, A. & Kneisel, C. 2006. Permafrost creep within a recently deglaciated glacier forefield: Muragl, Swiss Alps. *Permafrost and Periglacial Processes* 17(1): 79-85.

Keller, F. & Gubler, H.U. 1993. Interaction between snow cover and high mountain permafrost at Murtèl/Corvatsch, Swiss Alps. *Proceedings of the 6th International Conference on Permafrost (Bejing, China),* South China University of Technology Press, 332-337.

King, L., Gorbunov, A.P. & Evin, M. 1992. Prospecting and mapping of mountain permafrost and associated phenomena. *Permafrost and Periglacial Processes* 3/2: 73-81.

Kneisel, C. 2003. Permafrost in recently deglaciated glacier forefields – measurements and observations in the eastern Swiss Alps and in northern Sweden. Zeitschrift für Geomorphologie 47, 289-305.

Krautblatter, M. & Hauck, C. 2007. Electrical resistivity tomography monitoring of permafrost in solid rock walls. *Journal of Geophysical Research* 112, F02S20. doi:10.1029/2006JF000546.

Lautridou, J.P., Francou, B. & Hall, K. 1992. Present-day periglacial processes and landforms in mountain areas. *Permafrost and Periglacial Processes* 3/2: 93-101.

Lehning, M., Bartelt, P.B., Brown, R.L., Fierz, C. & Satyawali, P. 2002. A physical SNOWPACK model for the Swiss Avalanche Warning Services. Part III: meteorological boundary conditions, thin layer formation and evaluation. *Cold Reg. Sci. Technol.*, 35: 169-184.

Lüthi, M. & Funk, M. 1997. Wie stabil ist der Hängegletscher am Eiger? *Spektrum der Wissenschaft* 97(5): 21-24.

Lütschg, M., Bartelt, P., Lehning, M., Stoeckli, V. & Haeberli, W. 2003. Numerical simulation of the interaction processes between snow cover and alpine permafrost. *Proceedings of the 8th International Conference on Permafrost 2003*, Zurich, Switzerland, 697-702

Marchenko, S.S., Gorbunov, A.P. & Romanovsky, V.E. 2007. Permafrost warming in the Tien Shan mountains, Central Asia. *Global and Planetary Change* 56 (3-4): 311-327.

Noetzli, J., Gruber, S., Kohl, T., Salzmann, N. & Haeberli, W. 2007. Three-dimensional distribution and evolution of permafrost temperatures in idealized high-mountain topography. *Journal of Geophysical Research* 112, F02S13, doi:10.1029/2006JF000545.

Noetzli, J., Hoelzle, M. & Haeberli, W. 2003. Mountain permafrost and recent Alpine rock-fall events: a GIS-based approach to determine critical factors. *Proceedings of the 8th International Conference on Permafrost 2003*, Zurich, Switzerland, 827-832.

Noetzli, J., Hilbich, C., Hoelzle, M., Hauck, C., Gruber, S. & Krauer, M. 2008. Comparison of transient 2D temperature fields with time-lapse electrical resistivity data at the Schilthorn Crest, Switzerland, Proceedings of the 9th International Conference on Permafrost 2008, Fairbanks, Alaska, USA. This volume.

Noetzli, J., Huggel, C., Hoelzle, M. & Haeberli, W. 2006. GIS-based modelling of rock-ice avalanches from Alpine permafrost areas. *Computational Geosciences* 10: 161-178 (doi: 10.1007/s10596-005-9017z).

Roer, I. 2007. Rockglacier kinematics in a high mountain geosystem. Bonner Geographische Abhandlungen 117.

Roer, I., 2008. Observations and considerations on destabilizing active rockglaciers in the European Alps. Proceedings of the 9th International Conference on Permafrost 2008, Fairbanks, Alaska, USA. This volume.

Roer, I., Kääb, A. & Dikau, R., 2005. Rockglacier acceleration in the Turtmann valley (Swiss Alps) - probable controls. *Norwegian Journal of Geography* 59 (2), 157-163.

Sass, O. 2003. Moisture distribution in rockwalls derived from 2D-resistivity measurements. Z. *Geomorph. Suppl.* 132: 51- 69.

Salzmann, N., Noetzli, J., Hauck, C., Gruber, S. & Hoelzle, M. 2007. RCM-based ground surface temperature scenarios in high-mountain topography and their uncertainty ranges. *Journal of Geophysical Research* 112, F02S12, doi:10.1029/2006JF000527.

Trombotto, D. 2000. Survey of cryogenic processe, periglacial forms and permafrost conditions in South America. *Revista Instituto Geologico* 21(1/2): 35-55.

UNEP 2007. Global Outlook for Ice & Snow, UNEP, Nairobi, Kenya.

Vonder Mühll, D., Arenson, L.U. & Springman, S.M. 2003. Temperature conditions in two Alpine rock glaciers. *Proceedings of the 8th International Conference on Permafrost 2003*, Zurich, Switzerland, 1195-1200.

Vonder Mühll, D., Noetzli, J. & Roer, I. 2008. PERMOS – a comprehensive monitoring network of mountain permafrost in the Swiss Alps, Proceedings of the 9th International Conference on Permafrost 2008, Fairbanks, Alaska, USA. This volume.

Climate, Glaciers, and Permafrost in the Swiss Alps 2050: Scenarios, Consequences, and Recommendations

Wilfried Haeberli
Glaciology, Geomorphodynamics & Geochronology, Geography Department, University of Zurich, Switzerland
Roland Hohmann
Environment, Traffic and Energy Division, B,S,S. Economic Consultants, Basel, Switzerland

Abstract

Climate scenarios for the time horizon of 2050 in the Swiss Alps, as simulated by using high-resolution ensemble modeling, indicate most likely changes in temperature/precipitation by + 2°C / + 10% in winter and + 3°C / - 20% in summer. Such a development would lead to the vanishing of about 75% of the existing glacier surface and deep warming of permafrost in mountain peaks. Corresponding impacts would mainly concern rather dramatic changes in landscape appearance, slope stability, and the water cycle. The formation of lakes in the forefields of retreating or even collapsing glaciers, together with the decreasing stability of rock walls, leads to an increasing probability of major rockfalls impacting onto water bodies and triggering dangerous flood waves. A special recommendation was therefore provided to systematically assess the safety of natural, artificial, and newly forming lakes in the Alps.

Keywords: climate change; cold mountains; glaciers; permafrost; slope stability.

Introduction

Climate change in cold mountain areas is faster than on the global average and strongly affects one of their most characteristic aspects – surface and subsurface ice (UNEP 2007). Increasing concentrations of greenhouse gases are likely to cause accelerating rates of change, which would lead within decades to environmental conditions far beyond historical and Holocene precedence and to commitments for the future probably lasting for centuries if not millennia. A primary challenge to cope with such a rather clearly foreseeable development is the anticipation of impacts from the reaction of complex, highly interconnected, and more and more disequilibrated natural systems (Watson & Haeberli 2004).

In March 2007, the Advisory Body on Climate Change created in 1996 by the Swiss Academy of Sciences on behalf of the Swiss Federal Government published a report on climate change and Switzerland for the year 2050 (OcCC 2007). Based on corresponding assessments for various sectors of the environment, the economy and the society, recommendations were prepared for the Swiss Federal Government. The present contribution deals with glaciers and permafrost in the Swiss Alps as an example of corresponding analyses and assessments relating to cold high-mountain regions at lower latitudes. It briefly summarizes the now-available knowledge based on climate projection and glacier and permafrost changes, and possibly resulting impacts. An example (Stein Glacier) is provided to emphasize the importance of combined glacier/permafrost considerations within the framework of recommendations to governmental policy makers.

Projections

Climate

Excellent data document the climate and its recent change in Switzerland. Atmospheric temperature rise during the 20th century was > 1°C and, hence, about twice the global average of 0.6°C. During the same time period, annual precipitation increased by some 8%. Due to the fact that evaporation also increased, river runoff remained more or less constant. The topography of the Alpine Mountain Chain only introduces relatively minor spatial variability of these changes with time.

Regional and seasonal climate change scenarios for Switzerland and the years 2030, 2050, and 2070 (Fig. 1) were calculated by Frei (2004) on the basis of the results from the EU-funded PRUDENCE project (Christensen et al. 2002). Uncertainties were estimated based on the distribution of the results from 16 model chains representing different combinations of 2 emission scenarios, 4 global, and 8 regional climate models. The estimates are based on the assumption that mitigation policies will only have a major influence in the second part of the 21st century and that the time horizon of 2050 could mark a transition to much more severe conditions at later stages. According to the applied scenario, temperatures will increase until 2050 with respect to 1990 by 1.8°C in winter (95% interval 0.9°C to 3.4°C) and 2.8°C (1.4°C to 4.9°C) in summer, both, north and south of the Alps. As a result the 0°C-isotherm will rise during winter by about 360 m (180 m to 680 m). Precipitation will increase by about 10% (-1% to +26%) in winter and decrease by about 20% (-36% to -6%) in summer. A trend towards more frequent and intense heat waves, probably also droughts, is expected in summertime. Cold waves in wintertime will probably decrease in number and intensity.

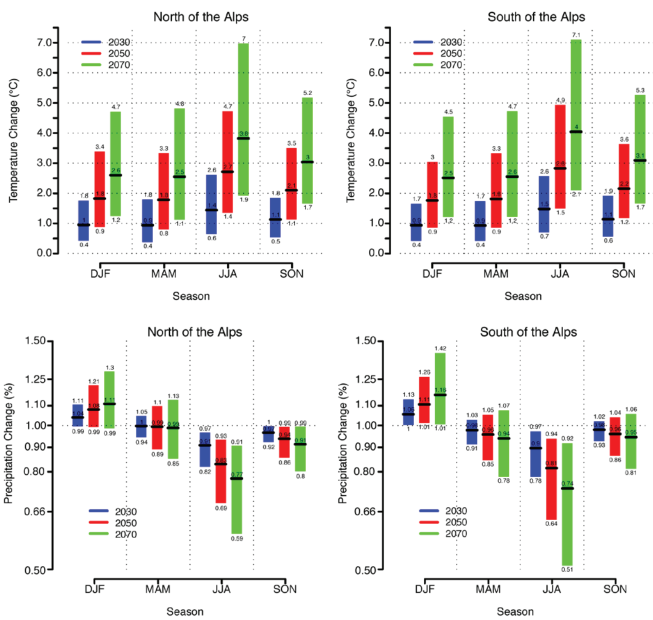

Figure 1. Seasonal climate scenarios (top: temperature, bottom: precipitation) for Switzerland and the years 2030, 2050, and 2070 for the parts north and south of the Alps (from OcCC 2007).

Glaciers

In the European Alps, a comprehensive database on glaciers and their long-term fluctuations has been built up over more than a century. This now enables the integration of *in situ* measurements (length change, mass balance), remote sensing (glacier inventories), digital terrain information, and numerical modeling for the entire mountain chain (Haeberli et al. 2007). The average loss in overall glacier volume was about 0.5% per year between 1850—the end of the Little Ice Age—and 1975, then increased to about 1% per year of the remaining volume between 1975 and 2000; and since the turn of the millennium, has accelerated to about 2–3% per year. The extremely hot and dry summer of 2003 alone eliminated some 8% of the remaining ice volume. Many glaciers started to waste down or even collapse and disintegrate rather than to actively retreat (Paul et al. 2007).

Alpine-wide estimates of future glacier evolution had first been made by Haeberli and Hoelzle (1995; cf. also Maisch et al. 2000, Maisch 2001) and proved to be rather robust. The latest and most differentiated model uses statistically calibrated relations between equilibrium line altitude as measured in long-term mass balance observations, summer temperature, and annual precipitation together with glacier inventory data and the SRTM3 digital elevation model (Zemp et al. 2006). Combination with the climate scenario applied for 2050 shows that the glacier surface area in the European Alps could be reduced with respect to conditions in 1971–1990 by a further 75% (50% to 95%) as soon as by 2050 (Fig. 2). Slightly smaller losses can be assumed for the Swiss Alps, where the largest glaciers exist. A remarkable part—roughly one-third—of this anticipated development has already taken place by now (in 2007).

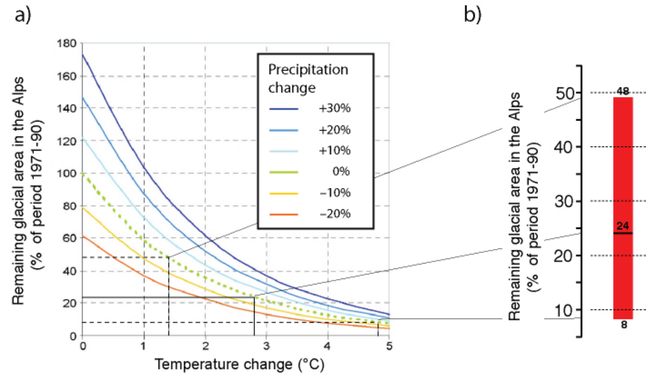

Figure 2. Glacier area in the Alps as a function of temperature and precipitation change: (a) as combined with the assumed climate scenario for 2050; (b) after Zemp et al. 2006, from OcCC 2007.

Permafrost

Systematic research on permafrost in the Alps only started well after World War II. First attempts to establish a long-term monitoring program began with the observation of borehole temperatures in the ice-rich debris of Murtèl rock glacier (Vonder Mühll & Haeberli 1991) and photogrammetric rock glacier monitoring (Haeberli et al. 1993). A decisive step forward was the installation of 100-m-deep bedrock boreholes in the permafrost of European mountains within the Permafrost and Climate in Europe (PACE) project (Harris et al. 2003). Numerical models for estimating spatial permafrost distribution patterns in the Swiss Alps were first applied by Keller et al. (1998). Most recently, a model simulation was done at a 1:50,000 scale for the entire Swiss Alps on behalf of the Federal Office for the Environment (FOEN). Permafrost in the Swiss Alps is now known to occupy a surface area, which is roughly twice as large as the glacierized area. Its development is observed within the framework of PERMOS (Permafrost Monitoring Switzerland; Vonder Mühll et al., 2008), one of the first networks of this kind.

Thermal conditions in commonly ice-rich permafrost in talus and moraines strongly depend on snow cover conditions and are thus difficult to predict. Because of latent heat effects, complete thawing of such frozen debris in any case takes many decades to centuries, even with warming to 0°C. Permafrost evolution in bedrock of steep mountain peaks with highly complex topography is less snow-dependent. The PACE boreholes indicate surface warming during the 20th century by about 0.5 to 1°C, and corresponding thermal anomalies (heat flow reduction) down to 50 70 m below surface. Future scenarios can be simulated using 3-dimensional transient heat diffusion models.

Corresponding calculations for idealized topographies (Noetzli et al. 2007) illustrate that the uppermost peaks are largely decoupled from the geothermal heat flow because of predominant lateral fluxes in strongly asymmetrical thermal fields and that warming trends can penetrate from two or more sides (Fig. 3). Due to the slow process of heat diffusion at depth, permafrost inside the mountains still persists after centuries, but with warmer if not near 0°C temperatures over wide altitudinal ranges and at great depths.

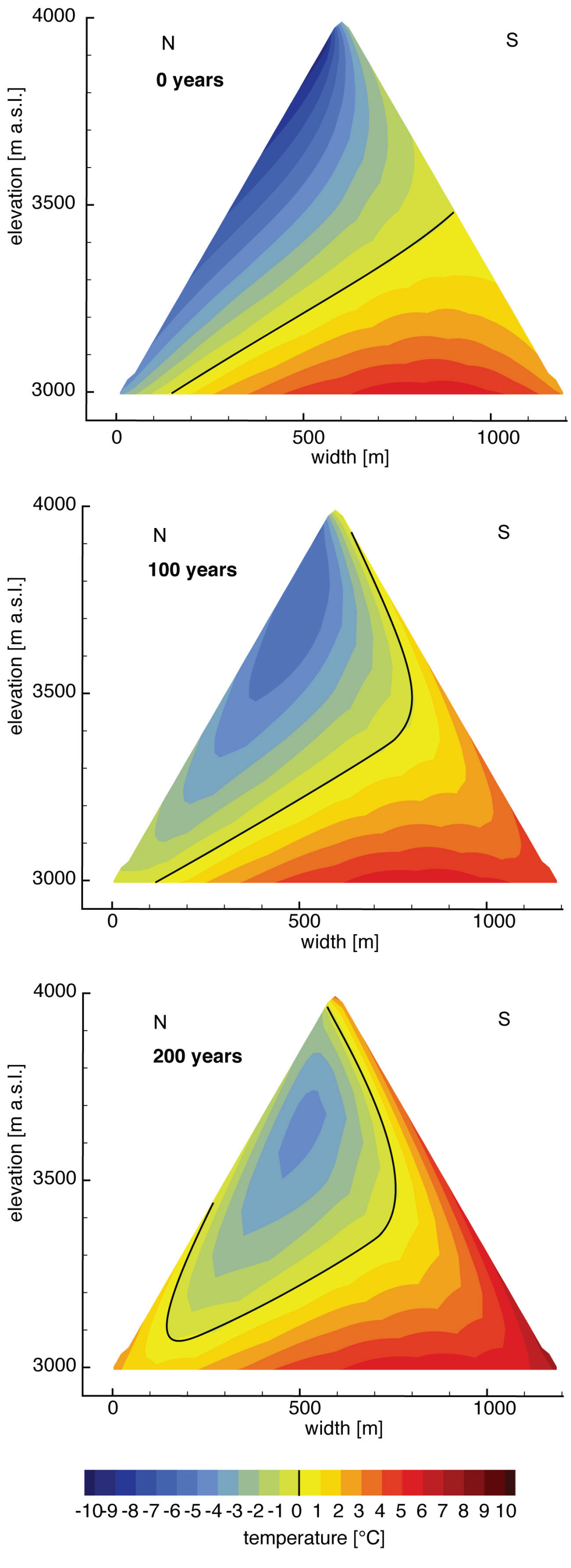

Figure 3. Model simulation (heat diffusion only) of the thermal field within a high Alpine mountain peak with realistic permafrost occurrence (from energy balance modeling), assumed centennial warming and idealized topography (after Noetzli et al. 2007; cf. OcCC 2007).

Impacts

Landscape and surface processes

Rapid glacier shrinkage is among the most obvious and visible phenomena related to ongoing warming trends. Already today, the perception of high-mountain landscapes is changing: the vanishing beauty of firn and ice as a symbol of an intact environment is more and more seen as a clear and easily understood indication of human-induced disturbance. In areas with a moderately humid to relatively dry climate, revegetation of newly exposed terrain is a slow process. For generations to come, therefore, deglaciated high-mountain chains will predominantly remain as areas of bare rock and debris without closed forests and mature soils (Egli et al. 2006). This will affect the attractiveness and touristic value of the respective landscape. Entire geo- and ecosystems as well as their individual parts have strongly different characteristics and time scales of response to fast climate change. This will undoubtedly lead to growing distances from conditions of dynamic equilibrium, which were able to form during the Holocene with its relatively stable climate.

One remarkable landscape element developing with continued atmospheric warming is the formation of new lakes with further glacier retreat and disintegration. Potential sites for future lake formation in over-deepened bed parts can be modeled by assuming constant basal shear stress along the central flow line, constant width-to-depth ratio of channel-type valley cross sections, and compressive flow connected with negative bed slopes. New lakes will thus most likely form where present-day low-slope ice surfaces, free of crevasses, have an enlarged width and grade into a narrower, steeper, and more or less heavily crevassed part in the flow direction (Fig. 4). Such lakes will be landforms of considerable attractiveness and, hence, to some degree compensate for the loss in landscape attractiveness from glacier disappearance. In many instances, however, they will be situated within an over-steepened and destabilized surrounding topography with enhanced periglacial-geomorphological activity. Corresponding slope stability problems would cause hazardous situations not known from the past. One example out of the number of possibilities is outlined below.

Natural hazards

Most critical stability conditions in perennially frozen rock walls are expected to be found in areas with warm permafrost (Davis et al. 2001, Noetzli et al. 2003, Gruber et al. 2004, Gruber & Haeberli 2007). Deep long-term warming of perennially frozen mountain peaks has the potential to bring steeply inclined rock layers to critical temperatures, not only over more extended vertical ranges but also to greater depths. As a consequence, the probability of large rockfalls is slowly increasing. Loss of support of steep slopes due to glacier disappearance leads to a reorientation of the stress field in adjacent slopes, and further contributes to the destabilization of rock walls above newly forming lakes. The possibility of flood waves from impacts of large rock, ice, snow or mixed avalanches must, therefore, be seriously considered.

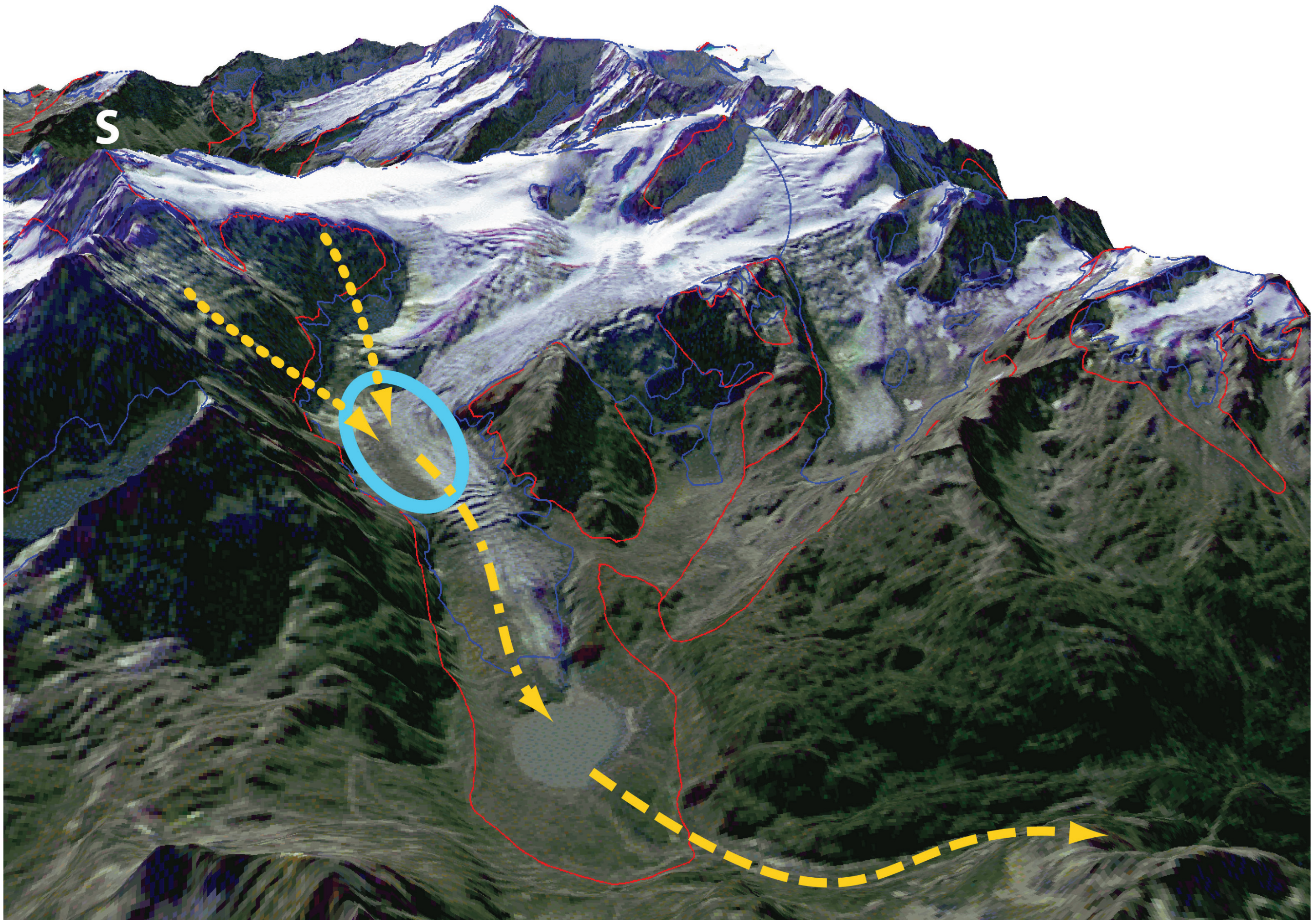

Figure 4: Modeled future development of a lake in an assumed overdeepened bed part of the Stein glacier near Sustenpass, Bernese Alps. Dotted lines indicate potential rock/ice avalanches from warming permafrost in the rock walls of Sustenhorn (S), dashed-dotted line related flood wave into the existing proglacial lake Steinsee, dashed line resulting flood wave from both lakes. Satellite image (combined SPOT/Landsat, September 1992) drawn over a DEM from swisstopo, image by F.Paul). Thin lines are former glacier margins (red 1850, blue 1973). Reproduced by permission of swisstopo (BA081042).

GIS-based models of trajectories from rock/ice avalanches can be applied for realistic assessments (Noetzli et al. 2006). The timing of the events, however, can involve long delays and is hardly predictable. The same is true, in principle, for debris flows, which can be triggered by intense convective summer precipitation events in, so far, glacier-covered starting zones with newly exposed moraine material. Examples of corresponding assessments for the Bernina group in the Upper Engadin were calculated by Rothen-Bühler (2006) within the framework of an integrative 4-dimensional geo-information system, which was built up as a tool for environmental planning in high mountain areas. Another case of a future hazard potential from flood waves caused by rock/ice avalanches from high/steep rock walls with warming permafrost into a modeled future lake replacing the now existing glacier surface is illustrated for Steingletscher/Sustenhorn (Bernese Alps) in Figure 4.

Water cycle

As a result of climate change, the maximum in river discharge will occur earlier in the year and will be less pronounced. The combined effect of increased precipitation and 0°C-isotherms at higher elevations will lead to a growing risk of winter flooding in lowlands surrounding the Alps, because greater percentages of liquid precipitation must be expected to runoff directly instead of being temporarily stored as snow. Drier summers, on the other hand, will lead to more frequent and especially more severe droughts. With conditions like in summer 2003 (stable high pressure over central Europe during several months) becoming near average in the second part of the century, the combination of missing precipitation, earlier snowmelt, and strongly reduced meltwater from disappearing glaciers could lower runoff to critical levels even in large Alpine rivers (Rhine, Rhone).

Despite the large water resources in the Alpine region, water stress could become a problem in some parts of Switzerland during the hot/dry season because of the decreasing availability of river water and its interconnection with soil humidity, water temperatures, lake/groundwater levels and aquatic ecosystems (fish, algae, etc.) and the increasing demands for domestic freshwater supply,

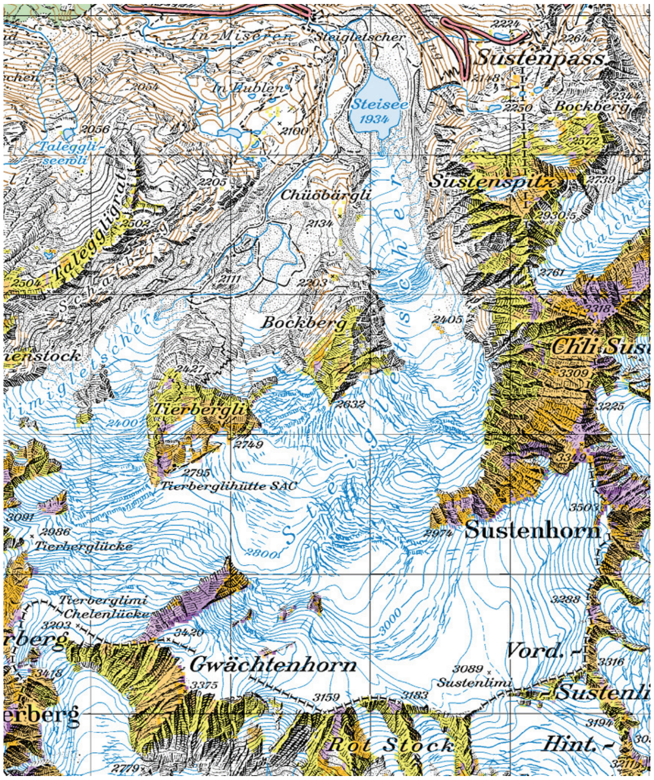

Figure 5: Detail of the map 1:50,000 with numerically simulated permafrost distribution as compiled for the entire Swiss Alps on behalf of the Federal Office for the Environment (BAFU/FOEN). The area is the same as on Figure 4. Yellow colors indicate relatively warm/thin, violet colors relatively cold/thick permafrost.

agriculture (irrigation), hydropower production, cooling of nuclear power plants, or even firefighting in desiccated forests. Conflicts about water use are likely to grow and options for adaptation—for instance, redefinition of the use of reservoirs at high-altitude (irrigation and summer power production rather than winter power production)—should be investigated as early as possible.

Conclusions and Recommendations

The "experiment with the global climate" has started. It cannot be stopped, but only be influenced. Grave consequences for cold mountain areas are unavoidable and are already developing at accelerating rates. Corresponding mitigation and adaptation measures must be planned. This primarily requires early and realistic anticipation of future developments and potential system reactions. The time scale to be considered involves several coming decades. As a consequence, rapid action is necessary. With modern digital terrain information, numerical and GIS-based models, and satellite imagery, all necessary technical means are available.

As a follow-up to the report on the climate in 2050 (OcCC 2007), a set of recommendations with respect to climate change impacts was provided to the Swiss Federal Government. Concerning Alpine glaciers and permafrost, the importance of adequate monitoring and the need for a systematic safety assessment of all existing natural and artificial lakes, as well as of all newly forming lakes, was emphasized. Perhaps the most important and most far-reaching statement, however, relates to the rights for the use of water, an aspect which may well become a central focus of living conditions and economic development in a rather near future.

At a national level, first steps have already been undertaken. The numerically modeled 1:50,000 permafrost map of the Swiss Alps, prepared on behalf of the Federal Office for the Environment (FOEN, Fig. 5), greatly helps with providing transparent information to authorities and raising public awareness. The Swiss Academy of Sciences, the Federal Office for the Environment, and MeteoSuisse, together, now definitely established the highly developed network Permafrost Monitoring in Switzerland (PERMOS), and the glacier monitoring network is being reorganized in order to integrate modern technologies and strategies according to international climate-related observing systems (GCOS 2003, 2004).

Acknowledgments

We thank all the numerous colleagues and experts who contributed to the original assessment reports. The interest, support, and excellent collaboration of the Swiss Academy of Sciences, the Federal Office for the Environment, and MeteoSuisse are gratefully acknowledged. Stephan Gruber, Jeannette Noetzli, Max Maisch, Frank Paul, and Isabelle Roer critically read an early draft of the present paper.

References

Christensen, J.H., Carter, T. & Giorgi, F. 2002. PRUDENCE employs new methods to assess European climate change. *EOS* 82: 147.

Davies, M., Hamza, O. & Harris, C. 2001. The effect of rise in mean annual air temperature on the stability of rock slopes containing ice-filled discontinuities. *Permafrost and Periglacial Processes* 12: 137-144.

Egli, M., Wernli, M., Kneisel, C., Biegger, S. & Haeberli, W. 2006. Melting glaciers and soil development in the proglacial area Morteratsch (Swiss Alps): II. Modeling the present and future soil state. *Arctic, Antarctic, and Alpine Research* 38/4: 510-521.

FOEN. 2007. Klimaänderung in der Schweiz – Indikatoren zu Ursachen, Auswirkungen, Massnahmen. Federal Office for the Environment, Switzerland.

Frei, C. 2004. Klimazukunft der Schweiz – eine probabilistische Projektion. (www.occc.ch/products/CH20250/CH2050-Scenarien.pdf).

GCOS. 2003. Second report on the adequacy of the Global Observing Systems for Climate in support of the UNFCCC. GCOS-82, WMO, Geneva.

GCOS. 2004. Implementation plan for the Global Observing System for Climate in support of the UNFCCC. GCOS-92, WMO, Geneva.

Gruber, S. & Haeberli, W. 2007. Permafrost in steep bedrock slopes and its temperature-related destabilization following climate change. *Journal of Geophysical Research* 112: F02S18 (doi:10.1029/2006JF000547).

Gruber, S., Hoelzle, M. and Haeberli W. 2004. Permafrost thaw and destabilization of Alpine rock walls in the hot summer of 2003. *Geophysical Research Letters*, 31/L13504.

Haeberli, W. & Hoelzle, M. 1995. Application of inventory data for estimating characteristics of and regional climate-change effects on mountain glaciers: a pilot study with the European Alps. *Annals of Glaciology* 21: 206-212. Russian translation in: *Data of Glaciological Studies*, Moscow, 82: 116-124.

Haeberli, W., Hoelzle, M., Keller, F., Schmid, W., Vonder Mühll, D. & Wagner, S. 1993. Monitoring the long-term evolution of mountain permafrost in the Swiss Alps. *Proceedings of the Sixth International Conference on Permafrost* 1: 214-219.

Haeberli, W., Hoelzle, M., Paul, F. & Zemp, M. 2007. Integrated monitoring of mountain glaciers as key indicators of global climate change: the European Alps. *Annals of Glaciology* 46: 150-160.

Harris, C., Vonder Mühll, D., Isaksen, K., Haeberli, W., Sollid, J.L., King, L., Holmlund, P., Dramis, F., Guglielmin, M. & Palacios D. 2003. Warming permafrost in European mountains. *Global and Planetary Change* 39: 215-225.

Keller, F., Frauenfelder, R., Gardaz, J.M., Hoelzle, M., Kneisel, C., Lugon, R., Phillips, M., Reynard, E. & Wenker, L. 1998. Permafrost map of Switzerland. *Proceedings of the 7th International Conference on Permafrost*, Yellowknife, Canada: 557-562.

Maisch, M., Wipf, A., Denneler, B., Battaglia, J. & Benz, Chr. 2000. Die Gletscher der Schweizer Alpen. Gletscherhochstand 1850, Aktuelle Vergletscherung, Gletscherschwund-Szenarien 21. Jahrhundert. NFP 31-Schlussbericht Teilprojekt 4031-033412, (1. Auflage 1999), 2. Auflage, 373p.

Maisch, M. 2001. The longterm signal of climate change in the Swiss Alps: Glacier retreat since the end of the Little Ice Age and future ice decay scenarios. *Geografia Fisisca e Dinamica Quaternaria* 23/2000, 139-151.

Noetzli, J., Gruber, S., Kohl. T., Salzmann, N. & Haeberli, W. 2007. Three-dimensional distribution and evolution of permafrost temperatures in idealized high-mountain topography. *Journal of Geophysical Research* 112: F02S13 (doi: 10.1029/2006JF000545).

Noetzli, J., Hoelzle, M. and Haeberli W. 2003. Mountain permafrost and recent Alpine rock-fall events: a GIS-based approach to determine critical factors. ICOP 2003 Permafrost: *Proceedings of the Eighth International Conference on Permafrost*, 21-25 July 2003, Zurich, Switzerland, A.A. Balkema Publishers 2, 827-832.

Noetzli, J., Huggel, C., Hoelzle, M. & Haeberli W. 2006. GIS-based modelling of rock-ice avalanches from Alpine permafrost areas. *Computational Geosciences* 10: 161-178 (doi: 10.1007/s10596-005-9017z).

OcCC. 2007. Klimaänderung und die Schweiz 2050 – erwartete Auswirkungen auf Umwelt, Gesellschaft und Wirtschaft. OcCC and ProClim, Swiss Academy of Sciences (Ed. R. Hohmann).

Paul. F., Kääb, A. & Haeberli, W. 2007. Recent glacier changes in the Alps observed by satellite: Consequences for future monitoring strategies. *Global and Planetary Change* 56: 111-122.

Rothenbühler, C. 2006. GISALP – räumlich-zeitliche Modellierung der klimasensitiven Hochgebirgslandschaft des Oberengadins. Schriftenreihe Physische Geographie (Universität Zürich), Glaziologie und Geomorphodynamik 50, 179p.

UNEP. 2007. Global outlook for ice and snow. United Nations Environment Programme, Nairobi (Kenya), Birkeland Trykkerri, Birkeland, Norway, 235 p.

Vonder Mühll, D. & Haeberli, W. 1990. Thermal characteristics of the permafrost within an active rock glacier (Murtèl/Corvatsch, Grisons, Swiss Alps). *Journal of Glaciology* 36/123: 151-158.

Vonder Mühll, D., Noetzli, J. and Roer, I. 2008. PERMOS: A comprehensive monitoring network of mountain permafrost in the Swiss Alps. This volume.

Watson, R. T. & Haeberli, W. 2004. Environmental threats, mitigation strategies and high-mountain areas. In: Royal Colloquium: Mountain Areas – a Global Resource; *Ambio* Special Report 13: 2-10.

Zemp, M., Haeberli, W., Hoelzle, M. & Paul, F. 2006. Alpine glaciers to disappear within decades? *Geophysical Research Letters* 33: L13504 (doi: 10.1029/2006GL026319).

Frost Boil Dynamics Using ^{210}Pb as a Tracer for Soil Movement

Birgit Hagedorn
University of Alaska Anchorage, Environment and Natural Resources Institute
Rolf Aalto
University of Exeter, Department of Geography
Ronald S. Sletten
University of Washington, Quaternary Research Center
Bernard Hallet
University of Washington, Quaternary Research Center

Abstract

Frost boils, also known as plugs or non-sorted circles, are non-sorted mineral soil centers surrounded by vegetation and occur throughout the Arctic. They influence surface albedo, soil temperature, soil stability, and consequently the distribution of vegetation; thus they are an important environmental factor in arctic landscapes. Numerous mechanisms for their initiation and maintenance have been proposed including: differential frost heave, convection cell-like cryoturbation, diapirism, and load casting; however, there are few techniques for direct observations. In this paper, we evaluate the natural, atmospheric-derived, radioactive isotope ^{210}Pb as a novel tracer of frost boil kinematics in a case study in northwestern Greenland, Pituffik Peninsula (76°N, 68°W). Once deposited, ^{210}Pb is strongly adsorbed to particle surfaces and decays with a half-life of 22.3 years; thus it is an excellent tracer for sediment motion up to approximately 80 years. Our first results confirm the usefulness of this tracer but also highlight necessary measurements and sampling strategies to fully interpret the ^{210}Pb distribution in frost boils.

Keywords: frost boil; High Arctic; patterned ground; ^{210}Pb tracer; plug.

Introduction

According to Washburn (1980:128), "Nonsorted circles are patterned ground whose mesh is dominantly circular and lacks a border of stones. The term mud-boil is frequently used in Canada for both nonsorted and sorted circles. Nonsorted circles are characteristically margined by vegetation, and occur singly or in groups…." Nonsorted circles, mudboils, or frost boils are found across the Arctic, where they are important environmental features (Walker et al. 2004). They influence microtopography, the abundance and distribution of vegetation, and therefore the temperature and moisture regime of the active layer (Roth & Boike 2001, Boike et al. 2002, Boike et al. 2007), which are important factors for the stability of permafrost as well as atmosphere-ground surface interaction. A thorough description of field observation and discussion of the diverse hypothesis of the genesis of plugs and plug circles is given by Washburn (1997).

From the 19 hypotheses for the formation of patterned ground reviewed by Washburn (1956), detailed descriptions during excavations and measurements of soil motion and soil physical parameters (Schmertmann & Taylor 1965, Washburn 1969, Nicholson 1976, Zoltai & Tarnocai 1981, Hallet & Prestrud 1986, Hallet et al. 1988, Washburn 1989, van Vliet-Lanoë 1991, Washburn 1997, Hallet 1998, Walker et al. 2004, Overduin & Kane 2006) as well as mathematical modeling approaches (Kessler et al. 2001, Kessler & Werner 2003, Peterson & Krantz 2003) indicate that cycles of freezing and thawing and of drying and wetting, inclined freezing fronts, buoyancy, and differential frost heave are the most important factors for the formation of circles, if sufficient fine soil (Goldthwait 1976) and water are present. In the case of unsorted circles (e.g., frost boils, mud boils, mud hummocks), gravity driven diapirism of water-oversaturated soil above permafrost has been suggested by Swanson et al. (1999) and Shilts (1978). Based on viscosity and density measurements, Swanson (1999) estimated that several decimeter of diapir movement could happen during a single thaw event (Swanson et al. 1999). Burial of organic rich surface material (e.g., Dyke & Zoltai 1980) along boil fringe suggests that some boils are closed systems where upward movement of soil in center causes lateral outward movement at surface and subsidence at the boil fringe (Mackay & MacKay 1976, Nicholson 1976, Dyke & Zoltai 1980, Mackay 1980, Zoltai & Tarnocai 1981, Washburn 1997). Such circulatory movement has mostly been attributed to inclining freezing front (Nicholson 1976), differential frost heave (Mortensen 1932, Hallet & Waddington 1991, van Vliet-Lanoë 1991), and freeze-thaw pumping (Mackay 1980, Veillette 1980). Dating of buried organic matter in three boils of central Canadian Arctic indicates subduction rates of organic material of ~1 mm yr^{-1} (Zoltai & Tarnocai 1981). However, even though distribution of organic material and radiocarbon dating gave indications of sediment motion, direct and detailed monitoring of sediment transport over longer (~100 years) time periods will greatly improve the understanding of the proposed mechanism.

Our study presents a new approach to trace sediment motion in frost boils using the radionuclide ^{210}Pb as tracer. ^{210}Pb is a natural product of the ^{238}U decay series and a direct daughter of ^{222}Rn ($T_{1/2}$ 3.8 d). During ^{238}U decay in the soil, part of ^{222}Rn emanates into atmosphere where it decays to ^{210}Pb ($T_{1/2}$ 22.3 y). The ^{210}Pb is scavenged by aerosols, washed out by rain and snow, and deposited on the ground surface where it is strongly adsorbed to sediment grain surfaces. These chemical and physical characteristics of ^{210}Pb make it an excellent tracer of sediment transport processes in time and space. ^{210}Pb has been used in numerous applications including sedimentation and erosion processes in lacustrine, marine, and terrestrial environments (Appleby et al. 1979, Dörr 1995, Hagedorn et al. 1999, Walling et al. 2003, Aalto et al. 2008). To our knowledge, however, it has not been used in patterned ground studies. The half-life of ^{210}Pb limits its applications to ~100 years within which surface expressions become evident based on modeling studies from Peterson & Krantz (2003) and estimates from heave and motion measurements on sorted circles in Thule NW Greenland by Schmertmann & Taylor (1965).

Study Site and Methods

The study was conducted near Thule Airforce Base in northwest Greenland (76°N, 68°W). The base is located on a ~800 km^2 ice-free peninsula between the Greenland Ice Sheet to the west and Baffin Bay to the south and east. The sampling site is in Nordfjeld (North Mountain), a high valley with average elevation of 180 m. Proterozoic sedimentary rocks (Dundas formation) dominate among glacial drift and the last glaciation was initiated around >32 Ka ago (Davies et al. 1963). A more recent glacial advance either from the fjord or ice sheet is debated (Davies et al. 1963, Kelly et al. 1999). Annual average air temperature and precipitation measured by Thule Air Base since 1978 are -11.7±3°C with July temperatures at 5.3±1°C and 124 mm$_{weq}$ precipitation of which ~40% falls as snow. For the years of sampling (2003 & 2004), the average annual air temperature was -9.2°C; average soil temperatures ranged from -9.1°C (surface) to -9.8°C (1.2 m) with a thaw depth reaching ~1.2 m in early August. Spring snow cover in 2003 and 2004 was 80 mm$_{weq}$ and 30 mm$_{weq}$, and rain was 71 mm and 106 mm, respectively.

Patterned ground at the study site is nonsorted a priori and appears as irregular stripes and frost boils. The frost boils are ~0.5 m to 2 m in diameter; they show little micro-relief during the summer and are bordered with vegetation. Some boils show slight enrichment of pebbles towards their edges, but abundance of coarse material is generally sparse. During the early summer when the surface is thawed, desiccation cracks and salt precipitates develop at the surface of the central portion of the boils. Soil of distinctive color than surface has been observed near the center of several boils and appears to be recently injected from below the surface, suggesting that soil movement can be very rapidly, which has also been suggested by Swanson et al. (1999).

The central portion of the frost boil discussed here is 1.5 m in diameter. A few pebbles rest on the surface; they are more abundant towards the fringe (Fig. 1). Near

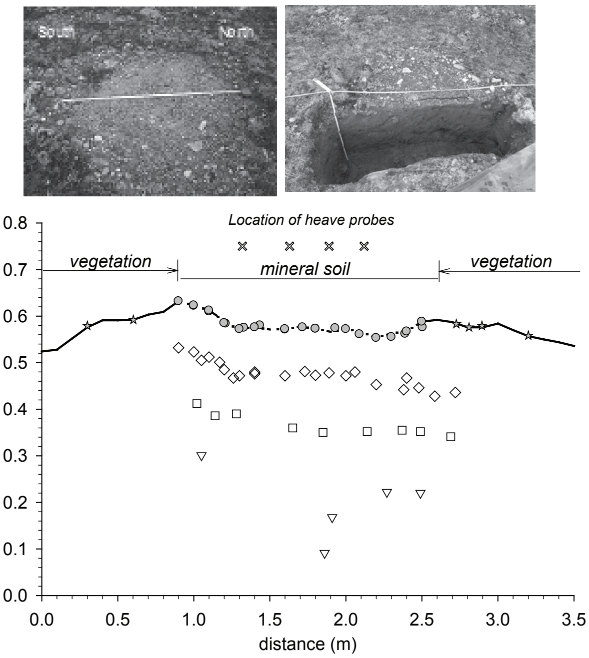

Figure 1. Upper: view of frost boil before and after excavation; note prominent crack in the image on the right developed after the excavation. Lower: detailed topography and position of samples. The different symbols refer to sampling depth in the following figures. Stars are in vegetation and dashed lines mark transition between mineral boil and vegetation. Circles with dots are measured elsewhere in vegetated areas close to frost boil. The dashed lines (Trans) mark transition from mineral soil to vegetated soil (see text). Location of boil: 78°33.241N, 68°33.596W.

the vegetated border, the mineral soil is covered with cryptogamic crust that locally forms small folds with axes paralleling the vegetation border. The center of boil consists of two apparent soil horizons: C1 (surface to 0.3 m depth) and C2 (>0.3 m depth). The C1-horizon tends to break into crumbs, shows silt caps, and has a weak platy structure. The C2- horizon has a well-developed platy structure. A few roots reach down to the frozen ground, which was at 0.69 m depth during time of excavation (June 29, 2004). A ~0.02 m O-horizon is developed in the vegetated area, and it is underlain by ~0.1 m A-horizon with weak crumb structure. A buried AB-horizon was found ~0.25 m below the vegetation. Surface samples were taken in 2003 without excavating the boil. After sampling, four heave probes were installed and left over winter, additional heave probes were installed in vegetated areas. The heave probes consist of 10 cm Plexiglas stick glued perpendicular on a 2.5 x 2.5 cm base. A Plexiglas sleeve is put over the stick and this ensemble is installed in the upper soil in the way that upper end of stick and sleeve are level with soil surface. Frost heave in upper soil will pull the sleeve up relative to the base buried deeper in the soil. The soil heave is then measured as distance between stick and outer sleeve. In 2004 the surface topography of boil was mapped and one half of boil was excavated and sampled in detail (Fig. 1). Most samples were collected undisturbed in 60 mL moisture cans to determine soil water content and bulk density gravimetrically. Dried samples were sieved to

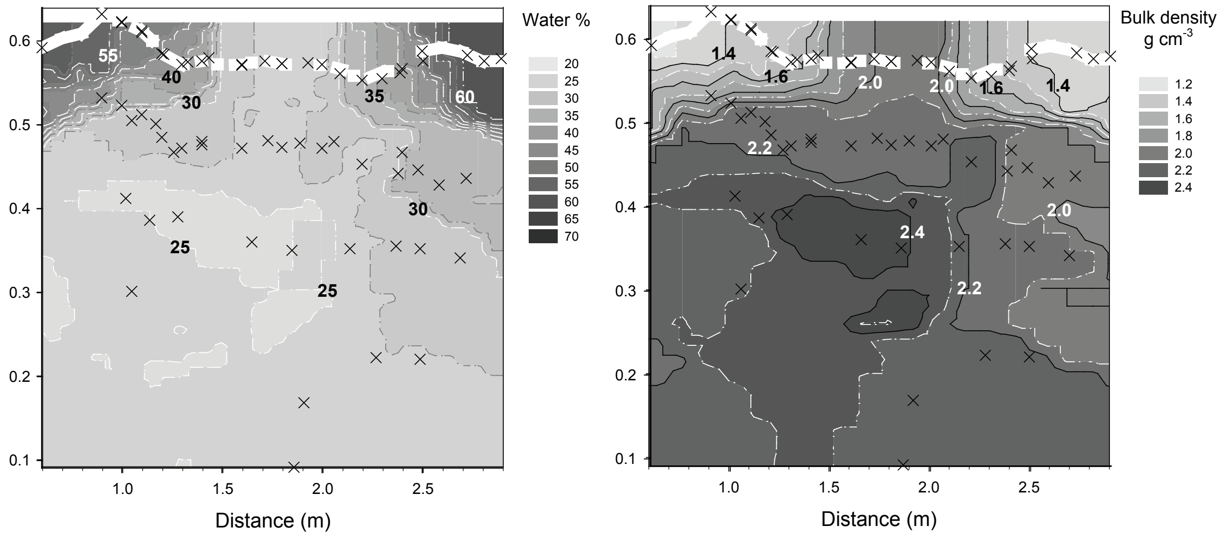

Figure 2. Vertical section through the frost boil showing contour maps of measured (A) water content and (B) wet bulk density in frost boil. Crosses mark position of measurements. The heavy white line shows the surface (topography) of the boil. Information above this line has no significance. The contours were generated by linear interpolation between nearest neighbor.

<2 mm and particle size distribution was determined by laser diffraction of the <2 mm fraction. Grain sizes of samples analyzed for ^{210}Pb were determined by Sedigraph 5100 on the <250 µm fraction. ^{210}Pb was analyzed on acid leachates of the <250 µm fraction by analyzing its granddaughter ^{210}Po using alpha spectroscopy (Aalto et al. 2008). This method only accounts for externally derived ^{210}Pb (adsorbed at grain surfaces) and the majority of it derives from atmospheric fallout. In addition to this excess unsupported ^{210}Pb, a smaller amount of supported ^{210}Pb is produced in situ by the decay of locally derived ^{222}Rn trapped in the soil atmosphere. This supported ^{210}Pb produces some background activity at depth.

Results and Discussion

Heave, grain size, and water content

Heave probes were installed in four positions (Fig. 1) across the mineral center on September 1, 2003. In addition, heave probes were also installed in vegetated areas in near proximity of the investigated frost boil. The total heave values on June 28, 2004 were 6, 12, 23, and 12 mm, while heaving rate measured in vegetated soil was <2 mm.

The grain size distribution of all samples (boil and vegetation) is loamy sand with sand: 59.5 ± 10%, silt: 30.1 ± 8.4%, and clay: 10.5 ± 4.7%. This grain size distribution is equal to low centered mud boils described by Zoltai and Tarnocai (1981) and has enough fine material to be suitable for frost heave and patterned ground formation (Goldthwait 1976). Although the frost boil appears as a nonsorted circle, there is a slight enrichment of pebbles towards the vegetated border and slight increase in the clay size fraction at depth.

The water content on June 29, 2004 is displayed in Figure 2A. It covers a range between 22 wt% and 78 wt% (on basis of wet weight) where surface samples from the center of the boil have lowest water content (22 wt% to 35 wt%). In contrast, surface samples close to surrounding vegetation are wetter (41-58 wt%) and the vegetated surfaces have highest water content (44-78 wt%). Volumetric water content calculated from bulk density and gravimetrical water content is between 13 vol% to 36 vol% indicating that soils are not water saturated at this time of the year.

The wet bulk density ranges between 990 kg m^{-3} to 2600 kg m^{-3} with lowest values below vegetation and cryptogamic crust-covered surfaces, and highest values in the bare central portion of the boil (Fig. 2A). The higher bulk density in the central portion of the boil and at depth is quite consistent with the theory that after thawing soil dries out and is compacted in center. The soil water distribution observed here is similar to water content measured in mud boils in Svalbard during and shortly after snowmelt (Boike et al. 2002). As shown by Boike et al. (2002) moisture content in these boils is quite dynamic during the season and it is difficult to draw conclusions from a single set of density/soil moisture measurements. However, using spatial distributed year-round measurements of soil moisture and soil temperature in the mud boil Boike et al. (2002) observed that moisture is transported to fringe in frozen ground and therefore leads to thawing and collapse of these regions (Boike et al. 2002). Such water dynamic seem to concurs well with freeze-thaw pumping as driving mechanism for boil development as discussed by Washburn (1997)

^{210}Pb systematics and distribution

Assuming that ^{210}Pb is deposited equally on the surface by continuous atmospheric flux, all surface samples should display the same activity if they have the same history of surface exposure. Due to its adsorption primarily on small grain sizes, lead will not infiltrate far into the ground (Stumm 1992) and therefore, surface samples collected from upper 0.1 m should contain almost all atmospheric deposited ^{210}Pb.

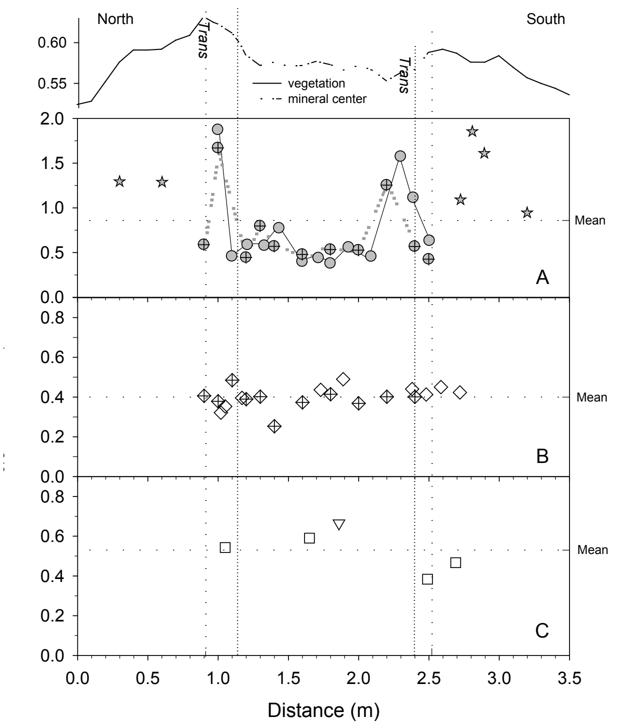

Figure 3. ^{210}Pb activity distribution in the investigated frost boil and surrounding area. The two lines delineate the transition between mineral surface and vegetation. (A) Surface samples, (B) Samples from ~0.1 to 0.15 m below surface, and (C) samples from >0.25 m below surface. Symbols refer to sampling depth (see Fig. 1); symbols with cross indicate samples collected in 2003.

If undisturbed, the ^{210}Pb activity in surface soil will begin to approach steady state conditions with ^{210}Pb deposition balanced by decay after $1/\lambda_{210}$ (τ_{210} residence time of ^{210}Pb, see Albarède (1996, p. 344 ff.)) which is 32.2 years. However, our alpha analytical techniques allow more accurate exposure determinations, or dating out to approximately $2.5/\lambda_{210}$. Hence, soil on surfaces that have been undisturbed for >80 years should closely approach the steady state ^{210}Pb activity. Furthermore, the ^{210}Pb activity at depth should be equal to background values from in situ decay of ^{222}Rn in soil atmosphere and will be lower than steady state ^{210}Pb activity at surface. Accepting that ^{210}Pb background flux is much lower than atmospheric flux, elevated ^{210}Pb values at depth indicate that surface material is transported to depth within the last 100 years and for these samples, the duration of burial can theoretically be estimated out to 80 years using the decay rate of ^{210}Pb. Following this line of reasoning, surface soil with ^{210}Pb activity lower than steady state activity has been at the surface less than 80 years.

^{210}Pb values of surface samples display a very distinct, almost symmetrical pattern with low values in center of the boil and higher values towards the vegetation border (Fig. 3A) and this pattern exists in samples collected in both years. The average ^{210}Pb activity in the inner center of the boil is 0.5 dpm g^{-1} and is much lower than the average ^{210}Pb in vegetation (1.65 dpm g^{-1}). Samples at ~0.10 to 0.15 m depth (Fig. 3B) have average ^{210}Pb values of 0.40 dpm g^{-1} with a range between 0.50 and 0.22 dpm g^{-1}. These samples do not show a systematic trend like the surface samples but scatter around the average activity. Samples collected from greater depth >0.25m (Fig. 3C) have slightly higher ^{210}Pb activity with average of 0.45 dpm g^{-1}. One sediment sample collected just above the permafrost table (triangle at ~ 60 cm in Fig. 1) has ^{210}Pb activity of 0.68 dpm g^{-1} higher than most samples at depth and higher than surface samples in the mineral center of the frost boil.

Following the ^{210}Pb systematics described above, the average ^{210}Pb activity in vegetation of 1.65 dpm g^{-1} reflects steady state. Since this surface is very stable the observed variability of ^{210}Pb activities may indicate accumulation processes due to topographic depressions or changes in plants which serve as natural sediment and dust traps.

Low ^{210}Pb activities in center part of boil suggest that sediments have recently been exposed to surface. As described above, freshly injected sediment in boil center has been observed during the thaw season on adjacent frost boils supporting the trend observed with the ^{210}Pb. Assuming that boil and its close perimeter is closed sediment system demands that the injected sediment is balanced by subduction; both motions have been assumed based on distribution of buried rocks and organic material (Dyke & Zoltai 1980) in non sorted circles. They lead to the assumption of a circulatory motion where soil subsides at boil fringe and rises from below in center of boil. According to this mechanism, the bottom of boil just above permafrost table would be replaced by material from the surface. If the circulation is fast enough (<80 years) the sediment at depth should have ^{210}Pb activity above background but lower than steady state activity. The subduction rates from Dyke and Zoltai (1980) on the order of 1 mm yr^{-1} infer that most of unsupported ^{210}Pb is decayed below a depth of 10 cm. The observed elevated ^{210}Pb activity in the one sediment sample at depth (at ~60 cm) may be due to remaining ^{210}Pb from subducted sediments and would suggest much higher subduction rates. However, elevated background activities can be reached at depth due to high moisture content which reduces ^{222}Rn diffusion out of soil and therefore, increases the in situ produced ^{210}Pb background activity. These results show the importance to accurately determine background levels of ^{210}Pb.

The fresh injected sediment in center of boil will be laterally transported towards fringe and therefore, accumulation of atmospheric ^{210}Pb with time would cause a constant increasing in ^{210}Pb activity toward the fringe. The slightly higher activity towards the northern fringe of boil could indicate lateral transport though this trend is missing in the southern part. Overall, a circularly motion in central mineral boil is not well documented by ^{210}Pb except for general low activities compared to stable surfaces which indicates that sediment has not been exposed to atmosphere for very long time and therefore, may have been injected recently from below.

In the area between stable vegetation and mineral boil, low ^{210}Pb activity in direct contact to stable vegetation also suggests injection of sediment from depth while the high

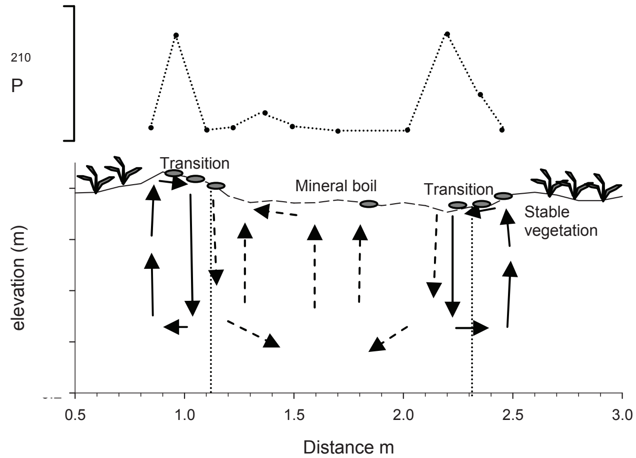

Figure 4. Schematic sketch of observed ^{210}Pb activity in surface sediments (upper) and possible sediment motion to produce observed ^{210}Pb activity trend (lower).

^{210}Pb activities in this area (Fig. 3A) indicate that sediment has been at surface for elevated time. A possible mechanism to create the observed ^{210}Pb distribution could be a circulatory cell opposite to that in mineral boil as indicated in Figure 4. The sediment is than subducted close to mineral center of boil (Fig. 4). Subduction at this location is supported by observed buried plant material (*Dryas spp.*) which was found in 12 cm depth at 1.21 m distance at north side of boil (X-axis, Fig. 3). Hallet and Prestrud (1986) proposed a similar circulatory motion ("rolling border") in the stone perimeter of sorted circles based on soil displacement measurements.

Conclusions and Outlook

The use of ^{210}Pb as a tracer for soil motion yields promising results. Compared to the radiocarbon tracer, ^{210}Pb is connected directly to sediment grains and not restricted to certain components in the sediment. It therefore can be sampled in as high resolution as needed for individual system. However, the time limit of ~80 years restricts its application to recent processes. Conclusions drawn from ^{210}Pb distribution in this study are in agreement with other field observations in this high Arctic site and with general mechanism proposed by other researchers for formation and sustainability of nonsorted circles. However, for developing this tracer to its full potential it is important to accurately determine the steady state and background ^{210}Pb activity, which are the upper and lower limits of unsupported ^{210}Pb activity within the frost boil system. Knowledge of these boundary values will allow more detailed interpretation of ^{210}Pb activities and their significance with respect to sediment motion. A way to do this would be to determine the ^{210}Pb inventory (dpm m^{-2}) by sampling continuous depth profiles rather than single points of activity. Together with boundary values sampling of continuous profiles will provide the opportunity to estimate sediment motion in time and space for the studied frost boil system.

Acknowledgments

We would like to thank Paul Overduin for his review of the manuscript, VECO, Thule Air Base for their logistical support, and A. Vigna for field assistance. This study was funded by the National Science Foundation Grant OPP-0221606 with partial support for dating by NSF EAR-0403722 and 0521774.

References

Aalto, R., Lauer, J.W. & Dietrich, W.E. 2008. Spatial and temporal dynamics of sediment accumulation and exchange along Strickland River floodplains (Papua New Guinea) over decadal-to-centennial timescales. *Journal of Geophysical Research* (in press).

Albarède, F. 1996. *Introduction to Geochemical Modeling*. Cambridge: Cambridge University Press.

Appleby, P.G., Oldfield, F., Thompson, R., Huttunen, P. & Tolonen, K. 1979. ^{210}Pb dating of annually laminated lake sediments from Finland. *Nature* 280: 53-55.

Boike, J., Ippisch, O., Overduin, P.P., Hagedorn, B. & Roth, K. 2007. Water, heat and solute dynamics of a mud boil, Spitsbergen. *Geomorphology* (in press).

Boike, J., Ippisch, O. & Roth, K. 2002. Thermal and hydrological dynamics of a mud boil - any clue about its formation? *Chinese Journal of Glaciology and Geocryology* 24 (5): 538-543.

Davies, W.E., Krinsley, D.B. & Nicol, A.H. 1963. Geology of the North Star Bugt area, northwest Greenland. *Meddelelser om Gronland* 12(162): 68.

Dörr, H. 1995. Application of ^{210}Pb in soils. *Journal of Paleolimnology* 13: 157-168.

Dyke, A.S. & Zoltai, S.C. 1980. *Radiocarbon-dated Mud-boils, Central Canadian Arctic.* Geological Survey of Canada, Current Research, Part B 80: 271-275.

Goldthwait, R.P. 1976. Frost sorted patterned ground: A review. *Quaternary Research* 6: 27-35.

Hagedorn, B., Harwart, S., van der Loeff, M.M.R. & Melles, M. 1999. *Lead-210 Dating and Heavy Metal Concentration in Recent Sediments of Lama Lake (Norilsk Area, Siberia).* Berlin, Heidelberg: Springer Verlag.

Hallet, B. 1998. Measurements of soil motion in sorted circles, western Spitsbergen. *Seventh International Conference on Permafrost, Yellowstone, Collect. Nordicana.*

Hallet, B., Anderson, S.P., Stubbs, C.W. & Gregory, E.C. 1988. Surface soil displacements in sorted circles, Western Spitzbergen. *Permafrost, Fifth International Conference, Trondheim, Norway*: Tapir Publishers.

Hallet, B. & Prestrud, S. 1986. Dynamics of periglacial sorted circles in Western Spitzbergen. *Quaternary Research* 26: 81-99.

Hallet, B. & Waddington, E.D. 1991. Buoyancy forces induced by freeze-thaw in the active layer: implications for diapirism and soil circulation. *Periglacial Geomorphology*. J.C. Dixon & Abrahams, A.D. London: John Wiley and Sons Ltd., 251-279.

Kelly, M., Funder, S., Houmark-nielsen, M., Knudsen, K. L., Kronborg, C., Landvik, J. & Sorby, L. 1999. Quaternary glacial and marine environmental history of northwest Greenland: a review and reappraisal. *Quaternary Science Reviews* 18(3): 373-392.

Kessler, M.A., Murray, A.B., Werner, B.T. & Hallet, B. 2001. A model for sorted circles as self-organized patterns. *Journal of Geophysical Research* 107(B7): 13,287-13,306.

Kessler, M.A. & Werner, B.T. 2003. Self-organization of sorted pattern ground. *Science* 299: 380-383.

Mackay, J.R. 1980. The origin of hummocks, western arctic coast. *Canadian Journal of Earth Sciences* 17(8): 996-1006.

Mackay, J.R. & MacKay, D.K. 1976. Cryostatic pressure in nonsorted circles (mud hummocks), Inuvik, Northwest Territories. *Canadian Journal of Earth Sciences* 13: 889-897.

Mortensen, H. 1932. Über die physikalische Möglichkeit der 'Brodel'-Hypothese. *Neues Jahrbuch für Mineralogie, Geologie und Paläontologie, Monatshefte Part B*: 417-422.

Nicholson, F.H. 1976. Pattern ground formation and description as suggested by low Arctic and subarctic examples. *Arctic and Alpine Research* 8(4): 329-342.

Overduin, P.P. & Kane, D.L. 2006. Frost boils and soil ice content: Field Observations. *Permafrost and Periglacial Processes* 17: 291-307.

Peterson, R.A. & Krantz, W.B. 2003. A mechanism for differential frost heave and its implications for patterned-ground formation. *Journal of Glaciology* 49(164).

Roth, K. & Boike, J. 2001. Quantifying the thermal dynamics of a permafrost site near Ny-Alesund, Svalbard. *Water Resources Research* 37: 2901-2914.

Schmertmann, J. & Taylor, S.R. 1965. *Quantitative Data from a Pattern Ground Site over Permafrost.* Technical Report Hanover, N.H., U.S. Army Cold Regions and Engineering Laboratory.

Shilts, W.W. 1978. Nature and genesis of mudboils, central Keewatin, Canada. *Canadian Journal of Earth Sciences* 15: 1053-1068.

Stumm, W. 1992. *Chemistry of the Solid-Water Interface*. New York: Willey.

Swanson, D.K., Ping, C.-L. & Michaelson, G.J. 1999. Diapirism in soils due to thaw of ice-rich material near the permafrost table. *Permafrost and Periglacial Processes* 10(4): 349-367.

van Vliet-Lanoë, B. 1991. Differential frost heave, load casting and convection: Converging mechanisms; a discussion of the origin of cryoturbation. *Permafrost and Periglacial Processes* 2: 123-139.

Veillette, J.J. 1980. *Nonsorted Circles on Cohesionless Fine Silty Sand, North Central District Keewatin.* Paper 80-1B, Geological Survey of Canada: 259-267.

Walker, D.A., Epstein, H.E., Gould, W.A., Kelley, A.M., Kade, A.N., Knudson, J.A., Krantz, W.B., Michaelson, G., Peterson, R.A., Ping, C.-L., Raynolds, M.K., Romanovsky, V.E. & Shur, Y. 2004. Frost-boil ecosystems: Complex interactions between landforms, soils, vegetation and climate. *Permafrost and Periglacial Processes* 15: 171-188.

Walling, D.E., Collins, A.L. & Sichingabula, H.M. 2003. Using unsupported lead-210 measurements to investigate soil erosion and sediment delivery in a small Zimbian catchment. *Geomorphology* 52: 193-213.

Washburn, A.L. 1956. Classification of patterned ground and review of suggested origins. *Geological Society of America, Bulletin* 67: 823-865.

Washburn, A.L. 1969. Patterned ground in the Masters Vig district, Northeast Greenland. *Biuletyn Periglacjalna* 18: 259-330.

Washburn, A.L. 1980. *Geochryology: A Survey of Periglacial Processes and Environments.* New York: Halsted Press, John Willey & Sons, Inc.

Washburn, A.L. 1989. Near-surface soil displacement in sorted circles, Resolute area, Cornvallis Island, Canadian High Arctic. *Canadian Journal of Earth Sciences* 26: 941-955.

Washburn, A.L. 1997. Plugs, and plug circles: A basic form of patterned ground, Cornwallis Island, Arctic Canada - origin and implications. *Geological Society of America.*

Zoltai, S.C. & Tarnocai, C. 1981. Some nonsorted pattern ground types in northern Canada. *Arctic and Alpine Research* 13(2): 139-151.

“Pingo-Like” Deformation, Vilaine Estuary, Britanny

Bernard Hallégouët
Géographie, Université de Bretagne Occidentale, 29793 Brest, France
Brigitte Van Vliet-Lanoë
UMR 6538, Domaines Océaniques, IUEM, 29280 Plouzané, France
Christian Hibsch
UMR CNRS 7566 G2R, BP239, Université H. Poincaré, 54506 Vandoeuvre-lès-Nancy cedex, France

Abstract

The Pénestin section (southern Brittany, France) presents large diapiric deformations initially attributed to pingos by several authors. We present tectonic, petrographic and stratigraphic arguments leading to a mechanical interpretation of the deformations. The area corresponds to an upper Neogene paleoestuary of the Vilaine River, in middle terrace position, incised into a kaolinitic saprolite. There is no evidence for recent transpressive tectonics or for periglacial pingos, despite the presence of MIS 8 ice wedge casts. Shale diapirism does exist. Deformation is favoured by the liquefaction of saprolite and a seaward mass movement triggered by an earthquake around 280,000 yr. BP. This kind of deformations is common in tectonically active regions. The development of permafrost during MIS 8 (Saalian I) allowed ice segregation of the porosity in sediments, which froze younger reactivation of the shale diapirism.

Keywords: Brittany; earthquake; neotectonic; periglacial; saprolite; shale diapirism.

Introduction

Distinguishing between tectonic deformations and periglacial disturbances in the Quaternary is a prerequisite for seismic hazard assessment in former periglacial areas. Among these deformations, we discuss whether a specific “folds” succession can be related to neotectonic activity or, periglacial forms. Examples exist in the southern Pénestin section (Brittany, N.W. France, Fig. 1) and the Bovey Tracey basin (Devon, UK), where deformation was first interpreted as pingo scars (Jenkins & Vincent 1981, Rivière and Vernhet 1962) or as complex features in Germany attributed to permafrost by Eissman (1981) and Strunk (1983). Recently, these “fold trains” have been interpreted as induced by seismic shaking (Van Vliet-Lanoë et al. 2004) or as Quaternary tectonic folding (Brault et al. 2001). This paper presents tectonic, petrographic and stratigraphic arguments leading to a mechanical interpretation of the Quaternary deformation processes at Pénestin, located south of the Vilaine estuary southwest of Pénestin city. The morphologic convergence with classical deep-seated shale diapirism is explained on the basis of earthquake-induced transient transformation of a basal saprolite.

Geology

The section of “la Mine d’or” is a fluvio-marine middle terrace complex from the Vilaine River, perched about 15 m above the Hercynian basement cropping out along the shore cliff. The basement is faulted in several compartments and deeply weathered (kaolinitic saprolite). The water table is commonly above it. The section is oriented roughly north-south. At the top of the section, the topography slopes 0.5% to the north and 1% to the west (seaward).

Pénestin is located close to a southern branch of the South Armorican Shear Zone (Fig. 1). This structure is one of the major Variscan dextral strike-slip faults of the European plate (Gapais et al. 1993). The seismicity is moderately active with intensities MSK reaching VII or even VII-VIII (SIRENE database, Fig. 1). to:

- Unit B**:** Scattered blocks of sandstones observed at the contact between the saprolite and the sediments with some sandy gravel generally attributed to Oligocene deposition.
- Unit C1: A beach conglomerate, prograding from the south. At its base, it includes flat-lying blocks of Laderes sandstones and vertical frost-jacked cobbles (cryoexpulsion) stacked into the saprolite, forming cryogenic pattern ground. The truncation by abrasion of the soft but coherent saprolite, with the absence of scouring, also argues for shore face

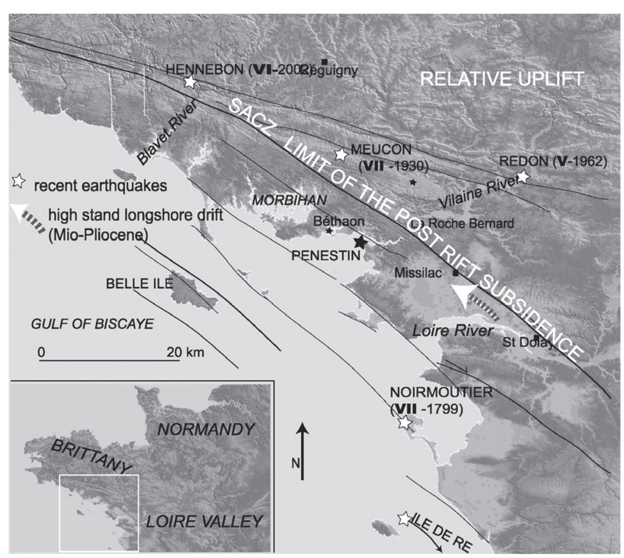

Figure 1. Location of the section.

deposition under a cold climate with block transportation by ice rafting (Van Vliet-Lanoë et al. in press). This unit yields an age of 6.7 ± 0.7 Ma by ESR. It is further locally consolidated by a hydromorphic ferricrete. This hard pan has a major impact on the deformations throughout the section by modifying the permeability and rheology above the saprolite.

- Unit C2: A prograding coarse sandy unit with an increasing charge of angular rock fragments constitutes a sedimentary progradation coming from the south. This unit is strongly rubified close to the surface by yellow-red podzolic pedogenesis. It corresponds to the top of a middle Pliocene estuarine, river-dominated braided fan formed during a major regression. It is covered by rhythmic red and grey silty clays, often wrinkled, unit C3; these tidalites represent the Gelasian/Pre-Tiglian high stand.

Unit D1: Unit C2 is eroded by a channel, consisting of fine-grained sands and clays lacking frost perturbation. This interglacial estuarine material has been dated at 445 ± 71 ka by ESR (Marine Isotope Stage 13) (Laurent 1994). The extent of the sands is visible at the base of some of the large “bowls.”. This unit is practically never deformed where it is thick, but is susceptible to stretching where it is thin and is sometimes faulted.

Unit D2: This sandy gravel belongs to a braided channel system with large blocks and covers most of the section. Blocks are ice-rafted. This periglacial river corresponds to the Pleistocene “middle” terrace of the Vilaine and is further weathered by a polygenetic red-yellow podzolic soil. The sediment has been dated at 317 ± 53 ka (MIS 10 to 8) by ESR (Laurent 1994).

Locally, Unit E1 appears. This is a loess-like khaki silt infilling wedges. These wedges are developed in specific tensional positions and post-date unit D2 and the deformations. (Van Vliet-Lanoë et al. 1997a). They correspond to ice wedge casts, which are truncated by an erosional surface, some recent loesses and heads (unit E2), and by recent dune sands (unit F), Holocene in age.

The geometry of the section revealed a paleosurface shaped at least since the Oligocene and further incised by three successive channel generations. C1 crops out as a marine strand flat, corresponding to a periglacial low stand, Late Miocene to Lower Pliocene in age. C2 is a temperate tidal channel, ending in a mud flat and coming from the south, Middle to Late Pliocene in age. D1 is a temperate tidal channel, 420 ka old. D2 is a conglomerate with more sandy layers, corresponding to a periglacial braided river, 307 ka old; it pre-dates the fold-like deformations. This stratigraphic interpretation makes the age range of the basement deformations clear. North of the bay, the weathered micaschists are truncated by a marine abrasion reaching 8 m NGF. In the middle part of the section, the substratum is weathered in bleached soft clayish silt. The main Kerfalher fault is located 50 m south of Poulante Point, the southern end of the section. A satellite fault outcrops at Poulante Point. Its orientation is roughly N120°E and it does not seem to have suffered recent slip reaching the surface.

Quaternary deformations

The wavy, fold-like deformations affecting the saprolite and the sedimentary units have been interpreted as pingo traces or as evidence for recent strike-slip faulting of the Kerfalher fault system (Brault et al. 2001). Deformations do not present a regular wavelength or strike-slip faulting. Some sectors are devoid of deformation, although others close to Poulante Point are smaller and more clustered (Fig. 2). It seems clear from our data that the more intense deformational features are almost always developed above faults affecting the basement. These pre-existing faults acted as specific water pathways to fault-controlled water migration for potential seismic pumping. Few striations have been observed along the faults. The slip movements reveal normal-sinistral kinematics, compatible with sliding toward the sea-side and incompatible with the supposed strike-slip faulting.

Deformations mostly developed in thick bleached saprolite. These are much less intense when the preserved overburden sediments are thick and more permeable. To the south, the geometry of the deformations is more or less continuous and is elongated roughly N60°E, like the basement faults. Short, often asymmetric, irregular “bowls” have developed due to the presence of the thick white saprolite below units D1 and D2 (Fig. 3a). Usually 2-3 m below the base of D1, the saprolite is undisturbed and porous. No deformation has developed where the conglomeratic ferricrete exists. The deformations are smoother and “longer” in wavelength where the saprolite is coherent (A2), larger and stronger for A3, and smaller but strong where the alluvial complex is thin. Wrinkling developed in unit C3 is related to saprolite injections and has been interpreted as due to the interaction of *P* and Rayleigh waves (Van Vliet-Lanoë et al. 2004). Deformations are thus controlled by (i) pre-existing faults; (ii) the overburden sedimentary load; (iii) the characteristics of its porosity, and (iv) the mechanical properties of the saprolite and the absence of C1 conglomeratic ferricrete.

Liquefaction can develop in clayish sands (Ruxton 2004), allowing incipient doming that stretches the overburden conglomerate cover and pinches out the flanking sandy units, simulating syn-sedimentary deformation. Locally, the D1 sand unit shows stretching with listric microfaults and bending. At the level of maximal curvature of the doming, tension gashes are injected with liquefied kaolinitic silts. Where the saprolite bursts out, load casts deform the extruded saprolite mass, with local wrinkling (Fig. 3b). At the apex of saprolite upward injection, ice wedge casts filled with khaki loess (unit E1) were later centred on tension bulges connected with the large undulations (Fig. 3c). Differential frost heaves may have deformed the structures later (Van Vliet-Lanoë et al. 2004). The clay fraction consists essentially of neoformed, silt-sized kaolinite with about 10% illite, leading to a low density and high porosity in the undisturbed saprolite. Such material has a much lower plasticity index than the other clay minerals (illite, smectite) (Skempton 1953). According to our

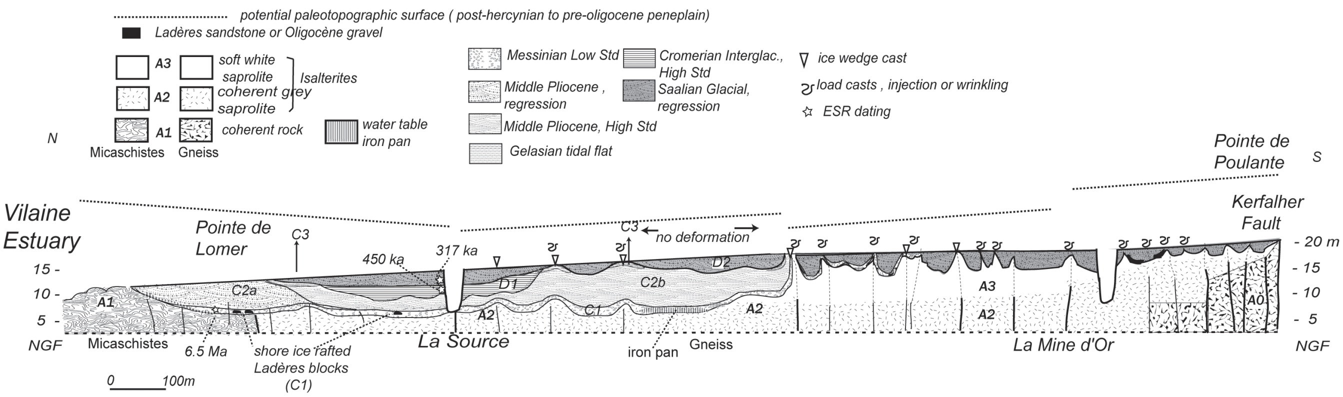

Figure 2. Global sketch of the main section at Pénestin.

laboratory data, the winter water content of unremoulded saprolite is around 23%, slightly above the water content at Atterberg plastic limit (20%, Cassagrande methodology). Liquefaction occurs above 30% in unremoulded sediment (28% at Atterberg liquid limit) where the water table seeps along most of the cliff. Shocks induced by storm waves can ease the collapse of original porous fabric of the saprolite, inducing mass wasting. The bulk density of the saprolite increases towards the surface. The undisturbed dark grey saprolite yields a 1.3 dry bulk density, which when slightly disturbed rises to 1.6, and for white, fully disturbed saprolite to 1.9. The dry bulk density of the coarse sand and the conglomerate are about 1.9 and 2.0, respectively. Cohesive kaolinitic silt is hard to liquefy in normal conditions (Skempton 1953); to destroy the fabric, we need an external trigger to induce liquefaction. To reach the liquid limit (30%) and equilibrate the pressure induced by the overburden conglomerates, we need to destroy the original porous fabric of the "light" saprolite to reach 23% water in the collapsed silt and to add at least 7% water without the possibility of water escape. The origin of this supplementary water supply is clearly connected to the basement faults. To induce mass movement, water needs to be confined in excess within the liquefied saprolite and oversaturation of the saprolite needs to be supplied with water for several days. Petrographic analysis of the saprolite is instructive, revealing no petrographic change in an undisturbed saprolite. The dense material with an unpreserved macro-fabric (A3) reveals interstitial porosity collapse. The material with a partly disturbed macro-fabric preserves most of the initial porosity, but deformed and partly crushed. At the contact with the D1 unit, the saprolite presents sliding planes, attesting to lateral movement of A3 mass with respect to D2. Other units, like C3 and D2, present late deep traces of ice lensing (paleopermafrostrelic permafrost). Frost-induced porosity usually promotes lateral drainage.

Discussion

Periglacial deformation

The deformations were first interpreted by Rivière and Vernhet (1962) as pingo scars relative to continuous permafrost, as indicated by ice wedge casts, but the clustered deformations do not fit the cone-in-cone internal fabric related to the ice-body collapse observed by De Gans (1995) and the isolated pingo. Other periglacial mounds like palsa occur in clustered locations, on wet silty or clayish surfaces, sometimes sloppy. The observed deformations do not fit those described by Pissart (1993). In pingo and palsa, scars, overturned layers exist inside the rims of the scars, sometimes disrupted by normal faults (pingo) with sedimentation or peat developed within the central depression.

Diapirs can also be induced at shallow depths with a residual thick ice cap decaying on oversaturated subglacial sediments like glacio-marine or glacio-lacustrine silts and clays (Brodzikowski & Van Loon 1980). This process is unrelated to the Pénestin paleoclimatic context, as the site is located at least 800 km from the southernmost extent of the British ice sheet. Hydrates diapirs in permafrost may also be responsible for those deformations but the section is too shallow to support this interpretation.

Liquefaction

In the southern section, liquefaction is evident from injections and the global geometry of the deposits reveals mostly a positive gradient in density with light unconsolidated saprolite overlain by dense gravely sedimentary units. However, the coarse-grained D2 unit shows mostly brittle behaviour, the sandy basal layer from D1 is stretched with brittle fracturing, and sliding planes exist close to the contact of the deformed saprolite. The occurrence of subsurface overconsolidation of the saprolite with reduction of microporosity, thin mud injection and fabric wrinkling suggests rapid deformation (Van Vliet-Lanoë et al. 2004) but the development of the large deformations with larger injections seems related to slower motion over several days. Liquefaction susceptibility reflects the relative resistance of soils to loss of strength when subjected to ground shaking. Co-seismic liquefaction is always associated with water-saturated sediments that can reach oversaturation by fabric collapse or with sediments oversaturated by co-seismic water supply (Muir-Wood & King 1993). Co-seismic liquefaction also leads to overconsolidated sediments at shallow depth, although the superficial layers are liquefied.

a)

b)

c)

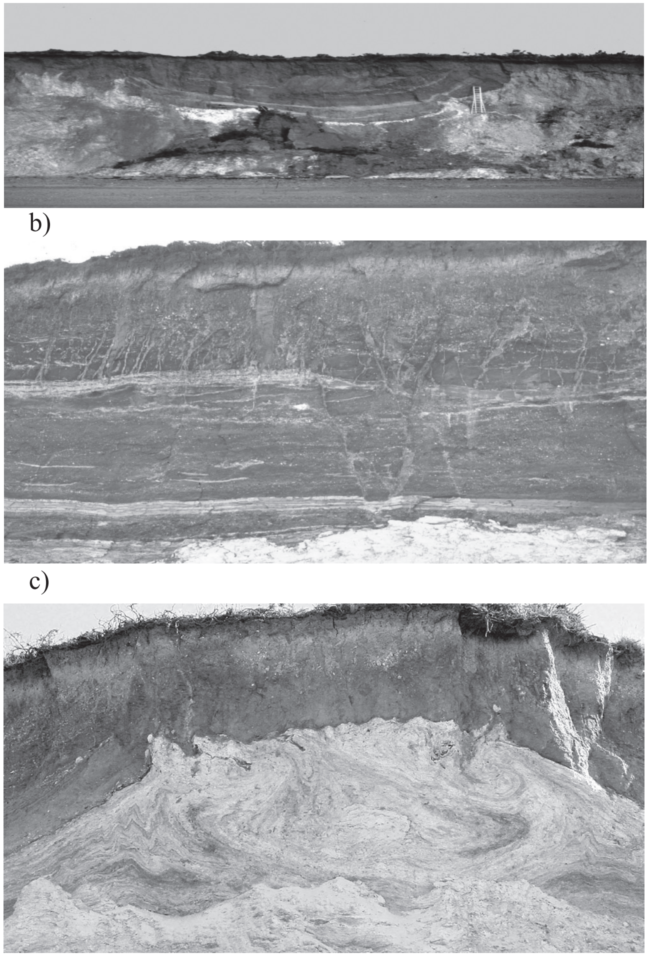

Figure 3. a): View of a "bowl" north of "la Mine d'or." Notice injection at the level of the ladder; b): Giant drop with lateral wrinkling in saprolite A3 (section height: 2 m); c): Clustered ice wedge casts above a diapir.

At Penestin, we interpret evidence of liquefaction and overconsolidation in initially cohesive sediments as resulting from fabric collapse and transient water supply. An external trigger for liquefaction and a complementary water supply is needed. As water is a non-compressible fluid, the alternating squeezing and suction from the local water table located in the faulted basement caused by P and Rayleigh waves caused a rise in excess pore water pressure in the overlying saprolite with subsequent liquefaction. This ejection of liquid mud is normally locked by overburden sediments. Here, the overburden weight of the D units is limited by erosional truncation so mud ejection was easier. Youd et al. (2004) observed that soil softening leads to a lengthening of the period of ground motion and that ground oscillation leads to a continued rise of pore water pressures after ground shaking ceases. The generated overpressure is confined at depth in the regional water table contained in a fractured substratum. An earthquake of strong magnitude can liquefy cohesive silty soils as demonstrated by recent major earthquakes. Liquefaction was also very important even on the gentle slope at the foot of the Turnagain hills with lateral spreading and sliding of a rafted suburb of Anchorage (Seed & Wilson 1967).

The remaining possible mechanisms are thus shale diapirism or folding. Tectonic transpressive folding does not fit our observations, as discussed previously. Disharmonic surface folding is difficult to apply to the geometry of deformation at Pénestin (apex of basement faults). After deformation, the whole system was truncated by a late erosional surface related to the periglacial regimes of MIS 8 and MIS 6, without younger evidence of "folding."

Shale diapirism

While often mimicking folding, shale diapirism usually develops in marine basin in association with fast sedimentation, the strong sedimentary overburden leading to water overpressure in unconsolidated sediments. Active shale diapirism occurs when the overburden layer is thinned by tension and the mobilized shales are pushed upward due to the rise in internal pressure (Vendeville & Jackson 1992). In these conditions, clay behaves as a fluid, with a very low viscosity, inducing hydraulic fracturing in the confining layer, with differential loading (Bolton & Maltman 1998). The initial diapir shape is modified by lateral or oblique upward migration of fluidized shales and may generate a network of clay dykes and sills, in the form of a ring or conical faults that help the rise of the diapir. When the hydraulic pressure drops, the diapirism stops, followed by drainage and consolidation with further collapse (Vendeville & Jackson 1992).

At Pénestin, there is no evidence of thick overburden sediments to justify confining, since sedimentation stopped at about 300 ka, prior to the main deformation. Most D1-D2 gravels behave as a confining system for the saturated saprolite. The extra pore-fluid was produced locally by seismic-induced water supply along the normal faults triggering the diapiric motion, as discussed above. This localized overpressure source induced a metric swell of the saprolite at the apex of the feeding fault, resulting in tension gashes at the apex of the bulging developed in the rigid and confining alluvial system. During the fracturing process, the inner hydraulic pressure gradient was probably involved in fracture opening, like in hydrofracturing. Nevertheless, it is difficult to determine if fracturing and fluidization were synchronous, although tension gashes were rapidly injected by the fluidised saprolite and locally extruded to the surface. The conical faulting developed further, marked and eased by injections of fluidized saprolite on the side of the diapirs; this has been confused with flower structures due to transpressive shear. In detail, shale diapirism should explain most of the deformational structures in the saprolite as well as deformation like stretching in D1 sands and sliding planes developed in the saprolite observed at the base of the bowl-like structures.

These mechanisms, co-seismic fluidization and diapiric motion, do not perfectly explain the elongation of the observed patterns and their higher frequency close to the summit of Poulante Point. The elongation develops in parallel with the main slope (E-W 1%) of the Pénestin peninsula. During the Anchorage earthquake, sliding of the whole liquefied saprolite mass (Seed and Wilson 1967) induced buoyancy and rafting of sedimentary bodies. For Pénestin, two raft models can be proposed. In the first, the sliding is orthogonal to the positive ridges that correspond to local mud diapirs in stretched areas (Fig. 4c), while in the second, the raft structures are groove-shaped and each is separated by and strikes along mud diapirs (Fig. 4d). This last model agrees with the topographic slope towards the sea (marine low stand at the time of deformation) and with the kinematics observed in NE-SW slickensides in the deformed saprolite.

Reconstitution of Pénestin event

With this succession of mechanisms, nearly synchronous, we can reconstitute the entire story. A major earthquake occurred around 280-290 ka when the climate was periglacial and the Vilaine River was prograding, but sea level was not yet too low and permafrost was absent. The regional water table was high, and during the event, fluids probably escaped along basement fault nets, locally bulging the saprolite and consequently weakening the rigid confining alluvial body. During the earthquake, water was supplied by the fractured weathered substratum, except above the ferricrete. The whole saprolite surpassed the plastic limit and, in the upper layer, the liquid limit; it began to rise, rapidly deforming the base of deposits C3, D1 and D2. This process probably continued to evolve with the continuing rise in pore water pressure after ground shaking ceased. The diapir movement probably persisted for several hours after the event and generated lateral spreading. Displacement may have been mostly south-westward, following the main slope. The sliding was groove-shaped by differential loading of the D1 gravels, parallel to the diapirs separating the various corrugations. The “folds” in the northern part of the section trace thus aborted shale diapirism.

The date of the paleo-earthquake, roughly marking the onset of a regional relaxation event after a regional compressional event (circa 430-280 ka) is somewhat disturbed by the building of major ice sheets on Britain (MIS 12 and 10; Van Vliet-Lanoë et al. 1997, 2002). After this event, the saprolite probably dried out during the Saalian I (MIS 8; 280-240 ka), by segregated ice development in the permafrost, also responsible for the development of ice wedges, and by subsequent drainage of the alluvial body when it thawed. Today, the water table is perched on the densified saprolite A3.

Such a development in a tectonically active region is basically linked to the existence of an unconsolidated clay body (sedimentary or saprolite) and to the presence of a rather shallow water table and a confining surface layer like consolidated clayish conglomerate or even a lodgement till. In formerly glaciated region, the normal load of dead ice bodies can be traced on unconsolidated mud (Brodzikowki & Van Loon 1980); seismic activity induced by glacio-isostatic rebound also provides evidence (Hasegawa & Basham 1989). Outside the glacial limits, large undulations of so-called periglacial diapirs in places like the Rhine Graben (Strunk 1983) or basins like Bovey Tracey (Devon) are more likely due to seismically induced shale diapirism.

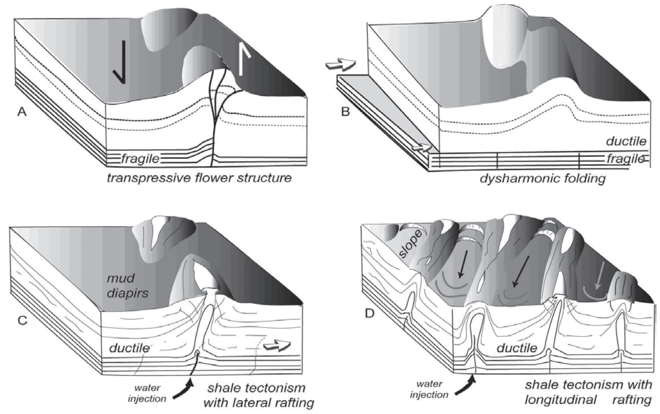

Figure 4. Hypothetic model of deformation at Pénéstin. D is the most evident from field data.

Conclusions

The deformations observed along the Mine d’or section at Pénestin represent the evidence of successive events triggered by the distant effects of an earthquake. One major deformational process is shale diapirism, initially triggered by seismic water supply, loading and lateral spreading, favoured by liquefaction of the saprolite basement that allowed the shale diapirism to develop. Traces of periglacial pingo and palsa are not observed at Pénestin, despite the presence of a paleo-relic permafrost. Neither Quaternary transpressive tectonics nor local ruptures are identified at this precise site.

During the seismic event, the phenomenon could have developed further. This whole process resulted, especially at the Mine d’or, in a liquefied mud leaded to a local mega-load cast on top of the saprolite outbursting, with lateral shortening induced by pulsated motion (wrinkling). Post-seismic relaxation, drainage and normal collapse of the stretched saprolite allowed some normal tension faulting to develop, probably also related to mass wasting, especially near “La Source.” Diapir motion probably persisted at a much lower rate for a few days or weeks, controlled by the main slope to the west, explaining the bulging of some of the diapirs exploited on the tension zone by younger ice wedge casts (260 ka), when permafrost developed and definitively blocked the motion. Seismically-induced shale diapirism seems to be frequent in active continental basins when a shallow water table is available to promote liquefaction.

References

Bolton, A. & Maltman, A., 1998. Fluid-flow pathways in actively deforming sediments: the role of pore fluid pressure and volume change. Mar.Petr.Geol., 15: 281-297.

Brault, N., Guillocheau, F., Proust, J.-N., Nalpas, T., Brun, J.-P., Bonnet, S. & Bourquin, S. 2001. Le système fluvio-estuarien Pléistocène moyen-supérieur de Pénestin (Morbihan): une Paléo-Loire? Bull. Soc. Géol. France 172: 563-572.

Brodzikowski, K. & Van Loon, A.J. 1980. Sedimentary deformations in Saalian glaciolimnic deposits near Wlostow (Zary area, W. Poland). Geol. Mijnb. 59: 250-272.

De Gans, W., 1988. Pingo scars and their identification. In: M.J. Clark (ed.), Advances in Periglacial Geomorphology. London: Wiley, 299-322.

Eissman, L., 1981. Periglaziäre Prozesse und Permafrost-strukturen aus sechs Kaltzeiten des Quartärs. Altenberger Naturwis. Forsch. 1: 171p.

Gapais, D., Lagarde, J.-L., Le Corre, C., Audren, C., Jegouzo, P., Casas Sainz, A. & Van Den Driessche, J. 1993. La zone de cisaillement de Quiberon. Témoin d'extension de la Chaîne Varisque en Bretagne méridionale au Carbonifère. C.R. Acad. Sci., Ser. II, 316: 1123-1129.

Hasegawa, H.S. & Basham, P.W. 1989. Spatial correlation between seismicity and postglacial rebound in Eastern Canada. In S. Gregersen,S. & P.W. Basham, P.W. (eds), Earthquakes at North-Atlantic Passive Margins: Neotectonics and Postglacial Rebound. Kluwer Acad. Publ., 483-500.

Jenkins, D.G. & Vincent, A. 1981. Periglacial features in the Bovey basin, south Devon. Proc. Ussher Soc. 5 : 201-205.

Laurent, M. 1993. Datation de quartz de formation quaternaires, comparaison avec le paléomagnétisme. PhD, MNHN, Paris, 104 p.

Muir-Wood, R. & King, G.C.P. 1993. Hydrologic signatures of earthquake strain, J. Geophys. Res. 98: 22035-22068.

Obermeier, S.F. 1996. Using liquefaction-induced features for paleoseismic analysis. In: J. McCalpin,J. (ed.), Paleo-Seismology. Acad.Press, 331-396.

Pissart, A. 1983. Remnants of periglacial mounds in the Hautes Fagnes, Belgique; structure and age of the ramparts. Geol. Mijnb. 62: 551-555.

Rivière, A., Vernhet, S. 1962. Accidents périglaciaires dans la région de Pénestin, (Morbihan). C.R. Acad.Sc. Paris, 255: 744-746.

Seed, H.B., Wilson, S.D. 1967. The Turnagain Heights landslide, Anchorage, Alaska. J Soil Mech. Found. Div., ASCE, 93 : 325-353.

SIRENE. 1996. Base de la macrosismicité française. CEA-IRSN-BRGM.

Skempton, A.W. 1953. The colloidal activity of clays. Proceedings of the 3rd International Conference on Soil Mech. & Found. Eng., Switzerland, 1: 57-61.

Strunk, H. 1983. Pleistocene diapiric upturnings of lignites and clayey sediments as periglacial phenomena in central Europe. Proceedings of the Fourth International Permafrost Conference, , Fairbanks, Alaska, July 17-22, 1983: ()1200-4.

Van Vliet-Lanoë, B., Bonnet, S., Hallégouët, B. & Laurent, M. 1997. Neotectonic and seismic activity in the Armorican and Cornubian Massifs: regional stress field with glacio-isostatic influence? J.O.Geodyn. 24: 219-239.

Van Vliet-Lanoë, B., Meilliez, F. & Maygari, A. 2004. Distinguishing between tectonic and periglacial deformations of Quaternary continental deposits in Europe. Glob.Planet.Ch. 43: 103-127.

Van Vliet-Lanoë, B., Hibsch, C., Csontos L., Jegouzo, S, Hallégouët, B, Laurent, M., Maygari, A., Mercier, D. & Voinchet, P., Seismically induced shale diapirism: the Mine d'or section, Vilaine estuary, southern Brittany. Int..J.Earth Sci., in press.

Vendeville, B.C. & Jackson, M.P.A. 1992. a) The rise of diapirs during thin skinned extension. b) The fall of diapirs during thin skinned extension. Mar. Petr. Geol. 9: 331-371.

Youd, T.L., Steidl, J.H., & Nigbor, R.L. 2004. Lessons learned and need for instrumented liquefaction sites. In: Soil Dynamics and Earthquake Engineering 24: 639-646.

The Rich Contributions of A.L. Washburn to Permafrost and Periglacial Studies

Bernard Hallet
Quaternary Research Center and Department of Earth and Space Sciences, University of Washington, Seattle

Abstract

Albert Lincoln Washburn, (1911–2007) contributed immensely to the fields of periglacial geomorphology and permafrost research through his studies, publications, leadership, and personal qualities. His deep interest in the "intimate workings of nature" is evident in his own meticulous and exhaustive field and laboratory studies of diverse types of periglacial processes, including patterned ground formation, slope movement, and ice growth in soils. This review focuses on these productive field studies in Greenland and on Cornwallis Island, and on his research in the Periglacial Laboratory at the University of Washington. Link's intense curiosity about periglacial processes and his untiring, generous effort to properly present the work and ideas of other researchers are clearly evident in his monographs and renowned books, which remain the standard references in the field decades after their publication (*Periglacial Processes and Environments* [1973], *Geocryology—A survey of periglacial processes and environments* [1979]). In addition, Link launched and directed research centers and scientific journals that have nurtured the study of cold landscapes. Significantly, his scientific legacy also includes an exceptional, more personal dimension: the emergence of the unusually cohesive and amiable permafrost/periglacial community, as it was fostered in part by Link and his wife Tahoe's warmth, generosity, and friendship, which graced many members of our worldwide community.

Keywords: active layer; frost heaving; frozen ground; patterned ground; periglacial geomorphology; periglacial processes; permafrost; upfreezing.

"To test the forefront of knowledge for even a brief period, particularly when the subject matter concerned the intimate workings of nature, provided both a motivation and challenge that ... are deep and real for me."

—From one of Lincoln Washburn's rare speeches, 1988

"Quietly content as we trotted beside the kamotik [large dog sled], I thought of some friends who would envy me, and others who would be at a loss to understand why I would wish to undergo what to them would be extreme hardship. I could not have explained my feeling to them then, nor can I do so now.… One is very close to the earth and one's companions but at the same time quite detached—an odd feeling of being free, yet an integral part of the nature of things. The Inuit know they belong to the Arctic. They are an integral part of the natural world around them. While, sadly, many of us have lost touch with it."

—From Tahoe Washburn's (1999) book relating experiences in the Canadian Arctic 1938–41

Introduction

Very sadly, Lincoln Washburn passed away on January 30, 2007, in Seattle; he was 95. He will be missed by many. We can, however, rejoice upon reflecting on his remarkably productive career.

Herein, I highlight his exceptional contributions to science and focus on his pioneering discoveries about processes shaping Arctic landscapes. I also mention his broader contributions to science, which extend well beyond his own research; they include his leadership role in the foundation of major interdisciplinary research centers and academic journals that have nurtured advances in understanding the Polar Regions, the Quaternary period, as well as permafrost and periglacial phenomena.

For more personal information about Link, as his many friends knew him, please refer to the thoughtful obituaries written by two of his long-term friends and colleagues, Steve Porter (2007) and Carl Benson (2007). Considerable material from these sources appears below.

Research Contributions: Field

Here, I focus on Link's productive field studies in Greenland and on Cornwallis Island. They comprise a wealth of detailed observations of surface exposures and excavations of diverse types of patterned ground, and extensive long-term studies of surface displacements to define quantitatively the kinematics of patterned ground activity and slope movement. It was Link's extensive fieldwork that provided the foundation and motivation for his unifying nomenclature and concept about periglacial soil patterns. He coined the term "patterned ground," provided rich and diverse examples, and summarized all ideas current at that time about their genesis (Washburn, 1950, 1956). Interestingly, "patterned ground" is now widely used not only by those working in periglacial features on Earth, but by the planetary community (e.g., Mangold et al. 2004), especially as the current stream of high-resolution images of Mars (e.g., Hi-Rise; http://hirise.lpl.arizona.edu) are revealing diverse forms of patterned ground, many of which resemble those in the hyper arid polar regions where, in contrast with Mars, the conditions and processes manifested in these patterns can be examined and monitored in detail.

Figure 1. Link and Tahoe Washburn in the late 1980s, Resolute, Cornwalis Island, Canada.

Mesters Vig

Link launched his fieldwork on periglacial processes and features near Mesters Vig in the King Oscar Fjord region of East Greenland, which he had first visited during the Louise Boyd expedition in 1937. He conducted a reconnaissance study in the summer of 1955, established instrumented sites in 1957, and made observations each year from 1957 through 1961, and again in 1964. The results of his studies are presented in three substantial monographs that appear in separate issues of the Danish journal *Meddelelser om Grønland* (Washburn, 1965, 1967, 1969). Collectively, these volumes comprise over 600 pages that record in detail his observations and measurements at more than 20 experimental sites.

His research was comprehensive in addressing a diversity of landforms and periglacial phenomena with a persistent focus on better understanding the formative processes. For example, Washburn (1969) systematically considered 11 forms of weathering, and 12 types of patterned ground. At his experimental sites, he deployed arrays of markers and established detailed photographic records that enabled him to monitor soil motion and surface changes over a period of many years. Moreover, he did not limit himself to landscape features; his outlook was interdisciplinary and included the vegetation and climate of the region, as well as its history of isostatic uplift.

Antarctica

He conducted research in Antarctica in 1957 and 1958 and was involved in planning the multinational, interdisciplinary Dry Valley Drilling Project in 1972-75, which succeeded in drilling a number of deep boreholes into permafrost, which gave revealing glimpses at the subsurface ice distribution, stratigraphy and chemistry, as well as temperature gradient over a large sector of the Dry Valleys near McMurdo. Valuable δ^{18}O data from the cores at three sites (DVDP cores 8–12) in the Taylor Valley emerged from a study led by his close colleague, Minze Stuiver, in the Quaternary Research Center (QRC, Stuiver et al. 1981). These early isotopic data and chronology continue to help fuel research within the QRC. They now render this location an ideal validation and calibration site for an ongoing effort by QRC scientists, R. Sletten, B. Hagedorn, and me, to understand the existence of subsurface ice in hyper-arid cold regions and to model the isotopic evolution of ground ice.

Resolute

His fieldwork on Cornwallis Island, Arctic Canada, in what is now Nunavut Territory, extended from 1981 to 1995. There, Link focused on solifluction and patterned ground activity. In the former, he established arrays of surface markers that he resurveyed periodically. The patterned ground work consisted of detailed mapping of extensive areas of sorted circles, establishing arrays of markers across individual circles that were repeatedly measured to monitor soil motion, and "bed-frames" that enabled him to monitor the spatial variation in surface heave and settling across a ~5 m^2 area. Washburn (1989) summarized his findings on soil displacements in sorted circles in a comprehensive paper that examines the spatial pattern of changes in position and tilt of dowels inserted in the soil surface. His research results inspired and guided much subsequent field work in diverse Arctic regions by a number of researchers (e.g., Anderson 1988a, Hallet & Prestrud 1986, Hallet et al. 1988, Hallet 1990, Hallet & Waddington 1991)

The culmination of this work is his last major written contribution, a monograph, "Plugs and plug circles: A basic form of patterned ground. Cornwallis Island Arctic Canada—Origin and implications." Washburn (1997) presents the results of years of observations and countless excavations of these soil domains, which develop spontaneously and ascend progressively through the active layer, and are likely to transform into more distinct types of patterned ground. He combines lucid, accurate descriptions with thoughtful and careful interpretations that shed light on the complexity of the principal formative processes active in the early stage of patterned ground development. Interestingly, recent numerical modeling shows sorted patterned ground initiating as plugs much like those depicted by Link (Kessler et al., 2001).

Research Contributions: Laboratory

His research in the Periglacial Laboratory at the University of Washington was focused on the effects of ice growth/thaw and frost heaving/thaw settling on solifluction, vertical textural segregation (sorting), and the development of deformational structures in layered soils. With the competent assistance of researchers, C.M. Burrous and R.G. Rein, Link Washburn used his specially designed laboratory for a comprehensive, long-term study of processes and features of the active layer, including soil deformation on horizontal surfaces and slopes. This laboratory featured a unique tilting slab capable of accommodating soil up to 1 m thick and 9 m^2 in area overlying a simulated permafrost table or an unfrozen substrate.

Next, I will describe two experiments conducted in the 1973–76 period in some detail not only because they yielded interesting sets of useful and unparalleled results, but because they illustrate the meticulous care taken in conducting the experiments in Link Washburn's Periglacial Laboratory, and in presenting the results. Unfortunately, these studies are essentially unpublished but considerable information is available in detailed internal QRC reports at the University of Washington. Two of these reports are used extensively here: "Soil deformation resulting from some laboratory freeze-thaw experiments" by A.L. Washburn, C.M. Burrous, and R.G. Rein, and "Experimental Upfreezing of Objects: Effects of Object Geometry" by C. M. Burrous. Few results from solifluction and horizontal slab experiments were published (Rein and Burrous 1980, Washburn et al. 1978).

Soil deformation, involutions

Through a number of well-designed, large-scale experiments, with thoroughly documented, simple initial conditions, Link and his co-workers were able to elucidate the rich interactions between soil texture, thermal regime, and soil deformation. Two comprehensive experiments were conducted using frost-susceptible silt on the 2.5 m by 3.6 m slab (Washburn et al. 1978). In experiment 2, for example, the slab was subdivided in plan view into 4 sectors differing in the nature of the upper 3 cm of material, but sharing the same base material, which consisted of 24 cm "clayey$_{12}$sandy$_{16}$silt$_{72}$ of predominantly eolian origin from eastern Washington" overlying 8 cm of "coarse, angular sand (Del Monte white sand) that served as a good basal aquifer. The upper 3 cm of each sector consisted, respectively, of A) clean gravel, B) silt mixed with gravel in the ratio of 6:4, C) white sand, and D) silt identical to base material. The slab was cycled through 10 freeze-thaw cycles, generally ranging from -15ºC to 15ºC while water was made available to the basal sand and remained unfrozen throughout most experiments with piezometric control at least at the onset of freezing

Figure 2 illustrates two sectors, C) with sand at the surface and D) all silt, viewed in a vertical cross-section. It demonstrates cleanly the important effect of surface soil texture on thermal behavior, and highlights the more rapid descent of the freezing front under the sand. This difference in thermal evolution, and associated surface heave, was well documented using a thermocouple probe and a displacement transducer in each sector (Fig. 3). These probes consisted of copper-constantan thermocouples spaced 2 cm apart.

The differential descent of the freezing front due to differences in soil texture results in an inclined freezing front (Fig. 4), which is important because it can induce lateral as well as vertical relative motion of relatively "large" particles in the soil. This lateral motion and inclined freezing fronts are widely recognized to be important in the development of sorted pattern ground. They also figure prominently in numerical models of patterned ground formation (Kessler et al., 2001; Kessler and Werner, 2003), and yet, with the notable exception of these poorly known results, there is a dearth of solid experimental or field data to guide the key assumptions that are required for realistic modeling of the texture-thermal feedbacks that are central to patterned ground formation.

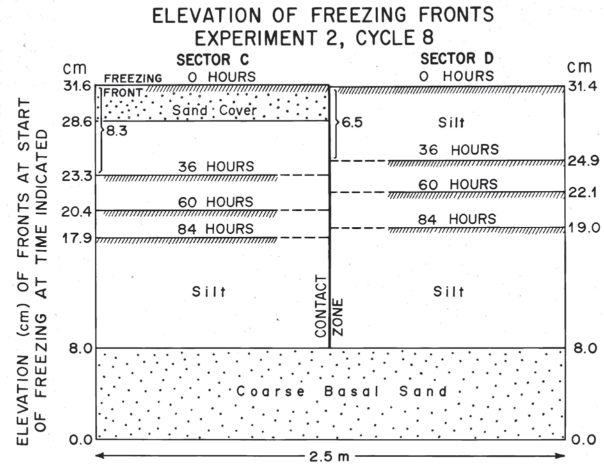

Figure 2. Initial configuration of soil in experiment 2, and descent of freezing front during a typical cooling period. After 36 hours the freezing front had descended 6.5 cm into the silt, and 8.3 cm below the sand cap. The freezing front depth was defined using temperature probes and frost tubes located in each sector, ~11 cm and 41 cm from the contact zone, respectively.

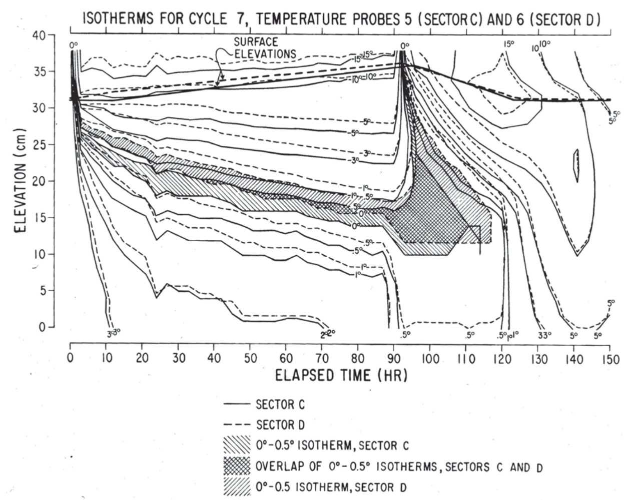

Figure 3. Contrasting thermal evolution and surface heave for the two soil sectors shown in Figure 2 through one representative freeze-thaw cycle.

Aside from important temperature data, these experiments also yielded a wealth of additional observations that were carefully described and interpreted. These are not new, but they gain importance because they arise in a system designed to be simple and uniform in terms of soil materials and moisture content at the onset, with initial conditions that are exceptionally well documented.

In a year-long study, experiment 3, Fairbanks silt, a well known frost-susceptible soil, was subjected to 32 controlled freeze-thaw cycles. The silt was underlain by 6 cm of sand that allowed for the controlled input of water at the base of the soil to fuel the ice lens growth and frost heaving. Typically, to begin freezing the surface temperature was lowered to -20ºC, while the base of the frost-susceptible soil was maintained at 2ºC. This thermal regime was maintained for 4 days, and then the soil was thawed over ~1.5 days by raising the room

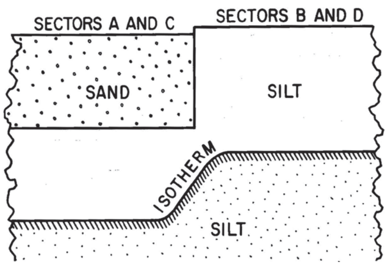

Figure 4. Hypothetical isotherm across the boundary between domains with contrasting surface materials.

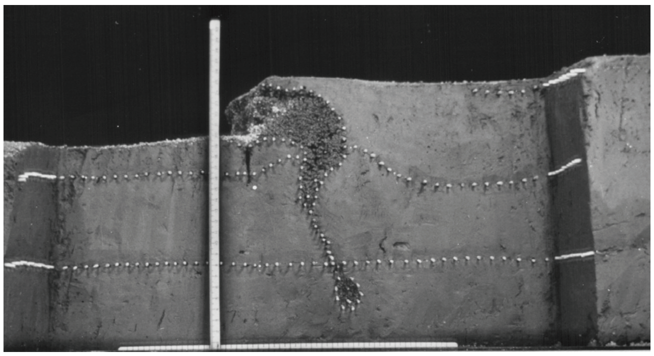

Figure 5. Vertical section at the end of 32 freeze-thaw cycles in experiment #3 highlighting a domain of sand that descended ~20 cm from the surface, a 6 cm-thick layer on the left side (removed before picture was taken). Arrays of white toothpicks delineate glitter surfaces in the soil that were initially horizontal at depths of 0.8, 8.5, and 16.6 cm. Scales are 32 cm long.

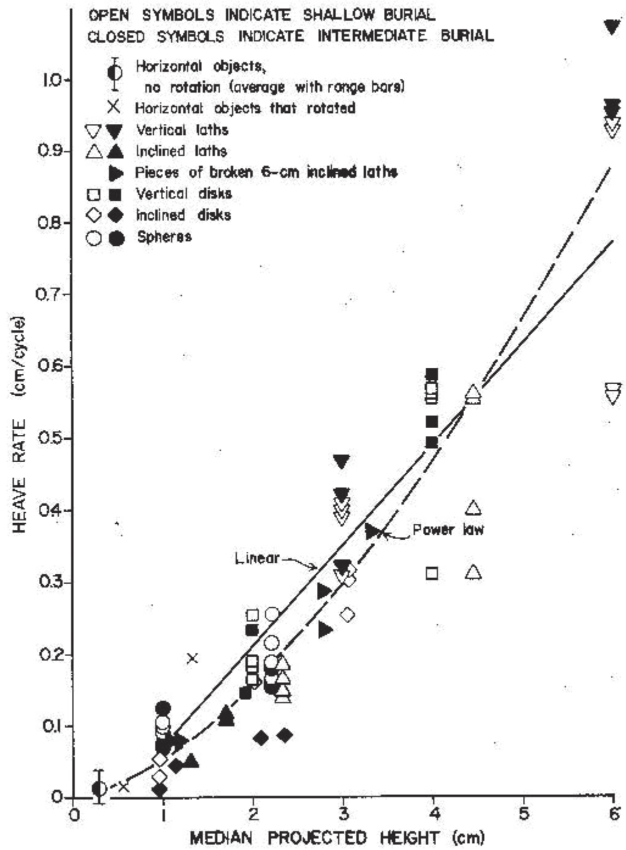

Figure 6. Combined upfreezing data as a function of median projected height of buried glass objects.

temperature and using infrared heaters above the soil surface. The silt surface generally heaved at a nearly uniform rate of 1.2 cm/day as the freezing front descended ~2.8 cm/day; the surface subsided 3.1 cm/day as it thawed. The total heave per cycle was roughly 5 cm, corresponding to a heaving strain of about 20%. Based on visual inspection, this strain is consistent with the volume ratio of visible ice lenses in cores that were taken of the frozen soil. Interesting phenomena developed largely at the boundary between domains with contrasting surface materials; they include A) involutions of sand that penetrated well below the surface, most probably during the thaw-settling phase of the experiments (Fig. 5), and B) shear displacement along a vertical surface and with limited descent of surface sand along this surface. In addition, Link and his co-workers noted details that are seldom mentioned, such as the tendency for bubbles to emerge at the soil surface near shallow up-freezing objects, and the appearance of a gleyed horizon at the silt base.

Upfreezing

Another exhaustive laboratory study examined systematically the dependence of size and shape of diverse objects on the rate at which they progressively ascend through the soil due to repeated cycles of heaving and settling. This was part of the year-long study just described, experiment 3. Prior to freezing, the Fairbanks silt was prepared carefully to permit the precise placement of 54 glass objects of different sizes and shapes (spheres, disks, and laths), with known initial position and orientation, on a 20 cm-grid at each of three levels in a silt layer ~25 cm thick.

A striking result (Fig. 6) is that the distance objects ascend through the silt per freeze/thaw cycle increases roughly linearly with their projected height. Surprisingly, the shape and orientation of the object have little effect. According to this clear result, larger stones are expected to move up toward the surface faster than smaller stones, and the upfreezing rate can be modeled as scaling with the product of the projected height of an object and the heaving strain of the soil. This powerful result inspired Anderson (1988a, b) to launch her own laboratory study of upfreezing, and guided her as she explored the role of upfreezing in sorted patterned ground. According to Figure 6, the net upfreezing of a stone with a projected height of 5 cm, for example, was ~0.6 cm per freeze/thaw cycle. This presumably resulted from an ascent of, at most, 1 cm (the product of the 20% heaving strain and the 5 cm projected height) during the freezing phase, followed by a descent of 0.4 cm during the thaw phase. Anderson (1988a) reported similar ascent/descent ratios during freeze-thaw experiments as long as the stones were well below the soil surface.

Several other findings from this study are noteworthy: 1) inclined tabular objects in these experiments rotated toward the horizontal, which was somewhat surprising in view of the common observation of steeply inclined stones emerging from the tundra that suggest a tendency for upfreezing to rotate stones toward the vertical; 2) all long (6 cm) inclined laths broke, indicating that these objects were subjected to large torques, presumably during the freezing phase; 3) for objects of the same projected height, laths heaved slightly faster than disks, which in turn heaved faster than spheres; and 4) the depth below the ground surface had little effect, which is counterintuitive because heaving strains were larger at depth due to the slower freezing while the surface heaving rate remained roughly constant; evidently greater upward heave during freezing was offset by greater settling during thaw.

Books and Monographs

Link's deep interest in periglacial processes and his untiring generous effort to present the work and ideas of other researchers properly are clearly evident in his monographs and books, which remain the standard authoritative references worldwide decades after their publication (Washburn 1973, 1979). His books are esteemed for their being thorough and for presenting the fruit of deep scholarly searches, as well as his own research findings. In contrast with most modern journal publications, Link's manuscripts are rich with lengthy presentations of multiple hypotheses and interpretations of diverse periglacial features and processes from researchers worldwide. His recent comprehensive monograph on the multitude of origins that have been proposed for the Mima Mounds in western Washington (Washburn 1987) exemplifies these qualities.

A Leader and a Visionary

Lastly, I wish to highlight Link Washburn's considerable contribution to science through his exceptional leadership and vision. He gained much recognition and appreciation while serving as the first director of the Arctic Institute (Dunbar 1952). Later, but still decades before the emergence of "earth system science" and the widespread concern about global warming, Link envisioned and launched the Quaternary Research Center at the University of Washington to promote interdisciplinary research about the global environment during the Quaternary. This fascinating period features the evolution of humans and the advent of civilization as well as massive abrupt changes in climate, sea level, global biota, and ice extent that still challenge our understanding and remind us of the difficulty of predicting climate and environmental change. Sensing the need for a scientific journal devoted to this important field, Link launched *Quaternary Research*, which appeared in 1970. "He shepherded the journal through its first 5 years, establishing for it a reputation for breadth and excellence, and making it one of the most widely cited earth science publications" (Porter 2007).

Link has been recognized and honored nationally and internationally. A few apt words by Albert Pissart (personal communication from Liège, Belgium, 2007) capture the essence of this worldwide recognition; reflecting on his deceased friend, he wrote: "j'avais conservé un culte pour ses travaux, son honnêteté scientifique, sa modestie et son extrême amabilité." Loosely translated, Albert worshipped Link's work, his scientific honesty, his modesty, and his extreme kindness. Moreover, Albert noted that with his appetite for learning and unusual fluency in German and French, he read and understood essentially all published material, and on his frequent trips to meetings in Europe between 1959 and 1985, he exchanged ideas and information freely within the European as well as the American scientific community. This exceptionally rich background contributed to his monographs and books, which were the first important syntheses of worldwide knowledge to date about periglacial processes and landforms and their connections with fossil periglacial features.

Albert also stressed that Link had received the highest scientific recognition possible in Belgium as an elected associate member of the Royal Academy. Steve Porter (2007) provides a listing of the numerous honors he received and the committees and organizations for which Link served as a directing officer, both nationally and internationally.

Summary

Highlights of Link's career include unfailing scholarship, research, administration, and careful detailed planning. His books and monographs catalyzed the emergence of periglacial geomorphology as a distinct scientific field, and solidified the field internationally by assembling and generously distilling results from a multitude of studies scattered in diverse sources worldwide, across national and linguistic boundaries. In addition to the research centers he directed and the scientific journals he launched, his rich scientific legacy includes the unusually cohesive and amiable permafrost and periglacial community, the emergence of which was fostered in part by Link and Tahoe's warmth, generosity, and friendship, which reached many members of this worldwide community.

Acknowledgments

I thank Steve Porter and Carl Benson for their thoughtful and comprehensive obituaries, sections of which I have borrowed from liberally, Ross Mackay and Albert Pissart for helpful communications, and Land Washburn for permitting use of the photograph of Link and Tahoe.

References

Anderson, S.P. 1988a. Upfreezing in sorted circles, western Spitsbergen. *Proceedings of the 5th International Conference on Permafrost,* Trondheim, Norway.

Anderson, S.P. 1988b. The upfreezing process; experiments with a single clast. *Geological Society of America Bulletin* 100 (4): 609-621.

Benson, Carl S. 2007. Albert Lincoln Washburn (1911–2007). *Arctic* 60(2).

Dunbar, M.J. 1952. A.L. Washburn. *Arctic* 5(1): 3.

Hallet, B. 1990. Self organization in freezing soils: from microscopic ice lenses to patterned ground. *Canadian Journal of Physics* 68: 842-852.

Hallet, B. & Prestrud, S. 1986. Dynamics of periglacial sorted circles in Western Spitsbergen. *Quaternary Research* 26: 81-99.

Hallet, B. & Waddington, E.D. 1991. Buoyancy forces induced by freeze/thaw in the active layer: implications for diapirism and soil circulation. In: J.C. Dixon & A.D. Abrahams (eds.) *Periglacial Geomorphology.* Proceedings, 22nd Binghampton Geomorphology Symposium 1991. New York: J. Wiley and Sons, 251-279.

Hallet, B., Anderson, S., Stubbs, C.W. & Gregory, E.C. 1988. Surface soil displacements in sorted circles, western Spitsbergen. *Proceedings, Fifth International Conference on Permafrost,* Trondheim, Norway 1: 770-775.

Kessler, M., Werner, B., Murray, B. & Hallet, B. 2001. A model for sorted circles as self-organized patterns. *Journal of Geophysical Research-Solid Earth* 106 (B7): 13287-13306.

Kessler, M. & Werner, B. 2003. Self-organization of sorted patterned ground. *Science* 299(5605): 380-383.

Mangold, N., Maurice, S., Feldman, W.C., Costard, F. & Forget, F. 2004. Spatial relationships between patterned ground and ground ice detected by the Neutron Spectrometer on Mars. *Journal of Geophysical Research* 109(E08001), doi:10.1029/2004JE002235.

Porter, S.C. 2007. In memoriam: A. Lincoln Washburn (1911-2007). *Quaternary Research* 67: 311-312.

Rein, R.G. Jr. & Burrous, C.M. 1980. Laboratory measurements of subsurface displacements during thaw of low-angle slopes of a frost-susceptible soil. *Arctic and Alpine Research* 12(3): 349-358.

Stuiver, M., Yang, I.C., Denton, G.H. & Kellog, T.B. 1981. Oxygen isotope ratios of Antarctic permafrost and glacier ice. *Antarctic Research Series: Dry Valley Drilling Project*. L.D. McGinnis. Washington, D.C., American Geophysical Union 33: 131-139.

Washburn, A.L. 1947. Reconnaissance geology of portions of Victoria Island and adjacent regions, Arctic Canada. *Geological Society of America Memoir* 22, 142 pp.

Washburn, A.L. 1950. Patterned ground. *Revue Canadienne de Géographie* 4: 5-54.

Washburn, A.L. 1956. Classification of patterned ground and review of suggested origins. *Geological Society of America Bulletin* 67: 823-866.

Washburn, A.L. 1965. Geomorphic and vegetational studies in the Mesters Vig District, Northeast Greenland. *Meddelelser om Grønland* 166(1), 60 pp.

Washburn, A.L. 1967. Instrumental observations of mass-wasting in the Mesters Vig District, Northeast Greenland. *Meddelelser om Grønland* 166(4), 296 pp.

Washburn, A.L. 1969. Weathering, frost action, and patterned ground in the Mesters Vig District, Northeast Greenland. *Meddelelser om Grønland* 176(4), 303 pp.

Washburn, A.L. 1970. An approach to a genetic classification of patterned ground. *Acta Geographica Lodziensia* 24: 437-446.

Washburn, A.L. 1973. *Periglacial Processes and Environments.* London: Edward Arnold, 320 pp.

Washburn, A.L. 1979. *Geocryology: A Survey of Periglacial Processes and Environments.* London: Edward Arnold, 402 pp.

Washburn, A.L. 1980. Permafrost features as evidence of climatic change. *Earth Science Reviews* 15: 327-402.

Washburn, A.L. 1987. Mima mounds: An evaluation of proposed origins, with special reference to the Puget Lowland. Washington Department of Natural Resources. Division of Geology and Earth Resources. *Report of Investigations* 29, 53 pp.

Washburn, A.L. 1989. Near-surface soil displacement in sorted circles, Resolute area, Cornwallis Island, Canadian High Arctic. *Canadian Journal of Earth Sciences* 26: 941-955.

Washburn, A.L. 1997. Plugs and plug circles: A basic form of patterned ground. Cornwallis Island Arctic Canada: Origin and implications. *Geological Society of America Memoir* 190, 183 pp.

Washburn, A.L., Sanders, J.E. & Flint, R.F. 1964. A convenient nomenclature for poorly sorted sediments. *Journal of Sedimentary Petrology* 33: 478-480.

Washburn, A.L., Burrous, C.M. & Rein, R.G. Jr. 1978. Soil deformation resulting from some laboratory freeze-thaw experiments. *Proceedings 3rd International Conference on Permafrost,* Trondheim, Norway.

Washburn, T.T. 1999. *Under Polaris: An Arctic Quest*. Seattle: University of Washington Press.

Advances in Permafrost and Periglacial Research in the Dry Valleys, Antarctica

Bernard Hallet, Ronald S. Sletten, Jaakko Putkonen
Quaternary Research Center, University of Washington, Seattle WA 98195, USA

Abstract

Extremely dry and cold conditions in continental portions of Antarctica lead to permafrost properties and periglacial processes that merit special attention because they are quite distinct from those in the Arctic, which are generally more familiar. Moreover, they resemble most closely those on Mars, providing powerful analogues that are helpful in interpreting the surface of the planet and the dominant surficial processes, as well as evidence for major recent change in the climate of Mars. Herein, we review recent studies of periglacial processes and implications for understanding the hyper-arid, cryogenic landscape typical of the non-ice covered portions of the Antarctic continent and beyond. Our review is selective as it is limited to the research we are familiar with in the Dry Valleys region; it includes 1) thermal and moisture states of Antarctic permafrost 2) factors affecting the formation, stability and longevity of ice below the ground surface, 3) nature and rates of patterned ground processes with a focus on sand-wedge polygons, 4) rates and mechanisms of permafrost creep, hillslope processes and sediment transport, and 5) specific analogues pertinent to permafrost and periglacial activity on Mars, and related inferences about Martian climate change.

Keywords: Antarctica; contraction cracks; Dry Valleys; Mars; patterned ground; periglacial; permafrost.

Introduction

In comparison with the Arctic, the Antarctic continent is very cold and extremely dry. In addition to leading to distinct thermal conditions below the ground surface, the cold and hyper-arid conditions cause major differences in permafrost properties and processes between the polar regions. The dearth of water in the Dry Valleys profoundly affects a suite of periglacial processes that are fueled by large volumetric changes associated with freezing and thawing in water-rich systems. Frost heaving is very limited, which curtails a suite of processes that are directly linked to ice lens or needle ice growth: weathering of bedrock and sediments, frost-induced sorting of material, formation of sorted patterned ground, and downslope motion of debris. On the other hand, the large seasonal temperature fluctuations, and in particular the very low soil temperatures attained in the winter because of the lack of thick insulating blanket of snow, lead to large thermal stresses in the upper part of the permafrost; the resulting thermal contraction cracks in the permafrost render polygonal patterned ground pervasive and often the dominant surface texture of extensive areas. The dry conditions also lead to two characteristics unusual in wetter cold regions: the accumulation of salts at and below the ground surface, and the importance of eolian processes in shaping the periglacial landscape. Moreover, under the cold conditions that prevail in the Dry Valleys, subsurface ice can form and persist for long periods of time, and landscape evolution can be extremely slow.

The relatively slow periglacial processes and stable landscapes typical of Antarctica merit special attention because they contrast with those in the Arctic, which are generally more familiar, and they resemble those on Mars most closely, providing an informative analogue environment that is helpful in interpreting the surface of that planet. Moreover, diverse techniques that have been developed for studying permafrost and periglacial systems in the Antarctic may prove useful in other cold regions. They include 1) analyses of cosmogenic nuclide concentrations in bedrock, sediment, soil and ice for diverse objectives: determining rates of weathering and sublimation of buried ice, ages of deposition, and duration of exposure or burial; 2) isotopic, trace and major element studies of subsurface ice to examine the origin and evolution of the ice, and 3) ground displacements using in situ instrumentation as well as space borne techniques (GPS, SAR Interferometry) to document the magnitude of thermally or gravitationally driven regolith motion.

Permafrost and periglacial process studies in the Antarctic also complement those in the Arctic in addressing questions that seldom emerge in the wetter and more dynamic frozen landscape of the Arctic. Why is there ice below the surface in this dry environment? What is the longevity of buried ice? What is the rate of sublimation of that ice? What is the origin of salts and how do they affect H_2O transport, and ionic transport and isotopic exchange in the ice? How stable is the ground surface or a landform?

Herein, we do not attempt to provide a comprehensive review but rather summarize the more substantial advances in terms of new approaches, methodology, or insight gained into key processes largely in the Dry Valleys of southern Victoria Land, near McMurdo, which contain the largest non-ice covered area on the Antarctic continent (Campbell & Claridge 2006).

Thermal Properties of Dry Valley Soils

Two primary factors distinguish the soil thermal regime in the Dry Valleys from that of a typical Arctic site: 1) soils are extremely cold in the winter, often dropping below -40ºC (Fig. 1), and 2) the near surface soil (the upper ~0–20 cm) often lacks H_2O, making the soil an effective, cohesionless

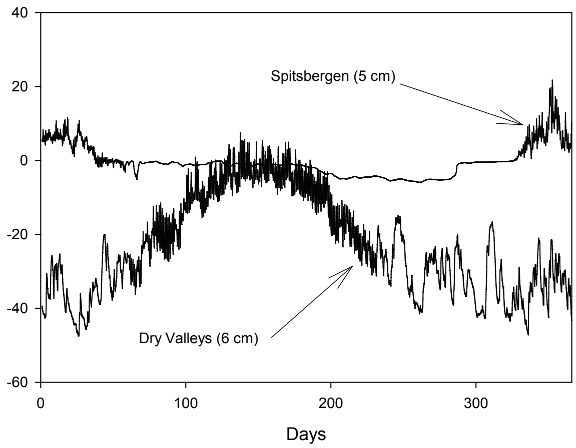

Figure 1. Soil temperatures 5 and 6 cm below the ground surface in Spitsbergen (Putkonen 1998), and in the Dry Valleys (Putkonen et al. 2003). The data span one year starting on the first of August. As the field sites are in opposite hemispheres, the summers are out of phase. Note very cold and variable conditions, and the conspicuous absence of the zero-degree curtain or other phase change effects close to 0ºC in the Dry Valleys.

insulator (Putkonen et al. 2003) with bulk soil thermal conductivities as low as 0.1–0.4 W m^{-1} K^{-1}. Laboratory measurements of typical dry surface soil samples, yield values of 0.3 W m^{-1} K^{-1} for the thermal conductivity 1000 J kg^{-1} K^{-1} for the heat capacity and 1200–1800 kg m^{-3} for the density; correspondingly, the thermal diffusivity is 0.17–0.25 x 10^{-6} m^2 s^{-1}

Such a low thermal conductivity promotes steep thermal gradients, which can reach 200 K m^{-1} near the soil surface, and limits the penetration of surface temperature variations (Putkonen et al. 2003). The dearth of near surface ice/water also eliminates all thermal effects related to the phase change of water that are characteristic of Arctic soils.

Due to the cold winters, short cool summers and low thermal conductivity of the dry soil, the active layer is thin, ranging from 30-60 cm for low altitude coastal sites to about 15 cm in the alpine valleys ~1400 m asl and about 70 km from the coast (Campbell et al. 1998, Putkonen et al. 2003). Snow may fall any time of the year, but the thin snow cover (typically less than 30 cm) lasts only days (Campbell et al. 1998, Hagedorn et al. 2007). Without the insulating snow cover, the near surface soil temperatures vary widely through the winter reflecting the large variations in atmospheric conditions.

Moisture State

Due to low precipitation and air temperatures, averaging around –20°C, in the Dry Valleys, liquid water is very limited; most snow sublimates and only a small amount melts, delivering little or no moisture to the ground (Gooseff et al. 2003, Hagedorn et al. 2007). Campbell and Claridge (1982) report that soil moisture moves mostly in the form of vapor with limited migration of snow melt. Nevertheless, salt horizons and salt crystallization beneath stones are prevalent in the Dry Valleys (Keys & Williams 1981); considering the limited solubility of the salts, these accumulations reflect significant long term fluxes of liquid water even under these extremely arid conditions.

Water persists in thin films on mineral surfaces to very low temperatures (Anderson & Morgenstern 1973, Yong et al. 1979, Fu et al. 1993) and considerable ion migration probably occurs along these films (Ugolini & Anderson 1973, Wettlaufer & Worster 1995, Claridge et al. 1996, Wettlaufer 1999, Wettlaufer 2001, Dickinson & Rosen 2003). The high solute content lowers the freezing point of water well below 0°C, and tends to increase the mobility of both water and solutes by thickening these films. To date only two studies of transport rates have been performed in the field. Using LiCl-tracers in Antarctic soils, Claridge et al. (1996) documented Li diffusion 15–25 cm into the soil and 5 m laterally in ≤ 3 years, with a strong dependence on the moisture content. Application of ^{36}Cl and ^{22}Na-labeled NaCl close to the ice-cemented permafrost in Wright Valley by Ugolini and Anderson (1973) revealed upward migration of both ions but significantly less movement of ^{22}Na than ^{36}Cl, presumably due to differences in diffusion coefficients and chemical behavior e.g., ion exchange and adsorption.

Subsurface Ice

Subsurface ice is pervasive in the Dry Valleys, where it occurs in various forms: pore ice, ice in permafrost cracks, and buried lake or buried glacial ice (Bockheim & Hall 2002, Campbell & Claridge 2006).

This ice is fundamental to diverse periglacial processes, including patterned ground activity and mass wasting, not only in Antarctica but also on Mars. Its existence within the top decimeters in soils that are 10^4 to 10^6 year old is enigmatic, however, since current models indicate that any ice within few meters of the surface would sublimate into atmosphere within several thousand years (van der Wateren & Hindmarsh 1995, Hindmarsh et al. 1998, Schorghofer 2005). Most recently, Hagedorn et al. (2007) explore mechanisms that slow or may reverse ice loss from the soil to the atmosphere, and incorporate them into a sublimation model that uses high-resolution climate and soil temperature data in Victoria Valley, where the surface is ~10 Ka old and the soil is ice cemented 0.22 m below the surface. According to this model, snow slows long-term sublimation but, due to the dearth of data on the duration and timing of snow cover, the potential of snow melt to offset vapor transport out of the soil cannot be assessed quantitatively at present. Studies of depth profiles of δD and $\delta^{18}O$ in pore ice are providing new insights into the origin and evolution of ground ice in the Dry Valleys (Hagedorn et al. 2003, Souchez & Lorrain 2006).

Massive subsurface ice occurs sporadically in the Dry Valleys. Much effort has been directed at dating and understanding the origin and longevity of this buried ice, especially in Beacon Valley where it has been interpreted as the oldest glacier ice on Earth. Such ancient ice would be of considerable interest because it may contain an unparalleled archive of paleoenvironmental conditions and lyophilized bacteria. Sugden et al. (1995) reported an 8.1 Ma volcanic ash in the sublimation till overlying this ice, and viewed it as a direct air-fall deposit. This interpretation implies slow sublimation for the survival of both the ice and the delicate layer of ash and hence, a persistent cold climate, which has broad implications about global climate stability since the Miocene. This extreme stability is not, however, consistent with independent estimates of sublimation rates of 50 m Ma^{-1} and ~10^3 m Ma^{-1}, respectively from measurements of cosmogenic nuclides in a 19-m ice core (Stone et al. 2000) and from theory (e.g., Hindmarsh et al. 1998). Moreover the use of the ash to constrain the age of the ice has been questioned by Sletten et al. (2007) who reported old tephra erratics within the sublimation till.

One way to resolve this age controversy is to decipher the history of the till overlying the massive ice from cosmogenic nuclide measurements. The till is a residue of debris-laden ice that sublimed. Ng et al. (2005) reinterpreted published ^3He depth profiles through the sublimation till in Beacon Valley, Antarctica, to derive rigorous constraints on the till-thickness history and on the amount and rate of ice loss by sublimation. The ^3He profiles show that the lower 80% of the till formed in the past 310–43 ka under sublimation rates averaging >7 m Ma^{-1}. Such rapid, recent growth of the till contradicts previous interpretations that it is older than 8.1 Ma at an adjacent site, where it encloses volcanic ash of this age, casting additional doubt on the validity of the ash in constraining the age of the ice.

Soil Distribution and Characteristics, and Weathering

Relative to many well studied portions of the Arctic, the spatial distribution of soils in the Dry Valleys region has received little attention until recently (Bockheim et al. 2007). A new soil map is being developed for selected regions of the McMurdo Dry Valleys (McLeod et al. 2007). As mentioned earlier, the active layer tends to be relatively dry and shallow (Paetzold et al. 2003); it is often ice-free particularly at the higher elevation sites near the ice sheet (Bockheim et al. 2007).

The paucity of liquid water in the Dry Valleys leads to soils sharing many characteristics with soils of arid regions with considerable salt accumulation. The dominant salts are chlorides, nitrates, and sulfate, mostly of direct marine origin (Bao et al. 2008); the latter two reflect oxidation in the atmosphere prior to deposition (Bao et al. 2000). The abundance of salts influences soil moisture (Hagedorn et al. 2007), weathering (Dickinson & Grapes 1997), and biology (Barrett et al. 2006).

The Dry Valleys Long Term Ecological Research site in Taylor Valley has served as a focus for studies of soil processes related to the soil fauna (Barrett et al. 2006, Wall et al. 2006) and to chemical weathering, which influences the chemistry of soil water, as well as streams and lakes (Lyons et al. 2002, Gooseff et al. 2007). Publications on the soils, hydrology, and biota are listed on the LTER web site (www.mcmlter.org).

The cold, hyper-arid conditions lead to some of the lowest known bedrock erosion rates on Earth. A powerful means of determining these rates has been exposure age dating using cosmogenic nuclides. Such research in the Dry Valleys area has shown that 1) the bedrock surfaces have been exposed sub-aerially for millions of years; notably they have not been buried by ice sheets or covered by water or sediments, and 2) these bedrock surfaces erode at rates of ~1 m Ma^{-1} (Nishiizumi et al. 1991, Brook et al. 1995, Summerfield et al. 1999, Smith et al. 2001, Schoenbohm et al. 2004). These bedrock erosion rates are among the lowest recorded on Earth and are 1-3 orders of magnitude slower than, for example, ~10 m Ma^{-1} in the Sierra Nevada, USA (Stock et al. 2005).

Patterned Ground

Polygonal patterned ground is ubiquitous in the Dry Valleys, even on steep hillslopes. In this and other arid, cold regions, thermal contraction cracks tend to open at the ground surface during cold periods. In contrast with regions where moisture is abundant and the cracks tend to fill with water and ice, the Dry Valley cracks fill partially with wind-blown sand and other fine-grained debris. This infilling prevents the cracks from fully closing during warm periods. During subsequent cooling periods, each crack reopens, permitting more sand infilling, thereby, incrementally forming a wedge of sand. With time, the ground surface on either side of the crack is warped upward by the growing sand wedge to form symmetrical ridges separated by a trough over the crack (Péwé 1959). These sand-filled cracks interconnect to form polygons (Fig. 2) that have received very little attention compared to the thoroughly studied ice-wedge polygons (Mackay 1971, 2002).

The progressive growth of sand-wedges can be examined by monitoring the distance between markers installed across contraction cracks. Recent measurements of 417 pairs of steel rods, which were hammered vertically into the ground on opposite sides of contraction cracks at 13 sites established in the early 1960s by Robert Black, show steady divergence across the sand-wedges of patterned ground in the Dry

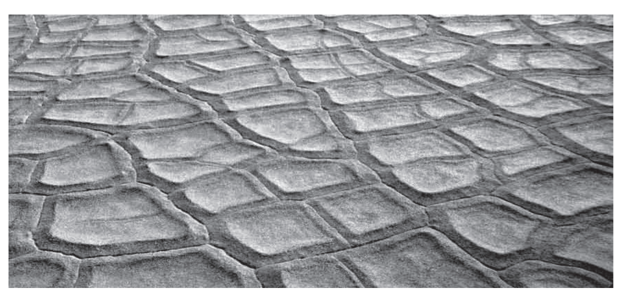

Figure 2. Polygonal patterned ground in upper Victoria Valley. These distinctive low-centered polygons form spontaneously from the recurrent opening and closing of cracks due to thermal strains, and the progressive addition of wind-blown sand into the cracks.

Valleys. Rod spacings were measured on several occasions from 1962 to 2002 (Berg & Black 1966, Black 1973, Black 1982, Malin & Rawine 1995, Sletten & Hallet 2004). Individual divergence rates between paired rods in lower Beacon Valley, for example, are highly variable, ranging from 0.1 to 1.8 mm a^{-1}. By 2002, the mean distance between rod tops increased 20–25 mm (std. dev. 16-18 mm) since their installation 39 years earlier. The rates are remarkably steady in time, and are essentially identical to those at sites recently established to continuously monitor contraction crack dynamics (Sletten et al. 2003).

The recurrent cracking and sustained addition of wind-blown sand to a depth of ~5 m generate long-term pervasive deformation in the permafrost and wedge material and net surface aggradation, or inflation, at rates of 0.05 to 0.1 mm a^{-1}. Evidence for both surface and sub-surface deformation includes the pair of ridges that commonly border each contraction crack (Fig. 2), and frozen soil layers that are often warped upward as they approach the wedge (Péwé 1959). Recent, high resolution instrumental measurements show significant thermally-induced permafrost deformation and are invaluable in studying the dynamics of this form of patterned ground (Fig. 3).

This soil deformation is complex, and constitutes a form of cryoturbation that is expected to pervasively disrupt geomorphic surfaces where sand-wedge polygons are active. The ratio of polygon size (~10 m) to typical sand-wedge growth rate (~1 mm a^{-1}) for lower Beacon Valley provides an indication of the time scale for the reworking of the ground surface, which is only ~10^4 years. Provided that the rates of wedge growth deduced from Black's data over the last few decades can be extrapolated to considerably longer time scales, they challenge the notion that similar nearby geomorphic surfaces have been stable for millions of years, as proposed by Sugden et al. (1995) and Marchant et al. (2002).

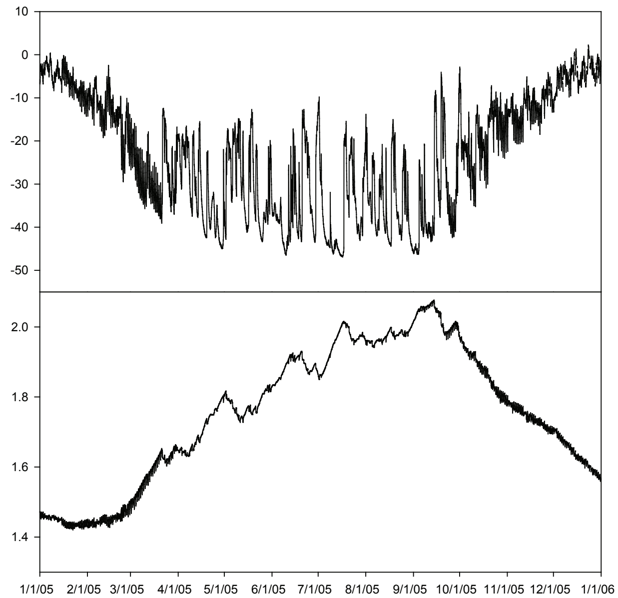

Figure 3. Air temperature (deg C) at 2 m and increase in distance between two markers (in cm) that are ~2 m apart across a contraction crack in central Beacon Valley. Displacements were measured with micrometer resolution using a linear motion transducer. Data were recorded hourly using a Campbell CR10X data logger.

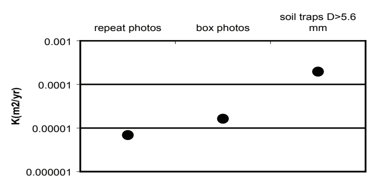

Figure 4. Mean topographic diffusivity for Dry Valleys determined using repeat photography and soil traps. These values approach the lowest known terrestrial values from hot deserts and they contrast strongly with those in the Arctic where regolith fluxes are among the highest on Earth. For additional details see (Putkonen et al. 2007).

Slope Processes

The stability of ground surfaces and preservation of deposits that record past events and environments are important to studies of the geologic and climatic history of Antarctica. Clear indications of downslope debris transport such as solifluction lobes and direct measurements of debris motion on slopes, which are common in the Arctic, are rare in the Dry Valleys; elongated polygons or sorted stripes, and solifluction terraces are uncommon. (Putkonen et al. in press).

Although the common occurrence of ancient volcanic ashes at or near ground surfaces suggests essentially perfect preservation of sedimentary deposits in the Dry Valleys (Marchant et al. 1993, Marchant & Denton 1996, Marchant et al. 1996) and negligible downslope debris motion, recent research suggests rates of downslope motion that approach those in hot deserts.

In contrast with the Arctic, all the downslope movement in the Dry Valleys is limited to the upper few centimeters of the dry soil (Putkonen et al. in press). Using repeat photographs, soil traps, and measurements of downslope displacements of rock fragments in the Dry Valleys, Putkonen et al. (2007) determined a sediment transport coefficient (topographic diffusivity) for the Dry Valleys that normalizes the debris flux per unit width of the slope for the local slope angle (Fig. 4). This contemporary diffusivity ranges from 10^{-5} to 10^{-4} $m^2 a^{-1}$; it is relatively low but approaches those previously reported from other sites worldwide (Oehm & Hallet 2005). Indirect observations in the Dry Valleys suggests that strong winds play a significant role in the downslope transport of dry debris as they can destabilize relatively large pebbles as evidenced by gravel dunes in the lower Wright valley and sediment recovered in soil traps (Lancaster 2002, Putkonen et al. 2007). The topographic diffusivities are highest in alpine valleys located farther inland from the coast, and lowest near the coast.

To determine the longer term downslope debris flux Putkonen et al. (2007) also analyzed concentrations of distinct rock fragments found downhill of eroding source boulders. These boulder trails yielded a lower limit for the

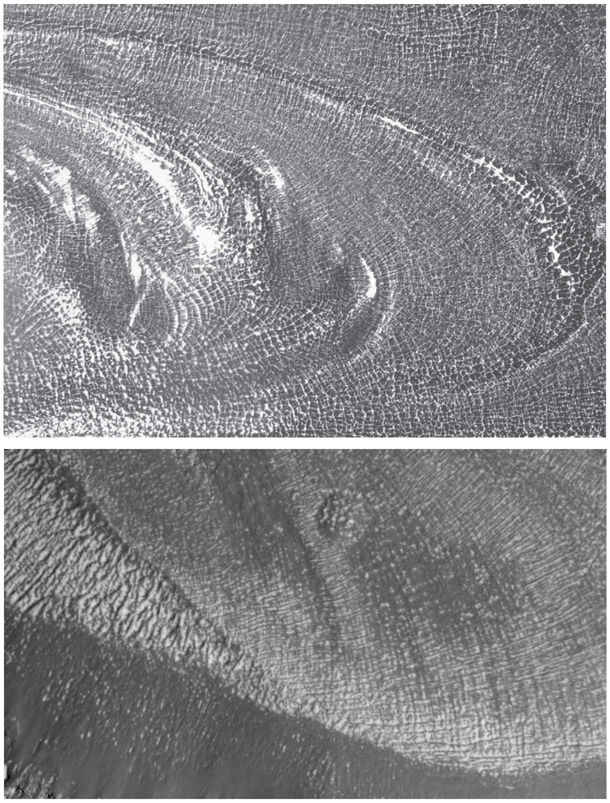

Figure 5. Upper picture shows accurate ridges and a pervasive system of near-orthogonal surface cracks on the rock glacier in upper Mullins, Valley, Antarctica. Similar terrain is observed on Mars (MOC S05-01603).

long term topographic diffusivity of order 10^{-8}–10^{-7} m^2 a^{-1}; actual diffusivities are likely much larger. Another source of information about the long-term mobility of surface debris can be extracted from braking blocks, which are partially exhumed boulders that have a typical bulge of regolith on the uphill side and a depression on the downhill side; they are ubiquitous in the Dry Valleys. Using a model of downslope motion governed by local slope, Morgan and Putkonen (2005) simulated the evolution of the microtopography toward a steady state, obtaining results resembling closely the microtopography observed in the field. They were able to assess minimum regolith transport rates; the corresponding topographic diffusivity was found to exceed 10^{-6} m^2 a^{-1}.

In conclusion, the rates at which debris moves downslope in Antarctica are generally the smallest known on earth; they strongly contrasts with those from wet Arctic that are among the highest. Despite these low rates, downslope debris transport can significantly alter landforms and disturb ancient deposits in the Dry valleys over a typical exposure time of millions of years.

Rock Glaciers – Permafrost Creep

The absence of vegetation, dearth of snow and stability of land surfaces in the Dry Valleys are ideal for the use of satellite-based Synthetic Aperture Radar studies of surface motion as the surface maintains excellent coherence of the radar returns over several years. Rignot et al. (2002) obtained a

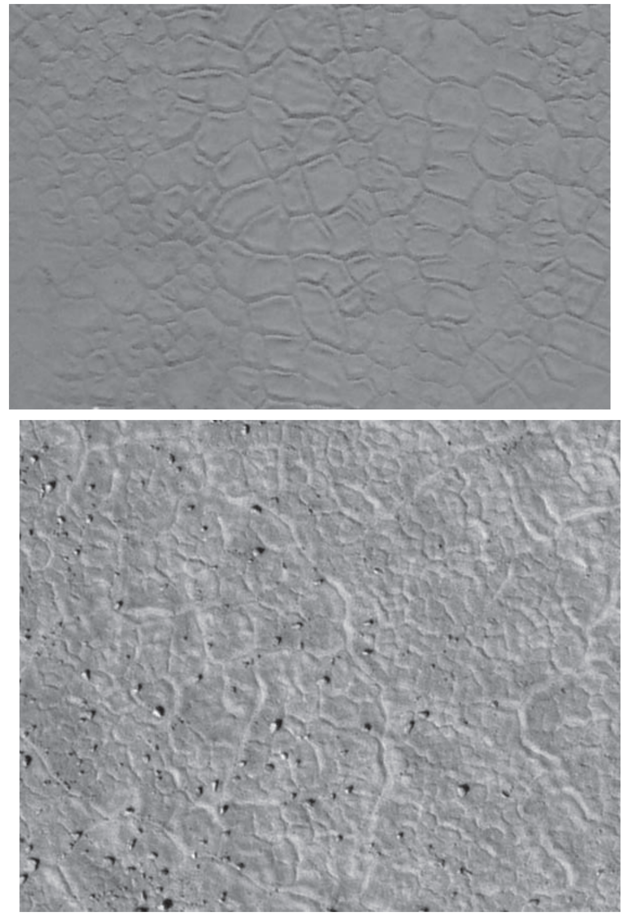

Figure 6. Aerial photograph of Victoria Valley (top) and analogous terrain on Mars (HiRise image TRA_000828_2495_IRB; illumination from the lower left). Shallow surface troughs outline polygons approximately 10–20 m across.

spatially continuous surface velocity field with a precision of fractions of a millimeter per year on rock glaciers (debris-covered glaciers) entering Beacon Valley. They found coherent velocity patterns, with peak velocities approaching 40 mm per year; these velocities are consistent with our unpublished GPS measurements of surface boulder motion.

The ice supply from these rock glaciers nourishes the central portion of Beacon Valley, where it sublimates. Interestingly, the ice supply balances the loss by sublimation provided sublimation rates are within the 0.02–0.2 mm a^{-1} range, which brackets the net sublimation rate of 0.05 mm a^{-1} obtained using cosmogenic isotopes in subsurface ice (Stone et al. 2000).

The surface of rock glaciers displays a series of features strikingly similar to those imaged on Mars suggesting the likely presence of debris-covered massive ice on Mars. Figure 5 illustrates many of these features including lobe-like forms, arcuate ridges, and complex dense patterns of surface cracks.

Studying Mars Using Antarctica Analogue

The cold and dry near-surface conditions typical of the Dry Valleys approach those on Mars. Studies of Antarctica as a useful analogue were initiated in the 1970s after the first images were taken by the Mariner and Viking spacecraft (e.g., Anderson et al. 1972). With additional successful missions and the recent acquisition of much higher resolution images, along with compelling evidence for widespread ice in the upper ~1 m of permafrost (Boynton et al. 2002), there is a considerable resurgence in interest to use the Dry Valleys as a popular natural laboratory to study landforms and processes that occur or may occur on Mars. They include rock glaciers and moraines (Head & Marchant 2003), the sublimation of subsurface ice (McKay et al. 1998, Hagedorn et al. 2007) that has much in common with the identical process on Mars (Schorghofer 2005), the formation of polygonal patterned ground (Fig. 6) and associated micro-relief (Mellon 1997, Sletten & Hallet 2003), and the occurrence and preservation of simple life forms under extreme polar conditions (e.g., Gilichinsky et al. 2007).

Acknowledgments

We acknowledge C. McKay, B. Hagedorn, D. Gilichinsky, M. Mellon and A. Gillespie for assisting us in the field and/or for informative discussions pertinent to this review. This material is based upon work supported by the National Science Foundation under Grant No. 9726139 & 0636998, and by NASA Grant NNX06AC10G. The authors acknowledge the use of Mars Orbiter Camera (MOC) images processed by Malin Space Science Systems that are available at http://www.msss.com/moc_gallery/.

References

Anderson, D.M., Gatto, L.W. & Ugolini, F.C. 1972. An antarctic analog of Martian permafrost terrain. *Antarctic Journal of the U.S.* 7: 114-116.

Anderson, D.W. & Morgenstern, N.R. 1973. Physics, chemistry, and mechanics of frozen ground: a review. *Permafrost; Second International Conference, Proceedings*, Yakutsk, USSR, National Academy of Sciences Press, Washington, D.C., 257-288.

Bao, H.M., Barnes, J.D., Sharp, Z.D. & Marchant, D.R. 2008. Two chloride sources in soils of the McMurdo Dry Valleys, Antarctica. *Journal of Geophysical Research-Atmospheres* 113(D3).

Bao, H.M., Campbell, D.A., Bockheim, J.G. & Thiemens, M.H. 2000. Origins of sulphate in Antarctic dry-valley soils as deduced from anomalous ^{17}O compositions. *Nature* 407(6803): 499-502.

Barrett, J.E., Virginia, R.A., Hopkins, D.W., Aislabie, J., Bargagli, R., Bockheim, J.G., Campbell, I.B., Lyons, W. B., Moorhead, D., Nkem, J., Sletten, R.S., Steltzer, H., Wall, D.H. & Wallenstein, M. 2006. Terrestrial Ecosystem Processes of Victoria Land, Antarctica. *Soil Biology and Biochemistry* 38(10): 3019-3034.

Berg, T.E. & Black, R.F. 1966. Preliminary measurements of growth of nonsorted polygons, Victoria Land, Antarctica. *Antarctic Soils and Soil Forming Processes*. J.C.F. Tedrow. Washington, D.C., American Geophysical Union 8: 62-108.

Black, R.F. 1973. Growth of patterned ground in Victoria Land, Antarctica. *Permafrost: The North American Contribution to the 2nd International Conference*, Yakutsk, Siberia, National Academy of Sciences, 193-203.

Black, R.F. 1982. Patterned-ground studies in Victoria Land. *Antarctic Journal of the U.S.* 17(5): 53-54.

Bockheim, J.G., Campbell, I.B. & McLeod, M. 2007. Permafrost distribution and active-layer depths in the McMurdo Dry Valleys, Antarctica. *Permafrost and Periglacial Processes* 18(3): 217-227.

Bockheim, J.G. & Hall, K.J. 2002. Permafrost, active-layer dynamics and periglacial environments of continental Antarctica. *South African Journal of Science* 98(1-2): 82-90.

Boynton, W.V., Feldman, W.C., Squyres, S.W., Prettyman, T.H., Bruckner, J., Evans, L.G., Reedy, R.C., Starr, R., Arnold, J.R., Drake, D.M., Englert, P.A.J., Metzger, A.E., Mitrofanov, I., Trombka, J.I., d'Uston, C., Wanke, H., Gasnault, O., Hamara, D.K., Janes, D.M., Marcialis, R.L., Maurice, S., Mikheeva, I., Taylor, G.J., Tokar, R. & Shinohara, C. 2002. Distribution of hydrogen in the near surface of Mars: Evidence for subsurface ice deposits. *Science* 297(5578): 81-85.

Brook, E.J., Brown, E.T., Kurz, M.D., Ackert-Jr, R.P., Raisbeck, G.M. & Yiou, F. 1995. Constraints on age, erosion, and uplift of Neogene glacial deposits in the Transantarctic Mountains determined from in situ cosmogenic ^{10}Be and ^{26}Al. *Geology* 23(12): 1063-1066.

Campbell, I.B. & Claridge, G.G.C. 1982. The influence of moisture on the development of soils of the cold deserts of Antarctica. *Geoderma* 28: 221-238.

Campbell, I.B. & Claridge, G.G.C. 2006. Permafrost properties, patterns and processes in the transantarctic mountains region. *Permafrost and Periglacial Processes* 17(3): 215-232.

Campbell, I.B., Claridge, G.G.C., Campbell, D.I. & Balks, M.R. 1998. The soil environment of the McMurdo Dry Valleys, Antarctica. *Ecosystem dynamics in a polar desert, the McMurdo Dry Valleys, Antarctica*. J. Priscu. Washington, D.C., American Geophysical Union 72: 369.

Claridge, G.G.C., Campbell, I.B. & Balks, M.R. 1996. Ionic migration in soils of the Dry Valley region. *International Workshop on Polar Desert Ecosystems*, Christchurch, New Zealand, A.A. Balkema, Rotterdam.

Dickinson, W.W. & Grapes, R.H. 1997. Authigenic chabazite and implications for weathering in Sirius group diamictite, Table mountain, dry valleys, Antarctica. *Journal of Sedimentary Research* 67((5) Part A): 815-820.

Dickinson, W.W. & Rosen, M.R. 2003. Antarctic permafrost: An analogue for water and diagenetic minerals on Mars. *Geology* 31(3): 199-202.

Fu, H., Dash, J., Wilen, L. & Hallet, B. 1993. The physics of liquid water in frozen powders and soils. *Permafrost; Sixth International Conference, Proceedings*, Beijing, 1117-1119.

Gilichinsky, D.A., Wilson, G.S., Friedmann, E.I., McKay, C.P., Sletten, R.S., Rivkina, E.M., Vishnivetskaya, T.A., Erokhina, L.G., Ivanushkina, N.E., Kochkina, G.A., Shcherbakova, V.A., Soina, V.S., Spirina, E.V., Vorobyova, E.A., Fyodorov-Davydov, D.G., Hallet, B., Ozerskaya, S.M., Sorokovikov, V.A., Laurinavichyus, K.S., Shatilovich, A.V., Chanton, J.P., Ostroumov, V.E. & Tiedje, J.M. 2007. Microbial Populations in Antarctic Permafrost: Biodiversity, State, Age, and Implication for Astrobiology. *Astrobiology* 7(2): 275-311.

Gooseff, M.N., Barrett, J.E., Doran, P.T., Fountain, A.G., Lyons, W.B., Parsons, A.N., Porazinska, D.L., Virginia, R.A. & Wall, D.H. 2003. Snow-patch influence on soil biogeochemical processes and invertebrate distribution in the McMurdo Dry Valleys, Antarctica. *Arctic Antarctic and Alpine Research* 35(1): 91-99.

Gooseff, M.N., Barrett, J.E., Northcott, M.L., Bate, D.B., Hill, K.R., Zeglin, L.H., Bobb, M. & Takacs-Vesbach, C.D. 2007. Controls on the spatial dimensions of wetted hydrologic margins of two antarctic lakes. *Vadose Zone Journal* 6(4): 841-848.

Hagedorn, B., Sletten, R.S. & Hallet, B. 2007. Sublimation and ice condensation in hyperarid soils: Modeling results using field data from Victoria Valley, Antarctica. *Journal of Geophysical Research Earth Surfaces* 112: F03017, doi:10.1029/2006JF000580.

Hagedorn, B., Sletten, R.S., Hallet, B. & Steig, E. 2003. Formation and characterization of ice-cemented soils in Victoria Valley. *9th International Symposium on Antarctic Earth Sciences*, Potsdam, Germany.

Head, J.W. & Marchant, D.R. 2003. Cold-based mountain glaciers on Mars: Western Arsia Mons. *Geology* 31(7): 641-644.

Hindmarsh, R.C.A., Van Der Wateren, F.M. & Verbers, A.L.L.M. 1998. Sublimation of ice through sediment in Beacon Valley, Antarctica. *Geografiska Annaler Series A: Physical Geography* 80(3-4): 209-219.

Keys, J.R. & Williams, K. 1981. Origin of crystalline, cold desert salts in the McMurdo region, Antarctica. *Geochimica et Cosmochimica Acta* 45(12): 2299-2309.

Lancaster, N. 2002. Flux of eolian sediment in the McMurdo Dry Valleys, Antarctica: a preliminary assessment. *Arctic Antarctic and Alpine Research* 34(3): 318-323.

Lyons, W.B., Nezat, C.A., Benson, L.V., Bullen, T.D., Graham, E.Y., Kidd, J., Welch, K.A. & Thomas, J.M. 2002. Strontium isotopic signatures of the streams and lakes of Taylor Valley, southern Victoria Land, Antarctica: Chemical weathering in a polar climate. *Aquatic Geochemistry* 8(2): 75-95.

Mackay, J.R. 1971. The origin of massive icy beds in permafrost, western Arctic coast, Canada. *Canadian Journal of Earth Sciences* 8: 397-422.

Mackay, J.R. & Burn, C.R. 2002. The first 20 years (1978-1979 to 1998-1999) of ice-wedge growth at the Illisarvik experimental drained lake site, western Arctic coast, Canada. *Canadian Journal of Earth Sciences* 39(1): 95–111.

Malin, M.C. & Rawine, M.A. 1995. Thirty years of measurements of sand wedge growth in lower Wright, Antarctica. *Antarctic Journal* Review 1994: 19-20.

Marchant, D.R. & Denton, G.H. 1996. Miocene and Pliocene paleoclimate of the Dry Valleys region, southern Victoria Land: a geomorphological approach. *Marine Micropaleontology* 27(1-4): 253-271.

Marchant, D.R., Denton, G.H., Sugden, D.E. & Swisher, C.C. III. 1993. Miocene glacial stratigraphy and landscape evolution of the western Asgard Range, Antarctica. *Geografiska Annaler* Series A 75A(4): 303-330.

Marchant, D.R., Denton, G.H., Swisher, C.C. III. & Potter, N. Jr. 1996. Late Cenozoic Antarctic paleoclimate reconstructed from volcanic ashes in the Dry Valleys region of southern Victoria Land. *Geological Society of America Bulletin* 108(2): 181-194.

Marchant, D.R., Lewis, A.R., Phillips, W.M., Moore, E.J., Souchez, R.A., Denton, G.H., Sugden, D.E., Potter, N. Jr. & Landis, G.P. 2002. Formation of patterned ground and sublimation till over Miocene glacier ice in Beacon Valley, southern Victoria Land, Antarctica. *Geological Society of America Bulletin* 114(6): 718-730.

McKay, C.P., Mellon, M.T. & Friedmann, E.I. 1998. Soil temperatures and stability of ice-cemented ground in the McMurdo Dry Valleys, Antarctica. *Antarctic Science* 10(1): 31-38.

McLeod, M., Bockheim, J.G. & Balks, M. 2007. A fifth-order reconnaissance soil map of ice-free areas of the Transantarctic Mountains, Antarctica. *A Keystone in a Changing World: Online Proceedings of the 10th ISAES*. A. K. Cooper, C. R. Raymond & ISAES Editorial Team**:** Extended Abstract 116, 4 pp.

Mellon, M. 1997. Small-scale polygonal features on Mars: seasonal thermal contraction cracks in permafrost. *Journal of Geophysical Research* 102(E11): 25617-25628.

Morgan, D.J. & Putkonen, J. 2005. Sediment transport in the McMurdo Dry Valeys, Antarctica. *Geological Society of America Abstracts with Programs* 37(7): 304.

Ng, F., Hallet, B., Sletten, R.S. & Stone, J.O. 2005. Fast-growing till over ancient ice in Beacon Valley, Antarctica. *Geology* 33(2): 121-124.

Nishiizumi, K., Kohl, C.P., Arnold, J.R., Klein, J., Fink, D. & Middleton, R. 1991. Cosmic ray produced 10Be and 26Al in Antarctic rocks: exposure and erosion history. *Earth and Planetary Science Letters* 104(2-4): 440-454.

Oehm, B. & Hallet, B. 2005. Rates of soil creep, worldwide: weak climatic controls and potential feedback. *Zeitchrift fur Geomorphologie* 49(3): 353-372.

Paetzold, R.F., Balks, M.R., Aislabie, J. & Sletten, R.S. 2003. Active Layer Thickness of Soils In The Ross Sea Region, Antarctica. *EOS Transaction of the Am. Geophys. Union*, San Francisco. Fall Meet. Suppl., Abstract C21B-0810.

Péwé, T.L. 1959. Sand-wedge polygons (Tesselations) in the McMurdo sound region, Antarctica; a progress report. *American Journal of Science* 257: 545-552.

Putkonen, J., Balco, G. & Morgan, D. In Press. Slow regolith degradation determined by cosmogenic-nuclide concentrations in Arena Valley, Antarctica. *Quaternary Research*.

Putkonen, J., Rosales, M., Turpen, N., Morgan, D., Balco, G. & Donaldson, M. 2007. Regolith transport in the Dry Valleys of Antarctica. *ISAES 2007 Proceedings. USGS OFR-2007,* doi:10.3133.

Putkonen, J., Sletten, R.S. & Hallet, B. 2003. Atmosphere/ ice energy exchange through a thin debris cover in Beacon Valley, Antarctica. *Permafrost; Eighth International Conference, Proceedings* Zurich. 8: 913-915.

Putkonen, J.K. 1998. Soil Thermal Properties and Heat Transfer Processes Near Ny Alesund, Northwestern Spitsbergen, Svalbard. *Polar Research* 17: 165-179.

Rignot, E., Hallet, B. & Fountain, A. 2002. Rock glacier surface motion in Beacon Valley, Antarctica, from synthetic-aperture radar interferometry. *Geophysical Research Letters* 29(12): 13,494-7.

Schoenbohm, L., Kurz, M., Ackert, R., Brook, E. & Brown, E. 2004. Erosion history from cosmogenic ^{10}Be 2^{6}Al, ^{3}He and ^{21}Ne depth profiles: Dry Valleys, Antarctica. *European Geosciences Union 1st General Assembly*, Nice, France.

Schorghofer, N. 2005. A physical mechanism for long-term survival of ground ice in Beacon Valley, Antarctica. *Geophysical Research Letters* 32: L19503, doi: 10.1029/2005GL023881.

Sletten, R.S. & Hallet, B. 2003. Surface stability and contraction crack development on various forms of ground ice in the Dry Valleys, Antarctica. *9th International Symposium on Antarctic Earth Sciences*, Potsdam, Germany.

Sletten, R.S. & Hallet, B. 2004. Extreme soil inflation in the Dry Valleys, Antarctica. *Geological Society of America Annual Meetings,* Invited Talk, Seattle.

Sletten, R.S., Hallet, B. & Fletcher, R.C. 2003. Resurfacing time of terrestrial surfaces by the formation and maturation of polygonal patterned ground. *Journal of Geophysical Research* 108(E4): 8044, doi:10.1029/2002JE001914.

Sletten, R.S., Mann, D.H., McIntosh, W.C., Dunbar, N.W., Prentice, M.L., Dickinson, W. & Stone, J. O. 2007. Possible redeposition of volcanic ashes in the Dry Valleys by glacier transport: in Antarctica. *A Keystone in a Changing World: Online Proceedings of the 10th ISAES*. A. K. Cooper, C. R. Raymond & ISAES Editorial Team**:** Extended Abstract 158, 4 pp.

Smith, M.E., Stone, J.O., Sletten, R. & Hallet, B. 2001. Cosmogenic Isotope Exposure Constraints on the Age and Sublimation Rate of Buried Ice in Beacon Valley, Antarctica. *Eos Transactions, American Geophysical Union,* Fall Meeting Supplement, 2001 82(47).

Souchez, R. & Lorrain, R. 2006. The environmental significance of deuterium excess in meteoric and non- meteoric Antarctic ice. *Glacier Science and Environmental Change*. P. Knight, Blackwell Publishing, 179-184.

Stock, G.M., Anderson, R.S. & Finkel, R.C. 2005. Rates of erosion and topographic evolution of the Sierra Nevada, California, inferred from cosmogenic 26Al and 10Be concentrations. *Earth Surface Processes and Landforms* 30: 985-1006.

Stone, J.O., Sletten, R.S. & Hallet, B. 2000. Old ice, going fast: Cosmogenic isotope measurements on ice beneath the floor of Beacon Valley, Antarctica. *Eos Transactions, American Geophysical Union, Fall Meeting Supplement,* Abstract H52C–21 81(48).

Sugden, D.E., Marchant, D.R., Potter, N., Jr., Souchez, R.A., Denton, G.H., Swisher, C.C., III & Tison, J.-L. 1995. Preservation of Miocene glacier ice in East Antarctica. *Nature* 376(6539): 412-414.

Summerfield, M.A., Stuart, F.M., Cockburn, H.A.P., Sugden, D.E., Denton, G.H., Dunai, T. & Marchant, D.R. 1999. Long-term rates of denudation in the Dry Valleys, Transantarctic Mountains, southern Victoria Land, Antarctica based on in-situ-produced cosmogenic ^{21}Ne. *Geomorphology* 27(1-2): 113-129.

Ugolini, F.C. & Anderson, D.M. 1973. Ionic migration and weathering in frozen Antarctic soils. *Soil Science* 115(6): 461-470.

van der Wateren, D. & Hindmarsh, R. 1995. Stabilists strike again. *Nature* 376(6539): 389-391.

Wall, D.H., Adams, B.J., Barrett, J.E., Virginia, R.A. & Hopkins, D.W. 2006. A synthesis of soil biodiversity and ecosystem functioning in Victoria Land, Antarctica. *Soil Biology & Biochemistry* 38(10): 3001-3002.

Wettlaufer, J.S. 1999. Impurity effects in the premelting of ice. *Physical Review Letters* 82(12): 2516-2519.

Wettlaufer, J.S. 2001. Dynamics of ice surfaces. *Interface Science* 9(1-2): 117-29.

Wettlaufer, J.S. & Worster, M.G. 1995. Dynamics of premelted films: frost heave in a capillary. *Physical Review E* 51(5): 4679-4689.

Yong, R.N., Cheung, C.H. & Sheeran, D.E. 1979. Prediction of salt influence on unfrozen water content in frozen soils. *Engineering Geology* 13: 137-155.

Spatial Analysis of Small-Scale Polygonal Terrain in Utopia Planitia, Mars: A Comparison with Terrestrial Analogues

T.W. Haltigin
Department of Geography, McGill University, Montreal, QC, Canada
W.H. Pollard
Department of Geography, McGill University, Montreal, QC, Canada
G.R. Osinski
Department of Earth Sciences, University of Western Ontario, London, ON, Canada
P. Dutilleul
Department of Plant Science, McGill University, Ste. Anne de Bellevue, QC, Canada
J.W. Seaquist
Department of Physical Geography, Lund University, Lund, Sweden

Abstract

This paper presents the results of a Spatial Point Pattern Analysis (SPPA) of small-scale polygonal terrain in Utopia Planitia, Mars, and draws comparisons with a number of terrestrial analogue sites. Utopia Planitia displays a wide variety of landforms interpreted as having periglacial origins, suggesting the past or present existence of large quantities of ground ice. Therefore, this region of Mars offers an excellent case study to assess the applicability of statistical analysis in quantifying and comparing terrestrial and Martian small-scale polygonal terrain, which in turn may yield insight about the processes responsible for their formation.

Keywords: Axel Heiberg Island; Canada; Mars analogues; polygonal terrain; spatial point pattern analysis.

Introduction

Polygonal terrain is one of the most common landscape features found in terrestrial polar environments (Mellon 1997a). These networks of interconnected trough-like depressions form through a process termed *thermal contraction cracking*—a result of complicated interactions between climatological and rheological processes (Lachenbruch 1962)—and often signify the presence of shallow subsurface ice deposits in the form of ice wedges (Mackay 1999).

Large polygonal patterns on the surface of Mars discovered by the Mariner missions were originally of great interest as they, too, were thought potentially to be implicit of ground ice deposits (Carr and Schaber 1977). However, subsequent analysis concluded that polygons with diameters ranging from 2-10km were too large to be associated with thermal contraction cracking and thus are now believed to be formed through a variety of other geological processes (e.g., Lane and Christensen 2000).

More recently, though, Mars Global Surveyor's Mars Orbiter Camera (MOC) had been used to identify and map polygons of much smaller size, revealing that these small-scale geometric networks are scattered throughout Mars' mid- to high-latitudes in both hemispheres (Kuzmin & Zabalueva 2003). With sizes ranging from 10–200 m, they are much more comparable to terrestrial polygons; as such, analysis of these features has prompted a revisiting of their analogical value.

Because polygons on Mars are often located in close proximity to other landforms thought to be representative of ground ice presence (e.g., Soare et al. 2007) and display strong visual similarities to terrestrial polygons, (Isaev and Abramenko 2003; Mangold 2005), the presence of these patterns on Mars has been used to suggest the possibility of near-surface ground ice deposits (e.g., Mellon 1997b; Seibert and Kargel 2001; Mangold et al. 2004).

Previous descriptions of polygonal terrain have tended to be qualitative in nature, and thus require some degree of subjectivity to analyze. However, by using quantitative techniques to describe polygonal geometry, it is possible to categorize various groups of networks and relate them to other factors.

Our goal for this study was to apply a statistical technique to surface patterns on the Martian surface, attempting to answer two overarching research questions pertaining to Martian polygonal terrain: "*is their geometry related to proximity to other periglacial landforms*?" and "*how similar are they to polygons found on Earth*?".

In essence, this study seeks not only to map the spatial distribution of polygonal terrain occurrence in relation to other features thought to be indicative of ground ice, but also to quantify the similarities and differences displayed between the geometry of the polygonal terrain observed on Earth and Mars.

Research Context

Terrestrial polygonal terrain and ice wedges

A detailed explanation of polygon formation via thermal contraction cracking is provided in the seminal works performed by Lachenbruch (1962), Pewe (1966), and Black (1974), summarized below. When tensile stresses due to seasonal decreases in surface and subsurface temperatures exceed the tensile strength of frozen ground, vertical cracks develop in order to relieve the stress. Over time, numerous cracks begin to join or intersect, resulting in closed polygonal geometrical shapes. As temperatures warm, the open cracks are filled with surface meltwater and groundwater that freezes when it reaches the permafrost within the crack. The vertical vein of ice that results represents the early stages of an "ice wedge."

As the surrounding climate warms later in the year, movements of near-surface soils induced by thermal expansion promote the formation of shoulder-like ridges bounding a linear depression in the ground above the wedge. Eventually, the cracks close again and the buildup of stresses due to freezing reinitiates the following winter. By repeating the process over hundreds or thousands of years, the ice wedge continues to thicken and the polygonal topographic patterns at the surface become more enhanced.

Martian polygons = ground ice?

It is conceivable that polygons found on Mars represent analogous geocryological systems to those found on Earth, based on converging lines of evidence suggesting that Martian polygons may be indicative of near-surface ground ice.

For example, it is possible that both terrestrial and Martian polygons are formed by similar processes. Mellon (1997a,b) showed that the conditions required for thermal contraction cracking could be exhibited poleward of 30 degrees latitude. Subsequently, Seibert & Kargel (2001) demonstrated that ice wedge cracking was potentially responsible for their formation.

In addition, polygons tend to be located in areas otherwise believed to be rich in ground ice. Mangold et al. (2004) noted that the majority of polygonal terrain is located poleward of 55 degrees, within the zone predicted to contain stable ice and spatially coincident with regions where Odyssey's Neutron Spectrometer detected near surface hydrogen enrichment (Boynton et al. 2002). Moreover, Langsdorf & Britt (2004) and Soare et al. (2007) showed that polygons are often found in close proximity to other landforms potentially associated with ground ice deposits (Fig. 1)

Comparing polygonal terrains on Earth and Mars

The apparent lack of quantitative comparisons between the geometry of terrestrial and Martian polygonal terrain may be a result of how polygonal ground has been categorized on either planet. On Mars, various combinations of geographical distribution, proximity to nearby landforms, and polygon size have been used to group polygonal networks (Kuzmin and Zabalueva 2003; Langsdorf and Britt 2004; Mangold 2005). On Earth, however, polygons tend not to be classified by their geometry, but rather by their relation to permafrost aggradation or degradation (Mackay 2000).

A selection of previous researchers have attempted to

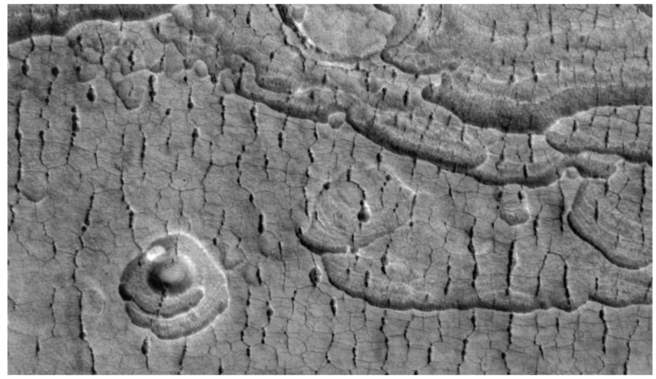

Figure 1: Example of polygons appearing within pitted and scalloped terrain (MOC image: R0301203). Image is approximately 3.5 km across.

use statistical analysis in their description of polygon morphology (e.g., Rossbacher 1986; Plug and Werner 2001; Yoshikawa 2003). Unfortunately, a universally accepted method to compare polygonal terrain on Earth and Mars has yet to be determined.

Refined statement of objectives

Through previous work, we have introduced the utility of a particular statistical method – Spatial Point Pattern Analysis – for quantifying a variety of polygonal terrain morphologies observed on Earth and Mars (Haltigin et al. 2007). We have now begun to apply the method more systematically to investigate differences in polygon morphology on a regional (rather than global) scale.

Therefore, our specific objectives for the present study are to: (1) explore variations in observed polygon morphologies displayed in the Utopia Planitia region of Mars, and; (2) compare the observed morphologies with a selection of those present in the Canadian High Arctic. By satisfying these objectives, it is possible that the inferred similarities and differences can be used to interpret some of the processes responsible for their formation.

Study Areas

Mars: Utopia Planitia

Utopia Planitia is a major topographic depression situated in the northern plains of Mars (Fig. 2). Although Odyssey's Gamma Ray Spectrometer (GRS) has revealed that this area is relatively free of hydrogen in the near-surface (Boynton et al. 2002), the large spatial resolution of GRS pixels may not be capable of identifying local ground ice occurrence.

A variety of geomorphic indicators do, in fact, suggest the presence of ground ice in Utopia Planitia. For example, small-sized polygons throughout the region and possible thermokarst features such as pitted terrain and scalloped terrain (Fig. 1) has led to the suggestion that this region contains ice-rich sedimentary deposits, whose emplacement could well be atmospheric and relatively recent (Costard & Kargel 1995; Soare et al. 2007).

Earth: Axel Heiberg Island

Fieldwork was conducted at four polygonal terrain sites near the McGill Arctic Research Station (M.A.R.S.) (79.383N, 91.067W). The region is set within a polar desert climate, having a mean annual air temperature of approximately -15°C and total annual precipitation of <100 mm (Bigras et al. 1995).

Although polygonal terrain is widespread throughout Axel Heiberg Island, the four sites near the mouth of Expedition Fjord were selected based on geomorphological considerations after a preliminary reconnaissance field campaign in 2005.

Specifically, the sites chosen display differing morphologies, but are located in extremely close proximity to each other (three of the four are separated by <1 km, while the fourth is <10 km away). Such a small geographical range removes variation in the two primary factors known to affect polygon geometry: surface age (Sletten et al. 2003) and climate (Mackay 1999).

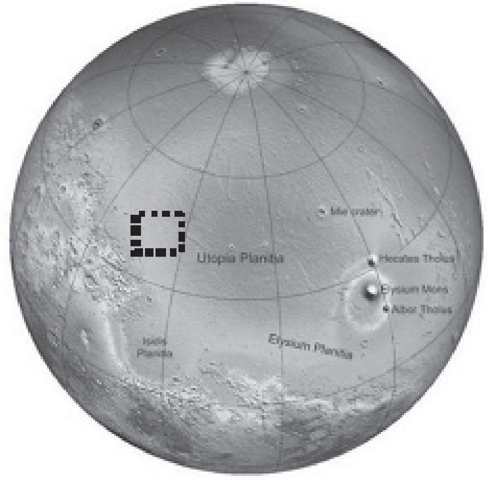

Figure 2: Topographic map of Mars centered on Utopia Planitia based on Mars Orbiter Laser Altimeter (MOLA) data. Dashed inset represents approximate region of interest for current study (Credit: MOLA Science Team, NASA, MOLA image gallery).

Methodology

Data collection

(a) Mars imagery

A systematic survey of all available Mars Global Surveyor MOC Narrow Angle images was performed for the region within Utopia Planitia between 80–90E and 40–50N. Images were downloaded from the online MOC database and visually inspected for the presence of polygonal terrain. The images selected represent a broad diversity of polygon morphologies, and thus are an ideal template upon which to examine the applicability of a statistical technique to detect and quantify geometrical variation. Of the 52 images on which polygonal terrain was identified, a subset of 22 images between 80–90E and 40–45N were selected for spatial analysis.

(b) Aerial photography

Prior to aerial photograph collection, the field sites were prepared by demarcating transects on the ground with a series of Ground Control Points (GCP)—a series of brightly colored markers that are easily identifiable on the photos. Depending on the width of the area required to be imaged, four to six transects spaced 40m apart were lined with alternating brightly-colored ground markers to provide readily visible flightlines for the helicopter pilot.

Vertical aerial photographs were taken from the helicopter using a Nikon D200 digital SLR camera equipped with a 50 mm Zoom-Nikkor lens. Images taken from an altitude of approximately 300 m resulted in image widths of approximately 100 m at sub-decimeter resolution. Between 15 and 20 photos were collected per transect, totaling 75–100 individual images per site.

(c) GPS surveys

A Trimble 5700 differential Global Positioning System (dGPS) was used to measure the spatial coordinates of the GCPs and selected polygon trough intersection point using the Post-Processed Kinematic survey method (Lantuit & Pollard 2005). Standard coordinate correction algorithms were applied using Trimble's TG-Office software. Processed dGPS coordinates were subsequently used to spatially reference the aerial images (see *Data analysis* section).

Data analysis

(a) MOC image processing

Each MOC image was imported into a Geographic Information System (GIS; ArcMap 9.1) and placed within an arbitrary coordinate system (units=meters); x-y coordinates of (0.00, 0.00) were assigned to the bottom left-hand corner of the image, while the remaining three corners were scaled according to the image height and width provided in the file's metadata.

Because of temporal and computational constraints, it was infeasible to perform the spatial analysis on the entire MOC image. Therefore, an initial visual inspection was performed in order to designate a representative area of the observed polygonal terrain. Within the selected area, all discernible polygon trough intersections were manually identified and digitized. Coordinates of the digitized points were exported and used for the statistical analysis.

(b) Aerial photo processing

Individual photos were imported into the GIS to be spatially referenced. Processed dGPS coordinates were assigned to the corresponding point on the images, causing the photos to be stretched and rotated to be oriented within Universal Transverse Mercator coordinate space. By performing this "georeferencing" on all images for a given site, an oriented and scaled photo mosaic was produced. Finally, all trough intersection points were manually digitized, with the coordinates exported for spatial analysis.

(c) Spatial point pattern analysis

A full explanation of spatial point patterns is provided by Diggle (2003). Tables of x-y coordinates for both the MOC and field images were analyzed using a customized code written for the statistical software package SAS. After the analysis area was defined, the analysis yields two key outputs: (1) a range of predicted nearest-neighbor distances (NND) that would satisfy the null hypothesis of a completely random distribution, and; (2) a table of observed NND for each trough intersection point.

By plotting a cumulative frequency distribution curve of the observed NND values, it is possible to determine whether the observed spatial distribution of trough intersection points is clustered, random, or regular, and the degree to which they are so designated.

Results and Discussion

Distribution of polygonal terrain in Utopia Planitia

Locations displaying polygonal terrain are spread quite evenly throughout the area within the transition zone grading from the cratered uplands to the basin below (Fig. 3a). Although the simple *occurrence* of polygons is widespread in the entire study area, the appearance of polygons in conjunction with other thermokarst features may be a function of surface elevation.

Specifically, the majority of instances where polygons appear independently of other features are found at higher elevations (lower left portion of Fig. 3a-c), with 10 of 14 cases found well above the basin floor. Furthermore, polygons in the vicinity of scalloped terrain appear primarily at lower elevations than do those found containing pitted chains. It is unsurprising, then, that a band of images displaying *both* pits and scallops is located in the zones of intermediate elevation.

Spatial point patterns of Utopia Planitia polygons

A great variation in polygon size is displayed clearly amongst the assorted terrains throughout the study area, with median NND span from 25.5 m to 64.4 m (Fig. 3b). The overall range of NND varied greatly as well, with minimum values ranging from 15.1 m to 32.8 and maximum values ranging from to 39.6 to 154.2 m.

A diversity of morphology is also evidenced by an examination of the observed spatial point patterns. Of particular interest is the recognition that in no cases are the observed patterns clustered; rather, the sites display varying degrees of randomness and regularity (Fig. 3c).

Sites were determined to be "primarily random" if at least 50% of the observed NND fell within the envelope predicted by the spatial point pattern analysis to satisfy the null hypothesis of complete randomness. Sites were identified as "mixed" if between 25% and 50% of the observed points satisfied this requirement and "primarily regular" if less than 25% of the observed NND satisfied the requirement.

In general, the majority of sites that displayed primarily regular patterns possessed the lowest median NND values

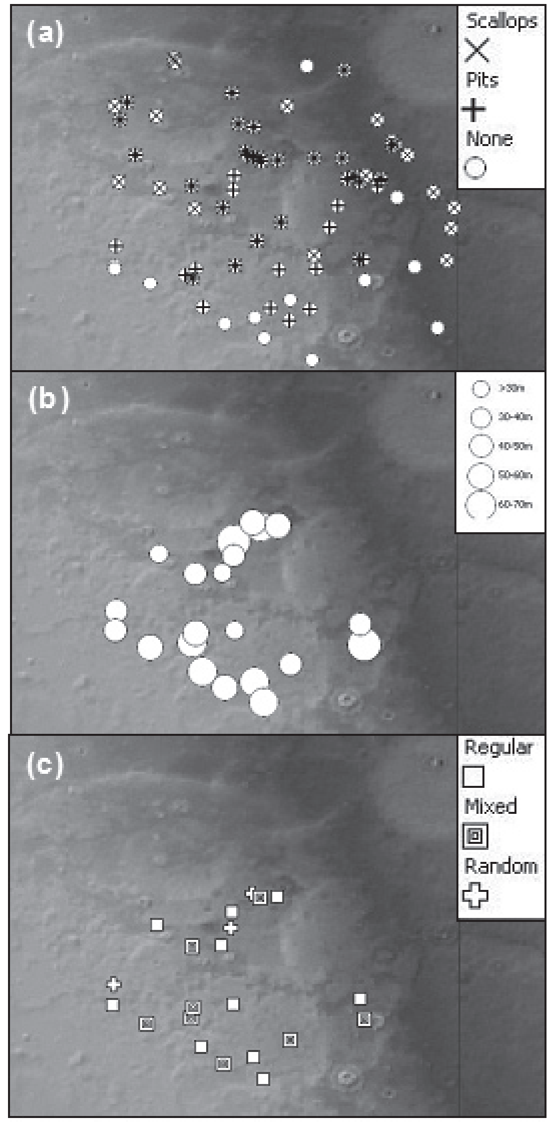

Figure 3: (a) Occurrence of polygonal terrain in relation to other periglacial features; (b) Median NND and (c) observed spatial point pattern of polygonal terrain field.

(averaging approximately 30 m), indicating that smaller polygons tend to be more regular. Conversely, the three sites determined to be primarily random had average median NND values of 40 m. Thus, a positive relationship can be inferred between polygon size and randomness of the network's geometry.

More trends emerge when comparing the observed spatial point patterns to proximity to other landforms. In particular, it is interesting to note that all three of the sites displaying primarily random geometry are found in conjunction with the pitted chains. In only one case each were pits found for sites with regular or mixed geometry, respectively. In addition, all sites that displayed scalloped terrain were found to contain regular patterning. No clear trend was apparent for sites with polygonal terrain appearing in the absence of other landscape features, having virtually an equal number of instances that were considered either mixed (5/9) or regular (4/9).

Spatial point patterns of Axel Heiberg polygons

As with the MOC images discussed above, size variation is displayed with the terrestrial polygons. It appears, though, that the terrestrial polygons are somewhat smaller. Median NND values range from 6.2 m to 19.5 m. Minimum NND values are comparable for the 4 sites, ranging from 2.2 m to 5.3 m; maximum NND values vary greatly, ranging from 15.2 m to 110 m.

Similar to the MOC images, in no cases did the terrestrial sites display a clustered distribution. However, while the MOC images tended mostly to vary between regular and random distributions, two of the four terrestrial sites were considered completely random.

It appears that a decrease in overall randomness occurs with decreasing polygon size for the field sites. Specifically, the two sites that were completely random had larger median NND than did the primarily regular sites.

Factors influencing polygon morphology

For both Martian and terrestrial polygonal terrain, spatial point pattern analysis was able to quantify variations in observed polygon morphologies. In both cases, polygons with smaller NND tended to be more regular, with increasing randomization occurring as the NND became greater. It is possible, then, that similar processes are responsible for polygon formation on both planets.

The two most well-documented factors influencing polygonal geometry are the surrounding climate (Mackay, 1999) and the amount of time that the polygons have been developing (Sletten et al. 2003). Given that the Utopia sites spanned a reasonably large range of elevation, it is evident that both climate and surface age of each site may not have been constant. As a result, it plausible that climate and age determinants may be responsible for the variations in observed polygonal size and regularity.

However, the same cannot be said for the Axel Heiberg sites. Because the polygonal terrain fields examined in this study are located so close together, climatic forcing would necessarily have been equal for each. Moreover, because their elevations are <10 m of each other, the estimated emergence age of the sites would also be virtually equal. Therefore, it is evident that some other factor must be responsible for the variation in observed morphologies.

We believe that substrate material may be as important as climate and age in determining the appearance of the polygons. Although polygonal terrain can develop in any type of ice-bonded sediment (Black 1974), varying substrate types have different rheological properties (Sletten et al. 2003). Namely, a soil's thermal contraction coefficient dictates the ground's response to thermally induced stresses (Lachenbruch 1962), and thus it will also determine the dimensions of the tension cracks and the rate and magnitude of surface sediment redistribution.

After a qualitative examination, it is possible that the sites' sediment distributions can be correlated with the polygonal morphology. In general, a decrease in maximum sediment size is associated with both a decrease in nearest neighbour distance and an increase in polygon regularity.

The use of spatial point patterns to analyze the distribution of trough intersection points may yield insight into the effects of age and substrate. As described by Lachenbruch (1962), the spacing of cracks depends on the local strength of the material and on the ground's ability to dissipate stress through the cracking process. Given that cracks initiate at local weaknesses that, theoretically, are randomly distributed throughout a particular field site, the earliest cracks to form (and thus the earliest intersections) should also be randomly distributed. Therefore, observations of random spatial distributions may indicate that the polygonal terrain under investigation is relatively young.

Similarly, point patterns may also be reflective of subsurface grain size distribution. Because cracking initiates at weaknesses, it is plausible that a more heterogeneous substrate would contain more randomly distributed points of weakness. Conversely, a more homogeneous substrate should have a more regular distribution of weaknesses. By using trough intersections as proxy indicators of the cumulative stress field that has acted over time on the site, more regular spatial point patterns may be used to infer a more uniform distribution of grain sizes in the ground.

Summary and Conclusions

The occurrence of polygonal terrain within Utopia Planitia, Mars, was characterized according to: (i) elevation; (ii) proximity to other landforms possibly indicative of ground ice, and; (iii) randomness/regularity of the spatial distribution of trough intersections.

Polygons found independently of other features tend to be located at the highest elevations, while polygons found within scalloped terrain tends to be located at lower elevations that those containing thermokarst pits. Generally, polygons within scalloped terrain are more regular than those found within pitted terrain.

Certain similarities were observed between terrestrial and Martian polygonal terrain. On both Earth and Mars, the polygons examined displayed varying degrees of regularity and randomness, but in no cases were the observed patterns considered statistically clustered.

Polygon "regularity" was found overall to have a negative relationship with polygon size. By examining the terrestrial analogue sites, a relationship was found between surface sediment size and the observed spatial point patterns. At the field sites, larger sediments were associated with larger, more irregular polygons. It is possible that similar characteristics could be evident on Mars.

The techniques outlined in this research can be applied to thousands of MOC images displaying polygonal terrain on the Martian surface, and would likely be even more effective on incoming HiRISE images. Potentially, spatial point patterns could be used to classify polygons found throughout the planet and provide a common platform by which to compare numerically the patterns observed on Mars and Earth.

Acknowledgments

Funding for this work was provided by the Canadian Space Agency's CARN program, NSERC, and ArcticNet. Logistical support in the field was provided by the Polar Continental Shelf Project (PCSP). Many thanks to Maude Oullet, Bimal Patel, and Geoff Pearce for painstakingly examining the MOC database in search of polygons. Finally, the authors acknowledge the use of the Mars Orbiter Camera images processed by Malin Space Science Systems that are available at http://www.msss.com/moc_gallery/.

References

Black, R.F. 1974. Ice-wedge polygons of northern Alaska. In D. Coates (ed.) *Glacial Geomorphology*. Binghampton, NY: State University of New York, 247-275.

Bigras, C., Bilz, M., Grattan, D.W. & Gruchy, C. 1995. Erosion of the geodetic hills fossil forest, Axel Heiberg Island, Northwest Territories. *Arctic*, 48(4): 342-353.

Boynton, W.V. & the GRS Team. 2002. Distribution of hydrogen in the near-surface of Mars: Evidence for subsurface ice deposits. *Science*, 297: 81-85.

Carr, M.H. & Schaber, G.G. 1977. Martian permafrost features. *Journal of Geophysical Research* 82: 4,039-4,054.

Costard F.M. & Kargel, J.S. 1995. Outwash plains and thermokarst on Mars. *Icarus* 114: 93-112.

Diggle, O. 2003. *Statistical Analysis of Spatial Point Patterns*. London, UK: Arnold.

French, H.M. 1996. *The Periglacial Environment*. Longman Group, Essex: 341pp.

Haltigin, T.W., Osinski, G.R., Pollard, W.H. & Dutilleul, P. 2007. Using spatial point patterns to quantify polar desert polygonal geometry. *Lunar and Planetary Science* XXXVIII: Abstract 1635.

Isaev, V.S. & Abramenko, O.N. 2003. Demonstration of polygonal ice-wedges [*sic*] terrain on the Tazovsky Peninsula in the Weastern [*sic*] Siberia and some polygonal patterns on the [*sic*] Mars. *Microsymposium on Comparative Planetology* 38, MS001, 1-2.

Kuzmin, R.O. & Zabalueva, E.V. 2003. Polygonal terrains on Mars: Preliminary results of global mapping of their spatial distribution. *Lunar and Planetary Science*, XXXIV: Abstract 1912.

Lachenbruch, A.H. 1962. Mechanics of thermal contraction cracks and ice-wedge polygons in permafrost. *Special paper to the Geological Society of America* 70: 69pp.

Lane, M.D. & Christensen, P.R. 2000. Convection in a catastrophic flood deposit as the mechanism for giant polygons on Mars. *Journal of Geophysical Research* 105: 17,617-17,627.

Langsdorf, E.L. & Britt, D.T. 2004. Periglacial processes in the southern hemisphere of Mars. *Lunar and Planetary Science* XXXV: Abstract 2115.

Lantuit, H. & Pollard, W.H. 2005. Temporal stereophotogrammetric analysis of retrogressive thaw slumps on Herschel Island, Yukon Territory. *Natural Hazards and Earth System Sciences* 5: 413-423.

Mackay, J.R. 1999. Periglacial features developed on the exposed lake bottoms of seven lakes that drained rapidly after 1950, Tuktoyaktuk Peninsula area, Western Arctic coast, Canada. *Permafrost and Periglacial Processes* 10: 39-63.

Mackay, J.R. 2000. Thermally induced movements in ice-wedge polygons, Western Arctic Coast: A long-term study. *Geographie Physique et Quaternaire* 54(1): 41-68.

Mangold, N. 2005. High latitude patterned grounds on Mars: Classification, distribution and climatic control. *Icarus* 174: 336-359.

Mangold, N., Maurice, S., Feldman, W.C., Costard, F. & Forget, F. 2004. Spatial relationships between patterned ground and ground ice detected by the Neutron Spectrometer on Mars. *Journal of Geophysical Research* 109(E08001).

Mellon. M.T. 1997a. Thermal contraction cracks in Martian permafrost: Implications for small-scale polygonal features. *Lunar and Planetary Science* (XXVIII): Abstract 1495.

Mellon, M.T. 1997b. Small-scale polygonal features on Mars: Seasonal thermal contraction cracks in permafrost. *Journal of Geophysical Research* 102(E11): 25,617-25,628.

Pewe, T.L. 1966. Ice wedges in Alaska – classification, distribution, and climatic significance. In *International Permafrost Conference Proceedings*: pp.76-81. *NAS-NRC Publication 1287*, National Academy of Science, Washington DC.

Plug, L.J. & Werner, B.T. 2001. Fracture networks in frozen ground. *Journal of Geophysical Research*, 106(B5): 8,599-8,613.

Rossbacher, L.A. 1986. Nearest-neighbour analysis: A technique for quantitative evaluation of polygonal ground patterns. *Geografiska Annaler, Series A, Physical Geography* 68(1/2): 101-105.

Seibert, N.M. & Kargel, J.S. 2001. Small-scale Martian polygonal terrain: Implications for liquid surface water. *Geophysical Research Letters* 28(5): 899-902.

Sletten, R.S., Hallet, B. & Fletcher, R.C. 2003. Resurfacing time of terrestrial surfaces by the formation and maturation of polygonal patterned ground. *Journal of Geophysical Research*, 108(E4): 8044, doi:10.1029/2002JE001914.

Soare R. J., Kargel J. S., Osinski G. R. & Costard F. 2007. Gully formation, periglacial processes and evidence of near-surface ground-ice in Utopia and western Elysium Planitia. *Icarus* in press.

Yoshikawa, K. 2003. Origin of the polygons and the thickness of Vastis Borealis formation in western Utopia Planitia on Mars. *Geophysical Research Letters* 30(12): 1603, doi:10.1029/2003GL017165.

Thermal and Water Conditions of the Active Layer after the 2002 Tundra Fire, Seward Peninsula, Alaska

Koichiro Harada
School of Food, Agricultural and Environmental Sciences, Miyagi University, Sendai, Japan
Yuki Sawada
Institute of Low Temperature Science, Hokkaido University, Sapporo, Japan
Kenji Narita
Faculty of Education and Human Studies, Akita University, Akita, Japan
Masami Fukuda
Institute of Low Temperature Science, Hokkaido University, Sapporo, Japan

Abstract

In order to clarify the effects of a tundra fire on the thermal and water conditions of permafrost and active layer, field observations were carried out on the Seward Peninsula, Alaska, between 2005 and 2007, where a 2002 tundra fire had burned up to a road that acted like a firebreak. Ground temperatures at burned sites were 4°C–5°C higher than those at unburned sites. Measurements of soil water content showed no significant tendency, increase or decrease. The depth of the active layer was significantly greater on the burned (60 cm) than the unburned (40 cm) side of the firebreak in 2005 and 2006. In 2007 the depths were 80 cm and 50 cm, respectively. The effect of fire on permafrost reaches only to the layer near ground surface, the active layer or upper part of the permafrost. Apparent electrical resistivity values up to 1 m at burned sites were relatively low. Resistivity values of unfrozen mineral soil in the active layer were calculated, and there was no significant difference of unfrozen soil between burned and unburned sites. The variation of calculated resistivity was small at burned sites, which may show the small variation of water content along the survey line due to the fire.

Keywords: active layer; permafrost; resistivity; wildfire.

Introduction

Due to its heat and disappearance of vegetation in the Arctic, wildfire affects the ground surface condition of permafrost and may cause its degradation. This degradation yields the emission of methane gas from the permafrost, which furthers global warming. Due to predicted warmer and dryer summers the area burned by tundra fire is expected to increase by as much as twice (Rupp et al. 2000), although current tundra fire activity is less frequent than the wildfires in boreal forests (Racine et al. 1985). Tundra fire disturbance and corresponding vegetation changes bring heat balance on the ground surface, and these may yield degradation of permafrost (Racine et al. 2004).

On the Seward Peninsula, large tundra fires occurred in 1971, 1997, and 2002, and a discontinuous permafrost area burned widely near the Kougarok River. In this area permafrost surveys were carried out in 2005, 2006, and 2007. The final goal of this study is to clarify effects of tundra fire on the thermal and water conditions of permafrost and active layer, and on vegetation recovery.

Study Area

Field observations were carried out in the Kougarok region, interior Seward Peninsula, Alaska (Fig. 1). There permafrost is discontinuously distributed and is considered to be sensitive to global and local climate changes. Mean annual air temperatures measured in this area range between –2.9°C and –5.5°C in 2000–2006 (Liljedahl et al. 2007).

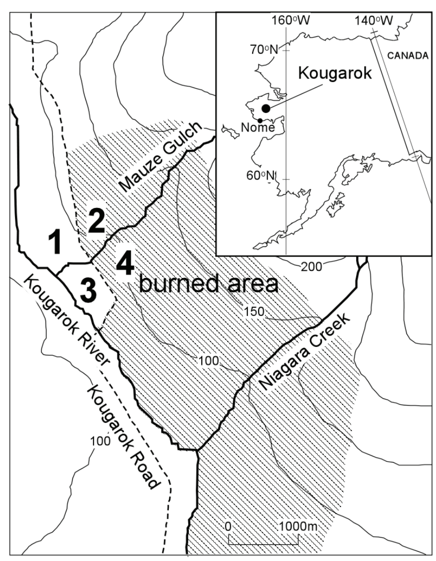

Figure 1. Location map of study sites.

In 2002, a wildfire occurred near Niagara Creek and Meuze Gulch. The fire began to burn at the east side of Kougarok Road and was stopped by the road, so the west side of the road did not burn and was considered to be undisturbed by the fire. Thus, four study sites were established near Meuze Gulch to compare the differences of thermal and moisture conditions in the active layer on the burned and unburned sides. The four sites in Figure 1 represent: unburned south-

Table 1. Average, minimum, maximum and median values of active layer thickness in 2005, 2006 and 2007.

	2005				2006				2007			
	average (cm)	minimum (cm)	maximum (cm)	median (cm)	average (cm)	minimum (cm)	maximum (cm)	median (cm)	average (cm)	minimum (cm)	maximum (cm)	median (cm)
1: US	40	24	59	40	37	24	60	34	44	28	66	44
2: BS	64	52	83	65	66	46	84	67	69	52	82	68
3: UN	40	22	62	41	39	16	66	38	52	27	79	52
4: BN	62	44	80	63	61	26	90	61	81	69	102	80

facing (Site 1: US), burned south-facing (Site 2: BS), unburned north-facing (Site 3: UN) and burned north-facing (Site 4: BN). It is assumed that vegetation cover was similar at all sites before the fire. Unburned sites (Sites 1 and 3) are now covered by tussock-shrub tundra.

Field Observations

In order to monitor present thermal and water conditions, ground temperatures, soil water contents, and thermal conductivities in the active layer were measured by pit excavations to the permafrost table at all four sites in July and August 2005, August 2006, and August 2007. The volumetric water content was measured by the TDR method, and the thermal conductivity by the thermal probe method. Depths of active layer were also measured by using a steel rod from the ground surface. We made 50 measurements within a 10 x 10 m area at each site.

Electromagnetic soundings were carried out in order to estimate the permafrost thickness in August 2005, which was 20–30 m at north-facing sites (Sites 3 and 4), but was not detected at south-facing sites (Sites 1 and 2) due to the shallow bedrock (Sawada et al. 2005).

Electrical resistivity values of the active layer and upper part of the permafrost (1 m deep) were obtained using the DC electrical sounding method. 2D measurements were conducted at all four sites. The electrode interval, the maximum depth, and the length of survey line were set to 1 m, 5 m, and 29 m, respectively.

Observational Results

In Figure 2, typical soil profiles to the permafrost table, obtained from pit surveys conducted in August 2007 at each site, are shown. The mineral soil consists mainly of clayey soil. The thickness of the organic layer ranges widely between 0 cm and 30 cm at each site.

The significant difference between burned and unburned sites is the presence or absence of a moss layer. The moss layer is not present at burned sites due to the fire. The thermal conductivities measured in 2007 in the moss, organic, and mineral layers were 0.1–0.5 W/mK, 0.3–1.2 W/mK and 0.5–1.3 W/mK, respectively. As the moss layer has a low thermal conductivity, this layer has an important role as a heat insulator and controls the depth of the active layer.

Thus, the measured active layer thicknesses were significantly different between the burned and unburned sites, about 60 cm and 40 cm in 2005 and 2006, and about 80 cm and 50 cm in 2007 (Table 1). Statistical analyses were also made and showed the availability of data (not shown

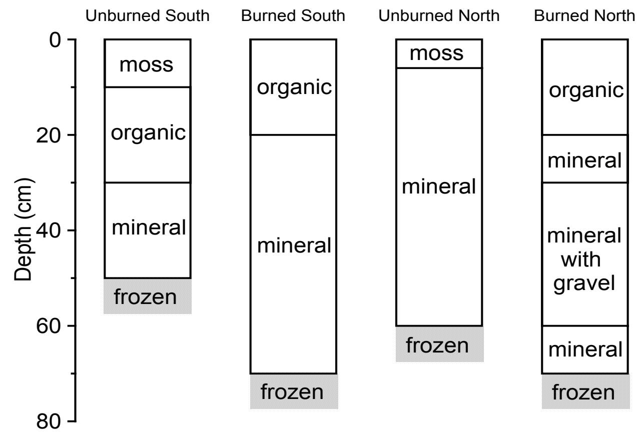

Figure 2. Typical soil profile at four sites in study area.

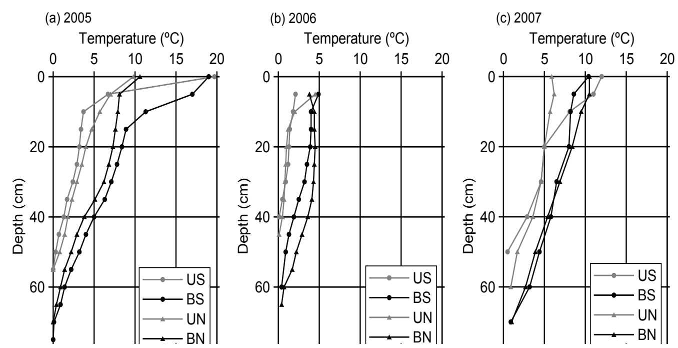

Figure 3. Ground temperature profiles in (a) 2005, (b) 2006 and (c) 2007.

here). The thickness at the burned sites was more than 20cm deeper than that at the unburned sites. This deep active layer at the burned sites was caused by the lack of the moss layer. Comparing the active layer thickness in 2005 and 2006, there is no significant increase. However, the thickness in 2007 at north-facing sites was more than 10–20 cm deeper than those in 2005 or 2006.

Figure 3 shows the ground temperature profiles measured using soil pits. The ground temperatures at the burned sites (black lines in Fig. 3) were 4°C–5°C higher than those at the unburned sites (gray lines in Fig. 3). The volumetric water contents of soil at the burned sites were higher than those at the unburned sites in 2005, but lower in 2006 (Fig. 4). The data observed in 2007 was complicated, and may have been affected by the rain fall just before the observations.

Apparent resistivity values up to 1 m deep obtained from 2D soundings conducted in 2006 are shown in Figure 5. There is an obvious difference between the burned and unburned sites. The apparent resistivity value at the burned sites was much lower than at the unburned sites.

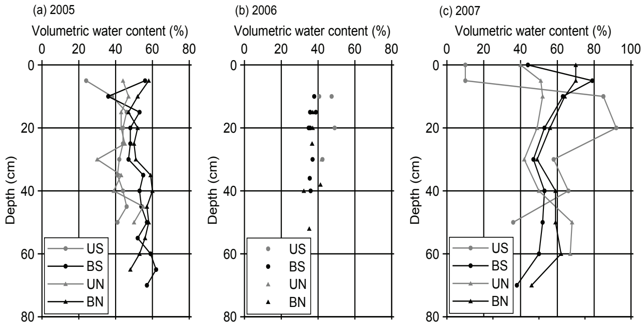

Figure 4. Volumetric water content at study sites in (a) 2005, (b) 2006 (point measurement) and (c) 2007.

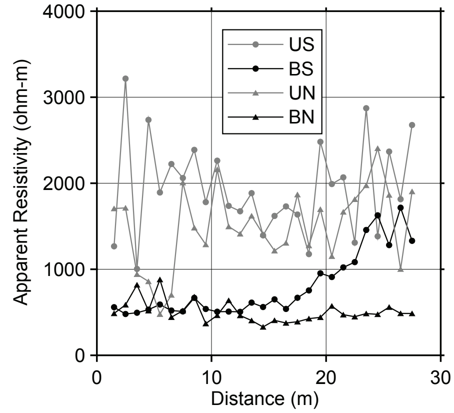

Figure 5. Apparent resistivity values up to 1 m deep along the 2D electrical sounding line conducted in August 2006. Horizontal axis shows the distance from the starting point of electrical sounding.

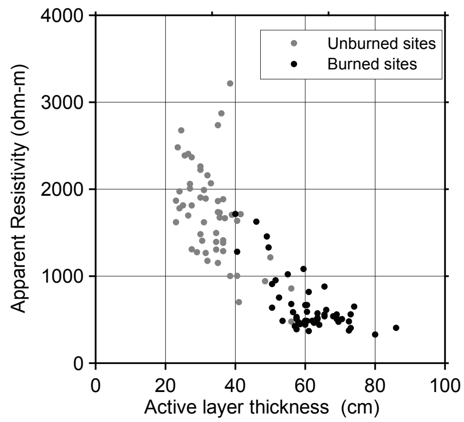

Figure 6. Relationship between active layer thickness and apparent resistivity measured in August 2006.

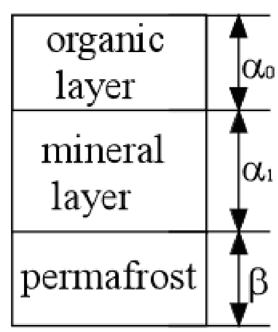

Figure 7. Estimation model for resistivity of unfrozen mineral layer.

Discussion

After the tundra fire, the thickness and ground temperature of the active layer at burned sites changed drastically due to the destruction of the surface moss layer. However, it is estimated that permafrost thickness has not changed between the burned and unburned sites (Sawada et al. 2005). These results suggest that the effect of fire on permafrost reaches only to the layer near ground surface, the active layer or upper part of the permafrost. In future, the active layer thickness may increase year by year, or the increase of active layer thickness will stop after recovery of surface vegetation. Thus, a continuous monitoring of ground temperature and a numerical calculation is needed to clarify the effect of fire on permafrost.

In 2007, the active layer thickness increased more than 10–20 cm, and this result with the other data (e.g. air temperature) should be discussed, but has yet to be. And more measurement will be needed to clarify the change of thickness of the active layer after a wildfire.

After the tundra fire, no significant tendency of change of water content was observed in this area, there was no drastic increase or decrease. As the water content is also an important factor in solving the permafrost's degradation or recovery, it is also necessary to measure water content continuously.

Here, as a resistivity value of soil depends on soil water content (e.g. Harada and Fukuda 2000), an estimation of the water condition was made using measured apparent resistivity values. Generally, an apparent resistivity value obtained from the DC sounding is produced from the combination of a true resistivity value and the thickness of the layer. In this study, relative low apparent resistivity values were obtained at the burned sites (Fig. 5). As a resistivity value of soil also depends on temperature, and the value of resistivity in the active layer or unfrozen material is conductive (e.g. Harada and Fukuda 2000), a thick active layer condition shows a low apparent resistivity value (Fig. 6). An apparent resistivity value strongly depends on the thickness of the active layer, so this apparent resistivity value does not affect the true resistivity value in the active layer directly.

In order to obtain the true resistivity value of the unfrozen mineral layer in the active layer, a simple calculation was carried out using the apparent resistivity value measured in 2006. The model used here is shown in Figure 7, and it was assumed that an apparent resistivity up to 1m, ρ_a, was produced from a resistivity value and thickness of each layer shown in Fig. 7, unfrozen organic layer, unfrozen mineral layer and permafrost,

$$\frac{1}{\rho_a} = \frac{\alpha_0}{\rho_0} + \frac{\alpha_1}{\rho_1} + \frac{\beta}{\rho_2} \qquad (1)$$

$$\alpha_0 + \alpha_1 + \beta = 1 ,$$

where ρ_0, ρ_1, and ρ_2 are true resistivity of the organic layer,

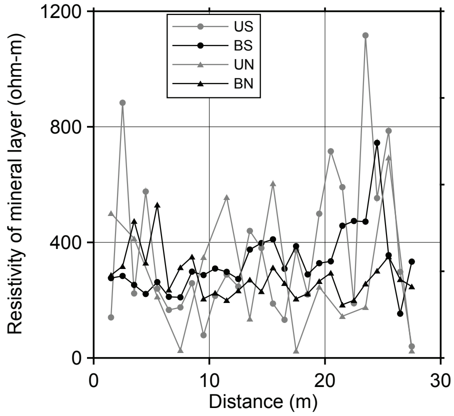

Figure 8. Estimated resistivity value of unfrozen mineral layer in 2006.

the mineral layer, and the permafrost, and α_0, α_1, and β are the thickness of each layer, respectively. Here, ρ_0 and ρ_2 were given as assumed values of 5000 and 10,000 ohm-m, respectively, and α_0, α_1, and β were given using measured thickness values were used. Then, the true resistivity value of unfrozen mineral layer ρ_1 was estimated using equation (1).

Figure 8 shows the calculated result of the true resistivity value of the unfrozen mineral layer in 2006. Comparing calculated values between the burned and unburned sites, there was no significant difference of the unfrozen mineral soil. Furthermore, the values ranged widely at the unburned sites, and a variation of resistivity was small at the burned sites. This may show the small variation of water content along the survey line due to the fire. In the future, a calibration between soil water content and resistivity will made, and this model will be developed to monitor the ground water content using the DC electrical sounding method.

Conclusions

Permafrost surveys were carried out in order to monitor the permafrost conditions after a wildfire at the discontinuous permafrost area on the Seward Peninsula, Alaska.

After a 2002 tundra fire, thermal conditions of the active layer at the burned sites changed drastically due to the destruction of the surface moss layer. The measured active layer thicknesses were significantly different between the burned and unburned sites, by more than 20 cm. There is no obvious increasing of the thickness between 2005 and 2006, however, the thickness in 2007 at north-facing sites was more than 10–20 cm deeper than those in 2005 or 2006.

The effect of fire on permafrost reaches only to the layer near ground surface, the active layer, or the upper part of permafrost.

The ground temperatures at the burned sites were 4°C–5°C higher than those at the unburned sites. Measurements of soil water content show no significant tendency, increasing or decreasing.

Measured apparent resistivity values at the burned sites show a lower value than those at the unburned sites, which was caused by the thick active layer. Using the estimation model, the true resistivity value of the unfrozen mineral layer was calculated, and there was no significant difference between burned and unburned sites. The resistivity values ranged widely at unburned sites, and the variation of resistivity was small at burned sites, which may show the small variation of water content along the survey line due to the fire.

Acknowledgments

We would like to express our sincere thanks to Prof. L. Hinzman, R. Busey, A. Liljedahl, and K. Yoshikawa of the University of Alaska Fairbanks for their support with the fieldwork. This research was financially supported by the Japan Aerospace Exploration Agency.

References

Harada, K. & Fukuda, M. 2000. Characteristics of the electrical resistivity of frozen soils. *Seppyo* 62: 15-22 (in Japanese with English Abstract).

Liljedahl, A., Hinzman, L., Busey, R. & Yoshikawa, K. 2007. Physical short-term changes after a tussock tundra fire, Seward Peninsula, Alaska. *Journal of Geophysical Research* 112: F02S07, doi: 10.1029/2006JF000554.

Racine, C.H., Patterson III, W.A. & Dennis, J.G. 1985. Tundra fire regimes in the Noatak River Watershed, Alaska: 1956–1983. *Arctic* 38: 194-200.

Racine, C.H., Jandt, R., Meyers, C. & Dennis, J. 2004. Tundra fire and vegetation change along a hillslope on the Seward Peninsula, Alaska, U.S.A. *Arctic, Antarctic, and Alpine Research* 36: 1-10.

Rupp, T.S., Chapin III, F.S. & Starfield, A.M. 2000. Response of subarctic vegetation to transient climatic change on the Seward Peninsula in north-west Alaska. *Global Change Biology* 6: 541-555.

Sawada, Y., Harada, K., Hinzman, L.D. & Fukuda, M. 2005. Permafrost degradation after the tundra fire in Seward Peninsula, Alaska - a perennial study-. *Proceedings of the 6th International Conference on Global Change: Connection to the Arctic (GCCA-6), Tokyo, Japan, December 12-13, 2005*: 148-151.

The Fate of Terrestrial Carbon Following Permafrost Degradation: Detecting Changes Over Recent Decades

Jennifer W. Harden and Christopher C. Fuller
U.S. Geological Survey, Menlo Park CA, USA

Martin Wilmking
University Greifswald, Greifswald, Germany

Isla Myers-Smith
University of Alberta, Edmonton, Alberta, Canada

Susan E. Trumbore
Univ. California, Irvine, CA, U.S.A.

Jill Bubier
Mount Holyoke College, South Hadley, MA, USA

Abstract

As boreal and arctic regions of North America have been undergoing considerable warming since the 1950s, a key question remains as to the fate of permafrost and carbon over this important time period. We used ^{137}Cs as an age constraint for soil carbon that has accumulated since the first occurrence of ^{137}Cs in 1954. We tested this approach by comparing profiles of $\Delta^{14}C$ to ^{137}Cs for soils of different plant communities near Delta Junction, central Alaska. Both isotopes indicate upward accumulating, organic systems that have little evidence for mixing or leaching. We then used inventories of these isotopes to normalize the C storage between frozen and thawed site-pairs. To date, we identified a net loss of carbon from a tundra-forest transition in northern Alaska. We measured net increases of C resulting from forest-bog and forest-fen transition in Alaska and Canada.

Keywords: boreal; carbon storage**;** discontinuous permafrost zone; peat; permafrost; soil carbon; thermokarst.

Introduction

Boreal regions in general and central Alaska in particular, encompass a broad range of ecosystems that are underlain by permafrost. There is an abundance of upland terrain with sporadic or discontinuous permafrost. Lowland terrain is also underlain by discontinuous permafrost, often with thicker peat deposits and ice-rich permafrost. Further nested within these landscapes are highly patchy vegetation and soil conditions that result from frequent fires. In central Alaska, recent results indicate that 7% of the landscape has undergone thermokarst, 47% has permafrost, 27% is unfrozen without a recent permafrost history, and 19% of the area has an uncertain thermal status (Jorgenson et al. 2005).

Permafrost degradation has been observed for the past decades when remotely-sensed and field observations have noted associated changes in vegetation (Vitt et al. 2000; Camill et al. 2001, Jorgenson et al. 2001, Turetsky et al. 2002, Christensen et al. 2004). Changes in air temperature, ground ice content, winter snowfall, and fire contribute to stabilization and destabilization of near-surface permafrost (Osterkamp & Romanovsky 1999). Discontinuous permafrost in Alaska may by particularly sensitive to climate warming in areas where soils are not blanketed by loess and ice-rich seasonal frost (Swanson 1996). Since 1949, thermokarst in the Tanana floodplain of Interior Alaska has increased by 21% and may result in the disappearance of permafrost in these landscapes (Jorgenson et al. 2001).

Thawing of near-surface permafrost has been associated with changes in patterned ground (Osterkamp et al. 2000) and conversion of forests to wetlands (Osterkamp et al. 2000, Jorgenson et al. 2001, Jorgenson & Osterkamp 2005). Permafrost thaw can also lead to the development of an open talik, or drained soil layer, involving shifts toward drier landscapes and ecosystems, for example, from moss- to lichen-dominated ground covers (Burn, 1998, Schuur et al, 2007).

Recent changes in northern climate systems have led to a piqued awareness of carbon stocks residing in near-surface permafrost and of their vulnerabilities to climate change. Since the 1960s, significant changes in air and surface temperatures have been documented for northern regions (see http://www.gtnp.org/pdf/icoppostergtnp). Upon significant warming, permafrost degradation can lead to either net accumulation or loss of carbon via shifts in ecosystems and C processing, and it is likely that both effects occur concurrently, yet heterogeneously, across the landscape. Evidence for net increases in carbon resulting from thermokarst, for example, include wetlands (Turetsky et al. 2007). Conversely, in systems that are becoming drier, there is the potential for aerobic respiration to reduce terrestrial carbon stocks.

Detecting changes in C storage using trace gas exchange requires long-term monitoring to decipher interannual variations from significant trends (Dunn et al. 2007). CO_2 budgets are particularly problematic because sources of respiration are numerous, and because detecting small changes in decomposition relative to large signals of

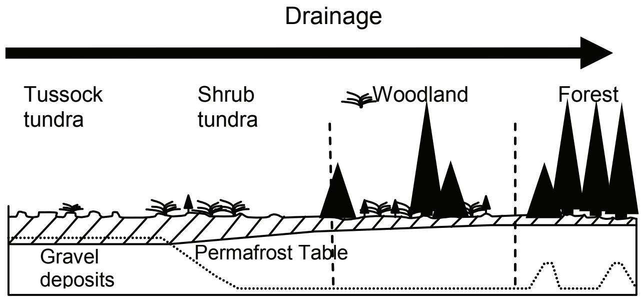

Figure 1a. Schematic drawing of permafrost degradation leading to drainage. Active layer in tundra on floodplain terrace deepens and leads to drainage of water through gravel deposits. Based on Wilmking et al. 2006.

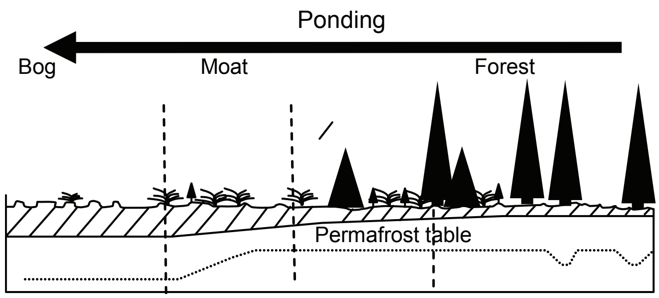

Figure 1b. Example of permafrost degradation leading to ponding. Based on Meyers-Smith et al. 2007.

respiration is difficult. Detecting changes in the solid carbon phase (e.g., vegetation and soil) is also challenging, owing largely to long-term variations in frozen ground, plant cover, and fire history (Harden et al. 2000).

Significantly, the recent warming trend in northern latitudes has been accompanied by atmospheric labeling by radiocarbon and radiocesium as a result of aboveground weapons testing. Such labeling of organic matter lends itself to assessments of carbon that has been fixed in recent decades. In context of landscape changes, such assessments can help to decipher the fate of carbon in the recent phase of northern latitude warming.

Approach

In Interior Alaska, the fate of terrestrial carbon over the next few decades likely will be determined by shifts in hydrology following permafrost thaw. Water plays a critical role in governing C cycling processes, including plant production (NPP), combustion (F), decomposition (kC or Rh), and leaching (DOC). Our goal is to test this hypothesis at the site scale, using radioisotopes of carbon and cesium to identify carbon stored in the past 50 years.

We examined a variety of ecosystems in Interior Alaska and northern Canada, including black spruce forests, tussock tundra, *Sphagnum* bogs, and a rich fen. We paired sites according to our interpretations of their near-surface permafrost and histories of thermokarst, and analyzed soils for radioisotopes.

Site scale measures of C stocks and isotopes are particularly helpful at establishing C accumulation rates over the last 50 years. ^{137}Cs is a product of uranium fission produced by weapons testing. The first significant atmospheric fallout occurred in 1952 with the maximum delivery occurring between 1963 and 1964. It can be used as a tracer for soil materials if the following conditions are met: (1) total cesium inventories are conserved in the soil, and (2) there is no significant movement of ^{137}Cs. These conditions are examined for a variety of soils before testing our hypotheses.

Radiocarbon was also produced by weapons testing and has been used as a tracer for carbon turnover in soils (Trumbore 2006). The main differences between Δ^{14}C and ^{137}Cs are: (1) Whereas fallout of ^{137}Cs declined precipitously after 1963, fallout of Delta^{14}C declined slowly owing to terrestrial C exchange with the atmosphere and fossil fuel emissions, And (2). Whereas ^{137}Cs is conserved in soil and sediment, Delta^{14}C can be retained via slow decomposition or effective stabilization or lost via rapid decomposition or combustion. ^{137}Cs in the atmosphere is generally bound to particulates, whereas Delta^{14}C in the atmosphere is present in gas phase. Isotopes of Cs and C therefore have different input mechanisms to the land surface.

Methods

In order to test the feasibility of using these isotopes to estimate recent changes in C storage, we first examined variations in soil ^{137}Cs and ^{14}C for patterns of storage, remobilization, and accumulation. Four sites were located in Interior Alaska near Delta Junction. Vegetation at all sites contained black spruce, but varied in tree density and abundance, owing mainly to variations in soil moisture and temperature (for more detail see Manies et al. 2004). Groundcover varies from a feather moss/lichen mix to feather moss.

In order to interpret the response of C storage to thaw, we sampled organic soils at sites with and without near-surface permafrost, interpreting sites as pairs of frozen and thawed landscapes. In Manitoba, Canada a frozen palsa was found adjacent to a collapse bog, a collapse fen, and a rich fen (Bubier et al. 1998, Trumbore et al. 1999). We assumed that the collapse fen originated as part of the palsa complex based on new collapse features on the side of the palsa that slumped into the fen. There was no direct evidence that the bog or rich fen had formed directly from the palsa, but cores at 2m depth were composed of *Sphagnum* peat and woody peat.

In Alaska, we sampled organic soils at permafrost/thawed pairs of soils in two locations. In the case of sites near the Kugururok River near treeline, sites from a tundra and a forest site (Wilmking et al. 2006) were used as frozen and thawed pairs. These sites were separated by shrub and shrub tundra ecosystems that were invaded by trees over the past 40 years; a deepening active layer along the tundra-forest transition indicates a transition from moderate to well-drained soil conditions (Fig. 1a). In the case of sites along the Tanana River near Fairbanks, a forest system underlain by permafrost was directly observed to burn and within a year to collapse into a wetland bog in 2001 (Myers-Smith et al. 2007). Environmental reconstructions from charcoal and diatoms indicated previous cycles of fire-induced collapse.

We used ^{137}Cs and $\Delta^{14}C$ to identify organic matter that accumulated since about 1964, a time when atmospheric enrichment from aboveground weapons testing reached a maximum. Radiocarbon was measured on bulk organic matter at the UC Irvine W. M. Keck Carbon Cycle AMS facility (KCCAMS) and at the Lawrence Livermore Laboratory following correction and calibration procedures (Trumbore et al. 1999). Splits of the same samples were analyzed for ^{137}Cs, total ^{210}Pb and ^{226}Ra activity by gamma spectrometery at the USGS Sediment Radioisotope Laboratory in Menlo Park (Fuller et al. 1999). ^{210}Pb data is not presented and is being evaluated as a chronometer for these profiles.

For samples from both Manitoba and Alaska, we calculated inventories of radiocarbon and Cs to compare C stocks and accumulation rates represented in the upper layers of the organic soils. Inventories were calculated as:

$$\Sigma(i{*}fC{*}\ BD{*}\ th)_{horizons} \qquad (1)$$

where i is the concentration of isotope in fraction modern (^{14}C) in soil; fC is the fraction organic C used for FM only; BD is bulk density (g m^{-3}); and th is the thickness of each horizon (m).

Soil horizons labeled by bomb-enriched concentrations of isotopes are defined by concentrations >0.04 pCi/g for ^{137}Cs, which represents the detection limit of the instrument, and concentrations >FM 1.0 for radiocarbon, where FM = Delta^{14}C/1000 + 1. In the case of Alaska samples, we assumed that the bomb-enriched layers were 50 years old (sampled in 2004; enriched by fallout since 1954). In the case of Manitoba samples collected in 1994, we used radiocarbon peak 1963 to estimate peat ages of 30 years (Trumbore et al. 1999). Inventories included only organic soil horizons.

Results

Depth profiles of both isotope profiles reach maximum and pre-bomb values at approximately the same depths in each core. Maximum values in both isotopes likely represent the time around 1963, when weapons testing reached peak-output to the atmosphere (Fig. 2). Deep soil horizons with radiocarbon values <1.0 FM likely indicate pre-bomb ages. These layers are essentially free of ^{137}Cs (Fig. 2), likely indicating that Cs was not re-mobilized from shallow to deeper layers. It also is possible, but unlikely, that ^{137}Cs and radiocarbon could have mobilized in tandem.

Mean ^{137}Cs inventories were 3.3 +/- 1.3 pCi/cm2 and mean $\Delta^{14}C$ inventories were 0.6 +/- 0.2 Delta^{14}C /cm^2 (data not shown). Variability in inventory of fallout materials among ecosystems in a given region ranged from 40 to 30% of the mean inventory for ^{14}C and Cs, respectively.

C inventories in bomb-labeled soil layers

Based on the site pairing where thermokarst led to drainage, there was a 64% loss of C in the near-surface soil (Table 1, example 1). Based on the examples where thermokarst led to ponding and formation of wetlands, there was a mixed response. In Manitoba, thaw resulted in -70% (loss) to +80% (gain) in C stocks in which fens accumulated C and the bog lost C (Table 1, examples 3–7). In Alaska, C stocks increased by 11% .Based on inter-site variations in Cs stocks (above), changes less than 30% are likely not significant.

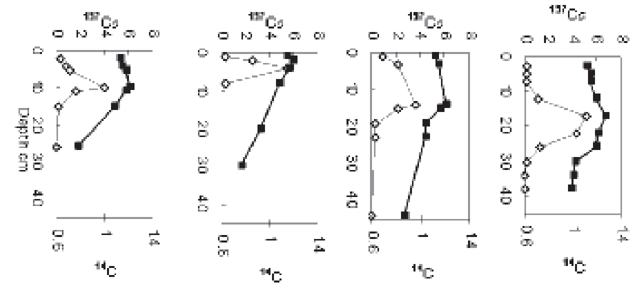

Figure 2. Radiocarbon (closed symbols) and radiocesium (open) concentrations versus basal horizon depths from 4 soils of differing ecosystem settings from the area around Delta Junction, Alaska. From left to right, profiles correspond to mature forest stands, sites DFTC6 (well-drained), DFTC23 (well-drained), DFCC15 (permafrost at ~50cm), DFDC1 (permafrost at 41 cm) from Manies et al. 2004. Samples collected in 2002. Cs measured in 2006.

Table 1. Recent soil carbon labeled with bomb-enriched isotopes and stored in pairs of frozen and unfrozen ground. Comparison 1: Frozen tundra (1Tundra) Unfrozen, drained forest soils (2Forest) based on Wilmking et al. 2006 using ^{14}C; Comparison 2: Frozen forest (3Forest) Unfrozen, ponded wetland bog (4WetlandBog) based on Myers-Smith et al, in press using ^{137}Cs. Comparison 3: Frozen palsa (5P) Unfrozen wetland bog (6WBog) Unfrozen wetland fen (7,8WFen) using ^{14}C. C stocks in g C m^{-2} Rates in gC m-2yr-1 calculated over 30 *(sites 7,8)* to 50 yrs *(sites 1–6)*.Changes calculated as difference in stock or rate between frozen and thawed state, divided by frozen state.

Site Pair		C Stock	Rate	Stock Change	Rate Change
1Frozen	1Tundra	10363	259		
Thawed	2Forest	3703	93	-64%	-64%
2Frozen	3Forest	5477	137		
Thawed	4Wetland Bog	6065	151	+11%	+11%
3Frozen	5Palsa	5413	258		
Thawed	6WetlandBog	1811	58	-67%	-77%
Thawed	7WetlandFen	9768	349	+80%	+35%
Thawed	8Wetland	9153	277	+69%	+8%

Table 2. Long-term total C stocks. Sites underscored in Table 1.

	Stock g m-2	Age Yr BP	Rate g m-2yr-1	Rate Change	Stock Change
1Tundra	19772	680	29		
2Forest	8649	635	14	-56%	-53%
3Forest	13933	585	24		
4Wetland	20701	25	84	+49%	+255%

C inventories of total soil profiles

Changes in total carbon stocks for the full soil profiles showed a net decrease in C stock where thermokarst led to drainage, and a net increase in C stocks where thermokarst resulted in wetlands.

Discussion

Based on Cs and C isotopes, it appears that either isotope may be used as labels for C that has entered the soil since about the 1950s when above-ground weapons testing introduced significant sources of ^{137}Cs and $\Delta^{14}C$. We interpret depth profiles of these isotopes (Fig. 2) as evidence for "upward accumulating" systems with little or no vertical mixing. As noted above, the soils from Delta Junction showed little or no sign that Cs was mobilized in the soil profile based on the agreement in depths where (1) peak values and (2) pre-bomb values of both ^{137}Cs and Delta^{14}C occurred. However, data from the Fairbanks site (Myers-Smith et al. in press) did show signs of remobilization in the deepest organic layers, based on a comparison to radiocarbon ages.

Albeit a preliminary finding with no replication, we found that soil C was lost (C source) where thaw water was drained and that there was a mixed response for C where thaw water was ponded. It is likely that drainage of thawed water resulted in aerobic decomposition, which outweighed plant production and resulted in a C source to the atmosphere. By contrast, where thaw resulted in ponding, changes from frozen state to anaerobic conditions for decomposition and changes in plant production may result in a mixed response, resulting in a C sink or C source.

There are at least three important limitations of this isotopic approach that limit our ability to constrain changes in carbon storage. First, mobilization of either radiocarbon or radiocesium would impact results of this approach. Input and decomposition of organic matter into and out of the soil layers causes most of the depth variations, because peaks and attenuations of both isotopes are coincident for 4 very different soil types. Nevertheless, some amount of both isotopes could move together through the profile via leaching or mixing. Second, any estimates of recent net carbon accumulation are overestimates, because C loss via decomposition of deep soil layers is not accounted for by this approach. Based on assessments by Rapalee et al. (1998), this overestimate may be quite small because decomposition rates are very slow in saturated systems. By the same logic, recent carbon losses resulting from thermokarst are underestimated, again because deep decomposition is not accounted for in this approach. Where systems are converting frozen and large C stocks to aerobic decomposition, such underestimates could be quite large. For example, turnover time in well-drained soil of 100 years applied to a carbon stock of the tundra soil of 10000 gC m^{-2} amounts to 100 gC m^{-2} yr^{-1}. Third, the time of initial thermokarst formation is not known for any of these sites. Therefore, if rates of C accumulation change over time-since-thermokarst, C accumulation rates should not be compared directly without finding a way to stratify the data according to post-thaw successional age.

In order to address these important limitations to our labeling approach, we recommend that C stocks be assessed for post-bomb labels, particularly in newly-formed thermokarst features of known age. Moreover, C inventories should be replicated for a variety of ecosystems. Methods also should be developed to account for the contribution that deep decomposition may make to offset near-surface accumulations of C. Owing to its powerful greenhouse potential and sensitivity to the water table, the role of methane in the trace gas budget of these systems will vary according to the fate of water upon thaw. For example, saturated collapse scars have significantly higher CH_4 emissions than palsas or non-permafrost wetlands (Wickand et al. 2006, Turetsky et al. 2002). As permafrost wetlands are dominant sources of CH_4, yet make up a small proportion of the total landscape, quantifying total green house gas emissions from remote sensing is a challenge that must be met for these boreal regions (Bubier et al. 2005).

Conclusions

Detection of change

Cesium and radiocarbon inventories lead us to expect 30 to 40% variability, respectively, in fallout inventories within a given region. Therefore, C stocks need to be >50% different from the control or baseline in order to be a significant detection of change. During the time period since the 1950s when the atmosphere warmed significantly, it is likely that significant soil C losses accompanied conversion of tundra to forest in our study site in Interior Alaska. By contrast, significant soil C uptake accompanied the conversion of black spruce forest to wetland in our study site in northern Manitoba.

Acknowledgments

Thanks go to Hugo Veldhuis for field insights; Ted Schuur, Peter Kuhry, and Jon O'Donnell for reviews; Ag. Canada NASA BOREAS; NSF Carbon-Water (solicitation no. NSF 06-514); and USGS (Earth Surface Dynamics Program) for funding.

References

Bubier, J.L., Crill, P.M., Moore, T.R., Savage, K. & Varner, R.K. 1998. Seasonal patterns and controls on net ecosystem CO_2 exchange in a boreal peatland complex. *Global Biogeochemical Cycles* 12: 703-714.

Bubier, J., Moore, T., Savage, K. & Crill, P. 2005. A comparison of methane flux in a boreal landscape between a dry and a wet year. *Global Biogeochemical Cycles* 19, GB1023, doi: 10.1029/2004GB002351.

Burn, C.R. 1998. The response (1958-1997) of permafrost and near-surface near-surface ground temperatures to forest fire, Takhini River valley, southern Yukon Territory. *Canadian Journal of Earth Sciences* 35(2):184-199.

Camill, P., Lynch, J.A., Clark, J.S., Adams, J.B. & Jordan, B. 2001. Changes in biomass, aboveground net primary production, and peat accumulation following permafrost thaw in the boreal peatlands of Manitoba. *Canada Ecosystems* 4: 461-478.

Christensen, T.R., Johansson, T., Åkerman, H.J., & Mastepanov, M.2004. Thawing sub-arctic permafrost: Effects on vegetation and methane emissions. *Geophys. Res. Lett.* 31: 1-4, doi 10.1029/2003GL018680.

Dunn, A.L, Barford, C.C., Wofsy, S.C., Goulden, M.L. & Daube, B.C. 2007. A long-term record of carbon exchange in a boreal black spruce forest: means, responses to interannual variability, and decadal trends. *Global Change Biology* 13(3): 577-590.

Fuller, C.C., vanGeen, A., Baskaran, M. & Anima, R. 1999. Sediment chronology in San Francisco Bay defined by 210Pb, 234Th, 137Cs, and 239,240Pu. *Marine Chemistry* 64: 7-27.

Harden, J.W., Trumbore, S.E., Stocks, B.J. Hirsch, A., Gower, S.T., O'Neill, K.P. & Kasischke. E.S. 2000. The role of fire in the boreal carbon budget. *Global Change Biology* 6(suppl.1): 174-184.

Jorgenson, M.T., Racine, C.H., Walters, J.C. & Osterkamp, T.E. 2001. Permafrost degradation and ecological changes associated with a warming climate in central Alaska. *Climatic Change* 48: 551-579.

Jorgenson, M.T. & Osterkamp, T.E. 2005. Response of boreal ecosystems to varying modes of permafrost degradation. *Can. J. Forest Res*. 35: 2100-2111.

Manies, K.L., Harden, J.W., Silva, S.R., Briggs, P.H. & Schmid, B.M. 2004. Soil data from Picea mariana stands near Delta Junction, AK of different ages and soil drainage type. U.S. Geological Survey Open File Report 2004-1271, 19 pp

Myers-Smith, I.H., Harden, J.W., Wilmking, M., Fuller, C.C., McGuire, A.D., Chapin, F.S.III. In press. Wetland succession in a permafrost collapse: interactions between fire and thermokarst. *European Biogeosciences.*

Osterkamp, T.E. & Romanovsky V.E. 1999. Evidence for warming and thawing of discontinuous permafrost in Alaska. *Permafrost Periglac*. 10: 17-37.

Osterkamp, T.E., Viereck, L., Shur, Y., Jorgenson, M.T., Racine, C., Doyle, A.,& Boone, R.D. 2000. Observations of thermokarst and its impact on boreal forests in Alaska, U.S.A. *Arctic Alpine Res*. 32: 303-315.

Rapalee, G., Trumbore, S.E., Davidson, E.A., Harden, J.W. & Velhuis, H. 1998. Scaling soil carbon stocks and fluxes at the BOREAS Northern Study Area. *Global Biogeochemical Cycles* 12(4): 687-701.

Schuur, E.A.G., Crummer, K.G., Vogel, J.G. & Mack. M.C. 2007. Plant productivity and species composition following permafrost thaw and thermokarst in Alaskan tundra. *Ecosystems,* doi:10.1007/s10021-007-9024-0.

Swanson, D.K. 1996. Susceptibility of permafrost soils to deep thaw after forest fires in Interior Alaska, U.S.A., and some ecological implications. *Arctic Alpine Res.* 28: 217-227.

Trumbore, S.E. 2006. Carbon respired by terrestrial ecosystems—recent progress and challenges. *Global Change Biology* 12: 141-153, doi:10.1111/j.1365-2486.2005.01067.x.

Trumbore, S.E., Bubier, J. Harden, J.W. & Crill, P.M. 1999. Carbon Cycling in Boreal Wetlands: A Comparison of Three Approaches. *Jour Geophys. Res. Atm.* 104: 27,673-27,682.

Turetsky, M.R., Wieder, R.K., & Vitt, D.H. 2002. Boreal peatland C fluxes under varying permafrost regimes, Soil Biol. *Biochem.* 34: 907-912.

Turetsky, M.R., Wieder, R.K., Vitt, D.H., Evans, R. & K. D. Scott. 2007. The disappearance of relict permafrost in boreal regions: effects on peatland carbon storage and fluxes. Global Change Biology 13: 1-13.

Vitt, D.H., Halsey, L.A. & Zoltai, S.C. 2000. The changing landscape of Canada's western boreal forest: the current dynamics of permafrost. *Can. J. Forest Res*. 30: 283-287.

Wickland, K.P., Striegl, R. G., Neff, J.C. & Sachs, T. 2006. Effects of permafrost melting on CO2 and CH4 exchange of a poorly drained black spruce lowland. *Jour. Geophys. Res.* 111:G02011, doi:10.1029/2005JG000099.

Wilmking, M., Harden, J. & Tape, K. 2006. Effect of tree line advance on carbon storage in NW Alaska. Journal of Geophysical Research 111:G02023, doi:10.1029/2005JG000074.

—Plenary Paper—

Recent Warming of European Permafrost: Evidence from Borehole Monitoring

Charles Harris
School of Earth, Ocean and Planetary Sciences, Cardiff University, Cardiff, CF10 3YE UK
Ketil Isaksen
Norwegian Meteorological Institute, P.O.Box 43 Blindern, NO-0313 Oslo, Norway

Abstract

Here we present a review of recent ground thermal data derived largely from the continent-scale network of instrumented boreholes within mountain permafrost established between 1998 and 2001 by the European Union PACE project. More recently, networks of intermediate and shallow boreholes in Switzerland, Norway, and Iceland have been added. A large number of complex variables determine permafrost temperatures, including altitude, topography, net radiation, and snow distribution. Thus, modeling the above-ground climate signal from observations of permafrost temperatures and coupling downscaled climate models to assess future permafrost thermal responses to climate forcing remain major research goals. Boreholes drilled in areas of steep mountain topography may penetrate complex three-dimensional thermal fields, making interpretation of thermal profiles in terms of changes in the upper thermal boundary extremely challenging. However, in the lower relief settings of the Scandinavian and Svalbard PACE boreholes, observed warm-side deviation in thermal profiles strongly suggests a period of sustained surface warming in the latter half of the 20th century and in the early 21st century. The significance of short-term extreme thermal events is illustrated with reference to the record-breaking summer of 2003 in the Alps and the anomalously warm winter-spring-summer period in 2005–2006 in Svalbard. It is concluded that such events may initially be more significant than the longer-term underlying trends in climate. Permafrost thermal responses to climate change occur at markedly different time scales, with changes in active layer thickness being more or less immediate, modification of thermal profiles below the depth of zero amplitude taking decades or centuries, and basal melting associated with progressive permafrost thinning requiring millennial time scales. However, as illustrated here by the example of Icelandic permafrost, where the frozen ground layer is thin and warm and the geothermal heat flux rates are high, permafrost decay and disappearance may be much more rapid.

Keywords: borehole monitoring; climate change; Europe; permafrost temperatures.

Introduction

In the present paper we review current evidence for permafrost warming within the European sector. In the mid-latitude high relief setting of the Alps, ground temperatures are only a few degrees below zero and permafrost may be thin near the lower permafrost boundary. Permafrost warming in alpine mountain slopes increases the risk of landslides, debris flows, and rockfalls (Noetzli at al. 2003, Gruber & Haeberli 2006). However, predicting the thermal response of mountain permafrost to climate change is challenging because of spatially complex topography and substrate properties (e.g. Hoezle et al. 2001). In contrast to the Alps, permafrost is continuous in the Arctic archipelago of Svalbard, outside the glaciated areas. Ocean-atmosphere coupling results in the climate being particularly sensitive to variations in sea-ice cover (Benestad et al. 2002, Isaksen et al. 2007b). Observed and predicted reductions in sea-ice (Stroeve et al. 2007, Serreze et al. 2007) suggest the onset of a rapid climate transition, with increasing frequency of anomalously high temperatures (Christensen et al. 2007, Isaksen et al. 2007b). The thermal response of permafrost may therefore exceed recent historical experience. Finally, the maritime setting of Iceland results in permafrost being restricted to higher elevations, and here geothermal heat flux increases the sensitivity of permafrost to changes in the upper boundary condition (Farbrot et al. 2007). This diversity of permafrost settings within Europe provides a background for this paper.

European Borehole Monitoring

A major stimulus to European permafrost research was provided by the PACE project (Permafrost and Climate in Europe), which commenced in 1997 (see Harris et al. 2001), and much of the more recent research reported here is a legacy of this program (Harris et al. submitted). Primary data have been collected through instrumented permafrost boreholes; the main borehole network of six instrumented bedrock boreholes drilled 100 m or more in depth was established between 1998 and 2001 through the PACE project (Fig. 1). The longest continuous European permafrost temperature time series is from the 32 m deep Murtèl Corvatsch borehole in Switzerland (Fig. 1) which was drilled in 1987, in an ice-rich rock glacier (Vonder Mühll and Haeberli 1990, Hoelzle et al. 2002). This borehole has been incorporated into the PACE network.

Over the past decade, the number of intermediate and shallow (less than 25 m) depth monitoring boreholes has increased steadily, particularly in Switzerland, where permafrost monitoring is coordinated by the PERMOS programme (Vonder Mühll et al. 2004, 2007). In Norway and Svalbard the IPY project "Thermal State of Permafrost" (TSP) (Christiansen this volume) has also instigated a

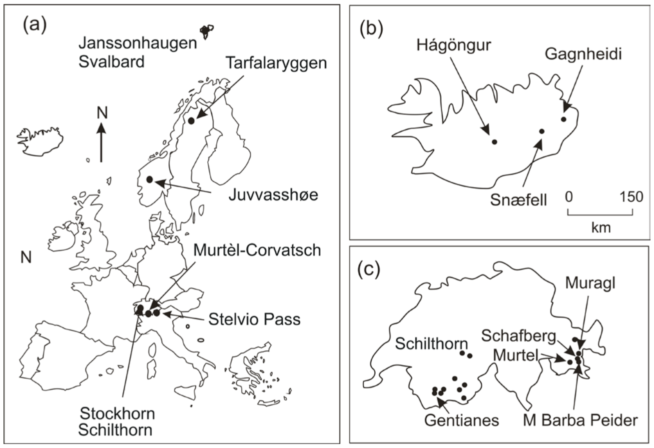

Figure 1. Distribution of boreholes mentioned in text. (a) PACE borehole network, (b) Icelandic boreholes, (c) Swiss boreholes.

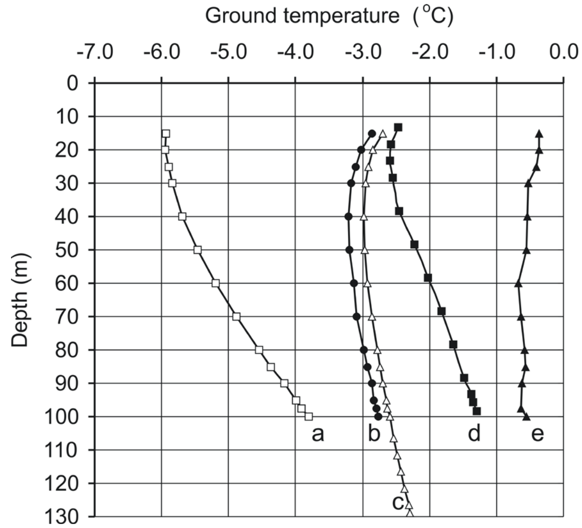

Figure 2. Ground temperature profiles in permafrost below 15 m at (a) Janssonhaugen, (b) Tarfalaryggen, (c) Juvvasshøe, (d) Stockhorn, (e) Schilthorn, and (f) Murtèl-Corvatsch. Data recorded 22 April 2005 (temperature profile at Juvvasshøe below 100 m depth recorded manually 1 October 2000).

program of permafrost monitoring through shallow boreholes. A total of 66 boreholes are listed from the European sector in the GTNP database (http://www.gtnp.org/); 31 of these are in Switzerland, 18 in Norway and Svalbard, and between 3 and 6 in Iceland, Italy, Spain, and Sweden. Not all are continuously monitored, and many have only short time series.

Instrumentation generally utilizes automatic logging of thermistor strings within cased boreholes. Recommendations on instrument specification, spacing, and logging frequencies may be found in the PACE Manual (see Appendix B, Vonder Mühll 2004), but all thermistors should be retrievable to allow periodic recalibration. In most PACE boreholes a second 15–20 m deep borehole was drilled adjacent to the deeper hole to allow more detailed higher frequency monitoring of the near surface (Isaksen et al. 2001, 2007a, Gruber et al. 2004c). In other borehole monitoring programs, a multimeter may be used to record thermistor temperatures periodically, or the borehole may be equipped with single-channel miniloggers, which are retrieved annually for downloading. Alternative approaches to monitoring the thermal status of permafrost include active layer thickness (e.g., the Circumpolar Active Layer Monitoring (CALM) program), and measurement of the Bottom Temperature of Snow (BTS) (e.g., Vonder Mühll et al. 2004, 2007).

Permafrost Geothermal Profiles

Since heat advection by ground water or air circulation is often negligible, permafrost geothermal profiles are primarily a function of heat conduction from the Earth's interior and heat fluxes at the ground surface. The annual ground surface thermal cycle penetrates to 15–20 m (the depth of zero amplitude), but larger perturbations of longer periodicity may penetrate much deeper and take much longer to do so (e.g., Lachenbruch & Marshall 1986). Perturbation of the thermal gradient below the depth of zero annual amplitude may provide direct evidence of thermal trends at the permafrost table during preceding decades or centuries (e.g., Cermak et al. 2000, Osterkamp & Romanovsky 1999). Where permafrost is thin (<100m), such thermal perturbation may extend to the base, causing basal melting, but in thicker permafrost, deeper penetration of climatically forced thermal cycles is likely to require millennial time scales.

In mountain permafrost, the thermal field is often strongly three-dimensional (Noetzli et al. 2007) and the thermal offset between mean ground surface temperature and mean permafrost table temperature reflects spatial heterogeneity in active layer composition and snow distribution, the latter also being subject to large inter-annual variations (Gruber et al. 2004c). Thus, modeling the above-ground climate signal from observations of permafrost temperatures, and coupling downscaled climate models to assess future permafrost thermal responses to climate forcing, remain major research goals (Harris et al. submitted). The greater altitudinal range and more complex topography in the Alps lead to greater variability in permafrost temperatures recorded by Swiss boreholes than those in Scandinavia and Svalbard. Figure 2 shows ground temperature profiles from PACE boreholes recorded in April 2005.

Ground temperatures in the Alpine boreholes Stockhorn and Schilthorn are highly disturbed by topography. Gruber et al. (2004c) have shown that for Stockhorn, marked differences in thermal gradient occur over short distances in response to a strongly three-dimensional temperature field. At Schilthorn, permafrost temperatures are very close to 0ºC and are influenced by latent heat effects and convective heat transfers by water as well as topographic effects. In contrast, the three Nordic boreholes have low relief within 100–200 m of the monitoring sites, relatively uniform bedrock and thin snow cover, suggesting that the climate signal dominates the observed geothermal gradients (Isaksen et al. 2007b). At greater depths than the boreholes, the effect of larger-scale relief may be significant and may in part explain

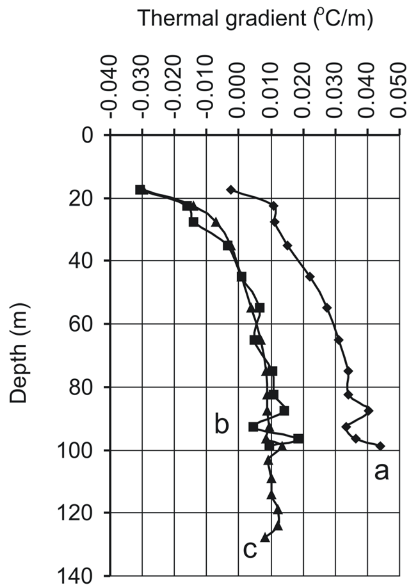

Figure 3. Thermal gradients at (a) Janssonhaugen, (b) Tarfalaryggen, (c) Juvvasshøe, calculated from profiles presented in Figure 2.

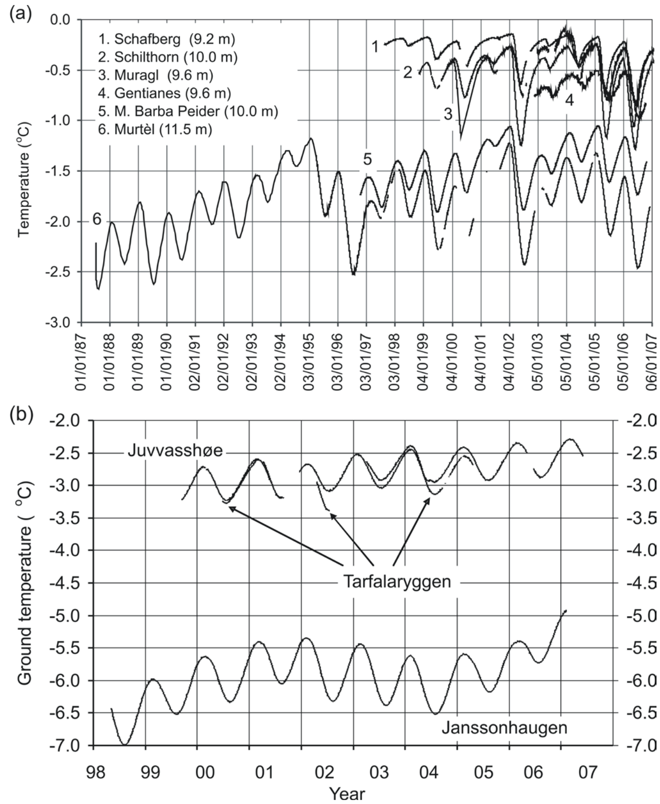

Figure 4. Permafrost temperature time series from around 10 m depth. (a) selected Swiss PERMOS boreholes. (b) Nordic PACE boreholes. For locations of boreholes, see Figure 1.

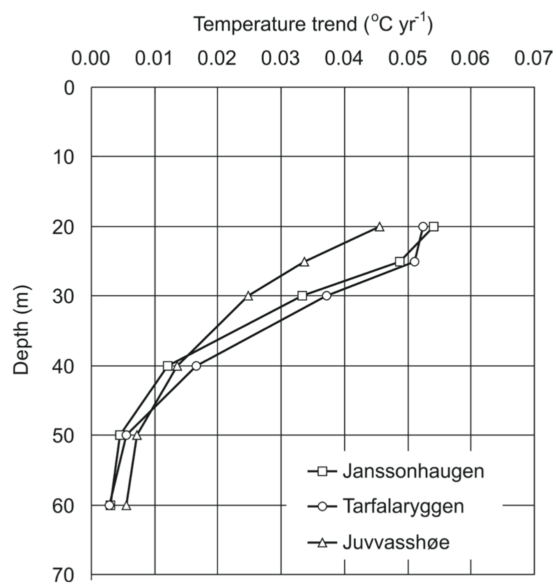

Figure 5. Observed linear trends in ground temperature as a function of depth. Time series at start in 1999 at Janssonhaugen, 2001 at Tarfalaryggen, and 2000 at Juvvasshøe, and they last for 6, 4, and 5 years, respectively.

the low thermal gradients observed at Tarfalaryggen and Juvvasshøe (Fig. 3). All three boreholes show a significant warm-side deviation in their thermal profiles to 70 m depth, with marked increases in thermal gradient with depth. Just below the depth of zero amplitude, gradients are negative (Fig. 3). These characteristics probably reflect surface warming since the mid 20th century (Harris et al. 2003, Isaksen et al. 2001, 2007a) and extrapolation to the surface of temperature gradients between 30–20 m depths and 70–100 m suggests surface warming of ~1.4°C, ~1.1°C and ~1.0°C for Janssonhaugen, Tarfalaryggen, and Juvvasshøe respectively.

Recent Trends in Permafrost Temperatures

Permafrost temperatures at depths of around 10 m in Swiss and Norwegian boreholes are illustrated in Figure 4(a) and (b). At Murtèl-Corvatsch in Switzerland, marked warming was recorded between 1987 and 1995 (Vonder Mühll & Haeberli 1990, Vonder Mühll et al. 1998, 2002, 2007, Hoelzle et al. 2002), but this was reversed in the winter of 1995–96 and more markedly so in 1996–97. Since then, at Murtèl and other Swiss boreholes, no marked overall warming trend is apparent, with periods of rising ground temperatures being cancelled out by marked winter cooling in 2002–03 and 2006–07. Harris et al. (2003) showed that snow-poor early winter periods rather than markedly lower atmospheric temperatures were largely responsible for these ground cooling events.

In the three Nordic boreholes, deflation maintains relatively thin snow cover in winter, so that ground temperatures are strongly coupled to atmospheric temperatures (Isaksen et al. 2007a). At Janssonhaugen especially, temperature records at 10 m depth show pronounced fluctuations and large inter-annual variability, making identification of longer-term trends more difficult. However, recorded ground temperature changes below the zero annual amplitude provide direct evidence of thermal trends at the ground surface during recent decades. At all three sites a clear trend towards warming ground temperatures is detected (Fig. 5). For instance, at 30 m depth, present warming rates are in the order of 0.025 - 0.035°C yr^{-1}. Isaksen et al (2007a) demonstrated that statistically significant ground warming may be detected to 60 m depth, the rate of warming being greatest at Tarfalaryggen and Janssonhaugen (Fig. 5).

The Significance of Extreme Events

Climate warming in the 20^{th} and 21^{st} centuries is likely to increase active layer thicknesses. However, an associated increase in frequency of high-temperature anomalies with sustained higher than normal temperatures may well dominate active layer evolution. Two examples of such extreme periods are discussed below: summer 2003 in the Alps, when temperatures during June, July, and August were approximately 3°C higher than the 1961–1990 average (Gruber et al. 2004c) and Svalbard in 2005–6 when anomalously high winter spring and summer temperatures caused significant permafrost warming (Isaksen et al. 2007b).

At the bedrock borehole of Schilthorn, Switzerland, active layer thickness ranged from around 4.4 m to around 4.9 m in the five years prior to 2003, but increased to nearly 9 m (Fig. 6a) during the 2003 extreme summer. In subsequent years the thickness has been around 4.8 m. At Stockhorn the active layer increased from around 3 m in the previous few years to 4.27 m in 2003. Numerical modeling has shown that in 2003 Alpine active layers were thicker than in the previous 21 years and were probably the greatest for several centuries (Gruber at al. 2004b). Rapid warming and thawing of bedrock containing ice-bonded joint planes led to a marked increase in rockfall events (Keller 2003) particularly on north-facing slopes where the effects of elevated atmospheric temperatures are greatest, and permafrost most widely distributed (Gruber et al. 2004b, Noetzli et al. 2007). The sharply increased depth of thaw during the summer of 2003 far outweighed the direct effect of gradually rising temperatures on the stability of the uppermost few metres of rock in most Alpine rock walls (Gruber et al. 2004c, Gruber & Haeberli 2006).

In contrast, active layer thickness changed much less dramatically at the ice-rich rock glacier of Murtèl-Corvatsch (Fig. 6b) in Switzerland where latent heat demand during thaw at the permafrost table provides an effective heat sink, limiting the active layer thickening. The general trend since 1987 has been towards increasing active layer thickness and in 2003 it reached 3.51m, around 11 cm thicker than in the previous summer and the greatest value since monitoring began in 1987. However, once thawed, meltwater drains away, leaving a thicker active layer with much lower ice content and therefore latent heat demand than the underlying permafrost. Thus, despite a much cooler summer in 2004, the active layer reached the same thickness as in 2003, and in 2005, which was cooler again, thaw penetration was only a few cm less than in 2003 (Vonder Mühl et al. 2007).

The winter-spring-summer period in 2005–6 on Svalbard provides a remarkable example of extreme atmospheric temperatures. The mean air temperature between December and May 2005–2006 was as high as −4.8°C, which is 8.2°C

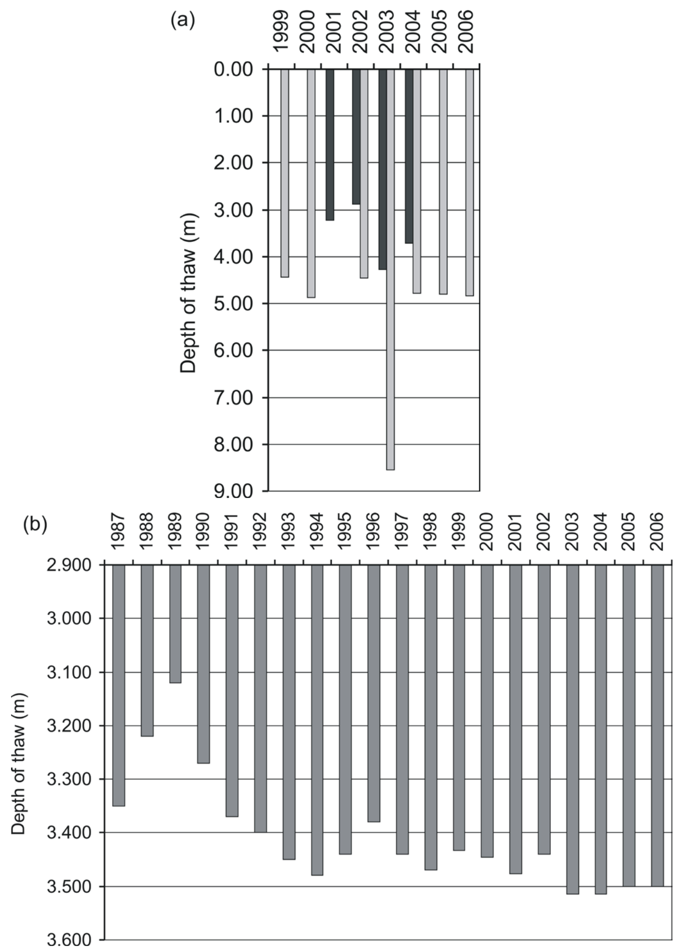

Figure 6. Active layer thickness: (a) Schilthorn (light bars) and Stockhorn (dark bars); (b) Murtèl-Corvatsch.

above the 1961–1990 average and 2.8°C higher than the previous record from 1954, amounting to an offset of 3.7 standard deviations from the mean (Isaksen et al. 2007b). The anomaly coincided with a marked reduction in sea-ice cover and an unusually large extent of marine open water around Svalbard during winter, spring, and summer 2005–2006. The warm winter was followed by warmer than average summer temperatures, which were around 2°C above the 1969–1990 normal. For calendar year 2006, the cumulative negative ground temperature at the permafrost table in the Janssonhaugen borehole (2 m depth) showed a 40% reduction compared with the average of the previous six years.

The effect on permafrost temperatures at Janssonhaugen is most clearly captured by considering the 12-month period from 1 December 2005 to 30 November 2006 (Isaksen 2007b). Plotting mean ground temperatures over this period, for instance the uppermost 3 meters, shows temperatures at the permafrost table 1.8°C above the 1999–2005 average, with the thermal anomaly traceable to a depth of at least 15 m. The start of active layer thawing was the earliest in the 8-year record and active layer thickness was 1.8 m, exceeding the mean of the previously recorded years by 0.18 m (an 11% increase).

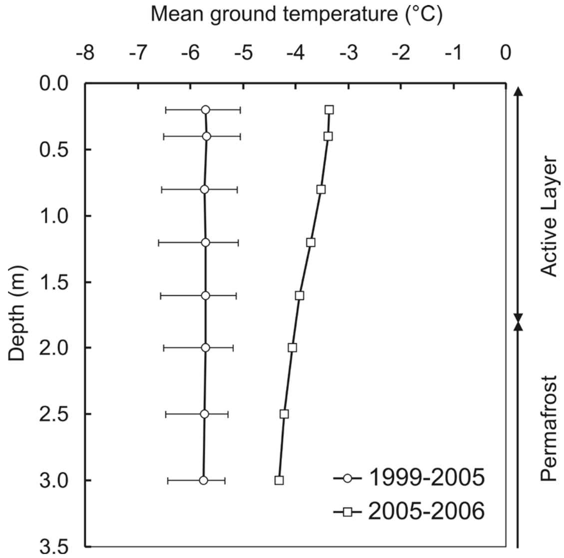

Figure 7. Mean ground temperature profile at Janssonhaugen for 2005–2006 compared with the mean for 1999–2005. Horizontal bars show the absolute variations of the previous years.

In order to place this anomaly into the context of climate change, Isaksen et al. (2007b) compared the accumulated degree day air temperature curve for 2006 at Svalbard airport with equivalent curves derived from empirical-statistical downscaling based on the multi-model World Climate Research Programme (WCRP) Coupled Model Intercomparison Project (CMIP3) of the most recent Intergovernmental Panel on Climate Change (IPCC) assessment in which atmospheric CO_2 reaches 720 parts per million by 2100. The 2006 accumulated degree day curve lay well within the range of the predicted scenarios for 2071–2100. Since 1999, accelerated warming has been observed at Janssonhaugen, the calculated rate at the top of the permafrost being in the order of 0.6–0.7°C/decade (Isaksen et al. 2007a). Thus the extreme temperatures of 2005–2006 were superimposed on a significant warming trend. If the frequency of such high temperature anomalies increases, then near-surface permafrost warming will be irregular rather than gradual and punctuated by rapid warming events such as that in 2005–2006.

Sensitivity to Geothermal Heat Flux

In Iceland, maritime conditions give cool summers and mild winters. The MAAT for 1961–1990 is around 4°–5° C in the south, and 2°–3°C in the north in lowland areas (Farbrot et al. 2007). Extensive non-glaciated mountain areas have MAAT below -3°C, indicating a potential for permafrost where snow cover is thin or absent. A regional model, calibrated against borehole thermal data and rock glacier inventories, suggests the presence of permafrost above around 800m a.s.l. in the north and above 1000m in the south (Etzelmüller et al. 2007, Etzelmüller et al. 2008), with the thickness of snow strongly modulating permafrost distribution.

Four monitoring boreholes in central and northeastern Iceland were established in 2004 (Farbrot et al. 2007,

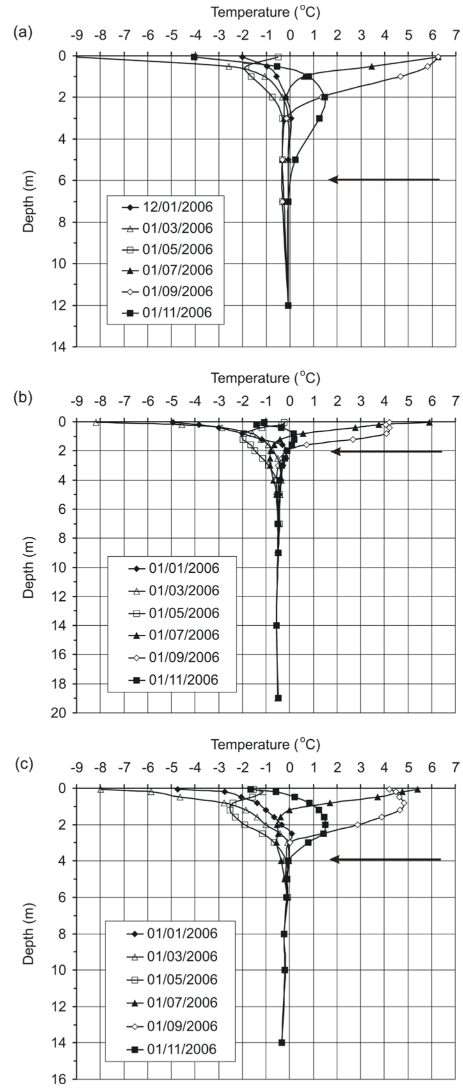

Figure 8. Temperature profiles in boreholes during 2006: (a) Hágöngur, (b) Snæfell, (c) Gagnheiði. Active layer thickness during the 2006 summer season indicated by arrows.

Etzelmüller et al. 2007, Etzelmüller et al. this volume), at altitudes of between 890–930 m a.s.l. (Fig. 1b). All boreholes are shallow (12–22 m deep) and penetrate thin sediment into basaltic bedrock. Permafrost was absent at the Vopnafjörður site due to excess snow cover, but at Snæfell and Gagnheiði it was estimated to be 30–35 m thick (Fig. 8b, c), with active layers around 2 m and 4 m respectively. At the Hágöngur borehole, permafrost was thin and the active layer thick (around 6 m) and permafrost temperatures close to zero degrees C (Fig. 7a). Meteorological data indicate that mean annual ground surface temperatures for the past few years in Iceland have been 0.5–1°C higher than those for the 1961–90 period (Etzelmüller et al. 2007). At the Gagnheiði and Snæfell boreholes, temperature profiles show warm-side deviation from steady state, suggesting recent rises in the upper boundary temperature (Fabrot et al. 2007).

Using a one-dimensional thermal model, Farbrot et al. (2007) showed that increases in mean daily surface air temperatures of (a) 0.01°C a^{-1} and (b) 0.03°C a^{-1} would cause permafrost to disappear at Snæfell in 160 and 100 yr respectively and at Gagnheiði in 125 and 75 yr respectively, the slower thermal response at Snæfell reflecting higher ice contents. Modeled temperature evolution since 1955 suggested that the present-day permafrost thicknesses reflect cooling in the late 1960s/early 1970s. This rapid permafrost thermal response is in part a reflection of the shallowness of the permafrost layer, but it is also due to the influence of high geothermal heat fluxes, which at Snæfell are around 170 mW m^2, approximately five times the values at the Scandinavian PACE borehole sites.

Conclusions

The spatial complexity of European mountain permafrost makes the representativeness of data from the small number of monitored boreholes extremely difficult to assess. The time series of borehole temperatures are mainly less than 10 yr, apart from Murtél-Corvatsch.

The addition of new boreholes provides the opportunity to sample a wider diversity of terrain and substrate character. However, prediction of permafrost distribution and response to climate change in European mountains requires further progress in physically-based numerical modeling coupled with remotely sensed data on relief, ground cover, and substrate characteristics.

PACE boreholes in Norway, Sweden, and Svalbard provide firm evidence for significant and accelerating ground warming. In addition, the importance of short-term extreme thawing events is emphasized. These have included the three-month period of sustained high temperatures during summer 2003 in the Alps, when active layers thickened significantly in bedrock sites and, in Svalbard, the anomalously warm year of 2005–6 when marked warming of permafrost occurred. Comparison of 2006 air temperatures in Svalbard with downscaled model scenarios of warming associated with enhanced greenhouse gases in the 21st century indicates that 2005–6 was well within the range predicted for the period 2071–2100, suggesting that the Svalbard archipelago may be in a critical location, with potential for particularly rapid climate change.

Given the variability of climate in the past and evidence for continued and possibly accelerated change in the future, permafrost is clearly in a transient state. More or less immediate response to extreme annual temperature variations may be anticipated in active layer thickness, while thermal profiles extending to several decimeters below the depth of zero amplitude reflect changes over many decades or centuries. Permafrost warming and basal melting are, however, likely to take several millennia, except where permafrost is thin and — as is the case in Iceland — where geothermal heat flux is unusually high.

Acknowledgments

The authors wish to thank Jeannette Noetzli, Dani Vonder Mühll, and Bernd Etzelmüller for supplying data presented in this paper.

References

Benestad, R.E., Førland, E.J. & Hanssen-Bauer, I. 2002. Empirically downscaled temperature scenarios for Svalbard, Atmosheric. *Science Letters* 3: 71–93, doi.10.1006/asle.2002.005.

Cermak, V., Safanda, J., Kresl, M., Dedecek, P. & Bodri, L. 2000. Recent climate warming: Surface air temperature series and geothermal evidence. *Studia geophysica et geodaetica* 44, 430–441.

Christensen, J.H. et al. 2007. Regional climate projections, in Climate Change 2007: The Physical Science Basis. Contribution of Working Group I to the Fourth Assessment Report of the Intergovernmental Panel on Climate Change, edited by S. Solomon et al., 849–940, Cambridge Univ. Press, New York.

Christiansen, H.H., Berthling, I., Blikra, L.H., Dehls, J., Etzelmuller, B., Farbrot, H., Humlum, O., Isaksen, K., Juliussen, H., Lauknes, T-R., Midttømme, K. & Rønning, J. 2008. Permafrost Observatory Project: A Contribution to the Thermal State of Permafrost in Norway and Svalbard, TSP NORWAY. Proceedings, *Ninth International Conference on Permafrost,* Fairbanks, Alaska, July 2008.

Etzelmüller, B., Farbrot, H., Guðmundsson, A., Humlum, O., Tveito, O.E. & Björnsson, H. 2007. The Regional Distribution of Mountain Permafrost in Iceland. *Permafrost and Periglacial Processes* 18: 185–199. DOI: 10.1002/ppp

Etzelmüller, B., Schuler, T.V., Farbrot, H. & Guðmundsson, Á. 2008. Permafrost in Iceland: Distribution. Ground Temperatures and Climate Change Impact. Proceedings, *Ninth International Conference on Permafrost,* Fairbanks Alaska, July 2008.

Farbrot, H., Etzelmüller, B., Gudmundsson, A., Schuler T.V., Eiken, T., Humlum, O. & Björnsson, H. 2007. Thermal characteristics and impact of climate change on mountain permafrost in Iceland. *Journal of Geophysical Research* 112, F03S90, doi:10.1029/2006JF000541.

Gruber, S. & Haeberli, W. 2007. Permafrost in steep bedrock slopes and its temperature-related destabilization following climate change. *Journal of Geophysical Research*, 112, F02S18, doi:10.1029/2006JF000547.

Gruber, S., Hoelzle, M. & Haeberli, W. 2004a. Permafrost thaw and destabilization of Alpine rock walls in the hot summer of 2003, *Geophysical Research Letters* 31: L13504, 4pp.

Gruber, S., Hoelzle, M. & Haeberli, W. 2004b. Rock wall temperatures in the Alps-modelling their topographic distribution and regional differences. *Permafrost and Periglacial Processes* 15(3): 299-307.

Gruber, S., King, L., Kohl, T., Herz, T., Haeberli, W. & Hoelzle, M. 2004c. Interpretation of geothermal profiles perturbed by topography: the Alpine permafrost boreholes at Stockhorn Plateau, Switzerland. *Permafrost and Periglacial Processes* 15(4): 349-357.

Harris, C., Haeberli, W., Vonder Mühll, D. & King, L. 2001. Permafrost monitoring in the high mountains of Europe: the PACE project in its global context. *Permafrost and Periglacial Processes* 12(1): 3-11.

Harris, C., Vonder Mühll D., Isaksen K., Haeberli W., Sollid J. L., King L., Holmlund P., Dramis F., Guglielmin M. & Palacios D. 2003. Warming permafrost in European mountains. *Global and Planetary Change* 39: 215-225.

Harris, C., Arenson, L.U., Christiansen, H.H., Etzelmüller, B., Frauenfelder, R., Gruber, S., Haeberli, W., Hauck, C, Hölzle, M., Humlum, O., Isaksen, K, Kääb, A., Lehning, M., Lütschg, M.A., Matsuoka, N., Murton, J.B., Nötzli, J., Phillips, M., Ross, N., Seppälä, M., Springman, S.M. & Vonder Mühll, D. Submitted. Permafrost and climate in Europe: geomorphological impacts, hazard assessment and geotechnical response Earth Science Reviews.

Hoelzle, M., Mittaz, C., Etzelmüller, B. & Haeberli, W. 2001. Surface energy fluxes and distribution models of permafrost in European mountain areas: an overview of current developments. *Permafrost and Periglacial Processes* 12(1): 53-68.

Hoelzle, M., Vonder Mühll, D. & Haeberli, W. 2002. Thirty years of permafrost research in the Corvatsch-Furtschellas area, Eastern Swiss Alps: a review. *Norwegian Journal of Geography* 56(2): 137-145.

Isaksen, K., Holmlund, P., Sollid, J.L & Harris, C. 2001. Three deep alpine-permafrost boreholes in Svalbard and Scandinavia. *Permafrost and Periglacial Processes* 12: 13-25.

Isaksen, K., Sollid, J.L., Holmlund, P. & Harris, C. 2007a. Recent warming of mountain permafrost in Svalbard and Scandinavia. *Journal of Geophysical Research* 112, F02S04, doi:10.1029/2006JF000522.

Isaksen, K., Benestad, R.E., Harris, C. & Sollid, J.L. 2007b. Recent extreme near-surface permafrost temperatures on Svalbard in relation to future climate scenarios Geophysical Research Letters, 34, L17502, doi:10.1029/2007GL031002, 2007.

Lachenbruch, A.H. & Marshall, B.V. 1986. Changing climate: Geothermal evidence from permafrost in the Alaskan Arctic. *Science* 234: 689-696.

Noetzli, J., Hoelzle, M. & Haeberli, W. 2003. Mountain permafrost and recent Alpine rock-fall events: a GIS-based approach to determine critical factors.

Noetzli, J., Gruber, S., Kohl, T., Salzmann, N. & Haeberli, W. 2007. Three-dimensional distribution and evolution of permafrost temperatures in idealized high-mountain topography. *Journal of Geophysical Research* 112,: F02S13, doi:10.1029/2006JF000545.

Osterkamp, T.E. & Romanovsky V.E. 1999. Evidence for Warming and Thawing of Discontinuous Permafrost in Alaska. *Permafrost and Periglacial Processes* 10: 17–37.

Serreze, M.C., Holland, M.M. & Stroeve, J. 2007. Perspectives on the Arctic's shrinking sea-ice cover,. *Science* 315: 1533, doi:10.1126/ science.1139426.

Stroeve, J., Holland, M.M., Meier, W., Scambos, T. & Serreze, M.C. 2007. Arctic sea ice decline: Faster than forecast. *Geophysical Research Letters* 34: L09501, doi:10.1029/2007GL029703.

Tveito, O. E. et al. 2000. Nordic temperature maps, report, 28 pp., Norwegian Meteorological Institute, Oslo.

Vonder Mühll, D. & Haeberli, W. 1990. Thermal characteristics of the permafrost within an active rock glacier (Murtèl/Corvatsch, Grisons, Swiss Alps). *Journal of Glaciology* 36(123): 151-158.

Vonder Mühll, D., Noetzli, J., Makowski, K. & Delaloye, R. 2004. Permafrost in Switzerland 2000/2001 and 2001/2002, Glaciological Report (Permafrost) No. 2/3 of the Glaciological Commission (GC) of the Swiss Academy of Sciences (SAS) and Department of Geography, University of Zurich, 86 p.

Vonder Mühll, D., Noetzli, J., Makowski, K. & Delaloye, R. 2007. Permafrost in Switzerland 200/2003 and 2003/2004, Glaciological Report (Permafrost) No. 4/5 of the Glaciological Commission (GC) of the Swiss Academy of Sciences (SAS) and the Department of Geography, University of Zurich.

Vonder Mühll, D., Stucki, T. & Haeberli, W. 1998. Borehole temperatures in Alpine permafrost: a ten years series, in Proceedings Seventh International Conference on Permafrost, Yellowknife, Canada, 23-27 June 1998, edited by A.G. Lewkowicz, and M. Allard, pp. 1089–1095, Centre d'Etudes Nordiques, Universite Laval, Collection Nordicana 57.

Full-Scale Physical Modeling of Solifluction Processes Associated with One-Sided and Two-Sided Active Layer Freezing

Charles Harris
School of Earth, Ocean and Planetary Sciences, Cardiff University, Cardiff CF10 3YE,UK
Martina Kern-Luetschg
School of Earth, Ocean and Planetary Sciences, Cardiff University, Cardiff CF10 3YE,UK
Julian Murton
University of Sussex, Dep tment of Geography, Brighton, BN1 9SJ, UK
Marianne Font
UMR CNRS 6143 M2C and University of Caen, Rue des Tilleuls, Caen, 14 032, France
Michael Davies
Faculty of Engineering, University of Auckland, Auckland 1142, New Zealand
Fraser Smith
School of Engineering, University of Dundee, Dundee, DD1 4HN, UK

Abstract

In this paper we present data from one typical cycle of freezing and thawing, derived from a 17-cycle full-scale experiment to simulate solifluction processes associated with two-sided active layer freezing and one-sided seasonal ground freezing. Two adjacent 12° slope models, each 5 m long, 1.5 m wide , and 35 cm thick were constructed using the same silt-rich natural soil. In the one-sided freezing model, the slope was formed above a sand substrate in an open hydraulic system, and the slope thawed completely between freezing cycles. The second model was constructed on a refrigerated plate that maintained permafrost in the lowermost 5 cm of soil and promoted bottom-upward soil freezing in addition to the top-down freezing induced by air temperature cycles. In the two-sided freezing model, downward moisture migration during the thaw period resulted in ice segregation immediately above and within the permafrost table. In the seasonally frozen slope model, ice segregation was greatest in the near-surface zones and decreased with depth. This contrasting distribution of soil ice caused marked differences in patterns of heave, thaw settlement, timing and style of downslope soil movement.

Keywords: one-sided freezing; physical modeling; solifluction; two-sided freezing.

Introduction

Here we present preliminary results from a three-year full-scale simulation experiment designed to investigate the influence of the distribution of segregation ice on the style and timing of periglacial solifluction (gelifluction and frost creep). These experiments form part of a larger program in which physical modeling coupled with field monitoring will provide detailed validation and calibration data for numerical modeling of solifluction processes (see also Kern-Luetschg et al. 2008).

Although the literature on periglacial solifluction is extensive, it is largely focused on areas with seasonally frozen ground or warm permafrost, where freezing takes place from the surface downwards. Field measurements (e.g., Washburn 1967, Benedict 1981, Smith 1988, Kinnard & Lewkowicz 2005, Jaesch et al. 2003) and laboratory simulations (Coutard et al. 1988, Harris et al. 1995, 1997) have shown that in seasonally frozen frost-susceptible soils, winter frost heave is followed by solifluction movements during summer thaw consolidation. Ice contents often decrease with depth, as do rates of soil movement. In cold permafrost regions, two-sided active layer freezing is observed, with freezing from the bottom upwards and the top downwards (Mackay 1981, Cheng 1983, Lewkowicz & Clark 1998, Schur 1988, Shiklomanov & Nelson 2007), and this commonly leads to a zone of ice segregation at the base of the active layer and top of the permafrost, termed the "transient layer" by Schur et al. (2005).

In Garry Island, Canada, Mackay (1981) described late summer plug-like solifluction, associated with displacement over the ice-rich zone at the base of the active layer. He showed that ice within this basal zone forms by early winter upward advance of a freezing front from the permafrost table, augmented by ice lensing in late summer as water migrates downward across the thaw front and into still-frozen basal active layer and upper permafrost. Similar observations of slow, annual downslope active layer movement over a deforming basal zone are reported by Lewkowicz & Clark (1998) and Matsuoka & Hirakawa (2000). Thaw consolidation may reduce the unfrozen thickness of this basal deforming zone, and resulting shear strains, accumulated over many annual freeze-thaw cycles, have been implicated in the reduction of local soil shear strength over time, promoting active layer detachment slides during anomalously warm summers (Harris & Lewkowicz 2000).

Table 1. Average test soil properties. *PL* is Plastic Limit, *LL* is Liquid Limit, c_v is coefficient of consolidation, and *k* is permeability.

% clay	% silt	% sand	PL %	LL %	ø degrees	c_v m^2/yr	k m/sec
25	65	10	22	33	26	18.4	4.4×10^{-8}

An early experiment to investigate the significance of ice distribution within the thawing active layer was reported by Rein & Burrous (1980), who used a tilting box containing a 25 cm thick layer of frost susceptible silt-loam. Two experiments were conducted, first with high ice contents in the mid profile, second with high ice contents at the base. Thaw consolidation and solifluction were shown to be concentrated within these ice-rich layers, with little shear strain occurring elsewhere in the profile. In the present paper we seek to test the hypothesis that similar processes of soil shear strain occur close to the surface in seasonally frozen ice-rich soil and at the base of the active layer in permafrost regions where two-sided freezing is associated with an ice-rich basal layer.

Experimental Design

Two identical 12° slope models were constructed adjacent to each other within a 5 m square freezing chamber, using the same frost susceptible soil (Fig. 1). Models were 5 m long, 1.5 m wide, and 35 cm thick. Soil properties are similar to those of many solifluction soils reported in the literature (see, for instance, the review by Harris, 1982) and are summarized in Table 1. Air temperatures were lowered to between -8°C and -12°C to simulate winter freezing, and were subsequently raised to between +15°C and +20°C to simulate the summer thaw period.

The two-sided freezing model was constructed above a refrigerated plate that maintained a 5–6 cm thick permanently frozen layer (permafrost) at the base of the model, with basal temperatures around -2.5°C during simulated summer conditions. Freezing was from the bottom upwards and the top-down (two-sided) during simulated winter cycles. Since the maximum thaw depth was only around 30 cm, active layer thickness was much less than in most field situations. When the active layer had reached its full thickness, water was added at the surface via a fine spray. Downward moisture migration led to basal ice segregation, simulating summer frost heave (e.g., Mackay 1983) and increasing the basal ice content. The one-sided freezing slope model was formed above a sand substrate in an open hydraulic system (basal water supply). Moisture contents prior to initiation of winter freezing averaged around 25% by weight in the two-sided freezing model, but were slightly higher in the one-sided model.

In this paper we present results of one freeze-thaw cycle from the final sequence of 8 cycles and contrast the soil response in the two-sided model with that in the one-sided model.

Figure 1. Two parallel slope models, far side, two-sided freezing model, near side, one-sided freezing model. Cross beams support pairs of LVDTs which form fixed base triangles, the apex of which is attached to a Perspex footplate embedded in the soil surface.

Instrumentation

Data were collected at half-hourly intervals via a PC-based data logging system. Instrumentation was similar to that used in earlier experiments (see Harris et al. 1997). Temperatures were measured using an array of stainless steel thermistor probes measuring to within ±0.38°C, (supplied by Campbell Scientific Ltd.) located at the surface and depths of 0 cm, 5 cm, 15 cm, 25 cm, and 35 cm in the central zone of each slope model. Pore water pressure monitoring used Druck PDCR 81 miniature pore pressure transducers consisting of stainless steel cylinders of diameter 6 mm and length 12 mm with a porous stone tip. Transducers were filled with low viscosity silicon oil and had a range of 350 mb, combined non-linearity and hysterics of ±0.2%, and thermal sensitivity of 0.2% of reading per °C. Pore pressure data are not included here but will be fully discussed in later papers.

Soil surface motion was recorded using pairs of longstroke (300 mm) captive guided armature linear variable differential transformers (LVDTs) with spherical end bearings supplied by RDP Electronics Ltd, UK. Pairs of LVDTs formed a fixed base triangle mounted on a slotted track parallel to the slope above each model, supported by a beam (Fig. 1). Both LVDTs were connected to an 8 cm square Perspex footplate embedded in the soil surface, forming the apex of the triangle. Frost heave, thaw consolidation, and downslope displacements of the soil surface were registered by changes in LVDT length and were resolved as orthogonal vectors perpendicular and parallel to the soil surface. Soil displacement profiles were observed through re-excavation of Rudberg columns.

Results

Soil temperatures

Typical responses of both slope models to cyclic freezing and thawing are illustrated below by reference to Cycle 16, between 20 April and 7 June 2007. For convenience, all soil depths are given here for the equivalent unfrozen soil. When frozen, soil depths increase as a result of frost heave, but this varies from one cycle to another. Contrasting thermal

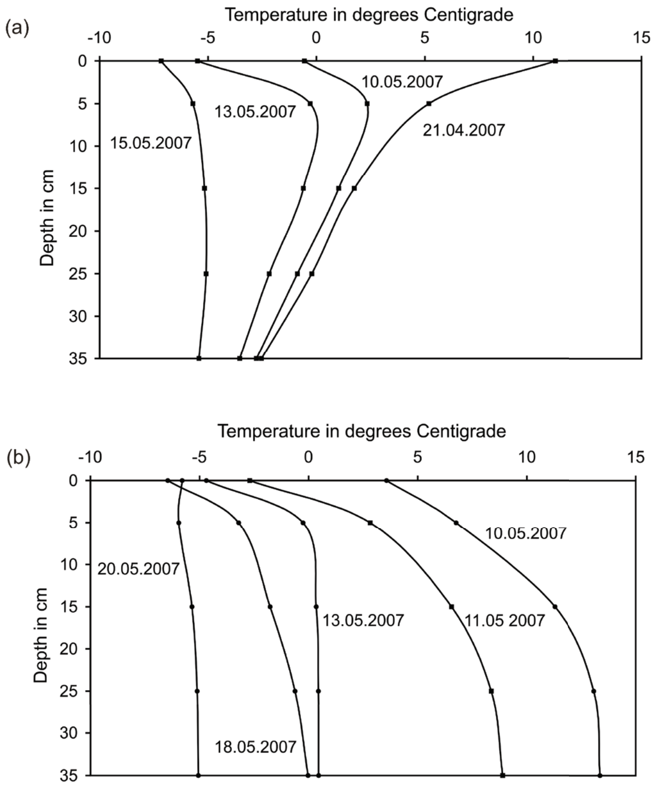

Figure 2. Thermal profiles during freezing. (a) two-sided freezing model, (b) one-sided freezing model.

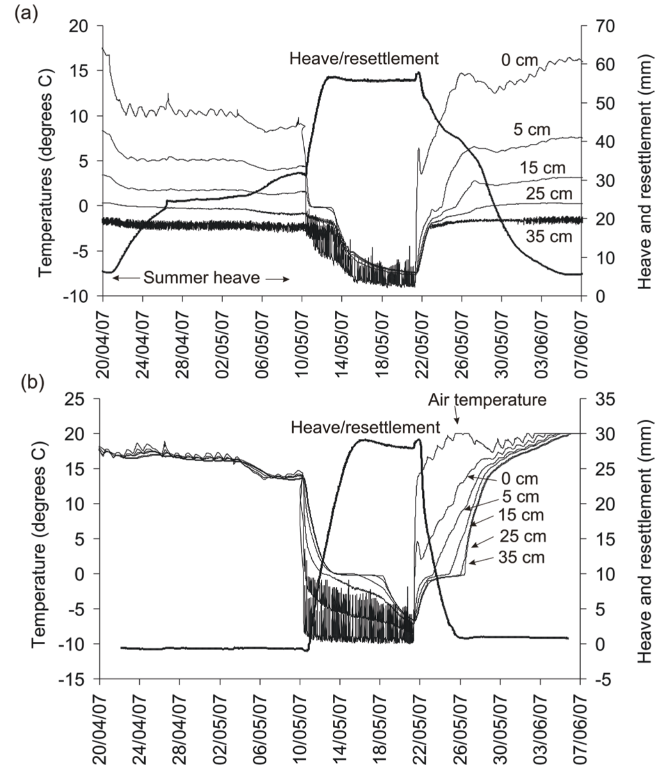

Figure 3. Frost heave followed by thaw settlement (heavy line) shown with soil temperatures through each model. (a) Two-sided freezing experiment. (b) One-sided freezing experiment.

regimes were observed during the freezing phase, reflecting the presence of permafrost in the two-sided freezing model, but its absence in the one-sided model (Figs. 2a, b). The basal temperature in the two-sided (permafrost) model was maintained at around -2.5°C, and active layer thickness was around 26 cm until air temperatures were lowered to approximately -10°C on May 10th. Winter freezing occurred over the next three days, with freezing fronts advancing from the permafrost table upwards and from the surface downwards. In the one-sided model downward freezing from the surface was initiated by the fall in air temperatures on May 10th and lasted some 5 days.

Frost heave and thaw settlement

A fall in surface temperatures of around 6°C on April 20, 2007, coupled with the addition of 5 litres of water sprayed across the entire surface, initiated the first phase of basal freezing in the two-sided freezing model and 18 mm of "summer heave" was recorded by April 26th (Fig. 3a). Further surface cooling on May 3rd, and the addition of 5 liters of water caused a second phase of ice segregation at the base of the active layer with an additional 6 mm of summer heave. Finally, the phase of two-sided freezing from May 10th–13th was associated with approximately 25 mm of frost heaving.

Surface downward frost penetration in the one-sided model, initiated on May 10th, led to a uniform rate of heaving with approximately 28 mm of surface frost heave recorded by May 16th (Fig. 3b) after which heave virtually ceased. The freezing front had penetrated to an unfrozen depth of between 15–20 cm by May 16th, so that little heave occurred during freezing of the lower 15 cm of the model. This was due to closure by freezing of the basal water supply tubes at the top of the model.

Thawing in both models was initiated by raising air temperatures to around 20°C on May 20, 2007. In the two-sided model the rate of thaw penetration increased through the uppermost 5 cm, was at a maximum between 5 and 15 cm depth, and then progressively decreased (Fig. 4a). Average thaw penetration rates are shown in Table 2. In the one-sided model, thaw penetration accelerated through the thaw period (Fig. 4b, Table 2) and was complete some 12 days before the maximum thaw depth was reached in the two-sided model.

By coupling the rate of thaw penetration with the rates of surface thaw settlement, and assuming that surface settlement during a given period was due to consolidation of the layer that thawed in that period, we were able to reconstruct ice contents within the thawing models (Table 2). Average heaving ratios (HR defined as frost heave divided by frozen thickness) were calculated from the amount of settlement recorded over a given soil depth range, divided by the frozen thickness. In the two-sided model, ice content was lowest within an ice-poor zone between unfrozen depths of 5 cm and 15 cm (HR 0.03), and highest in the basal zone between unfrozen depths of 25 cm and 26 cm (HR 0.66). In contrast, segregation ice was concentrated between 0 cm and 5 cm unfrozen depths in the one-sided freezing model, where the average heaving ratio was 0.25, and decreased to virtually zero in the lowermost 10 cm of the model.

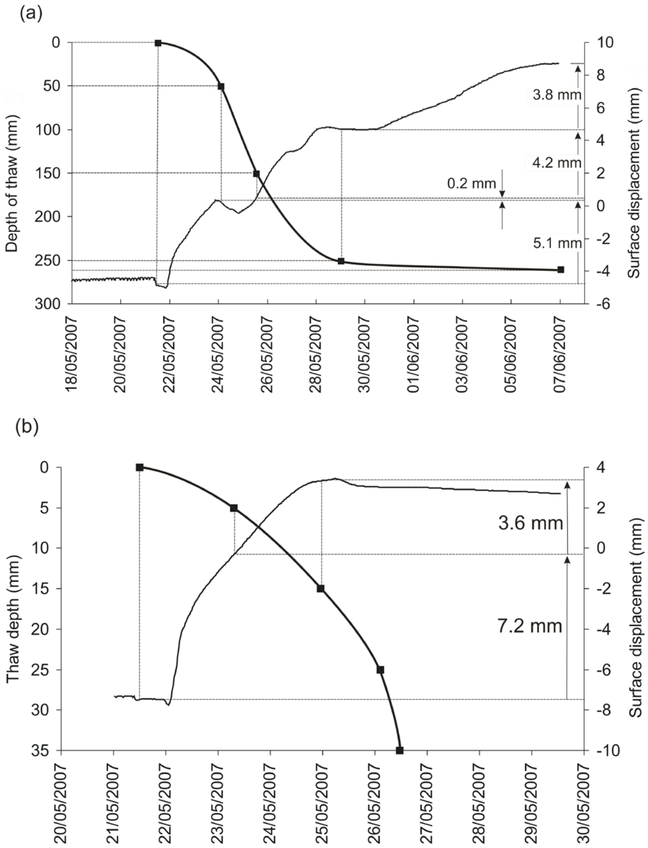

Figure 4. Rate of thaw penetration (heavy line) and measured surface downslope displacements. (a) Two-sided freezing model. (b) One-sided freezing model.

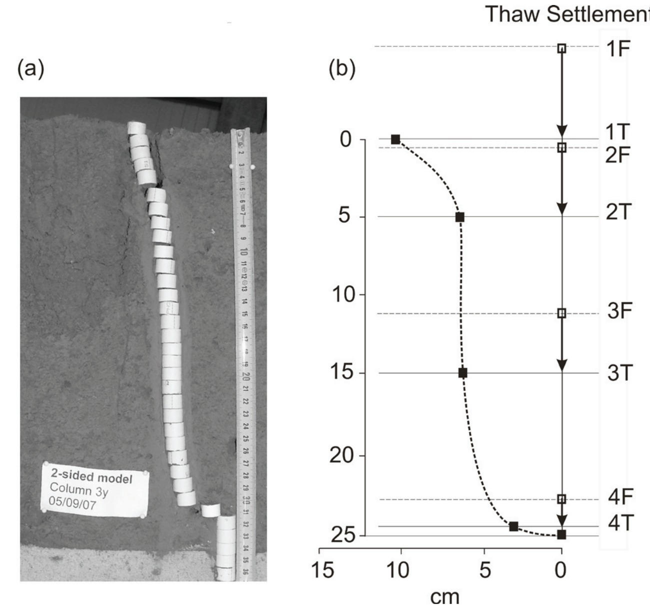

Figure 5. Soil displacement profiles, two-sided freezing model. (a) observed displacement profile after 8 cycles of freezing and thawing. (b) synthetic model derived from thaw penetration and displacement data (Figure 4[a]). Labels show levels of layer boundaries (surface, 5 cm, 15 cm, 25 cm and 26 cm) in frozen (1–4F) and thawed (1–4T) states.

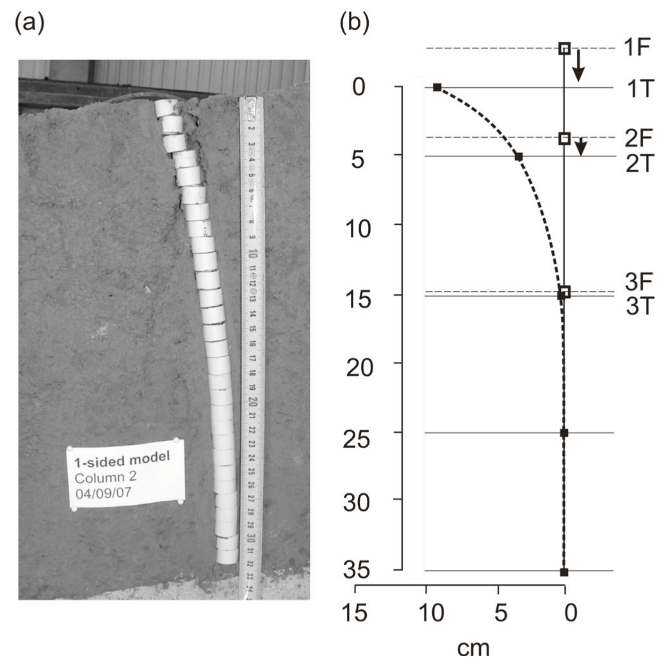

Figure 6. Soil displacement profiles one-sided freezing model. (a) observed displacement profile after 8 cycles of freezing and thawing. (b) synthetic model derived from thaw penetration and displacement data (Figure 4[a]). Labels show levels of layer boundaries (surface, 5 cm, 15 cm, 25 cm and 26 cm) in frozen (1–4F) and thawed (1–4T) states.

Downslope soil displacement

The distribution of soil shear strain within each model was assessed for the single thaw phase described here by attributing measured surface downslope surface displacement over a given time period to shear strain within the layer of soil that thawed over the same time period. In Figure 4(a) and (b), downslope surface displacement is plotted on a common time axis with the penetration of the thaw front. In the two-sided model, thawing of the upper 5 cm unfrozen thickness of soil was associated with some 5.1 mm downslope displacement, but thawing of the ice-poor region between 5 cm and 15 cm unfrozen depth caused virtually no net downslope movement, the recorded displacements probably reflecting changes in moisture status of the already thawed soil layer. As the thaw front penetrated to below 15 cm unfrozen depth, surface movement was again recorded, continuing over the prolonged period when the very ice-rich zone between 25 cm and 26 cm (unfrozen depths) thawed. In contrast, surface displacement in the one-sided model occurred only as the uppermost 15 cm of the model thawed, with displacement of 7.2 mm during thaw of the upper 5 cm, and 3.6 mm during thaw between 5 cm and 15 cm unfrozen depths.

Synthetic displacement profiles were generated for each model on the basis that the measured surface movements were attributed to the corresponding thawing soil layer. For clarity, displacements are multiplied by 8, to give the synthetic profiles that would arise following eight identical cycles of freezing and thawing in each model. These are compared with observed displacement profiles from excavated Rudberg Columns following the last eight freeze-thaw cycles of the

Table 2. Details of model freezing and thawing.

Model	Unfrozen depth mm	Unfrozen thickness mm	Frozen thickness mm	Thaw settlement mm	Heaving Ratio	Time to thaw hr	Thaw rate mm/hr
Two-sided	0						
	50	50	62.85	12.85	0.20	38	1.65
	150	100	102.65	2.65	0.03	35	2.93
	250	100	115.59	15.59	0.13	83	1.39
	260	10	29.85	19.85	0.66	240	0.12
One sided	0						
	50	50	66.48	16.48	0.25	43.5	1.53
	150	100	109.23	9.23	0.08	39.5	2.77
	250	100	101.99	1.99	0.02	27.5	3.71
	350	100	100.03	0.03	0.0003	9	11.11

modeling program (Figs. 5, 6). Clear similarities are revealed between synthetic profiles and observed profiles.

Discussion and Conclusions

The thaw consolidation theory of Morgenstern & Nixon (1971) and Nixon & Morgenstern (1973) provides a theoretical basis for prediction of pore water pressures induced during thawing of ice-rich soils, and in our experiments, maximum shear strains were observed within the ice-rich layers where thaw consolidation was greatest. However, since the rate of thaw penetration was governed largely by soil ice contents (which determined latent heat required for phase change), thaw consolidation ratios (R) were actually highest where ice contents were least and thaw penetration fastest (central active layer zone, two-sided freezing experiment, $R = 0.37$ and basal zone, one-sided experiment, $R = 0.26$). Conversely, the slower thaw penetration in the ice-rich layers in both models resulted in the release of more meltwater and induced more soil deformation, but was reflected in lower thaw consolidation ratios.

Although the model of two-sided active-layer freezing did not strictly represent the annual cycle of the lower thermal boundary, we were able to successfully simulate segregation ice distributions. The distribution of segregation ice within the two-sided freezing model was similar to field observations in natural permafrost active layers. For instance, Mackay (1981, Fig. 15, p. 1674) clearly illustrated a desiccated central zone within the active layer in Garry Island very similar to that observed here. In addition, continuous monitoring of a permafrost slope in Svalbard during 2005–2006 (Harris et al. 2006) has also demonstrated an ice-poor zone in the central part of the active layer, with very little thaw settlement or downslope movement being recorded as this layer thawed. As in the experimental results discussed here, the majority of movement at the Svalbard field site occurred during thaw of the ice-rich basal zone. Progressive soil freezing from the surface down and from the permafrost table upwards forms a closed hydraulic system within the central zone of the active layer, both in the field and in our model. Water migration towards the respective freezing fronts reduces moisture contents in the central zone, and pore water suction increases effective stress and hence unfrozen shear strength.

In this paper we have presented initial results from one freeze-thaw cycle in a series of 17 such cycles undertaken during a three-year laboratory simulation of solifluction processes. More detailed papers are in preparation in which data from all cycles will be considered and recorded pore water pressures discussed. The initial hypothesis was that solifluction-induced shear strain results from thaw consolidation of ice-rich soil, and that the distribution of segregation ice within a frozen profile largely determines where greatest thaw strain will occur. Continuous monitoring of heave, settlement, and surface displacement of identical slope models subjected to contrasting thermal regimes has provided compelling evidence, supporting the initial hypothesis and confirming that thawing of the basal ice-rich zone within the permafrost model generated basal shearing and "plug-like flow" similar in character to field observations.

Acknowledgments

This research was funded by the British Natural Environment Research Council (Grant NER/B/S/2003/00748). Laboratory assistance from Gerard Guillemet and Anthony Dubois is gratefully acknowledged.

References

Benedict, J.B. 1970. Downslope soil movement in a Colorado alpine region: rates, processes, and climatic significance. *Arctic and Alpine Research* 2: 165-226.

Cheng, G. 1983. The mechanism of repeated segregation for the formation of thick-layered ground ice. *Cold Regions Science and Technology* 8: 57–66.

Coutard, J-P., Van Vliet- Lanoe, B. & Auzet, A.V. 1988. Frost heaving and frost creep on an experimental slope: results for soil structures and sorted stripes. *Zeitschrift für Geomorphologie, Supplementband* 71: 13-23.

Harris, C. 1981. *Periglacial Mass Wasting: A Review of Research.* BGRG Research Monograph. Norwich: Geo Books. 204 pp.

Harris, C., Davies, M.C.R. & Coutard, J.-P. 1997. Rates and processes of periglacial solifluction: an experimental approach. *Earth Surface Processes and Landforms* 22: 849-868.

Harris, C. & Lewkowicz, A.G. 2000. An analysis of the stability of thawing slopes, Ellesmere Island, Nunavut, Canada. *Canadian Geotechnical Journal*, 37: 465-478.

Harris, C., Luetschg, M., Murton, J.B., Smith, F.W., Davies, M.C.R., Christiansen, H.H. & Ertlen-Font, M. 2006. Solifluction processes in arctic permafrost: results of laboratory and field experiments, *EOS Transactions AGU* 87(52), Fall Meeting Supplement, Abstract C43A-03.

Kern-Luetschg, M.A., Harris, C., Cleall, P., Li, Y. & Thomas, H. 2008. Scaled centrifuge modeling of solifluction in permafrost and seasonally frozen soils. *Proceedings of the Ninth International Conference on Permafrost, Fairbanks, Alaska, June 29–July 3, 2008* (this proceedings).

Kinnard, C. & Lewkowicz, A.G. 2006. Frontal advance of turf-banked solifluction lobes, Kluane Range, Yukon Territory, Canada. *Geomorphology* 73: 261-276.

Lewkowicz, A.G. & Clark, S. 1998. Late summer solifluction and active-layer depths, Fosheim Peninsula, Ellesmere Island, Canada. In: A.G. Lewkowicz & M. Allard (eds.), *Proceedings of the Sixth International Conference on Permafrost, Yellowknife, Canada*. Centre d'Etude Nordiques, Université Laval, Sainte-Foy: 641-666.

Mackay, J.R. 1980. The origin of hummocks, western Arctic coast, Canada. *Canadian Journal of Earth Sciences* 17: 996-1006.

Mackay, J.R. 1981. Active layer slope movement in a continuous permafrost environment, Garry Island, Northwest Territories, Canada. *Canadian Journal of Earth Sciences* 18: 1666-1680.

Mackay, J.R. 1983. Downward water movement into frozen ground, western arctic coast, Canada. *Canadian Journal of Earth Sciences* 20: 120-134.

Matsuoka, N. & Hirakawa, K. 2000. Solifluction resulting from one-sided and two-sided freezing: field data from Svalbard. *Polar Geoscience* 13: 187-201.

Matsuoka, N. 2001. Solifluction rates, processes and landforms: a global review. *Earth-Science Reviews* 55: 107-133.

McRoberts, E.C. & Morgenstern, N.R. 1974. The stability of thawing slopes. *Canadian Geotechnical Journal* 11: 447-469.

Morgenstern, N.R. & Nixon, J.F. 1971. One-dimensional consolidation of thawing soils. *Canadian Geotechnical Journal* 8: 558-565.

Rein, R.G. & Burrous, C.M. 1980. Laboratory measurements of subsurface displacement during thaw of low-angle slopes of frost-susceptible soil. *Arctic and Alpine Research* 12: 349-358.

Schur, Y.I. 1988. The upper horizon of permafrost soils. *Proceedings of the Fifth International Conference on Permafrost,.(e Tapir, Trondheim,*: 867-871.

Schur, Y.I., Hinkel, K.M. & Nelson, F.E. 2005. The transient layer: implications for geocryology and climate change science. *Permafrost and Periglacial Processes* 16: 5-17.

Shiklomanov, N.I. & Nelson, F. 2007. Active layer processes. In.: S.A. Elias (ed.), *Encyclopedia of Quaternary Science* Vol. 3, Elsevier, Oxford, 2138-2146

Smith, D.J. 1988. Rates and controls of soil movement on a solifluction slope in the Mt. Rae area, Canadian Rocky Mountains, *Zeitschrift für Geomorphologie, Supplementband* 71: 25-44.

Washburn, A.L. 1967. Instrumental observations of mass-wasting in the Mesters Vig district, Northeast Greenland. *Meddelelser om Grønland* 166: 318 pp.

Wireless Sensor Networks in Permafrost Research: Concept, Requirements, Implementation, and Challenges

Andreas Hasler
Glaciology, Geomorphodynamics, Geochronology; Geography Department, University of Zurich, Switzerland
Igor Talzi
Computer Science Department, University of Basel, Switzerland
Jan Beutel
Computer Engineering and Networks Laboratory, ETH Zurich, Switzerland
Christian Tschudin
Computer Science Department, University of Basel, Switzerland
Stephan Gruber
Glaciology, Geomorphodynamics, Geochronology; Geography Department, University of Zurich, Switzerland

Abstract

In a joint project of computer- and geo-scientists, wireless sensor networks (WSNs) are customized for permafrost monitoring in alpine areas. In this paper, we discuss requirements for a rugged setup of such a network that is adapted to operation in a difficult environment. The experiences with a first deployment at Jungfraujoch (Switzerland) show that, beside hardware modifications of existing WSN platforms, special emphasis should be given to the development of robust synchronization and low-power data routing algorithms. This results from the fact that standard software tools are not capable in dealing with the high-temperature fluctuations found in high-mountains without compromising the power consumption and the network topology. Enhancements resulted in a second deployment at Matterhorn (Switzerland), from where we expect results in the near future. Once the technology of WSNs is a science-grade instrument, it will be a powerful tool to gather spatial permafrost data in near real-time.

Keywords: measurement; permafrost; PermaSense project; wireless sensor networks.

Introduction

Spatially distributed measurements of permafrost parameters over long periods are time consuming in deployment and maintenance, vulnerable to environmental impacts, and create inhomogeneous data sets, as no standard and easy applicable measurement devices exist. The project *PermaSense* addresses the development of a new generation of monitoring equipment for remote and harsh environments (Fig. 1). In this paper, we present the design and implementation of a wireless sensor network (WSN) to measure temperatures, dilatation, and diverse hydrological parameters in rock faces of alpine permafrost.

A WSN generally consists of distributed *network nodes* with attached sensors that communicate by local UHF radio within each other and that are up-linked by one (or several) *base stations* via mobile communication (e.g., UMTS, GPRS), internet, or other data transfer systems to a *data sink server* (Fig. 2). Each node contains a microprocessor, a radio transceiver, a sensor interface, some local memory, and an independent power supply. The network topology depends on the radio connectivity between the nodes. If data is transmitted via intermediate network nodes to the base station, this is called *multi-hop,* while a pure star-topology around the base station is called a *single-hop* network. Compared to existing logging systems using single radio-connected measurement devices, WSNs are designed to adapt their network topology dynamically according to the connectivity constraints, allowing observation of a larger area with multi-hop connection. While the dataflow is generally out of the network through the base station into the data sink, commands, network parameters or even executable programs can potentially be pushed into the network.

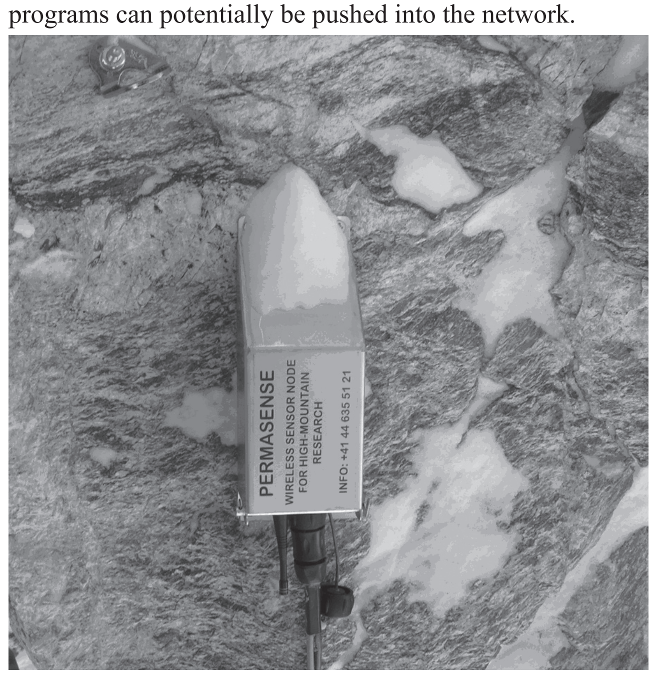

Figure 1. Network node at the field site Matterhorn – Hörnligrat.

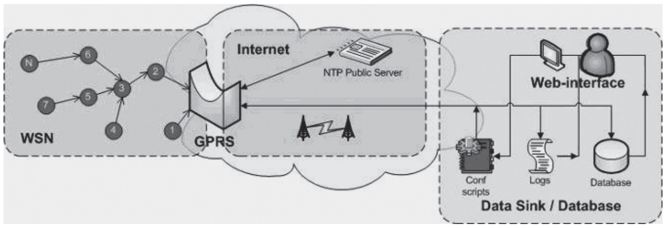

Figure 2. Framework of a WSN as used in our field deployments and test bed.

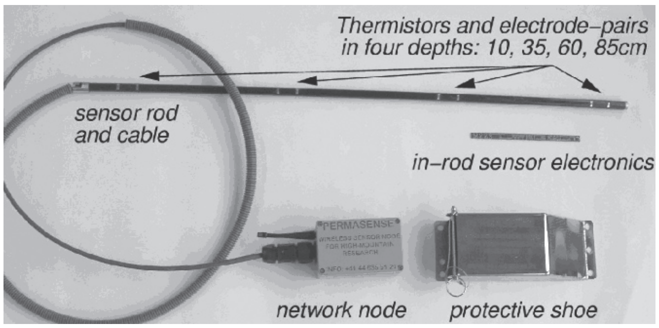

Figure 3. First-generation network node and customized sensor rod that measures temperatures and DC-resistivity as an indicator of liquid pore water at four different depths; the electronics and battery (lithium-thionyl) of the network node are mounted in a waterproof aluminum housing (125x80x57 mm) and protected from icefall and rockfall with a steel protective shoe. Measurement electronics are in the tip of the sensor rod to minimize temperature fluctuation errors.

Based on experiences with our first deployment on Jungfraujoch (3500 m a.s.l., Swiss Alps) during winter and spring 2006/2007, we specify requirements for yearlong stand-alone monitoring. WSN concepts and requirements for environmental use, and challenges for the implementation as well as the experiences from a second deployment generation are presented and discussed in this article.

Application of WSNs for Permafrost Research

Environmental WSNs

Environmental applications of WSNs have emerged in the past years following the general developments in mobile communication (Hart & Martinez 2006). Depending on the monitored variables and processes, the sensor networks differ in node size (e.g., from weather station to the futuristic "smart dust") as well as in spatial and functional extent of the network. In permafrost process research we are mainly interested in so-called localized multifunctional sensor networks. These systems are able to measure multiple parameters within an area of special interest. Despite the fast progress in the field of WSNs, only a limited number of application projects exists so far. The Projects *Glacsweb* (Martinez et al. 2004), *SensorScope* (http://sensorscope.epfl.ch/index.php), or the *Volcano monitoring project* (Werner-Allen et al. 2006) are such examples. A larger overview of existing environmental sensor network projects is given by Hart & Martinez (2006).

Potential of WSNs

For permafrost research and other remote environmental applications of WSNs, we identify the following potential:

- Once installed, maintenance and data acquisition is less time-consuming with WSNs than with standard logging systems, particularly at difficult accessible locations. The nodes inform the operator about battery level and functioning.
- Data is available all year-round at near real-time on a user interface. This is not only relevant for research, but can be very valuable for hazard monitoring.
- The data can be stored with redundancy, and not only locally on the logger. In case of destruction or loss of a sensor node, the data measured until this event is saved.
- Measurements are synchronous and arrive at one central database. No extensive manual post-processing and homogenization of the data is needed.
- Interval and mode of measurements do not require being statically predefined. They can be controlled by remote commands from the user interface or can be context-sensitive to other measurements of the network.

The project PermaSense

Wireless sensor networks have not yet been established for reliable, yearlong operation under cold climate and high alpine conditions. In PermaSense, computer- and geo-scientists upgrade in close cooperation the WSN platform *TinyNode* for permafrost research. Software for power-efficient operation of an adaptive multi-hop network topology is currently under development and being tested. Robust and reliable deployment hardware was designed, sensor interface hardware was developed, and software integration of sensors is being implemented. Customized sensors were manufactured, and compatible commercial sensors were evaluated and connected (Fig. 3). A detailed description of the network software of our first deployment, based on TinyOS, is given by Talzi et al. (2007).

Requirements for a permafrost WSN

Similar to standard logging systems for permafrost purposes, a WSN requires the following main features: Stable operation over a wide temperature range from -40°C to 40°C during at least one year or season, respectively (battery capacity). For analog measurements, a 12-bit analog-digital conversion (ADC) is generally sufficient, as the resulting resolution for temperature measurements over the indicated range is 0.02°C (a corresponding measurement accuracy can be reached with a zero-point calibration around 0°C). If pressure sensors are applied, a vibration wire (VW) compatible ADC, or frequency counter is of use. One or several digital interfaces (RS 232, RS 485, or SDI-12) for commercial sensors, allows the integration of diverse sensor types into the network. For power-intensive measurements (e.g., ERT), an incoming power supply line or solar panel control should be considered. All incoming and outgoing lines of this sensor interface should be lightning protected if the system operates at exposed locations.

As permafrost parameters typically change with slow rates, a temporal resolution of the measurements of some minutes to hours is required. Rarely, continuous measurements are needed (e.g., acceleration sensors), which is not further considered in this article. The mechanical setup should correspond to the operating conditions (e.g., Fig. 3).

WSN-specific requirements:

- The scale of the spatial extent ranges from decameters up to several hundred meters (depending on WSN limitations). To provide connectivity in complex alpine topography, a *multi-hop* system is preferable.
- Network topology is established automatically. A predefined topology is not applicable in practice and cannot adapt itself to a temporal lack of connection caused by snow cover, for example, of the devices.
- Connectivity through snow and ice is better with lower radio frequencies (<1GHz).
- Ultra low-power operation is supported. Sleeping cycles of the radio receiver, and consequently synchronization of the wake periods, are required.
- The measurements of different nodes are taken synchronically (in most cases, an accuracy of seconds is sufficient) and time-stamped.
- Nodes with no connectivity to neighbors store measured data locally on the node (capacity: 6 months).
- Data transmission capacity considers payload of the measured data with some margins to catch up data transmission from temporally invisible nodes. Generally, measured data does not exceed 2 kB per day.
- A *deployment mode* allows checking radio interconnectivity within the network during installation.
- A small form factor of the network node and a pluggable sensor interface ease the logistic effort for system maintenance.
- System health parameters (battery level, node temperature) inform the operator about network conditions and optimize the time of battery change.
- Command propagation into the network or context sensitivity allows to monitor periods of special interest in high resolution and to save power during less interesting periods.
- Data is stored in a database that provides metadata and has a safe backup strategy.
- A user interface supports the network maintenance (see above) and the database management.

Field Deployments

Energy balance models to estimate permafrost distribution and condition have recently been applied successfully to high-mountain topography (Gruber et al. 2004). Especially for steep and compact rock faces with little snow cover, modeling results correspond well with surface temperature measurements. Also mean annual subsurface temperature distribution and permafrost bodies are simulated satisfyingly with a 3D heat-conduction model (Noetzli et al. 2008). However, in such models processes of nonconductive heat transport are not considered despite their relevance for thawing depth and rate along fractures in the bedrock. The aim of our measurement site at Jungfraujoch is to quantify the spatial variability of thawing processes and heat transport in the near-surface layer.

First deployment: Jungfraujoch, winter 2006/2007

The influence of surface characteristics, fracturing, and meltwater availability is measured by eight of the above described sensor rods in gently steep (40°–70°) and fractured rock faces (general case in high alpine areas) around the Sphinx observatory at Jungfraujoch (ca. 3500 m a.s.l., Figs. 4, 5). Additionally, two thermistor chains are installed into the bordering ice faces.

The monitoring site consists of north and south faces of a ridge, which divide the network into two clusters with limited connectivity between them and differing thermal regimes (Fig. 4). Resulting from this topology, the thermal clock drift requires synchronization algorithms that let the node times converge even with such temperature deviations.

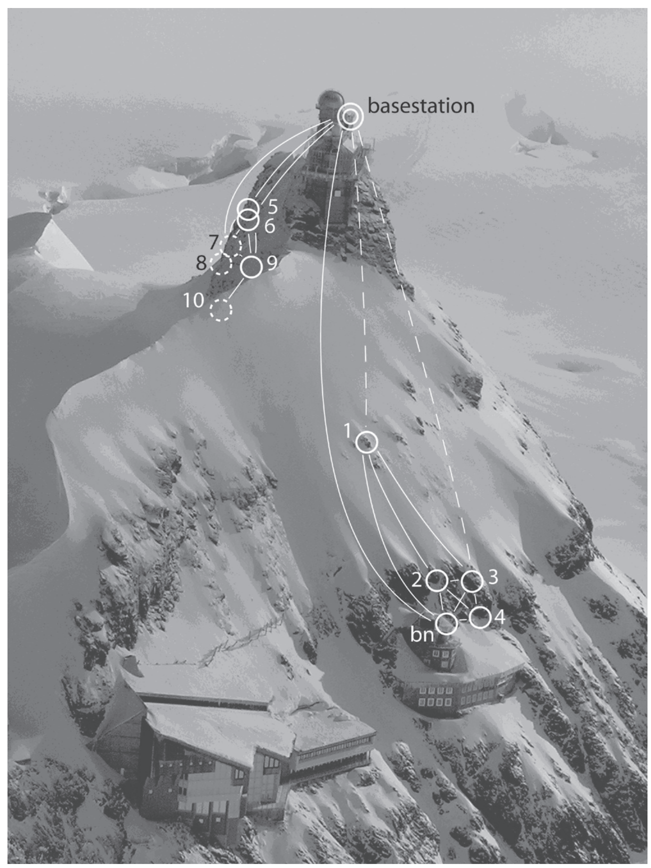

Figure 4. Deployment on Jungfraujoch (3500 m a.s.l., Swiss Alps) consisting of 10 sensor nodes with network topology; the base station is mounted on the Sphinx observatory. Each circle depicts a network node with its corresponding number. Lines indicate good radio connectivity between nodes; dashed lines indicate unstable connectivity; dashed circles are hidden nodes; and *bn* is a bridge node introduced to provide stable connection to the base station. The network is divided into to two clusters on the north-facing (left) and the south-facing (right) slopes of the ridge.

The initial installation of the sensors took place in fall 2006 after four months of system design and hardware production. We set up the first network at the same time, which, however, has not been successful due to the short development time and insufficient testing of the network software and hardware. In addition, a stability problem of the measurement values appeared under field conditions. After a debugging and testing phase over the winter of 2006/2007, first valid data could be gathered in April 2007 (Fig. 6). Yet no data transmission could be maintained over a period of more than two weeks. At this point, an extension of the project with the integration of network into a test bed prior to deployment was already planned for the second deployment in fall 2007. We decided to momentarily leave the network in a mode where data is stored locally to the node memory, and enhance and test the system for the second deployment.

Figure 5. Network node #4 and cable to the sensor rod, which is drilled one meter into the rock perpendicular to the surface. The network nodes can be easily exchanged and attached to the sensor by a waterproof plug.

Second deployment: Matterhorn "Hörnligrat" (3400 m a.s.l., Swiss Alps) in October 2007

Although public and research interests increased significantly following the hot summer of 2003, frost dynamics and natural hazards research in alpine permafrost areas has been discussed already a decade ago (e.g., Haeberli et al. 1997, Wegmann 1998). Frost weathering and rockfall activity is subject to yearlong field observations and measurements (e.g., Matsuoka & Sakai 1999, Matsuoka 2001) and lab experiments (Murton et al. 2006). These lab experiments have shown that ice segregation takes place also in solid (but porous) rock. Field data gave clear evidence for the contribution of temperature fluctuation and water to near-surface weathering and pebble fall. However, a direct physical linkage between temperature and rockfall disposition has not yet been demonstrated in the field. Different concepts of this linkage are discussed in Gruber & Haeberli (2007). The second deployment of PermaSense addresses this issue, to gather data of cleft ice and rock stability interaction.

The installation containing 13 sensor nodes with 6 sensor types, 2 bridge nodes, and 1 base station was made on the

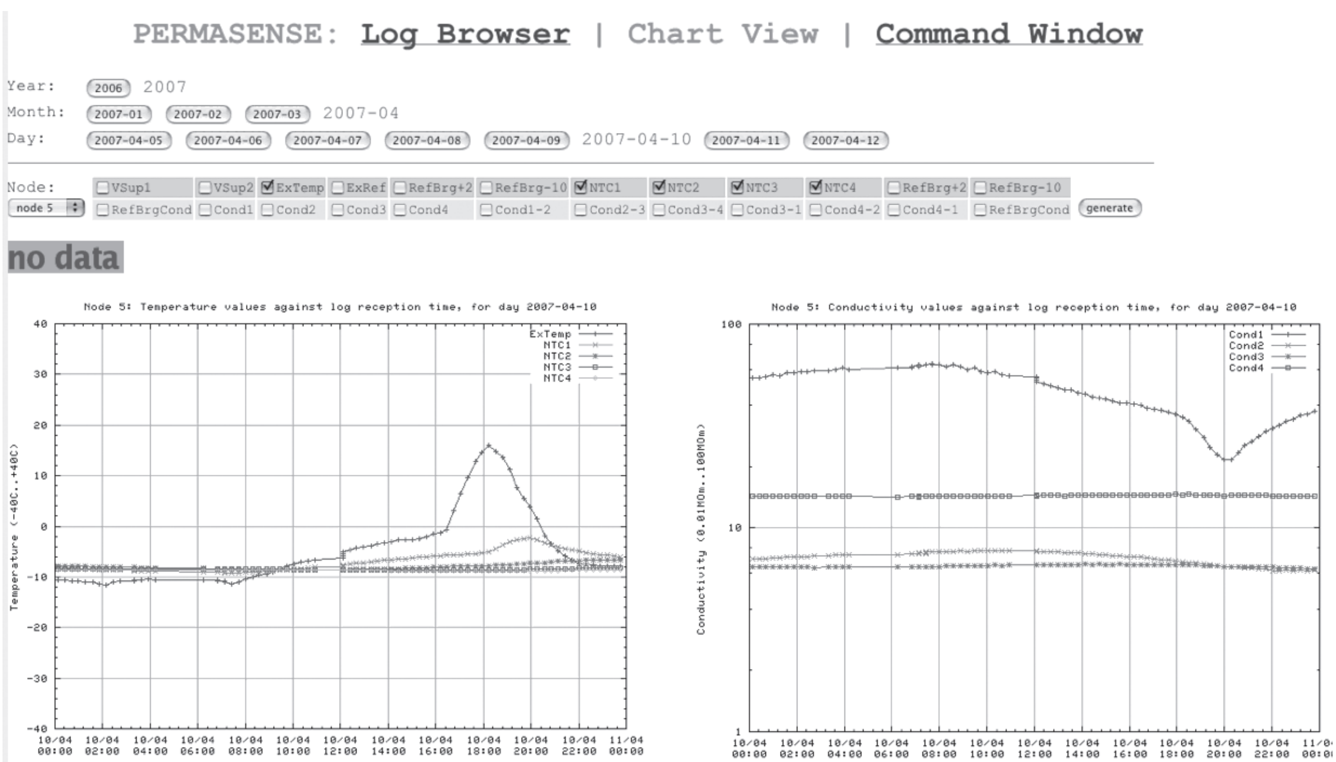

Figure 6. Screenshot of the user interface; direct visualization of one day of measurements from sensor rod #5 in the north-facing slope of the Sphinx. On the left, temperatures of the sensor rod thermistors (NTC1–NTC4) and the node temperature are plotted; the right diagram shows the corresponding rock resistivities. At the near-surface level (NTC/Cond 1), the temperature signal is clearly visible in the resistivity values.

northeast ridge of the Matterhorn at Hörnligrat in October 2007 (Fig. 7). At this site, a rockfall of some 1000 m^3 occurred in July 2003. Massive ice was observed at the surface of the detachment zone (Fig. 7) just after the event. This indicates the presence of stability-relevant ice-filled clefts in this area.

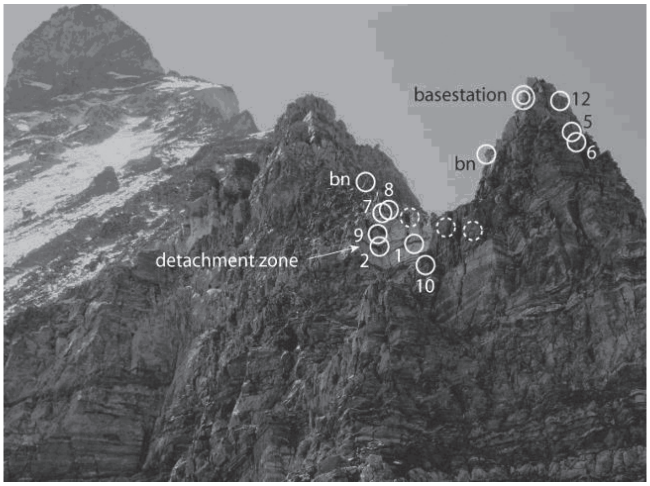

Figure 7. Deployment at Hörnligrat of the Matterhorn. Circles with numbers mark sensor nodes; dashed circles are sensors on the back (northwestern) side of the ridge; *bn* indicates bridge nodes.

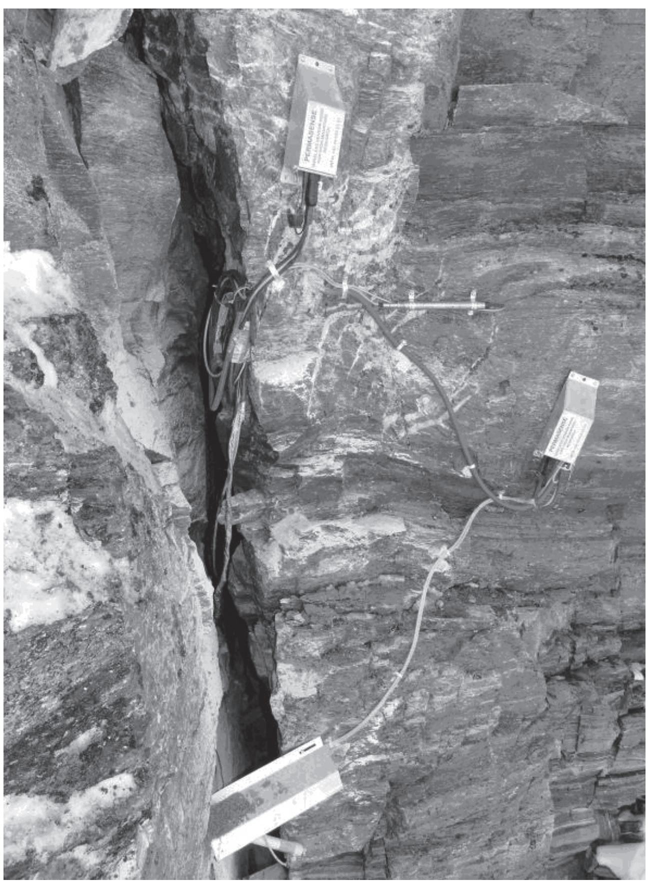

Figure 8. Installation site with multiple sensors: At the bottom, two crack meters measure dilatation. Within the cleft, potential water pressure and ice stress, as well as temperatures at different depths, are measured. The tube between the two nodes is the reference air pressure measurement.

In addition to the sensors used on Jungfraujoch, we integrated commercial sensors with a newly designed *sensor interface board* (SIB) into our network. With these sensors we measure crack dilatation, water pressure, ice pressure, and water movements in the clefts. Thermistor chains are mounted into clefts to measure temperature profiles together with the mentioned parameters. One node and SIB has a combination of this sensors attached resulting in a multiple sensor network node. The installation of more than one network node at one spot allows a flexible combination of sensors adapted to the situation in the field (Fig. 8).

Discussion of Experiences and Challenges of PermaSense

In the initial phase of PermaSense until April 2007, diverse problems were critical for the function of the WSN and the subject of debugging. The quality of the measurements and the instable operation of the base station are two examples of early-stage and hardware-related problems. Other system parts, such as the mechanical setup or the battery type, appeared well adapted to the conditions met in the field over the winter and spring 2006/2007.

The network setup at Jungfraujoch at the end of April 2007 and the subsequent test runs at the test bed in Zurich showed two main topics remaining critical for stable, long-term operation:

1. Time synchronization of the nodes.
2. Stability and power efficiency of the data routing.

As described above, the conditions in the field make time synchronization challenging due to large temperature fluctuations and deviations between installation spots. Short radio receiving slots compared to the sleeping intervals due to power limitations require a high quality of synchronization. The fact that the clock quartz are generally optimized for 25°C and have high drifts at negative temperatures makes a precise synchronization of a permafrost WSN even more challenging. Software-based temperature-drift compensation could be a possible solution, but needs extensive testing before application.

The currently used statically predefined data transmission slots, the radio communication as a power intense component, are used in a rather inefficient way. To optimize power consumption and consequently increase battery life-time, a dynamic organization of the data transmission slots is promising. This could also increase the data transmission capacity in areas of the network where it is required and, as a consequence, support more stable data routing as well.

Conclusions

Based on the experience gained from technology development and two high-mountain deployments, we can draw the following main conclusions for the application of WSNs in mountain permafrost research:

For a successful application of WSNs in permafrost research and in other environmentally challenging situations, an adapted software design and extensive testing of the network under realistic but well-monitored conditions are essential.

Due to large temperature fluctuations and large lateral temperature gradients, in combination with complex network topologies and power limitations, synchronization of the nodes is a very challenging task. Major algorithmic work, as well as specific testing, is needed here.

The power efficiency and the duration of operation without battery exchange in the field can be increased significantly with further software development.

Once we succeed in overcoming the current major problems, WSNs have the potential to become a powerful technology to gather spatially distributed field data in near-real time for permafrost research.

Acknowledgments

We would like to thank Sandro Schönborn, Roman Lim, and Mustafa Yücel for their contribution to PermaSense. The project is partly financed by the Swiss Federal Office for the Environment (FOEN) and the National Competence Center for Research – Mobile Information and Communication Systems (NCCR-MICS). We also acknowledge the helpful technical advice of Hansueli Gubler, ALPUG, in the initial phase of PermaSense.

References

Gruber, S. & Haeberli, W. 2007. Permafrost in steep bedrock slopes and its temperature-related destabilization following climate change. *Journal of Geophysical Research* 112. doi:10.1029/2006-JF000547.

Gruber, S., Hoelzle, M. & Haeberli, W. 2004. Rock wall temperatures in the Alps: Modelling their topographic distribution and regional differences. *Permafrost Periglacial Processes* 15(3): 299–307.

Haeberli, W., Wegmann, M. & Vonder Muehll D. 1997. Slope stability problems related to glacier shrinkage and permafrost degradation in the Alps. *Eclogae Geologicae Helvetiae* 90: 407–414.

Hart, J.K. & Martinez, K. 2006. Environmental sensor networks: A revolution in the earth system science? *Earth-Science Reviews* 78: 177–191.

Martinez, K., Hart, J.K. & Ong, R. 2004. Environmental sensor networks. *Computer* 37 (8): 50–56.

Matsuoka, N. 2001. Direct observation of frost wedging in alpine bedrock. *Earth Surface Processes and Landforms* 26: 601–614.

Matsuoka, N. & Sakai, A. 1999. Rockfall activity from an alpine cliff during thawing periods. *Geomorphology* 28: 309-328.

Murton, J.B., Peterson, R. & Ozouf, J-C. 2006. Bedrock fracture by ice segregation in cold regions. *Science* 314: 1127–1129.

Noetzli, J., Hilbich, C., Hauck, C., Hoelzle, M. & Gruber, S. 2008. Comparison of transient 2D temperature profiles with time-lapse electrical resistivity data at the Schilthorn Crest, Switzerland. *Proceedings.of the Ninth International Conference on Permafrost.*

Talzi, I., Hasler, A., Gruber, S. & Tschudin, C. 2007. PermaSense: Investigating permafrost with a WSN in the Swiss Alps. *In Proceedings for EmNets-07*: 8–12.

Wegmann, M. 1998. Frostdynamik in hochalpinen Feswänden am Beispiel der Region Jungfrau - Aletsch. Mitteilungen der Versuchsanstalt für Wasserbau, Hydrologie und Glaziologie an der ETH Zürich 161.

Werner-Allen, G., Lorincz, J., Johnson, J., Lees, J. & Welsh, M. 2006. Fidelity and yield in a volcano monitoring sensor network. *Proceedings of the 7th conference on USENIX Symposium on Operating Systems Design and Implementation* 7: 381–396.

A Four-Phase Model to Quantify Subsurface Ice and Water Content in Permafrost Regions Based on Geophysical Data Sets

Christian Hauck
Institute for Meteorology and Climate Research, University of Karlsruhe/Forschungszentrum Karlsruhe, Germany
Mathias Bach
Geophysical Institute, University of Karlsruhe, Germany
Christin Hilbich
Geographical Institute, University of Jena, Germany

Abstract

The indirect nature of geophysical soundings requires a relation between the measured variable (electrical resistivity, seismic velocity) and the rock/soil, water, air, and ice contents. In this contribution we present a model which determines the volumetric fractions of these four phases from tomographic electrical and seismic data sets. The so-called 4-phase model is based on geophysical mixing rules for electrical resistivity and seismic P-wave velocity. Observed resistivity and velocity data are used as input data on a two-dimensional grid; in the general case a porosity model has to be prescribed. First results confirm the good model performance, especially concerning the detection and quantification of ground ice as well as the detection of air cavities in the blocky surface layer. In addition, differences in ice content from time-lapse data can be determined. Examples from permafrost and non-permafrost sites with different morphologies (e.g., high mountain bedrock plateaus, scree slopes, moraines) are presented.

Keywords: electrical resistivity; four-phase model; geophysics; ice content; refraction seismics; water content.

Introduction

Based on the observational evidence of climate change in permafrost regions in recent years (e.g., Kääb et al. 2007, Marchenko et al. 2006, Fukui et al. 2007), it is now recognised that a detailed knowledge of the material composition of the subsurface in permafrost regions is required for (1) modeling of the future evolution of the ground thermal regime in permafrost areas, (2) a physically-based assessment of the hazard potential due to degrading permafrost, and (3) an optimal design of hazard mitigation measures. The important material properties in this context include the ice content, the unfrozen water content, and the porosity. The relative proportions between ice, water, and air content determines the thermal conductivity of the frozen material (e.g., Lachenbruch et al. 1982) which is needed for modeling of future thermal conditions of permafrost. Due to the commonly remote location of permafrost areas and corresponding logistical and financial difficulties in obtaining these properties from borehole logs, knowledge about the exact material composition of the subsurface in permafrost areas is scarce.

In frozen ground subsurface material may consist of four different phases: two solid phases (rock/soil matrix as well as ice), a liquid (unfrozen pore water), and a gaseous phase (airfilled pore space and cavities)(see Fig. 1). Except for laboratory and borehole data, the composition of the subsurface material can only be inferred through indirect geophysical investigations. Due to the complexity of the subsurface, a combination of complementary geophysical methods (e.g., electrical resistivity tomography and refraction seismic tomography) is often favoured to avoid ambiguities in the interpretation of the results (Maurer & Hauck 2007).

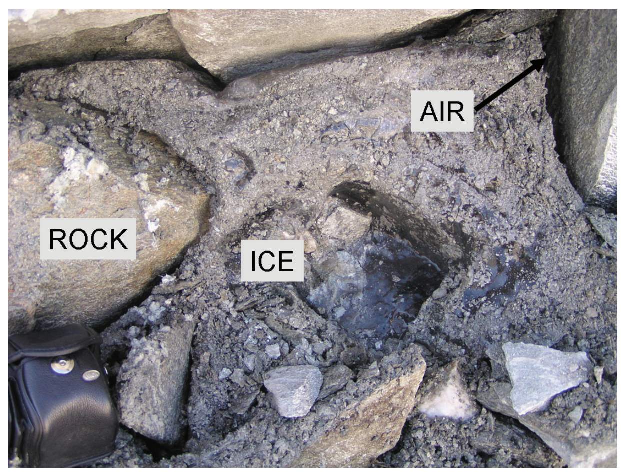

Figure 1. Photo of an ice-air-rock mixture within a rock glacier in the Swiss Alps. The camera in the lower left corner illustrates the scale.

However, the indirect nature of geophysical surveys requires a relation between the measured variable (electrical resistivity, seismic velocity) and the respective parts of the material composition (rock, water, air, ice). Such relations have been developed for the electrical properties; for example, the well-known relation between the electrical resistivity of the bulk material, the pore-water resistivity, the porosity and the saturation known as Archie's Law (Archie 1942), and for the elastic properties such as the mixing law for seismic P-wave velocities by Timur (1968).

In permafrost studies, quantitative combinations of electric and seismic data sets were introduced by McGinnis et al.

(1973) who used resistivity data for calculating the increase in seismic P-wave velocity due to the frozen layer. Oberholzer et al. (2003) used an index based on the ratio of resistivity and seismic P-wave velocity to differentiate between frozen and unfrozen morainic material in the Swiss Alps. However, up to now no physically-based relation between parameters commonly measured in surface geophysical surveys and the four phases present in permafrost material exists for practical applications in permafrost studies.

In the following a so-called 4-phase model (FPM) for explicit prediction of three of the four phases is presented which is based on two-dimensional tomographic electrical and seismic measurements. Results from the application of the 4-phase model to several periglacial morphologies will be shown to illustrate the performance of the model. In a further step the model is applied to time-dependent resistivity and seismic velocity data to determine the temporal change of ice and unfrozen water content between two measurement dates.

It is believed that the FPM serves as a useful tool for improved interpretation of geophysical data sets in frozen regions, and that it can be applied for determining quantitative information about the ice content and its temporal evolution.

Theory

The 4-phase-model is based on the well-known geophysical mixing rule for electrical resistivity (Archie 1942) and on an extension of the time-average formula for seismic P-wave velocities (Timur 1968) (Eqs. 1, 2):

$$\rho = a\rho_w \Phi^{-m} S_w^{-n} \tag{1}$$

$$\frac{1}{v} = \frac{f_w}{v_w} + \frac{f_r}{v_r} + \frac{f_i}{v_i} + \frac{f_a}{v_a} \tag{2}$$

where ρ and ρ_w are the electrical resistivities [in Ωm] of the bulk material and the pore water, respectively, Φ is the porosity, S_w is the saturation, n, m, and a are empirical constants, f_w, f_r, f_i, and f_a are the volumetric fractions of the water, rock, ice, and air content, and v, v_w, v_r, v_i, and v_a are the seismic P-wave velocities [in m/s] of the bulk material, water, rock, ice, and air, respectively. Under the condition

$$f_w + f_r + f_i + f_a = 1 \tag{3}$$

and using $\Phi = 1-f_r$ and $S_w = f_w/\Phi$, equations for the ice, water, and air content can be derived as a function of the rock content (1-porosity):

$$f_i = \frac{v_i v_a}{v_a - v_i}\left[\frac{1}{v} - \frac{f_r}{v_r} - \frac{1-f_r}{v_a} + \left(\frac{a\rho_w(1-f_r)^n}{\rho(1-f_r)^m}\right)^{1/n}\left(\frac{1}{v_a} - \frac{1}{v_w}\right)\right] \tag{4}$$

$$f_a = \frac{v_i v_a}{v_i - v_a}\left[\frac{1}{v} - \frac{f_r}{v_r} + \frac{1}{v_i}(f_r - 1) - \left(\frac{a\rho_w(1-f_r)^n}{\rho(1-f_r)^m}\right)^{1/n}\left(\frac{1}{v_w} - \frac{1}{v_i}\right)\right] \tag{5}$$

$$f_w = \left(\frac{a\rho_w(1-f_r)^n}{\rho(1-f_r)^m}\right)^{1/n}. \tag{6}$$

Equations (4), (5), and (6) allow then to explicitly compute ice, air, and unfrozen water content for each model block on a 2D-grid from seismic P-wave velocity and electrical resistivity data if a suitable porosity model can be prescribed. In the absence of ice or if the ice and rock content are considered as one (solid) phase, Equations (1) to (3) can be rearranged to determine the porosity. The seismic velocities for air (330 m/s) and ice (3500 m/s) are known—further material properties such as the P-wave velocity of the host rock material, the resistivity of the pore water, or the so-called cementation exponent m and the saturation exponent n have to be specified. Whereas the former two parameters can be measured in the field, the latter are often assumed to equal 2 for many rock materials (e.g., Archie 1942, Keller & Frischknecht 1966). In a further step these model parameters can be determined by a Monte Carlo approach, the results of which are used additionally as indicator for the reliability of the model results (Bach 2008).

The model was tested using electric and seismic data sets from two active rock glaciers in the Swiss Alps, where borehole data were available to verify the performance of the FPM. Sensitivity studies indicate a strong dependence of the quantitative model results on the pore water resistivity, which should be measured directly in the field, wherever possible.

Data Sets

Seismic and ERT data sets from various field campaigns on different periglacial morphologies were used to test the model performance and evaluate the applicability of the FPM to different rates of ice, water, air, and water within the subsurface. The geophysical data stem from a number of different projects, including the EU PACE project (Permafrost and Climate in Europe) and the geophysical monitoring network within PERMOS (Hilbich et al. 2008) and are described in the respective publications (Table 1). Data inversions were performed using the geoelectric Res2DINV software and a seismic inversion algorithm by Lanz et al. (1998). In the following we will present data from an ice-rich, coarse-grained moraine material from the South-Shetland Islands, Maritime Antarctica (further details can be found in Hauck et al. 2007), poor-ice bedrock slope with superficial fine-grained material on Schilthorn, Swiss Alps (described in Hauck 2001), frozen and unfrozen bedrock material from a long gentle slope in Jotunheimen, Norway (Hauck et al. 2004) and a low-altitude, cold-ventilated scree slope in the Black Forest, Germany (Hauck & Kneisel 2008). Examples of rock glaciers will be discussed in detail in a companion paper and will not be repeated here. Finally, a monitoring data set comprising measurements along the same survey line observed at two different times from the frozen bedrock plateau at Stockhorn, Swiss Alps (Hilbich et al. 2008) will be presented. The characteristics of the field sites are summarised in Table 1.

Four-Phase Model Results

Figure 2 shows inversion results for P-wave velocity and specific resistivity as well as the FPM results for the

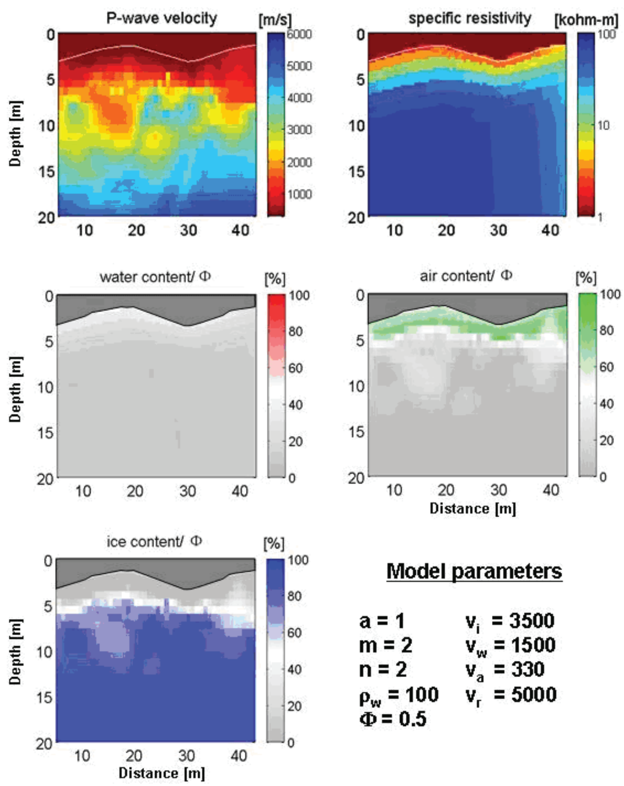

Figure 2. P-wave velocity and specific resistivity inversion results for the ice-cored moraine on Livingston Island, Maritime Antarctica. Ice, water, and air content are displayed relative to the available pore space of 50%.

volumetric contents with a prescribed constant porosity model of 50% for a blocky moraine on Livingston Island, Maritime Antarctica. Ice, water, and air contents are normalised by the porosity showing the percentage of the pore space which is filled by the respective material. Resistivities are high below the uppermost 2 metres, and seismic velocities show a low-velocity zone in this region, indicating an active layer without any frozen material. Consequently, the result for the ice content shows values up to 100% below the uppermost 2 m meaning that 100% of the pore space is filled with ice below the active layer. Within the active layer, mostly air and only little water is present within the available pore space. The results indicate clearly that the moraine is ice-cored—similar results were obtained for the ice-rich rock glacier Murtèl in the Swiss Alps (not shown here).

Figure 3 summarises the results for the other landforms, i.e., the frozen bedrock sites at Schilthorn and Juvvasshøe, the unfrozen bedrock slope 600 m below the top of Juvasshøe, and the low-altitude scree slope at Präg. All examples except Schilthorn were computed with different but constant porosity models, which may limit the significance for interpreting absolute values, but which can be used as indication to what extent the pore space is filled with the respective material. Based on results from a drilling in 1998 (Vonder Mühll et al. 2000), a porosity model that decreases with depth was used for the Schilthorn site. Table 2 provides an overview of the model parameters used for the different field sites.

The results for the frozen bedrock at Juvvasshøe show high ice contents below a 4 m thick active layer, which is mainly "filled" with air but only little water. The sharp transition between active layer and permafrost at 4 m can be seen both in the resistivity and in the seismic data. The permafrost layer consists almost completely of rock and ice with only little air and water. These results agree well with borehole logs and borehole temperatures from this site (Isaksen et al. 2001, Harris et al. 2001).

In contrast, the results for the frozen bedrock at Schilthorn indicate a much lower ice content relative to the available pore space and a significantly higher unfrozen water content (see also Noetzli et al. 2008, Hilbich et al. 2008). These model results are caused by the much lower resistivity values

Table 1. Characterization of the field sites and data sets used in this study.

	Livingston Island, Maritime Antarctica	Juvvasshøe/Jotunheimen, Norway PACE borehole	Juvvass/Jotunheimen, Norway	Schilthorn, Northern Swiss Alps PACE borehole	Stockhorn, Western Swiss Alps PACE borehole	Präg/Black Forest, Germany
Site description	ice-cored moraine	flat bedrock	north facing bedrock slope	north facing bedrock slope	bedrock plateau	cold ventilated scree slope
Lithology	boulderly diamicton with sands and silts	quartz monzonorite, 3-5 m weathered layer	quartz monzonorite, thick debris cover (vegetated)	limestone schists 0 to several m debris cover	Albit-Muskowit schists, > 1m debris cover	large blocks, gneiss
Altitude (a.s.l.)	30 m	1894 m	1300 m	2910 m	3410 m	600 m
Profile length, investigation depth	35 m 15 m	60 m 15 m	65 m 20 m	58 m 10 m	94 m 15 m	168 m 25 m
Literature	Hauck et al. 2007	Hauck et al. 2004	Hauck et al. 2004	Hauck 2001	Hilbich et al. 2008	Hauck & Kneisel 2008

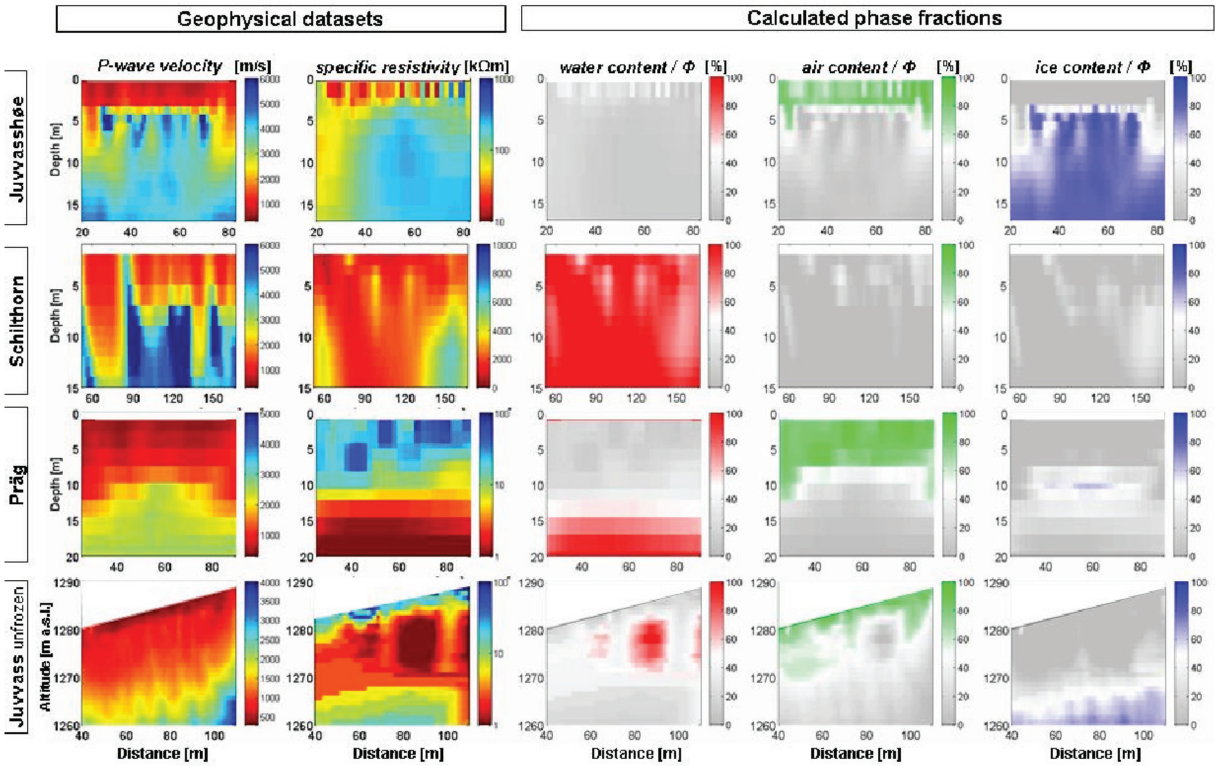

Figure 3. Geophysical data sets and 4-phase model results for four frozen and unfrozen mountain sites with different ice contents. Ice-, water- and air content are displayed relative to the available pore space Φ. The model parameters for the respective field cases are summarised in Table 2. Note, that the scales for seismic P-wave velocities and resistivities are different for the various sites.

yielding higher unfrozen water contents through Equation (1). Significant ice contents are found below a depth of 5 m, which agrees well with the observed active layer depth at the time of the measurements (Hauck 2001).

Blocky and ventilated scree slopes are known to sustain permafrost thermal regimes including substantial ground ice occurrences (Delaloye & Lambiel 2005). In the absence of excavations and boreholes, usually no indications are given as to whether ground ice is present or whether "dry permafrost conditions" prevail (Hauck & Kneisel 2008). Although the model results for the low-altitude scree slope at Präg indicate total ice contents of up to 25% (half of the available pore space of 50%) at around 10 m depth, this result has to be treated with care, as the model results for water and air show that the modeled ice-bearing zone is located right between the air-filled top layer (uppermost 7–10 m) and the ground water table at 12–15 m depth. Inversion results with a slightly deeper low-velocity top layer or a low-resistivity bottom layer reaching to slightly shallower depth would lead to a vanishing intermediate ice layer. Such inaccuracies in modeled layer depth are well within the uncertainty range of geophysical inversion models.

The unfrozen Juvvass slope is located along the northern slope of Juvvasshøe summit, but at an altitude where joint thermal and geophysical measurements proved the absence of permafrost (Hauck et al. 2004). The FPM results correctly predict no ice occurrences within the uppermost 10 m, where air is predominantly found in the upper 2 m with partly

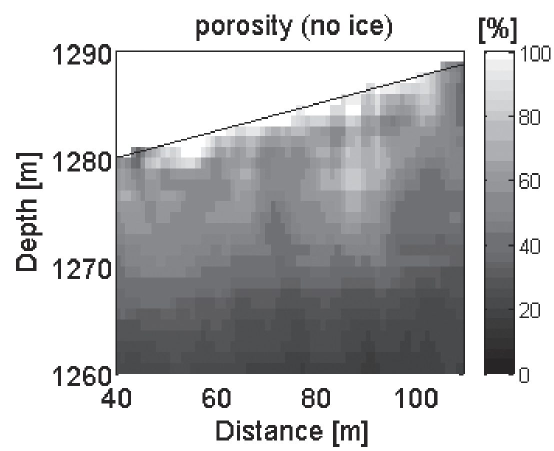

Figure 4. Calculated porosity for the unfrozen bedrock slope at Juvvass/Jotunheimen, Norway, under the assumptions of no ice and n = m = 2.

saturated conditions below. However, below a depth of 10 m modeled ice content values are increasing with depth. This obvious discrepancy to the thermal evidence has its causes in the increasing velocity and resistivity values measured at greater depth, which most probably corresponds to the bedrock layer. Assuming an ice content of zero and using the simplifications of n = m = 2, Equations (4)–(6) can be reformed to compute the porosity distribution over the model domain. In Figure 4 porosity values >50% are predicted for

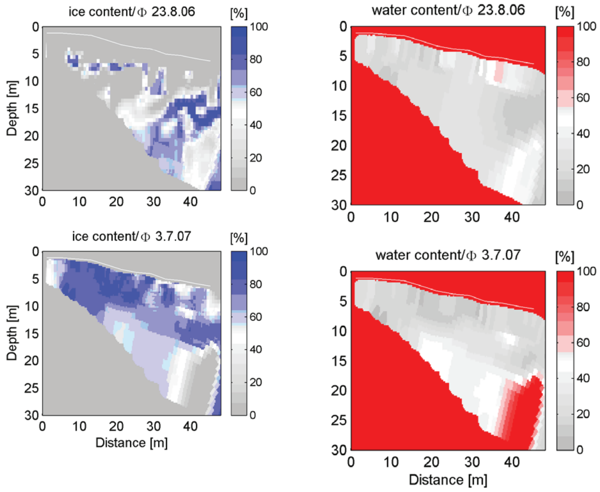

Figure 5. FPM Monitoring results for ice and water content at the bedrock plateau Stockhorn, Western Swiss Alps, for two measurement dates in summer 2006 and 2007.

the bouldery surface layer with decreasing porosity values below, indicating the more and more compacted rock material at greater depths. This much more probable scenario (no ice and decreasing porosity with depth as opposed to constant porosity and increasing ice content with depth) illustrates the main deficiency of the FPM in cases of low ice contents and unknown porosity distribution. Because rock and ice can exhibit similar seismic P-wave velocities and similarly high resistivity values, the differentiation between bedrock and ice occurrences is sometimes difficult, especially if no geological or glaciological *a priori* data are present.

Monitoring Results

The full potential of the FPM becomes evident for applications with time dependent data sets. Figure 5 shows the FPM results for two measurements at Stockhorn, Western Swiss Alps, where geoelectric and seismic measurements are regularly conducted within the geophysical monitoring network of PERMOS (Permafrost Monitoring Switzerland, see Hilbich et al. 2008). Due to different resolutions of seismic and ERT data sets, the coinciding model domain is triangular in this case.

Measurements were obtained in late summer 2006 and early summer 2007, representing different phases of the seasonal thawing of the active layer. The much higher ice contents in the uppermost 5 m in July 2007 compared to the ice-free conditions at the end of August 2006 are clearly visible in Figure 5. Furthermore, ice contents at greater depth (>15 m) are larger in August 2006 than in the beginning of July 2007, which may resemble the phase lag of winter temperatures. Corresponding water contents are generally low with maximum values near the surface in August and at greater depth in July. The saturated water anomaly in the lower right corner originates from a consistently occurring low-resistive anomaly in the ERT monitoring results, the cause of which has not yet been determined.

Table 2. Model parameters used for FPM calculations at the different field sites. In all cases the following values were used: $a = 1$, $m = 2$, $n = 2$, $v_i = 3500$ m/s, $v_a = 330$ m/s, $v_w = 1500$ m/s.

	ρ_w [ohm-m]	Φ	v_r [m/s]
Livingston Island,	100	0.5	5000
Juvvasshøe	100	0.2	6000
Schilthorn	300	0.5 – 0.25	4000
Präg	100	0.4	5200
Juvvass slope	100	0.5	6000
Stockhorn	100	0.3	5000

Conclusion

A new model for quantifying subsurface ice, water, and air contents in permafrost regions has been presented. The so-called 4-phase model (FPM) is based on tomographic specific resistivity and seismic P-wave velocity data sets and combines well-known petrophysical relationships of electric and elastic properties of the material on one hand and the relative phase fractions within the subsurface on the other hand. Field cases from a series of different permafrost sites were presented to evaluate the model performance. Key results from this study include:

- The model correctly delineates the ice, air, and water contents in cases of large ice occurrences such as ice-cored moraines and rock glaciers.
- Internal layers, especially the active layer, can be delineated because of strong contrasts in the vertical ice and air distribution. These contrasts can become more pronounced in the FPM results than in the original geophysical data, which facilitates the interpretation.
- Unfrozen water contents are generally low, except for the Schilthorn site, where modeled water content values are higher than the corresponding ice contents.
- In its present form, the absolute model results are strongly biased by the prescribed porosity model. As a consequence, phase fractions are shown relative to the available pore space. In a further step the free model parameters (including porosity) will be determined using a quasi Monte Carlo approach yielding more realistic porosity distributions.
- Deficiencies of the FPM have been found for cases of low ice contents in combination with an unknown porosity distribution. As rock and ice may exhibit similar seismic P-wave velocities and similar high resistivity values, the differentiation between bedrock and ice may become difficult, especially if no geological or glaciological *a priori* data are present.
- Promising results were obtained for geophysical monitoring data, where porosity remains unchanged and resistivity and velocity changes can unambiguously be related to changes in ice, air, and water content.

Acknowledgments

We would like to thank all field crews participating in the geophysical surveys, H. Maurer for providing the seismic inversion code and M. Böttcher for her contribution in developing the FPM. Fieldwork was partly financed by the EU-PACE, PERMOS (BAFU, Switzerland) and Permamodel (Spanish Antarctic Program and University of Zürich) projects.

References

Archie, G.E. 1942. The electrical resitivity log as an aid in determining some reservoir characteristics. *American Inst. of Mining and Metallurgical Engineers* 146*:* 55–62.

Bach, M. 2008. Modellierung von Eis- und Wassergehalt im Untergrund mittels seismischer und geoelektrischer Tomographie. M.Sc. Thesis. University of Karlsruhe.

Delaloye, R. & Lambiel, C. 2005. Evidence of winter ascending air circulation throughout talus slopes and rock glaciers situated in the lower belt of alpine discontinuous permafrost (Swiss Alps). *Norwegian Journal of Geography* 59(2): 194-203.

Fukui, K., Fujii, Y., Ageta, Y. & Asahi, K. 2007. Changes in the lower limit of mountain permafrost between 1973 and 2004 in the Khumbu Himal, the Nepal Himalayas. *Global Planet. Change* 55(4): 251-256.

Harris C., Davies M.C.R. & Etzelmüller, B. 2001. The assessment of potential geotechnical hazards associated with mountain permafrost in a warming global climate. *Permafrost and Periglac. Process*. 12: 145-156.

Hauck, C. 2001. Geophysical methods for detecting permafrost in high mountains. PhD Thesis. ETH Zürich, Switzerland, *VAW-Mitteilung* 171, 204 pp.

Hauck, C., Isaksen, K., Vonder Mühll, D. & Sollid, J.L. 2004. Geophysical surveys designed to delineate the altitudinal limit of mountain permafrost: an example from Jotunheimen, Norway. *Permafrost and Periglac. Process*. 15 (3), 191-205.

Hauck, C., Vieira, G., Gruber, S., Blanco, J.J. & Ramos, M. 2007. Geophysical identification of permafrost in Livingston Island, maritime Antarctica. *J. Geophys. Res*. 112: F02S19, doi: 10.1029/2006JF000544.

Hauck, C. & Kneisel, C. 2008. Quantifying the ice content in low-altitude scree slopes using geophysical methods. In: C. Hauck & C. Kneisel (eds.), *Applied geophysics in periglacial environments*. Cambridge University Press, *in press*.

Hilbich, C., Hauck, C., Delaloye, R. & Hoelzle, M. (2008): A geoelectric monitoring network and resistivity-temperature relationships of different mountain permafrost sites in the Swiss Alps. *Proceedings of the Ninth International Conference on Permafrost, Fairbanks, Alaska, June 29–July 3, 2008* (this proceedings).

Isaksen K., Holmlund P., Sollid J.L. & Harris C. 2001. Three deep alpine-permafrost boreholes in Svalbard and Scandinavia. *Permafrost and Periglac. Process*. 12: 13-25.

Kääb, A., Frauenfelder, R. & Roer, I. 2007. On the response of rockglacier creep to surface temperature increase. *Global Planet. Change* 56 (1-2): 172-187.

Keller, G.V. & Frischknecht, F.C. 1966. *Electrical Methods in Geophysical Prospecting*, Pergamon Press, Inc.

Lachenbruch, A.H., Sass, J.H., Marshall, B.V. & Moses, T.H.J. 1982. Permafrost, heat flow and the geothermal regime at Prudhoe Bay, Alaska. *J. Geophys. Res.* 87(B11): 9301-9316.

Lanz, E., Maurer, H.R. & Green, A.G. 1998. Refraction tomography over a buried waste disposal site. *Geophysics* 63(4): 1414-1433.

Marchenko, S.S., Gorbunov, A.P. & Romanovsky, V.E. 2007. Permafrost warming in the Tien Shan Mountains, Central Asia. *Global Planet. Change* 56(3-4): 311-327.

Maurer, H. & Hauck, C. 2007. Geophysical imaging of alpine rock glaciers. *J. Glac.* 53(180): 110-120.

McGinnis, L.D., Nakao, K. & Clark, C.C. 1973. Geophysical identification of frozen and unfrozen ground, Antarctica. *Proceedings of the Second International Conference on Permafrost*, *Yakutsk, Russia:* 136-146.

Noetzli, J., Hilbich, C., Hauck, C., Hoelzle, M. & Gruber, S. 2008. Comparison of transient 2D temperature fields with time-lapse electrical resistivity data at the Schilthorn Crest, Switzerland. *Proceedings of the Ninth International Conference on Permafrost, Fairbanks, Alaska, June 29–July 3, 2008* (this proceedings).

Oberholzer, P., Vonder Mühll D. & Ansorge J. 2003. Shallow structure of the lower Rossboden Glacier and its moraine dam (Valais, Swiss Alps). *Eclogae Geologicae Helvetiae* 96(2): 299-312.

Timur, A. 1968. Velocity of compressional waves in porous media at permafrost temperatures. *Geophysics* 33(4): 584-595.

Vonder Mühll, D., Hauck, C. & Lehmann, F. 2000. Verification of geophysical models in Alpine permafrost using borehole information. *Annals of Glaciology* 31: 300-306.

—Plenary Paper—

Rationalizing Climate Change for Design of Structures on Permafrost: A Canadian Perspective

Don W. Hayley
EBA Engineering Consultants Ltd., Canada
Bill Horne
EBA Engineering Consultants Ltd., Canada

Abstract

The design engineer is challenged by uncertainty when determining how a plethora of published trends indicating a warming arctic climate can affect future permafrost stability. A process was developed in Canada in 1998 for screening projects in an attempt to rationalize the effects of climate change. Two case histories from the authors' files are used to illustrate the screening process. One project is a government building with complex foundation conditions but a defined service life. The second example is a site reclamation project that relies on permafrost for stability. Reclamation requires confirmation that the risk of thaw can be managed to an acceptable level over the long term. Climate change trends for structures on permafrost with a defined service life can reasonably be predicted from historical climate data and climate normals developed over a period of years (30 years). Global Climate Models (GCM) can be a better choice when longer term analyses are required. Both methodologies have limitations that must be balanced with appropriate risk assessment. A geothermal analysis that includes appropriate climate trend input, coupled with a failure modes and effects analysis, can provide a useful tool for evaluating alternatives where long term environmental risks must be managed.

Keywords: Canada; climate change; GCM; permafrost; site reclamation; thermal analysis; thermosyphons.

Introduction

Concern about global warming has added a new layer of uncertainty to the current practice of cold regions engineering. Recent studies have clearly shown that climatic warming trends are more severe at higher latitudes, and regional data from northern Canada has identified that the mean annual air temperatures are most affected by warmer than normal winter conditions. Structures that rely on properties of permafrost and ice for long-term stability can be at risk if design processes do not recognize and rationalize future uncertainty from changing climatic conditions. It is no longer an accepted procedure to adopt historic thirty-year climatic normals as design parameters in regions of permafrost.

This paper describes a risk-based process for screening projects sensitive to climatic warming that was developed in 1998 for application in Northern Canada. In this paper, the process is described in general terms, and two representative projects are used as case histories to illustrate the strengths and limitations of the process.

Project Screening Process

Engineering projects in the north usually depend on permafrost as a structural material for foundation support, seepage retention or as a barrier for contaminant flow. The ability of the frozen ground to carry out these functions depends on site conditions and meteorological parameters that sustain the permafrost. Environment Canada initiated a three year study to review and document the factors that require consideration when designing new structures on permafrost in 1995. The author was a contributor along with a number of government scientists and university researchers with permafrost interests. The product was a report titled "Climate Change Impacts on Permafrost Engineering Design" (Etkin et al. 1998). The report is no longer available in print but can be provided by the authors in .pdf form on request.

The report is ten years old and much has changed in our understanding of how climate change is affecting our practice. The value in the 1998 report is the recognition that not all structures are exposed to the same risk level. The process requires the designer to systematically consider the sensitivity of the site and type of structure to damage resulting from changes to the permafrost regime. Each project is screened to categorize its site sensitivity and the consequences of failure resulting from permafrost warming or thaw following the schematic in Figure 1. The probability and consequences feed into a risk table, Figure 2, where the risk level, identified as a scale with four levels, is used to determine a reasonable level of analyses appropriate for the project.

The analyses range from non-concern through application of professional judgement to detailed quantitative analyses using state-of-practice numerical models. A simple classification system for relating soil type and initial ground temperatures to site sensitivity is shown in Figure 3. A table of consequences linked to potential failure modes is included in Figure 4.

Project Examples

Application of the process can be illustrated with two projects from the authors' files. The first project has been chosen to illustrate a complex foundation design for a new municipal building with a defined service life. The

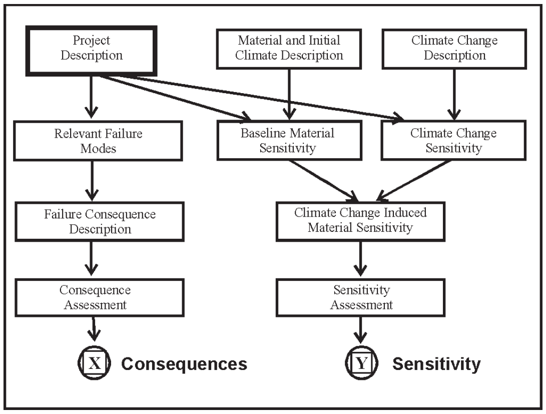

Figure 1. Screening process schematic.

Likelihood (Probability)	Consequence Negligible	Minor	Major	Catastrophic
Frequent	C	A	A	A
Probable	C	B	A	A
Occasional	D	B	B	A
Remote	D	C	B	A
Improbable	D	C	C	B

Risk Level	Analysis Prescribed
D	Not Required
C	Qualitative
B	Semi-quantitative
A	Detailed Quantitative

Figure 2. Risk assessment table (adapted from Canadian Standards Association, CSA-Q634-91).

Type of Soil	Permafrost Temperature Zone Zone 4 ($T < -7°C$)	Zone 3 ($-7 \leq T < -4°C$)	Zone 2 ($-4 \leq T < -2°C$)	Zone 1 ($-2 \leq T < 0°C$)
Any Soil containing massive ice	M	H	H	H
Peat and Organic	L	M	H	H
Lacustrine (silt or clay)	M	M	M	H
Morainal soils (till)	L	L	L	M
Marine Soils with Salinity	M	M	H	H
Alluvial and Glaciofluvial (sand or gravel)	L	L	L	M
Frost-shattered rock	L	L	M	M

Figure 3. Classification of sensitivity by soil type and permafrost zone.

Failure Mode	Project Type Tailings Ponds, Dams	Open Pit Mine	Roads	Foundations / Piles	Slopes, Embankments
Thaw Settlement	YES	NO	YES	YES	YES
Loss of strength / Creep	YES	YES	NO	YES	YES
Increased Permeability	YES	NO	NO	NO	NO
Accelerated frost effects	NO	NO	YES	YES	NO

Figure 4. Table of consequences linked to failure modes.

second project involves site reclamation that must address the implications of changes to the permafrost regime over the very long term. In both cases, the project cycle is well advanced such that they can be considered realistic case histories.

Inuvik Hospital

The Government of the Northwest Territories initiated replacement of the hospital in Inuvik with a new Regional Health Centre in the late 1990s. The chosen site was on the fringe of municipal development. The Inuvik area is typically covered with glacial materials with a high proportion of ground ice prevailing in continuous permafrost. The hospital site underlain by a granular soil with a relatively low ice content. Inuvik was developed as a new townsite in the 1950s, and the challenges of building on ice-rich permafrost were met at that time by establishing a procedure for installation of timber piles frozen into steamed holes (Philainen 1959). The construction could then proceed above the surrounding ground to provide a cold crawl space to allow natural air convection. These designs have functioned well but are now generally architecturally unacceptable for municipal and industrial buildings. The new hospital required its main floor to be on grade, with a crawl space excavated into permafrost soils. A thermosyphon heat exchange system was chosen to allow below grade foundation design.

The guideline screening process identified that Inuvik is a region of high sensitivity to climate warming and that the consequences of thaw-settlement on a structure of this type would be severe. Moreover, the lower Mackenzie Valley, in close proximity to the Beaufort Sea, is recognized as a “hot spot” for climatic extremes. An appropriate framework for design analyses was therefore state-of-practice geothermal modelling to select a thermosyphon configuration that would sustain the permafrost foundation soils. This must be coupled with consideration of the potential for future deformations attributed to permafrost warming. The building had a designated design life of thirty years; therefore, it was necessary to look forward to the year 2030 for climatic input to design analyses and to consider the probability that extreme events could upset the ground thermal regime during the thirty years of operation.

The building is a steel frame structure on concrete footings set below grade with a warm crawl space. The underlying permafrost is protected from thaw with a thick layer of rigid polystyrene insulation underlain by a horizontal looped thermosyphon system. Figure 5 shows the structure at the open foundation and framing stage in October 2001, and a foundation schematic is shown in Figure 6.

The thermal design requirements were to develop a combination of granular pad thickness, insulation thickness and thermosyphon spacing that would satisfy the design life requirements of preservation of the permafrost and minimal warming from initial ground temperatures. The design was based on two-dimensional finite element geothermal analyses that have been configured to include heat flux to a horizontal plane of thermosyphons (Hwang 1976). Heat is

Figure 5. Inuvik Hospital – open foundation and framing stage, October 2001.

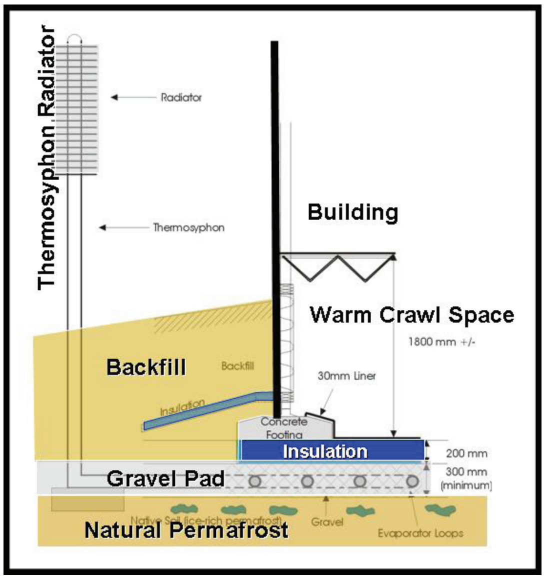

Figure 6. Foundation schematic.

removed from the foundation soils and dissipated to the air at the above-ground radiators whenever the air is colder than the ground below the building. The overall heat balance, therefore, becomes dependant on the outside air temperature and the efficiency of heat extraction process. That efficiency is expressed by a coefficient that can be determined from the literature (Haynes and Zarling 1988) or adapted from similar projects where performance records are available. The greatest uncertainty is the outside air temperature and wind velocity and how that might change in response to microclimatic effects from construction or macro-climatic effects from climate warming trends.

The foundation system was configured to satisfy thermal design criteria based on historic air temperature records for each of the following conditions:

- Five consecutive 1 in 5 warm years followed by a 1 in 100 warm year,
- Ten consecutive 1 in 5 years, and
- A linear warming trend over the life of the structure.

It was necessary to use the historical database to construct hypothetical annual air temperature inputs that were representative of each of the above conditions. A probabilistic analysis was carried out to determine the mean monthly temperatures representative of both the 1 in 5 and 1 in 100 return period warm years. The freezing and thawing indices for each of the years from 1957 to 2000 were calculated and ranked with a "best fit" linear regression on probability paper. The 1 in 5 and 1 in 100 warm indices were chosen and normal monthly air temperatures were scaled upward by the ratio of the respective freezing and thawing indices to their normals. These constructed new mean monthly air temperature annual cycles were considered representative of conditions with the chosen return periods.

The influence of a potential global warming trend was evaluated by starting at the mid-point of the thirty year Canadian Climate Normals available at the time (1961 to 1990) and ramping the mean annual temperatures upward in a linear function over the period from 1975 to 2030. The Environment Canada Report provided guidance for selecting either a best estimate case or a high sensitivity case global warming scenario and amplifying the effects based on season, and latitude. Inuvik lies at about 70°N latitude where the winter amplification increases the seasonal increase by a factor of 3 and the summer increases are attenuated by a factor of 0.5. The annual cycle is divided into four seasons of three months each and the air temperature increase applied for each month by cycle expressed as degree-C/month/decade was: Winter 0.95, Spring 0.66, Summer 0.16, and Fall 0.18. This allowed construction of a mean monthly air temperature representative of each year as the temperatures continued to increase in a linear fashion. The overall trend for the high sensitivity case chosen as a design basis could be expressed as a ramp increase in mean annual air temperature of 0.47°C/decade with most of the warming applied during the winter and spring months.

The resultant climatic design input is shown in Figure 7. The analyses and design were carried out in early 2001 using the best available information at that time. It is used here to illustrate a process rather than quantify climatic design parameters for the community of Inuvik. If the work were undertaken today, the most current data would be used. Figure 7 also shows mean annual air temperatures recorded in Inuvik since the design and construction was completed. The limited data suggests that with some excursions, the climate continues to warm following a near linear relationship that fits the extrapolated best fit line for the entire 50 year data set. That line falls slightly above and is parallel to the values chosen for design.

The ground temperatures below the warm crawl space under the structure have been monitored. Initial ground temperatures at a depth of 5 m were in the range of -2.6°C to -3.7°C and were predicted to rise slowly to -2.2°C over the thirty year term. Post-construction ground temperatures are reported elsewhere in these proceedings by Holubec et al, 2008. Performance has been better than design predictions for the first seven years of operation as the ground has been cooled by the thermosyphon system. There have been no movements reported for the foundations, although some water has migrated into the crawl space forming ice mounds under the insulation, and there has been some distress in the thermosyphon pipe attributed to manufacturing defects that are unrelated to the system design.

Reclamation of arctic military sites

Reclamation of decommissioned military defense sites across North America has been ongoing for the past twelve years. The most active program in Canada has been the Distant Early Warning (DEW) line of radar surveillance camps that stretched along the high arctic coastline from Baffin Island to Alaska. The sites typically lie about 69 degrees North Latitude where mean annual air temperatures range from -9°C to -15°C and corresponding ground temperatures range from -5°C to -12°C. The reclamation process often requires construction of secure landfills where contaminated soil is encapsulated in geomembrane liners and permafrost soils.

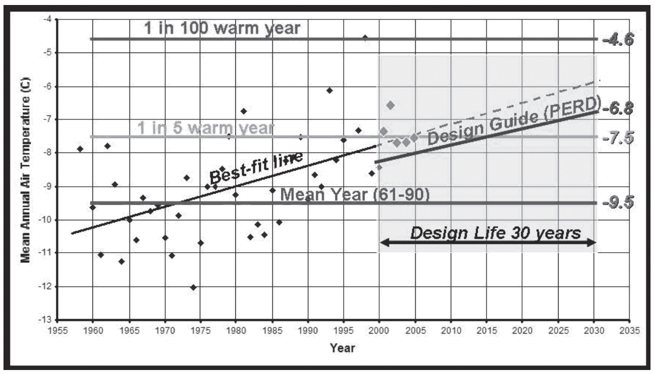

Figure 7. Mean annual air temperatures in Inuvik.

Unlike the Inuvik Hospital, these waste containment structures do not have a defined life but must function in perpetuity at a level of environmental risk that is acceptable to aboriginal people who use the nearby land for subsistence. Regulatory processes in the arctic require detailed technical review of all designs and consultation to ensure that best management practices are followed. Climatic uncertainty is therefore an important component in the design of waste containment structures that interface with permafrost. Stringent requirements must be met to achieve approvals.

A typical design developed jointly by EBA Engineering Consultants Ltd. (EBA) and UMA Engineering Ltd. for containment of contaminated soil is shown in Figure 8. The first defence against loss of contaminated pore fluid is a geomembrane liner. The second line of defence is the underlying ice-saturated permafrost soil. A final soil cover is configured to retain the active layer within the cover.

The screening process identifies most of these remote sites as moderate permafrost sensitivity; however, failure consequences could range from minor to major, depending on proximity to sensitive receptors. The risk posed from climatic warming is that the active layer thickness will increase with time allowing thaw to penetrate into the waste. A hypothetical worst-case failure mode could see the permafrost slopes supporting the liner thaw and slump,

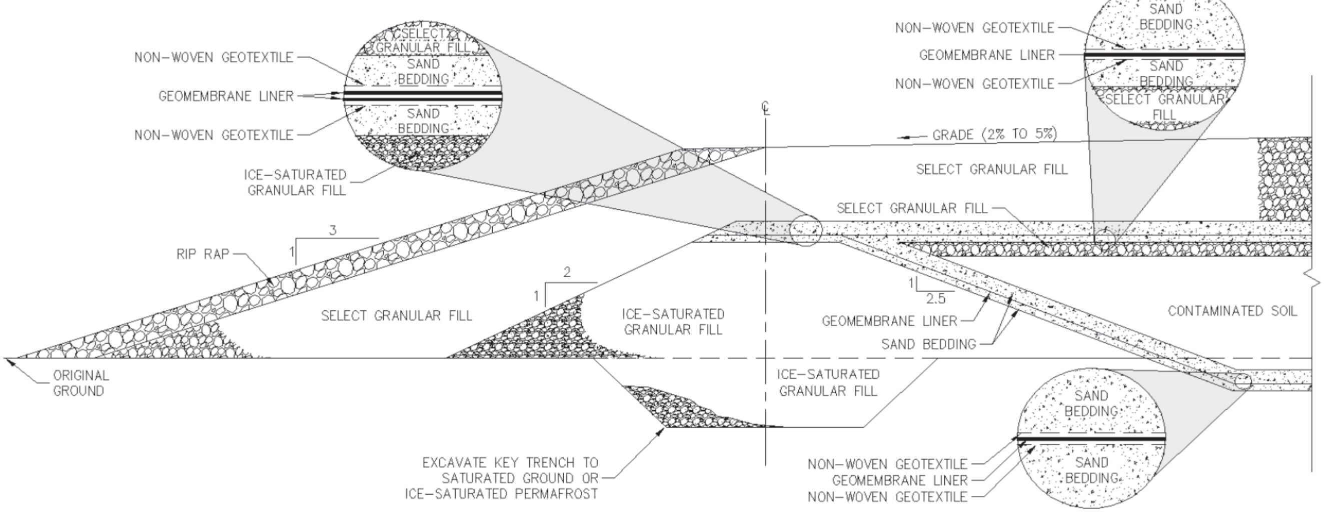

Figure 8. Design of soil containment landfill.

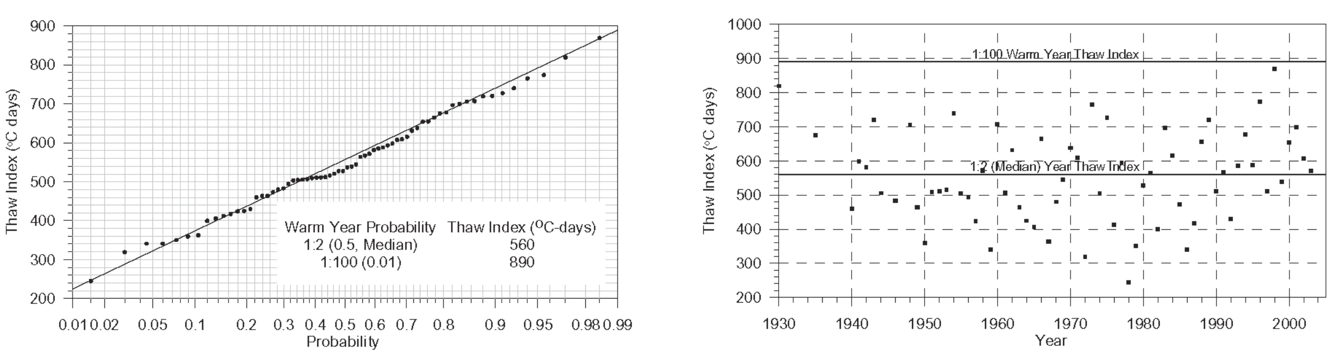

Figure 9. Historical thaw index probability.

resulting in failure of both the primary and secondary containment.

Geothermal analyses are required to substantiate the use of permafrost as a containment system for the landfills. Analyses are carried out to predict the short-term and long-term ground temperatures to determine the following:

- Length of time for landfill freezeback;
- Short-term thermal regime in the landfill;
- Long term thermal regime including an estimated amount of climate change; and
- Depth of annual thaw (active layer) in the cover material.

Geothermal analyses are carried out for each landfill using GEOTHERM, which is a proprietary two-dimensional finite element computer model developed by EBA. The model simulates transient, two-dimensional heat conduction with a change of phase for a variety of boundary conditions. The heat exchange at the ground surface is modelled with an energy balance equation considering air temperatures, wind velocity, snow depth, and solar radiation. The thermal analysis is calibrated to measured temperatures and/or observed active layers thicknesses.

Climatic data required for the thermal model include monthly mean air temperature, wind speed, solar radiation, and snow cover. Weather stations were maintained at the sites; therefore, climatic records dating back to the mid-1950s are available. The landfills are designed for mean conditions, warm conditions and long-term climate change.

Statistical analyses are carried out to determine mean monthly temperatures representative of a 1 in 100 warm year using the process described for the Inuvik Hospital. A historical thaw index probability analysis of a site is shown in Figure 9.

The influence of climate change on the landfill ground temperatures and active layer is evaluated by carrying out thermal analyses for a period of 100 years. The change in air temperature is estimated using a similar method, described in ACIA 2005. The air temperatures are estimated from Global Circulation Models, or GCMs. The GCMs are mathematical representations of the atmosphere, land surfaces, and oceans that have been developed to predict future climate behavior in response to changes in the composition of the atmosphere. Several scenarios have been developed to estimate the likely range of future emissions that may affect climate (IPCC 2000). Different GCMs have been developed, resulting in different degrees of projected climatic warming.

The outputs from various GCMs are posted on the web by the Canadian Climate Impact Scenario project (http://www.cics.uvic.ca/scenarios/index.cgi). Seasonal temperature changes are posted for the "B21 scenario" from four GCMs: a) CGCM2 (Canadian Centre for Climate Modelling and Analysis, Canada); b) GFDL-R30 (Geophysical Fluid Dynamics Laboratory, United States); c) ECHAM4 (Max-Planck Institute of Meteorology, Germany), and d) HadCM3 (Hadley Centre for Climate Prediction and Research, United Kingdom). Average seasonal changes in temperatures from the four GCMs for a central arctic site (69°N, 83°W) are listed in Table 1.

Table 1. Mean air temperature change (°C) over 110 years.

	December January February	March April May	June July August	September October November	Annual
Average of Four GCMs	6.4	4.2	3.8	5.1	4.9

Table 2. Predicted long-term maximum depth of thaw penetration into secure soil disposal landfills at a central arctic location.

Air Temperature Conditions	Predicted Active Layer Thickness (m)
After ten consecutive mean years	1.7
After one 1:100 warm year following ten mean years	2.2
After ten consecutive 1:100 warm years	2.4
After 100 years of global warming (average of four GCMs)	2.7
After 100 years of global warming plus one 1:100 warm year	3.3

The thermal analysis indicates that the permafrost remains during a 100-year period. The active layer depth continues to increase with time. Typical active layer thicknesses for a central arctic site are listed in Table 2 for the various climate conditions. The values are site specific. Thermal analysis are carried out for individual sites to take into account the local soil properties, ground temperatures, and climate.

The performance after 100 years becomes rather hypothetical because estimates of climate change scenarios seldom extend beyond 100 years. Longer term performance can only be bracketed by a range of climate potential climate extremes between 100 and 200 years. The project team has evaluated the following three alternatives:

- Air temperatures reach a stable condition and remain constant after 100 years;
- Warming rate continues on a linear ramp function similar the first 100 years; or
- Warming rate reduces to 50% of the 100 year warming rate.

Thermal analysis indicates that the permafrost at central arctic sites will be retained below a thickened active layer if the warming rate continues at a constant rate for a period of 200 years. The ground temperature warms at a rate similar to the air temperature at these sites. Degradation of the permafrost may begin to occur at sites that initially have warmer air and ground temperatures.

A failure modes effects analysis (FMEA) can be carried out to evaluate the effects climate change as well as other failure modes. Methods of FMEA are described by Nahir et al. 2005, and Roberson and Shaw, 2005. The FMEA considers the effects of retrogressive thaw of permafrost at a predicted rate on the performance of the landfill, including the potential for physical instability and contaminant flux out of the landfill. The potential consequences of these releases to the surrounding environment can then be considered.

The consequence of failure can be ranked as low, minor, moderate, major or critical, relative to financial costs, ecosystem impact, and health and safety of the local population. Each proposed design must provide a balance between potential long term environmental impacts and legal obligations with the overall site remediation costs.

A geothermal design that includes a conservative climate change scenario coupled with an FMEA analysis will provide a basis for a rational decision on adoption of a landfill construction plan at a particular site.

Limitations and Conclusions

The screening process described in this paper has no official status as an adopted guideline in Canada. Nevertheless, it has received reasonable acceptance by Canadian regulators as an appropriate framework for identifying projects where climate change effects on permafrost can put the environment at risk. The study is now ten years old and has been tested with operating structures such as complex buildings, dams reliant on permafrost and industrial site reclamation. The process has been shown to add value to projects and streamline regulatory assessments. The inputs to the process must, however, evolve with time as scientific knowledge pertaining to the magnitude of warming trends matures.

The design engineer's toolbox comprises historical air temperature data and output from a range of GCMs that simulate hypothetical changes to the composition of the atmosphere. The application of these parameters as inputs to engineering analyses must be kept in perspective with the risks involved. Straight line extrapolation of historic air temperature data is not realistic beyond a thirty-year climate normal period and should never be used beyond the length of the period of record.

The failure of GCMs to predict current climate on a regional scale is a significant drawback to the use of these models for engineering analyses. All numerical models used by design engineers must be rationalized at the input stage by calibration to existing known conditions. The failure of many models to calibrate effectively sheds doubt on their use as predictive tools. At the current time, a practical option is to establish initial conditions at remote sites from limited site data and use the future trends predicted by GCMs with appropriate judgement.

It becomes a design engineer's unprecedented challenge to look more than 100 years into the future to establish climate change trends. Science seldom provides projections deep into the next century, and linear extrapolation from current conditions into that grey zone can have a serious adverse effect on decision-making for arctic resource development. Those projects must be based on best practices for risk assessment. That requires a coupling of appropriate ground thermal analyses with failure modes and effects analyses. We must always be prepared to weigh the consequences of a long term retrogressive system failure against general landscape degradation that could accompany many of the worst-case climate change scenarios that are currently being contemplated.

References

ACIA, 2005. *Arctic Climate Impact Assessment*. Cambridge University Press, 1042 pp.

Etkin, D. 1998. *Climate Change Impacts on Permafrost Engineering Design,* funded by Panel on Energy Research and Development Canada, Environment Canada, 42 pp.

Haynes, F.D. & Zarling, J.P. 1988. Heat transfer performance of commercial thermosyphons with inclined evaporator sections. *Proceedings of the Seventh International Conference on Offshore Mechanics and Arctic Engineering,* Vol. IV, 275-280.

Hwang, C.T. 1976. Predictions and Observations of the Behavior of a Warm Pipeline on Permafrost. *Canadian Geotechnical Journal,* Vol. 13. No. 4, pp. 452-480.

IPCC 2000. *Emissions Scenarios: A Special Report of the Intergovernmental Panel on Climate Change Working Group III.* Nebojsa Hakicenovic & Rob Swart (eds.). Cambridge, UK: Cambridge University Press, 570 pp.

Nahir, M., van Aanhout, M. & Reineche S., 2005. Application of Risk Management to Northern Affairs Program (NAP) Contaminated Sites in the North. Assessment and Remediation of Contaminated Sites in Arctic and Cold Climates, 189-198.

Philainen, J.A. 1959. Pile Construction in Permafrost. ASCE, *J. Soil Mechanics* Foundation Division., Vol. 85, No. SM6, Part I, 75-95.

Robertson, A. & Shaw, S. 2005. Enviromine. Failure Modes & Effects Analysis (FMEA). Ed. Shannon Shaw <http://robersongeoconsultants.com/rgc_enviromine/Issues/cls_FMEA.asp>

Terrestrial Carbon Dynamics Along a Permafrost-Dominated North-South Transect in the Tibetan Plateau

Jicheng He
Institute of Tibetan Plateau Research, Chinese Academy of Sciences, Beijing, P. R. China
Department of Earth & Atmospheric Sciences and Department of Agronomy, Purdue University, West Lafayette, Indiana
Qianlai Zhuang
Department of Earth & Atmospheric Sciences and Department of Agronomy, Purdue University, West Lafayette, Indiana
Tianxiang Luo
Institute of Tibetan Plateau Research, Chinese Academy of Sciences, Beijing, P. R. China

Abstract

We selected a north-south transect in the Tibetan Plateau, comprised of six alpine tundra ecosystems underlain with permafrost, to examine the terrestrial carbon dynamics with the Terrestrial Ecosystem Model (TEM) for the period from 1967 to 2000. We find that the ecosystems act as a carbon small source in the most northern site, Wudaoliang (-0.87 g C m^{-2} a^{-1}), while the other five sites act as a carbon sink at 0.31, 2.49, 5.19, 5.35, and 4.21 g C m^{-2} a^{-1} at Naqu, Tuotuohe, Anduo, Dangxiong, and Gandansi, respectively. From north to south, the number of months with carbon sink increases along the temperature and precipitation gradient. Due to warmer and wetter soil conditions, all sites in the transect acted as a carbon sink in the 1990s. The future warming climate may enhance ecosystem carbon sequestration due to increase of soil temperature and moisture associated with permafrost thawing in the Tibetan Plateau.

Keywords: net ecosystem production; permafrost; Tibetan Plateau; transect.

Introduction

The Tibetan Plateau, the largest geomorphologic unit on the Eurasian continent, almost covers an area of 2.6 million km^2, with an average altitude more than 4000 m above sea level, and accounts for 26.8% of China's landmass (Zhang et al. 2002). From the southeast to northwest, supplies of heat and water decrease gradually, and forest, meadow, steppe, and desert ecosystems are developed (Zheng 1996). Meanwhile, there exists the largest area of mountainous permafrost worldwide with an area of 1.5 million km^2 in the plateau. Climatic warming on the plateau in past decades has been evident from meteorological observation and ice core records (Liu & Chen 2000, Thompson et al. 2000). It has been shown that the annual mean temperature of the Tibetan Plateau has risen at a rate of 0.26°C per decade in the last 40 years, which was much higher than those of whole china and the world (Du 2001); the winter temperature rose about 0.32°C per decade from 1955 to 1996 (Liu & Chen 2000). Consequently, the region experienced widespread permafrost degradation, and the thickness of the active layer has increased in the last few decades. Future warming will likely result in an even more extensive and rapid permafrost degradation in the region. Thus, the knowledge of ecosystem responses to the changes of permafrost and active layer depths in the past will help understand the contribution of regional carbon dynamics to global carbon cycling. However, few studies have been conducted to quantify the inter-annual variations and changing trend in carbon fluxes for the terrestrial ecosystems in the plateau. On the plateau, heat and moisture increase gradually from north to south, and these gradients provide a good opportunity to examine the variation pattern of net ecosystem production (NEP) during the past decades. In this study, we select a north-south transect in the permafrost region in the plateau, including six field sites dominated by alpine tundra (Wudaoliang, Tuotuohe, Anduo, Naqu, Dangxiong, and Gandansi) to examine the terrestrial carbon dynamics during the past few decades with the Terrestrial Ecosystem Model (TEM), which is coupled with a permafrost model (Zhuang et al. 2001, 2002, 2003). Our aims are (1) to explore whether the terrestrial ecosystems in the permafrost region are sequestering or releasing carbon, (2) to examine the temporal trends of NEP for each site along the transect and their relations with soil temperature and moisture, and (3) to provide information for simulating the response of alpine tundra ecosystems to projected climate variability across the range of permafrost region on the plateau.

Methods

Data preparation

The six sites with high altitudes are located in plateau permafrost region (Fig. 1) with heat-moisture gradients from north to south (Table 1). To drive the TEM, the monthly temperature and precipitation data for each site are calculated from the nearest meteorological station. Considering the elevation differences between the field site and the nearest meteorological station site, we have recalculated the monthly temperature using the month-specific elevation lapse rate of temperature (Fang 1992). As for precipitation, we haven't done any recalculations and used meteorological data directly. The cloudiness data are extracted from the gridded data of the Climatic Research Unit, University of

Table 1. Locations and climatic, soil and vegetation characteristics for the six sites along the north-south transect in the plateau permafrost region.

	Longitude	Latitude	Altitude (m)	Annual temperature (°C)	Annual precipitation (mm)	Soil texture (sand:silt:clay)	Vegetation type
Wudaoliang	93.07°E	35.22°N	4,626	-5.4	273.1	91:6:3	Alpine needlegrass steppe
Tuotuohe	92.55°E	34.31°N	4,582	-4.2	273.4	97:2:1	Alpine needlegrass steppe
Anduo	91.81°E	32.46°N	4,871	-2.9	434.1	91:2:7	Alpine needlegrass steppe
Naqu	91.93°E	31.57°N	4,636	-1.3	429.8	62:28:10	Alpine kobresia meadow
Dangxiong	91.15°E	30.50°N	4,288	1.6	460.9	53:32:15	Alpine kobresia meadow
Gandansi	91.49°E	29.75°N	4,100	6.3	421.8	49:36:15	Alpine kobresia meadow

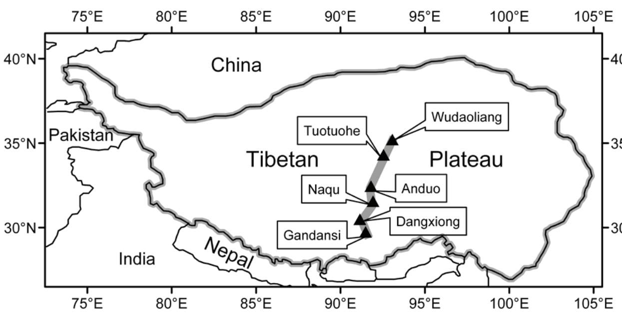

Figure 1. Locations of the north-south transect and field sites in the plateau permafrost region.

Norwich, U.K. (http://www.cru.uea.ac.uk/) based on the sites' geographic location. To parameterize model TEM, we have measured the net primary production (NPP), C in vegetation and soil, total N in vegetation and soil, and soil texture at Wudaoliang site (Luo et al., 2002a, b, 2004). We use the annual atmospheric CO_2 concentration data from Mauna Loa station (Keeling & Whorf 2005).

Model parameterization and simulations

As a process-based ecosystem model, the terrestrial ecosystem model (TEM) uses spatially referenced information on climate, elevation, soils, and vegetation to estimate the spatial and temporal distribution of major carbon and nitrogen fluxes and pool sizes at continental scales, and can be used to describe mechanistic processes of ecosystem carbon and nitrogen cycle and their dynamic responses to changes in environmental conditions. It was first applied to estimate the NPP of potential vegetation in South America (Raich et al. 1991) and then widely used in evaluating responses of terrestrial ecosystems to historical and projected changes in atmospheric CO_2 and climate for different spatial scales (Kicklighter et al. 1999, Tian et al. 2000, Schimel et al. 2000, Clein et al. 2000, McGuire et al. 2000, Clein et al. 2002), and modeling the carbon dynamics and emission of greenhouse gas in Alaska tundra ecosystems (Zhuang et al. 2007). In this study, we use version 5.0 of the model to quantify carbon dynamics for each field site along the north-south transect on the plateau permafrost region. We first parameterize TEM with the observations of vegetation and soil carbon and nitrogen and NPP for the alpine tundra ecosystem. The specific data used to parameterize the model

Table 2. Values and sources for estimated pools and fluxes used to parameterize the model for alpine tundra at Wudaoliang in the north-south transect. 93.1°E, 35.2°N. Elevation 4626 m.

Variable	Value*	Source and comments
C_v	347.5	Measured.
N_v	9.73	Measured.
C_s	2892	See Luo et al. (2004).
N_s	353	See Luo et al. (2004).
N_{av}	1.8	Based on 0.86%, the averaged N_{av}:N_s ratio from Wang et al. (2000) , Wang et al. (2006), Bai et al. (1999) and measured data of two Chinese Ecological Research Network's field stations.
GPP	233	Based on the NPP:GPP ratio in Table A1 by McGuire et al.(1992).
NPP	59.5	See Luo et al. (2004).
NPPSAT	119	Based on the NPP:NPPSAT ratio in Table A1 by McGuire et al.(1992).
NUPTAKE	1.24	Calculated from NPP_n, 75%NPP_n=NUPTAKE.

*Units for annual gross primary production (GPP), net primary production (NPP), and NPPSAT are g C $m^{-2}a^{-1}$. Units for annual N uptake by vegetation are g N $m^{-2}a^{-1}$. Units for vegetation carbon (C_v) and soil carbon (C_s) are g C m^{-2}. Units for vegetation nitrogen (N_v), soil N (N_s), and inorganic N (N_{av}) are g N m^{-2}.

are described in Table 2. The tundra parameterization of soil thermal dynamics in Alaska from our previous study is used for alpine tundra ecosystems in this study (Zhuang et al. 2003). The parameterization of carbon is verified with the observed data of NPP. Third, we simulate the monthly NEP from 1967 to 2000 for those six sites. Finally, we analyze the relationships between NEP, annual air temperature and precipitation, the averaged soil temperature in top 20 cm depth, and soil moisture.

Results

Temporal variation in simulated NEP

From 1967 to 2000, simulated annual NEP for Wuadaoliang, Tuotuohe, and Dangxiong decreased from -1.5, -11.3, and 13.2 to -3.3, -18.3, and 5.1 g.C.m^{-2}.a^{-1}, respectively. In contrast, annual NEP for Anduo and Gandansi increased from 3.3 and -10.2 to 30.9 and 16.4 g.C.m^{-2}.a^{-1}, respectively

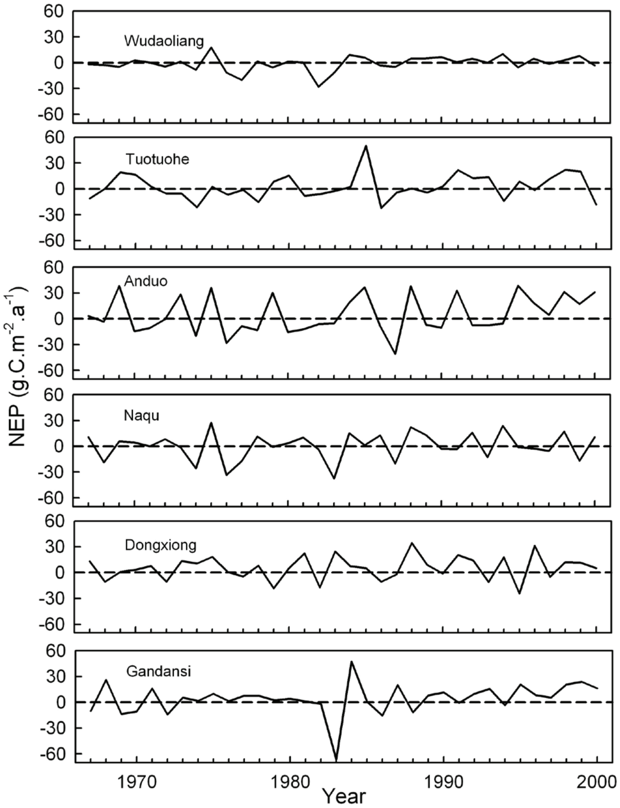

Figure 2. Changes in net ecosystem production (NEP) for the six sites along the north-south transect as simulated by the Terrestrial Ecosystem Model (TEM) during the period from 1967 through 2000.

(Fig. 2). During the past three decades, simulated NEP at the six sites differs in variation pattern, with small interannual variations in Wudaoliang and large variations in Anduo and Gandansi. The terrestrial ecosystem in Wudaoliang is a very weak carbon source with the average value of -0.87 $g.C.m^{-2}.a^{-1}$, while the terrestrial ecosystem in Naqu acts as a very weak sink with the value of 0.31 $g.C.m^{-2}.a^{-1}$. From north to south along the transect the terrestrial ecosystems in other the four sites are carbon sinks with values of 2.49, 5.19, 5.35 and 4.21 $g.C.m^{-2}.a^{-1}$ in Tuotuohe, Anduo, Dangxiong and Gandansi, respectively.

Monthly variation in NEP

We calculate the mean monthly NEP from 1990–2000 and compare the seasonal variation patterns in NEP among the six sites (Fig. 3). From January to May, most sites along the transect act as a carbon source, except that Dangxiong and Gandansi are weak sinks in May with the values of 1.37 and 0.26 $g.C.m^{-2}.month^{-1}$, respectively. The NEP for all sites has switched from a net source to a net sink in June except for Tuotuohe. In October, the NEP for all sites has switched from a net sink to a net source except that Gandansi acts as a sink with the value of 5.99 $g.C.m^{-2}.month^{-1}$. From north to south along the transect, the number of months with carbon sink increased gradually from three months in Wudaoliang (from June through August) and Tuotuohe (from July through September), four months in Anduo and Naqu (from

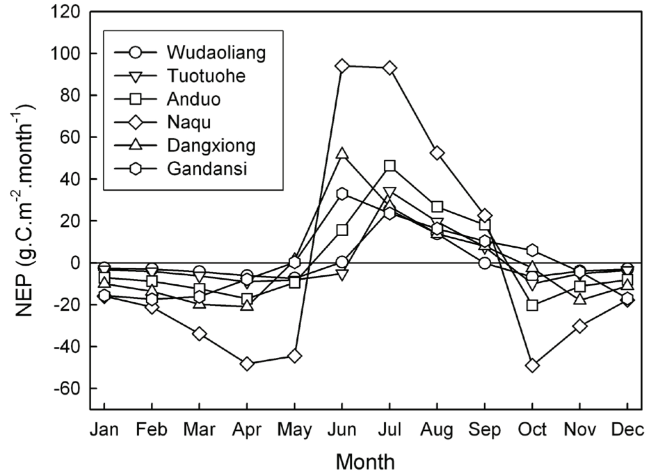

Figure 3. Mean monthly NEP values for the six sites along the north-south transect as simulated by the Terrestrial Ecosystem Model (TEM) during the period from 1990 through 2000.

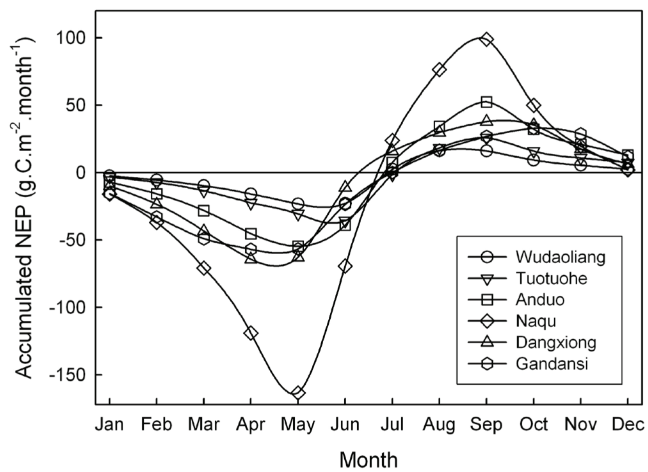

Figure 4. Accumulated mean monthly NEP values for the six sites along the north-south transect as simulated by the Terrestrial Ecosystem Model (TEM) during the period from 1990 through 2000.

June through September), five months in Dangxiong (from May through September), to six months in Gandansi (from May through October) due to water-heat increase trend from north to south along the transect. The mean NEP in months with sink increases from 13.18 $g.C.m^{-2}.month^{-1}$ in Wudaoliang to 65.59 $g.C.m^{-2}.month^{-1}$ in Naqu and then decreases to 14.97 $g.C.m^{-2}.month^{-1}$ in Gandansi. For the inter-annual variation pattern, the estimates of monthly NEP for Naqu vary between -49.02 $g.C.m^{-2}.month^{-1}$ in October and 94.13 $g.C.m^{-2}.month^{-1}$ in June, and demonstrate considerably more variation than for other five sites. As for the inter-annual variation in accumulated NEP values (Fig. 4), the alpine tundra ecosystem in all sites has offset the amount of carbon released to atmosphere and sequestered carbon from atmosphere in July except for Tuotuohe, which begin to store carbon in ecosystem until August. In all sites, the ecosystem sequestering carbon activities occurred first in Dangxiong (Fig. 4). Similar to the intra-annual variation pattern in monthly NEP, the accumulated monthly NEP for

Table 3. The correlations between NEP and climatic factors in six sites along the north-south transect during 1967–2000.

	WDL	TTH	AD	NQ	DX	GDS
Air T	0.23	-0.21	0.20	0.08	0.05	0.34*
Air P	-0.03	0.15	-0.05	-0.16	0.13	0.49**
Soil T	0.24	-0.23	0.17	0.09	0.10	0.32
Soil M	-0.20	-0.54**	-0.52**	-0.26	0.14	0.23
Air T_{5-9}	0.35*	0.04	0.43*	0.37*	-0.07	-0.17
Air P_{5-9}	-0.01	0.04	-0.07	-0.17	0.15	0.49**
Soil T_{5-9}	0.47**	0.04	0.61**	0.35*	-0.04	-0.13
Soil M_{5-9}	-0.15	-0.30	-0.47**	-0.24	0.20	0.37*

WDL: Wudaoliang; TTH: Tuotuohe; AD: Anduo; NQ: Naqu; DX: Dangxiong; GDS: Gandansi; Air T: annual mean air temperature; Air P: total annual precipitation; Soil T (M): annual soil temperature (moisture) within 20 cm soil depth; Air T_{5-9}: mean temperature from May through September; Air P_{5-9}: total precipitation from May through September; Soil T_{5-9} (M_{5-9}): mean soil temperature (moisture) within 20 cm soil depth from May through September; *indicates $p<0.05$, ** indicates $p<0.01$.

Naqu also shows considerably more variation than for the other five sites.

Temporal responses of NEP to climate

There are different temporal responses of NEP to temperature, precipitation, soil temperature, and moisture among the six sites. In general, climate in growing season (from May to September) plays a more important role than annual climate in affecting NEP in alpine tundra ecosystems (Table 3). For trends in annual climate during the past three decades (Table 3), simulated annual NEP and annual soil temperature within 20 cm depth are uncorrelated across six sites, and meanwhile simulated annual NEP and annual temperature and precipitation are also uncorrelated for all sites except for Gandansi. NEP trends are negatively correlated with annual soil moisture in Tuotuohe and Anduo. As for the relationships between NEP and climate in growing season (Table 3), estimates of annual NEP are positively correlated with the mean air temperature and soil temperature from May through September for Wudaoliang, Anduo, and Naqu. Mean soil moisture from May through September is negatively correlated with NEP for Anduo and positively with NEP in Gandansi. From the 1970s to the 1990s, mean temperature in growing season increased for all six sites (Fig. 5). In comparison to the 1970s, precipitation in growing season increased in the 1990s for all sites except for Tuotuohe in which the precipitation decreased by 36.32 mm. When both temperature and precipitation are considered, during the growing season five sites experienced warmer and wetter conditions over the three decades, and only one site (Tuotuohe) became warmer and drier (Fig. 5). In response to climatic change, NEP increased for all sites during the past three decades (Fig. 5). In the 70's, only two sites (Dangxiong and Gandansi) acted as a carbon sink, three sites (Tuotuohe, Naqu, and Dangxiong) became carbon sink in the 1980s, and all sites became carbon sink in the 1990s with the highest decadal NEP value of 11.20 in Gandansi.

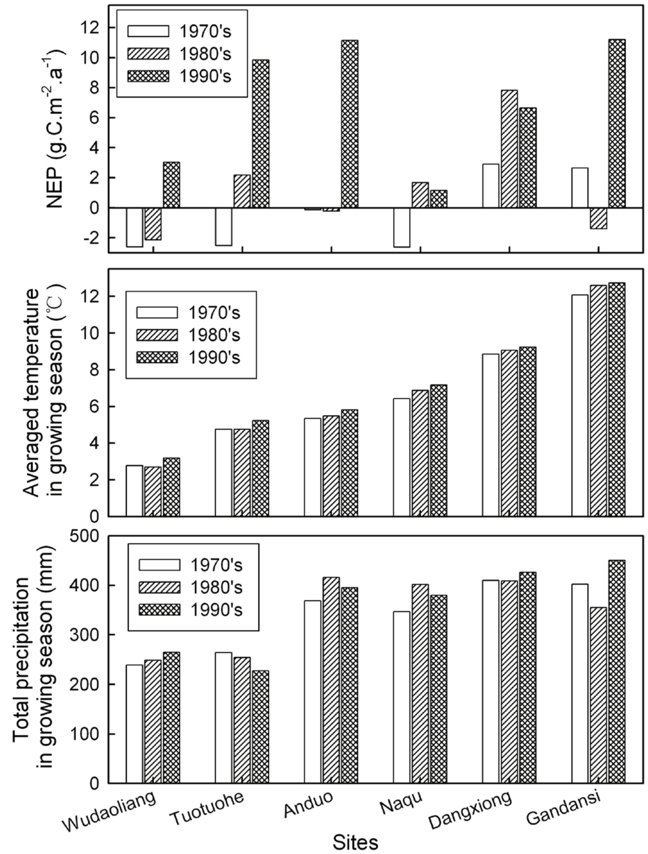

Figure 5. Mean NEP, averaged temperature and precipitation in growing season (May–September) in the 1970s, the 1980s and the 1990s for the six sites along the north-south transect.

Discussion

Using the TEM, we evaluate the NEP variation patterns in six sites dominated by alpine tundra in Tibetan permafrost region during the period from 1967 to 2000. Our results indicate that the alpine tundra ecosystems in the permafrost region mostly act as a carbon sink over the last three decades, which is consistent with the finding based on carbon flux measurements (Xu et al. 2005a, b, Zhao et al. 2005) and static closed chamber measurement data (Zhang et al. 2005) in other sites on the Tibetan plateau.

In the alpine shrub tundra ecosystem in Haibei of northeastern Tibetan plateau (101°19′E, 37°37′N, 3200 m), CO_2 flux observation data show that net CO_2 influx occurred from June to September, and net CO_2 efflux occurred from January to May and October to December with peak influx in August and peak efflux in April (Xu et al. 2005a, b). Our simulated NEP values show similar monthly variation pattern as that in Haibei. In our results, most sites along the transect acted as a carbon sink from June to September and had the lowest NEP in April and the highest NEP in June or July (Fig. 3). In comparison to the observation data in Haibei, our simulated mean NEP values during the 1990s for all sites, varying between 3.03 and 11.2 $g.C.m^{-2}.a^{-1}$ (Fig. 5), were less than 61.91 $g.C.m^{-2}.a^{-1}$ for alpine shrub ecosystem

(Xu et al. 2005a, b) and 76.91 $g.C.m^{-2}.a^{-1}$ for alpine meadow ecosystem, close to 14.45 $g.C.m^{-2}.a^{-1}$ for alpine shrub meadow ecosystem, and much higher than -130.36 $g.C.m^{-2}.a^{-1}$ for alpine swamp meadow ecosystem (Zhao et al. 2005) in Haibei. These differences in NEP values may be due to higher altitude, lower temperature, shorter growth period, and different plant species in the transect. Our simulated mean NEP during the 1990s is also less than the value of 71.12 $g.C.m^{-2}.a^{-1}$ for alpine grassland ecosystem, calculated from the empirical model between CO_2 emission amount and soil surface temperature in Pangkog (90.01°E, 31.23°N, 4800 m) on the Tibetan plateau (Zhang et al. 2005). This difference suggests that spatial variability in climate, soil, and vegetation is important in determining patterns of ecosystem NEP. Compared to the arctic tundra ecosystem, our estimates of mean NEP during the 1990s for Tuotuohe (9.85 $g.C.m^{-2}.a^{-1}$), Anduo (11.14 $g.C.m^{-2}.a^{-1}$), and Gandansi (11.20 $g.C.m^{-2}.a^{-1}$) are very close to the mean annual NEP of Pan-Artic (10 $g.C.m^{-2}.a^{-1}$) and substantially less than the value for moisture tundra in the Kuparuk River Basin, which fluctuated around 25 $g.C.m^{-2}.a^{-1}$ (McGuire et al. 2000).

In the Pan-Arctic, simulated NEP in moisture tundra is more correlated with soil moisture than with air temperature (McGuire et al. 2000), and the same relationships are also found in Tuotuohe and Anduo in our study. For tundra in northwestern Alaska, NEP trends during 1981–2000 are negatively correlated with air temperature trends and positively correlated with precipitation trends (Thompson et al. 2005). In contrast, we didn't find the same correlations in this research. The results from Thompson et al. (2005) indicated that NEP for tundra in northwestern Alaska decreased in warmer and drier conditions or warmer and wetter conditions while in colder and wetter conditions, NEP would increase. In this study, the alpine tundra ecosystems in five sites experienced warmer and wetter conditions over the three decades and one (Tuotuohe) experienced warmer and drier conditions (Fig. 5). However, in comparison to the values in the 1970s, NEP increased for all sites during the past three decades (Fig. 5). Contrary to the results of Thompson et al. (2005), our study indicates that the warmer climate states result in increases in NEP, rather than decreases. Future warming will result in an even more extensive and rapid permafrost degradation in the permafrost region. The warmer and wetter condition in the Tibetan Plateau will likely enhance its carbon sequestration in the terrestrial ecosystems.

Conclusion

In this study, we evaluate the terrestrial carbon dynamics for six sites in permafrost region from 1967 to 2000 with the biogeochemistry TEM. We find that the alpine tundra ecosystems in most sites act as a carbon sink varying between 5.35 $g.C.m^{-2}.a^{-1}$ in Dangxiong and 0.31 $g.C.m^{-2}.a^{-1}$ in Naqu during the past three decades. As for the seasonal variation patterns in NEP among the six sites, from January to May, most sites along the transect act as a carbon source. The NEP for all sites switches from a net source to a net sink in June except for Tuotuohe. In October, the NEP for all sites switches from a net sink to a net source except for Gandansi. Moreover, there are different temporal responses of NEP to changes of air temperature, precipitation, soil temperature, and moisture among the six sites. Generally, climate in the growing season (from May to September) plays a more important role than annual climate in affecting NEP in alpine tundra ecosystems. In comparison to the 1970s, precipitation in the growing season increases in the 1990s for all sites except for Tuotuohe. So the alpine tundra ecosystems in five sites experienced warmer and wetter conditions over three decades, and one site (Tuotuohe) experienced warmer and drier conditions. In response to climatic change, NEP increased at all sites during the three decades. In the 1970s, only two sites (Dangxiong and Gandansi) acted as carbon sinks, three sites (Tuotuohe, Naqu and Dangxiong) became carbon sinks in the 1980s. All sites became carbon sinks in the 1990s. Our analysis suggests that the changes of soil temperature and moisture conditions due to changes in permafrost conditions have significant effects on terrestrial ecosystem carbon dynamics. The future quantification of carbon budget in the Tibetan Plateau should consider the NEP spatial variability induced by changes of soil temperature and moisture associated with permafrost dynamics.

Acknowledgments

This research was supported by K.C. Wong Education Foundation, Hong Kong.

References

Bai, K., Han, J. & Wang, P. 1999. The distribution and growing seasonal dynamics of soil nitrogen fractions on Russian wild rye grass pasture under different grazing intensities (in Chinese). *Acta Agrestia Sinica* 7: 308-318.

Clein, J.S., Kwiatkowski, B.L. & McGuire, A.D. 2000. Modeling carbon responses of tundra ecosystems to historical and projected climate: a comparison of a fine- and coarse-scale ecosystem model for identification of process-based uncertainties. *Global Change Biology* 6 (suppl. 1): 127-140.

Clein, J.S., McGuire, A.D. & Zhang, X. 2002. Historical and projected carbon balance of mature black spruce ecosystems across North America: the role of carbon-nitrogen interactions. *Plant and Soil* 242: 15-32.

Du, J. 2000. Change of temperature in Tibetan Plateau from 1961 to 2000 (in Chinese). *Acta Geographica Sinica* 56(6): 682-690.

Fang, J. 1992. Study on the geographic elements affecting temperature distribution in China. *Acta Ecologica Sinica* 12(2): 97-104.

Keeling, C.D. & Whorf, T.P. 2005. Atmospheric CO_2 records from sites in the SIO air sampling network. In *Trends: A Compendium of Data on Global Change.* Carbon Dioxide Information Analysis Center, Oak Ridge National Laboratory, U.S. Department of Energy, Oak Ridge, Tenn., U.S.A.

Kicklighter, D.W., Bruno, M. & Doenges, S. 1999. A first order analysis of the potential role of CO_2 fertilization to affect the global carbon budget: a comparison of four terrestrial biosphere models. *Tellus* 51B: 343-366.

Liu, X. & Chen, B. 2000. Climatic warming in the Tibetan Plateau during recent decades. *International Journal of Climatology* 20: 1729-1742.

Luo, T., Li, W. & Zhu, H. 2002b. Estimated biomass and productivity of natural vegetation on the Tibetan Plateau. *Ecological Applications* 12: 980-997.

Luo, T., Pan, Y. & Ouyang, H. 2004. Leaf area index and net primary productivity along subtropical to alpine gradients in the Tibetan Plateau. *Global Ecology and Biogeography* 13: 345-358.

Luo, T., Shi, P. & Luo, J. 2002a. Distribution patterns of aboveground biomass in Tibetan alpine vegetation transects. *Acta Phytoecologica Sinica* 26(6): 668-676.

McGuire, A.D., Clein, J.S. & Melillo, J.M. 2000. Modeling carbon responses of tundra ecosystems to historical and projected climate: sensitivity of pan-arctic carbon storage to temporal and spatial variation in climate. *Global Change Biology* 6 (suppl. 1): 141-159.

McGuire, A.D., Melillo, J.M. & Joyce, L.A. 1992. Interactions between carbon and nitrogen dynamics in estimating net primary productivity for potential vegetation in North America. *Global Biogeochemical Cycles* 6(2): 101-124.

Raich, J.W., Rastetter, E.B. & Melillo, J.M. 1991. Potential net primary productivity in South America: application of a global model. *Ecological Applications* 1(4): 399-429.

Schimel, D., Melillo, J.M. & Tian, H. 2000. Carbon storage by the natural and agricultural ecosystems of the US (1980–1993). *Science* 287: 2004-2006.

Thompson, C.C., McGuire, A.D. & Clein, J.S. 2005. Net carbon exchange across the arctic tundra-boreal forest transition in Alaska 1981-2000. *Mitigation and Adaptation Strategies for Global Change* 11: 805-827.

Thompson, L.G., Yao, T. & Mosley-Thompson, E. 2000. A high-resolution millennial record of the South Asian monsoon from Himalayan ice cores. *Science* 289: 1916-1919.

Tian, H., Melillo, J.M. & Kicklighter, D.W. 2000. Climatic and biotic controls on interannual variations of carbon storage in undisturbed ecosystems of the Amazon Basin. *Global Ecology and Biogeography* 9: 315-336.

Wang, C., Wan, S. & Xing, X. 2006. Temperature and soil moisture interactively affected soil net N mineralization in temperate grassland in Northern China. *Soil Biology & Biochemistry* 38: 1101-1110.

Wang, Q., Li, L. & Bai, Y. 2000. Field experimental studies on the effects of climate change on nitrogen mineralization of meadow steppe soil (in Chinese). *Acta Phytoecologica Sinica* 24: 687-692.

Xu, S., Zhao, X. & Fu, Y. 2005a. Characterizing CO_2 fluxes for growing and non-growing seasons in a shrub ecosystem on the Qinghai-Tibet plateau. *Science in China (series D)* 48 (supp. 1): 133-140.

Xu, S., Zhao, X. & Li, Y. 2005b. Diurnal and monthly variations of carbon dioxide flux in an alpine shrub on the Qinghai-Tibet plateau. *Chinese Science Bulletin* 50(6): 539-543.

Zhang, X., Shi, P. & Liu, Y. 2005. Experimental study on soil CO_2 emission in the alpine grassland ecosystem on Tibetan plateau. *Science in China (series D)* 48 (supp. 1): 218-224.

Zhang, Y., Li, B. & Zheng, D. 2002. A Discussion on the boundary and area of the Tibetan Plateau in China (in Chinese). *Geographical Research* 21(1): 1-8.

Zhao, L., Li, Y. & Zhao, X. 2005. Comparative study of the net exchange of CO_2 in 3 types of vegetation ecosystems on the Qinghai-Tibetan plateau. *Chinese Science Bulletin* 50(16): 1767-1774.

Zheng, D. 1996. The system of physico-geographical regions of the Qinghai-Xizang (Tibeta) Plateau. *Science in China* (Series D) 39(4): 410-417.

Zhuang, Q**.**, Romanovsky, V.E. & McGuire, A.D. 2001. Incorporation of a permafrost model into a large-scale ecosystem model: Evaluation of temporal and spatial scaling issues in simulating soil thermal dynamics, *J. Geophys. Res*. 106(D24): 33,649-33,670.

Zhuang, Q., McGuire, A.D. & O'Neill, K.P. 2002. Modeling soil thermal and carbon dynamics of a fire chronosequence in interior Alaska. *Journal of Geophysical Research* 108: 8147, doi: 10.1029/2001JD001244.

Zhuang, Q**.**, McGuire, A.D. & Melillo, J.M. 2003. Carbon cycling in extratropical terrestrial ecosystems of the Northern Hemisphere during the 20th century: a modeling analysis of the influences of soil thermal dynamics, *Tellus*, 55B: 751-776.

Zhuang, Q., Melillo, J.M. & McGuire, A.D. 2007. Net emissions of CH_4 and CO_2 in Alaska: implications for the region's greenhouse gas budget. *Ecological Applications* 17(1): 203-212.

Changes of Permafrost and the Cold-Region Environment in Northeastern China

Ruixia He, Huijun Jin, Lanzhi Lü, Shaopeng Yu, Shaoling Wang, Dongxin Guo
State Key Laboratory of Frozen Soils Engineering, Lanzhou, China 730000

Abstract

Extensive air-temperature inversions in the winter affect the development and distribution of permafrost in the Xing'anling Mountains, Northeastern China. Permafrost is thicker and colder in lower topographic positions. Wetlands and permafrost are interdependent. Permafrost conditions are closely related to surface coverage conditions. The cold-region environment has been greatly affected by climate warming and human activities during the past 50 years. Permafrost has been degrading as evidenced by the deepening active layer, thinning permafrost, rising ground temperatures, expanding taliks, disappearance of patches of permafrost, and the significant northward shift of the southern limit of permafrost. Under the projected climate warming, there would be significant degradation of permafrost and resultant environmental changes. In particular, degradation of permafrost would lead to land desertification on the Hulun Buir Plateau at the west flank of the Da Xing'anling Mountains and on the northern edge of the Songnen Plain, adversely affecting the regional sustainable development.

Keywords: assessment; cold-region environment; engineering projects; permafrost; urbanization; Xing'anling Mountains.

Introduction

Systematic geocryological studies in Northeastern China began in the early 1950s. Several important projects were conducted in the 1960s and 1970s, and the distribution and evolution of permafrost became better understood. In the 1970s, field expeditions, observations, and monitoring which focused on the development and distribution of permafrost, ground temperature, and ground ice were organized and sustained. The first map of permafrost (1: 3,000,000) was compiled based on engineering explorations, investigations, and climatic data (Guo et al. 1981, NECPRT 1983).

During the period from 1979 to 1980, the southern limit of permafrost was studied in detail through correlations of climatic variables and through field investigations along the delineated southern limit of permafrost from the correlations. From 1989 to 1992, the impact of forest fires on permafrost was observed and analyzed. The impact of climate warming on permafrost and its environmental effects also were investigated preliminarily. From 1990 to 2004, permafrost study was initialized to meet the needs for building civil infrastructures and because of increased environmental concerns. Since 2004, permafrost research has been re-activated by the Third-Term Knowledge Innovative Project of the Cold and Arid Regions Environmental and Engineering Research Institute, Chinese Academy of Sciences. The need for better understanding the frozen-ground conditions for the construction of the China-Russia crude-oil pipeline project from Skovorodino, Russia, via Mo'he, China, to Daqing, China, and the Mo'he Airport provided further incentive and funding for geocryology.

At present, the research mainly focuses on relationships among climatic and environmental changes in permafrost regions, interactions of permafrost, forested wetland and snow cover, and the changes of land use in the northern part of Northeastern China. This paper reviews the changes of permafrost and the cold-region environment in Northeastern China, in which the latest data obtained during the surveys and studies of permafrost conditions for the China-Russia Pipeline and Mo'he Airport projects, and field investigations on permafrost and periglacial phenomena in July–August 2007 are incorporated. It also includes the interactions between permafrost and human activities.

Although the degradation of permafrost in Northeastern China has been of considerable concern during recent decades, the research on the mechanisms and the processed-based modeling and prediction of permafrost degradation and its impacts on the cold-region environment are not well established. The Xing'anling Mountains contain the largest cluster of forests and wetlands and, consequently, the habitats and national reserves of many endangered species particularly sensitive to changes of permafrost, climate, and anthropogenic disturbances. Several national key construction projects, including the China–Russia crude-oil pipeline, Hei'he to Dalian Expressway, high-speed railway from Harbin to Dalian, require further investigations on frozen-ground engineering to provide a timely scientific base for frost hazard mitigation. Therefore, the studies on the degradation, mechanisms, trends, and environmental impacts of permafrost in the mountains under influences of climate warming and anthropogenic activities can provide scientific bases for regional environmental management and societal and economic development.

Study Region

Permafrost in Northeastern China is located on the eastern margin of the Eurasian Continent. The Xing'anling Mountains are located in the northern and western parts of Northeastern China (Fig. 1). The elevation of the Da Xing'anling Mountains ranges from 500 to 600 m in the northern section to 1,000 to 1,400 m in the middle section, and further to more than 2000 m in the southernmost section, with its highest peak (Huanggangliang Mountains) at 2029

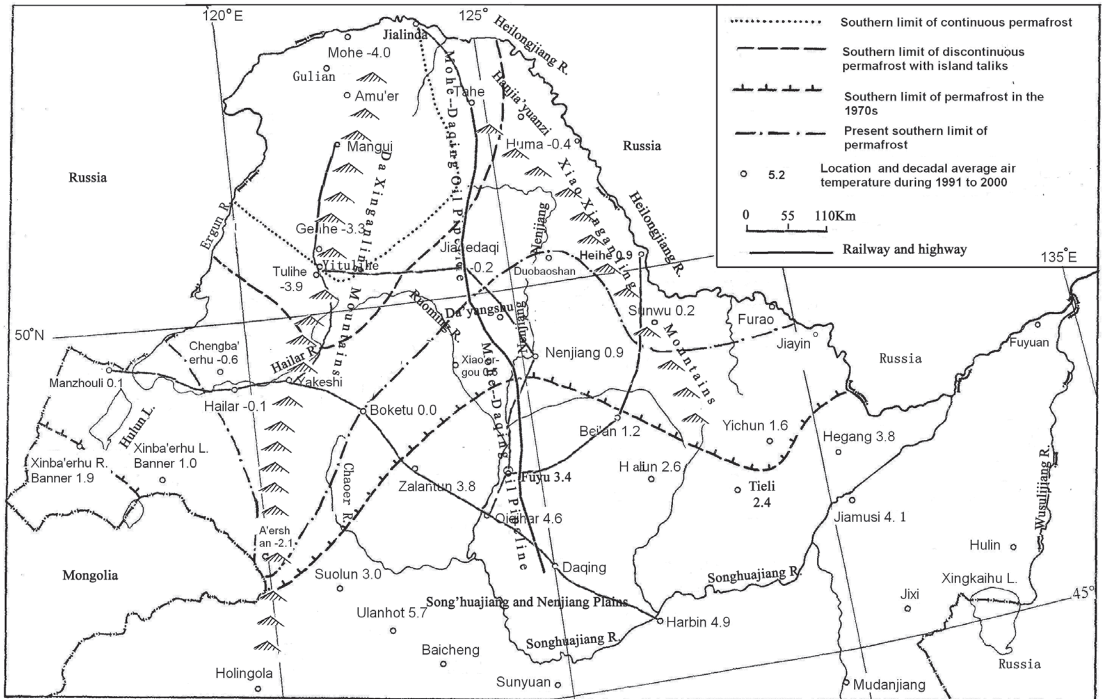

Figure 1. Study area map showing permafrost distribution and changes of the SLP in the Xing'anling (Hinggan) Mountains (revised from Jin et al. 2007a, with permission from the John Wiley & Sons, Ltd.).

m. In contrast, the Xiao Xing'anling Mountains are gentler in topography, with meandering river channels, elevations of 500 to 600 m, and few peaks higher than 800 m.

The mountains are comprised of Late Palaeozoic granites, and Cenozoic volcanic formations, with sporadic Paleozoic metamorphic and sedimentary rocks. Since the onset of the Quaternary, the mountains have been slowly and differentially uplifting, and have been subjected to long-term erosion and leveling. The slope deposits on the upper parts of the mountains are predominately angular gravel or sandy clay with gravel, generally only 1–2 m in thickness, and with a layer of humic topsoil 0.1–0.2 m in thickness. However, in piedmont areas, intermontane basins and valleys, deposits from debris flows, fluvial, and slope processes are as much as 10–15 m thick. In typical soil profiles, peat and humic soil are underlain by clayey sand and sandy clay with sand and gravel (Zhou et al. 2000).

The region is characterized by a temperate continental monsoonal climate with long, cold winters and short, hot summers. Mean annual air temperatures range from 0~+1°C in the south to -5~-6°C in the north. The average annual precipitation ranges from 500–700 mm in the southeast to less than 200 mm in the northwest. Rainfall in summers accounts for 80–90% of the annual precipitation. The Siberia high pressure in winter causes an extensive air temperature inversion which strongly affects the development and distribution of permafrost. A large part of the region is covered with dense forests, or shrubs, or wetlands.

The Hulun Buir Plateau is at the northwestern flank of the Da Xing'anling Mountains. It is gentler in topography with low relief and surrounded by hills. As a main body of the plateau, the Hailar platform is located in the central part. Loose Quaternary strata are widely distributed along the Hailar, Hui, and Wu'erxun Rivers. The upper part of soil profile is composed of silt and sand, generally its thickness varies from 20 to 50 m. The lower part consists of gravels, with thicknesses of 30–60 m. The landscape changes from forest to steppes to the west of the Yimin River.

Evidence of Permafrost Degradation

Although the features of permafrost are largely controlled by latitude, elevation, and longitude, they vary greatly within a relatively small area. The extensive air temperature inversion in winter greatly affects the development and distribution of permafrost. As a result, permafrost is thicker and colder in lower topographic positions than at higher elevations (Lu et al. 1981, Guo et al. 1981). Although the thickness of permafrost gradually increases northwards and northwestwards, it is further complicated by local geology, geography, snow cover, and vegetation. In addition, permafrost has been remarkably affected by anthropogenic activities.

Evidence of permafrost degradation

During the last few decades, permafrost has been remarkably affected by climate warming and increasing human activities. Permafrost degradation is shown by the deepening active layer, thinning permafrost, rising temperature, expanding taliks and the disappearance of permafrost patches (Zhou et al. 1996, Jin et al. 2006). The southern, or lower limit of permafrost has shifted significantly northward and upward (Jin et al. 2006, 2007a).

Northward shifts of the southern limit and areal reduction

Because of its marginal nature, permafrost in Northeastern China is very sensitive to external disturbances. Formation and degradation of permafrost has happened many times during the Pleistocene and Holocene (Guo & Li 1981). The main body of existing permafrost was formed during the Last Glaciation Maximum. There is a very statistically significant correlation between the mean annual air temperatures and the southern limit of permafrost (Guo et al. 1981). Based on the average air temperatures during 1991–2000, and extensive ground-truthing, the southern limit of permafrost has shifted evidently northwards, as much as 50–120 km in some areas (Jin et al. 2007a). The area of permafrost was reduced by 35%, from 390,000 km^2 in the 1970s (Lu et al. 1981) to 260,000 km^2 in the late 1990s (Jin et al. 2006, 2007a).

Deepening active layer and disappearing permafrost patches

The permafrost table has been lowering. The depths of maximum thaw have been increasing. For example, the depth of the active layer in the Amu'er area in the northern Da Xing'anling Mountains was less than 0.8 m during the 1970s. By 1991, it had increased to 1.2 m (Gu et al. 1994). Some patches of permafrost identified in the 1960s and 1970s have disappeared. For example, a permafrost island with the permafrost table at 1.7 m was observed near Jiagedaqi during railway construction in 1964, but by 1974 permafrost was absent under the rail roadbed. Many patches of permafrost from Dayangshu to Wuerqi, and even to Jiagedaqi, have disappeared according to the latest investigations and surveys in 2007.

Thinning and warming of permafrost

Borehole 14 at the former Yituli'he Permafrost Observatory is located in an undisturbed meadow on the first terrace of the northern bank of the Yituli'he River. The mean annual soil temperatures at shallow (<20 m in depths) have warmed as a result of the combined influence of rapid urbanization, disturbance from road construction and use, urban heat-island effects, and climate warming. Ground temperatures at 13 m increased by about 0.2°C between 1984 and 1997 (Jin et al. 2006). Permafrost degradation also has led to the change of its thermal stability types and the expansion of taliks. Some periglacial processes, such as thermokarsting and thaw-slumping, have been enhanced.

Factors Affecting Permafrost Degradation

Climate change

The main reason for extensive degradation of permafrost is climate warming (Gu et al. 1994, Jin et al. 2007). During the past century, the average temperature in Northeastern China had increased by 1.7°C. The mean annual air temperatures of the Da Xing'anling Mountains were increasing from 1954 to 1989 (Yan 1994). During the past 120 years, the mean annual air temperature in Heilongjiang Province has increased by 1.4°C; with the maximum increase in winter and spring (Pan et al. 2003). The warming during 1971–2000 was 1.4°C more than during the 30 years from end of the 19th century

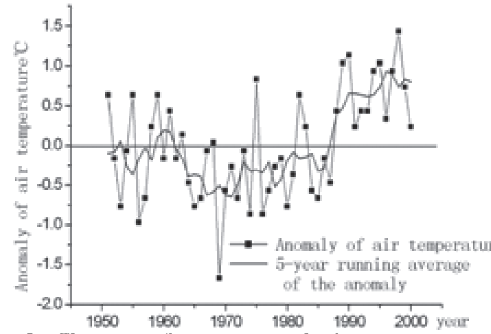

Figure 2. Changes of mean annual air temperature of the Da Xing'anling Mountains during 1961–2000.

to the early 20th century (Pan et al. 2003). Observations at 33 local stations confirmed a similar trend. The mean annual air temperatures during 1971–2000 were 0.9~2.2°C higher than those in the 1960s (Fig. 2) (Jin et al. 2007a). The intensity of warming in the north is more prevalent than that in the south, and the largest warming occurred in the northern Heilongjiang Province and eastern Inner Mongolia, where the mean increase rate was 0.08°C/year.

Increasing anthropogenic activities

There were few human activities in Northeastern China before the 19th century, and the natural environment was not significantly disturbed before the 20th century. During the 1930s to 1940s, the natural environments were devastated because of the Japanese occupation. Since the 1950s, the forest farming in Xing'anling Mountains has increased significantly. Town buildings, forestry, traffic, and transportation were constructed and expanded. In the late 1960s, large amounts of forests were felled for building the Nenlin Railway and the subsequent rapid expansion in population. Establishment and growths of new towns necessitated further deforestation. Long-term, illogical exploitation of forest resources has significantly reduced the forested areas, and remarkably and extensively changed the natural environments. The forested belts retreated northwards by as much as 150–200 km compared to those in the late 19th century. According to a forestry bureau in the Xiao Xing'anling Mountains, the percentage of local forest coverage decreased from 94% in 1957 to 10% in 1980 (Zhou et al. 2000). The extremely serious forest fire in May to June 1987 also changed the albedo of the ground surface and subsequent radiation balance, air and soil temperatures, and soil moisture, resulting in a significant change in the distribution and thickness of permafrost in the Da Xing'anling Mountains (Zhou et al. 1993).

There were about 20,600 people in the 1950s. This number increased to 540,000 by 1994 (Zhou et al. 2002). The population growth necessitated the construction of more infrastructures, such as railways, roads, and buildings. Engineering construction inevitably introduced disequilibrium in the thermal balance and temperatures of permafrost, resulting in various thawed zones, deepened active layers, and accelerated permafrost degradation. For example, in Yakeshi, Jiagedaqi, and Dayangshu near the southern limit of permafrost, there were patches of permafrost everywhere in the early 1950s and 1960s when the towns were

Table 1. Comparison of decadal average air temperature at the Gen'he (50°47′N, 120°30′E, 717 m) and Tuli'he (50°29′N, 120°04′°E, 733 m) meteorological stations during 1961–2000.

Station	Decadal average air temperature (°C)			
	1961–70	1971–80	1981–90	1991–2000
Gen'he	-5.5	-5.0	-4.0	-3.3
Tuli'he	-5.4	-5.0	-4.3	-3.9

Note: The average ground surface temperature at two stations from 1960–1980 was -4.1°C.

Table 2. Comparison of average of mean annual air temperature (AMAAT) and average ground-surface temperature (AGST), maximum frost depths (MFD), and date of thaw completion (DTC) at Gen'he and Tuli'he meteorological stations during 2000–2004.

Station	AMAAT (°C)	AGST (°C)	MFD (cm)	DTC
Gen'he	-3.4	-1.8	260	Late June
Tuli'he	-4.1	-2.6	300	Late July

booming. After 20–40 years of human activities, permafrost has been difficult to find. Urbanization and its "heat-island" effect on permafrost degradation were recognizable. The Gen'he and Tuli'he Forestry Bureaus were set up in 1953, in the discontinuous permafrost zone with natural *larch* forest. The mean annual and decadal average ground temperatures were little changed before 1980s. The Gen'he Forest Bureau had a population of 70,000 in the early 1990s. After the Gen'he City was founded in 1994, the population increased to 180,000 in an area of 19,929 km^2 (Zhou et al. 2002). The city dimensions are 3–4 times those of Tuli'he. It is apparent that the average temperature of Gen'he was 0.6°C higher than that of Tuli'he during 1991–2000 (Table 1). The depth of maximum seasonal frost penetration in Gen'he is 40 cm shallower than that in Tuli'he, and the completion of thawing of the seasonally frozen layer is 1 month ahead (Table 2).

Degradation of Permafrost and Environment

During recent decades, the rapid degradation of permafrost has led to a series of changes in local environments. The major impacts include wetlands degradation, grassland desertification, and shifts of forest types.

Permafrost degradation and changes in wetlands

Freshwater marshes and shallow lakes in Northeastern China, with a total area of 67,378 km^2, account for 17.5% of the total wetlands areas in China (Wang & Du 2006). Coexisting with permafrost, the wetlands in the Da Xing'anling Mountains, with a total area of 8,245 km^2, are mainly located in river valleys, on gentle slopes, and on divides of watersheds. The wetlands in the Xiao Xing'anling Mountains are mainly distributed in the wide valleys and the gulches adjacent to the watershed divides, more on the northern slopes than on the southern slopes.

The wetlands have been gradually shrinking due to the persistent climate warming and drying, permafrost degradation, deforestation, land reclamation, and other anthropogenic activities such as engineering construction and operation, urbanization, overgrazing, and land reclamation. According to a survey report, the area of rivers, marshes, and shrub wetlands in Wuma Forestry Bureau had decreased by 17.4 km^2 in 2001 compared to 1989 (Dai 2007). Further reduction in areal extent of herbaceous swamps was projected under climate change scenarios in the future.

Among the many factors contributing to the changes of wetland ecosystems in the Da Xing'anling Mountains, the single most important one was probably permafrost degradation . In permafrost regions, wetlands are developed in the active layer, which is the interactive interface for mass and heat transfers between permafrost and the external environments. The marsh vegetation layer and the underlying peat layer possess unique thermal properties for insulation and water conservation (Jin et al. 2007b). As a result, they facilitate the formation of permafrost and protect it.

At the meantime, the permafrost layer effectively withholds the downward infiltration of water into soil strata, resulting in ponding at ground surface. A variety of nutrients leached from the active layer enriched here is conducive to the growth of marsh plants. It again facilitates water collection on the surface and formation of an anaerobic environment with slow and decreased decomposition of organic matter.

The freeze-thaw processes have controlling effects on the development, distribution, and degradation of wetlands (Jin et al. 2007b). In recent decades, with the rapid degradation of permafrost, the frozen layer gradually has become thinner. When permafrost is less than 40 cm in thickness, it will be thawed by mid- to late April, before the marsh plants sprout in early May; the soil moisture quickly infiltrates and the ensued physiological drought of plants will adversely affect the swamp development (Zhao & Du, 1980). As a result, the degradation of permafrost inevitably leads to the shrinkage of wetlands, which degrades permafrost (Wang 1983).

Relationship between permafrost degradation and deterioration of the grassland ecosystem

The Hulun Buir Plateau consists of grasslands, wetlands, lakes, and deserts in a transitional zone between patchy permafrost and seasonally frozen ground. Located to the west of the Da Xing'anling Mountains, the Hulun Buir Sandy Land has an annual precipitation of about 350 mm but with good vegetation coverage. It is still considered one of the best pastoral areas in China. However, three sandy belts have developed and are expanding, eroding into the grasslands (Sun & Liu 2001).

According to the 3rd Grassland Resources Investigation, the total grassland area in the Hulun Buir was 112,980 km^2 during 1981–1985, in which the Aeolian-desertified area was 20,970 km^2. By the end of 2002, the area of existing grasslands was 100,878 km^2, with the sandy area of 38,828 km^2. About 12,102 km^2 of grasslands, or 10.7%, were lost during the past 20 years. The aeolian-desertified area increased from 20,970 km^2 (18.6%) in the 1980s to 38,828 km^2 (38.5%) in 2002 (Huang et al. 2003). A survey on desertification on the Hulun Buir Grassland indicates that the total area of aeolian-desertified land has been expanded, to 11,413 km^2, which is about 3.3% more than that in the 1990s (Nie et al. 2005).

The deterioration of the Hulun Buir grassland ecosystem is attributed not only to natural causes, such as climate warming and permafrost degradation, but also to human activities, such as over-exploitation of water, land, and biological resources, among which the degradation of permafrost may have played an important role in the deterioration of the grasslands ecosystems.

Permafrost degradation could lead to deeper freezing and thawing, and resultant thermokarst, solifluction, and thaw-slump. Freeze-thaw cycles weaken soils structurally, and strengthen the frost weathering and mineralization of organics, resulting in intensifying damages to soil surfaces. The bare soil surface becomes material sources for desertification and is conducive to soil erosion. Permafrost degradation causes the reduction of soil moisture at the plant roots layer, drying of surface soils and wetlands, rising ground temperatures, and changes in soil structures and composition, facilitating grassland degradation. Therefore, permafrost, to a certain degree, constrains and impacts the trends and intensity of changes in the grassland eco-systems. In the permafrost zone, when vegetation coverage is reduced, surface heat absorption increases, ground temperatures rise, and depths of seasonal thaw penetration increase, accelerating permafrost degradation.

Changes of forest ecosystem

The Xing'anling Mountains are the northernmost and largest forested areas in China, with an area of 84,600 km^2. As the representative of bright-leaved taiga in Northern China, it belongs to the taiga area characterized by cold climate and simple forest structure, which mainly includes *Larix gmelinii*, *Pinus sylvestris var. mongolica,* primeval *Betula platyphylla* forests, and secondary forests and other underwood, and underherb (Zhang et al. 1995).

In the Da Xing'an Mountains, where about 81% of frozen ground has Xing'an *larch* forests, is the largest continual coniferous forest in China. Permafrost is necessary for the natural evolution of the Xing'an *larch*, which relies on the suprapermafrost water to keep growing in a shallow-rooted pattern over a long time, and to store freshwater with permafrost, forming a typical frost-forest environment.

Natural forests in permafrost regions are controlled by a frozen-ground environment. However, the degradation or disappearance of permafrost can result in ground subsidence, drunken forests, or dead woods. In a forest farm of Gen'he Forestry Bureau, 6,000 m^3 of woods fell and the thermokarstic subsidence hollow expanded at a rate of 10 m/year, resulting in the losses of woods (Zhou et al. 2003).

The degradation of permafrost and shifts in the southern limit of permafrost can cause a change of vegetative distribution and types (Tan & Li 1995). Patchy permafrost used to exist in Dayangshu in the 1960s, but it had disappeared by 1978. Primeval Xing'an *larch* forests disappeared gradually and were replaced by secondary *Populus davidiana* and *Betula platyphylla* forests, and further became *lespedeza* and *hazelnut* forests (Zhou et al. 2003). The enhanced air and ground temperatures had an impact on forest. As a result, the Xing'an larch forest belt moved northwards. For example, the Xing'an larch used to be common in Yakeshi in the west, but it is seldom sighted. In Nenjiang in the south, primeval forests have already been replaced by secondary forests (Tang & Li, 1995).

At present, the degradation of permafrost is accelerating. As a result, the areal extent of forests in permafrost regions is shrinking, and the vegetation system of the original Xing'an *larch* is being threatened because of human activities such as tree felling, land reclamation, mine exploitation, road construction and operation, anthropogenically-enhanced occurrences of forest fires, and influences of climate warming and permafrost degradation.

Conclusions

1. Due to the pronounced climate warming and increasing anthropogenic activities, permafrost has been degrading rapidly in Northeastern China as evidenced by the deepening active layer, thinning permafrost, rising ground temperatures, expanding taliks, and disappearance of permafrost patches.
2. A series of cold-region ecological and environmental changes were observed, some with adverse consequences.
3. It was estimated on the basis of changes in mean annual air temperatures, and partially verified by field investigations, that the southern limit of permafrost in Northeastern China has shifted significantly northwards, as much as 50–120 km in some areas, during the last 30 years. However, most of the surveys were made along major linear engineering corridors, which may have been more impacted by construction and operation of engineering infrastructures and other human activities.
4. Cold-region ecological environments have changed noticeably, such as vanishing wetlands, deforestation, desertifying grasslands and wetlands, and enhanced water and soil erosion.
5. Human activities, typically represented by rapid urbanization and engineered infrastructures, have cast significant influences on permafrost and the cold-region environment in Northeastern China, as many more people were supported there that other permafrost regions on earth.
6. The key to the study of environmental management and protection in the northern part of Northeastern China is to understand permafrost dynamics and the changes of permafrost environments under a changing climate and intense anthropogenic activities. Long-term, in-depth, and integrated research should be conducted to manage, protect and rehabilitate the damaged ecological environment, in order to healthily sustain the socio-societal and economic development in the cold region in the northern Northeastern China.

Acknowledgments

This study was supported by the CAS Cold and Arid Regions Environmental and Engineering Research Institute Third-term Knowledge Innovation Project "*Climatic and environmental changes in cold and arid northeastern China* *and their adaptation*" (Grant No. O650445), National Science Foundation of China (NSFC) Glaciology and Geocryology Incubation Program "*Symbiosis and degradation of permafrost and wetlands ecosystems in northeastern China*" (Grant No. J0630966), and NSFC Project "*Symbiosis and degradation of Xing'an-type permafrost and peat bogs*" (Grant No. 40701031). Professor Max C. Brewer English-edited the paper. Two unidentified reviewers and Professor Douglas L. Kane provided insightful viewpoints and constructive advice for revisions. Their generous assistance is greatly appreciated and thus acknowledged.

References

Dai, B. 2007. Shallow analysis the current situation and protection of wetland in the Da Xing'anling Mountains. *Inner Mongolia Forestry Investigation and Design* 30(4): 68-73 (in Chinese).

Gu, Z., Zhou, Y., Liang, F., Liang, L. & Zhang, Q. 1993. Permafrost feature and their changes in Amuer Area, Da Xing'anling Moutains prefecture. *Journal of Glaciology and Geocryology* 15(1): 34-40 (in Chinese).

Gu, Z., Zhou, Y., Liang, F. & Liang, L. 1994. Permafrost features and their relationship to the environmental factors in Amuer, Da Xing'anling Mountains. *Impacts of Forest Fire on Environments in the Da Xing'anling Mountains and Their Mitigation*. Beijing, China: Science Press, 149-155 (in Chinese).

Guo, D. & Li, Z. 1981. Historical evolution and formation age of permafrost in northeastern China since the late Pleistocene. *Journal of Glaciology and Geocryology* 3(4): 1-6 (in Chinese).

Guo, D., Wang, S., Lu, G., Dai, J. & Li, E. 1981. Regionalization of permafrost in the Da- and Xiao-xing'anling Mountains in northeastern China. *Journal of Glaciology and Geocryology* 3(3): 1-9 (in Chinese).

Huang, G., Zhao, W. & Zhang, Z. 2003. Current situation and protection of grassland ecology in Hunlun Buir. *Inner Mongolia Prataculture* 15(4): 4-5 (in Chinese).

Jin, H., Yu, S., Lü, L., Guo, D. & Li, Y. 2006. Degradation of permafrost in the Da and Xiao Xing'anling mountains, Northeast China, and preliminary assessment of its trend. *Journal of Glaciology and Geocryology* 28(4): 467-475 (in Chinese).

Jin, H., Yu, Q., Lü, L., Guo, D., He, R., Yu, S., Sun, G. & Li, Y. 2007a. Changes of permafrost in the Da and Xiao Xing'anling Mountains, Northeastern China. *Permafrost and Periglacial Processes* 18(2): 245-258.

Jin, H., Yu, S., Jin, R. & Sun, G. 2007b. Symbiosis of marshes and permafrost in the Xing'anling Mountains, Northeastern China. *Chinese Geographical Science* 17(4): 376-382

Lu, G., Wen, B. & Guo, D. 1981. *Permafrost in Northeastern China*, Permafrost Expedition Team of Yakeshi Forestry Survey and Design Institute, Inner Mongolia, 69 pp. (in Chinese).

Nie, H., Yue, L. & Yang, W. 2005. Present situation, evolution trend and causes of sandy desertification in Hulunbuir Steppe. *Journal of Desert Research* 25(5): 635-639 (in Chinese).

Northeastern China Permafrost Research Taskforce (NECPRT). 1983. Major features of permafrost distribution in northeastern China. In *Proceedings of the Second Chinese Conference on Geocryology*. Lanzhou, China: Gansu People's Press, 36-42 (in Chinese).

Pan, H., Zhang, G. & Xu, N. 2003. A Preliminary analysis of climate warming in Heilongjiang Province since the 1980s. *Climatic and Environmental Research* 8(3): 348-355 (in Chinese).

Sun, J. & Liu, D. 2001. Desertification in the Northeastern China. *Quaternary Sciences* 21(1): 72-77 (in Chinese).

Tan, J. & Li, X. 1995. The study on the effects of the climate warming on permafrost degradation and *Larix gemillnii* northward shifts in the Da Xing'anling Mountains. *Inner Mongolia Forestry Investigation and Design* 1: 25-31 (in Chinese).

Wang, C. 1983. Relationships among freezing-thawing process swamp lands, and agriculture on the swampy Sanjiang Plain. *Proceedings of the Second Chinese Conference on Geocryology*. Lanzhou, China: Gansu People's Publishing House, 85-93 (in Chinese).

Wang, Q. & Du, M. 2006. Current situation and prospect of wetland restoration in Northeast China. *Forestry Investigate and Design* 140(4): 25-27 (in Chinese).

Yan, M.H. 1994. Climate changes in the Da Xing'anling Mountains in the recent 36 years. *Impacts of Forest Fire on Environments in the Da Xing'anling Mountains and Their Mitigation*. Beijing, China: Science Press, 143-148 (in Chinese).

Zhang, Y., Zhou, Y. & Ma, J. 1993. Insect taxonomy in forests in the Da Xing'anling Mountains and the impacts of forest fires on the insect taxonomy. *Impacts of Forest Fire on Environments in the Da Xing'anling Mountains and Their Mitigation*. Beijing, China: Science Press, 164-169 (in Chinese).

Zhao, Y. & Du, L. 1980. The study about the formation, type and distribution in the Da and Xiao Xing'anling Mountains. *Journal of Northeast Forestry University* 1: 27-34 (in Chinese)

Zhou, Y., Liang, L. & Gu, Z. 1993. Effects of forest fires on hydro-thermal regime of frozen ground, the Northern part of Da Xing'anling Mountains. *Journal of Glaciology and Geocryology* 15(1): 17-26 (in Chinese).

Zhou, Y., Guo, D., Qiu, G., Cheng, G. & Li, S. 2000. *Geocryology in China*. Beijing, China: Science Press, 171-194 (in Chinese).

Zhou, M., Yu, X. & Feng, L. 2002. Analysis on the driving forces of the permafrost degradation in the Da Xing'anling. *Journal of Arid Land Resources and Environment* 16(4): 44-47 (in Chinese).

Zhou, M., Yu, X. & Feng, L. 2003. Roles of permafrost and wetlands in forests in the Da Xing'an Mountains ecosystems. *Journal of Beijing Forestry University* 25(6): 91-93 (in Chinese).

A Geoelectric Monitoring Network and Resistivity-Temperature Relationships of Different Mountain Permafrost Sites in the Swiss Alps

Christin Hilbich
Department of Geography, University of Jena, Germany

Christian Hauck
Institute for Meteorology and Climate Research, University of Karlsruhe/Forschungszentrum Karlsruhe, Germany

Reynald Delaloye
Geosciences Department, Geography Unit, University of Fribourg, Switzerland

Martin Hoelzle
Glaciology, Geomorphodynamics and Geochronology, University of Zurich, Switzerland

Abstract

An Electrical Resistivity Tomography (ERT) monitoring network has been installed in different permafrost landforms in the Swiss Alps. Repeated ERT measurements yield information on changes occurring in the physical properties of the ground with changing temperature and time. Because the sensitivity of electrical resistivity to temperature is mainly due to the amount of unfrozen water in the pore space of the subsurface material, temporal resistivity changes can be related to freezing and thawing processes. The combined analysis of borehole temperature and ERT monitoring data is used to determine temporal changes of ice and unfrozen water. Key results from this approach include (a) the determination of site-specific total resistivity ranges (as a function of ice content) and amplitudes of seasonal resistivity changes, (b) the demonstration of 3D-topography effects on resistivity distribution in ridge situations, and (c) the identification of depth dependent resistivity-temperature relationships as a function of depth related unfrozen water contents.

Keywords: electrical resistivity tomography; monitoring; mountain permafrost; PERMOS; temperature.

Introduction

Within the context of climate change, the European Alps are affected by greater average warming than commonly projected for Europe as a whole (Beniston et al. 1997). The consequences of global warming for permafrost have been investigated and observed in polar regions for many years (e.g., Osterkamp et al. 1983, Nelson et al. 2001, Frauenfeld et al. 2004, IPCC 2007). In contrast to mainly flat polar lowlands, mountain permafrost is strongly influenced by topographic factors (aspect, slope angle, altitude) affecting net solar radiation and snow cover distribution (Hoelzle et al. 2001). Spatial and temporal heterogeneities of these factors cause complex permafrost distribution patterns that are complicated by heterogeneous subsurface material compositions (bedrock; fine- and coarse-grained debris). Consequently, also the ice content differs markedly between different permafrost landforms.

In addition to temperature, ice content is one of the most critical parameters for the evaluation of the impact of global warming on rockwall stability. Direct observations of ice content are scarce and difficult to obtain. Indirect information from Electrical Resistivity Tomography (ERT) has great potential for detecting the presence of ice, because the specific resistivities of frozen and unfrozen material are markedly different. With repeated ERT measurements under constant general conditions, temporal changes of resistivities are assessed and can be related to freezing and thawing processes (Hauck 2002, Hilbich et al. 2008).

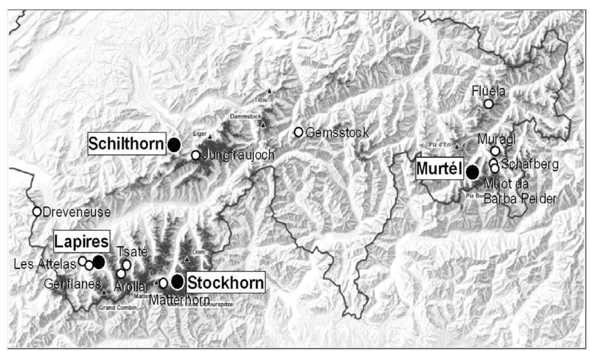

Figure 1. The PERMOS network in the Swiss Alps with borehole temperature monitoring sites (white dots) and combined borehole and ERT monitoring sites (black dots) (Map: BAFU 2007).

However, reliable and quantitative conclusions concerning climate-related changes in ice content can only be drawn when resistivity changes related to external water input (e.g., from precipitation, snowmelt, or lateral water flow) can be excluded (or distinguished from ice melt).

The newly installed ERT monitoring network within the Swiss permafrost monitoring network PERMOS (Fig. 1) provides a unique data set that facilitates study of the relations between measured resistivities and borehole tem

peratures in different permafrost landforms. Sites in the network include the *Schilthorn* (Bernese Alps) permafrost site, which has the longest (>8 years) record of ERT measurements (Hilbich et al. 2008). In this paper we analyze the potential of coupled ERT and temperature monitoring to improve resistivity-based estimates of total amounts and temporal changes of ice content in permafrost regions.

Theory and Methods

Borehole temperatures

In existing European and Swiss permafrost monitoring networks (PACE21, PERMOS (Harris 2001, Vonder Mühll et al. 2004)), subsurface temperature data are obtained in a network of shallow and deep (down to 100 m) boreholes. The PERMOS programme started in 1999 and involves 16 permafrost borehole-monitoring sites with the longest time-series at rockglacier *Murtèl* (Upper Engadine), recording since 1987. However, long-term climate-related degradation processes in terms of thawing phenomena cannot necessarily be identified by thermal permafrost monitoring alone, as the ice content depends on temperature evolution, and also on the availability of unfrozen water during the freezing period (Hilbich et al. 2008).

Electrical Resistivity Tomography (ERT)

The electrical resistance of the ground can be determined by passing a current between two electrodes and measuring the resulting potential difference between two other electrodes coupled to the ground. Repeating this procedure along an electrode array for a number of different 4-electrode combinations (quadrupoles) with different center points and spacing reveals a two-dimensional distribution of electrical resistances within a subsurface section. By multiplying a geometric factor representing the distance between the four electrodes, the apparent resistivity ρ_a is obtained for each data point of a certain multi-electrode configuration. Using the software package RES2D-INV (Loke & Barker 1995), a 2D model of specific resistivities ρ_s, i.e., the true resistivity distribution of the subsurface section, can be calculated from ρ_a by an iterative tomographic inversion process. All ERT data presented in this contribution were measured with the WENNER configuration, and the robust inversion scheme (Clairbout & Muir 1973) of the software RES2DINV was applied.

ERT monitoring

Within the ERT monitoring network a fixed electrode array was installed at four characteristic permafrost sites in the Swiss Alps. All electrodes of one array are permanently connected via cables to a contact box, which serves as an adaptor to a resistivity meter and can be accessed throughout the year (described in detail in Hilbich et al. 2008). Measurements can be carried out by only one person, even in winter, when the electrode array is covered with snow. ERT monitoring started in 1999 at the *Schilthorn* site, in 2005 at the *Murtèl* and *Stockhorn* sites, and in 2006 at the *Lapires* site (see section "Field Sites") and comprises roughly 10 measurements per site to date, except for *Schilthorn* with more than 100 measurements.

Dependence of resistivity on temperature

According to an empirical relationship called Archie´s Law, the resistivity of a medium (consisting of a rock or soil matrix and pore water) can be related to the resistivity of the water, the porosity, and the fraction of the pore space occupied by liquid water (Telford et al. 1990).

The sensitivity of electrical resistivity to temperature arises from different effects, above and below the freezing point. At positive temperatures, the resistivity of the pore water increases with decreasing temperature as a consequence of increasing viscosity of the pore water, which, in turn, decreases the mobility of the ions in the water. This can be quantitatively described as a linear function of the resistivity ρ_0 measured at a reference temperature T_0 and the temperature coefficient of resistivity α, which has a value of about 0.025 K^{-1} for most electrolytes (Telford et al. 1990):

$$\rho = \frac{\rho_0}{1+\alpha\,(T - T_0)} \qquad (1)$$

Below the freezing point, resistivities increase exponentially due to successive freezing of the pore water with decreasing temperatures. The subzero relationship between resistivity and temperature is given by:

$$\rho = \rho_0\, e^{-\,b(T)} \qquad (2)$$

where ρ_0 and b (in K^{-1}) are constants (e.g., Hauck 2002). The factor b controls the rate of decrease and can be determined from Equation (2) if resistivity data for different subzero temperatures are available.

Repeated ERT measurements therefore yield information on the changes occurring in the physical properties of the ground with changing temperature and time (Fortier et al. 1994). Plotting ground temperatures from boreholes (interpolated to the depths of the model blocks of the tomograms) against ρ_s extracted from ERT data at borehole positions (marked in Figs. 4–6) then allows comparison of the relation between T and ρ_s for different sites.

Field Sites

ERT monitoring sites have been chosen to represent different permafrost landforms, different climatic regions in the Swiss Alps, and with respect to the availability of deep boreholes (≥20 m). The landforms include the north-facing rock slope of *Schilthorn* (Bernese Alps), the rock plateau *Stockhorn* (Valais), the talus slope *Lapires* (Valais), and the active rock glacier *Murtèl* (Upper Engadine) (Fig. 1). All ERT profiles were placed close to at least one borehole to enable a calibration of the indirect geophysical measurements with direct observations of the subsurface material composition as made during drilling, and subsurface temperature records of the boreholes. A detailed description of the test sites is given in Table 1.

Results and Discussion

Eight-year ERT monitoring at Schilthorn

The ERT monitoring at *Schilthorn* started in September 1999 and comprises more than 100 datasets, making it the

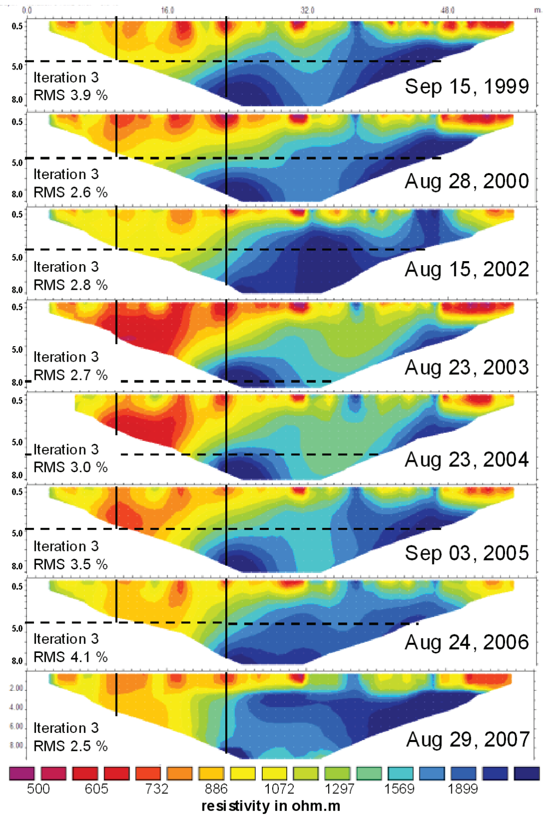

Figure 2. ERT monitoring results of Schilthorn: interannual comparison of late summer resistivity distribution (modified after Hilbich et al. 2008).

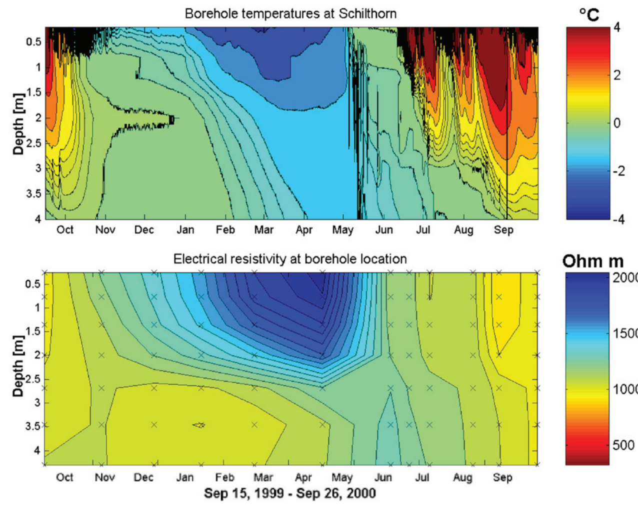

Figure 3. Comparison of temperatures (top) and interpolated resistivities at borehole location (bottom) for September 1999–September 2000 at *Schilthorn*. Resistivity data points used for interpolation are shown as black crosses.

longest ERT monitoring record in mountain permafrost research. A comprehensive analysis of this time series is given in Hilbich et al. (2008). Figure 2 shows the interannual changes between measurements in late summer for each year except 2001.

One of the most prominent features of the dataset is the effect of the extraordinarily hot summer of 2003 on mountain permafrost in the European Alps. According to the borehole temperatures, the summer of 2003 caused an immense deepening of the active layer to almost twice the depth of the years before (horizontal dashed lines in Fig. 2). But, in contrast to the subsurface temperatures, which returned rapidly to almost "normal" conditions in 2004, measured resistivities took about 4 years to recover to pre-2003 conditions. As stated before, temporal resistivity changes are assumed to be caused by freezing and thawing processes that are themselves controlled by temperature. The close relation between temperature and resistivity is evident from Figure 3, where borehole temperatures and specific resistivities at the borehole position are shown for the upper four meters and for a one year period (September 1999 to 2000).

ERT monitoring at different landforms

First results from ERT monitoring in different permafrost landforms reveal pronounced differences in total resistivity values and the amplitude of seasonal resistivity dynamics. The first is due mainly to site-specific material characteristics (lithology, pore volume, fractions of pores filled with air, ice, and unfrozen water, etc.), but the latter can have different causes. Besides local climatic effects controlled by altitude, aspect, snow regime, etc., such morphological characteristics as differences in substrate, active layer thickness, thermal conduction in the active layer, etc. play an important role for the amount to which seasonally variable atmospheric forcing is transferred into the ground. This becomes evident not only from the site-specific subsurface temperature regime but also from the resistivity changes throughout a year. Figures 4, 5, and 6 show tomograms with typical summer (top) and winter (bottom) resistivity distributions for the bedrock (*Stockhorn*), rockglacier (*Murtèl*) and talus slope (*Lapires*) sites. From the qualitative comparison, the most important site-specific characteristics are discussed qualitatively in the following paragraphs:

Stockhorn

The Stockhorn profile is located on a plateau between the steep (>80°) northern rock face, and the steeply inclined southern slope. Permafrost distribution is therefore assumed to be affected by 3D topography effects as described by Gruber et al. (2004) and Noetzli et al. (2008). Three-dimensional effects become evident in the ERT monitoring data by pronounced active layer freezing (increasing resistivities during winter) in the northern part, while similar characteristics are missing in the southern part. This corresponds well with observations of the snow cover, which is usually thicker and persists longer in the northern part. In general, the site is exposed to pronounced resistivity changes in the whole subsurface section (to about 20 m depth), which is attributed to 3D topographic effects of the ridge, influencing radiation and turbulent heat transfer to the ground.

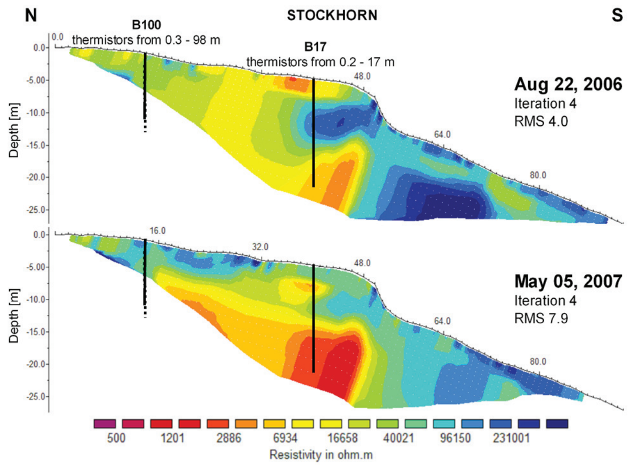

Figure 4. ERT tomogram for typical summer (top) and winter (bottom) conditions at rock plateau *Stockhorn*.

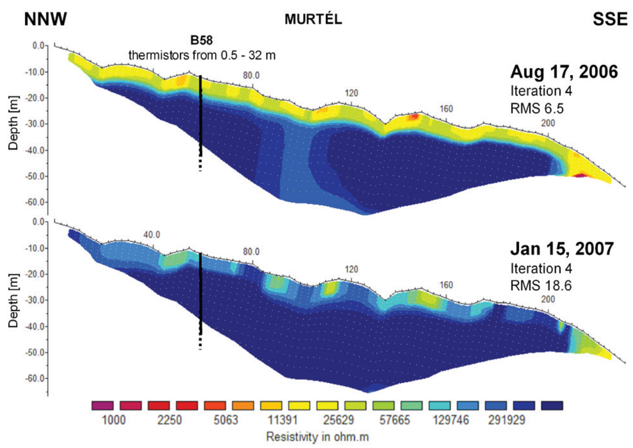

Figure 5. ERT tomogram for typical summer (top) and winter (bottom) conditions at rockglacier *Murtèl*.

Murtèl

Rock glacier Murtèl is generally characterized by extremely high resistivities (300 kΩm to > 2 MΩm) in the interior part caused by the large volume of massive ice. The air in the blocky top layer effectively isolates the ice core from summer heating. Consequently, seasonal resistivity changes are only observed in the active layer (ca. 3–3.5 m) and the tongue. Although changes in the inverted resistivities of the ice core can be quite high (not resolved by the color scale), no systematic seasonal change or trend can be observed from the monitoring data so far. Due to a limited sensitivity of the inversion model to high resistive zones at greater depth, spatial or temporal variations of such high resistivities on the order of MΩm should not be over-interpreted (Marescot et al. 2003). An exception concerns the slightly less resistive vertical zone below the depression at 100–105 m horizontal distance, which is observed in all ERT data (see upper panel in Fig. 5). In summer this resistivity contrast is usually more pronounced than in winter. Due to the uncertainties mentioned above, this zone with decreased (but still very high) resistivities is difficult to interpret but may be an indication of a slightly higher amount of unfrozen water (under subzero temperature conditions), possibly indicating water flow or a zone of higher debris content.

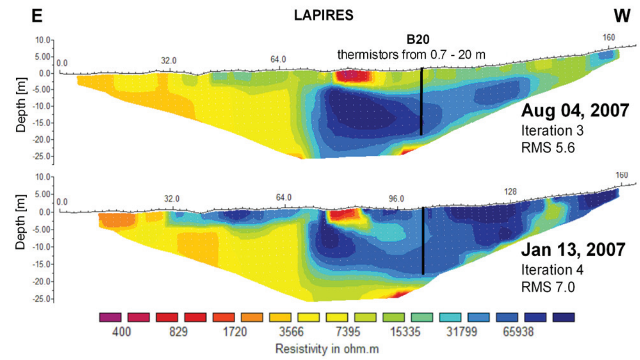

Figure 6. ERT tomogram for typical summer (top) and winter (bottom) conditions at talus slope *Lapires*.

Lapires

The *Lapires* site can be characterized as a talus slope thermally influenced by internal ventilation with a special pattern of permafrost and ground ice occurrence partially reflecting of this internal air circulation (reported in detail by Delaloye & Lambiel 2005). The highly resistive feature in the central part of the tomogram indicates the zone where ground ice is likely to be present. In general, such high resistivities (here >40 kΩm) can be caused by high amounts of ice or air within the pore space of the blocky talus slope (Hauck & Kneisel 2008). ERT monitoring results reveal substantial seasonal changes in resistivities within this zone, possibly indicating a change in material properties over the course of the year. In combination with direct observations during drilling of the borehole and subsurface temperature records, decreasing resistivities at the bottom of this feature during winter and increasing resistivities in summer appear to be related to the air circulation. This may indicate ice formation in summer and thawing processes in winter, but the process remains difficult to understand physically. However, the resistive anomaly can also be influenced by the presence of a cable car pylon in the middle of the profile, represented by very low resistivities in the upper few meters. This low resistive anomaly may cause a low confidence of the resistivity measurement and the inversion process beneath. Further tests are necessary to judge the significance of resistivity changes as indication for changes in material properties.

Active layer freezing during winter (up to 4 m) is, however, clearly evidenced at this site.

Resistivity-temperature relationships

Resistivity-temperature (ρ-T) relationships are plotted for all four test sites in Figures 7 and 8. Figure 7 shows the results for *Schilthorn* (active layer from 0–4.3 m depth), where the largest data set is available. For temperatures above the freezing point results agree well with theory (Eq. 1) with slightly but continuously increasing resistivities with decreasing temperature.

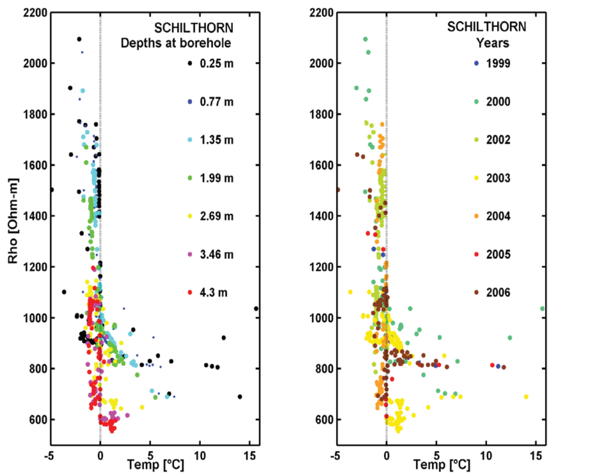

Figure 7. Resistivity at borehole location against subsurface temperatures for the 8-year *Schilthorn* dataset. Colors highlight depths (left panel) and years (right panel). Note that temporal resolution and number of measurements per year are not regular.

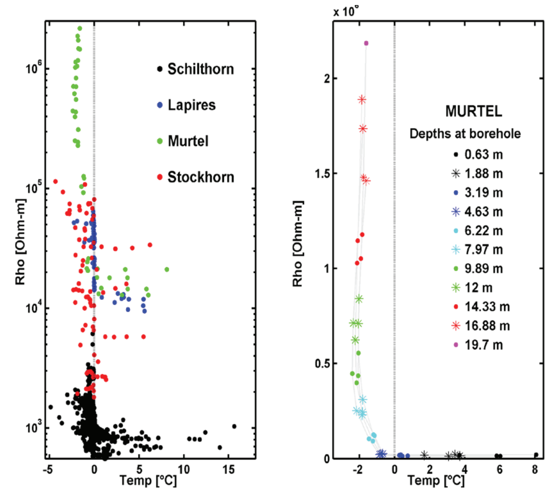

Figure 8. Left panel: comparison of amplitudes of resistivity-temperature relationships for all sites. Right panel: ρ-T relation for 4 different measurement dates at *Murtèl* with colors highlighting different depths. Note that temporal resolution and number of measurements per year are not regular.

At subzero temperatures the reverse effect is visible at all sites: starting at temperatures slightly below the freezing point; resistivities increase exponentially while temperature decrease is almost negligible. Comparing the ρ-T relationship for different depths it is apparent that although the shape of the curves is similar the resistivities are decreasing with depth, indicating higher amounts of unfrozen water at greater depths of the active layer (according to Archie's Law). During freezing unfrozen water contents remain higher in the deeper parts represented by the still lower resistivities (Hauck 2002). Analyzing the same data set with respect to different years, the exceptional low resistivity values of 2003 and the following years become evident as being completely below the main part of the ρ-T curve, again confirming the hypothesis of substantial ground ice degradation at *Schilthorn* in the summer of 2003.

Figure 8 shows the data from all monitoring sites. The amplitude of the resistivity increase for subzero temperatures differs significantly between the sites. While values approximately duplicate at *Schilthorn* from ca. 800 Ωm in unfrozen state to 1600–2000 Ωm in frozen state, they rise over more than an order of magnitude from <100 kΩm to >2 MΩm at *Murtèl*. Unfrozen values at *Lapires* and *Stockhorn* are similar to *Murtèl*, reflecting the blocky active layers, but frozen values are significantly lower due to the lower ice contents. Unfrozen resistivity values of *Stockhorn* cover a wide range due to high variations between dry and wet surface conditions.

The right panel in Figure 8 shows the ρ-T relationships for different measurement dates (lines) and depths (colors) at *Murtèl*. In contrast to *Schilthorn*, values are constant over time, showing almost the same relationship at all temporal reference points. This high degree of repeatability highlights the thermally inert role of the rockglacier and further confirms the reliability of the ERT monitoring approach, even on blocky and highly resistive terrain. A striking feature is the clear dependence of the ρ–T relation on depth. At *Murtèl* (and also at *Stockhorn* and *Lapires*, not shown here) the reverse pattern of *Schilthorn* is visible: Values increase with increasing depths. In contrast to *Schilthorn* (Fig. 7), values in Figure 8 mainly represent conditions below the permafrost table and are therefore interpreted as being due to decreasing unfrozen water contents with depth. However, also decreasing intensity of weathering, higher density and less pore space with depth may be contributing parameters.

Conclusion

Results from an ERT monitoring network at four sites in the Swiss Alps are presented and analyzed in combination with borehole temperature data. Key results from the landform-specific approach can be summarized as follows:

- Both total resistivity ranges and amplitudes of temporal resistivity changes differ markedly for the observed landforms. This is due to site-specific differences of material properties (lithology, pore volume, contents of air, ice and unfrozen water within the pore space, etc.), seasonal dynamics, temperature ranges and the hierarchy of dominating factors.
- Three-dimensional topographic effects influence radiation and turbulent heat transfer to the ground in ridge situations and complicate the pattern of resistivity distribution and seasonal changes, as shown by the example of the rock plateau *Stockhorn*.
- Small seasonal changes are recorded at the *Murtèl* site due to thermally inert characteristics of rockglaciers as opposed to high seasonal dynamics at the other sites as a consequence of internal ventilation (*Lapires* talus slope), high unfrozen water and low ice contents (*Schilthorn*) and 3D effects (*Stockhorn*).
- From the ρ-T relationships a significant dependence on depth becomes evident, with opposite behavior observed

in the active layer (at *Schilthorn*) and below the permafrost table (*Stockhorn*, *Lapires*, *Murtèl*) due to differences in unfrozen water content.

A long-term continuation of the ERT monitoring in the scope of PERMOS is intended and aims at a site-specific assessment of climate related ground ice degradation.

Acknowledgments

We thank Schilthornbahn AG, Zermatt Bergbahnen AG and Corvatsch AG for logistical, and the PERMOS network (BAFU, Switzerland) for financial support, and all students who helped in the field.

References

Beniston, M., Diaz, H.F. & Bradley, R.S. 1997: Climatic change at high elevation sites: An overview. *Climatic Change* 36(2): 233-251.

Bundesamt für Umwelt BAFU 2006. *Hinweiskarte Permafrost Schweiz*. http://www.bafu.admin.ch.

Claerbout, J.F. & Muir, F. 1973. Robust modeling with erratic data. *Geophysics* 38: 826-844.

Delaloye, R. & Lambiel, C. 2005. Evidences of winter ascending air circulation throughout talus slopes and rock glaciers situated in the lower belt of alpine discontinuous permafrost (Swiss Alps). *Norwegian Journal of Geography* 59(2): 194-203.

Fortier, R., Allard, M. & Seguin, M.K. 1994. Effect of physical properties of frozen ground on electrical resistivity logging. *Cold Regions Science and Technology* 22: 361-384.

Frauenfeld, O.W., Zhang, T. & Barry, R.G. 2004. Interdecadal changes in seasonal freeze and thaw depths in Russia. *Journal of Geophysical research* 109: 1-12.

Gruber, S., Hoelzle, M. & Haeberli, W. 2004. Permafrost thaw and destabilization of Alpine rock walls in the hot summer of 2003. *Geophysical Research Letters* 31: 1-4.

Harris, C. 2001. Permafrost and Climate in Europe (PACE), *Permafrost and Periglacial Processes* 12(1): 156.

Hauck, C. 2002. Frozen ground monitoring using DC resistivity tomography. *Geophysical Research Letters* 29(21): 2016.

Hauck, C. & Kneisel C. 2008a. *Applied geophysics in periglacial environments*. Cambridge: Cambridge University Press, in press.

Hilbich, C., Hauck, C., Hoelzle, M., Scherler, M., Schudel, L., Völksch, I., Vonder Mühll, D. & Mäusbacher, R. 2008. Monitoring of mountain permafrost evolution using electrical resistivity tomography: A seven-year study of seasonal, annual and long-term variations at Schilthorn, Swiss Alps. *Journal of Geophysical Research* 113: F01S90.

Hoelzle, M., Mittaz, C., Etzelmüller, B. & Haeberli, W. 2001. Surface energy fluxes and distribution of permafrost in European mountain areas: an overview of current developments. *Permafrost and Periglacial Processes* 12: 53-68.

Intergovernmental Panel on Climate Change (IPCC) 2007. *Climate change 2007: The physical science basis. Summary for policy makers.* http://www.ipcc.ch/.

Loke, M.H. & Barker, R.D. 1995. Least-squares deconvolution of apparent resistivity. *Geophysics* 60: 1682-1690.

Marescot, L., Loke, M.H., Chapellier, D., Delaloye, R., Lambiel, C. & Reynard, E. 2003. Assessing reliability of 2D resistivity imaging in mountain permafrost studies using the depth of investigation index method. *Near Surface Geophysics* 1.2: 57-67.

Nelson, F.E., Anisimov, O.A. & Shiklomanov, N.I. 2001. Subsidence risk from permafrost thaw. *Nature* 410: 889-890.

Noetzli, J., Hilbich, C., Hauck, C., Hoelzle, M. & Gruber, S. 2008. Comparison of Transient 2D Temperature Fields with Time-Lapse Electrical Resistivity Data at the Schilthorn Crest, Switzerland. *Proceedings of the Ninth International Conference on Permafrost, Fairbanks, Alaska, June 29–July 3, 2008* (this proceedings).

Osterkamp, T.E. 1983. Response of Alaskan permafrost to climate. *Proceedings of the Fourth International Conference on Permafrost, Fairbanks, Alaska*: 145-152.

Telford, W.M., Geldart, L.P. & Sheriff, R.E. 1990. *Applied geophysics*. 2nd edition, Cambridge: Cambridge University Press, 770 pp.

Vonder Mühll, D., Noetzli, J. Makowski, K. & Delaloye, R. (eds.) 2004. *Permafrost in Switzerland 2000/2001 and 2001/2002*. Glaciological Report (Permafrost) of the Glaciological Commission of the Swiss Academy of Sciences 2, 3.

Spatial and Interannual Patterns of Winter N-Factors Near Barrow, Alaska

Kenneth M. Hinkel
Department of Geography, University of Cincinnati, Cincinnati, OH 45221-0131 USA
Anna E. Klene
Department of Geography, University of Montana, Missoula, MT 59812 USA
Frederick E. Nelson
Department of Geography, University of Delaware, Newark, DE 19716 USA

Abstract

A 150-km^2 area near Barrow, Alaska, was monitored at hourly intervals between 2001 and 2005 using ~70 data loggers recording air and near-surface soil temperature as part of the Barrow Urban Heat Island Study. Data records for the winter period were used to calculate site-specific *n-factors*, the ratio between seasonally cumulated degree days at the ground surface to those at standard screen height at corresponding locations. Winter n-factors have similar magnitudes between sites and across years, with typical averages of 0.65-0.70. However, n-factor magnitudes are generally lower and their spatial variability much higher near the urbanized area, owing to heterogeneous snow accumulation and the effects of drifting snow.

Keywords: Alaska; air temperature; n-factor; permafrost; snow cover; urbanization.

Introduction

The surface energy balance in Arctic tundra is highly variable over relatively short distances owing to the localized effects of snow, vegetation, soil moisture content, and substrate properties. These variables affect the amount of heat conducted to depth and therefore have considerable influence on the soil thermal regime. In permafrost terrain, energy inputs in summer develop the active layer, which itself exhibits a high degree of spatial variability. One method to parameterize the surface energy balance and simplify calculations over longer time periods is the *n-factor*. Originally proposed by Carlson (1952), this is a simple ratio of seasonal degree days (°C-days) at the ground surface to seasonal degree days in the air over the same time period (Lunardini 1981). The n-factor's geographic variability has been analyzed at a variety of spatial scales. Shur & Slavin-Borovskiy (1993) examined summer n-factor patterns in western Siberia across more than 25 degrees of latitude, and noted a general increase in n-factors poleward. At the local plot scale, Klene et al. (2001) observed significant variation in summer n-factors between natural landscape-vegetation types, but relative consistency within the units.

This study was conducted at an intermediate scale, and uses a relatively dense network of temperature-measurement sites to map winter patterns of the n-factor. The purposes are to (1) quantify the degree of regularity in seasonal n-factor magnitude and spatial patterns between different years; and (2) identify conditions that influence winter n-factors at the scale of the study.

Study Area and Background

Barrow is a coastal village on the Chukchi Sea at 71.3°N, 156.5°W. With a mean annual temperature of -12.0°C (National Climate Data Center [NCDC] 2003), the area lies in the continuous permafrost zone, with permafrost thickness extending to depths of nearly 400 m. Active-layer thickness averages around 35 cm (Hinkel & Nelson 2003), but is highly variable between landscape types (Klene 2005). The snow cover is typically established by mid-September and averages about 40 cm in depth at the end of winter.

Barrow has a population of around 4600, with an urban settlement pattern typical of the U.S. Building density is relatively high in the older village center, while suburban-style housing of lower density dominates recent developments around the village's periphery and extends as a band along the coast for several km.

Most buildings are single-story and built atop piles driven into the underlying permafrost. The local road network consists of gravel berms elevated 1-2 m above the natural terrain. The urbanized area constitutes an artificial topography that exceeds the natural relief of the surrounding coastal plain and has significant impacts on snow-drift patterns, snow depth, and retention of water at the surface. Each of these factors, in turn, influences the n-factor.

As part of a larger study concerned with evaluating the impact of Barrow's urban heat island on soil temperatures and permafrost stability, HoboPro® data loggers were installed across a 150-km^2 area beginning in 2001. Fifty loggers were deployed in 2001, and by 2003 the network had expanded to nearly 70 loggers. About half were deployed in urban settings, with the remainder dispersed across the hinterland in a loose grid pattern (Hinkel et al. 2003, Hinkel & Nelson 2007). The two-channel loggers have an accuracy of ±0.2°C and precision of 0.02°C at the freezing point. Loggers were mounted on an instrument mast with one thermistor inside a radiation shield at standard screen height (1.8 m) to measure air temperature, and the other thermistor positioned 5 cm below the ground surface to measure near-surface soil temperature. Loggers were synchronized to record hourly measurements. The rate of instrument attrition was around

10% yearly, owing primarily to animal activity and logger failure.

Methodology

Because the date of snowmelt in spring and snow cover development in autumn varies between sites and years, it was first necessary to define seasonal boundaries. For each site, the mean daily air and soil temperature traces were plotted. Using these records in combination with graphs of daily soil temperature range, we defined the winter snowcover period as 15 Sept to 15 May (243 days; 244 days on leap year).

For each site with a complete record for the seasonal period, average daily air and soil temperatures were cumulated. The n-factor was then calculated for each site, summary statistics generated, and seasonal maps produced using a simple kriging algorithm (Golden Software 2002) to interpolate site values over the study area.

Sites were defined as urban or rural depending on whether they were within 30 m of any building, road, or other "built" structure.

Table 1. Winter air temperature (°C) summary statistics based on daily average for sites with a complete record over the period; winter is 15 Sept to 15 May.

	Winter-2001-02	Winter-2002-03	Winter-2003-04	Winter-2004-05
N	31	39	52	42
Mean	-17.98	-15.75	-17.89	-16.76
Median	-17.91	-15.60	-17.79	-16.63
Minimum	-19.09	-17.70	-19.00	-17.63
Maximum	-17.05	-15.05	-17.08	-16.20
Std_Dev	0.52	0.54	0.51	0.36

Table 2. Summary statistics for winter n-factors. Snow depth (cm) averages measured in either April or May.

	2001-02	2002-03	2003-04	2004-5
N	31	39	52	42
Minimum	0.36	0.34	0.32	0.28
Maximum	0.90	0.91	0.87	0.90
Range	0.54	0.57	0.55	0.63
Mean	0.66	0.66	0.65	0.66
Median	0.68	0.68	0.68	0.69
StdDev	0.13	0.15	0.13	0.16
Snow (cm)	31	30	38	31

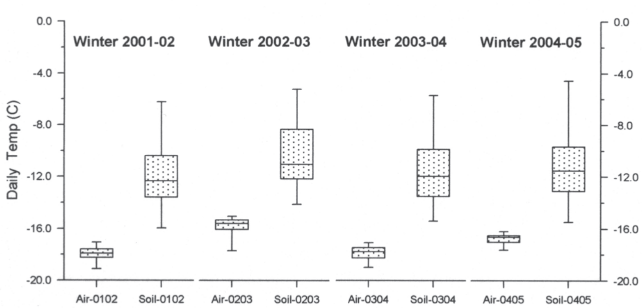

Figure 1. Box-and-whisker plots of average winter air and near-surface temperature for all valid sites.

Results and Discussion

In a region of relatively even and continuous tundra vegetation such as Barrow, winter n-factors can initially be treated as a homogenous group for analysis. N-factors near unity indicate close coupling between the soil and air temperature. Conversely, lower magnitudes indicate relatively warmer soil temperature in winter that reflects the insulating effects of the snow cover. Strong decoupling is induced by deep snow, with n-factors falling toward zero.

Annual summary statistics

Summary winter air temperature statistics are given in Table 1. The number of sites used in the calculations varied between winters owing to lost or partial records. Winter 2002-03 was about 2°C warmer than other years; this is also apparent in Figure 1, which shows the distribution of the daily air and soil temperature averages by winter period. There is limited variation in average daily air temperature in all winters, as can be expected within such a relatively small area. By contrast, the variability in near-surface soil temperature is substantial, and is related to local edaphic, vegetation, and snow conditions.

Summary n-factor statistics are given by winter period in Table 2, and the range of n-factors by year is shown in Figure 2. Winter n-factors have very similar measures of central tendency (0.65-0.69 for mean and medians), indicating little interannual variation. Winter snow-cover depth, measured each year at the 121 grid nodes of the ARCSS/CALM 1-km^2 grid within the study area, was consistently around 31 cm, except during the winter of 2003-04 when it averaged 38 cm. The thicker snow cover does not appear to impact the mean, median, or range of n-factors in that year, although values appear somewhat more clustered around the median (Fig. 2). Direct interannual comparison is difficult, however, because the number of operational sites varied between years.

Annual spatial patterns

Maps of the winter n-factor are shown in Figure 3. The winter pattern of n-factors demonstrates relatively consistent geographic patterns with (1) higher magnitudes (>0.70) near the coast, especially in the vicinity of Elson Lagoon; (2) lower magnitudes (<0.55) near the urban center, and (3) much higher spatial variability near the urbanized areas. This last point can be best appreciated by separating the urban and rural sites, and calculating summary statistical parameters of n-factors (N=164) for the two groups (Table 3). The urban sites have a lower mean and median n-factor (by about 0.10), and vary more around the measures of central tendency; the range is wider and the standard deviation is greater by a factor of two. A plot of the histograms for the two groups of sites (Fig. 4) verifies this interpretation and clearly illustrates the tight clustering of rural n-factors around the mean and median centered on 0.7.

In Barrow, strong winter winds (averaging ~11 knots or 5.5 m s^{-1}) are consistently from the NNE and snow drifting is common. Deflation of snow by wind on the northeastern

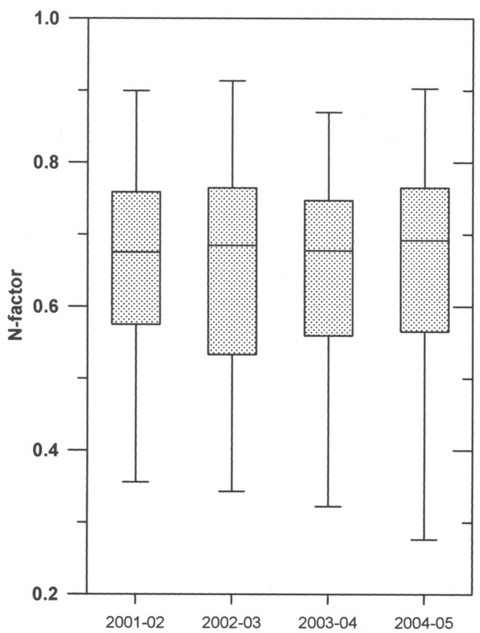

Figure 2. Box-and-whisker plots of winter (15 Sept-15 May) n-factor by year.

coast would tend to increase the winter n-factor at affected sites. Conversely, relatively large accumulations of snow in the lee of buildings, plowed roadways, and snow fences (Hinkel & Hurd 2006) reduce the magnitude of the n-factor and promote spatial variability. Because the number of sites used to construct these maps differs substantially, more detailed comparison is not prudent.

Forcing factors

During winter, snow depth and thermal properties have been found to be the dominant factors determining ground temperature in rural and urban environments (e.g., Gold 1967, Goodrich 1982, Woo & Debreuil 1983). In some environments, this is closely tied to vegetation, which traps snow in the canopy layer (Sturm et al. 2001). In Barrow, however, the relatively short tundra vegetation (seldom more than 20 cm and usually much less) reduces the importance of this factor. This study found snow to be the main determinant of winter soil temperatures and n-factors, with the artificial topography inducing snow accumulation and drifting, thus impacting the magnitude and variability of winter n-factors in the urban setting. Other urban factors that may complicate

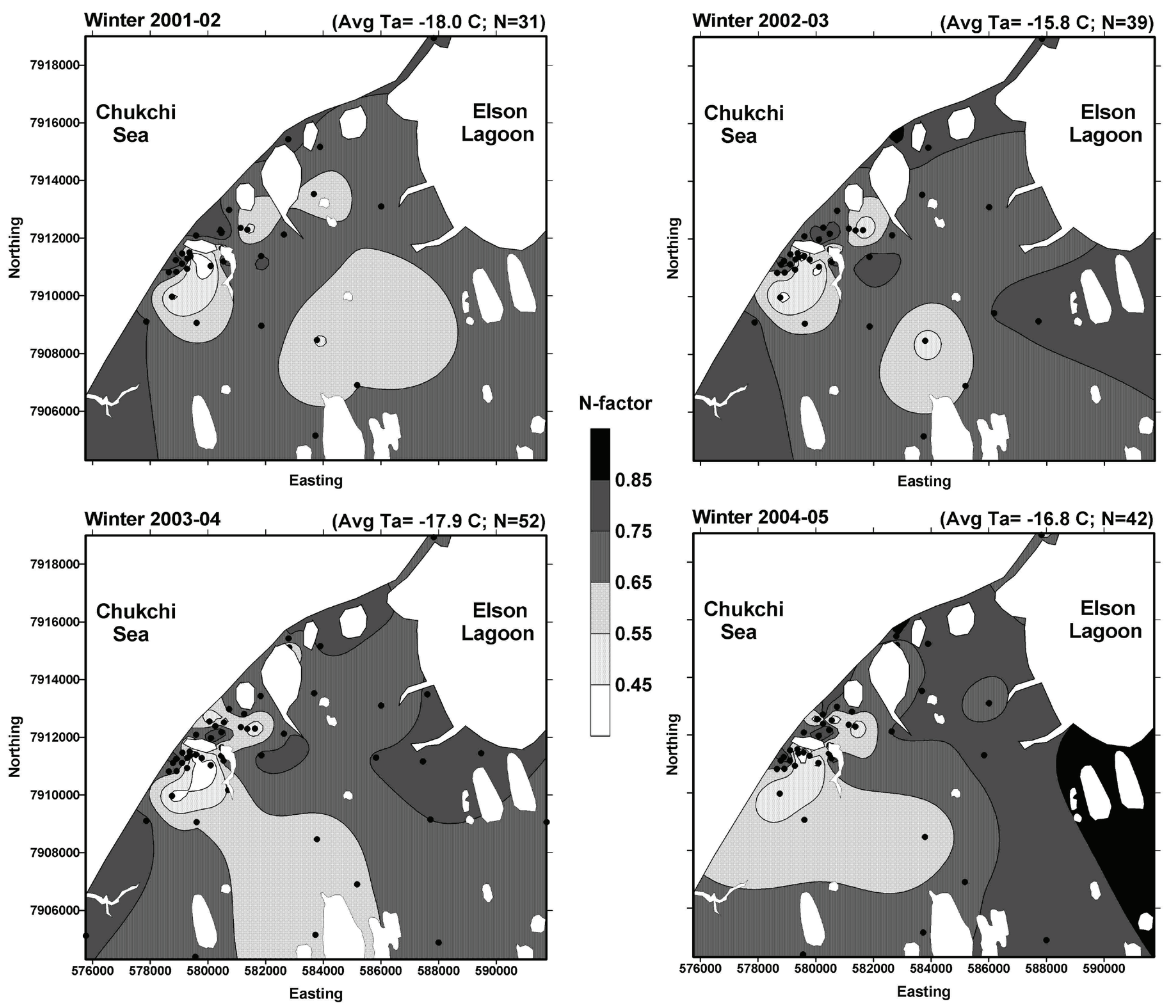

Figure 3. Isarithmic maps of winter n-factors; seasonal average air temperature and N indicated in upper right corner. Dots show instrument sites.

Table 3. Summary statistics of all winter n-factors (N=164) separated into either urban or rural setting.

	Urban	Rural
N	112	52
Minimum	0.28	0.50
Maximum	0.91	0.90
Range	0.64	0.41
Mean	0.63	0.71
Median	0.64	0.73
Std_Dev	0.16	0.08

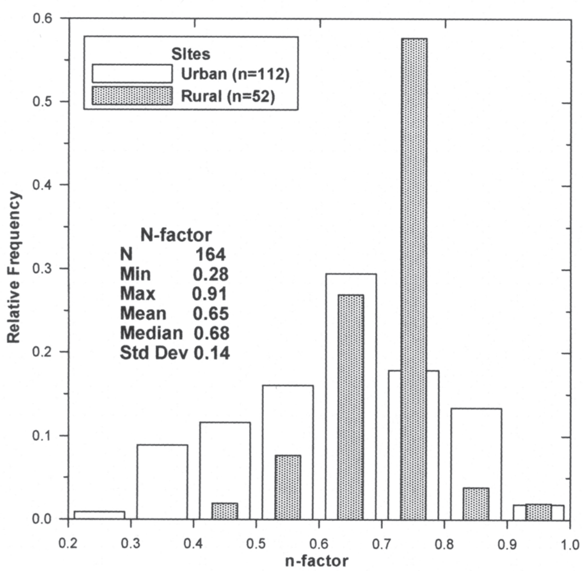

Figure 4. Histogram of n-factors by setting, with summary statistics for all sites.

the ground thermal regime include changes in subsurface soil water flow caused by construction of permafrost-stabilized road berms. Particularly in the newer subdivisions of Barrow, roads form a grid pattern that inhibits lateral meltwater runoff in spring and causes ponding. This results in such intensive flooding that tanker trucks proceed from block to block, pumping water to be dumped elsewhere. Other urban factors, such as the effects of dust on snow albedo (Dutton & Endres 1991), can also have an impact in this environment. Separation of n-factor regimes by rural and urban regions provides a useful first-approximation explanation.

Compared to results from previous studies, the rural values reported here are somewhat higher than those found by Taylor (1995), Karunaratne & Burn (2003, 2004) and Kade et al. (2006). Taylor (1995), for example, reported winter n-factors of 0.12–0.45 for forested sites in the Mackenzie River Valley. Karunaratne and Burn (2003) examined winter n-factors at several sites in the Yukon (forested, burned, meadow, snow fence, and cleared) between 1997 and 2000. They reported winter n-factors at the cleared sites (0.5) that were similar to those observed in the forested site, while the burned and snow fence sites had n-factors of ~0.3 and the meadow site had an intermediate value. Kade et al. (2006) examined n-factors in barren nonsorted frost circles and vegetated tundra along a climate gradient consisting of three sites in northern Alaska. They calculated tundra n-factors of about 0.3, 0.6, and 0.9 at Happy Valley, Franklin Bluffs, and Howe Island, respectively. This generally shows the impact of reduced snow depth, vegetation height, and soil organic layer thickness as one moves poleward from the Arctic Foothills towards the Arctic Ocean. Carlson (1952) calculated winter n-factors of 0.25-0.33 for three sites of differing land-covers (trees, shrubs, vegetation removed) with an undisturbed snow cover. At "urban" sites that were cleared of snow, he found n-factors of 0.62-0.76 at sites with a gravel surface and n-factors of 0.65–0.84 associated with concrete and asphalt surfaces. The high n-factors observed at Barrow likely reflect the effects of the relatively thin snow cover and tundra vegetation.

Conclusions

This study of n-factor magnitudes and spatial patterns is somewhat different from those conducted in the past in that (1) the analysis was performed at a spatial scale intermediate between the plot- and regional-scale studies reported in the literature; (2) it utilizes a relatively dense network of data loggers; and (3) the study took place over several years to examine the annual variability of winter n-factors. The spatial and temporal consistency of n-factors over a series of winters has been demonstrated empirically in the rural environment.

Conversely, individual sites within the urban environment were of lower magnitude and show greater variability. The anthropogenic impact on snow accumulation and drifting patterns induced by buildings, plowed roads, and snow fences is the likely cause. This indicates that n-factors may exhibit high variability across short distances in natural terrain of high relief, and merits further investigation. Other studies may focus on the impact of engineered structures or climate-induced vegetation changes. Spatial and temporal analysis of summer n-factors would likely require implementing a land cover classification scheme to fully understand the complex patterns (Klene et al. 2003, Hinkel et al. 2004).

Acknowledgments

This work was supported by the National Science Foundation (NSF) under grants OPP-9529783, 9732051 and 0094769 to KMH and OPP-0095088 and 0352958 to FEN. Any opinions, findings, conclusions, or recommendations expressed in this material are those of the authors and do not necessarily reflect the views of the NSF. Mention of any product does not constitute endorsement. We are grateful for support from the Barrow Arctic Science Consortium, the Ukpeagvik Inupiat Corporation, and the many Barrow residents who allowed us to use their backyards and parking lots. R. Beck, J. Bell, B. Jones, and C. Tweedie assisted in this study. Our thanks to an anonymous reviewer.

References

Carlson, H. 1952. Calculation of depth of thaw in frozen ground. In: *Frost Action in Soils: A Symposium*, pp. 192-223. *Highway Research Board Special Report 2* Washington, DC: National Research Council.

Dutton, E.G. & Endres, D.J. 1991. Date of snowmelt at Barrow, Alaska, U.S.A. *Arctic and Alpine Research* 23: 115-119.

Gold, L.W. 1967. Influence of surface conditions on ground temperature. *Canadian Journal of Earth Sciences* 4: 199-208.

Golden Software 2002. *Surfer 8 User's Guide: Contouring and 3D Surface Mapping for Scientists and Engineers*. Golden, CO: Golden Software.

Goodrich, L.E. 1982. The influence of snow cover on the ground thermal regime. *Canadian Geotechnical Journal* 19: 421-432.

Hinkel, K.M. & Nelson, F.E. 2003. Spatial and temporal patterns of active layer depth at CALM sites in Northern Alaska, 1995-2000. *Journal of Geophysical Research-Atmospheres* 108(D2), 10.129/2001JD000-927.

Hinkel, K.M., Nelson, F.E., Klene, A.E. & Bell, J.H. 2003. The urban heat island in winter at Barrow, Alaska. *International Journal of Climatology* 23: 1889-1905.

Hinkel, K.M., Klene, A.E. & Nelson, F.E. 2004. The summer climate of an arctic coastal village: Preliminary observations from the Barrow Urban Heat-Island study. *Polar Geography* 28(3): 197-221.

Hinkel, K.M. & Hurd, J.K., Jr. 2006. Permafrost destabilization and thermokarst following snow fence installation, Barrow, Alaska, U.S.A. *Arctic, Antarctic and Alpine Research* 38(4): 530-539.

Hinkel, K.M. & Nelson, F.E. 2007. Anthropogenic heat island at Barrow, Alaska, during winter: 2001-2005. *Journal of Geophysical Research-Atmospheres* 112, D06118, doi:10.1029/2006JD007837.

Kade, A., Romanovsky, V.E. & Walker, D.A. 2006. The n-factor of nonsorted circles along a climate gradient in Arctic Alaska. *Permafrost and Periglacial Processes* 17(4): 279-289.

Karunaratne, K.C. & Burn, C.R. 2003. Freezing n-factors in discontinuous permafrost terrain, Takhini River, Yukon Territory, Canada. In *Proceedings of the 8th International Conference on Permafrost. Zurich: University of Zurich-Irchel*: 519-524.

Karunaratne, K.C. & Burn, C.R. 2004. Relations between air and surface temperature in discontinuous permafrost terrain near Mayo, Yukon Territory. *Canadian Journal of Earth Sciences* 41: 1437-1451.

Klene, A.E., Nelson, F.E. Shiklomanov, N.I. & Hinkel, K.M. 2001. The N-factor in natural landscapes: Variability of air and soil-surface temperatures, Kuparuk River Basin, Alaska. *Arctic, Antarctic, and Alpine Research* 33(2): 140-148.

Klene, A.E., Hinkel, K.M. & Nelson, F.E. 2003. The Barrow heat island study: Soil temperatures and active-layer thickness. In *Proceedings of the 8th International Conference on Permafrost. Zurich: University of Zurich-Irchel*: 555-560.

Klene, A.E. 2005. *Climate and Urbanization in Barrow, Alaska*. Dissertation, Department of Geography. Newark, DE: University of Delaware.

Lunardini, V.J. 1981. *Heat Transfer in Cold Climates*. New York, NY: Van Nostrand Reinhold Company.

National Climate Data Center (NCDC) 2003. URL: http://www5.ncdc.noaa.gov [Available online at http://www5.ncdc.noaa.gov /pubs/publications.html#CLIM81.] "Monthly Normals (Climatography of the U.S. #81 and "SOD -Daily Surface Data (TD3200/3210 combined) for W. Post and W. Rogers Airport, Barrow, Alaska."

Shur, Y.L. & Slavin-Borovskiy, V.B. 1993. N-factor maps of Russian permafrost region. In *Proceedings of the Sixth International Conference on Permafrost, Vol.* 1. Wushan Guangzhou, China: South China University of Technology Press: 564-568.

Sturm, M., McFadden, J.P., Liston, G.E., Chapin, F. S. III, Racine, C.H. & Holmgren, J. 2001. Snow-shrub interactions in Arctic tundra: A hypothesis with climatic implications. *Journal of Climate* 14: 336-344.

Taylor, A.E. 1995. Field measurements of n-factors for natural forest areas, Mackenzie Valley, Northwest Territories. In *Geological Survey of Canada, Current Research,* 1995-B: 89-98.

Woo, M.-k. & Dubreuil, M.-A. 1983. Effects of an Arctic settlement on the snowpack. *40th Annual Meeting of the Eastern Snow Conference* 28: 143-156.

Spatial and Temporal Variation of Soil Temperatures and Arctic Hydrology in the Kuparuk River Basin, Alaska

Larry D. Hinzman
University of Alaska Fairbanks, International Arctic Research Center

Robert E. Gieck
University of Alaska Fairbanks, Water and Environmental Research Center

Douglas L. Kane
University of Alaska Fairbanks, Water and Environmental Research Center

Abstract

A series of environmental studies have been carried out in the northern foothills of the Brooks Range and the Arctic Coastal Plain in the Kuparuk River Basin, Alaska, to develop a better understanding of the physical and climatic dynamics of an arctic ecosystem. As part of these studies, soil temperature and snow depth measurements along a transect from near the Beaufort Sea coast across the Coastal Plain to the Brooks Range foothills were made continuously at three locations. Summarized here are trends observed in soil temperature spanning the last 15 years in this area. Soil temperature measurements were made in the active layer and permafrost to depths exceeding 10 meters. Data collection began at these sites in 1993. These datasets are of sufficient temporal length and quality to begin showing long-term trends in arctic soil temperature and the relationship between snow depth and winter soil temperature. All locations within the permafrost show a warming trend (average annual temperature) over the period of observations (depths greater than 50 cm at Franklin Bluffs and Sagwon Hill and 90 cm at Imnavait Ridge). Maximum soil temperatures in the active layer above the permafrost, however, show a slight cooling trend at all three sites. Minimum soil temperatures in the permafrost at each site are increasing as are average annual soil temperatures; maximum annual temperatures in the permafrost are mixed with Sagwon Hills decreasing. There is no significant overall trend in snow water equivalent (SWE) at the three sites. There is considerable variation in SWE and snow depth from year-to-year, which clarifies the dependence of the soil thermal regime on snow. The hydrologic cycle in these catchments has yet to show any response that can be documented.

Keywords: active layer; Alaska; climate change; hydrology; permafrost; soil temperature.

Introduction

Since 1985, continuous hydrologic research studies have been ongoing on the North Slope of the Alaskan Arctic (Fig. 1) in watersheds within and adjacent to the north-flowing Kuparuk River Basin (Kane et al. 2000). The hydrologic response of these basins is related to the major physical properties of the basin such as topography, soils, vegetation, and thermal state In this case the thermal state is probably the most important, as the area is underlain by continuous permafrost 250 to >600 m deep. It is clear from the published papers that the environment of this region is transitioning to a warmer climate (Serreze et al. 2000, Hinzman et al. 2005, and others). Heat and mass water fluxes in any environment are closely intertwined. Therefore, if the climate is warming, the hydrology of these Arctic basins will also be impacted. One could foresee greater precipitation with less spatial and temporal sea ice extent (sources of precipitable water increasing); perhaps increased evapotranspiration (ET) from land surfaces with increases in precipitation and air temperature; and the runoff response is debatable, depending upon what happens with precipitation. One of the major controversial areas is what will happen to the active layer and vegetation, as this has long-term implications to the hydrologic cycle of the Arctic.

Two decades ago, Lachenbruch and Marshall (1986)

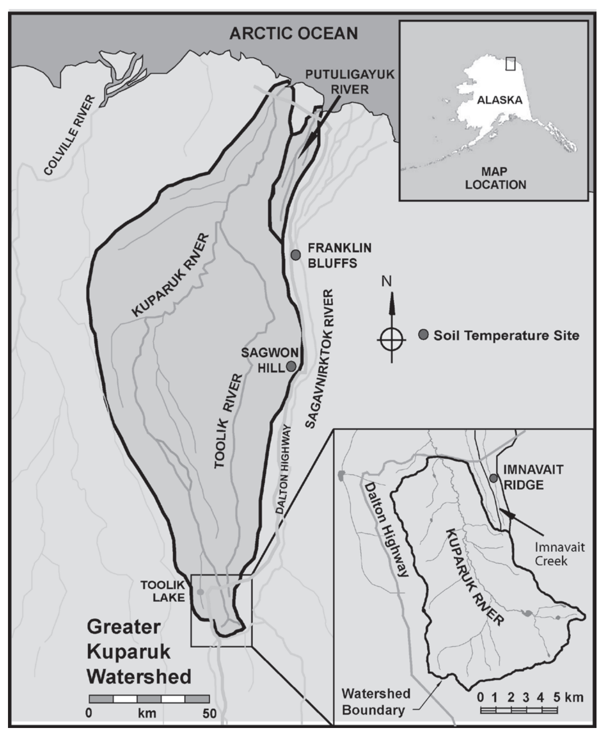

Figure 1. Map of the monitored watersheds and the borehole observations sites on the North Slope of Alaska, USA.

showed that permafrost on the North Slope of Alaska was warming. Clearly it took thousands of years for the permafrost to form, and it is not going to totally disappear for some time (except where it is quite warm and thin, but that is not the case in northern Alaska). Presently, the active layer in the Kuparuk basin is on average about 40 to 60 cm deep (Hinzman et al. 1998), greater in well-drained sites, and shallower in poorly drained sites. There is evidence, however, that change is ongoing near the ground surface. Sturm et al. (2001) described the increase in shrubs in the present tundra environment on the North Slope of Alaska; hydrologically this has implications for trapping snow, ET and soil moisture, and possibly runoff. A warmer climate should result in a deeper active layer initially, though there are some who would argue that shrubs will invade and provide ground shading and thus lower ground surface temperatures. It is more complex than this, however, as different plant communities have different soil water demands (drier soils typically have deeper active layers because less energy is needed for phase change). Overduin and Kane (2006) have shown that over a three-year period, no increase in the active layer thickness was observed for a site on the North Slope of Alaska from relative depth measurements at summer's end. However, more detailed analyses showed that areal ground surface subsidence rates of 2 to 5 cm/yr were due to the melting of ice at the base of the active layer, although not detected in simple active layer depth measurements relative to the surface with a probe.

Presented here are the results of 15 years of borehole data collected at sites on a north-south transect in the Kuparuk River basin. Most of the discussion will concentrate on three sites: Franklin Bluffs, Sagwon Hill, and Imnavait Ridge. At these three sites, measurements were made at depths greater than 10 m. Several thermistor strings were also installed at numerous other sites in the shallow active layer.

Setting

Four nested watersheds on the North Slope of Alaska, USA (Fig. 1), are instrumented with hydrologic and meteorological stations that support hydrologic and related process studies and data to complete water balance computations (Kane et al. 2004, Lilly et al. 1998, Kane et al. 2008a). These studies were initiated in 1985 in Imnavait Creek (2.2 km^2), 1993 in the Upper Kuparuk (142 km^2) and entire Kuparuk River (8,140 km^2), and in 1999 in the Putuligayuk catchment (471 km^2). The U.S. Geological Survey (USGS) started gauging the entire Kuparuk River near Deadhorse in 1971, and the record is continuous. They also started gauging the Putuligayuk River in 1971; however, in the 1980s some years of data are missing, and then they switched it to a crest gauge. During the early years of gauging by the USGS, there was very little complementary hydrologic data collected until this study was initiated.

The north draining Kuparuk basin transitions the northern extremities of the Brooks Range, through the foothills and finally into the Arctic Ocean after crossing the low-gradient Coastal Plain. The permafrost thickness increases from 250 m in the headwaters to 600 m along the coast. The active layer is generally about 40 to 60 cm deep, although it is quite variable, depending upon slope, aspect, soils, organic cover, etc. Vegetation is essentially continuous over the area, starting with alpine communities in the headwaters, tussock tundra in the foothills, and sedges and grasses on the Coastal Plain. Shrubs (~1 m high) can be found throughout the basin except at the high elevations and the northern extremes. More detailed description of these basins can be found in Kane et al. (2000).

Results

Franklin Bluffs is located approximately 25 miles south of the Arctic Ocean coastline in the Coastal Plain (Fig. 1). The terrain is low gradient and poorly drained. The daily soil temperatures are plotted since 1993 in Figure 2 (there is one gap in the dataset). Soils at this site displayed a cooling of the summer maximum annual temperature in the active layer and a warming of the permafrost soils (Fig. 3, Table 1). The winter minimum annual soil temperature showed a cooling trend for active layer soils and a warming trend of permafrost soils (Fig. 4). Overall the average annual soil temperature (Fig. 5) demonstrated a trend of cooling of the active layer soils and a warming of permafrost soils. With cooling of the active layer and warming of the permafrost, there was a convergence of the average annual temperature at each depth. Three winters had above-average SWE (Fig. 6) at this site after 2000; this would decrease deep winter cooling and delay ablation in the spring, thus possibly shortening summer.

The Imnavait Ridge site is located in the Imnavait Basin in the upland of the foothills of the Brooks Range near Toolik Lake (Fig. 1). The site is located on a well drained ridgeline on a gentle west facing slope.

Discussion

It is clear that the hydrology of the Kuparuk River Basin is dominated by deep continuous permafrost. First, the permafrost acts as an aquitard, and there is no hydraulic connectivity between the surface and the subsurface permafrost groundwater (Yoshikawa et al. 2007). In some neighboring watersheds, there are springs of subpermafrost groundwater origin that have apparently been flowing for thousands of years. The thick, ice-rich permafrost severely limits subsurface storage to just the active layer, where the volume of storage is quite close to the average total precipitation for just one year. Because of this limited storage, runoff ratios for these basins are much higher than found in more temperate climates (Kane & Yang 2004) for both snowmelt and rainfall

Kane et al. (2003a) discuss the impact of surficial permafrost features on the runoff response of arctic catchments. In general, these features (polygons, thaw lakes, strangemoor ridges, beaded drainage, etc.) reduce the hydrologic runoff response of these watersheds. However, as an example, the conversion of low-centered polygons to high-center polygons

Table 1. Trend line slopes (1993 to 2007) of annual maximum, minimum, and average temperature at two depths in boreholes on the North Slope of Alaska. *P*-values are in parentheses. The *p*-value represents a decreasing index of the reliability of a result (Brownlee 1960). The lower the *p*-value, the more we can believe that the trend line is significantly different from zero. A *p*-value of 0.01 implies the slope of the trend line is significantly different from zero at the 99% confidence level.

Annual	Imnavait Ridge		Sagwon Bluffs		Franklin Bluffs	
	20 cm	800 cm	20 cm	850 cm	20 cm	850 cm
	$°C \cdot yr^{-1}$		$°C \cdot yr^{-1}$		$°C \cdot yr^{-1}$	
Average	0.03 (0.7377)	0.17 (<0.0001)	0.05 (0.6052)	0.04 (0.2231)	-0.01 (0.9206)	0.12 (0.0011)
Minimum	0.16 (0.5771)	0.14 (0.0004)	0.29 (0.1961)	0.09 (0.0189)	0.20 (0.3145)	0.13 (0.0058)
Maximum	-0.14 (0.0338)	0.13 (0.0013)	-0.27 (0.0026)	-0.02 (0.6161)	-0.19 (0.0128)	0.11 (<0.0001)

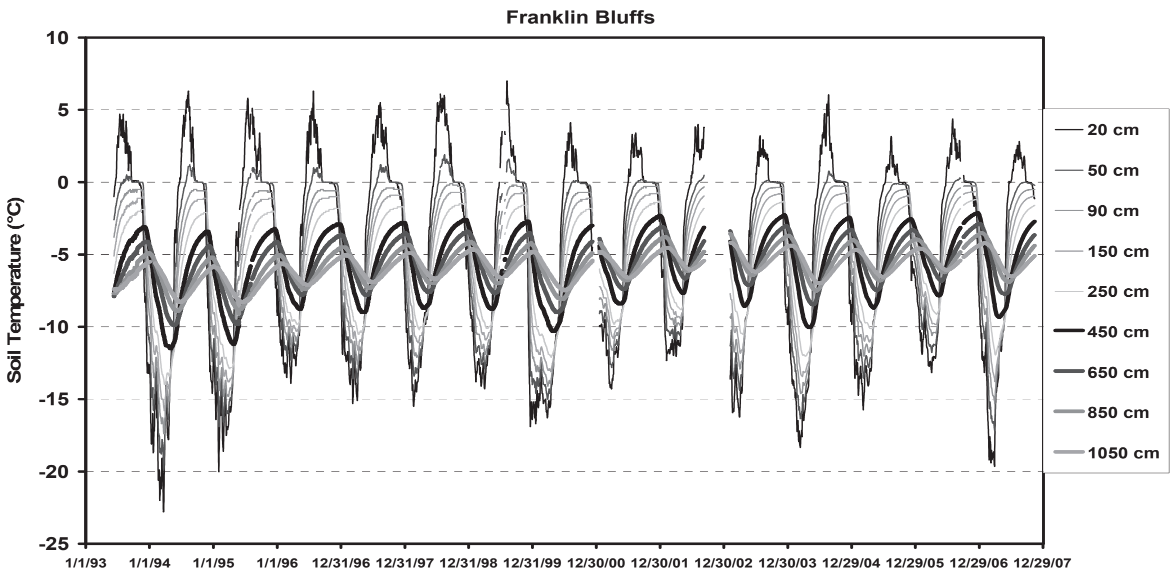

Figure 2. Daily variations in soil temperatures observed in a borehole near Franklin Bluffs, Alaska, from the surface down to 10.5 m from 1993 to 2007.

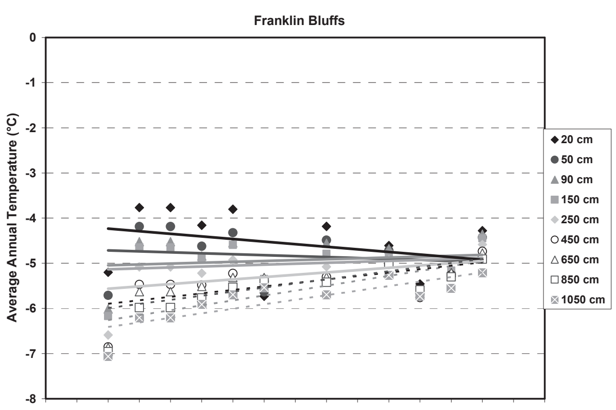

Figure 3. Trends observed in the average annual soil temperature profile of the borehole near Franklin Bluffs, Alaska.

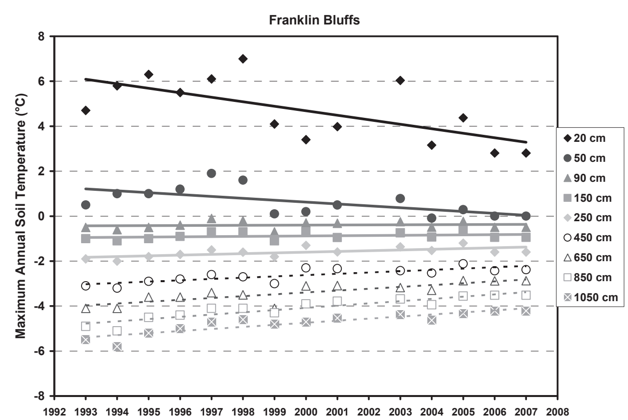

Figure 4. Trends observed in the maximum annual soil temperature profile of the borehole near Franklin Bluffs, Alaska.

could significantly increase the hydrologic runoff response of a watershed, including sediment yield. This process has been observed in several areas by the authors along the Dalton Highway outside the studied basin. McNamara et al. (1999) hypothesized that headwater drainages (water tracks) in the Arctic are immature channels that have not fully developed because of the underlying permafrost. The suggestion that permafrost is limiting channel maturity has many implications to the hydrologic response of arctic catchments in a changing climate, including runoff response and sediment (suspended and bed) yields.

In response to some imposed disturbance, such as a tundra fire or climatic warming, massive ice-rich permafrost may differentially thaw, creating irregular surface topography. Depressions forming on the surface soon form ponds, accelerating subsurface thaw through lower albedo and additional heat advected into the pond through runoff. In time, a talik (a layer of unfrozen soil above the permafrost and below the seasonally frozen soil) may form below such ponds as the depth of water becomes greater than the amount that can refreeze during the winter. If the talik grows to a size that completely penetrates the underlying permafrost or connects to a subsurface layer that allows continued drainage, the pond may then begin to drain. Over the past three to five decades, increased pond formation and shrinking have been observed in Alaska (Yoshikawa & Hinzman 2003, Jorgensen et al. 2001), Canada (Smol & Douglas 2007), and Siberia (Smith et al. 2001).

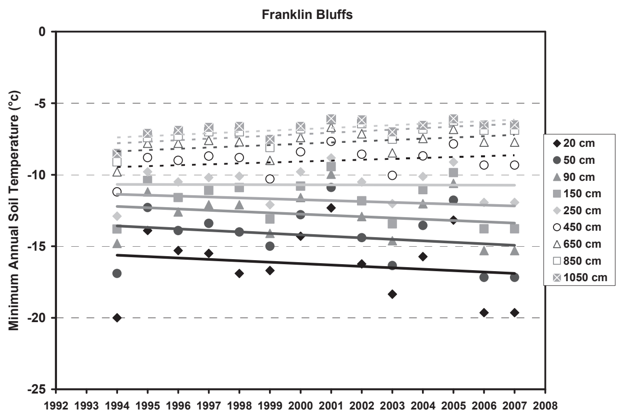

Figure 5. Trends observed in the minimum annual soil temperature profile of the borehole near Franklin Bluffs, Alaska.

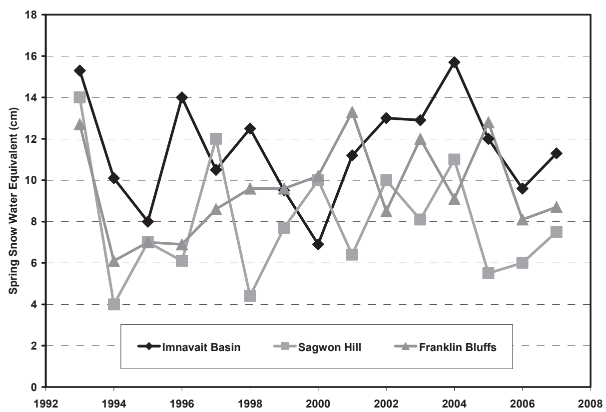

Figure 6. Annual variations in the maximum snowpack water equivalent measured near borehole sites just prior to spring melt.

Summary

The general trend of the thermal regime at the three research sites is one of overall warming; this is in agreement with other studies (Romanovsky et al. 2002). The warming was strongly statistically significant at the 850 cm depths for the minimum annual temperatures at all three sites. The deeper temperature probes (>400 cm) displayed significant warming in average, minimum, and maximum annual temperatures at Imnavait Creek and Franklin Bluffs, but was not consistent at Sagwon. To date, we do not see measurable responses of arctic hydrology to climate change in the form of changes in precipitation, runoff, soil moisture, storage, and ET. Clearly the permafrost is warming, thermokarsting is evident, and

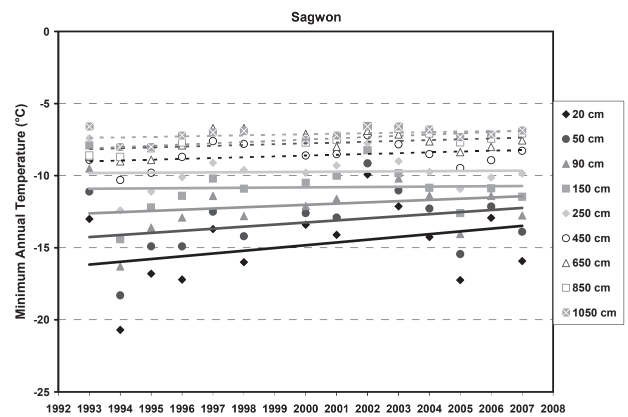

Figure 7. Daily variations in soil temperatures observed in a borehole near Sagwon Bluffs, Alaska, from the surface down to 10.5 m from 1993 to 2007.

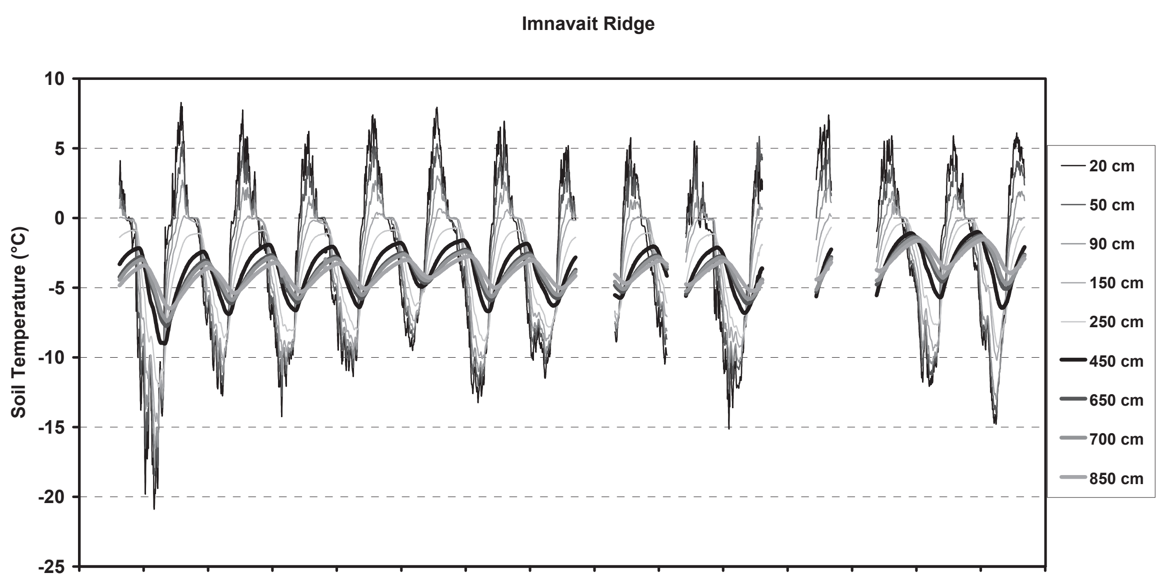

Figure 8. Daily variations in soil temperatures observed in a borehole near Imnavait Creek, Alaska, from the surface down to 8.5 m from 1993 to 2007.

thawing of the top of the ice-rich permafrost is ongoing. In an area of the world where frozen ground plays a dominant role in the physical structure of a watershed, this should be viewed ominously. Why do we not presently see this impact on arctic hydrology? First, it may not be extensive enough to reach a threshold value at the watershed scale. Second, changes in the hydrology will not be evident until the soil has progressed from frozen to thawed. Although warming is occurring, it appears that the small amount of thawing that has occurred at the base of the active layer has not significantly increased the available storage due to subsidence concurrent with thawing. Third, there is considerable natural variability in these hydrologic processes, plus we still struggle to make accurate estimates of hydrologic fluxes and stores. The natural variability in hydrological variables may be much greater than the subtle differences induced by a warming climate. We hypothesize that continued warming of the permafrost will bring significant changes to the hydrology of this region as we presently know it.

Acknowledgments

This paper is based on work supported by the National Science Foundation, Office of Polar Programs (Grants OPP-9814984, OPP-009615, OPP-0327664, and OPP-0335941), and the U.S. Army CRREL for borehole drilling support.

References

Hinzman, L.D. Bettez, N.D., Bolton, W.R., Chapin, F.S., Dyurgerov, M.B., Fastie, C.L., Griffith, B., Hollister, R.D., Hope, A., Huntington, H.P., Jensen, A.M., Jia, G.J., Jorgenson, T., Kane, D.L., Klein, D.R., Kofinas, G., Lynch, A.H., Lloyd, A.H., McGuire, A.D., Nelson, F.E., Oechel, W.C., Osterkamp, T.E., Racine, C.H., Romanovsky, V.E., Stone, R.S., Stow, D.A., Sturm, M., Tweedie, C.E., Vourlitis, G.L., Walker, M.D., Walker, D.A., Webber, P.J., Welker, J., Winker, K.S. & Yoshikawa, K. 2005. Evidence and implications of recent climate change in Northern Alaska and other Arctic regions. *Climatic Change* 72(3): 251-298.

Hinzman, L.D., Goering, D.J. & Kane, D.L. 1998. A distributed thermal model for calculating temperature profiles and depth of thaw in permafrost regions. *Journal of Geophysical Research – Atmospheres* 103(D22): 28,975-28,991.

Jorgenson, M.T., Racine, C.H., Walters, J.C. & Osterkamp, T.E. 2001. Permafrost degradation and ecological changes associated with a warming climate in central Alaska. *Climate Change* 48: 551-579.

Kane, D.L., Hinzman, L.D., McNamara, J.P., Zhang, Z. & Benson, C.S. 2000. An overview of a nested watershed study in Arctic Alaska. *Nordic Hydrology* 4/5: 245-266.

Kane, D.L., Gieck, R.E. & Bowling, L.C. 2003a. Impacts of surficial permafrost landforms on surface hydrology. *Proceedings of the Eighth International Conference on Permafrost, Zurich, Switzerland, 21–25 July 2003*, M. Phillips et al. (eds.). Lisse, The Netherlands: A.A. Balkema Publishers: 507-512.

Kane, D.L., McNamara, J.P., Yang, D., Olsson, P.Q. & Gieck, R.E. 2003b. An extreme rainfall/runoff event in Arctic Alaska. *Journal of Hydrometeorology* 4(6): 1220-1228.

Kane, D.L., Gieck, R.E., Kitover, D.C., Hinzman, L.D., McNamara, J.P. & Yang, D. 2004. *Hydrologic Cycle on the North Slope of Alaska*. International Association of Hydrological Sciences, IAHS Publication 290, 224-236.

Kane, D.L. & Yang, D. 2004. *Northern Research Basins Water Balance*. International Association of Hydrological Sciences, IAHS Publication 290, 271 pp.

Kane, D.L., Gieck, R.E. & Hinzman, L.D. 2008a. Water balance for a low-gradient watershed in Northern Alaska. *Proceedings of the Ninth International Conference on Permafrost, Fairbanks, Alaska, June 29–July 3, 2008* (this proceedings).

Kane, D.L., Hinzman, L.D., Gieck, R.E., McNamara, J.P., Youcha, E.K. & Oatley, J.A. 2008b. Contrasting extreme runoff events in areas of continuous permafrost. *Arctic Alaska. Hydrology Research* (in press).

Lachenbruch, A.H. & Marshall, B.V. 1986. Changing climate: geothermal evidence from permafrost in the Alaskan Arctic. *Science* 234: 689-696.

Lilly, E.K., Kane, D.L., Hinzman, L.D. & Gieck, R.E. 1998. Annual water balance for three nested watersheds on the North Slope of Alaska. *Proceedings of the Seventh International Conference on Permafrost*, *Yellowknife, Canada, June 1998*, A.G. Lewkowicz & M. Allard (eds.): 669-674.

McNamara, J.P., Kane, D.L. & Hinzman, L.D. 1999. An analyses of an Arctic channel network using a digital elevation model. *Geomorphology* 29: 339-353.

Overduin, P. P. & Kane, D.L. 2006. Frost boils and soil ice content: Field observations. *Permafrost and Periglacial Processes* 17: 291-307.

Romanovsky, V.E., Burgess, M., Smith, S., Yoshikawa, K. & Brown, J. 2002. Permafrost temperature records: indicators of climate change. *EOS* 83(50): 589 & 593-594.

Serreze, M. C., Walsh, J.E., Chapin, F.S. III, Osterkamp, T., Dyurgerov, M., Romanovsky, V., Oechel, W.C., Morison, J., Zhang, T. & Barry, R.G. 2000. Observational evidence of recent change in the northern high latitude environment. *Climate Change* 46: 159-207.

Smith, L.C., Sheng, Y., MacDonald, G.M. & Hinzman, L.D. 2005. Disappearing Arctic lakes. *Science* 308: 1429, (3 June 2005).

Smol, J.P. & Douglas, M.S.V. 2007. From controversy to consensus: Making the case for recent climatic change in the Arctic using lake sediments. *Frontiers in Ecology and the Environment* 5: 466-474.

Sturm, M., Racine, C. & Tape, K. 2001. Increasing shrub abundance in the Arctic. *Nature* 411: 546-547.

Yoshikawa, K. & Hinzman, L. 2003. Shrinking thermokarst ponds and groundwater dynamics in discontinuous permafrost. *Permafrost and Periglacial Processes* 14(2): 151-160.

Yoshikawa K., Hinzman, L.D. & Kane, D.L. 2007. Spring and aufeis (icing) hydrology in Brooks Range, Alaska *J. Geophys. Res*. 112: G04S43, doi:10.1029/2006JG000294.

Factors Controlling Periglacial Geodiversity in Subarctic Finland

Jan Hjort
Department of Geography, University of Helsinki, Helsinki, Finland
Miska Luoto
Thule Institute, University of Oulu, Oulu, Finland Department of Geography, University of Oulu, Oulu, Finland

Abstract

The aim of this study was to determine the environmental factors controlling the diversity of periglacial landforms on the landscape scale. The study was performed using an empirical dataset of periglacial landforms from an area of 600 km^2. Both distribution and abundance of landform diversity were modeled. The utilized statistical method was generalized linear modeling (GLM). A total of 40 different periglacial landform types and subtypes were identified. The number of different types in the 25-ha modeling squares varied from zero to nine. Based on GLM, the diversity of periglacial features increased with increasing moisture variability and altitude. Moreover, slope angle was an important correlate with cubic term; the diversity was highest on flat ground sites (0–2°) and on rather steep slopes (8–12°). The employment of GLM proved to be a useful approach to estimate the role of environmental factors in determining the periglacial geodiversity.

Keywords: generalized linear modeling (GLM); geodiversity; periglacial geomorphology; prediction; subarctic.

Introduction

Periglacial domain covers different features from large pingos to small sorted circles (French 2007). On a regional scale, the variety of periglacial phenomena can be substantial including several tens of features (e.g. Åkerman 1980). While the diversity of periglacial landforms is a well-known issue, rather few have studied the environmental factors behind the feature variability. One potential reason for the lack of research may be the difficulty in analyzing complex processes in extensive regions. The recent developments in combining the Geographic Information System (GIS), remote sensing (RS) data, and statistical techniques have improved the possibility of surveying extensive regions and studying different aspects of periglacial geomorphology (Luoto & Hjort 2005, 2008, Etzelmüller et al. 2006, Brenning et al. 2007, Hjort & Luoto, in press).

It would be profitable to develop spatial analysis techniques to map the sites of high geodiversity, because knowledge on the variability of geomorphological processes and landforms is important to conservation managers, engineers, and scientists (Walsh et al. 1998). Furthermore, in the context of geodiversity, the interest in variability on non-living nature has risen recently (e.g., Gray 2004). The concept of geodiversity is less well-appreciated in geomorphology, but is now developing momentum of its own. Geodiversity conservation is increasingly seen as important in its own right and as an essential support to biodiversity and cultural conservation programs (Gray 2004).

Here we examine the applicability of GIS-based datasets and generalized linear modeling (GLM) in determining the factors controlling the diversity of periglacial landforms on the landscape scale (Luoto & Hjort 2004, Hjort et al. 2007). The study is performed using an empirical dataset of periglacial landforms from an area of 600 km^2 at a 25-ha resolution (n = 2249). This rather coarse resolution was chosen based on data exploration and attempts to reduce the potential problems of spatial autocorrelation in statistical modeling (McCullagh & Nelder 1989). Both distribution (high- vs. low-diversity sites) and abundance (number of different types) of landform diversity were analyzed. Especially, we seek answers to the questions: (i) can we spatially predict the diversity of periglacial landforms and (ii) which environmental factors control the diversity in subarctic Finland on the landscape scale?

Study Setting

Background: factor-process-landform relationship

The complex relationship between environmental factors affecting the activity and presence of periglacial processes is presented in Figure 1A. In general, the most important environmental drivers are climate, topography, material, moisture conditions, snow and ice cover as well as vegetation (Washburn 1979, French 2007). Climatological conditions affect, for example, freeze-thaw cycles and moisture distribution and thus, all periglacial processes (Fig. 1B). Moreover, the wind has a significant role in snow redistribution, which affects ground temperatures and moisture conditions. Soil moisture, along with temperature, is one of the most important determinants of frost processes (e.g., Matthews et al. 1998). Soil material affects the moisture distribution and activity of periglacial process. Topography, snow cover, and vegetation influence the processes through the main factors: temperature and soil moisture (Fig. 1). However, topography directly affects slope phenomena, and vegetation on the slope as well as aeolian processes. Most of these environmental factors have a positive relationship with the process activity. Nonetheless, some factors (e.g., soil moisture) may reduce the activity of periglacial processes (e.g., aeolian phenomena).

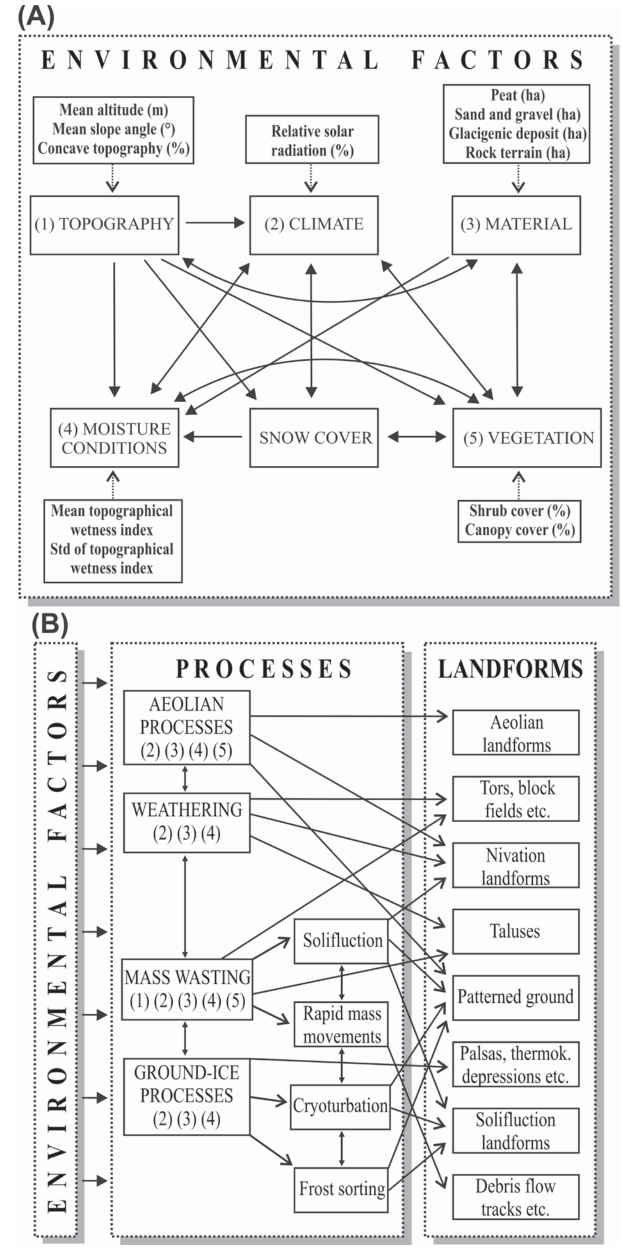

Figure 1. (A) The main interactions between environmental factors affecting periglacial processes and landforms on a regional scale. The environmental predictors and surrogates of factors used in this study are shown in outermost boxes. (B) Simplified conceptual model of the relationships between environmental factors, periglacial processes, and periglacial landforms commonly found from northern Fennoscandia (e.g., Lundqvist 1962, Harris 1982, Seppälä 2005). The main factors affecting processes are indicated with numbers (1 = topography, 2 = climate, etc.).

Study area

The study area is located in the northernmost Finnish Lapland within the zone of discontinuous permafrost (Fig. 2). The landscape of the area is characterized by rather rounded fells with elevations ranging from 110 to 641 m above sea level. The bedrock (ca. 1.9 billion-year-old) is covered by glacigenic till and peat, as well as sand and gravel deposits (Meriläinen 1976). Moreover, silty sediments are prevalent in the wide flat-bottomed valleys. The climate of the area is subarctic: the mean annual air temperature is -2.0°C, and mean annual precipitation ca. 400 mm (*Climatological Statistics in Finland 1961–1990* 1991). The vegetation of the area is characterized by subalpine mountain birch forests (*Betula pubescens* ssp. *czerepanovii*) and alpine heaths (*regio alpina*).

Modeling data

Periglacial landforms. The landforms were mapped and converted to grid-based modeling data in four steps (for details see Hjort 2006). First, a detailed stereoscopic interpretation of black-and-white aerial photographs (1:31,000) was performed to identify the potential sites of periglacial features. Second, the features were mapped utilizing pre-mapping results and a Global Positioning System (GPS) device (Garmin eTrex personal navigator with an accuracy of ca. 10 m) in the field during the summers of 2002 and 2003. Third, the field-mapping results were digitized in a vector format on orthorectified aerial photographs (ground resolution = 1 m) utilizing GIS software. Both active and inactive landforms were grouped together because the determination of activity of some feature types would have been a complicated task without several year-round field measurements. Finally, the created geomorphological database was used to produce two types of response datasets at the 25-ha resolution. In the first case, the datum was divided to the sites of high (coded 1) and low (coded 0) diversity using threshold values from 4 to 6 (e.g., high diversity ≥4 landform types present in the modeling square, low diversity <4 types present). In the second case, landform diversity was determined based on the number of different landform types in the modeling squares. The first type of datum was used to model the occurrence of high and low sites of diversity (distribution modeling) and the second type was used to analyze the intensity of diversity (abundance modeling).

Explanatory data. Taking into account the study aims, modeling resolution, and the complex relationships between environmental factors, periglacial processes, and periglacial landforms (Fig. 1), the explanatory variables (i.e., predictors) were compiled from commonly used and accessible information sources, namely a digital elevation model (DEM) (20-m grid size) (Hjort 2006), biotope database (Anonymous 2002), and digital soil map (Hjort 2006). Six topographical parameters (mean altitude, mean slope angle, mean and standard deviation of topographical wetness index, proportion of concave topography, and relative solar radiation), 4 soil-type variables (glacigenic deposit, sand and gravel, peat, as well as rock terrain cover), and 2 vegetation factors (shrub and tree cover) were computed using Arc/Info GRID at the 25-ha resolution (Fig. 1).

Data split. The final modeling data included 2249 squares, which were randomly divided into model- calibrating (50%, n = 1125) and model-evaluation sets (50%, n = 1124) (Guisan & Zimmerman 2000). A total of 151 squares were excluded due to the abundant water cover and deficiency in the explanatory data.

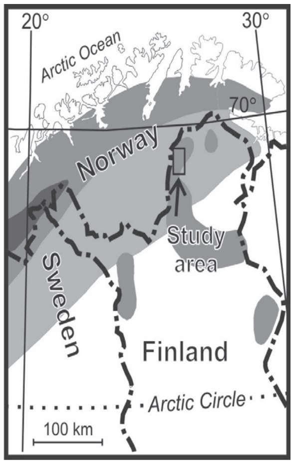

Figure 2. Location of the study area in northern Fennoscandia. Permafrost conditions are indicated with shades of gray: continuous (darkest), discontinuous, and sporadic (modified after Brown et al. 1998).

Generalized linear modeling

Generalized linear models (GLMs) are mathematical extensions of traditional least square (LS) regression models that do not force data into unnatural scales; they allow for nonlinearity and nonconstant variance (heteroscedasticity) structures in the data (McCullagh & Nelder 1989). In this study, the model calibration was performed utilizing the statistical package R version 2.3.0, with standard GLM function. The probability of curvilinear relationships between the explanatory and response variables was examined by including the quadratic and cubic terms of the predictors in the models (Crawley 1993). The variables were selected using a statistically focused backward elimination approach (see Crawley 1993). Elimination was based on a strict criterion ($p < 0.001$) for variable exclusion. The percentage of deviance explained [(null deviance – residual deviance / null deviance) * 100] was calculated for the final GLMs to gain an overall picture of the success of the fitting (for details see Hjort 2006).

Model evaluation. The distribution models were assessed utilizing evaluation data and the area under the curve (AUC) values of a receiver operating characteristic (ROC) plot (e.g., Pearce & Ferrier 2000). The AUC values range from 0.5 for models with no discriminative ability to 1.0 for models with perfect discrimination. Swets (1988) proposed a rough guide for classifying the AUC measures of the models: 0.50–0.70 = low model accuracy, 0.71–0.90 good model accuracy, > 0.90 = high model accuracy. The predictive ability of the abundance model was assessed by calculating Spearman's rank correlation coefficient (R_s) between the predicted and observed diversity using evaluation data (Guisan & Zimmermann 2000).

Results

Periglacial landforms

A total of 40 different periglacial landform types and subtypes were identified (Table 1). The most common landforms, if calculated by occupied modeling squares, were earth hummocks (n = 1636), peat pounus (n = 702), sorted nets (n = 631) and sorted sheets (n = 431). The rarest features were non-sorted lobes (n = 10), slushflow tracks (n = 4) and braking blocks (n = 4), respectively.

Table 1. Periglacial landforms mapped from the study area and their prevalence at the 25-ha modeling resolution (x = not determined).

Periglacial landforms	Present squares (%)
Palsas (4 subtypes)	134 (5.4%)
Thermokarst ponds	69 (2.8%)
Circles	
- convex non-sorted circles	229 (9.2%)
- stony earth circles	245 (9.8%)
- earth hummocks	1636 (65.4%)
- peat pounu	702 (28.1%)
- sorted stone circles	81 (3.2%)
- stone pits	252 (10.1%)
- debris islands	38 (1.5%)
Polygons	
- non-sorted polygons	18 (0.7%)
- sorted polygons	50 (2.0%)
Nets	
- sorted nets	631 (25.2%)
Boulder depressions	73 (2.9%)
Steps	
- non-sorted steps	111 (4.4%)
Stripes	
- non-sorted stripes	36 (1.4%)
- sorted stripes	198 (7.9%)
Debris flow slopes	17 (0.7%)
Slush flow tracks	4 (0.2%)
Solifluction features	
- non-sorted terraces	275 (11.0%)
- non-sorted lobes	10 (0.4%)
- ploughing blocks	15 (0.6%)
- braking blocks	4 (0.2%)
- sorted sheets (2 subtypes)	431 (17.2%)
- sorted terraces	74 (3.0%)
- sorted lobes	68 (2.7%)
- sorted streams	244 (9.8%)
Talus slopes	19 (0.8%)
Block fields	34 (1.4%)
Tors	127 (5.1%)
Nivation sites	x
Stone pavements	15 (0.6%)
Sand dunes (3 subtypes)	99 (4.0%)
Deflation sites (2 subtypes)	295 (11.8%)

The number of different periglacial landform types in the 25-ha modeling squares varied from 0 to 9 (Fig. 3). A total of 247 (9.9%) squares were without any periglacial features and 2253 (90.1%) sites were occupied by at least 1 landform type. Squares with only 1 landform type were commonly occupied by extensive fields of earth hummocks, peat pounus, palsas, or sorted nets. Considerably many of the modeling squares included 2 to 4 different landform types, which is mainly caused by the presence of feature continuums. Over 6 landform types were observed from only 58 (2.3%) squares.

Diversity GLMs

The results of the diversity modeling are summarized in Table 2. In distribution modeling, the amount of explained deviance varied between 16% and 18%. The abundance model was able to explain 21% of the deviance change. In model evaluation, the AUC measures of the distribution models ranged from 0.76 to 0.78, indicating fair discrimination ability between the sites of high and low diversity. The abundance model was moderate in predicting the number of different periglacial landforms present in the analysis squares (R_s = 0.52).

The number of the environmental factors varied from 2 to 4 in the final GLMs (Table 2). The most important correlates for both the distribution of high-diversity sites (≥4 landforms present) and abundance of landform types were mean altitude, mean slope angle, and soil moisture variability. The slope angle variable was included in 3 of the 4 models with cubic term, indicating that the diversity was highest on flat ground sites (0–2°) and on rather steep slopes (8–12°) (Fig. 4). Moreover, canopy and peat cover were shown to be connected to the diversity (Table 2).

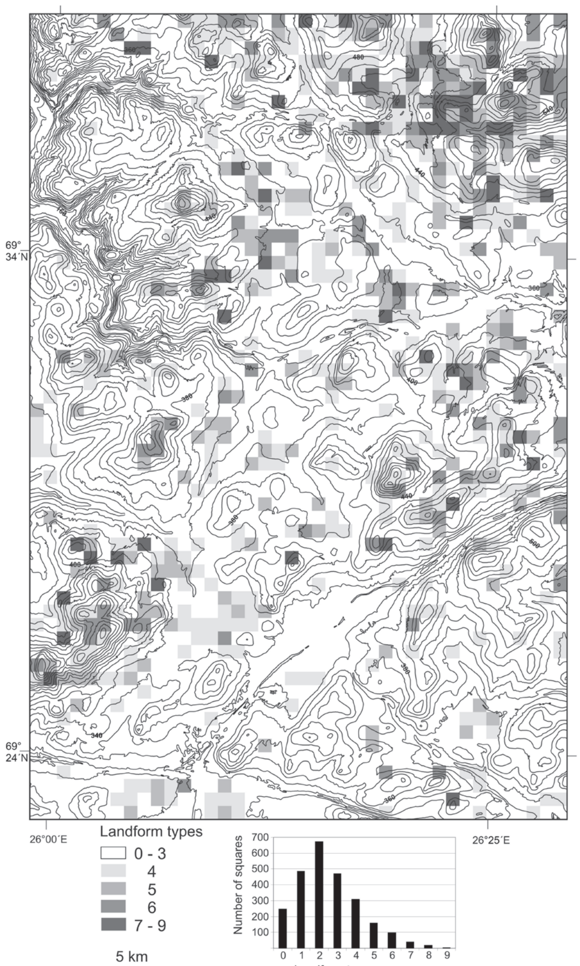

Figure 3. Number of different periglacial landform types at the 25-ha modeling resolution. The vertical interval of contours is 20 m (© National Land Survey of Finland).

Discussion

In general, knowledge on the diversity of geomorphological phenomena could be useful for academic, applied and economic applications (Gray 2004). In the context of global change, spatial models of geodiversity could be used to assess the impacts of changing environmental conditions on periglacial processes (Fronzek et al. 2006, Johansson et al. 2006). One would expect that declining frost conditions would decrease the feature variability, but the short-term effects of climate change on periglacial processes are rather unclear. For example, increasing temperature decreases frost severity. However, increasing precipitation could increase frost activity because moisture availability has shown to be one of the most important determinants for the occurrence

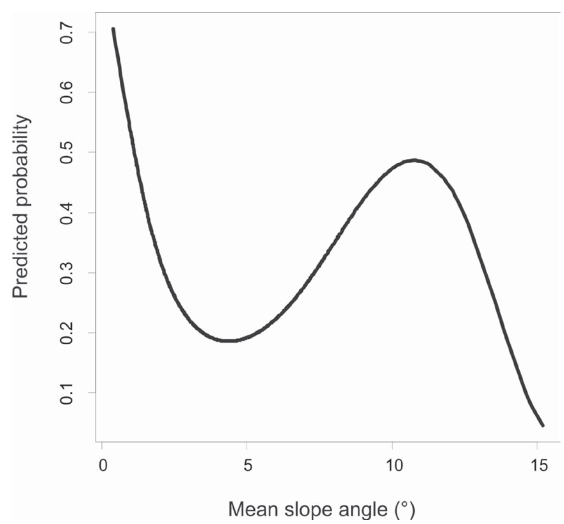

Figure 4. Relationship between diversity of periglacial landforms and slope angle. The predicted probability of diversity is derived from the distribution GLM (threshold value = 4) relating slope variable separately to the response variable.

Table 2. Summary of the final distribution (D_x) and abundance (A) models (x indicates the utilized threshold value in distribution modeling).

GLM	Mean altitude	Mean slope angle	Std of wetness index	Mean canopy cover	Peat cover	AUC cal / eval *$R_{(s)}$ cal / eval*
D_4	↗	− + −	↗	↘		0.79 / 0.76
D_5	↗	− + −	↗			0.78 / 0.76
D_6	↗		↗			0.79 / 0.78
A	↗	− + −	↗		∩	*0.48 / 0.52*

The direction of the effect of environmental factor ($p < 0.001$) is indicated with symbols (↗ = positive correlate, ↘ = negative correlate, ∩ = second-order correlate with a humped response curve, − + − = third-order correlate with a recumbent S-shaped response curve). The area under the curve (AUC) values and Spearman's rank correlation coefficient (R_s) were calculated with the calibration (cal) and evaluation (eval) data.

and activity of frost processes on a local (e.g., Matthews et al. 1998) and regional (Luoto & Hjort 2004) scale. Moreover, climate warming will probably increase the vegetation cover in sparsely vegetated arctic and subarctic regions (e.g., Liston et al. 2002). This would affect the periglacial processes, because feature occurrences have shown to be connected to shrub abundance, both positively and negatively, depending on the process type (Hjort 2006).

Periglacial phenomena have been mapped from numerous cold climate regions, but environmental factors controlling diversity have not been analyzed statistically previously (e.g. Lundqvist 1962, Karte 1979, Åkerman 1980, Harris 1982, Hjort 2006). Based on the modeling conducted in this study, the diversity of periglacial landforms was connected to altitude and soil moisture variability on the landscape scale. Moreover, the most diverse sites were either flat areas (0–2°) or rather steep slopes (8–12°). Different patterned ground features occur on flat topography, whereas moderate slopes are covered by sorted and non-sorted solifluction landforms. In proportion, gentle slopes are less suitable for most of the observed periglacial feature types (cf. Washburn 1979, French 2007).

The prediction and explanation power of the models were only on a moderate level (cf. Brenning & Trombotto 2006, Hjort et al. 2007). This is partly due to the complex process-environment relationships when landforms of different origin are grouped. Several different processes are responsible for the genesis of the observed periglacial landforms, and it is a challenging task to generate spatial datasets of causal factors of periglacial processes (Luoto & Seppälä 2002). Moreover, the correlation between environmental factors and periglacial landforms may be blurred by the fact that an environmental factor may be a positive or a negative correlate, depending on the feature type. On the other hand, the employment of a multivariate method and GIS-based data helped to draw a conclusion of factors affecting periglacial geodiversity, an issue that may be a complicated task using traditional descriptive methods.

Despite the fact that the prediction and explanation abilities of the models were rather low, the models were robust and gave parallel results. Therefore, the inferences of important environmental factors lie on fairly solid ground. However, the data-related limitations and method-based weaknesses may bias the modeling results, and the model outcomes should not be interpreted uncritically. In the context of geomorphological modeling, these important issues have been discussed, for example by Guzzetti et al. (1999) as well as Luoto & Hjort (2006).

Conclusions

The employment of GLM and GIS-based data proved to be a useful way to estimate the role of environmental factors in determining the diversity of periglacial features. However, the prediction and explanation power of the models were comparatively low due to the complex process-environment relationships when landforms of different genesis were grouped. Thus, there remains considerable room for further improvements in modeling the diversity of periglacial geomorphology. Improved models could be applied in geodiversity and environmental change studies.

Acknowledgments

The Kevo Subarctic Research Institute provided outstanding facilities during the field surveys. J. Hjort was funded by the Finnish Cultural Foundation.

References

Åkerman, J. 1980. Studies on periglacial geomorphology in West Spitsbergen. *Meddelanden Från Lunds Universitets Geografiska Institution, Avhandlingar* 89, 297 pp.

Anonymous, 2002. *Digital Biotope Data*. Helsinki: Metsähallitus.

Brenning, A. & Trombotto, D. 2006. Logistic regression modeling of rock glacier and glacier distribution: Topographic and climatic controls in the semi-arid Andes. *Geomorphology* 81: 141-154.

Brenning, A., Grasser, M. & Friend, D.A. 2007. Statistical estimation and generalized additive modeling of rock glacier distribution in the San Juan Mountains, Colorado, United States. *Journal of Geophysical Research* 112: F02S15.

Brown, J., Ferrians, O.J.J., Heginbottom, J.A. & Melnikov, E.S. 1998 (revised February 2001). *Circum-Arctic map of permafrost and ground-ice conditions*. Boulder, CO: National Snow and Ice Data Center/ World Data Center for Glaciology. Digital Media.

Climatological Statistics in Finland, 1961–1990. 1991. Supplement of meteorological yearbook of Finland. Helsinki: Finnish Meteorological Institute, 125 pp.

Crawley, M.J. 1993. *GLIM for Ecologists*. Oxford: Blackwell Scientific Publications, 379 pp.

Etzelmüller, B., Heggem, E.S.F., Sharkhuu, N., Frauenfelder, R., Kääb, A. & Goulden, C. 2006. Mountain permafrost distribution modelling using a multi-criteria approach in the Hövsgöl area, northern Mogolia. *Permafrost and Periglacial Processes* 17: 91-104.

French, H.M. 2007. *The Periglacial Environment* (3rd ed.) Chichester: Wiley, 458 pp.

Fronzek, S., Luoto, M. & Carter, T.R. 2006. Potential effect of climate change on the distribution of palsa mires in subarctic Fennoscandia. *Climate Research* 32: 1-12.

Gray, M. 2004. *Geodiversity. Valuing and Conserving Abiotic Nature*. Chichester: Wiley, 434 pp.

Guisan, A. & Zimmermann, N.E. 2000. Predictive habitat distribution models in ecology. *Ecological Modelling* 135: 147-186.

Guzzetti, F., Carrara, A., Cardinali, M. & Reichenbach, P. 1999. Landslide hazard evaluation: a review of current techniques and their application in a multi-scale study, Central Italia. *Geomorphology* 31: 181-216.

Harris, C. 1982. The distribution and altitudinal zonation of periglacial landforms, Okstindan, Norway. *Zeitschrift für Geomorphologie* 26: 283-304.

Hjort, J. 2006. *Environmental Factors Affecting the Occurrence of Periglacial Landforms in Finnish Lapland: A Numerical Approach*. Shaker Aachen: Verlag, 162 pp.

Hjort, J. & M. Luoto (In press). Can abundance of geomorphological features be predicted using presence-absence data? *Earth Surface Processes and Landforms* 33.

Hjort, J., Luoto, M. & Seppälä, M. 2007. Landscape scale determinants of periglacial features in subarctic Finland: a grid-based modelling approach. *Permafrost and Periglacial Processes* 18: 115-127.

Johansson, M., Christensen, T.R., Åkerman, J.H. & Callaghan, T.V. 2006. What determines the current presence or absence of permafrost in the Torneträsk region, a sub-arctic landscape in Northern Sweden? *Ambio* 35: 190-197.

Karte, J. 1979. Räumliche Abgrenzung und regionale Differenzierung des Periglaziärs (in German with English summary). *Bochumer Geographische Arbeiten* 35: 211 pp.

Liston, G.E., McFadden, J.P., Sturm, M. & Pielke Sr., R.A. 2002. Modelled changes in arctic tundra snow, energy and moisture fluxes due to increased shrubs. *Global Change Biology* 8: 17-32.

Lundqvist, J. 1962. Patterned ground and related frost phenomena in Sweden. *Sveriges Geologiska Undersökning, Serie C, Avhandlingar och Uppsatser* 583. 101 pp.

Luoto, M. & Hjort, J. 2004. Generalized linear models in periglacial studies: terrain parameters and patterned ground. *Permafrost and Periglacial Processes* 15: 327-338.

Luoto, M. & Hjort, J. 2005. Evaluation of current statistical approaches for predictive geomorphological mapping. *Geomorphology* 67: 299-315.

Luoto, M. & Hjort, J. 2006. Scale matters: A multi-resolution study of the determinants of patterned ground activity in subarctic Finland. *Geomorphology* 80: 282-294.

Luoto, M. & Hjort, J. 2008. Downscaling of coarse-grained geomorphological data. *Earth Surface Processes and Landforms* 33: 75-89.

Luoto, M. & Seppälä, M. 2002. Modelling the distribution of palsas in Finnish Lapland with logistic regression and GIS. *Permafrost and Periglacial Processes* 13: 17-28.

Matthews, J.A., Shakesby, R.A., Berrisford, M.S. & McEwen, L.J. 1998. Periglacial patterned ground on the Styggedalsbreen glacier foreland, Jotunheimen, southern Norway: micro-topographic, paraglacial and geoecological controls. *Permafrost and Periglacial Processes* 9: 147-166.

McCullagh, P. & Nelder, J.A. 1989. *Generalized Linear Models* (2nd ed.) New York: Chapman & Hall, 511 pp.

Meriläinen, K. 1976. The granulite complex and adjacent rock in Lapland, northern Finland. *Bulletin of Geological Survey of Finland* 281. 129 pp.

Pearce, J. & Ferrier, S. 2000. Evaluating the predictive performance of habitat models using logistic regression. *Ecological Modelling* 133: 225-245.

Seppälä, M. 2005. Periglacial environment. In: M. Seppälä (ed.), *The Physical Geography of Fennoscandia*. Oxford: Oxford University Press, 349-364.

Swets, J.A. 1988. Measuring the accuracy of diagnostic systems. *Science* 240: 1285-1293.

Walsh, S.J., Butler, D.R. & Malanson, G.P. 1998. An overview of scale, pattern, process relationships in geomorphology: a remote sensing and GIS perspective. *Geomorphology* 21: 183-205.

Washburn, A.L. 1979. *Geocryology: A Survey of Periglacial Processes and Environments*. London: Arnold, 406 pp.

Borehole and Ground Surface Temperatures and Their Relationship to Meteorological Conditions in the Swiss Alps

Martin Hoelzle
Glaciology, Geomorphodynamic, & Geochronology, University of Zurich
Stephan Gruber
Glaciology, Geomorphodynamics & Geochronology, University of Zurich

Abstract

In Switzerland, several boreholes are monitored within the framework of the Permafrost Monitoring Switzerland (PERMOS). Three of these boreholes, at Murtèl, at Schilthorn, and at Stockhorn, are at least 60 m deep. In addition, a number of shorter boreholes (c. 6 m deep) were drilled in other projects and have been continuously observed over several years. Results on long- and short-term behavior of these boreholes are presented and compared to standard meteorological components, such as air temperatures and snow cover, measured directly at these borehole sites or nearby. First analyses show the importance of the snow cover duration and thickness; more important on a local scale are different surface and subsurface characteristics influencing heat transfer by conduction and heat capacity. The concept of different offsets between atmosphere and lithosphere is discussed, and data reflecting these offsets are presented for typical alpine conditions.

Keywords: alpine permafrost; borehole temperatures; meteorological measurements; surface offset; thermal offset; total offset.

Introduction

Climatic and microclimatic factors control the surface temperature. In turn, the surface temperature is one of the major factors influencing the ground thermal regime. Usually, once the surface temperature regime is known, the thermal regime in the ground, provided it is homogenous, can be analyzed without further consideration of climate. However, snow cover as well as ground thermal properties that depend on surface and near-surface characteristics often strongly modify heat and energy fluxes in the ground (Brown & Péwé 1973, Harris & Brown 1978).

Since the early 1980s, climate–permafrost relationships in high-alpine areas have been in the focus of Alpine permafrost research (cf. Keller 1994, Haeberli et al. 1998, Hoelzle et al. 1999, Hoelzle et al. 2001, Hoelzle et al. 2003, Mittaz et al. 2000, Stocker-Mittaz et al. 2002). In recent years, mountain permafrost research has developed considerably. Main efforts are concentrated on improved modeling and attempting to couple regional climate models with local scale models (Salzmann et al. 2006, Noetzli et al. 2007, Salzmann et al. 2007). There is, however, still a considerable lack in process understanding of the complex interactions between atmosphere and lithosphere in high- mountain areas. This is mainly caused by the complex topography and the high variability of the spatial and temporal influences of snow and surface characteristics (Gruber et al. 2004, Hanson & Hoelzle 2005). The model-concept describing the offset between mean annual air temperature (MAAT) and temperature at the top of permafrost (TTOP) has been developed by several authors (Burn & Smith 1988, Smith & Riseborough 1996, Smith et al. 1998, Henry & Smith 2001, Riseborough 2002) and is a useful simplification to overcoming the problem of physically coupling the atmosphere and the ground. However, snow and surface/subsurface conditions in alpine areas differ quite strongly from the ones in the Arctic. First attempts to apply the concept of TTOP to mountain areas were made by Herz et al. 2003 and Juliussen & Humlum 2007. In the concepts of Lachenbruch & Marshall 1986, Burn & Smith 1988, and Smith & Riseborough 1996, the total offset between MAAT and TTOP is often expressed first by a surface offset between MAAT and the mean annual ground surface temperature (MAGST) and MAGST and TTOP. In reality, the surface offset consists of two separate offsets: one between MAAT and the mean annual surface temperature (MAST) and one between the MAST and MAGST. These two offsets are often treated as one, because they are hardly ever separately measured. The MAST can be expressed as the radiative surface skin temperature, which can be measured by an IR thermometer (see Table 1) measuring the thermal infrared radiating temperature of the ground surface in its field of view. This temperature is measured always at the variable current surface of the corresponding season; e.g., in winter mainly the snow surface and in summer mainly the bedrock surface.

Until today, no reliable information about long-term values of these offsets for alpine areas have been available that are based on long-term measurements. The long-term measurements presented in this paper should help to provide first approximations of the various offsets and a description of the general relationship between MAAT, snow depth, MAGST, and TTOP. This study also reveals the importance of long-term monitoring to improve our process understanding, which is required to develop useful but simple model concepts.

Measurements at Murtèl-Corvatsch and Schilthorn

Meteorological measurements at Murtèl-Corvatsch

The Murtèl-Corvatsch and Chastelets borehole sites are located northwest of the Murtèl cable car station within the ski area Silvaplana – Piz Corvatsch. The area is situated in the Upper Engadine (Eastern Swiss Alps). A steep northwest-facing rock wall surrounds the area, and the slopes below the rock walls are covered by several meters of loose debris. Several rock glaciers and protalus ramparts are situated at the foot of the slope below the ridge. The area is inside the periglacial belt with strong weathering intensity on the headwalls resulting in a large amount of debris feeding the active rock glaciers below.

One of these rock glaciers is the Murtèl rock glacier (46°26´N, 9°49´E), which has been well-investigated over many years (Hoelzle et al. 2002). A borehole was drilled in 1987 and has provided a ground temperature data record since then. In 1997 a first micrometeorological station was installed at the Murtèl-Corvatsch site (Mittaz et al. 2000). Such long-term micrometeorological studies at the borehole locations (Harris et al. 2003) are needed for process understanding, model development, and calibration (Hoelzle et al. 2001). They provide data on heat fluxes between the atmosphere and the active layer, and between the active layer and the underlying permafrost. Therefore, they have been included in the concept of the permafrost monitoring network Switzerland (PERMOS).

Air temperature, radiation, and wind speed among others have been measured directly at the borehole site on the rock

Table 1. Sensors used in this study.

Variables	Sensors (Company)	Sensor Type	Range	Accuracy
Air temperature	MP-100A (Rotronic)	RTD PT-100 1/3-Din ventilated	-40 - +60°C	±10 %
Snow height	SR50 (Campell)	Ultrasonic Electrostatic Transducer	0.5 – 10 m	±0.01 m
Surface temperature	Infrared thermometer	IRt/c.5	-35 – 10°C	±1.5°C
Ground temp. Murtèl-Schilthorn-Stockhorn boreholes	YSI 44006 Yellow Springs Instruments	NTC-Thermistors	-20 - +40°C	±0.02 °C
Ground temp. Active layer	UUB31J1 Fenwal	NTC-Thermistors	-20 - +40°C	±0.02 °C
Chastelets boreholes	YSI 44006 Yellow Springs Instruments	NTC-Thermistors	-20 - +40°C	±0.02 °C
Rocklogger	M-Log Geoprecision	PT1000	-55 - +85°C	±0.01°C

glacier since January 1997. In addition, there is a meteorological station on the summit cable car station that has been run by MeteoSwiss since 1983. With the help of this meteorological station the air temperature at Murtèl-Corvatsch was reconstructed from 1997 back until 1987, which is when the ground temperature measurements started. The same reconstruction is made for the surface temperature measurements, which have been recorded since 2001 by an IR thermometer. Since 1972, snow depths have been continuously measured in winter (October to May) at the middle station of the Corvatsch cable car by the Snow and Avalanche Research Institute in Davos. These data are compared and adjusted to the direct measurements made at the Murtèl-Corvatsch station, which allowed a continuous reconstruction of snow depth for the period 1988ñ2007. These reconstructions were necessary to have a continuous data record directly at the measurement site of the Murtèl borehole.

The micrometeorological station measures air temperature, wind speed and direction, humidity, snow depth, as well as all components of the radiation balance every 10 minutes which is logged every half-hour as a 30-minute mean (cf. sensor description in Table 1). Meteorological measurements in high-alpine environments are difficult because of the harsh climatic conditions. This results in many periods without data. Such periods are caused by lightning, avalanches, rime-ice, or burying of the instrumentation by snowfall.

Ground temperature masurements at Murtèl-Corvatsch

The Murtèl borehole from 1987 was drilled down to 58 m, but in this study only the uppermost thermistors, down to 6 m, are analyzed. The measuring interval is 24 hours.

Seven thermistors were placed in the uppermost 90 cm of the active layer less than 2 m from the microclimate station and in close vicinity of the borehole. Five thermistors are placed 5 cm deep in the boulders, while two thermistors are hanging in cavities between the boulders, thus measuring the ambient air temperatures. They are described in detail by Hanson & Hoelzle 2003, 2004. Temperatures were registered every minute and logged as a 5-minute mean. All thermistors were calibrated before their placement and are annually indirectly calibrated by the zero curtain in spring.

In the Chastelets area, five boreholes were drilled in the year 2002. These boreholes are described in detail by Hanson & Hoelzle 2005. The boreholes were selected using the criteria that aspect and climatic conditions should be the same and that only the surface characteristics are different, such as, for example, coarse debris or bedrock.

Meteorological measurements at Schilthorn

The study area in the Schilthorn massif is situated at the transition between the Prealps in the north and the principle chain of the Bernese Alps, which exceed 4000 m a.s.l. The Schilthorn summit reaches 2970 m a.s.l. and is located at 46°34′N, 7°50′E.

Today, only perennial snow patches can be found, which have been shrinking considerably as a consequence of the warm 1980s and 1990s (Imhof 2000).

Due to its geographic situation (exposed to moist western winds), the climate in the Schilthorn massif is of almost maritime alpine character; i.e., with fairly abundant precipitation, showing a distinct summer maximum. The mean annual accumulation in Lauterbrunnen (valley floor) is 1234 mm, whereas about 2700 mm were estimated on the highest summits, where about 90% of the precipitation falls as snow (Imhof 2000). Consequently, the surface is snow-covered for longer than in most of the comparable regions of the central Alps.

The microclimatological station was installed about 100 m to the northwest of the Schilthorn summit at 2900 m a.s.l. in 1998.

Ground temperature measurements at Schilthorn

Also in 1998, a 14-m deep borehole was drilled into bedrock a few meters to the northwest of the climate station and equipped with a thermistor chain. Two additional boreholes were drilled in the year 2000: a vertical one with a depth of 100 m and a horizontal one with a depth of 92 m. The borehole data show that the active layer reaches, in general, to a depth of about 5 m, and that the MAGT at 14 m depth is around -0.5 to -0.7°C. Thus, permafrost is present at the drill sites but is rather warm.

Results

Meteorological measurements at Murtèl-Corvatsch and Schilthorn

Tables 2 and 3 show the mean monthly values for the three variables (1) air temperature, measured 2 m above the ground, (2) snow height, and (3) ground temperature at 3.6 m and 5.0 m below surface at the top of permafrost.

As ground temperature data for Murtèl-Corvatsch exist from 1987 onwards, air temperature and snow depth were reconstructed as needed.

Schilthorn meteorological and ground temperature data recording started in 1998/99. The mean ground temperature at 3.6 m depth represents the TTOP. Air temperature has an annual peak amplitude at Murtèl-Corvatsch of 15.4°C and at Schilthorn of 13.5°C. Mean snow depth at Schilthorn is approximately double that of Murtèl-Corvatsch.

These values indicate that Murtèl-Corvatsch has a more continental climate than Schilthorn. Schilthorn is situated around 300 m higher than Murtèl-Corvatsch. Despite this elevation difference, the ground temperatures at Murtèl-Corvatsch are by far -1.2°C colder.

TTOP at Schilthorn is at a depth of around 5 m; however, in the year 2003, the active layer thickness increased to around 9 m. This was caused by the heat wave of 2003 which lead to warmer TTOP temperatures than normal. This can also be recognized in Figure 2.

Time series of air temperature, snow depth, and ground temperatures at Murtèl-Corvatsch

Figure 1 displays the continuous mean monthly data set from 1988 to 2007 for air temperature, snow depth, and ground temperature at TTOP 3.6 m below surface. The time series illustrates the influence of snow cover on the TTOP. The winters 1993/94, 1996/97, 2000/01, and 2002/03 had snow depths that far exceeded normal conditions. As a result, the TTOP were very warm, even in the year 2002/03 which had very cold winter air temperatures. In contrast, the winters 1988/89 and especially 2001/02 had below-average snow conditions, which resulted in very cold TTOP. An exception was the winter 2006/07, which had the lowest snow depth since the beginning of the snow measurements in 1972. It did not result in the coldest TTOP, because winter air temperatures were the warmest ever recorded at the meteorological stations in the Corvatsch area.

Table 2. Mean monthly values of different meteorological measurements at the Murtèl-Corvatsch site from 1988 to 2006.

Monthly mean 1988-2006	Air temperature [°C]	Snow height [m]	Borehole temperature (depth = 3.6 m) [°C]
January	-7.42	0.64	-2.24
February	-8.79	0.70	-2.84
March	-6.91	0.82	-3.20
April	-5.06	0.94	-3.57
May	0.24	0.67	-2.87
June	3.59	0.21	-0.75
July	6.50	0.02	-0.42
August	6.65	0.01	-0.29
September	2.81	0.02	-0.20
October	-0.09	0.08	-0.18
November	-5.31	0.32	-0.26
December	-7.38	0.52	-1.16
Average	**-1.76**	**0.41**	**-1.50**

Table 3. Mean monthly values of different meteorological measurements at the Schilthorn site from 1999 to 2007.

Monthly mean 1999-2007	Air temperature [°C]	Snow height [m]	Borehole temperature (depth = 5 m) [°C]
January	-9.60	1.10	-0.10
February	-9.27	1.12	-0.26
March	-7.62	1.25	-0.60
April	-4.79	1.48	-0.87
May	-0.33	1.59	-0.92
June	2.74	1.20	-0.77
July	3.87	0.29	-0.46
August	3.93	0.03	-0.25
September	2.6	0.02	0.07
October	-0.98	0.22	0.03
November	-5.86	0.50	-0.04
December	-7.88	0.88	-0.08
Average	**-2.77**	**0.81**	**-0.35**

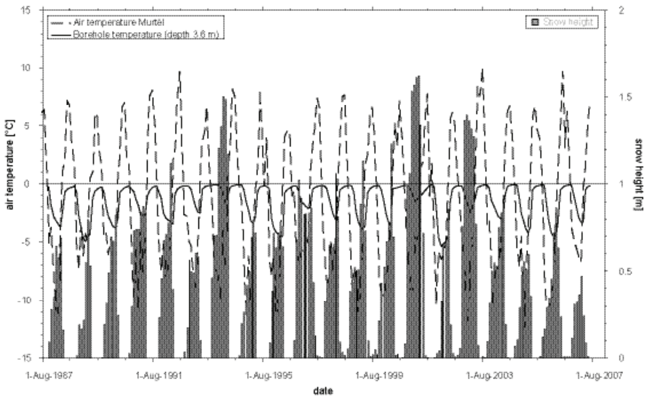

Figure 1. Monthly air temperature, snow depth and ground temperature at TTOP in 3.6 m depth at Murtèl-Corvatsch (borehole 2/87).

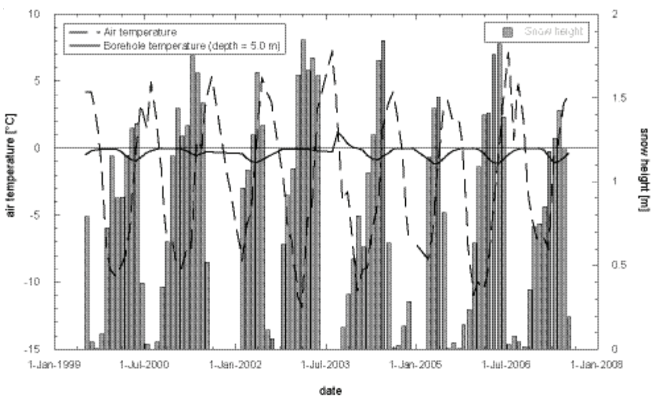

Figure 2. Monthly air temperature, snow depth and ground temperature at TTOP in 5.0 m depth at Schilthorn (borehole 51/98).

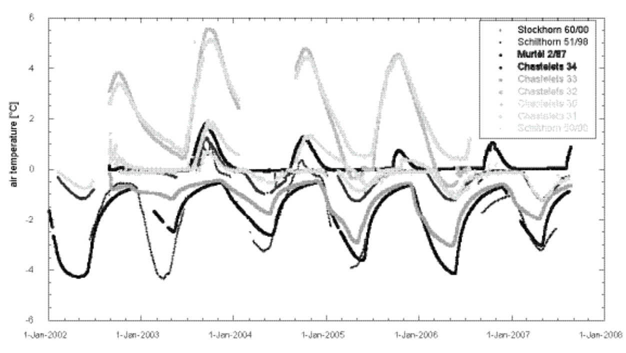

Figure 3. Daily ground temperatures in all boreholes at 5 m depth.

Time series of air temperature, snow depth, and ground temperature at Schilthorn

Figure 2 shows the mean monthly data set from 1999 to 2007 for air temperature, snow depth, and ground temperature at TTOP in a depth of 5.0 m. The time series from the Schilthorn does not reflect the influence of the snow cover on the TTOP temperature as well as the Murtèl-Corvatsch series does. The winter snow cover at Schilthorn shows less variability than at Murtèl-Corvatsch.

In general, winter snow cover at Schilthorn starts earlier and reaches greater snow thicknesses than at Murtèl-Corvatsch. This results in stronger warming than at Murtèl-Corvatsch. Additionally, the surface layer at the Schilthorn is composed of fine-grained material containing more unfrozen water and resulting, therefore, in reduced cooling because of latent heat effects.

Table 4. Surface offset (temperature at 0.5 m depth – air temperature) and total offset (including thermal offset) 1) temperature at 2.5 m depth – air temperature; 2) temperature at 4.5 m depth – air temperature) for different boreholes and years. The rows in grey show the values for the permafrost boreholes.

Borehole	Measurement period	Surface offset	Total offset 1	Total offset 2
Murtèl 2/87	1997/98	1.50	0.33	-0.12
Murtèl 2/87	2001/02	0.26	-0.33	-0.50
Murtèl 2/87	2002/03	1.33	0.02	-0.37
Murtèl 2/87	2003/04	1.40	0.73	0.28
Murtèl 2/87	2004/05	0.41	0.10	-0.37
Murtèl surface block	2003/04	2.08		
Murtèl surface block	2004/05	1.24		
Murtèl below surface block	2003/04	1.39		
Murtèl below surface block	2004/05	0.50		
Chastelets B30	2002/03	4.57	3.63	3.35
Chastelets B31	2002/03	2.89	1.85	1.38
Chastelets B32	2002/03	4.66	3.79	3.32
Chastelets B33	2002/03	2.49	0.62	0.32
Chastelets B34	2002/03	3.37	2.22	1.36
Chastelets B30	2004/05	3.52	3.62	4.06
Chastelets B31	2004/05	1.51	2.14	2.02
Chastelets B32	2004/05	3.41	3.56	3.72
Chastelets B33	2004/05	1.11	0.00	0.36
Chastelets B34	2004/05	2.21	2.11	1.94
Murtèl rock	2003/04	4.61		
Murtèl rock	2004/05	4.08		
Murtèl rock	2005/06	3.98		
Schilthorn 51/98	1999/00	2.49	2.70	2.49
Schilthorn 51/98	2005/06	2.85	2.72	2.66
Schilthorn 50/00	2005/06	2.90	2.88	2.77
Stockhorn 60/00	2002/03	-1.28	4.98	3.72

Time series of different ground temperatures at all investigation sites

Figure 3 shows the temperature development since 2002 within all boreholes investigated in this study. After the very warm summer 2003, a slight cooling trend is observed within all boreholes. This effect can mainly be attributed to less winter snow (see also Fig. 1).

Offset data at all sites

Table 4 shows the surface offset and total offset for several years and borehole sites. These selected data only include years that have less than 10% data gaps. The data show that at most permafrost sites the surface offset is less than at permafrost-free sites. The range of surface offset at the permafrost sites varies from less than 0 up to 2.9°C, but between 3.41 and 4.6°C at permafrost-free sites. Borehole 34 lies in between and should be treated as a special case, because this site is at the edge of a rock glacier within fine material and the lowest temperature sensor at 6 m depth is close to 0°C, indicating permafrost below but not in this borehole.

In Figures 4 and 5, the surface offset and thermal offset, including the offset between MAAT and MAST, are shown as an average over the whole measurement period for Murtèl-Corvatsch (Fig. 4) and Schilthorn (Fig. 5). The offset data reveal that the mean difference between MAAT and MAST is 1.12°C at Murtèl-Corvatsch and 1.24°C at Schilthorn, respectively. The offset between MAST and MAGST is 3.62°C at Murtèl-Corvatsch and 3.99°C at Schilthorn.

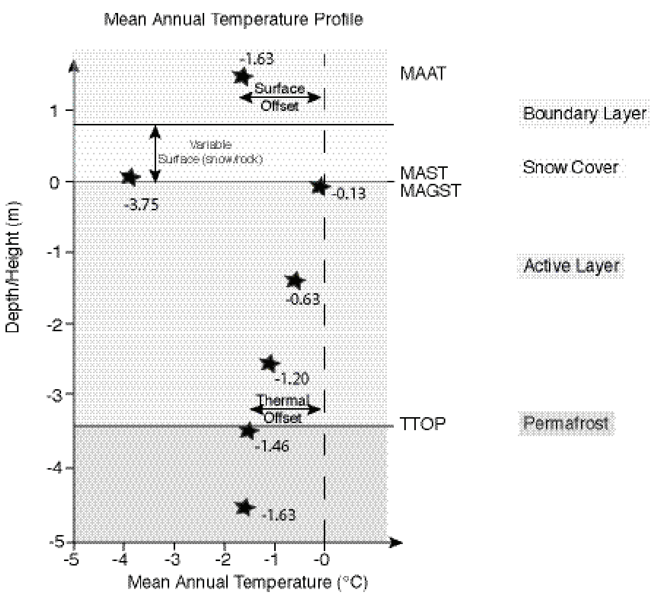

Figure 4. Different offset values shown from the mean data measured at the Murtèl-Corvatsch.

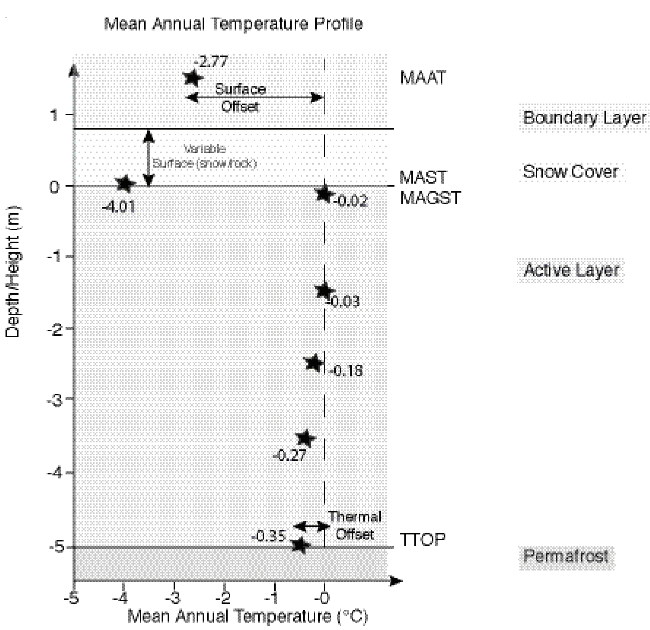

Figure 5. Different offset values shown from the mean data measured at the Schilthorn.

The offset usually called *surface offset* (MAGST – MAAT) is 1.50°C at Murtèl-Corvatsch and 2.75°C at Schilthorn. The offset usually called *thermal offset* (TTOP –MAGST) is 1.53°C at Murtèl-Corvatsch and 0.33°C at Schilthorn. The total offset (TTOP – MAAT) at Murtèl-Corvatsch with a value of 0.17°C is considerably smaller than at Schilthorn with 2.42°C.

Discussion and Conclusions

The long-term data sets collected in the last 20 years within the monitoring project PERMOS, together with the additional data, form a unique archive that is becoming more and more valuable. The time series at Murtèl-Corvatsch and Schilthorn not only reveal how the TTOP are related to snow cover and air temperature, but they also show the different behavior at the different investigation sites mainly caused by variable surface and subsurface characteristics.

However, the variability of the offsets between the permafrost sites is high. As an example, the surface offset at Murtèl-Corvatsch is more or less compensated by the thermal offset in the ground, which results in a very small total offset of only 0.17°C. In contrast, at Schilthorn the surface offset is dominating and the thermal offset is very small, resulting in a larger total offset of 2.42°C.

In the future, the concept of working with different offset values, based on long-term measurements, may help to better understand the processes between atmosphere and mountain permafrost and, therefore, will help to build up simple relationships for modeling mountain permafrost (Noetzli et al. this volume) and to better interpret the development of temperature and related ice content in the ground (Hilbich et al. this volume).

Acknowledgments

We would like to acknowledge the continuous support of the Permafrost Monitoring of Switzerland (PERMOS), the Corvatsch cable car company, and all students and colleagues at the University of Zurich. The very constructive review of the referees is kindly acknowledged.

References

Brown, R.J.E. & Péwé, T.L. 1973. Distribution of permafrost in North America and its relationship to the environment, a review 1963-1973. *Proceedings of* the *Second International Conference on Permafrost, Yakutsk, USSR*: 71-100.

Burn, C.R. & Smith, C.A.S. 1988. Observations of the 'thermal offset' in near-surface mean annual ground temperatures at several sites near Mayo, Yukon Territory Canada. *Arctic* 41: 99-104.

Gruber, S., King, L., Kohl, T., Herz, T., Haeberli, W. & Hoelzle, M. 2004. Interpretation of geothermal profiles perturbed by topography: The Alpine permafrost boreholes at Stockhorn Plateau, Switzerland, *Permafrost & Periglacial Proc.* 15(4): 349-357.

Haeberli, W., Hoelzle, M., Kääb, A., Keller, F., Vonder Mühll, D. & Wagner, S. 1998. Ten years after drilling through the permafrost of the active rock glacier Murtèl, Eastern Swiss Alps: Answered questions and new perspectives. *Proceedings of the Seventh International Conference on Permafrost*, *Yellowknife, Canada*: 403-410.

Hanson, S. & Hoelzle, M. 2003. The thermal regime of the coarse blocky active layer at the Murtèl rock glacier in the Swiss Alps. *Eighth International Conference on Permafrost, Zürich, Extended Abstracts*: 51-52.

Hanson, S. & Hoelzle, M. 2004. The thermal regime of the active layer at the Murtèl rock glacier based on data from 2002. *Permafrost & Periglacial Proc.* 15(3): 273-282.

Hanson, S. & Hoelzle, M. 2005. Installation of a shallow borehole network and monitoring of the ground thermal regime of a high alpine discontinuous permafrost environment, Eastern Swiss Alps. *Norwegian Journal of Geography* 59: 84-93.

Harris, C., Vonder Mühll, D., Isaksen, K., Haeberli, W., Sollid, J.L., King, L., Holmlund, P., Dramis, F., Guglielmin, M. & Palacios, D. 2003. Warming permafrost in European mountains. *Global and Planetary Change* 39: 215-225.

Harris, S.A. & Brown, R.J.E. 1978. Plateau Mountain: a case study of Alpine permafrost in the Canadian Rocky Mountains. *Proceedings of the Third International Conference on Permafrost*, *Edmonton, Canada*: 385-391.

Henry, K. & Smith, M. 2001. A model-based map of ground temperatures for the permafrost regions of Canada, *Permafrost and Periglacial Processes* 12: 389-398.

Herz, T., King, L. & Gubler, H. 2003. Thermal regime of coarse debris layers in the Ritigraben catchment, Matter valley, Swiss Alps. *Eighth International Conference on Permafrost, Zürich, Extended Abstracts*.

Hilbich, C., Hauck, C., R., D. & Hoelzle, M. 2008. Geoelectric monitoring network and resistivity-temperature relationships of different mountain permafrost sites in the Swiss Alps. *Proceedings of the Ninth International Conference on Permafrost, Fairbanks, Alaska (*this volume).

Hoelzle, M., Wegmann, M. & Krummenacher, B. 1999. Miniature temperature dataloggers for mapping and monitoring of permafrost in high mountain areas: First experience from the Swiss Alps. *Permafrost & Periglacial Proc.* 10(2): 113-124.

Hoelzle, M., Haeberli, W. & Stocker-Mittaz, C. 2003. Miniature ground temperature data logger measurements 2000-2002 in the Murtèl-Corvatsch area. *Proceedings of the Eighth International Conference on Permafrost*, *Zürich*: 419-424.

Hoelzle, M., Mittaz, C., Etzelmüller, B. & Haeberli, W. 2001. Surface energy fluxes and distribution models of permafrost in European mountain areas: an overview of current developments. *Permafrost & Periglacial Proc.* 12(1): 53-68.

Imhof, M. 2000. Permafrost investigation in the Schilthorn massif, Bernese Alps, Switzerland. *Permafrost & Periglacial Proc.*, 11(3): 189-206.

Juliussen, H. & Humlum, O. 2007. Towards a TTOP Ground Temperature Model for Mountaneous Terrain in Central-Eastern Norway. *Permafrost & Periglacial Proc.* 18: 161-184.

Keller, F. 1994. *Interaktionen zwischen Schnee und Permafrost - Eine Grundlagenstudie im Oberengadin*, Dissertation thesis, ETH Zürich, Zürich, 145 pp.

Lachenbruch, A.H. & Marshall, B.V. 1986. Changing climate: geothermal evidence from permafrost in the Alaskan Arctic. *Science* 234: 689-696.

Mittaz, C., Hoelzle, M. & Haeberli, W. 2000. First results and interpretation of energy-flux measurements of Alpine permafrost. *Annals of Glaciology* 31: 275-280.

Noetzli, J., Gruber, S., Kohl, T., Salzmann, N. & Haeberli, W. 2007. Three-dimensional distribution and evolution of permafrost temperatures in idealized high-mountain topography. *J. of Geophysical Res.*, 112 (F02S13): doi:10.1029/2006JF000545.

Noetzli, J., Hilbich, C., Hauck, C., Hoelzle, M. & Gruber, S. this volume. Comparison of transient 2D temperature profiles with time-lapse electrical resistivity data at the Schilthorn crest, Switzerland. *Proceedings of the Ninth International Conference on Permafrost, Fairbanks, Alaska* (this volume).

Riseborough, D.W. 2002. The mean annual temperature at the top of permafrost, the TTOP model, and the effect of unfrozen water. *Permafrost & Periglacial Proc.* 13: 137-143.

Salzmann, N., Frei, C., Vidale, P.L. & Hoelzle, M. 2006. The application of Regional Climate Model output for the simulation of high-mountain permafrost scenarios. *Global & Planetary Change* 56: 188-202.

Salzmann, N., Noetzli, J., Hauck, C., Gruber, S., Hoelzle, M. & Haeberli, W. 2007. RCM-based ground-surface temperature scenarios in high-mountain topography and their uncertainty ranges. *J. of Geophysical Res.* 112 (F02S12): doi:10.1029/2006JF000527.

Smith, C.A.S., Burn, C.R., Tarnocai, C. & Sproule, B. 1998. Air and soil temperature relations along an ecological transect through the permafrost zones of Northwestern Canada. *Proceedings of the Seventh International Conference on Permafrost, Yellowknife, Canada*: 1009-1015.

Smith, M.W. & Riseborough, D.W. 1996. Ground temperature monitoring and detection of climate change. *Permafrost & Periglacial Proc.* 7: 301-310.

Stocker-Mittaz, C., Hoelzle, M. & Haeberli, W. 2002. Permafrost distribution modeling based on energy-balance data: a first step. *Permafrost & Periglacial Proc.* 13(4): 271-282.

Soil Temperature and Thaw Response to Manipulated Air Temperature and Plant Cover at Barrow and Atqasuk, Alaska

Robert D. Hollister
Department of Biology, Grand Valley State University, 1 Campus Drive, Allendale, Michigan 49401-9403, USA
Patrick J. Webber
P.O. Box 1380, Ranchos de Taos, NM 87557-1380, USA
Robert T. Slider
Department of Biology, Grand Valley State University, 1 Campus Drive, Allendale, Michigan 49401-9403, USA
Fredrick E. Nelson
Department of Geography, University of Delaware, Newark, DE 19716-2541, USA
Craig E. Tweedie
Department of Biology and the Environmental Science and Engineering Program, University of Texas at El Paso, 500 University Avenue, El Paso, Texas 79968-0513, USA

Abstract

This paper examines the response of tundra systems to more than a decade of experimental warming, using International Tundra Experiment (ITEX) open-top chambers (OTCs) in wet and dry vegetation types near Barrow and Atqasuk, Alaska. The magnitude of chamber warming varied by site and changed over time. Maximum thaw depth varied little between OTC and control plots, except in recent years. To understand how vegetation controls air-soil heat exchange, we denuded the vegetation to bare ground in two chambers and added the removed vegetation to adjacent chambers to provide enhanced thermal insulation. Soil temperatures were coolest in chambers to which litter had been added. The difference between air and soil temperatures was similar between the chambers with added litter and chambers that had been in place for nine years. This experiment indicates that changes in vegetation due to a warmer climate may result in cooler soils.

Keywords: experimental warming; ITEX; open-top chamber, soil temperature; thaw depth; tundra; vegetation.

Introduction

Open Top Chambers (OTCs) have been used by the International Tundra Experiment (ITEX) since the early 1990s to simulate warmer snow-free growing conditions, which are expected to occur in the Arctic with climate change (Henry & Molau 1997, Arft et al. 1999, Hollister et al. 2005a, Walker et al. 2006). Recent studies have shown that the effect of OTCs on air and soil warming varies across sites of differing vegetation type (Marion et al. 1997, Hollister et al. 2006). Related studies document increased plant growth, changes in plant species composition and abundance, and an accumulation of leaf litter in response to warming (Hollister 2003, Hollister 2005a, b, Walker et al. 2006). This study aims to understand how changes in vegetation can alter the air-soil heat exchange properties of warmed plots and potentially explain the differential response of some vegetation types to OTCs.

We manipulated vegetation by removing the canopy and adding the clipped plant matter to adjacent plots to directly explore the impact of the plant canopy on air-soil heat exchange in a manner similar to Ng and Miller (1977). The relationship between air and soil warming is driven by soil type and vegetation (Gross et al. 1990, Walker et al. 2003). While dead plant litter is not a true substitute for a denser living plant canopy, it is easily manipulated and may provide insights into the insulating effect of the vegetation on soil temperature.

Study Area and Methods

Study sites were established in different years (see Table 1) in wet and dry plant communities near the villages of Barrow (71°18′N, 156°40′W) and Atqasuk (70°29′N, 157°25′W), Alaska. Barrow and Atqasuk are on the coastal plain of Alaska's North Slope and lie within the zone of continuous permafrost. Seasonal thaw varies with landscape position and is generally less than 1 meter (Nelson et al. 1998, Hinkel & Nelson 2003). Atqasuk is 100 km south and inland from Barrow and is on average 5^{o}C warmer in July than Barrow (Haugen & Brown 1980). The Barrow dry (BD) site lies on a former raised beach ridge. The soil is a moderately well drained xeric pergelic cryaquept underlain with fine silt, sand, and gravel. The vegetation is a dry heath dominated by prostrate shrubs and lichens. The Barrow wet (BW) site lies on the edge of a drained thaw lake basin. The soil is a poorly drained histic pergelic cryaquept underlain by fine silt. The vegetation is a wet meadow dominated by graminoids and mosses. The Atqasuk dry (AD) site lies on a raised rim of a drained thaw lake basin. The soil is a well drained pergelic cryopsamment underlain with aolian sand. The vegetation is a dry heath dominated by lichens and prostrate shrubs. The Atqasuk wet (AW) site lies on a pond margin. The soil is a poorly drained histic pergelic cryaquept underlain with aolian sand and silt. The vegetation is a wet meadow dominated by mosses and graminoids.

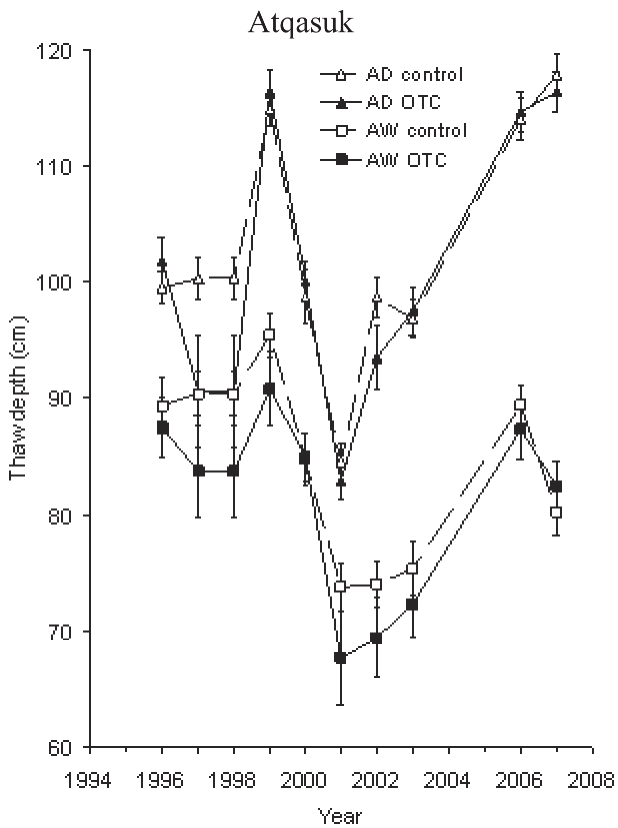

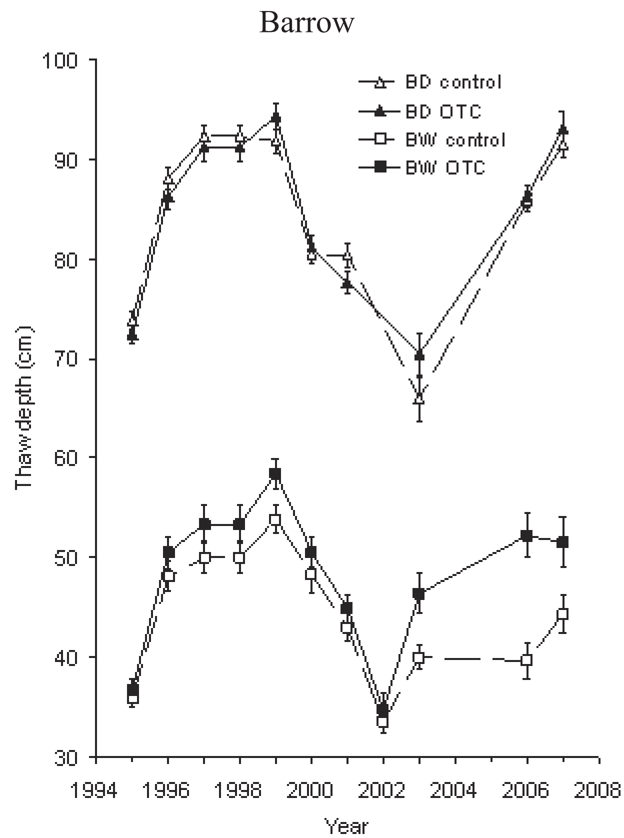

Figure 1. Mean annual maximum depth of thaw below OTC plots (filled symbols) and control plots (open symbols) at Atqasuk (left) and Barrow (right). Note the change in scale between locations; lines between readings for each year to allow for ease of delineating sites and treatments. Data were not collected in 2004 and 2005. Error bars represent the standard error of the mean and most sample sizes were 24.

Figure 2. Mean July temperature (°C) of air at +13 cm (circles) and soil at depths of 10 cm (triangles) and 45 cm (squares) in OTC plots (filled symbols) and control plots (open symbols) at the four study sites. Error bars represent the standard error of the mean (n=2). Missing data are represented by an M; a dot above and below the value to represent missing error bars.

Table 1. Years that sites were established, temperature and thaw measurements were initiated, and number of years in operation. Sites of 24 OTC and 24 control plots were established in different years. Plots where temperatures were recorded were established in the same year.

Site	Established		No. years	
	Site	Temp	Temp	Thaw
Atqasuk dry (AD)	1996	1998	9	11
Atqasuk wet (AW)	1996	1998	9	11
Barrow dry (BD)	1994	1998	9	13
Barrow wet (BW)	1995	1998	9	12

Each of the study sites consists of 24 OTC and 24 control plots in which standardized annual measurements, such as summer thaw depth, are made. The hexagonal OTCs are constructed of Sun-Lite HPTM fiberglass (Solar Components Corporation, Manchester, New Hampshire) to passively warm study plots. Chambers are approximately 35 cm high, 103 cm across at the base, and 60 cm across at the top (Molau 1993, Hollister 2003). The OTC and control plots cover an area of approximately 1 m^2. The magnitude of warming in the OTCs is driven by solar intensity and wind conditions (Marion et al. 1997, Hollister et al. 2006). For example, on calm sunny days the passive OTCs can warm the plant canopy up to 10°C above the ambient temperature. OTCs were installed soon after snowmelt and removed in mid to late August at the end of each field season. The length of the growing season and snow depths were not altered by the experimental manipulation. Additional plots for destructive sampling and sensor installation have been set up since the sites were established.

At each site two plots per treatment were established in 1998 to provide more detailed information on the effects of the OTCs on the air and soil microclimate. Since 1998 soil temperature has been measured at depths of 0 cm , 10 cm, and 45 cm using TP101M temperature probes (Measurement Research Corporation, Gig Harbor, Washington) connected to Campbell Scientific CR10X dataloggers. Prior to 2005, aerial sensors were housed in radiation shields placed within the plant canopy at approximately 13 cm above the ground surface and connected to HOBO® or StowAway™ loggers (Onset Computer Corporation, Pocasset, Massachusetts). In 2005 air temperatures were measured with Campbell 107 temperature probes connected to the CR10X at each site. The accuracy of each probe varies with temperature but is generally within 0.2°C. Temperatures were measured every 10 to 80 minutes. Averages and standard errors were calculated by averaging values for each plot and then comparing plots.

To explore the influence of the plant canopy on OTC performance between sites, two new treatments with two replicates each were established in 2007 at each site. In one treatment the plant canopy was removed down to bare ground in a 20 cm diameter circle in the center of the plot during late June. The removed vegetation was added to adjacent plots, forming a loose layer of litter that mixed in the existing plant canopy. This additional material may generally be considered as litter because the plants were unattached, although it contained lichens, mosses and vascular plants that remained green and appeared vigorous. These two new treatments of OTC plots were in place for one field season. Temperature was monitored in these plots at +13 cm, -1 cm, and -10 cm using StowAway™ loggers.

Depth of thaw was measured to the nearest cm by inserting a graduated metal rod into the ground until the ice-rich permafrost table was reached, usually in mid-August, at each of the 24 plots per treatment.

Results

Mean annual maximum thaw depth

Mean annual maximum thaw depth generally varied little between the OTC and control plots (Fig 1). Thaw was deeper at Atqasuk than Barrow and was deeper in dry sites than in wet sites. Thaw was deeper in warmer years (see mean July temperatures in Fig 2). Thaw in this study's wet sites, which are subject to periodic inundation and have thick insulating moss layers, is somewhat shallower than in dry sites, but large relative to thaw depths recorded in other land cover types in the region. At the dry sites the difference between OTC and control plots was generally indistinguishable. At the wet sites the average difference between OTC and control plots was more consistent across years. At the AW site the control plots generally showed deeper average thaw than OTCs, while at the BW site thaw was consistently deeper in the OTC plots compared with control plots. This difference was more pronounced in recent years.

Air and soil temperature

Mean July air temperatures were between 0.3°C and 4.3°C warmer within the OTC plots. The magnitude of this warming varied by site and over time, with the most pronounced warming in later years (Fig 3). The effect of OTCs on soil temperature varied by site and year. The OTCs cooled the soils at the AW site and warmed them at the AD site. At Barrow, OTCs warmed the soils in early years and cooled them in later years. The effect of OTCs on soil temperature diminished with depth.

The change from soil warming to cooling over time at Barrow warranted further examination. Table 2 represents the average difference in temperature between the control and OTC plots over the course of the experiment. Winter temperatures were consistently warmer under the OTC plots and this difference intensified over time. In summer, soil temperatures became increasingly cooler over time in the OTCs.

Table 2. Mean seasonal differences in soil temperature (°C) between OTC and control plots at the BD and BW sites. Differences were calculated by subtracting the mean of the control plots from that of the OTC plots.

	BD site			BW site		
Year	0 cm	-10 cm	-45 cm	0 cm	-10 cm	-45 cm
Winter (September–May)						
1998	0.5	0.5	0.3	0.1	0.1	0.2
1999	0.7	0.7	0.4	0.5	0.2	0.2
2000	0.3	0.4	0.3	0.3	0.1	0.2
2001	0.4	0.5	0.2	0.5	0.1	0.1
2002	0.5	0.5	0.3	0.4	0.0	0.1
2003	0.4	0.4	0.3	0.4	0.1	0.2
2004	0.5	0.6	0.3	0.4	0.2	0.2
2005	0.3	0.4	0.2	1.0	0.1	0.2
2006	0.3	0.4	0.3	---	---	---
2007	0.7	0.7	0.5	---	---	---
Summer (June–August)						
1998	-0.1	-0.1	0.1	0.3	0.3	0.4
1999	0.2	0.2	0.1	1.3	0.6	0.3
2000	-0.2	0.1	0.1	0.6	0.3	0.2
2001	-0.1	0.3	0.1	0.0	0.0	0.1
2002	-0.8	0.2	0.2	0.0	0.1	0.2
2003	-0.7	0.0	0.1	-0.3	-0.2	0.1
2004	-1.1	0.0	0.2	-1.6	-0.9	0.0
2005	-0.9	0.0	0.1	-0.6	-0.8	0.1
2006	-1.5	-0.1	0.0	---	---	---
2007	-2.0	-0.1	0.1	---	---	---

--- no data due to instrument malfunction

Note: recording begun in Aug of 1998 and data are missing between Aug 2004–June 2005 at the BW site.

Vegetation manipulation

The difference between air temperature and soil temperature at a depth of 10 cm was least in the control plots (Table 3). Regardless of whether or not the OTCs cooled or warmed the soils, the pattern across the three warming treatment types (bare ground, added plant matter, 9 years of warming) was consistent. Within the OTCs the soil temperatures were coolest under the plots receiving additional plant matter. The soils under the OTCs which had been in place for nine years were either warmer or similar in temperature to soil under OTCs where the vegetation was removed. The difference between air (13 cm height) and soil (10 cm depth) temperature within the OTCs was greatest in OTCs where plant matter was added, and this difference was similar to the OTCs which had been in place for 9 years.

Discussion

Previous studies have found that temperature enhancement by the OTCs varied significantly in different plant communities (Marion et al. 1997, Hollister et al.

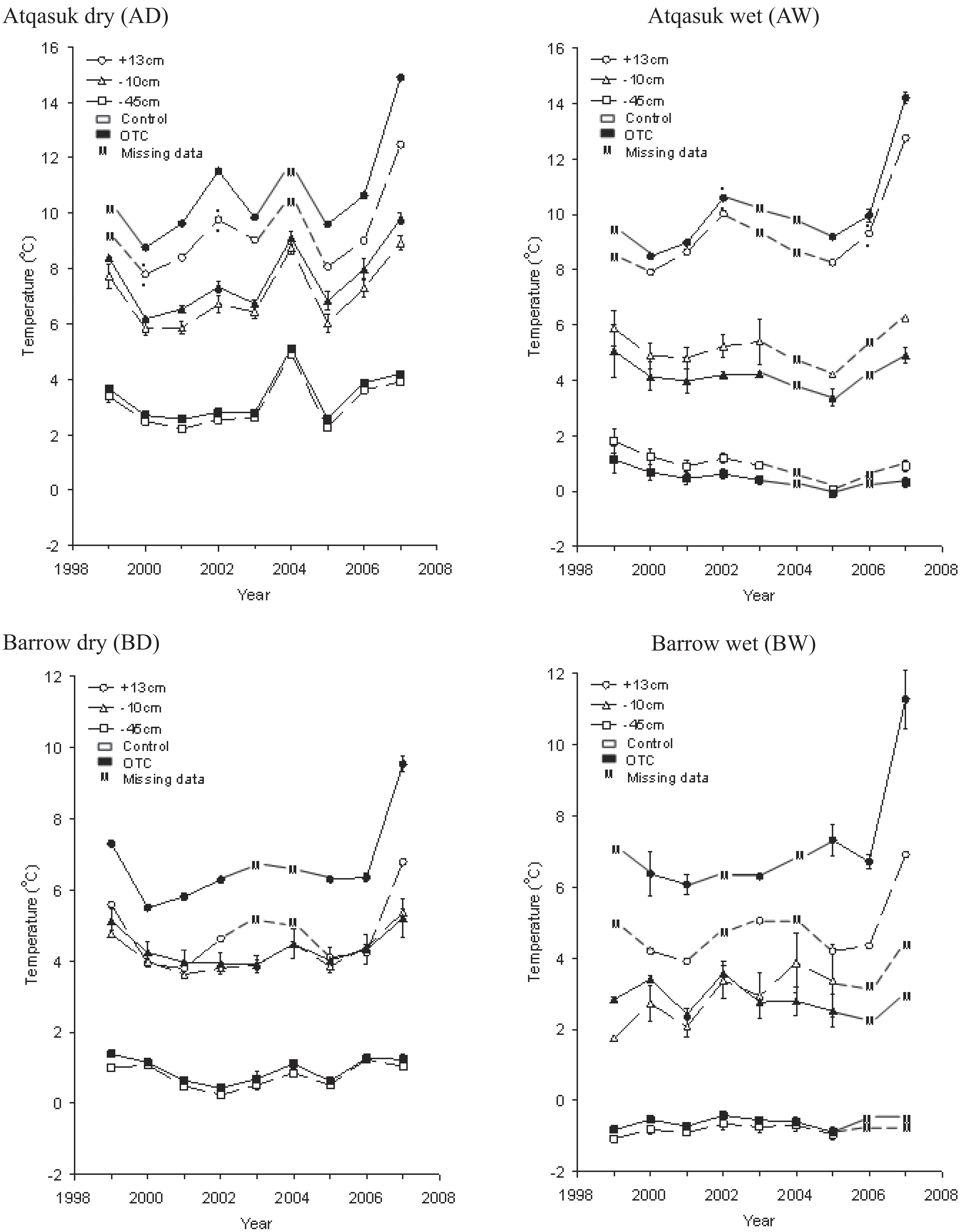

Figure 3. Mean July temperature (°C) of air at +13 cm (circles) and soil at depths of 10 cm (triangles) and 45 cm (squares) in OTC plots (filled symb ols) and control plots (open symbols) at the four study sites. Error bars represent the standard error of the mean (n=2). Missing data are represented by an M; a dot above and below the value to represent missing error bars.

Table 3. The effect of plant removal and addition on mean July canopy and soil temperature within the study plots (°C). Plots included control plots (Control) and OTC plots in place for 9 years (9 years) or in place for one year where the surface vegetation was removed to expose bare ground (Bare) and where the removed vegetation was added (Added) at the four study sites. Measurements were made at canopy height (+13), within 1 cm of the ground surface (0) and at a depth of 10 cm (-10). The difference between the temperature at the plant canopy and at a depth of 10 cm is shown (Diff). Values in parentheses represent the standard error of the mean (n=2).

		OTC		
	Control	**Bare**	**Added**	**9 Years**
		Atqasuk dry (AD)		
+13	12.5 (0.1)	13.4 ---	14.3 (0.2)	14.9 (0.0)
0	14.4 (0.4)	12.8 (0.3)	11.1 (0.3)	15.6 (1.8)
-10	8.9 (0.3)	9.8 (0.1)	8.9 (0.3)	9.8 (0.2)
Diff	**3.5 (0.2)**	**3.7 ---**	**5.4 (0.5)**	**5.1 (0.2)**
		Atqasuk wet (AW)		
+13	12.8 (0.1)	10.1 (2.9)	13.4 (0.1)	14.2 (0.2)
0	12.8 (1.1)	6.7 ---	7.2 (0.5)	11.1 (0.7)
-10	6.3 (0.1)	4.5 (0.1)	3.8 (0.3)	4.9 (0.3)
Diff	**6.5 (0.1)**	**5.6 (2.8)**	**9.7 (0.4)**	**9.3 (0.5)**
		Barrow dry (BD)		
+13	6.8 (0.1)	8.6 (0.0)	8.4 --	9.5 (0.2)
0	10.4 (0.4)	8.2 (0.4)	4.5 (0.9)	8.2 (1.1)
-10	5.4 (0.1)	5.4 (0.1)	3.1 (0.6)	5.2 (0.5)
Diff	**1.4 (0.0)**	**3.2 (0.1)**	**4.7 --**	**4.3 (0.3)**
		Barrow wet (BW)		
+13	6.8 (0.1)	8.9 (0.6)	9.7 (0.0)	11.0 (0.8)
0	--- ---	10.3 (2.3)	4.6 (0.8)	11.5 ---
-10	--- ---	3.7 (0.3)	3.0 ---	4.4 ---
Diff	**--- ---**	**5.3 (0.3)**	**6.7 ---**	**6.3 ---**

--- no data due to instrument malfunction

2006). The consistency of results from this study across sites indicates that the sites share a common response to changes in vegetation. At all sites the difference between air temperature and soil temperature measured at a depth of 10 cm was greatest in the OTC plots and greatest in either the OTC plots in place for 9 years or where plant matter was added. It appears, therefore, that vegetation is influencing both soil temperatures beneath the plots and long-term changes in the vegetation layer, such as increased leaf area index (Hollister 2003). Moreover, these significant changes resulting from experimental warming occurred over a period of less than ten years. The most likely explanation for the increase in soil temperature is increased insulation provided by enhanced vegetation growth and plant litter. This result is in agreement with that of the classic Ng and Miller (1977) experiment and modeling exercise, in which increased canopy and litter layers led to a cooling of the soil and a reduction of the active layer. The small size of the plots in this study probably reduced the impact on thaw depth.

These findings indicate that vegetation also plays a role in OTC warming. There was a tendency toward more warming in later years of the experiment, and the OTCs in place for nine years were warmer than the newly installed OTC plots where vegetation was manipulated. Presumably the vegetation minimizes heat loss from the warmed interior of the chamber. Vegetation becomes taller and denser over time, creating warmer conditions that are more conducive to tundra plant growth. Through this process the OTCs retain progressively more heat, leading to greater seasonal average differences between the OTCs and the control plots.

The increase in thaw depth at the BW site in later years of the experiment and the concomitant soil cooling during the summer months warrant further investigation. The two data sets were collected from different plots (temperature from 2 plots per treatment established in 1998 and thaw from 24 plots per treatment established in 1996). The change in temperature diminished with depth and was not significant at the depths near maximum thaw. It is also possible, although unlikely, that minor movements of the sensors due to cryoturbation may have influenced soil temperatures.

Taken together, the long-term warming experiment and short-term vegetation manipulation within the warming experiment demonstrate that vegetation is one of the dominant determinants of air-soil heat exchange at shallow depth at these sites, and that differences in OTC performance at the sites are strongly influenced by vegetation. As the vegetation responds to warming with increased growth, these changes appear to dampen air-soil heat exchange. Not only does this study reaffirm the importance of vegetation in influencing patterns of air-soil heat exchange in tundra regions, it also highlights the value of long-term experimental observations and how these can facilitate our understanding of how climate change may affect tundra ecosystem structure and function.

Acknowledgments

We thank the US National Science Foundation, Office of Polar Programs, Arctic System Science Program for its support of this work (OPP #9714103, #0632263), student assistants responsible for data collection, two anonymous reviewers, and our many ITEX colleagues for sharing their insights and constructive criticism. Any opinions, findings, conclusions, or recommendations expressed in this paper are those of the authors and do not necessarily reflect the views of the National Science Foundation. Identification of specific products and manufacturers in the text does not imply endorsement by the National Science Foundation.

References

Arft, A.M., Walker, M.D., Gurevitch, J., Alatalo, J.M., Bret-Harte, M.S., Dale, M.R.T., Diemer, M.C., Gugerli, F., Henry, G.H.R., Jones, M.H., Hollister, R.D., Jónsdóttir, I.S., Laine, K., Lévesque, E., Marion, G.M., Molau, U., Mølgaard, P., Nordenhall, U., Raszhivin, V., Robinson, C.H., Starr, G., Stenström, A., Stenström, M., Totland, Ø., Turner, P.L., Walker, L.J., Webber, P.J., Welker, J.M. & Wookey, P.A. 1999. Responses of tundra plants to experimental warming: Meta-analysis of the international tundra experiment. *Ecological Monographs* 64: 491-511.

Gross, M.F., Hardisky, M.A., Doolittle, J.A. & Klemas, V. 1990. Relationships among depth of frozen soil, soil wetness,and vegetation type and biomass in tundra near Bethel, Alaska. *Arctic and Alpine Research* 22 (3): 275-282.

Haugen, R.K. & Brown, J. 1980. Coastal-inland distributions of summer air temperature and precipitation in northern Alaska. *Arctic and Alpine Research* 12(4): 403-412.

Henry, G.H.R. & Molau, U. 1997. Tundra plants and climate change: The International Tundra Experiment (ITEX), Introduction. *Global Change Biology* 3(Suppl. 1): 1-9.

Hinkel, K.M. & Nelson, F.E. 2003. Spatial and temporal patterns of active layer thickness at circumpolar active layer monitoring (CALM) sites in northern Alaska, 1995–2000. *Journal of Geophysical Research-Atmospheres* 108: 81688168, DOI:10.1029/2001JD000927, 2003.

Hollister, R.D., Webber, P.J. & Bay, C. 2005a. Plant response to temperature in northern Alaska: Implications for predicting vegetation change. *Ecology* 86: 1562-1570.

Hollister, R.D. 2003. *Response of Tundra Vegetation to Temperature: Implications for Forecasting Vegetation Change.* Ph.D. Thesis. East Lansing, Michigan, USA: Michigan State University.. 385+XXIV pp.

Hollister, R.D., Webber, P.J., Nelson, F.E. & Tweedie, C.E. 2006. Soil thaw and temperature response to air warming varies by plant community: Results from an open-top chamber experiment in northern Alaska. *Arctic Antarctic and Alpine Research* 38: 206-215.

Hollister, R.D., Webber, P.J. & Tweedie, C.E. 2005b. The response of Alaskan arctic tundra to experimental warming: Differences between short- and long-term responses. *Global Change Biology* 11: 525-536.

Marion, G.M., Henry, G.H.R., Freckman, D.W., Johnstone, J., Jones, G., Jones, M.H., Lévesque, E., Molau, U., Mølgaard, P., Parsons, A.N., Svoboda, J. & Virginia, R.A. 1997. Open-top designs for manipulating field temperature in high-latitude ecosystems. *Global Change Biology* 3(Suppl. 1): 20-32.

Molau, U. (ed) 1993. *International Tundra Experiment (ITEX) Manual*. Copenhagen, Denmark: Danish Polar Center. 29+XV pp.

Nelson, F.E., Outcalt, S.I., Brown, J., Hinkel, K.M. & Shiklomanov, N.I. (1998). Spatial and temporal attributes of the active-layer thickness record, Barrow, Alaska, U.S.A. *Proceedings of the Seventh International Conference on Permafrost*. Québec: Centre d'études nordiques, Université Laval, Publication No. 57: 797-802.

Ng, E. & Miller, P.C. 1977. Validation of a model of the effect of tundra vegetation on soil temperatures. *Arctic and Alpine Research* 9 (2): 89-104.

Walker, D.A., Jia, G.J., Epstein, H.E., Raynolds, M.K., Chapin, F.S., III, Copass, C., Hinzman, L.D., Knudson, J.A., Maier, H.A., Michaelson, G.J., Nelson, F., Ping, C.L., Romanovsky, V.E. & Shiklomanov, N. 2003. Vegetation-soil-thaw-depth relationships along a low-Arctic bioclimate gradient, Alaska: Synthesis of information from the ATLAS studies. *Permafrost and Periglacial Processes* 14: 103-123.

Walker, M.D., Wahren, C.H., Hollister, R.D., Henry, G.H.R., Ahlquist, L.E., Alatalo, J.M., Bret-Harte, M.S., Calef, M.P., Callaghan, T.V., Carroll, A.B., Epstein, H.E., Jónsdóttir, I.S., Klein, J.A., Magnusson, B., Molau, U., Oberbauer, S.F., Rewa, S.P., Robinson, C.H., Shaver, G.R., Suding, K.N., Thompson, C.C., Tolvanen, A., Totland, Ø., Turner, P.L., Tweedie, C.E., Webber, P.J. & Wookey, P.A. 2006. Plant community responses to experimental warming across the tundra biome. *Proceedings of the National Academy of Sciences of the United States of America* 103: 1342-1346.

Flat Loop Evaporator Thermosyphon Foundations: Design, Construction, and Performance in the Canadian Permafrost Regions

Igor Holubec
I. Holubec Consulting Inc.
John Jardine
Arctic Foundations of Canada Inc.
Bill Watt
Arctic Foundations of Canada Inc.

Abstract

Climate change is rapidly warming permafrost in the Arctic, with the result that the traditional sand-slurry piles foundation may not be applicable for new structures with a design lifespan of 50 years or so. One foundation design that may be suitable for the warming trend of permafrost is the thermosyphon foundation design with flat loop evaporator pipes. There is limited published information on the design and performance of this foundation. To address the above points, the performance of several thermosyphon foundations with horizontal evaporator piping at several locations with varied climate conditions, foundation designs, and construction history is presented. Thermosyphon foundations presented herein are all located in Canada in Inuvik, NT, Iqaluit, and Pangnirtung, NU, and Kuujjuaq, QC. Mean annual air and ground temperatures are given for these projects along with design, construction schedule, and ground-temperature changes.

Keywords: flat-looped; foundation; performance; permafrost; thermosyphon.

Introduction

The design and construction of foundations for buildings is a challenge in permafrost with high ice content. The heat from the buildings may warm and thaw the frozen ground resulting in settlement of building; jacking of piles in raised buildings due to the annual freezing of the active layer; and settlement of piles due to creep of high ice-rich soils. There are limited windows for construction during the year, and a construction schedule is influenced by the availability of materials and equipment. Finally, the site and drainage conditions may change due to the construction that may impact the thermal conditions of the site.

The challenges have been increased by climate warming that is rapidly increasing the ground temperature in Arctic regions. The most recent Intergovernmental Panel on Climate Change (IPCC 2007) made the following statements: a) warming of the climate system is unequivocal; b) average Arctic temperatures increased at almost twice the global average rate; and c) temperatures at the top of the permafrost layer have generally increased since the 1980s in the Arctic by up to 3°C. Global air temperature increases since 1975 to 2001 and the future changes predicted by various models are shown in Figure 1. This figure illustrates two points that should be considered in the design of future foundations in permafrost: a) air temperature has increased appreciably since about 1975, and b) this rate of temperature increase will likely continue to about 2100.

Holubec (2007) looked at the mean annual air temperature (MAAT) records at 24 weather stations across the Canadian permafrost regions to obtain MAAT and establish the warming rate at these stations from 1985 on. Data were interpreted by means of linear trend lines to smooth out the MAAT variations from year to year. This provides an estimate of the present mean climate warming rate and allows determining MAAT for a specific year over the next 100 years. Mean annual ground temperatures (MAGT) were estimated for the same locations by assuming that the MAGT was 4.4°C warmer than the MAAT (Smith & Burgess 2000). Results grouped into four general Canadian areas with permafrost are given in Table 1.

Results in Table 1 indicate that permafrost will warm significantly and will start to thaw in most of Canada's mainland permafrost region in less than 50 years, which is the normal design period for new buildings.

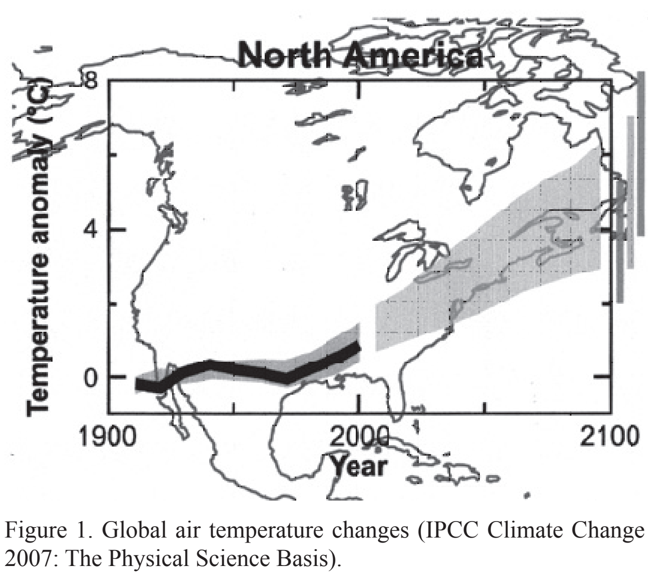

Figure 1. Global air temperature changes (IPCC Climate Change 2007: The Physical Science Basis).

Table 1. Climate conditions across Canadian Arctic in 2006.

Region [a]	MAAT [b] deg C	MAGT [b] deg C	Warming rate [c] deg C/10years
Western Arctic	- 3 to -9	1 to -5	0.7
Central Mainland Arctic	-9.8	-5.4	1.1
Eastern Arctic	-5.8	-1.4	1.7
Arctic Islands	-14.1	-9.7	0.9

a) Results based on average of 3 to 4 climate stations in each Region. b) MAAT & MAGT in 2006. c) Warming rate since 1985

The MAGT's at Inuvik, NT, and Iqaluit, NU, were at about -3.0°C in 2006. These are in general agreement with ground-temperature measurements. The -3°C is the ground temperature at which Johnston (1981) suggests that a passive cooling system should be considered for building foundations. The fact that most of the Canadian mainland permafrost region is in the range of 0 to -5°C and the climate warming rate is about 1°C every decade suggests a cooling system should be considered for building foundations.

Flat Loop Thermosyphon Design

Thermosyphon cooling is a passive thermal system that was first used in Alaska in 1960. Its benefit was clearly demonstrated on the Alaska pipeline, where over 120,000 thermosyphon tubes were installed within pipe piles (Heuer et al. 1985). Thermosyphon is a closed pipe, charged with a gas that is maintained in two phases: liquid and gas.

A thermosyphon continuously transfers heat during winter by evaporation and condensation of a liquid and gas, respectively. Heat transfer occurs when the top of the tube (radiator/condenser) is in an environment colder than the bottom part of the tube (evaporator) located in the ground. A vertical thermosyphon design, normally called thermopile/thermoprobe, expanded into sloped evaporator thermosyphon in 1978; and then in 1994, the flat loop thermosyphon design evolved. The three thermosyphon designs used in building foundations are illustrated in Figure 2.

Brief descriptions of the three designs are:

a) Buildings are supported on thermopiles with a 0.6 m to 1 m air space between the ground and building.

b) Conventional sloping evaporator (CSE) has an evaporator-condenser pipe that slopes beneath the building. The slope allows the condensate to flow to the bottom of the pipe. The building rests on a granular pad, and the evaporator pipes are covered with insulation to retard heat flow into the ground.

c) Flat looped evaporator (FLE) has a looped pipe (evaporator pipe) beneath the building that connects to a larger-diameter riser that functions as the condenser. Evaporator pipes are installed within a granular pad and covered with insulation and granular bedding. The building may be supported directly on the insulation or columns resting on footings on the bedding.

The principle of the flat looped evaporator thermosyphon is illustrated in Figure 3. The FLE design is a relatively recent development (Yarmak & Long 2002). Its performance was tested during the winter of 1993–1994 in Winnipeg, where it was observed to be 1.4 more efficient that the CSE. The FLE started to be installed in 1994 in Alaska and Canada.

The use of the FLE has been much greater in Canada than in Alaska because of different availability of access. The prevalent thermosyphon foundation design in Alaska is the thermopile because of ready access in most locations for large equipment to drill the large holes for these piles. The FLE design is more common in Canada because of the smaller weight of material that needs to be transported to the site and requires only small equipment for installation. Furthermore, the FLE protects a large building footprint at relatively low installation cost.

Since 1994 some 80 FLE systems have been constructed in Canada. Of these, 10 FLE have been placed at the bottom of dams to keep the foundation frozen and 70 FLE under buildings. The FLE system has been used in two configurations: either below slab-on-grade, where the lower building is founded on a gravel/insulation/evaporator pipe system, or the base of the building has a crawl-space that is followed by the gravel/insulation/evaporator pipe system. The majority of FLE have the buildings supported on the slab grade-on design.

The two foundation systems have different requirements for the installation of water and grey water pipes. In the slab-on-grade design, the services are installed in insulated conduits or utilidors below the floor slab. In the crawl-space design; the services are hung from the floor beams. The slab-

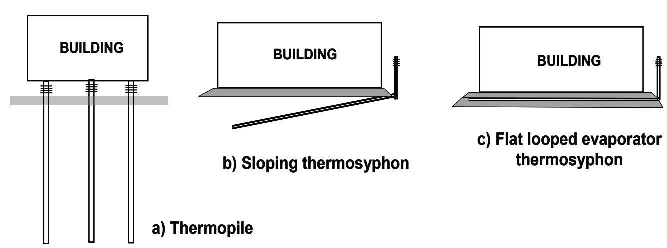

Figure 2. Three thermosyphon designs.

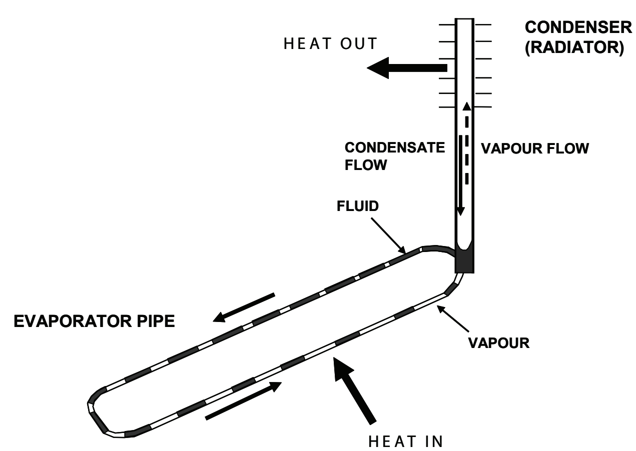

Figure 3. Operation of a flat looped thermosyphon.

on-grade may make repairs or changes to the services more difficult.

The foundation of the flat looped thermosyphon system consists of following basic components: a) 1- to 2-m thick compacted gravel pad; b) evaporator pipes; c) 150 mm bedding below and above the pipes; d) 100 to 200 mm rigid insulation; and e) a vertical radiator. A typical layout of the evaporator pipes and the location of the radiators for a flat looped thermosyphon installation is shown in Figure 4.

Performance

Only limited-performance information is available, because many installations are small buildings constructed on slab-on thermosyphon foundations. Due to the small size of the buildings and the remoteness of the sites, the installations are poorly monitored. Difficulties of the foundations are only noticed if drywalls in the building start to crack or if it is difficult to open or close doors. It appears that the majority of slab-on-grade thermosyphons are working well by the small number of known complaints.

Information on the facilities, their locations, temperatures at time of installation, and type of foundation discussed herein are given in Table 2.

Aurora College

The best performing flat looped thermosyphon foundation, with no problems and having ground-temperature records, is the Aurora College in Inuvik constructed in 2002. This is a slab-on-grade installation with a thick granular pad below the evaporator pipes and good surface drainage control. The natural ground before construction consisted of 0.5 m of granular fill, followed by nearly 2 m of peat and highly ice-rich soil with numerous ice lenses. A reference ground-temperature cable indicates the MAGT to have been about -2.5°C in 2002.

The native ground was excavated to about 3 m and replaced with compacted non-frost susceptible granular fill. Evaporator pipes were installed within a bedding layer and covered with 100 mm rigid insulation. The evaporator pipes were spaced at about 0.8 m. The excavation and granular backfill were completed in May 2002. This was followed by installing the thermosyphon system, charging it with carbon dioxide, and covering the evaporator pipes with insulation and about 1.25 m granular. This was completed in early June. Ground temperature performance from June 2002 to July 2003 is shown by means of ground-temperature profiles in Figure 5.

Figure 4. Typical thermosyphon flat loop, slab on ground installation at Pangnirtung, NU.

Ground-temperature profiles illustrate that the granular foundation started to cool right after it was covered with insulation and about 1.2 m of gravel. The thermosyphons started to cool and freeze the granular fill and natural ground below the evaporator pipes in mid-October and completed the conversion of all pore water to ice early in December. The coldest temperature at 6 m of -4.4°C was reached in May 2003; this warmed to -2.3°C on December 9, 2003. The warmest temperature at the base of the evaporator pipes (depth 0 m), -0.2°C, was reached in mid-September 2003.

One set of ground temperatures measured in September 2007 showed the ground temperature at the evaporator pipes and at 6 m depth to be -0.2°C and -3°C, respectively. The first temperature indicates the maximum ground temperature reached in 2007. However, the second is not representative of the MAGT because data for a whole 12 months is not available.

Inuvik Hospital

This case history has several aspects that are of interest. This is a flat looped thermosyphon foundation with a heated crawl space. The base of the foundation was excavated about 2 m below the ground surface and backfilled with 0.5 m granular fill. The evaporator pipes were installed within 300 mm of bedding and subsequently covered with 200 mm of rigid Styrofoam insulation. The insulation was covered with a membrane liner and 19 mm cement boards to protect the liner. Height from the cement board to the base of the main floor slab is about 1.9 m. The base of the crawl space is about 1 m below the outside ground level. Finally, the excavation between the natural ground and basement wall was backfilled with free draining granular material that was

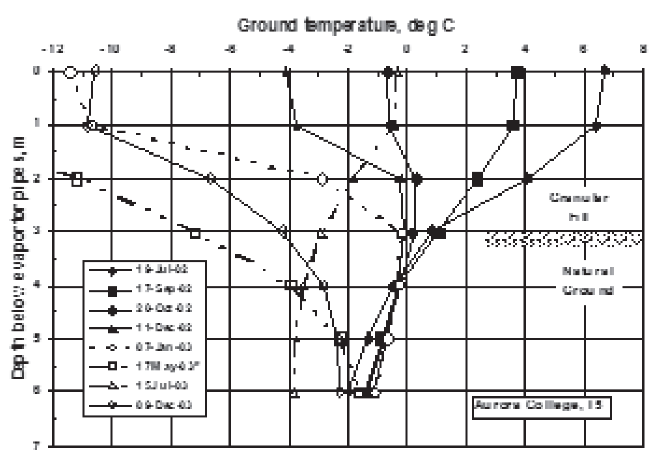

Note: Depth measured from evaporator pipe

Figure 5. Ground temperature profiles after installation of thermosyphon foundation at Aurora College.

Table 2. Information on facilities discussed in this paper.

Name	Aurora College	Hospital	RCMP Office	Pangnirtung Health Centre	Service Building	Air Terminal
Settlement Territory	Inuvik NT	Inuvik NT	Iqaluit NU	Pangnirtung NU	Kuujjuaq QC	Kuujjuaq QC
Year installed	2002	2001	2006	2006	1986	2006
Freezing Index, degree-days	4200	4200	3546	3400	3200	2568
MAAT °C @ installation	-7.5	-7.5	-7.3	-6.7	-5.2	-3.5
Estimated MAGT, °C	-3.1	-3.1	-2.9	-2.3	-0.8	+0.9
Insulation thickness ,mm	100	200	150	150	100	150
MAGT @ evaporator pipes, °C	-0.1	-1.0	-1.5	-2.0	-0.1	-0.6
Avg MAGT @ ~ 5m, °C	-4.3	-4.1	-6.1	-3.0	-2.5	-1.2
Max depth of MAGT readings, m	6	5	5.85	4.8	7.8	7.6
Avg MAGT at max'm depth, °C	-4.0	-4.1	-5.8	-3.0	-1.0	-0.4
Range of MAGT at maximum drill hole depth. °C	1.3 to -7.0	2.9 to -5.4	-2.9 to -7.6	-1.7 to -5.5	-0.5 to -2.1	-0.2 to -7.6
MAGT @ 5m colder than natural ground	1.2	1.0	3.2	0.7	1.7	2.1

Notes: MAAT – Mean annul air temperature, MAGT – Mean annual ground temperature.

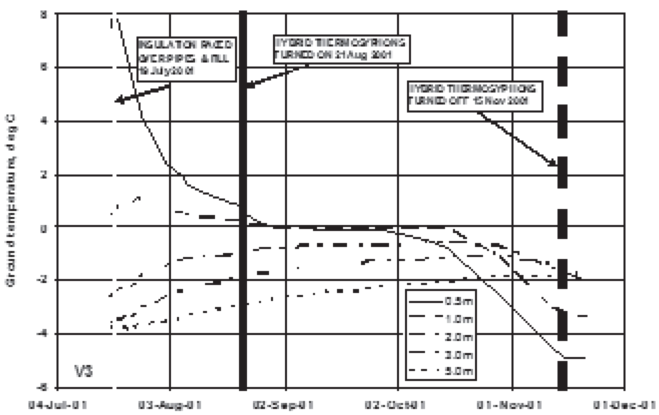

Figure 6. Ground cooling by hybrid system at Inuvik Hospital.

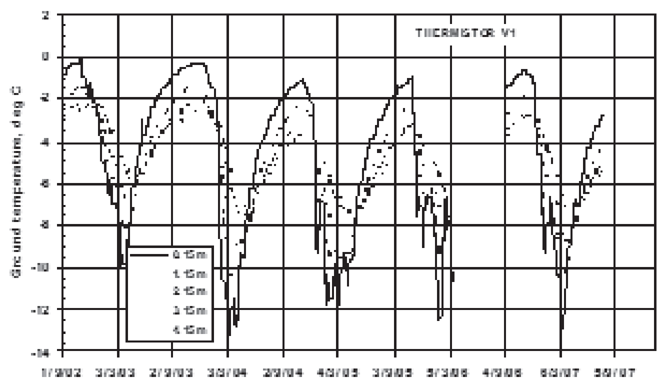

Figure 7. Ground temperature changes below evaporator pipes at Inuvik Hospital.

not covered with a low permeability soil zone to prevent surface water infiltrating the granular fill.

Excavation, granular fill, evaporator pipe, and insulation placement were completed by 19 July 2001. Since the project desired to have the ground below the thermosyphon foundation frozen as early as possible before pouring the footings, a hybrid thermosyphon system was installed. This consisted of cooling coils around the conductor pipes that were cooled by a mechanical refrigeration plant. The cooling plant was activated on 21 August 2001 and switched off permanently on 15 November 2001, when the foundations were completely frozen with a cold reserve. Ground cooling of the foundation by the hybrid system is illustrated in Figure 6. This shows that thaw within the natural ground did not exceed more than about 1 m below the base of the excavation, and the ground was completely frozen by 17 October 2001. The hybrid system was turned off on 15 November 2001, and the passive thermosyphon system started to operate.

The vertical thermistors at the hospital started to be monitored again in mid-September 2002. The changes in ground temperature, at five depths from this date on, are shown in Figure 6.

Graphs presented in Figures 7 and 8 show the warmest and coldest ground temperatures below the evaporator pipes during five years of operations.

Figure 8 illustrates that, for the first two years, the maximum ground temperature 0.15 m below the evaporator pipes was at about -0.3°C, and thereafter it varied between -0.6 and -1.0°C. At a depth of 4.15 m the ground temperature was about -2.5°C for the first two years and then cooled to about -3.5°C.

The minimum ground temperatures varied greatly just below the evaporator pipes, as expected, but steadied at 4.15 m depth after one year at about -7.5°C (Fig. 9).

Two problems developed at Inuvik Hospital. First, the mill that provided the evaporator pipes shipped defective welded A53B pipes that were found to leak slowly at the manufacturer's seam welds. This developed after the evaporator pipes were cooled when the thermosyphons started to operate, and resulted in a loss of refrigerant and some of the thermosyphon loops having to be recharged annually. Since that installation, the installer has used only seamless A104 pipe.

The second problem was caused by surface water penetrating the surface granular zone above the evaporator pipes during the summer. This water froze in the fall when the thermosyphons start to operate and produced localized ice boils between the top of gravel and insulation.

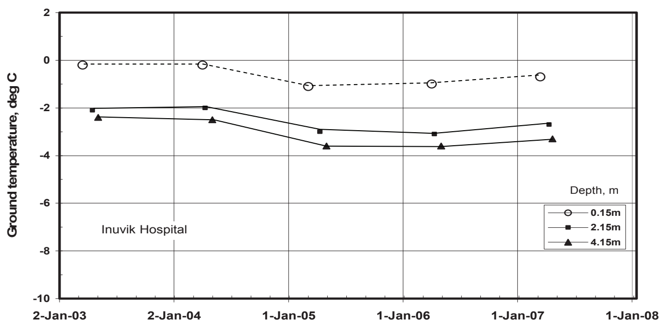

Figure 8. Maximum ground temperatures measured below the evaporator pipes.

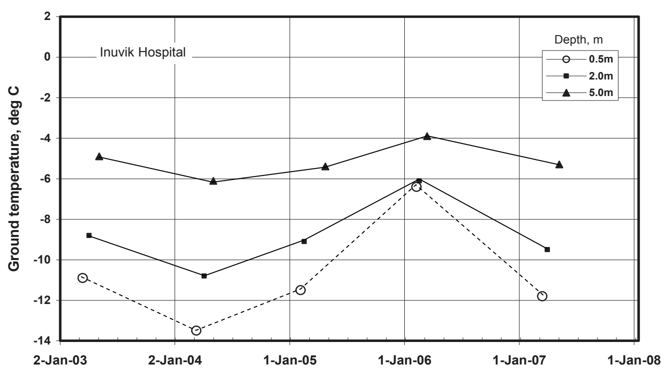

Figure 9. Minimum ground temperatures measured below the evaporator pipes.

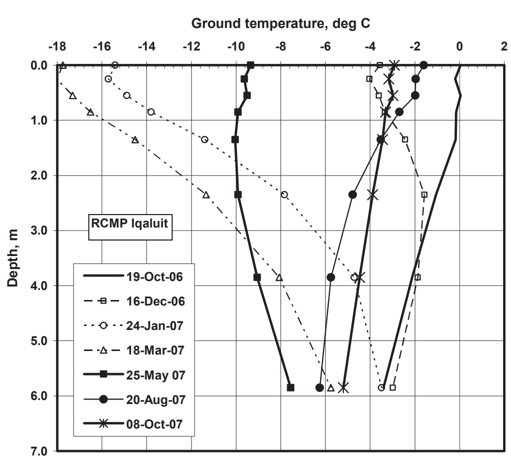

Figure 10. Ground temperature profiles after installation of thermosyphons at RCMP site, Iqaluit, NU.

Other troubled installations

Problems have been observed at three other flat loop thermosyphon installations: 1) In 1994 a FLE foundation with a crawl was constructed under a small Visitor Centre in Inuvik, NT. The central portion of the building started to settle, which is believed to be caused by locating the insulation above the base of the footing and not insulating the concrete columns that conducted heat to the frozen ground. 2) Another above-FLE foundation with crawl space constructed in Rankin Inlet, NU, in 1996 had routed extra heat from a power plant through trenches into the crawl space of the building. It is believed that the heat from the pipes and surface water infiltration through the trenches resulted in settlement of columns. Finally, 3) A Female Young Offender Facility constructed with slab-on-ground FLE foundation in Inuvik, NT, in 2001 exhibited considerable settlement under the eastern portion of the building. It appears that poor foundation cooling in this area was the result of introducing channel bends in the evaporator pipes during construction to accommodate a service piping trench. It is postulated that the four right-angle bends to accommodate the services reduced the efficiency of liquid/gas movement.

Construction scheduling

The normal practice in the construction of buildings on a FLE foundation has been to allow the FLE to operate over the first winter before putting up the structure of the building. The desire to start construction of the building the same year as the thermosyphon was built led to employing mechanical freezing during the summer (hybrid system) at the Inuvik Hospital. Three case histories of thermosyphon construction at Iqaluit, NU (RCMP), Pangnirtung, NU (Health Centre), and Kuujjuaq, QC (Air Terminal) illustrate the time required to develop permafrost with different construction schedules, MAAT, and soil type. Summary of relevant information and ground temperatures attained are given in Table 2.

The RCMP installation demonstrates the benefit in constructing the thermosyphon foundation in early summer. With this schedule, the subgrade froze completely by mid-October (Fig. 10). Since the foundation was left over the winter before adding the building, the absence of a heated slab during the first winter resulted in the coldest foundation at -6.1°C at 5 m below the evaporator pipes.

At Pangnirtung (Health Centre), the foundation with the thermosyphon and insulation was not completed until 24 August 2006. At this site complete freezing was attained in mid-December, and the building was enclosed and started to be heated mid-January 2007. In early October 2007, when thermosyphon cooling began again, the ground at the evaporator pipes was still frozen at -2.0°C, and the ground at 5 m depth was at -4°C.

The Air Terminal at Kuujjuaq differs from the previous two case histories because it has a higher MAGT and a smaller freezing index, and the soil is predominantly silt with higher water content. The thermosyphon installation at this location was completed at the end of August 2006, but was not completely frozen until mid-February 2007. It is estimated the MAGT was -1.2°C at 5 m depth.

Ground temperature regime with longer record of data is available from an earlier installation with sloped evaporator design (Service Building) in Kuujjuaq (Fig. 11). This installation was constructed in 1986, and ground temperatures are available to 1995. It needs to be noted that the MAAT was warmer in 1986, -5.5°C, and about -4.5°C in 1995 and only 100 mm of insulation was used. It is estimated that the MAGT at 5 m depth was about -2.5°C.

Conclusions

1. A majority of the 80 flat loop thermosyphon foundations have demonstrated that this design provides an economical foundation system that will function for some time even with climate warming affecting the permafrost.
2. Problems encountered in four installations were not associated with the flat loop evaporator thermosyphon concept. The problems were due to a) defective pipes provided by the mill; b)inadequate insulation around concrete columns; c)incorporating right angle channel geometry (in section) in the evaporator pipes to accommodate services; and d) allowing surface water into the evaporator granular pad.
3. The air terminal installation in Kuujjuaq shows that frozen ground can be developed, or maintained at MAAT at locations that are not conducive to permafrost. The effectiveness of the flat loop thermosyphon can be increased by increasing insulation thickness, decreasing evaporator spacing, and increasing condenser size.
4. A review of existing FLE installations show a past history of poor granular pad design and construction control, and insufficient attention has been given to surface water control around the building.

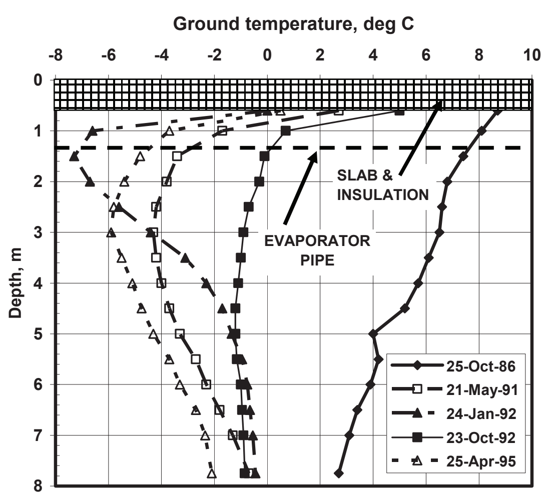

Figure 11. Ground temperature changes at FLE slab-grade at Service Building in Kuujjuaq, BC.

Acknowledgments

The authors would like to thank the Public Works and Services of Northwest Territories in providing information on the projects constructed in Inuvik, and other clients in providing ground-temperature data at their projects.

References

Heuer, C.E., Long. E.L. & Zarling J.P. 1985. Passive techniques for ground temperature control. Thermal Design Consideration in Frozen Ground Engineering. *Technical Council on Cold Regions Engineering Monogram*.

Holubec, I. 2007. Design requirements for climate warming in permafrost. *Yellowknife 2007 Symposium*. May 24, 2007 (unpublished).

IPCC 2007. Climate change 2007: The physical science basis. *Working Group I. Summary for Policymakers*. Published by WMO & UNEP, February 5, 2007.

Smith, S. & Burgess, M. 2000. Geological survey of Canada. *Open File Report 3954*, October 2000.

Yarmak, E. Jr. & Long, E.L. 2002. Recent developments in thermosyphon technology. *Proceedings of the Eleventh International Conference on Cold Regions Engineering, Anchorage, Alaska, May 2002*.

Thermal and Mechanical Erosion Along Ice-Rich Arctic Coasts

Md. Azharul Hoque
Department of Geography, McGill University, 805 Sherbrooke St. W, Montreal, QC, H3A 2K6, Canada
Wayne H. Pollard
Department of Geography, McGill University, 805 Sherbrooke St. W, Montreal, QC, H3A 2K6, Canada

Abstract

Block failure and retrogressive thaw slump activity are significant modifiers of Arctic costal morphology. This study investigates these erosional processes along ice-rich bluffs of the southern Beaufort Sea coast through a series of analytical models. Block failure potential is linked with different permafrost features like ice wedges and thermo-erosional niches. Failure often occurs along the ice wedge axis when wave erosion undercuts the base of the cliff. Model results indicate that low cliff heights tend to exhibit overturning failure, whereas high cliffs display sliding failure. Headwall retreat of retrogressive thaw slumps are also analyzed using parametric model calculations that incorporate energy balance activity to model melting ground ice. Model findings for block failure and headwall retreat are supported by field observations made in 2007 and previous studies. Using the approaches discussed in this paper, long-term morphologic patterns along Arctic coasts can be estimated using the spatial and rheological nature of permafrost materials and meteorological inputs.

Keywords: arctic coast; block failure; ice wedge; permafrost; retrogressive thaw slump.

Introduction

Coastal erosion in polar environments involves the synergistic interaction of wave-, thermal-, and gravity-induced mechanisms. The theory behind wave-induced erosion processes are reasonably well understood, and given the short open-water season that typically occurs in the Arctic, the magnitude of these effects are thought to be limited. However, the roles of morphologic and climatic coastal erosion processes are not as clearly understood. For example, field evidence indicates that mass wasting processes can occur almost year-round through gravity-driven processes, as large sediment blocks have been observed resting on sea ice as well as within shallow water. Similarly, thermal erosion processes, such as thermokarst, are readily observed when solar radiation raises ice-rich sediment surface temperatures above 0°C in spite of sub-0°C ambient temperatures. Ice-rich bluffs along the Yukon north coast display rates of coastal retreat that cannot be explained by wave action alone. The literature frequently refers to block collapse and retrogressive thaw slump activity as significant coastal erosion processes (Aré 1988, Walker 1988).

In this paper, we examine the potential role of two non-wave related erosional processes: block failure and thermokarst. The mechanics of block failure are studied through analytical models. The safety factor approach to slope-stability analysis is based on a series of widely recognized analytical and numerical solutions (Carson 1971, Chowdhury 1978). In this study, we apply different failure planes and mechanisms for a range of permafrost rheological characteristics, specifically exploring the role of ice wedge and thermo-erosional niche development in block failure. Strength parameters related to ice content and temperatures for coastal bluffs are then used to predict the failure potential for site-specific conditions. Additionally, we analyze the thermal erosion of exposed ground ice in retrogressive thaw slump headwalls through a computational model based on energy balance. Solar radiation and heat flux components are calculated to quantify the ablation of exposed ground ice as well as headwall retreat. The sensitivity of various factors affecting thermal and mechanical erosion of ice-rich coastal cliffs is examined. The complex processes of block failure and retrogressive thaw retreat of frozen cliffs are examined in a series of numerical solutions for a range of input conditions. We also discuss the implications of climate change on block failure and retrogressive thaw slumps and how the findings of this study can be used to predict long-term associated morphologic change under these conditions.

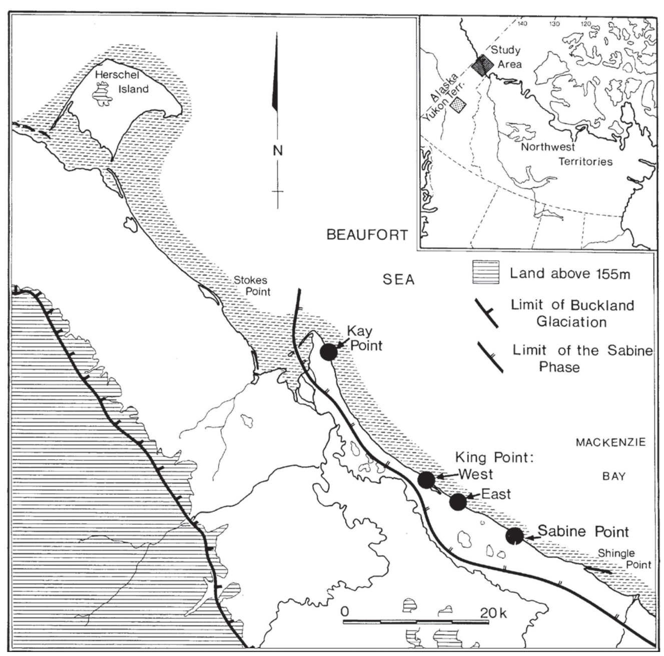

Figure 1. Study area: southern Beaufort Sea Coast.

Study Area

Our study focuses mainly on the southern Beaufort Sea coast (Fig. 1). The Beaufort Sea and its coastal region are the focus of considerable interest for a number of reasons, including human history, land claims, potential oil and gas development, permafrost and ground ice characteristics, and climate change. Extensive segments of the Beaufort Sea coast are characterized by bluffs ranging from 3–30 m in height (Solomon 1995). A previous study near King Point on the Beaufort Sea coast found an apparent spacing of modern ice wedges extending up to 15 m (Harry et al. 1985). This study also reported that most wedges have minimum heights between 4.5 m and 6.0 m. Other studies have described ground ice exposures and thermokarst activity (de Krom & Pollard 1988). Numerous recent block failures and active retrogressive thaw slumps were observed in this area during reconnaissance in 2007.

Block Failure

Model description

Two key features cause block failure along Arctic coasts: 1) the occurrence of horizontal thermo-erosional niches at the base of a bluff, and 2) the presence of ice wedges in backshore permafrost. Block failure is initiated by the development of an underlying niche, while ice wedge geometry determines the block size. The distance between two ice wedges along the coastline determines the length of the block. Figure 2 shows a two-dimensional cross section of a cliff with an ice wedge and horizontal niche. The cliff is characterized by H_c (cliff height), x_n (horizontal depth of the niche), z_n (height of the niche at the cliff face), and x_w (distance of ice wedge from the cliff face).

As a niche is formed at the base of a cliff, the toe of the cliff shifts from its initial position *P* to the new position *O*. According to the Culmann method of slope stability, the failure surface is a plane passing through the toe of the slope (Carson 1971). Following Culmann's assumption, Carson (1971) showed that the potential failure plane is inclined with an angle $\theta = (\alpha/2+\phi/2)$, where α is the slope angle of the cliff face and ϕ is the angle of internal friction of soil materials. In the areas where ice wedges are present, failure usually occurs along the ice wedge (Walker 1988). When an ice wedge and a thermo-erosional niche both are present, there are two possible modes of block failure: sliding and overturning.

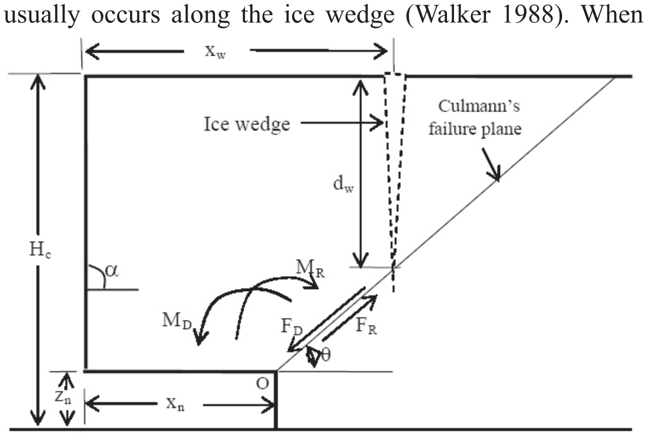

Figure 2. Two-dimensional cross section of a vertical cliff.

Sliding failure occurs when a block of frozen soil slides down the cliff on a relatively planar surface. The sliding mass is assumed to translate as a rigid body down the surface; it does not undergo rotation. When we apply a static balance of forces, the factor of safety against sliding is then defined as the ratio of resisting force to driving force. The driving force consists of the downslope component induced by weight, and the resisting force is the shear strength existant along the failure plane. The latter is comprised of two components: (1) cohesive strength of the soil, and (2) frictional forces derived from the angle of internal friction and the weight component perpendicular to the shear plane. If F_D is the driving force and F_R is the total resisting force, then the factor of safety against sliding is expressed as:

$$F_S=F_R/F_D \tag{1}$$

On the other hand, the cantilever action of the overhanging bluff induces an overturning moment (M_D) at the toe of the bluff. The resisting moments (M_R) are due to the weight of landward portion of the block and to the tensile strength (f_t) of the ice-rich permafrost soil. Overturning failure occurs if the overturning moment exceeds the resisting moment. In this case, the factor of safety against overturning is expressed as:

$$F_O=M_R/M_D \tag{2}$$

Strength of permafrost soils

The long-term strength of perennially frozen soils is of great importance in the evaluation of bluff stability. The strength of a frozen soil depends on its temperature, moisture content, mineral composition, and structure (Tsytovich 1975). Ground ice acts as cement in frozen soil; hence the widely used term "ice bonded." Temperature impacts ground ice physical properties, and therefore, in cases where ice contents are high, it influences soil strength. Tsytovich (1975) reported that the long-term compressive strength of frozen ground strongly depends on negative temperatures and can be expressed as:

$$\sigma_c = a + b(\theta)^n \tag{3}$$

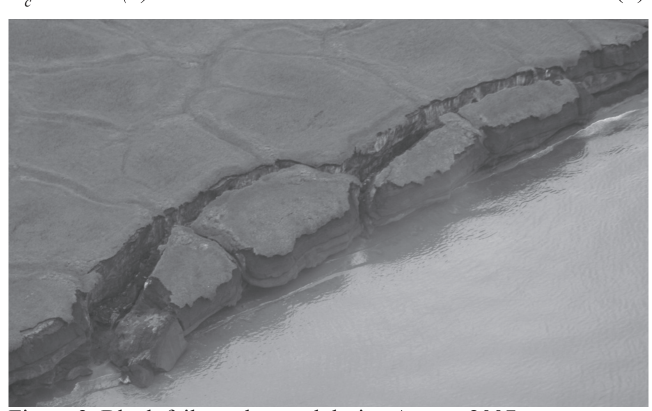
Figure 3. Block failure observed during August 2007.

where, a, b, and n are empirical parameters that depend on frozen soil types and θ is the absolute value of the negative temperature.

Long-term cohesion is expressed as $c = \sigma_c / 3^{0.5}$ (Vyalov 1966). There is limited information on long-term tensile strength of frozen soils, with the majority of available information related to compressive strength. The tensile strength of a frozen soil is substantially lower than its compressive strength (by a factor of 2–6) (Tsytovitch 1975). Based on Vyalov's experiment, Tsytovitch (1975) reported the long-term tensile strength for soils ranging from 30–180 kPa with temperature ranges of -0.2°C to -4.6°C.

Model calculations and discussions

For a given set of rheological conditions, block failures will be governed by the wave-eroded niche depth as well as the depth, location, and orientation of ice wedges. Aerial surveys along the Yukon coast revealed that failure usually occurs within the ice wedge (Fig. 3). Accordingly, the present study includes ice wedges as part of the block failure analysis. In this case, the ice wedge is assumed to have a recent thermal contraction crack and, therefore, no pressure or resisting force along the failure plane within the ice wedge. Thermal expansion pressure at the face of the ice wedge is also considered to be negligible.

Model calculations are performed for different cliff heights, ice wedge locations (distance from the bluff), and niche depths to: (1) obtain critical combinations of input parameters to induce cliff failure and (2) determine associated modes of failure (i.e., overturning vs. sliding). Permafrost soil strengths used in model calculations are based on Tsytovich's (1975) experimental results. A sample calculation using c=100 kPa, f_t=35 kPa, $\phi=20^0$, x_w=4 m indicates that cliff heights up to about 7.5 m exhibit overturning, whereas larger cliffs displayed sliding failure. Calculations using a range of input conditions show that for a given set of soil strength parameters and ice wedge distance, smaller cliffs are subjected to overturning whereas larger cliffs are subjected to sliding. The model is in general agreement with field conditions, as observed block failure in bluffs 3–6 m high were predominantly overturning-type failure. These results are supported by their mechanical nature: in smaller cliffs the sliding force exerted by the weight of soil is less than the total resisting force exerted by the cohesive strength of the soil. Therefore, block failure occurs when the niche extends to a critical distance causing overturning due to cantilever effect of the overhanging mass. The critical niche depth necessary for an overturning failure increases with the cliff height. This is because any increase in niche depth increases overturning moment (M_D) and decreases resisting moment (M_R). This agrees with the findings of Are′ (1988), in which the critical niche depth is calculated from the formula of curvature for an overhanging mass of frozen sediment.

Figure 4 depicts the model calculations for different cliff heights using c=200 kPa, f_t=70 kPa, $\phi=20^0$. It can be seen that, for a given cliff height and soil strengths, the relationship between niche depth and ice wedge distance is linear. It should be noted, however, that when ice wedges are closer to the shoreline, the critical niche depths are close for different cliff heights. In the present discussion, the maximum cliff height for overturning failure is denoted as H_0. Figure 5 shows the variation in H_0 with permafrost soil strength. Calculations are performed for niche dimensions x_n=2 m and z_n=1 m. Results indicate that H_0 increases with cohesive strength, meaning that higher cohesive strength increases the range of cliff heights subjected to overturning. The relationship between H_0 and cohesive strength are linear, meaning that the non-dimensional parameter given by $\gamma H_0/c$ can be considered constant for a given set of rheological properties of cliff materials. Model calculations with cohesive strength ranging from 100 kPa to 400 kPa, ϕ = 0, and an ice wedge distance x_w ranging from 2 m to 10 m show that the values of non-dimensional parameter $\gamma H_0/c$ varies from 0.95 to 1.1.

The calculations discussed above are for cases where the ice wedge depth intersects Culmann's failure plane. Calculations show that overturning can also occur for ice wedges with depths (d_w) less than the depth of Culmann's failure plane (d_{cl}). However in such cases, the ice wedge distance required for failure is less than that previously obtained. Calculations were performed for a cliff height of 10 m using niche dimensions and strength parameters as follows: z_n=1 m, x_n =2 m, c=200 kPa, f_t =70 kPa, and ϕ =20^0. Figure 6 shows variations in critical d_w that produce overturning under a varying x_w and displays that overturning can occur for a d_w less than the depth of Culmann's failure

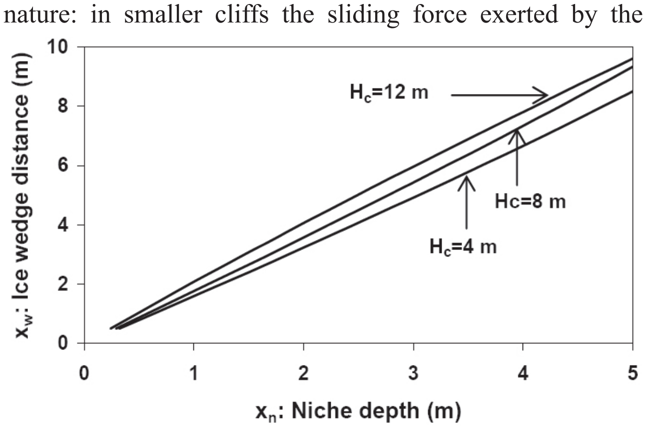

Figure 4. Ice wedge location and niche depth required for failure of cliffs of 4 m, 8 m, and 12 m heights.

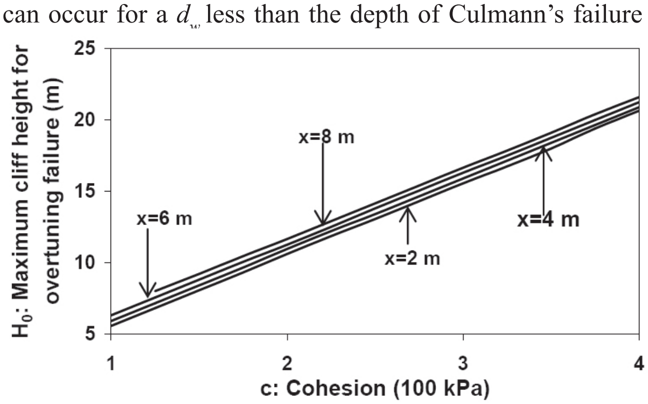

Figure 5. Ice wedge distance required for various cliff heights and material strength.

plane. In such cases, it is found that failure occurs along the plane passing through the toe of the slope and the bottom of the ice wedge and that the critical d_w for overturning increases with x_w.

Retrogressive Thaw Slumps

Model description

Retrogressive thaw slumps are a form of back-wasting slope retreat due to thawing ice-rich permafrost and are frequently observed in thermokarst landscapes. Their morphology consists of (i) a vertical headwall, (ii) a steeply inclined headscarp of ice-rich sediment, and (iii) a lobate mudflow at the base of the slump (de Krom 1989, Lantuit and Pollard 2005). Headwall retreat has previously been linked to thawing degree days (Robinson 2000) and net radiation flux (Lewkowicz, 1986b). Retrogressive thaw slumps have been the focus of several studies involving the field measurement of headwall retreat (e.g., French 1974, French & Egginton 1973, Lamothe & St Onge 1961, McRoberts & Morgenstern 1974), and additional studies have attempted to create empherical models for headwall retreat using energy flux (Lewkowicz 1986b), global radiation and degree-days (Egginton 1976), and thawing degree-hours (Kerfoot 1969). However, most of these cases are based on limited data. The present study formulates a computational model for headwall retreat using energy balance terms.

Headwall retreat can be calculated using the ablation rate of ground ice at the exposed face. The energy available for ground-ice ablation is represented by the following energy balance equation (Lewkowicz 1986a):

$$Q_m = Q_s + Q_l + Q_h + Q_e + Q_g + Q_p + Q_w \tag{4}$$

where, Q_m is energy flux available for ground ice ablation, Q_s is net shortwave radiation, Q_l is net long-wave radiation, Q_h is air convection (sensible heat), Q_e is vapor condensation (latent heat), Q_g is ground heat conduction, Q_p is the heat flux from precipitation, and Q_w represents the heat flux from water flowing down the headwall. Fluxes are measured as energy per time per unit area of the exposed surface (kJ/m^2-sec).

The summation of all sources of energy represents the total amount of energy (Q_m) available to melt the ground ice. The amount of headwall retreat *(R)* through ablation of ground ice can be expressed as:

$$\frac{dR}{dt} = \frac{Q_m}{c_i L B} \tag{5}$$

where, c_i is volumetric ice content in the headwall, L is volumetric latent heat of fusion of ground ice (kJ/m^3), B is thermal quality of the ground ice (e.g., ratio of heat required to melt a unit weight of the ground ice to that of ice at °C). The melting face consists of a mixture of ice, free water, and soil particles. The latent heat for fusion of ground ice is less than that of pure ice. This is because the relative proportion of the ice determines the thermal quality of ground ice. The relationship between ice content and volumetric latent heat reported by Lewkowicz (1986b) shows that latent heat decreases with lower ice contents.

Net shortwave radiation is an important source of ground ice ablation and consequentially, headwall retreat. The amount of energy available from the absorption of shortwave radiation for ground ice ablation is given by:

$$Q_s = (1-\alpha)\, I_i \tag{6}$$

where α is the albedo of ice-rich headwall soils and I_i is the incident solar radiation.

The longwave radiation component (Q_l) consists of the radiation emitted from the headscarp to the atmosphere (resulting in a net energy loss on clear days) and back-radiation reflected by the atmosphere and cloud cover. Longwave radiation (Q_a) from headscarp materials to the atmosphere can be expressed in accordance with the Stefan-Boltzman law:

$$Q_a = \varepsilon\sigma\, T_s^4 \tag{7}$$

where ε is the emissivity of headscarp materials, σ is the Sefan-Boltzman constant (5.735x10-11 kJ/m^{2}sK$^{4)}$, and T_s is the temperature of melting face (°K).

The transmission of back-radiation (Q_b) is a complex process based on experimental data and various assumptions. Snow investigations show that the downward longwave radiation can be adequately expressed by a single air temperature function as: $Q_b = 0.67\sigma\, T_s^4$ for clear skies and $Q_b = \sigma\, T_s^4$ for

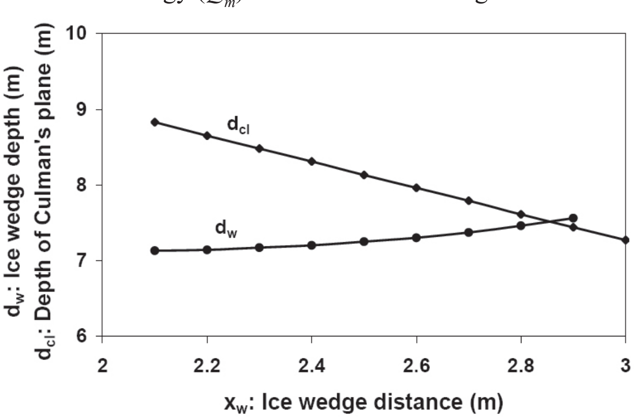

Figure 6. Critical ice wedge depth for failure under varying ice wedge distance.

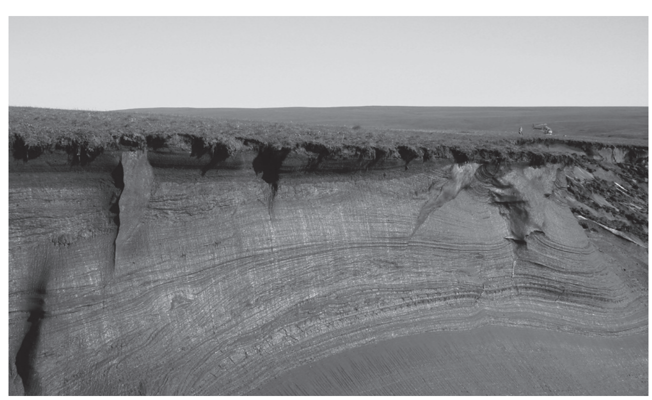

Figure 7. Headwall of an active retrogressive thaw slump on Herschel Island (photo taken on 11 August 2007).

cloud or forest cover (USACE 1998). By combining the findings from incoming and outgoing longwave radiation, the net longwave radiation can be determined using the following equation:

$$Q_l = Q_a - Q_b \tag{8}$$

Turbulent exchange, by convection (Q_h) and condensation (Q_e), varies widely depending on climate and local weather conditions. Following Gray & Prowse (1992), the sensible and latent heat transfer are expressed as:

$$Q_h = D_h u_z (T_a - T_s) \tag{9}$$

$$Qe = D_e u_z (e_a - e_s) \tag{10}$$

where D_h is the bulk transfer coefficient for sensible heat transfer (kJ/m^3 °C), u_z is the wind speed (m/s) measured upslope of the slump headwall at a chosen height, T_a is the air temperature (°C), T_s is the temperature at the melting face (°C), D_e is the bulk transfer coefficient for latent heat transfer (kJ/m^3 Pa), e_a is the vapor pressure of the air surface (Pa), and e_s is the vapor pressure at the melting ice face (Pa).

During periods of retrogressive thaw slump activity, it is reasonable to assume that T_s at melting face is 0°C and that e_s is the saturation vapor pressure at 0°C (6.108 mbar). This allows for the measurement of air temperature and vapor pressure at a single height to apply the bulk transfer method. According to Male & Gray (1981) there is wide range in variation in the bulk transfer coefficients reported by researchers, and these values are typically determined experimentally. However, Lewkowicz (1986a) considered the coefficients to be the same for both sensible and latent heat through the use of a psychrometer constant (mbar/°C), thereby allowing for the application of the bulk transfer method without obtaining field measurements for the coefficients.

Q_g is very small compared to the overall energy budget (USACE 1998). Using the measured ground temperature gradient, ground heat flux can be calculated by solving the one-dimensional, steady state conduction equation:

$$Q_g = -k\,(dT_g/dx) \tag{11}$$

where k is the thermal conductivity of the permafrost soil, dT_g/dx is the temperature gradient, and x is the depth to ground ice.

Q_p is encountered as precipitation falls upon and runs down the ice face(USACE 1998) and can be expressed as:

$$Q_p = C_p \rho_w P\,(T_r - T_s) \tag{12}$$

where C_p is the specific heat of rain (kJ/kg °C), ρ_w is the density of water (kg/m^3), P is the rainfall intensity (mm/unit time), T_r is the rain temperature (°C), and T_s is the temperature of the ice face (°C). The temperature of the rain is assumed to be air temperature or, if available, the wet bulb temperature.

As the temperature of the meltwater flowing down the headwall is close to the melting face temperature (0°C), the conductive heat transfer term Q_w in Eq. (4) is considered to be negligible compare to the overall energy budget.

Model calculation and discussions

Equation 5, supplemented by Equations 6–12, can be solved using a first-order explicit finite difference method in time to calculate the temporal variation of headwall retreat. Model calculations have applied hourly weather data obtained from King Point, Yukon Territory, Canada. Net shortwave radiation is calculated by assuming an albedo of 0.15 for the headscarp based on a regression analysis of field measurements reported by Lewkowicz (1986b). The coefficient for sensible heat transfer component (Q_h) was taken from Lewkowicz (1986b). The energy exchange components Q_e and Q_g are ignored in the present model calculations, as Lewkowicz (1986b) reported that these components are small compare to the total energy flux. Sample calculations are performed for the incoming shortwave radiation ranging from 0 to 400 W/m^2 on the sloping face of a headwall, a wind speed of 20 km/hr, and air temperatures of 2°C and 6°C. Results from model calculations are provided in Figure 8. For a given incoming shortwave radiation, higher temperatures correspond to higher retreat rates, which are due to the melting component of Q_h. Model calculations are on the same order of magnitude reported by other studies in the Arctic (e.g., Lewkowicz 1986a, 1986b).

Headwall retreat calculations were undertaken using data from King Point, Yukon Territory, over a 60-day

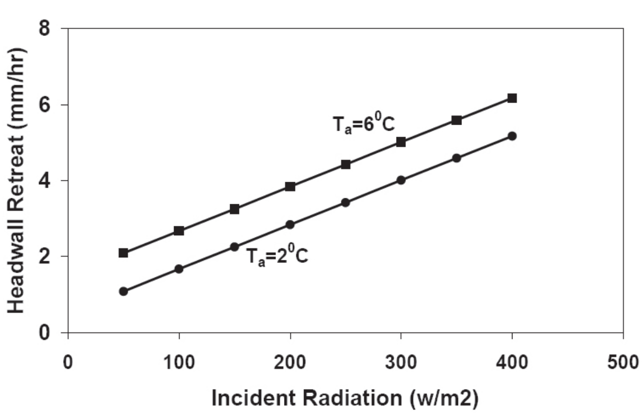

Figure 8. Headwall retreat rates for 2°C and 6°C under different incoming shortwave radiation.

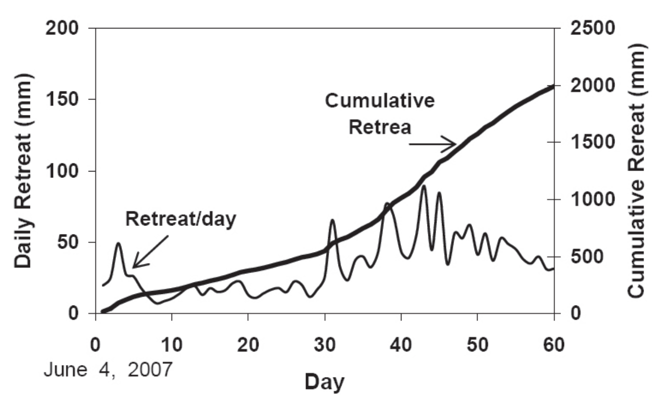

Figure 9. Calculated cumulative retreat using meteorological data at King Point.

period beginning June 4, 2007. Estimated values of daily and cumulative retreat are shown in Figure 9. July retreat is higher than that for June in response to increased solar energy and air temperatures. The calculated values of 34 mm and 90 mm of retreat for average and maximum daily retreat and 2 m of cumulative retreat over a 60-day period is an excellent average approximation of observed retrogressive thaw slump activity in this region.

Concluding Remarks

The present study provides computational models for two important erosion processes common to ice-rich Arctic coastal cliffs: (1) block failure, and (2) headwall retreat of retrogressive thaw slumps. Model calculations (supported by field observations) offer the following conclusions:

a) Block failure typically occurs along Culmann's failure plane, where ice wedges intersect Culman's plane. If ice wedge depth is less than the depth of Culmann's failure plane, failure occurs along the plane passing through the bottom of the wedge and the toe of the overhanging cliff.
b) Low cliffs are subjected to overturning failure, whereas the higher cliffs are subject to sliding failure.
c) In cases where ice wedges intersect the Cullman's failure plane, the maximum cliff height exhibiting overturning failure is dependent on the strength of cliff materials and can be expressed as a constant non-dimensional parameter $\gamma H_0/c$ for a given internal friction angle.
d) Headwall retreat of retrogressive thaw slump is governed by net shortwave radiation. Calculated headwall retreat based on weather data from King Point, Yukon Territories, gives an average value of 34 mm/day during summer 2007.

The block failure model is being enhanced by further quantifying the effects of ice content and ice wedge morphology. Field measurements of headwall retreat and microclimate data are being conducted for final model calibration and validation. Improvement of the thaw model will involve coupling with a slope irradiance model. Further studies relating block failure and headwall retreat are also needed to determine which process is predominant in specific permafrost regions. These models provide insight into morphological processes of Arctic coastlines and suggest potential responses to changing climate conditions by predicting changes in permafrost integrity and retrogressive thaw slump activity.

References

Are′, F.E. 1988. Thermal abrasion of sea coasts. *Polar Geography and Geology* 12(2): 87-155.

Carson, M.A. 1971. *The Mechanics of Erosion* (Monographs in spatial and environmental systems analysis). London: Pion Publisher, 174 pp.

Chowdhury, R.N. 1978. Slope Analysis. *Development in Geotechnical Engineering,* 22: Elsevier, 423 pp.

de Krom, V. & Pollard, W.H. 1989. The occurrence of ground ice slumps on Herschel Island Yukon Territory. *Musk-Ox* 37: 1-7.

French, M.H. 1974. Active thermokarst processes, eastern Banks Island, western Canadian Arctic. *Canadian Journal of Earth Science* 11: 785-794.

French, H.M. & Egginton, P. 1973. Thermokarst development, Bank Island, Western Canadian Arctic. In: *Permafrost: the North American Contribution*, *2nd International Conference*, *Yukutsk, USSR*. Washington, DC: National Academy of Sciences, Publication 211: 203-212.

Kerfoot, D.E. 1969. *The Geomorphology and Permafrost Conditions of Garry Island, N.W.T.*, Ph. D. Thesis. Vancouver, B.C.: The University of British Columbia.

Harry, D.G, French, H.M. & Pollard, W.H. 1985. Ice wedge and permafrost condition near King Point, Beaufort Sea Coast, Yukon Territory. In: *Current Research, Geological Survey of Canada* 85 (1A): 111-116.

Lamothe, C. & St Onge, D.A. 1961. A note on a periglacial erosional process in the Iscachen area, N.W.T. *Geological Bulletin* 16: 104-113.

Lantuit, H. & Pollard, W.H. 2005. Temporal stereo photogrammetric analysis of retrogressive thaw slumps on Herschel Island, Yukon Territory. *Natural Hazards and Earth System Sciences* 5: 413-423.

Lewkowicz, A.G. 1986a. Headwall retreat of ground-ice slumps, Banks Island, Northwest Territories. *Canadian Journal of Earth Sciences* 24: 1077-1085.

Lewkowicz, A.G. 1986b. Rate of short-term ablation of exposed ground ice, Bank Island, Northwest Territories, Canada. *Journal of Glaciolog* 32 (112): 511-519.

Male, D.H. & Gray, D.M. 1981. Snowcover ablation and runoff. In: D.M. Gray & D.H. Male (ed.), *Handbook of Snow: Principles, Processes, Management and Use*. Pergamon Press, 360-436.

McRoberts, E.C. & Morgenstern, N.R. 1974. The stability of thawing slopes. *Canadian Geotechnical Journal* 11: 447-469.

Robinson, S.D. 2000. Thaw slump derived thermokarst near Weather Creek, Ellesmere Island, Nunavut. *Geological Survey of Canada Bulletin* 529: 335-345.

Solomon, S.M. 1995. *Impact of the September 1993 Storm on the Beaufort Sea,* Geological Survey of Canada, Atlantic Geoscience Center, Nova Scotia, Canada

Tsytovitch, N.A. 1975. *The Mechanics of Frozen Ground*. George K. Swinzow (ed.), US Army Cold Regions Research and Engineering Laboratory. New York: McGraw-Hill, 426 pp.

USACE (U.S. Army Corps of Engineers). 1998. *Runoff from Snowmelt.* Engineering Manual, No.-110-2-1406.

Vialov, S.S., Gorodetskii, S.E., Ermakov V.F., Zatsarnaya, A.G., & Pekarskaya, N.K. 1966. *Method of Determining Creep, Long-term Strength and Compressibility Characteristics of Frozen Soils*. (Technical translation 1364, National Science Library, NRC, Canada) Moscow: Nakua Publisher, 106 pp.

Walker, H.J. 1988. Permafrost and coastal processes. *Proceedings of the Fifth International Conference on Permafrost* 3: 35-42.

The 2005 Mt. Steller, Alaska, Rock-Ice Avalanche: A Large Slope Failure in Cold Permafrost

Christian Huggel, Stephan Gruber
Glaciology, Geomorphodynamics & Geochronology, Department of Geography, University of Zurich
Jaqueline Caplan-Auerbach
Geology Department, Western Washington University, Bellingham WA, USA
Rick L. Wessels
U.S. Geological Survey, Alaska Science Center - Alaska Volcano Observatory, Anchorage AK, USA
Bruce F. Molnia
U.S. Geological Survey, Reston VA, USA

Abstract

This paper describes and analyzes the exceptionally large rock-ice avalanche of 40 to 60 million m^3 volume that occurred in 2005 from the south face of Mt. Steller (Bering Glacier region, Alaska), which has steep glaciers at the summit. Analysis of seismic signals revealed a series of precursory rock/icefalls and a special sequence interpreted as slip and deformation in glacier ice. Reconstruction of the thermal conditions based on regional climate and radiosonde data yielded mean annual ground surface temperatures of -10 to -15°C for the failure area. Because the slope failure was at depths of meters to decameters we also performed numerical modeling of a 2D temperature profile across the mountain. Results showed that the existence of a hanging glacier in the summit area induces a deep-seated thermal anomaly. We subsequently outline a number of processes that may be effective for slope destabilization with the given thermal conditions.

Keywords: cold permafrost; Mt. Steller, Alaska; rock-ice avalanche; seismic signals; steep glacier; thermal modeling.

Introduction

A large rock-ice avalanche of 40 to 60 million m3 occurred on 14 September 2005 from the southern flank of Mt. Steller in the Bering Glacier-Bagley Ice Field region. The initial failure from a maximum elevation of 3100 m a.s.l. involved significant volumes of both rock and ice from steep glaciers. The avalanche mass travelled for almost 10 km and was deposited on Bering Glacier. As we will show, the failure was from areas in cold permafrost conditions, with the area of failure being thermally disturbed by an overlying steep glacier. Understanding of such large slope failures is important in the context of atmospheric warming and the potentially severe consequences in case of similar events in populous regions.

Increasing temperatures can destabilize frozen rock (Gruber & Haeberli 2007). Recent studies have demonstrated that not only rock surface temperatures but also temperature distribution at depth should be considered for slope stability, and have simulated the effects of projected climate change on the thermal regimes of different mountain topography (Noetzli et al. 2007). In Alaska, atmospheric warming and a related increase of permafrost temperatures have been generally strong in the 20th century. According to borehole observations in low-land areas, permafrost temperatures in the 20th century warmed by 2–4°C by the early 1980s (Lachenbruch & Marshall 1986) and up to 2–3°C during the past two decades (Osterkamp & Romanovsky 1999, Osterkamp 2007). The rise of permafrost temperatures, however, has not been as consistent as the rise of air

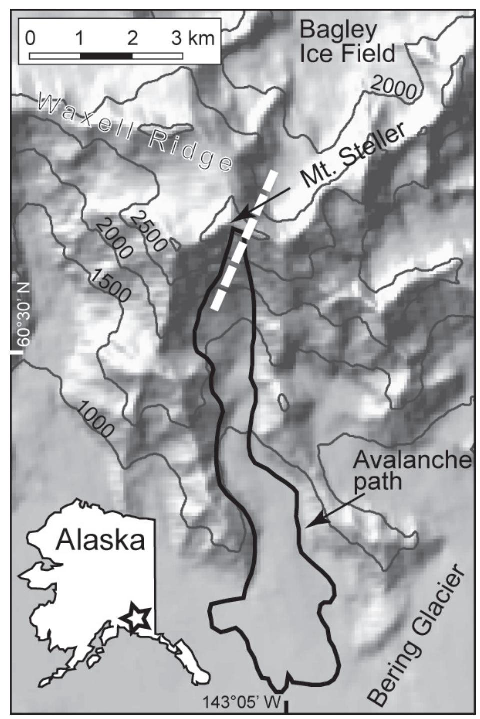

Figure 1. Map showing Mt. Steller and the extent of the 2005 rock-ice avalanche (dashed line indicates the cross section used for thermal modeling, cf. Fig. 5).

temperatures in Alaska, mainly because of the influence of local factors (e.g., snow cover) on the energy balance (Osterkamp 2007). Knowledge on the evolution of permafrost temperatures in Alaskan high-mountain areas is scarce.

Steep glaciers in mountain walls can induce complex thermal anomalies in perennially frozen bedrock. A limited number of studies have shown that even in cold permafrost conditions, overlying glaciers can create temperatures close to phase equilibrium at the ice-bedrock interface (Wegmann et al. 1998, Haeberli et al. 1999). Because on-site access to large high-mountain walls is very limited and often impossible, investigations are typically restricted to remotely based measurements and modeling, although systematic rock temperature measurements exist in the Alps where site access is comparably easy (Gruber et al. 2004).

Seismometers have been used to study rapid mass movements resulting from slope failures (e.g., Weaver et al. 1990, Norris 1994). More recently, seismology has been used as a tool to analyze slope failure processes up to two hours before avalanche initiation (Caplan-Auerbach et al. 2004, Caplan-Auerbach & Huggel 2007), thus revealing new possibilities for the investigation of slope failures.

This study aims at reconstructing the 2005 failure and avalanche at Mt. Steller and the factors that led to this event. Although the site geology is fundamental for the slope failure we will concentrate here on the thermal conditions at the failure site and related transient effects such as atmospheric warming and overlying glaciers. More generally, we want to improve our understanding of large slope failures in steep terrain in cold permafrost and discuss the possible influence of thermal disturbance.

The 2005 Mt. Steller Avalanche

Mt. Steller (3236 m a.s.l., 60°13′N, 143°05′W) is part of the Waxell Ridge, a bedrock massif that separates the Bagley Ice Field from Bering Glacier (Fig. 1). Climatically, Mt. Steller is located close to the divide between the warmer and more humid climate of coastal Alaska and the drier and colder interior of Alaska. Geologically, the Steller S-face consists of tertiary sedimentary rocks that are layered sub-parallel to the surface slope in the failure zone.

The Waxell Ridge is a very remote area with difficult access conditions and almost only visited from the air. The 14 September 2005 rock-ice avalanche from Mt. Steller was identified because its associated seismic signals were recorded at seismometers throughout Alaska and around the world. The Alaska Earthquake Information Center reported that the event had an equivalent local magnitude of 3.8, while analysis of global long period waves yielded a magnitude of 5.2 (G. Ekstrom, personal communication, 2005). Due to the complicated access conditions of Mt. Steller, we based the reconstruction of the rock-ice avalanche on available remotely operating systems such as satellite imagery, airborne observations, and seismic recordings. We used a Landsat ETM+ scene taken a few hours after the avalanche on 14 September 2005 and photographs from a fixed-wing flight the day immediately after the event, repeated in Summer 2006 and 2007. Topographic information was derived from the USGS NED (2 arc sec, ~60 m) digital elevation model (DEM) and available topographic maps. Data from climate stations and radiosonde measurements in the region were used for temperature reconstruction at the Steller site.

Figure 2. Upper section of the avalanche failure zone. The summit hanging glacier failed on a width of ~500 m and an elevation range of ~200 m. The ice thickness is in the range of 20–30 m. Note the liquid water on the exposed rock failure surface, and the large hollow-like cavity at the right margin, possibly indicating the existence of water (photo courtesy of Ruedi Homberger).

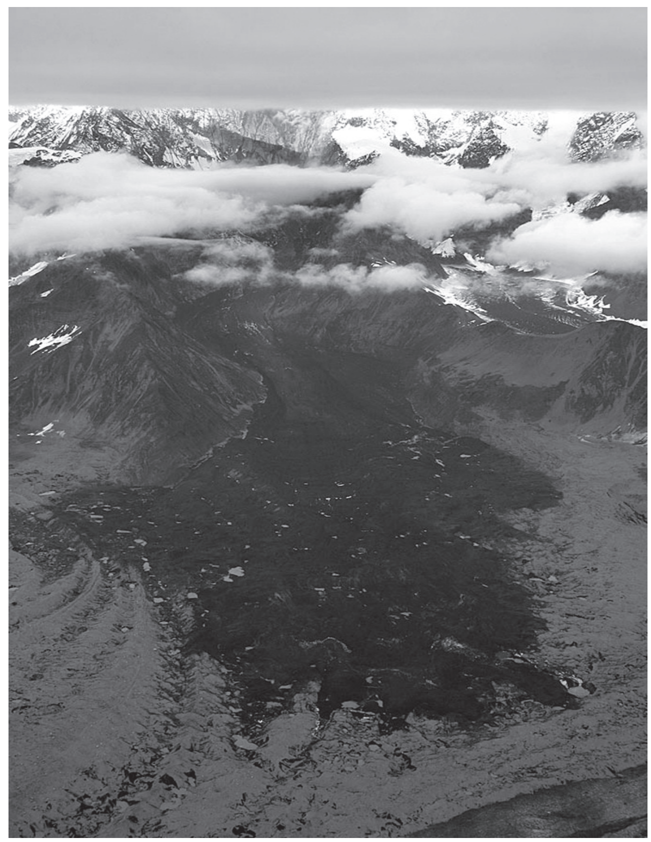

Figure 3. Photo showing the flow path through the glacial valley and the runout area of the rock-ice avalanche on the Bering Glacier For scale, refer to Fig. 1 (photo courtesy of Ruedi Homberger).

The 2005 rock-ice avalanche initiated in the S-face of Mt. Steller that has an average slope of 45° and an elevation drop of 1600 m. At the uppermost section, this face is covered by steep glacier ice which extends over the ridge to the northern side. At the time of the avalanche, the S-face of Mt. Steller was extensively covered by snow, as is typical of mountain walls in this region. The photographs taken the day after the event show that a significant part of the hanging glacier, along with large volumes of bedrock, was involved in the avalanche (Fig. 2). We estimate that 3 to 4.5 million m^3 of glacier ice with ice thickness of 20 to 30 m failed. The failure volume of rock is difficult to assess without precise topographic data. It is evident that almost the entire S-face was affected by the avalanche, but it is not clear which bedrock areas actually failed and which ones were only affected by the passing avalanche. We estimate that bedrock failed between 2500 and 3100 m a.s.l. und crudely estimate the initial rock volume at 10 to 20 million m^3. Additionally, another 2 million m^3 of snow may have been involved in the initial avalanche.

The rock and ice mass from the Mt. Steller avalanche impacted the glacier at the toe of the S-face that extends from ~1700 m a.s.l. towards the south, and eroded several millions of m^3 of glacier ice. The avalanche then traveled on the glacier surface in a laterally confined valley for about 4 km until it reached the relatively flat surface of Bering Glacier where the mass spread and stopped on the debris-covered ice (Fig. 3). The total horizontal run out distance was 9 km, whereas the drop height was 2430 m, with the uppermost failure point at ~3100 m a.s.l. and the lowest run.out point at 670 m a.s.l. The total avalanche volume deposited on Bering Glacier can be reconstructed with an area of 4 km^2 and an average deposit thickness of 10 to 15 m using the undulating topography of the moraine ridges that were filled by the avalanche deposits as a height reference. This yields a total avalanche volume of 40 to 60 million m^3; and thus, the 2005 Mt. Steller avalanche ranges among the largest avalanches observed in recent decades worldwide. These volume estimates furthermore indicate that the initially failed glacier ice made up about 10% of the total avalanche volume, and that probably about 5 to 30 million m^3 of ice, snow, and debris were entrained along the avalanche path.

Seismic Response

Seismic recordings played a particularly important role in the detection and analysis of the 2005 Mt. Steller avalanche. First analyses of seismic signals recorded at several Alaskan stations showed spindle-shaped seismograms typical of mass movements such as rockfall and debris avalanches (Weaver et al. 1990, Norris 1994, Caplan-Auerbach et al. 2004) or snow avalanches (Suriñach et al. 2001). Based on the duration of these signals and the horizontal runout distance, we estimated an avalanche speed of ~100 m/s or possibly even more. It is not completely clear why the avalanche produced such a large seismic signal that was recorded all over the world, but the steep topography with the high S-face and the resulting strong impact at the toe of the face must have contributed to this. The large size of the seismic signal also supports our estimate that a very large mass of >20 million m^3 was involved in the initial failure

Another remarkable aspect of the seismic signal analysis

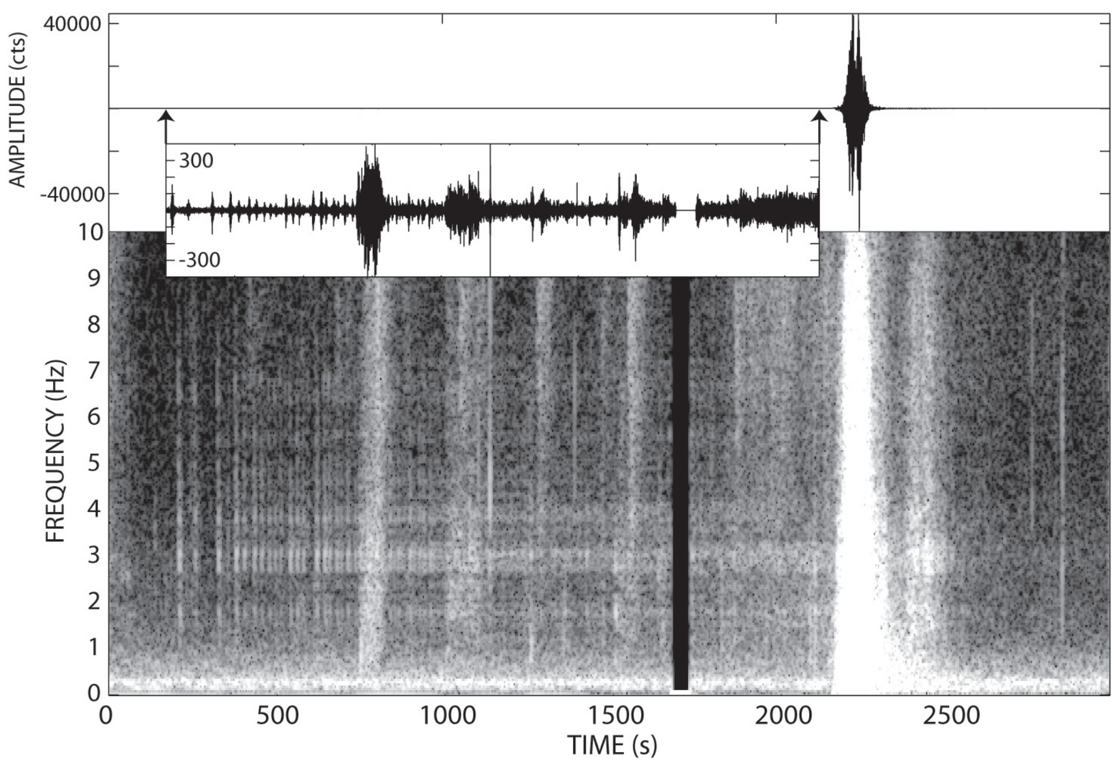

Figure 4. Seismic signal surrounding the 2005 avalanche at Mt. Steller. The top panel shows the time series of groundshaking as recorded at station KHIT, 12 km to the SW of Mt. Steller. The bottom panel is a spectrogram representing signal strength at different frequencies for the time series, with white representing stronger signals. The avalanche is visible at ~2150 seconds into the record. Because the amplitude of the avalanche is so large, a close-up of the precursory time series is shown in the inset. Note the different vertical scales on the two time series. (We acknowledge the Alaska Earthquake Information Center for operating the network and providing the data.)

at Mt. Steller was an unusual precursory seismic sequence occurring up to 30 minutes prior to failure. It should be noted that avalanches initiating in snow or rock have not been observed to exhibit precursory seismicity (Norris 1994, Suriñach et al. 2001, Caplan-Auerbach et al. 2004). Recent studies at Iliamna Volcano (3050 m a.s.l., 60.03°N, 153.09°W) in the Cook Inlet region of Alaska, however, have demonstrated that such precursory signals do occur with avalanches that initiate in ice or at the ice-bedrock interface (Caplan-Auerbach & Huggel 2007). The Mt. Steller precursory seismic signals mimic those at Iliamna in that they exhibit a series of discrete earthquakes which increase in occurrence rate for ~15 minutes before they gradually transform into a continuous ground-shaking (Fig. 4). The 15–20 minute continuous signal eventually culminates in a strong, broadband, spindle-shaped signal believed to represent the actual avalanche. At Iliamna, Caplan-Auerbach & Huggel (2007) interpreted the precursory seismic signals as deformation and slip movement in the ice with slip rates accelerating as failure approaches, and we propose the same mechanism for the Mt. Steller event. The evidence for relating the precursory seismic signals to failure in ice and not in rock supports a model in which the ice of the subsequently failed hanging glacier began to move over 30 minutes prior to failure. This, however, does not necessarily imply that the Mt. Steller avalanche initiated in ice and not in rock. Closer observation of the seismic signal (Fig. 4) shows that a number of smaller avalanches, represented by broadband, spindle-shaped signals, occurred prior to and during the precursory slip events. While the signals of these precursory slip events are well-defined at specific frequencies (i.e., at ~2, 3 and 4 Hz, Fig. 4) the smaller avalanches are identifiable by their broadband spectrum (i.e., all the way up to 10 Hz and more) at ~750, 1000, 1200 and 1500 seconds (Fig. 4). This suggests that the first stages of failure included rock, and that these initial slope failures could have triggered slip along the base of the hanging glacier. Unfortunately, because of the small (<M1) magnitude of the events and sparse nature of the regional seismic network, precise epicentral locations cannot be calculated for the precursory seismicity. However, examination of S-P times at station KHIT suggests a location at a distance consistent with a source at Mt. Steller.

Permafrost Analysis and Failure Interpretation

The purpose of this section is a first estimate of the permafrost conditions at the failure site, including the thermal regime at depth. Our thermal model presented here provides some general and basic insights but may have limitations compared to real conditions at Mt. Steller. We highlight the thermal interaction of permafrost with glacier ice and possible relations to slope stability and failure.

The reconstruction of the thermal ground conditions at the failure site was chiefly based on radiosonde data from Yakutat, located 270 km SE of Mt. Steller, and the closest regional meteorological stations (Cordova, Yakutat, McCarthy, Chitina, Ernestine, and Thompson Pass, 3 to 760 m a.s.l.). The Yakutat radiosonde data yielded a mean annual air temperature (MAAT) of -10.5°C at 3000 m a.s.l. considering the period 1994–2007. However, vertical temperature extrapolation from the closest meteorological stations in the warmer and more humid climate of the Alaskan S-coast using a lapse rate of 0.0065°C m^{-1} derived from radiosonde data resulted in a MAAT of -15.5°C at the 3000 m a.s.l. level. Some, but not all, of this temperature difference may be explained by the fact that the MAAT extrapolated from ground-based climate stations was derived from a 50-year record and, therefore, does not fully reflect the recent warming in Alaska. For subsequent assessment and thermal modeling, we applied the radiosonde-based MAAT value since it may reasonably be assumed that the temperature record of the more homogeneous troposphere is a more accurate approximation of conditions at Mt. Steller than are local ground stations. We set the mean annual ground

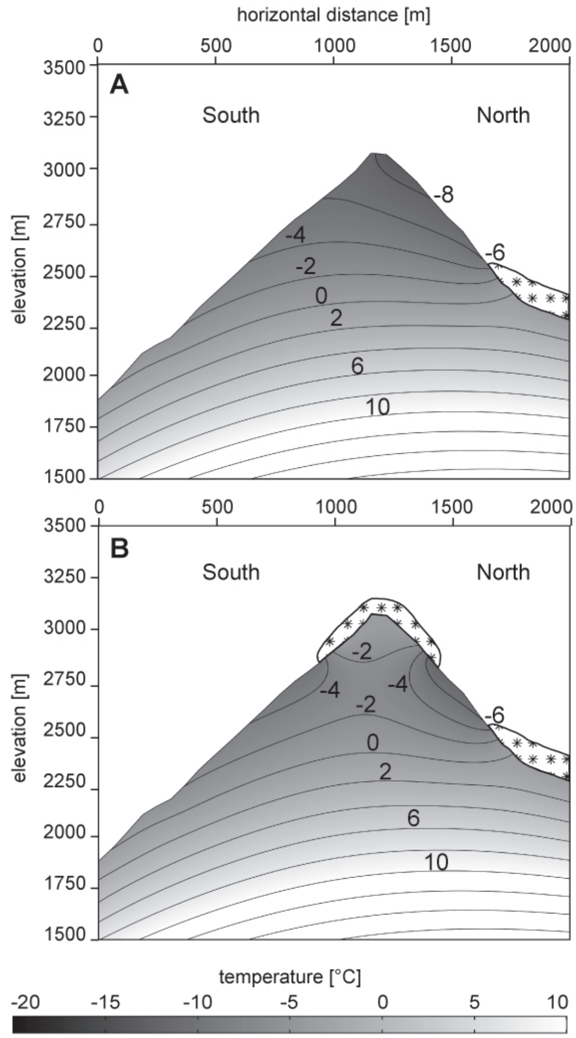

Figure 5. 2D rock temperature distribution in a N-S cross section of Mt. Steller. Distance and elevation a.s.l. are in meters, isotherms in °C. A: Rock temperature without considering overlying glaciers. B: Rock temperature with overlying glaciers (ice depth not in scale). Note the temperature differences at the summit area for A and B.

surface temperature (MAGST) 3°C warmer than MAAT for the S-face and 1°C warmer than MAAT for the N-face of Mt. Steller (Haeberli et al. 2003, Gruber et al. 2004).

Our analysis of thermal conditions at Mt. Steller was concerned with the temperature distribution at the surface and at depth since the failure depth reached meters to decameters depth. Recent studies using a modeling scheme with surface temperature (Gruber et al. 2004) and 3D subsurface heat conduction calculation (Noetzli et al. 2007) have demonstrated the distribution of temperature for idealized 3D topography such as ridges. For Mt. Steller, we calculated a 2D temperature profile along a N-S cross section. Subsurface temperatures were simulated using a steady-state, two-dimensional, finite-element, heat conduction model of 10.5 km width having a base 2000 m below sea level. The upper boundary condition was given by estimated surface temperature (see above), and an inward heat flux of 0.08 W/m^2 was set at the lower boundary. The thermal conductivity for rock was assumed to be homogeneous and isotropic at 2.5 W/m/K, a reasonable average value for sedimentary rock. Noetzli et al. (2007) have shown that realistically small variations of the thermal conductivity do not significantly affect the model result. Transient model runs were not considered because the corresponding boundary conditions for this remote area are poorly known and would introduce additional uncertainty.

We first modeled a temperature profile assuming there was no summit glacier on Mt. Steller (Fig. 5A). Results show steeply inclined isotherms at the summit area with heat flux from S to N, and less inclined isotherms below the summit. Studies in the Alps have demonstrated that steep glaciers in conditions with MAAT of about -5 to -10°C have a cold-based front frozen to the ground but can show much warmer or even phase-equilibrium temperatures at the upper part (Haeberli et al. 1997, 1999). This is due to latent heat dissipation from percolating and refreezing meltwater in the snow and firn layer. For the second model, which includes the summit glacier ice (Fig. 5B), we, therefore, assumed cold ice for the front of the S-face glacier; entirely cold ice conditions for the N-face glacier; and temperate ice for the upper part of the summit ice apron, as well as for the glaciers at lower elevations of the N and S face. Model results show the deep-seated thermal anomaly induced by the glacier ice with bedrock temperatures at the summit region close to phase transition up to several decameters depth (Fig. 5B). Exposed bedrock in the S-face below the hanging glacier is several degrees colder.

Based on our assumptions, the existence of temperate ice and liquid water at the Mt. Steller summit area is possible. Relatively large amounts of liquid water on the bedrock of the formerly glacier-covered failure zone (Fig. 2) photographed a few hours after the avalanche in cloudy weather conditions likely also hint at this; however, this water could also stem from immediate snow/ice melting after the event. Irrespective of the source of liquid water (i.e., from the base of the glacier and/or subsurface rock, or from recent snow/ice melting), it is evidence of quite significant melting conditions at the ~3000 m a.s.l. level at Mt. Steller.

Despite incomplete information, we hypothesize a temperature-related destabilization, with a likely influence of the strong recent warming in Alaska. A MAAT increase of 2–4°C during the past decades could have penetrated several decameters into the bedrock; additionally, the Mt. Steller summit glacier likely experienced a transition to warmer temperatures where infiltration has become more frequent and has warmed large portions of the glacier, possibly to phase equilibrium temperatures. The Yakutat radiosonde data, in fact, is evidence that temperatures above freezing repeatedly persisted at elevations of the Mt. Steller summit in the past few years as late as September. The ~10 days prior to the 2005 failure were characterized by particularly warm temperatures above freezing; and correspondingly enhanced melting could likely have contributed to the slope failure.

A system of well-developed cracks is observable in air photos and could have experienced corresponding effects of hydrostatic pressure variations. However, the 2005 slope failure also involved large parts of bedrock at lower elevation that was not glacier-covered but was in cold permafrost conditions (Fig. 5). It is not clear which mechanisms contributed to the slope failure in this zone, but an effect of the upper warmer part is imaginable. For instance, variations of hydrostatic pressure and effective stress induced by the upper part could cause micro fractures and progressive failure in the lower part (Eberhardt et al. 2004).

Discussion and Conclusions

We have described the 2005 rock-ice avalanche from Mt. Steller in the Bering Glacier region, Alaska, which was one of the world's largest slope failures and avalanches of the past decades. We have focused on the conditions of failure, with a particular eye on the surface and subsurface thermal regime. Seismic signals contributed to an improved understanding of the failure mechanism by providing evidence of precursory rock/ice-falls and indication of deformation and slip of the overlying glacier ice. It is only recently that such processes in glacier ice prior to failure were discovered in seismic signals and more investigation is needed to better constrain the involved mechanisms.

The MAGST reconstruction at the failure zone was mainly based on radiosonde data and yielded temperatures of about -4 to -8°C. Numerical modeling allowed us to estimate the subsurface temperature distribution at Mt. Steller, demonstrating the deep-seated thermal effect of overlying steep glaciers on bed rock temperatures at depth. The radiosonde data should well reflect the recent strong warming in Alaska, and, according to these temperatures, the assumption of polythermal and temperate ice in the S-face and on the summit is reasonable. Nevertheless, there is an uncertainty in the boundary conditions of the thermal model which may range within ~2–3°C.

Our understanding of temperature-driven slope destabilization processes at mountains with permafrost is still very incomplete. So far, based on this study and a number of recent similar slope failures (Haeberli et al. 2003, Huggel et al. 2005, Fischer et al. 2006), we conclude that the existence of steep glaciers in cold permafrost mountains is an important and quickly changing factor of slope stability.

Acknowledgments

These studies were partly supported by funds of the Swiss National Science Foundation and the USGS Mendenhall Postdoctoral Program. We very much thank R. Homberger and P.& D. Claus for providing photographs. Helpful comments by P. Deline, M. Wegmann, and the editor D. Kane are acknowledged.

References

Caplan-Auerbach, J., Prejean, S.G. & Power, J.A. 2004. Seismic recordings of ice and debris avalanches on Iliamna Volcano (Alaska). *Acta Vulcanologica* 16: 9-20.

Caplan-Auerbach, J. & Huggel, C. 2007. Precursory seismicity associated with frequent, large avalanches on Iliamna Volcano. *Alaska. Journal Glaciology* 53: 128-140.

Eberhardt, E., Stead, D. & Coggan, J.S. 2004. Numerical analysis and progressive failure in natural rock slopes - the 1991 Randa rockslide. *International Journal of Rock Mechanics & Mining Sciences* 41: 69-78.

Fischer, L., Kääb, A., Huggel, C. & Noetzli, J. 2006. Geology, glacier retreat and permafrost degradation as controlling factors of slope instabilities in a high-mountain rock wall: the Monte Rosa east face. *Natural Hazards and Earth System Science* 6: 761-772.

Gruber, S., Hoelzle, M. & Haeberli, W. 2004. Rock wall temperatures in the Alps: Modelling their topographic distribution and regional differences. *Permafrost and Periglacial Processes* 15: 299-307.

Gruber, S. & Haeberli, W. 2007. Permafrost in steep bedrock slopes and its temperature-related destabilization following climate change. *Journal of Geophysical Research* 112:F02S18, doi:10.1029/2006JF000547.

Haeberli, W., Wegmann, M. & Vonder Mühll, D. 1997. Slope stability problems related to glacier shrinkage and permafrost degradation in the Alps. *Eclogae Geologicae Helvetia* 90: 407- 414.

Haeberli, W., Huggel, C., Kääb, A., Polkvoj, A., Zotikov, I. & Osokin, N. 2003. Permafrost conditions in the starting zone of the Kolka-Karmadon rock/ice slide of 20 September 2002 in North Osetia (Russian Caucasus), *Proceedings of the 8th International Conference on Permafrost, Zürich, Switzerland, July, 2003*, *Extended Abstracts*: 49-50.

Haeberli, W., Kääb, A., Hoelzle, M., Bösch, H., Funk, M., Vonder Mühll, D. & Keller, F. 1999. Eisschwund und Naturkatastrophen im Hochgebirge. Zürich: VDF Hochschulverlag an der ETH Zürich, 190 pp.

Huggel, C., Zgraggen-Oswald, S., Haeberli, W., Kääb, A., Polkvoj, A., Galushkin, I. & Evans, S.G. 2005. The 2002 rock/ice avalanche at Kolka/Karmadon, Russian Caucasus: assessment of extraordinary avalanche formation and mobility, and application of QuickBird satellite imagery. *Natural Hazards and Earth System Sciences* 5: 173-187.

Lachenbruch, A.H. & Marshall, B.V. 1986. Changing climate: geothermal evidence from permafrost in the Alaskan Arctic. *Science* 234: 689-696.

Noetzli, J., Gruber, S., Kohl, T., Salzmann, N. & Haeberli, W. 2007. Three-dimensional distribution and evolution of permafrost temperatures in idealized high-mountain topography. *Journal of Geophysical Research* 112: F02S13, doi:10.1029/2006JF000545.

Norris, R. D. 1994. Seismicity of rockfalls and avalanches at three Cascade Range volcanoes: implications for seismic detection of hazardous mass movements, *Bulletin Seismological Society of America* 84: 1925-1939.

Osterkamp, T.E. 2007. Characteristics of the recent warming of permafrost in Alaska. *Journal of Geophysical Research* 112:F02S02.

Osterkamp, T.E. & Romanovsky, V.E. 1999. Evidence for warming and thawing of discontinuous permafrost in Alaska. *Permafrost and Periglacial Processes* 10: 17-37.

Suriñach, E., Furdada, G., Sabot, F., Biescas, B. & Vilaplana, J.M. 2001. On the characterization of seismic signals generated by snow avalanches for monitoring purposes. *Annals of Glaciology* 32: 268-274.

Weaver, C. S., Norris, R. D. & Jonientz-Trisler, C. 1990. Results of seismological monitoring in the Cascade Range, 1962–1989: earthquakes, eruptions, avalanches and other curiosities. *Geoscience Canada* 17: 158-162.

Wegmann, M., Gudmundsson, G. & Haeberli, W. 1998. Permafrost changes and the retreat of Alpine glaciers: A thermal modelling approach. *Permafrost and Periglacial Processes* 9: 23-33.

—Plenary Paper—

Alpine and Polar Periglacial Processes: The Current State of Knowledge

Ole Humlum
University of Oslo, Institute of Geosciences, Box 1047 Blindern, 0316 Oslo, Norway
and
UNIS, Box 156, NO-9171 Longyearbyen, Svalbard, Norway

Abstract

Recently the traditional view on the geomorphological evolution of periglacial landscapes has been questioned. The geomorphological processes considered most important for landscapes in periglacial regions, in general, are not unique for periglacial environments. On the other hand, there is a suite of geomorphological processes which may be seen as characteristic for periglacial environments. Based on what the author considers characteristic periglacial phenomena and landforms, this paper attempts to identify what might be conceived as the main characteristic periglacial processes. Seasonal or perennial freezing and conspicuous landforms such as extensive talus sheets, polygonal networks, and large-scale patterned ground, dominate descriptions of periglacial regions. Phenomena controlling bedrock disintegration, rockfall, thermal contraction cracking, and sorting of sediments are therefore all seen as the means to identify characteristic periglacial processes. Each of these periglacial processes is shortly described, and the present state of knowledge, or the lack of such, is outlined.

Keywords: climate; geomorphology; modeling; monitoring; periglacial; permafrost.

Introduction

Periglacial regions at high latitude or high altitude experience rapid changes in the ground thermal regime in response to daily and annual as well as long-term climatic variations. Changes in the ground thermal regime and the associated growth or decay of permafrost may destabilize rock slopes or mobilize sediment slopes, possibly leading to major geomorphic changes, accompanied by natural hazards (e.g., Harris et al. 2001, Haeberli and Burn 2002). One practical priority issue of periglacial geomorphology should therefore by to improve understanding of the climatic controls on geomorphic processes, to predict potential hazards. The ultimate scientific aim of periglacial geomorphology, however, remains the formulation of models for cold-climate landscape evolution (French and Thorn 2006).

By tradition, alpine and polar periglacial landscapes are regarded as characterized by efficient frost-driven geomorphological processes. The importance of frost shattering and related processes was equally emphasized. Hence, the geomorphology of periglacial areas was long regarded as controlled primarily by processes driven by freeze–thaw mechanisms.

Originally, the term periglacial was used to describe the climatic and geomorphic conditions of areas peripheral to Pleistocene ice sheets and glaciers. Modern usage refers, however, to a wider range of cold climatic conditions regardless of their proximity to a glacier, either in space or time. In addition, many, but not all, periglacial environments possess permafrost; but they appear all to be dominated by frost action processes (Dylik 1964, French 1976, Washburn 1979, French 2007). In line with this view, the English version of the Multi-Language Glossary of Permafrost and Related Ground-Ice Terms compiled by the IPA's Terminology Working Group (Everdingen 1998), defines the term periglacial as the conditions, processes and landforms associated with cold, nonglacial environments.

Periglacial landscapes

The origin of periglacial landscapes as traditionally defined is recently becoming a theme for renewed debate. The relationship of landscapes to climate is a topic which has simultaneously been regarded as a focus for research in geomorphology and an approach which has fruitlessly occupied the time of geomorphologists over the past several decades. The former view has characterized research by many French and German geomorphologists, whereas the latter has prevailed among Anglo-American researchers. There is little doubt that major differences in climate have a profound effect on landscape development. Disagreement comes with the finer distinctions between degrees of climatic differences evident in past attempts to identify morphoclimatic zones. For instance, if we examine a range of landscapes in periglacial environments, landscape diversity is often more apparent than uniformity. A further problem is the diversity of conditions under which apparently similar landforms can develop. Perhaps the most intractable problem in periglacial geomorphology is the logical temptation of explicit linking of a particular landform with a specific set of climatic conditions. The observation of periglacial phenomena such as, e.g. ice-wedge casts, in climatic environments in which they could not have developed obviously raises the question of climatic change in landform interpretation.

Any modern periglacial landscape should be considered as consisting of a number of landforms currently adjusting according to present climate, and a number of relict features, produced under past climatic conditions. Whether a climatic change is of geomorphic significance depends on its magnitude and duration, and on the properties of the landform considered. The larger or more resistant a landform, the longer, in general, it takes to adjust to a change in climate. In addition, the broad features of landscapes in periglacial environments are also highly influenced by lithological differences.

The validity of the traditionally view on the evolution of a typical periglacial landscape has therefore been questioned in recent times: The importance of geomorphological processes like chemical weathering, rainfall-induced slope processes and river action are emphasized, even though they are not unique for periglacial environments, but occur also in many other climatic settings. For example, Rapp (1960) in his classical study on weathering in northern Sweden demonstrated that solution was more important than mechanical processes. Later Thorn (1992) suggested that frost action may have been overestimated in relation to explaining the geomorphology of periglacial regions. Weathering and transport processes not related to frost may often modify the landforms resulting from frost action, or even preside over landform evolution in many periglacial environments. The action of wind and running water may be two important examples of such ubiquitous processes not limited to cold regions. This development in 2003 lead André to ask the pertinent question: Do periglacial landscapes evolve under periglacial conditions? The significance of this question was emphasized by French and Thorn (2006). On this background we might even begin to wonder what is understood by periglacial processes.

Periglacial processes

The André (2003) paper was published in a special issue of the journal Geomorphology, presenting a selection of papers originally presented at the general session "Glacial and Periglacial Geomorphology" of the Fifth International Conference on Geomorphology held in Tokyo, Japan, in August 2001 (Matsuoka et al. 2003). A study of these papers provide some assistance in identifying what is understood as periglacial processes at the beginning of the 21st century. Broadly the papers could be categorized into four themes: effects of diurnal frost, mountain permafrost, paleo-periglaciation and nonfrost processes in periglacial environments.

This suggests that many periglacial geomorphologists still have their research focus on frost-related processes. Low temperatures as a driving mechanism apparently remain a valid criterion for defining periglacial processes, even though the evolution of landscapes in periglacial environments may be controlled by other azonal processes. Also the steady interest in fossil periglacial features as indicators of past cold environments, points toward this conclusion. The validity of paleoclimatic indicators depends on precise description of, among other things, the climatic control on processes responsible for the landform or sedimentary structure studied. Otherwise, the periglacial feature observed would clearly be of little use as indicator for past cold environments.

So, at the beginning of the 21st century periglacial geomorphologists apparently are defining key periglacial processes as those related to seasonal or perennial frost, a point of view supported by French and Thorn (2006). At the same time, it is recognized that landscapes in periglacial regions are not always dominated by such periglacial processes, but quite often by more omnipresent processes such as wind and running water. On this background it might be considered if the future use of the term periglacial should be limited to describe processes and environments, rather than landscapes?

Having identified the modern implication of periglacial processes, we may proceed towards identifying a number of especially important or characteristic processes. To achieve this goal, we must first consider what is generally seen as characteristic landforms in periglacial environments. Due to space limitations, this will clearly not represent a comprehensive analysis, but will focus on a few landforms and phenomena, by the present author seen as characteristic for landscapes in periglacial environments.

Characteristic periglacial landforms and processes

The perhaps most obvious and impressive landforms in periglacial environments are those associated with steep slopes. In many mountain areas, glacial over-steepening, combined with weathering has led to rock slope instability and the production of large volumes of debris. Outside Holocene permafrost environments, a fundamental distinction is often recognized in valleys partly filled by glacier ice during Stadials of the last ice age. Within the former glacier limits, volumes of talus are limited relative to those at the foot of slopes outside the limits. By implication, the greater volumes of debris reflect the more severe periglacial conditions that prevailed during the Stadial and perhaps also during the deglaciation. Indeed, the impressive size of talus accumulations in periglacial highlands environments has led many researchers to conclude that rockfall is particularly pronounced under cold-climate conditions, due to release of debris from cliffs by frost wedging.

Low-relief periglacial areas are characterized by extensive polygonal networks, patterned ground and different types of frost mounds. All these phenomena are related to temperature induced volume changes of bedrock, sediments, ice, or mixtures of thereof. A highly diversified terminology is attached to the description of the surface expression of such phenomena. For example polygonal networks may appear in the literature under the headings of tundra polygons, frost-fissure polygons, ice-wedge polygons, and sand-wedge polygons, just to mention a few.

These observations suggest that frost-related non-glacial processes leading to rock disintegration, rockfall, rupturing by thermal contraction, and the deformation and sorting of thawed soil may be among what might be seen as characteristic periglacial processes. This assumption will provide the basis for the discussion below.

Characteristic Periglacial Phenomena

Rock disintegration

Evidence suggests that frost action is not the only weathering process leading to rock decay in periglacial environments. Cold-climate weathering is caused by the broader concept of cryogenic weathering, a collective term for a combination of little known physical and chemical processes which cause the in situ breakdown of rock under cold-climate conditions. Pressure release, salt weathering, chemical weathering, biological activity or thermal shocks may all play a role. In fact, chemical weathering (Roberts, 1968, Dixon et al., 2002) and biological processes (André, 2002) are more and more often considered as important actors in cold environments.

Field data on rock temperature and moisture content is essential for improved understanding of rock weathering in periglacial environments and for setting up realistic laboratory experiments. Unfortunately, such data are scarce in literature. In recent years, however, this situation is beginning to change through the publication of such data (e.g., Hall 1997, Hall 2006, Hall et al. 2002, Prick 2003).

This new accessibility of high-quality field data has provided the background for conducting realistic laboratory experiments, investigating the importance of ice segregation for low temperature bedrock breakdown under permafrost conditions (Murton et al. 2001). This experiment demonstrated that ice segregation, frost heave and brecciation in artificial permafrost formed in moist chalk are fundamentally similar to the processes associated with the growth of natural permafrost formed in frost-susceptible sediment. Similarities between the experimentally formed brecciation and naturally brecciated bedrock in areas of contemporary and former permafrost suggest that ice segregation during perennial and seasonal freezing is an important weathering process of frostsusceptible bedrock. By implication, the coarse, angular debris produced by ice segregation in bedrock during cold Quaternary periods was suggested being the sediment source for many of the coarse periglacial slope deposits. It is also very likely that bedrock fracture by ice segregation is significant for rockwall stability in regions of mountain permafrost, and for landform development in such areas in general. On this background Büdel's (1977) original 'Eisrinde' hypothesis absolutely deserves renewed research interest.

Rockfalls

The term rockfall describes the fall of relatively small (< 10 m^3) fragments of rock debris that are released from bedrock cliffs. By tradition, rockfall in periglacial environments has been widely attributed to frost wedging, the widening of cracks and joints by ice during freezing and detachment of debris from cliffs during thaw. Frost wedging is, however, only one of several processes operating on cliff faces (André 2003). Rockfall may also be triggered by stress-release, progressive failure along joints, or build-up of hydrostatic pressure within a rock mass. Indeed, some researchers view the role of freeze-thaw in rockfall as trivial in comparison with intrinsic controls such as stress release, weathering and build-up of joint-water pressures.

The timing of rockfalls remains the main reason for seeing frost wedging as the foremost cause of rockfall in cold environments. Rapp (1960) noted that rockfall at high latitudes is most frequent in spring and autumn, when cliffs was assumed to experience a maximum frequency of freeze-thaw cycles. Rockfall inventories in the Arctic and the Alps (e.g. Luckman, 1976, Coutard and Francou 1989) suggest maximum activity during the spring thaw. In Japan, Matsuoka and Sakai (1999) observed peak rockfall rate 5-15 days after meltout of the cliff face, when seasonal thaw reached an estimated depth of 1 m. Other rockfall inventories, however, emphasize diurnal variations, rather than seasonal trends. This is observed at alpine cliffs with frequent diurnal freeze-thaw cycles penetrating to depths of 50 cm (Coutard and Francou 1988). Rockfalls may also coincide with summer rainstorms, implying that build-up of joint-water pressures is also instrumental in releasing debris. Conversely, Matsuoka and Sakai (1999) in Japan found that intensive rockfall activity is rarely associated with either diurnal freeze-thaw cycles or precipitation events. So it is actually difficult to confirm the hypothesis regarding frost wedging as the main trigger of rockfall in periglacial environments.

Wind action

Due to the general lack of trees, many periglacial regions experience high wind speeds (Seppälä 2004), leading to the formation of different types of deflation surfaces. The vegetation, soil and fine material debris is removed to leave an armoured surface where large clasts are embedded within a matrix of finer sediment. Grains of sand and fine gravel can often be observed in motion during strong winds, blasting vegetation and rock surfaces. Sand dunes or sand sheets may occur downwind of such areas (Ballantyne and Harris 1994, Humlum and Christiansen 1998), but often much of the debris seems not to accumulate as dunes or sheets. Some may become temporarily resident in the snow pack, to thaw out in spring. Some probably finds its way into lakes and rivers on valleys floors. Some may be transported into the sea suspended in the air.

Another characteristic feature related to wind action in periglacial environments is wind-facetted blocks or wind polished bedrock surfaces (Christiansen and Svensson 1998). The wind-eroded surfaces are identified from their smooth and polished surfaces, together with facets and grooves (Christensen 2004). Blowing snow at low temperatures has apparently been the abrading agent for several examples of periglacial bedrock windpolish (Fristrup 1953).

Snowblow

Snowblow by wind is important in most periglacial environments, partly because of the typical absence of high vegetation providing lee at the ground surface, partly because many periglacial regions are found at high latitudes or high altitudes, where wind speed may be high.

The process of snow drifting is important in low-relief periglacial terrain, where the resulting distribution of snow controls heat exchange between atmosphere and the ground surface during the winter, for example on palsas (Seppälä 2004). The thermal importance of the snow cover for permafrost is well demonstrated by the efforts put into determining the n-factor, describing the thermal insulation provided by the snow cover (Smith and Riseborough 2002). In high-relief areas, snow accumulation on steep slopes contributes to the release of avalanches, especially on slopes downwind of extensive mountain plateaus (Humlum et al. 2007).

At low temperatures, the hardness of snow crystals increases, and wind transported snow may act as an efficient abrasive agent in relation to boulders and bedrock (Fristrup 1953). In addition, wind induced accumulations of snow are important as sources of water during the summer, as precipitation generally is low in periglacial environments.

Bagnold (1941) provided much of the groundwork for current steady-state models of sand drift (e.g. Sørensen 1991). The same physical basis has been applied to existing numerical models of snowdrift, such as SnowTran-3D (Liston and Sturm 1998) and the snowdrift index in SNOWPACK (Lehning et al. 2000, 2002a, 2002b). Snow drift prediction models using weather station data have also been developed for meteorological services (e.g., Li and Pomeroy 1997a, 1997b). These models, however, tend to consider snow drift as a probabilistic event and relate conditions to a measurement height, rather than to surface conditions.

Snow avalanches

Snow avalanches represent a periglacial transport process especially important during winter and spring. Although many shallow or midwinter avalanches contain only snow, deeper and late winter avalanches frequently incorporate and transport varying volumes of rock debris. As avalanches tend to follow gulleys, this debris accumulates on valley floors at the mouths of these gulleys in the form of avalanche boulder lobes (Rapp 1960), protalus ramparts (Ballantyne and Harris 1994), or rock glaciers (Humlum et al. 2006).

The meteorological control of snow avalanches represents a research theme in its own right, highly developed especially in Switzerland, Austria, USA and Norway. Several factors affect the likelihood of an avalanche, including weather, temperature, slope steepness, slope aspect, wind direction, terrain, vegetation, and the general snowpack conditions. Different combinations of these factors can create low, moderate or extreme avalanche conditions. Despite the existence of large databases with observations on avalanches, avalanche safety rules still are based mainly on empirical rules of thumb, rather that on strict meteorological-geotechnical analysis.

Another way of investigating the climatic control on avalanches is through analysis of avalanche deposits accumulated during the Holocene (e.g., Blikra and Selvik 1998). Such analyses, however, important as they are, only indicate that avalanches become more frequent during cold periods with frequent snow precipitation, but do not provide the means of detailed insights into meteorological controls on avalanche release. Indeed, some attempts at analysis simply assumes that the presence of what is interpreted as avalanche-derived debris indicate past periods with cold and snowy conditions.

Thermal contraction of frozen ground

Periglacial thermal contraction phenomena such as ice-wedge casts are widespread in periglacial environments. Fossil features in the form of ice-wedge casts are often used to estimate palaeotemperatures, specifically the maximum values of the mean annual air temperature or the mean air temperature of the coldest month (e.g., Washburn 1979, Vandenberghe et al. 1998). The now common use of ice-wedge casts as palaeotemperature indicators arose from an influential study by Péwé (1966a, 1966b) of ice-wedges in Alaska. As later pointed out by Murton and Kolstrup (2003), however, the validity of such attempts at reconstructions still remains uncertain because of limited knowledge of the frequency of thermal contraction cracking under contemporary permafrost environments. In addition, the perhaps complex controls other than meteorological on cracking are still incompletely understood. In fact, snow thickness appears to represent a decisive factor on ice-wedge cracking near the Western Arctic coast of Canada (Mackay 1993). Also the role of surface vegetation still needs to be quantified (Murton and Kolstrup 2003).

Progress in knowledge on thermal contraction cracking requires detailed field observations, supplemented by laboratory and numerical experiments, using real-world meteorological data on climate, landforms and sediments. A numerical modeling experiment on ice-wedge formation was recently presented by Plug and Werner (2001). This attempt at modeling ice-wedge growth turned out to be premature, because of lack of insight in real world conditions (Burn 2004).

Examples of how to expand knowledge on thermal contraction cracking of frozen sediments is given by careful field studies such as, e.g., Mackay (1993) and Christiansen (2005), in great detail describing meteorological and snow conditions related to thermal cracking of frozen ground.

Sediment sorting

Sorting of near-surface sediments in periglacial areas is responsible for the distinct, and often symmetrical geometric shapes known under the general heading patterned ground. The details of the sorting process and the origin of patterned ground has remained elusive for ages, despite much research effort.

Patterned ground is perhaps the most striking feature of the periglacial landscape, and can be found in a variety of forms: Polygons, circles, nets, steps, and stripes. The individual surface forms may range in size from a few centimeters to several meters in diameter. Typically, the type of patterned ground in a given area is related to the amount of larger stones present in local soils and the frequency of freeze-thaw cycles.

Polygons, circles and nets normally occur on level or gently sloping surfaces, while steps and stripes are found on steeper gradients. Both sorted and non-sorted varieties are recognized. The sorted varieties are typically outlined by coarse, stony material, and so are termed “stone circles,” “stone polygons,” “stone nets,” “stone steps,” and “stone stripes.”

The origin of patterned ground involves a complex interaction of several geomorphological processes, including differential frost heaving and mass movement. Recurrent freezing and thawing of water is usually believed to be critical for the development of patterned ground. In permafrost regions and non-permafrost regions affected by seasonal frost, repeated freezing and thawing of soil water transports larger stones toward the surface as smaller soils flow and settle underneath larger stones. At the surface, areas that are rich in larger stones contain less water than highly porous areas of finer grained sediments. These water saturated areas of finer sediments have greater ability to expand and contract as freezing and thawing occur, leading to lateral forces which ultimately pile larger stones into clusters and stripes. Through time, repeated freeze-thaw cycles form the common polygons, circles, and stripes of patterned ground.

There is still much debate as to the detailed mechanisms involved in freeze-thaw sorting, but it is widely agreed that the large scale patterned ground reflects the former existence of permafrost (Ballantyne 1996). Recurrent freezing and thawing of ground is also considered important for other periglacial phenomena such as solifluction and ploughing blocks.

The way ahead for periglacial geomorphology

Periglacial geomorphology is very special. It usually requires some mastery of geology, meteorology and geophysics to plan and carry out efficient investigations of complex geomorphological problems in periglacial environments. On the other hand, especially Quaternary geologists can in a very real sense be seen as applied periglacial (and glacial) geomorphologists. This relation emerges because periglacial (and glacial) geomorphologists combine the historical perspective so dear to geologists with an accentuated awareness and interest of contemporary geomorphological processes. In my opinion, it is exactly this study of geomorphological processes in periglacial environments which provides periglacial geomorphology with integrity, and upon which periglacial geomorphology relies for future scientific credibility.

Geomorphological processes clearly unique to periglacial environments relate to seasonal or perennial freezing, including the growth of segregated ice and associated frost heaving. Many of these processes operate in the near-surface layer subject to seasonal freezing and thaw; the active layer in permafrost regions. Ground seasonally frozen experience a range of special conditions associated with pore-water expulsion and thaw consolidation (French and Thorn 2006). On sediment slopes, this may promote rapid mass failures. On bedrock slopes, disintegration of exposed rock by mechanical frost weathering and several still poorly understood physical and biochemical processes may lead to rock falls. In addition to such characteristic periglacial processes the enhanced effect of wind in periglacial regions clearly deserves further study (Seppälä 2004).

Any study contributing to increased knowledge on geomorphological processes in periglacial environments are by definition important, no matter the specific theme chosen. From a strategic point of view, however, it appears that improved understanding of especially processes related to seasonal or perennial freezing should be seen as having tactical research priority within future periglacial research. Rock weathering in periglacial environments may be considered the mother of many types of sediments, and therefore a key factor for a range of other processes and landforms. Rock weathering in periglacial environments definitely deserves a concerted research effort, along with research on thermal contraction cracking and sediment sorting. These three phenomena together typify landscapes in most periglacial environments.

What is needed within periglacial geomorphology is a detailed monitoring scheme of meteorological parameters and geomorphological processes. Clearly, the use of dataloggers and other automatic equipment will have an important role in this development (Matsuoka 2006).

In this context, the organization in 2004 of a new Working Group (WG) on 'Periglacial Landforms, Processes and Climate' under the International Permafrost Association (IPA) may prove helpful. This WG is aiming at making a database for temporal and spatial variability of periglacial processes with special attention to meteorological controls and the impact of climatic change. To achieve this goal, the WG attempts to establish a global network for monitoring periglacial processes (Matsuoka and Humlum 2005, Matsuoka 2006), highlighting geomorphological processes associated with ground thermal regimes, inside and outside permafrost regions.

The recommended parameters to be measured depend primarily on the purpose of the study and the spatial scale. A cold-climate drainage basin is subjected to a variety of geomorphic processes, including glacial, periglacial, fluvioglacial, nival, gravitational and eolian processes. One research approach may focus on the mechanism of a specific process like rock fall, solifluction or ice-wedge growth, whereas other may aim at evaluating the sediment budget for the whole catchment. Whatever the approach chosen, the search for knowledge on past and present processes influencing landform evolution in periglacial regions is becoming increasingly influenced by more and more refined monitoring protocols, relying upon automatic and sophisticated equipment.

To the present author the common denominator for future periglacial research appears to be a coordinated research scheme embracing mapping, monitoring, experiments, and modeling, with focus on geomorphological processes relating to seasonal or perennial freezing.

Acknowledgments

Most of this paper was written during my sabbatical at University of St. Andrew (Scotland), where space facilities were kindly provided by Professor Colin Ballantyne. Both Professor Hugh French and Professor Norikazu Matsuoka have shared their thoughts on periglacial geomorphology with me during stays at UNIS (Svalbard), and in this way they have influenced the present paper. The responsibility for the actual content, and for any errors and omissions, however, remains fully with me. To everyone, I extend my warmest thanks.

References

André M.-F. 2002. Rates of postglacial rock weathering on glacially scoured outcrops (Abisko-Riksgränsen area, 68°N). *Geografiska Annaler* 84A, 3-4: 139-150.

André, M.-F. 2003. Do periglacial landscapes evolve under periglacial conditions? *Geomorphology* 52: 149-164.

Büdel, J. 1977. *Klima-Geomorphologie*. Berlin and Stuttgart: Gebrüder Borntraeger, 304 pp.

Bagnold, R.A. 1941. *The Physics of Blown Sand and Desert Dunes*. London: Chapman and Hall, 265 pp.

Ballantyne, C.K. 1996. Formation of miniature sorted patterns by shallow ground freezing: A field experiment. *Permafrost and Periglacial Processes* 7: 409-424.

Ballantyne, C.K. & Harris, C. 1994. *The Periglaciation of Great Britain*. Cambridge: Cambridge University Press, 330 pp.

Blikra, L.H. & Selvik, S.F. 1998. Climatic signals recorded in snow avalanche-dominated colluvium in western Norway: depositional facies successions and pollen records. *The Holocene* 8: 631-658.

Burn, C.R. 2004. A Field Perspective on Modelling 'Single-ridge' Ice-wedge Polygons. *Permafrost and Periglacial Processes* 15: 59-65.

Christiansen, H.H. 2004. Windpolished boulders and bedrock in the Scottish Highlands: evidence and implications of Late Devensian wind activity. *Boreas* 33: 82-94.

Christiansen, H.H. 2005. Thermal Regime of Ice-wedge Cracking in Adventdalen, Svalbard. *Permafrost and Periglacial Processes* 16: 87-98.

Christiansen, H.H. & Svensson, H. 1998. Windpolished boulders as indicators of a late Weichselian wind regime in Denmark in relation to neighbouring areas. *Permafrost and Periglacial Processes* 9: 1-21.

Coutard, J.P. & Francou, B. 1989. Rock Temperature-Measurements in 2 Alpine Environments: Implications for Frost Shattering. *Arctic and Alpine Research* 21: 399-416.

Dixon J.C., Thorn, C.E., Darmody, R.G. & Campbell, S.W. 2002. Post-glacial rock weathering processes on a rocke moutonnée in the Riksgränsen area (68°N), northern Norway. *Norsk Geografisk Tidskrift* 56: 257-264.

Dylik, J. 1964. Eléments essentials de la notion de 'périglaciaire'. *Biuletyn Peryglacjalny* 14 : 111-132.

Everdingen, R.v. 1998. *Glossary of Permafrost and Related Ground-Ice Terms*. Compiled by the IPA's Terminology Working Group and edited by Robert van Everdingen. Dr. Everdingen made some minor updates and corrections to the Glossary in 2002.

French, H.M. 1976. *The Periglacial Environment*. London: Longman, 308 pp.

French, H.M. 2007. *The Periglacial Environment*. Chichester: John Wiley & Sons, Ltd., 458 pp.

French, H.M. & Thorn, C.E. 2006. The changing nature of periglacial geomorphology. *Géomorphologie: relief, processus, environment* 3: 165-174.

Fristrup, B. 1953. Wind erosion within the Arctic deserts. *Geografisk Tidsskrift* 52: 51-56.

Hall, K. 1997. Rock temperatures and implications for cold regions weathering. 1: New data from Viking Valley, Alexander Island (Antarctica). *Permafrost and Periglacial Processes* 8: 69-90.

Hall, K. 2006. Perceptions of rock weathering in cold regions: a discussion on space and time attributes of scale. *Géomorphologie: relief, processus, environment* 3: 187-196.

Hall, K., Thorn, C.E., Matsuoka, N. & Prick, A. 2002. Weathering in cold regions: some thoughts and perspectives. *Progress in Physical Geography* 26: 577-604.

Haeberli, W. & Burn, C.R., 2002. Natural hazards in forests: glacier and permafrost effects as related to climate change. In: Sidle, R.C. (Ed.), Environmental Changes and Geomorphic Hazards in Forests. CABI Publishing, Oxfordshire: pp. 167-202.

Harris, C., Davies, M.C.R. & Etzelmüller, B. 2001. The assessment of potential geotechnical hazards associated with mountain permafrost in a warming global climate. Permafrost and Periglacial Processes 12: 145-156.

Humlum, O. & Christiansen, H.H. 1998. Mountain climate and periglacial phenomena in the Faeroe Islands. *Permafrost and Periglacial Processes* 9: 189-211.

Humlum, O., Christiansen, H.H. & Juliussen, H. 2007. Avalanche-Derived Rock Glaciers in Svalbard. *Permafrost and Periglacial Processes* 18: 75-88.

Lehning, M., Doorschot, J. & Bartelt, P. 2000. A snowdrift index based on SNOWPACK model calculations. *Annals of Glaciology* 31: 382-386.

Lehning, M., Bartelt, P., Brown, B., Fierz, C. & Satyawali, P. 2002a. A physical SNOWPACK model for the Swiss avalanche warning. Part II. Snow microstructure. *Cold Reg. Sci. Technol.* 35: 147-167.

Lehning, M., Bartelt, P., Brown, B. & Fierz, C. 2002b. A physical SNOWPACK model for the Swiss avalanche warning. Part III. Meteorological forcing, thin layer formation and evaluation. *Cold Reg. Sci. Technol.* 35: 169-184.

Li, L. & Pomeroy, J.W. 1997a. Estimates of threshold wind speeds for snow transport using meteorological data. *Journal of Applied Meteorology* 36: 205-213.

Li, L. & Pomeroy, J.W. 1997b. Probability of occurrence of blowing snow. *Journal of Geophysical Research* 102(D18): 21,955-21,964.

Liston, G.E. & Sturm, M. 1998. A snow-transport model for complex terrain. *Journal of Glaciology* 44: 498-516.

Luckman, B. H. 1976. Rockfalls and Rockfall Inventory Data: Some Observations from Surprise-Valley, Jasper-

National-Park, Canada. *Earth Surface Processes and Landforms* 1: 287-298.

Mackay, J.R. 1993. Air temperature, snow cover, creep of frozen ground, and the time of ice-wedge cracking, western Arctic coast. *Canadian Journal of Earth Sciences* 30: 1720–29.

Matsuoka, N. 2006. Monitoring periglacial processes: Towards construction of a global network. *Geomorphology* 80: 20–31.

Matsuoka, N. & Sakai, H. 1999. Rockfall activity from an alpine cliff during thawing periods. *Geomorphology* 28: 309-328.

Matsuoka, N., Iwata, S. & Haeberli, W. 2003. Periglacial geomorphology at the beginning of the 21st century: introduction. *Geomorphology* 52: 1-3.

Matsuoka, N. & Humlum, O. 2003. Monitoring Periglacial Processes: New Methodology and Technology. *Permafrost and Periglacial Processes* 14: 299-303.

Murton, J. B., Coutard, Ł J.-P., Lautridou, J.-P., Ozouf, J.-C., Robinson, D.A. & Williams, R.B.G. 2001. Physical Modelling of Bedrock Brecciation by Ice Segregation in Permafrost. *Permafrost and Periglacial Processes* 12: 255-266.

Murton, J.B. & Kolstrup, E. 2003. Ice-wedge casts as indicators of palaeotemperatures: precise proxy or wishful thinking? Progress in Physical Geography 27(2): 155-170.

Péwé, T.L. 1966a. *Ice wedges in Alaska: classification, distribution and climatic significance.* In: Proceedings, First International Conference on Permafrost. 11–15 November 1963. National Academy of Science: National Research Council of Canada, Publication 1287: 76–81.

Péwé, T.L. 1966b. Palaeoclimatic significance of fossil ice wedges. *Biuletyn Peryglacjalny* 15: 65-73.

Plug L.J. & Werner B.T. 2002. Nonlinear dynamics of icewedge networks and resulting sensitivity to severe cooling events. *Nature* 417: 929–933.

Prick, A. 2003. Frost weathering and rock fall in an arctic environment, Longyearbyen, Svalbard. In: Phillips, M., Springman, S.M., Arenson, L.U., eds., *Permafrost, Proceedings of the Eight International Conference on Permafrost*, 21-25 July, Zürich, Switzerland. Balkema, Lisse, vol.2: 907-159.

Rapp, A. 1960. Recent development of mountain slopes in Kärkevagge and surroundings, Northern Sweden. *Geografiska Annaler* 42: 71-200.

Roberts, D. 1968. Occurrences of weathering pits from Sørøy, Northern Norway. *Geografiska Annaler* 50A: 60-63.

Smith, M.W. & Riseborough, D.W. 2002. Climate and the Limits of Permafrost: A Zonal Analysis. *Permafrost and Periglacial Research* 13: 1-15.

Seppälä, M. 2004. *Wind as a geomorphic agent in cold climates*. Cambridge: Cambridge University Press, 358 pp.

Sørensen, M. 1991. An analytical model of wind-blown sand transport. *Acta Mech.*,1 (Suppl.): 67-81.

Thorn, C.E. 1992. Periglacial geomorphology: What? Where? When? In: Dixon, J.C. & Abrahams, A.D. (eds.). *Periglacial Geomorphology*. Chichester: John Wiley & Sons, 3-31.

Vandenberghe, J., Coope, R. & Kasse, K. 1998. Quantitative reconstructions of palaeoclimates during the last interglacial-glacial in western and central Europe: an introduction. *Journal of Quaternary Science* 13: 361-66.

Washburn, A.L. 1979. *Geocryology: A Survey of Periglacial Processes and Environments*. London: Edward Arnold, 406 pp.

Interseasonal Connection of Hydrothermal Components in a Permafrost Region in Eastern Siberia

Yoshihiro Iijima
Institute of Observational Research for Global Change, Japan Agency for Marine-Earth Science and Technology
Hoteak Park
Data Integration and Analysis Group, Japan Agency for Marine-Earth Science and Technology
Takeshi Yamazaki
Department of Geophysics, Graduate School of Science, Tohoku University
Hironori Yabuki
Institute of Observational Research for Global Change, Japan Agency for Marine-Earth Science and Technology
Trofim C. Maximov
Institute for Biological Problems of Cryolithozone, RB RAS
Tetsuo Ohata
Institute of Observational Research for Global Change, Japan Agency for Marine-Earth Science and Technology

Abstract

The present study aims to examine the interseasonal impacts of water cycle components on subsequent hydrothermal processes in permafrost, focusing on rainfall, snow amounts, and snow start and disappearance timings in the Lena River basin over recent decades. According to climatological analysis, there is a significant correspondence between the interannual variation in snow depth and soil temperature. In addition, both snow cover start and disappearance dates have negative correlations with soil temperature and moisture. These relationships indicate that a wetter climate with earlier snow season tends to produce an earlier start of subsequent growing season, which has been observed in the central Lena River basin in recent years. Based on a one-dimensional land surface model, earlier snow cover start and disappearance dates are correlated with significant increases in evapotranspiration from the boreal forest due to an earlier soil thawing and earlier plant growth and increased supply of soil moisture for plant uptake.

Keywords: active layer; eastern Siberia; evapotranspiration; rainfall in previous year; snow start and disappearance.

Introduction

The Eurasian continent has been a major topic of studies on land-surface-atmosphere interaction and the corresponding impact on not only the adjacent regional climate, such as Asia monsoon (Liu and Yanai 2002) and Arctic climate (Saito et al. 2001, Gong et al. 2007), but global climate change (Bonan et al. 1992, Yasunari et al. 1991). Especially, the variation in water cycle components in cold regions, containing rainfall, snow cover, soil moisture and frozen ground rich with ice, is a distinctive feature of the continental climate systems and has a delayed and durable influence on the overlying atmosphere through the land-surface fluxes of heat and moisture.

In eastern Siberia, which contains vast areas of permafrost, snow melt water directly contributes to the runoff of large rivers (Peterson et al. 2002, Ye et al. 2004) and evapotranspiration via soil moisture and photosynthesis in boreal forest following snow disappearance (Ohta et al. 2001, Sugimoto et al. 2003). These marked variations in water circulation play important roles in climatic feedback by modifying atmospheric anomalies. Thus, the preceding rain and snow conditions are very important for understanding variations in both the basin- and continental-scale water cycle and the climate system of neighboring regions. For instance, several statistical analyses have demonstrated that the timing of snow disappearance and increasing surface temperature in eastern Siberia is one of the possible candidates for long memory of an atmospheric anomaly from winter arctic oscillation and subsequent summer atmospheric circulation over the East Asia (Ogi et al. 2003, Arai & Kimoto 2005). However, few studies have investigated interactions between snow, permafrost, and climate or interannual variations in permafrost related hydrothermal conditions and water and energy cycle processes during the warm season that are possible effects of land memory in eastern Siberia.

The present study, therefore, aims to examine interseasonal impacts of water cycle components on subsequent land-surface processes, mainly focusing on the relationship between permafrost conditions and hydro-climatic components, such as rainfall in pre-winter, snow depth, snow starting timing in early winter and disappearance timing in spring at Yakutsk area in the central Lena River basin, based on observational meteorological data for recent decades. Our analysis is then extended to reveal the durable relationship and processes between these hydrothermal components influenced on the permafrost conditions and interannual variations in surface energy balance, using detailed land-surface energy balance model simulation.

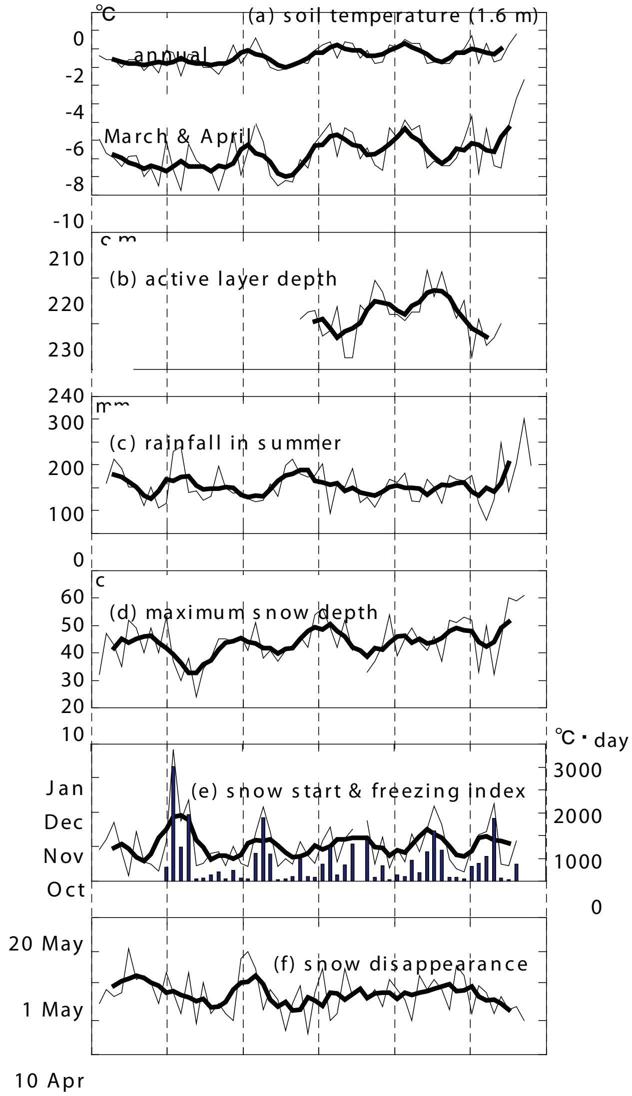

Figure 1. Long-term variations in hydrothermal components; (a) mean annual and minimum (average in March and April) soil temperature at 1.6 m depth at Pokrovsk, (b) active layer depth at Pokrovsk, (c) rainfall amount from July to September at Yakutsk, (d) maximum snow depth at Yakutsk, (e) snow start date with more than 10 cm snow depth (line) and freezing index until the date (bar), and (f) snow disappearance date at Yakutsk from 1950 to 2007. Bold lines denote 5–year running mean.

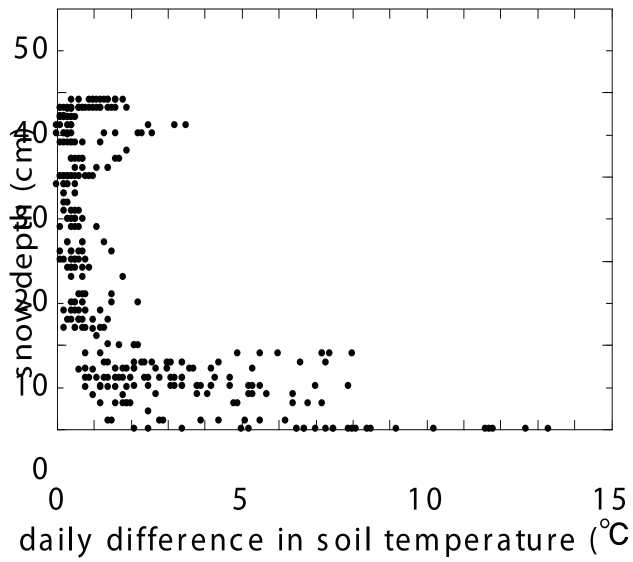

Figure 2. Relationship between daily difference in soil temperature at surface at larch forest site and daily snow depth at Yakutsk from October to December during four winters (2003–2006).

Data and Methods

We used the routine observational data at Yakutsk (62.01°N, 129.43°E) and Pokrovsk (61.48°N, 129.15°E) from a dataset of the Baseline Meteorological Data in Siberia Version 4 (BMDS; Suzuki et al. 2006). The dataset contains daily values of air temperature (°C), precipitation (mm), snow depth (cm) and soil temperature from 40 to 320 cm depth (°C) over a 19-year period (1986–2004). We used soil temperature data at only Pokrovsk since the data at Yakutsk shows strong influences of anthropogenic disturbances. After 2004, daily data was added from a dataset of the NCDC Global Summary of Day up to September 2007. Past data from 1950 to 1985 are added utilizing the Global Summary of Day for daily air temperature, the Global Synoptic Climatology Network of the former USSR (NCDC D9290C) dataset for daily precipitation, the Historical Soviet Daily Snow Depth (HSDSD) dataset for daily snow depth, and Roshydromet station data for monthly soil temperature. Based on the snow depth data, the first date of 0 cm of snow depth in each spring was defined as "snow disappearance date" and the first date of more than 10 cm of snow depth in early winter with lasting snow cover throughout the winter was defined as "snow start date" since this quantity of snow accumulation acts as an effective layer of thermal insulation.

The intensive hydrometeorological observation at larch forest at Spasskaya-pad, Yakutsk, Russia has been ongoing since 1998 by GAME-Siberia project and it continues up to the present. We used several components of the dataset from 1998 to 2007 for the present study. That is, soil temperature in the active layer (0, 0.1, 0.2, 0.4, 0.8, and 1.2 m depth) and volumetric soil moisture content (0.1, 0.2, 0.4, 0.6, and 0.8 m depth).

Before 1998, there is no information on water and energy balance conditions at the larch forest site. Thus, we used estimated surface energy flux calculated by a one-dimensional land surface model (Yamazaki et al. 2004). The model includes three submodels; vegetation, snow cover, and soil. The model divided the canopy into two layers and then represented the fluxes above and within the canopy. The model was applied to the larch forest site at Yakutsk. Daily forcing meteorological quantities of each grid were reconstructed based on the BMDS dataset from 1986 to 2000. Using the daily forcing data, the model simulated hourly water and energy fluxes above and within the forest. The more detailed settings for estimating energy and water flux using the model are documented in Yamazaki et al.

(2007). Yamazaki et al. (2007) demonstrated that the model could reasonably estimate diurnal and seasonal variations in surface energy fluxes at the larch forest.

Results and Discussions

Interannual variations in hydrothermal components

Figure 1 shows interannual variations in hydrothermal components in relation to permafrost conditions at Yakutsk and Pokrovsk sites from 1950 to 2007. Rainfall and snow amounts and variations show hardly any differences between Yakutsk and Pokrovsk.

Soil temperature variation at 1.6m depth indicates decadal fluctuations (Fig. 1a); that is, high temperature peak in 1971, 1981, 1991, and 2000 and low peak in 1966, 1974, 1988, 1994 and 2004. Soil temperatures in March and April at Pokrovsk show annual minimum value contributing to the amplification of the interannual variation in mean annual temperature. The active layer depth calculated by daily soil temperature data at Pokrovsk from 1977 to 2004 (Fig. 1b) has significant positive correlation with mean annual soil temperature ($R = 0.65$, $p < 0.001$). Deeper thawing occurred in early 1980s and early 2000s, corresponding with the warmer soil temperature.

Interannual variation in soil temperature has significant relationship with snow accumulation and its timing rather than rainfall amount in pre-winter (Fig. 1c). Maximum snow depths at Yakutsk (Fig. 1d) range between 15 cm and 50 cm. Basically, years with slow snow depths tend to show a decrease in annual minimum soil temperature ($R = 0.58$, $p < 0.001$). The significant relationship between soil temperature and snow depth indicates that variations in the timing and duration of the seasonal snow cover result in the ground thermal regime during winter (Frauenfeld et al. 2004, Zhang 2005). Snow start date with more than 10 cm of snow depth (Fig. 1e) fluctuates between early October and late January at Yakutsk. As shown in Fig. 2, a decrease in soil temperature is effectively enhanced by the longer duration of shallower snow depth with less than 10 cm during early winter (October to December) at Yakutsk. In fact, a large freezing index until the date with 10 cm of snow depth had significant impacts on the decrease in soil temperature. Namely, years with late timing of snow accumulation have longer and greater freezing intensity so that the soil temperature decreases significantly. It suggests that the thin snow cover has an effective cooling effect on the ground thermal regime when the air temperature is below 0°C until sufficient snow accumulation occurs. Also, soil temperatures tend to sustain cooling anomalies for several years after the large decrease in soil temperatures such as from 1973 to 1976, from 1985 to 1988, from 1994 to 1998, and from 2001 to 2004. During these periods, rainfall in pre-winter as well as snow depth was below average in most of the years. The result implies that durable cooling anomalies likely occurred under dry soil condition.

The snow disappearance date (Fig. 1f) shows relatively short interannual variation between mid-April to early May.

Table 1. Correlation matrix of rainfall, snow timings, soil moisture and soil temperature during 1998 to 2006 at the larch forest site, Spasskaya-pad, Yakutsk.

	Rain autumn	Snow start	Snow disap	Soil moisture	Soil temp
Rain autumn	1.00				
Snow start	−0.18	1.00			
Snow disap	−0.03	0.62	1.00		
Soil moisture	0.87*	−0.80*	−0.35	1.00	
Soil temp	0.38	−0.57	−0.53	0.75*	1.00

(*: $p < 0.05$)

Rain autumn – rainfall amount in pre-winter (July–September); Snow start – snow start date in previous year; Snow disp. – snow disappearance date; Soil moisture – volumetric soil moisture at 0–40cm depth in July and August; Soil temp. – soil temperature at 120 cm depth in July and August.

There is no significant relationship with maximum snow depth ($R = 0.20$, ns). According to Iijima et al. (2007) and Gong et al. (2007), the snow disappearance mainly depends on the atmospheric warming. The snow disappearance dateclosely relate with the date of soil thawing from surface to 80 cm depth at Pokrovsk, although no significant relationship with active layer depth which appears in September. It appears that the snow disappearance timing affects the soil thawing near the surface and also the soil moisture melting which directly affect evapotranspiration from vegetated surface.

Figure 3 shows interannual variations in soil temperature and soil moisture at the larch forest site in Spasskaya-pad near Yakutsk during 1998 through 2007 and variations in snow depth and snow start and disappearance date at Yakutsk. It is found that both soil temperature during wintertime (which indicates intensity of freezing) and soil moisture content at the beginning of warm season show simultaneous interannual variations. That is, there are warmer and wetter years in 2000, 2005, and 2006, while colder and drier years in 1998, 2003, and 2004. Table 1 demonstrates a correlation matrix between rainfall in pre-winter (from July to September), snow start date in previous winter, snow disappearance date, soil temperature and moisture in summer. As described above, it appears that there is a significant correspondence in interannual variation between soil temperature and soil moisture. It implies that thermal condition in active layer is strongly connected with hydro-climatic variations. In addition, rainfall in pre-winter has strong correlation with soil moisture in next summer. It appears that rainfall remains in the active layer through winter and possibly acts as climatic memory of soil moisture. Moreover, both snow start and disappearance timings have negative correlations with soil temperature and moisture. It might be suggested that snow start timing determines intensity of freezing in active layer during early winter, and wet condition during winter also affects soil freezing.

As shown in long-term variation in soil temperature at Pokrovsk, interannual warming and cooling trends are found at the larch forest site. These trends in successive years are basically due to the similar snow and rainfall conditions. These continuous hydro-climatic conditions may maintain

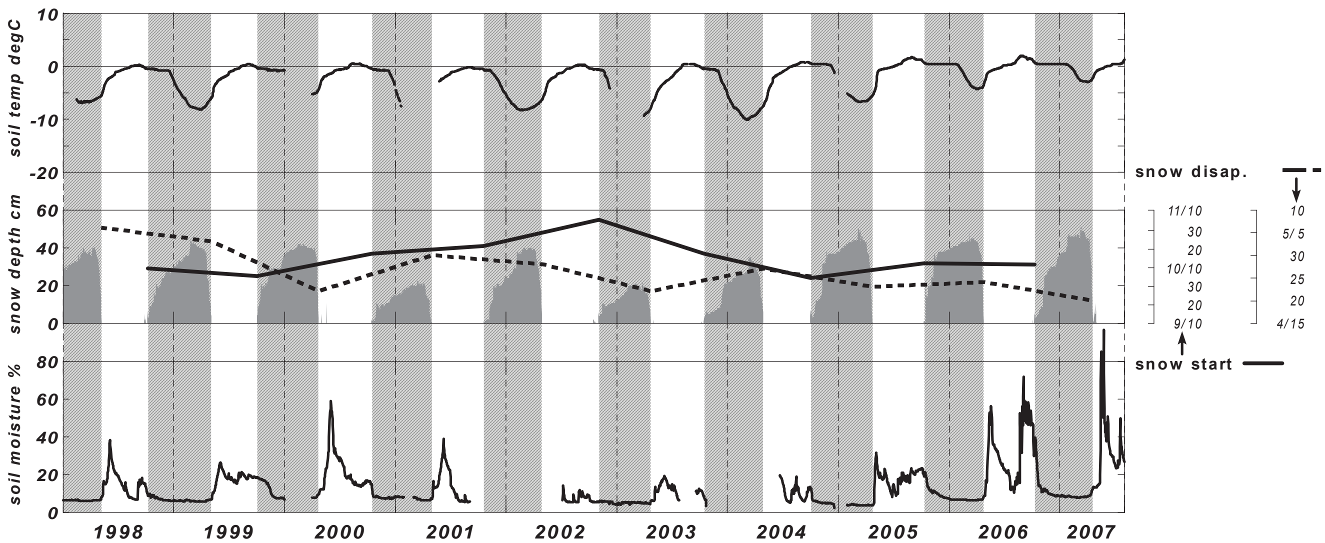

Figure 3. Nine-year (1998–2007) variation in (a) soil temperature, (b) snow depth, and (c) soil moisture. Soil temperature (120 cm depth) and soil moisture (10 cm depth) were observed at larch forest site in Spasskaya-pad, Yakutsk. Snow depth was observed at Yakutsk. Bold and dotted lines denote snow start date and snow disappearance date, respectively. Dark area denotes snow cover period in each winter.

the trend of previous soil temperature anomalies through reemergence in deeper soil layer through soil moisture anomalies (Schaefer et al. 2007).

Snow timing and evapotranspiration in spring

Estimated monthly average of latent heat flux above the larch forest canopy from 1986 to 2000 and its standard deviation are shown in Figure 4. Annual maximum appears in June or July due to the maximum activity of evapotranspiration from the forest. Interannual variation in latent heat flux is less variable in comparison with variation in precipitation. This tendency was recently confirmed by eight-year (from 1998 to 2006) variation in energy flux above the larch forest canopy at the same station based on micro-meteorological observation (Ohta et al. 2006). Though there is a small variation in latent heat flux, the maximum variation appears in May with the largest standard deviation (±6 Wm^{-2}).

Figure 5 shows the relationship between estimated latent heat flux in May normalized by net radiation above the larch forest canopy by the model and both snow starting date in previous winter and snow disappearance date from 1986 to 2000. It appears that both timings have significant negative correlations (snow start date: R = -0.76, p < 0.01, snow disappearance date: R = -0.59, P < 0.05). The relationship with snow disappearance date directly corresponds to the beginning of transpiration since the timing of soil warming after snow disappearance determines foliating of plants at forest floor and trees and also determines timing of soil thawing for supplying plant available soil moisture, which parameterized in the model (Yamazaki et al. 2007). On the other hand, the significant relationship with snow start date in previous winter suggests that the warmer (cooler) anomaly of soil temperature during winter remains until

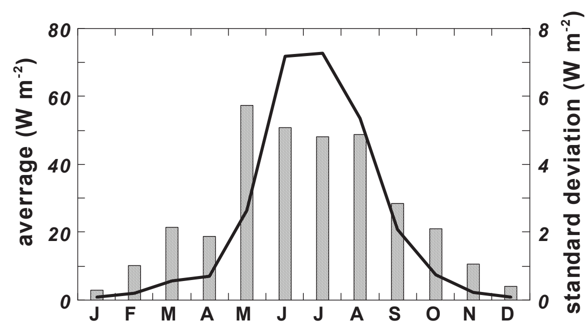

Figure 4. Monthly average and standard deviation of latent heat flux above the canopy at larch forest from 1986 to 2000 simulated by one-dimensional land surface model.

snow disappearance and also cause the earlier (later) timing of soil thawing. Thus, the relationship implies that soil temperature modulated by snow timing strongly influence the evapotranspiration processes in the early growing season.

Figure 6 exhibits the difference of hydrothermal conditions (mainly years with either high or low latent heat fluxes in May) from the difference between the average of the four high years (low years) and the average of the four prior years (same). These values were averaged using each four years (high years: 1990, 1992, 1994, and 2000; low years: 1987, 1989, 1995, and 1998) and the preceding four years in each case. The difference in latent heat flux in May between high and low years exceeds 10 W m^{-2} (Fig. 6a). Snow depth difference is apparent during snow disappearance timing (Fig. 6b). Namely, earlier melting appears in high years. Inversely, snow start timing in early winter shows earlier snow accumulation in high years. In addition, deeper snow depth appears during the winter two years ago. During the previous

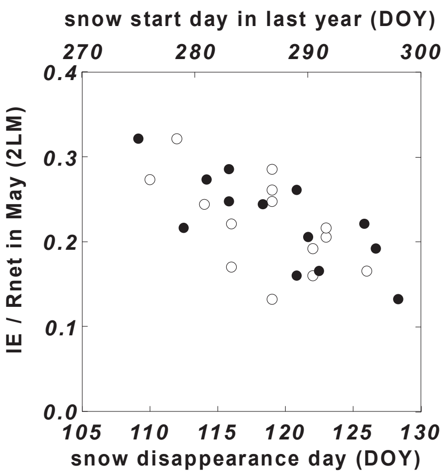

Figure 5. Relationship between snow timings and estimated mean monthly evapotranspiration ratio (latent heat/net radiation). Open and solid circles denote snow start date and snow disappearance date, respectively.

warm season, rainfall in the high years is larger than in low years (Fig. 6c). Due to the large difference in snow depth in the winter two years ago and earlier snow accumulation in previous winter, soil temperature shows large difference during the successive two winters (Fig. 6d). It should be noted that the warmer temperature continuously lasts throughout two years in deeper layer. These durable warming tends to enhance earlier thawing of frozen layer (Fig. 6e). Thus, it might be earlier start of evapotranspiration due to earlier soil moisture supply. Ohta et al. (2006) exhibited that there was a remarkable positive relationship between surface soil moisture and annual amounts of evapotranspiration. They also implied that the effects of snowfall from previous cold seasons and the permafrost conditions affect soil moisture into subsequent growing season and are important to the interannual variations in evapotranspiration.

Conclusions

The present study investigates climatological features of hydrothermal components in the Yakutsk region and its relationship with evapotranspiration during subsequent warming season. The results of the present study are summarized as follows:

1. Long-term variation in soil temperature at Pokrovsk indicates decadal fluctuations and has significant relationship with snow accumulation and its timing. The drier climate with later snow accumulation may produce an anomaly of lower soil temperature and thus shallower active layer.
2. There is a significant correspondence in interannual variation between soil temperature and soil moisture at the larch forest site. In addition, both snow start and disappearance dates have negative correlations with them.
3. Both snow start in previous winter and snow disappearance have significant negative correlation with latent heat flux from the boreal forest in May simulated by a one-dimensional land surface model associated with the start of subsequent plant growing season.

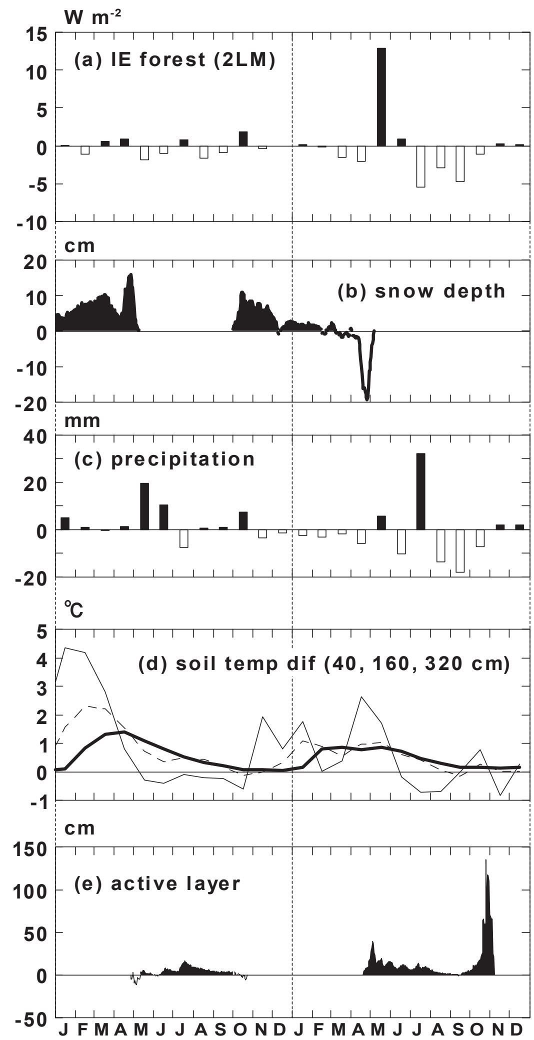

Figure 6. Differences of hydrothermal conditions for the average of the four highest years and the average of the previous for years for high evapotranspiration in May (left panel) and the same for low evapotranspiration in May (right panel); (a) latent heat flux from forest canopy by one-dimensional land surface model, (b) daily snow depth at Yakutsk, (c) monthly rainfall at Yakutsk, (d) monthly soil temperature at 40 cm (thin line), 160 cm (broken line), and 320 cm (bold line) depths at Pokrovsk, and (e) daily thawing depth at Pokrovsk.

Acknowledgments

We extend our appreciation to Prof. B. Ivanov of the Institute for Biological Problems of Cryolithozone for allowing us the opportunity to investigate in Siberia. This work was financially supported by Institute of Observational Research for Global Change, Japan Agency of Marine-Earth Science and Technology.

References

Arai, M. & Kimoto, M. 2005. Relationship between springtime surface temperature and early summer blocking activity over Siberia. *Journal of Meteorological Society of Japan* 83: 261-267.

Bonan, G. B., Pollard, D. & Thompson S. L. 1992. Effects of boreal forest vegetation on global climate. *Nature* 359 (6397): 716-718.

Frauenfeld, O.W., Zhang, T. & Barry R.G. 2004. Interdecadal changes in seasonal freeze and thaw depths in Russia, *Journal of Geophysical Research* 109: D05101, doi:10.1029/2003JD004245.

Gong, G., Cohen, J., Entekhabi, D. & Ge, Y. 2007. Hemispheric-scale climate response to Northern Eurasia land surface characteristics and snow anomalies. *Global and Planetary Changes* 56: 359-370.

Iijima, Y., Masuda, K. & Ohata, T. 2007. Snow disappearance in Eastern Siberia and its relationship to atmospheric influences. *International Journal of Climatology* 27: 169-177.

Liu, X, & Yanai, M. 2002. Influence of Eurasian spring snow cover on Asian summer rainfall. *International Journal of Climatology* 22: 1075-1089. doi:10.1002/joc.784.

Ogi, M., Tachibana, Y. & Yamazaki, K. 2003. Impact of the wintertime North Atlantic Oscillation (NAO) on the summertime atmospheric circulation. *Geophysical Research Letter* 30(13): 1704. doi:10.1029/2003GL017280.

Ohta, T., Hiyama, T., Tanaka, H., Kuwada, T., Maximov, T. C., Ohata, T. & Fukushima, Y. 2001. Seasonal variation in the energy and water exchanges above and below a larch forest in eastern Siberia. *Hydrological Processes* 15: 1459-1476.

Ohta, T., Kuwada, T., Dolman, H., Moors, E., Maximov, T. C., Kononov, A.V. & Yabuki, H. 2006. Interannual variation in water and energy exchanges at a larch forest in Spasskaya Pad, eastern Siberia. *International Workshop on H_2O and CO^2 Exchange I Siberia:* 67-70.

Peterson, B.J., Holmes, R.M., McClelland, J.W., Vorosmarty, C.J., Lammers, R.B., Shiklomanov, A.I., Shiklomanov, I.A. & Rahmstorf, S. 2002. Increasing river discharge to the Arctic Ocean. *Science* 298: 2171-2173.

Saito, K., Cohen, J. & Entekhabi, D. 2001. Evolution of atmospheric response to early-season Eurasian snow cover anomalies. *Monthly Weather Review* 129(11): 2746-2760.

Schaefer, K.M., Zhang, T., Tans, P.P. & Stockli R. 2007. Temperature anomaly reemergence in seasonally frozen soils. *Journal of Geophysical Research* 112: D20102, doi:10.1029/2007JD008630.

Sugimoto A., Naito, D., Yanagisawa, N., Ichiyanagi, K., Kurita, N., Kubota, J., Kotake, T., Ohata, T., Maximov, T.C. & Fedorov, A.N. 2003. Characteristics of soil moisture in permafrost observed in East Siberian taiga with stable isotopes of water. *Hydrological Processes* 17: 1073-1092.

Suzuki, R., Razuvaev, V.N., Bulygina, O.N. & Ohata, T. 2006. *Baseline Meteorological Data in Siberia Version 4.* Institute of Observational Research for Global Change, Japan Agency for Marine-Earth Science and Technology, Yokosuka, Japan.

Yamazaki, T., Yabuki, H., Ishii, Y., Ohta, T. & Ohata, T. 2004. Water and energy exchanges at forest and a grassland in Eastern Siberia evaluated using a one-dimensional land surface model. *Journal of Hydrometeorology* 79: 1107-1118.

Yamazaki, T., Ohta T., Suzuki R. & Ohata T. 2007. Flux variation in a Siberian taiga forest near Yakutsk estimated by a one-dimensional model with routine data, 1986–2000. *Hydrological Processes* 21: 2009-2015, doi:10.1002/hyp.6708.

Yasunari, T., Kitoh, A. & Tokioka, T. 1991. Local and remote responses to excessive snow mass over Eurasia appearing in the northern spring and summer climate – a study with the MRI GCM. *Journal of the Meteorological Society of Japan* 69: 473-487.

Ye, H., Yang, D., Zhang, T., Zhang, X., Ladochy, S. & Ellison M. 2004. The impact of climatic conditions on seasonal river discharges in Siberia. *Journal of Hydrometeorology* 5: 286-29

Zhang, T. 2005. Influence of the seasonal snow cover on the ground thermal regime: An overview. *Reviews of Geophysics* 43: RG4002, doi:10.1029/2004RG000157.

Topographical Controls on the Distribution and Size of Rock Glaciers in the Central Brooks Range, Alaska

Atsushi Ikeda
Graduate School of Life and Environmental Sciences, University of Tsukuba
Kenji Yoshikawa
Water and Environmental Research Center, University of Alaska Fairbanks

Abstract

Distribution, morphology, internal structure and thermal conditions of rock glaciers were studied in the central Brooks Range, Alaska, an area characterized by continuous permafrost. A positive size correlation was found between the active talus-derived rock glaciers and the source rock walls. The source rock walls of the inactive rock glaciers were limited to a relatively small size. These topographical relationships indicate that direct debris supply from the rock walls at least partly controls the size and activity of these rock glaciers. On six talus-derived rock glaciers, low mean annual ground surface temperatures (-3°C to -7°C) were monitored, and similar low ice content was indicated by DC resistivity measurements. The results approve the interpretation of the topographical analysis based on the assumption that a number of rock glaciers have similar creep property and composition. In contrast, rock glaciers interacting with glacial processes enlarged below the relatively small rock walls.

Keywords: Brooks Range; continuous permafrost; DC resistivity; GIS; rock glacier; rock wall.

Introduction

Distribution, size, and structure of rock glaciers probably reflect the complex input of debris, ground water, and snow which is controlled by local climate and geology. Rock glaciers have been often classified into active and inactive types to discuss the climatic and geological factors that control their long-term movement (e.g., Wahrhaftig & Cox 1959, Calkin et al. 1987, Ikeda & Matsuoka 2002). Active rock glaciers are moving downslope by internal ice deformation. Inactive rock glaciers are stagnant but still contain ice. Barsch (1992) suggested two kinds of inactivity: climatic and dynamic. The melting of ice in a rock glacier accounts for climatic inactivity. Dynamic inactivity results from reducing shear stress within the perennially frozen layer in a rock glacier, which is caused either by a temporal decrease in debris supply or by a downslope decrease in slope gradient. In continuous permafrost areas, where climatic inactivation rarely occurs, the inactivation of rock glaciers has been attributed to the dynamic concept (e.g., Calkin et al. 1987, Solid & Sørbel 1992).

Although size relationships between rock glaciers and their debris source (i.e., rock walls) have indicated quantitative rates of debris production and transportation in mountainous periglacial environments (e.g., Barsch 1977, Barsch & Jakob 1998, Humlum 2000), debris supply has been rarely explored to discuss the size and activity of rock glaciers (cf. Frauenfelder et al. 2003). A topographical analysis by Frauenfelder et al. (2003) indicated that the size of rock glaciers appears to reflect the temperature conditions rather than the size of the debris source. In addition, variable ice content in rock glaciers should be tested further to discuss this matter (Humlum 2000).

In this study the distribution and size of rock glaciers near Atigun Pass in the central Brooks Range, Alaska, were re-examined using recent technologies (see also

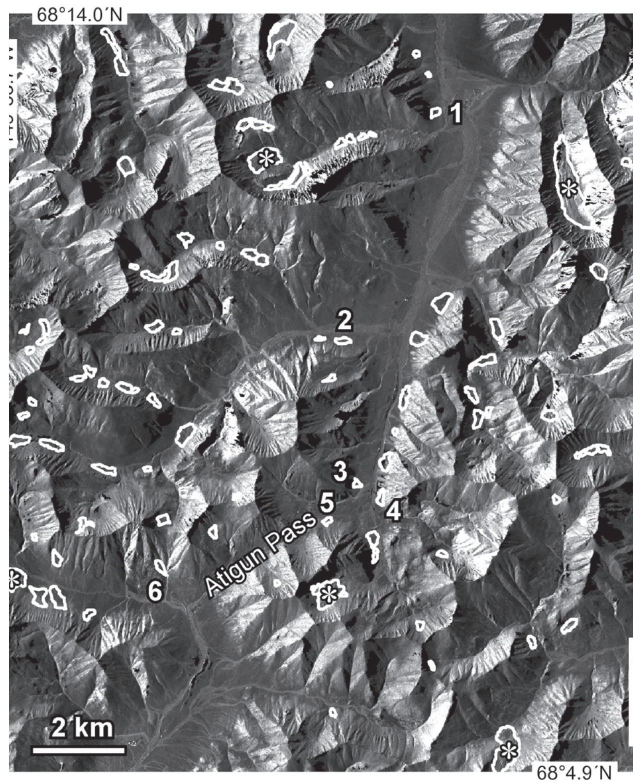

Figure 1. Distribution of rock glaciers (outlined in white) in the Atigun Pass area. An asterisk indicates a rock glacier overflowing from a cirque. The numbered rock glaciers underwent geophysical measurements.

Calkin et al. 1987, for the previous achievement), because the area characterized by simple geology and ubiquitous permafrost appeared suitable for testing 'dynamic' controls from topographical analysis. In addition, temperature conditions and internal structure were studied to assist in the

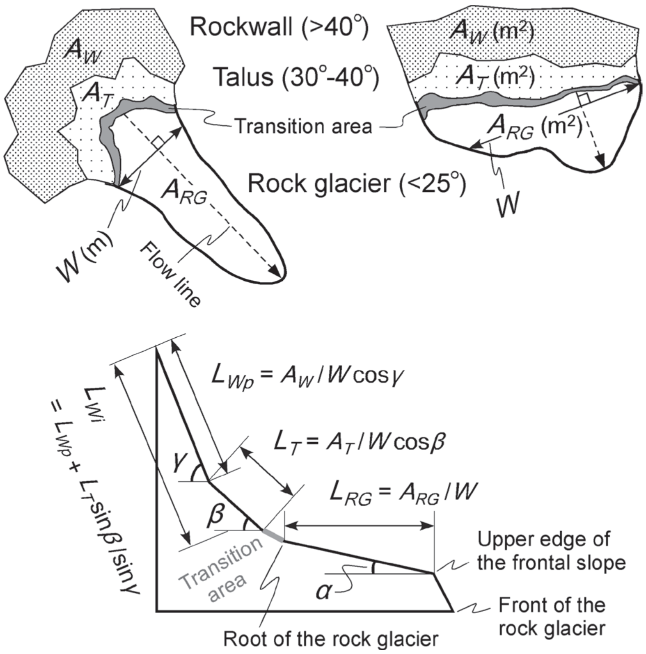

Figure 2. Definition of morphological parameters discussed in the text. Upper figures are plan views and lower figure is a cross section.

interpretation of the topographical analysis.

Atigun Pass lies on the continental divide between the Yukon Basin and Arctic basins (Fig. 1). Permafrost continuously underlies the study area having low mean annual air temperature (MAAT < -7°C) and low precipitation (400–700 mm a^{-1}). Cirque glaciers only remain on the north-facing slopes below the highest peaks ,which reach 2000 m above sea level (a.s.l.), whereas the area was mostly covered with glaciers until the Late Glacial (Hamilton & Porter 1975, Ellis & Calkin 1979). The area consists of sandstone or conglomerate, interbedding shale. The methods of this study are mapping on a digital elevation model (DEM), temperature monitoring on the ground surface and one- and two-dimensional (1D and 2D) geoelectrical resistivity measurements.

Distribution and Morphology

Mapping and measurement of terrain parameters

Using GIS software (ArcGIS ver. 9.2, ESRI Inc., USA), the distribution of rock glaciers was traced on 10 m grid DEM. Topographical parameters assumed to represent climatic and mechanical conditions of rock glaciers (altitude, length, slope angle, area, etc.) were measured for 99 rock glaciers which were clearly identified in 1/63,000 aerial photographs in a selected 13.8 km × 16.5 km area (Fig. 1). The areas of a source rock wall and a talus slope were unambiguously defined by the slope angle: a slope steeper than 40° as a rock wall and a slope between 30° and 40° as a talus slope. A relatively short slope 25°–30° below a talus slope indicated sedimentation by debris flows and avalanches; transportation by permafrost creep can also be responsible for such slope relaxation. Thus, the uppermost point of a slope gentler than 25° was defined as the root of a rock glacier. Besides the 99 rock glaciers, two rock glaciers developed from conspicuous terminal moraines in the selected area. Both of them were excluded from the measurements because they had no direct connection with the cirque walls.

The measured parameters for a rock glacier were: along the central flow line, the altitudes at the upper and lower ends (i.e., root and front), altitude of the upper edge of the frontal slope, horizontal length and aspect of the front (Fig. 2). Horizontal width (W) at the root and horizontal area (A_{RG}) were also measured. The average slope angle of the upper surface (α) was calculated from the horizontal length and the altitudes at the root and edge, and the average length (L_{RG}) from W and A_{RG}. The measured parameters for a source slope were the horizontal areas of the source rock wall (A_W) and the underlying talus slope (A_T), and the average angles of the talus slope (β) and the rock wall (γ). The present size of a source rock wall was represented by the average length of a source rock wall (L_{Wp}), which is A_W normalized by W (see Fig. 2). In addition, the average length of an initial source rock wall after the deglaciation (L_{Wi}) was roughly estimated from the average length of the underlying talus slope (L_T), which probably buried the lower part of the initial rock wall (see Fig. 2 for the calculation of L_{Wi}). Additional data on altitudes and aspect were obtained from 61 rock glaciers around the selected area.

The activity status of rock glaciers (i.e., active or inactive) must be determined by repeated geodetic surveys in the strict sense (Roer & Nyenhuis 2007). In many studies, however, the activity status has been presumed from visual features (e.g., Wahrhaftig & Cox 1959, Calkin et al. 1987, Ikeda & Matsuoka 2002). In this study, rock glaciers having a frontal slope steeper than 35° were classified into the active type and those having a frontal slope gentler than 35° into the inactive type. According to Ikeda & Matsuoka (2002), this classification mostly guarantees the inactive type, although the rock glaciers classified into the active type inevitably include some inactive rock glaciers (see also Roer & Nyenhuis 2007). If a frontal slope mostly steeper than 35° showed partly subsided form (i.e., having a much gentler and thinner part) and a rounded upper edge, the rock glacier was tentatively classified into the active/inactive type. In addition, two rock glaciers were also classified into the active/inactive type, because of the significant disagreement between the steep frontal slopes (c. 10 m high) on the aerial photographs and the gentle angles calculated from the DEM.

Distribution

The rock glaciers in the selected area were classified into 44 active, 40 inactive, and 15 active/inactive rock glaciers. The fronts of the rock glaciers were distributed in all aspects over elevations between 970 m a.s.l. and 1730 m a.s.l. (Fig. 3). The roots of the rock glaciers had a distribution pattern similar to the fronts, ranging between 1015 m a.s.l. and 1835 m a.s.l. The source rock walls mostly faced the same direction as the rock glaciers, whereas the sources of large rock glaciers often faced several directions. The upper limit of the distribution was 100–200 m lower than the major mountain ridges, and on the north-facing slopes it corresponded to

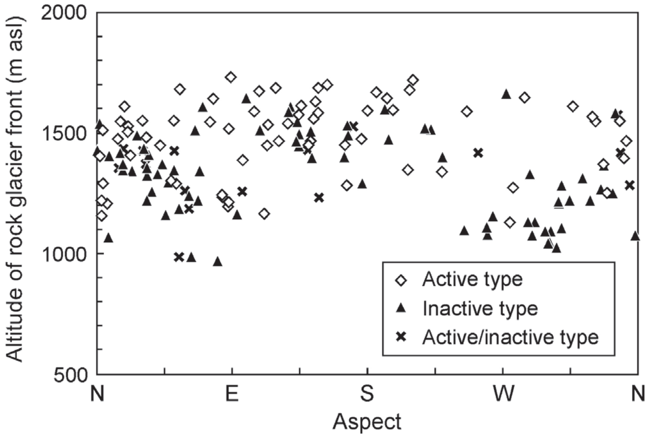

Figure 3. Distribution of the fronts of rock glaciers in the Atigun Pass area.

the present glacial equilibrium line. The lower limit of the distribution corresponded to the piedmont line. The active rock glaciers were distributed at relatively higher altitudes than the inactive rock glaciers, whereas the distributions were largely overlapping except for the west-facing slopes.

Sizes of rock glacier and source rock wall

The topographical parameters were analyzed in terms of the following concepts. The deformation of a rock glacier can be represented by the density, acceleration by gravity, thickness, sine of slope angle, and a creep parameter depending on temperature and structure, using a pseudoplastic flow law for glacier ice (e.g., Wagner 1992). In addition, the long-term (i.e., more than several hundred years) deformation has been assumed to result in a certain length of the rock glacier balancing with debris supply (Olyphant 1983, 1987, Haeberli et al. 1999).

In this study, the L_{RG} values were compared with the L_W (i.e., L_{Wi} or L_{Wp}) values. This was because the size of the rock walls was preliminarily assumed to mainly control the rate of debris supply (determining the thickness of the rock glacier under the balancing condition), although the rate reflected various conditions of the rock wall, such as size, strength, temperature variation, and water content. The assumption was made because parameters other than size were too difficult to evaluate on a large number of rock walls.

The active rock glaciers showed a linear relationship between L_W and L_{RG}, if large rock glaciers overflowing from a cirque were excluded (Fig. 4). In contrast, such a relationship was lacking for inactive rock glaciers. Even larger inactive rock glaciers (L_{RG} > 200 m) had small L_W values. This pattern was more distinct in the L_{Wp}–L_{RG} diagram than that of L_{Wi}–L_{RG}, because the ratios of L_{Wi} to L_{Wp} were, on average, 2:1 for the active type and 3:1 for the inactive type. This indicated the thickening of the talus slopes above the inactive rock glaciers.

The three longest rock glaciers (L_{RG} = 950, 1140 m and 1680 m), all of which overflowed from a cirque, are not within Figure 4a. The longest one was active and had a huge source (L_{Wi} = 2840 m and L_{Wp} = 1940 m); the others were inactive or active/inactive and had relatively small sources (e.g., L_{Wi} = 800 m and 1160 m). Such rock glaciers probably

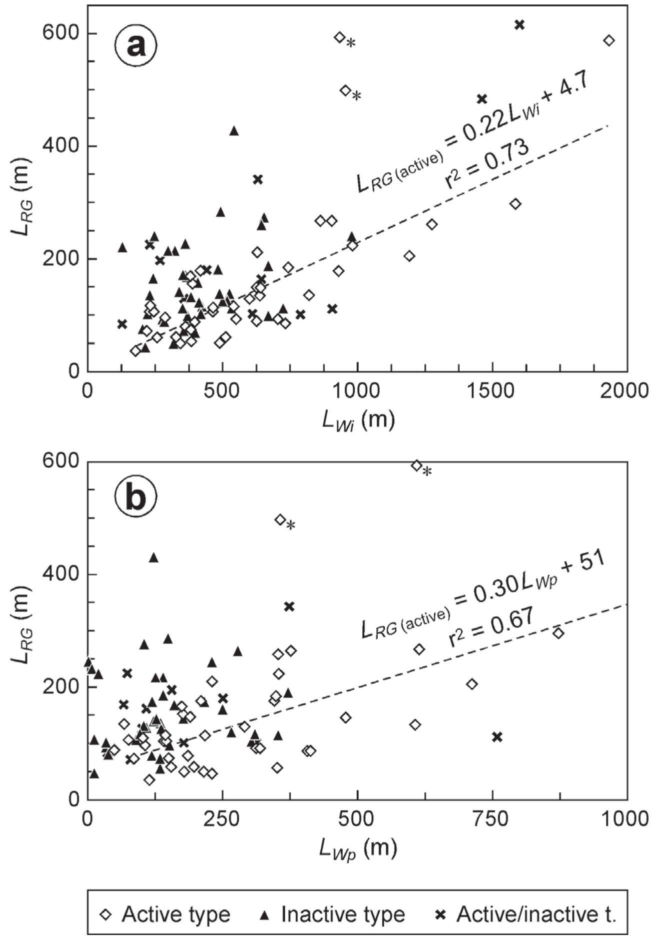

Figure 4. Relationship between average lengths of source rock walls (L_W) and rock glaciers (L_{RG}). Lengths of (a) initial rock walls (L_{Wi}) and (b) present rock walls (L_{Wp}) are examined. See Figure 2 for definition of parameters. *Data of rock glaciers overflowing from a cirque.

included significant amounts of debris that had once deposited as moraines. In addition, glacial ice was often observed at the roots of such large rock glaciers in the active status, which originated from altitudes close to the glacial equilibrium line (Calkin et al. 1987).

The upper surface of the rock glaciers sloped from 2° to 25°. The ranges of α were almost equal between the active type (12° ± 4°) and inactive type (13° ± 4°). The α values of the rock glaciers longer than 400 m also ranged from 8° to 15°. Thus, slope angle appeared to be a minor factor for inactivation and outgrowing.

Temperature and Internal Structure

Ground surface temperature

Ground surface temperatures were monitored on six rock glaciers (A1–6) using miniature data loggers, Thermo Recorder TR-51A (T & D, Japan) (see Fig. 1 for the location). On five rock glaciers (A1–4, A6), a data logger was placed at the surface that was 30–40 m distant from the upper edge of the frontal slope in mid May 2005. A data logger was also placed near the talus foot on A5 rock glacier in late August

Table 1. Mean annual ground surface temperature (MAGST) and DC resistivity stratigraphy of rock glaciers. ρ = calculated resistivity, D = depth of the layer base and AB/2 = half length of the sounding profile (roughly equal to the maximum depth of the sounding). Frontal altitude and aspect for each rock glacier are also displayed.

Site	Altitude	Aspect	MAGST	DC resistivity stratigraphy					
				First layer		Second layer		Third layer	AB/2
	(m a.s.l.)	(degree)	(°C)	ρ (kΩm)	D (m)	ρ (kΩm)	D (m)	ρ (kΩm)	(m)
A1	970	80	−5.1 ± 0.4	8.4–1.6	3.0	25	19	0.22	50
A2	1065	5	−3.3 ± 0.4	0.3	0.7	52	35	20	100
A3	1165	110	−3.6 ± 0.2	1.3	2.7	38			64
A4	1155	265	−6.6 ± 0.3	0.8	1.6	19			80
A5	1345	15	−4.8 ± 0.3	1.1	2.8	41			50
A6	1230	145	−3.9 ± 0.3	0.8	2.2	24	16	13	64

2005. These loggers recorded surface temperatures under a 2–4 cm thick clast at one-hour intervals with a resolution of 0.1°C until the beginning of July 2007. Then, the mean annual ground surface temperature (MAGST) values were determined.

The lack of daily variations in the ground surface temperatures indicated that snow covered the lower part of the rock glaciers from late September to mid May, whereas snow remained near the north-facing talus foot at 1350 m a.s.l. until mid June. The variations in the observed winter temperatures were largely different between the sites. The difference in the temperatures, however, hardly correlated with the elevation of the sites (see Table 1 for the altitudes), which implied irregular distribution of snow cover. As a result, MAGST on the rock glaciers ranged from −3°C to −7°C without correlation with the elevation (Table 1).

DC resistivity

On the six rock glaciers (A1–6), 1D DC resistivity measurements were performed in late July 2005 with the SYSCAL R1 resistivity meter (Iris Instruments, France). All of the rock glaciers were talus-derived and had no contact with glaciers during the Holocene (Ellis & Calkin 1979). The setting of the electrodes followed the Schlumberger array. Modeled resistivity curves fitting with measured values were calculated with WinSev6 software (W_GeoSoft, Switzerland). To compare resistivity stratigraphies, the settings of the inversion analysis were fixed as described in Ikeda (2006). In addition, 2D DC resistivity distributions at a shallow depth (<10 m deep) were estimated by a tomographical method for three rock glaciers (A3–5). The electrode configuration followed the Wenner array. The measurements were carried out with a lightweight resistivity meter, Handy-ARM (OYO, Japan), in early July 2007. Then, we computed the 2D distributions of modeled DC resistivities with RES2DINV software (Geotomo Software, Malaysia), employing the same settings of the inversion analysis as those in Ikeda & Matsuoka (2006).

The 2D resistivity distributions showed low resistivities (1–16 kΩm) within the uppermost layer (<2 m deep), probably corresponding to the active layer. The resistivities near the surface in the 1D profiles, which largely depend on the surface material at the center of the survey profiles, were close to 0.3 kΩm on A2, 1 kΩm on A3–6 and 8 kΩm on A1 (Table 1). Vegetated thin soil on the surface resulted in such low surface resistivities for rock glaciers, because the shale part of the source rock walls produced relatively fine and weathering-susceptible clasts on the rock glaciers. The main components of the debris, however, appeared to be boulders. In fact, the average intermediate-axis diameter of 25 clasts that were measured at intervals of 0.5 or 1 m along a line on a less vegetated part ranged from 25–45 cm for A3–5 rock glaciers (cf. pebbly rock glaciers composed of much smaller debris in Ikeda & Matsuoka 2006).

The resistivities of the layers below 2–3 m deep (i.e., permafrost) were 20–50 kΩm in the 1D profiles (Table 1), whereas those in the 2D distributions increased from 4–16 kΩm at 3 m depth to 30–250 kΩm at 10 m depth. In the case of A4, the exponentially increasing resistivities toward the bottom of the tomogram indicated resistivities higher than 250 kΩm for the permafrost below the measurement limit. The 1D sounding profiles of A3–5 were too short to detect the third layer.

Discussion and Perspectives

Topographical controls through debris supply

Topography of the mountain range roughly restricts the distribution of the rock glaciers. Besides the main divide and piedmont line of the mountain range (i.e., the uppermost and lowermost limits of the distribution), for example, the straight mountain slopes that lack enough concavity to lay rock glaciers strongly restricted the number of westbound rock glaciers above 1300 m a.s.l. (see Fig. 3). In the selected area, the area of the rock walls decreased from 8.8 km^2 on the north-facing slope (0°–45°, 315°–360°) to 3.7 km^2 on the south-facing slope (135°–225°), which may result in fewer rock glaciers on the south-facing slopes through less debris production from the rock walls (see Fig. 3).

The positive correlation between L_{RG} and L_W for the (talus-derived) active rock glaciers (Fig. 4) implies that the amounts of debris supply from the source rock walls control the size of these rock glaciers. This result is contrasted with that of a similar study in the Alps where such a relationship is unclear (cf. Frauenfelder et al. 2003). The correlation in this study partly accounts for the bedrock geology that is much more uniform than the case in the Alps. In fact, such a correlation was found in the Alps for a small number of rock glaciers under a limited geological condition (Ikeda & Matsuoka 2006).

In Figure 4, the L_{RG} values of the extremely long rock glaciers (overflowing from a cirque) are out of the linear trends for the active talus-derived rock glaciers. The lengths that appear not to balance with the relatively small rock walls are primarily attributed to former glacial deposits, which were probably incorporated into these rock glaciers. In addition, if these rock glaciers include glacial ice, the resulting high ice content also contributes to the large size in spite of low debris content. According to the field observation by Calkin et al. (1987), such interaction with glaciers probably occurred on large tongue-shaped rock glaciers in this area.

About two thirds of the data on the inactive rock glaciers (mostly shorter than 200 m) is plotted within the band of the talus-derived active type in the LW–LRG diagrams (Fig. 4). Thus, the difference in the classified activity is difficult to interpret from the size of the source rock walls alone. The LW values of the inactive rock glaciers, however, concentrate in relatively smaller values, which indicates the low potential of the debris supply. The talus thickening above the inactive rock glaciers, which was presumed from the difference in Figures 4a and 4b, is partly because the debris down-transportation by permafrost creep was terminated at the talus foots. This burial of the rock walls with the talus materials decreases the potential of the debris supply from the rock walls. The resulting small input of debris probably prevents the underlying rock glaciers from advancing further, although the initial cause of the inactivation remains unsolved.

As well as the data on the largest rock glaciers that were probably affected by glacial processes, the data on the large inactive and active/inactive rock glaciers (> 150 to 200 m in L_{RG}) in Figure 4 appear not to balance with the size of the source rock walls. This may indicate that the former rate of rock wall erosion per area was higher, or the present source slopes became smaller than the former slopes. Both processes can be responsible for the inactivation of the rock glaciers through decrease in debris supply, although we should exhibit additional data to discuss this matter, avoiding a vicious circle.

Significance of topographical controls in the Brooks Range

The inactivation and restriction of the lower distribution boundary found in Figure 3 cannot reasonably be attributed to the degradation and absence of permafrost in a study area that is classified continuous permafrost, although such phenomena mainly depend on the permafrost distribution and its temporal change in mid-latitude high mountains such as the Alps (e.g., Frauenfelder et al. 2001, Ikeda & Matsuoka 2002).

Additionally, Frauenfelder et al. (2003) found correlation between the length and velocity of active rock glaciers. The latter depended on the MAAT, which was estimated from the locality and altitude for each site, rather than the source area and slope angle. This is mainly because frozen ground softens significantly as the permafrost temperature increases in warm permafrost environments (MAAT > -4°C). In contrast, the dependence of velocity on temperature was insignificant in cold environments (MAAT < -7°C) such as the Brooks Range (Kääb et al. 2007). The MAGST, much lower in the Brooks Range than in the Alps (Fig. 5), also indicates that the creeping depth (mostly within a few tenth meters in depth) of the studied rock glaciers is much lower than the melting point in contrast to the case in the Alps (cf. Arenson et al. 2002). Thus, the difference in a creep parameter between the rock glaciers in the study area is assumed to be much smaller than that in the Alps. This means that in the Brooks Range the effect of debris supply on the size of rock glaciers can be tested using the L_W–L_{RG} diagrams without one major source of noise.

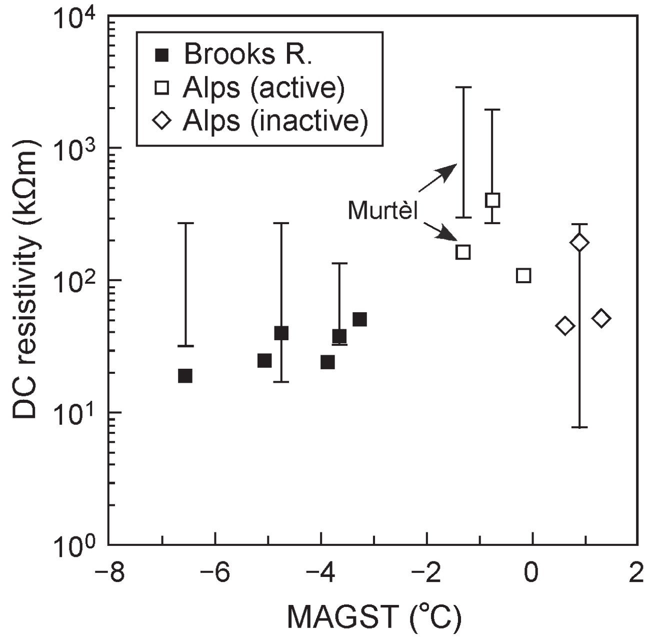

Figure 5. Relationship between MAGST and DC resistivity at 5–9 m depth in the Brooks Range and Swiss Alps. Resistivities from a one-dimensional method are indicated by symbols and ranges of resistivities from a two-dimensional (2D) method by bars. The data in the Alps are from Ikeda (2006) and Ikeda & Matsuoka (2006), except for the 2D data of the Murtèl site from Hauck (2001).

To examine the ice content of the studied talus-derived rock glaciers, the relationship between MAGST and DC resistivity of permafrost (5–9 m deep) of the rock glaciers is displayed with the data of typical talus-derived rock glaciers in the Alps in Figure 5. The DC resistivities from the 1D measurement in the Brooks Range (10–50 kΩm) are lower and less scattered than those in the Alps (50–400 kΩm). The absolute values of the resistivities derived from the 2D measurements are also within the smaller ranges in the study area than in the Alps. These results imply that the ice content in the studied rock glaciers is relatively small for rock glaciers, and the variation in ice content between different rock glaciers is also smaller than that in the Alps (see Haeberli & Vonder Mühll 1996, Hauck & Vonder Mühll 2003, Ikeda 2006, for the interpretation of DC resistivity). Thus, we can interpret the L_W–L_{RG} diagrams assuming that the size of the talus-derived rock glaciers in the study area is roughly proportional to the debris volume in the rock glaciers.

This study shows that the central Brooks Range is a suitable area to investigate topographical controls on rock glaciers. More detailed study will address the long-term rates of rock wall erosion and the advance of talus-derived rock glaciers, and will possibly evaluate the dynamic inactivation and interaction with glacial processes of the rock glaciers quantitatively.

Acknowledgments

This study was financially supported by the Grant-in-Aid for Research Fellow of the Japan Society for the Promotion of Science from the Ministry of Education, Science and Culture, Japan, and the Inoue Fund for Field Science from the Japanese Society of Snow and Ice. We acknowledge K. Koui, A. Mittermeier, and A. Kikuchi for field assistance; S. Berezovskaya, M. and M. Kawauchi, and S. Sawaguchi for logistical help; R. Busey, P. Prokein, L. Hinzman, D. Kane, Y. Hayakawa, N. Matsuoka, and K. Moriwaki for academic support.

References

Arenson, L., Hoelzle, M. & Springman, S. 2002. Borehole deformation measurements and internal structures of some rock glaciers in Switzerland. *Permafrost and Periglacial Processes* 13: 117-135.

Barsch, D. 1977. Nature and importance of mass-wasting by rock glaciers in alpine permafrost environments. *Earth Surface Processes* 2: 231-245.

Barsch, D. 1992. Permafrost creep and rockglaciers. *Permafrost and Periglacial Processes* 3: 175-188.

Barsch, D. & Jakob, M. 1998. Mass transport by active rock glaciers in the Khumbu Himalaya. *Geomorphology* 26: 215-222.

Calkin, P.E., Haworth, L.A. & Ellis, J.M. 1987. Rock glaciers of central Brooks Range, Alaska, U.S.A. In: J.R. Giardino, J.F. Shroder, Jr. & J.D. Vitek (eds.), *Rock Glaciers.* London: Allen and Unwin, 65-82.

Ellis, J.M. & Calkin, P.E. 1979. Nature and distribution of glaciers, neoglacial moraines, and rock glaciers, east-central Brooks Range, Alaska. *Arctic and Alpine Research* 11: 403-420.

Frauenfelder, R., Haeberli, W., Hoelzle, M. & Maisch, M. 2001. Using relict rockglaciers in GIS-based modelling to reconstruct Younger Dryas permafrost distribution patterns in the Err-Julier area, Swiss Alps. *Norsk Geografisk Tidsskrift* 55: 195-202.

Frauenfelder, R., Haeberli, W. & Hoelzle, M. 2003. Rockglacier occurrence and related terrain parameters in a study area of the Eastern Swiss Alps. *Proceedings of the Eighth International Conference on Permafrost*, *Zurich*, *Switzerland*, *July 21–25*, *2003*: 253-258.

Haeberli, W. & Vonder Mühll, D. 1996. On the characteristics and possible origins of ice in rock glacier permafrost. *Zeitschrift für Geomorphologie N. F. Suppl.-Bd.* 104: 43-57.

Haeberli, W., Kääb, A., Wagner, S., Vonder Mühll, D., Geissler, P., Haas, J.N., Glatzel-Mattheier, H. & Wagenbach, D. 1999. Pollen analysis and ^{14}C age of moss remains in a permafrost core recovered from the active rock glacier Murtèl-Corvatsch, Swiss Alps: geomorphological and glaciological implications. *Journal of Glaciology* 45(149): 1-8.

Hamilton, T.D. & Porter, S.C. 1975. Itkillik Glaciation in the Brooks Range, northern Alaska. *Quaternary Research* 5: 471-497.

Hauck, C. 2001. Geophysical methods for detecting permafrost in high mountains. *Mitteilungen der Versuchsanstalt für Wasserbau, Hydrologie und Glaziologie*, *ETH Zürich* 171: 204 pp.

Hauck, C. & Vonder Mühll, D. 2003. Inversion and interpretation of two-dimensional geoelectrical measurements for detecting permafrost in mountainous regions. *Permafrost and Periglacial Processes* 14: 305-318.

Humlum, O. 2000. The geomorphic significance of rock glaciers: estimates of rock glacier debris volumes and headwall recession rates in West Greenland. *Geomorphology* 35: 41-67.

Ikeda, A. 2006. Combination of conventional geophysical methods for sounding the composition of rock glaciers in the Swiss Alps. *Permafrost and Periglacial Processes* 17: 35-48.

Ikeda, A. & Matsuoka, N. 2002. Degradation of talus-derived rock glaciers in the Upper Engadin, Swiss Alps. *Permafrost and Periglacial Processes* 13: 145-161.

Ikeda, A. & Matsuoka, N. 2006. Pebbly versus bouldery rock glaciers: Morphology, structure and processes. *Geomorphology* 73: 279-296.

Kääb, A., Frauenfelder, R. & Roer, I. 2007. On the response of rockglacier creep to surface temperature increase. *Global and Planetary Change* 56: 172-187.

Olyphant, G.A. 1983. Computer simulation of rock-glacier development under viscous and pseudoplastic flow. *Geological Society of America Bulletin* 94: 499-505.

Olyphant, G.A. 1987. Rock glacier response to abrupt changes in talus production. In: J.R. Giardino, J.F. Shroder, Jr. & J.D. Vitek (eds.), *Rock Glaciers.* London: Allen and Unwin, 55-64.

Roer, I. & Nyenhuis, M. 2007. Rockglacier activity studies on a regional scale: comparison of geomorphological mapping and photogrammetric monitoring. *Earth Surface Processes and Landforms* 32: 1747-1758.

Solid, J.L. & Sørbel, L. 1992 . Rock glaciers in Svalbard and Norway. *Permafrost and Periglacial Processes* 3: 215-220.

Wagner, S. 1992. Creep of Alpine permafrost, investigated on the Murtel Rock Glacier. *Permafrost and Periglacial Processes* 3: 157-162.

Wahrhaftig, C. & Cox, A. 1959. Rock glaciers in the Alaska Range. *Bulletin of the Geological Society of America* 70: 383-436.

Geophysical Investigation of Saline Permafrost at Ilulissat, Greenland

Thomas Ingeman-Nielsen
Arctic Technology Centre, Department of Civil Engineering, Technical University of Denmark, DK-2800 Kgs. Lyngby, Denmark

Niels Foged
Arctic Technology Centre, Department of Civil Engineering, Technical University of Denmark, DK-2800 Kgs. Lyngby, Denmark

Rune Butzbach
ASIAQ, Greenland Survey, DK-3900 Nuuk, Greenland

Anders Stuhr Jørgensen
Arctic Technology Centre, Department of Civil Engineering, Technical University of Denmark, DK-2800 Kgs. Lyngby, Denmark

Abstract

The technical properties and general state of permafrost in Greenland is not well documented. A new coordinated investigation has been initiated for ground temperature measurements and permafrost mapping in Greenlandic towns in sporadic, discontinuous, and continuous permafrost zones. We present investigation results from one of the sites, located at Ilulissat in an area of discontinuous saline permafrost. We have established ground temperature measurement stations and conducted a shallow geoelectrical study. Our results show that the sediments in the study area mainly consist of frost susceptible silty clays. The area has permafrost with a maximum active layer thickness between 0.9 m and 1 m. In spite of low permafrost temperatures, a considerable part of the pore water is unfrozen due to high residual salt concentrations. Consequently, the unfrozen water content dominates the geotechnical properties, and the sediments have a limited heat capacity available should the temperature conditions change.

Keywords: ice content; resistivity survey; saline permafrost; temperature measurements.

Introduction

The variability in the thermal state of permafrost in Greenland is presently not very well mapped. A series of well-organized ground temperature stations were operated in a number of West Greenlandic towns from the late 1960s to the early 1980s; however only part of these datasets have ever been published, and no large coordinated investigations have been conducted since. With the NSF ARC-0612533 project, "Recent and future permafrost variability, retreat and degradation in Greenland and Alaska: An integrated approach," a new coordinated investigation has been initiated for ground temperature measurements in Greenlandic towns in sporadic, discontinuous, and continuous permafrost zones. The project conducted in cooperation between Asiaq Greenland Survey, the Danish Meteorological Institute (DMI), University of Alaska Fairbanks (UAF), and Technical University of Denmark (DTU).

Figure 1. Map of Greenland with the location of the field site (Ilulissat) indicated.

This paper concerns one of the locations studied in this project, a field site located close to the airport in the town of Ilulissat, West Greenland (Fig. 1). Here we present the first results from fieldwork conducted in the summer 2007, which included shallow drilling, installation of ground temperature sensors (thermistors), and a shallow geoelectrical survey. Furthermore, we compare these results with investigations conducted from 1978 to 1980 in connection with the construction of the airport.

Site Description

Ilulissat is situated in the inner part of the Disko Bay at approximately 69.2°N and 51.1°W. The climate is arctic with a Mean Annual Air Temperature (MAAT) around -3.3°C (average from 1997 to 2006) with an increasing trend. The long-term variation in MAAT is shown in Figure 2. In the most recent classification by Christiansen & Humlum (2000), Ilulissat is located in the discontinuous permafrost zone.

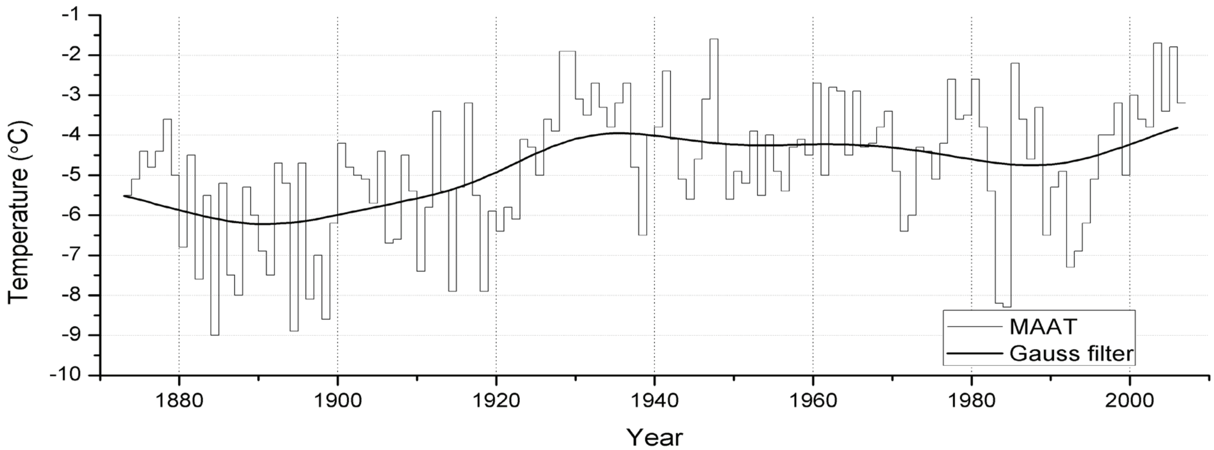

Figure 2. Mean Annual Air Temperature (MAAT) at Ilulissat from 1873 to 2006, as well as a Gauss filter with a filter width of 9 years (Cappelen 2007). These temperatures are measured at a DMI climate station (04216+04221) located in town, not at the airport field site.

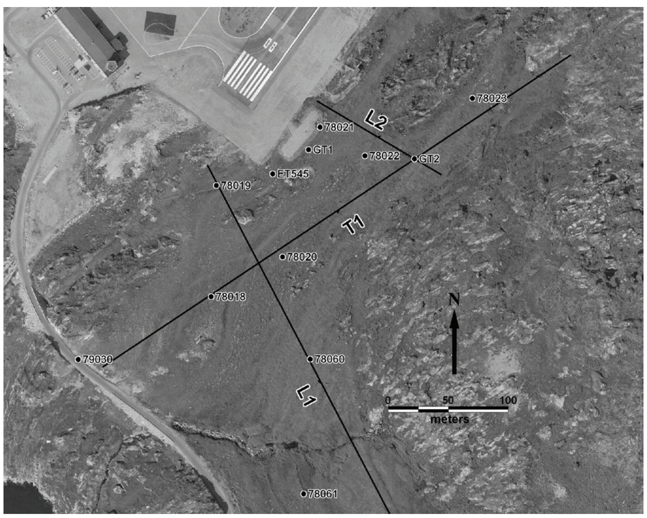

Figure 3. Aerial photo of field site with selected boreholes and survey lines included.

The bedrock in the area consists of Nagsugtoquidian gneisses with amphibolitic bands. It is affected by a series of fault and fracture systems, most importantly a northwest-southeast situated system. The entire area was ice covered during the last glaciation (Weichsel-Wisconsin), and the area was not deglaciated until approximately 9600 years BP (Bennicke & Björck 2002). A series of marine silt and clay rich sediments were later deposited at relatively high sea levels of <50 m. Interaction between eustatic changes and isostatic uplift raised the area above sea level about 5000 years ago (Rasch 2000), exposing the sediments to percolation of precipitation and possibly groundwater flow. This has resulted in depletion of salts in the upper part of the soil profile.

Permafrost was formed relatively early and the sediments have thereby been exposed to the consolidation and fracturing phenomena caused by ice lens formation in fine-grained sediments (Foged 1979).

Previous Investigations

In the period from 1978 to 1980, a series of investigations were undertaken in relation to the construction of the present airport facility. These investigations included drilling of a number of boreholes. Some of these boreholes were equipped with PT100 temperature sensors, which were manually logged at irregular intervals during the survey period. Furthermore samples from the boreholes were analyzed with respect to water content, pore water chemistry, freezing point depression, and consolidation parameters. A geoelectrical study was also conducted, including a number of electrical soundings at the borehole locations. Some of these results were previously published in Foged & Bæk-Madsen (1980), but many have never been published except in internal reports. In this paper, we present data from borehole 78020 as reference data for the new study.

Methodology and Instrumentation

In 2005, ASIAQ installed a ground temperature station (ET545, Fig. 3) next to their climate station at the airport site (climate station operational since 1993 and measures air temperature, humidity, and precipitation). This ground temperature station has PT100 temperature probes at the ground surface as well as depths of 0.25 m, 0.5 m, 1 m, 2 m, 3 m, and 4 m.

In 2007 we installed ground temperature sensors at locations GT1 and GT2 as well as at borehole locations 78020 and 78060 in order to establish information on the spatial variability in the area. All locations are equipped with Tinytag dataloggers with thermistors at 25 cm and 1.6 m depth. The new borehole at 78020, which is 4 m deep, is also equipped with Hobo U12 loggers with thermistors at the surface, 0.25 m, 0.5 m, 0.75 m, 1 m, 2 m, 3 m, and 4 m depths.

Our geophysical survey consisted of three Continuous Vertical Electrical Sounding (CVES) profiles conducted with Wenner and Wenner-Schlumberger configurations using an ABEM SAS4000 terrameter with the Lund Imaging system. This system consists of 61 electrodes on four cables with unit spacing on the two central cables and double spacing on the two outer cables. We used a unit electrode spacing of 5 m on profiles L1 and T1, and 1.5 m spacing on L2. We

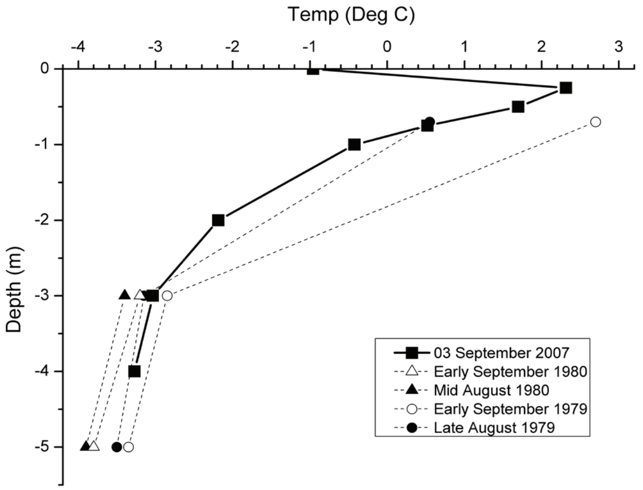

Figure 4. Ground temperature measurements from 1979–1980 (dashed lines) and 2007 (solid line).

have also made Vertical Electrical Soundings (VES) of the Schlumberger type at borehole locations 78018, 78020, and 78060, as well as at the intersection of L2 and T1, using the ABEM SAS4000 terrameter in standard setup. The CVES profiles have been inverted using Res2Dinv from Geotomo Software, and VES soundings using SELMA (Christensen & Auken 1992).

Results

Our continuous measurements of ground temperatures show that the present day maximum Active Layer Thickness (ALT) at the airport field site occurs in the beginning of September. At station ET545 the ALT was 1.0 m in 2006 and estimated to be 0.9 m in 2005 (the estimate is based on late August temperatures at surface and 1 m depth, as the sensors at 25 cm and 50 cm were not yet installed). Figure 4 shows a plot of the temperature measurements from the new installation at the old borehole 78020 location from September 3, 2007. This dataset indicates an ALT of 0.9 m in 2007. The same figure shows a plot of the temperature measurements from late August and early September of 1979 and 1980. In 1979 the ALT is estimated to have been between 1.0 m and 1.2 m. The estimate is based on temperatures at 0.7 m, 3 m, and 5 m depth. In 1980, the upper temperature probe had ceased functioning. The temperatures from the deeper probes were slightly lower than those observed in 2007, indicating a smaller ALT. We conclude that the ALT today is the same or slightly shallower than that observed in 1979 and 1980.

Olesen (2003) established and operated a ground temperature station (OBO) in Ilulissat from 1968 to 1982. It was equipped with 21 PT100 sensors at depths down to 15 m. In the upper 2 m, sensors were spaced at 0.25 m intervals. The sensors in the upper 1 m were only operational from 1969 to 1972. During this period, the average ALT was 1.1 m. This OBO site is located in town, some 3 km from the airport site. The airport site is slightly warmer than the DMI town station (0.4°C average 1997–2006). This shows that there may be significant local variations in air temperature.

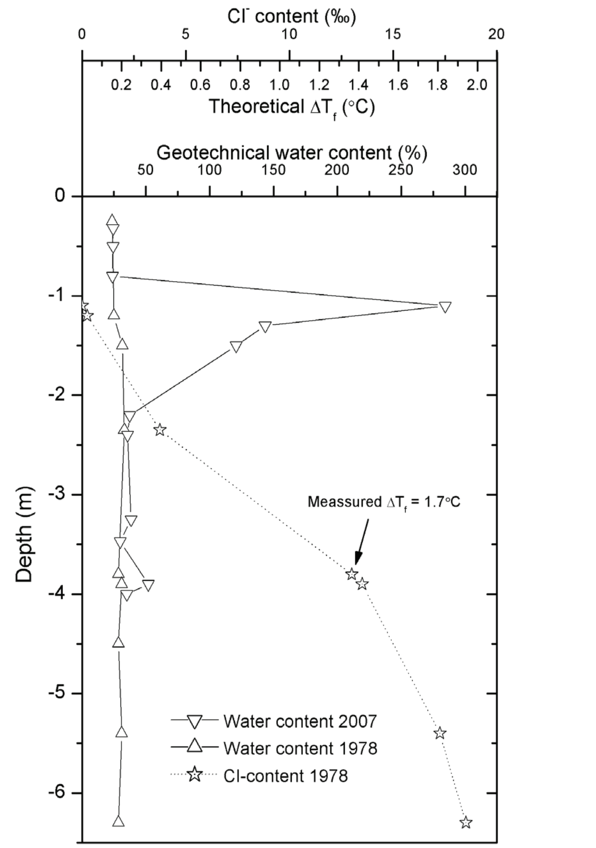

Figure 5. Water contents and Chloride (Cl^-) concentration from borehole location 78020, based on analysis from 1978 and 2007. The figure also shows the theoretical freezing point depression (ΔT_f) based on a pure NaCl solution of the same chloride concentration. Actual measured values of ΔTf are somewhat larger than the theoretical value.

The present ALT is apparently smaller than that observed in early 1970s at the OBO site. However, the difference may be related to a difference in air temperature . The old OBO station no longer exists, and the original location is crossed by a paved road. However, in order to obtain comparative measurements we have installed a new station as close as possible to the old OBO station.

Borehole 78020 was drilled July 26 1978, and is typical for the area. It showed a 6.9 m thick sequence of marine silty to very silty clay deposits, over gneiss bedrock. At the time of drilling, the active layer was 0.4 m thick, and the permafrost was very ice rich down to a dept of 4 m. Figure 5 shows the original water contents measured on samples collected from the borehole, as well as water contents from samples collected at the new drilling in 2007. Typical water contents lie between 23% and 35% and correlates well between the two datasets. However, from 1 m to 2 m depth, the new measurements show much larger water content when compared to the original measurements made in 1978. This is not necessarily due to temporal changes, but more to the fact that during the drilling in 1978, there was no focus on the importance of establishing the actual ice content. The collection of samples was organized to minimize the volume

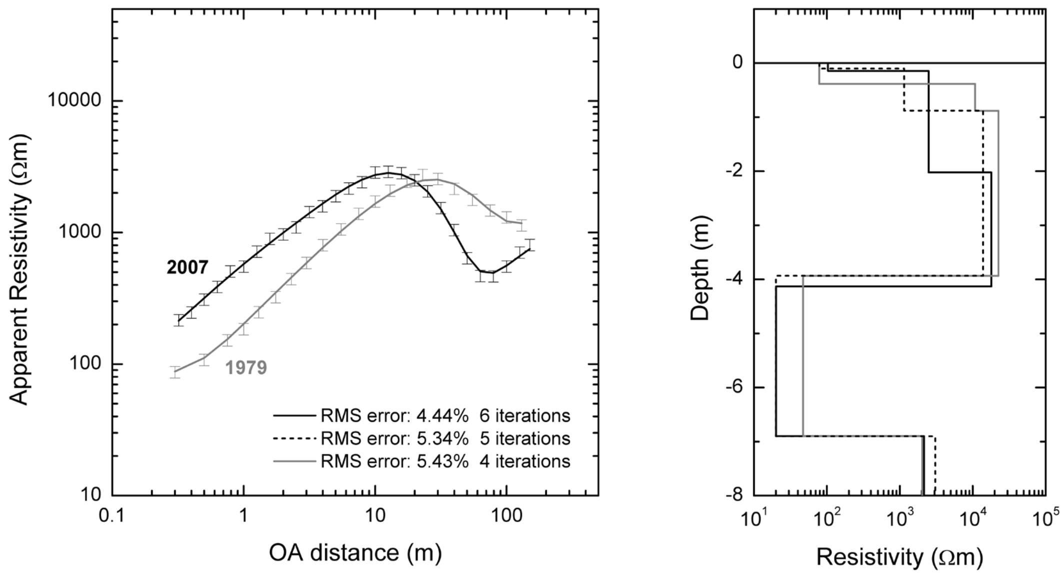

Figure 6. Inversion results from vertical electrical soundings at borehole location 78020, measurements from 1979 (grey lines) and 2007 (black lines). Five layer resistivity models are necessary in order to fit the datasets properly. However, the models are very poorly defined, and for the 2007 dataset two different models fitting the data equally well are indicated (black solid and dashed lines).

of ice lenses in the samples; however, the notes did record the occurrence of an ice rich zone.

Below the 4 m depth, ice was no longer observed in the samples, although temperatures are known to be subzero. The cause is the residual salt content in the marine clay deposits. Figure 5 also shows the variation of the pore water chloride content with depth in the borehole. It is seen to increase drastically from 3.75‰ at a depth of 2.35 m to 18.5‰, almost seawater concentration, at a depth of 6.3 m. These chloride concentrations have been used to calculate the theoretical freezing point depressions (ΔT_f) based on a pure NaCl solution of the same chloride concentration (see separate scale in Fig. 5), using the formula (adapted from Atkins 1994):

$$\Delta T_f = K \cdot c \cdot (1+\alpha) \quad ,$$

where K is the cryoscopic factor (1.86 $K \cdot kg \cdot mol^{-1}$ for water), c is the chloride concentration in mol/L, and α is the dissociation factor (assumed unity). The observed maximum concentration corresponds to a theoretical freezing point depression of 1.94°C. The actual measured values are somewhat lower however, due to a combination of other salts in the pore water solution, the electrochemical properties of the clay particles, and capillary tension in the pores.

The result of the freezing point depression below approximately 4 m depth is that the sediments are unfrozen as observed during drilling in 1978 and that unfrozen water content dominates the technical properties.

One of the effects of the unfrozen state is that the resistivity of the clay deposits is very low. This is observable on the Vertical Electrical Soundings (VES) collected at borehole 78020 location in 2007 and 1979 (Fig. 6). The two VES were collected June 6, 2007 and August 3, 1979. The different active layer thicknesses account for most of the difference observed in the apparent resistivity curves. The inverted resistivity models are also shown in Figure 6, and consist of five layers. Layer 1 is the unfrozen active layer, layers 2 and 3 are frozen sediments of varying but high resistivity, layer 4 is the technically unfrozen layer with low resistivity, and layer 5 is the bedrock. The models are highly undetermined when inverted with no constraints. The inversion of the 1979 data (solid grey line in Fig. 6) was strongly constrained at the depth of the bedrock interface, and loosely constrained within the depth of the active layer and the zone of frozen sediment. The 2007 dataset (solid black line) was first inverted with constraints on the depth to bedrock as well as the bedrock resistivity. In both datasets the apparent resistivity data could only be properly fitted, when the frozen zone was split into a shallow part with lower resistivity (layer 2), and a deeper part with higher resistivity (layer 3). Although poorly determined the depth to layer 3 corresponds well with the ALT in the 1979 data inversion, approximately 0.9 m, so that layer 2 corresponds to the frozen part of the active layer. For the 2007 data, the depth to layer 3 is much greater, and thus a similar interpretation is not possible. However, by constraining thicknesses of the layers, as well as the unfrozen active layer and bedrock resistivities, to fit the values obtained in the inversion of the 1979 data, it was possible to fit the 2007 dataset equally well (black dashed line, indistinguishable in apparent resistivity plot, see Fig. 6). Therefore, the VES results support the hypothesis that no significant changes have occurred in the permafrost conditions of the area over the period of study.

The inverted T1 CVES profile shown in Figure 7 (Fig. 3 shows the location of profile T1) shows the resistivity structure of the area. The upper part of the profile is highly resistive, with resistivities of more than 20 kΩm. Below is a conductive layer with resistivities between 50 Ωm and 600 Ωm. The lower part of the profile corresponds to bedrock at medium to high resistivity. Bedrock is outcropping immediately to the

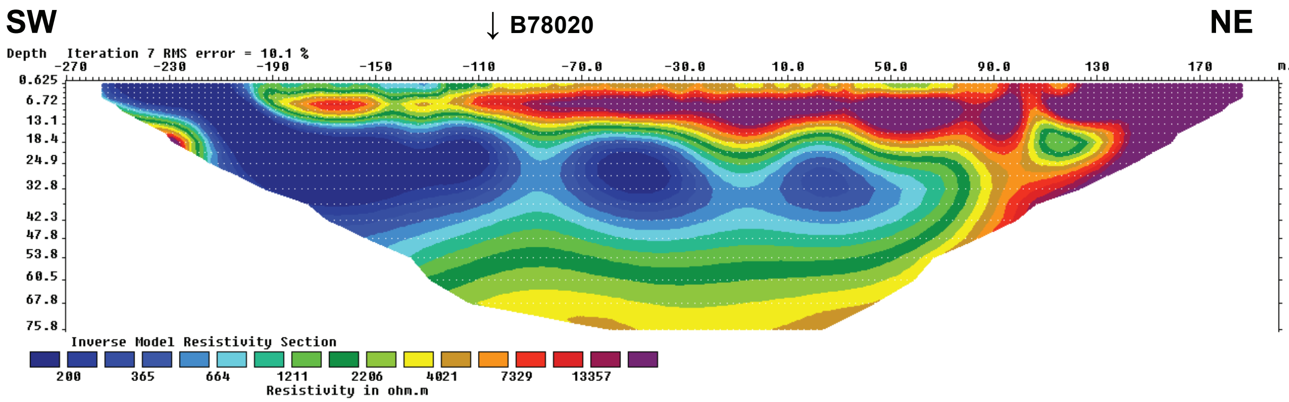

Figure 7. CVES profile (profile T1 in Fig. 3) with an electrode spacing of 5m using ABEM SAS4000 and LUND Imaging System. The profile clearly shows a low resistive layer corresponding to the technically unfrozen layer observed in soundings and boreholes. However the interpreted depths are invalid, due to macro anisotropy caused by ice lenses, and related equivalency problems.

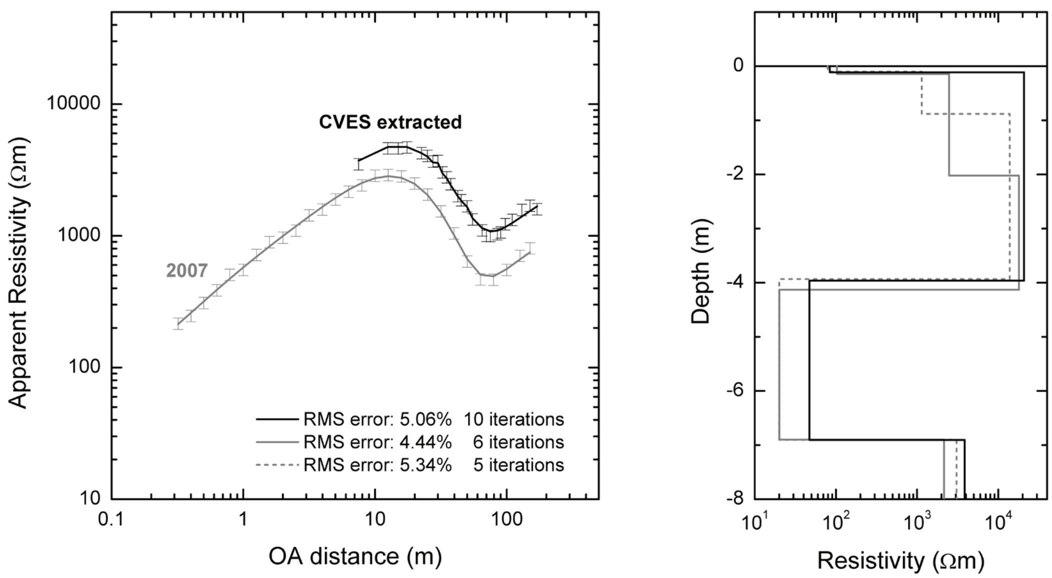

Figure 8. A dataset has been extracted from the CVES profile and inverted as a 1D sounding using a general array inversion scheme. The data could be fitted with essentially the same model as the normal Schlumberger sounding. Only a four layer model was used in this case, as the data density in the top of the profile is not large enough to support an extra layer. The reason for the offset between the Schlumberger sounding curve and the extracted data is the larger potential electrode distance used in the Wenner-Schlumberger configuration in the CVES profile.

southwest and northeast of the profile.

The general resistivity structure of the profile corresponds well with the collected VES. Nevertheless, the depths observed in the inverted resistivity model are much larger than the actual values. The bedrock interface for example is located at a depth of more than 35 m. No efforts to constrain the model resulted in a reasonable fit to the dataset. Similar problems have been observed previously in ice-rich permafrost areas in Greenland (Ingeman-Nielsen 2005, 2006), and are probably caused by pseudo anisotropy due to the presence of massive ice lenses. High ice content in the form of near horizontal ice lenses in the upper 2 meters of the permafrost gives rise to equivalency problems when the measurement system is geometrically large compared to the individual layers. In fact, a thin layered sequence with large resistivity contrasts is electrically equivalent to and indistinguishable from a thicker and isotropic sequence.

Combined with the normal equivalency problem of sandwiching a thin conductive layer between two thicker and resistive layers, this geoelectrical setting proves very difficult to resolve, as indicated by the wrong depths in the CVES inversion and the highly undetermined parameters in the VES inversions.

In order to substantiate this interpretation, we have extracted a subset from the CVES dataset, consisting of all measurements with a center point at the B78020 location plus or minus 10 m, and inverted this dataset using a 1D general array inversion scheme. As presented in Figure 8, it was possible to fit this dataset using essentially the same model as for the 2007 VES. In this case we used a four layer model, as the data density in the upper part of the profile is not large enough to support the extra layer. The only constraints on the inversion were a strong fix on the depth to the bedrock and very loose constraints on the resistivities of the conductive layer and the bedrock. All other parameters we left unconstrained.

This shows that it is indeed possible to construct a geoelectrical model that fits all the collected datasets. Furthermore it indicates that in this type of setting, a 1D laterally constrained inversion scheme could be superior to the more generally applied 2D blocky inversion scheme.

Conclusions

In order to determine permafrost properties in Ilulissat, we have established a number of ground temperature measurement stations and conducted a shallow geoelectrical study. Our results show that the sediments in the study area mainly consist of very frost susceptible, silty clays of marine origin. The area has permafrost with a maximum active layer thickness (ALT) between 0.9 m and 1 m. The ALT today is similar to that observed in 1979 and 1980, although ALT may have been smaller in the cold period during the early 1990s. Permafrost temperatures as low as -3°C to -4°C have been registered, but still a considerable part of the pore water is unfrozen at depths below 4 m, due to high residual salt concentrations and clay surface electrochemical properties. As a result, the unfrozen water content dominates the geotechnical properties. The unfrozen layer was observed directly while drilling in 1978 and in 2007 with vertical electrical soundings and CVES profiles as a low resistive layer. Consequently, these sediments have only a limited heat capacity available should the temperature conditions change.

Acknowledgments

This research was funded by the Polar Earth Science Program, Office of Polar Programs, National Science Foundation (ARC-0612533).

References

Atkins, P.W. 1994. *Physical Chemistry* (6th ed.). Oxford University Press, 1031 pp.

Bennike, O. & Björck, S. 2002. Chronology of the last recession of the Greenland Ice Sheet. *Journal of Quaternary Science* 17(3): 211-219.

Cappelen, J. 2007. *DMI Annual Climate Data Collection 1873-2006, Denmark, The Faroe Islands and Greenland.* Danish Meteorological Institute. Technical Report 07-05. www.dmi.dk/dmi/tr07-05.

Christensen, N.B. & Auken, E. 1992. SELMA - Simultaneous Electromagnetic Layered Modelling and Analysis. Proceedings of Interdisciplinary Inversion Workshop 1 Aarhus 1992, Methodology and Applications within Geophysics, Astronomy, and geodesy. *Geoskrifter*: 49-56.

Christiansen H.H. & Humlum, O. 2000. Permafrost. In: B.H. Jakobsen, J. Böcher, N. Nielsen, R. Guttesen, O. Humlum & E. Jensen (eds.), *Topografisk Atlas Grønland*. Copenhagen: C.A. Reitzets Forlag, 32-35.

Foged, N. 1979. *Engineering Geological Investigations of Quaternary Marine Clay Deposits on West Greenland.* Ph.D. Thesis (in Danish). The Institute for Applied Geology. Technical University of Denmark.

Foged, N. & Bæk-Madsen. 1980. Jakobshavn Airport thermal stability in marine deposits. *Second International Symposium on Ground Freezing, Trondheim, June 24–26.* Norwegian Institute of Technology.

Ingeman-Nielsen, T. 2005. *Geophysical Techniques Applied to Permafrost Investigations in Greenland.* Ph.D. Thesis. Department of Civil Engineering, Technical University of Denmark, 177 pp.

Ingeman-Nielsen, T. 2006. Mapping ice-bonded permafrost with electrical methods in Sisimiut, *West Greenland EAGE Near Surface 2006, Extended Abstracts*, 4 pp.

Olesen, O.B. 2003. *Shallow Borehole Temperatures, Ilulissat, Greenland. Copenhagen, Denmark: Greenlandic Geological Survey (GEUS).* Distributed by National Snow and Ice Data Center/World Data Center for Glaciology. Digital Media.

Rasch, M. 2000. Holocene Relative Sea Level Changes in Disko Bugt, West Greenland. *Journal of Coastal Research* 16(2): 306-315.

Climate Change and Arctic Infrastructure

Arne Instanes
Instanes Svalbard AS, N-9171 Longyearbyen, Norway
Oleg Anisimov
State Hydrological Institute, St. Petersburg, Russia

Abstract

Several authors report that impacts of climate change on infrastructure in the Arctic are already evident. Damage to infrastructure and engineering structures in permafrost regions are often linked to observed increase in air temperature over the last 10 to 20 years. However, these reports do not show in detail how the change in air temperature may affect the active layer thickness and permafrost temperature at specific sites and for specific structures in the Arctic. This paper presents the results of a study of the impact of climate change on Arctic infrastructure based on historical meteorological records. The temperature data are used together with a numerical model to evaluate the possible warming of permafrost at depth, and theoretical impacts on pile foundation capacity at specific sites in the Arctic. Results from permafrost model forced by several GCM-based climatic projections are used to construct the predictive map indicating threats to infrastructure due to potential weakening of the frozen ground.

Keywords: climate change; engineering; foundations; geotechnical; permafrost; warming.

Introduction

For several decades, air temperatures in the Arctic have warmed at approximately twice the global rate (McBean et al. 2005). Zonal-mean temperature north of 60°N has increased up to 2°C since the late 1960s. Contemporary warming in the Arctic is strongest (~ 1°C/decade) in winter and spring, and smallest in autumn. Such changes lead to warming, thawing, and degradation of permafrost. Observational data are limited, and are not available throughout the entire Arctic. Borehole measurements indicate that permafrost temperatures have increased markedly during the last 50 years, (Romanovsky et al. 2002), with rapid warming in Alaska (Hinzman et al. 2005), Canada (Beilman et al. 2001), Europe (Harris et al. 2003), and Siberia (Pavlov & Moskalenko 2002).

In the context of the future climate change one of the key concerns associated with the thawing of permafrost is the detrimental impact on the infrastructure built upon it. Several authors report that such impacts are already evident (Khrustalev 2001, Romanovsky & Osterkamp 2001, Zernova 2003, Gribchatov 2004, Vasilieva 2004). Instanes et al. (2005) and Instanes (2003) conclude that human interaction and engineering construction very often lead to extensive thawing of both continuous and discontinuous permafrost even if climatic conditions remain unchanged. The intergovernmental panel on climate change (Anisimov & Vaughan 2007) also points out that the effect of heated buildings on underlying ice-rich permafrost has been known for a very long time, and may be mistaken for an impact of climate change.

In this paper we used historical air temperature records from three different cities to investigate the change in pile foundation bearing capacity during the last 100 years. We upscaled the results of this historical analysis and constructed the map of potential threats to infrastructure using the hazard index that takes into account regionality of projected climatic and permafrost changes.

Pile Design

Design ground temperature

The strength and deformation characteristics of frozen soils are temperature dependent. It is, therefore, necessary to determine the thickness of the active layer (maximum thaw depth) and the maximum ground temperature along the embedded pile length (Andersland & Ladanyi 2004). These two parameters are incorporated into the site-specific design of foundations in permafrost regions. Conventional engineering design is based on the analysis of historical variations of climatic and permafrost data and accounts for the frequency of extreme events, such as abnormally high temperatures resulting in deeper seasonal thawing of permafrost. Each foundation is designed with construction-specific safety factors that depend on the probability of such extremes.

Adfreeze bonds

The adfreeze bond strength between the pile surface and surrounding frozen permafrost soil is temperature and time dependent. For a specific pile foundation design, this parameter should be determined from geotechnical field and laboratory investigations. For the purpose of this study, a simplified relationship is used, as shown in Figure 1.

Data in Figure 1 may be used to evaluate the effect of changing climatic conditions on the bearing capacity of piles and thus to predict the potentially detrimental impacts of warming and thawing permafrost on the structures built upon it.

Air Temperature Records

The climatic data used in the present analysis were mean monthly air temperatures from three different locations in the Arctic: (1) Fairbanks, Alaska (N64°15′, W147°37′);

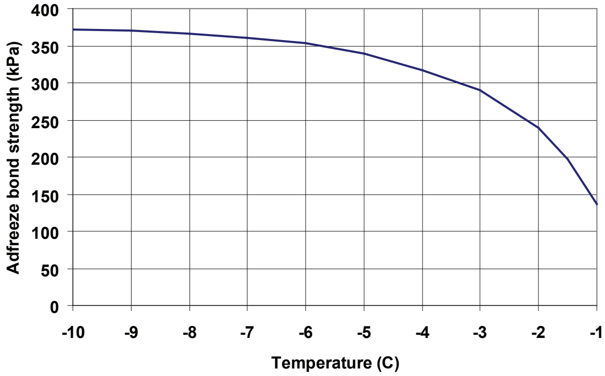

Figure 1. Adfreeze bond strength used in the analysis.

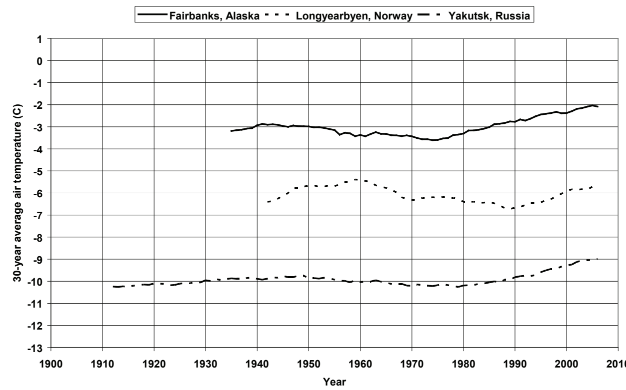

Figure 2. Mean annual air temperatures for Fairbanks, Alaska; Longyearbyen, Norway; and Yakutsk, Russia, smoothed with 30-years running filter.

(2) Longyearbyen, Norway (N78°25′, E15°47′); and (3) Yakutsk, Russia (N62°02′, E129°45′). The sites were chosen based on:

- station time series approximately 100 years or more,
- location near population concentrations and major infrastructure,
- locations representing different climatic and environmental conditions in the Arctic.

All three stations show some indication of increased air temperatures during the last 20 to 30 years. Yakutsk has the longest time series starting in 1829, while the time series for Fairbanks and Longyearbyen start in 1904 and 1912, respectively.

Figure 2 shows mean annual air temperatures for Yakutsk, Longyearbyen, and Fairbanks, smoothed with 30-years running filter. In the last three to four decades temperatures increased by almost 2ºC in Yakutsk, and by 1ºC in Fairbanks (see Fig. 2).

In Longyearbyen there was the decrease of the annual mean air temperature from the maximum of –5.2ºC in 1960 to the minimum of –6.8ºC in 1990 followed by rapid increase by ca. 1ºC since then. Based on Figure 2, the temperatures in the 1960s were still higher than now. However, Longyearbyen had a mean annual air temperature in 2006 that was the warmest on record (-1.6ºC).

Mean monthly air temperatures were used in the thermal model to calculate the changes in the ground temperature at different depth and to evaluate the effect on the bearing capacity of piles.

Permafrost Models and Results

Two permafrost models of different complexity were used in this study. The first is the TEMP/W, version 7.03 (Geo-Slope 2007) software that can model the thermal changes in the ground due to changing temperature or heat flux boundary conditions. This simple model is often used in practical engineering applications and gives good results at point locations given that the model is validated by observational data. More sophisticated model that was used for constructing predictive hazard map for Russian permafrost region is detailed in the next section. The TEMP/W model accounts for the effects of the temperature dependent thermal conductivity, volumetric latent heat of fusion, and soil unfrozen water content. In this study we used a simplified homogenous soil profile consisting of silty sand with the following parameters:

- dry density (γ_d): 16.7 kN/m^3 (ρ_d=1700 kg/m^3),
- water content (w): 20%,
- degree of saturation (S_r): 100%
- porosity (n): 37.1%,
- volumetric heat capacity frozen (c_{vu}): 2300 kJ/(m^{3}K),
- volumetric heat capacity unfrozen (c_{vu}): 3150 kJ/(m^{3}K).

Thermal conductivity and heat capacity was adjusted to changing ground temperature and unfrozen water content using simplified empirical relationships.

The soil profile was modeled using isoparametric 8-nodes quadrilateral finite elements. Mean monthly air temperatures were applied to the surface boundary of the finite element mesh. The initial ground temperature at the start of the analyses (1904 for Fairbanks, 1912 for Longyearbyen, and 1900 for Yakutsk) was set approximately equal to the mean annual air temperature in Figure 2.

It should be noted that n-factors of 1.0 was used in the analysis presented in this paper. Andersland & Ladanyi (2004) suggest that n-factors between 1.2 and 2.0 would be appropriate for sand and gravel surfaces during thawing.

The ultimate goal of the calculations was to evaluate the probability for the ground temperature to exceed the threshold beyond which the pile becomes unstable and is incapable of bearing the load of construction above it. Figure 3 presents the maximum ground temperatures along the embedded pile length for selected years in Fairbanks, Longyearbyen, and Yakutsk, respectively. Maximum ground temperatures for each decade are presented in Tables 1, 2, and 3. It can be observed from the figures and tables that all three locations have the highest ground temperatures after year 2000.

Computed and measured ground temperatures are in good agreement in Longyearbyen. For Fairbanks and Yakutsk the computed values seem to be lower than observed ground temperatures. This is probably due to the effect of the n-factor used in the analysis (see above). The thermal model

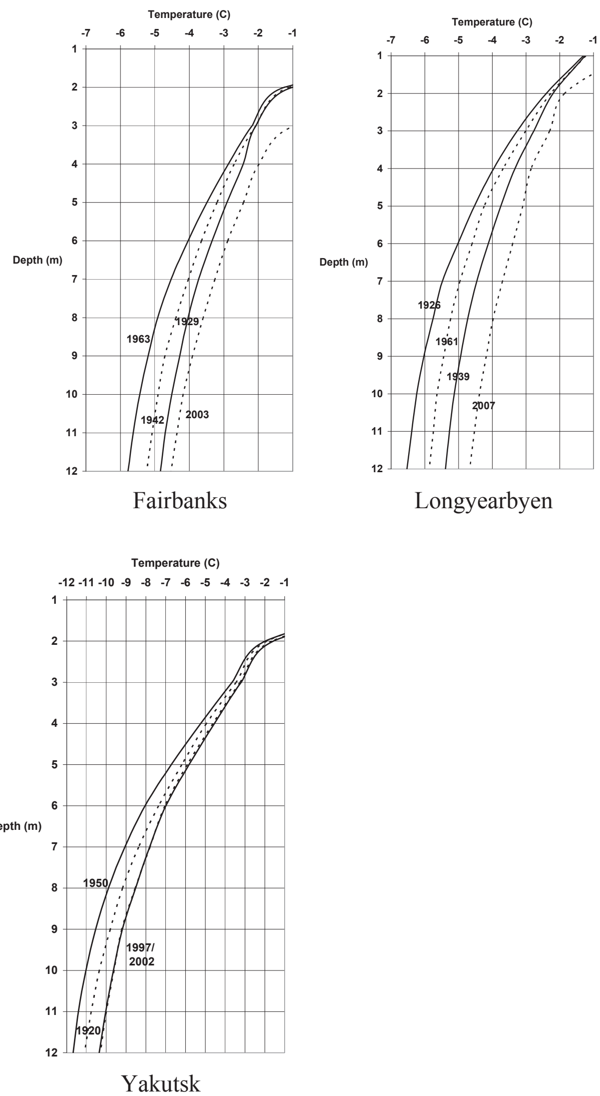

Figure 3. Maximum ground temperature along the embedded pile length, Fairbanks 1929, 1942, 1963, and 2003 (a); Longyearbyen 1926, 1939, 1961, and 2007 (b);and Yakutsk 1920, 1950, and 1997/2002 (c).

should, therefore, be tuned with actual ground temperature observations. However, the main purpose of the study was to look at the relative effect of variations in air temperature over the last 100 years for an idealized soil profile, and the results show that this goal has been achieved.

Pile Capacity

Based on the maximum ground temperatures presented in Tables 1, 2, and 3 and the adfreeze bond strength presented in Figure 1, theoretical pile capacities for a 200 mm diameter pile for the three locations are presented in Figure 4. As follows from the figure, for Fairbanks the theoretical pile capacity has been reduced by 6.5% from the maximum capacity of 627 kN in 1963 to 587 kN in 2003. In Longyearbyen the pile capacity has been reduced by 12.5% from the maximum capacity of 717 kN in 1977 (and 1926) to 636 kN in 2007.

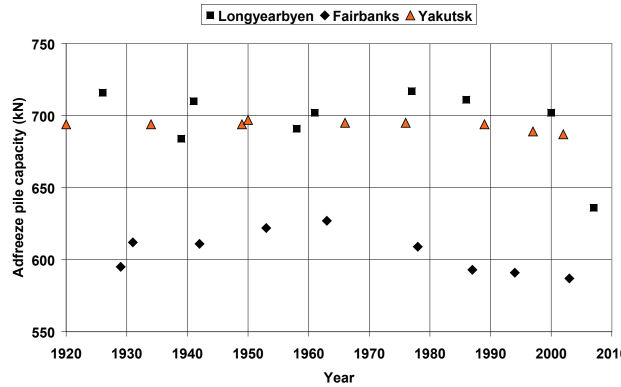

Figure 4. Theoretical adfreeze pile capacity for a 200 mm pile.

In Yakutsk, the theoretical pile capacity has remained almost unchanged, with only slight reduction by 1.5% in the period 1950–2002. This is because ground temperatures in Yakutsk are low (<-6ºC below 5 meters depth, see Table 3), while the adfreeze bond strength does not change much for temperatures below -5 to -6ºC (see Fig. 1). Pile capacities in Longyearbyen are higher than in Yakutsk because the active layer thickness here is much smaller due to the relatively cold summers in Spitsbergen compared to central Yakutia. It implies that the embedded length of the pile that has a temperature below -1ºC (also called the effective pile length) is bigger in Longyearbyen (approximately 11 m) than in Fairbanks and Yakutsk (approximately 10 m).

Hazard Map

Nelson et al. (2001) suggested the hazard index for predictive large-scale mapping of potential risks to infrastructure due to warming and thawing of permafrost. The more recent study by Anisimov & Lavrov (2004) uses modified hazard index, I_G, that is given by the following equation:

$$I_G = \Delta Z_{al} V_{ice} K_s \tag{1}$$

Here ΔZ_{al} is the projected change in the depth of seasonal thawing, expressed in relative units with respect to modern norm; V_{ice} is the volumetric ground ice content, and K_s is the coefficient that characterizes soil salinity.

Changes in the depth of seasonal thawing have been calculated using an equilibrium permafrost model forced by several climatic scenarios. The baseline algorithm developed by V. Kudryavtcev (1974) was modified to account for the presence of the organic layer and for the effects of the changing thermal conductivity of the snow cover. The mathematical formalism has been detailed in several preceding publications (i.e., Anisimov et al. 2007; Sazonova & Romanovsky 2003). All calculations were made in the nodes of 0.5° lat/long grid spanning the northern Eurasian permafrost region.

The model was forced by the contemporary and projected for the future climatic data. We used gridded monthly norms

Table 1. Maximum ground temperature along the embedded pile length for each decade, Fairbanks, Alaska.

Depth (m)	1929 (ºC)	1931 (ºC)	1942 (ºC)	1953 (ºC)	1963 (ºC)	1978 (ºC)	1987 (ºC)	1994 (ºC)	2003 (ºC)
1	+5.99	+5.54	+5.41	+5.31	+5.42	+6.30	+6.69	+6.39	+7.66
2	-1.00	-1.36	-1.09	-1.25	-1.24	-1.11	-0.92	-0.71	-0.89
3	-2.07	-2.19	-2.07	-2.15	-2.18	-2.02	-1.96	-1.93	-1.98
4	-2.44	-2.71	-2.70	-2.75	-2.87	-2.63	-2.48	-2.48	-2.43
5	-2.91	-3.18	-3.20	-3.34	-3.49	-3.20	-2.97	-2.96	-2.89
6	-3.34	-3.63	-3.65	-3.88	-4.04	-3.63	-3.42	-3.37	-3.26
7	-3.73	-4.02	-4.03	-4.37	-4.53	-4.04	-3.73	-3.76	-3.60
8	-4.04	-4.36	-4.39	-4.80	-4.92	-4.42	-4.05	-4.08	-3.91
9	-4.28	-4.57	-4.71	-5.04	-5.20	-4.74	-4.33	-4.32	-4.18
10	-4.51	-4.74	-4.91	-5.30	-5.44	-4.95	-4.58	-4.55	-4.36
11	-4.70	-4.92	-5.08	-5.52	-5.63	-5.16	-4.70	-4.72	-4.53
12	-4.84	-5.01	-5.24	-5.67	-5.78	-5.33	-4.81	-4.84	-4.68

Table 2. Maximum ground temperature along the embedded pile length for each decade, Longyearbyen, Norway.

Depth (m)	1926 (ºC)	1939 (ºC)	1941 (ºC)	1958 (ºC)	1961 (ºC)	1977 (ºC)	1986 (ºC)	2000 (ºC)	2007 (ºC)
1	-1.30	-1.25	-1.50	-1.30	-1.23	-1.43	-1.36	-1.08	-0.08
2	-2.40	-2.20	-2.49	-2.18	-2.27	-2.38	-2.34	-2.30	-1.86
3	-3.26	-2.77	-3.28	-2.84	-3.01	-3.20	-3.14	-2.98	-2.30
4	-3.96	-3.33	-3.88	-3.38	-3.68	-3.91	-3.80	-3.63	-2.85
5	-4.53	-3.75	-4.32	-3.85	-4.24	-4.55	-4.37	-4.23	-3.10
6	-5.02	-4.12	-4.76	-4.30	-4.60	-5.13	-4.83	-4.64	-3.40
7	-5.48	-4.46	-5.09	-4.71	-4.96	-5.48	-5.25	-5.03	-3.70
8	-5.76	-4.73	-5.29	-5.00	-5.24	-5.82	-5.56	-5.34	-3.98
9	-6.03	-4.94	-5.49	-5.23	-5.44	-6.05	-5.81	-5.60	-4.18
10	-6.24	-5.13	-5.59	-5.45	-5.64	-6.25	-6.00	-5.81	-4.38
11	-6.39	-5.27	-5.68	-5.60	-5.75	-6.40	-6.15	-5.98	-4.53
12	-6.53	-5.39	-5.74	-5.74	-5.87	-6.52	-6.28	-6.11	-4.67

Table 3. Maximum ground temperature along the embedded pile length for each decade, Yakutsk, Russia.

Depth (m)	1920 (ºC)	1934 (ºC)	1949 (ºC)	1950 (ºC)	1966 (ºC)	1976 (ºC)	1989 (ºC)	1997 (ºC)	2002 (ºC)
1	+4.89	+5.16	+5.36	+5.22	+4.80	+6.02	+5.15	+5.94	+5.95
2	-1.89	-1.88	-1.84	-1.97	-1.92	-1.93	-1.87	-1.65	-1.56
3	-3.45	-3.43	-3.46	-3.65	-3.51	-3.48	-3.51	-3.25	-3.19
4	-4.95	-4.93	-5.02	-5.23	-5.04	-5.00	-4.94	-4.62	-4.54
5	-6.19	-6.33	-6.38	-6.72	-6.47	-6.42	-6.29	-5.91	-5.82
6	-7.36	-7.60	-7.50	-8.04	-7.75	-7.69	-7.50	-7.04	-6.99
7	-8.37	-8.50	-8.50	-9.06	-8.57	-8.67	-8.37	-7.80	-7.81
8	-9.18	-9.26	-9.38	-9.89	-9.38	-9.38	-9.10	-8.54	-8.52
9	-9.80	-9.98	-10.10	-10.54	-10.12	-10.08	-9.80	-9.22	-9.19
10	-10.35	-10.47	-10.58	-11.03	-10.58	-10.59	-10.27	-9.61	-9.64
11	-10.76	-10.88	-11.00	-11.41	-11.02	-10.98	-10.68	-10.00	-10.03
12	-11.10	-11.23	-11.33	-11.67	-11.35	-11.33	-11.02	-10.30	-10.36

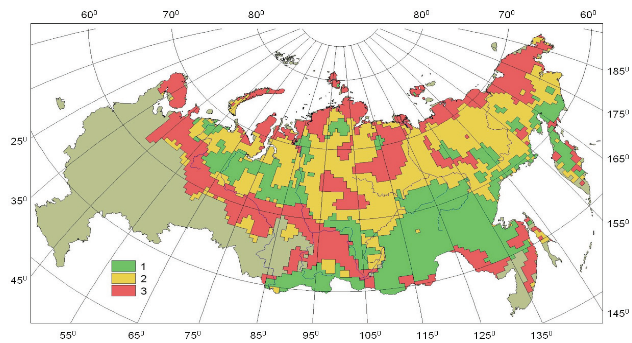

Figure 5. Predictive map of potential threats to infrastructure for 2050. Red, yellow, and green colors designate regions with high, moderate, and low susceptibility of buildings and engineered structures to the ongoing climatic and permafrost changes.

of air temperature and precipitation with 0.5° lat/long resolution as baseline data characterizing modern climate (New et al. 1999). Set of five scenarios of climate change for the 11-year long time periods centered on 2030, 2050, and 2080 has been constructed by superimposing predicted by CGCM2, CSM_1.4, ECHAM4/OPYC3, GFDL-R30_c and HadCM3 GCMs changes of climatic parameters on baseline data. These GCMs were selected as a result of the survey made in the course of the ACIA (Arctic Climate Impact Assessment) because they account for many key processes in the Arctic and provide reasonable fit to the observed climatic trends (Symon 2005). All climate models were forced by the B2 emission scenario. The climatic scenarios are fully documented in the ACIA report (2005) and are available on the web sites of the data distribution center of the Intergovernmental Panel on Climate Change (IPCC; http://ipcc-ddc.cru.uea.ac.uk/ and http://igloo.atmos.uiuc.edu/IPCC/).

Soil thermal properties were calculated using parameterizations that take into account soil type, soil moisture and ground ice content. We calculated winter-average snow depth at each node using monthly precipitation data. The density, thermal conductivity, and heat capacity of snow were prescribed at 300 kg m^{-3}, 0.23 W m^{-1} K^{-1} and 2090 J kg^{-1} K^{-1}, respectively. Vegetation types with prescribed thermal properties and soil type were obtained from the digital global ecosystems database (1992). The model was validated by the data from Circumpolar Active Layer Monitoring program (Brown et al. 2000) and used to calculate permafrost parameters under modern and projected for the future climatic conditions. Results of such calculations differ in detail depending on climatic scenario. Predictive map of hazard index in Figure 7 was constructed using the "median" climatic projection of GFDL model for 2050.

Summary and Conclusions

Historical air temperature records indicate warming during the last few decades in three selected locations representing different climatic and environmental conditions in Spitsbergen, in central Yakutia, and in Alaska. The results from this study suggest that piled foundations have not suffered sufficient loss in bearing capacity to become unstable due to the observed increase in air temperatures. However, the loss in capacity of piles in Longyearbyen from 702 kN to 636 kN in the period 2000–2007 is the early warning of the potentially detrimental impacts of changing climate.

One of the apparent features of the climate change impacts in permafrost regions is strong regionality. Susceptibility of permafrost to climatic changes and associated risks to infrastructure depend on the combinations of local soil, topographic, hydrological, vegetation, and snow conditions. In this paper the large-scale pattern of the future impacts was studied using the hazard index. Although such index provides highly generalized information about the potential impacts on the infrastructure, it may serve as effective tool for resource and land use planning, environmental risk management, and civil engineering in permafrost regions.

Areas of greatest hazard potential in Figure 5 include the Arctic coastline and parts of Siberia in which substantial development has occurred in recent decades. Particular concerns are associated with Yamal peninsula that falls into the highest risk zone, because of the ongoing expansion of the oil and gas extracting and transportation industry into this region. Although temperatures here are relatively low, frozen ground is already very unstable, largely because of its high salinity, and thus even small warming may cause extensive thawing of permafrost and ground settlement with serious impacts on the inrastructure.

Acknowledgments

Anisimov's research of the contemporary climatic changes in Russia and predictive modeling of the impacts of thawing permafrost on infrastructure is supported by the Russian Foundation for Basic Research, grants # 07-05-00209 and 07-05-13527.

References

Andersland, O.B. & Ladanyi, B. 2004. *Frozen ground engineering*. 2nd edition. New Jersey, USA: John Wiley & Sons, Inc. Published in cooperation with ASCE press, 363 pp.

Anisimov, O.A. & Lavrov, C.A. 2004. Global warming and permafrost degradation: risk assessment for the infrastructure of the oil and gas industry. *Technologies of oil and gas industry* (3): 78-83 (in Russian).

Anisimov, O.A. & Vaughan, D.G. 2007. Polar Regions. In: *Climate Change 2007: Climate change impacts, adaptation, and vulnerability. Contribution of Working group II to the Fourth Assessment Report of the Intergovernmental Panel on Climate Change*.

Anisimov, O.A., Lobanov, V.A., Reneva, S.A., Shiklomanov, N.I. & Zhang, T. 2007. *Uncertainties* in gridded air temperature fields and their effect on predictive active layer modeling. *Journal of Geophysical Research* 112 (F02S14), doi:10.1029/2006JF000593/

Beilman, D.W., Vitt, D.H. & Halsey, L.A. 2001: Localized permafrost peatlands in Western Canada: Definition, distributions, and degradation. *Arct. Antarct. Alp. Res.* 33(1): 7077.

Brown, J., Hinkel, K.M., Nelson, F.E. 2000. The Circumpolar Active Layer Monitoring (CALM) program: research designs and initial results. *Polar Geography* 24(3): 165-258.

Geo-Slope. 2007. Thermal modeling with TEMP/W 2007. An engineering methodology. Calgary, Canada: GEO-SLOPE International Ltd., 240 pp.

Global ecosystems database version 1.0 on CD-ROM. 1992. Series USDOC/NOAA National Geophysical Data Center, Boulder.

Harris, C., Vonder Mühll, D., Isaksen, K., Haeberli, W., Sollid, J.L., King, L., Holmlund, P., Dramis, F., Guglielmin, M. & Palacios, D. 2003: Warming permafrost in European mountains. *Global and Planetary Change* 39: 215-225.

Hinzman, L.D., Bettez, N.D., Bolton, W. Chapin III, R.F.S., Dyurgerov, M.B. Fastie, C.L., Griffith, B., Hollister, R., Hope, D.A., Huntington, H., Jensen, A.M., Jia, G.J., Jorgenson, T., Kane, D.L., Klein, D.R., Kofinas, G., Lynch, A.H., Lloyd, A.H., McGuire, A.D., Nelson, F.E., Nolan, M., Oechel, W.C., Osterkamp, T.E., Racine, C.H., Romanovsky, V.E., Stone, R.S., Stow, D.A., Sturm, M., Tweedie, C.E., Vourlitis, G.L., Walker, M.D., Walker, D.A., Webber, P.J., Welker, J., *Winker*, K.S. & Yoshikawa, K. 2005. Evidence and implications of recent climate change in northern Alaska and other arctic regions. *Climatic Change* 72: 251-298.

Instanes, A., Anisimov, O., Brigham, L., Goering, D., Ladanyi, B., Larsen, J.O. & Khrustalev, L.N. 2005. Chapter 16: Infrastructure: Buildings, Support Systems, and Industrial Facilities. In: *Arctic Climate Impact Assessment, ACIA*. Cambridge: Cambridge University Press, 907-944.

Intergovernmental panel on Climate Change (IPCC). 2007. *IPCC Working Group II Climate Change Impacts, Adaptation and Vulnerability Fourth Assessment Report, Chapter 15 Polar Regions (Arctic and Antarctic)*. www.ipcc.ch.

Khrustalev, L.N. 2001. Problems of permafrost engineering as related to global climate warming. In: R. Paepe & V. Melnikov (eds.), *Permafrost Response on Economic Development, Environmental Security and Natural Resources*. Dordrecht, the Netherlands: Kluwer Academic Publishers, 407-423.

Kudryavtsev, V.A., Garagulya, L.S., Kondrat'yeva, K.A. & Melamed, V.G. 1974. *Fundamentals of Frost Forecasting in Geological Engineering Investigations* Nauka, Moscow. (in Russian). English translation appears as U.S. Army Cold Regions Research and Engineering Laboratory Draft Translation 606 (1977).

Nelson, F.E., Anisimov, O.A. & Shiklomanov, N.I. 2001. Subsidence risk from thawing permafrost. *Nature* 410: 889-890.

New, M., Hulme, M. & Jones, P. 1999. Representing twentieth-century space-time climate variability. Part I: Development of a 1961–90 mean monthly terrestrial climatology. *Journal of Climate* 12(3): 829-856.

McBean, G., Alekseev, G., Chen, D., Førland, E., Fyfe, J., Groisman, P.Y, King, R., Melling, H., Vose, R. &.Whitfield, P.H. 2005: Chapter 2: Arctic Climate–Past and Present. *Arctic Climate Impacts Assessment (ACIA)*. C. Symon, L. Arris, B. Heal (eds.), Cambridge, UK:Cambridge University Press, 21-60.

Romanovsky, V.E. and Osterkamp, T.E. 2001. Permafrost: Changes and impacts. In: R. Paepe and V. Melnikov (eds.), *Permafrost Response on Economic Development, Environmental Security and Natural Resources*. Dordrecht, the Netherlands: Kluwer Academic Publishers, 297-315.

Pavlov, A.V. & Moskalenko, N.G. 2002: The thermal regime of soils in the north of Western Siberia. *Permafrost Periglacial Process* 13(1): 43-51.

Romanovsky, V.E., M. Burgess, S. Smith, Yoshikawa, K. & Brown, J. 2002: Permafrost temperature records: Indicators of climate change. *EOS, Transactions, American Geophysical Union* 83: 589-594.

Sazonova, T.S. & Romanovsky, V.E. 2003. A model for regional-scale estimation of temporal and spatial variability of active-layer thickness and mean annual ground temperatures. *Permafrost and Periglacial Processes* 14(2): 125-140.

Symon, C. (ed.). 2005. *Impacts of a Warming Arctic: Arctic Climate Impacts Assessment.* Cambridge: Cambridge University Press, 1042 pp.

Vasilieva, I. 2004: *Climate, thawing permafrost, and buildings in the Northern lands*. *Expert* - 9 *Siberia.* Yakutsk, pp. 2nd October 2004.

Zernova, L. 2003. *Has the frost cancelled the predicted global warming? The City*. St. Petersburg, Russia, 14-15.

Foundation Design Using a Heat Pump Cooling System

Bjarne Instanes
Instanes Svalbard AS, N-9171 Longyearbyen, Norway

Arne Instanes
Instanes Svalbard AS, N-9171 Longyearbyen, Norway

Abstract

On several locations in Svalbard, Norway, it is advantageous to design buildings with on-grade foundations over ice-rich permafrost soils. These types of foundations require insulation material underneath the concrete floor slab and a cooling system underneath the insulation to prevent thawing of the underlying ice-rich permafrost. This type of foundation design may also be beneficial to mitigate the effect of possible future climate warming on the structure. The heat pump cooling system presented in this paper is designed to decrease the temperature of the permafrost foundations soils to a design value. The heat extracted from the ground is used for heating of the building above. The foundation system has been installed at several locations in Longyearbyen and Sveagruva in Svalbard over the last 20 years. From our point of view the foundation design presents an attractive alternative to pile foundations both from an economical and a technical point of view. The paper describes in detail the foundation design using heat pumps, including case studies and cost comparison with conventional pile foundations of the frozen ground.

Keywords: engineering; foundations; geotechnical; permafrost; warming.

Introduction

Foundation design in Svalbard was traditionally based on pile foundations or shallow foundations. These foundation techniques require a ventilated air space of 0.5–1.0 m between the insulated floor and the ground surface. Pipelines for water supply and sewage were insulated and heated and attached outside under the insulated floor of the building. In this manner the heat flow from the building was restricted from entering the ice-rich permafrost soils.

The new technique described in this paper has several advantages compared to conventional piles or shallow foundations.

Climatic Conditions in Svalbard

The Svalbard archipelago is situated 74°N–81°N and 10°E–35°E. The land area is approximately 62,000 km^2 (Fig. 1). Svalbard has an exceptionally mild climate compared to North America and Russia at the same latitude, mainly due to the warming effect of the Gulf Stream and low pressures transporting heat northwards. Longyearbyen is located at 78°N, 11°E on Spitsbergen in the Svalbard Archipelago. Longyearbyen is the main settlement in Svalbard and has today approximately 2000 citizens. The main activities are coal mining, education, research and tourism.

Figure 2 shows the mean annual air temperature at the Longyearbyen/Svalbard Airport during the period 1912–2006. Monitoring of air temperature at the Svalbard airport commenced in 1975. Data earlier than 1975 is from air temperature monitoring in Longyearbyen. Figures 3 and 4 present the air freezing index and thawing index for Longyearbyen. It can be observed from the figures that there is a trend of increasing mean annual air temperatures during the last 20 to 30 years. In the same period the air freezing index is decreasing (indicating warmer winters) and the air thawing index is increasing (indicating warmer summers). However, Figures 2, 3, and 4 also show that the area has previously experienced warm periods, especially 1920 to the 1940s and 1950s.

It can also be observed from the figures that 2006 and 2007 have been extremely warm years, and this advocates a foundation design that can mitigate the effects of possible climate warming.

Conventional Foundation Design in Svalbard

Foundation design in Svalbard was traditionally based on pile foundations or shallow foundations. These foundation

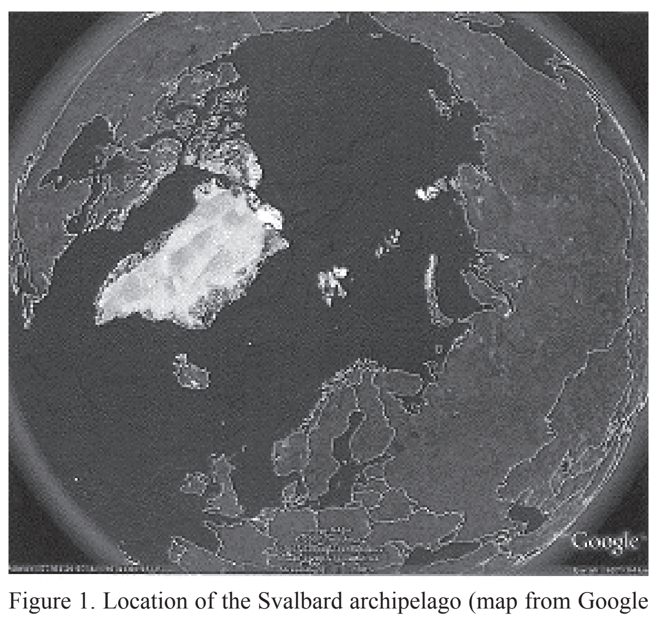

Figure 1. Location of the Svalbard archipelago (map from Google Earth, earth.google.com).

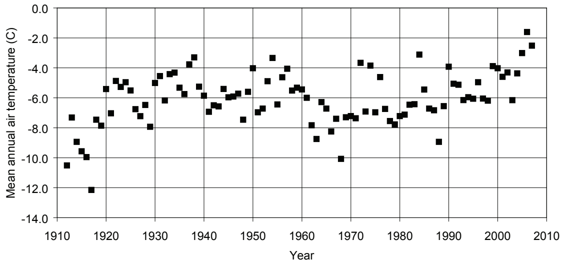

Figure 2. Mean annual air temperatures, Longyearbyen 1912–2007.

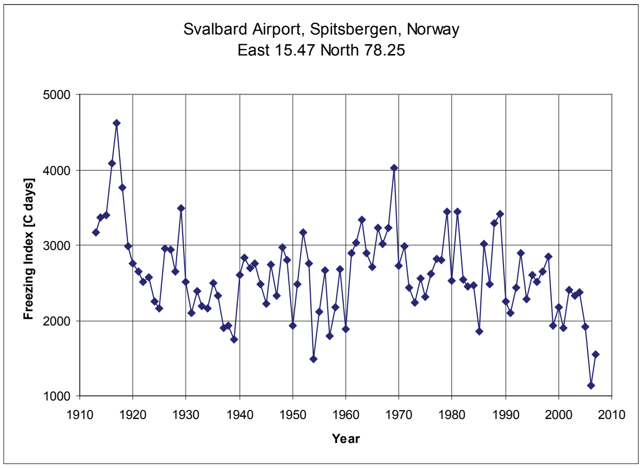

Figure 3. Air freezing index, Longyearbyen 1912–2006.

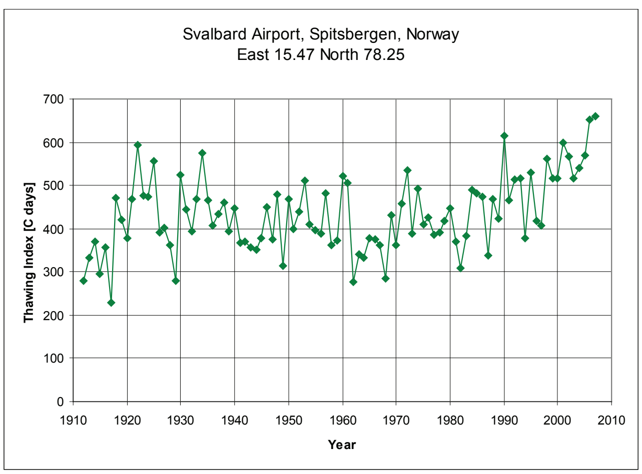

Figure 4. Air thawing index, Longyearbyen 1912–2007

techniques require a ventilated air space of 0.5–1.0 m between the insulated floor and the ground surface. Pipelines for water supply and sewage were insulated and heated and attached to under the insulated floor of the building. In this manner the heat flow from the building was restricted from entering the ice-rich permafrost soils.

In the 1980s the main author, in collaboration with a contractor and the local mining company, developed new equipment for predrilling boreholes for pile installation. The new drill rig was capable of drilling 300 mm diameter holes to a depth of 12 m beneath the surface. This meant that installation and grouting of prefabricated concrete, steel, or wooden piles became the preferred foundation technique in Svalbard.

However, this meant as mentioned above, that the building had to be elevated above the ground which is, in our opinion, not ideal from an esthetical, practical, or economical point of view.

Heat Pump Cooling System

Based on experience from the development of a district heating system utilizing heat pumps in Bergen Harbour, Norway, the idea of using heat pumps in permafrost areas was born. A heat pump will lower the ground temperature, and the heat extracted from the ground can be used in the heating of the interior of the building. In 1986 the first building using the new technique was constructed in Sveagruva, Svalbard (N77°53′, E16°41′) (Instanes 1988). The storage building had an area of 900 m^2. Because of the high foundation loads, pile foundations were not a good solution for this project. The building was therefore placed directly on the ground using heat pumps to artificially lower the ground temperature (Fig. 5).

The following procedure was used for clearing the site and installing the heat pump system (Fig. 6):

- The site was drained and leveled in order to lead surface water away from the building.
- A mimimum 0.5 m thick layer of sand, gravel fill was placed on the natural terrain and compacted.
- Forty mm PVC cooling pipes were placed on the sand, gravel layer in a 100 mm thick reinforced concrete slab.
- The cooling fluid circulated in the pipes is a mixture of glycol and water.
- Two hundred mm thick Styrofoam insulation was placed on top of the concrete slab.
- A plastic film was placed on top of the insulation in order to stop vapour diffusion.
- A 700 mm layer of fine sand was placed between the insulation and the floor of the building (gravel size can also be used in this layer). The thickness of this layer is governed by the necessary slope of drainage pipes.
- The concrete slab on top of the sand layer was reinforced and had a thickness of 150 mm. It was designed for large mobile loads from cranes and vehicles inside the building.

In addition to the first use in Sveagruva described above, the foundation system has been installed for three buildings in Longyearbyen: *Næringsbygget* (1989 and 1992), *Svalbardbutikken* (1990) and more recently in the ISS-building (20052006)(Fig. 7).

The technique is especially useful when the foundation loads are high and in areas with difficult foundation soils such as marine, saline, ice-rich, silts and clays, frequently found in Longyearbyen and Sveagruva (Instanes & Instanes 1998).

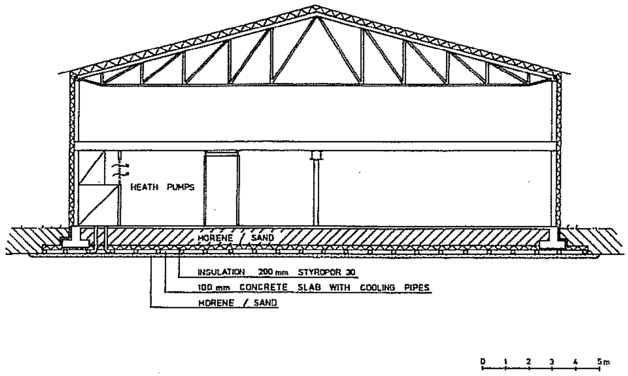

Figure 5. Cross-section of the storage building in Sveagruva.

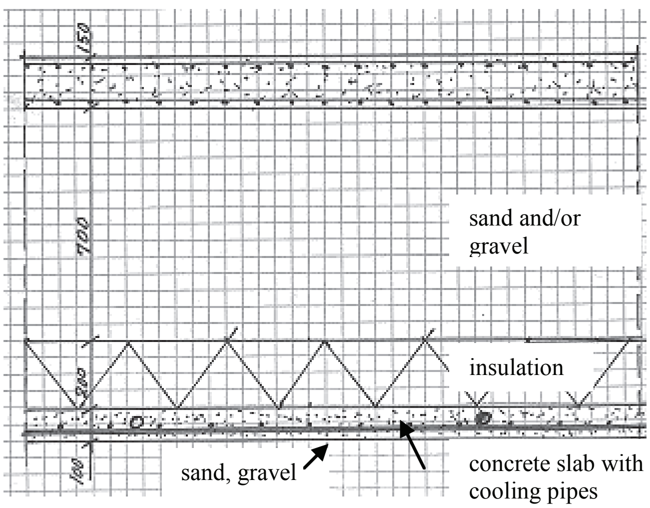

Figure 6. Detail of the foundation system.

ISS-Building, Longyearbyen

The ISS-building is a laundry that was constructed in 2004–2005. The site lies close to the Advetfjord and is thermally affected by the sea. The foundation soils consist of saline (3%–4%), ice-rich, silty clay. The permafrost temperature at 10 m depth is approximately -3°C to -4°C. The design criterion for the foundations was maximum settlement of 5 cm in 20 years. The foundation principle for this building is similar to what has been described in the previous section.

Figure 8 shows the layout of the cooling pipes for the ISS-building.

The total area covered by the cooling pipes is 600 m^2 (15 m x 40 m) and the total length of the pipes was 760 m. The maximum horizontal distance between parallel pipes was 0.75 m. Two parallel systems were installed, one primary main system and one secondary backup system

Pile foundations were considered for this building, but due to the difficult soil conditions, relatively warm permafrost, and the warm interior of the building (up to +40°C), it was not considered a technically safe solution during possible climate warming. The heat pump cooling system was therefore selected.

Figure 7. Overview of Longyearbyen. *Næringsbygget* and *Svalbardbutikken* are located in the center of the photo, ISS-building in the lower right corner.

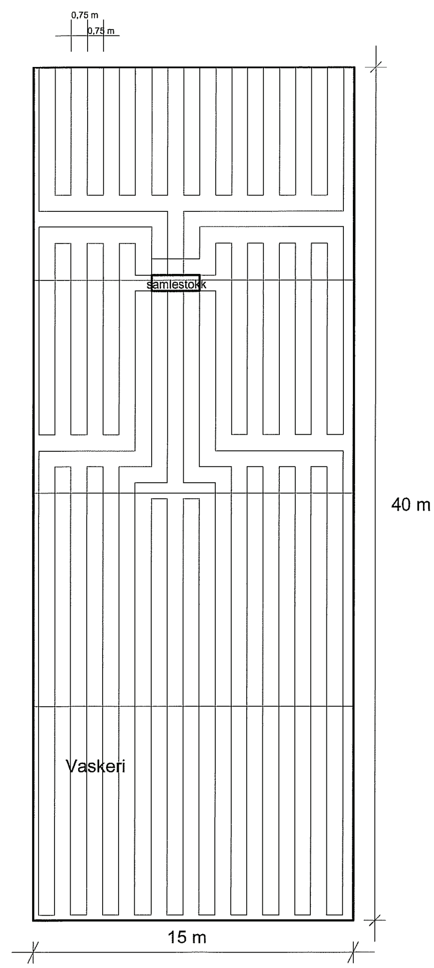

Figure 8. Layout of the cooling pipes at the ISS-buildings.

Thermal Considerations and Costs

The thermal design of the foundation system was based on the principle that the subsurface soils were to be cooled down to -5°C. To estimate the time needed to cool down the surface layers after construction, the thermal model TEMP/W, version 7.03 (Geo-Slope 2007) was used. TEMP/W is a finite element software that can model the thermal changes in the ground due to changing temperature or heat flux boundary conditions. It also accounts for the effects of the temperature dependent thermal conductivity, volumetric latent heat of fusion, and soil unfrozen water content.

Based on the thermal calculations and present climate warming, it was decided to let the cooling system run continuously with an internal fluid temperature varying between -5°C and -10°C.

The additional cost associated with the heat pump cooling system compared to conventional pile foundations was estimated to NOK1000 per m^2 (approximately USD180 per m^2).

Advantages Using a Heat Pump Cooling System

A foundation system in permafrost regions using a heat pump system is advantageous due to a number of reasons:

- The foundation design can be used in marginal zones with discontinuous permafrost or saline soils.
- The energy consumption is limited. The heat loss through the floor is regained by the heat pumps.
- The building can be constructed with the floor directly on the ground and the air space between the floor and the ground is avoided.
- The heat loss from the building because of wind blowing under the building is eliminated.
- The water supply and sewage pipes can be buried in the sand/gravel layer, making the access to the building and the entrance to the building easier.
- It becomes possible to have a warm "ground floor" in the building.
- Heating using hot water pipes can be installed in the floor; additional insulation may then be needed beneath the floor surface.
- For large buildings such as storage buildings and industrial facilities, it becomes costly to have floor structure spanning between piles or pillars. Using an embankment fill, the loads can be transferred directly to the embankment.
- Possible climate change and permafrost temperature increase can be mitigated.

References

Instanes, A. & Instanes, D. 1999. Pile design in saline permafrost at Longyearbyen. *Proceedings of the 10th International Conference on Cold Regions Engineering, Lincoln, NH, USA, August 16-19, 1999*: 222-231.

Instanes, B. 1988. Foundation design on permafrost with heat pumps. *Proceedings of the Fifth International Conference on Permafrost, Trondheim, Norway, August 2-5, 1988*: Volume 3: 73-74.

Geo-Slope. 2007. *Thermal Modelling with TEMP/W 2007. An Engineering Methodology.* Calgary, Canada: GEO-SLOPE International Ltd. 240 pages.

Five-Year Ground Surface Temperature Measurements in Finnmark, Northern Norway

Ketil Isaksen, Herman Farbrot
Norwegian Meteorological Institute, Oslo, Norway
Lars Harald Blikra
International Centre for Geohazards, Oslo, Norway
Bernt Johansen
Northern Research Institute Tromsø, Tromsø, Norway
Johan Ludvig Sollid, Trond Eiken
Department of Geosciences, University of Oslo, Oslo, Norway

Abstract

In 2002 a new permafrost monitoring program was initiated in Finnmark, northern Norway. A series of miniature temperature dataloggers were installed for continuous monitoring of ground surface and air temperatures. Results suggest that permafrost is widespread in Finnmark. However, the great areas of birch and pine forest in Finnmark appear to correspond to areas without permafrost, due to the forest acting as a snow fence and causing snow to accumulate. Above the timberline, snow depth seems to be the most critical factor for the formation of permafrost.

Keywords: mean ground surface temperatures; Northern Norway; permafrost distribution.

Introduction

Permafrost is widespread in the higher mountains of Norway. Extensive studies in southern Norway show that the lower regional altitudinal limit of mountain permafrost is strongly correlated to the mean annual air temperature (MAAT) and decreases eastwards with increasing continentally (e.g., Etzelmüller et al. 2003). However, there are, to date, few quantitative studies of the distribution of permafrost in northern Norway.

In 2002, a new permafrost monitoring program was initiated in Finnmark, which is the northernmost county of mainland Norway (Fig. 1). A series of miniature temperature dataloggers (MTDs) were installed for monitoring ground surface and air temperatures. Continuous ground surface monitoring was performed at five main sites in a transect starting at Varangerhalvøya in the extreme northeast of Norway, continuing southwest to the interior of Finnmarksvidda, and then northeastwards to the Gaissane.

The main aim of this study is to determine mean ground surface temperatures (MGST) at representative sites in Finnmark in order to provide an initial indication of the presence or absence of permafrost. The results are related to climate data, mainly air temperature and snow cover. In addition, a land-cover classification of the whole county is made that gives a first qualitative picture of the relationship between climate, vegetation and permafrost distribution in Finnmark. A review of the literature of permafrost occurrence in northern Scandinavia is presented, together with new results from 5 years of temperature monitoring.

Literature Review

Permafrost in northern Scandinavia

Until the 1980s, permafrost research in Northern Scandinavia was mainly concentrated on palsas, and a number of studies (cf. references in Åhman 1977) were undertaken following the pioneer work of Fries and Bergström (1910).

However, in the beginning of the 20th Century, field observations and theoretical considerations by Reusch (1901) suggested that permafrost was present in the mountains of Scandinavia. In the following decades few reports on permafrost occurrence in northern Scandinavia were published. A review of Scandinavian permafrost investigations up to 1950s is provided by Ekman (1957). During the drilling of a well at 1220 m a.s.l. in northern Sweden, permafrost was encountered at 70 m depth in bedrock (Ekman 1957). Frozen ground was also encountered during construction work in northern Finland and Sweden (e.g., Ekman 1957, Åhman 1977), but it is often difficult to decide whether these findings are perennially or only seasonally frozen ground (King & Seppälä 1988).

Since the beginning of the 1960s, research on permafrost outside the palsa mires has increased, with most reports on geomorphological indicators (Jeckel 1988).

In the 1980s, studies using geophysical methods encountered extensive permafrost at 50–100 m depth in bedrock in mountain areas of northern Sweden (e.g., King 1982) and Finland (King & Seppälä 1987). On a mountain in northern Sweden, Jeckel (1988) reported a mean ground temperature (MGT) at 2.3 m depth to be -0.8°C at 880 m a.s.l. In a 100 m deep borehole at Tarfalaryggen (1550 m a.s.l.) in northern Sweden, it has subsequently been shown that MGT is approximately -3 ºC and permafrost thickness is estimated to exceed 300 m (Isaksen et al. 2001). In northern Finland, Bottom Temperature of Snow (BTS) measurements suggested a lower limit of permafrost at 600-650 m a.s.l. on north-facing slopes (Jeckel 1988). In Finnmark, quantitative studies on permafrost distribution are limited and are

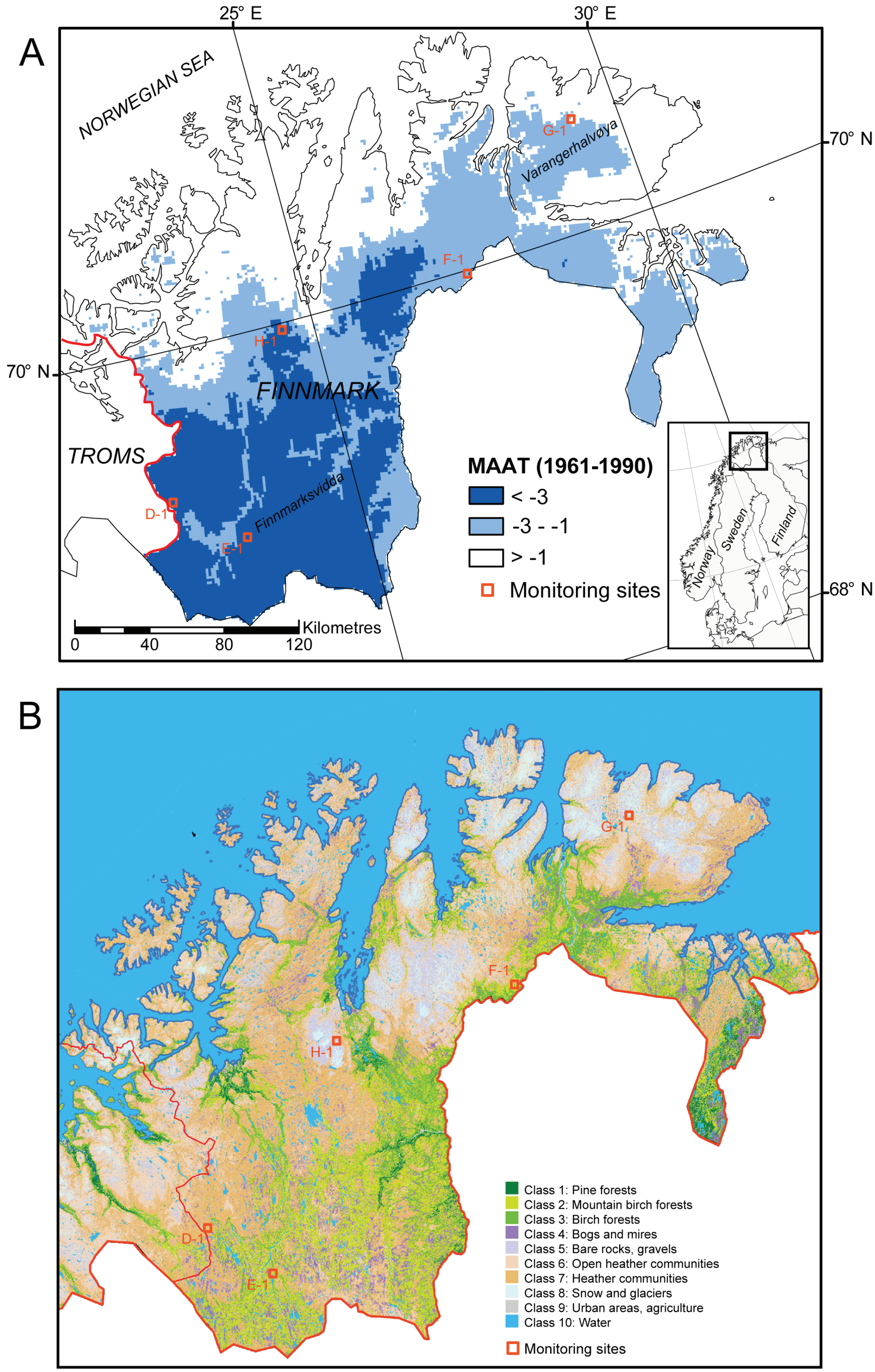

Figure 1. A) Location map showing the monitoring locations and three classes of the mean annual air temperature (MAAT, 1961-1990) in Finnmark (based on Tveito et al. 2000). (D-1) Biedjovággi; (E-1) Ávži; (F-1) Eliasvárri; (G-1) Basečearru; (H-1) Gaissane. The dark blue shows areas where MAAT is below -3°C, light blue shows areas where MAAT is between −3°C and −1°C and white is MAAT above -1°C. B) Classified land-cover map of Finnmark county based on Landsat TM/ETM+ satellite images (see text for details).

mostly restricted to palsa mires (e.g., Sollid & Sørbel 1998, Hofgaard 2007). In some settlements, however, permafrost degradation has caused problems during construction work (e.g., Lien 1991).

Study Sites

Three of the sites (D, G, and H), were chosen to optimize comparability and to ensure that the thermal properties were not excessively complex (Fig. 1). These were located at exposed locations, in the main ridge-crest or plateau areas, where snow accumulation is low. The last two sites are located in open (F) and dense (E) mountain birch forest.

The inner part of Finnmark (Finnmarksvidda, site E) is a plain having strong continentally and has the lowest MAAT when reduced to sea level in Norway. Typically, in this area, MAAT is -2.5°C to -4°C, with mean summer temperatures of 8°C to 10°C and mean winter temperatures of -15°C to -20°C. In winter, mean maximum snow depth is 25–75 cm. Towards the N (Site H) and NW (Site D), continentality decreases, with more mountains and more complex climate settings. Towards the NE, at Varangerhalvøya (Site G), mountain plateaus dominate, and the area is in the Arctic climate zone.

Methods

Land-cover classification

In this study, a land-cover map of Finnmark county (Fig. 1B) is developed (in 200 x 200 m resolution), reflecting degrees of density in the vegetation cover. The land-cover map is a subsection of the vegetation map produced for the entire country of Norway. In this map, a total number of 45 Landsat TM/ETM+ images were processed during six operational stages: (1) spectral classification, (2) spectral similarity analysis, (3) generation of classified image mosaics, (4) ancillary data analysis, (5) contextual correction, and (6) standardization of the final map products (Johansen & Karlsen 2005). Analysis performed on the spectral-only data is often denoted as the pre-classification stage of the process, whereas the post-classification process involves analysis and subsequent contextual corrections of the pre-classified image using ancillary data. In the final standardization part of the process, the defined classification units are related and described according to classification schemes well-established in the Norwegian botanical literature (Fremstad 1997). From the overall vegetation map of Norway, different thematic maps can be extracted.

Continuous temperature measurements

Nine (out of 20 in total) UTL-1 (Geotest, Switzerland) MTDs were used to determine the mean ground surface temperatures (MGST). They were buried at the surface (c. 0.05 m depth) and installed in Autumn 2002 and 2003. In addition, one logger was used to monitor the air temperature at G-1. At the other sites, air temperatures were obtained by interpolation from nearby weather stations (Table 1). The thermistors in the MTDs are of the type TMC-1T, with accuracy better than the 0.27°C given by

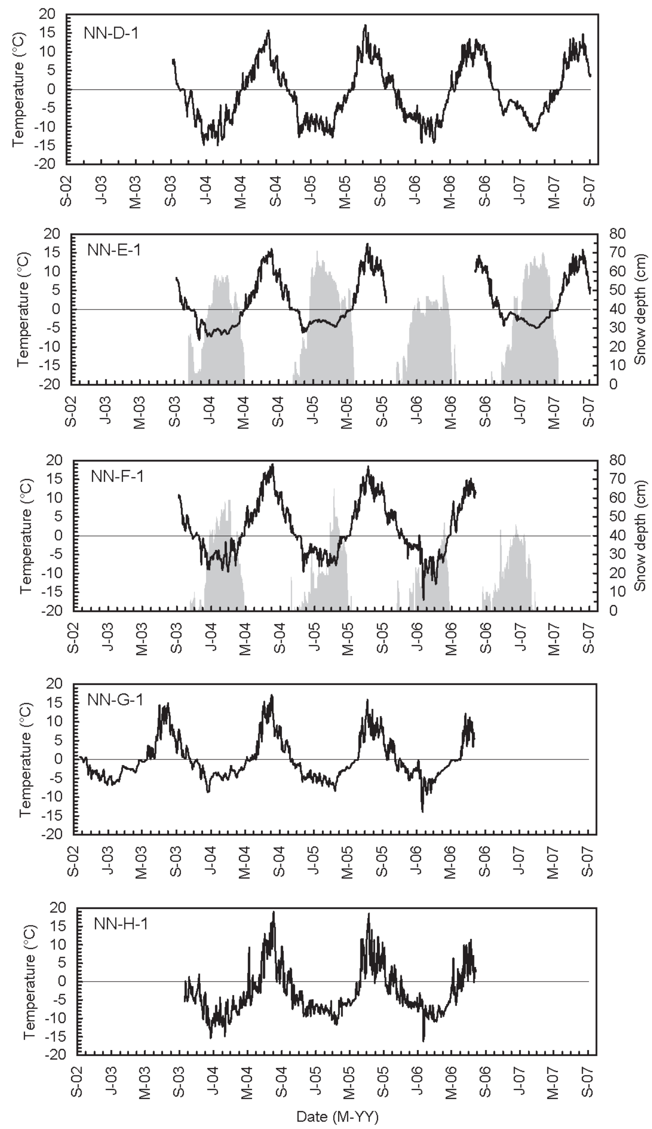

Figure 2. Daily ground surface temperatures obtained at the 5 main locations in Finnmark during 2002–2007. For E-1 and F-1, observed snow depth (grey bars) from nearby official stations are shown.

the manufacturer (Hoelzle et al. 1999). The MTDs were programmed to record the ground surface temperature every 6 hours (2 hours in Gaissane). In addition, the MTDs gave important information concerning damping of short-term air temperature fluctuations through the snow (reflecting the development and thickness of snow cover), the time when melting occurred at the bottom of the snowpack, and when snow disappeared.

Climate data from official weather stations were used to normalize the data sets in respect to the normal standard period 1961–1990, in order to establish the long-term MGST. The method is described by Ødegård et al. (2008). From the MTDs, monthly mean of ground surface temperatures were calculated and analyzed with the best nearby correlated air temperature from an official meteorological station having long-time series (e.g., 30-year period or more). A high correlation suggests low influence of snow and latent heat effects, which give a strong coupling between the air

Table 1. Key temperatures observed at monitoring sites. MGST = Mean ground surface temperature for observation period, maximum and minimum of 12-months running mean of MGST during observation period. MAT = Mean air temperature observed (Obs) and interpolated from nearest station (Int). MAT-anomaly: Air temperature deviation for observation period from nearest station. Air temperature at G-1 is for the period Sep03–Jun06. For interpolation of air temperature at G: 2,3,4, a gradient 0.53°C/100 m was used from G-1 (Laaksonen 1976). For the other interpolated values, the same gradient was used from nearest official weather station. H-1 and H-2 were from Farbrot et al. (2008). Type = Land type class (cf. Fig. 1B).

Site	Type	Alt. m a.s.l.	Period observed	MGST Obs.	MGST max Obs.	MGST min Obs.	MAT Obs.	MAT Int.	MAT-anomaly	MAGST Normal	MAAT Normal
D-1	6	739	Oct 03-Aug 07	-1.1	-0.1	-1.7	-	-3.4	1.5	-2.2	-4.9
E-1	3	355	Oct 03-Aug 07	1.6	2.0	1.0	-1.2	-	1.5	1.2	-2.6
F-1	2	130	Oct 03-Jun 06	2.2	2.5	1.9	-	0.6	1.9	0.8	-1.3
G-1	5	502	Oct 02-Jun 06	0.3	0.7	-0.2	-1.2	-	1.4	-1.0	-2.9
G-2	5	480	Oct 02-Jun 06	1.0	1.2	0.5	-1.1	-	1.4	-0.4	-2.8
G-3	5,6	415	Oct 02-Jun 06	1.3	2.1	0.5	-0.8	-	1.4	-0.3	-2.4
G-4	6	355	Oct 02-Jun 06	1.7	2.2	1.2	-0.5	-	1.4	0.1	-2.1
H-1	5	1034	Oct 03-Jun 06	-2.4	-2.1	-2.8	-	-2.9	1.6	-3.6	-4.5
H-2	5	618	Oct 03-Jun 06	-0.9	-0.6	-1.2	-	-0.9	1.6	-2.2	-2.5

and ground surface temperatures. Monthly air temperature anomalies (in respect to the 1961–1990 average) can then be used to correct the monthly observed ground surface temperature during the observation period (see Table 1).

Results

Vegetation types in Finnmark

The land cover map of Finnmark portrays the density of the vegetation cover at different levels. The coniferous pine forests are mainly located to the southern, continental parts of the county, constituting the largest areas along the main rivers in the area. In addition, the Pasvik area, south of Varangerhalvøya, is characterized by well-developed pine forests. The mountain birch forest, occupying large areas on Finnmarksvidda, is characterized by an open forest layer with heather and lichen species dominating the ground layer. The more dense and fertile birch forests are located mainly in the coastal regions. The differentiation in the mountain belt generally reflects the low-, the mid-, and the high-alpine belt of the region. Heather communities, with a closed vegetation cover, characterize the low-alpine belt. In the mid-alpine belt, the vegetation cover is more scattered due to harsher climate conditions. The high-alpine belt has bare rocks, boulder fields, and gravel ridges. Few vascular species are adapted to the climate conditions found here. This belt is characterized by mosses and lichen species.

Mean ground surface temperature (MGST)

Mean ground temperatures from 3–5 years of continuous monitoring (Fig. 2 and Table 1) show that:

a) the highest MGST were found in the forested areas (G-1 and E-1);
b) the lowest MGST were observed at the two highest sites (H-1) Gaissane and (D-1) Biedjovággi were bare rock and boulder fields dominate;
c) 12-month running means of MGST show large variation within the observation period at all sites. The difference between the highest and lowest 12-month MGST are between 0.6°C and 1.6°C; and
d) the mean air temperature (MAT) is generally 1–2.5°C lower than MGST. The largest difference is found at the two forested sites (2.8°C), while at the most exposed locations (H) the difference is only 0–0.4°C.

Correlation between ground surface temperature and air temperatures at G-1 is shown in Fig. 3. The results indicate a strong correlation. In general, the site is exposed to strong winds, leading to only a thin snow cover in late winter, probably not more than 0.3–0.5 m.

Data from official weather stations close to the monitoring sites show that the MAT during the observation period was 1.4–1.9°C above the 1961–1990 normal. By normalizing the observed MGT-values (Ødegård et al. 2008), data suggest that mean annual ground surface temperature (MAGST) is below 0°C at six sites. Only the two sites located in forest (E and F) and the lowermost site at Varangerhalvøya (G-4) have positive MAGST.

Discussion

In Norway, the Nordic mountain birch limit is close to the 8°C tetratherm (mean air temperature for June–September) (Wielgolaski 2005). However, the tetratherm limits decrease in relatively continental areas with high day temperatures during summer. This means that continental sites generally have a higher forest limit than more maritime sites even though the MAAT is equal (Meier et al. 2005, Wielgolaski 2005). Forest (mainly birch) is present in the interior of Finnmark where MAAT is far below 0°C (Fig. 1). The timberline is located at about 500 m a.s.l. on Finnmarksvidda (Meier et al. 2005).

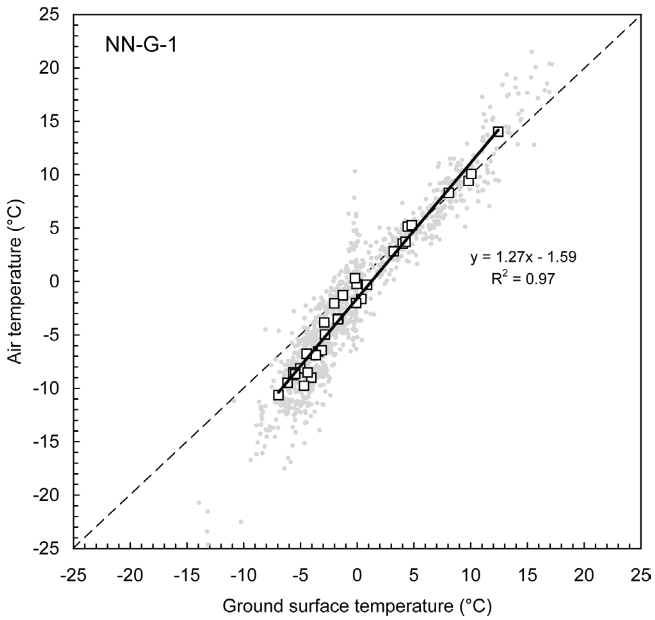

Figure 3. Mean daily (grey small dots) and monthly (open squares) ground surface temperature versus mean daily and monthly air temperature (2 m) during the period of record at G-1 Basečearru (Varangerhalvøya). Linear least squares regression coefficients and coefficient of determination (R^2) for the monthly values are shown.

Two sites, E-1 and F-1, are significantly warmer than the other study sites. The reason is the influence of the forest, which collects snow and therefore has a quite different energy-balance compared to wind-swept locations. Although cooler in summer due to radiation interception and higher evaporation (e.g., Rouse 1984), the near-surface ground temperatures in the forest are considerably warmer in winter than the other locations (Table 1). Hence, the forest in Finnmark largely prevents permafrost formation, making the forest line altitude very important in defining the permafrost limits. Although Scandinavian treelines are expected to advance in response to climate warming, there are indications of recessive treelines in northern Norway in contrast to southern Norway (Dalen & Hofgaard 2005). Above timberline, snow depth appears to be the most critical factor for the formation of permafrost (cf. King & Seppälä 1988). Results from Farbrot et al. (2008) and this study (Table 1) suggest that MGST above timberline in Finnmark can differ by 1–2°C due to variations in snow thickness. This is somewhat lower than values reported from southern Norway (e.g., Hauck et al. 2004, Ødegård et al. 2008).

King (1984) suggests that mountain permafrost in Scandinavia may be divided into continuous, discontinuous and sporadic. Their lower limits correspond to MAAT of -6°C and -1.5°C and sporadic permafrost may occur even in areas with positive MAATs. The transition between these belts is gradual. The temperature values for the lower limits are valid for the central Scandinavian mountain areas with moderately continental climate. The climate of Finnmark shows strong continentality, with generally thin snow cover. The results obtained from the MTDs and Farbrot et al. (2008) suggest that the proposed limits suggested by King (1984) can be adjusted in this region by lowering the limit of discontinuous permafrost to a MAAT of -1°C (Fig. 1). In areas colder than -3°C, permafrost seems to be widespread above timberline.

Conclusions

Miniature temperature dataloggers recording ground surface temperatures have been shown to provide data suitable for mapping the spatial variation in mean annual ground surface temperatures in Finnmark, and thus the possible presence or absence of permafrost at the sites. Results suggest that:

- Permafrost is widespread in Finnmark. The lower limit of discontinuous permafrost outside the palsa mires corresponds to mean annual air temperatures (MAAT) of approximately -1°C,
- Permafrost is probably present in the interior part of Varangerhalvøya. This is probably the northernmost permafrost area in north-western Europe (outside Russia) and can be regarded as polar permafrost
- Birch and pine forest in Finnmark appears to correspond with areas without permafrost. Trees cause snow to accumulate and insulate against strong ground cooling. Below the timberline and beside the palsa mires, formation of permafrost is possible at local exposed sites where snow does not accumulate, or cleared areas (in villages, on roads etc),
- Snow depth seems to be the most critical factor for the formation of permafrost above the timberline. However, variations in mean annual ground surface temperatures due to variations in snow depth seem to be lower in Finnmark (cf. Table 1) than in southern Norway, probably due to generally lower precipitation. Permafrost is apparently widespread in Finnmark in areas above timberline having MAAT lower than -3°C,
- Air temperatures for the previous 3–5 years have been 1.5–2.0°C warmer than the 1961–1990 average. In Finnmark permafrost is "warm" as it is only a few degrees below 0°C, which makes it very vulnerable to warming (cf. Isaksen et al. 2007), and
- The present monitoring program in Finnmark is being continued and will be included within the Norwegian funded IPY-project *Permafrost Observatory Project: A Contribution to the Thermal State of Permafrost in Norway and Svalbard*, (Christiansen et al. 2007). The relation between MGST and snow and vegetation should be further investigated, and similar measurements should be made at other sites to see if these findings can be generalized to larger areas.

Acknowledgments

This study is part of a Norwegian network project, *Permafrost og ustabile fjellsider,* supported by the Geological Survey of Norway, Norwegian Meteorological Institute and the University of Oslo. In addition, part of the study was financed by the Norwegian Research Council (project no.

157837/V30). C. Harris smoothed the English, and two anonymous reviewers gave important improvements to the manuscript. The contributions of all persons and institutions mentioned are gratefully acknowledged by the authors.

References

Åhman, R. 1977. Palsar i NordNorge. Meddelanden från Lunds universitets Geografiska institution avhandlingar LXXVIII.

Christiansen H et al. 2007. Permafrost Observatory Project: A Contribution to the Thermal State of Permafrost in Norway and Svalbard, TSP NORWAY. *Eos Trans. AGU* 88(52), Fall Meet. Suppl., Abstract C21A-005.

Dalen, L. & Hofgaard, A. 2005. Differential Regional Treeline Dynamics in the Scandes Mountains. *Arctic, Antarctic and Alpine Research* 37: 284-296.

Ekman, S. 1957. Die Gewässer des Abisko-Gebietes und ihre Bedingungen. Kungl. Sv. Vetenskapsakademiens Handlingar 6:6 (Stockholm).

Etzelmüller, B., Berthling, I. & Sollid, J.L. 2003. Aspects and Concepts on the Geomorphological Significance of Holocene Permafrost in Southern Norway. *Geomorphology* 52: 87-104.

Farbrot, H., Isaksen K & Etzelmüller B. 2008. Present and Past Distribution of Mountain Permafrost in Gaissane Mountains, Northern Norway. *Proceedings of the Ninth International Conference on Permafrost, Fairbanks, Alaska, June 29-July 3, 2008* (this proceedings).

Fremstad, E. 1997. Vegetasjonstyper i Norge. *NINA Temahefte* 12: 1-279.

Fries, T. & Bergström, E. 1910. Några iakttagelser öfver palsar och deres förekomst i nordligaste Sverige. – Stockholm, Geol. Fören. Förh. 32: 195-205.

Hauck, C., Isaksen, K., Vonder Mühll, D. & Sollid, J.L. 2004. Geophysical surveys designed to delineate the altitudinal limit of mountain permafrost; an example from Jotunheimen, Norway. *Permafrost and Periglacial Processes* 15: 191-205.

Hoelzle, M., Wegmann, M. & Krummenacher, B. 1999. Miniature temperature dataloggers for mapping and monitoring of permafrost in high mountain areas: First experience from the Swiss Alps. *Permafrost and Periglacial Processes* 10, 113-124.

Hofgaard, A. 2007. Monitoring of palsa peatlands. Initial investigation in Goahteluoppal, West-Finnmark 2006. *NINA Report* 257, 33 pp.

Isaksen, K., Holmlund, P., Sollid, J.L. & Harris, C. 2001. Three deep alpine-permafrost boreholes in Svalbard and Scandinavia. *Permafrost and Periglacial Processes* 12: 13-25.

Isaksen, K., Sollid, J.L., Holmlund, P. & Harris, C. 2007. Recent warming of mountain permafrost in Svalbard and Scandinavia. *Journal of Geophysical Research* 112: doi:10.1029/2006JF000522.

Jeckel, P.P. 1988. Permafrost and its altitudinal zonation in N. Lapland. In: Senneset, K. (ed.), *Permafrost Fifth International Conference,* 170-175.

Johansen, B. & Karlsen S.R. 2005. Monitoring vegetation changes on Finnmarksvidda, Northern Norway, using Landsat MSS and Landsat TM/ETM+ satellite images. *Phytocoenologia* 35: 969-984.

King, L. 1982. Qualitative and quantitative Erfassung von Permafrost in Tarfala (Schwedisch-Lappland) und Jotunheimen (Norwegen) mit Hilfe geoelektrischer Sondierungen. *Zeitschrift für Geomorphologie, N. F.*, Suppl.-Bd. 43: 139-160.

King, L., 1984. Permafrost in Skandinavien. Untersuchungs-ergebnisse aus Lappland, Jotunheimen und Dovre/Rondane. *Heidelberger Geographische Arbeiten* 76: 174.

King, L. & Seppälä, M. 1987. Permafrost thickness and distribution in Finnish Lapland; results of geoelectric soundings. *Polarforschung* 57: 127-147.

King, L. & Seppälä, M. 1988. Permafrost sites in Finnish Lapland and their environment occurrences. *Permafrost, ICOP IV*, Trondheim, 1988, Vol 1.

Laaksonen, K. 1976. The dependence of mean air temperatures upon latitude and altitude in Fennoscandia (1921-50). *Ann. Academ. Scient. Fennicae A III* 119, 19 pp.

Lien, R. 1991. Investigation on permafrost in Kautokeino (in Norwegian). *Statens Vegvesen*, 91/3114-01.

Meier, K.-D., Thannheiser, D., Wehberg, J. & Eisenmann V. 2005. Soils and nutrients in northern birch forests: A case study from Finnmarksvidda, northern Norway. In: Wielgolaski, F.E. (ed*.), Plant ecology, herbivory, and human impact in Nordic mountain birch forests*. Berlin: Springer-verlag. P. 19-34.

Ødegård, R.S., Isaksen, K., Eiken, T. & Sollid, J.L. 2008. MAGST in Mountain Permafrost, Dovrefjell, Southern Norway, 2001-2006. *Proceedings of the Ninth International Conference on Permafrost, Fairbanks, Alaska, June 29-July 3, 2008* (this proceedings).

Reusch, H. 1901. Some contributions towards an understanding of the manner in which the valleys and mountains of Norway were formed (in Norwegian). In *NGU Yearbook 1900*. Norwegian Geological Survey, Kristiania, 124-263.

Rouse, W.R. 1984. Microclimate of Arctic tree line. 2: Soil microclimate of tundra and forest. *Water Resources Research* 20: 67-73.

Sollid, J.L. & Sørbel, L. 1998. Palsa bogs as a climate indicator—examples from Dovrefjell, southern Norway. *Ambio* 27: 287-291.

Tveito, O.E., Førland E.J., Heino, R., Hanssen-Bauer, I., Alexandersson, H., Dahlström, B., Drebs, A., Kern-Hansen, C., Jónsson, T., Vaarby-Laursen, E. & Westman, Y. 2000. Nordic Temperature Maps. *DNMI Klima 9/00 KLIMA*. 54pp.

Wielgolaski, F.E. 2005. History and environment of the Nordic mountain birch. In: Wielgolaski, F.E. (ed.), *Plant ecology, herbivory, and human impact in Nordic mountain birch forests*. Berlin: Springer-verlag. P. 3-18.

Comparable Energy Balance Measurements on the Permafrost and Immediately Adjacent Permafrost-Free Slopes at the Southern Boundary of Eurasian Permafrost, Mongolia

Mamoru Ishikawa
Institute of Observational Research for Global Change, JAMSTEC, Japan
Faculty of Environmental Earth Science, Hokkaido University, Japan

Yoshihiro Iijima
Institute of Observational Research for Global Change, JAMSTEC, Japan

Yinsheng Zhang
Institute of Observational Research for Global Change, JAMSTEC, Japan

Tsutomu Kadota
Marine Work Japan, Japan

Hironori Yabuki
Institute of Observational Research for Global Change, JAMSTEC, Japan

Tetsuo Ohata
Institute of Observational Research for Global Change, JAMSTEC, Japan

Battogtokh Dorjgotov
Institute of Geography, Mongolian Academy of Science, Mongolia

N. Sharkhuu
Institute of Geoecology, Mongolian Academy of Science, Mongolia

Abstract

Mongolian *Larch* forests are situated at the southern boundary of the Eurasian Taiga that vulnerably coexists with the permafrost. This paper describes hydro-meteorological situations at the permafrost underlying forested areas and also in the immediately adjacent permafrost-free pasture slopes, and evaluates the vulnerable and reciprocal features of permafrost and forest. Records spanning nearly two years showed considerably reduced net radiation onto the ground surface, lower air and soil temperatures, and wetter soils at the forest site. The analysis showed small imbalances of energy balance components between atmospheric and active layer heat fluxes estimated independently, if the effects of organic matter and porosity are considered for the soil thermal parameters. This indicates the importance of considering thermal properties of the forest soil in the preservation of permafrost when the forest shading, which greatly reduces incoming solar radiation, is well known.

Keywords: active layer; energy budget; forest; pasture; southern boundary of Eurasian permafrost.

Introduction

In northern Mongolia, the distribution of permafrost is mosaic-like, yielding ecological contrast even over small geographic areas. *Larch* forests dominate on the north-facing permafrost slopes, while pastures dominate the south-facing slopes. Ongoing degradation of permafrost due to recent climatic warming (Sharkhuu 2003) is expected to lead to reduced forested area and to influence the regional hydro-ecological system.

Since 2002, the Institute of Observational Research for Global Change, of the Japan Agency of the Marine-Earth Science and Technology (JAMSTEC) has continuously made hydro-meteorological observations at sites in northern Mongolia, with the aim of understanding the water cycle on the basin-scale and predicting future changes. The distribution and vulnerability of permafrost are the major focuses of this project, because changes in these parameters would significantly alter river runoff regimes and soil wetness, resulting in the degradation of ecosystem services of this region. This paper describes hydro-meteorological situations at the permafrost underlying forested areas and also in the immediately adjacent permafrost-free pasture slopes, and evaluates the vulnerable and reciprocal features of permafrost and forest.

Regional Settings and Observations

The observation sites used in this study are located on the northern forested (NF site) and southern pasture (SP site) slopes east of Ulaanbaatar (Fig. 1a). The nearest meteorological station, approximately 2 km away from these sites, had a mean annual air temperature of -3.5°C from 1992 to 2000. Mean annual total precipitation at Ulaanbaatar, where most of the precipitation occurs from June to August, was only 300 mm.

Analyzing cores obtained by drilling investigation, Ishikawa et al. (2005) found ice-rich permafrost and nearly

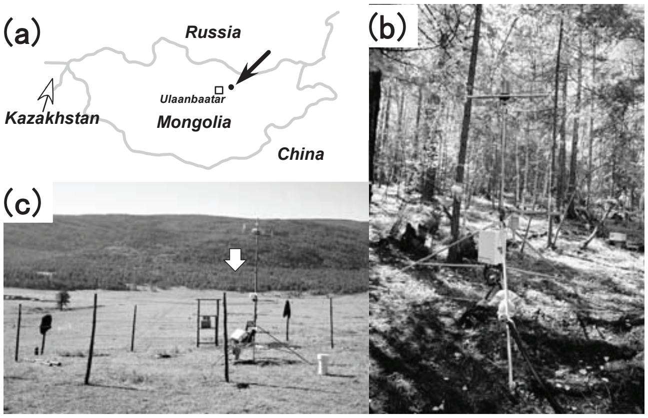

Figure 1. (a) Location of the observational site. Views of the setting of AWS (automatic weather monitoring system) on the (b) NF site and (c) SP site. The arrow in (c) indicates the location of the NF site.

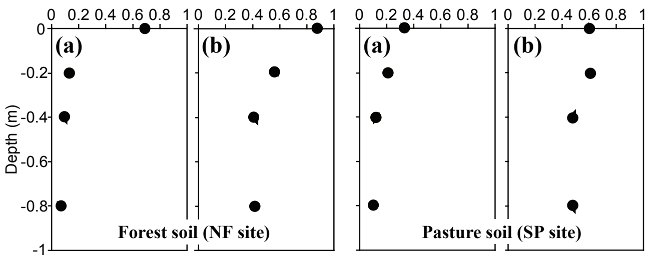

Figure 2. Soil properties at the NF and SP slope sites, based on laboratory analyses. (a) Organic ratio of soil particles (m^3/m^3), (b) porosity (m^3/m^3).

saturated active layer with a thickness of 2.4 m beneath the NF site, while cores showed the SP site to be permafrost-free, highly unsaturated, seasonally frozen ground beneath this site.

In summer 2003, an automatic weather monitoring system (AWS) with a capacity to measure four radiation components, air temperature, relative humidity, wind speed at two heights and surface soil heat flux, soil temperatures at depths of 0, 0.2, 0.4, 0.8, 1.2, 2.4, and 3.2 m, and moistures at 0, 0.2, 0.4, 0.8, and 1.2 m was installed at both sites (Figs. 1b, 1c). Soils at both sites comprised mainly sand cobbles covered with an organic-rich layer of several centimeters. We sampled undisturbed upper-layer soils and analyzed porosity, density, and organic contents in the laboratory (Fig. 2).

Analysis

Neglecting heat supplied by rainfall, the surface energy balance equation during the snow-free period is

$$Q_n = Q_h + Q_e + Q_g \tag{1}$$

where Q_n is net radiation calculated simply by adding the four radiation components; sensible heat flux, Q_h, latent heat flux, Q_e, and the ground heat flux from heat pile, Q_g. The turbulent fluxes Q_h and Q_e were estimated by the Bowen ratio method. The Bowen ratio, B, is expressed after approximating fluxes using gradients in the following manner:

$$B = Q_h / Q_e = C_a \Delta T / (L^{lv} \Delta q), \tag{2}$$

where C_a is the specific heat of air, L^{lv} is the latent heat for vaporization, and ΔT and Δq are the vertical gradients of air temperature and specific humidity, respectively. Combining equations (1) and (2), the latent heat flux is

$$Q_e = \rho_w (Q_n - Q_g)/(1+B), \tag{3}$$

where ρ_w is the density of water. Q_n was estimated from measurements of the four radiation components. We used surface soil heat flux sensor data as Q_g, relative humidity and air temperatures taken at two (for NF site) and three (SP site) heights, removing spurious data from original 10-minute-interval datasets as indicated by Ohmura (1982).

The conductive (sensible) soil heat flux was calculated using Fourier's law of heat transport,

$$j_h^i = -k_h^i \frac{\partial T}{\partial z} \tag{4}$$

where k_h is bulk thermal conductivity, T is temperature, and z is depth for the i-th soil layer from the surface downward. The non-conductive heat component, r_h, is expressed in terms of heat production in W/m^3, and is estimated by considering the one-dimensional energy conservation as formulated by:

$$r_h^i = \frac{\partial}{\partial t}[c_h^i T] + \frac{\partial}{\partial z} j_h^i \ , \tag{5}$$

where c_h is bulk heat capacity and t is time. Total thermal energy stored in the soil layer, $Q_{g\text{-}c}$, is the summation of conductive and non-conductive heats of each layer as

$$Q_{g-C} = \sum_i (j_h^i + r_h^i d^i), \tag{6}$$

where d^i is thickness of the i-th layer. The mid-depth of the i-th layer was set to be at the i-th depth measurement from the surface. Neglecting energy flux in the deepest soil layer, we calculated energy flux components in the upper three layers, having thicknesses of 0.3, 0.3 and 0.4 m from the surface. The finite element formulation used to solve equation (6) is described in Ishikawa et al. (2006).

Calculation of $Q_{g\text{-}C}$ requires data on the bulk thermal conductivity (k_h) and bulk heat capacity (c_h) of each soil layer. The spatio-temporal variations of the above variables are known to be largely dependent on the ratio between soil particle, water, and ice. Two models with different numbers of parameters were evaluated. The first model used conventional parameterization, which does not include the effects of thermal parameters of air occupying porosity and organic matter (Farouki 1981):

$$k_h^i = k_m^{1-n} k_s^{\theta_s} k_w^{\theta_w}\ , \tag{7}$$

$$c_h^i = (1-n)\rho_m c_m + \theta_s \rho_s c_s + \theta_w \rho_w c_w \tag{8}$$

In a second model, we modified equations (7) and (8) in order to consider mineral, water, ice, organic contents, and thermal parameters of air as,

$$k_h^{i'} = k_a^{n-\theta_s-\theta_w} k_o^{\theta_o} k_m^{1-n-\theta_o} k_s^{\theta_s} k_w^{\theta_w}, \tag{9}$$

$$c_h^{i'} = (1-n-\theta_o)\rho_m c_m + \theta_s \rho_s c_s + \theta_w \rho_w c_w + \theta_o \rho_o c_o, \tag{10}$$

where θ is volumetric fraction, n is porosity, ρ is density, k is thermal conductivity, c is specific heat (for subscripts, as follows: m, mineral; o, organic matter; s, ice; w, water). The ρ, c, and k for the mineral, organic matter, ice, and water components of soil modeled in equations (7) ~ (10) were set as $\{\rho_m, \rho_s, \rho_w, \rho_o\} = \{1.55, 0.92, 1.0, 1.3\} \times 10^3$ kg/m^3, $\{c_m, c_s, c_w, c_o\} = \{0.733, 2.11, 4.22, 1.93\} \times 10^3$ J/kg/K, and $\{k_m, k_s, k_w, k_o\} = \{0.54, 2.2, 0.57, 0.026\}$ W/m/K. We used laboratory soil analysis data for the volumetric fraction of organic matter and porosity (Fig. 2).

Results

Due to forest shading, the summer net radiation at the NF site was greatly reduced, corresponding to 26% of that at the SP site (Figs. 3, 4). This was more pronounced in the winter period. We found nearly zero downward shortwave radiation due to further reductions by topographic relief at this site. Mean T_a during the first December, January, and February was -19.4°C at the NF site and -18.1°C at the SP site.

The forest canopy intercepted rainfalls on the forest floor; the NF site received 87.5% and 97.4% of rainfall of that of the SP site during the summers 2003 and 2004, respectively. The interception loss of snow was not obvious; rather, snow depth (SD) at the SP site remained less than for the forest, possibly due to redistribution by wind.

Permafrost condition was found to occur at below 280

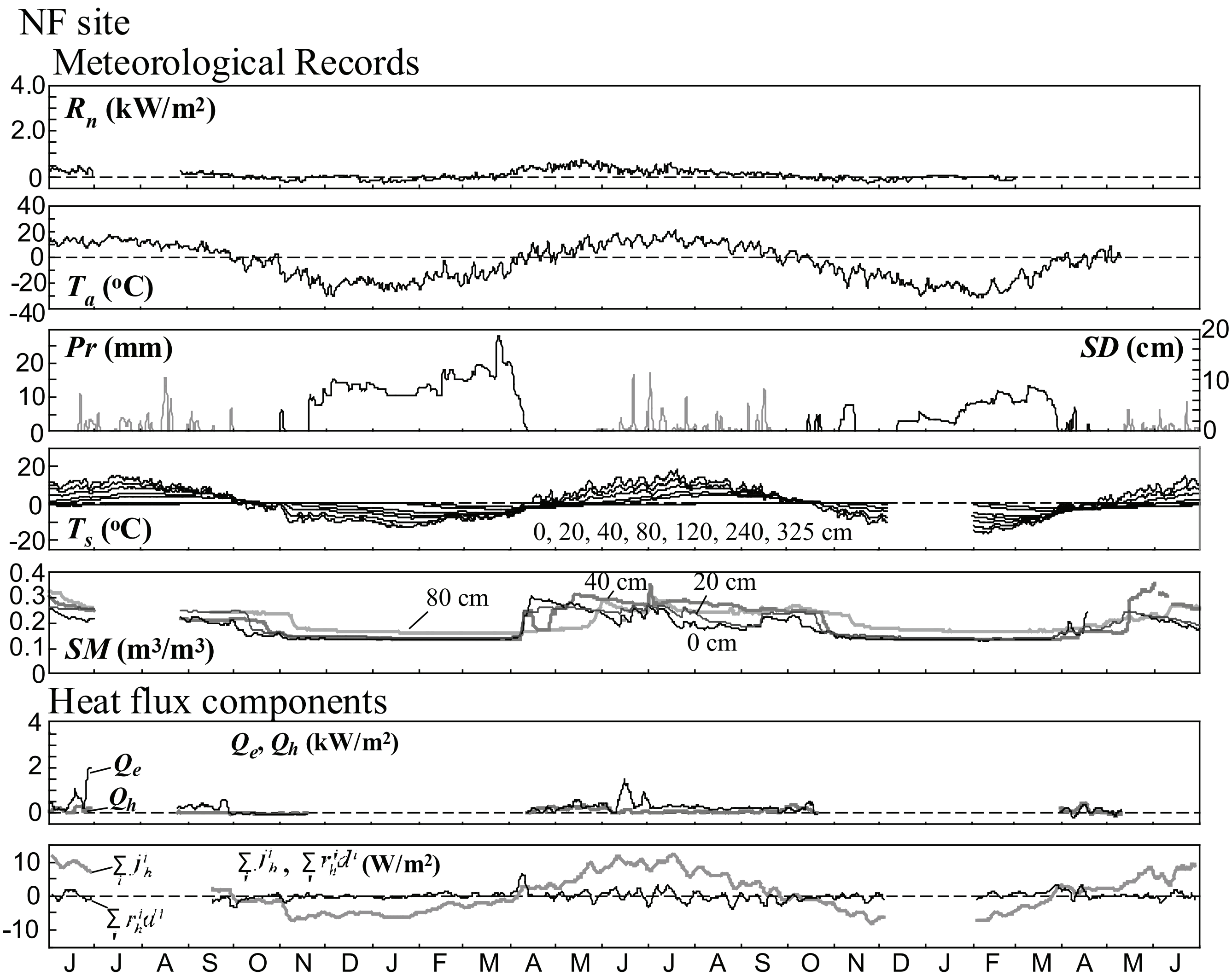

Figure 3. Data and estimated heat flux components at the NF site. See Figure 1b for a picture of the site. Data are missing for some periods due to instrument failure. R_n: net radiation, T_a: air temperature, P_r: rainfall, SD: snow depth, T_s: soil temperatures, SM: soil moistures. For soil moisture, we showed only the upper four depths that were used for calculating soil heat flux components. Q_e: atmospheric latent heat flux, Q_h: atmospheric sensible heat flux, Σj_h^i: total soil conductive heat flux, $\Sigma r_h^i d^i$: non-conductive heat fluxes transferred into the upper three soil layers (0.3, 0.3 and 0.4m in thickness, respectively, extending down from the surface). Five-day running mean values are plotted for each of the heat flux components. For Q_e and Q_h, only results obtained during snow-free period are shown. Calculations of Σj_h^i and $\Sigma r_h^i d$ by equations (9) and (10) are plotted.

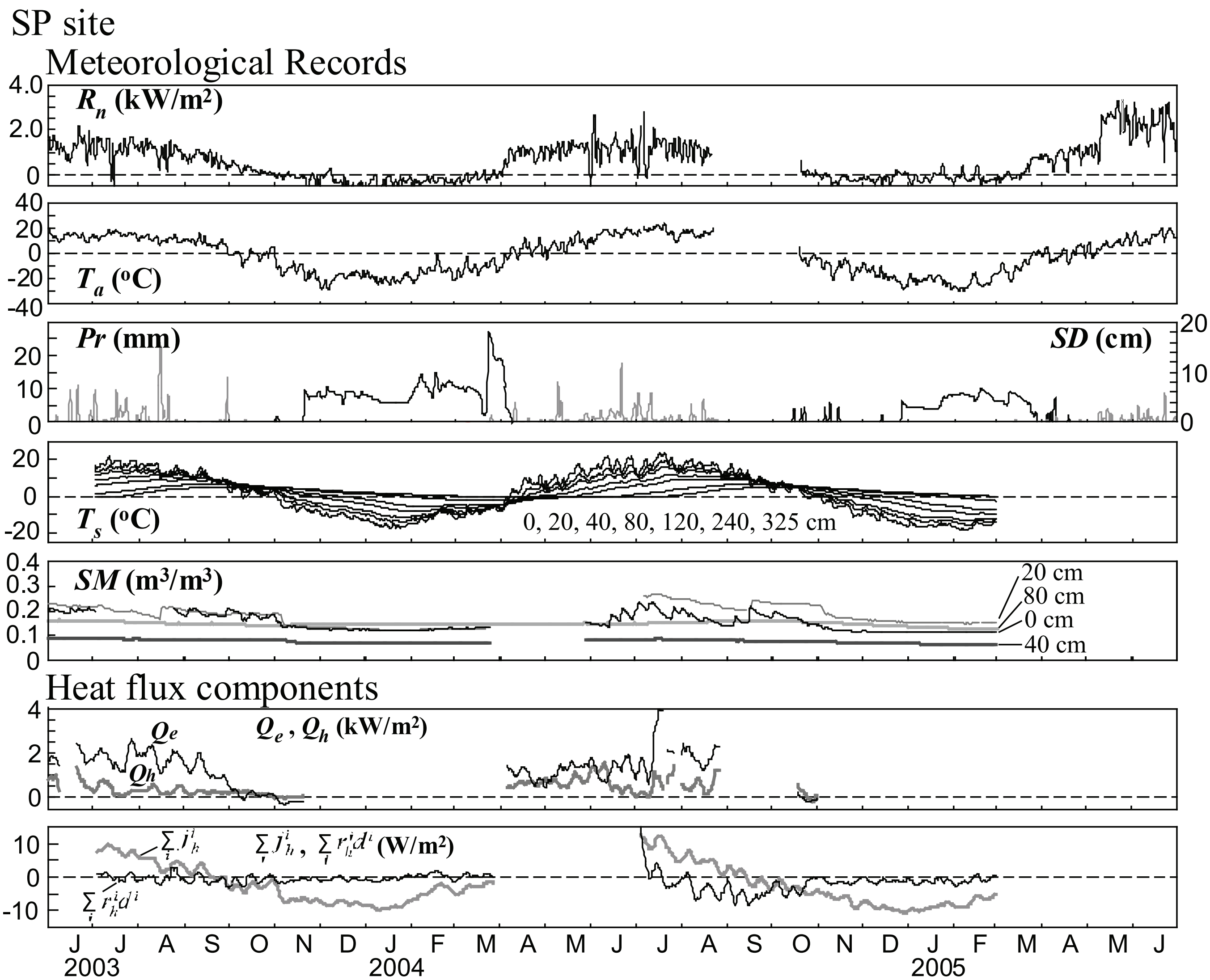

Figure 4. Data records and estimated heat flux components at the southern pasture slope (SP) sites. See Figure 1c for the environments. Same caption as Figure 3.

cm at the NF site, where soil moisture becomes greater for the deeper soils. This is probably due to the impermeability of the underlying permafrost. Contrastingly with the permafrost-free SP site, wet soils were restricted near the surface soil layers. At this site, the regions with significant short-term fluctuation in soil moisture contents are restricted to the shallowest depths (0 and 20 cm), even during the rainy season. Greater net radiation would modulate immediate evaporative soil water loss, as indicated in the greater sensible heat flux at the SP site.

The wet soils at the NF site are probably maintained by lesser atmospheric latent heat (Figs. 3, 4). The ratio of summer evaporation at the FP and SP sites was 0.22; this estimation was approximated with eventual lysimetric measurements. Q_e remained at levels similar to Q_h until the end of May when water for evaporation was mostly derived from snowmelt infiltration and seasonal thawing of the active layer.

Thereafter, Q_h decreased, possibly due to reduced downward shortwave radiation due to the growing forest canopy. Concurrent Q_e, on the other hand, remained higher than Q_h, largely due to water supply from rainfall. The seasonal development of atmospheric heat flux components mentioned here was generally similar to that at the SP site, which experienced greater evaporation from snowmelts, with higher moisture in the seasonal soil thaw and rainfalls.

The origin of soil latent heat is very complicated (e.g., Kane et al. 2001). Consumption of soil latent heat, $r_h < 0$, possibly arises from evaporation and thawing processes, whereas release, $r_h > 0$, arises from condensation and freezing. Furthermore, r_h reflects the heat transfer accompanied by liquid (water, vapor) movements. Identification and quantification of these processes are required for further comparisons between the energy equivalent of water phase changes and changes in soil moisture contents (e.g., Roth & Boike, 2001).

In our study, more negative r_h for JAS 2004 at the SP site than that at the NF site indicates a larger evaporative water loss at the SP site, as suggested by atmospheric heat fluxes (Figs. 3, 4). At the NF site, the most obvious latent heat releases occurred during the snow disappearance period of April 2004, when the temperature over the active layer

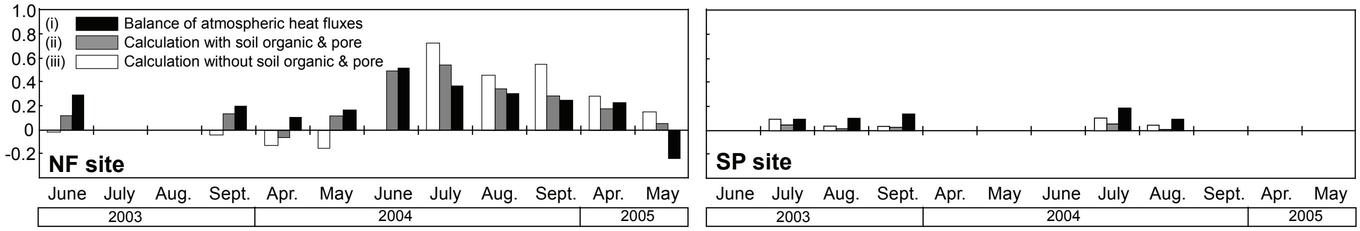

Figure 5. Total soil heat flux transferred into the soil layers (Q_{g-c} up to depth of 1.0m) as expressed in decimal fractions to the net radiation for the northern forested (NF) and southern pasture (SP) sites during the snow-free period (June to September).

increased due to considerable subfreezing to nearly the thawing point in a short period. Similarly, the active layer was warmed in the second snow disappearance period, but this warming was less obvious. Both warming events were probably triggered by pipe-like snowmelt infiltration, which is controlled by snow cover thickness and thus by soil moisture of the near surface soil layer (Beven & Germann 1982, Ishikawa et al. 2006).

Discussion

Figure 5 demonstrates the relative importance of the heat flux components transferred into the upper three soil layers (up to depth of 1.0 m), comparing three calculations: (i) from the balance of atmospheric heat balance components, (ii) without soil organic matter and pores occupied by air (using equations 7 and 8), and (iii) with these parameters (equations 9 and 10). For the NF site, the ratio of soil energy storage to net radiation throughout the period was 22.0%. This value agreed well with that from calculation (iii) (22.1%), but differed with that from calculation (iii) (26.5%). These values approximate the observations at other permafrost sites (e.g., Rouse 1984, Boike et al. 1998, Iwahana et al. 2005, Ishikawa et al. 2006).

For the SP site, the ratio of soil energy storage to net radiation was considerably smaller than that at the NF site, indicating soil heat storage to be a minor contributor. The average value through the period from calculations (i), (ii) and (iii) was 11.5, 5.7 and 2.9%, respectively. We postulate that larger energy difference encountered by calculations (i) and (iii) at the NF site reflect unrealistic parameterization of the soil thermal properties (i.e., thermal conductivity and heat capacity). On the other hand, the difference was not obvious at the SP site where the conventional soil parameterizations without organic and pore effects are probably still accurate.

These findings indicate that energy interaction at the forest site greatly depends on the surface organic-rich layers that prevent the active layer from undergoing further warming during the summer period. Furthermore, this shows the importance of thermal properties of forest soils for preservation and development of the permafrost underlying this slope with well-known forest shading that greatly reduces incoming solar radiation to the ground surface. The pore- and organic-rich forest soil would be fed by fallen leaves and branches from *Larch* trees during autumn. Degrading such soils would accelerate permafrost degradation, even though the forests still shade the ground surface.

Acknowledgments

Local residents and members of the Institute of Hydrology and Meteorology near the observational sites kindly assisted with year-round maintenance of the meteorological instruments. This work was financially supported by the Institute of Observational Research for Global Change, Japan Agency of Marine-Earth Science and Technology.

References

Beven, K. & Germann, P. 1982. Macropore and water flow in soils. *Water Resources Research* 18: 1311-1325.

Boike, J., Roth, K. & Overduin, PP. 1998. Thermal and hydrologic dynamics of the active layer at a continuous permafrost site (Taymyr Peninsula, Siberia). *Water Resources Research* 34: 355-363.

Farouki, O.T. 1981. *Thermal Properties of Soils*. CRREL Monograph No. 81-1, 136 pp.

Ishikawa, M., Zhang, Y., Kadota, T. & Ohata, T. 2006. Hydrothermal regimes of the dry active layer. *Water Resources Research* 42: W04401, doi:10.1029/2005ER004200.

Ishikawa, M., Sharkhuu, N., Zhang, Y., Kadota, T. & Ohata, T. 2005. Ground thermal and moisture conditions at the southern boundary of discontinuous permafrost, Mongolia. *Permafrost and Periglacial Processes* 15: 1-8.

Iwahana, G., Machimura, T., Kobayashi, Y., Fedrov, A.N., Konstantinov, P.Y. & Fukuda, M. 2005. Influence of the forest-cutting on the thermal and hydrological regimes of the active layer near Yakutsk, eastern Siberia. *Journal Geophysical Research* 110: G02004, doi:10.1029/2005JG000039.

Kane, D., Hinkel, K.M., Goering, D.L., Hinzman L.D. & Outcalt, S.I. 2001. Non-conductive heat transfer associated with frozen soils. *Global Planetary Change* 29: 275-292.

Ohmura, A. 1982. Objective criteria for rejecting data for Bowen ratio flux calculations. *Journal of Applied Meteorology* 21: 595–598.

Roth, K. & Bioke, J. 2001. Quantifying thermal dynamics of a permafrost site near Ny-Ålesund, Svalbard. *Water Resources Research* 37: 2901-2914.

Rouse, W.R. 1984. Microclimate at arctic tree line: 2, Soil microclimate of tundra and forest. *Water Resource Research* 20: 67-73.

Sharkhuu, N. 2003. Recent changes in the permafrost of Mongolia, *Proceedings of the Eighth International Conference on Permafrost:* 1029-1034.

Developing a Digital Hydrogeological Map of Central Yakutia (The Lena-Aldan Watershed)

L.D. Ivanova
Melnikov Permafrost Institute, SB RAS, Yakutsk, Russia
N.M. Nikitina
Melnikov Permafrost Institute, SB RAS, Yakutsk, Russia

Abstract

A digital hydrogeological map of Central Yakutia is being developed in *ArcView* GIS at scale of 1:1,000,000. This project was initiated in 2005 by the Groundwater Laboratory of Permafrost Institute. To implement the project, a *Microsoft Access* database was created containing information obtained from hydrogeological drill holes and on talik water and subpermafrost water in central Yakutia. The digital map model contains the following main themes: *Hydrogeological Zoning*, *Local Talik Aquifers of the Permeable Zone*, *Subpermafrost Aquifers of the Poorly Permeable Zone*, *Local Talik Aquifers Talik-to-Area Rate, Drill Holes, Possible Use of Groundwater for Drinking Purposes, Water in Intrapermafrost and Open Taliks* and others.

Keywords: aquitard; groundwater; permafrost; subpermafrost; talik; zoning.

Introduction

The Lena-Aldan watershed is situated in the southeastern part of the Yakutian artesian basin, a first-order hydrogeological unit (Tolstikhin 1970). The average thickness of permafrost is 300–400 m, and maximal is 600–800 m. This area contains suprapermafrost and intrapermafrost water in the permeable zone and subpermafrost waters in the poorly permeable zone. Suprapermafrost water of lake and river taliks occurs virtually under all lakes and rivers that are common to abundant in the Lena-Aldan watershed. They yield little water, generally of poor quality. Under the largest lakes and rivers of Lena and Amga, open taliks occur that are hydraulically connected with subpermafrost water. Taliks beneath the Lena River present a stable water supply resource and the water is used for drinking. Intrapermafrost water is found in the fourth fluvial terrace of the Lena River in sand deposits along the surface of the contact with carbonate bedrock. It has good quality and is used for drinking. Subpermafrost water of the Lena-Aldan watershed is sterile, because the permafrost protects it from human contamination. Nevertheless, quality and quantity of water depend on complex litho-tectonic, cryohydrogeologic and hydrodynamic factors. In some cases, subpermafrost water can contain high concentrations of natural occurring chemical elements, which limits its use for drinking.

Classification and analysis of voluminous and diverse data is required in support of groundwater quality management and both municipal and industrial water supply use in Central Yakutia. This task is accomplished by developing a digital groundwater map. The digital hydrogeological map of Central Yakutia, at a scale of 1:1,000,000, is visualized in ArcView GIS for users, and is accessible for editing and updating. Compilation and modeling of geological, hydrogeological and geocryological information have been made by standard methods (Vasiliev et al. 1999, Torgovkin & Fedorov 1999) using the Microsoft Access program and the ArcInfo and ArcView GIS technologies. This map is the first digital groundwater map being developed for a permafrost region.

Methods of Thematic Mapping

During the first phase of the project, a talik and subpermafrost water database was created in *Microsoft Access* compatible with *ArcView* GIS mapping software. The database contains information for more than 200 drill holes. The holes are scattered unevenly over the map area. Most of them are concentrated in major river valleys and lake basins, while the fewest are near watershed divides. The database consists of electronic tables which contain the drill hole identification number and geographic coordinates, hydrogeological unit, lithostratigraphic column, permafrost characteristics, aquifer parameters, and groundwater hydrochemistry.

The next stage was to digitize the Central Yakutia sheet of the Geological Map of Yakutia, 1:500,000 scale (Grinenko et al. 2000) and adjust it to a mapping scale of 1:1,000,000 with generalization of stratigraphic units. The digitized geological contours were used as a raster background for vectorization of thematic layers with consideration of permafrost conditions. Then, statistical processing of data, and analysis and interpretation of general geographical information (descriptive, qualitative and quantitative characteristics, and identification of parameters) were made. This allowed us to integrate the informational resources to the geospatial model and compile the hydrogeological stratification schemes to develop a digital model of the hydrogeological map.

To construct thematic layers of the map, paper maps were first drawn using common mapping methods. Where only sparse data were available, correlation and extrapolation techniques were used (Zarutskaya & Krasilnikova 1988). Then, the layers were scanned and digitized. Numerous and diverse thematic data are referenced in a common spatial coordinate system in the Gauss-Kruger projection (129 central meridian).

Content of the Digital Map

The digital map consists of two components. The Basic component includes several layers: frame, grid, inhabited places, roads and hydrographic features. The Thematic Maps component will have the following layers: *Geological Map, Hydrogeological Zoning, Local Talik Aquifers of the Permeable Zone, Subpermafrost Aquifers of the Poorly Permeable Zone, Local Talik Aquifers Talik-to-Area Rate, Chemistry of Local Talik Aquifers of the Permeable Zone, Chemistry of Subpermafrost Aquifers of the Poorly Permeable Zone, Water in Intrapermafrost and Open Taliks, Drill Holes, Permafrost Thickness Isolines, Possible Use of Local Talik Aquifers of the Permeable Zone*, *Possible Use of Subpermafrost Aquifers of the Poorly Permeable Zone*.

Hydrogeological Zoning layer; the limits of hydrogeological structures of second order correspond to the *Hydrogeological Zoning Map of Russian Federation* scaled 1:2,500,000. In the Lena-Aldan and Lena-Vilyui artesian basins of second order, third and fourth orders of hydrogeological structural units have been identified (Fig. 1 and Table 1), based on our earlier studies (Shepelev et al. 1984, Ivanova & Nikitina 2000).

Local Talik Aquifers of the Permeable Zone layer; aquifers in Cenozoic, Mesozoic, and Paleozoic rocks are mapped in accordance with litho-stratigraphic principle. The aquifer's color in the map corresponds to the stratigraphic subunit color. In case if aquifer is presented by two stratigraphic subunits, two colors are used (Fig. 2)

Subpermafrost Aquifers of the Poorly Permeable Zone layer: maps the first subpermafrost aquifer. The map demonstrates subpermafrost groundwater units in Mesozoic, Paleozoic and Proterozoic formations and the aquitard of Archean metamorphic rock. The color of the aquifer or aquifer unit corresponds to the stratigraphic subunit color.

Local Talik Aquifers' Talik-to-Area Rate layer: the cross-hatching shows the talik-to-area rate value, which is calculated as a percentage ratio of total talik area in a given geomorphological unit to its area, and ranges between 0.5 and 4.0%.

Chemistry of Local Talik Aquifers of the Permeable Zone and *Chemistry of Subpermafrost Aquifers of the Poorly Permeable Zone* layers: background speckle shows the combination of dissolved solids concentration (TDS)

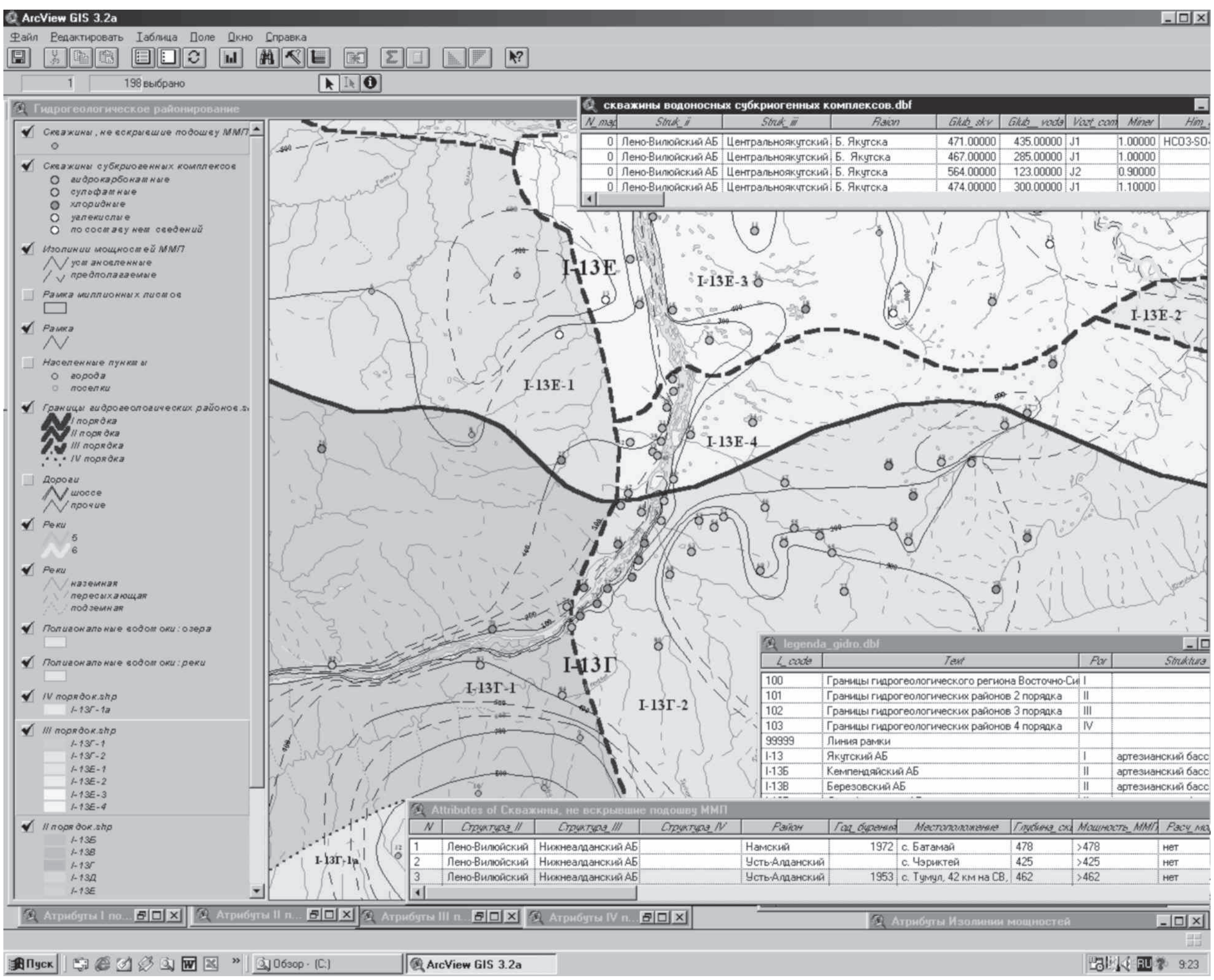

Figure 1. A fragment of *Hydrogeological Zoning* thematic layer combined with *Permafrost Thickness Isolines.*

Table 1. Third- and fourth-order hydrogeological units.

Hydrogeological Unit		Stratigraphic age	Thickness of frozen aquitard, m	Groundwater flow type	Groundwater quality
Lena-Vilyui artesian basin I-13E (I order)	Vilyui artesian basin I-13E-1 (III order)	K	400-600	Tabular-pore and tabular in terrigenous sediments and poorly lithified rocks	Fresh
	Pre-Verkhoyansk artesian basin I-13E-2 (III order)	K_1-J_1	350-450	Tabular and tabular-fissured in terrigenous poorly lithified and fissured rocks	Fresh
	Lower Aldan artesian basin I-13E-3 (III order)	N-K	350-500	Tabular-pore in terrigenous sediments	Fresh
	Central Yakutian artesian basin I-13E-4 (III order)	J, T, Є, A	200-500	Fissure and fissure-vein in terrigeneous in fissured rocks and fissure and fissure-karst in terrigenous-carbonate rocks	Fresh and slightly saline
Lena-Aldan artesian basin I-13Г (I order)	Middle Lena aretesian basin I-13Г-1 (III order)	J, $Є_{1-2}$	310-490	Fissure-tabular and fissure in terrigeneous fissured rocks and fissure-karst in karsted and saline rocks	Fresh and slightly saline
	Buotama-Amga cryogeological basin I-13Г-1a (IV order)	A	600-880	Lithologic aquitard of metamorphic rocks	–
	Lena-Amga artesian basin I-13Г-2 (III order)	J, $Є_{1-2}$	200-500	Fissure-tabular, fissure and fissure-karst in terrigeneous fissured and karsted carbonate rocks	Fresh and slightly saline

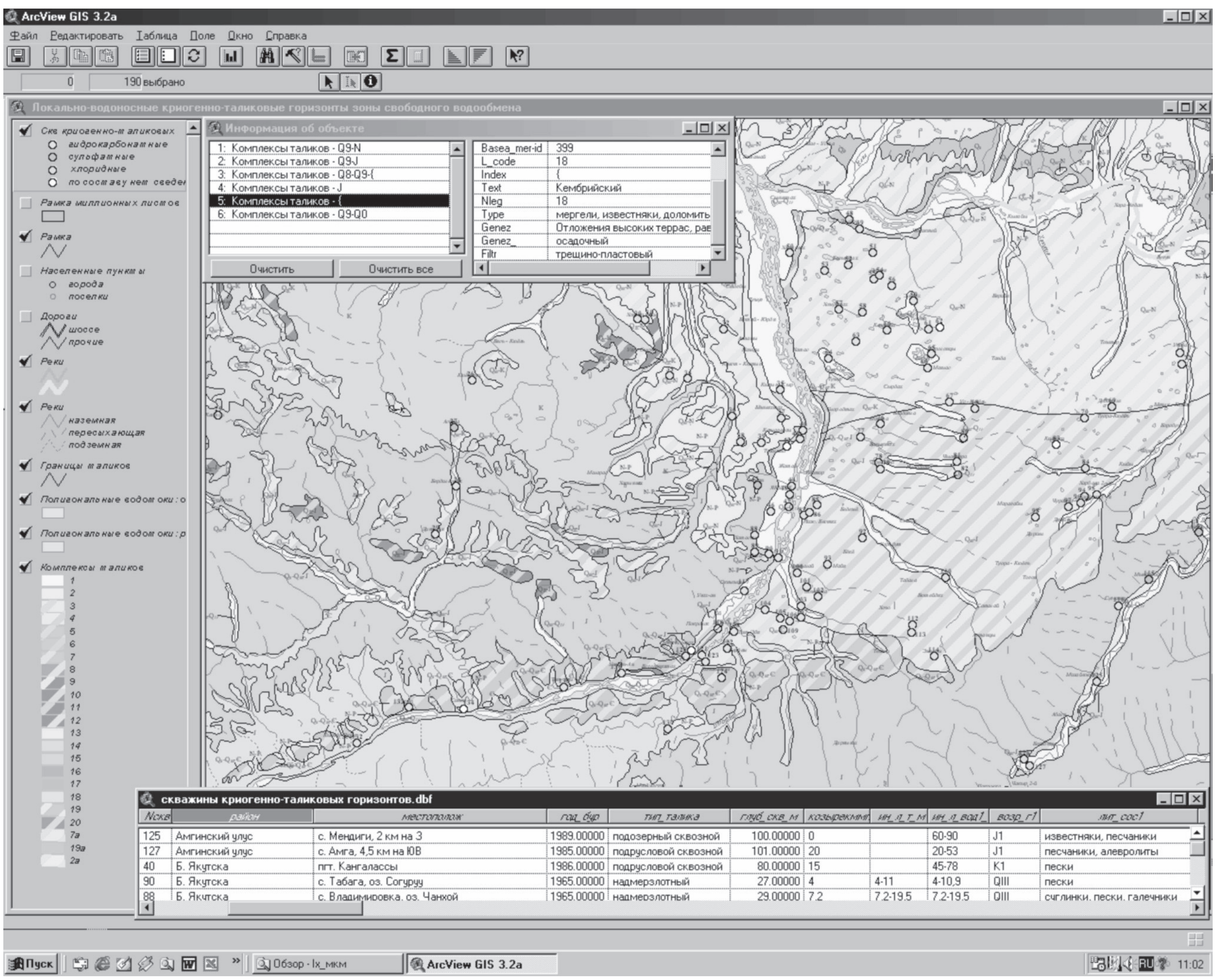

Figure 2. A fragment of *Local Talik Aquifers of the Permeable Zone* thematic layer combined with *Drill Holes* theme.

and anionic composition of underground water in the following gradation (g/dm^3): nearly pure freshwater (up to 0.5), freshwater (0.5–1.0), slightly saline water (1.0–3.0), moderately saline water (3.0–10.0), and very saline water (10.0–50.0).

Water in Intrapermafrost and Open Taliks layer: not-to-scale symbols show intrapermafrost, river and lake open taliks, springs, icings and glades. In *Drill Holes* layer, different symbols show (a) borings through closed talik, open talik and subpermafrost aquifers; and (b) holes that failed to reach the base of permafrost.

Permafrost Depth Isolines layer: shows the depth to the base of permafrost at 100 m intervals. Isolines were constructed based on analysis of measurement data and the well-known method of geographic interpolation.

Possible Use of Local Talik Aquifers of the Permeable Zone and *Possible Use of Subpermafrost Aquifers of the Poorly Permeable Zone* layers: delineate the areas where groundwater quality meets drinking water standards.

Each layer contains an attribute table, which is formed automatically and contains a standard data set. These tables are linked to thematic data in the Microsoft Access database. It is possible to connect attribute tables between the layers, to join the layers, and to add table and raster drawing images to the layer layout.

Conclusions

The digital hydrogeological map will become a more effective tool for accomplishing hydrogeological tasks brought about by groundwater exploration and use in permafrost regions. The map will allow users to change scales without quality loss, abandon the overwhelming integrated maps in favor of interrelated thematic layers in versions that meet their specific purposes, and easily access the data via attribute tables. Information can be stored and added in electronic format and is accessible for analysis and modeling. The digital hydrogeological map will be useful for those involved in water supply, monitoring, conservation, and contamination abatement.

References

Grinenko, V.S. 2000. *The Geological Map of Yakutia*. Saint-Petersburg: VSEGEI.

Ivanova, L.D. & Nikitina, N.M. 2000. More precise permafrost hydrogeological zonation of the southern portion of the Yakutian artesian basin. *Kriosfera Zemli* IV(2): 52-56.

Kurennoy, V.V., Golitsyn, M.S., Tikhonenkov, Y.E., Shakhnova, R.K., Shpak, A.A. & Leonenko, L.V. 2001. *Construction of Hydrogeological Maps Using Computer Technologies*. Moscow: Russian Ministry of Natural Resources, 196 pp.

Shepelev, V.V., Tolstikhin, O.N., Piguzova, V.M., Nikitina, N.M., Nekrasov, I.A., Lomovtseva, N.S. & Ivanova, L.D. 1984. *Groundwater in the Permafrost Regions of East Siberia*. Novosibirsk: Nauka, 192 pp.

Tolstikhin, O.N. 1970. Hydrogeological Zoning. In: A.I. Efimov & I.K. Zaitsev (ed.), *Hydrogeology of the USSR*. *Vol. XX: Yakut ASSR*. Moscow: Nedra, 91-99.

Torgovkin, Y.I. & Fedorov, A.N. 1999. An application of GIS-technologies in permafrost-landscape studies (exemplified by Spasskaya Pad study area, Central Yakutia). *INTERCARTO-5. GIS for sustainable development of territories (June. 1999). Papers of the International Conference, part 4. GIS in Regional Research/ - Yakutsk, Yakutsk Universitiy Press*: 68-77.

Zarutskaya, I.P. & Krasilnikova, N.V. 1988. *Mapping of Natural Conditions and Resources*. Moscow: Nedra, 299 pp.

Sensitivity of Permafrost Landscapes to Anthropogenic Impacts in the Northern Verkhoyansk Area, Subarctic Yakutia

Rozaliya N. Ivanova
Melnikov Permafrost Institute SB RAS

Abstract

Three sensitivity levels to human impacts such as deforestation and agricultural practices have been distinguished for permafrost landscapes in the northern Verkhoyansk area situated within the Northern Taiga subzone. Sensitivity of permafrost landscapes is estimated based on cryoindicators such as volumetric ice content, active layer thickness, depth to wedge ice, and thaw subsidence. An essential criterion of permafrost landscape sensitivity is the ground ice: its form, depth, amount, and pattern of distribution in the ground. Sensitivity of landscapes in the northern Verkhoyansk area is the integral characteristic of its geoecological condition.

Keywords: anthropogenic impacts; cryoindicators; geoecological condition; permafrost landscape; sensitivity.

Introduction

The northern Verkhoyansk is a vast northern area that has received little study in terms of permafrost ecology. It is the world's coldest region "called the "cold pole of Eurasia." It has the whole variety of landscapes, ranging from lowland bogs to high mountains, both natural and anthropogenic.

To understand the microclimatic and thermal conditions, as well as the ecological state of natural and anthropogenic permafrost landscapes in the central part of the Yana River valley, monitoring observations on four sites were conducted by the Permafrost Institute during the period of 1989 to 1992. The study area was located in the vicinity of Batagai, at 67°31′N latitude, 134°41′E longitude, 130 m elevation a.s.l. (Ivanova 2003).

Permafrost landscape is defined as a homogeneous natural complex which functions under the influence of cryogenesis, with unique combinations of permafrost characteristics (Fedorov 1991). Permafrost landscape sensitivity is referred to as the degree of its reaction to anthropogenic impacts (Grave 1980).

The geoecological state of permafrost landscapes is deteriorated by disruption of the ground surface, as well as by formation of numerous polygonal structures, thermokarst depressions, cracking of the ground and heaving of peat soils due to anthropogenic factors (frequent fires, damage to the surface vegetation and soil by off-road movement of vehicles, agricultural practices, etc.).

Forest clearing and surface cover disturbances cause strong changes in ice-rich soils. Among the effects are three- to four-fold increase in seasonal thaw depth, melting of wedge ice and development of thaw depressions up to 0.8 m in depth.

Results and Discussion

Three sensitivity levels have been distinguished for permafrost landscapes in the northern Verkhoyansk area situated within the Northern Taiga subzone, based on permafrost landscapes classifications according to terrain sensitivity to anthropogenic impacts and environmental changes (Grave & Melnikov 1989, Fedorov 1991, 1996, Zotova & Tumel 1996, Gavriliev et al. 2001) (Table 1).

The low sensitivity landscapes have low volumetric ice contents (less than 20%). Ice wedges occur below 2.0 m from the ground surface. The thickness of the active layer is 1.0 m or more. The development of adverse cryogenic processes is not expected.

The landscapes of moderate sensitivity have volumetric ice contents of 20% to 40%. The active layer is less than 1.0 m in thickness, surface subsidence is 0.2 to 0.5 m and the top of ice wedges occurs below 1.0 m depth.

The highly sensitive landscapes are characterized by volumetric ice contents of over 40%. Adverse soil and cryogenic processes are present, such as thermokarst depressions 0.5 to 0.8 m in depth, soil disruption and erosion. Ice wedges occur within 1.0 m from the ground surface. The active layer thickness does not exceed 0.5 m.

Moderate sensitive landscapes prevail in the Kumakh site with natural, undisturbed conditions (12 km southwest of Batagai, situated in the intermontane saddle in the Yansk Upland). The site is covered by very wet and swamp meadows and bogs with such growth as *Carex*, *Eriophorum* and *Calamagrostis*. Highly sensitive landscapes occupy some part of the site and include meadows and grass-moss bogs (Fig. 1, Table 2).

Table 1. Cryoindicators for sensitivity estimation of Northern Verkhoyansk permafrost landscapes (the Northern Taiga subzone).

Condition of permafrost landscapes	Volumetric ice content, %	Thickness of active layer, m	Depth to wedge ice, m	Surface subsidence, m
Low sensitive	<20	>1.0	>2.0	<0.2
Moderate sensitive	20-40	0.5-1.0	1.0-2.0	0.2-0.5
Highly sensitive	>40	<0.5	<1.0	>0.5

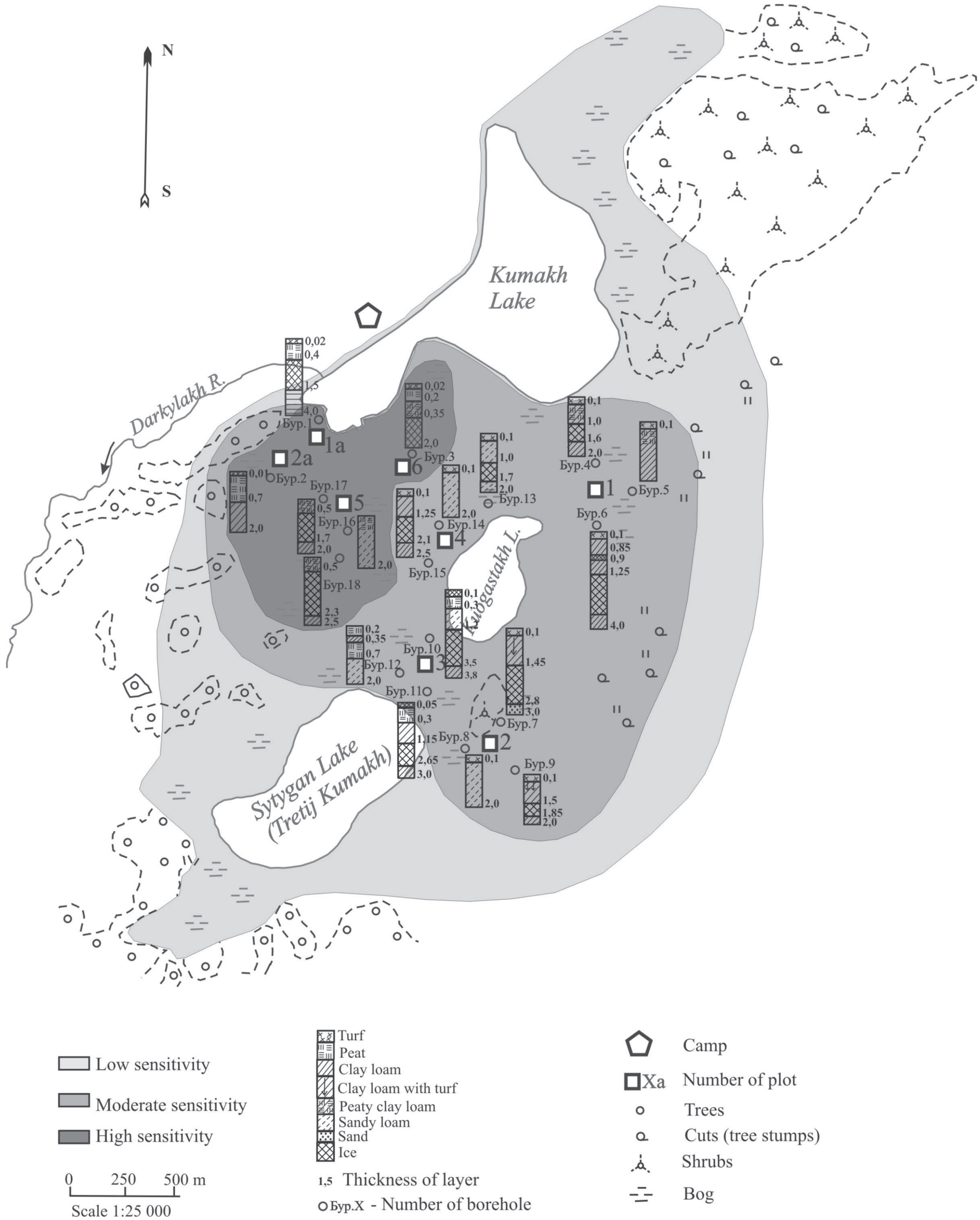

Figure 1. A sensitivity map of meadow landscapes at Kumakh site.

Table 2. Estimation of permafrost landscape sensitivity in Kumakh site.

Plot	Landscape	Volumetric ice content, %	Thickness of active layer, m	Depth to wedge ice, m	Surface subsidence, m	Condition of permafrost landscapes
1	*Carex-Calamagrostis* very wet meadow	>40	0.55	0.85-1.0	0.45	Moderate sensitive
2	*Calamagrostis-Carex* meadow	30	0.65	1.45-1.5	0.35	
3	Waterlogged bog with grass vegetation	>40	0.6	1.15-1.2	0.3	
4	*Carex-Eriophorum* swamp meadow	>40	1.15	1.0-1.25	0.5	
5	Grass-moss bog with low-centered polygons	50-80	0.56	0.5	0.5-0.6	Highly sensitive
6	*Carex-Calamagrostis* swamp meadow	>40	0.55	0.35	0.5-0.7	
1a	*Carex-Calamagrostis* meadow	20-40	0.45	0.4	0.4-0.6	
2a	*Calamagrostis-Carex* flood meadow	20-40	0.46	2.5	0.3-0.6	

The lack of agricultural lands in the Yana River valley causes the clearing of north-taiga forests. We observed agricultural landscapes in the Batymakh and Yuttyakh sites, which are situated on the first terrace of the Yana River. Forest clearing and soil cover disturbance result in intense changes in the soils with high ice content. In the Batymakh site the top 5-10 cm of humus soil was partially removed together with tree roots. Thus the permafrost soils lost 30%-50% of humus reserves that considerably reduced the soil fertility. Ground cover disturbance caused a 3-4 times increase of seasonal thaw depth, from 0.3 to 0.9-1.2 m. Ice content of frozen sandy loams in the site varies from 40% to 60% by volume. The central part of the site is underlain by ice wedges. Here thaw depressions developed up to 0.5 m in depth and 5 m in width. Thus, we can conclude that the top of ice wedges thawed. According to geocryological conditions and sensitivity to anthropogenic impacts, the landscapes in this site are also subdivided to low sensitive, moderate sensitive and highly sensitive categories (Ivanova 2005).

Landscape sensitivity in northern Verkhoyansk area is the integral characteristic of its geoecological condition. The estimation of the sensitivity of permafrost landscape is based mainly on thaw subsidence which directly depends on volumetric ice content of the active layer.

Subsidence is caused by activization of cryogenic phenomena and processes, such as frost cracking in the active layer (width of cracks varies from 0.5 to 6 cm and its depth often penetrates the top of perennially frozen ground); fissured polygons (depth of fissures extends up to 0.5 m); small polygons (depth of cracks extends up to 0.6 m); ice segregation (especially the formation of wedge ice in the top part of permafrost); low-centered polygons and subsidence troughs; block polygons (normally from tens of centimeters to 4-6 m; and occasionally 8-12 m in diameter).

Conclusion

Present-day climatic variations and anthropogenic impacts (tree removal, surface disturbance, ploughing, etc.) add to the effect of cryogenesis on the adverse processes that disturb and modify the landscapes, as well as on the reduction of ecological and economic values of the landscapes in northern Verkhoyansk.

Terrain zoning according to permafrost landscape sensitivity is essential for geoecological monitoring at a local level. It can provide useful contributions to cryoecological databases, as well as help develop environmental protection standards for subarctic regions.

References

Fedorov, A.N. 1991. *Permafrost Landscapes in Yakutia: Location Technique and Mapping Issues.* Yakutsk: SB RAS Permafrost Institute Press: 140.

Fedorov, A.N. 1996. Impact of Present Bioclimatic Changes on Permafrost Landscapes Development. In: V.T. Balobaev, *Climatic Impact on Permafrost Landscapes in Central Yakutia*. Yakutsk: SB RAS Permafrost Institute Press, 86-106.

Gavriliev, P.P., Ugarov, I.S. & Efremov, P.V. 2001. *Permafrost and Ecological Characteristics of Agricultural Lands in Central Yakutia*. Yakutsk: SB RAS Permafrost Institute Press, 196.

Grave, N.A. 1980. Place and concept of geocryological researches of environment control and conservation issues in permafrost area. *Terrain Sensitivity to Anthropological Impact in Permafrost Area.* Yakutsk, 6-12.

Grave, N.A. & Melnikov, P.I. 1989. *Criteria and Predictions of Permafrost Landscapes Sensitivity. Factors and Techniques of Geosystems Sensitivity.* Moscow: Academy of Science Press: 163-171.

Ivanova, R.N. 2003. Seasonal thawing of soils in the Yana River valley, northern Yakutia. *Proceedings of the Eighth International Conference on Permafrost, Zurich, Switzerland, 21-25 July 2003, Vol. 1*: 479-482.

Ivanova, R.N. 2005. Sensitivity of permafrost terrain to clearing of North-Taiga forests in the Yana Valley, Northern Yakutia. *Programme and Abstracts of 2nd European Conference on Permafrost (EUCOP II), Potsdam, German, 12-16 July 2005*: 182-183.

Zotova, L.I. & Tumel, N.V. 1996. Permafrost ecological evaluation of landscapes condition affected by anthropogenic impacts. *Proceedings of the First Conference of Geocryologists in Russia,* Moscow: Moscow State University Press, Vol.2: 374-383.

Micrometeorological Measurements on Mountain Permafrost in the Daisetsu Mountains, Hokkaido, Japan

Go Iwahana
Graduate School of Engineering, Hokkaido University, Sapporo, Japan
Yuki Sawada
Institute of Low Temperature Science, Hokkaido University, Sapporo, Japan
Mamoru Ishikawa
Graduate School of Environmental Science, Hokkaido University, Sapporo, Japan
Fumitaka Katamura
Kyoto Prefectural University, Kyoto, Japan
Toshio Sone
Institute of Low Temperature Science, Hokkaido University, Sapporo, Japan
Tetsuo Sueyoshi
Institute of Low Temperature Science, Hokkaido University, Sapporo, Japan
Koichiro Harada
Miyagi University, Sendai, Japan

Abstract

We commenced micrometeorological measurements in the Daisetsu Mountains, Hokkaido, Japan, including the monitoring of thermal and hydrological conditions in the ground down to 5 m depth, in July 2005. The temperature conditions at the site were as cold as those within a continuous permafrost zone. Persistent, driving westerly winds prevent snow from accumulating on the mountain permafrost site. The depth of the permafrost base was deeper than 5 m. Relative humidity was high, with large amounts of summertime precipitation (~ 700–1000 mm). It is likely that the soil water condition in the active layer is kept high or nearly saturated during the thawing season due to frequent rainfall and the existence of permafrost. The observed and future long-term data are expected to be used to model the ground thermal and hydrological processes and thereby lead to a better understanding of the relation between permafrost and vegetation ecology.

Keywords: active layer; Japan; micrometeorology; mountain permafrost.

Introduction

The occurrence of perennially frozen ground in Japan has been studied by numerous researchers, as summarized by Ishikawa et al. (2003), who categorized the distribution of mountain permafrost in Japan into three groups in terms of geographic location. Mountaintop permafrost occurs in certain summit areas where the mean annual temperature is sufficiently low to allow the occurrence of permafrost. Such areas commonly have little snow cover because of strong winds. Mountainside permafrost occurs mainly on slopes or depressions such as deglaciated cirques in the Japanese Alps (e.g., Fukui 2003). Extra-zonal permafrost occurs upon certain block slopes at low altitudes, where the mean annual air temperature is considerably above 0°C (e.g., Sawada et al. 2003). The mountain permafrost in the Daisetsu Mountains of Hokkaido, Japan is categorized as mountaintop permafrost and is considered to be highly sensitive to global warming because air temperature has a direct control on the ground thermal regime of mountaintop permafrost (Ishikawa et al. 2003), and because the site is located near the southern limit of permafrost occurrence in the Northern Hemisphere (Fig. 1).

Mountain permafrost within the Daisetsu Mountains is

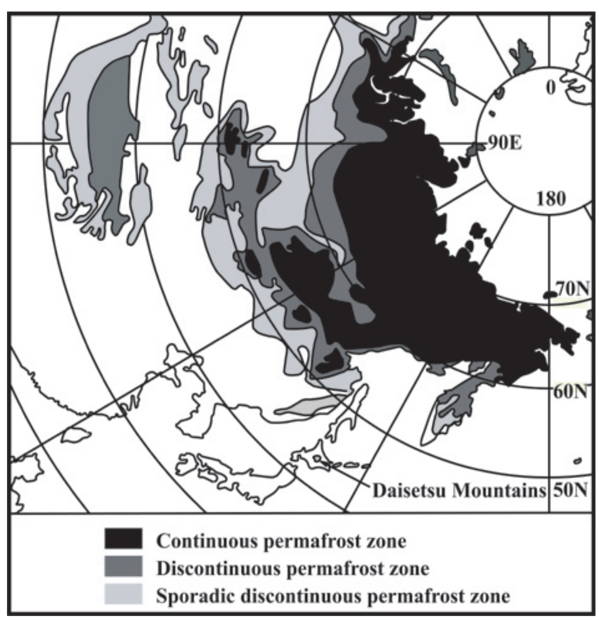

Figure 1. Location of the Daisetsu Mountains. Modified from Harris (1986).

distributed in a complex manner over a large area at altitudes above approximately 1700 m above sea level (a.s.l.). The occurrence of permafrost in this area has been examined by borehole and geophysical testing, as well as the BTS (bottom temperature of snow cover) measurements (e.g., Fukuda & Kinosita 1974, Sone et al. 1988, Ishikawa & Hirakawa 2000). Numerous periglacial features, including patterned ground (e.g., Koaze 1965, Sone & Takahashi 1986, Fukuda & Sone 1992) and palsa bog (e.g., Takahashi & Sone 1988, Sone 2002) have been studied in the Daisetsu Mountains, suggesting the extensive occurrence of perennially frozen ground; however, long-term variations in permafrost temperature have yet to be reported, and the extent of permafrost remains unclear.

Global climate change could alter the physical factors that control the surface energy and water balance, such as air temperature, precipitation, vegetation, radiation, and wind conditions. Such changes could in turn affect the thermal and hydrological regime of the active layer and underlying permafrost. Koizumi & Shinsho (1983) reported a correlation between vegetation distribution and level of ground water table, which is determined by the depth of the permafrost table, in the mountaintop permafrost area of the Daisetsu Mountains. Kudo (1990) noted the importance of soil temperature as a control of vegetation distribution in the southern part of these mountains.

We initiated micrometeorological measurements with the aim of understanding the physical processes controlling the surface energy and water balance in the mountaintop permafrost area of the Daisetsu Mountains. Similar micrometeorological studies have been conducted in many cold regions (Eugster et al. 2000), although the summit areas of mountains have rarely been targeted. The observed data will be used to model the ground thermal and hydrological processes and thereby lead to a better understanding of the relation between permafrost occurrence and vegetation ecology. The data provide fundamental information for process-based modeling of mountain permafrost distribution. Basic meteorological measurements and geophysical surveys of mountain permafrost have been performed in this range over the past 30 years; however, the available information remains insufficient in terms of discussing environmental controls on the occurrence and temporal variation of mountain permafrost.

This paper describes micrometeorological characteristics, including the current thermal and hydrological status of the active layer and upper permafrost, of a site at which a 4 m tower equipped with micrometeorological instruments was installed at a representative point in the area of mountain permafrost in July 2005.

Study Site

The Daisetsu Mountains (43°N, 142°E) are located in central Hokkaido, northern Japan (Fig. 1). The current morphology of the mountains formed during early to middle Quaternary volcanic activity that saw the eruption of andesite lavas. The lava flows formed plateaus at 1700 to 2000 m a.s.l. during early to middle Quaternary, followed by the formation of various volcanic cones. The highest peak in the area is Mt. Asahi (2290 m a.s.l.); the timberline occurs at about 1600 m a.s.l.

An automatic micrometeorological observation system is installed about 400 m northeast of the peak of Mt. Goshiki (Fig. 2) at 2015 m a.s.l. The plateau atop of Mt. Goshiki is relatively flat and is one of the most suitable places in the area for micrometeorological measurements, with a 300–

Figure 2. Summertime view of the study site looking toward the west. The peak in the background is Mt. Hakuun.

Table 1. Description of employed instruments.

<table>
<tr><th>Elements</th><th>Model</th><th>Manufacture</th><th>Height or depth (m)</th><th>Logging interval</th><th>Scan interval</th></tr>
<tr><td>Air temperature & Relative humidity</td><td>HD9009TR-5</td><td>Delta OHM</td><td>1.5</td><td rowspan="7">30 min.</td><td rowspan="7">10 s.</td></tr>
<tr><td>4-elements radiation</td><td>CNR-1</td><td>Kipp & Zonen</td><td>1</td></tr>
<tr><td>Ground heat flux</td><td></td><td>Huske</td><td>0.01</td></tr>
<tr><td>Rainfall</td><td>52203</td><td>R. M. Young</td><td>1</td></tr>
<tr><td>Wind direction</td><td>05103-47</td><td>R. M. Young</td><td>4</td></tr>
<tr><td>Wind speed</td><td>03101Y-5</td><td>R. M. Young</td><td>4</td></tr>
<tr><td>Soil temperature</td><td>thermistor probes</td><td>Isizuka denshi</td><td>16 depths</td></tr>
<tr><td>Soil water content</td><td>EnviroSMART</td><td>Sentek</td><td>6 depths</td><td>6 h.</td><td>6 h.</td></tr>
</table>

400 m fetch in the direction of the prevailing wind. About half of the plateau is covered by patchy vegetation colonies (Fig. 2) of *Diapensia Lapponica* var. *oboata*, *Loiseleuria procumbens, Oxytropis japonica* Maxim. var. *sericea* Koidz, lichens, etc. The heights of the colonies are 20–50 mm. Areas of bare ground reveal volcanic pebble conglomerate (clasts of ~5–20 mm in diameter).

Methods

The data used in this paper were obtained between 2 July 2005 and 14 October 2006. Data losses of several hours were linearly interpolated. Long-term data loss due to instrumental malfunction occurred over periods ranging from several days to months.

Four-component radiation (shortwave incoming radiation Si, shortwave outgoing radiation So, longwave incoming radiation Li, and longwave outgoing radiation Lo) was measured, and net radiation Rn was calculated as $Rn = Si + Li - So - Lo$. Ground heat flux at the soil surface was measured using a heat flux plate installed at a depth of 10 mm. Surface albedo α was calculated every 30 minutes as $\alpha = So/Si$, taking the minimum values from 10:00 to 14:30 (during which time α values were almost constant) to obtain a daily representative midday value. Those values which were thought to be influenced by the accumulation of snow on the upper sensor were removed from the dataset. Air temperature and relative humidity were measured using Pt100 sensors and a capacitance probe, respectively. Rainfall was measured using a tipping bucket rain gauge with a resolution of 0.1 mm. Wind speed and direction were measured using a propeller-type anemometer. These instruments were installed upon a 4 m tripod.

Soil temperature was measured using thermistor probes (104ET; Ishizuka Denshi, Japan) calibrated in an ice-water bath with a precision of 0.02°C and an overall accuracy of less than ± 0.09°C in the temperature range between –20 and 30°C. Measurements were taken at depths of 0.01, 0.05, 0.10, 0.20, 0.30, 0.50, 0.70, 0.90, 1.10, 1.30, 1.50, 1.70, 1.90, 3.00, 4.00, and 5.00 m. Volumetric soil water content was estimated using FDR (Frequency Domain Reflectometry) sensors at depths of 0.10, 0.20, 0.30, 0.40, 0.60, 0.80, 1.00, and 1.20 m.

The model numbers, manufacturer details, heights of measurements, and recording intervals for all meteorological instruments used in this study are summarized in Table 1. Data were recorded using a data logger (CR10X; Campbell Scientific Inc., USA) with a multiplexer (AM16/32; Campbell Scientific Inc., USA). Soil moisture data were measured every 6 hours and recorded; other parameters were measured every 10 seconds, with 30-minute averages being recorded.

Results and Discussion

Air temperature and humidity

Air temperature and relative humidity were measured from July 2005 to October 2006. Figure 3 (upper) shows the seasonal monthly mean, maximum, and minimum air temperature. The mean annual air temperature from October 2005 to September 2006 was -4.6°C. The maximum values of 18.5°C and 17.8°C were observed in August 2005 and August 2006, respectively; the highest daily minimum values of 3.6°C and 6.2°C were observed in the same months, and the minimum air temperature of -27.4°C was recorded in January 2006. The degree of daily variation in air temperature was small in mid-summer and large in winter. For the period from October 2005 to October 2006, the freezing and thawing indexes were 2727 and 1050 degree days, respectively.

Relative humidity was very high. Figure 3 (lower) shows seasonal changes in monthly mean, maximum, and minimum relative humidity. The maximum daily values of relative humidity were 100% on every day of the observation period, meaning that the atmosphere close to the ground was at the dew point especially at night. Daily variations in relative humidity were relatively minor (less than 15%) from mid-November to mid-February, but large (up to 95%) during other periods. The relative humidity fell below 20% only during the daytime on fine days during the snow-free period. Values fluctuated close to the saturation point after every rainfall event.

Largely continuous monitoring of air temperature was undertaken at Hakuun hut (2000 m a.s.l.; ~2 km south of the study site) from 1985 to 1993 (Sone et al. 1988, Tachibana et al. 1991, Nakayama & Sone 1992, Sone & Nakayama 1992, Sone 1994). The mean annual air temperatures in 1985, 1987, and 1988 were -3.8°C, -4.9°C, and -5.2°C, respectively. According to the diagram of Harris (1981), if snow barely covers the ground surface in winter, our study area is characterized as a continuous or discontinuous permafrost zone (Sone 1992). Our temperature measurements also support his conclusion.

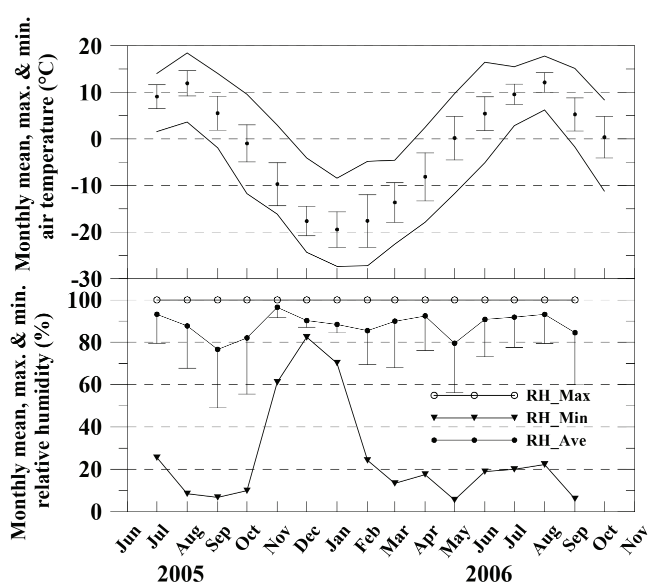

Figure 3. Seasonal changes in monthly mean, maximum, and minimum air temperature (upper) and relative humidity RH (lower). Error bars indicate standard deviations.

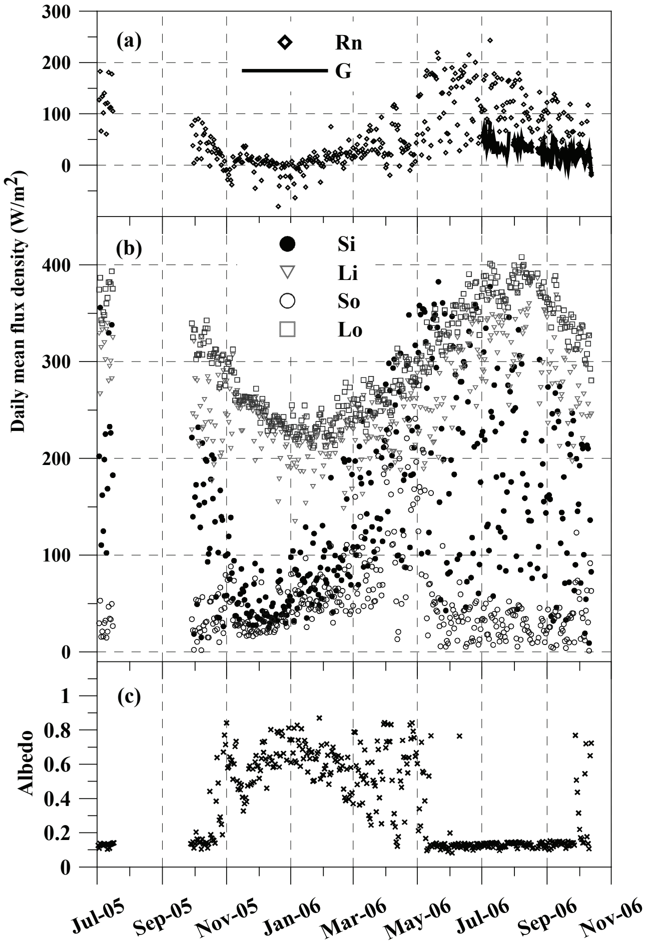

Figure 4. (a) Seasonal changes in daily mean net radiation Rn and daily mean ground heat flux G. (b) Seasonal changes in daily mean values of radiation components (shortwave incoming radiation Si, shortwave outgoing radiation So, longwave incoming radiation Li, and longwave outgoing radiation Lo). (c) Seasonal changes in daily representative albedo (calculated over the period 10:00–14:30).

Radiation environment and ground heat flux

Daily mean Rn values were close to or below 0 W/m^2 in winter and above 200 W/m^2 in early summer (Fig. 4a). These values were strongly dependent on the weather, fluctuating between 50 and 220 W/m^2 during summer. Measurements of ground heat flux were initiated in July 2006. The daily mean value was around 50 W/m^2 during July 2006, decreasing gradually to 0 W/m^2 during the middle of October 2006 (Fig. 4a). The large fluctuations in daily net radiation values were accompanied by similar fluctuations (of 20%–50%) in the ratio of ground heat flux G to Rn (G/Rn). The obtained range in the ratio G/Rn is similar to that reported in some tundra regions, and much higher than that in boreal forests (Eugster et al. 2000).

On fine days from May to July 2006, the maximum values of 30-minute mean Si were about 1100 W/m^2, and Rn was calculated to be about 750 W/m^2 (data not shown). The daily maximum Si and Rn decreased, respectively, to about 200 and 100 W/m^2 on days of bad weather. Si values near the upper envelope were measured on fine days. The recording of Si values lower than those on fine days indicates a large number of days with cloudy or stormy weather (Fig. 4b).

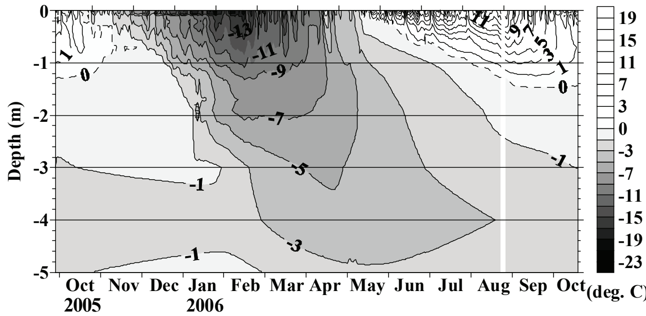

Figure 5. Seasonal variations in the soil temperature profile to a depth of 5 m at the study site from October 2005 to October 2006. Solid isotherms are drawn with increments of 2°C; the dashed line indicates the 0°C isotherm.

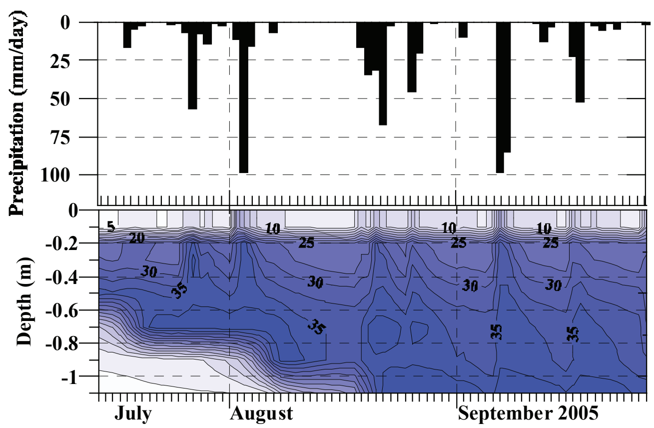

Figure 6. Seasonal changes in daily precipitation (upper) and profile of the volumetric soil water content in the liquid phase (lower; values are given in %).

Albedo values were relatively stable (0.08–0.15) in summer but showed large variations in winter related to snow coverage (Fig. 4c).

Wind direction and speed

Wind data are limited to the period between July and November 2005 because of sensor malfunction during other periods. Two predominant wind directions were recorded: strong westerly winds and relatively weak south-westerly winds. About 30% of the westerly wind velocities (30-minute averages) were in the range of 10–20 m/s, 40% in the range of 5–10 m/s. The equivalent percentages for the south-westerly wind were about 10 and 40%, respectively. The winds during other periods were of lower velocities. Persistent, strong westerly to south-westerly winds were also reported by Sone (unpubl.), who described strong winds from October to April. It has been observed that most of the summit plateaus in the Daisetsu Mountains have little snow cover because of persistent westerly driving winds (Takahashi & Sato 1994).

Ground temperature and water conditions

The ground began to freeze from the surface at the beginning of October 2005 and from the permafrost upward in the middle of the same month (Fig. 5). The entire active layer fell below 0°C in November, reaching -9°C in February. Thawing of the frozen ground commenced in the middle of May 2006. The thaw front developed at an almost constant average rate of 12.2 mm/day until the end of August. A freezeback from the deeper layer was also observed, induced by prolonged cold weather at the end of June.

The active layer thickness was 1.28 m and 1.46 m in 2005 and 2006, respectively, and the depth of the permafrost base was greater than 5 m. The permafrost temperature at a depth of 4 m fluctuated between -1.70°C and -4.84°C during the observation period.

Large amounts of summertime precipitation were recorded at the study site. The 4-month cumulative rainfall amounts from June to September were 813 mm in 2005 and 693 mm in 2006. Sone (unpubl.) measured 4-month rainfall amounts of 929 mm in 1995 and 976 mm in 1996 at a point located about 1 km west of our study site. Soil water content was close to saturated throughout 2005, and variations in soil water showed a strong correlation with rainfall events (Fig. 6). The values of soil moisture presented in this paper were calculated using default calibration curves for sandy soil; however, *in situ* calibration is required for a more accurate discussion of the absolute amount of soil moisture in the active layer.

Although we did not obtain data on evapotranspiration and runoff ET + R at the study site (with regard to discussing the water budget), we roughly estimated ET + R by differentiation of the water balance equation P = dS + ET +R. P and dS are precipitation and change in the amount of soil water storage in a certain period, respectively. The value of dS in the active layer from 15 July to 27 September 2005 was determined from the measured profiles of soil water content (40 mm). The values of P and ET + R in the same period were 770 and 810 mm, respectively. A relatively minor change in soil water storage was observed; almost all of the precipitation water that fell during this period was likely to have been lost to evapotranspiration or discharged laterally. Rapid changes in soil moisture within the deeper active layer indicate the high permeability of the soil (Fig. 6). It is likely that the soil water condition in the active layer at the site was kept high or near-saturated during the thawing season because of frequent rainfall and the existence of permafrost. However, rapid changes in soil moisture throughout the active layer probably reflect the high permeability of the volcanic soil. A degree of lateral runoff may also have occurred, strongly influencing the hydrological regime of the active layer.

Changes in surface conditions

Albedo depends on surface conditions such as snow coverage, soil moisture at the surface, and vegetation phenology. Snowfall began in October 2005 and continued until May of the following year (Fig. 4c). Two snowfall events probably even occurred during June of 2006. Considering that the albedo of fresh snow is 0.75–0.95 (Campbell & Norman 1998), the fact that the measured values were often below 0.7 indicates only partial snow coverage on most days in winter. The large variations in daily mean albedo during winter indicate repeated cycles of snow cover followed by the snow being blown away or sublimated. The observed variations in minimum wintertime albedo values indicate that snow coverage on the ground was highest from the end of December to the beginning of January; most of the accumulated snow had disappeared by the end of February. However, the December–February snow coverage must be confirmed by an alternative method, as the albedo of old snow can be 0.4–0.7 (Campbell & Norman 1998). The summertime albedo showed minor fluctuations (0.08–0.15) relative to those in winter. The summertime day-to-day variations in albedo reflect the moisture conditions of the surface soil: moist soil is darker, with a lower albedo. The albedo values during the snow-free period showed a gradual increase (by about 0.02 on average), together with day-to-day variations. The seasonal change in albedo can likely be attributed to the phenology of surface vegetation. It should be noted that albedo values also depend on the zenith angle and cloud cover (Goodin & Isard 1989); these factors must be considered in further discussions.

Surface temperature

Ground surface temperature was obtained using a directly installed thermistor sensor (Tsurf) at a depth of 10 mm and the Lo values from the radiometer (Trad). Trad is calculated using the Stefan–Boltzmann equation with an emissivity of 0.98. The maximum Tsurf was 33.1°C, recorded in June 2006; the maximum daily range in Tsurf (35.3°C) was observed on the same day. The daily range in Tsurf during mid-summer is about twice that in Ta, and monthly averaged Tsurf is 1.1°C –6.0°C higher than Ta. Trad values agreed well with Ta values for the snow-covered period. Trad in summer showed similarly large daily variations to those for Tsurf, but maximum values of Trad showed an increasing trend during mid-summer. Large differences between Ta and ground surface temperature were found in both winter and summer.

Perspectives

State-of-the-art automatic micrometeorological instruments are able to precisely monitor physical conditions in severe mountaintop areas, where measurements are rarely conducted. We commenced micrometeorological measurements, including the monitoring of thermal and hydrological conditions in the ground down to 5 m depth, with the intention of characterizing the features of the surface energy and hydrological balance at a mountaintop permafrost site in Japan. The information will be used to simulate future changes in the environment.

The newly obtained data support the conclusions proposed in previous studies of wind, rainfall, and air temperature undertaken by other Japanese scientists in areas of mountain permafrost. In addition, we recorded the year-round thermal regime of the active layer and the upper layer of permafrost. We also present, for the first time, continuous and simultaneous measurements of the profile of volumetric water content in the active layer, surface radiation, and air moisture condition at a Japanese mountaintop site. These data will be a base of future long-term monitoring of mountain permafrost and its environment. Additional measurements are required to determine the characteristics of surface energy and hydrological balance at the site.

Acknowledgments

This work was initially funded by the Leadership Fund of the Institute of Low Temperature Science, Hokkaido University, in 2004. Financial support was thereafter provided by a Sasakawa Scientific Research Grant from the Japan Science Society (in 2005) and the Northern Advancement Center for Science & Technology and Asahi Breweries Foundation (in 2006).

References

Campbell, G.S. & Norman, J.M. 1998. *An Introduction to Environmental Biophysics*. New York: Springer-Verlag, 286 pp.

Eugster, W., Rouse, W.R., Sr, R.A.P., Mcfadden, J.P., Baldocchi, D.D., Kittel, T.G.F., III, F.S.C., Listion, G.E., Vidale, P.L., Vaganov, E. & Chambers, S. 2000. Land-atmosphere energy exchange in Arctic tundra and boreal forest: available data and feedbacks to climate. *Global Change Biology* 6(S1): 84-115.

Fukuda, M. & Kinoshita, S. 1974. Permafrost at Mt. Taisetsu, Hokkaido and its climatic environment. *The Quaternary Research (in Japanese with English abstract)* 12(4): 192-202.

Fukuda, M. & Sone, T. 1992. Some characteristics of alpine permafrost, Mt-Daisetsu, Central Hokkaido, Northern Japan. *Geografiska Annaler Series A-Physical Geography* 74(2-3): 159-167.

Fukui, K. 2003. Investigating mountain permafrost distribution by ground temperature measurements in the Tateyama Mountains, the northern Japanese Alps, central Japan. *Zeitschrift Fur Geomorphologie*, 47: 179-193.

Goodin, D.G. & Isard, S.A. 1989. Magnitude and Sources of Variation in Albedo within an Alpine Tundra. *Theoretical and Applied Climatology* 40(1-2): 61-66.

Harris, S.A. 1981. Distribution of active glaciers and rock glaciers compared to the distribution of permafrost landforms, based on freezing and thawing indices. *Can. J. Earth Sci.* 18: 376-381.

Harris, S.A. 1986. *The Permafrost Environment*. Ottawa: Barnes & Noble Books, 276 pp.

Ishikawa, M., Fukui, K., Aoyama, M., Ikeda, A., Sawada, Y. & Matsuoka, N. 2003. Mountain permafrost in Japan: distribution, landforms and thermal regimes. *Zeitschrift Fur Geomorphologie* 47: 99-116.

Ishikawa, M. & Hirakawa, K. 2000. Mountain permafrost distribution based on BTS measurements and DC resistivity soundings in the Daisetsu Mountains, Hokkaido, Japan. *Permafrost and Periglacial Processes* 11(2): 109-123.

Koaze, T. 1965. The patterned grounds on the Daisetsu volcanic group, Central Hokkaido. *Geographical Review of Japan (in Japanese with English abstract)* 38(3): 179-199.

Koizumi, T. & Shinsho, H. 1983. Plant communities on permafrost areas in the alpine zone of the Daisetsu Mountains, Central Hokkaido, Japan. *Jap. J. Ecol. (in Japanese with English abstract)* 33: 357-363.

Kudo, G. & Kodama, Y. 1990. Annual transition of soil temperature in the Taisetsu Mountains. *Low Temperature Science, Ser. A. Data Report (in Japanese)* 49: 15-32.

Nakayama, T. & Sone, T. 1992. Characteristics of air temperature variation. *Low Temperature Science, Ser. A (in Japanese with English abstract)* 51: 173-181.

Sawada, Y., Ishikawa, M. & Ono, Y. 2003. Thermal regime of sporadic permafrost in a block slope on Mt. Nishi-Nupukaushinupuri, Hokkaido Island, Northern Japan. *Geomorphology* 52(1-2): 121-130.

Sone, T. 1992. Permafrost environment of the Daisetsu mountains, Hokkaido, Japan. *Permafrost and Periglacial Processes* 3: 235-240.

Sone, T. 1994. Air temperature data at Hakuun Hut in the Daisetsu Mountains, Central Hokkaido in 1990-1993. *Low Temperature Science, Ser. A (in Japanese with English abstract)* 53: 33-50.

Sone, T. 2002. Internal structure of a palsa in the bog to the south of Mt. Hiragatake, the Daisetsu Mountains, Hokkaido, Japan. *Journal of Geography (in Japanese with English abstract)* 111(4): 546-554.

Sone, T. & Nakayama, T. 1992. Air temperature data at Hakuun Hut in the Daisetsu Mountains, Central Hokkaido, 1987-1989. *Low Temperature Science, Ser. A (in Japanese with English abstract)* 51: 31-48.

Sone, T. & Takahashi, N. 1986. Winter field observations of the frost-fissure polygons on Hokkai-Daira Plataeu, Daisetsu volcanic massif, Hokkaido. *Geographical Review of Japan, Ser. A (in Japanese with English abstract)* 59(11): 654-663.

Sone, T., Takahashi, N. & Fukuda, M. 1988. Alpine permafrost occurrence at Mt. Taisetsu, Central Hokkaido, Northern Japan. In: *Permafrost, Proceedings of Fifth International Conference on Permafrost*, *Trondheim*: 253-258.

Tachibana, Y., Kodama, Y. & Yamada, T. 1991. Variation of air temperature in the Taisetsu Mountains in winter. *Low Temperature Science, Ser. A. Data Report (in Japanese)* 50: 33-45.

Takahashi, N. & Sato, K. 1994. Tail-shaped vegetation patch as an indicator to estimate the winter prevailing wind in the alpine bare ground. *Quarterly Journal of Geograph (in Japanese with English abstract)y* 46: 136-146.

Takahashi, N. & Sone, T. 1988. Palsas in the Daisetsuzan mountains, Central Hokkaido, Japan. *Geographical Review of Japan, Ser. A (in Japanese with English abstract)* 61(9): 665-684.

Influence of Temperature and Groundwater Fluctuation on LNAPL Migration at Colomac Mine Site

Olumide Iwakun
Civil and Environmental Engineering Department, University of Alberta, Canada
Kevin W. Biggar
BGC Engineering, Edmonton, Alberta, Canada
David C. Sego
Civil and Environmental Engineering Department, University of Alberta, Canada

Abstract

The ongoing site characterization of spilled petroleum hydrocarbon at the abandoned Colomac gold mine site in a discontinuous permafrost region shows variable distribution of accumulated light non-aqueous phase liquid (LNAPL) in the monitoring wells across the site and over time. The site is adjacent to a lake and has between 0 to 4.6 m of overburden soil underlain by fractured greywacke. Different mechanisms, including groundwater fluctuation and thermal regime, have been proposed to account for spatial and temporal variation of the LNAPL at the site. The measured LNAPL showed increased thickness in the winter period. Multiple linear regression was used to correlate the accumulated LNAPL in one of the most yielding monitoring wells with temperature data from a dedicated thermistor-borehole and measured groundwater elevation. The accumulated LNAPL showed significant correlation with both the temperature data and the groundwater water elevation at the site.

Keywords: freeze; LNAPL; migration; mine; permafrost.

Introduction

Discovery of valuable minerals in the Northwest Territory (NWT) in Canada has led to increased mining activities. The adverse environmental impacts of the mining operations during and after closure are a widespread problem, which has received major attention recently. Many of the mining sites used are located in remote areas where a large percentage of the operating cost is due to logistics of moving and maintaining personnel and materials at the site. To offset some of the logistic issues in transporting petroleum fuel as the main energy source to the site and smooth operation of the mine, large volumes of fuel are stored in tanks on site. The designated area of the site where several fuel storage tanks are located is called the *tank farm*. Accidental fuel spillage during transportation or leakage of the fuel tanks in the tank farm area is a looming problem, which is complicated by the presence of permafrost.

To this effect, various studies have been conducted to understand the behavior of spilled fuel in frozen and freezing environment. Permafrost has been shown to be an effective barrier to water flow but not a barrier to the flow of petroleum hydrocarbons (Biggar et al. 1998, McCarthy et al. 2003). Studies conducted with petroleum hydrocarbon (PHC) contaminated soils in freezing conditions showed that the concept of LNAPL exclusion forward of freezing front is applicable (Konrad & Seto 1991, Tumeo & Davidson 1993, Biggar & Neufield 1996, Chuvilin 1999, Barnes et al. 2004). In addition to the concept of LNAPL exclusion, Barnes et al (2004) stipulated physical displacement of the mobile phase PHC from the pore spaces as water expands on freezing. Chuvilin et al (2001a) showed that spreading and transportation of oil in regions of frozen ground is dependent on oil composition, soil temperature, and type of mineral surface.

Literature on migration of spilled fuel within fractured bedrock in a permafrost environment is limited. Iwakun & Biggar (2007) suggested that a lower groundwater table in the winter period may enhance drainage of mobile free phase PHC as light non-aqueous phase liquid (LNAPL) from the overburden soil and fractured bedrock surface at Colomac mine. However, in this study, the measured petroleum LNAPL thickness was correlated with the measured ground temperature to understand the influence of thermal fluctuation on LNAPL migration at the site.

Site Background

Colomac mine was an open-pit gold mine located in a discontinuous permafrost region approximately 220 km northwest of Yellowknife in the Northwest Territories. It operated between 1990 and 1997. When it became uneconomical to operate the mine site, it was closed and abandoned in 1999. It is now the responsibility of the Contaminated Site Office (CSO) of Indian and Northern Affairs Canada (INAC) to remediate the site. The site is underlain by fractured bedrock identified as greywacke, and has between 0 to 4.6 m overburden soil made up of sands and gravel. There are different aspects of the site under remediation but this paper will focus on the tank farm area where fuel spillage occurred.

Between 1990 and 2003, over 24 spills of diesel and gasoline around the tank farm were reported at the site (Fig. 1). Of these spills, two were significant. These include 18,000

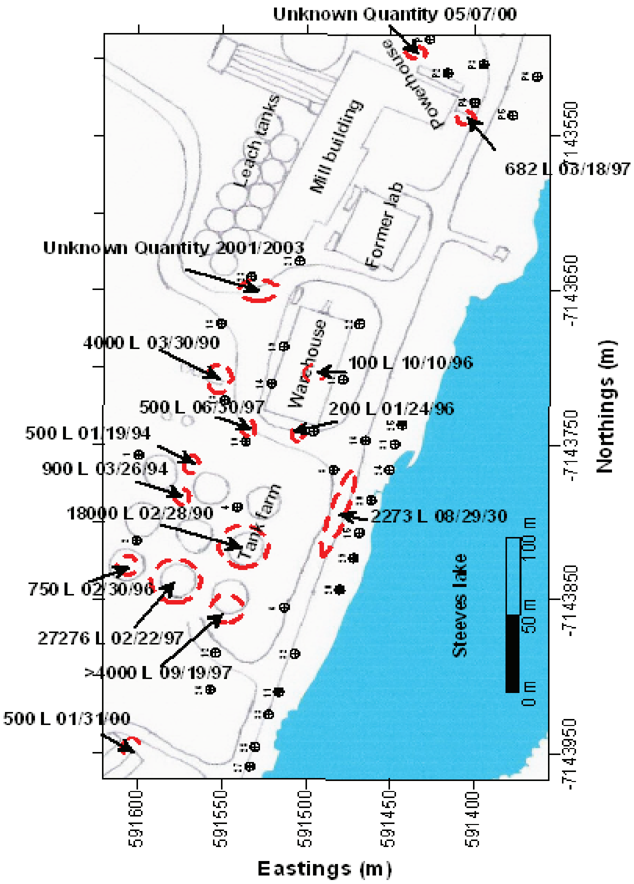

Figure 1. Summary of historical spillage at Colomac mine.

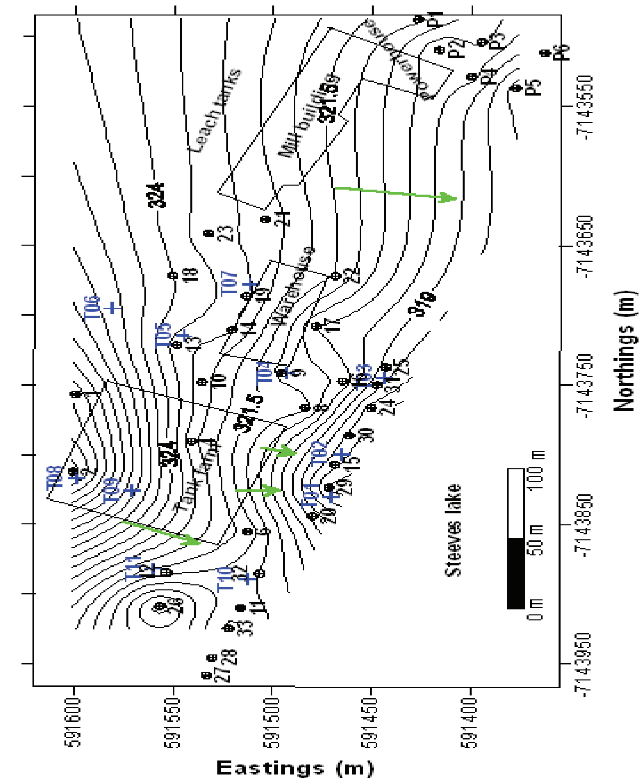

Figure 2. Water table contour for August 2006 showing spatial location of installed monitoring wells and thermistors strings. (Note: thermistor strings are preceeded with T.)

L and 27,276 L in February of 1990 and 1997, respectively, as a result of leakage of one of the fuel storage tanks. After these spills, some measures were taken to curb migration of PHC to Steeves Lake adjacent to the site. These include:

- Installation of 5 m deep interceptor trench lined with corrugated pipe at the west berm of the tank farm in late 1990.
- Placement of skirted boom with absorbent pad along the Shore of Steeves Lake when PHC sheen was observed in late 1990/1991.
- Detailed site characterization and installation of monitoring wells across the site in 2000, shown in Figure 2.
- Replacement of interceptor trench with a frozen soil barrier in 2004 to contain down-gradient migration of mobile phase PHC.
- Removal and biopile treatment of overburden soil at the tank farm area in 2005.

Details of these measures were discussed by Iwakun & Biggar (2007). However, in spite of these measures, petroleum LNAPL is still being observed in some of the monitoring wells across the site. Sheen of PHC at the shore of the lake is also being observed in the summer. Limited effectiveness of these measures shows that knowledge of subsurface behavior of spilled fuel at the site is inadequate. Thus, to improve this understanding, further site investigation was initiated by the University of Alberta Geotechnical Centre and Environment Canada in June 2005.

Site Investigation

Subsurface investigation at this site includes periodic monitoring of depths to petroleum LNAPL, water, and bottom/ice in the wells; thermistor cable installation and thermal profiling; groundwater sampling; hydraulic testing; borehole imaging; rotary coring; and product recovery. These activities have been discussed by Iwakun & Biggar (2007) and Iwakun et al. (2007). However, for completeness of this paper, summaries of pertinent activities and major findings will be given in this paper with particular emphasis on thermistor installation and monitoring of depths to petroleum LNAPL and water.

Depths to product and water

An interface probe was used to measure the depths to petroleum LNAPL, water, and well-bottom. When the measured depth to well-bottom was less than the known depth of the well, ice was inferred at that depth. A summary plot of some of the measurements is shown in Figure 3. The apparent groundwater flow pattern in the summer was inferred from the interpreted isopleths of the groundwater elevation as shown in Figure 2. However, it should be noted that the actual flow pattern may be substantially different from that presented because the fracture networks control the flow direction. In the winter period, apparent flow patterns cannot be inferred because of different thermal distribution at the site as discussed in the subsequent section. Elevated groundwater was noticed in the spring but gradually declined

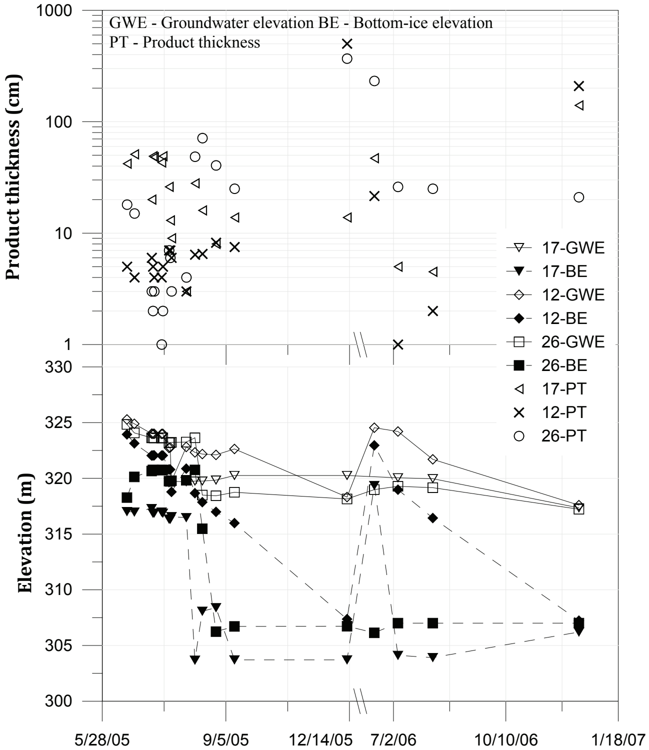

Figure 3. Well-probe data in selected monitoring wells at the site.

as winter approached before freezing.

It was also observed that in early spring, some of the wells were not thawed to well-bottom resulting in an artificial increase in groundwater elevation due to a perched groundwater condition. Thus, at this site, a suprapermafrost water table condition existed from early spring through the summer period. As winter approached, an intrapermafrost water table condition existed across the site except at the warehouse area where the thermal regime was influenced by heat from a generator in the southwest corner of the warehouse building. Due to nearness of the site to the lake, the intrapermafrost water condition may also be influenced by the unfrozen thaw bulb (i.e. talik) adjacent to and beneath the lake.

Ground temperature profiling

To understand the influence of the thermal regime on contaminant distribution, Solinst level loggers, baraloggers, and thermistor strings were initially installed in some of the wells to corroborate the monitored depths to water and bottom-ice at the site between June 2005 to April 2006. Between April and June 2006, new boreholes with dedicated thermistor strings were installed across the site as shown in Figure 2. Each thermistor string consists of eight sensors at specific depths with battery operated datalogger. The boreholes were backfilled with bentonite pellets and water after installation of thermistor string. Sensitivity of the thermistor strings were tested in the laboratory and found to be within ±0.2°C of actual melting point of ice at 0°C.

Summary of other pertinent activities

Some of the wells were hydraulically tested using a packer assembly at discrete intervals in the summer of 2005 and 2006. The results showed higher transmissivity (in the range of 10^{-3} to 10^{-6} m^2/s) within the upper 7 m of the bedrock. At depth, the bedrock has very low transmissivity (in the order of 10^{-9} m^2/s). Rotary bedrock coring at the site corroborates this inference. The fractured upper section of the bedrock appears localized because the transmissivity varied from one well to the other. Borehole imaging using a Well-Vu camera showed what looks like near vertical and horizontal fractures with depth. However, due to drilling method of most of the wells (i.e. percussion hammer drilling), it is difficult to correlate fracture width from post image analysis to that of the hydraulic test. Fissures observed may be due to well-bore scaring during installation. With borehole imaging, zones with marked discoloration were noticed in the upper section of the bedrock but no pooled free phase PHC was observed at the bottom of the wells.

Methodology

From the activities stated above, the observed apparent LNAPL thickness in the monitoring wells (MW) showed that MWs 12, 26, and 17 are the highest yielding wells at the site. Of these, MW 12 and 26 are very close (Fig. 2) but MW 12 is closer to the installed thermistor string. MW 17 is close to the warehouse and its thermal profile may be influenced by the heat generated southwest of the warehouse building. Thus, the measured apparent LNAPL thickness of MW 12 and its thermal profile are used for this study.

The measured thermal profile close to MW 12 and 26 is shown in Figure 4. This thermal profile was used for a simple statistical test with the measured apparent LNAPL thickness using multiple linear regression. Since the measured apparent LNAPL also varies with groundwater elevation as shown in Figure 3, a multiple linear regression test with both temperature and groundwater elevation as independent variables was also undertaken. For this study, the temperature value used for the regression analysis was determined by averaging the temperature value in the upper 7 m of the subsurface. This decision was made because other tests conducted at the site including hydraulic tests, bedrock coring, and borehole imaging, showed that the upper section of the bedrock is highly fractured.

The implication of this is that the apparent petroleum LNAPL in the monitoring wells is assumed to come from the overburden soil and fractured upper section of the bedrock.

Multiple linear regression

This method of analysis was chosen because of perceived dependency of the measured apparent LNAPL in the wells on temperature and groundwater elevation.

Multiple regression demonstrates the consequence of one independent variable with the other independent variable kept constant. The regression coefficients of the variables are calculated using the equation below:

$$\Sigma X_1 Y = b_1 \; \Sigma X_1^2 + b_2 \; \Sigma X_1 X_2$$
$$\Sigma X_2 Y = b_1 \; \Sigma X_1 X_2 + b_2 \; \Sigma X_2^2 \tag{1}$$

where $X_j = x_j - x_m$, $Y_j = y_j - y_m$, and both represent deviation of independent and dependent variables (x, y) respectively; b_j is the regression coefficient of j-th variable. The regression coefficients are used to construct equation to the regression plane given by:

$$\bar{y} = b_0 + b_1 \bar{x}_1 + b_2 \bar{x}_2 \tag{2}$$

where b_0 is a constant. Finding b_1 and b_2 in equation 1 leads to simultaneous equations which can be represented with a matrix of the form AN=B, where N represents a matrix tensor of the unknown regression coefficients and is solved by multiplying the inverse of its coefficient matrix (A) with the known vector (B); i.e., N=A^{-1}B. The tensor of the inverse matrix (i.e., e_{jj} terms) is used in the computation of standard deviation of each regression coefficient (S_{bj}) in combination with the residual variance ($S_{y/x}$), and ultimately used in calculating its level of significance using the t-test. If the calculated t is greater than the tabulated t (from statistical table), then the null hypothesis that the regression coefficient is insignificant is rejected. The relevant equations are shown below:

$$A^{-1} = \begin{bmatrix} e_{11} & e_{12} \\ e_{21} & e_{22} \end{bmatrix} \tag{3}$$

$$e_{11} = \frac{\Sigma x_2^2}{\Sigma x_1^2 \; \Sigma x_2^2 \; - (\Sigma x_1 \; x_2)^2}$$
$$e_{22} = \frac{\Sigma x_1^2}{\Sigma x_1^2 \; \Sigma x_2^2 \; - (\Sigma x_1 \; x_2)^2}$$
$$e_{12} = e_{21} = \frac{\Sigma x_1 \; x_2}{\Sigma x_1^2 \; \Sigma x_2^2 \; - (\Sigma x_1 \; x_2)^2} \tag{4}$$

$$S_{y/x}^2 = \frac{\Sigma Y^2 \; - \; b_1 \, \Sigma Y X_1 - \; b_2 \, \Sigma Y X_2}{n - 3} \tag{5}$$

$$S_{bj} = S_{y/x} \sqrt{e_{jj}} \tag{6}$$

$$t = \frac{b_j}{S_{bj}} \tag{7}$$

An F-test was used to test the level of significance of the multiple regression as a whole using the equation below:

$$F = \frac{b_1 \, \Sigma Y X_1 + \; b_2 \, \Sigma Y X_2}{S_{y/x}^2} \tag{8}$$

The computed F-value is compared with that given in statistical table at a given level of significance. If the computed value is greater than tabulated value, then the null hypothesis that the partial regression coefficients are insignificant is rejected.

Finally, the degrees of association of the variables were tested using multiple correlation coefficients given by the formula below:

$$r^2 = \frac{b_1 \, \Sigma Y X_1 \; + \; b_2 \, \Sigma Y X_2}{Y^2} \tag{9}$$

$$r_{yx_j} = \frac{\Sigma \, x_j \, Y}{\sqrt{x_j^{\,2} + \Sigma \, Y^2}} \tag{10}$$

where r and r_{xyj} are sample and any two variable correlation coefficients, respectively. The computed value is also compared with tabulated value in statistical table to draw inference on the null hypothesis as discussed earlier.

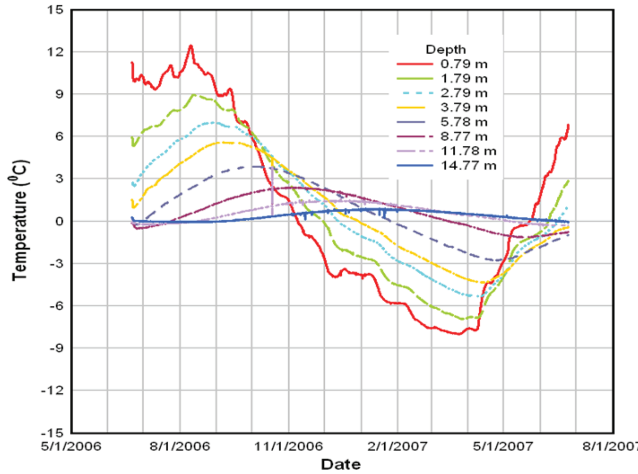

Figure 4. Temperature profile in one of the dedicated thermistor strings "T11" adjacent to MW 12.

Results

The data used for the regression analysis are shown in Table 1. The averaged integral temperature in the upper 7 m was also divided into two, because there is an inflection in the temperature profile between 3 m and 4 m depths from the ground surface due to heat lag effect as shown in Figure 4. The results of the statistical parameters are shown in Table 2. The calculated F-value of the regression equation and the sample multiple-correlation coefficient are greater than the tabulated value for 5% significant level. Thus, the regression equation is statistically significant, and the measured apparent LNAPL thickness correlates well with groundwater elevation and temperature profile at the site within 95% confidence limit as shown in Figure 5.

The partial regression coefficients of the apparent LNAPL (or product) thickness in the well are negative for both groundwater elevation and temperature. This implies that the product thickness increases with decreasing groundwater elevation and decreasing temperature. The absolute partial regressions of product thickness with groundwater elevation and temperature within the upper 3 m of the subsurface

Table 1. Data from MW 12 used for correlation regression.

Date	PT (cm)	GWE (m)	T 1-7 (°C)	T 1-3 (°C)	T 3-7 (°C)
06/17/05	5.0	325.3	0.240	2.414	-0.793
06/23/05	4.0	324.9	2.231	5.804	0.539
07/07/05	6.0	324.0	3.236	6.779	1.553
07/08/05	5.0	324.0	3.283	6.795	1.614
07/09/05	4.0	324.0	3.321	6.810	1.663
07/15/05	4.0	324.0	3.689	7.079	2.079
07/16/05	5.0	324.0	3.772	7.210	2.139
07/21/05	7.0	322.7	4.110	7.677	2.417
07/22/05	7.0	322.8	4.181	7.784	2.470
07/23/05	6.0	319.7	4.261	7.894	2.535
08/04/05	3.0	322.8	4.848	8.262	3.225
08/11/05	6.4	322.3	5.341	9.052	3.578
08/17/05	6.5	322.2	5.486	8.828	3.898
08/28/05	8.2	322.1	5.700	8.569	4.338
09/12/05	7.5	322.6	5.655	7.952	4.564
12/12/05	501.0	318.3	0.220	-1.909	1.231
06/15/06	21.5	324.5	0.047	2.024	-0.893
07/06/06	1.0	324.2	3.194	6.766	1.498
08/06/06	2.0	321.7	4.997	8.523	3.320
12/14/06	209.0	317.6	0.130	-1.939	1.114

PT – Product thickness; GWE – Groundwater elevation.
T a-b – Average integral temperature from a-b m depth.

Table 2. Summary of statistical parameters from analysis.

b0	-38.68	e11	0.012	Sy/x	85.15
b1	-6.76	e22	0.003	Sb1	9.45
b2	459.61	e21	0.0003	Sb2	4.92
t1	-4.09	F-sample	9.58	F-table	3.590
t2	-1.37	r-sample	0.728	r-table	0.456
				t-table	2.110

Summary of partial correlation coefficients

Variables	GWE	T 1-7	T 1-3	T 3-7	PT
PT	-0.691	-0.537	-0.769	-0.200	1.000

are 0.691 and 0.769, respectively, and above the tabulated regression value of 0.456 from statistical table at 5% significant level (Table 2). The absolute partial regression of integral temperature from 3 to 7 m depth is 0.2, and below the tabulated r-value. Thus, the product thickness is more sensitive to changes in groundwater elevation and temperature within the upper 3 m of the subsurface than that at depth.

Discussion

Correlation of the product thickness with both the groundwater elevation and temperature profile only depicts association with the variables and does not necessarily imply causation. However, because other tests have been conducted at the site, inference can be drawn on how the decreasing groundwater elevation and temperature contributes to increased product thickness in the monitoring wells. Increased correlation with temperature in the upper 3 m of the subsurface suggests causative active mechanism at that section based on the premise of LNAPL exclusion due to freezing of water in soil matrix (Barnes et al. 2004) and fractures. However, this premise must be further explored experimentally for fissured media under laboratory condition.

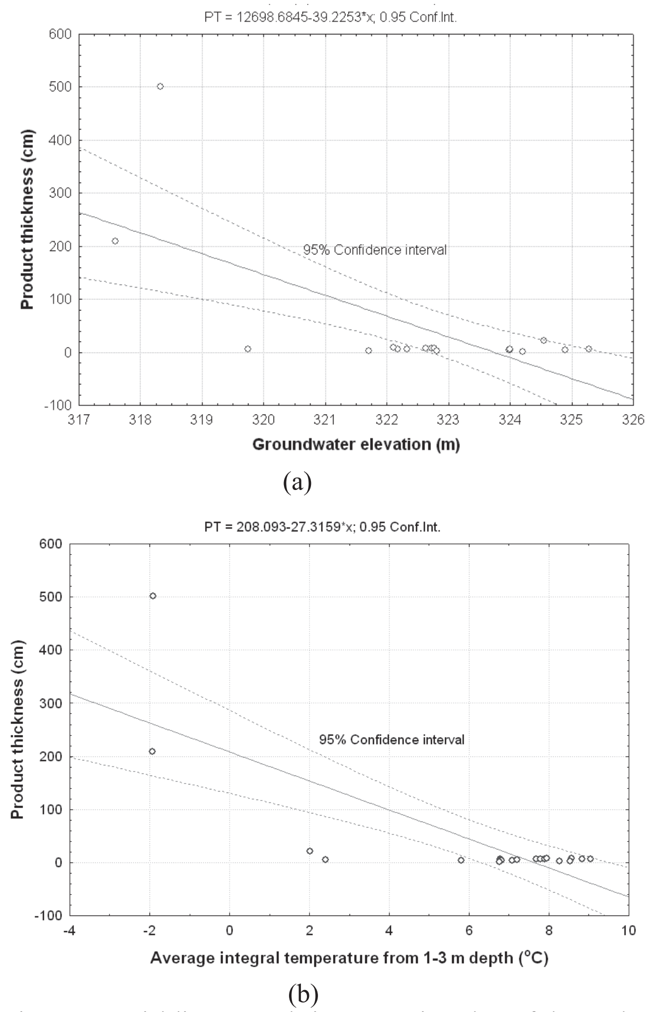

Figure 5. Partial linear correlation regression plots of the product thickness with (a) Groundwater elevation (b) Average integral temperature from 1-3 m depth.

Gravity drainage of mobile residual petroleum LNAPL in the formation due to a decrease in groundwater elevation coupled with LNAPL exclusion forward of the freezing front are hereby proposed as active mechanisms contributing to increased product thickness in the monitoring wells. The associative strength of these mechanisms is downplayed because of continual purging of the accumulated petroleum LNAPL from the monitoring wells. The overburden soil around MW 12 is 2.3 m thick and consists of gravel fill with sand. The well-log showed that multiple fractures exist between the upper 0.7 m of the bedrock surface with strong odor of petroleum hydrocarbon (PHC). Previous site characterization at the site by URS (2002) suggested that LNAPL being observed at the site are the residual LNAPL in the unsaturated zone of the subsurface. Thus, increased correlation of temperature fluctuation in the upper section of the subsurface affirms this.

Lower correlation between the product thickness and averaged integral temperature between 3 and 7 m from the subsurface does not necessarily imply poor influence on the product thickness because other factors such as fracture pattern and network may be masking its association. Though linear regression was used for this analysis, the actual association between the varied parameters may be non-linear. The practical significance of this study is that fluctuation of the groundwater table and freeze thaw cycle may increase recovery of mobile residual petroleum hydrocarbon from the subsurface at this site.

Conclusions

In this study, accumulated mobile LNAPL thickness in the monitoring well is shown to significantly correlate with the groundwater elevation and temperature at Colomac mine site. The petroleum LNAPL thickness increased with decreasing groundwater elevation and temperature. It was hypothesized that gravity drainage of mobile residual petroleum LNAPL at decreased groundwater elevation coupled with LNAPL exclusion are key mechanisms contributing to the observed behavior. The study suggests that product recovery may be enhanced by engineered fluctuation of the groundwater table and thermal regime at the site.

Acknowledgments

This study was sponsored by Program for Energy Research and Development (PERD), Indian and Northern Affairs Canada (INAC) and Environment Canada. The contributions by Greg Bickerton and Dale Van Stempvoort of Environment Canada, field assistance provided by Rob Duschene, Ross Neureuther, John Voralek, and Ron Breadmore of INAC are gratefully acknowledged.

References

Barnes, D.L., Wolfe, S.M. & Filler, D.M. 2004. Equilibrium of petroleum hydrocarbons in freezing ground. United Kingdom. *Polar Record* (214): 245-251.

Biggar, K.W., Haidar, S., Nahir, M. & Jarrett, P.M. 1998. Site investigations of fuel spill migration into permafrost. *Journal of Cold Regions Engineering* 12: 84-104.

Biggar, K.W. & Neufeld, J.C.R. 1996. Vertical migration of diesel into silty sand subject to cyclic freeze-thaw. Cold Regions Engineering: *Proceedings of the Eighth International Conference on Cold Regions Engineering. August 12-16:* 116-127.

Chuvilin, E.M. 1999. Migration of ions of chemical elements in freezing and frozen soils. *Polar Record* 35(192): 59-66.

Chuvilin, E.M., Naletova, N.S., Miklyaeva, E.C., Kozlova, E.V. & Istanes, A. 2001a. Factors affecting the spreadibility and transportation of oil in regions of frozen ground. *Polar Record* 37(202): 229-238.

Iwakun, O. & Biggar, K.W. 2007. Behaviour of spilled petroleum hydrocarbon at Colomac mine site, NWT. Canada. *60th Canadian Geotechnical and 8th joint CGS/IAH-CNC Groundwater Conferences.* Paper No. 565: 8 pp.

Iwakun, O., Biggar, K.W., Van Stempvoort, D. & Bickerton, G. 2007. Fuel contamination characterization in permafrost fractured bedrock at the Colomac mine site. Submitted to Cold Region Science and Technology (CRST-D-06-00119R1). 26 pp.

Konrad, J.M. & Seto, J.T.C. 1991. Freezing of a clayey silt contaminated with an organic solvent. *Journal of Contaminant Hydrology* 8(3-4): 335-356.

McCarthy, K., Walker, L. & Vigoren, L. 2004. Subsurface fate of spilled petroleum hydrocarbon in continuous permafrost. *Cold Regions Science and Technology* 38: 43-54.

Tumeo, M.A. & Davidson, B. 1993. Hydrocarbon exclusion from ground water during freezing. *Journal of Environmental Engineering* 119(4): 715-724.

URS, Norecol, Dames & Moore Inc. 2002. Assessment of hydrocarbons within fractured bedrock at the lakefront and waste oil areas and development of a remedial action plan, Colomac Mine, NWT. Report for Public Works & Government Services Canada. Vancouver, BC: 21 pp. + appendices.

The Temperature Regime in Boreholes at Nalaikh and Terelj Sites, Mongolia

Ya Jambaljav, A. Dashtseren, D. Solongo, A. Saruulzaya, D. Battogtokh
Permafrost laboratory at Institute of Geography, MAS, Mongolia

Y. Iijima, M. Ishikawa, Y. Zhang, H. Yabuki, Ts. Kadota
Institute of Observational Research for Global Change, JAMSTEC, Japan

Abstract

Since 2002, long-term field research of joint Japan-Mongolian IORGC projects have been concentrated and conducted in Nalaikh and in Terelj near Ulaanbaatar, Mongolia. There are two sites in Terelj (Terelj GL, Terelj FA) and one site in Nalaikh. At these sites we have been measuring the meteorological and permafrost parameters. This paper presents the temperature regime from 2003 to 2007 in boreholes located at these sites. The air temperature trend has increased by 1.9°C in Ulaanbaatar since 1969.

Keywords: active layer; geocryological; near-surface temperature; permafrost; temperature regime.

Introduction

Mongolia is a country of predominated by high and middle height mountains with continental climate, which promote the occurrence and development of permafrost. Permafrost underlies almost two thirds of the country and comprises the Province of Hovsgol, the Hangai, Hentei, and Altai mountains, and surrounding areas. Therefore, there is predominately mountain and arid land permafrost from sporadic to continuous distribution which is spread along the southern fringe of the Siberian permafrost region (Sharkhuu 2001). The permafrost in Mongolia is changing very rapidly under the influence of human activities such as open and close-pit coal mining, forest fires, etc. (Sharkhuu 2004).

This paper presents the temperature regimes between 2003 and 2007 from three observation sites (Terelj FA, Terelj GL, and Nalaikh) located near Ulaanbaatar. Long-term field research of joint Japan-Mongolian IORGC projects has been concentrated and conducted in Nalaikh and in Terelj. Nalaikh is located approximately 40 km to the southeast of Ulaanbaatar and is characterized by sparsely grassed pasture plate area. The elevation is about 1420 m a.s.l. Terelj is located approximately 40 km to the east of Ulaanbaatar and approximately 70 km from Ulaanbaatar by main road. Terelj is characterized by mountainous area with heights of 1550–2195 m a.s.l. In Terelj the south facing slopes are characterized by sparsely grassed grasslands with granite appearing in some places. South facing slopes and adjacent valleys have no permafrost. North facing slopes are covered by boreal forest, beneath which the permafrost occurs.

The objectives of this paper are to review the recent temperature regimes and to compare the air, near-surface, and ground temperature curves at selected sites.

Description of observation sites

According to the geocryological map of Mongolia (scale 1:1,500,000) the study area is located in an insular and sparsely insular permafrost region (Gravis et al. 1971). The insular and sparsely insular permafrost occupies 1%–50% of the total area. There are 18 observation sites in Terelj and 1

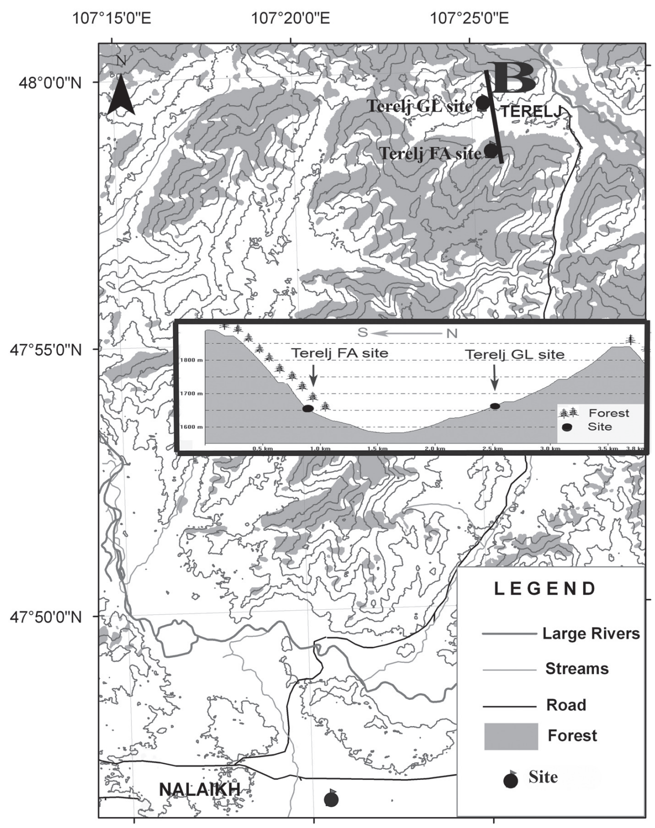

Figure 1. Location of sites. Also the profile along the B line is shown.

site in Nalaikh. In this paper we used the temperature data from 2 sites in Terelj (Terelj GL, Terelj FA) and from the Nalaikh site (Fig. 1).

Terelj FA site lies on a north facing forested slope of 10°–20°. The upper slope is 25°–40°. The elevation is 1656.5 m a.s.l. A 7.5 m deep borehole was drilled at this site in 2002. The ground temperature has been measured in this borehole using the CR-10X datalogger, datamark, and thermorecorder TR52. Terelj GL site lies on a south facing grassland slope of 10°–15°. The upper slope is 20°–35°. The elevation is 1664.4

m a.s.l. A 10 m deep borehole was drilled at this site in 2002. The ground temperature has been measured in this borehole using the datamark and CR-10X datalogger. The Nalaikh site lies on sparsely grassed pasture plate area of the Nalaikh depression. The elevation is 1420 m a.s.l. Boreholes 30.0 m and 7.0 m deep were drilled at this site in 2002. At these sites we also have measured the meteorological parameters at automatic weather stations (AWS).

Used data

In this paper we have used the air temperature and borehole temperature data measured at the Terelj FA and Terelj GL observation sites and at the Nalaikh site. The air temperature has been measured 1 and 2 m above the ground surface at Terelj FA, 1, 2, and 4 m above the ground surface at Terelj GL, and 0.5, 1, 2, and 4 m above the ground surface at Nalaikh. The air temperature data 2 m above the ground surface was used for this paper. Also we have used the temperature data from the 7.0 m deep and 30.0 m deep boreholes at the Nalaikh site, the 7.5 m deep borehole data at Terelj FA, and the 10.0 m deep borehole temperature data at Terelj GL site.

Climate Condition

According to climate change studies during the last 60 years, the mean annual air temperature has increased by 1.56° in Mongolia. Winter temperature has increased by 3.61° and spring, autumn temperature by 1.4°–1.5°. However the summer temperature has decreased by 0.3° (Natsagdorj 2000).

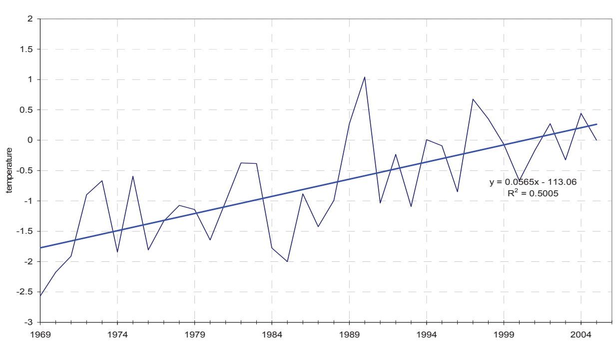

Figure 2. Mean annual air temperature in Ulaanbaatar between 1969 and 2005.

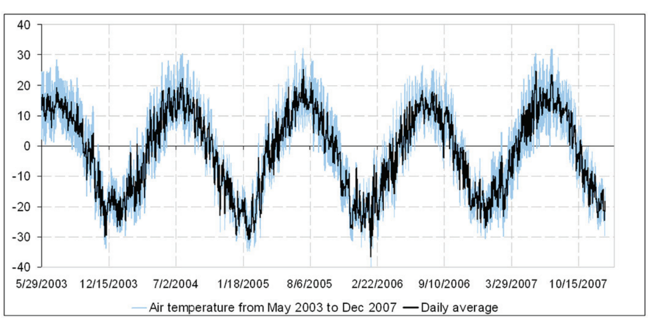

Figure 3. Air temperature at Terelj FA site.

Air temperature trend increased by 1.9° from 1969 to 2005 in Ulaanbaatar (Fig. 2).

Temperature Regimes of Sites

Air temperature

The maximum air temperature has been about +30.0°, and the minimum air temperature about -30.0° for the last 5 years at the Terelj FA site (Fig. 3). The mean annual air temperature was -2.9° for 2003, -2.1° for 2004, -2.97° for 2005, -3.35° for 2006, and -1.69° for 2007.

The maximum air temperature has been about +30.0° and the minimum air temperature is about -30.0° for the last 5 years at the Terelj GL site (Fig. 4). The mean annual air temperature was -1.21° for 2004, -1.36° for 2005, -1.5° for 2006, and +0.63° for 2007.

The maximum air temperature has been about +40.0° and the minimum air temperature is about -35.0° for the last 5 years at the Nalaikh site (Fig. 5). The mean annual air temperature was +0.96° for 2003, +5.82° for 2004, +4.94° for 2005, and +5.41° for 2006.

The air temperature curves are similar for the Terelj sites excepting the mean annual air temperature. But the air temperature curves are significantly different between the Terelj and the Nalaikh sites. The winter air temperature of the Nalaikh site increased rapidly over the last 5 years. At the Nalaikh site over the last 5 years the mean annual air temperature was plus 4.3°, which is disequilibrium with present permafrost in the Nalaikh depression. Mean annual air temperature of the Terelj FA site is minus 2.6° and mean annual air temperature of the Terelj GL site was minus 0.7° for the last 5 years.

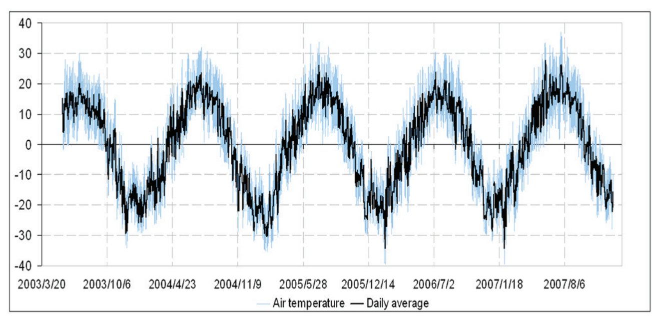

Figure 4. Air temperature at Terelj GL site.

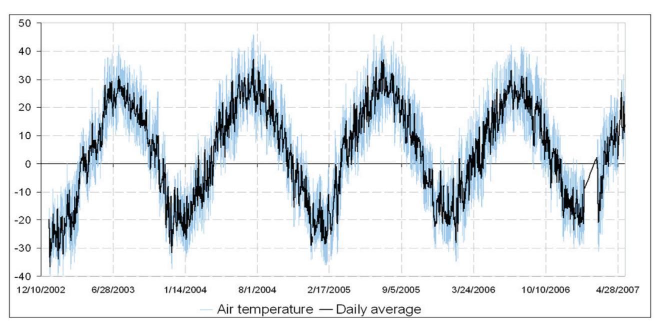

Figure 5. Air temperature at Nalaikh site.

Near-surface temperature

In wintertime the day-night temperature fluctuation is smoother than it is in summertime, because the temperature sensors are under the snow in wintertime (Figs. 6, 7, 8). Therefore, the winter near-surface temperature was higher than the winter air temperature. It means that snow cover has a warming effect at all three sites. So the minimum rate of the winter near-surface temperature was about -22°C at Terelj FA, about -19°C at Terelj GL, and about -26°C at Nalaikh.

In summertime day-night temperature fluctuation is higher than it is in wintertime especially at the Nalaikh site because of sparsely grassed area in Nalaikh. The maximum rate of the summer near-surface temperature was about +38°C at Terelj FA, about +35°C at Terelj GL, and about +60°C at Nalaikh.

Temperature on bottom of seasonally freezing and thawing

At the Terelj FA site the active layer thickness was about 3.8 m for 2004, 3.5 m for 2005, 3.25 m for 2006, and 3.55 m for 2007. The ground temperature ranged from -2.9°C to +0.1°C at a depth of 3.5 m between 2004 and 2007 (Fig. 9).

At the Terelj GL site the seasonal freezing depth was 3.90 m for 2004, 4.0 m for 2005, 4.2 m for 2006, and 3.85 m for 2007. The ground temperature ranged from -0.3°C to +4.9°C at a depth of 4.0 m between 2004 and 2007 (Fig. 10).

At the Nalaikh site the active layer thickness is more than 7.0 m. As shown on Figure 11, at the Nalaikh site the minimum rate of ground temperature was -0.3°C at a depth of 7.0 m between 2003 and 2007. The maximum rate of ground temperature was not possible to determine due to no data in the summertime.

As shown by Figures 9 and 11 above, the active layer thickness is different due to different topography, ground thermal condition, water content, ice content, and surface cover of the sites. The active layer thickness is about 3.5 m at the Terelj FA site. The Terelj FA site is characterized by north facing forested slope 10°–20°. Active layer thickness is about 7.5 m by borehole with a depth of 30.0 m at the Nalaikh site. The Nalaikh site is characterized by sparsely grassed plate area. As shown in Figure 10, the seasonal freezing depth is about 4.0 m at the Terelj GL site. Therefore the thicknesses of active layer and the seasonal freezing depths are different from place to place within a short distance in the mountain area.

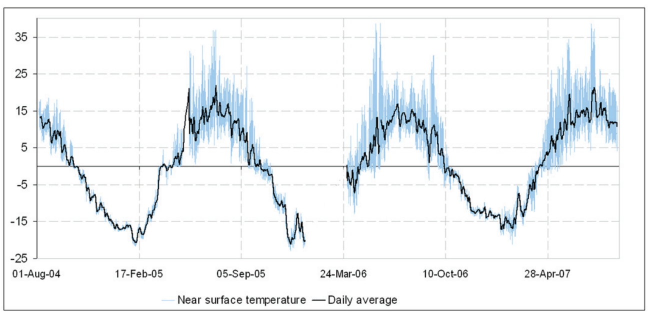

Figure 6. Near-surface temperature at Terelj FA.

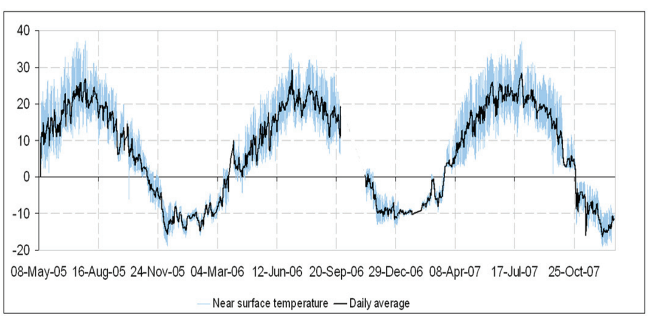

Figure 7. Near-surface temperature at Terelj GL.

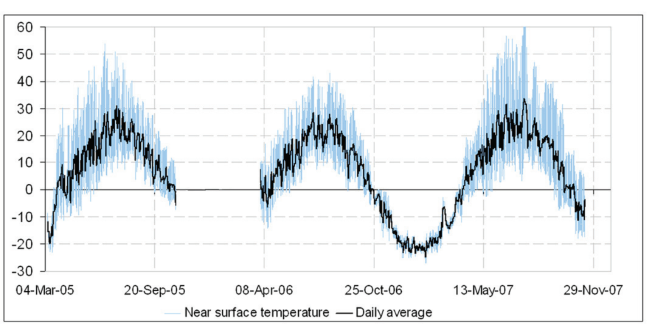

Figure 8. Near-surface temperature at the Nalaikh site.

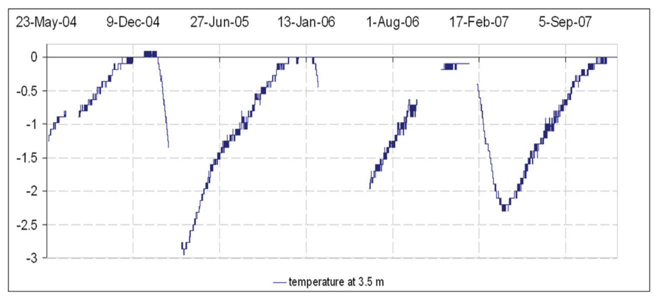

Figure 9. Ground temperature on a depth of 3.5 m at Terelj FA site.

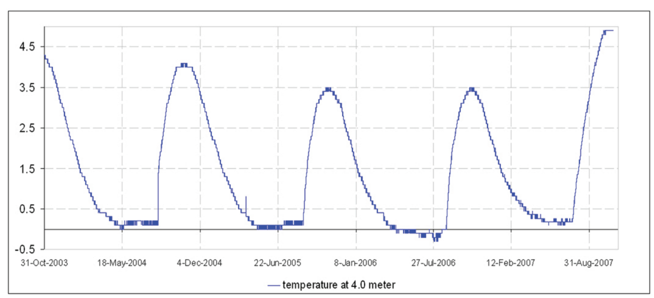

Figure 10. Ground temperature on depth of 4.0 meter at Terelj GL.

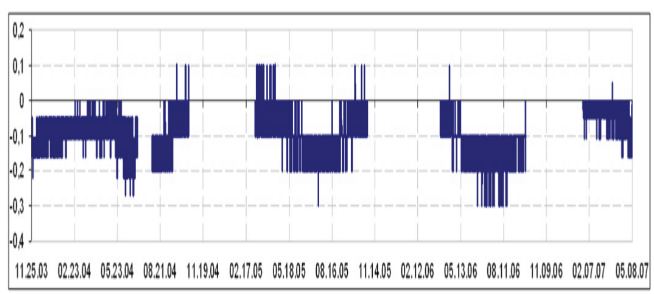

Figure 11. Ground temperature on a depth of 7.0 m at the Nalaikh site.

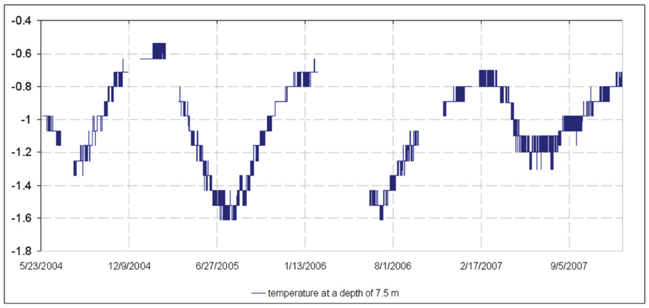

Figure 12. Temperature curve on a depth of 7.5 m from May 2004 to December 2007 at the Terelj FA site.

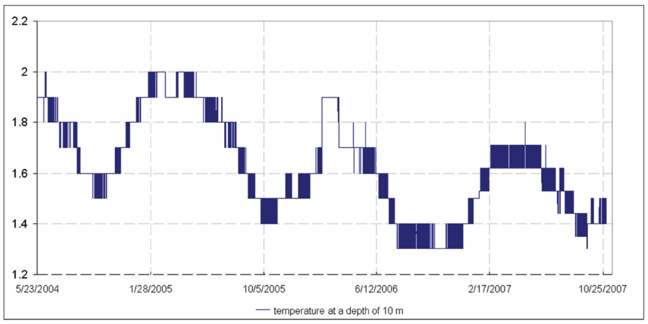

Figure 13. Temperature curve on a depth of 10.0 m from May 2004 to November 2007.

Deep temperature curves at three sites

Figure 12 shows the temperature curve on a depth of 7.5 m at the Terelj FA site. As shown in Figure 12, the depth of yearly temperature penetration is more than 7.5 m at the Terelj FA site. The maximum temperature was -0.55°C and the minimum temperature was -1.6°C between 2004 and 2007. The minimum temperatures were higher in 2004 and in 2007 than they were in 2005 and 2006. The maximum temperatures ranged from -0.55°C to -0.7°C.

Figure 13 shows the temperature curve on a depth of 10.0 m at the Terelj GL site. The depth of yearly temperature penetration is more than 10.0 m. The maximum temperature was +2°C in January of 2005. It had decreased between 2004 and 2007.

The minimum temperature was +1.3°C in September of 2006. It also had decreased between 2004 and 2007. Both temperatures (maximum and minimum) decreased from year to year between 2004 and 2007 because the snow thickness and the duration of snow cover became thicker and shorter in this period of time.

Figure 14 shows the temperature profile of the 30 m deep borehole at the Nalaikh site. The temperature below 5.0 m, is close to 0°. As shown in Figure 14, the active layer thickness was 7.5 m. By this temperature profile there are two layers of permafrost. The first layer is from 7.5 m to 11.4 m; the second layer is from 15.5 m down.

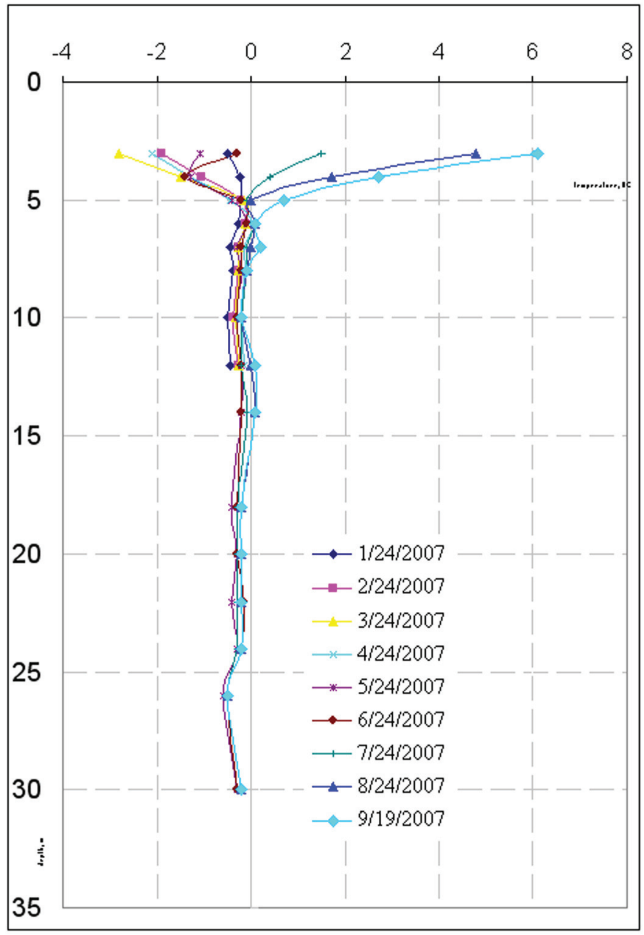

Figure 14. Temperature profile of 30.0 m deep borehole at Nalaikh.

Conclusion

- There are very high amplitudes of air and near-surface temperature at the three sites. Also there are very high day-night fluctuations of air and near-surface temperature. Day-night temperature fluctuation became low in wintertime at the surface, because the sensors lie under the snow cover.
- Near-surface temperature was a little higher than the air temperature in wintertime. So thin snow cover has a warming effect. The snow thickness was about 5–20 cm depending on the topography of the sites.
- The active layer thickness and the seasonal freezing depth are different due to topography, ground thermal conditions, surface cover, water, and ice content. There is a thick active layer at the Nalaikh site.
- Deep temperature is close to 0° at the Nalaikh site. The minimum temperature is -1.6°C on a depth of 7.5 m.
- There are two layers of permafrost at the Nalaikh site.

Acknowledgments

The author wishes to thank the Japan Agency for Marine-Earth Science and Technology and the Institute of Geography of the Mongolian Academy of Sciences who supported this research.

References

Kudryavtsev, V.A. 1978. *General Geocryology.* Moscow: Moscow University Press, 462 pp.

Ishikawa, M., Sharkhuu, N. & Zang, Y. 2006. Ground thermal and moisture conditions at the southern boundary of discontinuous permafrost, Mongolia. *Permafrost and Periglacial Processes* (Number 2) Volume 16 (ISSN 1045-6740): 209-216.

Sharkhuu, N. 2001a. Permafrost mapping in Mongolia, *Extended abstracts of International Symposium on Mountain and Arid Land Permafrost, Ulaanbaatar, Mongolia, September 2-7, 2001*: 63-67.

Sharkhuu, N. 2001b. Geocryological monitoring in Mongolia, *Extended abstracts of International Symposium on Mountain and Arid Land Permafrost, Ulaanbaatar, Mongolia, September 2-7, 2001*: 63-67.

Sharkhuu, N., Battogtokh, D., Ishikawa, M., Kadota, T. & Zang, Y. 2004. Dynamics of active layer and spring icing at Terelj observation sites, Mongolia *Proceedings of the International Symposium on Terrestrial and Climate Change in Mongolia, Tokyo, Japan, November 9-10, 2004* 5: 29-30.

Recent Changes in Hydrologic Response Observed in Permafrost Regions of Northwest Canada

J. Richard Janowicz
Water Resources Section, Yukon Department of Environment, Whitehorse, Yukon Territory, Canada

Abstract

Air temperature trends have been observed to change over the last several decades in northern North America. Both summer and winter air temperatures have increased in most regions. An assessment was carried out to determine if corresponding trends of hydrologic response are apparent within permafrost regions of North America. Hydrograph characteristics were assessed using the Mann-Kendall trend test. The greatest changes to hydrologic response were observed with winter low flows. The greatest changes in winter streamflow appear to be occurring within the continuous permafrost zone, where flows from the majority of sampled streams have increased. Winter low flow trends in streams within the discontinuous permafrost zone generally exhibit positive trends, but are more variable. Winter streamflow trends within the sporadic permafrost zone are not consistent. Increasing winter streamflow trends have occurred from some mountainous regions of alpine permafrost. Other streams exhibit no discernable change, while some streams exhibit a negative change.

Keywords: continuous; discontinuous; Mann-Kendall; 7-day low flow; sporadic permafrost; trend analysis.

Introduction

The primary control over hydrologic response in northern regions is permafrost distribution, permafrost thickness, and thickness of the active layer (Hinzman et al. 2005). Thick underlying permafrost and a thin active layer produce short pathways to the stream channel, with little or no interaction with subsurface processes. Ice-rich permafrost restricts rain or snowmelt infiltration to subsurface zones, resulting in surface storage in the form of ponds or wetlands. A thicker active layer enhances infiltration and associated groundwater recharge, which in turn would result in greater groundwater contributions to streamflow. Yukon hydrologic response follows this principle, and is closely tied to the underlying permafrost.

Changing climate appears to be resulting in a likewise change in the permafrost distribution of northern regions, including the Yukon Territory. Increasing air temperatures are resulting in permafrost warming and associated thawing, which in turn results in a thicker active layer. Permafrost degradation is expected to be greatest within the discontinuous and sporadic permafrost zones, since these permafrost classes are warmer; and therefore, more susceptible to thawing (Hinzman et al. 2005). Observations within the discontinuous permafrost regions of Alaska disclose the development of extensive areas of thermokrast terrain due to thawing permafrost (Osterkamp & Romanovsky 1999).

Yukon temperature and precipitation trends have been observed to change over the last several decades (Janowicz 2001). Winter and summer temperatures have increased in all regions, with greater winter temperature increases in northern Yukon, and greater summer increases in southwestern Yukon. Winter precipitation has increased slightly in all regions, while summer precipitation is more variable, decreasing in northern Yukon and increasing in southern Yukon. The greatest changes have occurred in western, mountainous regions where both summer and winter temperatures and winter precipitation have increased significantly. These observed trends are in the general order of projections developed by a Canadian Climate Centre global climate model (GCMII), which is based on a 100 percent increase of CO_2 in the atmosphere (Taylor 1997, Intergovernmental Panel on Climate Change 2001).

There have been a number of studies carried out in northern regions of North America on the impact of climate change on hydrologic response (Kite 1993, Burn 1994, Loukas & Quick 1996, 1999, Leith & Whitfield 1998, Whitfield & Taylor 1998, Spence 2002)). Whitfield & Cannon (2000) & Whitfield (2001) assessed climatic and hydrologic variations between two decades (1976–1985; 1986–1995) for stations in British Columbia and Yukon. Hydrologic response was generally found to be characterised by higher year round flows. Mountainous streams were found to have the timing of the freshet advanced, followed by lower summer and fall discharge. Zhang et al. (2001) and Yue et al. (2003) assessed the streamflow records for 243 Canadian hydrometric stations making up the Reference Hydrometric Basin Network, including some Yukon stations, over the period 1967 to 1996. While most of these stations were in southern Canada, they found winter low flows in northern British Columbia and Yukon to have increased significantly. Annual mean and peak flows were observed to have increased in glacerized basins of southern Yukon and northern British Columbia. Burn et al (2004), in the comparison of streamflow of the Liard and Athabasca Rivers in the mountainous, headwater regions of the Mackenzie River basin, found both streams to exhibit increases in winter discharge and some increase in the snowmelt freshet. Dery & Wood (2005) investigated the discharge of 64 arctic or subarctic Canadian rivers from 1964 to 2003. They found a general 10 percent decline in mean annual discharge to the Arctic and North Atlantic Oceans over that period, which is consistent with a decline in annual precipitation in northern Canada over that period. The decline in streamflow was less pronounced in northwestern Canada, where the results were not statistically significant. Their work indicated there were links between annual discharge and Arctic Oscillation, El Nino/South Oscillation (ENSO), and the Pacific Decadal Oscillation (PDO) at interannual to decadal timescales.

There has been only limited work to date on the impact of climate change specific to Yukon hydrology. Janowicz & Ford (1994) used the CCC GCM temperature and precipitation projections, and a correlation approach to assess the impacts of climate change on the water supply to the upper Yukon River. Their analyses indicated that annual inflows to the glacierized upper Yukon River would increase by 39 percent, primarily in summer months, due to increasing temperature and precipitation. Janowicz (2001) carried out an analysis of streamflow to assess the response of the observed temperature and precipitation changes on peak flows, which normally occur as a result of spring snowmelt. The assessment revealed that there has been a dramatic change in mean annual flood (MAF) in some regions of Yukon over the last 20 years, with a progressive decrease in the parameter moving from south to north. The greatest increases in MAF were observed to occur within the sporadic permafrost zone, from predominantly glacierized systems in western Yukon. Smaller increases were noted in southeastern Yukon. These increases correspond to the observed increase in both summer temperatures and winter and summer precipitation. Peak flows from central and eastern Yukon, within the discontinuous permafrost zone, exhibit very little change. Within the continuous permafrost zone, peak flows were observed to decrease progressively moving northward to the Arctic coast.

This paper summarizes the results of a study carried out to assess apparent trends of annual minimum flows in Yukon and adjacent areas of northwestern Canada over the last few decades.

Setting and Methodology

The analyses were carried out using data from the Yukon Territory and the western Northwest Territory west of the 125th parallel of longitude, an area covering approximately 920,000 km^2. This region consists of three permafrost zones: continuous, discontinuous, and sporadic (Fig. 1). Continuous permafrost areas have greater than 90% coverage; discontinuous areas have between 50 and 90% coverage; and sporadic areas have 10 to 50% coverage (Brown et al. 1997). The continuous, discontinuous, and sporadic zones represent 30, 45, and 25 percent of Yukon, respectively (Natural Resources Canada 1995). Hydrometric data from all active and recently discontinued (<5 years) Environment Canada, Water Survey of Canada (WSC), stations on unregulated streams, with at least 25 years of record were used in the analyses. The data were obtained from the WSC website. Because of numerous station discontinuations in

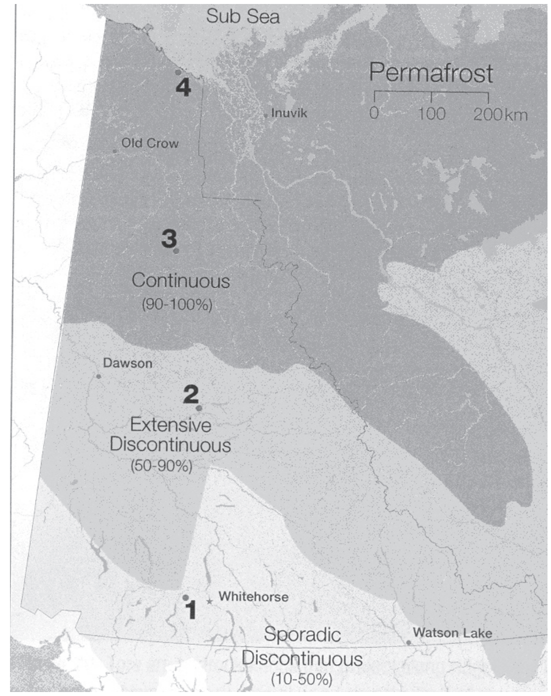

Figure 1. Study area and permafrost zones (from Smith et al. 2004).

the mid-1990s, only 21 stations were available for analyses. These were equally distributed between the three permafrost classes. The 7-day average minimum annual low flow, which normally occurs in late winter or early spring, was assessed in the present study. The 7-day average low flow parameter is a commonly used, minimum flow measure which reduces the variability over a single value.

Trend analysis

The Mann-Kendall trend test was used to assess trends in the 7-day minimum annual low flow parameter. The Mann-Kendall test is a non-parametric test used for the assessment of trends in time series. It is a simple, robust tool which can readily handle missing values. The calculated standard normal variate value (Z) is associated with a specific level of significance. The significance level provides an indication of the strength of the trend. A significance level of 0.001 indicates a very strong trend; 0.01 indicates a strong trend; 0.05 indicates a moderate trend; and 0.1 indicates a weak trend. A level of significance of less than 0.1 indicates there is no discernable trend.

Results and Discussion

Table 1 provides a summary of the trend analyses. Positive trends in winter low flows are generally evident in all Yukon permafrost regions, with the occurrence of this trend inversely related to latitude. Winter baseflows are also generally related to drainage area. In cold regions, the relationship is more pronounced, with smaller drainages having less groundwater inputs to baseflow; therefore, smaller winter flows. While

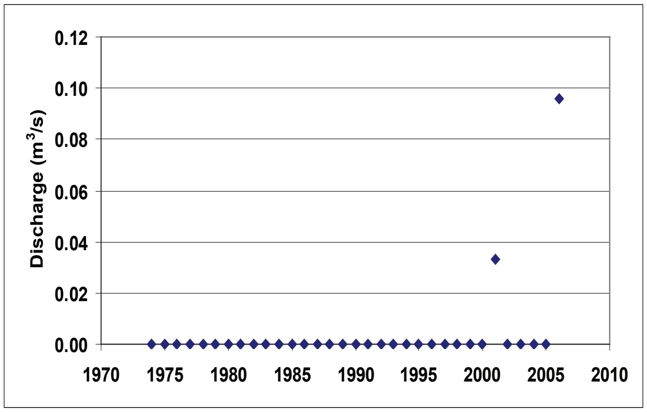

Figure 2. Seven-day average minimum low flow – Rengleng River at Dempster Highway.

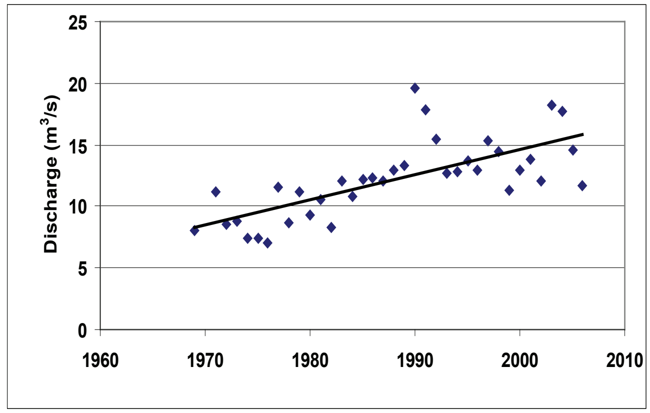

Figure 3. Seven-day average minimum low flow – Arctic Red River at Fort McPherson (r^2=0.49).

summer and winter precipitation have generally increased and decreased, respectively, in permafrost regions, annual precipitation has increased slightly, and there has been a corresponding slight observed increase in annual runoff in continuous and discontinuous permafrost regions. Both precipitation and annual discharge increases are slight, and cannot provide the basis for winter low flow increases. Summer and winter air temperatures have been observed to increase in most regions, and may attribute to the increase in winter low flows. Climate warming produces permafrost degradation, which enhances the interaction between surface and groundwater systems, allowing for greater groundwater contributions to baseflow.

The greatest positive trends in winter low flows appear to have occurred in the continuous permafrost zone, where streams with drainage areas in the order of 5,000 km^2, generally have streamflow throughout the winter. There is an exception for streams along the Arctic coast, where larger streams often experience "zero" winter flows. It is not possible to statistically validate trends from study streams which have had predominately "zero" winter flows in past decades. As with many statistical techniques, the Mann-Kendall test is not able to handle "zero" flows. Figure 2 provides an illustration of low flow trends for a small stream, the Rengleng River (station number 10LC003), with a drainage area of 1310 km^2. Winter low flows in past decades have been nonexistent, while measurable flow during recent winter periods has been observed. The winter flow regime for Caribou Creek (10ND002), with a drainage area of 68.3 km^2, has remained unchanged, with "zero" flows throughout the entire 29 year monitoring period.

Figure 3 provides an illustration of the positive winter low flow trend for the Arctic Red River (10LA002), with a drainage area of 18,600 km^2.

Trends of winter low flow regimes, with increasing flows, are generally exhibited by streams within the discontinuous permafrost zone. Four of the seven assessed streams have statistically significant positive winter low flow trends. Figure 4 illustrates the increasing trend for the Klondike River (09FA003). Even the smallest streams within the discontinuous permafrost zone normally have winter flows, so drainage area is not as strong a factor in influencing winter streamflow, as in the continuous permafrost zone.

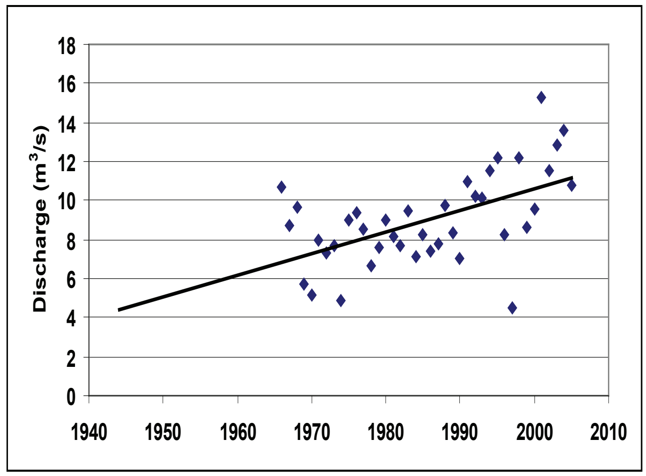

Figure 4. Seven-day average minimum low flow – Klondike River above Bonanza Creek (r^2=0.30).

Trends of increasing winter low flows are not generally strong within the sporadic permafrost zone. Two of the seven represented streams have statistically significant positive trends. Both of these streams are transitional with the discontinuous permafrost zone, and one of these drains a mountainous region with significant alpine permafrost. Other streams exhibit no discernable change, while one stream exhibits a negative change.

Conclusions

An assessment of streamflow response was carried out to determine if there are apparent trends in permafrost regions as a result of observed temperature changes. As permafrost properties change with climate warming, hydrologic response in northern regions would likewise presumably change. Degrading permafrost increases the thickness of the active layer, decreases the overall thickness of the permafrost and, in certain areas, eliminates the presence of

Table 1. Mann-Kendall trend statistics.

Permafrost Class	Station Name	Drainage Area (km^2)	Record Period	n	Z Statistic	Significance Level
Continuous	Old Crow R nr Old Crow	13900	1977-05	27	0.83	> 0.1
	Porcupine R nr Border	59800	1962-05	40	1.81	0.1
	Arctic Red R nr Mouth	18600	1969-06	37	4.89	0.001
	Rengleng R bl Hwy #8	1310	1973-05	32	"0"	-
	Caribou Cr ab Hwy #8	625	1975-06	31	"0"	-
	Peel R ab Ft McPherson	70600	1975-06	31	3.65	0.001
	Trail Valley Cr nr Inuvik	68.3	1977-06	29	"0"	-
Discontinuous	Ross R at Ross R	7250	1961-05	44	1.42	> 0.1
	Pelly R at Pelly Crossing	49000	1953-05	52	2.12	0.1
	Pelly R bl Vangorda Cr	22100	1973-05	33	2.43	0.1
	Stewart R at Mouth	51000	1964-05	42	1.23	> 0.1
	Klondike R ab Bonanza Cr	7800	1966-05	40	3.44	0.001
	Flat R nr Mouth	8560	1961-06	39	0.94	> 0.1
	S Nahanni R ab Virginia	14600	1964-06	42	2.3	0.1
Sporadic	Dezadeash R at Haines Jnc	8500	1953-05	53	2.95	0.01
	Giltana Cr nr Mouth	194	1981-05	25	0.82	> 0.1
	Alsek R ab Bates R	16200	1975-05	31	0.29	> 0.1
	Wheaton R nr Carcross	875	1958-05	44	-0.67	> 0.1
	Takhini R nr Whitehorse	6930	1949-05	56	1.49	> 0.1
	White R at Alaska Hwy	6240	1975-05	30	2.43	0.05
	Liard R at Upper Crossing	33400	1961-05	45	0.73	> 0.1

underlying permafrost entirely. These actions place a greater reliance on the interaction between surface and subsurface processes. Annual minimum flows were assessed, which were represented by the mean 7-day low flow. The Mann-Kendall test was used to statistically validate observed trends. Winter low flow trends have experienced significant apparent changes over the last three decades. The greatest changes in winter low flows appear to be occurring within the continuous permafrost zone, where flows from the majority of sampled streams have increased. Winter low flow trends in streams within the discontinuous permafrost zone generally exhibit positive significant trends, but are more variable. Winter streamflow trends within the sporadic permafrost zone are not consistent. Increasing winter streamflow trends have occurred from some mountainous regions of alpine permafrost. Other streams exhibit no discernable change, while one stream exhibits a negative change.

Acknowledgment

The work carried out by Cam Malloch in performing much of the data extraction and manipulation is greatly appreciated.

References

Brown, J., Ferrians, O.J., Heginbottom, J.A. & Melnikov. 1997. *Circum-Arctic map of permafrost and ground ice conditions.* 1:10,000,000. International Permafrost Association.

Burn, D.H. 1994. Hydrologic effects of climate change in west-central Canada. *Journal of Hydrology* 160: 53-70.

Burn, D.H., Cunderlik, J.M. & Pietroniro, A. 2004. Hydrological trends and variability in the Liard River basin. *Hydrological Sciences Journal* 49: 53-67.

Dery, S.J. & Wood, E.F. 2005. Decreasing river discharge in northern Canada. *Geophysical Research Letters* 32:L10401.

Hinzman, L.D., Bettez, N.D., Bolton, W. R., Chapin, F. S., Dyurgerov, M.B., Fastie, C. L., Griffith, B., Hollister, R.D., Hope, A., Huntington, H.P., Jensen, A.M., Jia, G.J., Jorgenson, T., Kane, D.L., Klein, D.R., Kofinas, G., Lynch, A.H., Lloyd, A.H., McGuire, A.D., Nelson, F.E., Nolan, M., Oechel, W.C., Osterkamp, T.E., Racine, C.H., Romanovsky, V.E., Stone, R.S., Stow, D.A., Sturm, M., Tweedie, C.E., Vourlitis, G.L., Walker, M.D., Walker, D.A., Webber, P.J., Welker, J., Winker, K.S. & Yoshikawa K. 2005. Evidence and implications of recent climate change in northern Alaska and other Arctic regions. *Climate Change* 72: 251-298.

Intergovernmental Panel on Climate Change 2001. In: J.T. Houghton et al. (eds.), *Climate change 2001: The Scientific Basis.* Cambridge University Press, 881 pp.

Janowicz, J.R. & Ford, G. 1994. Impact of climate change on water supply in the upper Yukon River. *Proceedings of the 62nd Annual Western Snow Conference, Sante Fe, New Mexico, April 18–21, 1994*.

Janowicz, J.R. 2001. Impact of recent climatic variability on peak streamflow in northwestern Canada with implications for the design of the proposed Alaska Highway gas pipeline. *Proceedings of the 13th Northern Research Basins International Symposium & Workshop, Saariselka, Finland and Murmansk, Russia, August 19–24, 2001*: 161-169.

Kite, G.W. 1993. Application of a land class hydrological model to climate change. *Water Resources Research* 29(7): 2377-2384.

Leith, R.M. & Whitfield, P.H. 1998. Evidence of climate change effects on the hydrology of streams in south-central B.C. *Canadian Water Resources Journal* 23: 219-230.

Loukas, A. & Quick, M.C. 1996. Effect of climate change on hydrologic regime of two climatically different watersheds. *Journal of Hydrological Engineering* 1(2): 77-87.

Loukas, A. & Quick, M.C. 1999. The effect of climate change on floods in British Columbia. *Nordic Hydrology* 30: 231-256.

Natural Resources Canada. 1995. *National Atlas of Canada*. 5th Ed., MCR 4177. Geological Survey of Canada, Terrain Sciences Division, Ottawa.

Romanovsky, V.E. & Osterkamp, T.E. 1999. Evidence for warming and thawing of discontinuous permafrost in Alaska. *Permafrost and Periglacial Processes* 10: 17-37.

Smith, C.A.S., Meikle, J.C. & Roots, C.F. 2004. *Ecoregions of the Yukon Territory – biophysical properties of Yukon landscapes.* Agriculture and Agri-food Canada, PARC Technical Bulletin 04-01, Summerland, British Columbia, 313 pp.

Spence, C. 2002. Streamflow variability (1965–1998) in five Northwest Territories and Nunavut rivers. *Canadian Water Resources Journal* 27: 135-155.

Taylor, B. 1997. Climate change scenarios for British Columbia and Yukon. In: E. Taylor & B. Taylor (eds.), *Responding to global climate change in British Columbia and Yukon, Canada Country Study: Climate Impacts and Adaptation,* Vol. 1. Environment Canada.

Whitfield, P.H. 2001. Linked hydrologic and climate variations in British Columbia and Yukon. *Environmental Monitoring and Assessment* 67: 217-238.

Whitfield, P.H. & Cannon, A.J. 2000. Recent climate moderated shifts in Yukon hydrology. In: D.L. Kane (ed.), *Proceedings AWRA Conference Water Resources in Extreme Environments, Anchorage, Alaska, May 1–3, 2000.*

Whitfield, P.H. & Taylor, E. 1998. Apparent recent changes in hydrology and climate of coastal British Columbia. In: Y. Alila (ed.), *Mountains to Sea: Human Interaction with the Hydrologic Cycle. Proceedings of the 51st Annual Canadian Water Resource Conference*: 22-29.

Yue, S., Pilon, P. & Phinney, B. 2003. Canadian streamflow trend detection: impacts of serial and cross-correlation. *Hydrological Sciences* 48: 51-63.

Zang, X., Harvey, K.D., Hogg, W.D. & Yuzyk, T.R. 2001. Trends in Canadian streamflow. *Water Resources Research* 37: 987-998.

Factors Contributing to the Long-Term Integrity of Drilling-Mud Sump Caps in Permafrost Terrain, Mackenzie Delta Region, Northwest Territories, Canada

R.E.L. Jenkins
Water Resources Division, Indian and Northern Affairs Canada, Yellowknife, NT, Canada
J.C.N. Kanigan
Department of Geography and Environmental Studies, Carleton University, Ottawa, ON, Canada
S.V. Kokelj
Water Resources Division, Indian and Northern Affairs Canada, Yellowknife, NT, Canada

Abstract

In this study, we examine the operational and environmental factors associated with the cap performance of 110 drilling-mud sumps constructed between 1965 and 2005 in the Mackenzie Delta region, Northwest Territories. Thawing of ice-rich cover materials can cause cap subsidence and surface ponding, and may increase the potential for migration of sump contents. To control for the effects of degradation over time, we examined data for the 77 sumps constructed between 1968 and 1977. Significant ponding (>20% of cap area) characterized 65% of the sumps in warm permafrost (>-3.9°C) and alluvial terrain. The largest proportion of sumps with good cap integrity were in cold permafrost (<-7.0°C) on tundra uplands. Many sumps that were operated in summer maintained good cap integrity, and were situated in cold permafrost, further highlighting the importance of site environmental conditions. Variable long-term cap performance suggests that a long-term approach to managing sumps in permafrost terrain is necessary.

Keywords: cap integrity; drilling-mud sumps; Mackenzie Delta region; permafrost.

Introduction

Drilling wastes produced during land-based hydrocarbon exploration in the Canadian arctic and subarctic have been disposed of to in-ground sumps (French 1978a, b) in accordance with Federal legislation. Sumps are excavated into permafrost and are generally situated adjacent to the wellhead. Following the completion of the drilling program, the drilling fluids, cuttings and rig wash are deposited to the sump which is then backfilled to form a cap (Fig. 1). The design intent is to confine the active layer within the cover materials and maintain the saline drilling wastes in the underlying permafrost (French 1980, Dyke 2001).

Operational and environmental factors combine to influence sump performance (French 1985). For example, sumps constructed in cold permafrost are more likely to maintain saline drilling fluids in a frozen state even if climate or vegetation conditions change with time. The potential for sump collapse is enhanced where permafrost is ice-rich because thawing of cover materials or adjacent terrain can lead to surface subsidence and ponding. Accumulation of surface water on or around the sump cap may lead to thermal instability promoting additional subsidence. The capping of unfrozen materials can cause fluids to be squeezed out of the sump. Under contemporary practices, the fluids deposited to the sump in winter are assumed to freeze in situ and the wastes are capped prior to warming air temperatures in spring (Fig. 1). Terrain disturbance adjacent to sumps can lead to surface subsidence and ponding around the cap, but impacts can be minimized by operating on a protective ice pad.

Since 1965, about 150 drilling-mud sumps have been constructed in the Mackenzie Delta region. Sump cap collapse and ponding suggests that permafrost, the primary containment medium, has partially degraded and that the drilling wastes are no longer encapsulated by permafrost (Fig. 2) (Kokelj & GeoNorth 2002).

In this paper we summarize information on the construction practices, environmental conditions and cap integrity for 110 drilling-mud sumps constructed over the past 40 years in the Mackenzie Delta region. Our primary objectives are: 1) To provide a summary of sump cap performance; and 2) to examine the influence of construction practices and environmental conditions on long-term sump cap integrity. This investigation is timely because the proposed Mackenzie Gas Pipeline has stimulated renewed hydrocarbon exploration in the region and sumps remain a waste disposal option in the north.

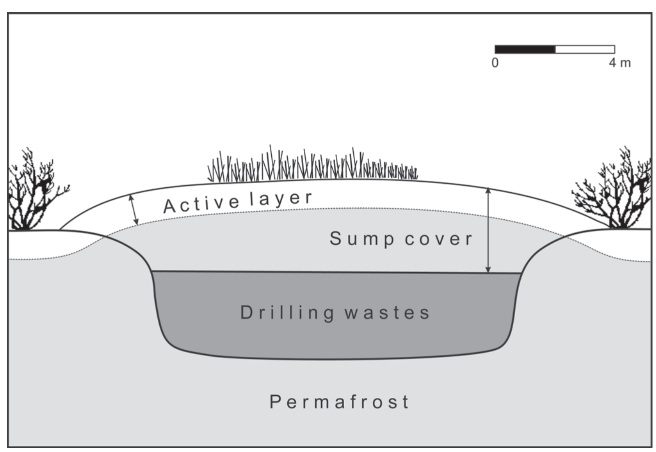

Figure 1. Generalized cross-section of a northern drilling-mud sump.

Figure 2. Drilling-mud sump in the outer Mackenzie Delta. The sump cap has collapsed causing a large pond to form. The arrow indicates submerged willows in the pond. Willows on sump cap in background are approximately 2 m in height.

Study Area

The drilling-mud sumps we examined are located in the Mackenzie Delta and the adjacent uplands in a diverse range of terrain, permafrost and ecological conditions (Fig. 3). Mean annual air temperatures at Inuvik and Tuktoyaktuk are -8.8°C and -10.2°C, respectively (Environment Canada 2007). Mean annual ground temperatures range from -9°C in upland terrain near the Beaufort Sea coast to above 0°C in point bar willow communities of the Delta (Mackay 1974, Smith 1975).

Most of the drilling-mud sumps in alluvial terrain of the Mackenzie Delta are subject to periodic flooding in spring and those in the low-lying northern delta may also be inundated by storm surges in summer (Fig. 3) (Burn 2002). North of treeline, low shrubs grow along point bars, and sedge wetlands occupy the delta plain. Thermal disturbance associated with the numerous lakes and channels, early removal of snow due to spring flooding, and the growth of tall shrubs and associated deep snow on point bars can account for warmer ground temperatures in the Delta than in the adjacent tundra uplands (Mackay 1974, Smith 1975). Ground temperatures at undisturbed sites in the outer delta range from -2 to -3°C (Mackay 1974). Southward the elevated delta plain is vegetated by spruce forests underlain by permafrost between about -2°C and -4°C (Mackay 1974, Kanigan et al. 2008). In the delta, wedge ice and near-surface aggradational ice is associated with spruce forests and sedge wetlands (Kokelj & Burn 2005, Kokelj et al 2007a).

The uplands east of the Mackenzie Delta, including the Tuktoyaktuk Coastlands, are characterized by low arctic shrub tundra (Ritchie 1984). Mean annual ground temperatures are lower than in the delta due to the absence of flooding and thinner snow cover. Ground temperatures decrease northwards with vegetation height and snow cover, so that permafrost on the Tuktoyaktuk Coastlands and on northern Richards Island may be below -8°C (Mackay 1974). The terrain is hummocky and the fine-grained materials are frost susceptible (Kokelj et al. 2007b). Upland sediments

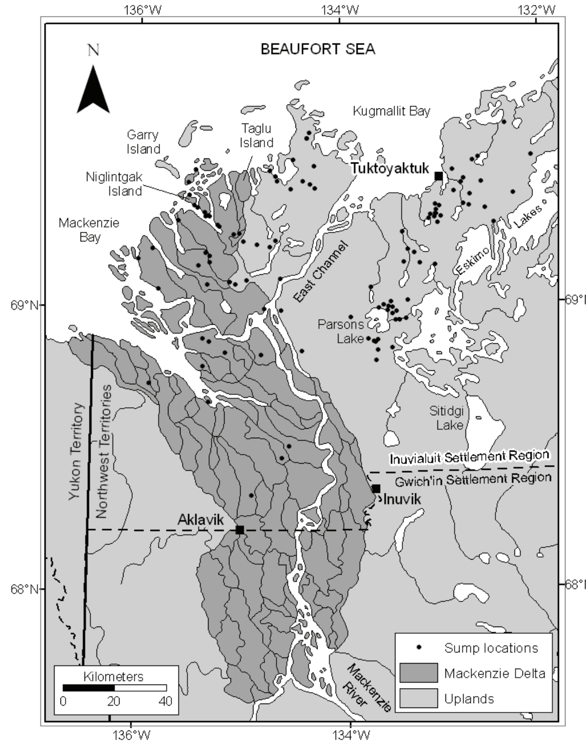

Figure 3. Mackenzie Delta region and drilling-mud sumps examined in this study.

of morainal, glaciofluvial or lacustrine origin contain large volumes of ground ice including massive ice, wedge ice, and near-surface aggradational ice (Mackay 1963, Rampton 1988).

Methods

We examined operational and environmental data for 110 sumps in the Mackenzie Delta region (Fig. 3). Information on the drilling-mud sumps was extracted from an Indian and Northern Affairs Canada (INAC) compilation of sump data and an inventory of sumps in the Inuvialuit Settlement Region (ISR) funded by the Environmental Studies Research Fund (ESRF) and industry (AMEC Earth and Environmental 2005, Komex International & IEG Environmental 2005). The inventory and field methodologies were developed by an ESRF Technical Advisory Group which included government, Inuvialuit and industry representatives. National Energy Board information on site locations and operating dates was used. The sump information collected via these initiatives is publicly available at (http://nwt-tno.inac-ainc.gc.ca/wrd_e.htm).

Permafrost has been utilized as a primary containment medium in northern drilling-mud sumps (French 1980, Dyke 2001). Sump cap collapse and cap ponding strongly suggest that the underlying permafrost is degrading and that the original design intent is not being achieved. Conversely, a sump cap with no ponding suggests frozen ground has been maintained within and around the sump. Field and aerial photograph based estimates of ponding within the sump perimeter was grouped into the three categories of 0% to 5% ponding, 6% to 20% ponding and greater than 20% ponding. We suggest that these categories reflected good, moderate and poor cap integrity, respectively.

The timing of sump closure is of interest because the potential for terrain disturbance is greater during the thaw season and air temperatures at the time of capping influence the thermal state of sump contents. Sump construction and closure dates were not recorded but through consultation with industry and regulators it was determined that commencement and completion dates of drilling provide reasonable estimates for the duration that a sump remained open and the subsequent timing of sump closure. In this study, the "summer operating season" was defined as those months in which the Inuvik monthly climate normals from 1971 to 2000 were above 0°C, which includes May 1 to September 30 (Environment Canada 2007). Sumps were grouped by year of construction into those constructed prior to 1980 (1965-1979), those constructed in the 1980s and recently constructed sumps (1990–2005). The intervals are uneven so the few sumps constructed in the 1960s (5) and 2000s (5) could be grouped into adjacent time intervals.

Mean annual permafrost temperatures may be associated with sump performance since areas of cold permafrost are more likely to maintain sump contents in a frozen state and areas with warm permafrost are more susceptible to thawing after disturbance (Smith & Burgess 2004). Sumps were grouped into three ground temperature classes (-1.0 to -3.9°C, -4.0 to -6.9°C, -7.0 to -9.9°C) based on a generalized map of mean annual ground temperatures (Mackay 1974). Historical ground temperature measurements were also obtained from wellheads adjacent to 14 of the sump sites (Taylor et al. 1998).

Associations between sump-cap ponding and environmental and operational variables were determined using an X^2 test of independence:

$$X^2 = \sum (O - E)^2 / E \qquad (1)$$

where O is the observed frequency in the sample, and E is the expected frequency in the population (Sokal & Rohlf 1995). A test statistic that is larger than the critical value reflects significant differences between the observed and expected frequencies, indicating that there is an association between the two variables.

Results

Table 1a shows that about half of the sumps had minor ponding, while the other half were characterized by moderate to significant ponding. The majority of sumps were constructed and capped between 1965 and 1979 (Table 1b), and the time period for which a sump is open has decreased over the past four decades (Table 1b). All sumps constructed since 1980 were capped within four months of excavation. Only 20% of all sumps were capped in summer and there have been no summer operations since 1986.

Table 1a. Degree of sump-cap ponding.

Percent sump- cap ponding	Minor (0-5%)	Moderate (6-20%)	Significant (20%)
Percent of total sumps	48 (n=53)	21 (n=23)	31 (n=34)

Table 1b. Sump construction practices.

Year of construction	Percent of total sumps	Sump open >5 mos. (%)	Sump capped in summer (%)
1965-79	73 (n=80)	25	25
1980-89	20 (n=22)	0	10
1990-2005	7 (n=8)	0	0

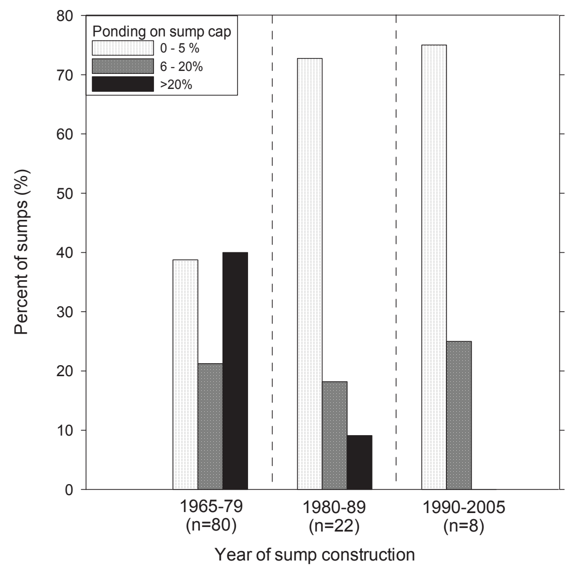

Figure 4. Percentage of sumps affected by minor, moderate and major ponding by period of sump operation. Note that time intervals are uneven.

Sumps constructed since 1990 are characterized by generally good cap integrity in contrast to sumps capped before 1980, most of which have moderate to significant ponding (Fig. 4). There is a statistical association between sump age and cap ponding at the 0.05 level of significance ($X^2_{(4,110)}$ = 13.569; p = 0.009). The good cap conditions of recently constructed sumps may reflect improvements in site selection, construction and closure practices, but may indicate that sump covers degrade with time (Fig. 2).

To investigate the effects of environmental conditions and operating practices on long-term sump integrity and to control for the influence of sump age we reduced the study scope to 77 drilling-mud sumps constructed between 1968 and 1977. Figure 5 shows that the magnitude of cap ponding decreases with ground temperatures. Over 60% of the sumps in warm permafrost (-1.0°C to -3.9°C), coincident with alluvial terrain, were characterized by significant ponding.

Only 30% of the sumps underlain by cold permafrost in upland terrain have significant ponding, and more than half were well intact (Fig. 5). Sump-cap ponding and mean annual ground temperature are associated at the 0.10 level of significance ($X^2_{(4,77)}$ = 8.302; p = 0.08).

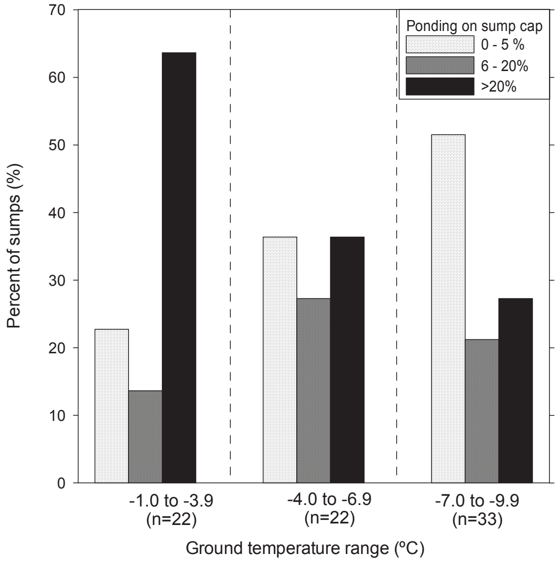

Figure 5. Percentage of sumps affected by minor, moderate and major ponding by mean annual ground temperature class for sumps constructed between 1968 and 1977.

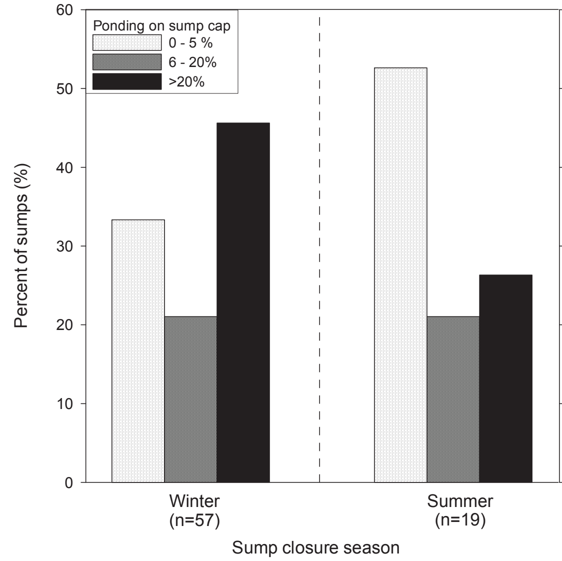

Figure 6. Percentage of sumps affected by minor moderate and major ponding by season of sump closure for sumps constructed between 1968 and 1977.

The sumps constructed from 1968 to 1977 were dichotomized on the basis of the season in which they were closed (summer or winter) (Fig. 6). About 50% of the sumps capped in summer showed minor cap ponding and only 25% were characterized by significant ponding. In contrast, almost half of the sumps capped in winter have significant ponding. Sump-cap ponding is statistically independent of the timing of sump closure ($X^2_{(2,76)} = 2.692$; $p = 0.26$) at the 0.05 level of significance, indicating that the two factors are not associated.

Discussion

Most of the 110 drilling-mud sumps we examined in Mackenzie Delta region were constructed and capped in the 1970s (Table 1). About 40% of these sumps have ponding on or around the sump cap that exceeds 20% of the cap dimensions (Fig. 4). Cap collapse and ponding indicate that the drilling wastes are no longer completely encapsulated by frozen ground and that the primary waste containment medium has been compromised.

The strong association between cap ponding and sump age can partially be explained by improvements to construction and closure practices since the 1970s. These improvements include: a) a reduction in the amount of fluids utilized during drilling and deposited to the sump; b) more efficient drilling operations and reduction to the length of time a sump is open; c) avoidance of summer operations; and d) minimizing disturbance to terrain adjacent to the sump by operating on a protective ice pad. Irrespective of improved practices, there is evidence that sumps deteriorate with time. Submerged willows in many of the sump ponds suggest that collapse occurred subsequent to cap revegetation, possibly after decades of cap stability (Fig. 2). Sumps covers that are presently intact have the potential to subside if permafrost were to thaw as the result of shrub growth and increased snow accumulation, or due to climate warming (Kokelj & GeoNorth 2002).

Cap subsidence and significant ponding was most common on sumps in warm permafrost of the alluvial delta, whereas the zone of coldest permafrost on northern Richards Island and the Tuktoyaktuk Coastlands had the lowest proportion of sumps with significant ponding, and the highest proportion of intact sump caps (Fig. 5). It appears that potential impacts of high ice content permafrost on sump cap integrity in the northern part of the study region was offset by thermal stability associated with cold permafrost (Mackay 1970, Rampton 1988).

The difficulty of maintaining good sump-cap integrity in a warm permafrost environment is indicated by Figure 5 and corroborated by the poor cap conditions observed at many historical drilling-mud sumps in the central Mackenzie Valley where mean annual ground temperatures are above -3°C (C. Baetz - INAC, pers. com.). In our study area, the warmest permafrost coincides with alluvial terrain of the Mackenzie Delta which is also characterized by naturally poor drainage, probably strengthening the observed association between significant cap ponding and warm permafrost.

No significant association was found between the timing of sump closure and sump-cap ponding (Fig. 6). This result was surprising because various complications have been documented in association with summer operations (French 1980, 1985), including a) thawing and loss of frozen backfill; b) degradation of ice-rich permafrost in exposed sump sidewalls; and c) squeezing and seepage of unfrozen fluids up and out of the sump at the time of capping. Closer inspection of the data reveals that most of the summer sumps were located in cold upland terrain. Only four were located in warm permafrost and alluvial terrain and three of these were characterized by significant ponding (Fig. 2). Furthermore, some of the summer sumps may have been contoured or recapped in the years immediately following abandonment. The relatively good condition of several summer constructed sumps in cold permafrost highlights the importance of good site selection.

Regardless of site conditions or construction practices there is a strong association between cap ponding and sump age which suggests that sump conditions can deteriorate over time (Fig. 2). Almost 30% of the sumps constructed during winter in cold permafrost between 1965 and 2005 presently have more than 20% of the cover occupied by ponded water. Many sumps constructed under ideal site and operating conditions have degraded, so it is apparent that other factors may lead to the thawing of a sump over time. For example, well-drained exposed mineral soils that characterize the sump cover favour the growth of tall shrubs which trap snow redistributed by winds (Johnstone & Kokelj 2008). Colonization by tall shrubs can transform a cold snow-free cap surface into one with annual snow accumulation of over 1m thickness causing ground warming and possible thawing of sump contents (Johnstone & Kokelj 2008). Natural sites in the study region characterized by mineral soils and deep snow are often associated with a talik (Gill 1972). It is also possible that rising air temperatures and associated ground warming in the western Arctic has contributed to the degradation of sumps (Osterkamp & Romanovsky 1999, Smith et al. 2005).

Decadal scale sump cap performance in the Mackenzie Delta region strongly suggests that if long-term freezing of drilling wastes in permafrost remains an intended waste disposal option, warm permafrost and alluvial terrain must be avoided. Factors that influence the thermal evolution of drilling-mud sumps such as vegetation succession and climate change cannot be directly controlled by best practices, so the necessity for long-term observation and management of sumps in permafrost terrain should be anticipated. Furthermore, the environmental consequences of sump cap collapse should be better understood so that sump cap degradation can be appropriately managed.

Conclusions

Based on our results and discussion we make the following conclusions:

1. Recent sumps are characterized by good cap integrity, but 40% of sumps constructed prior to 1980 have more than 20% ponding on their surface. The data suggest an improvement of operating and abandonment practices; however this trend may actually reflect the gradual degradation of sump covers over time.

2. For the 77 sumps constructed during the period from 1968 to 1977, poor cap integrity was most prevalent in poorly-drained, alluvial terrain where permafrost temperatures were above -4°C. Sump cap conditions were best at upland sites in cold (<-7.0°C) permafrost. If the objective of a sump is to encapsulate wastes in permafrost, construction in warm permafrost and alluvial environments should be avoided.

3. The season in which a sump was capped was not associated with sump-cap ponding and cap integrity. This is probably because site environmental conditions subsumed the effect of capping season.

4. About one third of the sumps constructed during winter operations in cold permafrost are characterized by significant cap ponding. Factors such as cap revegetation and climate warming may impact long-term sump-cap integrity indicating that a long-term management approach to drilling-mud sumps constructed in permafrost is necessary.

Acknowledgments

This work was supported by the Aurora Research Institute; Natural Sciences and Engineering Research Council of Canada, Northern Chairs program (C.R. Burn, Carleton University) and the Northern Internship Program; and the Water Resources Division, Indian and Northern Affairs Canada. Data used in these analyses were compiled through an Environmental Studies Research Fund initiative with participation from Indian and Northern Affairs Canada, the Inuvialuit Joint Secretariat, and Industry.

References

AMEC Earth and Environmental. 2005. Inuvialuit Settlement Region drilling waste disposal sumps study. Submitted to Government of Canada, *Environmental Studies Research Fund, ESRF* 04-046, 54 pp.

Burn, C.R. 2002. Mackenzie Delta. In: S. Black & A. Fehr (eds.) *Natural History of the Western Arctic, Part 1: Land and Water*. Inuvik, Northwest Territories: Western Arctic Handbook Committee, 24-29.

Dyke, L.D. 2001. Contaminant migration through the permafrost active layer, Mackenzie Delta area, Northwest Territories, Canada. *Polar Record* 37 (202): 215-228.

Environment Canada. 2007. *Canada Climate Data* [online], Ottawa. Available from: http://climate.weatheroffice.ec.gc.ca/climateData/canada_e.html [cited 01 August 2007].

French, H.M. 1978a. Terrain and environmental problems of Canadian arctic oil and gas exploration. *Musk-ox* 21: 11-17.

French, H.M. 1978b. *Sump Studies: 1, Terrain Disturbances. Environmental Studies No. 6.* Ottawa: Department of Indian Affairs and Northern Development, 52 pp.

French, H.M. 1980. Terrain, land-use and waste drilling fluid disposal problems, Arctic Canada. *Arctic* 33: 794-806.

French, H.M. 1985. Surface disposal of waste drilling fluids, Ellef Ringnes Island, NWT: short term observations. *Arctic* 38(4): 292-302.

Gill, D. 1972. The point bar environment in the Mackenzie River delta. *Canadian Journal of Earth Sciences* 9: 1382-1393.

Johnston, J. & Kokelj, S.V. 2008. Environmental conditions and vegetation recovery at abandoned drilling-mud sumps in the Mackenzie Delta region, NWT, Canada. *Arctic* (In press).

Kanigan, J.C.N., Burn, C.R. & Kokelj, S.V. 2008. Permafrost response to climate warming south of treeline, Mackenzie Delta, Northwest Territories, Canada (*this proceedings*).

Kokelj, S.V. & Burn, C.R. 2005. Near-surface ground ice in sediments of the Mackenzie Delta, Northwest Territories, Canada. *Permafrost and Periglacial Processes* 16: 291-303.

Kokelj, S.V., Burn, C.R. & Tarnocai, C. 2007b. The structure and dynamics of earth hummocks in the subarctic forest near Inuvik, Northwest Territories, Canada. *Arctic, Antarctic, and Alpine Research* 39(1): 99-109.

Kokelj, S.V. & GeoNorth Limited. 2002. *Drilling Mud Sumps in the Mackenzie Delta Region: Construction, Abandonment and Past Performance.* Submitted to Water Resources Division, Indian and Northern Affairs Canada, Yellowknife, Northwest Territories, 55 pp.

Kokelj, S.V., Pisaric, M.F.J. & Burn, C.R. 2007a. Cessation of ice-wedge development during the 20th century in spruce forests of the Mackenzie Delta, Northwest Territories, Canada. *Canadian Journal of Earth Sciences* 44: 1503-1515.

Komex International & IEG Environmental. 2005. *Inventory of Drilling Waste Disposal Sumps*. Submitted to Imperial Oil Resources, Conoco-Phillips, Shell and BP, 6 volumes.

Mackay, J.R. 1963. The Mackenzie Delta area, Northwest Territories, Geographical Branch, Memoir 8. Department of Mines and Technical Surveys, Ottawa.

Mackay, J.R. 1970. Disturbances to the tundra and forest tundra environment of the western Arctic. *Canadian Geotechnical Journal* 7 (4): 420-432.

Mackay, J.R. 1974. *Seismic Shot holes and Ground Temperatures, Mackenzie Delta Area, Northwest Territories.* In Geological Survey of Canada Paper 74-1, Part A, Report of Activities, April to October 1973. Ottawa: Geological Survey of Canada, Department of Energy, Mines and Resources, 389-390.

Osterkamp, T.E., & Romanovsky, V.E. 1999. Evidence for warming and thawing of discontinuous permafrost in Alaska. *Permafrost and Periglacial Processes* 10: 17-37.

Rampton, V.N. 1988. *Quaternary Geology of the Tuktoyaktuk Coastlands, Northwest Territories, Memoir 423.* Ottawa: Geological Survey of Canada, Department of Energy Mines and Resources Canada.

Ritchie, J.C. 1984. *Past and Present Vegetation of the Far Northwest of Canada*. Toronto: University of Toronto Press, 251 pp.

Smith, M.W. 1975. Microclimate influences on ground temperatures and permafrost distribution, Mackenzie Delta, Northwest Territories. *Canadian Journal of Earth Sciences* 12: 1421-1438.

Smith, S. & Burgess, M. 2004. *Bulletin 579: Sensitivity of Permafrost to Climate Warming in Canada*. Ottawa: Geological Survey of Canada, Natural Resources Canada.

Smith, S.L., Burgess, M.M, Riseborough, D. & Nixon, F.M. 2005. Recent trends from Canadian permafrost thermal monitoring network sites. *Permafrost and Periglacial Processes* 16: 19-30.

Sokal, R.R. & Rohlf, F.J. 1995. *Biometry*, 3rd ed. New York: W.H. Freeman and Co., 887 pp.

Taylor, A., Burgess, M.M., Allen, V. & Wilkinson, A. 1998. *Canadian Geothermal Data Collection: Deep Permafrost Temperatures and Thickness of Permafrost* [online]. Boulder, CO: National Snow and Ice Data Center/World Data Center for Glaciology. Available from: http://nsidc.org/data/docs/fgdc/ggd503_boreholes_ncanada/data.html [cited 01 August 2007].

Studies on the Cooling Effect of Diatomite in the Protection of Permafrost Embankment

Chen Ji
State Key Laboratory of Frozen Soil Engineering, Cold and Arid Regions Environment and Engineering Institute, Chinese Academy of Sciences, Lanzhou, China 730000

Sheng Yu
State Key Laboratory of Frozen Soil Engineering, Cold and Arid Regions Environment and Engineering Institute, Chinese Academy of Sciences, Lanzhou, China 730000

Qihao Yu
State Key Laboratory of Frozen Soil Engineering, Cold and Arid Regions Environment and Engineering Institute, Chinese Academy of Sciences, Lanzhou, China 730000

Anhua Xu
Institute for Highway Survey-Design and Research of Qinghai, Xi'ning, China 810000

Huang Bo
Institute for Highway Survey-Design and Research of Qinghai, Xi'ning, China 810000

Abstract

Preservation of permafrost is one of the principles adopted in permafrost geotechnical engineering. Using a thermal semiconductor can help toward this purpose. The thermal semiconductivity property of water near 0°, diatomite is used for making a kind of thermal semiconductor after it absorbs water. Experiments on the thermal conductivity difference between frozen and unfrozen diatomite, and on the water retention ability of diatomite, were carried out in a laboratory. The results showed that under the condition of water content equal to 140% (its saturation higher than 70%), thermal conductivity of frozen diatomite is about 1.66 times that of thawed diatomite. However, its water retention ability is inferior. For the purpose of improving the long-term cooling effect of saturated diatomite in field experiment engineering, a 0.1 m thick sand layer was covered on the diatomite protection-slope layer. Four years of data monitoring a 120 m long experimental road arranged at Hongtupo section between K391+000 and K391+120 of 214th National Highway, showed that a diatomite slope-protection layer can delay the degradation of the underlying permafrost and improve the stability of the embankment. In order to improve its performance and reduce future maintenance, it is necessary to pay more attention to the construction season, construction techniques, and local climate.

Keywords: diatomite; permafrost embankment; thermal semiconductor.

Background

Preserving permafrost is one of the most basic principles that are adopted in a cold permafrost area. Prethawing techniques can be an alternative for a small portion or shallow, thin permafrost layer, but excepting such conditions, preservation of the permafrost is frequently used in practice. In order to preserve the permafrost, many researchers and engineers have proposed measures which cool down the permafrost by means of adjusting radiation, convection, or conduction. From the point of adjusting conduction, increasing thermal resistance is often used in a cold permafrost area to raise the permafrost table and prevent the frozen soil below the permafrost table from thawing. For example, EPS and PU are often used because of their low conductivity, but warm permafrost dominates the Qinghai-Tibet Plateau. The above measure is very difficult to ensure the stability of a frozen soil ground-foundation. Active cooling measures are essential for preserving permafrost in this area (Cheng 2005, 2007). Construction material with special thermal conductivity features, with conductivity which is higher at low temperatures than at normal temperatures, can be particularly effective in utilizing "thermal offsets" in the active layer soils.

There is a large difference of thermal conductivity between water (0.6 W/m·K) and ice (2.3 W/m·K). Thus, the water can be regarded as a thermal diode with the critical temperature of 0°C. However, as a construction material, it is unsuitable because of its many known disadvantages in foundation engineering. Light, porous media with strong water absorption ability provide an ideal alternative for utilizing the special property of water. For example, peat soil and urea-formaldehyde have been used as thermal semiconductors in arctic and subarctic permafrost regions (Ersoy 1980, Mchattie 1983, Feklistov & Rusakov 1996). Many field experiments and engineering practices have proven their cooling effects (Ma et al. 2002). However, this method has never been applied in the permafrost region in the Qinghai-Tibet Plateau because of the scarcity of those materials (Ma 2005). Diatomite has high porosity and a great capacity for water absorption. Previous tests have shown that the water content of diatomite can easily reach about 200%.

Strong absorption capacity implies its potential as a thermal semiconductor.

Test on Thermal Conductivity of Diatomite

The testing sample was a kind of coarse-grain diatomite (Fig. 1), produced in Jilin province, China. It has a strong water-absorption capacity and high stability after water saturation. Its bulk density varies from 0.35 to 0.43 g/cm^3; its specific gravity is about 2.1. The bulk density of the testing sample is about 0.4 g/cm^3. Thermal conductivities of the diatomite with different water contents were measured both in the frozen and unfrozen states. Test results are listed in Table 1.

From Table 1, it can be seen that with the increase of water content, the difference in thermal conductivity of diatomite between frozen and thawed states also increases. When the water content reaches 140% (saturation about 70%), the ratio of thermal conductivities between frozen and thawed diatomite is 1.66.

Water Retaining Ability of Diatomite

The thermal conductivity ratio between frozen and unfrozen diatomite is associated with its water content. In the engineering practice, it is necessary for the constructor to know its water retaining ability.

Water retaining ability tests were conducted in the laboratory. Ambient temperature was about 20°. Wind was simulated by fan. Wind direction was parallel to the sample's top surface; wind speed was about 5m/s, which is similar to the field environment. Naked diatomite, diatomite covered by a 2 cm thick sand layer, and a 5 cm thick sponge were monitored. From Figure 2, water loss rate all increased with time under the above three experiment conditions. For naked diatomite, the evaporation rate is faster than the one covered by sand or sponge the first four days. Ten days later, all evaporation rates nearly approximate the same value at 55%. Owing to the availability of sand and its early good effect, sand cover was recommended in the field.

Figure1. Diatomite sample for testing.

Table 1. Thermal conductivity test of diatomite with different water content.

Water content (%)		60	100	140	180	208
Saturation (%)		30	50	70	90	100
Thermal conductivity (w/m·k)	Frozen	0.26	0.53	0.76	1.08	2.33
	Thawed	0.24	0.35	0.46	0.44	0.78
	ratio	1.08	1.51	1.66	2.47	2.98

Introduction of Experiment Engineering

The field experiment was conducted on a northern slope of Hongtupo Mountains between milestone 391+000 and 391+120 along the National Highway 214 (Figs. 3, 4). It was constructed on the upper part of a gentle permafrost slope. The longitude and latitude of the center of experimental section is 98º58.154′E and N35º14.136′N. This section extended 10° SW. The road surface is asphalt paved. On the left, grass grows well, and vegetation coverage is about 70%; on the right, the earth surface is moist, and the vegetation coverage is about 40%. The roadbed is 2.5 m high on the left and 3.5 m high on the right. Annual rainfall is less than 100 mm, and mean annual air temperature is about -4.5 ºC.

The experiment site is located in permafrost area. The volumetric ice content there is 10%–20%. The natural permafrost table is about 2.4 m; the artificial table is about 8.0 m under the road surface; and the mean annual ground temperature is -0.9ºC. The diatomite experimental section has a total length of 50 m. Diatomite layers 0.4 m thick cover both side slopes.

Construction work can be divided into two parts. At the first stage in November 2003, the dry diatomite was laid on the side slope. In April, 2004, water was sprayed for the

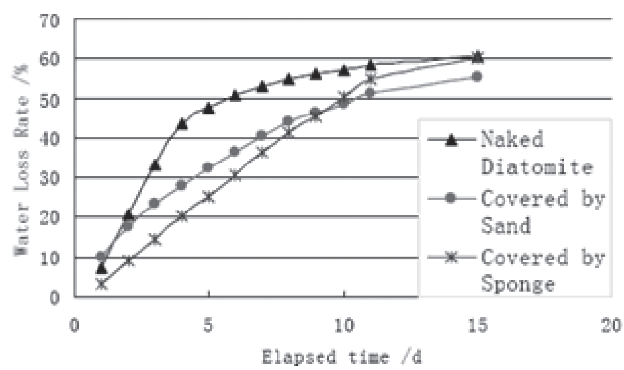

Figure 2. Curves of evaporation ratio changing with time.

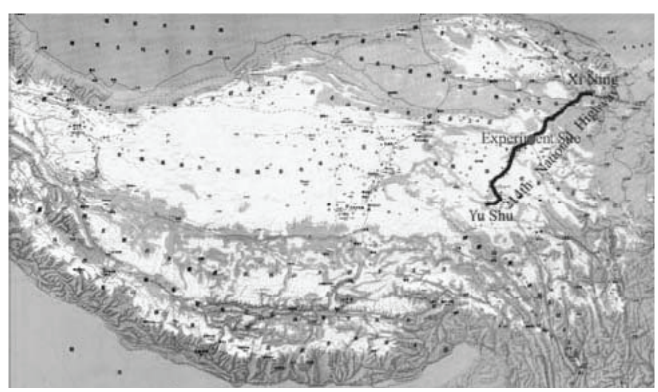

Figure 3. Location of 214th National Highway and the experiment site in the Tibet Plateau.

Figure 4. Experimental section of diatomite protection-slope.

first time. Water content of diatomite reached about 140% at that time. A 0.1 m thick sand soil was put on the diatomite layer to keep the stability of the diatomite cover and reduce evaporation (Fig. 4).

Three monitoring sections were arranged. Two sections (K391+085, K391+100) were the diatomite experiment; another one (K391+050) was a reference. Four monitoring boreholes were drilled for each section. There were located at the east slope-toe, east shoulder, centerline, and left shoulder. Temperature probes were installed in the boreholes at an interval of 50 cm. On both side slopes, 10 temperature probes were installed 50 cm beneath the surface. Monitoring work was conducted between June 2003 and September 2006. Except for a monitoring borehole for measuring natural ground temperatures at K391+085, all monitoring items were identical in the three sections.

Analysis of the Cooling Effect of the Diatomite

Surface temperatures of side slopes

Side slope surface plays a very important role in the thermal balance of a roadbed. High surface temperature is bound to result in the degradation of underlying permafrost. Figure 5 displays the curves of 50 cm deep surface temperature changing with time.

It is evident in Figure 5 that: (1) in a year, slope surface temperatures of reference and diatomite sections behave differently. Compared with the diatomite section, the temperature of the reference section is higher in the summer and lower in the winter. This phenomenon is similar to what happens to the roadbed using EPS or PU. It shows that diatomite can effectively increase the thermal resistance and drop the annual temperature amplitude. Therefore, diatomite can raise the permafrost table and enhance the stability of frozen soil foundation. (2) With time elapsing, the temperature difference between the reference and diatomite sections increased in the summer and declined in the winter. From this point, the diatomite layer served as a thermal insulator and prevented insolation heating from the side slopes into the roadbed in the summer. It served, also, as a thermal conductor and facilitated heat release in the winter.

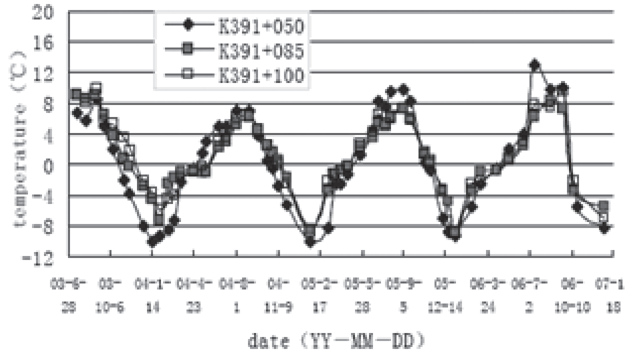

Figure 5. Curves of slope surface temperature changing with the time.

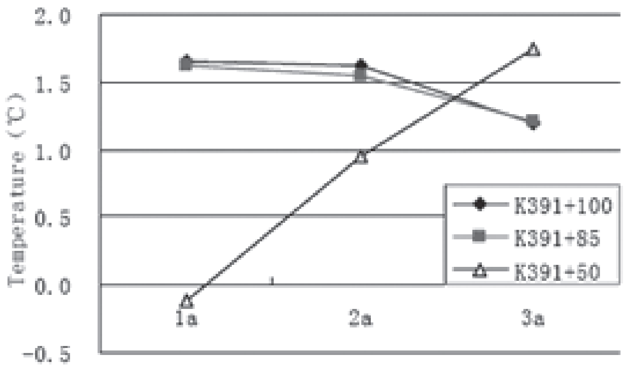

Figure 6. Curves of mean annual temperature of slope surface temperature changing with time.

This phenomenon demonstrates the thermal semiconductor effect of diatomite.

Temperature curves are not adequate proof of the cooling effect of diatomite because the whole year effect is not yet determined. Mean annual temperature is an essential index to affecting the developing trends of the underlying permafrost. In the first two years, the mean annual temperature of the slope surface was lower in the reference section than in the diatomite section, but in the third year, the result was reversed. The mean annual temperature of the diatomite section began to be lower than the reference section (Fig. 6). It can be concluded from the feature of temperature curves that the temperature of diatomite will decline continuously in the next few years, and the temperature difference between the diatomite and the reference section will increase. The cooling effect of the diatomite layer will be confirmed strongly.

The permafrost table

A permafrost table is an often-used index to characterize the cooling effect of engineering measures. It can directly indicate the final effect of diatomite. Figure 7 indicates the permafrost table observed in the boreholes in the reference and diatomite sections.

The permafrost table in a natural state changed little from 2003 to 2004. Therefore, the effect of air temperature changes on the cooling effect of diatomite is minor and can be omitted. The permafrost table dropped abruptly beneath the roadbed in the first year. Although the permafrost table

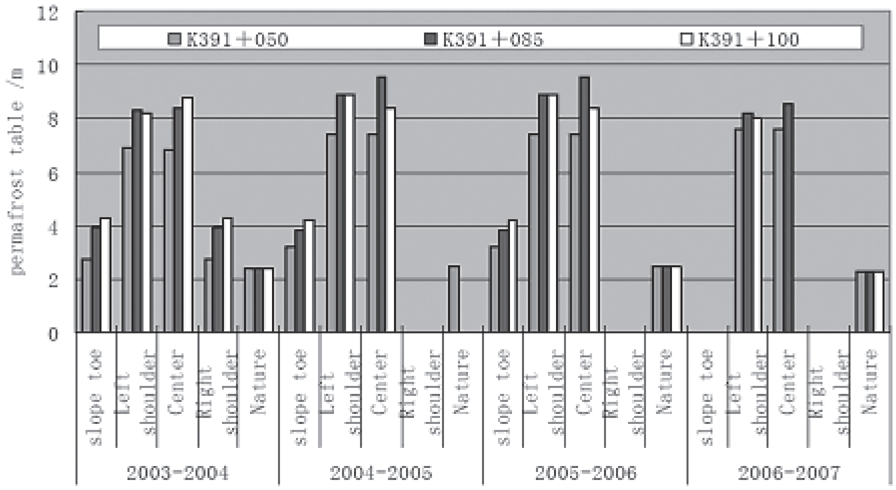

Figure 7. Contrast of the permafrost table between the experiment and comparing section.

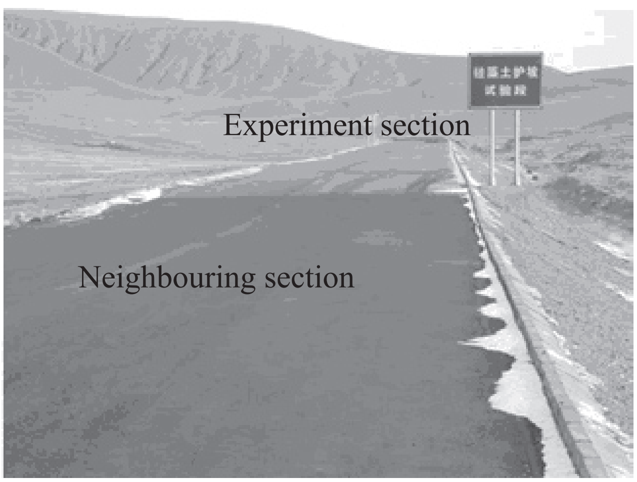

Figure 8. Operational status of experimental section and neighboring section.

in the reference section was higher at the beginning, the trends are more beneficial to the diatomite section than the reference section. In the second and the third year, the permafrost table in the diatomite section fluctuated greatly, but that in the reference section kept lowering. In the fourth year, the permafrost table in the reference section continued to decline, but that in the diatomite section rose. Considering the trend of mean annual surface temperature, the permafrost table will go up continuously over the next several years. The rise of the permafrost table shows that the diatomite layer can act as a good thermal semiconductor when it is saturated with water/ice.

Operational status

As of this year, the experimental section with diatomite has worked for four years. The roadbed kept its stability, and the road surface needed little maintenance. This section kept its good performance. However, in the neighboring section, the asphalt pavement has been repaired one time only two years after construction finished (Fig. 8). Investigation at the end of 2006 showed that waves appeared here.

Problems and Discussions

Although four years of field data prove that the diatomite layer can effectively protect the underlying permafrost, early data are disappointing. It is necessary to analyze the phenomenon in order to avoid future mistakes and to find solutions to problems not previously noticed.

Previous research showed that the construction season plays an important role in the ground temperature under the roadbed and embankment in the initial stage. Its effect can last three or more years (Wen 2006). This is especially true for a roadbed using insulation. In the early spring, ground temperature is relatively low, but topsoils begin to thaw and construction is easier than in the winter. If EPS or PU is added, it can effectively reduce the incoming heat in the coming warm season. On the contrary, if insulation is constructed in the late autumn when ground temperatures are relatively high, it would help prevent heat within the roadway from releasing. In this experiment, diatomite was constructed in the adverse season. Consequently, the permafrost table was deeper and the side slope surface temperature was higher in the diatomite section in the initial several years.

Construction techniques also are important. From November 2003 to April 2004, the diatomite was dry. The dry diatomite is just a thermal insulator and retains the internal heat releasing. Thus, the permafrost table in the diatomite section decreased abruptly in the first year. Furthermore, laboratory test results suggest that the water retaining ability of diatomite is less satisfactory than expected. Due to the lack of maintenance and water-tight measures, the water content changed greatly after April 2004. Investigation in the winter of 2005 and 2006 showed that, although the total water content was more than 100%, the top 3 cm diatomite layer was only about 1%. This layer played a role in insulation during winter. It depressed the semiconductivity performance of diatomite.

Climate also affected the cooling effect of diatomite. The experimental section is located in a cold and arid region. Evaporation potential is far greater than the precipitation.

For diatomite only covered by 10 cm sand, it is impossible to maintain the state of high water content in the diatomite if maintenance is scarce.

Conclusions

Diatomite can be used as a thermal semiconductor. The performance of a diatomite semiconductor improves with the increase of water content. A diatomite semiconductor can delay the degradation of the underlying permafrost and improve the stability of a road embankment; however, because the period of observation was only four years, its long-term effect needs more validation. This experiment demonstrated that it is necessary to pay more attention to construction season, construction techniques, local climate, and maintenance before a thermal semiconductor is utilized to cool down the permafrost embankment.

Acknowledgments

This work was supported by the Hundred Young Talented Scientists Program of the Chinese Academy of Sciences granted to Dr. Jilin Qi.

References

Ersoy T. & Haist G. 1980. Statilization of a Highway embankment in a permafrost area. *Proceedings of the 2nd International Symposium on Ground Freezing. 1980:* 1076-1088.

Feklistov, V.N. & Rusakov, N.L. 1996. Application of foam insulation for remediation of degraded permafrost. *Cold Regions Science and Technology* 24: 205-212.

Guodong C. 2005. A roadbed cooling approach for the construction of Qinghai–Tibet Railway. *Cold Regions Science and Technology* 42(2): 169-176.

Ma, W., Guo-dong, C. & Qing-bai, W. 2002. Preliminary Study on Technology of Cooling Foundation in Permafrost Regions. *Journal of Glaciology and Geocryology* 24 (5): 579-587.

Ma, W., Shi, C., Wu, Q. et al. 2006. Monitoring study on technology of the cooling roadbed in permafrost region of Qinghai–Tibet plateau. *Cold Regions Science and Technology* 44(1): 1-11.

Mchattie, R.L. & Esch, D.C. 1983. Benefits of peat underlay used in road construction on permafrost. *Proceedings of the Fourth International Conference on Permafrost*: 826-831.

Zhi, W. 2006. *Evaluation on the Application of Thermal Insulator in the Embankment in the QTP*. Doctoral thesis for the degree of GUCAS (Graduate University of Chinese Academy of Sciences).

Identification and Mitigation of Frost Hazards Along the China-Russia Oil Pipeline

Huijun Jin, Jianming Zhang, QihaoYu, Yu Sheng, Zhi Wei, Guoyu Li, Yanjun Ji, Ruixia He, Lanzhi Lü
State Key Laboratory of Frozen Soils Engineering, 326 W. Donggang Rd., Lanzhou, China 730000
Jiaqian Hao, Youchang Chen, Wei Wu, Yimin Zhao
Daqing Oilfield Engineering Company, PetroChina Corporation Limited, Daqing, China 163712

Abstract

The China-Russia oil pipeline is designed to transport 603,000 barrels of Siberian crude oil per day using a buried pipeline 914 mm in diameter across 1030 km of permafrost and seasonally frozen ground. Construction was scheduled to be between March 2008 and August 2009. The design was significantly challenged by differential frost heaving and thaw settlement. About 500 boreholes to depths of 5 to 20 m were drilled and cored for analyses, and frozen ground conditions were evaluated. Conventional burial construction modes were adopted after detailed surveys and analyses of permafrost conditions along the pipeline route**.** Permafrost forecasts, thermal and strain/stress analyses, measures to mitigate frost hazards, and a design for long-term monitoring and early detection of developing frost hazards were conducted. Mitigative measures using excavation and backfill of non-frost-susceptible soils, insulation, and drainage control were proposed and adopted. A review of the engineering activities and measures undertaken to address these concerns is presented herein.

Keywords: China-Russia oil pipeline; engineering geology; frost heaving; mitigation; permafrost; thaw settlement.

Introduction

A key component of the Siberian-Pacific oil pipeline is a 1030 km-long, 914 mm-diameter spur pipeline to transport 603,000 barrels of oil daily from Skovorodino, Siberia (54.0°N, 123.6°E, 398 m in elevation) to Daqing, China (46.6°N, 125.0°E, 151 m). The spur pipeline will enter Northeastern China near Mo'he (53.5°N, 122.4°E, 350 m) (Fig. 1) and cross 965 km of permafrost and seasonally frozen ground in China.

Potential pipeline routes were hotly debated in the past 12 years. The Mo'he to Daqing route was chosen because it offered the shortest distance through ice-rich permafrost and wetlands reserves, generally more favorable terrain conditions, and easier access to existing transportation corridors. The pipeline, using conventional burial, is designed to transmit unheated crude oil, with an estimated incoming oil-temperature range of -6°C to +10°C at the Mo'he inlet. It traverses 530 km of warm permafrost, of which about 118 km in China is ice-rich. Permafrost features vary greatly over short distances. In the south, it traverses about 500 km of seasonally frozen ground, with maximum frost penetration depths of 1.8 m to 4.0 m. Preliminary and detailed designs were completed by August and December 2007 respectively. Construction is scheduled in 2008–2009.

The design along an unheated pipeline buried in frozen ground required mitigation of frost heaving in the cold season and thaw settlement in the warm season. A series of resultant environmental impacts and geohazards on pipeline foundation stability needed to be economically minimized after the massive pipeline construction and during the operation period. Therefore, proper designs needed to compromise between long- and short-term investments. Since 2004, the permafrost research activities have been focused on the prediction and mitigation of frost heaving and differential thaw settlement of pipeline foundation soils in order to provide technical support for the pipeline design. This paper reviews the overall research activities and engineering measures addressing these concerns.

Study Regions

Topography, geology, and climate

The pipeline route crosses about 965 km of mountains and plains in Northeastern China. In typical soil profiles, peat and humic soils are underlain by clayey sands and sandy clays. The region along the pipeline route is characteristic of a temperate continental monsoon climate with long, dry, cold winters and short, moist, warm summers. Mean annual air temperatures range from 0°C to 1°C in the south to -5°C to -6°C in the north. Annual precipitation ranges from about 400 to 700 mm, 80%–90% of which falls in summer. The vegetation is comprised of cold to temperate mountain needle-leaf forest. Needle and broad-leaf mixed forests and forest steppes gradually appear when moving southwards into the piedmont area. They are eventually replaced by agricultural land at the southern end of the pipeline route.

Permafrost features

Permafrost conditions are characterized by latitudinal and elevational zonation, with local marked variations. The areal extent of permafrost increases northwards from 0% to 65%, and mean annual ground temperatures decrease from 0°C to -2.6°C (Table 1). The observed thickness of permafrost varies from about 1 to 60 m; occasionally permafrost extends to 120 m. Permafrost zones range from isolated patches to widespread discontinuous zones of permafrost. In the northern Da Xing'anling Mountains, tussocks and moss layers are dense, and the thicknesses of surficial deposits are 8–12 m on the shaded slopes of intermontane basins, in wetlands or in lowlands, and on low river terraces. Permafrost

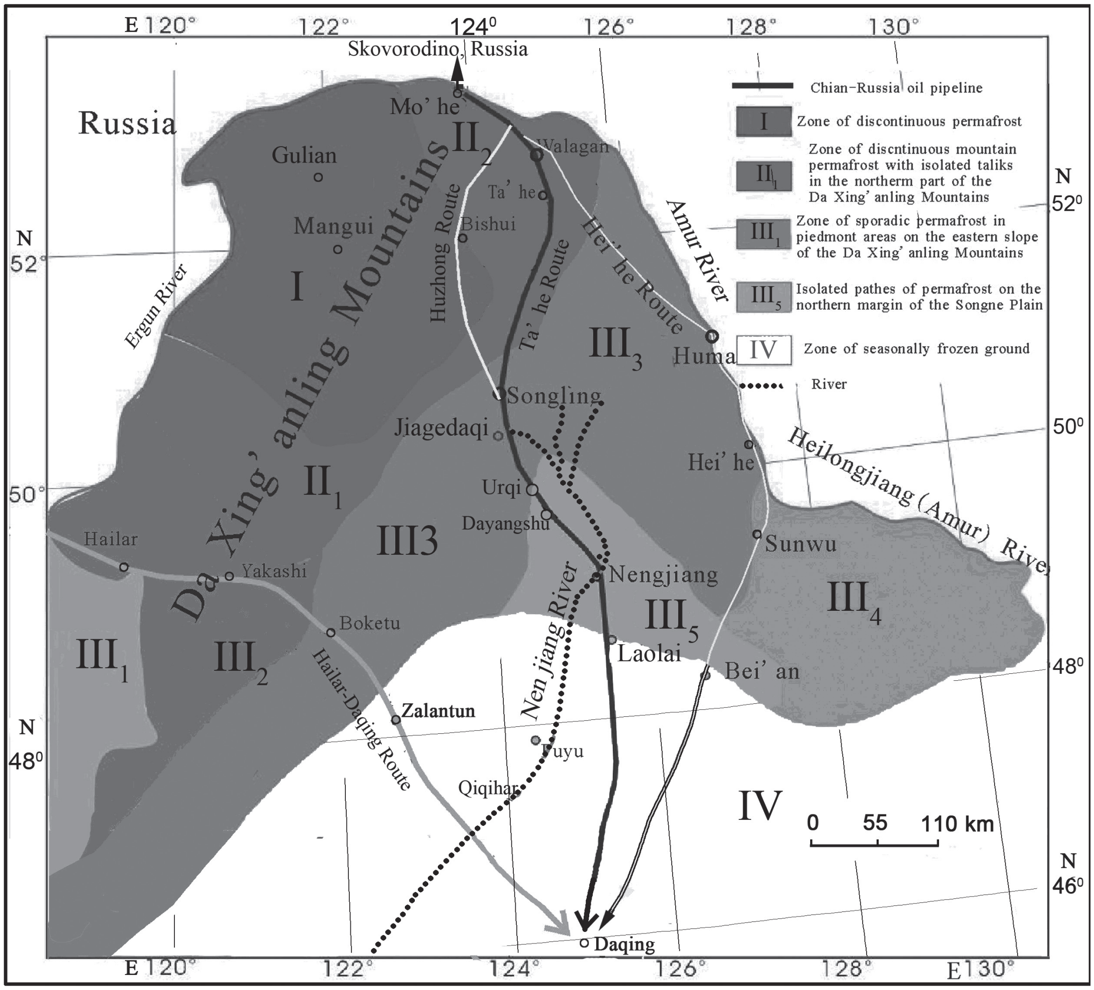

Figure 1. China-Russia oil pipeline routes in Northeastern China (revised from Guo et al. 1981 & Jin et al. 2007a).

can be as thick as about 50 m to 60 m. In contrast, on treeless or sparsely vegetated sunlit slopes with thick surficial deposits, permafrost is either thin or absent. On shaded slopes with dense vegetation, permafrost conditions are intermediate between valley bottom lowlands and sunlit slopes.

Seasonally frozen ground

When moving southwards, the maximum thaw depths in river taliks in increasingly fragmented discontinuous permafrost is 2.5 m to 4.0 m, depending on surface cover, soil moisture conditions, and lithology. Seasonally frozen ground largely replaces permafrost from Da'yangshu southwards (Fig. 1). Topographically, this is the transition between the eastern slopes of the Da Xing'anling Mountains and the northern Nen Jiang River Plain. The lithology consists of silt and/or silty clay. The ground water table is generally shallow, and long, cold winters favor frost heaving when moisture and soil conditions suffice. The maximum depth of frost penetration is 1.8 m to 3.5 m, occasionally to 4.0 m.

Study Methods

Survey and investigation of permafrost

The distribution and thickness of warm, ice-rich permafrost; the types, distribution, genesis and features of hazardous periglacial phenomena and assessment of their potentially adverse impacts on pipeline infrastructures were of particular interest in the surveys and investigations (DOE 2007a). During the feasibility, preliminary, and detailed survey stages, about 500 boreholes with depths of 5 m to 20 m were drilled and cored for analyses.

Assessment and forecast of permafrost conditions

The assessment and forecast of permafrost included evaluation of the present conditions of permafrost along the pipeline route and their possible changes during the next 50 years (DOE 2007b). The assessment was based on 1951 topographic maps, permafrost data obtained during the 1970s, field engineering explorations in 2006–2007, and aerial mapping at 1:2000 along the pipeline route in 2006–2007. The assessment covered soil strata, topography and geomorphology, permafrost features, engineering geology, classification of frost heaving and thaw settlement of foundation soils, overall assessment, and advice on pipeline construction modes (Jin et al. 2007a). The overall assessment considered the genetic types, water/ice contents, and thaw-sensitivity and/or frost-susceptibility of the pipeline foundation soils.

The zonation has three hierarchical levels: zone, subzone, and section of frozen ground engineering geology (Jin et al.

Table 1. Permafrost features along the pipeline route.

Location	Lat. (N)	Elev. (m)	MAAT (°C)	MAGT (°C)	PT (m)
Xing'an	52°25′	260		-1.8	
Amur	52°50′	747	-5.4	-0.1~-4.2	21~120
Station 22	52°45′	370		2.0	
S of Walagan	52°30′	445		-1.8	
JMH K276	52°26′	410		-0.7	
Tafeng	52°25′	560	-2.8	-0.3	15
N of Cuigang	52°19′	440		-0.6	
S of Dawusu	51°47′	500		-0.4	
Cuiling	51°40′	1072	-4.6	-1.3	50
N of Xinlin	51°40′	517		-1.2	
N of Tayuan	51°26′	585		-2.6	
N of Xintian	51°08′	545		-1.2	
JMH K34-35	50°41′	400		2.0	
Jiagedaqi	50°23′	382	-4.0	-0.1	7~16
Dayangshu	50°08′	360	-0.2	0.1	1~7

Note: MAAT—mean annual air temperature; MAGT—mean annual ground temperature; PT—permafrost thickness; N—North; S—South; JMH—Jiagedaqi to Mo'he Highway. The depth of zero annual amplitude of ground temperature, which generally ranges from 10 to 15 m. Air temperatures were based on meteorological data from 1970 to 2005.

2007a in press). Frozen ground along the pipeline route was first divided into zones of seasonally frozen ground, isolated patches, sporadic, and discontinuous permafrost based on the areal extent of permafrost. The zones of permafrost were divided into thermal stability subzones of very unstable (>-0.5°C), unstable (≥-1°C), and stable (<-1°C) permafrost. The 3rd-tier of permafrost zones was based on the soil moisture content. The overall and by-segment assessment synthesized available information.

Changes of permafrost were projected for Northeastern China during the 21st century using GIS-aided equivalent-latitude models (Wei et al. 2008). Possible changes of permafrost conditions at selected sites along the pipeline route were forecasted using the finite-element method. The prediction considered typical boundary and initial conditions based on the observed present conditions along the pipeline route (Jin et al. 2007a). These conditions included air, ground surface, ground temperature and their seasonality; ice-contents, types of permafrost, and a climate warming scenario of 2.4°C during the next 50 years, and influences of anthropogenic activities represented by removal of vegetation and pipeline operation.

Simulations on pipeline-soil interactions

According to the best estimation, crude oil temperature will vary from -6°C to +10°C at the Mo'he inlet at the start of oil transmission in August 2009. It was assumed that oil temperatures would have seasonal sinusoidal variations for 50 years, and that the top of the pipeline would be buried at a depth of 1.5 m. Thermal analyses focused on temperatures of crude oil in the pipeline and of foundation soils along the pipeline route; and resultant seasonal and long-term freeze-thaw processes around the buried pipe and along the route, both without engineering measures and with some mitigative measures (insulation, backfill of non-frost-susceptible (NFS) soils, and drainage control). Stress/strain analyses included studies on the coupled thermo-mechanical interactions between the pipeline and foundation soils, possible weak segments along the pipeline with and without the mitigative measures, and checks against the design criteria for steel pipeline integrity, safety, and long-term stability.

Mitigation of frost hazards

Engineering measures for mitigation included: 1) stress and strain constraints for pipeline safety; 2) excavation and backfill of NFS-soils at segments with significant frost hazards; 3) drainage and flood controls; 4) insulation; 5) burial depth; 6) transition zones; 7) river and other crossings of linear infrastructures; 8) slope stability; 9) periglacial hazards; and 10) project management in permafrost regions.

Monitoring of pipeline foundation soils

Permafrost temperatures along the pipeline route were measured generally on a weekly basis, using thermistor cables fixed in cased boreholes during the 1970–1980s. During 2007–2008, 12 exploratory boreholes with depths of 15 m to 20 m were chosen for ground temperature measurements using thermistor cables (Jin et al. 2007a).

A program for long-term monitoring of pipeline foundation soils was established to ensure pipeline long-term safety through early detection and proactive mitigations of pipeline foundation soil problems. The monitoring elements included ground temperatures, soil moisture contents, and deformation of the pipeline foundation soils, both in the proximity of the pipeline and under natural conditions, for comparison. There were 20 cross-sections designed and they were to be implemented during and/or after pipeline construction.

Results and Discussions

Assessment and forecasts of permafrost

Permafrost along the pipeline route has been in degradation during the past 40 years due to significant climate warming of about 0.9°C to 2.5°C and increased human activity (Jin et al. 2007b). Frozen ground and engineering geology conditions along the pipeline route were inadequately understood for pipeline design prior to the survey in 2006–2007. Recent surveys indicated that about 118 km of warm, ice-rich permafrost along the route needed particular attention. Generally, these segments are associated with wetlands underlain by thick silts or clays.

The major frozen ground zones included: 1) Mo'he-Walagan zone of discontinuous (65% to 80%) permafrost with isolated taliks; 2) Walagan-Songling zone of discontinuous (35% to 65%) permafrost with extensive taliks; 3) Songling-Jiagedaqi zone of sporadic (10% to 35%) permafrost; 4) Jiagedaqi-Dayangshu zone of patchy (<10%) permafrost; and 5) Dayangshu-Daqing zone of seasonally frozen ground (Fig. 1).

The forecast of permafrost conditions considered permafrost types and cover conditions representative of the pipeline route, the removal of forest vegetation during pipeline construction, and climate warming of about 2.4°C during the pipeline lifespan. It is evident that the permafrost tables will deepen; the rates of temperature increase will slow with operating time, increasing ice contents, and decreasing ground temperatures. However, thaw settlements of pipeline foundations will increase with higher ice contents.

Thermal analyses

Oil temperatures at the incoming Mo'he Pump Station and along the pipeline route will be subject to seasonal and interannual variations due to the heat exchanges along the routes in Siberia and China.

Distribution of oil temperatures along the 965 km route during the pipeline lifespan was a key issue to pipeline-soil interactions and pipeline foundation design due to its control on areal extents and developing trends of seasonal and interannual freeze and thaw cylinders around the operating pipeline. These further control the deformations and stresses on the pipeline, and the mitigative measures required. The simulations results indicated that oil temperatures cool southwards in the warm season, but that they warm southwards during the cold seasons (Sheng et al. 2007, 2008). As a result, the amplitudes of seasonal variations will decrease southwards and reach a quasi-stable state at about Km-870 (Fig. 2). Oil temperatures could slightly increase with elapsing time due to climate warming. However, the average annual oil temperature decreases southwards in the north, then starts to increase from about Km-488. This is because ground temperatures along the pipeline route are low before reaching Km-366, roughly 0°C at Km-366 to Km-431, and above 0°C southwards.

The thaw depth beneath the pipeline in the cold (<1.0°C) permafrost area north of Ta'he generally will be small (1.3 m to 2.3 m), but will increase southwards. In the warm (>1.0°C) permafrost area, the thaw depth will increase sharply. With elapsing time, thaw settlement prevails due to thermal impacts from pipeline operation. Changes of the ice-rich permafrost table will be 0.5 m to 2.0 m. The resultant thaw settlement in the north (Km-0 to Km-317) will be large and will need to be mitigated. In the southern part (Km-317 to Km-630), frost heaving in the wetlands will be a major challenge. The depth of ground freezing beneath the pipeline will decrease from about 0.4 m at Km-317 to 0 m at Km-580. By Km-700 minimum oil temperatures will be greater than 0°C.

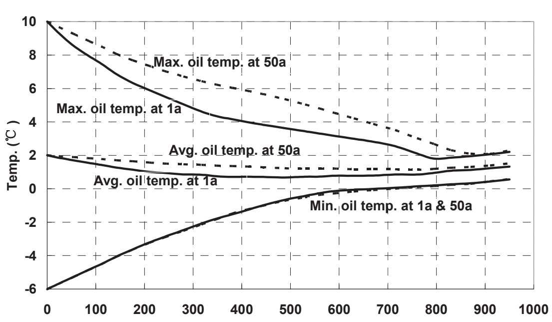

Figure 2. Predicted changes of oil temperatures along the proposed route of un-insulated pipeline.

Two-directional freezing in winter and thawing in summer will occur in soils surrounding the buried pipeline. The thaw cylinder around the pipeline will enlarge with elapsing time but at a decreasing rate with increasing ice contents. The frozen cylinder around the pipeline will diminish with elapsing time, with increasing soil water content, and when moving southwards. Insulation can effectively reduce the development of freeze-thaw cylinders during the early years of operation.

Strain/stress analyses and pipeline safety constraints

Frost heaving and differential thaw settlement will result due to spatiotemporal seasonality of oil and soil temperatures and differences of soils and pipelined oil at certain sections (AGRA Earth & Environmental Limited and Nixon Geotech Limited 1999). However, the pipeline is more tolerant of differential thaw settlement than frost heaving. The largest stress would occur in the center of thaw settlement or in the transition zone between frost heaving and non-frost heaving sections; the largest allowable deformation will increase with section length of frost heaving (Sheng et al. 2007). Therefore, frost mounds pose greater threats to the pipeline. The transition zone between frost heaving and thaw settlement is also hazardous. The length of frost-heaving zones has a significant impact on the pipeline bending moment. Any increase in the length of the transition would mitigate frost heaving on the pipeline.

Numerical analyses were conducted on effective stresses on pipeline under various combinations of oil pressure, pipe-wall thickness, length of transition, frost heaving and differential thaw settlement conditions, to determine the maximum allowable deformations under certain combinations of oil pressures and pipe-wall thicknesses (Sheng et al. 2007, 2008).

The stress/strain criteria for designing pipeline foundations were provided according to the best estimates of potential frost heaving and thaw settlement of soils along the pipeline and analytical results of frost heaving and thaw settlement. A linear transition zone model in which the coefficients of frozen and unfrozen ground were 23.4 and 6 MPa, was used, and the length of the transition zone was 40 m. Pipeline foundation safety with and without mitigative measures and its classification under differential deformation, and under various wall thicknesses, oil pressures, and lengths of transition, were analyzed using numerical models for the pipe-soil interactions (Sheng et al. 2007). Reducing the intensity of longitudinal differential deformations using proper insulation, backfill of NFS soils (bedding), and increasing the wall-thickness of the pipe could effectively mitigate the damage from frost hazards (Jin et al. 2007a, Sheng et al. 2007).

Mitigative measures and construction mode

During route selection, the engineers chose locations with less-frost-susceptible soils, less soil moisture, deeper ground water tables, and sun-lit slopes. Patchy or sporadic permafrost was avoided or crossed in the shortest distance possible. Other considerations included avoidance of solifluction, icings, frost mounds, wetlands and maintenance of slope stability.

During the design phase, insulation was considered for permafrost areas with high ice contents and susceptibility to frost heaving, to minimize the freeze-thaw extent around the pipeline and thermal impacts of heat exchanges with the underlying permafrost. Differential deformations in interfaces of ice contents, soil types, frost-susceptibility, and construction modes required special attention. In sections with shallow, ice-rich permafrost, backfilling with NFS-soils was accomplished. In the section with thick, ice-rich permafrost, a combination of localized backfill of NFS soils, proper insulation, and drainage control were considered. In sections with extensive frost-susceptible soils, drainage control was critical.

During the construction phase, all designs or changes in design were managed strictly according to the opinions of experienced cold regions engineers. The proper construction season for burial of pipeline in permafrost was in late winter and early spring. Careful examinations of excavated soil profiles were important, as surveys were often inadequate in revealing special permafrost conditions. Removal of vegetation adjacent to the pipeline, operation of large equipment, and necessary drainage were controlled.

The burial depth of the pipeline was designed according to the "*Code for Design of Oil Transportation Pipeline Engineering*" (People's Republic of China National Standard 2003), and to accommodate the local conditions such as thickness of frozen ground, geological conditions, transported oil temperatures, and farmland and woodland. The pipeline was conventionally buried in ice-poor and -medium permafrost areas, or areas with shallowly buried bedrock and the total length is 124.9 km. When passing through forests, the top of the pipe was buried deeper than 1.6 m (below the depth that could be impacted by local forest fires) (Zhou et al. 1994). The pipe ditch was 0.2 m deeper than regular areas, and the fine-grained backfill reached a depth of 0.3 m above the pipe top. In areas north of the Jiagedaqi, the pipe top was buried at depths of 2.2–2.4 m because the measured maximum depth of seasonal frost penetration is 2.6 m to 2.8 m in taliks with frost-susceptible soils.

In the seasonally frozen ground areas south of Jiagedaqithe burial depth of pipeline top was set at the depth of 0.4 m above the maximum local depth of seasonal frost penetration from Jiagedaqi to Ne'he, 1.9 m in Yi'an County, 1.8 m in the Lindian and Daqing areas.

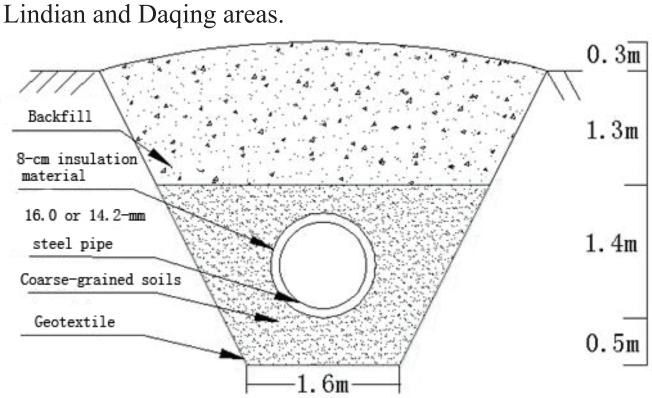

Figure 3. Burial using backfill and insulation for wetlands underlain by thick, high-ice-content permafrost.

The modified burial using coarse-grained (bedding) sand and gravel beneath the pipe was adopted for the ice-saturated and ice-rich permafrost areas. Elevation was not considered because of frequently-occurring forest-fire concerns. The top of the pipe is 1.5 m and the total length of the modified burial is 3.63 km.

In high-ice-content permafrost areas with large active layer thickness, modified burial with insulation and backfill of NFS soils was adopted (Fig. 3) for a total length of 28.3 km. In wetlands underlain by permafrost (total length of 39.2 km), or with frequently-occurring outflow springs (total length of 1.59 km), a similar approach was adopted.

Areas of very ice-rich patchy permafrost, generally less than 3.7 m in thickness, were backfilled with coarse-grained soils (bedding materials). The pipe top was buried 2.0 m. When the thickness of permafrost was large, the pipe top was at 1.8–2.0 m in areas with weakly thaw-sensitive permafrost, or where ice-rich permafrost was partially removed (Tables 2, 3).

Table 2. Results from thermal and strain/stress analyses on backfill and insulation (Sheng et al. 2007).

Mitigative measures	Wall thickness of pipe	Frozen depth beneath pipe	Stress on pipe (MPa)	Thickness (m) of backfill beneath pipe
Backfill, 8-cm Insulation	16.0 mm	0.75 m	315	0.3
	14.2 mm		308	0.5

Table 3. Statistics on mitigative measure for permafrost hazards along the China-Russia oil pipeline..

Type of frozen ground	Mitigative measures	Length (km)
Talik (Seasonally frozen ground)	Pipeline top 0.4 m above the local frost penetration; 0.2 m excess backfill of NFS soils beneath pipe. Pipeline top at 1.6 m in bedrocks	142.86
Ice-poor,-medium permafrost	Conventional burial, pipe top at 1.8 m	209.46
Ice-rich permafrost (non-wetlands areas)	Pipeline top at 1.6 m, 8-cm-thick insulation around the pipe, 0.5 m backfill of coarse soils beneath pipe of 14.2-mm-wall thickness	40.73
	Backfill of NFS soils, 14.2-mm-pipe-wall thickness	21.18
Wetlands with ice-rich permafrost	Pipe top at 1.8 m, 8-cm-thick insulation around pipe, 0.3 m backfill of coarse soils beneath pipe of 16.0-mm-wall-thickness	42.72
Areas with springs		1.59

In ice-rich permafrost areas, the top of the pipeline was buried 1.6 m with backfill of NFS-soils, insulation, and other measures. In wetlands underlain by the ice-rich permafrost or with frequent occurrence of outflow springs (potential icings and frost mounds), frost hazards and pipeline floating due to hydrostatic pressure were mitigated using the modified burial with NFS-soil backfill, insulation, and drainage control. If only partial backfill of NFS-soils was required, its depth was chosen based on local engineering geological conditions. When partial backfill of NFS-soils and insulation was required for protection of permafrost and maintenance of a preset, engineered permafrost table, the depths of backfill of NFS soils and insulation parameters were optimized by thermal and strain/stress analyses (Table 2) (Sheng et al. 2007).

Summary and Conclusions

The China-Russia oil pipeline traverses warm permafrost regions with significant frost hazards in Northeastern China. Significant changes of permafrost were observed or projected along the pipeline route.

Pipeline oil temperatures are expected to generally increase southwards and with time; the effects of climate warming are anticipated to be overshadowed by oil temperature variations; insulation tends to constrain the oil temperature variations and the freeze-thaw cylinder around the pipeline early in the pipeline operation period. Differential thaw settlement is anticipated to have a lesser impact than frost heave on the pipeline.

Conventional burial was chosen for the pipeline in spite of possible significant frost heaving and thaw settlement because of concerns about frequent forest fires, inevitably posing substantial risk to pipeline integrity. Therefore, a system for long-term monitoring and assessment of foundation stability was deemed indispensable for early detection and subsequent proactive mitigation of developing problems.

Acknowledgments

This study was supported by the Chinese Academy of Sciences (CAS) 100 Talents Program "Stability of linear engineering foundations in warm permafrost regions under a changing climate"; CAS Knowledge Innovation Key Project "Mechanisms and mitigation of frost heaving and thaw settlement of pipeline foundation soils in permafrost regions" (Grant No. KZCX2-YW-311); and PetroChina Technological Development Program on Permafrost Research along the China-Russia Crude Oil Pipeline Route. Dr. Max C. Brewer, Professor Emeritus with the U. S. Geological Survey, Anchorage, kindly English-edited the manuscript.

References

AGRA Earth & Environmental Limited and Nixon Geotech Limited. 1999. *Monograph on Norman Wells Pipeline Geotechnical Design and Performance.* Geological Survey of Canada Open File 3773, 142 pp.

Daqing Oilfield Engineering (DOE) Co. 2007a. *Report on the Expedition of Frozen Ground Engineering Geology Along the China-Russia Crude Oil Pipeline (Mo'he to Daqing)*. Daqing, China: Daqing Oil Engineering, Company (edited), 122 pp. (in Chinese).

DOE. 2007b. *Review on the Progress of Preliminary Design of the China-Russia Pipeline (Mo'he-Daqing Segment)*. Daqing, China: Daqing Oil Engineering, Company (edited), 428 pp. (in Chinese).

Guo, D.X., Wang, S.L., Lu, G.W., Dai, J.B. & Li, E.Y. 1981. Regionalization of permafrost in the Da- and Xiao-xing'anling Mountains in Northeastern China. *J. Glaciology and Geocryology* 3(3): 1-9 (in Chinese).

Jin, H.J., Zhang, J.M., & Tong, C.J. 2007a. *Final Report on the Assessment and Prediction of Frozen Ground Engineering Geology Along the Mo'he to Daqing Oil Pipeline*. Lanzhou, China: PetroChina Daqing Oil Engineering Company & Chinese Academy of Sciences Cold and Arid Regions Environmental and Engineering Research Institute edited, 309 pp. (in Chinese).

Jin, H.J., Yu, Q.H., Lü, L.Z., Guo, D.X. & Li, Y.W. 2007b. Degradation of permafrost in the Da and Xiao Xing'anling Mountains, Northeastern China. *Permafrost and Periglacial Processes* 18(2): 245-258. Doi: 10.1002/ppp.589.

Jin, H.J., Wei, Z., Yu, Q.H., Lü, L. Z. & Wang, S.L. in press. Assessment of frozen ground engineering geology conditions along the Qinghai-Tibet Highway/Railway, China. *Engineering Geology.*

People's Republic of China. 2003. *Code for Design of Oil Transportation Pipeline Engineering*. PetroChina Co., Ltd. and PRC Ministry of Construction edited, Beijing, China: China Planning Press, 158pp. (in Chinese).

Sheng, Y., Jin H.J., Wen, Z. & Li, G.Y. 2007. *Thermal and Stress Analyses of Foundations Soils Along the Buried Pipeline in Permafrost Regions*. Lanzhou: China: PetroChina Daqing Oil Engineering Company & Chinese Academy of Sciences Cold and Arid Regions Environmental and Engineering Research Institute (edited), 127pp.

Sheng, Y., Wen, Z., Li, G.Y., Hao, J.Q. & Wu, W. 2008. Thaw settlement behavior of permafrost along the proposed China-Russia crude oil pipeline route in Northeastern China. *Proceedings of the Ninth International Conference on Permafrost, Fairbanks, Alaska, June 29–July 3, 2008* (this proceedings).

Wei, Z., Jin, H.J., Zhang, J.M., Ji, Y.J., Yang, S.Z. & He, R.X. 2008. Forecasting changes of permafrost in Northeastern China during the next 50 years using the combination of GIS-aided equivalent-latitude and finite-element models. *Proceedings of the Ninth International Conference on Permafrost, Fairbanks, Alaska, June 29–July 3, 2008* (this proceedings).

Zhou, Y.W., Liang, L.H., Gu, Z.W., Liang, F.X. & Zhang, Q.B. 1994. Changes of thermal regimes of permafrost after forest fires in the northern Da Xing'anling Mountains. In: Q. Zhao, W. Zhang, Y.W. Zhou, & Y. Yang (eds.), *Environmental Impacts of Forest Fires in the Da Xing'anling Mountains and Their Mitigation*. Beijing, China: Science Press, 25-35 (in Chinese).

Increasing Permafrost Temperatures in Subarctic Sweden

Margareta Johansson
Dept. of Physical Geography and Ecosystem Analyses, Lund, Sweden and Abisko Scientific Research Station, Abisko, Sweden

H. Jonas Åkerman
Dept. of Physical Geography and Ecosystem Analyses, Lund, Sweden

Christer Jonasson
Abisko Scientific Research Station, Abisko, Sweden

Torben R. Christensen
Dept. of Physical Geography and Ecosystem Analyses, Lund, Sweden and Abisko Scientific Research Station, Abisko, Sweden

Terry V. Callaghan
Abisko Scientific Research Station, Abisko, Sweden and Dept. of Animal and Plant Sciences, Sheffield, UK

Abstract

This paper reports permafrost temperatures from three peat mires in subarctic Sweden. There were trends of increasing ground temperatures in the boreholes between 1980 and 2002 of 0.04°C a^{-1} to 0.05°C a^{-1} in the upper 1 m and 0.03°C a^{-1} to 0.04°C a^{-1} in the lower 12–15 m. However, no trend was detected in the middle of the profile. To verify the trends from the mires (with scarce temporal resolution), we use ground temperatures from Abisko Scientific Research Station recorded in an area currently nearby permafrost. Here, ground temperatures have increased on an annual basis and at all seasons apart from the summers, where decreasing temperatures were detected. The changes in ground temperatures could be correlated to increasing air temperature and increasing summer precipitation, but surprisingly not with snow depth. At lower depths the increases may be due to possible increased heating from slightly warmer or more freely flowing ground water.

Keywords: Abisko; ground temperatures; subarctic Sweden.

Introduction

Increases in air temperatures in the Arctic region have been almost twice as high as for the rest of the world during the last decades. This arctic amplification is expected to continue (ACIA 2005). These increases have had and will have profound effects on ground temperatures and, hence, on permafrost distribution (Anisimov et al. 2007). Even though it is widely known that there is a mismatch between air and ground temperatures, as there are other parameters of importance to ground temperatures, increasing air temperature in general increases ground temperatures (e.g., Thorn et al. 1999). For time scales up to a decade, the climatic changes of primary importance for ground temperatures are the changes in air temperatures and snow cover (Osterkamp & Romanovsky 1999). Increasing snow depth increases the insulation of ground from prevailing low winter temperatures and, hence, increases the ground temperatures. In contrast, late snowfall decreases soil temperatures due to the high albedo and the consumption of latent heat during snowmelt (Zhang et al. 2001a). In areas of discontinuous permafrost where air temperatures are close to 0°C, shallow permafrost is especially sensitive to climate warming. In such areas, snow depth and duration are particularly important and, together with air temperature, determine the presence or absence of permafrost.

Increasing ground temperatures have been reported from around the Arctic (e.g., Walsh et al. 2005, Romanovsky et al. 2007, Isaksen et al. 2007, Osterkamp & Romanovsky 1999), but information is underrepresented for the lowland discontinuous permafrost area of northern Fennoscandia. This paper reports permafrost temperatures from three peat mires in subarctic Sweden. Here, important changes in permafrost distribution and active layer depth have been recorded in lowland mires (Akerman & Johansson, submitted). We use the relationships between air temperatures, precipitation, and snow depth to explain the recorded changes in ground temperatures found during the last decades.

Research area

Abisko is located in subarctic Sweden and lies within the zone of discontinuous permafrost (Brown et al. 1998). Mountain permafrost determined mainly by air temperatures is found approximately above 880 m a.s.l. (Jeckel 1988), whereas at lower elevations permafrost is only likely to exist in peat mires (due to the peat's insulating effect) and underneath wind-exposed ridges (due to lack of snow) (Johansson et al. 2006). Ground temperatures have been recorded in peat mires around Abisko (Storflaket and Kursflaket, Table 1), which is located in an area of rain shadow, with a mean annual precipitation of 303 mm a^{-1} (1913–2006) and a mean annual air temperature of -0.6°C (1913–2006). In similar climatic conditions 6 km west of the mires at the Abisko Scientific Research Station, ground temperatures have been recorded in an area currently without permafrost (Abisko AWS, Table 1).

Table 1. The location, depth of measurements and observation periods for the four sites.

Site name	Coordinates (Lat/Long)	Measured at depth (m)	Observation period
Storflaket mire	68º20′51″N 18º57′55″E	0, 0.5, 1, 1.5, 2, 3, 4, 5, 6, 7, 8, 9, 12	1980-1982, 1984-1989, 1994-1997, 2000-2002
Katterjokk mire	68º25′31″N 18º10′29″E	0, 0.5, 1, 1.5, 2, 3, 4, 5	1980-1982, 1984-1989, 1994-1998, 2000-2002
Kursflaket mire	68º21′05″N 18º52′42″E	0, 0.5, 1, 1.5, 2, 3, 4, 5, 6, 7, 8, 9, 12, 15	1980-1982, 1984-1989, 1992, 1994-1997, 2000-2002
Abisko AWS (Automatic Weather Station)	68°21′20″N 18°49′14″E	0.05, 0.2, 0.5, 1	1985 until present

In addition, ground temperatures have been recorded at a mire located 35 km west of Abisko (Katterjokk, Table 1). Due to a very strong climatic gradient that occurs in the area, this site experiences a maritime climate with a mean annual precipitation of 848 mm a^{-1} and a mean annual air temperature of –1.7°C (1960–1990: Alexandersson et al. 1991). The depth of the peat is similar at all mires ~90 cm and is underlain by silt.

Snow depth in winter has increased by 2 cm/decade from 1913 until present in the area, but no statistically significant trend was detected in the start and end date of the snow season (Kohler et al. 2006).

The depth of permafrost ranges from a few meters in the mire located west of Abisko down to 16 m in the other mires close to Abisko (Akerman & Johansson submitted).

Methods

Air temperature monitoring

Air temperatures have been recorded manually at the Abisko Scientific Research Station from 1913 until present (at the outset, every third hour using the same method as used at the Swedish Meteorological and Hydrological Institute, 2 m screen air temperature). In 1984 an automatic weather station was installed and air temperatures have been recorded automatically every 10 minutes since then.

Ground temperature monitoring

At the mires, Copper-Constantan thermocouples were installed in boreholes at depths described in Table 1 and ground temperatures were recorded hourly, the third week of May and September using Campbell loggers.

At Abisko AWS, ground temperatures were recorded using a resistance temperature sensor Pt100 that was connected to an Automatic Weather Station. Data was recorded automatically every 10 minutes.

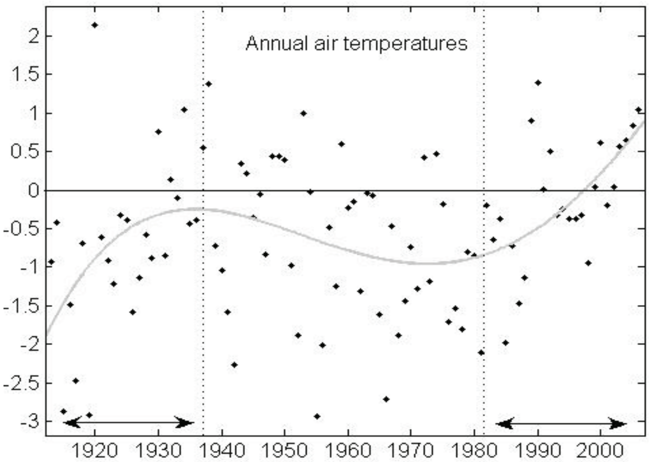

Figure 1. Annual air temperatures and a 4th degree polynomial fit from the Abisko Station, 1913 to 2006. The vertical dotted lines depict the two warming periods for which independent regression analysis was performed.

Data analysis – determining trends and attributing causes of the observed changes

Trends were calculated for the ground temperatures from the three mires and from the Abisko Station by using a robust linear regression, as implemented in the software package MATLAB R2006a. Trends were assumed to be significant for *p* levels ≤0.05. For air temperatures a 4th degree polynomial curve fit was used. To attribute the causes of the observed changes in the ground temperatures, correlation between ground temperatures, air temperatures, snow depth, and precipitation were calculated using multiple regressions (REGRESS) also within the software package MATLAB. All data were normalized and standardized prior to analysis.

Results

Air temperatures from Abisko

The mean annual air temperature at Abisko was -0.6°C between 1913 and 2006. The annual air temperatures at Abisko have during the 20th century experienced an increase in the beginning of the century that lasted until the late 1930s, which was then followed by a slight cooling trend until the mid 1970s and then again followed by an increase that is still ongoing. The regressed mean annual air temperature has been below zero degrees more or less throughout the 20th century, but in the last seven years the regressed annual air temperature has increased above the critical 0°C boundary (Fig. 1). There is an increase in air temperatures during the period of observation of 0.03°C a^{-1} (regression estimate of temperatures). Due to the distinct warming and cooling periods that have occurred throughout the last century, the overall increase in air temperature was not statistically significant (R^2 0.20 *p-value* 0.07). However, when analyzing the two warming periods that correspond roughly with the first 26 years of the record and the last 26 years, statistically significant increases were found (0.09°C a^{-1} for 1913–1938

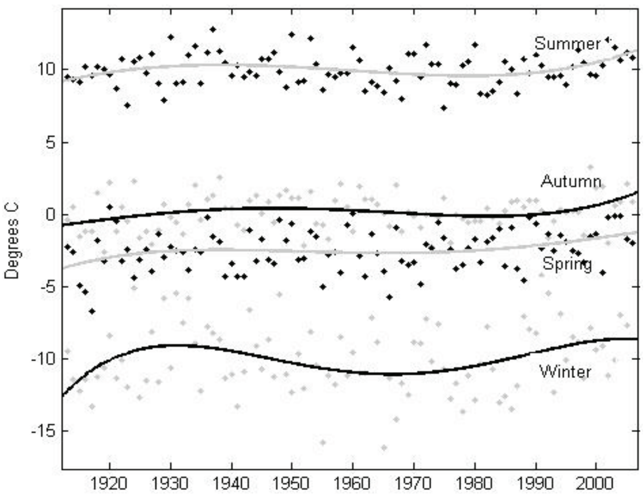

Figure 2. Seasonal air temperatures and a 4th degree polynomial fit from the Abisko Scientific Research Station, 1913–2006.

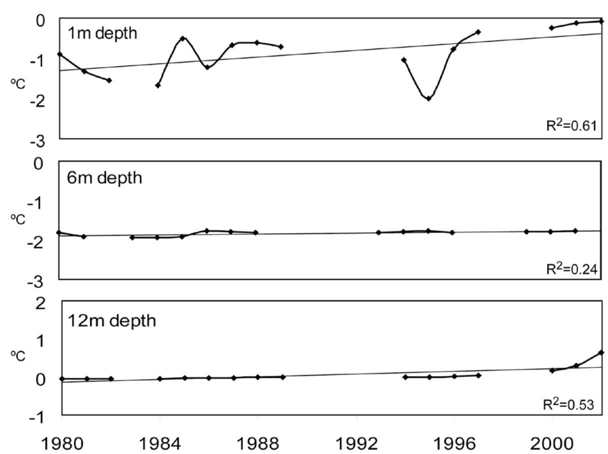

Figure 3. Ground temperatures at 1 m, 6 m, and 12 m depths and linear trends at Storflaket mire measured in September from 1980 to 2002.

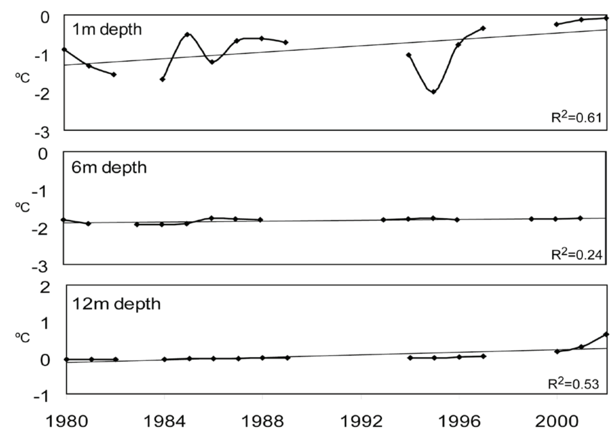

Figure 4. Ground temperatures at 1 m, 6 m, and 15 m depths and linear trends at Kursflaket mire measured in September from 1980 to 2002.

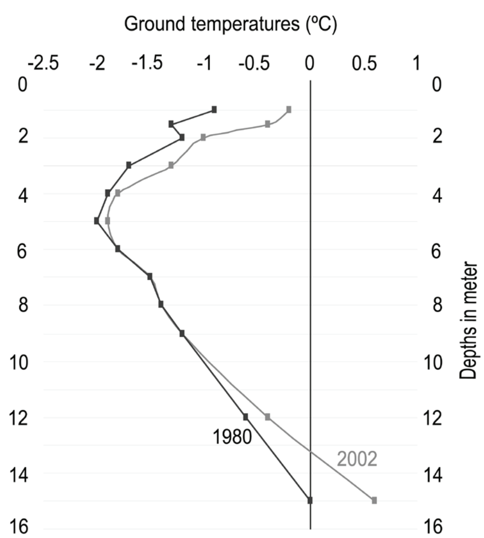

Figure 5. Ground temperatures in September 1980 and 2002 from Kursflaket mire. (Note: There was no subsidence of the ground surface where the temperatures were measured.)

(R^2 0.28 *p-value* 0.005) and 0.10°C a^{-1} for 1981–2006 (R^2 0.43 *p-value* 0.001).

For the whole period of observations there has been an increase in air temperatures in all four seasons that follows the same trend as the annual air temperatures (Fig. 2). The largest increases in temperatures are found in winter (December, January and February) 0.04°C a^{-1} (regression estimates), in autumn (September, October and November) and summer (June, July, and August) an increase of 0.02°C a^{-1} was found. Spring (March, April and May) experienced the lowest increase of 0.01°C a^{-1}. As the seasonal trends follow the annual trends with increases in the beginning of the century, followed by a cooling period and then again a warming period, the trends in increasing air temperatures are not statistically significant for the whole period of observation at all seasons (MAM R^2 0.06 *p-value* 0.02; JJA R^2 0.003 *p-value* 0.6; SON R^2 0.02 *p-value* 0.19; DJF R^2 0.005 *p-value* 0.48). However, over shorter periods of the temperature records, statistically significant trends, like the increases in the beginning and end of the century can be found. In general it is the lower temperatures that have increased.

Ground temperatures from the mires

At Storflaket mire, the ground temperature monitoring has been conducted down to 12 m. There is a statistically significant trend towards warmer September ground temperatures in the upper 1 (0.05°C a^{-1}; R^2 0.61 *p-value* 0.004) and the lower 12 m (0.04°C a^{-1}; R^2 0.53 *p-value* 0.001) depths. In the middle of the borehole no statistically significant trend could be detected (Fig. 3).

In May, statistically significant increasing trends were found at one (0.09°C a^{-1}; R^2 0.38 *p-value* 0.01) and 12 m

Table 2. Regression statistics of ground temperatures between 1985 and 2006 for Abisko AWS including estimates from the regressions of initial and final temperatures and the differences between them.

Time	Depth (cm)	R^2	*p-value*	Regression estimate of temp °C in 1985	Regression estimate of temp °C in 2006	Difference estimated from the regression °C a^{-1}
Annual	5	0.06	0.253	1.86	2.26	0.02
	20	0.20	0.039	1.46	2.10	0.03
	50	0.29	0.009	1.44	2.23	0.04
	100	0.38	0.002	1.38	2.30	0.04
Spring (March, April, May)	5	0.01	0.744	-0.56	-0.40	0.007
	20	0.11	0.127	-1.22	-0.58	0.03
	50	0.34	0.004	-1.30	-0.14	0.05
	100	0.49	0.000	-0.84	0.28	0.05
Summer (June, July, August)	5	0.52	0.000	9.90	7.73	-0.1
	20	0.40	0.002	8.23	6.45	-0.08
	50	0.19	0.043	5.93	4.84	-0.05
	100	0.00	0.856	3.48	3.58	0.005
Autumn (September, October, November)	5	0.37	0.003	1.81	3.01	0.05
	20	0.48	0.000	2.07	3.41	0.06
	50	0.58	0.000	2.73	4.08	0.06
	100	0.57	0.000	3.07	4.48	0.06
Winter (December, January, February)	5	0.24	0.022	-3.72	-1.29	0.11
	20	0.29	0.009	-3.24	-0.89	0.11
	50	0.34	0.004	-1.59	0.14	0.08
	100	0.45	0.001	-0.20	0.87	0.05

(0.004°C a^{-1}; R^2 0.89 *p-value* 0) depth, but again not for the depths in between.

At Kursflaket mire, ground temperature monitoring has been conducted down to 15 m. The ground temperatures in September have increased in the upper 1 m (0.04°C a^{-1}; R^2 0.46 *p-value* 0.003) and in the lower part of the borehole at 12 m and 15 m (0.03°C a^{-1}; R^2 0.91 *p-value* 0), while there is no significant trend at depths in between (Figs. 4, 5). In spring no trends were detected at 1 m and 6 m depths. At 15 m there was a statistically significant increasing trend (0.03°C a^{-1}; R^2 0.91 *p-value* 0).

At Katterjokk mire the permafrost is very shallow ranging from 2 m to 5 m; hence, no deeper temperature recordings have been made. The same trend as found in the other two mires was detected, with statistically significant increasing ground temperatures in September in the upper 1 m (0.04°C a^{-1}; R^2 0.53 *p-value* 0.001); but below no significant trend was detected (Fig. 6). In May, statistically significant trends were detected at both 1 m and 5 m depths, and increases of 0.07°C a^{-1} (R^2 0.66 *p-value* 0.0001) and 0.01°C a^{-1} (R^2 0.71 *p-value* 0), respectively, were recorded.

Ground temperatures from the Abisko Scientific Research Station

At the Abisko AWS, the ground temperatures have on an annual basis, increased at all depths (Table 2), but only at 50 cm and 100 cm depth is there a statistically significant trend. In spring, increasing statistically significant trends occur for the same depths, but not in the upper 50 cm. In summer, a decreasing trend in ground temperatures is detected, and down to 50 cm it is statistically significant. In autumn, again we see an increasing trend in ground temperatures, and it is statistically significant for all depths. In winter, there is also an increasing trend that is statistically significant for all depths.

Correlations of air temperatures and ground temperatures, snow depth and precipitation

On an annual basis, we could detect a statistically significant correlation between air temperature and ground temperature at Abisko. The highest correlation is found at the 20 cm depth (R^2 0.66) and the lowest, at the 1 m depth (R^2 0.42). The same pattern is detected for the spring. For summer, no correlation could be found between air temperature and soil temperatures. In autumn, statistically significant correlations could be detected at 5 cm (R^2 0.45) and 20 cm (R^2 0.36) depths, but not at lower depths. In winter, statistically significant correlations between air temperature and ground temperature were found at all depths, 5 cm = R^2 0.64, 20 cm = R^2 0.62, 50 cm = R^2 0.55, and 100 cm = R^2 0.45.

No statistically significant correlations were detected between snow depth and the ground temperature in any of the seasons or on an annual basis at the Abisko AWS.

On an annual basis, a weak statistically significant trend could be detected between precipitation and soil temperature at the 20 cm depth, but not at any other depths. In spring, autumn, and winter no correlations between precipitation and ground temperatures were found, but in summer, a statistically significant trend could be detected at 5 cm and 20 cm depths (R^2 0.30 and R^2 0.23).

Discussion

Mean annual air temperatures at Abisko (Fig. 1) follow the same trend as shown for the Northern Hemisphere (Houghton et al. 2001, IPCC 2007), with a warming period in the beginning of the 20th century continuing until about 1940, followed by slight cooling until the 1970s, and then a second warming period that is still ongoing. Although interannual variation is so large during the last century that the overall increase is not statistically significant, temperature increases are statistically significant in the two warming periods when they are analyzed separately. Similarly, Kohler et al. (2006) did not detect a trend for the whole period (apart from the spring record) but also found statistically significant increases over a shorter time period (1956–2000). The recent increase at the end of the century, mainly due to increases in lower air temperatures, has resulted in a current temperature that is possibly higher than those since at least the Medieval Warm Period (Grudd et al. 2002).

The temporal pattern of mean annual air temperature is repeated in each of the seasons (Fig. 2). For example, Holmgren & Tjus (1996) reported an increase in summer air temperatures from the beginning of the century to about 1940, which was as high as 1.5°C. In addition to the increases in seasonal and mean annual air temperatures, increases in snow depth (Kohler et al. 2006) and active layer depth (Akerman & Johansson Submitted) have occurred in the area.

Increasing ground temperatures could be detected from all four sites, but in the mires, increases in ground temperatures only occurred in the upper and lower parts of the permafrost (Figs. 3, 4). This is accompanied by an increase in active layer depth (Åkerman & Johansson submitted). In the middle, no significant trend was found. Isaksen et al. (2007) also found increases in ground temperatures in mountain permafrost in northern Scandinavia. They detected significant warming down to at least 60 m in depth. Statistically significant correlations were found between the seasonal ground and air temperatures (Isaksen et al. 2007).

We hypothesized that ground temperatures would have been determined by snow depth in addition to air temperatures. This hypothesis was based on studies such as that by Thorn et al. (1999), who worked in a valley close to the Katterjokk mire and concluded that air temperatures could explain as much as 95% of the variance in ground temperatures at shallow depths at some sites. However, at other sites with differing microclimate determined by variation in elevation, aspect, and vegetation cover, air temperatures could only explain as little as 20%. This was suggested to be due to a role of seasonal snow cover (although this was not measured) (Thorn et al. 1999). In addition, Josefsson (1990) found a relationship between ground temperatures and climatic parameters, especially snow cover at four sites near Abisko. Both Thorn et al. (1999) and Josefsson (1991) have interpreted snow cover

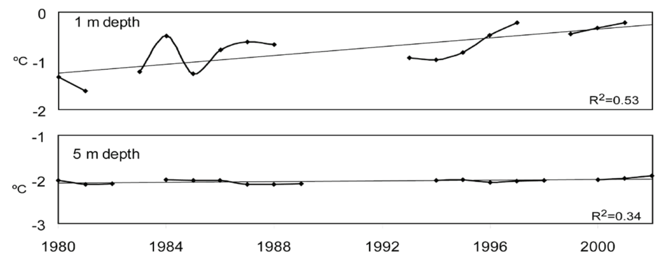

Figure 6. Ground temperatures at 1 and 5 m depth and linear trends at Katterjokk mire measured in September from 1980 to 2002.

as one of the most important parameters that determine ground temperatures in our study area.

We also found correlations between air and ground temperatures. Surprisingly we could not detect any correlation between snow depth and ground temperature even though we used two unique snow datasets from Abisko. Changes in starting and ending dates of snow cover could affect the ground temperatures at Abisko, but no such changes were detected at Abisko (Kohler et al. 2006); hence these cannot explain increases in ground temperatures.

As we found a decrease in summer ground temperatures (Table 2) that could not be correlated to snow depth and air temperature, and the correlations that were found between air temperature and ground temperature explained little of the variance, it can be concluded that other factors also determine the ground temperatures in the Abisko region. The decrease in summer ground temperatures could be caused by a change in vegetation which alters the albedo, shading, and soil moisture. Vegetation has not shifted at the Abisko AWS and, hence, cannot explain the decreasing trend in summer ground temperatures. The decrease in ground temperature was correlated, however, with increases in summer precipitation that have occurred during the last decades. An increase in precipitation increases evaporation which in turn increases the energy consumption resulting in cooler ground temperatures. Similar trends with decreasing summer ground temperatures have been reported from Irkutsk in southcentral Siberia, where they were also attributed to increases in summer precipitation (Zhang et al. 2001b).

The increases in ground temperatures in the lower part of the permafrost might be due to a slight "heat wave" as a result of the warming period at the end of the century. More likely though, there is a possible heating affect from slightly warmer or more freely flowing ground water around and below the frozen bodies of silt and turf. Although, there are no direct measurements of surface and ground water temperatures, temperatures at 12 m and 15 m of just above 0°C indicate that liquid water is flowing at the bottom of the permafrost. However, observations of seasonal variations in ground temperatures at the base of the permafrost are needed to confirm this. If the relatively high temperatures at the base of the permafrost in the mires reflect the movement of liquid water, then the permafrost is even more vulnerable than we first expected because of the influences of warming from above and below.

Acknowledgments

This work contributes to the IPY "Back to The Future" (BTF; ID No: 512) and we gratefully acknowledge support from the Swedish Environmental Agency (Naturvårdsverket). This work was partly funded by the EU financed project ALARM–Assessing large-scale environmental risks for biodiversity with tested methods, contract no GOCE-CT-2003-506675.

References

ACIA. 2005. *Arctic Climate Impact Assessment.* Cambridge University Press, 1042 pp.

Akerman, H.J. & Johansson, M. Submitted*.* Thawing permafrost and deepening active layer in sub-arctic Sweden. *Submitted to Permafrost and Periglacial Processes.*

Alexandersson, H., Karlström, C. & Larsson-McCann, S. 1991. *Temperature and precipitation in Sweden 1961-90 Reference Normals, SMHI Meteorologi Klimasektion* No 81.

Anisimov, O.A., Vaughan, D.G., Callaghan, T.V., Furgal, C., Marchant, H., Prowse, T.D., Vilhjálmsson, H. & Walsh, J.E. 2007. Polar Regions (Arctic and Antarctic). *Climate Change 2007: Impacts, Adaptation and vulnerability*. Contribution of Working Group II to the Fourth Assessment Report of the Intergovernmental Panel on Climate Change. M.L Parry, O.F. Canziani, J.P. Palutikof, P.J. van der Linden & C.E. Hanson, (eds.), Cambridge: Cambridge University Press, 653-685.

Brown, J., Ferrians, O.J., Jr., Heginbottom, J.A. & Melnikov, E.S. 1998. Circum-Arctic Map of Permafrost and Ground-Ice Conditions. In: M. Parsons & T. Zhang (eds.), *International Permafrost Association Standing Committee on Data Information and Communication (comp.)*. 2003. Circumpolar Active-Layer Permafrost System, Version 2.0. Boulder, Colorado: National Snow and Ice Data Center/World Data Center for Glaciology. CD-ROM.

Grudd, H., Briffa, K.R., Karlen, W., Bartholin, T.S., Jones, P.D. & Kromer, B. 2002. A 7400-year tree-ring chronology in northern Swedish Lapland: natural climatic variability expressed on annual to millennial timescales. *Holocene* 12: 657-665.

Holmgren, B. & Tjus, M. 1996. Summer air temperatures and tree line dynamics at Abisko. *Ecological Bulletins* 45: 159-169.

Houghton, J.T., Ding, Y., Griggs, D.J., Noguer, M., van der Linden, P.J., Dai, X., Maskell, K. & Johnson, C.A. (eds.), 2001. *Climate Change 2001: The Scientific Basis*. Cambridge: Cambridge University Press, 881 pp.

IPCC 2007. Climate Change 2007: The Physical Science Basis-Contribution of Working Group I to the Fourth Assessment. In: S. Solomon, D. Qin, M. Manning, Z. Chen, M. Marquis, K.B. Averyt, M. Tignor & H.L. Miller (eds.), *Report of the Intergorvernmental Panel on Climate Change*. Cambridge, United Kingdom and New York, NY, USA: Cambridge University Press.

Isaksen, K., Sollid, J.L., Holmlund, P. & Harris, C. 2007. Recent warming in mountain permafrost in Svalbard and Scandinavia. *Journal of Geophysical Research* 112: F02S04, doi:10.1029/2006JF000522.

Jeckel, P.P. 1988. Permafrost and its altitudinal zonation in N. Lapland. *Proceedings of the Fifth International Conference on Permafrost, Vol. 1, Trondheim, Norway, August 2–5, 1988:* 170-175.

Johansson, M., Christensen, T.R., Akerman, H.J. & Callaghan, T.V. 2006. What determines the current presence or absence of permafrost in the Torneträsk Region, a sub-arctic landscape in northern Sweden. *Ambio* 35: 190-197.

Josefsson, M. 1990. Ground Temperature Variations in a Subarctic Mountain Valley, Abisko, Northern Sweden. *Geografiska Annaler*, Series A 72(2): 179-190.

Kohler, J., Brandt, O., Johansson, M. & Callaghan, T.V. 2006. A long-term Arctic snow depth record from Abisko, northern Sweden, 1913-2004. *Polar Research* 25: 91-113.

Osterkamp, T.E. & Romanovsky, V.E. 1999. Evidence for warming and thawing of discontinuous permafrost in Alaska. *Permafrost and Periglacial Processes* 10: 17-37.

Romanovsky, V.E., Sazonova, T.S., Balobaev, V.T., Shender, N.I. & Sergueev, D.O. 2007. Past and recent changes in air and permafrost temperatures in eastern Siberia. *Global and Planetary Change* 56: 399-413.

Thorn, C.E., Schlyter, J.P.L., Darmody, R.G. & Dixon, J.C. 1999. Statistical relationship between daily and monthly air and shallow-ground temperatures in Kärkevagge, Swedish Lapland. *Permafrost and Periglacial Processes* 10: 317-330.

Walsh, J.E., Anisimov, O., Hagen, J.O.M., Jakobsson, T., Oerlemans, J., Prowse, T., Romanovsky, V., Savelieva, N., Serreze, M., Shiklomanov, A., Shiklomanov I. & Solomon, S. 2005. Cryosphere and hydrology. In: *Arctic Climate Impact Assessment*. Cambridge University Press. 183-242.

Zhang, T., Barry, R.G., Gilichinsky, D., Bykhovets, S.S., Sorokovikov, V.A. & Ye, J. 2001a. An amplified signal of climatic change in soil temperatures during the last century at Irkutsk, Russia. *Climate Change* 49: 41-76.

Zhang, T., Barry, R.G. & Haeberli, W. 2001b. Numerical simulations of the influence of the seasonal snow cover on the occurrence of permafrost at high latitudes. *Norsk Geografisk Tidsskrift* 55: 261-266.

—Plenary Paper—

Permafrost-Related Performance of the Trans Alaska Oil Pipeline

Elden R. Johnson, PE
Alyeska Pipeline Service Co, Fairbanks, AK
Lorena A. Hegdal, PE
Alyeska Pipeline Service Co, Fairbanks, AK

Abstract

The Trans Alaska Oil Pipeline System crosses 1287 km (800 mi) of Alaska, from the Prudhoe Bay oil field on the Beaufort Sea (latitude 71°N) to the marine terminal at the ice-free port of Valdez. Approximately 75% of the route consists of permafrost, transecting the full range of conditions from cold, deep and continuous in the north, discontinuous in the interior, and sporadic to frost-free in the south. The pipeline has operated for over 30 years, transporting nearly 2.5 billion cubic meters (16 billion barrels) of warm crude oil in a harsh, technically problematic, and fragile arctic environment. The lifetime operating reliability of the pipeline has been nearly 99%, with only 12 lifetime spills exceeding the 50-barrel definition. This remarkable performance record attests to the functional, environmental and economic success of the project. This paper describes permafrost-related experiences and engineering lessons learned regarding the performance of the pipeline.

Keywords: crude oil; lessons; permafrost; pipeline; Trans Alaska Pipeline System (TAPS).

Introduction

The Trans Alaska Pipeline System (TAPS) is owned by a consortium of major oil companies and operated by the Alyeska Pipeline Service Co, (Alyeska). The route of TAPS spans the full range of permafrost conditions from continuous and cold, to sporadic and marginal. The 48 inch NPS (nominal pipe size, 122 cm diameter) pipeline has transported up to 334 thousand cubic meters per day (2.1 million barrels per day) at peak throughput and currently operates at about 111 thousand cubic meters per day (700 thousand barrels per day). Oil temperatures have ranged from 63ºC (145ºF) at the northern inlet to 7ºC (45ºF) at the southern outlet. TAPS has now transported nearly 2.5 billion cubic meters (16 billion barrels) of crude oil across the State of Alaska since startup in June of 1977. The safe and effective transportation of these huge quantities of warm crude oil over 1287 kilometers (800 miles), 75% of which contains permafrost, was the primary engineering problem faced by the TAPS designers and operators.

Some permafrost related maintenance problems were recognized shortly after startup (Johnson 1983) including buried pipeline settlement; non-condensable gas blockage of thermo-siphons (heat pipes), and buried insulation system failures. Some of these early issues have been resolved as the immediate effect of initial permafrost thawing has diminished over time. Other time-related issues have been corrected by ongoing maintenance programs.

Designing and building a pipeline across the harsh environment of Alaska has distinguished itself as one of the great engineering achievements of history. Many untried and innovative technical solutions were needed. The design was not perfect, however, and has required consistent monitoring and adjustment over the last 30 years. The remarkable success story of TAPS provides important lessons to those planning similar permafrost sensitive pipeline projects in the future.

Design Challenges

The primary function of the pipeline is to efficiently transport tariff grade crude oil under all environmental and operating conditions experienced over the life of the project. The design life of TAPS was originally stated as 30 years, but as with many infrastructure projects, is now expected to perform well beyond that period (Norton and Miller 2002). In 2004, the federal and state government renewed the grant and lease of pipeline right-of-way for another 30 year period after determining that with proper maintenance the pipeline could safely and efficiently operate for an additional 30 years (Norton et al. 2002).

When oil was first discovered in economic quantities on the North Slope of Alaska in 1968, the pipeline design concept first envisioned consisted of a full length buried pipeline. The pipe itself was purchased assuming a completely buried design. As experts and engineers were engaged, it became clear that warm oil and unstable permafrost were not compatible. The true magnitude of engineering challenge to building a pipeline on permafrost emerged.

The extent and nature of permafrost could not be known until route finding was completed and geotechnical information obtained. Over 5,000 soil borings (1 per 250 m on average) were conducted for characterization and testing of over 15,000 soil samples. Once this information was compiled, frozen and thawed locations could be identified and permafrost found along the route was characterized for engineering purposes as either cold, warm, stable, or unstable.

Permafrost north of the Brooks Range (northern 270 km or 168 miles of the pipeline) was determined to be continuous and cold (Fig. 1). The permafrost temperature on the North Slope is typically about -7ºC near the surface (20ºF) and extends to a depth of nearly 670 meters (2,200 ft). South of the Brooks Range permafrost becomes discontinuous, and then sporadic with varied depth below the active layer.

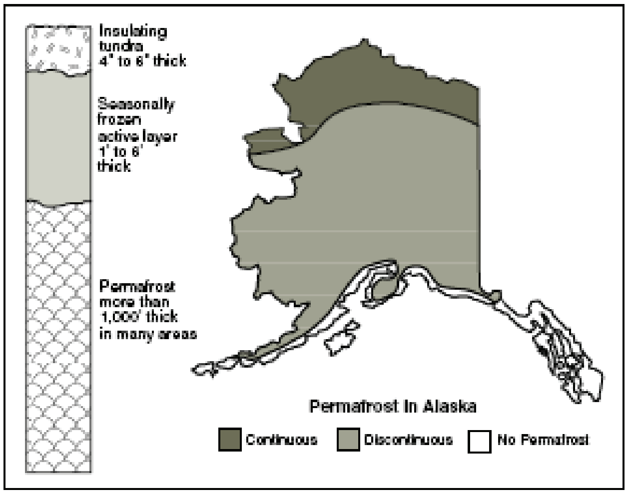

Figure 1. Distribution of permafrost in Alaska.

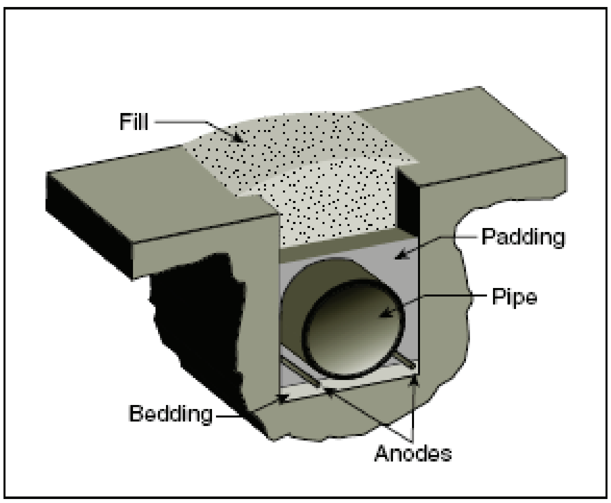

Figure 2. Buried pipeline construction.

Temperatures below the active layer can be near the freezing point and assumed to be -0.3°C (31.5°F) for engineering purposes. Active layer depths vary depending on soil surface material and temperature, from several centimeters to several meters.

Stable permafrost was defined as frozen rock, or clean granular material with no visible ice. Clean granular material was defined as sand or gravel with less than 6% fine material by weight (passing the # 200 sieve). In varied soil profiles, stability was also determined on the basis of a calculated 30-year settlement over the expected depth of thaw of less than 30 centimeters (1 ft).

The key initial design challenge was route finding and mode selection to avoid or minimize the threat to pipeline integrity caused by permafrost. Three basic pipeline design modes were developed and applied depending on permafrost condition (Johnson 1983). These included conventional buried pipelines, above-ground pipeline construction and special insulated buried pipeline construction. Other modes, including bridges and river crossings, special fault crossing, road crossings and animal crossings were employed for unique situations.

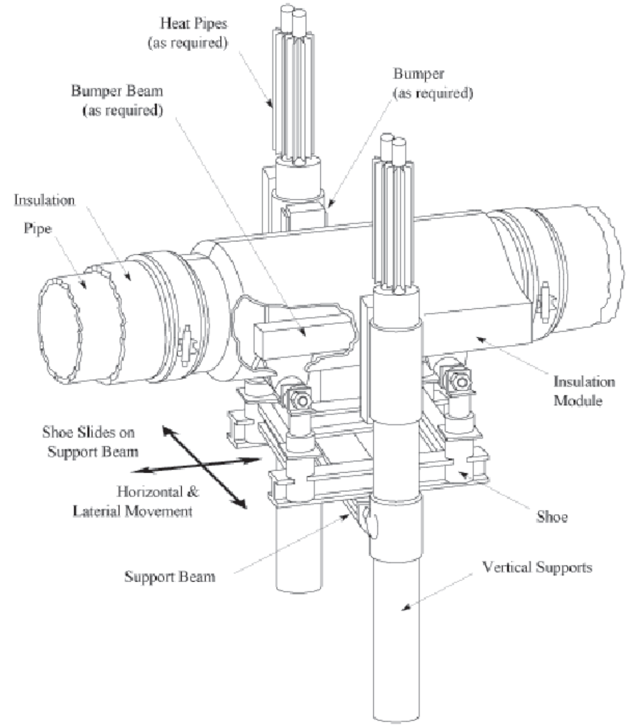

Figure 3. Above-ground pipeline construction.

Buried pipeline construction mode was the preferred mode because it was less costly than others (Fig. 2). The pipeline was buried where thawed or thaw stable ground was encountered. Burial depth averaged 1.5 m (5 ft) and ranged between 1 and 12 m. Buried pipeline required the placement of a cathodic protection system (anodes) to control corrosion. On the North Slope and through mountain passes, the pipeline was often routed along river floodplains because thawed or thaw stable sand and gravel could often be found to allow buried construction. A total of 612 km (380 of 800 miles) or 48% of TAPS was constructed below ground.

The above-ground mode was used where unstable permafrost was encountered. This design avoids permafrost threats by completely bridging over it (Fig. 3). The elegant zigzag configuration (Fig. 4), with thermo-siphon radiators (heat-pipes) often protruding from support pilings visually distinguishes TAPS from all others and makes it one of the most photographed in the world. The zigzag configuration controls the amount of movement associated with thermal expansion, and limited ground movement (static or dynamic). A total of 676 km (420 of 800 miles) or 52% of TAPS was constructed above ground.

Special design constraints dictated the burial of the pipeline at three locations with unstable permafrost which would normally employ an above-ground design. The above-ground mode was thought to interfere with wildlife migration and was not allowed. In this special buried mode, an insulated pipeline was designed with mechanical refrigeration to maintain frozen conditions below the pipe (Fig. 5).

Figure 4. Zigzag configuration of above-ground pipeline.

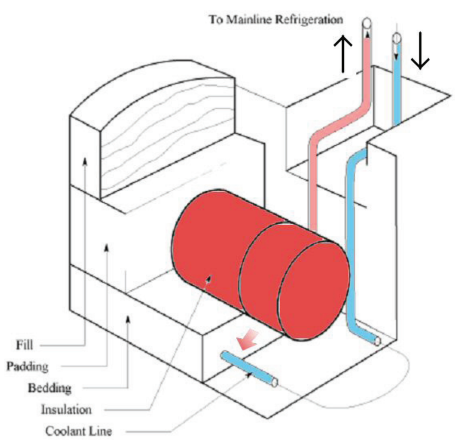

Figure 5. Special buried pipeline construction.

Other environmental conditions and operating hazards

A number of additional environmental conditions besides permafrost had to be considered in the design of TAPS. These included natural hazards such as earthquakes, floods, icings, ground movement, extreme weather, fire, corrosion, and material defects. Human related hazards such as incorrect operation, maintenance error, support system structural damage, vehicle or aircraft impact, third party damage, and deliberate sabotage were also considered.

The design of TAPS considered extreme conditions and events which could be expected within the 30-year project life. Design criteria were used to assure the pipeline could withstand normal operating conditions within safe limits, and withstand extreme contingency conditions without failure.

Operating and Maintenance Experience

Permafrost related operating hazards require ongoing monitoring and maintenance because the nature and magnitude of the threat is constantly changing over time. Alyeska conducts regular monitoring, surveillance, and maintenance activities to inspect the pipeline for changes and to maintain it within specified operating limits. Functional limits are determined for each system component based on principals of Reliability Centered Maintenance (RCM) (Moubray 1997). Monitoring and maintenance strategies are determined based on failure consequence, likelihood, and hazard rate (rate of hazard advance over time such as corrosion or settlement rate).

Monitoring and maintenance strategies are incorporated within written integrity management program procedures. The integrity management plan (IMP) is divided into broad categories for organization and management purposes. The IMP addresses all perceived threats including corrosion, floods, earthquakes, human error, and mechanical breakdown, as well as those related to permafrost. The following integrity management categories are directly or indirectly influenced by permafrost and are described in further detail in the remainder of this paper.

1. Mainline above-ground support systems,
2. Mainline integrity management (curvature, mechanical damage and corrosion),
3. Right of way and facilities civil monitoring,
4. Fuel gas pipeline.

Subject matter experts identified for each program direct scheduled activities, maintain records, assess results and monitor performance. An annual report is prepared to describe previous results, evaluate asset condition, recommend future activities, and recommend improvements in overall program management practice.

Mainline above-ground support system

The above-ground support system is a unique component of TAPS which allows it to bridge over unstable permafrost. Were it not for the presence of permafrost, such a support system would not be needed and TAPS would be similar to most other pipelines. Above-ground portions make up 52% of TAPS.

Key system components include the zigzag configuration, intermediate pipeline supports, anchors, vertical support members, and heat-pipes. The zigzag configuration of the pipeline itself (Fig. 4) is designed to allow controlled pipe movement in response to temperature changes or seismic events. Intermediate supports spaced normally every 18 m (60 ft) provide vertical support. Anchors provide for controlled lateral and longitudinal movement and are spaced typically 550 m (1800 ft) apart.

Intermediate supports consist of two vertical support members (VSM) with support brackets, a cross beam, a sliding shoe assembly and intermediate pipe clamp (Fig. 3). The pipe is allowed to slide laterally and longitudinally through the use of low friction Teflon pads. Anchors consist of four vertical support members with support brackets, anchor platform assembly, and anchor clamp. The anchor assembly is designed to release and absorb energy if differential longitudinal loading exceeds the design level.

The primary function of the above-ground system is to support the pipeline under all operating and contingency loadings. Support system components themselves may fail or sustain limited damage during contingency events as long as the pipeline itself does not fail.

Vertical support members (Fig. 6) are the basic units of vertical and lateral support linking the pipe to the ground. VSM consist of 46 cm diameter (18 inch) pipe piles drilled or driven into the ground to a depth which is determined by soil conditions. VSM depths vary between 5 to 15 m (15 to 50 ft) below ground surface with 11 m (35 feet) being the average.

VSM are designed to resist vertical loads in either up or down direction. A typical 2 m (5–7 ft) active layer is assumed to have no load bearing capacity. Upward frost jacking loads are generated in the active layer and control the minimum embedment depth. Vertical loads are resisted in the region below the active layer, by ad-freeze forces where the ground is frozen, and friction forces where thawed. End-bearing resistance is utilized in some cases. The ad-freeze strength used in design is based on a 30 year estimate of viscous creep in frozen soil and depends on permafrost temperature assumptions (warm or cold). A 30-year creep limit of 8 cm (3 inches) of downward movement was used to determine frozen strength.

A total of 78,000 VSM were used in the construction of the above-ground support system. Of these, approximately 97% rely on maintenance of a frozen soil condition for stability. In warm permafrost, heat pipes are used to maintain a permanently frozen condition. VSM with heat pipes are known as thermal VSM (Fig. 6) and make up about 80% of all VSM used. Heat pipes are closed loop, passive heat exchangers, charged initially with ammonia, and now recharged with CO_2. They are designed to remove heat in the winter when air temperatures are colder than the ground. They super-cool the soil in the load bearing zone compensating for long term heat loss at the ground surface. A single heat pipe is designed to maintain a frozen condition; two heat pipes are installed in each VSM for redundancy. A total of nearly 124,000 heat pipes were used in the construction of the above-ground pipeline support system.

Above-ground support system components are monitored on a frequency which depends on risk and hazard rate. Monitoring consists of observations which may indicate permafrost degradation such as the following;

1. VSM vertical movement determined by elevation survey, load cell testing, or observed out of level cross beam.

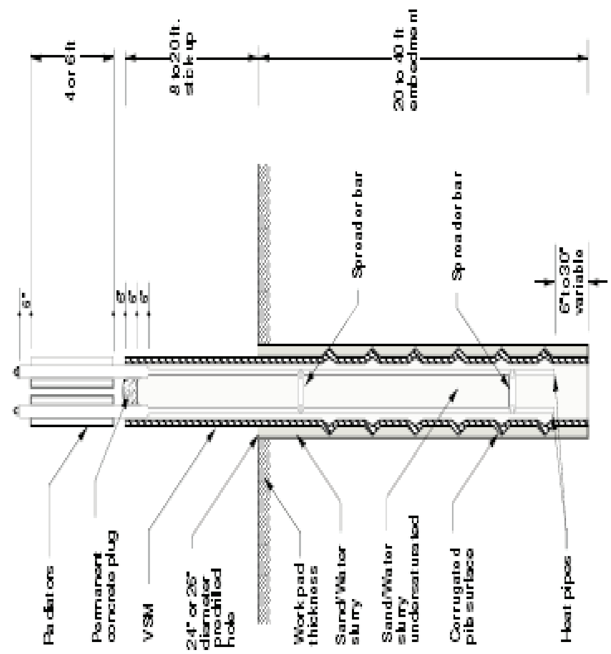

Figure 6. Typical thermal VSM.

2. VSM out of plumb.
3. Heat pipe degradation determined by infrared survey.
4. Tripped anchors, caused by excess lateral load.
5. Intermediate shoes off-center
6. "Floating shoes" not supporting vertical loads.
7. Damaged Teflon sliding base.

Where conditions are observed outside of designated operating limits, maintenance is performed to restore the component to within acceptable parameters. Maintenance may vary from minor adjustments to replacement of system components. A key performance feature of TAPS is its maintainability. Many components are specifically designed for ease of maintenance. The 2007/2008 maintenance year is considered typical of the scale of maintenance activities, consisting of the following;

1. Replace 2 VSM
2. Reposition 4 tripped anchors
3. Load adjust 8 intermediate supports (floating shoes)
4. Repair 9 out-of-location intermediate shoes
5. Replace 1,000 degraded Teflon slide plates
6. Recharge 2,000 degraded heat pipes

Heat pipes have experienced blockage by non-condensable hydrogen gas (a by-product of corrosion). They are monitored by infrared camera able to detect a "cold top" condition indicative of radiator blockage by non condensable gas (Sorensen et al. 2002). Repair of heat pipes is performed by recharging them with CO_2. Repairs are prioritized for southern areas where permafrost is marginal, concentrated blockage zones, slopes sensitive to movement, or locations where VSM movement is observed.

The level of maintenance noted above is considered manageable and provides evidence that permafrost degradation is not a current problem in the operation of above-ground portions of TAPS. Increased maintenance may be anticipated in the future with additional degradation of marginally frozen areas.

Mainline integrity management

While the above-ground pipeline avoids most permafrost related risk by bridging over it, the buried pipeline must adapt to differential settlement of the pipeline caused by permafrost thawing. The buried pipeline design required that foundation soils be either thawed or thaw stable. Thousands of pre-construction boreholes and soil tests were conducted to assure that the pipeline was buried only in suitable locations. Boreholes were closely spaced, averaging 250 m (820 ft) along the length of the line, to help detect random pockets of unstable permafrost.

The long-term (30-year) thaw depth for buried TAPS was estimated to vary from 20 to 37 m (70 to 120 ft) depending on soil type and ice content. Frozen soils were not considered thaw stable if calculated thaw settlement exceeded about 30 cm (1 ft). Geologists logged the pipeline ditch during installation to confirm thaw stability of any frozen soil discovered below pipe depth. The pipeline design had to be radically changed to the above-ground mode on multiple occasions due to the discovery of ice-rich or unstable permafrost.

Some areas of unstable permafrost went undetected in spite of all soil data gathered prior to and during construction. In 1979, after 2 years of operation during the most rapid thaw bulb development, the pipe buckled and leaked at two locations. In each case, short pockets of undetected ice rich permafrost caused approximately 1.3 m (4 ft) of pipe settlement over a span of nearly 122 m (400 ft). The pipe was excavated, encapsulated with a steel sleeve and underpinned using a steel support system to prevent further settlement. One leak location was later cut out and replaced. The other is still operating in a safe and stable condition.

Following these initial leaks, an integrity management program (IMP) was developed to detect, measure and assess other potential settlement locations. The program initially consisted of settlement monitoring rods placed on top of the pipe at suspected locations and extended to the ground surface for survey monitoring. Surveys were used to observe the settlement rate and estimate pipe curvature. Pipe curvature was used as the key performance indicator of potential pipe buckling. The program was also supported by numerous additional soil borings to determine subsurface conditions.

A later enhancement incorporated the use of deformation monitoring, in-line inspection (ILI) pigs (instrumented devices) placed in the pipeline which could detect deformation indicative of incipient buckling. The program was instrumental in detecting a dozen locations requiring repair in the decade between 1980 and 1990.

Later in the 1990s, curvature/deformation in-line inspection tools using inertial guidance systems were developed for use on TAPS. These tools are capable of accurately detecting and measuring high curvature areas (Hart et al. 2002).

Settlement repairs initially involved extensive structural support systems, or excavation and replacement in an above-ground mode. One solution involved the use of chemical grouting, and active ground freezing (Thomas et al. 1982) to restore a frozen condition, and then supplemented with numerous free standing heat pipes to permanently maintain the frozen ground. Another solution where the pipe had settled up to 4.6 m (13 ft), involved abandonment of a short section of buried pipeline and replacement with an 800 m (0.5 mile) section of elevated pipe (Simmons & Ferrell 1986). Less severe settlement locations were corrected by excavating the pipe and returning it to a safe curvature using either mechanical lifting or air bags. A detailed description of pipeline settlement repairs is provided by Ferrell and Thomas (1988). Only about 1.5 km out of 612 km (0.9 miles of 380 miles) or 0.25%) of buried pipe required maintenance as a result of permafrost subsidence.

Now with diminished pipeline throughput, the oil takes longer to reach Valdez and thus experiences greater environmental cooling. The thaw bulb below the pipeline has reached its maximum extent and is no longer growing by an appreciable amount. A concern for future low throughput conditions if oil temperatures drop below freezing, is that frost may penetrate to pipe depth, causing increased wax precipitation and freezing of small amounts of water in the oil. In the extreme case, frost jacking forces could develop if frost penetrates below pipe depth.

The special buried insulated pipeline mode presented a different set of permafrost related issues. An annular, shop fabricated, close-celled polyurethane insulation, encapsulated by a fiber reinforced plastic (FRP) outer jacket was used to insulate unstable permafrost from the heat of the pipe. Brine refrigerant is circulated in 15 cm (6 in) diameter refrigeration piping placed below the mainline pipeline (Fig. 5). Refrigeration plants continuously operate to circulate chilled brine. This design relies on the FRP outer jacket to maintain a waterproof pipe environment. This mode is used on about 6 km (4 miles) of the pipeline.

In some cases the FRP outer shell has not effectively prevented water ingress into the insulation. The insulation has become wet, losing its thermal resistance, and causing increased thermal demand on the mechanical refrigeration plants. Refrigeration plants have had to be overhauled and upgraded. Water ingress has also created pipe corrosion concerns that have required excavation, inspection and replacement of the insulation system. Cathodic protection has been added to control corrosion as part of the repair.

Right of way and facility maintenance

The pipeline work pad used for access during construction and maintenance was constructed on permafrost, roughly in proportion to the construction mode mix (52% above ground, 48% buried). Five of the 10 original pump stations were constructed on unstable permafrost. Several integrity and maintenance related concerns have been identified in conjunction with permafrost along the right of way and at facilities.

A total of 55 sensitive pipeline slopes were identified where soil instability could pose a threat to the pipeline. Many of these slopes depend on frozen ground to assure continued stability. Of the 55 sensitive slopes, 6 were deemed high priority and subject to special slope monitoring activities. Maintenance has been required (Tart & Ferrell 2002), including the replacement of several dozen VSM, drainage enhancements and use of surface insulation and heat pipes to maintain permafrost and control down slope movement.

During design of the pipeline, it was divided into segments based on changes in pipeline risk factors. One concern affecting the design was the potential for soil liquefaction under seismic conditions. The preferred solution for buried pipeline was to place the pipeline at a depth below where liquefaction was predicted to occur. In the above-ground mode, the solution was to either avoid liquefiable soils altogether, or maintain them in a frozen condition.

In November 2002, a 7.9 M earthquake, the largest in the world that year, occurred along the Denali Fault which runs directly under the pipeline (Hall et al. 2003). This large earthquake ruptured the ground 5 m (18 ft) laterally and 1.1 m (3.5 ft) vertically at the fault crossing and produced ground motions slightly in excess of design criteria. The pipeline support system was damaged, but the pipe itself did not leak. The pipeline was shut down for 66 hrs for inspection.

Liquefaction was observed at several locations but all above-ground and buried designs performed within expectations. Following the event, an inertial guidance (curvature/deformation) ILI tool was run to identify areas of hidden damage with none found (Johnson et al. 2003). Also, each of the roughly 1500 original design segments deemed sensitive to liquefaction were reassessed in light of the earthquake experience. One concern was that marginally frozen slopes may have thawed over time, creating increased liquefaction risk. This reassessment is now nearly complete with no unstable areas identified at this time.

The gravel work pad constructed alongside the pipeline for access purposes was designed primarily for short term use during the construction period (Metz 1983). A design objective was to minimize use of hard to obtain gravel materials. In some cases, board stock insulation was used either in the work pad itself or around VSM. The purpose of insulation was to reduce thawing of natural materials to maintain trafficability, while minimizing gravel requirements. It was also used around VSM to minimize active layer depth, decrease jacking loads, and increase lateral load resistance.

Insulation used around VSM has been effective in reducing thaw, but adjacent areas of the uninsulated work pad have settled causing depressions, ponding and limiting access. Maintenance has been required to fill some of the deepest depressions in certain areas.

Pump station facilities were built on permafrost at 5 locations (PS 1, 2, 3, 5, and 6). The remaining pump stations were built on thawed or thaw stable ground. Permafrost pump stations were designed with mechanical refrigeration systems to maintain stability of buildings and piping. Routine survey monitoring is used to determine facility settlement. Settlement of buildings and piping has occurred, in some cases requiring maintenance. Free standing heat pipes have been used to maintain permafrost around buildings.

The most serious challenge for the pump stations has been with the buried annular insulated systems similar to those used on the mainline. Water has penetrated the outer jacket, wetting the insulation and creating corrosion concerns. Nearly all buried insulated facility piping has been excavated and replaced with an "insulated box" system (Johnson 1983). This system uses board stock insulation placed under the pipeline but above the refrigeration piping. Board stock insulation is then placed at the sides of the pipe and the annulus filled with a lean mix concrete grout. Cathodic protection anodes and a CP monitoring system are placed within the grout. Board stock is used to cover the box. This reinsulation system has generally performed well, preventing further thaw settlement and inhibiting corrosion since completion in the early 1980's.

Fuel gas line maintenance

Alyeska operates a 238 km (148 mile) long fuel gas pipeline to provide natural gas fuel for turbines at the four northern pump stations. The line is 10 inch NPS (nominal pipe size, 25.4 cm diameter) for the first 55 km (34 miles) and 8 inch NPS (20.3 cm diameter) for the last 183 km (114 miles). The line was constructed in winter with a snow and ice work pad. It was buried to a depth of 1 meter (36 in) in cold unstable permafrost. Board stock insulation was placed at the estimated active layer depth of 46 cm (18 inches) over the line to help maintain it in a continuously frozen condition at pipe depth.

The gas line is placed adjacent to the Dalton Highway for much of its route. Disturbance of the surface soil during construction combined with dust from the highway has increased surface heat exchange, and caused a deepened active layer in places. Disturbance of drainage paths has caused some erosion and ponding of water over the line. The gas is chilled to -2ºC (28ºF), but chiller upsets have occasionally allowed periods of above freezing gas temperature (0º–20ºC or 32º–68ºF) in the summer.

The overall affect has been a long term deterioration of permafrost in some locations, subsidence of the surface, and thawing to a depth at or below pipe depth in some places. This has resulted in heaving of the line due to thermal expansion, frost jacking during freeze-back and loss of cover over the pipe. However, there has never been a gas line leak from the pipe.

Maintenance activities have consisted of excavation and reburial of the line to repair heaving locations, and/or replacement of fill over the line to restore depth of cover. Maintenance resulting from permafrost degradation has been required on 10%–20% of the line, primarily where it runs next to the Dalton Highway.

Lessons Learned: TAPS and Permafrost

Over 30 years ago the owners of TAPS faced the daunting task of engineering and building a pipeline across the breadth of Alaska under harsh arctic conditions along a route consisting mostly of permafrost. A project of this nature had never before been done. The wisdom of the project was severely questioned at the time, all the way to the President of the United States who authorized it in 1973 only after a tie-breaking vote in Congress. Public expectations were expressed for the highest level of environmental and pipeline safety performance and enforced by strict government agreement and regulation.

The operating history of TAPS now reveals that a warm oil pipeline can be constructed and operated on permafrost. The Trans Alaska Pipeline has been a huge and persistent success over its more than 30 year operating life. It has transported between 10% and 25% of the US domestic crude oil supply, providing a measure of energy security to the people of the United States. It has produced revenues to the State of Alaska to operate the government, generating 80% of the budget, while contributing to a $40 billion Permanent Fund paying annual dividends to Alaska citizens.

Only two pipeline leaks are attributed to permafrost, a 636 cubic meter (4,000 bbl) spill and a 238 cubic meter (1,500 bbl) spill, both occurring in 1979. Careful monitoring and maintenance has been required to mitigate the affects of permafrost hazards. The scale of maintenance attributed to permafrost has been reasonable and manageable, historically estimated to range between 5% and 10% of operating costs. A notable sum, but small compared with the overall benefit generated by the pipeline.

The following lessons regarding TAPS and permafrost are summarized based on the author's experience.

1. The TAPS above-ground design has performed all its functions with relatively minimum maintenance. Its robust and redundant design, built for maintainability, is a beautiful thing in both form and function.
2. The TAPS buried design is more sensitive to permafrost than the above-ground design, requiring comparably more maintenance to address permafrost issues. It is difficult, if not impossible, to find all random pockets of unstable soil using preconstruction boreholes and close construction inspection. Less than 1% of the buried pipeline has required maintenance associated with permafrost subsidence. The advent of inertial instrumented In-Line-Inspection (ILI) tools effectively detects subsidence locations, allowing preventive maintenance to be performed and mitigating subsidence risk.
3. The TAPS special buried, insulated and refrigerated design is maintenance intensive and recommended only as a last resort. Mechanical refrigeration is costly to operate, and buried insulation can not be made reliably waterproof. Wet insulation not only aggravates thaw subsidence, but contributes to corrosion problems which are very difficult to mitigate with cathodic protection. The environmental benefit afforded by this design in facilitating animal migration is questionable.
4. Permafrost related operating hazards require ongoing monitoring and maintenance because the nature and magnitude of the threat is constantly changing over time. An integrity management plan is needed to identify risks, assess condition, and outline permafrost related maintenance options.
5. Any global climate change is not expected to threaten the future operation or integrity of TAPS. Increased maintenance may be expected on above-ground portions, and possibly buried insulated portions especially in marginally frozen southern zones. The above-ground design readily accommodates maintenance and should not experience significantly increased risk. Permafrost risks on buried portions have been largely diminished as thawing has reached its maximum extent.
6. The TAPS fuel gas line provides a small scale view of problems to be anticipated by a larger gas transmission pipeline. More than 10% of the gas line has required permafrost related maintenance attention. The tundra is fragile and is degraded by many construction and operating factors.

Final advice for arctic pipeline engineers is summarized in the words of Dr. Harold Peyton, acclaimed pioneering designer of TAPS: "Engineers must balance the heat flow equation or Mother Nature will do it for them."

Acknowledgments

The authors wish to thank Alyeska Pipeline Service Company for permission to publish this paper and reviewers for their thoughtful comments and suggestions. Additional details of the history and performance of the pipeline can be found on the corporate web site (Alyeska, the Facts 2007).

References

Alyeska Pipeline Service Co. 2007. *The Facts, Trans Alaska Pipeline System,* publicly available at Alyeska-pipe.com.

Ferrell, J.E. & Thomas, H.P. 1988. Remedial Solutions for Pipeline Thaw Settlement. International Conference on Pipeline Infrastructure.

Hall, W.J., Nyman D.J., Johnson, E.R. & Norton, J.D. 2003. Performance of the Trans Alaska Pipeline in the Nov 3, 2002 Denali Fault Earthquake. *6th US Conference on Lifeline Earthquake Engineering.* American Society of Civil Engineers (ASCE) Technical Conference, Long Beach CA.

Hart, J.D., Powell G, Hackney, D. & Zulfiqar, N. 2002. Geometry Monitoring of Trans Alaska Pipeline. *11th International Conference on Cold Regions Engineering,* Anchorage AK.

Johnson, E.R., Metz, M.C. & Hackney, D.A. 2003. Assessment of Below Ground Trans Alaska Pipeline Following the Magnitude 7.9 Denali Fault Earthquake. *6th US Conference on Lifeline Earthquake Engineering.* ASCE Technical Conference, Long Beach CA

Johnson, E.R.. 1983. Performance of the Trans-Alaska Oil Pipeline. *Proceedings of 4th International Conference on Permafrost,* Fairbanks AK. National Academy of Sciences, 109-111.

Metz, M.C. 1983. Pipeline Workpads in Alaska. *Proceedings of 4th International Conference on Permafrost,* Fairbanks AK. National Academy of Sciences, 106-108.

Moubray, J. 1997. *Reliability Centered Maintenance,* 2nd Edition, Industrial Press, Inc.

Norton J.D. & Miller J. 2002. Useful Life of Trans Alaska Pipeline, *11th International Conference on Cold Regions Engineering,* Anchorage AK.

Norton, J.D., Jokela, B., Hass, E. & Dugan, R. 2002. Environmental Impact of 25 years of Trans-Alaska Pipeline Operation. *11th International Conference on Cold Regions Engineering,* Anchorage AK.

Simmons, G.G. & Ferrell, J.F. 1986. Alyeska Reroutes Trans Alaska Pipeline at MP 200. *Proceedings of Fourth International Conference on Cold Regions,* ASCE Anchorage, AK.

Sorensen, S., Smith, J. & Zarling, J. 2002. Thermal Performance of TAPS Heat Pipes with Non Condensable Gas Blockage. *11th International Conference on Cold Regions Engineering,* Anchorage AK.

Tart, R.G. & Ferrell, J.F. 2002. Performance of the Squirrel Creek Slopes on Discontinuous Permafrost. *11th International Conference on Cold Regions Engineering,* Anchorage AK.

Thomas, H.P., Johnson, E.R., Stanley, J.M. & Shuster, J.A. 1982. Pipeline Stabilization at Atigun Pass. *Proceedings of the Third International Conference on Ground Freezing,* Hanover NH.

The Impact of Light-Colored Pavements on Active Layer Dynamics Revealed by Ground-Penetrating Radar Monitoring

Anders Stuhr Jørgensen
Arctic Technology Centre, Department of Civil Engineering, Technical University of Denmark, DK-2800 Kgs. Lyngby, Denmark.

Thomas Ingeman-Nielsen
Arctic Technology Centre, Department of Civil Engineering, Technical University of Denmark, DK-2800 Kgs. Lyngby, Denmark.

Abstract

Ground-penetrating radar (GPR) has been used to study the variations in the depth of the frost table throughout a complete thaw-freeze season at Kangerlussuaq Airport, western Greenland. In autumn 2000, three test areas were painted white on the parking area of the airport in order to reduce further development of depressions in the asphalt pavement. One of these areas has been used in the GPR investigations to compare the variations of the frost table underneath a normal dark asphalt surface to that below a more reflective surface. Results clearly indicate a correlation between the use of the reflective surface and a reduced depth of the frost table. In late summer, the difference in the depths of the frost table is approximately 0.9 m. The results should promote interest in the development and use of light-colored pavement materials.

Keywords: active layer; ground-penetrating radar; permafrost; reflective surface.

Introduction

The presence of permafrost is an important aspect in civil engineering in arctic regions. Thawing of ice-rich permafrost leads to consolidation of the active layer above. The construction of road and airport embankments changes the thermal regime of the ground, and may lead to permafrost degradation under or adjacent to such structures. This problem is now amplified by the effects of climate warming. Mapping the lateral and vertical extent of permafrost as well as actual ice-content is, therefore, an important part of geotechnical site investigations in arctic regions. Ground-penetrating radar (GPR) has proved to be a useful method for mapping the distribution of permafrost (Annan 2002, Annan & Davis 1976, Pilon et al. 1992); especially the frost table is often observed as a strong reflection in the GPR data (Jørgensen & Andreasen 2007, Ingeman-Nielsen 2005, Arcone et al. 1998). Thus, repeated GPR surveys can reveal yearly variations in thickness of the active layer.

Figure 1. Kangerlussuaq Airport. The investigated area is surrounded by the circle.

This paper is based on repeated GPR investigations from May until October 2007 on the southern parking area at Kangerlussuaq Airport, western Greenland (Fig. 1). The objectives of the measurements were to study variations in the depth of the frost table throughout a complete thaw-freeze season and to compare the differences of the depth underneath a normal dark asphalt and a more reflective surface (a white painted area).

Site Description

Kangerlussuaq Airport is built on a river terrace (altitude 30–50 m) at the head of the 170 km long fjord, Kangerlussuaq (Søndre Strømfjord), located just north of the Polar Circle at 67°00′N and 50°42′W. In the western part of the area the terrace is made up of fine-grained glaciomarine sediments partly covered with fluvial deposits of sand and gravel. In the eastern part fine-grained marine deposits are absent.

The climatic conditions at Kangerlusssuaq are arctic continental, determined by its northern location and its position in a 2-3 km wide valley surrounded by mountains (plateau altitude 400–600 m). To the east the Greenlandic ice sheet, with altitudes up to 3 km, has a dominant influence on precipitation and winds. These conditions result in a dry sub-arctic climate with winter temperatures down to -40°C (-40°F) and summer temperatures up to 20°C (68°F). From 1977–99, the mean annual temperature was -5.7°C and the mean annual precipitation was 151 mm (Danish Meteorological Institute 2007). Since the middle of the 1990s the mean annual temperature in Kangerlussuaq has increased to -4.0°C (Fig. 2). Nevertheless, Kangerlussuaq is still underlain by 100-150 m of continuous permafrost (Tatenhove & Olesen 1994). The entire active layer is frozen during the winter, but in late summer the depth of the frost

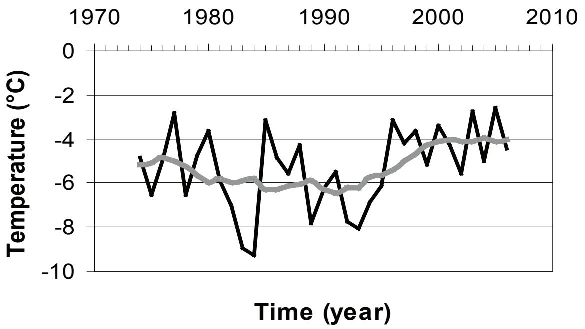

Figure 2. Mean annual air temperature (black) and nine year average temperature (gray) in Kangerlussuaq, 1974-2006 (Danish Meteorological Institute 2007).

table is up to 3.0 m in the open terrain (Ingeman-Nielsen et al. 2007). However, under areas covered with asphalt the depth of the frozen surface is greater, and in some areas this causes melt-water to concentrate under the pavement.

Methodology

In the period from May until October 2007, eight GPR investigations were carried out at the southern parking area of Kangerlussuaq Airport (Fig. 1). In addition, one investigation was carried out in July 2005 and three investigations were carried out in a period from May until August 2006 (Jørgensen & Andreasen 2007, Jørgensen et al. 2007).

GPR systems produce a short pulse of high frequency electromagnetic energy which is transmitted into the ground. The propagation of the signal depends on electrical properties of the ground, which are mainly controlled by the water content of investigated materials. Changes in the dielectric properties will cause a reflection of parts of the transmitted signal, while the rest of the signal will continue to propagate into the ground. Reflection will occur at each successive interface in the ground, until the signal has been damped by losses in the ground. The reflected signal is detected by the GPR receiver, and travel times for individual radar waves can be used to display the results in a radargram, in terms of received amplitude as a function of travel time.

Results from a GPR investigation give insight into the structural changes in the ground but do not directly show the composition or type of the materials investigated. To calibrate the GPR results from Kangerlussuaq Airport, a borehole was drilled and a trench was dug in August 2005.

We applied a GSSI Model SIR-20 with two ground coupled 400 MHz and 900 MHz (GSSI Model 5103 and GSSI Model 3101) antennas. All measurements were conducted along the same profile (Figs. 3A, 3B) with the antennas towed about 3 m behind a car. The GPR profiles were recorded by survey wheel, and traces were collected every 0.05 m (20 traces per meter).

The post-processing included band-pass trace-filtering to reduce electronic and antenna-to-ground coupling noise, spatial filtering to remove coherent background noise, and

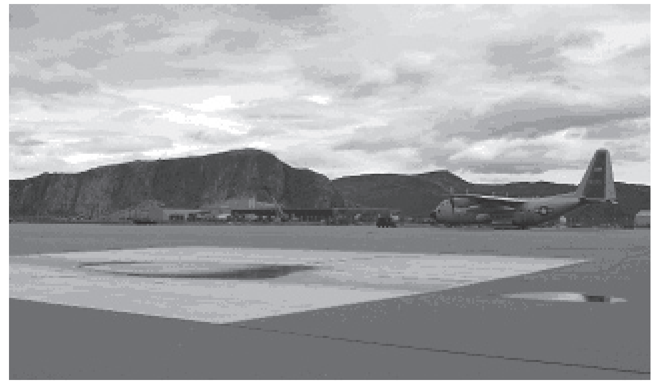

Figure 3A. White painted asphalt surface on the southern parking area of Kangerlussuaq Airport.

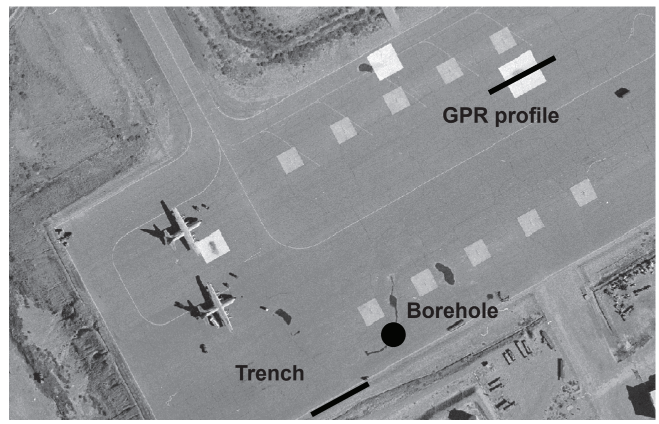

Figure 3B. Placement of GPR measurements across the white painted asphalt surface shown in Figure 3A. The location of the trench and borehole is also shown.

a running average to make a horizontal smoothing of the recorded signal. The processing was carried out using the program ReflexW 3.5 from Sandmeier Scientific Software.

Results

Figure 4 illustrates the difference in the depth of the frost table underneath the normal black asphalt surface and the more reflective surface (white painted area). The variations of the depth of the frost table throughout the thaw-freeze season are illustrated in Figure 5.

According to borehole data from August 2005, top soils were unsaturated and unfrozen until a depth of 3.5 m. The trench revealed a depth of the frost table close to 4.0 m. The velocity of the radar waves in the unfrozen sediments underneath the southern parking area was estimated to be 0.13 m/ns by combining the GPR results with the results from the borehole logs and the trench.

The GPR results (Fig. 5) illustrate the progressive lowering of the frost table. The results also show the effect of the white surface on the depth to the frost table. The fact that the changes in depth to the strong reflection on the radargrams are aligned with the boundaries of the painted area (26 m wide) confirms that this reflection is actually the interface between the frozen and unfrozen ground.

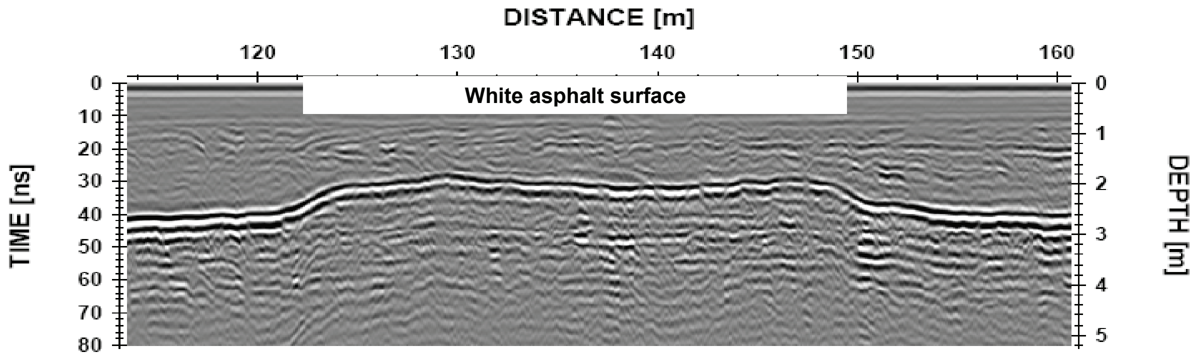

Figure 4. Radargram from July 2007 showing the depth of the frost table. The frost table is seen as a strong reflector in the depth of approximately 2.7 m underneath the normal dark asphalt surface (left and right parts of the radargram) and 2.1 m underneath the white painted area (middle of the radargram).

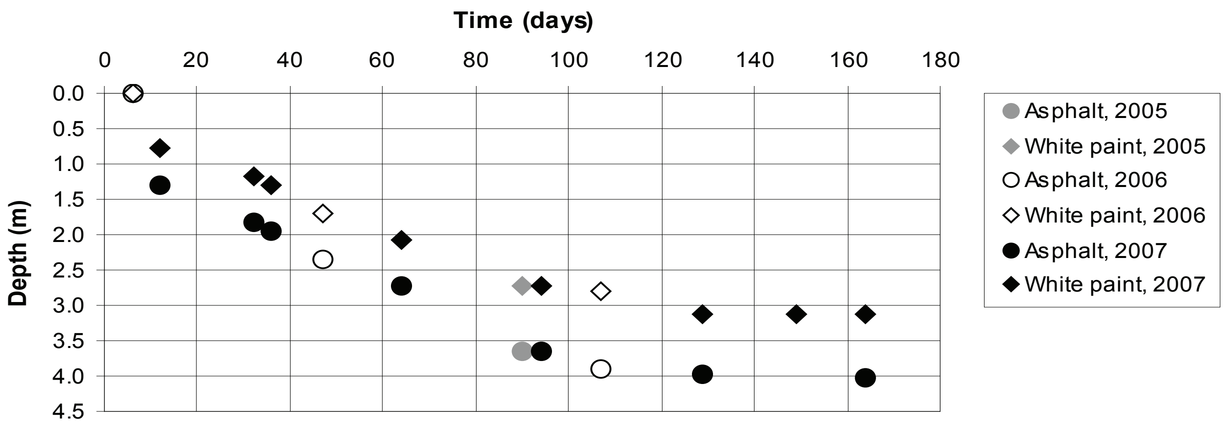

Figure 5. Variations of the depth of the frost table underneath the normal black asphalt surface and the white painted area. The time is shown as number of days from May 1st.

It appears that a stable situation is approached underneath the surfaces between the two measurements carried out in September (Fig. 5). The maximal difference between the depths to the frost table is found as approximately 0.9 m at the end of the thawing period (Fig. 5).

Discussion

We have performed GPR measurements across a reflective surface (white paint) eight times in the period from May until October 2007. The measurements have shown a clear correlation between the use of the reflective surface and a reduced depth to the frost table. At the end of the thawing period the difference in the depths to the frost table is approximately 15 ns.

Based on borehole information, the measured depth of the frost table (procured by the trench excavation) and GPR data collected at the locations of the borehole and the trench in August 2005, the radar wave velocity in the unfrozen sediments was found to be 0.13 m/ns, which corresponds to a permittivity of 5.3. The top soils at the borehole location were unsaturated sorted sand until a depth of 3.5 m with water content in the range of 2%–5% (Jørgensen and Andreasen, 2007). Using a calibration curve empirically determined by Topp et al. (1980) and soil parameters (density 2.70 g/cm^3 and porosity 30%), which is generally used for sandy materials in the area, a permittivity of 5.3 result in a water content of 4.75% for the material. This value lies within the interval of the water content measured in the soil samples from the borehole.

The low water content and well sorted sandy material, which result in a low adherence of the water particles, gives us a situation close to dry conditions and temporal changes in the velocity due to changing pore-water content in the unfrozen sediments were therefore neglected in the present study. An increase in water content will result in an increased permittivity of the material, which will lead to a decreased velocity of the radar waves. A water content of 9.50%, twice the amount of the determined value, would have reduced the maximal difference between the depths to the frost table underneath the two investigated surfaces to approximately 0.2–0.3 m.

Our results have shown that the change in active layer thickness due to the increased reflectivity of surface amounts to approximately 0.9 m in late summer. This constitutes a major difference in the thermal conditions below the reflective surface and the normal dark asphalt surface, and the results should promote interest in the development and use of light-colored pavement materials to reduce settlements under arctic infrastructures caused by the annual thaw-freeze cycle and increasing thickness of the active layer.

Acknowledgments

This research was mainly funded by the Commission for Scientific Research in Greenland (Kalaallit Nunaani ilisimatuutut misissuinernut kommissioni) and partly funded by the Polar Earth Science Program, Office of Polar Programs, National Science Foundation (ARC-0612533).

We would like to thank the Greenlandic Airport Department (Mittarfeqarfiit) for granting us access to the airport area in Kangerlussuaq, and the Municipality of Sisimiut (Sisimiut Kommunianut) for help with accommodation and transportation.

References

Annan, P. 2002. GPR – History, Trends, and Future Developments. *Subsurface Sensing Technologies and Applications* 3(4): 253-270.

Annan, P. & Davis, J. 1976. Impulse radar sounding in permafrost. *Radio Science* 11(4): 383-394.

Arcone, S.A., Lawson, D.E., Delaney, A.J., Strasser, J.C. & Strasser, J.D. 1998. Ground-penetrating radar reflection profiling of groundwater and bedrock in an area of discontinuous permafrost. *Geophysics* 63(5): 1573-1584.

Danish Meteorological Institute 2007. Climate data acquired through www.dmi.dk on August 20, 2007.

Ingeman-Nielsen, T. 2005. *Geophysical Techniques Applied to Permafrost Investigations in Greenland*. Ph.D. Thesis. Technical University of Denmark.

Ingeman-Nielsen, T., Clausen, H. & Foged, N. 2007. Engineering geological and geophysical investigations for road construction in the municipality of Sisimiut, West Greenland. *Proceedings, International Conference on Arctic Roads, Sisimiut, Greenland*: 53-61.

Jørgensen, A.S. & Andreasen, F. 2007. Mapping of permafrost surface using ground-penetrating radar at Kangerlussuaq Airport, western Greenland. *Cold Regions Science and Technology* 48: 64-72.

Jørgensen, A.S., Ingeman-Nielsen, T. & Brock, N. 2007. Annual variations of frost table in Kangerlussuaq Airport, western Greenland. *Proceedings, International Conference on Arctic Roads, Sisimiut, Greenland*: 79-83.

Pilon, J. A., Allard, M. & Levesque, R. 1992. Geotechnical Investigations of Permafrost in Ungava with Ground Penetrating Radar. Innovation & Rehabilitation, *Proceedings of the 45th Canadian Geotechnical Conference*, Canadian Geotechnical Society: 19/1-19/9.

Topp, G.C., Davis, J.L. & Annan, A.P. 1980. Electromagnetic determination of soil water content: measurements in coaxial transmission lines. *Water Resources Research* 16(3): 574-582.

Van Tatenhove, F.G.M. & Olesen, O.B. 1994. Ground Temperature and Related Permafrost Characteristics in West Greenland. *Permafrost and Periglacial Processes* 5: 199-215.

—Plenary Paper—

Thermokarst in Alaska

M. T. Jorgenson
ABR, Inc., Fairbanks, AK 99709
Y. L. Shur
Department of Civil Engineering, University of Alaska Fairbanks
T. E. Osterkamp
Geophysical Institute, University of Alaska Fairbanks

Abstract

Knowledge of the varying surface patterns (landforms), extent, and expansion rate of thermokarst is essential to understanding the response of northern ecosystems to climate change and human impacts. Field studies and airphoto analysis have revealed 22 thermokarst landforms associated with varying heat and mass transfer processes, terrain conditions, and ground ice. These include deep and shallow thermokarst lakes, thaw-lake basins, thaw-lake sinks, thermokarst pits, thermokarst troughs and pits, collapsed pingos, thermokarst shore bogs, thermokarst bogs and fens, thermokarst gullies, thermokarst water tracks, beaded streams, thaw slumps, detachment slides, sink holes and tunnels, glacial thermokarst, collapse-block shores, block landslides, thermokarst conical mounds, irregular mounds, and nonpatterned thawed ground. The extent of permafrost degradation was assessed using airphotos taken across the discontinuous zone, revealing 5% of the area has thermokarst, 62% has permafrost, 21% is unfrozen with no recent permafrost, and 12% remains undetermined. In continuous permafrost of arctic Alaska, thermokarst terrain was evident on 13.5% of the area, and 1.5% was unfrozen under deep non-thermokarst lakes. The rate of degradation based on airphoto analysis at four sites revealed the area affected by thermokarst increased 3.5–8 % over ~50-yr.

Keywords: Alaska; classification; degradation; extent rate; permafrost; thermokarst.

Introduction

Permafrost is an integral component of many northern ecosystems because it supports the ground surface, modifies microtopography, influences soil temperature and moisture, subsurface hydrology, rooting zones, and nutrient cycling (Van Cleve & Viereck 1983, Ford 1987). It is sensitive to climate directly through changes in air temperature, snow cover, or moisture's effects on soil thermal properties, or indirectly from fire frequency or human disturbance with numerous positive and negative feedbacks (Brown and Grave 1979, Osterkamp 1983, Lawson 1986, Esch & Osterkamp 1990, Nelson et al. 2001). Of particular concern for thermokarst, is the warming of permafrost in Alaska by up to 4°C during the last three decades, 2-4°C since the Little Ice Age, and 10°C or more since the end of the Pleistocene (Anisimov & Nelson 1996, Osterkamp 2007). Thawing of ice-rich permafrost can lead to wholesale conversion of ecosystems from terrestrial to aquatic or wetland systems, or conversely cause wetlands to become better-drained (Van Cleve & Viereck 1983, Burn 1998, Osterkamp et al. 2000). In Alaska, 28% of the land has continuous (>90% area), 51% discontinuous, and 8% sporadic/isolated permafrost (Brown et al. 1997).

Where ground ice in fine-grained sediments exceeds the pore space of the soil, thawing of the permafrost can cause the surface to settle or liquefy. The amount of settlement is directly related to the amount and type of ice. These in turn are related to complex interactions of slope position, soil texture, hydrology, and vegetation over time (Shur and Jorgenson 1998). Due to these interactions, the pattern and rate of permafrost degradation can be highly variable. As a result, the nature, extent, and rates of permafrost degradation in Alaska have been poorly quantified.

This paper tries to improve our understanding of thermokarst in Alaska by: (1) classifying and characterizing landforms associated with surface permafrost degradation; (2) estimating the extent of the thermokarst across Alaska, and (3) assessing the rate of degradation in selected areas.

Thermokarst Landforms

Twenty two thermokarst landforms associated with specific processes of permafrost degradation have been identified based on their microtopography and vegetation characteristics (Shur 1977, Jorgenson & Osterkamp 2005, Jorgenson et al. 2007, Shur & Osterkamp 2007). These are discussed below with respect to their distribution, characteristics, processes, and lateral rates of degradation. Terminology is mostly from Everdingen (1998). We focus here on surface changes, yet recognize that permafrost also can degrade from the bottom and that ice-poor permafrost can degrade without creating visible thermokarst.

Thermokarst lakes (alas lakes) are common throughout Alaska (Wallace 1948, Hopkins 1949, Osterkamp et al. 2000, Yoshikawa & Hinzman 2003, Jorgenson et al. 2006) and northern Yukon (Burn & Smith 1990). In Alaska, they are particularly abundant on the Innoko, Koyukuk, and Yukon Flats in central Alaska, on the Seward Peninsula and Yukon-Kuskokwim Delta in western Alaska, the western

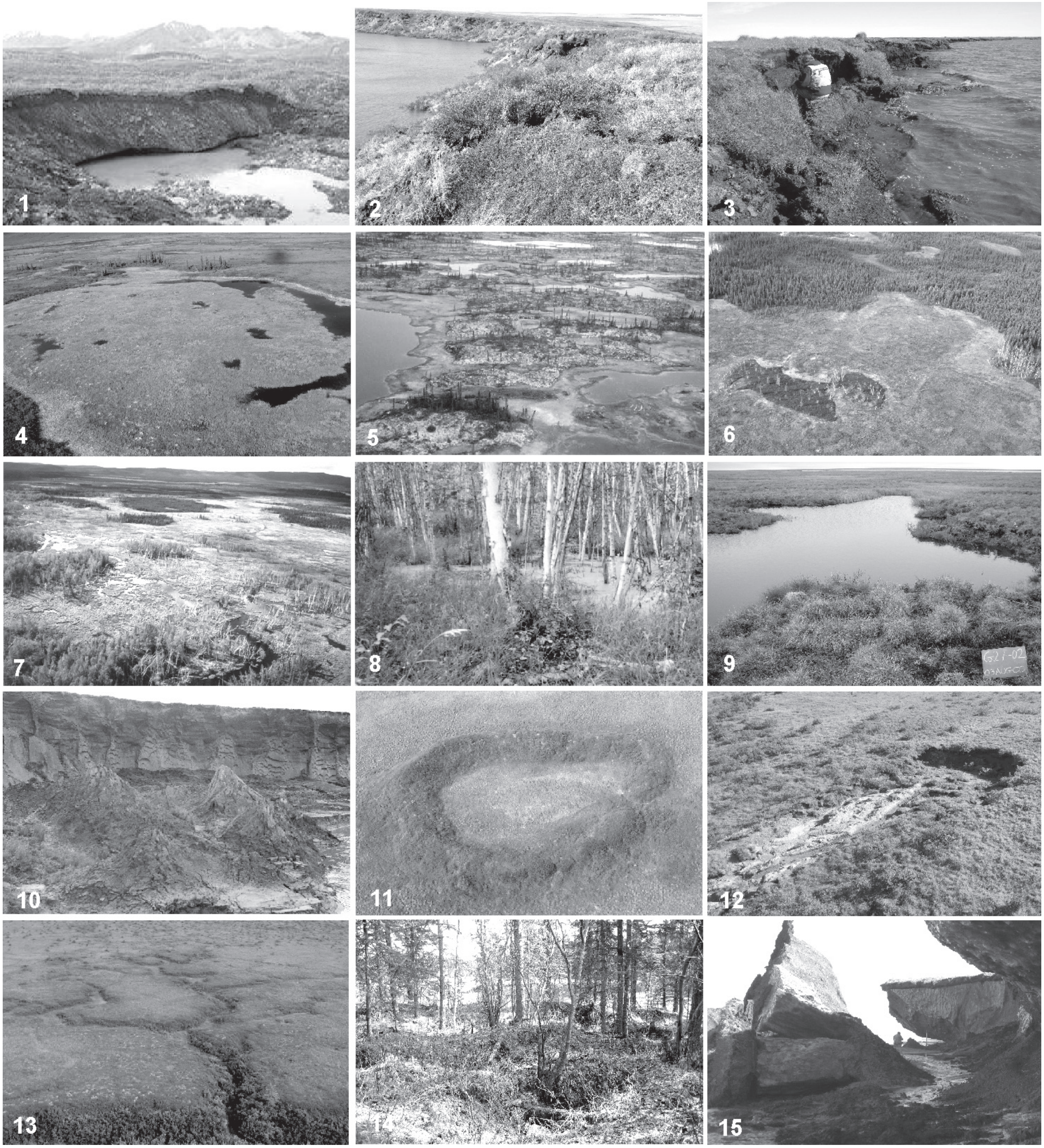

Figure 1. Fifteen thermokarst landforms in Alaska (from left to right on succeeding rows); including: (1) glacial thermokarst on the Muldrow moraine; (2) deep thermokarst lake in yedoma near Cape Espenberg; (3) shallow thermokarst lake near Teshekpuk Lake; (4) thaw-lake basin in Kobuk Valley; (5) thermokarst shore bogs near Innoko River; (6) thermokarst bog in Kobuk Valley; (7) thermokarst fen on Tanana Flats; (8) thermokarst pits on Tanana Flats; (9) polygonal thermokarst trough near Colville Delta; (10) thermokarst conical mounds near Colville River; (11) collapsed pingo near lower Noatak River; (12) thaw slump that started as a detachment slide in Noatak Basin; (13) thermokarst gullies in Kobuk Valley; (14) irregular mounds near Chena River; and (15) collapse blocks undercut by thermo-erosional niche along eroding coast near Cape Halkett.

Beaufort Coastal Plain near Barrow, and the northern Brooks Foothills (Hopkins 1949, Britton 1957, Black 1969, Tedrow 1969, Carter 1988). Permafrost degrades both laterally along the shores, and vertically beneath the water. Rates of lateral degradation range from 0.1 to 2 m/yr depending on ice content, soil texture, and thickness of the surface organic mat, slumping of the banks, and removal of shoreline material by waves. Water depths for shallow thermokarst lakes are typically 1−3 m. Deep thermokarst lakes have water depths >3 m and are classified as a separate thermokarst landform. They typically are found in areas with thick Pleistocene loess deposits, such as at the lower portions of the western Brooks Foothills (Carter 1988) and Seward Peninsula (Hopkins 1949).

Table 1. Thermokarst landforms and processes associated with permafrost degradation.

Landform	Mass Transfer	Heat Source[1]	Hydrologic Regime	Dominant Ice Type	Typical Size	Settlement (m)	Lateral Rate (m/yr)[2]
Deep Thermokarst Lake	Colluvial Waves	Water	Flooded, precip., surface flow	Segregated, ice wedge, other massive ice	1−1000s ha	2–10	0.5−2
Shallow Thermokarst Lake	Waves	Water	Flooded, precip., surface flow	Segregated and wedge ice	1−1000s ha	1–2	0.2−2
Thaw-lake Basin	Colluvial Waves	Water	Drained lake, laterally	Same as above	1−1000s ha	1–10	Banks stabilized
Thaw-lake Sink	None	Water	Drained out bottom	Same as above	1−1000s ha	1–10	Banks stabilized
Thermokarst Pits	None	Still Water	Flooded, precipitation	Ice wedges, thick layered ice	10s of m^2	1–2	na
Thermokarst Troughs and Pits	None	Still Water	Partially flooded, precipitation	Ice wedges	10s of m^2	0.5–2	na
Collapsed Pingo	None	Still Wat., Air	Flooded to drained	Intrusive Ice	ha	3–10	Little after collapse
Thermokarst Bogs	None	Still Water	Saturated by precipitation	Thick layered, Reticulate,	ha	1–2	0.1–0.5
Thermokarst Shore Bogs	None	Still Water	Saturated by precipitation	Thick layered, Reticulate,	ha	1–2	0.1–0.5
Thermokarst Fens	None	Flowing water	Groundwater	Thick layered, Reticulate,	10s of ha	1–2	0.5–1
Thermokarst Water Tracks	None	Flowing Water	Surface flow	Ataxitic, reticulate ice at permafrost surface	100s of m^2	0.2–1	na
Thermokarst Gullies	Fluvial	Flowing Water	Surface flow	Ice wedges	100s of m^2	1–3	na
Beaded Stream	Fluvial	Flowing Water	Surface flow	Ice wedges	ha	1–3	na
Sink Holes and Tunnels	Fluvial	Flowing Water	Groundwater	Ice wedges, cave (tunnel) ice	10s m^2 at surface	Pits 2–5	Little after collapse
Thaw Slumps	Colluvial	Air, Water	Surface flow	Ataxitic, reticulate, ice wedges	100s of m^2	1−5	Highly variable
Detachment Slides	Colluvial	Air	Drained, surface flow	Ataxitic, reticulate,	100s of m^2	0.5–2	Little after slide
Block Landslide	Colluvial	Air	NA	Ice wedges,	100s of m^2	3–10	2−10
Collapse-block Shore	Colluvial Fluvial	Air	Flowing water, waves	Ice wedges	10s of m^2	na	2−10
Conical Thermokarst Mounds	Colluvial	Air	Drained	Ice wedges	10s of m^2	2–5	na
Glacial Thermokarst	Colluvial	Air	Flooded by precipitation	Massive glacial ice	10s of ha	5–30	Highly variable
Irregular Thermokarst Mounds	None	Air	Drained	Lenticular, Reticulate, Ataxitic	m^2	0.2–1	na
Nonpatterned Ground (non-thermokarst)	None	Air	Drained, precipitation	Lenticular, Pore	na	<0.2	na

[1] Direct solar radiation effects not included. Heat is transferred through soil or sediment in most cases; directly to ice in cliff exposures.
[2] Thaw settlement values, and lateral degradation rates are generalized estimates based on limited data.

Thaw-lake basins develop after a thermokarst lake is breached by stream channels and drained (Britton 1957, Jorgenson et al. 2006). A distinct outlet is evident. They are prevalent in the northern boreal forest transition zone and arctic tundra, in contrast to southern thermokarst lakes, which usually paludify with bog vegetation.

Thaw-lake sink is a special type of thaw-lake basin caused by thawing of permafrost below or surrounding a lake, and drainage through subsurface sediments. These lakes may only partially drain and the water level becomes controlled by groundwater (Yoshikawa & Hinzman 2003). They are particularly abundant on abandoned floodplains on the Yukon Flats, where thick, frozen fine-grained overbank deposits overlie alluvial gravels. Once surface deposits thaw and hydrologic connections are made through the underlying gravel, water drains out the bottom.

Thermokarst pits form as small depressions on ice-rich deposits in the discontinuous zone. They often coalesce to form larger bogs and fens. Degradation is primarily vertical from increases in the active layer, and a talik, the unfrozen zone between the seasonally frozen active layer and the permafrost, quickly develops underneath the pits. Thaw settlement typically is 1–3 m and the pits fill with water.

Thermokarst troughs and pits are abundant in northern Alaska (Black 1969, Billings & Peterson 1980, Jorgenson et al. 2006). They form as a result of the degradation of ice wedges, and at an advanced stage, the thawed ice wedges form a polygonal network of water-filled or drained troughs surrounding high-centered polygons. Degradation occurs vertically as the active layer deepens and melts the underlying ice. Settlement generally is 1–2 m, although in areas where water flow through the trough network reinforces the degradation, settlement may reach 3–4 m. During initial stages of ice-wedge degradation, only scattered pits may be evident where they form at ice-wedge intersections. These features are uncommon in boreal regions due to the sporadic occurrence of ice wedges.

Collapsed pingos form by rapid thawing of massive ice in the cores of the pingos. Water is usually impounded in the center of the collapsed pingo and eventually breaches the rim of thawed material. Pingos are common across northern Alaska (Carter & Galloway 1979), but collapsed pingos are rare, except near the lower Noatak River.

Thermokarst bogs are circular depressions that are widespread on flats throughout central Alaska (Drury 1956, Jorgenson et al. 2001). They are associated with ice-rich, fine-grained soils on abandoned floodplains, lowland loess, and sloping retransported deposits. Vegetation is dominated by ombrotrophic Sphagnum and ericaceous shrubs. Bogs slowly degrade laterally at rates of 0.1–0.5 m/yr and thaw settlement typically is 1–3 m (Jorgenson et al. 2001).

Thermokarst shore bogs occur along slowly degrading margins of shallow thermokarst lakes in the boreal forest region (Drury 1956). Shore bogs are considered distinct because the bogs can expand both into the lake and outward toward the collapsing margin. Thus, the lakes may appear to shrink due to paludification even as the adjacent permafrost continues to degrade.

Thermokarst fens occur on flat to gently sloping terrain where groundwater discharges to surface springs, particularly along the northern foot-slopes of the Alaska Range (Racine & Walters 1994, Jorgenson et al. 2001). The fens are associated with degradation of thick-layered ice in silty abandoned floodplains and lowland loess. They form long, linear depressions often associated with birch forests. Vegetation is dominated by minerotrophic herbaceous vegetation (Racine et al. 1998). Degradation is initiated by lateral degradation at rates of 0.5–1 m/yr and thaw settlement typically is 1–3 m and up to 5 m (Jorgenson et al. 2001). Collapse along the margins of the fens forms a distinctive moat with slowly flowing water.

Water tracks are shallow, linear, parallel depressions that form on gently sloping hillsides in areas with continuous permafrost or on toe slopes with retransported deposits in the discontinuous zone. They are formed by the thawing of ice-rich soils near the surface by supra-permafrost groundwater movement. They are not associated with degrading ice wedges.

Thermokarst gullies form when channelized surface-water flow has deepened the active layer and thawed the ice-rich upper permafrost. They are abundant throughout northern and central Alaska. Where water becomes sufficiently channelized on ice-rich soils, gullies 1–5 m deep may develop that include some mechanical soil erosion (Tsuyuzaki et al. 1999). They are typically associated with thawing ice wedges.

Beaded streams are formed by the melting of wedge ice by flowing water in small lowland streams on flat terrain with formation of pools at the intersection of ice-wedges. They are very identifiable features of arctic lowland terrain with distinctive water quality (Oswood et al. 1989).

Sink holes and tunnels (pipes) occur in gently sloping areas where groundwater flow from hillsides encounters ice-rich colluvium and retransported deposits in the valley bottoms (Carey and Woo 2002, Fortier et al. 2007). Groundwater flow can thaw massive ice (Holocene ice wedges or Pleistocene massive ice deposits) at considerable depth. Removal of the ice leads to rapid collapse (days to weeks except in forests where roots can form a supporting structure for years) of the overlying soil and creation of sink holes. The distribution, extent, and mechanism of these features are not well known.

Thaw slumps are caused by the retrogressive thawing of ice-rich permafrost at a steep head-scarp face. Thaw slumps occur throughout northern and central Alaska and northern Canada (Burn & Friele 1989, Brease 1995, Huscroft et al. 2004, Lantuit & Pollard 2005, Kokelj et al. 2005). They occur on gentle to steep slopes. Typically they are initiated by detachment slides. Removal of the active layer exposes permafrost to rapid thawing. After initial degradation, the thawed area often expands laterally upslope along the exposed headwall. While thaw slumps may be limited in extent they can have important consequences on the water quality of downslope lakes and rivers (Kokelj et al. 2005). They are common adjacent to rivers, lakes, and coastlines.

Detachment slides involved the flow or slide of material associated with thawing of the ice-rich intermediate layer, increase in pore pressure in the active layer, and subsequent flow of thawed material (Lewkowicz & Harris 2005). Some slides initially can be limited to the active layer without thawing of ice-rich material at the permafrost surface, in cases where heavy rain has increased the soil moisture content and submerged weight. However, after detachment, thawing of the permafrost ensues. Detachment slides often transform into retrogressive thaw slumps. Slides were numerous in both Alaska and the Yukon after extensive forest fires in 2004 (Lipovsky et al. 2005).

Block landslides are created by the cracking and falling of ice-rich blocks of permafrost from tall, steep faces (Dyke 2000). The fallen or sliding blocks thaw or erode away to maintain a steep cliff face.

Collapse-block shores are associated with shoreline erosion that degrades permafrost soils and is common in northern Alaska along the Beaufort and Chukchi seas (Leffingwell 1919, Reimnitz et al. 1988, Jorgenson & Brown 2005, Mars & Houseknecht 2007). In ice-rich soils, thermo-erosional niches are formed by the thermal and mechanical erosion of ice-rich sediments along riverbanks, lake shores, and coastlines (Leffingwell 1919, Walker & Arnborg 1966). The undercut bluffs often crack off in large blocks. Shoreline retreat often is rapid (m/yr).

Conical thermokarst mounds (baydzherakhs) form from thawing of extremely ice-rich permafrost, where the ice wedges are very old and large (UAS 1959). Soil remaining in the center of polygons thaws and slumps into cone-shape mounds. Mounds often disappear in short time. They are indicative of extremely ice-rich, Pleistocene-age permafrost.

Glacial thermokarst forms highly uneven topography and kettle lakes and is common on ice-cored moraines in the Brooks, Alaska, and Chugach ranges. Numerous kettle lakes of early Holocene age and related to retreat of Wisconsin-era glaciers from their terminal moraines are well known throughout previously glaciated regions. Contemporary kettle lakes form in moraines formed during the Little Ice Age, such as at the terminus of the Muldrow Glacier. Water depths are highly variable, ranging from 5 to 30 m, and the water usually is turbid from slumping banks.

Irregular thermokarst mounds are common throughout lowland forests in central Alaska, although they are often indistinct and easily overlooked. They occur on all types of permafrost terrain where soils are ice-poor or where the active layer thaws sufficiently to equilibrate with changed climatic conditions. Usually, the mounds are 0.2−1 m high and 1−3 m across. Where permafrost persists at depth, the mounds become better drained and the lower-lying hollows become wetter. In warmer areas where permafrost has degraded to deep depths, or been entirely eliminated, all microsites become well-drained.

Nonpatterned thawed ground presumably is common on rocky hillsides, gravelly lowlands (abandoned glacial outwash), or gravelly floodplains, where thawing of ice-poor permafrost results in little to no thaw settlement. Detection is difficult because no surface changes are evident, the rocky soils resist penetration for thaw depth or temperature measurements, and evidence of a previously frozen state is often lacking. Permafrost degradation can still cause large ecological changes because increased subsurface drainage improves soil aeration.

The large variation in landforms associated with surface permafrost degradation is a result of the many complex and interacting factors found across the broad geomorphic environments of Alaska (Jorgenson & Osterkamp 2005, Shur & Osterkamp 2007). These include differing climates and rates of warming, physiography, soil texture, mass and heat transfer processes, hydrology, and ice content and morphology. Fire also has a widespread role because changes to the surface energy balance and soil properties are large and instantaneous (Burn 1998, Hinzman et al. 2001).

Extent

Assessment of the extent of thermokarst features is difficult due to the heterogeneity of ecological responses, diverse spectral characteristics, varying thaw settlement depths, and a wide-range of sizes of thermokarst features, ranging from 1 m^2 to 1000s of ha. To overcome these issues, Jorgenson et al. (2007) used airphoto interpretation and point-sampling on 655 airphotos to determine the abundance of thermokarst features across Alaska (Fig. 2).

Interpretation of 387 airphotos from the discontinuous zone (subarctic climate) revealed that 5% of the area has thermokarst terrain, 62% has permafrost unaffected by thermokarst, and 21% is unfrozen with no recent permafrost (e.g., active floodplains, south-facing slopes). In 11.9% of the area, permafrost status could not be determined (primarily bedrock areas that are thaw-stable). When considering only areas where current or recent permafrost was evident (67%), 7% of permafrost-affected areas have degraded. The most common types of thermokarst included: thermokarst fens (1.8% of total area); thermokarst bogs (1.0%); thermokarst lakes (1.0%); thaw-lake basins (0.3%); glacial thermokarst (0.5%); and thermokarst pits (0.3%) within the subarctic zone.

In the continuous permafrost zone, 13.5% of the terrain showed recent or old (early-mid Holocene) permafrost degradation on 268 airphotos. Common landforms included: thaw-lake basins (7.1 %), deep and shallow thermokarst lakes (1.9 %), thermokarst troughs and pits (2.3 %), thermokarst gullies (1.1%), water tracks (0.7%), and beaded streams (0.4%).

Some commonly described thermokarst features, however, were not encountered by the sampling indicating that overall coverage of the features was negligible. Thaw slumps, detachment slides, and thermokarst gullies were not encountered, although they were evident adjacent to a few sampling points. Conical thermokarst mounds, collapse blocks, and sink holes were not encountered.

While photo-interpretation is effective at identifying distinctive thermokarst features, there are two major types of terrain in which permafrost degradation is particularly

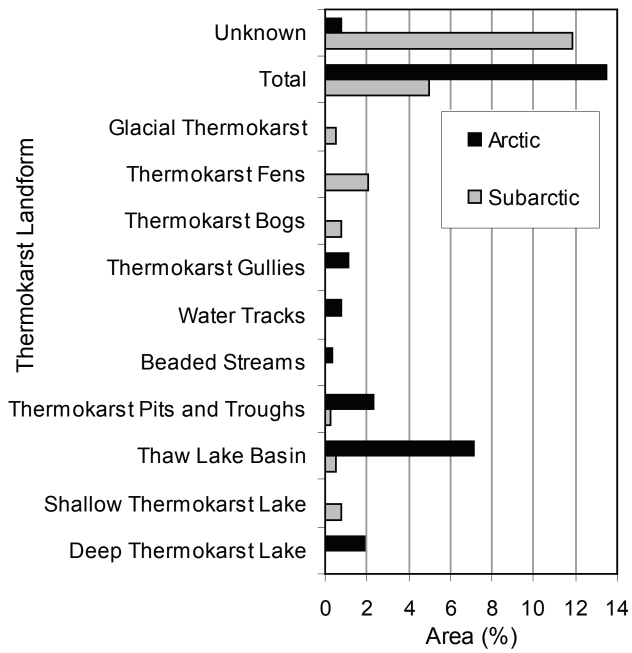

Figure 2. The extent of thermokarst features in arctic and subarctic, Alaska.

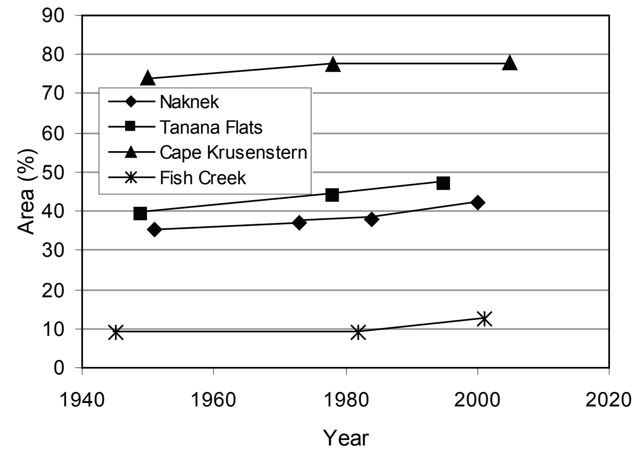

Figure 3. Changes in extent (% area) of thermokarst features from circa 1950 to circa 2000 at four sites in Alaska.

problematic to interpret. First, interpretation of thawing of ice-poor, thaw-stable permafrost is not possible because of the lack of thermokarst. This condition is prevalent in bed-rock controlled upland and alpine terrain in the discontinuous zone. In the discontinuous zone, degradation status of 11.9% of the terrain was unknown because of the lack of surface patterns indicative of thermokarst. Second, determination of thermokarst lakes and thaw-lake basins is problematic because not all lakes and basins in permafrost terrain develop from thawing and collapsing of ice-rich permafrost. In particular, lakes occurring in sand dunes and sheets can occur as simple impoundments in low-lying swales. Ground-ice data from Lawson (1983) and Pullman et al. (2007) show that eolian sand has negligible amounts of excess ice and the terrain is not capable of sufficient thaw settlement for thermokarst-lake formation. In addition, many shallow waterbodies are infilling remnant water in drained-lake basins (Jorgenson and Shur 2007). The photo-interpretation indicated 5.1% of the terrain had lakes, but only 1.9% was classified as thermokarst because a large portion of the Beaufort Coastal Plain is covered by eolian sand and slightly pebbly sand sheets. Areas with lakes interpreted to be thermokarst lakes are limited to extremely ice-rich deposits of limited distribution, such as delta overbank and glaciomarine deposits. The Pleistocene loess deposits in the Brooks Foothills have deep thermokarst lakes, but lakes in this hilly terrain are very limited in extent. Similarly, 7.1% of the basins were classified to be of thermokarst origin, while 7.5% to be of non-thermokarst origin.

Rates

The rate of thermokarst formation has yet to be assessed comprehensively due to the huge area, varying landforms, and lack of sufficient high-resolution imagery. Rates determined for a few areas, however, provide insight into degradation rates over the last half century. Below we provide rates across a climatic gradient from the zone of isolated permafrost, where mean annual air temperatures (MAAT) are 2°C, to the continuous zone, where MAATs are as low as -12°C (Fig. 3).

At Naknek in southwestern Alaska, thermokarst bogs have been developing in glacio-lacustrine deposits that have ice-rich permafrost dominated by layers of thick, clear, horizontal ice. Total area with thermokarst features has increased from 35.5% in 1951 to 42% in 2000 within the 9 km^2 study area. On the Tanana Flats, where thermokarst fens and bogs are abundant on abandoned floodplain deposits, thermokarst terrain has increased from 39% in 1949 to 47% in 1995 (Jorgenson et al. 2001). On the coastal plain near Cape Espenberg, where thermokarst lakes and thermokarst pits and troughs are abundant on eolian silt and thaw-lake deposits, thermokarst terrain has increased from 73.9% in 1950 to 78.1% in 2005. The high percentage of thermokarst terrain was due to the prevalence of old, drained thaw-lake basins. Finally, tundra near Fish Creek, where thermokarst polygonal troughs are common on flat upland terrain and drained lake basins are common on sandy soils in lowland terrain, thermokarst showed little change between 1945 and 1982 (9%), but had expanded to 12.5% in 2001 due to thawing of the top of ice wedges (Jorgenson et al. 2006). Overall, thermokarst terrain increased in percent area by 3.5 to 8%. The Naknek and Fish Creek areas showed more rapid thermokarst from ~1980 to ~2000, compared to the earlier ~1950 to ~1980 period, while Tanana Flats and Cape Espenberg showed more constant rates of increase between the periods.

Conclusions

There is a broad diversity of patterns and processes associated with surface permafrost degradation and its ecological consequences. Twenty-two thermokarst landforms have been identified that vary in relation to climate, geomorphic environments and soil texture, hydrologic regime, ice morphology and content. The extent of thermokarst varies from 5% of the surface area in the discontinuous zone to 13.5% in the continuous zone. The age of thermokarst features remains unknown. Overall, thermokarst terrain increased in percent area by 3.5 to 8% at four sites over a ~50-yr period, and at two of the sites the rate of thermokarst development increased during the last 20-25 yrs relative to the first 20-25 yrs since ~1950. This diversity complicates the analysis and modeling of the response of permafrost to climate change.

Acknowledgments

This research was supported by the Arctic Natural Sciences Program, National Science Foundation (OPP 0454985). We thank Tom George for acquiring the airphotos and for Dorte Dissing's help with GIS. Steve Kokelj and Jim Walters provided many helpful improvements.

References

Anisimov, O.A. & Nelson, F.E. 1996. Permafrost distribution in the northern hemisphere under scenarios of climatic change. *Glob. Planet. Change* 14: 59–72.

Billings, W.D. & Peterson, K.M. 1980. Vegetational change and ice-wedge polygons through the thaw lake cycle in Arctic Alaska. *Arctic Alpine Research* 12(4): 413–432.

Black, R.F. 1969. Thaw depressions and thaw lakes, a review. *Biuletyn Peryglacjalny* 19: 131–150.

Brease, P.F. 1995. Description, character, and rates of movement of the drunken forest slump-earthflow, Denali National Park and Preserve, Alaska (abstract). *Proceedings of Geological Society of America Meeting, 1995.* Geological Society of America.

Britton, M.E. 1957. Vegetation of the Arctic tundra. In: Hansen, H.P. (ed.) *Arctic Biology*: 18th Biology Colloquium, Oregon State Univ. Press, 67–113.

Brown, J., Ferrians, O.J., Heginbottom, J.A. Jr. & Melnikov, E.S. 1997. Circum-Arctic map of permafrost and ground ice conditions. U.S. Geol. Surv., *CP–45*.

Brown, J. & Grave, N.A. 1979. Physical and thermal disturbance and protection of permafrost. U.S. Army CRREL, Hangover, NH. *Spec. Rep. 79–5.* 42 pp.

Burn, C.R. 1998. The response (1958-1997) of permafrost and near-surface ground temperatures to forest fire, Takhini River valley, southern Yukon Territory. *Canadian Journal of Earth Sciences* 35: 184–199.

Burn, C.R. & Friele, P.A. 1989. Geomorphology, vegetation succession, soil characteristics and permafrost in retrogressive thaw slumps near Mayo, Yukon Territory. *Arctic* 42(1): 31–40.

Burn, C.R. & Smith, M.W. 1990. Development of thermokarst lakes during the Holocene at sites near Mayo, Yukon Territory. *Perm. Peri. Proc.* 1: 161–176.

Carey, S.K. & Woo, M. 2002. Hydrogeomorphic relations among soil pipes, flow pathways, and soil detachments within a permafrost hillslope. *Physical Geography* 23(2): 95-114.

Carter, L.D. 1988. Loess and deep thermokarst basins in arctic Alaska. *Proceedings Fifth International Conference on Permafrost, Trondheim, Norway.* Tapir Publishers, 706–711.

Carter, L.D. & Galloway, J.P. 1979. Arctic Coastal Plain pingos in National Petroleum Reserve in Alaska. K. M. Johnson, and J.R. Williams (eds.). *The U.S. Geological Survey in Alaska; accomplishments during 1978, U. S. Geological Survey Circular 804-B.* U.S. Geological Survey, 804-B: B33–B35.

Drury, W.H. 1956. Bog flats and physiographic processes in the upper Kuskokwim River region, Alaska. *Contributions from the Gray Herbarium of Harvard University, No. CLXXVIII*, 130 pp.

Dyke, L.D. 2000. Stability of permafrost slopes in the Mackenzie Valley. In: Dyke, L.D. & Brooks, G.R. (eds.). *The physical environment of the Mackenzie Valley, Northwest Territories: a base line for the assessment of environmental change*. Geological Survey of Canada, Bulletin 547: 177–186.

Esch, D.C. & Osterkamp, T.E. 1990. Cold regions engineering: climatic warming concerns for Alaska. *Journal Cold Regions Engineering* 4: 6–14.

Everdingen, R. van (ed.). 1998. Multi-language glossary of permafrost and related ground-ice terms. National Snow Ice Data Center for Glaciology, Boulder, CO.

Ford, J. & Bedford, B.L. 1987. The hydrology of Alaskan wetlands, USA.: A review. *Arct. Alp. Res.* 19: 209–229.

Fortier, D., Allard, M. & Shur, Y. 2007. Observation of rapid drainage system development by thermal erosion of ice wedges on Bylot Island, Canadian Arctic Archipelago. *Permafrost Periglacial Proc.* 18: 229–243.

Hinzman, L., Yoshikawa, K., Fukuda, M., Romanovsky, V., Petrone, K. & Bolton, W. 2001. Wildfire in the subarctic boreal forests, ecosystem impacts and response to a warming climate. *Tokohu Geophysical Journal* 36(2): 119–131.

Hopkins, D.M. 1949. Thaw lakes and thaw sinks in the Imuruk Lake area, Seward Peninsula, Alaska. *Journal of Geology* 57: 119–131.

Huscroft, C.A., Lipovsky, P.S. & Bond, J.D. 2004. A regional characterization of landslides in the Alaska Highway Corridor, Yukon. Yukon Geol. Surv., Whitehorse. *Open File Rep. 2004–18*, 61 pp.

Jorgenson, M.T., Pullman, E.R. & Shur, Y.L. 2003. Geomorphology of the Northeast Planning Area of the National Petroleum Reserve-Alaska, 2002. Second Annual Report prepared for Phillips Alaska, Inc., Anchorage, AK, by ABR, Inc., Fairbanks, AK, 67 pp.

Jorgenson, M.T. & Osterkamp, T.E. 2005. Response of boreal ecosystems to varying modes of permafrost degradation. *Can. J. Forest Research* 35: 2100–2111.

Jorgenson, M.T. & Shur, Y. 2007. Evolution of lakes and basins in northern Alaska and discussion of the thaw lake cycle. *Journal of Geophysical Research* 112:F02S17, doi 10.1029/2006JF000531.

Jorgenson, M.T. & Brown, J. 2005. Classification of the Alaskan Beaufort sea coast and estimation of sediment and carbon inputs from coastal erosion. *GeoMarine* 482: 32–45.

Jorgenson, M.T., Racine, C.H., Walters, J.C. & Osterkamp, T.E. 2001. Permafrost degradation and ecological changes associated with a warming climate in central Alaska. *Climatic Change* 48: 551–579.

Jorgenson, M.T., Shur, Y. & Pullman, E.R. 2006. Abrupt increase in permafrost degradation in Arctic Alaska. *Geophysical Res. Letters* 33: L02503, 2005GL024960.

Jorgenson, M.T., Shur, Y.L., Osterkamp, T.E. & George, T. 2007. Nature and extent of permafrost degradation in the discontinuous zone of Alaska. *Proceedings of Seventh International Conference on Global Change.* University of Alaska, Fairbanks, AK. pp. 120–125

Kokelj, S.V., Jenkins, R.E., Milburn, D., Burn, C.R. & Snow, N. 2005. The influence of thermokarst disturbance on the water quality of small upland lakes, Mackenzie Delta region, Northwest Territories, Canada. *Permafrost and Perigla. Process.* 16: 343-353.

Lantuit, H. & Pollard, W.H. 2005. Temporal stereo-photogrammetric analysis of retrogressive thaw slumps on Herschel Island, Yukon Territory. *Natural Hazards and Earth System Science* 5: 413-423.

Lawson, D.E. 1983. Ground ice in perenially frozen sediments, northern Alaska. *Proceedings Fourth International Conference on Permafrost.* National Academy Press, Washington, D.C., 695-700.

Lawson, D.E. 1986. Response of permafrost terrain to disturbance: a synthesis of observations from northern Alaska, U.S.A. *Arctic and Alpine Research* 18: 1–17.

Lewkowicz, A.G. & Harris, C. 2005. Frequency and magnitude of active-layer detachment failures in discontinuous and continuous permafrost, northern Canada. *Permafr. Periglacial Proc.* 16(1): 115-130.

Leffingwell, E. de K. 1919. The Canning River region of northern Alaska. U.S. Geol. Surv., Washington, D.C. *Prof. Pap. 109*, 251 pp.

Lipovsky, P.S., Coastes, J., Lewkowicz, A.G. & Trichim, E. 2005. Active-layer detachments following the summer 2004 forest fires near Dawson City, Yukon. *Yukon Exploration and Geology 2005.* Yukon Geological Survey, Whitehorse, Yukon: 175-194.

Mars, J.C. & Houseknecht, D.W. 2007. Quantitative remote sensing study indicates doubling of coastal erosion rate in past 50 yr along a segment of the Arctic coast of Alaska. *Geology* 35: 579–582.

Nelson, F.E., Anisimov, O.E. & Shiklomonov, O.I. 2001. Subsidence risk from thawing permafrost. *Nature* 410: 889–890.

Osterkamp, T.E. 1983. Response of Alaskan permafrost to climate. *Permafrost Fourth International Conference Proc.* National Academy Press, Wash., D.C., 145–152.

Osterkamp, T.E. 2007. Characteristics of the recent warming of permafrost in Alaska. *J. Geophys. Res*. 112, F02S02, doi 10.1029/2006JF000578.

Osterkamp, T.E., Viereck, L., Shur, Y., Jorgenson, M.T., Racine, C., Doyle, A. & Boone, R.D. 2000. Observations of thermokarst and its impact on boreal forests in Alaska, USA. *Arc. Ant.. Alp. Res.* 32: 303–315.

Oswood, M.W., Everett, K.R. & Schell, D.M. 1989. Some physical and chemical characteristics of an arctic beaded stream. *Holarctic Ecology* 12(3): 290-295.

Pullman, E.R., Jorgenson, M.T. & Shur, Y. 2007. Thaw settlement in soils of the Arctic Coastal Plain, Alaska. *Arctic, Antarctic, and Alpine Research* 39(3): 468-476.

Racine, C.H., Jorgenson, M.T. & Walters, J.C. 1998. Thermokarst vegetation in lowland birch forests on the Tanana Flats, Interior Alaska, U.S.A. *Proceedings Seventh International Conference on Permafrost.* Collection Nordicana 57: 927–933.

Racine, C.H. & Walters, J.C. 1994. Groundwater-discharge fens in the Tanana lowlands, Interior Alaska, U.S.A. *Arctic and Alpine Research* 26: 418–426.

Reimnitz, E.S., Graves, M. & Barnes, P.W. 1988. Map showing Beaufort Sea coastal erosion, sediment flux, shoreline evolution, and the erosional shelf profile. U.S. Geol. Surv., Denver, CO. *Misc. Invest. Series Map I-1182-G:* 22

Shur, Y.L. 1977. *Thermokarst*. Moscow: Nedra Publishing House (in Russian).

Shur, Y. & Osterkamp, T.E. 2007. Thermokarst. Institute of Northern Engineering, University of Alaska Fairbanks, Fairbanks, AK. *Rep. INE06*.11, 50 pp.

Shur, Y.L. & Jorgenson, M.T. 1998. Cryostructure development on the floodplain of the Colville River Delta, northern Alaska. *Proceedings Seventh International Conference on Permafrost.* Collection Nordicana 57: 993–1000.

Tedrow, J.C.F. 1969. Thaw lakes, thaw sinks, and soils in northern Alaska. *Biuletyn Peryglacjalny* 20: 337–345.

Tsuyuzaki, S., Ishizaki, T. & Sato T. 1999. Vegetation structure in gullies developed by the melting of ice wedges along Kolyma River, northern Siberia. *Ecological Research* 14: 385–391.

Van Cleve, K. & Viereck, L.A. 1983. A comparison of successional sequences following fire on permafrost-dominated and permafrost-free sites in Interior Alaska. *Proc. Fourth International Conference on Permafrost.* National Acad. Press, Wash.,D.C., 1292–1297.

USSR Academy of Sciences (UAS). 1959. *Fundamentals of Geocryology (Permafrost Science).* Moscow, 431 pp.

Walker, H.J. & Arnborg, L. 1966. Permafrost and ice-wedge effect on riverbank erosion. *Proceedings, Permafrost, International Conference.* National Academy of Sciences, Washington, D.C., 164–171.

Wallace, R.E. 1948. Cave-in lakes in the Nabesna, Chisana, and Tanana River Valleys, eastern Alaska. *Journal of Geology* 56(3): 171–181.

Yoshikawa, K. & Hinzman, L. 2003. Shrinking thermokarst ponds and groundwater dynamics in discontinuous permafrost. *Permafrost Perigla. Proc.* 14: 151–160.

Thermal Processes in the Active Layer of the Larsbreen Rock Glaciers, Central Spitsbergen, Svalbard

Håvard Juliussen
The University Centre in Svalbard (UNIS)
Ole Humlum
Institute of Geosciences, University of Oslo, Norway
Lene Kristensen
The University Centre in Svalbard (UNIS)
Hanne H. Christiansen
The University Centre in Svalbard (UNIS)

Abstract

A recent scientific focus on the thermal regime of openwork blocky deposits has lead to the conclusion that air circulation in the pore spaces and exchange with the atmosphere may be particularly important processes of heat transfer in such materials. This contradicts our data from the coarse openwork active layer of the Larsbreen rock glaciers. Visual observations and temperature data give inconsistent results on air circulation activity at this site, and we conclude that this process seems less important here compared to what is reported from other areas. Other thermal processes at the site, in addition to conduction, include water vapour transport and subsequent sublimation, and meltwater infiltration followed by several refreezing and melting events. More data is needed to understand the complex process pattern in the coarse active layer of these rock glaciers, and further instrumentation is planned as part of the IPY-project 'TSP Norway – Thermal State of Permafrost in Norway and Svalbard.'

Keywords: active layer; coarse debris; heat transfer; non-conductive processes; rock glacier; Svalbard.

Introduction

In openwork blocky debris such as rock glaciers, coarse talus deposits, and block fields, reported mean annual temperatures are often lower than in adjacent finegrained material (Harris & Pedersen 1998, Hanson & Hoelzle 2005). A recent scientific focus has lead to the conclusion that this temperature anomaly is due to air exchange between the blocky debris and the atmosphere and circulation of air within the material (Harris & Pedersen 1998). Circulation could be by free or forced convection (Nield & Bejan 2006). Free convection is driven by temperature-induced density differences of the air and may operate in gravel-sized materials or coarser if the degree of water saturation is less than about 40% (Johansen 1975), while forced convection is driven by pressure gradients as, for example, induced by high wind speeds (Ping et al. 2007). However, the general importance of this process is still largely unknown (cf. Juliussen & Humlum, in press) as many studies consider extreme cases with large pore spaces (Gorbunov et al. 2004) and steep slopes (Delaloye et al. 2003).

In this paper, we identify and discuss thermal processes operating in the coarse openwork active layer of some rock glaciers near the glacier Larsbreen in Svalbard (Fig. 1), based on visual observations from the active layer in Spring 2006 and temperature data from the active layer 2005–06.

Study Site

In Svalbard, low mean annual air temperatures (MAAT) of -5.1 to -7.1°C (1961–1990, ©Norwegian Meteorological Office) result in continuous permafrost except beneath temperate parts of glaciers. The permafrost is typically some tens of meters to 100 m thick in major valley bottoms and close to the sea, but up to 400–500 m thick in the mountains (Humlum et al. 2003).

Rock glaciers are common features in Svalbard (Sollid & Sørbel 1992). At the study site, rock glaciers are creeping out from the talus slope in front of and in a lateral position to the Larsbreen glacier (78°12′N, 15°36′E, 250 m a.s.l.) (Fig. 1). The rock glaciers in front of the glacier were deformed by the glacier advance during the Little Ice Age, but still each individual rock glacier can be traced back to the talus cone from which it is creeping, while the longitudinal furrows separating the rock glaciers are all associated with inter-cone depressions.

In the winter, snow accumulates in the depressions to depths of several meters. The rock glacier fronts, on the other hand, are covered by only a thin and sporadic snow cover. Avalanches are frequent in the study area, and cover the rooting zone of the rock glaciers with snow in the winter. By bringing snow and rock debris to the rock glacier rooting zone, they are probably a driving factor for the rock glacier development at this site (Humlum et al. 2007).

The rock debris in the rock glacier is talus material composed of Tertiary sandstones and shales (Hjelle 1993). Average clast size (b-axis) is 15.0 cm at the surface and 8.5 cm close to the permafrost table, and the clasts are slabby (c:a axial ratio of 0.24 to 0.32 and b:a axial ratio of 0.66 to 0.73, see also Fig. 2). The active layer is openwork, and the pore volume is filled with air in summer and a mix of air

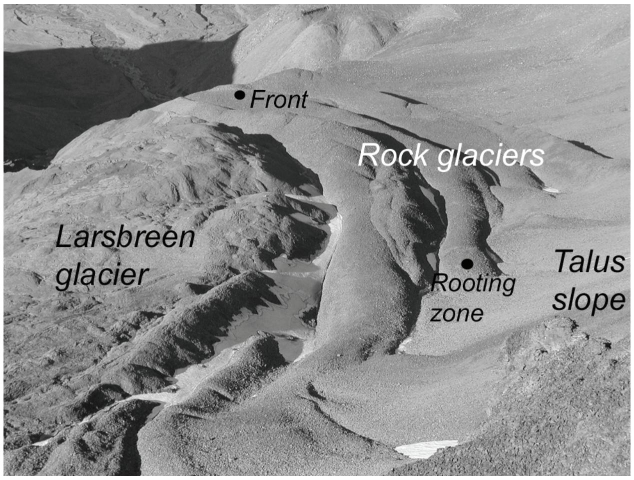

Figure 1. Photo showing the debris-covered front of the Larsbreen glacier, the rock glaciers, and the sites with active layer temperature measurements at the front and at the rooting zone.

and ice in the winter. The active layer is about one meter thick on the rock glaciers, and less than half a meter in the depressions between the rock glaciers.

Methods

Visual observations

The active layer was manually excavated at irregular time intervals during Spring 2006 to visually observe spatial and temporal changes in ice content and the structure of the ice during the melting season.

Temperature measurements

The active layer thermal regime on the rock glacier has been monitored close to the front (at the surface and at depths 0.35 m, 0.70 m, and 0.90 m) since Autumn 1999 and just below the rooting zone (at the surface and at depths 0.30 m, 0.60 m, and 1.15 m) since Summer 2005 (Fig. 1). Air temperature at the site was measured in a 0.15 m high naturally-ventilated stone cairn. Tinytag miniloggers with a precision of ±0.2°C were used both for air and active layer temperature monitoring. Temperature was logged at hourly intervals.

Since active layer temperatures were logged at two sites only, ground surface temperatures below the snow cover were measured manually at irregular time intervals through the winter and Spring 2006 to detect any spatial variability not recorded in the logger series. High spatial variability in winter ground surface temperature may reflect zones with rising and sinking pore air within individual convection cells (e.g., Goering 2002), while low variability would be against a hypothesis of effective, distinct convections cells.

Calculation of Rayleigh numbers

The potential for free air convection in a porous medium can be explored by estimating the Rayleigh number, which determines if heat transfer in a fluid is mainly by convection or conduction (Nield & Bejan 2006). It is given by:

$$Ra = \frac{C\beta gKH\Delta T}{\nu k} \tag{1}$$

where $C, \beta,$ and ν are the volumetric heat capacity, expansion coefficient, and kinematic viscosity of the pore fluid (in this case air); g is gravitational acceleration; K is the intrinsic permeability of the blocky debris layer; H is the thickness of the layer; ΔT is the temperature difference between the top and bottom of the layer (warmer boundary below); and k is the effective thermal conductivity.

Free convection can be expected if the Rayleigh number exceeds a critical value. In the case of closed upper and lower boundaries, such as represented by a continuous snow cover and the permafrost table, respectively, this critical value is $4\pi^2 \approx 40$ (Nield & Bejan 2006). When there is no snow, and the pore volume is open to the atmosphere (open boundary), the critical value is 27 (Serkitjis & Hagentoft 1998).

The Rayleigh number is estimated from the temperatures logged at the front and at the rooting zone. The effective thermal conductivity was estimated with an empirical relationship to porosity n (Johansen 1975):

$$k = 0.039n^{-2.2} \tag{2}$$

A value of 0.3 was used for the porosity. The hydraulic permeability was estimated with the approach of Fair & Hatch (1933), also used by Goering (2002):

$$K = \frac{1}{5}\left[\frac{(1-n)^2}{n^3}\left(\frac{\alpha}{100}\sum\frac{p}{d_m}\right)^2\right]^{-1} \tag{3}$$

where α is a particle shape parameter; p is the percentage of particles held between adjacent size limits; and d_m is the geometric mean size of those limits. These parameters are estimated from clast size measurements. The Rayleigh number estimates are conservative, as a minimum estimate of the hydraulic permeability was used.

Results

Visual observations

Visual observations from the active layer excavations in spring indicated that several types of non-conductive heat transfer processes had operated in the previous winter: infiltration and refreezing of meltwater, and sublimation of water vapour, the latter forming delicate hoar.

Interstitial ice was found in distinct zones, filling the open pore spaces or forming icicles (Fig. 2). Ice accumulations were largest beneath thin snow. Initially, the ice accumulations occurred in distinct zones as extensions of localized meltwater pathways through the snowpack (e.g., Conway & Benedict 1994, Albert et al. 1999). Thus, the ice formed by refreezing of infiltrating surface meltwater reaching the cold active layer. As the melting season progressed, ice accumulations became more widespread. After the snow cover was completely melted, the ice in the active layer started to melt from the surface.

Figure 2. Photos showing icicles and interstitial ice in the pore volume of the active layer. Vertical section of ruler is 17 cm. Photos taken 26.04.2006 (left) and 04.05.2006 (right).

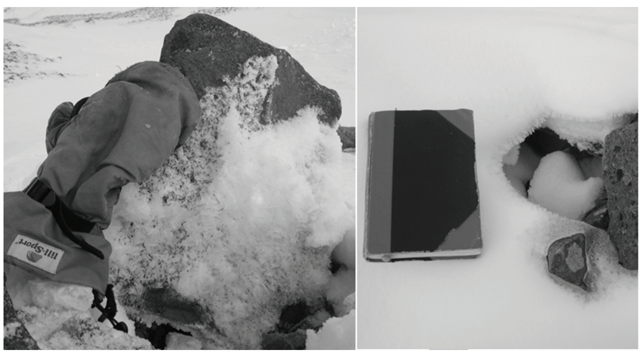

Figure 3. Left panel: Large hoar crystals occupying the pore volume and the base of the tilted block. Glove for scale. Photo taken 24.04.2006. Right panel: Funnel through the snow cover. Note the hoar on the funnel rim. Notebook (width 10cm) for scale. Photo taken 10.05.2006.

Well-developed hoar was found in the upper part of the active layer, in places filling the entire pore volume, and on snow funnel rims (Fig. 3). The hoar crystals were largest and most common near the surface of the rock glaciers where snow was thin or absent and active layer cooling was most effective. Hoar was also superimposed on some of the icicles, but not all, suggesting several episodes, both in the early winter and in the spring, of meltwater infiltration and refreezing. The prevalence of hoar suggests transport of water vapour in the pore volume towards the colder upper part of the active layer and subsequent sublimation.

Funnels through thin snow covers were frequently observed after snowfall (Fig. 3). Funnels indicate exchange of air between the pore volume and the outside (Keller & Gubler 1993).

Active layer temperatures

Average daily temperature in the air (at 15 cm height) and in the active layer at the rock glacier front and at the rooting zone for the period Sept. 2005–June 2006 are given in Figure 4. Active layer freeze-back occurred in the middle of September and was immediate, due to the lack of water in the coarse materials. At the front, negative temperatures prevailed in the active layer until May, and active layer temperatures followed the ambient air temperature throughout the winter. The shift to positive temperatures in May was immediate down to 0.35 m depth, but at 0.70 m depth there was a zero curtain period (stable temperature at 0°C) of about a week. This indicates that the upper 0.35 m was more or less free of ice, while some ice existed deeper in the active layer that required energy to melt before the temperature could switch to positive values.

At the rooting zone, the temperatures followed the air temperature until the onset of December, when the site was covered with avalanche snow. For the rest of the winter, the active layer temperatures followed only the main trends in the air temperature as high-frequency fluctuations were masked by the snow. The temperature curves from both sites show several episodes of sudden temperature increase, indicating meltwater infiltration and refreezing during the winter season, forming the observed ice accumulations (Fig. 2). These episodes occurred in periods of warm weather in the autumn, in January during an unusually warm and wet period, and in the spring melt season. In May and June, a snowmelt and zero curtain period of at least one month delayed active layer warming at the rooting zone. The zero curtain period started more or less at the same time at all depths, reflecting the abrupt nature of the infiltration process. The zero curtain period was significantly longer at 1.15 m depth, reflecting that melting occurs from the surface only and possibly indicating a higher ice content than at shallower depths.

The estimated Rayleigh numbers are also given in Figure 4. Since the Rayleigh number is a function of the active layer temperature gradient, it fluctuated in rhythm with the active layer temperatures through the winter. At the front, the theoretical critical Rayleigh number (open boundary) was frequently exceeded, indicating possible episodes of free convection at this site. The estimated Rayleigh numbers for the period 2000–2005 were of comparable size (not shown).

At the rooting zone, the Rayleigh number fluctuated in rhythm with that at the front and with the ambient air temperature, with the highest values well above the critical value (open boundary), until the site was covered by avalanche snow. Below avalanche snow, the Rayleigh number increased to a maximum just above the critical value (closed boundary) and showed less fluctuation than at the snow-free site. Keeping in mind that the Rayleigh number estimate was conservative, there is a potential for free convection also at this site.

Ground surface temperatures (GST)

The manually measured ground surface temperatures are displayed in Figure 5 as average values for each date with one standard deviation. Between 7 and 22 measurements were made at each visit. Continuous ground surface temperature measurements at two sites within 20–30 m from the rooting zone profile are also given (GST1 and GST2), along with the surface temperatures at the rooting zone and air temperature. The standard deviation of the manual measurements was mostly below 1°C, even when Rayleigh number estimates show a potential for convection. This suggests that there were no highly effective convection cells. Moreover, the temporal evolution of the ground surface temperatures was

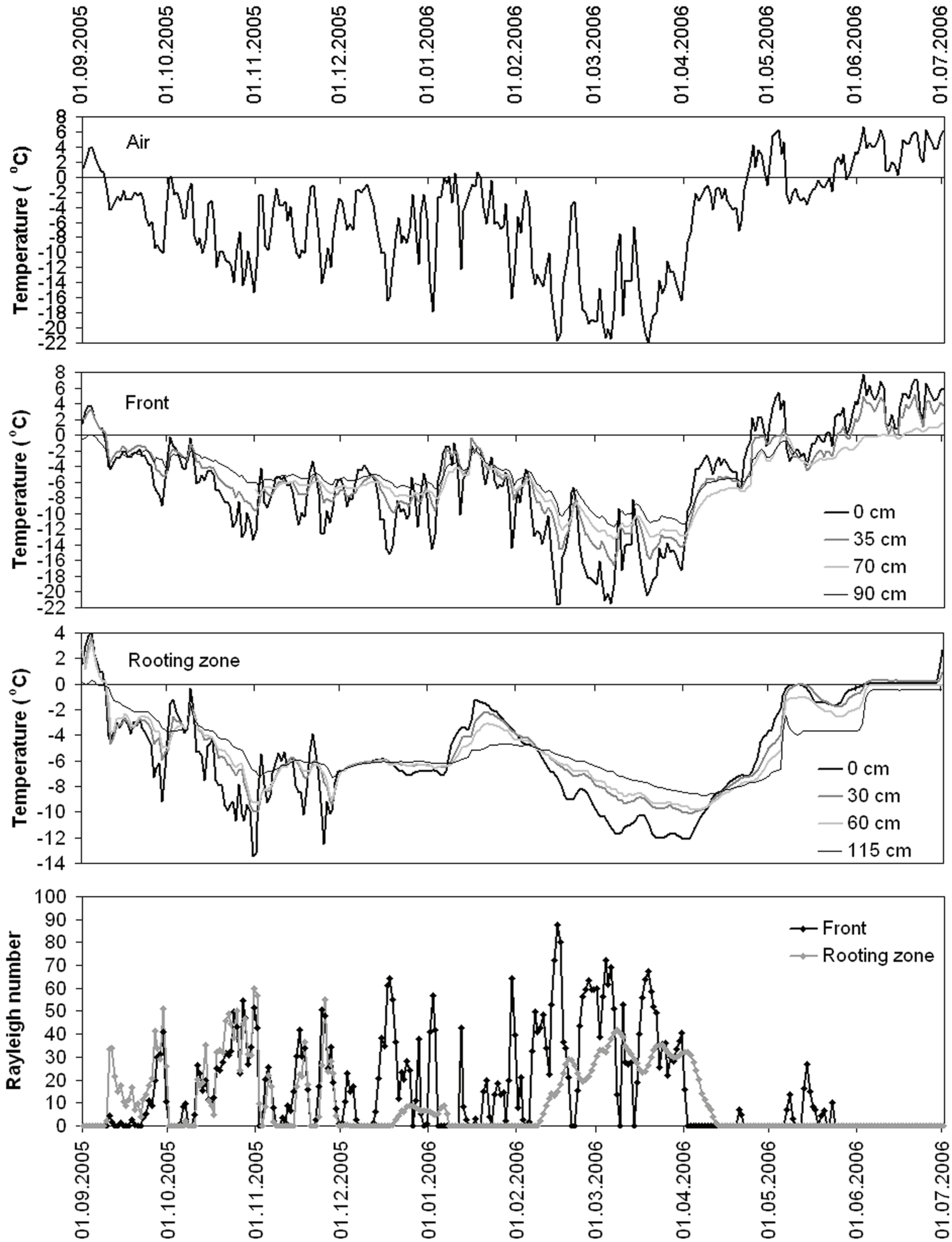

Figure 4. Daily air temperatures (at 15 cm height), active layer temperatures and estimated Rayleigh numbers at the front and at the rooting zone for the period Sept. 2005 – June 2006.

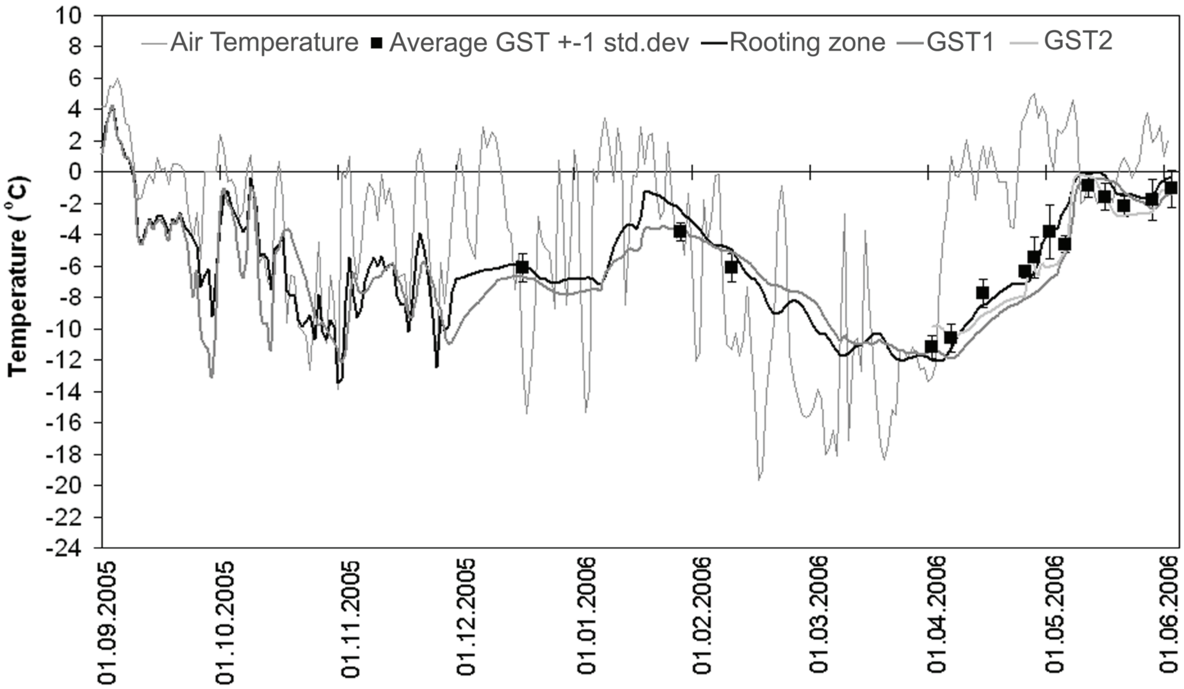

Figure 5. Average GST ± one standard deviation, based on measurement campaigns at irregular time intervals. Continuous ground surface temperatures at two sites with thick snow (GST1 and GST2), surface temperature at the rooting zone and air temperature (official temperatures from Svalbard airport, provided by the Norwegian Meteorological Office) are also given. GST2 starts on April 1.

the result of heat conduction through snow, as shown by snow temperature measurements, rather than by circulation of pore air in the active layer. The highest spatial variability in manually measured ground surface temperatures was due to a differential snowmelt pattern.

Discussion

Considering air convection in the active layer, the Rayleigh number and the spatially distributed GST revealed inconsistent results. While convection should be expected according to the Rayleigh number, both under open and closed boundary situations, no distinct convection cells were identified in the GST data. Funnels indicate that air exchange with the atmosphere is operating where the snow cover is thin (<10 cm). No funnels were found in thick snow covers. A possible explanation for the discrepancy between the Rayleigh number estimate and the GST data could be that the convection process is less efficient than described by e.g., Goering (2002), so that it is not detected in the spatially distributed GST data. Preservation of the delicate hoar supports that. The convection process may, perhaps, rather be viewed as a series of releases of 'heat bubbles' as described by Hanson & Hoelzle (2004), having negligible influence on the thermal regime. Instead, conduction is probably the main thermal process (cf. Gruber & Hoelzle 2008).

The presence of hoar in the upper part of the active layer indicates transport of water vapour and subsequent sublimation. Transport of water vapour may be by diffusion or air convection. Test measurements of relative humidity in the active layer pore volume, show saturated conditions for most of the winter, except for three shorter periods totalling 11–12 days, when the relative humidity decreases to 93–98% in the upper 0.35 m. Some upward vapour diffusion can be expected, at least during these periods, but it is at present not known to which degree this process can explain the amount of hoar in the upper part of the active layer. The drops in relative humidity nicely give the timing of air exchange between the pore volume and the atmosphere.

As the snow melts in spring, meltwater infiltrates the highly permeable active layer. The (initially small amount of) meltwater will first refreeze close to the surface in the active layer due to the cold content of the active layer. The observed icicles and extensions of meltwater pathways through the snow pack (Fig. 2) are formed in this way. As more meltwater is released and the cold content of the active layer decreases, the meltwater may infiltrate deeper into the active layer and eventually reach the base of the active layer, where it refreezes due to the colder permafrost below. Sawada et al. (2003) measured an accumulation of about 0.2 m of ice in only a few days in a block slope in Japan. This ice requires energy to melt and further delays active layer development (cf. Woo & Xia 1996).

Other processes, such as wind-forced convection (Humlum 1997) and heat radiation (Johansen 1975), may also be important for the thermal regime of coarse-grained active layers. Lack of relevant data precluded a discussion of these processes here.

Further studies are planned at the site as part of the IPY-project "TSP Norway—Thermal State of Permafrost in Norway and Svalbard." This involves an attempt to measure relevant energy fluxes (cf. Smith & Burn 1987, Rist & Phillips 2005).

Conclusions

Heat transfer processes in the coarse-grained active layer of the Larsbreen rock glaciers in Svalbard have been discussed based on visual observations of ice in the active layer and temperature data. The following conclusions can be drawn:

- Considering air convection in the active layer, the Rayleigh number and the spatially distributed GST data reveal inconsistent results. Convection of air in the pore volume of blocky debris seems less important here compared to what is reported from other areas. Winter air exchange between the pore volume of the blocky layer and the atmosphere may operate through snow covers thinner than about 10 cm.
- Hoar in the upper part of the active layer indicates transport of water vapour, by diffusion or air convection, and subsequent sublimation.
- Water from snowmelt infiltrates and refreezes in the active layer. Melting of this ice delays active layer development.

References

Albert, M., Koh, G. & Perron, F. 1999. Radar Investigations of Meltwater Pathways in a Natural Snowpack. *Hydrological Processes* 13: 2991-3000.

Conway, H. & Benedict, R. 1994. Infiltration of Water into Snow. *Water Resources Research* 30: 641-649.

Delaloye, R., Reynard, E., Lambiel, C., Marescot, L. & Monnet, R. 2003. Thermal Anomaly in a Cold Scree Slope (Creux du Van, Switzerland). *Proceedings of the Eighth International Conference on Permafrost, Zürich, Switzerland, July 21–25, 2003*: 175-180.

Fair, G.M. & Hatch, L.P. 1933. Fundamental Factors Governing the Streamline Flow of Water through Sand. *Jour. American Water Works Assoc.* 25: 1551-1565.

Goering, D.J. 2002. Convective Cooling in Open Rock Embankments. *Cold Regions Engineering*: 629–644.

Gorbunov, A.P., Marchenko, S.S. & Severskiy, E.V. 2004. The Thermal Environment of Blocky Materials in The Mountains of Central Asia. *Permafrost and Periglacial Processes* 15: 95-98.

Gruber, S. & Hoelzle, M. 2008. The Cooling Effect of Coarse Blocks Revisited. *Proceedings of the Ninth International Conference on Permafrost, Fairbanks, Alaska, June 29- July 3, 2008* (this proceedings).

Hanson, S. & Hoelzle, M. 2004. The Thermal Regime of the Active Layer at the Murtèl Rock Glacier Based on Data from 2002. *Permafrost and Periglacial Processes* 15: 273-282.

Hanson, S. & Hoelzle, M. 2005. Installation of a Shallow Borehole Network and Monitoring of the Ground Thermal Regime of a High Alpine Discontinuous Permafrost Environment, Eastern Swiss Alps. *Norwegian Journal of Geography* 59: 84-93.

Harris, S.A. & Pedersen, D.E. 1998. Thermal Regimes beneath Coarse Blocky Materials. *Permafrost and Periglacial Processes* 9: 107-120.

Hjelle, A. 1993. *Geology of Svalbard*. Oslo: Norsk Polar-Institutt. 162 pp.

Humlum, O. 1997. Active Layer Thermal Regime at Three Rock Glaciers in Greenland. *Permafrost and Periglacial Processes* 8: 383-408.

Humlum, O., Instanes, A. & Sollid, J.L. 2003. Permafrost in Svalbard: a Review of Research History, Climatic Background and Engineering Challenges. *Polar Research* 22: 191-215.

Humlum, O., Christiansen, H.H. & Juliussen, H. (2007). Avalanche-derived Rock Glaciers in Svalbard. *Permafrost and Periglacial Processes* 18(1)*:* 75-88.

Johansen, Ø. 1975. *Varmeledningsevne av jordarter. (Thermal Conductivity of Soils),* Trondheim: NTH (Norw. Tech. Univ.) Licentiat-Thesis. 231 pp. (in Norwegian).

Juliussen, H. & Humlum, O. In press. Thermal Regime of Openwork Block Fields on the Mountains Elgåhogna and Sølen, central-eastern Norway. *Permafrost and Periglacial Processes* 19(1).

Keller, F. & Gubler, H. 1993. Interaction between Snow Cover and High Mountain Permafrost, Murtel-Corvatsch, Swiss Alps. *Proceedings of the Sixth International Conference on Permafrost, Beijing*, 332-337.

Nield, D.A. & Bejan, A. 2006. *Convection in Porous Media*. New York: Springer Science and Business Media Inc, 640 pp.

Ping, H., Zhao, Z., Guodong, C. & Hui. B. 2007. Ventilation Properties of Blocky Stones Embankments. *Cold Regions Science and Technology* 47(3): 271-275.

Rist, A. & Phillips, M. 2005. First Results of Investigations on Hydrothermal Processes within the Active Layer above Alpine Permafrost in Steep Terrain. *Norwegian Journal of Geography* 59(2): 177-183.

Sawada, Y., Ishikawa, M. & Ono, Y. 2003. Thermal Regime of Sporadic Permafrost in a Block Slope on Mt. Nishi-Nupukaushinupuri, Hokkaido Island, Northern Japan. *Geomorphology* 52, 121-130.

Serkitjis, M. & Hagentoft, C.E. 1998. The Influence of Natural Convection on the Heat Transfer in an Air Filled Porous Medium Bounded by an Air Layer. *Nordic Journal of Builduing Physics* 1: 1-24.

Smith, M.W. & Burn, C.R. 1987. Outward Flux of Vapour from Frozen Soils at Mayo, Yukon, Canada: Results and Interpretation. *Cold Regions Science and Technology* 13: 143-152

Sollid, J.L. & Sørbel, L. 1992. Rock glaciers in Svalbard and Norway. *Permafrost and Periglacial Processes* 3: 215-220.

Woo, M. & Xia, Z. 1996. Effects of Hydrology on the Thermal Conditions of the Active Layer. *Nordic Hydrology* 27: 129-142.

Water Balance for a Low-Gradient Watershed in Northern Alaska

Douglas L. Kane
Water and Environmental Research Center, University of Alaska Fairbanks, USA
Robert E. Gieck
Water and Environmental Research Center, University of Alaska Fairbanks, USA
Larry D. Hinzman
International Arctic Research Center, University of Alaska Fairbanks, USA

Abstract

Water balance computations are a tool for developing a better understanding of hydrologic processes and their interaction for all types of environments. In this case study, water balance computations are carried out for an Arctic watershed characterized by continuous permafrost, lack of trees, low hydraulic gradient, negative mean annual temperature, and a snow cover for eight to nine months. The Putuligayuk River is a north draining river that drains 471 km^2 and empties into the Arctic Ocean. The snowmelt event, in late May or early June, is the major hydrologic runoff event of the year that results in 80% of the snowpack leaving the basin as surface flow. During the summer months, evapotranspiration (ET) exceeds precipitation with 60% of rainfall precipitation leaving the basin as ET and 40% as runoff. Annually, 60% leaves as runoff and 40% as ET.

Keywords: Arctic; evapotranspiration; continuous permafrost; precipitation; runoff; surface storage; water balance.

Introduction

It is abundantly clear that the Arctic is undergoing change from permafrost warming (Lachenbruch & Marshall 1986) to glacier mass wasting (Arendt et al. 2002), to snow cover reduction (Robinson et al. 1993), to reduction in sea ice extent (Maslanik et al. 1999, Vinnikov et al. 1999), to increasing shrub abundance (Sturm et al. 2001), to later freeze-up and earlier break-up (Magnuson et al. 2000), to many other changes (Hinzman et al. 2005). Hinzman et al. (2005) summarizes numerous kinds of evidence of environmental change, what the climatic drivers are and what are the implications. During this environmental change, hydrologist struggle with quantifying various hydrologic fluxes to improve our understanding of the Arctic hydrologic cycle with methods prone to error and considerable year-to-year natural variability. Water balance computation, generally at the small watershed scale, is one tool used to advance our knowledge of Arctic hydrology (Kane & Yang 2004). Unfortunately these studies are of short duration (no trends observed) and only at the small catchment scale (~400 km^2 or smaller).

Both the domestic and industrial demand for water and the impact that climate change is having on the hydrologic cycle in the Arctic warrants that we improve our hydrologic understanding. The number of hydrologic stations in the Arctic is quite low, the longevity of these stations is relatively short (except in Russia), and most stations are located at low elevations along the coasts or major drainages. Since 1999, we have been monitoring the runoff from the Putuligayuk River, including other complementary hydrologic and meteorological data. Reported here is the seasonal water balance for this 471 km^2 low-gradient catchment (Fig. 1) draining into the Arctic Ocean.

Setting

The Putuligayuk River (Fig. 1) is part of a nested watershed study (Kane et al. 2000) on the North Slope of Alaska that drains an area south of the Prudhoe Bay oil field

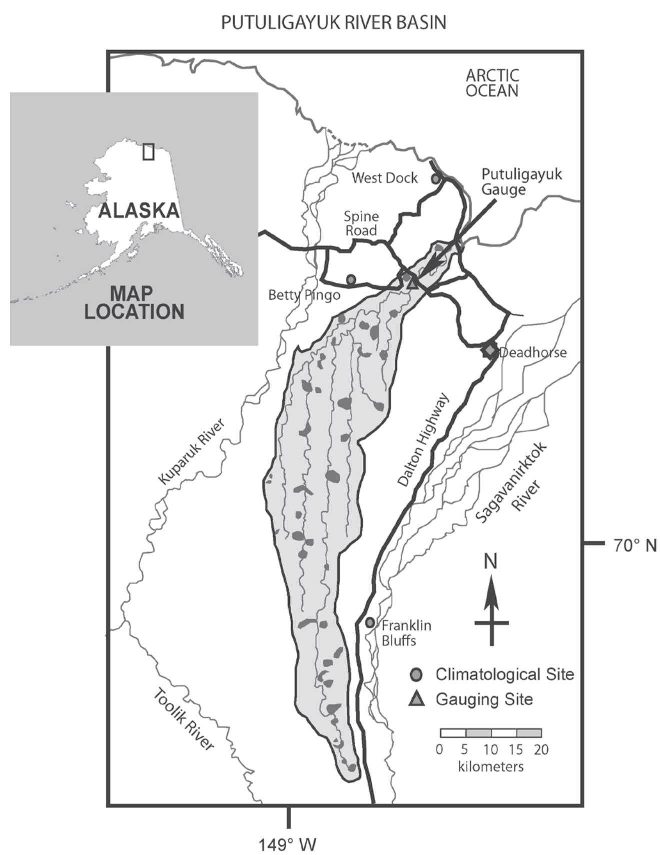

Figure 1. Location map of the north–draining Putuligayuk watershed on the North Slope of Alaska.

before flowing northward through the middle of the field and into the Arctic Ocean. It is a patchwork of lakes, drained lakes, and numerous other permafrost features such as high and low centered polygons, pingos, strangmoor ridges, frost boils, and hummocky terrain. This is an area of continuous permafrost with a maximum measured depth of 600 m, treeless and mostly vegetated with sedges with some shrubs in riparian areas. The elevation at the top of the watershed is 109 m and at the gauging site, 7 m. The active layer is typically around 35 to 55 cm at summer's end (Hinzman et al. 1998) and is composed of surficial organic soils (~20 cm although quite variable) over mineral soils.

Flow ceases in this basin during the winter months with breakup occurring in late May or the first two weeks in June, just prior to the summer solstice. The snowmelt breakup is the biggest runoff event of the year; this is substantiated by the U.S. Geological Survey, which first gauged this stream from 1971 through 1986 (1980 and 1981 missing). Little or no other complementary data were collected during this gauging period. For the past few years, snowfall precipitation has averaged about 40% of the annual precipitation. Redistribution by wind is a major component of the hydrologic cycle of this region. Elevational depressions (drainages, drained lakes, ponds, etc.) are depositional areas for blowing snow, and exposed areas are eroded. Snow damming in the river and smaller drainages (including lake outlets) delays the runoff event by several days; typically the tundra snowcover is almost completely absent before any runoff of significance is measured at the gauge.

During the summer months, evapotranspiration exceeds precipitation. This means that the surface storage of water in the ponds, wetlands and lakes decreases over the summer. Some late summer precipitation may replenish some of this deficit; however, most of the deficit will be made up during the following spring break-up (Bowling et al. 2003). In the summer, as the watershed dries out, the drainage network becomes fragmented. This explains why there is minimal runoff response during the summer months to precipitation, although it comprises 60% of annual precipitation.

Methods

Since 1999, we have been collecting hydrologic and meteorological data on the central coastal plain on the North Slope of Alaska in the near vicinity of the Arctic Ocean. One objective of this data was to perform a water balance determination of a low-gradient watershed that is in an area of continuous permafrost. The three main features of the water balance equation are the input (P), changes in various storage terms (ΔS), and outputs (ET and R); if we ignore storage terms, this equation can be simplified to:

$$P - ET - R \pm \Delta S = \eta \qquad (1)$$

where

P = precipitation, both snowfall and rainfall (possibly condensation)
ET = evapotranspiration (possibly sublimation)
R = discharge throughout the entire period of flow
ΔS = Change in surface storage
η = error term on closure

Summer liquid precipitation gauges exist at three sites (Fig. 1) immediately adjacent the Putuligayuk catchment: at Franklin Bluffs, Betty Pingo and West Dock. In addition there are meteorological measurements at each of these sites that collect 10 m profiles of air temperature, relative humidity and wind speed profiles; incoming and outgoing long- and short-wave and net radiation fluxes, wind direction, soil temperature, barometric pressure, and soil moisture data are also measured. Snow surveys of snow water equivalent (SWE) on the ground are carried out the last week of April. For the Putuligayuk catchment there are several measurements sites (number varied from year to year) where 50 snow depth and 5 density measurements are made at each site to get an estimate of the average SWE for that area.

The Putuligayuk River is gauged on the Prudhoe Bay oilfield where it crosses the Spine Road. A stage-discharge relationship has been developed with the stage being measured continuously during the warm summer season with both a float-type water level recorder and a pressure transducer, both located in a stilling well in the center of the river. During break-up the stage-discharge relationship is not reliable as there is some ice and considerable wind redistributed snow in the channel that slowly erodes as flows increase during the ablation season. Snow damming, both at the outlet of lakes and in the river channel, is an important hydrologic process as it delays the runoff response by several days. Typically, most of the shallow snow cover on the tundra disappears before the runoff has increased significantly (initially there is some local runoff along the roadway). The flow is gauged each day during the breakup once the flow seriously starts to increase. Once the flow starts to significantly increase during ablation, the flow continues to increase and peak even if a cold period sets in (Bowling et al. 2003). Historically, there are several years of stream gauging data as this site was operated from 1970 to 1979 and 1982 to 1986 by the U.S. Geological Survey. From the work by Bowling et al. (2003), it is clear that meltwater from the snowpack is responsible for recharging the copious number of lakes in the catchment and also producing the observed runoff. The flow gradually recedes over the summer with only small peaks in response to summer precipitation.

Studies carried out by researchers associated with the Water and Environmental Research Center at the University of Alaska (Rovansek et al. 1996, Mendez et al. 1998, Bowling et al. 2003) have demonstrated that in this part of the Arctic, it is common for summer evapotranspiration (ET) to exceed precipitation. Therefore a drying of the watershed (shrinkage of wetlands, ponds, and lakes) and fragmentation of the drainage network takes place during the summer. Meteorological data are collected so estimates of ET can be made over the basin as reported on by several groups working in the area (Kane et al. 1990, Rovansek et al. 1996, Mendez et al. 1998). Shutov et al. (2006) also presents methods conveniently adapted for calculating evaporation when detailed information on the hydrology and meteorology is missing.

Here we are going to use the Priestley-Taylor (Priestley & Taylor 1972) method to estimate the catchment ET:

$$-Q_e = \alpha(\Delta/(\Delta + \gamma))\ (Q_{net} + Q_g) \quad (2)$$

where

α = empirical parameter elating actual and equilibrium evaporation
Δ = slope of saturated pressure curve
γ = psychometric constant
Q_{net} = net radiation
Q_g = ground heat flux
Q_e = latent heat flux

The amount of water lost over the catchment from the watershed is equal to:

$$ET = Q_e/(\rho_w * \lambda) \quad (3)$$

where

ET = evapotranspiration
ρ_w = density of water
λ = latent heat of vaporization

The value of α varies with both space and time (Mendez et al. 1998); it was highest for lakes, intermediate for wetlands, and lowest for uplands; for wetlands and uplands it decreases during the summer.

It is very difficult to make field estimates of storage changes in this watershed at the seasonal or annual time scale. The numerous lakes, ponds, and wetlands represent a distributed storage reservoir for both rainfall and snowmelt. The amount of snowmelt water stored in a watershed each spring depends upon the ET and precipitation amounts the previous summer. In this water balance analyses we assume that the difference between the incoming precipitation (both rainfall and snow on the ground at winter's end) and export from the watershed (runoff and ET) represent the change in storage. Or it is assumed that there is no closure error.

Results and Discussion

Table 1 shows the water balance computations for the Putuligayuk catchment for a 9-year period from 1999 to 2007. An examination of the runoff hydrographs for the years gauged (Kane et al. 2000, Bowling et al. 2003) shows a significant runoff response to snowmelt, with very little response to summer precipitation; typical snowmelt and summer hydrographs for 3 years are shown in Figure 2. The hydrograph for 2003 shows a very high peak runoff that corresponds to the maximum SWE measured in the watershed. Also the average of the runoff from snow divided by SWE or the snow runoff ratio (0.78) is much greater than the average rainfall runoff ratio (0.36). This is true for each year also.

Although, the 9-year averages of SWE at winter's end (9.5 cm) and summer rainfall (8.5 cm) are very similar, a majority of the runoff is generated from snowmelt. Of the total precipitation, 60% left the basin as runoff over the 9-year period. This is considerably higher than found in more temperate climates and is partially due to the continuous permafrost in the basin. The global average for runoff has been reported as 36% (Baumgartner & Reichel 1975). However, there was considerable year-to-year variation in annual runoff, from 33% to 79% of annual precipitation. Part of this annual variation can be explained by changes in surface storage, magnitude of SWE and summer rainfall, and the timing of some of these events. If one looks at the data in Table 1, it can be seen that in the summer of 2005, with the second lowest warm season precipitation, the runoff ratio the following year was the second lowest for the 9-year duration. This is due to snowmelt water going back into surface storage after the previous dry summer when ET was equivalent to the summer precipitation. Wet years generally have high runoff ratios and dry years just the opposite; this is due to limited storage. In addition to the amount of precipitation, the timing is important; SWE is more likely to run off while summer precipitation is more likely to result in ET that produces a surface storage deficit. Late summer precipitation when ET is low can also significantly reduce the surface storage deficit that can develop over the summer when ET exceeds precipitation. The likelihood is that the wettest month of the year will be at the end of summer; however in any single year it can be September, July, or even June.

SWE at the end of winter averaged 9.5 cm and varied from a low of 8.2 cm to a high of 11.2 cm. Summer precipitation has averaged 8.5 cm the past 9 years; the range is quite wide as it ranges from 1.5 to 13.7 cm. There were three years when the summer precipitation was very low and produced drought conditions, at least for part of the summer: 6.0 cm in summer 2000, 5.0 cm in summer 2005 and 1.5 cm in summer 2007. The importance of the low summer precipitation is reflected in the amount of water stored in the watershed, both as surface and subsurface stores, and the deflated hydrologic runoff response to snowmelt the next year.

It is not clear why both the snow and rainfall runoff ratios are so low the first summer in 1999. As we were not monitoring the hydrology and meteorology in 1998, we have to rely on limited data from outside the catchment. There is some evidence that 1998 was a dry summer, but that does not explain the low rainfall runoff ratio. One weakness of this study is our inability to quantify the surface storage in the myriad of lakes, ponds, and wetlands that cover this landscape. Bowling et al. (2003) showed that in a 3-year period, 1999 to 2001, 24% to 42% of the snowmelt water went into storage. This water is lost back to atmosphere over the following summer, mainly to ET.

Table 1. Water balance components for Putuligayuk watershed, North Slope of Alaska, 1999 to 2007.

Year	SWE (cm)	Rainfall (cm)	ET (cm)	Snowmelt Runoff (cm)	Summer Runoff (cm)	Total Runoff (cm)	Storage Change (cm)	Total Runoff Ratio	Snow Runoff Ratio	Rainfall Runoff Ratio
1999	10.4	10.0	5.6	5.1	1.6	6.7	8.1	0.33	0.49	0.16
2000	9.9	6.0	5.8	9.7	2.8	12.5	-2.4	0.79	0.98	0.47
2001	8.4	7.5	5.4	6.8	2.3	9.1	1.3	0.57	0.81	0.31
2002	9.4	13.7	6.3	7.4	6.3	13.7	3.1	0.59	0.79	0.46
2003	11.2	10.8	5.4	10.5	6.8	17.3	-0.8	0.79	0.94	0.63
2004	9.2	11.1	6.3	7.6	7.1	14.8	-0.8	0.73	0.83	0.64
2005	8.9	5.0	5.0	8.4	0.5	8.8	0.0	0.64	0.94	0.10
2006	9.5	10.7	8.0	5.5	2.8	8.3	3.9	0.41	0.58	0.26
2007	8.2	1.5	6.6	5.2	0.3	5.5	-2.5	0.57	0.63	0.21
Max.	11.2	13.7	8.0	10.5	7.1	17.3	8.1	0.79	0.98	0.64
Min.	8.2	1.5	5.0	5.1	0.3	5.5	-2.5	0.33	0.49	0.10
Ave.	9.5	8.5	6.1	7.4	3.4	10.8	1.1	0.60	0.78	0.36
Std. Dev.	0.9	3.8	0.9	1.9	2.7	4.0	3.4	0.16	0.17	0.20

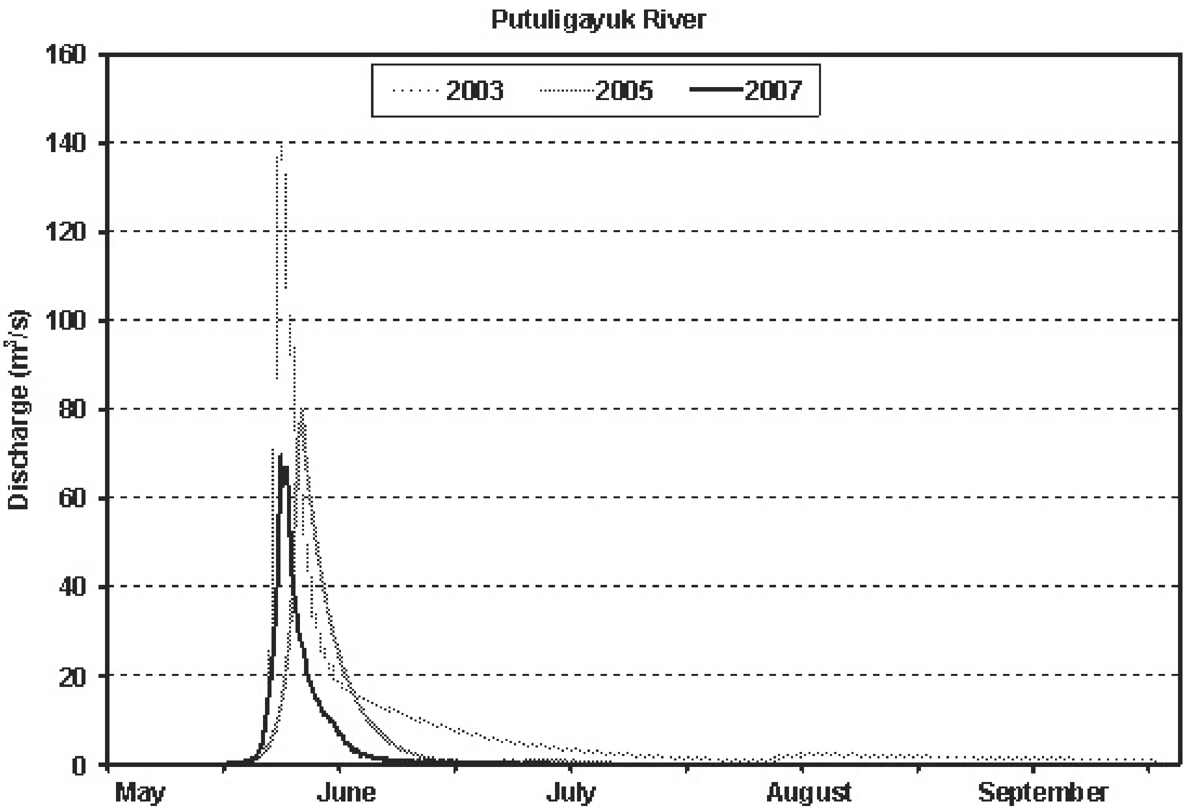

Figure 2. Typical annual hydrographs demonstrating the dominance of snowmelt runoff in the annual hydrologic cycle for the Putuligayuk River catchment.

There have been several water balance determinations for what is referred to as the nested watersheds of the Kuparuk basin (Lily et al. 1998, Kane et al. 2004), although the Putuligayuk catchment is just outside to the east. There are similarities in the water balance of other neighboring watersheds (Imnavait, Upper Kuparuk and Kuparuk) and this watershed; however there are also interesting contrasts. It can be anticipated that snowmelt will be a significant runoff event in these watersheds with average runoff ratios exceeding 0.5 and for individual years near 0.8 (Table 2). One interesting feature of the Putuligayuk catchment is the high average runoff ratio of 0.8 for the snowmelt period. This value is both surprising because this is a low-gradient watershed and it has much more surface storage (lakes, ponds, and wetlands) than the other three watersheds mentioned above.

It is clear that the snowmelt runoff response of the Putuligayuk catchment depends on the timing and amounts of precipitation the previous summer. Typically precipitation increases monthly throughout the summer and any deficits that develop in storage are partially replenished by summer precipitation, particularly at summer's end when ET is minimal. Significant precipitation at the end of summer produces high runoff response the next spring, while summer

Table 2. Summary of runoff ratios for 3 watersheds on the North Slope of Alaska.

Basin	Total Runoff Ratio	Snow Runoff Ratio	Rainfall Runoff Ratio
Putuligayuk River [1] (n = 9 years)	0.60	0.80	0.40
Upper Kuparuk River [2] (n = 7 years	0.62	0.49	0.68
Imnavait Creek [2] (n = 19 years)	0.50	0.66	0.41
Kuparuk River [3] (n = 4 years)	0.58	0.86	0.35

1. This paper 2. Kane et al. (2004) 3. Lilly et al. (1998)

drought conditions will result in a low runoff yield during the following ablation.

The summer runoff response of the Putuligayuk River can only be described as not impressive (Fig. 2). From the end of snowmelt to summer's end, the discharge is generally in recession with only a few very small responses to precipitation. Kane et al. (2003) discussed how permafrost land forms could retard surface runoff, and McNamara et al. (1998) described how the active layer slowly yields water during the summer and results in an extended recession that lasts through freeze-up in the fall. Otherwise the stream would cease flowing during the summer; this is actually a possibility in the summer of 2008 because of the extreme drought conditions of the summer of 2007.

Conclusions

This low-gradient river has a surprisingly high runoff ratio, both annually and during snowmelt. A majority of this runoff leaves the basin during and immediately after snowmelt, but first any surface storage deficit from the previous warm season must be replenished. Summer runoff response is minimal and generally ET exceeds P, which results in drying out of the basin and fragmentation of the drainage network. This is particularly true earlier in the summer when the probability of precipitation is lower than at the end of summer. Drought conditions during a summer result in lower than expected runoff response the following year. Storage is the most significant unknown in this computation; we just do not have adequate tools for getting quantitative estimates of subsurface (active layer) and surface storage. However, it is clear that the amount of surface storage is low in terms of average annual precipitation. Estimates of ET spatially over the watershed could be improved with more data, but the likelihood of this happening is quite low. With the record low summer precipitation in 2007, it is predicted that the snow runoff ratio for 2008 will be quite low unless the SWE is considerably above the 9-year average of 9.5 cm.

Acknowledgments

This paper is based on work supported by the National Science Foundation, Office of Polar Programs, Grants OPP-9814984 and OPP-0335941. We are also grateful to all faculty, staff, and students who helped collect the data that made these computations possible.

References

Arendt, A.A., Echelmeyer, K.A., Harrison, W.D., Lingle, C.S. & Valentine, V.B. 2002. Rapid wastage of Alaska glaciers and their contribution to rising sea level. *Science* 297: 382-386.

Baumgartner, A. and Reichel, E. 1975. The world water balance. Elsevier Scientific Publishing Company, New York, U.S.A.

Bowling, L.C., Kane, D.L., Gieck, R.E. Hinzman, L.D. & Lettenmaier, D.P. 2003. The role of surface storage in a low-gradient Arctic watershed. *Water Resources Research* 39(4): 1087.

Hinzman, L.D., Goering, D.J. & Kane, D.L. 1998. A distributed thermal model for calculating soil temperature profiles and depth of thaw in permafrost. *Journal of Geophysical Research* 103(D22):28,975-28,991.

Hinzman, L.D., Bettez, N., Boulton, W.R., et al. 2005. Evidence and implications of recent climate change in northern Alaska and other Arctic regions. *Climatic Change* 72: 251-298.

Kane, D.L., Gieck, R.E. & Bowling, L.C. 2003. Impacts of surficial permafrost landforms on surface hydrology.

Kane, D.L., Gieck, R.E. & Hinzman, L.D. 1990. Evapotranspiration from a small Alaskan Arctic watershed. *Nordic Hydrology* 21: 253-272.

Kane, D.L., Hinzman, L.D., McNamara, J.P., Zhang, Z. & Benson, C.S. 2000. An overview of a nested watershed study in Arctic Alaska. *Nordic Hydrology* 31(4/5): 245-266.

Kane, D.L., Gieck, R.E., Kitover, D.C., Hinzman, L.D., McNamara, J.P. & Yang, D. 2004. Hydrological cycle on the North Slope of Alaska. In: *Northern research basins water balance.* Kane, D.L & Yang, D. Eds., IAHS Publication 290, pp. 224-239.

Kane, D.L. & Yang, D. (eds.). 2004. *Northern research basins water balance.* International Association of Hydrological Sciences, IAHS Publication 290, 271 pp.

Lachenbruch, A.H. & Marshall, B.V. 1986. Changing climate: geothermal evidence from permafrost in the Alaskan Arctic. *Science* 234: 689-696.

Lilly, E.K., Kane, D.L., Hinzman, L.D. & Gieck, R.E. 1998. Annual water balance for three nested watersheds on the North Slope of Alaska. Proc., Permafrost, Seventh International Conference, Yellowknife, Canada, pp. 669-674.

Magnuson, J., Robertson, D. Son, B., Wynne, R., Livingstone, D., Arai, T., Assel, R., Barry, R., Card, V., Kuusisto, E., Grannin, N., Prowse, T., Steward, K. & Vuglinski, V. 2000. Historical trends in lake and river ice cover in the Northern Hemisphere. *Science* 289: 1743-1746.

Maslanik, J.A., Serreze, M.C. & Agnew, T. 1999. On the record reductions in western Arctic sea ice cover in 1998. *Geophys. Res. Lett.* 26(13): 1905-1908.

McNamara, J. P., Kane, D.L. & Hinzman, L.D. 1998. An analysis of stream flow hydrology in the Kuparuk River basin, Arctic Alaska: A nested watershed approach. *Journal of Hydrology* 206:39-57.

Mendez, J., Hinzman, L.D. & Kane, D.L. 1998. Evapotranspiration from a wetland complex on the Arctic coastal plain of Alaska. *Nordic Hydrology* 29(4/5): 303-330.

Priestley, C.H.B & Taylor, R.J. 1972. On the assessment of surface heat flux and evaporation using large scale parameters. *Monthly Weather Review* 100(1):81-92.

Robinson, D.A., Dewey, K.F. & Heim, R.R. 1993. Global snow cover monitoring: an update. *Bull. Am. Meteorol. Soc.* 74: 1689-1696.

Rovansek, R.J., Hinzman, L.D. & Kane, D.L. 1996. Hydrology of a tundra wetland complex on the Alaskan Arctic coastal plain, U.S.A. *Arctic and Alpine Research* 28(3): 311-317.

Shutov, V., Gieck, R.E., Hinzman, L.D. & Kane, D.L. 2006. Evaporation from land surface in high latitude areas: a review of methods and study results. *Nordic Hydrology* 37(4/5): 393-411.

Sturm, M., Racine, C. & Tape, K. 2001. Increasing shrub abundance in the Arctic. *Nature* 411: 546-547.

Vinnikov, K.Y., Robock, A., Stouffer, R.J., Walsh, J.E., Parkinson, C.L., Cavalieri, D.J., Mitchell, J.F.B., Garrett, D. & Zakharov, V.K. 1999. Global warming and Northern Hemisphere sea ice extent. *Science* 286: 1934-1937.

Detailed Cryostratigraphic Studies of Syngenetic Permafrost in the Winze of the CRREL Permafrost Tunnel, Fox, Alaska

Mikhail Kanevskiy
University of Alaska Fairbanks Institute of Northern Engineering, Fairbanks, Alaska, USA
Daniel Fortier
University of Alaska Fairbanks Institute of Northern Engineering, Fairbanks, Alaska, USA
Yuri Shur
University of Alaska Fairbanks Department of Civil and Environmental Engineering, Fairbanks, Alaska, USA
Matthew Bray
University of Alaska Fairbanks Department of Civil and Environmental Engineering, Fairbanks, Alaska, USA
Torre Jorgenson
ABR, Inc., Fairbanks, Alaska, USA

Abstract

The CRREL Permafrost Tunnel is a well-known location for studies of Late Pleistocene syngenetic permafrost. Our detailed cryostratigraphic mapping in the winze of the tunnel was based on study of cryogenic structure, ice content of the sediments, and different types of massive ice. The results show that original ice-rich syngenetically frozen silts were partly reworked by thermal erosion, which proceeded mainly along the large ice wedges. Gullies and underground channels, formed at various depths, were filled with ice and sediments, the structure and properties of which differ from the original syngenetic permafrost. In the winze, thin peat layers underlain by distinct ice lenses were observed. These layers mark the former positions of the permafrost table during peat accumulation, which occurred during slower sedimentation periods.

Keywords: Alaska; cryofacial analysis; cryostructure; mapping; syngenetic permafrost; thermal erosion.

Introduction

The well-known CRREL Permafrost Tunnel located near Fairbanks, Alaska, offers exposures of the Late Pleistocene syngenetically frozen silts with large ice wedges. The tunnel, constructed more than 40 years ago, consists of a main horizontal adit, which reaches 110 m in length, and an inclined winze 45 m long.

Ice-rich silts exposed in the tunnel belong to Goldstream Loess Formation of Wisconsinan age and are underlain by the gold-bearing Fox Gravel (Péwé 1975, Long & Péwé, 1996). Silts of eolian origin were partly reworked and retransported by slope and fluvial processes (Péwé 1975, Hamilton et al. 1988).

Similar syngenetic ice-rich permafrost with huge ice wedges was observed in many unglaciated areas of Siberia and Northern America. In Russian literature they are known as "Yedoma" or "Ice Complex" sediments (Katasonov 1978, Popov et al. 1985, Romanovskii 1993). Such permafrost has been studied in the continuous permafrost zone, and its occurrence in central Alaska is a rare phenomenon.

The tunnel, and particularly its adit, has been extensively studied by geologists and recently by permafrost scientists. Sellmann (1967) made general sketches of the exposures and characterized the stratigraphy and main types of ground ice observed in the tunnel. Detailed geological and paleoenvironmental studies of Quaternary sediments in the tunnel were performed by Hamilton et al. (1988).

Shur et al. (2004) identified features related to original syngenetic permafrost and showed the impact of thermo-erosion processes on the structure of the permafrost. Bray et al. (2006) performed mapping of permafrost in the main adit. Both works were focused on identification of differences between original permafrost and later modifications of it. However, in-depth understanding of syngenetic permafrost formation requires more detailed studies of permafrost properties and cryogenic structures. This paper presents detailed cryostratigraphic studies performed in the winze, where the original syngenetic permafrost is preserved better than in the main adit.

The main goals of our study were: (a) to compile a cryostratigraphic map of the winze, (b) to describe cryostructures of the permafrost, (c) to reconstruct events of the permafrost and sedimentary history of the study area, and (d) to estimate the ice content of the sediments.

Methods

The section of the winze 38 m long and from 12 to 18 m below the surface was studied in 2005–2006. The cryostratigraphic mapping used a cryofacial analysis proposed by Katasonov (1978). This analysis is based on the close relationship between cryostructure assemblages and specific terrain units, and reveals the way permafrost was formed. Cryofacial analysis has been especially useful for study of syngenetic permafrost (Katasonov, 1978).

The mapping of one wall and ceiling of the winze was performed in the scale 1:20; several sections were studied

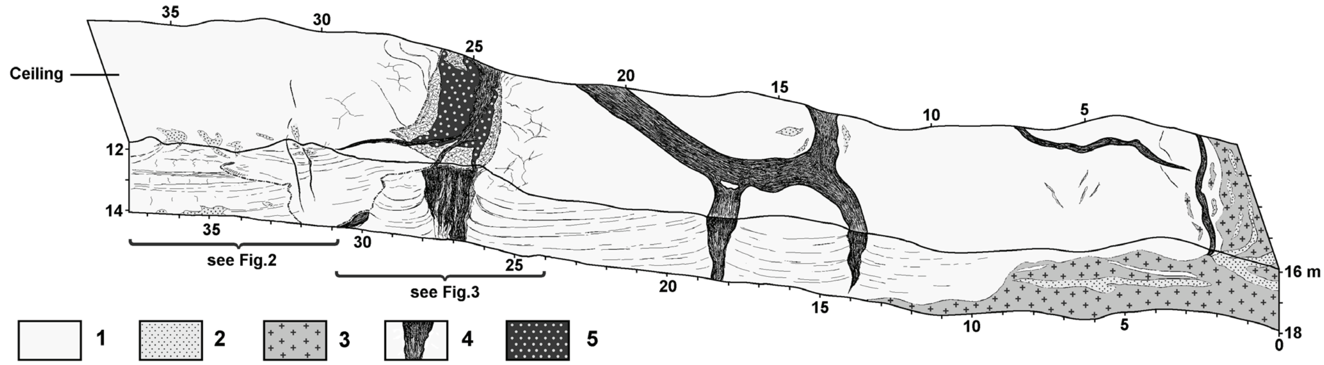

Figure 1. General view of the left wall and the ceiling of the winze. 1–silt; 2–sand; 3–Fox Gravel; 4–ice wedge; 5–thermokarst-cave ice.

greater detail (scale 1:4). Figure 1 shows the general view of the winze; more detailed fragments are shown in Figures 2 to 4. AMS radiocarbon dating (Fig. 2) was performed at the University of Arizona.

Results

The permafrost soils in the winze are mainly silts with sand lenses. The main cryostructure is micro-lenticular (Shur et al. 2004, Bray et al. 2006), which is characterized by occurrence of very small sub-horizontal (sometimes wavy) discontinuous ice lenses. The thickness of uniformly distributed ice lenses (and vertical spacing between them as well) usually does not exceed 0.5 mm.

Several varieties of micro-lenticular cryostructure can be distinguished in the winze (e.g., latent micro-lenticular, micro-braided). Micro-lenticular cryostructure (including all its varieties) is the most typical cryostructure of syngenetic permafrost; usually it occupies not less than 50–60% of the entire thickness of such sections (Kanevskiy 1991, 2003).

In the winze, gravimetric moisture content of the sediments with micro-lenticular cryostructure varies from 100% to 240% (Fig. 4a, Ssection 1). The similar range (80–180%, average 130%) was found in the adit of the tunnel (Bray et al. 2006). Organic content of the sediments varies from 3.3% to 9.5% by weight (Fig. 4a); the greatest values are specific to the organic-rich layers. The radiocarbon dates for these layers vary from 31, 000 to 35,000 y BP (Fig. 2).

Seven thin organic-rich horizons were observed in the upper part of the winze, at a depth of 12–14 m from the ground surface (Fig. 2). At the depth of about 0.4 to 0.6 m below each peat horizon, there are distinct ice (or ice-rich) layers (referred to as *belts* in the Russian literature). Numerous thin cracks partially filled with ice (ice veins) extend downward from the peat layers to a depth of up to 0.5 m. These cracks form polygons up to 0.5 m across.

Numerous sites of former gullies and underground channels were observed at various depths. They had been cut by running water in the silty sediments and afterwards filled with thermokarst-cave ice and soils, the structure and properties of which differ from the original syngenetic permafrost (Shur et al. 2004, Bray et al. 2006, Fortier et al. 2008).

In the winze, the gully filled with sediments was observed at the interval 29–35 m (Figs. 1 to 3). A truncated ice wedge affected by thermal erosion is located under this gully. The sediments filling the gully are mostly ice-poor stratified silts with lenses of sands. They contain numerous inclusions of organic material, which were interpreted as having been reworked by water. The organic content of the sediments in the gully varies from 7.0% to 22.8% and is much higher in comparison with the original permafrost (Fig. 4b).

Cryostructures in the lower part of section 2 (Fig. 4b, 60-165 cm) vary from latent micro-lenticular to porous. The gravimetric moisture content of this part of section 2 varies from 70% to 100% which is smaller than the water content of the original syngenetic permafrost. Such water content is unusual for sediments with very small amount of visible ice. It can be attributed to the higher organic content (Fig. 4b). Sediments with an organic content of 9–12% have a gravimetric moisture content of 70–80%, whereas sediments with organic content of 14–16% have a moisture content of 90–100%.

The cryostructures and ice contents of the upper part of the section 2 (Fig. 4b, 0–60 cm) are similar to those of the original permafrost; the gravimetric moisture contents here vary from 110% to 140%. This indicates change of sedimentation mode and decrease of sedimentation rate at the last stages of gully infilling.

Ice wedges observed in the winze have width of up to 1.8 m; their apexes terminate at the stratigraphic contact between the silts and the underlying alluvial gravels (Fig. 1). The exposure of ice wedges at the ceiling of the winze allows for an estimation of the shape and size of polygons, which reaches 8–12 m.

A horizontal body of thermokarst-cave ice crosscutting the ice wedge is exposed on the ceiling in the upper part of the winze (Fig. 3, section A-B). Its thickness varies from 0.2 to 0.35 m and it is underlain by a silt layer (0.1–0.4 m thick) with a reticulate-chaotic cryostructure (Shur et al. 2004, Fortier et al. 2008). This ice body is aligned with the ice wedge; however, it is wider than the wedge and therefore incised in the permafrost surrounding the ice wedge. The thermokarst-cave ice body is crossed by numerous sub-vertical ice veins, forming a small secondary ice wedge (Fig. 3, section A-B). Similar structures were observed in the adit (Shur et al. 2004, Bray et al. 2006).

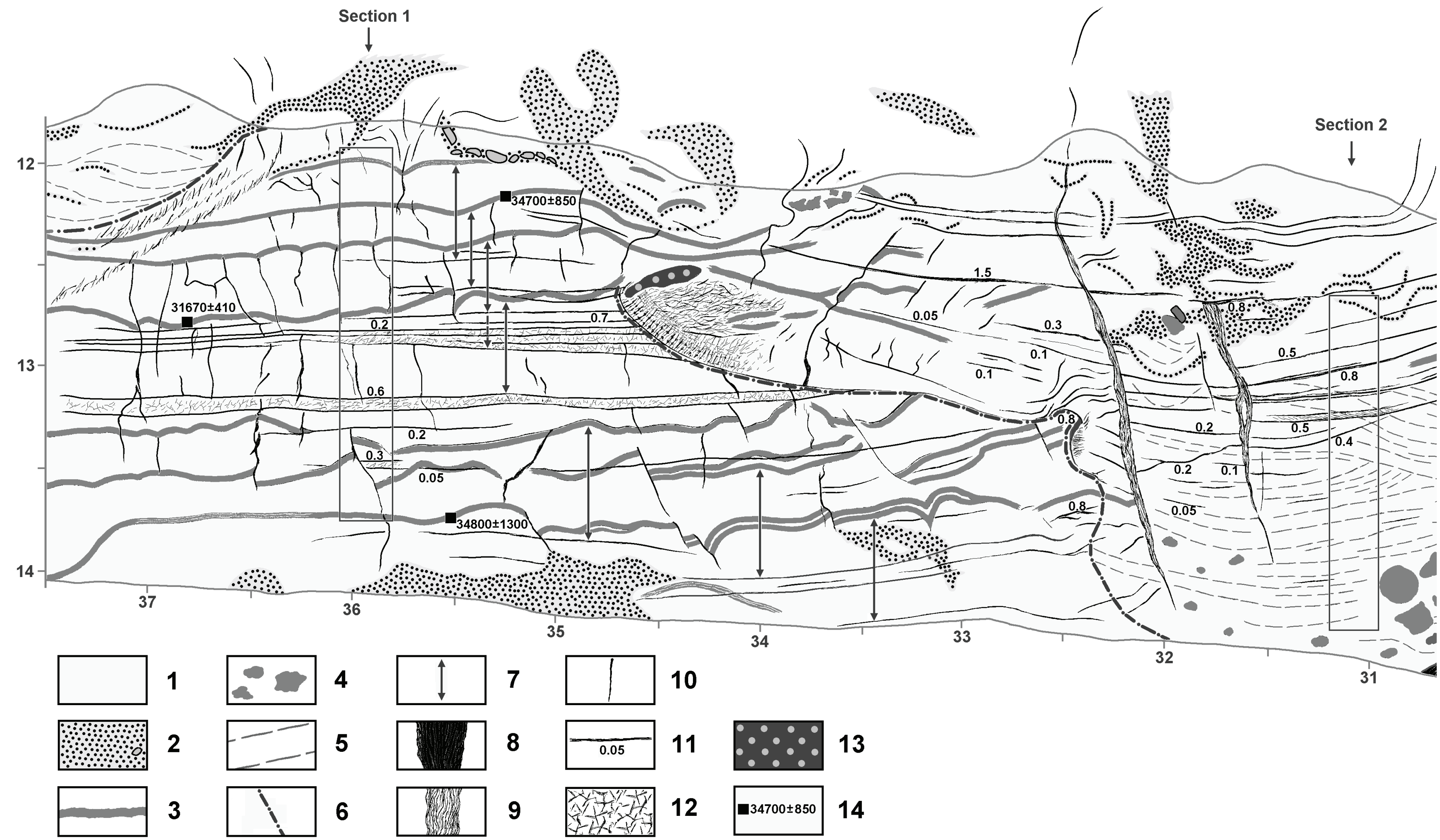

Figure 2. Cryostratigraphic map of the left wall of the winze, interval 31–37 m. 1–silt; 2–sand, gravel inclusion; 3–in situ peat layers; 4–inclusions of re-transported organic matter; 5–lamination in silt; 6–erosion boundary; 7–approximate position of active layer at the periods of slower sedimentation; 8–ice wedge; 9–composite wedge (ice/silt); 10–isolated ice vein; 11–ice layer (belt), thickness in cm; 12–reticulate-chaotic cryostructure; 13–thermokarst-cave ice; 14–uncalibrated radiocarbon age in y BP.

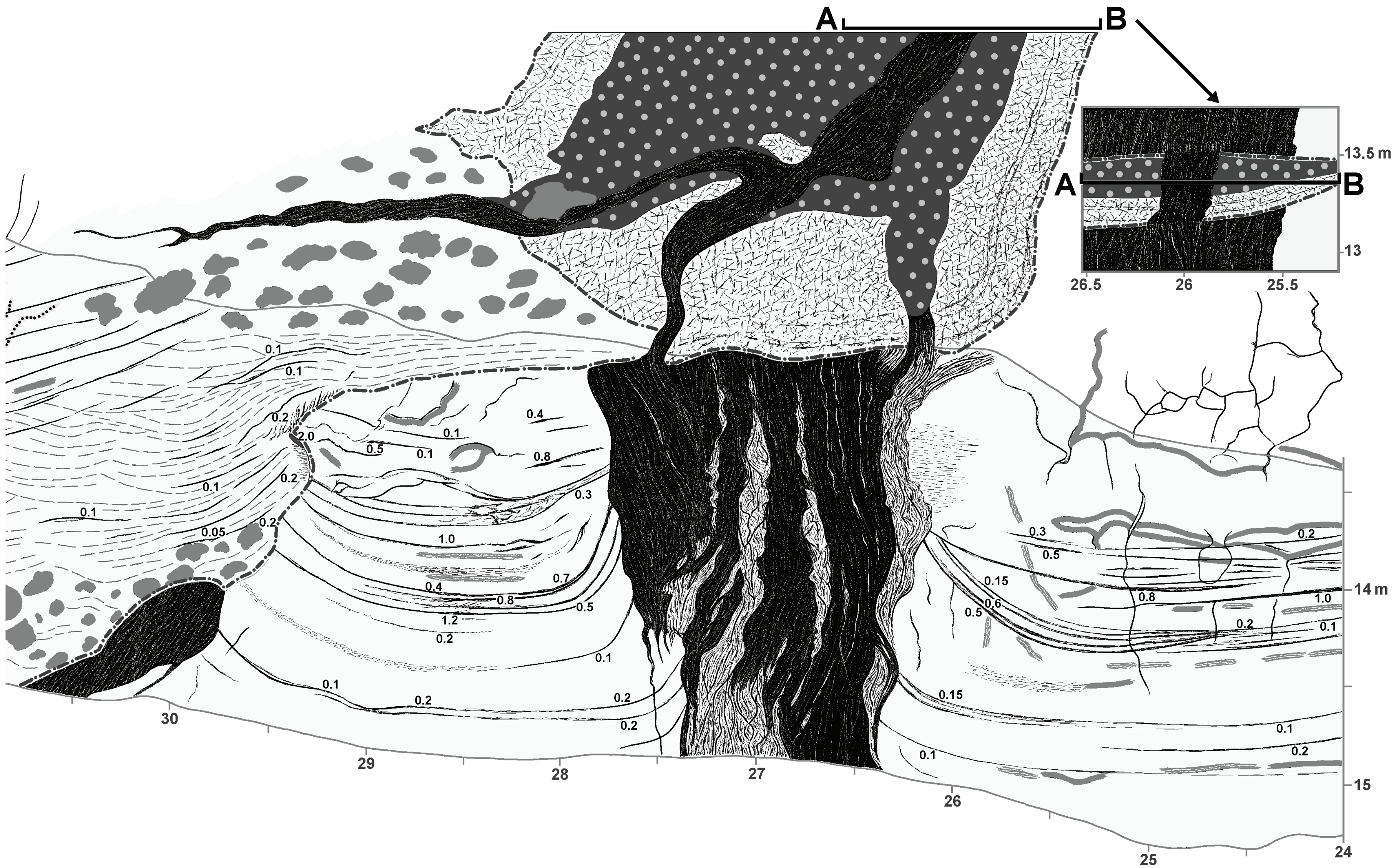

Figure 3. Cryostratigraphic map of the left wall of the winze, interval 24–31 m. For the legend, see Figure 2. A–B–schematic reconstruction of vertical section through the thermokarst-cave ice body, located at the ceiling of the winze.

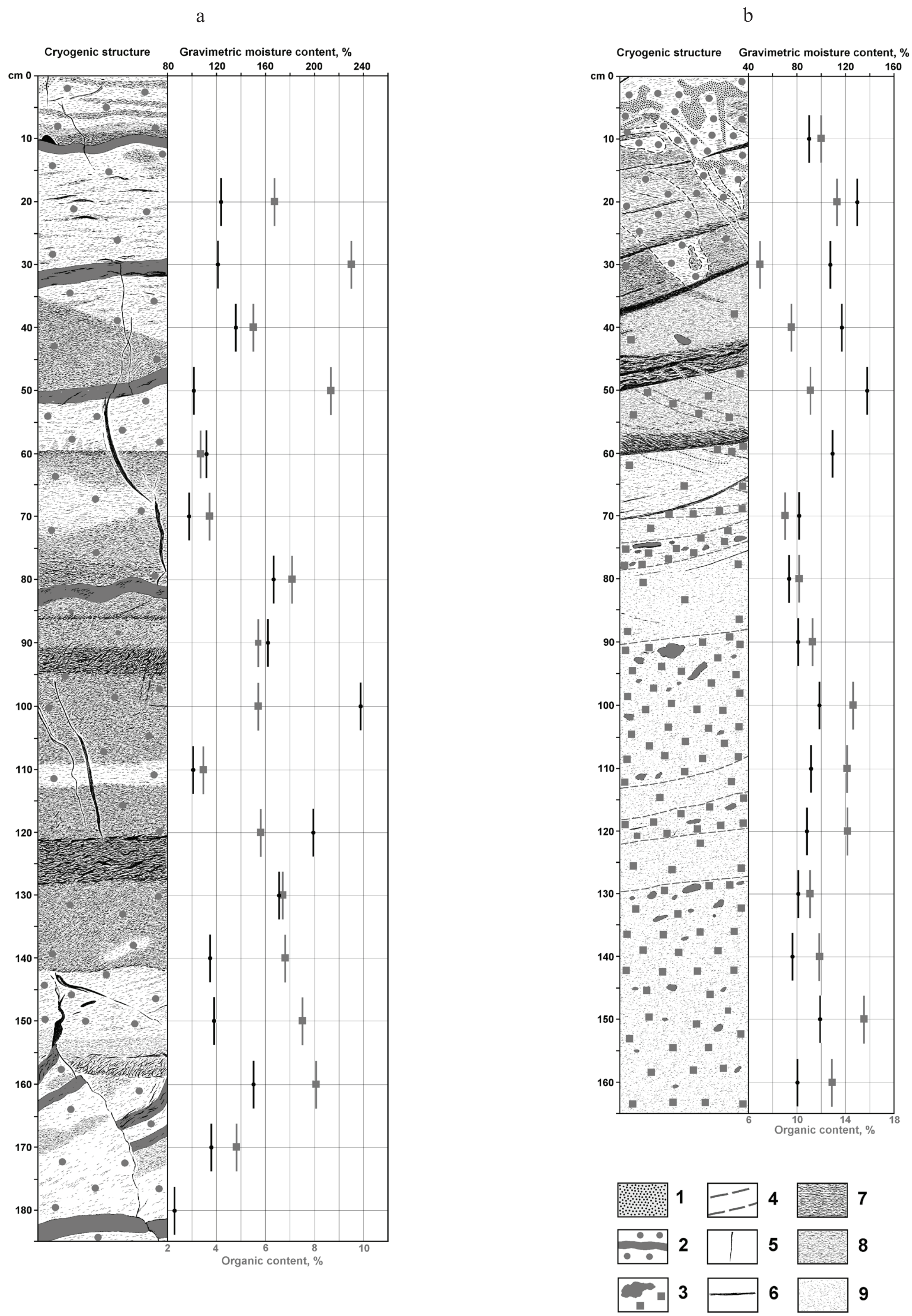

Figure 4. Details of cryogenic structure and properties of sections 1 (a) and 2 (b); location of sections is shown at Figure 2. 1–sand; 2–*in situ* peat layer and inclusions of organic matter; 3–inclusions of retransported organic matter; 4–lamination in silt; 5–isolated ice vein; 6–distinct ice layer (belt); 7–micro-braided cryostructure; 8–micro-lenticular cryostructure; 9–latent micro-lenticular/porous cryostructure.

Discussion

The study shows the prevalence of ice-rich syngenetically frozen silts with some areas partly reworked by thermal erosion, which proceeded mainly along large ice wedges. The evidences of syngenetic freezing, including undecomposed tiny rootlets and the prevalence of a micro-lenticular cryostructure, were observed directly above the contact between silts and poorly sorted alluvial gravels. The occurrence of micro-lenticular cryostructure varieties is typical for syngenetic permafrost, and is mostly linked to different rates of sedimentation (Kanevskiy 1991, 2003). The great variability of gravimetric moisture content of silts can be associated with the different cryostructures.

We associate the ice layers (belts), located beneath organic-rich horizons (Fig. 2), with the bottom of the active layer at the periods of temporary stabilization of the ground surface which occurred during periods of slower sedimentation favorable to peat accumulation. Approximate positions of the active layer at this time are denoted with arrows in Figure 2. During periods of very slow sedimentation, small polygons were formed due to shallow cracking at the stabilized surface.

There are several lines of evidence to suggest thermal erosion processes were going simultaneously with syngenetic permafrost formation. First, the occurrence of ice veins in the thermokarst-cave ice body suggests that the ice wedge continued to grow after its partial destruction by thermo-erosion and the subsequent formation of the thermokarst-cave ice. Second, the cryogenic structure of the upper part of the "gully" section (Fig. 4b) is identical to the cryogenic structure of the original permafrost.

Conclusions

Mapping in the winze of the CRREL permafrost tunnel shows the prevalence of ice-rich syngenetically frozen silts with micro-lenticular cryostructure. Periods of slow sedimentation were marked by peaty horizons and distinct ice layers, located at a depth of about 0.4 to 0.6 m below every peat horizon. These ice layers show the former positions of the permafrost table during the peat accumulation. Small ice veins extend downward from peaty horizons, forming polygons up to 0.5 m across.

The original syngenetic permafrost was partly reworked by thermal erosion, which proceeded mainly along ice wedges. No clear evidence of thermokarst was observed. Thaw unconformities are connected with the development of gullies and underground channels. These cavities were filled with water and soils, which froze back in situ, and which differ in structure and properties from the original syngenetic permafrost. Thermal erosion processes were going simultaneously with accumulation of syngenetically frozen silts and ice wedge development.

Acknowledgments

We thank the Cold Regions Research and Engineering Laboratory (CRREL) and its Fairbanks office for the opportunity to perform our studies in the tunnel. We are grateful to Margaret Cysewski, Eva Stephani, and Matthew Dillon for their field and laboratory assistance. This work was supported by the National Science Foundation under grant ARC-0454939 and Alaska EPSCoR, funded by the NSF award #0701898 and the state of Alaska. Any opinions and findings expressed in this material are those of the authors and do not necessarily reflect the views of the NSF.

References

Bray, M.T., French, H.M. & Shur, Y. 2006. Further cryostratigraphic observations in the CRREL permafrost tunnel, Fox, Alaska. *Permafrost and Periglacial Processes* 17(3): 233-243.

Fortier, D., Kanevskiy, M. & Shur, Y. 2008. Genesis of reticulate-chaotic cryostructure in permafrost. *Proceedings of the Ninth International Conference on Permafrost, Fairbanks, Alaska, June 29–July 3, 2008* (this proceedings).

Hamilton, T.D., Craig, J.L. & Sellmann P.V. 1988. The Fox permafrost tunnel: a late Quaternary geologic record in central Alaska. *Geological Society of America Bulletin* 100: 948-969.

Kanevskiy, M.Z. 1991. The role of quasi-syngenesis in formation of Quaternary sediments cryogenic structure in Northern Yakutia. In: P. Melnikov, & Y. Shur, (eds.), *The Upper Horizon of Permafrost.* Moscow: Nauka, 47-63 (in Russian).

Kanevskiy, M. 2003. Cryogenic structure of mountain slope deposits, northeast Russia. *Proceedings of the Eighth International Conference on Permafrost, Zurich, Switzerland, July 21-25, 2003*: 513-518.

Katasonov, E.M. 1978. Permafrost-facies analysis as the main method of cryolithology. *Proceedings of the Second International Conference on Permafrost, July 13-28, 1973, USSR Contribution*. Washington: National Academy of Sciences, 171-176.

Long, A. & Péwé, T.L. 1996. Carbon dating by high-sensitivity liquid scintillation counting of wood from the Fox permafrost tunnel near Fairbanks, Alaska. *Permafrost and Periglacial Processes* 7(3): 281-285.

Péwé, T.L. 1975. *Quaternary geology of Alaska. Geological survey professional paper 835*. Washington,D.C.: United States Government Printing Office, 145 pp.

Popov, A.I., Rozenbaum, G.E. & Tumel, N.V. 1985. *Cryolithology*. Moscow: Moscow University Press, 239 pp. (in Russian).

Romanovskii, N.N. 1993. *Fundamentals of cryogenesis of lithosphere*. Moscow: Moscow University Press, 336 pp. (in Russian).

Sellmann, P.V. 1967. *Geology of the USA CRREL permafrost tunnel, Fairbanks, Alaska.* Hanover, New Hampshire: US Army CRREL Technical Report 199, 22 pp.

Shur, Y., French, H.M., Bray, M.T. & Anderson, D.A. 2004. Syngenetic permafrost growth: cryostratigraphic observations from the CRREL Tunnel near Fairbanks, Alaska. *Permafrost and Periglacial Processes* 15(4): 339-347.

Interactive Stress Between Frost Bulb and Chilled Pipe by an Axis-Symmetric Freezing Experiment

Shunji Kanie
Graduate School of Engineering, Hokkaido University, Sapporo, Japan
Satoshi Akagawa
Graduate School of Engineering, Hokkaido University, Sapporo, Japan
Motohiro Sato
Graduate School of Engineering, Hokkaido University, Sapporo, Japan
Hikaru Okamoto
Graduate School of Engineering, Hokkaido University, Sapporo, Japan

Abstract

It has been known that a chilled gas pipeline buried in frost susceptible soil can be subjected to frost heave deformation. Frost heave itself has been studied by various researchers, but experimental observations of the mechanical interaction between the gas pipeline and the surrounding frost bulb has been rarely reported. The purpose of this study is to experimentally observe the interactive behavior between a chilled pipe and frost bulb under simplified conditions. The authors carried out an axis-symmetric freezing experiment which promotes formation of a concentric frost bulb. It is obviously difficult to measure the interactive stress, as well as the stress distribution, in the specimen. Therefore, the authors adopted complementary calculations for stress evaluation. Though the specimen is assumed elastic and homogeneous in the calculation, changes in the interactive stress between frost bulb and the pipe are estimated during frost bulb formation based on the observation results and analysis.

Keywords: experiment; frost bulb; mechanical modeling; pipeline; stress.

Introduction

A chilled gas pipeline installed underground may be subjected to frost heave, since a frost bulb forms around the pipe in frost-susceptible soil. This phenomenon has been studied by numerous researchers. Even in recent studies, Razaqpur and Wang (1996) proposed their practical models for frost heave estimation considering water migration based on the Clausius-Clapeyron equation; for example. Mikkola (2001) demonstrates the applicability of a mathematical model in which a physicochemical structure of the soil is described by using remeshing techniques for the Galaerkin method. As an engineering approach, various evaluation methods applying the segregation potential theory have been developed by Nixon (1982, 1987a-b), Konrad (1987), Shen & Ladanyi (1991), and Selvadurai & Shinde (1993). The authors also have been studying engineering estimation based on Takashi's equation, as a practical evaluation method with a beam on an elastic foundation model. Though frost heave behavior of the pipe with growth of a frost bulb has been researched, interactive stress acting between the frost bulb and chilled pipe has been rarely measured directly.

The purpose of this study is to experimentally observe the interactive behavior under a simplified condition and to consider an engineering evaluation method for interactive stress estimation. The axis-symmetric experiment proposed in this paper aims to promote concentric formation of the frost bulb and to measure stresses acting on the pipe with the growth of the frost bulb. Since it has been known that volumetric change in the frost bulb shows anisotropic properties and is affected by the constraining stress acting in the growing direction of ice lens, the pipe and the surrounding specimen were set vertically to exclude the effect of the force of gravity. As a result, the formation of a concentric frost bulb could be expected in the horizontal plane. Considering the difficulty in measuring the interactive stress at the boundary between the frost bulb and the pipe, the authors adopted a mechanical model for reasoning the interactive stress with known boundary conditions at the inner surface of the pipe and at the periphery of the specimen.

This mechanical model was also applied to examine the anisotropic properties in frost heave ratio during freezing. The calculated stresses on the inner surface of the pipe were compared with the observed stresses and the anisotropic properties of frost heave are discussed.

Axis-Symmetric Freezing Experiment

In multi-dimensional freezing of frost-susceptible soil, frost heave ratio is depending on the direction of freezing and the constraining stress. If the pipe is set horizontally and frost bulb forms in vertical plane, concentric formation of frost bulb cannot be expected, because the constraining stresses vary with the location in the vertical plane due to gravity force. In order to consider the interactive behavior between pipe and frost bulb, simplified condition without the effect of gravity force is preferable for both empirical and analytical evaluations. Therefore, the pipe and the cylindrical specimen surrounding the pipe were set vertically to promote concentric frost bulb formation in the horizontal plane to realize a quasi-one-dimensional behavior.

Table 1. Experimental conditions for consolidation.

Material	Kaolin	
Specific gravity of particle	2.64	g/cm^3
Water content Before consolidation	70	%
Water content After consolidation	50	%
Amplitude of load	80	kPa
Time for consolidation	170	hrs

Consolidation phase

First, frost susceptible material, kaolin, is filled in the mold and vertical load is applied from the top of specimen. Water contained in the specimen is drained from the top and the bottom through porous stones. The temperature of the laboratory is kept at +1°C during consolidation, and the temperature of the specimen is expected to be the same at anywhere in the specimen at the beginning of the freezing phase. The experimental conditions are tabulated in Table 1.

Freezing phase

After the consolidation, the outer mold is removed. The specimen keeps its position with constraint by a rubber membrane covering the outer surface of the specimen. Then, cold antifreeze starts to run through the pipe to promote the formation of the frost bulb. In the freezing phase, the top plate of the specimen is replaced with a thick acrylic plate to prevent vertical growth of a frost heave and to observe the formation of a horizontal frost bulb. The temperature of cold antifreeze is controlled to gradually decrease to keep the freezing rate in radial direction of 1 mm/hr based on the heat transfer analysis in advance. The final temperature of cold antifreeze was set at -10°C. Photo 1 shows the experimental apparatus during the consolidation phase and the freezing phase.

Measurement and observation

On the inner surface of the pipe, four sets of strain gauges for circumferential and vertical directions were set at the middle height of the specimen. The temperature distribution within the specimen was measured by four thermo-meters to confirm the growth of the frost bulb.

The change in peripheral length of the specimen was recorded by a wire gauge and was used for estimating the constraining stress at the outer boundary based on the spring coefficient of rubber membrane. In addition, frost bulb formation can be observed through the acrylic top plate.

If one wants to directly observe the interactive stress between the outer surface of the pipe and the inner surface of the specimen, installing a pressure gauge at the boundary may be a solution. However, the contact condition for adfreeze strength is affected by the gauge. In this paper, the authors adopt a mechanical model for reasoning interactive stresses using known boundary conditions at the inner surface of the pipe and the periphery of the specimen. This mechanical model will be introduced in the following section.

Experimental result

Pictures of the specimen during the freezing phase and after the experiment are shown in Photo 2. The size of the

(a) Consolidation phase

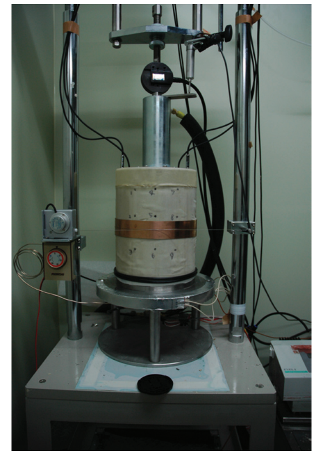

(b) Freezing phase

Photo 1. Experimental apparatus.

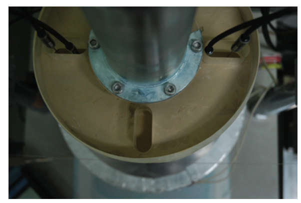

(a) During the freezing

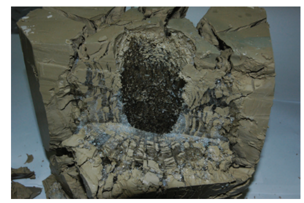

(b) After the freezing

Photo 2. Observed frost bulb: Picture (a) was taken during the freezing phase. Picture (b) is a photo after the freezing.

frost bulb was almost the same as that anticipated by thermal analysis, and the final outside diameter of the frost bulb became about 150 mm.

The stress in circumferential direction on the inner surface of the pipe varies with the growth of the frost bulb. Figure 1 illustrates the change in circumferential stress with time, and it can be found that tensile stress is gradually increasing. The interactive stress between the pipe and the frost bulb will be discussed with the evaluation model introduced in the following section.

The pipe was set at the center before removing, and the front upper part of the specimen was cut out to confirm ice lens formation within the specimen. It is found that a concentric frost bulb was successfully formed.

Mechanical Model and Analysis

The cylindrical specimen including the pipe is completely axis-symmetric so that a quasi-one-dimensional model with polar coordinates on a horizontal plane was applied. Because the material is assumed homogeneous and isotropic, nonlinear large deformations such as tensile cracks cannot be evaluated. However, anisotropic property in frost heave ratio is considered by giving appropriate radial and circumferential strains for corresponding volumetric change.

Formulation for stress evaluation

It can be assumed that the displacement in circumferential direction is zero and no body force is acting. Then, the equilibrium equation is expressed by equation (1).

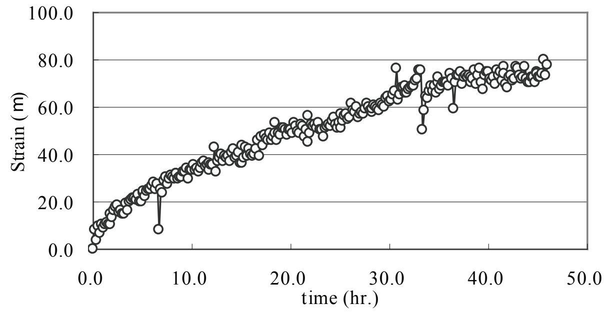

Figure 1. Change in circumferential stress on the inner surface of the pipe with the growth of the frost bulb.

$$\frac{d\sigma_r}{dr}+\frac{1}{r}\left(\sigma_r-\sigma_\theta\right)=0 \tag{1}$$

where r stands for the radial coordinate, and σ_r, σ_θ are stresses in radial and circumferential directions. The stress strain relation is given as follows.

$$\begin{Bmatrix}\varepsilon_r\\ \varepsilon_\theta\end{Bmatrix}=\frac{1+\nu}{E}\begin{bmatrix}(1-\nu) & -\nu\\ -\nu & (1-\nu)\end{bmatrix}\begin{Bmatrix}\sigma_r\\ \sigma_\theta\end{Bmatrix}+\begin{Bmatrix}\varepsilon_{rt}\\ \varepsilon_{t\theta}\end{Bmatrix} \tag{2}$$

ε_r, ε_θ are strains in radial and circumferential directions. E and ν are elastic modulus and Poisson's ratio, respectively. The strains are defined with displacements as equation (3).

$$\varepsilon_r=\frac{du}{dr},\ \varepsilon_\theta=\frac{u}{r} \tag{3}$$

Introducing equations (2) and (3) into (1), we can get the following equation (4).

$$\frac{d}{dr}\left[\frac{1}{r}\frac{d(ru)}{dr}\right]=0 \tag{4}$$

If equation (4) is integrated twice, the displacement u is described as a function of r with two constants.

$$u=\frac{1}{2}C_1 r+C_2\frac{1}{r} \tag{5}$$

Introducing a discrete model in the radial direction, the two constants can be related with the displacements at two nodes next to each other. The radial coordinates for those nodes are assumed as a and b respectively. The strains at r between two nodes are given by the following equation.

$$\begin{Bmatrix}\varepsilon_r\\ \varepsilon_\theta\end{Bmatrix}=\frac{1}{a^2-b^2}\begin{bmatrix}1/2 & -1/r^2\\ 1/2 & 1/r^2\end{bmatrix}\begin{bmatrix}2a & -2b\\ -ab^2 & a^2b\end{bmatrix}\begin{Bmatrix}u_a\\ u_b\end{Bmatrix} \tag{6}$$

In order to take the anisotropic property in frost heave ratio into consideration, parameter β, the ratio of inflation strain in θ direction to that in r direction, is introduced.

$$\beta=\varepsilon_{t\theta}/\varepsilon_{tr},\ \varepsilon_v=\varepsilon_{tr}+\varepsilon_{t\theta} \tag{7}$$

ε_v is the volumetric strain. Finally, we can get the following equation (8) for the discrete model.

$$\begin{Bmatrix}\sigma_r(a)\\ -\sigma_r(b)\end{Bmatrix}=[K]\begin{Bmatrix}u_a\\ u_b\end{Bmatrix}-\frac{\alpha}{1+\beta}\begin{Bmatrix}1-\nu(1-\beta)\\ -1+\nu(1-\beta)\end{Bmatrix}\varepsilon_v \tag{8}$$

Where

$$[K]=\alpha\frac{1}{a^2-b^2}\begin{bmatrix}a+(1-2\nu)b^2/a & -2(1-\nu)b\\ -2(1-\nu)a & b+(1-2\nu)a^2/b\end{bmatrix}$$

$$\alpha=\frac{E}{(1+\nu)(1-2\nu)}$$

Two boundary conditions are necessary for solving the discrete model. At the inner surface of the pipe, no radial stress is assumed because the pressure due to antifreeze is negligible. As another boundary condition, the constraining stress due to the membrane is adopted at the periphery of the specimen

Volumetric strain

If no water migration is considered, and contained water in the specimen is completely frozen, the volumetric strain is easily determined based on the water content and inflation ratio of ice. In this study, we applied Takashi's equation for estimating the volumetric strain. Takashi's equation was originally derived from numerous one-dimensional experiments to relate the frost heave ratio with the constraining stress and freezing rate as equation (9).

$$\xi=\xi_0+\frac{\sigma_0}{\sigma}\left(1+\sqrt{\frac{U_0}{U}}\right) \tag{9}$$

ξ : frost heave ratio, σ : constraining stress, U : freezing rate and ξ_0, σ_0 and U_0 are constants for the material obtained by experiment regulated by Japan Geomechanical Standard.

Though the frost heave ratio in Takashi's equation stands for volumetric change in one-dimensional frost heave, it is also introduced as volumetric strain ε_v in this study with the anisotropic parameter β. The constraining stress σ varies with the growth of the frost bulb. Then, it was calculated by the mechanical model with the growth and was applied into Takashi's equation to decide the volumetric change. The calculation conditions are tabulated in Table 2.

Evaluation of Results

Circumferential stress of pipe

The observed circumferential stress acting on the inner surface of the pipe has already been introduced in Figure 1. The estimated stresses by the mechanical model are added to the observation results as shown in Figure 2. In this figure, estimations with several variations in β based on Takashi's equation (case 1 to case 3) are illustrated, as well as the estimation results (case 0) in which in-situ freezing without water migration is assumed with isotropic inflation due to freezing. As shown in the figure, the estimation by Takashi's equation with β=0.0 shows good coincidence with the observation.

Table 2. Calculation conditions.

Radius	pipe		20 mm - 25 mm
	specimen		25 mm - 100 mm
Elastic Modulus	pipe		210 GPa
	specimen	unfrozen	150 MPa
		frozen	300 MPa
Poisson's ratio	pipe		0.3
	specimen	unfrozen	0.2
		Frozen	0.2
Number of element			76

Though the setting of appropriate β requires further study, it is understood that the estimation based on Takashi's equation may give satisfactory estimation for stress interaction.

Interactive stress between the frost bulb and the pipe

Figure 3 shows the estimation results for interactive stress in the radial direction between the frost bulb and the pipe based on Takashi's equation with β=0.0. It can be found that the radial interactive stress is tensile and is increasing with time. However, the amplitude of tensile stress is about 20% of the circumferential stress in the pipe. It may be that the frost bulb prevents stress transfer in the radial direction with its inflation. In this analysis, perfect continuity condition at the boundary for the interaction has been assumed, so that further discussion including adfreeze strength at the boundary may be necessary.

Figure 4 shows the stress distribution within the specimen estimated by the mechanical model. It is found that tensile stress in a radial direction is acting near the pipe, and its value reaches the maximum compression at the freezing front. On the other hand, circumferential stress is compressive in the frost bulb, and it becomes tensile in unfrozen soil.

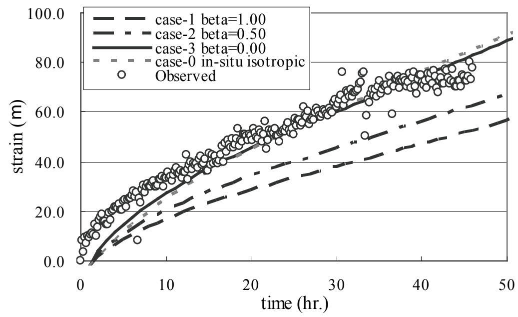

Figure 2. Estimated circumferential stress.

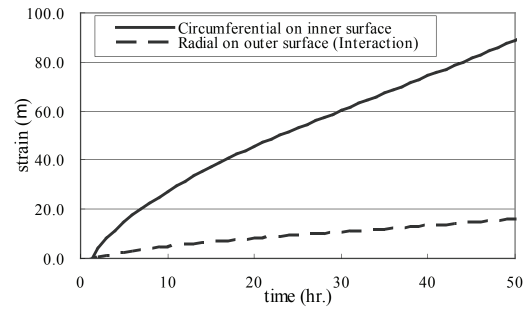

Figure 3. Estimated interactive radial stress.

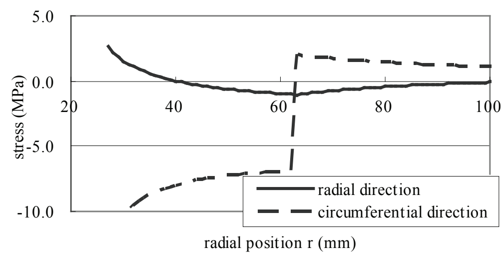

Figure 4. Stress distribution in the specimen (36 h after freezing).

Conclusion

Important findings obtained through this study are summarized as follows:

The newly-developed axis-symmetric freezing apparatus contributes to concentric formation of a frost bulb, and the interactive stress between frost bulb and pipe is successfully examined.

Evaluation of stress acting on the pipe shows good coincidence with the observation result by introducing Takashi's equation to the estimation of frost heave ratio.

In this study, introducing anisotropic property to frost heave yields better estimation in stress evaluation.

The interactive stress between frost bulb and pipe is tensile stress in the radial direction and is increasing with the growth of the frost bulb.

In this experiment, the specimen was covered with a rubber membrane, and the constraining stress due to the membrane was comparatively small due to its low spring coefficient. For further study, experiments under higher constraint pressure are preferable to scrutinize the interactive action.

References

Konrad, J.M. 1987. Procedure for determining the segregation potential of freezing soils. *Geotechnical Testing Journal, ASTM* 10: 51-58.

Konrad, J.M. & Shen M. 1996. 2-D frost action modeling using the segregation potential of soils. *Journal of Cold Regions Science and Technology* 24: 263-278.

Mikkola, M. & Hartikainen, J. 2001. Mathematical model of soil freezing and its numerical implementation. *International Journal for Numerical Methods in Engineering* 52: 543-557.

Nixon, J.F. 1982. Field frost heave predictions using the segregation potential concept. *Canadian Geotechnical Journal* 19: 526-529.

Nixon, J.F. 1987a. Thermally induced frost heave beneath chilled pipelines in frozen ground. *Canadian Geotechnical Journal* 24: 260-266.

Nixon, J.F. 1987b. Pipeline frost heave prediction using the segregation potential frost heave method. *Proceedings of Offshore Mechanics and Arctic Engineering* 1-6.

Razaqpur, A.G. & Wang, D. 1996. Frost-induced deformations and stresses in pipeline. *International Journal of Pres Ves & Piping* 69: 105-118.

Selvadurai, A.P.S. & Shinde, S.B. 1993. Frost heave induced mechanics of baried pipelines. *Journal of Geotechnical Engineering, ASCE* 119: 1929-1951.

Shen, M. & Ladanyi, B. 1991. Soil-pipeline interaction during frost heave around a buried chilled pipeline. In: D.S. Sodhi (ed.), *Cold Regions Engineering, ASCE 6th International Specialty Conference*. ASCE Publications, New York, 11-21.

Permafrost Response to Climate Warming South of Treeline, Mackenzie Delta, Northwest Territories, Canada

J.C.N. Kanigan
Department of Geography and Environmental Studies, Carleton University, Ottawa, Canada
C.R. Burn
Department of Geography and Environmental Studies, Carleton University, Ottawa, Canada
S.V. Kokelj
Water Resources Division, Indian and Northern Affairs Canada, Yellowknife, Canada

Abstract

The mean annual ground temperature (MAGT) at two sites in the Mackenzie Delta, south of treeline, has increased by 0.3°C and 0.7°C over the past 40 years. This ground warming is less than reported from the adjacent tundra uplands. The hypothesis that MAGTs in the boreal forest region of the delta may have a reduced response to climate warming due to the thermal influence of numerous water bodies has been investigated with an equilibrium geothermal model. The model indicates that water bodies have a warming influence on MAGTs up to 750 m from the lake or channel. If lake-bottom temperatures do not respond to climate warming, or warm more slowly than ground surface temperatures, then MAGTs at sites close to water bodies will warm more slowly than sites located greater than 750 m away. This may partly explain the apparent dampening of ground thermal responses to climate change in the delta.

Keywords: climate warming; ground temperature; Mackenzie Delta; modeling; thermal regime; water bodies.

Introduction

This paper examines the sensitivity of permafrost to climate change in an area where different surfaces may vary in their response to warming. The southern and central Mackenzie Delta is forested, and approximately 40% of the area is occupied by water bodies (Mackay 1963, Emmerton et al. 2007) (Figs. 1, 2). The delta region is experiencing relatively rapid climate warming, and the annual mean air temperature has increased from about -10°C to -7°C between 1960 and 2005 (Fig. 3) (Environment Canada 2007). Ground temperatures at 24 to 29 m depth at three shrub tundra sites northeast of the delta have responded to this warming, increasing by 0.2°C, 0.4°C, and 0.8°C between 1990 and 2002 (Smith et al. 2005). We hypothesize that mean annual ground temperatures (MAGT) in the delta may differ in their response to climate warming from those in the tundra uplands due to the physical characteristics of the forest cover, and the thermal influence of the more numerous water bodies. Annual mean lake-bottom temperatures may be more stable over time than similar land-surface temperatures because the climatic warming is dominantly in winter, when lakes are ice covered and lake-bottom temperatures remain close to 0°C and are insensitive to fluctuations in air temperature (Maxwell 1997, Burn 2002).

In this paper we report recent ground temperature change in the boreal forest regions of the Mackenzie Delta. Ground temperatures measured in 2006 at two forested sites near Inuvik and Reindeer Station (Fig. 1) are compared with data collected in 1961 and 1969. Previous studies have acknowledged that ground temperatures are higher in the delta than in the adjacent tundra uplands due to the thermal influence of water bodies, and have attempted to remove this influence by situating ground temperature measurement sites away from water (Mackay 1974). In this study, an equilibrium model was used to determine the distance from water bodies at which the thermal disturbance is negligible, and a spatial analysis was conducted to quantify the area

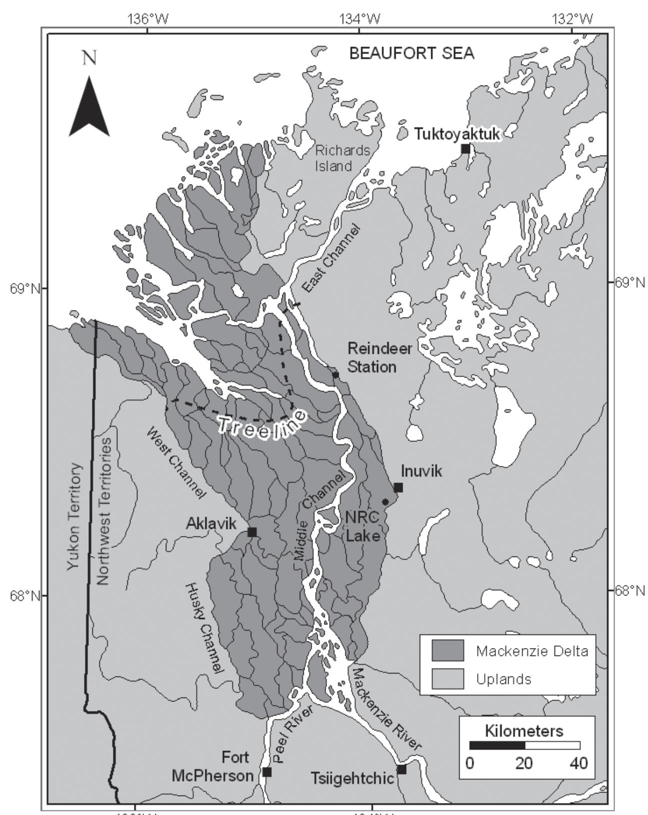

Figure 1. Mackenzie Delta region. Dark grey shading bounds the delta, and treeline is delimited by the dotted line (Mackay 1963).

Figure 2. Mackenzie Delta south of treeline. Land surfaces dominated by spruce forest are separated by channels and lakes.

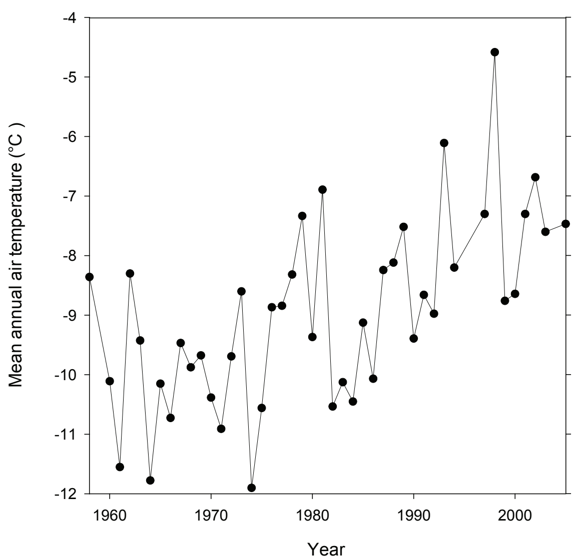

Figure 3. Mean annual air temperatures at Inuvik, 1958 to 2005. Data from Environment Canada (2007).

of the delta which is unaffected by the warming of water. We discuss whether ground temperatures in the delta will respond less to climate warming than in upland terrain, where there is a lower density of lakes.

The Mackenzie Delta Region

A variety of permafrost and terrain conditions exist in the Mackenzie Delta region, with a principal distinction between the alluvial delta and the shrub-tundra uplands to the east (Fig. 1). The delta is flooded annually by waters from the Mackenzie and Peel Rivers. Infiltration of flood water contributes to higher MAGT in the delta (-2°C to -4°C) than in the tundra uplands northeast of the delta (-6°C to -9°C) (Mackay 1974). The deposition of nutrients during the flood contributes to a northern extension of treeline, which forms the boundary between the central and northern delta (Fig. 1) (Mackay 1963).

The ground is warmer in the delta than in the surrounding uplands principally due to the high density of lakes and channels (Smith 1975). The late winter ice thickness on lakes in the central delta is less than 1 m, and most lakes do not freeze through (Mackay 1963, Marsh & Lesack 1996). As a result, an unfrozen talik forms in the sediments underneath most lakes of the Mackenzie Delta. The ground temperature beside lakes and channels is affected by heat flowing from the warmer sediments under the water body to the surrounding permafrost (Williams & Smith 1989).

South of treeline, white spruce (*Picea glauca*) communities occupy the majority of the land surface above the level of annual flooding. These communities are associated with colder permafrost than lower elevation sites because of surface conditions related to reduced flooding, including a thicker organic layer and a thinner snow cover due to canopy interception (Mackay 1974, Smith 1975, Pearce et al. 1988). The uppermost 1 to 2 m of permafrost in most spruce-forest communities are characterized by high ground-ice content, and, in places, syngenetic ice wedges (Kokelj & Burn 2005). Land surfaces of the central and southern delta located well away from water bodies have been used to measure ground temperatures that are relatively undisturbed by warming related to the presence of water (Mackay 1974).

Methods

Field methods

Ground temperatures were measured at two spruce-forest sites in the east central delta for comparison with data collected in 1961 and 1969 (Fig. 1) (Johnston & Brown 1964, Smith 1973). The site near Reindeer Station is located 101 m from the nearest lake, and 110 m from a channel, and the site at NRC Lake is located 77 m from the nearest lake and 72 m from a channel. These sites are representative of forested surfaces in the delta. Both sites were re-instrumented in 2004 by drilling a hole with a water-jet within 50 m of the original location and installing thermistors at comparable depths. Steel pipe was used to case the hole, which was filled with low conductivity silicone oil, and seven calibrated thermistors were installed at 0.5, 1.0, 3.0, 5.0, 7.0, 9.0, 11.0, 13.0, and 15.0 m depths. Steel pipe was used because it is sufficiently robust to withstand environmental stresses in the field. Temperatures at 15 m depth were of interest since this is near the depth of zero annual amplitude (Mackay 1974). It is assumed that the conductivity of the black iron pipe has a minimal influence at 15 m. The temperature at this depth corresponds with the MAGT and responds to long-term changes in air temperature or surface conditions, rather than seasonal fluctuations. Temperature measurements were made in 2006 to ensure that thermal equilibrium had re-established after drilling.

Analytical methods

The warming effect of water bodies on ground temperatures was modeled using equations developed by Lachenbruch (1957) and modified by Burn (2002). In the absence of water bodies, the undisturbed ground temperature profile is:

$$T_z = T_g + z/I \quad (1)$$

where T_z is the temperature (°C) at depth z (m), T_g is the mean annual ground surface temperature (°C), and I is the geothermal gradient (m°C^{-1}).

In the delta, the configuration of land and water can be modeled as a strip of a specified width of land that is bounded by a wide channel on one side, and a large lake on the other (Fig. 4). This is a conservative approach, as it assumes that the permafrost is a disturbance to ambient conditions governed by water bodies, not vice-versa. Many diagrams of the distribution of permafrost in the delta are consistent with this position (e.g. Smith & Hwang 1973, Fig. 4; Smith 1976, Fig. 14). This is a simplified representation of field conditions as modeled by Brown et al. (1964), who required a specific configuration for water bodies surrounding the site. In this paper, we are interested in a more general case. Under steady-state conditions, the ground temperature profile at a point on this strip of land is:

$$T_z = T_w + z/I + [(T_g - T_w)/\pi]\,[\tan^{-1}(H_{p1}/z) + \tan^{-1}(H_{p2}/z)] \qquad (2)$$

(modified from Burn 2002, eq. 4) where T_w is the mean annual water temperature (°C), H_{p1} is the width (m) of the strip of land from the lake to the point of measurement, and H_{p2} is the width (m) of the strip of land from the point of measurement to the channel. Current conditions are described by T_g = -3°C, T_w = 6°C, and I = 45 m°C^{-1} (Burn 2002). Ground temperatures were measured at 50 cm below the ground surface at the two delta spruce forest sites at Reindeer Station and NRC Lake between January 2005 and December 2006 to obtain T_g. The T_w was estimated from the mean annual lake-bottom temperature at NRC Lake, a small lake near Inuvik, measured from August 2005 to August 2007. NRC Lake is representative of the size and depth of most lakes in the delta (Johnston & Brown 1964, Marsh et al. 1999, Emmerton et al. 2007), and is representative of the flooding frequency of approximately 33% of lakes in the central delta, which is about once in five years (Marsh & Hey 1989). Smith (1976) reports less than 1°C difference between the T_w for a delta lake-bottom and T_w in channels.

A GIS analysis of topographic maps of the central and southern delta was conducted to determine the extent of terrestrial surfaces influenced by water bodies using ArcMap™ version 9.2. (Environmental Systems Research Institute 2007). National Topographic Database 1:50,000 scale vector data were used (Canada Center for Topographic Information, http://maps.nrcan.gc.ca), applying delta boundaries and treeline defined by Mackay (1963) (Fig. 1). Most aerial photographs used to generate the maps were taken during the early 1950s. Buffers were placed around channels and lakes in order to calculate the percentages of land in the delta located greater than 0, 50, 75, 100, 150, 300, 500, and 750 m away from a water body.

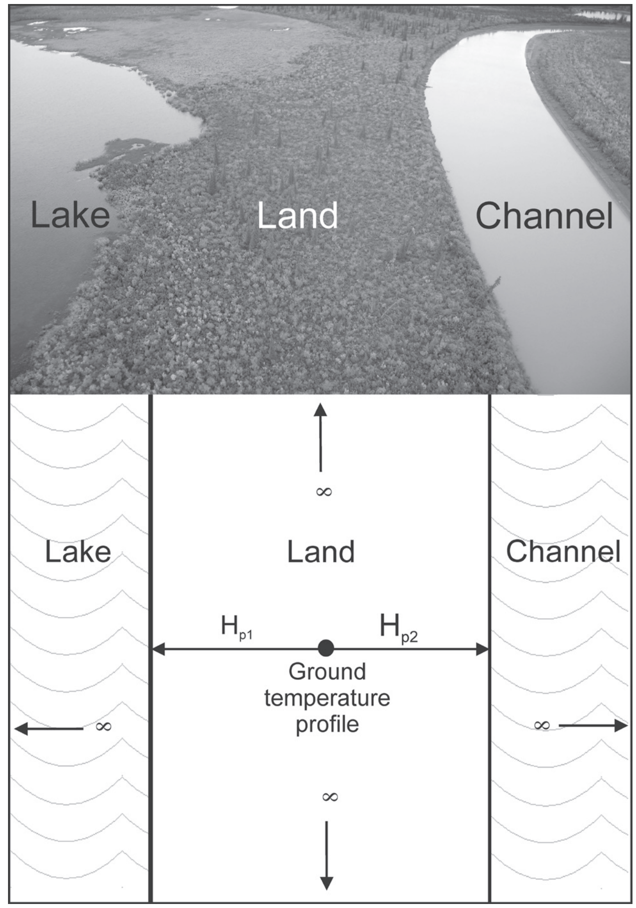

Figure 4. Configuration of ground and water bodies for simplified calculation of thermal disturbance from water in the delta environment.

Results

Field results

To characterize the current thermal regime, maximum and minimum ground temperatures recorded between January 2005 and December 2006 are presented in Figures 5 and 6. The 15 m ground temperature at the NRC Lake site increased from -3.5°C in May 1961 to -2.8°C in April 2006, a total increase of 0.7°C, or about 0.2°C per decade. At the site near Reindeer Station, ground temperature at 15 m depth increased by about 0.1°C per decade, from -2.3°C in September 1969 to -2.0°C in September 2006, a total increase of 0.3°C. Surface conditions at the time of the historical measurements were similar to those at present (Johnston & Brown 1964, Smith 1973); so it is likely that climate warming has contributed to the higher present day ground temperatures. Based on these two sites, it appears that ground temperatures in the delta have increased at a slower rate than on the adjacent shrub tundra (Smith et al. 2005). Data from the shrub tundra were obtained from below the depth of zero annual amplitude (24 and 29 m), and it is likely that even greater increases would have been recorded at the depth of zero annual amplitude.

Analytical results

Comparison of 15 m depth ground temperatures for various horizontal distances from water bodies with the undisturbed ground temperature are presented in Figure 7. The results indicate that in close proximity to water bodies (H_{p1}=H_{p2} = 0 to 200 m) the warming influence of the water decreases greatly as the horizontal distance from

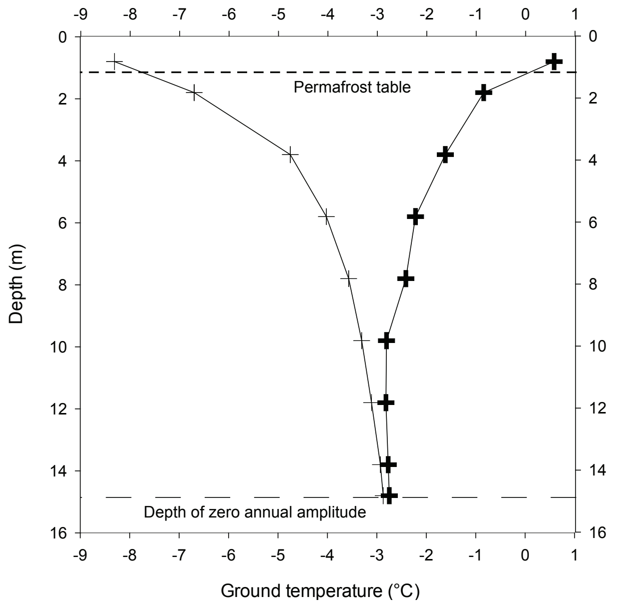

Figure 5. Ground temperature envelope from NRC Lake site, January 2005 to December 2006.

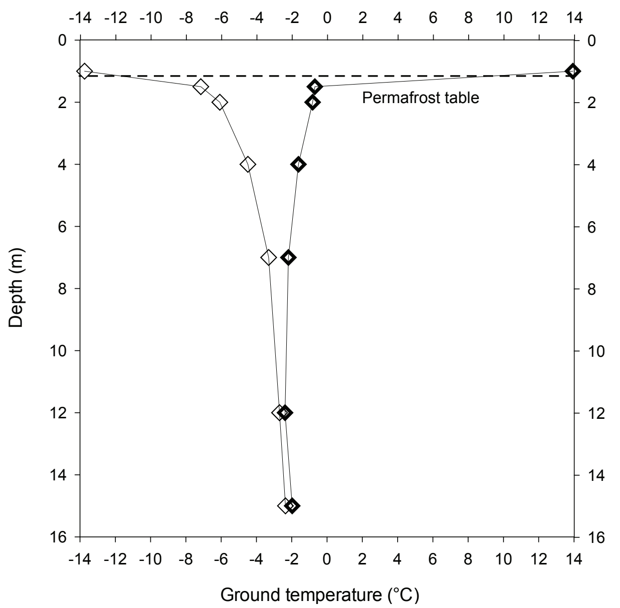

Figure 6. Ground temperature envelope from Reindeer Station site, January 2005 to December 2006.

water bodies increases. With further increases in horizontal distance (H_{p1}=H_{p2} = 200 to 1000 m), the ground temperature decrease is much reduced. If the distance from one water body remains small (H_{p1} = 50 m), as the distance from the second water body (H_{p2}) is increased, then the 15 m depth ground temperature remains above the undisturbed ground temperature despite further increases in H_{p2}, due to the close proximity of the first water body. The undisturbed ground temperature is approached where there is a large distance from both water bodies (H_{p1}=H_{p2} = 750 m).

Figure 7 shows that the difference between the disturbed and undisturbed ground temperature at 15 m depth is 0.1°C, 750 m from a water body. This difference approximates the precision of a thermistor, so at this distance the warming

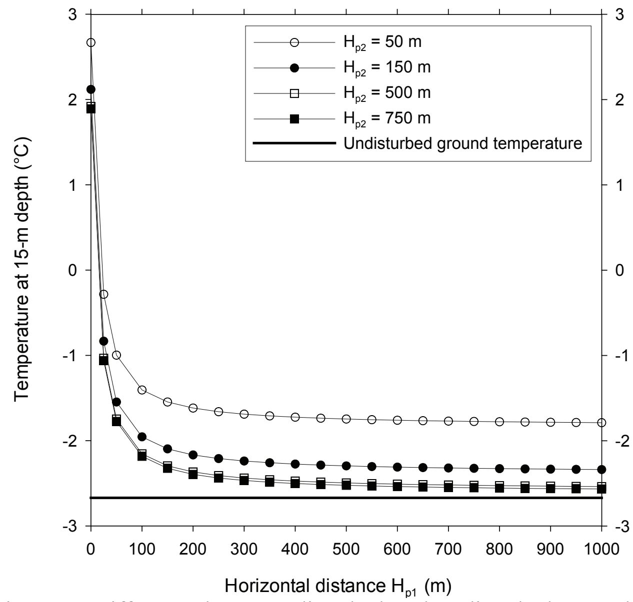

Figure 7. Difference between disturbed and undisturbed ground temperature as distances from channel and lake increase.

effect of water bodies is not detectable. The thermal influence of water bodies is detectable up to distances of about 750 m.

Spatial analysis of the central and southern delta indicated a total area of approximately 7900 km², of which about 58% is land. Only about 2% of land surfaces in the central and southern delta are located more than 750 m away from a water body (Fig. 8). This suggests that in the delta south of treeline, almost all ground temperatures at 15 m depth are affected to some extent by the thermal disturbance of water. The thermal effect is significant for most land areas, since a large proportion (81%) of terrestrial surfaces in the delta are located less than 150 m from a water body. The calculated 15 m depth ground temperature at a site located 150 m from a water body, given current T_g and T_w, is 0.6°C higher than the undisturbed ground temperature.

To test the hypothesis that ground where the temperature is affected by water bodies will warm less than unaffected ground, the equilibrium model was used to simulate the response of ground temperatures at 15 m depth to changes in T_g and T_w. Sites 50 and 150 m away from water bodies were used to simulate disturbed ground, and sites 750 m from water bodies to simulate undisturbed ground (Table 1). Data in Table 1 indicate that if the T_g and T_w are increased by the same amount, there is an equivalent increase in the temperature at 15 m depth, regardless of the horizontal distance from water bodies. So if ground and water temperatures respond to climate warming at the same rate, then MAGTs will respond uniformly throughout the delta.

The remaining scenarios simulate different responses of ground and water to climate warming. If T_g increases but T_w remains constant, the full increase in T_g is propagated to 15 m at sites located 750 m away from water bodies. However, the unchanged T_w is important at sites located 150 m or less from water bodies. The second scenario in Table 1 describes an increase of 1°C in T_g, and no change in T_w. At a site located 150 m from a water body, the temperature at 15 m depth is 0.1°C less than the corresponding temperature when T_g and T_w are both increased by 1°C. There is a reduction in the warming at 15 m depth, but at 150 m, this effect is comparable to the precision of measurement. A greater difference is produced when the T_g is increased by scenario, at 150 m from water, the 15 m ground temperature 3°C while the T_w remains unchanged (#4, Table 1). In this scenario at 150 m from water, the 15 m ground temperature is 0.2°C less than if T_g and T_w are both increased by 3°C. This is a physically significant effect since approximately 81% of land in the southern delta is located less than 150 m from a water body (Fig. 8).

The impact of no change in water temperatures is amplified at a distance of 50 m from a water body. At this distance, an unchanged T_w, coupled with a T_g increase of 1°C (#2, Table 1) leads to a 15 m ground temperature 0.2°C less than if the T_w also increased by 1°C. Similarly (#4, Table 1), under a T_g increase of 3°C, the 15 m ground temperature is 0.6°C less than if the T_w had also increased by 3°C. It appears that the response of water bodies to climate warming is physically significant at 50 m from a water body, and by implication, also at lesser distances. Such distances represent approximately 34% of the terrestrial area in southern delta (Fig. 8).

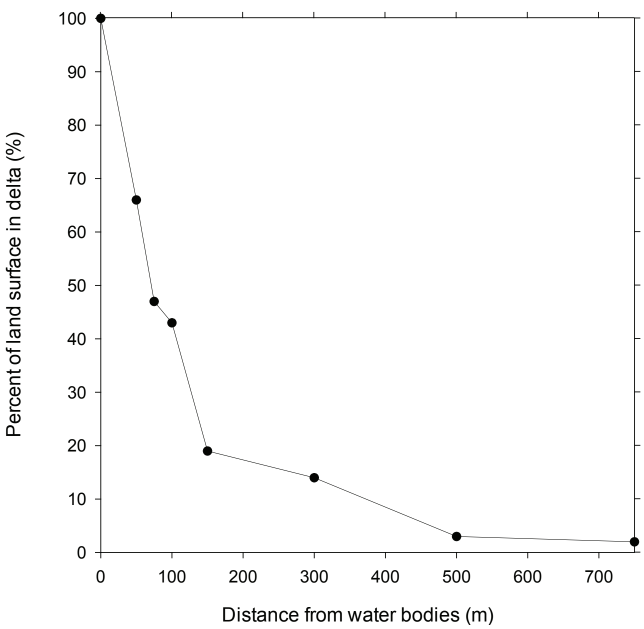

Figure 8. Percentages of land surface in the central and southern Mackenzie Delta that are located at distances greater than those specified from water bodies.

In the previous scenarios, T_w remained unchanged despite warming air temperatures in order to provide a distinction between the response of T_g and T_w to climate warming. It is perhaps more likely that water temperatures will respond to climate warming, but at a slower rate than ground temperatures. In the fifth scenario, the T_w was increased by half the change in T_g. The reduction in 15-m temperature of 0.1°C at 150-m distance may be undetectable due to instrument precision, but the reduction of 0.3°C at 50-m distance is measurable.

When water temperature warms more slowly than ground temperature, the modeling indicates that the thermal effect of water dampens the effect of climate warming, and that the dampening increases with proximity to the water body. In the Mackenzie delta, lakes are relatively static features, but the channels shift following bank erosion during the spring flood. There is a characteristic vegetation succession on point bars opposite cut banks which has been associated with various stages of permafrost aggradation (Smith 1975). Many sites within 50 m of channels may not support an equilibrium thermal regime, and at these locations the departure from undisturbed conditions will be greater than the equilibrium results presented in Table 1.

Conclusions

Field evidence from two sites in the forested Mackenzie delta indicates that recent ground temperature change in the delta, has been less than at three sites in the adjacent shrub tundra. Ground temperature modeling and spatial analysis indicate that almost all of the land in the delta is affected to some degree by water bodies. The reduced ground temperature changes measured in the delta may be related to the slow response of lakes to climate warming.

Based on the results that have been presented, the following conclusions are made:

1. Ground temperatures at 15 m depth have increased by 0.3°C and 0.7°C at two spruce-forest sites in the southern Mackenzie Delta since the 1960s. The warming rates of 0.1°C and 0.15°C per decade are slower than in the adjacent upland.
2. An equilibrium model for 15 m ground temperatures shows that the warming effect of water bodies extends to distances of 750 m from water bodies.

Table 1. Ground temperatures and ground temperature change in brackets at 15 m depth calculated at 50, 100, and 750 m from water bodies using equation 2, assuming different warming scenarios.

Horizontal distance from	Current conditions	1	2	3	4	5
Water bodies $H_{p1}=H_{p2}$ (m)	T_g=-3ºC T_w=6ºC (ºC)	T_g=-2ºC(+1) T_w=7ºC (+1) (ºC)	T_g=-2ºC(+1) T_w=6ºC (0) (ºC)	T_g=0ºC(+3) T_w=9ºC (+3) (ºC)	T_g=0ºC(+3) T_w=6ºC (0) (ºC)	T_g=0ºC(+3) T_w=7.5ºC (+1.5) (ºC)
50	-1.0	0.0 (+1)	-0.2 (+0.8)	2.0 (+3)	1.4 (+2.4)	1.7 (+2.7)
150	-2.1	-1.1 (+1)	-1.2 (+0.9)	0.9 (+3)	0.7 (+2.8)	0.8 (+2.9)
750	-2.6	-1.6 (+1)	-1.6 (+1)	0.4 (+3)	0.4 (+3)	0.4 (+3)

3. Spatial analysis indicates that about 2% of terrestrial surfaces in the delta are located at distances greater than or equal to 750 m from a water body, and therefore, almost all terrestrial sites in the delta experience the thermal influence of water bodies to some extent.

4. Results from an equilibrium model indicate that if lake-bottom temperatures do not respond to climate warming, or warm more slowly than ground surface temperatures, then mean annual ground temperatures at sites close to water bodies will warm more slowly than undisturbed sites. This may explain why ground thermal responses to recent climate warming appear to be damped in the Mackenzie Delta in comparison with the adjacent tundra uplands.

Acknowledgments

The research was supported by the Natural Sciences and Engineering Research Council of Canada, the Polar Continental Shelf Project (Natural Resources Canada), the Aurora Research Institute, and the Water Resources Division and Northern Scientific Training Program, Indian and Northern Affairs Canada. We thank Douglas Esagok, Larry Greenland, William Hurst, Les Kutny, and Thai Nguyuen for field assistance, and M.F.J. Pisaric and D.W. Riseborough for comments on the M.Sc. from which this work developed. This paper is Polar Continental Shelf Project contribution number 00908.

References

Brown, W.G., Johnston, G.H. & Brown, R.J.E. 1964. Comparison of observed and calculated ground temperatures with permafrost distribution under a northern lake. *Canadian Geotechnical Journal* 1: 147-154.

Burn, C.R. 2002. Tundra lakes and permafrost, Richards Island, western arctic coast, Canada. *Canadian Journal of Earth Sciences* 39: 1281-1298.

Emmerton, C.A., Lesack, L.F.W. & Marsh, P. 2007. Lake abundance, potential water storage, and habitat distribution in the Mackenzie River Delta, western Canadian Arctic. *Water Resources Research* 43: W05419.

Environment Canada 2007. Canada climate data [online]. Ottawa, Canada. Available from http://climate.weatheroffice.ec.gc.ca/climateData/canada_e.html [accessed 08 August 2007].

Johnston, G.H. & Brown, R.J.E. 1964. Some observations of permafrost at an arctic lake in the Mackenzie Delta, N.W.T., Canada. *Arctic* 17: 163-175.

Kokelj, S.V. & Burn, C.R. 2005. Near-surface ground ice in sediments of the Mackenzie Delta, Northwest Territories, Canada. *Permafrost and Periglacial Processes* 16: 291-303.

Lachenbruch, A.H. 1957. *Three-dimensional Heat Conduction Beneath Heated Buildings.* U.S. Geological Survey Bulletin 1052-B. U.S. Geological Survey.

Mackay, J.R. 1963. *The Mackenzie Delta area, Northwest Territories, Geographical Branch, Memoir 8.* Ottawa: Department of Mines and Technical Surveys.

Mackay, J.R. 1974. Seismic shot holes and ground temperatures, Mackenzie Delta area, Northwest Territories. *Geological Survey of Canada Paper 74-1, Part A, Report of Activities, April to October 1973.* Ottawa: Geological Survey of Canada, Department of Energy, Mines and Resources, 389-390.

Marsh, P. & Hey, M. 1989. The flooding hydrology of Mackenzie Delta lakes near Inuvik, NWT, Canada. *Arctic* 42: 41-49.

Marsh, P. & Lesack, L.F.W. 1996. The hydrologic regime of perched lakes in the Mackenzie Delta: potential responses to climate change. *Limnology and Oceanography* 41: 849-856.

Marsh, P., Lesack, L.F.W. & Roberts, A. 1999. Lake sedimentation in the Mackenzie Delta, NWT. *Hydrological Processes* 13: 2519-2536.

Maxwell, B. 1997. Responding to global climate change in Canada's Arctic. *The Canada Country Study: Climate Impacts and Adaptation. Vol. 2.* Downsview, Ontario: Atmospheric Environment Service, Environment Canada.

Pearce, C.M., McLennan, D. & Cordes, L.D. 1988. The evolution and maintenance of white spruce woodlands on the Mackenzie Delta. *Holarctic Ecology* 11: 248-258.

Smith, M.W. 1973. *Factors Affecting the Distribution of Permafrost, Mackenzie Delta, N.W.T.* Ph.D. thesis. Vancouver, B.C.: Department of Geography, The University of British Columbia.

Smith, M.W. 1975. Microclimate influences on ground temperatures and permafrost distribution, Mackenzie Delta, Northwest Territories. *Canadian Journal of Earth Sciences* 12: 1421-1438.

Smith, M.W. 1976. *Permafrost in the Mackenzie Delta, Northwest Territories.* Geological Survey of Canada Paper 75-28. Ottawa: Geological Survey of Canada, Department of Energy, Mines and Resources.

Smith, M.W. & Hwang, C.T. 1973. Thermal disturbance due to channel shifting, Mackenzie Delta, N.W.T., Canada. *Permafrost: The North American Contribution to the Second International Conference*: 51-60.

Smith, S.L., Burgess, M.M, Riseborough, D. & Nixon, F.M. 2005. Recent trends from Canadian permafrost thermal monitoring network sites. *Permafrost and Periglacial Processes* 16: 19-30.

Williams, P.J. & Smith, M.W. 1989. *The Frozen Earth: Fundamentals of Geocryology*. Cambridge: Cambridge University Press, 360 pp.

Near-Surface Permafrost Conditions near Yellowknife, Northwest Territories, Canada

K.C. Karunaratne
Ottawa-Carleton Geoscience Centre, Carleton University, Ottawa, Canada
S.V. Kokelj
Water Resources Division, Indian and Northern Affairs Canada, Yellowknife, Canada
C.R. Burn
Department of Geography and Environmental Studies, Carleton University, Ottawa, Canada

Abstract

Yellowknife, NWT, lies in the discontinuous permafrost zone, in the southern portion of the Slave Geologic Province of the Canadian Shield. There are few data on permafrost temperature from the Yellowknife area. Thermistors connected to miniature dataloggers were installed to measure air, near-surface, and permafrost temperatures at nine sites in four peatlands near Yellowknife, for two years. Annual mean ground surface temperatures were above 0°C at all sites, but annual mean temperatures in permafrost ranged from -1.9 to -0.2°C. The presence of permafrost at these sites is therefore due to the thermal offset, which ranged between 1.3 and 4.0°C. Annual mean air temperature was about 4.5°C higher in the second year and the surface offset declined by 2.6°C. The thermal offset increased by 1.2°C.

Keywords: n-factors; peatlands; permafrost; surface offset; thermal offset; Yellowknife.

Introduction

The city of Yellowknife, NWT, is located at the southern boundary of the Slave Structural Province of the Canadian Shield. The area is known for its Archean bedrock and the long history of mining. Currently, the region is experiencing rapid industrial development and the effects of global warming, which both affect and are affected by permafrost. Our understanding of permafrost conditions near Yellowknife is based largely on Brown (1973) and Wolfe (1998). The purposes of this paper are (1) to present field measurements of air and ground temperatures at several peatlands in the Yellowknife area for two consecutive years; and (2) to discuss the spatial variation in the surface and thermal offsets over the period of record. The field data presented in this paper were collected at sites along the Ingraham Trail up to 70 km east of the city.

Climate and Permafrost

The climate-permafrost system can be described by the difference between the annual mean temperatures of the air (Ta_a) and ground surface (Ts_a), the surface offset, and the difference between Ts_a and the annual mean temperature at the top of permafrost (Tp_a), or the thermal offset (Lachenbruch et al. 1988, Smith & Riseborough 1996). The surface offset is a function of the surface energy balance and therefore varies with vegetation, moisture, snow, and soil thermal properties (Klene et al. 2001, Karunaratne & Burn 2004). In winter, the surface offset is controlled by snow cover, and the latent heat released during ground freezing (Karunaratne & Burn 2004). The thermal offset is controlled by seasonal differences in the thermal conductivity of the active layer and the extent of winter cooling (Romanovsky & Osterkamp 1995, Riseborough 2002). The thermal conductivity of soil increases upon freezing because the thermal conductivity of ice is four times that of liquid water. Thus soil moisture content controls the difference between frozen and thawed conductivities of a soil, and thereby, the thermal offset as well. The thermal offset is negligible in bedrock and relatively high in peat. A large thermal offset can result in the presence of permafrost where annual mean surface temperature is greater than 0°C (Burn & Smith 1988).

Numerical models of the climate-permafrost relation have been developed that parameterize the surface and thermal offsets. The TTOP model, proposed by Smith & Riseborough (1996), represents the surface offset through freezing and thawing n-factors. The n-factor is a ratio of surface to air freezing or thawing indices (e.g., degree-days) (Karunaratne & Burn 2004). In the literature, thawing n-factors (n_t) range from 0.26 at a fen, to greater than 1.0 at open sites with well-drained mineral surfaces, and freezing n-factors (n_f) from 0.12 for wet sites with thick snow covers, to 0.48 for dry sites with little snow (Karunaratne & Burn 2004, Klene et al. 2001, Taylor 1995). The thermal offset depends on the ratio of thawed to frozen thermal conductivity (Romanovsky & Osterkamp 1995, Riseborough 2002), which can be estimated from soil characteristics.

Study Area

Yellowknife has a continental climate, with a mean annual air temperature (MAAT) of -4.6ºC (Environment Canada 2007). The mean daily maximum temperature for July is 21°C but can reach 30°C, while the mean daily minimum temperature for January is -31°C, and has dropped as low as -51°C (Environment Canada 2007). The mean total annual precipitation is 280 mm, of which more than half arrives as rain. Snow cover develops in October, persists until

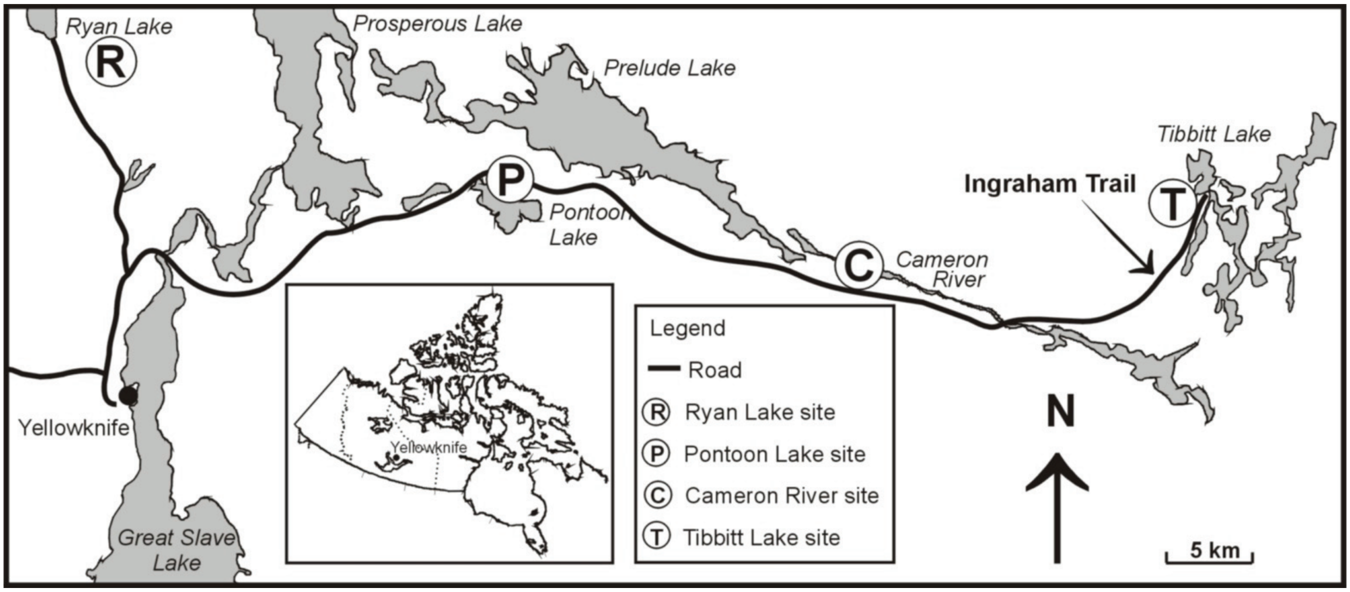

Figure 1. Location of peatland sites near Yellowknife.

the end of April, and approaches a depth of 40 cm in late winter (Environment Canada 2007). The terrain surrounding Yellowknife predominantly consists of peatlands populated by *Picea mariana*, and upland bedrock outcrops colonized by *Pinus banksiana*. The area lies in the extensive discontinuous permafrost zone (Heginbottom et al. 1995). Brown (1973) determined that permafrost is encountered near Yellowknife in peatlands, but not in outcrops or unconsolidated material. He recorded permafrost 50 m thick beneath a 30–cm active layer in a black-spruce peatland, and 30 m thick beneath a 68–cm active layer in a sedge peatland. In both cases the surficial peat was more than 1 m thick. Permafrost was absent in a nearby burnt peatland where the organic horizon was only 30 cm thick. Brown (1973) determined that mean annual ground temperatures were interannually variable, possibly due to differences in snow cover.

Study sites

Four sites were chosen along the Ingraham Trail east of Yellowknife to examine near-surface permafrost conditions. The sites were near Ryan Lake (R), situated 10 km north of Yellowknife, and at Pontoon Lake (P), Cameron River (C), and Tibbitt Lake (T), which were 30, 50, and 70 km east of Yellowknife respectively (Fig. 1). The sites were located in peatlands with *Sphagnum sp*. mosses and *Cladina sp*. lichens, and open-canopy *Picea mariana* forest. Low-lying shrubs commonly included *Ledum groenlandicum*, *Vaccinium vitis-idaea*, *Andromeda polifolia*, and *Empetrum nigrum*. *Rubus chamaemorus* was also ubiquitous. Although the peatlands are classified as basin bogs under the Canadian Wetland Classification System (1997), for the most part, the moss surface was dry, and the base of the active layer was commonly saturated. However, moisture conditions varied spatially and interannually.

Study period

The study period consisted of two years from October 2004 to September 2005, and from October 2005 to September 2006.

Precipitation differed between the years at the Yellowknife Airport. Summer 2004 was dry, receiving only 61mm of rain. The following summers were wetter, with 232 mm of rain in 2005, and 180 mm in 2006.

Snowfall was similar for both years but higher than normal, with maximum snow depth at the airport of 66 cm in both years.

Field Methods

Thermistors connected to miniature dataloggers were installed in 2003 and 2004 to measure air and near- surface temperatures at the peatlands. In total, nine sets of thermistors were installed at the four peatlands. Air temperatures were measured in radiation shields 1.5 m above the ground surface at peatlands T, C, and R. The thermistors measuring near-surface and ground temperatures were mounted on a wooden dowel and inserted into an augered hole. Near-surface temperatures were measured 2 to 5 cm beneath the living moss layer, and ground temperatures were measured at 50 and 100 cm depths. Temperature was recorded every 2 hours (Onset Computing, HOBO®, H08-006-04). The thermistors had a precision of ±0.38°C at 20°C, but random error associated with instrument precision is reduced in long-term averages because of the number of individual measurements (4380 measurements year^{-1}). The accuracy of the thermistors was reported to be ±0.5°C, but was found to be ±0.3°C of 0°C when they were calibrated in an ice bath.

In September 2006, soil samples of known volume were collected at each instrumented site at 10, 20, 30 and 50 cm depths. The soil samples were dried for 48 hours at 105°C to determine the volumetric soil moisture. Surveys of vegetation within 10 m^2 of each site were conducted in 2005, and included visual estimates of the canopy cover. Active-layer depths were determined at each of the instrumented sites in late summer by probing to resistance. In April 2005, snow depths were measured nine times along a 4x4 m cross-transect centered on the point of ground temperature measurements.

Table 1. Active layer depths , and the mean annual ground temperature at 50 cm (T_{50a}) and 100 cm (T_{100a}), and the annual maximum temperature at 100 cm (T_{100max}) for 2004–05 and 2005–06.

Site	Active Layer Depth (cm)	T_{100max} (°C)	T_{100a} (°C)	T_{50a} (°C)	T_{100a} - T_{50a} (°C)
2004-05					
T-01	50	-0.6	-1.9	-1.9	0.1
C-02	60	-0.6	-0.7	-0.2	-0.4
C-03	61	-0.2	-0.2	0.7	-0.8
C-04	44	-0.6	-1.7	-1.9	0.2
P-05	54		-	-1.3	
P-06	40	-0.2	-1.2	-1.6	0.4
R-07	48	-0.6	-0.8	-0.9	0.1
R-08	44	-0.6	-1.8	-1.8	0.0
R-09	40	-0.6	-1.8	-1.8	0.0
Mean	49	-0.5	-1.3	-1.2	-0.1
2005-06					
T-01	59	-0.6	-1.0	-0.8	0.3
C-02	68	-0.6	-0.6	0.3	0.9
C-03	70	-0.2	-0.2	0.9	1.0
C-04	50	-0.6	-0.7	-0.4	0.2
P-05	62	-	-	0.3	
P-06	45	-0.2	-0.3	-0.5	0.2
R-07	61	-0.6	-0.6	0.2	0.8
R-08	57	-	-1.1	-0.1	1.0
R-09	45	-	-1.1	-0.1	1.0
Mean	57	-0.5	-0.7	0.0	0.7

Permafrost at the Sites

Permafrost was established in the peat, but its thickness and that of the peat was unknown. Active-layer depths varied spatially and interannually and ranged from 40 to 70 cm (Table 1). The annual maximum temperature at 100 cm was below 0°C for both years at all the sites, indicating the presence of permafrost (Table 1). In 2004–05, the mean annual temperature at 100 cm (T_{100a}) ranged from -0.2°C at C-02 to -1.9°C at T-01; a difference of 1.7°C (Table 1). T_{100a} was between 0.7 and 1.0°C colder in 2004–05 than in 2005–06 except at C-02 and C-03 where it was nearly the same temperature in both years. At the coldest site, T-01, freezeback of the active layer did not occur until mid-January 2005 and until late February 2006, as indicated by a sudden decrease in the temperature at 50 and 100 cm depth (Fig. 2). At C-03, the warmest site, the temperature at 100 cm remained at -0.2°C throughout both years.

Air Temperature

Ta_a (October to September) at Yellowknife Airport (YZF) was -5.1°C for 2004–05, slightly below the MAAT of -4.6°C. The following year was warmer, with Ta_a of -0.6°C. The mean air temperature for the freezing (October to April) season (Ta_f) was 5.5°C lower in 2004–05 than in 2005–06, while the mean air temperature for the thawing (May-September) season (Ta_t) was 3.3°C lower in 2005 than in 2006 (Table 2). On average YZF was 0.9°C warmer than the study sites throughout the year, due to differences in microclimate conditions between the airfield and peatlands. The maximum difference between the peatlands for Ta_a and seasonal average temperatures (Ta_f and Ta_t) in both years was 0.8°C, but it was usually less than 0.3°C. The air temperatures at the study sites were similar, with differences in air temperature amongst the study sites, for the most part, within the accuracy of the instruments. Deviations in Ta_a beyond ±0.3°C were not consistent between sites, years, or seasons.

Table 2. Annual (October to September) mean air temperature (Ta_a), mean air temperature for the freezing season (Taf) and thawing season (Ta_t) for the Yellowknife Airport (YZF), and the Ryan Lake (R), Cameron River (C), and Tibbitt Lake (T) sites for 2004–05 and 2005–06.

	Ta_a (°C)		Ta_f (°C)		Ta_t (°C)	
Site	2004-05	2005-06	2004-05	2005-06	2004-05	2005-06
YZF	-5.1	-0.6	-16.0	-10.5	10.1	13.3
R	-5.7	-1.3	-16.6	-11.2	9.3	12.4
C	-6.1	-1.4	-17.1	-11.2	9.1	12.0
T	-6.1	-1.3	-17.4	-11.3	9.5	12.6
Mean	-5.8	-1.2	-16.8	-11.1	9.5	12.6

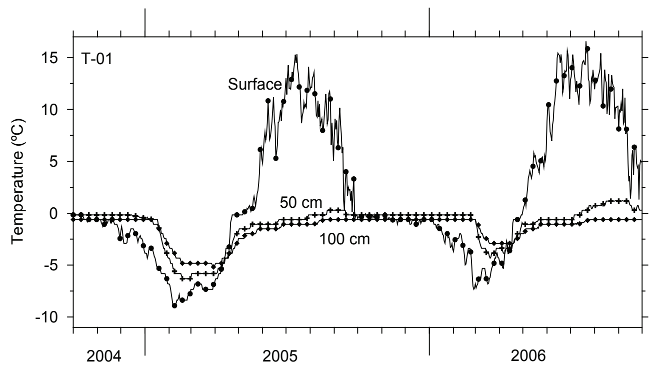

Figure 2. Mean daily surface and ground temperatures at 50 and 100 cm at site T-01 from October 2004 to September 2006. For clarity, the symbols are presented every 10 days while the plot is continuous throughout the two years.

Surface Temperature

The temperature of the surface is common to both the surface and thermal offsets and therefore is integral to the climate-permafrost relation. Surface temperature is measured at the base of the living mosses, approximately 2 to 5 cm from the ground surface to avoid radiative heating. This method is attractive because it positions the sensor close to the relatively warm ground surface during the summer, and is appropriate for measuring winter surface temperature,

Table 3. Mean near-surface temperatures for the year (Ts_a), freezing season (Ts_f) and thawing season (Ts_t), in 2004-05, and associated site characteristics.

Site	Ts_a (°C)	Ts_f (°C)	Ts_t (°C)	Snow Depth (cm)	Soil Moisure (g cm^{-3})	Canopy Cover (%)
T-01	0.8	-3.8	7.3	60	0.69	6-15
C-02	2.4	-1.6	7.9	56	0.74	6-15
C-03	2.0	-1.6	7.0	62	0.74	1-5
C-04	0.1	-4.0	5.9	45	0.70	51-75
P-05	1.0	-4.3	8.4	60	0.44	16-30
P-06	0.4	-5.1	8.2	42	0.41	51-75
R-07	1.9	-2.9	8.6	60	0.68	1-5
R-08	0.3	-4.1	6.5	41	0.67	51-75
R-09	-0.5	-5.0	5.8	41	0.67	76-100

Table 4. Rank order of the sites by annual mean surface temperature (Ts_a), and the mean surface temperature for the freezing season (Ts_f) and thawing season (Ts_t) for 2004–05 and 2005–06.

2004–05		2005–06	
Ts_a (°C)			
R-09	-0.5	R-09	2.3
C-04	0.1	C-04	2.5
P-06	0.4	P-06	2.5
T-01	0.8	T-01	2.7
C-02	2.4	C-02	3.3
Mean	0.6	Mean	2.7
Range	2.9	Range	1.1
Ts_f (°C)			
P-06	-5.1	T-01	-2.2
R-09	-5.0	P-06	-2.0
C-04	-4.0	C-04	-2.0
T-01	-3.8	R-09	-1.9
C-02	-1.6	C-02	-1.1
Mean	-3.9	Mean	-1.8
Range	3.5	Range	1.0
Ts_t (°C)			
R-09	5.8	R-09	8.1
C-04	5.9	C-04	8.8
T-01	7.3	T-01	9.6
C-02	7.9	C-02	9.6
P-06	8.2	P-06	9.6
Mean	7.0	Mean	9.1
Range	2.4	Range	1.5

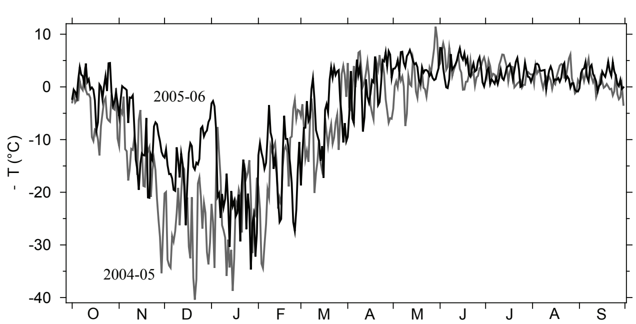

Figure 3. Difference between air and surface mean daily temperature at site C-02 for 2004–05 and 2005–06.

near the peat-snow interface. Such data can also be used to compare organic and exposed mineral surfaces.

Spatial variability of surface temperature

Annual mean and seasonal mean near-surface temperatures at each of the sites for 2004–05 are presented in Table 3, along with snow depth, mean volumetric soil moisture of the active layer, and estimated canopy cover. One measurement site was located in peatland T (T-01); three sites were in peatland C (C-02, -03, -04); two sites were in peatland P (P-05, -06); and three were in peatland R (R-07, -08, -09).

The range in Ts_a was 2.9°C among all nine sites, and 2.3°C among the sites at C and 2.4°C among the sites at R. Similarly, the variation in Ts_f, and Ts_t within peatlands C and R was no less than 60% of the total variation between peatlands. This suggests that the surface thermal regime was the same amongst the peatlands, and that variations in surface temperature among the instrumented sites were due to differences in microclimate.

The lowest Ts_a, and Ts_f, were measured at sites with over 50% canopy cover, and with thinner snow covers in winter due to interception of snow (Table 3). At sites where the snow depth was ≤ 45 cm, Ts_a were 0±0.5°C, and at sites with more than 50 cm of snow, Ts_a were between 0.8 and 2.4°C. The lowest Ts_t were also found at sites with high canopy cover, except at sites P-05 and P-06 which had the lowest soil moistures (Table 3). Canopy cover appears to control surface temperatures in peatlands through shading in summer and its influence on snow distribution in winter.

Interannual variation in surface temperature

Surface temperatures for 2004–05 and 2005–06 were examined at T-01, C-02, C-04, P-06 and R-09 to determine the year-to-year variability (Table 4). The surface temperature sensors at R-07, R-08, C-03, and P-05 did not produce reliable records in 2005-06 and were eliminated from this analysis. The average Ts_a, Ts_f, and Ts_t at the sites were 2.0°C lower in 2004–05 than in the following year (Table 4). The difference in annual mean surface temperature between the years was less than half of that for air temperature (Table 2). This is likely due to both the impact of snow cover in

Table 5. Surface offset (Ta_a-Ts_a), and freezing (n_f) and thawing (n_t) n-factors calculated from freezing and thawing degree-days at the sites.

Site	Surface Offset (°C) 2004-05	Surface Offset (°C) 2005-06	n_f 2004-05	n_f 2005-06	n_t 2004-05	n_t 2005-06
T-01	6.8	4.1	0.22	0.19	0.79	0.76
C-02	8.4	4.7	0.09	0.10	0.85	0.76
C-03	8.0	-	0.09	-	0.75	-
C-04	6.1	3.9	0.24	0.18	0.64	0.70
P-05	7.0	-	0.25	-	0.90	-
P-06	6.5	3.9	0.30	0.18	0.88	0.68
R-07	7.9	-	0.17	-	0.93	-
R-08	6.5	-	0.24	-	0.64	-
R-09	5.3	3.7	0.29	0.14	0.51	0.62
Mean	6.9	4.0	0.21	0.16	0.76	0.70

buffering the ground from variations in the air temperature regime, and to the impact of permafrost in restricting increases in surface temperature (Karunaratne & Burn 2004). The rank order of the five sites by Ts_a and Ts_t, was the same for both years (Table 4). The rank order of the sites by Ts_f, was similar for both years because the differences between four of the sites in 2005–06 did not exceed 0.3°C; the accuracy of the thermistors. Thus the interannual differences in surface temperature are consistent between the instrumented sites. Ts_a for all the sites was above 0°C for both years, except for R-09 in 2004–05. This indicates that the presence of permafrost in the Yellowknife area is due to the thermal, rather than the surface, offset. The thermal offset causes mean annual ground temperatures to decrease with depth through the active layer allowing permafrost to exist with mean annual surface temperatures above 0°C. Without the thermal offset, mean annual ground temperatures would increase with depth and therefore never extend below the mean annual surface temperature.

Surface Offset

The surface offset and the freezing (n_f) and thawing (n_t) n-factors were calculated for 2004–05 and 2005–06 based on surface temperatures measured at the sites and the average air temperature from T, C, R (Table 5). In 2004–05, the surface offset ranged from 5.3°C at R-09 to 8.4°C at C-02. The following year the surface offset was lower; between 3.7 and 4.7°C. The differences in surface offset between the two years can be attributed to differences between air and surface temperatures in early winter, since snow conditions were similar. In 2004–05, air temperatures had dropped below -20°C by mid-November, before the active layer had refrozen, which resulted in large differences between air and surface temperature (Fig. 3). In 2005–06, air temperatures were consistently higher than -20°C until the beginning of January, and thus closer to the surface temperature during freeze-back of the active layer.

Table 6. Thermal offsets calculated with ground temperatures at 50 cm (T_{50a}) and 100 cm (T_{100a}) for 2004–05 and 2005–06.

Site	T_{Sa}-T_{50a} (°C) 2004-05	T_{Sa}-T_{50a} (°C) 2005-06	T_{Sa}-T_{100a} (°C) 2004-05	T_{Sa}-T_{100a} (°C) 2005-06
T-01	2.5	3.3	2.7	3.8
C-02	2.4	2.7	3.0	4.0
C-03	1.1	-	2.2	-
C-04	1.8	2.8	1.8	3.2
P-05	1.9	-	-	-
P-06	1.9	3.0	1.6	2.8
R-07	2.6	-	2.7	-
R-08	2.0	-	2.3	-
R-09	0.8	2.3	1.1	2.4
Mean	1.9	2.8	2.2	3.2

Values of n_f ranged from 0.09 at C-02 and C-03 to 0.30 at P-06, and for n_t from 0.51 at R-09 to 0.93 at R-07 (Table 5). Both n_f and n_t for the study sites are within the range of n-factors reported in the literature for spruce peatlands (Jorgenson & Krieg 1988, Taylor 1995, Karunaratne & Burn 2004). Wet sites with thick active layers had the lowest values of n_f, and high values of n_f were calculated for sites with high canopy cover and subsequent thin snow covers. Values of n_t were related to canopy cover, with shaded sites having lower n_t than open sites. Sites P-05 and P-06 had higher n_t than their canopy cover would suggest possibly because of their low soil moisture. This suggests that moisture availability has a strong influence on n_t in peatlands.

Thermal Offset

The annual mean temperature at the top of permafrost (T_{Pa}) is required to calculate the thermal offset, but since the depth of the active layer varies spatially and interannually (Table 1), it is difficult to measure T_{Pa}. Fortunately, ground temperatures within the uppermost metres of permafrost can be used instead, as the ground warms very slowly with depth in this part of the temperature profile (Willams & Smith 1989), and temperatures several metres below the top of permafrost are similar to that at the top of permafrost. In 2004–05, slightly more than half of the sites had active layers thinner than 50cm, and the mean annual temperatures at 50 and 100 cm depths (T_{50a} and T_{100a}) were generally within 0.5°C, except at C-03 which had the deepest active layer (Table 1). The following year, most of the sites had active layers that were thicker than 50 cm, and the difference between T_{50a} and T_{100a} was 0.4°C higher than in 2004–05 (Table 1). The average difference in the thermal offset between that calculated with T_{50a} as opposed to T_{100a} was 0.1°C for the sites with active layers thinner than 50 cm, and 0.9°C for the sites with active layers thicker than 50 cm (Table 6). Thus the thermal offset calculated with T_{100a} is more appropriate to compare values between sites and years. The thermal offset (T_{Sa}-T_{100a}) was lower in 2004–05 than the following year for all of the sites; between 1.1 and 3.0°C in

2004–05 and between 2.4 and 4.0°C in 2005–06 (Table 6). The rank of the sites by the thermal offset was the same both years, with the highest value found at C-02 and the lowest at R-09. Sites with thick active layers had large thermal offsets (Table 1).

Conclusions

Air, surface and ground temperatures were measured in four peatlands near Yellowknife during 2004–05 and 2005–06. The following are the principal results of the study:

(1) The lowest annual mean surface temperatures were measured at sites with high canopy cover.
(2) The mean annual mean permafrost temperature among the sites was -1.3°C in 2004–05 and 0.7°C the following year.
(3) The mean surface offset among the sites was 5.9°C.
(4) The mean thermal offset among the sites was 2.6°C.
(5) Since the mean annual ground surface temperature in the peatlands was above 0°C, permafrost near Yellowknife is sustained by the thermal offset.

Acknowledgments

The research has been supported by the Natural Sciences and Engineering Research Council of Canada, and the Northern Scientific Training Program of Indian and Northern Affairs Canada. Field assistance from numerous individuals, especially Jesse Farlane and Krystal Thompson, is acknowledged with gratitude.

References

Brown, R.J.E. 1973. Influence of climatic and terrain factors on ground temperatures at three locations in the permafrost region of Canada. *Proceedings of the Second International Conference on Permafrost, North American Contribution, Yakutsk, U.S.S.R., July 13-28, 1973*: 27-34.

Burn, C.R. & Smith, C.A.S. 1988. Observations of the 'Thermal Offset' in near-surface mean annual ground temperatures at several sites near Mayo, Yukon Territory, Canada. *Arctic* 41: 99-104.

Environment Canada. 2007. Available from http://climate.weatheroffice.ec.gc.ca/.

Heginbottom, J.A., Dubreuil, M.A. & Harker, P.A. 1995. Canada-Permafrost. In: *National Atlas of Canada 5th Edition*. Ottawa: National Atlas Information Service, Natural Resources Canada, Plate 2.1 MCR 4177.

Jorgenson, M.T. & Kreig, R.A. 1988. A model for mapping permafrost distribution based on landscape component maps and climatic variables. *Proceedings of the Fifth International Conference on Permafrost, Trondheim, Norway, August 2-5, 1988*: 176-182.

Karunaratne, C.K. & Burn, C.R. 2004. Relations between air and surface temperature in discontinuous permafrost terrain near Mayo, Yukon Territory. *Canadian Journal of Earth Sciences* 41: 1437-1451.

Klene, A.E., Nelson, F.E. & Shiklomanov, N.I. 2001. The N-factor in natural landscapes: variability of air and soil-surface temperatures, Kuparuk river basin, Alaska, U.S.A. *Arctic, Antarctic and Alpine Research* 33: 140-148.

Lachenbruch, A.H., Cladouhos, T.T. & Saltus, R.W. 1988. Permafrost temperature and the changing climate. *Proceedings of the Fifth International Conference on Permafrost, Trondheim, Norway, August 2-5, 1988*: 9-17.

National Wetlands Working Group. 1997. *The Canadian Wetland Classification System, Second Edition.* B.G. Warner & C.D.A. Rubec (eds.), Waterloo, Ontario: Wetlands Research Centre, University of Waterloo, 68 pp.

Riseborough, D.W. 2002. The mean annual temperature at the top of permafrost, the TTOP Model, and the effect of unfrozen water. *Permafrost and Periglacial Processes* 13: 137-143.

Romanovsky, V.E. & Osterkamp, T.E. 1995. Interannual variations of the thermal regime of the active layer and near surface permafrost in Northern Alaska. *Permafrost and Periglacial Processes* 6: 313-335.

Smith, M.W. & Riseborough, D.W. 1996. Permafrost monitoring and detection of climate change. *Permafrost and Periglacial Processes* 7: 301-309.

Taylor, A.E. 1995. Field measurements of n-factors for natural forest areas, Mackenzie Valley, Northwest Territories. *Geological Survey of Canada, Current Research, 1995-B*: 89-98.

Williams, P.J. & Smith, M.W. 1989. *The Frozen Earth: Fundamentals of Geocryology.* New York: Cambridge University Press, 306 pp.

Wolfe, S.A. 1998. *Living with frozen ground: A field guide to permafrost in Yellowknife, Northwest Territories*. Geological Survey of Canada, Miscellaneous Report No. 64. 71 pp.

The Schmidt-Hammer as a Relative Age Dating Tool for Rock Glacier Surfaces: Examples from Northern and Central Europe

Andreas Kellerer-Pirklbauer
Institute of Geography and Regional Science, University of Graz, Austria

Abstract

This paper presents new data of measurements of Schmidt-hammer rebound values (*R*-values) on rock glacier surfaces and adjacent landforms from one site in northern Norway (Lakselv) and two sites in central Austria (Dösen and Weissenkar). The obtained *R*-values reveal long and complex rock glacier formation histories with initiations in the early Holocene. At least the large studied rock glaciers were formed continuously during most of the Holocene, whereas for small rock glaciers this is more difficult to prove. This implies that the Schmidt-hammer method seems to be a powerful tool in surface dating, particularly for large rock glaciers where multiple measurement sites along a longitudinal profile are possible to sample. *R*-values from such profiles enable the establishment of relative chronologies with high temporal resolution. Reliable absolute dating is possible when surfaces of known age with similar vegetation and climate history and comparable lithology are available. The more surfaces of known age are available, the better is a resulting age-calibration curve.

Keywords: Holocene landscape development; rock glacier formation; rock glacier surface dating; Schmidt-hammer.

Introduction

Rock glaciers originate from thick debris accumulations (talus and/or till) in high-relief environments that are under cryogenic conditions for a substantial period of time. Surface morphology, extent, and shape are the cumulative result of their entire genesis and thus climatic past. Temporal dates regarding their initiation and evolution period are the key to valuable palaeoclimatic information. Precise dating of rock glaciers is difficult but can be best achieved by applying an integrated approach, using a combination of relative—thereby distinguishing between fieldwork-based approaches (Schmidt-hammer rebound value, lichenometry, and weathering-rind thickness) and photogrammetry-based approaches (displacement rates and interpolated streamlines)—and absolute (luminescence, exposure/cosmogenic, and radiocarbon) dating methods (Haeberli et al. 2003). Absolute dating methods for rock glacier surfaces are still at an initial stage (Haeberli et al. 1999), are time-consuming, and have their own suites of assumptions and errors (cf. Shakesby et al. 2006), whereas relative dating methods are used more frequently (e.g., Haeberli et al. 2003, Frauenfelder et al. 2005, Kellerer-Pirklbauer et al. 2007). The combination of the Schmidt-hammer and photogrammetry-based approaches seems to be a powerful relative age-dating approach allowing—up to a certain extent—also absolute age estimations (Frauenfelder et al. 2005, Kellerer-Pirklbauer et al. 2007). However, Kellerer-Pirklbauer et al. (2007) pointed out that the main drawback of photogrammetry-based calculations of displacement rates and, derived from that, interpolated streamlines, is the crude assumption of constant velocity during the entire period of formation. Age estimations derived from Schmidt-hammer measurements seem to substantially reduce this drawback.

In this study the Schmidt-hammer method was applied at five rock glaciers and adjacent landforms in different environmental and geological settings. Results and age estimates are presented and compared with each other. The study areas are located at the following sites in Europe:

(1) One rock glacier near Lakselv, Gaissane Mountains, northern Norway (69°57′N, 24°47′E). Age dating based on cosmogenic isotope analysis is currently in progress from surface samples of a nearby rock glacier (LA-B in Fig. 1A) by Frauenfelder (pers. com.). No results are available so far.

(2) Three rock glaciers in the Dösen Valley, Ankogel Mountains, central Austria (46°59′N, 13°26′E). No detailed age estimations have been reported previously from there.

(3) One rock glacier in the Weissenkar Cirque, Schober Mountains, central Austria (46°57′N, 12°45′E). Crude age estimations were reported previously by Buchenauer (1990) suggesting a postglacial formation age.

Study Areas

Northern Norway – Lakselv

The study area near Lakselv, Gaissane Mountains, is characterised by a steep escarpment (caused by faulting) with some hundreds of meters in vertical dimension. This escarpment separates a high plateau from the broad glacially modified Balgesvag´gi valley (Fig. 1A). The high plateau is gently dipping towards the west with smooth summits reaching elevations above 800 m a.s.l. The bedrock at the study area consists of Precambrian and Palaezoic sandstones and silts. A number of gravitationally induced landforms can be identified at the foot of this escarpment reaching a lower elevation of ca. 380–400 m a.s.l. Such landforms are in particular two talus-derived, lobated rock glaciers (LA-A and LA-B in Fig. 1A) and four distinct avalanche boulder tongues (ABT in Fig. 1A). At this study area the intact (i.e. containing permafrost but presumably no current movement; Farbrot 2007), monomorphic and lobated rock glacier LA-A with a surface area of 0.09 km² was studied. For a detailed site description refer to Farbrot (2007).

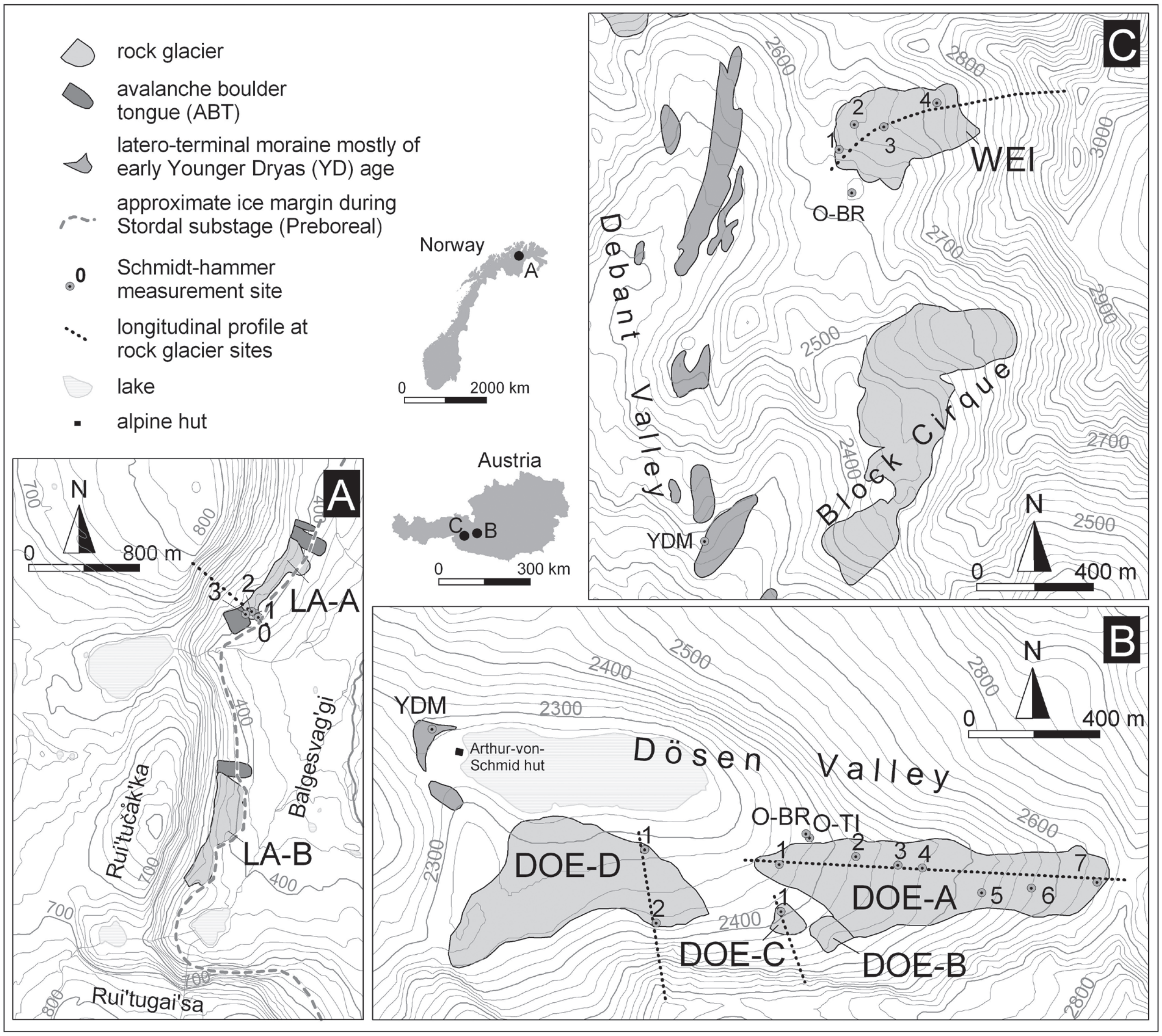

Figure 1. The study areas near (A) Lakselv, Gaissane Mountains in northern Norway and (B) Dösen Valley and (C) Weissenkar Cirque, both in central Austria: (A) Both rock glaciers (LA-A and LA-B=rock glacier Lakselv A and B) occur in close vicinity to avalanche boulder tongues indicating their close genetic relationship. Two Schmidt-hammer measurement sites are located at LA-A (1 & 2) and two nearby (0 & 3). The margin of the Fennoscandian Ice Sheet during the Stordal substage (Preboreal) was at the foot of the escarpment coming from east as indicated in the map. Age dating based on cosmogenic isotope analysis is currently in progress at LA-B. (B): Schmidt-hammer readings were carried out at two active, monomorphic, tongue-shaped (DOE-A and DOE-B) and one intact, monomorphic, lobated rock glacier (DOE-D) in the Dösen Valley. Dots at the rock glaciers, near rock glacier DOE-A (O-BR=bedrock outside rock glacier; O-TI=till boulders outside rock glacier) and at the terminal moraine of early Younger Dryas age (YDM) indicate sites of Schmidt-hammer measurements. (C) Schmidt-hammer readings were carried out at the surface of Weissenkar Rock Glacier (WEI), slightly outside the rock glacier at a roche moutonée (O-BR) and at a latero-terminal moraine ridge of early Younger Dryas age (YDM). Depicted landforms based on (A & B) field work and aerial photograph interpretation, and on (C) Buchenauer (1990). Dotted lines in the maps indicate longitudinal profiles.

Central Austria – Dösen

The second study area is situated in the Ankogel Mountains at the inner part of the glacially shaped, E-W trending Dösen Valley. This part of the valley is characterised by four north-to-west facing rock glaciers, a cirque floor with a tarn lake, and distinct terminal moraines (Fig. 1B). The moraines were presumably formed during the Egesen-maximum advance and are thus of early Younger Dryas (YD) age (Lieb 1996). The elevation ranges between 2270 m a.s.l. at the cirque threshold to more than 3000 m a.s.l. at the nearby Säuleck peak. The four rock glaciers predominantly consist of granitic gneiss (Kaufmann et al. 2007). Three of these rock glaciers (DOE-A, B, and C in Fig. 1B) are considered to be active, and one (DOE-D in Fig. 1B) is regarded as climatic inactive (Lieb 1996). In this study, the focus was on the two active and monomorphic rock glaciers, DOE-A (0.19 km²) and DOE-C (0.007 km²), and on the inactive and monomorphic rock glacier DOE-D (0.17 km²). Previous permafrost research—including velocity measurements—focused particularly on the rock glacier DOE-A (for details see Lieb 1996 or Kaufmann et al. 2007).

Central Austria – Weissenkar

The third study area is located in the Schober Mountains at a west-exposed cirque in the Debant Valley. As indicated by the high number of rock glaciers (n=126), the Schober Mountains provide suitable topoclimatic and geological (crystalline rocks) conditions for rock glacier formation (Lieb 1996). The cirque is dominated by the tongue-shaped Weissenkar Rock Glacier (WEI in Fig. 1C) which is fed by active scree slopes. Until the late 1990s, the rooting zone of WEI was occupied by a large perennial snow field. WEI consists of an active upper lobe overriding an inactive lower lobe. Different types of mica schist form the lithological component of the rock glacier. WEI is characterized by well developed furrows and ridges at its entire lower half, a lower limit at 2615 m a.s.l., a length of 500 m, and a surface area of 0.11 km². WEI creeps from the cirque to a plateau-like area composed of roches moutonées. Latero-terminal moraine ridges of Late Glacial age are frequent in the area. At this study area the rock glacier, one roche moutonée, and a distinct moraine ridge of supposed Egesen/early YD age located at the lower end of the Block Cirque were studied (cf. Buchenauer 1990, Lieb 1996, Kaufmann et al. 2006).

Methods

A Schmidt-hammer (or sclerometer) is a light and portable instrument traditionally used for concrete stability testing by recording a rebound value (R-value) of a spring-loaded bolt impacting a surface. Beginning in the 1980s (e.g., Matthews & Shakesby 1984, McCarroll 1989), this method has been increasingly applied in glacial and periglacial studies for relative rock surface dating. The obtained R-value is proportional to the compressive strength of the rock surface and gives a relative measure of the surface hardness and thus provides information on the time since surface exposure and the degree of weathering. High values are indicative of a lower age and vice-versa.

Analogue L-type Schmidt-hammers have been used at all three study areas using products of the companies "PROCEQ," Switzerland (Norwegian site) and "Controls," Italy (Austrian sites). On each of the larger rock glaciers (LA-A, DOE-A, DOE-D, and WEI), two to seven locations close to the central flow line between the frontal ridge and the rooting zone were measured. Sites were kept as small as possible. Measurements on rock glaciers were made on ridge crests and high spots to minimise the possible influence of late-lying snow on weathering rates.

Complementary measurements were carried out on a smaller rock glacier (DOE-C), on boulders at the active talus of the rooting zone of DOE-A, on an active ABT (LA-A3), and at outside sites located adjacent or down-valley from the rock glacier termini. These outside sites were located twice on bedrock (2 x O-BR: Dösen and Weissenkar) and four times on glacigenic boulders (LA-A0, O-TI and 2 x YDM: Dösen and Weissenkar). Sampled stable boulders and bedrock sites in each of the three study areas were selected on the basis of comparable lithology with dry, flat and clean surface, free of lichens, visual fissures and cracks (McCarroll 1989, Haeberli et al. 2003, Shakesby et al. 2006).

Arithmetic means of 50 individual readings (4 impacts per boulder; only the two middle values were noted) with 95% confidence interval were examined at all sites (Matthews & Shakesby 1984, Shakesby et al. 2006). Arithmetic means are representative for the effective hardness of the analyzed surface. The 95% confidence interval is indicative for the standard error and statistically significant age differences between measurement sites.

Results

The Schmidt-hammer results of all three study areas are summarised in Fig. 2A to 2C. Frequency distribution of only one sample shows low bimodality (LA-A3), and skewness is generally low to moderate. Negative skewness may point to a somewhat lower mean R-value (higher age) than observed; positive skewness may indicate a somewhat higher mean R-value (lower age) than observed.

Rock glaciers near Laksekv

Mean R-values range from 48.8 outside LA-A (LA-A0) to 54.8 at the active ABT (LA-A3) adjacent to the rock glacier with low 95% confidence limits. The four samples cover a R-value range of only 6.0. R-values taken at the rock glacier surface are significantly higher than the ones taken from the outside site close to a moraine ridge of Preboreal age, and they are significantly lower than the ones from the ABT.

Rock glaciers in the Dösen Valley

Mean R-values range from 29.7 at the YDM site to 47.7 at the active talus above DOE-A (DOE-A7) covering a R-value range of 18.0. The 95% confidence limits are generally below ±1.00. A decrease in R-values can be discerned at the inactive rock glacier DOE-D and, in particular, at the active rock glacier DOE-A (δR-value 12.3).

Rock glacier in the Weissenkar Cirque

Mean R-values range from 21.5 at the YDM site to 38.0 at site WEI4 located in the active rooting zone of the rock glacier covering a R-value range of 16.4. The rooting zone was occupied by a glacier during the Little Ice Age (~1850 AD) and a large perennial snow field until the late 1990s indicating a rather young age of the deposits at site WEI4. The 95% confidence limit at site WEI4 (1.77) is the highest of all 23 measured sites. A clear decrease in R-values can be discerned at the rock glacier WEI (δR-value 13.5).

Discussion

When analyzing Schmidt-hammer literature, it becomes obvious that R-value decrease over time is quite heterogeneous in alpine climates and in different lithologies. However, R-value differences of >10 suggest time periods of some thousands to more than ten thousand years even in competent rocks such as gneiss (e.g., Aa & Sjåstad 2000, Frauenfelder et al. 2005, Kellerer-Pirklbauer et al. 2007).

Rock glaciers near Lakselv

The formation of the studied rock glaciers in Lakselv

(LA-A) was initiated sometime after the retreat of the Fennoscandian Ice Sheet from the study area. During the YD period, the site of the rock glacier LA-A was situated well inside the glacier limit (Sollid et al. 1973). Marginal moraine ridge systems belonging to the Post-Main (Stordal) substages (Sollid et al. 1973) of suggested Preboreal age (9-10 ka BP, uncalibrated ^{14}C years; Andersen 1979) were deposited in very close vicinity to the present rock glaciers LA-A and LA-B (see Fig. 1A). Later these moraine ridges acted as natural barriers for the development of both lobated rock glaciers and were partly incorporated into them.

The interpretation of the obtained *R*-values is difficult, and the dating here is very speculative. Aa & Sjåstad (2000) calculated for a site in southern Norway that the *R*-value was reduced by 20.5 over a period of 9730 a. Their study site is to some extent climatically comparable to the Lakselv site but with different lithology (gneiss). They inferred a (hypothetical) linear surface weakening rate of 2.1 *R*-values per 1 ka. However, complications arise because the increase in the degree of weathering over time (i.e. weathering rind thickness) and the role of flaking of the weathering rind are not easy to quantify. Schmidt-hammer mean values seem to correlate with weathering rind thickness almost linearly (Laustela et al. 2003) allowing good comparison. Weathering rind thickness increases nonlinearly with time although this nonlinear weathering-time relationship seems to occur on very long timescales often exceeding 100 ka (Skakesby et al. 2006). The role of flaking of weathering rinds might be more important for shorter time periods (Etienne 2002). The *R*-value differences of 3.4 between LA-A1 and LA-A3 (site at the ABT) and 2.6 between LA-A1 and LA-A0 (site close to the Preboreal moraine ridge) is statistically significant. They allow the conclusion that the rock glacier surface is significant younger than Preboreal but significant older than the currently still active ABT. The low δR-value of 6.0 between the ABT site and the site adjacent to the moraine ridge also might be explained by occasional dispersing of rock material over the entire rock glacier LA-A and its foreland by powerful debris-charged snow avalanches. Judging from the morphology of the rock glacier itself, the glacial and periglacial landforms in close vicinity, and the considerations by Kääb (2005) – total age of rock glaciers might be 2–5 times higher than the minimum age obtained for the surface – a long and complex formation history and a rock glacier initiation soon after the Preboreal is suggested.

Rock glaciers in the Dösen Valley

The initiation of all rock glaciers in this study area occurred after the Egesen advance in the early YD period as indicated by the moraines downvalley from the four rock glaciers. In Austria, the early YD is 10Be-dated to around 12.3–12.4 ka (Kerschner & Ivy-Ochs 2007). Thus the maximum and the minimum R-values in this study area can be absolute dated to 12.3–12.4 ka at the YDM site and ~0 a at the active talus site DOE-A7. In this regard, one should not forget the time lag between initial crack formation in the rock face above the rock glacier (exposure to weathering) and the eventual release of a clast to the talus below. Quantification of this period is difficult.

By using a linear relationship between *R*-value and time, a tentative age-calibration curve with a mean decrease of 1.46

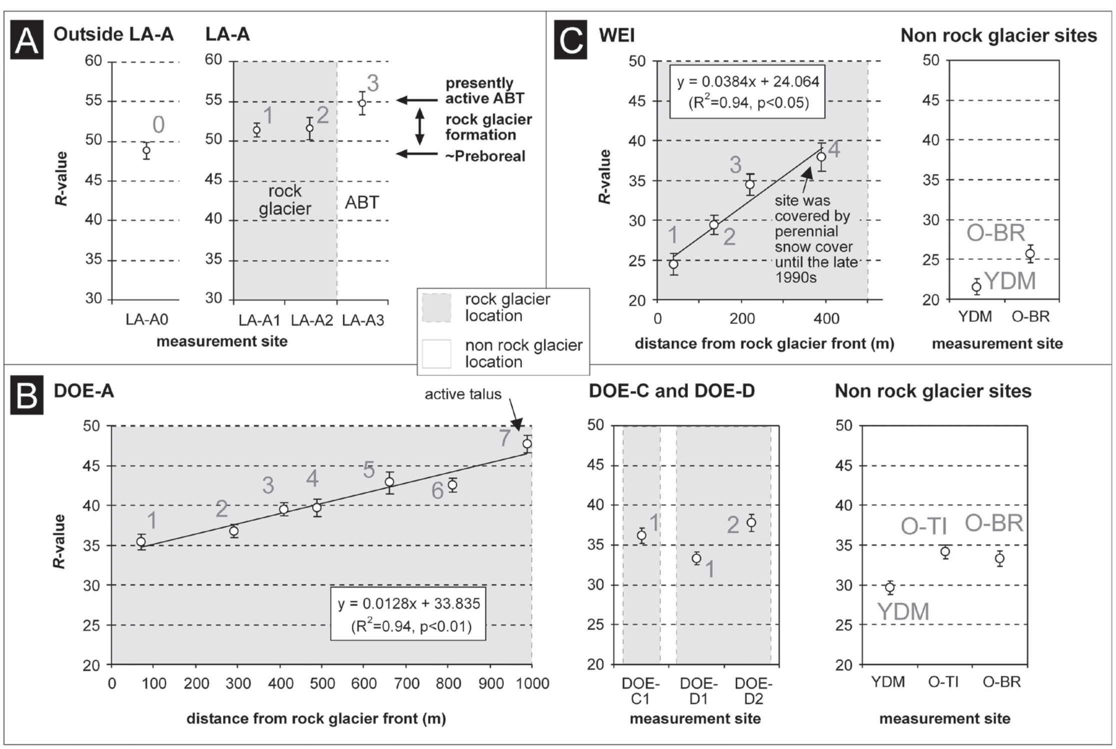

Figure 2. Results of the Schmidt-hammer measurements at the studied rock glaciers and nearby non-rock glacier locations in (A) northern Norway (LA-A) and (B-C) in central Austria (DOE-A, DOE-C, DOE-D and WEI): *R*-values show the arithmetic mean and 95% confidence limits at each measurement site. At the large monomorphic rock glaciers, DOE-A and WEI, *R*-values are plotted against distance from rock glacier front. Best-fit correlations are indicated. Numerals in the graph refer to locations in Figure 1. Estimated age ranges for (A) are given.

R-values per 1 ka can be inferred (Fig. 3A). Skakesby et al. (2006) introduced a simple method to investigate the likely size of error of the absolute age estimates derived by the linear relationship. According to their approach, error limits for the predicted ages are determined separately for the YD and present sites from the corresponding 95% confidence intervals of *R*-values by a straight line. The error limits in the predicted age based on this approach is ±607 years for YDM and ±774 years for DOE-A7. Thus a predicted age error of ca. ±0.7 ka for all sites should be considered.

A substantially and statistically significantly lower mean *R*-value at the YDM site compared to all other sites (δ≥3.6) suggests that during the YD and Preboreal periods, the head of the Dösen Valley was covered by a glacier terminating between the YDM and the present rock glacier front. The following glacier retreat deglaciated the bedrock site O-BR and deposited the coarse boulders at site O-TI. Identical *R*-values from site DOE-D1 suggest that the rock glacier DOE-D reached its lower end at a similar time. This further suggests that due to its lower position along the valley axis, this valley stretch was not glaciated in the preceding Preboreal period but allowed the formation of DOE-D.

The insignificant *R*-value difference between the outside site O-TI and the lowest site on DOE-A is difficult to interpret when considering the assumption that the total age of a rock glaciers is 2–5 times higher than the minimum age obtained for the surface (Kääb 2005). The obtained minor difference suggests that the surface and total landform age of DOE-A seems to be similar. The same seems to be true for DOE-C and DOE-D. Explanations might be: (a) a less effective "conveyor belt" mechanism (Haeberli et al. 2003), (b) debris-covered glacier tongues which were later incorporated in the rock glacier, (c) mineral variations in the bedrock, or (d) differences in the surface weakening rate between sites due to different vegetation /snow cover histories in the Holocene.

The regression line at DOE-A indicates that this rock glacier was formed continuously during most of the Holocene. Recent velocity data (1954–2005) from the rock glacier DOE-A show mean annual velocity rates of 13.4–37.4 cm a^{-1} (Kaufmann et al. 2007). If these velocities are taken as (questionable) constant over time and combined with the length of DOE-A, ages of 2.7–7.5 ka are calculated. These age values are lower than the age estimate of the lowest rock glacier site (DOE-A1) obtained by the tentative age-calibration curve presented in Fig. 3A (8.4±0.7 ka).

Rock glacier in the Weissenkar Cirque

The *R*-values from the third study area suggest a comparable landscape history to the one from the Dösen Valley. The initiation of the rock glacier WEI occurred after the Egesen advance in the early YD period as indicated by the YD moraines downvalley from the cirque. The linear relationship between the *R*-value of the YD moraine site (YDM: 21.5) and the uppermost measurement site in the rooting zone of the rock glacier (WEI4: 38.0) reveals a mean decrease of 1.33 R-values per 1 ka (Fig. 3B).

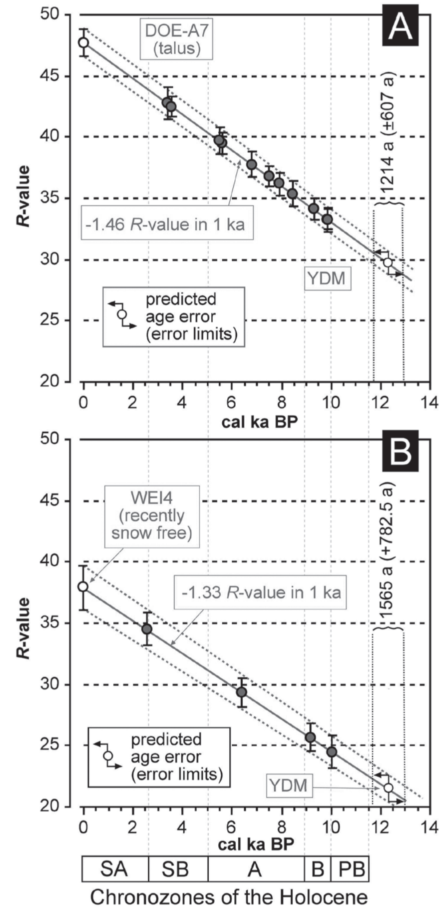

Figure 3. Tentative age-calibration curves for the *R*-values of the study areas Dösen (A) and Weissenkar (B) based on two surfaces of known age indicated as open circles. The calculation of predicted age error including error limits is illustrated for the YDM locations. Grey circles indicate calculated ages based on this approach. Holocene chronozones: SA=Subatlantic, SB=Suboreal, A=Atlantic, B=Boreal and PB=Preboreal.

This rate is only slightly less than the one from the Dösen Valley which indicates that the reduction in the mean *R*-value during the Holocene in central Austria was similar for granitic gneiss (Dösen) and mica schist (Weissenkar) despite substantially different absolute *R*-values.

At Weissenkar Cirque the bedrock site just outside the rock glacier (O-BR) suggests a younger age than the lowest site at the rock glacier (WEI1). Reasons for that might be explanations (a) to (d) presented above. The statistically significant decrease in R-values along a profile at WEI points to a long formation history of the landform starting in the early Holocene. At WEI, the lowest measurement site reveals an age of about 10 ka (cf. Fig. 3B). Therefore, WEI might be even older than the large rock glacier DOE-A in the Dösen Valley. Recent velocity data (1974–2004) from WEI were summarised by Kaufmann et al. (2006) showing low mean annual velocity rates of 1.6–11.6 cm a^{-1}. Assuming constant velocities and using a length of 500 m, rock glacier ages of 4.3–31.1 ka can be estimated. This maximum age is certainly far too high, highlighting the weakness of the assumption of constant surface velocity.

Conclusions

The Schmidt-hammer method seems to be a powerful tool in rock glacier dating, particularly for large rock glaciers where multiple measurement sites along a longitudinal profile are sampled. *R*-value data from such profiles enable the establishment of relative chronologies with high temporal resolution. For small and short rock glaciers this method is more difficult to apply, and additional palaeoclimatic information is required to constrain age estimates. At the study sites in Austria it was possible to estimate relatively accurately the age for Holocene features. However, possible incorporation of older clasts in the rock glacier surface or dispersing of "fresh" rock material by powerful debris-charged snow avalanches can lead to errors. Furthermore, mineral variations in the bedrock or differences in the rate of surface weakening between sites due to different vegetation/snow cover histories might significantly influence *R*-values. Reliable absolute surface age dating is only possible when surfaces of known age with similar vegetation and climate history, and comparable lithology are available. The more surfaces of known age are available, the better is a resulting age-calibration curve.

Acknowledgments

This study was carried out within the project ALP-CHANGE (www.alpchange.at) financed by the Austrian Science Fund (FWF) and by an international research scholarship by the Research Council of Norway. Research at the Weissenkar site was supported by students of my institute who are kindly acknowledged. The comments of both reviewer and the editor were highly appreciated.

References

Aa, R. & Sjåstad, J.A. 2000. Schmidt hammer age evaluation of the moraine sequence in front of Bøyabreen, western Norway. *Norsk Geologisk Tidsskrift* 80: 27-32.

Andersen, B.G. 1979. The deglaciation of Norway 15 000–10 000 BP. *Boreas* 8: 79–87.

Buchenauer, H.W. 1990. Gletscher- und Blockgletschergeschichte der westlichen Schobergruppe (Osttirol).- *Marburger Geographiche Schriften* 117: 276 pp.

Etienne, S. 2002. The role of biological weathering in periglacial areas: a study of weathering rinds in south Iceland. *Geomorphology* 47: 75-86.

Farbrot, H. 2007. *Distribution, thermal regime and geomorphic significance of mountain permafrost in northern Europe - examples from Iceland, northern Norway & Svalbard.* PhD. Thesis. University Oslo, 141 pp.

Frauenfelder, R. Laustela, M. & Kääb, A. 2005. Relative dating of Alpine rockglacier surfaces. *Zeitschrift für Geomorphologie* 49: 145-166.

Haeberli, W., Kääb, A., Wagner, S., VonderMühll, D., Geissler, P., Haas, J.N., Glatzel-Mattheier, H. & Wagenbach, D. 1999. Pollen analysis and 14C age of moss remains in a permafrost core recovered from the active rock glacier Murtèl-Corvatsch, Swiss Alps: geomorphological and glaciological implications. *Journal of Glaciology* 45: 1-8.

Haeberli, W., Brandovà, D., Burga, C., Egli, M., Frauenfelder, R., Kääb, A. & Maisch, M. 2003. Methods for absolute and relative age dating of rock-glacier surface in alpine permafrost. *Proceedings of the Eighth International Conference on Permafrost, Zurich, Switzerland, July 21-25, 2003:* 343-348.

Kääb, A. 2005. Remote sensing of mountain glaciers and permafrost creep. *Schriftenreihe Physische Geographie Glaziologie und Geomorphodynamik* 48: 266 pp.

Kaufmann, V., Ladstädter, R. & Lieb, G.K. 2006. Quantitative assessment of the creep process of Weissenkar rock glacier (Central Alps, Austria). *Proceedings of the Eight International Symposium High Mountain Remote Sensing Cartography, La Paz, Bolivia, March 21–28, 2005:* 77-86.

Kaufmann, V., Ladstädter, R. & Kienast, G. 2007. 10 years of monitoring of the Doesen rock glacier (Ankogel group, Austria) - A review of the research activities for the time period 1995-2005. *Proceedings of the Fifth Mountain Cartography Workshop, Bohinj, Slovenia, March 29–April 1, 2006:* 129-144.

Kellerer-Pirklbauer, A., Wangensteen, B., Farbrot, H. & Etzelmüller, B. 2007. Relative surface age-dating of rock glacier systems near Hólar in Hjaltadalur, Northern Iceland. *Journal of Quaternary Science* 23 (2): 137-151.

Kerschner, H. & Ivy-Ochs, S. 2007. Palaeoclimate from glaciers: Examples from the Eastern Alps during the Alpine Lateglacial and early Holocene. *Global and Planetary Change* 60(1-2): 58-71.

Laustela, M., Egli, M., Frauenfelder, R. & Haeberli, W. 2003. Weathering rind measurements and relative age dating of rock-glacier surfaces in crystalline regions of the Swiss Alps. *Proceedings of the Eighth International Conference on Permafrost, Zurich, Switzerland, July 21-25, 2003:* 627-632.

Lieb, G.K. 1996. Permafrost und Blockgletscher in den östlichen österreichischen Alpen. *Arbeiten aus dem Institut für Geographie, Univerisät Graz* 33: 9–125.

Matthews, J.A. & Shakesby, R.A. 1984. The status of the 'Little Ice Age' in southern Norway: relative-dating of Neoglacial moraines with Schmidt hammer and lichenometry. *Boreas* 13: 333-346.

McCarroll, D. 1989. Potential and limitations of the Schmidt hammer for relative dating. Field tests on Neoglacial moraines, Jotunheimen, southern Norway. *Arctic and Alpine Research* 21: 268-275.

Shakesby, R.A., Matthews J.A. & Owen, G. 2006: The Schmidt hammer as a relative-age dating tool and its potential for calibrated-age dating in Holocene glaciated environments. *Quaternary Science Reviews* 25: 2846-2867.

Sollid, J.L., Andersen, S., Hamre, N., Kjeldsen, O., Salvigsen, O., Sturod, S., Tveita, T. & Wilhelmsen, A. 1973. Deglaciation of Finnmark, North Norway. *Norsk Geografisk Tidsskrift* 27: 233-325.

Scaled Centrifuge Modeling of Solifluction in Permafrost and Seasonally Frozen Soils

Martina Kern-Luetschg
Cardiff University, School of Earth Sciences, Cardiff CF10 3YE,UK
Charles Harris
Cardiff University, School of Earth Sciences, Cardiff CF10 3YE,UK
Peter Cleall
Cardiff University, School of Engineering, Cardiff, CF24 3AA, UK
Yuchao Li
Cardiff University, School of Engineering, Cardiff, CF24 3AA, UK
Hywel Thomas
Cardiff University, School of Engineering, Cardiff, CF24 3AA, UK

Abstract

The technique of centrifuge modeling allows accurate simulation of full-scale geotechnical processes in small-scale models under correct self weight. Here we report results from two scaled 10 g centrifuge modeling experiments, designed to simulate solifluction processes associated with one-sided and two-sided freezing of an active layer of 1 m thickness at prototype scale. A distinct dry intermediate layer was observed in the two-sided experiment where only very small displacement and thaw settlement occurred. The overall rate of thaw in the two-sided model was significantly slower compared to the one-sided experiment. The total soil deformation profiles after five freeze-thaw cycles show a plug-like sliding component immediately above the permafrost table in the two-sided experiments, but shear strain decreasing with depth in the one-sided experiment. Data from these experiments are currently being used to calibrate and validate newly developed numerical constitutive modeling algorithms designed to predict soil behavior during solifluction.

Keywords: active layer; centrifuge modeling; solifluction.

Introduction

Here we present first results of scaled centrifuge simulation of solifluction processes associated with one-sided and two-sided soil freezing, allowing detailed comparison of hydrothermal processes and downslope displacement rates. These experiments are part of a research program designed to predict styles and rates of periglacial solifluction and their relationship to factors such as climate, hydrology, geology, and topography. New process-based numerical models are being developed and validated against well-controlled full-scale simulations (Harris et al., this volume) and reduced-scale centrifuge modeling.

Freezing and thawing of frost-susceptible, soil-covered slopes cause slow downslope soil movement which is highly significant to slope evolution. In areas of warm or no permafrost, seasonal freezing is from the surface downwards (one-sided freezing), whereas in cold permafrost areas, large thermal gradients in the uppermost permafrost layer can cause active layer freezing in two directions: from the permafrost table upwards and from the ground surface down (two-sided freezing) (e.g., Lewkowicz 1988, Shiklomanov & Nelson 2007). Bottom-upward freezing is most widespread where mean ground temperatures are below -5°C and usually precedes freezing from the surface (Shur 1988). In the case of one-sided freezing, ice lens formation occurs near the ground surface, but during two-sided freezing, ice lenses accumulate in a transition zone that includes the basal zone of the active layer and the upper part of the permafrost (Shur et al. 2005). Thaw penetration into this zone causes deeper soil movements and "plug-like" solifluction (Mackay 1981, Lewkowicz & Clarke 1998).

Numerous field studies of solifluction processes have emphasized the factors controlling spatial variability, and a global review is given by Matsuoka (2001). More detailed exploration of the mechanisms of periglacial solifluction under one-sided freezing has been achieved in large-scale laboratory simulations with controlled soil properties and boundary conditions (Coutard et al. 1988, Harris et al. 1996). The potential of using geotechnical centrifuge modeling technique for the simulations of mass movement processes in thawing slopes has been demonstrated in recent studies (Harris et al. 2001, Harris et al. 2003a,b, Harris et al. 2008). The present experiments were designed to simulate solifluction following one-sided and two-sided freezing conditions under correct slope self weight in the centrifugally accelerated gravity field and under well-controlled soil and boundary conditions.

Numerical Modeling

For stability problems in cold regions, such as periglacial solifluction, it may be difficult to accurately measure the field stresses in thawing soils with the limitation of current instruments and methods. The rates and styles of periglacial solifluction apparently depend to some degree on the depth at which ice lenses develop during frost heaving, (Matsuoka 2001). An accurate prediction of ice lensing is therefore of great importance to model the process of periglacial solifluction. A fully coupled thermo-hydro-mechanical numerical approach for modeling solifluction in freezing and thawing soils is under development, based on the existing software, COMPASS (Cleall et al. 2007). Numerical models will be calibrated against laboratory physical models, including centrifuge studies, and assessed via simulation of field data from monitored natural slopes in Svalbard and Norway (Harris et al. 2007).

Centrifuge Modeling Technique

Geotechnical centrifuge modeling allows detailed studies of real processes under defined boundary conditions, providing an excellent tool for verifying numerical methods. In the rotating centrifuge, a $1/N$ scaled model is subjected to a centrifugal force equivalent to N gravities (g) which increases the self-weight of the soil and thus generates a gravitational stress distribution in the model, which is equal to that in the prototype. In a centrifuge test at Ng, model linear dimensions scale as $1/N$, area $1/N^2$, stress 1/1, temperature 1/1, time for convective and conductive heat transfer $1/N^2$, and time for seepage force similarity $1/N^2$ (Croce et al. 1985, Savidou 1988). A 1/10 scale centrifuge model tested at 10 g therefore extrapolates to the correct prototype scale.

Accurate scaled modeling requires similitude in soil properties between model and prototype, which is achieved by using the same soil with the same stress history. In the present context, the thaw consolidation theory (Morgenstern & Nixon 1971) provides a framework for the analysis of effective stress within thawing ice-rich soils, the governing factors being thaw penetration rate (controlling rate of meltwater release) and consolidation rate (controlling rate of dissipation of excess pore-water pressure). Since time for seepage force similarity and for heat transfer both scale as $1/N^2$, no scaling conflicts arise in modeling the thaw consolidation process, and model time is reduced by a factor of N^2 (Harris et al. 2000, 2001).

However, the time scaling factor for viscous flow is 1/1, so potential temporal scaling conflicts arise if the dynamic response of the thawing soil to gravitational stress is a function of its viscosity. A series of "modeling of models" centrifuge experiments, in which solifluction processes were simulated at different scales and gravitational accelerations, showed virtually identical profiles of shear strain and identical soil transport rates in all models when scaled to prototype, leading to the conclusion that shear strains during solifluction reflect an elasto-plastic response of the thawing soil to gravitational stress, controlled by pore-water pressures, and not fluid flow controlled by viscosity (Harris et al. 2003a). Thus, no significant scaling conflicts arise during centrifuge modeling. An additional advantage of the method is that processes which would take many days or months at prototype scale can be simulated in a few hours.

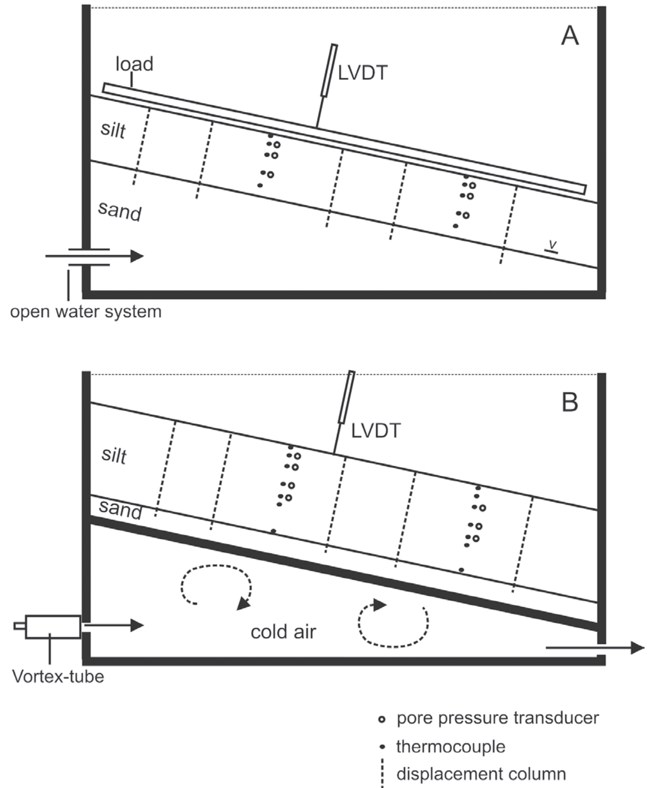

Figure 1. Experimental design during model freezing on the lab floor. (A) one-sided freezing and (B) two-sided freezing. The sides and base of the test box were surrounded in polystyrene insulation, and the surface temperature lowered to between -5°C and -10°C.

Design of Centrifuge Experiments

The Cardiff University geotechnical centrifuge consists of a beam centrifuge of 2.7-m radius for testing model packages of up to 1000 kg at an acceleration of up to 100 gravities. 1/10 scale slope models with gradient 12° were constructed in Perspex boxes of internal dimensions 0.74 m x 0.45 m x 0.44 m (Fig. 1) using the same silty soil that was used for equivalent full-scale laboratory simulations (see Harris et al., this volume). For this study, two different model types were prepared to simulate (a) the response of the thawing soil to ice distribution generated by seasonal one-sided freezing and (b) the response of the thawing soil to ice distribution generated by two-sided freezing under cold permafrost conditions. Soil was placed over a basal sand layer forming a 9-cm-thick model (scaling to 90 cm) for the one-sided experiments and a 14-cm-thick model (scaling to 140 cm) for the two-sided experiment.

In each, 2 vertical arrays of 5 and 7 type-K thermocouples, respectively, and three Druck pore pressure transducers were inserted. Thermocouples were placed at 5 cm above the box for air temperatures and at depths 0, 1, 3.5, 6, and 7 cm in the one-sided and at 0, 2, 3.5, 6, 8, and 9 cm in the two-sided model. Columns of 5 mm plastic cylinders were inserted perpendicular to the slope surface to measure soil deformation. A regular grid of 1 cm circular markers was distributed on the surface to monitor surface downslope displacement during thawing.

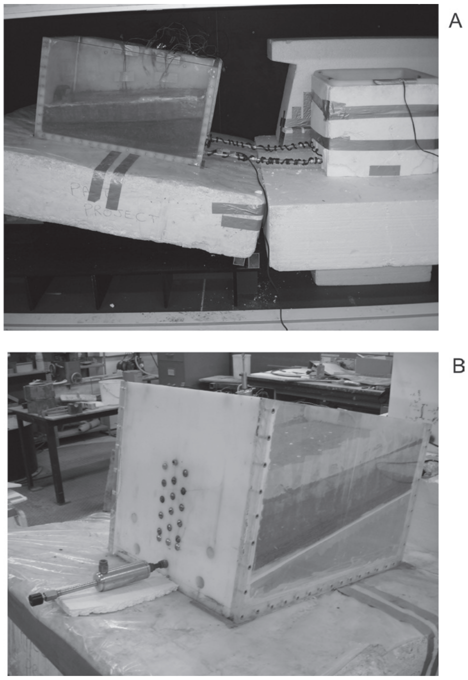

Figure 2. Model preparation. (A) One-sided set-up for freezing with an open-water system. (B) Two-sided freezing with a basal cooling system using vortex tubes.

Two linear voltage transducers (LVDT, LDC 1000C) were placed perpendicular to the soil surface to monitor frost heave during freezing. The model boxes were thermally insulated with polystyrene, and the soil slopes were frozen from the surface downwards at air temperatures between -5°C and -10°C in a freezing chamber under 1 g.

The one-sided model was frozen from the top under a confining load of 1.5 kPa and with an open-water system through the basal sand layer allowing ice segregation in the soil layer. During freezing, the model was tilted to give a horizontal soil surface, and water level was maintained at the sand-soil interface (Fig. 2A). In the two-sided model, a cold permafrost table was simulated using a basal cooling system of cold compressed air generated by three vortex tubes (Fig. 2B). During each cycle of two-sided freezing, summer heave was simulated by sprinkling water on the surface with air temperatures above 0°C and with the basal cooling system running, maintaining base temperatures around -3°C. Pore-water pressures, soil temperatures, air temperature, and frost heave were monitored through the data logger (Campbell CR1000).

The frozen model slopes were placed in the centrifuge gondola and thawed under a gravitational field of 10 gravities. Thawing was from the soil surface downwards at air temperatures between 10°C and 15°C and with an open drainage system. A laser (OADM20) was mounted above the slope surface to monitor thaw settlement. Every 30 minutes the grid of surface markers was captured by an automatic camera to trace the ground surface downslope displacement during thawing. During each freezing cycle, all sensors were monitored at 10-s intervals via the on-board centrifuge data logging system (Campbell CR10X). Each model was subjected to 5 freeze-thaw cycles.

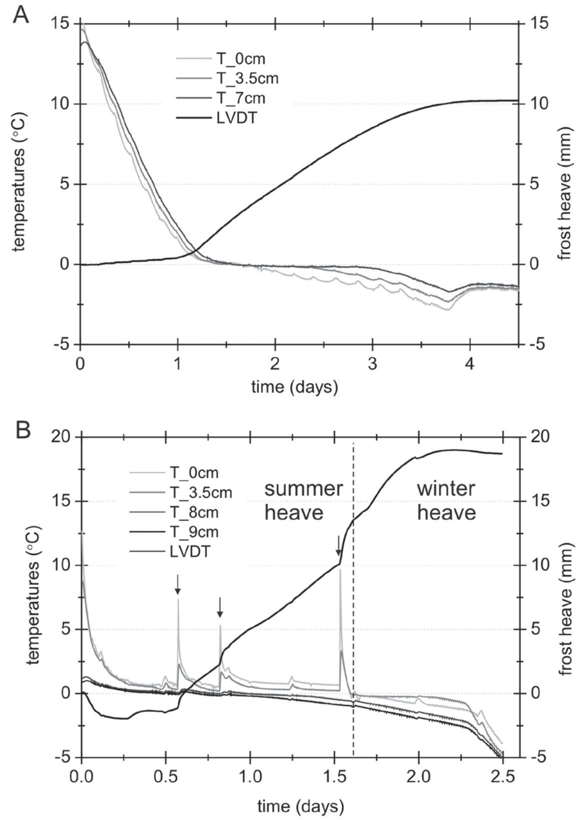

Figure 3. Frost heave and soil temperatures. (A) One-sided freezing experiment showing progressive frost heave over time and freezing from the surface downwards. (B) Two-sided freezing experiment in which heave can be divided into summer and winter components with active layer freezing from the surface downwards and from the permafrost table upwards. For summer, heave water was added to the surface (marked by arrows).

Results

Thermal regime and frost heave

During freezing of the soil models at 1g, the one-sided experiment showed a significant difference in frost heaving rate and thermal regime compared to the two-sided experiment, illustrated in Figure 3. Surface-downwards freezing of the one-sided model over a four-day period is indicated by the temperature-time series at depths 0, 3.5, and 7cm. Ice segregation occurred throughout the soil layer, reflected by uniform frost heaving rates (LVDT) over the freezing period (Fig. 3A). In the two-sided experiment, where basal temperatures were maintained below zero, active layer freezing took place over two days (Fig. 3B) and total heave was due (a) to summer heave with positive air temperatures and ice accumulation at the active layer base followed by (b) winter heave with active layer freezing from the surface downwards and from the permafrost table upwards.

A total of 10 mm (scaling to 10 cm at prototype) frost heave was measured in the one-sided and 19 mm (scaling to 19 cm) in the two-sided experiment. Heaving ratios (i.e., frost heave divided by thickness of the frozen layer) for different depths are listed in Table 1.

Table 1. Frost heave and thaw settlement measurements from the one-sided and two-sided experiment.

Test	Thaw depth (m)	Thaw settlement (mm)	Heaving ratio	Thaw rates (mm/hr)	Displacement (mm)	Ratio displacement/ settlement
1-sided	0	10.8	-	0.72	7.8	0.72
	0.1	31.3	0.24	0.33	9.3	0.30
	0.35	17.2	0.06	0.23	6.0	0.35
	0.6	22.4	0.08	0.39	3.9	0.18
	0.7	49.3	0.33	0.23	1.1	0.02
2-sided	0	7.1	-	0.28	0.0	0.0
	0.2	29.9	0.23	0.30	-3.1	-0.11
	0.35	6.4	0.04	0.07	3.8	0.60
	0.6	4.0	0.02	0.03	-0.7	-0.18
	0.8	5.4	0.03	0.02	2.5	0.45
	0.9	63.3	0.39	0.25	17.0	0.27

Thaw rates and thaw settlement

In Figure 4, thaw-penetration and thaw-settlement rates are shown during thawing at 10 g of the one-sided and the two-sided experiments in the centrifuge. Nearly linear thaw-settlement rates were monitored in the one-sided experiment. However, temperature profiles showed an apparent deceleration of thaw penetration close to the surface and between 0.6 and 0.7 m depths (prototype scale), associated with depths of slightly increased ice formation in the model. For each thawed layer (i.e., between two instrumentation depths), total thaw settlement, average thaw rates (i.e., thaw settlement per time), and heave ratio (i.e., thaw settlement per frozen layer thickness) are listed in Table 1. In the two-sided experiment, higher settlement rates were monitored near the surface and between depths 0.8 and 0.9 m (prototype scale) (Fig. 4B). In the relatively drier ice-poor layer (i.e., small heave ratios) between depths 0.35 and 0.6 m, lower rates of thaw settlement were measured. A very similar pattern was observed in recent field measurements on a permafrost solifluction slope in Svalbard (Harris et al. 2006) where moisture migration upwards and downwards during two-sided freezing had also left an ice poor central layer.

Rates of surface movement and displacement profiles

Table 1 shows surface displacement (at prototype scale) for each thaw depth during the one-sided and the two-sided experiment, based on time-lapse photographs of the displacement of one marker located in the center part of the model, where minimal boundary effects were expected. In the one-sided experiment, more than three-quarters of total displacement occurred during thaw of the uppermost 0.35 m, whereas in the two-sided experiment, most displacement occurred during thaw below 0.6 m. At these depths, highest ratios of displacement to thaw settlement were observed. However in the two-sided cycle, at depths between 0.2 to 0.6 m apparent upslope and downslope displacements were observed, which could have been caused by soil desiccation and crack formation during thaw progression into the relatively drier layers at these depths. From the displacement values in Table 1, and assuming that surface displacements were due to displacement of the thawed layer immediately

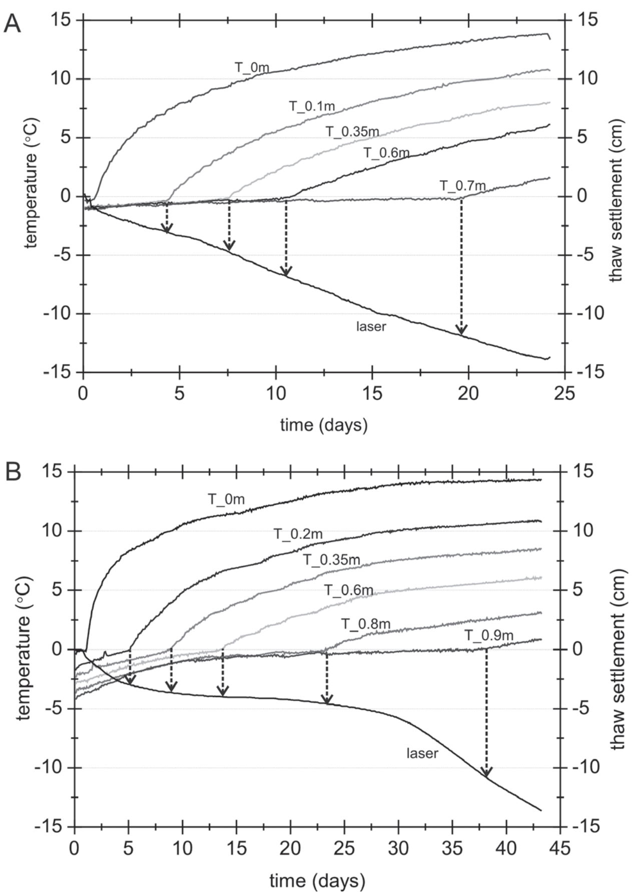

Figure 4. Temperature and settlement measured during thawing in the centrifuge for (A) the one-sided and (B) the two-sided experiment.

above the thaw front, subsurface displacement profiles were derived. Figure 5(a) shows profiles after one freeze-thaw cycle, (b) after five cycles of repeated freezing and thawing. The one-sided profiles show highest displacement near the surface, whereas in the two-sided experiment displacement occurs at deeper depths generating profiles similar to the plug-like movement of an active layer over an ice-rich basal shear zone as was described by Mackay (1981), Lewkowicz & Clarke (1998), and Matsuoka (2001).

Displacement columns were excavated after 5 freeze thaw cycles. Figure 6 shows an example for each experiment: the one-sided (a) and the two-sided (b). Although reflecting the generic shape of the calculated profiles (Fig. 5), the profile shapes exhibited by the columns also show some deviations especially for the two-sided experiment. This is due to the fact that the freezing cycles are not exactly reproducible: cycle-to-cycle variation in frost heave and depths of ice accumulation cause variation in total displacement and in the location of main displacement horizon (Fig. 6B). It should be noted that the active-layer thickness simulated in the two-sided freezing experiment was 9–10 cm model scale, 90–100 cm prototype. This is marked by an arrow in Figure 6B. Disturbance of the marker column below this depth reflects the final thawing of the model following the five-cycle experiment.

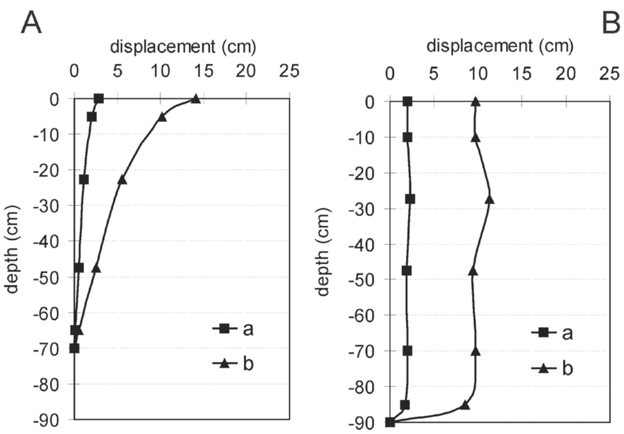

Figure 5. Calculated displacement profiles after (a) one freeze-thaw cycle and (b) five repeated cycles for (A) the one-sided and (B) the two-sided experiment.

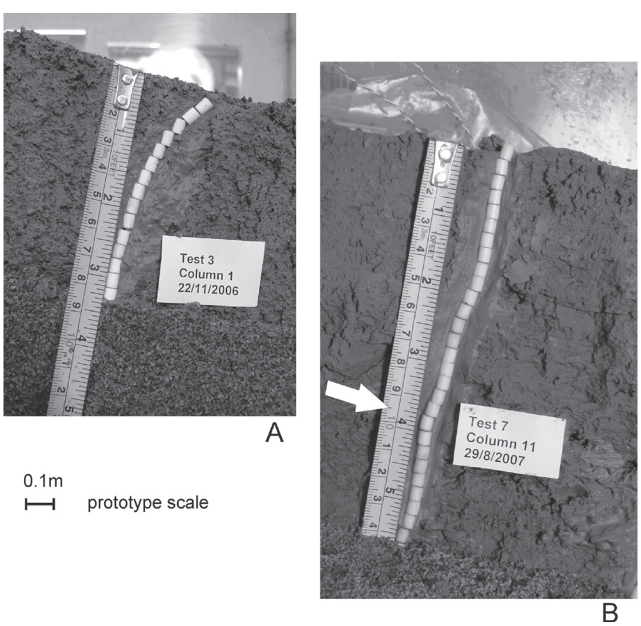

Figure 6. Observed subsurface displacement following five cycles for (A) the one-sided and (B) the two-sided experiment. The base of each column corresponds to the base of the model and top of the underlying sand layer.

Discussion

Subsurface displacement profiles resulting from the one-sided and two-sided experiments presented above exhibit significant differences regarding the depths where main displacement took place (Fig. 6). Matsuoka (2001) classified shapes of displacement profiles from field observations into four subgroups: needle ice creep, diurnal frost creep, annual frost creep with possible gelifluction, and plug-like flow. The typically convex shaped displacement profiles developed during five freeze-thaw cycles in our one-sided experiment (Fig. 6A) are similar to the one-sided seasonal freezing, gelifluction type of displacement profiles described by Matsuoka (2001). This profile shape typically originates from shear strain concentrated in the uppermost few centimeters to decimeters, depending on the duration of the freeze-thaw period which controls the depth of ice lens formation during freezing. In contrast, the two-sided experiments typically show concave-shaped profiles (Fig. 6B) similar to the plug-like displacement reported from cold permafrost areas where the basal active layer is ice-rich. In the two-sided freezing experiment (and in nature), the maximum summer active layer depth varied from cycle to cycle, leading to basal displacements occurring over a depth range of around 15 mm at model scale, or 15 cm at prototype scale, rather than being concentrated in one distinct layer. In general, the scaled experiments show similar shapes to those observed in full-scale experiments of one-sided and two-sided freezing and thawing (Harris et al., this volume). Scaled displacement rates and depths are in the same order of magnitude as field observations of solifluction in both seasonal frost and cold permafrost areas (see for instance Matsuoka & Hirakawa, 2000).

Conclusion

1. From these first results, we may conclude that the principle processes of solifluction associated with two-sided and one-sided active layer freezing were successfully physically modeled in small-scaled centrifuge experiments.
2. In the two-sided experiments, a distinct ice-poor intermediate layer was associated with very little thaw settlement downslope displacement.
3. Significantly different shapes of the one- and two-sided displacement profiles can be related to distribution of soil ice in the frozen models and subsequent consolidation during thaw. First qualitative comparisons indicate that scaled displacement rates and profile shapes are consistent with displacement profiles observed in field and full-scale laboratory experiments.
4. The geotechnical centrifuge modeling technique has proven an important tool for further systematic investigations of active layer behavior under controlled and repeatable conditions.
5. Further detailed validation through the principle of modeling of model analysis (Ko 1988) is in process and being produced in the near future.

6. Calibration and validation of numerical modeling with the scaled centrifuge physical modeling are in process, and further simulations of field monitoring and full-scale laboratory simulation experiments will be conducted.

Acknowledgments

This research was funded by the British Engineering and Physical Sciences Research Council Research Grant GR/T22964. Technical support from Harry Lane in the geotechnical centrifuge laboratory is gratefully acknowledged.

References

Cleall, P.J., Seetharam, S.C. & Thomas, H.R. 2007. Inclusion of some aspects of chemical behaviour of unsaturated soil in thermo/hydro/chemical/mecha-nical models. I: Model development. *ASCE Journal of Engineering Mechanics* 133(3): 338-347.

Coutard, J.-P., Van Vliet-Lanoe, B. & Auzuet, A.V. 1988. Frost heaving and frost creep on an experimental slope: results for soil structures and sorted stripes. *Zeitschrift fur Geomorphologie, Supplementband* 71: 13-23.

Croce, P.V., Pane, V., Znidarcic, D., Ko, H-Y., Olsen, H.W. & Schiffman, R.L. 1985. *Applications of Centrifuge Modelling to Geotechnical Design*, W.H.Craig, Ed. Balkema, Rotterdam, 381-401.

Harris, C., Davies, M.C.R. & Coutard, J.-P. 1996. An experimental design for laboratory simulation of periglacial soliflucton processes. *Earth Surf. Process. Landforms* 21: 67-75.

Harris, C., Rea, B.R. & Davies, M.C.R. 2000. Geotechnical centrifuge modelling of gelifluction processes: validation of a new approach to periglacial slope studies. *Annals of Glaciology* 31:263-268.

Harris, C., Rea, B.R. & Davies, M.C.R. 2001. Scaled physical modeling of mass movement processes. *Permafrost and Periglacial Processes* 12:125-136.

Harris, C., Davies, M.C.R. & Rea, B.R. 2003a. Gelifluction: viscous flow or plastic creep? *Earth Surf. Process. Landforms* 28: 1289-1301.

Harris, C. & Smith, J.S. 2003b. Modelling gelifluction processes: the significance of frost heave and slope gradient. *Proceedings of the Eighth International Conference on Permafrost, Zurich, Switzerland. Balkema, Lisse*: 355-360.

Harris, C., Luetschg, M., Murton, J.B., Smith, F.W. Davies, M.C.R., Christiansen, H.H. & Ertlen-Font, M. 2006. Solifluction processes in Arctic permafrost: Results of laboratory and field experiments. *EOS Trans., AGU, 87*(52), Fall Meeting Supplement, Abstract C43A-03.

Harris, C., Luetschg, M., Davies, M.C.R. Smith, F., Christiansen, H.H. & Isaksen, K. 2007. Field instrumentation for real-time monitoring of periglacial solifluction. *Permafrost and Periglacial Processes* 18: 105-114.

Harris, C., Smith, J.S., Davies, M.C.R. & Rea, B. 2008. An investigation of periglacial slope stability in relation to soil properties based on physical modelling in the geotechnical centrifuge. *Geomorphology* 93: 437-459.

Harris, C., Kern-Luetschg, M., Murton, J., Font, M., Davies, M. & Smith, F. 2008. Full-scale physical modeling of solifluction processes associated with one-sided and two-sided active layer freezing. *This volume.*

Ko, H.-Y. 1988. Summary of the state of the art in centrifuge model testing. In: W.H. Craig, R.G. James, & A.N. Schofield (eds.), *Centrifuges in Soil Mechanics*. Rotterdam: Balkema, 11-18.

Konrad, J.M., & Morgenstern, N.R. 1980. A mechanistic theory of ice lens formation in fine-grained soils. *Canadian Geotechnical Journal* 17: 473-486.

Lewkowicz, A.G. 1988. Slope processes. In: M.J. Clark (ed.), *Advances in Periglacial Geomorphology*. Chichester: Wiley, 325-368.

Lewkowicz, A.G. & Clarke, S. 1998. Late summer solifluction and active layer depths, Fosheim Peninsula, Ellesmere Island, Canada. *Proceedings the Seventh International Conference on Permafrost, Yellowknife, Canada*, 641-646.

Mackay, J.R. 1981. Active layer slope movement in a continuous permafrost environment, Garry Island, Northwest Territories, Canada. *Canadian Journal of Earth Sciences* 18: 1666-1680.

Matsuoka, N. & Hirakawa, K. 2000. Solifluction resulting from one-sided and two-sided freezing: field data from Svalbard. *Polar Geosci.* 13: 187-201

Matsuoka, N. 2001. Solifluction rates, processes and landforms: A global review. *Earth-Science Reviews* 55: 107-134.

Morgenstern, N.R. & Nixon, J.F. 1971. One-dimensional consolidation of thawing soils. *Canadian Geotechnical Journal* 8: 558-565.

Savidou, C. 1988. Centrifuge modelling of heat transfer in soil. *Centrifuge 88*. Rotterdam: Balkema, 583-591.

Shur, Y.I. 1988. The upper horizon of permafrost soils. *Proceedings of the Fifth International Conference on Permafrost*, *Trondheim, Norway,* 867-871.

Shur, Y., Hinkel, K.M. & Nelson, F.E. 2005. The transient layer: Implications for geocryology and climate-change science. *Permafrost and Periglacial Processes* 16: 5-17.

Shiklomanov, N.I. & Nelson, F. 2007. Active layer processes. In: S.A. Elias (ed.), *Encyclopedia of Quaternary Science,* Vol. 3, Oxford: Elsevier, 2138-2146.

Snow and Temperature Relationships on Polygonal Peat Plateaus, Churchill, Manitoba, Canada

G. Peter Kershaw
Department of Earth & Atmospheric Sciences, University of Alberta, Edmonton, AB, Canada, T6G 2E3

Abstract

Polygonal peat plateaus are a common landform in the Hudson Bay Lowlands and are diagnostic of continuous permafrost. The polygons are formed by ice wedge troughs that have different surface water and plant cover characteristics. In winter the low troughs accumulate more snow than the raised wind-deflated centers. This variation in snowpack drives temperature differences that can be dramatic. When thermokarst subsidence results from ice wedge melting, the snow accumulation is greater and the enhanced insulation traps more of the heat gained in summer. The mean annual temperature beneath the snow can rise above 0°C and the potential for a positive feedback occurs where further thermokarst subsidence traps more insulating snow. Ice wedges cease cracking and after degradation of the ice wedges, the raised polygon centres or baydjarakh have an external morphology that has resulted in them being mistakenly identified as palsas.

Keywords: baydjarakh; frost cracking; ice wedge polygon; microclimate; snowpack; temperature; thermokarst.

Introduction

Polygonal peat plateaus are relatively flat-topped features that have been dissected by ice wedge polygons and that often rise <2 m above the surrounding terrain (Brown 1970, van Everdingen 2005, Zoltai & Tarnocai 1975). The polygons are the ice wedge troughs that often have a different plant community from that which dominates the polygon centres.

One of the first descriptions of polygonal patterns was from Siberia by Figurin in 1823 (Washburn 1979). Since then they have been described from around the circumpolar North (French 1996, Mackay & Black 1973, Washburn 1979). They are formed by thermal contraction of the host sediments during winter followed by water entering the crack to freeze and form an ice veinlet that, given enough time for the cycle to repeat, develop into ice wedges (Fortier & Allard 2005, Fortier & Allard 2004, Kerfoot 1972, Lachenbruch 1966, Lachenbruch 1962, Leffingwell 1915, Mackay 1993, Mackay 1986, Mackay 1974, Mackay & Burn 2002, Mackay & MacKay 1974).

Thermal contraction has been observed with air temperature declines of 14°C d^{-1} over 34 h to 3.7°C d^{-1} over 102 h in peaty sands of northern Québec (Allard & Kasper 1998); 12°C d^{-1} over 18 h in peaty silts on Bylot Island, Nunavut (Fortier & Allard 2005); and 1.8°C d^{-1} over 96 h in ice-rich peat on islands in the Mackenzie Delta, NWT (Mackay 1993). In his 1993 paper Mackay concluded there was little correspondence between the mean daily air temperature and cracking of ice wedges; however, he noted that ice wedge cracking occurs when the mean minimum temperatures at 50 cm depth fall between -17°C and -23°C (the number and dates of readings were not specified).

Several factors can affect the magnitude and frequency of cracking, but there is a consensus that snowpack is a critical variable. One must be careful since in some studies the polygons are low-centered so that the snow insulates the polygon centres as well as the depressed ice wedge troughs (Allard & Kasper 1998, Fortier & Allard 2005). In high-centered polygons such as those at Churchill, the snowpack is thinner in the centers than the bordering ice wedge troughs. In general, a deeper, more continuous and long-lasting snowpack will insulate the ground against heat loss in winter (Goodrich 1982, Nicholson & Granberg 1973, Smith 1975).

Study area

The study features were ~2 km apart at similar elevation (~15 m a.s.l.) (Fig. 1). They were within the forest-tundra ecotone between the open forest and tundra near the Churchill Northern Studies Centre.

Excavations at one site in 1997 revealed ice nipples (Péwé 1962) extending from the tops of the larger ice wedges. These secondary wedges were more vein shaped—consistently ~2 cm thick and extending approximately 15 cm above the main wedge. Due to their morphology and lack of indications of

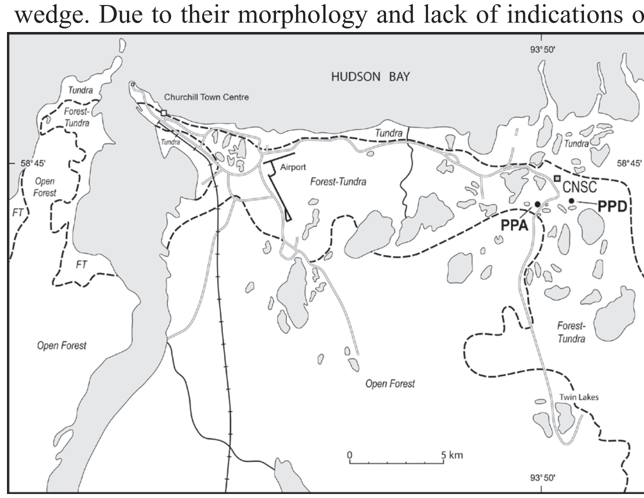

Figure 1. The study features were ~20 km east of the town of Churchill. Polygonal peat plateaus with degrading ice wedges (PPD) and aggrading ice wedges (PPA) were ~2 km south of the Churchill Northern Studies Centre (CNSC).

rapid peat accumulation, they were interpreted as evidence of active layer thinning and so can be classified as epigenetic ice wedges (Dostovalov & Popov 1966, French et al. 1982, Mackay 1974). The shallow (~20 cm) depressions over the ice wedges and the ice nipples are evidence of permafrost aggradation (Mackay 1976).

The ice wedges at the other site were degrading, as evidenced by the linear thermokarst depressions (0.8–1.5 m deep and 2–7 m wide) surrounding isolated remnant polygon centres (baydjarakhs). As with the aggrading site, the polygon centers were at the same height and flat topped. However, at the degrading site, the edges of intact and former ice wedge troughs were steep-sided, ending in a sedge wetland. When viewed from the air, the pattern of the original ice wedges was clearly polygonal. At both sites the polygons were 5–10 m in diameter. In 1997, and annually since 2002, ground-penetrating radar and coring at both sites have confirmed the presence of ice wedges within frozen peat of 1.25–2.5 m depth overlying marine sediments (clasts imbedded in a silty clay matrix) topped by a thin to 15 cm layer of poorly-decomposed marine algae. Coring confirms that the peat is dominantly well-decomposed to poorly-decomposed sedge peat with minor amounts of fine woody material, probably dwarf shrubs. Given the isostatic history (Dredge 1992), internal characteristics, basal marine algae deposits, and setting, the site history is probably much like reported for similar polygonal peat plateaus on Devon Island (Somr & King 1990).

Thaw depths were measured with a graduated probe in October 2007 at both sites. The polygon centers had 45.7 (n = 98) and 41.6 (n = 108) cm active layer on the polygonal peat plateau degrading and aggrading respectively. The mean active layer depth on the ice wedges at the aggrading peat plateau was 37 (n = 20) cm. Thaw depth in the troughs around the baydjarakhs could not be reliably determined since the underlying marine sediments were stony which prevented deep probing. Ground-penetrating radar surveys suggest a 10 to 12 m active layer between the remnant polygon centers.

In most cases the raised polygon centers were dominated by lichens (*Alectoria nigricans, A. ochroleuca, Cetraria nivalis, C. cucullata, Cladina* spp. and *Cladonia* spp.), dwarf ericaceous shrubs (*Ledum decumbens, Rhododendron lapponicum*) and the forb *Rubus chamaemorus*. The depressed ice wedge troughs on the aggrading permafrost site were dominated by mosses (*Sphagnum* spp. and *Dicranum* spp.), *Betula glandulosa*, *L. decumbens, Rubus chamaemorus* and *Salix* spp. On the degrading permafrost site the drier subsided troughs have similar plant cover to the aggrading site but where they extend to the water table the plants are dominated by wetland species (*Calliergon* spp. and *Carex aquatilis*).

Methods

Midwinter snowpack surveys were conducted over eight days in February each year from 2002 to 2007. Although the data collection included full snowpit stratigraphic descriptions, the data presented here are from the snow core (Adirondack) sampling. Sampling was stratified by microsite on the two polygonal peat plateaus–polygon centre and wedge troughs. Annual sample sizes varied between 30 and 132 and over the six years a total of 475 to 558 samples were taken on the four microsites–polygon centres and ice wedge troughs at both the aggrading and degrading polygonal peat plateaus.

Temperature was monitored with Campbell Scientific International CR10X data loggers and type T thermocouples connected through a multiplexer in the enclosure with the logger (AM416 or AM16/32) with reference junction on the 10X wiring panel. Readings were taken every 5 min with the mean daily temperature used in this analysis. Air temperature was recorded at 1.5 m height while surface temperatures were at 0 cm, shielded by moss or lichen. Near-surface permafrost temperature was measured at 80 cm depth; however, at the degrading permafrost site the sensor was severed by an animal after installation so no mean could be calculated for 2004.

A microclimate station was installed at the aggrading polygonal peat plateau in June 2001 and at the degrading polygonal peat plateau in June 2003. Mean annual temperatures were calculated for only those years where there was a full record: 2002–2006 and 2004–2006 for the aggrading and degrading sites, respectively.

A synthetic value was derived to facilitate comparison of the potential for heat conduction through the snowpack (Kershaw 2001). The Heat Transfer Coefficient (HTC) uses depth and density to estimate the potential heat loss from the soil; higher values indicate greater heat conduction and less insulation.

$$\mathrm{HTC} = k/d \quad (1)$$

where k is the thermal conductivity (Abel's 1893) of the snowpack and d is the snowpack depth

$$k = (2.94\ 10^{-6}\ \mathrm{W\ m^{-1}\ °K^{-1}})(\rho)^2 \quad (2)$$

where ρ is snowpack density (kg m^{-3})

Mean annual temperatures were calculated from the daily means during the year. Freezing degree-day totals were calculated by accumulating the mean daily values <0°C for the year.

Results

Interannual snowpack characteristics of depth and the potential for heat conduction were rarely significantly different (Figs. 2, 4). Consequently, comparisons among microsites were made with means of the six years of data.

Snowpack depth

Comparing microsites, snowpack depth varied little among years (Fig. 2). However, there were great differences between polygon centres and ice wedge troughs at both study sites. In the subsided ice wedge troughs at the degrading

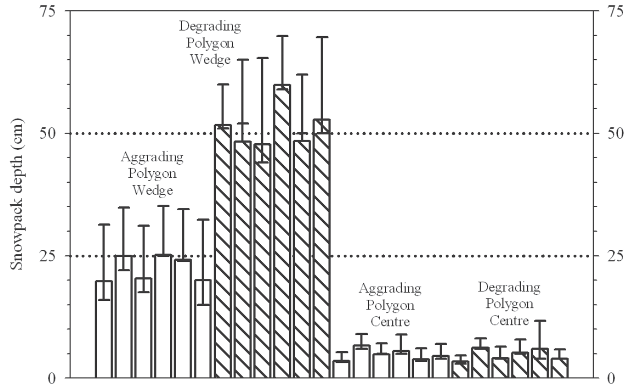

Figure 2. Midwinter snowpack depth 2002–2007 for the two ice wedge troughs and polygon centres on aggrading and degrading polygonal peat plateaus. Mean with capped lines for median (bottom) and standard deviation (top).

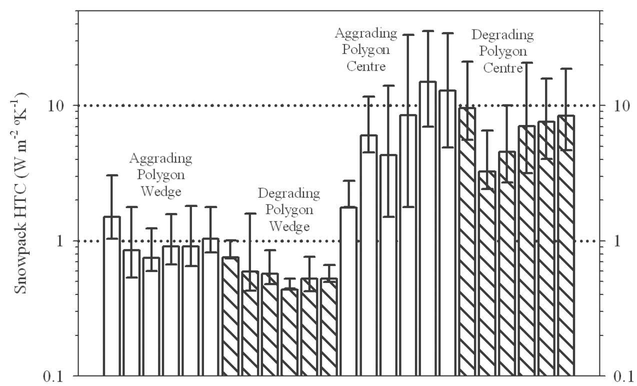

Figure 4. Midwinter snowpack heat transfer coefficient (HTC) (2002–2007) for the two ice wedge troughs and polygon centres on aggrading and degrading polygonal peat plateaus. Mean with capped lines for median (bottom) and standard deviation (top).

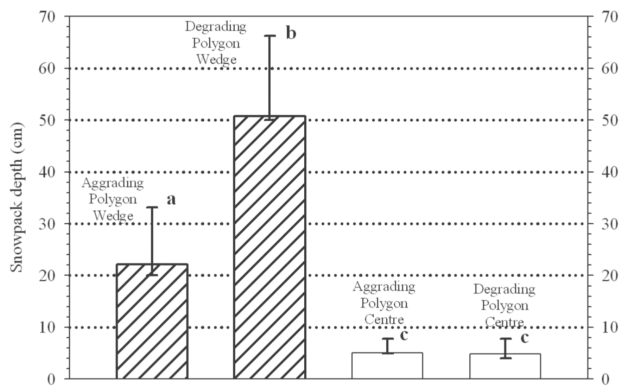

Figure 3. Midwinter snowpack depth (mean of six years) for the two ice wedge troughs and polygon centres on aggrading and degrading polygonal peat plateaus. Mean with capped lines for median (bottom) and standard deviation (top). Significantly different ($p < 0.05$) values have different letters.

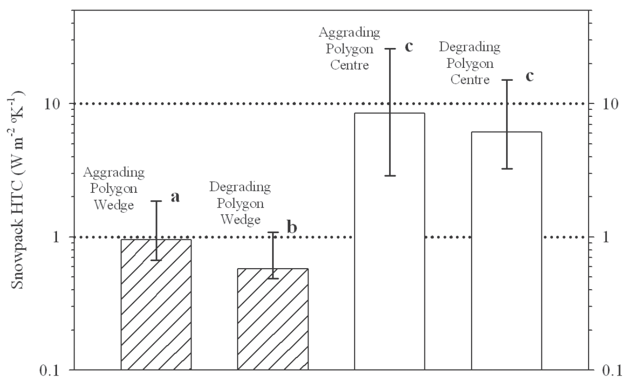

Figure 5. Midwinter snowpack heat transfer coefficient (HTC) (mean of six years) for the two ice wedge troughs and polygon centres on aggrading and degrading polygonal peat plateaus. Mean with capped lines for median (bottom) and standard deviation (top). Significantly different ($p < 0.05$) values have different letters.

polygonal peat plateau there was ~10x more snow than on the adjacent polygon centres. At the aggrading polygonal peat plateau there was 4x–5x more snow in the troughs. The polygon centre snowpack was similar between the two sites while the ice wedge troughs had significantly deeper snow (Fig. 3).

Snowpack heat conduction

Regardless of the year, there was ~10x higher potential for heat loss from the polygon centers compared to the adjacent ice wedge troughs (Fig. 4). The potential for heat loss from the wedge troughs on the degraded peat plateau was 40% lower that on the aggrading features (Fig. 5).

Temperature characteristics

Except for 2004, the mean annual air temperature was similar for the two sites (Fig. 6). Both the mean annual polygon centre surface temperatures and the near-surface permafrost temperatures were very similar. However, the mean annual surface temperatures of the ice wedge troughs differed by 5.5 to 6.5°C with the degrading ice wedges having mean annual temperatures well above 0°C at 2 and 3.5°C.

Freezing degree-days were greatest in 2004 and least in 2006 (Fig. 7). The polygon centres and the near-surface permafrost had similar values. Despite similar air temperatures, the ice wedge troughs were much colder on the aggrading peat plateau.

Discussion

The two study sites were close enough to share the same climatic characteristics and yet differed greatly in their geomorphic status—aggrading vs. degrading permafrost.

Snowpack – temperature relations

Snowpack on the polygon centres was similar in depth and potential heat conduction on the two sites (Figs. 3, 5). As a result, their surface temperature characteristics were similar with the same freezing degree-day totals (Figs. 6, 7). The mean annual temperature of the near-surface permafrost differed by only 0.2°C (Fig. 6).

The main difference between the sites was the snowpack and temperature characteristics of the ice wedge troughs. With at least double the snowpack and almost half the heat conduction, the degrading ice wedges had mean annual

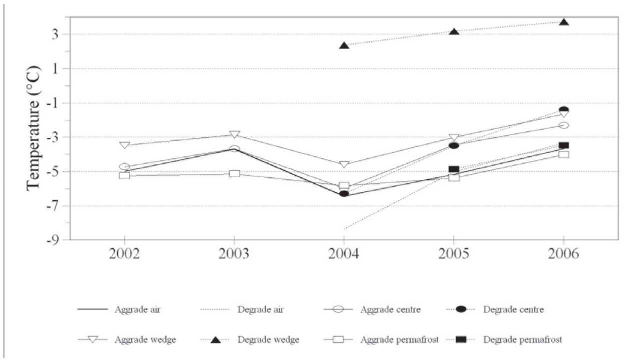

Figure 6. Mean annual temperature on polygonal peat plateau with aggrading permafrost (Aggrade) and degrading permafrost (Degrade). Temperatures measured at 150 cm height (air), ground surface of polygon ice-wedge trough (wedge) and ground surface of polygon centre (centre).

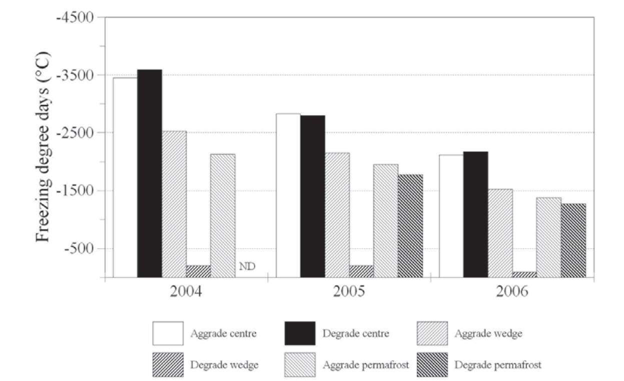

Figure 7. Accumulated freezing degree-days (<0ºC) on polygonal peat plateaus with aggrading permafrost (Aggrade) and degrading permafrost (Degrade). Temperatures measured at 150 cm height (Air), ground surface of polygon ice wedge trough (wedge) and ground surface of polygon centre (centre). No 2004 data available for near-surface permafrost on the degrading peat plateau.

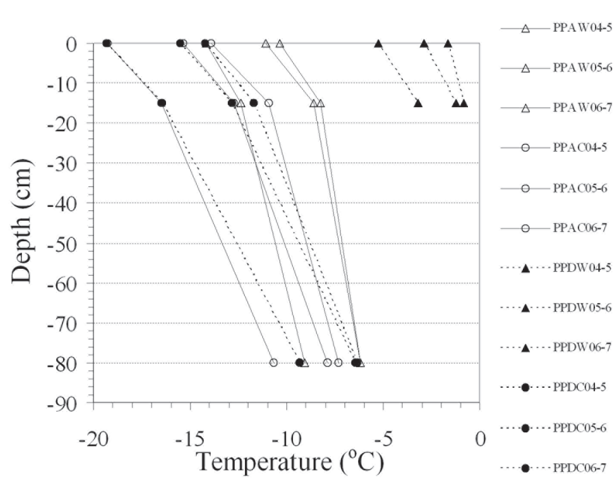

Figure 8. November to March mean temperatures for three winters (2004–2007) on polygonal peat plateaus with aggrading (PPA) and degrading (PPD) ice wedges (W) and their associated polygon centres (C). Measurements at the ground surface, 15 and 80 cm depth except for depressions associated with degraded ice wedges (PPDW).

surface temperatures above 0°C (Fig. 6). Winter temperatures (November–March) confirm that the degrading wedges were warmer than the polygon centres and the wedges on the aggrading site (Fig. 8). There was an average gradient of between 6.6°C and 10°C between the ground surface and 80 cm depth on the polygon centres.

The plant cover and near-surface peat characteristics were similar at both sites on the polygon centres but differed on the adjacent ice wedge troughs. The polygon centres had a thin snowpack with high heat conduction potential and consequently surface temperatures were similar to the air (Figs. 3, 5, 6). In 2003 open thermal contraction cracks were observed on the aggrading site but no cracks have ever been found at the degrading site. With no difference in polygon centre characteristics it must be the ice wedge trough characteristics that allow cracking to occur and the degrading site no longer possess these characteristics. The snowpack characteristics appear to set the limits to thermal contraction cracking.

Geomorphic implications

It is clear that the current state of the features is heavily influenced by surface topography interactions with snowpack and its thermal characteristics.

At the degrading site, it appears that a threshold has been achieved in the thermokarst depressions whereby thermal-contraction cracking has ceased. The snowpack prevents the magnitude and rate of cooling required for cracking of the residual ice wedges. It is also the case that many of the ice wedges have completely melted (Fig. 9). As thermokarst subsidence occurs the trough's ability to trap insulating snow increases and winter soil heat loss declines. Further degradation of the ice wedges eventually drops the surface to that of the surrounding fen and the local water table. The snow insulates so effectively that the mean annual temperature was from 7°C to 10.7°C warmer beneath the snow resulting in a mean annual surface temperature that was well above 0°C (Fig. 7). In contrast, on the aggrading site the difference was 1.9°C to 2.2°C with the mean annual surface temperature well below 0°C (Fig. 7).

Between ice wedge aggradation and complete degradation, there is a shift in snowpack characteristics over the wedges from offering little resistance to heat loss to effective insulation. At Churchill the study features provide examples of the two endpoints of this continuum. Given the dramatic differences between the two sites it might be that the switch between the two states occurred abruptly (a few years) after a threshold of snow thermal properties was achieved.

Conclusions

Two polygonal peat plateaus that were <2 km apart had similar plant cover, internal composition and mesoclimate; however, they differed in that one had degrading while the other had aggrading ice wedges. The ice wedge troughs in the baydjarakh field were often >1 m deeper than the aggrading site due to thermokarst subsidence.

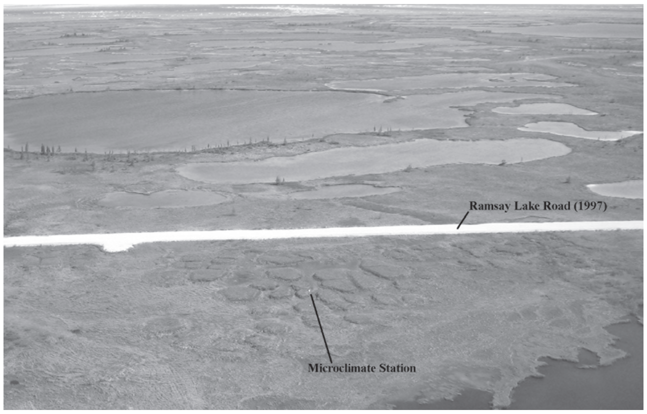

Figure 9. The former ice wedge pattern is still apparent at the degrading ice wedge site. The baydjarakh field developed as the original ice wedges degraded several decades prior to the construction of the Ramsay Lake Road. Hudson Bay is visible on the horizon.

The midwinter snowpack over the degrading ice wedges insulated against heat loss to the extent that the mean annual temperature was 2°C to 3°C above 0°C. Under these circumstances the ice wedges cannot reform. A new paradigm prevails at this site where the residual polygon centers remain elevated with shallow active layers and internal temperatures similar to the aggrading ice wedge site. The thermal contraction that would normally cause ice wedge cracking can occur on the raised mound of the residual polygon centre without affecting the area that surrounds it and which is under >50 cm of insulating snow. Under these circumstances the raised polygon centres are stable unless other processes such as change in plant cover or deflation of the peat lead to a change in their thermal state.

The residual polygon centres or baydjarakh (Czudek & Demek 1970) have been locally incorrectly identified as palsas. Their external morphology resemble palsas but their origin precludes this classification (van Everdingen 2005).

Polygonal peat plateaus are ubiquitous in the Hudson Bay Lowland (Dredge & Mott 2003) and are common throughout the rest of Canada (Tarnocai & Zoltai 1988, Zoltai et al. 1988). They are also common in Russia (Romanovskij 1985). Where they are sustaining thermokarst subsidence, interactions with increasing snowpack and its ability to trap summer heat could amplify the degradation process to the point that the ice wedges completely melt out. This positive feedback would be arrested if the polygon centre was lowered through such processes as deflation of the peat by wind (Seppälä 2004). However, it appears that progression of the process to a point whereby the ice wedges completely degrade is facilitated by snowpack interactions. In the area where polygonal peat plateaus are common and where future climate warming starts thermokarst subsidence, snowpack feedbacks could amplify the process and accelerate the effects of climate warming.

Acknowledgments

Earthwatch Institute volunteer teams along with students from the University of Alberta and Churchill Northern Studies Centre staff collected the snowpack data. In 1997 Dr. Michel Allard and Stewart Brown conducted initial excavations of the ice wedges and the first GPR surveys. Funding for this research has been through Earthwatch Institute, Churchill Northern Studies Centre, NSERC, IPY PPS Arctic Canada, and Canadian Circumpolar Institute.

References

Abel's, G. 1893. Daily variation of temperature in snow and the relation between the thermal conductivity of snow and its density. *Meteorologicheskii Vestnik* 3.

Allard, M. & Kasper, J.N. 1998. Temperature conditions for ice wedge cracking: field measurements from Salluit, northern Québec. In: A.G. Lewkowicz & M. Allard (eds.), *Proceedings of the 7th International Permafrost Conference, Collection Nordicana, No. 57*. Québec: Centre d'études nordiques, Université Laval.

Brown, R.J.E. 1970. Occurrence of permafrost in Canadian peatlands. *Proceedings of the Third International Peat Congress,Quebec*. Ottawa: National Research Council Canada.

Czudek, T. & Demek, J. 1970. Thermokarst in Siberia and its influence on the development of lowland relief. *Quaternary Research* 1(1): 103-120.

Dostovalov, B.N. & Popov, A.I. 1966. Polygonal systems of ice wedges and conditions of their development. *Proceedings Permafrost International Conference*, *Lafayette, Indiana.*

Dredge, L.A. 1992. *Field guide to the Churchill Region, Manitoba: glaciations, sea level changes, permafrost landforms, and archeology of the Churchill and Gillam areas, Miscellaneous Report 53*. Ottawa: Geological Survey of Canada.

Dredge, L.A. & Mott, R.J. 2003. Holocene pollen records and peatland development, Northeastern Manitoba. *Géographie Physique et Quaternaire* 57(1): 7-19.

Fortier, D. & Allard, M. 2005. Frost-cracking conditions, Bylot Island, Canadian Arctic Archipelago. *Permafrost and Periglacial Processes* 16: 145-161.

Fortier, D. & Allard, M. 2004. Late Holocene syngenetic ice-wedge polygons development, Bylot Island, Canadian Arctic Archipelago. *Canadian Journal of Earth Sciences* 41: 997-1012.

French, H.M. 1996. *The Periglacial Environment*. Essex, England: Addison Wesley Longman Limited.

French, H.M.; Harry, D.G. & Clark, M.J. 1982. Ground ice stratigraphy late-Quaternary events, southwest Banks Island, Canadian Arctic. *Proceedings Fourth Canadian Permafrost Conference*, *Calgary, Alberta*.

Goodrich, L.E. 1982. The influence of snow cover on the ground thermal regime. *Canadian Geotechnical Journal* 19: 421-432.

Kerfoot, D.E. 1972. Thermal contraction cracks in an Arctic tundra environment. *Arctic* 25: 142-150.

Kershaw, G.P. 2001. Snowpack characteristics following wildfire on a simulated transport corridor and adjacent subarctic forest, Tulita, N.W.T., Canada. *Arctic, Antarctic, and Alpine Research* 33(2): 131-139.

Lachenbruch, A.H. 1966. Contraction theory of ice-wedge polygons: a qualitative discussion. *Proceedings Permafrost International Conference, Lafayette, Indiana*. U.S. National Academy of Sciences, Publication 1287.

Lachenbruch, A.H. 1962. *Mechanics of thermal contraction cracks and ice-wedge polygons in permafrost. GSA Special Paper* 70, 69 pp.

Leffingwell, E.D.K. 1915. Ground-ice wedges: the dominant form of ground-ice on the north coast of Alaska. *Journal of Geology* 23: 635-654.

Mackay, J.R. 1993. Air temperature, snow cover, creep of frozen ground, and the time of ice wedge cracking, Western Arctic Coast. *Canadian Journal of Earth Sciences* 30: 1720-1729.

Mackay, J.R. 1986. The first seven years (1978–1985) of ice-wedge growth, Illisarvik experimental drained lake site, western Arctic coast. *Canadian Journal of Earth Sciences* 23(11): 1782-1795.

Mackay, J.R. 1976. Ice-wedges as indicators of recent climatic change, Western Arctic coast. *Geological Survey of Canada, Report of Activities, Paper 76-1A*: 233-234.

Mackay, J.R.1974. Ice-wedge cracks, Garry Island, Northwest Territories. *Canadian Journal of Earth Sciences* 11: 1366-1383.

Mackay, J.R. & Black, R.F. 1973. Origin, composition, and structure of perennially frozen ground and ground ice: A review. *Permafrost: North American Contribution, Second International Conference*, *Yakutsk*.

Mackay, J.R. & Burn, C.R. 2002. The first 20 years (1978–1979 to 1998–1999) of ice-wedge growth at the Illisarvik experimental drained lake site, western Arctic coast, Canada. *Canadian Journal of Earth Sciences* 39: 95-111.

Mackay, J.R. & MacKay, D.K. 1974. Snow cover and ground temperatures, Garry Island, N.W.T. *Arctic* 27(4): 287-296.

Nicholson, F.H. & Granberg, H.B. 1973. Permafrost and snowcover relationships near Schefferville. *North American Contribution Permafrost Second International Conference*. *Yakutsk.*

Péwé, T.L. 1962. Ice wedges in permafrost, lower Yukon River area, near Galena, Alaska. *Biuletyn Peryglacjalny* 11: 65-76.

Romanovskij, N.N. 1985. Distribution of recently active ice and soil wedges in the USSR. In: M. Church & O. Slaymaker (eds.), *Field and Theory Lectures in Geocryology*. Vancouver: University of British Columbia.

Seppälä, M. 2004. *Wind As a Geomorphic Agent in Cold Climates*. Cambridge: Cambridge University Press.

Smith, M.W. 1975. Microclimatic influences on ground temperatures and permafrost distribution, Mackenzie Delta, Northwest Territories. *Canadian Journal of Earth Sciences* 12: 1421-1438.

Somr, C.H. & King, R.H. 1990. Origin of polygonal peat plateaus under conditions of continuous permafrost, Truelove Lowland, Devon Island, N.W.T. In: M.M. Burgess, D.G. Harry & D.C. Sego (eds.), *Permafrost, Canada, Proceedings of the Fifth Canadian Permafrost Conference, Collection Nordicana 54*. Québec: Centre d'études nordiques, Université Laval.

Tarnocai, C. & Zoltai, S.C. 1988. Wetlands of Arctic Canada. In: C.C.A. Rubec (ed.), *Wetlands of Canada*. Montreal: Polyscience Publications Inc..

van Everdingen, R.O. (ed.). 2005. *Multi-Language Glossary of Permafrost and Related Ground-Ice Terms*. Boulder: National Snow and Ice Data Center/World Data Center for Glaciology.

Washburn, A.L. 1979. *Geocryology: A Survey of Periglacial Processes and Environments*. London: Edward Arnold Publishers Ltd.

Zoltai, S.C. & Tarnocai, C. 1975. Perennially frozen peatlands in the western Arctic and Subarctic of Canada. *Canadian Journal of Earth Sciences* 12(1): 28-43.

Zoltai, S.C., Tarnocai, C., Mills, G.F. & Veldhuis, H. 1988. Wetlands of Subarctic Canada. *Wetlands of Canada*. Montreal: National Wetlands Working Group, Canada Committee on Ecological Land Classification, Polyscience Publications.

Changes in Surface Topography and Active Layer Following Partial Gravel Removal in the Prudhoe Bay Oilfield, Alaska

Janet G. Kidd
ABR, Inc. – Environmental Research & Services, Fairbanks, AK, USA

Abstract

To promote the development of wetland plant communities on abandoned sites in the Prudhoe Bay Oilfield, Alaska, gravel has been partially removed to create suitable soil and hydrological conditions. This study focused on changes in surface topography and thermal regime following gravel removal at 6 sites over the past 17 years. We established transects across each site to monitor the relative surface elevation and depth of the active layer. The sites range in age from 4–16 years, and the depth of residual gravel fill varies from 8–60 cm. Results varied widely among the sites surveyed, with changes in surface topography and thaw depth ranging from minimal to extensive. In some cases, thaw settlement continued for more than 15 years after gravel removal. The deep thaw penetration likely was preserved due to the absence of an insulative surface organic mat. Despite the potential for promoting thermokarst, gravel removal is an effective approach for creating wetland ecosystems on disturbed sites.

Keywords: active layer; gravel fill; relative surface elevation; thaw depth; thermokarst; wetlands.

Introduction

Over the past 30 years, research has been conducted in the Prudhoe Bay Oilfield to develop strategies for rehabilitating land disturbed by oil extraction and oilfield operations (e.g., Mitchell 1979, Moore & Wright 1991, unpubl., McKendrick 1991, Jorgenson & Joyce 1994, Jorgenson 1997, Jorgenson et al. 2003a). Part of this effort has involved assessing the potential for restoring tundra wetland plant communities by removing gravel from abandoned sites and applying plant materials (Jorgenson & Joyce 1994, Kidd et al. 2004, 2006). Removing the gravel reestablishes a hydrologic connection with adjacent, undisturbed tundra communities and improves site characteristics for plant establishment and growth.

Although gravel removal can help facilitate the restoration of wetland plant communities on disturbed sites, the disruption of the thermal regime following gravel removal, and the resulting subsidence, can limit vegetation recovery in some cases (Jorgenson & Joyce 1995, Kidd et al. 2004, 2006). The absence of a thick, insulative gravel layer or tundra vegetative mat subjects the underlying permafrost to melting. In some cases, ponding is extensive, with water levels too deep to support emergent plant species. Compression of the underlying tundra soil by the weight of gravel fill also can result in the creation of impoundments (Kidd et al. 2004). When the gravel is removed, the depression that remains promotes the impoundment of water, which can further promote thaw subsidence by conducting and convecting heat away from the ground (Hopkins 1949).

To better predict the extent of changes in surface topography and permafrost following gravel removal and the effect on restoration efforts, we surveyed the relative surface elevation and depth of the active layer (thaw depth) of 6 gravel removal sites in the Prudhoe Bay Oilfield. The sites range in age from 4–16 years and include abandoned airstrips, access roads, an operations pad, and an exploratory well site (Fig. 1).

The survey sites are located in a variety of landscape settings, including Old Alluvial and Alluvial-Marine terraces and Basin Complexes (Jorgenson et al. 2003b, unpubl.). Adjacent plant communities include Moist Sedge-Shrub Tundra, Fresh Sedge and Grass Marsh, and Wet Sedge Meadow Tundra. Dominant plant species are *Carex aquatilis*, *C. bigelowii*, *Eriophorum* spp., *Arctophila fulva*, and *Salix* spp. Large waterbodies also are present near many of the sites. Based on data collected at Deadhorse and Prudhoe Bay (1990–2007), mean annual air temperature in the study area is -11°C, and mean annual total precipitation is 17.6 cm (National Climate Data Center 2007). The mean depth of the active layer in tundra ranges from 30.5–60.6 cm, based on measurements collected near West Dock (Fig. 1) and Deadhorse (1995–2005) (Streletskiy et al. 2008).

Methods

Prior to gravel removal, the gravel fill thickness at all sites was approximately 1.5 m, which is typical for roads and pads in the Prudhoe Bay Oilfield. After gravel removal, the residual gravel fill thickness ranged from 8–60 cm, except at the North Prudhoe Bay State No. 2 Exploratory Well Site (hereafter referred to as North State 2) and the Mobil W/Z airstrip. Shallow and deep basins were excavated in portions of these sites, resulting in complete gravel removal. Gravel was removed in winter or early spring, and the following summer, various plant cultivation treatments were applied. Treatments included applying fertilizer alone, seeding native-grass cultivars, transplanting tundra plugs, and seeding indigenous (locally collected) species. Fertilizer was applied with all the planting treatments. At one site, an area was left untreated as a control. Note that not all of the treatments listed above were applied at each site.

Relative surface elevations and thaw depths were measured from 1990–2006 along permanent transects established in each gravel removal area. The transects varied in number

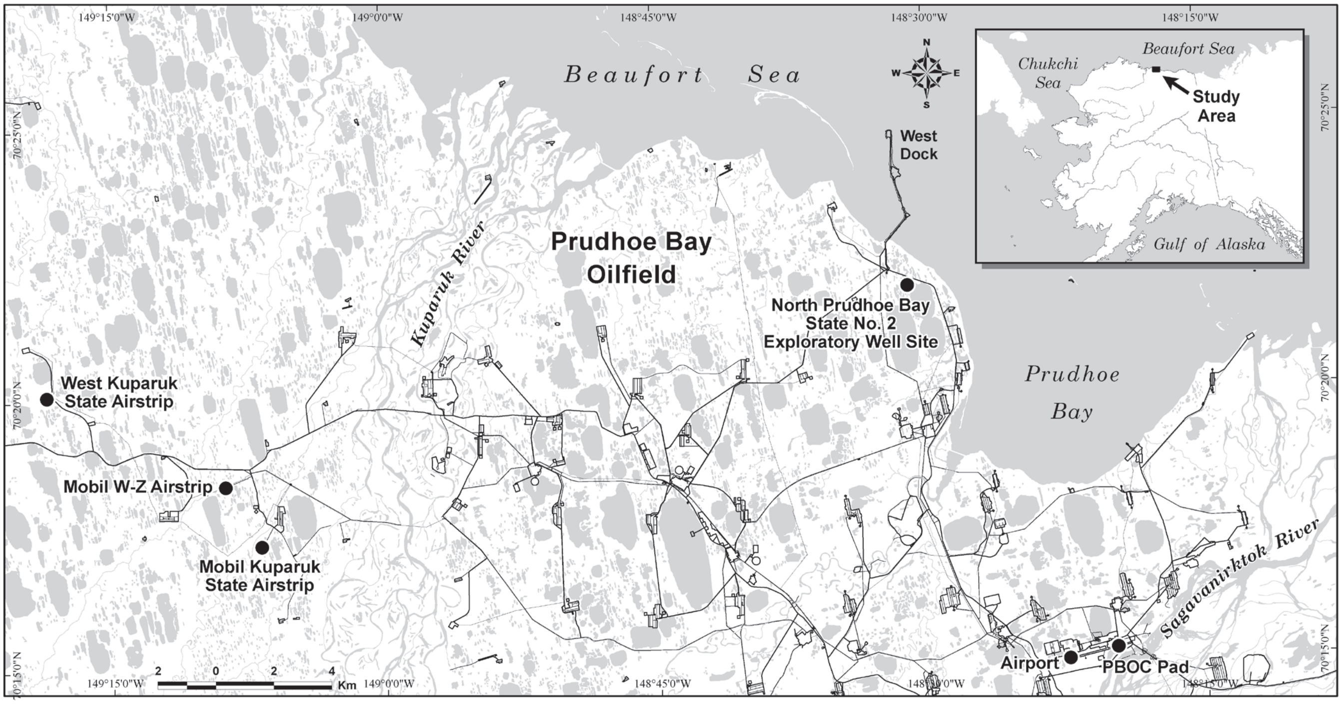

Figure 1. Locations of gravel removal sites surveyed for surface elevation and thaw depth, Prudhoe Bay Oilfield, Alaska, USA, 1990–2006.

and length, depending on the size of each site, and extended into the adjacent, undisturbed tundra approximately 5–10 m. Elevations were recorded at 1–2 m intervals along a meter tape using an auto-level or a laser level and survey rod. Thaw depths generally were measured every 5 m to the depth of resistance using a steel probe, which follows the methodology used in the Circumpolar Active Layer Monitoring (CALM) Program (Nelson et al. 1996). Additional thaw-depth measurements were made at prominent terrain breaks in the gravel removal areas and in the adjacent, undisturbed tundra in later years. The surveys were conducted in early to mid-August. Permanent benchmarks were not available at each location, so elevations were tied to the mean surface elevation of the adjacent, undisturbed tundra. Collection of geotechnical and ground temperature data was beyond the scope of this study.

Results and Discussion

Changes in surface elevation and thaw depth following gravel removal varied widely among the 6 sites surveyed, and were independent of site age (Figs. 2–5 & 7; Table 1). The greatest thaw settlement measured occurred at Mobil Kuparuk State Airstrip (-0.55 m, Fig. 2), where only 4 years had lapsed since gravel removal. In contrast, at North State 2, the southern transect only subsided 0.15 m in the 16-year period following gravel removal (Fig. 3). The topography of the 2 basins excavated also changed very little during this period. Changes in surface elevation on the northern transect were more notable, and included the development of several deep ponds.

The presence of deep troughs and depressions at Mobil Kuparuk Airstrip, the northern transect at North State 2, the Airport (Road 2, Fig. 4), and PBOC Pad (Fig. 5), indicate that ice wedges are present and in the process of melting. Flooded polygons form in response to the thawing wedges and are particularly evident at the Airport (Fig. 6). Elsewhere, more moderate subsidence has occurred (Fig.7), although the active layer is deep at all sites. Mean thaw depths range from 0.7–1.2 m (Table 1) and have yet to stabilize, even at the oldest sites (Airport, PBOC, North State 2). Mean thaw

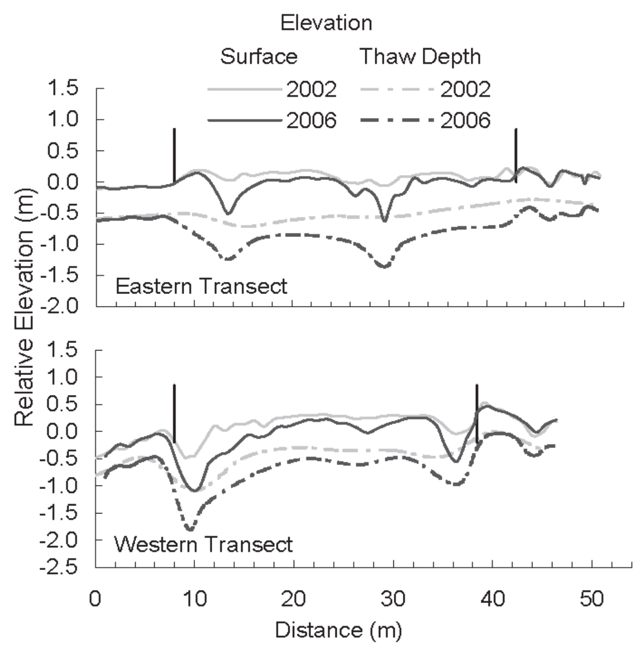

Figure 2. Profiles of relative surface and thaw depth elevation across Mobil Kuparuk State airstrip, 2002 & 2006. Brackets indicate boundaries between gravel removal areas and adjacent, undisturbed tundra.

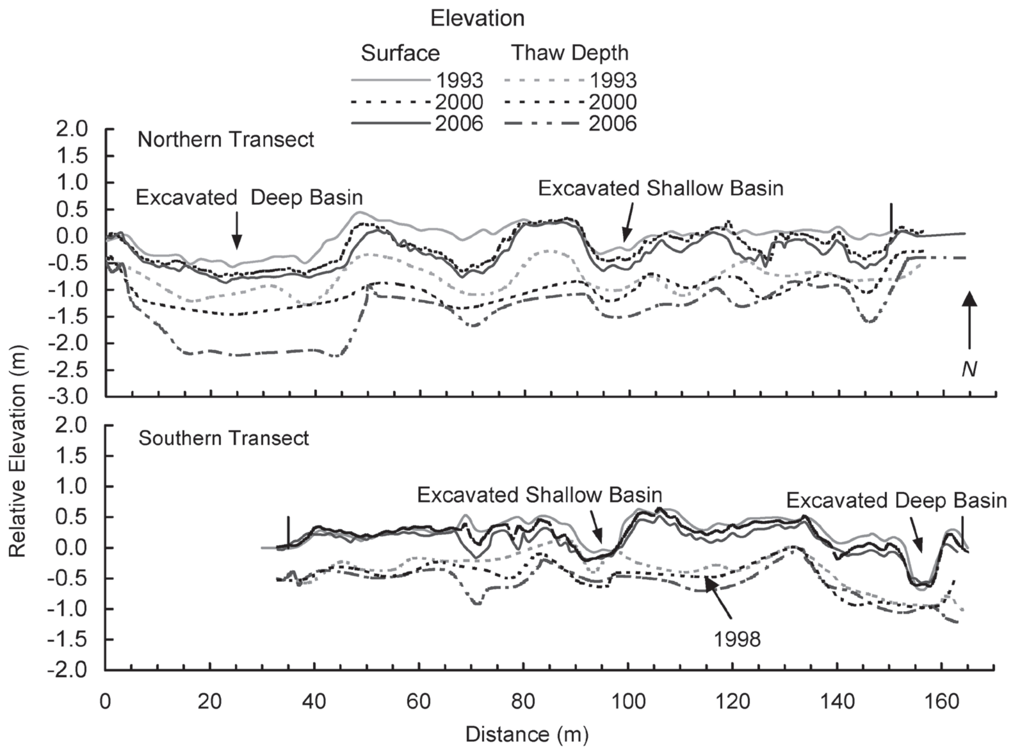

Figure 3. Profiles of relative surface and thaw depth elevation across North State 2, 1993, 2000, & 2006. Brackets indicate boundaries between gravel removal area and adjacent, undisturbed tundra.

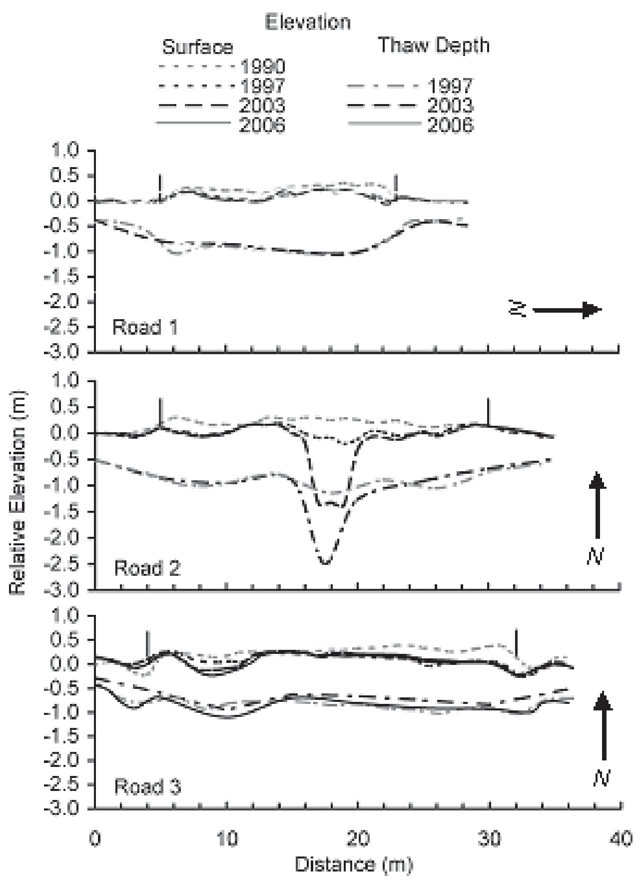

Figure 4. Profiles of relative surface and thaw depth elevation across Airport access roads 1990, 1997, 2003, and 2006. Brackets indicate boundaries between gravel removal areas and adjacent, undisturbed tundra.

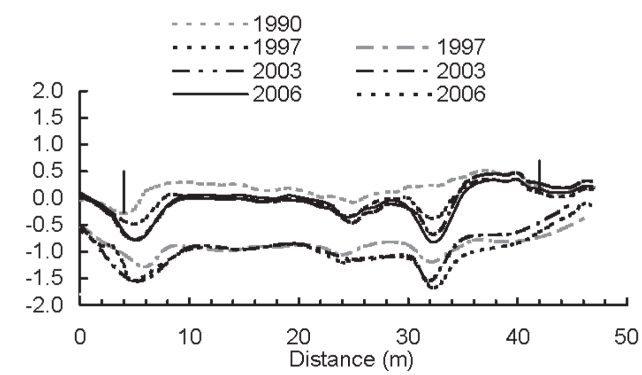

Figure 5. Profiles of relative surface and thaw depth elevation across PBOC Pad, 1990, 1997, 2003, & 2006. Brackets indicate boundaries between gravel removal areas and adjacent, undisturbed tundra.

depth in adjacent, undisturbed tundra in 2006 ranged from 0.49 m (± 0.02 m, n = 35) at Mobil W-Z to 0.73 m (± 0.03 m, n = 8) at the Airport.

The thawing and subsequent settlement of ice wedges at some of the sites is consistent with what has been observed elsewhere in terrain with similar characteristics. The 3 airstrips and the Airport access roads are all located in fine-grained, abandoned floodplain deposits, which are known to be ice rich (Jorgenson et al., 1996, unpublished). Compared with other terrain units in the region, the alluvial marine deposits associated with North State 2 are known to have some of the highest volumes of both ground and wedge ice (Pullman et al. 2007); this partly explains the extensive thermokarst on the northern half of the site. The southern

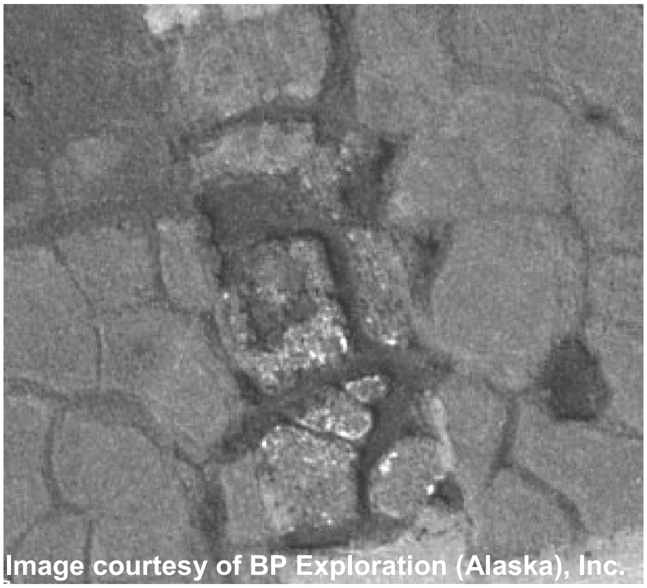

Figure 6. Aerial view of Road 3, Airport, showing deep, flooded polygon troughs, 2006.

half has experienced considerably less thaw settlement, however, suggesting that the processes governing surface stability at North State 2 are complex. The site is located in an old drained-lake basin, and the uneven thermokarst pattern probably reflects an irregular distribution of wedge ice in the sediments.

The differential settlement reveals the importance of varying types of ice. The settlement in the polygon centers between the ice wedges, which have varying forms of segregated ice, usually was only 10–30 cm. This is consistent with the thaw settlement estimates of 8–53 cm for a range of terrain types (Pullman et al. 2007). Settlement of the centers probably has achieved equilibrium with the new surface thermal regime. In contrast, the surface over ice wedges settled as much as 1.5 m. Ice wedges are particularly sensitive to disturbance (and climate change) because the wedge ice lies immediately below the active layer, and thus, there is little additional soil that can be thawed and added to the active layer to achieve a new stable equilibrium (Jorgenson et al. 2006). In addition, impoundment of water provides a positive feedback on heat gain and melting of ice. Jorgenson et al. (2006) found that aquatic sedges can rapidly colonize and stabilize the troughs within 30–50 yr, but troughs in the gravel removal areas are slow to vegetate. Consequently, they may be slower to stabilize until the wedge ice is almost completely melted out.

The absence of a deep organic soil layer has probably also played an important role in the maintenance of deep active layers and continued thaw settlement at these sites. Although productive communities of mosses and vascular plants have established in some of the treatment areas at the oldest sites, soil development has been minimal. The top 15–60 cm is still composed almost exclusively of coarse gravel, with varying amounts of sand. In addition,

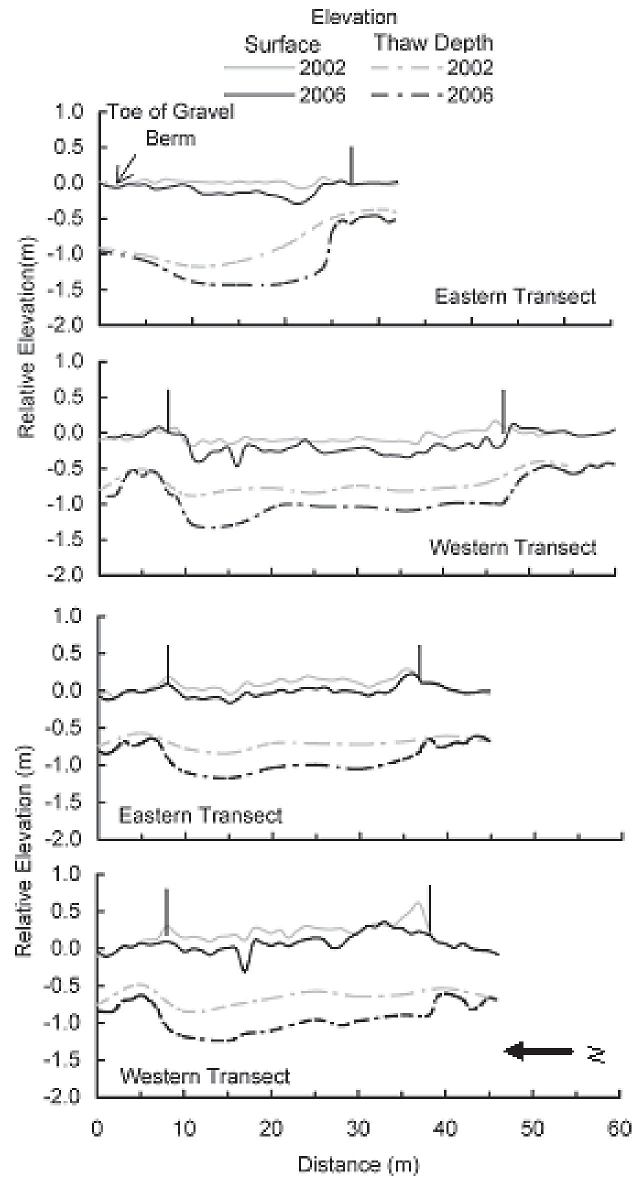

Figure 7. Profiles of relative surface and thaw depth elevation across Mobil W-Z (a) and West Kuparuk State (b) airstrips, 2002 and 2006. Brackets indicate boundaries between gravel removal areas and adjacent, undisturbed tundra.

plants have been unable to establish in deep ponds and troughs. As a result, during the relatively warm summers, heat can penetrate deeply into the exposed soil. The soils are saturated, and the high water content also serves as an excellent conductor of heat. Given the poor soil conditions and short growing season of the Arctic, it likely will be several decades before a sufficient moss and sedge peat mat develops on these sites to effectively insulate the soil. Consequently, we can expect that the volume of wedge ice will be substantially reduced before the sites become thermally stable.

Table 1. Mean (± SE) relative surface elevations and thaw depths for six study sites, Prudhoe Bay Oilfield, Alaska, 1990–2006.

	Surface Elevation (m)				Thaw Depth (m)			
Site	Initial		Final		Initial		Final	
Airport	Mean (±SE)	n[a]	Mean (±SE)	n	Mean (±SE)	n	Mean (±SE)	n
Road 1 (1990, 2003)	0.26 (0.01)	16	0.09 (0.02)	19	0.98 (0.22)	22	1.06 (0.02)	3
Road 2 (1990, 2003)	0.22 (0.01)	24	-0.22 (0.10)	25	0.80 (0.25)	24	0.98 (0.05)	5
Road 3 (1990, 2006)	0.49 (0.01)	26	0.10 (0.03)	27	0.85 (0.23)	25	0.93 (0.02)	7
PBOC Pad (1990, 2006)	0.22 (0.02)	36	-0.11 (0.05)	36	0.93 (0.22)	30	0.94 (0.04)	11
North State No. 2 Exploratory Well Site (1993, 2006)								
North	-0.03 (0.03)	80	-0.36 (0.03)	149	0.81 (0.04)	16	1.11 (0.04)	33
South	0.26 (0.03)	70	0.11 (0.02)	130	0.66 (0.04)	27	0.70 (0.04)	32
Mobil Kuparuk State Airstrip (2002, 2006)								
East	0.10 (0.01)	38	-0.07 (0.03)	40	0.64 (0.05)	8	0.81 (0.03)	10
West	0.44 (0.04)	31	-0.11 (0.06)	34	0.62 (0.01)	6	0.66 (0.04)	7
Mobil W-Z Airstrip (2002, 2006)								
Middle	0.01 (0.01)	24	-0.11 (0.02)	24	1.04 (0.06)	5	1.16 (0.07)	5
West	-0.08 (0.01)	37	-0.23 (0.02)	39	0.70 (0.01)	8	0.80 (0.02)	9
West Kuparuk State Airstrip (2002, 2006)								
East	0.11 (0.01)	28	-0.04 (0.02)	28	0.84 (0.03)	6	1.03 (0.02)	6
West	0.26 (0.02)	31	0.10 (0.02)	31	0.92 (0.03)	6	1.11 (0.04)	8

[a] n = sample size.

Conclusions

The results of long-term monitoring of surface stability and permafrost of gravel removal sites indicate that the observed changes in the thermal regime are long lasting and should be considered when planning land rehabilitation efforts to promote vegetation recovery. At sites where the probability of extensive thermokarst and thaw settlement occurring is high, the application of plant-cultivation treatments should be postponed until conditions are relatively stable. This delay will allow plant materials to be established in areas where conditions are likely to remain suitable over the long term. This effort can be assisted by assessing the terrain characteristics and the pattern of change in surface topography at each site following gravel removal. For many sites, the network of ponds and troughs that form is apparent relatively soon after gravel removal (within the first 3 years), although determining the ultimate water depth of ponds and troughs is more challenging.

Despite the potential for promoting thermokarst, gravel removal is an effective approach for creating wetland ecosystems on disturbed sites, for several reasons. First, a hydrologic connection with the adjacent, undisturbed tundra is established, facilitating the exchange of nutrients, seeds, plant propagules, and soil microbes. Second, the wetland hydrology encourages colonization by tundra plant species, primarily sedges and grasses. Finally, the heterogeneous surface topography that results from thermokarst creates a range of site conditions from moist to wet to ponded, allowing for the establishment of a diversity of plant species, with varying life-history characteristics. This diversity helps ensure some plasticity in the plant communities that establish, allowing them to respond to changing surface conditions while the thermal regime stabilizes. A potential concern is that the thermokarst associated with gravel removal sites might destabilize adjacent areas. However, although some thaw settlement is evident along the margins of gravel removal sites, we have not observed any dramatic changes in the surface stability of these areas.

Acknowledgments

Funding for this study was provided by BP Exploration (Alaska), Inc., and managed by Bill Streever, Environmental Studies Leader. Initial financial support for data collection was provided by ARCO Alaska, Inc. Torre Jorgenson designed the land rehabilitation studies that are the sources of the long-term datasets and provided a valuable technical review. Sue Bishop assisted with fieldwork and reviewed the manuscript. Additional field support and graphical assistance was provided by Tim Cater, Kate Beattie, and Allison Zusi-Cobb.

References

Hopkins, D.M. 1949. Thaw lakes and thaw sinks in the Imuruk Lake area, Seward Peninsula, Alaska. *Journal of Geology* 57: 119-131.

Jorgenson, M.T. 1997. Patterns and rates of, and factors affecting natural recovery on land disturbed by oil development in arctic Alaska. *Disturbance and Recovery in Arctic Lands: an Ecological Perspective*. NATO ASI Series 2 Environment, Vol. 25, Dordrecht: Kluwer Academic Publishers, 421-442.

Jorgenson, M.T. & Joyce, M.R. 1994. Six strategies for rehabilitating land disturbed by oil development in the arctic Alaska. *Arctic* 47: 374-390.

Jorgenson, M.T., Aldrich, J.W., Pullman, E.R., Ray, S.R., Shur, Y., Smith, M.D., Stickney, A.A. & Walker, H.J. 1996. Geomorphology and hydrology of the Colville River Delta, Alaska, 1995. Final report prepared for ARCO Alaska, Inc., Anchorage, AK, by ABR, Inc. and Shannon & Wilson, Inc., Fairbanks, AK, 136 pp.

Jorgenson, M.T., Kidd, J.G., Cater, T.C., Bishop, S.C. & Racine, C.H. 2003a. Long-term evaluation of methods for rehabilitation of lands disturbed by industrial development in the Arctic. In: R.O. Rasmussen & N.E. Koroleva (eds.), *Social and Environmental Impacts in the North*. Dordrecht: Kluwer Academic Publishers, 173-190.

Jorgenson, M.T., Roth, J.E., Emers, M., Schlentner, S.F., Swanson, D.K., Pullman, E.R., Mitchell, J.S. & Stickney, A.A. 2003b. An ecological land survey in the Northeast Planning Area of the National Petroleum Reserve–Alaska, 2002. Final report prepared for ConocoPhillips Alaska, Inc., Anchorage, AK, by ABR, Inc., Fairbanks, AK, 124 pp.

Jorgenson, M.T., Shur, Y.L. & Pullman, E.R. 2006. Abrupt increase in permafrost degradation in Arctic Alaska. *Geophysical Research Letters* 33: L02503, doi:10.1029/2005GL024960.

Kidd, J.G., Streever, B., Joyce, M.R. & Fanter, L.H. 2004. Wetland restoration of an exploratory well on Alaska's North Slope: a learning experience. *Ecological Restoration* 22: 30-38.

Kidd, J.G., Streever, B. & Jorgenson, M.T. 2006. Site characteristics and plant community development following partial gravel removal in an arctic oilfield. *Arctic, Antarctic, and Alpine Research* 38(3): 384-393.

McKendrick, J.D. 1991. Arctic tundra rehabilitation—observations of progress and benefits to Alaska. *Agroborealis* 23(1): 2-40.

Mitchell, W.W. 1979. *Three varieties of native Alaskan grasses for revegetation purposes.* University of Alaska, Alaska. Alaska Agricultural Experiment Station Circular 32.

Moore, N. & Wright, S.J. 1991. *Revegetation with Arctophila Fulva, 1985–1989*. Final report prepared for ARCO Alaska, Inc., Anchorage, AK, by Plant Materials Center, Alaska Dept. Natural Resources, Palmer, AK.

National Climate Data Center. 2007. U.S. Dept. of Commerce. Website address (accessed February 2007): http://www.ncdc.noaa.gov/oa/ncdc.html

Nelson, F., Brown, J., Lewkowicz, T. & Taylor, A. 1996. Active Layer Protocol. In: U. Molau & P. Molgaard (eds.), *ITEX Manual,* 2nd Ed. Danish Polar Center.

Pullman, E.R., Jorgenson, M.T. & Shur, Y. 2007. Thaw settlement in soils of the Arctic Coastal Plain, Alaska. *Arctic, Antarctic and Alpine Research* 39: 468-476.

Streletskiy, D.A., Shiklomanov, N.I. & Nelson, F.E. 2008. 13 years of observations at Alaskan CALM sites: long-term active layer and ground surface temperature trends. *Proceedings of the Ninth International Conference on Permafrost, Fairbanks, Alaska, June 29–July 3, 2008* (this proceedings).

Vegetation Differentiation Across a Topographic Yedoma–Alas Transect in the High Arctic Tundra of Oyogos Yar, East Siberia

Frank Kienast
Research Institute and Museum for Natural History Senckenberg, Research Station for Quaternary Palaeontology Weimar, Weimar, Germany

Lutz Schirrmeister
Alfred Wegener Institute for Polar and Marine Research, Potsdam, Germany

Sebastian Wetterich
Alfred Wegener Institute for Polar and Marine Research, Potsdam, Germany

Abstract

Excessive moisture is regarded as the main cause for the fall of Pleistocene tundra-steppe and the rise of modern tundra. The arctic tundra of Oyogos Yar is low in diverse plant species (ca 100). The floral composition is mainly the result of differences in moisture or drainage, respectively. We describe a vegetational profile recorded in August 2007 along a 10 km transect from the top of a yedoma ridge down to the adjacent alas depression between 40 m to 10 m a.s.l. Six main landscape units are described with respect to their floristic composition: yedoma top with thermokarst mounds, mud boils, yedoma slopes, small thermokarst ponds, thermo-erosional valleys, and the bottom of thermokarst depressions. Arctic thermokarst landscapes with yedoma ridges and alas depressions can be well-classified according to their vegetation. The main constituents of the plant cover at well-drained sites are grasses and polar willows, whereas excessively wet sites are occupied by sedges, cotton grass, and peat moss.

Keywords: alas depression; bioindication; moisture regime; thermokarst; tundra vegetation; yedoma elevation.

Introduction

The arctic vegetation cover reflects very well the small-scale periglacial landscape differentiation. Detailed surveys of plant associations are essential for the understanding of biotic responses to changes in permafrost landscapes. Around Beringia, the great influence of topography on arctic vegetation has been described from Alaska (Walker 2000, Kade et al. 2005) and from the Taymyr Peninsula (Matveyeva 1994). Such studies of modern tundra vegetation are, however, little-known from Arctic Yakutia. Within the frame of the joint Russian-German expedition, “Lena–New Siberian Islands 2007,” we studied relief-vegetation interactions at the coast of the Dimitrii Laptev Strait in August 2007.

Regional Setting

Oyogos Yar is the name of the mainland coast of the Dimitrii Laptev Strait (Fig. 1) between the mouth of the Kondrat’eva River in the east and Cape Svyatoy Nos in the west. This landscape is part of the Yana-Indigirka Lowland in Northeastern Siberia. Up to 500 m thick continuous permafrost and wide spread thermokarst characterize the coastal lowland. Oyogos Yar’s topography is dominated by extremely flat plains covered by mires and shallow lakes.

There are two main topographic elements: low elevations, so-called yedoma, which represent the Pleistocene ground level, and thermokarst depressions (alases), which formed as a result of thermal degradation of the ice-rich permafrost that constitutes the yedoma.

According to Aleksandrova (1980), Oyogos Yar belongs to the Sellyakh Inlet–Indigirka Delta district of the East Siberian province of the southern arctic tundra characterized by the dominance of *Alopecurus alpinus* and *Salix polaris*, the presence of *Carex ensifolia* ssp. *Arctisibirica,* and the absence of subarctic elements like *Betula nana* s.l. According to the Circumpolar Arctic vegetation map (CAVM Team 2003), the study area is covered with sedge/grass, moss wetland (W1) with *Carex aquatilis*, *Arctophila fulva*, *Dupontia*, and *Eriophorum* spp.

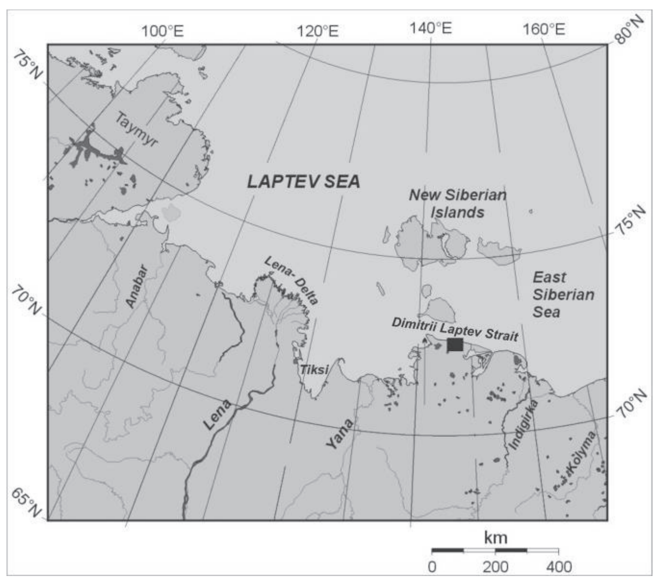

Figure 1. Position of the study area (black square corresponds to Fig. 2) at the mainland coast of the Dimitrii Laptev Strait.

The study area is located about 8 km west of the Kondrat’eva River mouth (Fig. 2) opposite to Cape

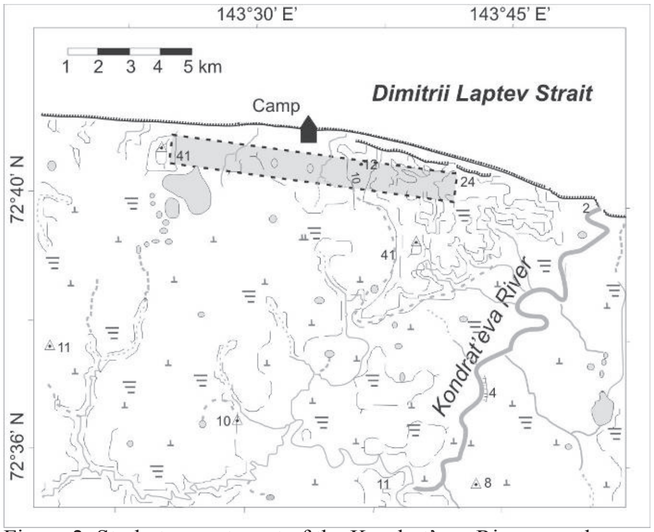

Figure 2. Study transect west of the Kondrat'eva River mouth.

Shalaurova, the eastern edge of Bol'shoy Lyakhovsky Island. The climate is characterized by cold winters, cool summers, and low precipitation. Climate data from the weather station Cape Shalaurova, about 80 km north of the study site, reflect a mean July air temperature of 2.8°C, a mean January air temperature of -32.2°C, and an annual precipitation of 253 mm (Rivas-Martínez 1996–2004).

Site Description

The study transect extends across the bottom of a large alas depression about 10 km in diameter (5 to 10 m a.s.l.) and the adjacent slope and top areas of a yedoma hill of up to 40 m in height (Figs. 2, 3). The alas bottom dominantly consists of polygonal wetland tundra with a 0.5 to 1.0 m thick peat cover. The thermokarst depression is cut by the coast of the Dimitrii Laptev Strait in the north, and additionally intersected by several thermo-erosional valleys that drained to the coast.

Within the recorded transect, the following six main landscape units are described with respect to their floristic composition: the yedoma with thermokarst mounds, mud boils, yedoma slopes, small thermokarst ponds, thermo-erosional valleys, and the bottom of thermokarst depressions.

Vegetation Characteristics

Thermokarst mounds on the yedoma

Thermokarst mounds are the best-drained habitats in the study area (Fig. 4). Their plant cover is mainly composed of *Salix polaris*, *Dryas punctata,* and *Alopecurus alpinus*. Other grasses, such as *Festuca brachyphylla* and *Deschampsia borealis,* and dicots, like *Potentilla hyparctica, Oxyria digyna, Papaver polare,* and *Valeriana subcapitata,* also occur.

Mud boils

Mud boils are the result of cryoturbation caused by frost pressing. In consequence, muddy soil flooded the ground.

Figure 3. View from the alas bottom to the yedoma hill.

Figure 4. Thermokarst mounds on the yedoma at Oyogos Yar.

The substrate is silty and well-drained. Mud boils occur at places most exposed and windswept on the Yedoma. Plants occur here only between such mud spots; the coverage is consequently very low with 20 to 40% (Fig. 5). *Potentilla hyparctica, Salix polaris,* and low growing grasses, and rushes like *Festuca brachyphylla, Deschampsia borealis,* and *Luzula confusa* are the main constituents of such habitats In addition, herbs such as *Lloydia serotina, Cardamine bellidifolia, Androsace triflora*, and *Tephroseris atropurpurea* occur in lower abundance.

This vegetation is similar in composition to cryptogam, herb barren (B1) or to the gramioid tundra (G1), described in the Circumpolar Arctic vegetation map (CAVM Team 2003).

Yedoma slopes

At yedoma slopes, the coverage is in general >80%. In the upper parts of slopes in SW exposition, *Dryas punctata* is one of the main constituents. *Salix polaris* and several grass species (*Alopecurus alpinus, Deschampsia borealis,* and *Festuca brachyphylla)* and *Luzula confusa* are characteristic of yedoma slopes. In lower parts of the slopes, where it is less drained and, consequently, moister, *Arctagrostis latifolia, Petasites frigidus,* several saxifrages (*S. nelsoniana, S. cernua, S. hieracifolia*) and other herbs (*Gastrolychnis apetala, Tephroseris atropurpurea, Ranunculus spp.*) are typical (Fig. 6).

Figure 5. Mud boil at the top of the yedoma visible in Figure 3.

Figure 6. Lower part of a yedoma slope with dominating *Arctagostis latifolia.* In the background, a thermo-erosional valley with reddish spectral signature (here: dark) is visible.

Figure 7. Thermokarst pond with dominating *Pleuropogon sabinei* growing immersed in the water (inserted photo).

Small thermokarst ponds

In small depressions on the yedoma, ponds with *Pleuropogon sabinei* and on the shore, *Arctophila fulva*, *Arctagrostis latifolia, Ranunculus hyperboreus, Dupontia fischeri*, *Eriophorum polystachion,* and *E. scheuchzeri* occur (Fig. 7).

Interestingly, genuine aquatics were widely lacking. Only *Hippuris vulgaris* was solitarily found in a sterile form. The white-flowered *Ranunculus pallasii* and *Caltha palustris* grew immersed in some ponds within the Alas depressions.

Figure 8. Thermo-erosional valley intersecting the yedoma of Oyogos Yar. Main constituent here is *Eriophorum scheuchzeri* causing a green spectral signature.

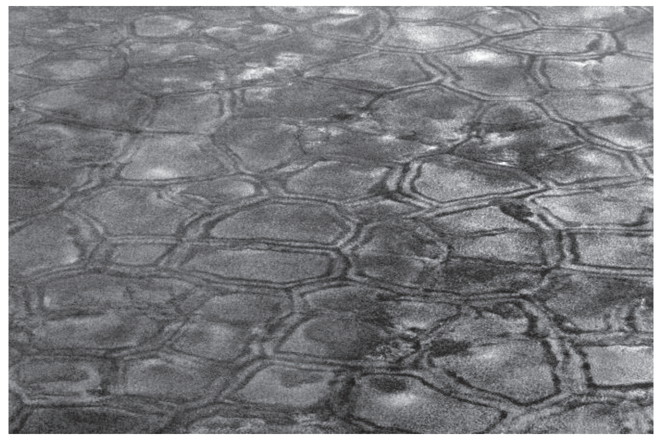

Figure 9. Bottom of a thermokarst depression with a water table above the ground. The polygonal surface patterns are visually strengthened by vegetational differentiation (compare Fig. 10).

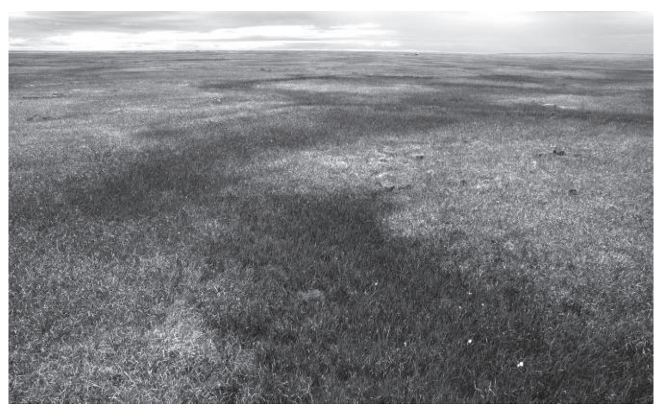

Figure 10. The wettest places in high center polygonal wetland tundra are the inter-polygonal trenches. Here, *Eriophorum polystachion* is the main constituent, causing a reddish (here dark) pattern.

Thermo-erosional valleys

Thermo-erosional valleys are permanently supplied by running water. They are characteristically colored and recognizable from a far distance (Fig. 6). Dark green and reddish signatures are mainly caused by different *Eriophorum* species: green – *E. scheuchzeri*, and red – *E.*

polystachion (Figs. 6, 8). Other plants of thermo-erosional valleys are *Petasites frigidus* and several crowfoot and grass species (*Dupontia fischeri, Calmagrostis holmii*).

Bottom of thermokarst depressions

The bottom of thermokarst depressions, alases, is in contrast to thermo-erosional valleys characterized by stagnant water and covered mainly with sedges (*Carex ensifolia* ssp. *arctisibirica*) and cotton grass (*Eriophorum polystachion*).

The vascular plant diversity here is the lowest in the study area. *Sphagnum* moss is widely present, causing irregular pale green spots in polygonal wetlands where the surface of water is above the ground (Fig. 9).

At sites outside water bodies, rushes (*Luzula nivalis, L. confusa*) cover large areas, together with several grasses (*Dupontia fischeri, Calamagrostis holmii, Poa alpigena,* and *Arctophila fulva*). The wettest places are almost exclusively occupied by *Eriophorum polystachion*, which produces reddish patterns on the ground indicating the water trenches between polygons from afar (Figs. 9, 10).

Conclusions

The main landscape units in thermokarst-affected landscapes can be well distinguished by their vascular plant cover.

Moisture or drainage, respectively is the most important ecological factor in the study area resulting in the strongest vegetation differentiation.

Subordinate factors are exposure and declination. There were no really dry places in the study area.

Excessive wetness is well-indicated by plants with characteristic spectral properties and, therefore, visible from far distances.

The plant species composition can alter quickly on short distances reflecting moisture changes resulting from the damming effect of the frozen ground.

The existence of such small-scale variations in the plant cover has important implications for the interpretation of palaeobotanical records.

Acknowledgments

We thank all participants of the joint Russian-German expedition, *Lena–New Siberian Islands 2007*, who helped us collecting, drying, and preparing the plants for the herbarium. The studies were supported by the German Science Foundation (KI 849/1).

References

Aleksandrova, V.D. 1980. The Arctic and Antarctic: their division into geobotanical areas. Cambridge University Press, Cambridge.

CAVM Team. 2003. Circumpolar Arctic Vegetation Map. 1:7,500,000. Conservation of Arctic Flora and Fauna (CAFF) Map No. 1. Anchorage, Alaska: U.S. Fish and Wildlife Service.

Kade, A., Walker, D.A.& Raynolds, M.K. 2005. Plant communities and soils in cryoturbated tundra along a bioclimate gradient in the Low Arctic, Alaska. *Phytocoenologia* 35(4): 761-820.

Matveyeva, N.V. 1994. Floristic classification and ecology of tundra vegetation of the Taymyr Peninsula. Northern Siberia. *Journal of Vegetation Science* 5: 813-828.

Rivas-Martínez, S. 1996–2004. Climate diagrams, Worldwide. *Bioclimatic Classification System*. Phytosociological Research Center, Spain. Online database, http://www.globalbioclimatics.org/plot/ru-mys-s.htm.

Walker, D.A. 2000. Hierarchical subdivision of Arctic tundra based on vegetation response to climate, parent material and topography. *Global Change Biology* 6 (Suppl. 1): 19-34.

A Two-Dimensional Numerical Heat Transfer Solution for Frost Heave Prediction Using the Segregation Potential Concept

Koui Kim

Dept. of Civil and Environmental Engineering, University of Alaska Fairbanks, Fairbanks, AK, USA

Wei Zhou

Dept. of Geology and Geological Engineering, Colorado School of Mines, Golden, CO, USA

Scott L. Huang

Dept. of Mining and Geological Engineering, University of Alaska Fairbanks, Fairbanks, AK, USA

Abstract

The Segregation Potential (SP) concept has been widely used to predict frost heaving for engineering projects, such as the design of buried chilled gas pipelines or ground freezing. It is of utmost importance for the SP concept to calculate an accurate temperature gradient in the frozen fringe. The authors developed a modified apparent heat capacity method using temperature-dependent unfrozen water contents. The model was implemented using the finite element method (FEM) with very fine mesh. The numerical results of the model have shown satisfactory accuracy as compared with the analytical solution. In addition, the model eliminates oscillations of the temperature gradient in the frozen fringe.

Keywords: chilled gas pipeline; frost heave; phase change; segregation potential.

Introduction

Frost heave is a mass and heat transfer phenomenon. The ice lens grows behind the freezing front. The transitional partially frozen zone between the ice lens and the unfrozen soil is called the *frozen fringe* (Miller 1972). Secondary frost heave theory (Miller 1978) is based on well-established principles of soil physics, hence it is the most popular theory. The secondary frost heave theory was successfully developed for numerical modeling (O'Neill & Miller 1985). However, the input parameters are difficult to obtain. Konrad & Morgenstern (1980, 1981) developed the Segregation Potential (SP) concept to overcome this problem. The SP concept succeeded in obtaining the overall frozen fringe characteristics including the suction gradient and the hydraulic conductivity through laboratory frost heave tests. The velocity of the pore water migrating to the frozen fringe, v, was proportional to the temperature gradient in the frozen fringe, gradT_{ff}, provided the suction at the pore-freezing front was constant:

$$v = \frac{P_w - P_u}{d} K_{ff} = \left(\frac{P_w - P_u}{T_s - T_f} K_{ff} \right) \mathrm{grad}T_{ff} = \mathrm{SP} \times \mathrm{grad}T_{ff} \tag{1}$$

where P_w = suction pressure at the active ice lens; P_u = suction at the freezing front; K_{ff} = overall hydraulic conductivity of the frozen fringe; d = thickness of the frozen fringe; T_s = segregation temperature; T_f = freezing temperature; and SP = segregation potential.

It was confirmed in a previous study by Konrad & Morgenstern (1982) that the SP value near thermal steady state is dependent on the following variables:

$$\mathrm{SP} = \mathrm{SP}\left(\dot{T}_f, P_u, P_e, etc\right) \tag{2}$$

where $\dot{T}_f$ = the cooling rate of the frozen fringe; P_e = confining pressure acting on the freezing front.

The cooling rates are very small in the field condition. It is reasonable to apply the cooling rates at the formation near thermal steady state obtained by constant temperature boundary frost heave tests for the field condition (Konrad & Morgenstern 1984). From Equation 1, the SP value decreases with increasing P_u. In most field conditions, P_u is fairly small as long as the freezing front is below the water table. Therefore, it would be reasonable to use the SP value determined by a laboratory frost heave test in which the warm plate temperature is close to freezing point, because the thermal boundary condition creates a small P_u value due to the short unfrozen soil length. The effect of P_e is taken into account empirically by Konrad & Morgenstern (1982):

$$\mathrm{SP} = \mathrm{SP}_0 \exp\left(-aP_e\right) \tag{3}$$

where a = a soil constant; SP_0 = the maximum value of segregation potential that occurs at zero external pressure.

Since the proposed model is based on the SP concept, the migrated water amount depends on the temperature gradient, the rate of cooling, and the stress state. To simplify the simulation process, numerically uncoupled temperature solution from the stress–strain analysis or mass transfer solution can be applied. For any particular time step, the non-linear temperature distribution is first calculated with an iterative procedure, and then this temperature solution is used to determine the location of the freezing front. With the freezing front position determined, the SP concept is then used to calculate the volume of water flow to the segregation freezing front.

The precise calculation of the temperature gradient in the frozen fringe is of utmost importance for the SP concept. Also, the coupled stress state has a strong dependence on thermal regime. Therefore, a numerical procedure for the transient heat transfer is first presented in this paper. Second, the verification of the developed heat transfer model is described. Finally, a new technique to calculate the temperature gradient in the frozen fringe is discussed.

Heat Transfer Model with Phase Change

Governing differential equation

The three basic modes of heat transfer are conduction, convection, and radiation. Heat conduction is the primary mode in soils (Konrand & Shen 1996). Although heat convection was considered in some models (e.g. Harlan 1973), it is usually negligible in soil heat transfer studies (Farouki 1981). Nixon (1975) reported that the convection component is two or three orders of magnitude smaller than the conduction component. Radiation components hardly contribute to the amount of heat transfer at all. Radiation accounts for less than 1% of the total heat transfer in sands and even less in fine-grained soils (Farouki 1981).

For the above mentioned reason, the developed two-dimensional heat transfer model with isotropic thermal properties is based on conduction only and is governed by the following equation:

$$C\frac{\partial T}{\partial t} + L = \frac{\partial}{\partial x}\left(k\frac{\partial T}{\partial x}\right) + \frac{\partial}{\partial y}\left(k\frac{\partial T}{\partial y}\right) \tag{4}$$

where C = volumetric heat capacity of soil; L = volumetric latent heat; T = soil temperature; t = time; and k = effective thermal conductivity of soil.

Alternatively, Equation 4 can be expressed as:

$$C_a\frac{\partial T}{\partial t} = \frac{\partial}{\partial x}\left(k\frac{\partial T}{\partial x}\right) + \frac{\partial}{\partial y}\left(k\frac{\partial T}{\partial y}\right) \tag{5}$$

where C_a = the apparent volumetric heat capacity.

The traditional apparent heat capacity is defined as:

$$C_a = C + \frac{L}{TI} \tag{6}$$

where $TI = T_f - T_s$: the temperature interval.

In this study, unfrozen water effect is taken into account in the phase change.

$$C_a = C + L'\rho_w\frac{\partial \theta_w}{\partial T} \tag{7}$$

where L' = latent heat of fusion per unit mass of water ($3.337*10^5$ J/kg); ρ_w = density of water (1000 kg/m^3); and θ_w = volumetric fraction of water.

This method is applied for fine-grained soils (Nixon 1983, Shen 1988). This method produces latent heat release over a range of subfreezing temperature.

Unfrozen water content in Fairbanks silt

Anderson and Morgenstern (1973) described a two-parameter power equation to determine unfrozen water content as:

$$w_u = m \times \left(T_f - T\right)^n \tag{8}$$

where w_u = unfrozen water content; m,n = characteristic soil parameters.

Michalowski & Zhu (2006) developed a first order exponential decay function:

$$w_u = w_1 + \left(w^t - w_1\right)\exp\left(\frac{T - T_f}{b}\right) \tag{9}$$

where w^t = the water content in an unfrozen state; w_1 = the asymptotic value; and b = the rate of decay.

With decreasing temperature, the unfrozen water content reaches the asymptotic value.

Equations 8 and 9 can describe the unfrozen water content of the soil, with which a clayey soil would be expected to have a relatively high unfrozen water content. However, the laboratory results of Fairbanks silt at the UAF pipeline experiment site showed a relatively low unfrozen water content and a very steep gradient around the freezing temperature (Huang et al. 2004). Therefore the authors applied a second order exponential decay given by:

$$\begin{cases} w_u = w_1 + w_2\exp\left(\dfrac{T - T_f}{t_1}\right) + w_3\exp\left(\dfrac{T - T_f}{t_2}\right) \\ w_1 + w_2 + w_3 = w^t \end{cases} \tag{10}$$

where t_1, t_2 = rate of decay.

Figure 1 shows the comparison between the calculated unfrozen water content curve and the measured results of Fairbanks silt at the UAF pipeline experiment site. The unfrozen water affects the soil's thermal properties.

Verification of Proposed Model

As shown in Equation 1, the precise calculation of the temperature gradient in the frozen fringe is the most important step for the SP concept. Nixon (1986) developed a two-dimensional geothermal model, named HAL, and conducted quadratic function fitting through three temperature points near the freezing front to determine gradT_{ff}. However, the proposed method produced oscillations of gradT_{ff} (Carlson & Nixon 1988). Coutts (1991) proposed that gradT_{ff} should be determined at the segregation temperature, which is the coldest temperature in the phase change range. This

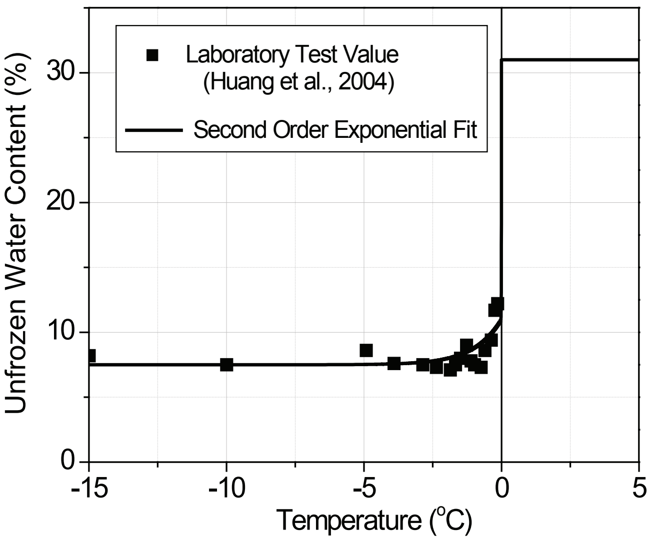

Figure 1. Unfrozen water contents of Fairbanks silt.

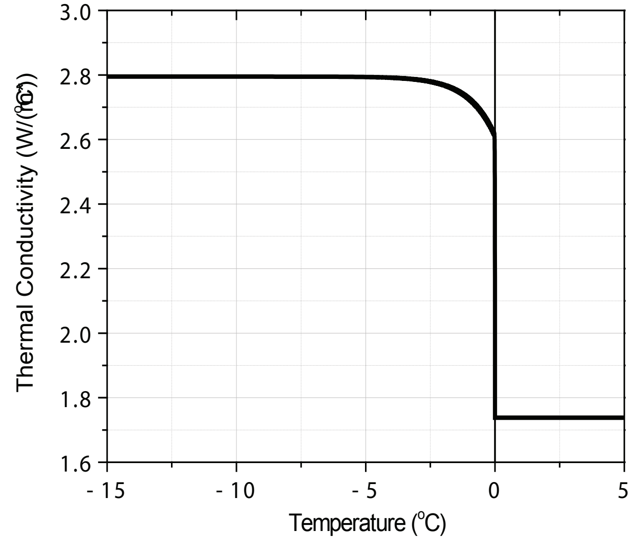

Figure 2. Thermal conductivity of Fairbanks silt for the proposed solution.

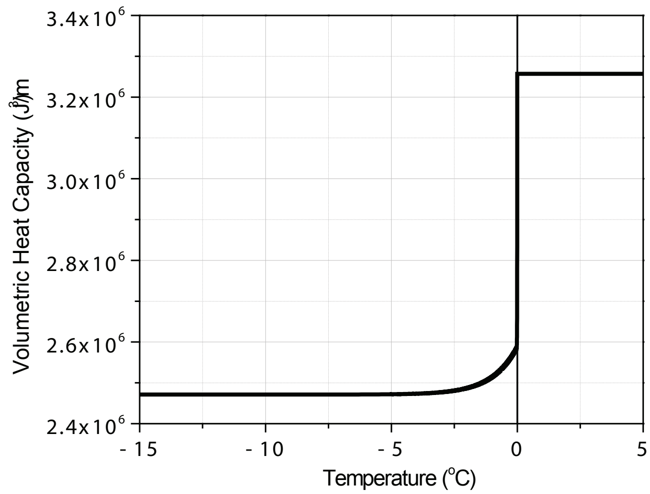

Figure 3. Volumetric heat capacity of Fairbanks silt for the proposed solution.

approach, however, could not eliminate oscillations. Konrad and Shen (1996) modified Coutts's model, and eliminated oscillations of gradT_{ff} using forced mesh adjustment. However, the procedure was very complicated to manage. Also, the adjusted mesh had numerical instability, because the stiffness term of the adjusted mesh had a very large range compared with that of the unfrozen or totally frozen mesh (Hawlader et al. 2004). The authors propose a new approach applying a fine mesh and considering the effects of unfrozen water.

The proposed model is implemented by ABAQUS/ Standard-6.7 finite element code. The soil geometry is a 0.0005 m by 10 m column. The two-dimensional four-node linear heat transfer element (DC2D4) is applied. The soil is divided into 0.0005 m square meshes. The mesh is only one element wide. The initial soil temperature is 1°C. The temperature boundary at the top is set at –1°C, and kept constant for 2000 hours. Zero heat flux is applied at the bottom and side boundaries. For the boundary conditions defined above, the two-dimensional heat transfer model is verified as a one-dimensional solution.

The unfrozen water contents shown in Figure 1 are taken into account in the thermal conductivities and volumetric heat capacities. Figures 2 and 3 show thermal conductivities and volumetric heat capacities of the Fairbanks silt at the UAF pipeline site, respectively. Thermal conductivity values were obtained by the thermal conductivity needle-probe method, then calibrated using the correlations of Johansen (1977). Those values are applied for the proposed model using the apparent heat capacity in Equation 7.

The proposed model is compared with the case using the traditional apparent heat capacity method with Equation 6, and verified against the Neumann solution. The Neumann solution is not valid for non-linear thermal properties but rather for materials that exhibit constant values in both the frozen and unfrozen states. Frozen thermal properties are determined at the asymptotic point. Latent heat generation was a concern in the frozen water amount from the freezing temperature to the asymptotic point (= w^t – w_1). The thermal conductivities of the frozen and unfrozen phase are determined as 2.79 and 1.74 W/(m*°C), the volumetric heat capacities were $3.26*10^6$ and $2.47*10^6$ J/(m^3*°C), respectively. The volumetric latent heat is $1.16*10^8$ J/m^3. Those constant properties are also used for the traditional apparent heat capacity method. The calculations are made by TI = 0.01°C, 0.05°C, and 0.1°C.

The freezing front penetration in each case is compared in Figure 4. While the traditional apparent heat capacity method for the case of TI = 0.01°C is identical to the result obtained from the Neumann solution, its accuracy is sensitive to the magnitude of TI. With increasing TI, the freezing front penetrates deeper.

Figure 5a shows the temperature profiles of Neumann and the proposed solution at 2000 hours. The proposed solution agrees

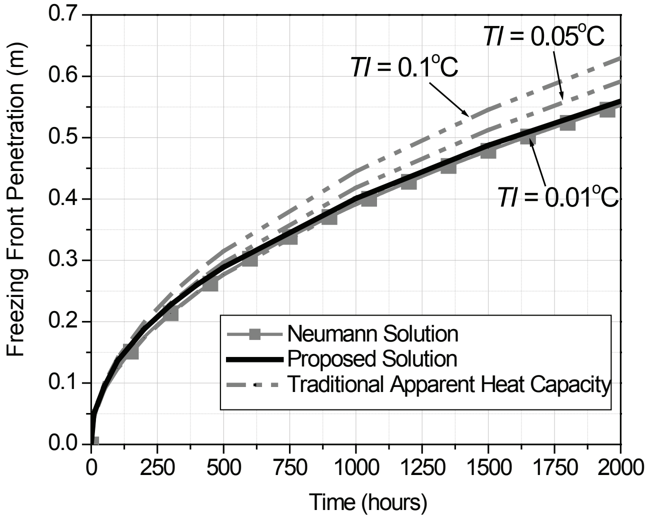

Figure 4. Comparison of freezing front penetration.

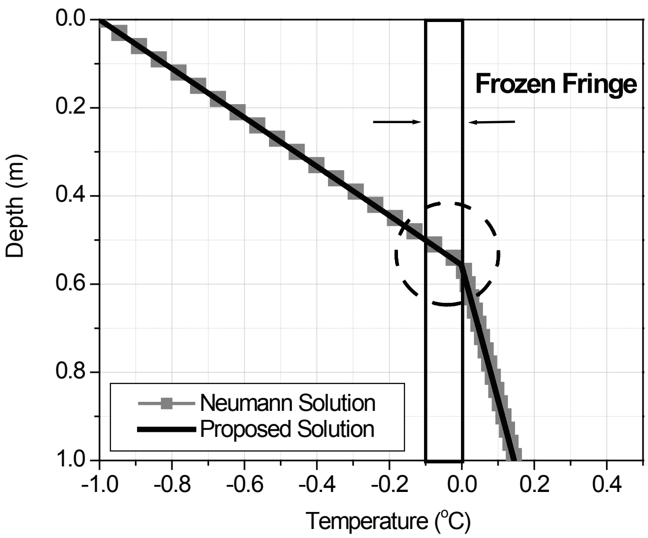

Figure 5a. Comparison of temperature distribution at 2000 hours.

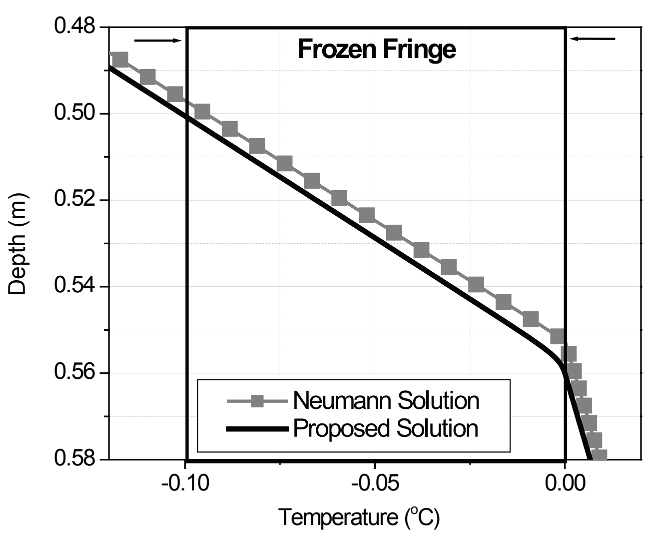

Figure 5b. Comparison of temperature distribution in frozen fringe at 2000 hours.

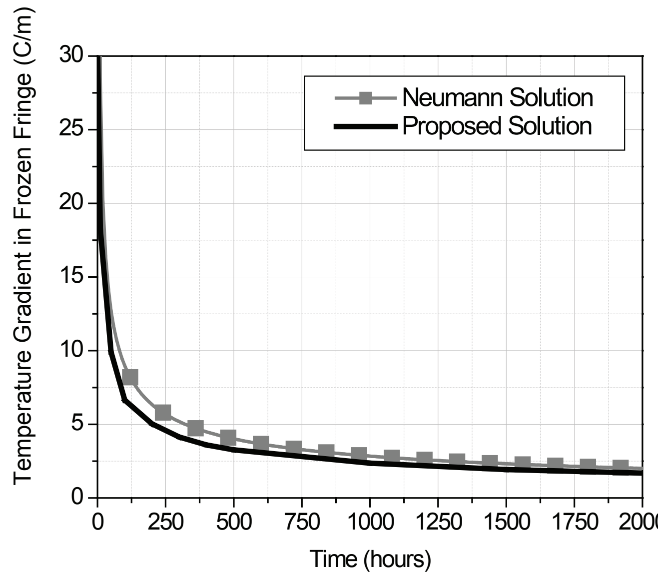

Figure 6. Comparison of temperature gradient in frozen fringe between Neumann and the proposed solution.

well with the Neumann solution. Figure 5b shows the close-up view of temperature distribution in the frozen fringe. T_s is assumed as –0.1°C to define the frozen fringe. Since the square mesh size is 0.0005 m, there are approximately 100 points in the frozen fringe. The effect of the fine mesh gives two advantages. First, it is the accuracy of the temperature distribution in the frozen fringe. The freezing front of the proposed solution is slightly deeper than that of Neumann solution as shown in Figures 4 and 5b. Also, the temperature distribution of the proposed solution is non-linear. This is due to the non-linear thermal properties of the unfrozen water content. The second advantage is the elimination of oscillations of gradT_{ff}. The history of gradT_{ff} between the proposed and Neumann solution is shown in Figure 6. The precision of the proposed solution is quite satisfactory and stable. Because of the precise and stable gradT_{ff}, it will be possible to adequately conduct water migration prediction using the SP concept.

It is true that the proposed solution requires considerable calculation time because of the fine mesh size. However, this issue was solved by using an IBM p690 computer at the Arctic Region Supercomputing Center in the University of Alaska Fairbanks.

The proposed solution was used to simulate the UAF frost heave experiment. Figures 7 and 8 show the finite element mesh and simulated temperature distribution with a deformed mesh in a steady state, respectively. The details of the mechanical model coupling and simulation results will be presented in a future paper.

Conclusion

A transient heat transfer model was developed to determine the temperature gradient in the frozen fringe with high precision using the SP concept. The proposed approach was implemented using a FEM model with a

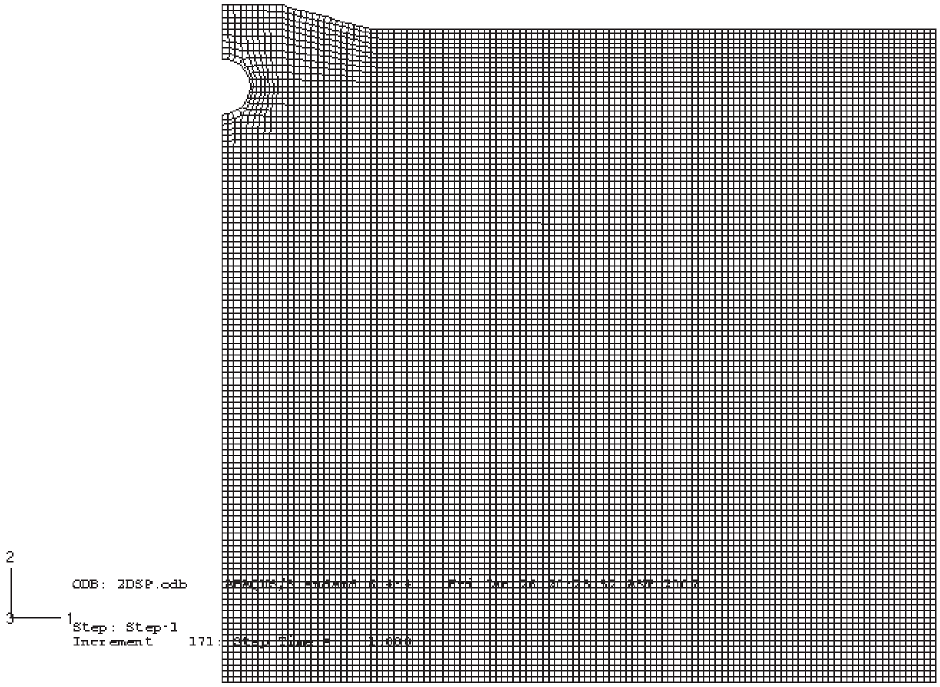

Figure 7. Finite element mesh for the simulation of the UAF pipeline experiments.

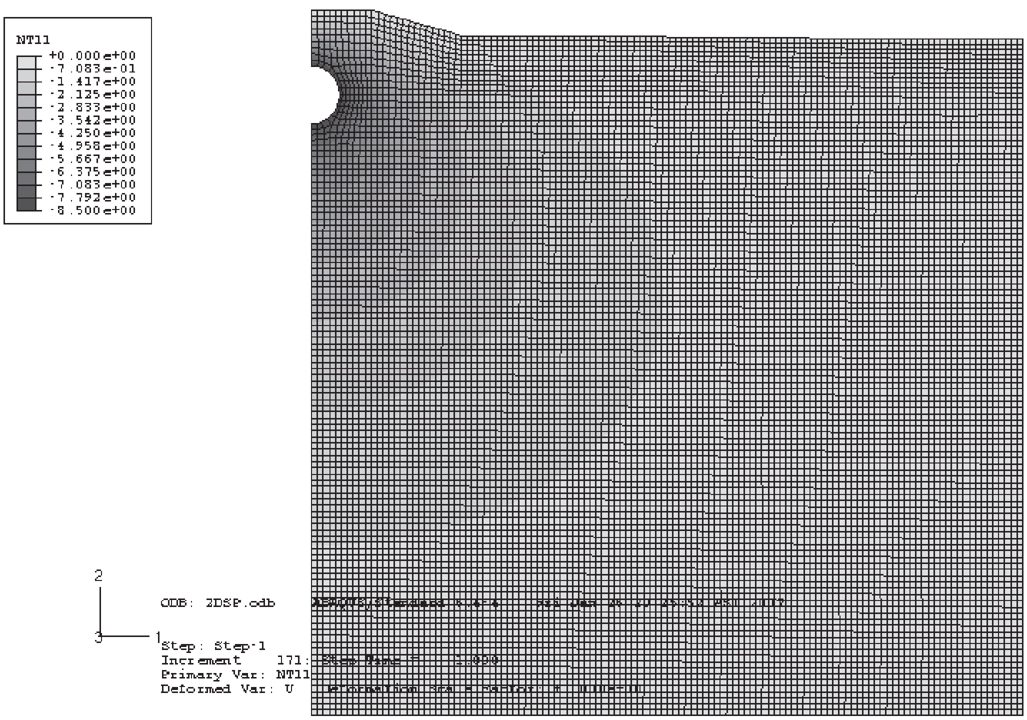

Figure 8. Simulated deformed mesh and temperature distribution in steady state.

fine mesh. A modified apparent heat capacity method considering unfrozen water contents was applied in the model. The model developed in this study has achieved the following improvements:

1. The proposed method can properly simulate the non-linear temperature distribution in the frozen fringe.
2. The calculated gradT_{ff} does not exhibit oscillations.
3. The simulated results agree well with the Neumann solution.

Acknowledgments

The numerical simulation of the study was supported by an Alaska EPSCoR Graduate Research Fellowship. The financial assistance is appreciated. The authors would also like to thank Dr. Xiong Zhang, University of Alaska Fairbanks, for his suggestions regarding the numerical simulation.

References

Anderson, D.M. & Morgenstern, N.R. 1973. Physics, chemistry and mechanics of frozen ground. *Proceedings of 2nd International Conference Permafrost, Yakutsk, Russia*: 257-288.

Carlson, L.E. & Nixon, J.F. 1988. Subsoil investigation of ice lensing at the Calgary, Canada, frost heave test facility. *Canadian Geotechnical Journal* 25: 307-319.

Coutts, R.J. 1991. *Development of Two-dimensional Finite Element Model to Calculate Temperatures and Stresses in Frost Susceptible Soils around a Chilled Pipeline.* M.S. Thesis. Ontario, Canada: University of Waterloo.

Farouki, O.T. 1981. *Thermal Properties of Soils.* CRREL Monograph 81-1. Hanover, NH: U.S. Army Cold Regions Research and Engineering Laboratory.

Harlan, R.L. 1973. Analysis of coupled heat-fluid transport in partially frozen soil. *Water Resources Research* 9: 1314-1323.

Hawlader, B.C., Morgan, V. & Clark, J. 2004. A simplified solution for frost heave prediction of chilled pipelines. *Proceedings of the Cold Regions Engineering & Construction Conference & Expo, Alberta, Canada.*

Huang, S.L., Bray, M.T., Akagawa, S. & Fukuda, M. 2004. Field investigation of soil heave by a large diameter chilled gas pipeline experiment, Fairbanks, Alaska. *Journal of Cold Regions Engineering* 18: 2-34.

Johansen, O. 1975. *Thermal Conductivity of Soils.* Draft translation 637, Hanover, NH: U.S. Army Cold Regions Research and Engineering Laboratory.

Konrad, J.M. & Morgenstern, N.R. 1980. A mechanistic theory of ice lens formation in fine-grained soils. *Canadian Geotechnical Journal* 17: 473-486.

Konrad, J.M. & Morgenstern, N.R. 1981. The segregation potential of a freezing soil. *Canadian Geotechnical Journal* 18: 482-491.

Konrad, J.M. & Morgenstern, N.R. 1982. Effect of applied pressure on freezing soils. *Canadian Geotechnical Journal* 19: 494-505.

Konrad, J.M. & Morgenstern, N.R. 1984. Frost heave prediction of chilled pipelines buried in unfrozen soils. *Canadian Geotechnical Journal* 21: 100-115.

Konrad, J.M. & Shen, M. 1996. 2-D frost action modeling using the segregation potential of soils. *Cold Regions Science and Technology* 24: 263-278.

Michalowski, R.L. & Zhu, M. 2006. Frost heave modelling using porosity rate function. *International Journal for Numerical and Analytical Methods in Geomechanics* 30: 703-722.

Miller, R.D. 1972. Freezing and heaving of saturated and unsaturated soils. *Highway Research Record* 393: 1-11.

Miller, R.D. 1978. Frost heaving in non-colloidal soils. *Proceedings of 3rd International Conference on Permafrost, Edmonton, Alberta, Canada*: 708-713.

Nixon, J.F. 1975. The role of convective heat transport in the thawing soils. *Canadian Geotechnical Journal* 12: 425-429.

Nixon, J.F. 1983. Practical application of a versatile geothermal simulator. *Journal of Energy Resources Technology* 105: 442-447.

Nixon, J.F. 1986. Pipeline frost heave predictions using a 2-D thermal model. *ASCE Research on Transportation Facilities in Cold Regions*: 67-82.

O'Neill, K. & Miller, R.D. 1985. Exploration of a rigid ice lens model of frost heave. *Water Resources Research* 21: 281-296.

Shen, M. 1988. Numerical analysis of temperature field in a thawing embankment in permafrost. *Canadian Geotechnical Journal* 25: 163-166.

Methane Emission from Siberian Wet Polygonal Tundra on Multiple Spatial Scales: Process-Based Modeling of Methane Fluxes on the Regional Scale, Lena Delta

Stefanie Kirschke
German Aerospace Center, German Remote Sensing Data Center, Wessling, Germany
Kurt P. Guenther
German Aerospace Center, German Remote Sensing Data Center, Wessling, Germany
Klaus Wisskirchen
German Aerospace Center, German Remote Sensing Data Center, Wessling, Germany
Torsten Sachs
Alfred Wegener Institute for Polar and Marine Research, Potsdam, Germany
Stefan Dech
German Aerospace Center, German Remote Sensing Data Center, Wessling, Germany

Abstract

Uncertainties in the carbon budget of high latitude ecosystems are partly due to difficulties in assessing the spatially and temporally highly variable methane emissions of permafrost soils. CH_4 contributes significantly to global warming. Arctic regions are most critically influenced by a changing climate. Modeling approaches are important tools to determine CH_4 fluxes of arctic environments. We present two process-based models to calculate methane emission from permafrost soils. Model forcing consists of ECMWF (European Center for Medium-Range Weather Forecasts) meteorological data which are validated against field measurements. Auxiliary input data is derived from satellite imagery and field measurements. A MERIS-FR land classification scheme is used to upscale emissions. Model results are validated using methane flux measurements on the landscape and small scale carried out in 2006 in the Lena Delta (72°N, 126°E) by Alfred Wegener Institute for Polar and Marine Research. The study site is characterized by arctic tundra ecosystems and continuous permafrost.

Keywords: Arctic; climate change; methane emissions; modeling; permafrost; tundra.

Introduction

Introduction

The radiative forcing due to methane—the second largest of the long-lived greenhouse gases after carbon dioxide—and its Global Warming Potential (GWP), which is about 20 times higher than the GWP of CO_2 (IPCC 2001), demonstrate the significant contribution of methane to warming of the atmosphere. The global atmospheric methane concentration has risen from a pre-industrial value of about 715 ppb to a current value of about 1774 ppb (IPCC 2007).

The observed increase in methane concentrations is very likely due to anthropogenic activity, mainly agriculture, burning of fossil fuels, and landfills. Contributions of further sources to the global atmospheric methane budget are not well determined yet (IPCC 2007) due to the difficulty in assessing the global emission rates of the natural sources, the strengths of which are highly variable in space and time (IPCC 2001).

Permafrost soils represent a large carbon reservoir, with an estimated carbon pool of about 900 Gt for frozen yedoma (ice-rich soils with high labile carbon content [Walter et al. 2003]) and non-yedoma soils excluding peatlands. The permafrost carbon reservoir exceeds that of the atmosphere (~730 Gt) and vegetation (~650 Gt) (Zimov et al. 2006).

Due to high sensitivity of the arctic soil carbon reservoir to increasing temperatures and to the large surface area, arctic regions are most critically influenced by changing climate. In thawed permafrost soils, methane is produced by specially adapted microbes under anaerobic conditions and released into the atmosphere. Extensive thawing of permafrost will release the carbon contained in the soils, hence further affecting the global carbon cycle. Model scenarios predict a severe degradation of permafrost in the Northern Hemisphere, including a northward shift of the permafrost boundary as well as an increase in active layer depth (Lawrence & Slater 2005, Zhang et al. 2007).

Studies on measuring methane flux on the landscape scale using the eddy covariance technique have been conducted by only by a few research groups (Fan et al. 1992, Friborg et al. 2000, Hargreaves et al. 2001, Harazono et al. 2006, Wille et al. 2007). Very few studies on modeling methane emission in Siberian permafrost regions on the regional scale have been performed (Bohn et al. 2007).

This study aims at modeling the methane budget of a high latitude permafrost-affected region for determining source strength, and at understanding emission patterns on a regional scale. Remote sensing techniques and ground-truth measurements are used to derive information needed as input for process-based models and to upscale modeling from single point to regional scale. We present a new approach where the methane model by Walter (1998) is modified for permafrost conditions and applied to a study site characterized by continuous permafrost.

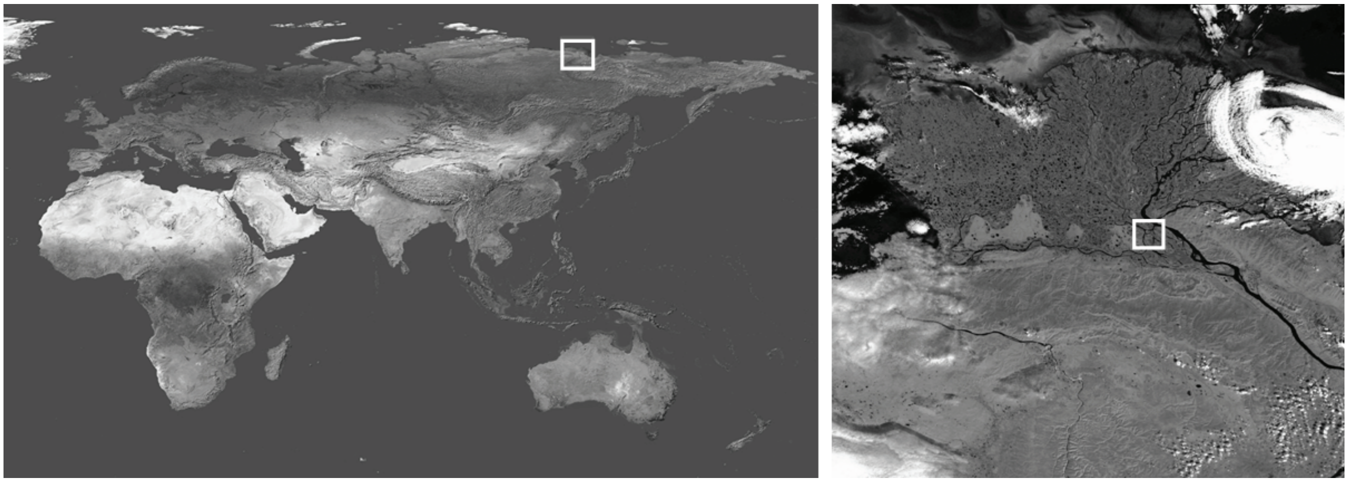

Figure 1. Geographical settings of the Lena River Delta and Samoylov Island shown in boxes (left panel: RGB composite of the globe based on MODIS data; right panel: RGB image for August 26, 2006, based on MERIS-FR data).

Materials and Methods

Study site

The Lena River Delta is located at the Laptev Sea coast in northeast Siberia (Fig. 1). It is considered a key region for understanding the underlying processes of the development and dynamics of permafrost in the Arctic under a warming climate. The region is characterized by arctic tundra ecosystems and is underlain by deep continuous permafrost.

The delta, situated at the north coast of Siberia, is the largest delta in the Arctic and one of the largest in the world (Walker 1998). It is characterized by a highly heterogeneous landscape of smaller and wider river branches and channels, as well as more than 1500 islands of various sizes on an area of about 32,000 km^2 (Walker 1998). Three major fluvial terraces with different geomorphological characteristics form the delta (Schwamborn et al. 2002). The 30-year (1961–1990) averages of mean air temperature and total precipitation measured at the meteorological station in Tiksi (eastern delta) are -13.5°C and 323 mm, respectively (Roshydromet 2004). The vegetation is mainly characterized by sedge/grass/moss wetland and sedge/moss/dwarf-shrub wetland, as well as dwarf-shrub tundra (CAVM Team 2003). The growing period is short, lasting for 60–80 days (Grigoriev 1993). The surface is characterized by wet polygonal tundra with a pronounced micro-relief (Wille et al. 2007).

Since 1998, yearly expeditions have been conducted by Alfred Wegener Institute for Polar and Marine Research, Potsdam (AWI) to study carbon dynamics and involved microbial processes and communities as well as the energy and water budget of Arctic tundra. Campaigns have been carried out on Samoylov Island (Fig. 1). Samoylov (72°22′N, 126°28′E) is representative of the active and youngest part of the Lena Delta and covers an area of approximately 7 km^2.

Model description

The methane emission model (Walter 1998) is a one-dimensional process-based climate-sensitive model to derive methane flux from natural wetlands. The processes leading to methane emission are modeled within a one-dimensional soil column which is discretized in 1 cm thick soil layers. Three different transport mechanisms that contribute to methane release from soils are taken into account and modeled explicitly; namely diffusion, ebullition, and plant-mediated transport.

Methane production strongly depends on the position of the water table (Roulet et al. 1992, Bubier et al. 1995), which is a measure for dividing the soil column into an anaerobic and aerobic zone (Fig. 2). Methane is only produced under the absence of oxygen and, hence, only in water-saturated parts of the soil column (Fig. 2a). The production of methane by methanogenic bacteria is a function of substrate availability, pH and temperature (Walter 1998). The temperature dependence of methane production rates can be described by Q_{10} values which depict the relative increase in activity after a temperature rise of 10°C (van Hulzen et al. 1999). The gas is then transported to the soil/water interface by molecular diffusion, ebullition and, if vascular plants occur, by plant-mediated transport. When the water table drops below the soil surface, oxygen can enter the soil pores, and the methane produced in lower, still water saturates (anaerobic) parts of the soil body and is transported upwards and oxidized in the aerobic zone by methanotrophic bacteria (Fig. 2b). Methane oxidation can be described by Michaelis-Menten kinetics (Bender & Conrad 1992).

The model is driven by meteorological data and needs auxiliary input data, such as vegetation and soil characteristics, land classification schemes, fraction of cover, and Net Primary Productivity (NPP). NPP is parameterized as a measure for substrate availability and, thus, is an important input parameter. Since the model was modified for permafrost conditions, many parameters are time-dependent with successive thawing of the soil body, and only a few fixed parameters are used in the simulation runs.

NPP of high latitude tundra ecosystems is calculated by the process-based vegetation model BETHY/DLR (Biosphere Energy Transfer Hydrology Model) (Knorr 1997,

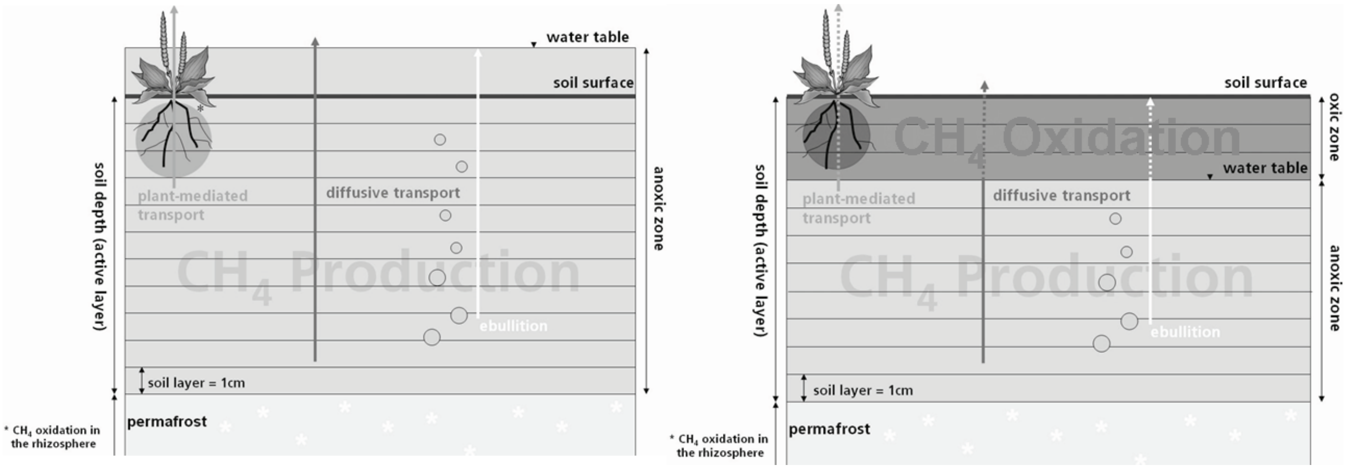

Figure 2. Schematic presentation of a soil column in the methane model. (a) Methane production and different transport mechanisms under water saturated conditions (anaerobic); (b) methane production and consumption as well as different transport mechanisms under partly aerobic conditions.

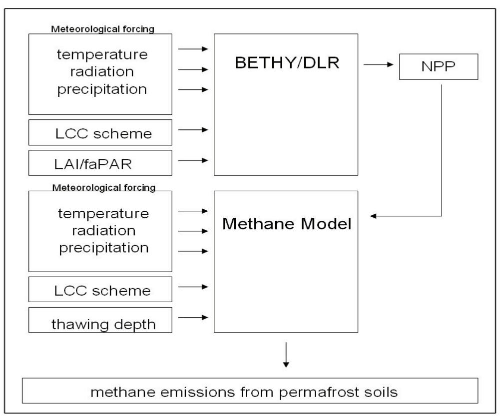

Figure 3. Flow chart illustrating the coupling of the BETHY/DLR model (NPP), the methane model, and their required input data.

Wisskirchen 2005). For simulations with BETHY/DLR, information about the state of vegetation is required; for example, time series of LAI (Leaf Area Index). Figure 3 shows the methodical structure of how the two models are coupled to work as a stand-alone package for modeling methane emission in permafrost regions.

Data

Both models need meteorological forcing data. Datasets provided by the European Centre for Medium Range Weather Forecast (ECMWF) are applied in modeling NPP and methane fluxes.

Auxiliary input data must be provided for both models. For simulations with the vegetation model BETHY/DLR, information about vegetation type and the state of vegetation (time series of LAI) is required. Running the methane model, additional input data such as vegetation parameters (e.g., rooting depth), soil characteristics (e.g., pore volume), land classification schemes (e.g., wetland distribution), fraction of cover, and NPP are needed.

Thawing of permafrost is described in the model by using measurements of active layer depth taken during field campaigns. Thawing/freezing is accounted for in order to characterize permafrost-related processes more realistically. The simulation starts with the first thawing of permafrost soil. Methane emission increases with increasing thawing depth, subsequently slowly decreases, and eventually comes to an end with permafrost re-freezing.

During the field campaign "System Laptev Sea – LENA2006" carried out from May to September 2006, Medium Resolution Imaging Spectrometer Full Resolution (MERIS-FR) data were acquired for the full growing season. MERIS-FR data were processed to derive information on vegetation characteristics needed as model input.

Vegetation characteristics

Vegetation characteristics play an important role in the presented modeling approach. In the vegetation model BETHY/DLR, LAI is used to describe the seasonal development of vegetation. It is needed as a continuous input variable to assess NPP.

In order to obtain realistic time series of LAI for the growing season 2006 of the Lena Delta, an approach using the MERIS Global Vegetation Index (MGVI), also called Top of the Atmosphere Vegetation Index (TOAVI), was used. FAPAR (Fraction of Absorbed Photosynthetically Active Radiation) can be retrieved by remote sensing techniques with acceptable accuracy using TOAVI values (Gobron et al. 2004) and can subsequently be used to estimate LAI. For homogeneous vegetation cover, LAI_{hom} is calculated using the equation (Monteith & Unsworth 1990):

$$LAI_{\mathrm{hom}_i} = LAI_{\max} \cdot \frac{\log(1 - FAPAR_i)}{\log(1 - FAPAR_{\max})} \tag{1}$$

$LAI_{\max}$ is chosen according to in situ measurements (Eq. 3). $FAPAR_i$ and $FAPAR_{\max}$ are derived from MGVI values.

During the field campaign 2006, field spectral measurements were taken using a portable ASD FieldSpecFR spectrometer (Analytical Spectral Devices Inc.). The spectrometer covers a wide spectral range from 350–2500 nm. Due to the highly heterogeneous surface patterns of wet polygonal tundra, different plant communities with different vegetation cover have evolved on a small scale in high and low center polygons and polygon rims, depending on changes in substrates and hydrologic regimes. Spectral measurements were taken in order to derive data on vegetation characteristics such as NDVI (Normalized Difference Vegetation Index) and LAI which can then be used to differentiate between plant communities as well as to validate satellite data.

Spectra have been processed using ENVI software. Processing is inevitable in order to correct for sensor properties and reference measurements using a spectralon panel. Biophysical indices (NDVI and LAI) were calculated and compared with NDVI and LAI values derived from MERIS-FR data.

NDVI was calculated from spectral data using the equation (Rouse et al. 1974):

$$NDVI = \frac{(R_{864} - R_{671})}{(R_{864} + R_{671})} \tag{2}$$

where R_{864} and R_{671} denote the reflectance at wavelengths 864 nm (near infrared) and 671 nm (red), respectively.
LAI was then calculated after Gardner & Blad (1986):

$$LAI = -1.248 + 5.839 * NDVI \tag{3}$$

LAI_{max} in equation (1) was set according to LAI values derived from equation (3).

Results and Discussion

Leaf Area Index (LAI)

Figure 4 shows results of the two approaches described above and presents a comparison between LAI calculated from field spectra and remote sensing data, respectively. The datasets compare reasonably well with slightly higher LAI values derived from in situ measurements. Additionally, a steeper slope can be observed in the in situ dataset. Possible explanations might be (1) an inaccurate atmospheric correction of MERIS-FR data due to high sun zenith angles and (2) the spatial resolution of MERIS-FR data (300 m) being unable to capture the high spatial heterogeneity of wet polygonal tundra.

However, it can be seen that the temporal variation of LAI during the vegetation period of 2006 is represented realistically. After slowly increasing at the beginning of the growing season, LAI reaches its maximum in mid-August (DOY 229) and then starts decreasing again. This agrees with ground truth observations from field campaigns in the delta.

Handling optical satellite data for high-latitude regions is often problematic due to high cloud contamination and high sun zenith angles. Here it is shown that for arctic regions like the Lena River Delta, information on vegetation characteristics can be retrieved from optical satellite-based measurements. Ground-truth data are useful for validating satellite-derived plant biophysical parameters. Working with

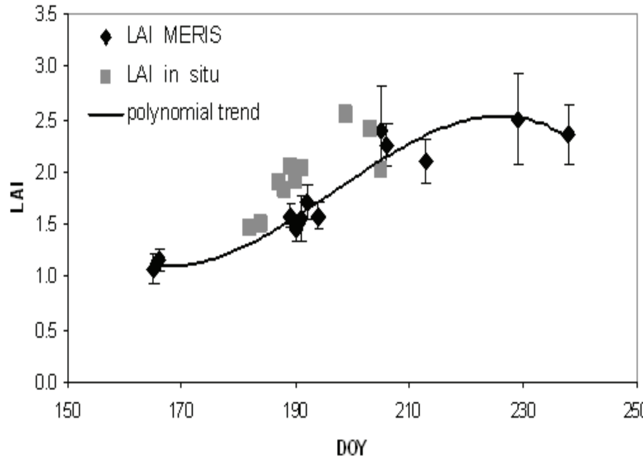

Figure 4. Time series of LAI for Samoylov Island for the growing season 2006. Diamonds: seasonal course of LAI derived from MERIS FAPAR values and polynomial fit, error bars indicate SD; triangles: LAI derived from field spectral measurements.

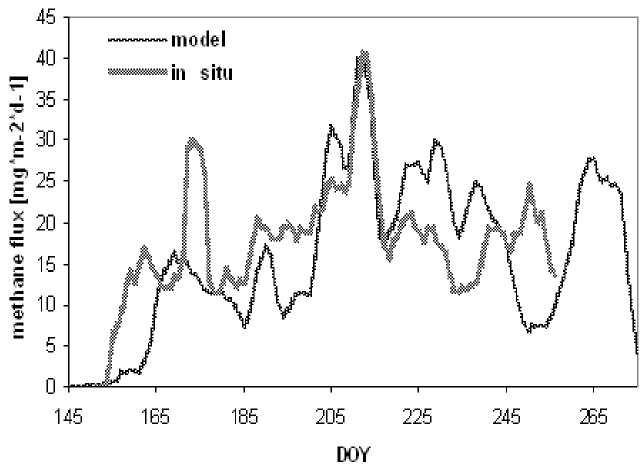

Figure 5. Measured and modeled methane fluxes (5-day running means) from a one-dimensional model run for the growing season 2006 and model coordinates 72°N, 126°E (Samoylov Island).

both ground-truth and remote sensing approaches as presented here provides a powerful tool to estimate vegetation characteristics on the small scale and to upscale these characteristics to the regional scale.

Realistic time series of plant canopy characteristics like LAI can be used as model input and to validate literature values when information about the state and seasonal variation of vegetation is required (BETHY/DLR).

Methane flux modeling

Methane flux was modeled one-dimensionally for the growing seasons of 2003–2006. Figure 5 shows a comparison of measured and modeled fluxes for the growing season of 2006. Flux measurements on the landscape scale using eddy covariance technique were carried out on Samoylov Island from June 9, 2006, through September 19, 2006, (Sachs et al. 2008). An eddy flux tower 3.6 m in height was used for methane flux measurements as well as for additional meteorological measurements. The seasonal course of modeled methane fluxes is limited by soil thawing and freezing.

In situ flux time series are used to validate the methane model and adjust model parameters, like Q_{10} values characterizing methane reduction and oxidation, to the study site. Between DOY 151 and 256, during overlap of the two curves, modeled methane flux is in good accordance with observed data. Flux integrals for both curves for the overlapping period are 1686 mg CH_4 m^{-2} (model) and 1895 mg CH_4 m^{-2} (measurements), respectively, which indicates a model underestimation of about 10%. This result agrees well with other studies using the same methane emission model; for example, when applied in Western Siberia (Bohn et al. 2007).

As can be seen in Figure 5, the time series of modeled methane emission shows less variation between days than the measured flux. This difference in seasonal fluctuation is due to the high variability of methane emission, both spatially and temporally (Joabsson et al. 1999, Wagner et al. 2003) and can be explained by the main factors controlling methane release. Wille et al. (2007) identified soil temperature and near-surface turbulence to be the driving parameters of methane emission in the Lena Delta.

The observed small-scale variability shown in the in situ data cannot fully be represented in the model results. Model input data on soil temperatures derived from ECMWF have a spatial resolution of 0.5°, and thus, variations in soil temperature due to the micro-relief of wet polygonal tundra cannot be taken into account.

Additionally, no data on wind distribution, wind direction, and wind speed are considered in the methane model.

However, since the project aims at quantifying methane emission on a regional scale, well-founded knowledge of small-scale process variability is an important factor for model understanding but cannot be fully implemented in the model.

Conclusions

For the growing season 2006, methane fluxes were modeled using two process-based models, a vegetation, and a methane emission model. Simulated methane fluxes are in agreement with in situ flux measurements ($r^2 = 0.63$). Time-integrated fluxes are 1686 mg CH_4 m^{-2} (model) and 1895 mg CH_4 m^{-2} (measurements), respectively. This indicates a model underestimation of about 10% which agrees with results of a study conducted in Western Siberia using the same methane emission model, where a model underestimation of about 10% was observed as well (Bohn et al. 2007).

Leaf Area Index needed as input for the vegetation model was calculated using two different approaches. LAI was derived (1) from satellite-based measurements and (2) by processing field spectral measurements. In situ data were applied in validating satellite data. It could be shown that information about the state and seasonal variation of the vegetation in arctic regions can be retrieved by remote sensing techniques. Used for deriving time series of LAI for the study site, the satellite measurements provide realistic results and compare reasonably well with LAI calculated from in situ spectral measurements.

The results demonstrate the important role of modeling techniques in assessing methane emissions for High Arctic permafrost-influenced ecosystems. Understanding of micro-scale processes studied through scientific field work is absolutely necessary when applying process-based models.

Acknowledgments

This project is conducted in the frame of the Helmholtz Research Network "Integrated Earth Observing System" (Helmholtz-EOS). Thanks to colleagues from AWI Potsdam for their in situ measurements and for getting the chance to participate in the LENA2006 campaign. Thanks to Dr. Dirk Wagner (AWI) who graciously provided data on Q_{10} values. The MERIS-FR data presented in this paper were acquired within the ESA-AO 3909.

References

Bender, M. & Conrad R. 1992. Kinetics of CH_4 oxidation in oxic soils exposed to ambient air or high CH_4 mixing ratios. *FEMS Microbiology Ecology* 101: 261-270.

Bohn, T.J, Lettenmaier, D.P., Sathulur, K. & Bowling, L.C. 2007. Large scale modeling of wetland methane emissions. *Integrated Land Ecosystem – Atmosphere Processes Study Newsletter* 4: 40-42.

Bubier, J.L., Moore, T.R., Bellisario, L., Comer, N.T. & Crill M.C. 1995. Ecological controls on methane emissions from a northern peatland complex in the zone of discontinuous permafrost, Manitoba, Canada. *Global Biogeochemical Cycles* 9(4): 455-470.

CAVM Team, 2003. Circumpolar Arctic Vegetation Map. Scale 1:7,500,000. Conservation of Arctic Flora and Fauna (CAFF) Map No. 1. U.S. Fish and Wildlife Service, Anchorage, Alaska.

Fan, S.M., Wofsky, S.C., Bakwin, P.S. & Jacob, D.J. 1992. Micrometeorological Measurements of CH_4 and CO_2 exchange Between the Atmosphere and Subarctic Tundra. *Journal of Geophysical Research* 97(D15): 16627-16643.

Friborg, T., Christensen, T.R., Hansen, B.U., Nordstroem, C. & Soegaard, H. 2000. Trace gas exchange in a high-arctic valley 2. Landscape CH_4 fluxes measured and modeled using eddy correlation data. *Global Biogeochemical Cycles* 14(3): 715-723.

Gardner, B. & Blad, B. 1986. Evaluation of spectral reflectance models to estimate corn leaf area while minimizing the influence of soil background effects. *Remote Sensing of Environment* 20:183-193.

Gobron, N., Mélin, F., Pinty, B., Taberner, M. & Verstraete, M.M. 2004. MERIS Global Vegetation Index: Evaluation and Performance. *Proceedings of the MERIS User Workshop, Frascati, Italy, November 10-13, 2003*.

Grigoriev, M.N. 1993. Cryomorphogenesis in the Lena Delta. Yakutsk (in Russian), 173 pp. In: J. Schneider, 2005, *Bilanzierung von Methanemissionen in Tundragebieten am Beispiel des Lena-Deltas, Nordostsibirien, auf der Basis von Fernerkundungsdaten und Gelaendeuntersuchungen*. Alfred Wegener Institute for Polar and Marine Research, Research Unit Potsdam, Master Thesis, 103 pp.

Harazono, Y., Mano, M., Miyata, A., Yoshimoto, M., Zulueta, R.C., Vourlitis, G.L., Kwon, H. & Oechel, W.C. 2006. Temporal and spatial differences of methane flux at arctic tundra in Alaska. *Mem. Natl Inst. Polar Res., Spec. Issue* 59: 79-95.

Hargreaves, K. J., Fowler, D., Pitcairn, C.E.R. & Aurela, M. 2001. Annual methane emission from Finnish mires estimated from eddy covariance campaign measurements. *Theoretical and Applied Climatology* 70: 203-213.

IPCC 2001. Climate Change 2001: The Scientific Basis. Contribution of Working Group I to the Third Assessment Report of the Intergovernmental Panel on Climate Change. J.T. Houghton, Y. Ding, D.J. Griggs, M. Noguer, P.J. van der Linden, X. Dai, K. Maskell, & C.A. Johnson (eds.), Cambridge, UK & New York, NY: Cambridge University Press, 881 pp.

IPCC 2007. Climate Change 2007: The Physical Science Basis. Contribution of Working Group I to the Fourth Assessment Report of the Intergovernmental Panel on Climate Change S. Solomon, D. Qin, M. Manning, Z. Chen, M. Marquis, K.B. Averyt, M. Tignor & H.L. Miller (eds.), Cambridge, UK & New York, NY: Cambridge University Press, 996 pp.

Joabsson, A., Christensen, T.R. & Wallén, B. 1999. Vascular plant controls on methane emissions from northern peat forming wetlands. *Trends in Ecology & Evolution (TREE)* 14(10): 385-388.

Knorr, W. 1997. Satellitengestützte Fernerkundung und Modellierung des globalen CO2-Austauschs der Landbiosphäre: Eine Synthese. Max-Planck-Institute for Meteorology, Examensarbeit Nr. 49 (in German), Hamburg, Germany.

Lawrence, D.M. & Slater, A.G. 2005. A projection of severe near-surface permafrost degradation during the 21st century. *Geophysical Research Lett*ers 32: L24401.

Monteith, J.L. & Unsworth, M.H. 1990. Principles of environmental physics. In: E. Arnold (ed.), London, 291 pp. In: P.J. Sellers, S.O. Los, C. Tucker, C.O. Justice, D.A. Dazlich, G.J. Collatz & D.A. Randall, 1996. *A Revised Land Surface Parameterization (SiB2) for Atmospheric GCMs.* Part II: The Generation of Global Fields of terrestrial Biophysical Parameters from Satellite Data. *Journal of Climate* 9(4): 706-737.

Roshydromet, Russian Federal Service for Hydrometeorology and Environmental Monitoring (2004). http://www.worldweather.org/107/c01040.htm.

Roulet, N., Moore, T.R., Bubier, J.L. & Lafleur, P. 1992. Northern fens: methane flux and climatic change. *Tellus* 44(B): 100-105.

Rouse, J.W., Haas, R.H., Schell, J.A. & Deering, D.W. 1974. Monitoring vegetation systems in the Greta Plains with ERTS. *Proceedings of the Third Earth Resources Technology Satellite-1 Symposium, Greenbelt, NASA SP-351,*301-317.

Sachs, T., Giebels, M., Wille, C., Kutzbach, L. & Boike, J. 2008. Methane emission from Siberian wet polygonal tundra on multiple spatial scales –vertical flux measurements by closed chambers and eddy covariance, Samoylov Island, Lena Delta. (this proceeding).

Schwamborn, G., Rachold, V. & Grigoriev, M.N. 2002. Late Quaternary sedimentation history of the Lena Delta. *Quaternary International* 89: 119-134.

Van Hulzen, J.B., Segers, R., van Bodegom, P.M. & Leffelaar, P.A. 1999. Temperature effects on soil methane production: an explanation for observed variability. *Soil Biology and Biochemistry* 31: 1919-1929.

Wagner, D., Kobabe, S., Pfeiffer, E.-M. & Hubberten , H.-W. 2003. Microbial Controls on Methane Fluxes from a Polygonal Tundra of the Lena Delta, Siberia. *Permafrost and Periglacial Processes* 14: 173-185.

Walker, H. J. 1998. Arctic deltas. *Journal of Coastal Research* 14(3): 718-738.

Walter, B. 1998. Development of a process-based model to derive methane emissions from natural wetlands for climate studies. Max-Planck-Institute for Meteorology, Examensarbeit Nr. 60, Hamburg, Germany, 160 pp.

Walter, K. M., Chapin III, F.S., White, D.M. & Zimov, S.A. 2003. Stratification of Thermokarst Lakes in NE Siberia based on Diffusive CH_4 Emissions. *Proceedings of the Arctic System Science Program All-Hands Workshop, Seattle, Washington, February 20–23, 2002:* 222.

Wille, C., Kutzbach, L., Sachs, T., Wagner, D. & Pfeiffer, E.-M. 2007. Methane Emission from Siberian arctic polygonal Tundra: Eddy Covariance Measurements and Modeling. *European Geosciences Union General Assembly 2007*, Abstract No. EGU2007-A-10277.

Wisskirchen, K. 2005. Modellierung der regionalen CO2-Aufnahme durch Vegetation. Dissertation (in German), Meteorologisches Institut der Rhein. Friedr.-Wilh.-Universität Bonn, 129 pp.

Zhang, Y., Chen, W. & Riseborough, D.W. 2007. Transient projections of permafrost distribution in Canada during the 21st century under scenarios of climate change. *Global and Planetary Change* (in press).

Zimov, S.A, Schuur, E.A.G. & Chapin III, F.S. 2006. Permafrost and the Global Carbon Budget. *Science* 312(5780): 1612-1613.

Interannual Variability of Winter N-Factors in the Kuparuk River Basin, Alaska

Anna E. Klene
Department of Geography, University of Montana, Missoula, MT 59812, USA
Frederick E. Nelson, Nikolay I. Shiklomanov, Dmitry A. Streletskiy
Department of Geography, University of Delaware, Newark, DE 19716, USA

Abstract

Hourly air and soil temperatures were monitored using arrays of miniature data loggers within eight 1-ha plots representing natural land cover types in northern Alaska's Kuparuk River watershed between 1995 and 2006. For each plot, mean daily air and soil temperatures were used to calculate mean winter *n*-factors, the ratio of seasonal freezing degree-day sums at the ground surface to those in the air. Mean 12 year *n*-factors ranged from 0.32 to 0.58 within the various plots, with ranges of 0.18 to 0.28 over the period of record. A distinct latitudinal gradient of *n*-factor values exists along this continentality gradient. Although direct measurements of snow cover are not available at the sites, temperature patterns indicate that snow cover is a major determinant of winter *n*-factor values.

Keywords: air temperature; Alaska; n-factor; permafrost; snow cover; soil-surface temperature.

Introduction

Transfer of heat between the atmosphere and ground in arctic environments can be complex. Large differences in vegetation and soil characteristics can occur over very short distances, leading to highly variable near-surface soil temperatures. In permafrost regions, however, it is often critical to be able estimate soil temperatures over large geographic areas. The *n*-factor, the ratio of freezing (or thawing) degree-day sums at the soil surface to those in the air at standard instrument height, was proposed (Carlson 1952) as a way of summarizing the seasonal winter (or summer) surface energy balance. Although the n-factor was introduced for engineering purposes, there has been considerable recent interest in its application to natural surfaces (Taylor 1995, Klene et al. 2001a, Karunaratne & Burn 2003, 2004, Kade et al. 2006). This, in turn, has led to its use in modeling exercises (e.g., Buteau et al. 2004, Juliussen & Humlum 2007).

Most previous studies have focused on series of plots in different latitudes, soil, and vegetation types over one or two seasons. This study utilizes multiple soil temperatures within a series of plots and examines the mean *n*-factor for each plot over 12 winter seasons to reveal information about interannual variability.

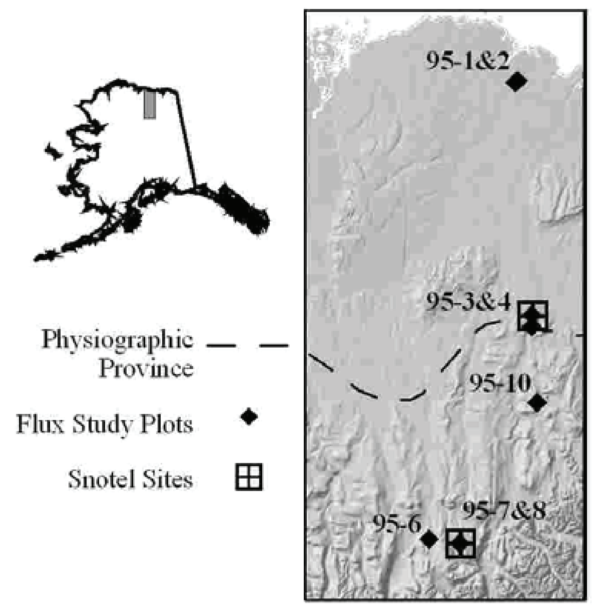

Figure 1. A shaded relief map of the study area showing locations of the Flux Plots, SNOTEL sites (see text), and the physiographic boundary between the coastal plain in the north and foothills in the south are depicted.

Study Area and Background

The Kuparuk River Basin of northern Alaska stretches from the Brooks Range to the Beaufort Sea, just west of the Dalton Highway (Fig. 1). This watershed was the focus of the U.S. National Science Foundation's (NSF) Arctic System Study Flux Project, an integrated mid-1990s study of the flux of greenhouse gases from terrestrial to atmospheric and marine environments (Kane & Reeburgh 1998).

Several of the projects utilized the "Flux Plots," a series of ten 1-ha plots arrayed along a climatic gradient from north to south. These plots were selected to represent common land-cover/soil associations and detailed vegetation and soil characterization was done on each. During the years the Flux Study was operating, these plots were incorporated into the NSF-funded Circumpolar Active-Layer Monitoring (CALM) program, allowing climate and active layer thickness measurements to continue in subsequent years. One plot on an island in the Sagavanirktok River was abandoned after flooding washed away the instrumentation, and another was discontinued due to difficulty in accessing a mountain top.

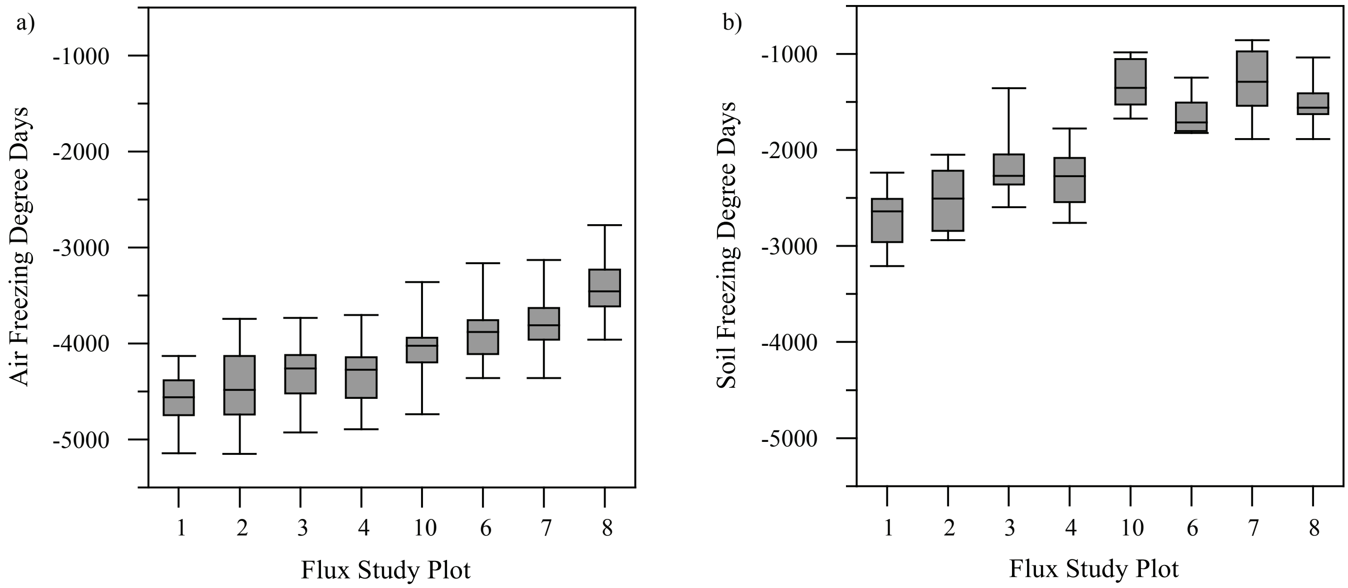

Figure 2. Box-and-whisker plots show the median, quartiles, and range of freezing degree-day sums in the air (a) and soil (b) at each of the eight Flux Plots observed between 1995 and 2006. Sites are arranged by latitudinal position; a distinct north-to-south (left-to-right) progression of values is apparent.

Elevations at the Flux plots used here ranged from 12 to 938 m a.s.l. Ten-year mean February and July air temperatures ranged from -18.3°C to -28.2°C and 7.3°C to 10.8°C, respectively, at the plots observed. Snow depths measured along a N-S transect in 1994–1996 varied from 0 m to 2 m within the basin (Taras et al. 2002). Permafrost underlies the entire region, with depths of about 600 m reported near Prudhoe Bay (Lachenbruch et al. 1982). Mean active layer thickness at the Flux Plots ranged from 42.2 cm to 60.3 cm during the 1995–1997 period (Klene et al. 2001). Vegetation was classified into four main categories: wet tundra, moist acidic tundra, moist nonacidic tundra, and shrublands (Walker & Bockheim 1995). Mean vegetation heights within the eight plots examined here ranged from 2.2 cm to 13.8 cm. Organic layer thickness ranged from 0 cm to 34 cm at the Flux Plots. Physiographically, the plots lie in the Arctic Coastal Plain province in the north and the Arctic Foothills province in the south (Wahrhaftig 1965). Observed soils included pergelic cryaquepts, cryorthents, cryoborolls, and histic pergelic cryaquolls (Walker & Bockheim 1995).

Klene et al. (2001) examined within- and between-plot variability of summer *n*-factors calculated for 1995–1997 at these plots. They found that mean n-factors within plots were robust when more than five soil-surface temperatures were available, and that the values were systematically related to land cover type. Mean summer *n*-factors calculated from 3 seasons of data ranged from 0.73 to 1.00 at the eight Flux Plots examined in this study (Klene et al. 2001).

Methodology

As part of the Flux Study, ten Stowaway© data loggers were installed at each Flux Plot in 1995. One monitored air temperature inside a six-gill radiation shield at standard screen height (1.8 m) while nine recorded soil-surface temperature in a range of microenvironments (Klene et al. 2001). The Stowaway loggers have gradually been replaced with five two-channel HoboPro© data loggers. The two-channel loggers have an accuracy of ±0.2°C and precision of 0.02°C at the freezing point. Thermistors at ground level were positioned approximately immediately below the ground surface to measure near-surface soil temperature. This placement was generally within an organic soil, though this varied from plot to plot. Water infiltration and animal damage led to high attrition rates initially, but recent records have generally been more reliable, although animal damage still causes losses each year. Observations were taken hourly until 1998, when a two-hour interval was adopted to extend battery life.

The hourly observations were summarized into daily means from which freezing degree-day sums (DDF) were calculated from air and soil records for the winter season, defined as 15 Sept to 15 May (243 days), following Hinkel et al. (2008). Adoption of this protocol results in inclusion of the entire snow cover period for most years. Statistics were computed for each winter season when more than 165 days with at least five of the nine soil-surface measurements were available at each plot. Freezing degree days (DDF) are calculated by summing mean daily temperatures for those days in which the mean was less than 0°C. Units are °C·days. Winter *n*-factors are based on freezing degree-day sums, thus warmer soil temperatures will lead to smaller winter *n*-factors, often attributable to the insulating effects of the snowpack. This is in contrast to thawing (summer) *n*-factors which are calculated using thawing degree days, which results in warmer soils leading to larger n-factors.

Snow depth is usually cited (e.g., Benson 1969; Goodrich 1982) as an important determinant of winter soil-surface temperatures and thus *n*-factors. However, snow depth records are rare in the Arctic. Two SNOTEL stations have

Table 1. Summary statistics for mean winter 1995–1996 through 2006–2007 at the eight Flux Plots.

	Flux 1	Flux 2	Flux 3	Flux 4	Flux 6	Flux 7	Flux 8	Flux 10
N winters	10	10	12	12	12	12	10	10
Minimum	0.49	0.47	0.33	0.42	0.33	0.22	0.30	0.24
Mean	0.58	0.56	0.51	0.54	0.43	0.35	0.44	0.32
Median	0.58	0.55	0.51	0.54	0.43	0.37	0.46	0.33
Maximum	0.70	0.64	0.61	0.68	0.51	0.48	0.54	0.42
Range	0.21	0.18	0.28	0.26	0.18	0.26	0.24	0.18
Stand. Dev.	0.05	0.05	0.07	0.07	0.06	0.08	0.08	0.05

been operating within the study area over the period of record at the Sagwon Hills and Imnavait Creek. These sites are part of the SNOwpack TELemetry program run by the U.S. Natural Resources Conservation Program. Direct snow depth observations were unavailable but accumulated monthly precipitation has been archived (NRCS 2007). Precipitation was summed from October to May and used as a crude estimate of winter snowfall. Although this does not account for local variability resulting from vegetation, drifting, or scouring, it provides a basis for initial assessment.

Results and Discussion

The basic components of the n-factor are air and soil degree-day sums. These are plotted in Figure 2 to illustrate the variability of these parameters over the 12 winter seasons at each of the Flux Plots. The climatic gradient of colder air temperatures on the coastal plain and warmer inland temperatures is readily apparent (Fig. 2a). The air-temperature gradient is a simple manifestation of the north-south continentality gradient in the region; the fact that the surface-temperature gradient shows a corresponding trend indicates that air and surface temperatures are more strongly coupled than elsewhere on Alaska's North Slope (Hinkel et al. 2008).

The soil degree-day sums (Fig. 2b) are systematically warmer than the air temperatures by approximately 2000°C·days. Twelve-year mean differences ranged from 1897°C·days at Plot 1 to 2756°C·days at Flux 10. They also reveal a distinct warming from north to south. The four most southerly sites are more similar in their soil DDF ranges and means than were the air degree-day sums.

Analysis of mean winter n-factors at each plot revealed a substantial interannual variability considering that the soil temperatures were averages from multiple individual microsites within each 1-ha plot. Table 1 lists summary statistics. Mean values at the more northerly sites are larger (0.51 to 0.58) while the southerly sites have mean values of 0.32 to 0.44. Ranges in the mean winter *n*-factors at each plot varied from 0.18 to 0.28.

Box and whisker plots were calculated for the mean winter *n*-factors at each site and revealed, once again, a strong gradient from north to south (Fig. 3). A broader distribution of mean *n*-factors at the four southerly sites is reflected in the increased area within the quartile box. While the latitudinal

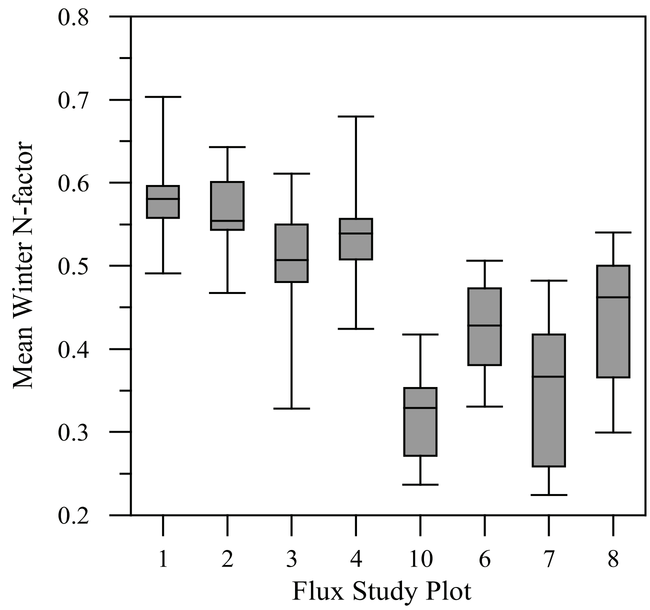

Figure 3. Box-and-whisker plots show the median, quartiles, and range of mean winter *n*-factors at each of the eight Flux Plots observed between 1995 and 2006.

gradient appears very distinct, snow depth at regional and microtopographic scales is an important factor determining ground temperature (Benson 1967, Gold 1967, Goodrich 1982). Vegetation should also be examined, as it can act to "trap" snow and prevent it from further displacement by wind gusts.

To examine these relationships, mean winter n-factors were plotted against the air and soil degree-day sums from which they were calculated (Fig. 4). DDF_{air} values show general trends of warmer air temperatures, leading to higher n-factors (Fig. 4a). The magnitude of the n-factor varies strongly by site (Plot 1 having the largest and Plots 6 and 10 the smallest) while DDF_{air} varies over a similar range. It is clear, therefore, that air temperature is not the sole determinant of the latitudinal gradient apparent in Figures 2 and 3.

The plot of DDF_{soil} (Fig. 4b) indicates that soil temperature constitutes a much stronger control over mean *n*-factor values. The data have an almost linear relationship, with warmer soils corresponding to lower *n*-factors. The data cluster tightly by plot, with northern sites having larger *n*-factor values and southern sites being lower.

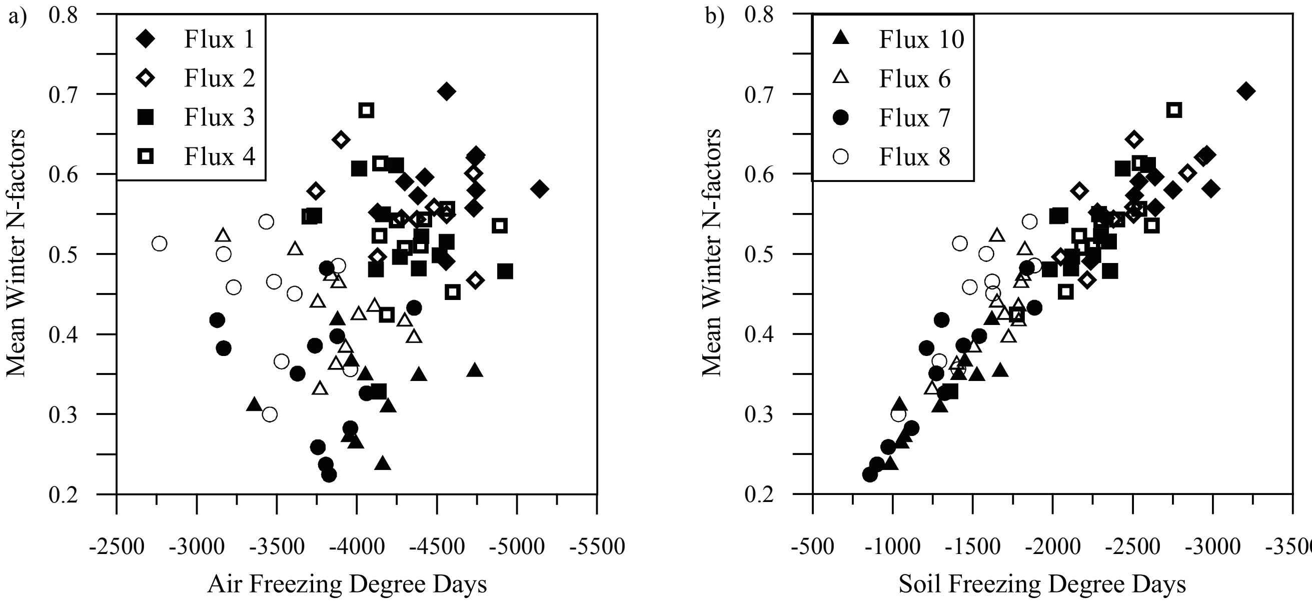

Figure 4. Mean winter air (a) and soil (b) degree days of freezing measured at each Flux Plot and graphed against mean winter n-factors. While air temperatures show no clear relationship, soil temperatures are directly related, reflecting the thermal influence of snow. X-axes have the same scale but different ranges.

Land cover within the region shows a general trend from moist nonacidic and wet sedge tundra complexes on the flat coastal plain, to a mix of acidic and shrub tundras in the foothills. The Flux Plots reflect these patterns (Walker & Bockheim 1995). Flux Plots 1 and 2 were chosen to include moist and wet complexes on the coastal plain. Plots 3 and 4 were selected as homogenous 1-ha areas of nonacidic and acidic tundra within close geographic proximity to each other (Walker & Bockheim 1995). The nonacidic tundra is characterized by the presence of Carex, Dryas, Eriophorum, and Hylocomium, while the acidic tundra has Eriophorum, Ledum, Betula, Hylocomium, and Salix with distinct tussock development (Walker & Bockheim 1995). Plots 6 and 8 are mixed acidic and shrub tundra and were included because of previous research done at those locations. Plot 7 is an acidic wetland. Site 10 was selected to represent a water-track, a shrubby wet first-order stream channel complex. The lower soil DDFs and n-factors at Plots 7 and 10 reflect their higher soil moisture contents. In the foothills, all 4 sites have the potential for drifting and scouring of snow, with slope angles ranging from 0° (Plot 7 in the bottom of a valley) to 15° at Plot 8. Sites 3, 6, 8, and 10 have slopes of more than 3°.

Taras et al. (2002) found that snow depth means and standard deviations were lower and less variable on the coastal plain than in the foothills. They were also able to categorize the amount of decoupling between air and soil temperatures using snow depth classes: 0–25 cm (highly coupled), 25–80 cm (coupled), and 80–200 cm (decoupled).

Although several studies have examined snow patterns on the North Slope, plot-level data were not available. Two SNOTEL sites, Sagwon and Imnavait, are located within the study area and have records covering the period 1995–2006. Each of these lies in close proximity to a pair of Flux Plots, in the Sagwon Hills (Plots 3, 4) and at Imnavait Creek (Plots 7, 8). Table 2 presents summary statistics of the accumulated precipitation (Oct–May) between 1995 and 2006 at these sites. While the mean winter precipitation at these sites is similar (approximately 8.7 cm), the range at Sagwon is just 1.0 while the Imnavait site range is 6.4 in.

Table 2. Summary statistics of the winter precipitation (Oct–May) accumulated at the available SNOTEL sites (cm). Seasons missing any monthly accumulation data were not used.

	Sagwon	Imnavait
N	6	10
Minimum	6.9	4.3
Mean	8.4	9.0
Median	8.8	7.2
Maximum	9.4	20.6
Range	2.5	16.3
Stand. Dev.	0.9	5.0

A crude assumption was made that the Sagwon site could represent general winter snow conditions in the northern portion of the study area while the Imnavait site would represent the southern. The Sagwon Hills are effectively the end of the coastal plain and beginning of the foothills province. Figure 5a shows the relationship between accumulated winter precipitation at Sagwon and mean winter n-factors at the four northern sites, while Figure 5b shows Imnavait and the southern sites.

Interestingly, the coastal sites furthest away from the Sagwon site seemed most closely related to interannual changes in snow depth. This presumably reflects that regional differences are important in areas that tend to be wind-blown with relatively shallow snowpack. In the south, no clear relationship is apparent. The documented variability of snow depth in the foothills (Taras et al. 2002) resulting

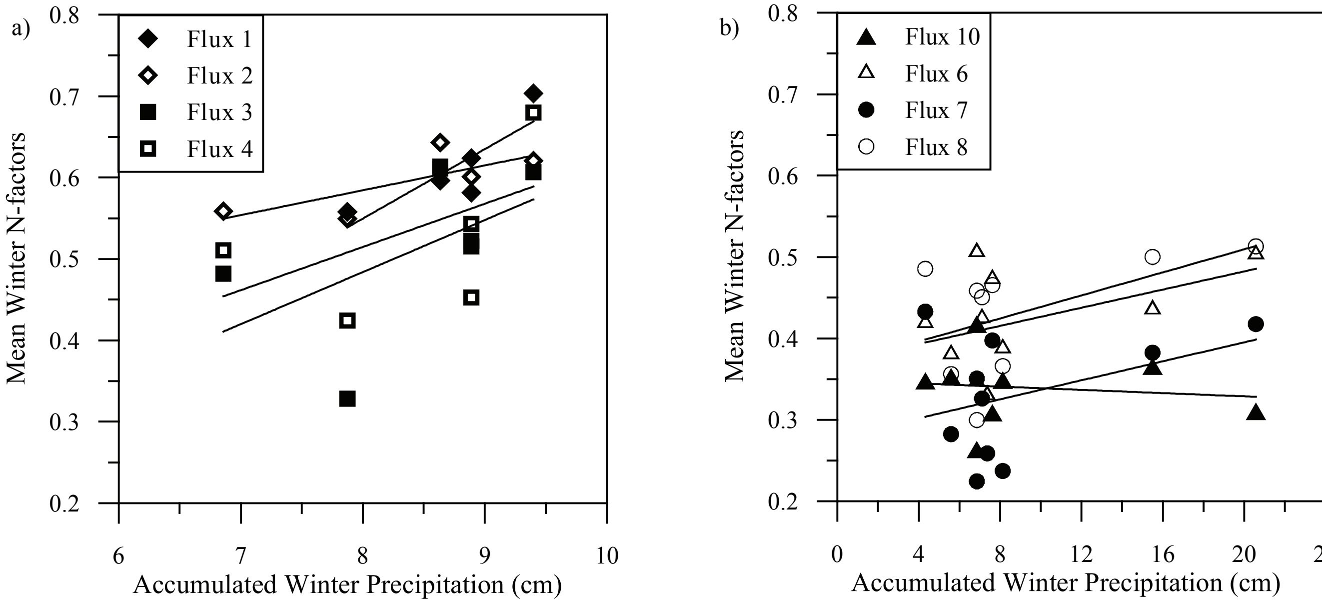

Figure 5. Accumulated winter precipitation (Oct–May) at SNOTEL sites plotted against mean winter *n*-factors in the northern (a) and southern (b) portion of the study area, represented by the Sagwon and Imnavait SNOTELs, respectively. The *x*-axes differ in scale.

from microtopography, vegetation, and wind-action is obfuscating the general interannual variability in snowpack conditions.

In comparison to previous work, the mean winter n-factors are higher than those found by Carlson (1952) and Taylor (1995) in central Alaska and the Mackenzie River Valley but similar to those observed by Karunaratne and Burn (2003, 2004) and Kade et al. (2006) in the Yukon Territory and northern Alaska. Snow depths may be thicker at Carlson's and Taylor's sites. In the study by Karunaratne and Burn (2003) in the Yukon between 1997 and 2000, n-factors ranged between 0.3 and 0.5 while the mean maximum snow depth observed ranged from 19–28 cm. Kade et al. (2006) calculated n-factors at a transect of three sites in northern Alaska overlapping the central and northern portions of the study area and found values of 0.3 and 0.6 at tundra sites bracketing the locations of Plots 3 and 4 and Sites 1 and 2.

Conclusions

The unusual set of geographically diverse observations used in this study allowed interannual quantification of n-factor variability at a range of tundra sites over 12 winter seasons. The latitudinal gradient in mean winter *n*-factors values are related not just to air temperatures, but also to vegetation and snow depth, as previous work and theory suggest. However, the lack of in situ snow depth measurements prevents further detailed analysis of within-plot variability. Future work should consider methods for improving quantification of snowpack characteristics, both spatially and temporally in the region.

Acknowledgments

This work was supported by the National Science Foundation under grants OPP-0095088 and 0352958. Opinions, findings, conclusions, and recommendations expressed in this paper are those of the authors and other CALM investigators, and do not necessarily reflect the views of the National Science Foundation. We are grateful for assistance with fieldwork from J. Riverstone (Mueller) and many graduate students and colleagues over the years.

References

Benson, C.S. 1969. *The Seasonal Snow Cover of Arctic Alaska*. Washington D.C.: Arctic Institute of North America, 96 pp.

Buteau, S., Fortier, R., Delisle, G. & Allard, M. 2004. Numerical simulation of the impacts of climate warming on a permafrost mound. *Permafrost and Periglacial Processes* (15)1: 41-47.

Carlson, H. 1952. Calculation of depth of thaw in frozen ground. In: *Frost Action in Soils: A Symposium*, Highway Research Board Special Report 2 Washington, DC: National Research Council, 192-223.

Gold, L.W. 1967. Influence of surface conditions on ground temperature. *Canadian Journal of Earth Sciences* 4: 199-208.

Goodrich, L.E. 1982. The influence of snow cover on the ground thermal regime. *Canadian Geotechnical Journal* 19: 421-432.

Juliussen, H. & Humlum, O. 2007. Towards a TTOP ground temperature model for mountainous terrain in central-eastern Norway. *Permafrost and Periglacial Processes* (18)2: 161-184.

Kade, A., Romanovsky, V.E. & Walker, D.A. 2006. The n-factor of nonsorted circules along a climate gradient in Arctic Alaska. *Permafrost and Periglacial Processes* 17(4): 279-289.

Kane, D.L. & Reeburgh, W.S. 1998: Introduction to special section: Land-Air-Ice Interactions (LAII) Flux Study. *Journal of Geophysical Research* 103: 28913-28915.

Karunaratne, K.C. & Burn, C.R. 2003. Freezing n-factors in discontinuous permafrost terrain, Takhini River, Yukon Territory, Canada. In: *Proceedings of the 8th International Conference on Permafrost. Zurich: University of Zurich-Irchel*: 519-524.

Karunaratne, K.C. & Burn, C.R. 2004. Relations between air and surface temperature in discontinuous permafrost terrain near Mayo, Yukon Territory. *Canadian Journal of Earth Sciences* 41: 1437-1451.

Klene, A.E., Nelson, F.E., Shiklomanov, N.I. & Hinkel, K.M. 2001. The n-factor in natural landscapes: variability of air and soil-surface temperatures, Kuparuk River Basin, Alaska. *Arctic, Antarctic, and Alpine Research* 33(2): 140-148.

Lachenbruch, A.H., Sass, J.H., Marshall, B.V. & Moses, T.H. Jr. 1982. Permafrost, heat flow, and the geothermal regime at Prudhoe Bay, Alaska. *Journal of Geophysical. Research* (87)B11: 9301-9316.

NRCS 2007. *Accumulated Precipitation for Sagwon, Alaska.* URL: http://www.ak.nrcs.usda.gov/ Snow/snowsites.html.

Sturm, M., McFadden, J.P., Liston, G.E., Chapin, F. S. III, Racine, C.H. & Holmgren, J. 2001. Snow-shrub interactions in Arctic tundra: A hypothesis with climatic implications. *Journal of Climate* 14: 336-344.

Taras, B., Sturm, M. & Liston, G.E. 2002. Snow-ground interface temperatures in the Kuparuk River Basin, arctic Alaska: measurements and model. *Journal of Hydrometeorology* (3):44, 377-394.

Taylor, A.E. 1995. Field measurements of n-factors for natural forest areas, Mackenzie Valley, Northwest Territories. In: *Geological Survey of Canada, Current Research,* 1995-B: 89-98.

Wahrhaftig, C. 1965. *Physiographic Divisions of Alaska.* Washington, DC: United States Geological Survey.

Walker, D.A. & Bockheim, J.G. 1995: *Vegetation-Soil Characterization at the 12 Flux Tower Sites. ARCSS/LAII/Flux Study.* LAII Science Management Office, University of Alaska Fairbanks, Fairbanks, AK.

Geophysical Mapping of Isolated Permafrost Lenses at a Sporadic Permafrost Site at Low Altitude in the Swiss Alps

Christof Kneisel
Department of Physical Geography, University of Würzburg, Germany
Daniel Schwindt
Department of Physical Geography, University of Trier, Germany

Abstract

Results of geophysical mapping of isolated permafrost lenses at a vegetated scree slope below the timberline using electrical resistivity tomography and refraction seismics are presented. In total, 20 geoelectrical and 10 seismic surveys were performed. Using 5 m spacing, survey length resulted in 175 m and 265 m arrays for the geoelectrical surveys and 115 m for the refraction seismic surveys. With respect to the large heterogeneity of the permafrost distribution, tomographic inversion schemes were used for data analyses and interpretation. Both electrical resistivity and refraction seismic surveys showed isolated anomalies of high resistivity and high velocity within the subsurface, especially in the lower parts of the scree slope. P-wave velocities of the isolated anomalies were between 1700-4300 m/s in a host material with velocities between 1000-1500 m/s. In most cases these locations coincide with the high-resistivity anomalies of the 2D resistivity tomography.

Keywords: electrical resistivity tomography; geophysical mapping; isolated permafrost; refraction seismics; scree slope; Swiss Alps.

Introduction

The Upper Engadine is one of the mountain regions in Switzerland with widespread alpine permafrost occurrence. Discontinuous permafrost is encountered above 2400 m a.s.l. Below the timberline, sporadic permafrost is assumed to exist only at very shaded sites. One of these special places is situated in the Bever valley, which represents one of the few sites in Switzerland where isolated permafrost lenses could be confirmed by several geophysical techniques (Kneisel et al. 2000, Kneisel 2003, Kneisel & Hauck 2003). For a detailed geophysical mapping of the sporadic permafrost distribution joint application of electrical resistivity tomography and seismic refraction surveys have been applied.

There are several publications concerning joint application of geoelectrical surveys and refraction seismics for sounding of rock glacier permafrost using one-dimensional techniques (e.g., Vonder Mühll 1993, Wagner 1996, Ikeda 2006). Similar to electrical resistivity tomography, a tomographic variant of seismic refraction which has become increasingly important in the past few years can be applied yielding two-dimensional velocity distributions of the subsurface (e.g., Musil et al. 2002, Kneisel & Hauck 2003, Hauck et al. 2004, LeBlanc et al. 2004, Maurer & Hauck 2007).

With respect to the known small-scale heterogeneity as many as 20 geoelectrical and 10 seismic surveys were performed, of which characteristic profiles are shown. This paper significantly extends the earlier studies presented by the author (see above) by introducing a larger number of 2D geophysical surveys using tomographic inversion schemes for data analyses allowing for more detailed interpretation and conclusions.

Site Description

The sporadic permafrost site below the timberline is located in the Bever Valley, a trough-shaped valley with bottom elevation between 1730 m and 1800 m a.s.l. at its lower end. Both the north- and south-exposed valley sides are wooded. At present the upper timberline is between 2200 m and 2300 m a.s.l. Larch (*Larix decidua*) and cembra pine (*Pinus cembra*) are the dominant tree species of the forest. Most parts of the scree slopes which occur below the rock walls are well covered with vegetation (Fig. 1). The soils are poorly developed and covered by an organic layer up to 30 cm thick. Below the organic layer, only a few centimeters of mineral soil exist. Mean annual air temperature at a nearby climate station in the Bever village at 1710 m a.s.l. is +1°C.

Methods

Electrical resistivity tomography (ERT)

Since geoelectrical methods are most suitable for

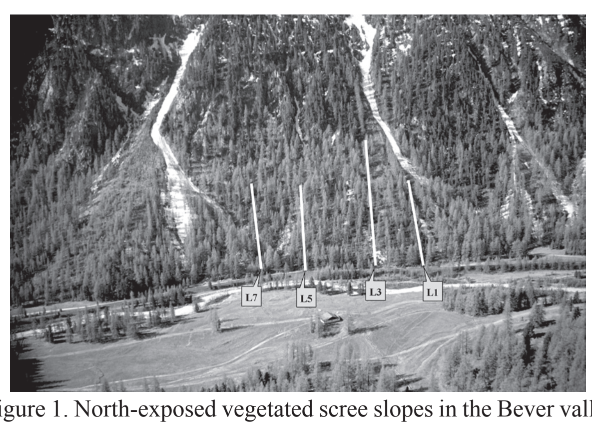

Figure 1. North-exposed vegetated scree slopes in the Bever valley. Lines indicate location of survey profiles.

investigating a subsurface with distinct contrasts in conductivity and resistivity, geoelectrical soundings constitute one of the traditional geophysical methods which have become standard in permafrost research to detect mountain permafrost. Since a marked increase of the electrical resistivity occurs at the freezing point, the method is expected to be most suitable to detect, locate, and characterize structures containing frozen material. Based on the number of scientific publications in the last decade and the large variety of applications, the tomographic variant of the method (electrical resistivity tomography, ERT) is maybe the most universally applicable method in mountain studies (Kneisel & Hauck 2008).

Resistivity values of frozen ground can vary over a wide range depending on the ice content, the temperature, and the content of impurities. The dependence of resistivity on temperature is closely related to the amount of unfrozen water. Perennially frozen silt, sand, gravel, or frozen debris with varying ice content show resistivity values between 5 kOhm.m to several hundred kOhm.m (e.g., Haeberli & Vonder Mühll 1996, Hauck & Kneisel 2008).

For the presented research the two-dimensional (2D) electrical surveys were performed using the Wenner and Wenner Schlumberger configurations with 5 m spacing and an IRIS SYSCAL Junior Switch resistivity-meter. The measured apparent resistivities are used to build up a vertical contoured section showing the lateral and vertical variation of resistivity over the section. The conventional method of plotting the results for the interpretation is the so-called pseudosection which gives an approximate image of the subsurface resistivity distribution. High gradients in the subsurface resistivity distribution usually indicate interfaces between different layers. The measured sets of apparent resistivities were inverted using the software package RES2DINV. This inversion software tries to reduce the difference between the calculated and measured apparent resistivity values by adjusting the resistivity of the model blocks. Topographic corrections can be incorporated into the inversion algorithm which is an essential point for studies in alpine periglacial environments with often complex and heterogeneous topography. Further details on different array geometries and data processing are given for instance in Reynolds (1997) and Kneisel (2006).

Refraction seismics

Similar to the resistivity investigated by electric methods, the sharp increase of the seismic primary wave (P-wave) velocity at the freezing point is used to differentiate between frozen and unfrozen material. The P-wave velocity distribution can be used as a complementary indicator to resistivity for the presence of frozen material. The method is especially useful to determine the top of the permafrost layer, as the contrast for the P-wave velocity between the unfrozen top layer (= active-layer, 400-1500 m/s) and the permafrost body (2000-4000 m/s) is usually large. On the other hand, the values for most common rock types (e.g., gneiss or granite) are similar to the values for ice, so the detection of mountain permafrost is often difficult by using refraction seismic data alone. From this it becomes clear that for some permafrost applications refraction seismic has to be combined for instance with electric methods, in order to get unambiguous results in terms of permafrost delineation. A Geometrics Geode 24-channel seismograph and a cable with 5 m spacing were used for data acquisition. A total number of 10 shot points enabled the data set to be inverted with tomographic inversion schemes. The Pickwin and Plotrefa software was used for data processing and analyses. To create the starting model for each profile a 1D-time-term inversion was performed. The tomographic inversion scheme is based on a least squares algorithm. Topographic corrections were incorporated into the inversion algorithm. Further details on seismic data analyses are given in Palmer (1986) and Reynolds (1997).

Results and Discussion

Profile L1 is situated in a clearing (Fig. 1) where the thickness of the organic layer varies between 15 and 25 cm. Two isolated high resistivity anomalies with a thickness of 10-15 m and a horizontal extent between 10-20 m are present in the ERT (Fig. 3). Maximum resistivities of more than 160 kOhm.m point to permafrost. This interpretation is confirmed by the results of the refraction seismic tomography with P-wave velocities of 4300 m/s for the lower anomaly. Though the upper anomaly shown in the ERT is not completely displayed in the refraction seismic tomogram, relatively warm permafrost (-0.2°C) is confirmed by temperature measurements in an 8 m deep borehole at this location (Fig. 2).

Both tomograms show a thin active-layer of 2-4 m depth, which is due to the isolating properties of the thick organic layer. This modelled active-layer depth compares well with the temperature measurements in the borehole. Measured in late October 2006, the maximum thaw depth had been reached.

High velocities and resistivities usually indicate high ice

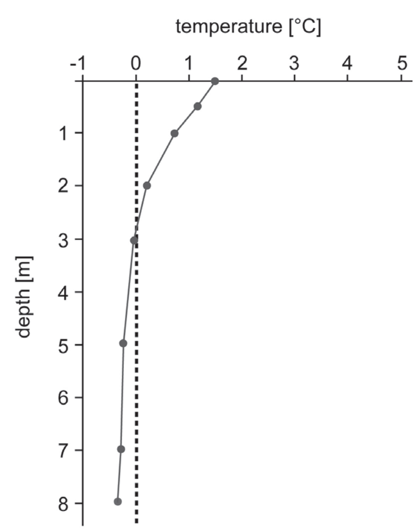

Figure 2. Borehole temperatures measured on 25.10.2006.

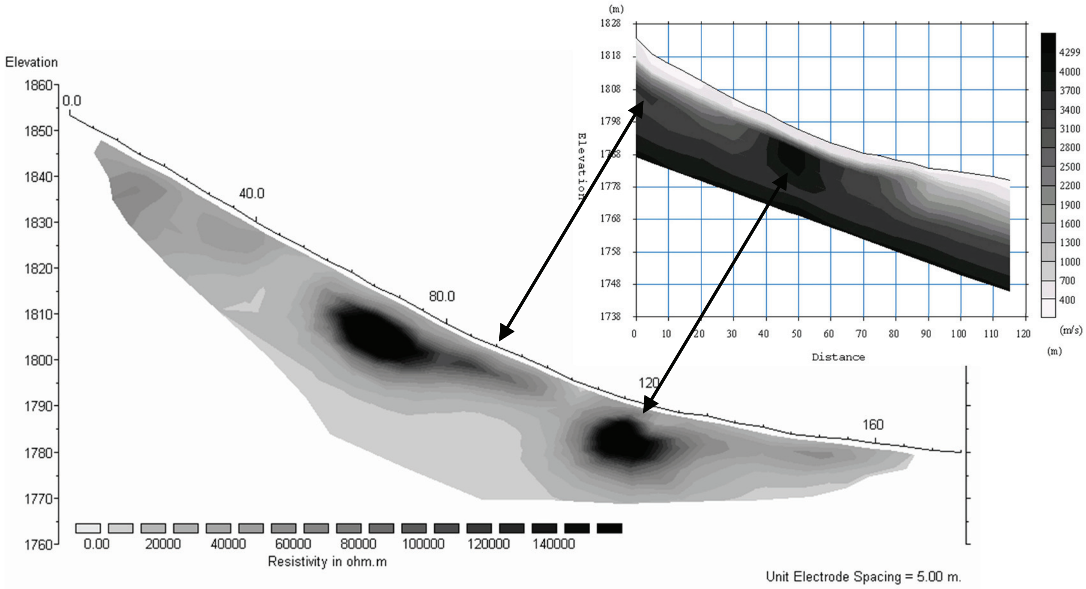

Figure 3. Electrical resistivity and refraction seismic tomograms of profile L1.

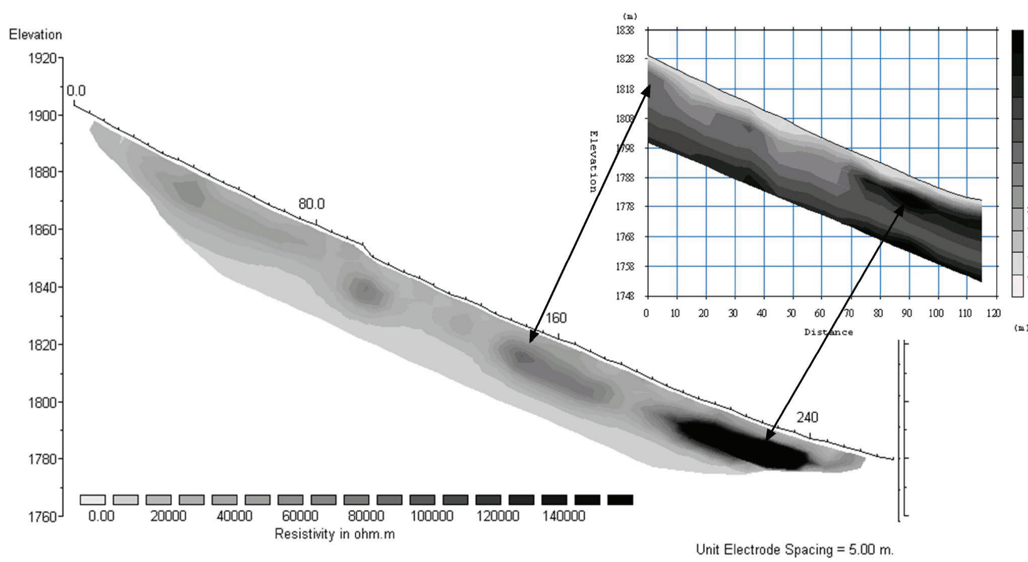

Figure 4. Electrical resistivity and refraction seismic tomograms of profile L3.

contents. Despite permafrost temperatures of only -0.2°C, the unfrozen water content is assumed to be relatively low, in the areas of the high resistivity and high velocity anomalies. The nearly linear decrease of resistivity values at greater depth indicates increasing unfrozen water content due to rising temperatures.

The ERT profile L3 (Fig. 4) shows two elongated high resistivity anomalies in the lower part of the scree slope. With resistivities of more than 160 kOhm.m the anomaly between 205 and 240 m of the ERT array is, situated in an area of coarse blocky material with low rates of fine grained material, covered with a thick organic layer of up to 30 cm. Despite relatively low P-wave velocities of 1900-2000 m/s this anomaly is assumed to represent permafrost. Low P-wave velocities at this place are most likely due to high contents of air filled voids. Profile L3 is assumed to be situated at the margin of a permafrost lens (Fig. 7). This is supported by results of a cross- and a parallel-measured profile, not shown in this paper.

The anomaly between 145 and 180 m of the ERT array and resistivities of 80-100 kOhm.m can be correlated with two anomalies in the refraction seismic tomogram. Unlike the lower parts of the profile, this area can be characterized by higher rates of fine grained material and an organic layer of about 20 cm. Despite of low P-wave velocities between 1500-1600 m/s permafrost can be assumed. If the high resistivities in this area were only due to air filled voids, seismic velocities should be much lower.

Without further research the anomalies above 1820 m a.s.l. in profile L3 cannot clearly be confirmed as permafrost, however the high resistivities are probably due to air filled voids and permafrost also in the upper parts of the scree slope.

The organic layer thickness in the area of profile L5 is comparatively thin, varying from 10-15 cm. In the ERT of profile L5 (Fig. 5) three anomalies with comparatively low resistivities of 60-100 kOhm.m are shown. The lower anomaly between 90 and 150 m can be compared with a more homogeneous area of high velocities (3000-3200 m/s) in the refraction seismic tomogram, hence are interpreted as permafrost. Below a depth of 10-15 m resistivities decrease nearly linear, indicating a decrease in ice content and/or increasing unfrozen water content. Ice rich, but "warm" permafrost can be assumed. High P-wave velocities exclude high amounts of air filled voids. The lower resistivities as compared to the other profiles could be due to comparatively higher unfrozen water content. Due to comparable conditions, concerning surface and subsurface properties, permafrost can also be assumed for the anomalies in the upper parts of the profile.

Very shaded conditions and a homogenous subsurface, with higher amounts of blocky material and an organic layer of about 20 cm is found in most parts of profile L7. Both, the ERT and the refraction seismic tomogram of profile L7 show an elongated high resistivity/high velocity anomaly between 1780 and 1815 m a.s.l., confirming probably ice-rich permafrost (Fig. 6). A thin active-layer of less than 2 m is

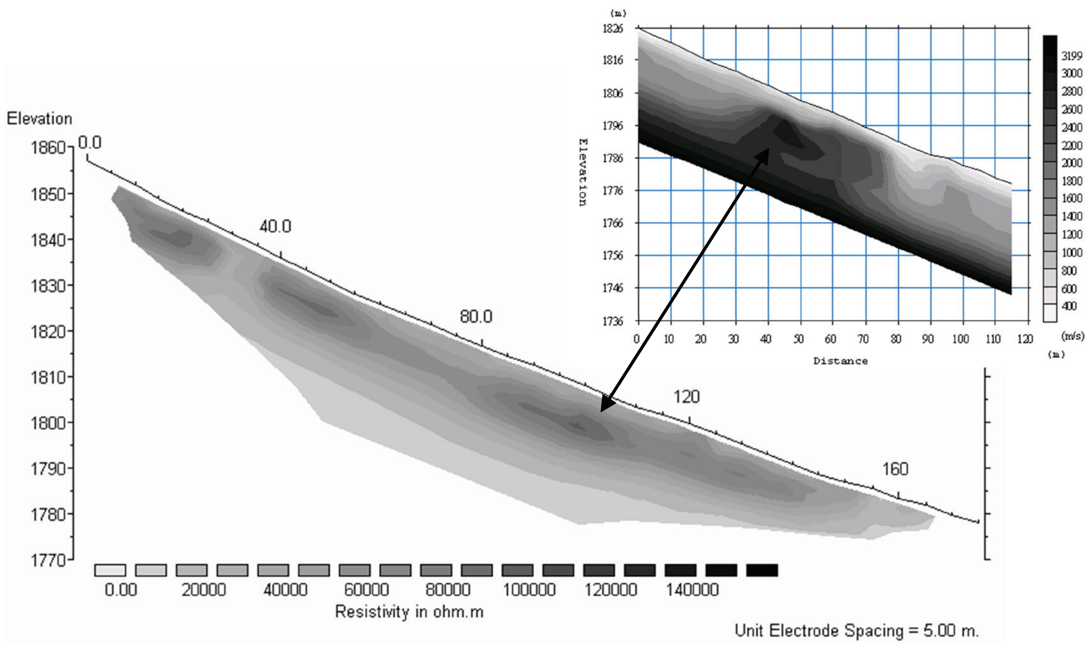

Figure 5. Electrical resistivity and refraction seismic tomograms of profile L5.

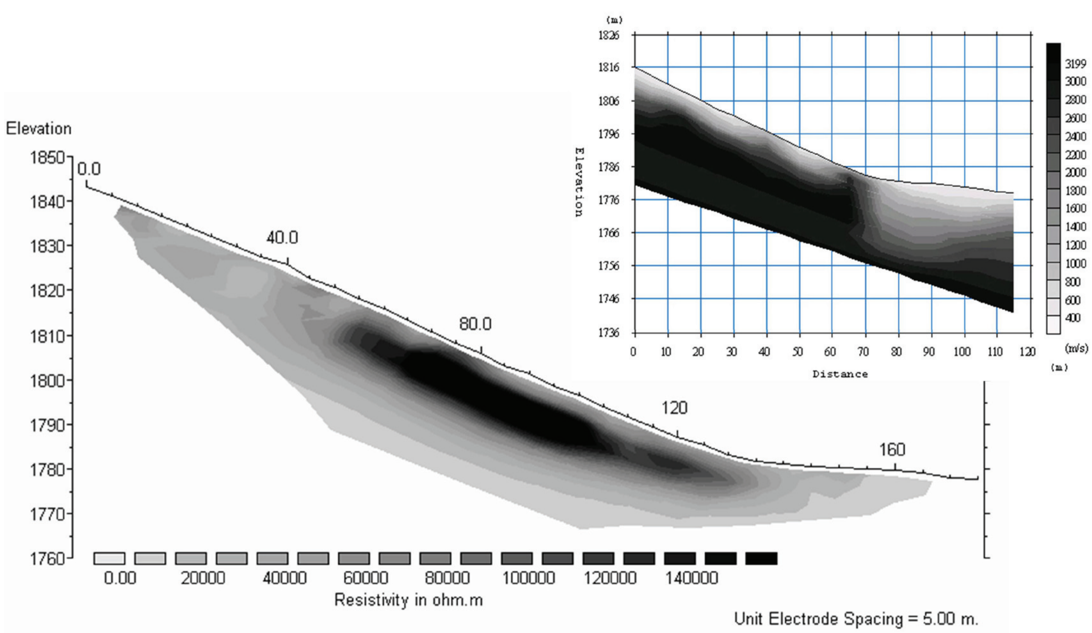

Figure 6. Electrical resistivity and refraction seismic tomograms of profile L7.

detected. However, these profiles had been measured in May 2007 and maximum thaw depth had not yet been reached. In contrast to the ERT, where resistivities slowly decrease up and down slope from the center of the permafrost lens, a sharp decrease to lower velocities is shown in the refraction seismic tomogram. Low resistivities and gradually increasing low P-wave velocities in the gently inclined lower parts of the profile could point to higher amounts of fine grained material in the subsurface.

Permafrost has been detected all over the investigated scree slope below 1840 m a.s.l. by extensive geophysical mapping (Fig. 7) however, permafrost distribution and characteristics are heterogeneous. In profiles L1 and L7 high resistivity/high velocity permafrost is present (Table 1, Fig. 7). Ice-rich permafrost with low amounts of unfrozen water and air cavities can be assumed. Lower resistivities but high P-wave velocities in profile L5 can be interpreted as ice-rich but warm permafrost with higher amounts of unfrozen water reducing the electrical resistivity. High resistivity/low velocity permafrost is to be found in profile L3. Due to very low amounts of fine grained material between the boulders many air cavities lead to high resistivities but low P-wave velocities.

Table 1. Comparison of maximum resistivities and P-wave velocities.

Profile	maximum resistivity (kOhm.m)	maximum P-wave velocity (m/s)
L1	>160	4100
L3	>160	1900-2000
L5	90-100	2900
L7	140->160	3100

Conclusions

Joint application of electrical resistivity and refraction seismics has proven to be a useful approach at this heterogeneous permafrost site as they provide complementary information about the subsurface. With respect to the large heterogeneity of the permafrost distribution, tomographic inversion schemes were used for data analyses and interpretation for both methods.

Both, electrical resistivity and refraction seismic surveys showed isolated anomalies of high resistivity and high velocity within the subsurface, especially in the lower parts of the scree slope. P-wave velocities of the isolated anomalies were between 1700-4300 m/s in a host material with velocities between 1000-1500 m/s. These locations coincide with the high-resistivity anomalies of the 2D resistivity tomography. Due to the P-wave velocities between 1700-4300 m/s, the high-resistive anomalies can be characterised as permafrost lenses, because air cavities would result in much smaller P-wave velocities. In most cases the results of both techniques coincide very well. Results of the refraction seismic tomography also point to a thin active-layer, especially in the lower parts of the scree slope. This can be due to the isolating properties of the thick layers of organic material which is, among other factors, responsible for the occurrence of this sporadic permafrost at low altitude.

The ground thermal regime is assumed to be a result of the interaction of climatic conditions with topography (northern exposure, small amount of incoming radiation, frequent temperature inversions in winter, distribution and duration of snow cover) as well as surface and subsurface factors (organic layers, coarse blocky material).

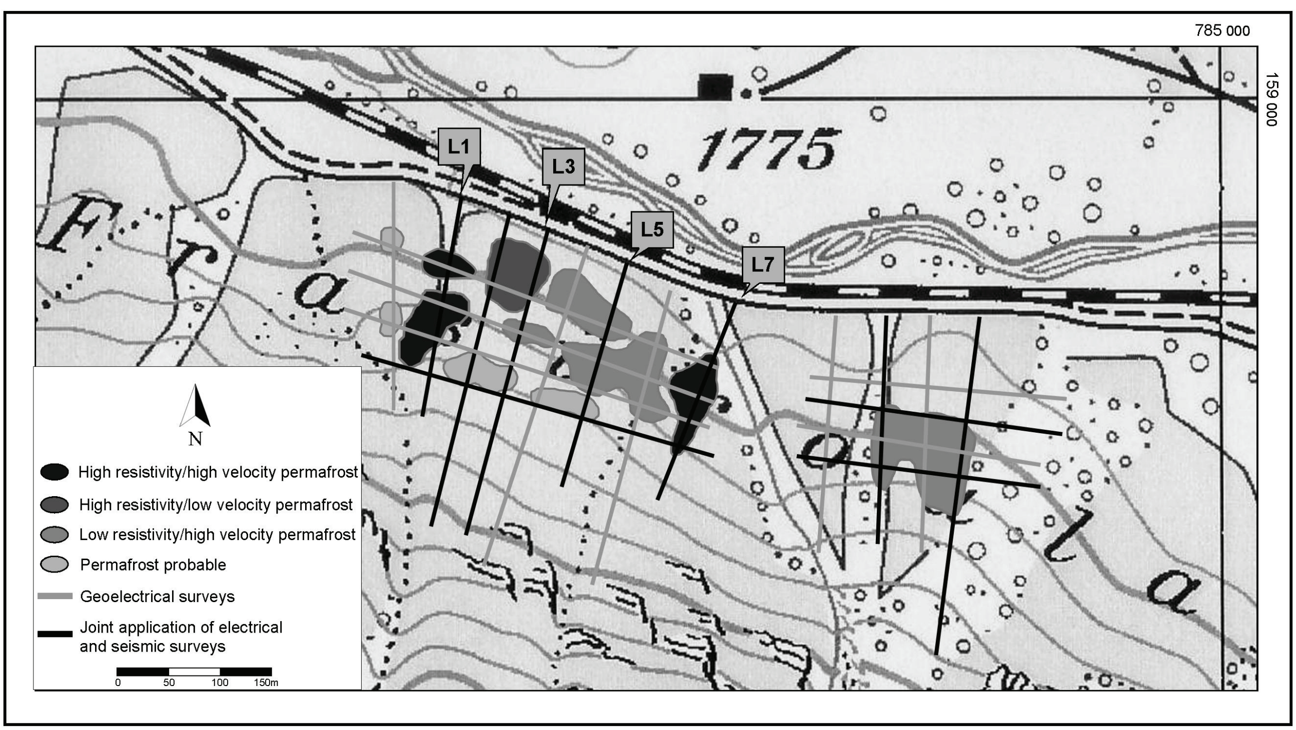

Figure 7. Location of geophysical surveys and inferred permafrost lenses in the Bever Valley.

References

Haeberli, W. & Vonder Mühll, D. 1996. On the characteristics and possible origins of ice in rock glacier permafrost. *Zeitschrift für Geomorphologie* N.F. Suppl. 104: 43-57.

Hauck, C., Isaksen, K., Vonder Mühll, D. & Sollid, J.L. 2004. Geophysical surveys designed to delineate the altitudinal limit of mountain permafrost: an example from Jotunheimen, Norway. *Permafrost and Periglacial Process* 15(3): 191-205.

Hauck, C. & Kneisel, C. 2008. *Applied geophysics in periglacial environments.* Cambridge University Press, in press.

Ikeda, A. 2006. Combination of conventional geophysical methods for sounding the composition of rock glaciers in the Swiss Alps. *Permafrost and Periglacial Processes* 17: 35–48.

Kneisel, C. 2003. Sporadic and discontinuous mountain permafrost occurrence in the Upper Engadine, eastern Swiss Alps. *Proceedings of the 8th International Conference on Permafrost*, *Zurich, Switzerland*: 561-566.

Kneisel, C. 2006. Assessment of subsurface lithology in mountain environments using 2D resistivity imaging. *Geomorphology* 80: 32-44.

Kneisel, C., Hauck, C. & Vonder Mühll, D. 2000. Permafrost below the timberline confirmed and characterized by geoelectrical resistivity measurements, Bever Valley, eastern Swiss Alps. *Permafrost and Periglacial Processes* 11(4): 295-304.

Kneisel, C. & Hauck, C. 2003. Multi-method geophysical investigation of a sporadic permafrost occurrence. In: L. Schrott, A. Hoerdt, & R. Dikau (eds.), Geophysical methods in geomorphology. *Zeitschrift für Geomorphologie*, Suppl. 132: 145-159.

Kneisel, C. & Hauck, C. 2008. Electrical methods. In: C. Hauck & C. Kneisel (eds.), *Applied Geophysics in Periglacial Environments.* Cambridge University Press, in press.

LeBlanc, A.M., Fortier, R., Allard, M. & Cosma, C.G. 2004. Seismic cone penetration test and seismic tomography in permafrost. *Canadian Geotechnical Journal* 41: 796-813.

Maurer, H. & Hauck, C. 2007. Geophysical imaging of alpine rock glaciers. *Journal of Glaciology* 53(180): 110-120.

Musil, M., Maurer, H., Green, A.G., Horstmeyer, H., Nitsche, F., Vonder Mühll, D. & Springman, S. 2002. Shallow seismic surveying of an Alpine rock glacier. *Geophysics* 67(6): 1701-1710.

Palmer, D. 1986. Refraction Seismics. In: Helbig & Treitel (eds.), *Handbook of Geophysical Exploration. Seismic Exploration 13*. London-Amsterdam: Geophysical Press.

Reynolds, J.M. 1997. *An Introduction to Applied and Environmental Geophysics*. Chichester: Wiley.

Vonder Mühll, D. 1993. Geophysikalische Untersuchungen im Permafrost des Oberengadins. - Mitt. Versuchsanst. Wasserbau, Hydrologie und Glaziologie, ETH Zürich, 122: 222 pp.

Wagner, S. 1996. DC resistivity and seismic refraction soundings on rock glacier permafrost in northwest Svalbard. *Norsk Geografisk Tidsskrift* 50: 25-36.

Thawing Permafrost and Temporal Variation in the Electrical Conductivity of Water in Small Tundra Lakes, Mackenzie Delta Region, N.W.T., Canada

S.V. Kokelj

Water Resources Division, Indian and Northern Affairs Canada, Yellowknife, NT, Canada

B. Zajdlik

Zajdlik and Associates, Inc.

M.S. Thompson

Water and Climate Impacts Research Centre, Department of Geography, University of Victoria, Victoria, Canada

R.E.L. Jenkins

Water Resources Division, Indian and Northern Affairs Canada, Yellowknife, NT, Canada

Abstract

Temporal variation in the late summer water quality of 21 small tundra lakes in the Mackenzie Delta region was investigated from 2003 to 2007. Ten lakes were undisturbed, eight had thaw slump scars in their catchments, and three were impacted by highly active thaw slumps. The electrical conductivities (EC) of lake waters from 2003–2007 varied significantly between most lakes. The greatest differences were between the disturbed lakes with elevated EC and undisturbed lakes with relatively low EC. Over the study period, the lowest and highest late-summer lake water EC were recorded in 14 of 21 lakes in association with the wettest preceding year (2006), and driest preceding winter (2003), respectively. This suggests that the chemistry of small tundra lakes is sensitive to variations in the annual water balance. Over time, the greatest relative variation in EC within lakes was associated with undisturbed lakes with unique catchment characteristics and lakes with large active thaw slumps. Intense slumping caused lake water EC to increase, and stabilization was associated with a decreasing trend.

Keywords: climate change; lake chemistry; Mackenzie Delta region; retrogressive thaw slumping; tundra lakes.

Introduction

Impacts to northern aquatic systems are anticipated with climate warming due to the modification of hydrological processes, increases in water temperature and terrestrial biomass, and intensification of disturbance regimes (Rouse et al. 1997, Jorgenson et al. 2006, Lantz & Kokelj, 2008). It is well documented that water in small tundra lakes is generally low in ionic concentration because runoff derived from snowmelt and rainfall is rapidly transported through a thin nutrient-poor active layer (Quinton & Marsh 1999, Kokelj & Burn 2005). Interannual variations in precipitation and catchment runoff should then influence the chemistry of these lakes (Rouse et al. 1997). Furthermore, there is a geochemical contrast between the leached active layer soils and the underlying ion-rich permafrost so that degradation of near-surface permafrost due to -active layer deepening or thaw slumping (Fig. 1) may modify the chemistry of soils, slope runoff, and waters in adjacent lakes and ponds (Kokelj & Lewkowicz 1999, Kokelj et al. 2002, Kokelj et al. 2005, Keller et al. 2007).

The physical and chemical characteristics of small lakes affected by retrogressive thaw slumps and adjacent undisturbed tundra lakes were described by Kokelj et al. (2005), and here we examine temporal variations in the electrical conductivity (EC) of water in these lakes from 2003 to 2007. Since runoff from areas affected by thawing permafrost is solute-rich (Kokelj & Lewkowicz 1999), we hypothesized that the ionic concentrations as indicated by EC would increase with time in lakes affected by active thaw slumps, whereas the stabilization of a slump may cause lake water ionic concentration to stabilize or decrease. It is reported that solute concentrations in lakes with stable thaw slumps are elevated with respect to undisturbed lakes (Kokelj et al. 2005), but relative interannual variability of the two populations may be similar due to the influence of regional climate conditions. To test these hypotheses, the chemical characteristics of water in the ten undisturbed lakes and the 11 lakes affected by recently stabilized and active slumps between Inuvik and Richards Island were evaluated in late summer from 2003 to 2007 (Fig. 2). Temporal patterns in EC are examined with respect to precipitation patterns and disturbance status. The implications of climate-induced permafrost degradation on lake chemistry are discussed and variability in water quality conditions is considered with respect to defining baseline water quality conditions for assessing environmental impacts of northern development.

Environmental Setting

The study lakes are in upland terrain east of the Mackenzie River Delta between Inuvik and the Beaufort Sea coast (Fig. 2). Kokelj et al. (2005) described the study area so that only a brief overview is provided here. The region is characterized by thousands of small lakes and ponds, most of which occur in glaciogenic deposits derived from carbonate and shale bedrock of the Mackenzie Basin (Rampton 1988, Mackay 1992, Burn 2002). As a result, calcium and sulphate are dominant ionic constituents of lake water (Kokelj et al. 2005).

Figure 1. Large, recently stabilized retrogressive thaw slump, Lake 10B. The thaw slump scar is about 7 ha in area. Note active slumps are developing in the scar zone in the upper part of photograph.

Lakes occupy between 10 and 20% of the landscape in the vicinity of the study lakes and median lake areas are on the order of a few hectares (Kokelj et al. 2005). Terrain is underlain by ice-rich permafrost and thaw slumps are common throughout the region (Fig. 1) (Mackay 1963, Rampton 1988). From 8 to 17% of water bodies in the vicinity of the study lakes are influenced by thermokarst slumping (Kokelj et al. 2005).

Study Lakes

Twenty-one study lakes between Inuvik and Richards Island were selected following analysis of aerial photographs and field reconnaissance in 2002 (Fig. 2). Small lakes with first-order catchments were selected (Table 1). Catchment, lake. and thaw slump disturbance areas were estimated by digitizing respective parameters on georeferenced, orthorectified, 1:30,000 scale, colour aerial photographs from 2004. Field reconnaissance and re-correction of aerial photographs has resulted in minor modifications to the aerial estimates of catchment and disturbance areas reported in Kokelj et al. (2005) (Table 1).

The lakes are in shrub and low shrub tundra environments in rolling terrain (Ritchie 1984). The small lakes (1 to 18 ha) are within headwater catchments that range from 7 to 92 ha. Eleven of the catchments (Lakes 1B to 11B) contain retrogressive thaw slumps, which occur on slopes surrounding the study lakes and occupy from 4 to 35% of the respective watershed areas (Fig. 1, Table 1). Lakes 5B, 9B and 10B were impacted by highly active slumping for at least a portion of the five-year study period. Slumping at 5B and 10B stabilized in 2004 and 2003, respectively, with activity at 10B increasing again in 2007. Lake 9B had a large and highly active slump for the first three years of study, but as the slump grew upslope, the headwall diminished and activity decreased in 2006 and 2007. Ten undisturbed lakes (Lakes 1A to 11A) are situated near disturbed catchments (Fig. 2). Time series data were not available for Lake 7A. The

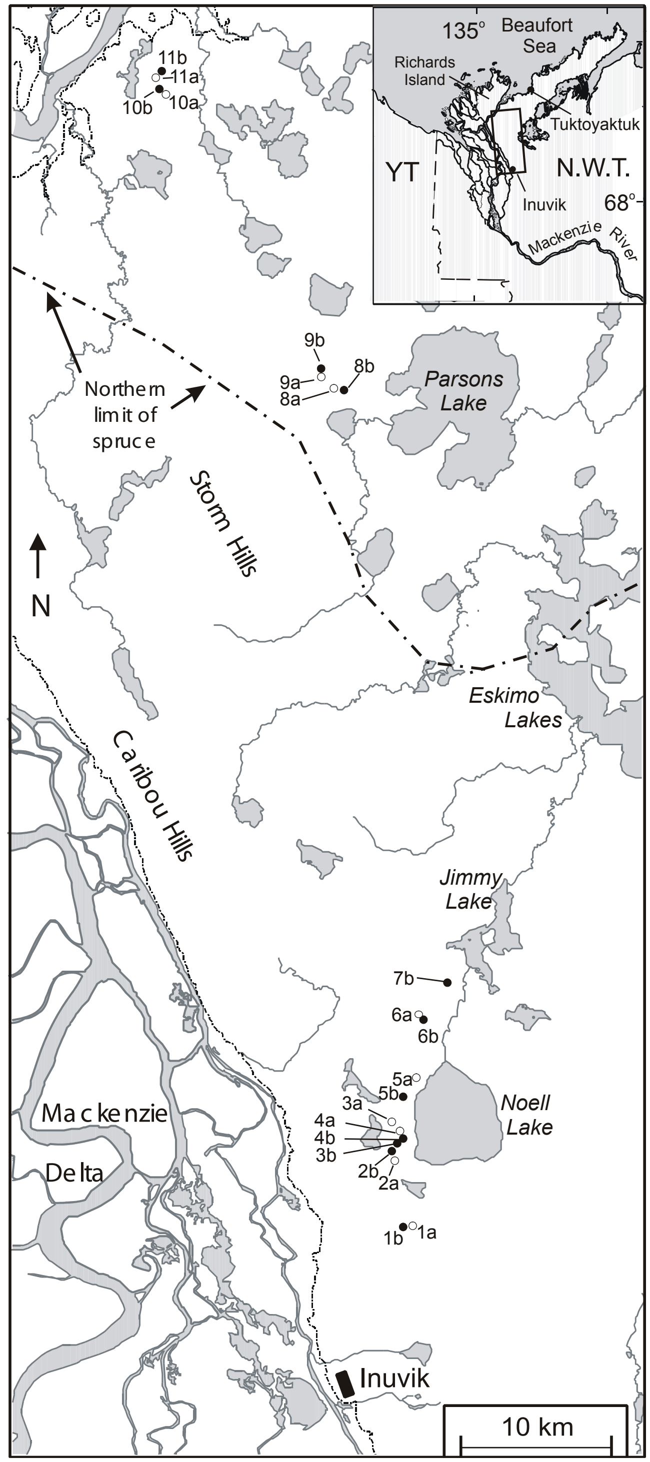

Figure 2. Map of tundra upland study lakes east of Mackenzie Delta, NWT.

southern portion of the study area was burned by wildfire in 1968, affecting catchments 1A, 1B, 2A, 2B, 3A, 3B, 4A, and 4B (Landhäuser & Wein 1993, Mackay 1995). Burned areas are colonized by dense alder and willow bush and active-layeractive layer thicknesses are generally greater than in the nearby tundra (Landhäuser & Wein 1993). Lake depth, determined at the centre of each lake, ranged from 11.3 m at Lake 3B to 1.6 m at Lake 8A, but the deepest parts of small lakes and ponds may be located away from the centre. Maximum late winter ice thickness in 2003 and 2007 did not exceed 1.5 m, and therefore, even the shallowest lakes did not freeze to the bottom. Profiles obtained during late summer surveys suggest that portions of lakes over about 6 m deep may be thermally and chemically stratified in late summer (Kokelj et al. 2005, Fig. 3).

Methods

From 2003 to 2007, during late August or the first week of September, surface water samples were obtained from the centre of each lake using a helicopter equipped with floats. Water samples were collected in 1 L polyethylene bottles rinsed three times with sample site water prior to collection. Sampling depth was about 50 cm. Following collection, sample bottles were placed in a cooler with ice packs and returned to the laboratory for analysis. Water samples were analyzed following standard methods taken from Clesceri et al. (1998). Specific EC and total alkalinity were measured on unfiltered samples in the laboratory using a Titralab radiometer. Anions and cations were evaluated by ion chromatography and hardness was calculated as the sum of inorganic calcium and magnesium using:

$$\text{Hardness (mg/L)} = 2.497 \times \text{Ca(mg/L)} + 4.117 \times \text{Mg(mg/L)}$$

Potential effects of lake and year on EC in undisturbed and disturbed lakes were tested using a randomized complete block design with years as blocks (Sokal & Rohlf 1995) followed by *post hoc* multiple comparisons using Tukey's test to control the experiment-wise Type 1 error rate. As lakes were not replicated, the interaction between year and lake could not be tested. Since multiple comparisons of means among lakes collapse data over years, the assumption of no year-lake interaction must be met if there is a significant effect. Although this assumption could not be tested, time series graphics of EC by lake provide no evidence of lake-year interaction. Residual diagnostics including Shapiro-Wilk's test of normality, visual assessment of leverage, plot residuals versus observed values, and a plot of fitted versus observed values indicate no concerns with assumptions of the statistical model (Sokal & Rohlf 1995). Relative variation in the conductivity of individual lakes over time was described by the coefficient of variation (CV) (Sokal & Rohlf 1995). Relations between water quality parameters and temporal variation in EC between lakes were explored using Spearman's rank correlations (Sokal & Rohlf 1995). Interpretation of the correlation results were regarded as tentative due to the likely low power of the between-lake EC tests because of small sample size and the large number of tests which adversely affect Type 1 error rate. Statistical analyses were conducted in R (R Development Core Team, 2007).

Results

Lake water ionic concentrations, 2003–2007

Electrical conductivity (EC) in late summer surface water samples collected from 2003–2007 was strongly correlated with major ions (Ca, Mg, K, Na, and SO_4; $P < 0.0001$) (also, see Kokelj et al. 2005; Table 3). This indicates that EC is a good descriptor of ionic strength in the water of the study lakes. In the undisturbed lakes, the highest late summer conductivities from 2003–2007 were observed in Lake 3A (160 to 185 µS/cm), which is one of the more southerly catchments and was burned in 1968 (Fig. 3). The lowest conductivities over this period were observed in Lake 9A (38.9 to 44.2 µS/cm), located in hilly upland tundra on the eastern slope of the Storm Hills (Fig. 2). The mean EC of undisturbed lakes from 2003 to 2007 was 104.5, 94.7, 93.2, 87.2, and 96.7 µS/cm, respectively. Analysis of variance shows that EC in undisturbed lakes varies significantly with year and lake, with the largest variation being associated with between lake differences (Table 2a, Fig. 3). Tukey's honest significant difference procedure indicates that, with four exceptions, the disturbed lakes, across years, are significantly different from one another. The *post hoc* testing also showed that in 2003, the mean EC of undisturbed lakes was significantly higher than in 2004 through 2006, but not 2007, and that EC in 2006 was significantly lower than that in 2007.

Ionic concentrations in lakes affected by retrogressive thaw slumping were always elevated with respect to undisturbed lakes (Figs. 3 & 4) (Kokelj et al. 2005). Lake 10B, had the highest lake water EC of any disturbed lake

Table 1. Lake area and catchment characteristics and coefficients of variation (CV) of late summer EC, 2003–2007, for ten undisturbed lakes and 11 lakes affected by retrogressive thaw slumping, tundra uplands, Mackenzie Delta region.

Lake No.	Lake area (ha)	Catchment area (ha)	Slump area (ha)	Slump status Active - A Stable - S	CV
Undisturbed					
1A	1.1	10.9	-	-	0.0737
2A	2.0	17.2	-	-	0.1007
3A	1.3	13.1	-	-	0.0669
4A	1.2	15.5	-	-	0.0979
5A	2.9	20.9	-	-	0.0799
6A	3.6	19.7	-	-	0.1144
8A	2.1	24.4	-	-	0.0947
9A	3.1	29.3	-	-	0.0547
10A	2.3	26.3	-	-	0.0475
11A	9.8	70.1	-	-	0.1034
Disturbed					
1B	18.0	91.6	3.3	A/S	0.0644
2B	4.9	15.9	0.9	S	0.0397
3B	4.0	15.3	3.6	S	0.0499
4B	5.0	17.8	2.5	S	0.0495
5B	2.8	27.7	2.0	A	0.1418
6B	1.2	7.5	0.8	S	0.0349
7B	3.1	34.7	1.0	A/S	0.0600
8B	6.5	32.7	4.0	A/S	0.0482
9B	3.6	7.2	2.5	A	0.0650
10B	11.4	23.3	7.2	A/S	0.0318
11B	10.5	39.4	2.5	A/S	0.0378

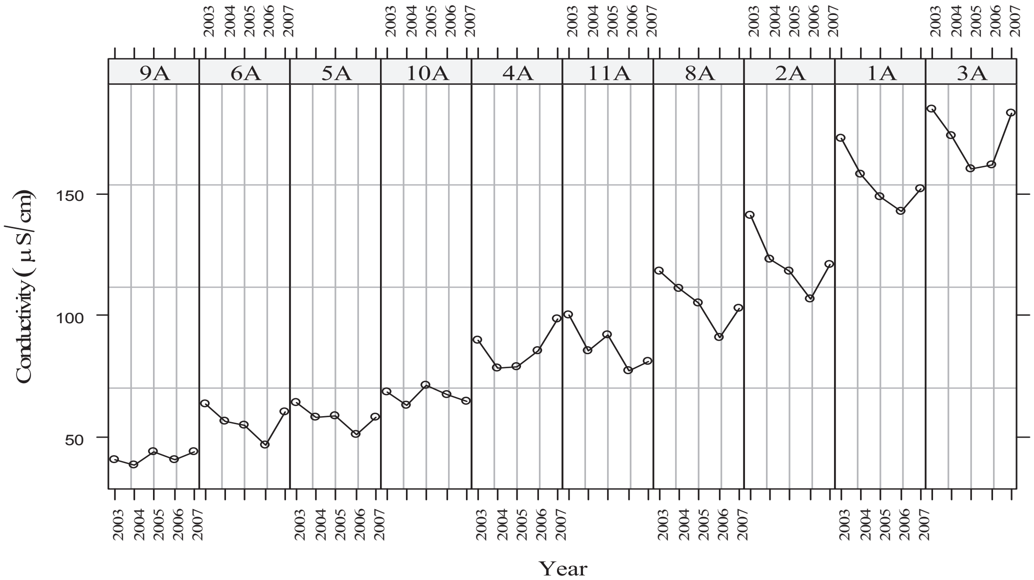

Figure 3. Electrical conductivity of lake water, undisturbed lakes 2003–2007, Mackenzie Delta region.

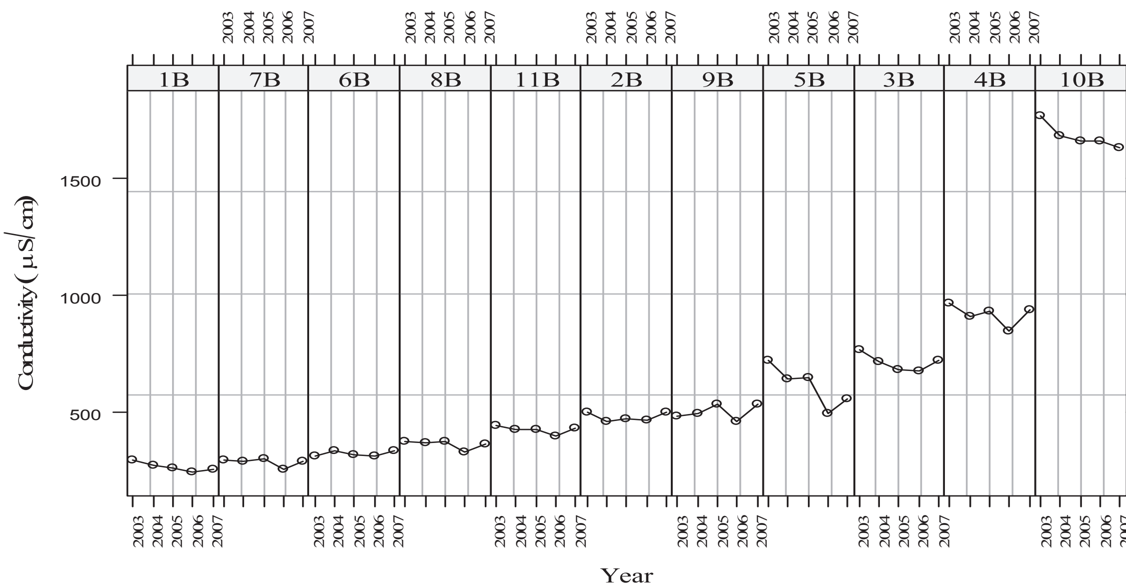

Figure 4. Electrical conductivity of lake water, lakes affected by slumping 2003–2007, Mackenzie Delta region.

and the greatest proportion of catchment area affected by slumping (Fig. 4, Table 1). The most southerly lake, 1B, had the smallest proportion of catchment area influenced by slumping and the lowest EC values. Yearly mean EC of the 11 lakes impacted by slumping from 2003 to 2007 was 631.7, 600.8, 602.5, 561.0, and 597.0 µS/cm, respectively. Table 2b shows that both lake and year are significant factors describing conductivity in the disturbed lakes and as expected the effect of lake (Kokelj et al. 2005) is much larger than that of year. The *post hoc* testing indicated that most lakes are significantly different from one another and that conductivity in 2006 is significantly lower than in 2003 through 2005.

Spearman's rank correlations of late summer lake water EC from 2003 to 2007 indicated significant positive associations between 36 pairs of lakes (Figs. 3, 4). It is also interesting to note the highest late summer EC was measured in 2003 for 14 of the 21 lakes, and the lowest lake water EC was also measured in 14 of 21 lakes in summer 2006 (Figs. 3, 4). Variability in late summer EC over years was described for each of the 21 lakes by calculating their CV (Table 1). Electrical conductivities of lakes 6A and 11A had the highest CV for the undisturbed population. The EC of lakes affected by retrogressive thaw slumping appear to be less variable than the undisturbed lakes, but this is due to the much higher ionic concentrations in disturbed lakes (Figs. 3, 4, Table 1) (Kokelj et al. 2005). Among the disturbed lakes, the highest CV for EC occurred in lakes 5B, 9B, and 1B. The first two lakes were characterized by large areas of highly-active slumping, and Lake 1B is in the largest study catchment and has a relatively large slump that reactivated in 2006 (Table 1).

Table 2. ANOVA table for conductivity in a) undisturbed lakes and b) lakes affected by thaw slumping.

Source	Degrees of freedom	Mean square	F-statistic	P-value
a)Undisturbed lakes				
Lake	9	9488	9.8968	<0.0001
Year	4	391	240.0757	<0.0001
Error	36	40		
b)Disturbed lakes				
Lake	10	836065	874.3637	<0.0002
Year	4	6964	7.2826	<0.0001
Error	40	956		

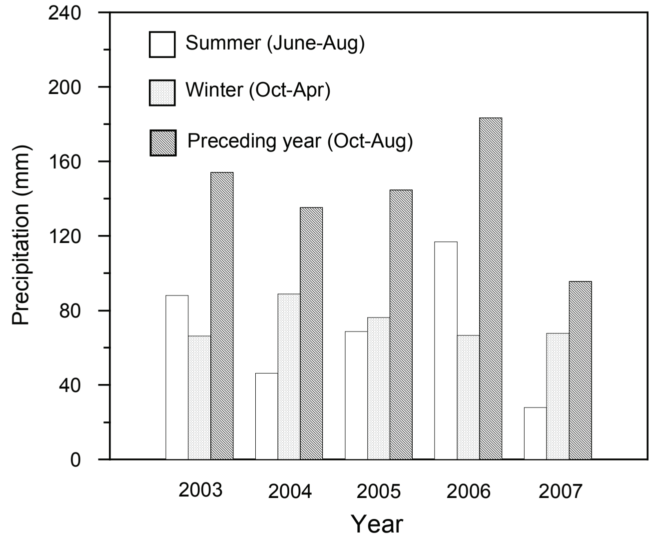

Figure 5. Precipitation for preceding summer, winter and year, Tuktoyaktuk, NWT (Environment Canada 2007).

Discussion

In the study region, tundra lakes are characterized by low ionic concentrations typically less than 100 µS/cm (Pienitz et al. 1997, Kokelj et al. 2005). Local variations in terrain and catchment conditions contribute to between lake differences in the EC of lake water (Figs. 3, 4, Table 2). For example, amongst undisturbed lakes, the highest lake water EC (1A, 2A, 3A) was associated with catchments that were burned in 1968 (Kokelj et al. 2005). Active layer deepening and thawing of near-surface permafrost can release soluble materials which may be transported to the lakes by surface runoff. Amongst the undisturbed lakes, the greatest relative variation in late summer EC (Table 1) was associated with lakes that possess unique catchment characteristics, including the influence of periodic icings and flooding by a nearby stream (6A), and large catchment areas which may experience interannual variation in contributory areas (11A).

End of summer EC from 2003–2007 covaried between many disturbed and undisturbed lakes (Figs. 3, 4). Although we interpret these results cautiously, the correlations suggest the influence of a regional driver. Mean conductivities of both disturbed and undisturbed lakes were notably high in 2003 and low in 2006. The minimum end of summer EC occurred in 14 of 21 lakes in August 2006, which was preceded by the wettest summer and year (Fig. 5). In contrast, EC highs in 14 of 21 individual lakes were recorded in August 2003, which was preceded by the driest winter. These observations suggest that the ionic chemistry of these lakes is sensitive to annual variations in the seasonal water balance.

Regardless, Table 2 emphasizes that between-lake differences have a greater relative influence over EC than does year. Figures 3 and 4 highlight the importance of permafrost degradation on between lake differences in EC as well as on the temporal variations in the chemistry of disturbed lakes. Lakes affected by retrogressive thaw slumping possess elevated ionic concentrations and EC with respect to undisturbed lakes because soluble materials released from thawing permafrost are transported to the lakes by surface runoff (Figs. 3, 4) (Kokelj et al. 2005). The intensity of ionic effects on lake water is positively associated with the proportion of catchment area affected by disturbance (Kokelj et al. 2005). Slumping also appeared to influence temporal variability in lake water EC. The highest coefficients of variation in late summer EC of disturbed lakes were associated with lakes affected by active slumping (Table 1). As hypothesized, intense slumping activity was associated with increasing EC (9B, 2003–2005) because thaw slumping exposes soluble materials that may be transported from disturbed slopes to the lake by surface runoff (Kokelj & Lewkowicz 1999). Stabilization of large active slumps was associated with a decreasing trend in EC, likely because the source of soluble materials is diminished with time (5B, 2005–2007; 10B, 2003–2007) (Fig. 4). It should be pointed out that temporal variation in ionic strength of water in the lakes 9B and 10B did not correlate with any of the other study lakes. In these lakes, effects of slumping subsumed the effects of a regional driver which appears to be influencing the EC of many other study lakes.

Permafrost temperatures are rising in response to 20th Century climate warming in Alaska and northwestern Canada and the frequency and magnitude of terrain disturbances associated with thawing permafrost is increasing (Serreze et al. 2000, Jorgenson et al. 2006, Lantz & Kokelj, 2008). An acceleration of thermokarst activity in conjunction with the geochemical response of lakes to slump growth (Fig. 4) suggests that permafrost disturbance could grow in importance as a driver of lake water chemistry.

In addition to anticipating impacts of climate change on tundra lakes, understanding factors that influence temporal variation in water chemistry is critical to establishing baseline water quality conditions for aquatic effects-monitoring programs. These programs are becoming regulatory requirements for assessing impacts and determining effectiveness of mitigations associated with resource development projects in Canada's North. The study lakes highlight the importance of considering catchment characteristics such as thaw slumping and lake sensitivity to interannual variations in the water balance when selecting reference lakes for the establishment of baseline conditions.

Conclusions

From these results the following conclusions are drawn:

1. Small lakes affected by thermokarst slumping have elevated EC relative to undisturbed lakes.

2. The largest degree of temporal variation in ionic strength of undisturbed tundra lakes occurred in association with unique catchment characteristics.

3. Patterns of variation in late summer EC appeared to be similar amongst many small tundra lakes. End of summer lake water EC may be sensitive to the annual water budget.

4. Amongst the disturbed lakes, those influenced by active slumping showed the greatest degree of variability in lake water EC. Increasing lake water EC was observed in a lake with a large rapidly growing slump and a decline in lake water EC was observed in lakes where large slumps have recently stabilized.

Acknowledgments

This work was supported by the Department of Indian Affairs and Northern Development, the Inuvialuit Joint Secretariat, the Natural Sciences and Engineering Research Council of Canada, the Northern Chair, C.R. Burn, and the Aurora Research Institute. Field assistance by Douglas Esagok and Nathen Richea is gratefully acknowledged.

References

Burn, C.R. 2002. Tundra lakes and permafrost, Richards Island, western Arctic coast, Canada. *Canadian Journal of Earth Sciences* 39: 1281-1298.

Clesceri, L.S., Greenberg, A.E. & Eaton, A.D. 1998. *Standard methods for the examination of water and wastewater, 20th Edition.* American Public Health Association. Washington, D,C.: United Book Press.

Environment Canada. 2007. *Canadian climate data online*. Available from http://www.climate.weatheroffice.ec.gc.ca/climateData/monthlydata_e.html

Jorgenson, M.T., Shur, Y.L. & Pullman, E. R. 2006. Abrupt increase in permafrost degradation in Arctic Alaska. *Geophysical Research Letters* 33.

Keller, K., Blum, J.D. & Kling, G.W. 2007. Geochemistry of soils and streams on surfaces of varying ages in Arctic Alaska. *Arctic, Antarctic and Alpine Research* 39: 84-98.

Kokelj, S.V. & Burn, C.R. 2005. Geochemistry of the active layer and near-surface permafrost, Mackenzie delta region, Northwest Territories, Canada. *Canadian Journal of Earth Sciences* 42: 37-48.

Kokelj, S.V., Jenkins, R.E., Milburn, D., Burn, C.R. & Snow, N. 2005. The influence of thermokarst disturbance on the water quality of small upland lakes, Mackenzie Delta region, Northwest Territories, Canada. *Permafrost and Periglacial Processes* 16: 343-353.

Kokelj, S.V. & Lewkowicz, A.G. 1999. Salinization of permafrost terrain due to natural geomorphic disturbance, Fosheim Peninsula, Ellesmere Island. *Arctic* 52: 372-385.

Kokelj, S.V., Smith, C.A.S. & Burn, C.R. 2002. Physical and chemical characteristics of the active layer and permafrost, Herschel Island, western arctic coast, Canada. *Permafrost and Periglacial Processes* 13: 171-185.

Lantz, T.C. & Kokelj, S.V. 2008. Increasing rates of retrogressive thaw slump activity in the Mackenzie Delta region, N.W.T. Canada. *Geophysical Research Letters* (in press).

Landhäusser, S.M. & Wein, R.W. 1993. Postfire vegetation recovery and tree establishment at the Arctic treeline: climate-change-vegetation-response hypotheses. *Journal of Ecology* 81: 665-672.

Mackay, J.R. 1963. The Mackenzie Delta area, N.W.T. Geographical Branch, Department of Mines and Technical Surveys, Ottawa, Canada, Memoir 8.

Mackay, J.R. 1992. Lake stability in an ice-rich permafrost environment: examples from the western Arctic coast. In *Aquatic Ecosystems in Semi-Arid Regions: Implications for Resource Management*. Robarts RD, Bothwell ML. (eds.) N.H.R.I. Symposium Series 7, Environment Canada, Saskatoon. 1-25.

Mackay, J.R. 1995. Active layer changes (1968 to 1993) following the forest-tundra fire near Inuvik, N.W.T., Canada. *Arctic and Alpine Research* 27: 323-336.

Pienitz, R., Smol, J.P. & Lean D.R.S. 1997. Physical and chemical limnology of 59 lakes located between the southern Yukon and the Tuktoyaktuk Peninsula, Northwest Territories (Canada). *Canadian Journal of Fisheries and Aquatic Science* 54: 330-346.

Quinton, W.L. & Marsh, P. 1999. A conceptual framework for runoff generation in a permafrost environment. *Hydrological Processes* 13: 2563-2581.

R Development Core Team. (2007). *R: A language and environment for statistical computing, V.2.3.1.* Vienna, Austria: R Foundation for Statistical Computing. ISBN 3-900051-07-0. http://www.R-project.org.

Rampton, V.N. 1988. *Quaternary geology of the Tuktoyaktuk Coastlands, Northwest Territories.* Memoir 423. Geological Survey of Canada.

Ritchie, J.C. 1984. *Past and present vegetation of the far northwest of Canada.* Toronto: University of Toronto Press, 251 pp.

Rouse, W., Douglas, M., Hecky, R., Kling, G., Lesack, L., Marsh, P., McDonald, M., Nicholson, B., Roulet, N. & Smol, J.P. 1997. Effects of climate change on freshwaters of Region 2: Arctic and sub-arctic North America. *Hydrological Processes* 11: 873-902.

Serreze, M.C., Walsh, J.E., Chapin, F.S., III, Osterkamp, T., Dyurgerov, M., Romanovsky,V., Oechel, W.C., Morison, J., Zhang, T., & Barry, R.G. 2000. Observational evidence of recent change in the northern high-latitude environment. *Climate Change* 46: 159-207.

Sokal, R.R. & Rohlf, F.J. 1995. *Biometry*. 3rd edition. New York: W.H. Freeman and Company, 876 pp.

Cryolithosphere on Mars and the Thickness of Frozen Rock

Ilya Komarov
Moscow State University, Faculty of Geology, Department of Geocryology, Russia
Vladislav Isaev
Moscow State University, Faculty of Geology, Department of Geocryology, Russia
Oleg Abramenko
Moscow State University, Faculty of Geology,Department of Geocryology, Russia

Abstract

The primary conceptualization of a cryolithosphere on Mars and a thickness of frozen rocks were introduced by Kuzmin (1983), Krass and Merzlikin (1990), and Clifford and Parker (2001). All evaluations of thickness of the Martian cryolithosphere were based on a stable temperature field model. The thickness of frost rocks (H_m) was found following the profile of gradual temperature distribution with depth for one- and two-layered lithological models. The average annual surface temperature, temperature of phase transition for water, temperature of heat transfer, and heat flux to the lower permafrost boundary were taken into account. The revised estimates of the frozen rock thickness are much reduced.

Keywords: cryolithosphere; heat transfer; modeling; temperature field; thermal conductivity coefficient.

Introduction

The greater distance of Mars from the Sun (1.5 times more than Earth) and strong rarefaction of the Martian atmosphere determines the existence of a large region with negative temperatures—a cryosphere. It begins at a height of 130–140 km above the surface, and extends deep inside across the entire planet. Many relief forms can be interpreted by the presence of a thick layer of frozen rock and consequent cryological processes. The relief is characterized by highly elongated forms which are up to 10 times larger in size then their terrestrial analogues. Considerable differences in the ice formation processes within the frozen rocks, and the scale of ice-saturated layers destruction on Mars and on Earth, could possibly explain such a significant difference in size.

Current ideas about the cryolithosphere of Mars and a frozen rock layer are mainly based on the work of Kuzmin (1983), Krass and Merzlikin (1990), and Clifford and Parker (2001). It has been estimated based on a stable thermal field model.

The thickness of a massive frozen rock layer ($H_м$) was found by the profile of stationary distribution of temperature T (K) with depth for models with one- and two-layered lithological cross-sections. The average surface temperature T_{av} and the temperature of phase transition of water, T_{ph} , and values of heat flux to the lower boundary of the cryolithosphere, q, are known. The main differences in these calculations were caused by the choices the various authors have made for the following parameters.

Coefficient of thermal conductivity (λ) for the upper rock layers. λ_m=1.8 W m^{-1} K^{-1} according to Merzlikin, and λ_m = 2.0 W m^{-1} K^{-1} according to Parker. In both calculations, a correction for the influence of temperature on the thermal conductivity of ice and upper layer porosity (0.35±0.15) has been used. Kuzmin set an average of λ_m=2.1 8 W m^{-1} K^{-1}, and using λ_{min} =0.59 and λ_{max} =3.47 8 W m^{-1} K^{-1}.

The magnitude of heat flux from depth (q) is 0.04 W m^{-2} or q = 0.03 W m^{-2} according to Krass and Clifford, respectively. q = 0.039 W m^{-2} (minimum = 0.022; maximum =0.055 W m^{-2}).

The average surface temperature (T_{av}) is equal to - 63°C. T_{av} = -29°C at the equator and T_{av} = -90°C at the poles in the works of Kuzmin, while T_{av}= - 82.5°C; T_{av} = -55°C at the equator and T_{av}= -119°C at the poles in the work of Clifford and Parker.

The presence of water-saturated layers in a cross-sectional model was considered by Kuzmin, Clifford, and Parker in their last publications.

The resulting average thickness of frozen rock varies from 2.7 km (Krass & Merzlikin 1990) to 3.23 km (Kuzmin 1983), changing from 1.5 km to 2.3–4.7 km in equatorial regions to 5 km (Kuzmin 1983) to 6.5–13 km (Clifford and Parker) under the polar caps.

According to the data of remote probing obtained recently (Mars Climate Database of the European Space Agency), and according to our ideas, it seems reasonably to precict the depth of the cryolithosphere and to reduce the estimated thickness of the frozen rock layer on Mars.

For the final evaluations, the following data were taken into account: (a) corrected means of surface temperature observed along meridians; (b) the pressure of upper layers on the lower boundary of frozen rock; (c) the presence on the surface of a dehydrated regolith layer with a thickness from 0.2 to 2.0 m. This layer is characterized by extremely low thermal conductivity (thermal resistance of a 1.5 m thick layer of regolith is equal to 5–10 m of freshly deposited snow); and (d) mineralization of pore solutions, taking the presence of highly mineralized solutions on Mars as a vital hypothesis. There appear to be salty “crusts” in study areas observed by landing craft such as Viking 1 and 2, and the Mars Pathfinder. Also, x-ray spectrometer (APXS) in the

Ares valley, and spectrometer Mossbauer in Gusev crater, registered high salinity in areas where the Mars Rovers, the Mars Pathfinder, and the Spirit landed.

The actual thickness of the frozen rock cryolithosphere on Mars is estimated to average around 2300 m, which is less than what was earlier assumed and similar to values observed on Earth. Frozen rocks contain cryohydrates that have no analogues on Earth.

For the analysis and interpretation of properties of Martian surface rocks, a set of laboratory experiments was carried out for terrestrial samples across a wide range of negative temperatures (from -60 to -120°C); these included measurement of thermal conductivity, heat capacity, and coefficient of linear expansion.

Discussion

Temperature conditions on the surface of Mars

The Martian Global Database (MGD) (www.lmd.jussieu.fr/mars.html) was used for evaluation of spatiotemporal mutability of components of surface energy (radiation-heat) balance, the surface temperature, and the temperature of the near-surface atmospheric zone for high latitude regions of Mars based on General Circulation Models (GCM) to model climate and atmosphere circulation. GCMs are also widely used for weather predication and climate research on Earth.

The Martian version of GCM is the result of cooperative work of LMD (Laboratoire de la Meteorologie Dynamique du CNRS, LMD, Paris) and AOPP (Atmospheric, Oceanic and Planetary Physics, Department of Physics, Oxford University, Oxford, England UK). They are based on actual data received from orbital stations and landing rovers from Mars Pathfinder, Mars Global Surveyor, and Viking 1 and 2.

The influence of atmosphere dustiness and dust storms were taken into account by adding some corrections for different scenarios: "dust" year and "clear" year, average and strong global dust storms The database is an information-searching system equipped with a calculation module for receiving current data on climatic parameters and during a period for a precise site, region, or across the planet.

The analyses of temperature conditions on the surface and in the near-surface atmosphere layers show that the dynamics of seasonal temperature have some characteristic features (Table 1). Maximum temperatures were observed at the end of the Martian summer, while the warmest season is autumn (for the North hemisphere).

Winter temperature tends to decrease with some variations for different areas. It is the coldest period for the region 64°N, 48°E with the peak of negative temperatures at -128.9°C. The coldest time for more southern areas 58°N, 48°E, as well as for 64°N, 30°E, is spring with the temperatures around -123°C.

In the extremely cold period (Ls = 330–360), diurnal temperature fluctuates within 1°C for the area 65°N, 68°N, within 50°C for the latitudes 47°N, and reaches the most significant values up to 100°C at latitude 43°N. Diurnal surface temperature for latitudes 65°N, 68°N achieve a minimum at 10 a.m. and a maximum at 12 p.m. The lower latitudes 43°N, 47°N are characterized by a minimum at 8 a.m., while maximums are differentiated according to the albedo. The lowest temperatures on the Utopia area (43°N, 91°W), for example, were observed at mid-day and the highest temperature at 18 a.m.; with 100°C of temperature fluctuation. In the areas of low albedo, temperatures are minimal at 8 a.m. and maximal at 14–16 p.m., and vary some 40–50 degrees.

Existence of dry soft regolith on the Martian surface

In accordance with data from the High Energy Neutron Detector (HEND) (Feldman et al. 2002), there is a dry soft regolith layer on the surface of Mars. The depth varies from 0.2 m close to the polar caps to 1.5–2.0 m on the equator. It was formed by physical weathering and has andesite or andesite-basaltic composition. The regolith layer at the Viking-1 landing site is composed mainly of clay particles or dusty fraction up to 60% (from 0.05–0.001 to less 0.001 mm), and by a sand fraction of up to 30% (from 0.1 to 2 mm). Some stone-like rounded inclusions with a size of 3–4 cm were noticed.

The thermal inertia (I) is the main thermal parameter of rocks, where $I = (\lambda C_{vhc})^{1/2}$. Here, C_{vhc} is the volumetric heat capacity in J cm^{-3} K^{-1}). Maps of thermal inertia compiled with the help of MCD and the data received by rovers (Jakovsky et al. 2000) allows generalizing a character of varying thermal inertia.

In particular, a significant increase of *I* values was observed from background values 100 J m^{-2} K^{-1} $s^{-1/2}$ (for 80% of the surface) to 400 J m^{-2} K^{-1} $s^{-1/2}$ for areas in northern latitudes from 86ºN, and to 2000 J m^{-2} K^{-1} $s^{-1/2}$ for some regions in the Southern Hemisphere.

As the data on thermal inertia is a *sine qua non* condition for regolith thermal conductivity, some experimental data obtained by differential scanning calorimetry (Komarov 2003, Isaev et al. 2006) for terrestrial samples were used in mathematic modeling of the thermal fields.

Values of volumetric heat capacity (C_{vhc}) do not depend on rarefaction and forces of gravitation. Samples of rocks were tested in an air-dry state because analyses of spectral lines of water in the short-wave part TES spectrums of the Martian surface showed that the amount of water in regolith is less than 0.1–0.2 weight percent (Christensen et al. 2001).

According to the data from neutron spectroscopy collected by the Mars Odyssey (Feldman et al. 2002), the total water content in the regolith layer on Mars is only up to first percents. Therefore, it appears to be chemically bound water.

Values of thermal inertia (I) vary between 330–380 J m^{-2} K^{-1} $s^{-1/2}$, the rock density (ρ) between 1.0–1.6 g cm^{3} for areas of Viking-1 and 2 landings. Taking into account the magnitude of the volumetric heat capacity (C) as 0.42 kJ kg^{-1} K^{-1}, and the dependence of C on the temperature, theoretical values of the thermal conductivity coefficient λ were in the range of 0.12 to 0.2 W m^{-1} K^{-1} were realized.

These estimates are similar to those actually evaluated on Mars by landing stations. For other sites located in middle and high latitudes of the Northern Hemisphere, values of λ are between 0.07–0.15 W m^{-1} K^{-1}.

Therefore, in spite of the shallow thickness and owing to the low thermal conductivity, the thermal resistance of the regolith layer is very high and could be compared to the resistance of a fresh snow on the Earth with a thickness of 3–5 m.

Results of laboratorial measurements of properties of terrestrial rocks at subzero temperatures

For the analysis and interpretation of rock properties of the subsurface layer on Mars, along with the data on heat capacity (C) obtained for terrestrial samples, it is possible to use experimental measurements of thermal conductivity and the coefficient of linear expansion (Komarov 2003, Isaev et al. 2006). It was determined for a wide range of negative temperatures (down to -120°C) by calorimeter and dilatometer equipment. Values of thermal conductivity for terrestrial rocks were re-estimated in accordance with the average value of near-surface atmospheric pressure (6 mbar). An account was based on the method of Dulnev and Zarichnyak (1974) under the conditions of transitional mode of gaseous medium flux ($2 \geq Kn \geq 0.1$, where Kn os the Knudsen criterion). The coefficient of accommodation was taken for the CO_2 – SiO_2 system (for the Martian atmosphere the main constituent is CO_2 – 95%).

This, with some corrections for rarefaction, corresponds to the coefficient of thermal conductivity of dusty particles.

According to our point of view, the thermal conductivity of the subsurface layer corresponds to coefficient values for dusty particles with a density in the range of 1.15 ± 0.15 g cm^{-3}. The density of surface rocks evaluated by orbital stations, and based on thermal inertia, is 1.2 g cm^{-3}. According to polarimetric analysis, it is 1.0 g cm^{-3} for the layer of some part of mm. Radar shows 1.4 g cm^{-3}, while the analyses of dielectric permittivity estimates 1.2 cm^{-3} for waves in the range of 3.8 to 70 cm.

Calculated evaluations of the thermal conductivity of ice-saturated rocks on Mars by Clifford and Parke were based on the generalized conductivity method. It was taken into account the dependence of ice thermal conductivity on the temperature which is, by far, significantly increased with the lowering of temperature. In our opinion, the value of λ was dramatically overestimated and, as a consequence, the thickness of permafrost was overestimated as well. As provided by experimental data ,some increase of λ can be noted exclusively for the pure hexagonal polycrystalline ice in a volume.

Among the possible explanations for actual decrease of λ in spite of the increase in conductivity of ice, are the following reasons:

(1) Loss of plastic properties of ice and formation of micro cracks within the body of ice starting at -12°C;

(2) Under low temperatures, a different coefficient of linear expansion (α) for ice and for mineral structures plays an important role, resulting in the formation of micro cracks at the mineral-ice interface; and

(3) A coefficient of linear expansion (α) specific to different minerals leads also to the formation of micro cracks.

The total effect of these processes becomes dominant and drives to decreasing of bulk thermal conductivity λ (Komarov 2003, Isaev et al. 2006).

The upper boundary of frozen rocks and ice content in the upper layers

The upper boundary of the frozen rocks was determined by the "impact method" developed in the analyses of surface images of Mars (scale from 1:5000000 to 1:250000) that were collected by Mariner-9, Mars-5 and Viking-1 and -2. This method is based on geomorphologic criterion. Morphological impact features revealed an alteration of upper layers of frozen rocks at different latitudes.

Thus, it was found that geologically young impact sites are often surrounded by radial fluid-like fluxes. It seems to be a result of a melting process in the underlying ice-saturated rocks that appeared after meteoritic explosion in ice-containing rocks. Evaluation of comparative ice-content was proposed by Kuzmin & Zabalueva (2002), who set up the ratio of the debris flow area to the diameter of the impact crater itself. A depth of frozen rock confining layers was also mapped (Kuzmin & Zabalueva 2002). Along with the data from the HEND equipment collected during the Mars Odyssey mission (Feldman et al. 2002), it has been used in our work for the evaluation of ice content in the frozen rocks.

This data shows a significant decrease of epithermal neutrons flux (energy rate 1eV - 0.1 MeV) in the areas of high latitudes caused by the presence of water ice within the subsurface rocks. The water content in a 2 m surface layer was evaluated as 40% by weight for Northern Hemisphere and 23% for Southern hemisphere (for 1-layer model), and to 55% (for two-layer model where dry regolith layer with 2% of water content overlies the subsurface strata).

Influence of overlying rock layers on the occurrence of low margin of frost rocks

Due to well-known peculiarities of ice formation in capillary-pore medium and in independent volume, a modified equation of Claiperon–Clauzius was used for evaluation of pressure (P) on temperature of phase transfer between water and ice. The equation takes into account the possibility of phase equilibrium for the phases under different pressure. In other words, it was assumed that ice of water can be liberated under the Martian atmospheric pressure while the water is subjected by the pressure of overlying layers.

This situation is characteristic for Mars, where strongly dissected basalts and andesites are abundant in subsurface layers due to impact activity. High rarefaction on Mars results in increasing density in liquid and solid phases during the process of degassing, though it makes a negligible correction in evaluations. Therefore, in the estimation of

Table 1. Monthly temperature on Mars according to latitude and season.

Ls	0-30	30-60	60-90	90-120	120-150	150-180	180-210	210-240	240-270	270-300	300-330	330-360	T av. K	T av. C
90 N	148	155	184	217	208	174	152	148	148	148	148	148	165	-108
60 N	174	212	222	224	218	204	186	160	150	150	150	151	183	-90
30 N	220	225	220	220	220	220	215	210	205	205	205	215	215	-58
0	215	215	210	210	215	230	230	230	230	225	225	220	221	-52
30 S	215	205	194	194	205	220	235	245	245	245	240	230	223	-50
60 S	178	150	147	146	146	146	152	210	242	242	228	205	183	-90
90 S	145	145	145	144	143	143	144	145	168	239	223	171	163	-110
average	185	187	189	194	194	191	188	193	198	208	203	191	193	-80

Table 2. Estimated thickness (m) of frosty, frost, and frozen rocks.

Coordinate	Close to North polar cap	60N	30N	0	30S	60S	Close to South pole cap
Average temperature of surface, ºC	-119	-94	-62	-55	-63	-96	-123
Average thickness of regolith, m	0	0.6	1.5	1.8	1.5	0.6	0
Average thickness of frosty rock, m	0	0	150	300	150	0	0
False thickness of frost rock (evaluate on value of thermal resistance), m	0	25	210	370	210	25	0
Average thickness of frozen cryohydrate-content rocks, m	2520	1470	0	0	0	1550	2680
Average thickness of frozen ice-content rocks, m	1250	1250	1100	570	1140	1250	1250
Average summarized thickness of frost rocks, m	3770	2720	1100	570	1140	2800	3930
Average thickness of cryolithosphere (with average thickness of cooled rocks 600 m), m	4370	3320	1850	1470	1890	3400	4530

the temperature on the low margin of frozen rocks and cryolithosphere, terrestrial values were taken for the density of ice and water. The effect of low gravitation on Mars was taken into account when the pressure of overlying strata was evaluated. By operation of the additivity rule, the influence of overlying layer pressure and mineralization of pore solutions could be calculated. The possibility of potential presence of gas hydrates within the frozen rocks was not appreciated.

Effect of mineralization of pore solutions (based on the hypothesis of the existence of brines at depth on Mars)

Salt crusts found by Viking 1 and 2 and by Mars Pathfinder evidence the existence of brines close to the surface. It is characterized by high chlorine and sulfur content in comparison with background rocks. Salt crust formation can be explained by the mechanism of capillary inflow of salty solutions up to the layer subjected to summer temperature fluctuations, as well as by irregular frost penetration. The latter leads to the formation of closed volumes of mineralized brines.

This formation is accompanied by increasing hydrostatic pressure and by subsequent cracking of frost rocks under mechanical stress. Mineralized solutions can be discharged on the surface forming salty crusts after evaporation.

Mineralization of surface layers was observed by Mars Pathfinder and Spirit rovers equipped by alfa-proton spectrometer (APEX) (Rieder et al. 1997) and by Mossbauer spectrometer in Ares valley and in the area of the Gusev impact.

Seasonal monitoring of radar reflectivity in the area of Solar Gulf also confirms the presence of brines in the frozen rocks.

In our opinion, the mechanism of formation of "martian cryopegs" is similar to the terrestrial analogues observed in regions of Central Yakutia, where considerable cryogenic concentration of pore solutions was taking place due to strong evaporation. Salt migration down along the sequence is forced out by frost penetration as a result of the "piston mechanism". Accumulation of mineralized solutions leads to the formation of cryopegs characterized by high salt concentrations that exceed 250 ml/l.

The composition of these brines is presumably magnesium-chlorine-sulfate: ice H_2O + $CaCl_2$ x $6H_2O$ + $MgCl_2$ x 12 H_2O

(the point of the eutectic is around 217K). This isotherm (217K) can be selected as a potential boundary between the zone of frozen H_2O- ice contained and frost cryohydrate contained rocks. It has no analogues on Earth.

The existence of mineralized waters set conditions for the zone of cooled rocks with no ice-content close to the low boundary of frozen rocks which is determined by the 273K isotherm. The upper boundary can be evaluated as additive value of temperature of ice to water phase transfer - 258 K (overlying rocks pressure and mineralization of pore solutions were taken into account).

Conclusions

Based on the estimated values of rocks which are tabulated (Table 2), it is concluded:

1. The average thickness of the frozen rock layer (cryolithosphere) is 2300 m, with some corrections caused by heat flux inflow. This value exceeds the terrestrial analogue but is significantly less than assumed earlier. A hypothesis of the existence of highly mineralized brines on Mars, the influence of the thermal resistance of a dry surface layer of regolith and overlying rocks on the temperature of water-ice formation, was taken into account.

2. The sequence is constrained by layers (from surface): frosty (thickness up to 300 m), frost (thickness up to 3900 m); cooled rocks (thickness up to 600 m) and thawed rocks. Within the frost rocks a cryohydrate-contained layers were identified. It has not been observed on Earth.

The presence of gas hydrates in the frozen rocks of Mars was not discussed due to lack of data.

References

Christensen, P.R. et al. 2001. The Mars Global Surveyor Thermal Emission Spectrometer experiment: Investigation description and surface science results. *J. Geophys. Res*. 106: 23823–23871.

Clifford, S.M. & Parker, T.J. 2001. *Icarus* 154: 40-78.

Dulnev G.N. & Zarychnyak Y.P., 1974, Heatconductivity of fusions and composed materials. *Energia*, 261 pp.

Feldman, W.C., Boynton W. V. & Tokar, R. L.. 2002, Global distribution of neutrons from Mars: results from Mars Odyssey, *Science* 297: 82-84.

Isaev, V.S., Komarov I.A. & Abramenko, O.N. 2006. *Planetary Chronology Workshop*, Abstract #6009.

Jakovsky, B.M. et al. 2000. The thermal inertia of Mars from the Mars Global Surveyor Thermal Emission Spectrometer. *J. Geophys. Res*. 105: 9643.

Komarov, I.A. 2003. *Proceeding of Third Mars Polar Science Conference*, Abstract #8015.

Komarov, I.A. 2003. Thermodynamic and heat mass transfer in disperse frozen grounds. *Scientific Worlds*. 608 pp.

Krass, M. & Merzlikin, V. 1990. *Hydrometeoizdat*, p. 361.

Kuzmin, R.O. 1983. *Cryolithosphere of Mars.* Moscow: Science.

Kuzmin, R.O. & Zabalueva, E.V. 1999 *LPSC*, Abstract 2104.

Kuzmin, R.O. & Zabalueva E.V. 2002. *Computational modeling of ice redistribution process in subsurface layer of Martian regolith on equator under quasi periodical fluctuations of planet axial inclination.* Herald of the Academy of Sciences Department of Geoscience, 1(20).

Rieder, R., Economou, T., Wanke, H. et al. 1997. The chemical composition of Martian Soil and Rocks returned by the Mobile Alpha Proton x-ray spectrometer: Preliminary results from x-ray Mode. *Science* 228: 1771-1774.

www.lmd.jussieu.fr/mars.html.

Geocryological Problems Associated with Railroads and Highways

V.G. Kondratiev
TransEGEM, Moscow, Russia

Abstract

Over the last 10 years, significant new construction of railroads and highways has occurred in Transbaikal and the adjacent territories, including China. Examples of geocryological problems associated with selected railroad and highway locations are presented. Operational reliability, assessment, and monitoring needs are discussed. Emphasis is given to providing comprehensive geocryological exploration efforts, utilizing innovative and intelligent design solutions, allowing for timely and quality construction procedures as well as making provisions for necessary ongoing maintenance. Experience with anti-deformation measures, used for both the Russian and Chinese railroads and highways, utilizing both active and passive methods for strengthening the embankments on ice-rich permafrost, is also presented. In addition, technical solutions involving anti-frost heaving devices for electrical contact-line railway and power line tower supports, is reviewed.

Keywords: embankments; geocryological monitoring; highways; permafrost; railroads; thaw settlement.

Introduction

The history of railways constructed in permafrost regions exceeds more than 100 years: Transbaikalian, Amur, Alaska, Norilsk, Gudson, Labrador, Baikal–Amur (BAM), Amur–Yakut (AЯМ), Yamal, and some other railways in Russia, the USA, and Canada. Construction of each of these railroads provides examples of frozen-ground construction and attempts to provide stable subgrade soils in areas of permafrost and deep seasonal freezing.

Construction in China of the Qinghai–Tibet Railway along the Golmud–Lhasa segment occurred in 2000–2006. This is the newest stage of major railway construction, involving conditions of permafrost and deep seasonal freezing of the soils. The project has included new, large-scale attempts to solve some of the specific problems.

The author was involved with Chinese experts on addressing problems of geocryological concerns along the Qinghai–Tibet Railway and the Qinghai–Tibet Highway over the last 14 years, and in Russia, has been actively engaged in these problems since 1986. Results of his research are reflected in more than 60 technical papers and reports, as well as 5 monographs published in the USSR, Russia, the USA, Canada, Norway, China, Japan, and Finland. Information from these projects and various studies are briefly reviewed in this paper.

Geocryological Problems Associated with Railroads

There has been very limited success in building a railway line that would not undergo deformations resulting from thawing of ice-rich soils or frost heave, induced by freezing of wet foundation soil. These problems are characteristic for all railroads regardless of the length of time in operation. The Transbaikalian Railroad has been in operation more than 100 years, the BAM and the Amur–Yakutsk Main Line, well over tens of years, and the connecting lines Chara–Cheena and Ulak–Elga, only several years. The Qinghai–Tibet Railway has only recently been completed.

Figure 1. Deformations of a track and power line tower support along an electrified section of the Transbaikalian Railroad, km 6278, November 2006.

One of the major problem areas on the Transbaikalian Railroad, located at route segment 6277 to 6278 km, is shown in Figure 1. This segment is known as the “golden” kilometer. At this location, continuing deformation of the embankment and rail-sleeper grating have been occurring since 1949. Train speed limitations of 40 km/h, and sometimes as low as even 15 km/h, have been imposed since 1969, while addition of ballast and rail adjustments are executed annually.

In some places, the ballast has already subsided 5 to 6 m, and subsidence of the railbed has not ceased. This condition is expected to continue for many years, since the embankment was constructed on permafrost soils having a thickness of 25 to 30 m.

On the East Siberian Railroad, in the region of the Kazankan sidings at 1374 km on the BAM, major railway track deformation has been taking place for nearly two decades. From the original four-track lines on this segment, only one remains in service; however, as shown in Figure 2, it also requires nearly-continual maintenance and recurrent refitting. For the last 7 years, 360 million rubles (about 15

Figure 2. Area of severe deformation on the East Siberian Railroad at 1374 km of BAM, September 2003 (photo by E.A. Kozyreva).

Figure 3. Track and power line tower deformation along the Chara–Cheena Railroad, October 2003.

million dollars) have been spent to refit this section of the railroad, but the problem of stabilization remains unsolved. Train speeds are still limited to 15 to 40 km/h, since the threat of unacceptable deformation of the track on this side hill-slope remains. Since this segment of the BAM is electrified, it is critical that the electric contact net and supporting power line towers be repaired as well.

To the north of the Transbaikalia, the Chara–Cheena Railroad was constructed in 2001. The route extends over an area having extremely complex engineering-geocryological conditions involving ice-rich permafrost. In some areas, the underground ice has a thickness of 5 to 10 m. An example of this railway track deformation, occurring under the adverse influence of cryogenic warming processes, is shown in Figure 3.

Sun-Precipitation Protective Sheds

The thawing of permafrost soil under railroad and highway embankments is usually caused by: 1) increased absorption of solar radiation into the subgrade when compared to the natural surface; 2) the infiltration of precipitation through the embankment; 3) an increase in the thickness of snow cover at the base of the embankment and adjacent area; and 4) the migration of surface and subsurface water into the body and base of the subgrade in side-hill slope areas.

Figure 4. Sun-precipitation protective sheds on the Qinghai–Tibet Railway, August 2006.

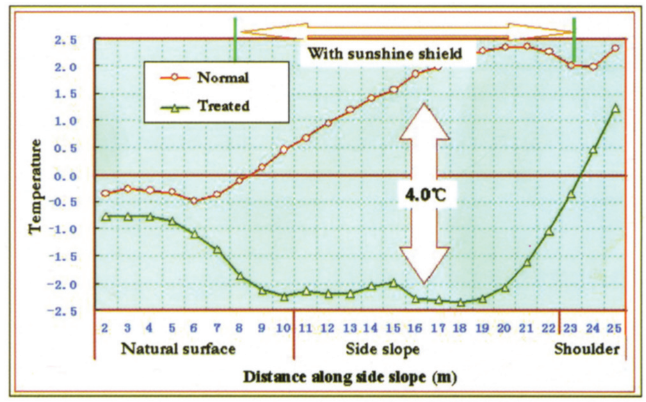

Figure 5. Cooling influence of the sun-precipitation protective sheds, constructed on the embankment slopes of the Qinghai–Tibet Railway.

Several methods of strengthening the base of embankments on ice-rich permafrost have been developed. These methods cause a decrease in the average annual temperature of soils and assist in preserving the permafrost state in a way that reduces warming and improves cooling impacts.

These technical solutions have been presented in articles, reports, and monographs, both in domestic and foreign publications (Kondratiev 1994, 1996, 1998, 2002, 2004, & 2006). The solutions have been applied on experimental projects while constructing the Amur–Yakutia trunk line and the connecting Ulak–Elga Railroad, and while preparing a feasibility study of stabilization measures for use on the Transbaikalian Railroad. Some of these solutions have been applied also on the Qinghai–Tibet Railway in China. An example of the sun-precipitation protective shed applied to side slopes is shown in Figure 4. Data from observations at the full-scale site indicates temperature reductions ranging from 3 to 5ºC in the subgrade soil. This cooling influence, as shown in Figure 5, serves to improve the stability of the subgrade soil on the highly ice-rich permafrost soil (Niu & Shen 2006).

Application of sun-precipitation protective sheds has also been accomplished on Russian railways and highways. On the Amur–Yakut Railway at the approach to the Lena River for tens of kilometers of the railroad, there exists a so-called ice complex, having a thickness of several tens of meters. Excavation or mechanical pre-thawing of this ice thickness is considered to be impractical. Therefore, it has been concluded that this section should be protected from thawing during all periods of railroad operation.

In 2007, a technical study of the application of sheds for preventing degradation of ice-rich permafrost, at the base of an embankment along the Tommot–Kerdem Railway, was initiated at five separate sites. These involved three embankments having heights of 3.48, 6.64, and 7.31 m and two excavations having depths of 2.38 and 5.5 m.

For comparison, at the same sites, thermotechnical calculations of the cooling influence of convective stone/rock covering on the embankments and excavated slopes were executed. Results were found to show a higher efficiency with the sun-precipitation protective sheds for cooling soils in the subgrade of an embankment and prevention of degradation in the underlying permafrost soil, particularly when used in combination with dolomite powder (light-reflecting painting) placed on the surfaces of the basic platform and employment of an antifiltering membrane underneath. Results further indicate that:

- On slopes of both embankments and excavations, the shed-only application provided a decrease of 10 to 31% (average 22.4%) in the depth of the bedding and cover over the permafrost soils along the axis in comparison with the rock covers.
- On the slopes of both embankments and excavations, use of sheds in combination with dolomite powder painted on the surface of the basic platform provided a 25 to 35% (average 30.6%) decrease in the depth of the bedding and cover over the permafrost soils along the axis in comparison with the rock covers.
- On the slopes of both embankments and excavations, use of sheds in combination with the dolomite power painted on the surface of the basic platform and with placement of an antifiltering membrane underneath provided a 28 to 40% (average 34.6%) decrease in the depth of the bedding and cover over the permafrost soils along the axis in comparison with the rock covers. In this case, cooling of the embankment and subgrade soil occurs more rapidly than at sites having rock covers. After only 5 years, the subgrade soils and a substantial part of the body of the embankment exist in the permafrost state, whereas under the rock covers the embankment remained unfrozen, and complete freezing will only occur after 50 years.

Thermotechnical calculations for the Amur–Yakut Highway, as well as experimental research in Tibet, demonstrate that sun-precipitation protective shed applications represent an effective treatment as an anti-deformation device for embankments on railroads and highways at sites containing icy permafrost soils. The positive effect of the shed application is accomplished by both allowing the intensive winter cooling of the embankment and its subgrade, and by both the reduction in infiltration of summer precipitation and the exclusion of direct solar radiation. This helps to preserve the higher strength properties of the frozen soils in the subgrade during all periods. Thus, the design of an embankment becomes simpler, traffic volume and safety improves, and maintenance and repair needs decrease.

Figure 6. Adverse deformation of power line tower supports along the electrified section of the Transbaikalian Railroad, August 2001.

Operational Reliability and Monitoring

Operational reliability of railways and highways in regions of permafrost is predetermined by the choice of constructive-technological solutions and methods of effective execution during construction and subsequent maintenance operations. Constant protection of roads from adverse engineering-geocryological processes, particularly in areas of ice-rich soil, is important in order to provide stability and maintain traffic design speeds. To be most effective, such protection needs to be carried out systematically with emphasis on engineering and geocryological monitoring of the routes. This includes providing regular reviews and controls, technical analysis, and estimations and forecasts of changes in freezing conditions. Such a procedure allows detection and mitigation of undesirable and adverse cryogenic processes. The concept of such a monitoring system was developed for the constructed Berkakit–Tommot–Yakutsk Railroad (Kondratiev and Pozin 2000). In 2001, the concept and process were presented in Beijing and then applied to the Qinghai–Tibet Railway route.

Anti-Frost Heaving Tower Supports

The provision and effective utilization of basic facilities of railways in areas of a permafrost and deep seasonal soil freezing is associated with significant difficulties. As an example, on the Transbaikalian Railroad during the past 10 years (1997 to 2006) at least 17,192 power line tower supports required corrective repairs and 3,294 were replaced. In most cases deformation of support structures were caused by frost jacking within wet friable sediments of seasonally thawed (STL) or seasonally frozen (SFL) layers. Figure 6 provides an example of the extent of tower deformation.

In responding to this problem, a patented solution for an anti-frost heaving measure was developed for the purpose of decreasing the influence of frost heaving forces. This is accomplished by the simultaneous increase in lateral forces on the tower support in STL by freezing and by cooling within long-term frozen soils by means of (a) thermosyphon support in STL, inserted into a hollow reinforced concrete support or metal base; (b) wrapping of an anti-frost heaving sleeve made of nonfreezing grease and a protective casing

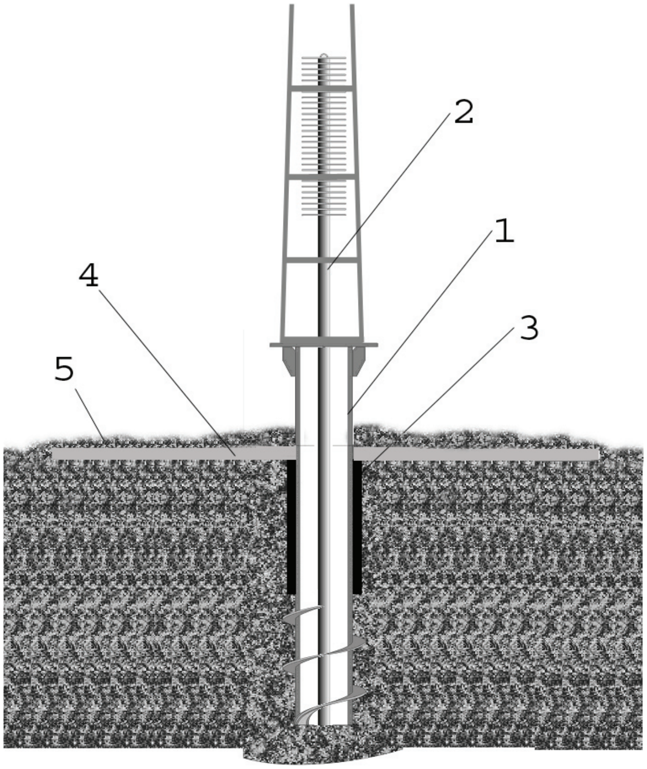

Figure 7. Metal support with screw base (1), with thermosyphon inset (2), anti-frost heaving sleeve (3), thermal insulation (4), and a covering soil layer (5).

made of frost-resistant material; (c) placement of heat and hydroinsulation at the soil surface around the support; and (d) inclusion of a sun-precipitation protective shed around the support and anti-frost heaving sleeve (Kondratiev, 2005).

The anti-frost heaving device design for a metal tower support having a screw base (as shown in Fig. 7) consists of three basic elements: the thermosyphon, the thermal insulation, and the anti-frost heave sleeve.

In October 2003, anti-frost heaving devices consisting of the thermosyphon structure and a 1.25 m long anti-frost heaving sleeve were installed on five tower support pile bases along the Erofey–Pavlovich–Sgibievo segment of the Transbaikalian Railroad.

Work on placing the insulation layer around the support bases and protective soil cover was performed in April 2004, after allowing maximum winter freezeback of the soil around the metal support bases. The elevated portion of the supports was then painted with a white cover.

Analysis of the data recovered since November 2004 shows that, owing to the cooling influence of the thermosyphons, soil freezing near the base (at 0.1 to 0.2 m from the surface) occurred more quickly than at 0.55 to 0.65 m. Around one support, the frozen soil mass, which normally thaws to a depth of 2.5 to 4 m by late autumn, was found to preserve the soil in a constantly-frozen state around the lower portion of the support at a depth of 1.5 to 3 m.

Periodic level surveys were conducted on the top part of the tower supports and have shown that the tower bases having anti-frost heaving devices have remained stable under varying conditions of soil freezing and thawing cycles. Measurements indicate that the vertical movement does not exceed 10 mm, based on a measurement accuracy of a Class III level survey. Whereas, 20 to 30% of the tower bases not having anti-frost heaving devices have begun to heave after 2 to 3 years following installation. Their vertical moving for 5 annual cycles of freezing-thawing have ranged from 10 to 280 mm.

Following verification of the experimental anti-frost heaving devices for the tower support bases, applications have now been extended to electrified rail line projects such as the Karimakaya–Borzya, Burinda–Magdagachi, Mogocha–Amazar, Chernovskaya, and Karimskaya stations. This solution also has the potential for use on other types of tower structures such as signal system devices, high voltage transmission lines, communication structures, and elevated pipelines which are exposed to the negative influence of soil frost heaving.

Geocryological Problems Associated with Highways

Problems with embankment stability of subgrade soils are characteristic for highways within permafrost regions as well. Particularly for the newer “Amur” Highway extending from Chita to Khabarovsk (shown in Figs. 8–10) and the Qinghai–Tibet Highway (shown in Fig. 11).

The federal “Amur”–Chita to Khabarovsk Highway is one of the largest contemporary construction efforts in Russia. Construction of the road, having a length of 2165 km, began in 1978 and is planned for completion in 2010. However, even now, many sections of the road are subject to constant repairs that are not always successful. As an example, the high embankment on the “Amur” Highway, where it passes over Chichon Stream at 247 km, is presented. Here, the uneven subsidence of the 20 m high embankment has been observed since May 2001, soon after the delivery of this highway section. Since that time, as shown in Figure 8, subsidence of the road surface in some places has approached about 2 m, in spite of the periodic addition of soil and the re-leveling to profile grade.

Both transverse and diagonal cracks, having widths of up to 15 to 20 cm, are opening within the roadway, shoulders, and embankment slopes. The pavement surface is also highly deformed. This highway section is in a very distressed condition. The traffic speed for vehicles is now limited to 40 km/h for this section, while the designated design speed is 100 km/h.

During September 2006, the innovative repairs of this 200 m of failing section, as shown in Figure 9, was completed.

Almost 10 million rubles have been spent on repairs to date; however, as shown in Figure 10, deformation of the embankment section continues. The subgrade soil in this section consists of 15 to 20 m of permafrost, with the larger part being ice-rich soils that settle and flow upon thawing. As a result, permafrost degradation and corresponding deformation of the road under the prevailing conditions is expected to continue indefinitely.There are a number of other such examples along the “Amur” Highway. Since much of the route passes through the southern fringe of discontinuous permafrost and also lies within a region of deep seasonal soil freezing, it is evident that an ongoing change in permafrost conditions and deep seasonal freezing will continue. Thus, it is important to identify permafrost conditions along the route, develop systematic means to address or control the cryogenic dynamics that adversely influence elements of the roadway, and initiate the timely application of protective measures. Therefore, in order to provide for a more effective operation of this highway, the system of engineering-geocryological monitoring of the “Amur” Highway was developed under the designation SIGMA “Amur.”

In 2006, the TransEGEM organization developed and submitted to Rosavtodor the concept of SIGMA “Amur.” Following is a summary of the developed concept (Kondratiev et al. 2007):

- The SIGMA “Amur” structure includes information gathering, processing and analysis of information, assessment and information storage, forecasting and projection of protective measures, and application of protection (implementation of protective measures).
- The operating scheme of SIGMA “Amur” provides for a number of regular procedures arranged into cycles for data gathering and processing, assessment of hazardous engineering-geocryological processes, forecasting their future development, and management of unfavorable processes.
- The operating structure of SIGMA “Amur” consists of several subsystems designed for different purposes: hierarchical, project monitoring, and operating subsystems, productive work, and methodical and technical support.
- Primary subjects of SIGMA “Amur” engineering-geocryological inquiry consists of three interrelated parts: geology-geographical, permafrost, and highway conditions.
- The overall program of the SIGMA “Amur” organization emphasizes optimal structure and consistency in practical operations, both with regard to organization and function.
- The plan is to implement a complex program with the aim to set up SIGMA “Amur.” The program has three stages: preliminary stage, setup of information database, and the SIGMA “Amur” operation stage.
- Address proposals on the organization of SIGMA “Amur” operation.

The early creation and functioning of SIGMA “Amur” was intended to provide a more reliable and safe highway that will reduce less unproductive expenditures and improve its operations. Without application of such a concept, the “Amur” Highway will be subject to continuing repairs, constant traffic speed limitations for vehicles, and major financial and material losses.

Figure 8. A section of road on the “Amur”–Chita to Khabarovsk Highway, km 247, before repairs, July 2006.

Figure 9. Same section of road on the “Amur”–Chita to Khabarovsk Highway, km 247, one month after completing innovative repairs, October 2006.

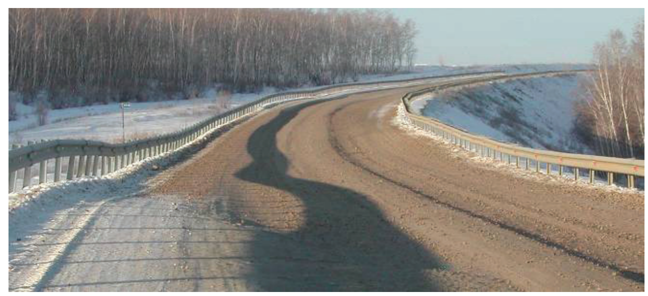

Figure 10. Same section of road on the “Amur”–Chita to Khabarovsk, km 247, eighteen months after completing innovative repairs, March 2008.

Figure 11. Deformation and displacement of an embankment slope on the Qinghai–Tibet Highway as a result of permafrost degradation outside the influence area of the thermosyphons, August 2006.

In the 1950s the Qinghai–Tibet Highway was constructed with a gravel-crushed stone coating. In the 1980s, it was reconstructed, and in may sections, asphalt pavement was applied. This black pavement surface accelerated degradation of permafrost within the subgrade, producing significant surface deformations in those sections having ice-rich soils. Also, those subgrades having frost heaving soils were adversely impacted (Wu et al. 1988). Recently the highway was reconstructed to meet contemporary high-speed vehicle standards. The highway, in essence, traverses parallel with the Qinghai–Tibet Railway. The highway has a hard-surfaced pavement and utilizes anti-frost heaving measures in the sections having ice-rich soils. At some of these locations, thermosyphons have been placed in the form of one or two lines along roadway shoulders; however, as can be seen in Figure 11, some embankment problems have begun to occur. It is also expected that the thermosyphons will not protect the road from thermokarsts because of their limited radius of cooling.

Conclusions

In conclusion, it is felt that the above information again demonstrates that, in order to achieve stable and reliable transportation routes in regions of permafrost and deep seasonal frozen soils, it is critical that a system be utilized which provides comprehensive geocryological exploration and evaluation, uses innovative and intelligent design solutions, allows timely and quality construction procedures, and provides for necessary ongoing maintenance.

References

Kondratiev, V.G. 1994. Strengthening of roadbed base on very icy permafrost soils. *Abstracts of International Conference on Arctic Margins, Magadan, 1994.*

Kondratiev, V.G. 1996. Strengthening railroad roadbed bases constructed on icy permafrost soils. *Proceeding of Eighth International Conference on Cold Regions Engineering, Fairbanks, Alaska, 1996*.

Kondratiev, V.G. 1998. Measures to control deformation of roadbeds on icy rich permafrost. *Proceeding 8th Congress of International Association for Engineering Geology and the Environment. Vol. V. Vancouver, Canada, 1998:* 3365-3371.

Kondratiev, V.G. 2002. Design and experience controlling railroad embankment deformation on ice-rich permafrost. *Proceeding of the Eleventh International Conference, Cold Regions Impacts on Transportation and Infrastructure, Anchorage, 2002:* 467-482.

Kondratiev, V.G. 2004. Problems and ways of permafrost preservation in the roadbed basis. *Journal of Glaciology and Geocryology* (26) Supplement Aug. 2004: 8-11.

Kondratiev, V.G. 2005. Stabilization of roadbed and contact-line and air line supports on permafrost. Chita: Chitgu, 241 pp. (in Russian).

Kondratiev, V.G. 2006. The active methods of stabilization of roadbed and contact-line and air line supports on permafrost. *Abstracts of Asian Conference on Permafrost. Lanzhou, China, August 7–9, 2006:* 57-58.

Kondratiev, V.G. & Pozin V.A. 2000. *Concept of the System of Engineering-eocryological Monitoring of the Berkakit–Tommot–Yakutsk Railway.* Chita: Zantrans, 84 pp. (in Russian).

Kondratiev, V.G., Soboleva, S.V. & Dementiev A.D. 2007. Concept of the engineering-geocryological monitoring of the Chita–Khabarovsk federal highway “Amur.” *Proceedings of the 8th International Symposium on Cold Region Development. Tampere, Finland, September 25–27, 2007:* 199-200.

Niu, F. & Shen, Y. 2006. *Guide of Field Excursion after Asian Conference on Permafrost (August 10–16, 2006).* Lanzhou, China.

Wu, Z. et al. 1988. *Roadbed Engineering in Permafrost Regions*. Lanzhou University.

The Influence of the Winter Season on Active Layer Depth in Taiga Landscapes, the Yakutsk Vicinity, East Siberia

P.Y. Konstantinov
Melnikov Permafrost Institute SB RAS, Yakutsk, Russia
R.N. Argunov
Melnikov Permafrost Institute SB RAS, Yakutsk, Russia
E.Y. Gerasimov
Melnikov Permafrost Institute SB RAS, Yakutsk, Russia
I.S. Ugarov
Melnikov Permafrost Institute SB RAS, Yakutsk, Russia

Abstract

This paper presents the results of investigations on interannual variability of seasonal thaw depth in the taiga landscapes on the Lena-Kenkeme watershed in the vicinity of Yakutsk (East Siberia). The results of our investigations indicate that the depth of seasonal thaw is more strongly related to the interannual variation of winter ground heat loss than to the interannual variation of air thawing index or total summer precipitation.

Keywords: active layer; ground heat storage; ground temperature; seasonal thaw depth; soil moisture content.

Introduction

The necessity of considering wintertime heat losses from the ground when analyzing seasonal thaw patterns is dictated by the specifics of the heat balance of the ground layer in contact with the atmosphere. The greater the winter heat loss from the ground (within the entire depth of annual heat exchange), the larger the amount of heat required for preliminary ground warming in the summer. Correspondingly, there will be some reduction in the proportion of the heat expended on phase transformation of soil moisture, and hence less energy will be available for deep summer thawing of the soil.

The winter heat loss from the ground shows strong variations from year to year. It is greater in years with thin snow cover and lower in those with deep snow. There are, however, no accurate methods for measuring or estimating this quantity. The intensity of winter cooling can be qualitatively characterized by the mean annual ground temperature at the active layer–permafrost boundary (t_ξ), because in permafrost areas the winter season plays a decisive role in the development of the ground thermal regime. Compared to the amount of ground heat exchange, t_ξ is easier to determine experimentally and is found by standard measurements with temperature sensors permanently installed in the ground. The t_ξ value is lower in the years of increased winter heat losses from the ground and is higher in years with reduced winter heat losses. Thus, the effect of variations in the winter ground heat loss on summer thaw depth can be estimated by investigating the relationship between thaw depth and interannual variation in mean annual ground temperature.

Methods

A modified design of the Danilin-type frost gage developed for Russian weather stations was used in this study. This device determines the 0°C isotherm within the ground from the position of the thawed/frozen interface in the measuring tube with distilled water, which is removed for reading from the pipe that is permanently installed in the ground. The Danilin frost gage has two important advantages. First, determination of the 0°C isotherm in the surrounding ground from phase change of water in the measuring tube provides a sufficiently reliable measurement, requires no preliminary calibration, and has virtually unlimited time stability. Even if there is some difference between the position of the 0°C isotherm determined by the frost gage and the actual position of the phase boundary (or the top of plastic frozen soil in clay material) due to different freezing points of the soil and the tube water, this will not affect statistical parameters of the time series since the error will be systematic. Second, the use of the frost gage ensures that measurements are made at the same location each year; this eliminates the potential effects of spatial variation.

Many years of experience have shown that the Danilin frost gage provides accurate estimates of thaw depth, but that it is not satisfactory for the study of active layer freezing. Therefore, a considerably simplified design of the Danilin frost gage intended exclusively for determination of summer thaw depth has been used in this study. This design does not use an extractable measuring tube, eliminating air convection into the soil. The simplified version of the frost gage consists of a polypropylene tube with an outer diameter of 25 mm and an inner diameter of 20 mm, whose length exceeds the maximum possible thaw depth at a site. The tube is waterproof and sealed at the bottom. The sealed bottom is lowered into a small-diameter hole drilled for thaw depth measurement. The annulus is backfilled and thoroughly compacted. Then the tube is filled with distilled water to the ground surface level. The position of the 0°C isotherm in the ground is determined by a metal tape whose end is lowered into the frost gage tube to the water/ice interface at the time of measurement.

Experimental investigations were conducted in taiga landscapes in the vicinity of Yakutsk (East Siberia, 62°N, 129°E). The thermal research program was initiated in 1996 (Konstantinov et al. 2001, Konstantinov & Fukuda 2001, Fedorov et al. 2003).

Experimental sites 1, 2, and 3 are located on the erosional plain (southern part of the study area) where the active layer consists predominantly of fine-grained sands (dry density 1100-1800 kg/m^3; 75%–85% sand, 8%–11% silt, and 6%–15% clay) and silty sands (dry density 1200–1750 kg/m^3; 61%–67% sand, 25%–29% silt and 6%–10% clay). Sites 4, 5, and 6 are located in the erosional-aggradational plain (northern part of the study area) where the soils consist mainly of silts (dry density 960-1700 kg/m^3; 19%–47% sand, 41%–66% silt, and 7%–20% clay).

Experimental site 1: Middle part of a long, gentle north-facing slope. Soils: sands and silty sands. Vegetation: *Laricetum arctouso-vacciniosum*.

Experimental site 2: Ridge crest. Soils: sands. Vegetation: *Lariceto-pinetum limnoso-arctostaphylosum*.

Experimental site 3: Upper part of a long, gentle north-facing slope. Soils: sands and silty sands. Vegetation: *Lariceto-betuletum limnoso-vacciniosum*.

Experimental site 4: Inter-alas surface surrounded by mature and growing thermokarst depressions. Soils: silts. *Mixtoherboso-graminosum* meadow.

Experimental site 5: Dry area on the bottom of a large thermokarst depression (alas). Soils: silts. *Mixtoherboso-graminosum* meadow.

Experimental site 6: Inter-alas surface. Large clear-cut area in larch forest where tree stands were removed in the early 1990s. Soils: silts. Vegetation: secondary growth of grasses and fragments of the low-shrub layer.

Results

The values of basic meteorological variables for the period of investigation are presented in Table 1, using a provisory year starting from 1 October and ending on 30 September, so that one winter season would not fall in two different calendar years. Double figures are used; e.g., 1997/1998, 1998/1999, etc. The data indicate that the main meteorological parameters have strong interannual variability in the study area, resulting in significant interannual variations of mean annual ground temperature (Table 2). The maximum difference in t_ξ has been 1.5°C–3.2°C in absolute values.

Interannual variations in maximum annual thaw penetration at experimental sites are given in Table 3. For the observation period, the standard deviation of thaw depth is 0.07–0.14 m, and the coefficient of variation is 0.04 to 0.09. As is seen, seasonal thaw depth is less variable than mean annual ground temperature, whose coefficient of variation is 0.25–0.47 for the same period. This fact imposes more stringent requirements on the instruments and methods used in field experiments. The use of only mechanical probing or soil temperature profiles in the study of interannual variation in seasonal thawing can result in errors, since these methods give less accurate estimates than the frost gage. This is especially critical in southern permafrost regions where active layer thicknesses exceed 1 m.

Tables 1 and 3 show that there is no obvious relationship between the active layer thickness and the air thawing index. Data for the period 2005–2007 confirm this conclusion. Interannual variations in the degree-days sum at the ground cover surface (May-September) are plotted in Figure 1. It is seen that the surface thawing index decreased in 2005–2007, but the depth of thaw and the mean annual ground temperature increased.

There is also no strong relationship between the seasonal thaw depth and the total summer precipitation. The years with the deepest (1999/2000) and shallowest (2000/2001) thaw penetration had total summer rainfall of 126 and 68 mm, respectively. The effect of precipitation on seasonal thaw depth appears not to be a major determinant here with this small difference in precipitation totals, considering that their range over the observation period was 68 to 256 mm. A distinct relationship between thaw depth and summer precipitation was only observed at Site 1 located in the middle part of a long, gentle slope with a larch stand on sandy soils (Tables 1, 3). In 1998/1999, 2004/2005, 2005/2006, and 2006/2007 high suprapermafrost groundwater flow occurred at this site after heavy rains, resulting in the deepest thaw.

Tables 2 and 3 and Figure 1 show that seasonal thaw depth increased in years with higher mean annual ground temperatures (1999/2000, 2004/2005, 2005/2006, and 2006/2007) and decreased in years with lower t_ξ (2000/2001, 2001/2002, 2002/2003, and 2003/2004). During the period of observations, t_ξ was warmest in 1999/2000. In that year most sites experienced maximum thaw depths, while air thawing indices and rainfall totals were within the average range of the series variation. The best agreement between the interannual variability of thaw depth and that of mean annual temperature was observed at sites with the minimum t_ξ difference over the observation period (Site 6).

If we compare thaw development in four years with the coldest ground temperatures (2000/2001, 2001/2002, 2002/2003, and 2003/2004), it is seen that the depth of thaw was not shallowest in the coldest year 2002/2003. This discrepancy can be explained if one compares pre-summer soil moisture contents in these years, which were 1.5–1.8 times higher in 2000/2001 and 2003/2004 compared to 2001/2002 and 2002/2003 (Fig. 2). This is the reason for minimum thaw in 2000/2001 and 2003/2004: greater heat loss is required for phase change of soil moisture under the conditions of increased seasonal ice content in the active layer. Shallower thaw depth at Site 2, which experienced warmer ground temperatures in 2006/2007 compared to 2005/2006 can also be attributed to the effects of variations in seasonal ice content. Many investigators have shown that opposite trends in thaw depth can occur over short distances. One possible explanation is the effect of seasonal ice content in the active layer, because ground conditions vary greatly over

Table 1. Meteorological parameters over the observation period.

Meteorological parameter	1997 / 1998*	1998 / 1999*	1999 / 2000*	2000 / 2001*	2001 / 2002*	2002 / 2003*	2003 / 2004*	2004 / 2005*	2005 / 2006*	2006 / 2007*
Σ_{-t}	-5051	-5341	-5026	-5529	-4658	-5022	-5109	-5394	-5053	-4709
Σ_{+t}	2158	1964	1941	2014	2139	1996	1821	2087	2034	2019
$t_{m.a.}$	-8.0	-9.4	-8.6	-9.8	-7.0	-8.4	-9.2	-9.2	-8.4	-7.5
R_s	146	196	126	68	89	243	128	199	256	191
h_{sn}	0.27-0.29	0.29-0.32	0.32-0.38	0.16-0.20	0.22-0.25	0.10-0.16	0.15-0.18	0.40-0.45	0.38-0.42	0.36-0.40
$h_{sn\ max}$	0.40-0.45	0.43-0.48	0.40-0.45	0.27-0.30	0.42-0.48	0.26-0.29	0.30-0.38	0.50-0.60	0.43-0.47	0.50-0.55

Explanations: * - the annual period from 1 October to 30 September; Σ_{-t}, Σ_{+t} - sum of freezing and melting degree-days (Yakutsk station); $t_{m.a.}$ - mean annual air temperature (Yakutsk station), °C; R_s - summer precipitation, mm (Yakutsk station); h_{sn} - depth of snow cover at the experimental sites (data are as December 1), m; $h_{sn\ max}$ - maximum depth of snow cover at the experimental sites (data are as March 1), m.

Table 2. Mean annual ground temperature at experimental sites over the observation period.

Site	Mean annual ground temperature, °C										Average value	Standard deviation	Coefficient of variation
	1997 / 1998	1998 / 1999	1999 / 2000	2000 / 2001	2001 / 2002	2002 / 2003	2003 / 2004	2004 / 2005	2005 / 2006	2006 / 2007			
1	-2.5	-2.6	-1.6	-2.9	-3.0	-3.4	-3.2	-2.6	-1.4	-1.2	**-2.4**	**0.77**	**0.32**
2	-1.7	-1.7	-0.9	-2.2	-2.0	-2.7	-2.4	-1.7	-1.0	-0.6	**-1.7**	**0.68**	**0.40**
3	-1.6	-1.6	-0.8	-1.9	-1.9	-2.3	-2.2	-1.8	-0.9	-0.6	**-1.6**	**0.59**	**0.38**
4	-2.2	-2.0	-1.5	-1.8	-1.7	-2.7	-2.3	-1.6	-1.5	-1.1	**-1.8**	**0.47**	**0.25**
5	-2.6	-2.4	-1.4	-2.5	-2.6	-3.2	-3.0	-2.0	-1.5	-0.8	**-2.2**	**0.76**	**0.35**
6	-1.8	-2.0	-1.2	-2.8	-3.4	-4.4	-3.4	-2.1	-1.4	-1.1	**-2.4**	**1.10**	**0.47**

Table 3. Maximum depth of summer thaw at experimental sites over the observation period.

Site	Depth of summer thaw, m										Average value	Standard deviation	Coefficient of variation
	1997 / 1998	1998 / 1999	1999 / 2000	2000 / 2001	2001 / 2002	2002 / 2003	2003 / 2004	2004 / 2005	2005 / 2006	2006 / 2007			
1	1.50	1.57	1.52	1.46	1.52	1.54	1.37	1.62	1.60	1.67	**1.54**	**0.09**	**0.06**
2	2.01	1.97	2.08	1.91	1.92	2.01	1.94	2.12	2.17	2.10	**2.02**	**0.09**	**0.04**
3	1.83	1.88	1.91	1.73	1.83	1.80	1.71	1.90	1.97	1.98	**1.85**	**0.09**	**0.05**
4	1.85	1.77	2.07	1.63	1.86	1.81	1.79	1.96	2.00	2.03	**1.88**	**0.14**	**0.07**
5	1.76	1.80	1.84	1.66	1.77	1.76	1.71	1.82	1.84	1.90	**1.79**	**0.07**	**0.04**
6	1.53	1.49	1.66	1.39	1.43	1.44	1.39	1.62	1.65	1.77	**1.54**	**0.13**	**0.09**

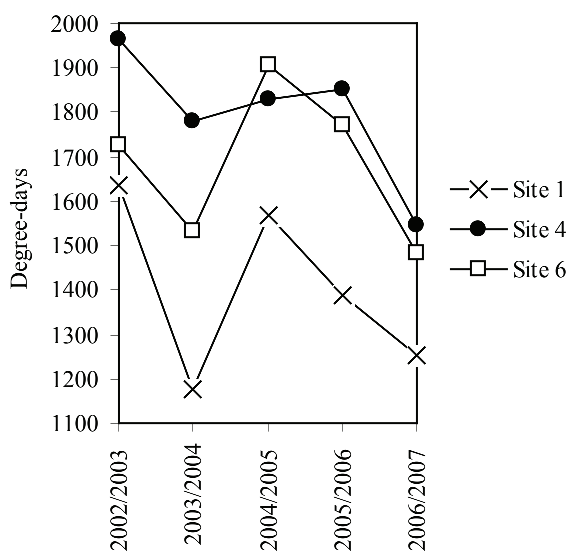

Figure 1. Interannual variations of degree-days sum at the ground cover surface.

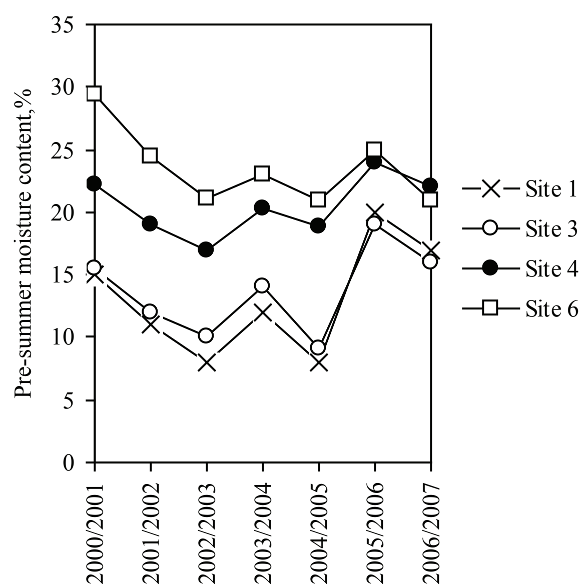

Figure 2. Interannual variation in the pre-summer moisture contents of the active layer (averages for the entire active layer profile).

space. Adjacent sites can therefore experience very different thaw rates if they show dissimilar variations in seasonal ice content from year to year. These examples demonstrate that soil moisture is an important consideration in the study of interannual variability of seasonal thaw depth.

Data on the effect of winter factors on active layer thickness are available mostly for the regions with a continental climate, such as Central Yakutia and northern Tian Shan (Blagoobrazov 1964, Skryabin et al. 1998, Marchenko 2002, Konstantinov et al. 2006). For the coastal regions of the permafrost zone, the depth of thaw has been found to be more sensitive to summer factors, mainly the thawing index (Brown et al. 2000, Leibman 2001, Fedorov-Davydov et al. 2004, Mazhitova & Kaverin 2007).

Conclusions

The results of our investigations indicate that in the taiga landscapes of the Yakutsk area, the depth of seasonal thaw is more strongly related to the interannual variation of winter ground heat loss than to the interannual variation of the air thawing index or total summer precipitation. This suggests that in years with warmer summers, the heat surplus at the ground surface is largely expended to increase eddy heat flux and latent heat flux, with only a small portion spent on heat flow into the soil. One of the major factors controlling seasonal thaw depth is soil moisture content in the active layer, which deserves a more in-depth study to develop a better understanding of the problem.

The findings of this study and other studies indicate that the relationship of active layer depth to winter factors is much stronger in the continental areas than in the coastal regions.

Acknowledgments

This study received partial financial support from Japan Science and Technology Corporation (JST) and Japan Agency for Marine-Earth Science and Technology (JAMSTEC).

References

Blagoobrazov, V.A. 1964. Seasonal and long-term fluctuations of the permafrost table in flatlands of Central Tien Shan. In: *Glaciological Investigations in Tien Shan.* Frunze: Kyrghyz Academy of Sciences Press, 65-76.

Brown, J., Hinkel, K.M. & Nelson, E.F. 2000. The Circumpolar active layer monitoring (CALM) program: research designs and initial results. *Polar Geography* 24(3): 165-258.

Fedorov, A.N., Gavriliev, P.P. & Konstantinov, P.Y. 2003. Study of permafrost-landscape dynamics at Spasskaya Pad. *J. Nauka I Obrazovanie* 3: 62-65.

Fedorov-Davydov, D.G., Davydov, S.P. & Davydova, A.I. 2004. Spatial and temporal regularities of soil seasonal thawing in the north of the Kolyma lowland. *Kriosfera Zemli* VIII(4): 15-26.

Konstantinov, P.Y., Argunov, R.N. & Gerasimov, E.Y. 2006. On the relationship between seasonal thaw depth and interannual variation of mean annual ground temperature. *Kriosfera Zemli* X(3): 15-22.

Konstantinov, P.Y., Rusakov, V.G. & Fukuda, M. 2001. Thermal Regime of the Upper Permafrost Layers in Taiga Landscapes, Yakutsk Area, 1996-2000. *Proceedings of the 9th Symposium on the Joint Siberian Permafrost Studies between Japan and Russia in 2000*. Sapporo: Hokkaido University, 204-209.

Konstantinov, P.Y. & Fukuda, M. 2001. Temperature Regime of the Upper Permafrost in the Yakutsk Area *Proceedings of the Second International Workchop on Global Change: Connection to the Arctic.* Sapporo: Hokkaido University, 103-106.

Leibman, M.O. 2001. Active-layer dynamics and measurement technique at various landscapes of central Yamal. *Kriosfera Zemli* V(3): 17-24.

Marchenko, S.S. 2002. Results of monitoring of active layer in the northern Tien Shan Mountains. *J. Kriosfera Zemli* VI(3): 25-34.

Mazhitova, G.G. & Kaverin, D.A. 2007. Thaw depth dynamics and soil surface subsidence at a Circumpolar active layer monitoring (CALM) site, the European north of Russia. *Kriosfera Zemli* XI(4): 20-30.

Skryabin, P.N., Varlamov, S.P. & Skachkov, Y.B. 1998. *Interannual Variations in the Ground Thermal Regime, Yakutsk Area.* Novosibirsk: SB RAS Press, 144 pp.

Landscape Geochemical Features and Peculiarities of ^{137}Cs Distribution in Tundra Landscapes of the Lower Pechora Reaches

E.M. Korobova
Vernadsky Institute of Geochemistry and Analytical Chemistry, Russian Ac. of Sciences
N.G. Ukraintseva
All-Russia Research Institute for Pipelines
V.V. Surkov
Moscow State University

Abstract

Distribution of natural and man-made chemical elements in soils and vegetation of modern landscapes of the Lower Pechora floodplain and the adjacent terrace was studied along landscape transects crossing the floodplain and terrace zones at different distances from the coast (Bolvansky Cape) to the settlement of Bol'shaya Sopka to reveal peculiarities due to landscape structure and natural migration processes. River water was characterized by low salinity (35–131 mg/l) and hydrocarbonate-calcium composition, while groundwater was comparatively enriched in magnesium, sodium, chlorine ions (39, 26, 31 meq%) and water-soluble organics (peaty areas, 540–2450°, Pt-Co scale). The concentration of ^{137}Cs in soils and vegetation was within the global fallout level, but varied considerably (2.5–215 Bq/kg and 24–365 Bq/kg dry weight, correspondingly) in relation to hydrological, landscape, and soil features of the area, the plant species enabling discussion of the recent history of migration processes in landscapes after man-made contamination.

Keywords: ^{137}Cs in soils and plants; landscape geochemistry; Lower Pechora; radioecology; radionuclide profiles.

Introduction

Draining vast areas, the rivers of the Arctic basin play an important role in its material balance on its margins rich in bioresources. The Pechora River basin belongs to an area with minor man-made impact and is, therefore, of interest for monitoring global man-made contamination and its history in high-latitude permafrost regions. Being a ubiquitous artificial marker of contamination, ^{137}Cs has been included in natural processes for more than 50 years and can serve as the tracer of spatial transformation of aerial contamination in modern landscapes. The objectives of this study were to reveal landscape heterogeneity and peculiarities of ^{137}Cs redistribution in the Lower Pechora area. The two main morphological elements, namely the floodplain and terrace area, were selected to compare the river transport and in situ migration with permafrost impact.

Study Area and Methods

Field studies were performed in the area of the Lower Pechora basin in 2003 and 2004. The strategy of investigation was similar to that applied in the Lower Yenisey reaches (Korobova et al. 2007). A series of landscape transects crossing the floodplain and terrace zones were located at different distances from the coast: Cape Bolvansky, Yushino settlement on the right river side, the upper delta Ekushnaky (EK) and Kermundei (KM) Islands, the right river side near Naryan Mar, and on the left high terrace near Bol'shaya Sopka (Table 1). Soil, water, and plant samples were taken at the selected sites characterizing the two main geomorphological levels. They correspond to terraces and flooding zones in order to compare radiocesium distribution in landscape components under atmospheric water migration and river transport. The location of study sites in a meridional seaward direction was to follow the marine impact and the delta island formation.

Soil profiles were sampled continuously, with sampling increments ranging from 2–10 cm to a depth of 40–100 cm. Vegetation was described by species composition and abundance and sampled at 0.25 m^2 plots located over the soil profiles. Surface and groundwater samples collected at selected points of the cross section were filtered, sealed, and preserved in a dark freezer (-5°C) for transportation to the laboratory. Ion composition of water samples was determined with the help of ion selective electrodes (NO_3^-, Cl^-), titrimetry (HCO_3^-), nephelometry (SO_4^{2-}), photometry (NH_4^+, PO_4^{3-}) techniques and AES-ICP (cations). Accuracy of determination did not exceed 5%.

^{137}Cs and ^{40}K were determined in soil and plant samples with the help of a Canberra gamma-spectrometer with an HPGe detector. ^{137}Cs determination error equaled on the average 31% and 33% (soils and plants), ^{40}K – 19% (soils), correspondingly, depending upon the concentration level.

Chemical Composition of the Surface and Ground Water on Terrace and Flood Plain

Water samples were analyzed to characterize ^{137}Cs water migration conditions (Sanchini 1988). Salinity and colority of water, as well as suspended load, considerably varied in their type, landscape position, and distance from the sea

Table 1. Sampling plots location.

Location	Sampling plots indices	Geomorphology	Soil and vegetation cover	Active layer depth, cm	Sampling depth, cm
Cape Bolvansky, 3,5 south from the Pechora mouth	A3p	III marine terrace, top of the hill	Polygonal undershrub-lichen tundra	110	120
	A11	Terrace backslope	Shrubby tundra, peaty soil on buried peaty gley	>180	180
	P1	Alluvial-marine floodplain, flat ridge on its shoulder	Polygonal undershrub-lichen tundra, lichen polygon with alluvial humus-peaty gley soil	80	30
	P2	Inter-ridge depression on the riverside coastal floodplain	Willow with horsetail-reedgrass-sedge tussock cover on humus-peaty soil with buried humus-peaty layer	Bed talik	30
Lower delta, near set. Yushino	Yu1	Low glacial-marine terrace, flat rise on the summit	Polygonal lichen tundra with undershrub, peaty gley loamy soil with detritus	>90	70
	Yu2	The talf close to the edge of the terrace	Undershrub-sphagnum-lichen peat on humus-peaty soil	42	45
Lower delta, Gluboky Island	Gl1	Frontal part of the plain 1.5 m above low water level (LWL)	Willow stand with horsetail-reedgrass-meadow sweet overground cover on soddy-gley sandy loam soil	Bed talik	125
Southern suburbs of Naryan Mar	NM2-03	II High terrace	A fragment of the old spruce forest with thick moss-lichen cover on tundra forest sandy soil	>80	-
Medium delta, 200 m from set. Iskateli	NM3	I high terrace, 11.6 m above LWL	Birch-larch elfin forest with moss-lichen cover on oddy-weakly podzolized soil developed on humus-podzolic illuvial-ferrugenous sandy soil	>140	120
	NM6	Sandy dunes on the edge of the terrace 4.3 m above LWL	Exposed profile Aeolian sand covering buried soddy-podzolic soil	>400	125
Medium delta, right side coastal floodplain	NM4	Inter-ridge abandoned channel 1,0 m above LWL	Willow shrubs sedge-herbaceous on soddy laminated loamy sand soil	Bed talik	30
	NM5	Riverside alluvial ridge of the low level floodplain	Willow shrubs with pioneer herbages on primitive weakly soddy laminated sandy soil	Bed talik	50
	NM1a	Inter-ridge depression	Herbaceous-sedge wet meadow with horsetail and willow restoration on silty-gley soil	Bed talik	80
Medium delta, Ekushansky Island	EK1	Exposed profile of the low level floodplain	Light herbaceous-grass cover (surface coverage – 10%), soddy sandy soil on laminated alluvium	Bed talik	190
	EK2	Exposed profile of the medium-level coastal floodplain	Herbaceous-grass meadow with high willow, soddy sandy soil overlain buried soody gley soil underlain by peaty silty gley soil	Bed talik	66
Medium delta, Kermundej Island	KM1	Edge of abandoned channel between the two former isles, 27 cm above LWL	Wet tussock sedge meadow on silty-gley soil	Bed talik	67
	KM2	Western toeslope to central depression	Herbaceous-reedgrass-sedge meadow on soddy-gley loamy soil on sandy alluvium	Bed talik	85
	KM3	Riverside ridge of the high floodplain 3,90 m above LWL	Thin high willow with horsetail stand on primitive weakly sod laminated soil	Bed talik	90
	KM4	Wide inter-ridge depression.	Bushy willow thicket with grass and horsetail on soddy gleyish loamy soil on sandy and loamy alluvium	Bed talik	125
	KM5	Ridge on the medium-level floodplain abruptly sloping to the young depression	Bushy willow with herbaceous-leguminous-grassy cover on soddy light loamy laminated soil on sandy alluvium	Bed talik	90
	KM6	Medium level floodplain 3,6 m above LWL.	High willow with alder and herbaceous-leguminous-grassy cover stand on soddy sandy loam soil	Bed talik	90
Near set. Bolshaya Sopka	BS1	High terrace on the left riverbank	Polygonal moss-lichen tundra with undershrubs on peaty gley soil developed on pebbled moraine loams	86	90
	BS2	Flat shallow depression on the terrace	Undershrub-lichen-moss peat on humus-peaty-gley soil	43	53

(Table 1). The Pechora River water was characterized by neutral pH value, low salinity (0.07–0.13 g/l) and colority except for its deep inlet at Kermundej Island (Table 2). Water salinity was the highest in the soil water on Cape Bolvansky terrace (0.193 g/l) close to the sea aquatory. The adjacent terrace foot and the lower floodplain groundwater were much fresher (<0.06 g/l) due to river impact. Low water salinity not exceeding 0.05 g/l was observed on the peaty watersheds upstream, while soil water of the islands and the river water were two times the value. Salinity correlated

Table 2. General characteristics of water samples

Sampling places	Water type	Suspension, g/l	Colority, grad	Salinity, mg/l
1. Cape Bolvansky	r*			70
2. Gluboky Shar	r	0,172	35	131
3. Gorodetsky Shar	r	0,116	16	129
4. Kermundej Island	r	0,106	35	131
5.Creek at Kermundej Island	r	0,099	135	109
6. Naryan Mar (2003 year)	r			94
7. Naryan Mar (2004 year)	r	0,083	26	131
8. Naryan Mar	tap	-	10	118
9. Yushino terrace (Yu2)**	gr	0,891	2450	39
10. Yushino terrace peat	pt	0,141	620	45
11. Yushino Lake	l	0,165	82	35
12. Kermundej low floodplain (KM1)**	gr	0,420	26	164
13. Kermundej Island , abandoned channel	l	0,120	55	113
14. Ekushansky Island, Rybnoe Lake	l	0,121	45	87
15. Bolshaya Sopka peat	pt	0,419		70

* r – *Pechora River*; l – *lake*; pt - *peat*; gr –*ground*.
** Sampling plots indices – see Table 1.

with pH (r=0.701, n=14) and water hardness (r=0.895). A tendency of negative relation was observed between salinity and colority (r=-0.528, n=13).

Peaty areas were noted for enhanced colority of water (up to 2450º, Pt-Co scale) due to soluble organic substances most abundant in the active layer of tundra humic gley soils. Suspended load determined varied from 0.1 to 0.8 g/l and increased in the groundwater of organic soils (Tables 1, 2).

Ion composition

Ion composition of ground-water presented in Figure 1 proved considerable leaching of the former marine sediments developed on Cape Bolvansky terrace. However, relatively high chlorine, magnesium, and low hydro-carbonate ion content indicate the marine contribution. The Pechora water near Cape Bolvansky was relatively enriched in sodium. A higher percentage of sodium and potassium ion content was found in the groundwater of Yushino soils. Pechora River water was relatively enriched in chlorine (up to 0.4 meq/l) and sodium (maximum 0.28 meq1/l) as compared to groundwater collected from soil cuts on the adjacent coastal zone and terraces (0.23 meq/l and 0.17 meq/l correspondingly). Chlorine, sulphate ions, and strontium content in the river water slightly decreased upstream, while potassium concentration in river water increased upstream (from 0.6 mg/l to 1.1 mg/l) being in general lower as compared to groundwater (up to 1.7 mg/l in the latter).

Terrestrial water compared to the river was noted for enhanced content of NH_4^+ (0.4–2.6 mg/l) and PO_4^{3-}, the highest nitrate ion amount NO_3^- (0.03–013 meq/l), and a large value of chemical oxygen demand (130–433 mgO_2/l,) in

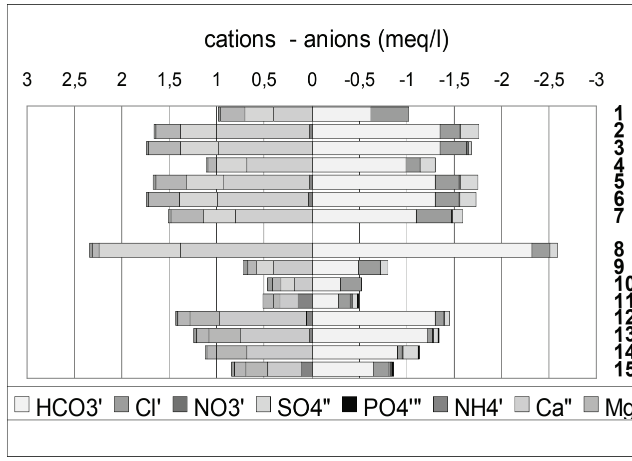

Figure. 1. Chemical composition of water samples positioned in southward direction. 1–15 - sampling places, see Table 2.

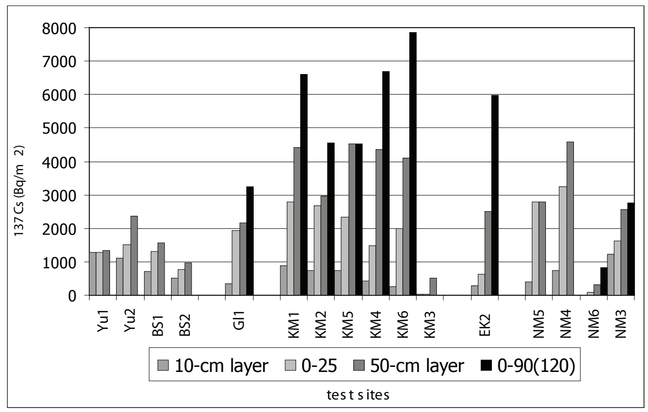

Figure 2. ^{137}Cs inventory in soil layers of different thickness. Sampling plots indices – see Table 1.

water of the peaty terraces (Pechora–17 mg/l, determination by V. Filonenko). It was at least twice as rich in silicon and iron as compared to the river. Performed analysis showed chemical signatures of the increasing influence of the marine environment that can be direct (aerial and water) and indirect (marine sediments) on both the terrace landscapes and river water and a considerable enrichment of the Pechora tundra terrace soils in water-soluble organic compounds and mobile iron. Similar water migration conditions due to vicinity of the sea seaward increase of salinity, chlorine and sodium in water and soil water extractions) and cryogene concentration of salts (enrichment of the tundra soils in water-soluble organic compounds and iron) were found earlier for the Lower Yenisey landscapes (Ivanov & Vlasov 1974, Korobova et al. 2003, 2004).

^{137}Cs Distribution in Soils

^{137}Cs inventory in soils

^{137}Cs activity determined in 203 samples collected from different soil layers was within the global fallout level and varied from 0.58 to 215 Bq/kg (dry weight – dw).

Radiocesium contamination density varied within sixteen studied plots from 0.8 to 7.8 kBq/m^2, V = 57% (Fig. 2). Mean

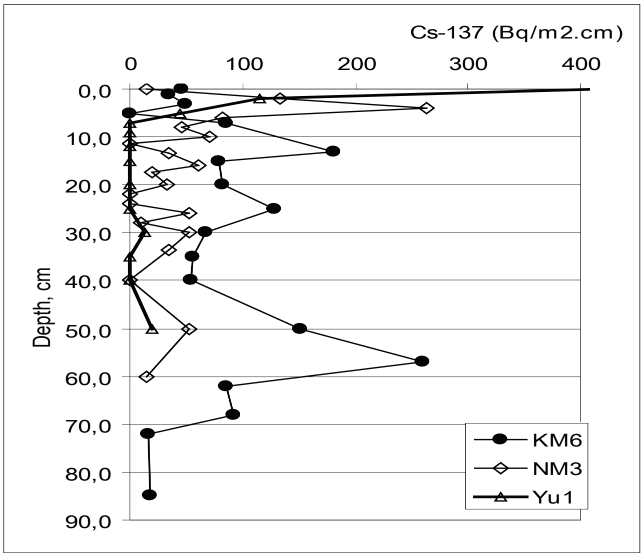

Figure 3. Three main types of ^{137}Cs profiles at the studied in Lower Pechora region. Sampling plots indices – see Table 1.

value equaled 4.8 ± 0.6 kBq/m^2 that corresponded to the data published in the *Atlas of Radioactive Contamination of Russia* (*Atlas* 1998, Wright et al. 1997, Strand et al. 1998).

Topsoil layers were most contaminated at watersheds (over 1 kBq/m^2, plots Yu1, 2; NM3, terrace landscapes). However, the contamination density within the total sampled depth was found the highest for the floodplain plots. The floodplain soils appeared to contain in total several times the amount of ^{137}Cs determined in the active layer of the terrace soils (Kermundej Island, Fig. 2).

^{137}Cs is known to be easily adsorbed by clay particles via ion exchange of interlayer cations or on the mineral edge defects (Evans et al. 1983, Cornell 1993, Bostick et al. 2002). Therefore, it seemed interesting to compare its inventory with that of natural ^{40}K since in sands, potassium concentration is in general three times lower than that in clay sedimentary rocks.

^{40}K inventory was the lowest in fresh sandy deposits of the medium-level sandy bars (KM3, NM6). In the organic soils of the peaty terraces, especially most distant from the coast (plot BS), ^{40}K inventory was the lowest. Positive correlation was established between ^{137}Cs and ^{40}K in 10–25 cm soil layer for all plots (0.760, n=14), in the lower (50–130 cm) mineral layers (0.640, n=8) and the total layer (0–130 cm, 0.708, n=9) in floodplain landscapes. In the top 10–cm layer of floodplain ^{137}Cs and ^{40}K relation was negative, while in watershed top organic horizons it had a positive tendency (r=0.653, n=5).

^{137}Cs profiles in terrace and floodplain soils

Our earlier investigations performed in the Lower Yenisey River basin showed that distribution in soil profiles significantly depended upon the origin of contamination (global fallout or regional river discharge) and geomorphological position of the plot (Korobova et al. 2004, 2007). In the Lower Pechora reaches the highest ^{137}Cs values were characteristic for terrace landscapes (215 Bk/kg, Yu2; 65–120 Bq/kg, NM3). Specific ^{137}Cs activity of the floodplain soil layers did not exceed 20 Bq/kg, reaching maximum in the buried layers sampled on Kermundej Island

Table 3. Fraction and ^{137}Cs distribution in pedon NM3 (see Table 1).

Horizon index, depth (cm)	Fraction (mm* %)				Cs-137 in fractions (%)			
	Coarse organic debris		Mineral fraction		Coarse organic debris		Mineral fraction	
	1*	2	2	3	1	2	2	3
0i	35	0,0	9,4	5,6	33	0,0	0,0	67
OeA1(0-2)	12	7,9	0,0	80	19	15	0,0	66
A (2-4)	10	0,0	5,2	8,5	13	0,0	9,3	77
A (4-6)	6,7	0,0	12	81	19	0,0	29	52
A/Eol(6-8)	3,7	0,0	9,2	87	24	0,0	19	57
Eol(8-10)	2,9	1,5	13	82	39	7,7	26	28
Ab(12-14)	3,7	13	0,0	84	27	73	0,0	0,0
A/Eb(14-16)	2,1	0,0	14	84	48	0,0	16	36
Eb (16-18)	37	0,0	7,1	56	57	0,0	21	23
B1s(18-20)	0,5	0,0	16	83	0,0	0,0	100	0,0
B2hs(24-26)	0,4	0,0	27	72	0,0	0,0	100	0,0
BChs(26-28)	0,8	0,0	35	65	100	0,0	0,0	0,0
BCs(28-30)	1,2	0,0	29	70	24	0,0	0,0	77
BC(30-33,5)	3,6	0,0	30	66	0,0	0,0	100	0,0
C(40-50)	0,1	11	0,0	89	0,0	28	0,0	72
C(50-60)	0,0	0,0	7,9	92	0,0	0,0	100	0,0

*1- <1mm; 2 - 1–.25 mm; 3 - >0.25 mm.

Concentration peaks in the terrace undisturbed tundra peaty and humus-peaty gley soils corresponded to the top 2-cm layer, to the boundary of the organic and gley mineral horizons (from 20 to 45 cm), and to the bottom of the active layer (40–60 cm) with the maximum radiocesium specific activity in the top organic horizon.

In the southern part of the study area, where the terrace soils are subjected to strong wind erosion and sand deposition, the soil profile (NM3) consisted of a sequence of organic layers or lenses interlacing with pure sands. Easy leaching of these horizons cause formation of podzolized, illuvial organic and ferric layers forming beneath the humic one. The most pronounced ^{137}Cs peak corresponded to the top organic layer (13–29 Bq/kg). Below the ^{137}Cs curve acquires a saw-tooth character with double increase in the buried humus horizon (5.5 Bq/kg). Contamination density of each layer reduced to its thickness allowed compare the horizons of the terrace and floodplain soils by ^{137}Cs fixation ability within the volume unit and demonstrated that maximum ^{137}Cs fixation in floodplain and terrace soil layers are of similar order (Fig. 3).

To study ^{137}Cs fixation in particles bound to organic matter, we undertook dry sieving of samples from profile NM3 and measured ^{137}Cs in fractions >1, 1, 1–0.25 and <0.25 mm. The coarse fraction consisted mainly of organic debris (litter, bark, roots) in various stages of decomposition. Fraction 1–0.25 mm, referred to as coarse and medium sand fraction according to U.S.D.A (Shaetzl & Anderson 2006), was a mixture of humified organic debris and organo-mineral aggregates which were separated visually into two parts: one enriched in organic debris and one not enriched. The smallest sandy fraction was

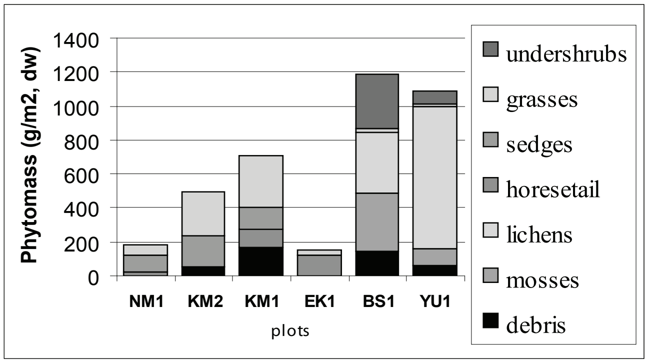

Figure 4. Phytomass of the selected plots and its composition. Plots indices – see Table 1.

mainly mineral. However, organic and ferric coating and charcoal particles were also present.

Fraction <0.25mm dominated by weight throughout the whole pedon (Table 3). Fine fraction played the main role in ^{137}Cs fixation in the top, newly formed organic horizon. In the buried organic lenses the major radionuclide portion (73%) was associated with slightly decomposed and humified organic debris. Mineral grains and aggregates 1–0.25 mm in diameter, enriched in ^{137}Cs, were found in textured illuvial horizons with humus and ferric iron accumulation. In transition to parent alluvium and sandy alluvium, all cesium supply was retained in this mineral fraction. Such distribution clearly showed that the organic matter is able to conserve ^{137}Cs for a long time. The form of the curve below the buried horizon and the low value of ^{137}Cs concentration give reason to suggest periodic deposition of slightly contaminated sediments by wind or water. However, a simple downward radionuclide migration in highly permeable sandy soils cannot be excluded.

Floodplain soils had several peaks of ^{137}Cs at definite depths (KM6, Fig. 3). On Kermundej Island, most profiles had three peaks, that is, 1, 15, and 30 cm in the silty gley soil on low-level floodplain (KM1) and 8–13, 25–30 and 52–57 cm on the medium level (KM4, KM5, KM6). The primitive sandy soil of the riverside high ridge (KM3) had the first pronounced peak at the depth of 50–60 cm. Similarity in radiocesium curves suggests synchronic sedimentation of the layers with the corresponding depth peak concentration. Higher ^{137}Cs deposition during flooding is usually explained by river erosion of the contaminated sediments and soil layer over vast areas. Using hydrological data helps to reconstruct maximum local flooding periods and to evaluate erasing and depositing capacity of the river.

The low contribution of the Chernobyl accident cannot be separated out from the total contamination using our data. However, this does not contradict the suggestion that the upper peak in soil profiles includes the Chernobyl contribution.

Three cuts were investigated on the left bank of Ekushansky Island severely eroded by the Pechora opened (1) old peaty deposits 1.5–3 m thick, (2) the young soddy sandy soil of the medium level floodplain, and (3) a fresh sandy alluvium. In old peat deposits ^{137}Cs was detected fragmentally (3 to 9 Bq/kg) to the depth of 23 cm. In the young soddy soil the layer with 13–14 Bq/kg of ^{137}Cs was buried at the depth of 62–75 cm under the less contaminated ones. In sandy alluvium only

Table 4. ^{137}Cs in plant groups.

Plant groups	n	m	s	min	max	V,%
Mosses	19,0	88,9	20,4	14,0	364,9	89
Lichens	11,0	36,9	11,1	7,1	79,4	72
Willow*	4,0	74,9	37,5	35,3	141,7	62
Horsetail	11,0	49,0	14,8	6,2	118,7	84

*leaves, Cape Bolvansky

a minor amount (2–2.5 Bq/kg) was determined in horizon 70–100 cm deep.

Performed analysis revealed roughly two to three contamination levels of the alluvial soil layers: (1) small (2–5 Bq/kg) or close to small (7–10 Bq/kg) and (2) medium (16–18 Bq/kg). The depths of the layers with similar sequence of contamination levels were believed to correspond to similar contamination events either due to direct aerial deposition or secondary deposition during flooding. An additional analysis of the appropriate hydrological data would help to reconstruct the flooding and to estimate sedimentation rates at the study plots.

^{137}Cs Accumulation in Vegetation Cover and Plant Species

Vegetation cover of the studied plots, described in Table 1, varied in total biomass from 0.15 to 5.77 kg/m^2 dw (excluding the tree layer at plots NM2 and NM3). The largest phytomass (mostly presented by willow shrubs - 81%–95%) developed on the medium and high level floodplains. Willow biomass sequentially increased from locations of the young rare willow growth pioneering high ridges (1, 2 kg/m^2, KM3) to mature willow thickets at the head of Gluboky Island (maximum value, GL1). In woodless areas the main mass contribution in floodplain landscapes belonged to mosses (30%) and lichens (up to 75%) on high terraces and to grasses and sedges (20%–53%) (Fig. 4).

Mean concentration of radiocesium in plant groups formed the row: mosses>horsetail>lichens (Table 4). High variation of the mean value within a group (62%–89%) was caused by considerable diversity in contamination level, landscape conditions, and species composition.

Site-specific ^{137}Cs accumulation by plant species

Radiocesium values exceeding 100 Bq/kg were found in plant species collected on the high terrace landscapes on Cape Bolvansky (mosses, horsetail, willow, grasses) near Yushino (Yu2, peaty soil, mosses) and Naryan Mar under old spruce forest (NM2, moss).

The moss species growing on terraces formed a row: *Hylocomium splendens>Pleurozium schreberi≥Sphagnum sp.* The highest ^{137}Cs accumulation was found in *Hylocomium* growing on Cape Shaitansky (365 Bq/kg). Sphagnum sampled in 5-cm layers in marshy depression near Yushino contained maximum ^{137}Cs amount in the top layer (95 Bq/kg against 45–49 Bq/kg down to 20 cm) that moss and lichen growing on Cape Bolvansky and near Yushino, as well as horsetail species collected on the floodplain were at least twice richer in ^{137}Cs as compared to Naryan Mar and Bolshaya Sopka sites. At Naryan Mar and Bolshaya Sopka sites, radiocesium content in the upper litter layer did not exceed 45%, while on Plot Yu2 it reached 80%. This can be caused by a difference in precipitation between the forest-tundra and tundra zones, leading to better leaching of the upper layers. The age of the ecosystem was also significant for ^{137}Cs fixation by plant species. Both *Hylocomium* and *Cladonia* species were 3 and 5 times richer when collected on plot NM2-03 located in old spruce forest with highly developed overgrown cover as compared to young coniferous forest near Naryan Mar (NM3). Correlation between ^{137}Cs-specific activity in the plant and the top 10 cm layer was significant for horsetail (r=0.710; n=11). Unlike the Lower Yenisey, ^{137}Cs content in horsetail increased seaward. This supported our earlier conclusion that horsetail is a suitable species for monitoring purposes (Korobova et al. 2007).

Conclusion

Low ^{137}Cs specific activity of soils and plants in the Pechora delta terrace and floodplain landscapes proved the global character of contamination. ^{137}Cs maximum content in terrace landscapes and their topsoil layer indicated aerial pollution that was higher in the soils and moss cover of the northern plots. Despite different water migration conditions and a pronounced marine influence increasing seaward that can be followed in chlorine content both in river and groundwater samples, ^{137}Cs fallout was strongly fixed by organo-mineral soil particles, reflected in maximum concentration of radiocesium in the undisturbed terrace organic horizons and particles enriched in organic debris, ^{137}Cs depth peaks in floodplain soils. Floodplain accumulation of ed ^{137}Cs was comparable and exceeded the inventories on the adjacent terraces that could occur due to both the direct fixation by dried surfaces and secondary accumulation of contaminated sediments. The most pronounced ^{137}Cs peaks in the lower layers covered by clean sandy alluvial or wind deposits are likely to correspond to the period of maximum ^{137}Cs global fallout (the year of 1963; Walling & He 1999). In case of constant flux, this allows a rough comparison of the deposition rates. Similar to the Yenisey, the Pechora terrace soils had pronounced minor ^{137}Cs peaks at the bottom of the active layer water, presumably due to ^{137}Cs sorption by suspension during concentration of water solution above the permafrost table due to freezing.

Acknowledgments

Authors are much obliged to Dr. I. Studenov and his colleagues who made field investigations possible. Thanks are due to E. Sedykh, N. Starchinova, N. Korsakova (Vernadsky Institute), and S. Kirov (Institute of Global Ecology, Russian Ac. of Sci.) for chemical analysis.

References

Anisimova, N.P. 1981. *Cryohydrogeochemical Peculiarities of the Frozen Zone.* Novosibirsk: Nauka, 89 pp.

Atlas of Radioactive Contamination of the European Part of Russia, Belarus and Ukraine. 1998. Moscow: FSGK, IGKE, 80 pp.

Bostick, B.C., Vairavamurthy, M.A., Karthikeyan, K.G. & Chorover, J. 2002. Cesium Adsorption on Clay Minerals: An EXAFS Spectroscopic Investigation. *Journal of Environment and Science Technology* 36(12): 2670 -2676.

Cornell, R.M. 1993. Adsorption of cesium on minerals: a review. *Journal of Radioanalytical and Nuclear Chemistry* 171(2): 483-500.

Dubikov, G.I. & Ivanova, N.V. 1990. Salty frozen deposits and their distribution in the USSR. In: *Salty Frozen Sediments as the Basement for Constructions*. Moscow: Nauka, 3-9.

Evans, D.W., Alberts, J. & Clark III R.A. 1983. Reversible ion-exchange fixation of cesium-137 leading to mobilization from reservoir sediments. *Geochimica et Cosmochimica Acta* 47: 1041-1049.

Ivanov, A.V. & Vlasov, N.A. 1974. Influence of cryogene processes on formation of hydro-carbonate-sodium waters. *Hydrochemical Materials* 60: 55-61.

Korobova, E.M., Ukraintseva, N.G., Surkov, V.V. & Linnik, V.G. 2004. Radionuclides in soils of the Yenisey river Gulf and delta coast. In: Engineering Geology and Environmental Protection. Sergeev Readings. Moscow: *GEOS* 6: 259-263.

Korobova, E.M., Brown, J.B. Ukraintseva, N.G. & Surkov V.V. 2007. ^{137}Cs and ^{40}K in the terrestrial vegetation of the Yenisey Estuary: landscape, soil and plant relationships. *Journal of Environmental Radioactivity* 96: 144-156.

Korobova, E.M., Ukraintseva, N.G., Surkov, V.V. & Brown, J.B. 2003. Geochemical study of the tundra landscapes in the Yenisey delta and gulf area Permafrost. *Proceedings of the Eight International Conference on Permafrost, Zurich, July 21–25*: 601-606.

Nifontova, M.G. 1998. Content of long-lived artificial radionuclides in moss-lichen cover of the terrestrial ecosystems in the Urals-Siberia region. *Ekologia* 3: 196-200.

Sanchini, P.H. 1988. Factors controlling the biogeochemical cycles of trace elements in fresh and coastal marine waters as revealed by artificial isotopes. Limnol. *Oceanogr* 33: 848-866.

Shaetzl, R. & Anderson, S. 2006. *Soils: Genesis and Geomorphology*. New York: Cambridge University Press, 817 pp.

Strand, P., Balonov, M., Aarkrog, A., et al. 1998. *AMAP Assessment Report: Arctic Pollution Issues*. Radioactivity. Oslo.

Walling, D.E. & He, Q. 1999. Investigating spatial patterns of overbank sedimentation on river flood plains. *Water, Air and Soil Pollution* 99: 9-20.

Wright, S.M., Howard B.J., Strand, P., et al. 1997. Prediction of ^{137}Cs deposition from atmospheric nuclear weapons tests within the Arctic. *Environmental Pollution* 4: 131-143.

Thermal State of Permafrost in the Eastern Arctic

G. Kraev, A. Abramov, S. Bykhovets, D. Fyodorov-Davydov, A. Kholodov, A. Lupachev, V. Mamykin, V. Ostroumov, V. Sorokovikov, D. Gilichinsky
Soil Cryology Laboratory, Institute of Physicochemical & Biological Problems in Soil Sciences, Russian Academy of Sciences, Pushchino, Russia

G. Zimova, N. Zimov
Northeast Scientific Station, Pacific Institute of Geography, Russian Academy of Sciences, Far Eastern Branch, Cherskii, Sakha Republic, Russia

Abstract

The thermal state of the permafrost of the Eastern Arctic lowlands lying between the Lena Delta and the mouth of the Kolyma River is described in this paper. Three datasets were considered: (a) soil temperature from 12 federal weather stations at 0.2 to 3.2 m depths, (b) the thawing depth dynamics from 20 various environmental Circumpolar Active Layer Monitoring (CALM) sites, and (c) the permafrost temperature of the upper 25 m measured in about 100 boreholes. The stability of the permafrost's thermal state during the last 25–30 years was revealed. In spite of the slow increase in the mean annual air temperature (0.01°C/yr to 0.02°C/yr), only cyclic fluctuations in soil temperature and depth of thawing rather than notable trends were observed.

Keywords: active layer; boreholes; climate change; soil temperature; thermal state of permafrost.

Introduction

Monitoring of the thermal state of ground outside the permafrost zone is performed occasionally according to special needs only. The necessity of such activities in the area of permafrost expansion (at 20% of the land) increases due to the projected permafrost response to climate change. Since the thermal capacities of the upper permafrost are controlled by climate, the climatic change tendencies are believed to be spatiotemporally reflected in the thermal state of permafrost. This study concerns the permafrost response to these changes during the last quarter of the 20th century, which was the period of global warming.

Object of Study

The thermal state of permafrost is known to respond to climate fluctuations by changes in the upper layers, as follows (Fig.1):

I. The active (seasonally thawing) layer, matching with the profile of modern cryosol, and is characterized by above-zero temperatures during summer and below-zero temperatures during winter. It ranges from ground surface to maximal depth reached by the thawing front in a given year by the end of the warming period. The maximal depth referred to as the active layer thickness (ALT) is usually implemented to models.

II. The layer of annual temperature oscillations. The temperature oscillations penetrate into the layer allowing the temperature to redistribute along the vertical axis in accordance with the basic Fourier conduction law. The bottom of the layer is referred to as the depth of zero annual amplitudes of temperature (H), which usually varies from 15 to 20 m depending on the thermal capacities of the ground and soil covers. The temperature fluctuations gradually lower to the bottom, and the temperature at the H depth is thought to represent the mean annual temperature of the permafrost (T_0).

III. Deeper layer of constant annual temperatures, where upper boundary condition changes are reflected with attenuation. It changes non-linearly and is believed to reflect the decadal to centennial fluctuations of soil temperature (Lachenbruch & Marshall 1986). The lower boundary is the permafrost bottom. The thermal pattern in this layer is usually characterized by the geothermal gradient (g) taken from the slope of the temperature curve.

Study Area

Investigations were carried out at Seaside Lowlands in the eastern Arctic in tundra, forest-tundra, and north taiga between the Lena Delta and the mouth of the Kolyma River (125–162°E, 65–72°N) at elevations up to 100 m above sea level. They spread up to 400 km latitudinally from the coasts of the Laptev and East-Siberian Seas to the mountainous areas of the Verkhoyansk and Cherskogo Ranges and the Yukagir Plateau (Fig. 2).

The topography of the study area is as follows: (a) drained watersheds composed of the late Pleistocene Ice Complex, (b) alas depressions, the result of subsidence of watersheds in the Holocene, (c) river flood plains, and (d) sand plains (like Khallerchinskaya Tundra) in the lower streams of the Indigirka, and Kolyma Rivers and the Lena Delta. The climate at the lowlands is arctic continental. According to Cherskii, Chokurdakh, and Tiksi weather stations the mean annual air temperature varies from -10°C to -16°C; the mean temperature of the warmest month (July) varies 8°C to 12°C, and that of the coldest month (January) varies -32°C to -34°C. The transition to above zero mean daily temperatures usually occurs in the second half of May, and the thermal

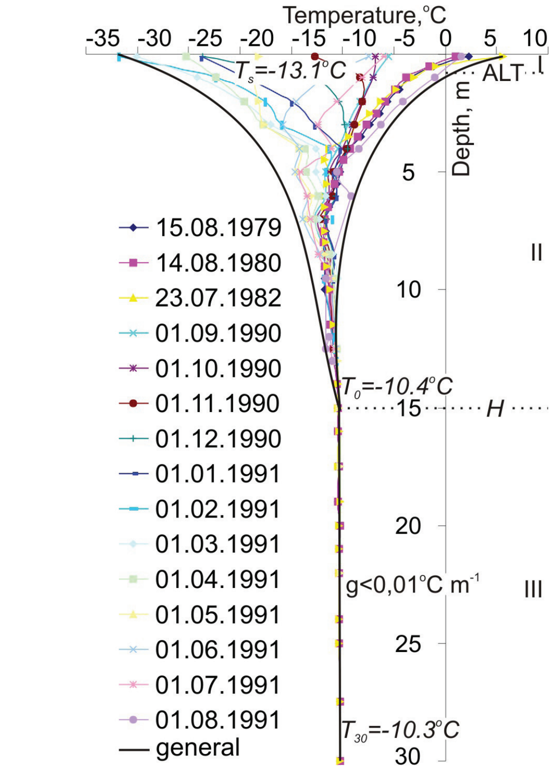

Figure 1. Temperature regime of the drained tundra watershed (Chukchee River, 69.48°N, 147.04°E). I-active layer; II-layer of annual temperature oscillations; III-layer of constant annual temperature. Data on every measurement are provided to assure the "general" envelopes are lined adequately; g was counted by dividing the difference in permafrost temperature, T_0, and the deepest temperature measured by the difference in depths of both measurements.

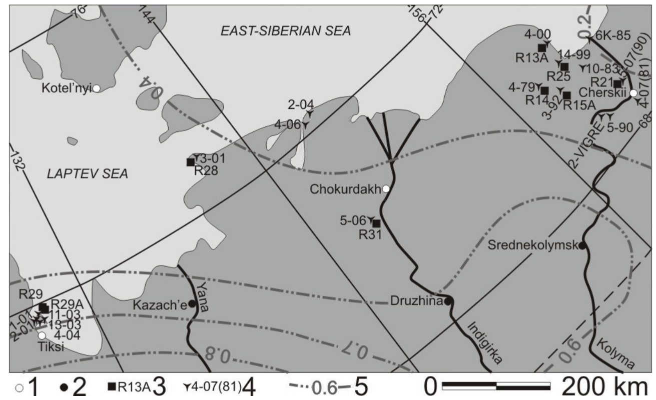

Figure 2. Locations of federal weather stations, boreholes and active layer monitoring sites considered in this paper. Key: 1–air temperature monitoring sites; 2–soil temperature monitoring sites; 3–active layer monitoring sites according to the CALM program numeration, with A designating the alas depression sites; 4–permafrost temperature monitoring in boreholes; the number after the dash is the year of drilling, which would be the starting year of the measurements if the other is not shown in brackets; 5–the current air temperature increase trends (Pavlov & Malkova 2005).

regime reverts to dominantly subzero temperatures at the end of September. The duration of the period with positive mean daily air temperatures is about 115–140 days. The mean annual atmospheric precipitation is 200–300 mm, with 80–130 mm of the total occurring during the warm season.

Snow cover is present from the end of September to mid-June having a maximal thickness of 30–70 cm, increasing eastwards, with more snow accumulating in depressions.

Continuous permafrost occurs to 290–420 m depths along the Kolyma River valley as found by Russian Geological Survey drilling in taiga at the southern margin of the study area and goes to 600–800 m along the Arctic coast in tundra, as calculated from the mean annual temperature and the geothermal gradient.

Materials and Methods

To estimate the thermal state of permafrost in the last 2–3 decades, three independent datasets were used:

1. ALT measured in variously located Circumpolar Active Layer Monitoring (CALM) sites, where observations have been held during the last 10–15 years since 1989.

2. The long-term soil temperature records at 0.2–3.2 m depth from the federal weather stations network, which represent long-term soil temperature observations since the 1960s. They characterize both the active layer and the upper part of the layer of annual temperature oscillations in permafrost.

3. Permafrost temperature measured in boreholes since the 1970s. It characterizes both the layer of annual oscillations and the layer of constant annual temperature down to 25–50 m.

Soil temperature data are available for 12 weather stations located in taiga north of the Polar Circle, surrounding the area of study. They can be obtained from the Frozen Ground Data Center (http://nsidc.org/fgdc/). Srednekolymsk, Druzhina, and Kazaché are located at Seaside Lowlands (Fig. 2). Kazaché operated in the 1930s–1950s and further data are absent, though it was excluded from our consideration. The Druzhina and Srednekolymsk stations, located in taiga, have records continuous enough to consider. Soil temperature measurements were made with outtake mercury thermometers (for detailed description of the measurement technique see Gilichinsky et al. 1998, 2000; Zhang et al. 2001, 2005; Frauenfeld et al. 2004; Bykhovets et al. 2007). In spite of being out of date, the monitoring system has distinctive preference of long-term continuous observations. The Srednekolymsk and Druzhina sites measure soil temperature since 1960 more or less constantly. The longest datasets of mean annual soil temperature have been chosen at 0.4 and 1.6 m depths. Gaps in the datasets were interpolated from neighboring depths, when the temperature correlation exceeded 0.7 (n>10; n – number of years). Ten-year averaging gave poorly representable results, and thus to acquire reflection of the 11-year sun cycle we used the 5-year running averages to compile the dataset for each depth.

ALT was measured at the CALM sites. All sites consist of the square net of regular observation points occupying 1 ha. Sampling points are arrayed with 10 m spacing in rows aligned with the cardinal directions and probed according to the CALM protocol (Nelson et al. 1996). The resulting datasets consist of 121 values for each site. Data are available at http://www.udel/geog/CALM. There are 20 sites located at the study area (for detailed site description see Brown et al. 2000, Fyodorov-Davydov et al. 2004). The detailed analysis of spatial and temporal patterns of seasonal thawing at the area under study could be found in the paper of Fyodorov-Davydov et al. in these proceedings. Only the sites having permafrost temperature boreholes in the vicinity were taken into account in this paper, as follows: R14 - tundra watershed on Chukochya River, R15A - alas depression on Kon'kovaya River, R21 - shrub tundra growing at sandy plain near Akhmelo Lake were measured since 1996, and R25 at the watershed residual hill slope near Yakutskoe Lake did from 1999. Site R13A - alas at Chukochii Cape was established in 2000. Several sites were established after 2000, as follows: R28 – polar tundra watershed at Svyatoi. Nos Cape measured only once in 2001; R29 and R29A at Bykovskii Peninsula in the Lena delta at watershed and alas, respectively, introduced in 2003, and R31 site at the left bank of the Indigirka River valley measured since 2004.

Single temperature measurements in boreholes started in 1979 according to the Techniques of Permafrost Survey (1979), as a rule to the depth of 25 m, using copper resistance thermometer strings and DC bridge (Russia) at each 0.5 m to 5 m depth, 1 m - from 5 m to 15 m depth, and 2.5 m down to borehole bottom. Boreholes diameter varied from 78 mm in the top to 63 mm in the bottom. Liners were installed to three meters only to prevent water leaking from the permafrost table. Later the resistance thermometers were replaced by thermoresistors with the same accuracy of ±0.1°C, but the measurements still were carried out once per year during 4–5 years. To determine the depth of constant annual temperatures with these means is possible in deep holes. Thus the necessary depth of the boreholes was not less than 25 m, and the period of observation has to be several years at least. The shallower of several measurements at neighboring measuring depths showing similar temperature were considered the depth of zero annual amplitudes. Since the mid-90s the boreholes have been step-by-step equipped by dataloggers for continuous year-round observations. At the moment two and four channel HOBO Pro series dataloggers with 0.25°C accuracy and ten-channel loggers with 0.01°C accuracy (LPC, Geomonitoring, Russia) are used. One sensor is usually installed at the surface, the others at various depths inside the borehole. Temperatures were measured four times per day.

The study area had more than 100 monitoring boreholes in 1979–92. Unfortunately most of them are lost nowadays. The new boreholes were drilled since 2000 at the same places and equipped with modern instruments for temperature measurements to re-involve the old data and quantitatively estimate the changes in the thermal state of permafrost. The changes were estimated using the 25-year old temperature records and the recent data.

Geothermal gradient measurements were measured to the depth 250 m in Geological Survey parametric borehole 2-VIGRE in 1979.

Results and Discussion

Soil temperature

Soil temperature measured at Srednekolymsk and Druzhina stations are shown in Figure 3. Two synchronous for both measuring depth and station periods of warming roughly at 1970–1975 and 1980–85, and those of cooling during 1975–80 and 1985–87 were revealed. The 1990s warming started earlier at more continental and cold Druzhina. The mean annual soil temperature in Srednekolymsk is -1.5±0.3°C (n=25, 1969–94) at 0.4 m (within the active layer), and 2.4±0.3°C (n=25) at 1.6 m (within permafrost). The mean annual soil temperature in Druzhina is -5.2±0.5°C at 0.4 m (active layer), and -4.6± 0.6°C (n=25) at 1.6 m (permafrost). The maximal difference in soil temperature during cold and warm periods reached 1°C in Srednekolymsk and up to 2°C in Druzhina. The soil temperature seems to be stable in Srednekolymsk, experiencing cyclic fluctuations during the study period of 1969–94. So does soil temperature in Druzhina at 0.4 m, while at 1.6 m it was warming with the rate of 0.03°C/yr.

Analysis of soil temperature trends at 0.4, 0.8, 1.6, and 3.2 m depths at 10 surrounding-the-lowlands weather stations located in Larix taiga north of the Polar Circle showed the maximal trend being 0.027°C /yr at 1.6 m in Druzhina, with most of thee stations having negligible (less than 0.01°C/yr) trends, while 3 stations showed even slightly negative trend. Chudinova et al. (2006) analyzing trends in soil temperature to the east of Lena River found a variety of tendencies for soil temperatures at 0.2–3.2 m depths have concluded the least soil temperature increase during 1960s–1990s beneath all the Federal weather stations. It could only be explained by the active layer having successful amounts of summer moisture and winter cold to discharge supplementary heat through the phase transitions. We let alone the discussion on reasons of trend variability in the study area. Above mentioned results confirm the fact that no significant changes occurred in soil temperature during the last 30 years.

Monthly time series of soil temperature at 0.4 and 1.6

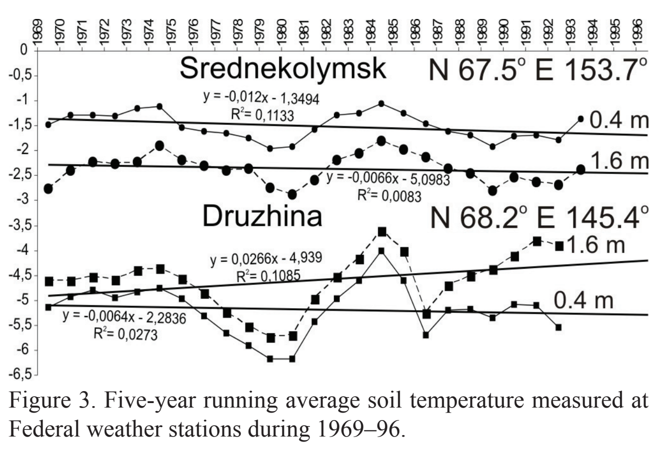

Figure 3. Five-year running average soil temperature measured at Federal weather stations during 1969–96.

Table 1. Mean annual soil temperature at the drilling sites according to monthly monitoring data.

	1981		Sep 1990-Aug 1991	
	active layer 0.4 m	perma-frost 1.6 m	active layer 0.4 m	perma-frost 1.6 m
Flood plain (4-07)	-4.7	-4.5		
Sand plain (5-07)			-0.9	-1.1
Watershed (4-79)			-11.9	-11.6
Srednekolymsk	-1.6	-1.3	-0.7	-2.0
Druzhina	-7.2	-6.7	-4.5	-3.7

m depths in our boreholes in tundra conducted in 1981, 1990–1991 correlate well ($r2>0.9$, $5<n<12$) with those made at the weather stations in taiga. Mean annual soil temperatures on tundra watersheds are much (more than 5°C) lower than in taiga (Table 1). Thermal regime of soils in taiga flood plain is colder than Srednekolymsk, while warmer than the Druzhina, lying south and characterized as more continental, having severe winters and less precipitation (data not shown). Borehole 5-07 showed abnormal, high soil temperature which is a subject of discussion below. However, the data are insufficient to reproduce the temperature, in our boreholes from the years of measurements at the weather stations only.

Active layer observations

Mean values of active layer thickness in the northern part of the Kolyma lowland vary significantly (see Fig. 4).

The largest discrepancies within tundra are associated with texture of parent materials. Sand plain tundra thaws two to three times deeper than wetter loams of watersheds. Besides the influence of lithology, the effect of locally higher permafrost temperatures, which promote deeper thawing, can be observed (Fyodorov-Davydov et al. 2004). Significant latitudinal differences within single topographic levels occurred only in 2005, when the deepest thawing occurred at all watersheds but the westernmost R29 site at Bykovskii Peninsula and R31 at the left bank of the Indigirka valley. The least ALT occurred in 1998 when only three of the sites were in operation. The longest dataset available is for the sand plain R21 site (see Fig. 3 in Fyodorov-Davydov et al., these proceedings). It shows the cyclic fluctuations of ALT. Decreasing of the ALT occurred through the 1990s, when the soil temperature remained relatively stable or even slightly decreased at both weather stations (Fig. 3). However, passing the highest value in 2004-05, the curve in 2007 returns to 1990s 101 cm ALT.

The influence of latitudinal irradiance on the spatial pattern of ALT is rather obvious in watersheds having relatively homogeneous texture (Table 2). Active layer thickness increases from north to south. At the R28 and R29 sites in grass-dominated tundra the ALT was 32±5 cm. Shrub tundra of R31, R14, and R25 had the mean ALT of 42±7 cm. Thaw depressions formed by thermokarst are usually waterlogged and accumulate peat, leading to a decrease of ALT. Thaw depths in alas are similar or slightly lower than on watershed.

In the area of study the close correlation between active layer thickness and thermal characteristics was observed at Site R25 ($r2>0.7$ for air temperature) and all other sites for the sum of summer above-zero temperature, but for R13A (Fyodorov-Davydov et al. 2004; see also Fyodorov-Davydov et al., these proceedings).

Permafrost temperature

The data on permafrost temperature at the depth of zero annual amplitudes are presented in Table 3. The depth of zero annual amplitude (H) was found at various depths: 8–10 m in alas depressions, 12–15 m at loamy watersheds, and 18–20 m within ice wedges and at the sand plain.

Temperature measurements conducted show the mean temperature on tundra watersheds of -10.5±0.9°C (n=8). The temperature rises up to -6.2°C in taiga watershed (5_90). Watershed permafrost temperature has significant negative correlation with latitude ($r2$=-0.79, n=8) designating the falling of permafrost temperature with latitude.

Alas depressions show the mean of -9.2±1.0°C (n=6), with the lowest temperature found at the highest alas at Chukochii Cape. The correlation with latitude is -0.55 (n=6),

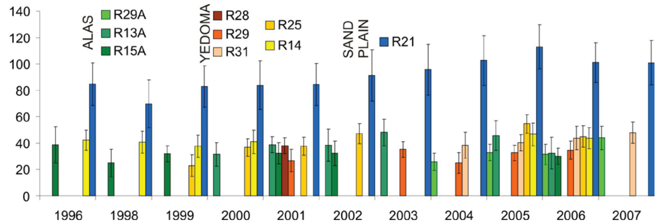

Figure 4. Mean annual ALT data (cm) monitored at the CALM sites. Green, red-yellow and blue colors represent different topographic levels. Sites are listed according to latitude southwards. Bars indicate ±1 standard deviation of 121 to 600 measuring points annually.

Table 2. Active layer thickness (cm) at the drilling sites according to monitoring data.

	72.87°	71.78°	70.55°	69.85°	69.48°
	R28	R29	R31	R25	R14
1996					42±8
1998					41±8
1999				23±8	38±8
2000				37±7	41±9
2001	38±6	27±9		38±7	
2002				47±8	
2003		35±6			
2004		25±8	38±10		
2005		33±6	40±6	55±7	47±8
2006		35±7	44±9	45±8	44±8
2007			48±8		

Table 3. Temperature monitoring of permafrost in boreholes.

	Hole	Lat.	Long.	Temperature, ºC 1980s	2000s
	4_04	71.7	129.4		-9.3
	13_03	71.7	129.4		-9.8
alases	2_01	71.8	129.4		-9.5
	3_92	69.4	158.6	-7.9	-7.4
	4_00	70.1	159.8		-10.2
	14_99	69.9	159.5		-9
	11_03	71.7	129.4		-11.3
	2_04	72.3	141.1		-11.2
	5_90	68.7	158.9	-6.2	
water-	4_06	72.3	141.1		-10.3
sheds	3_01	72.9	141		-11.7
	1_01	71.8	129.4		-10.9
	5_06	70.6	147.4		-9.5
	4_79	69.5	157.0	-10.5	-10.4
flood	6K_85			-6.1	
plains	4_07	68.6	161.4	-5.6	-5.7
sand	5_07	68.8	161	-7.9	-3.9
plain	10_83	69.4	159.5	-9.4	

Notes: 1980s involve temperature measurements made before 1990, while the 2000s include measurements made after 1995.

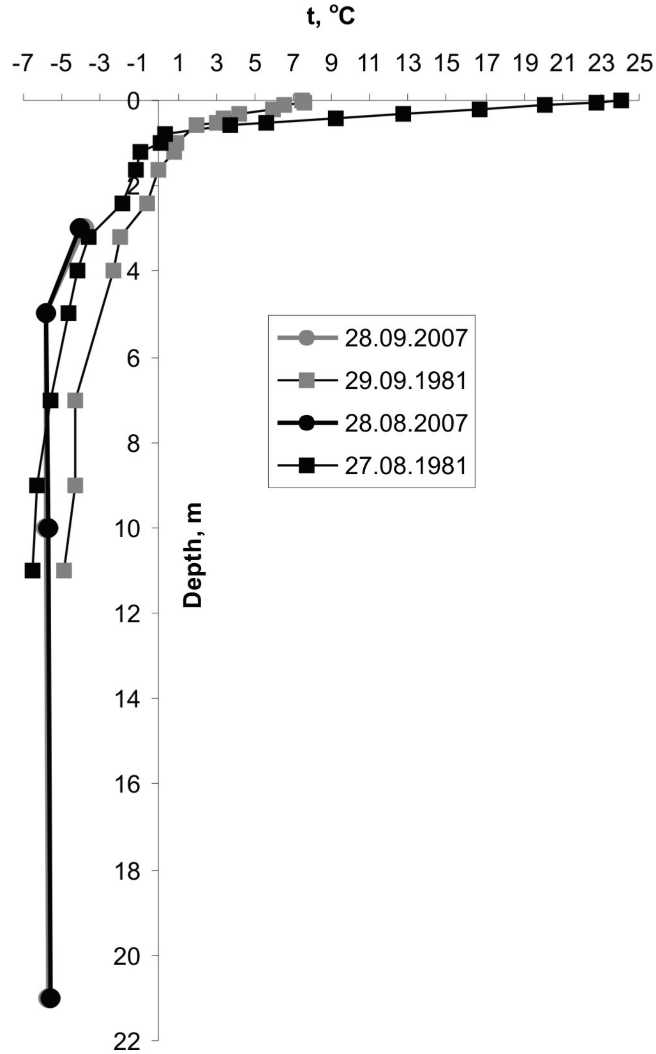

Figure 5. Temperature regime in 4_07 borehole at the Kolyma River flood plain.

which suggests other controls on permafrost temperature like wetness, relative depth of alas depression within the watershed, and peat thickness.

Permafrost temperature at levels experiencing present day sedimentation and syncryogenic formation of permafrost at flood plains and in Kamenka Island in the Kolyma delta is -5.9±0.2°C (n=2).

Measurements of permafrost temperature performed in the 1980s and 2000s differ by 0.1°C at watersheds and flood plains (Fig. 5), about 0.5°C in alas depressions.

From the bottom of the layer of zero temperature amplitudes (H) to 100 m depth g = 0, followed with the stepwise temperature rise, giving the mean g of 0.015°C /m.

Sand plain temperature is -9.4°C at the northernmost site, while it was suggested to be out of order at the 5_07 borehole representing the thermal anomaly site (see Tables 1, 3). Having the data on surface thermal capacities change through the years, we suppose the location of the borehole above the geological fault where the heat flux from the earth crust warms permafrost up to about -4°C. 3_92 borehole drilled in the very deep alas depression to 55 m depth shows positive gradient g down from the depth of zero annual amplitudes, which allows us to suggest the alas continuing to thaw having the long period heat wave penetrating to permafrost. Hence the temperature increase of 0.5 in alas depression is thought to be measured in atypical environment.

Permafrost warming was reported for many surrounding regions. For example Osterkamp (2005) reported on recent warming of Alaskan permafrost. The mean annual temperature of Eastern Arctic permafrost is in equilibrium with present-day climate. Long-term measurements do not reveal significant changes in permafrost temperature or even the timing of thermal wave penetration through the soils. We should not forget the stability of permafrost in the study area during Pleistocene. Even when regional permafrost degradation has occurred during climatic optimums, it was stable in the study area. However, as temperatures rise faster in the high-latitude continental regions, permafrost could be greatly impacted.

Conclusion

Today depths of seasonally thawing, soil and permafrost temperatures on wide eastern Arctic lowlands indicate the stable thermal state of permafrost during the last 30 yrs. The periods of warming of nearly 1970–75, 1980–85, 1989–93, and since 1999 till present, are reflected in the increase of less than 20% in ALT and 1°C–2°C in soil temperature.

This stability allows us to use data of single measurements in characteristics of permafrost thermal state in the Eastern Arctic. It is as follows.

Upper soils, permafrost temperature, and ALT are subject to change latitudinally, with the highest change occurring at sandy drained plains and between tundra and taiga. Watersheds usually have around -11°C temperature of permafrost and less than 0.6 m ALT. Widespread alas depressions have -9°C cold permafrost and nearly the same depth of seasonal thawing as watersheds. Flood plains characterize with -6°C cold permafrost.

The study area had more than 100 monitoring boreholes in 1980s with the network being recreated currently. Extensive temperature monitoring of permafrost allows the exclusion of temperature anomalies from modeling of thermal response of permafrost to climate changes. Reconstruction of old borehole networks gives the most precise evidence of permafrost thermal state change.

Acknowledgments

This study was supported by the Russian Academy of Sciences and also funded by the Polar Earth Science Program, Office of Polar Programs, National Science Foundation (ARC-0632400, ARC-0520578) and CALM (Circumpolar Active Layer Monitoring) Program (RUG2-1468-MO-04).

References

Brown, J., Hinkel, K.M. & Nelson, F.E. 2000. The Circumpolar Active Layer Monitoring (CALM) program: Research designs and initial results. Polar Geogr. 24(3): 165-258.

Bykhovets, S.S., Sorokovikov, V.A., Martuganov, R.A., Mamykin, V.G. & Gilichinsky, D.A. 2007. The history of soil temperature studies by the Russian weather station network. *Earth's Cryosphere* 11(1).

Chudinova, S.M., Frauenfeld, O.W., Barry, R.G., Zhang, T. & Sorokovikov, V.A. 2006. Relationship between trends and periodical components in air and soil temperature time-series over the permafrost-occupied regions of the Asian Territory of Russia. *J. Geophys. Res.*

Frauenfeld, O.W., Zhang, T., Barry, R.G. & Gilichinsky, D. 2004. Interdecadal changes in seasonal freeze and thaw depths in Russia. *J. Geophys. Res.* 109.

Fyodorov-Davydov, D.G., Sorokovikov, V.A., Ostroumov, V.E., Kholodov, A.L., Mitroshin, I.A., Mergelov, N.S., Davydov, S.P., Zimov, S.A. & Davydova, A.I. 2004. Spatial and temporal observations of seasonal thaw in the northern Kolyma Lowland. *Polar Geogr.* 28(4): 308-325.

Fyodorov-Davydov, D.G., Kholodov, A.L., Ostroumov, V.E., Kraev, G.N., Sorokovikov, V.A., Davydov, S.P. & Merekalova, A.A. 2007. Seasonal thaw of soils in North Yakutian Ecosystems. *Proceedings of the Ninth International Conference on Permafrost, Fairbanks, Alaska, June 29-–July 3, 2008* (these proceedings).

Gilichinsky, D.A., Barry, R.G., Bykhovets, S.S., Sorokovikov, V.A., Zhang, T., Zudin, S.L. & Fyodorov-Davydov, D.G. 1998. A century of temperature observations of soil climate: methods of analysis and long-term trends. In: A.G. Lewkowicz & M. Allard (eds.), *Proceedings of the Seventh International Conference on Permafrost:* 313-317.

Gilichinsky, D.A., Bykhovets, S.S., Sorokovikov, V.A., Fyodorov-Davydov, D.G., Barry, R.G., Zhang, T., Gavrilova, M.K. & Alekseeva, O.I. 2000. Weather station data: estimation of perennial changes in soil temperature in seasonally frozen grounds and permafrost zone of Russia. *Earth's Cryosphere* 4(3): 59-65.

Lachenbruch, A.H. & Marshall, B.V. 1986. Changing climate: geothermal evidence from permafrost in the Alaskan Arctic. *Science* 234: 689-696.

Nelson, F.E., Brown, J., Lewkowicz, T. & Taylor, A. 1996. Active layer protocol. In: U. Molau & P. Molgaard (eds.), *ITEX Manual, second edition*. Copenhagen: International Tundra Experiment: 14-16.

Osterkamp, T.E. 2005. The recent warming of permafrost in Alaska. *Global Planet. Change* 49: 187-202.

Pavlov, A.V. & Malkova, G.A. 2005. Current climate change in Northern Russia. The collection of maps. Novosibirsk, Russia: Geo, 54 pp.

Techniques of Permafrost Survey. 1979. Moscow State University Publishers, 328 pp.

Zhang, T, Barry, R., Gilichinsky, D., Bykhovets, S., Sorokovikov, V. & Ye, J. 2001. An amplified signal of climatic change in ground temperatures during the last century at Irkutsk, Russia. *Climate Change* 49: 41-76.

Zhang, T, Barry, R., Frauenfeld, O., Gilichinsky et al. 2005. Spatial and temporal variability in active layer thickness over the Russian Arctic drainage basin. *J. Geophys. Res.* 110.

Rock Permafrost Geophysics and Its Explanatory Power for Permafrost-Induced Rockfalls and Rock Creep: A Perspective

M. Krautblatter
Institute of Geography, University of Bonn, Germany

Abstract

Rockfalls and rock creep in permafrost-affected bedrock are an increasing hazard in high mountain areas. Besides temperature measurements and physically-based temperature modeling, geophysics in permafrost rocks provides a new methodology for investigating spatial and temporal patterns of permafrost rocks. First examples of 2D electrical resistivity tomographies and refraction seismic tomographies in permafrost rocks are displayed as well as 3D electrical tomographies. ERT time-lapse inversion routines allow for a direct comparison of subsequent time-sections and provide insight into temporal phenomena of heat propagation and permafrost aggradation and degradation. This article aims to show that in the case of ice-filled discontinuities and hydrological pressures geophysical results can potentially be linked to parameters that control rock stability.

Keywords: ERT; ice-mechanics; permafrost; refraction seismics; resistivity; rock creep; rockfalls.

Introduction

Degrading permafrost in rock walls is hazardous, partly due to the amount of potential energy that is released in case of instabilities (Harris et al. 2001). In 2002, the Dzhimarai-khokh rock/ice avalanche (Russian Caucasus) detached approximately 4 million m³ from a 1 km wide starting zone and caused more than 140 casualties (Haeberli, 2005, Kääb et al. 2003). Even smaller permafrost rockfalls, such as the 2003 Matterhorn rockfall, are considered major hazards in densely populated high mountain areas (Gruber et al. 2004). Inventories show that the frequency of these rockfalls has considerably increased in the warm 1990s and was boosted by the hot summer of 2003 (Schoeneich et al. 2004). Moreover, slow rock creep in permafrost rocks causes significant damage especially to tourist infrastructure in high mountain areas.

Besides temperature logger data, borehole information, and rock temperature modeling approaches, the geophysical applications described here provide a new tool for the spatial and temporal analysis of rock permafrost. In some cases, information on the thermal state of permafrost reveals sizeable information for stability consideration (Davies et al. 2001), but changing hydrological properties of ice, such as water content, may also play a vital part in decreasing resistive forces of ice-contained rock masses (Gruber & Haeberli 2007). This paper combines a review of existing geophysical techniques that are applicable in permafrost rocks and a perspective on how these can contribute to understanding mass movements in permafrost-affected bedrock in future. It will address three questions:

(1) What geophysical methods can be applied in permafrost rocks? (2) What properties do they detect? (3) What is their explanatory power for permafrost-induced mass movements?

Investigation Sites

Methods described in this article were tested at three investigation sites: the "Steintälli," a N-S exposed crestline (Matter/Turtmann Valleys, Switzerland) at about 3070–3150 m a.s.l. with slaty paragneiss (see Fig. 1); the North Face of the Zugspitze limestone summit (Wetterstein Mountains, Germany/Austria) at about 2800 m a.s.l., and the gneissic Gemsstock crestline (Switzerland) at 2900 m a.s.l. in collaboration with Marcia Phillips. Figure 1 shows a typical arrangement of a 2D-ERT in steep, permafrost-affected bedrock. More detailed site characteristics can be sourced from Krautblatter and Hauck (2007) and Gude and Barsch (2005). Problems associated with the comparison of different field sites and extrapolation of results are discussed in Krautblatter & Dikau (2007).

Figure 1. Electrical resistivity measurement at the Matter/Turtmann Valleys crestline, 3150 m a.s.l., Switzerland. 41 large steel screws serve as electodes along each transect.

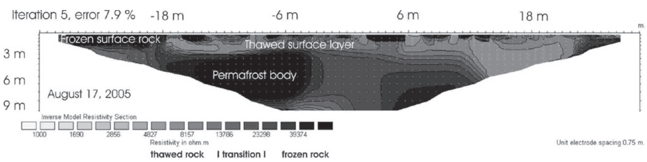

Figure 2. ERT in an east-facing rock wall recorded at August 17, 2005, at the Matter/Turtmann Valleys crestline, 3130 m a.s.l. Switzerland).

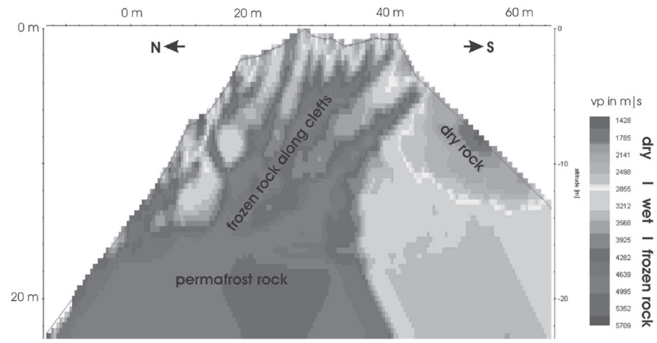

Figure 3. RST – north-south transect 9 (September 20, 2006), measured at the Matter/Turtmann Valleys crestline, 3150 m a.s.l.

Geophysical Methods for Rock Permafrost and Detectable Properties

Surface-based geophysical methods represent a cost-effective approach to permafrost mapping and characterisation (Harris et al. 2001). Hauck (2001) provided a systematic comparison of different geophysical methods for monitoring permafrost in high-mountain environments. However, the application of geophysical methods to permafrost rock walls just began in 2005 (Krautblatter & Hauck 2007). This section will give a quick overview of methods that have successfully been applied to permafrost rocks in the last three years. Data used for Figures 2, 6, and 8 were previously published in Krautblatter & Hauck (2007) and are described there in detail.

Electrical resistivity tomography (ERT)

ERT is a key method in permafrost research, as freezing and thawing of most materials are associated with a resistivity change that spans one order of magnitude, which is, in turn, easily detectable. The first approach to derive spatial information from rock faces by ERT was applied by Sass (2003). In subsequent studies he provided further evidence that ERT measurements are capable of measuring the degree of rock moisture (Sass 2005) and temporal and spatial variations of freeze and thaw limits (Sass 2004) in rock faces. These ERT measurements were confined to the monitoring of the upper weathering crust (centimeter- to decimeter-scale) of non-permafrost rock faces. Krautblatter and Hauck (2007) extended this method to a decameter-scale and applied it to the investigation of active layer processes in permafrost-affected rock walls.

Arrays with centimeter-long steel screws as electrodes were drilled into solid rock (see Fig. 1) and were measured repeatedly with high voltages (mostly 10^2–10^3 V) to improve the signal to noise ratio. A detailed survey of hardware and software adaptations and a systematic discussion of error sources is provided by Krautblatter and Hauck (2007). Errors associated with different ERT-arrays were assessed along with the impact of topography and other geometric error sources (Krautblatter & Verleysdonk 2008a). The Res2DInv software was chosen, as it is capable of topographic correction and "real" time-lapse inversion of subsequent measurements. To cope with high resistivity gradients, inversions models with mesh size smaller than the electrode distance and robust inversion routines provide better results. Resistivity values that correspond to the transition between frozen and thawed rock were measured repeatedly at the rock surface along different arrays and yielded evidence that the transition occurs between 13 and 20 kΩm for the gneissic rocks at the Steintälli (Krautblatter & Hauck 2007) and are in the same range as those established for carbonate rocks at the Zugspitze by Sass (2004) and our own measurements (Krautblatter & Verleysdonk 2008b). Figure 2 shows an ERT that was measured close to Figure 1 at an east-facing part of the rock crestline between Matter and Turtmann Valleys. It shows a 3 m thick thawed surface layer of rock above a constantly frozen permafrost layer; a plunge in temperature following August 14th is evident due to frozen rock close to the surface in all parts of the transect. Resistivity–temperature patterns of rock samples of all field sites are currently tested in a freezing chamber in the laboratory.

The relation between measured resistivity and rock temperature is straightforward. For temperatures below the freezing point, resistivity (p) depends mainly on unfrozen water content until most of the pore water is frozen. In Alpine environments resistivity can be calculated based on a reference value p_o as an exponential response to the temperature below the freezing point (T_f) according to McGinnis et al. (1973):

$$\rho = \rho_0 e^{b(T_f - T)} \tag{1}$$

The factor b in Equation (1) determines the rate of resistivity increase and can be derived empirically (Hauck 2001, Hauck 2002). Short-term changes in resistivity can be attributed to changes in pore water content and temperature, while changes in porosity and water chemistry can be neglected over daily to monthly measurement intervals in low-porosity rocks. Due to the exponential response of resistivity to temperatures below 0°C, freeze-thaw transitions correspond to an increase in resistivity by one order of magnitude and are thus a very sensitive method for detecting the state of rock permafrost close to 0°C. On the other hand, deeply frozen bedrock (below -5°C) along the measured transects causes problems for the electrode contact.

Refraction seismic tomography (RST)

The application of refraction seismics in permafrost studies is based on the interpretation of refracted headwaves that indicate the transition of a slower, unfrozen top layer

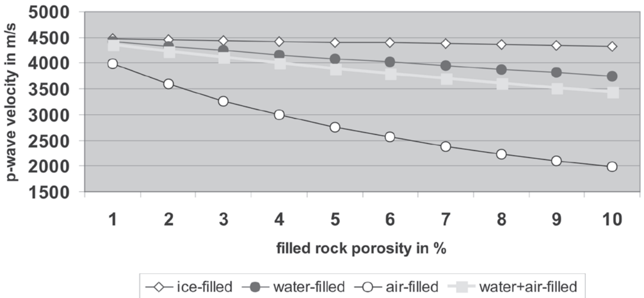

Figure 4. Estimation of P-wave velocities of rock with different porosity and pore content.

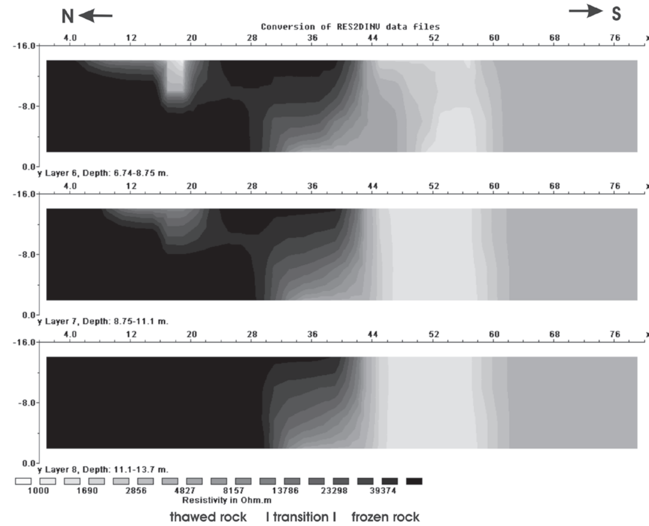

Figure 5. 3D-ERT cross sections at three different depths cutting the Turtmann/Matter Valley crestline N-S. Measured with ca. 1000 datum points from ca. 200 electrodes at September 5–9, 2006.

to a frozen layer with faster P-wave propagation below. Recent approaches apply tomographic inversion schemes (Otto & Sass 2006) often based on high-resolution datasets (Maurer & Hauck 2007, Musil et al. 2002). Seismics are also applied to determine 2D and 3D rock mass properties and potential instabilities (Heincke et al. 2006). Preliminary results from Krautblatter et al. (2007) indicate that refraction seismics are applicable for permafrost detection in solid rock walls, even if they provide less depth information than ERT measurements. On the other hand, it appears that they resolve small-scale features such as ice-filled clefts in more detail. For instance, Figure 3 shows a cross-cut through the E-W trending Steintälli crestline at Transect 9. Thoroughly frozen rock aligns along ice-filled discontinuities indicating the good thermal conduction (k = 2.2 W/(m*K)) without latent buffers in the readily frozen ice in clefts.

In practice P-Waves were stimulated with a 5 kg sledgehammer. Per transect, 24 drilled geophone positions in bedrock and 40 marked and fixed shot positions were arranged in line with the ERT transects so that RST and ERT were measured simultaneously (Krautblatter et al. 2007). A direct comparison of ERT and RST showed that frozen high-resistivity rocks in the ERT typically have P-wave velocities significantly above 4000 m/s (see section below) while wet and dry rock masses indicate a significantly slower propagation. As P-wave velocities of frozen and thawed rock differ only by a few hundred m/s in velocity, it is important to define the geometry of shot and recording position exactly, which was done using a high-resolution tachymeter. High P-wave velocities in rock necessitate high temporal resolution of geophone signals. Surface waves are not decelerated by a soft surface layer, such as soil, and thus often disturb signals recorded by geophones close to the shot position. We applied REFLEXW, Version 4.5 by Sandmeier Scientific Software, with model settings, such as initial P-wave velocity assumption, adjusted to bedrock conditions.

Air-, water-, and ice-filled pores in rock lead to significantly different attenuation of P-wave velocities. This is especially true for air-filled porosity. Figure 4 shows theoretical P-wave velocity for different pore-fillings and rock porosities derived from mixing laws. However, it appeared in simultaneous ERT and RST measurements that carefully conducted RST can resolve the difference between water and ice-filled rock even in low-porosity (2%–3%) bedrock, and that velocity differences are larger than expected from mixing laws for certain rock porosities. This could be due to the fact that melting in low-permeability rocks leads to a small gas content in pores to compensate the ice-water volume reduction or that the seismic velocities provide a more integral signal that includes ice in discontinuities in the rock mass.

The third dimension: 3D ERT and RST

ERT and RST can be conducted in 3D. Figure 5 shows three horizontal sections cut at depths of 7–9 m, 9–11 m and 11–14 m with N-S orientation that indicate a sharp divide between frozen rock to the north and thawed rock to the south at meter 44. Problems that arise when conducting three-dimensional geophysics in permafrost rocks are time-consuming measurements (ca. one week of uninterrupted measurements), the necessity of highly precise topographic information, and the required high resolution due to the enormous resistivity/seismic velocity gradients present in permafrost rock systems. Moreover, traditional 3D arrays (e.g., Pole-Pole or Dipol-Dipol ERT) result in bad signal to noise ratios (Krautblatter & Verleysdonk 2008a) and electrode/geophone spacing and arrays must be adjusted to local conditions. Therefore, the first 3D ERT and 3D RST array in permafrost rocks, which was conducted in 2006, relied on a very close (2 m) arrangement of geophones (120), electrodes (205), and shot positions (200) (Fig. 6) (Krautblatter et al. 2007) and is based on Wenner-arrays that yield much better signal to noise ratios than Pole or Dipole-type arrays.

The fourth dimension: Time-lapse ERT

The installation of permanent electrodes and modeling of subsequent resistivity datasets within the same inversion routine (so-called time-lapse inversion) allows for a direct assessment of spatial and temporal permafrost variability (Hauck 2002, Hauck & Vonder Mühll 2003). Figure 6 shows the freezing of the previously thawed surface rock up to 3 m

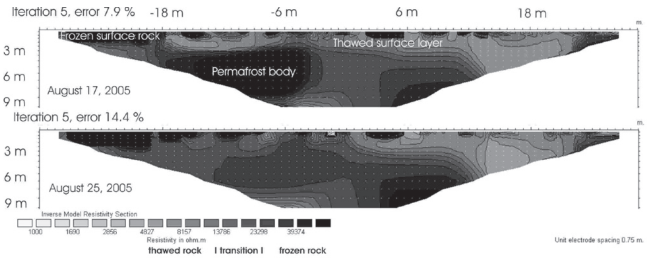

Figure 6. Freezing of surface rock from August 17 (top) to August 25, 2005 (bottom) due to a severe drop in air temperature recorded at the Steintälli E-transect (3130 m a.s.l., Matter/Turtmann Valleys, Switzerland).

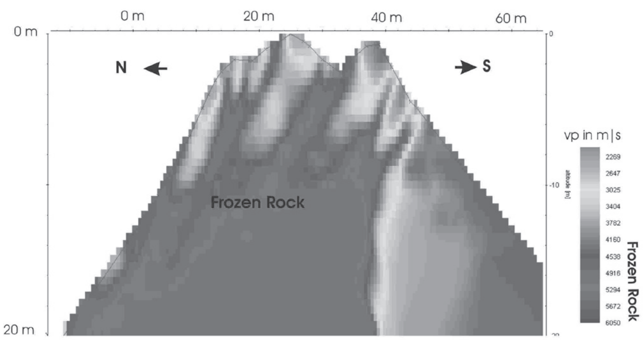

Figure 7. RST – north-south transect 7 (August 31, 2006) of the Matter/Turtmann Valleys crestline, 3150 m a.s.l. Mention the disposition of the frozen discontinuity zones as possible detachment zones with daylighted bedding.

depth following a plunge in temperature after August 14, 2005. While time-lapse routines for ERT are already in place, time-lapse routines for RST are still more difficult to perform.

Time-lapse inversion of subsequent measurements provides insights into short-term and long-term freeze-thaw thermal regimes (Krautblatter & Hauck 2007), response times (Krautblatter & Verleysdonk 2008b), changes in hydrological rock conductivity, and permafrost aggradation and degradation (Krautblatter 2008). Moreover, changes in subsequent time sections can definitely be attributed to changes in rock moisture or the state of freezing, while changes in geological properties can be ruled out for short-timescales.

Explanatory Power for Permafrost-Induced Mass Movements

We define permafrost-induced mass movements as those whose kinematical behavior is at least partly influenced by ice mechanics and permafrost hydrology. The most common types are rockfalls and rock block creep. These are usually explained (1) by a reduction of the resisting force, e.g., shear-strength in ice-filled clefts (Davies et al. 2001, Davies et al. 2000) or (2) an increase in the driving force, e.g., hydrological pressure (Fischer et al. 2007).

Ice-filled discontinuities

Figure 7 shows a cross-cut through the E-W trending Steintälli crestline. Geometrical position, orientation, and

Table 1. Geophysically detectable properties of permafrost rocks

ERT	Space-referenced integral tomography of frozen and thawed rock and hydrological conductivity at all measured depths. Temperature estimation (0° to -5°C) in combination with laboratory measurements (McGinnis).
RST	Space-referenced integral tomography of air-, water-, and ice-filled rock porosity. Exact positions of the uppermost freezing/thawing front and dominant air-, water-, and ice-filled rock discontinuities.
3D-measurements	3D spatial information on the freezing/melting front, hydraulic conductivity, and the persistence/ importance of discontinuity zones.
Time-lapse inversions	Development of heat fluxes, the permafrost system (aggradation/degradation), and the hydraulic system over time.

persistence of ice-filled clefts in the upper 10 m can be well detected in RST surveys. It is assumed that ice-filled discontinuities react according to stress-strain behavior of weight-loaded polycrystalline ice. The deformation of ice at constant stress is characterized by four phases: (1) elastic deformation that is followed by permanent deformation, first at a decreasing rate (2) primary creep, then at a constant rate (3) secondary creep, and finally at an increasing rate (4) tertiary creep (Budd & Jacka 1989). Mostly secondary creep and tertiary creep occur at speeds relevant for mass movements. The flow relation for secondary creep relates the shear strain rate ε_{xy} to the shear stress τ_{xy},

$$\varepsilon_{xy} = A\tau_{xy}^{n} \tag{2}$$

where A depends mainly on ice temperature, anisotropic crystal orientation, impurity content, and water content, and n increases at shear stresses greater than 500 kPa (Barnes et al. 1971). Crystal orientation, impurity content, and shear stresses remain more or less constant over short timescales. In contrary, ice temperature and water content in mass movement systems are subject to major annual and interannual changes. Thus, for temperatures above -10°C, A can be approached by

$$A = A_0 \exp(-\frac{Q}{RT}) \approx A_0 \exp(-\frac{16700}{T}) \tag{3}$$

where A_0 is independent of temperature, R is the universal gas constant, and Q is the activation energy (Weertman

1973) and A_{0t} for tertiary creep

$$A_{0t} = (3.2 + 5.8W) * 10^{-15} (kPa)^{-3} s^{-1} \quad (4)$$

can be related to the percentage water content W. It must be stressed that the water content strongly decreases with temperature. Paterson (2001) states -2°C as the lowest temperature at which the effect of water in the ice is relevant for the stress-strain behavior.

Equations (3) and (4) show that both ice temperature and water content play a dominant role in the mechanical behavior of ice-filled clefts at temperatures close to -0°C. Assuming moderate water content of 0.6%, the creep rate at 0°C is three times the rate at -2°C (Paterson 2001), which has serious effects on displacement rates and factors of safety considerations of mass movements.

As has been shown above, ERT and refraction seismics are highly susceptible to water/ice content inside the rock system just below the freezing point. Thus, the susceptibility range of seismic velocity and resistivity (ca. -0°C to -5°C) corresponds to the most important changes in ice-mechanical properties. This means the values temperature and water content, which are relevant for stability considerations in well-jointed permafrost rocks, are targeted by ERT and refraction seismics and combined interpretation strategies.

Hydrological pressure

Figure 8 shows light-colored, low-resistivity cleft water zones percolated by glacial meltwater that were observed to persist over several years and to limit the spatial extension of permafrost bodies (Krautblatter 2008). While pressure effects only have a small effect on the stress-strain behavior of ice itself (resisting force) (Weertman 1973), the reduction of applied normal stress and the increase in shear stress (driving force) may play a key role in preparing and triggering mass movements (Fischer et al. 2007, Terzaghi 1962). According to Wegmann (1998), permafrost degradation and aggradation in rocks in response to altered hydraulic conductivity occurs at all depths and quickly responds to annual melting patterns. He could also show that rock deformation quickly responds to spatial changes in permafrost rock conductivity.

Unfrozen cleft zones can easily be detected at the surface with RST and with ERT measurements possibly up to the maximum depth of the applied array (e.g., 80 m at the Zugspitze, 400 m Schlumberger-array). As shown in Figure 8, resistivity in water-filled cleft zones and frozen rock typically differs by 1–2 orders of magnitude and is, thus, easily detectable even at greater depths (Krautblatter & Hauck 2007). This opens up a whole range of new possibilities e.g., for the investigation of rock permafrost hydrology (Wegmann 1998), glacier-permafrost inter-connectivity (Moorman 2005), and rock deformation processes that are closely linked to freeze-thaw processes by latent heat transfer in clefts (Murton et al. 2006, Wegmann 1998).

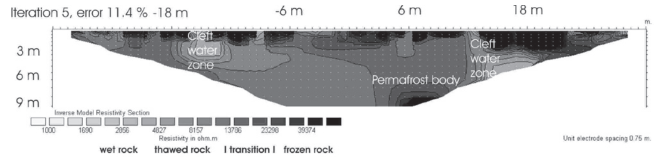

Figure 8. ERT of Transect NE (September 13, 2005). Mention the persistently thawed deep- reaching cleft water zones.

Conclusion

Resistivity monitoring may provide indications on temperature changes and water saturation, while refraction seismics help to gain insight into discontinuity zones and exact geometric properties of instable bodies. Repeated time-sections reveal interannual, annual, and multiannual time-patterns as well as response times, the fourth dimension of rock permafrost systems.

For permafrost-induced mass movements, with secondary and tertiary creep of ice close to -0°C, three highly-variable forces play a key role in unbalancing resisting and driving forces. The resisting force of ice-creep in clefts is mainly controlled by (1) temperature and (2) water content in the ice. Due to the laws of electrolytic conductivity, resistivity values assessed by ERT react sensitively to both parameters, and water content is a key control for P-wave velocity. The highly variable driving force, (3) hydrological pressure, is well detectable in ERT time-sections as pore and cleft space supersaturation lead to a plunge in electrolytic resistivity. However, many other anisotropic factors distort ERT and seismic measurements, and further field and laboratory experience is needed for the allocation of their influence and for the “suppression” of such noise.

Acknowledgments

This work has been funded by the German Research Foundation as part of the graduate school 437 “Relief.” Special thanks to C. Hauck, J.-C. Otto, R. Dikau, M. Moser, S. Wolf, S. Verleysdonk, and all who participated in the fieldwork.

References

Barnes, P., Tabor, D. & Walker, J.C.F. 1971. Friction and creep of polycrystalline ice. *Proceedings of the Royal Society of London, Series A*, 324(1557): 127-155.

Budd, W.F. & Jacka, T.H. 1989. A review of ice rheology for ice-sheet modeling. *Cold Regions Science and Technology* 16: 107-144.

Davies, M.C.R., Hamza, O. & Harris, C. 2001. The effect of rise in mean annual temperature on the stability of rock slopes containing ice-filled discontinuities. *Permafrost and Periglacial Processes* 12(1): 137-144.

Davies, M.C.R., Hamza, O., Lumsden, B.W. & Harris, C. 2000. Laboratory measurements of the shear strength of ice-filled rock joints. *Annals of Glaciology* 31: 463-467.

Fischer, L., Huggel, C. & Lemy, F. 2007. Investigation and modeling of periglacial rock fall events in the European Alps. *Geophysical Research Abstracts* 9(08160).

Gruber, S. & Haeberli, W. 2007. Permafrost in steep bedrock slopes and its temperature-related destabilization following climate change. *Journal of Geophysical Research - Earth Surface* 112(F2): F02S13.

Gruber, S., Hoelzle, M. & Haeberli, W. 2004. Permafrost thaw and destabilization of Alpine rock walls in the hot summer of 2003. *Geophys. Res. Lett.* 31(13): L15054.

Gude, M. & Barsch, D. 2005. Assessment of geomorphic hazards in connection with permafrost occurrence in the Zugspitze area (Bavarian Alps). *Geomorphology* 66: 85-94.

Haeberli, W. 2005. Investigating glacier-permafrost relationships in high-mountain area: historical background, selected examples and research needs. In: C. Harris & J.B. Murton (eds.), *Cryospheric Systems: Glaciers and Permafrost.* London: Geological Society Special Publication, 29-37.

Harris, C., Davies, M.C.R. & Etzelmüller, B. 2001. The assessment of potential geotechnical hazards associated with mountain permafrost in a warming global climate. *Permafrost and Periglacial Processes* 12(1): 145-156.

Hauck, C. 2001. Geophysical methods for detecting permafrost in high mountains. *Mitt. Versuchsanst. Wasserbau, Hydrologie und Glaziologie, PhD-thesis ETH Zürich* 171: 1-204.

Hauck, C. 2002. Frozen ground monitoring using DC resistivity tomography. *Geophys. Res. Lett.* 29, 2016, doi: 10.1029/2002GL014995: 12-1.

Hauck, C. & Vonder Mühll, D. 2003. Inversion and interpretation of two-dimensional geoelectrical measurements for detecting permafrost in mountainous regions. *Permafrost Periglac. Process.* 14(4): 305-318.

Heincke, B., Maurer, H., Green, A.G., Willenberg, H., Spillmann, T. & Burlini, L. 2006. Characterizing the fracture distribution on an unstable mountain slope using shallow seismic tomography: 2-D versus 3-D approaches. *Geophysics* 71(6): B241-256.

Kääb, A., Wessels, R., Haeberli, W., Huggel, C., Kargel, J.S. & Khalsa, S.J. 2003. Rapid aster imaging facilitates timely assessments of glacier hazards and disasters. *EOS* 13(84): 117, 121.

Krautblatter, M. 2008. Permafrost aggradation in the rock crest "Steintälli" (Valais, Switzerland) as a multiannual response to cool summers recorded by a three-year monitoring of rock permafrost by 2D/3D ERT and refraction seismics. *Geophysical Research Abstracts* 10: A-10496.

Krautblatter, M. & Dikau, R. 2007. Towards a uniform concept for the comparison and extrapolation of rock wall retreat and rockfall supply. *Geografiska Annaler* 89A(1): 21-40.

Krautblatter, M. & Hauck, C. 2007. Electrical resistivity tomography monitoring of permafrost in solid rock walls. *Journal of Geophysical Research-Earth Surface* 112. doi:10.1029/2006JF000546.

Krautblatter, M., Hauck, C. & Wolf, S. 2007. Geophysical 2D and 3D-monitoring of permafrost in rock walls. *Geophysical Research Abstracts* 9: A-09884.

Krautblatter, M. & Verleysdonk, S. 2008a. Rock wall permafrost monitoring with high-resolution 2D-ERT: lessons learnt from error estimates and a comparison of Wenner, Schlumberger, Gradient and Dipole-type arrays. *Geophysical Research Abstracts* 10: A-10383.

Krautblatter, M. & Verleysdonk, S. 2008b. Thawing regime and response time of present-day and relict permafrost revealed by monthly geophysical monitoring (Zugspitze, German/Austrian Alps). *Geophysical Research Abstracts* 10: A-10455.

Maurer, H. & Hauck, C. 2007. Instruments and methods: geophysical imaging of alpine rock glaciers. *Journal of Glaciology* 53(180): 110-120.

McGinnis, L.D., Nakao, K. & Clark, C.C. 1973. Geophysical identification of frozen and unfrozen ground, Antarctica. *2nd Int. Conf. on Permafrost, Yakutsk, Russia*, 136-146.

Moorman, B.J. 2005. Glacier-permafrost hydrological interconnectivity: Stagnation Glacier, Bylot Island, Canada. In: C. Harris & J.B. Murton (eds.), *Cryospheric Systems: Glaciers and Permafrost*, London: Geological Society Special Publication, 63-74.

Murton, J.B., Peterson, R. & Ozouf, J.-C. 2006. Bedrock fracture by ice segregation in cold regions. *Science* 314: 1127-1129.

Musil, M., Maurer, H., Green, A.G., Horstmeyer, H., Nitsche, F., Vonder Mühll, D. & Springman, S. 2002. Shallow seismic surveying of an alpine rock glacier. *Geophysics* 67(6): 1701-1710.

Otto, J.C. & Sass, O. 2006. Comparing geophysical methods for talus slope investigations in the Turtmann valley (Swiss Alps). *Geomorphology* 76(3-4): 257-272.

Paterson, W.S.B. 2001. *The Physics of Glaciers.* Oxford: Butterworth & Heinemann.

Sass, O. 2003. Moisture distribution in rock walls derived from 2D-resistivity measurements. *Z. Geomorph. N.F.*, Suppl.-Bd. 132(51-69).

Sass, O. 2004. Rock moisture fluctuations during freeze-thaw cycles: preliminary results from electrical resistivity measurements. *Polar Geography* 28(1): 13-31.

Sass, O. 2005. Rock moisture measurements: techniques, results, and implications for weathering. *Earth Surf. Process. Landforms* 30(3): 359-374.

Schoeneich, P., Hantz, D., Vengon, M., Frayssines, M., Deline, P., Amelot, F. & Savary, J. 2004. *A New Rlpine Rockfall Inventory.* Swiss Geoscience Meeting, Lausanne.

Terzaghi, K. 1962. Stability of steep slopes in hard unweathered rock. *Geotechnique* 12: 251-270.

Weertman, J. 1973. Creep of ice. In: E. Whalley, S.J. Jones & L.W. Gold (eds.), *Physics and Chemistry of Ice*. Ottawa: Royal Soc. of Canada, 320-337.

Wegmann, M. 1998. *Frostdynamik in hochalpinen Felswänden am Beispiel der Region Jungfraujoch - Aletsch.* Ph.D. Thesis. Mitt. Versuchsanst. Wasserbau, Hydrologie und Glaziologie, ETH Zürich 161: 1-144.

Temperatures in Coastal Permafrost in the Svea Area, Svalbard

Lene Kristensen
The University Centre in Svalbard, UNIS, Longyearbyen, Norway
Hanne H. Christiansen
The University Centre in Svalbard, UNIS, Longyearbyen, Norway
Fabrice Caline
The University Centre in Svalbard, UNIS, Longyearbyen, Norway

Abstract

Temperature data from three boreholes located on an ice-cored moraine near sea level are analyzed. One of these boreholes was drilled 6 m from the shore and shows significantly higher temperatures than the holes about 150 m from the shore. Using meteorological data and measurements of water temperatures, we model the permafrost distribution into the fjord as well as the influence of the sea on permafrost temperatures near the shore. The model results suggest that permafrost, as defined solely on temperature, is present beneath Van Mijenfjorden.

Keywords: borehole temperatures; coastal; geothermal modeling; permafrost; subsea permafrost; Svalbard.

Introduction

Permafrost on Svalbard is classified as continuous. It is more than 500 m thick in the highlands and less than 100 m near the coasts (Humlum et al. 2003). While considerable knowledge of permafrost conditions in the mountains exists from the extensive coal mining, little has been published on the permafrost in the shore areas of Svalbard. Exceptions are Gregersen & Eidsmoen (1988) that compares deep borehole temperatures at the shore with inland boreholes in Longyearbyen and Svea, and Harada & Yoshikawa (1996) that uses DC resistivity soundings to estimate the permafrost thickness of marine terraces at the shore of Adventfjorden near Longyearbyen.

The aim of this paper is to describe the permafrost conditions in the ice-cored moraine, Crednermorenen,a peninsula in Van Mijenfjorden in central Spitsbergen (Fig. 1). Since April 2005 temperatures have been logged every two hrs in three boreholes on the moraine each with 16 thermistors down to eight m. One of the boreholes is located only six m from the shoreline. Permafrost conditions in the shore area are important since the permafrost here is "warm" and thin. When constructing in such areas, particular attention must therefore be given to the permafrost conditions. In most other parts of Svalbard, permafrost is thicker, colder and more stable.

Due to the few previous studies of near-shore permafrost on Svalbard, an attempt was made to model both the effect of the sea on the onshore permafrost as well as the possibility of subsea permafrost. We use a transient 2D finite element geothermal model (TEMP/W from Geoslope International, Calgary, Canada; Krahn 2004) that is forced with meteorological data and measured water temperatures as boundary conditions.

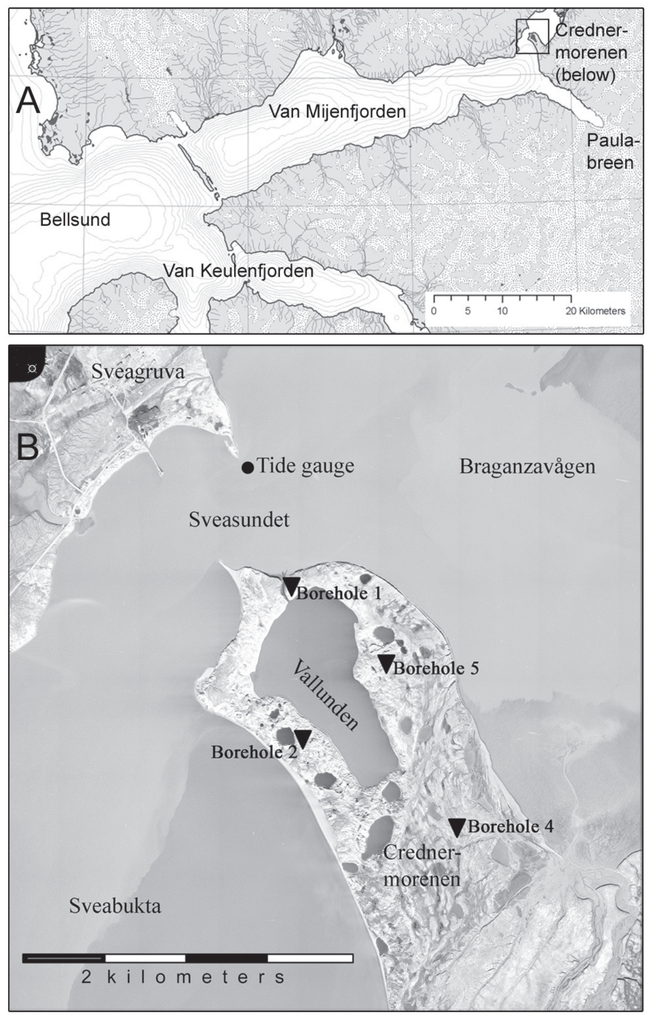

Figure 1. Field site. A) Van Mijenfjorden with Crednermorenen (in upper right corner). Map from: http://www.iopan.gda.pl. B) Crednermorenen with the location of the boreholes and the tide gauge. Air photo: Norsk Polarinstitutt, 1977.

Field Site

Crednermorenen is a lateral moraine deposited by a surge of the tidewater glacier Paulabreen (Fig. 1) around 1300 A.D. (Hald et al. 2001). The moraine forms a peninsula (1x3 km),

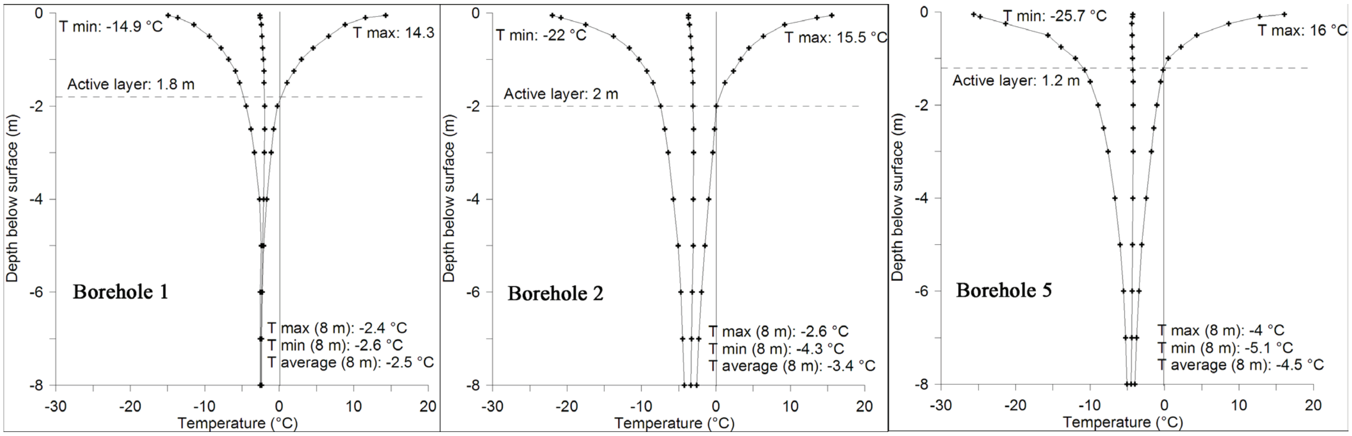

Figure 2. Maximum, minimum, and average temperatures in all depths from 10 September 2006 to 9 September 2007 for Boreholes 1, 2, and 5.

Table 1. Average annual temperature at the ground surface, at the top of the permafrost (TTOP).

	(Air)	Hole 1	Hole2	Hole 5
T surface (°C)	-4.6	-2.6	-3.7	-4.2
TTOP (°C)		-2.0	-3.1	-4.3

partly ice-cored and partly consisting of proglacially pushed marine clays (Kristensen et al., in press). It is surrounded by water on three sides and in its northern part lies a 1 km long lagoon, —Vallunden—that, is connected to the sea by a 15m-wide channel near Borehole 1. The water in Vallunden is salty as the tide flows in and out through the channel.

The oceanography in Van Mijenfjorden is strongly affected by an island at the fjord mouth, Akseløya (Fig. 1A), which nearly blocks the water exchange between the fjord and the warmer Atlantic water outside (Nilsen 2002). The water column is thus dominated by cold local water. Shore-fast ice is usually present from December to June. Bottom water salinity is around 34‰ (Hald et al. 2001), and July temperatures of -1.53°C and and -1.27°C have been measured in two basins in Van Mijenfjorden at 112 m and 74 m depth (Gulliksen et al. 1985). The climate in Sveagruva is slightly colder and more humid than in Longyearbyen 45 km to the NNE, but the meteorological record is shorter and more irregular. Mean annual air temperature close to sea level was -5.4°C in the period 1997–2006, and precipitation in the period 1995–2002 was on average 244 mm/y (www.met.no).

Temperature Measurements in Boreholes

Four 10 m deep boreholes (Fig. 1B) were drilled on Crednermorenen in March 2005 using an air pressure driven drilling rig. Coring was not possible, but the pulverized blown up sediment was collected from three of the holes, described and analyzed for water content and salinity. Borehole 1 was located two m above sea level and six m from the channel that connects Vallunden with Sveasundet. Borehole 2 was drilled into the ice-cored part of the moraine 17 m a.s.l. and 150 m from Sveabukta. Borehole 5 was established on top of the moraine ridge 145 m from Vallunden and 20 m a.s.l. Hole four was located on the marine clay part of Crednermorenen, but was destroyed by a bear in October 2006, and therefore no data are presented from that hole. In each borehole an eight m thermistor string (EBA Engineering, Edmonton, Canada) with 16 thermistors at decreasing spacing towards the surface was inserted. The uppermost sensor in each hole was placed at roughly three cm depth, and was measuring the surface temperature in this paper. Temperatures have been logged every two hour using Lakewood dataloggers; the accuracy of the thermistors is around 0.1°C. The annual temperature envelopes recorded in the three boreholes are shown in Figure 2. The maximum surface temperature for holes one and five occurred on 16 July 2007, and for hole two on 18 June 2007. The maximum temperature was very similar for the three holes, probably indicating that the barren surface provided similar summer conditions. The minimum surface temperature for all three holes occurred on 23 January 2007, which was contemporary with the minimum air temperature (-32.9°C) being recorded. The minimum surface temperature was much lower in hole two and five than in hole one. The latter had usually a snow cover of around 20 cm whereas both holes two and five were usually snow-free in winter due to wind redistribution in these more exposed sites. In Borehole 1 the seasonal temperature fluctuation became insignificant (0.25°C) below six meters depth, whereas the difference between annual maximum and minimum temperature at eight m in Boreholes 2 and 5 were 1.7°C and 1.1°C respectively.

Table 1 shows that all ground surface temperatures in the investigated period were higher than the mean air temperature. Hole one was warmest, reflecting the thickest snow cover during winter. The snow insulated the surface against cold winter temperatures creating a positive surface offset as demonstrated by, for example, Smith & Riseborough (1996). Hole 5 had the smallest surface offset as this site is usually never snow covered.

Smith & Riseborough (1996) also demonstrated that, due to higher thermal conductivity in frozen ground than in unfrozen, temperatures will tend to decrease from the ground surface to the top of the permafrost table (TTOP). Table 1 shows

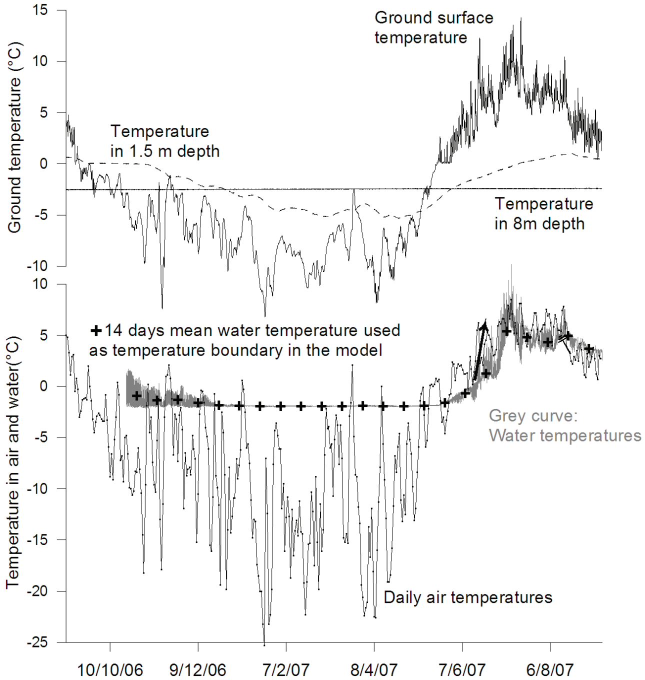

Figure 3. Upper part: Temperatures in Borehole 1 at the surface, in 1.5 m depth (dotted line) and in 8 m depth (no variation). Lower part: Air temperatures and water temperatures.

that in Boreholes 1 and 2 TTOP was higher than the surface temperature whereas in hole five it was practically the same. The active layer offset therefore seemed not to be important for the ground temperatures on the moraine, whereas snow depth in winter certainly was.

Tide and Water Temperature Measurements

Water temperatures in the narrow and shallow strait Sveasundet were measured and recorded every 20 min from 10 October 2006 to 9 September 2007 by a tidal gauge placed at two m water depth. The data can be seen in Figure 3 together with temperature measurements from Borehole 1 from three selected depths and air temperature measurements over the same time interval.

The freshwater from Kjellstrømsdalen passes the Sveasundet strait, and strong tidal currents flowing in and out of Braganzavågen ensure mixing of salt and fresh water here. For this reason the summer water temperatures were high compared to what has been measured in the deep basins in the fjord during summer. Winter temperatures however appeared to be constant around -1.93°C in most of the fjord.

The measured water temperatures can be divided in three distinct periods:

1) An autumn period when the temperature fluctuated in relation to the tide between -1.9 and +1.7°C lasting from 21 October to 26 December. Temperatures rose when the tide was moving through Sveasundet into the tidal flat Braganzavågen and fell when the tide flowed out again. This is consistent with observations that sea ice started forming in Braganzavågen before other places in the fjord. An example

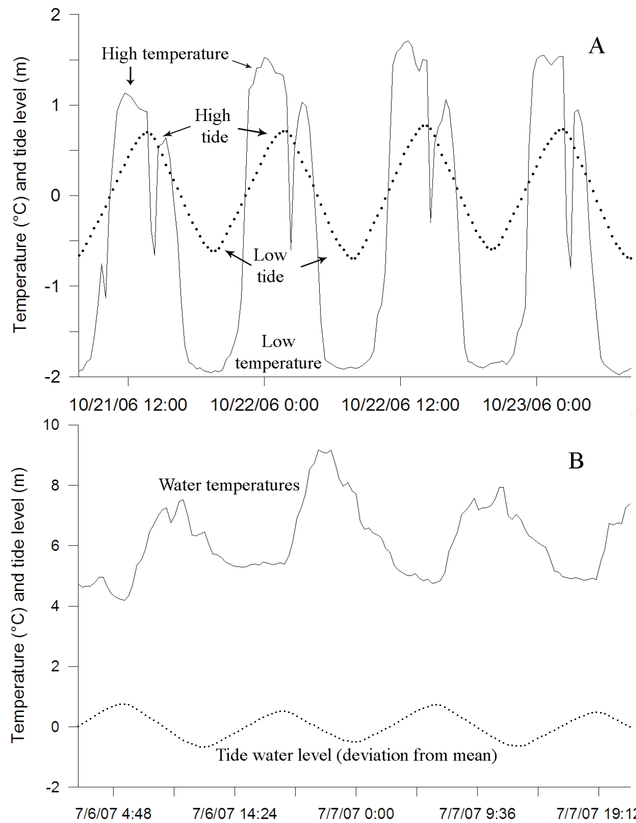

Figure 4. Examples of the relationship between water temperatures and the tide. A: Autumn conditions when the first sea ice forms, B: summer conditions.

of the coupling between tide and temperatures in the autumn can be seen in Figure 4A**.** November 28 was the last time the temperature rose above zero.

2) A winter period from 26 December to 22 May 2007. The temperature was nearly constant around -1.93, and no temperature fluctuations with tide were observed. The temperature corresponded to the freezing point of sea water and the fjord was covered by ice throughout this time. This winter period with constant water temperatures is easily identifiable in Figure 3.

3) A summer period from 22 May 2007 to the end of the measurements. Here the water temperatures increased and gradually approached the air temperature. The water temperature rose above zero for the first time on 13 June 2007. The temperature fluctuations were again controlled by tidal currents and were opposite in phase to those of the autumn. Now rising tide was associated with lower temperatures and falling tide with increasing temperatures (Fig. 4B). The reason is that water was now heated in the tidal flat Braganzavågen, where it was cooled during the autumn.

Modeling the Effect of the Sea on the Permafrost Temperatures

Studying the measured borehole temperatures, one can see that Borehole 1 deviated significantly from Boreholes

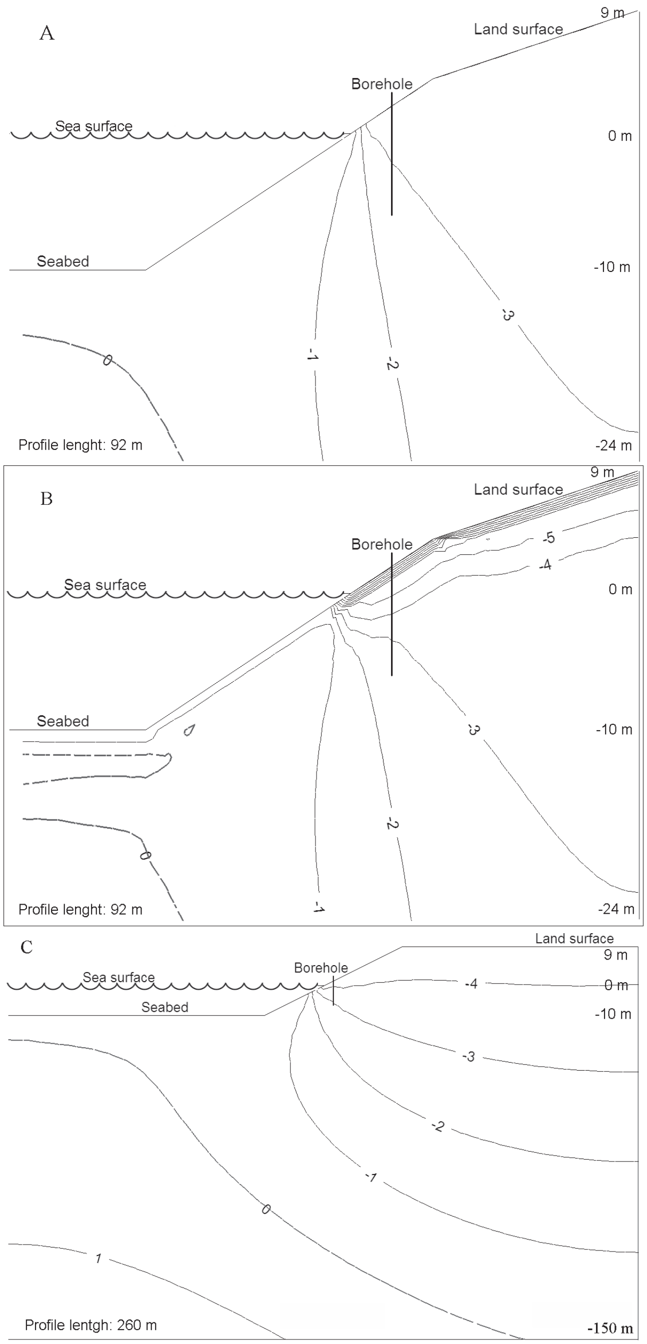

Figure 5. Three model output results. A: Steady state simulation of the ground temperatures in the immediate shore area. B: The same section but run in a transient mode forced with measured climatic data and sea water temperatures. Snapshot from 7 April 2007. C: Steady state simulation of a wider and deeper section with the boundary conditions the same as in A.

2 and 5 in respect both to the thermal regime and the depth of zero annual amplitude. While some of this deviation can be explained by a thicker snow cover during winter, most likely the proximity (6 m) to the sea affected the permafrost temperatures here. Located two m a.s.l. and being eight m deep, most of the borehole also lay below sea level. At eight m depth in Borehole 1, the temperature was -2.5°C. This indicates that permafrost probably extends into the seabed

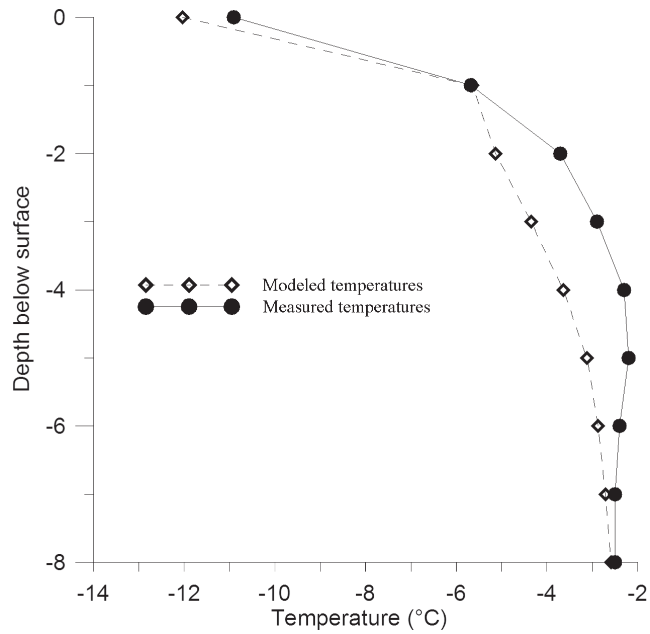

Figure 6. Comparison of the temperatures measured in Borehole 1 on 7 April 2007 and the modeled temperatures on the same day.

from the shore. An attempt was made to model both the effect of the sea on the onshore permafrost temperatures as well as the possibility of subsea permafrost existence. Gregersen & Eidsmoen (1988) previously tried to model the possible subsea permafrost in the area, but they had no information on the water temperatures in the fjord.

Model description and input

A 2D finite element program (TEMP/W) was used to model the permafrost thickness in Crednermorenen and the extent below the fjord bottom. The model is described in detail by Krahn (2004). Two temperature-dependent input functions (unfrozen water content and thermal conductivity) and overall water content are laboratory data from a nearby moraine, Damesmorenen, four km from hole 1, published by Gregersen et al. (1983). Volumetric heat capacity was set to 2000 and 3000 kJ/(m^3 x K) for frozen and unfrozen states respectively. Only one set of thermal properties was supplied to the model. It is obviously incorrect to assume homogeneous subsurface conditions, but we have no other thermal properties data available nor information on the subsea stratigraphy. A geothermal gradient of 35 mW/m^2 was set as a flux boundary condition at the bottom of the profiles. The vertical profile sides were set as zero flux boundaries.

To obtain a first estimate of the subsurface temperatures, the model was initially run in a steady state mode (Figs. 5A, 5C) using an estimated annual surface temperature and the average water temperatures as upper boundary conditions. A ground surface temperature of -4°C was used; this is slightly warmer than the mean annual air temperature due to the surface offset demonstrated in Table 1. A temperature of -0.1°C was used as the seabed boundary condition; this is the mean annual measured water temperature with interpolated temperatures for the missing 1.5 months of data.

The model was also run in a transient mode (snapshot in Fig. 5B) to compare the model results with the temperatures measured in Borehole 1. In the transient mode, eight simulations were run per day, and each node result was input to the next model run. Here the model was forced with meteorological data from 1 Jan 2006 to 10 September 2007. The meteorological inputs were maximum and minimum daily temperature, maximum and minimum daily humidity, and average wind speed. Latitude and longitude were supplied and the TEMP/W program used an energy balance approach to model the surface energy balance. To simulate the seabed temperature, a time dependent te mperature function was supplied as boundary condition, consisting of the average measured water temperature on 14 day basis. These are seen as crosses in the lower part of Figure 3.

No attempts were made to simulate the tidal fluctuation and its affect on the ground temperatures.

The model was run on two profile sections of different lengths and depths to both obtain detailed information on the near surface conditions, and impressions of the larger-scale ground temperatures in the coastal zone. The profiles were 92 m and 260 m long respectively and simplify a profile across the moraine and into Vallunden crossing Borehole 1.

Model results

Figure 5A shows a steady-state simulation for the immediate shore area. A high horizontal thermal gradient is seen in a narrow zone just below the shoreline. Since the mean annual water temperature is slightly below zero (-0.1°C), permafrost is modeled to be present in a thin layer below the seabed.

Figure 5B shows a snapshot plot from the transient model run from 7 April 2007. The sharp decrease of near surface temperatures reflects the winter freezing on land. A -1 °C isotherm has formed close below the seabed reflecting that the water temperatures approach -2°C during winter.

Figure 5C is a model run of the larger and deeper section but with the boundary conditions as those of Figure 5A. The pattern is similar as the one in Figure 5A but suggests that at depth, the presence of the sea will affect the ground thermal conditions more than 100 m from the shore, and similarly, that the cold temperatures from land will affect the sub-seabed temperatures at a similar distance offshore.

Figure 6 compares the measured and modeled temperatures in Borehole 1 for 7 April 2007. The discrepancy of model temperatures near the surface and towards the bottom is quite small, whereas the modeled temperature is up to 1.4°C wrong in the middle of the borehole. This and other snapshots throughout the year show that, while the general pattern is simulated reasonably well, there are discrepancies. These are often larger than those shown in Figure 6. However, the reasonable agreement of the modeled to the measured temperatures gives us some confidence in the general modeling results.

Discussion

The pronounced sill, Akseløya, restricts warm coastal water from entering Van Mijenfjorden and probably makes this fjord colder than other western Spitsbergen fjords. Sea ice cover is longer-lasting and more stable here. Therefore, this fjord is a primary candidate for possible subsea permafrost in western Spitsbergen fjords.

The modeling results of the subsea permafrost extend presented here should be seen as a minimum scenario. This is because the water temperatures were measured in a shallow, high-current strait, where the fjord water is strongly mixed with warmer fresh water during the summer. July temperature measurements from two deep basins in Van Mijenfjorden (Gulliksen et al. 1985) of -1.53°C and -1.27°C, respectively, indicate that water temperature in the deeper parts of the fjord remains below 0°C all year.

Permafrost, as defined solely on the basis of temperature, may not necessarily indicate cryotic subsea conditions. Sea water freezes at temperatures slightly above -2°C but capillarity and adsorption—in particular in fine-grained sediments—can further reduce the freezing point (Williams & Smith 1989). Thus, depending on the sediment properties, the seabed may well have permafrost by definition but still remain unfrozen. If the seabed consists of saline marine deposits, they will not be cryotic, even if thermally defined permafrost exists.

The 1300 A.D. surge of Paulabreen deposited lateral moraines in a rim around the inner parts of the fjord. A new detailed bathymetric survey indicates that glacial deposits also occupy the seabed here (Ottesen et al., in prep.). A seabed consisting of terrestrial sediments of glacial origin and with fresh rather than saline porewater could actually be frozen, but this hypothesis has not yet been tested.

The Crednermorenen moraine contains large amounts of buried glacier ice. It is possible that the unusual cold water conditions in Van Mijenfjorden are influencing the preservation potential of the ice-core in this moraine.

Conclusions

The permafrost temperatures measured in three boreholes in the ice-cored Crednermorenen moraine were studied for a period of a year. The surface temperatures in all holes were higher than the corresponding air temperature. The highest surface temperature was measured in Borehole 1 that normally has a snow cover of 20 cm while the two other boreholes are nearly snow free during winter. Most likely the warmer surface temperature in Borehole 1 is due to a surface offset (Smith & Riseborough 1996) caused by the insulating effect of snow.

Increasing temperatures were observed from the surface down through the active layer to the top of the permafrost in two of the boreholes. This is opposite to what would be expected if higher thermal conductivity of frozen ground compared to unfrozen ground causes an active layer (or thermal) offset. So this offset appears not to be important here; probably the ground is too dry.

Borehole 1 is located six m from the shore and is significantly warmer than two other boreholes both about 150 m away from the shoreline. To investigate the effect of the proximity to the sea, the finite element program TEMP/W was used to model the ground temperatures at the shore and below the seabed in both a steady-state and transient mode. Meteorological data and water temperature measurements were used to force the model.

The program manages reasonably well to simulate the ground temperatures in the near-shore borehole. The simulations indicate that permafrost, as defined solely on temperature, is present in a thin layer beneath the seabed of Van Mijenfjorden. Whether it is frozen or unfrozen will depend on the material properties.

At depth, the warming effect of the sea on the ground temperatures is modeled to penetrate more than 100 m inland and the cooling effect of land is affecting the seabed at an equal distance. The temperatures closer to the surface, however, are primarily locally controlled.

Acknowledgments

Many thanks to Store Norske Spitsbergen Kulkompani for funding the drilling and instrumentation of the boreholes and for providing logistical support when collecting data. LNSS, local contractor, preformed the drilling. Jomar Finseth, NTNU, supervised the drilling, sediment sampling, and laboratory work. John Inge Karlsen, logistics at UNIS, dived twice in muddy waters to emplace and recover the tide gauge that also recorded the water temperatures. The manuscript was improved by comments of an anonymous reviewer.

References

Gregersen, O. & Eidsmoen, T. 1988. Permafrost conditions in the shore area at Svalbard. *Proceedings of the Fifth International Conference on Permafrost, Trondheim, Norway, August 2-5,1988*: 933-936.

Gregersen, O., Phukan, A. & Johansen, T. 1983. Engineering properties and foundation design alternatives in the marine Svea clay, Svalbard. *Proceedings of the Fourth International Conference on Permafrost, Fairbanks, Alaska, July,17-22, 1983*: 384-388.

Gulliksen, B., Holte, B. & Jakola, K.J. 1985. The soft bottom fauna in Van Mijenfjorden and Raudfjorden, Svalbard. In: J.S. Grey & M.E. Christiansen (eds.), *Marine Biology of Polar Regions and Effects ofStress on Marine Organisms.* Oslo: John Wiley & Sons, 199-215

Hald, M., Dahlgren, T., Olsen, T.E. & Lebesbye, E. 2001. Late Holocene palaeoceanography in Van Mijenfjorden, Svalbard. *Polar Research* 20(1): 23-35

Harada, K. & Yoshikawa, K. 1996. Permafrost age and thickness near Adventfjorden, Spitsbergen. *Polar Geography* 20(4): 267-281

Humlum, O., Instanes, A. & Sollid, J.L. 2003. Permafrost in Svalbard: a review of research history, climatic background and engineering challenges. *Polar Research* 22(2): 191-215. ‘

Krahn, J. 2004. *Thermal modeling with TEMP/W–An engineering methodology*. Calgary, Alberta, Canada: Geo-slope International Ltd., 282 pp.

Kristensen, L., Juliussen, H., Christiansen, H.H. & Humlum, O. 2008. The structure and composition of a tidewater push moraine, Svalbard, revealed by DC resistivity profiling. *Boreas* (in press).

Nilsen, F. 2002. Measured and Modeled Tidal Circulation Under Ice Cover Van Mijenfjorden. Abstract: www.cosis.net/abstracts/EGS02/06395/EGS02-A-06395-2.pdf

Ottesen, D., Dowdeswell, J.A., Benn, D.A., Kristensen, L., Christiansen, H.H., Christensen, O., Hansen, L. & Lebesbye, E. Submarine landforms characteristic of glacier surges in two Spitsbergen fjords (in prep.).

Smith, M.W. & Riseborough, D.W. 1996. Permafrost monitoring and detection of climate change. *Permafrost and Periglacial Processes* 7(4): 301-309.

Williams. P. J. & Smith, M.W. 1989. *The Frozen Earth: Fundamentals of Geocryology.* Cambrigde: Cambridge University Press, 306 pp.

Thermal Deformation of Frozen Soils

G.P. Kuzmin
Melnikov Permafrost Institute, SB RAS, Yakutsk, Russia
V.N. Panin
Melnikov Permafrost Institute, SB RAS, Yakutsk, Russia

Abstract

A relationship between temperature deformations of frozen soil and physical characteristics that change with increasing or decreasing temperature has been derived. This relationship is based on the assumption that the volumetric expansion of the soil is equal to the sum of the volume changes of its components. The gaseous component is assumed to change in volume due to both thermal deformation of the gas and elastic deformation caused by a change in thermal stresses in the soil. This assumption is confirmed by the results of experiments.

Keywords: gaseous constituent; phase change; soil components, temperature deformation.

Introduction

Frost cracking of frozen soils subject to sub-freezing temperature fluctuations is a common phenomenon in permafrost regions. It is responsible for the formation of widely occurring polygonal features and affects various types of engineering structures (Ershov 2002).

Prediction of frost cracking in frozen ground requires knowledge of the thermal expansion coefficients, along with temperature data, and the soil thermal and mechanical properties (Grechishchev 1972).

The purpose of this paper is to derive an equation for obtaining the thermal deformation coefficients for frozen soils instead of time-consuming experimental determinations.

Thermal deformation of frozen soils, which generally consist of solid mineral particles, ice, water, and gases, determine the processes of the cryogenic rebound and formation and development of frost cracks.

Temperature change causes all frozen soil components to change volume in conditions of free or finite deformation. The most significant soil volumetric changes happen as a result of the water phase change, accompanied with the volume change accounting some 9% (Votyakov 1975). However frost penetration is accompanied with frost heave only if there is sufficient water-saturation (Votyakov 1975). When the water content is less than the plastic limit, freezing clay soils compress. When the water content is more than this limit, expansion develops during the freezing, and compression develops after freezing. Thus, the final deformation can be either positive or negative depending on initial in-situ water content.

No data is available on the influence of the soil gaseous constituent that reaches more than 10% in volume (Brodskaya 1962) on temperature deformations of frozen soils. Internal structural transformations of soil at freezing can not but influence the elastic deformations of gaseous constituent.

The Dependence of Temperature Deformations on Physical Characteristics of Frozen Soils

The resulting volumetric change of the frozen soil with temperature is not the direct sum of thermal deformations of its components (Ershov 2002). However, the internal structural transformations in the soil caused by changes in its temperature should have an effect on elastic deformations of the gaseous component. Therefore, the increment of volume change of the frozen soil at a change of temperature from t_1 to t_2 can be written as the sum of its components volume increments

$$\Delta V = \Delta V_d + \Delta V_W + \Delta V_i + \Delta Va \tag{1}$$

where ΔV_d, ΔV_W, ΔV_i, and ΔV_a are the increment of volume of soil skeleton, water, ice, and gaseous constituent, respectively.

Volumes of frozen soil components can be expressed through the physical characteristics and the whole soil volume.

$$V_d = \frac{\rho_d}{\rho_S} V \tag{2}$$

$$V_W = \frac{w_W \rho_d}{\rho_W} V \tag{3}$$

$$V_i = \frac{\left(w - w_W\right)\rho_d}{\rho_i} V \tag{4}$$

where ρ_d, ρ_S, ρ_W, and ρ_i are densities of the soil, mineral particles, water, and ice accordingly; w and w_W are the total water content and unfrozen water content.

Equation (1) in view of Equations (2)–(4) can be given as:

$$V_2 - V_1 = \left(\frac{\rho_{d,2}}{\rho_{S,2}} V_2 - \frac{\rho_{d,1}}{\rho_{S,1}} V_1 \right) + \left(\frac{w_{W,2}\rho_{d,2}}{\rho_{W,2}} V_2 - \frac{w_{W,1}\rho_{d,1}}{\rho_{W,1}} V_1 \right) + \left(\frac{w - w_{W,2}}{\rho_{i,2}} \rho_{d,2} V_2 - \frac{w - w_{W,1}}{\rho_{i,1}} \rho_{d,1} V_1 \right) + (V_{a,2} - V_{a,1}) \tag{5}$$

Characteristics for t_2 can be expressed through the corresponding parameters for t_1 in Equation (5).

The soil volume at t_2 can be presented as:

$$V_2 = (1 + \beta \Delta t) V_1 \tag{6}$$

where β=coefficient of volumetric temperature deformation; $\Delta t = t_2 - t_1$.

At temperature change the soil skeleton weight remains unchanged, hence:

$$\rho_{d,1} V_1 = \rho_{d,2} V_2. \tag{7}$$

The volume change of the closed-form gaseous constituent of frozen soils is the result of both its temperature deformations and action of temperature induced stress. Hence

$$\rho_{a,2} V_{a,2} = \rho_{a,1} V_{a,1} k \tag{8}$$

where ρ_a is soil gaseous constituent density; k is the coefficient considering the gases elastic deformations under the action of soil temperature stress.

The frozen soil components density for t_2 can be expressed through corresponding components for t_1

$$\rho_{S,2} = \frac{\rho_{S,1}}{1 + \beta_S \Delta t} \tag{9}$$

$$\rho_{W,2} = \frac{\rho_{W,1}}{1 + \beta_W \Delta t} \tag{10}$$

$$\rho_{a,2} = \frac{\rho_{a,1}}{1 + \beta_a \Delta t} \tag{11}$$

$$\rho_{i,2} = \frac{\rho_{i,1}}{1 + \beta_i \Delta t} \tag{12}$$

The coefficient of volumetric temperature deformation for frozen soils is related to the linear coefficient of deformation as

$$\beta = 3\alpha \tag{13}$$

In view of Equations (6)–(13) we find formula of coefficient of linear soil temperature deformation from Equation (5).

$$\alpha = -\frac{1}{3\Delta t} \left\{ \begin{array}{l} \rho_{d,1} \left[\begin{array}{l} \dfrac{3\alpha_S \Delta t}{\rho_{S,1}} + \dfrac{w_{W,2}(1 + 3\alpha_W \Delta t) - w_{W,1}}{\rho_{W,1}} + \\ \dfrac{(w - w_{W,2})(1 + 3\alpha_i \Delta t) - (w - w_{W,1})}{\rho_{i,1}} \end{array} \right] + \\ \dfrac{V_{a,1}}{V_1} \left[(1 + 3\alpha_a \Delta t) k - 1 \right] \end{array} \right\} \tag{14}$$

In Equation (14) gaseous constituent abundance in the soil $V_{a,1}/V_1$ can be evaluated as follows. We present the total soil volume as the sum of volumes of its components.

$$V = V_d + V_W + V_i + V_a \tag{15}$$

Having substituted in Equation (15) formulas of volumes of components Equations (2)–(4), we get

$$\frac{V_{a,1}}{V} = 1 - \rho_{d,1} \left(\frac{1}{\rho_{S,1}} + \frac{w_{W,1}}{\rho_{W,1}} + \frac{w - w_{W,1}}{\rho_{i,1}} \right). \tag{16}$$

Then the temperature deformation coefficient Equation (14) in view of Equation (16) is:

$$\alpha = \frac{1}{3\Delta t} \left\{ \begin{array}{l} \rho_{d,1} \left[\begin{array}{l} \dfrac{3\alpha_S \Delta t}{\rho_{S,1}} + \dfrac{w_{W,2}(1 + 3\alpha_W \Delta t) - w_{W,1}}{\rho_{W,1}} + \\ \dfrac{(w - w_{W,2})(1 + 3\alpha_i \Delta t) - (w - w_{W,1})}{\rho_{i,1}} \end{array} \right] + \\ \left[1 - \rho_{d,1} \left(\dfrac{1}{\rho_{S,1}} + \dfrac{w_{W,1}}{\rho_{W,1}} + \dfrac{w - w_{W,1}}{\rho_{i,1}} \right) \right] * \\ \left[(1 + 3\alpha_a \Delta t) k - 1 \right] \end{array} \right\} \tag{17}$$

Results, Analysis, and Summary

The coefficient k is unknown in Equation (17) and can be determined from experimental data. To this end, the thermal deformation coefficients were determined experimentally for artificially prepared frozen samples of loam and sandy loam, at two moisture contents, and sand, at one moisture content (Table 1). To prevent water drainage, the samples were insulated with a polyethylene film. After rapid freezing at low temperatures (20 C–30 C below zero), they were placed in a chamber with temperature t_1= -17°C, and maintained until

Table 1. The soil characteristics and results of definitions of coefficients and *k*.

Type of soil	ρ_d, g/cm^3	ρ_S, g/cm^3	w, fraction	$\alpha \cdot 10^6$, gr^{-1}	$w_{W,1}$ fraction	$w_{W,2}$ fraction	k
Loam	1.524	2.7	0.25	417	0.083	0.068	0.834
Loam	1.301	2.7	0.35	465	0.083	0.068	0.832
Sand loam	1.918	2.65	0.13	113	0.048	0.031	0.707
Sand loam	1.320	2.65	0.34	143	0.048	0.031	0.830
Sand	1.698	2.65	0.19	71	0.016	0.009	0.836

stabilization. Then, the samples were moved to a chamber with temperature t_2= -4.1 C, and the changes in length were observed until the cessation of deformation. The changes in length of the samples were measured using a dial gage with an accuracy of 0.01 mm.

The temperature deformation coefficient was calculated by the formula

$$\alpha = \frac{\Delta l}{l_1 \Delta t} \tag{18}$$

where $\Delta l = l_2 - l_1$; l_1 and l_2 are initial and final lengths of the sample; $\Delta t = t_2 - t_1$.

The *k* values were calculated by Equation (17) using the experimentally determined α values. Herewith the following values were introduced: α_S=10•x 10^{-6}gr.$^{-1}$; α_W=17.4•x 10^{-6} gr.$^{-1}$; α_i=50•x 10^{-6} gr.$^{-1}$; α_a=1217•x 10^{-6} gr.$^{-1}$. The unfrozen water content at t_1 and t_2 for all types of tested soils were taken from Votyakov (1975).

Experimental values of the coefficient of the temperature deformation, the deformations of samples received after stabilization, rather exceed the one-daily values, given in the paper by Votyakov (1975). The changes in the internal structure of the frozen soils with increasing thermal stresses caused elastic compression of the gaseous component, as is indicated by the values *k*<1.

Conclusion

1. The dependence of the frozen soils temperature deformation coefficient on its physical characteristics, where the gaseous constituent elastic deformations come into account, has been received.
2. The elastic compression of the jammed gaseous constituent occurs when the cooling of frozen soils in the range of water change phase.
3. The *k* values, obviously, depend on conditions of the frozen soil cooling.

References

Brodskaya, A.G. 1962. *The Compressibility of the Frozen Soils.* Moscow: Academy of Science Press: 83 pp.

Crechishchev, S.E. 1972. *Methodological Recommendations for Predicting Frost Cracking in Soils.* Moscow: VSEGINGEO: 38 pp.

Ershov, E.D. 2002. *General Geocrylogy: Manual for High School.* Moscow: Moscow Universiti Press: 682 pp.

Votyakov, I.N. 1975. *Physiomechanical Properties of the Frozen and Thawing Soils in Yakutia.* Novosibirsk: Nauka: 177 pp.

Channel Realignment Using Natural Channel Design Principles

Alexandre Lai
Alyeska Pipeline Service Company, Fairbanks, Alaska, USA
Marc N. Gaboury
LGL Limited environmental research associates, Nanaimo, British Columbia, Canada

Abstract

The Trans-Alaska Pipeline crosses Hess Creek on a 180 foot steel plate girder bridge. Thermal and hydraulic erosion altered the stream pattern with formation of a meander bend upstream of the bridge, leading to misalignment of the stream with the bridge abutments. To meet diverse stakeholder needs, an innovative approach to river engineering was implemented. Instead of a traditional riprap revetment, redirectional flow vanes were installed along an 800 foot meander bend. The vanes manipulate flow direction upstream of the bend, nudging the stream to a shallower curvature prior to entering the bridge opening. This new alignment improved conveyance through the bridge, created an active floodplain between eroding bank and the active channel, and over time will reestablish a functional riparian zone. Besides ecological benefits of a functioning floodplain, the riparian zone creates a buffer that insulates the ice-rich stream bank from further thermal and hydraulic erosion.

Keywords: erosion; floodplain; meander; realignment; stream; vanes.

Introduction

Hess Creek is located 85 miles north of Fairbanks, Alaska at Dalton Highway milepost 24 and is approximately 32 miles south of the Yukon River. The Trans-Alaska Pipeline crosses Hess Creek at pipeline milepost 375 on its 800 mile journey from the Beaufort Sea at Deadhorse, Alaska, to the port of Valdez. At the pipeline crossing, the creek corridor is 130 ft wide, and the pipeline is supported by a 180 ft single span steel plate girder bridge. The drainage basin is 508 mi^2 and the bankfull discharge is 3375 ft^3/s (cfs), based on a flood frequency analysis for gauged station USGS 15457800 on Hess Creek near Livengood, Alaska (1970–86; 662 mi^2). The area has discontinuous permafrost, and a typical floodplain soil profile consists of an organic layer, followed by silts, and alluvial gravels and sands down to bedrock.

At the time of construction in 1976, the pipeline crossing was in a stable reach of the creek with well-vegetated banks and no signs of bank erosion. A decade later, bank erosion upstream of the pipeline bridge was observed, and remedial action was taken to protect the north bridge abutment. But thermal and hydraulic erosion continued upstream of the bridge abutment and accelerated in the early years of 2000, most likely due to wildfires in the area. Continued erosion resulted in formation of a meander bend upstream of the bridge that previously was a relatively straight reach at the time of construction. This resulted in a misalignment of the bridge with the upstream and downstream reaches of the creek that could outflank the bridge abutment in a major flood event (Fig. 1). To meet the various stakeholder needs, such as protection of critical infrastructure, habitat preservation, and protection of an ecologically delicate region, an innovative approach to river engineering was used.

Figure 1. Hess Creek looking downstream, spring 2005 breakup. Hydraulic and thermal erosion of right bank resulting in misalignment with pipeline bridge.

Design Concept

A riprap revetment is typically used to halt streambank erosion (Alyeska Pipeline Service Company 1973). However, unless a new bank and floodplain are built, rip-rapping the existing bank will lock in a radius of curvature for the meander bend that will continue to be misaligned with the pipeline bridge opening. Instead of a traditional riprap treatment of the streambank, a series of flow deflector vanes were installed in Hess Creek to readjust the existing stream alignment into a smooth curvature with the bridge orientation. The vane design was based on an approach applied by the Rural Water Commission of Victoria in Australia (Standing Committee on Rivers and Catchments 1991). The design relied on a visual estimation of the critical line of attack (i.e., notional straight lines of maximum stream velocity that align the riverward tip of the upstream vane to the base of the next consecutive vane downstream to ensure the eroding bank is not attacked directly during floods) on

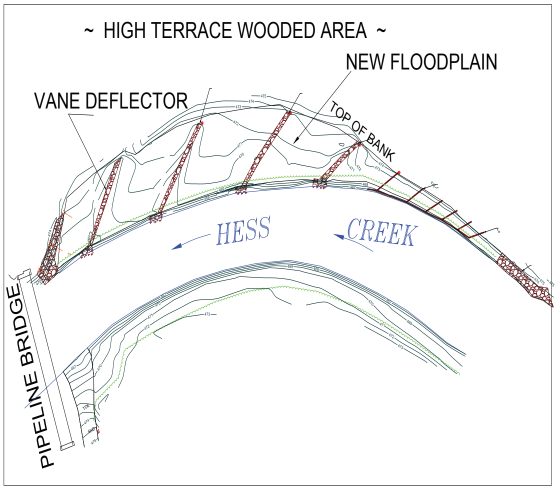

Figure 2. Plan view of 10 deflector vanes, new floodplain, and alignment of meander bend.

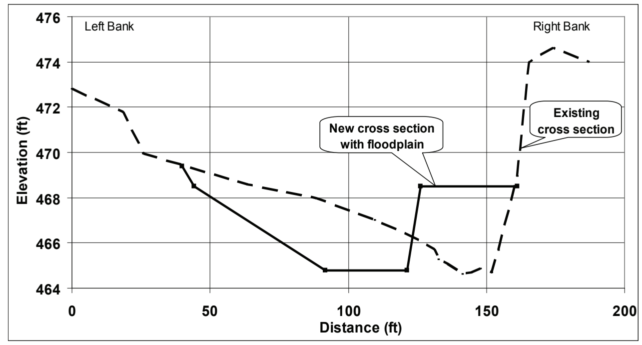

Figure 3. New cross section superimposed over existing eroding bank. A floodplain on the right bank was created from realignment of the meander bend.

Figure 4. Hess Creek upstream of pipeline bridge. Willows were planted along the bank and on the newly created floodplain.

the outside streambank of the meander during flood stage. Detailed planimetric drawings, based on topographic surveys, and aerial photographs were used to estimate the critical line of attack and to position, through an iterative process, the location of the deflector vanes (Fig. 2). The guidelines followed during the design stage were that: (1) the radius of curvature for the eroding meander bend would be realigned with the bridge orientation, (2) the new channel design width and meander radius would mimic stable channel and meander radii upstream and downstream of the project site, (3) each deflector vane would be spaced so the flow passing around and downstream from the riverward end of the vane intersected the next vane and not the eroding bank, and (4) vanes would be angled approximately 10° downstream of the perpendicular to the estimated critical line of attack.

Prior to construction of the deflector vanes, the channel was realigned laterally towards the south (left bank looking downstream), gradually from 0 ft at the upstream end to 40 ft at the downstream end, just before the bridge abutments (Fig. 3).

Based on reference reach surveys upstream and downstream of the work site, the bankfull channel width of the new channel was set at 82 ft. The channel realignment was about 800 ft long and gravel excavated from the point bar was used to build a floodplain terrace along the right bank in space created by the channel realignment. To provide a stable transition from the new floodplain to the existing terrace on the north banks, a 3H:1V slope was shaped.

After the new floodplain footprint was established, 10 riprap directional flow vanes, 10–98 ft long and up to 6 ft wide and 6 ft deep, were installed orienting downstream along the 800 ft meander bend. The vanes manipulated flow direction, nudging the stream into a shallower curvature prior to entering the pipeline bridge opening. The vanes were constructed of riprap, ranging in diameter from 1–4 ft. Spacing and length of the vanes increased from upstream to downstream in the meander bend. Vane spacing and length were dependent on the estimated critical line of attack and the existing and proposed radius of curvatures for the meander bend. A riprap-armored guidebank was constructed along a 50 ft section at the upstream end of the meander to prevent flood flows from outflanking the vanes located downstream. The tops of the vanes were generally level with bankfull elevation along much of their length, with a gradual slope at the landward end to the top of the shallow streambank. Height of the vanes was approximately 4 ft above the new channel thalweg (defined as the deepest point in a given cross-section). The vane was keyed into the streambed and bank about 3 ft with riprap. About 650 yd^3 of riprap were used to build the vanes, and an additional 100 yd^3 were used to reinforce the existing guidebank on the north bank. To enhance instream cover for fish, logs were buried into the floodplain between the downstream vanes. The logs extended instream about 12 ft and were submerged at low-water level.

Once the vanes were completed, willow cuttings were installed along the riverward edge of the new right bank. In addition, the floodplain was vegetated with live stakes and willow transplants the following summer (2006) (Fig. 4).

Post-Construction Monitoring

Although additional time is needed to properly assess the success of the design concept, initial results based on two full years of monitoring, since their installation in the fall of 2005, are encouraging. No additional bank erosion has occurred, and the active floodplain is slowly becoming vegetated with natural riparian species. Deflector vanes have effectively nudged the thalweg away from the eroding terrace. Cross section surveys confirm that the thalweg is along the tip of the vanes as can be seen from Figure 5, where the main current is away from the right bank and flowing in the middle of the flooded channel during breakup.

Continuous riprap treatments typically halt bank erosion entirely, while discontinuous measures like deflector vanes or bank barbs deflect flows with discreet instead of continuous hardpoints. Therefore, some limited adjustments between structures after construction are expected until a stable "scalloped" bank line is formed (McCullah & Gray 2005).

A scalloped bank line developed in between the constructed deflector vanes on the newly constructed floodplain in Hess Creek (Fig. 6). This occurred after the first snowmelt flood following construction, but has remained stable since 2006. These scallops are a result of flow separation due to expansion of flow lines downstream of the rock deflector vanes. The expansion zones are beneficial to the aquatic ecosystem because they provide back eddies, hydraulic complexity, refuge and resting areas for fish.

The low profile deflector vanes provide flood capacity during peak flows when the floodplain is overtopped relieving stresses along the bank and the vane structures. These floodplain overflows result in deposition of seeds and woody material, which over time will hopefully result in a healthy riparian zone.

Figure 5. Post-construction spring breakup 2006, as compared with Figure 1. Overbank flow completely submerged floodplain and deflector vanes. No bank erosion, and main flow current is along the tip of deflection vanes, away from the right bank (note location of white "bubble line").

Figure 6. Looking upstream from the bridge, September 2007, showing scallops between deflector vanes and woody material that accumulated along the bank and floodplain.

Conclusion

The deflector vanes provided bank protection by realigning the channel thalweg away from the eroding streambank and by providing a riprap key tie-in of the vane to the streambank. The former measure provided stability along the toe of the bank, and the latter safeguarded against outflanking of the vane structures during extreme floods. The new alignment improved conveyance through the bridge, created an active floodplain between the eroding bank and the active channel, and will reestablish over the long term a stable streambank and functional riparian zone. By adopting a channel width and meander radius based on channel morphology in undisturbed natural reaches in Hess Creek, it is expected that the stability of the channel and constructed works will be maintained under the range of existing hydrological conditions. Incorporating these natural channel characteristics in the meander realignment will also help to create and maintain some of the key physical components of a healthy aquatic ecosystem. These key components could include, for example, deep residual pool depth along the bend to provide high-quality holding pools for fish, sorting and distribution of substrates to obtain suitable sizes and quantities of spawning gravels, and over-stream deciduous vegetation and recruitment of woody debris from the new floodplain to provide cover for rearing fish. In addition to the ecological benefits of a functioning floodplain, the constructed works also created a buffer to insulate the exposed ice-rich streambank from further thermal and hydraulic erosion. There is also a direct economic benefit to this design approach, because only one third of the rock quantity typically used in a traditional riprap revetment was needed to build the structures.

Acknowledgments

Many individuals provided invaluable input to the design of this project, among them are, Wim Veldman, P.E., Philip Hoffman, P.E., and Habitat Biologist Kenneth Wilson. Their diligent review and suggestions contributed to improvement of the overall design and satisfying stakeholder needs.

References

Alyeska Pipeline Service Company. 1973. *Summary Report River and Floodplain Design Criteria for the Trans Alaska Pipeline System*.

McCullah, J. & Gray, D. 2005. *Environmentally Sensitive Channel and Bank-Protection Measures*. Washington, D.C.: National Cooperative Highway Research Program, NCHRP, Rep. 544.

Standing Committee on Rivers and Catchments. 1991. *Guidelines for Stabilizing Waterways*. Rural Water Commission of Victoria, Australia: 32 pp.

ERS InSAR for Assessing Rock Glacier Activity

Christophe Lambiel
Institute of Geography, University of Lausanne, Switzerland

Reynald Delaloye
Dept. of Geosciences, Geography, University of Fribourg, Switzerland

Tazio Strozzi
Gamma Remote Sensing, Switzerland

Ralph Lugon
Kurt Bösch University Institute, Sion, Switzerland

Hugo Raetzo
Federal Office for the Environment, Bern, Switzerland

Abstract

The potential of space-borne synthetic aperture radar interferometry (InSAR) to estimate both magnitude and spatial pattern of slope motion in a periglacial environment has been evaluated over a large area of the western Swiss Alps, using data from the ERS-1 and ERS-2 satellites. About 280 active rock glaciers with different classes of velocities have been identified on the analyzed interferograms. The velocities range from a few centimeters per year to several meters per year. These data were validated by some differential GPS measurements and compared to numerous field observations. The resulting classification permits a better description of the full range of rock glaciers velocities and dynamics. Therefore, ERS InSAR reveals itself to be an efficient remote sensing technique, not only for inventorying active rock glaciers over a wide area, but also for estimating and categorizing rock glacier displacement velocities.

Keywords: InSAR; permafrost creep; rock glacier activity; Swiss Alps.

Introduction

The study of rock glacier dynamics constitutes one of the major topics in alpine periglacial research (e.g., Haeberli et al. 2006). The abundant literature related to the creeping of ice-rich permafrost attests the great diversity of rock glacier velocities, from a few centimeters per year for the slowest ones to more than 5 m per year for the fastest ones (e.g.. Roer 2005). Recent studies in the European Alps have evidenced (1) the great inter-annual variation of rock glacier velocities (Delaloye et al. 2008a), (2) an acceleration since the 1980s (Kääb et al. 2007), and (3) the partial or complete destabilization of some rock glaciers (e.g., Delaloye et al. 2008b, Roer et al. 2008). For these reasons, it appears that the usual classification—active, inactive, relict—does not permit the whole range of rock glacier velocities and dynamics to be described accurately. Therefore, a more precise classification of rock glacier velocities would be desirable.

Space-borne Synthetic Aperture Radar Interferometry (InSAR) is a well-established technique for mapping centimeter temporal changes in surface topography (Bamler & Hartl 1998, Rosen et al. 2000, Strozzi et al. 2001). In mountain areas above the tree line, it is possible to detect mass movements mostly during the snow-free period (Rott et al. 1999, Delaloye et al. 2007a). In particular, several studies have demonstrated the efficiency of InSAR for estimating rock glacier displacements (e.g., Kenyi & Kaufmann 2003, Strozzi et al. 2004, Kääb et al. 2005, Kaufmann et al. 2007). In the framework of the ESA (European Space Agency) SLAM (Service for Landslide Monitoring) project and with the support of the Swiss Federal Office for the Environment, the potential of InSAR to inventory mass wasting in the alpine periglacial belt has been tested. Both magnitude and spatial pattern of slope instabilities have been evaluated over a large area of the western Swiss Alps (50 x 30 km) (Fig. 1), using data of the European Remote Sensing satellites ERS-1 and ERS-2 dating from 1995 to 2000.

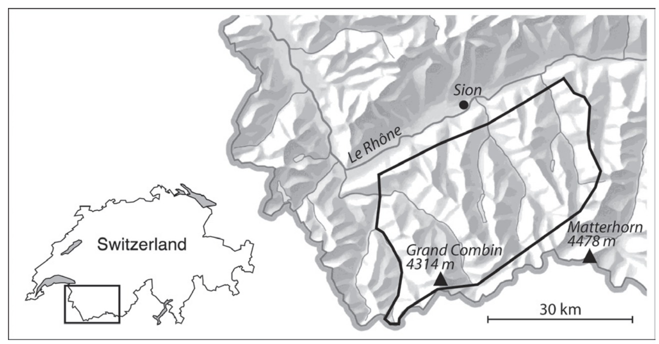

Figure 1. Area investigated.

This paper focuses on the various rates of rock glacier activity, which can be evaluated by ERS InSAR. After presenting the method and the dataset, the paper proposes a classification of rock glaciers, according to their typical ERS InSAR signals and morphological characteristics. Special attention was put on destabilization signs, which indicate a change in rock glacier dynamics.

Methods and Datasets

For this study, a total of 34 interferograms computed from ERS SAR images acquired at C-band (wavelength: 5.6 cm) between 1995 and 2000, with baselines shorter than 100-150 m, were used. Time lapse ranges between 1 day and 1085 days (in fact multiples of 35 days ± 1 day). The topographic reference was determined from an external digital elevation model with a spatial resolution of 25 m and an estimated vertical accuracy of 3 m (DHM25 © 2003 swisstopo). The InSAR products were also computed at 25 m spatial resolution. A change of the InSAR phase of one cycle is related to a movement of half the wavelength (2.8 cm) in the satellite line-of-sight direction, which is inclined at ~23° from the nadir and, in the western Swiss Alps, oriented toward the east +~12° for ascending orbits and toward the west -~12° for descending orbits. Thus, phase signals (i.e., change in the InSAR phase) detected on 1-day lag, 35-day lag, and 1-year lag interferograms can be interpreted as three orders of velocities, that is, respectively, centimeters per day, per month, and per year.

Important limiting factors of InSAR in mountainous terrain arise from temporal decorrelation, the satellite viewing geometry, and inhomogeneities in the tropospheric path delay. Atmospheric perturbations may cause phase changes related to the altitude. Among the other disruptive parameters, the wet snow, typically, can strongly reduce the reliability of an interferogram. This problem is especially present when working in alpine periglacial areas. In the Alps, above 2500 m a.s.l., the snow-free period is reduced to a few months, between July and early October. In addition, summer snowfalls are not uncommon at these altitudes, which can make many acquisitions unusable. On the other hand, cold snow is almost transparent to a radar wave. Thus, if the snow cover does not evolve, which may be possible only for few days, rapid movements can be identified in winter (Strozzi et al. 2004). Another limitation is the vegetation, which disturbs the radar backscatter and prevents any analysis in forest areas. Rock walls appear also strongly decorrelated, because of topographic effects. Finally, it is not possible to identify creeping landforms smaller than at least 2 x 2 grid cells (i.e., 50 x 50 m).

In order to identify the various rates of activity of active rock glaciers, different steps were followed:

- Evaluation of the reliability of the different interferograms. In particular, it was necessary to select the images for which the signal was not perturbed by the snow cover (both from the previous winter and from recent snowfalls). As a result, several interferograms could not be used in this study. The eight most reliable interferograms are listed in Table 1.
- Identification and delimitation of areas showing signals of potential slope motion by analysing the selected interferograms with various time scales and with different zoom levels.
- Determination of the corresponding geomorphological process (or landform) by orthophoto analysis or field observations.
- When available, comparing the InSAR estimated velocities to differential GPS data or airborne photogrammetric analysis.

Table 1. Dates of the best suited ERS SAR interferograms.

Dates	Direction	Days
11-12 March 1997	asc./desc.	1
29-30 July 1997	asc./desc.	1
3 Sept. - 8 Oct. 1997	descending	35
29 July - 3 Sept. 1997	ascending	35
18 Sept. 1996 - 30 July 1997	descending	315
8 Oct. 1997 - 23 Sept. 1998	descending	350
15 July 1998 - 8 Sept. 1999	descending	420
7 Oct. 1997 - 14 July 1998	ascending	279

InSAR-Detected Velocities

About 600 polygons corresponding to spatially limited slope movements were identified throughout the whole investigated area. Among these polygons, about 280 were attributed to "active" rock glaciers. The other ones correspond to landslides, solifluction, push moraines, or debris-covered glaciers.

For four rock glaciers of the inventory, an obvious phase signal is detected on 1-day lag interferograms. Figure 2 illustrates the data for the Tsaté-Moiry rock glacier. The summer interferogram displays a very clear signal all along the rock glacier (Fig. 2a). On the winter interferogram (Fig. 2b), the signal is a little less marked, which may indicate slower winter velocities. These data mean that the motion is in the cm range per day, which corresponds to more than 3 m a^{-1}. Terrestrial measurements with differential GPS carried out on the rock glacier revealed velocities even up to 7 m a^{-1} between 2006 and 2007. Similar InSAR signals were observed on the Petit Vélan rock glacier, where seasonal velocities up to 2 cm per day were measured in summer 2005 and 2007 (Delaloye et al. 2008b).

Some rock glaciers display a low 1-day phase signal, whereas the 1-month signal is decorrelated, that is larger than 1-phase cycle (2.8 cm). This is, for example, the case for the Tsarmine rock glacier (Fig. 3). In Figure 3a, a low signal can be detected on the 1-day summer interferogram (arrow), even if it is close to the noise level. The corresponding velocity can be estimated to a few millimeters per day, that is 1-2 m a^{-1}, which is confirmed by differential GPS measurements carried out since 2004 (see also Lambiel 2006). On the 1-month interferogram, the decorrelation is widespread over the landform (Fig. 3b).

Rock glaciers with velocities corresponding to the two previous categories constitute 5% maximum of the sample. On most of the InSAR-identified rock glaciers, a signal can only be detected with a 1-month interval. These rock glaciers can appear widely decorrelated, as it is the case for the Becs-de-Bosson rock glacier (Fig. 4) (Perruchoud & Delaloye 2007). This corresponds to minimum velocities of 20-30 cm a^{-1}. Another example is the Milon east rock glacier (Fig. 5a).

On numerous rock glaciers, the signal is hardly detectable at a 35-day lag, but is evident at a 1-year interval. The Milon west rock glacier is a nice example of this type (Fig. 5). Whereas only a very low signal occurs on the

1-month interferogram, the signal is evident on the 1-year interferogram. However, it remains rather correlated on the major part of the landform, which indicates a surface velocity of 2-3 cm a^{-1}.

Finally, rock glaciers showing only a low 1-year ERS InSAR signal or no signal at all creep with velocities slower than the phase cycle, i.e., 2.8 cm a^{-1}.

Interpretation

The presented examples show the strength of InSAR for distinguishing the large range of active rock glaciers velocities. Table 2 summarizes the ERS InSAR-detected velocities and the corresponding classification which can be proposed. The frequency of destabilization indices for each category, which attests a change in the rock glacier dynamics, is also reported in the table.

Very high velocity

Phase signals observed on 1-day lag interferograms allowed movements in the order of a centimeter per day, which means several meters per year, to be identified. This magnitude of velocities, which can be qualified of *very high*, has rarely been mentioned hitherto. However, recent studies have reported the existence of other unusually rapid rock glaciers (e.g., Roer et al. 2008). Landslide-like features, like well-developed scars and crevasses, are often observed on these landforms (Fig. 2c), which indicates a strong destabilization and a complete change in the rock glacier dynamics.

High velocity

Rock glaciers showing a low 1-day and a decorrelated 1-month ERS InSAR signal move with a speed of 1-2 m a^{-1}. Such velocities are in the upper range of the typical rock glacier velocities. These landforms may creep with such velocities because of a large amount of ice, relatively warm temperature, or steep slope, but some of them display indices of a recent acceleration. Among these indices, the thinning of the upper part and associated thickening of the lower part is frequently observed, as it is the case for the Tsarmine rock glacier (Fig. 3c). On such landforms, destabilization signs, like scars and crevasses, are frequent, but are often not as pronounced and obvious as for rock glaciers of the previous category.

Medium velocity

Rock glaciers only detected with a 1-month interval and for which the signal is decorrelated correspond to the classical active rock glaciers. Velocities are comprised between 20 cm a^{-1} and about 1 m a^{-1}. Indices of destabilization are occasionally observed. They may result from strong activity periods, as for the Mont Gelé B rock glacier, which moved with velocities of 120 cm a^{-1} between 2003 and 2004, whereas the velocities measured since 2000 are normally comprised between 20 to 60 cm a^{-1} (Lambiel 2006, Delaloye et al. 2008a).

Low velocity

Rock glaciers showing a correlated or a low signal on 35-day interferograms and a decorrelated signal on 1-year interferograms are active, but the deformation rate is only a few cm a^{-1} (max. 0.2 m a^{-1}). A cold permafrost temperature, low ice content or low inclined slope generally explain these moderate velocities. Even if they are rare, destabilization indices occur in some cases, as for example on Les Lués Rares rock glacier (Fig. 6). On this landform, which is located below the regional lower limit of permafrost (front at 2320 m a.s.l), numerous indices, such as subsidence features, blocks densely covered with lichens and bushes on the front should indicate a very low activity. However, fresh scars in the front underline the current instability of the rock glacier (Fig. 6c), which is confirmed by the obvious and coherent signal visible on the 35-day lag interferogram, indicating velocities of about 10-20 cm a^{-1} (Fig. 6a). Both these velocities and the limit of the moving area are confirmed by GPS measurements. About ten rock glaciers of the inventory display such characteristics. They all show evidences of a former inactivity or at least a very low activity (like vegetation growth and abundance of lichens), but display some recent destabilization indices.

Very low velocity

The rock glaciers which are only detected on 1-year lag interferograms correspond to the classical *inactive* landforms. Their velocity is in the cm range per year.

Discussion

The inventory of creeping frozen debris bodies over a wide area is rarely exhaustive and the delimitation of the landforms can be highly subjective, whatever the method used. This is particularly the case with InSAR, as a potential signal may be due to other causes than a change in topography (atmospheric perturbations, vegetation, snow cover, etc.). Thus, the successfulness of such a study depends mainly on the availability of reliable interferograms. In this project, the discovery of a few very rapid rock glaciers was possible thanks the availability of very good quality summer and winter 1-day lag interferograms. Likewise, two excellent 35-day interval images, both in the ascending and descending mode, permitted us to delimitate classical active rock glaciers with a good accuracy. On the other hand, 1-year interferograms were not as reliable, but the identification of several low active rock glaciers was nonetheless possible.

In some cases, the signal is very low, such as, for example, the Tsarmine rock glacier on the 1-day interferogram (Fig. 3a) and the Milon west rock on the 35-day interferogram (Fig. 5a). For the Tsarmine rock glacier, the reliability of the signal was confirmed by GPS measurements. In the absence of terrestrial data, only the analysis of several interferograms and a good knowledge of the corresponding geomorphology allow the signal to be interpreted as a movement and not attributed to noise or atmospheric artefacts. However, the presence of a clear signal on a wider time interval,

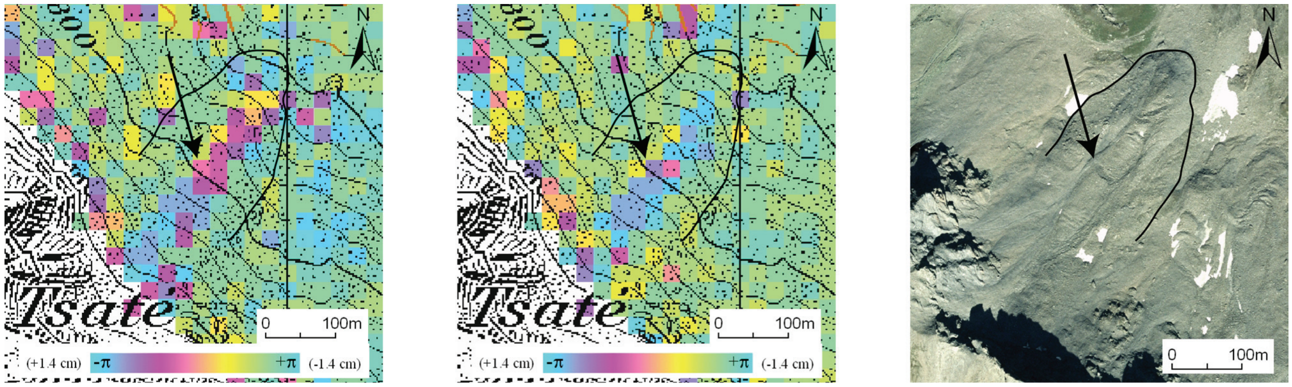

(a) (b) (c)

Figure 2. The active Tsaté-Moiry rock glacier. (a) 29-30 July 1997 (1d), ascending orbit; (b) 11-12 March 1997 (1d), ascending orbit; (c) orthoimage (Sept. 1999); scars are clearly visible on the centre of the rock glacier (arrow). Reproduced by permission of swisstopo (BA081058).

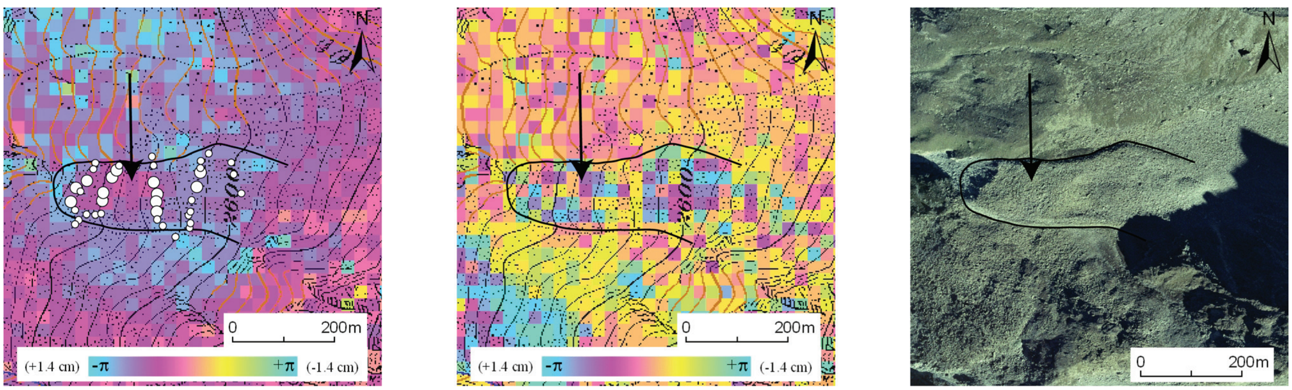

(a) (b) (c)

Figure 3. The active Tsarmine rock glacier. (a) 29-30 July 1997 (1d), descending orbit; white dots indicate horizontal surface velocities measured with differential GPS between 2004 and 2005; big dots = velocities > 4 mm/day; small dots = velocities < 4 mm/day; (b) 3 Sept..-8 Oct. 1997 (35d), descending orbit; (c) orthoimage (Sept. 1999). Reproduced by permission of swisstopo (BA081058).

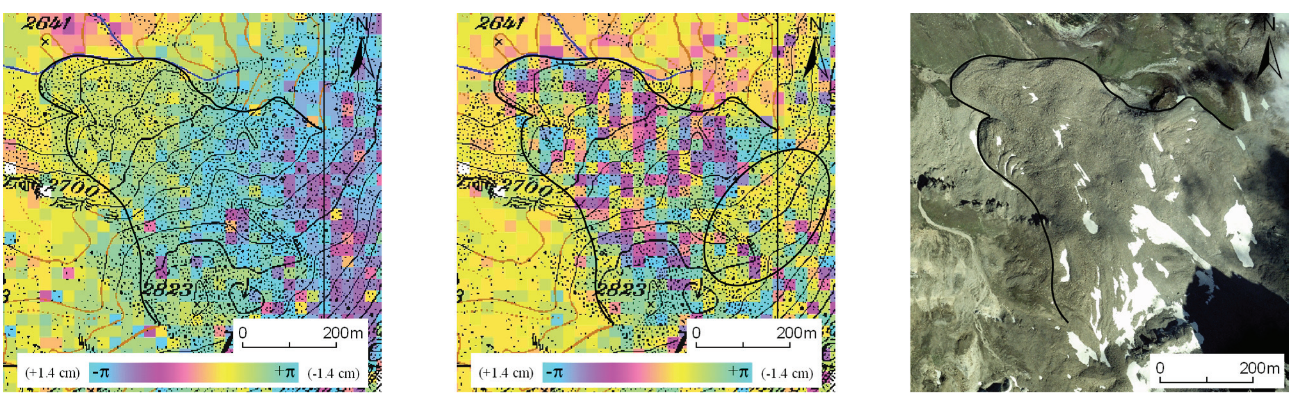

(a) (b) (c)

Figure 4. The active Becs-de-Bosson rock glacier. (a) 29-30 July 1997 (1d), descending orbit; (b) 3 Sept..-8 Oct. 1997 (35d), descending orbit; the circled area indicates an absence of movement, which is confirmed by GPS data (Perruchoud & Delaloye 2007); (c) orthoimage (Sept. 1999). Reproduced by permission of swisstopo (BA081058).

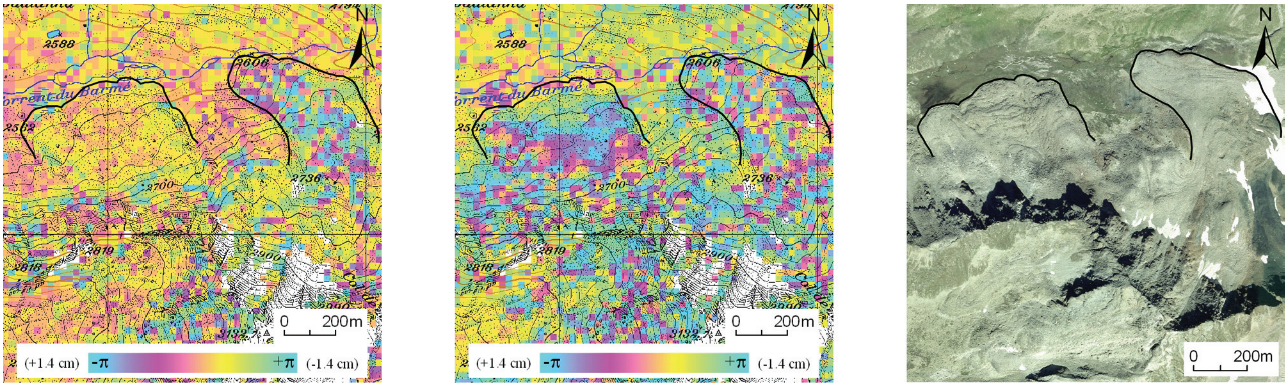

(a) (b) (c)

Figure 5. The active Milon east (right) and low active Milon west (left) rock glaciers. (a) 3 Sept..-8 Oct. 1997 (35d), descending orbit; (b) 18 Sept. 1996-30 July 1997 (315d), descending orbit; (c) orthoimage (Sept. 1999). Reproduced by permission of swisstopo (BA081058).

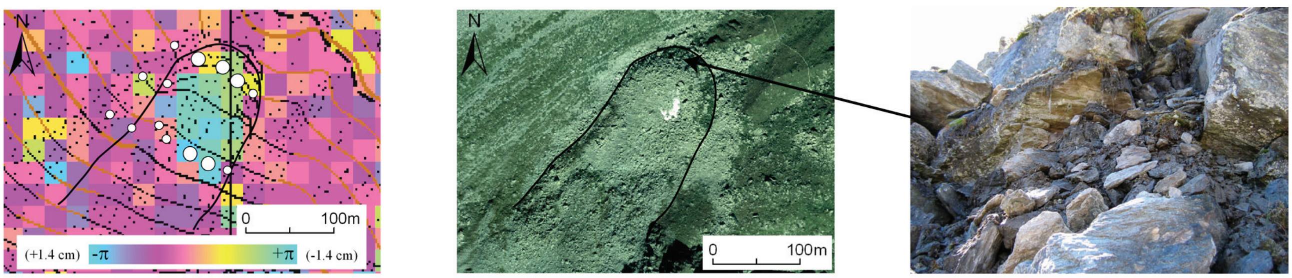

(a) (b) (c)

Figure 6. Les Lués Rares rock glacier. (a) 29 July-3 Sept. 1997 (35d), ascending orbit; white dots indicate horizontal surface velocities measured with differential GPS between 2006 and 2007; big dots = velocities of 1-2 cm/35 days; small dots = velocities < 0.5 cm/35 days or no movement; (b) orthoimage (Sept. 1999); (c) view on the destabilised front. Reproduced by permission of swisstopo (BA081058).

Table 2. Classification of the rock glaciers according to their surface velocities.

Classical classification	ERS InSAR signal	Estimated surface velocity	Velocity classification	Destabilization
Active	1 day	> 2 m a^{-1}	very high	very frequent
	(1 day)/ 35 days decorrelated	1-2 m a^{-1}	high	Frequent
	35 days	0.2-1 m a^{-1}	medium	Possible
	(35 days correlated) / 1 year	0.03-0.2 m a^{-1}	low	Rare
Inactive	(1 year)	up to a few cm a^{-1}	very low	No
Relict	No	-	-	No

which confirms the activity of the landform, is an absolute prerequisite for attributing the signal to a change in the topography rather to noise.

One limiting factor for using InSAR in the study of rock glacier velocities is the fact that this technique gives an estimation of the movement for a time-delimited period. For this study, most of the interferograms used correspond to the period 1996–1997. Thus, the observed velocities should be valid only for this period. In addition, numerous active rock glaciers are in an acceleration phase since the 1980s (Kääb et al. 2007), and some of them are suffering strong changes in the process regime (Roer et al. 2008). Thus, the phase signal detected on the available interferograms may no longer reflect the current state of activity of the corresponding rock glaciers. However, the comparison of the ERS InSAR-detected signals to velocities measured with differential GPS on 15 landforms since 2004, that is nearly 10 years later, permitted us to validate the InSAR data. Moreover, additional field observations on several tens of rock glaciers allowed us to understand the cause of such and such range of velocities, like, for instance, the observation of destabilization processes, which are clearly connected to the very high velocities observed on some rock glaciers (Roer et al. 2008). Thus, even if the velocities may have changed since the end of the 1990s, it is very probable that most of the rock glaciers are still in the same range of velocities as ten years before.

Conclusion and Perspectives

ERS InSAR has revealed itself to be an efficient remote sensing technique, not only for inventorying active rock glaciers over wide areas, and more generally the creeping landforms of the alpine periglacial belt, but also for estimating and categorizing their displacement velocities. Thus, InSAR constitutes an interesting tool for the study of rock glacier dynamics in the context of a general acceleration of these landforms. However, the detected signal can be sometimes close to the noise level. Thus, reliable interferograms, orthophotos, and a good knowledge of the local geomorphology are necessary to interpret the detected signal correctly.

Further InSAR studies are feasible with the SAR sensors on board of the European Environmental Satellite ENVISAT (C-band, 5.6 cm wavelength, 35 days repeat cycle), the Japanese Advanced Land Observing Satellite ALOS (L-band, 23.6 cm wavelength, 46 days repeat cycle) and the German TerraSAR-X mission (X-band, 3.1 cm wavelength, 11 days repeat cycle), in orbit since 2002, 2006, and 2007, respectively. They should permit recent data on rock glacier velocities throughout wide areas to be obtained. However, no one is able to provide reliable data on rock glaciers with very high velocities anymore (Delaloye et al. 2008b), as did the ERS-1/2 tandem between 1995 and 1999.

Acknowledgments

We would like to thank the Associate Editor and the two anonymous reviewers for their useful feedback, and Meredith Blake for proofreading the English.

References

Bamler, R. & Hartl, P. 1998. Synthetic aperture radar interferometry. *Inverse Problems* 14: 1-54.

Delaloye, R., Lambiel, C., Lugon, R., Raetzo, H. & Strozzi, T. 2007a. Typical ERS InSAR signature of slope movements in a periglacial mountain environment (Swiss Alps). *Proceedings Envisat Symposium 2007, Montreux, Switzerland 23–27 April 2007* (ESA SP-636, July 2007), 3P7.

Delaloye, R., Lambiel, C., Lugon, R., Raetzo, H. & Strozzi, T. 2007b. ERS InSAR for detecting slope movement in a periglacial mountain environment (western Valais Alps, Switzerland). *Proceedings HMRSC-IX, Grazer Schriften der Geographie und Raumforschung*. 43: 113-120.

Delaloye, R., Perruchoud, E., Avian, M., Kaufmann, V., Bodin, X., Hausmann, H., Ikeda, A., Kääb, A., Kellerer-Pirklbauer, A., Krainer, K., Lambiel, C., Mihajlovic, D., Staub, B., Roer, I. & Thibert, E. 2008a. Recent interannual variations of rockglaciers creep in the European Alps. *Proceedings of the Ninth International Conference on Permafrost, Fairbanks, Alaska, June 29-July 3, 2008* (this proceedings).

Delaloye, R., Strozzi, T., Lambiel, C. & Perruchoud, E. 2008b. Landslide-like development of rockglaciers detected with ERS-1/2 SAR interferometry. *Proceedings ESA FRINGE Symposium 2007* (in press).

Haeberli, W., Hallet, B., Arenson, L., Elconin, R., Humlum, O., Kääb, A., Kaufmann, V., Ladanyi, B., Matsuoka, N., Springman, S. & Vonder Mühll, D. 2006. Permafrost creep and rock glacier dynamics. *Permafrost and Periglacial Processes* 17: 189-214.

Kääb, A., Huggel, C., Fischer, L., Guex, S., Paul, F., Roer, I., Salzmann, N., Schlaefli, S., Schmutz, K., Schneider, D., Strozzi, T. & Weidmann, Y. 2005. Remote sensing of glacier- and permafrost-related hazards in high mountains: an overview. *Natural Hazards and Earth System Science* 5: 527-554.

Kääb, A., Frauenfelder, R. & Roer, I. 2007. On the response of rockglacier creep to surface temperature increase. *Global and Planetary Change* 56(1-2): 172-187.

Kaufmann, V., Ladstädter, R. & Kienast, G. 2007. 10 years of monitoring of the Doesen rock glacier (Ankogel group, Austria) - A review of the research activities for the time period 1995-2005. In: D. Petrovič, (ed.), *Proceedings of 5th Mountain Cartography Workshop, 29 March-1 April 2006, Bohinj, Slovenia*: 129-144.

Kenyi, L. & Kaufmann, V. 2003. Measuring rock glacier surface deformation using SAR Interferometry. *Proceedings of the Eighth International Conference on Permafrost, Zürich, Switzerland, June 2003*. Balkema 1: 537-541.

Lambiel, C. 2006. *Le Pergélisol Dans les Terrains Sédimentaires à Forte Déclivité: Distribution, Régime Thermique et Instabilités*. Thèse, Université de Lausanne, Institut de Géographie, coll. "Travaux et Recherches" 33: 260 p.

Perruchoud, E. & Delaloye, R. 2007. Short-term changes in surface velocities on the Becs-de-Bosson rock glacier (western Swiss Alps). *Proceedings HMRSC-IX, Grazer Schriften der Geographie und Raumforschung* 43: 131-136.

Roer, I. 2005. *Rockglacier Kinematics in a High Mountain Geosystem*. PhD Thesis. Rheinischen Friedrich-Wilhelms Universität Bonn, 217 pp.

Roer, I., Avian, M., Delaloye, R., Lambiel, C., Haeberli, W., Kääb, A. & Kaufmann, V. 2008. Observations and considerations on collapsing active rockglaciers in the Alps. *Proceedings of the Ninth International Conference on Permafrost, Fairbanks, Alaska, June 29-July 3, 2008* (this proceedings).

Rosen P., Hensley, S., Joughin, I., Li, F., Madsen, S., Rodriguez, E. & Goldstein, R. 2000. Synthetic aperture radar interferometry. *Proceedings of the IEEE*, 88(3): 333-382.

Rott, H., Scheuchl, B., Siegel, A. & Grasemann, B. 1999. Monitoring very slow slope movements by means of SAR interferometry: A case study from a mass waste above a reservoir in the Ötztal Alps, Austria. *Geophysical Research Letters* 26(11): 1629-1632.

Strozzi, T., Wegmüller, U., Tosi, L., Bitelli, G. & Spreckels, V. 2001. Land Subsidence Monitoring with Differential SAR Interferometry. *Photogrammetric Engineering & Remote Sensing (PE&RS)* 67(11): 1261-1270.

Strozzi, T., Kääb, A. & Frauenfelder, R. 2004. Detecting and quantifying mountain permafrost creep from in situ inventory, space-borne radar interferometry and airborne digital photogrammetry. *International Journal of Remote Sensing* 25(15): 2919-2931.

Sensitivity of Coastal Erosion to Ground Ice Contents: An Arctic-Wide Study Based on the ACD Classification of Arctic Coasts

Hugues Lantuit
Alfred Wegener Institute for Polar and Marine Research, Potsdam, Germany
Pier Paul Overduin
Alfred Wegener Institute for Polar and Marine Research, Potsdam, Germany
Nicole Couture
Dept. of Geography, McGill University, Montréal, Canada
Rune Strand Ødegård
Gjøvik University College, Gjøvik, Norway

Abstract

Changing sea ice conditions and thawing permafrost in the Arctic could lead to dramatic changes in coastal erosion dynamics. To address this issue, the Arctic Coastal Dynamics (ACD) project brought together experts from all circum-Arctic countries around a common project: the ACD classification of Arctic coasts. This paper uses 545 segments from the beta version of the ACD classification to investigate statistical relations between coastal erosion rates on Arctic coasts and ground ice content. Ground ice content and retreat rates are only weakly correlated statistically ($r = 0.48$, relationship statistically significant at $\alpha = 0.01$), but the multifactor nature of coastal erosion in the Arctic shows us that ground ice is a major factor affecting erosion processes. The current study integrates several geographical settings and time scales and is therefore integrative enough to be used as a benchmark for future empirically based models

Keywords: Arctic; coastal erosion; GIS; ground ice.

Introduction

Arctic coasts are among the most vulnerable environments to climate change. Changing sea ice conditions and thawing permafrost could lead to dramatic changes in coastal erosion dynamics. To address this issue, ACD was initiated to provide a comprehensive review of coastal erosion processes at the Arctic scale. This paper uses data from the beta version of the ACD classification to investigate statistical relations between coastal erosion rates on Arctic coasts and ground ice content. Close to 600 segments were used to systematically compare and plot ground ice content and coastal erosion rates. The specific aims of this paper are to document the statistical relation between ground ice and coastal erosion rates and to compare those relations with previously published studies. The statistical relationship extracted from this study will be used as a benchmark for empirical models of coastal erosion.

Background

Arctic coastal erosion

Coastal erosion in the Arctic is different from its counterpart in temperate regions due to the short open-water season (3-4 months) and to the presence of permafrost, and thus of ground ice, in coastal sediment.

Coastal retreat rates are also highly variable both spatially and temporally (Lantuit & Pollard 2008, Rachold et al. 2000, Solomon 2005). Spatial variability is mainly due to changes in the lithology, cryology, and geomorphology of coastal cliffs, including ground ice content.

Ground ice is a unique feature of polar coastal systems. It is present in the subaerial part of the shore profile, but also underneath the water column, as submarine ground ice (Mackay 1972, Rachold et al. 2007). Its presence affects both the response of the shore to thermal-hydrodynamical forcing and the sediment budget of the coast (Are 1988, Dallimore et al. 1996). The presence of ground ice leads to a process termed "thermal abrasion" (Are 1988) which encompasses the combined action of waves and thawing of the permafrost. It has been shown to facilitate erosion (Héquette & Barnes 1990, Kobayashi et al. 1999), through the presence of ice in coastal cliffs, or through the occurrence of large thermokarst features in the coastal zone (Lantuit and Pollard 2005, Lantuit & Pollard 2008, Wolfe et al. 2001). Dallimore et al. (1996) suggested that thaw settlement of ice-rich sediments in the nearshore zone could induce a change in the shoreface profile, hence enhancing wave efficiency during storms.

However, not all Arctic coastlines are characterized by subsea ice-rich permafrost and other explanations must be sought. Héquette and Barnes (1990) attributed those to the occurrence of ice scours and sediment entrainment by sea ice in the offshore zone, which as shown by Forbes and Taylor (1994) can alter significantly the coastal sediment budget. They based their hypothesis on the weak correlation between retreat rates and several factors including ground ice, wave height, and grain size (Fig. 1). This paper attempts at providing an expanded characterization (Arctic-wide) of the statistical relation between ground ice contents and re-evaluating the relation proposed by Héquette and Barnes (1990) for the southern Beaufort Sea by using the ACD classification of Arctic coasts.

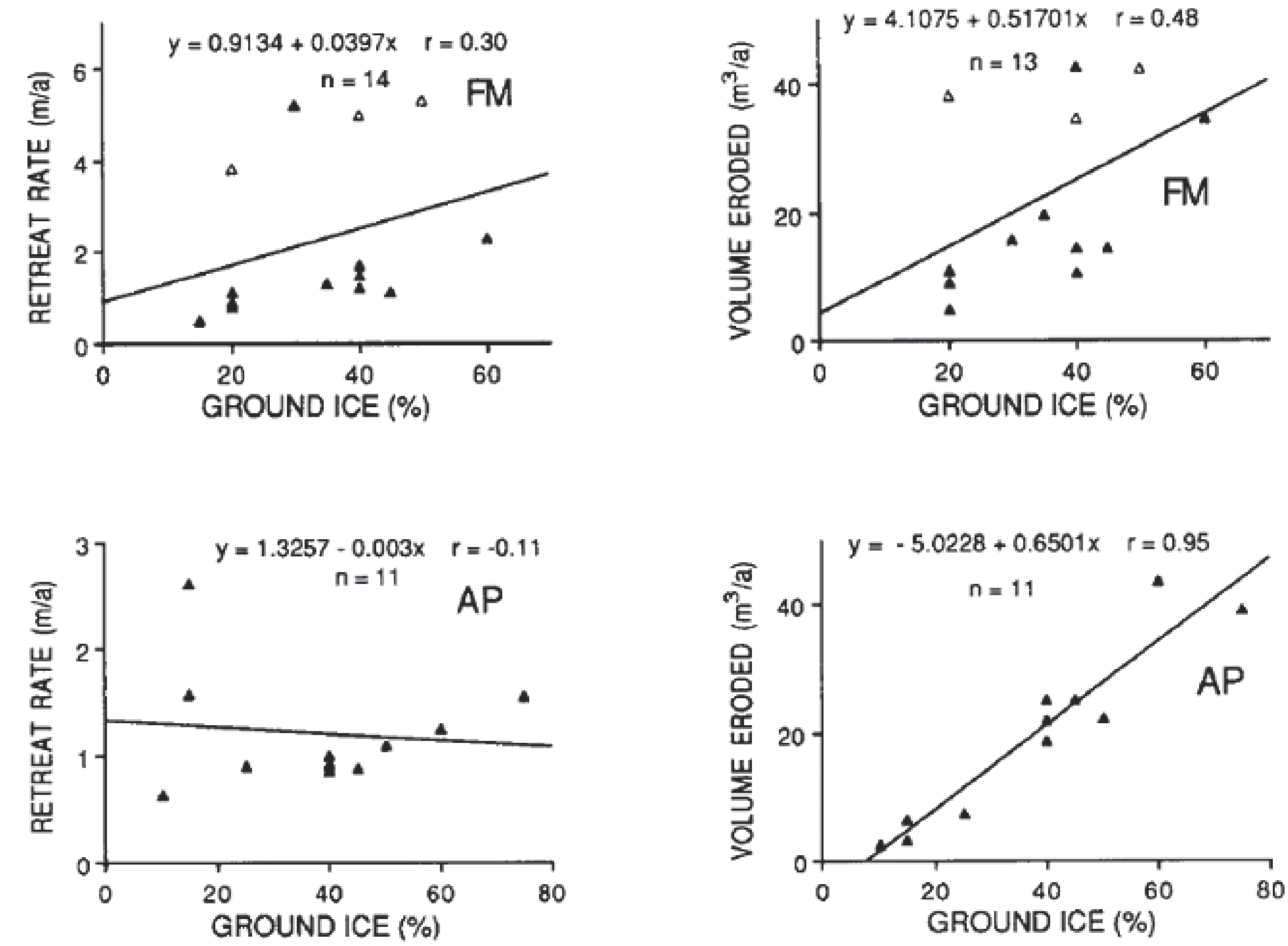

Figure 1. Coastal retreat and erosion as a function of visible ground ice in the bluffs. FM - field measurement sites; AP - aerial photograph sites; open triangles indicate minimum values of retreat rate (after Héquette & Barnes, 1990).

The ACD classification of Arctic coasts

The ACD classification was conceived as a broad enough framework to encompass existing classification schemes while capturing fundamental information for the assessment of climate change impacts and coastal processes. The implementation of the classification was done by so-called “regional experts”, who, based on digital and paper products and personal knowledge provided information which was subsequently gathered into a circum-Arctic coastal database. The classification was primarily geomorphological in nature and considered: (1) the shape or form of the subaerial part of the coastal tract, (2) the marine processes acting upon the coast, (3) the shape or the form of the subaqueous part of the coastal tract and (4) the lithofacies of the materials constituting the coastal zone

The beta version of the classification is made of 1331 segments each characterized by a series of geomorphological quantitative and qualitative variables. The classification is stored as an ISO 19115-compliant personal geodatabase and is therefore mappable in off-the-shelf Geographical Information Systems (GIS) (e.g., Fig. 2).

Methods

The first step of the processing consisted in reducing the dataset to a set of usable segments: Of the 1331 segments available in the beta version of the ACD classification of Arctic coasts, only segments for which ground ice content, coastal erosion rate, and backshore elevation (i.e. cliff height) were conjointly available were retained. The resulting dataset was reduced to 561 segments.

Subsequently, we consolidated the dataset by removing segments for which the presence of permanent sea ice cover in the summer hampered the development of erosion. The objective was to remove segments for which ground ice contents can be medium to high, yet unaffected by erosion due to sea ice presence in the summer. We used the NSIDC 1979-2000 median sea ice edge position and simply excluded segments located within the permanent sea ice zone in the dataset. We chose not to take into account the marked decreases observed in recent years in order to remain consistent with the times at which coastal erosion rates were mostly determined in the ACD classification.

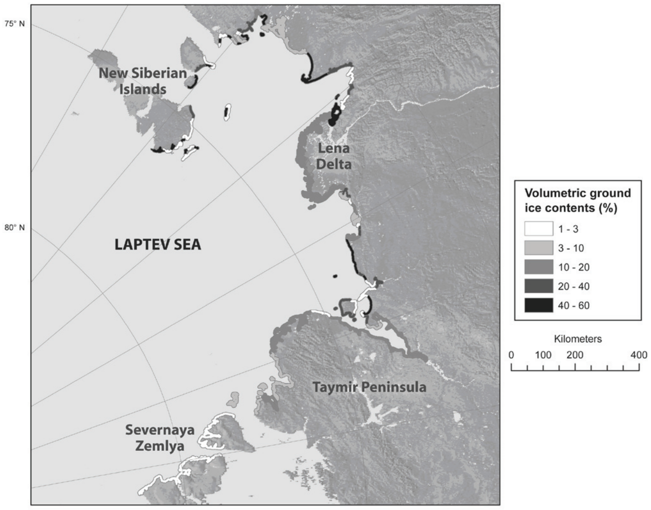

Figure 2. An example of the ACD classification capabilities: Volumetric ground ice contents of shore sediments in the Laptev Sea region (after Lantuit et al. 2008).

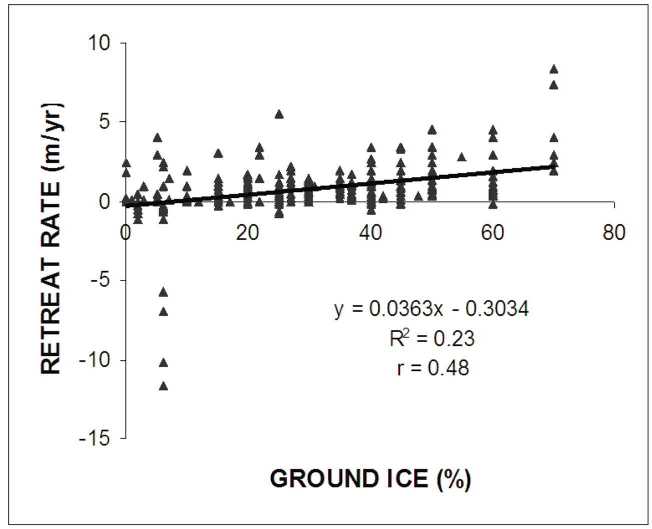

Figure 3. Retreat rate as a function of volumetric ground ice contents.

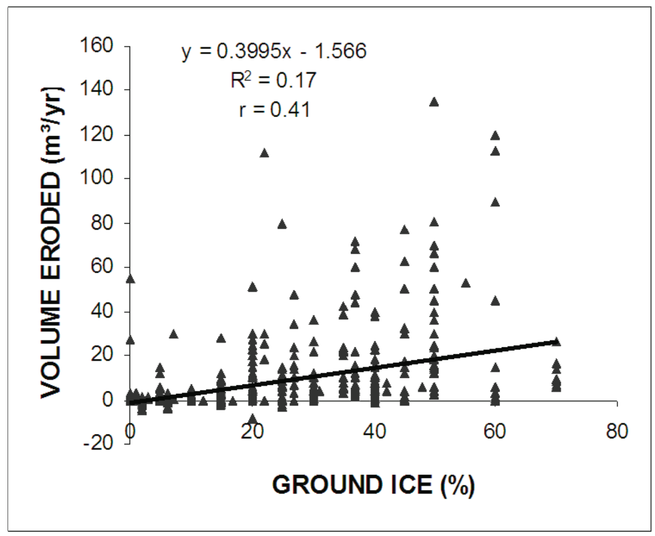

Figure 4. Volume eroded as a function of volumetric ground ice contents.

Using this criterion to consolidate the datasets we brought down the number of segments for analysis to 545. The resulting segments were remarkably ubiquitously distributed along coastal regions of the Arctic and can therefore be considered to be spatially unbiased. The Coast of the Canadian Archipelago was the only section, for which the entire coastline was not retained, due to the presence of sea ice throughout the summer season. At least 50 segments were used for each of the seven other sectors considered in the Analysis (Barents Sea, Kara Sea, Laptev Sea, East Siberian Sea, Chukchi Sea, Beaufort Sea)

We then ran two sets of analysis using retreat rates in m/yr and eroded volumes in m^3/yr (for a 1 m stretch of coastline). Eroded volumes were calculated by combining backshore elevations and retreat rates and constraining artificially the calculation to a 1 km stretch of coastline:

$$V = l \cdot h \cdot CRR \tag{1}$$

where V is the yearly eroded volume, h the backshore elevation, and CRR the annual coastal retreat rate. In our calculation, we normalized all l values to 1 km to facilitate comparison of segments

Results and Discussion

Simple regression analyses

The analysis of the retreat rates versus the percentages of visible ground-ice revealed a relatively weak relationship with a correlation coefficient r = 0.48 (R^2 = 0.23) (Fig. 3). The correlation between volumes eroded and ground ice was weaker (r = 0.41, R^2 = 0.17) (Fig. 4).

Both relations were statistically significant at α=0.01. Though weak, the correlation coefficient relating ground ice contents to retreat rates is considerably greater than the coefficients published by Héquette and Barnes (1990) (Fig. 1). In contrast, the correlation coefficient relating ground ice contents to eroded volumes is lower than the one observed by Héquette and Barnes (1990).

One can logically conclude that coastal erosion in the Arctic is not uniquely related to the presence of ground ice, but that the presence of ground ice significantly influences the process. The data available in the classification doesn't include hydrodynamic forcing and a multi-regression analysis is not currently possible. It should nevertheless be conducted in the future to better assess the statistical weight of ground ice in the thermal abrasion process.

Discussion

The lack of a correct indicator for ground ice in the nearshore zone is a strong deterrent in attempting to establish such relationships. The complex nature of ground ice, including its temperature and cryostructure, makes it difficult to correctly statistically relate ground ice to other variables using volumetric ice contents. One would gain from incorporating heat transfer and temperature properties for instance. For the lack of a better dataset, the relationship established using the ACD classification of Arctic coasts is probably the most detailed attempt at establishing such a relation.

These contradictory results between this paper and Héquette and Barnes (1990) can be explained by the multifaceted interaction of ground ice with coastal processes. Ground ice presence in the nearshore zone influences the course of erosion by modifying the shoreface profile (see above) when it thaws. It also provides the sediments at sea level with a transient strength which lasts until beach sediments are removed during storms and ice-rich sediments are exposed. Most importantly it induces the presence of large thermokarst processes in the subaerial part of the nearshore zone.

Thermokarst processes in the nearshore zone, such as retrogressive thaw slumps, are cyclic and their activity is intimately linked to the removal of sediment by storms. Following periods of large activity, the amount of sediment released by direct melting of ground ice by short-wave radiation influx above water accumulates at the foot of these landforms and progressively impedes the development of new slumps. This lasts until large storms occur and remove the sediment lobes, providing room for a new cycle of activity (Wolfe et al. 2001, Lantuit & Pollard 2008). The timescales at which these processes occur are comprised between 10^1 and 10^2 years (Lantuit & Pollard 2008) and are necessarily larger than the time spans used to calculate erosion rates or eroded volumes. Furthermore, because the cycle is strongly associated with storm activity, it is necessarily local.

This paper hypothesizes that the statistical relations extracted from the ACD classification of Arctic coasts, by their wide geographic distribution integrate this cyclic dimension better than the data from the Beaufort Sea only and should therefore be used in future applications. The two correlation coefficients obtained in this study are much closer to one another than the ones obtained by Héquette and Barnes (1990).

Conclusion

Ground ice content and retreat rates are only weakly correlated statistically, even though the relationship is statistically significant at $\alpha = 0.01$. However, due to the presence of multiple factors acting upon the coast in the Arctic realm, one cannot exclude that ground ice is a major, if not the most important, factor affecting erosion processes. Further studies will be needed to assess the role of each factor in a single integrated framework.

The relation presented in this paper should contribute to parameterization of future empirical models of coastal erosion as the most extensive effort to relate ground ice to retreat rates.

Acknowledgments

The authors wish to thank F. Steenhuisen, from the Arctic Centre, Groningen, The Netherlands and the members of the ACD group for their contribution to the beta version of the ACD classification of Arctic coasts. This paper is a contribution to the Fourth International Polar Year (IPY), 2007-2008.

References

Aré, F.E. 1988. Thermal abrasion of sea coast. *Polar Geography and Geology* 12. VH. Winston & Sons, 157 pp.

Dallimore, S.R., Wolfe, S.A. & Solomon, S.M. 1996. Influence of ground ice and permafrost on coastal evolution, Richards Island, Beaufort Sea coast, N.W.T. *Canadian Journal of Earth Sciences* 33: 664-675.

Forbes, D.L. & Taylor, R.B. 1994. Ice in the shore zone and the geomorphology of cold coasts. *Progress in Physical Geography* 18: 59-89.

Héquette, A. & Barnes, P.W. 1990. Coastal retreat and shoreface profile variations in the Canadian Beaufort Sea. *Marine Geology* 91: 113-132.

Kobayashi, N., Vidrine, J.C., Nairn, R.B. & Solomon, S.M. 1999. Erosion of frozen cliffs due to storm surge on Beaufort sea coast. *Journal of coastal research* 15: 332-344.

Lantuit, H. & Pollard, W.H. 2005. Temporal stereophotogrammetric analysis of retrogressive thaw slumps on Herschel Island, Yukon Territory. *Natural. Hazards and Earth System. Sciences* 5: 413-423.

Lantuit, H. & Pollard, W.H. 2008. Fifty years of coastal erosion and retrogressive thaw slump activity on Herschel Island, southern Beaufort Sea, Yukon Territory, Canada. *Geomorphology* doi:10.1016/j.geomorph.2006.07.040.

Lantuit, H., Steenhuisen, F., Graves-Gaylord, A., Ødegård, R. & Atkinson, D. accepted. 2008. The Arctic Coastal Dynamics geospatial framework. In: W.H. Pollard, N. Couture, H. Lantuit & V. Rachold (eds.), *Arctic Coasts - Circum-Polar Processes and Dynamics*. Montréal, Canada: McGill-Queens University Press.

Mackay, J.R., 1972. Offshore permafrost and ground ice, southern Beaufort Sea, Canada. *Canadian Journal of Earth Sciences* 9: 1550-1561.

Rachold, V., Grigoriev, M.N., Are, F.E., Solomon, S., Reimnitz, E., Kassens, H. & Antonow, M. 2000. Coastal erosion vs. riverine sediment discharge in the Arctic shelf seas. *International Journal of Earth Sciences* 89: 450-460.

Rachold, V., Bolshiyanov, D.Y., Grigoriev, M.N., Hubberten, H.-W., Junker, R., Kunitsky, V.V., Merker, F., Overduin, P.P. & Schneider, W. 2007. Near-shore Arctic subsea permafrost in transition, *EOS Transaction of the American Geophysical Union* 88(13): 149-156.

Solomon, S.M. 2005. Spatial and temporal variability of shoreline change in the Beaufort-Mackenzie region, northwest territories, Canada. *Geo-Marine Letters* 25(2-3): 127-137.

Wolfe, S.A., Kotler, E. & Dallimore, S.R. 2001. *Surficial Characteristics and the Distribution of Thaw Landforms (1970 to 1999), Shingle Point to Kay Point, Yukon Territory.* Open File 4115, Geological Survey of Canada.

The Kind and Distribution of Mid-Latitude Periglacial Features and Alpine Permafrost in Eurasia

Frank Lehmkuhl
Department of Geography, RWTH Aachen University, Templergraben 55, D-52056 Aachen, Germany

Abstract

The distribution of different periglacial landforms in various mid-latitude mountains of Eurasia is described. Alpine discontinuous and continuous permafrost is present in all these mountains, but in the humid mountains, this zone is very small due to the lower elevation of the glacier snowline (or ELA). In the more continental regions of Asia, this zone is much broader due to high elevation of the ELA. In these areas cryoplanation terraces, patterned ground, and rock glaciers occur in relative low elevations and are also widespread within the forest ecotone. On the other hand, solifluction features occur in higher regions due to arid conditions and especially the lack of soil humidity during the freeze-thaw cycles. In the Verkhoyansk Mountains further north in latitude, even in the mountain foreland and in the boreal forest of the Lean-Aldan Basin, periglacial features are widespread on continuous permafrost.

Keywords: Central Asia; European Alps; mid-latitude; periglacial features; permafrost.

Introduction

This paper presents a comprehensive review study concerning the kind and distribution of periglacial phenomena of mid-latitude mountains of Eurasia. New results are from continental Asia, in particular the mountain areas of Western Mongolia, the Russian Altai, and the Verkhoyansk Mountains (Fig. 1). The distribution of different periglacial landforms in these mountains is compared to the European and Japanese Alps. A first overview concerning mid-latitude periglacial landforms is given by Höllermann (1985); an overview for the high Asian mountains is given by Matsuoka (2003).

Periglacial Landforms in Mountain Areas

Concerning periglacial phenomena in mountain environments, especially small-scale periglacial or cryogenic landforms, are studied in the literature (e.g., Washburn 1979). Active solifluction (or gelifluction) generally occurs above the timberline as the forests stabilise and protect the ground. In general, the periglacial zone can divide into two sub-belts: First, the lower periglacial sub-belt, which includes mainly bound or turf-banked solifluction (steps, benches, terraces, lobes), and second, the upper sub-belt. The latter is characterized by unbound (or free) solifluction, blockfields, debris, stone pavements, and patterned ground (Troll 1973, Höllermann 1985). This periglacial zonation is obvious in most mid-latitude mountains above the timberline and provides information on the geoecology of high mountain environments, as the distribution of these landforms depends on several different factors (e.g., topography, geology and substrate, climate, vegetation, and soil water; see Fig. 2). Periglacial phenomena are generally controlled by cold climatic conditions, where the mean annual air temperature (MAAT) as well as the duration and depth of snow cover are low. The modern altitudinal belts of the vegetation, the soils, and the geomorphological processes are controlled by these general climatic conditions, but also by the different radiation on the northern and southern slopes (Höllermann 1985). However, new results from the European Alps show that active soil movements only occur in the upper sub-belt (Veit 2002).

Besides the different small-sized landforms of solifluction rock glaciers are typical landforms of high mountain environments. Two types are distinguished: (1) ice-cemented rock glaciers built up by unconsolidated rock or talus, and (2) morainic deposits. They are generated by the creep of mountain permafrost saturated or supersaturated with ice. Ice-cored rock glaciers consist of glacier ice mantled with a debris cover and originate from dead ice (Ishikawa et al. 2001). Rock glaciers affect unconsolidated but frozen rock fragments, creating characteristic landforms with a tongue or lobate shape and a surficial pattern of furrows and ridges that indicate the internal flow process (Barsch 1996, Fort 2002, Haeberli 2000). In addition, protalus ramparts, and talus slope or talus cone rock glaciers are described in the literature (e.g., Barsch 1996).

It is generally accepted that the distribution of rock glaciers is a good marker of discontinuous mountain permafrost (e.g., Barsch 1996). However, Fort (2002) mentioned that the identification of rock glaciers in the Himalayas is similar to other features such as rockslides and/or debris covered glaciers and, therefore, it is sometimes difficult to distinguish these landforms. Rock glaciers are described in detail especially in the European Alps and in mountain regions of North America (see reference in Barsch 1996). The knowledge of the distribution of rock glaciers in the different mountain systems on Earth is still very incomplete (Barsch 1996). Nevertheless, mountains with a continental climate, and thus the greatest differences between timberline and snowline (up to 1500 m) are more favourable for rock glaciers than those with a difference of less than 500 m (Höllermann 1985, Barsch 1996).

The upper limit of the periglacial belt results from steep high mountain topography or from the extent of perennial snow and ice in the higher altitudes (glacial belt).

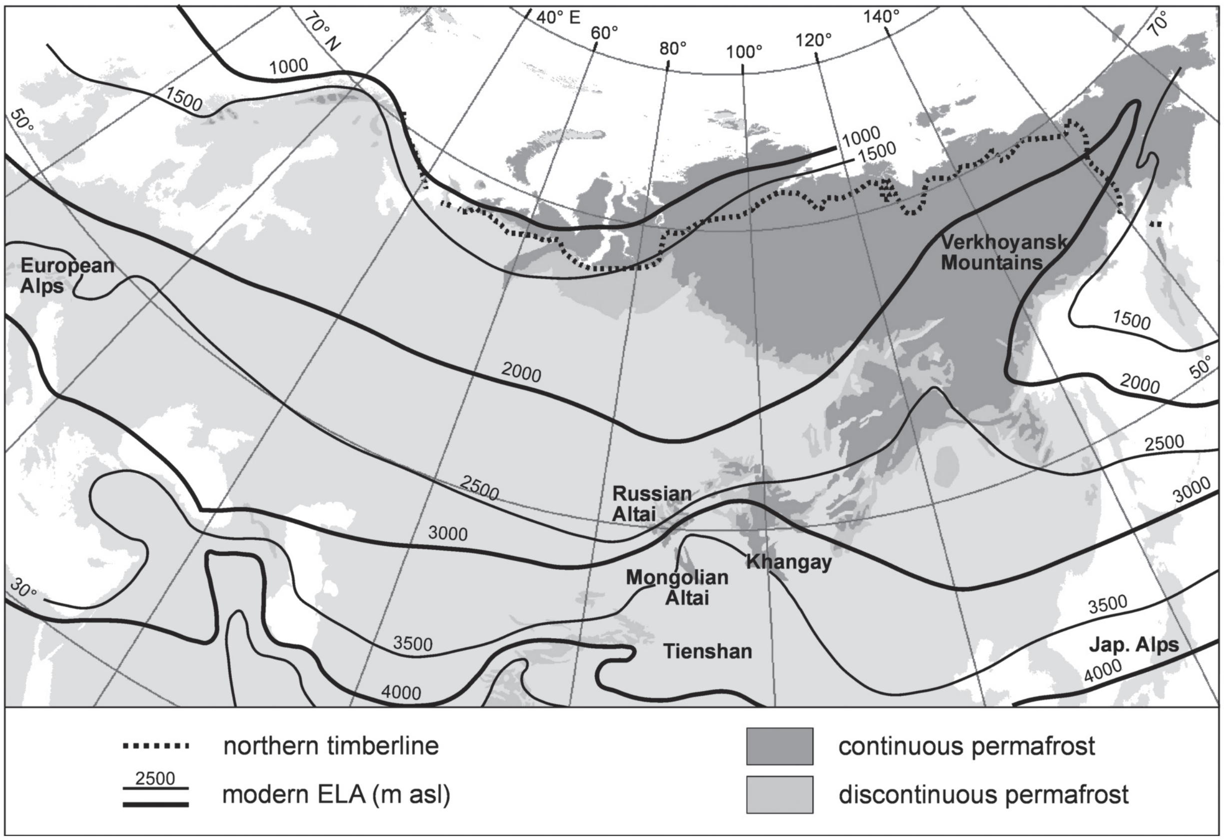

Figure 1. Map of study areas including the distribution of permafrost (modified according to Brown et al. 2001) and the modern ELA (m a.s.l., modified according to Wilhelm 1995).

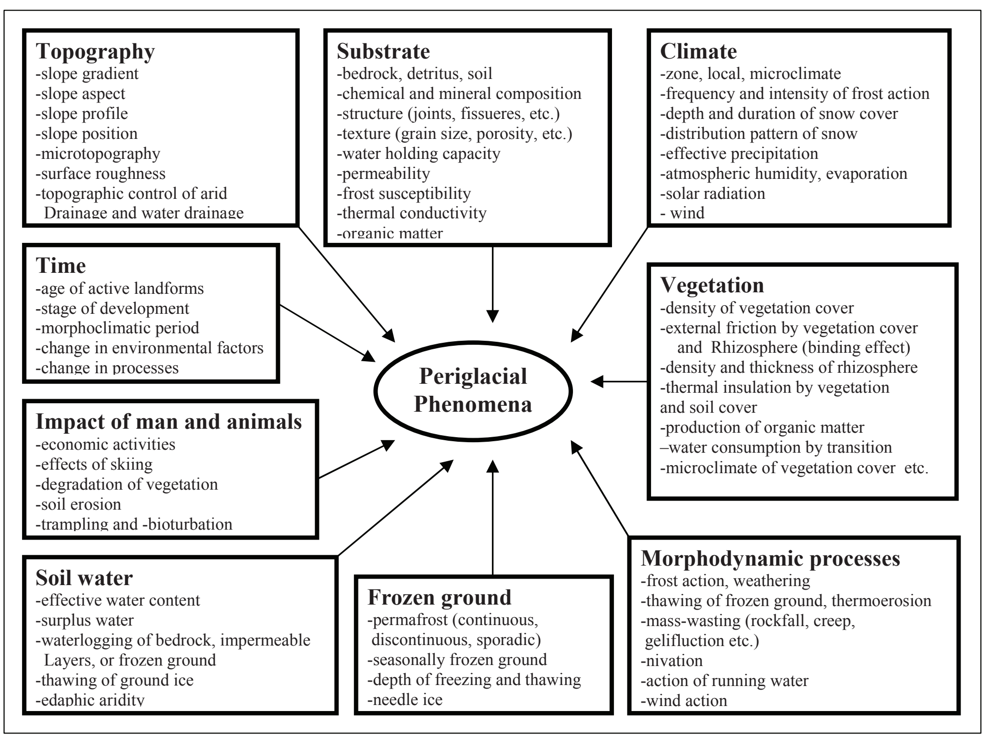

Figure 2. Main factors for the development and distribution of periglacial phenomena. Modified according to Höllermann (1985).

Results

In the following, the distribution of periglacial phenomena, such as lower limit of solifluction and rock glaciers, are described for the different mountain areas. The details for the lower limit of different periglacial and glacial features are given in Fig. 5 and Table 1.

European Alps

In the European Alps there are several studies regarding the periglacial phenomena. Veit (2002) summarized the current state of research for the European Alps. The periglacial phenomena can be divided in the humid European Alps into two sub belts: the lower limit of bound or turf-banked solifluction (occurs roughly above the timberline, Fig. 3) and the zone of unbound solifluction, dominated by blockfields, patterned ground, and bare bedrock. Active rock glaciers and other indicators of discontinuous permafrost are assumed to be generally in the upper periglacial sub-belt of the European Alps and of similar mountains. Active solifluction (or gelifluction) generally occurs above the timberline (see above). However, studies concerning the processes show that active movements occurs only in the upper part of the periglacial sub-belt (unbound solifluction); the turf-banked solifluction are fossil landforms (Jaesche 1999, Veit 2002).

Figure 3. Solifluction lobe (bound or turf-banked solifluction) in the Grossglockner region, European Alps, Elevation: 2200 m a.s.l.

Figure 4. Rock glacier in the Khangay Mountains, Mongolia. Granite bedrock on the eastern slope of the Otgon Tenger. Elevation: about 3000 m a.s.l.

In this paper the results from own field work from two mountain areas with the central part of the European Alps are described (Lehmkuhl 1989). These are the southernmost glaciated areas in the western part of the Alps (Pelvoux Mountains, France, 45°N/6°30′E) and the easternmost glaciated part of the Alps (Hohe Tauern, Austria, 47°N/13°E). Both regions are situated in the central part of the Alps, having more continental climatic conditions much more suitable for rock glaciers than the more humid margin ranges of the Alps (Barsch 1986, Höllermann 1985). The mean monthly air temperature in 2000 m a.s.l. varies between -4°C in January and +12°C in July (MAAT around 0°C). Annual precipitation ranges between 900 mm in valleys and >2000 mm in the mountains.

Rock glaciers occur in 2400 to 2500 m a.s.l., turf-banked solifluction in 2350 and 2200 m a.s.l. and unbound solifluction in 2750 and 2500 m a.s.l. (see Table 1 and Fig. 5).

Tianshan and Russian Altai

There are only a few studies regarding periglacial features in the Russian Altai. Schröder et al. (1996) and Fickert (1998) summarized in a north-south transect the distribution of periglacial phenomena. Their results concerning Tienshan (Sailijskij-Alatau, 42°N/77°E) and the results from own observations from the central part Russian Altai (Katun Ridge, 50°N/86°E) are given in Figure 5 and Table 1. The latter region is characterized by continental conditions with mainly summer precipitation and low winter temperatures resulting in the distribution of rock glaciers down to elevations of about 1600 m a.s.l. These low elevation rock glaciers occur in the forest belt indicating the high amplitude of temperatures with winter temperatures below -20°C and relative high summer precipitation. The precipitation values above 1000 mm/a are similar to those of the central European Alps. Further references see Marchenko et al. (2007).

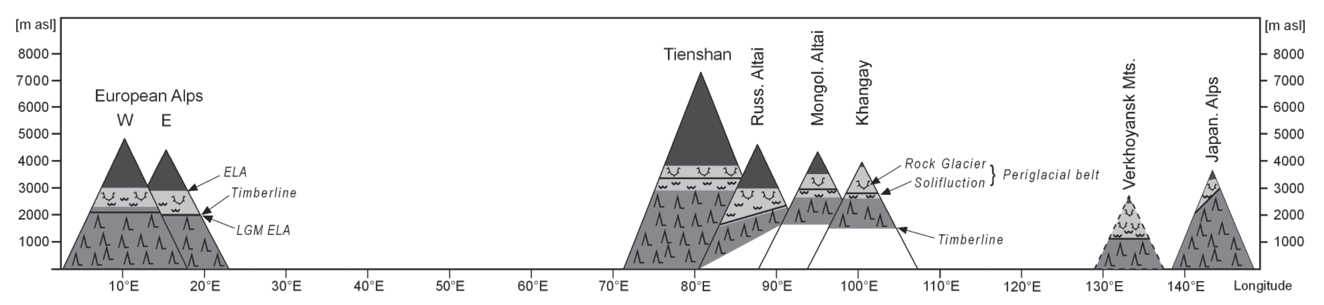

Figure 5. Periglacial belt (rock glacier and solifluction), timberline and snowline (modern ELA and Last Glacial Maximum ELA) of mid-latitude mountains from the European Alps to the Japanese Alps.

Table 1. Elevations (m a.s.l.) of snowline (ELA), timberline and selected lower limits of rock glaciers and solifluction (for the Alps: unbound solifluction in parentheses) from selected mid-latitude mountains between 40 and 50°N.

	Western European Alps	Eastern European Alps	Tienshan	Russian Altai	Mongolian Altai	Khangay	Verkhoyansk
Modern snowline (ELA)	3000	2900	3700-3900	2900-3000	3500	>3800	2500
Timberline	2300	2050	2900 (N)	2200-2400	2600–2700 (N)	2600 (N)	1100
Late Pleistocene ELA	ca. 2100	ca. 2000	2700?	1800-2200	2900–3000	2700-2900	1200
Pleistocene ELA-depression	ca. 1200	ca. 1100	1000?	800–1200	600	1000-1200	1300
Diff. Timberline-ELA	700	750	800	700	800–900	>1200	1400
Rock glaciers	2400	2500	2900	1600	2600	3200	--
Solifluction	2350 (2750)	2200 (2500)	2600	2200	2700	2900	800

Mongolian Altai and Khangay

Due to the low winter temperatures and the small amount of snow, frost weathering occurs in the mountains of Mongolia down to the basins below 900 m a.s.l. Other periglacial phenomena, such as solifluction, palsas, and earth hummocks are related to soil moisture, and therefore occur in higher elevations or exceptional geoecological sites with a higher water supply; for example, on north-facing slopes below larch forest spots. However, the distribution of rock glaciers in the continental climate conditions of western Mongolia is determinate on low temperatures, and mainly on the occurrence of granite and metamorphic rocks (Fig. 4). The detailed observations concerning the distribution of periglacial landforms and processes are based on several joint field expeditions and studies of the processes (Lehmkuhl 1999). Detailed investigations from the Mongolian Altai and Khangay are presented, for example, by Klimek & Starkel (1980), Pekala & Repelewska-Pekalowa (1993), Lombroinchen (1998), Lehmkuhl & Klinge (2000), Klinge (2001), Lehmkuhl et al. (2003) and Sharkhuu (2003). Further references can be found therein.

Hourly measurements of the soil temperatures of different depths at distinct geoecological sites in elevations between 1775 and 2760 m a.s.l. were carried out in two measuring cycles (Lehmkuhl & Klinge 2000). The main difference in the intensity of periglacial processes in the basins and mountains areas, respectively, can be seen in the freeze-thaw cycles in springtime. In this time the precipitation in the mountains is still snowfall, and moisture can infiltrate into the soils. Due to higher temperatures the precipitation (mainly rain) in the basins evaporates and rapid drying out of the soils occurs. Therefore, the main controlling factor for the cryogenic and especially solifluction processes in the mountains is the amount of precipitation during springtime. The freeze-thaw cycles during the relatively dry autumn season are a subordinated factor for the periglacial activity. At sites with low radiation, as caused for example, through shading effects in relief, the freeze-thaw cycles displace towards the summer with more precipitation. Therefore, periglacial processes on low-radiation sites are laced to the strength of the summer precipitation. On the other hand, the frequent freeze-thaw cycles at sites with high radiation drop towards the dry winter season, and therefore, the periglacial activity is low at such sites. Accumulation of snow (e.g., in nivation hollows) and/or the occurrence of frozen ground could guarantee sufficient soil humidity apart from the distribution of precipitation during the highest freeze-thaw cycles in the spring and autumn seasons and determines cryogenic processes and periglacial forms (e.g., earth hummocks, patterned grounds). This local influence can be reinforced by effects of radiation. In the larch forests at northern slopes, a cooler local climate with reduced transpiration in the summer allows the preservation of frozen ground and/or permafrost.

The details presented for this paper (Table 1) are based on two mountains ranges: (1) the Turgen-Kharkhiraa Mountains (49°30′N/91°E) as the northernmost part of the Mongolian Altai and (2) the Angarkhoy Mountains (47°N/101°E) as the central part of the Khangay. Mean monthly air temperature varies between -20°C in January and +20°C in July. The MAAT is, for example, about -4°C in the basin of the Uvs Nuur. Annual precipitation ranges between 200 mm in the basins and up to >400 mm in the mountain ranges. Solifluction and rock glaciers occur in elevations above 2600 m. Initial observations from other parts of the Mongolian Altai and the western Russian Altai show that such landforms can be found in almost every mountain system which comprise granite or other metamorphic rocks.

Verkhoyansk Mountains

The Verkhoyansk Mountains are much further north in latitude, and the climate is extremely continental. Mean monthly air temperature varies between -40°C in January and +20°C in July. Annual precipitation ranges between 220 mm in the lowlands around Yakutsk and up to 700 mm on the western flank of the Verkhoyansk Mountains. The observations presented in this paper focused on the central part of the Verkhoyansk Mountain range (64–65°N, 126–130°E) and based on fieldwork and remote sensing analysis (Stauch 2006, Stauch et al. 2007). Permafrost features such as pingos and thermokarst depressions and lakes (alases) are widespread on continuous permafrost even in the mountain foreland and in the boreal forest of the Lean-Aldan Basin. However, solifluction, nivation, and cryoplanation terraces can be found in elevations above 800 m a.s.l. only. No rock glaciers can be found in this study area.

Japanese Alps

Studies concerning mountain permafrost in Japan are summarised in Ishikawa et al. (2003). Mountain permafrost seems to be restricted mainly to north-facing slopes above 3000 m a.s.l. and in some rock glaciers. Matsuoka (2003) presents some more details concerning other periglacial features.

The details presented for this paper (Table 1) based also on own observations and discussions during an excursion led by Y. Ono in 2001 in the central Japanese Alps. MAAT in 2600 m a.s.l. is about 0°C, mean temperature in January and July were estimated to be -11.3 and +12.6°C, respectively. Annual precipitation is rather high (no data published) and northwestly wind across the Japan Sea provides a large amount of snow on the northern and eastern ranges in winter, the Pacific part of the mountains is much drier (Ishikawa et al. 2003).

Solifluction and rock glaciers occur in elevations above 2600 m a.s.l.; there are no modern glaciers in this part of the Japanese Alps.

Conclusion

As stated above, the distribution of various periglacial landforms depends on several different factors (e.g., climate, topography, geology and substrate, vegetation, and soil water; see Fig. 2). Periglacial phenomena are generally controlled by cold climatic conditions, where the mean annual air temperature is below 0°C and the duration and depth of snow cover are low.

The distribution of the periglacial belt in Eurasia at 40 to 50°N is given in the schematic profile in Fig. 6. All altitudinal lines are drawn relatively to the timberline as base level. Alpine discontinuous and continuous permafrost is present in all these mountains, but in the humid this zone is very small due to the lower elevation of the snowline (or recent equilibrium line of glaciers = ELA). In the more continental regions of Asia, like the Altai Mountains, this zone is much broader due to high elevation of the ELA. In addition, cryoplanation terraces, patterned ground, and rock glaciers occur in relative low elevations and are also widespread within the forest ecotone (Table 1).

The Verkhoyansk Mountains are further north in latitude and much drier. In this region, even the mountain foreland and in the boreal forest, permafrost activity and pingos are widespread. However, periglacial features, especially solifluction, occur only in mountain ranges above 800 m a.s.l. There are no active rock glaciers, as the humidity is not sufficient. These results fit recent observations in 2007 in the Gobi Altai, a mountain range within the driest part

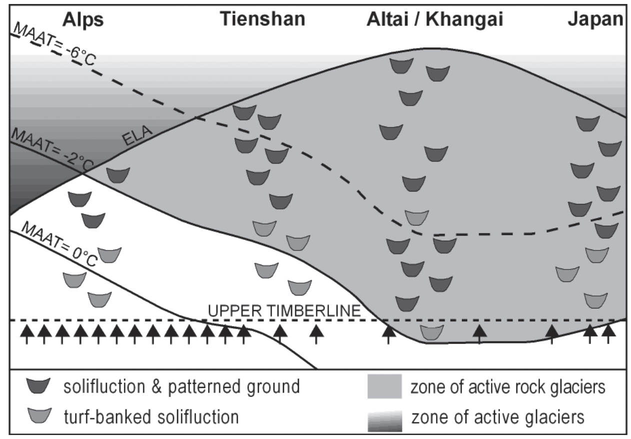

Figure 6. Schematic profile of the periglacial belt in Eurasia at 40 –50°N. All altitudinal lines are drawn relatively to the timberline as base level. Modified according to Höllermann (1985).

of Mongolia, where a few rock glaciers occur only in the highest and more humid parts of the Ikh Bogd Mountain above 3500 m a.s.l. (44°57′N, 100°18′E).

The Japanese Alps are more humid, and especially the thick winter snow cover reduced periglacial activity and permafrost distribution, including rock glaciers, toward a small zone in the highest mountain areas.

These results show that periglacial phenomena occur in the continental part of Asia even in the forest zone. Especially solifluction, but also rock glaciers, are determined through existence of soil humidity during the freeze-thaw cycles. Therefore the distribution of these features in the continental areas of Asia is smaller than in the humid European and Japanese Alps and, for example, restricted to northern slopes or higher elevations. Observations and soil temperature measurements in the Altai Mountains show that active rock glaciers and discontinuous permafrost occur in lower elevations than solifluction features. Thus, solifluction landforms in continental Asia depend more on moisture supply than rock glaciers. However, towards the arid regions of Central Asia, the lower limit of solifluction landforms, glaciers, and the lower timberline are rising in general; whereas the distribution of rock glaciers is even lower than in the humid parts of Europe and Pacific parts of Asia including Japan.

The modern ELA has the lowest position in the humid European Alps. The most significant difference between the timberline and the modern ELA occurs in the Khangay and Verkhoyansk Mountains. (Fig. 5, Table 1). The smallest amount of Pleistocene ELA-depression is in the arid regions of the Altai. However, the distribution of glaciers is related to temperature and moisture supply. The generalised contour lines of the modern ELA in Figure 1 show the influence of the humid mountains of the Altai and the dry part of eastern Siberia on the elevation of the snowline. As the northern timberline is related to summer temperatures and the humidity is even sufficient in the continual parts of Asia, this line shows a west–east latitudinal trend.

Acknowledgments

The fieldwork in Asia was funded by the Deutsche Forschungsgemeinschaft (DFG, LE 730/2-1,2; 7-1; 10-1,2). For help during fieldwork and several discussions, the author would like to thank especially Dr. O. Batkhishig, Mongolian Academy of Sciences, and Dr. N. Lachinski from the Siberian Botanical Garden, Russian Academy of Sciences, and the other Mongolian and Russian colleagues and co-workers. In addition, I would like to thank G. Stauch (Aachen) for discussions.

References

Barsch, D. 1996. *Rock Glaciers: Indicators for the Present and Former Geoecology in High Mountain Environments*. Berlin: Springer, 331 pp.

Brown, J., Ferrians, O.J., Heginbottom, J.A. & Melnikov, E.S. 2001. *Circum-arctic map of permafrost and ground ice conditions*. National Snow and Ice Data Center/World Data Center for Glaciology, Boulder, Colorado.

Fickert, T. 1998. Vergleichende Beobachtungen zu Solifluktions- und Frostmustererscheinungen im Westteil Hochasiens. *Erlanger Geogr. Arb.* 60: 1-150.

Fort, M. 2002. Are high altitude, lava stream-like, debris mixtures all rock glaciers? A perspective from the western Himalaya. *Z. f. Geomorph. N.F.,* Suppl. 130: 11-29.

Haeberli, W. 2000. Modern research perspectives relating to permafrost creep and rock glaciers: a discussion. *Permafrost and Periglacial Processes* 11: 290-293.

Höllermann, P. 1985. The periglacial belt of mid-latitude mountains from a geoecological point of view. *Erdkunde* 39: 259-270.

Ishikawa, M., Fukai, K., Aoyama, M., Ikeda, A., Sawada, Y. & Matsuoka, N. 2003. Mountain permafrost in Japan: distribution, landforms and thermal regime. *Z. f. Geomorph. N.F.,* Suppl. 130: 99-116.

Ishikawa, M., Watanabe, T. & Nakamura, N. 2001. Genetic differences of rock glaciers and the discontinuous mountain permafrost zone in Kanchanjunga Himal, Eastern Nepal. *Permafrost and Periglacial Processes* 12: 243-253.

Jaesche, P. 1999. Bodenfrost und Solifluktionsdynamik in einem alpinen Periglazialgebiet (Hohe Tauern, Osttirol). *Bayreuther Geowis. Arb.* 20: 1-136.

Klimek, K. & Starkel, L. (eds.) 1980. Vertical zonality in the Southern Khangai Mountains (Mongolia). Results of the Polish-Mongolian physico-geographical expedition, Vol. I. *Geographical Studies* 136: 1-107.

Klinge, M. 2001. Glazialgeomorphologische Untersuchungen im Mongolischen Altai als Beitrag zur jungquartären Landschafts- und Klimageschichte der Westmongolei. *Aachener Geogr. Arb.* 35: 1-125.

Lehmkuhl, F. 1989. Geomorphologische Höhenstufen in den Alpen unter besonderer Berücksichtigung des nivalen Formenschatzes. *Göttinger Geogr. Abh.* 88: 1-113.

Lehmkuhl, F. 1999. Rezente und jungpleistozäne Formungs- und Prozeßregionen im Turgen-Charchira, Mongolischer Altai. *Die Erde* 130: 151-172.

Lehmkuhl, F. & Klinge, M. 2000. Bodentemperaturmessungen aus dem Mongolischen Altai als Indikatoren für periglaziale Geomorphodynamik in hochkontinentalen Gebirgsräumen. *Z. f. Geomorph. N.F.,* Suppl. 44: 75-102.

Lehmkuhl, F., Stauch, G. & Batkhishig, O. 2003. Rock glacier and periglacial processes in the Mongolian Altai. *Proceeding of the Eighth International Conference on Permafrost, Zurich, Switzerland, July 21–25, 2003*: 639-644.

Lombroinchen, R. 1998. Short communication: periglacial processes and physical (frost) weathering in Northern Mongolia. *Permafrost and Periglacial Processes* 9: 185-189.

Marchenko, S.S., Gorbunov, A.P. & Romanovsky, V.E. 2007. Permafrost warming in the Tien Shan Mountains, Central Asia. *Proceeding of the Eighth International Conference on Permafrost, Zurich, Switzerland, July 21–25, 2003*: 311-327.

Matsuoka, N. 2003. Contemporary permafrost and periglaciation in Asian high mountains: an overview. *Z. f. Geomorph. N.F.,* Suppl. 130: 145-166.

Pekala, K. & Repelewska-Pekalowa, J. 1993. Solifluction and related slope processes in the mountains of Central Asia (Mongolia). *Paläoklimaforschung/ Palaeoclimate Research* 11: 87-101.

Schröder, H., Gunia, A. & Fickert, T. 1996. Vergleichende Periglazialmorphologie im zentralen Teil des nördlichen Tien-Shan. *Mitt. der Fränkischen Geogr. Ges.* 43: 275-300.

Serebryanny, L.R. & Gravis, G.F. 1993. Solifluction in northern Eurasia: a review. *Paläoklimaforschung/ Palaeoclimate Research* 11: 103-382.

Sharkhuu, N. 2003. Recent changes in the permafrost of Mongolia. *Proceeding of the Eighth International Conference on Permafrost, Zurich, Switzerland, July 21–25, 2003*: 1029-1034.

Stauch, G. 2006. Jungquartäre Landschaftsentwicklung im Werchojansker Gebirge, Nordost Sibirien. *Aachener Geogr. Arb.* 45: 1-176.

Stauch, G., Lehmkuhl, F. & Frechen, M. 2007. Luminescence chronology from the Verkhoyansk Mountians (North-Eastern Siberia). *Quaternary Geochronology* 2: 255-259.

Troll, C. 1973. High mountain belts between the polar caps and their definition and lower limit. *Arctic and Alpine Research* 3: A19-A27.

Veit, H. 2002. *Die Alpen – Geoökologie und Landschaftsentwicklung.* Stuttgart: Eugen Ulmer, 352 pp.

Washburn, A.L. 1979. *Geocryology.* London: Edward Arnold, 406 pp.

Wilhelm, F. 1995. *Schnee- und Gletscherkunde.* Berlin, New York: Walter de Gruyter, 434 pp.

Coastal Processes at the Tabular-Ground-Ice-Bearing Area, Yugorsky Peninsula, Russia

Marina Leibman
Earth Cryosphere Institute SB RAS, Tyumen, Russia
Anatoly Gubarkov
Tyumen State Oil and GAS University, Tyumen, Russia
Artem Khomutov
Earth Cryosphere Institute SB RAS, Tyumen, Russia
Alexandr Kizyakov
Institute VNIIIST, Moscow, Russia
Boris Vanshtein
FGUP Vniiokeangeologia, St-Petersburg, Russia

Abstract

Observations on Yugorsky Peninsula since 1998 cover periods with changing climatic controls of coastal processes. Coastal dynamics are connected to the activation of thermal denudation, the most widespread process in the area with tabular ground ice enclosed in geological sequences. Thermodenudation comprises cryogenic landslides, slumps, and earth flows resulting from tabular ground ice thaw. Thermoabrasion is a less common mechanism of coastal retreat in the study area. The dominating mechanism allows subdivision of coasts into thermodenudation, thermoabrasion, and mixed types. Coast types are time-dependent, and alternation of types depends on climate fluctuations. For the bluffs with tabular ground ice exposures, the increase of sediment yield onto the beach is determined on the one hand, by a relative amount of tabular ice in a section, and on the other, by increase in the thaw index. Activation of thermoabrasion depends on sea ice coverage along with wind speed and direction. Activation of thermoerosion results from heavy winter precipitation followed by a bursting spring.

Keywords: climatic controls; coastal dynamics; earth flows; thermoabrasion; thermodenudation; thermoerosion.

Introduction

Observations on Yugorsky Peninsula since 1998 cover the basic climatic controls of various coastal processes in the study area (Kizyakov et al. 2006): periods with changing summer temperature, ice coverage of the Kara Sea, amount of summer and winter precipitation, wind speed and direction, and wave action.

Coastal dynamics result from the activation of thermal denudation, the most widespread process in the area with tabular ground ice enclosed in geological sequences. The importance of the massive (tabular) ground ice occurrence as a major factor in coastal retreat is recognized in the literature (Lantuit & Pollard 2003, Solomon 2003, Lantuit et al. 2005, Kizyakov et al. 2006). Thermal denudation comprises cryogenic landslide/slump/earth flow processes, resulting from tabular ground ice thaw and removal of meltwater and waste material onto the beach and into the sea by gravitation (Leibman & Kizyakov 2007). Depending on climate fluctuations, coastal dynamics result from alternating or coinciding cryogenic landslide/slump/earth flow, thermoabrasion, and thermoerosion mechanisms. According to the dominating mechanism, coasts are subdivided into thermodenudation, thermoabrasion and mixed types (Sovershaev 1992, Kizyakov et al. 2003). Coasts are affected by nivation, earth falls, and aeolian processes as well, though they play subordinate roles.

Thermodenudation assumes special features in the tabular ground ice areas. These features are the formation of specific thermodenudation landforms such as thermocirques and thermoterraces, resulting from the tabular ground ice thaw and slope mass waste. The rate of coastal retreat at the backwalls of these forms is much higher than the coastal retreat rate at the adjacent portions of the coastal bluffs (Kizyakov et al. 2006).

This paper deals with coastal dynamics at the Yugorsky Peninsula coast. Field observations and monitoring reveal the main mechanisms which determine coastal types and destruction rates.

Study Area, Terms, and Methods

The study area, Yugorsky Peninsula at the southern coast of the Kara Sea (Fig. 1), is located on the Pai-Khoi Mountain range piedmont, a relief of rolling hills being affected by thermokarst and various slope and coastal processes. According to the records of the Amderma weather station, mean annual (summer) temperature for the period of observation ranged from -5.8 to -7.7°C (5.0–6.7°C); summer wind speed may exceed 20 m/sec, mainly in a southwestern direction; and the perennial average of annual/summer precipitation is rather low: 314/148 mm.

The area is characterized by continuous permafrost

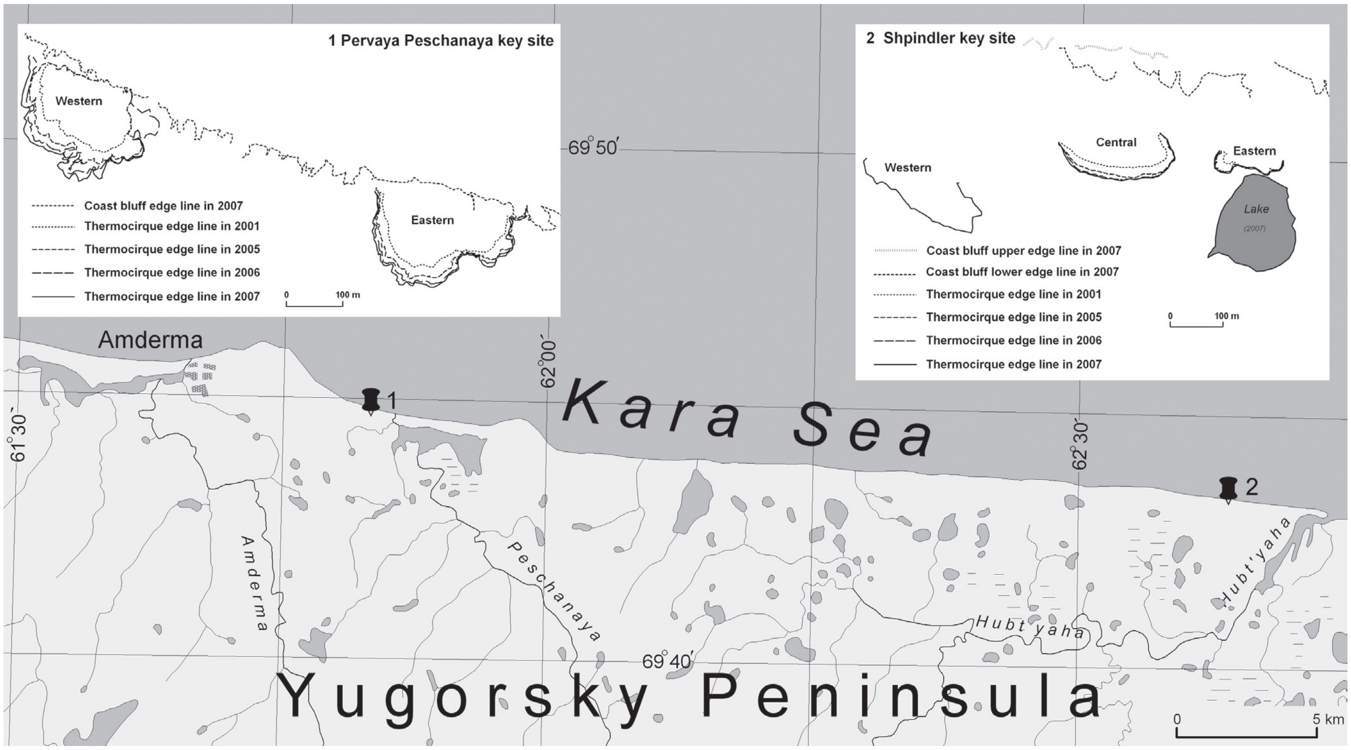

Figure 1. Yugorsky Peninsula. Pervaya Peschanaya (1, left inset map), and Shpindler (2, right inset map) key sites. Thermocirque configuration as well as annual coastlines are shown on inset maps.

distribution with ground temperature as low as -5°C, up to 400 m thickness, with an active-layer depth maximum exceeding 1.5 m, with average around 1 m, and widespread tabular ground ice in layers of 3–12 m thick enclosed in sandy-clayey deposits of glacial (?), marine, fluvial, Aeolian, and slope-wash genesis (Manley et al. 2001, Leibman et al. 2003). Two key sites are under study: Shpindler site is located west of the Hubt'Yakha River at the easternmost end of the coastal zone under study. The westernmost end is Pervaya Peschanaya site, west of the Pervaya Peschanaya River. At both key sites several thermocirques are mapped, four of which are monitored: the western and eastern thermocirques of Pervaya Peschanaya site, and the eastern and central thermocirques of Shpindler site (Fig. 1, inset maps). The coastal zone between these two key sites was described and the thermocirque/bluff edge position measured during a foot and boat trip along the coast.

The methods applied were as follows: A network of transects perpendicular to the edge of most actively retreating thermocirques and flat coastal bluffs was established. Repeated accurate tacheometric surveys were used to create a digital model of thermocirque relief at several time slices so that coastal dynamics were characterized not only in one dimension as a shoreline retreat, but also in two and three dimensions, as area and volume losses. The area loss allows better determination of the average retreat for an edge of complicated configuration, while volumetric loss allows calculation of the volume of material transported onto the beach during the period between two survey dates (Kizyakov et al. 2006).

Retreat measurements were performed in July and August. To better understand climate controls, retreat rates and thaw index were calculated for the entire period between measurements and thus include the warm period of the preceding and following year, not of a calendar warm period.

A tacheometric survey was implemented in 2001, 2003, 2005, and 2006. In the intermediate years, a GPS survey was used to measure the shoreline position and to extend transects farther inland after stakes closer to the edge were lost through the retreat. GPS is of less accuracy compared to tacheometry, but it is still within 1 m, due to repeated measurements in a closed loop.

In Russian literature, different terms are used for coastal and lateral thermoerosion, which make coastal mechanisms easier to understand; in this paper we will use the term *thermoabrasion* for coastal thermoerosion which is the formation of wave-cut niches followed by earth falls resulting in coastal bluff retreat. The term *thermoerosion* will be used to indicate only lateral thermoerosion (linear or ravine thermoerosion produced by running water/mud flows).

A substantial portion of the coast is represented by thermocirques and thermoterraces. Mechanisms of their formation are revealed by A. Kizyakov as depending on the localization of the initial thaw. Thermocirques are formed when the tabular ground ice body gets exposed by thermodenudation inland, and waste material is transported to the shore by local streams. While thermoterraces are formed by ice exposures directly on the bluff planes facing the sea; retrogressive thaw slumps and earth flows deliver waste material directly onto the beach (Fig. 2).

Thermodenudation landforms at the coasts are step-

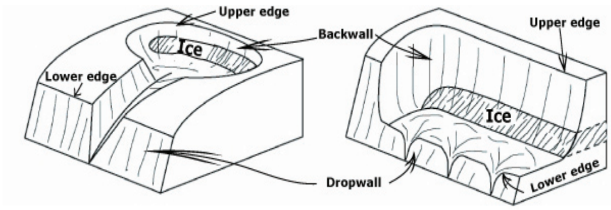

Figure 2. Thermocirque (left) and thermoterrace (right) landforms.

shaped with two retreating planes and respective edges: a thermocirque/thermoterrace backwall (retreating "upper" edge) and a dropwall to the beach (retreating "lower" edge) (Fig. 2).

Results

Table 1 shows the retreat rate in relation to air temperature fluctuations. As instrumental measurements of coastal retreat were performed in mid-summer, long before the coastal processes "winter sleep," we applied a special procedure to make interannual data comparable: thaw index is calculated as a sum of positive temperatures of the preceding year, starting immediately after the date of measurement, plus a sum of positive temperatures of the next year up to the date of measurement. If a period between measurements was more than a year, both total sum and annual average are calculated. The length of the period with positive temperatures is highly variable and depends, along with climate fluctuations, on field logistics. For this reason, we are using a diurnal "thaw index" as a measure of air temperature impact on retreat rate.

Calculations indicate that maximum retreat rate depends directly on degree-days. Each period of measurements is characterized by about 0.8–0.9 cm of retreat per one degree-day of summer temperature.

According to our observations, in 1998–2005, the lower edge retreat was minimal. A boat trip along the coastline did not show any niches or failures, except for several thermocirques. This was most likely related to rather high sea ice coverage till late summer in 1998–1999, and moderate wind speed in 1998–2005. A summer 2003 trip indicated an increase in the number and size of thermocirques and thermoterraces, mainly due to a warm summer (Kizyakov et al. 2003, 2004). But climatic events of spring–summer 2006 changed the rate of the process, especially in the dropwall along the entire 43 km of shoreline observed. That year was marked by extreme wind speed with direction toward the coast, with northern winds prevailing in frequency and speed (Leibman et al. 2006).

In 2007, winter was snowier and spring was cooler than usual. Snow patches covered a significant portion of coastal bluffs preventing wave action. At the same time, snow patches provided active thermoerosion by meltwater. This was made possible by a bursting spring with June–July diurnal temperature some days as high as 24°C. That high temperature stayed only for a few days; the rest of the days the air temperature was below 10°C, thus most snow patches were preserved, but meltwater was abundant. Thermoerosion activated retrogressive thaw slumps and earth flows with mud streams running over snow patches directly onto the beach. Thus processes of coastal destruction proceeded by the alternation of thermodenudation in 2000–2005, thermoabrasion in 2006, and joint thermoerosion and thermodenudation in 2007.

Table 2 presents the average annual retreat at all 4 key thermocirques for various periods of measurement.

Analysis of Table 2 indicates that the maximum annual retreat rate of the backwall was observed in 2005–2006 when the thaw index was maximum. Thermocirques at Pervaya Peschanaya site show a higher retreat rate compared to Shpindler site. Though the thaw index reduces in 2006–2007, retreat at Pervaya Peschanaya site is rather essential (almost 4 m average). Extremes of 2005–2006 were not only due to the high summer temperature (see Table 1, thaw index per day), but also because of strong wave uprush (Leibman et al. 2006). The lower edge started retreating fast, niches were formed, earth falls occurred, and ice exposures appeared at formerly stable slopes (Fig. 3).

Table 1. Shpindler monitoring key site, Yugorsky Peninsula, Russia. Central thermocirque backwall retreat in relation to thaw index.

Period	Average* backwall retreat, m	Days between measurement	Warm period**	Thaw index total/ diurnal degree-days
16.09.2001 10.08.2002	1.6	328	77	398.4/5.2
11.08.2002 22.08.2003	4.2	377	122	755.2/6.2
23.08.2003 05.08.2005	7.65 (3.83)	714	252	1401.9/5.6
06.08.2005 28.07.2006	3.74	358	120	839.3/7
29.07.2006 15.07.2007	1.25	353	93	502.4/5.4

*Calculated as average from retreat measured along the fixed transects, in parentheses annual value if period exceeds 1 year.
**Calculated for the period between measurements including preceding and following year's warm period.

Table 2. Retreat rate of the thermocirque's upper edge at key sites "Shpindler" and "Pervaya Peschanaya," Yugorsky Peninsula in 2001–2007.

Thermocirque	Average linear retreat, m*		
	2001–2005/annual		2006–2007
Shpindler, Central	14/3.5	4	1.25
Shpindler, Eastern	4/1	1	0.48
Pervaya Peschanaya, Eastern	14/3.5	5	3.00
Pervaya Peschanaya, Western	18/4.5	10	3.83

*Calculated as retreat area divided by a bluff edge length in 2001

Figure 3. The wave uprush in 2006 caused thermoabrasion and exposed tabular ground ice at the base of the coastal bluff, Yugorsky Peninsula, Kara Sea coast.

Figure 4. Snow patches in 2007 protect coastal bluffs from thermoabrasion at Yugorsky Peninsula, Kara Sea coast.

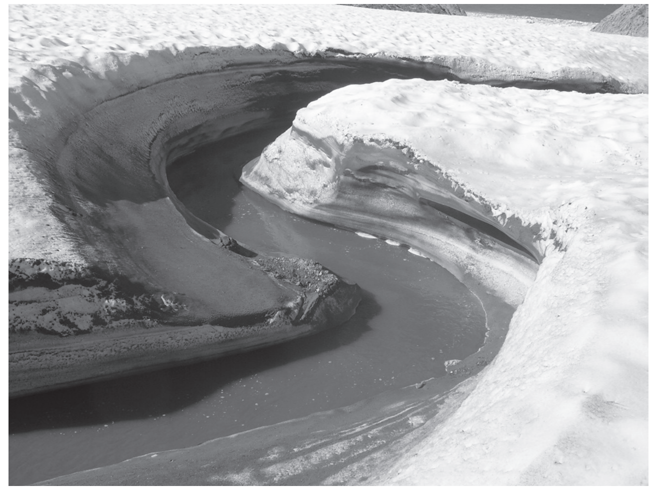

Figure 5. Snow patches filling coastal thermocirque bottoms in 2007 cut through by the meltwater streams bearing and transporting sediment load towards the beach at Yugorsky Peninsula, Kara Sea coast.

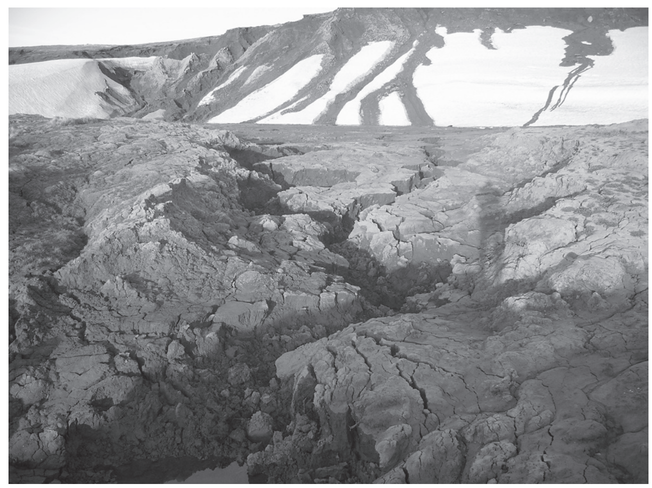

Figure 6. Snow patches in 2007 provide domination of mudflows and thermoerosion in destruction of coastal bluffs at Yugorsky Peninsula, Kara Sea coast.

Summer of 2007 was very different compared to 2001–2006. Snow patches covered most of the coastal bluffs (about 50% of the shoreline) protecting them from thermoabrasion (Fig. 4).

The high retreat rate at Pervaya Peschanaya in summer 2006–2007 is explained by both extreme wave action of fall 2006 and the increased effect of thermoerosion through the meltwater from snow patches in spring 2007 (Fig. 5). Also, nivation promotes retrogressive thaw slump/earth flow activity. Earth flows cut the surface of snow patches (Fig. 6) or run over the snow surface onto the beach. Thus, in 2007 landslides/slumps/earth flows and thermoerosion canals, promoted by snowmelt and nivation, dominate in coastal destruction mechanisms. Calculations show that a 2-week snowmelt period due to thermoerosion, transports as much sediment downslope as earth flow/slump activity during the entire warm period of any previous year.

While thermoerosion provides more intensive sediment transport compared to earth flows and retrogressive thaw slumps, thermoabrasion is quite a sparse and sporadic process at Yugorsky coast, though with an extensive mass waste due to earth falls (Fig. 7).

The rates of coastal retreat for thermocirque edges may be 2–5 times higher than thermoabrasion retreat rates. Sediment transport through a narrow (10–30 m) exit from thermocirque onto a beach is equal to the sediment yield from 500–1000 m portion of a flat-bluff coast (Kizyakov et al. 2006).

Discussion

Observations in the key area with tabular ground ice occurrence show results close to those obtained in the Canadian Arctic by Lantuit & Pollard (2003), Lantuit et al. (2005), and Solomon (2003): tabular ground ice through thermodenudation (retrogressive thaw slumps) essentially increases the rate of coastal retreat, not only in the area of their direct occurrence, as in our study, but in the nearest vicinity (Lantuit & Pollard 2003).

The long-term retreat rate calculated from analysis of remote-sensing data at the Yugorsky coast (Kizyakov et al.

2006) was close to that obtained for various arctic areas and is around 1 m/yr for the period 1948–2001. Rather similar areas of the Canadian Arctic, as mentioned above, show a retreat rate of 1.03 m/yr in 1970–2000 (Lantuit et al. 2005). Though records averaged for a long period (53 years for Yugorsky Peninsula after Kizyakov et al. 2006, and 30 years after Lantuit et al. 2005) show a relatively low retreat rate, annual data at the coasts with tabular ground ice and respective retrogressive thaw slumps (thermal denudation in Russian terminology) display much higher rates. The highest rates are not directly connected to immediate climate warming. Lewkowizc (1987) reported retreat rates for slumpy slopes on Banks Island at 8.6–11.4 m/yr in average with a maximum 15.5 m/yr in 1983–1984. Lantuit & Pollard (2003) noted that the retreat rate was much higher in 2000–2001 (average 7.6 m) and even higher in 2001–2004 (9.6 m/yr).

These data correlate with our observations of increased retreat rates in the 2000s (up to 10 m/yr average, Table 2), exceeding a 55-year average by an order of magnitude. An order of magnitude difference between perennial average retreat rate and seasonal rates at the years of process activation shows that coastal retreat is of a cyclic character, and after several years of thermodenudation activity (12–15 years as in Lewkowicz 1987), a period of recession follows, compensating high rates of coastal destruction on the long-term scale.

High retreat rates result from tabular ground ice representing an essential part of the geological section. At Yugorsky Peninsula this part may be as high as 30–35% of the section as at the Central thermocirque of Shpindler site (Leibman et al. 2003).

As retreat rates appear to depend essentially on the tabular ground ice amount, it is critical to subdivide coastal types based on the existing exposures. At the coast under study, there are one or two ice layers depending on the marine terrace origin, age, and height. At the high terraces (35 to 45 m above sea level) two ice layers are exposed, the upper being 8–12 m thick at depths 15–25 m from the hilltop surface.

The lower ice layer dips westward, with the lower limit from 5–10 m above sea level at the Shpindler key site, and to below sea level at the Pervaya Peschanaya key site. The lower ice layer is found at practically all the terraces, both low and high ones. Flat coastal bluffs separating areas with tabular ground ice exposures may contain ground ice as well, only well insulated by thick scree deposits separating the ice surface from seasonal thaw even in warm years. But of course it should be taken into consideration that these areas are potential resources for activation of coastal destruction in a case of considerable climate warming. One more way to trigger the ice thaw is active thermoabrasion at the now stable flat bluffs.

A two-layer ice distribution pattern produces a specific shape of the coastal profile. The sea-facing macro-slope may consist of several steps with hanging thermocirque/thermoterrace bottoms formed by the thawed upper ice layer, and lower steps based on the toe of the lower ice layer. Only in the case of ice occurrence below sea level, as at Pervaya Peschanaya key site no steps are formed, but rather a thermokarst depression (Leibman et al. 2003, Leibman & Kizyakov 2007).

Figure 7. Intensive mass waste due to thermoabrasion (frozen-block falls) at Yugorsky Peninsula, Kara Sea coast.

Upper thermocirque/thermoterrace edges are located at a distance (several dozen to several hundred meters away) from the shoreline, they are not interacting with the sea. Even low terraces with thermocirques formed due to lower ice layer thaw are not affected by wave action and develop only due to air temperature and precipitation.

An overview of the flat coastal bluffs, thermocirques/thermoterraces, and thermoabrasion coasts during 7 years at the key sites, as well as observations during a long-shore trip showed the following: There were 2 periods of active coastal destruction. The summers of 2000 and 2001 were noted for re-activation of thermodenudation and exposure of tabular ground ice at the eastern (2000) and western (2001) thermocirques of Pervaya Peschanaya key site.

The summer of 2006 changed the whole coastal type structure. Most of the stable dry slopes, as well as dropwalls of thermodenudation slopes, turned into thermoabrasion coastal types with niches, frozen block falls, and cracks at the bluff edges, which prepared continuous failures for the remaining summer months of 2006. In 2007 about 50% of the coasts turned into the thermodenudation-thermoerosion type, thermoabrasion being almost entirely suppressed because wave action was prevented by abundant sea ice and snow patches armoring the dropwalls.

Thus, a combination of coasts of various types at any given time slice constitute the Yugorsky coasts. Coasts are represented by flat to convex bluffs, retreating parallel to themselves due to slow gravitation processes (scree and slopewash) or thermoabrasion (formation of niches followed by earth falls), combined with stepped, concave coasts with thermocirques/thermoterraces and ravines developing due to thermodenudation and thermoerosion. Material transported to the beach is evacuated, depending on the wave activity, in a few days under a strong wind and open sea conditions, to a few weeks if none of the above occur.

After a year of active thermoabrasion in 2006, the lower tabular ice layer was exposed, and this started thermodenudation at the dropwall, which continued in 2007 beneath the snow patches when the melt season started.

The basic conditions for proceeding activation are: (1) presence of rather thick ice layers; and (2) removal of the material delivered from the bluff onto the beach. For the bluffs with tabular ground exposures, the increase of material yield to the beach is determined on the one hand, by a relative amount of tabular ice in a section, and on the other hand, by an increase in summer air temperature, surface-thaw rate, summer atmospheric precipitation, speed and sediment load of eroding flows, and accordingly, amount of sediment and distance of its transportation.

The dual role belongs to winter precipitation. Plentiful snow preserves slopes from thaw. However, the snow contributes to thermodenudation through the nivation process, and provides excessive meltwater flow, increasing sediment yield to the bluff toe, at the same time speeding up the sediment removal from the beach.

Air temperature acts dually as well. High summer temperature prolongs the ice-free period, and along with the intensive wind enhances wave action, promoting both thermoabrasion and removal of sediment. If the summer temperature rise is not accompanied by significant atmospheric precipitation, then sediment yield and removal are slowed down by landslide bodies in the transition zone.

The activity of cryogenic processes unequivocally amplifies only at increase of the thickness and proportion of tabular ground ice.

Conclusions

A coastal dynamics study at the Yugorsky Peninsula coast (Kara Sea) was performed in 2001–2007. Tabular ground ice in the geological sections is responsible for the essential role of thermodenudation in the coastal destruction. Two commonly subdivided types of coasts: thermoerosion and thermodenudation cannot be applied in a study devoted to time-related patterns. Any portion of the coastline in a short-term dynamic under the climate fluctuations cannot only be transformed from stable into actively retreating, but also into a different type or into a mixed type existing within one time slice. Years with a wave uprush increase the proportion of coastal bluffs with the thermoabrasion mechanism dominating. Mixed type occurs when the "upper" edge is retreating according to thermodenudation pattern, while the "lower" edge is destructed by thermoabrasion.

From climatic controls, the main forcing factor for the rate of coastal retreat is summer air temperature (thaw index). The dominating mechanism for the time-dependent coastal destruction (dynamic type of coasts) is determined by different climatic parameters such as wave uprush caused by low sea ice coverage and strong landward winds, intensive winter precipitation resulting in numerous snow patches, which in the conditions of a bursting spring cause domination of thermoerosion and earth flows.

Acknowledgments

Research was supported by Russian Federal Agency of Science and Innovations, Federal Program "World Ocean."

References

Kizyakov, A.I., Perednya, D.D., Firsov, Yu.G., Leibman, M.O. & Cherkashov, G.A. 2003. Character of the costal destruction and dynamics of the Yugorsky Peninsula coast. In: *Reports on Polar and Marine Research* 443: 47-49.

Kizyakov, A.I., Leibman, M.O. & Perednya, D.D. 2006. Destructive relief-forming processes at the coasts of the Arctic plains with tabular ground ice. *Kriosfera Zemli* X(2): 79-89 (in Russian).

Kizyakov, A.I., Zimin, M.T., Leibman, M.O. & Cherkashov, G.A. 2004. Mapping of the coasts of Yugorsky peninsula, Kara Sea. In: *Reports on Polar and Marine Research* 482: 80-83.

Lantuit, H. & Pollard, W. 2003. Remotely sensed evidence of enhanced erosion during the twentieth century on Herschel Island, Yukon Territory. *Reports on Polar and Marine Research* 443: 54-59.

Lantuit, H., Couture, N., Pollard, W.H., Haltigin, T., De Pascale, G. & Budkewitsch, P. 2005. Short-term evolution of coastal polycyclic retrogressive thaw slumps on Herschel Island, Yukon Territory. *Reports on Polar and Marine Research* 506: 72-75.

Leibman, M.O. & Kizyakov, A.I. 2007. *Cryogenic landslides of the Yamal and Yugorsky Peninsular*. Moscow-Tyumen: IKZ SO RAN, 206 pp. (in Russian).

Leibman, M.O., Hubberten, H.-W., Lein, A.Yu., Streletskaya, I.D. & Vanshtein, B.G. 2003. Tabular ground ice origin in the Arctic coastal zone: cryolythological and isotope-geochemical reconstruction of conditions for its formation. *Permafrost. Proceedings of the 8th International Conference, Zurich, July 21–25 2003*. Lisse, *Netherlands*: A.A. Balkema Publishers, I: 645-650.

Leibman, M.O., Khomutov, A.V., Cherkashev, G.A. & Vanshtein, B.G. 2006. Advantages of various land-based methods to study dynamics of the ice-bearing coasts. *Program and Abstracts of the 6th ACD Workshop, 22-26 October 2006, Groningen, Netherlands*: 29.

Lewkowicz, A.G. 1987. Nature and Importance of Thermokarst Processes, Sand Hills Moraine, Banks Island, Canada. *Geografiska Annaler. Series A, Physical Geography* 69(2): 321-327.

Manley, W.F., Lokrantz, H., Gataullin, V.N., Ingolfsson, O., Forman, S.L. & Andersson, T. 2001. Quaternary stratigraphy, radiocarbon chronology, and glacial history at Cape Shpindler, southern Kara Sea, Arctic Russia. *Global and Planetary Change* 31: 239-254.

Solomon, S.M. 2003. A new shoreline change database for the Mackenzie-Beaufort region, NWT, Canada. *Reports on Polar and Marine Research* 443: 108-109.

Sovershaev, V.A. 1992. Coastal zone of the Arctic seas. In: *Geoecologia Severa*. Moscow: Moscow State University Press, 55-60 (in Russian).

Gully-Polygon Interactions and Stratigraphy on Earth and Mars: Comparison of Cold-Desert, Near-Surface, Fluvial, and Periglacial Processes

Joseph Levy
Brown University Department of Geological Sciences, Providence, RI, USA
James W. Head
Brown University Department of Geological Sciences, Providence, RI, USA
David R. Marchant
Boston University Department of Earth Sciences, Boston, MA, USA

Abstract

We examine the distribution and structure of composite-wedge polygons in the South Fork region of Wright Valley, Antarctica, in order to document the manner in which patterned ground contributes to the flow of water in cold desert gully systems. These gully-polygon systems are comparable to terrains observed in high-resolution images of the martian surface. We find that thermal contraction crack polygons contribute to the generation, transport, and storage of water in the Wright Valley gully systems. Further, we evaluate the formation sequence of gully-polygon systems. Similar relationships between gully alcoves, channels, and fans, and patterned ground on Mars suggest that many martian gullies formed on patterned surfaces, cross-cutting a continuous permafrost layer. Therefore, these gullies may result from the melting of atmospherically derived ice under appropriate microclimate conditions.

Keywords: Antarctica; Dry Valleys; gullies; Mars; microclimates; polygons.

Introduction

Gullies on Mars are a class of young features, initially interpreted to have formed by the surficial flow of rapidly released groundwater (Malin & Edgett 2000, 2001), and which may still be active (Malin et al. 2006). Although numerous alternative formation mechanisms have been proposed, however, many workers conclude that an aqueous phase is involved in gully erosion, making gullies features of great astrobiological interest (Malin et al. 2001, SR-SAG 2006). Recent terrestrial analog fieldwork in the Antarctic Dry Valleys (ADV) of Southern Victoria Land, Antarctica, has reported on the primacy of top-down melting of snow as a source for water flowing through the active layer and hyporheic zone of terrestrial gullies (Dickson et al. 2007, Head et al. 2007a, Levy et al. 2007, Morgan et al. 2007).

Although the role of ice wedge polygons in the development of Arctic fluvial systems has been addressed (e.g., Lachenbruch 1962, Fortier et al. 2007), the effects of patterned ground on cold desert fluvial systems have not been broadly discussed, despite the observation of gullies in periglacial terrains on Earth and Mars (e.g., Bridges & Lackner 2006, Levy et al. 2008). Physical models constraining the deposition and behavior of ice-rich soils under present Mars surface conditions suggest that ice deposition and melting can occur on pole-facing slopes at high latitudes under suitable microclimate conditions (Hecht 2002) and that ice-rich soils can undergo thermal contraction cracking, generating patterned ground (Mellon 1997). We present the results of ADV gully-polygon interaction studies, outlining the use of polygons as for determining the stratigraphic sequence of gullied landscape evolution. This analysis provides a baseline for interpreting relationships between gullies and polygons observed in 70 HiRISE images of the martian surface. Analysis indicates that thermal contraction crack polygons play a similar role in the accumulation and transport of gully materials on both Earth and Mars, and that some gullies form or evolve in the continuous presence of actively expanding thermal contraction crack polygons.

ADV Analog Studies

The South Fork of Wright Valley, Antarctica is located at 77°33′36″S, 161°17′24″E in the Intermediate Mixed Zone of the ADV (Marchant & Head 2007) (Figure 1). Gullies, composed of a broad alcove, a sinuous channel, and a distal fan (e.g., Malin & Edgett 2000) are common on the southern wall of the valley (elevation spanning: ~300–1000 m) (Levy et al. 2007). Continuous permafrost is present in the South Fork region beneath a dry active layer 20–45 cm deep (McGinnis & Jensen 1971). Composite-wedge polygons are common on the unconsolidated colluvium surfaces of Wright Valley and show a wide variety of sub-forms. Climatically, the South Fork study area is a cold, hyper-arid desert, with mean annual temperatures of -20°C (Ragotzkie & Likens 1964).

Gully-polygon processes

Monitoring of polygonally patterned ground covering all components of the South Fork gully systems (alcoves, channels, and fans), suggests that polygons modulate the accumulation, transport, and storage of meltwater in the Antarctic gully systems.

Previous work has shown that windblown snow accumulated in gully channels and alcoves is the primary source of meltwater for ADV gullies (Dickson et al. 2007,

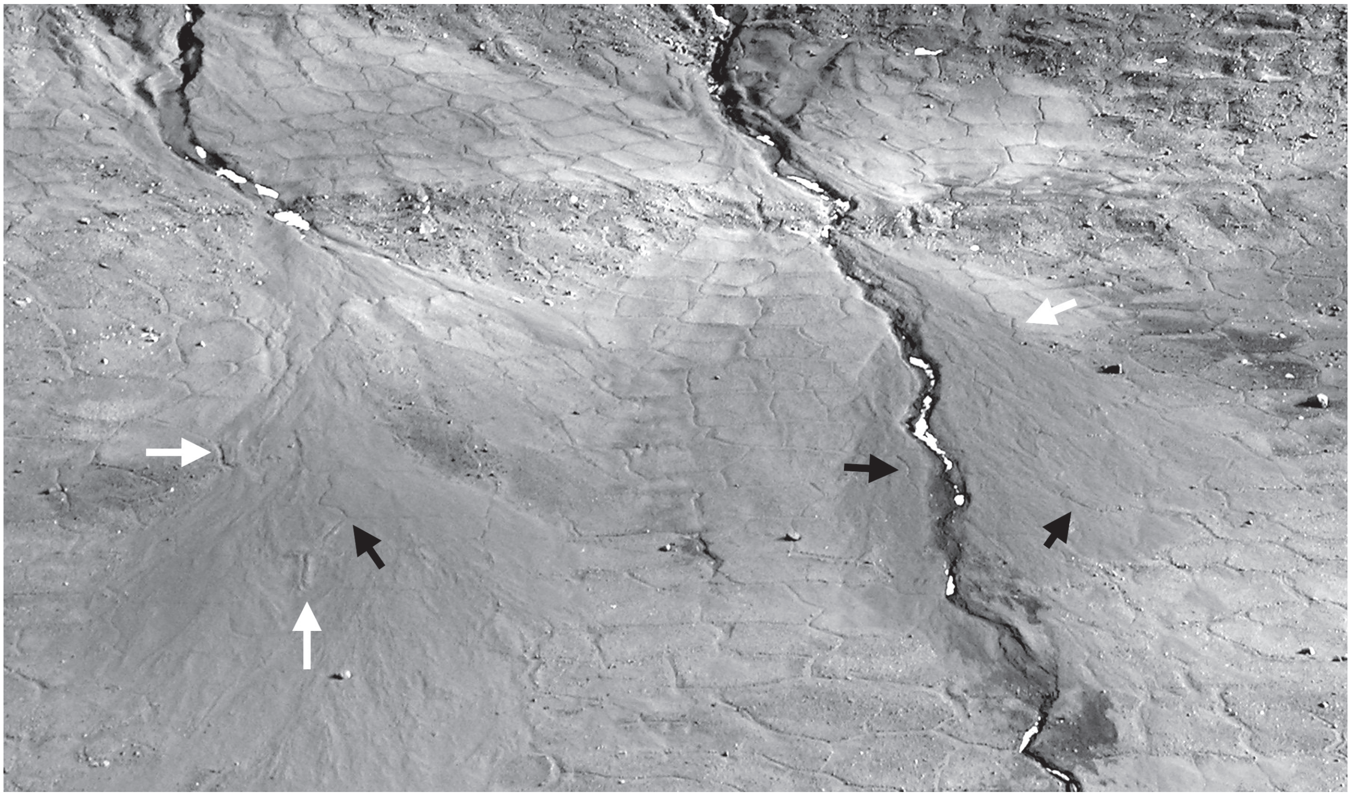

Figure 1. Gullies in the South Fork region of Wright Valley, ADV. Polygons are ~16 m wide. White arrows indicate embayment of patterned surfaces by fan deposits; black arrows indicate dissection of fans by thermal contraction crack polygons.

Levy et al. 2007, Morgan et al 2007, Head et al. 2007a). Windblown snow also accumulates in polygon troughs (~5–30 cm deep) in the South Fork study site, and ablates by melting and sublimation over the course of the austral summer (Levy et al. 2008). Polygon troughs intersecting a gully channel were measured, and the maximum volume of trapped snow was calculated to be comparable to or exceed the volume of windblown snowbanks calculated to be stored in the gully channel (~135 m^3). Where polygon trough snowbank melt-water can be transported into the channel, it becomes available to augment gully flow.

Water transport within South Fork gullies is enhanced by changes to ice-cement-table topography produced by polygon trough evolution. In some sediment excavations, liquid water is observed to flow along the base of the ice-cement table, through the active layer overlying depressed polygon troughs (the surficially depressed region above the polygon wedge). The ice-cement table depth and gradient are locally steepened by the development of polygon troughs, resulting in the concentration of meltwater derived from the melting and infiltration of overlying snow banks (Levy et al. 2008). Where water sources are large enough to initiate overland, channelized flow (i.e., gully channels), polygons directly contribute to gully water transport. At locations where gully channels intersect down-slope-oriented polygon troughs, the troughs are "annexed," as surface flow is transferred into the polygon troughs (Fig. 1). Annexed polygon troughs are generally wider, and more sinuous than adjacent non-annexed polygon troughs.

Water storage in the South Fork gullies is influenced by the presence of polygons in the distal hyporheic zone (Levy et al. 2007, 2008). Colluvium darkening in the distal hyporheic zone results from darkening of clay and silt-rich polygon interiors due to enhanced water content (~5% water by mass) (Levy et al. 2008). In contrast, pebble-rich polygon-wedge materials are bright and considerably drier (0.3–0.5% water by mass) than average colluvium surfaces in the South Fork study area (1.1–1.3% water by mass) (Levy et al. 2008). The concentration of wet, fine-grained colluvium in distal hyporheic zone polygon interiors and coarse, dry colluvium in distal hyporheic zone polygon troughs suggests that localized freeze-thaw processing is sorting grains within gully-terminal composite-wedge polygons, modulating spatial water distribution within the distal hyporheic zone.

Gully-polygon stratigraphic relationships

Relationships between polygon troughs and gully channels in Wright Valley indicate cross-cutting of pre-existing polygons by the gully channel. Polygon troughs intersect gully channels at oblique and near-orthogonal angles, and polygon wedge material is exposed on both sides of the gully channel. Some polygons are cut twice by the same gully channel (on up-slope and down-slope margins). Further, annexed polygon troughs could only develop if polygons preceded the presence of the gully channel. Taken together, these observations suggest that South Fork region gully channels were incised into previously extant polygons.

Contacts between gully fan surfaces and inter-gully,

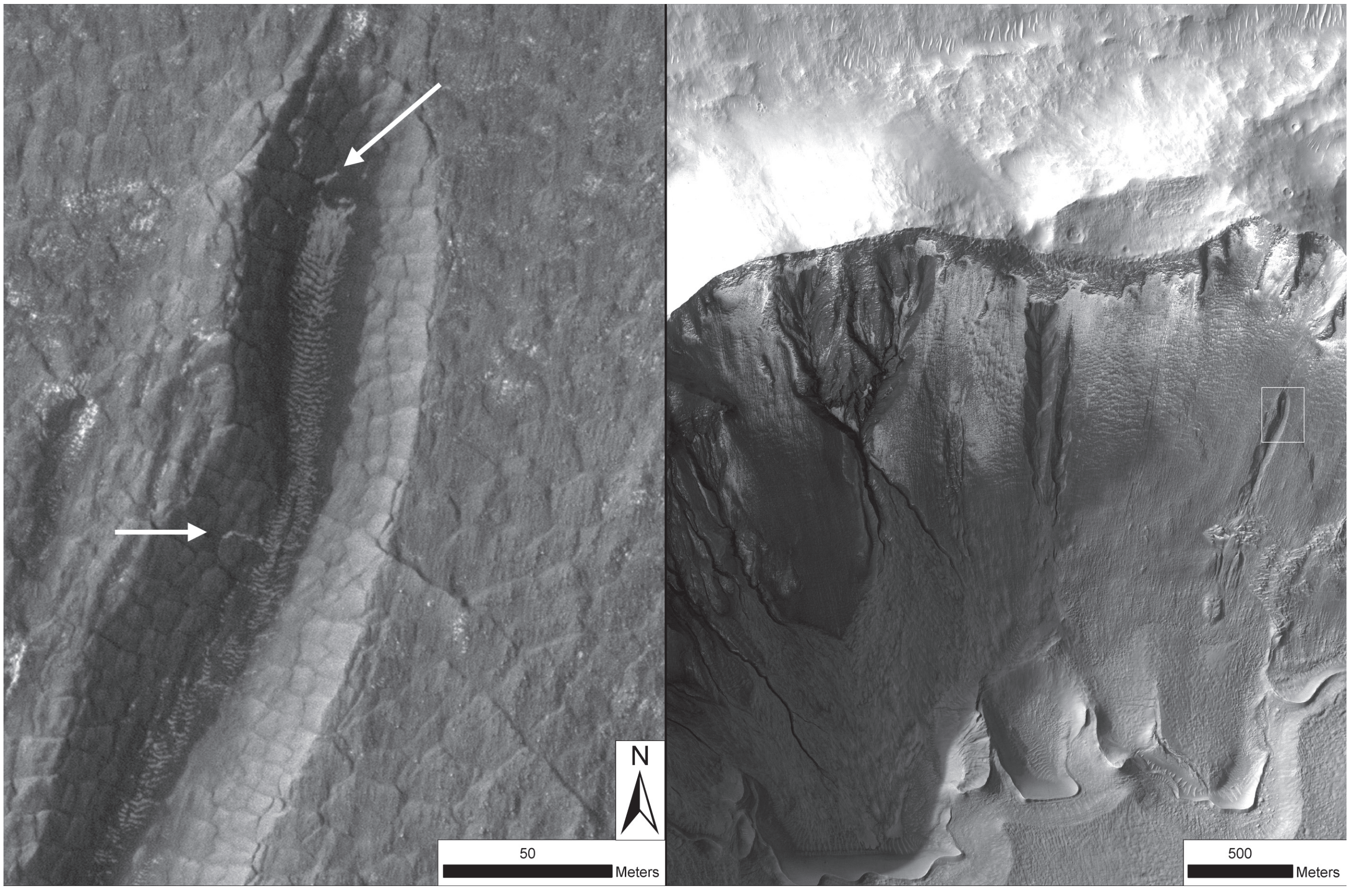

Figure 2. Left: Gully alcove surface with patterned ground. Arrows indicate frost preferentially present in polygon troughs during southern hemisphere winter. Right: Crater interior with gully-polygon suite. Area shown at left is boxed. Both images are from PSP_001882_1410. Illumination from left.

polygonally-patterned colluvium deposits can be used to trace the formation sequence of gully fans (Fig. 1). Local topographic high areas of patterned colluvium, including raised polygon shoulders, are embayed by gully fan deposits. Fan deposition is also blocked in places by the presence of a deep polygon trough (Fig. 1). Fan deposits are dissected by fine thermal contraction cracks which form a polygonal network continuous with the polygon network on the inter-fan surfaces. Taken together, these observations suggest that South Fork region gully fans formed in the presence of polygonally patterned ground, and that the expansion of thermal contraction cracks has kept pace with the aggradation of the gully fans, implying the continued presence of near-surface ice-cemented sediment during the entire process of gully channel and fan formation and evolution.

Gully-Polygon Interactions on Mars

Polygonally patterned ground is a ubiquitous surface feature of high-latitude terrains on Mars (Mangold 2005). Thermal contraction cracking is expected in ice-cemented regolith polewards of ~30° (Mellon 1997), and features interpreted as thermal contraction crack polygons are mapped to within ~10° of the martian poles (Mangold 2005); higher latitudes are dominated by polar cap processes.

A survey of high-resolution (30 cm per pixel) images of the martian surface between 30°–80° latitude was conducted, comprising 537 HiRISE camera images from the primary science phase of the HiRISE mission. Gullies are present in 118 of the images, and occur in conjunction with polygons in 70 of the images: primarily in the southern hemisphere (on account of higher topographic roughness). In both hemispheres, gully-polygon suites commonly occur within multi-kilometer impact craters. Northern hemisphere gullies have little aspect preference at the scale of MOLA gridded altimetry data (~460 m per pixel), while southern hemisphere gullies have a strong pole-facing preference, consistent with the extensive survey results of Dickson et al. (2007). Gullies forming in association with polygonally patterned ground show an equally strong pole-facing preference in the southern hemisphere (58%), and little aspect bias in the northern hemisphere.

Three gully-polygon suites were selected for initial stratigraphic and process analysis. Physical characteristics for the three sites are summarized in Table 1.

Mars gully-polygon process

Morphological analysis of HiRISE images shows relationships between martian polygonally patterned ground and gullies analogous to those observed in Antarctica.

Polygons in and around the alcoves of two gullies (Figs. 2, 3) are outlined by bright deposits which have accumulated preferentially in polygon troughs (either through direct deposition of frost, after Hecht 2002, or wind-capture of ice or particulates, after Morgan et al., 2007): a process analogous to the accumulation of windblown snow in Antarctic polygon troughs. Polygon-modified transport of gully materials on Mars is evidenced by the presence of sinuous, sub-linear, bright features interpreted to be analogous to annexed polygon troughs (Fig. 4). High-albedo material with a similar texture and brightness to the primary gully fan deposits is present in polygon troughs which extend down-slope of the gully fans. The polygon troughs filled by the material are wider than adjacent troughs, have less angular intersections between polygon trough segments, and are more sinuous along the lengths of the trough segments than neighboring troughs. Taken together, we interpret these features as evidence of preferential transport of gully-fan-forming material through these polygon troughs, and erosion of pre-existing polygon troughs during gully fan formation. Preferential storage of gully-related fluids within polygons is not directly observed in HiRISE images. Sorting of polygon-forming sediments by freeze-thaw/sublimation processes may be occurring below martian gullies, however, this process is not visible at 30 cm pixel scales. Alternatively, little grain-size dependent partitioning of water within polygons in martian gully distal hyporheic zones may be occurring on account of the precarious metastability of water at the martian surface (e.g., Hecht 2002).

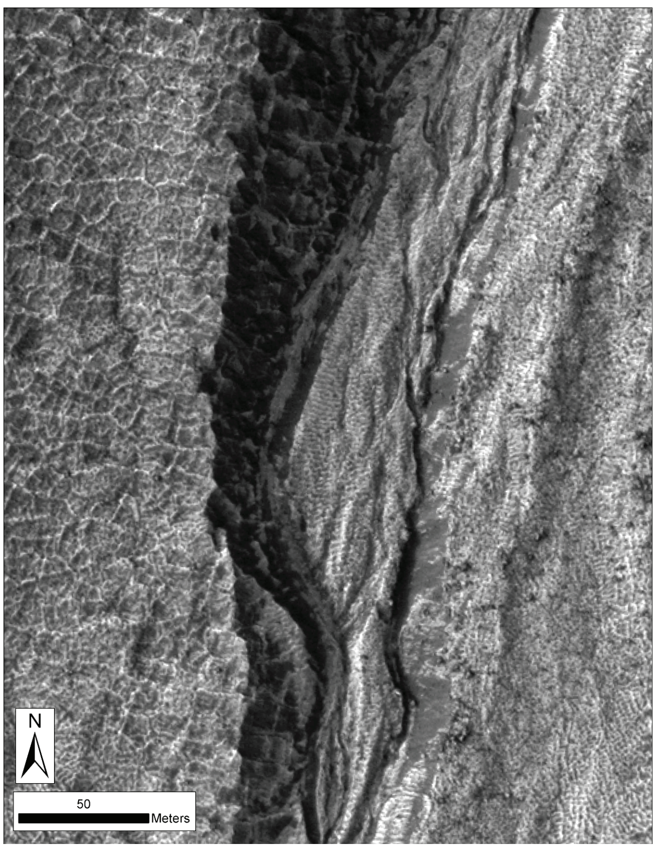

Figure 3. Portion of PSP_002368_1410 showing frost preferentially present in gully-alcove polygon troughs.

No evidence of any gully-polygon interaction is observable within gullies on equator-facing slopes, even those present within the same craters as gully-polygon suites on pole-facing slopes (Fig. 5). When present, equator-facing gullies appear to be extensively softened by sublimation and deflated by aeolian modification.

Mars gully-polygons stratigraphic relationships

As on Earth, polygons present in gullied terrains can be used to determine the formation sequence of landscape elements. A continuous network of polygonally patterned ground is commonly present across gully alcoves and inter-gully surfaces (Fig. 2). This relationship suggests that formation of polygonally patterned ground has continued through the period of gully alcove incision, making these polygons the youngest elements within the gully polygon system (in contrast to previous observations by Malin & Edgett, 2000, suggesting gullies exclusively overlie polygons). Contacts between gully fans and polygons (Fig. 4) show blocking of fan expansion by polygon troughs, annexation of polygon troughs (and filling with fan-like sediments), and incision of gully fans by polygons. Polygons present within gully fans 1) have narrower trough widths than polygons on inter-gully walls, 2) have subdued topographic relief, and 3) have interiors surfaced by gully fan material. Taken together, these observations suggest that these gully fans formed in the presence of polygonally patterned ground, overprinted the previously extant polygons, and were incised by continuously expanding thermal contraction crack polygons during fan emplacement.

Conclusions

Polygonally patterned ground in the South Fork of Wright Valley was analyzed as a component of a near-surface hydrological system in which channelized, subaerial water flow occurs under cold desert conditions. Patterned ground

Table 1. Summary of gully-polygon suite characteristics.

Image Number	PSP_001846_2390	PSP_002368_1275	PSP_001882_1410
Image Location	South of Copias Palus	South of Porter Crater	East of Gorgonum Chaos
Latitude, Longitude	58.7° N, 82.4°E	52.1°S, 246.8°E	38.7°S, 194.0°E
Altitude	-3800 m	2000 m	1000 m
Aspect	Pole-Facing and Equator-Facing	Pole-Facing	Pole-Facing
Gully Slope	9.3°	10.0°	17.5°
Image L_s	152 (Northern Summer)	174 (Southern Winter)	154 (Southern Winter)

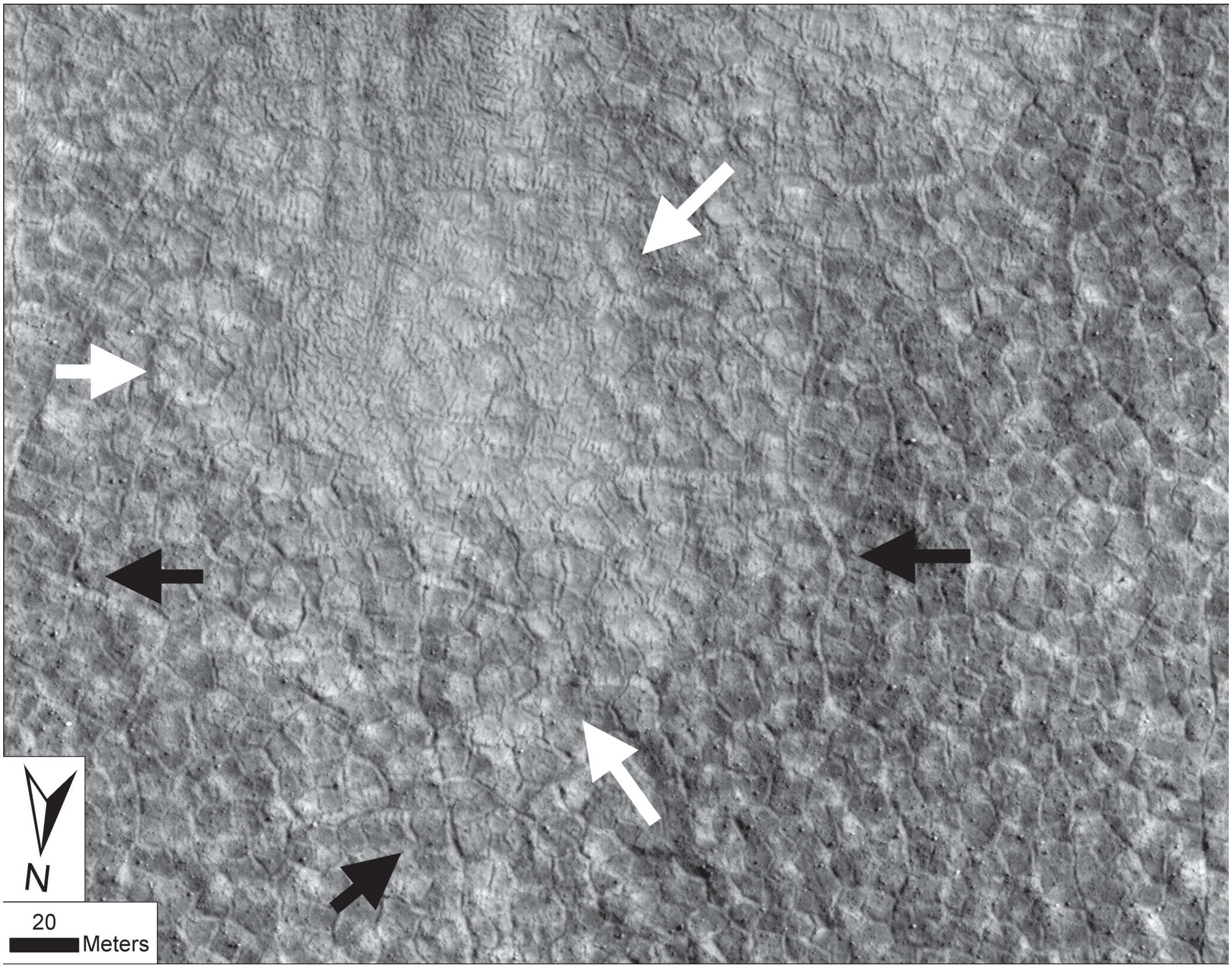

Figure 4. Gully fan from PSP_001846_1410. White arrows indicate extent of bright continuous fan deposit. Black arrows indicate annexed polygon troughs. Illumination from right.

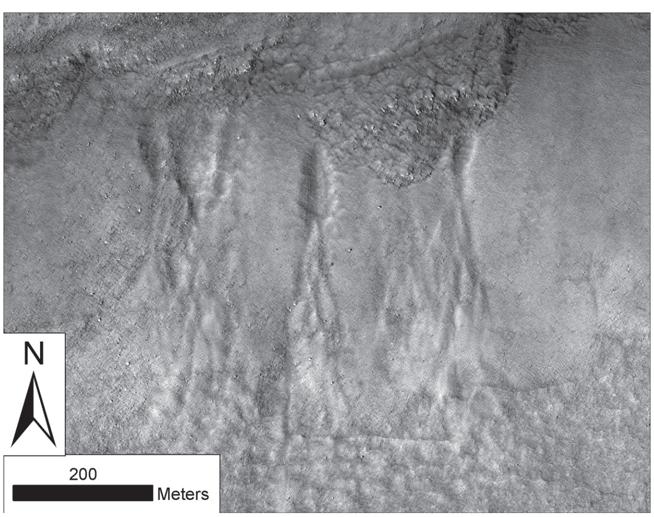

Figure 5. Gullies on equator facing slope, opposite gullies in Figure 4 (PSP_001882_1410). Illumination from left.

was found to play a significant role in the accumulation, transport, and storage of atmospherically-derived gully meltwater. Gully-polygon stratigraphic relationships indicate that patterned ground formation preceded gully formation and continued throughout gully evolution. This suggests the continuing presence of climate conditions permitting the expansion of composite-wedge polygons. Further, these results suggest the continuous presence of an impermeable ice-cemented sediment permafrost layer during the entire course of gully evolution.

Analysis of 537 HiRISE images in the 30°–80° latitude range revealed 70 gullies on the martian surface interacting with polygonally patterned ground. Our analysis indicates that patterned ground on Mars plays an analogous role in the accumulation and transport of martian gully materials to those observed on Earth. Further, stratigraphic relationships between gullies and polygons on Mars indicate that some gullies have formed in the presence of continuously expanding thermal contraction crack polygons. In some gullies, thermal contraction cracks are the youngest stratigraphic element in the gully system. The processes of frost-trapping by polygon troughs, polygon trough annexation, polygon overprinting by gully fans, and dissection of gully fans by thermal contraction crack polygons, have all been observed in martian gullies, suggesting that some martian gullies have formed and evolved on surface units underlain by a continuous layer of shallow permafrost during the most recent period of gully activity. No evidence of catastrophic water release was observed. Polygon-gully interactions and fresh-looking gully structures were found to form preferentially on pole-facing slopes in the presence of shaded alcoves. Taken together these lines of evidence suggest an atmospheric origin for some gully volatiles, consistent with the model of gully activity observed in the Antarctic Dry Valleys.

Acknowledgments

This work was made possible with support of JSL by the Rhode Island Space Grant Consortium, by NSF Grant ANT-0338291 to David Marchant and James Head, and by NASA MFRP Grant NNX06AE32G. Thanks to J. Dickson, D. Kowalewski, G. Morgan, D. Shean, and K. Swanger for field and data support. Thanks to A. McEwen and the HiRISE team for Mars image data. Also, thanks to PHI, the staff of RPSC, and the personnel of McMurdo Station.

References

Bridges, N.T. & Lackner, C.N. 2006. Northern hemisphere martian gullies and mantled terrain: implications for near-surface water migration in Mars' recent past. *Journal of Geophysical Research* 111: doi: 10.1029/2006/JE002702.

Dickson, J.L., Head, J.W., Marchant, D.R., Morgan, G.A., & Levy, J.S. 2007. Recent gully activity on Mars: Clues from late-stage water flow in gully systems and channels in the Antarctic Dry Valleys. *LPSC 38*, Houston, TX, March 12-16, 2007: 1678.

Fortier, D., Allard, M., & Shur, Y. 2007. Observation of rapid drainage system development by thermal erosion of ice wedges on Boyt Island, Canadian Arctic Archipelago. *Permafrost and Periglacial Processes* 18: 229-243.

Head, J.W., Marchant, D.R., Dickson, J.L., Morgan, G.A., & Levy, J.L. 2007a. Mars gully analogs in the Antarctic Dry Valleys: Geological setting and processes. *LPSC 38*, Houston, TX, March 12-16, 2007: 1617.

Hecht, M.H. 2002. Metastability of water on Mars. *Icarus* 156: 373-386.

Lachenbruch, A.H. 1962. Mechanics of thermal contraction cracks and ice-wedge polygons in permafrost. *GSA Special Papers* 70: 1-69.

Levy, J.S., Head, J.W., Marchant, D.R., Morgan, G.A., & Dickson, J.L. 2007. Gully surface and subsurface structure in the south fork of Wright Valley, Antarctic Dry Valleys: Implications for gully activity on Mars. *LPSC 38*, Houston, TX, March 12-16, 2007: 1728.

Levy, J.S., Head, J.W., Marchant, D.R., Morgan, G.A., & Dickson, J.L. 2008. The Role of Thermal Contraction Cracks in Cold-Desert Fluvial Systems. *Antarctic Science*, In Press.

Malin, M.C. & Edgett, K.S. 2000. Evidence for recent groundwater seepage and surface runoff on Mars. *Science* 288 (5475): 2330-2335.

Malin, M.C. & Edgett, K.S. 2001. Mars Global Surveyor Mars Orbiter Camera: Interplanetary cruise through primary mission. *Journal of Geophysical Research* 106 (E10): 23,429-23,540.

Malin, M.C., Edgett, K.S., Pasiolova, L.V., McColley, S.M., & Dobrea, E.Z.N. 2006. Present-day impact cratering rate and contemporary gully activity on Mars. *Science* 314 (5804): 1573-1577.

Mangold, N. 2005. High latitude patterned grounds on Mars: Classification, distribution, and climatic control. *Icarus* 174: 336-359.

Marchant, D.R. & Head, J.W. 2007. Antarctic Dry Valleys: Microclimate zonation, variable geomorphic processes, and implications for assessing climate change on Mars. *Icarus* 192: 187-222.

McGinnis, L.D. & Jensen, T.E. 1971. Permafrost-hydrogeologic regimen in two ice-free valleys, Antarctica, from electrical depth sounding. *Quaternary Research* 1: 31-38.

Mellon, M.T. 1997. Small-scale polygonal features on Mars: Seasonal thermal contraction cracks in permafrost. *Journal of Geophysical Research* 102 (E11): 25,617-25,628.

Morgan, G.A., Head, J.W., Marchant, D.R., Dickson, J.L., & Levy, J.S. 2007. Gully formation on Mars: Testing the snowpack hypothesis from analysis of analogs in the Antarctic Dry Valleys. *LPSC 38*, Houston, TX, March 12-16, 2007: 1656.

SR-SAG. 2006. Findings of the Mars special regions science analysis group. *Astrobiology* 6(5): 677-732.

Ragotzkie, R.A. & Likens, G.E. 1964. The heat balance of two Antarctic lakes. *Limnology and Oceanography* 9(3): 412-425.

Computation of Critical Heights of Embankments on High-Temperature Permafrost Regions in the Eastern Tibetan Plateau

Dongqing Li
SKLFSE, Cold and Arid Regions Environmental and Engineering Research Institute, CAS, Lanzhou 730000, China
Jin Chen
SKLFSE, Cold and Arid Regions Environmental and Engineering Research Institute, CAS, Lanzhou 730000, China
Qingzhou Meng
SKLFSE, Cold and Arid Regions Environmental and Engineering Research Institute, CAS, Lanzhou 730000, China
Jiankun Liu
School of Civil Engineering and Architecture, Beijing Jiaotong University, Beijing 100044, China
Jianhong Fang
Highway Research and Survey Design Institute of Qinghai Province, Xining, 810008, China

Abstract

Ccritical embankment heights were computed for warm permafrost regions in the eastern Tibetan Plateau using geographical and geological conditions. The resulting modeled results agree well with the data collected on the Qinghai-Xizang Highway over the past 30 years. At first, for concrete and gravel road surfaces, the thermally-stable critical heights of embankments were estimated to be 2.50 m for concrete surfaces and 2.00 m for gravel surfaces, using regression analysis. When the heights of embankments are higher than the critical heights, the degrading permafrost table will gradually stabilize after construction. However there is no critical height of embankments for the asphalt pavement road in warm permafrost regions according to our models.

Keywords: degrading permafrost table; embankment stability; highway engineering; mathematical models; pavements; permafrost; thermal analysis.

Introduction

When the natural ground surface is changed by roadway embankment construction, the thermal balance of the permafrost is also altered. Thermal equilibrium will not be reached for many years. As a result, the permafrost table under the roadbed is also degraded. As thermal balance is achieved, the permafrost table may rise or lower depending on roadway thickness and surface. For example, after construction of the Qinghai-Xizang Highway, the permafrost temperature under the roadbed increased, and the permafrost table was lowered. The roadway was paved with asphalt, which absorbs heat resulting in higher surface temperatures. Thaw settlement of the embankment occurred, destroying the road (Li & Wu 1997). Consequently, it is very important to understand the thermal stability of embankments after construction in permafrost regions, especially warm permafrost regions where the mean annual ground temperature is higher than or equal to -1.0°C. This corresponds to a mean annual air temperature of -3.5°C or higher.

The Qinghai-Sichuang Highway crosses the eastern part of the Qinghai-Xizang Plateau, China. The highway crosses about 300 km of mostly warm permafrost. The thickness of the permafrost has been degrading in this region since the 1960s (Zhu 1995, Li 1996).

We analyzed the thermal stability of embankments on permafrost in an effort to predict the temperature of the permafrost with different road surfaces and estimate critical heights.

Methods and Conditions

Mathematical model

Since Harlan (1973) presented the first model for coupled heat and mass transfer in freezing soils, his strategy has been referred to and further developed by many other researchers (Guyman & Luthin 1974, Outcalt 1977, Taylor & Luthin 1978, Jame & Norum 1976, Nixon 1975, Li & Wu 1996). These authors applied two partial differential equations, using temperature and water (ice) content or water pressure to describe the transient heat and water flows in freezing soils. The two equations are coupled through the relationship between unfrozen water content and temperature. If vapor transfer and heat convection are omitted, the application of the laws of heat balance to saturated or unsaturated soil and the mass conservation of water in soil pores result in the following two equations:

$$\frac{\partial}{\partial x}(\lambda_x \frac{\partial T}{\partial x}) + \frac{\partial}{\partial y}(\lambda_y \frac{\partial T}{\partial y}) = C\rho \frac{\partial T}{\partial t} - L\rho_i \frac{\partial \theta_i}{\partial t} \tag{1}$$

$$\frac{\partial}{\partial x}(K_x \frac{\partial \psi}{\partial x}) + \frac{\partial}{\partial y}(K_y \frac{\partial \psi}{\partial y}) = \frac{\partial \theta_u}{\partial t} + \frac{\rho_i}{\rho_w}\frac{\partial \theta_i}{\partial t} \tag{2}$$

where ρ_w, ρ, and ρ_i are the densities of water, soil, and ice, respectively; t, x, and y denote the time and two space coordinates; θ_i and θ_u are the volumetric fractions of the ice content and the unfrozen water content; $\lambda x(\lambda y)$ and $Kx(Ky)$ are the thermal and the hydraulic conductivities in the x and y directions; T is the temperature; C is the specific heat; L is

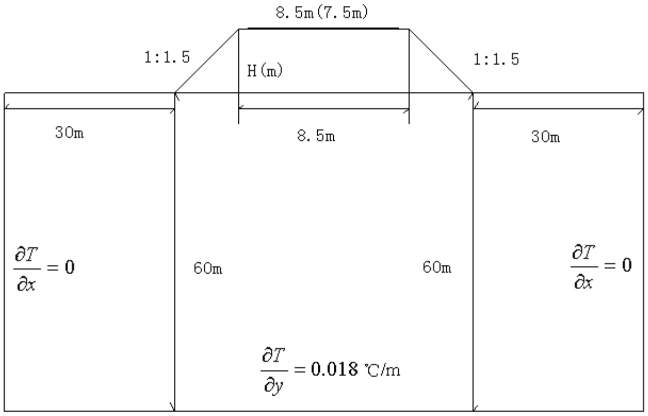

Figure 1. The profile of embankment for calculations.

the latent heat; ψ is the total potential of water in soil; $\psi=\varphi+Z$, where φ and Z denote the volumetric potential of water in the soil and the gravitational potential, respectively.
In general, Z can be omitted and therefore $\psi=\phi$.

According to the characteristic relationship, $\theta_u=f(T)$ between the unfrozen water content θ_u and the temperature T, we obtain the following differential relationship:

$$\frac{\partial\theta_u}{\partial t}=\frac{\partial\theta_u}{\partial T}\frac{\partial T}{\partial t} \tag{2a}$$

Substituting this differential relationship into Equation (2) and reducing Equation (1), we can derive:

$$\begin{gathered}(C\rho+L\rho_w\frac{\partial\theta_u}{\partial T})\frac{\partial T}{\partial t}=\\ \frac{\partial}{\partial x}(\lambda_x\frac{\partial T}{\partial x})+\frac{\partial}{\partial y}(\lambda_y\frac{\partial T}{\partial y})+L\rho_w\left[\frac{\partial}{\partial x}(\mathrm{K}_x\frac{\partial\psi}{\partial x})+\frac{\partial}{\partial y}(\mathrm{K}_y\frac{\partial\psi}{\partial y})\right]\end{gathered} \tag{3}$$

Equations (2) and (3) can be solved when given the function ψ and the characteristic relationship between the unfrozen water content and temperature. The temperature is determined empirically. From these equations, we can develop several models.

Taylor (1976, 1978) investigated the volumetric potential of unfrozen water in frozen soil. He showed the volumetric potential could be determined using the characteristic relationship between the unfrozen water content and temperature, similar to the volumetric potential of unfrozen soil, when the action of ice in the frozen soil is omitted. The characteristic relationship of moisture for unfrozen soil is suitable for frozen soil.

By introducing the new differential relationship:

$$\frac{\partial\psi}{\partial T}=\frac{\partial\psi}{\partial\theta_u}\frac{\partial\theta_u}{\partial T} \tag{3a}$$

and using the terms of the differential water capacity $c=\partial\theta/\partial\psi$ and the soil-water diffusivity $D=\mathrm{K}/c$, we reduce Equation (3) to:

$$C(T)\frac{\partial T}{\partial t}=\frac{\partial}{\partial x}(\beta_x(T)\frac{\partial T}{\partial x})+\frac{\partial}{\partial y}(\beta_y(T)\frac{\partial T}{\partial y}) \tag{4}$$

where:

$$C(T)=C\rho+L\rho_w\frac{\partial\theta_u}{\partial T}$$

$$\beta_x(T)=\lambda_x+L\rho_w D_x\frac{\partial\theta_u}{\partial T}$$

$$\beta_y(T)=\lambda_y+L\rho_w D_y\frac{\partial\theta_u}{\partial T}$$

$$D_x=\frac{\mathrm{K}_x}{\frac{\partial\theta_u}{\partial\psi}},D_y=\frac{\mathrm{K}_y}{\frac{\partial\theta_u}{\partial\psi}}$$

Since the characteristic relationship between the unfrozen water content and the temperature can be determined by testing, the set nonlinear Equations (2) and (4) can be solved. The implicit finite difference method was used to derive the results reported in this paper.

Boundary and initial condition

The input for the derived equations is established in part by Chinese standards and in part based on experience. According to the Chinese standards for designing and building national highways, road surface width is 8.5 m, and shoulder width is 0.5 m. The height of embankment varies. The side-slope is 1:1.5. Finally, the bottom boundary is located at 60 m depth. Based on drilling records, the temperature and the heat flux at the bottom of the permafrost were found to be constant on the Eastern Tibetan Plateau (Li et al. 1998). The ground temperature gradient at the lower boundary was estimated to be 0.018°C per meter. The lateral boundary (30 m from the slope corner) is situated so far from the road that the temperature gradient is regarded as 0.0°C/m horizontally (see Fig. 1).

The initial ground temperature field under the road was obtained from a borehole. The ground temperature without embankment was simulated using the boundary conditions noted until stable temperature field under the natural ground surface was established. This initial temperature profile was used to estimate the transient temperature field after road construction. The initial temperature in the embankment was assumed to be -1.0°C. The mean annual temperature of the embankment slope is 0.5°C lower than the upper boundary temperature of road surface, because that is often influenced by traffic.

Using meteorological information from Hua Shixia Valley and Ma Duo County in the Eastern Tibetan Plateau (Yu 1993), and by regression analysis of the sine function, we can reduce the upper boundary temperature of road surface to the following sine function:

$$T=T_s+G(t)+12.2\sin\left(\frac{2\pi}{8640}t+\frac{4\pi}{3}\right)$$

Here, T_s is the mean annual temperature at the ground surface; t is the time in hours of the annual cycle after the construction of embankment, respectively ranging from 0 to 8640 hours; $G(t)$ is the mean annual climate warming rate; here $G(t)=0$.

The mean annual air temperature in the warm permafrost regions was taken as -3.5°C. Ground temperature in the eastern part of the Qinghai-Xizang Plateau, T_s is -1.0°C for natural ground, +3.0°C for an asphalt surface, +1.5 for a concrete surface and +1.0°C for a gravel road surface (Wu 1988). The natural permafrost table is about 2.00–2.20 m in the Hua Shixia Valley, a continuous permafrost region.

The hydrogeological conditions and heat parameters are as follows:

1. 0.00–2.00 m, organic clayey soil, water content 40.0%, dry density 0.9 g/cm3, heat capacities of unfrozen and frozen soils 1.17 J/cm^3·°C and 1.34 J/cm^3·°C and thermal conductivities of that 13.97 J/cm·h·°C and 16.72 J/cm·h·°C, respectively.
2. 2.00–3.30 m, clayey soil, water content 178.5%, dry density 0.36 g/cm^3, heat capacities of unfrozen and frozen soils 1.03 J/cm^3·°C and 0.89 J/cm^3·°C, and thermal conductivities of that 26.36 J/cm·h·°C and 77.40 J/cm·h·°C, respectively.
3. 3.30–7.60 m, gravel, water content 24.5%, dry density 1.52 g/cm^3, heat capacities of unfrozen and frozen soils 2.82 J/cm^3·°C and 2.23 J/cm^3·°C, and the thermal conductivities of that 40.59 J/cm·h·°C and 56.90 J/cm·h·°C, respectively.
4. Below 7.60 m, mantle rock, water content 4.0%, heat capacity of soil 2.29 J/cm^3·°C, thermal conductivity of soil 97.20 J/cm·h·°C.
5. Fill materials of embankment contain clayey soil with coarse-grained gravel; water content 8.0%–10.0%, dry density 2.0 g/cm^3. The capacities and conductivities of unfrozen and frozen soils were taken as those in 3.30–7.60 m deep gravel soil.

The relationships between unfrozen water content, temperature, total moisture, and thermal properties are taken from experimental research on moisture transfer in frozen soil (Xu & Deng 1991).

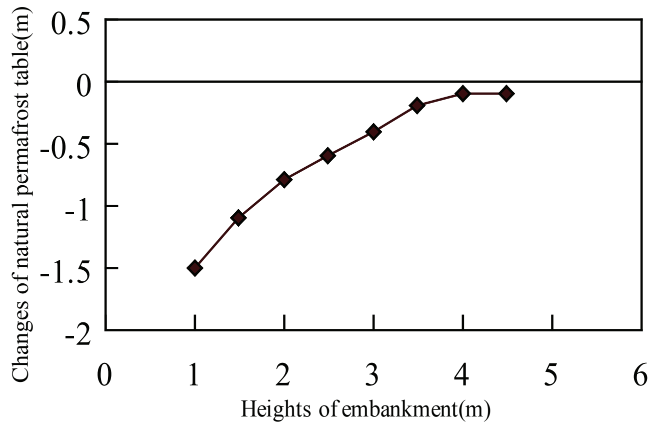

Figure 2a. Relation between height of embankment and the changes of natural permafrost tables under roadbed (asphalt).

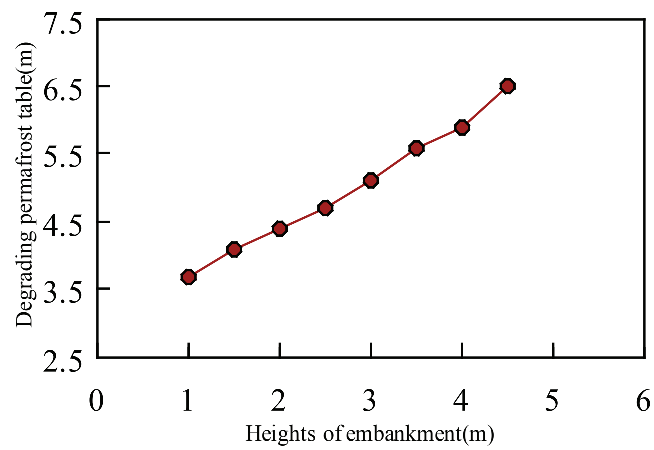

Figure 2b. Relation between height of embankment and the degrading permafrost table of embankment (asphalt).

Results and Discussion

Because traffic is increasing, replacing the existing gravel surface with pavement is necessary. To keep the road surface smooth, the fill stability must be maintained. In order to prevent thaw settlement, the permafrost table under the roadbed must be maintained and not lowered. Frost heaving of the active layer above the permafrost must be controlled to less than 1%. The calculations in this paper use the two principles as guidelines. Using the different types of road surface and embankment heights, changes in the level of the permafrost table as a function of time are analyzed. Using the results, the critical design heights of the embankment for a 30-year period after construction are determined using linear regression analysis between heights of embankment and changes of the natural permafrost table.

The analysis is summarized in Figures 2–6. Figures 2a–4a show for asphalt, concrete, and gravel road surface the relation between the height of embankment and the changes of the level of the natural permafrost table under the middle sections of road in the 30 years after construction on the high-temperature permafrost sections. On the other hand, Figures 2b–4b show the relation between the height of embankment and the degrading permafrost table (changed permafrost table under the roadbed) under the middle sections of the road; that is, the critical design heights have a relationship with the age of the road after construction. Figures 5 and 6 show the zero degree isothermal curves under the roadbed with asphalt pavement at the embankment height of 4.0 m and 3.5 m in 30 years.

From Figure 3 to Figure 4, for concrete and gravel surface embankments, when the embankment height is lower than 3.0 m, it can be seen that there is an almost linear relation between the height of embankment and change in the natural permafrost table and degrading permafrost table under the road in the thirtieth year after construction. This is in agreement with that for low-temperature permafrost regions (Li et al. 1998); therefore, from a linear regression analysis, the heat-stable critical heights of embankment for concrete and gravel roads are figured out as 2.50 m and 2.00 m in the thirtieth year after construction.

From Figure 2, however, for the asphalt pavement road, the above-mentioned relation is nonlinear. After 10 years the permafrost table under the roadbed is always lower than the natural permafrost table. As shown in Figures 5 and 6, when the height of embankment is higher than 3.5 m for an asphalt

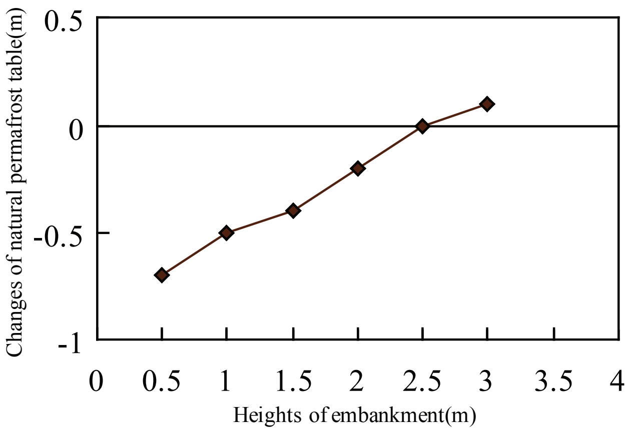

Figure 3a. Relation between height of embankment and the change of natural permafrost tables under roadbed (concrete).

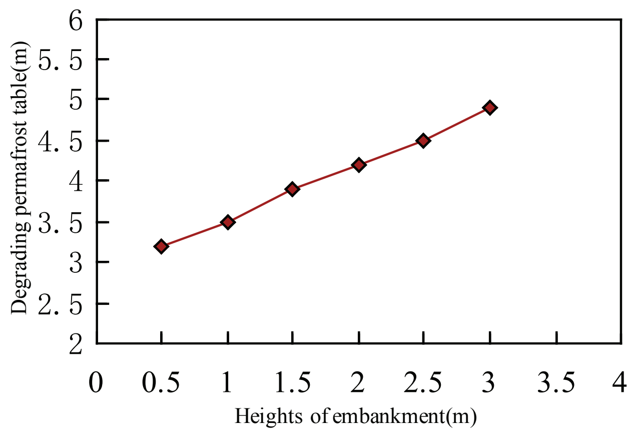

Figure 3b. Relation between height of embankment and the degrading permafrost table of embankment (concrete).

road, there will be a residual thaw zone (an upper thawed course) (Huang 1983) above the degrading permafrost table in the embankment more than 10 years after construction. Again, the predicted permafrost table is lower than the natural permafrost table under the road from that point forward. Consequently, the degrading permafrost table under the roadbed was always lower than the natural permafrost table under the roadbed after 10 years following construction or in the thirtieth year; we cannot get any critical height for asphalt pavement, as we did for concrete-surface and gravel-surface roads. Because of the existence of the upper thawed course (an unfrozen area in the embankment above the degrading permafrost table), the frost deformation of the embankment, therefore, would be largely increased making it impossible to maintain smoothness specifications. In other words, it is not desirable to build an asphalt-pavement road in the warm permafrost regions of the Tibetan Plateau.

For concrete and gravel surface roads, there is no upper thawed course (an unfrozen area in the embankment above the degrading permafrost table) in the embankment for embankment heights less than 3.0 m; that is, there are critical heights of embankment. These are in correspondence with the observed results on high-temperature permafrost regions in the Qinghai-Xizang Highway during the 30 years or more of the last century (Wu et al. 1988).

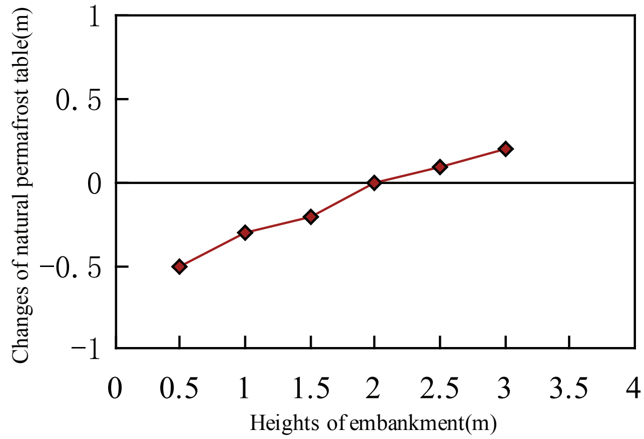

Figure 4a. Relation between height of embankment and the changes of natural permafrost tables under roadbed (gravel).

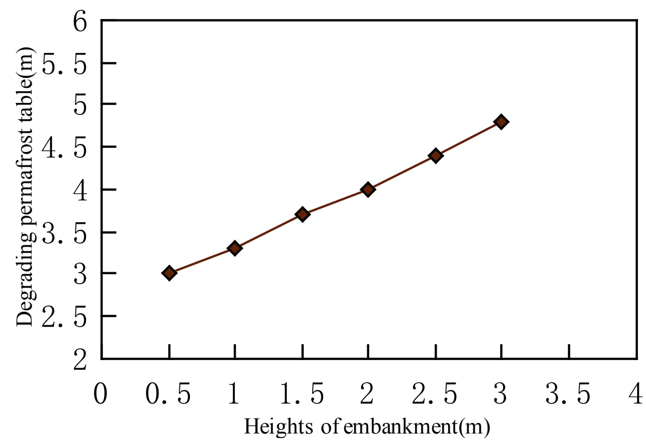

Figure 4b. Relation between height of embankment and the degrading permafrost table of embankment (gravel).

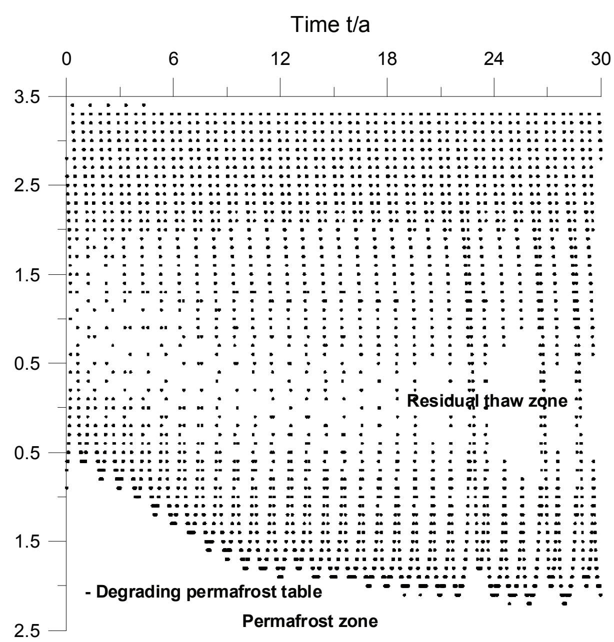

Figure 5. The zero degree isothermal curves under the roadbed at the embankment height of 3.5 m in 30 years (asphalt).

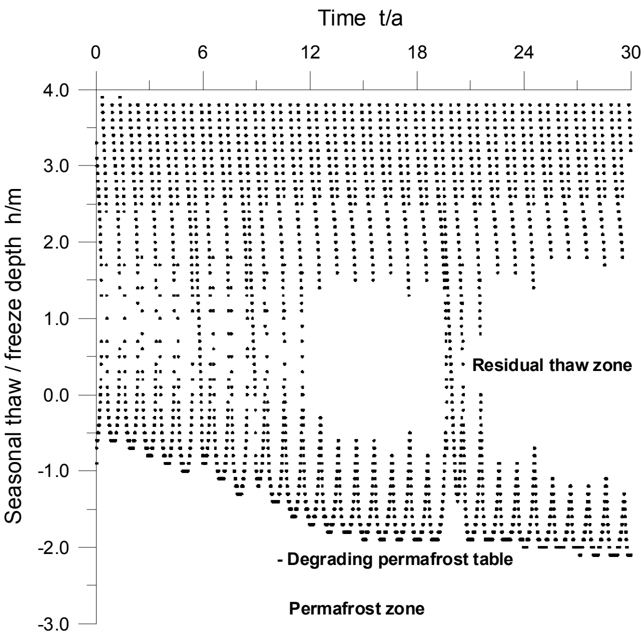

Figure 6. The zero degree isothermal curves under the roadbed at the embankment height of 4.0 m in 30 years (asphalt).

Conclusions

1. It is important to predict permafrost change under the road with running time after construction. The applied numerical model provides the ability to predict and estimate critical heights of embankment in cold regions.

2. The heat-stable critical heights of embankment on the high-temperature permafrost regions in the Eastern Tibetan Plateau are 2.50 m and 2.00 m for a 30-year analysis period after construction for concrete and gravel road surfaces, respectively.

3. According to the principle of protecting the permafrost, it is not desirable to build an asphalt pavement road in the area; that is, there is no critical height of embankments for the asphalt pavement road in high-temperature permafrost regions in this area.

Acknowledgments

The research was supported by the National Natural Science Foundation of China (No. 40671039), the Talent Project of Cold and Arid Regions Environmental and Engineering Research Institute (No. 2004122), the program for New Century Excellent Talents, NCET-05-0092, the grant of the Knowledge Innovation Program of the Chinese Academy of Sciences (No. KZCX3-SW-351), the grant of the Western Project Program of the Chinese Academy of Sciences (No. KZCX2-XB2-10), and the National Science Supporting Project of the Ministry of Science and Technology of China (2006BAC07B02).

References

Guyman, G.L. & Luthin, J.N. 1974. A coupled heat and moisture transport model for arctic soils. *Water Resources Research* 10: 1314-1323.

Harlan, R.L. 1973. An analysis of coupled heat-fluid transport in partially frozen soil. *Water Resources Research* 9: 1314-1323.

Huang, X.M. 1983. Determination of the critical height of embankment for highway in permafrost regions of Tibetan Plateau. *Proceedings of the second national conference on permafrost (selection)*. China: Gansu People's Publishing House, 391-397.

Jame, Y.W. & Norum, D.I. 1976. Heat and mass transfer in freezing unsaturated soil in a closed system. *Proceedings of the 2nd Conference on Soil Water Problem in Cold Region, Edmonton, Alba*: 1-18.

Li, D., Wu, Z., Fang, J. et al. 1998. Heat stability analysis of embankment on the degrading permafrost district in the East of Tibetan Plateau, China. *Cold Regions Science and Technology* 28: 183-188.

Li, D.Q. & Wu, Z.W. 1996. Numerical calculation on permafrost degradation. *Proceedings of the fifth chinese conference on Glaciology and Geocryology*, Vol.2, China: Gansu Culture Press, 1082-1086.

Li, S. & Wu, Z. 1997. The forming and changing property of thawed course under roadbed on the permafrost regions of Tibetan Plateau. *Journal of Glaciology and Geocryology* 19(2): 133-140.

Ma, Y. 1993. The reconfirmation on climatic change of Qinghai Province. *Meteorology of Qinghai* 3: 13-19.

Nixon, J.F. 1975. The role of convective heat transport in the thawing of frozen soils. *Canadian Geotechnical Journal* 12(4): 425-429.

Outcalt, S. 1977. Numerical modelling of the ice lensing processes. *Proc., Int. Symp. On Frost Action in Soils*, *Lulea, Sweden, Feb 1977*. Lulea University of Technology, Vol. 2: 75-91.

Taylor, G.S. & Luthin, J.N. 1976. Numeric results of coupled heat mass flow during freezing and thawing. *IProc. 2nd. Conf. on Soil Water Problems in Cold Regions*, Edmonton Alta: 1-2.

Taylor, G.S. & Luthin, J.N. 1978. A model for coupled heat and moisture transfer during soil freezing. *Canadian Geotechnical Journal* 15(3): 548-555.

Wu, Z.W., Cheng, G.D., Zhu, L.N. & Liu, Y.Z. 1988. Adhere layer and engineering signification. *Road Engineering of Frozen Soil*. Lanzhou, China: Lanzhou University Press, 48-60.

Xu, X.Z. & Deng, Y.S. 1991. Driving force of water migration in freezing and frozen soils. *Experimental Study on Water Migration in Freezing and Frozen Soil.* Pecking, China: Science Press, 9-29.

Zhu, L.N., Wu, Z.W. & Liu, Y.Z. 1995. Permafrost degeneration in the east of Tibetan Plateau. *Journal of Glaciology and Geocryology*, Pecking, China: Science Press, 17(2):120-124.

Author Index

Subject Index